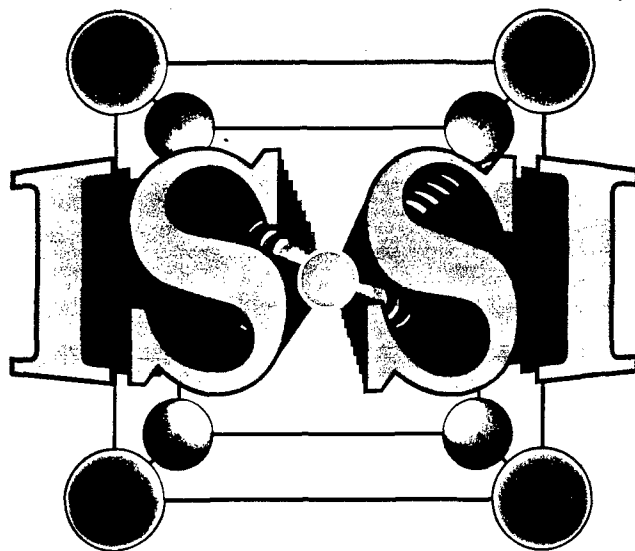


19981204 038



# **STRUCTURAL INTERMETALLICS 1997**

**EDITED BY**

**M.V. Nathal  
R. Darolia  
C.T. Liu  
P.L. Martin  
D.B. Miracle  
R. Wagner  
M. Yamaguchi**

**DISTRIBUTION STATEMENT A:  
Approved for Public Release -  
Distribution Unlimited**

**Reproduced From  
Best Available Copy**

**DTIC QUALITY INSPECTED 3**

## REPORT DOCUMENTATION PAGE

AFRL-SR-BL-TR-98

88

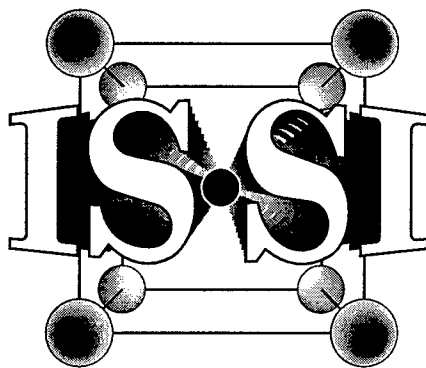
Public reporting burden for this collection of information is estimated to average 1 hour per response, including the time for reviewing the collection of information, gathering and maintaining the data needed, and completing and reviewing the collection of information, including suggestions for reducing this burden, to Washington Headquarters, Davis Highway, Suite 1204, Arlington, VA 22202-4302, and to the Office of Management and Budget, Paperwork Project, Washington, DC 20503.

0837

g data sources,  
in aspect of this  
1215 Jefferson  
20503.

1. AGENCY USE ONLY (Leave blank)		2. REPORT DATE September 1997		3. REPORT TYPE AND DATES COVERED Final Technical Report	
4. TITLE AND SUBTITLE Second International Symposium on Structural Intermetallics				5. FUNDING NUMBERS F49620-97-1-0317	
6. AUTHOR(S) M. V. Nathal, R. Darolia, C. T. Liu, P. L. Martin, D. B. Miracle, R. Wagner, and M. Yamaguchi					
7. PERFORMING ORGANIZATION NAME(S) AND ADDRESS(ES) Structural Materials Division Minerals, Metals & Materials Society 420 Commonwealth Drive Warrendale, PA 15086-7514				8. PERFORMING ORGANIZATION REPORT NUMBER	
9. SPONSORING/MONITORING AGENCY NAME(S) AND ADDRESS(ES) AFOSR/NA 801 N. Randolph Street Room 732 Arlington, VA 22203-1977				10. SPONSORING/MONITORING AGENCY REPORT NUMBER  F49620-97-1-0317	
11. SUPPLEMENTARY NOTES					
12a. DISTRIBUTION AVAILABILITY STATEMENT Approved for public release; distribution unlimited				12b. DISTRIBUTION CODE	
13. ABSTRACT (Maximum 200 words) These proceedings represent the written record of the Second International Symposium on Structural Intermetallics which was held at the Seven Spring Mountain Resort, Champion, Pennsylvania1 from September 21, through September 25, 1997. The intent of the symposium was to provide a detailed and in-depth perspective of the approaches, results and progress toward the structural application of intermetallic compounds and their composites. Longer presentations which focused on real progress and trends rather than recent results, and extended discussion periods formed the centerpiece of this symposium. Emphasis was placed on a balance of presentations covering basic research, alloy development and applications. There was an excellent international representation in the presentations as well as in the attendees. To meet the objective of making this symposium a premier event to be held every four years, very stringent requirements were applied in the selection of the papers. Only two thirds of the papers were accepted for the presentation at the symposium. Our intent was to publish a first class proceedings, therefore, each manuscript was critically reviewed by at least two reviewers. Guidance given to the reviewers was to follow procedures used by well-established journals so as to ensure: 1) the subject matter was adequately covered, 2) the manuscript contained significant findings or original unpublished research, and 3) the work presented was of technological significance. We believe that we have succeeded in meeting our objective based on the quality of the papers that appear in these proceedings.					
14. SUBJECT TERMS				15. NUMBER OF PAGES 977	
				16. PRICE CODE	
17. SECURITY CLASSIFICATION OF REPORT UNCLASSIFIED		18. SECURITY CLASSIFICATION OF THIS PAGE UNCLASSIFIED		19. SECURITY CLASSIFICATION OF ABSTRACT UNCLASSIFIED	
				20. LIMITATION OF ABSTRACT UL	





# **STRUCTURAL INTERMETALLICS 1997**

Proceedings of  
the Second International Symposium on Structural Intermetallics  
sponsored by  
The High Temperature Alloys and Titanium Committee  
Structural Materials Division  
The Minerals, Metals & Materials Society  
held September 21 -25, 1997  
at Seven Springs Mountain Resort, Champion, Pennsylvania

EDITED BY

M.V. Nathal  
R. Darolia  
C.T. Liu  
P.L. Martin  
D.B. Miracle  
R. Wagner  
M. Yamaguchi

A Publication of  
**TMS**  
Minerals • Metals • Materials

**A Publication of The Minerals, Metals & Materials Society**  
420 Commonwealth Drive  
Warrendale, Pennsylvania 15086  
(412) 776-9000

The Minerals, Metals & Materials Society is not responsible for statements or opinions and is absolved of liability due to misuse of information contained in this publication.

Printed in the United States of America  
Library of Congress Catalog Number 97-71555  
ISBN Number 0-87339-375-9

Authorization to photocopy items for internal or personal use, or the internal or personal use of specific clients, is granted by The Minerals, Metals & Materials Society for users registered with the Copyright Clearance Center (CCC) Transactional Reporting Service, provided that the base fee of \$3.00 per copy is paid directly to Copyright Clearance Center, 27 Congress Street, Salem, Massachusetts 01970. For those organizations that have been granted a photocopy license by Copyright Clearance Center, a separate system of payment has been arranged.

**TMS**  
Minerals • Metals • Materials

© 1996

If you are interested in purchasing a copy of this book, or if you would like to receive the latest TMS publications catalog, please telephone 1-800-759-4867 (U.S. only) or 412-776-9000, EXT. 270..

## **PREFACE**

These proceedings represent the written record of the Second International Symposium on Structural Intermetallics which was held at the Seven Spring Mountain Resort, Champion, Pennsylvania, from September 21, through September 25, 1997. The intent of the symposium was to provide a detailed and in-depth perspective of the approaches, results and progress toward the structural application of intermetallic compounds and their composites. Longer presentations which focused on real progress and trends rather than recent results, and extended discussion periods formed the centerpiece of this symposium. Emphasis was placed on a balance of presentations covering basic research, alloy development and applications. There was an excellent international representation in the presentations as well as in the attendees. To meet the objective of making this symposium a premier event to be held every four years, very stringent requirements were applied in the selection of the papers. Only two thirds of the papers were accepted for the presentation at the symposium. Our intent was to publish a first class proceedings, therefore, each manuscript was critically reviewed by at least two reviewers. Guidance given to the reviewers was to follow procedures used by well-established journals so as to ensure: 1) the subject matter was adequately covered, 2) the manuscript contained significant findings or original unpublished research, and 3) the work presented was of technological significance. We believe that we have succeeded in meeting our objective based on the quality of the papers that appear in these proceedings. These proceedings describe the results from extensive research and development programs which are being carried out throughout the world to develop intermetallics for structural applications. Considerable progress has been made in understanding as well as solving the ductility and toughness issues, component and engine tests have been successfully completed, and examples of introduction into service are becoming more common. The recent successes bode well for ISSI-2001.

## ACKNOWLEDGMENTS

### Organizing Committee

This symposium would not have been possible without the tireless work of the members of the organizing committee. The support of the TMS staff in organizing this symposium is also gratefully acknowledged. The following committee members organized this conference.

General Committee .....	M.V. Nathal, Chairman R. Darolia D.B. Miracle
Treasurer .....	P. Heitman
Technical Program .....	R. Darolia, Chairman M.V. Nathal C.T. Liu P.L. Martin D.B. Miracle R. Wagner M. Yamaguchi
Arrangements .....	K.S. Kumar
Publicity .....	J.D. Whittenberger
International Steering .....	M. Yamaguchi D. Banerjee M.Y. Nazmy G. Sauthoff T. Khan

### Financial Support

We gratefully acknowledge the financial support by the NASA Lewis Research Center, Oak Ridge National Laboratory, US Air Force Office of Scientific Research, Commonwealth Scientific and Industrial Research Organization (Australia), Rockwell Science Center, ABB Power Generation, Allison Engine Company, Allison Advanced Development, General Electric Company, Allied Signal, Plansee Aktiengesellschaft, R & D Institute of Metals and Composites for Future Industries (Tokyo, Japan), and the Structural Materials Division of TMS.

## **BEST PAPER AWARD (Co-Winners)**

The paper "The Effect of Heat Treatments on Microstructures and Primary Creep Deformation of Four Investment Cast Titanium Aluminide Alloys" by D.Y. Seo, T.R. Bieler, and D.E. Larsen, and the paper "Effects of Microstructure, Temperature and Environmental on Fatigue Crack Growth in Ti-46.5Al-3Nb-2Cr-0.2W  $\gamma$  Titanium Aluminide" by A.H. Rosenberger, B.D. Worth, and J.M. Larsen, were selected by the Technical Program Committee as the Best Papers of the Second International Symposium on Structural Intermetallics. The selection of the best papers was based on the following criteria: originality, technical content, relevance to the field, clarity and style.

# TABLE OF CONTENTS

## KEYNOTE ADDRESS

Intermetallics for Structural Applications: Potential, Reality and the Road Ahead .....	3
J.C. Williams	

## INTERDISCIPLINARY TOPICS

Constraint Effects on Fracture Toughness of Intermetallic Alloys and In-Situ Composites .....	11
K.S. Chan	
Mechanisms of Dislocation Creep in Single Phase Nickel and Titanium Aluminides .....	21
K.J. Hemker and W.D. Nix	
Fatigue Crack Growth in Intermetallics .....	33
N.S. Stoloff	
Equilibrium Point Defects in NiAl and Similar B2 Intermetallics Studied by PAC .....	43
G.S. Collins, J. Fan, and B. Bai	
Characterization of Segregation in Nickel and Titanium Aluminides .....	53
M.K. Miller, D.J. Larson, and K.F. Russell	
Vaporization Studies of Nickel and Titanium Aluminides .....	63
K. Hilpert, M. Albers, M. Eckert, and D. Kath	
Constitution of Ternary Aluminide Systems as Basis for Materials Development .....	73
M. Palm and G. Inden	
Complicated Kinetics of L1 <sub>0</sub> -Ordering and -Disordering Due to Structural Changes Caused by Lattice Distortion .....	83
M. Spanl, B. Sprusil, and W. Pfeiler	
Ductility Enhancement in Structural Intermetallics from First Principle Calculation .....	91
R. Asokamani and R. Rita	
Ductility and Toughness Considerations in Intermetallics .....	99
Y. Kimura and D.P. Pope	

## MICROSTRUCTURE AND PROPERTIES OF TIAL

Microstructural Design of Near $\gamma$ -TiAl for Creep Resistance .....	109
J. Beddoes, L. Zhao, P. Au, D. Dudzinski, and J. Triantafillou	
HREM Investigation on Deformation Twinning and Twin Intersection in a Ti-45Al-10Nb Alloy Deformed at Elevated Temperatures .....	119
J.G. Wang, L.C. Zhang, G.L. Chen, H.Q. Ye, and T.G. Nieh	

The Role of Interfacial Substructure in the Creep Deformation of a Fully-Lamellar TiAl Alloy .....	129
L.M. Hsiung and T.G. Nieh	
<b>Best Paper Award Co-Winner:</b>	
The Effect of Heat Treatments on Microstructures and Primary Creep Deformation of Four Investment Cast Titanium Aluminide Alloys .....	137
D.Y. Seo, T.R. Bieler, and D.E. Larsen	
Deformation Processes and Dislocation Motion in $\gamma$ -TiAl .....	147
K.J. Hemker, M. Lu, and M. Zupan	
Deformation Substructure Evolution Pertaining to $1/2\langle 110 \rangle$ Unit Dislocations in TiAl Alloys .....	157
S. Sriram, D.M. Dimiduk, and P.M. Hazzledine	
The $\alpha$ - $\gamma$ Phase Transformation Mechanisms in Two-Phase $\gamma$ -TiAl Based Intermetallic Alloys .....	167
E. Abe, T. Kumagai, and M. Nakamura	
Morphology of Discontinuous Coarsening in Fully Lamellar Ti-44Al (at%) Alloy.....	177
S. Mitao and L.A. Bendersky	
Structural Evolution of Titanium Di-Borides in Wrought Ti-47at%Al-2at%Mo-0.2at%B .....	185
M. De Graef, D.A. Hardwick, and P.L. Martin	
Defect Sub-Structures in Lamellar Ti48Al After "Hard" Orientation Loading at Room and Elevated Temperatures .....	195
J.M.K. Wiezorek, X.-D. Zhang, and H.L. Fraser	
Atomic Mobility and Point Defects in Gamma Titanium Aluminides .....	205
G. Sattonnay, C. Dimitrov, and O. Dimitrov	
The Effect of Cooling Rate During Casting on Microstructural Development in Ti-48Al-2Cr-2Nb Type Alloys .....	215
K. Muraleedharan, L.L. Rishel, M. De Graef, A.W. Cramb, T.M. Pollock, and G.T. Gray III	
Mechanical Behavior and Microcrack Formation in $\gamma$ -TiAl Alloys as a Function of Strain Rate and Temperature .....	225
Z. Jin, G.T. Gray III, Y.-W. Kim, and M. Yamaguchi	
Microstructure Evolution in Gamma Titanium Aluminides Containing Beta-Phase Stabilizers and Boron Additions .....	235
M. Krishnan, B. Natarajan, V.K. Vasudevan, and D.M. Dimiduk	
Stability of Ultrafine Lamellar Microstructures During Aging in Two-Phase $\gamma$ -TiAl Alloys .....	245
P.J. Maziasz, C.T. Liu, and J. L. Wright	
A Preliminary Study on the Decomposition of the Beta Phase in Ti-44Al-8Nb and Ti-44Al-4Ta-4Zr-0.2Si Alloys .....	253
T.T. Cheng and M.H. Loretto	

## PROCESSING OF TiAl

Processing of Intermetallic Alloys .....	263
S.L. Semiatin, J.C. Chesnutt, C.M. Austin, and V. Seetharaman	
Processing and Properties of Gamma Titanium Aluminides .....	277
H. Clemens, N. Eberhardt, W. Glatz, H.-P. Martinz, W. Knabl, and N. Reheis	
Directional Solidification of TiAl-Based Alloys .....	287
D.R. Johnson, Y. Masuda, Y. Shimada, H. Inui, and M. Yamaguchi	
Multilayer Coating for Protection of Titanium Aluminides from Oxidation and Hydrogen Embrittlement .....	295
B.D. Prasad, S.N. Sankaran, K.E. Wiedemann, and D.E. Glass	
Measurement of Deformation-Induced Residual Strains and Stresses in PST-Crystals of the Intermetallic Alloy TiAl .....	305
M. Riemer, H. Biermann, R. Kowalewski, and H. Mughrabi	
Development of Third Generation Castable Gamma Titanium Aluminides: Role of Solidification Paths .....	313
S. Naka, M. Thomas, C. Sanchez, and T. Khan	
Diffusion Brazing of a Ti-45Al-2Nb-2Mn+0.8vol.%TiB <sub>2</sub> XD Alloy .....	323
Q. Xu, M.C. Chaturvedi, N.L. Richards, and N. Goel	
Spray Processing and Mechanical Behavior of $\gamma$ -TiAl .....	331
B. Li and E.J. Lavernia	
Improvement on Oxidation Resistance of Titanium Aluminide Intermetallics by Coatings .....	341
Z. Tang, F. Wang, and W. Wu	
Numerical Simulation of Thermal Stress Formation in Investment Cast $\gamma$ -TiAl .....	347
L. Würker, M. Fackeldey, and P.R. Sahn	
The Influence of Ion Implantation upon High Temperature Oxidation Behavior of Ti-48at.%Al Alloy .....	353
Y.G. Zhang, X.Y. Li, C.Q. Chen, X.J. Zhang, T.H. Zhang, and H.X. Zhang	
Study on Superplasticity of Deformed Ti <sub>3</sub> Al and TiAl Base Alloys .....	361
S. Li, J. Zhang, B. Wang, J. Zhang, D. Zou, T. Jia, and Z. Gong	
Microstructural Evolution During Thermomechanical Processing of TiAl .....	369
D.L. Anton	
New Surface Treatment Using a Fluidized Bed Furnace for Improving Oxidation Resistance of TiAl-Base Alloys .....	377
H. Kawaura, K. Nishino, and T. Saito	
Scale-up of Ingot Metallurgy Wrought $\gamma$ -TiAl .....	387
P.L. Martin, D.A. Hardwick, D.R. Clemens, W.A. Konkel, and M.A. Stucke	



Infrared Brazing of a TiAl-Base Alloy Using Ti and Al Foils and the Joint Microstructural Evolution .....	395
S. Annaji and R.Y. Lin	

Oxidation Behaviour of Highly Alloyed $\gamma$ -TiAl Alloys .....	405
A. Partridge and M.R. Winstone	

## PROPERTIES AND APPLICATIONS OF TIAL

Aircraft Engine Applications for Gamma Titanium Aluminide .....	413
C.M. Austin, T.J. Kelly, K.G. McAllister, and J.C. Chesnutt	

Automotive Application of TiAl Intermetallics .....	427
S. Isobe and T. Noda	

Surface Damage Due to Impact and Fatigue Strength Reduction in Gamma Titanium Aluminides .....	435
P.S. Steif, J.W. Jones, T. Harding, M.P. Rubal, V.Z. Gandelsman, N. Biery, and T.M. Pollock	

Effects of Alloying on the Mechanical Properties of Gamma-Based Titanium Aluminides .....	443
W.O. Soboyejo, C. Mercer, Y. Ni, and A.B.O. Soboyejo	

Production of Titanium Aluminide Valves for Automotive Engines by Reactive Sintering .....	453
D. Schneider, T. Jewett, C. Gente, K. Segtrop, and M. Dahms	

Creep Behaviour of a Cast $\gamma$ -TiAl Based Alloy for Gas Turbine Applications .....	461
D. Lundström and B. Karlsson	

Influence of Microstructure, Environment and Temperature on Fatigue Crack Propagation in TiAl Alloys .....	469
G. Hénaff, C. Mabru, A. Tonneau, and J. Petit	

Tensile and Low Cycle Fatigue Properties of Ti-48Al-2W-0.5Si Gamma Titanium Aluminide .....	479
V. Recina and B. Karlsson	

Application of Cast Gamma Alloy for Turbochargers .....	489
T. Tetsui	

Fatigue Crack Growth in TiAl Intermetallics with Equiaxed, Duplex and Lamellar Microstructures at Elevated Temperatures .....	495
Y. Mutoh, S. Kurai, T. Hansson, T. Moriya, S.J. Zhu, and Y. Mizuhara	

An Approach to Ductility Improvement of TiAl and Ti <sub>3</sub> Al Titanium Aluminides Based on Microstructure Control .....	505
V.M. Imayev, G.A. Salishchev, R.M. Imayev, M.R. Shagiev, N.K. Gabdullin, and A.V. Kuznetsov	

High Temperature Mechanical Properties Evaluation of a $\gamma$ -TiAl Base Industrially Developed Intermetallic Alloy .....	515
V. Lupinc, M. Marchionni, M. Nazmy, G. Onofrio, L. Rémy, M. Staubli, and W.M. Yin	
Manufacturing-Performance-Cost Relationships in Gamma TiAl Castings .....	523
P. McQuay and D.E. Larsen	
Designing Gamma TiAl Alloys: Fundamentals, Strategy and Production .....	531
Y.-W. Kim and D.M. Dimiduk	
Alloying Effects and Deformation Processes in Duplex $\gamma$ -TiAl Alloys .....	545
C.T. Forwood, M.A. Gibson, P.R. Miller, C.J. Rossouw, and A.J. Morton	

#### **Best Paper Award Co-Winner:**

Effects of Microstructure, Temperature and Environmental on Fatigue Crack Growth in Ti-46.5Al-3Nb-2Cr-0.2W $\gamma$ Titanium Aluminide .....	555
A.H. Rosenberger, B.D. Worth, and J.M. Larsen	
Threshold Fatigue Crack Growth Behavior of the Gamma Titanium Aluminide Alloy Ti-46.5Al-3Nb-2Cr-0.2W Under High Cycle Fatigue Conditions .....	563
B.D. Worth, J.M. Larsen, and A.H. Rosenberger	

### **NIAL ALLOYS**

Prospects for the Development of Structural NiAl Alloys .....	573
R.D. Noebe and W.S. Walston	
Development and Characterization of High Strength NiAl Single Crystal Alloys .....	585
R. Darolia and W.S. Walston	
Creep Deformation Behavior and Microstructure Evolution of NiAl/Ni <sub>3</sub> Al Multiphase Alloys .....	595
H. Senba and M. Igarashi	
Misfit Control in NiTi/Ni <sub>2</sub> TiAl $\beta/\beta'$ Alloys .....	605
M.A. Peters and C.J. Humphreys	
Impact Resistance of NiAl Alloys .....	613
W.S. Walston and R. Darolia	
The Effect of Volume Fraction Reinforcement and Annealing on the Strength of Cryomilled NiAl Containing AlN Particles .....	621
M.G. Hebsur, J.D. Whittenberger, and A. Garg	
Effect of Chemistry, Microstructure and Orientation on 1100 - 1400 K Plastic Flow Properties of Hf-Doped NiAl Single Crystals .....	631
J.D. Whittenberger, A. Garg, R.D. Noebe, W.S. Walston, and R. Darolia	
Microscopic Fracture Behavior of Single Crystalline Intermetallics .....	641
M. Göken, M. Maßmann, F. Thome, and H. Vehoff	

Point Defect Concentrations and Solid Solution Hardening in NiAl with Fe Additions .....	649
L.M. Pike, C.T. Liu, and Y.A. Chang	
Progress in the Modeling of NiAl-Based Alloys Using the BFS Method .....	655
G. Bozzolo, R.D. Noebe, J. Ferrante, and A. Garg	
Deformation and Microstructure of Ni-Rich and Hf-Doped NiAl Single Crystals in the Hard Orientation .....	665
R. Srinivasan, M.F. Savage, M.S. Daw, R.D. Noebe, A. Garg, and M.J. Mills	
Toughening Mechanisms in Directionally Solidified B2-NiAl-Based EutecticAlloys .....	673
A. Misra, Z.L. Wu, R. Gibala, R.D. Noebe, and B.F. Oliver	
Tensile Behavior of $\beta$ -NiAl: Intrinsic vs. Extrinsic Properties .....	683
V.I. Levit and M.J. Kaufman	

### **Ni<sub>3</sub>Al AND IRON ALUMINIDES**

Mechanical Properties of Ni <sub>3</sub> Al and FeAl: Recent Developments .....	693
E.P. George and C.T. Liu	
Microstructure and Mechanical Properties of Fe-40Al-0.6C .....	703
L. Pang and K.S. Kumar	
Development and Engineering Application of a DS Cast Ni <sub>3</sub> Al Alloy IC6 .....	713
Y.F. Han, Z.P. Xing, and M.C. Chaturvedi	
Defect Properties and Defect Analysis in Iron Aluminides .....	721
J. Wolff, M. Franz, A. Broska, B. Köhler, and Th. Hehenkamp	
Protective Coatings Based on FeAl Intermetallic Obtained by a Gas Detonation Method .....	727
Z. Bojar, W. Przetakiewicz, R.A. Varin, and J. Bystrycki	
How to Obtain Some Room Temperature Ductility of FeAl (B2) IntermetallicAlloys .....	735
A. Fraczkiewicz, A.-S. Gay, S. Launois, and M. Biscondi	
High Temperature Mechanical Properties and Microstructure of Fe <sub>3</sub> Al Based Intermetallic Alloys .....	741
A.A. Couto and P.I. Ferreira	
High Temperature Yield Strength of Binary Stoichiometric and Al-Rich Ni <sub>3</sub> Al Single Crystals .....	749
D. Golberg, M. Demura and T. Hirano	
Elasticity and Internal Friction of Fe <sub>70</sub> Al <sub>30</sub> -Single Crystals .....	759
W. Hermann, T. Ort, and H.-G. Sockel	
Observation of Quenched-in Vacancies in the B2 Intermetallic Compounds FeAl .....	769
T. Haraguchi and M. Kogachi	

## ADVANCED INTERMETALLICS AND COMPOSITES

The Mechanical Behaviour of the Intermetallic $\text{Ti}_2\text{AlNb}$ .....	777
T.K. Nandy and D. Banerjee	
Environmental Effects on the Fracture Toughness of the Ternary Cubic ( $\text{Ll}_2$ ) Titanium Trialuminide Intermetallics .....	787
R.A. Varin and L. Zbroniec	
Phase Evolution, Stability, and Microstructure-Creep Relations in An Orthorhombic Ti-23Al-27Nb Alloy .....	795
C.J. Boehlert, B.S. Majumdar, V. Seetharaman, D.B. Miracle, and R. Wheeler	
Platinum Group Metals-Base Refractory Superalloys for Ultra-High Temperature Use .....	805
Y. Yamabe-Mitarai, Y. Ro, T. Maruko, T. Yokokawa, and H. Harada	
Structure-Property-Application Relationships in Ruthenium Aluminide RuAl .....	815
I.M. Wolff, G. Sauthoff, L.A. Cornish, H. DeV. Steyn, and R. Coetzee	
Effects of Al on $\omega$ Formation in Transition Metal Intermetallic Alloys .....	825
G. Shao, E. Passa, P. Tsakirooulos, A.P. Miodownik, D.N. Manh, and D.G. Pettifor	
Phase Stability in High Temperature Mo-Rich Mo-B-Si Alloys .....	831
C.A. Nunes, R. Sakidja, and J.H. Perepezko	
A Study of the Microstructure and Mechanical Behaviour of Ductile Nb-Al-V Alloys .....	841
D.N. Horspool, D.K. Tappin, and M. Aindow	
Atomic Structure and Deformation of Nb-Ti-Al Alloys .....	851
R. Wheeler, S. Perungulam, S. Banerjee, D.-H. Hou, R.J. Grylls, and H.L. Fraser	
Mechanical Properties and Oxidation Resistance of Binary $\text{Al}_2\text{Ti}$ Intermetallic Compound .....	859
J.E. Benci and J.C. Ma	
Oxidation Studies on $\text{MoSi}_2\text{-X}$ ( $\text{X}=\text{Al}, \text{Ta}, \text{W}$ ) Alloys .....	869
A. Stergiou and P. Tsakirooulos	
Microstructural Characterization of NiTi-Based $\beta_2$ /Ni <sub>2</sub> TiAl-Based $\beta'$ Two Phase Alloys .....	877
H. Murakami, P.J. Warren, T. Kumeta, Y. Koizumi, and H. Harada	
Structure and Mechanical Properties of Ti-Al-Fe Alloys at Ambient and High Temperatures .....	885
M. Palm, A. Gorzel, D. Letzig, and G. Sauthoff	
Microstructure Evolution, Phase Transformations and Oxidation of an Orthorhombic Titanium Aluminide Alloy .....	895
J. Kumpfert and C. Leyens	

Microstructure and Mechanical Properties of Ultra SCS™ Fiber Reinforced Orthorhombic Ti-22Al-26Nb Composites .....	905
A. Chatterjee, J.R. Roessler, L.E. Brown, P.W. Heitman, and G.E. Richardson	
Mission Cycle Behavior of Orthorhombic Titanium Matrix Composite .....	913
T.P. Gabb, J. Gayda, A. Chatterjee, and R. Ress	
Microstructure and Creep Resistance of Nb <sub>3</sub> Al/Nb In-situ Composites .....	923
N. Nomura, K. Yoshimi, and S. Hanada	
Fabrication and Mechanical Behaviors of SiC <sub>CVD</sub> /TiAl Composite .....	929
Y. Mizuhara, K. Hashimoto, H. Nakatani, and Y. Shimada	
An Investigation of Fatigue and Fracture in NiAl/Mo Composites .....	939
P. Ramasundaram, R. Bowman, and W.O. Soboyejo	
Strong, Tough, and Pest Resistant MoSi <sub>2</sub> -Base Hybrid Composite for Structural Applications .....	949
M.G. Hebsur and M.V. Nathal	
Molybdenum and Titanium Silicide Based Composites and Alloys .....	959
R. Mitra, N.E. Prasad, A.V. Rao, and Y.R. Mahajan	
Subject Index .....	969
Author Index .....	975

## **KEYNOTE ADDRESS**

## INTERMETALLICS FOR STRUCTURAL APPLICATIONS; POTENTIAL, REALITY AND THE ROAD AHEAD

J. C. Williams  
GE Aircraft Engines  
Cincinnati, OH 45241

### **Abstract**

Intermetallic compounds represent a new and essentially not yet implemented class of materials. This paper describes the status of these materials with respect to their readiness for introduction and outlines some of the barriers that must be addressed and overcome. Emphasis is placed on non-technical barriers such as organizational culture, since these aspects of materials acceptance are less commonly discussed. Some suggestions to accelerate progress also are offered along with some cautions. In the final section, a prognosis for implementation of intermetallic compounds is offered.

### **Introduction**

Intermetallic compounds have been the subject of study for the past thirty-five years, both as intellectually interesting phases from an alloy theory standpoint and as materials that have unusual physical and mechanical properties. More recently, there has been recognition that intermetallics have promise as high temperature structural materials because they exhibit excellent strength retention at high homologous temperatures. The status of intermetallics as structural materials was reviewed at ISSI-1 four years ago. The purpose of this paper is to update the status of this class of materials and to attempt to review, in capsule form, some of the lessons that have been learned in this ensuing period and the realities of the application potential for these materials. Following this, some speculation will be offered about the future applications of intermetallics and the time frame in which these materials may be potentially realized.

It turns out that the barrier issues to implementation of any new class of materials, intermetallics being one example, are of several types. These are technical, economic and a third which here will be called "cultural" for lack of a more precise term. There is some overlap in these categories, but it still is useful to discuss the barrier issues in this way. The focus of this paper will be weighted in favor of the latter two categories (economic and cultural) because these are matters less frequently discussed and because there are many better qualified authors (a number of which are attending ISSI-2) to write a detailed technical treatise on intermetallics. There also is interaction between discrete issues in these categories and these must be addressed and overcome if real progress is to be made. Many of these issues have been discussed in a National Materials Advisory Board report that examines the process of commercializing new materials (1).

### **Brief Assessment of Leading Candidate Intermetallics**

From the standpoint of maturity both in terms of cumulative effort expended, progress and continuing application potential, there are essentially five classes of intermetallic materials, at least in the opinion of the author. These are three Ti base systems: Alpha-2 ( $\text{Ti}_3\text{Al}$  based), Orthorhombic ( $\text{Ti}_2\text{AlNb}$  based) and Gamma ( $\text{TiAl}$  based) and two Ni base systems: Gamma prime ( $\text{Ni}_3\text{Al}$  based) and Beta ( $\text{NiAl}$  based). There are many other intermetallic compounds that have been the object of basic research studies, e.g.  $\text{Al}_3\text{Nb}$  and  $\text{MoSi}_2$ , but most of these appear to be have considerably less ductility and, as a result, have not yet been the subject of detailed evaluation for specific components. Thus they are a long way from implementation in actual products. This section is not intended as a detailed assessment, but rather a discussion of these materials together with enough examples of the issues to establish some credibility of the assessment.

Among the five systems mentioned, there are two systems that appear to be the front runners: Gamma and Gamma-prime. Gamma is attractive because of its low density, which leads to good specific stiffness and strength. It is currently being aggressively pursued as an airfoil material, both for the compressor and the low pressure turbine section of gas turbine engines. Gamma-prime has good high temperature strength and oxidation resistance and is very cost competitive relative to advanced superalloys. It does not compete well with the highest performance PM superalloys for highly stressed component applications such as disks, but is very attractive as a replacement for stainless steel and lower temperature capability Ni base alloys. In these latter cases it provides affordable performance improvement. Orthorhombic Ti aluminide has good strength in the range 675-750° C and is less susceptible to environmental embrittlement than Alpha-2 (2). Orthorhombic Ti aluminide also is more ductile and easier to shape than the Alpha-2 materials. Orthorhombic Ti aluminides also have a lower ( $\approx 50\%$ ) coefficient of thermal expansion than Ni based alloys. This system appears promising for applications in casings and other static parts that operate in the temperature range just mentioned. It also is attractive as a matrix for SiC fiber reinforced composites, but these materials are considerably further from commercialization due to some unresolved technical issues still being worked and for cost reasons.

Structural Intermetallics 1997  
Edited by M.V. Nathal, R. Darolia, C.T. Liu, P.L. Martin,  
D.B. Miracle, R. Wagner, and M. Yamaguchi  
The Minerals, Metals & Materials Society, 1997

Beta NiAl has been studied and extensively evaluated both in polycrystalline and monocrystalline forms. These studies have led to significant improvements in the understanding of this material, and a successful factory demonstrator engine test has been conducted with NiAl turbine vanes. However, the low toughness including impact resistance and the limited ductility of NiAl are sufficient barriers that further development for application in turbine airfoils has been abandoned at GE. Having said this, it is important to recognize the important learning that the NiAl effort has allowed. For example, the learning regarding the design of attachments described in more detail later has been accomplished using NiAl. When dealing with new classes of materials the concept of cumulative learning is important, especially when assessing the value of discontinued development investments. This is important not only for company funded efforts but also for government sponsored programs. The materials community should assert some leadership in establishing the value of cumulative learning as a metric.

Work on the Alpha-2 materials also has been discontinued in favor of the similar, but constitutionally different Orthorhombic Ti Aluminides. The Alpha-2 materials exhibit a large reduction in tensile ductility during tensile testing in air between  $\approx 600$  and  $800^\circ\text{C}$  (6). This has been traced to an environmentally induced embrittlement effect. As mentioned earlier, the Orthorhombic materials do not show such a pronounced effect. This, coupled with more attractive properties, has prompted a shift in most active efforts to apply the  $\approx 25$  atom Al Ti based intermetallics from Alpha-2 to the Orthorhombic materials. In some regards, this can be viewed as an evolutionary step in materials system development and the distinction between the Orthorhombic and Alpha-2 materials classes may only be important to materials specialists. The maturation of Orthorhombic was significantly aided and accelerated by the learning gained during the extensive investigation of Alpha-2. This is a good example of the use of cumulative learning.

### **Barrier Issues**

As already mentioned, it is convenient to address the barrier issues in three distinct categories. One reason for this is to call attention to the "softer", but essential, issues of economics and organizational culture, both of which can severely impede the acceptance and implementation progress of a technically acceptable material.

**Technical:** The technical issues which remain as barriers to wide spread applications of intermetallics include some familiar ones mentioned in a variety of earlier papers (2-5). Among these are limited ductility at low temperatures, inadequately developed methods for designing load bearing components using materials with such limited ductility, lack of experience (and therefore confidence) in using such materials for load bearing applications, limited manufacturing experience for making components from intermetallic compounds and a plethora of ancillary, application and material system specific questions that require answers before committing any new material to product introduction. Answering many of these questions is not technically demanding, but providing the answers takes time and consumes resources. Thus the cost of obtaining

these answers enters into the cost:benefit calculation and can become a barrier.

Structural materials with limited ductility are anathema to design engineers because of the perceived and real increase in risk of catastrophic failure. One of the long-standing difficulties in this area has been the inability of the design and materials communities to separate reality from perception. Clearly, there is a real requirement for enough ductility at component features such as attachments to allow re-distribution of loads. It also is necessary to have enough ductility to achieve damage tolerance in service and robustness during manufacturing including assembly. The divergence of reality and perception comes when the definition of "enough" is attempted. A significant part of this is because the greatest ductility often is needed at locations or under conditions that are most difficult to analyze, i.e. at attachments where there is multi-axial loading or under less well understood loading conditions, such as impact. Analytical tools to deal with these situations are evolving, but are not mature enough yet to allow analysis to supplant component and product testing as the final verification step. Further, the availability of detailed failure modes that can be properly represented in analytical routines is limited to say the least.

There also are issues related to design paradigms (paradigm has become an overworked word, but it still has real meaning) that can interfere with acceptance of a new material. For example, the "requirement" for tensile ductility levels that are as large as those that have become accepted through years of successful use of metallic alloys. In reality, this is not a requirement but only a level that has been shown through experience to be large enough to work. It is much harder to estimate the margin that is present in successful applications, yet it is frequently argued that this is a minimum. The unwillingness to use materials with less than these levels of ductility certainly is a paradigm problem, but is not necessarily a technical one. As described earlier, it is very difficult to analytically determine what the minimum required ductility is. However, there are experiments that can be performed to bound the ductility requirement and to concurrently obtain data on the relation between detailed feature geometry, required ductility and failure modes. For example, in the case of turbine blades, simple pull tests on attachments (dove tails) have showed that changes in geometry can permit the breaking loads to increase by several hundred per cent. These data, coupled with analysis of the maximum operating loads, allows a suitable geometry to be defined without specifically invoking ductility or failure modes. A factory engine test is the ultimate step in determining if the new attachment geometry is suitable. Clearly, this empirical approach is less elegant, more expensive and consumes more time than analysis, but at the moment it is the only reliable approach. The ability to accelerate qualification of advanced materials by analysis, simulation and modeling should assume a higher priority in the materials community. This requires close cooperation with design engineers who understand component behavior. If this capability is developed it will aid accelerating the acceptance of new materials. Similarly, design methods are evolving to handle anisotropic materials, but the convergence between these methods and the required types of materials property data still creates additional effort if not uncertainty about the accuracy of the analysis.



The object of this paper is not to provide a complete or detailed litany of the application or material specific technical issues that have been encountered in the attempts to introduce intermetallics into service. However, it is instructive to mention some examples, which will be done in the following paragraphs.

Chemical composition control is an issue for all metal based materials. For intermetallics, the compositions frequently lie in alloy content domains where there is little experience in controlling composition or, even, for which reliable chemical analysis methods exist. Usually this is not an large technical barrier, but development of analytical methods and compositional standards takes time and costs money. In some instances, small concentrations of alloying additions are beneficial to the performance of the material. Realization of the benefit of small alloying additions also can lead to narrow composition limits which may be difficult to achieve in production heats. In these cases the analytical sensitivity required may require special techniques that are not generally available. Again, this is manageable but creates another special case which is not conducive to acceptance of the material.

Methods for manufacturing components from new classes of materials must be understood and the applicability of past practices need to be determined. The availability of shape making techniques such as forging and casting and the capability of these processes (in a statistical variation sense) must be known. Applicability of secondary shaping processes such as machining or grinding also must be understood. For example, the machining or grinding conditions used during manufacturing of an intermetallic component are potentially different than for an alloy, if these processes can be used at all. Feeds, speeds, coolants and tools all need to be evaluated and the propensity for cracking or burning must be determined. In many cases acceptable conditions can be identified and processing practices can be defined. In such cases, the main point of discussion becomes availability of the necessary machine tools and the cost differences associated with machining the new material. Similar evaluations and comparisons must be made for surface treatments including both coatings and vapor blasting or shot peening. Relatively speaking, intermetallics pose fewer major challenges in these types of matters than other advanced materials such as composites. Nevertheless, evaluating all of the processes required to make a component from a new material takes time, costs money and, therefore, represents another barrier to acceptance and implementation. The importance of cost will be discussed in the next section on economics.

**Economic:** In the past 4 years (since ISSI-1) the realities and consequences of the "New World Order" have become clearer. As a result, there has been a rapid transition away from military driven applications to dual use (military and commercial) or purely commercial applications of many high performance materials. The tried and proven practice has been the introduction of new materials into a military system or product and then transitioning them to commercial applications. There is growing recognition that this cycle can no longer support the development schedule for competitive commercial products. This is finally becoming the new "conventional wisdom" for most managers and technologists in aerospace companies. Concurrently, the emergence of the airlines from a multi-year period of record financial losses has increased the cost sensitiv-

ity in the aircraft and aircraft engine producers. Today, introduction of a new material into a product requires a much better cost:benefit analysis than was the case ten or even five years ago. In recognition of this, preliminary cost:benefit estimates are being used by some companies to guide selection of R&D projects. In the long term, this new level of discipline in choosing development projects should lead to fewer projects that are technical successes but economic failures and more that are outright successes. To contribute to this result and to sustain the role of materials and processes in competitive products, the materials community needs to learn how to better quantify and depict the benefit of their output. One promising but little used method is option value pricing which gives more appropriate results than discounted cash flow or internal rate of return calculations used to guide other types of investment decisions (e.g., machine tools and acquisitions).

In a reduced or fixed sum funding environment, there naturally will be an element of competition for funds between the engineering disciplines, especially those that provide the so-called product enabling technologies. The author perceives the materials case to be somewhat more difficult to make, in part because it is distributed between materials developers, users and producers. In the U.S. few vertically integrated enterprises exist for structural materials. Whether the above perception is accurate or not, it is clear that establishing the methodology for representing the benefit of materials and process development investment should be a high priority for the materials community. For advanced materials such as intermetallics, this is even more important because the incremental investment is larger than for a true evolutionary material, e.g. a next generation Ni or Ti alloy. Clearly the incremental benefit associated with a new class of material also is larger, and quantifying this should become the centerpiece of the discussion.

The cost of development and introduction of a new material consists at least of three discrete elements or phases: (1) development and definition of the desired composition and structure and getting representative preliminary property data; (2) answering the (myriad) application specific technical questions and developing high enough quality data to use in preliminary component designs; (3) obtaining a design data base and demonstrating that components can be made from the material in representative production scale facilities and at acceptable component cost. With each of these successive steps the cost increases by a factor of 5 to 10. Yet the availability of federal funding usually is heavily biased toward phase one. Today, there are numerous interesting concepts that have been "stuck" at the end of phase 1 with no funding available to move them forward. In addition, many phase 1 activities are conducted at universities and national laboratories and transitioning these concepts to product making organizations is essential if they are to be implemented in real products. This transition process including third party (federal) funds to support the product demonstration has been an uneven one at best. The current "corporate welfare" stigma is only making this matter worse. From an industrial perspective, there needs to be some company provided "risk capital" available to stimulate this transition process, but there is little such funding available today.

The U.S. research and development community continues to decry the reductions in funding for basic research, but there seems to be little attention given to the growing "backlog" of

ideas, discoveries and inventions that are stalled in the phase 1 / phase 2 transition zone due to lack of funding for transition to products. It seems that phase 2 activities are high enough risk that use of federal funding is appropriate to help offset this risk. After that, promising concepts that emerge from phase 2 should be reduced to practice using some combination of public and private sector funds. (In past times the public funds often came from large systems development projects as opposed to discrete funding for materials commercialization. The results were the same but the "visibility and optics" with regard to the use of public funds were very different.) Today, there also is the uncertainty of market size, at least where military programs are concerned. This creates a natural reluctance by materials producers to make capital investments to produce a new material because of the vagaries of the pay-back analysis. To understand this point, one only has to contemplate the recent fate of the A-12, the P-7 and the dramatic reductions in quantities or production rates of the V-22, B-2 and F-22 to begin to appreciate the severity of this problem.

One might ask, "What does this have to do with intermetallics?". One reply is that factors that inhibit transition from phase 2 to phase 3 are economic focused barrier issues for introduction of a new material. For intermetallics, the extent to which the capital base for manufacturing components is a limitation depends significantly on the particular compound under consideration. For the Alpha-2 and Gamma titanium aluminides and for  $\text{Ni}_3\text{Al}$ , conventional metal working and casting facilities are adequate, although not optimum. For other compounds such as  $\text{NiAl}$ ,  $\text{Al}_3\text{Nb}$  and  $\text{MoSi}_2$ , there are basically no production scale facilities available. Thus even if the prospect for commercialization of these latter compounds were strong, the barrier to transitioning them from phase 2 to phase 3 would be significantly higher. It is reasonable to speculate that the absence of production capability for these materials is related to their immaturity, but it is harder to know whether, if there were real niche markets for one or more of these compounds, if there would be capital available to establish facilities to produce them.

A key factor in the decision process for facility investment is market size. One way to increase market size is for the user community to cooperate in developing materials and to commit early in the development process to using common materials. Many advanced materials including intermetallics will have relatively small volume requirements at best. Sub-division of this volume between several similar, but discrete, compositions only heightens the commercialization barriers. The current realities (at least as perceived by the author) are that this type of cooperation needs to accelerate if the implementation of advanced materials is to keep pace with the needs of new products.

**Organization Culture:** Perhaps the "softest" aspect of commercializing a new material is the role of organizational culture. Organizational culture has its basis in history and tradition and in the ingrained attitudes of the employees and leaders of an organization. Therefore, anything written in detail about this subject is, of necessity, specific to one organization or even a unit of a larger organization. Most aspects of the culture of an organization cannot be represented quantitatively and even can be difficult to describe. Organizational culture nevertheless has a great deal to do with the acceptance of

change, the willingness to assume reasonable risk, the willingness to engage in technology sharing/cooperation for mutual gain and many other less tangible characteristic traits such as top down vs. bottom up decision making processes.

There is a relationship between organizational culture and the nature and persistence of paradigms. As discussed earlier, the acceptance of new materials with different characteristics extends beyond the ability to satisfactorily address the technical issues and ultimately depends on the existence of a few influential individuals to "champion" the new material and move beyond their paradigm based rejection. The existence and influence of champions is unto itself a measure of organizational culture. Without such champions it is unlikely that the opportunity to provide enough answers to technical questions will occur. This is more so today than it was five years ago because the availability of risk capital is less. The role of the champion ranges from saying "just go do it" to influencing the allocation of the necessary resources needed to address the technical questions. All organizations have a formal structure and a (separate) power structure. The champion may or may not hold a position of authority in the formal structure, but he or she must have significant influence within the power structure.

The speed with which an organization recognizes the need for change is a cultural matter and is usually related to the way success and failure have been and are rewarded and punished. Organizations that deal in high technology content products must permit employee teams to tackle very hard problems without unreasonable fear of failure. They also should recognize that an excellent effort which leads to a negative result is not a failure if the effort contributes significantly to cumulative learning. This is the mark of a striving, progressive organizational culture. Such organizations are destined to operate at the frontier of their domains. Organizations that only tackle sure things are, at best, destined to be followers (and not fast followers at that). Other organizations seem to foster a culture that seems not to differentiate activity from accomplishment. This often is characterized by doing some work on literally all new concepts. These organizations either have too many resources or no strategy. In a limited resource environment, strategy really means choice and excellent execution of a sound strategy is the mark of winning organizations.

Another aspect of organizational culture is the degree to which conformity is encouraged or rewarded. Conformity, except where compliance and legal issues are concerned, can stifle creativity. The current use of Integrated Product Development (IPD) teams is sometimes argued to encourage conformity. This does not have to be the case. A good team member contributes the best he or she has to offer and communicates both output and approach to the rest of the team. This does not seem to necessitate conformity.

So what does all of this have to do with acceptance and implementation of a new material such as an intermetallic? Simply put, it has a lot if not everything to do with it! For example, an organization that allows the metallic alloy ductility paradigm to impede the evaluation of a less ductile, but otherwise attractive, material is destined to fall behind organizations that move out and try the material. Risk mitigation can be achieved through selection of low risk initial applications. Similarly, organizational cultures that are preoccupied with always succeeding (no matter how small the successes) will

stifle the willingness of designers to devote time, energy and creativity to re-thinking their methods and approaches to enable a new material with different characteristics to function successfully. This situation or culture places rules above reason. Paradigm bound organizations will experience difficulty operating in new domains, even though they may have world class track records in incremental product improvements. The key to moving beyond existing domain boundaries is having leadership with vision and that empowers employees and having creative, energetic employees who see excitement in calculated risk taking. These organizations will be more successful in implementing new materials such as intermetallics and will realize the benefit of new materials with different characteristics in their products.

Universities and government or non-profit research organizations also have their own cultures. The best of these institutions clearly have on staff some of the most creative materials scientists and engineers available anywhere. In these institutions\*, there has been a tendency to focus on concept or knowledge creation. This is an essential first step in creation of any new material. In terms of cost, however, it also is the least expensive step. Also, there are aspects of commercializing a new material and/or introducing it into a product that are hard to appreciate without doing them. One of these is understanding the cultural characteristics of a product making organization; some of these have been described earlier. The acceptance and transition of materials concepts created in universities and in research institutions has been and continues to be a slow and uneven process. As product making organizations continue to focus more and more on current and next generation products, it will become increasingly important to remedy this situation. One possibility is a more regular interchange of people which will provide a "grass roots" understanding of other organizational cultures. Industrial sabbaticals for university faculty is one specific suggestion. A standard objection to this is the perceived need by product organization to protect their proprietary information. While this issue has real dimensions, the perception is substantially larger than reality. In fact, some of the organizations that are most vocal on this point have become so insular that they no longer realize how little proprietary information they truly have! This becomes a culture clash and is a good example of the unwillingness of an organization to share to gain.

### The Road Ahead

The prospect of major breakthroughs in intermetallic compounds that lead to simultaneous retention or improvement of high temperature strength and substantial improvement in low temperature ductility seem unlikely if not scientifically unfounded. Thus, the focus on continuing to learn how to use the materials that are available today through improved design methods and more consistent (lower variation) processing seems to be the more productive use of the available resources.

---

\* Corporate Research Laboratories have been excluded from this category because they are part of a larger product making enterprise. The integration (or lack thereof) of corporate laboratories into the larger enterprise is a corporate culture issue unto itself.

The ability to sustain investment in advanced materials such as intermetallic compounds and the future of advanced materials over the next ten to twenty years will depend on successful implementation of a few production applications. This is why low risk introduction strategy is needed to complement higher risk, higher pay-off applications. Another critical element of near term success will be the ability to get the cost of production components within an acceptable range. The growing cost stringency in the aerospace industry makes achieving this even more challenging, but current progress provides reason for cautious optimism. While there will be future generations of intermetallics both from a compositional and a constitutional standpoint, there is real merit in focusing on a very few first generation materials. Coupled with the discipline to avoid proliferation of compositions with marginal (at best) improvements in performance must come agreements to cooperate more extensively in pre-competitive development activities, particularly those in phase 2 and some aspects of phase 3 such as data bases. Similar focus on a very small number of fabrication methods will be needed to amass critical concentration of resources to truly productize a few manufacturing processes. Today, this seems essential, given the relatively small total volume of material that will be used in the next five years.

The road ahead for advanced materials including intermetallics has some potholes in it, but these can be circumnavigated. Attention to cost, better cooperation across the materials community, using low risk introductions and creation of the "right" culture will help. What cannot be tolerated, metaphorically speaking, is a number of unproductive detours driven by false pride, technical curiosity or lack of discipline. Funding is the fuel for this journey and it is a finite resource. The high performance materials community must have the vision, discipline and constancy of purpose to stay the course and not deviate. That is, we must identify a few successful production applications before the fuel supply is exhausted. This is a high stakes game that impacts the competitiveness of future products. Many of the key drivers are factors that have very little to do with technology *per se*. Recognition of this point represents new territory for most materials technologists, but is one of the important keys to success.

### Acknowledgments

The author acknowledges with gratitude the constructive comments from his colleagues, Ram Darolia, Lyman Johnson and Doug Konitzer, who read earlier versions of this paper and suggested improvements.

### References

1. "Commercialization of New Materials for a Global Economy", National Research Council, NMAB Report #465, National Academy Press, Washington, DC, 1993.
2. A. Woodfield and B. Lawless, "Orthorhombic Titanium Alloy Microstructure/Property Relationships", Proc. 40<sup>th</sup> Sagamore Army Materials Research Conf., 1993, Pgs 89-100.
3. C. M. Austin and T. J. Kelly, "Gas Turbine Engine Implementation of Gamma Titanium Aluminide", Superalloys

- 1996, Kissinger, et al, eds, TMS Warrendale PA, 1996, Pgs.539-543.
4. P. K. Wright, "designing with Gamma Ti Aluminide", Structural Intermetallics, R. Darolia et al, eds, TMS Warrendale PA, 1993, Pgs. 885-895.
  5. J. C. Williams, "Intermetallic Compounds: an Assessment of Progress and Potential", Structural Intermetallics, R. Darolia et al, eds, TMS Warrendale PA, 1993, Pgs. 839-844.
  6. C. H. Ward, J. C. Williams and A. W. Thompson, "Dynamic Environmental Embrittlement of an  $\alpha_2$  Titanium Aluminide", Scripta Met., 28, 1017-1021, (1993).

## **INTERDISCIPLINARY TOPICS**

# CONSTRAINT EFFECTS ON FRACTURE TOUGHNESS OF INTERMETALLIC ALLOYS AND IN-SITU COMPOSITES

Kwai S. Chan

Southwest Research Institute  
P. O. Drawer 28510  
San Antonio, TX 78228-0510

## Abstract

This overview paper presents a summary of the effects of constraint on the near-tip fracture process in intermetallic alloys and in-situ composites. In addition to geometry, constraint can arise from the crystallography of slip in single crystal alloys and from the microstructure in polycrystalline alloys and in-situ composites. The dependence of constraint on the phase morphology in the microstructure is illustrated with experimental evidence, and its role in ductile phase toughening is summarized for both intermetallic alloys and composites. Various means for mitigating constraint in these materials are examined to investigate possible impact on fracture resistance. Particular attention is focused on the effects of constraint on the initiation fracture toughness and the onset of crack instability. Relations between constraint, microstructure, and resistance-curve fracture behavior are examined and compared against experimental data in the literature.

## Introduction

Constrained plastic flow is a term used to describe a deformation state where plastic straining is impeded in a certain direction. Classical examples of constrained plastic flow are rolling of a plate and deformation at a notch root, ahead of a crack tip, or under a hardness indenter. In these cases, the constraint arises from the deformation geometry that induces a triaxial state of stress in the deformation zone. Because of the triaxial stress state, the stress for constrained plastic flow is higher than that for the unconstrained. A common measure of plastic constraint is the ratio,  $\sigma_1/\sigma_0$ , of the maximum principal stress,  $\sigma_1$ , in constrained flow to the flow stress,  $\sigma_0$ , in uniaxial deformation; such a ratio is generally referred to as the plastic constraint factor. Another common indicator of plastic constraint is the triaxiality parameter, which

is the ratio,  $\sigma_m/\sigma_y$ , of the hydrostatic or mean stress,  $\sigma_m$ , to the yield stress,  $\sigma_y$ . For both cases, a highly constrained deformation field like a deep notch root or a crack has a plastic constraint factor on the order of three. Both parameters are used interchangeably in this paper.

The development of the crack-tip plastic constraint due to geometry effects has been examined and summarized in two recent symposia [1, 2]. The geometrical effects can arise from a crack-tip geometry change, which is related to the amount of crack-tip blunting and the specimen dimensions [3]. Figure 1 illustrates the plastic constraint near a crack tip as measured by the triaxiality parameter,  $\sigma_m/\sigma_y$ , for three different crack-tip geometry changes [3]. In the Hutchinson, Rice, and Rosengren (HRR) field [4, 5], a plastic constraint factor of three is present at the crack-tip because of the assumption of small strain and little geometry change. In the case of small scale yielding, only small amounts of crack-tip blunting and geometry change are allowed. The plastic constraint is highest when the size of the plastic zone is small compared to other characteristic dimensions (i.e., thickness and width) so that small scale yielding prevails. Under this condition, the fracture processes near crack tip are dominated by the leading singular term in either the K-field or the J-field, and the maximum hydrostatic stress developed near the crack tip can be as high as three times the flow stress [3]. In contrast, the fully plastic field is nonunique [6] and exhibits a geometry dependence [3]. As the crack-tip plastic zone size increases, a loss in the plastic constraint results when crack-tip yielding changes from small to large scale and becomes uncontained (Figure 1).

Beside geometric constraints, a high plastic constraint can be induced by nondeformable constituents in the microstructure, particularly at the interfaces of deformable and nondeformable phases. This type of constraint, which is microstructural in nature, is prevalent in alloys or

composites that contain a less deformable or rigid phase in a more deformable phase. Metal-matrix composites and ductile-phase toughened intermetallic alloys and in-situ composites fall into this category. The amount of plastic constraint that develops within the ductile phase depends on the volume fraction, size, and morphology of the less deformable or rigid phase [7-10].

A high plastic constraint factor also exists under certain crack-tip slip conditions [11, 12]. The high plastic constraint does not arise from geometry or microstructure, but originates from the crystallography of slip and its interaction with the crack tip stress field. Crystallographic constraint can exist in single crystal alloys, even those with a single phase microstructure. It is prevalent in planar slip materials. As a result, ordered alloys and intermetallics that exhibit planar slip behavior and have limited independent slip systems can be vulnerable to brittle fracture resulting from a high crystallographic constraint.

In summary, plastic constraint in metals and deformable intermetallics can arise from three sources: (1) geometric, (2) crystallographic, and (3) microstructural origins. The objective of this paper is to give an overview of the effects of plastic constraint on the near-tip fracture processes in intermetallic alloys and in-situ composites. Since the geometric constraint is well known [1, 2], it is included in this paper for completeness and comparison purposes only. The concept of crystallographic constraint is new and is therefore examined in greater detail than its geometric and microstructural counterparts. The paper is divided into two main parts, one on crystallographic constraint and the other on microstructural constraint. For each type of constraint, attention will be focused on (1) the origin of the particular constraint, (2) relaxation of the plastic constraint, and (3) the role of plastic constraint in fracture resistance in intermetallics and its composites.

### Crystallographic Constraint

#### (A) Origin

In Figure 1, crack-tip plastic flow is described by continuum plasticity theory for a power-law hardening material characterized by the Ramberg-Osgood constitutive equation. For a crack in a single crystal alloy, the crack-tip blunting process is dictated by crystal plasticity and significantly influenced by crystallography. The strong influence of crystallography on the plastic constraint and fracture process in single crystal alloys exhibiting planar slip has been analyzed [11-13] by considering the propagation of a mixed-mode crack along a coplanar slipband, as shown in Figure 2 [11]. The salient feature of a mixed mode slipband crack is the formation of a plastic zone containing slip on a plane that is coplanar with the crack plane and a region of both coplanar and out-of-plane slip as depicted in Figure 2. The size of the coplanar slip zone is considerably larger than that of the out-of-plane slip zone, but the latter is located closer to the crack tip. The shear stresses within the plastic zone are relaxed and prevented from increasing by coplanar slip. The coplanar slip, however, does not relax the normal stresses. As a consequence, the normal and hydrostatic stresses within the plastic zone continue to build up until out-of-plane slip is activated near the crack tip. The resulting elastic-plastic stress field is described by [11]

$$\sigma_{ij} = \begin{bmatrix} \sigma_{xx}^+ & \sigma_{xy}^+ & \sigma_{xz}^+ \\ \sigma_{xy}^+ & \sigma_{yy}^+ & \sigma_{yz}^+ \\ \sigma_{xz}^+ & \sigma_{yz}^+ & \sigma_{zz}^+ \end{bmatrix} \quad (1)$$

where  $\sigma_{xy}^+$ ,  $\sigma_{yz}^+$ , and  $\sigma_{xz}^+$  are the shear stresses relaxed by coplanar slip;

$\sigma_{xx}^+$ ,  $\sigma_{yy}^+$ , and  $\sigma_{zz}^+$  are the normal stresses that must be relaxed by out-of-plane slip. At the out-of-plane slip plastic zone

$$\sigma_{xx}^+ = \sigma_{yy}^+ = \frac{\sigma_{zz}^+}{2\nu} = \frac{K_I}{\sqrt{2\pi r_p}} \quad (2)$$

where  $\nu$  is the Poisson's ratio and  $r_p$  is the out-of-plane plastic zone size. The corresponding triaxiality factor is then given by

$$\frac{\sigma_m}{\sigma_y} = \frac{2(1+\nu)K_I}{3\sigma_y\sqrt{2\pi r_p}} \quad (3)$$

where the yield stress,  $\sigma_y$ , is taken to be twice the critical resolved shear stress,  $2\tau_y$ , for coplanar slip. From Eq. (3), it is apparent that the plastic constraint factor depends on the size of the out-of-plane slip plastic zone, which in turn, is controlled by crystallography and the ease of activating out-of-plane secondary slip. When activation of out-of-plane secondary slip is difficult and  $r_p$  is small, the plastic constraint factor at the secondary slip zone boundary can be large. The presence of this type of constraint at the crack tip provides the driving force for continual propagation of the mixed mode crack along the slip plane and the formation of cleavage-like fracture facets, despite the occurrence of coplanar slip directly ahead of the crack plane [11].

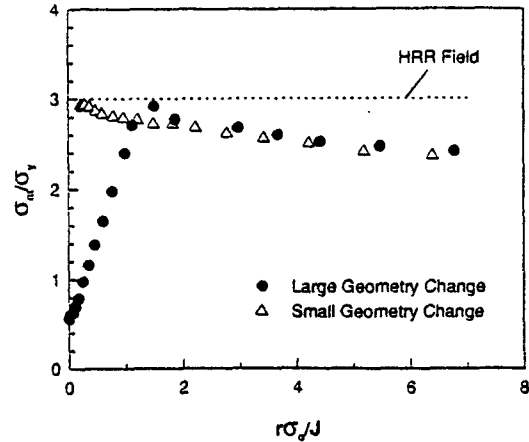


Figure 1: A comparison of the triaxiality ahead of a crack as given by small and large geometry change boundary layer formations. The triaxiality of the HRR field is independent of  $r$  and is indicated by the horizontal straight line. From Hancock et al. [3].

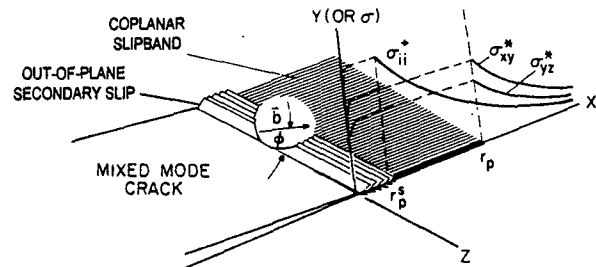


Figure 2: A schematic illustration of the stress state ahead of a mixed mode crack with a coplanar slip band characterized by a slip vector  $b$  at an angle  $\phi$  to the crack front. The coplanar slip extends to  $r_p$  while secondary slip is activated to  $r_p$ . From Koss and Chan [11].

Table I: Calculated triaxial constraint factors for a mixed Mode I and II crack ( $\psi_1 = \psi_2 = 45^\circ$ ,  $\psi_3 = 90^\circ$ ) in L1<sub>0</sub> (TiAl) and B2 (NiAl) single crystals compared against those for fcc, bcc, and hcp crystals

Crystal Structure	Coplanar Slip System	Out-of-plane Secondary Deformation System	$\sigma_m/2\tau_y$
L1 <sub>0</sub> (TiAl) [18]	(111) $\langle\bar{1}10\rangle$	( $\bar{1}11$ ) $\langle\bar{1}10\rangle$	1.65
B2 (NiAl) [49]	(110) [001]	( $\bar{1}10$ ) [ $\bar{1}11$ ] (011) [100]	1061 $\infty$
fcc	(111) [ $\bar{1}01$ ]	( $\bar{1}11$ ) [101]	1.65
bcc	(110) [ $\bar{1}11$ ]	(121) [ $\bar{1}11$ ]	2.0
hcp	(0001) [1120]	(1012) [ $\bar{1}101$ ] twins	3.3

Table I presents the triaxiality constraint factor for a mixed mode I and II crack along a coplanar slipband for several crystal structures and material systems, including those of intermetallic compounds like L1<sub>0</sub> (TiAl) and B2 (NiAl). These calculations are based on the assumption that  $\tau_y$  and  $\tau_y^*$  are equal. Large values of the triaxiality constraint factor are obtained for the fcc, bcc, hcp, and L1<sub>0</sub>. For B2, the triaxiality constraint factor for coplanar slip on (110) [001] is extremely large because of difficulty in activating out-of-plane slip in this crystal structure for the crack/slip configurations considered.

#### (B) Relaxation of Crystallographic Constraint

When crystallography is favorable for out-of-plane secondary slip, the triaxiality constraint buildup near a coplanar slipband crack is strongly influenced by the ease of the activation of the out-of-plane slip, the size of the secondary slip zone,  $r_p^*$ , and the size of the coplanar slip zone,  $r_p$ . Both of these plastic zone size parameters have been derived by Koss and Chan [11]. In this analysis, a uniaxial stress,  $\sigma$ , is applied along a y' direction such that y' is at angles of  $\psi_1$ ,  $\psi_2$ , and  $\psi_3$  with the x, y, and z axes of the mixed-mode crack, respectively. The angles between the x, y, and z coordinate system of the crack and the slip plane normal are  $\alpha_1$ ,  $\alpha_2$ , and  $\alpha_3$ , while those for the slip direction are  $\beta_1$ ,  $\beta_2$ , and  $\beta_3$ . The analysis indicates that the size of the coplanar slip zone,  $r_p$ , is given by [11]

$$r_p = \frac{\sigma^2 a}{2\tau_y^2} f_c(\psi_i, \phi) \quad (4)$$

where  $f_c$  is a function of the orientations of the crack ( $\psi_i$ ,  $i = 1, 2$ , and 3) and the coplanar slip direction ( $\phi$ ) with respect to the stress direction (see Figure 2). In addition, the size of the secondary slip zone,  $r_p^*$ , can be expressed as [11]

$$r_p^* = \frac{\sigma^2 a}{2\tau_y^2} f_s(\chi, \psi_i, \alpha_i, \beta_i) \quad (5)$$

with

$$\chi = \frac{\tau_y^*}{\tau_y} \quad (6)$$

where  $\tau_y^*$  is the critical resolved shear stress for out-of-plane secondary slip;  $f_s$  is function of  $\chi$ ,  $\alpha_i$ ,  $\beta_i$ , and  $\psi_i$  with  $i = 1, 2$ , and 3. The expressions for  $f_c$  and  $f_s$  are given by [11]

$$f_c = \cos^2 \psi_2 (\cos \psi_1 \sin \phi + \cos \psi_3 \cos \phi)^2 \quad (7)$$

where

$$f_s = \left[ \frac{E}{\chi - (C \cos \psi_2 \cos \psi_1 + D \cos \psi_2 \cos \psi_3)/B} \right]^2 \quad (8)$$

$$B = \cos \psi_2 \cos \psi_1 \sin \phi + \cos \psi_2 \cos \psi_3 \cos \phi \quad (9)$$

$$C = \cos \alpha_1 \cos \beta_2 + \cos \alpha_2 \cos \beta_1 \quad (10)$$

$$D = \cos \alpha_2 \cos \beta_3 + \cos \alpha_3 \cos \beta_2 \quad (11)$$

$$E = \cos^2 \psi_2 (\cos \beta_1 \cos \alpha_1 + \cos \beta_2 \cos \alpha_2 + 2v \cos \beta_3 \cos \alpha_3) \quad (12)$$

The mode I stress intensity factor for the mixed mode crack is given by [11]

$$K_I = \sigma \cos^2 \psi_2 \sqrt{\pi a} \quad (13)$$

which can be combined with Eqs. (3) and (5) to obtain the triaxial constraint factor,  $\Sigma$ , leading to

$$\Sigma = \frac{\sigma_m}{\sigma_y} = \frac{\sigma_m}{2\tau_y} = \frac{(1+v)\cos^2 \psi_2}{3\sqrt{f_s}} \quad (14)$$

where  $\sigma_y$  is taken to be  $2\tau_y$ ,  $a$  is crack length, and  $v$  is Poisson's ratio.

This model has been used to elucidate the role of slip anisotropy, as measured by the  $\chi$  parameter defined in Eq. (6), in the relaxation of plastic constraint of a mixed mode slipband crack. Figure 3 presents the calculation of the triaxiality constraint parameter for a mixed mode I and II crack in an fcc crystal [11, 13]. This result is also applicable to the L1<sub>0</sub> system found in a TiAl single crystal. For this calculation,  $\psi_1 = \psi_2 = 45^\circ$ ,  $\psi_3 = 90^\circ$ , and  $\phi = 90^\circ$ . Coplanar slip is taken to occur on (111) [ $\bar{1}01$ ], while out-of-plane secondary slip occurs on ( $\bar{1}11$ ) [101]. The corresponding values for  $\alpha_1$ ,  $\alpha_2$  and  $\alpha_3$  are  $35.26^\circ$ ,  $70.53^\circ$ , and  $61.87^\circ$ ; they are  $90^\circ$ ,  $35.26^\circ$ , and  $125.26^\circ$  for  $\beta_1$ ,  $\beta_2$ , and  $\beta_3$ , respectively [11, 13].



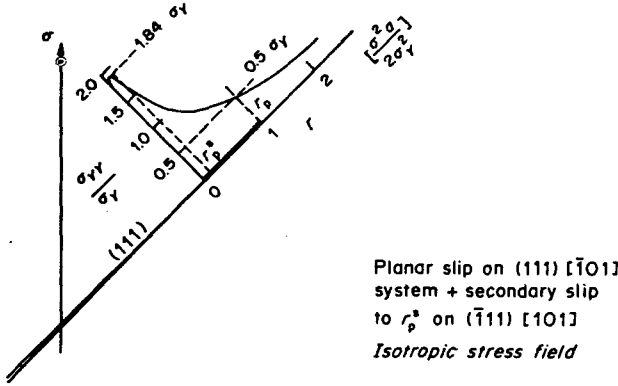


Figure 3: Approximate normal stress distribution ahead of a coplanar crack for  $(\bar{1}11)[101]$  slip in an isotropic single crystal. The result is applicable for fcc and  $L1_0$  crystals. From Chan [13].

Figure 4 indicates that the value of the triaxiality constraint factor increases linearly with increasing values of  $\chi$ . It has a value of 1.6 when the critical resolved shear stresses for coplanar slip and out-of-plane secondary slip are both equal ( $\chi = 1$ ). For comparison, the triaxiality factor for the corresponding mixed mode crack in a von Mises solid is 0.5 only. Thus, the triaxiality factor is elevated by a factor of more than 3 due to coplanar slip and the difficulty in activating out-of-plane slip. This constraint factor is further increased if out-of-plane slip is more difficult than the coplanar slip (i.e.,  $\chi > 1$ ). In contrast, the constraint factor is decreased when out-of-plane slip is easier than coplanar slip ( $\chi < 1$ ). At  $\chi = 0.67$ , extensive out-of-plane slip relaxes the triaxiality stresses to zero so that the crack-tip region is essentially under pure mode II.

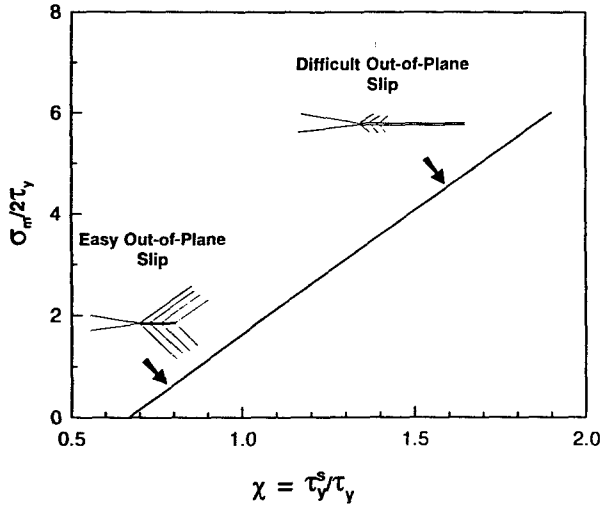


Figure 4: Calculated values of the triaxiality constraint factor,  $\sigma_m/2\tau_y$ , as a function of the slip anisotropy parameter,  $\chi = \tau_y^s/\tau_y$ .

### (C) Constraint Relaxation and Fracture Resistance

The driving force for propagating a slipband crack can be evaluated using the J-integral approach pioneered by Rice [14]. First, a fictitious cut is made to extend the slipband crack into the out-of-plane slip zone. The newly created crack surface is then superimposed with appropriate normal and shear tractions. Evaluating the J-integral around the crack surface by taking a counterclockwise path gives

$$J_c = \sigma_{yy}^+ \delta_y + \sigma_{yz}^+ \delta_z + \sigma_{zx}^+ \delta_x \quad (15)$$

where  $\sigma_{yy}^+$  is the normal traction;  $\sigma_{yz}^+$  and  $\sigma_{zx}^+$  are the shear tractions on the extended crack surfaces;  $\delta_y$ ,  $\delta_z$ , and  $\delta_x$  are the corresponding crack tip opening displacements. At the onset of crack extension, the J-integral is represented by a critical value,  $J_c$ , which is a measure of the material's resistance against fracture. The  $\sigma_{yy}^+ \delta_y$  term in Eq. (15) corresponds to the work done in opening up the slipband crack, which contains both the surface energy,  $\Gamma_p$ , and the plastic energy,  $\Gamma_o$ , dissipated by out-of-plane slip, while the  $\sigma_{yz}^+ \delta_z$  and  $\sigma_{zx}^+ \delta_x$  terms correspond to the plastic energy,  $\Gamma_o$ , dissipated by coplanar slip. The condition at the onset of slipband fracture is thus given by

$$J_c = \Gamma_p + \Gamma_o + \Gamma_o \quad (16)$$

which corresponds to the effective surface energy [15] or to the work of crack separation per unit area [16]. The distinction between the two types of slip in the plastic zone provides additional insight into the slipband cracking process. A significant implication of Eq. (16) is that the  $\Gamma_c$  term due to coplanar slip is essentially decoupled from the mode I fracture term, which is the sum of  $\Gamma_p$  and  $\Gamma_o$ . In general, the fracture resistance of a slipband crack depends on the plastic energy dissipated by both out-of-plane and coplanar slip. In the extreme limit that out-of-plane slip is difficult, the out-of-plane slip zone is negligibly small ( $\Gamma_o = 0$ ) and mode I opening of the slipband crack occurs when  $\sigma_{yy}^+ \delta_y = \Gamma_p$ . Since coplanar slip takes place prior to the condition of  $\sigma_{yz}^+ \delta_z = \Gamma_o$ , the resulting  $J_c$  has a value equal the sum of  $\Gamma_p$  and  $\Gamma_o$ , with  $\Gamma_c \gg \Gamma_p$ . Hence, the fracture resistance of the slipband crack is dictated by plastic energy dissipated by coplanar slip, even though mode I opening of the slipband crack, which occurs elastically, controls the crack surface separation process. When  $\Gamma_p \ll \Gamma_o$ , Eq. (16) can be expressed as

$$J_c = \int_0^{\gamma_p^*} \tau_y^s r_p^s d\gamma_o + \int_0^{\gamma_o^*} \tau_y r_y d\gamma_c \quad (17)$$

where  $\gamma_p^*$  and  $\gamma_o^*$  are the critical shear strains to fracture for the out-of-plane and coplanar slip, respectively. Ignoring strain hardening, Eq. (17) leads one to

$$J_c = \tau_y^s \gamma_p^* r_p^s + \tau_y \gamma_o^* r_y \quad (18)$$

which can be rewritten as

$$\frac{J_c}{J_o} = 1 + \frac{\tau_y^s \gamma_p^* r_p^s}{\tau_y \gamma_o^* r_y} \quad (19)$$

and combined with Eqs. (4)-(6) to give

$$\frac{J_c}{J_o} = 1 + \frac{\chi f_s}{f_c} \quad (20)$$

with

$$J_o = \tau_y \gamma_o^* r_y \quad (21)$$

when  $\gamma_s^*$  and  $\gamma_c^*$  are set to be identical. This assumption is only valid when the triaxial stress states associated the two types of fracture are similar. Figure 4 indicates that the triaxiality constraints are likely different and, as a result,  $\gamma_s^*$  and  $\gamma_c^*$  would generally have different values. The fracture strains are assumed to decrease with increasing triaxial constraint according to the relations given by [17]

$$\gamma_s^* = \gamma_s \exp[-a_1 \Sigma(r_p^*)] \quad (22)$$

and

$$\gamma_c^* = \gamma_c \exp[-a_1 \Sigma(r_p)] \quad (23)$$

where  $\gamma_s$  and  $a_1$  are material constants and the triaxial constraint factor,  $\Sigma$ , given in Eq. (14), is a function of the relevant plastic zone size. Substituting Eqs. (22) and (23) into (19) gives

$$\frac{J_c}{J_s} = 1 + \frac{\chi f_s}{f_c} \left\{ \exp[a_1(\Sigma(r_p) - \Sigma(r_p^*))] \right\} \quad (24)$$

which differs from Eq. (20) by the inclusion of the triaxial constraint term.

Figure 5 presents the calculated value of  $J_c/J_s$  as a function of  $\chi$  using Eq. (24) for the mixed mode I and II crack considered earlier in Figure 4 using  $a_1 = 3/2$  [17]. In addition, Figure 5 also shows the ratio of the out-of-plane plastic zone size to the coplanar slip plastic zone size. When  $\chi \geq 1$ , the amount of plastic work dissipated by out-of-plane slip is negligible due to difficulty in activating this mode of slip because of unfavorable crystallographic orientation and a higher critical resolved shear stress. As a consequence, the fracture resistance is entirely contributed by the plastic work done in fracturing the coplanar slipband and is relatively independent of  $\chi$ . When  $\chi < 1$ , the amount of plastic work dissipated by out-of-plane slip increases with decreasing values of  $\chi$ . The increase corresponds to increases in the out-of-plane slip plastic zone size and decreases in the triaxial stresses. Increase in the out-of-plane slip makes fracture along the coplanar slipband difficult. At  $\chi = 0.6667$ , all plastic dissipation is spent on out-of-plane slip and fracture along the coplanar slipband becomes impossible.

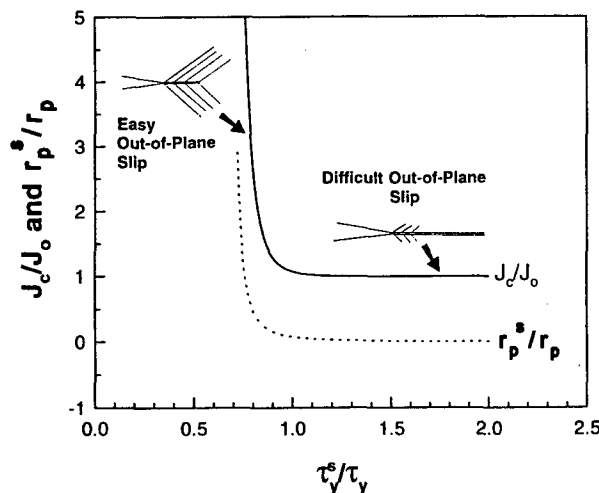


Figure 5: Calculated value of  $J_c/J_0$  and  $r_p^*/r_p$  as a function of the slip anisotropy parameter,  $\chi = \tau_y^*/\tau_y$ .

#### (D) Relationships Between Slip Anisotropy, Constraint Relaxation, and Fracture Resistance

The strong influence of slip anisotropy on the stress triaxiality near the tip of a mixed mode crack is summarized in Figure 6. When  $\chi \gg 1$ , coplanar slip is considerably easier than out-of-plane slip. Near-tip stress relaxation is primarily by coplanar slip, which produces no relaxation against the buildup of elastic normal stresses. As a result, the triaxiality constraint factor is extremely high. Since the slipband is subjected to a large unrelaxed elastic normal stress, separation of the slipband is relatively easy and fracture occurs along the coplanar slipband, Figure 6(a), and results in a relatively low fracture resistance, Figure 5. The lack of out-of-plane slip and the presence of large triaxial stresses are conducive to the formation of a cleavage-like fracture appearance without evidence of plastic flow. When  $\chi = 1$ , small amounts of out-of-plane secondary slip are activated, thus limiting a large buildup of triaxial stresses near the crack-tip. The near-tip constraint is still high, however. Consequently, fracture still occurs along the coplanar slip and the fracture resistance remains low, Figure 5. The stress triaxiality is sufficiently high to produce a cleavage-like fracture appearance, but exhibits evidence of out-of-plane secondary slip, i.e., slip steps. When  $\chi \ll 1$ , out-of-plane slip dominates and relaxes the normal stresses near the crack tip. The lack of a buildup of triaxial stresses near the crack tip makes fracture along the coplanar slip band difficult. The fracture resistance is also increased considerably as the result of out-of-plane slip, Figure 5.

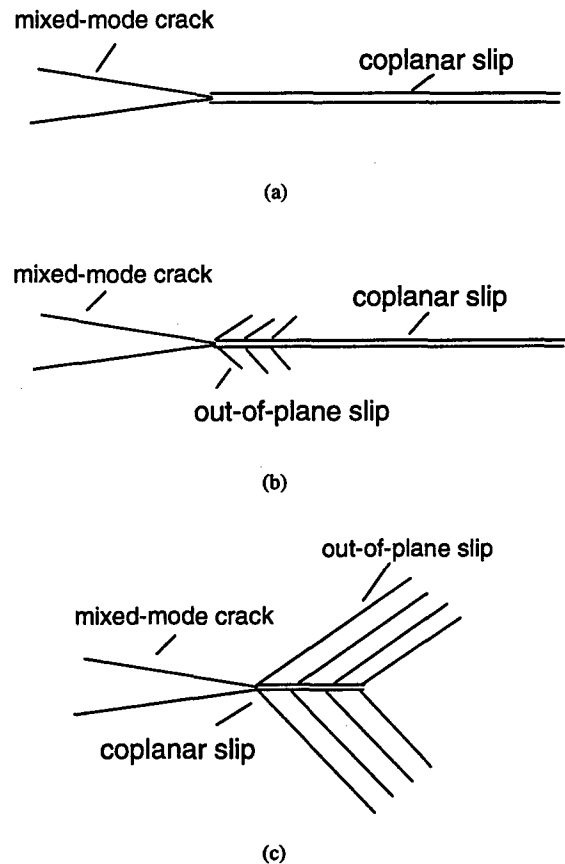


Figure 6: Crack-tip slip morphology for different values of the slip anisotropy parameter,  $\chi = \tau_y^*/\tau_y$ , and the resulting fracture resistance: (a)  $\chi \gg 1$ ,  $J_c/J_0 = 1$ ; (b)  $\chi = 1$ ,  $J_c/J_0 = 1$ , and (c)  $\chi \ll 1$ ,  $J_c/J_0 \gg 1$ .

### (E) Application of the Model to the Lamellar TiAl Microstructure

Slip in the  $\gamma$  phase in the lamellar  $\gamma + \alpha_2$  microstructure of TiAl-based alloys occurs predominantly on the (111) planes [18-23]. Because of the aligned nature in the lamellar microstructure, (111) slip parallel to the  $\gamma/\alpha_2$  would be easy, while that across the lamellae would be more difficult. The lamellae interface can also be a (111) plane in  $\gamma$  [24] and serve as a slip plane. Thus, interlamellar (111) slip is easy, but translamellar (111) is more difficult in lamellar TiAl alloys. This slip anisotropy leads to anisotropic fracture characteristics that can be readily explained on the basis of crystallographic constraint and its relaxation by slip anisotropy.

Figure 7 shows a mixed mode slipband crack propagated on a (111) plane in the interlamellar direction of a lamellar TiAl grain [25]. For this crack configuration, coplanar slip occurs in the easy slip direction. Relaxation of the normal stress of the K field must be accomplished by hard slip in the translamellar direction. Since activation of out-of-plane hard slip is considerably more difficult than coplanar easy slip,  $\chi > 1$  and a large buildup of triaxial stresses near the crack tip is expected. Inui et al. [26] reported that the CRSS for ordinary slip, superlattice slip, and twinning in PST Ti-56Al crystals is in the range of 80-120 MPa. The variation arose because the CRSS was dependent on the crystallographic orientation of the crystals. If the CRSS for easy slip is taken to be 80 MPa and that for hard slip is 120 MPa, the  $\chi$  ratio is estimated to be 1.5; the corresponding triaxial constraint factor,  $\Sigma$ , is 4 and the normalized fracture toughness,  $J/J_0$ , is one. Thus, continual crack extension along the coplanar slip is favored and most, if not all, of the fracture toughness arises from plastic dissipation associated with easy slip in the coplanar slip zone. Because of the large triaxial constraint at the crack-tip, the fracture resistance is expected to be low. Indeed, crack extension occurred at a K level of 6-9 MPa  $\sqrt{m}$  [25], which is considerably lower than the  $K_{IC}$  value of 18-20 MPa  $\sqrt{m}$  for fracture that does not follow exclusively along a slip plane [25, 17]. Additionally, out-of-plane microcracks formed near the tip of the slipband cracks as shown in Figure 7.

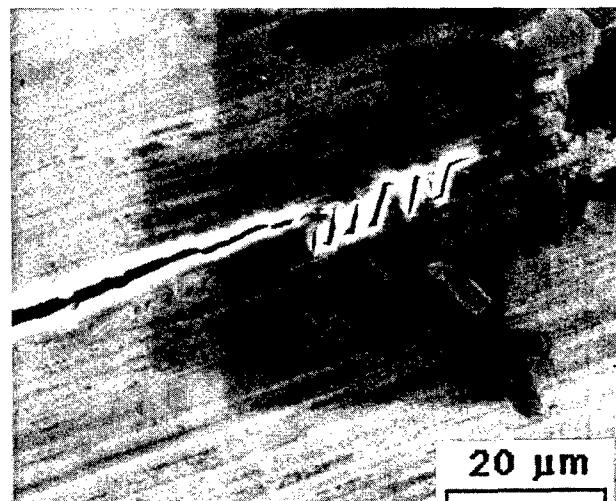


Figure 7: Slipband cracking in a lamellar TiAl grain with the formation of out-of-plane microcracks due to a high crystallographic constraint near the crack tip. From Chan and Shih [32].

When crack extension occurs in the translamellar direction, crystallography dictates that coplanar slip takes place in the hard slip direction but out-of-plane slip occurs in the easy slip direction. For this crack configuration,  $\chi < 1$  and the out-of-plane easy slip keeps the triaxial constraint near the crack tip to a low value ( $\Sigma \approx 0$ ) and the normalized fracture toughness is improved substantially ( $J/J_0 > 5$ ) due to extensive out-of-plane slip in the interlamellar direction. As a result, crack extension along a coplanar slipband on a hard slip plane cannot occur. This crack process is illustrated in Figure 8, which shows a mixed mode crack propagated in the translamellar direction (areas A and B) [28], hard slip occurs ahead of the crack but most of the crack-tip deformation is manifested as interlamellar, easy slip. As a result, the

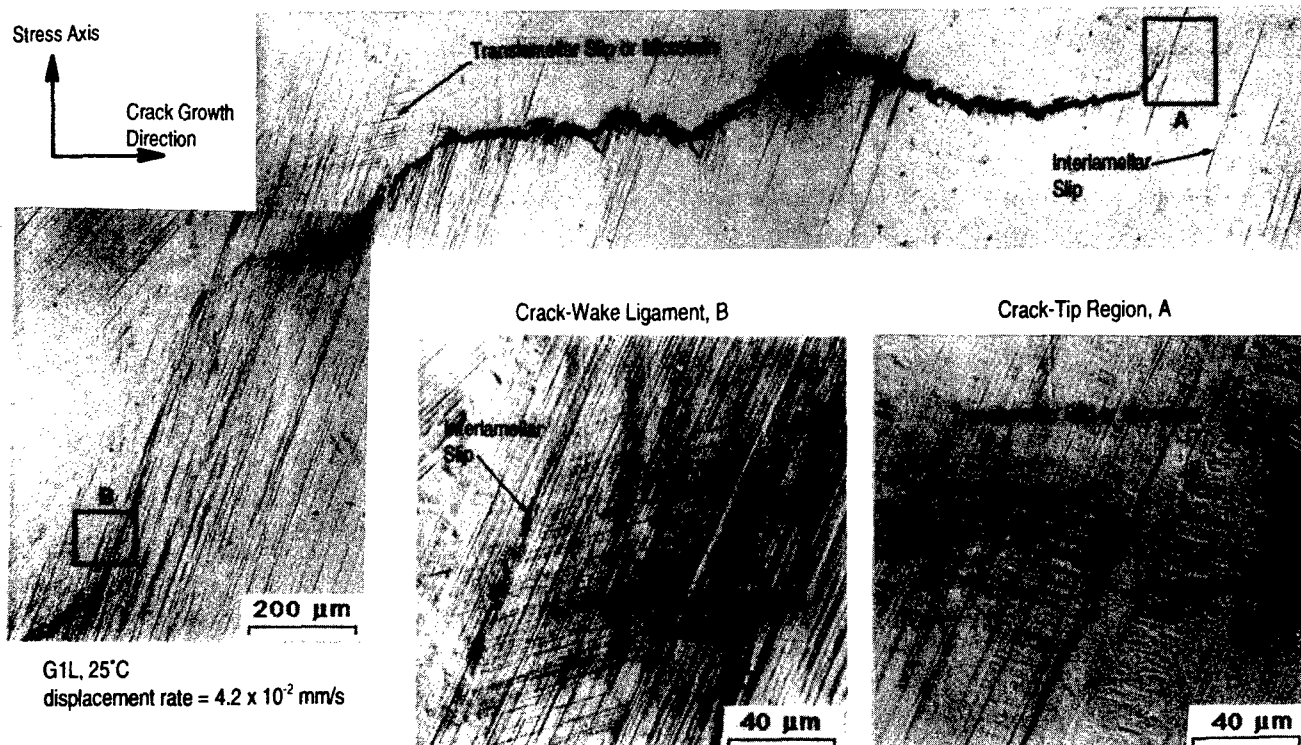


Figure 8: Interlamellar and translamellar slip in the crack-tip region and a crack-wake ligament in a lamellar TiAl alloy. From Chan and Kim [28].

crack could not propagate translamellarly, but deflected to propagate interlamellarly. As explained earlier, this anisotropic fracture behavior is the consequence of crystallographic constraint and its relaxation by slip anisotropy. It is important to note that slip anisotropy can increase or decrease the crack-tip stress triaxiality, depending on the value of  $\chi$  ( $\tau_y^s/\tau_y$ ). When the stress triaxiality is reduced to zero, plastic dissipation increases rapidly and can lead to shear ligament toughening [29, 30].

### Microstructural Constraint

#### (A) Origin

Plastic constraint occurs in a microstructure where plastic incompatibility exists between phases. In maintaining compatibility, hydrostatic stresses build up in the more deformable phase so that higher stresses are required to further deformation. Metal or intermetallic matrix composites formed by phase mixing to give hard particles in a ductile matrix is one example where triaxial stresses lead to strengthening. In-situ composites formed by phase transformation to give a microstructure of hard particles in a deformable matrix is another case where plastically incompatible phases are used for improving strength.

The relation between strength improvement and hydrostatic stress in the matrix is illustrated in Figure 9, which shows results of a finite-element calculation of the stress-strain response of a composite microstructure simulated by a unit cell of spherical  $\text{Cr}_2\text{Nb}$  particles in a Nb matrix [31]. The geometry of the unit cell is presented as an insert in Figure 9(a). The von Mises effective stress of the composite is normalized by the yield stress of the Nb matrix and plotted as a function of logarithmic strain in Figure 9(a). As expected, the flow stress of the composite increases with increasing volume fraction of the intermetallic phase. A major enhancement in the strength occurs when the volume fraction,  $f$ , of the intermetallic phase is increased from 60% to 80%. The triaxial constraint at the interface of the Nb matrix and  $\text{Cr}_2\text{Nb}$  particle that is presented as a function of the angle  $\vartheta$  in Figure 9(b) indicates that a buildup of large hydrostatic stresses at  $f = 0.8$ . Thus, the improvement in the composite strength is accompanied by a large increase in the hydrostatic stress in the matrix and at the matrix/particle interface. It is evident that the manner by which the triaxial constraint develops in a two-phase microstructure is quite different from those induced by geometrical and crystallographic effects.

In addition to volume fraction, the triaxial stress distribution in particulate composites also depends on the shape, size, and distribution of the reinforcement, as well as the externally imposed constraint [7-10]. FEM calculations based on a uniform size, shape, and distribution of particles, which are used in unit cell calculations, usually do not agree with experimental results even though the size, shape, and volume fraction of the reinforcement are modeled precisely because of local clustering of particles in real materials [7]. Nonetheless, unit cell calculations have provided a qualitative description of the triaxial constraint in particulate composites, even though local clustering effects needed to be factored in also. In terms of reinforcement shape, finite-element calculations have shown that whiskers are more effective in increasing composite strength than spherical particles, but the triaxial constraint is also higher in the whisker-reinforced composites [7-10]. Triaxial stresses also tend to concentrate at corners of irregular particles [7-10]. Variation in the spacing between particles can lead to horizontal and vertical clustering, and both affect the strength of the composite [7]. Tensile and compressive hydrostatic stress fields generally exist in the composite. Horizontal clustering does not result in overlapping of the tensile and compressive stress fields, while vertical clustering usually does. The consequence is that vertical clustering can cause a more drastic reduction in strength than horizontal clustering [7].

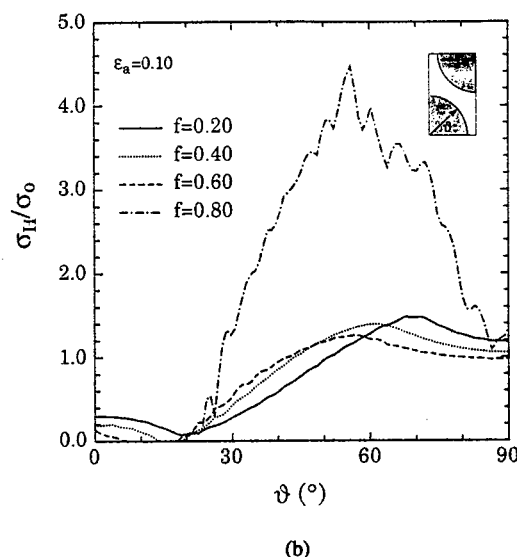
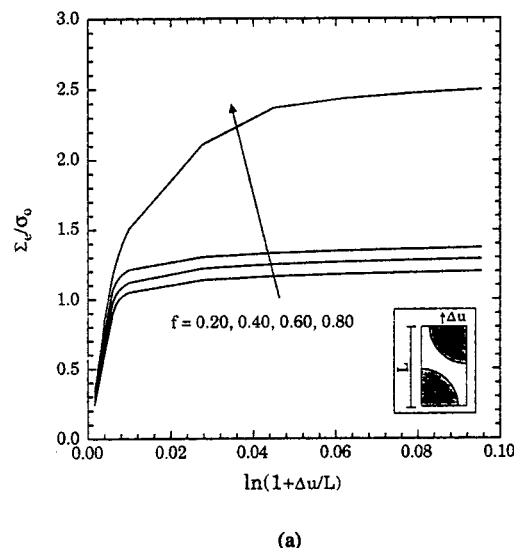


Figure 9: FEM results for  $\text{Cr}_2\text{Nb}/\text{Nb}$  in-situ composites based on a unit cell containing a spherical  $\text{Cr}_2\text{Nb}$  particles in a Nb solid solution alloy matrix: (a) calculated stress-strain curves, and (b) triaxial stresses.

#### (B) Role of Constraint in the Fracture Process

While they contribute to strength, triaxial stresses also increase the propensity for composite fracture and low fracture toughness. For particulate composites, the failure mechanisms include fracture of the reinforcement particles [32] and void nucleation, growth, and coalescence in the matrix [8, 10]. In ductile-phase toughened materials [33, 34] and laminated composites [35-39], the high triaxial constraint localizes plastic flow in the matrix phase and hastens fracture of bridging ligaments in the crack wake, thereby reducing the effectiveness of the ductile phase in improving fracture resistance. Since fracture of laminated composites has been the topic of several recent articles [36-39], only fracture of particulate composites and in-situ composites is discussed here due to lack of space.

For composites with strong particles, void nucleation in the matrix or at the particle/matrix interface may be the dominant failure mechanism.

Interface void nucleation has been observed at the end of whiskers where the hydrostatic stress is highest [9]. For spherical particles, a recent FEM calculation indicates that the plastic strains are highest in the region located at  $\theta = 45^\circ$  near the particle/matrix interface (D) and in the matrix region above the pole of the spherical particle (C), Figure 10 [10]. The triaxial constraint is, however, higher above the pole. Song et al. [10] postulated that void nucleation would take place both at regions C and D. Void growth in region C would be unstable and occur at a faster rate than voids in region D. Complete separation of the reinforcement particle from the matrix would occur when the larger voids from region D link with the smaller voids in region C, resulting in a fracture surface containing a bimodal distribution of void sizes, as observed experimentally.

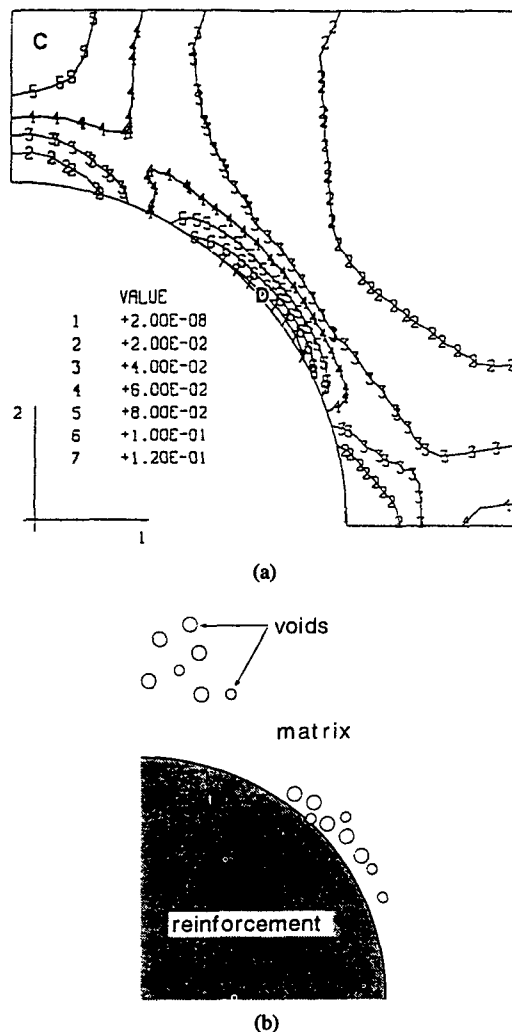


Figure 10: Void nucleation in a ductile matrix containing hard particles: (a) a contour plot of hydrostatic stresses, and (b) postulated void nucleation sites. From Song et al. [10]

When the particles are angular, higher stresses are carried by the particles and the surrounding matrix exhibits higher triaxial stresses also. As a result, the failure mechanism is dominated by particle fracture rather than by void nucleation, growth, and coalescence at the matrix/particle interface. The detrimental effect of the triaxial constraint on the fracture toughness of an in-situ composite is illustrated in Figure 11, which shows the fracture toughness of  $\text{Cr}_2\text{Nb}/\text{Nb}$  composite as a function of  $\text{Cr}_2\text{Nb}$

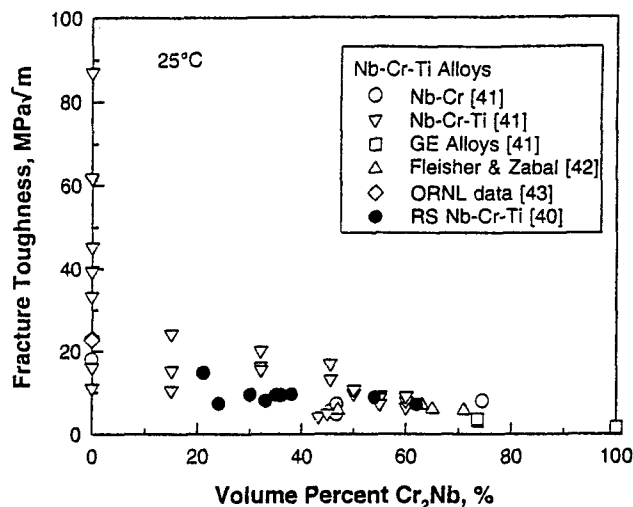


Figure 11: Comparison of fracture toughness values of RS and conventionally processed Nb-Cr-Ti materials [40-43] as a function of volume percent of  $\text{Cr}_2\text{Nb}$ . From Chan et al. [41].

particles [40, 41]. At low volume fraction, the  $\text{Cr}_2\text{Nb}$  intermetallic particles are embedded within the more ductile Nb solid solution phase. In contrast, ductile Nb solid solution alloy particles are embedded in a brittle  $\text{Cr}_2\text{Nb}$  surround when the volume fraction of  $\text{Cr}_2\text{Nb}$  is high. Without  $\text{Cr}_2\text{Nb}$  particles, the fracture toughness of the Nb solid solution alloy ranges from 18 to 87  $\text{MPa}\sqrt{\text{m}}$ , depending on the amount of Ti addition [40]. The fracture toughness of the in-situ composites [40-43] decreases with increasing volume fraction of  $\text{Cr}_2\text{Nb}$  particles. The role of the hard  $\text{Cr}_2\text{Nb}$  particles in the fracture process can be understood on the basis of FEM calculations [31] that indicate that the particles are highly stressed and a relatively high plastic constraint is prevalent in the Nb matrix located between the two particles. As a result, the  $\text{Cr}_2\text{Nb}$  particles ahead of the crack-tip fractured and the plastic flow in the resulting ligaments are highly localized, as shown in Figure 12 [32].

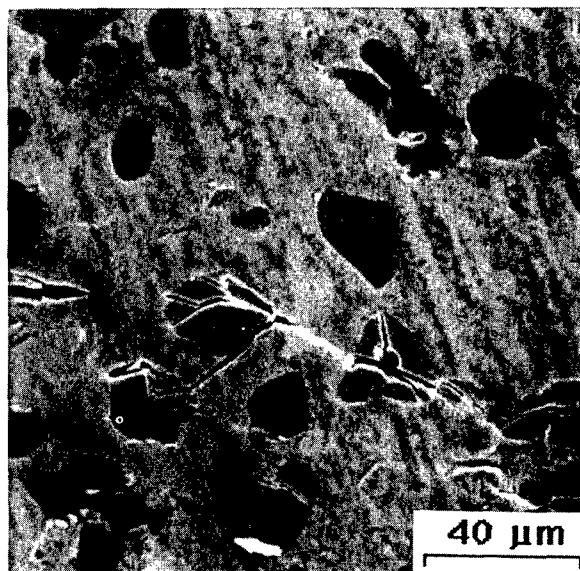


Figure 12: Fracture of angular particles in a Nb-Cr-Ti in-situ composite with a microstructure of  $\text{Cr}_2\text{Nb}$  particles in a Nb(Cr, Ti) solid solution alloy matrix. From Chan [32].

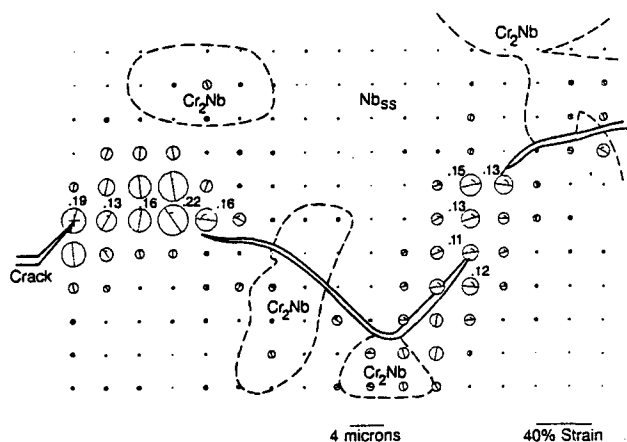


Figure 13: Near-tip strain distribution obtained by the stereomaging technique for the in-situ composite, Nb-36Cr-27Ti. The strains are presented in terms of Mohr's circles of strains at various locations in the near-tip process zone. The von Mises effective strains are indicated at locations of high strain concentration. From Chan [31].

Figure 13 shows the local strains in the bridging ligaments in the form of Mohr's circle of strains that were obtained using a machine-vision stereomaging technique [32]. In addition, the von Mises effective strains are also indicated for selected locations in the bridging ligaments. Figure 13 indicates that the von Mises effective strain as high as 22% existed in the bridging ligaments prior to their fracture. The highly strained region was, however, quite small, indicating that the plastic strain was fairly localized. As a result, fracture of the ligaments occurred easily without substantial amounts of plastic dissipation, leading to a low fracture resistance for the composites.

One possible means of eliminating particle fracture is to reduce the particle size. A recent work [41] on  $\text{Cr}_2\text{Nb}$  composites demonstrated that rapid solidification techniques can be used to reduce the particle size from  $\approx 20 \mu\text{m}$  to  $2 \mu\text{m}$  so that fracture of the intermetallic size becomes more difficult. High triaxial constraint still exists in the refined microstructure so that the fracture resistance of the RS in-situ composites has not been improved compared to those processed by conventional routes. A high oxygen content might have embrittled the RS in-situ composites also.

### (C) Relaxation of Constraint and Fracture Toughness

Relaxation of triaxial stresses is important for increasing the plastic dissipation in the bridging ligaments formed in the crack wake. For both particulate and laminated composites, an effective means for relaxing the triaxial stresses in the crack wake ligaments is by limited debonding at the matrix/reinforcement interface [33-35]. Numerical analyses have demonstrated that partial interface debonding leads to a significant increase in the plastic dissipation and to enhanced fracture resistance [33, 34]. Results of rigid/plastic [33] and elastic/plastic [34] formulations both predict increasing fracture energy when the interface is allowed to partially debond. The enhancement in fracture toughness due to ductile particle bridging also increases with particle size, yield stress, and volume fraction of the ductile phase [34].

Work on  $\text{Nb}_5\text{Si}_3$  in-situ composites [44-48] has indicated that hot extrusion followed by heat-treatment to obtain a microstructure of recrystallized Nb solid solution alloy and  $\text{Nb}_5\text{Si}_3$  particles leads to a resistance-curve fracture behavior and a relatively high fracture resistance. The resistance-curve fracture behavior is the result of crack

bridging by Nb particles in the crack wake, as shown in Figure 14 [32]. Limited interface debonding has been observed on some particle/matrix interface; necking of the Nb particles down to a point has also been observed on the fracture surfaces [45]. Figure 15 presents the fracture toughness of  $\text{Nb}_5\text{Si}_3$  composites as a function of silicide content for both hot-pressed [44] and extruded materials [40, 44, 45, 48]. Comparison of the fracture toughness of  $\text{Cr}_2\text{Nb}$  and  $\text{Nb}_5\text{Si}_3$  composites presented in Figures 14 and 15 indicates that the  $\text{Nb}_5\text{Si}_3$  composites are more fracture-resistant than the  $\text{Cr}_2\text{Nb}$  composites in the presence of small amounts of intermetallic particles ( $\approx 20\text{-}30\%$  intermetallic particles). The higher fracture toughness in the  $\text{Nb}_5\text{Si}_3$  composites appears to arise from the presence of ductile ligament bridging in this material and the lack of it in the  $\text{Cr}_2\text{Nb}$  composite. The difference in the crack bridging behavior may be attributed to these factors: (1) more small spherical particles in the  $\text{Nb}_5\text{Si}_3$  composites and large angular particles in the  $\text{Cr}_2\text{Nb}$  composites, (2) recrystallized Nb matrix in the  $\text{Nb}_5\text{Si}_3$  composites and unrecrystallized microstructure in the  $\text{Cr}_2\text{Nb}$  materials, (3) strong particle/matrix interface in the  $\text{Cr}_2\text{Nb}$  composites, and (4) a higher fracture toughness for  $\text{Nb}_5\text{Si}_3$  ( $\approx 3 \text{ MPa}\sqrt{\text{m}}$ ) when compared to  $\text{Cr}_2\text{Nb}$  ( $\approx 1 \text{ MPa}\sqrt{\text{m}}$ ). Thus, the fracture resistance of intermetallic in-situ composites depends on the fracture properties of the intermetallics, the ductile phase, and the microstructure. Many microstructural parameters affect the distribution of triaxial stresses in the microstructure, which, in turn, influence the fracture process and the material's resistance against fracture.

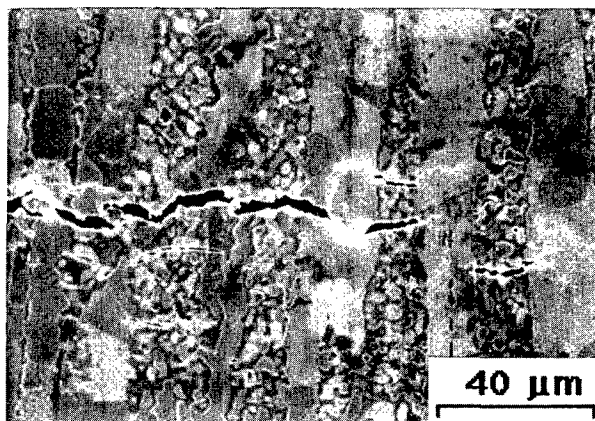


Figure 14: Crack bridging by ductile Nb particles in a  $\text{Nb}_5\text{Si}_3/\text{Nb}$  in-situ composites. From Chan [32].

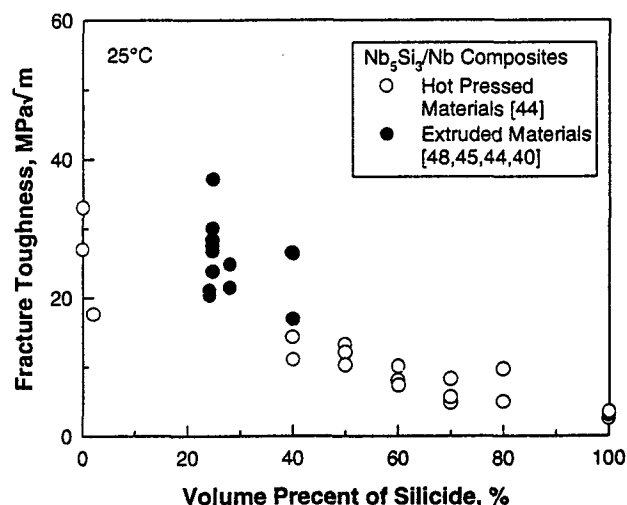


Figure 15: Fracture toughness of  $\text{Nb}_5\text{Si}_3/\text{Nb}$  in-situ composites.

## Conclusions

Plastic constraint can arise from geometrical, crystallographic, and microstructural means. Crystallographic constraint originates from the crystallography of slip in single crystals, and it can be mitigated by slip anisotropy. Microstructural constraint, which exists in microstructures containing plastically nondeformable and deformable phases, depends on the volume fraction, size, shape, distribution, and local clustering of the hard phase. High triaxial constraint can lead to particle fracture, as well as void nucleation, growth, and coalescence or cleavage in the ductile phase, leading to low fracture resistance in metal and intermetallic matrix composites. Mitigating the triaxial constraint in the ductile phase during fracture is an important consideration in improving the fracture resistance of intermetallic in-situ composites.

## Acknowledgements

Work was supported by the Air Force Office of Scientific Research (AFSC) under Contract No. F49620-95-0043, Dr. Charles H. Ward, Program Monitor. The United States Government is authorized to reproduce and distribute reprints for governmental purposes notwithstanding any copyright notation hereon. Clerical assistance by Ms. Patty Soriano of Southwest Research Institute is appreciated.

## References

1. E. M. Hackett, K.-H. Schwalbe, and R. H. Dodds, eds., Constraint Effects in Fracture, ASTM STP1171 (Philadelphia, PA: ASTM, 1993).
2. R. K. Mahidhara, A. B. Geltmacher, P. Matic, and K. Sadananda, eds., Recent Advances in Fracture (Warrendale, PA: TMS, 1997).
3. J. W. Hancock, W. G. Reuter, and D. M. Parks, Constraint Effects in Fracture, ASTM STP1171, edited by E. M. Hackett, K.-H. Schwalbe, and R. H. Dodds (Philadelphia, PA: ASTM, 1993) 21-40.
4. J. W. Hutchinson, J. Mech. Phys. Solids, 16 (1968), 13-31.
5. J. R. Rice and G. F. Rosengren, J. Mech. Phys. Solids, 16 (1968), 1-12.
6. F. A. McClintock, Fracture, Vol. 3, edited by H. Liebowitz (London, U. K.: Academic Press, 1991), 47-225.
7. T. Christman, A. Needleman, and S. Suresh, Acta Metall., 37 (1989), 3029-3050.
8. T. Christman, a. Needleman, S. Nutt, and S. Suresh, Mat. Sci. Eng. A107 (1989), 49-61.
9. J. Llorca, A. Needleman, and S. Suresh, Acta Metall. Mater., 39 (1991), 2317-2335.
10. S. G. Song, N. Shi, G. T. Gray III, and J. A. Roberts, Met. Mat. Trans. A, 27A (1996), 3739-3746.
11. D. A. Koss and K. S. Chan, Acta Metall., 28 (1980), 1245-1252.
12. D. A. Koss and K. S. Chan, Dislocation Modeling of Physical Systems, (Oxford, UK: Pergamon Press, 1981) 18-22.
13. K. S. Chan, Acta Metall., 35 (1987), 981-987.
14. J. R. Rice, Fracture: An Advanced Treatise, edited by H. Liebowitz (New York, NY: Academic Press, 1968), Vol. 2, 191-311.
15. E. Orowan, Welding Journal, 34 (1955), 1575-1605.
16. V. Tvergaard and J. W. Hutchinson, J. Mech. Phys. Solids, 40 (1992), 1377-1397.
17. J. W. Hancock and A. C. Mackenzie, J. Mech. Phys. Solids, 24 (1976), 147-169.
18. Y.-W. Kim, JOM, 41 (7) (1989), 24-30.
19. D. Shechtman, M. J. Blackburn, and H. A. Lipsitt, Met. Trans., Vol. 5 (1974), 1373-1381.
20. H. A. Lipsitt, D. Shechtman, and R. E. Schafrik, Met. Trans., Vol. 6A (1975), 1975-1991.
21. M. Yamaguchi and Y. Umakoshi, Progress in Material Sciences, Vol. 34 (1990), 1-148.
22. E. L. Hall and S.-C. Huang, Microstructure/Property Relationships in Titanium Aluminides and Alloys, Y.-W. Kim and R. R. Boyer, eds., TMS, Warrendale, PA, (1990), 47-64.
23. H. Inui, M. H. Oh, A. Nakamura, and Y. Yamaguchi, Acta Met. Mat., Vol. 40 (1992), 3095-3104.
24. Y.-W. Kim, MRS Proceedings, Vol. 213 (Pittsburgh, PA: MRS, 1991), 477-494.
25. K. S. Chan and D. S. Shih, Met. Mat. Trans. A, 28A (1997), 79-90.
26. H. Inui, M. Matsumuro, D.-H. Wu, and M. Yamaguchi, Phil. Mag. A, 75(2) (1997), 395-423.
27. K. S. Chan, Gamma Titanium Aluminides, edited by Y.-W. Kim, R. Wagner, and M. Yamaguchi (Warrendale, PA: TMS, 1995), 835-847.
28. K. S. Chan and Y.-W. Kim, Metall. Mat. Trans. A, 25A (1994), 1217-1228.
29. K. S. Chan, Met. Trans. A, 22A (1991), 2021-2029.
30. K. S. Chan, Metall. Mat. Trans. A, 26A (1995), 1407-1418.
31. G. Lin, GKSS Research Center, Geesthacht, Germany, and K. S. Chan, Southwest Research Institute, San Antonio, Texas, Unpublished Research, 1997.
32. K. S. Chan, Met. Mat. Trans. A, 27A (1996), 2518-2531.
33. G. Bao and C.-Y. Hui, Int. J. Solids Struct., 26 (1990), 631-642.
34. V. Tvergaard, Int. J. Mech. Sci., 34 (1992), 635-649.
35. M. F. Ashby, F. J. Blunt, and M. Bannister, Acta Metall., 37 (1989), 1847-1857.
36. K. T. Venkateswara Rao, G. R. Odette, and R. O. Ritchie, Acta Metall. Mater., 42 (1992), 893-911.
37. L. Xiao and R. Abbaschian, Metall. Trans. A, 24A (1993), 403-415.
38. M. Y. He, F. E. Heredia, D. J. Wisnuchek, M. C. Shaw, and A. G. Evans, Acta Metall. Mater., 41 (1993), 1223-1228.
39. K. S. Chan, MRS Proceedings, Vol. 364, edited by J. A. Horton, I. Baker, S. Hanada, R. D. Noebe, and D. S. Schwartz (Pittsburgh, PA: MRS, 1994), 469-480.
40. D. L. Davidson, K. S. Chan, and D. L. Anton, Met. Mat. Trans. A, 27A (1996), 3007-3018.
41. K. S. Chan, D. L. Davidson, and D. L. Anton, Met. Mat. Trans. A, 1997 (in press).
42. R. L. Fleischer and R. J. Zabala, Metall. Trans. A, 21A (1990), 2149-2154.
43. V. K. Sikka, S. Viswanathan, and E. A. Loria, Superalloys 1992, edited by S. D. Antolovich, R. W. Strusrud, R. A. MacKay, D. L. Anton, T. Khan, R. D. Kissinger, and D. L. Klarstrom (Warrendale, PA: TMS 1992), 423-431.
44. R. M. Nekkanti and D. M. Dimiduk, MRS Symposium Proceedings, Vol. 194 (Pittsburgh, PA: MRS, 1990), 175-182.
45. M. G. Mendiratta, J. J. Lewandowski, and D. M. Dimiduk, Met. Trans. A, 22A (1991), 1573-1583.
46. M. G. Mendiratta and D. M. Dimiduk, Met. Trans. A, 24A (1993), 501-504.
47. J. D. Rigney, P. M. Singh, and J. J. Lewandowski, JOM, 44 (1992), 36-41.
48. J. D. Rigney and J. J. Lewandowski, Met. Mat. Trans. A, 27A (1996), 3292-3306.
49. R. Darolia, K.-M. Chang, and J. E. Hack, Intermetallics, 1 (1993), 65-78.

## MECHANISMS OF DISLOCATION CREEP IN SINGLE PHASE NICKEL AND TITANIUM ALUMINIDES

K. J. Hemker\* and W. D. Nix\*\*

\*Department of Mechanical Engineering, Johns Hopkins University, Baltimore, MD 21218

\*\*Department of Materials Science and Engineering, Stanford University, Stanford, CA 94305-2205

### Abstract

The high temperature creep properties of some of the single-phase, intermetallic alloys found in the Ni-Al-Ti ternary system are discussed. The creep characteristics of these ordered alloys are reviewed and compared with those of pure metals. Although the general shapes of the creep curves for intermetallic alloys are similar to those observed for pure metals, the underlying creep mechanisms may be quite different. In many instances, the diffusion-assisted recovery processes that lead to steady-state creep in pure metals are replaced by a gradual evolution of the deformation microstructure with creep strain in intermetallics. In such cases, creep of intermetallics has been found to be controlled by the glide mobility of dislocations, the immobilization or multiplication of dislocations, or, in some cases, by dynamic recrystallization. In these cases, the Dorn description of power-law creep is no longer valid and attempts to characterize the creep behavior with activation energies and stress exponents, derived from minimum creep rates, have met with limited success. In such cases, the development of fundamental constitutive equations for creep should be based on microstructural observations of the development of substructure as a function of creep strain. In the small number of cases where diffusion-controlled power-law creep of intermetallic alloys has been observed, the creep behavior is not remarkably different from that observed for single-phase metals, provided the effects of diffusivity and elastic shear modulus are taken into account.

### Introduction

Research on intermetallic alloys has been motivated in part by the expectation that these materials can be used for high temperature structural applications. The high melting temperatures, low densities and excellent oxidation properties of some intermetallic alloys, compared to high temperature structural metals and alloys, have made them attractive candidates for further development as high temperature structural materials. Among the mechanical properties of interest for these materials is the resistance to creep deformation, particularly at high temperatures. In the present paper we review briefly the present state of understanding dislocation creep in some of the single-phase, intermetallic alloys found in the Ni-Al-Ti ternary system. The alloys of interest are shown in Table 1, along with the crystal structure, lattice parameter and density of each phase. We note a wide spectrum of crystal structures among these phases, thus providing an opportunity to explore dislocation creep of intermetallics with a variety of different crystal structures.

The focus of this paper is on the creep deformation of either single crystals or coarse-grained, polycrystalline materials. In particular, we do not discuss the technically important role of grain boundaries, twins or second phase particles on the creep of intermetallics. We limit our attention to simple crystalline states in an effort to examine the basic role of dislocation processes in creep of intermetallics. In particular,



we seek to understand dislocation creep in intermetallic alloys and to compare the controlling mechanisms with those typical of coarse-grained pure metals. Our focus on creep of single-phase intermetallics can also be justified on the basis that these processes are important in the creep of intermetallic alloys with more complex microstructures.

For pure metals it is well known that high temperature, power-law creep is controlled by lattice self diffusion. Typically, at the beginning of creep, dislocations glide and cross-slip rapidly on their slip planes until they are stopped by their interactions with other dislocations. Usually the creep rate declines rapidly in this primary stage of creep, as dislocation networks and substructures are formed. Lattice diffusion-controlled climb allows dislocations to rearrange and annihilate, thus permitting more dislocations to move and multiply. In this way a steady-state condition may be reached in which the hardening effects of dislocation generation and interaction are balanced by the softening effects of recovery. This is sometimes called recovery-controlled creep. The entire creep process may be controlled by the climb motion of the dislocations which, in turn, is controlled by long-range lattice diffusion. This diffusion-controlled, power-law creep can be described by the Dorn equation, a phenomenological equation for the steady-state strain rate:

$$\left( \frac{d\epsilon}{dt} \right)_s = AD_L \frac{\mu b}{kT} \left( \frac{\sigma}{\mu} \right)^n$$

Here  $D_L$  is the lattice self diffusion coefficient,  $A$  is a factor that depends on stacking fault energy, and the other terms have their usual meaning. For many pure metals the stress exponent in the power-law regime is about 4-5 and the activation energy for creep is about the same as that for lattice self diffusion. This equation may be derived by considering the competition between strain hardening and recovery. Such derivations invariably lead to a creep equation of the form of the Dorn equation but with a natural power-law stress exponent of 3, rather than the 4-5 observed experimentally. Nevertheless, the model of diffusion-controlled dislocation climb has provided a solid foundation for understanding power-law creep of pure metals.

The prominence of the Dorn equation in the creep literature has had a strong influence on the study of creep of intermetallic alloys. In many studies it has been common to first measure the activation energy and stress exponent for creep deformation to determine if the Dorn equation is obeyed. Often the stress exponents for creep and the creep activation energies are taken to indicate that creep might be controlled by climb, as in the case of pure metals. Usually such equally important factors as the transients associated with primary creep and with stress and temperature changes have received less attention and the microstructural evolution associated with creep is often not studied. As noted above, ordinary pure-metal-type creep of the kind described by the Dorn equation involves strain hardening processes and microstructural changes during creep. If these characteristics are absent from the creep response, then the relevance of the Dorn equation and the assumption that creep is controlled by ordinary dislocation recovery must then be questioned.

Table 1: Crystal Structures, Lattice Parameters and Densities of Several Ni-Al-Ti Intermetallic Alloys

Alloy	Structure	Lattice Parameters		Density (g/cm <sup>3</sup> )
		a (nm)	c (nm)	
NiAl	B2	0.288	-	5.96
Ni <sub>2</sub> AlTi	L2 <sub>1</sub>	0.585	-	6.38
Ni <sub>3</sub> Al	L1 <sub>2</sub>	0.357	-	7.40
TiAl	L1 <sub>0</sub>	0.398	0.405	3.89
TiAl <sub>3</sub>	DO <sub>22</sub>	0.395	0.860	3.36
Ti <sub>3</sub> Al	DO <sub>19</sub>	0.577	0.464	4.23

Also, if the softening processes leading to steady-state flow involve recrystallization, then the Dorn equation is not applicable, in spite of any similarities with the stress exponents and activation energies for climb-controlled creep.

In the present paper we seek to understand dislocation creep of single-phase intermetallic alloys. The atomic ordering found in intermetallic compounds causes both ordinary and superlattice dislocations to form and their motion leads to the formation of antiphase boundaries (APB's), superlattice intrinsic stacking faults (SISF's) and complex stacking faults (CSF's). The dislocations in these crystals have core structures that are much more complex than those typically found in pure metals. The reader is referred to the work of Yamaguchi and Umakoshi [1] for an excellent description of the faults and dislocation core structures in the intermetallics under consideration here. These core structures and faults are expected to alter both the glide and climb characteristics of dislocations, thus changing the basic mechanisms by which dislocation creep can occur. In addition, the ordering in intermetallics is expected to alter the diffusion process associated with dislocation climb, as more than one element must be transported to or from a dislocation for it to climb. This too could have effects in creep, although atomic mobility in intermetallic alloys does not seem to differ greatly from that in close-packed metals with similar melting temperatures.

In the following we briefly review the creep properties of several intermetallic alloys of the Ni-Al-Ti ternary system. We begin with Ni<sub>3</sub>Al, in part because the discovery of the yield strength anomaly in that material motivated much of the early interest in the high temperature strength properties of intermetallics. Much of our discussion of Ni<sub>3</sub>Al will be based on our own work. This is followed by a discussion of the creep properties of  $\gamma$ -TiAl, perhaps the most promising of these intermetallics for elevated temperature structural applications. That part of our review is based partly on our own work and partly on the work of others, most notably Oikawa and his colleagues. We also discuss the current state of understanding of creep of Ti<sub>3</sub>Al and TiAl<sub>3</sub>, although much less is known about the mechanisms of creep deformation in these materials compared to other intermetallics. In the last part of the paper we review the creep properties of NiAl and ternary alloys containing Ti, involving both solid solutions and the Heusler phase Ni<sub>2</sub>AlTi. This review is also based largely on our own work, but we relate our results to the early work of Strutt who first elucidated the creep properties of these materials.

## Ni<sub>3</sub>Al (L1)

Early work on the creep behavior of Ni<sub>3</sub>Al was based on the assumption of steady-state creep [2-4], but subsequent work by Anton et al. [5] and Schneibel and Horton [6] has shown that steady-state creep is not achieved at temperatures corresponding to the peak in the flow strength anomaly. Instead, they [5,6] reported that the creep rate increases continually with creep strain and termed this behavior "inverse creep". The elimination of pure-metal-type steady-state creep as the controlling process greatly aided our understanding of creep in this alloy, but a microstructural model describing inverse creep in Ni<sub>3</sub>Al was not developed until some time later.

The present authors, have studied the creep behavior of Ni<sub>3</sub>Al(Hf,B) single crystals oriented along different tensile axes (TA) in the temperature regime where the yield strength increases anomalously with increasing temperature [7]. Typical creep curves from that work are shown in Fig. 1. The creep rate of this alloy was found to increase normally with increasing temperature, and the general shapes of all of the creep curves were found to be the same. The specimens strained rapidly at the beginning of the test, but the creep rate quickly decreased and appeared to go to zero. Surprisingly, after 10-15 hours the creep rate started to increase again and it continued to increase until the creep rate reached a value almost two orders of magnitude higher than the minimum. This latter observation is consistent with the earlier observations of inverse creep in the polycrystalline specimens [5,6].

TEM studies of specimens crept for only a few hours showed that almost all of the dislocations were aligned along their screw direction and found to be cross-slipped into Kear-Wilsdorf (KW) lock configurations, see Fig. 2(a). It should be noted that these dislocations were homogeneously distributed. No evidence of subgrain formation could be found in these specimens. The absence of subgrains and the presence of KW locks are clear indications that the mechanism responsible for the decrease in creep rate during primary creep of Ni<sub>3</sub>Al differs from that for pure metals. The observation of KW locks suggests that cross-slip pinning, the mechanism responsible for the anomalous yield strength, is also the controlling process for primary creep. This microstructural observation is supported by the fact that the amount of creep strain associated with primary creep decreases anomalously with increasing temperature [7].

Additional insight into the nature of primary creep of Ni<sub>3</sub>Al and the anomalous temperature dependence of the yield stress has been gained by studying the creep response at much lower temperatures, where only octahedral glide and cross-slip pinning are allowed to occur. Here we review some of the creep experiments on Ni<sub>3</sub>Al that have been conducted at room temperature in an effort to develop a better understanding of that stage of creep.

Thornton et al. [8] studied creep of polycrystalline Ni<sub>3</sub>Al at low temperatures, but where the yield stress increases with temperature. On loading to just above the yield stress, they

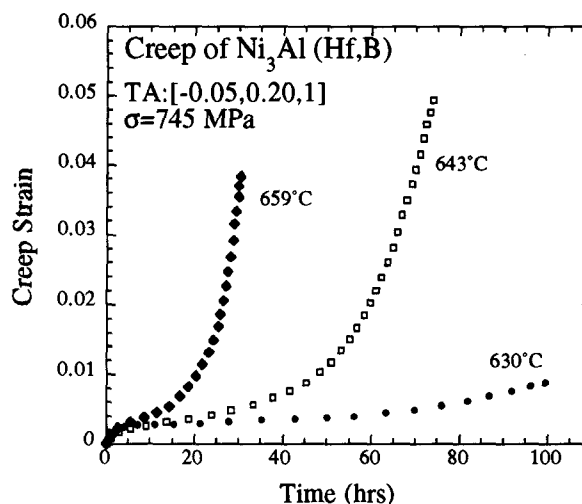


Fig. 1 Intermediate temperature creep curves for Ni<sub>3</sub>Al(Hf,B) showing a normally shaped primary transient and a transition to an extended period of inverse or accelerating creep. Primary creep decreases anomalously with temperature, but inverse creep has a very strong normal temperature dependence.

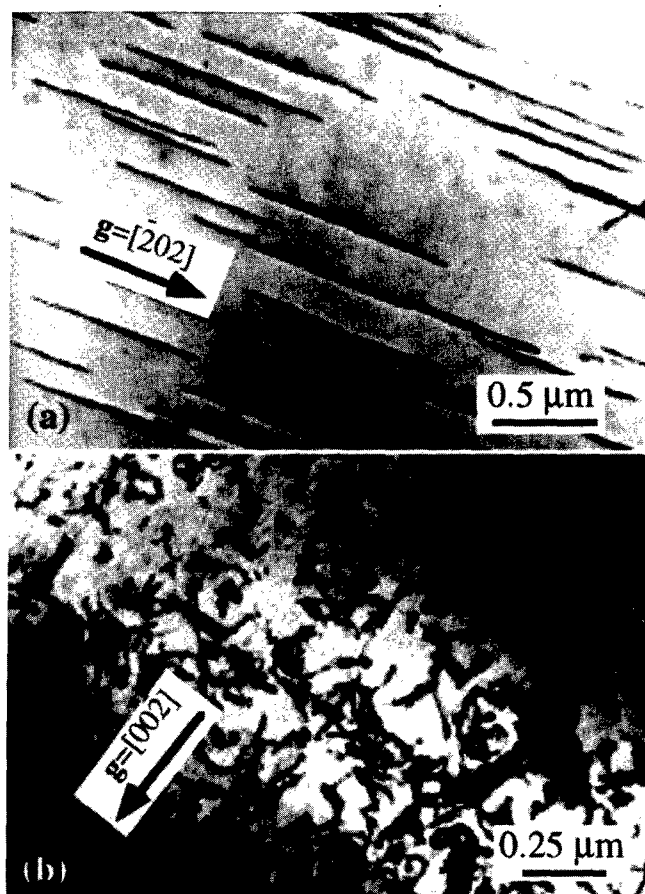


Fig. 2. The deformation microstructure associated with (a) primary and (b) inverse creep in Ni<sub>3</sub>Al(Hf,B). Super-dislocation motion is exhausted by KW lock formation during primary creep, but bowing out and subsequent motion of these dislocations on the (010) cube cross-slip results in inverse creep.

found very high initial creep rates, which then declined rapidly with until they became immeasurably small. At intermediate stresses they observed the creep rate to decline according to a logarithmic creep law. This exhaustion process can be described naturally by the superkink model of anomalous yielding developed by Chrzan and Mills [9]. In their description of plastic deformation, dislocations move by the lateral motion of non-screw superkinks which remain mobile only if their lengths exceed a critical value that depends on the applied stress. The competition between the creation of new kinks and the annihilation of old ones determines how far a given dislocation will travel before it becomes void of mobile superkinks and, thus, completely locked. Uchic and Nix [10] have recently studied this exhaustion process by conducting room temperature creep experiments on oriented single crystals of  $\text{Ni}_3\text{Al}$ . Figure 3, taken from their work, shows a creep curve for an applied stress of 85.1 MPa, just above the yield stress. The points along the curve result from fitting their data using a single fitting parameter that was suggested by Chrzan [11] for a logarithmic type of creep response. The match with the data indicates that creep exhaustion is well described by the dynamics of kink motion and that a single relaxation time provides a good description of the primary creep process.

According to the superkink model, creep can be re-initiated if the applied stress is raised slightly, whereupon a whole new cycle of dislocation motion and subsequent immobilization will occur. Uchic and Nix [10] have shown that an incubation time is associated with the re-initiation of creep for such a stress increment. Fig. 4 taken from their work shows that for a stress increment of 2.2 MPa, from a stress of 85.9 MPa, where exhaustion had occurred, a sigmoidal creep response is observed. Initially the creep rate is low because the density of mobile superkinks is low. Only after some multiplication has occurred does the creep rate rise dramatically before again declining in a new exhaustion process. The creep experiments provide a different way to study the processes that control the anomalous temperature dependence of the yield strength. By studying the evolution of the creep rate under constant stress and temperature conditions, it is possible to directly observe the kinetic behavior of moving dislocations.

We consider now the inverse stage of creep, which is observed only at elevated temperatures. Creep tests conducted in the region of inverse creep have been interrupted for microstructural evaluation [7]. TEM observations of specimens crept to 5% creep strain indicated an absence of structural coarsening. As was the case for primary creep, subgrains were not observed. Surprisingly, the KW locks formed during primary creep could not be found during inverse creep; all of the dislocations associated with inverse creep were found to be curved in nature, see Fig. 2(b). Tilting experiments have shown that these curved dislocations bow out and glide on the (010) cube cross-slip plane and that the Burgers vector of these curved dislocations is the same as for the original KW locks. These observations have been interpreted to mean that the KW locks that are formed during primary creep act as sources for the cube cross-slip plane and that inverse creep is caused by the bowing out and subsequent glide of these dislocations on

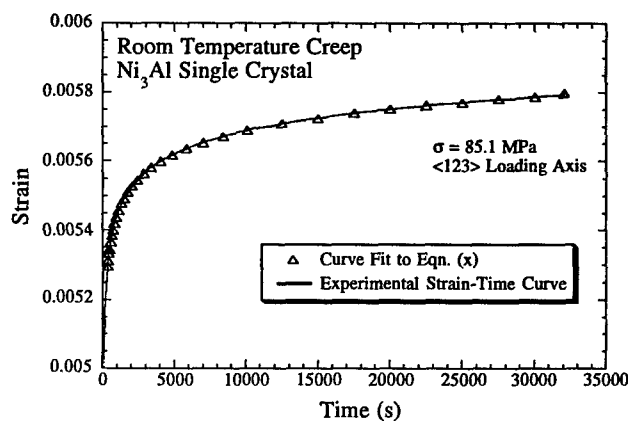


Fig. 3 Room temperature creep curve for single crystal  $\text{Ni}_3\text{Al}$  [10] and comparison with model of Chrzan [11].

the (010) cube cross-slip plane. Glide on the (010) plane involves a high Peierls stress (because the superpartials must dissociate on  $\{111\}$  planes), which results in the very high temperature dependence, as evidenced in Fig. 1.

In contrast to the inverse creep observed at intermediate temperatures, steady-state creep of  $\text{Ni}_3\text{Al}$  single crystals has been observed at 1273 K, above the peak in the yield stress-temperature curve [12]. The steady state was reached in less than 1% creep strain and observed to last for the duration of the creep tests (~25% creep strain), see Fig. 5. The creep transient associated with the start of the test was found to be slightly inverted and thus more consistent with Class I, alloy-type creep behavior than pure-metal-type behavior. TEM observations of specimens undergoing steady-state creep indicated that subgrain formation did not play an important role in deformation. A small number of subgrains were observed but they are much larger (about 100 to 200  $\mu\text{m}$  in diameter) than subgrains that are known to control deformation in pure metals, see for example [13]. Matrix dislocations were also associated with the region of steady-state creep, but the relatively small density and homogeneous distribution of these dislocations were not suggestive of processes that could be related to Dorn creep.

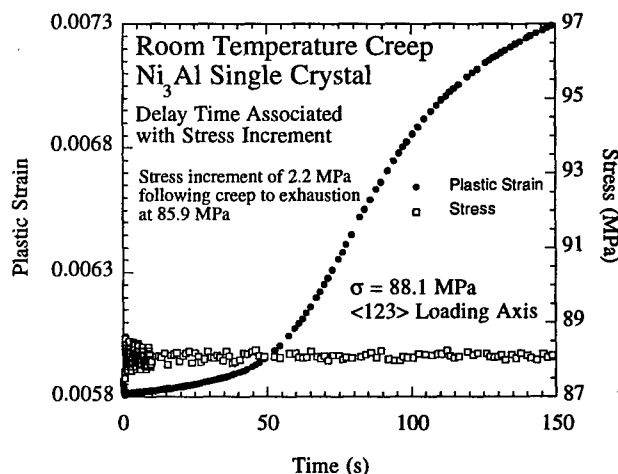


Fig. 4 Delay time for room temperature creep of single crystal  $\text{Ni}_3\text{Al}$  after a stress increment [10].

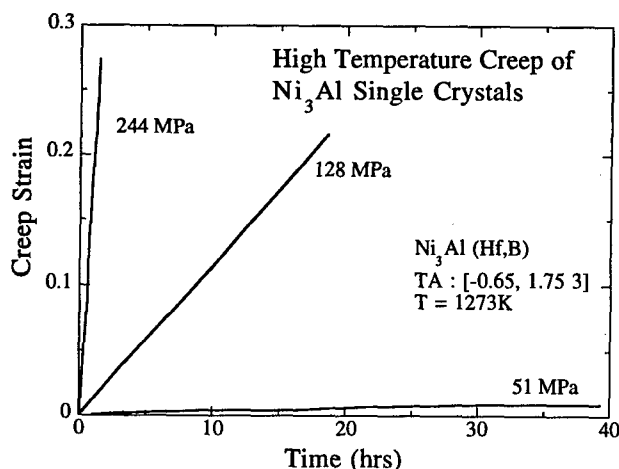


Fig. 5 High temperature creep of  $\text{Ni}_3\text{Al}$  single crystals. Steady state creep is observed from the beginning of the tests.

An orientation dependence of the creep rate has been noted, as the specimen aligned near the  $[001]$  direction crept at a rate that was orders of magnitude lower than those oriented along  $[-123]$  [14]. Efforts to explain this difference in terms of resolved shear stresses were unsuccessful. Attempts to identify a single dislocation mechanism with TEM have also been unsuccessful, as a number of slip systems were found to be active. Observations of the shape and morphology of the dislocations were used to rule out the importance of the  $\{110\}$  slip that had been reported in earlier work [14], and it was concluded that multiple slip systems are active during high temperature creep.

The TEM observations and the measured values of  $n = 4.3 \pm 0.1$  and  $Q_{\text{creep}} = 398 \pm 40$  kJ/mole [14] all suggest that high temperature creep may involve both dislocation mobility and the recovery of dislocation substructure. The observed steady-state creep activation energy is higher than the activation energy for Ni diffusion in  $\text{Ni}_3\text{Al}$ , reported to be in the range 300-340 kJ/mol [15]. The suggestion that this high activation energy is related to Al diffusion [12] has been supported by Wolfenstein et al. [16] who made an analysis of the relative diffusivities in  $\text{Ni}_3\text{Ge}$ , and concluded that the activation energy for Al diffusion in  $\text{Ni}_3\text{Al}$  should be about 408 kJ/mol. This result is in close agreement with the experiments of Hemker and Nix [12] and it suggests that climb-controlled processes are important in  $\text{Ni}_3\text{Al}$  at high temperatures.

#### $\gamma\text{-TiAl (L1}_0\text{)}$

To date, most studies of the creep behavior of  $\gamma\text{-TiAl}$  have been based on the phenomenological description of steady-state creep in pure metals [17-18]. Attempts to identify and model the deformation mechanisms associated with power law creep have met with very limited success. Representing the minimum creep rate as a power function of stress and an exponential function of reciprocal temperature has yielded stress exponents in the range ( $n=3-8$ ) and a correspondingly wide range of activation energies ( $Q_{\text{creep}} \sim 192-700$  kJ/mol).

These parameters are quite different from those that would be expected if  $\gamma\text{-TiAl}$  were exhibiting pure-metal-type creep behavior. Stress exponents of  $\sim 4.5$  are often associated with recovery-controlled creep and the activation energy for the diffusion of Ti in TiAl is  $Q_{\text{diffusion}} = 291$  kJ/mol [19].

Oikawa and his associates have conducted the most extensive studies of the creep properties of single phase, polycrystalline  $\gamma\text{-TiAl}$  at elevated temperatures [17, 20-24]. In reviewing his work and the work of others, Beddoes et al. [25] have called attention to the problem of extracting basic information about the controlling mechanisms from the minimum creep rate data. The importance of grain size [21,23], Al content [22,23], internal threshold stresses [26], precipitate formation [27], and diffusion-assisted climb [25] have all been addressed and evaluated in terms of the existing descriptions of pure-metal-type creep. These studies have provided a starting point for understanding the factors that control the creep behavior of  $\gamma\text{-TiAl}$ , but a fundamental description of creep has not been forthcoming.

Figure 6 is taken from the paper of Ishikawa and Oikawa [24] and shows the regimes of creep that have been identified in these studies. The minimum creep rate is plotted as a function of stress for three different compositions at one temperature. The slopes of the curves indicate three different regimes of behavior. At the highest stresses and strain rates, regime I, the power law exponent is about 4.7, close to the value typically observed for pure metals. Also, the activation energy for creep in regime I is found to be about 320 kJ/mol [28], somewhat higher than, but close to, the activation energy for Ti diffusion in  $\gamma\text{-TiAl}$ . In addition, the shapes of the creep curves at the highest stresses (see Fig. 7) are suggestive of ordinary recovery-controlled creep, as the creep rate declines in the course of primary creep to a steady-

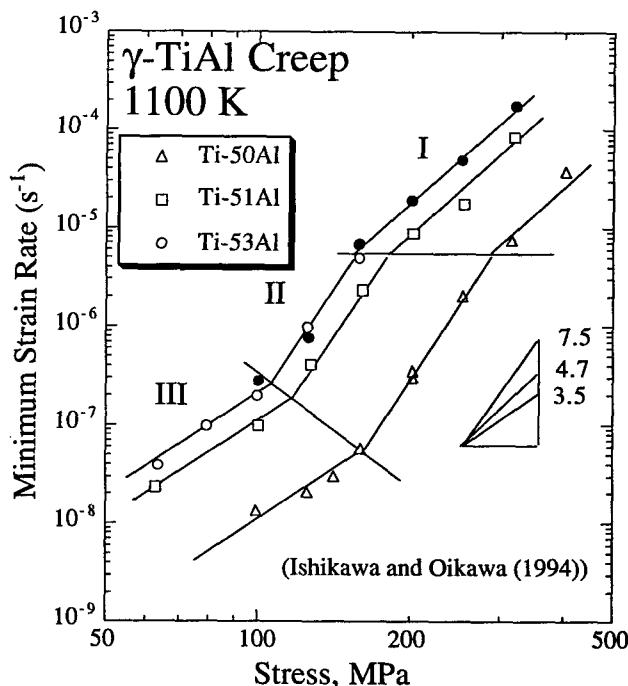


Fig. 6 Creep regimes for TiAl solid solutions at 1100K based on minimum strain rates [24].

state value. Although these parameters and characteristics suggest the applicability of the Dorn equation, the report of extensive recrystallization under these testing conditions [28] clearly indicates that dislocation climb is not the principal recovery mechanism.

At lower stresses, in regime II, both the stress exponent [28] and the activation energy [26] are nearly twice the values expected for climb-controlled creep. In addition, as shown in Fig. 7, the creep curves show inverse or accelerating creep [22]. These results, together with the observation of some local grain boundary migration [25], suggests that ordinary climb-controlled creep is not occurring at the intermediate stresses either.

Only at the lowest stresses, in regime III, does the creep response seem to be completely controlled by the behavior of dislocations. No evidence of recrystallization has been reported for creep at these lower stresses [28]. But in this regime the stress and temperature dependence of the minimum creep rate is of questionable mechanistic significance because inverse creep is observed. For such a creep response, the creep rate depends not only on the stress and temperature but also the amount of accumulated creep strain. Thus, a controlling mechanism cannot be identified on the basis of the stress and temperature dependence of the minimum creep rate.

The success of these phenomenological studies has been limited, at least in part, by the fact that they have not been fully supported by the type of microstructural analysis that is needed to reach mechanistic conclusions. Recent TEM studies [18,24,29] have indicated that, for  $\gamma$ -TiAl, the dislocation substructure evolves with creep strain and differs fundamentally from the steady-state behavior of most pure metals. The need for microstructural observations of the development of substructure during creep can also be seen by comparing the creep behavior of  $\gamma$ -TiAl with that of  $\text{Ni}_3\text{Al}$ , see Figs. 1 and 8. In both cases, the creep rate decreases rapidly during primary creep, passes through a minimum, and then accelerates through a region of extended inverse creep. Although the general shapes of these curves are similar to those for pure metals, the limited nature of secondary creep and increased importance of inverse or accelerating creep is not. These observations suggest that a more complete description of creep in  $\gamma$ -TiAl might be obtained by identifying and modeling the underlying mechanisms that control primary and inverse creep.

The creep curves in Fig. 8 have been taken from the work of Lu and Hemker [30], who have interrupted creep experiments at various amounts of creep strain, prepared thin foils, and performed TEM studies of the deformation microstructure associated with the various stages of creep (primary, secondary, and inverse). Comparing microstructural observations with the shape and macroscopic features of the creep curves allowed them to identify the underlying dislocation mechanisms that govern both primary and inverse creep.

In  $\gamma$ -TiAl, the exhaustion of the creep rate by strain hardening during primary creep has been shown to be

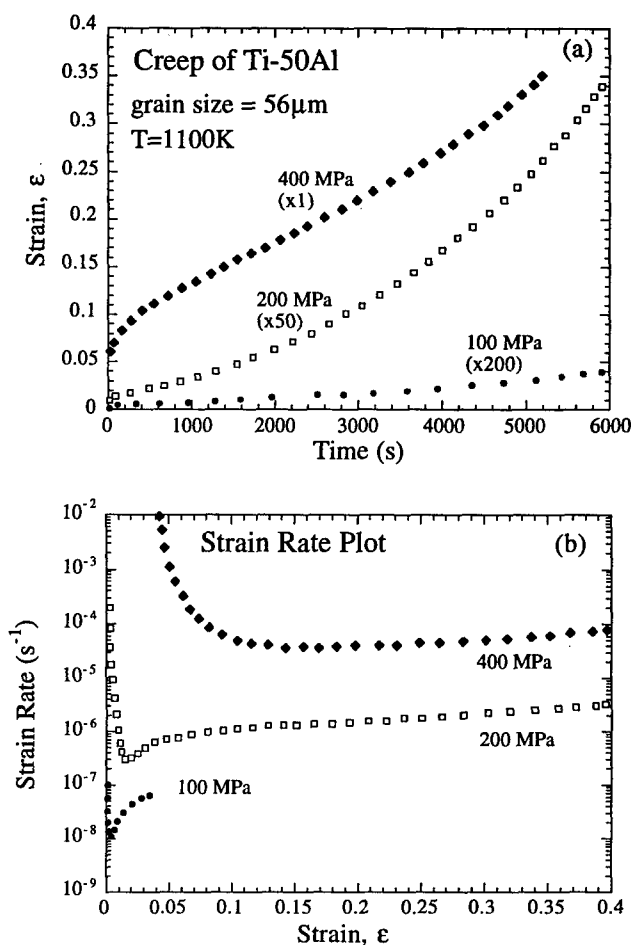


Fig. 7 Shapes of creep curves for TiAl at stresses corresponding to the three regimes identified in Fig. 6. [24].

unusually high [30]. Specimens unloaded during primary creep were found to contain ordinary dislocations, superdislocations, and faulted dipoles, see Fig. 9(a). The homogeneous distribution of these dislocations and the distinct absence of subgrains have been noted and taken to mean that the primary creep behavior of  $\gamma$ -TiAl differs fundamentally from the hardening that occurs by subgrain formation in pure metals. Hug [31] and Viguier and Hemker [32] have shown that the formation of faulted dipoles is related to the motion of superdislocations; thus, the presence of faulted dipoles in the creep microstructure is a strong indication that superdislocations are mobile during the early stages of primary creep [29]. By comparison, the superdislocations observed in the latter stages of primary creep were all found to be cross-slip locked, suggesting that the exhaustion of superdislocation motion may be responsible for the dramatic hardening that occurs in the primary creep of  $\gamma$ -TiAl, in a manner similar to that which occurs in  $\text{Ni}_3\text{Al}$ . However, the availability of ordinary dislocations must also be accounted for in the case of  $\gamma$ -TiAl. The ordinary dislocations that are associated with primary creep in Fig. 9(a) can be seen to contain a large number of pinning points that align themselves along the screw orientation of the ordinary dislocations. These features are similar in nature to the intrinsic pinning points that have been associated with the anomalous yielding behavior of

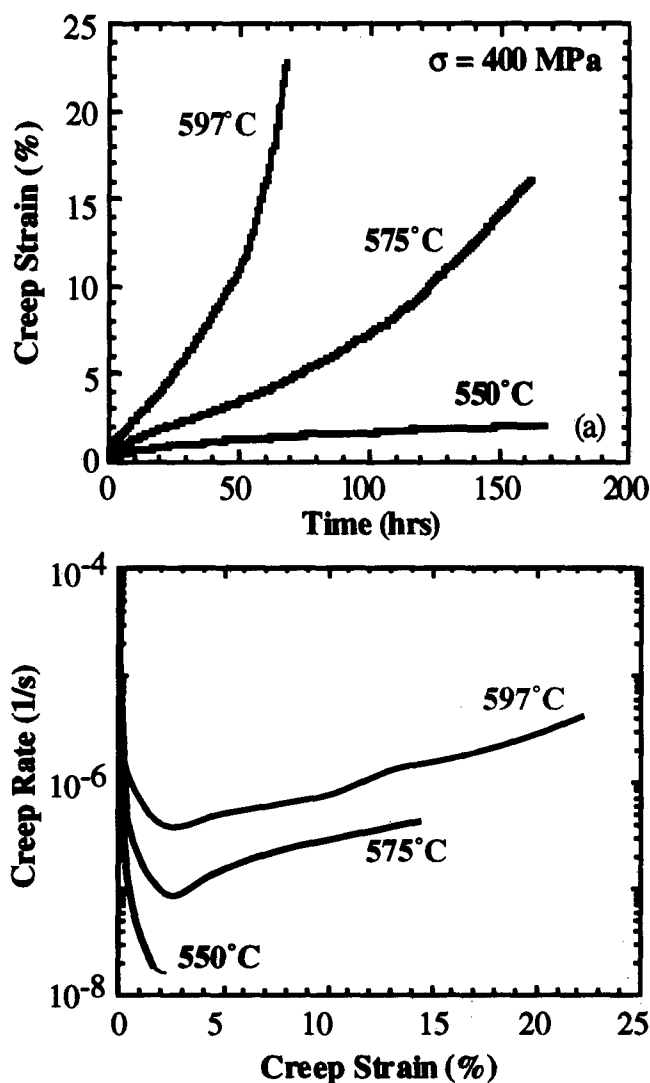


Fig. 8 Creep curves for Ti-51Al-2Mn with evidence of primary, secondary, and inverse creep, but not steady-state creep.

polycrystalline  $\gamma$ -TiAl [33,34], and their presence in the crept specimens suggests that they inhibit the motion of ordinary dislocations during primary creep as well. In this way, the primary creep of  $\gamma$ -TiAl can best be described in terms of the activation and subsequent exhaustion of superdislocation motion and by the intrinsic pinning of ordinary dislocations.

Specimens interrupted at the minimum creep rate exhibit the following microstructural features: (1) the faulted dipoles that were prevalent during primary creep have disappeared, (2) superdislocations appear to be the same as those observed during primary creep, (3) ordinary dislocations are found to have increased in both number and degree of bowing, and (4) a modest number of twins are observed, see Fig. 9(b). The absence of faulted dipoles and the unchanged appearance and number of superdislocations indicate that exhaustion of superdislocation motion during primary creep is an irreversible process. HREM observations [35] of "roof barriers" in  $\gamma$ -TiAl have shown the superdislocation cores in

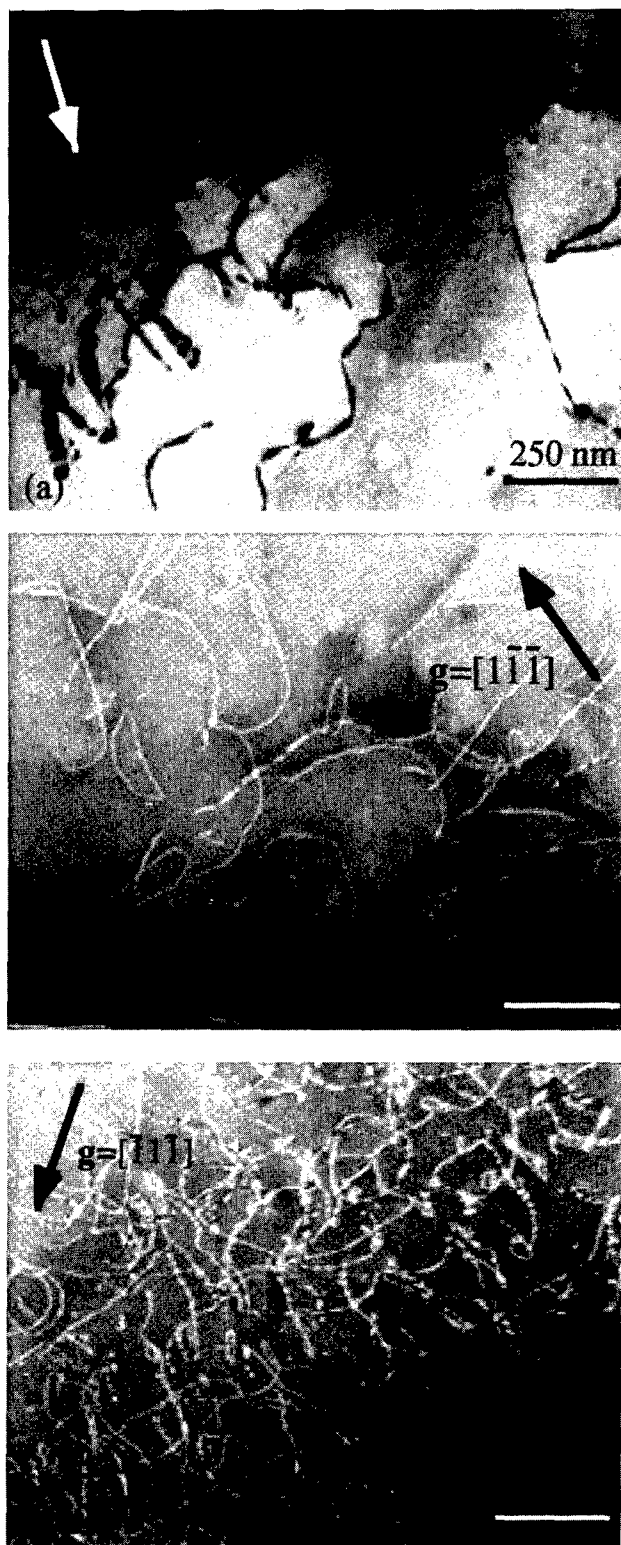


Fig. 9 The deformation microstructure associated with (a) primary, (b) secondary, and (c) inverse creep in Ti-51Al-2Mn. Both ordinary and superdislocation motion are exhausted during primary creep, but increased ordinary dislocation activity appears to govern inverse creep.

$\gamma$ -TiAl to be dissociated into an extended non-planar configuration which is substantially larger and more formidable than the KW locks observed in  $\text{Ni}_3\text{Al}$ . For this reason, the activation of cube cross-slip can not be used to explain the inverse creep of  $\gamma$ -TiAl.

A larger number of twins were observed during inverse creep, but, as is shown in Fig. 9(c), inverse creep is dominated by ordinary dislocation motion. The pinning points that were observed in primary and secondary creep are still present, but they are farther apart and no longer appear to be as strong a deterrent to dislocation motion. Instead, evidence for spiral like by-passing and the pinching off and subsequent growth of dislocation loops suggests that the pinning points actually serve as nucleation sites for the multiplication of ordinary dislocations. The dislocation densities associated with creep have been measured as a function of creep strain [29], and the results of that work indicate that the density of superdislocations remains constant at approximately  $2 \times 10^{10} \text{ cm}^{-2}$ , while the density of ordinary dislocations was observed to increase by an order of magnitude in the same creep experiment. Lu and Hemker [27] have compared the acceleration of the creep rate with the difference in the density of ordinary dislocations that occurs between 5% and 22% creep strain. They found that the increase in the creep rate cannot be explained solely in terms of dislocation multiplication; the creep rate increased three times faster than the dislocation density. Modeling the creep rate with an Orowan relation suggests that changes in both the velocity and density of ordinary dislocations are responsible for the creep acceleration. These creep processes differ completely from those typical of pure metals, and in this light it is not surprising that attempts to model the creep response of this alloy in terms of the climb-assisted recovery of dislocations and the Dorn equation have met with limited success.

#### $\text{Ti}_3\text{Al}$ ( $\text{DO}_{19}$ )

Mendiratta and Lippsett were the first to study the high temperature creep properties of polycrystalline  $\text{Ti}_3\text{Al}$  [36]. They observed power law creep behavior with stress exponents in the range  $n=4-5$  and creep activation energies of about 200 kJ/mol. The more recent work of Ohtsuka et al. [37] and Maruyama and Oikawa [38] have included studies of the shapes of the creep curves and microstructural observations. These latter studies show that the creep properties of  $\text{Ti}_3\text{Al}$  are similar to those of  $\gamma$ -TiAl. Three different creep regimes have been identified on the basis of the stress dependence of the creep rate at 1100K [38]. The stress exponent in the high stress regime is about  $n=7$  while the creep activation energy is about 340 kJ/mol, both too high to justify a climb-controlled creep process. As in the case of  $\gamma$ -TiAl, normally-shaped creep curves and recrystallization are found at the highest stresses and temperatures. Thus, ordinary recovery processes do not appear to control creep in the high stress regime. At low stresses the observed stress exponent is even higher ( $n=9$ ) and the creep activation energy is much too high to be associated with diffusion ( $Q_{\text{creep}}=480 \text{ kJ/mol}$ ). Also, as in the case of TiAl, inverse creep is observed at low stresses, suggesting that some form of dislocation mobility might be controlling creep of this material. A mechanistic

understanding of the creep process in  $\text{Ti}_3\text{Al}$  will not be achieved without additional experiments, especially ones involving single crystals and accompanied by suitable microstructural analysis.

#### $\text{TiAl}_3$ ( $\text{DO}_{22}$ )

Although  $\text{TiAl}_3$  has the lowest density of any of the intermetallics considered here, very little is known about its high temperature creep properties. Yamaguchi et al. [39] explored plastic deformation of this material at temperatures up to 860°C and identified both twinning and slip as deformation mechanisms. More recently, Takahashi et al. [40-41] have studied the compression flow properties at temperatures as high as 1300K. This work was part of a larger study of the effects of Vanadium on the deformation properties of  $\text{TiAl}_3$ . They observed both dynamic recrystallization and inverse creep for these materials, showing that ordinary recovery-controlled creep is not observed.

#### NiAl ( $\text{B}_2$ )

The number of lattice translation vectors ( $\langle 100 \rangle$ ,  $\langle 110 \rangle$  and  $\langle 111 \rangle$ ) available for dislocation motion is significantly higher in NiAl than for either  $\text{Ni}_3\text{Al}$  or  $\text{TiAl}$ . At high temperatures slip in the  $\langle 111 \rangle$  direction is not observed, in part because of the high ordering energy of NiAl. For crystals oriented to allow slip in  $\langle 100 \rangle$  directions, the preferred slip system is  $\langle 100 \rangle \{110\}$  at all temperatures. For crystals loaded along the "hard",  $\langle 001 \rangle$  axis there is no resolved shear stress for slip involving  $\mathbf{b} = \langle 100 \rangle$ ; Bevk et al. [42] showed that  $\langle 101 \rangle \{101\}$  slip is activated at high temperatures for crystals loaded in this direction.

Strutt et al. [43] published the first comprehensive study of creep of NiAl single crystals loaded in both hard and soft orientations. They found the creep rates for crystals loaded in the soft,  $\langle 111 \rangle$  and  $\langle 110 \rangle$ , directions to be much higher than those for crystals loaded in the hard,  $\langle 001 \rangle$ , direction, consistent with expectations based on plastic deformation at lower temperatures [44]. Figure 10 shows a similar comparison for loading in the  $[223]$  and  $[001]$  directions, taken from the work of Forbes et al. [45]. The steady-state deformation data are presented in normalized form using the Dorn equation as a guide. The creep data for each orientation were obtained at different temperatures ranging from 900°C to 1200°C, but normalizing by the lattice diffusion coefficient and the temperature dependent elastic shear modulus brings all of the data for a given orientation onto a single curve. The normalized creep rates for the soft,  $[223]$ , orientation are about 50 times faster than for the hard,  $[001]$  orientation at the same stress. The creep rates for other soft orientations,  $[111]$  and  $[110]$ , were found to be close to those for the  $[223]$  orientation.

The normalized form of the data shown in Fig. 10 allows us to compare the creep properties of NiAl with those of metals having similar crystal structures. In particular, it is of interest to compare the power law creep properties of NiAl with those of BCC metals. Nix and Gibeling [46] have collected the steady state creep data of various BCC metals



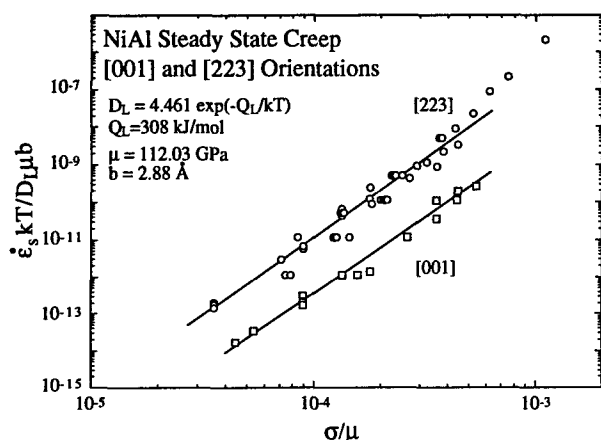


Fig. 10 Steady state creep properties of NiAl single crystals loaded along the [223] and [001] axes [45]. Normalization of the data using the lattice diffusivity and shear modulus bring the data for a single orientation onto a single curve.

and have plotted the data in the same way as Fig. 10. A comparison of Fig. 29 from their paper with Fig. 10 shows that the data for NiAl fall in the same range as for BCC metals. Indeed, the results for the two orientations shown in Fig. 10 bracket the creep properties of several BCC metals. From this it can be concluded that the steady state creep properties of NiAl are not remarkably different from those of pure metals, when the diffusivities and shear moduli are taken into account.

Because the Dorn equation provides no guidance about the orientation dependence of creep, it is necessary to inquire about the origin of the strong anisotropy of the creep resistance for NiAl crystals. A study of the transients associated with creep deformation and the corresponding structural changes during creep has been conducted by Forbes et al [47] and Glatzel et al. [48]. These results provide some understanding of the creep anisotropy in NiAl single crystals, but they also raise some questions about the applicability of the Dorn equation as well.

A creep curve taken from the work of Forbes et al. [49] for

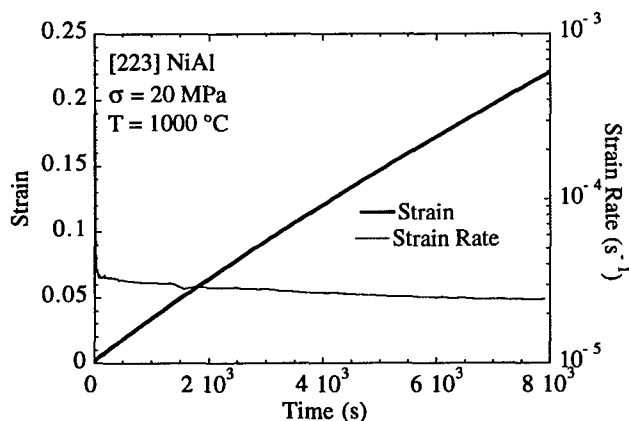


Fig. 11 Creep curve for a NiAl single crystal loaded along the soft, [223], axis [45]. No significant transients are observed.

tension creep in the soft, [223] direction is shown in Fig. 11. Note that the strain rate varies only slightly over the entire course of the test. This suggests a viscous kind of deformation with almost no strain hardening occurring during creep. TEM studies [48] revealed an almost complete absence of dislocation substructure after creep for this and other soft orientations. The small number of subgrains that were observed in tested samples ranged in size from 100 to 500 nm in diameter [48], much larger than would be expected for creep of similar BCC metals. Thus, although the steady state creep properties seem to be well described by the Dorn equation, the absence of a normal primary creep stage and a corresponding development of dislocation substructure raises questions about the controlling mechanism. If creep of NiAl in the soft orientations is controlled by dislocation recovery, then any microstructural evidence of the controlling recovery event does not seem to remain in the material after creep.

A creep curve for the hard, [001] orientation is shown in Fig. 12 [45]. It shows that the creep rate varies considerably during the course of creep. Initially the creep rate is very low but it increases quickly to a maximum before declining steadily during the course of creep. The creep rate continues to drop with increasing strain toward the steady-state value, which is about an order of magnitude lower than the maximum creep rate shown in the figure. TEM observations reported by Glatzel et al. [48] revealed extensive dislocation network formation during the course of creep in the  $\langle 001 \rangle$  orientation, consistent with the strain hardening evidenced by the falling creep rate during most of the primary creep stage.

The low creep rate at the very beginning of the test was not expected. Forbes et al. [45] provided an understanding of that effect in terms of the mobility of  $b = \langle 101 \rangle$  dislocations. Analysis of the elastic energies of dislocations in NiAl shows that edge dislocations of the type  $b = \langle 101 \rangle$  have the same energy as the two component dislocations:  $b = \langle 100 \rangle$  and  $b = \langle 001 \rangle$  [50]. This suggests that dislocations of the type  $b = \langle 101 \rangle$  might break apart during the course of creep. Dislocations with cores extended in this way would not be free to glide under  $\langle 001 \rangle$  loading; dislocation motion would

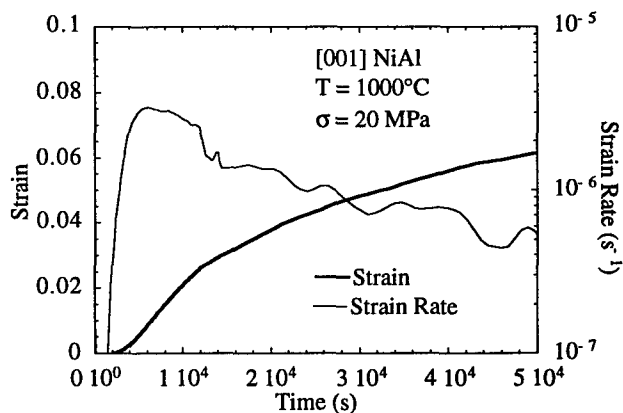


Fig. 12 Creep curve for a NiAl single crystal loaded along the hard, [001], axis [45]. A sigmoidal creep curve is observed.



require climb. Indeed, Mills et al. [51] have observed core splitting of this kind for  $b=\langle 101 \rangle$  edge dislocations in bicrystals deformed at 650°C. Later Mills et al. [52] observed that some edge dislocations in these crystals completely decompose and separate into their  $b=\langle 100 \rangle$  components. These observations help to explain the very low creep rates observed in the early stages of creep. The  $b=\langle 101 \rangle$  dislocations that are responsible for creep can be pinned because their cores are extended out of their glide plane. The rise in creep rate is apparently caused by the multiplication of moving dislocations.

Although the activation of  $\langle 101 \rangle$  slip was expected for high temperature deformation in the hard orientation [42], the Burgers vectors of the dislocations observed by Forbes et al. [45] in samples crept in the  $\langle 001 \rangle$  direction seemed inconsistent with this expectation. Invariably the dislocation networks found in crept samples involved Burgers vectors of the type  $b=\langle 100 \rangle$ , for which there is no resolved shear stress for loading in the  $\langle 001 \rangle$  direction. Dislocations with  $b=\langle 101 \rangle$  Burgers vectors were observed only rarely, and then the dislocation segments in question seemed to be the result of reactions of  $b=\langle 100 \rangle$  and  $b=\langle 001 \rangle$  dislocations. A closer examination showed that for loading along the  $[001]$  direction the combination of dislocations with  $b=[100]$  and  $b=[010]$  was never observed. The observed dislocation types were those that would result from the decomposition of gliding  $b=[101]$  or  $b=[011]$  dislocations. Observations of Laue spot streaking and cross-section shape changes led Forbes et al. [45] to conclude that deformation must have taken place by the glide of  $b=[101]$  or  $b=[011]$  dislocations. After reacting to form dislocation networks, the  $b=\langle 101 \rangle$  dislocations decompose completely into  $b=\langle 100 \rangle$  type dislocations. Thus the observed dislocation substructures do not reveal the dislocations active during creep deformation. Only the products of the dislocation decomposition reaction are left in the crystal for observation. Also, the process of decomposition requires edge dislocations to climb. Thus a climb controlled recovery process can be identified for the hard orientation and

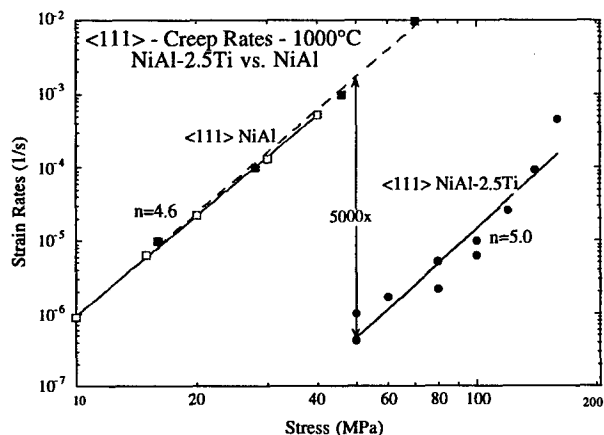


Fig. 13 Steady state creep properties of a NiAl-Ti solid solution compared with the creep properties of stoichiometric NiAl, both loaded along the  $\langle 111 \rangle$  axes [52]. The solid solution is observed to be much stronger than the stoichiometric material.

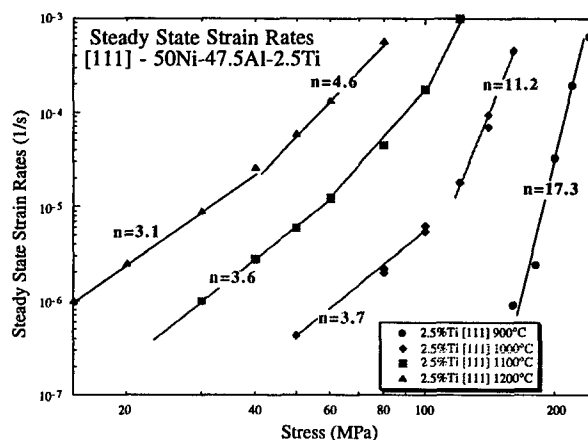


Fig. 14 Stress dependence of the steady state creep rate of a NiAl-Ti solid solution as a function of temperature [52]. Stress exponents of 3 are approached at high temperatures and low stresses.

the use of the Dorn equation can be justified.

The creep properties of NiAl single crystals containing small amounts of Ti as a solid solution strengthening element have also been studied recently by Kitabjian et al. [53]. As shown in Fig. 13, the addition of 2.5% Ti decreases the steady-state creep rate at a given stress by a factor of about 5000. Kitabjian et al. [53] have shown that this dramatic strengthening of Ti may be due to the strong elastic interactions between Ti solutes and dislocations. Using lattice parameter measurements, they determined the size of Ti atoms as they substitute for Al on the Al sublattice. They found a 34% size mismatch, sufficiently large to produce significant drag on the glide motion of dislocations. As shown in Fig. 14, at the highest temperatures and lowest stresses the stress exponent for deformation of NiAl-Ti single crystals approaches a value of 3, consistent with the solute drag hypothesis. Also, the numerous dislocations created during creep of these solid solutions do not readily form dislocation networks, a characteristic of solute drag-controlled creep of metallic solid solutions. For classical solute drag-controlled creep, such as that exhibited by Al-Mg solid solutions, dislocation networks are not a prominent feature of the dislocation substructure. Rather, gently curved dislocation segments and loops dominate the dislocation structure in such solid solutions. These same dislocation structures are observed in NiAl-Ti solid solutions. While all of these observations point to solute controlled-drag as a controlling creep mechanism for the Ti solid solution, the creep transients associated with stress changes show only marginal indications of solute drag controlled creep. Generally, the creep transients associated with stress changes are more like those found for pure metals. Thus, the controlling mechanism for creep has not been identified unambiguously.

### Ni<sub>2</sub>AlTi (L<sub>2</sub>)

The intermetallic Heusler phase, Ni<sub>2</sub>AlTi, shows not only simple ordering of the B2 type, with Ni atoms at cube

corners, but also ordering of the Al and Ti atoms in alternate cube centers. Because of this additional ordering,  $a_{\text{NiAl}}\langle 100 \rangle$  is not a perfect lattice translation and the  $\langle 100 \rangle$  direction is not an easy slip direction, as it is for NiAl crystals. Instead, slip is expected to occur in the  $\langle 110 \rangle$  direction and to involve ordinary dislocations with Burgers vectors of the type  $a_{\text{NiAl}}\langle 110 \rangle$ . The consequences of this type of ordering for creep were first explored by Strutt et al. [54] who studied high temperature creep of polycrystalline stoichiometric  $\text{Ni}_2\text{AlTi}$  as a function of stress and temperature. They found a creep activation energy of 280 kJ/mol and stress exponents ranging from 3 to 13, depending on the stress and temperature. They also observed normal creep primaries and dislocation network formation. All of their results suggested pure-metal-type creep behavior. However, a comparison of the creep properties of polycrystalline  $\text{Ni}_2\text{AlTi}$  with those of NiAl single crystals loaded in the hard,  $\langle 001 \rangle$ , direction revealed a much higher creep resistance for  $\text{Ni}_2\text{AlTi}$  (stress increase by a factor of three) which could not be explained on the basis of the factors that appear in the Dorn equation. Instead, Strutt et al. [54] suggested that the inability of  $b = a_{\text{NiAl}}\langle 110 \rangle$  dislocations to cross-slip from one  $\{110\}$  plane to another was the cause of the greater strength in the Heusler phase. Deformation by slip on systems of the type  $\langle 110 \rangle\{001\}$  was ruled out by Strutt et al. [54] on the basis of a hard sphere analysis of slip and the high APB energies that would be involved if  $\langle 110 \rangle$  dislocations were to dissociate into their  $\langle 100 \rangle$  and  $\langle 010 \rangle$  components. In summary we can conclude that the creep properties of  $\text{Ni}_2\text{AlTi}$  cannot be fully explained using the Dorn equation as a guide, again showing the need for a different type of approach for understanding creep of intermetallics.

### Concluding Remarks

Our review of the creep properties of single-phase intermetallics of the Ni-Al-Ti ternary system has revealed that steady-state, recovery-controlled creep of the kind observed for most pure metals is only rarely observed. Instead creep of many of the intermetallics we have considered is characterized either by dynamic recrystallization (at high stresses and temperatures) or by the competition between dislocation immobilization and multiplication (at intermediate stresses and temperatures). The complexity of the dislocation cores in these materials appears to be the cause of this different kind of creep behavior. For many of these intermetallics dislocations become locked through cross-slip pinning long before any network formation can occur. Since the structure that typically drives recovery in pure metals is not present in many intermetallics, ordinary recovery-controlled creep does not occur. Given enough time at a high enough temperature, dislocations that are locked during primary creep, by processes related to anomalous yielding, are observed to glide on other slip planes or cause other dislocations to do so, which produces an accelerating creep response. Because the minimum creep rate for these materials does not define a unique state and is not controlled by recovery, the stress and temperature dependence of the minimum creep rate does not have any special significance, as it does for the case of recovery-controlled creep.

Of the alloys that were studied, a strong case for ordinary climb-controlled creep can be made only for the case of  $\langle 001 \rangle$  NiAl single crystals. Here the creep behavior is not remarkably different from that observed for single-phase metals, provided the effects of diffusivity and elastic shear modulus are taken into account. But even for this case the core structures of the dislocations play a much more significant role than they do for pure metals. For other intermetallics that appear to behave like pure metals, the absence of dislocation networks after creep raises questions about the applicability of pure-metal creep as a guide. These findings suggest that the Dorn equation, which has provided such a useful guide for understanding steady-state creep of pure metals, should not be used generally for intermetallics. Instead, the constitutive creep properties of intermetallics should be based on a full accounting of all of the creep stages revealed by the creep curve and on microstructural observations of the dislocation mechanisms responsible for these different stages.

### Acknowledgments

The authors gratefully acknowledge the financial support of the Air Force Office of Scientific Research under AFOSR Grants Nos. F49620-95-1-0280 (KJH) and F49620-92-J-0009 (WDN). The support and encouragement of Capt. Charles H. Ward of AFOSR is very much appreciated. Additional support for KJH was provided by the NSF under Grant No. CMS-9409538. The assistance of Mr. M. Lu in connection with the preparation of this manuscript is also gratefully acknowledged.

### References

1. M. Yamaguchi and Y. Umakoshi, *Prog. Mat. Sci.*, **34**, 1, (1991).
2. P. A. Flinn, *Trans. AIME*, **233**, 714, (1960).
3. R. G. Davies, and T. L. Johnston, in Ordered Alloys, Ed. B. H. Kear et al, 447, Baton Rouge LA, Claitor's Publishing, (1970).
4. R. K. Ham, R. H. Cook, G. R. Purdy, and G. Willoughby, *Met. Sci. J.*, **6**, 205, (1972).
5. D. L. Anton, D. D. Pearson, and D. B. Snow, *MRS Symp. Proc.*, Pittsburgh PA, **81**, 287, (1987).
6. J. H. Scheibel, and J. A. Horton, *J. Mat. Res.*, **3**, 4, (1988).
7. K. J. Hemker, M. J. Mills, and W. D. Nix, *Acta metall.*, **39**, 1901, (1991).
8. P.H. Thornton, R.G. Davies and T.L. Johnson, *Metall. Trans.*, **1**, 207 (1970).
9. D.C. Chrzan and M.J. Mills, *Mat. Sci. & Engr.*, **A164**, 82 (1993).
10. M.D. Uchic and W.D. Nix, Proc. Sixth Intl. Conf. on Creep and Fracture of Engineering Materials and Structures, Irvine, CA, Ed: J.C. Earthman, The Institute of Metals, (1997).
11. D.C. Chrzan (private communication)
12. K. J. Hemker, and W. D. Nix, *Metall. Trans. A*, **24A**, 335, (1993).
13. S.V. Raj and G.M. Pharr, *Mat. Sci and Eng. A*, **A122**, no. 2, 233, (1989).

14. P. Caron, T. Kahn and P. Veyssier, *Phil. Mag. A*, **60**, 267 (1989).
15. K. Hoshino, S.J. Rothman and R.S. Averbach, *Acta Metall.*, **36**, 1271 (1988).
16. J. Wolfenstein, H.J. Kim and J.C. Earthman, *Metall. Mater. Trans. A*, **25A**, 2477 (1994).
17. H. Oikawa, *Mat. Sci. & Eng.*, **A153**, 427, (1992).
18. R. W. Hayes, and P. L. Martin, *Acta metall. et mater.*, **43**, 2761, (1995).
19. H. Mehrer, W. Sprengel, and M. Denking, *Diffusion in Ordered Alloys*, TMS, Warrendale PA, 51, (1993).
20. T. Takahashi, H. Nagai, and H. Oikawa, *Mat. Sci. & Eng.*, **A114**, 13, (1989).
21. T. Takahashi, H. Nagai, and H. Oikawa, *Mat. Sci. & Eng.*, **A128**, 195, (1990).
22. Y. Ishikawa, K. Maruyama, and H. Oikawa, *Mat. Trans., JIM*, **33**, 1182, (1992).
23. K. Maruyama, T. Takahashi, and H. Oikawa, *Mat. Sci. & Eng.*, **A153**, 433, (1992).
24. Y. Ishikawa, and H. Oikawa, *Mat. Trans., JIM*, **35**, 336, (1994).
25. J. Beddoes, W. Wallace, and L. Zhao, *Int. Mat. Rev.*, **40**, 197, (1995).
26. T. Takahashi, H. Nagai and H. Oikawa, *Mat. Sci. & Engr.*, **A114**, 13 (1989).
27. M. Kaufman, D. G. Konitzer, R. D. Shull, and H. L. Fraser, *Scripta metall.*, **20**, 103, (1986).
28. Y. Ishikawa, K. Maruyama, and H. Oikawa, in *Structural Intermetallics*, Ed. R. Darolia, J. J. Lewandowski, C. T. Liu, P. L. Martin, D. B. Miracle, and M. V. Nathal, TMS, Warrendale PA, 345, (1993).
29. M. Lu, and K. J. Hemker, *Metall. Mater. Trans. A*, in press, (1997).
30. M. Lu, and K. J. Hemker, *Acta mater.*, in press, (1997).
31. G. Hug, A. Loiseau, and A. Lasalmonie, *Phil. Mag. A*, **54**, 47, (1986).
32. B. Viguier, and K. J. Hemker, *Phil. Mag. A*, **73**, 575, (1996).
33. B. Viguier, K. J. Hemker, J. Bonneville, F. Louchet, and J. L. Martin, *Phil. Mag. A*, **71**, 1295, (1995).
34. S. Sriram, D. M. Dimiduk, P. M. Hazzledine, and V. K. Vasudevan, *Phil. Mag. A*, in press, (1997).
35. K. J. Hemker, B. Viguier, and M. J. Mills, *Mat. Sci. & Eng.*, **A164**, 391, (1993).
36. M.G. Mendiratta and H.A. Lipsitt, *J. Mat. Sci.*, **15**, 2985 (1980).
37. M. Ohtsuka, T. Fukuda and H. Oikawa, in *Strength of Materials, Fundamental Physical Aspects of the Strength of Crystalline Materials*. Proc. ICSMA 10, Eds: H. Oikawa, K. Maruyama, S. Takeuchi and M. Yamaguchi, Japan Inst. Metals, 733 (1994).
38. K. Maruyama and H. Oikawa, *MRS Symp. Proc.*, Pittsburgh PA, **288**, 653 (1993).
39. M. Yamaguchi, Y. Umakoshi and Y. Yamane, *Phil. Mag. A*, **55**, 301 (1987).
40. T. Takahashi, K. Endo, S. Kaizu and T. Hasagawa, *MRS Symp. Proc.*, Pittsburgh PA, **288**, 711 (1993).
41. T. Takahashi, K. Iwami and T. Hasagawa (unpublished research)
42. J. Bevk, R.A. Dodd and P.R. Strutt, *Metall. Trans.*, **4**, 159 (1973).
43. P.R. Strutt, G.M. Rowe, J.C. Ingram and Y.H. Choo, *Electron Microscopy and Structure of Materials* (ed. G. Thomas) p. 722, University of California Press, Berkeley, CA (1976).
44. R.J. Wasilewski, *Trans. AIME*, **236**, 455 (1966).
45. K.R. Forbes, U. Glatzel, R. Darolia and W.D. Nix, *MRS Symp. Proc.*, Pittsburgh PA, **288**, 45 (1993).
46. W.D. Nix and J.C. Gibeling, in *Flow and Fracture at Elevated Temperatures*, ed: R. Raj, American Society for Metals, Metals Park OH, 1 (1985).
47. K.R. Forbes and W.D. Nix, *MRS Symp. Proc.*, Pittsburgh PA, **288**, 385 (1993).
48. U. Glatzel, K.R. Forbes and W.D. Nix, *MRS Symp. Proc.*, Pittsburgh PA, **288**, 749 (1993).
49. K.R. Forbes, U. Glatzel, R. Darolia and W.D. Nix, *Metall. Mater. Trans. A*, **27A**, 1229 (1996).
50. U. Glatzel, K.R. Forbes and W.D. Nix, *Phil. Mag.*, **A67**, 307 (1993).
51. M.J. Mills and D. B. Miracle, *Acta metall. et mater.*, **41**, 85 (1993).
52. M.J. Mills, J.E. Angelo, M.S. Daw, J.D. Weinberg and D.B. Miracle, *Mat. Sci. & Eng.*, **A 192-193**, 134, (1995).
53. P.H. Kitabjian, A. Garg, R. D. Noebe and W.D. Nix, Proc. Sixth Intl Conf. on *Creep and Fracture of Engineering Materials and Structures*, Irvine, CA, Ed: J.C. Earthman, The Institute of Metals, (1997)
54. P.R. Strutt, R.S. Polvani and J.C. Ingram, *Metall. Trans. A*, **7A**, 23 (1976).

# FATIGUE CRACK GROWTH IN INTERMETALLICS

N. S. Stoloff

Rensselaer Polytechnic Institute  
Troy, New York 12180-3590

## Abstract

The fatigue crack growth behavior of intermetallics and intermetallic matrix composites is described. Most of the available literature is concerned with TiAl alloys, MoSi<sub>2</sub> alloys, including composites, and Fe<sub>3</sub>Al alloys, such that these are the focus of this review. However, limited studies of Ni<sub>3</sub>Al, Ti<sub>3</sub>Al, Nb<sub>3</sub>Al and of some complex composite alloys also are discussed. As a class, most intermetallics have very low fatigue crack growth resistance in comparison to current structural high temperature alloys. Among variables that affect fatigue crack growth resistance, composition, microstructure, temperature and test environment are the most significant. Effects of R ratio (minimum to maximum stress intensity range) also are discussed because of the impact of this variable on closure effects. General guidelines for increasing fatigue crack growth resistance are discussed.

## Introduction

Much attention has been directed towards the fracture behavior of intermetallic compounds under monotonic loading. It is well known that most of the intermetallics of interest for structural applications are relatively brittle, although in many cases brittleness is the result of an environmental effect.[1,2] Similarly, under cyclic loading conditions crack growth is usually very rapid, with unusually high stress exponents noted in the Paris-Erdogan [3] equation:

$$da/dN = C\Delta K^m \quad (1)$$

Again, the test environment can play a major role, especially in the case of aluminides and silicides.[2] However, the study of crack

growth resistance under cyclic loading conditions has lagged investigations of monotonic behavior. Only in the case of a few intermetallic systems has a comprehensive study of the factors influencing crack growth been carried out. Previous reviews of fatigue behavior in intermetallics have demonstrated just how sparse are data in the literature[4,5]. However, there is now an appreciable data base for TiAl[6-15] and some Fe<sub>3</sub>Al alloys[16,17] and for MoSi<sub>2</sub>/Nb composites of differing morphologies[18,19]. Unfortunately, data for other intermetallic systems remain sparse. Due to space limitations, this paper will summarize the most recent developments in the field of fatigue crack growth (FCG) only.

## Crack Growth in Specific Systems

### Titanium Aluminides

The mechanical behavior of both TiAl and Ti<sub>3</sub>Al alloys is very dependent upon the microstructure. Unfortunately, those microstructural features that maximize strength may have an adverse effect upon fracture behavior under both cyclic and monotonic conditions. In this review we emphasize those factors that affect the fatigue crack growth behavior of the titanium aluminides.

#### a. TiAl Alloys

In the case of gamma TiAl alloys, the best combination of mechanical properties is obtained in two phase microstructure alloys in the composition range of 44-49a%Al[10]. For wrought alloys, fully lamellar material exhibits higher fracture toughness, creep resistance and fatigue resistance than a duplex microstructure. In a recent review, Sadananda and Vasudevan[8] have pointed out that there is a

trend to higher FCG thresholds as Al content increases, especially as Al increases from 48a% to 50a%. The latter alloy is single phase, while all others compared at lower Al contents were two phase. However, as R ratio increases, thresholds drop sharply. Also, crack growth exponents in TiAl are extremely high, as shown in Fig. 1 for several binary and ternary alloys[12]. Therefore, once initiated, cracks grow extremely rapidly. A range of stress exponents,  $m$ , from 8.2 to 56.2 is obtained with different test conditions for a 48Al-2Mn-2Nb alloy, values that are in all cases much higher than for conventional structural materials[20]. Under such conditions, flat S-N curves also are to be expected, so that knowledge and control of stresses is extremely important. High values of the exponent are typical of many brittle ceramics and intermetallics. For TiAl alloys, high growth rates have been attributed to low energy fracture modes such as cleavage of gamma grains at room temperature and transgranular decohesion of the gamma and alpha two phases at 700 or 800C. It was concluded that microstructures with a large proportion of gamma grains have much poorer fatigue properties than lamellar gamma/alpha two alloys[14].

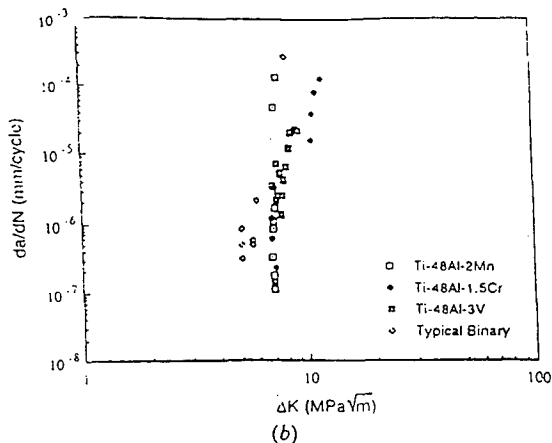


Fig. 1. Summary of fatigue crack growth rate data in  $\gamma$ -TiAl alloys.[12]

It has been shown repeatedly that a lamellar structure exhibits higher crack growth resistance than either duplex or equiaxed microstructures, as shown in Fig. 2 for a two phase Ti-47.3Al-2.3Nb-1.5Cr-0.4V alloy[10]. For both fine duplex and coarse lamellar structures FCG rates are higher at 650°C than at either 25°C or 800°C. The superior performance of lamellar microstructures under both cyclic and monotonic loading has been attributed to extrinsic shielding from crack deflection, microcrack nucleation ahead of the crack tip and resultant bridging by lamellar

colonies in the crack wake, similar to the behavior of aligned composites[6].

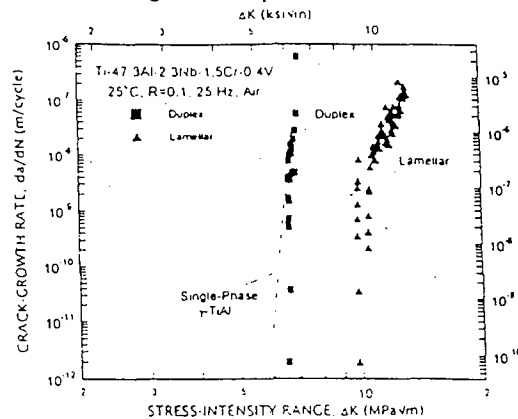


Fig. 2. Fatigue-crack growth behavior of the two-phase  $\gamma$ -TiAl alloy in the duplex and lamellar microstructures at room temperature in air ( $R = 0.1$ , 25 Hz).[10]

When TiAl is reinforced with ductile particles (20vol% TiNb), fatigue crack growth resistance is reduced if pancake shaped particles are oriented with their edges perpendicular to the crack plane, see Fig. 3[13]. R ratio is clearly a factor; only for  $R = 0.1$  does reinforced material behave similarly to unreinforced TiAl. On the other hand, when particles are oriented with their faces normal to the crack plane, fatigue crack growth resistance is modestly enhanced. The degradation of fatigue resistance with unfavorably oriented ductile particles, seen also with  $\text{MoSi}_2$ [18,21], is attributed to one or more of several factors: the absence of crack bridging, the influence of the ductile reinforcements in decreasing the crack opening displacement (COD) under cyclic loading and the accumulation and partitioning of inelastic strains.

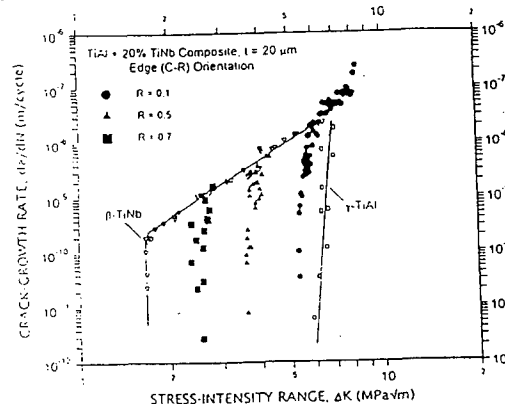


Fig. 3. Influence of load ratio,  $R = 0.1$ , 0.5 and 0.7, on the cyclic fatigue-crack growth behavior in a  $\gamma$ -TiAl composite reinforced with 20 vol.%( $t \sim 20\mu\text{m}$ ) TiNb particles in the edge (C-R) orientation.[13]

Only one study of the effect of brittle reinforcements on crack growth of TiAl has been reported; XD TiAl + 7v%TiB<sub>2</sub> has a fatigue crack threshold of 7 MPa $\sqrt{m}$ <sup>1/2</sup>[22], which is higher than for many unreinforced TiAl alloys.

In summary, fatigue crack growth thresholds are low and exponents are high in TiAl alloys. In general, lamellar two phase microstructures provide the highest fatigue crack growth resistance. Both ductile (Nb or TiNb) and brittle particles have been incorporated into TiAl alloys. The effectiveness of these reinforcements depends upon microstructural variables such as volume fraction and orientation of the particles.

#### b. Ti<sub>3</sub>Al Alloys

As in the case of TiAl alloys, microstructure plays a major role in fatigue crack growth resistance of Ti<sub>3</sub>Al alloys.[23]. A coarse Widmanstätten structure provides better crack growth resistance than an equiaxed microstructure.

Evidence for environmental effects on crack growth of alpha two alloys both at room and at elevated temperatures has been provided in several studies[24-26]. There is an effect of frequency on growth rates in lab air as well as in 10<sup>-5</sup> torr vacuum for a Ti-24Al-11Nb alloy tested at 649 C, see Fig. 4[24]. Cracks grow much more rapidly in air than in vacuum in this alloy. Similar observations have been made at temperatures in the range between 650 and 800 C[25,26]. There is a significant effect of frequency on growth rates in this alloy; lowering of frequency from 100Hz to 0.01Hz causes growth rates to increase by a factor of ten. In general, growth rates in alpha two alloys increase with moist environments, lower test frequencies, increased hold times and increased test temperatures[27,28].

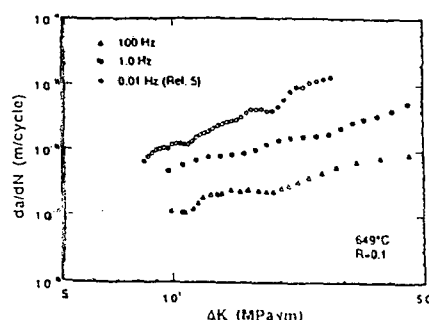


Fig. 4. Variation of fatigue crack growth rates of Ti-24Al-11Nb with frequency at 649°C.[24]

Limited work has been done on small crack behavior in Ti<sub>3</sub>Al alloys[29,30]. Small cracks in super alpha two grow at a slightly higher rate than in the nickel-base superalloy Astroloy, but about 10-100 times slower than in 7075 Al[29]. Small cracks in Ti-24Al-11Nb develop arbitrary shapes that are affected by microstructure and texture; these shapes, in turn, affect crack growth rates. With a basketweave microstructure as well as with two other microstructures, small and long crack data correlate well when crack closure is accounted for[30]. However, small crack growth rates were always higher than those for long cracks in an aligned colony structure.

Perhaps the single factor most likely to influence the crack growth resistance of titanium aluminides is the use of fibrous reinforcements. A continuous SCS-6 SiC fiber-reinforced Ti-24Al-11Nb alloy (longitudinal orientation) is far more resistant to crack growth than is nickel-base superalloy IN-100, as shown in Fig. 5[31]. However, transversely oriented fibers result in higher growth rates than in conventional  $\alpha_2$ ,  $\gamma$  and IN100 alloys.

In summary, crack growth rates in alpha two alloys are lowest for Widmanstätten microstructures, dry environments and low test temperatures. Fibrous reinforcements improve crack growth resistance only when oriented parallel to the applied stress axis.

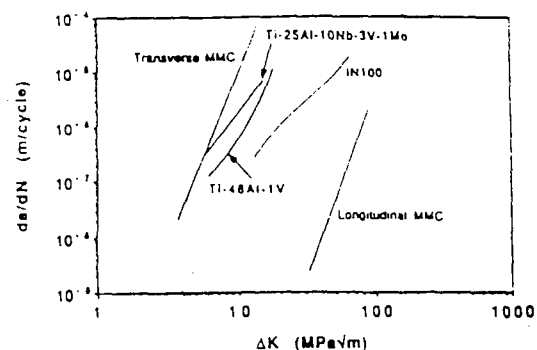


Fig. 5. Comparison of crack-growth rates of titanium aluminides,  $\alpha_2$  composites, and IN-100; tests at 650°C, R = 0.1,  $\nu$  = 0.2 Hz except for the composite, for which  $\nu$  = 3.33 Hz.[31]

#### c. Orthorhombic Ti-Al-Nb Alloys

The orthorhombic (O) phase is found in Ti alloys containing 20-30a%Al and 14-30%Nb. These alloys display an interesting combination of room temperature ductility and high

temperature creep strength. Majumdar et al[32] have reported that an alloy consisting of a mixture of alpha two of composition Ti-24Al-11Nb and orthorhombic Ti-24.5Al-15Nb has superior FCG resistance to an alpha two Ti-24Al-11Nb alloy, especially for  $\Delta K$  values of 20 MPam<sup>1/2</sup> or higher; the difference is reduced at lower  $\Delta K$  values. Fractography showed that the improved FCG resistance of the two phase path alloy was due to a rough and tortuous crack and less cleavage fracture.

### Iron Aluminides

The fatigue behavior of iron aluminides has been extensively studied, over a range of aluminum contents from 16-35a% [16,17,32-35]. Effects of ternary solutes, microstructure, temperature and R ratio (minimum to maximum stress intensity) have been studied under both aggressive (i.e. moist air or hydrogen gas) and inert (i.e. dry) environments. Most of the work has been carried out on compositions that exhibit Fe<sub>3</sub>Al type order, although some work has been done on the FeAl alloys Fe-35a%Al. We review here the most recent findings, emphasizing the role of Cr and Zr additions to crack growth behavior.

The alloys studied, all of which were supplied by the Oak Ridge National Laboratory (ORNL), are listed in Table 1. Note that some alloys are partially recrystallized so as to maximize tensile ductility. Alloy FAP-Y is disordered, Fe-35a%Al is a B2 ordered intermetallic and all of the other alloys are ordered Fe<sub>3</sub>Al type, tested in either the fully ordered DO<sub>3</sub> condition or in the partially disordered B2 condition. All tests were run at a frequency of 20 Hz and an R

ratio of 0.5; atmospheres varied between laboratory air, oxygen gas and hydrogen gas, as well as moderate vacuum.

A summary of FCG data for all alloys listed in Table 1 appears in Fig.6[34]. The highest FCG rates are exhibited by the disordered FAP-Y alloy, while the lowest rates are found in the B2 ordered 0.5%ZrC alloy. Work on alloy FA-129 has shown that FCG rates are lower in the B2 than the DO<sub>3</sub> condition, and that there is little difference between rates for fully and partially recrystallized microstructures[17,33].

The effects of environment are shown for the alloy containing 0.5%Zr in Fig.7[34]. Note the adverse effect of moist air. Zirconium has its major effect in high  $\Delta K$  region (above threshold) and 1%Zr is less effective than is 0.5%Zr. The presence or absence of carbon seems to have little influence, perhaps because of the high Zr/C ratios used in this work. No evidence of carbides was seen by TEM.

Sikka[36] has previously shown that additions of 0.1a%Zr + 0.01%C and 0.2a%Zr + 0.02a%C give higher ductilities than 1 or 2a%Zr. There may be a similar effect of these elements on fatigue behavior, especially since high crack growth exponents are usually associated with brittle intermetallics and ceramics.

Fractographic examination showed that dimpled rupture is predominant in all environments for the Zr-containing alloys, except for 0.5%Zr and 1%ZrC in hydrogen[34]. By contrast, FA-129 and the ternary alloy showed predominantly cleavage in all environments. Dimpled rupture was only evident i FA-129 when that alloys is tested in oxygen[17,33,34].

TABLE 1 Composition of Iron Aluminide Alloys (Atomic %)

	FAP-Y	FA-129	Fe-35%Al	Ternary	1%ZrC	0.5%ZrC	0.5%Zr
Fe	77.07	66.17	65.0	67.0	65.95	66.45	66.5
Al	16.12	28.08	35.0	28.0	28.0	28.0	28.0
Cr	5.44	5.04	-	5.0	5.0	5.0	5.0
Zr	0.11	-	-	-	1.0	0.5	0.5
C	0.13	0.20	-	-	0.05	0.05	-
Mo	1.07	-	-	-	-	-	-
Nb	-	0.51	-	-	-	-	-
Y	0.06	-	-	-	-	-	-
Grain Size	42μm	*	385μm	180μm	*	*	*

\* - partially recrystallized

Fatigue crack growth rates of iron aluminides are very sensitive to composition and the test environment. Tests in oxygen provide the lowest growth rates. Fracture tends to be by transgranular cleavage in all test environments, although Zr promotes a more fibrous fracture appearance.

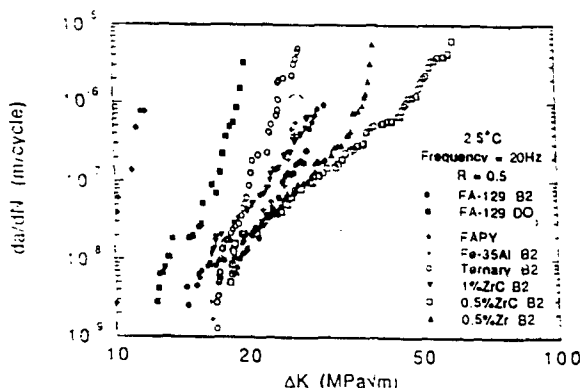


Fig. 6. Fatigue crack growth curves for several Fe-Al Alloys.[34]

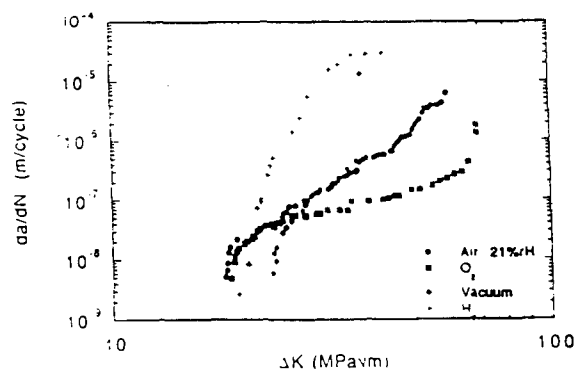


Fig. 7. Effects of environment on FCG of  $\text{Fe}_3\text{Al}$  alloy 0.5% Zr.[34].

#### Nickel Aluminides

In spite of the overwhelming interest in the mechanical behavior of nickel aluminides, little has been published in the past five years on their fatigue behavior. However, for the sake of completeness, we include here a brief summary of what is known about the crack growth behavior of  $\text{Ni}_3\text{Al}$ . No published FCG data are available for  $\text{NiAl}$ .

It has been known for some time that crack growth rates in  $\text{Ni}_3\text{Al}$  alloys are lower than for many superalloys, and that rates of growth increase with increasing temperature[37]. Detailed studies of an alloy designated IC-221 ( $\text{Ni-8w\%Al-7.74\%Cr-0.008\%B}$ ) showed that

environmental effects are very important, in that oxygen accelerates crack growth at elevated temperatures[38]. Creep processes also contribute to growth rates at temperatures above  $700^\circ\text{C}$ . Crack growth rates increase with decreasing frequency in both vacuum and air for this alloy at  $800^\circ\text{C}$ , but the rates always are higher in air. Intergranular fracture occurs in air at all test frequencies, while transgranular fracture is noted in vacuum. Secondary cracking is enhanced at lower frequencies, suggesting that diffusion of oxygen contributes to their initiation.

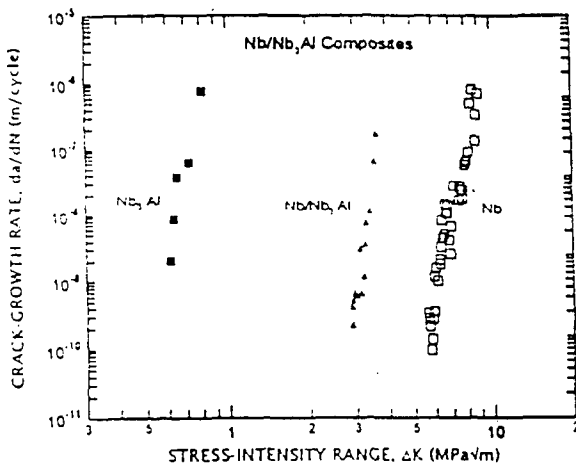


Fig. 8. Crack growth rates for  $\text{Nb/Nb}_3\text{Al}$  as well as  $\text{Nb}_3\text{Al}$  and  $\text{Nb}$ .[40].

#### Niobium Aluminides

Considerable work has been done on the fracture and fatigue of  $\text{Nb}_3\text{Al}$  and several composite alloys with  $\text{Nb}$  or  $\text{Ta}$ [39-43.] These have generally shown the characteristic high crack growth exponents associated with brittle materials. A study of FCG in a  $\text{Nb/Nb}_3\text{Al}$  in-situ composite showed crack growth rates that were much lower than for the unreinforced intermetallic, although not nearly as low as for pure  $\text{Nb}$ , see Fig. 8[40]. Aging of a hot pressed  $\text{Nb}_3\text{Al/Nb}$  alloy caused a slight drop in FCG rate but crack growth was much slower in pure  $\text{Nb}$ [39]. As with other intermetallics, particles of a ductile phases are not nearly as effective in increasing toughness, compared to fibers or layered reinforcements. The toughness and fatigue threshold values for three  $\text{Nb-Al-Ti}$  alloys in which  $\text{Nb}_3\text{Al}$  precipitates of unknown volume fraction are dispersed in a B2 matrix have been reported[41]. FCG rates are similar to those of mill annealed  $\text{Ti-6Al-4V}$ , although lower



thresholds were noted in the former. The fatigue threshold of Nb-15Al-25Ti was only 3 MPam<sup>1/2</sup>, compared to a toughness of about 20 MPam<sup>1/2</sup>. Data for Nb-18a%Al-10%Ta in-situ composites also show an improvement over Nb<sub>3</sub>Al, but FCG exponents are very high and Nb remains superior.[42]

## Silicides

### a. MoSi<sub>2</sub>

Several investigations of fatigue crack growth resistance of MoSi<sub>2</sub>[21] and its composites with Nb[18,19] or SiC[44,45] particles have been published. Soboyejo et al[21] reported that at room temperature, stable crack growth occurs in MoSi<sub>2</sub> delta K values as low as 1.7 MPam<sup>1/2</sup>. The crack growth exponent was 14, consistent with the high values reported for other brittle intermetallics. The same study revealed that the fatigue resistance was lowered by the addition of 20v% Nb particles, even though the monotonic fracture resistance was increased slightly by the particles. This work was important in that it confirmed that improvements in fracture toughness by the use of ductile particles do not necessarily lead to improved fatigue crack growth resistance.

Crack bridging is observed under monotonic conditions but not under cyclic loading of particle reinforced MoSi<sub>2</sub>. It has been shown by the same group that crack growth rates increase with increasing Nb fiber diameter, and that growth rates with 750 micron fibers are 100 times greater than for laminated composites reinforced with 200 micron thick Nb lamellae[21]. The varying effects of different microstructures were attributed to differences in reinforcement spacing and crack tip blunting by the Nb fibers. The latter results in much lower Paris exponents for the composites, compared to unreinforced MoSi<sub>2</sub>. In the near threshold regime, the laminates had similar crack growth resistance to the particulate reinforced material. Interestingly, the crack growth resistance of pure Nb, a weak but ductile metal, is much greater than that of any of the composites[18.] By way of contrast, fibers and laminates provide higher monotonic toughnesses than for monolithic MoSi<sub>2</sub>.

Another recent finding is that a wire mesh Nb reinforcement provides much lower crack growth rates than do Nb particles, see Fig.9[18.] Increasing load ratios from 0.10 to 0.70 results in much higher growth rates and reduced fatigue thresholds; such behavior is

characteristic of other metals and ceramics, but the data for this system are much more sensitive to  $K_{max}$  than for metals. A modified Paris power law relation which includes the effects of both  $\Delta K$  and  $K_{max}$  has been established:

$$da/dN = C'(K_{max})^n(\Delta K)^p \quad [2]$$

where  $C'$  is a scaling constant which is independent of  $K_{max}$ ,  $\Delta K$  and  $R$ , while  $n$  and  $p$  are experimental constants, calculated to be 13.2 and 7.5, respectively. The improved properties of the wire mesh-reinforced MoSi<sub>2</sub> has been attributed to extensive crack deflection at the interface between the matrix and the reinforcements, interface debonding and frictional sliding between mating crack face asperities. Therefore, increased crack tip shielding is believed to result from crack deflection and roughness-induced crack closure. Another feature of the fatigue crack growth resistance of the composites is that stable crack growth readily occurred, while stable crack growth is very difficult to obtain in monolithic MoSi<sub>2</sub>.

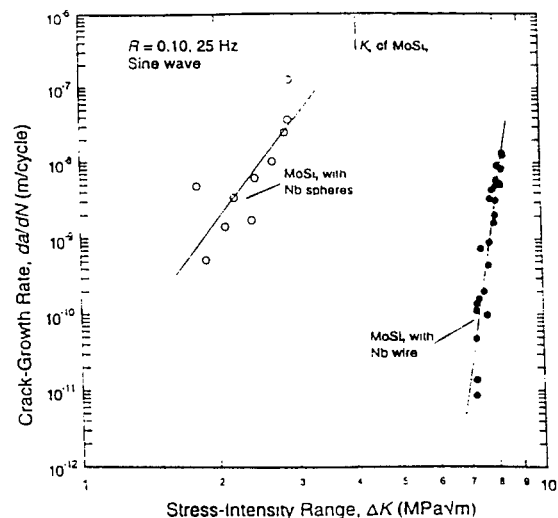


Fig. 9. Variation in cyclic fatigue-crack growth rates,  $da/dN$ , as a function of the nominal  $\Delta K$  at  $R = 0.1$  for MoSi<sub>2</sub> reinforced with 20 vol pct Nb in the form of high-aspect ratio wire mesh (Nb<sub>w</sub>/MoSi<sub>2</sub>) and as spherical particulates (Nb<sub>p</sub>/MoSi<sub>2</sub>).[18]

Silicon carbide particles, unlike Nb particles, reduce FCG rates in (Mo,W)Si<sub>2</sub> at 1200°C[44]. Later work showed that the fatigue resistance of (Mo,W)Si<sub>2</sub>-SiC composites at elevated temperatures can be improved by addition of 2 wt% C, see Fig.10. Other work had shown a

similar improvement in fracture toughness with carbon additions[46]. Both effects seem to result from the prevention of formation of silica during processing as well as during exposure to air and the formation of a ternary Nowotny phase that contributes to toughening. The presence of carbon increased the threshold for fatigue crack growth initiation and lowered crack growth rates. Further, carbon reduced the incidence of cavitation at crack tips in the composite samples[45].

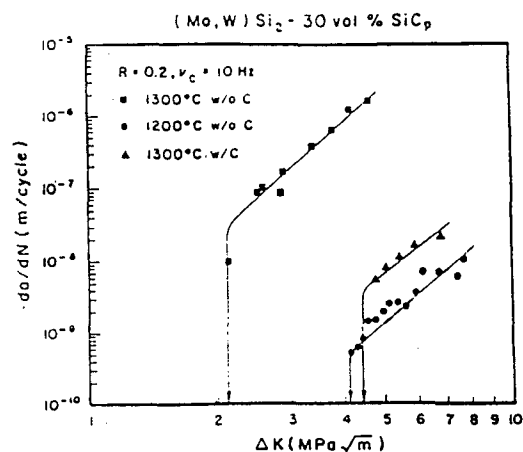


Fig. 10. Variation of crack growth rate per cycle,  $da/dN$ , plotted as a function of the applied stress intensity range,  $\Delta K$ . [45]

TABLE 2  
Fatigue Crack Growth Data, Air

ALLOY	TEMP.	FREQUENCY	R	$\Delta K_{th}$	$\Delta K_{max1}$	m	Ref.
Ti-48Al	25	--	--	5	8	--	12
Ti-47.3Al-2.3Nb-1.5Cr-0.4v d	25	25	0.1	6.5	7.5	50	10
Ti-47.3Al-2.3Nb-1.5Cr50.4v l	25	25	0.1	10.	20	15*	10
TiAl-7v%TiB2	25	--	--	7	22		22
TiAl-10v%TiNb	25	25	0.1	5.5	8		13
TiAl-20v%TiNb	25	25	0.1	5	9.6		13
Ni <sub>3</sub> Al+B+Hf	25	20	0.1	20	60		17,33
Fe-28Al-5Cr-0.5Nb B2	25	20	0.5	14.5	29.9	6.9	17,33
Fe-28Al-5Cr-0.5Nb DO3	25	20	0.5	13.3	19.8	11.3	16,34
Fe-28Al-5Cr-0.5Zr-0.5C B2	25	20	0.5	18	60		16,34
Fe-28Al-5Cr B2	25	20	0.5	16.9	26.4		16,34
Nb <sub>3</sub> Al	25	25	0.1	0.6	1		40
Nb <sub>3</sub> Al/Nb	25	25	0.1	3	4	5	40
Nb-18Al-10Ta	25	--	--	4	5		42
Nb-12.5Al-41Ti-1.5Mo(L,S)	25	20	0.1	4-7-5*	30		41
MoSi <sub>2</sub>	25	25	0.1	1.7	3	14	21
MoSi <sub>2</sub> -20v%Nb <sub>p</sub>	25	25	0.1	2	3	14	18
MoSi <sub>2</sub> -20v%Nb <sub>mesh</sub>	25	25	0.1	7.2	8.5		18
(Mo,W) Si <sub>2</sub> -30v%SiC <sub>p</sub>	1200	10	0.2	4.1	9	3.9	44
MoSi <sub>2</sub> -20v%SiC <sub>w</sub>	1200	10	0.2	0.8	1.3	155.6	50
TiAl	800	25	0.1	5.5	9	6.3	11
TiAl-20v%TiNb	800	25	0.1	4.9	8	6.9	11
Ti-47.3Al-2.3Nb-1.5Cr-0.4V(l)	800	25	0.1	12	18		49
Ti-47.3Al-2.3Nb-1.5Cr-0.4V(d)	800	25	0.1	8	12		49
Ti-48Al-2Mn-2Nb (as cast)	700					10.	20
Rene' N4 (single crystal)	21	0.5	0.1	22	35	3.8	55
Rene' N4 (single crystal)	704	0.5	0.1	20	80	2.4	55
Rene' N4 (single crystal)	927	0.5	0.1	22	40	4.4	55
Rene' 95	650	0.33	0.05	10	60	--	51
IN 100	650	0.2	0.1	~12	60	--	31
Ti-6Al-4V(mill anneal)	25			8.5	25	5	53
Hip Astroloy (fine grain)	25	40	0.1	5.7	28	--	52
Hip Astroloy (coarse grain)	25	40	0.1	12	32	--	52

\*depends on orientation, heat treatment

## b. Other Silicides

There do not appear to be any published fatigue data for other silicides in spite of considerable research on the deformation and fracture of the Nb-Si[47] and Cr-Si[48] systems.

### Discussion

A summary of crack growth data for many of the alloy systems described in this paper appears in Table 2. Note that in many cases the FCG exponent has not been reported. Also shown are data for some commercial Ti and Ni-base alloys.

To put the data of Table 2 in perspective, it should be noted that many ferritic and austenitic steels display fatigue thresholds of the order of 5.5-8 MPam<sup>1/2</sup> for R=0.1, and the thresholds drop to as low as 2 MPam<sup>1/2</sup> as R increases to 0.8 [54]. Much more distinctive about the intermetallics than the low thresholds are the very high stress exponents, *m*, observed in several such alloys. In one case, MoSi<sub>2</sub> reinforced by 20v%SiC whiskers, an exponent of 155.6 was observed [50], about 50 times higher than typical values for structural metals, including nickel-base single crystals such as Rene 'N4 (see Table 2).

While there has been considerable effort devoted to obtaining fatigue data for TiAl alloys, Fe<sub>3</sub>Al alloys and MoSi<sub>2</sub> composites, there still remains a serious lack of comprehensive crack growth data for most intermetallics. In order for intermetallics or their composites to achieve status as commercial materials, more effort needs to be placed upon obtaining fatigue data bases that include crack growth along with stress and strain controlled fatigue data. However, certain guidelines are evident in judging the fatigue crack growth resistance of these materials. High FCG exponents and low thresholds can be expected pending improvements in ductilities and fracture toughness. Unless high ductilities and fracture toughnesses are achieved, FCG exponents will be high and thresholds will be low. Environmental effects are a serious problem which must be addressed in all of these alloy systems. Hydrogen introduced directly or by breakdown of water vapor causes severe embrittlement of iron aluminides under both cyclic and monotonic conditions [16,17,33].

Similarly, Ni<sub>3</sub>Al, TiAl and Ti<sub>3</sub>Al alloys are sensitive to hydrogen environments under monotonic conditions[1,2]. Therefore, hydrogen contact must be avoided to determine intrinsic FCG rates. Oxygen also causes problems with Ti<sub>3</sub>Al and Ni<sub>3</sub>Al at elevated temperatures[2,38]. The effects of hydrogen and oxygen on FCG in other intermetallic alloy systems have not been studied. Nevertheless, the use of ductile Nb reinforcements to improve toughness of silicides can be expected to lead to serious problems in both monotonic and cyclic properties. This is because of the strong affinity of Nb and other group Va metals of the periodic table for hydrogen, oxygen and nitrogen and the known embrittlement of Nb by these elements.

The role of microstructure in FCG has been studied extensively only in titanium aluminides[6,10,12,23]; lamellar structures clearly are superior in their FCG resistance to all other microstructures. While grain size effects on FCG are not expected to be large, the distribution of strengthening phases will be a significant factor[18, 19, 21]. Other variables that affect FCG resistance are temperature, frequency and R ratio. In most cases, FCG rates increase as temperature increases (in aggressive environments or when creep may occur) and as R ratio increases. However, there are exceptions to these general observations, as has been noted for TiAl[10] and Fe<sub>3</sub>Al[35], for which temperature effects are complex.

### Acknowledgements

The author is grateful to the U. S. Dept. of Energy, Fossil Energy Program and to DARPA/ONR for financial support of research on fatigue and fracture over many years.

### REFERENCES

1. N. S. Stoloff and C. T. Liu, *Intermetallics*, 2, (1994), 75-87.
2. T. Takasugi, in *Critical Issues in the Development of High Temperature Materials*, N. S. Stoloff, D. J. Duquette and A. F. Giamei, Eds., TMS, Warrendale, PA, (1993), 399-414.
3. P. C. Paris and F. Erdogan, *J. Basic Eng.*, Trans. ASME Ser. D. 85 (1963), 528-534.
4. N. S. Stoloff, in *Critical Issues in the Development of High Temperature Materials*, N. S. Stoloff, D. J. Duquette and A. F. Giamei,

- Eds., TMS, Warrendale, PA, (1993), 367-384.
5. N. S. Stoloff, in *Physical Metallurgy and Processing of Intermetallic Compounds*, N. S. Stoloff and V. K. Sikka, Eds., Chapman and Hall, New York, 1996, 126-155.
6. R. Gnanamoorthy, Y. Mutoh and Y. Mizuhara, *Intermetallics*, 4, (1996), 525-529.
7. S. J. Balsone, J. M. Larsen, D. C. Maxwell and J. Wayne Jones, *Mat. Sci. and Eng. A192/193*, (1995), 457-464.
8. K. Sadananda and A. K. Vasudevan, *Mat. Sci. and Eng. A192/193*, (1995), 490-501.
9. W. O. Soboyejo, J. E. Deffeyes and P. B. Aswath, *Mat. Sci. and Eng.*, A138, (1991), 95-101.
10. K. T. Venkateswara Rao, Y. W. Kim, C. L. Muhlstein and R. O. Ritchie, *Mat. Sci. and Eng.*, A192/193, (1995), 474-482.
11. K. T. Venkateswara Rao and R. O. Ritchie, in *Fatigue and Fracture of Ordered Intermetallics II*, T. S. Srivatsan, W. O. Soboyejo and R. O. Ritchie, Eds., TMS, Warrendale, PA (1995).
12. W. O. Soboyejo, C. Mercer, K. Lou and S. Heath, *Metall. Trans. A*, 26A, (1995), 2275-2291.
13. K. T. Venkateswara Rao, G. R. Odette and R. O. Ritchie, *Acta Metall.*, 42, (1994), 893-911.
14. S. J. Balsone, J. M. Larsen, D. C. Maxwell and J. W. Jones, *Mat. Sci. and Eng.*, A192/193 (1995) 457-464.
15. K. S. Chan and D. S. Shih, *Metall. Trans.*, 28A (1997) 79-90.
16. D. A. Alven and N. S. Stoloff, *Scr. Metall.*, 34, (1996), 1937-1942.
17. A. Castagna and N. S. Stoloff, *Scr. Metall.*, 25, (1992) 673-678.
18. K. Badrinarayanan, A. L. McKelvey, K. T. Venkateswara Rao and R. O. Ritchie, *Metall. Trans.* 27A, (1996), 3781-3792.
19. W. O. Soboyejo, F. Ye and D. S. Schwartz, *Metall. Trans. A*, 26A, (1995), 2263-2273.
20. A. W. James and P. Bowen, *Mat. Sci. and Eng. A153*, (1992) 486-492.
21. W. O. Soboyejo, K. T. Venkateswara Rao, S. M. L. Sastry and R. O. Ritchie, *Metall. Trans.*, 24A, (1993) 585-600.
22. K. S. Kumar in *Composites Science and Technology*, 52, (1994) 127-150.
23. P. B. Aswath and S. Suresh, *Mat. Sci. and Eng. A114*, (1989) L5-L10.
24. B. K. Parida and T. Nicholas, *Materials Sci. and Eng.*, 153, (1992) 493-498.
25. R. J. T. Penton, M. T. Cope and P. Bowen, *Mat. Sci. and Eng. A153*, (1992), 508-513.
26. S. J. Balsone, D. C. Maxwell, M. Khobaib and T. Nicholas, in *Fatigue 90*, H. Kitagawa and T. Tanaka, Eds., *Materials and Components Eng. Publ. Ltd.*, Waverly, UK, III, (1990) 1905-1910.
27. J. F. Wessels, B. J. Marquardt and D. D. Krueger presented at TMS-AIME Symp. on Creep and Fracture of Titanium Aluminides, TMS, Indianapolis, IN, (1989).
28. S. Vekaturaman, AFWAL-TR-87-4103, Air Force Materials Lab, Wright Patterson Air Force Base, OH, (1987).
29. D. L. Davidson, J. B. Campbell and R. A. Page, *Metall. Trans. A*, 22A, (1991), 377-391.
30. K. S. Ravichandian and J. M. Larsen, *Mat. Sci. and Eng.*, A153, (1992), 499-507.
31. J. M. Larsen, K. A. Williams, S. J. Balsone and M. A. Stucke in *High Temperature Aluminides and Intermetallics*, S. H. Whang et al, Eds., Warrendale, PA, TMS (1990), 521-556.
32. B. S. Majumder, C. Boehlert, A. K. Rai and D. B. Miracle, in *High Temperature Ordered Intermetallic Alloys VI*, J. A. Horton, et al, Eds., MRS Symp. Proc. 364, part 2, (1995), 1259-1264.
33. A. Castagna, P. J. Maziasz and N. S. Stoloff, in *High Temperature Ordered Intermetallic Alloys V*, I. Baker, R. Darolia, J. D. Whittenberger, M. H. Yoo, Eds., MRS Symp. Proc., Pittsburgh, 288, (1993), 1043-1048.
34. N. S. Stoloff and D. A. Alven, in *Proc.*

Symp. on Corrosion-Deformation Interactions, Nice, France, Sept. 24-26 1996, (in press).

35. A. Castagna and N. S. Stoloff in High Temperature Ordered Intermetallic Alloys VI, MRS Symp. Proc., Pittsburgh, 364, part 2, (1995) 1171-1176.

36. V. K. Sikka, Oak Ridge National Laboratory, (1996), unpublished.

37. N. S. Stoloff, G. E. Fuchs, A. K. Kuruvilla and S. J. Choe, in High Temperature Ordered Intermetallic Alloys II, N. S. Stoloff, C. C. Koch, C. T. Liu and O. Izumi, Eds, Mat. Res. Soc. Symp. Proc. 81, Pittsburgh, PA, MRS, (1987), 247-261.

38. W. Matuszyk, G. Camus, D. J. Duquette and N. S. Stoloff, Metall. Trans. A., 21, (1990), 2967-2976.

39. L. Muruges, K. T. Venkateswara Rao, L. C. DeJonghe and R. O. Ritchie, in Intermetallic Composites II, MRS Symp. Proc. 273, MRS, Pittsburgh, PA, (1992).

40. L. Muruges, K. T. Venkateswara Rao and R. O. Ritchie, Scripta Metall. 41 (1993), 1107-1112.

41. J. Dipasquale, D. Gahutu, D. Konitzer and W. Soboyejo, in High Temperature Ordered Intermetallics VI, J. A. Horton et al, Eds., MRS Symp. Proc. 364, part 2, Pittsburgh, PA, (1995), 1347-1352.

42. S. Hanada, T. Tatsuo and R. Gnamamoorthy, Acta Metall. Sinica (English Letters) 8, (1995) 477-487.

43. D. L. Davidson and K. S. Chan, Final Report, AFOSR Contract No. F49620-92-C-0022, April 1995.

44. U. Ramamurty, A. S. Kim, S. Suresh, and J. J. Petrovic, J. Am. Ceram. Soc., 76, (1993), 1953-1964.

45. U. Ramamurty, S. Suresh, and J. Petrovic, J. Am. Ceram. Soc., 77, (1994), 2681-2688.

46. S. Maloy, A. Heuer, J. Lewandowski and J. Petrovic, J. Amer. Cer. Soc., 74 (1991) 2704-2706.

47. M. G. Mendiratta, J. J. Lewandowski and D. M. Dimiduk, Metall. Trans. 22A (1991), 1573-1583.

48. M. Nazmy, C. Nosedo, G. Sauthoff, B. Zeumer and D. Anton in High Temperature Ordered Intermetallic Alloys VI, J. A. Horton, et al, Eds., MRS Symp. Proc. 364, part 2, (1995) 1333-1338.

49. K. T. Venkateswara Rao, Y-W Kim and R. O. Ritchie, Scripta Metall., 33 (1995) 459-465.

50. G. Y. Lu, R. Lederich and W. Soboyejo, in Deformation and Fracture of Ordered Intermetallic Alloys III, W. O. Soboyejo, T-S. Srivatsan and H. L. Fraser, Eds., Warrendale, PA, TMS (1997) 507-535.

51. B. A. Cowles, J. R. Warren and F. K. Haake, NASA-CR-165123, July (1980).

52. C. W. Brown, J. E. King and M. A. Hicks, Met. Sci., 18 (1984) 374.

53. W. O. Soboyejo, Metall. Trans. 23A, (1992) 1773-1750.

54. J. M. Barsom and S. T. Rolfe, Fracture and Fatigue Control in Structures, 2nd Ed. Prentice-Hall, Englewood Cliffs, NJ (1987) 285.

55. B. A. Lerch and S. D. Antolovich, Metall. Trans. 21A (1990) 2169-2177.

# EQUILIBRIUM POINT DEFECTS IN NiAl AND SIMILAR B2 INTERMETALLICS STUDIED BY PAC

Gary S. Collins\*, Jiawen Fan† and Bin Bai

Department of Physics  
Washington State University  
Pullman, WA 99164-2814, USA

## Abstract

Point defects in NiAl and other structural intermetallics have been studied using perturbed angular correlation of gamma rays (PAC), by which signals are detected from antisite atoms and/or lattice vacancies in the first few atomic shells of probe atoms. For samples of quenched NiAl having 50 to 54 at.% Ni, site-fractions of Ni-vacancies (proportional to the vacancy concentration) were found to be independent of composition, indicating that the equilibrium, high-temperature defect is the Schottky vacancy pair and not the so-called triple defect. An effective formation enthalpy of 1.11(4) eV was measured for Ni-vacancies after equilibrating and quenching samples from temperatures in the range 700-1400 C. The formation enthalpy of the Schottky pair is two times larger. Quenched-in vacancies exhibit striking, novel behavior at low temperature: vacancies start to become mobile at about 350 C in 15-minute anneals, as observed by trapping at the probe atoms, but are only able to anneal out appreciably at temperatures of about 700 C. This behavior is attributed to different mobilities of Ni and Al vacancies. Recent data suggests that the Al-vacancy becomes thermally activated at about 350 C, converting into a Ni-vacancy and Ni-antisite atom when it comes near the probe atom. The Ni-vacancy becomes mobile only at about 700 C. Thermal activation of motion of quenched-in and confined vacancies at low temperature, observed here for the first time, offers an explanation for the well-known transition from brittle-to-ductile mechanical behavior in NiAl near 300 C. The explanation is supported by a study of vacancy interactions with Zr solutes that is briefly described. Results for other B2 intermetallics are also briefly described.

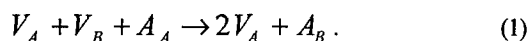
## Introduction

There is considerable interest in developing highly-ordered intermetallic compounds such as NiAl as high-temperature structural materials. Properties of these materials are affected by intrinsic point defects such as antisite atoms and lattice vacancies. Because vacancies mediate diffusion and diffusion-related processes such as creep, it is particularly important to understand their properties. The present paper describes experiments carried out toward that end.

NiAl and other compounds such as CoAl and PdIn that have the CsCl (B2) structure and are formed from group VIIIA and IIIB are well-ordered up to their melting temperatures. We shall use the notation AB to generically identify these compounds, with A= Ni, Co, Pd, and B= Al, In, et cetera. They exist as single phases for compositions typically extending to several atomic percent on either side of stoichiometry. Deviations from stoichiometry are accommodated by introduction of structural point defects. Density and lattice parameter measurements on annealed samples have shown (1) that compounds deficient in element A (A-poor) normally contain vacancies on the A-sublattice ( $V_A$ ) whereas A-rich compounds contain A atoms as antisite defects on the B-sublattice ( $A_B$ ). (Symbols identify the type of atom or defect and subscripts indicate the sublattice on which it sits.) For a review of this data, see Chang and Neumann (2). It should be noted that the concentrations of structural defects needed to accommodate deviations from stoichiometry can be very large: annealed NiAl having 49 or 51 at.% Ni will have mole fractions equal to 4 at.% for  $V_{Ni}$  or 2 at.% for  $Ni_{Al}$ , respectively. (Mole fractions are defined in this paper with respect to the total number of sites on a single sublattice.)

\* Corresponding author, email: [collins@wsu.edu](mailto:collins@wsu.edu);  
research group URL: <http://defects.physics.wsu.edu/>  
† Now with North American Scientific, North Hollywood, CA.

Equilibrium point defects become thermally activated at elevated temperature to minimize the free energy of the crystal. Considering single-phase systems like B2 NiAl, equilibrium defects can only be created as combinations of elementary defects that maintain strictly equal numbers of lattice sites on all sublattices. Possible defects include the Schottky defect and so-called triple defect. Excluding interstitial defects because of their high energy, the available elementary defects are vacancies and antisite atoms on the two sublattices. Of these,  $B_A$  (e.g.,  $Al_{Ni}$ ) will be excluded from consideration because it is unobserved as a structural defect in A-poor alloys and therefore must have high energy. From the three remaining elementary defects  $V_A$ ,  $V_B$  and  $A_B$  can be formed two defect combinations: the Schottky vacancy-pair,  $V_A + V_B$ , and the triple-defect originally proposed by Wasilewski (3),  $2V_A + A_B$ . The triple defect can be imagined to form from a Schottky defect by transfer of an  $A_A$  atom to a neighboring B-vacancy, thereby creating a second A-vacancy and A-antisite atom:

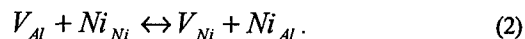


The Schottky and triple defects are homogeneous defects in the sense that they can be generated without changing the local atomic composition. The principal defect activated will be the one having the lower formation enthalpy. In the following we shall assume that electron-screening leads to small interaction energies between the elementary defects, as borne out by calculations (e.g., ref. 5). However, little is known experimentally on this point.

Other mechanisms for forming defects must also be considered. A possible mechanism is preferential evaporation of a constituent, modifying the composition. A second mechanism is formation of low-dimensional phases at surfaces, grain boundaries or dislocations. A simple example of the latter mechanism would be termination of a NiAl lattice with Ni-sites at surfaces and grain-boundaries. In effect, this would make for a greater number of sites on the Ni sublattice. As a consequence, the Ni composition within the grains would be reduced. In our experiments, described below, the typical grain size was about 150 microns (4), for which there is a ratio of  $10^{-5}$  surface to volume sites. Thus, even complete enrichment of the surface with Ni would modify the composition within the grains by a small, undetectable amount. Formation of enriched multilayers amounts to phase separation, and so is ruled out for these B2 systems by the phase diagrams. We therefore expect that presence of heterogeneous defects will only lead to small and unimportant shifts in the elemental composition within grains. For our grain size, enrichment of a Ni monolayer could cause formation of a mole fraction of  $10^{-5}$  Ni-vacancies. Vacancy defect concentrations in quenched NiAl are much greater, of the order of  $10^{-3}$ , so that mole fractions of heterogeneous elementary defects such as might be produced by surface enrichment are expected to be small in comparison to concentrations of homogeneous Schottky or triple defects.

Equilibrium concentrations of defects become established by diffusion. Atom movement in NiAl and similar compounds almost certainly occurs by vacancy diffusion. A recent calculation for stoichiometric NiAl indicates that the dominant diffusion mechanism involves Ni and Al vacancies making near-neighbor jumps on their own sublattices (that is, second-neighbor jumps on the underlying bcc lattice), (5) and we will assume this is true for slightly Ni-rich compositions (50-53.5

at.% Ni) considered below. As a consequence, in order to form either Schottky or triple-defects during heating, vacancies on both sublattices must diffuse in from the surface. As long as equal numbers of both vacancies diffuse in, the composition remains homogeneous. Once inside, an Al-vacancy may react with a host Ni atom to form, in effect, a triple-defect (cf. eq. 1):



Since there is no other obvious way for triple-defects to form, diffusion of  $V_{Al}$  appears to be essential even if the triple-defect were the dominant equilibrium defect. Interestingly, recent calculations of defect energies in NiAl (5,6) indicate that the triple-defect has a formation energy lower than the Schottky defect, but that Al-vacancies have a migration energy lower than Ni-vacancies. Thus, equilibrium could be established under the triple-defect model as follows:  $V_{Al}$  diffuse rapidly from the surface and convert into  $V_{Ni}$  and an immobile  $Ni_{Al}$  (eq. 2 above). Later, either the same  $V_{Ni}$  or other  $V_{Ni}$  migrating nearby may undergo the reverse reaction with the immobile  $Ni_{Al}$ , recreating the more mobile  $V_{Al}$ . Such serial conversion between mobile and immobile states is akin to the problem of hydrogen diffusion in a medium with shallow traps. Therefore,  $V_{Al}$  may contribute significantly to diffusion even when its instantaneous concentration is low. To summarize, diffusion of both types of vacancies is necessary under either model.

What is known about the equilibrium defect in NiAl? Considering NiAl, Wasilewski used qualitative arguments to show that the triple-defect might be the dominant equilibrium defect in compounds like NiAl.(3) However, from the extensive review of properties of NiAl by Miracle (7), identification of the equilibrium defect to date appears inconclusive. This is because experimental methods used have been indirect. Recent computations of defect structures and energies in NiAl (e.g. refs. 5,6,8) find that the Schottky defect has a higher formation enthalpy than the triple-defect.

In the present work, we apply a microscopic method, perturbed angular correlation of gamma rays (PAC), to study equilibrium defects in NiAl directly. With this method, we are able to observe signals due to elementary defects near probe atoms sitting on the Al-sublattice. These signals have been identified with  $V_{Ni}$  in the first atomic shell and  $Ni_{Al}$  or  $V_{Al}$  in shell 2, and with combinations of those defects. Following a description of the method, we describe four experiments on NiAl with goals and results as follows:

(1) Nature of the equilibrium defect. Five samples with compositions spanning the range 50.3-53.5 at.% Ni were quenched rapidly after equilibration at a fixed temperature of 1050 C. The site-fraction of probe atoms having a  $V_{Ni}$  neighbor (proportional to the Ni-vacancy concentration) was found to be independent of composition. This result is shown to be consistent with the Schottky-defect model and not the triple-defect model.

(2) Formation enthalpy of the equilibrium defect. Two samples having 50.7 at.% Ni were equilibrated and quenched from high temperatures. Site-fractions of  $V_{Ni}$  increase with quenching temperature in the range 700-1400 C, with an effective activation enthalpy equal to 1.11(4) eV. This effective formation enthalpy for  $V_{Ni}$  translates to an activation enthalpy for a Schottky pair equal to 2.22(8) eV.

(3) Low-temperature equilibrium regime for quenched-in defects. Annealing out of excess defects was studied in samples having 50.6 at.% Ni. Vacancy mobility was first observed at 350 C in 15 min. isochronal anneals by formation of increasing numbers of  $V_{Ni}$  defects next to the probe atoms. Additional studies showed, unexpectedly, that over the range of 350-650 C vacancies are unable to anneal out to any appreciable extent. Further measurements elucidated for the first time a novel low-temperature equilibrium regime in which a concentration of mobile vacancies is confined in the lattice. A possible explanation for this phenomenon is that one of the two vacancy species migrates at 350 C while the other migrates at 650 C. In the intervening temperature range, one of the two species is mobile with a constant concentration. The mobile vacancy species may therefore contribute in novel ways to diffusion processes at low temperature. Existence of this regime offers a possible explanation for the onset of ductile mechanical behavior at about 300 C.

(4) Identity of the vacancy species diffusing at 300 C. Annealing quenched samples at 350 C leads to an increase in the site-fraction of  $V_{Ni}$  complexes, and was initially therefore naturally attributed to migration and trapping of  $V_{Ni}$ . (9) However, recent measurements show that, when trapping starts, there is a significant increase in the site fraction of a new signal attributed to a complex of  $V_{Ni}$  and  $V_{Al}$  defects near the probe. This and other data can be explained by migration of  $V_{Al}$  to a position close to a probe atom (in shell 2, 3 or 5, belonging to the Al-sublattice) followed by conversion into a first-shell  $V_{Ni}$  defect and immobile  $Ni_{Al}$  antisite atom in shell 2, 3 or 5 (see eq. 2). Therefore, the more mobile vacancy is identified as  $V_{Al}$ .

## Methods

### Sample preparation.

NiAl samples of about 100 mg total mass were made by arc-melting ~5N pure foils of Ni and Al together with radioactive  $^{111}In$  under argon. Nominal compositions were taken to be the actual ones since mass losses during arc-melting were very small and lead only to uncertainties in the composition of about 0.1 at.%. After melting, samples were annealed for 1 hour under hydrogen at 1200 C in a tube furnace in order to coarsen the grains and improve sample homogeneity. Based on inhomogeneous broadening of PAC signals caused by distant defects in a series of alloys from 48-52 at.% Ni, (9) compositional uniformity across the samples is believed to have been better than 0.2 at.%.

Samples were quenched rapidly from temperatures up to 1400 C using a vertical drop-furnace (10) having a quenching rate estimated to be approximately  $10^4$  K/s.

### Perturbed angular correlation of gamma rays (PAC).

General approach. Defects are detected via the radiations emitted by radioactive probe atoms introduced for this purpose in the host. For the  $^{111}In/Cd$  probe used in this study, mole fractions of probes are typically about  $10^{-8}$ , excluding any appreciable disturbance of defect behavior by probes. A crystal defect produces an electric-field gradient (efg) in its vicinity

that falls off with distance  $r$  qualitatively as  $r^{-3}$ . The most significant and best-resolved efg's will therefore be produced by defects in neighborhoods of a few atomic shells around the PAC probes. A defect's efg interacts with the quadrupole moment of the nuclear PAC level, which has spin-5/2 and a half-life of 84 ns. This so-called hyperfine interaction can be considered to cause the probe's nuclear spin to precess over lifetime with a frequency characteristic of the defect type and its distance from the probe (atomic shell). The interaction is detected through the time and angular correlation of gamma radiations emitted when the PAC level is formed and decays. One measures a lifetime decay curve for the PAC level that is modulated by a perturbation function  $G_2(t)$ . The perturbation function contains all the information about the defects. Further information on methods may be found in ref. (11).

For a unique efg, the perturbation function of a spin-5/2 PAC level is given by

$$G_2(t) = s_0 + s_1 \cos \omega_1 t + s_2 \cos \omega_2 t + s_3 \cos \omega_3 t, \quad (3)$$

in which the three frequency harmonics are related via  $\omega_3 = \omega_2 + \omega_1$  and  $1 \leq \omega_2 / \omega_1 \leq 2$ , and the amplitudes  $s_0$ - $s_3$  sum to unity. The fundamental frequency  $\omega_1$  is proportional to the principal component of the efg tensor,  $V_{zz}$ , and the ratio  $\omega_2 / \omega_1$  is related to the asymmetry parameter of the efg tensor,  $\eta = |(V_{xx} - V_{yy}) / V_{zz}|$ . When there is a three-fold or higher axis of charge symmetry through the probe nucleus, the interaction is said to be axially symmetric ( $\eta = 0$ ),  $\omega_1 : \omega_2 : \omega_3$  are in the proportion 1:2:3, and the amplitudes  $s_0$ - $s_3$  are 1/5, 13/35, 10/35 and 5/35, respectively. In that case,  $\omega_1 = \frac{3\pi}{10} \frac{eQV_{zz}}{h}$ , in which  $Q$  is the quadrupole moment of the nucleus. For lower symmetry,  $0 < \eta < 1$ . Finally  $\omega_1 = 0$  if the point symmetry is cubic as in the perfect B2 crystal.

In a typical measurement there is a variety of local environments of probes due to the presence of structural and/or thermal defects. Each environment produces a characteristic value of  $\omega_1$  and  $\eta$ . In practice one observes a superposition of perturbation functions for all environments, each multiplied by an amplitude proportional (in a known way) to the fraction  $f$  of probes in that site. The hyperfine parameters  $\omega_1$  and  $\eta$  and site fractions  $f$  are obtained by fitting experimental spectra by computer to a sum of  $G_2(t)$  functions.

PAC spectrometer. We used a four-detector spectrometer of standard design with BaF<sub>2</sub> scintillators. A more detailed description of instrumentation is given in ref. (11).

### Defect identification

Identifying signals with underlying geometrical arrangements of atoms was mostly made through measurements on annealed samples having 48-52 at.% Ni. (12,9) The  $^{111}In$  probes are almost certainly located on the Al sublattice because In is isovalent with Al and has a large atomic size like Al. Since the  $Al_{Ni}$  antisite is an unobserved high-energy defect, an even larger  $In_{Ni}$  impurity is *a fortiori* less likely. In table I are given atom types and distances of atoms from shells near  $In_{Al}$  probes



in perfect, stoichiometric NiAl. Distances are in units of the near-neighbor distance  $r_{nn}$ . Also listed are inverse-cubed distances to indicate the relative strengths of efg's that might be expected from defects in different shells.

Table I. Atom shells near  $\text{In}_{\text{Al}}$  probes in perfect NiAl.

Shell	Atom	Number	$r/r_{nn}$	$(r_{nn}/r)^3$
1	Ni	8	1.0000	1.000
2	Al	6	1.1547	0.650
3	Al	12	1.6330	0.230
4	Ni	24	1.9149	0.142
5	Al	8	2.0000	0.125

The experimental efg of a defect may be taken to be proportional to the product of  $r^{-3}$  in the table and a (shell-dependent) effective charge. Table I shows that stronger efg's are likely to come preferentially from defects in the first and second shells. Indeed, we believe this is the case in our measurements. More distant defects produce weaker efg's that lead only to inhomogeneous broadening of signals due to nearby defects.

Local configurations anticipated for defects are shown by diagrams in Figure 1. Attention is restricted to defects in the two closest shells. Lines in the diagrams show the Ni-sublattice, with Ni sites at cube corners and Al sites at cube centers (Ni and Al atoms on their normal sites are not drawn.) Symbols indicate  $\text{In}_{\text{Al}}$  probes (large shaded circles),  $\text{V}_{\text{Ni}}$  in the first atomic shell (open squares), and  $\text{Ni}_{\text{Al}}$  (small shaded circles) and  $\text{V}_{\text{Al}}$  (stippled square) in the second atomic shell. Thick lines are drawn between probes and defects to make the geometries of the defect-probe complexes clearer.

Experimental hyperfine interactions measured at 295 K are listed in Table II together with identifications of sites in terms of local environments of the probes. A relative measure of interaction strength is indicated by the ratio of  $\omega_1$  to the monovacancy frequency. The  $\text{V}_{\text{Al}}$  configuration was not observed by itself, but the analogous  $\text{V}_{\text{In}}$  site that has been unambiguously identified in PdIn (13,14) has a very low frequency, so that a correspondingly low frequency is expected in NiAl. Diagrams from Fig. 1 are also listed.

Table II. Quadrupole interactions and environments of probes

$\omega_1$ (Mrad/s)	$\eta$	$\omega_1 / \omega_1^{\text{IV}}$	Local Environment <sup>a</sup>	Figure
~0	-	~0	defect-free $\text{In}_{\text{Al}}$	1.a
128(1)	0	(1)	$\text{V}_{\text{Ni}}$	1.b
187(1)	0.64(1)	1.46(1)	2 $\text{V}_{\text{Ni}}$ (a)	1.c
222(2)	0.89(1)	1.73(1)	2 $\text{V}_{\text{Ni}}$ (b)	1.d
19(2)	0.1(1)	0.15(2)	$\text{Ni}_{\text{Al}}$	1.e
unobserved	-	(0.15) <sup>b</sup>	$\text{V}_{\text{Al}}$	1.f
141(2)	0.20(5)	1.10(2)	$\text{V}_{\text{Ni}} + \text{Ni}_{\text{Al}}$	1.g&h
158(2)	0.20(5)	1.23(2)	$\text{V}_{\text{Ni}} + \text{V}_{\text{Al}}$	1.j&k

a.  $\text{V}_{\text{Ni}}$  are in shell 1 and  $\text{Ni}_{\text{Al}}$  and  $\text{V}_{\text{Al}}$  are in shell 2.

b. Ratio measured in PdIn, refs. (13,14).

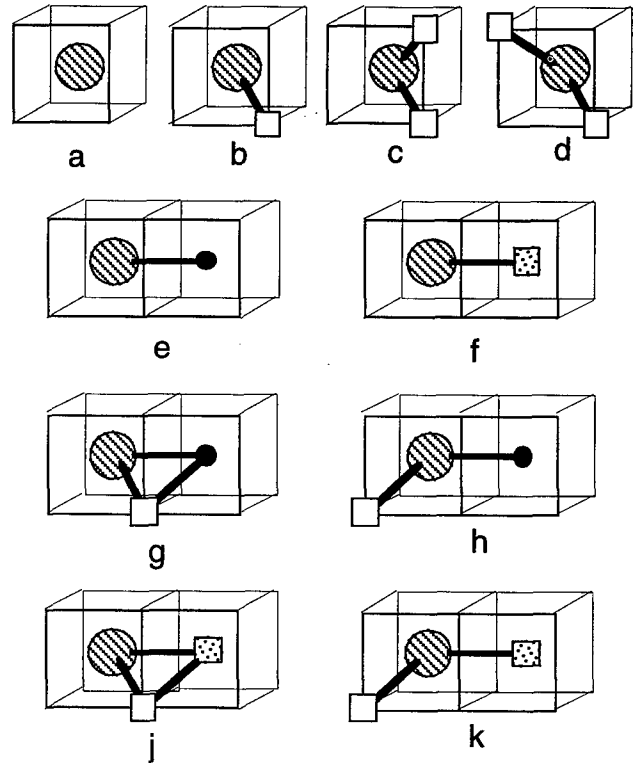


Figure 1: Possible configurations of In probe atoms and nearby point defects. Symbols: In-probe (large shaded circle); Ni-vacancy (open square); Al-vacancy (stippled square); Ni-antisite atom (small black circle). The cubic grid represents the Ni sublattice. Host atoms on normal sites are not drawn.

Most configurations were first observed in measurements made on a series of five NiAl alloys with compositions in the range 48-52 at.% Ni. PAC spectra measured after annealing at 1200 C and cooling in furnace to room temperature over about 12 hours are shown in Figure 2.(9,11,12)

Knowledge of structural defects in Ni-poor and Ni-rich samples,  $\text{V}_{\text{Ni}}$  and  $\text{Ni}_{\text{Al}}$  respectively,(1) helps identify signals with sites. The arguments for identification are given briefly here. More information can be found in refs. (9,11,12).

**Defect-free and  $\text{V}_{\text{Ni}}$  sites.** The 50.1% sample exhibits a zero-frequency signal (raised baseline) for about 50% of the probe atoms that is consistent with cubic point symmetry and is attributed to defect-free, stoichiometric NiAl (Fig. 1.a). The perturbation with period ~50 ns has axial symmetry and is attributed to one  $\text{V}_{\text{Ni}}$  in the first atomic shell (Fig. 1.b). The interaction frequency, 128 Mrad/s, is comparable to frequencies observed for near-neighbor vacancies trapped to  $^{111}\text{In}$  probes in pure metals.(15) (The large site fraction of  $\text{V}_{\text{Ni}}$  is not obviously expected for this composition, it is attributed to incomplete annealing out of vacancies during furnace-cooling and/or to the presence of structural vacancies in parts of the sample caused by chemical inhomogeneity that made portions of the sample slightly Ni-poor.)

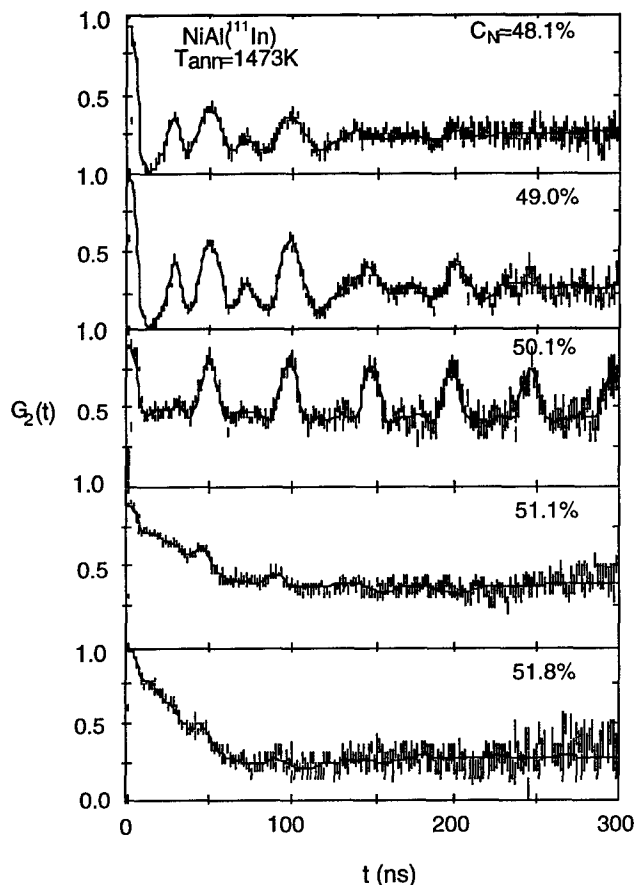


Figure 2: PAC spectra of annealed NiAl (48.1-51.8 at.% Ni). From ref. 11.

**Double  $V_{Ni}$  sites.** Ni-poor spectra (48.1 and 49.0%) exhibit a large site fractions of the 128 Mrad/s signal and, as well, the higher frequency 187 and 222 Mrad/s signals. The expected mole fractions of structural  $V_{Ni}$  are 7.6% and 4.0%, respectively. The high frequency signals are attributed to two distinct configurations of two  $V_{Ni}$  in the first shell (Figs. 1.c and 1.d). The  $V_{Ni}$  defects bind with  $In_{Al}$  probes. Evidence for binding comes from the fact that site fractions of the  $V_{Ni}$  in both Ni-poor spectra are greater than what would be expected if the structural vacancies were at random. At a value of 45%, the site-fraction of the 128 Mrad/s signal exceeds the maximum possible probability for having a single defect neighbor assuming that defects are located at random, confirming nonrandomness.

**$Ni_{Al}$  site.** Ni-rich spectra (51.1 and 51.8%) exhibit mostly low-frequency interactions that were originally attributed to distant defects (11,12). However, among these is a unique 19 Mrad/s signal that was attributed more recently (9) to one  $Ni_{Al}$  in the second shell (Fig. 1.e). The site fraction of the unique 19 Mrad/s signal is always much greater than expected on the basis of a random distribution of antisite atoms. This will be discussed further below.

**Mixed  $V_{Ni}$  and  $Ni_{Al}$  sites.** Ni-rich spectra in Fig. 2 have small site fractions of a signal with 141 Mrad/s and small efg

asymmetry parameter. Since the only high-frequency structural defect is the first-shell  $V_{Ni}$ , it is assumed to involve a quenched-in  $V_{Ni}$  and a second shell  $Ni_{Al}$  structural defect in configurations Fig. 1.g or 1.h. Both configurations lead to the same efg calculated in the point-charge approximation, and are therefore equivalent in our measurements. The point-charge calculations show that one can explain the 128, 19 and 141 Mrad/s signals reasonably well using an effective charge of the  $Ni_{Al}$  defect equal to -0.4 of the charge of  $V_{Ni}$ . (9)

Signal identifications from the past work described above are believed to be fairly robust. The remaining signal in Table II, with 158 Mrad/s, was observed for the first time only recently. Its tentative identification as a first-shell  $V_{Ni}$  and second-shell  $V_{Al}$  complex is discussed separately below under experiment 4. Among the simple configurations shown in Fig. 1, only the single  $V_{Al}$  complex has not been observed.

### Thermodynamics of Defects

Thermodynamic properties of the point defects can be related to the observed site fraction of  $V_{Ni}$  using the law of mass action. Further details will be found in ref. (9). We write for the composition  $Ni_{1+2x}Al_{1-2x}$ , in which x marks the deviation from stoichiometry. Defining mole fractions of the defects with respect to the number of sites on one sublattice, and assuming  $[Al_{Ni}]=0$ , it is easy to show that mole fractions of defects obey the following equation of constraint:

$$4x + (1 - 2x)[V_{Ni}] - (1 + 2x)[V_{Al}] = 2[Ni_{Al}]. \quad (4)$$

The reaction for formation of a Schottky defect and its equilibrium constant are

$$0 \rightarrow V_{Ni} + V_{Al}, \quad K_S = [V_{Ni}][V_{Al}] = \exp(-G_S / k_B T) \quad (5)$$

and similarly for the triple-defect,

$$0 \rightarrow 2V_{Ni} + Ni_{Al}, \quad K_T = [V_{Ni}]^2[Ni_{Al}] = \exp(-G_T / k_B T), \quad (6)$$

in which 0 specifies the defect-free lattice. Substituting  $[V_{Al}]$  from eq. 5 and  $[Ni_{Al}]$  from eq. 6 into eq. 4 leads to a general, cubic equation in  $[V_{Ni}]$ .

Measurements were made on slightly Ni-rich samples. Under the Schottky defect model, only structural  $Ni_{Al}$  are present, so that  $[Ni_{Al}]=2x$ , and one obtains for small positive x:

$$[V_{Ni}] = [V_{Al}] = \exp(S_S / 2k_B) \exp(-E_S / 2k_B T). \quad (7)$$

Thus vacancy mole-fractions on the two sublattices are equal and, moreover, independent of composition. Under the triple-defect model, on the other hand,  $[V_{Ni}]$  depends significantly on x for small x. Therefore, measurement of the x-dependence of  $[V_{Ni}]$  can be used to distinguish between the two defect models, as we do in experiment 1 below.

Ni-vacancies tend to bind with In probes, as already demonstrated by enhanced site fractions in Fig. 2. This can be modeled by a reaction for forming a vacancy-probe complex:

$$V_{Ni} + In \rightarrow InV_{Ni}, \quad K_B = \exp(-G_B / k_B T) \quad (8)$$

where  $G_B$  is the free energy of binding of the first vacancy. Similar reactions can be written down for binding of additional vacancies (with different binding enthalpies). Defining the site fractions for probes that have  $n$  near-neighbor vacancies as  $f_n$ , it can be shown (9) that the monovacancy site-fraction has a remarkably simple relation to thermodynamic quantities after it has been normalized by the defect-free fraction,  $f_0 = 1 - f_1 - f_2 - \dots$ :

$$\frac{f_1}{1 - f_1 - f_2} = zK_B[V_{Ni}], \quad (9)$$

in which  $z$  is the coordination number (8 here). Nontrivially, Equation 9 is independent of the defect model or of binding of additional vacancies to the probe atom;  $f_1/f_0$  is simply proportional to the product of the vacancy concentration and the equilibrium constant for binding of the first vacancy.

### Experiments and results

Experiments reported below were made on samples with 50.3-53.5 at.% Ni. Thus, the only expected structural defects are  $Ni_{Al}$  antisite atoms.

#### 1. Identity of the equilibrium defect in NiAl

Five samples of NiAl were each equilibrated at 1050 C and then rapidly quenched to room temperature. (9) Special care was taken to ensure that all samples received the same thermal treatment. In Figure 3 is shown the normalized monovacancy site fractions versus  $x$ , the deviation from stoichiometry. In the next paragraph it is explained that  $K_B$  in equation 9 depends only on the quenching rate. Since quenching rates were the same for all samples, then, from equation 9, site fractions should be proportional to the vacancy concentration. The figure shows that quenched-in site fractions are independent of composition. Drawn over the figure are curves showing expected trends for the Schottky and triple-defect models. (The triple-defect curve was calculated assuming a vacancy mole fraction of about  $10^{-3}$ .) As can be seen, the lack of dependence of the quenched-in site fraction on composition is in excellent agreement with the Schottky model and, at least for our samples, appears to rule out the triple-defect model. Additional measurements in ref. 9 (not shown) obtained after quenching from in the range 800-1000 C exhibit the same lack of dependence on composition. Alternative explanations for this independence include possibilities that (1) defects might form by an unknown, heterogeneous mechanism in our samples, or (2) there might exist a significant dependence of the defect formation or vacancy migration enthalpies on  $x$  that compensates by accident for the dependence based on the defect model.

#### 2. Formation enthalpy of the equilibrium defect

PAC measurements were made on 50.6 at.% Ni samples after rapid quenching from temperatures in the range 200-1400 C. (9) Some spectra from in the high-temperature range 700-1400 C are shown in Figure 4. Samples were equilibrated for 1 hour and were determined by comparison with spectra measured after different equilibration times to be in equilibrium prior to quenching. The summed site-fraction of first-shell single-

vacancy defects (128 and 141 Mrad/s) increases rapidly with temperature. The normalized monovacancy site fraction is plotted versus inverse temperature in Figure 5. As can be seen, the site fraction has a well-defined Arrhenius behavior above about 750 C with activation enthalpy 1.11(4) eV. To interpret the activation enthalpy, it was assumed that the quenching rate was rapid enough that no defects could anneal out during the quench. However, defects will certainly be able to jump many times on an atomic scale during the quench, maintaining a local defect equilibrium, until all motion ceases at a much lower temperature. If one assumes Newton's law of cooling, it can be shown that  $K_B$  depends only on the quenching rate and is independent of the quench temperature, as long as the quenching temperature is greater than an effective temperature below which all motion is frozen. Thus, according to eq. 9, the activation enthalpy should equal the effective formation enthalpy of the Ni-vacancy, independent of binding of the vacancy with the probe. For Schottky equilibrium defects, it equals half the formation enthalpy of the vacancy-pair.

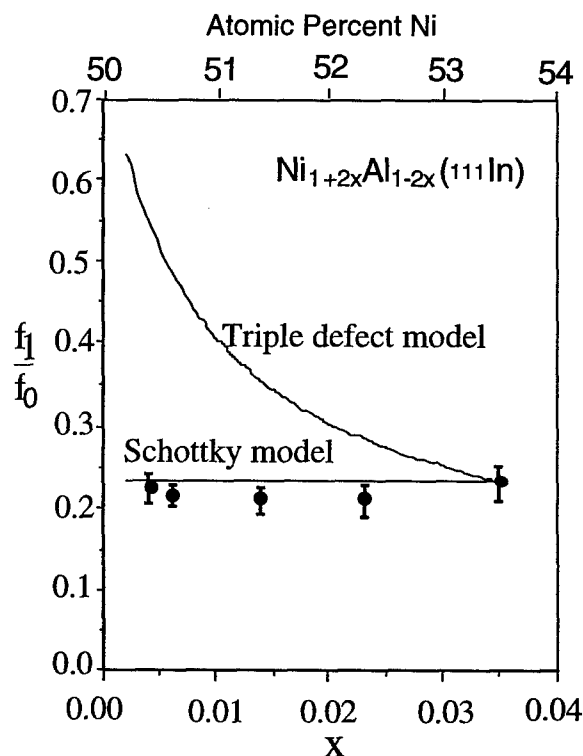


Figure 3: Site fractions of In probes having one Ni-vacancy neighbor as a function of composition measured after quenching from 1050 C. Site fractions, normalized with the defect-free site fraction, are proportional to the vacancy concentration.

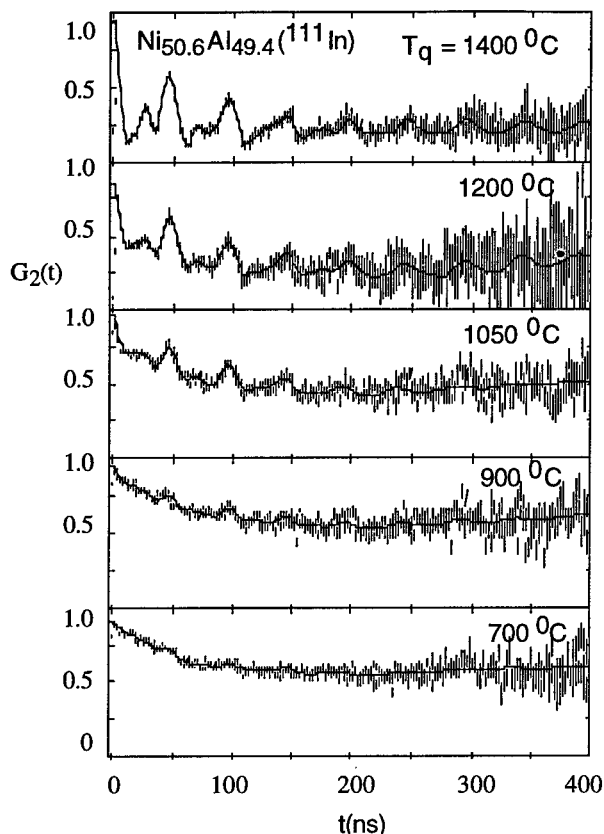


Figure 4: PAC spectra of NiAl after quenching from the indicated temperatures.

### 3. Low-temperature vacancy mobility

Initial studies of the first stages of annealing-out of quenched-in vacancies led to perplexing results. After quenching a 50.5 at.% Ni sample from 950 C, formation of  $V_{Ni}$ -probe complexes was observed to take place at 350 C in 15 min isochronal anneals. This is exhibited in Figure 6, which shows annealing curves for site fractions of the 128 and 141 Mrad/s single-vacancy sites as well as for the sum of both sites. The summed vacancy site-fraction doubles from about 12% to 25% near 350 C, which is attributed to thermal activation and migration of vacancies at that temperature. (9) However, there is no clear-cut evidence of detrapping during annealing at higher temperature that is customarily observed, for example in metals. (15) To understand this odd behavior, a new experiment was undertaken in which samples were prequenched from 950 C to introduce vacancies. Then the samples were equilibrated for 15-minute periods at temperatures at or above 300 C and quenched to room temperature, after which PAC spectra were measured and monovacancy site-fractions determined. It was found that, in the range 350 to 700 C, site-fractions of  $V_{Ni}$  could reach equilibrium in 15 minutes and could be altered reversibly by subsequent quenches from higher or lower temperatures. This means that the vacancy concentration remained constant over the entire 350-700 C range, although vacancies were already mobile at 350 C. Site fractions were reversibly found to

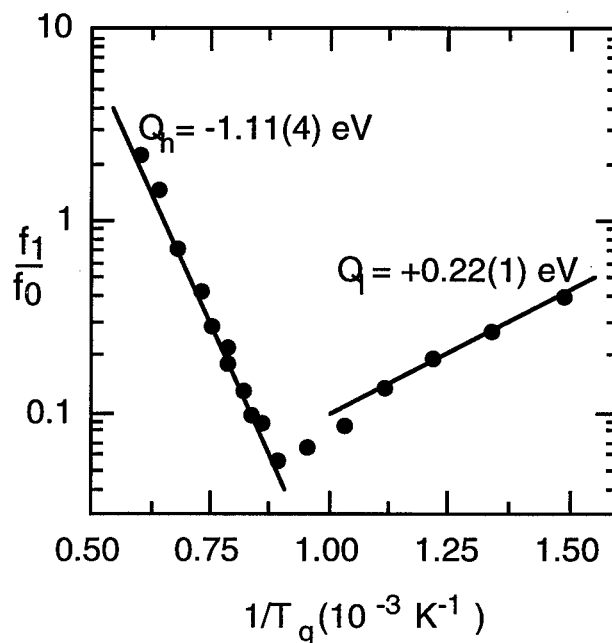


Figure 5: Site fractions of near-neighbor Ni-vacancies versus the inverse quenching temperature. Fractions are normalized by the defect-free fraction. Two equilibrium regimes are observed.

be lower for higher quenching temperature  $T_q$  and higher for lower  $T_q$ , as expected due to vacancy-probe binding (cf. eq. 9). Finally, irreversible annealing-out of vacancies commenced above about 700 C. In Fig. 5, the low-temperature range shows reversible data obtained in this way. The data were fitted and found to have an activation enthalpy of 0.22(1) eV. According to eqs. 8 and 9, if  $[V_{Ni}]$  is constant, the activation enthalpy is the binding enthalpy of the first vacancy.

Such a low-temperature equilibrium regime, in which defects move without annealing out, has not to our knowledge been observed or considered before. It has, however, a natural explanation in terms of different mobilities of the vacancies on the two sublattices: one vacancy species starts to move over atomic distances at 350 C, but is unable to anneal out until the other species becomes mobile at 700 C.

### 4. Nature of the vacancy species mobile at low-temperature

Which vacancy species becomes mobile at 350 C? The increase in site fraction of  $V_{Ni}$  complexes during annealing of quenched NiAl suggests at first sight that  $V_{Ni}$  becomes mobile and traps at In impurities at 350 C while  $V_{Al}$  becomes mobile at 700 C. However, recent measurements lead us instead to the opposite conclusion: that  $V_{Al}$  is mobile at lower temperature.

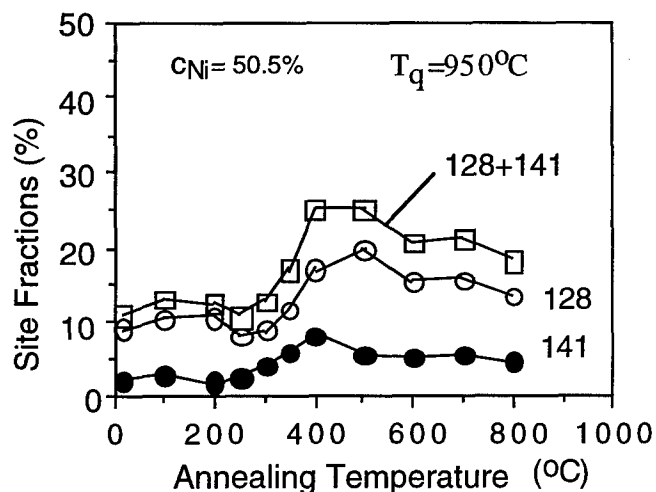


Figure 6. Site fractions for two complexes involving a single Ni-vacancy, and their sum, measured after isochronal annealing of a NiAl sample with quenched-in vacancies. Migration and trapping of vacancies is observed near 350 C.

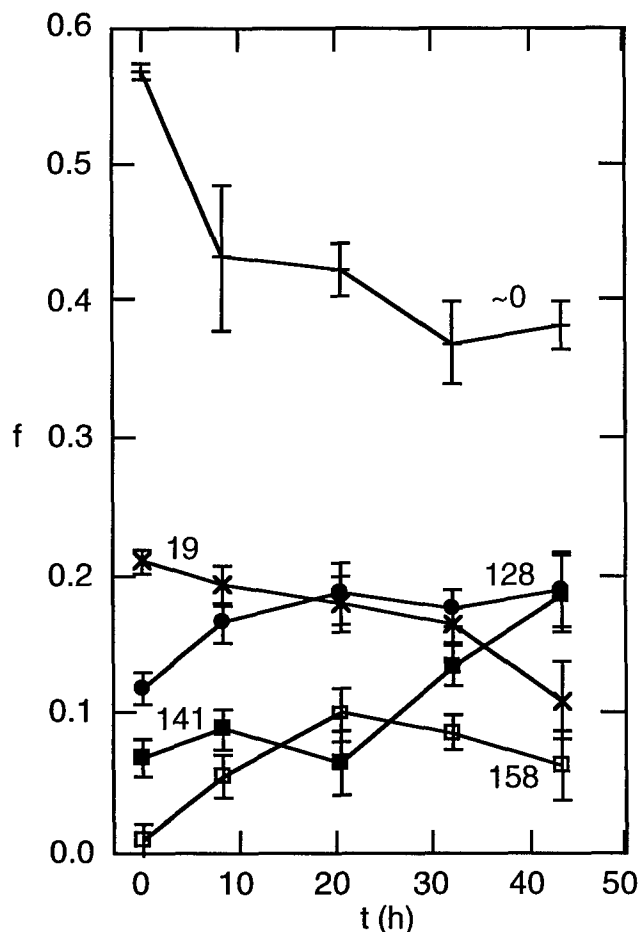


Figure 7: Site fractions of In probes during isothermal annealing at 200 C. Defect identifications are given in Table II.

Recently, we began PAC measurements in equilibrium at elevated temperature instead of on quenched samples. These include measurements undertaken to shed more light on the low-temperature regime as follows. A sample was first prequenched from 950 C. Afterwards, the evolution of site fractions was monitored following annealing for different times at 200 C (see Fig. 7). The equilibration time can be seen from the figure to be of the order of 1 day as opposed to about 15 min. at 350 C, so that atomic motion is indeed very slow even on an atomic length scale. Our findings are as follows:

(1) A new 158 Mrad/s signal is observed during annealing at 200 C that has not previously been detected in very many studies, either after annealing at higher temperature or quenching from high temperature. We conclude that it is not some combination of  $V_{Ni}$  and/or  $Ni_{Al}$  defects, and that it therefore must involve  $V_{Al}$ , the other mobile defect. Most likely, the defect is not an isolated nearby  $V_{Al}$  because the observed 158 Mrad/s frequency appears to be too high. In the analog system PdIn we previously detected both  $V_{In}$  and  $V_{Pd}$  defects and the frequency ratio observed there is only 0.15, much less than 1.23 observed here (cf. Table II). The high frequency therefore suggests that  $V_{Ni}$  must be involved. We attribute the signal to complexes involving one  $V_{Ni}$  and  $V_{Al}$  defect each, as pictured in Fig. 1.j and 1.k. Both configurations have equal efg's in the point-charge approximation. Point charge calculations indicate that the observed frequency can be explained for the two configurations using an effective charge of the  $V_{Al}$  equal either to -0.6 or +0.7, which magnitude seems quite reasonable. Therefore, the new signal is attributed to  $V_{Al}$  migration and trapping at 350 C.

(2) Site-fractions of both single- $V_{Ni}$  complexes (128 and 141 Mrad/s) are observed to increase during annealing in Fig. 7. While in principle they could form by migration and trapping of  $V_{Ni}$ , we found just above that  $V_{Al}$  migrates at the lower temperature instead of  $V_{Ni}$  and therefore we seek an explanation consistent with a mobile  $V_{Al}$  defect. The results can be reconciled by the hypothesis that  $V_{Al}$  defects diffuse on the Al lattice until they reach positions in either of Al-shells 2,3 or 5 about the probes. From there, each may react according to eq. 2 with a Ni atom in the first shell, leaving one  $V_{Ni}$  in shell 1 and one  $Ni_{Al}$  in shell 2,3 or 5. The driving force for the reaction is binding of  $V_{Ni}$  to the probes. The reaction and final state are pictured in Figure 8 for  $V_{Al}$  reacting after diffusion into shell 3. Depending on the shell from which  $V_{Al}$  reacts, the antisite atom may be left in shell 2,3 or 5. If left in shell 2, the final state would be as pictured in Fig. 1.g, with known frequency 141 Mrad/s. If left in shells 3 or 5, then the antisite atom is probably far enough away that the efg's hardly differs from the efg for a lone  $V_{Ni}$  (Fig. 1.b) so that the signals are unresolved from the lone  $V_{Ni}$  signal at 128 Mrad/s. Therefore, the increases in site fraction of both the 128 and 141 Mrad/s signals in Figs. 6 and 7 can be understood to be caused by migration of  $V_{Al}$  with reaction at the probe site.

(3) Conversion of  $V_{Al}$  into first-shell  $V_{Ni}$  described just above indicates that the 158 Mrad/s complex attributed to the double  $V_{Ni} - V_{Al}$  complex may be a less stable state that is only observable during long-time annealing at the very low temperature of 200 C. We suppose that it is unstable at higher temperature, reacting quickly to form one of the double- $V_{Ni}$

complexes (Fig. 1.c or 1.d). Small increases in double- $V_{Ni}$  site fractions were detected that are not shown in Figs. 6 or 7.

### Discussion

1. What is the equilibrium defect in NiAl? Recent theoretical calculations of defect energetics in NiAl, e.g. by local density-functional (16) or embedded atom (5,6) methods find that the triple-defect has lower formation enthalpy than the Schottky vacancy-pair, in contradiction of our findings (Fig. 3 and discussion). Perhaps the best other data for comparison with our measurements are from a high-temperature dilatometric study by Fukuchi and Watanabe (17) who found for samples having 50.9 and 54.5 at.% Ni that, respectively, effective vacancy formation enthalpies were 1.08(6) and 0.96(3) eV, close to our value 1.11(4) eV for 50.6 at.% Ni. They found no increase in the vacancy concentration as the Ni composition decreased toward 50 at.% (indeed a slight decrease was observed), in agreement with our observations in Fig. 3 and in disagreement with the triple-defect model (such as shown in Fig. 2 of ref. 16.) While our identification of a new signal for Al-vacancies near probe atoms supports the Schottky defect model, the attribution is not as direct as we would like. On the experimental side we cannot rule out the possibility of some unknown heterogeneous defect formation mechanism. However, our samples are not atypical of metallurgical samples with regard to grain size, so that if such a mechanism is active here, it should be active in general. On the theoretical side, if, as calculated in ref. 16, the Al-vacancy mole-fraction were never greater than about  $10^{-20}$ , it is difficult to see how a sample could develop an equilibrium concentration of triple-defects in a short time given the presumed second-neighbor diffusion mechanism. To sum up our observations, the Schottky vacancy-pair appears to be the high-temperature equilibrium defect in NiAl.

2. Higher mobility of the aluminum vacancy in NiAl. Our conclusion that the Al-vacancy is more mobile than the Ni-vacancy in NiAl is supported by, and supports, recent embedded-atom-method calculations of energetics of vacancies in NiAl by Mishin and Farkas (5,6) They find that the migration energy of the Al-vacancy should be 0.37 eV lower.

3. Antisite enrichment and diffusion mechanisms. The experiments provide microscopic evidence for migration of both Ni- and Al-vacancies in NiAl and defect interactions with impurity In probes. The reaction  $V_{Al} \rightarrow V_{Ni} + Ni_{Al}$  followed by diffusion of the newly-created  $V_{Ni}$  away on the Ni sublattice offers a mechanism for enriching local neighborhoods of probes with  $Ni_{Al}$  antisite atoms. The fact that observed antisite signals in slightly Ni-rich NiAl have nearly always been much greater than expected for a random distribution of structural defects support this enrichment mechanism. Enrichment might occur because there is binding between antisites and probes or due to an asymmetry between rates of arrival and departure of  $V_{Ni}$  and  $V_{Al}$  defects.

4. The brittle-to-ductile transition in NiAl. Many intermetallics exhibit a transition from brittle to ductile mechanical behavior at low temperature. In NiAl, this occurs at temperatures of the order of 300 C (see, e.g., 7,18,19). It has been variously attributed to thermal-activation of dislocation

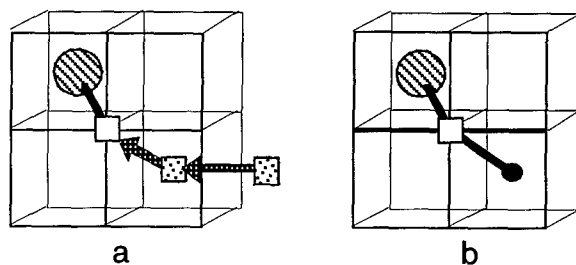


Figure 8: Mechanism by which diffusion of an Al-vacancy can increase the number of Ni-vacancies in the first shell of In probe atoms. (a) Al-vacancy migrates into shell 3 of the In probe and then reacts with a Ni atom (open circle) in shell 1. Vacancy jumps are shown by the arrows. (b) Final defect configuration, with a Ni-vacancy in shell 1 and Ni-antisite atom in shell 3.

motion on new slip systems (18) or to processes mediated by point-defect diffusion (19). Our observation that one of two vacancy species becomes mobile at about 350 C and our identification of the species helps elucidate the nature of the transition. We have demonstrated the presence of a mobile and confined vacancy species,  $V_{Al}$ , that can, moreover, transform into the other species,  $V_{Ni}$ , at the modest expense of creating an antisite  $Ni_{Al}$  defect. As a consequence, the transition to ductile behavior can be explained by the presence of quenched-in (and hard to remove) lattice vacancies that become thermally activated above the transition temperature but which are unable to easily anneal out until the other vacancy species becomes thermally activated. "Free" and mobile vacancies should make possible a broad range of unexpected diffusion processes such as point-defect assisted enhancement of dislocation motion and climb. Brittle-to-ductile transitions in other intermetallics may likewise originate in the different mobilities of point defects.

5. Zirconium solute interactions with vacancies in NiAl. Small amounts of solutes in NiAl cause large changes in mechanical properties. For example, the brittle-to-ductile transition is raised from 300 to 600 C by introducing 0.20 at.% of Zr. (20) Recently we made measurements to determine whether vacancies interact with Zr solutes. (21) In brief, three samples of  $Ni_{52}Al_{48}$  having 0, 0.05 and 0.20 at.% Zr were given identical thermal treatments in order to introduce equal, small amounts of excess vacancies, estimated to be about 0.05 at.%. The site fraction of vacancies detected at the  $^{111}In$  probes (at a mole fraction of only about  $10^{-8}$ ) was observed to decrease by a factor of three with increasing Zr content. A thermodynamic analysis showed that the trends can be explained by a vacancy-Zr binding enthalpy close to 0.25 eV. In effect, Zr solutes appear to trap and immobilize "free" excess vacancies and make them unavailable to trap at In PAC probes. In the context of our explanation for the brittle-to-ductile transition given just above, presence of Zr solutes (or other solutes that bind with vacancies) depletes free vacancies, thereby making them unavailable to assist in the novel diffusional processes described above, and thus raising the transition temperature.

6. Other B2 intermetallics. PAC measurements have been carried out in this laboratory also on CoAl, FeAl, CoGa and PdIn, with selected results as follows. Annealed stoichiometric samples of CoAl and PdIn exhibit little

inhomogeneous broadening and are therefore very well-ordered in the same way as NiAl. FeAl and CoGa, by contrast, exhibit many signals indicating the presence of intrinsic and/or quenched disorder. Signals analogous to many of those in NiAl were identified in CoAl and PdIn. (22)

CoAl. (ref. 9) Defect behavior was found to be qualitatively similar to NiAl. A high-temperature equilibrium regime was found to extend from 1050 to above 1400 C in which an effective formation enthalpy of 1.55(6) eV for Co-vacancies was obtained from a fit of Co-vacancy site-fractions as in Fig. 5. A low-temperature regime was detected between 550 and 800 C with an activation enthalpy of 0.19(1) eV attributed to vacancy-probe binding.

PdIn. (refs. 14,24,25) The In probe is not an impurity here, so defect concentrations can be determined in a direct way from site-fractions. Supposing that defects are located more-or-less at random, the site fraction of probes having one near-neighbor Pd-vacancy defect, for example, is given by the binomial probability  $f_1 = 8[V_{Pd}](1 - [V_{Pd}])^2$ . Our measurements follow up on an earlier study by Müller and Hahn. (23) Signals for both  $V_{Pd}$  and  $V_{In}$  vacancies were detected in quenched PdIn, with thermally activated vacancies detected between 550 and 1250 C. (24) Roughly equal site fractions for the two vacancies were detected, from which it was concluded that the Schottky vacancy-pair is the dominant equilibrium defect. Between 550 and 1000 C, the effective activation enthalpy for formation of Pd-vacancies was determined to be 0.65(9) eV. Above 1000 C, defect concentrations were observed to saturate and not increase further, with  $[V_{Pd}] = 1.5$  at.%. A study was also made of defect concentrations in mechanically-milled PdIn. (25) It was found that Pd-vacancy concentrations increase rapidly during the first stages of milling and saturate at a mole fraction of 3.5 at.% after 10 minutes of milling.

### Summary

We applied a hyperfine-interaction method with atomic sensitivity, perturbed angular correlation of gamma rays, to study point defects in annealed and quenched NiAl. Because the method differentiates clearly among defects, it can lead to a more model-independent understanding of defect behavior.

Point defects were identified through measurements on annealed, off-stoichiometric samples. Effective formation enthalpies for transition-metal vacancies were determined through analysis of site-fractions of probe atoms in vacancy complexes obtained from quenched samples. The composition dependence of quenched-in vacancies in Ni-rich samples was found to be consistent with the Schottky defect model or, which cannot be excluded, some unidentified heterogeneous formation process.

An explanation was provided for the brittle-to-ductile transition in NiAl (other similar highly-ordered B2 intermetallics) in terms of mobility of quenched-in vacancies: Vacancies are readily quenched into NiAl at levels of the order of 0.1 at.%. Ductility commences at a temperature where one vacancy species, but not the other, can begin to move. This explanation is supported by the finding, briefly described, that Zr solutes trap excess vacancies. Unfortunately, this

explanation does not lead to an obvious solution of the problem of low-temperature brittleness in NiAl. Brittleness can only be made worse by introducing solutes that trap excess vacancies, such as Zr. Solutes that do not trap vacancies should have little effect. PAC experiments are now underway at high temperature to test the assumptions used and conclusions reached here using quenched samples.

### Acknowledgments

This work was supported in part by the National Science Foundation under grants DMR 90-14163, 93-13702 and 96-12306 (Metals Program).

### References

1. E.g., for NiAl, see A.J. Bradley and A. Taylor, *Proc. Roy. Soc. (London)* A159 (1937) 56.
2. Y. Austin Chang and Joachim P. Neumann, *Prog. Solid St. Chem.* 14 (1983) 221-301.
3. R.J. Wasilewski, *J. Phys. Chem. Solids* 29 (1968) 39-49.
4. Jiawen Fan, PhD dissertation, Washington State University, 1992 (unpublished).
5. Yuri Mishin and Diana Farkas, *Phil. Mag.* A75 (1997) 187-199
6. Yuri Mishin and Diana Farkas, *Phil. Mag.* A75 (1997) 169-185
7. D. B. Miracle, *Acta metall. mater.* 41 (1993) 649-684.
8. C.L. Fu, Y.-Y. Ye, M.H. Yoo and K.M. Ho, *Phys. Rev.* B48 (1993) 6712-6715.
9. Jiawen Fan, PhD dissertation, Washington State University, 1992 (unpublished).
10. B. Lengeler, *Phil. Mag.* 34 (1976) 259.
11. G.S. Collins, S.L. Shropshire and J. Fan, *Hyperfine Interactions* 62 (1990) 1.
12. Jiawen Fan and Gary S. Collins, *Hyperfine Interactions* 60 (1990) 655.
13. Gary S. Collins and Praveen Sinha, *Mat. Res. Soc. Symp. Proc.* 364 (1995) 59.
14. Praveen Sinha, PhD dissertation, Washington State University 1995 (unpublished).
15. F. Pleiter and C. Hohenemser, *Phys. Rev.* B25 (1982) 106.
16. C.L. Fu, Y.-Y. Ye, M.H. Yoo and K.M. Ho, *Phys. Rev.* B48 (1993) 6712.
17. M. Fukuchi and K. Watanabe, *J. Japan Inst. Metals* 43 (1979) 1091 (in Japanese).
18. R.D. Field, D.F. Lahrman and R. Darolia, *Acta metall. mater.* 39 (1991) 2951.
19. R.W. Margevicius and J.D. Cotton, *Acta metall. mater.* 43 (1995) 645.
20. S. V. Raj et al., *Scripta Metallurgica* 23 (1989) 2049.
21. Bin Bai and Gary S. Collins (unpublished).
22. G.S. Collins, P. Sinha and M. Wei, *Hyperfine Interactions* C1 (1996) 580.
23. H.-G. Müller and H. Hahn, *Philos. Mag.* A50 (1984) 71.
24. G.S. Collins and P. Sinha, *Mat. Res. Soc. Symp. Proc.* 364 (1995) 59.
25. G.S. Collins and P. Sinha, *Materials Science Forum* 225-227 (1996) 275.

## CHARACTERIZATION OF SEGREGATION IN NICKEL AND TITANIUM ALUMINIDES

M.K. Miller, D. J. Larson and K.F. Russell

*Metals and Ceramics Division,  
Oak Ridge National Laboratory,  
Oak Ridge, TN 37831-6376, USA*

### Abstract

Atom probe field ion microscopy has been used to characterize the distributions of microalloying additions in the microstructure of a variety of nickel and titanium aluminides. In  $\text{Ni}_3\text{Al}$ , boron additions were found to segregate to dislocations, low angle boundaries, stacking faults, antiphase boundaries, and grain boundaries. The boron and aluminum levels at grain boundaries were found to vary both from boundary to boundary and also along an individual boundary segment. In some cases, a boron-enriched film up to  $\sim 3$  nm thick was observed. In aluminum-enriched  $\text{Ni}_3\text{Al}$ , ultrafine clusters containing up to approximately 10 boron atoms were detected in the matrix.

In contrast, the majority of the boron additions in  $\text{NiAl}$  was determined to be in the form of ultrafine  $\text{MB}_2$ -type precipitates. These precipitates offset the benefits of the boron segregation to the high angle grain boundaries. In molybdenum-doped  $\text{NiAl}$ , atom probe analyses indicated extremely low solubilities of the molybdenum and other trace impurities in the matrix and significant enrichments of molybdenum, nitrogen and silicon, boron, and iron at the grain boundaries.

In boron-doped two phase  $\alpha_2$ - $\gamma$   $\text{TiAl}$  containing chromium, niobium, and tungsten, the boron level was found to be significantly depleted from the bulk level in both the  $\alpha_2$  and  $\gamma$  phases and a variety of coarse borides including  $\text{TiB}$ ,  $\text{TiB}_2$  and a finer chromium-enriched  $(\text{Ti,Cr})_2\text{B}$  precipitate was observed. The tungsten and chromium were determined to partition preferentially to the  $\alpha_2$  phase and also to segregate to the  $\alpha_2$ - $\gamma$  and  $\gamma$ - $\gamma$  interfaces. These results indicate that a significant proportion of the microalloying elements are consumed by the boride precipitates.

### Introduction

Nickel and titanium aluminides have attractive potential for technological applications due to their superior high temperature properties. However, the brittleness of these materials at room temperature makes fabrication difficult and therefore limits their application. One of the traditional methods of improving the properties of these types of materials is to add microalloying elements.

A variety of microalloying elements including boron and molybdenum have been used to improve the mechanical properties of both  $\text{Ni}_3\text{Al}$  and  $\text{NiAl}$ . Boron additions to the  $\text{L}_{12}$ -ordered  $\text{Ni}_3\text{Al}$  of as little as 200 parts per million produce dramatic improvements in ductility [1,2]. However, boron additions to the  $\text{B}_2$ -ordered  $\text{NiAl}$  have a significantly different effect on the microstructure and the mechanical properties [3]. Although additions of as little as 20 parts per million of boron improve the ductility, larger amounts significantly increase the yield strength. The addition of between 0.4 and 1.6% molybdenum to  $\text{NiAl}$  has been shown to significantly improve the room temperature ductility and high temperature yield strength [4].

Efforts to enhance the ductility and refine the grain size in  $\text{TiAl}$ -based materials have focused on the addition of a variety of microalloying elements such as boron, silicon, tungsten, chromium, vanadium, manganese and molybdenum [5]. Boron additions of greater than  $\sim 0.5$  at. % are effective in refining the grain size in cast materials [5,6] and additions at the level of only a few hundred parts per million have been shown to refine and stabilize the lamellar structure in  $\gamma$ -based  $\text{TiAl}$  alloys [7-10]. Tungsten additions to  $\text{TiAl}$  enhance oxidation resistance and improve creep resistance and strength whereas chromium additions enhance the ductility. However, the exact mechanism by which these



refinements are accomplished for these various elements is not understood [11]. In order to understand these mechanisms, one of the first requirements is to determine the distribution of these microalloying additions in the microstructure.

The atom probe field ion microscope (APFIM) is well suited to the characterization of the segregation and partitioning behavior of the microalloying elements in the microstructure due to its near atomic spatial resolution, light element sensitivity, high mass resolution, and low detection levels [12,13]. These atom probe characterizations have focused on the quantification of the solubility levels of the microalloying elements in the matrix, the estimation of the levels of segregants at grain boundaries and other interfaces, and the determination of the size and composition of precipitates. This approach is required to determine the actual distribution of the microalloying elements in the microstructure so that their effectiveness may be more thoroughly evaluated.

### Experimental

Atom probe field ion microscopy analyses were performed in the Oak Ridge National Laboratory energy-compensated atom probe field ion microscope [14]. Field ion specimens of these materials were produced by standard electropolishing procedures of either material cut from bulk samples or, in the case of  $\text{Ni}_3\text{Al}$ , wires produced by rapid solidification techniques [12]. The field ion micrographs were recorded with the use of neon as the imaging gas. Due to the low probability of randomly encountering some of these microstructural features in the atom probe, some field ion specimens were initially screened in the transmission electron microscope and suitable specimens were then selected for examination in the atom probe. This pre-selection process also provided additional information as to the precise nature of the defect. The compositions of the matrix and the precipitates were determined by selected area atom probe analysis. Experimental conditions were chosen to prevent systematic errors due to preferential evaporation and retention of any solute.

In the case of grain boundary segregation, the solute coverage may be fundamentally determined with a method based on the Gibbsian interfacial excess. The Gibbsian interfacial excess [15,16] of element  $i$ ,  $\Gamma_i$ , is defined as

$$\Gamma_i = \frac{N_{i(\text{excess})}}{A} = \frac{N_i - N_{i(\alpha)} - N_{i(\beta)}}{A}, \quad (1)$$

where  $N_{i(\text{excess})}$  is the excess number of solute atoms associated with the interface,  $A$  is the interfacial area over which the interfacial excess is determined,  $N_i$  is total number of solute atoms in the volume analyzed,  $N_{i(\alpha)}$  and  $N_{i(\beta)}$  are the number of solute atoms in the two adjoining regions  $\alpha$  and  $\beta$  either side of the dividing surface. The interfacial area  $A$  that is sampled in a typical atom probe experiment is given by  $A = \pi r_a^2 / \cos \phi$ , where  $r_a$  is the effective radius of the probe aperture and  $\phi$  is the angle between the unit normal to the interface plane and the unit vector parallel to the cylinder of analysis ( $\phi \neq 90^\circ$ ) and is determined from either the projection of the interface in the field ion micrographs or examination of the field ion specimen in the transmission electron microscope. The actual number of atoms collected must take account of the less than perfect detection efficiency of the single atom detector. The detection efficiency of the atom probe used in these investigations has been determined to be 0.62. The interfacial excess can be related to the fractional monolayer coverage of solute,  $\Phi$ , by comparing it to the saturation value of the excess,  $\Gamma_{i(\text{sat})}$ , i.e.,  $\Phi = \Gamma_i / \Gamma_{i(\text{sat})}$ . There are a number of interpretations of what constitutes a monolayer [17]. The method used in this paper was based on the number of atoms expected on the closest packed plane of the crystal structure. For example, in  $\text{NiAl}$  this is the (110) plane and therefore a monolayer coverage consists of  $1.72 \times 10^{19}$  atoms  $\text{m}^{-2}$  with a width  $w = d_{(110)} = 0.20$  nm.

### Results and Discussion

#### $\text{Ni}_3\text{Al}$

In boron-doped  $\text{Ni}_3\text{Al}$ , atom probe analysis revealed that most of the boron addition remained in solid solution in the matrix. In addition, field ion microscopy revealed that boron was found to segregate to

dislocations, Fig. 1, low angle boundaries, Fig. 2, stacking faults (SISF), Fig. 3, antiphase boundaries, Fig. 4, and grain boundaries Figs. 5 and 6 [18-21]. All the dislocations and boundaries shown in these field ion micrographs are decorated with brightly-imaging spots. The unique single atom identification capability of the atom probe was used to determine that these brightly-imaging spots are individual boron atoms. In the cases of the low angle boundary and the stacking fault, the boron decoration is more clearly revealed in field ion micrographs that were taken during field evaporation, shown in Figs. 2b and 3b, since the contrast due to the individual atomic terraces (i.e., the concentric rings) is minimized rendering the brightly-imaging boron atoms more prominent. It is evident from the narrow width of the segregation exhibited in these field ion micrographs that the boron segregation is confined to the interface plane. Boron segregation to the dislocations, low angle boundaries, stacking faults and antiphase boundaries should influence the mechanical properties through a solute drag type mechanism.

A pair of field ion micrographs of two different grain boundaries is shown in Fig. 5. It is evident from the distribution of the brightly-imaging atoms in the field ion micrographs that the boron coverage at the grain boundaries varies significantly. This variation was also observed along different regions of the same grain boundary as shown in Fig. 6. For example, in some regions the coverage was extremely low, e.g., Figs. 6a and 6d, whereas in other regions there was significantly higher coverage, e.g., Fig. 6c and 6e. Atom probe quantification of the boron level and the nickel to aluminum ratio at two grain boundaries is summarized in Table 1. In addition the local solute distribution along a single grain boundary is shown. The boron coverage along this grain boundary was found to vary from over a significant range of 9.4 to 61.9%. Similar wide variations have been observed at other grain boundaries. The Ni:Al ratio was found to vary from 2.2 to 3.4. It should be noted that the Ni:Al ratio of the matrix in these aluminum-depleted materials was 3.1. No simple correlation between the Ni:Al ratio and the boron coverage was found.

Table 1. The Gibbs interfacial excesses of boron at grain boundaries in  $\text{Ni}_3\text{Al}$ .

Analysis	Ni:Al Ratio	Gibbs Interfacial Excess, $\Gamma_i$ atoms $\text{m}^{-2}$	Coverage %
1a	3.40	$4.5 \times 10^{18}$	26.7
1b	2.92	$4.2 \times 10^{18}$	24.0
1c	2.23	$4.8 \times 10^{18}$	27.0
1d	2.30	$1.7 \times 10^{18}$	9.4
1e	2.81	$3.6 \times 10^{18}$	20.4
1f	2.70	$1.1 \times 10^{19}$	61.9
1 (avg.)	2.73	$5.0 \times 10^{18}$	28.2
2 (avg.)	2.73	$2.3 \times 10^{18}$	13.0

Some grain boundaries exhibited evidence of more extensive boron segregation, as shown in Fig. 7. In most cases, the boron segregation appeared as extended brightly-imaging lenticular regions at the grain boundary. The maximum thickness of these regions was estimated to be  $\sim 3$  nm and their length was often larger than the field-of-view of the image, i.e., greater than  $\sim 100$  nm. The composition of these regions was determined to be 26-31 at. % Al and up to 5 at. % B. Although the possibility of multilayer segregation cannot be totally excluded, it is more likely that this boron-enriched region is an ultrathin precipitate or grain boundary film. However, the measured composition does not appear to be consistent with the tau phase (nickel-aluminum-boride).

In addition to this extended morphology, some shorter (5 to 10 nm in length) boron-enriched regions were also observed, as shown in Figs. 7b and 7c. Most of the segment of the grain boundary shown in Fig. 7b exhibited low coverage with only an isolated boron atom evident. However, a small facet that exhibited significantly higher boron coverage was also observed on this grain boundary. This observation indicates that the local boundary plane can have a strong influence on the segregation behavior. These smaller boron-enriched regions were also observed to be located preferentially on one side of the grain boundary as shown in Fig. 7c. It should be noted that the absence of

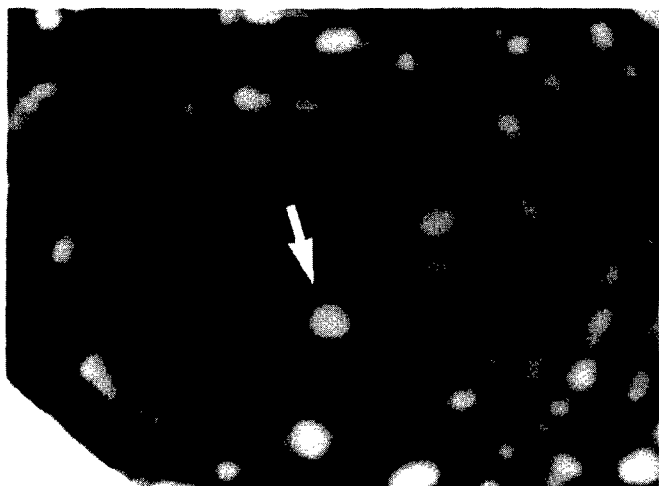


Fig. 1. Field ion micrograph of a boron-decorated dislocation in  $\text{Ni}_3\text{Al}$ .

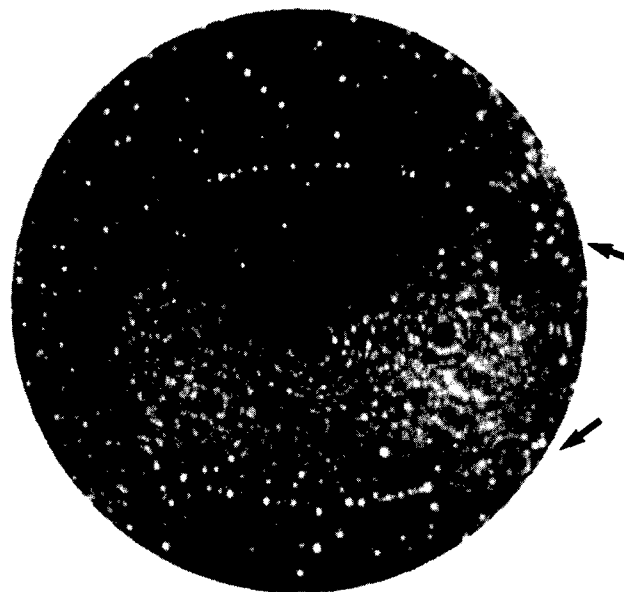


Fig. 4. Field ion micrograph of a boron-decorated antiphase boundary in  $\text{Ni}_3\text{Al}$ .

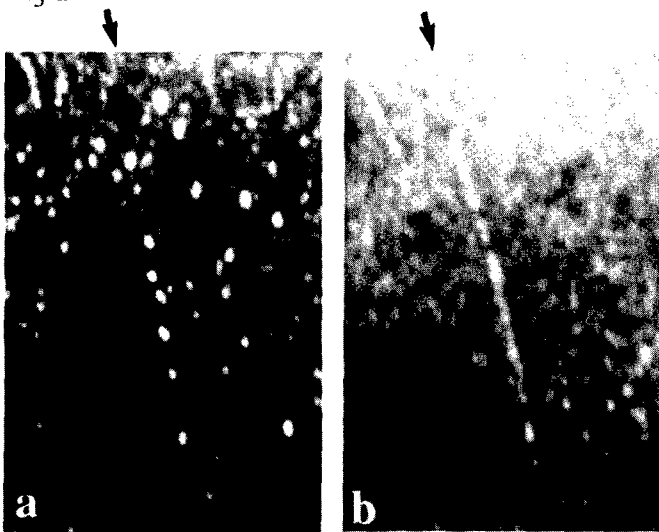


Fig. 2. Field ion micrograph of a boron-decorated low angle boundary (misorientation  $<1^\circ$ ) in  $\text{Ni}_3\text{Al}$ .

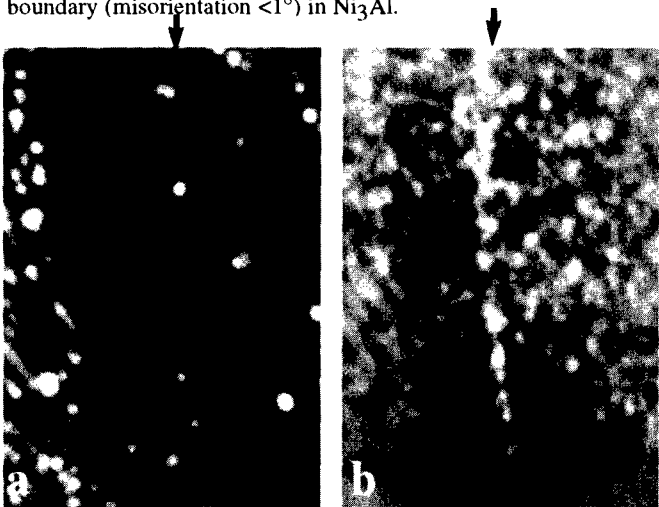


Fig. 3. Field ion micrograph of a boron-decorated stacking fault in cold worked  $\text{Ni}_3\text{Al}$  annealed for 1 h at  $800^\circ\text{C}$ .

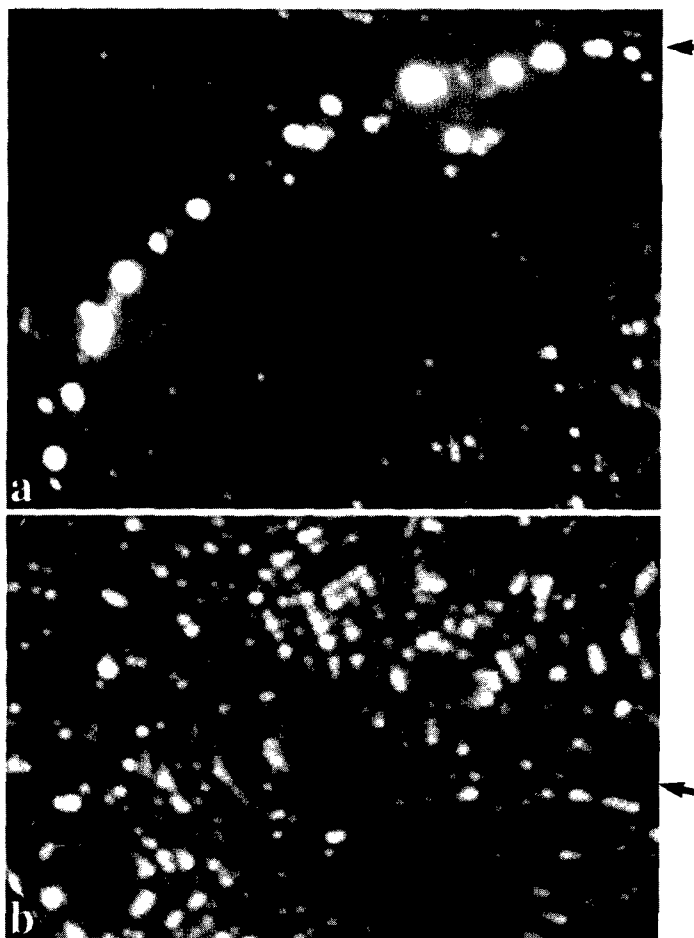


Fig. 5. Field ion micrographs of boron-decorated grain boundaries in  $\text{Ni}_3\text{Al}$ .

rings in the field ion images of these boron-enriched regions does not necessarily indicate that they are amorphous regions since the imaging behavior of boride phases (see below) is such that few if any rings are normally observed in the field ion images of crystalline boride precipitates.

No ultrafine intragranular precipitates have been observed in these boron-doped Ni-24.2 at. % Al alloys. However, boron clustering has been observed in alloys with higher aluminum contents (Ni-25 at. % Al and Ni-26 at. % Al), as shown in Fig. 8 [18]. These features were found to contain up to approximately 10 boron atoms and were classified as clusters due to their small size and the absence of any other elements. The presence of these clusters suggests that there is a abrupt change in the boron matrix solubility at the stoichiometric composition.

## NiAl

In boron-doped NiAl, atom probe analyses revealed that boron segregates to the grain boundaries, as shown in Fig. 9. As in the case of Ni<sub>3</sub>Al, the variation of the brightly-imaging boron atoms indicated that the boron coverage varied along the grain boundary. Due to the favorable orientation of this grain boundary,  $\phi = 90^\circ$ , several analyses at different positions along its length were possible. The results are summarized in Table 2 in order of analysis position along the boundary. The boron coverage was found to vary by a factor of ~5 from 5.2 to 27.4% or  $\Gamma_i = 8.7$  to  $46.3 \times 10^{17}$  atoms  $m^{-2}$ . Most sections of the boundary exhibited nickel depletion (Ni:Al = 0.84) with one section exhibiting a significant nickel enrichment (Ni:Al = 1.27). Boron enrichment was observed in both nickel depleted and nickel enriched sections. No strong correlation between the Ni:Al ratio and the coverage was apparent in these data. It should be noted that despite the extremely small radius of the cylinder of analysis used in these grain boundary analyses,  $r_a = 0.4$  to  $r_a = 0.75$  nm, a significant number of atoms from the grain interior on either side of the boundary were also collected. Although this extended radius does not affect the coverage, it influences the accuracy of the Ni:Al ratio at the exact boundary plane.

Table 2. The Gibbs interfacial excesses of boron at a  $\Sigma 3$  coincident site lattice grain boundary in NiAl + 0.04 at. % B aged 1 h at 900°C.

Analysis	Ni:Al Ratio	Gibbs Interfacial Excess $\Gamma_i$ atoms $m^{-2}$	Coverage %
1	0.77	$9.7 \times 10^{17}$	5.8
2	0.91	$1.0 \times 10^{18}$	6.1
3	1.27	$8.7 \times 10^{17}$	5.2
4	0.79	$8.7 \times 10^{17}$	5.2
5	0.80	$1.2 \times 10^{18}$	7.3
6	0.88	$1.3 \times 10^{18}$	7.7
7	0.84	$2.3 \times 10^{18}$	13.6
8	0.94	$1.5 \times 10^{18}$	9.1
9	0.82	$1.8 \times 10^{18}$	10.8
10	0.81	$4.6 \times 10^{18}$	27.4
Average	0.88	$1.6 \times 10^{18}$	9.8

Previous atom probe characterization of a binary Ni-49 at. % Al alloy by Camus et al. demonstrated that approximately two thirds of the analyzed grain boundaries were depleted in aluminum to  $\sim 40 \pm 1\%$  Al (Ni:Al = 1.5) at the boundary and the remaining one third did not exhibit any significant depletion [24,25].

Unlike boron-doped Ni<sub>3</sub>Al which exhibits significant matrix boron solubility, atom probe analysis of the matrix in an NiAl + 0.15 at. % B alloy revealed that the boron solubility was extremely low ( $0.003 \pm 0.007$  at. % B after aging for 1 h at 500°C and  $0.026 \pm 0.003$  at. % B after aging for 1 h at 1100°C) [22]. However, the boron in the matrix and at the grain boundaries does not fully account for the total boron in the material and indicates that the remaining boron must be associated with another microstructural feature.

The majority of the boron was determined to be partitioned to ultrafine precipitates ranging in size from 1 to 20 nm, as shown in Fig. 10. Atom probe analysis revealed that the precipitate composition was consistent with a MB<sub>2</sub> type precipitate where the metallic content M was a mixture of titanium, vanadium, chromium and tungsten. The metallic content was found to vary significantly from precipitate to precipitate suggesting that these precipitates were formed from the trace elements in the material. Some carbon was also detected in these precipitates. Similar ultrafine MC precipitates have also been observed in carbon-doped NiAl [22] and undoped single crystal NiAl [23].

Due to their small size and relatively high number density, these precipitates produce significant precipitation hardening and are therefore detrimental to the mechanical properties. This precipitation hardening also offsets the benefits of the boron segregation to the high angle grain boundaries. It has been shown that the number density of these precipitates can be decreased by reducing the quantities of trace impurities in the alloy by zone refinement [23]. Alternatively, the number density of these precipitates can be reduced and their size increased with an appropriate heat treatment [22].

In NiAl containing 0.7 at. % Mo annealed 1 h at 1000°C and 1 h at 500°C, atom probe analysis [26] indicated extremely low solubilities of the molybdenum and other trace impurities in the matrix: Ni- 50.4  $\pm$  1.2 at. % Al - 0.005  $\pm$  0.001 % Mo, 0.007  $\pm$  0.002 % Fe, 0.005  $\pm$  0.001 % Si and N and 0.0004  $\pm$  0.0004 % V. The large error on the aluminum content indicates a significant variation from one region to another.

The majority of the molybdenum in this alloy was found to be concentrated in a low number density ( $\sim 1$  to  $2 \times 10^{21} m^{-3}$ ) of 10- to 50-nm-diameter spherical molybdenum precipitates. The composition of these body-centered cubic precipitates was determined to be Mo- 3.3  $\pm$  0.6 at. % Al with residual amounts of 0.06  $\pm$  0.03% B, 0.04  $\pm$  0.02% Ni, 0.01  $\pm$  0.01% Fe, and 0.04  $\pm$  0.02% V. The precipitates were observed both in the NiAl matrix, as shown in Fig. 11, and also at grain boundaries. Calculations based on an Orowan mechanism indicate that these precipitates generate a significant increase in yield stress of between 82 and 210 MPa depending on the measured minimum and maximum size of the precipitate. These values are in good agreement with the differences in the yield stresses of the molybdenum-doped (254 MPa) and undoped alloys (154 MPa) since a larger number of the smaller diameter precipitates was observed.

A field ion micrograph of a  $\Sigma 3$  coincident site lattice grain boundary in NiAl containing 0.7 at. % Mo annealed 1 h at 1000°C and 1 h at 500°C is shown in Fig. 12. Due to the favorable orientation of the grain boundary plane with respect to the specimen axis,  $\phi = 90^\circ$ , extensive characterization of this boundary was possible. The Gibbsian interfacial excesses of the solutes along this boundary are summarized in Table 3. These coverages were significantly lower than the boron coverages observed in the boron-doped NiAl. Despite the relatively low coverages, significant enrichments of molybdenum, nitrogen and silicon, carbon, boron, and iron are evident at the grain boundary.

Table 3. The Gibbs interfacial excesses of solute at a  $\Sigma 3$  coincident site lattice grain boundary in NiAl + 0.7 at. % Mo aged 1 h at 1000°C and 1 h at 500°C.

Element	Gibbs Interfacial Excess, $\Gamma_i$ atoms $m^{-2}$	Coverage %
Mo	$9.9 \times 10^{16}$	0.58
N/Si	$6.5 \times 10^{16}$	0.38
C	$1.1 \times 10^{16}$	0.07
B	$5.7 \times 10^{15}$	0.03
Fe	$3.8 \times 10^{15}$	0.02

A 2 1/2 D reconstruction of the solute distribution along this grain boundary is shown in Fig. 13. This reconstruction was created by taking the z coordinate of each solute atom as position along the composition profile. The solutes were then assumed to be randomly distributed along the grain boundary plane to give the x coordinate (y=0). Since the diameter of the cylinder of analysis varied from 3.4 to 4.3 nm during this

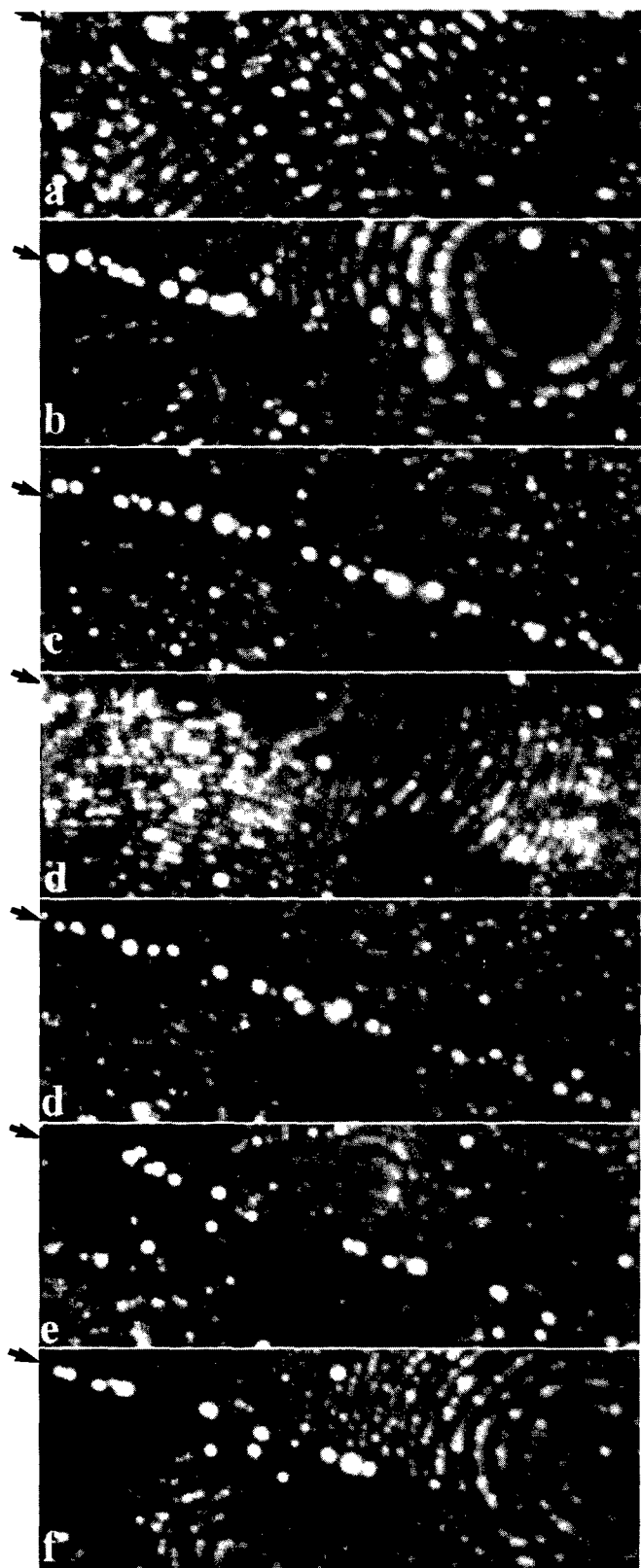


Fig. 6. Field ion micrograph of a boron-decorated grain boundary in  $\text{Ni}_3\text{Al}$ .

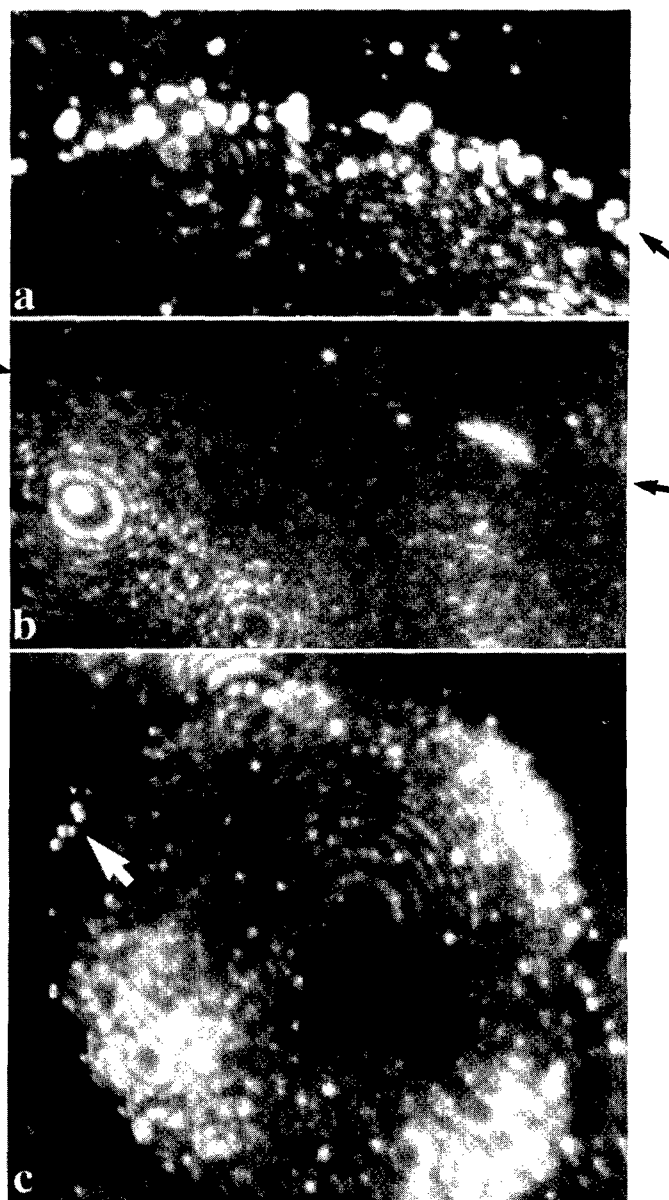


Fig. 7. Field ion micrographs of a grain boundary boron-enriched phase in  $\text{Ni}_3\text{Al}$ .

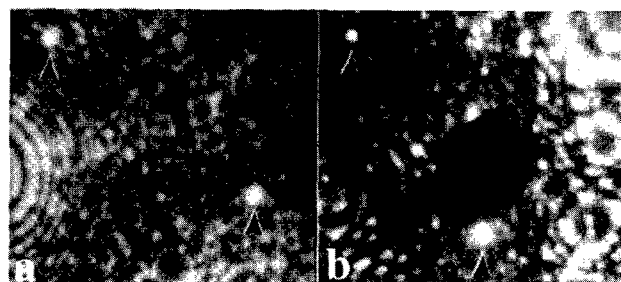


Fig. 8. Field ion micrographs of boron clusters in (a)  $\text{Ni}_3\text{Al}$  and (b)  $\text{Ni}_{74}\text{Al}_{26}$ .

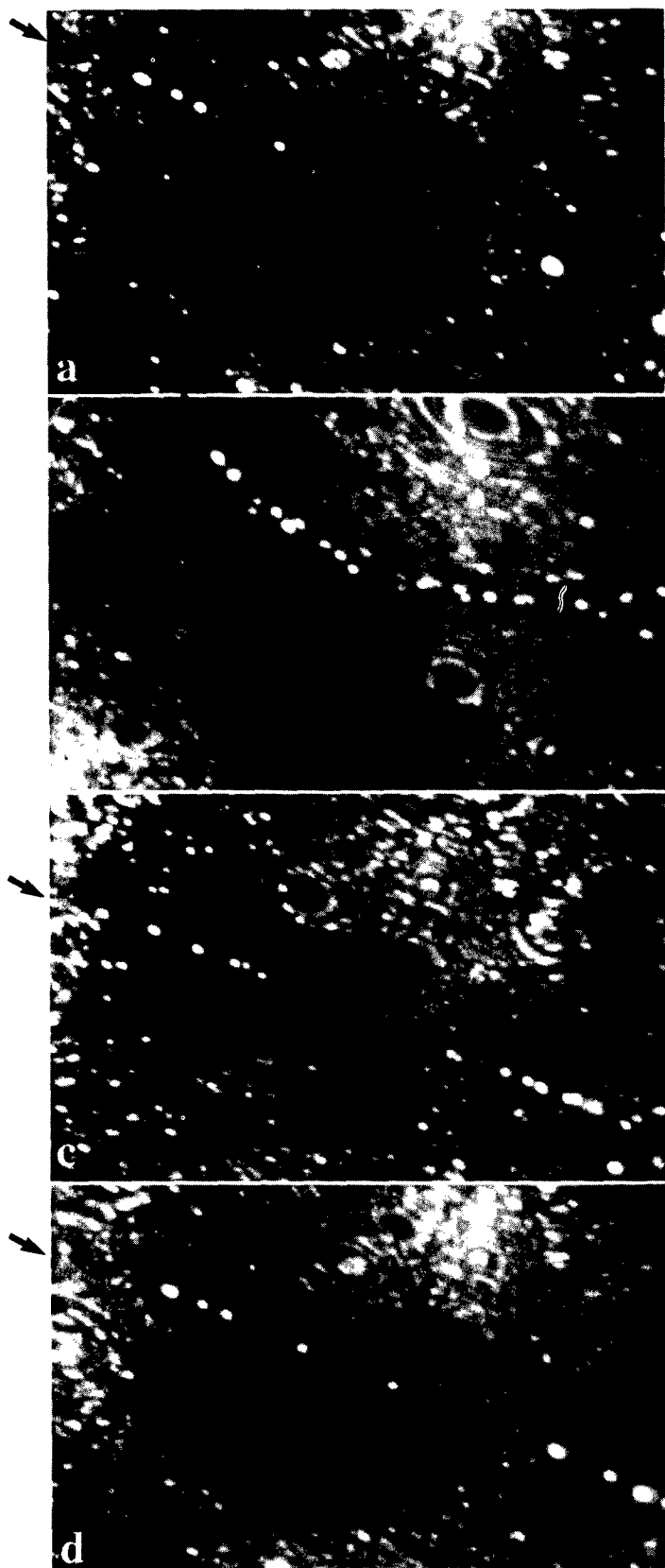


Fig. 9. Field ion micrographs of a boron-decorated grain boundary in NiAl.

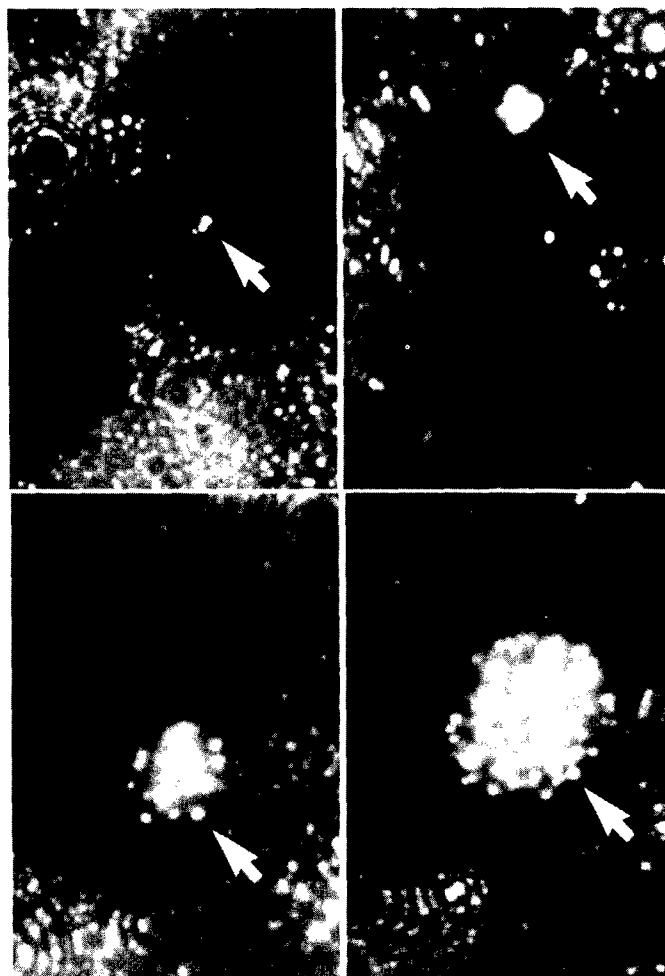


Fig. 10. Field ion micrographs of MB<sub>2</sub>-type precipitates in NiAl.

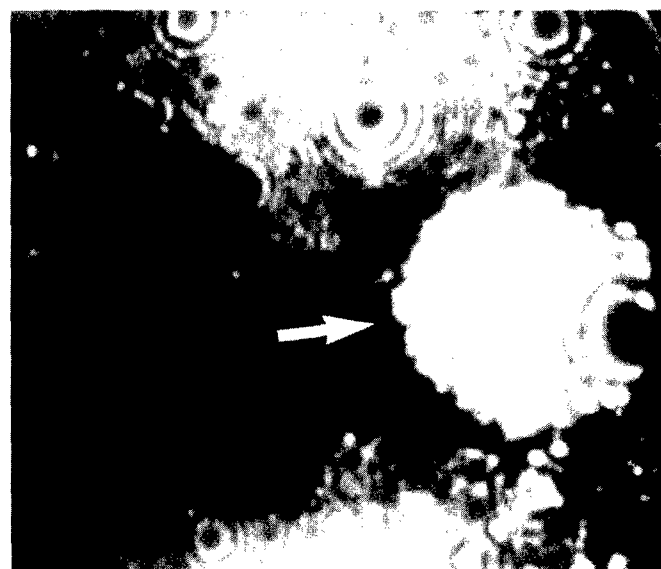


Fig. 11. Field ion micrograph of a molybdenum precipitate in molybdenum-doped NiAl.

analysis, this randomization will only introduce a small one-dimensional uncertainty in the reconstruction. Although most of the solute was distributed uniformly along the grain boundary, there was some visual evidence of regions of higher than average local concentrations of iron, molybdenum, nitrogen and carbon. There was also some evidence of molybdenum-nitrogen enrichment. This small non-uniformity in the solute distribution may arise from small changes in the boundary plane or the presence of grain boundary dislocations which changes the local atomic environment and thereby influence the segregation behavior.

## TiAl

These materials differ from the previous examples in that they contain two primary phases: an  $L1_0$ -ordered  $\gamma$  phase and a  $DO_{19}$ -ordered  $\alpha_2$  phase. In addition, the compositions of these phases vary significantly depending on the heat treatment and may be far from their equilibrium or steady state values. For example, in the materials examined, the aluminum content of the  $\gamma$  phase was found to vary from ~40-50 at. % Al and that of the  $\alpha_2$  phase was typically 34-36 at. % Al. Due to these variations, the identity of phase based solely on the aluminum content alone was not reliable. Since the  $\alpha_2$  phase is known to scavenge oxygen and other interstitial elements [27,28], it typically has an oxygen content of one to two orders of magnitude higher than the  $\gamma$  phase. For example, the oxygen content of the  $\alpha_2$  phase in a Ti-47% Al-2% Cr-1.8% Nb-0.2% W-0.15 % B alloy was found to be ~33 times that of the  $\gamma$  phase. Therefore, phase identification was based on the measured aluminum content in conjunction with the measured oxygen levels as well as the appearance of the phase in the field ion image.

Field ion micrographs of the  $\gamma$  and brightly-imaging  $\alpha_2$  phases are shown in Fig. 14. The width of these  $\alpha_2$  laths was found to vary from less than 5 nm (Fig. 14b) to more than 20 nm (Fig. 14a) in Ti-47% Al-2% Cr-1.8% Nb-0.2% W-0.15 % B that was stress-relieved for 2 h at 900°C. No evidence for boron segregation to the  $\gamma$ - $\alpha_2$  phase interface has been obtained from atom probe analysis of the interface.

These materials also contain a significant number of  $\gamma$ - $\gamma$  interfaces as shown in Fig. 15. However, no evidence for boron segregation to the  $\gamma$ - $\gamma$  phase interface has been obtained. The segregation behavior of the other microalloying elements is discussed below.

The boron levels in the  $\gamma$  and  $\alpha_2$  phases were found to be significantly depleted from the bulk alloy concentration. For example, the solubilities of boron in the  $\gamma$  and  $\alpha_2$  matrix phases were found to be  $0.011 \pm 0.006$  at. % B and  $<0.003$  at. % B, respectively in Ti-47% Al-2% Cr-1.8% Nb-0.2% W-0.15 % B that was stress-relieved for 2 h at 900°C.

The majority of the boron was concentrated in a variety of borides including TiB, TiB<sub>2</sub> and a chromium-enriched (Ti,Cr)<sub>2</sub>B precipitate [29]. A field ion micrograph of a M<sub>2</sub>B precipitate in a Ti-47% Al-2% Cr-1.8% Nb-0.2% W-0.15 % B alloy that was stress-relieved for 2 h at 900°C is shown in Fig. 16. With the exception of the smaller ( $< 50$  nm thick) chromium-enriched (Ti,Cr)<sub>2</sub>B precipitates, most of the borides were larger than the field of view of the field ion microscope, i.e., greater than ~100 nm. The compositions of some of the precipitates are summarized in Table 4. It is evident that a significant proportion of the microalloying additions is present in these boride precipitates. The partitioning of the microalloying elements to these borides may reduce their availability for other more beneficial mechanisms. Although these coarse borides may help pin the grain boundaries and retard grain growth, it is likely that improvements could be made in the effectiveness of the boron additions.

Table 4. Composition of boride precipitates as measured in the atom probe. (atomic %)

Alloy	Measured Composition	Type
Ti-47% Al-2% Cr-1.8% Nb-0.2% W-0.15 % B	(Ti <sub>94.3</sub> Nb <sub>3.2</sub> Cr <sub>1.1</sub> W <sub>1.1</sub> Al <sub>0.3</sub> )B <sub>1.7</sub>	MB <sub>2</sub>
	(Ti <sub>92.6</sub> Nb <sub>2.5</sub> Cr <sub>0.6</sub> W <sub>0.6</sub> Al <sub>3.7</sub> ) <sub>0.95</sub> B	MB
	(Ti <sub>59.5</sub> Nb <sub>9.5</sub> Cr <sub>23.0</sub> W <sub>5.3</sub> Al <sub>2.7</sub> ) <sub>2.06</sub> B	M <sub>2</sub> B

A field ion micrograph of an  $\alpha_2$ - $\gamma$  interface in a tungsten containing Ti-47% Al-2% Cr-1.8% Nb-0.2% W-0.15 % B alloy that was stress-relieved for 2 h at 900°C is shown in Fig. 17. Several brightly-imaging atoms are apparent both at the interface and in the near boundary region in the  $\alpha_2$  phase. Since this alloy contains boron and several refractory elements that all exhibit similar brightly-imaging behavior, it is not possible to positively identify these brightly-imaging atoms from their appearance in the field ion image. The average tungsten content of the  $\gamma$  phase in this material was determined to be  $0.16 \pm 0.02$  at. % W. The tungsten content of the  $\alpha_2$  phase was found to vary significantly from one region to another [30]. The measured compositions ranged from  $0.17 \pm 0.15$  at. % W to  $0.39 \pm 0.08$  at. % W with an average of  $0.33 \pm 0.06$  at. % W. Part of this variation may be due to a tail in the segregation profile at the  $\alpha_2$ - $\gamma$  interface as indicated by the width of the decoration in the field ion micrograph. These results indicate that tungsten is partitioning to the  $\alpha_2$  phase. The  $\alpha_2$ - $\gamma$  interface region was found to be enriched to a level of  $0.68 \pm 0.45$  at. % W. The tungsten interfacial segregation supports the previous observation that tungsten additions stabilize the  $\alpha_2$  lamellae against dissolution during thermal aging [8-10].

Tungsten segregation to the  $\gamma$ - $\gamma$  interfaces was also observed in these materials [30]. A composition profile taken such that the axis of the cylinder of analysis was aligned almost precisely along a  $\gamma$ - $\gamma$  interface is shown in Fig. 18. The orientation of the interface with respect to the specimen axis is shown in the transmission electron micrograph of the needle-shaped field ion specimen shown in Fig. 19. This orientation permitted the distribution of solute along the interface to be examined. It is evident from the composition profile that there was a significant and relatively uniform enrichment of tungsten at this  $\gamma$ - $\gamma$  interface. The average coverage at this interface was determined to be 4.6% W (Gibbsian interfacial excess  $\Gamma_1 = 6.4 \times 10^{17} \text{ m}^{-2}$ ). This coverage gives an enhancement factor of ~29 over the  $\gamma$  matrix level. A tungsten composition profile taken across a  $\gamma$ - $\gamma$  interphase is shown in Fig. 20a. The average coverage at this interface was determined to be 3.7% W (Gibbsian interfacial excess  $\Gamma_1 = 4.7 \times 10^{17} \text{ m}^{-2}$ ). This coverage gives an enhancement factor of ~23 over the  $\gamma$  matrix level. The chromium and niobium composition profiles taken across this  $\gamma$ - $\gamma$  interphase are also shown in Fig. 20b. Although the chromium indicates some enrichment at this  $\gamma$ - $\gamma$  interface, the niobium does not. The variation in chromium enrichment from interface to interface is in agreement with previous results from Yamaguchi et al. [31, 32].

The chromium and niobium additions were also found to partition between the  $\gamma$  and  $\alpha_2$  phases. In Ti-47% Al-2% Cr-1.8% Nb-0.2% W-0.15 % B that was stress-relieved for 2 h at 900°C, the average chromium content of the  $\alpha_2$  phase was  $2.9 \pm 0.2$  at. % Cr and that of the  $\gamma$  phase was  $1.6 \pm 0.06$  at. % Cr indicating that chromium is enriched in the  $\alpha_2$  phase. In the Ti-47% Al-2% Cr-1.8% Nb-0.2% W-0.15 % B alloy, the niobium was also found to have a slight preference for the  $\gamma$  phase ( $1.9 \pm 0.06$  at. % Nb) over the  $\alpha_2$  phase ( $1.6 \pm 0.13$  at. % Nb).

Atom probe analyses of the chromium and niobium levels at both the  $\gamma$ - $\gamma$  and  $\gamma$ - $\alpha_2$  phase interfaces revealed that some interfaces were enriched in both niobium and chromium and some interfaces exhibited no enrichments.

## Conclusions

In boron-doped Ni<sub>3</sub>Al, the boron additions were found to segregate to dislocations, low angle boundaries, stacking faults, antiphase boundaries, and grain boundaries. The boron and aluminum levels at grain boundaries were found to vary both from boundary to boundary and also along an individual boundary segment. In some cases, a boron-enriched thin film up to 3 nm thick was observed. In aluminum-enriched Ni<sub>3</sub>Al, ultrafine clusters containing up to approximately 10 boron atoms were detected in the matrix.

In contrast, the majority of the boron in boron-doped NiAl was determined to be in the form of ultrafine MB<sub>2</sub>-type precipitates. These precipitates are detrimental to the mechanical properties and offset the benefits of the boron segregation to the high angle grain boundaries. In molybdenum-doped NiAl, atom probe analyses indicated extremely low



Fig. 12. Field ion micrograph of a  $\Sigma 3$  grain boundary in molybdenum-doped NiAl.

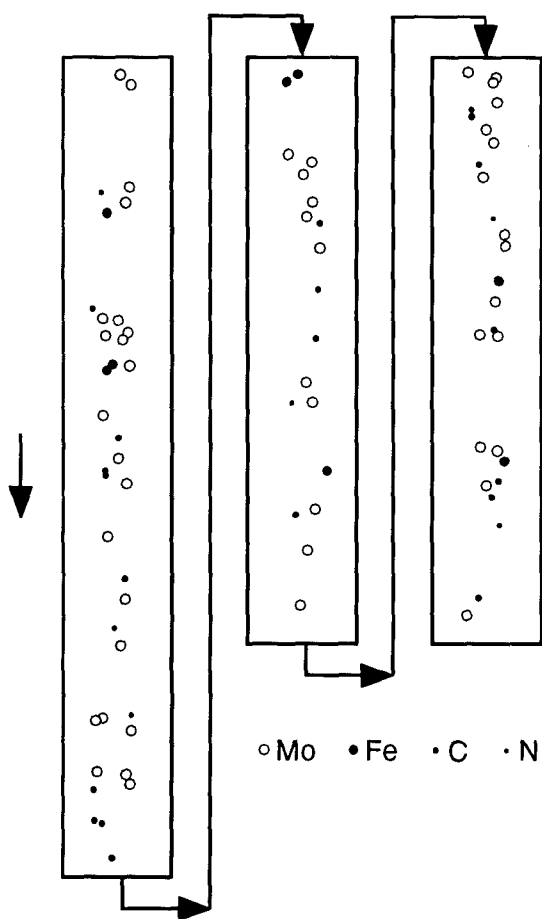


Fig. 13. Reconstruction of the solute segregation along a  $\Sigma 3$  grain boundary in molybdenum-doped NiAl. Each symbol is an individual atom.

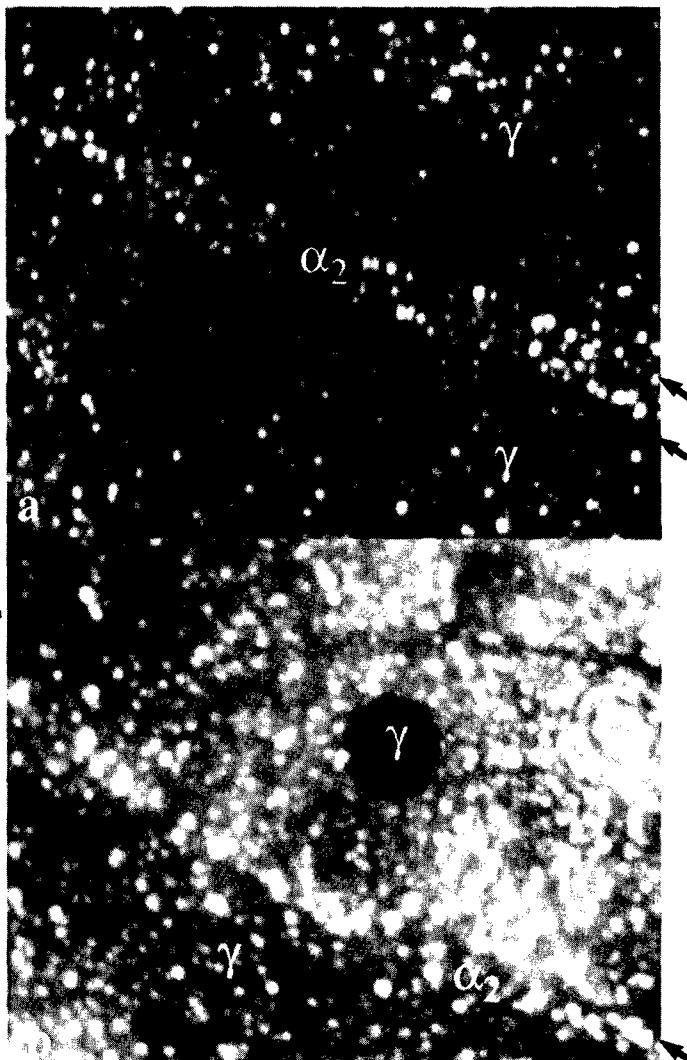


Fig. 14. Field ion micrograph of brightly-imaging  $\alpha_2$  laths in TiAl. (a) 5 nm and (b) 20 nm thick.



Fig. 15. Field ion micrograph of a  $\gamma$ - $\gamma$  interface in TiAl.

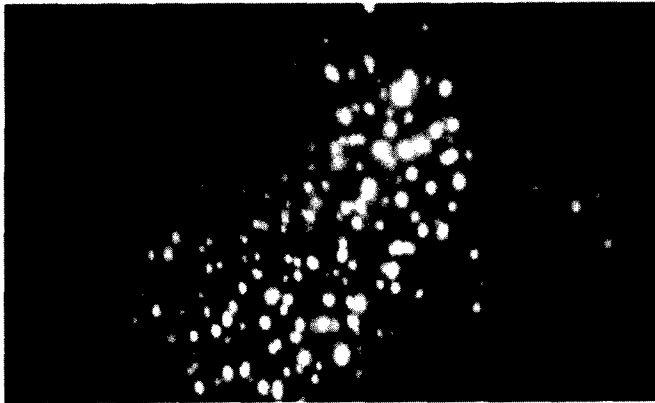


Fig. 16. Field ion micrograph of a chromium-enriched  $M_2B$  precipitate in TiAl.

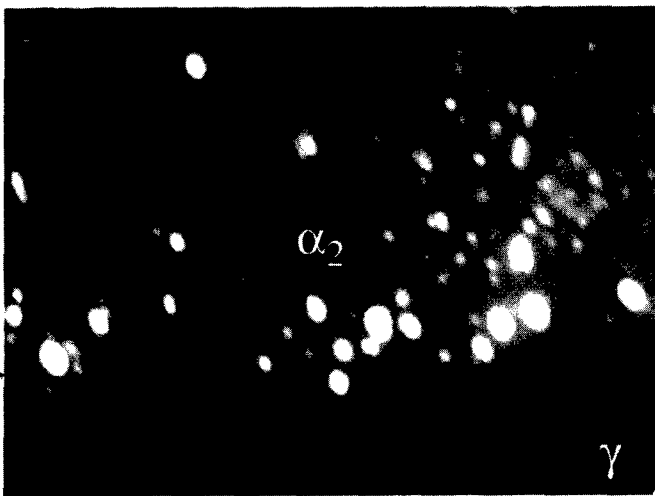


Fig. 17. Field ion micrograph of an  $\alpha_2$ - $\gamma$  interface in TiAl.

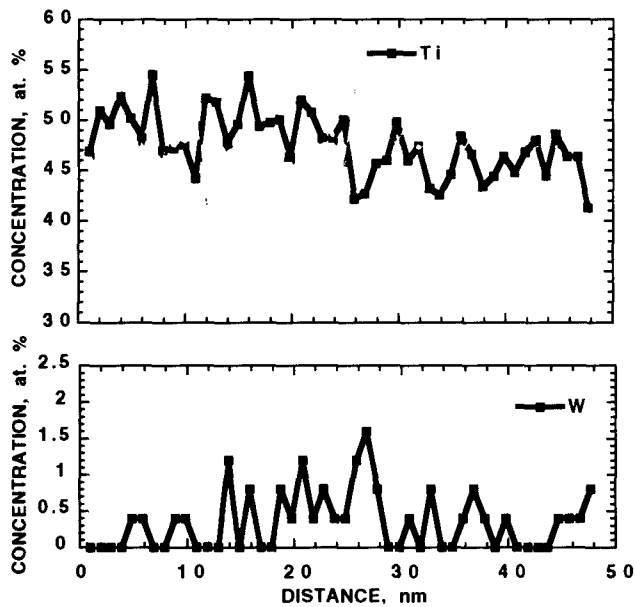


Fig. 18. Composition profile along a  $\gamma$ - $\gamma$  interface in TiAl.

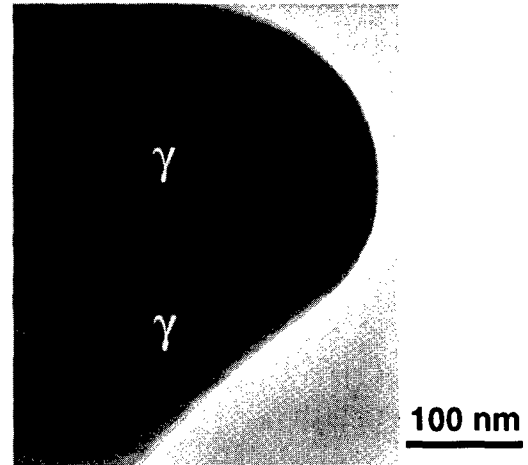
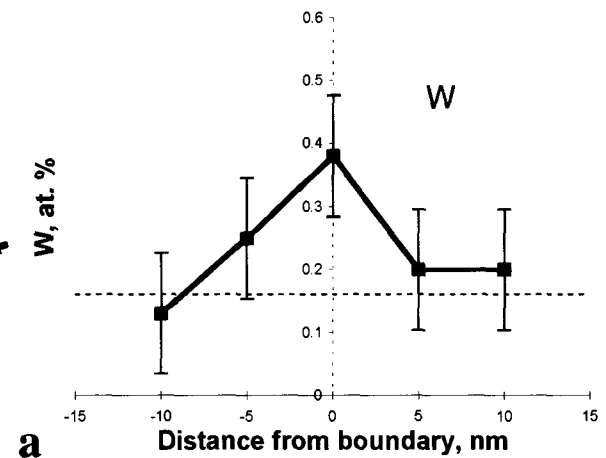
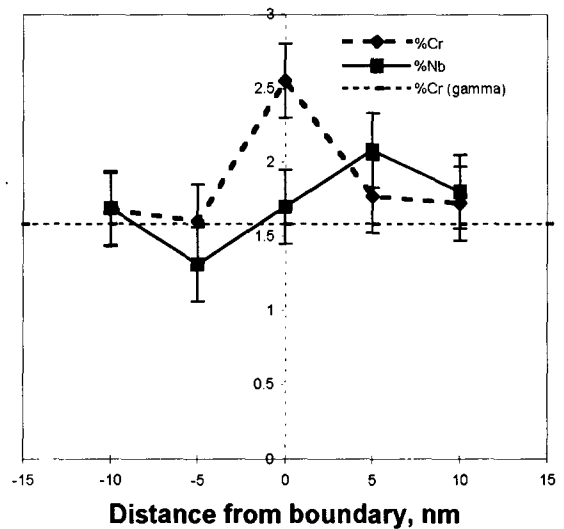


Fig. 19. Transmission electron micrograph of the field ion specimen used to produce the composition profile shown in Fig. 18



a



b

Fig. 20. Composition profiles for tungsten, chromium and niobium across a  $\gamma$ - $\gamma$  interface in TiAl.



solubilities of the molybdenum and other trace impurities in the matrix and significant enrichments of molybdenum, nitrogen and silicon, boron, and iron at the grain boundaries.

In boron-doped two phase  $\alpha_2$ + $\gamma$  TiAl containing chromium, niobium, and tungsten, the boron level was found to be significantly depleted from the bulk level in both the  $\alpha_2$  and  $\gamma$  phases and a variety of coarse borides including TiB, TiB<sub>2</sub> and a finer chromium-enriched (Ti,Cr)<sub>2</sub>B precipitate was observed. The tungsten and chromium were determined to partition preferentially to the  $\alpha_2$  phase and also to segregate to the  $\alpha_2$ - $\gamma$  and  $\gamma$ - $\gamma$  interfaces. These results indicate that a significant proportion of the microalloying elements are consumed by the boride precipitates.

#### Acknowledgments

The authors would like to thank Drs. J. A. Horton, C. T. Liu, I. M. Anderson, A. J. Duncan and R. Jayaram for their contributions to the results presented in this paper. This research was supported by the Division of Materials Sciences, U. S. Department of Energy under contract DE-AC05-96OR22464 with Lockheed Martin Energy Research Corp. and through the SHaRE Program under contract DE-AC05-76OR00033 with Oak Ridge Associated Universities.

#### References

1. K. Aoki and O. Izumi, *Nippon Kinzoku Gakkaishi*, **43** (1979) 1190.
2. C. T. Liu, C. L. White and J. A. Horton, "Effect of Boron on Grain Boundaries in Ni<sub>3</sub>Al", *Acta Metall.*, **33** (1985) 213-229.
3. R. D. Noebe, R.R. Bowman and M.V. Nathal, "Physical and Mechanical Properties of the B2 compound NiAl", *Inter. Mater. Rev.*, **38** (1993) 193-232.
4. C.T. Liu and J.A. Horton, "Effect of refractory alloying additions on mechanical properties of near-stoichiometric NiAl", *Mater. Sci. Eng. A*, **192/193** (1995) 170-178.
5. S. C. Huang, "Alloying Considerations in Gamma-Based Alloys" *Structural Intermetallics*, eds. R. Darolia, J. Lewandowski, C. T. Liu, P. Martin, D. Miracle and M. Nathal, TMS, Warrendale, PA, 1993, p. 299-308.
6. S.C. Huang and E.L. Hall, "Structure and Properties of TiAl Alloys Containing Interstitial Elements", *Proc. High Temperature Ordered Intermetallic Alloys IV*, Boston, December 1990, vol. 213, L. Johnson, D.P. Pope and J.A. Horton, (eds.) (Pittsburgh, PA, Materials Research Society, 1991), pp.827-832.
7. T. Nakano, and Y. Umakoshi, "Effect of Boron Addition on the Plastic Behavior of PST Crystals in TiAl", *Intermetallics*, **2** (1994) 185-191.
8. R. V. Ramanujan, P. J. Maziasz, and C. T. Liu, "The Thermal Stability of the Microstructure of Gamma-Based Titanium Aluminides", *Acta Metall.*, **44** (1996) 2611-2642.
9. C. T. Liu, J. H. Schneibel, P. J. Maziasz, J. L. Wright and D.S. Easton, "Tensile Properties and Fracture Toughness of TiAl Alloys with Controlled Microstructures", *Intermetallics*, **4** (1996) 429-440.
10. P. J. Maziasz, R. V. Ramanujan, C. T. Liu and J. L. Wright, "Effects of Boron and Tungsten Alloying Additions of the Formation and Stability of Lamellar Structures in Two-Phase Gamma-TiAl", *Intermetallics*, **5** (1997) 83-95.
11. Y.-W. Kim, "Ordered Intermetallic Alloys, Part III: Gamma Titanium Aluminides", *JOM*, **46** (1994) 30-40.
12. M. K. Miller and G. D. W. Smith, *Atom Probe Microanalysis: Principles and Applications to Materials Problems* (Pittsburgh, PA, Material Research Society, 1989).
13. M.K. Miller, A. Cerezo, M.G. Hetherington and G. D. W. Smith, *Atom Probe Field Ion Microscopy* (Oxford, England, Oxford University Press, 1996).
14. M. K. Miller, "The ORNL Atom Probe", *J. de Physique*, **47-C2** (1986) 493-498.
15. J. W. Gibbs, *The Collected Works of J. Willard Gibbs*, vol. I, (New Haven, CT, Yale University Press, 1948).
15. M. K. Miller and G. D. W. Smith, "Atom Probe Analysis of Interfacial Segregation", *Appl. Surf. Sci.*, **87/88** (1995) 243 -250 and references therein.
16. D. McLean, *Grain Boundaries in Metals* (London, England. Oxford University Press, 1957) 116.
17. E.D. Hondros and M.P. Seah, "Segregation to Interfaces", *Inter. Mater. Rev.*, **22** (1977) 262-301.
18. M.K. Miller and J. A. Horton, "An Atom Probe Field Ion Microscope Study of Boron Decorated Grain Boundaries in Ni<sub>3</sub>Al", *Scripta Metall.*, **20** (1986) 789-792.
19. J. A. Horton and M. K. Miller, "Atom Probe Analysis of Grain Boundaries in Rapidly-solidified Ni<sub>3</sub>Al", *Acta Metall.*, **35** (1987) 133-141.
20. J. A. Horton and M. K. Miller, "An Atom Probe Study of Boron Segregation to Line and Planar Defects in Ni<sub>3</sub>Al", *Proc. High Temperature Ordered Intermetallic Alloys II*, Boston, December 1987, vol. 81, N. S. Stoloff, C. C. Koch, C. T. Liu and O. Izumi, (eds.) (Pittsburgh, PA, Materials Research Society, 1987), pp. 105-110.
21. M. K. Miller and J. A. Horton, "Direct Observation of Boron Segregation to Line and Planar Defects in Ni<sub>3</sub>Al", *J. de Physique*, **48-C6** (1987) 379-384.
22. R. Jayaram and M.K. Miller, "An Atom Probe Study of Grain Boundary and Matrix Chemistry in Microalloyed NiAl", *Acta Metall.*, **42** (1994) 1561-1572.
23. A. Duncan, M. J. Kaufman and M. K. Miller, "Segregation of Interstitial Impurities in Single-crystal NiAl", *Appl. Surf. Sci.*, **76/77** (1994) 160-164.
24. P.P. Camus, I. Baker, J.A. Horton and M.K. Miller, Grain Boundary Chemistry in NiAl, *J. de Physique*, **49-C6** (1988) 329-333.
25. M.K. Miller, R. Jayaram and P.P. Camus, "Grain Boundary Composition in NiAl", *Scripta Metall.*, **26** (1992) 679-684.
26. M. K. Miller, I. M. Anderson and K. F. Russell, "Precipitation and Grain Boundary Segregation in Molybdenum-doped NiAl", *Appl. Surf. Sci.*, **94/95** (1996) 288-294.
27. R. Uemori, T. Hanamura and H. Morikawa, "Oxygen Scavenging Effect of the  $\alpha_2$  Phase in the TiAl Intermetallic Compound", *Scripta Metall.*, **26** (1992) 969-974.
28. A. Menand, S. Huget and A. Nerac-Pertaix, "Interstitial Solubility in  $\gamma$  and  $\alpha_2$  Phases of TiAl-Based Alloys", *Acta Mater.*, **44** (1996) 4729-4737.
29. D.J. Larson, C. T. Liu and M. K. Miller, "Boron Solubility and Boride Compositions in Two-Phase Titanium Aluminides", *Intermetallics*, in press.
30. D.J. Larson, C. T. Liu and M. K. Miller, "Tungsten Segregation in  $\alpha_2$ + $\gamma$  Titanium Aluminides", *Intermetallics*, in press.
31. M. Yamaguchi and H. Inui, "TiAl Compounds for Structural Applications", *Structural Intermetallics*, eds. R. Darolia, J. Lewandowski, C. T. Liu, P. Martin, D. Miracle and M. Nathal, TMS, Warrendale, PA, 1993, p. 127-142.
32. H. Inui, K. Kishida, M. Kobayashi, M. Yamaguchi, M., Kawasaki, and K. Ibe, "Compositional Variations at TiAl-TiAl Lamellar Boundaries in Binary and Some Ternary PST TiAl", *Phil. Mag. A*, **74** (1996) 451-464.

# VAPORIZATION STUDIES OF NICKEL AND TITANIUM ALUMINIDES

K. Hilpert, M. Albers, M. Eckert, and D. Kath

Research Center Jülich, Institute for Materials in Energy Systems,  
52425 Jülich, Germany

## Abstract

Vaporization studies were carried out by Knudsen effusion mass spectrometry on the alloys of the Ni-Al, Ti-Al, and Ti-Al-Nb systems. In addition, the ternary solid solutions of Co, Fe, Hf, or Ti in  $\text{Ni}_3\text{Al}$  and of Nb in TiAl were investigated. Partial pressures of alloy components were measured in the temperature range between 1200 and 1700 K. Partial and integral thermodynamic properties were obtained from these pressures such as chemical activities or enthalpies and Gibbs energies of formation. The partial thermodynamic properties are used for a better understanding of high temperature corrosion and the substitution behavior of Fe in  $\text{Ni}_3\text{Al}$  and Nb in TiAl. The results obtained agree with direct measurements of the lattice site occupation. Phase boundaries were derived from the vapor pressure measurements in addition to thermochemical data.

## Introduction

The nickel aluminides  $\text{Ni}_3\text{Al}$  and  $\text{NiAl}$  as well as the titanium aluminides  $\text{Ti}_3\text{Al}$  and TiAl are of interest for the development of structural alloys on the basis of ordered intermetallic phases. The ternary solid solutions formed by these phases are of particular interest for practical applications. The basic properties of the nickel and titanium aluminides, except the thermodynamic properties, are summarized in the recent extensive review article by Sauthoff (1) and the references quoted therein. The thermodynamic properties known so far need complementation. This refers particularly to the determination of partial thermodynamic properties.

Besides integral thermodynamic properties, partial thermodynamic properties are generally determined by vaporization and electromotive force (EMF) studies (see e.g. Refs 2 and 3). This is in contrast to calorimetry (see e.g. Ref. 2) which usually only yields integral values. The vaporization and EMF studies make it possible to directly determine the change of the Gibbs energy,  $\Delta G$ , of the reactions considered. The changes of the enthalpy and the entropy,  $\Delta H$  and  $\Delta S$ , additionally result in many cases. The direct determination of enthalpies of reaction,  $\Delta H$ , and specific heats,  $c_p$ , is carried out by calorimetry.

The vaporization studies of nickel and titanium aluminides carried out so far have been conducted by using Knudsen effusion mass spectrometry and the isopiestic method. General reviews of the method of Knudsen effusion mass spectrometry are given for example by Hilpert (4) and Chatillon et al. (5). These two articles also contain comprehensive surveys of the results obtained by this method on intermetallic phases and systems. The application of the isopiestic methods is based upon the equilibration of different alloy samples with a given well defined Al partial pressure at different temperatures and the subsequent chemical analysis of the alloy samples. Thermodynamic activities of Al in solid alloys of the Ni-Al system resulted by using this method. The results and the experimental procedure are described in the pioneering work by Steiner and Komarek (6). The isopiestic method is limited to alloys with a highly volatile component such as Al or

Hg which are used for equilibration via the vapor phase. Knudsen effusion mass spectrometry does not have this limitation.

The potential of Knudsen effusion mass spectrometry can be summarized as follows:

- identification of the gaseous species forming the equilibrium vapor in the Knudsen cell,
- determination of partial pressures in the range from generally between  $10^{-5}$  and 10 Pa and up to temperatures above 2500 K, and
- computation of thermodynamic properties from the measured partial pressures and their temperature dependencies, as for example, thermodynamic activities, chemical potentials, as well as enthalpies and entropies of dissociation or formation.

Knudsen effusion mass spectrometry is used by the first author's group. This paper summarizes the results obtained by this group on the alloys of

- the binary Ni-Al and Ti-Al systems,
- the ternary solutions of Co, Fe, Hf, and Ti in  $\text{Ni}_3\text{Al}$  as well as
- the ternary solution of Nb in TiAl, and the Ti-Al-Nb system.

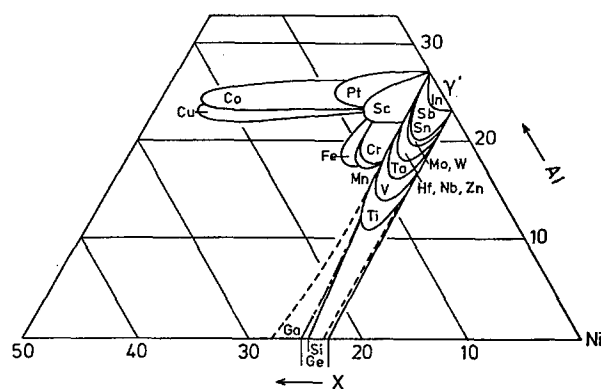


Figure 1: Schematic representation of the solubility lobes of the  $\gamma'$ - $\text{Ni}_3\text{Al}$  phase in the Ni-Al-X systems for different elements according to Ochiai et al. (7).

The solid solutions of Co, Fe, Hf, and Ti in  $\text{Ni}_3\text{Al}$  were selected on the basis of the different directions of the solubility lobes of the  $\gamma$ - $\text{Ni}_3\text{Al}$  phase reported by Ochiai et al. (7) (Figure 1). The solubility lobe of Co extends in the direction  $\text{Ni}_3\text{Al}-\text{X}_3\text{Al}$ , the solubility lobes of Hf and Ti extend in the direction  $\text{Ni}_3\text{Al}-\text{Ni}_3\text{X}$ , and the direction of the lobe for Fe is in between these two boundary directions. According to Ochiai et al. these different directions mean substitution of Co predominantly for Ni in  $\text{Ni}_3\text{Al}$ , substitution of Hf and Ti predominantly for Al, and of Fe for Ni and Al. The Ti-Al-Nb system was selected due to the importance of Nb additives to titanium aluminides for corrosion (see e.g. Ref. 8). Moreover, Nb gives some solid solution strengthening and improves creep resistance.

Structural Intermetallics 1997

Edited by M.V. Nathal, R. Darolia, C.T. Liu, P.L. Martin,  
D.B. Miracle, R. Wagner, and M. Yamaguchi  
The Minerals, Metals & Materials Society, 1997

The results obtained are discussed with respect to the site preference of the ternary additives in the Ni<sub>3</sub>Al and TiAl lattices and the oxidation behavior of Nb-Ti-Al alloys. In addition, results of phase diagram studies are reported for the alloy systems mentioned above.

### Experimental

The measurements were carried out with a substantially modified Knudsen cell - mass spectrometer system supplied by Finnigan MAT, Bremen, Germany. The Knudsen cell - mass spectrometer system used is denoted as MSI in Ref. 9 and the modifications are reported there. It allowed the determination of silver partial pressures in the Knudsen cell of less than 10<sup>-8</sup> Pa (9). The mass spectrometer is a single-focusing, 90° sector field instrument of the CH5 type. The vapor species were ionized with an electron emission current of 0.6 mA and an electron impact energy of 70 eV.

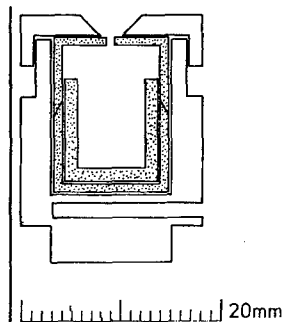


Figure 2: Knudsen cell composed of an outer metallic cell and an inner ceramic cell with ceramic crucible.

Figure 2 shows the selected cylindrical Knudsen cell used in the measurements. The outer molybdenum cell contains an inner cell with a crucible, both made of the same ceramic material. High-density zirconia stabilized by calcium oxide, supplied by Friedrichsfeld, Mannheim, Germany, or high-density yttria, supplied by Mazek, Jülich, Germany, are used as ceramic materials in order to avoid chemical reactions with the alloys to be investigated. This is a very important aspect since the alloys considered as structural intermetallics are very reactive with most of the crucible materials at the high temperatures of the measurements. Yttria was a particularly inert material. Temperatures in the Knudsen cell were measured with an optical pyrometer on the bottom of a black body cavity placed laterally close to and below the bottom of the cell (see Figure 2).

Partial pressures  $p(i)$  of the alloy components  $i$  resulted from the measured ion intensities  $I^+(i)$ , corrected for the isotopic distribution, by the equation

$$p(i) = E \frac{1}{\sigma(i)} I^+(i) T$$

where  $E$  is the pressure calibration factor and  $\sigma(i)$  is the ionization cross section of  $i$ . The pressure calibration factor results from the vaporization of a pure metal with known vapor pressure. The ionization cross sections were taken from the tables by Mann (10). They do not have to be taken into account if the metal used for the calibration is the same as the alloy component  $i$  for which the partial pressure is evaluated. The uncertainties introduced by the use of ionization cross sections in the evaluation of partial pressures over alloys are generally less than 35 per cent.

Partial and integral thermodynamic properties result from the partial pressures and their temperature dependencies by the standard equations given for example in Ref. 2. The mixing properties of melts and solid solutions also result directly from measured ion intensities, i.e. without calibration of the mass spectrometer - Knudsen cell system, by the use of the ion intensity ratio methods (see e.g. Ref. 11 and references quoted therein). The Gibbs-Duhem relation is used to obtain, for example, the activity coefficient  $f(A)$  of the component  $A$  in the mixture  $\{xA + (1-x)B\}$  from the ion intensity ratio  $I(A^+)/I(B^+)$  by the equation

$$\ln f(A) = - \int_{x=1}^x (1-x) d \ln \frac{x I(B^+)}{(1-x) I(A^+)}$$

Ion intensity ratio methods have been used successfully for the study of numerous systems (see e.g. Ref. 4). The accuracy of the data obtained by this method is generally better than 10 per cent.

The samples were prepared by induction melting of the pure alloy components in a purified argon atmosphere using the levitation technique.

### Results and Discussion

#### The Ni-Al System

Fifteen alloy samples of different compositions covering the complete composition range of the Ni-Al system between  $x(\text{Ni})=0.7$  and  $x(\text{Ni})=1$  were investigated by Knudsen effusion mass spectrometry and high temperature differential thermal analysis. Only the species Ni and Al were detected in the gaseous phase over the different alloy samples. Figure 3 shows the phase diagram of the nickel-rich part of the Ni-Al system obtained by the vapor pressure measurements and high temperature differential thermal analysis. The dashed lines and the error bars represent the estimated uncertainties of the results obtained by Knudsen effusion mass spectrometry. The uncertainties of the results obtained by differential thermal analysis are smaller than the size of the dots. Details of the determination of phase boundaries from the concentration and temperature dependencies of the Ni and Al partial pressures and from differential thermal analysis are reported in Ref. 12. The phase diagram shown in Figure 3 differs from that given in the compilation by Hansen and Anderko (13). In contrast to the diagram by Hansen and Anderko, the diagram in the present work shows the same phase equilibria and fundamental structure as that proposed by Schramm (14), which was rejected in Hansen and Anderko's compilation. The following peritectic and eutectic reactions exist according to Hansen and Anderko:



These reactions, which were generally used until about 1990, differ from those shown in Figure 3. The phase reactions in the present work have recently been supported by Ref. 15 and are now incorporated into recent compilations (Refs 16 and 17).

Ni and Al partial pressures were determined over each of the 15 alloy samples (18). Figure 4 shows as an example those over the Ni<sub>3</sub>Al phase of stoichiometric composition. Pressures for the melt, the solid  $\gamma'$  phase, and the two phase fields in between the two (cf. Figure 3) are given. Similar vapor pressure curves were obtained for the remaining samples. The equilibrium vapor pressures of pure nickel and aluminum are additionally given for comparison. The Ni partial pressure over the alloy exceeds that of Al over the alloy in contrast to the corresponding equilibrium pressures over the pure metals. This is caused by the very high reduction of the Al pressure by the alloy formation in contrast to the Ni pressure; at 1600 K the reduction amounts to more than three orders of magnitude.

Integral and partial thermodynamic properties, such as enthalpies, chemical activities, and chemical potentials, were evaluated for the solid phase and the melt from the partial pressures determined (18). The correlation between the partial and integral enthalpies of formation of Ni<sub>3</sub>Al, for example, is given by the relation

$$\Delta_f H_m^0(\text{Ni}_3\text{Al}) = 0.75 \Delta_f h_{\text{Ni}} + 0.25 \Delta_f h_{\text{Al}}$$

The data evaluated from the pressures in Figure 4 are shown as an example in Table I. The partial enthalpies obtained (cf. Table I) reveal that the high value for the integral enthalpy of formation is due to the increase of the bond strength of the Al atoms in the alloy as compared to pure Al metal; the bond strengths of the Ni atoms in the alloy and the pure Ni metal are practically the same. This is also reflected by comparing the enthalpies of

dissociation given in parentheses of the gaseous species  $\text{Al}_2$  ( $150 \pm 14$ , Ref. 19),  $\text{Ni}_2$  ( $230 \pm 21$ , Ref. 20), and  $\text{AlNi}$  ( $228 \pm 21$ , Ref. 21). The values in parentheses are the molar enthalpies of dissociation in  $\text{kJ mol}^{-1}$  at 0 K and were obtained by separate gas phase measurements using Knudsen effusion mass spectrometry. The values show an increase of the Al-Ni bond as compared to that of Al-Al unlike that of Ni-Ni.

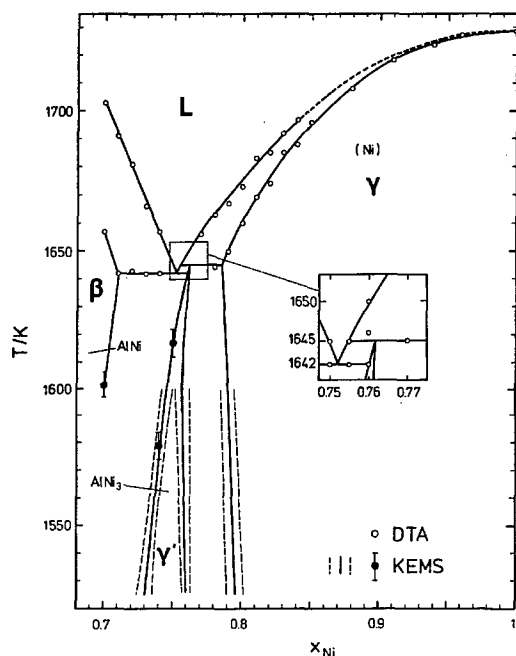


Figure 3: Ni-rich part of the Ni-Al phase diagram obtained by high temperature differential thermal analysis (DTA) and Knudsen effusion mass spectrometry (KEMS) (Ref. 12).

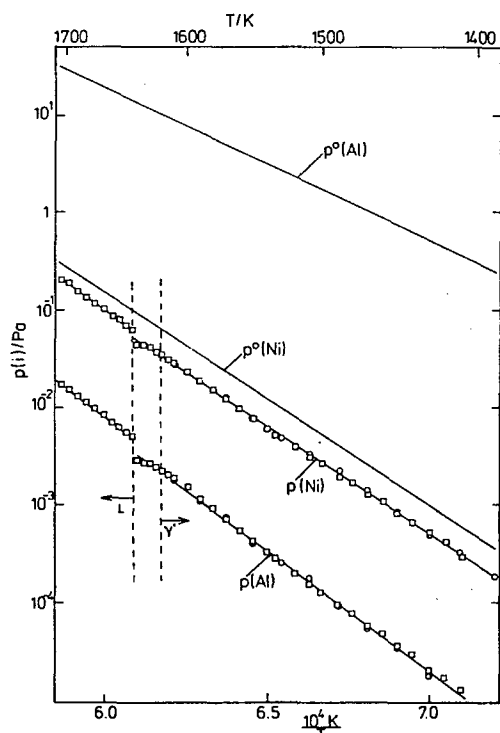


Figure 4: Temperature dependence of the Ni and Al partial pressures over  $\text{Al}_{1-x}\text{Ni}_x$ ,  $x = 0.75$ , ( $p(i)$ ) and over pure nickel and aluminum ( $p^o(i)$ ) (Ref. 18).

The enthalpy of formation of  $\text{Ni}_3\text{Al}$  at room temperature,  $\Delta_f H_m^\circ(298.15 \text{ K}) = -153 \pm 20 \text{ kJ mol}^{-1}$ , is obtained from the corresponding enthalpy value in Table I and ancillary data. Values of,  $\Delta_f H_m^\circ(298.15 \text{ K}) = -149.2 \pm 8.0$  (Ref. 22) and  $-155.2 \text{ kJ mol}^{-1}$  (Ref. 23) result from calorimetric measurements. The values agree well with those in the present work obtained for the first time by vapor pressure measurements. The different uncertainties of the data demonstrate that calorimetry is usually the best method for the determination of enthalpies of formation. However, the vapor pressure methods have the advantage that they allow the determination of partial quantities and precise  $\Delta G$  values. The good agreement of the enthalpies of formation demonstrates the consistency of results obtained by different methods.

Table I: Partial and integral thermodynamic properties of formation of the  $\text{Ni}_3\text{Al}$  phase with  $x(\text{Ni})=0.75$  at 1600 K according to the reaction:  $3 \text{ Ni(s)} + \text{Al(l)} = \text{Ni}_3\text{Al(s)}$ . (Errors are probable overall errors.)

i	$\Delta_f h_i/(\text{kJ mol}^{-1})$	$\Delta_f s_i/(\text{J mol}^{-1} \text{ K}^{-1})$
<i>Partial quantities</i>		
Ni	$2.1 \pm 10.0$	$6.6 \pm 6.3$
Al	$-171.9 \pm 9.1$	$-35.8 \pm 6.2$
<i>Integral quantities</i>		
	$\Delta_f H_m^\circ/(\text{kJ mol}^{-1})$	$\Delta_f S_m^\circ/(\text{J mol}^{-1} \text{ K}^{-1})$
	$-165.6 \pm 19.6$	$-15.9 \pm 12.5$

The partial pressures determined by us over  $\text{NiAl}$  of stoichiometric composition are shown in Figure 5. The equilibrium pressures of pure  $\text{Ni(s)}$  and  $\text{Al(l)}$  are shown for comparison as in Figure 4 for  $\text{Ni}_3\text{Al}$ . The partial pressures of Ni and Al and their ratio change significantly on going from  $\text{Ni}_3\text{Al}$  to  $\text{NiAl}$ .

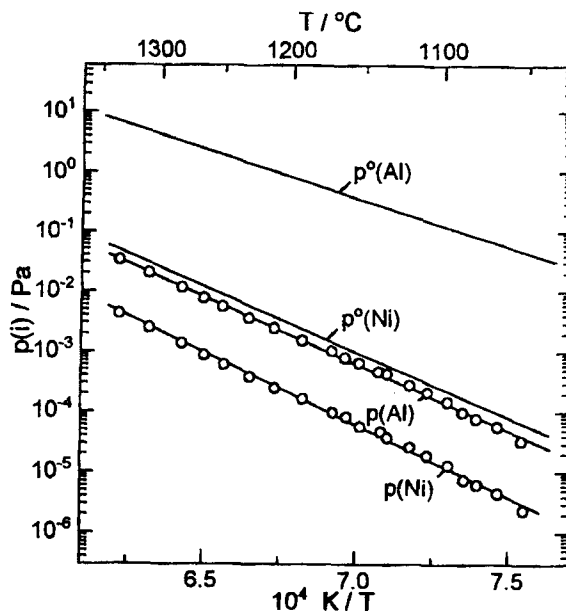


Figure 5: Temperature dependence of the Ni and Al partial pressures over  $\text{Al}_{1-x}\text{Ni}_x$ ,  $x=0.50$ , ( $p(i)$ ) and over pure nickel and aluminum ( $p^o(i)$ )

The mass spectrometric work carried out on the Ni-Al system by Jacobson (24, 25), Johnston and Palmer (26), and Oforka (27) as well as on the Ni-Al-Cr system by Argent and Oforka (28) should be mentioned here. Johnston and Palmer investigated the melt of the Ni-Al system. They used Knudsen cells made of graphite which led to the dissolution of carbon in the melt as reported in Ref. 12 thereby causing uncertainties. Only three alloy compositions were investigated by Argent and Oforka as well as Oforka in

the nickel-rich part of the Ni-Al system. The results agree fairly well with the data obtained by us (cf. Ref. 18). Jacobson used a double Knudsen cell system for the vaporization studies. The results obtained agree well with those reported in Ref. 18.

### The Ti-Al System

The first vaporization studies of the Ti-Al system by Knudsen effusion mass spectrometry were carried out by Hoch and Usell (29). These authors only determined the Al activity for one temperature of 1780 K over a limited concentration range of the system. We, therefore, studied the vaporization of 19 alloy samples of different compositions covering the complete composition range of the Ti-Al system in the temperature range between 1100 and 1650 K. Figure 6 shows the sample compositions and the temperature ranges of the measurements. The partial pressures of Ti and Al were determined. The pressures obtained and the thermodynamic data evaluated are given in detail in Ref. 31. Figure 7 shows as an example the thermodynamic activities of Ti and Al in different solid alloys of the Ti-Al system for the mean temperature of the measurements of 1473 K. The phase composition of the different alloys at 1473 K is also given in the diagram. The thermodynamic activities of Ti and Al resulted according to the relation  $a(i) = p(i)/p^{\circ}(i)$  ( $i = \text{Ti, Al}$ ) by comparing the pressures over the alloy samples,  $p(i)$ , with those of pure Ti(s) and Al(l),  $p^{\circ}(i)$ . In addition, the thermodynamic activity of Ti was evaluated from the measurement results by the ion intensity ratio method (cf. Section Experimental). The results obtained by this method are also shown in the diagram. The two different evaluation methods which are independent of each other, agree in general very well showing the accuracy of the method. Recently Jacobson et al. (24, 25) determined the thermodynamic activities of Al in 3 alloys of the Ti-Al system belonging to the  $\gamma$ -TiAl,  $\{\gamma\text{-TiAl} + \text{TiAl}_3\}$ , and  $\{\gamma\text{-TiAl} + \text{TiAl}_2\}$  phase fields. The results obtained by Jacobson et al., as well as Hoch and Usell (29) agree reasonably well with those in the present work. A detailed comparison is given in Ref. 31.

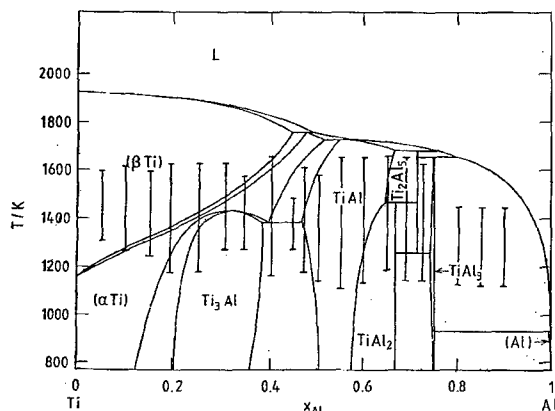
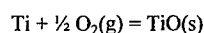
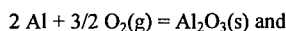


Figure 6: Phase diagram by Kattner et al. (30) with the composition of the prepared alloy samples and the temperature ranges of the vaporization measurements (Ref. 31).

The formation of a stable  $\text{Al}_2\text{O}_3$  scale is a critical issue in the technical application of titanium aluminides. Knowledge of the thermodynamic activities of Ti and Al in the alloys is necessary for predictions of the stability of oxide scales. Such predictions have been carried out so far by Rahmel and Spencer (32) as well as Luthra (33). Only estimated activities were, however, used by these authors. The computations by Rahmel and Spencer were repeated by employing the thermodynamic activities determined in the present work. The oxygen partial pressures of the reactions



were computed (see Figure 8). The computation was carried out at 1373 K in order to permit a comparison with the results obtained by Rahmel and Spencer (32). It is obvious that the oxygen partial pressures belonging to the two oxidation reactions intersect at an Al concentration of about  $x(\text{Al}) = 0.54$ . Rahmel and Spencer (32) determined the Al concentration for this intersection as  $x(\text{Al}) = 0.61$ , while Luthra (33) obtained  $x(\text{Al}) = 0.55$  at 1073 K. This means that the results of the present work lead to the prediction of a stable  $\text{Al}_2\text{O}_3$  scale for lower Al concentrations than by Rahmel and Spencer (32). Moreover, the data obtained by us show that this concentration decreases with decreasing temperature.

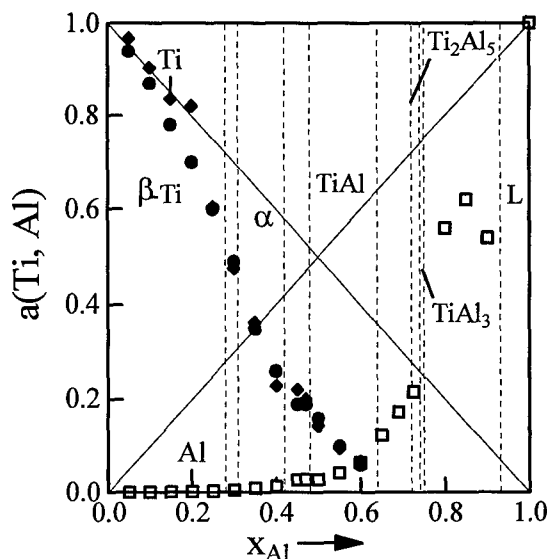


Figure 7: Thermodynamic activities of Ti and Al at 1473 K in solid Ti/Al alloys of different compositions obtained by the ion intensity ratio method (•) and by the equation  $a(i) = p(i)/p^{\circ}(i)$  (♦, □) (Ref. 31).

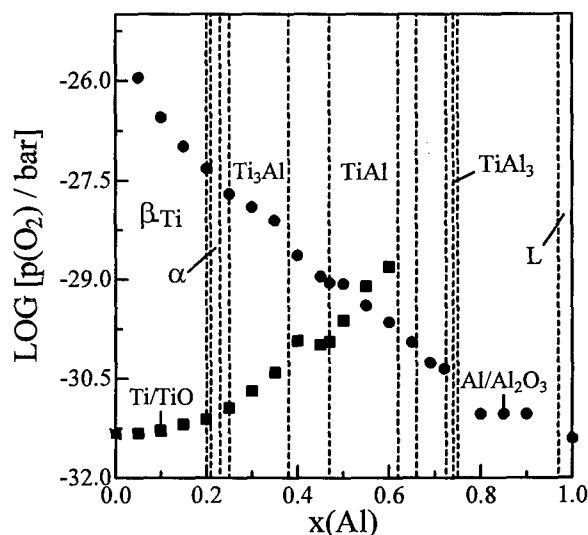


Figure 8:  $\text{O}_2$  partial pressures for different metal/oxide equilibria and Al concentrations in Ti-Al alloys (Ref. 31).

### Ternary Solid Solutions of Co, Fe, Hf and Ti in $\text{Ni}_3\text{Al}$

Partial pressures of Ni and Al were determined over all the alloys of different compositions at temperatures between 1300 and 1700 K. Co and Fe partial pressures were additionally obtained for the solutions of Co or Fe in  $\text{Ni}_3\text{Al}$ . Thermodynamic activities and other thermodynamic properties were evaluated from the partial pressures determined. Such properties are,

for example, the excess chemical potentials of Ni and Al in the solubility range of the  $\text{Ni}_3\text{Al}$  phase for the alloy compositions  $(\text{Ni}_3\text{Al})_{1-x}\text{M}_x$  ( $\text{M} = \text{Hf}, \text{Fe}, \text{Co}$ ) (Figure 9) and the excess partial enthalpies and entropies in the same alloys for  $\text{M} = \text{Fe}$  (Figures 10 and 11). The determination of partial enthalpies and entropies was only possible for the solution of Fe in  $\text{Ni}_3\text{Al}$ . The composition series  $(\text{Ni}_3\text{Al})_{1-x}\text{M}_x$  were considered since they allow the determination of the change of the thermodynamic properties on adding the third component M to  $\text{Ni}_3\text{Al}$ . Compositions with  $\text{M} = \text{Ti}$  could not be considered due to the shape of the solubility lobe in the Ni-Al-Ti system at the temperatures of the measurements. The alloys consist of two phases if comparatively small amounts of Ti are added to  $\text{Ni}_3\text{Al}$ . The alloy compositions  $\text{Ni}_{0.75}\text{Al}_{0.25-x}\text{Ti}_x$ ,  $0 \leq x \leq 0.25$ , obtained by substituting Ti for Al, were, therefore, investigated in this system. The results obtained for the compositions  $\text{Ni}_{0.75}\text{Al}_{0.25-x}\text{Ti}_x$  are reported in Ref. 34. A detailed presentation of the data for the alloy compositions  $(\text{Ni}_3\text{Al})_{1-x}\text{M}_x$  ( $\text{M} = \text{Hf}, \text{Fe}, \text{Co}$ ) is given in Refs. 35, 36 and 37.

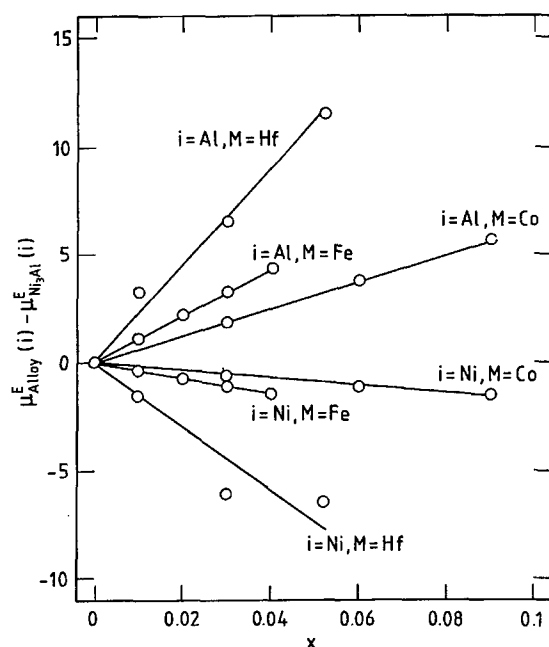


Figure 9: Excess chemical potentials of Ni and Al in the solubility range of the  $\gamma'$ - $\text{Ni}_3\text{Al}$  phase for 1473 K and the compositions  $(\text{Ni}_3\text{Al})_{1-x}\text{M}_x$  ( $\text{M} = \text{Hf}, \text{Fe}, \text{Co}$ ),  $\mu_{\text{Alloy}}^E(i)$ , relative to the value of  $\text{Ni}_3\text{Al}$  of stoichiometric composition,  $\mu_{\text{Ni}_3\text{Al}}^E(i)$ .

In addition, phase diagram studies concerning the extension of the different ternary solubility ranges were carried out for the temperatures of the vaporization measurements in order to obtain the correct assignment of the measured data to the  $\gamma'$  phase. Figure 12 shows a vertical section in the Ni-Al-Hf system as an example of the results obtained by the phase diagram studies.

It is interesting to note that the excess chemical potentials of Ni or Al shown in Figure 9 change in the same way for each of the three elements. The excess chemical potentials of Al increase and those of Ni decrease if Hf, Fe or Co is added to  $\text{Ni}_3\text{Al}$ . It is well known that the transition metals are dissolved in  $\text{Ni}_3\text{Al}$  by the substitution for Ni and Al.

The following question arises: What is the correlation between the substitution behavior of the added Hf, Fe, or Co and the excess chemical potentials determined?

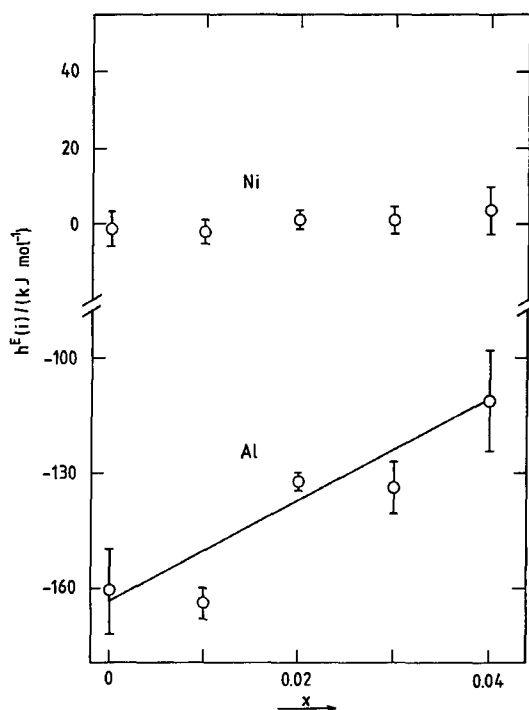


Figure 10: Excess partial enthalpies of Ni and Al in the  $\gamma'$  solid solution for the alloys  $(\text{Ni}_3\text{Al})_{1-x}\text{Fe}_x$  (Ref. 36).

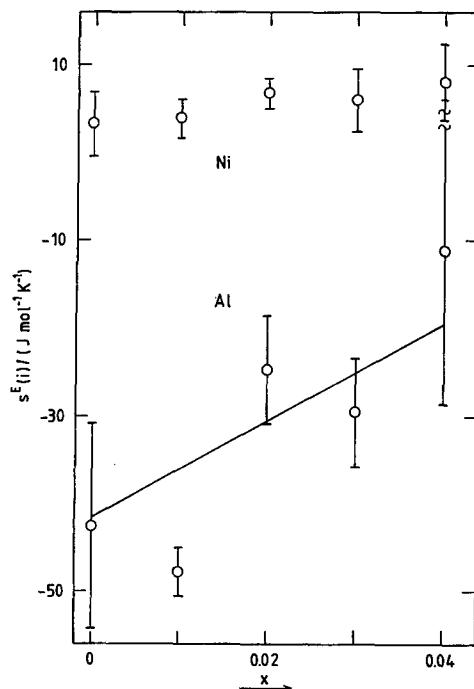


Figure 11: Excess partial entropies of Ni and Al in the  $\gamma'$  solid solution for the alloys  $(\text{Ni}_3\text{Al})_{1-x}\text{Fe}_x$  (Ref. 36).

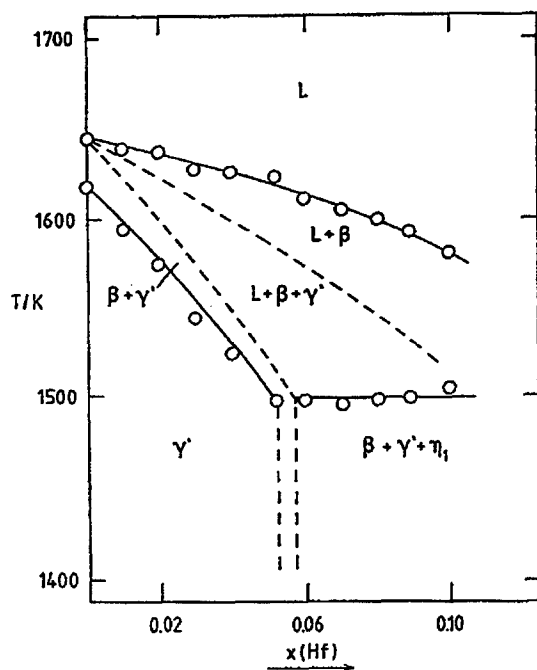


Figure 12: Vertical section in the Ni-Al-Hf system for the compositions  $(\text{Ni}_3\text{Al})_{1-x}\text{Hf}_x$ ,  $0 \leq x \leq 0.25$ .

The excess chemical potential of the component  $i$  is determined by two contributions according to the relation

$$\Delta\mu^E(i) = \Delta h^E(i) - T \Delta s^E(i).$$

The partial excess enthalpy  $\Delta h^E(i)$  determines the strength of the bond forces of the component  $i$  in the alloy. The partial excess entropy  $\Delta s^E(i)$  is determined by the degree of order of the component  $i$  in the crystal lattice. The  $\text{Ni}_3\text{Al}$  phase has a face-centered cubic  $\text{L1}_2$  structure. All Al atoms are situated at the cube corner sites and all Ni atoms at the face center sites if there is complete order. The partial entropies of Ni and Al are then lowest. If a third component is added to this structure, which substitutes for example predominantly for Al, disorder is introduced in the Al sublattice thereby increasing the partial entropy of Al. A similar situation is valid for the partial entropies of Ni if the added component substitutes predominantly for Ni. Figure 11 shows that Fe substitutes predominantly for Al in  $\text{Ni}_3\text{Al}$ , which is in agreement with the results obtained by Mössbauer effect measurements (38, 39), axial electron-channeling microanalysis (40), and atom probe field-ion microscope measurements (41). The answer to the question posed above is that the change of the chemical potentials does not allow predictions concerning the substitution behavior of a third component in  $\text{Ni}_3\text{Al}$ . This is determined by the change of the entropy. The change of  $\mu^E$  depends on the changes of the enthalpy and entropy contributions (see above equation for  $\Delta\mu^E(i)$ ). The change originating from the entropy can, therefore, be compensated and obtain a different direction by the enthalpy contribution. This explains why the changes in the excess chemical potentials for Hf, Fe, and Co in Figure 9 show the same trend though Fe and Hf substitute predominantly for Al and Co for Ni (see e.g. Ref. 41).

The calorimetric study on ternary  $\text{Ni}_3\text{Al}$ -based alloys leading to enthalpies of formation (42) should be mentioned in this section.

#### Ternary Solid Solutions of Nb in TiAl and the Ti-Al-Nb System

Twenty-four alloy samples were prepared within the Ti-Al-Nb system. The compositions of these alloy samples are shown in Figure 13. Emphasis was laid on the  $\gamma$ -TiAl phase and on the alloys with the compositions

$(\text{Ti}_{1-x}\text{Al}_x)_{1-y}\text{Nb}_y$  ( $0.20 < x < 0.62$ ;  $y = 0.1$ ). Using these alloys the influence of Nb on the activities of Ti and Al in the different phase fields was investigated.

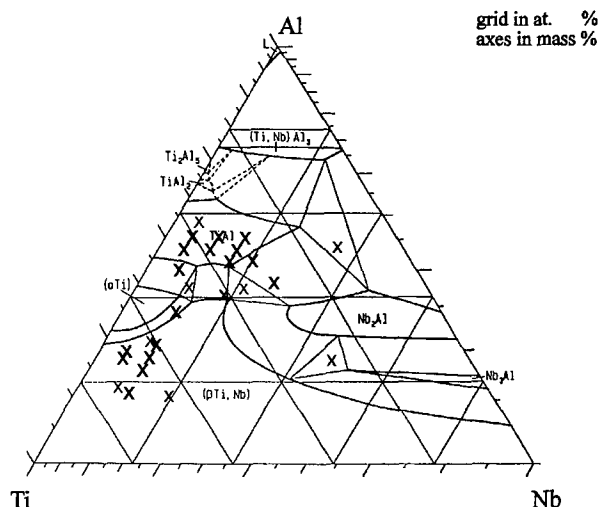


Figure 13: Phase diagram of the Ti-Al-Nb system by Hellwig (43) for a temperature of 1200 °C (The crosses (x) represent the prepared and investigated alloy samples.)

Figure 14 shows the influence of the Nb content in the  $\gamma$ -TiAl phase on the activities of Ti and Al for the alloy compositions  $(\text{Ti}_{0.38}\text{Al}_{0.62})_{1-x}\text{Nb}_x$ . These compositions result by adding Nb to  $\text{Ti}_{0.38}\text{Al}_{0.62}$ . The composition  $\text{Ti}_{0.38}\text{Al}_{0.62}$  was selected since it allows comparatively large amounts of Nb to be added to a Ti/Al alloy with constant composition within the  $\gamma$ -TiAl solubility range (cf. Figure 13). The Ti activity increases while the Al activity decreases in the  $(\text{Ti}_{0.38}\text{Al}_{0.62})_{1-x}\text{Nb}_x$  alloys if the Nb content is raised (Figure 14).

Figure 15 shows the influence of Nb on the activities of Ti and Al in different phase fields. The alloys with constant Nb content of the compositions  $(\text{Ti}_{1-x}\text{Al}_x)_{1-y}\text{Nb}_y$  ( $0.20 < x < 0.62$ ;  $y = 0.1$ ) were compared with binary Ti-Al alloys with the same Ti/Al ratio. Alloy samples with the same Ti/Al ratio with and without Nb additive were measured successively several times. Thermodynamic activities with a precision of less than 5 per cent resulted in this way. In no case does the activity of Al increase relative to the activity of Ti. This and the results shown in Figure 14 mean that Nb additives do not favor the formation of a stable  $\text{Al}_2\text{O}_3$  scale as compared to the formation of a stable  $\text{TiO}_2$  scale. The formation of a stable  $\text{Al}_2\text{O}_3$  scale is an important aim of alloy development since mixed  $\text{TiO}_2/\text{Al}_2\text{O}_3$  scales do not protect the alloy from corrosion (8).

#### Prediction of the Lattice Site Occupation in the $\gamma$ -TiAl Phase of the Ti-Al-Nb System

The site preference of Nb in the  $\gamma$ -TiAl phase and the distribution of the Ti and Al atoms on the different sites of the crystal lattice can be computed with a statistical model based on the Bragg-Williams approximation. Mixing properties determined by Knudsen effusion mass spectrometry are very useful for the determination of the input parameters used in the model computations. The species chemical potential/bond energy (SCPBE) model (44) can be very useful for parameterizing the thermodynamic properties of phases which can be represented by a multiple sublattice model. The SCPBE model for phases which are taken to be comprised of two sublattices is considered in Refs 45 and 46 by Oates and Wenzl. The development of the equations given in these references to the general case of any number of sublattices is given in Ref. 44. These equations are used for the  $\gamma$ -TiAl phase considered here. The TiAl phase crystallizes with the tetragonal  $\text{L1}_0$  structure, i.e. it is basically a cubic structure which is tetragonally distorted because of the particular stacking of the atom planes. The  $\gamma$ -TiAl phase can

be described by two Al-containing sublattices and two Ti-containing sublattices which penetrate each other.

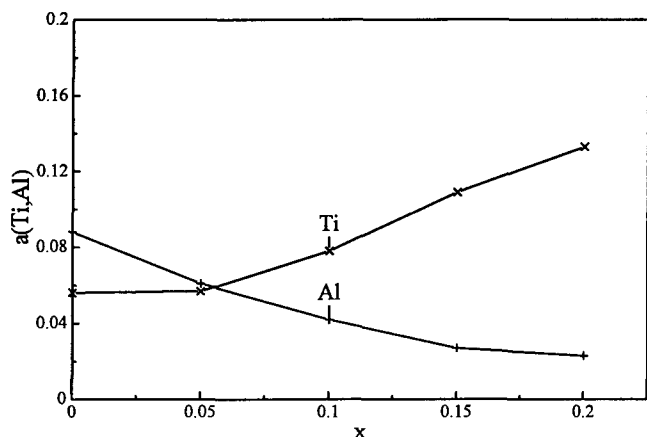


Figure 14: Thermodynamic activities of Ti and Al in the  $\gamma$ -TiAl phase for the compositions  $(\text{Ti}_{0.38}\text{Al}_{0.62})_{1-x}\text{Nb}_x$ ,  $x = 0 - 0.2$ , at 1473 K.

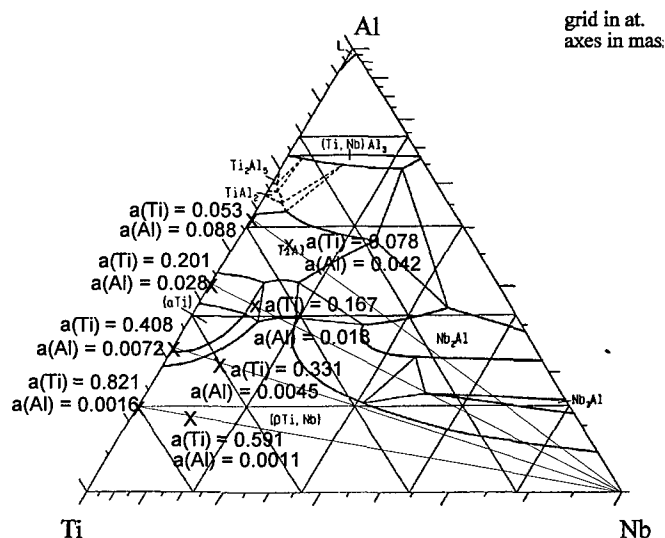


Figure 15: Comparison of the thermodynamic activities of Ti and Al in ternary Ti-Al-Nb alloys with constant Nb content of 10 per cent with those in binary Ti-Al alloys for different Ti/Al ratios at a temperature of 1473 K.

The input parameters for the computations are the binary interaction parameters  $\Omega(\text{Ti-Al})$ ,  $\Omega(\text{Ti-Nb})$ , and  $\Omega(\text{Al-Nb})$  between the nearest Ti-Al, Ti-Nb, and Al-Nb neighbors, respectively. The following interaction parameters were used in the computations:

$$\Omega(\text{Ti-Al}) = -55.5 \text{ kJ mol}^{-1},$$

$$\Omega(\text{Ti-Nb}) = -10 \text{ kJ mol}^{-1}, \text{ and}$$

$$\Omega(\text{Al-Nb}) = -90 \text{ kJ mol}^{-1}.$$

$\Omega(\text{Ti-Al})$  resulted from the chemical potentials determined by us for the alloys of the binary Ti-Al system reported in one of the preceding sections. The value of  $\Omega(\text{Ti-Nb})$  is obtained from the computations for the modeling of the binary Ti-Nb system in Ref. 47. The given value for  $\Omega(\text{Al-Nb})$  resulted by the fitting of the activities of Ti and Al in the alloys  $(\text{Ti}_{0.38}\text{Al}_{0.62})_{1-x}\text{Nb}_x$  ( $x = 0 - 0.2$ ) computed with the model on those determined experimentally (Fig. 14). The parameters  $\Omega(\text{Ti-Al})$  and  $\Omega(\text{Ti-Nb})$  obtained from the results of the binary systems are used in these computations and the value for  $\Omega(\text{Al-Nb})$  was varied.

The interaction parameters obtained are used to compute the concentrations of the Ti and Al atoms on the Al and Ti sublattices of the binary  $\gamma$ -TiAl phase in the homogeneity range of this phase (see Figure 16). In addition, the concentrations on the Ti and Al sublattices for the ternary  $\gamma$ -TiAl phase, which is obtained by the addition of Nb, are computed for the alloys of the compositions  $(\text{Ti}_{0.38}\text{Al}_{0.62})_{1-x}\text{Nb}_x$  (see Figure 17).

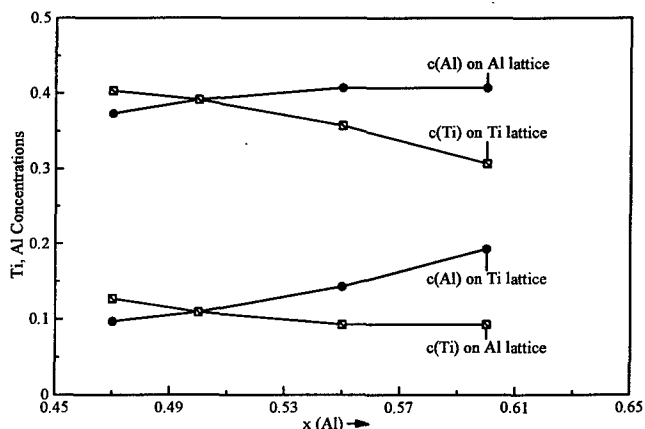


Figure 16: Concentrations of Ti and Al in the Ti and Al sublattices of the binary  $\gamma$ -TiAl phase at 1473 K with different Al contents.

The lattice site occupations for the binary  $\gamma$ -TiAl phase show that the Al sublattice contains 38% Al atoms and 12% Ti atoms for TiAl of stoichiometric composition, the Ti sublattice contains 38% Ti atoms and 12% Al atoms (see Figure 16). The high value for the concentration of antistructure atoms of 12% is caused by the high thermal energy at 1473 K. The concentration of antistructure atoms is diminished if the temperature decreases. The larger change of the Al concentration on the Ti sublattice as compared to the Al sublattice with increasing Al content means that the added Al atoms form predominantly antistructure atoms on the Ti sublattice thereby leading to a strong decrease of the Ti concentration on this lattice.

The occupation of the Ti and Al sublattices shown in Figure 16 for  $x(\text{Al}) = 0.62$  equals that in Figure 17 for  $(\text{Ti}_{0.38}\text{Al}_{0.62})_{1-x}\text{Nb}_x$  with  $x = 0$ . The added Nb atoms obviously prefer the occupation of sites on the Ti sublattice. This agrees with Konitzer's results (48) obtained by X-ray emission/channeling experiments. The occupation of sites on the Ti sublattice by Nb causes changes of the Ti and Al concentrations on the Ti and Al sublattices. It is interesting to note that these changes obviously particularly concern the

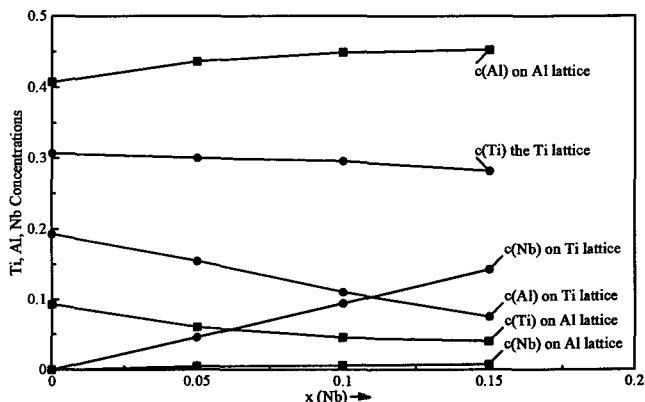


Figure 17: Concentrations of Ti, Al, and Nb in the Ti and Al sublattices of the ternary  $\gamma$ -TiAl phase at 1473 K for the alloy compositions  $(\text{Ti}_{0.38}\text{Al}_{0.62})_{1-x}\text{Nb}_x$  with different Nb contents.



concentrations of the antistructure atoms on the two sublattices. In contrast to this, the occupation of the Ti and Al sublattices with atoms of the same kind as the sublattice show very small changes if the Nb concentration in the alloy is raised.

### Conclusions

Vaporization studies render possible the determination of partial and integral thermodynamic properties with emphasis on Gibbs energies. The most complete information on vaporization processes is obtained by the use of Knudsen effusion mass spectrometry. This method allows the identification of the vaporizing species and the determination of their partial pressures at high temperatures over a large dynamic range of generally more than 6 orders of magnitude up to temperatures above 2500 K. Mixing properties and other thermodynamic properties of alloys can be evaluated from the partial pressures. The application of this method to structural intermetallics yields valuable information at high temperatures.

This potential for the study of intermetallics is demonstrated by reporting the authors' results on nickel and titanium aluminides.

The Ni and Al partial pressures over the phases NiAl and Ni<sub>3</sub>Al give information on the possible depletion of one component during the alloy production process at high temperature. A complete set of thermodynamic data for the formation of Ni<sub>3</sub>Al ( $\Delta G$ ,  $\Delta H$ ,  $\Delta S$ ) was determined. Phase boundaries resulted from the temperature and concentration dependencies which lead to a new phase diagram for the nickel rich part of the Ni-Al system after combining the results of Knudsen effusion mass spectrometry and high temperature differential thermal analysis. Thermodynamic activities of Ti and Al were obtained in the alloys of the Ti-Al-Nb and the Ti-Al boundary system. These data are necessary for the understanding of high temperature corrosion of titanium aluminides.

The importance of mass spectrometric vaporization studies for fundamental research is shown by the data determined for the ternary solutions of Co, Fe, Hf, or Ti in Ni<sub>3</sub>Al and of Nb in TiAl. The partial entropies of mixing of the alloy components render possible predictions on the substitution behavior of a third component in ordered intermetallic phases. This was demonstrated for the solid solution of Fe in Ni<sub>3</sub>Al. The predicted site preference of Fe for Al agrees with the results of direct measurements by different methods. The thermodynamic activities determined in the alloys of the solubility range of Nb in TiAl are used for the evaluation of the input parameters for the application of a thermodynamic model, which rendered possible the computation of the lattice site occupation in the solubility range of the  $\gamma$ -TiAl phase.

### References

- G. Sauthoff, in: "Materials Science and Technology", eds R.W. Cahn, P. Haasen, and E.J. Kramer, from Structure and Properties of Non Ferrous Alloys, vol. 8, ed. K.H. Matucha, (Weinheim, Germany: VCH Verlagsgesellschaft mbH, 1996), 643-802.
- Oswald Kubaschewski and Charles B. Alcock, *Metallurgical Thermochemistry*, (Oxford: Pergamon Press, 1979).
- H. Kleykamp, "Experimental Aspects of Solid Galvanic Cell Methods for Thermodynamic Studies on Alloys", *Ber. Bunsenges. Phys. Chem.*, 87 (1983), 777-781.
- K. Hilpert, in: "Structure and Bonding", vol. 73, "Noble Gas and High Temperature Chemistry", eds J. Clarke et al. (Berlin, Germany: Springer, 1990), 97-198.
- C. Chatillon, A. Pattoret, and J. Drowart, "Thermodynamic Studies of Condensed Phases by High Temperature Mass Spectrometry: Analysis of the Method and Review of Results", *High Temp. - High Pressures*, 7 (1975) 119-148.
- A. Steiner and K.L. Komarek, "Thermodynamic Activities of Solid Nickel-Aluminium Alloys", *Trans. Met. Soc. AIME*, 230 (1964), 786-790.
- S. Ochiai, Y. Oya, and T. Suzuki, "Alloying Behaviour of Ni<sub>3</sub>Al, Ni<sub>3</sub>Ga, Ni<sub>3</sub>Si, and Ni<sub>3</sub>Ge", *Acta metall.*, 32 (1984), 289-298.
- A. Rahmel, W.J. Quadackers, and M. Schütze, "Fundamentals of TiAl-Oxidation - A Critical Review", *Mater. and Corr.*, 46 (1995), 271-285.
- K. Hilpert and K. Ruthardt, "Determination of the Dissociation Energy of the Cr<sub>2</sub> Molecule", *Ber. Bunsenges. Phys. Chem.*, 91 (1987), 724-731.
- J.B. Mann, in: Recent Developments in Mass Spectrometry, eds K. Ogata and T. Hayakawa, (Tokyo: University of Tokyo Press, 1970), 814-823.
- A. Neckel, "Mass-Spectrometric Determination of Thermodynamic Mixing Effects of Alloys", in: *Thermochemistry of Alloys*, eds H. Brodowski and H.-J. Schaller, (Kluwer Academic Publishers, 1989), 221-246.
- K. Hilpert, D. Kobertz, V. Venugopal, M. Miller, H. Gerads, F.J. Bremer, and H. Nickel, "Phase Diagram Studies on the Al-Ni System", *Zeitschrift für Naturforsch.*, 42a (1987), 1327-1332.
- Max Hansen and Kurt Anderko, *Constitution of Binary Alloys*, 2nd edition (New York, NY: McGraw-Hill Book Company, 1958), 118-121.
- J. Schramm, "The Binary System Nickel-NiAl", *Zeitschrift für Metallkunde*, 33 (1941), 347-355.
- J.D. Verhoeven, J.H. Lee, F.C. Laabs, and L.L. Jones, "The Phase Equilibria of Ni<sub>3</sub>Al Evaluated by Directional Solidification and Diffusion Couple Experiments", *J. Phase Equilibria*, 12 (1991), 15-23.
- Handbook of Binary Phase Diagrams*, vol. 1 (Schenectady, NY: General Electric Company, 1983); update 12/94.
- Günter Petzow and Günter Effenberg, *Ternary Alloys*, vol. 7 (New York, NY: VCH Publishers, 1993), e.g. 441 and 452.
- K. Hilpert, M. Miller, H. Gerads, and H. Nickel, "Thermodynamic Study of the Liquid and Solid Alloys of the Nickel-Rich Part of the Ni-Al Phase Diagram Including the AlNi<sub>3</sub> Phase", *Ber. Bunsenges. Phys. Chem.*, 94 (1990), 40-47.
- C.A. Stearns and C.A. Kohl, "Mass Spectrometric Determination of the Dissociation Energies of Gaseous Al<sub>2</sub>, AlSi, and AlSiO", *High Temp. Science*, 5 (1973), 113-127.
- A. Kant, "Dissociation Energies of Diatomic Molecules of the Transition Elements. I. Nickel", *J. Chem. Phys.*, 41 (1964), 1872-1876.
- L.N. Gorokhov, A.M. Emel'yanov, Yu.S. Khodoev, E.S. Levin, M.S. Petrushevskii, and P.V. Geld, "Mass Spectrometry of Evaporating Nickel Monoaluminide and Microinhomogeneity in the Liquid", *High Temp.*, 14 (1976), 355-358.
- F.J. Sommer, "Modern Methods in High Temperature Calorimetry", *J. Thermal Analysis*, 33 (1988), 15-28.
- P.D. Desai, "Thermodynamic Properties of Selected Binary Aluminium Alloy Systems", *J. Phys. Chem. Ref. Data*, 16 (1987), 109-124.
- N.S. Jacobson, "Double Knudsen Cell System for Alloy Activity Measurements by Mass Spectrometry", 188th Meeting of The Electrochemical Society, Chicago, Oct. 1995, Extended Abstracts vol. 95-2, (Pennington, NJ: The Electrochemical Society, 1995), 1094-1095.
- Nate S. Jacobson, private communication with author, NASA Lewis Research Center, Cleveland, Ohio, 27 February 1997.
- G.R. Johnston and L.D. Palmer, "Quad-Cell Mass Spectrometry: Thermodynamic Properties of Liquid Aluminium - Nickel Alloys", *High Temp. - High Pressures*, 12 (1980), 261-266.
- N.C. Oforika, "Thermodynamics of Aluminium-Nickel Alloys", *Indian Journal of Chemistry*, 25A (1986), 1027-1029.
- N.C. Oforika and B.B. Argent, "Thermodynamics of Ni-Cr-Al Alloys", *J. Less-Common Met.*, 114 (1985), 97-109.
- M. Hoch and R.J. Usell, "Thermodynamics of Titanium Alloys: II. Titanium and Aluminium Activities in the bcc  $\beta$  Phase of the Ti-Al System", *Met. Trans.*, 2 (1971), 2627-2632.
- U.R. Kattner, J.C. Lin, and Y.A. Chang, "Thermodynamic Assessment and Calculation of the Ti-Al System", *Metallurg. Trans.*, 23A (1992), 2081-2090.
- M. Eckert, L. Bencze, D. Kath, H. Nickel, and K. Hilpert, "Thermodynamic Activities in the Alloys of the Ti-Al System", *Ber. Bunsenges. Phys. Chem.*, 100 (1996), 418-424.
- A. Rahmel and P.J. Spencer, "Thermodynamic Aspects of TiAl and TiSi<sub>2</sub> Oxidation: The Al-Ti-O and Si-Ti-O Phase Diagrams", *Oxid. Met.*, 35 (1991), 53-68.

33. K.L. Luthra, "Stability of Protective Oxide Films on Ti-Base Alloys", Oxid. Met., 36 (1991), 475-490.
34. J. Kapala, D. Kath, and K. Hilpert, "Thermodynamic Activities and Phase Boundaries for the Alloys of the  $\text{Ni}_3\text{Al}$ - $\text{Ni}_3\text{Ti}$  Pseudobinary Section in the Ni-Al-Ti System", Metallurg. Mat. Trans., 27A (1996), 2673-2677.
35. M. Albers, M. Sai Baba, D. Kath, M. Miller, and K. Hilpert, "Chemical Activities in the Solid Solution of Hf in  $\text{Ni}_3\text{Al}$ ", Ber. Bunsenges. Phys. Chem., 96 (1992), 1663 - 1668.
36. M. Albers, D. Kath, and K. Hilpert, "Thermodynamic Activities and Partial Enthalpies of Mixing in the Solid Solution of Fe in  $\text{Ni}_3\text{Al}$ ", Metallurg. Mat. Trans., 27A (1996), 3569 - 3575.
37. M. Albers, K. Hilpert, H. Nickel, and K.G. Weil: "Determination of Activities of Components in the Ternary Alloys Al-Ni-M (M = Co, Fe, Hf) by Knudsen Effusion Mass Spectrometry" (Report Jül-2974, Forschungszentrum Jülich GmbH, Jülich, Germany, 1994).
38. J.W. Drijver and F. van der Woude, "Mössbauer Effect Measurements on the Intermetallic Compounds  $\text{Ni}_3\text{Al}$  and  $\text{Ni}_3\text{Ga}$ ", J. Phys. F: Metal Phys., 3 (1973), L206-L211.
39. J.R. Nicholls and Rees D. Rawlings, "A Mössbauer Effect Study of  $\text{Ni}_3\text{Al}$  with Iron Additions", Acta metall., 25 (1977), 187-194.
40. J. Bentley, "Axial Electron Channeling Microanalysis of  $\text{L}_{12}$  Ordered Alloys", (Kyoto, Japan: Proc. XIth Cong. on Electron Microscopy, 1986), 551-552.
41. M.K. Miller and J.A. Horton, "Site Occupation Determinations in  $\text{Ni}_3\text{Al}$  by Atom Probe", (Mat. Res. Symp. Proc. vol. 81, 1987 Materials Research Society), 117-122.
42. S. Keck, C. Rzyman, and F. Sommer, "Determination of the Enthalpy of Formation of Ternary  $\text{Ni}_3\text{Al}$ -Based Alloys", Anales de Physica, Series B, 86 (1990), 31-38.
43. A. Hellwig, "Experimental Investigations for the Constitution of the Aluminium-Titanium-Niobium System" (Ph.D. thesis, University of Dortmund, Germany, 1990).
44. M. Albers, L. Bencze, W.A. Oates, and H. Wenzl, "A Note on Applying the Species Chemical Potential Bond Energy Model to Multiple Sublattice Solutions", Calphad, 19 (1995), 153-154.
45. W.A. Oates and H. Wenzl, "The Bond Energy Model for Ordering in a Phase with Sites of Different Coordination Numbers", Calphad, 16 (1992), 73-78.
46. W.A. Oates and H. Wenzl, "Bond Energy Model of Multiple Sublattice Solutions Using Species Chemical Potentials. Basic Theory and Relation to Compound Energy Model", Calphad, 17 (1993), 35-46.
47. K.C. Hari Kumar, P. Wollants, and L. Delaey, "Thermodynamic Calculation of Nb-Ti-V Phase Diagram", Calphad, 18 (1994) 71-79.
48. D.G. Konitzer, J.P. Jones, and H.L. Fraser, "Site Occupancy in Solid Solutions of Nb in the Intermetallic Compounds  $\text{TiAl}$  and  $\text{Ti}_3\text{Al}$ ", Scripta Metall., 20 (1986), 265-268.

CONSTITUTION OF TERNARY ALUMINIDE SYSTEMS  
AS BASIS FOR MATERIALS DEVELOPMENT

Martin Palm & Gerhard Inden  
Max-Planck-Institut für Eisenforschung GmbH  
D-40237 Düsseldorf, Germany

Abstract

An overview about fundamental research carried out on the constitution of Ti-Al-X (X = Fe, Cr, Nb), Fe-Al-Y (Y = C, Cr, Ti) and Ni-Al-Z (Z = Ta) systems is presented. Except for the Fe-Al-Cr system at least two isothermal sections for each system were experimentally determined. Experimental techniques employed include metallography, X-ray diffraction at room temperature as well as at high temperatures up to 1200°C, electron probe microanalysis and transmission electron microscopy. The respective isothermal sections are presented and their significance with respect to the development of new structural materials is discussed.

Introduction

Knowledge about the constitution of a system, i.e. information about phase stability, phase equilibria and phase transformations in dependence of temperature and composition, is the basis for a target development of new alloys. The limited availability of those data often hinders a purposeful alloy development [1]. Also in recent activities aiming at the development of new structural materials based on intermetallic phases, it is the phase diagram in the first place, which tells, whether a given system contains intermetallic phases or not and provides ranges of stability in dependence of temperature and composition.

But not all intermetallic phases are suitable candidates for an alloy development. Several criteria have been established, which have to be fulfilled in order for an intermetallic compound to be promising for the development of new materials. As these criteria were recently compiled and discussed in detail [2], only a short summary of those criteria is given here: ideal candidate phases should have sufficient strength at service temperature, have a low density, should not be too brittle and

should be corrosion resistant. In order to fulfill these requirements, selection criteria for a phase in question are a high melting point, a high crystal symmetry combined with a small unit cell size and a sufficient corrosion resistance or the ability to form protective scales in corrosive media.

As only few phases fulfill all those criteria, methods for optimizing promising candidates have to be considered. Those are, e.g. variations in compositions by alloying to improve the oxidation resistance, consideration of two- or multi-phase alloys for an increase in ductility or strength or optimization of the microstructure by oriented precipitates. All those measures require precise knowledge about the stability ranges of those phases and about phase equilibria in dependence of temperature. The latter point implies, that phase equilibria have to be known at least in the whole range anticipated as service temperature for the materials in question. With respect to ternary systems, this requires the availability of more than one isothermal section.

Therefore, with the exception of the Fe-Al-Cr system, at least two isothermal sections have been experimentally determined in the temperature range, in which appropriate Al-base materials might be used. Al containing systems were chosen since aluminum is a light weight element, tends to form protective alumina scales, and forms intermetallic phases with the subgroup elements.

Ti-Al-X systems

Ti-Al

The phase diagram, which is commonly accepted as standard reference, was compiled by Murray [3]. This assessed diagram contains several phase boundaries which were considered as uncertain by the author, e.g. the Al-rich boundaries of  $Ti_3Al$  and  $TiAl$ , phase equilibria between the phases  $Ti_3Al$ ,  $\alpha$ -Ti and  $TiAl$ ,

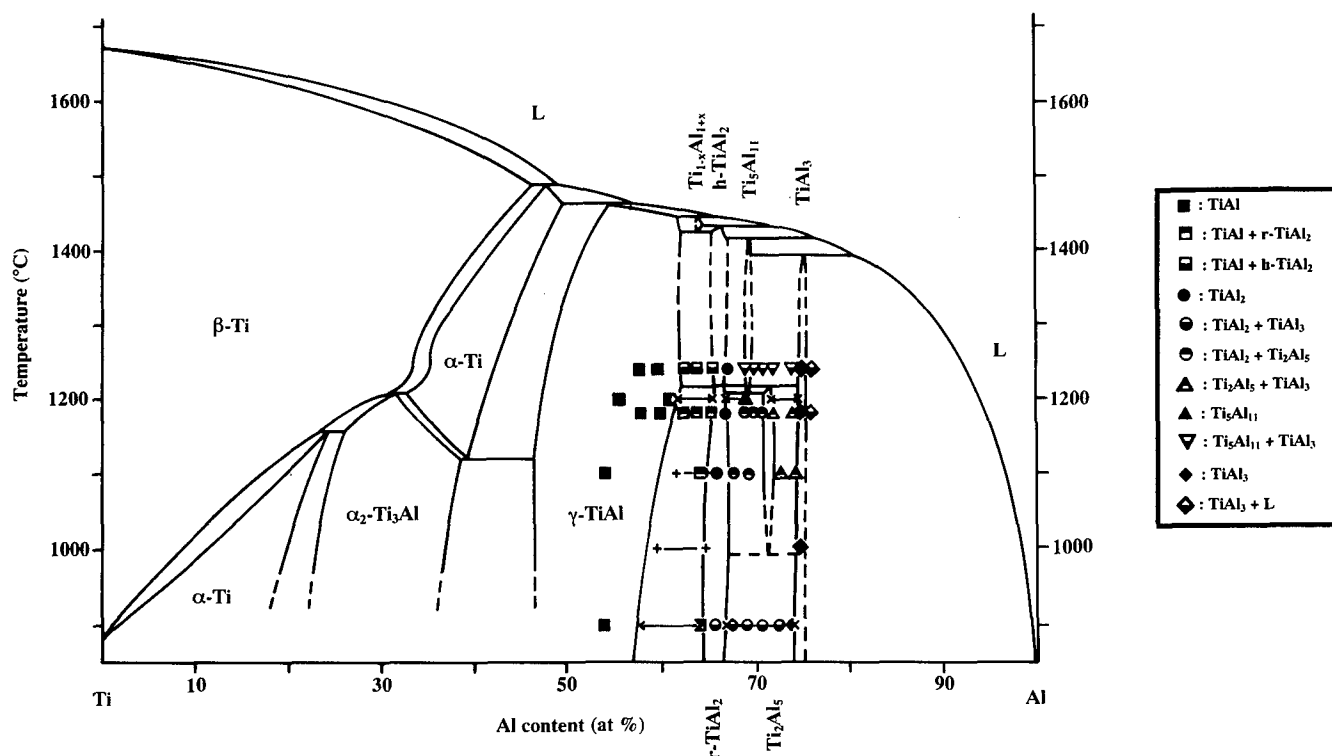


Figure 1: Revised phase diagram of the Ti-Al system. Phase equilibria on the Ti-rich side are taken from [8]. The stability range of  $Ti_{1-x}Al_{1+x}$  was established by [11,13]. Experimental results of bulk alloys for 1240°C and 1180°C are taken from [11], for 1200°C from [10,20], for 1100°C and 900°C from [9]. Tie lines were determined by [14] (+—+) and [10,20] (x—x).

and composition ranges and phase equilibria of the Al-rich phases  $Al_2Ti$  and  $Al_5Ti_2$ . They were therefore given as broken lines in [3]. The suggested eutectoid formation of  $\alpha$ -Ti [4-6] was experimentally verified [7]. Phase relationships among the phases  $\alpha$ -Ti,  $\beta$ -Ti,  $Ti_3Al$  ( $\alpha_2$ -Ti) and  $TiAl$  ( $\gamma$ -Ti) were evaluated in a detailed experimental study [8]. The structures of the phases as well as phase equilibria on the Al-rich side have also been established by now [9-13]. On the basis of those results a revised Ti-Al phase diagram is presented in Fig. 1. This diagram is corroborated by the results obtained for the ternary systems.

#### Ti-Al-Nb

The Ti-Al-Nb system has become of considerable interest for recent alloy developments, because alloying  $Ti_3Al$  and  $TiAl$  with Nb improves the oxidation resistance [15] and the mechanical properties [2,16-18]. Because of this interest there have been several investigations of the Ti-Al-Nb system, but most of them were restricted to a single temperature - 1200°C - and they partially yielded contradicting results. Isothermal sections of the Ti-Al-Nb system published in the standard reference source for ternary phase diagrams [19] are mainly based on data by Hellwig [10]. These data are presented here in a revised form. Revisions concern new results obtained in the binary subsystem and a partial re-evaluation as well as additional investigations at 1000°C. A detailed investigation on alloys of fixed composition as well as on diffusion couples by optical microscopy, electron probe microanalysis (EPMA), transmission electron microscopy (TEM), and X-ray diffraction (XRD) yielded two isothermal sections for 1000°C (Fig. 2) and 1200°C (Fig. 3; all experimental details can be found in [10,20]). In this temperature range the

phases  $TiAl$  and  $Ti_3Al$  have a marked solubility for Nb. The complete miscibility between the phases  $NbAl_3$  and  $TiAl_3$  is confirmed and the corresponding solid-solution,  $(Nb,Ti)Al_3$ , exhibits a solubility for Al of up to 2.0 at.% Al at 1000°C and 3.0 at.% Al at 1200°C. At 1200°C (Fig. 3) phase equilibria between the phases  $TiAl$ ,  $TiAl_2$ ,  $Ti_2Al_5$ , and  $(Nb,Ti)Al_3$  were determined for the first time. No ternary intermetallic phase was detected at this temperature and the existence of ternary phases reported earlier, i.e.  $\gamma_1$  ( $NbTiAl_3$ ) [21,22],  $T_1$  (" $Ti_{45}Al_{35}Nb_{20}$ ") [23] and  $T_2$  (" $Ti_{45}Al_{45}Nb_{10}$ ") [23], has to be ruled out. The predominant feature of the isothermal section at 1000°C (Fig. 2) is the presence of an isolated island of ordered B2-type  $\beta$  ( $\beta^*$ ). It is assumed that it forms by a eutectoid-like reaction between 1200°C and 1000°C.

With respect to an alloy development on the basis of the Ti-Al-Nb system the isothermal sections indicate following prospects: In the temperature range under consideration there is a considerable solid solubility for Nb in  $TiAl$  and  $Ti_3Al$ . This gives the possibility to develop single-phase materials on the basis of those two phases within a wide composition range by variation of the chemistry. If two-phase alloys are considered, there is a comparatively broad two-phase field of  $Ti_3Al/\alpha$ -Ti +  $TiAl$  available for variations of the Nb content. To obtain two-phase  $TiAl$  alloys containing  $Nb_2Al$  or  $\beta$ -(Nb,Ti) as the second phase, comparatively large amounts of Nb have to be added. Comparison of the two isothermal sections also reveals that the composition of  $\beta$ -(Nb,Ti) varies substantially in dependence of temperature. Alterations of the microstructure with temperature are thus to be expected. This fact is not desirable for an alloy development at these temperatures.

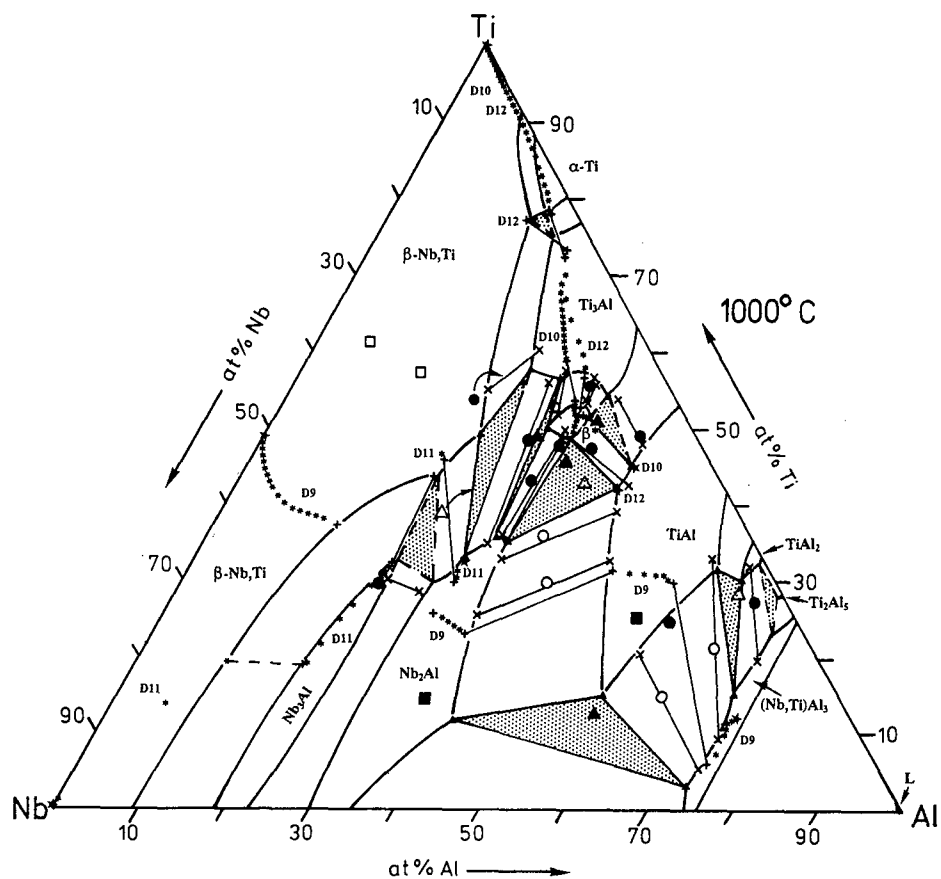


Figure 2: Isothermal section of the Ti-Al-Nb system at 1000°C [20].

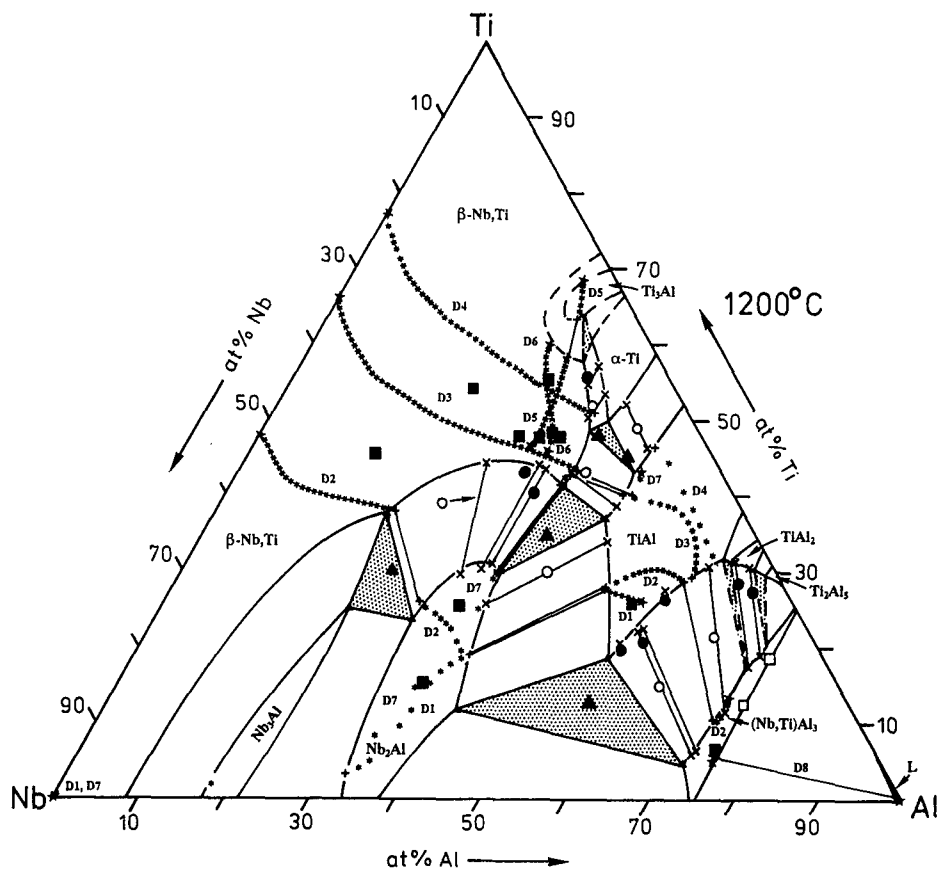


Figure 3: Isothermal section of the Ti-Al-Nb system at 1200°C [20].

## Ti-Al-Cr

Like Nb, Cr is considered as an additive to Ti-Al based alloys to improve the oxidation resistance. In contrast to Ti-Al-Nb alloys, not only alloying with Cr but also coatings of a second phase have been suggested [24] to protect TiAl based alloys from oxidation. Materials under consideration for such coatings include TiCrAl<sub>2</sub> and two-phase  $\gamma$  + Ti(Cr,Al)<sub>2</sub> based alloys which form protective alumina scales. The critical assessment of the Ti-Al-Cr system [25] revealed, that only scarce information exists about phase equilibria in this system. Recent investigations of phase equilibria in the Ti-Al-Cr system focused mainly on phase equilibria involving the phase TiCrAl<sub>2</sub> with L<sub>12</sub>-structure [24-29]. A detailed investigation on quenched samples by EPMA, TEM and XRD [30] yielded two isothermal sections for 1000° and 1150°C (Figs. 4 and 5). They show a considerable solubility for Cr in TiAl and Ti<sub>3</sub>Al but this solubility is smaller compared to Nb. The L<sub>12</sub>-ordered phase TiCrAl<sub>2</sub> is the only isolated ternary intermetallic phase. It has a marked composition range. The solubility for Cr in D<sub>022</sub>-(Ti,Cr)Al<sub>3</sub> is also considerable. No continuous solid solubility between  $\beta$ -Ti and  $\beta$ -Cr exists at 1000°C because the Laves phase Ti(Cr,Al)<sub>2</sub> "interrupts" the single-phase region, but at 1150°C there is a complete miscibility in the  $\beta$  phase.

With regard to a development of single-phase materials on the basis of the titanium aluminides, it is only for TiAl that the solubility for Cr is large enough to allow for a variation of the alloy chemistry within a considerable range. For two-phase alloys consisting of TiAl + Ti<sub>3</sub>Al the composition range is limited < 3 at.% Cr. Another prospect may be two-phase alloys with the cubic  $\beta$  phase, which is in equilibrium with TiAl over the whole temperature range under consideration. There is also a direct two-phase equilibrium between TiAl and the L<sub>12</sub> phase TiCrAl<sub>2</sub> at both temperatures. This is important in view of the development of protective coatings for TiAl. However, at lower temperatures at least some of those alloys may become TiAl<sub>2</sub> based due to the shrinkage of the TiCrAl<sub>2</sub> single-phase field with decreasing temperature [24,26].

In the context of the discussion of alloys based on the Ti-Al-Nb and Ti-Al-Cr systems it has to be mentioned, that a  $\gamma$ -TiAl alloy of composition Ti-48Al-2Cr-2Nb (in at.%; also known as GE-alloy) has already been successfully developed for use in gas turbine engines [31].

## Ti-Al-Fe

While the former two alloy systems are already in the center of interest for a material development, the Fe-Al-Ti system has attracted less attention up to now. One reason may have been the lack of a reliable phase diagram, as has been stated in recent compilations of this system [32-34]. Two isothermal sections have been experimentally determined for the Fe-Al-Ti system at 800°C (Fig. 6) and 1000°C (Fig. 7) [35] and an additional section at 900°C is presented at this conference [36]. In contrast to the other Ti-Al-X systems discussed here, TiAl and Ti<sub>3</sub>Al have only a limited solubility for iron in the temperature range under consideration. Two ternary intermetallic phases exist. Besides the cubic L<sub>12</sub> phase ( $\tau_2$ , "FeTiAl<sub>2</sub>") a second cubic phase with complex fcc-structure of D<sub>8h</sub>-type exists. All binary phases of the Fe-Ti subsystem -  $\beta$ -Ti, FeTi and Fe<sub>2</sub>Ti - show a considerable solubility for Al. The homogeneity range of the  $\alpha$  solid solution can accommodate a considerable amount of Ti. The ordered polymorphs of the  $\alpha$  solid solution - B2 and L<sub>21</sub>, the latter being the ternary

equivalent of D<sub>03</sub> - are stabilized to much higher temperatures with respect to the disordered (A2) polymorph by the introduction of Ti.

Because of the limited solubility of Fe in TiAl and Ti<sub>3</sub>Al possibilities of developing single-phase materials by variations of the compositions are quite limited. Also no two-phase equilibrium between the L<sub>12</sub> phase ( $\tau_3$ ) and TiAl exists. This impedes the development of respective coatings. On the other hand there seems to be some potential for an alloy development of two-phase alloys containing the phase  $\tau_2$  or FeTi as a second phase. About the results of mechanical testing of appropriate alloys a separate report will be given on this conference [36]. Besides these prospects with respect to alloy developments based on titanium aluminides, the Fe-Al-Ti system may offer additional potential for iron aluminide based materials. The  $\alpha$  solid solution is stable over a considerable composition range and the ordered polymorphs (B2, L<sub>21</sub>) of the  $\alpha$ -solid solution are substantially stabilized in respect to higher temperatures by the introduction of Ti.

## Fe-Al-X systems

### Fe-Al-Cr

Only limited information is available for the Fe-Al-Cr system and phase equilibria in the Al rich part adjacent to the solid solubility range of the  $\alpha$  solid solution were not established [37]. From metallographic, EPMA, and XRD investigations on quenched samples an isothermal section at 1000°C (Fig. 8) was established [38]. No ternary intermetallic phase exists at this temperature, but all binary compounds exhibit marked solid solubility ranges for the third component. This holds especially for the phase Al<sub>8</sub>Cr<sub>5</sub>, where three quarters of Cr can be substituted by Fe. As all phases in the Al-rich part of the Fe-Al-Cr system have low crystallographic symmetries their brittleness may sustain an alloy development.

### Fe-Al-C

While the main emphasis in the development of materials based on intermetallic phases lies on the combination of different metal atoms, comparably little effort has been put forward up to now to combine metals and non-metals. In this respect the Fe-Al-C system is quite promising. From the early investigations by Morral (1934) [39] and Nishida (1968) [40] it was clear, that three cubic phases are present in this system. Besides the bcc  $\alpha$  solid solution and the fcc  $\gamma$  solid solution a ternary intermetallic phase, denoted as K phase ("Fe<sub>3</sub>AlC"), exists. The lattice of this perovskite-type phase can be considered as an ordered fcc arrangement of Fe and Al of type L<sub>12</sub>, with C atoms occupying the octahedral interstices. Because the compiled data about the phase diagram [41,42] showed the need for further investigations, three isothermal sections for 800°, 1000° and 1200°C (Fig. 9) as well as several vertical sections were determined [43]. They were established from metallography, EPMA and XRD investigations. Additional DTA and high temperature XRD experiments were carried out to gain information about phase equilibria between the isothermal sections [43, 44]. The perovskite-type phase is stable in a considerable composition range, which shifts only slightly towards lower carbon concentrations with increasing temperature. The  $\alpha$  solid solution has a limited solubility for carbon of up to 1 at.% C. The introduction of carbon stabilizes the B2-ordered polymorph is by to higher temperatures.

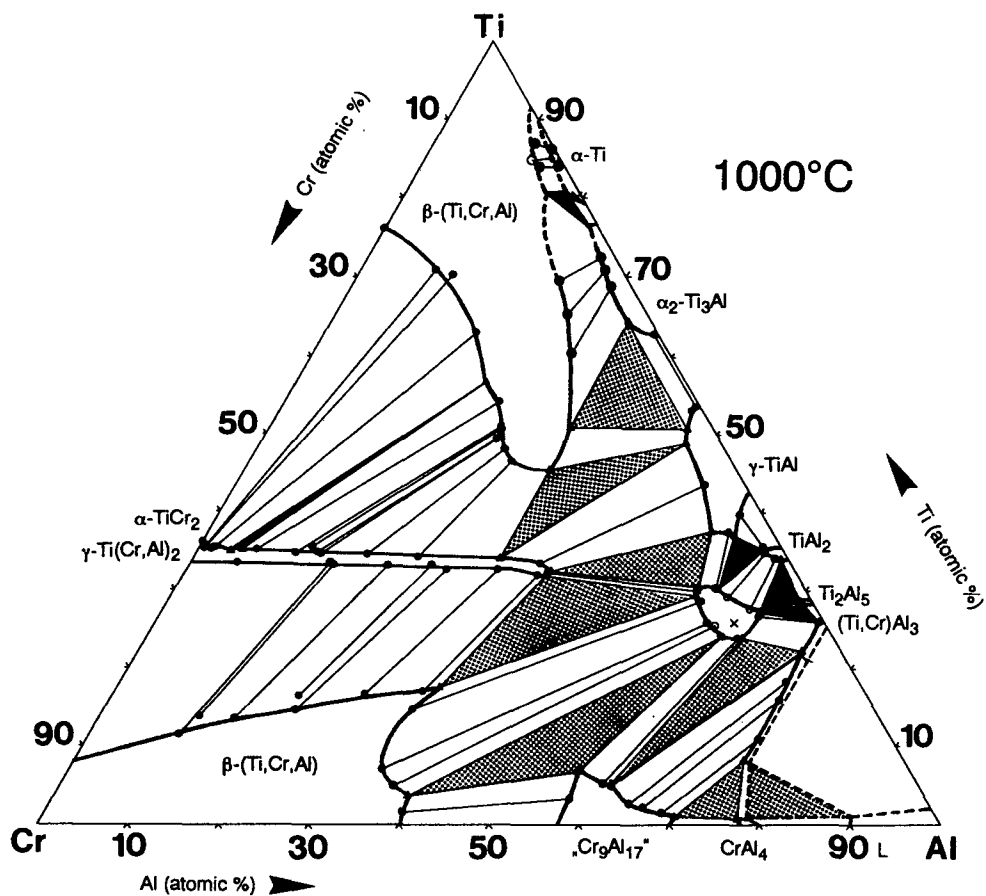


Figure 4: Isothermal section of the Ti-Al-Cr system at 1000°C. Revised diagram from [30].

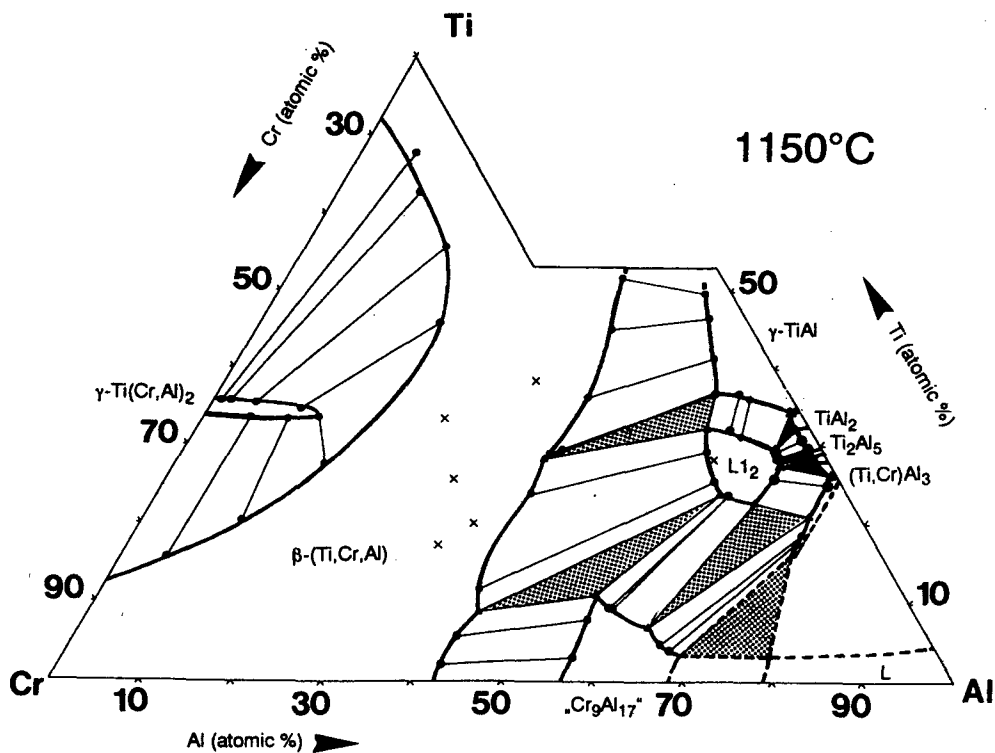


Figure 5: Isothermal section of the Ti-Al-Cr system at 1150°C. Revised diagram from [30].

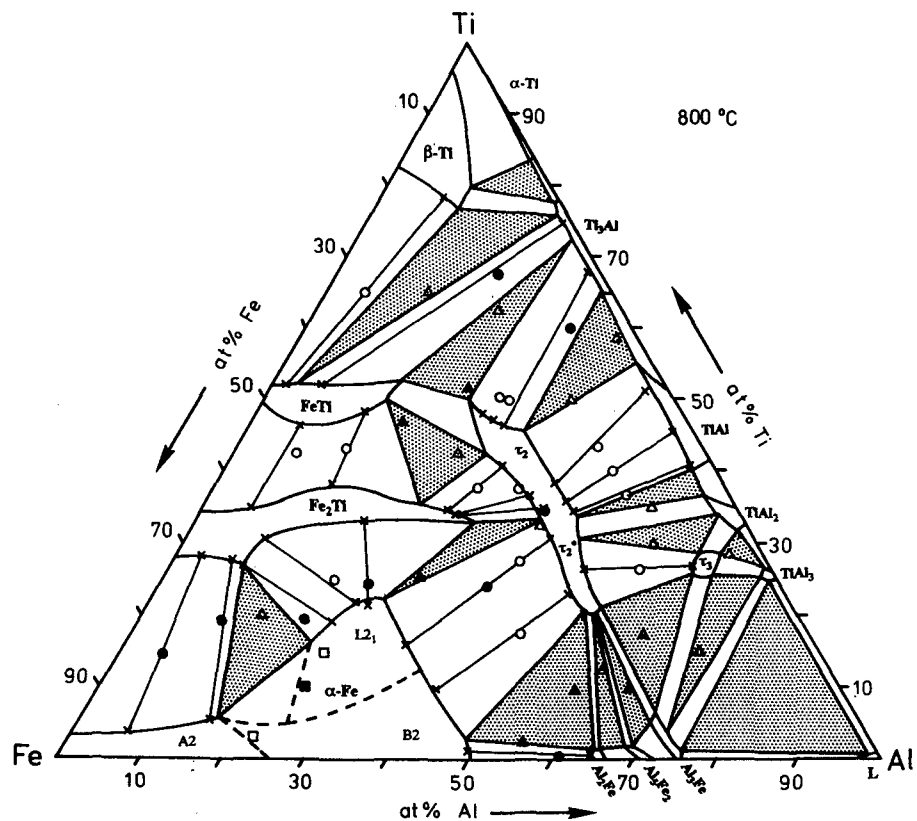


Figure 6: Isothermal section of the Ti-Al-Fe system at 800°C [35].

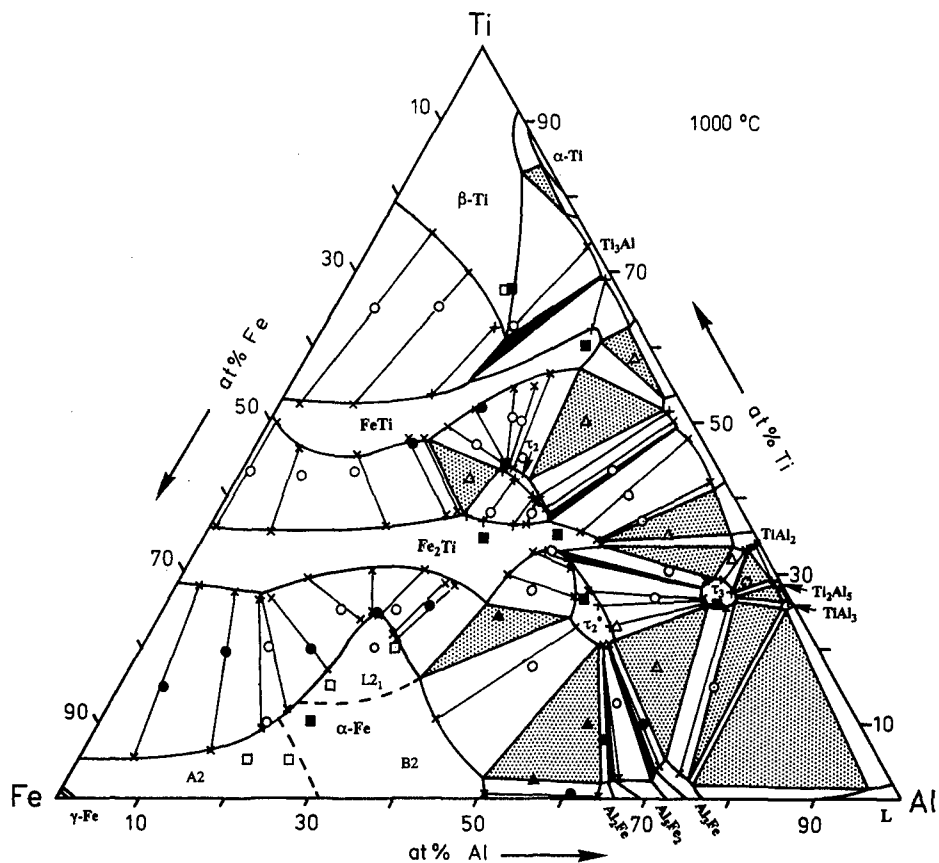


Figure 7: Isothermal section of the Ti-Al-Fe system at 1000°C [35].



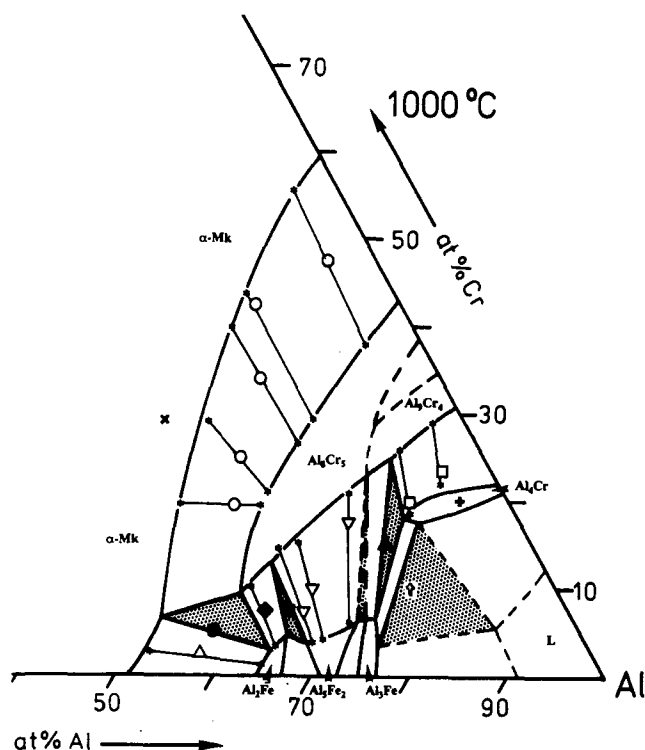


Figure 8: Partial isothermal section of the Fe-Al-Cr system at 1000°C [38].

Parallel to the investigation of the phase equilibria the high temperature deformation behaviour of the K phase [45] and of two-phase alloys  $\alpha + K$  [46,47] was examined. Such two-phase alloys, where the K phase acts as strengthening phase in a matrix of  $\alpha$  solid solution, are stable over wide temperature and composition range. In contrast, alloys containing the  $\gamma$  phase will undergo drastic changes in phase equilibria, and therefore in microstructure, as the stability range of the  $\gamma$  phase is strongly dependent on temperature and expands considerably with increasing temperature (Fig. 9).

#### Ni-Al-Ta system

Together with Ti-Al based systems nickel aluminides are the major topic for the development of structural materials on the basis of intermetallic phases. Here the B2-ordered phase NiAl and the L<sub>12</sub>-ordered compound Ni<sub>3</sub>Al are of special interest. In order to improve the creep resistance of NiAl at high temperatures, particle hardening is considered to have beneficial effects. In this respect the Ni-Al-Ta system may offer some prospects, as several ternary phases exist. Again a recent summary of the relevant literature [48] revealed, that the knowledge about phase equilibria is sketchy. Therefore two isothermal sections for 1000°C and 1250°C (Fig. 10) were determined in the Ni-Al-Ta system from metallography, EPMA and XRD investigations [49]. The composition ranges of three ternary intermetallic compounds - the Laves phase NiAlTa (C14-type structure), the Heusler phase Ni<sub>2</sub>AlTa (L<sub>21</sub>) and the phase Ni<sub>6</sub>AlTa (D<sub>024</sub>) - were established. Other ternary phases reported before, i.e. NiAl<sub>2</sub>Ta ( $\tau_6$ ), Ni<sub>2</sub>Al<sub>2</sub>Ta, NiAlTa<sub>2</sub> and Ni<sub>2</sub>Al<sub>3</sub>Ta<sub>5</sub> ( $\tau_4$ ), have not been observed. NiAl and Ni<sub>3</sub>Al both have a marked solid solubility for Ta, but in the for-

mer phase the solubility for Ta is strongly dependent on stoichiometry. At Ni contents below the stoichiometric composition of 50 at.% Ni the solubility for Ta is limited to less than 1 at.%, while at Ni contents beyond 50 at.% Ni, 3.3 at.% Ta (1000°C) and up to 7.3 at.% Ta (1250°C) can be solved in NiAl.

All three ternary intermetallic phases are suitable for strengthening of NiAl. Among those Ni<sub>6</sub>AlTa may be the least promising candidate as this phase is extremely brittle and exhibits only a narrow two-phase field Ni<sub>6</sub>AlTa + NiAl. In contrast, there exists a broad two-phase field between NiAl and the Laves phase NiAlTa offering a wide range of alloy compositions. Appropriate alloys have already been successfully tested [50-52]. The Heusler phase Ni<sub>2</sub>AlTa has been taken as strengthening phase as well [53]. Ta containing two-phase NiAl + Ni<sub>3</sub>Al alloys have not received much attention up to now.

#### References

1. F. Aldinger and H.J. Seifert, "Konstitution als Schlüssel zur Werkstoffentwicklung," *Z. Metallkd.*, 84 (1993), 1-10.
2. G. Sauthoff, "Intermetallics," in: K.H. Matucha, ed., "Structure and Properties of Nonferrous Alloys," Materials Science and Technology, vol. 8, (VCH, Weinheim, Germany, 1996), 643-803.
3. J.L. Murray, *Phase Diagrams of Binary Titanium Alloys* (ASM International, Metals Park, OH, 1987), 12-24.
4. R.D. Shull, A.J. McAlister, and R.C. Reno, "Phase Equilibria in the Ti-Al System," (Proc. 5th Int. Conf. on Titanium, Munich, 1984, eds. G. Lütjering, U. Zwicker and W. Bunk, DGM, Oberursel, Germany, 1985), 1459-1466.
5. S.A. Jones et al., "Microstructural Studies of Ti-Al Alloys in the Vicinity of the 'Eutectoid' Reaction ( $\alpha \rightarrow \alpha_2 + \gamma$ )," *Scripta Met.*, 22 (1988), 1235-1240.
6. R.D. Shull and J.P. Cline, "High Temperature X-Ray Diffractometry of Ti-Al Alloys," *High Temp. Sci.*, 26 (1990), 95-117.
7. A. Hellwig, M. Palm, and G. Inden, "The Invariant Reaction between  $\alpha$ ,  $\alpha_2$  and  $\gamma$  in the Ti-Al System," *Scripta Met. Mat.*, 27 (1992), 143-148.
8. R. Kainuma, M. Palm, and G. Inden, "Solid-phase Equilibria in the Ti-rich Part of the Ti-Al System," *Intermetallics*, 2 (1994), 321-332.
9. K. Kaltenbach et al., "A Contribution to the Al-Ti Phase Diagram," *Z. Metallkd.*, 80 (1989), 511-514.
10. A. Hellwig, "Experimentelle Untersuchungen zur Konstitution des Systems Al-Ti-Nb," (Doctoral thesis Universität Dortmund, Germany 1990).
11. J.C. Schuster and H. Ipser, "Phases and Phase Relations in the Partial System TiAl<sub>3</sub>-TiAl," *Z. Metallkd.*, 81 (1990), 389-396.
12. J.E. Benci, J.C. Ma, and T.P. Feist, "Structure and Microstructure of Al<sub>2</sub>Ti Intermetallic Alloy," *Mat. Res. Soc. Symp. Proc.*, 288 (1993), 397-402.
13. J. Braun, M. Ellner, and B. Predel, "Zur Struktur der Hochtemperaturphase Ti<sub>1-x</sub>Al<sub>1+x</sub>," *J. Alloys Compounds*, 203 (1994), 189-193.
14. F.J.J. van Loo and G.D. Rieck, "Diffusion in the Ti-Al System - II. Interdiffusion in the Composition Range between 25 and 100 at.% Ti," *Acta Metall.*, 21 (1973), 73-84.
15. J. Subrahmanyam, "Cyclic Oxidation of Aluminized Ti-14Al-24Nb Alloy," *J. Mat. Sci.*, 23 (1988), 1906-1910.

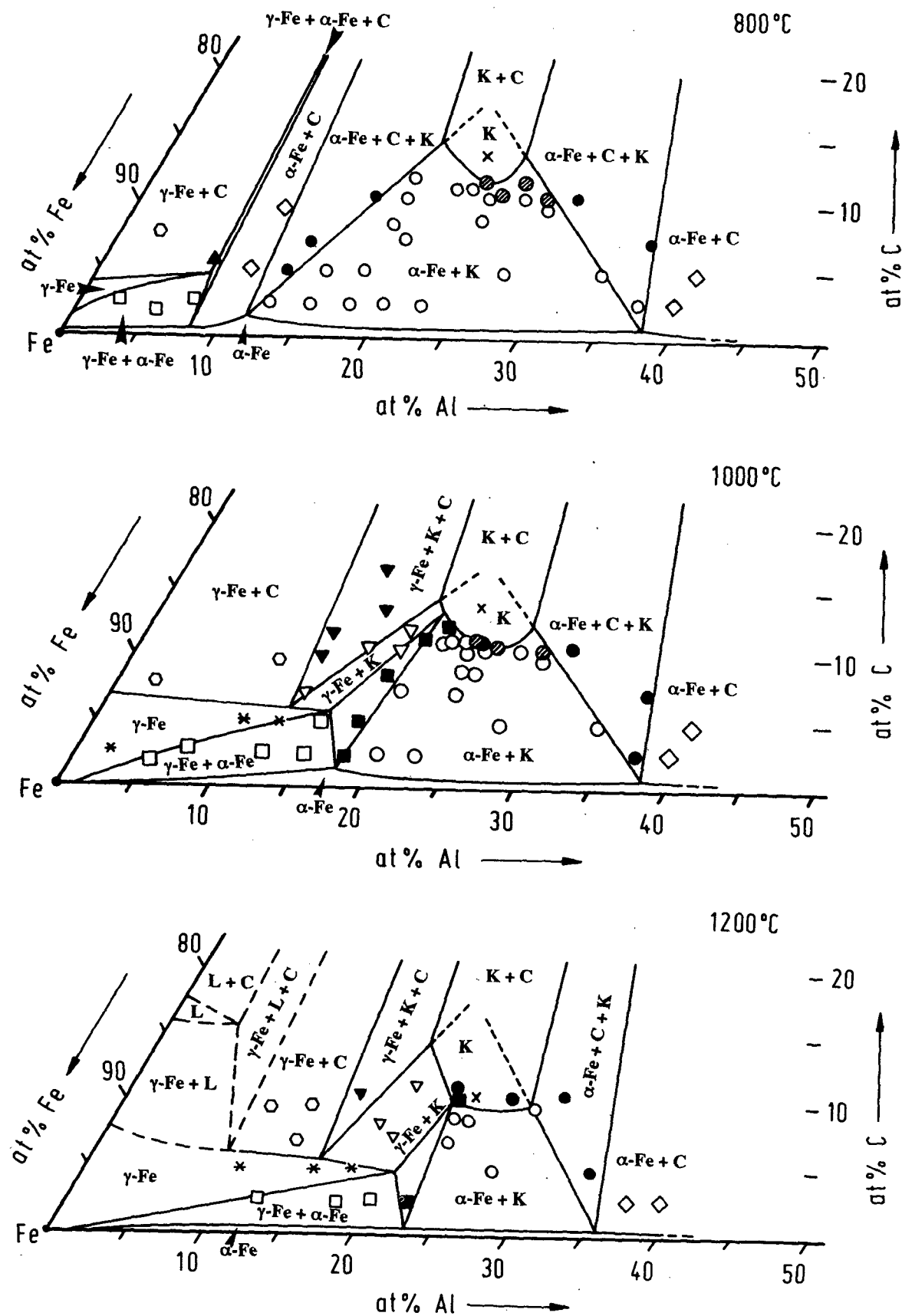


Figure 9: Partial isothermal section of the Fe-Al-C system at 800°C, 1000°C, and 1200°C redrawn from [43].

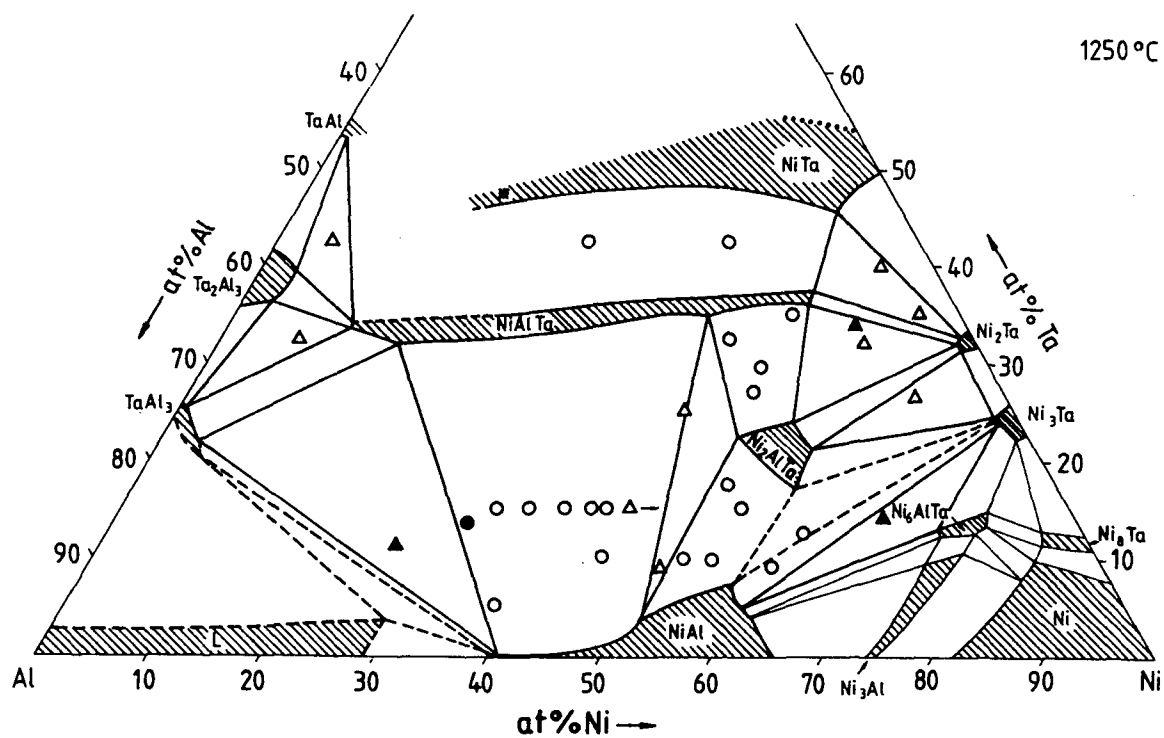
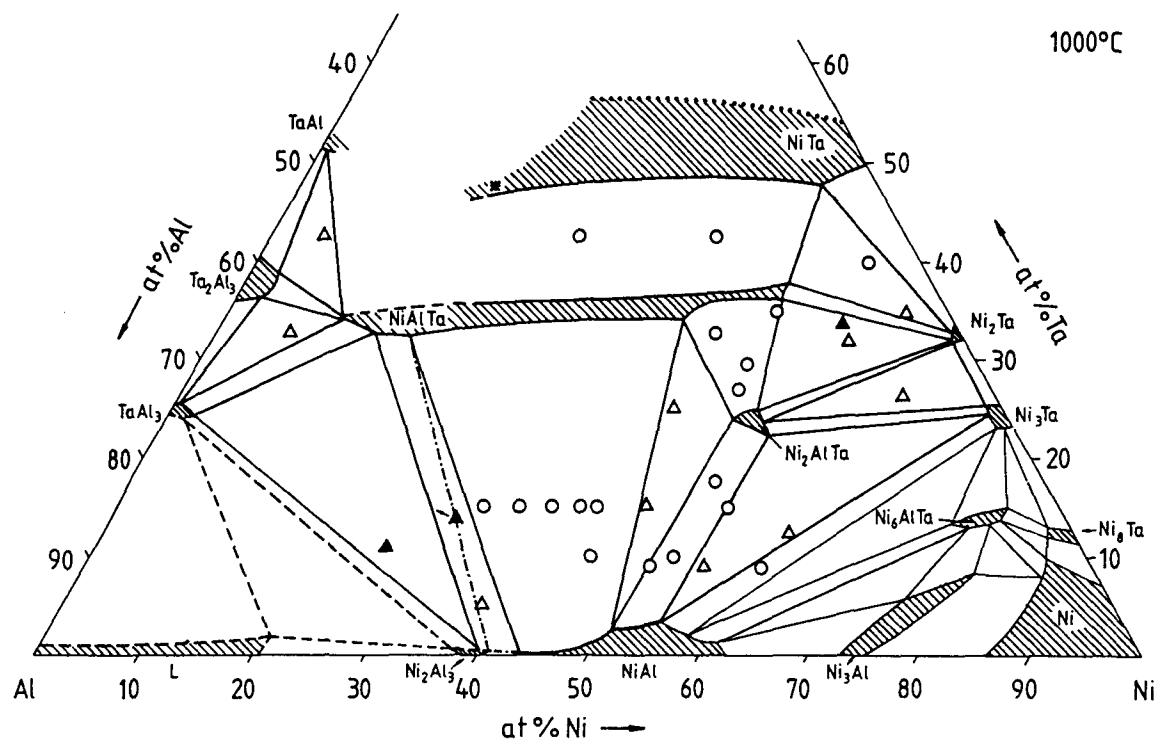


Figure 10: Partial isothermal section of the Ni-Al-Ta system at 1000°C and 1250°C [49].

16. Y.-W. Kim and F.H. Froes, "Physical Metallurgy of Titanium Aluminides," in High Temperature Aluminides and Intermetallics eds. S.H. Whang et al. (TMS Warrendale, USA, 1990), 465-492.
17. K. Hashimoto and M. Kimura, "Effects of Third Element Additions on Mechanical Properties of TiAl," in Structural Intermetallics, eds. R. Darolia et al. (TMS Warrendale, USA, 1993), 309-318.
18. D. Banerjee et al., "The Physical Metallurgy of Ti<sub>3</sub>Al Based Alloys," ibid. 19-33.
19. S. Gama, "Aluminium-Niobium-Titanium," in Ternary Alloys, vol. 7, eds. G. Petzow and G. Effenberg (VCH, Weinheim, 1993), 382-398.
20. A. Hellwig, M. Palm, and G. Inden, "Phase Equilibria in the Al-Nb-Ti System at High Temperatures," submitted for publication in Intermetallics.
21. L.A. Popov and V.I. Rabezova, "Equilibrium Diagram of the Al-Nb-Ti System," Russ. J. Inorg. Chem., 7(2) (1962), 222-224.
22. G.L. Chen et al., "Investigation on the 1000, 1150 and 1400°C Isothermal Section of the Ti-Al-Nb System," Intermetallics, 4 (1996), 13-22.
23. T.J. Jewett et al., "Experimental Determination of the Ti-Nb-Al Phase Diagram at 1200°C," in "High Temperature Ordered Intermetallic Alloys," eds. C.T. Liu et al., Mat. Res. Soc. Symp. Proc., 133 (1989), 69-74.
24. M.P. Brady, J.L. Smialek, and F. Terepka, "Microstructure of Alumina-forming Oxidation Resistant Al-Ti-Cr Alloys," Scripta Met. Mat., 32 (1995), 1659-1664.
25. F.H. Hayes, "Aluminium-Chromium-Titanium," in Ternary Alloys vol. 4, eds. G. Petzow and G. Effenberg (VCH, Weinheim, 1991), 430-440.
26. T.J. Jewett, B. Ahrens, and M. Dahms, "Phase Equilibria Involving the  $\tau$ -L1<sub>2</sub> and TiAl<sub>2</sub> Phases in the Ti-Al-Cr System," Intermetallics, 4 (1996), 543-556.
27. T.J. Jewett, B. Ahrens, and M. Dahms, "Stability of the L1<sub>2</sub> Phases at 800°C in the Ti-Al-Cr System," Scripta Mat., 34 (1996), 395-399.
28. T.J. Jewett and M. Dahms, "Stability of the Ti(Cr,Al)<sub>2</sub> Phase," Z. Metallkd., 87 (1996), 254-261.
29. S. Hao and N. Zeng, "Isothermal Section of Phase Diagram in Ti-Al-Cr Ternary System at 1000°C," Acta Metall. Sinica, 31 (1995), B152-B158.
30. G. Schwanold and G. Inden, "Phase Equilibria in the Ti-Cr-Al system at 1273 and 1423K," Revue Metall., SF2M - JA96 (1996), 196.
31. J.C. Chesnutt, C.M. Austin, and K.G. McAllister, "Gamma Titanium for Gas Turbine Engines. A GE Aircraft Engines Perspective," Revue Metall., SF2M - JA96 (1996), 67.
32. V. Raghavan, "The Fe-Al-Ti System," Phase Diagrams of Ternary Iron Alloys, Part 1 (ASM International, Metals Park, OH, 1987), 12-24.
33. K.S. Kumar, "Ternary Intermetallics in Aluminium-Refractory Metals-X Systems (X = V, Cr, Mn, Fe, Co, Ni, Cu, Zn)," Int. Met. Rev., 35 (1990), 293-327.
34. G. Ghosh "Aluminium-Iron-Titanium," in Ternary Alloys, vol. 5, eds. G. Petzow and G. Effenberg (VCH, Weinheim, 1992), 456-469.
35. M. Palm, G. Inden, and N. Thomas, "The Fe-Al-Ti System," J. Phase Equilibria, 16 (1995), 209-222.
36. M. Palm et al., "Structure and Mechanical Properties of Ti-Al-Fe Alloys at Ambient and High Temperatures," ISSI-2 (1997).
37. G. Ghosh, "Aluminium-Chromium-Iron," in Ternary Alloys, vol. 4, eds. G. Petzow and G. Effenberg (VCH, Weinheim, 1991), 324-343.
38. M. Palm, "The Al-Cr-Fe System - Phases and Phase Equilibria in the Al-rich Corner," J. Alloys Compounds, in the press.
39. F.R. Morral, "The Constitution of Iron-rich Fe-Al-C Alloys," J. Iron Steel Inst., 130 (1934), 419-428.
40. K. Nishida, "A Study of Fe-Al-C Alloys," Technical Reports Hokaido University, 48 (1968), 71-108.
41. V. Raghavan, "The Fe-Al-C System," Phase Diagrams of Ternary Iron Alloys, Part 1 (ASM International, Metals Park, OH, 1987), 89-97.
42. V. Raghavan, "Al-C-Fe," J. Phase Equilibria, 14 (1993), 615-617.
43. M. Palm and G. Inden, "Experimental Determination of Phase Equilibria in the Fe-Al-C System," Intermetallics, 3 (1995), 443-454.
44. M. Palm, "Konstitutionsuntersuchungen zum System Fe-Al-C," (Doctoral thesis Universität Dortmund, Germany 1990)
45. I. Jung and G. Sauthoff, "High-temperature Deformation Behaviour of the Perovskite-type Phases Fe<sub>3</sub>AlC and Ni<sub>3</sub>AlC," Z. Metallkd., 80 (1989), 490-496.
46. W. Sanders and G. Sauthoff, "Deformation Behaviour of Perovskite-Type Phases in the System Fe-Ni-Al-C - I. Strength and Ductility of Ni<sub>3</sub>AlC<sub>x</sub> and Fe<sub>3</sub>AlC<sub>x</sub> Alloys with Various Microstructures," Intermetallics, 5 (1997), in the press.
47. W. Sanders and G. Sauthoff, "Deformation Behaviour of Perovskite-Type Phases in the System Fe-Ni-Al-C - II. Deformation Behaviour of a Two-Phase Fe<sub>3</sub>AlC<sub>0.45</sub> Alloy," Intermetallics, 5 (1997), in the press.
48. A. Zakharov, "Aluminium-Nickel-Tantalum," in Ternary Alloys, vol. 7, eds. G. Petzow and G. Effenberg (VCH, Weinheim, 1993), 483-497.
49. M. Palm, W. Sanders, and G. Sauthoff, "Phase Equilibria in the Ni-Al-Ta System," Z. Metallkd., 87 (1996), 390-398.
50. G. Sauthoff, "The High Temperature Deformation of Intermetallic Alloys," in Structural Intermetallics, eds. R. Darolia et al. (TMS Warrendale, USA, 1993), 845-860.
51. D.R. Johnson et al., "Directional Solidification and Mechanical Properties of NiAl-NiAlTa Alloys," Intermetallics, 3 (1995), 141-152.
52. B. Zeumer and G. Sauthoff, "Intermetallic NiAl-Ta Alloys with Strengthening Laves Phase for High-Temperature Applications: I. Basic Properties," submitted for publication in Intermetallics.
53. M. Igarashi and H. Senba, "High Temperature Deformation and Oxidation Resistance of NiAl Based Intermetallic Compounds," in Structural Intermetallics, eds. R. Darolia et al. (TMS Warrendale, USA, 1993), 533-542.

## COMPLICATED KINETICS OF L1<sub>0</sub>-ORDERING AND -DISORDERING DUE TO STRUCTURAL CHANGES CAUSED BY LATTICE DISTORTION

M. Spanl<sup>1</sup>, B. Sprusil<sup>2</sup> and W. Pfeiler<sup>1</sup>

<sup>1</sup> Institut für Materialphysik, University of Vienna, Strudlhofgasse 4, A-1090 Vienna, Austria

<sup>2</sup> Institute of Metal Physics, Charles University, Ke Karlovu 5, CZ-121 16 Praha, Czech Republic

### Abstract

Differential scanning calorimetry (DSC) and microhardness measurements were used to study the kinetics of L1<sub>0</sub>-ordering in CuAu. During dynamic heating a *decrease* of order/disorder transition temperature T<sub>OD</sub> was observed with *increasing* heating rate. This is just opposite to what one would expect for a first order phase transition usually yielding an effect of superheating. It is shown that this 'retro'-effect is caused by a shift of T<sub>OD</sub> to lower temperatures during *heating* which was initiated during previous *cooling* cycle. The origin appears to be the stabilisation of CuAuI ordered phase against complete transformation into CuAuII during heating by twinning and loss of coherency of ordered domains during previous cooling cycle.

### Introduction

It is well known that CuAu exhibits two regions of long range order (LRO), up to about 385°C the ordered tetragonal CuAuI phase (L1<sub>0</sub>) and between 385°C and 410°C the ordered orthorhombic CuAuII phase. The equilibrium state above 410°C is disordered (DO) face centred cubic [1]. Considering intermetallic alloys for technical application, their thermal stability and mechanical behaviour is of great interest, and there is need especially for a systematic study of ordering kinetics in those alloys. Nyström [2] has shown that the transformation from one ordered phase into the other (CuAuI and CuAuII) is much more sluggish than the transformation between order and disorder. Furthermore, a great influence of thermal treatment above the order/disorder transition temperature T<sub>OD</sub> on the re-ordering behaviour was reported by Kuczynski et al. [3]. Previous studies have shown that ordering into L1<sub>0</sub>-ordered structure is accompanied by volume changes, which arise from growth of coherent ordered domains in the disordered matrix inducing great lattice distortion. It was also reported that increase of annealing temperature and/or annealing time within the ordered temperature region leads to a relaxation of the produced lattice distortion due to dislocation generation and twinning [4,5].

In a comparison between calorimetric and resistometric measurements of the order/disorder transition in CuAu and Cu<sub>3</sub>Au, Sprusil et al. [6] observed a similar shape of specific heat and first derivative of the temperature dependence of resistivity, but slight differences in the T<sub>OD</sub> values and the dependence on heating rate. Therefore a detailed investigation of the ordering kinetics of CuAu was carried out dynamically for well-defined starting conditions by means of in-situ resistometry and differential scanning calorimetry (DSC) [7] which showed an expected undercooling behaviour, but an unexpected decrease of T<sub>OD</sub> with increasing heating rate, the so-called 'retro' effect [7,8]. It was the aim of the present work to study by means of DSC and measurements of microhardness the influence of different thermal treatments on the characteristics of LRO-DO transition observed upon heating and its dependence on heating rate and (previous) cooling rate.

### Experimental

Sample material (chemical analysis: 49.4±0.5at%Cu, 50.6±0.6at%Au) was supplied by DEGUSSA via the Institut für Physikalische Chemie, University of Munich, Germany. The samples were rolled at room temperature to about 0.3mm thickness with intermediate and final annealings at 600°C in purified argon atmosphere. For DSC and microhardness measurements a disc-shaped specimen of about 3mm in diameter was mechanically punched out from the rolled sheet and a pure (99.99%) Au sheet, which was used as a reference specimen. Calorimetric measurements were carried out with DSC7 apparatus from Perkin Elmer. Great care was taken to avoid oxidation effects of sample surface. Therefore the measuring chamber was first evacuated and then filled with purified 99.999% Argon gas. For microhardness measurements a Zeiss-Axioplan light microscope was used together with a PAAR MHT-4 microhardness tester. Microhardness values were obtained as an average of 20 widely spaced indentations made on each sample using a 42.5g load with constant indentation rate (10g/s) and equal indent time of 10s.

Table 1 gives the thermal treatments of different measuring runs of the present study.

Table 1: Thermal treatments of different measuring runs.

measuring series	cooling rate $Q_c$ [K/min]	isothermal annealing time/temperature	heating rate $Q_H$ [K/min]	starting condition (each run)
DSC I	1 2 5 10 20	-	2, 5, 10	10min at 450°C
DSC II	2  10	0min/250°C 30min/250°C 60min/250°C 0min/250°C 30min/250°C 60min/250°C	10	10min at 450°C
DSC III	20	60min/250°C 60min/280°C 60min/290°C 60min/300°C 60min/310°C 60min/320°C 60min/330°C 60min/340°C 60min/350°C 60min/360°C	10	10min at 450°C
Micro-hardness (measured at RT)	isochronal $\Delta T=10K$ $\Delta t=10min$	-	isochronal $\Delta T=10K$ $\Delta t=10min$	48h at 600°C, slow cooled to 450°C, quenched  10min at 450°C cooled to RT with 1K/min

## Results

DSC cycles of heating/cooling runs starting from the ordered state with various rates from 0.2 to 20K/min were made in a previous study [7]. The results of the heating runs are shown in Figure 1. The above mentioned 'retro' effect, a shift of  $T_{OD}$  to lower temperatures with increasing heating rate, is obvious.

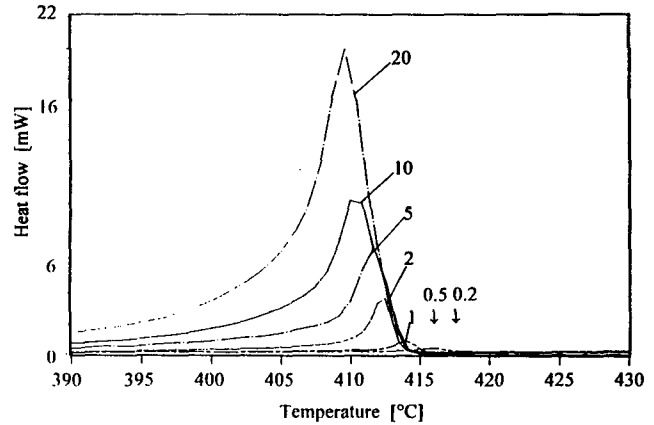


Figure 1: Heat flow during DSC heating runs from 0.2 to 20K/min versus temperature (arrows mark the peak positions of the low rates not visible in this scale)

### DSC-Series I

To study the influence of previous cooling rate the first series [I] of DSC measurements were cycles with cooling rates  $Q_c$  (1, 2, 5, 10, 20K/min) followed by three different heating runs with rates  $Q_H$  (2, 5, 10K/min). Each cooling run started with a 10min anneal at 450°C to achieve equal starting conditions. The results are shown in Figure 2a-e. For the low cooling rate of 2K/min (Figure 2b) a marked retro effect is observed during subsequent heating runs. With increasing cooling rate the retro effect decreases ( $Q_c=5K/min$ ) and vanishes for  $Q_c=10$  and 20K/min (Figure 2c-2e). For the very low cooling rate of 1K/min, however, a total shift of  $T_{OD}$  to lower temperatures is observed, which does not depend considerably on heating rate (Figure 2a).

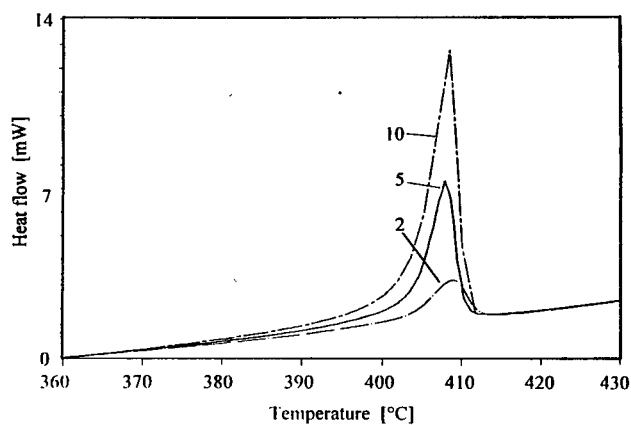
### DSC-Series II

In this series the influence of annealing time at 250°C on the  $T_{OD}$  was investigated for two initial cooling rates of  $Q_c$  (2, 10K/min). The starting condition was again a 10min anneal at 450°C. The isothermal annealing time at 250°C was  $t_a=0, 30, 60min$  with subsequent heating ( $Q_H=10K/min$ ) to 450°C. The results of this DSC runs are given in Figure 3, where it can be seen that isothermal annealing at 250°C is of minor importance on  $T_{OD}$  during subsequent heating. A total shift, however, is observed for previous cooling at a low rate of 2K/min. In contrast, for previous cooling with the higher rate of 10K/min no such peak shift is obtained.

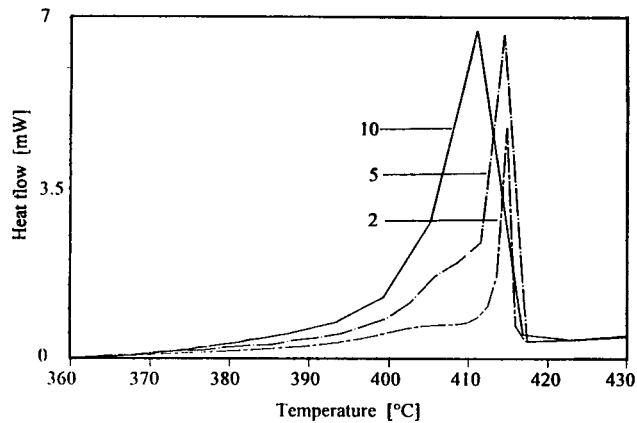
### DSC-Series III

In a third series (Figure 4) DSC-cycles were measured which should yield the influence of intermediate annealing temperature for a constant annealing time of 1h at different temperatures. To avoid that previous cooling lowers  $T_{OD}$  during subsequent heating, a fast cooling rate of 20K/min (see Figure 2e) was used. The heating run was performed with  $Q_H=10K/min$ . The intermediate annealing temperature was decreased in steps of 10K from 390°C to 250°C, respectively. In Figure 4 a quite small but continuous shift of the disordering temperature to lower temperatures with decreasing annealing temperature can be detected.

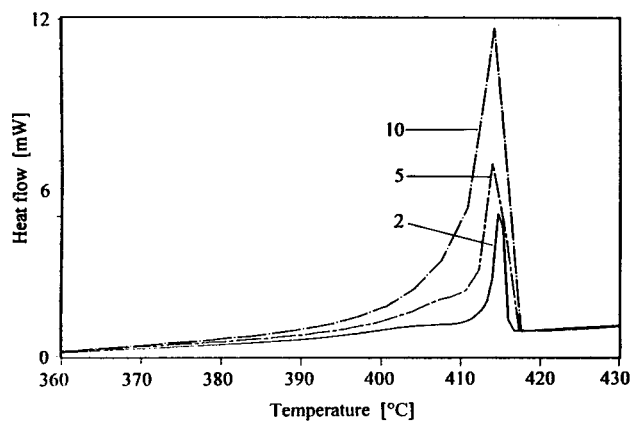
Table 2 gives a compilation of  $T_{OD}$ -peak temperatures during heating obtained for the various DSC-measuring series.



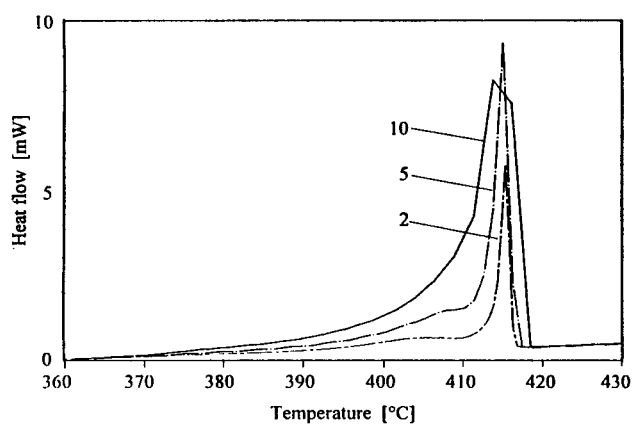
a) Heating runs for previous cooling at 1K/min



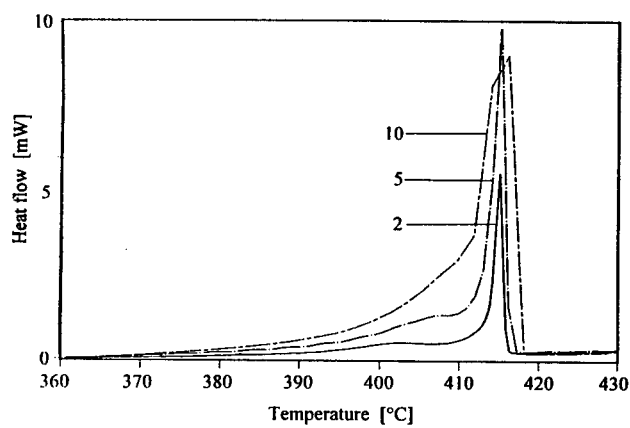
b) Heating runs for previous cooling at 2K/min



c) Heating runs for previous cooling at 5K/min



d) Heating runs for previous cooling at 10K/min



e) Heating runs for previous cooling at 20K/min

Figure 2: DSC runs with different heating rates  $Q_H=2, 5, 10$  K/min for various previous cooling conditions; a)  $Q_C=1$  K/min, b)  $Q_C=2$  K/min, c)  $Q_C=5$  K/min, d)  $Q_C=10$  K/min, e)  $Q_C=20$  K/min. Temperature treatment before each cooling/heating cycle: 10min anneal at 450°C.

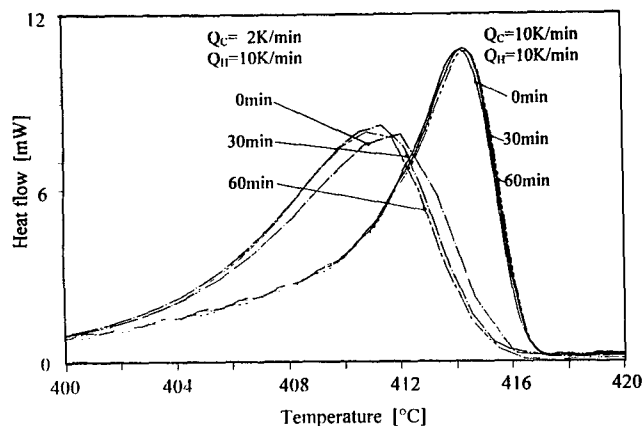


Figure 3: DSC runs using two cooling rates of  $Q_c=2, 10\text{K/min}$  and a constant heating rate of  $Q_h=10\text{K/min}$  with variation of intermediate annealing time at  $250^\circ\text{C}$  ( $t_a=0, 30, 60\text{min}$ ). Temperature treatment before each cooling/heating cycle: 10min anneal at  $450^\circ\text{C}$ .

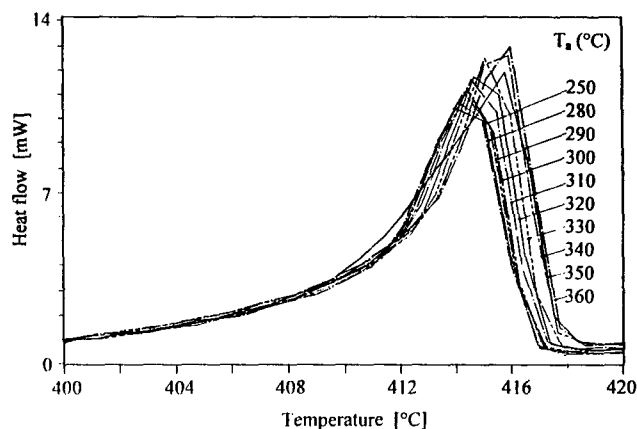


Figure 4: DSC runs using constant cooling and heating rates ( $Q_c=20\text{K/min}$  and  $Q_h=10\text{K/min}$ ) for intermediate anneals of 1h at various temperatures as indicated. Temperature treatment before each cooling/heating cycle: 10min anneal at  $450^\circ\text{C}$ .

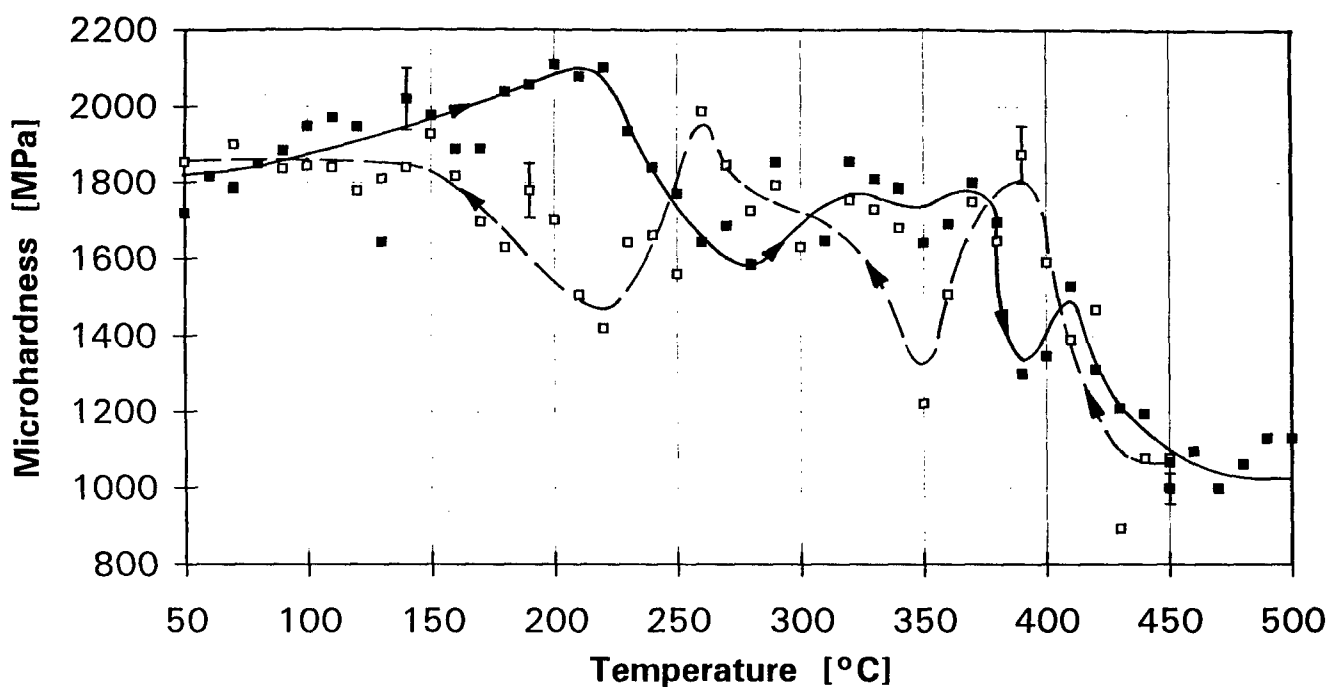


Figure 5: Changes in microhardness during isochronal annealing ( $\Delta T=10\text{K}$ ,  $\Delta t=10\text{min}$ ). Open squares: cooling; full squares: heating. Accuracy: about 4%.

#### Microhardness:

Microhardness tests give a picture of mechanical changes like grain-growth, dislocation generation and twinning in a material which undergoes an order/disorder transition when this transformation is accompanied by considerable lattice distortion as observed for CuAu. To obtain information about the temperature region where such essential structural processes occur which may influence the retro-effect, microhardness was measured during isochronal cooling and heating cycles. During an isochronal temperature

treatment the sample was annealed for equal amounts of time at a stepwise changed temperature.

In Figure 5 the changes of microhardness are plotted versus annealing temperature during isochronal annealing ( $\Delta T=10\text{K}$ ,  $\Delta t=10\text{min}$ ) at falling (450 to  $50^\circ\text{C}$ ,  $\square$ ) and raising temperatures (50 to  $500^\circ\text{C}$ ,  $\blacksquare$ ). It has to be noted that two different samples have been used for both runs. The initial temperature treatment for the cooled sample was 48h at  $600^\circ\text{C}$ , slowly cooled to  $450^\circ\text{C}$  and quenched. The other sample was annealed for 10min at  $450^\circ\text{C}$  and then cooled at  $1\text{K/min}$  to room temperature. The initial hardness



value of about 1100MPa of the cooling curve coincides with the final one of the heating curve. For the final hardness of the cooling curve and the starting value of the heating curve the same value of about 1800MPa is obtained

For both runs three ranges can be distinguished which are somewhat shifted in temperature between cooling and heating:

*range I:* 350 - 430°C (cooling)

390 - 450°C (heating)

In this temperature range a hardness peak is observed. It may be attributed to the formation/dissolution of CuAuII.

*range II:* 220 - 350°C (cooling)

280 - 390°C (heating)

For both runs a broad (double-) peak is observed, showing a drastic decrease below 260°C (cooling) and above 370°C (heating), respectively.

*range III:* 50 - 220°C (cooling)

50 - 280°C (heating)

During cooling first a gradual increase of hardness is observed until a final saturation is reached. Heating starts with a slight increase until the maximum value of hardness, followed by a gradual decrease

### Discussion

It is known from the literature that the transformation of disordered CuAu into its LRO-state is of the nucleation and growth type [3,9]. For this type of phase transition, during heating an increase of the transition temperature with increasing heating rate for dynamic measurements is to be expected (effect of superheating). In contrast, a slight 'retro-effect' of lower transition temperature with increase of heating rate has been observed for cooling/heating cycles under well-defined starting conditions [7,8] (Figure 1). From a series of detailed in-situ resistivity measurements [8] it was presumed that the retro-effect is a consequence of incomplete transformation of CuAuI into CuAuII during the heating part of the cycle. In the present paper several measuring series by DSC are reported and compared with microhardness measurements during cooling and heating.

### DSC-Measurements

As a main result of the present investigation the strong influence of previous *cooling* rate on the order/disorder transition temperature  $T_{OD}$  measured during the following *heating* run was obtained. The following details arise from DSC-series:

- A retro-effect of decreasing  $T_{OD}$  with increasing heating rate is observed for 'low' cooling rates of  $Q_c$  (1, 2, 5K/min) only, with a maximum dependence on heating rate for previous cooling at 2K/min (Figure 2).
- An overall shift of  $T_{OD}$ -values to lower temperatures with lower cooling rate is observed (see Table 2). For 'high' cooling rates of  $Q_c$  (10, 20K/min) no such shift is observed (Figure 2).
- Isothermal annealing at 250°C is of minor importance, but a previous cooling at a 'low' rate of 2K/min leads to a considerable lowering of  $T_{OD}$  during subsequent heating if compared with a 'fast' cooling at 10K/min (Figure 3).
- 'Fast' cooling (20K/min) with subsequent isothermal annealing for 1 h at temperatures between 250 and 360°C yields only a very small shift of  $T_{OD}$  to lower temperatures during heating at 10K/min (Figure 4).

Whereas our former investigations showed the existence of the retro-effect [7,8], there is now evidence that for low *cooling* rates a peak-shift of  $T_{OD}$  to lower temperatures during subsequent heating is observed, which

Table 2: Estimated peak-temperatures of DSC-series I, II and III  
(Accuracy:  $\pm 0.3K$ )

series	cooling/heating rate [K/min]	isothermal annealing time/temperature	peak-temperature [°C]
DSC I	1/2	-	408.8
	1/5	-	407.8
	1/10	-	408.1
	2/2	-	415.0
	2/5	-	414.1
	2/10	-	410.6
	5/2	-	415.0
	5/5	-	413.8
	5/10	-	413.8
	10/2	-	415.1
	10/5	-	415.0
	10/10	-	415.0
	20/2	-	415.0
	20/5	-	415.0
	20/10	-	415.2
DSC II	2/10	0min/250°C	411.5
	2/10	30min/250°C	411.0
	2/10	60min/250°C	411.0
	10/10	0min/250°C	414.3
	10/10	30min/250°C	414.3
	10/10	60min/250°C	414.4
DSC III	20/10	60min/250°C	414.5
	20/10	60min/280°C	414.7
	20/10	60min/290°C	414.9
	20/10	60min/300°C	415.0
	20/10	60min/310°C	415.1
	20/10	60min/320°C	415.2
	20/10	60min/330°C	415.5
	20/10	60min/340°C	415.7
	20/10	60min/350°C	416.0
	20/10	60min/360°C	416.0

does not significantly depend on the heating rate. Such a shift is not observed for fast heating rates; additionally, in this case for intermediate annealings between 250 and 360°C no marked peak-shift during heating is initiated.

It seems clear from (1) the DSC-measurements and (2) the above contention that the retro-effect is caused by incomplete transformation of CuAuI into CuAuII during heating [8], that 'stabilising' processes during the *cooling*

cycle exist which protect the CuAuI-phase against complete transition into CuAuII during the subsequent heating run.

#### Microhardness Measurements

Microhardness measurements give information on how a material reacts during small plastic deformation, where the measured hardness values depend on the shear stress as well as on work-hardening processes. This way, microhardness essentially measures the rates of dislocation generation and annihilation and is a test for the mobility of dislocations and their interaction with various obstacles. In CuAu the situation with respect to its mechanical behaviour during long-range ordering is somewhat complicated. It is known from the literature [3,4] that the increase of order first proceeds by nucleation and growth of ordered domains remaining coherent with the disordered matrix. At a certain state of ordering, however, further ordering is accompanied by twinning, and the coherency of ordered domains is progressively lost [5]. For the microhardness values measured during ordering, this means an increase or a decrease depending on the current microstructure of the alloy. Internal stresses, e.g. around small coherent particles, hinder dislocation motion and therefore increase the microhardness. On the other hand, breakdown of coherence and generation of misfit dislocations increase dislocation motion and so decrease the microhardness. The observed results from microhardness measurements especially during the cooling run, therefore, can be used to detect the origin of the above processes stabilising the CuAuI-phase during cooling.

The microhardness curves in Figure 5 below 220°C, each read in the respective measuring direction (decreasing or increasing temperature), show a gradual increase of hardness which is thought to be correlated with a further increase of degree of order (order hardening) following the previous heat treatment, but without major structural changes.

Both microhardness curves above 220°C show a two-peak structure, a rather sharp peak at about 390°C for cooling and 410°C for heating and a broad (double-) peak between 220 and 350°C for cooling and between 280 and 390°C for heating. The differences in the position of these peaks between cooling and heating hint at a Hysteresis originating without doubt from the order/disorder transitions which occur in these temperature ranges. It is known [10] that the critical resolved shear stress during changes in the degree of LRO is at maximum for intermediate values of order parameter. Therefore the two-peak character of the microhardness curves can be understood by formation and transformation of the ordered phases CuAuII (sharp peak) and CuAuI (broad double-peak).

Various authors correlate the strong decrease of hardness during ordering (cooling curve) with the relief of internal stress being accompanied by the growth of originally coherent ordered domains in the sample [3-5]. The processes enabling this stress relief are essentially twinning and an accompanying progressive loss of coherence of the ordered domains. It can be observed in the microhardness curve during cooling that there are two such ranges of decreases in hardness, which may mark the onset of such stress-accommodation. Below 390°C twinning may start in CuAuII and below 260°C twinning seems to start in CuAuI, both in agreement with optical investigation [3].

These observations which correlate with the literature [3-5], now lead to a consistent interpretation of the origin of the peak-shift of  $T_{OD}$  during heating including the retro-effect. The effect which stabilises the CuAuI-phase against transformation into CuAuII during *heating* arises from the processes of stress relief during *cooling*. These processes are thought to be essentially twinning and loss of coherence of ordered domains. When this stress accommodation has occurred, the re-transformation into CuAuII during heating, which means the generation of regularly spaced antiphase boundaries, is hindered. This is not the case if the ordered domains of CuAuI during heating are coherent with the disordered matrix. This may also be seen from the differences in microhardness (peak temperature and peak height) between cooling and heating. The peak during (slow) cooling at 390°C, which is attributed to the formation of CuAuII has a height of about 1800 MPa. During heating it is shifted to 410°C and the hardness is reduced

to about 1500 MPa. In addition, the decrease of microhardness proceeds until 450°C. This may be a further indication of incomplete transformation of CuAuI into CuAuII and a continuing dissolution of twinned CuAuI-microstructure up to at least 450°C. A detailed optical investigation for clarification of twinning processes as a function of different thermal pre-treatments is under way.

#### Conclusions and Summary

From the findings of the DSC-measurements that isothermal annealing between 250 and 360°C after fast cooling are of minor importance for the discussed peak-shift, it must be concluded that prolonged annealing in this temperature range does not lead to the stabilisation of CuAuI-phase by stress relief. In contrast, it seems that cooling through the temperature interval between 410 and 360°C is critical for the behaviour during subsequent heating.

What is the reason for the dependence of CuAuI phase being stabilised by twinning on the cooling rate in the temperature interval between 410 and 360°C? The rate of cooling between 410 and 360°C critically influences the size of nucleated ordered domains of CuAuI.<sup>\*)</sup> A low cooling rate means longer nucleation time at smaller undercooling, which leads to comparably large domain size. However, it is known from the literature [3-5], that twinning and loss of coherence are linked to large ordered domains, and these are prohibited in the presence of very small ordered domains.

The result may be summarised as follows:

- (i) DSC-measurements show that the retro-effect observed in a previous investigation is a consequence of a shift of  $T_{OD}$  to lower temperatures during *heating* which was initiated during previous *cooling*.
- (ii) The origin for the shift of  $T_{OD}$  to lower temperatures is the stabilisation of CuAuI-phase against its complete transition into CuAuII during heating.
- (iii) The microhardness measurements indicate that the stabilisation of the CuAuI-phase arises from relief of internal stresses, which have been accumulated during nucleation of ordered domains, by twinning and loss of coherence of ordered domains with the disordered matrix.
- (iv) The marked influence of cooling rate on the peak-shift during heating can be correlated with the size of nucleated ordered domains.

#### Acknowledgement

M. S. and W. P. are grateful for the financial support by the 'Hochschuljubiläumsstiftung der Gemeinde Wien' and the Austrian 'Fonds zur Förderung der wissenschaftlichen Forschung'.

#### References

- [1] M. Hansen and K. Anderko, „Constitution of binary alloys,“ 2<sup>nd</sup> Edition, McGraw-Hill, New York 1958.
- [2] J. Nyström, „A calorimetric and resistometric study on the transformations in CuAu,“ Arkiv Fysik 2, 151 (1950).
- [3] G.C. Kuczynski, R. F. Hochman and M. Doyama, „Study of the kinetics of ordering in the alloy CuAu,“ J. Appl. Phys. 26, 871 (1955).

<sup>\*)</sup> It has to be noted that this interpretation cannot directly be concluded from present microhardness curves. These curves have been measured during isochronal annealing treatment which as a quasi-static procedure will yield some differences in peak temperatures in comparison to dynamic linear heating treatment.

- [4] M. Hirabayashi and S. Weissmann, „Study of CuAu by transmission electron microscopy,“ *Acta Met.* **10**, 25 (1962).
- [5] V.S. Arunachalam and R.W. Cahn, „Order-hardening in CuAu,“ *J. Mater. Sci.* **2**, 160 (1967).
- [6] B. Sprusil, V. Sima and B. Chalupa, „ Phase transformations in CuAu and Cu<sub>3</sub>Au: A comparison between calorimetric and resistometric measurements,“ *Z. Metallkd.* **84**, 118 (1993).
- [7] B. Chalupa, F. Chmelik, V. Sima, B. Sprusil, M. Spanl H. Lang and W. Pfeiler, „ Hysteresis of long-range ordering in CuAu,“ *Mat. Res. Soc. Symp. Proc. Vol. 398*, eds. J.S. Im, B. Park, A.L. Greer, G.B. Stephenson, 581-586 (1996).
- [8] B. Sprusil and W. Pfeiler, „The Retro-effect in stoichiometric CuAu: a resistometric study“, submitted to *Intermetallics*.
- [9] J.L. O'Brien and G.C. Kuczynski, „ X-ray study of the kinetics of ordering in CuAu,“ *Acta Met.* **7**, 803 (1959).
- [10] N. Brown, „ The yield point of a super-lattice,“ *Phil. Mag.* **4**, 693 (1959).

# DUCTILITY ENHANCEMENT IN STRUCTURAL INTERMETALLICS FROM FIRST PRINCIPLE CALCULATION

R. ASOKAMANI AND R. RITA\*

Physics Department, Anna University, Chennai, India.

\* C.T. Thomas Elizabeth College for Women, Perambur, Chennai, India.

## Abstract

A theoretical investigation on the enhancement of the ductility of the potentially useful aerospace intermetallic compounds  $Ti_3Al$  and  $Ni_3Al$  has been made using band structure results obtained from Tight Binding Linear Muffin Tin Orbital (TBLMTO) method.

Eventhough  $Ti_3Al$  and  $Ni_3Al$  have excellent high temperature properties, still they suffer from poor ductility which is due to intragranular fracture (lack of sufficient number of operable slip systems) and intergranular fracture (grain boundary weakness).

Inspite of having sufficient number of independent slip systems, polycrystalline  $Ni_3Al$  is brittle. As  $Ti_3Al$  crystallizes in hcp structure, it does not satisfy the Von Mises criterion and hence, has poor ductility. In the case of  $Ni_3Al$ , eventhough the above said criterion is fulfilled the ductility is poor because of the  $pd\sigma$  covalent bonding existing between  $Ni-3d$  and  $Al-2p$  electrons.

To enhance ductility, the strength of  $pd\sigma$  interaction has

to be decreased by increasing the  $d-d$  interaction by insertion of either  $3d$  or  $4d$  atoms into the host material.

In the present work  $Nb$  is added to  $Ni_3Al$  and we try to find out to what extent this addition could be made without destroying the cubic symmetry with the help of heat of formation studies. The correlations that exist between ductility and Fermi energy as well as the density of states at the Fermi level are also discussed with the overall goal of understanding the mechanisms for increasing the ductility of these intermetallics.

## Introduction

The ordered intermetallic compounds possess many interesting high temperature properties which make them useful for structural applications at high temperatures. However a major barrier to the widespread use of these ordered intermetallics is that most of them lack room temperature ductility and toughness [1]. The two major factors which have been found responsible for brittleness in ordered intermetallics are (i) intergranular fracture due to grain boundary weakness (ii) transgranular fracture due to insufficient number of operable slip systems [2].

In this paper we discuss the methods of improving the ductility in the ordered intermetallics which suffer from the above mentioned defects.

The ordered intermetallic compounds of the Ti-Al system, are particularly important for aerospace applications. In addition to their excellent high temperature properties like high melting point, high strength and oxidation resistance at elevated temperatures, these alloys are about half as dense as the Ni-based super alloys which have traditionally been used in aerospace industry. In spite of having these desirable properties  $Ti_3Al$  suffers from poor ductility. This is because of its ordered hexagonal  $DO_{19}$  structure, which does not satisfy the requirement of five independent slip systems as demanded by the Von Mises criterion for greater ductility. By making  $Ti_3Al$  to possess  $L1_2$  structure so as to have enough slip systems one can fulfill the requirement of ductility. This crystal structural transformation in  $Ti_3Al$  is discussed in section 2.

Another intermetallic compound with desirable properties to be used at high temperatures is  $Ni_3Al$ . Though it exists in the cubic  $L1_2$  structure with required number of slip systems, it suffers from poor ductility which is mainly arising from  $Pd\sigma$  bonding. The ductility of  $Ni_3Al$  can be improved by reducing the strength of the  $Pd\sigma$  bonding by alloying it with proper element. The ductility is improved by alloying  $Ni_3Al$  with Nb. The solubility range of Nb in  $Ni_3Al$  and its influence in improving the ductility of  $Ni_3Al$  are discussed in section 3.

The choice of the alloying element and the extent to which it should be added play an important role in improving the ductility of the ordered intermetallic compounds. In section 4, we bring out some of the correlations between ductility and Fermi energy as well as the density of states at the Fermi level which will serve as guiding factors in deciding the alloying elements to be used to enhance the ductility.

## Section 1: Electronic structure and total energy calculations

The method employed here to compute the band structure is semi-relativistic Tight Binding Linear Muffin Tin Orbital Method (TBLMTO) within Atomic Sphere Approximation (ASA) [3,4]. Von Barth-Hedin exchange correlation scheme has

been used to compute the exchange correlation potential. The short ranged Screened Muffin Tin Orbitals (which are exactly transformed from the conventional long ranged MTOs) are the basis for this method.

The screened TB-MTO's take the form

$$\begin{aligned} |\chi^s(E)\rangle &\sim |\phi(E)\rangle N^s(E) + |J^s\rangle \tilde{P}^s(E) r \leq W \\ &\sim |n^s\rangle \quad r \geq W \end{aligned} \quad (1)$$

Where  $|\phi(E)\rangle$  is the solution of the radial Schrodinger equation for spherically symmetric potential centred at  $W$ , the Wigner-Seitz radius.

$$\begin{aligned} N^s(E) &= (W/d)^{1/2} (P^s(E))^{1/2} \\ \text{and } P^s(E) &= P^0(E) (1 - \alpha P^0(E))^{-1} \end{aligned} \quad (2)$$

Here  $P^0(E)$  is the conventional potential function,  $\alpha$  is the screening parameter,  $|n^s\rangle$  is the screened Neumann function and  $|J^s\rangle$  is the augmented screened Bessel function and  $d$  is  $|R_i - R_j|$ . The details of the method can be found in ref (3) and (4)

In all our calculations we assumed equal Wigner-Seitz radii for both transition metals and aluminium as the degree of overlap between the atoms lies within the allowed range. The basis set includes  $s, p$  and  $d$  orbitals at each atomic site and the fully relativistic core states are recalculated at every iteration. The combined correction terms are included in all our calculations. The valence electrons are treated in a semi relativistic way.

The total energy of the solid is calculated using the following expression.

$$E_{\text{tot}} = T_{\text{kin}} + \sum_R U_R + \sum_{R,R'} \sum_Z Z_R \sum_T |R-R'-T|^{-1} \quad (3)$$

where the first term is the kinetic energy of the valence electrons which should be expressed as the difference between the total energy and the potential energy of the non-interacting electrons.

$$T_{\text{kin}} = \int_0^{E_F} E N(E) dE - \sum_R \int_0^{S_R} v_R(r) n_R(r) 4\pi r^2 dr \quad (4)$$

where  $N(E) = \sum_{R1} N_{R1}(E)$  is the sum of the projected Density Of

States (DOS).  $v_R(r)$  is the one electron potential in the sphere at  $R$  and  $n_R(r)$  is the spherically averaged charge density. The second term in equation (3) is the sum of the intra-sphere interaction energy between the electrons themselves and between the electrons and the nucleus in that sphere and it can be expressed as

$$U_R = \int_0^{S_R} n_R(r) [E_{\infty} - \frac{Z_R}{r}] 4\pi r^2 dr + \int_0^{S_R} n_R(r') |r-r'|^{-1} 4\pi r'^2 dr' \quad (5)$$

The third term in equation (3) is the intersphere coulomb (or Medelung) energy. Here  $Z_R$  is the difference between the nuclear charge and the electronic charge in the sphere at  $R$ .

## Section 2: Crystal structural transformation in $Ti_3Al$

It has been established that the intermetallic compound  $Ti_3Al$  which has an ordered hexagonal  $DO_{19}$  structure (Figure 1a) does not satisfy the requirement of five independent slip systems for general ductility. The cubic  $L1_2$  phase (figure 1b) has more number of slip systems than the  $DO_{19}$  phase because of its higher symmetry. It has also been found that the materials with isotropic charge density distribution are more ductile than materials with anisotropic charge density distribution [5]. Further, from a comparison between the charge densities of  $L1_2$  and  $DO_{19}$  structures of  $Ti_3Al$ , the observed homogeneous charge density distribution in the  $L1_2$  structure is an encouraging sign to improve the ductility of  $Ti_3Al$  by stabilizing the cubic phase [6]. So it is of great interest to examine the possibility of a  $DO_{19} \rightarrow L1_2$  transition [7] in  $Ti_3Al$ .

In order to achieve this, attempts have been made by alloying the host either with 3d elements or 4d elements by which one changes the chemical pressure. Instead, we try to achieve the hexagonal to cubic structural transformation by applying external pressure. The electronic band structure calculations were carried out for both  $L1_2$  and  $DO_{19}$  structures for both extended and reduced cell volumes. The total energy calculations obtained from the above studies clearly show that  $Ti_3Al$  crystallizes in  $DO_{19}$  structure and a crossover observed in their total energy curves indicates a structural transformation from  $DO_{19}$  to  $L1_2$  at high pressures. The lattice constants  $c$  and  $a$  agree very well with the

experimental values. The  $c/a$  ratio is calculated to be 0.803 which is in good agreement with the experimental value of 0.8007 of Pearson [8] and 0.807 of the other theoretical work [6].  $Ti_3Al$  exists in the low symmetric  $DO_{19}$  structure because of the directional bonding.

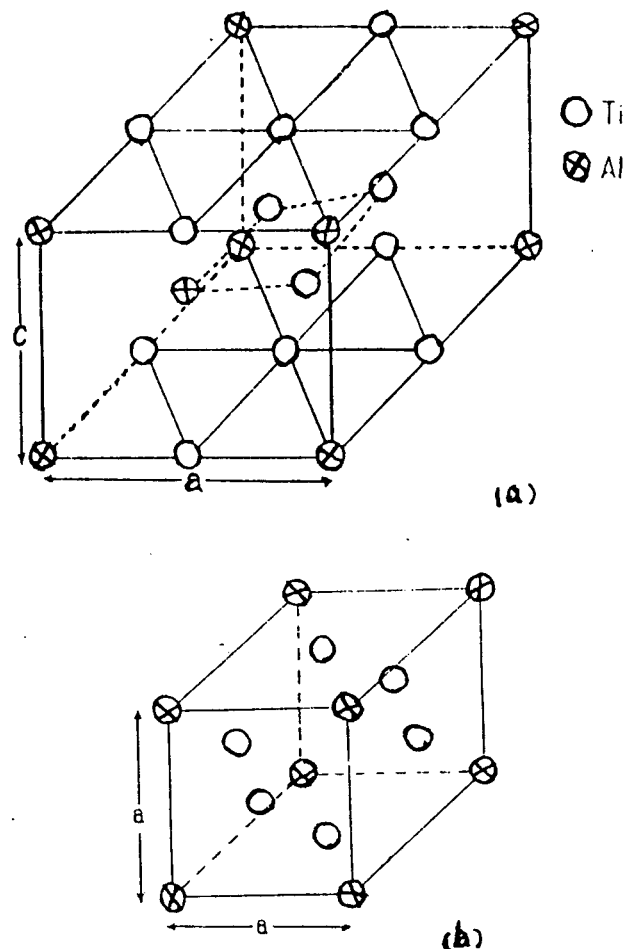


Fig. 1 : Crystal structure of  $Ti_3Al$  in (a) hexagonal  $DO_{19}$ , and (b) cubic  $L1_2$  structure.

The strong Ti-Ti and Ti-Al bondings weaken under compression owing to loss of convalency and hence,  $Ti_3Al$  transforms from somewhat low symmetric  $DO_{19}$  structure to high symmetric cubic  $L1_2$  structure. This structural transformation is shown in the figure 2 where, the above said cross-over occurs for  $v/v_0$  around 0.9 which indicates that at high pressure  $Ti_3Al$  will go to cubic  $L1_2$  structure as it has lower energy. As the charge density is much more uniformly distributed in  $L1_2$  structure [6] the high pressure phase of  $Ti_3Al$  should be ductile [5]. Further, it has been observed that materials which have more d-d interaction than p-d interaction should have more ductility [9]. From the above observations and because of the

stronger Ti (d) - Ti(d) interaction in the high pressure  $L1_2$  phase than in  $DO_{19}$  phase of  $Ti_3Al$ , we believe that one can improve ductility of  $Ti_3Al$  by stabilizing it in the cubic phase.

In support of our theoretical findings of pressure induced structural transition in  $Ti_3Al$ , it has been observed that the  $A_3B$  type isostructural compounds such as  $Fe_3Sn$ ,  $Ni_3Sn$  and  $Ni_3In$  also follow the  $DO_{19} \rightarrow L1_2$  structural transition at high pressures [10,11].

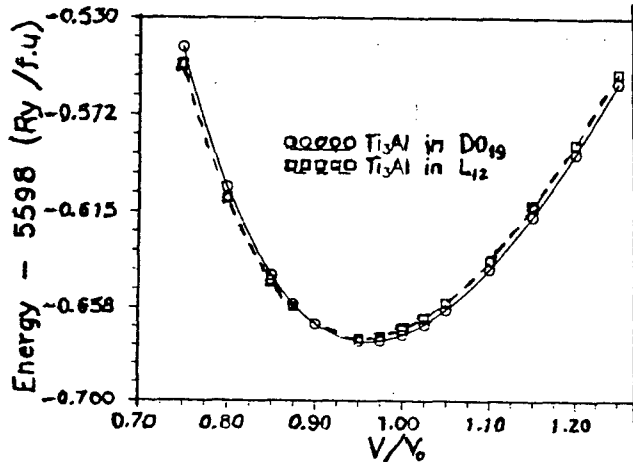


Figure 2 : The volume variation of total energy curves for  $Ti_3Al$  in the cubic  $L1_2$  and hexagonal  $DO_{19}$  structures.

### Section 3 : Ternary addition to $Ni_3Al$

It is well known that single crystal  $Ni_3Al$  is highly ductile whereas polycrystalline  $Ni_3Al$  is brittle.  $Ni_3Al$ , which is in the cubic structure, possesses enough number of independent slip systems to satisfy the Von Mises criterion for better ductility. So, the intergranular fracture should be mainly responsible for the poor ductility in polycrystalline  $Ni_3Al$ .

Aluminium atom is covalently bonded with the Ni atom in  $Ni_3Al$  via  $pd\sigma$  interaction and on account of electronegativity difference, the Al atom draws more charge from the Ni atom. As a result of this, less charge is available to participate in the Ni-Ni bonding in the grain boundaries and this leads to weakening of the grain boundaries [12]. On the otherhand, if the Nb like transition metal atom is added to the Ni-Al matrix, the covalent character of the Ni-Al bond will be weakened and hence, the suppression of grain boundary embrittlement can be expected [9]. The weakening of  $Pd\sigma$  covalent interaction by Nb alloying in  $Ni_3Al$  will lead to

more uniform charge density distribution in  $Ni_3(Al,Nb)$ . Thus,  $Ni_3(Al,Nb)$  will be more ductile than  $Ni_3Al$ .

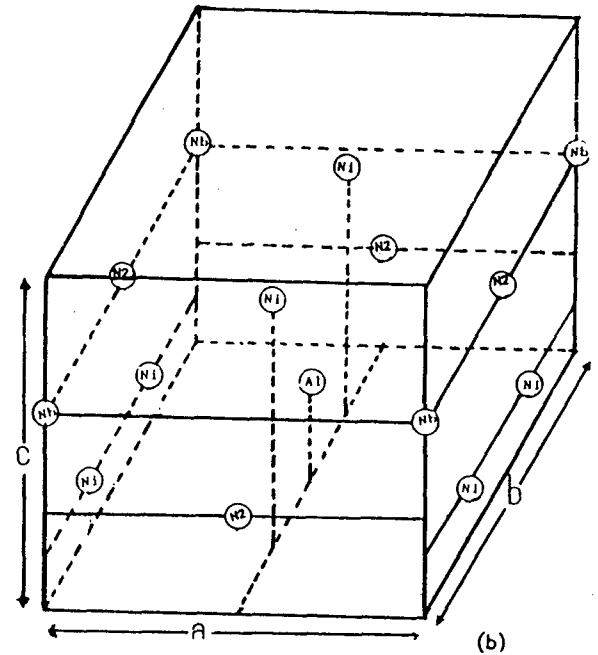
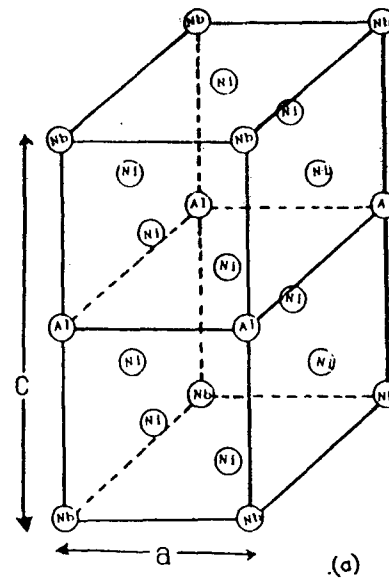


Fig. 3 : The supercells of  $Ni_3(Al, Nb)$  in (a)  $L1_2$  ( $Ni_3Al_{0.5}Nb_{0.5}$ ) (b)  $DO_{19}$  ( $Ni_3Al_{0.5}Nb_{0.5}$ )

The ternary alloying of transition metals sometimes changes  $Ni_3Al$  from high symmetry cubic structure to low symmetry structures. Under such circumstances, as the transgranular fracture mechanism predominates, the system will be more brittle.  $Ni_3Nb$

crystallizes in the low symmetry orthorhombic (DOa) structure. The relative stability between cubic and orthorhombic phases of  $\text{Ni}_3\text{Al}$  as a function of Nb substitution is studied here to determine the critical concentration upto which the cubic phase is retained.

The electronic band structures were carried out for  $\text{Ni}_3\text{Al}$ ,  $\text{Ni}_3\text{Al}_{0.75}\text{Nb}_{0.25}$ ,  $\text{Ni}_3\text{Al}_{0.5}\text{Nb}_{0.5}$ ,  $\text{Ni}_3\text{Al}_{0.25}\text{Nb}_{0.75}$  and  $\text{Ni}_3\text{Nb}$ . These calculations were performed for both the  $\text{Ll}_2$  structure of  $\text{Ni}_3\text{Al}$  and the orthorhombic structure of  $\text{Ni}_3\text{Nb}$  by considering the supercells which are shown in figure (3).

The heat of formation for  $\text{Ni}_3(\text{Al}, \text{Nb})$  compounds is estimated from the energy difference between the compound and the weighted sum of their constituents. i.e.

$$\Delta H = E_{\text{Ni}_3\text{AlNb}_x} - (XE_{\text{Ni}} + YE_{\text{Al}} + ZE_{\text{Nb}}) \quad (6)$$

where, X, Y and Z are the chemical composition of Ni, Al and Nb respectively.

In order to understand the relative stability between  $\text{Ll}_2$  and  $\text{DO}_a$  structures of  $\text{Ni}_3\text{Al}$  as a function of Nb substitution, the heat of formation of  $\text{Ni}_3\text{Al}$  as a function of Nb substitution is plotted for both  $\text{Ll}_2$  and  $\text{DO}_a$  structures in figure (4). From the figure it is clearly seen that the  $\text{Ll}_2$  structure is retained upto 14.75% of Nb substitution in  $\text{Ni}_3\text{Al}$  and the corresponding chemical substitution is  $\text{Ni}_3\text{Al}_{0.41}\text{Nb}_{0.59}$ . There exists an empirical correlation between valence electron concentration  $e/a$  and the  $\text{DO}_a \rightarrow \text{Ll}_2$  structural transition in intermetallic compounds [13,14]. Our present quantum mechanical calculations reported here estimates the critical  $e/a$  ratio for the above composition as 8.545 which is in good agreement with that obtained from the empirical observations [14,15].

The calculated value of heat of formation for  $\text{Ni}_3\text{Al}$  obtained from our total energy study (50.74 kcal/mol) is found to be comparable with the experimental values 36.6 kcal/mol [16] and 37.5 kcal/mol [17] and is in good agreement with the earlier theoretical total energy studies 44.8 kcal/mol [18]. Similarly, the heat of formation theoretically obtained for  $\text{Ni}_3\text{Nb}$  is 31.9 kcal/mol and is in very good agreement with the experimental value of 30.4 kcal/mol [16]. The value of heat of formation for  $\text{Ni}_3\text{Al}_{0.25}\text{Nb}_{0.75}$  is small for both  $\text{Ll}_2$  and  $\text{DO}_a$  structures indicating that the system is likely to go to the disordered state more easily as has been

observed by Xu et al in the case of  $\text{Fe}_3\text{Ti}$  system [19]. Our heat of formation study on  $\text{Ni}_3(\text{Al}, \text{Nb})$  shows that the ordering decreases by Nb substitution in  $\text{Ni}_3\text{Al}$ . This is a positive indication for the improvement of ductility of  $\text{Ni}_3\text{Al}$  by the Nb substitution.

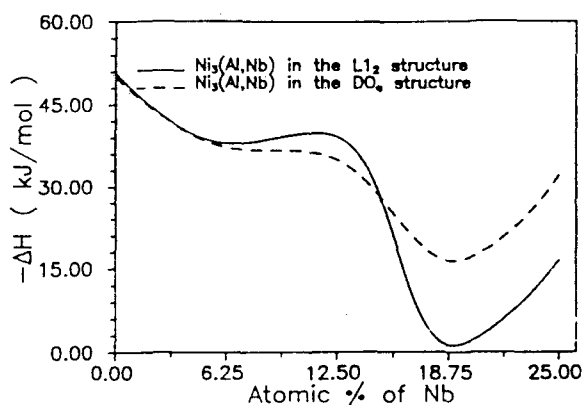


Fig. 4 : The variation of heat of formation as a function of Nb substitution in  $\text{Ni}_3\text{Al}$  for  $\text{Ll}_2$  (continuous line) and  $\text{DO}_a$  (dashed line) structures.

#### Section 4 : Correlation between density of states and structural stability

Figure (5) clearly shows that the  $\text{DO}_{19}$  structure has a lower  $N(E_F)$  value.

Compared to  $\text{Ll}_2$  structure which brings out a correlation between  $N(E_F)$  and structural stability. The values of  $N(E_F)$  corresponding to  $\text{Ll}_2$  and  $\text{DO}_{19}$  structures are calculated to be 60.387 and 15.354 states  $\text{Ryd}^{-1} \text{ F.U}^{-1}$  respectively. Further the experimental works of Kuentzler and Waterstrat and that of Wang et al [20,21,22] also clearly demonstrate that the system will prefer that structure which has a lower  $N(E_F)$ . Table (1) gives the experimentally measured electronic specific heat coefficient ( $\nu$ ) and the melting point for the different transition metal diborides which clearly shows that the lower the  $\nu$  value, (lower  $N(E_F)$  value) greater is the melting point and the corresponding structure is stable. The electronic structure calculations performed for a number of intermetallics exhibit what is called a pseudogap (PG), a valley in the vicinity of the Fermi level which supports the above mentioned experimental observations. This has been verified in some of our studies on Laves phase compounds and other systems such as  $\text{Zr}_3\text{Al}$ ,  $\text{Ti}_3\text{Al}$  etc. [23,24]. This point has been emphasized repeatedly by Freeman and his co-workers [25,6].



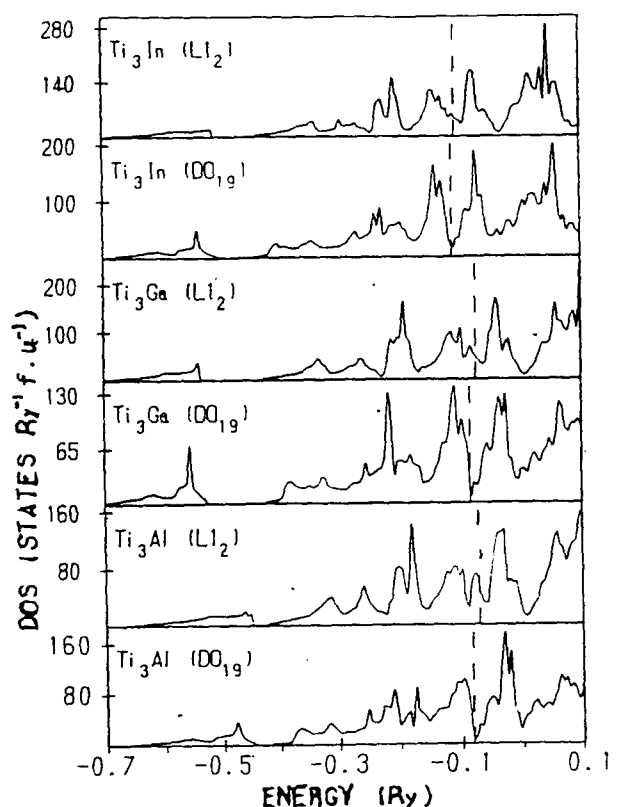


Figure 5 : Total density of states of  $Ti_3X$  ( $X=Al, Ga, In$ ) compounds in  $L1_2$  and  $DO_{19}$  structures.

These studies imply that the macroscopic property namely the high melting point possessed by the ordered intermetallic compounds corresponds to a microscopic low  $N(E_F)$  value. Hence in the search for high temperature intermetallics to be used for aerospace applications one should look for materials which have low  $N(E_F)$  values.

Table I : The  $T_m$  and  $\nu$  values of transition metal diborides

Compound	$\nu$ (exp) mJ/mol/K <sup>2</sup>	$T_m$ (°C)
ScB <sub>2</sub>	2.2	-
TiB <sub>2</sub>	1.08	2980
V B <sub>2</sub>	4.84	2400
Cr B <sub>2</sub>	13.6	2200
Mn B <sub>2</sub>	4.45	

The position of the Fermi level plays a very important role as it is able to discriminate between ordered and disordered systems.

If  $E_F$  lies exactly at the PG, it indicates an ordered intermetallic compound with high melting point. On the other hand if it lies to the right of the PG the system has greater glass forming ability [26] which is a requirement for shape memory alloys.

### Conclusion

From the above studies, one finds that the ductility of the intermetallic compounds such as  $Ti_3Al$  and  $Ni_3Al$  can be improved by the application of external pressure or chemical substitution. The ductility of  $Ti_3Al$  is improved by  $DO_{19} \rightarrow L1_2$  structural transformation which is realised by the application of external pressure. In the case of  $Ni_3Al$ , the ductility is improved by alloying it with Nb wherein the d-d interaction strength is enhanced at the expense of p-d interaction. The critical concentration of Nb to be added to  $Ni_3Al$  which will enhance the ductility by reducing the p-d interaction without any change in its  $L1_2$  structure using the Heat of formation studies.

The microscopic model calculation which has been performed is able to successfully determine the critical concentration of Nb which could be added to  $Ni_3Al$ . But it should be noted that this model calculation has not taken into account temperature and the two phase or multiphase regions actually observed in the phase diagram. The grain size effects should also be incorporated and they remain at present as unsolved problems. However one hopes that ternary, quaternary additions to Ti-Al and Ni-Al systems with suitable alloying elements and proper degree of alloying and with the guidance of the Hume-Rothery rules will ultimately result in improved materials which could be used for aerospace applications.

The relationship between ductility and the position of Fermi level in the DOS histogram has been determined with the idea of pseudogap. Our theoretical calculations show that the density of states at the Fermi level should be small for a material to have high melting point. But if the PG is sharp which clearly separates bonding states from the antibonding states, ductility will be very much decreased as the above indicates strong covalent bonding character. Hence if the ductility is to be improved, the density of states around  $E_F$  should be flat as in the case of metals like Cu or Ag[27], which gives rise to a uniform electron density rather than the directional Pd-d bonding present in the intermetallics [28]. Hence we conclude that a lower  $N(E_F)$  and a flat Dos histogram around  $E_F$  will be one of the stringent requirements for higher melting point and greater ductility. We believe that the pseudogap

concept which has not been given its due importance hitherto should be seriously taken into consideration in all the future calculations.

### Acknowledgement

One of the authors (R.Asokamani) wishes to thank the Department of Science and Technology for the financial support. We are thankful to Mr. C.Ravi and Mr.C.V. Bhaskar for their timely help.

### References

1. Yamaguchi M. and Umakoshi Y. "The deformation behaviour of intermetallic superlattice compounds", Prog. Mater. Sci. Vol.34 pp. 1-148. (1990).
2. Von Mises R., Angew. Z., "Materials Sci. and Eng.", 3rd ed., by V. Raghavan, p. 251 (1928)
3. Andersen O.K. and Jepsen, O., "Explicit first principles Tight binding theory", phys. Rev. Lett. Vol.53, pp.2571-2574 (1984).
4. Andersen O.K., Pawłowska Z., and Jepsen O., "Illustration of the linear-muffin-tin-orbital tight-binding representation compact orbitals and charge density in Si", Phys. Rev. B, Vol.34, PP. 5253-5269 (1986).
5. Eberhart M.E. and Vvedensky D.D., "Environmentally specific mechanical properties Beyond atomic parameters", Phys. Rev. B, Vol.37, pp. 8488 - 8490 (1988).
6. Hong T. et al., "Crystal structure, phase stability and electronic structure of Ti-Al intermetallics:  $Ti_3Al$ ", Phys. Rev. B, Vol.43, pp. 1940-1947 (1991).
7. Hong T., Watson-Yang T. J. and Freeman A.J., "Crystal structure, phase stability and electronic structure of Ti-Al intermetallics:  $Ti_3Al$ ", Phys. Rev. B, 41, 12462 (1990).
8. W.B. Pearson, A Hand book of Lattice spacings and structures of metals and Alloys (Pergamon, New York, 1958).
9. Morinaga M et al., "Electronic effect on the ductility of alloyed TiAl compound", Acta Metall. Mater, Vol.38 (1990).
10. Cannon J.F. "High press. sci. and Technol", Eds. C.Homan, R.K. Mac Crone and E. Whalley, Mat. Res. Soc. Symp Proc. Vol.22, pp. 113-118 (1984).
11. Webb A.W. et al., "Compressibility of  $Ni_3In$ ", Physical Vols. 139 & 140B, pp. 311 - 313 (1986).
12. Izumi Q. and Takasugi. T. "Deformability improvements of  $L1_2$ -type intermetallic compounds", Mat. Res. Soc. Symp. Proc., "High Temperature Ordered Intermetallic Alloy". Eds. Koch. C.C, Liu C.T. and Stoloff N.S, Vol.81 pp. 173-182 (1987).
13. Sinha A.K. "Close-packed ordered  $AB_3$  structures in ternary alloys of certain transition metals", Trans. Am. Inst. Mech. Eng. Vol. 245, pp. 911-917 (1969).
14. Liu C.T. and Inouye H., "control of ordered structure and ductility of (Fe, Co, Ni), V alloys," Metall. Trans. Vol. 10A, pp. 1515-1525 (1979)
15. Liu C.T., "physical metallurgy and mechanical properties of ductile ordered alloys (Fe, Co, Ni), V" Int. Met. Rev. Vol.29, pp. 168-194 (1984).
16. Smithells Metals Reference Book, 6th ed., edited by E.A. Brands (Butterworth, London, 1983).
17. Kubaschewski, O., Evans E.L.L., and Alcock C.B. (1979), Metallurgical Thermochemistry, 4th ed. (Pergamon, Oxford).
18. Xu J.H et al., "Phase stability and magnetism of  $Ni_3Al$ ", Phys. Rev. B, Vol.41, PP.5010-5016 (1990).
19. Xu J.H. Lin.W. and Freeman A.J., "Electronic structure and phase stability of  $A_3Ti$  ( $A = Fe, Co, Ni$  and  $Cu$ )", Phys. Rev. B, Vol. 48, pp. 4276-4288 (1993)
20. Kuentzler R., and Waterstrat R.M., "Electronic properties, superconductivity and stability of the ordered alloys of the Ti-Rh, Zr-Rh and Hf-Rh isoelectronic systems", Solid State Commun., Vol. 68, pp. 85-91 (1988)
21. Kuentzler R. and Waterstrat R.M., "Electronic properties, Superconductivity and stability of the Zr-Rh alloys", solid state commun., Vol.54, pp 517-524 (1985)
22. Wang X.B., Tian D.C. and Wang L., "The electronic structure and chemical stability of the  $AlB_2$ -type transition-metal diborides", J. Phys, condensed Matter 6, 10185, (1994)
23. Pauline S. et al, "Electronic structure and properties of the Laves phase compounds  $YRh_2$  and  $LaRh_2$ ", Solid State Comm., Vol. 83, No.3, pp. 235-240 (1992).
24. Ravindran P., and Asokamani R., "Electronic structure, Phase stability, equation of state and pressure dependent superconducting properties of  $Zr_3Al$ ", Phys. Rev. B, Vol.50, pp. 668-678 (1994).
25. Xu J.H. and Freeman A.J., "Phase stability and electronic structure of  $ScAl_3$  and  $ZrAl_3$  and of Sc-Stabilised Cubic  $ZrAl_3$  precipitates", Phys. Rev. B, Vol.41, PP.12553-12561 (1990).
26. Moruzzi V.L. Oclhafa, P. and Williams. A.R., " Stability of ordered and amorphous transition metal compounds", Phys. Rev. B, Vol.27, PP.7194 (1983).
27. Calculated Electronic properties of metals, Moruzzi V.L. Janak J.F., Williams A.R. (New York, 1978).
28. Ravindran P, and Asokamani R, "Suppression of superconductivity by carbon addition to  $La_3X$  ( $X=Al, Ga, In$  or  $Ti$ )", J.Phys. Condensed Matter, Vol.7, pp. 5567-5577 (1995)

# DUCTILITY AND TOUGHNESS CONSIDERATIONS IN INTERMETALLICS

Yoshisato Kimura and David P. Pope

Department of Materials Science and Engineering  
University of Pennsylvania  
Philadelphia, PA 19104, U.S.A.

## **Abstract**

Limited ductility and toughness at low temperatures are serious disadvantages in intermetallics. As in other metallic materials, the two major brittle failure modes in intermetallics are cleavage and intergranular fracture. We focus on cleavage fracture and the corresponding brittle-to-ductile transition mechanism. To prevent cracking, a "sufficient number" of dislocations must be generated at the crack tip, and this "sufficient number" appears to be very large. This event is more like a phase transition than an ordinary thermally activated process.

In this paper a new theoretical model, proposed to explain the BDT based on a thermally-driven stress-assisted homogeneous dislocation nucleation mechanism, is summarized. The microstructural implications of this model are presented and the means of achieving an acceptable combination of strength and toughness through microstructural control are then discussed.

## **Introduction**

Intermetallic compounds are good candidate structural materials for high temperature applications, but first the basic problem of brittleness at low temperatures must be overcome. Of course, high temperature strength cannot be sacrificed in the process of ductilization. The question is: is this brittleness an intrinsic unchangeable property of most intermetallics?

Many intermetallics are known to have simple crystal structures based on bcc, fcc, hcp and their derivatives; however, the Burgers vectors observed in intermetallics are usually twice as long as the equivalent ones in disordered metals due to the existence of the superlattice. The formation of superlattice dislocations involves not only a very large self-energy but also other energies, like the anti-phase boundary energy and other fault energies that become important when the dislocation is dissociated. We suspect that this large self-energy is the biggest reason why many intermetallics do not have sufficient plastic deformability, even though they might possess simple crystal structures similar to pure metals.

Fault energies, such as the complex stacking fault energy and antiphase boundary energy, tend to be high in intermetallic compounds with high melting temperatures. Consequently, the energy of a dissociated dislocation is high, and therefore dislocation dissociation becomes very difficult in these materials.

The key factor in determining the mechanical properties of most crystalline materials is the microstructure. In this sense, microstructure can be referred to as the "architecture" of the material. Microstructural control is well known to be an excellent way to improve the ductility and toughness without deteriorating the strength of a material, and sometimes both the strength and toughness can be increased. The improvement of the strength and toughness of TiAl-based alloys through the use of lamellar microstructures is a well-known example [1-9]. We include in microstructural control three rough categories of processes, which, of course, relate to each other.

The first category of processes pertains to single phase materials, for example, the addition of alloying elements and the use of off-stoichiometric compositions to control fault energies. Another is grain size control, a well-known process which has been extended in recent years, ranging from sub-micron grains to the total elimination of grain boundaries, i.e., single crystals. Recently, nanophase materials with grain sizes in the *nm* range have been intensively developed [10,11]; these exhibit increases in both strength and ductility over their coarser grained counterparts. Specific directional alignment of the microstructure, as in the case of textured materials, also belongs in this category.

The second category uses a two-phase or multi-phase microstructure, which is commonly the most effective and useful method of constructing a desirable architecture. Microstructures with excellent toughness and strength compared to their single phase counterparts, such as eutectoid (pearlite) steels, tempered martensitic steels and lamellar TiAl alloys, are limited to lamellar structures and martensitically transformed structures. To the best of our knowledge, traditional commercial alloys based on metals with limited toughness for structural use have microstructures belonging to these architectures with high

densities of interfaces. Conventional multi-phase microstructures involving precipitates are very widely used in many alloy systems, but this hardening mechanism invariably leads to decreases in ductility and toughness.

There is also a third, special kind of microstructural control that is important to intermetallics: crystal structure conversion from a complex structure to a more simple close packed structure, for example,  $DO_{22}$  to  $L1_2$  by the addition of substitutional elements, such as Fe, Cr, Mn, and so forth, to  $Al_3Ti$  [12,13],  $A15$  to  $E2_1(L'1_2)$  in  $V_3Au$  [14,15] and even from "none" to  $E2_1$  in  $Co_3AlC$  [16,17] by interstitial elements.

In some cases, impurities or environmental effects become important, especially at grain boundaries and phase interfaces. An example of the environmental effect seen in the fracture properties of  $Ni_3Al$ , which is well-known to be susceptible to embrittlement by hydrogen coming from atmospheric  $H_2O$  [18,19]. In this paper we ignore these effects and concentrate on the factors that we believe are most important to transgranular fracture processes.

The purpose of this paper is to provide an overview of what we believe to be important in transforming an intrinsically low toughness material to a strong, tough material. The attention is focused on the brittle-to-ductile transition (BDT) from the standpoint of dislocation activity related to generation and mobility because many intermetallics have a very high BDT. Our group at the University of Pennsylvania has proposed a new model that provides a rational explanation of the BDT which we believe has important practical implications [20-24]. For the purpose of this discussion we ignore the obvious cases of materials that do not have enough active slip systems and materials which are grain boundary-brittle. We recognize that the viewpoint of this paper is highly controversial, and that much experimental work is required to test these ideas. Nonetheless, there is substantial theoretical evidence for its veracity, and the practical implications of the theory are consistent with metallurgical experience in many metallic-based systems.

### The Brittle-to-Ductile Transition in Intermetallics

#### Cleavage Failure and Toughness

The most common brittle failure mode observed in intermetallic compounds is cleavage fracture. The alternative mode is intergranular fracture, which is also a widespread problem in intermetallic compounds, e.g., in  $L1_2$   $Ni_3Al$ . The dominant mode varies from material to material, depending on the competition of fracture stress between transgranular cleavage and intergranular separation, in other words, the strength of the grain interior and the grain boundary. Each mode has its specific temperature dependence at the BDT. At the brittle-to-ductile transition temperature (BDTT) materials typically exhibit a drastic increase in the fracture toughness within a relatively narrow

temperature range. The fracture toughness increase is commonly (but not always) accompanied by a transition from cleavage fracture to ductile fracture associated with microvoid coalescence above the BDTT, owing to a dramatic increase in dislocation activity. In many cases, however, the toughness simply increases but the fracture mode remains cleavage [12]. In this paper, we focus on cleavage failure and the control of plasticity through dislocation generation and motion, and we ignore intergranular failure.

A material fails by cleavage fracture because the rate of energy dissipation from dislocation activity taking place near the crack tip during crack growth is insufficient. It is clear that there is commonly very substantial dislocation activity below the BDTT. Above the BDTT there are, of course, massive amounts of plasticity. Thus it is not a question of no dislocation activity below the BDTT and massive amounts above. The actual phenomenon is much more complex. The extensive experimental work on  $Al_3Ti$  gives one good example [12,25-29]. Binary  $Al_3Ti$  has the tetragonal  $DO_{22}$  type crystal structure in which there are insufficient active slip systems. To improve this situation,  $Al_3Ti$  can be converted and stabilized in the fcc-based  $L1_2$  type crystal structure through the addition of small amounts of ternary elements, such as Fe and Cu.  $Al_3Ti$  modified in this way might be expected to show substantial ductility, similar to fcc metals. In fact, substantial numbers of dislocations are generated in the region around a crack tip in  $Al_3Ti + Fe$ . Furthermore, the critical resolved shear stress of  $L1_2$   $Al_3Ti$  is not too high and not very temperature dependent above room temperature. Nevertheless this alloy still exhibits very brittle cleavage failure by cleavage on many low index planes, up to 1000 K or more. The temperature dependence of the fracture toughness of forged  $L1_2$   $Al_3Ti + Mn$  or  $Cr$  is shown in Fig. 1, reported by

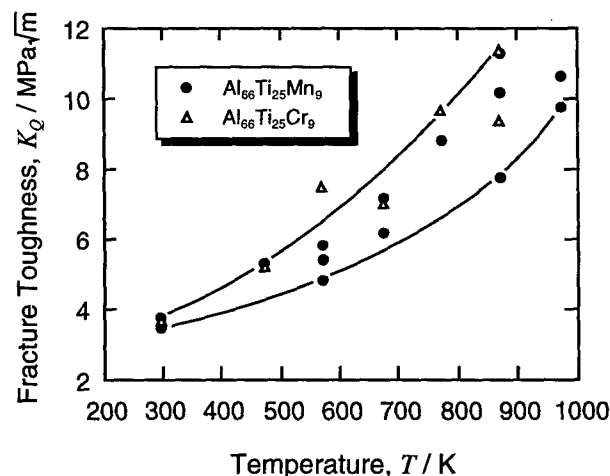


Fig. 1 The temperature dependence of the fracture toughness of forged  $Al_3Ti$  alloys modified into the  $L1_2$  structure by additions of Mn or Cr, Kumar et al. [12]

Kumar et al.[12]. The fracture toughness does not exceed  $12 \text{ MPa m}^{1/2}$  at temperatures below 1000 K. These results show the complexity of the problem: large numbers of dislocations are already generated well below the BDTT, in spite of the fact that cleavage failure occurs. This behavior, cleavage failure with low toughness but with substantial dislocation activity, is called "quasi brittle" as first proposed by Hack et al.[30]. These results, and similar results on many other materials, raise the question of how many dislocations must be generated in order to prevent cleavage crack propagation and catastrophic failure. We have come to the conclusion that the answer is an "unlimited number," as discussed below.

### **Traditional Approaches to Explaining the BDTT**

The models proposed heretofore to explain the BDT can be broadly divided into two categories: (i) dislocation nucleation controlled models and (ii) dislocation mobility controlled models.

In category (i), the most widely used model is the one originally proposed by Rice and Thomson [31] and subsequent extensions [32,33], in which the brittle or ductile behavior results from a competition between crack propagation and spontaneous dislocation emission at the crack tip. The thermally activated generation of one dislocation at the crack tip is considered to be the necessary and sufficient condition for crack blunting at the BDT. It is traditionally assumed that each loop is nucleated and driven to an unstable configuration by the applied stress, and thermal fluctuations merely help to overcome the energy barrier associated with the nucleation. The activation barrier for the formation of a single dislocation loop determines the frequency of dislocation emission. Evaluation of the critical temperature ( $T_c$ ) requires additional assumptions about a specific rate of dislocation generation at the very sharp transition. No strain rate effects can be explained explicitly in this model since mobility effects are not considered in this analysis of dislocation emission.

The strain rate dependence of  $T_c$  and its correlation with dislocation mobility is the predominant characteristic of the BDT as explained by models belonging to category (ii). In contrast to the dislocation nucleation model, the generation of dislocations at the crack tip is assumed to be relatively easy in the mobility-based models. These models involve numerical simulations of the dislocation dynamics in the vicinity of the crack tip. A closer examination of the simulations reveals that the sudden transition at a critical temperature is essentially caused by the introduction of an avalanche of dislocations and not only by mobility effects. The mobility of dislocations influences the strain rate dependence of  $T_c$ , but we believe that this does not necessarily imply that the BDT is a mobility-controlled event.

Consequently, thermally activated processes must necessarily be taken into account, especially below the BDTT, but they are not sufficient to elucidate the entire

phenomenon of the BDT. The issue that needs to be resolved is not whether dislocation nucleation or dislocation mobility is the controlling factor of the BDT but how the two effects can be treated simultaneously to attain a rational description of the BDT. The main problem with both models, in our opinion, is the sharpness at the transition in many materials, a clear indication to us that thermally activated processes are not involved.

### **Thermal and Stress Driven**

#### **Dislocation Generation Model,**

#### ***the Khantha, Pope, Vitek (KPV) Model***

The traditional thermal activation process alone cannot explain an abrupt, massive change in dislocation activity at the BDT because exponentials do not change dramatically over small changes in temperature. Figure 2 shows the temperature dependence of ductility of various intermetallic compounds with high melting temperatures, all exhibiting very sharp BDTs [34]. This rapid change of dislocation activity is more similar to a phase transition than to a thermally activated event. A new model for the BDT has been proposed by Khantha et al.[20-24], in which the burst of dislocation activity is considered to be associated with a thermally-driven, stress-assisted cooperative instability of many dislocation loops. The three principal features which distinguish this present approach from the existing models are:

- (1) The onset of ductile behavior is not a thermally activated event but a cooperative instability driven primarily by thermal fluctuations in the presence of a high applied stress. Thus for a given applied stress, there is a critical temperature at which additional dislocations can be formed with no increase in free energy of the system.
- (2) Interactions between many dislocation loops result in screening, which produces an effective softening of the medium. That is, it is the interaction between the many (small) growing dislocation loops that leads to the decrease in free energy for additional loops.
- (3) The prediction of the instability is based on the linear elastic theory of dislocations combined with statistical mechanics.

The fact that the unstable massive emission of dislocations takes place in a narrow temperature range suggests that the onset of ductile behavior is not a thermally activated phenomenon in the usual sense but is, rather, a thermally driven instability which results in an enormous increase in the dislocation density. The idea that massive dislocation emission can be driven by thermal fluctuations contradicts traditional dislocation theory in the sense that the thermal barrier for the spontaneous nucleation of a single dislocation loop and its expansion into an

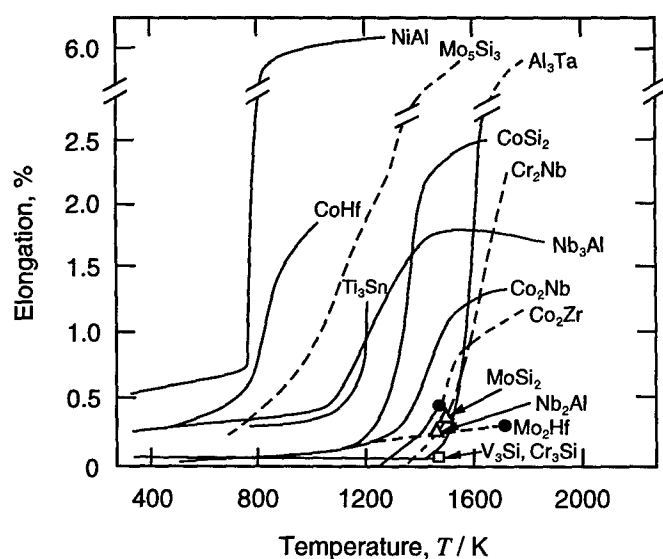


Fig. 2 The temperature dependence of the ductility of various intermetallic compounds with high melting points, exhibiting very sharp BDTs [34].

unstable configuration can be shown to be extremely high for stresses much smaller than the theoretical shear strength. Hence, in this case dislocation generation is appreciable only if the temperature is very high, commonly greater than the melting temperature. This is the basis for the commonly-held assumption that homogeneous nucleation of dislocations is unimportant during plastic deformation. However, the situation for many interacting loops is completely different from the case of a single dislocation loop. Kosterlitz and Thouless (K-T) considered such a situation and proposed a model which depends on the cooperative instability that occurs in the dislocation population as a whole, not on the instability of a single loop [35]. This model contains the assumptions that (i) dislocation loops interact elastically without entangling with each other, and (ii) the crystal is initially dislocation-free, except for the thermally-produced loops. The mutual interactions among dislocation loops give rise to a screening effect which lowers the energy required for the formation of additional loops. This screening effect is physically distinct from dislocation shielding of the stress field in the vicinity of the crack tip. Without the aid of an applied stress, cooperative dislocation generation occurs close to the melting temperature and causes a dislocation-mediated melting transition.

In order to decrease the temperature at which the K-T type collective dislocation emission instability occurs, the external stress is introduced explicitly into the KPV model. A loaded elastic solid at finite temperatures contains a certain concentration of dislocation dipoles (loops) of different sizes, which can be nucleated by thermal agitation as metastable defects; i.e., a given loop forms, then decays, but the total population is constant. The creation of each

loop induces in the medium a certain amount of plastic strain in addition to the elastic strain. The energy reduction occurs because the growth of one loop induces growth of other loops. This synergistic effect leads to a decrease in the "effective modulus" which relates incremental stresses to incremental strains in the medium. This decrease in the effective modulus is important, even though it is a slight change, because when a dislocation loop forms among other dislocation loops, its energy is proportional to the effective modulus, and thus its energy is lower than the energy of an isolated dislocation loop. The presence of an applied stress influences the dislocation emission by decreasing the enthalpic contribution to the free energy and inducing a further increase in the density of dislocation loops and a concomitant decrease of the effective modulus. The critical point, or the BDTT, is reached when the effective modulus goes to zero. The corresponding critical temperature or transition temperature is then substantially lower than the melting point when the applied stress is of the order of  $\mu_0/1000 - \mu_0/100$ , where  $\mu_0$  is the shear modulus.

In this model, the BDTT is determined primarily by the shear modulus and the burgers vector (along with the dislocation core radius and core energy), all of which are fixed for a given single phase material. However, in a two-phase material, dislocations can be produced in one phase and injected into the second phase, if the interfaces between the two phases are coherent. Furthermore, if the interfaces in a single phase material are "special," in the sense that the shear modulus has a very low magnitude in the region of the interface (boundary), then dislocation generation can be very easy near the interfaces. In this case, dislocations would be generated near the interface, then injected into the bulk, and if the interfaces are sufficiently closely spaced, i.e., fine grain size, the interfaces (grain boundaries) will dominate the overall behavior. The essential feature of this argument is that the dislocations are preferentially produced in the interfacial regions, and therefore, a polycrystalline single phase material can also deform via dislocation injection from the interfacial regions. In the balance of this paper, we will explore the consequences of this assumption and relate these consequences to the behavior of some alloy systems.

### Microstructural Aspects

The minimal requirements for a strong, tough material for structural applications at elevated temperatures are the following: (i) the yield and creep strength must be sufficiently high, (ii) the fracture stress, both cleavage and intergranular, must be higher than the proof stress, (iii) the energy of interfaces, if they exist, must be low so that the microstructure remains stable, even at high temperatures, and (iv) the high-temperature oxidation resistance must be sufficient.

As stated in the introduction, there are not many microstructures which can impart both strength and toughness to a low-toughness material. The only examples

we are aware of are microstructures with high densities of interfaces: lamellar structures, martensitically transformed structures and fine-grained structures. In these microstructures, we believe that the interfaces play very important roles as both the nucleation sites for dislocations as well as the obstacles to dislocation motion. How might interfaces become preferred dislocation nucleation sites? Since the energy to nucleate a dislocation is proportional to  $\mu_0 b^2$ , where  $\mu_0$  is the shear modulus and  $b$  the Burgers vector, the rate of nucleation can be increased by locally decreasing  $\mu_0$ , for example at an interface. If the shear modulus near a particular type of interface is low, such an interface could be a preferred dislocation nucleation site, and a high density of interfaces would produce large numbers of dislocations above a critical stress. Thus if the critical stress for interfacial nucleation is below the Griffith stress, the material will deform, not cleave. A material containing a high density of such special interfaces spaced, say, at sub-micron distances, might be regarded as a "two-phase" solid in which one "phase" is the bulk and the other "phase" consists of the interfaces. As shown in Fig. 3, at a stress

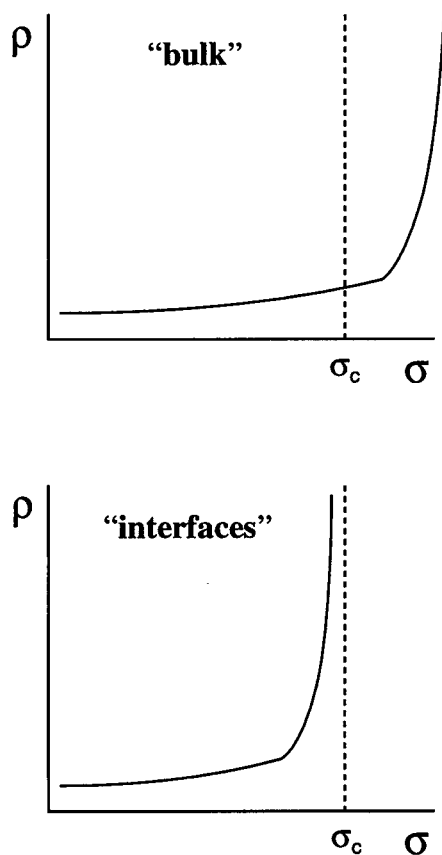


Fig. 3 Schematic drawing of the relation ship between dislocation generation and the cleavage stress for "two-phase" solid consisting of "bulk" and "interface," where  $\rho$  is the mobile dislocation density,  $\sigma$  is the applied stress and  $\sigma_c$  is the cleavage stress.

below the bulk cleavage stress, dislocations are nucleated in the many interfaces and propagate into the bulk. Such an approach might provide a means for designing materials for toughness and strength through microstructural control. It would involve calculating the shear modulus of different interfaces, then finding a way to produce a very high density of the desirable interfaces (those with low shear modulus) in the material. This is complicated, of course, since a fine spacing of lamellae might possibly decrease the creep resistance at elevated temperature depending on the stability of the interfaces. These interfaces must have a low energy so that the microstructure does not coarsen during exposure at high temperatures.

This model is admittedly still very controversial, but nevertheless assuming it to be correct, the ductility and toughness of several intermetallic alloys are discussed below.

### Ni-based Superalloys:

Ni-base superalloys are among the most well-known and successful materials in the history of this field. The microstructure of this alloy is the well-known  $\gamma/\gamma'$  structure, consisting of a  $\gamma$ -Ni solid solution matrix and typically cuboidal  $\gamma'$ -Ni<sub>3</sub>Al precipitates having volume fractions of more than 60% in most cases. A scanning electron microscopic image showing a typical  $\gamma/\gamma'$  superalloy microstructure is presented in Fig. 4. The high temperature strength of this alloy comes about because creep occurs through dislocation motion in the narrow Ni-base solid solution channels between the cuboidal

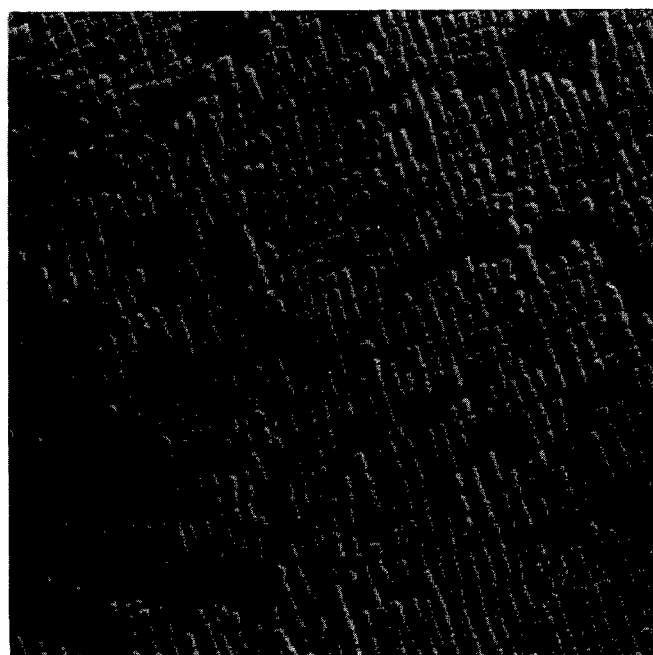


Fig. 4 A scanning electron micrograph showing a typical  $\gamma/\gamma'$  microstructure of a Ni-base superalloy, MAR-M200, photographed from replica. (Courtesy of Dr. D. M. Shah, Pratt and Whitney Aircraft Corp.)

precipitates. The fact that those are ordinary dislocations precludes their penetration into the precipitates, except at higher stresses, and the effects of curvature make motion difficult within the narrow channels [36-39]. The most important feature of this microstructure from the current standpoint is that the matrix can deform, and moreover, a local increase in stress, say at a crack tip, can cause successive ordinary dislocation pairs to cross the interface before cleavage initiates. Furthermore, dislocations can be homogeneously nucleated in the matrix at low temperatures at stresses well below the Griffith stress. In this case the Ni solid solution matrix acts as the dislocation sources for deformation of the precipitates, when such deformation is required; i.e., dislocations are "injected" into the precipitates. We believe that a similar mechanism probably happens in Fe-C pearlite. In this case, the  $\alpha$ -Fe acts as the source of dislocations, injecting them into the normally-brittle  $\text{Fe}_3\text{C}$ , especially during severe plastic deformation under extremely high stresses, like during wire drawing. As is well known, fine pearlitic microstructures are both very strong and relatively tough. The main difference between the  $\gamma/\gamma'$  and  $\alpha$ -Fe/ $\text{Fe}_3\text{C}$  microstructures from the point of view of high temperature application is the interfacial energy. In the  $\gamma/\gamma'$  system it is very low, owing to the coherence of the interfaces, and in pearlite the  $\alpha$ -Fe/ $\text{Fe}_3\text{C}$  interfacial energy is much higher. As a result, the former coarsens very slowly at high temperatures while the latter coarsens quickly, leading to a coarse, soft spheroidized structure.

#### **Lamellar TiAl-Based Alloys:**

TiAl is emerging as one of the most likely candidate intermetallic materials for industrial application, for example, in the intermediate temperature sections of gas turbine engines. TiAl-based alloys display dramatically different microstructures depending on composition near the 50:50 Ti:Al ratio. Aluminum-rich alloys have a single-phase  $\text{L1}_0$  structure, but stoichiometric and titanium-rich alloys exhibit a two-phase microstructure, consisting of layers of tetragonal,  $\text{L1}_0$  TiAl and hexagonal,  $\text{D0}_{19}$   $\text{Ti}_3\text{Al}$ . Interestingly, the best combination of strength and toughness is found in the two-phase lamellar microstructure, although its components are quite brittle in single crystalline form, and the properties improve greatly as the microstructure is refined to the point where the lamellae are of sub-micron thickness. A typical lamellar structure is shown in Fig. 5. The relatively high toughness and ductility have been achieved by inventive metallurgical processing [1-9], but a microscopic understanding of the underlying deformation process is still only rudimentary. Since the various interfaces in the structure are all coherent TiAl/TiAl or TiAl/ $\text{Ti}_3\text{Al}$  interfaces, they have relatively low energies [40] and are quite stable at high temperatures. This results in good creep resistance. We believe the reasons for the improved toughness imparted by the microstructure are also related to the nature of the interfaces themselves. Since neither phase is very tough or ductile in single phase form, we suggest that the interfaces between the phases are

important features in the toughening. All these interfaces are well-known to have special orientations because of the symmetries of the phases as they join together (the interfaces are all (111) planes in the TiAl and (0001) planes in the  $\text{Ti}_3\text{Al}$ ). There are the total of four different types of interfaces in the microstructure; three TiAl/TiAl interfaces due to the tetragonality of the  $\text{L1}_0$  structure and one TiAl/ $\text{Ti}_3\text{Al}$  interface. We suspect that at least one of these interfaces is a preferred site for homogeneous dislocation nucleation, resulting from a decreased shear modulus near the special interface. Thus we believe that it is likely that the improved deformability of lamellar TiAl alloys is a direct result of the nature and density of at least one of the four lamellar interfaces in the microstructure.

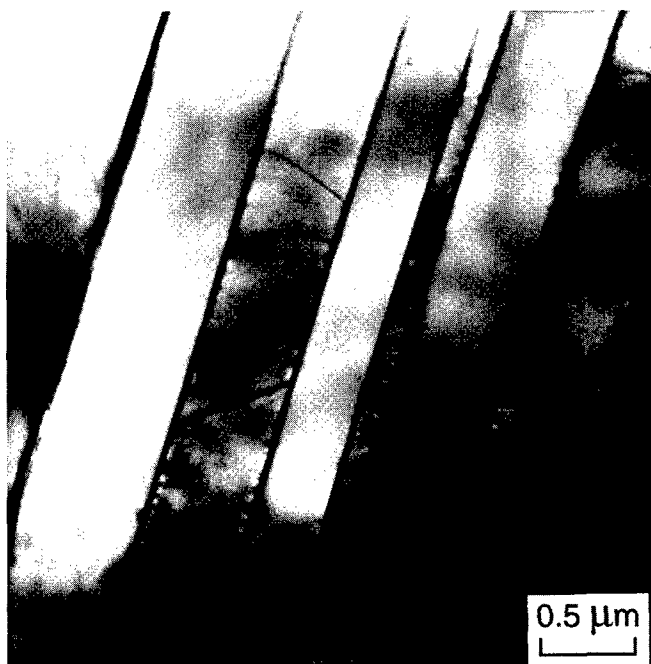


Fig. 5 A transmission electron micrograph showing a typical lamellar microstructure of a TiAl-based alloy. (Courtesy of Mr. Lei Lu, Graduate Student, Materials Science and Engineering, University of Pennsylvania.)

#### **NiAl-Based Alloys:**

We now contrast the behavior of  $\gamma/\gamma'$  Ni-base superalloys with that of alloys based on B2 NiAl, intended to operate at higher temperatures than  $\gamma/\gamma'$  alloys. These alloys have an NiAl-base matrix which is precipitation hardened by  $\text{L2}_1$  cuboidal Heusler phase precipitates. See the review by Darolia for an overview of the mechanical properties of a two-phase NiAl/Heusler- $\text{Ni}_2\text{AlTi}$  ( $\beta/\beta'$ ) alloy [41]. At elevated temperatures the NiAl matrix undergoes slow deformation, strengthened by the Heusler precipitates, but in this case the intrinsic ductility of the matrix is limited, especially at low temperatures, for two reasons: (i) the B2 NiAl deforms primarily by [100] slip, which provides an insufficient number of slip systems, and (ii) the



"intrinsic" BDTT of B2 NiAl is high owing to its strongly ordered structure. Consequently, a sharp increase in stress, as at a crack tip, cannot be relieved by massive local dislocation generation in the same way as in  $\gamma/\gamma'$  alloys. Furthermore, it appears that the NiAl/Heusler interfaces are not preferred dislocation nucleation sites. Thus the NiAl/Heusler alloys have the necessary dislocation-blocking characteristics for high strength, but there appears to be no place for dislocations to be preferentially generated at stresses below the cleavage stress. If a way could be found to "engineer" the NiAl/Heusler interfaces such that they become preferred dislocation nucleation sites, then these alloys might attain the necessary combination of ductility and strength for structural applications.

### Summary

#### *Implications for Design of Intermetallic-Based Alloys*

If we are to use intermetallics which, in single phase form, have an excessively high BDTT as the basis for developing structural materials, we believe that the key lies in interfacial properties, not in bulk properties. Even though much of the research effort to date has concentrated on improving the toughness of different bulk intermetallics through control of, say, fault energies, we know of no case where this has been successful in disordered alloys. However, we can point to a number of examples in different alloy systems where toughnesses and strengths have been improved by the introduction of a high density of "special" interfaces. While our explanation of how those interfaces contribute to improved toughness is admittedly highly speculative, the practical success of the method is clear.

Therefore we suggest that a similar route should be followed to produce strong, tough intermetallic-based alloys. Fine lamellar microstructures must be designed that are thermally stable to provide good creep resistance and, at the same time, these lamellar interfaces must be preferred sites for dislocation nucleation, i.e., the volume near the interface must have a low shear modulus. There is the possibility of designing such interfaces, see, for example, the work of Vitek and Bassani [42], who have shown that the local shear modulus near an interface can either be higher than or lower than the bulk shear modulus by a substantial margin.

### Acknowledgments

This work was supported by the office of Naval Research, the Department of Energy and the Air Force Office of Scientific Research.

### References

1. C. T. Liu, J. H. Schneibel, P. J. Maziasz, J. L. Wright and D. S. Easton, *Intermetallics*, **4**(1996), 429.
2. Y. W. Kim, *J. Metals*, **41**(1989), 24.
3. *idem.*, *Acta Metall. Mater.*, **40**(1992), 1121.
4. *idem.*, *J. Metals*, **46**(1994), 30.
5. M. Yamaguchi and H. Inui, "Structural Intermetallics", eds. R. Darolia, J. J. Lewandowski, C. T. Liu, P. L. Martin, D. B. Miracle and M. V. Nathal, TMS, Warrendale, (1993), 127.
6. M. Takeyama, T. Kumagai, M. Nakamura and M. Kikuchi, *ibid.*, 167.
7. S. C. Huang, *ibid.*, 299.
8. T. Fujiwara, A. Nakamura, M. Hosomi, S. R. Nishitani, Y. Shirai and M. Yamaguchi, *Phil. Mag. A*, **61**(1990), 591.
9. M. Yamaguchi and H. Inui, S. Yokoshima, K. Kishida, D. R. Johnson, *Mater. Sci. Eng.*, **A213**(1996), 25.
10. R. W. Siegel and G. E. Fougere, *Nanostructured Mater*, **6**(1995), 205.
11. C. Suryanarayana, *Intl. Mater. Rev.*, **40**(1995), 41.
12. K. S. Kumar, "Structural Intermetallics", eds. R. Darolia, J. J. Lewandowski, C. T. Liu, P. L. Martin, D. B. Miracle and M. V. Nathal, TMS, Warrendale, (1993), 87.
13. D. G. Pettifor, "Intermetallic Compounds - Structure and Mechanical Properties," ed. O. Izumi, JIM, Sendai, (1991), 149.
14. H. T. Chen, S. A. Myers and C. C. Koch, *Mater. Sci. Eng.*, **98**(1988), 277.
15. Y. Fahmy, J. C. Russ and C. C. Koch, *J. Mater. Res.*, **6**(1991), 1856.
16. Y. Kimura, M. Takahashi, S. Miura, T. Suzuki and Y. Mishima, *Intermetallics*, **3**(1995), 413.
17. Y. Kimura, M. Takahashi, S. Miura and Y. Mishima, "High-Temperature Ordered Intermetallic Alloys VI," eds. J. A. Horton, I. Baker, S. Hanada, R. D. Noebe, D. S. Schwartz, MRS Symp. Proc. Vol. **364**, Mater. Res. Soc., Pittsburgh, (1995), 1371.
18. E. P. George, C. T. Liu and D. P. Pope, *Phys. Stat. Sol. (a)*, **160**(1997), in press.
19. *idem.*, *Acta Mater.*, **44**(1996), 1757.
20. M. Khantha, D. P. Pope and V. Vitek, *Phys. Rev. Lett.*, **73**(1994), 684.
21. *idem.*, *Scr. Metall. Mater.*, **31**(1994), 1349.
22. *idem.*, *Mater. Sci. Eng.*, **A192/193**(1995), 435.
23. M. Khantha and V. Vitek, *Acta Mater*, (1997), in press.
24. M. Khantha, D. P. Pope and V. Vitek, *Acta Mater*, (1997), in press.
25. Z. L. Wu, D. P. Pope and V. Vitek, *Scr. Metall. Mater.*, **24**(1990), 2187.
26. *idem.*, *ibid.*, **24**(1990), 2191.
27. *idem.*, *High-Temperature Ordered Intermetallic Alloys IV*, eds. L. A. Johnson, D. P. Pope and J. O. Stiegler, MRS Symp. Proc. Vol. **213**, Mater. Res. Soc., Pittsburgh, (1991), 487.
28. Z. L. Wu and D. P. Pope, *Acta Metall. Mater.*, **42**(1994), 509.

29. *idem.*, *ibid.*, **42**(1994), 519.
30. J. E. Hack, S. P. Chen and D. J. Srolovitz, *Acta Metall. Mater.*, **37**(1989), 1957.
31. J. R. Rice and R. Thomsom, *Phil. Mag.*, **29**(1974), 73.
32. D. D. Mason, *Phil. Mag. A*, **39**(1979), 455.
33. P. M. Anderson and J. R. Rice, *Scr. Metall. Mater.*, **20**(1986), 1467.
34. D. L. Anton and D. M. Shah, "Development Potential of Advanced Intermetallic Materials," final report to Air Force, Contract F33615-87-C-5214, Project 2420 (1990).
35. J. M. Kosterlitz and D. J. Thouless, *J. Phys. C: Sol. Stat. Phys.*, **6**(1973), 1181.
36. D. P. Pope and S. S. Ezz, *Intl. Met. Rev.*, **29**(1984), 136.
37. T. M. Pollack and A. S. Argon, *Acta Metall. Mater.*, **40**(1992), 1.
38. *idem.*, *ibid.*, **42**(1994), 1859.
39. F. R. N. Nabarro, *Metall. Mater. Trans.*, **27A**(1996), 513.
40. L. Lu, R. Siegl; A. Girshick, D. P. Pope and V. Vitek, *Scr. Metall. Mater.*, **34**(1996), 971.
41. R. Darolia, "Structural Intermetallics", eds. R. Darolia, J. J. Lewandowski, C. T. Liu, P. L. Martin, D. B. Miracle and M. V. Nathal, TMS, Warrendale, (1993), 495.
42. E. S. Alber, J. L. Bassani, V. Vitek and G. J. Wang, *Phys. Rev. B*, **53**(1996), 8398.

## **MICROSTRUCTURE AND PROPERTIES OF TIAL**

# MICROSTRUCTURAL DESIGN OF NEAR $\gamma$ -TiAl FOR CREEP RESISTANCE

J. Beddoes, L. Zhao\*, P. Au\*, D. Dudzinski, J. Triantafillou

Department of Mechanical & Aerospace Engineering, Carleton University

1125 Colonel By Drive, Ottawa, K1S 5B6, Canada

\*Structures, Materials and Propulsion Laboratory, Institute for Aerospace Research

National Research Council, Ottawa, K1A 0R6, Canada

## Abstract

Preliminary guidelines for microstructural design of creep resistant near  $\gamma$ -TiAl intermetallics are developed from creep tests at 760°C. Lamellar microstructures with even small amounts of  $\gamma$  grains have decreased creep resistance due to preferential deformation and dynamic recrystallization of  $\gamma$  grains. Decreasing the lamellar grain size increases  $\dot{\epsilon}_{\text{MIN}}$  only for grain sizes  $<150 \mu\text{m}$ , indicating a change from an intra- to intergranular controlled strain rate. Reducing the interlamellar spacing lowers the strain rate. High and low stress regimes are delineated, in which the creep rate is thought to be controlled by dislocation glide and recovery respectively. The boundary between these two regimes occurs at a higher stress level when finer lamellae exist. Planar grain boundaries lead to brittle intergranular failure with minimal tertiary creep, while well interlocked lamellae along grain boundaries provide resistance to intergranular cracking, allowing additional intragranular deformation, resulting in greater tertiary creep. The results indicate that optimum creep resistance requires: a fully lamellar microstructure with grains  $<200 \mu\text{m}$ , elimination of single phase  $\gamma$  grains, narrow lamellae and interlocked lamellar grain boundaries.

## Introduction

The technology related to near  $\gamma$ -TiAl intermetallics has advanced sufficiently that gas turbine applications are imminent, with several application trials successfully completed [1-

3]. The temperature/stress domain of the envisaged applications is such that creep deformation is inevitable. However, creep resistance is a major barrier to increasing the service temperature for near  $\gamma$ -TiAl alloys [3]. Consequently, the creep properties of near  $\gamma$ -TiAl alloys have been studied extensively, with the major results summarized elsewhere [4]. Despite this increasing volume of creep data, a comprehensive understanding of the influence of individual microstructural features on creep is lacking. To help alleviate this situation, this paper presents the results of a series of creep tests on near  $\gamma$ -TiAl designed to highlight the effect of individual microstructural parameters. From these results, a set of preliminary guidelines for the microstructural design of near  $\gamma$ -TiAl alloys for creep resistance are developed, which will contribute to the knowledge base required for successful gas turbine application of near  $\gamma$ -TiAl alloys. An eventual aim of the current research is to develop a mechanistic understanding of near  $\gamma$ -TiAl creep, without which there is greater risk associated with the use of  $\gamma$ -TiAl alloys in the envisaged critical propulsion applications. Furthermore, from a mechanistic understanding constitutive models with a predictive capability applicable to the design of new alloy/microstructure combinations can be developed.

This paper develops the microstructural guidelines from creep tests on four near  $\gamma$ -TiAl alloys, heat treated to various microstructural conditions. The creep tests utilize monotonic loads, the consecutive stress reduction method and the stress increment technique. The test results are interpreted in terms of:

primary creep resistance, minimum creep strain rate ( $\dot{\epsilon}_{\text{MIN}}$ ), extent of time at which  $\dot{\epsilon} \approx \dot{\epsilon}_{\text{MIN}}$ , and fracture strain and time.

### Materials & Experimental Procedure

The compositions of the four alloys used in this investigation are summarized in Table I. The material was supplied as gas atomized powder produced by Crucible Compaction Metals. The maximum powder particle size was 500  $\mu\text{m}$ . Details of the powder microstructure are summarized elsewhere [5-7].

Table I  
Composition of Powder Alloys

Element	TiAl	TiAl+W	TiAl+Cr	Ti-4822
Al (at%)	48.1	48.4	47.1	47.7
W (at%)	-	1.9	-	-
Cr (at%)	-	-	2.9	1.97
Nb (at%)	-	-	-	2.03
Fe (wppm)	1000	400	130	900
C (wppm)	110	330	440	180
N (wppm)	30	110	110	70
O (wppm)	530	2090	2190	660
Ti	bal.	bal.	bal.	bal.

The powder was hermetically sealed under vacuum in CP Ti tubes and consolidated by hot isostatic pressing (HIP) at 1250°C and 200 MPa for 2 hours. This HIP cycle produced material with >99.9% density [8]. Post-HIP compositional analysis showed no increase in oxygen, nitrogen or carbon contents, indicating that powder cleanliness was maintained. The HIP'ed microstructure and mechanical properties are presented elsewhere [9].

The microstructures of interest were developed by heat treating HIP'ed material in the  $\alpha$  or  $\alpha+\gamma$  phase fields. Samples were prepared for heat treating by wrapping in Ta foil and sealing in quartz tubes backfilled with Ar to  $\approx 220$  mm Hg. Metallographic preparation utilized standard techniques [10].

Creep samples with a gauge length of 22 mm and 4 mm diameter were machined by low stress grinding and tested under tension in air at 760°C. Creep strain was measured by a linear variable differential transducer equipped extensometer attached to the specimen shoulders, giving strain resolution of at least  $\pm 1.5 \times 10^{-5}$ . Constant load was applied for monotonic tests corresponding to an initial stress of 240 or 276 MPa.

The stress exponents were determined using the stress increment technique. The initial stress was 105 MPa and stress increments of  $\approx 15\%$  were applied after sufficient strain to determine the creep strain rate ( $\dot{\epsilon}$ ). Time at each stress level varied from >250 h at low stress to <100 h at high stress. The stress levels reported are corrected to account for the accumulated sample strain.

The consecutive stress reduction technique was used to investigate the response to a decrease in the applied stress. After sufficient time that the initial stress of 276 MPa caused a constant creep  $\dot{\epsilon}$ , the applied stress was reduced  $\approx 5\%$ . Once a positive  $\dot{\epsilon}$  was re-established another stress reduction was applied. Depending on the mechanism controlling creep, an incubation period of zero  $\dot{\epsilon}$  or either positive or negative creep may follow the stress reduction [11,12]. For the current work it is informative to examine the relationship between the remaining stress level and the incubation period associated with each stress level.

### Results and Discussion

#### Influence of $\gamma$ Grain Volume Fraction

It is well established that  $\alpha_2/\gamma$  lamellar microstructures exhibit the best creep resistance [4]. However, small  $\gamma$  grain volume fractions are effective at increasing the tensile ductility [13]. Therefore, it is of interest to compare the creep properties of fully lamellar (FL) structures with nearly lamellar (NL) structures containing low volume fractions of  $\gamma$  grains. To achieve this the binary TiAl alloy was heat treated to produce the microstructures of Figure 1. These microstructures span the range from the duplex (DP) condition (Figure 1a), through various nearly lamellar conditions that contain  $\gamma$  grain volume fractions between 7 and 25% (Figures 1b to 1d), to the FL condition (Figure 1e) that contains <1%  $\gamma$  grains. Table II summarizes the microstructural parameters resulting from the heat treatments of Figure 1, which are also described in more detail elsewhere [10].

Table II  
Microstructural Parameters & Creep Results  
(760°C/240 MPa)

Property	DP	NL1	NL2	NL3	FL
% $\gamma$ Grain	80-85	20-25	15-20	7-10	<1
$\gamma$ Grain Size ( $\mu\text{m}$ )	<35	<30	<25	<20	-
Lamellar Grain Size ( $\mu\text{m}$ )	60	94	170	234	290
$\dot{\epsilon}_{\text{MIN}}$ ( $\text{h}^{-1}$ )	$1.7 \times 10^{-3}$	$8 \times 10^{-4}$	$3.6 \times 10^{-4}$	$1.2 \times 10^{-4}$	$6 \times 10^{-5}$
Rupture Life (h)	68.5	145.5	255	455	608
Fracture Strain (%)	36.4	23.4	20.5	11.7	6.5

The creep results for the microstructures of Figure 1 are illustrated in Figure 2 and summarized in Table II. Increasing

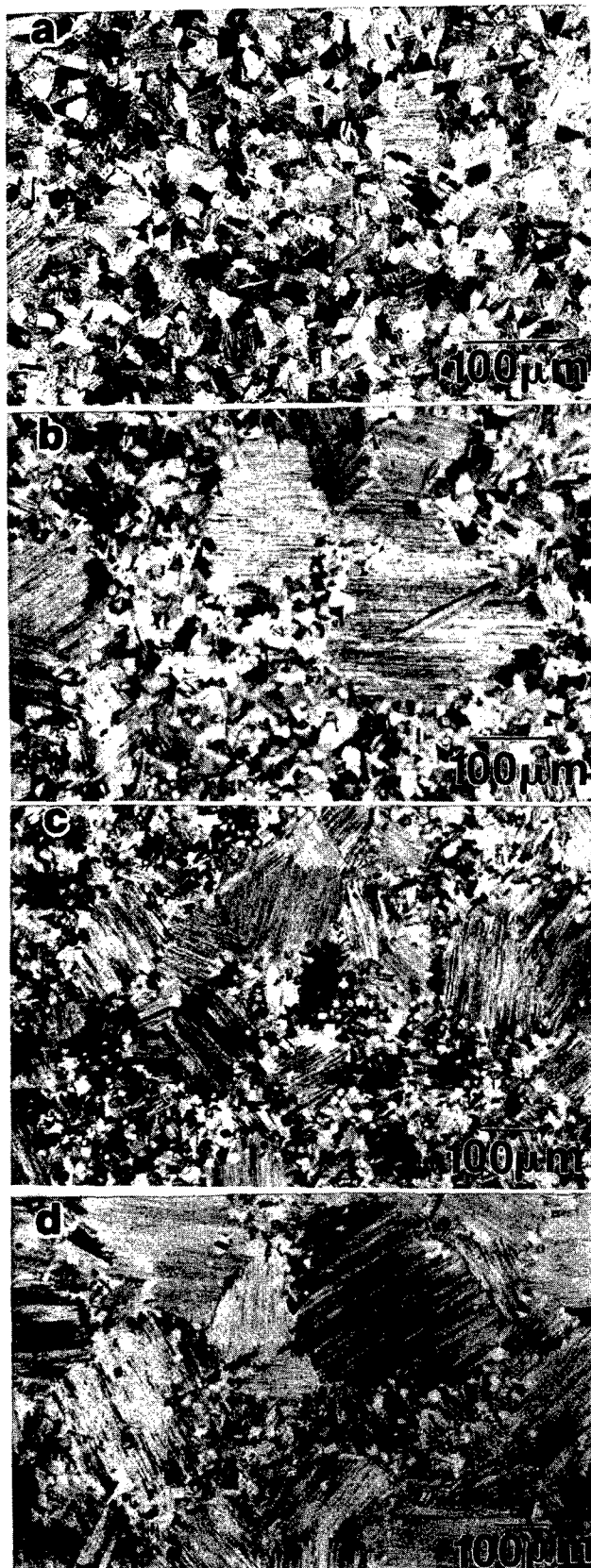


Figure 1. Binary TiAl microstructures, (a) DP - 2h/1350°C AC, (b) NL1 - 1h/1365°C AC, (c) NL2 - 1h/1370°C AC, (d) NL3 - 1h/1375°C AC, continued next page.



Figure 1 (e) FL - 1h/1380°C AC. All conditions stabilized 48h/950°C.

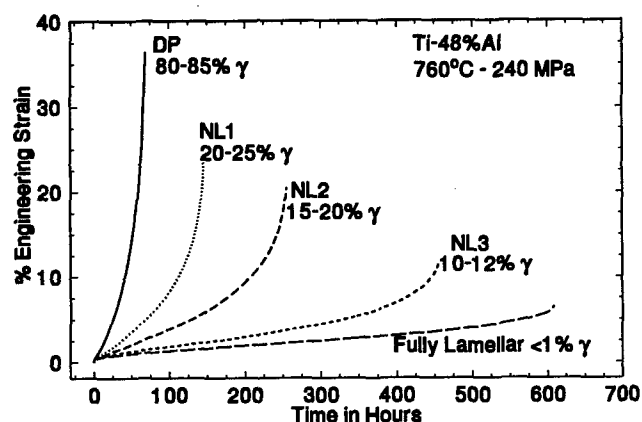


Figure 2. Creep curves for TiAl microstructures of Figure 1.

resistance corresponds to a decrease in the  $\gamma$  grain volume fraction and an increasing lamellar grain size. Even a small volume fraction of  $\gamma$  grains (7-10%) causes substantially less creep resistance. Examination of creep deformed material reveals that it is the  $\gamma$  grain volume fraction, rather than the decreasing grain size, that is responsible for the lower creep resistance. As seen in Figure 3,  $\gamma$  grains are preferentially deformed during creep, which causes dynamic recrystallization (DRX) of  $\gamma$  grains. The smaller DRX grains can then easily deform further through grain boundary sliding (GBS). The microstructural instability of DRX-GBS leads to an early onset of tertiary creep. In contrast, the FL structure can be very stable. FL TiAl+W tested at 760°C for 1840 h at between 136 and 274 MPa, exhibited no microstructural changes detectable via optical microscopy [14]. The results of Figure 2 indicate that the longest creep life and lowest  $\dot{\epsilon}_{\text{MIN}}$  are obtained with a FL microstructure.

Few results pertaining to primary creep of near  $\gamma$ -TiAl alloys are available. For FL microstructures, large primary creep strains have been attributed to the abundance of interfaces [15]. However, as shown in Figure 4, at 240 MPa the FL

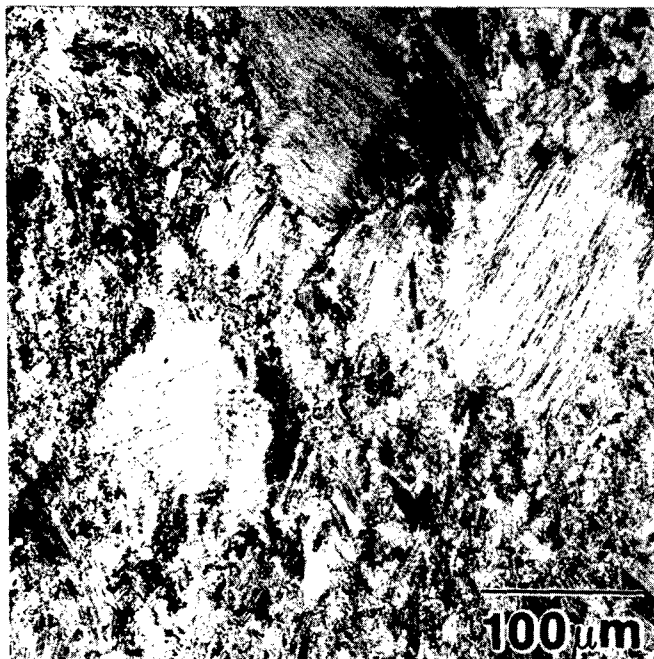


Figure 3. Deformed structure of NL1 after creep fracture (760°C/240 MPa/24.4% strain). Lamellar grains remain relatively undeformed and  $\gamma$  grains are heavily deformed.

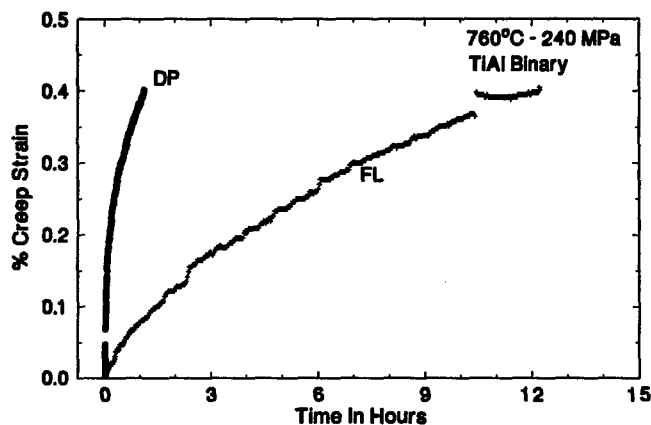


Figure 4. Primary creep of DP and FL conditions of Figures 1(a) and 1(e) respectively.

condition has a longer time to 0.4% creep compared to the DP condition. Therefore, in addition to the longest creep life and lowest  $\dot{\epsilon}_{\text{MIN}}$ , the FL condition exhibits the best primary creep behaviour. Given the superior creep properties of the FL condition, the remainder of this paper concentrates on this microstructure.

#### Influence of Lamellar Grain Size

Typically near  $\gamma$ -TiAl FL microstructures are coarse grained, with lamellar grain sizes of  $>500 \mu\text{m}$  not uncommon [4]. However, FL microstructures with lamellar grain sizes of  $<500 \mu\text{m}$  are of particular interest, since the reduced grain size improves tensile ductility [16]. Therefore, the creep properties

are presented for near  $\gamma$ -TiAl alloys heat treated to produce a range of lamellar grain sizes  $<500 \mu\text{m}$ .

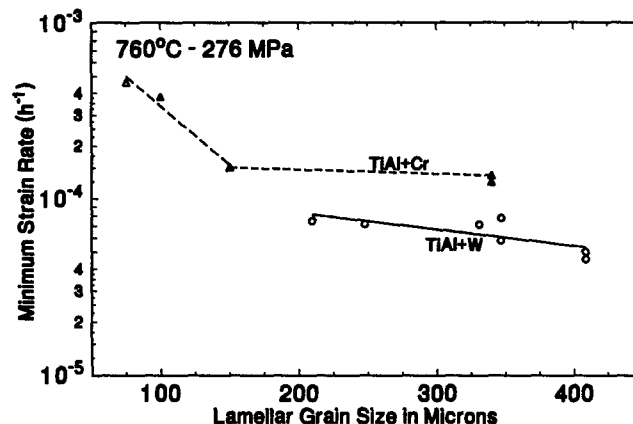


Figure 5.  $\dot{\epsilon}_{\text{MIN}}$  as a function of grain size for FL TiAl+W and TiAl+Cr.

Figure 5 presents  $\dot{\epsilon}_{\text{MIN}}$  for TiAl+Cr and TiAl+W. Most creep tests of near  $\gamma$ -TiAl alloys do not exhibit a steady state strain rate, but an extended time period during which  $\dot{\epsilon} \approx \dot{\epsilon}_{\text{MIN}}$  is typical [4]. In Figure 5,  $\dot{\epsilon}_{\text{MIN}}$  remains nearly constant for lamellar grain sizes  $>150 \mu\text{m}$ . This concurs with previous results for a near  $\gamma$ -TiAl alloy for lamellar grain sizes between 600 and 1200  $\mu\text{m}$  [17]. The results of Figure 5 are interpreted as indicating that at 760°C and 276 MPa  $\dot{\epsilon}_{\text{MIN}}$  is not dependent on grain boundary reaction controlled creep mechanisms. Therefore, the creep strain rate should be influenced by intragranular microstructural features, as outlined in a later section.

Reducing the lamellar grain size does improve the creep life due to an increase in the extent of tertiary creep, Figure 6. The more pronounced tertiary creep is associated with deformation occurring in a larger volume of material and extensive secondary cracking [14]. The minimal tertiary creep of coarse grained structures is attributed to strain incom-

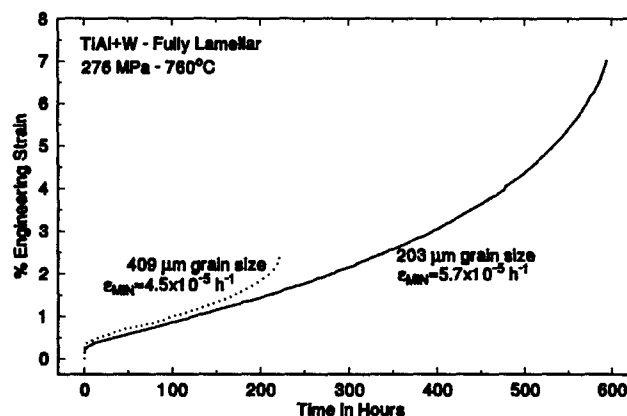


Figure 6. Creep curves of FL TiAl+W to illustrate effect of lamellar grain size on extent of tertiary creep.

patibility at the grain boundaries between 'hard' and 'soft' oriented lamellar grains. This incompatibility causes intergranular or interlamellar cracking that, due to the relatively large grain size, can grow to greater than the critical crack size before arrest at a grain boundary or triple point. With a finer lamellar grain size, cracks are arrested and become dormant before they cause fast fracture, allowing more homogeneous deformation in a larger volume of material, leading to greater tertiary creep strain and increased creep damage tolerance.

By utilizing an innovative heat treatment cycle, fine grained fully lamellar (FGFL) microstructures with grain sizes  $<150\text{ }\mu\text{m}$  can be produced without hot working [18]. At these lamellar grain sizes  $\dot{\epsilon}_{\text{MIN}}$  for TiAl+Cr increases, Figure 5. This indicates that grain boundary reaction controlled creep mechanisms may influence the creep strain rate of TiAl+Cr at grain sizes  $<150\text{ }\mu\text{m}$ . However, for Ti-4822, the FGFL microstructure possesses a useful balance of mechanical properties, Table III [18], exhibiting: superior creep properties compared to the coarse grained FL condition; fracture toughness much better than the DP condition and nearly equivalent to the FL condition; and the highest ultimate tensile strength, with ductility significantly better than the FL condition. The results of Table III illustrate that the FGFL microstructure largely eliminates the trade-off of mechanical properties that exists between the DP and FL microstructures, but depending on the composition, the FGFL condition does not necessarily provide the best creep properties.

Table III  
Mechanical Property Comparison for  
Fine Grained Fully Lamellar Ti-48Al-2Cr-2Nb [18]

Property	FGFL	DP	FL
Creep-276 MPa/760°C $\dot{\epsilon}_{\text{MIN}}$ ( $\text{h}^{-1}$ )	$1.2 \times 10^{-4}$	$2.2 \times 10^{-3}$	$2.5 \times 10^{-4}$
Rupture Life (h)	438	42	206
Room Temp. Tensile 0.2% Y.S. (MPa)	382	414	347
UTS (MPa)	509	477	403
% Elongation	1.7	2.6	1.3
Plane Strain Fracture Toughness ( $\text{MPa}\cdot\text{m}^{1/2}$ )	26.4	17	30.5

From the results presented it is clear that the lamellar grain size has a major influence on the creep of near  $\gamma$ -TiAl alloys. A relatively small lamellar grain size improves creep life by increasing the creep damage tolerance, without significantly influencing  $\dot{\epsilon}_{\text{MIN}}$ . The results suggest that  $\dot{\epsilon}_{\text{MIN}}$  for FL structures is not controlled by creep mechanisms that rely on grain boundary reactions.

### Influence of Lamellar Interface Spacing

The previous section alluded to the role of intragranular microstructural features on the creep strain rate. For the FL condition, the lamellar interface spacing is a major microstructural parameter. Appropriate heat treatment of the TiAl binary alloy produced FL structures with narrow lamellae (FLn) or relatively wide lamellae (FLw), as shown in Figure 7, with the features summarized in Table IV. The major microstructural differences of the two conditions in Figure 7 are the lamellar interface spacing and the grain boundary morphology. Figure 8 shows the creep curves for the microstructures of Figure 7, with the relevant creep properties summarized in Table IV. It is clear that the change in lamellar interface spacing and/or grain boundary morphology causes a major change in both  $\dot{\epsilon}_{\text{MIN}}$  and creep life.

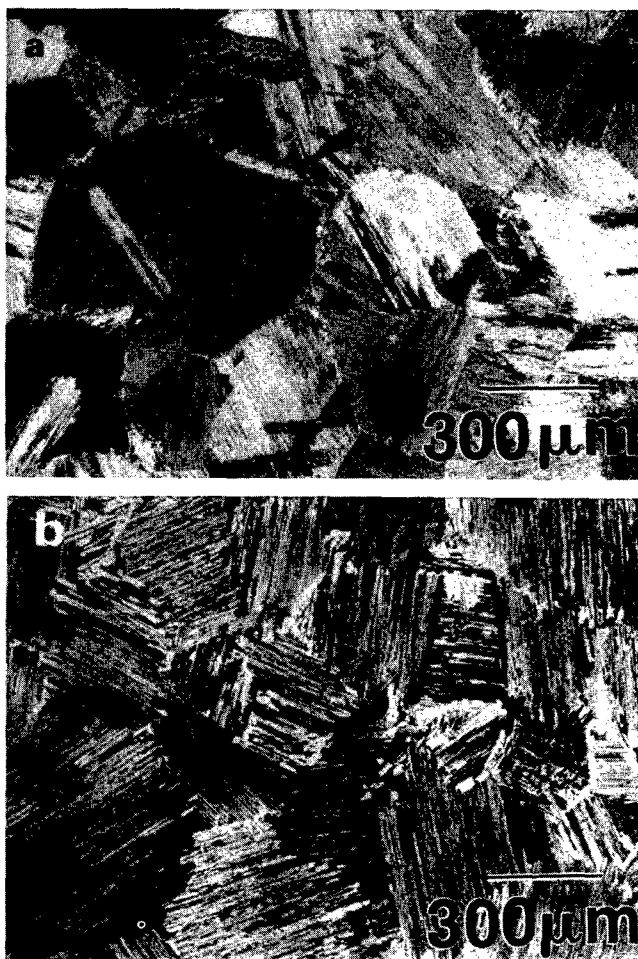


Figure 7. Microstructures of FL conditions, (a) FLn (1h/1380°C AC, and (b) FLw (1/2h/1400°C FC). Both conditions stabilized 48h/950°C.



Table IV  
Microstructure & Creep Results (760°C/240 MPa)

Property	FLn 1h/1380°C AC	FLw ½h/1400°C FC
Lamellar Grain Size	300 µm	300 µm
Avg. Interface Spacing	120 nm	450 nm
γ Lath Width	50-300 nm	200-1000 nm
Grain Boundary Morphology	planar	interlocked
Creep Life	608 h	279 h
$\dot{\epsilon}_{\text{MIN}}$	$5.9 \times 10^{-5} \text{ h}^{-1}$	$2.7 \times 10^{-4} \text{ h}^{-1}$
$\epsilon_f$	6.5 %	18.4 %

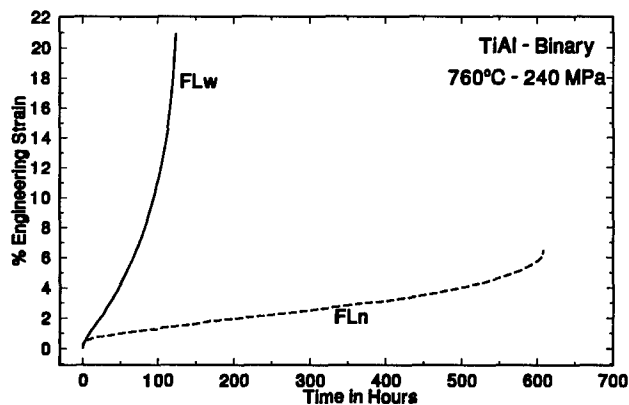


Figure 8. Creep curves for microstructures of Figure 7.

The results of the previous section highlight that  $\dot{\epsilon}_{\text{MIN}}$  is independent of grain size, implying that prior to the onset of tertiary creep grain boundary reaction controlled creep mechanisms have a minimal affect on the creep  $\dot{\epsilon}$ . Therefore, the difference in  $\dot{\epsilon}_{\text{MIN}}$  between the FLn and FLw conditions is associated with the change in lamellar morphology, rather than the grain boundary structure.

To better define the influence of lamellar interface spacing, the results of stress increment tests for the FLn and FLw conditions are presented in Figure 9. The results indicate that  $\dot{\epsilon}_{\text{MIN}}$  for the FLn condition is lower, by a factor of  $\approx 2$  at 105 MPa and  $\approx 6$  at 290 MPa. At low stress the stress exponent is  $\approx 1$ , consistent with recovery controlled creep. At high stress, the stress exponent approaches 10, which may be interpreted as indicating an increasing contribution of dislocation glide with increasing stress, to a combined dislocation climb and glide creep mechanism [19]. However, the gradual increase in

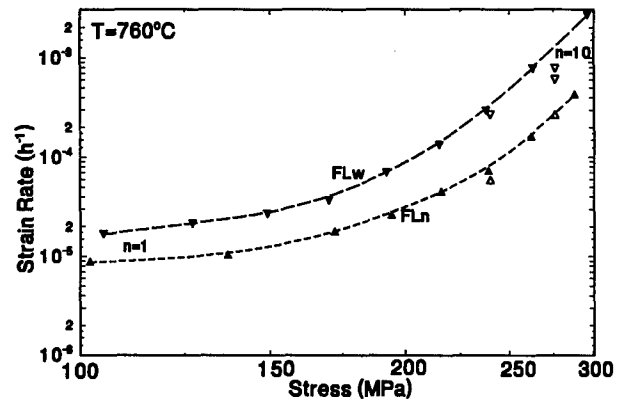


Figure 9. Results of stress increment creep tests. Closed symbols - stress increment results, open symbols -  $\dot{\epsilon}_{\text{MIN}}$  from monotonic tests.

the stress exponent at intermediate stresses, makes identification of the creep mechanism difficult. Intermediate stresses (i.e. 140 to 180 MPa) are of particular importance, since envisaged gas turbine applications have similar stress levels.

The results of consecutive stress reduction tests on the FLn and FLw conditions are shown in Figure 10. At high stress, a short incubation period of zero strain rate occurs following the stress reduction, consistent with creep occurring via dislocation glide, which following the stress reduction continues, albeit at a slower rate [12]. The deformed structure corresponding to the high stress region, Figure 11, contains considerable dislocation activity within  $\gamma$  lamellae, with many dislocations segments spanning individual  $\gamma$  lamellae and interacting with lamellar interfaces. These dislocation structures are consistent with glide controlled creep. At low stress the increasing incubation period of zero strain rate with decreasing stress, Figure 10, indicates that creep is increasingly controlled by recovery processes [12]. The stress at which the mechanism changes from recovery to glide

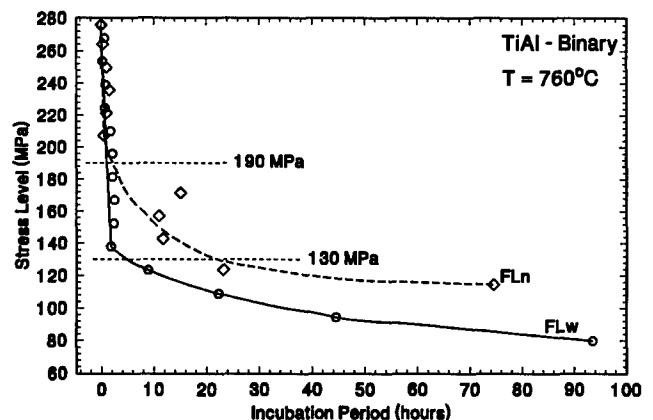


Figure 10. Incubation period following each stress reduction.

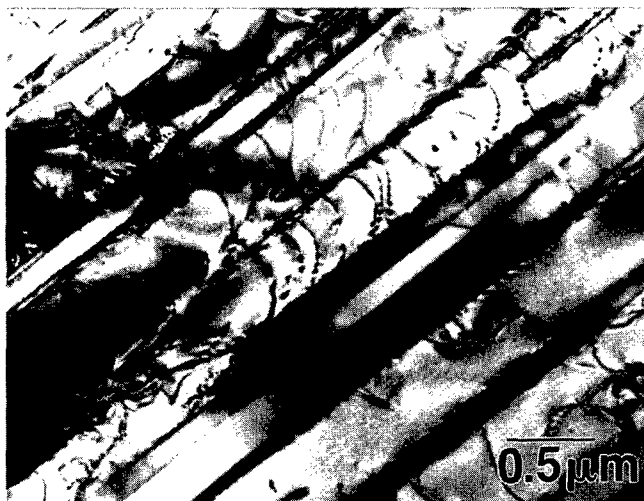


Figure 11. Creep deformed substructure in FLn. (760°C/240 MPa/6.5% strain)

controlled creep is delineated in Figure 10 by the change in the response to the stress drop. As such, for the FLn and FLw conditions glide controlled creep occurs at stress levels >190 MPa and >130 MPa respectively. These stress levels agree reasonably well with the shear stress required for Orowan bowing of dislocations between lamellar interfaces [19]. This implies that the interaction between dislocations in the  $\gamma$  lamellae and lamellar interfaces resists the dislocation glide. The beneficial effect of the reduced lamellar interface spacing is to raise the internal stress required to initiate glide controlled creep. Consequently, with a finer lamellar interface spacing deformation will occur at the slower  $\dot{\epsilon}$  associated with recovery creep to a higher stress level.

Figure 8 and Table IV clearly illustrate that improved  $\dot{\epsilon}_{\text{MIN}}$  and creep life result from a finer lamellar interface spacing. Primary creep is also an important parameter, since the maximum allowable strain for many envisaged applications is <1%. Figure 12 shows the primary creep response for the FLn and FLw conditions, from which it is apparent that fine lamellar interface spacing also improves the resistance to

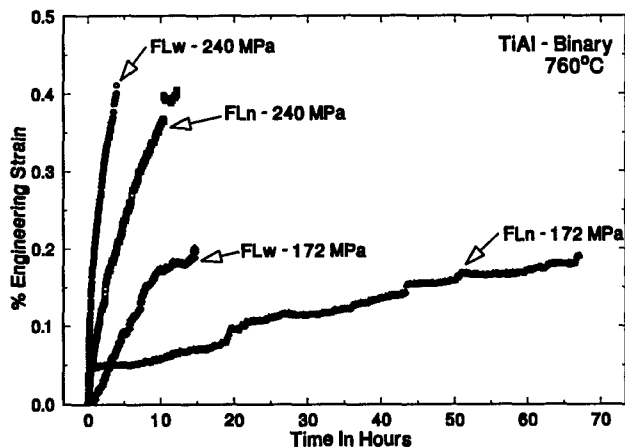


Figure 12. Primary creep response of fully lamellar microstructures.

primary creep. A DP microstructure crept to the maximum strain levels shown in Figure 12 in much shorter times than the FL conditions [20]. The microstructure of the FLn condition after deformation to 0.4% strain exhibited dislocations spanning  $\gamma$  lamellae, similar to Figure 11. However, it is not clear if the difference in time to 0.4% strain for the FLn and FLw conditions is due to the lamellar spacing altering the motion of these dislocations (as discussed in the previous paragraph), or due to a change in the rate at which dislocations are generated during primary creep. The dislocation generation rate may be influenced by the interface structure, which depends on the cooling rate applied to produce the FLn (air cool) and FLw (furnace cool) conditions. Further research is required to clarify this issue.

The results presented highlight the influence of lamellar morphology on creep resistance. It is also of interest to evaluate the role of composition. Although the current work was not designed to elucidate compositional effects, some useful results have been generated. Heat treatments involving air and furnace cooling from the single phase  $\alpha$  region applied to TiAl+W produced average lamellar spacing of 75 and 200 nm respectively [21]. However, as shown in Figure 13 the reduction in lamellar spacing from 200 to 75 nm did not cause as large an increase in creep resistance as that caused by reducing the lamellar spacing in the binary alloy (Figure 8). These results indicate that the W addition may partially overshadow the influence of lamellar spacing. Depending on the creep mechanism involved, W solute might hinder the glide of dislocations, or due to the low diffusivity of W solute the recovery rate may be reduced. In either case, it appears that W solute has a large influence on the creep rate, which is about an order of magnitude lower for TiAl+W than for binary TiAl. This is consistent with previous conclusions regarding the influence of W [22]. Importantly, this result may indicate that ternary or quaternary additions may reduce the sensitivity of creep on microstructure, since solute elements may provide greater resistance to dislocation glide than the lamellar interfaces.

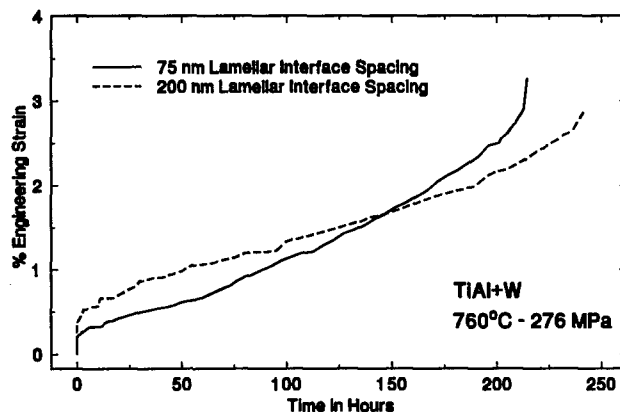


Figure 13. Effect of lamellar interface spacing on the creep behaviour of TiAl+W.

### Influence of Grain Boundary Morphology

As well as the change in lamellar interface spacing, the microstructures of Figure 7 have different grain boundary structures. Well interlocked lamellae exist along the grain boundaries of the FLw structure, while the grain boundaries of the FLn condition are more planar. Interlocked lamellae along grain boundaries have been concluded to improve creep resistance [23]. For binary TiAl, it has been established, in the previous section, that  $\dot{\epsilon}_{\text{MIN}}$  is controlled by the lamellar interface spacing. Therefore, it would not be expected that grain boundary morphology would have a substantial influence on  $\dot{\epsilon}_{\text{MIN}}$  and it is worth considering the influence of grain boundary morphology on the creep of these two conditions.

The planar grain boundaries of the FLn structure, Figure 7, offer little resistance to intergranular cracking and brittle intergranular failure occurs at low strain (6.5%) with minimal deformation of the grains adjacent to the fracture, Figure 14. In contrast, the well interlocked lamellae along grain boundaries of the FLw condition, Figure 7, are more resistant to cracking, forcing further strain to occur within the grains and resulting in greater total creep strain (18.4%), Figure 8 and Table IV. Therefore, the grain boundary morphology influences the onset of tertiary creep and the extent of tertiary creep.

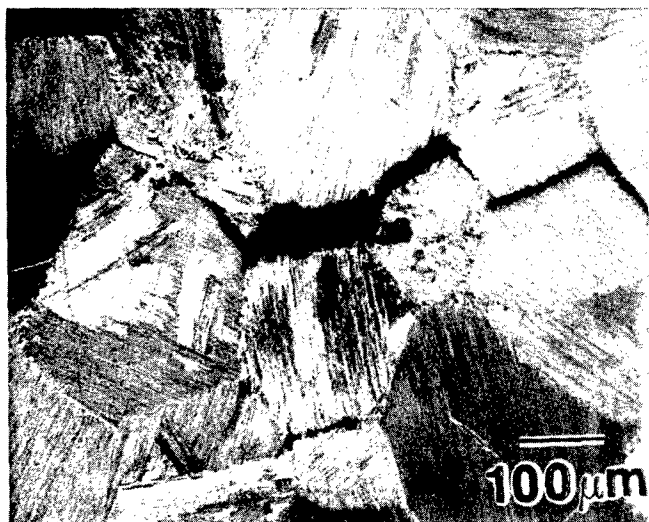


Figure 14. Intergranular creep failure of FLn condition. (760°C/240 MPa/6.5% strain)

A consequence of the greater intragranular deformation associated with interlocked grain boundaries, is the formation of shear bands across lamellae, such as shown in Figure 15. Similar shear band formation has been noted in other near  $\gamma$ -TiAl alloys with interlocked grain boundaries [24]. In the current work, shear band formation only occurs in grains with lamellae oriented nearly parallel to the applied load ('hard' mode), so that shear bands form  $\approx 45^\circ$  to the load axis corresponding to the maximum shear stress direction. This result

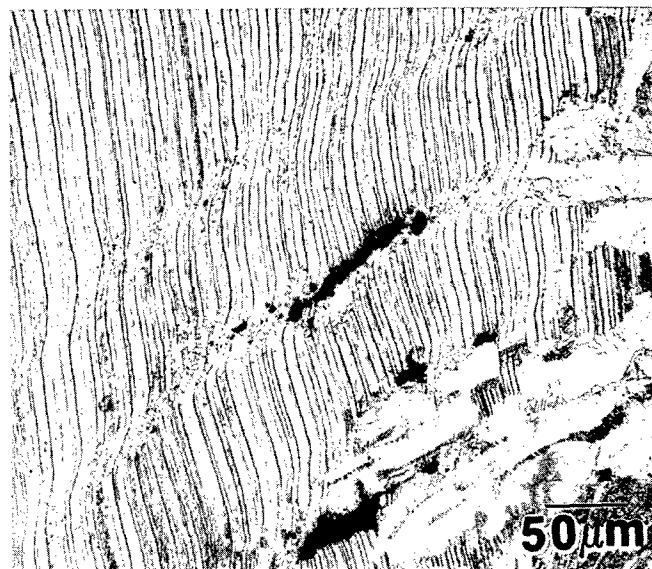


Figure 15. Shear bands in creep deformed FLw, loading direction is vertical. (760°C/240 MPa/18.4% strain)

highlights the anisotropic properties of the  $\alpha_2/\gamma$  FL structure. The effect of lamellar anisotropy is discussed in greater detail elsewhere [25].

### Summary & Conclusions

The results presented highlight that several microstructural attributes of near  $\gamma$ -TiAl intermetallics with fully lamellar structures influence creep properties. Especially noteworthy is that for near  $\gamma$ -TiAl compositions several microstructural attributes must be specified to achieve the optimum creep resistance available from the fully lamellar microstructure.

### Microstructural Design for Creep Resistance

The results derived from these creep studies allow development of preliminary guidelines for microstructural design of creep resistant near  $\gamma$ -TiAl intermetallics. For best creep resistance the following microstructural attributes are required:

1. A *fully lamellar microstructure* with as low a volume fraction of single phase  $\gamma$  grains as possible. Even volume fractions of  $<10\%$   $\gamma$  grains will reduce the creep resistance, due to preferential deformation of the  $\gamma$  grains.
2. A relatively *fine lamellar grain size* ( $<200 \mu\text{m}$ ). Reducing the grain size improves the creep damage tolerance, thereby increasing the tertiary creep strain and creep life. The balance of creep resistance and other mechanical properties required will determine the optimum grain size below  $200 \mu\text{m}$ .
3. *Narrow lamellar interface spacing*. This improves the primary creep resistance and lowers the minimum creep strain rate. Reducing the lamellar interface spacing increases the internal stress necessary for dislocation glide.

4. *Interlocked lamellar grain boundaries*. This feature enhances the resistance to intergranular cracking, leading to increased tertiary creep and potentially greater creep life.

A microstructure possessing all these features may be difficult to achieve via conventional heat treatment cycles. Therefore, there is a requirement for the development of innovative processing options that produce the desired microstructures for the intended applications.

#### Acknowledgements

Financial assistance was received from the Natural Science and Engineering Research Council of Canada and the Department of National Defence (Canada). Elements of this work have been completed as part of National Research Council Project IAR-SMPL JHR-01.

#### References

1. C.M. Austin, T.J. Kelly, Progress in Implementation of Gamma Titanium Aluminides, Gamma Titanium Aluminides I, eds. Y-W. Kim, R. Wagner, M. Yamaguchi, TMS (1995) 21.
2. W. Smarsly, "Titanium Aluminides for Gas Turbines", Proc. European Propulsion Forum: The Influence of New Materials and Manufacturing Processes on the Design of Future Aero Engines, Royal Aeronautical Soc. (1993) Paper 22.
3. D.E. Larsen, D.A. Wheeler, "Investment Cast Gamma and XD™ Gamma Titanium Aluminide Component for Aerospace and Automotive Applications", Proc. 42<sup>nd</sup> Annual Tech. Meeting, Investment Casting Institute (1994) Paper 8.
4. J. Beddoes, W. Wallace, L. Zhao, "Current Understanding of Creep of Near  $\gamma$ -Titanium Aluminides", Int. Mat. Rev., 40 (1995) 197-218.
5. J. Beddoes, W. Wallace, M.C. de Malherbe, "Densification of  $\gamma$ -TiAl Powder By Hot Isostatic Pressing", Int. J. of Powder Metallurgy, 28 (1992) 313-326.
6. L. Zhao, J. Beddoes, W. Wallace, "The Deformation and Dynamic Recrystallization in a Hot Isostatically Pressed Ti-48Al-2W Powder Alloy", High Temperature Intermetallics-V, Mat. Res. Soc. Symp. Proc. Vol. 288, eds. I. Baker, R. Darolia, J.D. Whittenburger, M.H. Yoo, (1993) 921-926.
7. W. Wallace, L. Zhao, J. Beddoes, D. Morphy, "Densification and Microstructural Control of Near  $\gamma$ -TiAl Intermetallic Powders By HIP'ing", Hot Isostatic Pressing'93, eds. L. Delaey, H. Tas, (1993) 99-108.
8. L. Zhao, J. Beddoes, D. Morphy, W. Wallace, "The Microstructure and Mechanical Properties of a Near Gamma-TiAl Powder Alloy Processed By Hot Isostatic Pressing", Mat. Sci. Eng., A192/193 (1995) 957-964.
9. J. Beddoes, L. Zhao, W. Wallace, "The Microstructure and Properties of Hot Isostatically Consolidated Near  $\gamma$ -TiAl Powder", Advancements in Synthesis & Processing, eds. F.H. Froes, W. Wallace, SAMPE (1992) M657-M670.
10. J. Triantafillou, J. Beddoes, W. Wallace, "Creep Properties of Lamellar Near  $\gamma$ -Titanium Aluminides", Canadian Aeronautics & Space J., 42 (1996) 108-115.
11. J.J. Gibeling, W.D. Nix, "The Description of Elevated Temperature Deformation in Terms of Threshold Stresses and Back Stresses: A Review", Mat. Sci. Eng., 45 (1980) 123.
12. D.O. Northwood, I.O. Smith, "Experimental Techniques For Probing The Micromechanisms of Creep: A Review", Metals Forum, 8 (1985) 237.
13. T. Tsuzuku, T.W. Clyne, "Effects of Microstructure on Failure of TiAl During Testing at ambient and Elevated Temperatures", Fatigue and Fracture of Ordered Intermetallic Materials I, eds. W.O. Soboyejo, T.S. Srivatsan, D.L. Davidson, TMS (1994) 239-252.
14. J. Beddoes, L. Zhao, J. Triantafillou, P. Au, W. Wallace, "Effect of Composition and Lamellar Microstructure on the Creep Properties of TiAl+W", Gamma Titanium Aluminides, eds. Y-W. Kim, R. Wagner, M. Yamaguchi, TMS (1995) 959-966.
15. M. Es-Souni, A. Bartels, R. Wagner, "Creep Behaviour of a Fully Transformed Near  $\gamma$ -TiAl Alloy Ti-48Al-2Cr", Acta metall. mater., 41 (1995) 153.
16. Y-W. Kim, "Microstructural Evolution and Mechanical Properties in Gamma Titanium Aluminides", Microstructure/Property Relationships in Titanium Aluminides and Titanium Alloys, eds. Y-W. Kim, R.R. Boyer, TMS (1991) 91-103.
17. D.I. Kimm, J. Wolfenstine, "Effect of Grain Size on The Creep Behavior of Fully Transformed  $\gamma$ -TiAl", Scripta metall. mater., 30 (1994) 615-619.
18. L. Zhao, P. Au, J. Beddoes, W. Wallace, "Method to Produce Fine Grained Lamellar Structures in Gamma

Titanium Aluminides", US Patent, granted, number to be assigned.

19. J. Beddoes, J. Triantafillou, L. Zhao, "Effect of Stress on Creep of Lamellar Near  $\gamma$ -TiAl" High Temperature Ordered Intermetallic Alloys VII, Mat. Res. Soc. Symp. Proc. Vol. 460 (1997).
20. D. Dudzinski, J. Beddoes, L. Zhao, "Primary creep and Anelastic Recovery of a Near  $\gamma$ -TiAl Intermetallic", Proc. 7<sup>th</sup> Int. Conf. on Creep & Fracture of Engineering Structures & Materials, eds. J. Earthman, TMS (1997).
21. J. Triantafillou, J. Beddoes, L. Zhao, W. Wallace, "The Creep Properties of TiAl+W with a Lamellar Microstructure", Scripta metal. mater., 31 (1994) 1387-1392.
22. P.L. Martin, H.A. Lipsitt, "Deformation and Fracture of TiAl+W at Elevated Temperatures", Proc. of 4<sup>th</sup> Int. Conf. on Creep & Fracture of Engineering Structures & Materials, eds. B. Wilshire, R.W. Evans, Institute of Materials (1990) 255-263.
23. S. Mitao, S. Tsuyama, K. Minakawa, "Effect of Aluminum Content on Creep Deformation Behavior of  $\gamma$ -Titanium Aluminides", Microstructure/Property Relationships in Titanium Aluminides and Alloys, eds. Y-W. Kim, R.R. Boyer, TMS (1991) pp.297-311.
24. R.W. Hayes, P.A. McQuay, "A First Report on The Creep Deformation and Damage Behavior of a Fine Grained Fully Transformed Lamellar Gamma TiAl Alloy", Scripta metal. mater., 30 (1994) 259-264.
25. W.R. Chen, J. Beddoes, J. Triantafillou, L. Zhao, "Creep of Polycrystalline Near  $\gamma$ -TiAl With A Lamellar Microstructure", Acta Metallurgica Sinica (English Letters) 9 (1996) 565-570.

# HREM INVESTIGATION ON DEFORMATION TWINNING AND TWIN INTERSECTION IN A Ti-45Al-10Nb ALLOY DEFORMED AT ELEVATED TEMPERATURES

J. G. Wang<sup>1,2)</sup>, L. C. Zhang<sup>1)</sup>, G. L. Chen<sup>1)</sup>, H. Q. Ye<sup>2)</sup> and T. G. Nieh<sup>3)</sup>

1)State Key Laboratory for Advanced Metals and Materials, University of Science and Technology Beijing, Beijing, 100083, P. R. China

2)Laboratory of Atomic Imaging of Solids, Institute of Metal Research, Academia Sinica, Shenyang, 110015, P. R. China

3)Lawrence Livermore National Laboratory, P.O. Box 808, L-369, Livermore, CA 94551-9900, USA

## Abstract

Deformation twinning and twin intersection in the hot-deformed Ti-45Al-10Nb alloy were investigated by using high resolution transmission electron microscopy (HREM). Two types of deformation twinning (type P and type Q) were observed. Type P twin can be formed either through dislocation mechanisms or at grain boundaries. In the former case, twin was formed by either a pole mechanism or a perfect dislocation dissociation mechanism. It can also formed at grain boundary by bowing out of twinning dislocations at the grain boundary and propagated through the sequential emission of twinning dislocations on adjacent twinning planes. The  $1/3[111]$  Frank partial dislocations were observed at ledges in the incoherent twin boundary of some type P twins. A mechanism was proposed to illustrate the propagation of type P twin with or without  $1/3[111]$  Frank Partials at the ledges in the incoherent twin boundary. In contrast, type Q twins usually formed at the lamellar interfaces. In this case, twinning dislocations form a discontinuous segment of tilt wall moving in concert as a superdislocation to create a shear microband.

In the case of twin intersection, two types (type I and type II) of twin intersection were also observed. For type-I twin intersection, three intersection configurations have been noted, deflections have been found either in only one of the twin bands or in both twin bands. In some parts of the intersection zone crystal lattice has been observed to rotate a

small angle with respect to the lattice of the deflected twin. No structure change and secondary twinning in the barrier twin were noted. For type-II intersection, three intersection configurations were also observed. Secondary twinning is noted to be the dominant mechanism, the incident twin has often been split into several thinner twins after crossing the barrier twin, the shear is not fully transmitted across the intersection.

## Introduction

Deformation twinning is considered to be an important deformation mode in  $\gamma$ -TiAl alloys. Since it is an easy deformation mode, twinning may play a role in ductilization of the TiAl alloy, which is the major challenge for the industrial utilization of TiAl. The propagation of twins through movement of  $1/6\langle 11\bar{2} \rangle$  dislocations on  $\{111\}$  plane in  $L1_0$ -TiAl was proposed by Shechtman *et al.* [1], and recent *in situ* TEM observations by Farenc *et al.* [2,3] and Jin *et al.* [4,5] seem to confirm this prediction. Twin nucleation can be observed from either superdislocation dissociation or bowing out one or two twinning dislocations at grain boundaries. Alloy composition, microstructure and deformation temperature also have an influence on twinning, but various opinions prevail on the relative importance of these variables [6-8].

On the other hand, since twins can act as obstacles to the propagation of both dislocations and other twins systems, twinning may also cause brittleness. Recently,

the crystallography of deformation twinning, dislocation-twin interaction and twin-twin intersections have been studied both theoretically and experimentally [9~12]. Many features created by the deformation twinning intersections were observed. Both types of deformation twinning intersection observed in TiAl alloys can be accomplished by basal or cubic plane slips or by shearing on the (111) plane in a barrier twin.

Ti-45Al-10Nb is a high-performance alloy with an excellent high temperature strength and oxidation resistance[13,14]. By adding 10% Nb the stacking fault energy of the alloy is decreased and twinning and twin intersection are enhanced [15]. In the present work, the deformation twinning and twin intersection in the alloy deformed at high temperatures are examined using HREM.

### Experimental Procedure

The alloy with a composition 45at.% Ti, 45at.% Al and 10at.% Nb was prepared from high purity Ti (99.9%), Al (99.9%) and Nb(99.9%) by non-consumable electrode arc-melting in a purified argon atmosphere. The as-cast ingot was wrapped in a steel foil and heated to 1250°C for 30 mins, quasi-isothermally forged to more than 40%. The temperature of forge hammer was 1050°C. The strain rate was about  $5 \times 10^{-1} \text{ s}^{-1}$ . The forged ingot was cooled to room temperature in air.

TEM specimen were prepared by standard twin jet polishing and/or ion-milling and observed in a JEOL-2000EXII electron microscope operating at 200kV with a spherical aberration coefficient of 0.7 mm. Interfaces in the samples were examined in either  $\langle \bar{1}10 \rangle$  or  $\langle \bar{1}01 \rangle$  orientations with the lamellar interfaces edge on.

### Deformation Twinning

The phases in the quasi-isothermal forged Ti-45Al-10Nb alloy are  $\gamma$ -TiAl and  $\alpha_2$ -Ti<sub>3</sub>Al [14,15], which composed of a nearly fully lamellar microstructure shown in Fig. 1. Two types of deformation twins can be observed in the hot-deformed alloy. One type is that the twinning plane is (111)<sub>γ</sub> parallel to lamellar interfaces (referred as type P deformation twin, herein), the other is that the twinning plane is (1 $\bar{1}$ 1)<sub>γ</sub>, having an inclining angle of about 70.5° with respect to lamellar interfaces (referred as type Q deformation twin, herein); they are illustrated in Fig. 2.

#### *Formation of type P twin*

##### Formation of type P twin in the $\gamma$ lamellae

Type P twins can be formed either through dislocation mechanisms or at grain boundary. In the former case, twin formation can be further described by two mechanisms. One is the pole mechanism, in which an imperfect

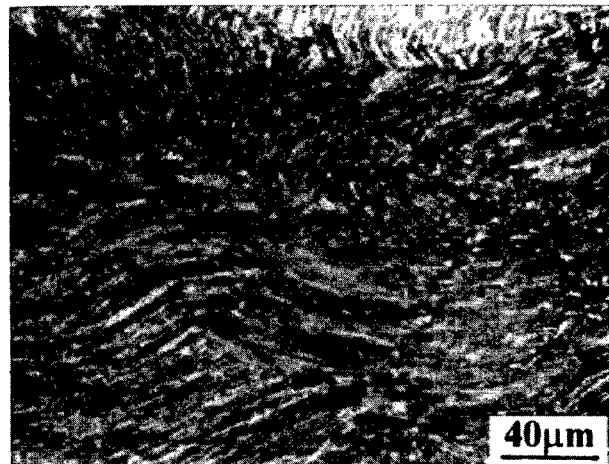


Fig. 1 Optical microstructure of hot-deformed Ti-45Al-10Nb alloy.

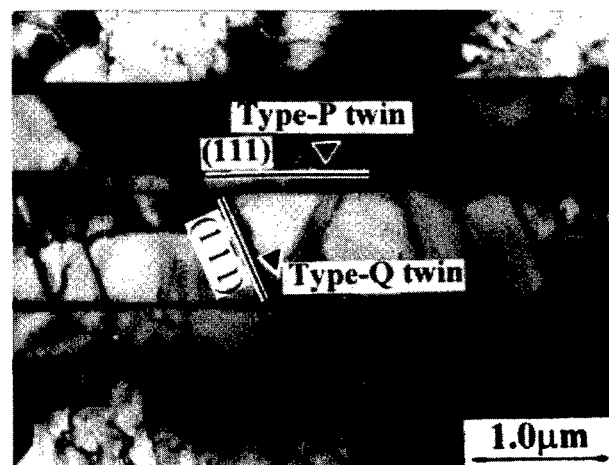


Fig. 2 Two types of deformation twins: type P twins (twinning plane is (111)<sub>γ</sub>) and (b) type Q twins (twinning plane is (1 $\bar{1}$ 1)<sub>γ</sub>).

dislocation winds around a (pole) screw dislocation leaving behind a twinned material [16]. The other is the dissociation mechanism in which a perfect dislocation  $1/2[110]$  lying on the primary slip plane (111), dissociates in the twinning plane ( $1/2[110] \rightarrow 1/3[111] + 1/6[11\bar{2}]$ ) and results in a twinning dislocation  $1/6[11\bar{2}]$ . This dislocation moves on the twinning plane and leaves behind the twinned material. The dissociated  $1/3[111]$  Frank partial dislocation can be observed by HREM. Figure 3 (a) shows a thin type P twin  $\gamma_D$  formed in the matrix  $\gamma_C$ , which is four atomic planes thick. Four  $1/3[111]$  Frank partial dislocations can be shown in Fig. 3 (b) (beam direction  $[10\bar{1}]_M$ ). This mechanism is similar to the homogeneous glide of twinning dislocations proposed by Fourie *et al.* [17] and Price[18], as schematically illustrated in Fig. 3 (c).

##### Formation of type P twin at grain boundary

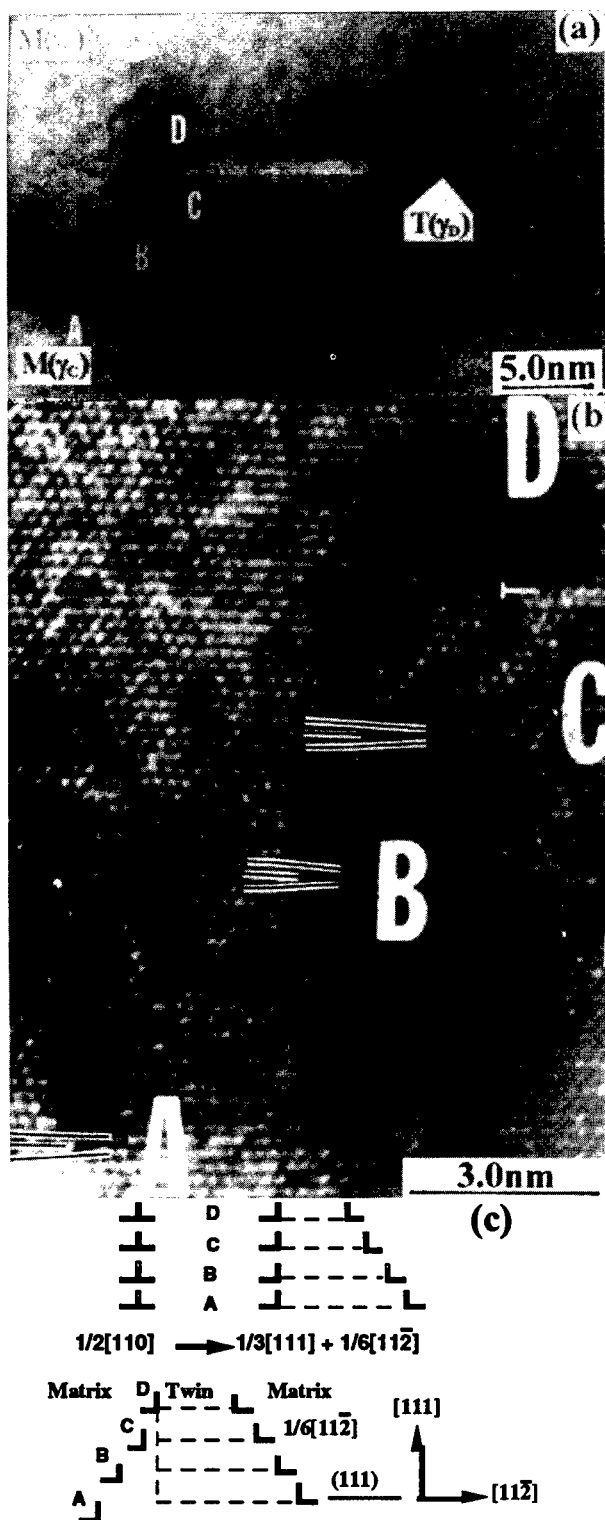
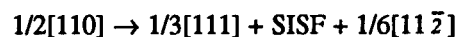


Fig. 3 (a) HREM image of a thin type P twin formed within  $\gamma$  lamellae, (b) high magnification of the left part of the thin twin in (a) showing the  $1/3[111]$  Frank partials at sites A, B, C and D (beam direction  $[10\bar{1}]_M$ ), (c) schematic representation of a perfect dislocation dissociation mechanism to illustrate the formation of thin twin in (a).

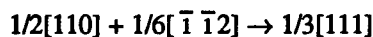
Type P twins can nucleated not only in  $\gamma$  lamellae through dislocation mechanisms, but also at grain boundaries. In fact, in the present study, most of the type P twins were observed to nucleated at grain boundaries. Figure 4 (a) shows a typical type P deformation twin  $T(\gamma_b)$  nucleated at a small-angle, tilted  $\gamma_A / \gamma_C$  grain boundary (as indicated by a dashed line), and penetrated into the  $\gamma$  lamellae matrix. The twin has its tip as stacking fault of the matrix. The twin layers near the twin tip exhibit a semi-lenticular shape. The twinning dislocations which are characterized by ledges [19~21] glide only on one side of the twin layers. The tip of the twins has an incoherent twin boundary on one side and a flat coherent twin plane on the other side. The mean distance between ledges at incoherent twin boundary is about 3.8 nm. This is consistent with the observation of Jin *et al.* [4,5] in a creep-deformed Ti-48at.%Al-2at.%Nb-2at.%Cr alloy. Their results showed that mechanical twins can be nucleated by bowing out of twinning dislocations at grain boundary resulting from a local stress concentration, and propagated by sequential emission of twinning dislocations from grain boundaries and the homogeneous glide of the twinning dislocations on every adjacent twinning plane.

According to Marcinkowski and Sree Harsha[22], based upon the traditional symmetric twin morphology (lenticular), twinning dislocations pile up at the twin tip are distributed more densely than those away from the tip. However, by examining the ledge (twinning dislocations) distribution in the incoherent twin boundary of twin  $T(\gamma_b)$  in Fig. 4(a), we find that the spacing between any two neighboring ledges is rather homogenous. This may be because the morphology of these twins are semi-lenticular and the stacking fault energy for TiAl was decreased greatly by the addition of 10 at.% Nb [15] (The stacking fault energy is about 20 mJ/m<sup>2</sup>).

Figure 4(b) is a higher magnification of a local region in Fig. 4(a).  $1/3[111]$  Frank partial dislocations can be observed at ledge A and B. This illustrates that ledges at incoherent twin boundary contain  $1/3[111]$  Frank partials and when the twin grows during hot-working  $1/3[111]$  Frank partials can move away from the incoherent twin boundary to the twin interior or the matrix through climbing. These  $1/3[111]$  Frank partials were introduced either by the dissociation of  $1/2[110]$  dislocations at the interface through the following reaction:



or by the reaction of  $1/2[110]$  with  $1/6[\bar{1}\bar{1}2]$  at the interface described by



The formation of ledges with or without  $1/3[111]$  Frank partials at type P mechanical twin boundaries can be



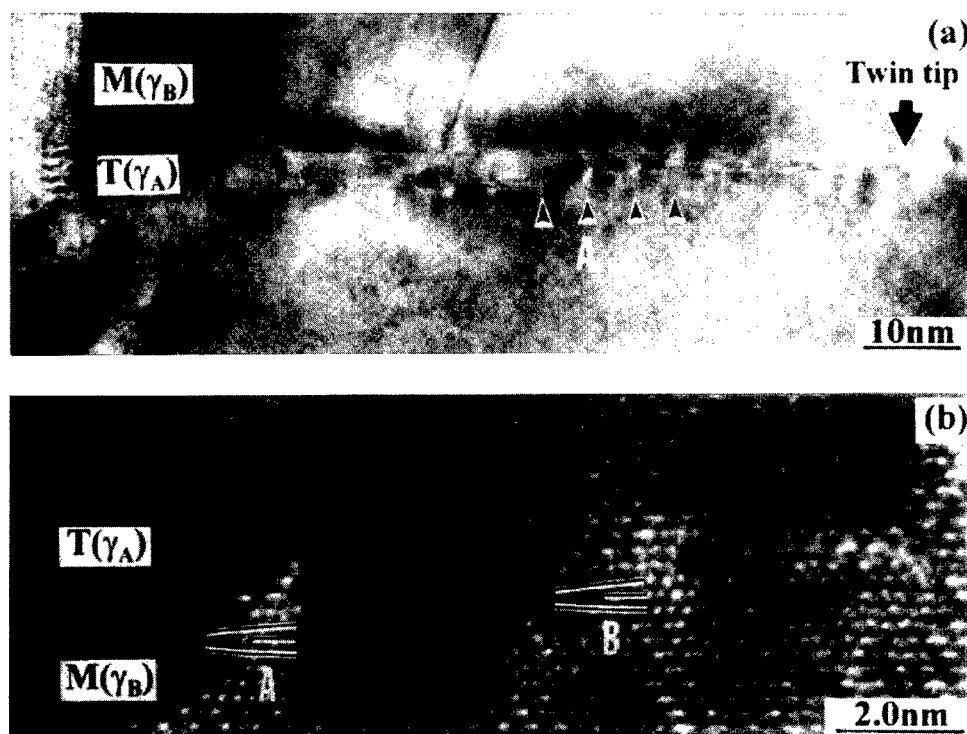
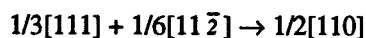


Fig. 4 (a) A type P twin  $T(\gamma_B)$  nucleated at a small-angle, tilted  $\gamma_A/\gamma_C$  grain boundary (as indicated by a dashed line), (b) high magnification HREM image of the ledges A and B at incoherent twin boundary of the twin in (a) showing  $1/3[111]$  Frank partials.

schematically illustrated in Fig. 5. During hot deformation of two-phase ( $\gamma+\alpha_2$ ) alloys, the  $1/3[111]$  Frank partial dislocations can move away from the ledges by climb, and react with another  $1/6\langle 112 \rangle$  Shockley partial dislocation at opposite interface as follows:



This reaction yields an ordinary dislocation  $1/2[110]$ , moving away from the incoherent twin boundary. This is a typical mechanism of moving dislocation passing through a twin boundary during deformation [23].

#### Formation of type Q twins

Type Q twins usually formed at the lamellar boundary, i.e.  $\alpha_2/\gamma$  interface, and existed type P  $\gamma/\gamma_T$  twin boundary. Figure 6 shows HREM images of type Q twins formed at lamellar interfaces, in which (a) is two twins formed at semi-coherent type P twin boundary with a high density of ledges and (b) is a twin formed at the ledge of  $\alpha_2/\gamma$  interface. Usually, type Q twin is very thin and its morphology can be characterized as a rod (or stick). Both sides of the twinning planes are coherent twin boundaries and no ledges were observed at the twinning boundaries. The twin plane is  $(1\bar{1}1)$  plane and the twin dislocation is  $1/6[1\bar{1}\bar{2}]$  Shockley partial dislocation. In Fig. 6 (b), a type Q twin  $T_2$  is propagating into the  $\gamma$  lamellae. The

morphology of the twin 'tip' can no longer be characterized as pile-up-like. Instead, twinning dislocations at the twin 'tip' form a square front array configuration. A tilt array of twinning dislocations emit simultaneously from the lamellar boundary and move in concerts as a superdislocation forming a discontinuous segment of tilt wall to create a shear microband [24,25]; this is illustrated in Fig. 6 (c) (where D denotes the spacing of  $(1\bar{1}1)$  plane,  $d(1\bar{1}1)$ ).

As reported by Zhao *et al.* [26], the defect structures on the lamellar boundaries were composed of mainly three closely spaced  $1/6\langle 112 \rangle$  Shockley partial dislocations inside  $\gamma$  lamellae. The interfacial dislocations can be characterized as ledges at the lamellar boundary. As discussed previously [14], there exist a high density of ledges with two and three atomic planes high at the  $\alpha_2/\gamma$  and  $\gamma/\gamma_T$  interfaces in the hot-deformed alloy studied, which correspond to the Shockley partials and the superdislocations containing Frank partials, respectively. Ordinary dislocation loops with Burgers vector  $b=1/2\langle 110 \rangle$  were observed to emit from the semicoherent twin-related  $\gamma/\gamma$  boundaries, microtwins are heterogeneously nucleated at misfit interfacial dislocations [27,28]. The process is certainly supported by the localized stress field of the misfit dislocations. Ledges at lamellar interfaces (including  $\alpha_2/\gamma$  and  $\gamma/\gamma_T$  interfaces) are expected to be the region of localized stress concentration during deformation. These

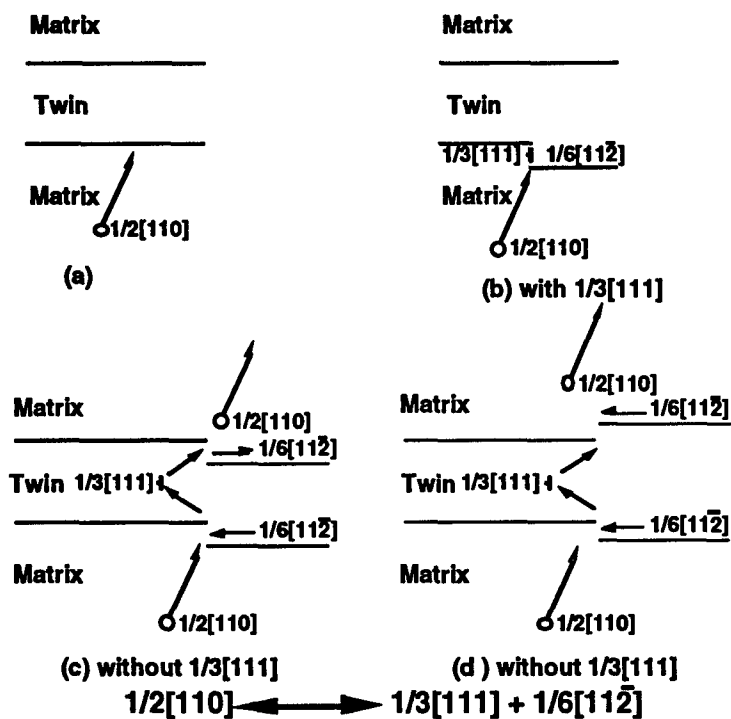


Fig. 5 Schematic diagrams showing the interaction of  $\frac{1}{2}[110]$  dislocation with twin boundaries.

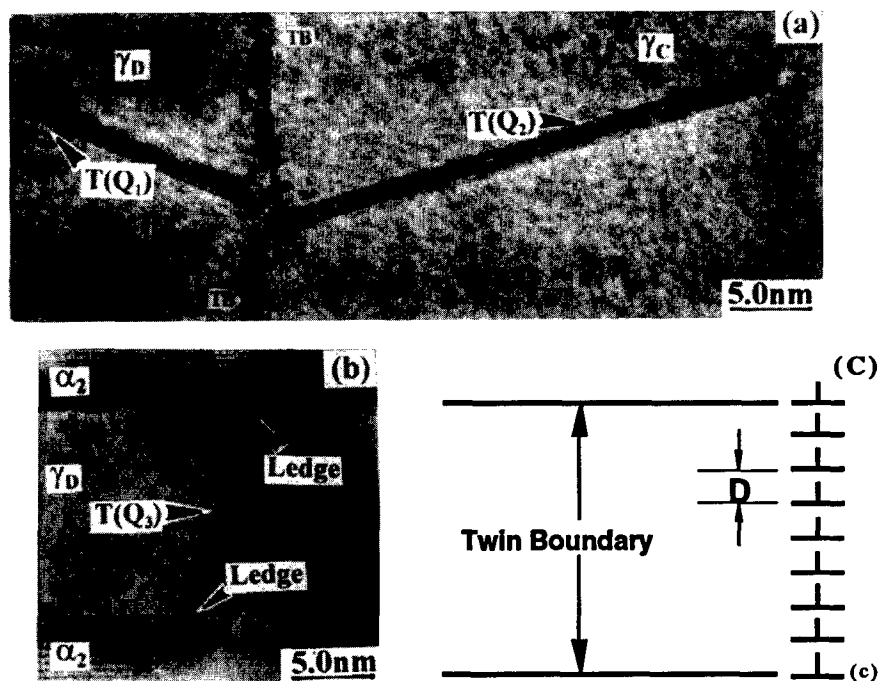


Fig. 6 HREM images of type Q twins formed at (a) semicoherent type P twin boundary with a high density of ledges, (b) ledges on  $\alpha_2/\gamma$  interfaces, (c) configuration of dislocations at the tip of type Q twin forming a discontinuous segment of tilt wall (where D denotes the spacing of  $(1\bar{1}1)$  plane,  $d(1\bar{1}1)$ ).

ledges can act as sources to emit the misfit interfacial dislocations which are mainly  $1/6\langle 112 \rangle$  Shockley partials. These interfacial Shockley partials with Burger vector  $b=1/6[1\bar{1}\bar{2}]$  emitted from the ledges can move on  $(1\bar{1}1)$  planes and resulted in the nucleation of type Q twin at ledges.

The  $(111)$  plane is the primary slip plane in the lamellae microstructure. The  $(1\bar{1}1)$  plane, in contrast, is a conjugate slip plane which is not the easiest direction for deformation. Twins in these  $(1\bar{1}1)$  planes would require a much higher stress concentration. Thus, the nucleation of type Q twin is more difficult than that of type P twin, and type Q twins are usually thinner than type P twins.

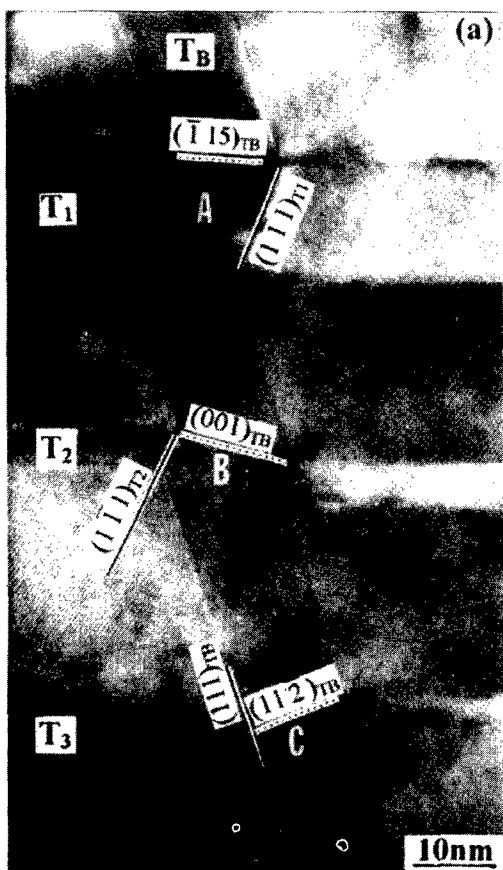


Fig. 7 (a) HREM image of type-I twin intersection viewed in  $[\bar{1}10]_M$  direction, in which twin band  $T_B$  (barrier twin) are intersected by  $T_1$ ,  $T_2$  and  $T_3$ . Three kinds of intersection configuration at A, B and C are schematically illustrated in (b), (c) and (d) respectively.

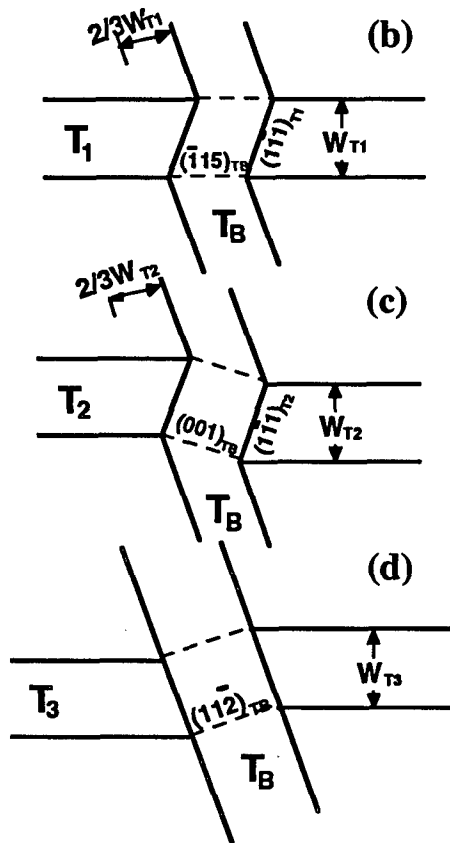
different kinds of intersection configuration are noted at A, B and C. At A, it is observed that twin  $T_1$  does not undergo a displacement normal to its habit plane across the intersection as a result of intersection with twin  $T_B$ . This suggests that the twin  $T_1$  may trespass into the barrier twin  $T_B$  without deflection. The trace of the boundary between twin  $T_1$  and the intersection region is nearly parallel to trace of  $(1\bar{1}1)_{T_1}$ . A displacement of the twin  $T_B$  (barrier twin) normal to its habit plane across the intersection is measured to be two thirds of the width of twin  $T_1$  (incident). At B,

## Twin Intersections

Two types of deformation twin intersection were observed in the hot-deformed Ti-45Al-10Nb alloy: intersection occur along  $\langle 110 \rangle$  (type-I) and  $\langle 101 \rangle$  directions (type-II).

### Type-I Intersection

Figure 7 (a) is a HREM image of type-I twin intersection viewed in the  $[\bar{1}10]_M$  direction, in which twin band  $T_B$  (barrier twin) intersected with  $T_1$ ,  $T_2$  and  $T_3$ . Three



the trace of the twinning plane of twin  $T_2$  across the intersection is nearly parallel to the trace of the  $(001)_{TB}$  plane (marked in Fig. 7 (a)), which indicates that twin  $T_2$  may penetrate into twin  $T_B$  by gliding of perfect dislocations on the  $(001)_{TB}$  basal plane. It is worth noting that the boundary between twin  $T_2$  and the intersection region is not flat; it exhibits a zigzag pattern, and the average trace (indicated by a broken line) is a few degrees away from the trace of the  $(1\bar{1}1)_{T_2}$ . The displacement of the twin  $T_B$  (barrier twin) normal to its habit plane has been

measured to be larger or equal to two thirds of the width of twin  $T_2$ . The displacement of twin  $T_2$  normal to its habit plane was measured to be about a third or less of the width of twin  $T_B$ . At location C, the trace of the twinning plane of twin  $T_3$  across the intersection is nearly parallel to the trace of the  $(11\bar{2})_{TB}$  plane (indicated in Fig. 7 (a)). While the twin  $T_B$  remains undeflected, the boundary between twin  $T_3$  and the intersection region is flat, it is just the basal twinning plane  $(111)_{TB}$  of twin  $T_B$  (barrier). The displacement of twin  $T_3$  normal to its habit plane was measured to be about half of the width of twin  $T_B$ . The above three intersection geometry at position A, B and C are schematically illustrated in Figs. 7 (b), (c) and (d), respectively.

Intersection mechanisms for type-I intersection have been proposed by several researchers [9-12]. Accommodation on the  $(001)_{TB}$  basal plane mechanism and the straight penetration mechanism can be used to well illustrate the observed intersection configurations at positions A and B (in Fig. 7). For configuration at location C, detailed studies are underway [16]. Figure 8 is a HREM image of several incident twins cross a barrier twin, it can all be elucidated by the above three kinds of intersection configuration A, B, and C. It should be noted that no structure change or secondary twinning is observed in the intersection (in barrier twin), only a small rotation of the lattice with a few degrees can be seen in type-I intersection (as indicated in Fig. 8)

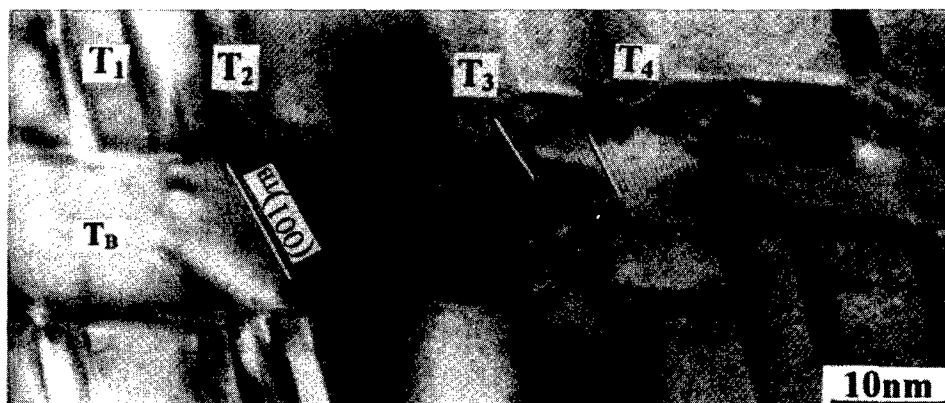
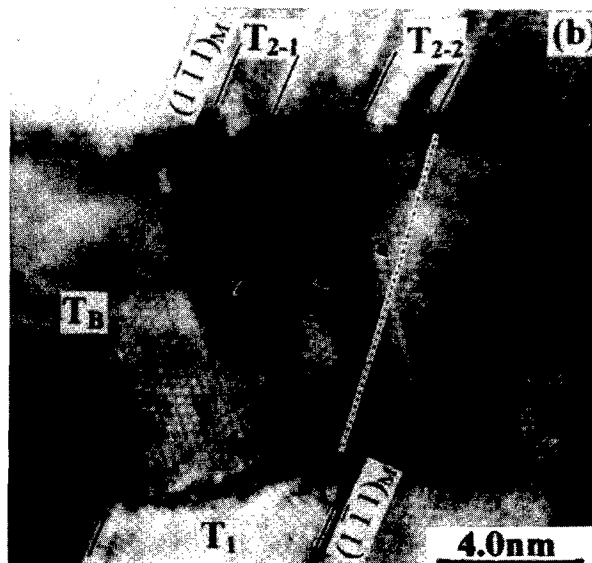
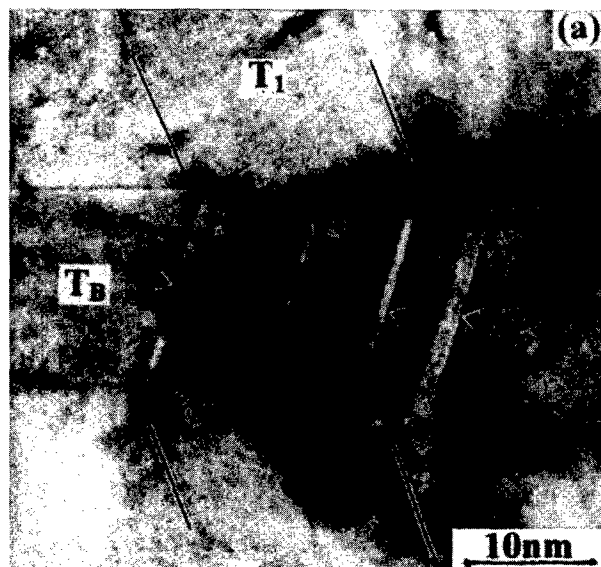


Fig. 8 HREM image of several incident twins crossing a barrier twin, a small rotation of lattice with a few degrees observed in the type-I intersection.

### Type-II Intersection

Figures 9 (a) and (b) show typical type-II intersections accomplished by secondary twinning (the beam direction is  $[10\bar{1}]_M$  and  $[\bar{1}01]_M$  respectively). In Fig. 9 (a), twin  $T_B$

(barrier twin) was intersected by twin  $T_1$  and secondary twins can be seen as fine twin layers distributed in  $T_B$ . The incident twin  $T_1$  is interrupted at the intersection, the shear



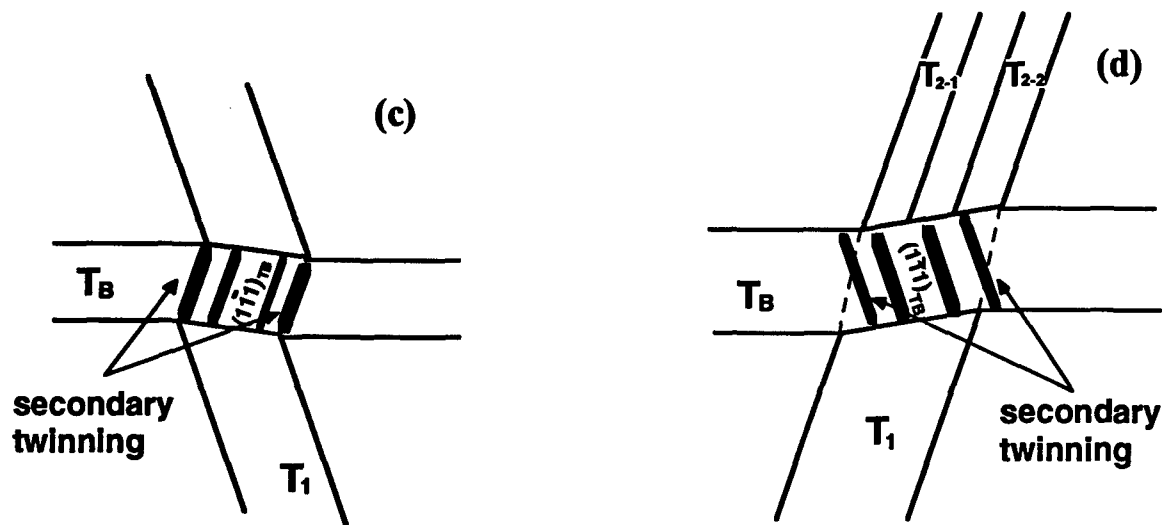


Fig. 9 HREM images of typical type-II intersections accomplished by secondary twinning, the beam direction is  $[10\bar{1}]_M$  and  $[\bar{1}01]_M$  in (a) and (b) respectively (secondary twinning is indicated by arrows), (c) and (d) are schematic illustrations of the intersection geometry for (a) and (b) respectively.

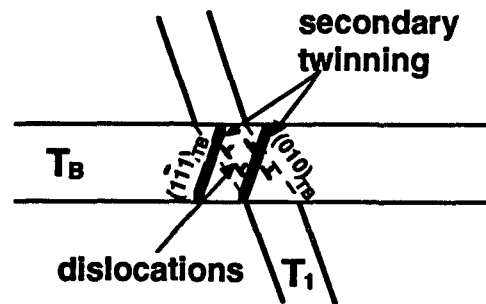
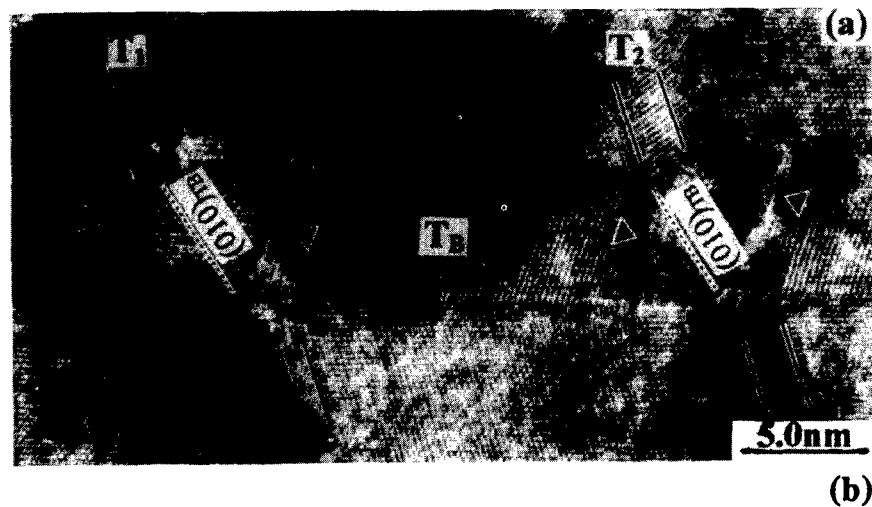


Fig. 10 (a) HREM image of type-II intersection accomplished by  $\{100\}_{TB}$  cubic plane penetration, the beam direction is  $[10\bar{1}]_M$  (secondary twinning is indicated by arrows), (b) schematic illustration of the intersection geometry in (a).

has been transmitted in the barrier twin by secondary twinning. As a result, the barrier twin was distorted. The

boundaries between the intersection region and the incident twin are characterized by step and the coherency of the

barrier twin boundaries in the intersection region is demolished. The incident twin was also deflected. In Fig. 9 (b), thin secondary twinning layers were observed in the intersection, but the incident twin  $T_1$  appears to be undeflected. It should be noted that the incident twin  $T_1$  has been split into two thinner twins  $T_{2-1}$  and  $T_{2-2}$  after trespassing the barrier twin  $T_B$ . Also, the incident twin changes its width after crossing the barrier twin. The width of the incident twin  $T_1$  was 22 (111) plane layers which is more than the total width of the incident twins  $T_{2-1}$  and  $T_{2-2}$  (14 (111) plane layers). This indicates that the incident twin propagates on the  $(111)_M$  plane from the bottom to the top, and the shear action is not fully transmitted across the intersection. The intersection geometry of Figs. 9 (a) and (b) are schematically illustrated in Figs. 9 (c) and (d) respectively. Figure 10 (a) shows a type-II intersection accomplished by  $\{100\}_{TB}$  cubic plane penetration, the beam direction is  $[10\bar{1}]_M$ . The twin bands  $T_1$  and  $T_2$  penetrate the twin band  $T_B$  along  $(010)_{TB}$  since the intersection bands in the twin  $T_B$  are parallel to the trace of  $(010)_{TB}$  plane. The twin band  $T_1$  did not fully trespass the intersection, and  $T_2$  is fully interrupted across the intersection. It should be noted that very thin secondary twinning layers (indicated by arrows) can also be observed in the barrier twin  $T_B$ ; this is schematically illustrated in Fig. 10 (b).

Dislocation mechanism concerning the accommodation by secondary twinning and on the  $\{100\}_{TB}$  cubic plane for type-II twin intersection [9-12] can be used to analyze the intersection configurations in Figs. 9 and 10.

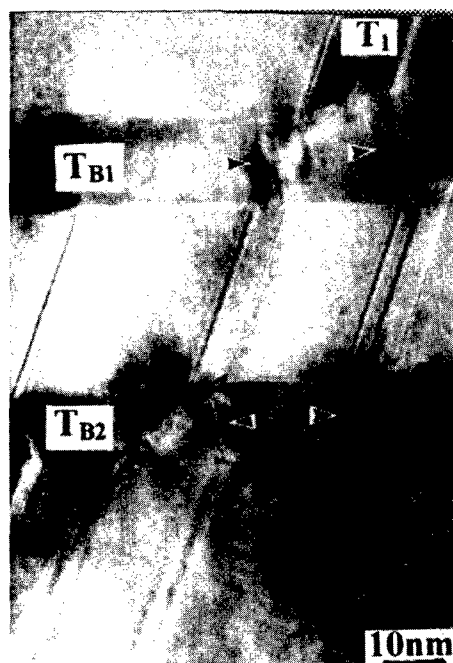


Fig. 11 HREM image of a type-II twin intersection, where two barrier twins  $T_{B1}$  and  $T_{B2}$  are intersected by an incident twin  $T_1$  (secondary twinning is indicated by arrows).

Figure 11 shows a HREM image of a type-II twin intersection configuration, in which two barrier twins  $T_{B1}$  and  $T_{B2}$  are intersected by an incident twin  $T_1$ . It can be readily seen that secondary twinning is the dominant mechanism for type-II intersection. Also, the incident twin is noted to split into several thinner twins after crossing the barrier twin, the total width of these thinner twins is less than that of the initial incident twin, suggesting the shear action is not fully transmitted across the intersection.

### Summary

Two types of deformation twinning (type P and type Q) in the hot-deformed Ti-45Al-10Nb alloy have been investigated by using HREM. Type P twin can be formed either through dislocation mechanisms or at grain boundary. In the former case, twin can be formed through either a pole mechanism or a dislocation dissociation mechanism. In the latter case, the twin can be nucleated by bowing out of twinning dislocations at the grain boundary, caused by a local stress concentration. The twin propagates by the further emission of twinning dislocations on every adjacent twinning plane. Type Q twins usually formed at the lamellar interfaces, i.e.  $\alpha_2/\gamma$  interfaces and existed type P  $\gamma/\gamma(T)$  twin boundary. The twinning plane is  $(1\bar{1}1)$  and the twinning dislocation is  $1/6[1\bar{1}\bar{2}]$ . The ledges on these lamellar interfaces are the common sites for the nucleation of type Q twins. The propagation of type Q twin is that the moving of  $1/6[1\bar{1}\bar{2}]$  twinning dislocations on the twinning plane  $(1\bar{1}1)$  in concert as a superdislocation to create a shear microband.

Two types of twin intersection have also been investigated. For type-I, three intersection configurations were observed. Twin deflection has been observed either in only one of the twin bands or in both twin bands. In some parts of the intersection zone crystal lattice has been observed to rotate a small angle with respect to the lattice of the deflected twin, and no structure change and secondary twinning in the barrier twin were noted. For type-II intersection, three intersection configurations also have been observed. Secondary twinning appears to be the dominant mechanism. An incident twin was often split into several thinner twins after crossing the barrier twin, and the shear action was not fully transmitted across the intersection.

### Acknowledgements

This work was supported by the National Nature Sciences Foundation of China (NNSFC). TGN's part was performed under the auspices of the U.S. Department of Energy by LLNL (contract No. W-7405-Eng-48).

## References

1. D. Shechtman, M. J. Blackburn and H. A. Lipsitt, *Metall. Trans.*, **5A** (1974), 1373.
2. S. Farenc, A. Coujou and A. Couret, *Phil. Mag. A*, **67** (1993), 127.
3. A. Couret, S. Farenc, D. Caillard and A. Coujou, in *Twinning in Advanced Materials*, edited by M. H. Yoo and M. Wuttig, Proceedings of a symposium held at Pittsburgh, Pennsylvania, October 18-20, 1993, The Minerals, Metals and Materials, 1994, p. 361.
4. Z. Jin and T. R. Bieler, in *Twinning in Advanced Materials*, edited by M. H. Yoo and M. Wuttig, Proceedings of a symposium held at Pittsburgh, Pennsylvania, October 18-20, 1993, The Minerals, Metals and Materials, 1994, p. 375.
5. Z. Jin and T. R. Bieler, *Phil. Mag. A*, **71** (1995), 925.
6. H. A. Lipsitt, D. Shechtman and R. E. Schafrik, *Metall. Trans.*, **6A** (1975), 1991.
7. S. Sriram, G. B. Viswanathan and V. K. Vasudevan, in *Twinning in Advanced Materials*, edited by M. H. Yoo and M. Wuttig, Proceedings of a symposium held at Pittsburgh, Pennsylvania, October 18-20, 1993, The Minerals, Metals and Materials, 1994, p. 383.
8. M. Yamaguchi and H. Inui, in *Structural Intermetallics*, edited by R. Darolia, J. J. Lewandawski, C. T. Liu, P. L. Martin, D. B. Miracle and M. V. Nathal, (The Minerals, Metals & Materials Society), 1993, p. 127.
9. S. Wardle, I. Phan and G. Hug, *Phil. Mag. A*, **67** (1993), 497.
10. Y. Q. Sun, P. M. Hazzledine and J. W. Christian, *Phil. Mag. A*, **68** (1993), 471.
11. Y. Q. Sun, P. M. Hazzledine and J. W. Christian, *Phil. Mag. A*, **68** (1993), 495.
12. Y. G. Zhang and M. C. Chaturvedi, *Phil. Mag. A*, **68** (1993), 915.
13. G. L. Chen, W. J. Zhang, Y. D. Wang, J. G. Wang and Z. Q. Sun, in *Structural Intermetallics*, edited by R. Darolia, J. J. Lewandawski, C. T. Liu, P. L. Martin, D. B. Miracle and M. V. Nathal, (The Minerals, Metals & Materials Society), 1993, p. 319.
14. G. L. Chen, J. G. Wang, L. C. Zhang and H. Q. Ye, *Acta Metall. Sinica*, **8** (1995), 273.
15. J. G. Wang, Ph.D. Thesis, University of Science and Technology Beijing, 1994.
16. J. G. Wang, unpublished work, 1997.
17. J. T. Fourie, F. Weiberg and F. W. C. Boswell, *Acta Metall.*, **8** (1960), 851.
18. P. B. Price, *Proc. R. Soc. A*, **60** (1961), 251.
19. G. J. Mahon and J. M. Howe, *Metall. Trans. A*, **21** (1990), 1655.
20. H. Iuni, A. Nakamura, M. H. Oh and M. Yamaguchi, *Ultramicroscopy*, **39** (1991), 268.
21. S. R. Singh and J. M. Howe, *Phil. Mag. A*, **66** (1992), 739.
22. M. J. Marcinkowski and K. S. Sree Harsha, *Trans. Metall. Soc. AIME*, **242** (1961), 1405.
23. J. P. Hirth and J. Lothe, *Theory of Dislocations*, Second Edition, 1982, New York, Wiley.
24. J. P. Hirth, *Appl. Mech. Rev.*, **45** (1992), S71.
25. J. P. Hirth, in *Twinning in Advanced Materials*, edited by M. H. Yoo and M. Wuttig, Proceedings of a symposium held at Pittsburgh, Pennsylvania, October 18-20, 1993, The Minerals, Metals and Materials, 1994, p. 107.
26. L. Zhao and K. Tangri, *Phil. Mag. A*, **65** (1992), 1065.
27. F. Appel, P. A. Beaven and R. Wagner, *Acta Metall. Mater.*, **41** (1993), 1721.
28. F. Appel and R. Wagner, in *Twinning in Advanced Materials*, edited by M. H. Yoo and M. Wuttig, Proceedings of a symposium held at Pittsburgh, Pennsylvania, October 18-20, 1993, The Minerals, Metals and Materials, 1994, p. 317.

## THE ROLE OF INTERFACIAL SUBSTRUCTURE IN THE CREEP DEFORMATION OF A FULLY-LAMELLAR TiAl ALLOY

L. M. Hsiung and T. G. Nieh

Lawrence Livermore National Laboratory, P.O. Box 808, L-370  
Livermore, CA 94551-9900

### Abstract

The substructure of a fully-lamellar (FL) TiAl alloy creep deformed at 760°C has been examined using transmission electron microscopy (TEM). The deformation of the FL-TiAl alloy at the primary creep stage is mainly accommodated by the movement of lattice dislocations in the  $(111)_\gamma$  easy-glide planes and interfacial dislocations in the  $\gamma/\gamma$  and  $\gamma/\alpha_2$  interfaces. When the alloy is deformed into the secondary creep stage, the density of interfacial dislocations continues to increase and deformation twins nucleate and grow from the lamellar interfaces. It is suggested that deformation twinning in lamellar TiAl can be viewed as a stress-relief process due to the pile-up of interfacial dislocations gliding along the lamellar interfaces during deformation. The deformation twins in  $\gamma$  lamellae are accordingly formed as a result of a interfacial dislocation reaction based upon a stair-rod cross-slip mechanism. The FL-TiAl alloys become more resistant to creep deformation after prestraining is due mainly to the sessile stair-rod dislocations formed at the intersection between the deformation twin and  $\gamma$  or  $\alpha_2$  lamella. These stair-rod dislocations act as effective barriers for the movement of interfacial dislocations during deformation.

### Introduction

For potential high-temperature engineering applications, TiAl components are limited to undergo less than 0.5% total creep elongation. However, it has been reported that the existing FL-TiAl alloys can deform to such a strain even at a low stress (< 150 MPa) within a short period of time during primary creep regardless of their low steady-state creep rate (<  $10^{-8}$ ) at such a stress[1]. Thus, the reduction of primary creep of FL-TiAl alloys has become a critical issue before their high temperature applications can be realized. It has recently been reported that the primary creep of fully-lamellar (FL) TiAl alloys can be significantly reduced by a prestraining technique[1,2]. That is, when an FL-TiAl specimen is first crept to a few percent of strain at high stresses (> 240 MPa), the specimen become more resistant to a subsequent creep deformation at lower stresses (< 240 MPa) even after a prolonged loading. Although the physical mechanism remains to be clarified, it can be postulated from the fact that creep is governed by a continually changing int-

-eraction between strain hardening and recovery processes [3,4] which strongly affect the creep strain rate at a given temperature and stress.

A preliminary study reported previously has suggested that the mobility of interfacial dislocations played a dominant role in the creep deformation of a powder metallurgy (P/M) FL-TiAl alloy[5]. Since the movement of lattice dislocations within the  $\gamma$  lamellae is largely restricted by a refined lamellar spacing within the P/M FL-TiAl alloy, the deformation strain is considered to be mainly resulted from the motion of interfacial dislocations. The creep resistance of the alloy significantly increases when the movement of interfacial dislocations in the twin-related ( $\gamma/\gamma$ ) or interphase ( $\gamma/\alpha_2$ ) interfaces is effectively impeded by deformation twins. To clarify the role of interfaces in the deformation twinning of FL-TiAl, more analyses have been performed on the deformation substructure as well as the interfacial substructure developed within the creep deformed FL-TiAl alloy. A possible mechanism for deformation twinning in lamellar TiAl is proposed in order to rationalize the prestraining effect.

### Experimental Procedure

#### Material and creep test

A fully-lamellar TiAl alloy [a nominal composition of Ti-47Al-2Cr-2Nb (at.%)] were fabricated at Oak Ridge National Laboratory by a powder metallurgy (P/M) process involving a hot-extrusion of gas-atomized titanium aluminide powder produced by Pratt & Whitney, West Palm Beach, FL. After extrusion, the alloys were annealed at 900°C in a vacuum of  $10^{-4}$  Pa for 2 h. Creep tests were conducted at 760°C in a dead-load creep machine with a lever arm ratio of 16:1. Detailed information regarding procedures of specimen preparation, creep experiment and part of the experimental data was reported elsewhere [1,2]. For current study, the deformation substructures of two tested specimens [one crept into the primary creep stage at a maximum stress of 138 MPa (creep strain: 0.5%) and one crept into the secondary creep stage at a maximum stress of 518 MPa (creep strain: 4.5%)] were investigated.

Structural Intermetallics 1997  
Edited by M.V. Nathal, R. Darolia, C.T. Liu, P.L. Martin,  
D.B. Miracle, R. Wagner, and M. Yamaguchi  
The Minerals, Metals & Materials Society, 1997



### Substructure characterization

TEM foils were first cut from the gauge section of tested specimens so that the edge of gauge section (which is parallel to the stress axis) was retained on the foils. The foils were finally prepared by twin-jet electropolishing in a solution of 60% methanol, 35% butyl alcohol and 5% perchloric acid at 15 V and -30°C. The microstructures of both as-fabricated and crept alloys were examined using a JEOL-200CX transmission electron microscope equipped with a double-tilt goniometer stage. It is noted here that TEM examinations of crept specimens were carried out with the thin foils tentatively oriented so that the retained (gauge section) edge was parallel to a tilting axis. During TEM observations, the angle between the longitudinal (edge-on) lamellae and the stress axis was accordingly determined with an error within 5°. Images of dislocations were recorded using a weak-beam dark field (WBDF) imaging technique under  $g(3g)$  two-beam diffraction conditions.

## Results and Discussion

### Substructure in an as-fabricated alloy

There are generally three types of thermally-grown lamellar interfaces in FL-TiAl alloys, i.e. i)  $\gamma/\alpha_2$  interphase interface with the orientation  $(0001)_{\alpha_2} // (111)_{\gamma}$  and  $\langle 11\bar{2}0 \rangle_{\alpha_2} // \langle 1\bar{1}0 \rangle_{\gamma}$ , ii)  $\gamma/\gamma_T$  true-twin ( $180^\circ$  rotational) interface, and iii)  $\gamma/\gamma$  pseudo-twin ( $60^\circ$  or  $120^\circ$  rotational) interface. The types ii) and iii) interfaces are also referred as twin-related interfaces hereafter. A typical edge-on lamellar substructure consisting of  $\gamma$ ,  $\gamma_T$ , and  $\alpha_2$  lamellae within an as-fabricated alloy sample is shown in Fig. 1(a). Several lattice dislocations (LD hereafter) can be observed in the  $\gamma$  lamellae, and the LD lines are mostly terminated their two ends at either  $\gamma/\alpha_2$  interphase or  $\gamma/\gamma$  twin-related interfaces. This is more clearly shown in Fig. 1(b). These LD are termed hereafter as threading dislocations. In addition to the LD, a considerable number of the tips of interfacial dislocation lines (which terminate their ends with the free surface of the sample) can be found along the  $\gamma/\gamma$  and  $\gamma/\alpha_2$  interfaces. As can be seen more readily in a micrograph where the lamellar interfaces are inclined (Fig. 2), the density of interfacial dislocations (ID hereafter) is much greater than that of LD. It is noted here that the intrinsic ID are mostly Shockley partials of either  $1/6\langle 1\bar{1}2 \rangle$  or  $1/3\langle 1\bar{1}2 \rangle$  type. Since the Burgers vectors of ID are parallel to the  $(111)_{\gamma}$  plane, they are considered to be mobile especially at elevated temperatures. The movement of ID could be impeded by barriers such as impinged LD, interface ledges and grain (or twin) boundaries. In general, dislocation density in the  $\gamma/\alpha_2$  interface is much greater than that in the  $\gamma/\gamma$  twin-related interface. This is because of a greater lattice and thermal misfit between the  $\gamma$  and  $\alpha_2$  phases. It is also worthy noting that a recent *in-situ* TEM straining experiment published elsewhere [6] has indicated that the interfacial dislocations in the  $\gamma/\gamma$  twin-related interface are mobile even at room temperature. In addition, the migration of twin interface (i.e. thickening of the  $\gamma$  lamellae) was observed to be associated with the movement of interface dislocations.

### Substructure in a creep deformed alloy

Generally, the creep curve of a FL-TiAl exhibits three stages. For an illustration purpose, a schematic representation of a normal creep strain/time curve at temperatures above  $0.5T_m$  is shown in Fig. 3. After the initial instantaneous strain ( $\epsilon_0$ ), alloy

undergoes a period of transient response where the strain rate decreases with time to a minimum steady-state value ( $\dot{\epsilon}_s$ ) that persists for a period of time from  $t_1$  to  $t_2$ . The primary creep strain ( $\epsilon_p$ ) is noted to depend upon the applied stress. Normally, at a fixed temperature, the higher the applied stresses, the greater is  $\epsilon_p$ . Final failure with a rupture life ( $t_f$ ) occurs soon after the creep rate increases during the third (or tertiary) creep stage.

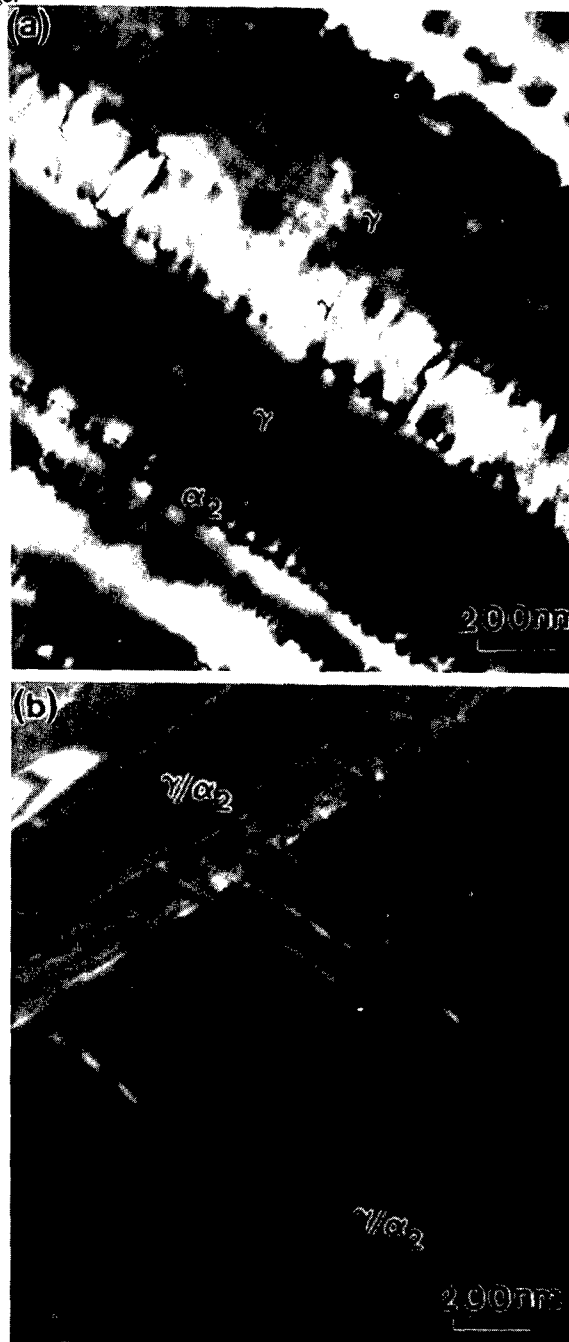


Fig. 1 (a) A bright-field TEM image showing a typical edge-on lamellar substructure consisting of  $\gamma$ ,  $\gamma_T$  and  $\alpha_2$  lamellae within an as-fabricated alloy sample,  $Z$  (zone axis) =  $[0\bar{1}1]_{\gamma}$ ; (b) a dark-field TEM image showing some threading lattice dislocations within a lamella ( $\gamma/\alpha_2$  denotes the interface between  $\gamma$  and  $\alpha_2$  phases).



Fig. 2 A WBDF image showing a typical interfacial dislocation substructure of an as fabricated alloy. The appearance of fringe contrast is due to inclined interfaces.

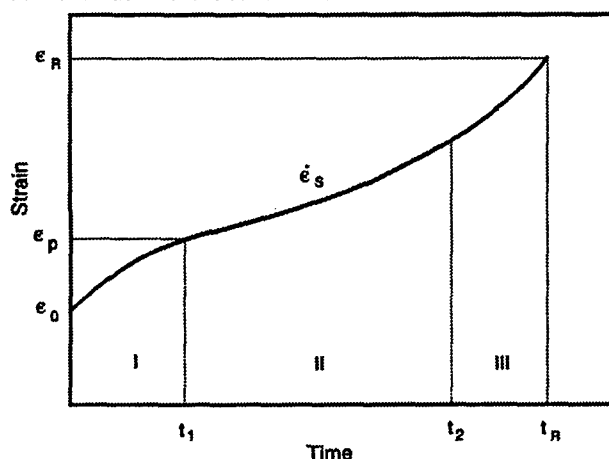


Fig. 3 A typical strain-time creep curve for FL-TiAl showing three stages.

#### Substructure developed at the primary creep stage

For specimen tested into the primary creep stage, the deformation substructures of two lamellar orientations,  $\sim 0^\circ$  and  $25^\circ$  with respect to the stress axis, were examined. It is designated hereafter the nearly  $0^\circ$ -oriented one as a hard grain, and the nearly  $25^\circ$ -oriented one as a soft grain based upon the work by Yamaguchi *et al.* on the polysynthetically twinned (PCT) crystals: the yield strength of the  $0^\circ$ -oriented PCT crystals is twice as high as that of the  $25^\circ$ -oriented ones [7,8]. A typical substructure developed within a hard lamellar grain is shown in Fig. 4, and it shows no significant difference compared to the undeformed substructure shown in Fig. 2. This indicates that hard grains accommodate insignificant deformation at primary creep stage. Since the resolved shear stress on the  $(111)_\gamma$  slip plane and the interfaces is negligibly small for the nearly  $0^\circ$ -oriented lamellar grains, deformation will have to be accommodated by multiplying dislocations (mostly threading dislocations) located in the slip planes intercepting the lamellar

interfaces. The critical shear stress ( $\tau_b \sim \mu b/l$ , where  $l$  is the distance between pinning points) required to bow the threading dislocations is considerably high. For example, for an approximation, taking  $\mu \sim 59$  GPa (at  $760^\circ\text{C}$ ),  $b \sim 0.56$  nm, and  $l \sim 150$  nm (average lamellar spacing),  $\tau_b \sim 220$  MPa. This yields approximately a critical stress ( $\sigma \sim 2\tau_b$ ) of 440 MPa for bowing the threading dislocations. This value is greater than the applied stress of 138 MPa.

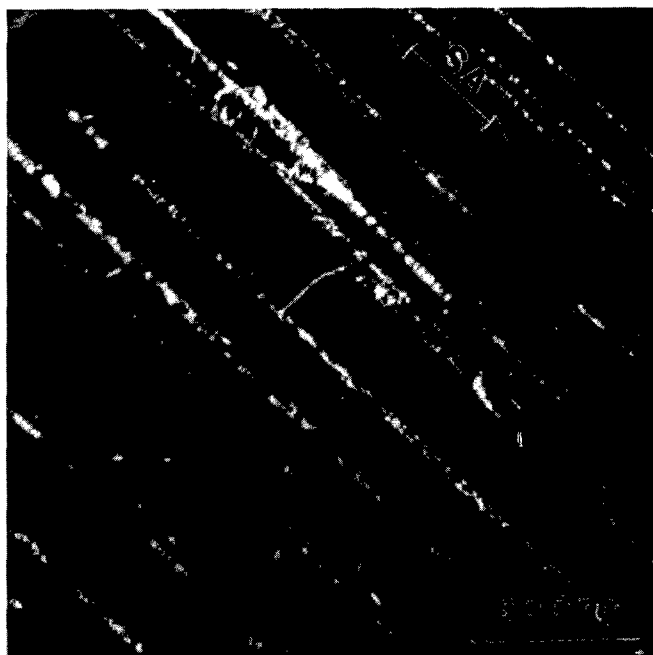


Fig. 4 A typical substructure of a nearly  $0^\circ$ -oriented lamellar grain in sample I (SA denotes the stress axis).

Typical microstructures observed within a soft lamellar grain are shown in Figs. 5(a) and (b). For this orientation, dislocations in the interfaces as well as the  $(111)_\gamma$  slip plane are readily to move. Figure 5(a) is a weak-beam image showing the multiplication of lattice dislocations in the  $(111)_\gamma$  slip plane. A typical example of ID piled up by an LD impinged on a twin-related interface is shown in Fig. 5 (site A). It is interesting to note here that some IDs had overcome the obstacle and moved across the impinged LD. The wavy appearance of those dislocation lines (below LD 1) may suggest that they were severely dragged during their motion presumably by lattice imperfections such as solute atoms or vacancies. Since the ID piled up by single lattice dislocation line impinged on lamellar interfaces can be easily remobilized through a thermally-activated process, such a dislocation barrier is considered to be ineffective. On the other hand, a more effective dislocation barrier may be formed if a considerable number of impinged LD react with intrinsic ID to generate dislocation nodes. A typical example is shown in Fig. 6(a). Here many dislocation nodes are formed in a  $\gamma/\alpha_2$  interface as a result of the dislocation reaction between impinged LD of the  $(\bar{1}\bar{1}1)[\bar{1}01]$  type and intrinsic ID. Consequently, the ID become less mobile and start to pile up [Fig. 6(b)]. Notice that the impinged LD become invisible in Fig. 6(b) since the imaging condition here is  $g \cdot b = 0$ . It is, therefore, suggested that the deformation of the FL-TiAl alloy at the primary creep stage is mainly accommodated by soft

lamellar grains through the operations of mobile dislocations in the lamellar interfaces and  $(111)_\gamma$  slip planes. Their mobility is mainly retarded by grain boundaries and a limited number of dislocation barriers generated by a secondary slip within lamellae.

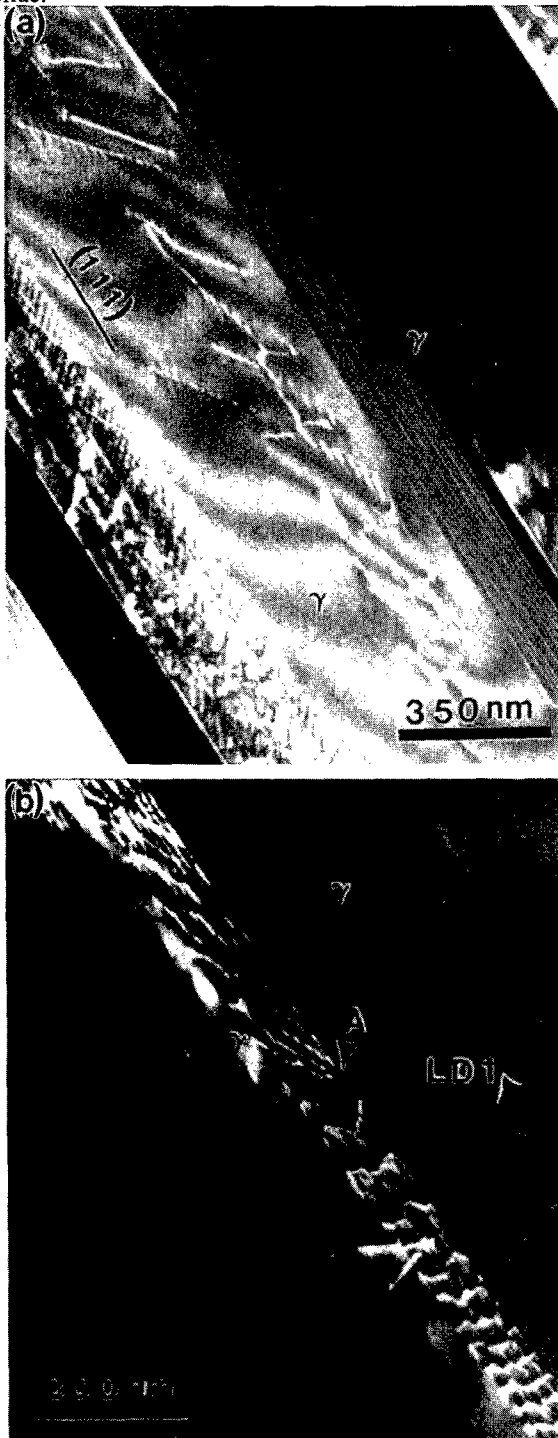


Fig. 5 Typical substructures of a nearly 25°-oriented lamellar grain in an alloy sample deformed into the primary creep stage ; (a) a WBDF image showing the multiplication of lattice dislocations in the  $(111)_\gamma$  plane; (b) a WBDF image showing the pile-up of interfacial dislocations (site A) in a twin-related interface.

#### Substructure developed at the secondary creep stage

When specimens were tested into the secondary creep stage, both soft and hard lamellar grains were deformed. A deformation substructure associated with deformation twins (DT hereafter) within  $\gamma$  lamellae was developed. A typical deformation substructure observed within a nearly 20°-oriented lamellar grain is shown in Fig. 7. Notice that there is no significant increase of the dislocation density compared with that in specimens deformed at the primary creep stage. The density of DT is noted to be higher in  $\gamma$  lamellae (of the same orientation variant) with a thinner dimension. This indicates that deformation in lamellar grains at the secondary creep stage is mainly accommodated by deformation twinning, and it is even greater in extent in thinner  $\gamma$  lamellae. This is due mainly to either an insufficient dislocation source or a difficulty of dislocation multiplication within thin  $\gamma$  lamellae. The mechanically twinned alloys are expected to be more resistant to creep deformation when they are subsequently tested at a lower stress since (i) the twins further impede the movement of lattice dislocations within the  $\gamma$  lamellae [Fig. 8(a)], and (ii) the boundary dislocations formed at the intersection between DT and the  $\gamma$  or  $\alpha_2$  lamellae provide additional and more effective barriers for the movement of interfacial dislocations [Fig. 8(b)]. This may offer an explanation for the prestraining effect reported previously[2].



Fig. 7 A WBDF image showing the formation of deformation twins (some are marked by arrows) within a nearly 20°-oriented lamellar grain.

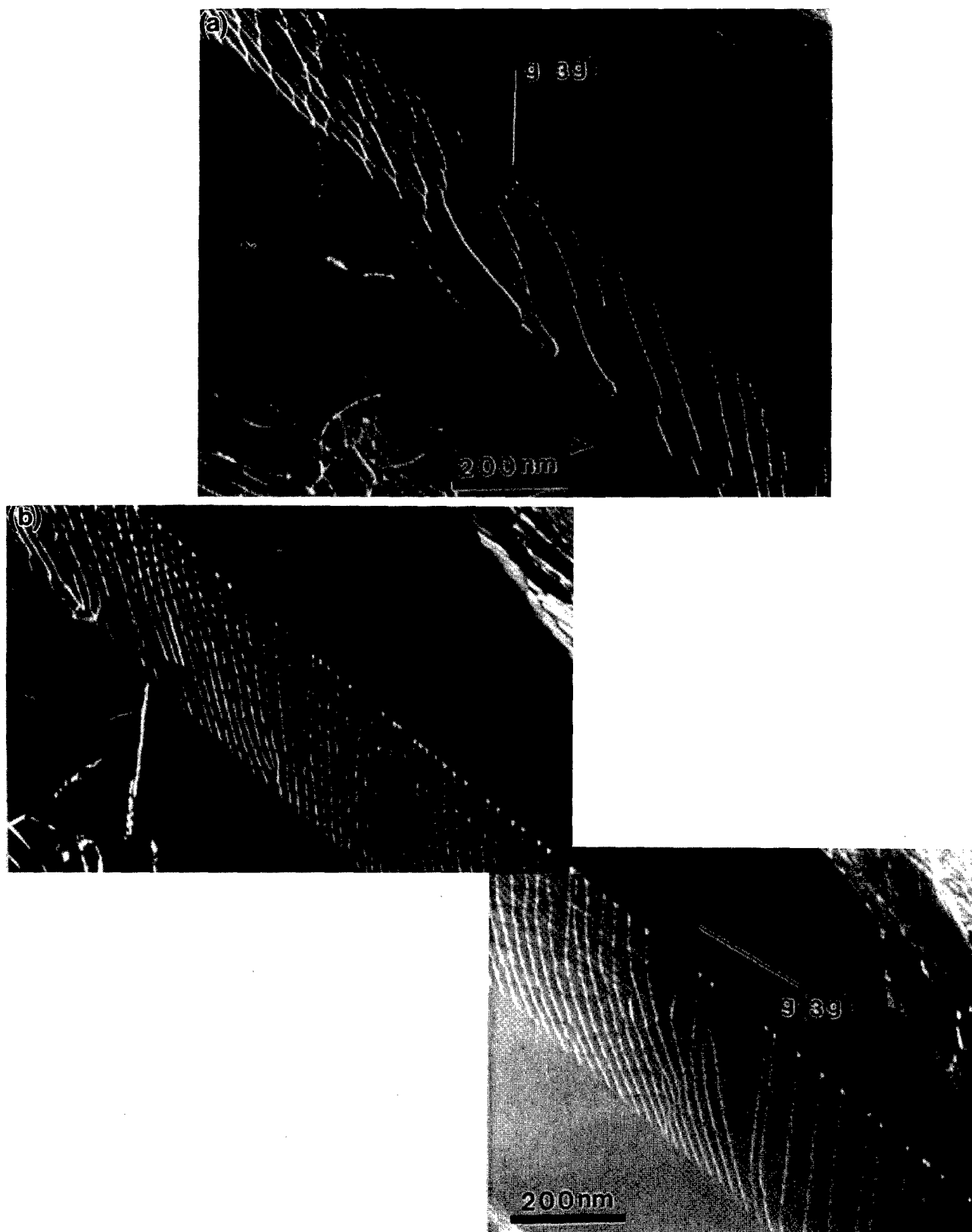


Fig. 6 WBDF images, a)  $g = 00\bar{2}$  and b)  $g = 020$ , showing that the mobility of interfacial dislocations is retarded as a result of the formation of dislocation nodes due to the reaction between the impinging lattice dislocations and (intrinsic) interfacial dislocations. Noted that the impinged LD become invisible in b).

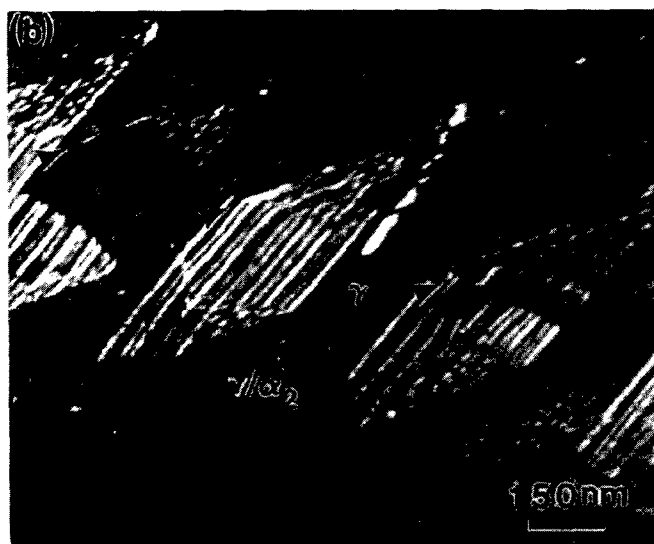


Fig. 8 (a) Deformation twins (marked by arrows) act as barriers to the movement of lattice dislocation within the  $\gamma$  lamellae, and (b) boundary dislocations (marked by arrows) formed at the intersections between deformation twins and  $\alpha_2$  lamellae provide additional barriers to the movement of interfacial dislocations.

#### A proposed mechanism for deformation twinning in lamellar TiAl

Based upon the above observations, it is proposed that deformation twinning in lamellar TiAl can be viewed as a stress-relief process due to a pile-up of interfacial dislocations gliding along the lamellar interfaces [parallel to the  $(111)_\gamma$  plane] during deformation. The effective stress ( $\tau_e$ ) at the tip of the pile-up of  $n$  dislocations is  $\tau_e \sim n\tau_i$ [9], where  $\tau_i$  is the resolved shear stress acting on the interface. To relieve the stress, DT in  $\gamma$  lamellae is formed by a dislocation reaction based upon a stair-rod cross-slip mechanism[10-12]. As for an example of the  $(\bar{1}11)$ -type DT

formed in an alloy deformed into the secondary creep stage (see Fig. 9(a)), the corresponding dislocation reaction (dissociation) is proposed to be  $1/6[\bar{1}\bar{2}1]_{(111)} \rightarrow 1/6[0\bar{1}\bar{1}]_{(100)} + 1/6[\bar{1}\bar{1}2]_{(\bar{1}11)}$ . The  $(\bar{1}11)$   $[\bar{1}\bar{1}2]$ -type DT is accordingly formed by a successive cross-slip of the twinning dislocations  $1/6[\bar{1}\bar{1}2]$  in the  $(\bar{1}11)$  plane and leaving the stair-rod dislocations  $1/6[0\bar{1}\bar{1}]$  in the  $(100)_\gamma$  plane. Twin (stacking) faults are accordingly formed in the interfaces between the  $\gamma$  lamellae and DT. A schematic representation of the growth of a DT from one  $\gamma/\alpha_2$  interface toward the other (illustrated in Fig. 9(a)) is shown in Fig. 9(b). Although it has been demonstrated previously in Fig. 8(b), there is a high density of boundary dislocations, presumably stair-rod dislocations, formed at the intersection between DT and an  $\alpha_2$  lamella, the density of the dislocations is too high to be resolvable using weak-beam imaging techniques. The existence of the stair-rod dislocations, however, is indirectly evidenced in Figs. 10(a) and (b). Here, a pair of approximately aligned DT is originally formed on the opposite side of an  $\alpha_2$  lamella. These two aligned DT eventually coalesce at the joints adhered to the  $\alpha_2$  lamella. This coalescence is considered to be resulted from the annihilation of stair-rod dislocations (with opposite Burgers vectors) through a thermally-activated process. A schematic representation of a pair of approximately aligned DT on the opposite side of an  $\alpha_2$  lamella, and the formation of stair-rod dislocations with opposite Burgers vectors is shown in Fig. 11.

While additional work is underway to elaborate the twinning mechanism, the significance of the proposed mechanism is to reveal that there are several barriers to be overcome in order to activate the twinning reaction. These barriers include (i) the repulsive force between the interfacial (Shockley) and stair-rod dislocations, (ii) the increase of line energy due to the dislocation dissociation, and (iii) the increase of interfacial energy due to the twin (stacking) faults associated with the gliding of twinning dislocations in the  $(\bar{1}11)$  plane. The resolved shear stresses ( $\tau_i$ ) on both the interfacial and cross-slip planes ( $\tau_e$ ) and a local stress concentration ( $\tau_e$ ) due to the pile-up of interfacial dislocations are considered to be important factors for the formation of deformation twins. Accordingly, the prestaining effect can be rationalized based upon the proposed mechanism. That is, the DT can only be formed above a critical stress level so that the barriers for the twinning reaction are readily overcome. The twinning reaction is subsequently ceased when the applied stress is lower than the critical stress level. Consequently, the sessile stair-rod dislocations formed between the DT and  $\gamma/\alpha_2$  interfaces within the prestrained alloy act as effective dislocation barriers for the movement of interfacial dislocations when the alloy deforms at a lower stress level.

#### Conclusions

The deformation substructure of a fully-lamellar TiAl alloy creep deformed at 760°C have been examined using transmission electron microscopy (TEM). Two different creep loading conditions were employed: one at a low stress level (138 MPa, total creep strain: 0.5%, deformed into the primary creep stage), and the other at a high stress level (518 MPa, total creep strain: 4.5%, deformed into the secondary creep stage). The deformation of the FL-TiAl alloy at the primary creep stage is mainly accommodated by soft lamellar grains through the operations of mobile dislocations in the lamellar interfaces and  $(111)_\gamma$  slip planes. Their mobility is mainly retarded by grain boundaries and a limit number of dislocation barriers generated by secondary slip systems within  $\gamma$  lamellae. When the alloys is

tested into the secondary creep stage, deformation twins are formed within both soft and hard lamellar grains. It is suggested that deformation twinning in lamellar TiAl can be viewed as a stress-relief process due to the pile-up of interfacial dislocations gliding along the lamellar interfaces during deformation. The deformation twins in lamellae are accordingly formed as a result of an interfacial dislocation reaction based upon a stair-rod cross-slip mechanism. The resolved shear stresses on both the interfacial and cross-slip planes and a local stress concentration due to the pile-up of interfacial dislocations are considered to be important factors for the formation of deformation twins. The FL-TiAl alloys become more resistant to creep deformation after prestraining is due mainly to sessile stair-rod dislocations formed at the intersection between the deformation twin and the  $\gamma$  or  $\alpha_2$  lamella. These sessile stair-rod dislocations act as effective barriers for the motion of interfacial dislocations during deformation.

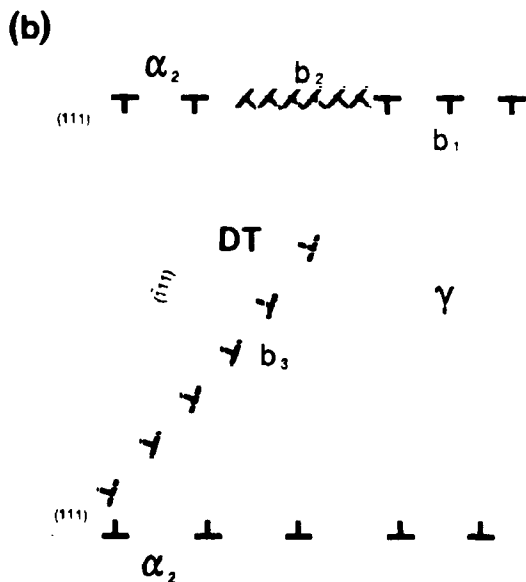
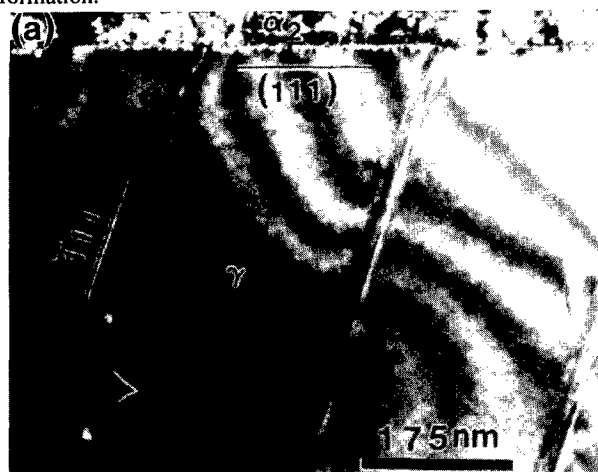


Fig. 9 A bright-field TEM image showing several  $(\bar{1}11) [1\bar{1}2]$ -type deformation twins formed within  $\gamma$  lamellae. Notice that the growth of a DT from one  $\gamma/\alpha_2$  interface toward another. The other is marked by an arrow, and is schematically illustrated in (b), where  $b_1$ ,  $b_2$ , and  $b_3$  denote the interfacial, strained, and twinning dislocations, respectively.

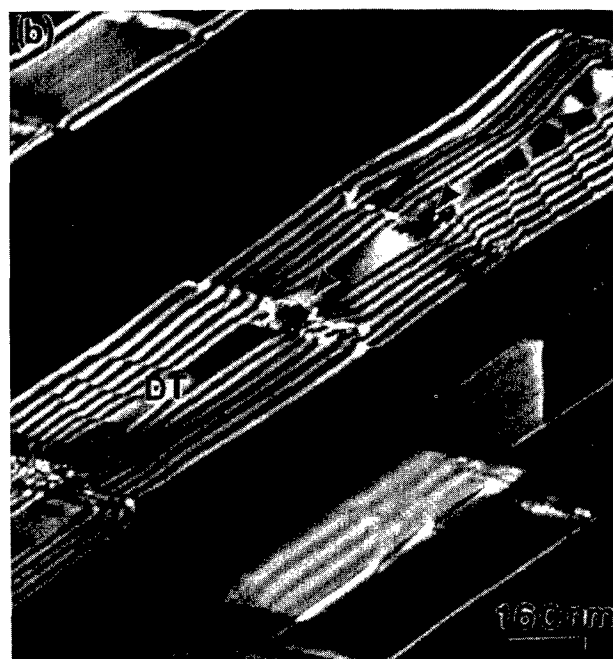


Fig. 10 WBDF images showing the faulting of  $\alpha_2$  lamellae [indicated by an arrow in (a)] resulted from the coalescence of two approximately aligned DT at the joints adhered to an  $\alpha_2$  lamella [indicated by an arrow in (b)]. Images generated from the same region using  $\gamma$  and  $\gamma_T$  reflections, respectively.

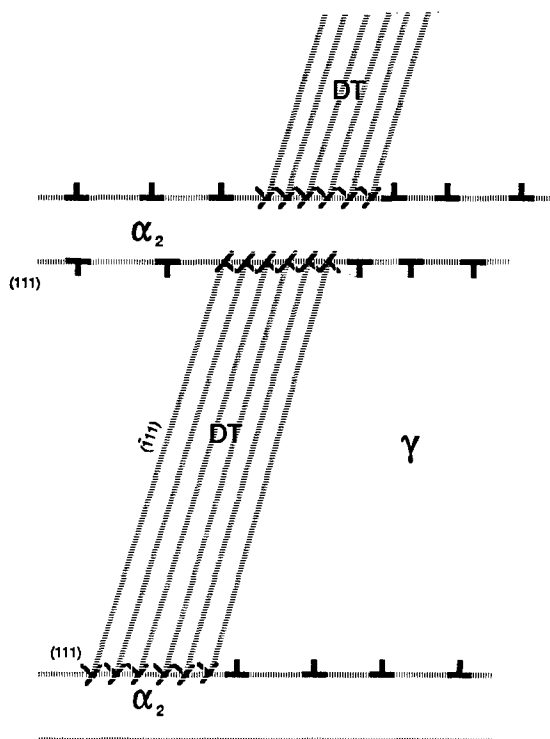


Fig. 11 A schematic representation of a pair of approximately aligned DT formed on the opposite side of an  $\alpha_2$  lamella and the existence of stair-rod dislocations (with opposite Burgers vectors) at the intersections between DT and an  $\alpha_2$  lamella.

#### Acknowledgments

This work was partly performed under the auspices of the U.S. Department of Energy through contract # W-7405-Eng-48 with Lawrence Livermore National Laboratory.

#### References

1. J. N. Wang, A. J. Schwartz, T. G. Nieh, C. T. Liu, V. K. Sikka and D. R. Clemens, in *Gamma Titanium Aluminides*, ed. Y-W. Kim *et al.*, TMS, Warrendale, PA, 949 (1995).
2. J. N. Wang, A. J. Schwartz, T. G. Nieh and D. R. Clemens, *Mater. Sci. & Engrg.*, **A206**, 63 (1996).
3. E. Orowan, *J. W. Scott. Iron Steel Inst.*, **64**, 45 (1946).
4. J. H. Gittus, *Phil. Mag.*, **21**, 495 (1970).
5. L. M. Hsiung and T. G. Nieh, *Scripta Mater.*, **36**, 323 (1997).
6. L. M. Hsiung, A. J. Schwartz and T. G. Nieh, *Scripta Mater.* (1997). – in press
7. M. Yamaguchi and Y. Umakoshi, *Progress in Materials Science*, **34**, 1 (1990).
8. M. Yamaguchi and H. Inui, in *Structural Intermetallics*, ed. R. Darolia *et al.*, TMS, Warrendale, PA, 127 (1993).
9. E. O. Hall, *Yield Point Phenomena in Metals and Alloys*, Plenum Press, New York, 1970.
10. H. Fujita and T. Mori, *Scripta Metall.*, **9**, 631 (1975).
11. T. Mori and H. Fujita, *Acta Metall.*, **28**, 771 (1980)
12. T. Mori, H. Fujita and S. Takemori, *Phil. Mag. A*, **44**, 1277 (1981).

## BEST PAPER AWARD (Co-Winner)

### THE EFFECT OF HEAT TREATMENTS ON MICROSTRUCTURES AND PRIMARY CREEP DEFORMATION OF FOUR INVESTMENT CAST TITANIUM ALUMINIDE ALLOYS

D.Y. Seo, T.R. Bieler, and D.E. Larsen\*

Department of Materials Science and Mechanics  
Michigan State University, East Lansing, MI 48824-1226, USA

\* Howmet Corporation, Whitehall, MI, 49461, USA

#### Abstract

Several heat treatments were developed and applied to investment cast Ti-45Al-2Nb-2Mn(at%)+0.8v%TiB<sub>2</sub> XD<sup>TM</sup>, Ti-47Al-2Nb-2Mn(at%) + 0.8v%TiB<sub>2</sub> XD<sup>TM</sup>, Ti-47Al-2Nb-2Cr(at%), and Ti-47Al-2Nb-1Mn-0.5W-0.5Mo-0.2Si alloys in an effort to enhance creep properties and decrease heat treatment time compared to current practices. Results show that the creep resistance of WMoSi can be improved by 10 times with heat treatment, and 47-2-2 can be improved by 3 times, and the XD alloys can be improved slightly, or not at all with lower Al level. The variation, or lack of variation, in creep resistance with heat treatment can be explained by differences observed in the microstructures and textures produced by the various heat treatments. Quantitative microscopic comparisons were made between microstructures in undeformed and deformed regions in creep specimens deformed to strains between 0.1 and 1.5% strain, using optical, SEM and TEM techniques. The lamellar spacing in lamellar grains systematically decreased by 15-35%, with increasing stress, during the first 0.1-2% strain. Precipitates containing W, Mo, and/or Si nucleated and grew at a faster rate in the deformed part of the specimen, as compared to the grip section, with approximately twice the volume fraction in the deformed region, and the precipitates were generally smaller and more homogeneously dispersed. These observations indicate that strain assisted nucleation of precipitates accounts for much of the excellent creep resistance of the WMoSi alloy.

#### Introduction

Cast near gamma titanium aluminides are gaining acceptance as potential replacements for superalloy and steel components in aerospace, automotive and industrial applications since it has high specific strength at high temperatures [1-3]. Components cast from these alloys can operate at temperatures up to 815 °C(1500 °F) at half the weight of the components they replace. Most applications of cast gamma components require good primary creep resistance to meet component life requirements.

The microstructure is an important factor that is sensitive to composition, heat treatment, and strongly affects creep properties. Gamma titanium aluminide can be heat treated to obtain four types of microstructures [4]. The best creep resistance has been observed in fully lamellar microstructures [5]. However, the duplex microstructure is preferred for many applications since it provides desirable room temperature ductility [2].

The addition of Cr, Nb, V, Mn, W, Mo and Si, in two phase Ti-Al alloys is also an important factor in order to control the material properties. Cr can improve the ductility of duplex alloys with additions of 1-3% at%. [6,7]. The additions of 1-3at% V and Mn are the most common elements for improving plasticity in two phase TiAl alloys [8,9,10,11] but V generally reduces the oxidation resistance[12]. Nb greatly enhances the oxidation resistance[13,14,15] and slightly improves the creep resistance [14]. The addition of 0.5-1 at.% Si enhances creep strength, the oxidation resistance, and room-temperature fracture toughness of 48at% Al two phase alloys [16,17,18,19]. Si also increases fluidity, and reduces the susceptibility to hot cracking [20]. Mo provides a good balance of strength and ductility in TiAl having very fine equiaxed gamma grains with the  $\alpha_2$  and  $\beta$  phase [21,22]. Addition of W greatly improves oxidation resistance, and enhances creep resistance [23].

Most of these studies have focused on either room temperature properties, minimum creep rate conditions or stress-rupture properties. However, primary creep resistance is important for practical applications. Gamma based TiAl exhibits primary creep strains that are typical for metals, where the minimum is reached after about 1% strain. In an effort to decrease the creep rate during primary creep deformation, additions of W, Mo, and Si have increased the time to reach 0.5% strain due to a dynamic precipitation process [13,24]. In several related studies, observations of lamellar refinement indicate that primary creep deformation includes a significant amount of mechanical twinning parallel to lamellar interfaces that occurs as an easy mode of deformation that hardens the microstructure at low strains [25,26,27,28]. In this paper the primary creep resistance (time to 0.5% creep strain) is compared between four alloys having different kinds of strengthening strategies, including ceramic particles, solid solution elements and precipitates, which affect the ways the microstructure can be manipulated by heat treatment. After primary creep to 0.5% we quantify changes in the different lamellar and equiaxed microstructures,  $\gamma$  interface and  $\alpha_2$  lath spacing, mechanical twinning, interstitial composition, precipitate size, composition, shapes, and dislocation interactions with precipitates.

#### Materials and Experimental Procedure

The investment cast gamma TiAl alloys used are described in Table I. Some specimens with varying interstitial content were investigated and they are hereafter identified as med-O or high-O alloys. All materials were hot isostatically pressed (HIPed) at 1260°C for 4 hours at 172 MPa (2300°F, 25 ksi) in order to eliminate casting porosity. The heat treatments used were in the  $\alpha_2+\gamma$  phase field at 900 or 1010°C(1650 or 1850°F) for 10, 20 or 50 hours, and cooled in a static argon



atmosphere (SAC). A two step heat treatment was also used consisting of 1177°C (in the  $\alpha+\gamma$  phase field) for 5 hours and then in the  $\alpha_2+\gamma$  field for 10 hours at 1010°C (2150 and 1850°F), respectively, and cooled in static argon. These heat treatments all provided duplex microstructures. These specimens were then subjected to creep tests at 760°C, 138 MPa (1400°F, 20 ksi) and 649°C, 276 MPa (1200 °F, 40ksi). The creep specimens were cooled under load once 0.5 % strain was reached. Some additional 5x5x3 mm brick shaped specimens of Ti-47Al-2Nb-1Mn-0.5W-0.5Mo-0.2Si alloy were cut using EDM machining from a piece of an as-HIPed casting gate for compression-shear creep tests. They were deformed on a 45° inclined stage in a compression cage fixture developed for evaluating creep in a PST crystal [25].

Table I. Nominal chemical composition of investment cast TiAl alloys (at%)

Abbreviation	Ti	Al	Si	Nb	Mn	Cr	Mo	W	B	O	N	H	Fe
47-2-2	Balance	47		2		2							
47Al XD (low O)	48.54	46.19	0.04	1.87	1.86	0.02			1.15	0.203	0.026	0.012	0.07
med-O	48.55	45.43	0.04	2.02	1.95	0.02			1.14	0.227	0.032	0.012	0.10
high-O	47.66	47.16	0.04	1.81	1.88	0.02			1.07	0.289	0.037	0.012	0.03
45Al XD	Balance	45		2	2				0.8*				
WMoSi	Balance	47	0.2	2	1		0.5	0.5					

\* Vol. Fraction of TiB<sub>2</sub>

Compression-shear creep tests were conducted at 650 and 750°C with shear and compression stress components of 61, 91.5 and 122 MPa in air using an ATS series 2710 creep testing machine. Tests were stopped once 0.2 - 1.5% creep strains were reached. The creep data were recorded by a PC based data acquisition system developed for creep tests. The specimen shape change was measured using external extensometry connected to the compression cage and SLVC transducers located outside of the furnace. Specimen load, temperature, displacement, and time data were reduced, assuming simple shear deformation with the aid of spreadsheet and plotting programs.

For optical and SEM analysis, deformed samples were obtained from the gage section of the creep deformed specimen. Some undeformed samples were also cut from the grip section of tensile test specimens. A modified Kroll's reagent [29] was used to reveal the microstructure in this material. For analysis of different phases, polished and unetched specimens were used in a JSM-6400V scanning electron microscope (SEM) at 25kV, using the Backscattered electron (BSE) technique. For microanalysis by transmission electron microscopy (TEM) the specimens were prepared as follows: 0.7 mm thick slices were taken from the specimen using a diamond saw. 3 mm discs were produced using an EDM cutting machine such that the foil normal was parallel to the tensile axis. After mechanical polishing, thin foils for electron microscopy were prepared by the twin jet polishing method using a solution consisting of methyl alcohol and 10% sulfuric acid at 20 volts at -25 °C. These foils were examined in a Hitachi H-800 transmission electron microscope operated at 200kV. Texture measurements were made on selected specimens and analysis was made using popLA software [30].

## Results and Analysis

### A. Primary creep behavior

#### Tensile creep

The time to 0.5% creep of the four alloys varies with composition and heat treatment as shown in Figure 1. The average value of three samples is plotted with the line, and high and low values are also plotted. From this plot, it is apparent that the 45 Al composition is insensitive to heat treatment. The 47 Al (low O) samples exhibit different responses to heat treatment. With TiB<sub>2</sub>, the heat treatment for 10 hours at 900°C is damaging to primary creep resistance, but otherwise there is no significant improvement with increasing time at temperature in heat treatment, other than a beneficially smaller range of values with the two step heat treatment. But for the 47Al with high O alloys, creep resistance is significantly improved with increasing amounts of O. The alloys with medium and high O exhibit creep times to 0.5% that are more than twice as long. The scatter is similar in magnitude for all alloys except the low O alloy after the two-step heat treatment. For the 47-2-2 alloy, the creep resistance

is substantially improved with increasing amounts of time and temperature in heat treatment, but the variability in the samples is not significantly improved with heat treatment. For the WMoSi alloy, the primary creep resistance is the best (295 hours) as show in Figure 1. In WMoSi alloy, tensile creep deformation at low temperature and high stress (649°C, 276 MPa), the material deformed quickly up to 0.2% strain, where the strain rate slowed considerably. At the higher temperature and lower stress, (750°C, 138 MPa) the trend was similar, but the change was less dramatic. This effect is clearly shown in Figure 2. The strain rate vs strain curve was obtained by differentiating a least squares curve fit of the creep data using the equation ( $\epsilon = a(1-\exp(bt))+c(1-\exp(dt))$ ) [31]. All alloys exhibit a rapid decrease in strain-rate below about 0.2%. The creep rates of the higher O alloys were lower and decreasing

more rapidly at 0.5% strain. At low strains, the creep curves for both higher O alloys cross at a strain of 0.1%, indicating that the high O alloy had a faster initial creep rate. The WMoSi alloy also shows a cross over in the curve creep around at 0.2% strain due to different stress and temperature conditions shown in Figure 2 b. The most dramatic reductions of strain rate occurred in the alloys having better primary creep resistance.

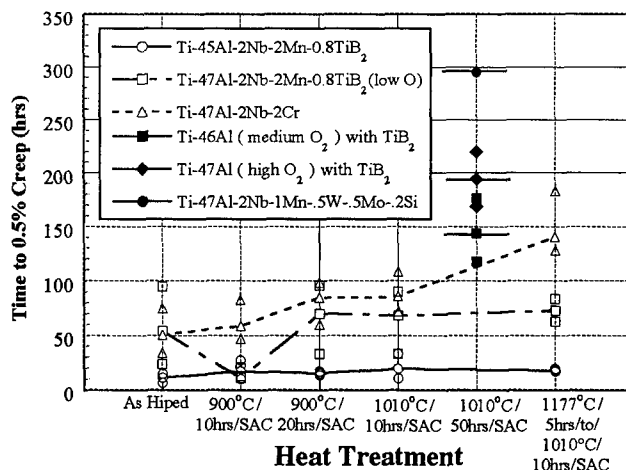


Figure 1: Time to 0.5% creep strain with respect to heat treatment. The lines go through the average of 3 values, high and low values are indicated by additional symbols (tested at 760°C/138 MPa)

#### Compression-shear creep

For the larger strain compression-shear creep conditions in Figure 3, the initial creep rates are similar, but the 750°C specimen reached 0.8% about 20 times faster than the 650°C specimen at the same stress. From Figure 2 b, the initial creep rate and shape of the creep deformation curve for stresses larger than 86 MPa is similar, indicating a rapid decrease in the creep rate. At 86 MPa, the strain rate decreases more slowly to an initial saturation strain that is reached at a larger strain. At the lower temperature, the saturation of the initial creep rate is reached at a smaller strain, and the decrease in strain rate is larger.

The initial saturation strains depend on the temperature and stress. A higher stress at the same temperature or a higher temperature with same stress make the saturation strain shift toward smaller strain. The curvature of the creep curves is similar at the same temperature or stress level. A higher stress

results in a greater drop in the strain rate at the saturation strain. The effect of heat treatment on the creep rate for the WMoSi alloy reduces the creep rate by more than a factor of 10.

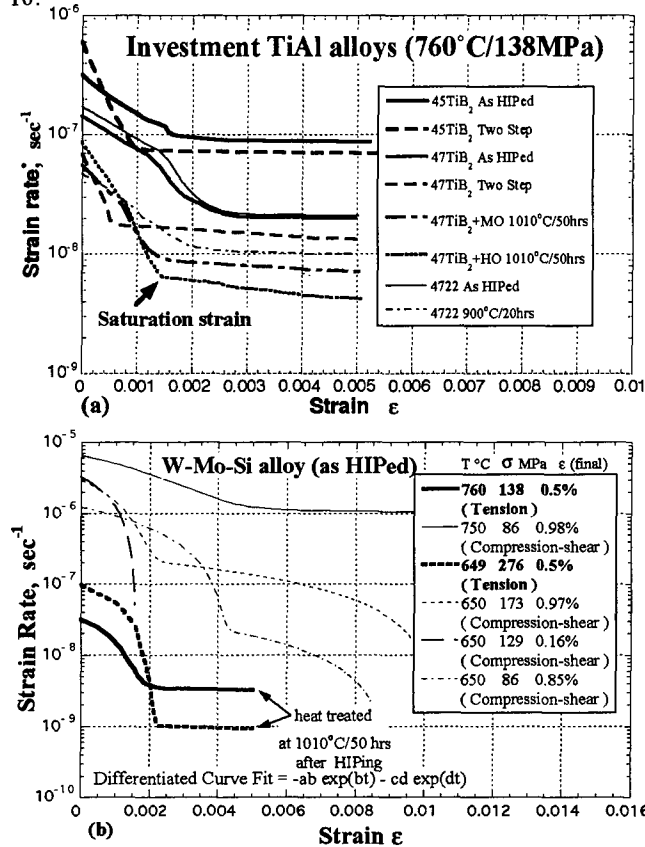


Figure 2: Differentiated curve fits of creep data exhibit a decreasing strain rate to a saturation strain between 0.1 and 0.5% strain, whereafter the decrease in strain rate is less rapid.

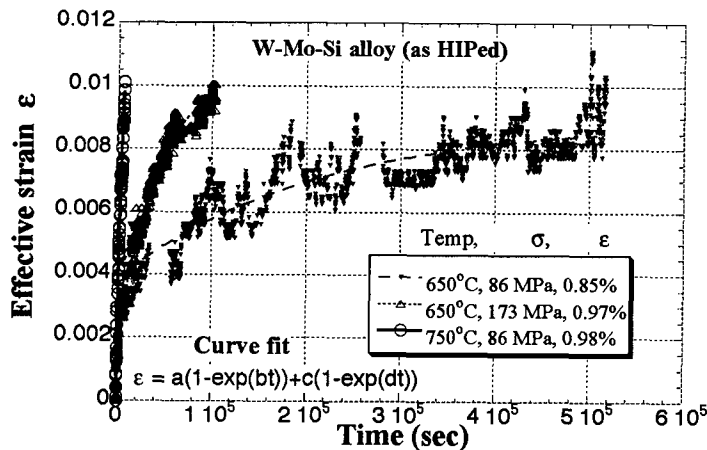


Figure 3: The strain rate following the saturation strain is very sensitive to stress and temperature.

## B. Microstructures

### Ti-45Al-2Nb-2Mn-0.8TiB<sub>2</sub>

From optical micrographs, a very fine duplex microstructure was observed in all specimens as shown in Figure 4 a, regardless of heat treatment. There is a homogeneous distribution of 10-50  $\mu\text{m}$  equiaxed and 20-100  $\mu\text{m}$  lamellar grains. The volume fraction of lamellar grains

generally decreases with increasing amounts of heat treatment (Figure 5).

From analysis of backscattered images of undeformed and deformed specimens obtained in the SEM, there are no distinguishable changes in the microstructure resulting from creep deformation. Optical micrographs of the crept specimen show that many TiB<sub>2</sub> particles are distributed randomly. There are several types of particles such as equiaxed, needle, and irregular shaped precipitates with a spacing of 30-50  $\mu\text{m}$ , and they are located inside gammagrains, in grain boundaries

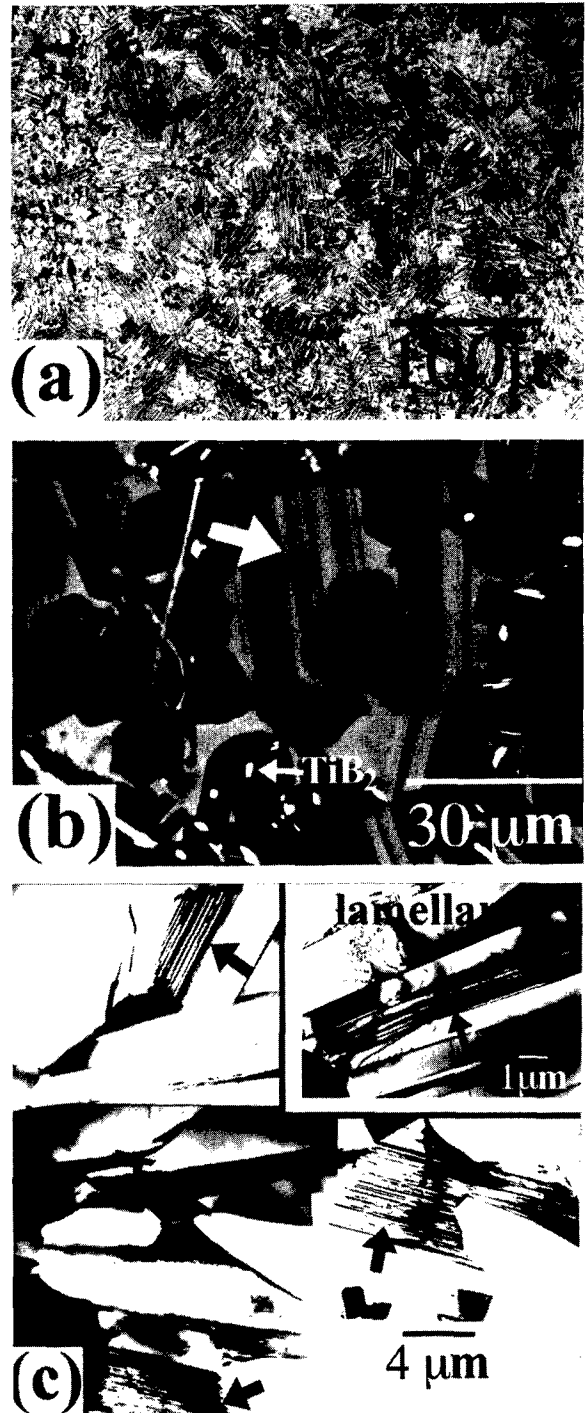


Figure 4: Microstructures of As HIPed 45Al XD (a) optical micrographs before creep test (b) BSE images and (c) BF image after creep test.

between gamma (dark phase) and  $\alpha_2$  (bright phase) grains and in lamellar grains, but not inside  $\alpha_2$  grains, as shown in Figure 4 b. As annealing time increased no distinct change in the particles was observed, but in the case of the two-step heat treatment there appeared to be fewer particles. Single phase  $\gamma$  and  $\alpha_2$  grains represent about 40% of the volume fraction. The  $\alpha_2$  grains have angular shapes, but the  $\gamma$  grains tend to be more round and equiaxed. This indicates that equiaxed  $\gamma$  grains nucleate in several places in a given parent  $\alpha_2$  grain, and that some of the parent  $\alpha_2$  region transform into lamellar grains, but others do not. Very fine lamellar features are observed in some  $\alpha_2$  grains in both deformed and undeformed specimens (see arrows in Figure 4 b). These regions also exhibit contrast indicating formation of extremely fine lamellar microstructures consisting of both  $\alpha_2$  and  $\gamma$  lathes. Since they are much finer than the obvious lamellar grains, they are not likely to have resulted from thermally induced transformation, so they are more likely to have resulted from local stress concentrations [26,28,32]. These features were observed in all heat treatments. Since the  $\alpha_2$  grains have an angular shape, stress concentrations are more likely to be focused at triple points in  $\alpha_2$  grains, where fine mechanical twinning is most often observed [26,28,32]. The fine twinned regions are also observed in TEM images. They occur in the angular shaped  $\alpha_2$  grains, as illustrated in Figure 4.c. Regions of extremely fine mechanical twinning are also observed in some lathes of the lamellar grains (Figure 4. c).

Table II Grain sizes of four investment TiAl alloys (unit:  $\mu\text{m}$ )

Alloys	lamellar	equiaxed
Ti-45Al-2Nb-2Mn-0.8TiB <sub>2</sub>	20~50	10~50
Ti-47Al-2Nb-2Mn-0.8TiB <sub>2</sub> (low O)	20~200	10~50
Ti-46Al-2Nb-2Mn-0.8TiB <sub>2</sub> (medium O)	20~200	10~50
Ti-47Al-2Nb-2Mn-0.8TiB <sub>2</sub> (high O)	100~200	25~100
Ti-47Al-2Nb-2Cr	50~500	20~200
Ti-47Al-2Nb-1Mn-0.5W-0.5Mo-0.2Si	100~500	5~200

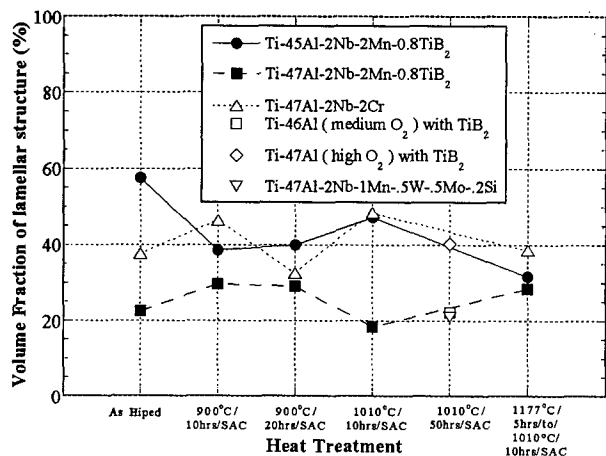


Figure 5: Volume fraction of lamellar grains in TiAl alloys with respect to heat treatment.

#### Ti-47Al-2Nb-2Mn-0.8TiB<sub>2</sub>

Microstructures of as-HIPed specimens exhibit a heterogeneous microstructure illustrated in Figure 6 a. There are clusters of small equiaxed grains in some regions where there are fewer lamellar grains, and conversely, a few fine  $\gamma$  grains are observed in regions dominated by lamellar grains. After heat treatment the microstructures exhibit fewer small grain clusters. The volume fraction of equiaxed grains changes, and after the two step heat treatment, the lamellar volume fraction increased slightly as described in Figure 5. As time and temperature of heat treatment increase, microstructures became more homogeneous. The equiaxed grain size distribution becomes more homogeneous, and fewer clusters of finer  $\gamma$  grains were observed. The microstructures of medium O alloys are similar to that of the low O alloy shown in Figure 6. a. The low and medium O alloy has a lower volume fraction of

lamellar grains than the high O alloy (25%, 22% and 40%) which is contrary to the common observation that lower aluminum (~46at% Al) causes more lamellar grains. However, this result is consistent with the observation that oxygen is an alpha phase stabilizer in Ti alloys [8,33]. From Table II the higher O levels have fewer small grains, which correlates with improved creep resistance [34].

Backscattered electron (BSE) images of the higher O alloys after creep deformation in Figure 6.b and c illustrate differences in  $\alpha_2$  morphology (white phase, see arrows). The largest  $\alpha_2$  regions in the high O alloy are smaller than those in medium O alloy, and angular shaped 3-7  $\mu\text{m}$   $\alpha_2$  grains (arrow) were commonly observed in the medium O alloy (it also has lower aluminum). Angular  $\alpha_2$  grains correlate with faster primary creep [34]. In the alloys with boron, two types of boride particles were found, needle and round; the round type is 1.5-3.5  $\mu\text{m}$ , and the needle type is 3-60  $\mu\text{m}$  long. The needle particles have been identified as TiB and equiaxed particles as TiB<sub>2</sub> [35]. The heat treatment or interstitial content did not affect the size and distribution of these particles. From analysis of SEM BSE images and TEM images, these particles appear to provide nucleation sites for lamellar lathes (fine lamellar colonies were frequently found near particles), and they also block and entangle dislocations.

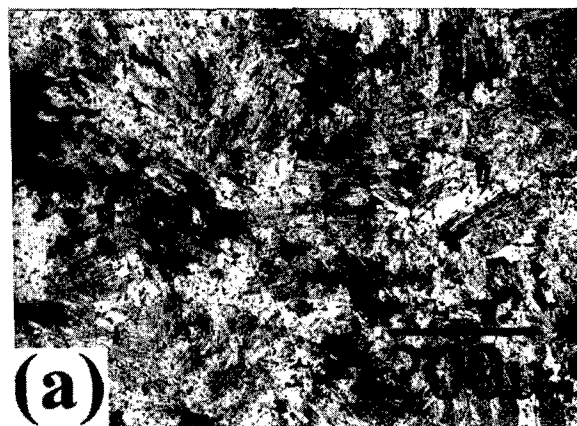


Figure 6: (a) optical micrographs of As HIPed 47Al XD before creep test.

#### Ti-47Al-2Nb-2Cr

In contrast to the microstructures containing TiB<sub>2</sub>, the as-HIPed microstructure exhibits very large (up to 500  $\mu\text{m}$ ) lamellar grains and about 200  $\mu\text{m}$  pockets of equiaxed 10-20  $\mu\text{m}$  equiaxed  $\gamma$  grains (Figure 7 a). The microstructure is extremely heterogeneous, and it exhibits some of the same types of heterogeneities (clusters of small equiaxed grains) observed in Figure 7 a. As shown in Figure 5, with heat treatment, the volume fraction of the lamellar grains increases and decreases with increasing time and temperature, and the microstructure becomes less heterogeneous. The pockets of equiaxed grains become fewer and there are fewer fine grains in the pockets.

In the backscattered electron SEM images of this alloy there is a smaller volume fraction of angular equiaxed  $\alpha_2$  grains between gamma grains (Figure 7 b). The very fine twins seen in the 45 Al sample (Figure 4 b and c) were not observed in the smaller  $\alpha_2$  equiaxed grains in the 47 Al specimens. Very small bright phases can be seen either in  $\alpha_2$  equiaxed grains or boundaries of gamma grains (indicated by arrows) and these phases are  $\beta$  phase which is produced by addition of Cr. They have an orientation relationship of (0001)  $\alpha_2$  // {111}  $\gamma$  // {110}  $\beta$ , and  $\langle 1120 \rangle \alpha_2$  //  $\langle 110 \rangle \gamma$  //  $\langle 111 \rangle \beta$  [36]. Since Cr is known to strengthen the  $\alpha_2$  and  $\gamma$  phases, this may account for the lack of mechanical twinning observed in the  $\alpha_2$  phase in the Ti-47Al-2Nb-2Cr alloy [36]. There appears to be a decrease in the amount of  $\beta$  phase with the increasing amounts of heat treatment.

TEM investigations indicate that a 170° angle relationship between lamellae is frequently observed in the as-HIPed and heat treated conditions. Typically, one of the

two lamellar lathes has a finer spacing described in the reference [34]. Subboundaries developed in larger regions of lamellar grains during high temperature deformation. No subgrains had developed fully in equiaxed grains even though there were regions exhibiting a dislocation density greater than  $2 \times 10^{12}/\text{m}^2$ . After the two-step heat treatment, dynamic precipitation was observed in grain interiors and interfaces, and this may account for some the improved creep resistance [27].

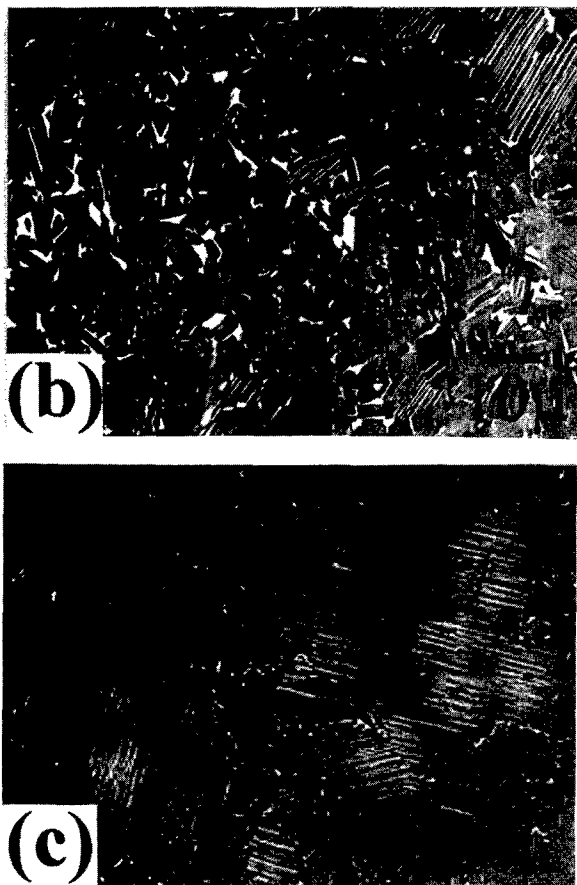


Figure 6: (b) BSE images of medium O alloy and (c) high O alloy after creep test.

Ti-47Al-2Nb-1Mn-0.5W-0.5Mo-0.2Si

The microstructure of the undeformed as-HIPed alloy showed a similar feature as shown in Figure 8 a. Since the strains were small, there was no obvious change in the microstructure after creep deformation. However, reductions in the lamellar spacing were systematically observed in higher magnification observations after deformation. Figure 8 shows the microstructure of the tensile crept specimen in the gage section with equiaxed grains ranging from 5 - 200  $\mu\text{m}$ . The lamellar colonies are on the order of 100 - 500  $\mu\text{m}$ , but many have smaller equiaxed grains interspersed among the lamellar grain boundaries. These groups of small equiaxed grains are produced during HIP treatment due to large local strains associated with pore closure. The volume fraction of lamellar grains in the two crept tensile specimens are  $21 \pm 2\%$  and with the balance being equiaxed grains. Macroscopically the only differences between specimens deformed at 750 °C, 138 MPa and 649 °C, 276 MPa, were the observation of more twins in the larger equiaxed grains of the deformed sample compared to the microstructure in the undeformed grip section. Also, there appeared to be more twinning at the lower temperature, higher stress condition.

Backscattered electron images in Figure 8 b indicated that the  $\beta$  phase (whitest phase) were found in grain

boundaries between  $\gamma$  grains and lamellar grains or in lamellar colony interfaces in both the as-HIPed and heat treated specimens as observed in a related study [19,27,37]. As shown in Figure 8 c, precipitates in the heat treated alloy after HIPing are located in various places such as lamellar

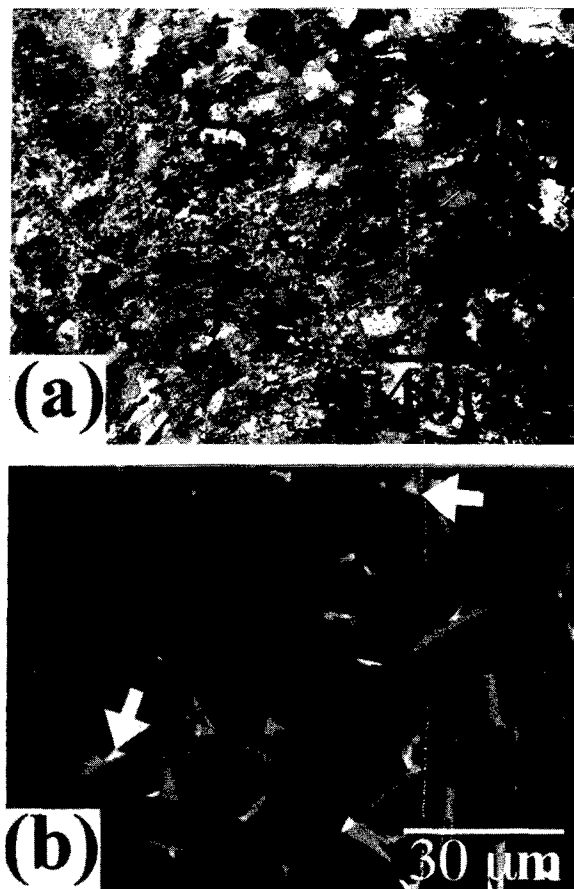


Figure 7: Microstructures of As HIPed 47-2-2 (a) optical micrographs before creep test (b) BSE images after creep test.

interfaces, grain boundaries, and within equiaxed grains, and precipitates were found only in the heat treated alloy. The as-HIPed deformed specimens exhibited no precipitates. This indicates that subsequent heat treatment facilitates the formation of the precipitates. The precipitates in lamellar interfaces vary from 0.05-0.45  $\mu\text{m}$  and tend to be smaller, and many of them have a needle shape (Figure 8 c). In equiaxed grains, precipitates are larger, and tend to have an aspect ratio of 2-3. Thus the precipitates have various shapes with dimensions ranging from 0.2-2  $\mu\text{m}$ . These precipitates have been identified as  $\text{Ti}_5\text{Si}_3$  in several studies [19,27,37]. After analyzing the distribution of precipitates in at least 5 lamellar grains, about 35% more precipitates were found in the deformed sample. This observation suggests that precipitates were formed with the assistance of strain during creep deformation. These observations taken together indicate that precipitation is facilitated by heat treatment, and that a more homogeneous nucleation and growth process occurs in the presence of strain. As with  $\text{TiB}_2$  particles, the precipitates always have a high density of dislocations in their vicinity.

From TEM analysis, twins appear to have initiated from a grain boundary at the boundary region between an equiaxed and a lamellar grain and propagated through equiaxed grains..

#### C. Lamellar spacing

250 - 500  $\alpha_2$  spacing counts in more than 20 - 25 lamellar regions and at least 100  $\gamma$  lamellar interfaces in about 6 different regions near grain boundaries before and after creep

deformation were used to compute the average spacing of  $\alpha_2$  and  $\gamma$  interfaces before and after creep deformation. The  $\alpha_2$  spacing was measured by using BSE imaging. These measurements are upper bounds of the actual spacing, since the lamellar plane normal direction was not determined to make the

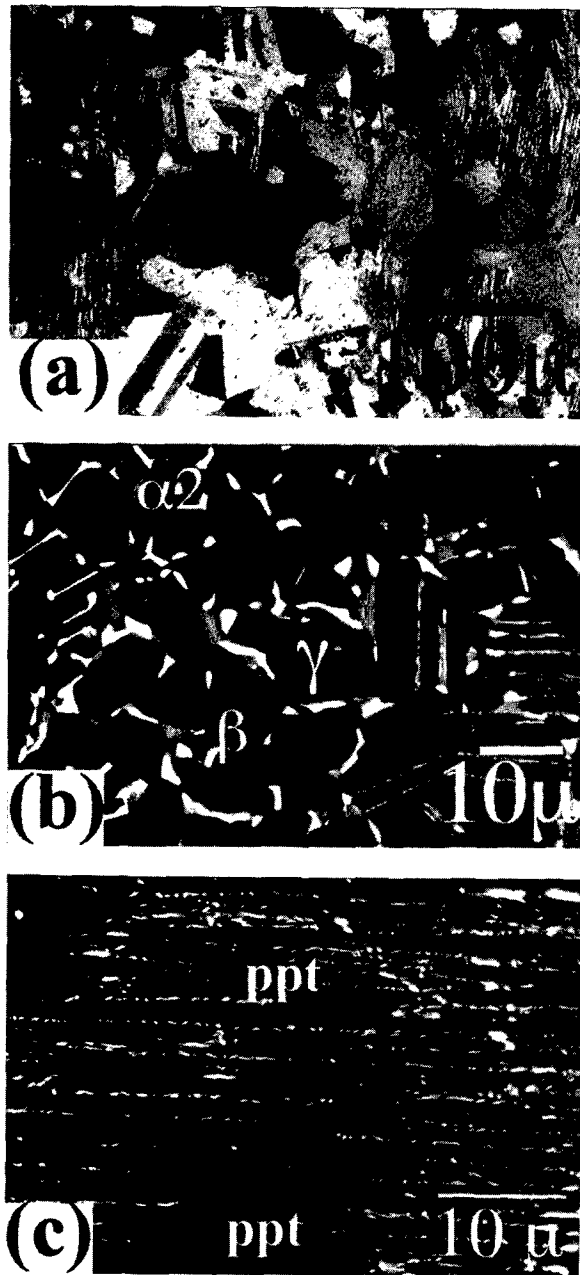


Figure 8: Microstructures of heat treated WMoSi alloy after creep test (a) optical micrographs, (b) and (c) BSE images.

parallax correction needed to determine the actual  $\alpha_2$  spacing. However, this is a systematic way to compare  $\alpha_2$  spacings in specimens with similar microstructures. The TEM was used for measuring the true  $\gamma$  interfaces and  $\alpha_2$  thickness (by tilting the foil so that a  $\langle 110 \rangle$  direction in a lamellar plane was parallel to the beam) and about 50  $\alpha_2$  laths were counted in several lamellar regions for this measurement.

In the case of Ti-47Al-2Nb-2Cr alloy, by using the dark field method and tilting techniques, the spacing of  $\gamma$  laths,  $\alpha_2/\alpha_2$  laths and the thickness of  $\alpha_2$  laths in several lamellar grains were measured. The data was obtained by measuring about 100-350 laths and taking the average.

#### Ti-47Al-2Nb-2Mn-0.8TiB<sub>2</sub>

The  $\alpha_2$  spacing was reduced in these alloys after creep deformation and this reduction varies with heat treatment and interstitial content [34,38]. The average  $\alpha_2$  spacing before deformation in the alloy with high O is 1.37  $\mu\text{m}$ , which is nearly as large as the 1.57  $\mu\text{m}$  spacing of the low O alloy which showed the poorest creep resistance. The average  $\alpha_2$  thickness is larger (0.2  $\mu\text{m}$ ) in the high O alloy than the low O alloy (0.15  $\mu\text{m}$ ). This also suggests that oxygen stabilizes the  $\alpha_2$  phase.

The distribution of  $\alpha_2$  and  $\gamma$  interface spacings before and after creep deformation are shown in Figure 9.a. From this plot, the reduction of the  $\alpha_2$  and  $\gamma$  interface spacings after deformation at the early stage of creep can be easily visualized since the dashed line shows the highest frequency of lamellae with fine spacing. During the first 0.5% strain, more reduction in the strain-rate correlates with more reduction in lamellar spacing in the low O alloy. The high O alloy does not follow the same relationship between the reduction in spacing and the reduction in strain-rate: The high O alloy exhibits a larger reduction in strain-rate, and a greater amount of reduction in the  $\gamma$  interface. The high O alloy exhibits more reduction of  $\gamma$  interface than the alloy heat treated at 900°C for 10 hours, which gave poor creep resistance. If the reduction in lamellar spacing occurs by mechanical twinning, then more twinning appears to cause a greater amount of strain at early times. The effect of the high O is that more refinement in the  $\gamma$  interface spacing occurs in primary creep, but it occurs more slowly.

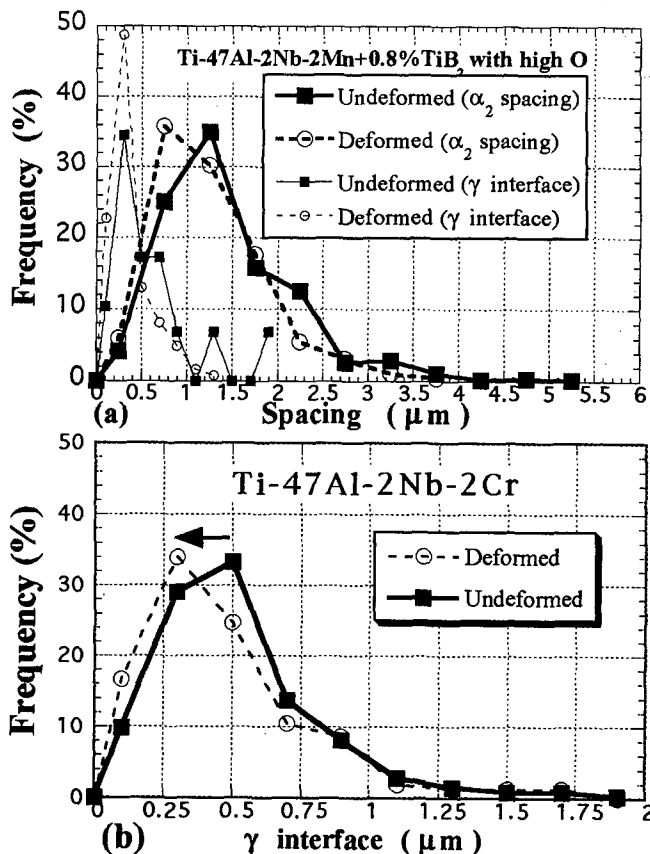


Figure 9: distribution of  $\alpha_2$  and  $\gamma$  interface spacings in TiAl alloys before and after creep deformation (a) high O (b) 47-2-2.

#### Ti-47Al-2Nb-2Cr

The  $\alpha_2$  and  $\gamma$  interface spacings decrease with heat treatment and after creep deformation [34]. In the case of  $\gamma$  interface, there was only 8% reduction of spacing from heat treatment and a 4% reduction of  $\gamma$  interface after creep deformation in the 900°C/20hr heat treated alloy as determined

from Figure 9.b. From the reference 34, measured averaged  $\alpha_2$  spacing shows that the spacing decreases from about 5% to 18% from the As HIPed condition to the one and two-step heat treatments. From Table III, after deformation, in the one-step heat treatment there was a 22% reduction of the  $\alpha_2/\alpha_2$  spacing, and a 10% reduction in the  $\alpha_2$  thickness. This may result from nucleation of new  $\alpha_2$  lamellae initiated by mechanical twinning, since a mechanical twin has the crystal structure of the  $\alpha_2$  phase for three layers in each interface [28]. In general, heat treatment and creep deformation cause the lamellar scale to become more refined.

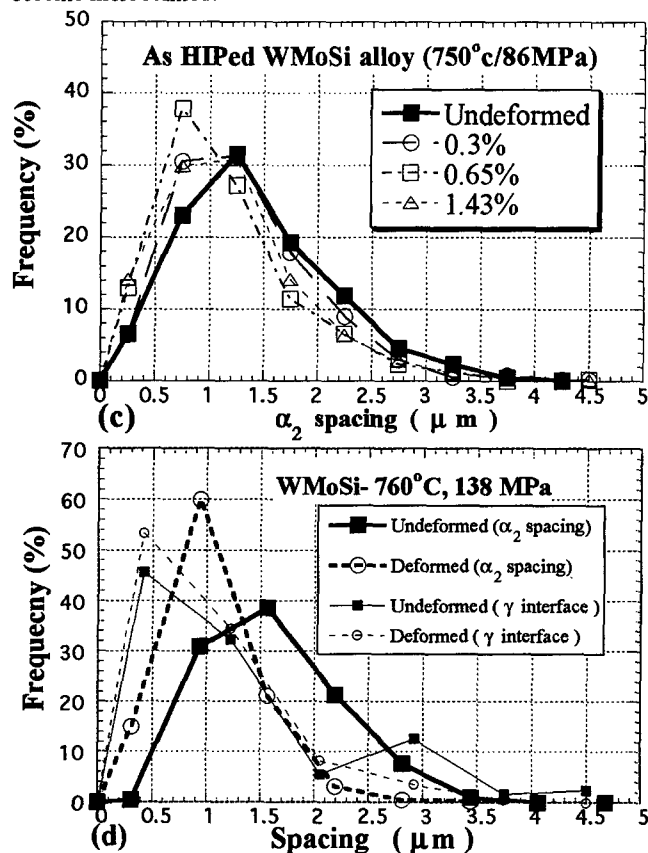


Figure 9: Distribution of  $\alpha_2$  and  $\gamma$  interface spacings in TiAl alloys before and after creep deformation (c) WMoSi under compression-shear (d) WMoSi alloys.

Ti-47Al-2Nb-1Mn-0.5W-0.5Mo-0.2Si

#### a. lamellar spacing in compression-shear creep deformation

The distribution of  $\alpha_2$  spacings before and after deformation is represented in Figure 9. c. The undeformed representation shows the same trend for three samples characterized before deformation, and the average is indicated by a bold line. In every case, there is a nominally similar shift of the frequency distribution toward smaller spacings due to small creep strains. The average of about 500 observations of  $\alpha_2$  spacings is plotted with respect to effective strain and load in Figure 10. There is a 23% reduction in lamellar spacing with strain that saturates at effective strains between 0.1 and 0.3%, whereafter the spacing remains relatively constant. For the same strain of 0.1%, the amount of refinement at 750°C is about half of the amount that occurred at 650°C. The amount of refinement at 650°C decreases with decreasing stresses.

#### b. lamellar spacing in tensile creep deformation

From Table III, there was a reduction in spacing of 34 % in  $\alpha_2$  and 24 % in  $\gamma$  interfaces for the specimen deformed at 760°C, 138 MPa. Contrary to the observations in the

compression-shear specimens, the reduction in  $\alpha_2$  spacing was smaller (18%) in the 650°C 276 MPa specimen, in part, due to a lower undeformed lamellar spacing. However, the deformed lamellar spacing for this specimen (0.9  $\mu\text{m}$ ) is smaller than the spacing for the deformed 760°C 138 MPa specimen (1.03  $\mu\text{m}$ ).

Unlike the compression shear specimens, the undeformed lamellar spacing was measured in the grip section of the creep specimens, which experienced the same thermal history with presumably no stress. The compression-shear specimens all came from the same physical region of the casting, but nothing is known about the relative positions of the two tensile specimens in the casting, where the initial lamellar spacing may have differed due to differences in cooling rates, or other unidentified process parameters. The  $\alpha_2$  spacing and  $\gamma$  interface distribution curves before and after deformation are represented as a bold and a dotted line, respectively, in Figure 9 d. As with the compression-shear specimens, there is a nominally similar shift of the frequency distribution toward smaller spacing due to small creep strains.

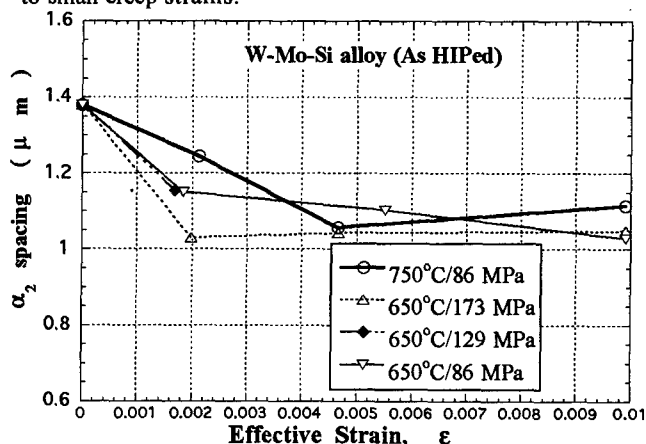


Figure 10: The plot of  $\alpha_2$  spacing respect to different effective strains and different loads at 650°C and 760°C.

#### D. Effect of Anisotropic Crystal Structure on Deformation

Figure 11 a shows the maximum Schmid factor for true  $\langle 112 \rangle$  twinning and dislocation deformation systems. A high Schmid factor indicates that a deformation system will operate to carry strain. The operation of true twinning depends strongly on the orientation of a crystal with respect to the loading axis. In tension, orientations close to  $\langle 441 \rangle$  (near tail of arrow) are likely to twin. However, upon twinning, the crystal rotates to an orientation near  $\langle 118 \rangle$  (near head of arrow). Once the crystal is twinned, the Schmid factor for true twinning is zero. The same phenomena occurs in compression, in the opposite sense. In the twinned orientation, the Schmid factor for ordinary dislocations is also small, and only superdislocations have a high Schmid factor, so twinning increases the volume fraction of crystals where only super dislocations can operate. Luster and Morris observed that superdislocations were active only in crystals having a Schmid factor greater than 0.35, and they only nucleated from interfaces where efficient slip transfer from neighboring crystals was possible [39]. Ordinary dislocations and true twinning were observed in grains where the Schmid factor was larger than 0.25. In lamellae thinner than 0.5  $\mu\text{m}$ , only deformation systems with Burgers vectors in the lamellar plane were operative. These criteria were applied in Figure 11. b to determine the volume fraction of a set of randomly oriented crystals that could deform with 4 or more deformation systems active, excluding superdislocations. Deformation in tension has only 19 vol% of crystals with 4 Schmid factors operative, while in compression, 28 vol % have 4 systems active. In contrast, 33 vol % of crystals in a FCC metal have 4 systems with  $m > 0.32$  (inverse Taylor factor). These observations imply that compression of TiAl should be less prone to cracking than tension, since superdislocation activity is restricted as indicated above.

Table III Average lamellar spacing and reduction % of TiAl alloys

	$\gamma$ interface	$\alpha_2$ spacing	$\alpha_2$ thickness	Creep test condition
4722	0.49 $\mu\text{m}$ , 4%*	1.29 $\mu\text{m}$ , 22%	0.11 $\mu\text{m}$ , 10%	Tension 760 ° C/138 MPa
	900 ° C/20 hrs	900 ° C/20 hrs	900 ° C/20 hrs	
	0.38 $\mu\text{m}$ , 24%	1.33 $\mu\text{m}$ , 22%	0.15 $\mu\text{m}$	
	900 ° C/20 hrs	900 ° C/20 hrs		
47Al XD (low O)		1.42 $\mu\text{m}$ , 24% As HIPed		Tension 760 ° C/138 MPa
high O	0.59 $\mu\text{m}$ , 40% 1010 ° C/50 hrs	1.37 $\mu\text{m}$ , 14% 1010 ° C/50 hrs	0.2 $\mu\text{m}$	Tension 760 ° C/138 MPa
WMoSi	1.30 $\mu\text{m}$ , 24% 1010 ° C/50 hrs	1.57 $\mu\text{m}$ , 14% 1010 ° C/50 hrs		Tension 760 ° C/138 MPa
WMoSi	0.46 $\mu\text{m}$	0.74 $\mu\text{m}$ , 18%** 1010 ° C/50 hrs		Tension 649 ° C/276 MPa
WMoSi		1.38 $\mu\text{m}$ , 23% As HIPed		Compression-shear 760 ° C/138 MPa

\* about 3 lamellar regions sampled, more than 3 in other specimens. \*\* initial lamellar spacing was fine in this specimen.

• initial values of  $\alpha_2$  and  $\gamma$  interface spacing, and  $\alpha_2$  thickness are indicated before %.

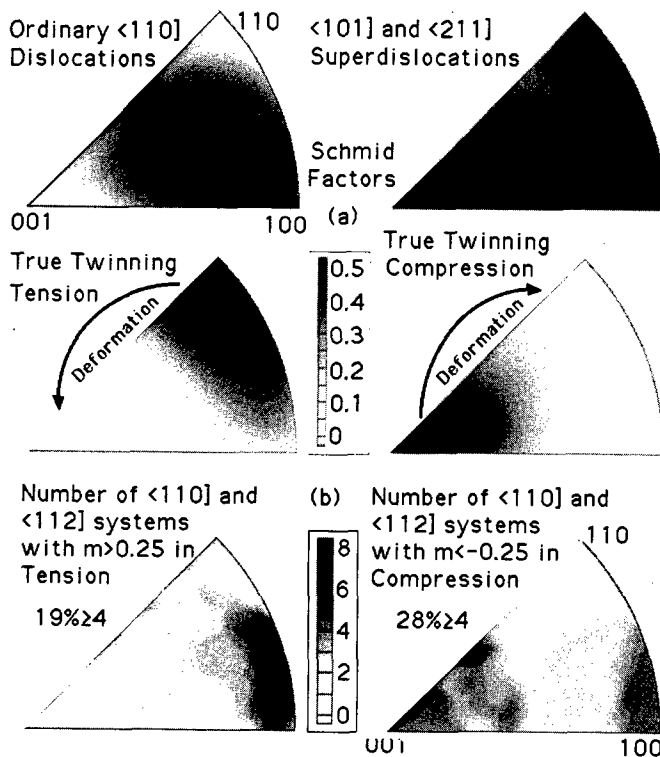


Figure 11: (a) The maximum Schmid factor for deformation in a given crystal direction is plotted for ordinary and super dislocations, and for true twinning, which depends on deformation mode. (b) There are no operative ordinary dislocation or true twinning systems near <001> for tension, and none near <110> for compression

### Discussion

The above review of several investigations indicate that many microstructure features affect primary creep. The impact of the following microstructural features will be assessed for the alloys investigated: Lamellar refinement, reduction of lamellar volume fraction, removal of small equiaxed gamma grains, effect of heat treatment, and the effect of dynamic precipitation. With understanding of how these microstructural changes

affect creep properties, optimal microstructural design criteria for creep resistance can be balanced with other design constraints.

#### a. Lamellar refinement

Lamellar refinement occurs in all materials examined. Lamellar refinement can only occur by a mechanical twinning process, or by a strain induced transformation similar to twinning [40,41]. These processes cause new interfaces to be created as strain occurs. Most of the refinement occurs in the first 0.1-0.2% of strain, where the strain rate is high. Comparing Figure 2b with 10 shows that the initial fast strain rate drops rapidly as the lamellae are refined, and that the strain rate decreases more slowly with strain after the initial refinement process has saturated, as indicated by the discontinuity in the strain rate in Figure 2b. The amount of refinement depends on the initial lamellar spacing, stress and temperature. A greater amount of lamellar refinement occurs in materials with higher initial lamellar spacing, and consequently, the time to reach 0.5% is reduced, since more of the 0.5% strain occurs in the initial high strain rate process of lamellar refinement. Therefore, reducing the lamellar spacing will reduce the initial amount of strain that can be accommodated by lamellar refinement, and it will take longer to reach 0.5% strain. Heat treatment can be used to reduce initial lamellar spacing; more heat treatment reduces lamellar spacing [34]. Pre-straining can also refine the lamellar spacing in exactly the same way as in creep deformation, by taking up the easy refinement strain before the creep process begins. The most creep resistant TiAl based alloys developed to date have extremely fine lamellar spacings of 0.1  $\mu\text{m}$  [42].

Lamellar refinement hardens the material in two ways, by orientation hardening due to twinning, and by restriction of deformation to modes parallel to the lamellar plane. The volume fraction of hard orientations, where only superdislocations have a high Schmid factor increases with the amount of strain accommodated by mechanical twinning. In addition to orientational hardening, creation of more finely spaced interfaces strengthens the material by a Hall-Petch effect. In addition to strengthening, very fine lamellar regions have been shown to deflect cracks propagating across lamellae [43]. The greatest amount of lamellar refinement observed in the studies described above occurred in the high oxygen XD alloy. From Figure 9a and Table III, the reduction in  $\gamma$  spacing was 40%. The high interstitial content may restrict ordinary dislocation mobility more than in the other alloys, and the more difficult operation of ordinary dislocations would increase the probability for strain accommodation by mechanical twinning. Even though mechanical twinning has a lower critical resolved shear stress than ordinary dislocations in binary TiAl single crystals [44], twin nucleation requires a high stress concentration, which exists in grain boundary regions [45].

The reduction in the spacing between  $\alpha_2$  layers and the reduction in  $\alpha_2$  thickness indicated in Table III indicates that



new  $\alpha_2$  layers are being formed in the process of lamellar refinement. This is possible by a strain induced phase transformation that required subsequent diffusion of Ti into the transformed crystal structure, which has been proposed by [31]. A true twin interface can serve as a nucleus for this process, since a true twin interface consists of 4 atomic layers of  $\alpha_2$  crystal structure [28]. Strain accomplished by a moving ledge mechanism has been proposed by Wang and Nieh [42]

#### b. Effects of Heat Treatment on Grain size and Lamellar Volume Fraction

Heat treatments shown in Figures 1 and 5 indicate that more heat treatment improves or does not adversely affect creep resistance (with one notable exception for the 10 hr 900°C in the 47Al XD alloy in Figure 1). A major source of this improvement is due to removal of fine equiaxed grains that provide regions where boundary diffusional processes are more significant. The presence of the  $\text{TiB}_2$  inhibits grain growth, which causes a limiting effect on improving creep resistance. However the degrading effect of larger grain size on room temperature ductility is well established, so the improved creep resistance in the 47-2-2 alloy in Figure 1 may occur at the expense of ductility.

Since the lamellar grains are the source of the lamellar refinement deformation mechanism, a higher lamellar volume fraction should cause a greater amount of strain at the initial high strain rate. In low temperature, low stress creep of duplex microstructures, the steady state creep rate was observed to increase with lamellar volume fraction [46]. A larger strain at the high strain rate will reduce the time to 0.5%. Evidence for this is effect is found in Figures 1 and 5. Figure 5 shows that the lamellar volume fraction is affected by heat treatment, though it is difficult to ascertain how intrinsic microstructural variations may obscure these measurements. The data in Figure 5 were taken from several regions and multiple cross sections of a sample, and they are nominally similar to the trends observed when fewer observations were used. The most consistent feature was the differences in volume fraction between the 10 hr 1010°C and the 2 step heat treatment conditions. The 47-2-2 alloy exhibits the best improvement in creep resistance with the 2-step heat treatment, and correspondingly, the lamellar fraction was reduced by this heat treatment. The same thing occurred in the 45Al XD alloy, and the effect of reducing the lamellar volume fraction was a big reduction in the experimental scatter in the times to 0.5%, but no substantial improvement was measured with any heat treatment in this alloy. Conversely, the lamellar volume fraction increased with the 2 step heat treatment in the 47 Al XD alloy, and this would suggest a degrading effect on creep resistance. Since the 2 step heat treatment also reduced the number of fine grains, these two changes apparently balanced each other so that no net improvement in creep resistance was obtained.

#### c. Effects of Heat Treatment on Precipitation, and Dynamic Precipitation

The most creep resistant alloy is the heat treated WMoSi alloy. The heat treatment causes nucleation of precipitates. The growth of the precipitates is affected by the stress state, where the stressed region of the material stimulates a more homogeneous and faster growth of the precipitates. Moving dislocations acting as pipes for transport of solute atoms to precipitates enhance and homogenize their growth. This effect is beneficial for developing a creep resistant microstructure that does not develop larger harder inclusions that would degrade ductility. The 47-2-2 alloy also developed fine precipitates with the two-step heat treatment, but the substantial improvement in creep resistance is also correlated with a much larger grain size.

The WMoSi alloy in the as-HIPed condition exhibited strain rates more than 10 times faster with a smaller stress, giving it a creep resistance similar to the 45Al XD alloy. The lack of precipitates in this alloy indicates that most of the silicon is still in solution, which implies that Si in solution degrades creep resistance. This has also been demonstrated by Wang and Nieh [47]. They showed that Si in solution would

facilitates ledge mobility in lamellar interfaces, which was proposed as a rate limiting creep deformation process.

### Conclusion

Changes in the microstructure have been analyzed to determine how heat treatment and alloy composition affect primary creep resistance in several near- $\gamma$  TiAl alloys.

All alloys exhibit lamellar refining that causes an initially rapid creep rate up to strains between 0.1 and 0.2%. This undesirable rapid creep strain can be reduced by refining the lamellar spacing by heat treatment or pre-straining.

Lamellar refining occurs by mechanical twinning or similar processes that transform the crystal orientation by a moving interface. The microstructure is hardened by a Hall-Petch effect which results in prevention of deformation across thin lamellae when they are smaller than 0.5  $\mu\text{m}$ , and by orientation hardening, since mechanical twinning rotates crystals into hard orientations where only superdislocations have a high Schmid factor.

Heat treatment homogenizes the grain size distribution by removing fine grains. This results in a more homogeneous creep deformation that can reduce the scatter in some alloys. There is limited evidence for degraded primary creep resistance with higher lamellar volume fraction.

Precipitation provides a large benefit for creep resistance. The use of silicon can be detrimental to creep resistance if it is kept in solution. Precipitation is complex, and heat treatment can provide appropriate conditions for a desirable homogeneous dynamic growth of precipitates during creep deformation.

### Acknowledgment

This research was supported by a research contract with Howmet Corp., Whitehall, MI.

### References

1. H.A. Lipsitt, D. Shechtman and R. E. Schafrik, *Metall. Trans.* 6A, (1975), 1991.
2. Y. W. Kim, *JOM*, vol. 41, No.7, (1989), 24.
3. Y-W. Kim and F.H. Froes, *High Temperature Aluminides and Intermetallics*, eds. S.H. Whang, et al., TMS, (1990), 465.
4. Y. W. Kim and D.M. Dimiduk, *JOM*, vol. 43, No.8, (1991), 40.
5. S.C. Huang and Y.W. Kim, *Scripta Metall.* 25, (1991), 1901.
6. S.C. Huang and E.L. Hall, *Metall. Trans. A*, 22A (1991), 1619.
7. T. Kawabata, T. Tamura, and O. Izumi, *Metall. Trans. A*, 24A, (1993), 141.
8. M. Yamaguchi and H. Inui, *Structural Intermetallics*, eds. R. Darolia, et al., (TMS, Warrendale, PA, 1993), 127.
9. M.J. Blackburn and M.P. Smith, U.S. Patent 4294615, (1981).
10. S.C. Huang and E.L. Hall, *Acta Metall. Mater.*, 6, (1991), 1053.
11. T. Tsujimoto and K. Hashimoto, *Mat. Res. Soc. Symp. Proc.*, 133, (1989), 391.
12. G.H. Meier, D. Appalonia, R.A. Perkins, and K.T. Chiang, in *Oxidation of High-Temperature Intermetallics*, ed. T. Grobstein and J. Doychak (TMS, Warrendale, PA 1988), 185.
13. D.W. McKee and S.C. Huang, *Corrosion Sci.*, 33, (1992), 1899.
14. J. B. McAndrew and H.D. Kessler, *J. Metals*, 8, (1956), 1348.
15. W. Zhang, G. Chen, and Z. Sun, *Scripta Metall.*, 28, (1993), 563.
16. S. Tsuyama, S. Mitao and K. Minakawa, *Mater. Sci. Eng.*, A153, (1992), 427.



17. S.C. Huang, D.W. McKee, D.S. Shih and J.C. Chestnutt, Intermetallic Compounds-Structure and Mechanical Properties, ed. O. Izumi, (The Japan Institute of Metals, Sendai, 1991), 363.
18. S. Tsuyama, S. Mitao, and K. Minakawa, Mater. Sci. Eng., A153, 1992, 451.
19. K. Kasahara, K. Hashimoto, H. Doi, and T. Tsujimoto, J. Japan Inst. Metals, 53, 1990, 948
20. Y. G. Nakagawa, S. Yokoshima, and K. Mastuda, Mater. Sci. Eng., A153, (1992), 722.
21. T. Maeda, M. Okada, Y. Shida and M. Nakanishi, Proc. 1989 Sapporo Meeting, (The Japan Institute of Metals, Sendai, 1989), 238.
22. T. Maeda, M. Okada and Y. Shida, MRS Symp. Proc., vol 213, (MRS Pittsburgh, PA, 1991), 555.
23. P.L. Martin, M.G. Mendiratta, and H.A. Lipsitt, Metall. Trans. A, 14A (1983), 2170.
24. R.A. Perkins, K.T. Chiang, and G.H. Meier, Scripta Metall., 21, (1987), 1505.
25. T.R. Bieler, D.Y. Seo R.S. Beals, C.H. Wu, and S.L. Choi, Gamma Titanium Aluminides, ed. Y.W. Kim, et al. (TMS, Las Vegas, NV 1995), 795.
26. Z. Jin, S.W. Cheong and T.R. Bieler, Gamma Titanium Aluminides, ed. Y-W. Kim, et al. (TMS, Las Vegas, NV 1995), 975.
27. D.Y. Seo, S.U. An, T.R. Bieler, D.E. Larsen, P. Bhowal, H. Merrick, Gamma Titanium Aluminides, ed. Y-W. Kim, et al. (TMS, Las Vegas, NV 1995), 745.
28. Z. Jin and T.R. Bieler, Phil Mag., 70, (1995), 819-836.
29. K. Muraleedharan and T.M. Pollock, unpublished research, PRET home page, <http://titan.mems.cmu.edu/etch.html>.
30. T.S. Kallend, U.F. Kocks, A.D. Rollett, and H.R. Wenk, Mater. Sci. Eng., A132, 1991, 1-11.
31. D. Y. Seo, T.R. Bieler and D.E. Larsen, Proceedings of 7th International Conference on Creep and Fracture of Engineering Materials and Structures in Irvine, CA, Aug. 1997, in press.
32. Z. Jin, R. Beals and T.R. Bieler, Structural Intermetallics, eds. R. Darolia et al., (TMS, Warrendale, PA 1993), 275.
33. S. Yamaguchi and H. Shiraishi, Mater. Sci. Eng., A152, 283, (1992).
34. D.Y. Seo, T.R. Bieler and D.E. Larsen, Advances in the Science and Technology of Titanium Alloy Processing, eds. I. Weiss, R. Srinivasan, P. Banja, and D. Eylon, (TMS Warrendale, PA, 1997), 605-24.
35. D.E. Larsen, S.L. Kampe, Christodoulou, MRS Symp. Proc., 194, 285, (1990).
36. Y. Zheng, L. Zhao and K. Tangri, Scripta Metall., 26, (1992), 291.
37. T. Noda, M. Okabe, S. Isobe, and M. Sayashi, Mater. Sci. Eng., A192/193, (1995), 774.
38. D. Y. Seo, T.R. Bieler and D.E. Larsen, Mater. Res. Soc. Symp. Proc. Vol. 460 (Pittsburgh, PA, 1997) in press.
39. J. Luster and M.A. Morris, Metall. Trans. A, 26A, (1995), 1745-1756.
40. Z. Jin and T.R. Bieler, Phil Mag. A, 72, (1995), 1201-19.
41. C.R. Feng, D.J. Michel and C.R. Crowe, Scripta Metall., 23, 1989, 241-246.
42. T.G. Nieh, J.N. Wang, Scripta Metal. et Mater. 33, (1995), 1101-7.
43. Z. Jin and G.T. Gray III, TMS symposium on Fundamentals of Gamma Titanium Aluminides, Feb. 1997, eds. K.S. Chan, V.K. Vasudevan, Y.-W. Kim, to be published in Mater. Trans.
44. Mahapatra Scripta Mater.
45. Z. Jin and T.R. Bieler, Phil Mag. A, 71, (1995), 925-47.
46. R. A. MacKay and I. E. Locci, unpublished research, NASA Lewis.
47. Wang and Nieh, TMS symposium on Fundamentals of Gamma Titanium Aluminides, Feb. 1997, eds. K.S. Chan, V.K. Vasudevan, Y.-W. Kim, to be published in Mater. Trans.

## DEFORMATION PROCESSES AND DISLOCATION MOTION IN $\gamma$ -TiAl

K.J. Hemker, M. Lu, and M. Zupan

Department of Mechanical Engineering, Johns Hopkins University,  
Baltimore, MD 21218

### Abstract

Ordinary dislocations, superdislocations, and deformation twinning have all been identified as active deformation processes in  $\gamma$ -TiAl. Studies of these processes can generally be divided into one of two types, those associated with yielding and those which are focused on the long term creep behavior. This paper is an attempt to combine these two subjects in hopes of realizing a more unified description of the rather complicated nature of dislocation motion in this alloy. Works on both yielding and creep are revisited, and new experiments involving both microsample tensile testing and TEM observations of microstructural evolution during both creep and Cottrell-Stokes experiments are presented. The microsample experiments are being used to study the orientation and temperature dependence of the CRSS, and preliminary results have shown the tension-compress asymmetry of single crystalline Ti-55.5%Al to be negligible at 500 K. The TEM observations have greatly expanded our understanding of the development of dislocation substructure in this alloy. The results from these studies have been combined in an attempt to characterize dislocation motion in a way that can be used to describe both the yielding and creep behavior of this alloy.

### Introduction

TiAl-base alloys are currently being considered for use in automotive engine valves, turbocharger rotors, turbine engine compressor components and turbine engine

exhaust system components [1]. Although commercial TiAl alloys will most commonly be two phase fully lamellar structures, similarities in the dislocation mechanisms of gamma and two phase lamellar alloys have recently been noted [2]. The present study concentrates on single phase gamma alloys in hope of synthesizing the current understanding of the dislocation processes that govern the mechanical response of this important family of intermetallic alloys.

In this paper, the relationship between mechanical properties and deformation mechanisms is considered from two complementary vantage points. Investigations characterizing this relationship are presented with respect to the manner of deformation (i.e. yielding or creep) in the first part of this manuscript. The findings of these collective studies will then be reviewed in terms of the underlying dislocation mechanisms, here the intent is to identify and characterize dislocation motion in a way that will render a fundamental description of both yielding and creep in this intermetallic alloy.

### Yielding Behavior

#### Polycrystalline studies

The mechanical behavior of aluminum rich single-phase polycrystalline  $\gamma$ -TiAl alloy obeys three distinct temperature domains. The strength decreases with temperature at low temperatures, increases moderately at intermediate temperatures, and reaches a peak above which it falls off precipitously at higher temperatures, see for example [3]. The ordered  $L1_0$  crystal structure of  $\gamma$ -TiAl gives rise to both ordinary ( $b_{\text{ordinary}} =$

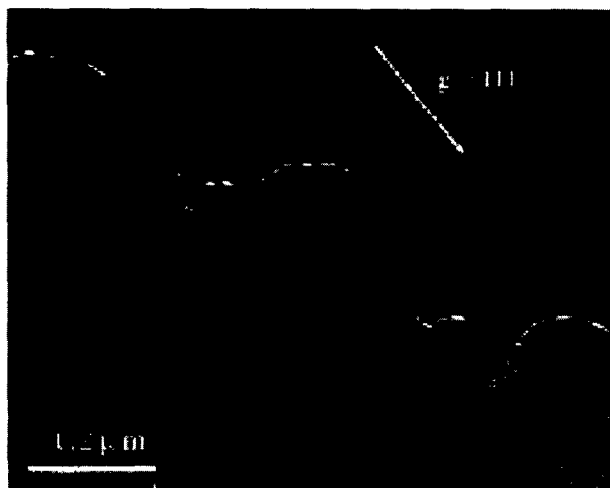


Figure 1: Dragging out of faulted dipoles on a superdislocation in Ti-53Al-1Nb that was deformed at  $-150^{\circ}\text{C}$ . Taken from Viguier and Hemker [7].

$\frac{1}{2}\langle 110 \rangle^1$  and super ( $b_{\text{super}} = \langle 101 \rangle$ ) dislocations. It was originally assumed that the normal decrease in strength with temperature at low temperatures is related to ordinary dislocation motion and that the anomalous behavior observed at intermediate temperatures is related to the cross-slip locking of superdislocations [5], but this has not proven to be the case. At low temperatures, the deformation microstructure of this alloy is dominated by the formation of faulted dipoles [2-4,6]. Detailed analysis of these faulted dipoles indicates they are formed by the localized pinning of a superdislocation, the bypassing of that pinning point, and the drawing out of a dipole whose energy is then reduced by the passage of two subsequent partial dislocations and the formation of an extrinsic stacking fault [4,7]. The weak-beam image in Fig. 1, which was taken from Viguier and Hemker [7], is an experimental observation of the formation of faulted dipoles in Ti-53Al-1Nb that was deformed at  $-150^{\circ}\text{C}$ . The curved shape of the parent superdislocation ( $b_{\text{super}} = \langle 101 \rangle$ ) indicates that the faulted dipoles are drawn out on the trailing edge of the dislocation and can be taken as clear evidence that these faulted dipoles impede the motion of the superdislocation.

At intermediate temperatures, the mechanical response of polycrystalline  $\gamma$ -TiAl has been found to exhibit an anomalous temperature dependence of the flow stress at intermediate temperatures [2,3,8,9], but this anomalous behavior does not appear to be related to the formation of faulted dipoles nor the cross-slip locking of superdislocations. The importance of ordinary dislocations, not superdislocations, has manifested itself in a wide number of TEM studies [2,3,9-13] of specimens that were yielded in the anomalous temperature regime.

<sup>1</sup> The  $\langle \rangle$  notation indicates that the first two indices are interchangeable while the third is not and is taken from [4].

These ordinary dislocations have been observed to be pinned along their length. The pinning points appear to align along the screw orientation, but are clearly different in nature than the cross-slip locking that is often associated with superdislocations. Viguier et al. [3] have shown that the density of pinning points increases with temperature up to a peak temperature that corresponds to a peak in the flow stress, and they have concluded that the pinning of ordinary dislocations is an intrinsic process that is related to the nucleation and lateral expansion of double kinks. Subsequent observations by Sriram et al. [2] have confirmed the temperature dependence of these pinning points and shown them to be pinned along a three dimensional stair-case. In considering the three dimensional configuration of these dislocations the latter authors have outlined three distinct types of pinning points: atomic level jogs, those associated with dipole creation, and jogs large enough to allow by-passing and multiplication. Models which describe the yield strength anomaly of  $\gamma$ -TiAl in terms of ordinary dislocation motion have been forthcoming [2,14].

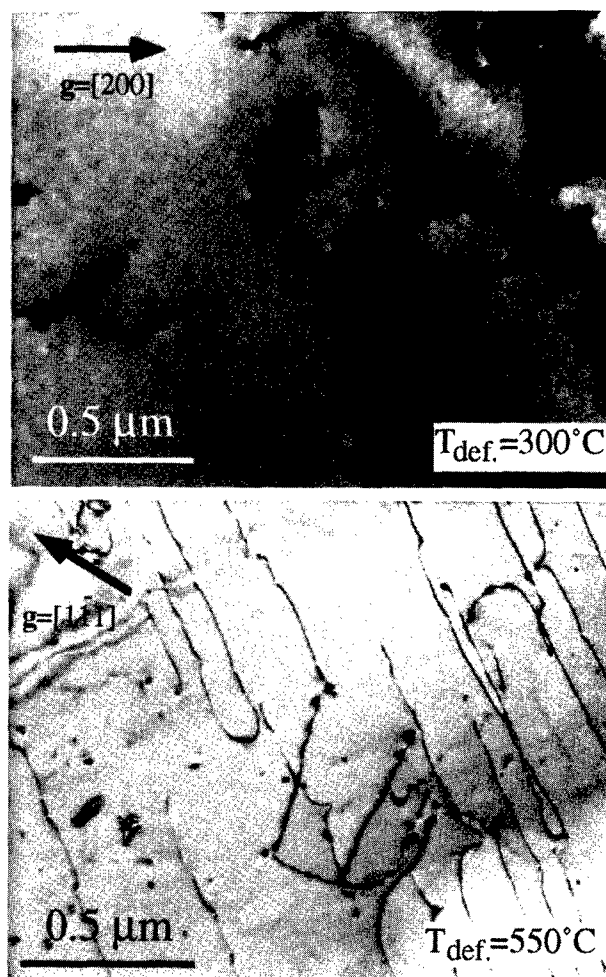


Figure 2: Faulted dipoles are the dominant feature associated with low temperature ( $300^{\circ}\text{C}$ ) deformation, while ordinary dislocations are the dominant feature for intermediate temperature ( $550^{\circ}\text{C}$ ) deformation.

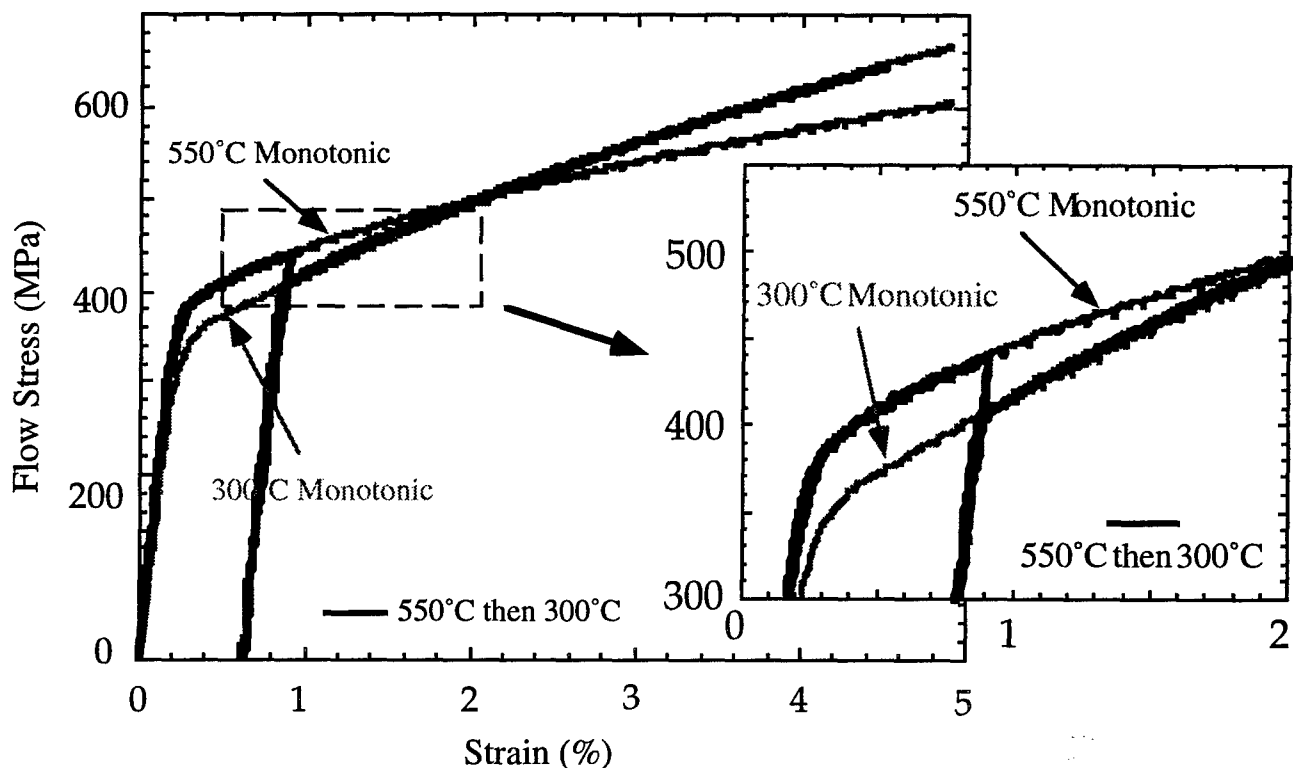


Figure 3: Cottrell-Stokes type temperature drop experiment shows a fully recoverable flow stress behavior of single-phase polycrystalline Ti-51Al-2Mn. The specimen was prestrained at 550°C, unloaded, and reloaded at 300°C. Taken from Lu and Hemker [15].

The yield strength anomaly and the distinction between low temperature and intermediate temperature deformation has also been evidenced in a recent set of temperature change experiments [15]. Monotonic and transient Cottrell-Stokes experiments on polycrystalline  $\gamma$ -Ti<sub>47</sub>Al<sub>51</sub>Mn<sub>2</sub> have been conducted at 300°C and 550°C, and TEM observations of these specimens indicate that deformation at 300°C is associated with superdislocation motion and the formation of faulted dipoles, while ordinary dislocation motion dominates at 550°C, see Fig. 2. As is illustrated in Fig. 3, the transient associated with a temperature drop experiment suggests that ordinary dislocation motion is a fully reversible process [15]. Further inspection of this curve indicates that the stress-strain response of this material is independent of prior deformation history, as transient and monotonic curves were found to be nearly identical at the higher strains. This finding suggests that strain hardening can also be described as a dynamic, fully reversible, process.

In polycrystalline TiAl, when the deformation temperature is increased to beyond the peak temperature, the substructure has been found to be dominated by highly curved ordinary dislocations [3,16]. Although cusps and pinning points can still be found on these dislocations, the density of these points are greatly reduced and the bowed nature of these dislocations greatly exaggerated. These dislocations no longer exhibit a preferred orientation. These high temperature ordinary

dislocations have been described as dislocation helices by Kad and Fraser [16], and it appears that their formation occurs by a natural progression of the pinning and bypassing mechanisms observed at intermediate temperatures. The influence of climb has been debated but is still unclear.

Twinning has also been reported in a number of yielding studies [3,11,17]. An excellent description of the microscopic formation of twins in TiAl is presented in [4,17]. The percentage of grains containing twins and the density twins within a given grain have both been observed to increase with temperature in the anomalous temperature regime, see for example [3]. The occurrence of twinning decreases at higher temperatures, and it is interesting to note that twinning activity has been found to be highest at a temperature that coincides with the peak in the yield strength [3]. These observations are rather surprising given the athermal nature of twinning. However, it is important to note that twinning does not occur in all grains and that it is an additional deformation mechanism. That is to say that twinning occurs in addition to but does not replace dislocation activity.

#### Single Crystal Studies

To date, understanding of the relation between microscopic deformation processes and macroscopic mechanical performance of  $\gamma$ -TiAl has been somewhat hindered by the difficulty associated with obtaining high quality single crystals of this alloy. Single crystals of  $\gamma$ -

TiAl, 6-10 mm in diameter and ~50 mm in length, can now be grown by the optical float zone technique [18] but the relative small size of these crystals precludes the orientation and machining of standard tensile specimens. The first study to employ single crystals [19] did report a yield strength anomaly for a variety of orientations. More recently, Li and Whang [20], Wang, Li and Whang [21], and Stucke, Vasudevan and Dimiduk [22] have all measured a yield strength anomaly in single crystals that were oriented for super lattice slip. In the most comprehensive study involving single crystals of  $\gamma$ -TiAl performed to date, Inui, Matsumuro, Wu and Yamaguchi [23] have shown that both ordinary and superlattice dislocations exhibit an anomalous increase in their CRSS with temperature.

Similar to what has been observed in polycrystals, Inui et al. [23] also reported that the yield stress-temperature profile of all orientations could be divided into three temperature regimes. Their observations suggest that superdislocation motion is easiest at low and intermediate temperatures but that the CRSS for superdislocations becomes prohibitively high at temperatures approaching the peak in the yield strength anomaly. Ordinary dislocations and twinning were found to have increased importance at these intermediate and high temperatures. Inui et al [23] also reported an orientation dependence of the CRSS, but all single crystal studies performed to date have employed compression tests. The lack of single crystal tensile data is unfortunate because it prohibits the measurement of the tension-compress asymmetry of the yield strength and prevents the development of a dislocation model for TiAl that is similar to the highly successful description of superdislocation cross-slip in  $\text{Ni}_3\text{Al}$  [24].

A newly developed microsample tensile testing machine has been shown to be ideal for measuring mechanical properties with limited amounts of material [25], and we are in the process of using this novel apparatus to measure the tension and compression strength of TiAl as a function of specimen orientation and

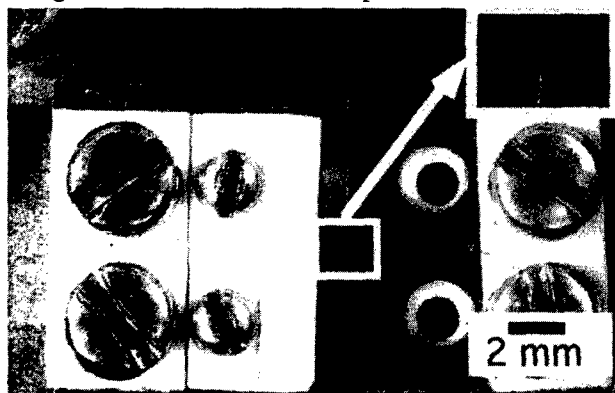


Figure 4: Microsample in the grips and awaiting testing, these grips are specially designed to isolate the specimen and allow for resistive heating of the sample.

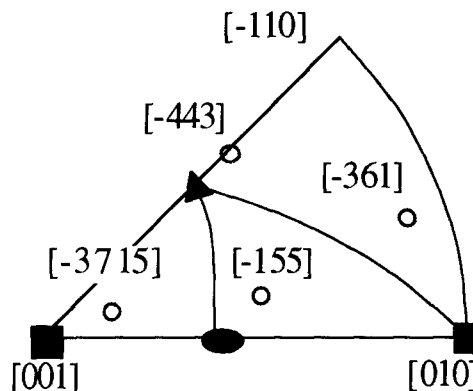


Figure 5: Standard stereographic triangle showing the tension and compression orientation of the microsamples that have been tested.

test temperature. There are three main challenges associated with the tensile testing of very small specimens: i) specimen preparation and handling, ii) applying and measuring a uniaxial load while minimizing effects of bending and friction in the loading mechanism, and iii) strain measurement. The specimens used in the present study were grown in the optical float zone furnace at the University of Pennsylvania [18], oriented using Laue and TEM, sliced and punched with an EDM, electro-polished to a mirror finish, coated with 6  $\mu\text{m}$  Ni and indented with microindents that act as the markers for the strain measurement.

The small size of the microtensile specimens precludes the use of most standard gripping mechanisms. In the present study, self-aligning grips, which match the ends of the dog-bone specimens, hold the specimens while a linear air bearing insures proper alignment of the load frame, greatly reduces friction in the loading mechanism, and permits accurate measurement of the load with an in-line miniature load cell. A photograph of a micro-tensile loading device and specimen are shown in Fig. 4, and a more detailed description of this device are given in [26,27].

Strain is measured by use of an interferometric strain/displacement gage (ISDG); a non-contact optical technique for measuring the relative displacement of two reflective markers. When illuminated with a laser, the diffracted reflections from the facets of these pyramidal-shaped indents overlap and interfere to produce fringes in a manner that is equivalent to Young's two-slit interference phenomenon [28]. A tensile strain causes the fringes to move towards the incident laser beam, and the strain is measured by monitoring the motion of the fringes with linear diode arrays. Rigid body motions and bending will also cause the fringes to move, but these effects can be negated by averaging the motion of two fringe patterns on each side of the specimen. The ISDG used in this study was found to have an uncertainty of  $\pm 3\%$  and a strain resolution of  $\sim 5$  microstrain. A more complete description of the optical principles and the practical

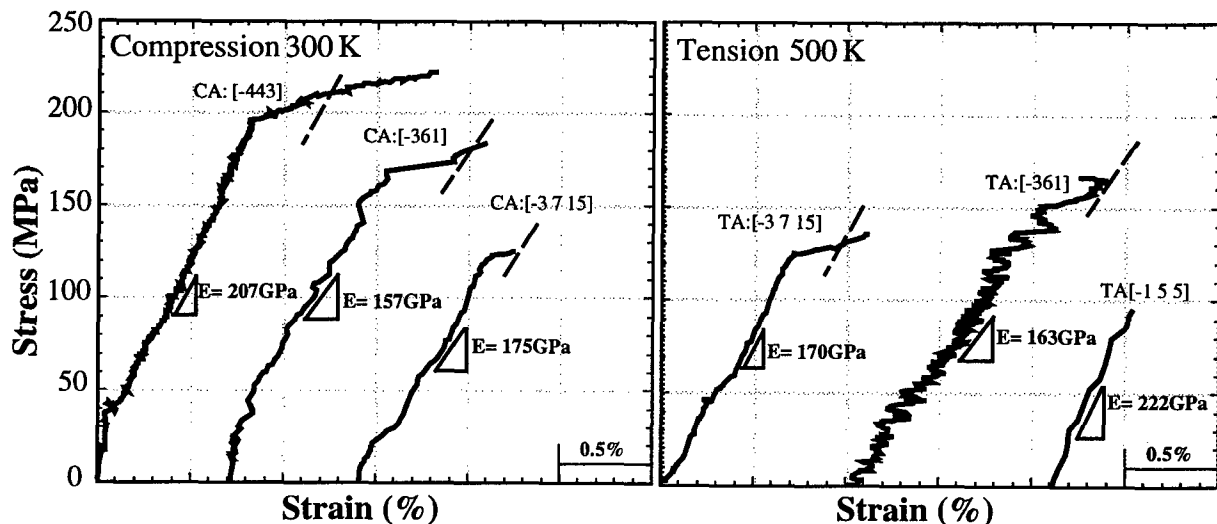


Figure 6: Compression and tension stress-strain curves for  $\gamma$ -Ti-55.5%Al single crystals deformed at 300 and 500 K. The 0.2% off-set for each of the different orientations are given by the dotted lines. The [-155] oriented sample fractured before yielding and no flow stress was measured, but values of  $s_{0.2\%}$  were obtained for the other orientations. Taken from Zupan and Hemker [27].

aspects of an ISDG measurement system are given in review article [29] and NASA report [30].

Microsample tensile specimens of single crystal  $\gamma$ -Ti-55.5%Al have been tested at four different orientations, two different temperatures, and in both tension and compression. The loading axes of these tests are indexed and shown graphically in Fig. 5. The compressive stress-strain curves for three room temperature microsample tests are shown in Fig. 6(a). All tensile tests conducted at room temperature failed in a brittle manner, but the stress-strain curves for three 500 K microsample tensile test are given in Fig. 6(b).

The fact that the ISDG measures strain directly on the gage of the microsample specimens greatly facilitates the measurement of Young's modulus ( $E$ ). Values for  $E$  have been measured on the elastic portion of the curves in Fig. 6 and are listed in Table 1. Literature values of measured [31,32] and calculated [31,33] values of the anisotropic elastic constants have been used to calculate  $E$  for each of the four orientations, and are included in Table 1. A comparison of these values shows the microsample test results to be in very good agreement with the previously reported values.

The 0.2 flow stress ( $\sigma_{0.2\%}$ ) for the microsample tensile tests have been taken from the stress-strain curves. The maximum resolved shear stress (RSS) for both  $\langle 110 \rangle$  and  $\langle 101 \rangle$  slip has been determined for each experiment, and these values are compared with reference values of similar orientations in Table 1. The similarity between the measured and literature values for  $\langle 101 \rangle$  slip is encouraging and can be taken as an indication that superdislocation activity is the controlling deformation mechanism in all of the microsample tests. The absence of a single value of the CRSS is an indication that Schmid's law varies with orientation in TiAl. This

variation is reflected in the literature [23,34], and further experiments are under way to quantify this variation.

The [-3 7 15] microsample tensile test that was run at 500 K and is shown in Fig. 6(b) is, to the author's knowledge, the first plastically deformed tensile curve for single crystal  $\gamma$ -TiAl. It is interesting to note that the measured value of  $\sigma_{0.2\%}$  is nearly identical to the value that was measured in compression at 300 K, because this suggests that the tension-compression asymmetry for this orientation is negligible.

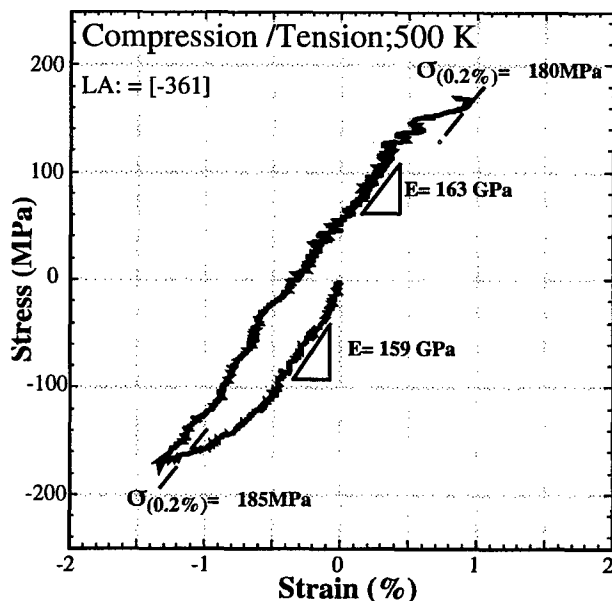


Figure 7: Stress-strain curves for the cyclic loading of single crystal along the [-361] orientation at 500 K. The specimen was compressed until it yielded ( $\sigma_c=180$  MPa) and then pulled until it yielded in tension ( $\sigma_t=185$  MPa).

Table 1 Comparison of the measured and reference values of E (GPa),  $\sigma_{0.2\%}$  (MPa) and RSS (MPa) for TiAl

Loading Axis	E <sub>measured</sub>	E <sub>calc</sub> Exp. (GPa)		E <sub>calc</sub> Theory		σ <sub>(0.2%)</sub>	RSS Super	RSS Ordinary	RSS Reference Values	
[-443]	207	206	206	182	220	-216	76	52		
[-361]	163,157,159	165	165	134	148	-188, -185 +180	94	61	98	
[-3 7 15]	175,170	169	169	173	157	-131 +130	65	36		68
[-155]	222	202	201	205	206	—	N/A	N/A		
Refs.		[32]	[31]	[33]	[31]				[23]	[34]

In order to further investigate this point, a reverse cycle tension-compression microsample experiment has been designed and the first results from that test are given in Fig. 7 (note: the tensile portion of this curve is repeated in Fig. 6). In this experiment, a [-3 6 1] microsample specimen has been pushed until it yielded in compression and then pulled until it yielded in tension. In this way, the compressive and tensile yield strength of the crystal was measured on the same specimen. The measured values of  $\sigma_{0.2\%}$  are noted on the graph and listed in Table 1. The difference in the measured values of the yield strength is only 5 MPa. This test will have to be repeated for a number of orientations and temperatures, but this preliminary result indicates that the tension-compression asymmetry is minimal at 500 K.

#### Creep Behavior

The majority of studies on the creep behavior of polycrystalline binary [35] and ternary [36] alloys of  $\gamma$ -TiAl have been based on the phenomenological description of steady-state creep in pure metals. Measured changes in the minimum creep rate of  $\gamma$ -TiAl have been correlated with variations in temperature, stress, grain size and Al content, but these attempts to identify and model the deformation processes associated with power law creep have met with little success. The need for microstructural observations of the development of substructure during creep has been echoed by a number of authors [37-39].

Creep curves that have been obtained at intermediate temperatures (550, 575, and 597°C) under an applied stress of 400 MPa are shown in Fig. 8 (a). These tests temperatures are in the region of the anomalous yielding behavior, but the overall creep strength of this alloy was found to have a normal temperature dependence. The overall shape of these creep curves is composed of three parts: primary creep where the creep rate decreases rapidly, secondary creep in which the creep rate goes through a minimum, and tertiary creep in which the creep rate increases with time. The general shape is similar to that associated with steady-state power law creep in a number of pure metals and solid solution alloys, but the deformation microstructure is not. Subgrains were not

observed in these specimens, and the dislocation structure was found to evolve throughout the duration of the creep experiments, see Fig. 8 (b,c).

Specimens that were interrupted during primary creep and sectioned for TEM observations were found to contain superdislocations, ordinary dislocations, and faulted dipoles, see Fig. 8 (b). The observation of fault dipoles during creep was unexpected, but their presence has been taken as a strong indication of the activity of superdislocations during primary creep. The role of superdislocations is further evidenced by the fact that the densities of superdislocations and fault dipoles were generally found to be comparable with that of ordinary dislocations. The ordinary dislocations that were observed were found to contain a substantial number of pinning points that aligned along screw orientation. These pinned ordinary dislocations are very similar to those associated with yielding at these temperatures [2,3].

A micrograph of a specimen unloaded during secondary creep is shown in Fig. 8 (c), and observations like this one have led to the following microstructural characterization of secondary creep. The faulted dipoles that were prevalent during primary creep could not be found. Superdislocation were observed and were noted to be almost identical in nature to those observed during primary creep. Ordinary dislocations were observed and were found to have increased in both number and degree of bowing. A modest number of twins were also observed. The density of ordinary dislocations in the grains containing twins was visibly lower than in those which do not.

The microstructure in tertiary creep has been found to be dominated by ordinary dislocation motion, see Fig. 8(d). A large number twins were observed in the tertiary specimens, but the extensive bowing, looping, and multiplication of ordinary dislocations during tertiary creep is the most profound finding of our microstructural study of creep in  $\gamma$ -TiAl. The ordinary dislocations associated with tertiary creep do not exhibit a strong preferred orientation, instead they seem to be expanding in a manner that is consistent with what has been observed in high temperature yielding experiments. Evidence of by-passing and the pinching off of dislocations at local

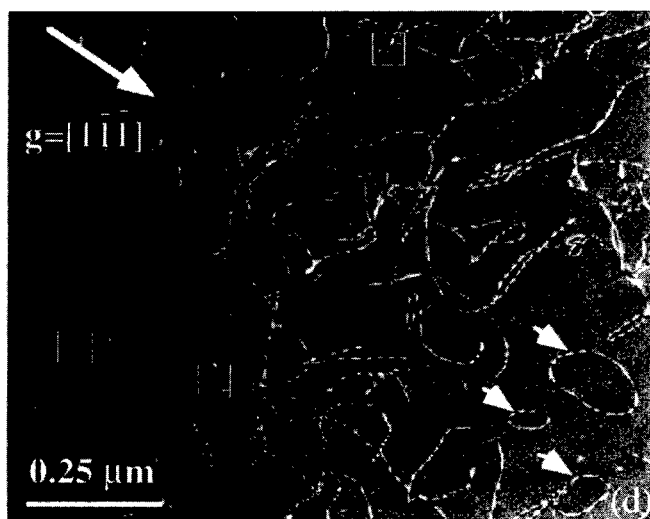
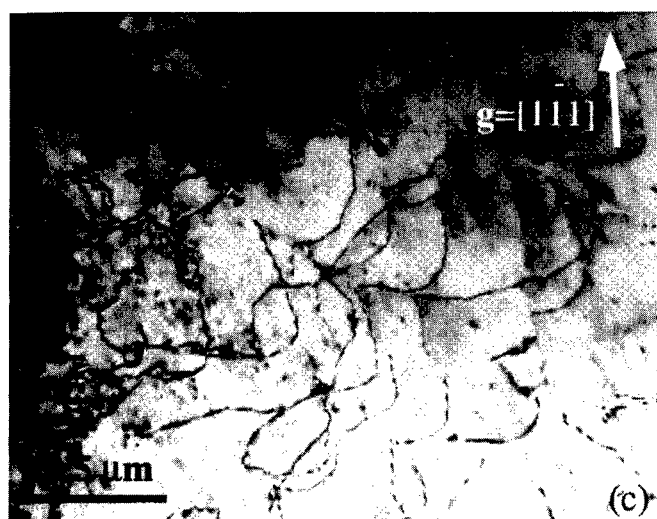
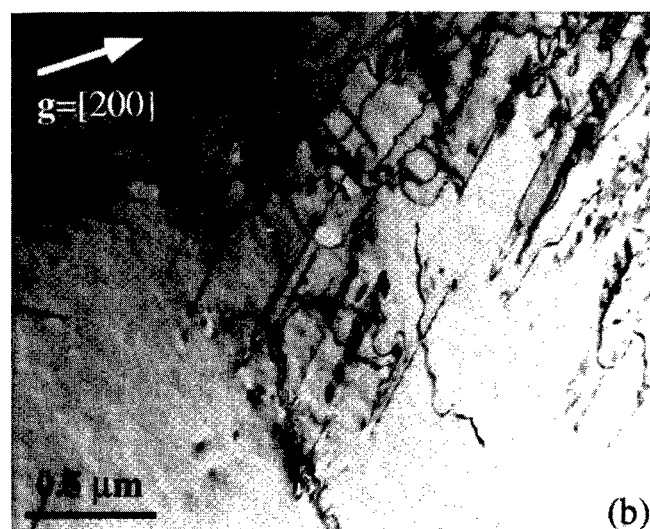
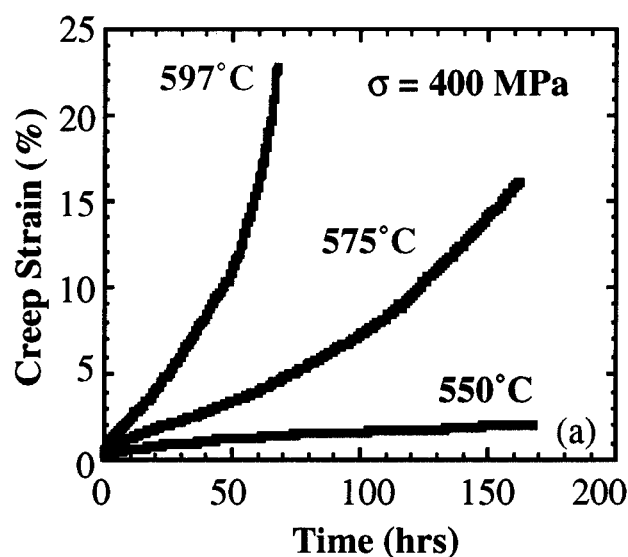


Figure 8: (a) Creep strain vs. time for creep experiments conducted at 550°C, 575°C and 597°C, and at 400 MPa. The deformation substructure associated with a test conducted at 597°C of: (b) primary creep (0.6% strain) where faulted dipoles, superdislocations and ordinary dislocations are present, (c) secondary creep (5.0% strain) evidencing the increased bowing of ordinary dislocations and the absence of faulted dipoles, and (d) tertiary creep (22% strain) where ordinary dislocation bowing multiplication dominates the substructure.

pinning points are highlighted with boxes in Fig. 8 (d). The creation and expansion of small loops are also highlighted (with arrows) in this figure. Tilting experiments, not shown here, have shown these loops to be expanding by glide on (111) planes, and the continual generation and multiplication of ordinary dislocations appears to be the underlying cause of tertiary creep in this material.

We have measured the densities of superdislocation and ordinary dislocations as a function of creep strain, and the results of this exercise are given in Table 2. The density of superdislocations was found to maintain a constant value of approximately  $2 \times 10^{10} \text{ cm}^{-2}$ . By contrast, the density of ordinary dislocations was

found to increase by an order of magnitude over the life of the creep experiment. An Orowan relation has been used to compare the increase in ordinary dislocation density with the corresponding increase in creep rate, and the results of this comparison indicate that the creep rate increases three times as fast as the density [40]. This observation suggests that processes other than the increase in dislocation density play an important role in the acceleration of the creep rate. The observed change in the configuration of ordinary dislocations suggests that both the density and mobility of these dislocations are responsible for tertiary creep.



Table 2 Dislocation densities ( $\times 10^{10}/\text{cm}^2$ ) of ordinary dislocations and superdislocations measured in specimens deformed to various amounts of creep strain

	Primary	Secondary	Tertiary
<b>b=1/2&lt;110]</b>			
550°C	5.9±0.9	18.9±5.1	
597°C	5.9±1.4	23.4±5.0	60.2±8.1
703°C	17.1±3.2	24.0±6.2	
<b>b=&lt;101]</b>			
550°C	2.1±0.5	2.5±0.3	
597°C	2.4±0.3	2.6±0.5	
703°C	2.0±0.3	1.9±0.6	

### Superdislocation Motion

Superdislocations in  $\gamma$ -TiAl have been proposed [5] and observed [41] to cross-slip into non-planar "roof type" barriers. HREM observations of these "roof barriers" have shown the superdislocation core to be dissociated into an extended  $\text{SESF}_{(111)}\text{-APB}_{(010)}\text{-SISF}_{(-11-1)}$  non-planar configuration that is substantially wider and more formidable than the KW locks that have been observed in  $\text{Ni}_3\text{Al}$ . The formation of these roof barriers is a thermally activated process, and the CRSS of superdislocation motion has been shown to rise sharply at temperatures above 800 K [23]. This dramatic increase in the CRSS and the fact that cross-slipped superdislocations remain immobile in the latter stages of creep can both be attributed to the extended nature of the superdislocation core in the cross-slipped configuration.

The motion of superdislocations in the early stages of creep and in low temperature yielding experiments deserves further attention. The drawing out of faulted dipoles that is depicted in Fig. 1 is a clear indication that the creation of faulted dipoles is tied to the motion of superdislocations. Detailed studies [4,7] have shown that the formation of these faulted dipoles occurs by the localized pinning, by-passing, and subsequent relaxation of a superdislocation, but the origin of localized pinning is still unknown. The disappearance of faulted dipoles at higher temperatures can be related to their thermal instability and the fact that localized pinning is supplanted by cross-slip at higher temperatures. In this light, the observation and subsequent disappearance of faulted dipoles during creep are suggestive of superdislocation motion during the early stages of primary creep, the exhaustion of superdislocation activity through cross-slip, and the self annihilation of the faulted dipoles during the high temperature test. The role of faulted dipole formation in low temperature yielding has been well documented [2-4,6], but the formation of faulted

dipoles has not been reported for single crystal yielding, and this discrepancy deserves further attention.

Inui et al. [23] have shown that the compressive CRSS for  $\langle 101 \rangle$  slip depends on crystal orientation and suggested that the asymmetric  $\text{SISF}_{(111)}\text{-APB}_{(111)}\text{-CSF}_{(111)}$  dissociation of superdislocations in TiAl should lead to a tension-compression asymmetry of the yield strength. The Schmid's law violations have been found in both tension and compression in the current study, and more tests aimed at measuring the CRSS at a large number of orientations and temperatures is currently underway. The microsample tests also indicated that the tension-compression asymmetry of  $\gamma$ -TiAl is negligible at 300-500 K. Additional tests at higher temperatures are also being pursued.

### Ordinary Dislocation Motion

Measured [23] and theoretical [42] estimates of the Peierls stress for ordinary dislocation motion in  $\gamma$ -TiAl are in the range of 175 - 250 MPa. The absence of ordinary dislocations in the low temperature yielding studies and the observation of highly curved dislocations in post-mortem TEM observations can also be taken as evidence of the high lattice friction associated with ordinary dislocation motion in  $\gamma$ -TiAl. The activation of BCC-like thermally activated glide can be expected to play an important role in overcoming lattice friction, and the rapid decrease in the CRSS of  $\langle 110 \rangle$  slip with temperature that is observed at low temperatures [23] is an indication of the thermally activated glide processes.

Unlike normal BCC motion, the mobility of ordinary dislocations in  $\gamma$ -TiAl has been found to be reduced by the formation of intrinsic pinning points at intermediate temperatures. Evidence for strengthening associated with these pinning points can be found in both the yield strength anomaly that occurs at intermediate temperatures and in the unusually large amount of strain hardening that is observed during primary creep. In both instances, ordinary dislocation motion was found to be inhibited by the presence of the pinning points; the dislocations were observed to bow out between a densely packed array of pinning points that are roughly aligned along the Burgers' vector of the dislocation.

The strength and effectiveness of these pinning points has been found to depend on both time and temperature. While the density of pinning points has been observed to increase with temperature at intermediate temperatures, the precipitous fall of the CRSS for  $\langle 110 \rangle$  slip that occurs above the peak in the yield stress is a strong indication that there is a critical temperature, above which pinning is defeated by thermally activated motion. The observation of intrinsically pinned ordinary dislocations during both yielding and primary creep is a clear indication that yielding and creep are related processes. Many of the processes that have been used to describe yielding (i.e. intrinsic pinning points, unzipping, jog dragging, prismatic loop formation) can also be used

to explain the creep behavior, and the enhanced bowing of ordinary dislocations that occurs during the latter stages of creep can be used to characterize the thermally activated motion of ordinary dislocations.

The reversible nature of deformation and strain hardening illustrated in Fig. 3 suggests that pinning points are continuously defeated and reformed during yielding. The overcoming of pinning has also been observed in the secondary and tertiary regions of the creep curves, but here the constraints of the experiment (constant stress and temperature) suggest that the pinning points are defeated by a thermally activated process, most likely the lateral unzipping of pinning points that results in increased bowing and further motion of these dislocations. The intrinsic pinning points have also been observed to serve as initiation sites for dislocation multiplication. Evidence for multiplication through spiral like by-passing and loop formation and growth have both been observed, see Fig. 8(d). In summary, it appears that the three dimensional nature of pinning that results in the yield strength anomaly at intermediate temperatures naturally leads to dislocation multiplication and a decrease in strength when given enough time at high enough temperatures.

### Twinning

The temperature dependence of twinning and observation that the density of twins increases with creep strain are rather unusual findings given the fact that twinning is usually considered to be an athermal process. It is important to note that increased twinning is also tied to conditions where ordinary dislocation motion dominates the dislocation behavior, i.e. near the anomalous peak in polycrystalline alloys and during tertiary creep. The observation that twinning is associated with the absence of superdislocation motion and the activity of ordinary dislocation systems, which are too few in number to accommodate general deformation, suggests that twinning may be explained in terms of geometric constraints and incompatibility stresses. The finding that the volume fraction of grains containing twins and the total density of twins both increase with creep strain [39] also suggests that these twins are nucleated by the misfit stresses that build up in the crystal as ordinary dislocation motion progresses.

### Summary and Conclusions

The mobility of both ordinary dislocations and superdislocations has been found to have a profound effect on the macroscopic mechanical behavior of both yielding and creep, and the following relationships have been noted:

- The motion of superdislocations is related to localized pinning and faulted dipole formation at low

temperatures and cross-slip locking and the formation of rather formidable "roof-type" barriers at high temperatures.

- Preliminary attempts at characterizing superdislocation motion by measuring the tension-compress asymmetry with microsample tensile tests indicate that this effect is small in single crystalline Ti-55.5%Al at 500 K.
- The mobility of ordinary dislocations is restricted by lattice friction at low stresses and the intrinsic formation of pinning points at intermediate temperatures. At higher temperatures and longer times these pinning points naturally act as sources for multiplication.
- Twinning has been observed to occur during both yielding and creep. Increased activity at large strains and high temperatures suggests that twinning may be associated with the need for strain accommodation.
- Low temperature yielding in polycrystalline TiAl occurs by superdislocation motion and the formation of faulted dipoles. Superdislocation activity has also been identified in single crystal studies, but the formation of faulted dipoles has yet to be verified. In both cases, the yield strength anomaly can be related to both the cross-slip locking of superdislocations and the intrinsic pinning of ordinary dislocations. The drop in high temperature strength can be related to the thermally activated multiplication and increased mobility of ordinary dislocations.
- The unusually high strain hardening that is observed during primary creep is due to the exhaustion of superdislocation motion and the pinning of ordinary dislocations. With time and temperature, the pinching off and by-passing of pinning points lead to dislocation multiplication and increased mobility. This increase in ordinary dislocation activity governs tertiary creep and controls the overall creep performance of this alloy.

### Acknowledgments

This work was supported by the Air Force Office of Scientific Research, the NSF Mechanics and Materials Program, and the NSF Division of Materials Research.

### References

- 1 Y. W. Kim, *JOM*, **46**, 30 (1994).
- 2 S. Sriram, D. M. Dimiduk, P. M. Hazzledine, and V. K. Vasudevan, in press, (1997).
- 3 B. Viguier, K. J. Hemker, J. Bonneville, F. Louchet, and J. L. Martin, *Phil Mag A*, **71**, 1295 (1995).
- 4 G. Hug, A. Loiseau, and A. Lasalmonie, *Phil Mag. A*, **54**, 47 (1986).

- 5 B. A. Greenberg and M. A. Ivanov, *Structural Intermetallics*, TMS, 293 (1993).
- 6 H. A. Lipsitt, D. Shechetman, and E. Schafrike, *Metall. Trans. A*, **6**, 1991 (1975).
- 7 B. Viguier and K. J. Hemker, *Phil. Mag. A*, **71**, 575 (1996).
- 8 P. Prasad Rao and K. Tangri, *Mat. Sci. & Eng.*, **A132**, 49 (1991).
- 9 S. A. Court, V. K. Vasudevan, and H. L. Fraser, *Phil. Mag. A*, **61**, 141 (1990).
- 10 S. Farenc and A. Couret, *MRS Symp. Proc.*, **288**, 465 (1993).
- 11 M. A. Morris, *Phil. Mag. A*, **68**, 259 (1993).
- 12 U. Messerschmidt, M. Bartsch, D. Haussler, M. Aindow, R. Hattenhauer, and I. P. Jones, *MRS Symp. Proc.*, **364**, 47 (1995).
- 13 F. Appel, U. Sparka, and R. Wagner, *MRS Symp. Proc.*, **364**, 623 (1995).
- 14 F. Louchet and B. Viguier, *Phil. Mag. A*, **71**, 1255 (1995).
- 15 M. Lu and K. J. Hemker, *Phil. Mag. A*, submitted, (1997).
- 16 B. K. Kad and H. L. Fraser, *Phil. Mag. A*, **69**, 689 (1994).
- 17 S. Wardel, I. Phan, and G. Hug, *Phil. Mag. A*, **68**, 471 (1993).
- 18 R. Mahapatra, H. Lin, D. P. Pope, and Y. T. Chou, *MRS Symp. Proc.*, **364**, 813 (1995).
- 19 T. Kawabata, T. Kanai, and O. Izumi, *Acta Metall.*, **33**, 1355 (1984).
- 20 Z. X. Li and S. H. Whang, *Mater. Sci. Eng.*, **A152**, 182 (1992).
- 21 Z.-M. Wang, Z. X. Li, and S. H. Whang, *Mat. Sci. & Eng.*, **A192/193**, 211 (1995).
- 22 M. A. Stucke, V. K. Vasudevan, and D. M. Dimiduk, *Mat. Sci. & Eng.*, **A192/193**, 111 (1995).
- 23 H. Inui, M. Matsumuro, D.-H. Wu, and M. Yamaguchi, *Phil. Mag. A*, **75**, 395 (1997).
- 24 V. Paidar, D. P. Pope, and V. Vitek, *Acta Metall.*, **32**, 435 (1984).
- 25 B. Yuan and W. N. J. Sharpe, *Journal of Testing and Evaluation*, in press, (1996).
- 26 M. Zupan, D. LaVan, and K. J. Hemker, *MRS Symp. Proc.*, in press (1996).
- 27 M. Zupan and K. J. Hemker, *Metall. & mater. Trans., A*, submitted, (1997).
- 28 D. Halliday and R. Resnick, *Fundamentals of Physics*, 2 ed. John Wiley and Sons, (1977).
- 29 W. N. J. Sharpe and R. O. Fowler, in *Small Specimen Test Techniques Applied to Nuclear Reactor Vessel Thermal Annealing and Plant Life Extension*, edited by W. R. Corwin and F. M. Haggag (American Society for Testing and Materials, Philadelphia, Pa, 1993), p. 386-401.
- 30 W. N. J. Sharpe, "An Interferometric Strain/Displacement Measurement System," Report No. 101638 (1989).
- 31 K. Tanaka, T. Ichitsubo, H. Inui, M. Yamaguchi, and M. Koiwa, *Phil. Mag. Lett.*, **73**, 71 (1996).
- 32 Y. He, R. B. Schwarz, A. Migliori, and S. H. Whang, *J. Mater. Res.*, **10**, 1187 (1995).
- 33 C. L. Fu and M. H. Yoo, *Phil. Mag. Lett.*, **62**, 159 (1990).
- 34 M. A. Stucke, D. M. Dimiduk, and P. M. Hazzledine, *MRS Symp. Proc.*, **288**, 471 (1993).
- 35 H. Oikawa, *Mat. Sci. & Eng.* **A153**, 427 (1992).
- 36 R. W. Hayes and P. L. Martin, *Acta metall. et mater.*, **43**, 2761 (1995).
- 37 J. Deddoes, W. Wallace, and L. Zhao, *Int. Mat. Rev.*, **40**, 197 (1995).
- 38 Y. Ishikawa and H. Oikawa, *Mater. Trans., JIM*, **35**, 336 (1994).
- 39 M. Lu and K. J. Hemker, *Acta mater.*, in press (1997).
- 40 M. Lu and K. J. Hemker, *Metall. & mater. Trans., A*, submitted, (1997).
- 41 K. J. Hemker, B. Viguier, and M. J. Mills, *Mat. Sci. & Eng.*, **A164**, 391 (1993).
- 42 J. P. Simmons, M. J. Mills, and S. I. Rao, *MRS Symp. Proc.*, **288**, 335 (1995).

## DEFORMATION SUBSTRUCTURE EVOLUTION PERTAINING TO 1/2<110] UNIT DISLOCATIONS IN TiAl ALLOYS

Seshagiri Sriram \*, Dennis M. Dimiduk, and Peter M. Hazzledine†  
Materials Directorate, Wright Laboratory, WL/MLLM  
Wright-Patterson AFB OH 45433-7817

\*SYSTRAN Corporation, 4126 Linden Ave., Dayton OH 45432

†UES Inc., 4401 Dayton-Xenia Road, Dayton OH 45432

### Abstract

In single-phase, coarse grained TiAl, at room temperature (RT) and above, much of the plastic strain is carried by 1/2<110] unit dislocations. They undergo double cross-slip forming jogs with a variety of heights. The rise in the yield stress with temperature, in the temperature range RT-600°C is linked to the increased frequency of double cross-slip. Observations in this paper suggest that in ( $\alpha_2$ + $\gamma$ ) lamellar TiAl the same mechanisms operate within  $\gamma$  lamellae, but now dislocations must overcome both point (jog) obstacles and planar (lamellar boundary) obstacles. As the lamellar thickness decreases, the planar obstacles become increasingly important. There is some evidence that the two obstacles are linked, that cross-slip is more frequent in thinner lamellae. This is consistent with the observation that in the thinnest lamellae, deformation is mostly carried by twins instead of by 1/2<110] unit dislocations.

### Introduction

Polycrystalline, single-phase  $\gamma$ -TiAl alloys with or without alloying additions, typically have equiaxed grains, with an average size ranging from ~50-500 $\mu$ m, and exhibit a pronounced flow-stress anomaly (between 500 and 800°C) (1-5). The thicknesses of individual  $\gamma$ -lamellae variants in two-phase ( $\alpha_2$ + $\gamma$ ) fully-lamellar materials, on the other hand, follow a log-normal distribution (6,7), with an *average* value ranging from ~1.0-0.6 $\mu$ m in PST (polysynthetically twinned) crystals grown at different rates (6,8,9), and ~0.04-0.5 $\mu$ m in polycrystalline alloys subjected to cooling rate controlled heat treatments (7). Further, in fully-lamellar materials, in which the deformation of  $\gamma$  lamellae is constrained by the presence of  $\alpha_2$  lamellae and alternating  $\gamma$  variants, there is no flow-stress anomaly (10), and the yield-strength value is strongly dependent on the lamellar orientation relative to the stress axis (8,11).

In order to gain insight into the yielding behavior of the  $\gamma$  phase in these distinct microstructural forms, it is essential to have a detailed knowledge of the deformation substructure, and concomitant changes if any, with changes in the microstructural length scales.

The deformation behavior of  $\gamma$ -TiAl is complex since it is dictated often by *simultaneous* operation of the <011>{111}, 1/2<112>{111}, and 1/2<110>{111} slip systems, and 1/6<112] twinning. However, neither the temperature, strain, nor strain-rate dependencies, nor the influence of Al content (hence microstructure), on these individual and/or collective deformation modes, are well understood. The present study is part of an overall initiative aimed at understanding fundamental deformation characteristics of TiAl alloys, paying particular attention to the substructure associated with 1/2<110] unit dislocations.

TEM observations in single crystals (12,13), textured polycrystals (2,14) and equiaxed, coarse-grained polycrystals (15,16), all show that 1/2<110] unit dislocations are a dominant part of the deformation substructure. The presence of unit dislocations has also been reported in deformed two-phase alloys (17-20), and PST crystals (10,21). These dislocations have numerous pinning points along their screw-character segments, and the mixed-character dislocation segments bow about these pinning points giving rise to a distinct cusped morphology. Further, the pinning points appear to align roughly along the screw direction, and dislocation debris in the form of prismatic loops and elongated dipoles are generally observed in the vicinity of the pinning points (2,12,15,16,19,20). The pinning-point density is temperature dependent, increasing from ~2-5  $\mu$ m<sup>-1</sup> at room temperature (RT) to ~15 $\mu$ m<sup>-1</sup> at 600°C (3,16).

Regarding the substructure evolution of unit dislocations, two mechanisms have been reported so far (16,22-23). Louchet and Viguier (21,22) view substructure evolution as a result of collisions between kinks nucleated

along the screw-character dislocation segments, but gliding on separate primary and cross-slip  $\{111\}$  planes, giving rise to pinning points. In this mechanism, the flow-stress is related to the aggregate behavior of a population of pinned dislocations, having a restricted mobility because of pinning. Sriram et al. (16) view substructure evolution as a double cross-slip process, giving rise to jog obstacles (or pinning points) with a range of heights. As a result of this, the screw dislocations experience variable jog-height dependent glide resistance, which accounts for the flow-stress. In both these models, the temperature-dependent pinning frequency, or alternatively, the free segment length of the dislocation between the pinning points is a critical parameter relating substructure to the flow-stress. In the latter model, the dimensions of individual pinning points are critical in establishing the substructure flow-stress correlation. In the case of two-phase alloys, lamellar  $\gamma$  thicknesses are of the same order as the free segment length of the dislocation between the pinning points in coarse-grained alloys at RT. Under these conditions, it is important to know how the substructure and the mechanism giving rise to pinning points changes, in order to correlate these to the flow-stress in lamellar TiAl alloys.

Hence, the purpose of this paper is two-fold: (i) to highlight the three-dimensional substructure of unit dislocations in deformed coarse-grained TiAl, and show that this substructure can account for the flow-stress reasonably well; and (ii) to extend these observations to  $\gamma$  lamellae of the two-phase alloys, in order to study the effect of microstructural length scale on the evolution of deformation induced unit-dislocation substructure.

### Experimental Methods

For the purpose of this study, three types of materials were used: (i) the first set consisted of polycrystalline Ti-50Al and 52Al (all compositions are in at%) alloys containing low levels of interstitials (O, C and N contents in weight ppm. were ~250, ~200 and ~50, respectively), obtained from vacuum arc-melted buttons. Details of the heat treatment and their purpose are reported elsewhere (5). (ii) The second type consisted of a fully lamellar Ti-48Al PST crystal, grown (at 4mm/hr.) using the induction float-zone technique. Cylindrical rods approximately 12mm in diameter, machined from a previously induction skull-melted and HIP'd binary alloy was used as the starting material to obtain this crystal. Finally, (iii) an alloy containing Ti-45.3Al-2.1Cr-2Nb, heat treated to produce a fully-lamellar microstructure (7) and subsequently stabilized at 900°C/24hrs., was examined.

Parallelepipeds for compression testing were sectioned from the bulk heat-treated alloy sets (i) and (iii). For the PST crystal, sections were made from the as-grown crystal with the lamellae oriented perpendicular ( $\phi=90^\circ$ ) to the compression axis. Sample sets (i) and (iii) were deformed to a plastic strain of ~2-3% at room

temperature (RT), and samples from set (i) were also deformed at 300°C and 600°C, respectively. All the compression tests were done under a nominal strain rate of  $1.7 \times 10^{-4} \text{ s}^{-1}$ . Sample (ii) was RT deformed up to a permanent strain of ~0.2%, which was measured with precision microstrain gauges glued to the specimen surfaces. Details pertaining to the microstrain experiments are discussed elsewhere (7). TEM observations of the thin foils obtained from the deformed samples (i), (iii) (at an angle of  $45^\circ$  to the compression axis), and (ii) (parallel to the compression axis) were made using conventional bright-field (BF), dark-field (DF), and weak-beam dark-field (WBDF) techniques.

### Results

The three types of materials used in this study offered a broad range of microstructural scales: the coarse-grained alloys had an average grain size of ~300 $\mu\text{m}$  (50Al) and 500 $\mu\text{m}$  (52Al), respectively;  $\gamma$  thickness in the PST crystal was ~2 $\mu\text{m}$  and that in the fully lamellar, multicomponent alloy (iii), was ~0.6-0.1 $\mu\text{m}$ . Grain sizes were determined from optical micrographs using the standard linear intercept method. Lamellar thicknesses were determined from TEM micrographs, obtained by tilting the foil with lamellae in the edge-on orientation. The thickness of the  $\gamma$  variant is defined as the edge-to-edge distance, measured perpendicular to the adjacent variant, or  $\alpha_2$  boundary.

#### Unit Dislocation Substructure in the Coarse-Grained Alloys

Figure 1 shows  $\mathbf{b}=\pm 1/2[\bar{1}10]$  dislocations obtained from the 600°C deformed 50Al alloy. In this figure, several features of  $\mathbf{b}=1/2<110>$  unit dislocations are highlighted, as mentioned previously. The micrograph shows that: 1) the dislocations tend to align roughly along the  $[\bar{1}10]$  screw-dislocation line direction; 2) the dislocation line contains numerous pinning points, particularly along the screw-dislocation portion, which are indicated by the arrow-heads; 3) in the vicinity of the pinning points, dislocation debris exists in the form of prismatic loops (L), some of which appear as drawn out dipole segments (D). Further, these loop and dipole debris do not necessarily align with the pinning points. Finally, 4) the dislocation line develops cusps having a mixed-character between the pinning points.

The three-dimensional substructure of these dislocations was determined by analyzing a series of weak-beam images, obtained by tilting about the axis of the Burgers vector of the dislocations. Figure 2 shows one of several such images, recorded from the 52Al alloy deformed at 300°C. The dislocation segments marked A, B and C in the figure have  $\mathbf{b}=\pm 1/2[\bar{1}10]$  Burgers vector, and are gliding on the  $(11\bar{1})$  primary slip plane. They are pinned at points  $j_1, j_2, j_3$ , etc., on A, B, C, with bowed segments between these pinning points. The schematic of the three-dimensional structure, resulting from stereo-observations, and the detailed analysis (16), is shown in

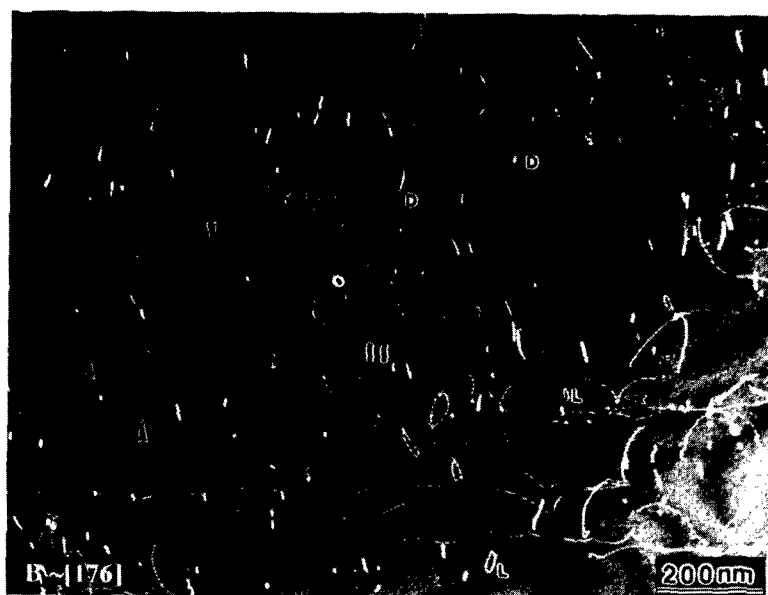


Figure 1: Weak-beam image of  $b=\pm 1/2[110]$  unit dislocations in the 600°C deformed 50Al alloy, showing the characteristic morphological features of these dislocations.



Figure 2: Weak-beam image of  $b=\pm 1/2[110]$  unit dislocations in the 300°C deformed 52Al alloy. The bowed segments A, B, C are gliding on the  $(11\bar{1})$  primary slip-plane. The jogs  $j_1, j_2, j_3$  etc., pin the dislocations.

Figure 3. In this schematic, all the bowed segments lie on parallel  $\{111\}$  octahedral planes and the pinning points ( $j_1, j_2$  etc., in Figure 2) are jogs with varying heights, of the order of  $\sim 20\text{nm}$  in height.

The linear density of pinning-points, i.e., the average number of *visible* pinning-points per unit length of the dislocation segment, were measured from the RT,  $300^\circ\text{C}$  and  $600^\circ\text{C}$  deformed sample micrographs, and were found to be  $\sim 2\mu\text{m}^{-1}$ ,  $10\mu\text{m}^{-1}$ , and  $12\mu\text{m}^{-1}$ , respectively. This is equivalent to the dislocation free segment length ( $\lambda_s$ ), (defined as the length of the dislocation between the visible pinning points) of  $\sim 0.5\mu\text{m}$ ,  $0.1\mu\text{m}$ , and  $0.08\mu\text{m}$ , respectively. Finally, radii of curvature of bowed segments were used to estimate the friction stress. For these measurements an isotropic elasticity approximation was assumed and the radius of curvature was directly read off by fitting them to circles with different radii. Such segments in Figure 2 were measured to have radii between  $45$  and  $125\text{nm}$ , with a mean value of  $84 \pm 20\text{nm}$ . Similar measurements in the RT deformed 50Al alloy yielded a mean radius of  $200 \pm 40\text{nm}$ .

#### Unit Dislocations in the Fully Lamellar Material

In order to determine the morphological characteristics of unit dislocations in  $\gamma$  lamellae with large differences in their thicknesses ( $\lambda_t$ ), weak-beam images of these dislocations were obtained from individual lamellae in the RT deformed PST crystal and the polycrystalline alloys.

Figure 4(a) is an image obtained from the Ti-48Al PST crystal. The micrograph shows that unit dislocation loops emerge from the lamellar interface and glide across the thickness ( $\lambda_t \sim 2\mu\text{m}$ ) of the lamella. Pinning points along the screw segments, indicated by the arrows, and dislocation debris (D) are evident. These morphological features are similar to those observed in the coarse-grained alloys (Figures 1, 2). Further, the linear density of pinning points is  $\sim 4\mu\text{m}^{-1}$ , which is in the same range as that recorded in the RT deformed coarse-grained Ti-50/52Al alloys.

Figure 4 (b) and (c) show hard-mode unit dislocation images obtained from the fully-lamellar polycrystalline alloy. Figure 4(b) is an example in which the screw dislocation line direction is nearly normal to the lamellar interface. The characteristic pinned morphology, and debris loops are clearly seen. Pinned screw dislocations with their line direction parallel to the lamellar interface are also observed, shown in Figure 4(c) (the inset shows an enlarged view), with pinched-off dipole loops in the vicinity of these dislocations. The lamellar thicknesses ( $\lambda_t$ ) were  $\sim 0.6\mu\text{m}$  in (b) and  $\sim 0.4\mu\text{m}$  in (c). The linear pinning-point densities of the dislocations in both the orientations were the same, and were found to be  $\sim 11\mu\text{m}^{-1}$ .

Attempts to observe unit dislocations in much finer  $\gamma$  ( $\lambda_t$  in the range of  $\sim 0.05$ - $0.1\mu\text{m}$ ) lamellae of the polycrystalline material, were unsuccessful. The substructure was dominated by deformation twins, and amongst the several lamellae examined, none of them

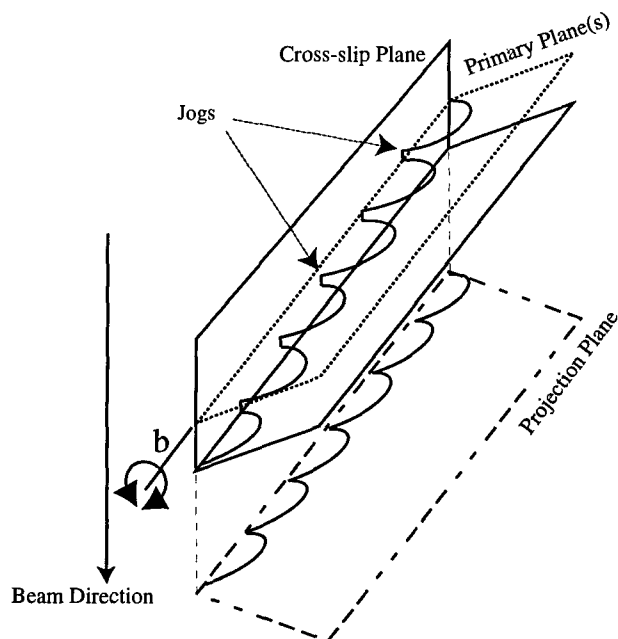


Figure 3: Schematic of the substructure determined from a detailed analysis of the unit dislocation images obtained by tilting about the axis of the Burgers vector. All the bowed segments lie on parallel  $\{111\}$  planes and the jogs lie on the cross-slip plane.

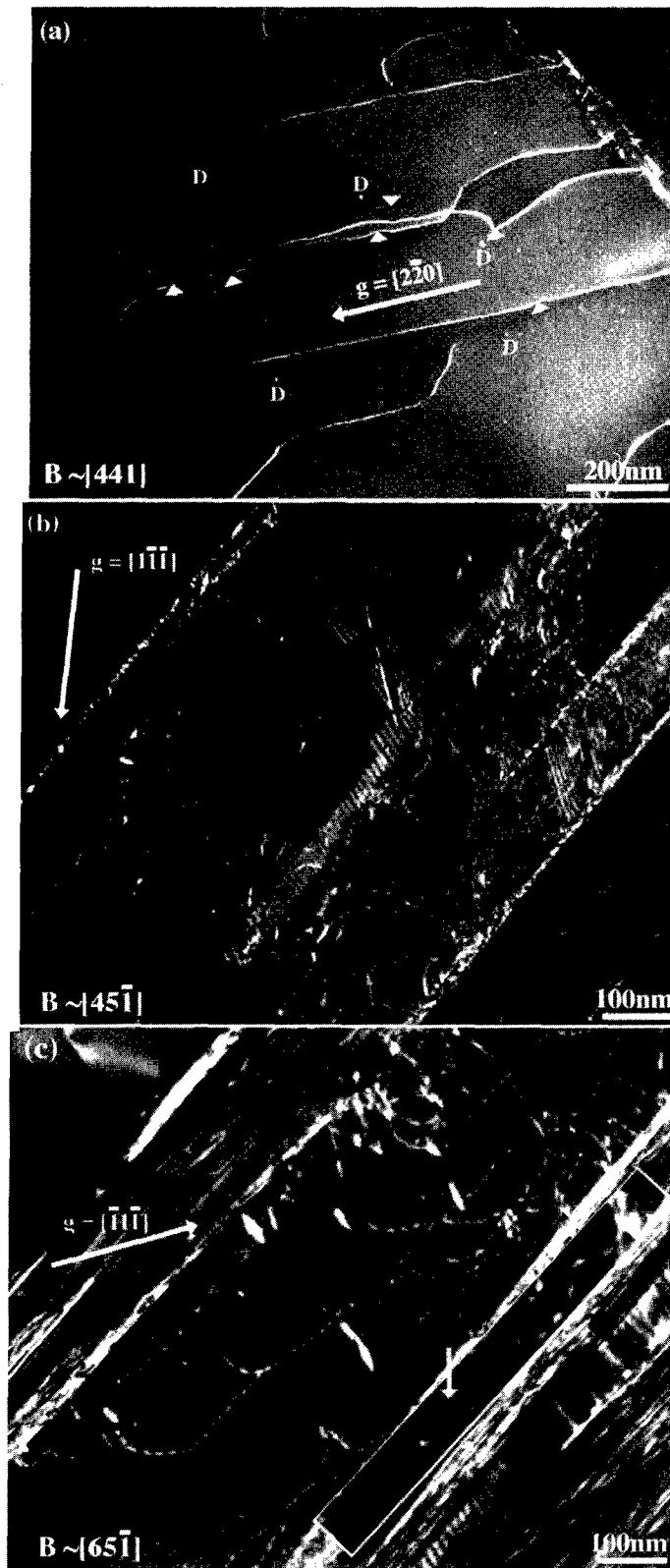


Figure 4: Weak-beam images of  $b=\pm 1/2[\bar{1}10]$  unit dislocations in the fully-lamellar materials: (a)- dislocation loops emerging from the lamellar interface of a  $\sim 2\mu\text{m}$  thick lamella in the PST crystal. (b,c)- hard-mode screw dislocations in the polycrystalline alloy. The screw dislocation line direction with respect to the lamellar interface is nearly normal in (b), and parallel in (c), respectively. The lamellar thickness is  $\sim 0.6\mu\text{m}$  in (b), and  $\sim 0.4\mu\text{m}$  in (c).



contained dislocations with characteristics similar to those shown in Figures 1, 2 and 4.

## Discussion

### Three-Dimensional Characteristics of Unit Dislocations

In the present study, observations of the unit dislocations projected onto the primary plane show features similar to those reported in several earlier studies (2,12,15,16,19,20). Their essential features are 1) numerous pinning points along the screw dislocations, 2) the screw dislocation segments bow between the pinning points, 3) the pinning points align roughly, but not exactly, along the Burgers-vector direction, and 4) there are small prismatic dislocation loops and elongated dipoles with the same Burgers vector as the primary dislocations.

Our interpretation of the three dimensional structure of the unit dislocations is that all the bowed segments lie on the primary plane and that the pinning points are jogs, as shown in Figure 3. This structure is similar to the one reported in Be (which also shows a yield stress anomaly) by Beuers, Johnson and Petzow (24). The occurrence of jogs along the dislocations suggests that profuse *double cross-slip* has occurred and that the resulting jogs act as obstacles, impeding the motion of the primary screw dislocations. The fact that the screw dislocations may slip on the primary plane, transfer to the cross-slip plane and then back to the primary plane so readily is not surprising in view of the very compact screw dislocation core, as suggested by simulation results (25) and experimental observations (on a 60° mixed segment) (26,27). Double cross-slip, in which most of the dislocation motion (and hence strain) occurs on the primary plane, is expected in samples for which the primary Schmid factor significantly exceeds that on the cross-slip plane.

Using the characteristic features of the substructure described above, an attempt is made to account for the observed flow-stress in the 300°C deformed 52Al alloy. In order to do this, the possible components of the substructure contributing to the flow-stress need to be determined; these are discussed below.

### Jog-Height Dependent Drag Processes

Based on the above results, it is concluded that the pinning points are jogs, and that they exist in a range of heights. Under the force of the applied stress, the jogs can move laterally along the dislocation line (conservative glide), or move forward non-conservatively, the latter leading to jog-height dependent drag processes. Regarding the former, a detailed force analysis (16) on the jogs (considering the line tension on the bowed segments, the motion of the bowed segments (under the applied stress) and the drag force normal to the screw direction) showed that, lateral motion is possible only for short jogs (of the order of few atomic spacings) with fairly large cusp asymmetries. Outside of this restrictive regime, the jogs become trapped between the bowed segments and are strong obstacles to dislocation glide.

Depending upon the jog height, different drag processes (28) may be envisaged during the forward motion of the dislocations. These are shown schematically in Figures 5 (a-c). First, (Figure 5a) for elementary jog heights,  $h_v$ , up to a maximum height of a few atomic spacings, a sufficiently high stress will move the jog with the dislocation, either emitting or absorbing vacancies depending upon the sign of the dislocation and the direction of movement. Next, (Figure 5b) for intermediate height jogs,  $h_d$ , the gliding dislocation bows around the jog forming edge-dislocation segments. The elastic interaction between the segments connecting the jogs is strong, preventing them from passing each other, hence the process would involve dragging or extending a dipole. Finally (Figure 5c), for jogs with large heights ( $h_f$ ), the separation between the dislocation segments connecting the jogs is large enough that they act as independent dislocation sources.

### Short Jogs and Friction Stress

The smooth, curved shapes of the dislocations in stress-free foils observed in Figures 1 and 2, and earlier observations (2,12,15,16,19,20) indicate two things: first, the friction stress is high, and second, the friction stress is not entirely a Peierls stress ( $\tau_p$ ). For the purposes of interpreting these observations, it is postulated that the friction stress ( $\tau_f$ ) consists of three components; a Peierls stress ( $\tau_p$ ), a solid solution stress ( $\tau_{ss}$ ) and the part of the pinning stress ( $\tau_j$ ) caused by small vacancy-producing atomic jogs which move with the dislocations (Figure 5(a)). Further, friction stress is a part of the flow-stress which can reverse sign without macroscopic dislocation motion. The friction stress can be estimated from the radius of curvature of the bowed segments from the relationship

$$\tau_f \geq T/bR_m \quad (1)$$

Using the measured average radius of  $84 \pm 20 \text{ nm}$  (Figure 2), a line tension ( $T$ ) of  $Gb^2/2$ , and setting  $G=65.2 \text{ GPa}$  (at 573K) (29),  $b=0.28 \text{ nm}$ , the reversible friction stress on these bowed out dislocations is estimated to be at least  $114 \pm 30 \text{ MPa}$ . This stress estimate may be compared with experimental stress values obtained in this 52Al alloy deformed at 300°C. The flow-stress value at a maximum deformation of  $\sim 1.6\%$  is  $325 \text{ MPa}$  (30), which, when resolved on the primary slip system, gives an upper limit of  $163 \text{ MPa}$ . This implies that the friction stress accounts for at least 70% of the slow stress. Despite the isotropic elasticity approximation for the line tension, the comparison suggests that the friction stress accounts for most of the flow-stress.

### Intermediate Height Jogs and Dipole Formation

For intermediate jogs with height ( $h_d$ ) greater than one unit, an alternative to producing vacancies is for them to create dipoles as the screw dislocation moves (Figure 5(b)). The upper limit to the height of a dipole

may be estimated from the fact that when  $h_d$  is large enough, the applied stress may break the dipole apart. In this case the dipole becomes a dislocation source (Figure 5(c)). Dipoles become unstable when

$$h_d > Gb/[8\pi(1-\nu)(\tau_a - \tau_f)] \quad (2)$$

where  $\tau_a$  is the applied stress. The average height of the tallest jog that was measured is 40nm. Using Equation (2) together with the measured jog height, and setting  $\nu=0.236$  (29), the calculated value for  $(\tau_a - \tau_f)$  is 24MPa, once again confirming that the friction stress accounts for most of the flow stress.

#### Substructure-Flow-Stress Correlation in Coarse-Grained TiAl

From the results and discussion presented in the foregoing, the following idea of yielding in TiAl emerges when  $b=1/2<110\rangle$  unit dislocations are controlling. The cores of these screw dislocations are so compact that cross-slip and double cross-slip are profuse. The result is a jogged screw dislocation which emits point defects from short jogs and drags dipoles from tall jogs. The jogs of different heights provide a spectrum of point forces resisting the motion of the screw dislocation.

At 300°C the separation between the pinning points, (i.e., the visible jogs), is close to 100nm. The forces exerted by the pinning points vary from  $6.4 \times 10^{-10}$  N for a unit jog emitting vacancies to  $5.5 \times 10^{-9}$  N for a dipole of maximum height, 40nm (16). The first estimate for the pinning stress

therefore lies between 23MPa (for all unit jogs) and 192MPa (for all 40nm tall jogs), the actual value depending on how the heights of the jogs are distributed. These numbers may be compared with the measured friction stress of  $114 \pm 30$ MPa and the estimated upper limit of the flow-stress,  $\sim 163$ MPa. As mentioned earlier, the friction stress is that part of the flow-stress which can reverse sign without macroscopic dislocation motion. This stress consists of the Peierls stress, a solid solution stress and the part of the pinning stress caused by jogs that can move with the dislocation. The flow-stress is the friction stress plus the pinning stress from tall, dipole forming jogs. The experimental stresses are not precise enough to enable exact conclusions to be drawn but, taking them at face value, it seems that most of the jogs are short at 300°C because the tall jogs only contribute  $163 - 114 = 49$ MPa to the flow-stress. As the temperature rises, the increase in the flow-stress (2-5) can be explained by either a shift in the distribution of jog heights towards larger heights (and therefore larger pinning forces) and/or an increase in the friction stress  $\tau_f$  due to a larger number of short jogs. These simple considerations show that it is possible to work out the yield stress from the properties of a single screw dislocation subjected to a spectrum of pinning forces from jogs produced by double cross-slip.

#### Substructure Flow-Stress Correlation in the Fully-Lamellar Material

The coarse-grained TiAl alloys (16) show that pinning-point formation on unit dislocations is intrinsic to these

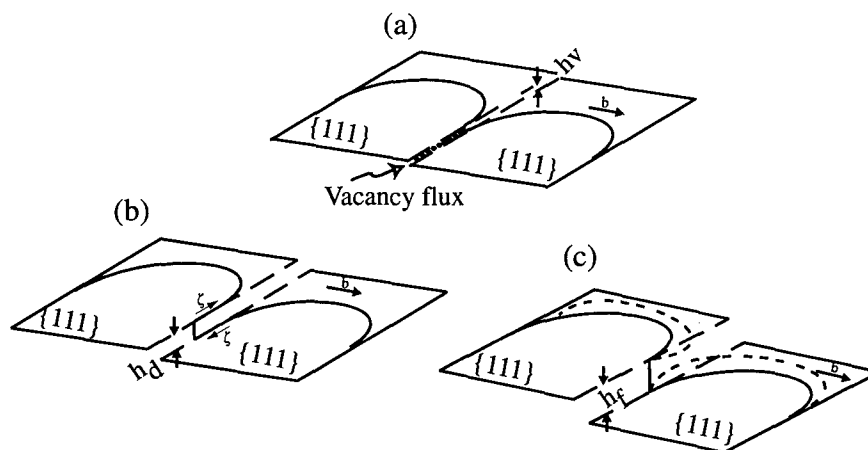


Figure 5: Schematic of the various jog-height dependent drag processes during forward motion of the bowed segments: (a) elementary jog-height (short jogs,  $h_v$ ) dragging involving generation of point defects; (b) intermediate jog-height (tall jogs,  $h_d$ ) involving dipole dragging; (c) large jog-height ( $h_f$ ) involving dislocation-dipole by-pass.

alloys, independent of alloy chemistry and grain size, but dependent on deformation temperature alone. Assuming this holds true in the fully-lamellar material, it is expected that for a given deformation temperature, the spacing of strong jog obstacles along unit-dislocation segments ( $\lambda_s$ ), would be in the same range as that in the coarse-grained material, for  $\gamma$  lamellae thicknesses ( $\lambda_t$ ) greater than  $\lambda_s$ . However, when  $\lambda_t$  is similar to or less than  $\lambda_s$ , one may speculate that the dislocation segments would contain a negligible number of pinning points along their length, giving rise to practically straight, free screw-character dislocation segments. In order to investigate these hypotheses, unit-dislocation segments were imaged in  $\gamma$  lamellae having thicknesses greater than (case (i)), similar to (case (ii)), and less than (case (iii)), the free segment length of dislocations in the coarse-grained material. A full study would include such observations as a function of deformation temperature. However, the present study is restricted to RT observations. The linear pinning density in the RT deformed coarse-grained alloy was  $\sim 2\mu\text{m}^{-1}$  (16), giving a free segment length of  $\sim 0.5\mu\text{m}$ .

#### Case (i)- $\lambda_t > \lambda_s$

Gamma ( $\gamma$ ) lamellae thicknesses ( $\lambda_t$ ) greater than the free segment lengths ( $\lambda_s > 0.5\mu\text{m}$ ) were only present in the PST crystals. Morphological characteristics of unit dislocations in a  $\sim 2\mu\text{m}$  thick PST lamella (Figure 4(a)) were similar to those observed in the coarse-grained alloys, and the linear pinning-point density was of the order of  $\sim 4\mu\text{m}^{-1}$ , which is in the same range as that in the coarse-grained alloys. It appears that at least in  $\gamma$  lamellae with these thicknesses, the morphological characteristics of unit dislocations do not change, compared with the coarse-grained alloys, as expected.

However, differences exist in terms of the relative contribution of the substructure to the measured flow-stress in both the material forms. Estimates of the friction stress in the RT deformed 50Al alloy yields a value of  $\sim 105\text{MPa}$ . The flow-stress at a maximum deformation of  $\sim 1.8\%$  is  $365\text{MPa}$ , which, when resolved on the primary slip system, gives an upper limit of  $183\text{MPa}$ . Comparing this value with the friction stress shows that the latter accounts for  $\sim 60\%$  of the flow-stress, similar to results obtained in the 52Al alloy deformed at  $300^\circ\text{C}$ . Friction stress determined from the radius of curvature of the bowed segments in the PST crystal, on the other hand, is  $\sim 78\text{MPa}$ . The RT yield strength of this crystal was  $\sim 540\text{MPa}$ , and using the Taylor factor of 3.4 for this particular orientation ( $\phi = 90^\circ$ ) (7), the resolved shear-stress is  $\sim 158\text{MPa}$ . Hence, the friction stress accounts for roughly only half the flow-stress. Though there are large uncertainties in these numbers, the result suggests that in the case of lamellar materials, dislocation processes at the glide barriers (lamellar boundaries) play an important role in contributing to the flow-stress. This is consistent with a recent analysis (7) showing lamellar-boundary spacing as an important microstructural parameter contributing to strengthening in fully-lamellar alloys. This was also pointed out earlier by Yamaguchi and Umakoshi (31).

#### Case (ii)- $\lambda_t \sim \lambda_s$

As the lamellar thickness  $\lambda_t$  approaches  $\lambda_s$ , as seen in the polycrystalline fully-lamellar alloys (Figure 4(b,c)), morphological changes in terms of pinning points and debris density, are evident. The gliding of hard-mode unit dislocations with their screw direction across the thickness ( $\sim 0.6\mu\text{m}$ ) of the lamella (i.e., short screw dislocation segments), and those with their line direction parallel to the lamellar boundary (i.e., long screw dislocation segments), in a neighboring lamella ( $\sim 0.6\mu\text{m}$  thick), are shown in Figures 4 (b) and (c), respectively. In both cases, the pinning density was the same,  $\sim 11\mu\text{m}^{-1}$ , but higher than that in both, the coarse-grained material (by roughly five times), and the PST crystal (by roughly three times). This observation suggests that the pinning frequency might not be solely temperature dependent, as expected from studies based on coarse-grained materials (2,3,16), but at the scale of the microstructure considered herein, other effects might become important. It is conceivable that at finer microstructural scales, internal stresses become increasingly significant (32), and that these stresses promote cross-slip.

The RT yield strength for this polycrystalline alloy was  $\sim 769\text{MPa}$ . Assuming a Taylor factor of  $\sim 3.4$  (7) the resolved shear stress is  $\sim 225\text{MPa}$ . Regarding the friction stress, direct measurements were not made, but assuming that the value was similar to that of the PST crystal ( $78\text{MPa}$ ), it accounts for only 35% of the flow stress, suggesting that long-range hardening from the lamellar boundaries is more important.

#### Case (iii)- $\lambda_t < \lambda_s$

Attempts to image unit-dislocations in lamellae typically of the order of  $\sim 0.1\mu\text{m}$  in the fully-lamellar polycrystalline alloys, surprisingly, did not reveal any of these dislocations. The substructure was found to be dominated by deformation twins. The reason for their absence in such fine lamellae is not clear and studies are underway to look at this aspect in more detail. Based on the present observations, one may conclude that twinning is the dominant deformation mode in such fine lamellae, possibly because  $1/2<110]$  unit dislocations are hard to move.

### Conclusions

1.  $b=1/2<110]$  unit dislocations are a dominant part of the deformation substructure in coarse-grained TiAl, and in lamellar TiAl alloys with  $\gamma$  lamellar thicknesses of the order of  $\sim 0.5\mu\text{m}$  or more. In thinner lamellae, twinning dominates.
2. The rate-controlling dislocations have screw character, and bow out on primary planes between discrete pinning points by a double cross-slip process.
3. The observed flow-stress in coarse-grained alloys can be accounted for, in a simple 'one dislocation' model, by the presence of jogs with a temperature-dependent spectrum of heights and

spacings, consequently a spectrum of pinning forces.

4. In lamellar TiAl alloys, the dislocation must overcome both point (jog) and planar (lamellar boundary) obstacles. There is some evidence that these obstacles are linked, in that the pinning frequency increases as lamellar thickness decreases.
5. In lamellar TiAl alloys, dislocation processes at the lamellar boundaries, and internal stresses that develop as the result of the microstructure becomes increasingly important in determining the flow-stress as their thickness gets finer.

#### Acknowledgments

The authors acknowledge the Materials Directorate, WL/MLLM, Wright-Patterson AFB, OH, and the Air Force Office of Scientific Research, for supporting this work. SS acknowledges support through AFOSR contract # F33615-94-C-5804, awarded to SYSTRAN Corp., Dayton OH. We would like to thank Professor Vijay K. Vasudevan for many helpful discussions, and Drs. T.A. Parthasarathy and Madan G. Mendiratta for part of the PST crystal results.

#### References

1. P. Prasad Rao and K. Tangri, Mat. Sci. & Engg., A132, 49, (1991).
2. B. Viguier, J. Bonneville, K. J. Hemker, and J. L. Martin, Mat. Res. Soc. Symp. Proc., 364, 629 (1995).
3. B. Viguier, K. J. Hemker, J. Bonneville, F. Louchet, and J. L. Martin, Phil. Mag. A., 71, 1295, (1995).
4. S. Sriram, V. K. Vasudevan, and D. M. Dimiduk, Mat. Res. Soc. Symp. Proc., 364, 647, (1995).
5. S. Sriram, V. K. Vasudevan, and D. M. Dimiduk, Mat. Sci. & Engg., A192/193, 217, (1995).
6. S. Sriram, Contributive Research and Development, Volume 26, Deformation Behavior and Dislocation mechanisms in TiAl Alloys, report, SYSTRAN Corporation, Contract No.F33615-94-C-5804, Materials Directorate, Wright-Laboratory, Wright-Patterson AFB, OH, p.11-15, (1996).
7. D. M. Dimiduk, P. M. Hazzledine, T. A. Parthasarathy, S. Sriram, and M. G. Mendiratta, Met. & Mat. Trans. A., (submitted) (1997).
8. T. Fujiwara, A. Nakamura, M. Hosomi, S. R. Nishitani, Y. Shirai, and M. Yamaguchi, Phil. Mag. A., 61, 591, (1990).
9. Y. Umakoshi and T. Nakano, Acta Metall. et Mater., 41, 1155, (1993).
10. H. Inui, K. Kishida, M. Misaki, M. Kobayashi, Y. Shirai, and M. Yamaguchi, Phil. Mag. A., 72, 1609, (1995).
11. H. Inui, M. H. Oh, A. Nakamura, and M. Yamaguchi, Acta. Metall. Mater., 40, 3095, (1992).
12. N. Bird, G. Taylor, and Y. Q. Sun, Mat. Res. Soc. Symp. Proc., 364, 635, (1995).
13. H. Inui, M. Matsumoro, and M. Yamaguchi, Phil. Mag. A., 75, 395, (1997).
14. B. Viguier, M. Cieslar, K. J. Hemker, and J. L. Martin, Mat. Res. Soc. Symp. Proc., 364, 653 (1995).
15. S. Sriram, V. K. Vasudevan, and D. M. Dimiduk, Mat. Res. Soc. Symp. Proc., 213, 375, (1991).
16. S. Sriram, D. M. Dimiduk, P. M. Hazzledine, and V.K. Vasudevan, Phil. Mag. A., (1997) (in print).
17. V. K. Vasudevan, M. A. Stucke, S. A. Court, and H. L. Fraser, Phil. Mag. Lett., 59, 299, (1989).
18. W. Wunderlich, T. Kresmer, and G. Frommeyer, Z.Metall., 81, 802, (1990).
19. F. Appel, U. Sparka, and R. Wagner, Mat. Res. Soc. Symp. Proc., 364, 623, (1995).
20. M. A. Morris, Phil. Mag. A., 68, 259, (1993).
21. H. Inui, A. Nakamura, M. H. Oh, and M. Yamaguchi, Phil. Mag. A., 66, 557, (1992).
22. F. Louchet and B. Viguier, Scripta Metall. et Mater., 31, 369, (1994).
23. F. Louchet and B. Viguier, Phil. Mag. A., 71, 1313, (1995).

24. J. Beuers, S. Johnson, and G. Petzow, Acta Met., 32, 435, (1987).
25. J. P. Simmons, S. I. Rao, and D. M. Dimiduk, Mat. Res. Soc. Symp. Proc., 288, 335 (1993), *Ibid.*, Alloy Modeling and Design, G.M. Stocks, and P. E. A. Turchi, (Eds), TMS, 183, (1994).
26. K. J. Hemker, B. Viguier, and M. J. Mills, Mat. Sci. Engg., 164A, 391, (1993).
27. J. P. Simmons, M. J. Mills, and S. I. Rao, Mat. Res. Soc. Symp. Proc., 364, 137, (1995).
28. J. J. Gilman and W. G. Johnston, Solid State Physics, 13, 147, (1962).
29. H. A. Lipsitt, D. Shechtman, and R.E. Schafrik, Met. Trans., 6A, 1991, (1975).
30. Sriram Seshagiri., Ph.D. Thesis, University of Cincinnati, (1994).
31. M. Yamaguchi and Y. Umakoshi, Prog. Mat. Sci., 34, 1, (1990).
32. P. M. Hazzledine, B. K. Kad, H. L. Fraser, and D. M. Dimiduk, Mat. Res. Soc. Symp. Proc., 273, 81, (1992).

## THE $\alpha$ - $\gamma$ PHASE TRANSFORMATION MECHANISMS IN TWO-PHASE $\gamma$ -TiAl BASED INTERMETALLIC ALLOYS

E. Abe, T. Kumagai and M. Nakamura

The 3rd Research Group, National Research Institute for Metals,  
1-2-1 Sengen, Tsukuba 305, Japan

### Abstract

The  $\alpha \leftrightarrow \gamma$  phase transformations in a Ti-48at.%Al alloy, which occur during quenching and subsequent aging, are discussed based on detailed systematic analyses of accompanied microstructures from a micron scale to an atomic scale. All the transformation mechanisms were interpreted to be based on the hcp  $\leftrightarrow$  fcc shear-like motion of atoms, which are fine lamellae formation ( $\alpha \rightarrow \alpha_2 + \gamma$ ) and massive transformation ( $\alpha \rightarrow \gamma_m$ ) during quenching, and fine plates formation ( $\gamma_m \rightarrow \alpha(\alpha_2)$ ) during isothermal aging. Besides, these transformations include the diffusion and ordering of atoms, and characteristic features caused by this process were found in the product microstructures. Taking these facts into consideration, possible pathways of the  $\alpha \leftrightarrow \gamma$  phase transformations are discussed.

### Introduction

It is well known that mechanical properties of two-phase  $\gamma$ -TiAl (L1<sub>0</sub>) -  $\alpha_2$ -Ti<sub>3</sub>Al (D0<sub>19</sub>) intermetallic alloys are strongly dependent upon microstructure, and the microstructure of these two-phase alloys can widely be changed by utilizing the phase transformations, especially, the  $\alpha$  (disordered hcp)  $\leftrightarrow \gamma$  transformations [1-4]. In order to establish an effective method of microstructural control to realize the required properties, total understanding of the possible  $\alpha \leftrightarrow \gamma$  phase transformations in these two-phase alloys is quite important. In this view, we have systematically studied the phase transformation mechanisms as well as the accompanied microstructure evolution in a Ti-48at.%Al alloy. From a series of these studies, it was found that several microstructural features can be produced only by a combination of quenching and aging heat treatment [5, 6].

When the Ti-48at.%Al alloy is water-quenched after solution treatment in the  $\alpha$  phase field for a certain period of time, a fully massively transformed ( $\alpha \rightarrow \gamma_m$ ) single phase structure consisting of randomly oriented fine  $\gamma$  grains is formed (Fig. 1(a)) [5,7,8]. Since the massively transformed  $\gamma$  phase is in a metastable state with Ti supersaturation, the  $\alpha_2$  phase is formed by the  $\gamma_m \rightarrow \alpha(\alpha_2)$  transformation on subsequent aging (Fig. 1(b)) [4, 9]. Thus, by utilizing these process, a further possibility of microstructural control is expected. Although a detailed mechanism of the  $\alpha \rightarrow \gamma$  massive transformation has not been clarified yet, the nucleation - growth of the massive transformation is known to start at grain boundaries of the parent phase so that the massive reaction does not completed when the sample is solution treated for an extend period of time, which has grown the parent  $\alpha$  grains larger in size. As a result of this, so-called untransformed region appear within the sample together with the massively transformed area (Fig. 1(c)). This untransformed region was found to comprise extremely fine  $\alpha_2 - \gamma$  lamellar structure (fig. 2) [5] ; this is by contrast with the case of quenched Ti-Al alloys with aluminum content of 40 ~ 47at.%, where the metastable  $\alpha_2$  single phase with aluminum supersaturation is frozen-in [10, 11]. Since Liu et al. recently reported that the refined microstructure with an extremely fine lamellar spacing shows excellent mechanical properties [12], it becomes very important to understand how these fine lamellae have been formed during quenching.

In this paper, we will discuss the  $\alpha \leftrightarrow \gamma$  phase transformations accomplished within a very short time on quenching/heating and produce some characteristic microstructural features described above, which is made by the detailed microstructural analyses. It should be mentioned here that these transformations are regarded as the disordered hcp  $\leftrightarrow$  ordered fcc transformations. This is an interesting aspect

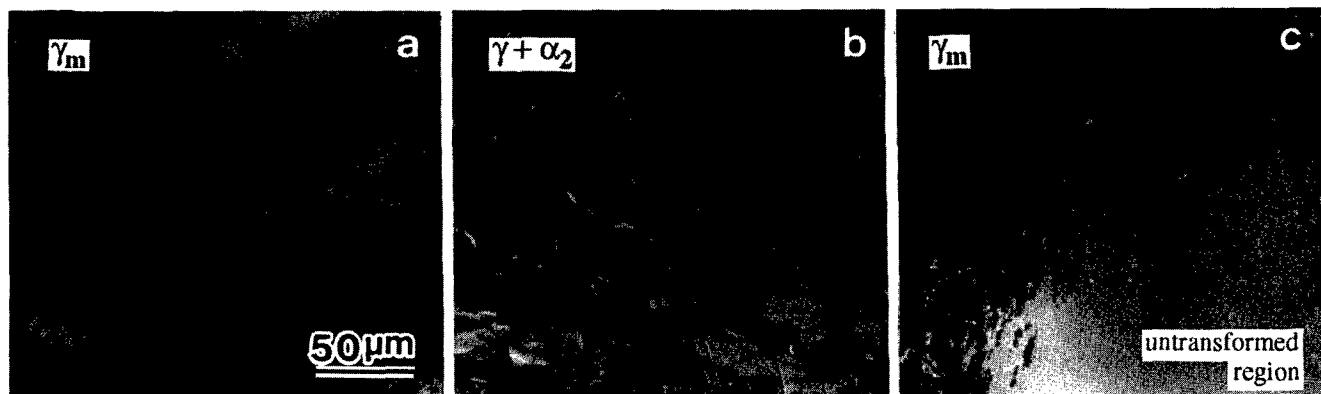


Fig. 1 Optical microstructures of ice-water quenched Ti-48Al alloy after (a) heat treated at 1683K for 1.8ks, (b) subsequently aged at 1473K for 1 day on sample (a) and (c) heat treated at 1683K for 14.4ks.

## Results and Discussion

### Fine lamellae formation : $\alpha \rightarrow \alpha_2 + \gamma$

Fig. 3(a) shows a schematic drawing of the untransformed region in the sample shown in fig. 2. As seen in this figure, the distribution of the  $\gamma$  plates was found to be inhomogeneous in the untransformed region. That is, the density of the  $\gamma$  plates is high near the massively transformed/untransformed boundary and becomes lower at the area far from this boundary. TEM micrographs obtained from these regions are shown in figs. 3(b) and (c) together with the corresponding selected area electron diffraction (SAED) patterns. In fig. 3(b), one can see a very fine lamellar structure consisting of thin plates with a few nm - a few tens nm in thickness. From the SAED pattern, these plates are found to be the  $\alpha_2$  and twin-related  $\gamma$  phases satisfying the crystallographic orientation relationship  $\{111\}\gamma // (0001)\alpha_2$  and  $\langle 110 \rangle \gamma // \langle 11\bar{2}0 \rangle \alpha_2$ , which is referred to as Blackburn's relationship for the Ti-Al system. The interfaces are flat in a wide range, and the interfacial lattice misfit between the  $\alpha_2$  and  $\gamma$  plates are considered to be very small, which can be known from the straight alignment of the diffraction spots from the both phases with streaks, as indicated by arrows [13]. This extremely fine lamellar structure is formed through the  $\alpha \rightarrow \gamma$  phase transformation during rapid cooling, however, this transformation has not proceeded to completion in the area shown in fig. 3(c), where the  $\gamma$  plates are located sparsely in the  $\alpha_2$  matrix. Thus, the early growth stage of the  $\gamma$  plates is frozen-in in this region, and it is evident from this micrograph that the lamellar structure has been formed by the "rapid" platelet precipitation of the  $\gamma$  phase. This microstructural feature is similar to those observed in the early stage of formation of the  $\gamma$  plates during isothermal annealing of Ti-40Al, which requires an incubation time following C-curve kinetics typical of a thermally activated process [14, 15]

Fig. 4 shows a high-resolution image obtained from the growth edge of the  $\gamma$  plate, as indicated by the arrow in fig. 3(c) [16]. In this image, one can notice that steps which are always found to be two (111) or (0001) planes high are formed at both side of the  $\gamma$  plate as indicated by arrows. Except for these steps, we can say that the interfaces are flat and coherent at the atomic level in the early stage of the formation of the  $\gamma$  plate. These steps are the Shockley partial dislocation ledges to accomplish the hcp (AB..) - fcc (ABC..) structural change. From this fact, it can be said that the growth of the platelet precipitation of the  $\gamma$  phase proceeds by migration of each



Fig. 2 TEM micrograph showing massively transformed/untransformed boundary

because these transformations involve two processes which are hcp  $\leftrightarrow$  fcc structural change and ordering of atoms. From this viewpoint, it can be said that these transformations are worth studying as occurring in intermetallic alloy systems.

### Experimental Procedures

A Ti-48at.%Al alloy was prepared by argon arc melting, using high purity (99.9%) Ti and high purity (99.99%) Al chips. The chemical composition of the ingot obtained by wet chemical analysis was 48.0at.%Al with 300wtppm O. The ingot was cut into small pieces with the size of about 7×7×15mm. These pieces were wrapped with Ta foils, heated at 1683K (for 1.8ks and 14.4ks) in a vertical furnace under a high purity argon atmosphere, followed by quenching by dropping into ice water. The as-quenched sample was cut into about 300μm slices, and some of them were subsequently annealed. Thin foils for TEM were prepared by standard twin-jet electropolishing using 10% perchloric acid-ethanol solution at 253K. High-resolution electron microscope observations were made on a 400kV electron microscope (JEM-4000EX) having a point-to-point resolution of 0.17nm. Microchemical analysis using energy-dispersive X-ray spectroscopy (EDS) were performed by a 200kV electron microscope (JEM-2010F) with a field emission gun.

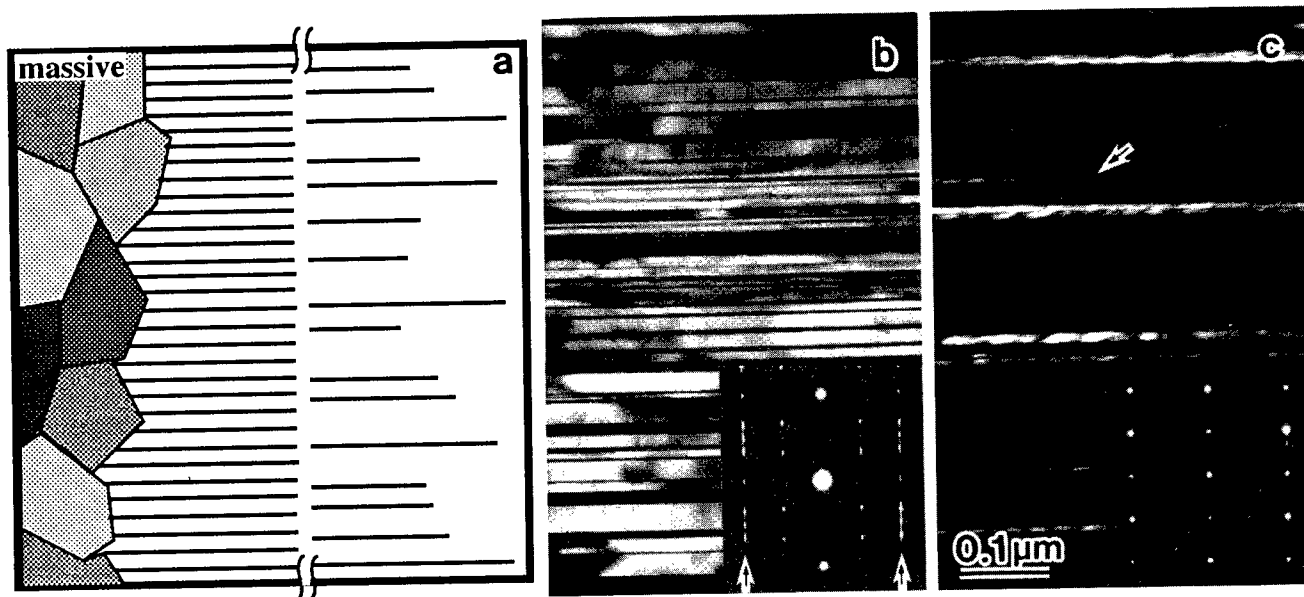


Fig. 3 (a) Schematic illustration showing distribution of the  $\gamma$ -plates in the untransformed region. (b), (c) Bright-field images corresponding to the regions with a (b) high-density and (c) low-density of the  $\gamma$ -plates.

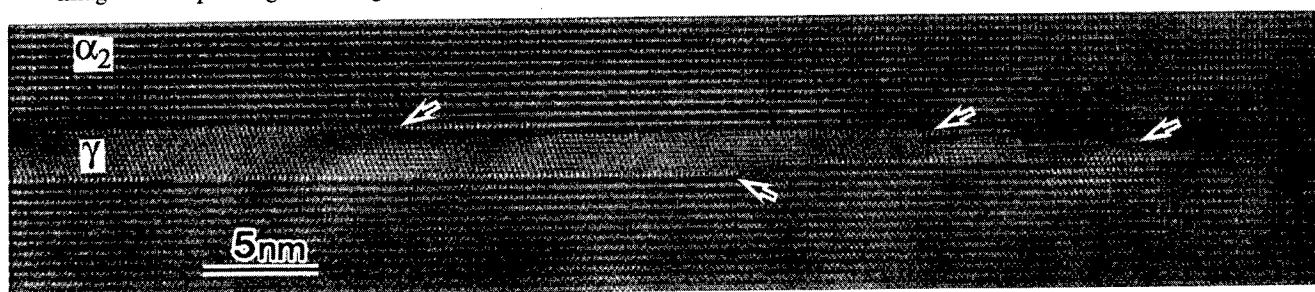


Fig. 4 High-resolution image of the growth edge of the  $\gamma$ -plate taken with the incident beam parallel to the  $\langle 101 \rangle_\gamma$  axis

Shockley partials on alternate (0001) planes, resulting in apparently perfect planar lamellar structure described above.

High-resolution image of the extremely fine lamellar structure is shown in fig. 5(a). In this image, one can see very thin  $\alpha_2$  and  $\gamma$  twin platelet crystals, and no single stacking fault can be recognized. The  $\alpha_2 - \gamma$  and  $\gamma - \gamma$  interfaces were found to be atomically flat without dislocation ledges in a wide range [17], which was confirmed from the image of wider area of fig. 5(a). This is by contrast with the case of the lamellar structure annealed in the two-phase field or slowly cooled from the  $\alpha$  phase field, where a high-density of ledges are formed at the  $\alpha_2 - \gamma$  interfaces [18-20]. In addition, based on the analysis of the ordered contrasts, the interesting feature can be recognized in fig. 5(a) that the antiphase domain boundaries (APDBs) are continuously formed across the  $\alpha_2 - \gamma$  and  $\gamma - \gamma$  interfaces, as schematically drawn in fig. 5(b). This feature of the APDBs can be explained by the  $\alpha \rightarrow \alpha_2 \rightarrow \alpha_2 + \gamma$  transformation pathway during quenching, that is, the  $\gamma$  plates growing by migration of partials can inherit the APDBs those formed by the  $\alpha \rightarrow \alpha_2$  ordering which occurs before nucleation of the  $\gamma$  plates [13]. It should be noted that the APDBs are continuous through the lamellae at the atomic level in fig. 5(a) [13, 21]; this situation is generally expected as a result of lattice invariant shear mechanism. However, the present  $\alpha \rightarrow \gamma$  transformation involves atomic rearrangement process to order finally for the L1<sub>0</sub> type, so that the question arises when and how this process has been accomplished. This will be discussed later in this section.

All of the characteristic features of the present fine lamellar structure described above, such as crystallographic relationship between the parent and product and growth by a shear mechanism, strongly indicate phenomenologically a martensitic transformation. In fact, the apparent microstructural features are very similar to those formed by the hcp - fcc martensite transformation in pure Co or Co-Ni alloys [22,23]. However, the microchemical analyses of the present lamellar structure using EDS showed a considerable compositional change has already occurred between the  $\alpha_2$  and  $\gamma$  phases, as shown in fig. 5(c). This suggests that the diffusion of atoms is involved in the  $\alpha \rightarrow \gamma$  transformation during quenching [13, 24]. It is interesting to note that no significant concentration gradient can be recognized within the  $\alpha_2$  plate, indicating diffusion of Al atoms to the growing  $\alpha_2 - \gamma$  interfaces is fast. On these basis, it is evident that the  $\alpha \rightarrow \gamma$  transformation during quenching has a dual nature both of crystallographic-shear mechanism and diffusion of atoms, just like the platelet precipitate mechanism reported in Cu-Zn, Cu-Zn-Al and Ag-Cd alloys ( $\beta_2$  (B2)  $\rightarrow$   $\alpha_1$  (9R) transformation) [25,26].

Fig. 5(d) is a schematic illustration for explaining the formation mechanism of the  $\gamma$  plates. As seen in this figure, the growth of the  $\gamma$  plate proceeds by shear for plate lengthening and diffusion of atoms for plate thickening [25]. The  $\gamma$  precipitation mechanisms in both cases, during isothermal aging for Ti-40Al [14,15] and during continuous cooling (rapid cooling) for the present Ti-48Al, are considered



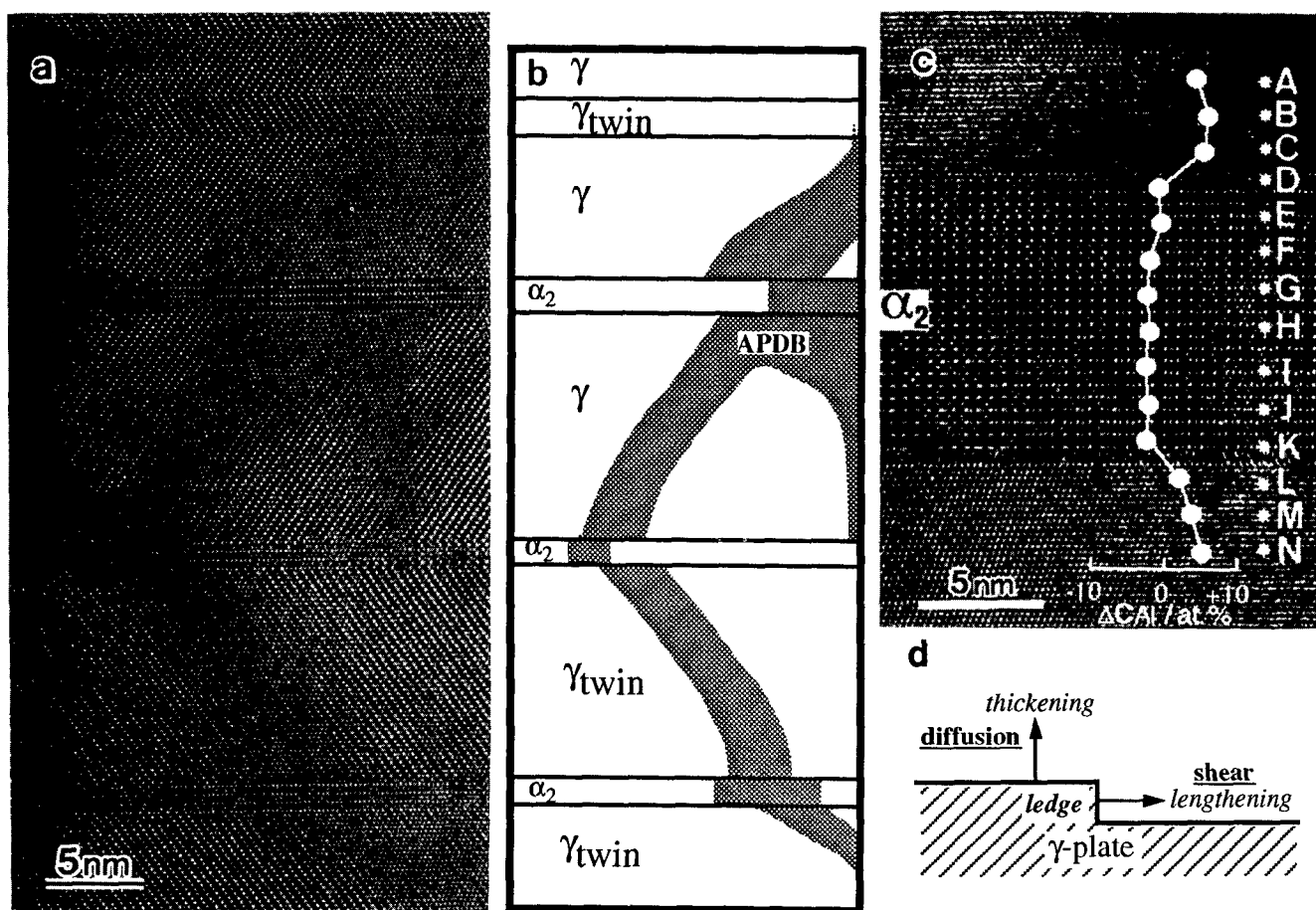


Fig. 5 (a) High-resolution image of the extremely fine  $\alpha_2$ - $\gamma$  lamellar structure in the ice-water quenched Ti-48Al alloy. (b) Schematic drawing of distribution of APDBs in (a). (c) Microchemical analysis by EDS. (d) Mechanism of the plate growth.

to be basically the same. It is evident from rapid lengthening growth of the  $\gamma$  plates (fig. 3(c), fig. 4) that the transformation has been mostly dominated by shear, producing extremely flat and perfectly coherent interfaces in a wide area as observed in the present work. Since the amount of resultant macroscopic shear of this hcp-fcc transformation is fairly large (about 0.35), a high-density of twin is generated during the transformation to accommodate this shear (fig. 5(a)). This implies that most of the partial dislocations at the edges of the  $\gamma$  plates for the hcp-fcc transformation (fig. 4) might have the same Burgers vector. It is confirmed in Ti-40Al that this transformation shows surface reliefs as a result of this shear component [15]. It should be mentioned here, in the case of lamellar structure formed by slow cooling, that relatively high-density of partial dislocation ledges are formed at the  $\alpha_2$ - $\gamma$  interfaces. This is due to a rather diffusion-controlled growth of the plates during slow cooling, that is, plate thickening took place mainly at the later stage of the precipitation, which requires diffusion of atoms and formation of new ledges at the  $\alpha_2$ - $\gamma$  interfaces (fig. 5(d)). In this process, partial dislocations is considered to be introduced to the interfaces to reduce  $\alpha_2$ - $\gamma$  interfacial lattice misfit which is actually observed for the lamellar structure formed by slow cooling [27]. These partials are sessile being not able to move without diffusion of atoms, and a ledge-kink mechanism was proposed to explain the diffusion and ordering process of the  $\alpha \rightarrow \gamma$  transformation [18,19].

The present  $\alpha \rightarrow \gamma$  transformation which occurs during quenching and produces extremely fine lamellar structure involves diffusion of atoms (fig. 5(c)). However, the parent( $\alpha_2$ )/product( $\gamma$ ) interfacial lattice misfit was found to be very small, and this can be one of the factor to suppress formation of new ledges at the interfaces. As mentioned earlier, diffusion of atoms seems to be very fast during quenching so that a ledge-kink mechanism can occur even in the present case, accomplishing ordering for the L1<sub>0</sub> as well as the hcp-fcc structural change by shear. Considering that APDBs are continuous across the  $\alpha_2$ - $\gamma$  interfaces at the atomic level (figs. 5(a) and (b)), it can be said that atomic site correspondence is highly maintained during the present ledge mechanism in the process of  $\alpha_2$ - $\gamma$ , although there does not exist a complete one-to-one correspondence [28]. This indicates that the atom transfer to the migrating partial dislocation ledges take places within a very narrow area around ledges.

It is important fact that the extremely fine  $\alpha_2$ - $\gamma$  lamellae can change into  $\gamma$ - $\gamma$  twin lamellae by short time aging (30sec) at 1273K [5, 16]. Thus, apparently the present  $\alpha \rightarrow \gamma$  transformation seems to be martensitic of time-dependent type. Although the detailed mechanism of this process is not clear, the existence of the metastable  $\gamma$  single phase field in the composition of Ti-48Al at low temperatures may allow the distribution of this  $\gamma$ - $\gamma$  twin lamellae. In addition, the platelet precipitation of the  $\gamma$  phase during

quenching can probably occur only when the  $\alpha$  or  $\alpha_2$  phase are undercooled and cross the metastable extension of the  $\gamma$  single phase field.

As for the nucleation stage of the  $\gamma$  plates during rapid cooling, grain boundaries seem to be most favorable sites (fig. 3(a)). The pre-existing stacking faults in the hcp grain can also be nucleation sites [29], which can construct a fcc stacking at local area. Furthermore, locally ordered B19 regions which were found in the metastable  $\alpha_2$  phase with a high-degree of Al supersaturation (close to Ti-48Al) [30] can also be nucleation sites for the formation of L1<sub>0</sub> structure, because only the change in stacking sequence of the B19 structure will produce the L1<sub>0</sub> structure. The latter two cases indicate a possibility of nucleation from grain interiors. In view of lamellar spacing control, applying a certain amount of external stress will be effective and enhance the nucleation of the plates, which is naturally expected from a nature of the  $\alpha \rightarrow \alpha_2 + \gamma$  lamellar transformation involving shear mechanism that dominates the early stage of the transformation.

#### Massive transformation : $\alpha \rightarrow \gamma_m$

The massive transformation is known to be a composition invariant transformation and generally occur at high-temperatures. Since this transformation shows macroscopically an advancing parent/product interface (fig. 1(b)) and produces the randomly oriented grains of the product phase, it is also known that both shear displacements and short-range diffusion are involved in the atomic movement (individual motion type) during the transformation [31]. The  $\alpha \rightarrow \gamma$  massive transformation in TiAl-based alloys is regarded as the transformation from the disordered hcp ( $\alpha$ ) phase to the ordered fcc (L1<sub>0</sub>) phase, and this is an interesting aspect because this type of transformation has never been reported in any other alloy systems.

As seen in fig. 2, averaged grain size of the  $\gamma_m$  is about a few microns. In the  $\gamma_m$  grains, a high-density of defects caused by the  $\alpha \rightarrow \gamma$  massive transformation is formed. Figs. 6 (a)-(c) show TEM micrographs taken from the  $\gamma_m$  grains. In fig. 6(a), one can see a large number of fine line contrasts aligned parallel to one another, lying on the (111) plane. This microstructural feature is apparently similar to that of the fine  $\alpha_2 - \gamma$  lamellae (figs. 3(b) and (c)) in the untransformed region. In the SAED pattern obtained from the region of fig. 6(a), all diffraction spots can be indexed by twin-related crystals of the  $\gamma$  phase, and no reflections from other phases can be recognized. Thus, we can say that these line contrasts are mostly twins having a wide range of thicknesses, as shown in a dark-field image of fig. 6(b). It should be noted that a density of twins is smaller than that in the fine lamellae in the untransformed region. In addition, in fig. 6(b), one can also notice some of the fine line contrasts which do not correspond to the twins. The nature of these will be described later. On the other hand, in the dark-field image of fig. 6(c) formed with 001 superlattice reflection, some curves showing characteristic fringe contrasts are seen. These fringes were firstly attributed to the APDBs [7, 8], however, recent detailed analysis showed that the nature of these fringes is not a simple antiphase boundary (APB) but is a thin rotated domain (RD) [32]. Since the ordered arrangement of Ti and Al atoms of the  $\gamma$  phase is generally known to be stable up to its melting point, this is the one of the most interesting defects caused by the  $\alpha \rightarrow \gamma$  massive transformation. The problem of interest is how these order-disorder-related defects are formed during the massive transformation.

HREM observation showed that the extremely fine line contrasts are mostly associated with thin platelet crystals (0.8 - 3nm) of twin and hcp, and single stacking faults are rarely observed within the  $\gamma_m$  grain. This fact indicates that the present  $\alpha \rightarrow \gamma$  massive transformation involves hcp - fcc

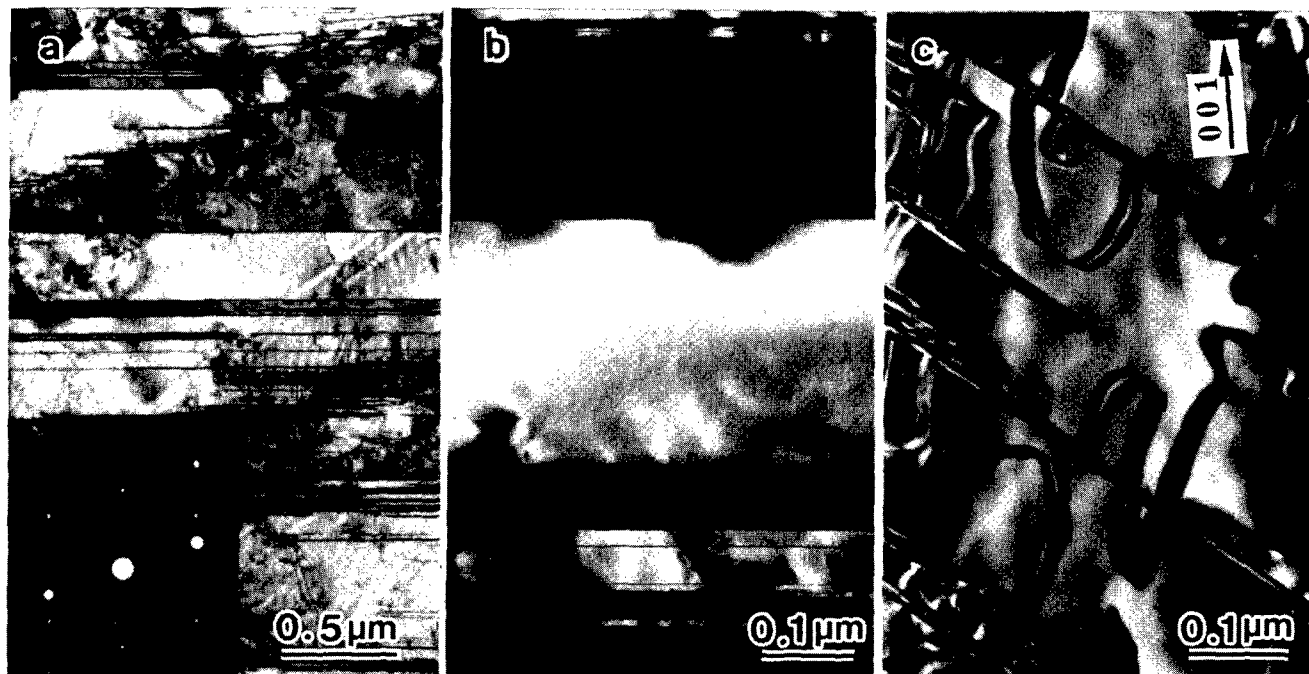


Fig. 6 TEM microstructure of a massively transformed  $\gamma$  grain. (a) Bright-field image taken with the incident beam slightly tilted from the  $[10\bar{1}]$  axis and the corresponding SAED pattern. (b) Dark-field image formed with  $1\bar{1}1$  reflection of the twin crystal. (c) Dark-field image formed with 001 superlattice reflection.

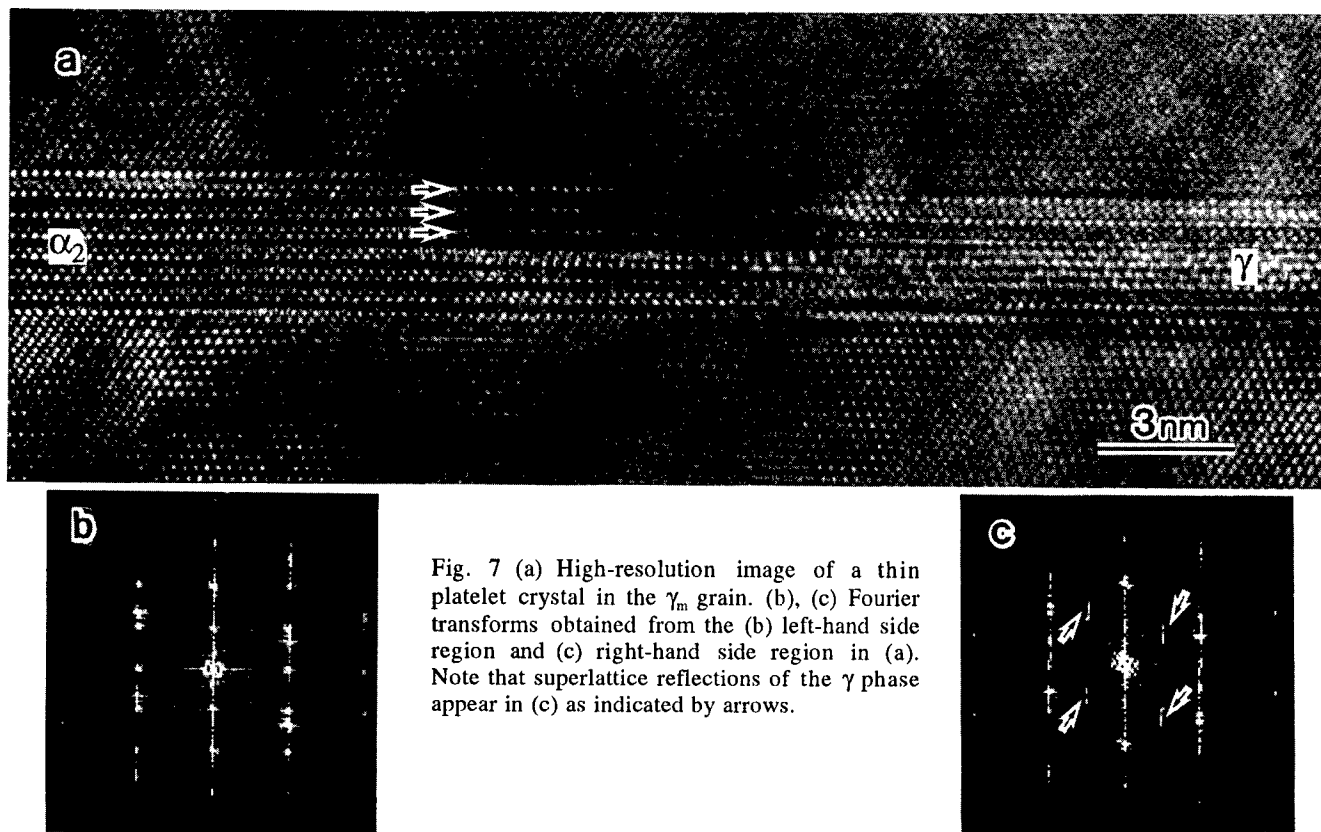


Fig. 7 (a) High-resolution image of a thin platelet crystal in the  $\gamma_m$  grain. (b), (c) Fourier transforms obtained from the (b) left-hand side region and (c) right-hand side region in (a). Note that superlattice reflections of the  $\gamma$  phase appear in (c) as indicated by arrows.

shear displacements, and it can be deduced that these thin hcp crystals are a retained parent phase. In order to accommodate the macroscopic shear as described in the previous section, a large number of twins aligned parallel to one another are considered to be formed during the  $\alpha \rightarrow \gamma$  massive transformation. Fig. 7(a) shows a high-resolution image of thin platelet crystal where the hcp-fcc transformation is frozen-in. In this image, one can notice that this thin plate has a hcp structure at the left-hand side and has a ordered  $L1_0$  structure at the right-hand side with pseudo twin relation ( $[110] \parallel [101]$ ), which can be confirmed by Fourier transforms obtained from the both regions, as shown in figs. 7(b) and (c). On this basis, we can say that the hcp-fcc transitional state exist at the middle of this plate. It is interesting to note that the structure of this transitional region is complex [33]; this situation is in contrast to that of growth of the  $\gamma$  plates for the lamellae formation, where Shockley partial dislocation ledges with two close-packed planes high are clearly observed (fig. 4). This indicates the mechanism of the present massive transformation is not simply interpreted as migration of each partial dislocations. In terms of this, one can find an interesting feature in the transitional area that the two-layer periodic contrasts are recognized along six layers of the close-packed plane as indicated by arrows in fig. 7(a). As is known in the case of hcp-fcc shear involving process, the elastic strain energy and macroscopic shear will be minimized if the three different Shockley partials of  $a/3 \langle 1\bar{1}00 \rangle$  hcp type which cancel with each other migrate during the transformation (self-accommodation) [22, 28]. That is, ledges with six close-packed layers constructed by these three Shockley partials having different Burgers vector will be formed during nucleation and growth stage. According to this interpretation, the periodic contrasts along six layers appeared in the transient region may be associated with this six layer ledge.

Although the massive transformation involves a short-range diffusion of atoms, this kind of self-accommodation mechanism could occur during transformation, and this proposition is in agreement with the relatively low density of twins in the  $\gamma_m$  grain compared with that in the untransformed region, as mentioned earlier.

A detailed analysis of the twin in the  $\gamma_m$  showed that multiple large ledges are frequently formed at the boundaries as shown in fig. 8(a) [34]. In this image, one also find at the twin boundary that three-layer periodic contrasts due to overlapping twin along the incident beam appear. This means that twin interface is inclined and are not on the (111) mirror plane. This situation is attributed to the existence of twinning partial dislocations at the boundaries, and, as a natural extension of this interpretation, it is known that formation of large ledges is caused by piling up of a number of partial dislocations, as schematically drawn in fig. 8(b). From this fact, we can say that the stacking fault energy in the  $\gamma_m$  phase is high. These large ledges on the twin interfaces may be caused by the six-layer ledge mechanism described above.

On the basis of the fact that APDBs (thin RD walls) exist in the  $\gamma_m$  grain (fig. 6(c)), several papers proposed a pathway of the  $\alpha \rightarrow \gamma$  massive transformation as  $\alpha$  (disordered hcp)  $\rightarrow$  disordered fcc  $\rightarrow \gamma$  ( $L1_0$ : ordered version of fcc) [35,36]. Consequently, antiphase domains are formed by fcc- $L1_0$  ordering. One might expect from this pathway that twins will be generated to reduce the elastic strain caused by this fcc-fcc ( $L1_0$ ) ordering. In this case, twins are formed by deformation so that it is most probable twinning takes place on {111} planes of the  $\gamma$  phase. This is not consistent with the present result that twins are always found to be on one of the {111} planes, (111), as described earlier (figs. 6(a), (b)). Thus, the existence of an intermediate disordered fcc state during the massive transformation becomes controversial. In addition,

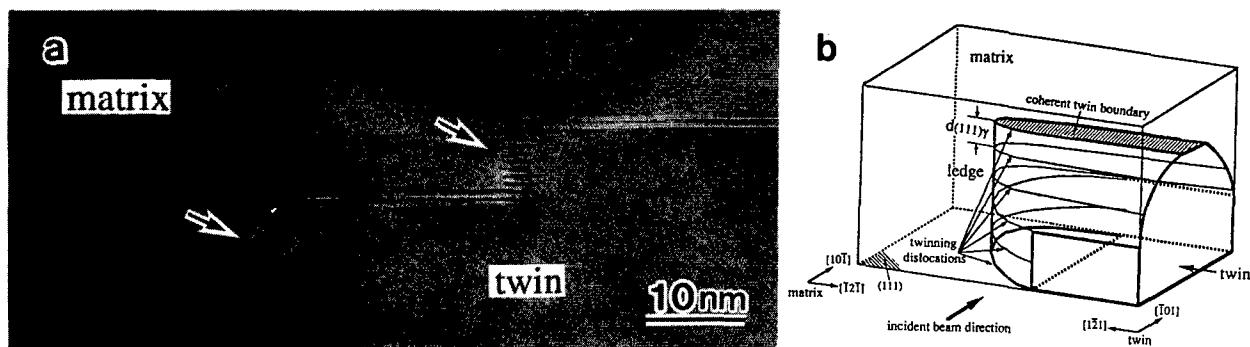


Fig. 8 (a) High-resolution image of a twin boundary in the  $\gamma_m$  grain, showing formation of large ledges at the boundary as indicated by arrows. (b) Large ledge structure model constructed by a number of twinning partial dislocations.

Zhang et al. found that the APB-like fringe contrasts are actually the thin RDs, and based on this, they proposed a model that large RDs formed firstly by fcc - L1<sub>0</sub> ordering become thinner as ordered domain growing [32, 36]. However, we found a simple APDB in the  $\gamma_m$  phase and showed that this APDB can easily change to the thin RD by short-range diffusion process, as shown in fig. 9 [37]. This indicates simple APDBs have been firstly formed during the transformation. All of these facts obtained in the present work seem to support that these defects, twins and thin hcp platelet crystals aligned parallel with each other and APDBs, have been formed directly during the  $\alpha \rightarrow \gamma$  massive transformation, not via intermediate disordered fcc state. This direct formation mechanism of the  $\gamma_m$  phase from the

disordered  $\alpha$  phase was already proposed in the early work by Jones and Kaufman [8].

Here, the question arises why this transformation can produce randomly oriented grains in spite of the fact that the transformation involves hcp-fcc shear like movement of atoms. As seen in fig. 2, the grains seem to have random orientation, and we did not find any significant orientation relationships between the  $\gamma_m$  grains and fine lamellae in the untransformed region. At this stage, there is no clear answer for this question. However, if the twinning in the  $\alpha$  phase take place prior to the massive transformation [38], apparently randomly oriented product grains could be obtained. In this case, the driving force for this twinning will be a problem.

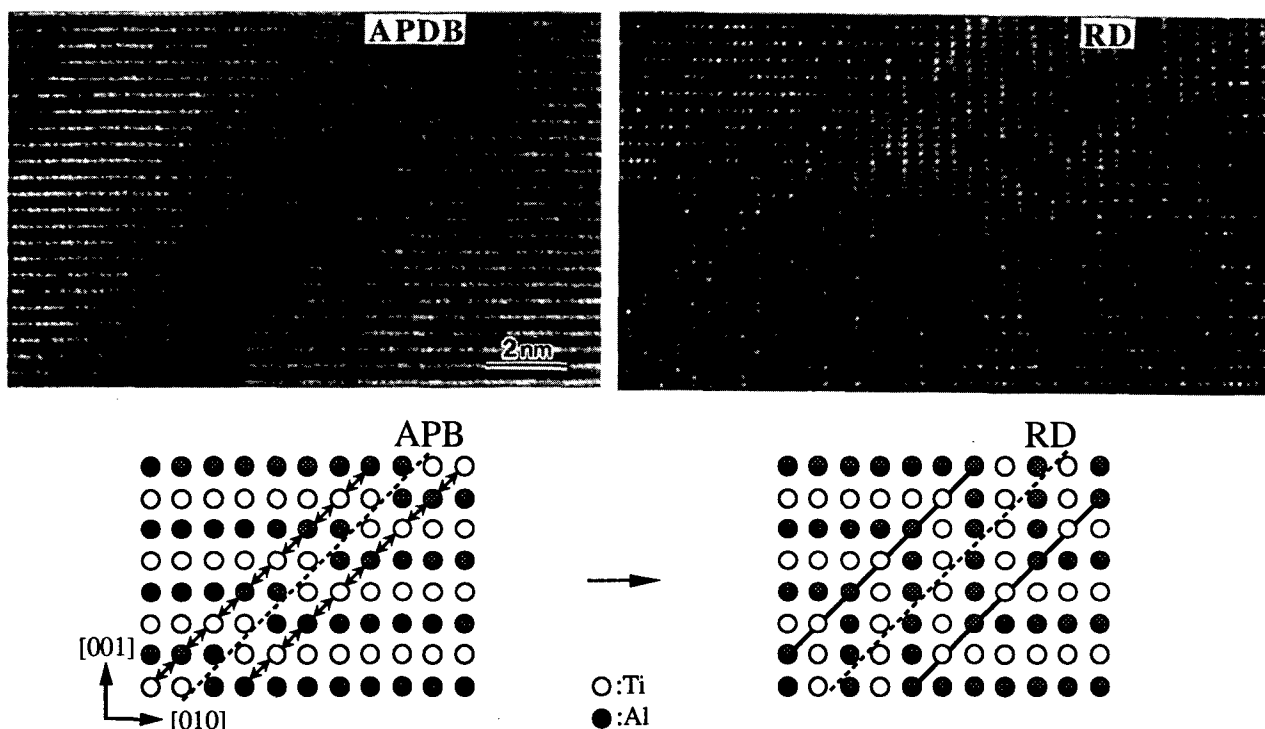


Fig. 9 High-resolution images of the boundaries showing fringe contrasts in the  $\gamma_m$  grain as shown in fig. 6(c), which are simple APDB and thin RD wall [37]. Antiphase relationships between the domains are known from the shift of ordered contrasts, and the corresponding atomic models are drawn schematically below. Note that the RD growth proceeding by the short-range diffusion process indicated by arrows will never change the antiphase relationship between the domains.

### Formation of the $\alpha_2$ plate from the $\gamma_m$ phase : $\gamma_m \rightarrow \gamma + \alpha(\alpha_2)$

In our recent paper [9], we have investigated the microstructural change during the isothermal aging (1473K) of the  $\gamma_m$  phase. By this treatment, both the particles and plates of the  $\alpha_2$  phase were found to be formed in the  $\gamma_m$  grain interiors. An intensive discussion was given of the formation mechanism of the  $\alpha_2$  particles, and the present paper will describe the formation of the  $\alpha_2$  plates.

In the early stage of the isothermal aging (10min), the fine  $\alpha_2$  plates and particles are formed at the grain interiors and grain boundaries, respectively. As the aging time extended (~1 day), the thickness of the plates hardly changes (less than a micron), whereas the particles grow and become coarse (a few microns). On the basis of these facts, we concluded that the growth of the plates seems to be almost completed in the early stage, and these are thermally stable in this condition [9]. Figs. 10 (a) and (b) show a TEM micrograph of the fine  $\alpha_2$  plates in the early stage of isothermal aging and the corresponding SAED pattern, respectively. In this image, one can see very fine plates (about 10nm thickness) as well as a thick plate (about 0.2 $\mu$ m thickness), lying on the variant planes of the {111}. This microstructural feature is interpreted as the nucleation and growth of the  $\alpha$  plates proceeded by the ledge mechanism on every {111} plane during isothermal aging, which involves fcc-hcp shear and diffusion of atoms.

It should be noted that very thin plates about 10nm in thickness exhibit a very small aspect ratio, indicating lengthening growth was fast and dominated the early stage, just like the case of the  $\gamma$  plate precipitation discussed earlier. At the  $\alpha_2 - \gamma$  interfaces of these thin plates, strain contrasts due to the existence of a high-density of partial dislocation ledges can be recognized in fig. 10(a). This implies the  $\alpha_2 - \gamma$  interfacial lattice misfit is relatively large comparing with the case of fine lamellae (figs. 3 (b) and (c), fig. 4), and the straight alignment of the diffraction spots of the both phases (fig. 3(b)) can not be seen in the SAED pattern of fig. 10(b).

It is interesting to note that the edges of some fine plates reach the thick plate and are terminated at the interfaces, as indicated by arrows. Fig. 10(c) shows a high-resolution image of such region in fig. 10(a). At the area where two  $\alpha_2$  plates denoted A and B meet with, one can clearly recognize a large ledge formed at the interfaces of the thick plate (A). From this characteristic feature, the formation of these plates are deduced as follows. Firstly, plate A was nucleated on the (111) plane and grew by migration of ledges. After that, plate B was nucleated on the different plane of  $\{111\}$ , and, when the growth edge reached the plate A, lengthening growth was terminated. Since the migrating ledges on the plate A can not across the plate B, the partial dislocations were piled up at this area and formed the large ledge. Once the lengthening growth is terminated, only the thickening is permitted for the plate

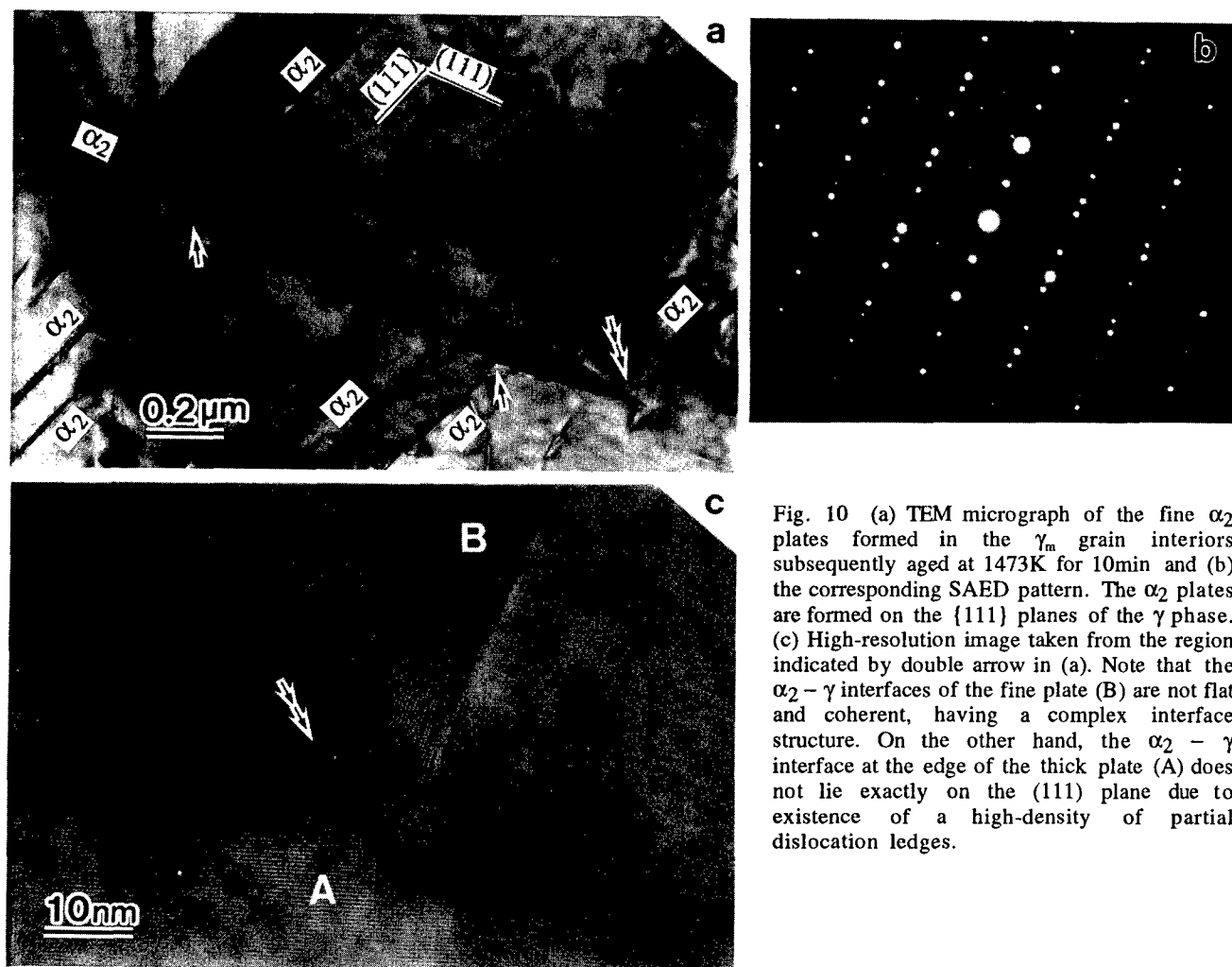


Fig. 10 (a) TEM micrograph of the fine  $\alpha_2$  plates formed in the  $\gamma_m$  grain interiors subsequently aged at 1473K for 10min and (b) the corresponding SAED pattern. The  $\alpha_2$  plates are formed on the {111} planes of the  $\gamma$  phase. (c) High-resolution image taken from the region indicated by double arrow in (a). Note that the  $\alpha_2 - \gamma$  interfaces of the fine plate (B) are not flat and coherent, having a complex interface structure. On the other hand, the  $\alpha_2 - \gamma$  interface at the edge of the thick plate (A) does not lie exactly on the (111) plane due to existence of a high-density of partial dislocation ledges.

growth. As discussed in the case of the  $\gamma$  plate precipitation (fig. 5(d)), this process requires not only the diffusion of atoms but also formation of new ledges at the interfaces which may hardly takes place in the early stage. This situation, terminating the plates with each other, is highly expected because the plates can nucleate on every  $\{111\}$  plane. Thus, apparently the plates growth is suppressed during further aging. In addition, the complex  $\alpha_2 - \gamma$  interface structure of the fine plates as seen in fig. 10(c) may be responsible for the thermal stability [9], which will be a barrier for the nucleation of new ledges at the interfaces. This interface structure is considered to be associated with the existence of a number of partial dislocations due to a high fault energy of the  $\gamma_m$  phase [34].

In terms of nucleation sites in the  $\gamma_m$  grain interiors, pre-existing hcp thin plates and stacking faults described in the previous section can be favorable site (we confirmed that the single stacking faults are formed on the  $\{111\}$  planes, including those not aligned parallel to the twins). Here, it should be noted that the plates are formed by the  $\gamma$  ( $L1_0$ )  $\rightarrow \alpha$  (disordered hcp) shear-involved transformation during the isothermal aging (the  $\alpha \rightarrow \alpha_2$  ordering takes place during quenching after the aging). Considering that  $a/6\langle 112 \rangle$  partial dislocations are not equivalent for the  $\gamma$  phase because of the  $L1_0$  ordering, it is expected only  $a/6[112]$  partial dislocations will be allowed for this shear-involved transformation in the early stage, which could produce the macroscopic shear and strain as discussed earlier. This strain causes the internal stress field at local area, which can induce the nuclei in the grain interiors on every  $\{111\}$  plane. According to this interpretation, nucleation of the plates will be enhanced under a certain external stress, so that one can obtain a microstructure with a high-density of fine  $\alpha_2$  plates distributed in  $\gamma$  grains using this technique.

#### Acknowledgment

This research was performed as a part of the research and development project of Basic Technology for Future Industries under the Agency of Industrial Science and Technology, sponsored by Ministry of International Trade and Industry in Japan. Helpful discussions with Professor W. T. Reynolds, Jr. and Professor J. M. Howe are gratefully acknowledged.

#### References

1. Y. W. Kim, "Microstructural Evolution and Mechanical Properties of a Forged Gamma Titanium Aluminide Alloy", *Acta Metall. Mater.*, 40 (1992), 1121-1134.
2. S. C. Huang, in R. Darolia et al. eds., *Structural Intermetallics*, (Warrendale, PA, TMS, 1993), 299.
3. M. Takeyama, "Microstructural Evolution and Tensile Properties of Titanium-rich TiAl Alloy", *Mat. Sci. and Engn. A152* (1992), 269-276.
4. M. Takeyama et al., in R. Darolia et al. eds., *Structural Intermetallics*, (Warrendale, PA, TMS, 1993), 167.
5. T. Kumagai et al., in J. A. Horton et al., eds., *Symp. Proc. High-Temperature Ordered Intermetallic Alloys*, vol. 364, (MRS, 1995), 181.
6. T. Kumagai et al., "The  $\gamma \rightarrow \alpha$  Phase Transformation in  $\gamma$ -Based TiAl Alloy", *Scripta Materialia*, 34 (1996), 235-242.
7. P. Wang, G. B. Viswanathan, and V. K. Vasudevan, "Observation of a Massive Transformation from  $\alpha$  to  $\gamma$  in Quenched Ti-48 At. Pct Al Alloys", *Metall. Trans.*, 23A (1992), 690-697.
8. S. A. Jones and M. J. Kaufman, "Phase Equilibria and Transformations in Intermediate Titanium-Aluminum Alloys", *Acta Metall. Mater.*, 41 (1993), 387-398.
9. T. Kumagai et al., "Microstructural Evolution of Massively Transformed  $\gamma$ -TiAl during Isothermal Aging", *Scripta Materialia*, in press (1997).
10. P. Wang and V. K. Vasudevan, "Composition Dependence on the Massive Transformation from  $\alpha$  to  $\gamma$  in Quenched TiAl Alloys", *Scripta Metall. Mater.*, 27 (1992), 89-94.
11. Y. Yamabe, M. Takeyama, and M. Kikuchi, "Determination of  $\alpha$  ( $A3$ )  $\rightarrow \alpha_2$  ( $D019$ ) Transition Temperatures in Ti-(40-45)at%Al Alloys", *Scripta Metall. Mater.*, 30 (1994), 553-557.
12. C. T. Liu et al. in Y. W. Kim, R. Wagner, and M. Yamaguchi, eds., *Gamma Titanium Aluminides*, (Warrendale, PA, TMS, 1995), 679.
13. E. Abe, T. Kumagai, and M. Nakamura, in R. Bormann et al., eds., *Symp. Proc. Metastable Phases and Microstructures*, vol. 400, (MRS, 1996), 281.
14. Y. Yamabe, M. Takeyama, and M. Kikuchi, in Y. W. Kim, R. Wagner, and M. Yamaguchi, eds., *Gamma Titanium Aluminides*, (Warrendale, PA, TMS, 1995), 111.
15. K. Nakai et al., "Formation Process of Lamellar  $\gamma$  Phase in a Ti-40at.%Al Alloy", *Mat. Trans. JIM*, 37 (1996), 813-820.
16. E. Abe, T. Kumagai, and M. Nakamura, "Studies on the  $\alpha \rightarrow \gamma$  Phase Transformation Mechanism in Ti-48at.%Al Alloy by High-Resolution Electron Microscopy", *Phil. Mag. Lett.*, (1995), 291-296.
17. E. Abe et al. in Y. Ishida et al. eds., *Interface Science and Materials Interconnection (iib-96, JIMIS-8)*, (Sendai, Japan, JIM, 1996), 319.
18. G. J. Mahon and J. M. Howe, "Transmission Electron Microscopy Investigation of Interfaces in a Two-Phase TiAl Alloy", *Metall. Trans.*, 21A (1990), 1655-1662.
19. S. R. Singh and J. M. Howe, "High-Resolution Electron Microscopy of  $\gamma - \alpha_2$  Interfaces in Titanium Aluminide", *Phil. Mag. A*, 66 (1992), 739-771.
20. Y. S. Yang, S. K. Wu, and J. Y. Wang, "A Study by High-Resolution Electron Microscopy of an  $\alpha_2 + \gamma$  Two-Phase Ti-40at.%Al Alloy", *Phil. Mag. A*, 67 (1993), 463-478.
21. E. Abe et al., in preparation (1997).
22. J. W. Christian, ed., *The Theory of Transformations in Metals and Alloys* (Oxford: Pergamon Press, 1965).
23. C. Hitzenberger and H. P. Karnthaler, "Weak-Beam TEM Study of the H.C.P. to F.C.C. Martensitic Phase Transformation Lamellae in CoNi", *Phil. Mag. A*, 64 (1991), 151-163.
24. K. Hono et al., "Chemical Compositions of Ultrafine Lamellae in the Water-Quenched Ti-48Al Alloy", *Scripta Materialia*, 35 (1996), 495-499.
25. M. H. Wu, Y. Hamada, and C. M. Wayman, "Transformation Characteristics of  $\alpha_1$  Plates in Cu-Zn-Al Alloys", *Metall. Mater. Trans.*, 25A (1994), 2581-2599.
26. T. Tadaki and K. Shimizu, "High-Resolution Analytical Electron Microscopy Study of Isothermal Plate-Shaped Products in Some  $\beta$ -Phase Alloys", *Metall. Mater. Trans.*, 25A (1994), 2569-2579.
27. E. Abe et al., unpublished results (National Research Institute for Metals, 1997).
28. J. M. Howe, U. Dahmen, and R. Gronsky, "Atomic Mechanism of Precipitate Plate Growth", *Phil. Mag. A*, 56 (1987), 31-61.

29. A. Denquin and S. Naka, "Phase Transformation Mechanisms Involved in Two-Phase TiAl-Based Alloys-I. Lamellar Structure Formation", *Acta mater.*, 44 (1996), 343-352.
30. E. Abe, T. Kumagai, and M. Nakamura, "New Ordered Structure of TiAl Studied by High-Resolution Electron Microscopy", *Intermetallics*, 4 (1996) 327-333.
31. C. S. Barrett and T. B. Massalski, eds., Structure of Metals, (New York: McGraw-Hill, 1966), 507.
32. X. D. Zhang et al. "The Structure and Origin of Boundaries between Antiphase Regions in L1<sub>0</sub> Intermetallics", *Acta mater.*, 44 (1996), 3735-3747.
33. E. Abe, T. Kumagai, and M. Nakamura, in C. C. Koch et al., eds., Symp. Proc. High-Temperature Ordered Intermetallic Alloys, (MRS, 1997), in press.
34. E. Abe et al., "High-Resolution Electron Microscopy of Twin Interfaces in Massively Transformed  $\gamma$ -TiAl Phase", *Phil. Mag. A*, 75 (1997), 975-991.
35. A. Denquin and S. Naka, "Phase Transformation Mechanisms Involved in Two-Phase TiAl-Based Alloys-II. Discontinuous Coarsening and Massive-Type Transformation", *Acta mater.*, 44 (1996), 353-365.
36. X. D. Zhang et al. "The Massive Transformation in Ti-Al Alloys : Mechanistic Observations", *Acta mater.*, 44 (1996), 3723-3734.
37. E. Abe and M. Nakamura, "The Structure of Antiphase Domain Boundaries in Massively Transformed  $\gamma$ -TiAl Studied by High-Resolution Electron Microscopy", *Phil. Mag. Lett.*, 75 (1997), 65-73.
38. P. Wang, D. Veeraraghavan, and V. K. Vasudevan, "Observation of Twins in the  $\alpha_2$  Phase in a Quenched Ti-46.54at.% Al Alloy", *Scripta Mater.*, 34 (1996), 1601-1607.

## MORPHOLOGY OF DISCONTINUOUS COARSENING IN FULLY LAMELLAR Ti-44Al (at%) ALLOY

S. Mitao <sup>\*1</sup> and L. A. Bendersky <sup>\*2</sup>

<sup>\*1</sup> Advanced Materials Engineering Lab., Materials & Processing Research Center  
NKK Corporation, Fukuyama 721, Japan.

<sup>\*2</sup> Metallurgy Division, National Institute of Standards and Technology,  
Gaithersburg, MD 20899-0001, U. S. A.

### Abstract

The morphology of discontinuous coarsening in the  $\text{Ti}_3\text{Al}$  ( $\alpha_2$ ) /  $\text{TiAl}$  ( $\gamma$ ) fully lamellar Ti-44at%Al alloy has been studied. Three types of morphology were observed in discontinuously coarsened lamellar structures (secondary lamellae). Type-(I) lamellae have the low energy habit plane as their lamellar interfaces, and have the same lamellar direction as the original primary lamellae. Type-(II) lamellae have the same crystallographic orientation of the  $\alpha_2$  plates as that in the original primary lamellae, but have a different lamellar direction from the original primary lamellae, and have irregular faceted lamellar interfaces. Type-(III) lamellae have a different lamellar direction and a different crystallographic orientation of the  $\alpha_2$  plates from that in the original primary lamellae, but have the low energy habit plane as their lamellar interfaces. Geometric conditions for formation of these types of secondary lamellae were analyzed based on the Livingston and Cahn treatment [Acta Metall. 22, 495 (1974)], taking misorientation between the penetrated primary lamellae, the advancing secondary lamellae and the lamellar colony boundaries.

### Introduction

$\gamma$ -based titanium aluminides consisting of ordered hexagonal  $\alpha_2$  ( $\text{Ti}_3\text{Al}$ ) and ordered fct  $\gamma$  ( $\text{TiAl}$ ) phases with a fully lamellar structure have been recognized as having an attractive combination of mechanical properties such as high fracture toughness and creep resistance [1-3]. The lamellae consisting of low energy semicoherent  $(0001)_{\alpha_2} / \{111\}_{\gamma}$  interfaces have good thermal stability because of the small curvature effect that promotes volume diffusion controlled coarsening. However, it is documented that pronounced discontinuous coarsening (DC), which proceeds by lamellar colony boundary (LCB) migration leaving behind coarser lamellae [4-8],

occurs in the lamellar structure [9-13].

In this paper, the morphology of the discontinuously coarsened lamellar structure in the fully lamellar Ti-44at%Al alloy has been studied. Morphologies of the secondary lamellar structure were characterized and classified based on microstructural observations. Geometric factors for formation of each type of secondary lamellae were analyzed based on the Livingston and Cahn treatment [4] taking misorientation and strong interfacial anisotropy of the lamellae into consideration.

### Experimental Procedures

The material used in this study was Ti-44at.%Al alloy prepared by non-consumable electrode arc melting in a cold hearth. The resulting ingot (approximately 10mm x 10mm x 150mm) was solution treated in the single  $\alpha$  phase region, at 1623K for 30 minutes, then argon gas purge quenched to room temperature. Formation of the lamellar structure (primary lamellae) during the gas quenching was not suppressed. The sample was sliced into 3mm thick pieces and encapsulated into quartz tubes backfilled with helium, then held at 1273K for 1 hour or 1 day, followed by water quenching. Microstructural characteristics were examined by light microscopy, scanning electron microscopy (SEM) and transmission electron microscopy (TEM).

### Microstructural Observation Results

An example of the secondary lamellae observed in the Ti-44at%Al alloy annealed at 1273K for 1 day is shown by light microscopy in Fig. 1. It is noted that the DC cells tend to show blocky shapes surrounded by LCBs which are mostly perpendicular or parallel to the penetrated primary lamellar orientation as indicated by "A" and "B" in the micrograph. This trend is also recognizable in Figs. 2(a,b) which are the back-



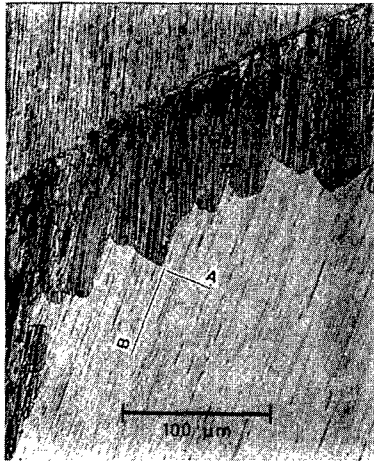


Figure 1: Light micrograph of discontinuous coarsening in the Ti-44at%Al alloy held at 1273K for 1 day. Note that the cell shape tends to be rectangular surrounded by lamellar colony boundaries which are perpendicular (A) or parallel (B) to the penetrated primary lamellae.

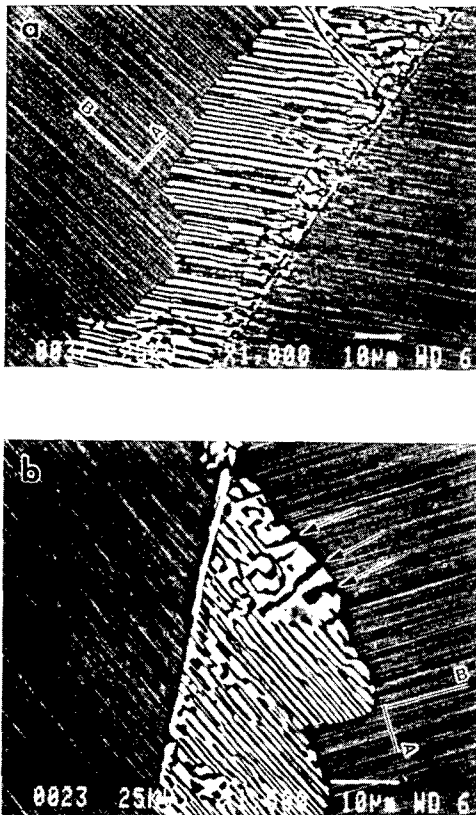


Figure 2: SEM backscattered electron images of discontinuous coarsening in the Ti-44at%Al alloy held at 1273K for 1 day. The bright and dark phases are  $\alpha_2$  and  $\gamma$  phases, respectively.

scattered electron images by SEM. The bright and dark phases are the  $\alpha_2$  and  $\gamma$  phases, respectively. The greater part of advancing LCBs are nearly perpendicular or parallel to the penetrated primary lamellar orientation (marked "A" and "B", respectively). Additionally, many imperfections such as bent lamellae are seen in DC structure, especially in Fig. 2(b), and some parts of the cell have even a different lamellar orientation as indicated by arrows in Fig. 2(b).

A typical example of the DC structure is demonstrated by the TEM bright field image in Fig. 3. The dark and bright lamellae are the  $\alpha_2$  and  $\gamma$  phases, respectively. The DC lamellae are an extension of the primary lamellae of the growing grain (on the lower left part of the micrograph), preserving their crystallographic orientations (see inset selected area diffraction patterns; (a) for the original primary lamellae, and (b) for the DC lamellae). The crystallographic orientation of the growing grain is  $[011]_\gamma // [2110]_{\alpha_2} // \text{beam direction}$ , with the planar lamellar interfaces, edge-on close to  $\{111\}_\gamma // (0001)_{\alpha_2}$  plane (parallel to the direction A). In addition to the secondary lamellae growing close to the direction A with a predominantly low energy habit plane (marked "I" for  $\alpha_2$  plates), one also observes lamellae growing in a different direction (marked "II" for  $\alpha_2$  plates). This type of secondary lamellae is recognizable not only by the growth direction but also by their irregular interfaces and larger lamellar spacing.

We classify the DC lamellae having predominantly planar interfaces with the habit plane parallel to that of original primary lamellae as Type-(I). The lamellae having a different growth direction from the original primary lamellae, with irregular, presumably high energy interfaces are classified as Type-(II). Since the crystallographic orientation of the  $\alpha_2$  plates in the Type-(I) and (II) lamellae are the same, Type-(I) and (II) can alternate in a single lamella during the growth process.

Formation of the Type-(II) lamellae apparently occurs when following two growth controlling factors become significant : 1) the penetrated primary lamellae meet the LCB plane almost perpendicularly, providing a large driving force in the primary lamellar direction ; 2) Type-(I) secondary lamellae and the LCB plane are close to parallel, imposing too large a diffusion distance for Type-(I) growth in the direction (large projected secondary lamellar spacing of Type-(I) lamellae on the LCB). The secondary lamellar spacing can be corrected not only by the bending of the  $\alpha_2$  plates, but also by reprecipitation of the  $\alpha_2$  phase on additional  $\{111\}$  planes of the  $\gamma$  phase in the secondary lamellae. Fig.4 shows a typical example of changing growth direction by reprecipitation of the  $\alpha_2$  phase (marked III in the figure). We classify this type of secondary lamellae as Type-(III), in which both lamellar direction and crystallographic orientation of the  $\alpha_2$  phase are different from the original primary lamellae, but lamellar interfaces consist of the low energy habit plane. In Fig.4, the habit plane of Type-(III) lamellae is  $(111)\gamma // (0001)_{\alpha_2}$ , while that of primary lamellae is  $(111)\gamma // (0001)_{\alpha_2}$  (for  $[011]_\gamma // [2110]_{\alpha_2}$  zone axis of the primary lamellae).

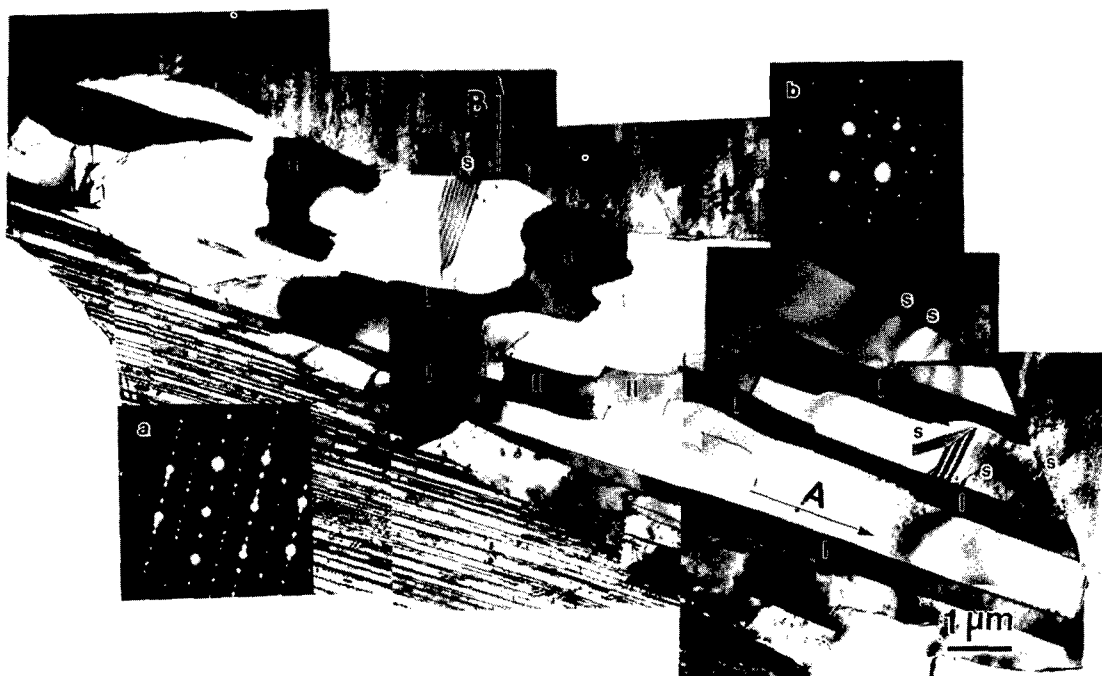


Figure 3. TEM micrograph and SAD patterns (a: original primary lamellae, b: secondary lamellae) for the DC structure observed in the Ti-44at%Al alloy held at 1273K for 1 h. The darker-contrast phase is the  $\alpha_2$  phase. DC lamellae with the low energy habit plane (Type-(I)) and ones with irregular shaped interfaces (Type-(II)) are observed.

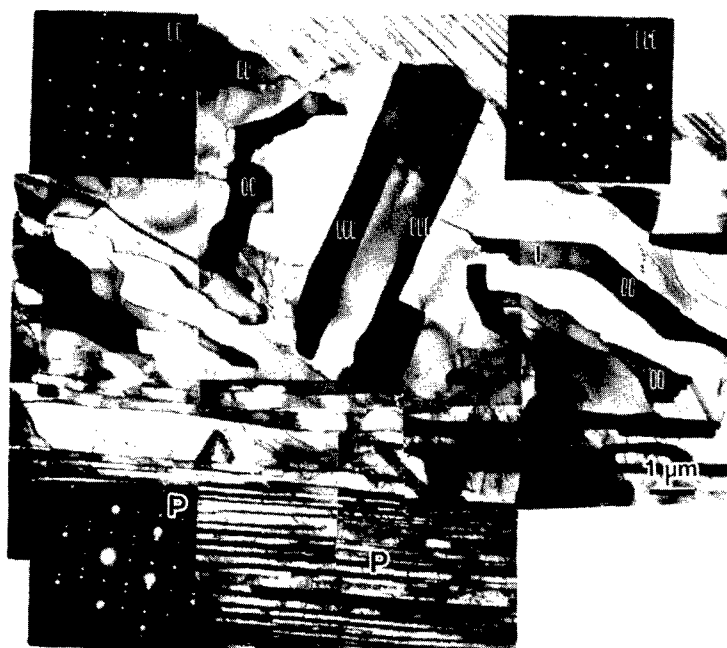


Figure 4. TEM micrograph of discontinuous coarsened structure in the Ti-44at%Al alloy held at 1273K for 1 day. Note the  $\alpha_2$  plates marked III (type-(III) lamellae) have the low energy habit plane as their lamellar interfaces, but they are not parallel to the original primary lamellae (marked P). The  $\alpha_2$  plates marked I and II are of type-(I) and (II) lamellae, or their combined form.

### Discussion

Three types of lamellar growth morphology observed in DC structure of the Ti-44at%Al alloy are schematically drawn in Fig.5.

Type-(I) :  $\alpha_2/\gamma$  lamellae consisting of the low energy habit plane lamellar interfaces, and the interfaces are parallel to those in the original primary lamellae.

Type-(II) : The lamellae have the same crystallographic orientation to those in the original primary lamellae, but with irregularly shaped high energy lamellar interfaces.

Type-(III) :  $\alpha_2/\gamma$  lamellae consisting of the low energy habit plane lamellar interfaces, but crystallographic orientation of the  $\alpha_2$  plates and the lamellar direction are different from those of the original primary lamellae. This kind of lamellae is formed by reprecipitation of  $\alpha_2$  plates in the  $\gamma$  matrix.

In this section, we will discuss geometric factors for formation of Type-(I) and (II) lamellae in terms of their dependence on misorientation between the penetrated primary and growing secondary lamellae, and on orientation of the LCB, based on the Livingston and Cahn treatment [4]. Two primary factors are taken into consideration : 1) the Gibbs-Thomson effect along the LCB between the primary and secondary lamellae establishing the driving force for the boundary migration; 2) the diffusion distance along LCB for the secondary lamellar growth (secondary lamellar spacing projected onto the LCB) satisfying the material balance between rejection of solute atoms in front of the migrating LCB and redistribution of the atoms behind the LCB through boundary diffusion. Hereafter, the  $\alpha_2$  and  $\gamma$  phase are referred to simply as  $\alpha$  and  $\gamma$ , respectively.

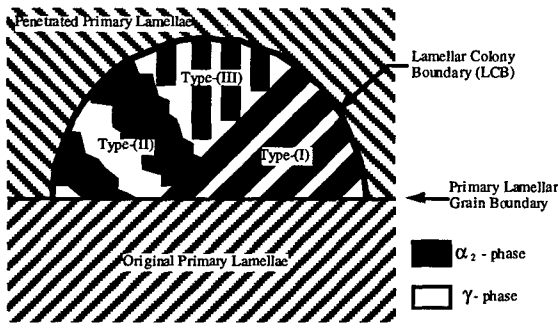


Figure 5: Schematic drawing of type-(I), (II) and (III) lamellae in a single DC cell.

### Growth Kinetics for Type-(I) DC

Fig.6 shows a schematic drawing of Type-(I) lamellae.  $\beta$  is the angle between the LCB plane and the normal to the secondary lamellar plane, and  $\phi$  is the angle between the primary and secondary lamellar planes.

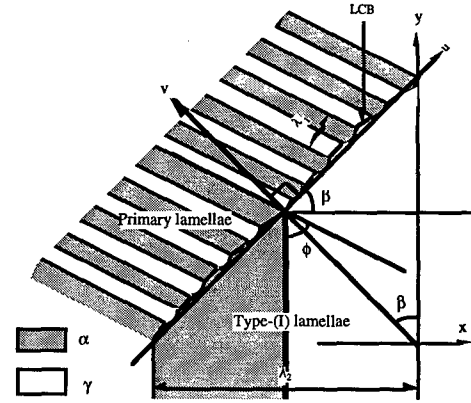


Figure 6: Schematic drawing of LCB between penetrated primary and Type-(I) lamellae.

All the primary and Type-(I) secondary lamellar planes and the LCB planes are assumed to be in edge on orientation. The maximum solute concentration difference along the LCB due to the Gibbs-Thomson effect ( $\Delta C_b$ ) is given by the following equation using the curvatures at the tip of each plate facing to the LCB.

$$\Delta C_b = \frac{C_b^e \sigma V_m}{RT} \left[ \left( \frac{1}{r_{1\alpha}} + \frac{1}{r_{1\gamma}} \right) - \left( \frac{1}{r_{2\alpha}} + \frac{1}{r_{2\gamma}} \right) \right] \quad (1)$$

where  $C_b^e$  is the equilibrium boundary concentration of aluminum without curvature,  $\sigma$  is the interfacial energy of the LCB,  $V_m$  is the molar volume,  $R$  is the gas constant,  $T$  is the temperature,  $r_i$  ( $i=1$ (primary),  $2$ (secondary));  $j=\alpha$  or  $\gamma$  phase) is the radius of curvature at the boundary between the tip of the  $j$  phase and the other phase having infinite thickness. The curvature and spacing relations are given in the following equations.

[primary lamellae]

$$\frac{1}{r_{1j}} = \frac{\gamma}{\sigma} F_1(\phi, \beta) \quad (2-a)$$

[secondary lamellae]

$$\frac{1}{r_{2j}^{(n)}} = \frac{\gamma}{\sigma} F_2^{(n)}(\beta) \quad (2-b)$$

From trijunction equilibrium, the  $F_1(\phi, \beta)$  and  $F_2^{(n)}(\beta)$  functions will be approximated as follows :

$$F_1(\phi, \beta) = \frac{\cos^2(\phi - \beta)}{f_j \lambda_1} \quad (j = \alpha \text{ or } \gamma) \quad (3-a)$$

$$F_2^{(n)}(\beta) = \frac{\cos^2 \beta}{f_j \lambda_2} \quad (j = \alpha \text{ or } \gamma) \quad (3-b)$$

Substituting these equations to equation (1) yields

$$\Delta C_b = \frac{C_b^* \gamma V_m}{RT f_\alpha f_\gamma} \left[ \frac{\cos^2(\phi - \beta)}{\lambda_1} - \frac{\cos^2 \beta}{\lambda_2} \right] \quad (4)$$

On the other hand, the LCB migration velocity normal to the boundary ( $v$ ) is given by

$$v = -\frac{D_b \delta}{(C_0 - C_j)} \frac{d^2 C_b^{2j}}{du_b^2} = -\frac{D_b \delta \cos^2 \beta}{(C_0 - C_j)} \frac{d^2 C_b^{2j}}{dx^2} \quad (j = \alpha \text{ or } \gamma) \quad (5)$$

where  $C_b^{2j}$  is the solute concentration in the boundary in front of the secondary  $j$  phase ( $j = \alpha$  or  $\gamma$ ),  $C_0$  is the sample composition,  $C_j$  is the solute concentration in the secondary  $j$  phase ( $j = \alpha$  or  $\gamma$ ,  $C_\alpha < C_0 < C_\gamma$ ),  $u_b$  is distance along the LCB, and  $x$  is distance normal to the secondary lamellar plane ( $dx \sim \cos \beta du_b$ ). Double integration gives the maximum solute concentration difference along the boundary ( $\Delta C_b$ ) as

$$\Delta C_b = \frac{v(C_\gamma - C_\alpha) f_\alpha f_\gamma \lambda_2^2}{8 D_b \delta \cos^2 \beta} \quad (6)$$

Combining equations (4) and (6) yields

$$v = \frac{8 D_b \delta C_b^* \gamma V_m}{(C_\gamma - C_\alpha) RT f_\alpha^2 f_\gamma^2 \lambda_2^2} \cos^2 \beta \left[ \frac{\cos^2(\phi - \beta)}{\lambda_1} - \frac{\cos^2 \beta}{\lambda_2} \right] \quad (7)$$

By taking  $dv/d\lambda_2 = 0$ , the value of  $\lambda_2$  maximizing  $v$  is found to be

$$\lambda_2 = \frac{3 \cos^2 \beta}{2 \cos^2(\phi - \beta)} \lambda_1 \quad (8)$$

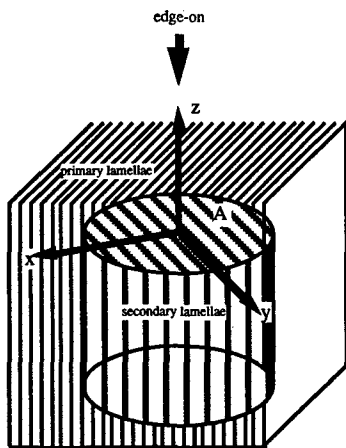


Figure 7: Schematic drawing of Type-(I) lamellar growth accompanied with the twisted LCB plane migration (marked "A").

However, because of three-dimensionality of the DC growth, the lamellar spacing is considered to be determined by the primary / secondary lamellar relations on the plane A in Fig. 7. For this orientation, where the primary and secondary lamellar planes are normal to LCB planes, the secondary lamellar spacing maximizing the growth velocity can be approximated to the value for  $\phi = \beta = 0$  in equation (8) assuming no twist angle dependency of the LCB migration velocity. The coarsening ratio,  $\lambda_2^{(I)}/\lambda_1 = 3/2$ , based on the maximum velocity assumption, is about 6 times smaller than the experimentally obtained value in this study ( $\lambda_2^{(I)}/\lambda_1 = 8.8$ ). Factors affecting the kinetics of the coarsening reaction such as the residual chemical driving force [14] and geometry of the lamellar front and contact angles [15-17] are considered to be causes for the discrepancy.

By substituting the calculated coarsening ratio into equation (7), the growth velocity of Type-(I) lamellae normal to the LCB ( $v(I)$ ) is given by

$$v^{(I)} = \frac{32 D_b \delta C_b^* \gamma V_m}{27 (C_\gamma - C_\alpha) RT f_\alpha^2 f_\gamma^2 \lambda_1^3} \cos^2 \beta [3 \cos^2(\phi - \beta) - 2 \cos^2 \beta] = G V_I \quad (9-a)$$

$$G = \frac{32 D_b \delta C_b^* \gamma V_m}{27 (C_\gamma - C_\alpha) RT f_\alpha^2 f_\gamma^2 \lambda_1^3} \quad (9-b)$$

$$V_I = \cos^2 \beta [3 \cos^2(\phi - \beta) - 2 \cos^2 \beta] \quad (9-c)$$

#### Growth kinetics for Type-(II) DC

In the type-(II) lamellae, the morphology and growth direction are not restricted by the favorable orientation of interfaces. This comes in the cost of extra interfacial energy of the lamellar interface which is assumed to be  $M$  times larger than that of the low energy  $(0001)\alpha_2 // \{111\}\gamma$  habit plane. Since growth direction of the Type-(II) lamellae is adjustable, the lamellae are assumed to be always perpendicular to the LCB ( $\beta = 0$ ;  $\beta'$ : the angle between the LCB plane and the normal to the Type-(II) secondary lamellar plane) to maximize the growth velocity (Fig. 8). The curvature at the tip of Type-(II) secondary lamellae ( $1/r_{2j}^{(II)}$ ) will be

$$\frac{1}{r_{2j}^{(II)}} = \frac{\gamma}{\sigma} F_2^{(II)} \quad (10-a)$$

$$F_2^{(II)} = \frac{M}{f_j \lambda_2} \quad (j = \alpha \text{ or } \gamma) \quad (10-b)$$

Substituting equations (2-a), (3-a), (10-a) and (10-b) to (1) yields

$$\Delta C_b = \frac{C_b^* \gamma V_m}{RT f_\alpha f_\gamma} \left[ \frac{\cos^2(\phi - \beta)}{\lambda_1} - \frac{M}{\lambda_2} \right] \quad (11)$$

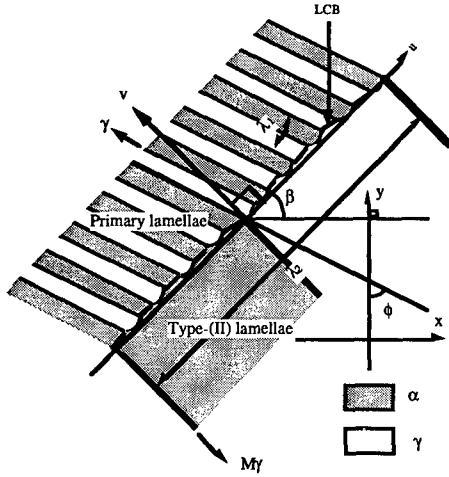


Figure 8: Schematic drawing of LCB between penetrated primary and Type-(II) lamellae. Note that the Type-(II) lamellae contact nearly normal to the LCB, but their lamellar interfacial energy is  $M$  times larger than that of the low energy habit plane.

On the other hand, since  $\Delta C_b$  has to satisfy equation (6), the growth velocity normal to the LCB is given by

$$v = \frac{8D_b \delta C_b \epsilon \gamma V_m}{(C_\gamma - C_\alpha) R T f_\alpha^2 f_\gamma^2 \lambda_2^2} \cos^2 \beta \left[ \frac{\cos^2(\phi - \beta)}{\lambda_1} - \frac{M}{\lambda_2} \right] \quad (12)$$

The  $\lambda_2$  value maximizing the growth velocity of Type-(II) lamellae ( $\lambda_2^{(m)}$ ) which will be dependent on  $\phi$  and  $\beta$  is obtained by taking  $dv / d\lambda_2 = 0$ .

$$\lambda_2^{(m)} = \frac{3M}{2 \cos^2(\phi - \beta)} \lambda_1 = \frac{3}{2} L_{II} \lambda_1 \quad (13-a)$$

$$L_{II} = \frac{M}{\cos^2(\phi - \beta)} \quad (13-b)$$

By combining equations (12) and (13-a), the growth velocity normal to the LCB in Type-(II) lamellae ( $v^{(m)}$ ) is given by

$$v^{(r)} = \frac{32D_b \delta C_b \epsilon \gamma V_m}{27(C_\gamma - C_\alpha) R T f_\alpha^2 f_\gamma^2 \lambda_1^3} \frac{\cos^6(\phi - \beta)}{M^2} = G V_{II} \quad (14-a)$$

$$V_{II} = \frac{\cos^6(\phi - \beta)}{M^2} \quad (14-b)$$

#### Geometric conditions for Type-(I) and (II) growth

Figs.9(a-c) show polar plots of the geometric factors for the LCB migration velocities for Type-(I) and (II) lamellae,  $V_I$  and  $V_{II}$ , as a function of LCB orientation ( $\beta$ ) for the given misorientations between the Type-(I) secondary lamellae and surrounding primary lamellae ( $\phi=0, 45$  and  $90$  degrees, respectively), taking  $M=2$  for Type-(II) lamellae.

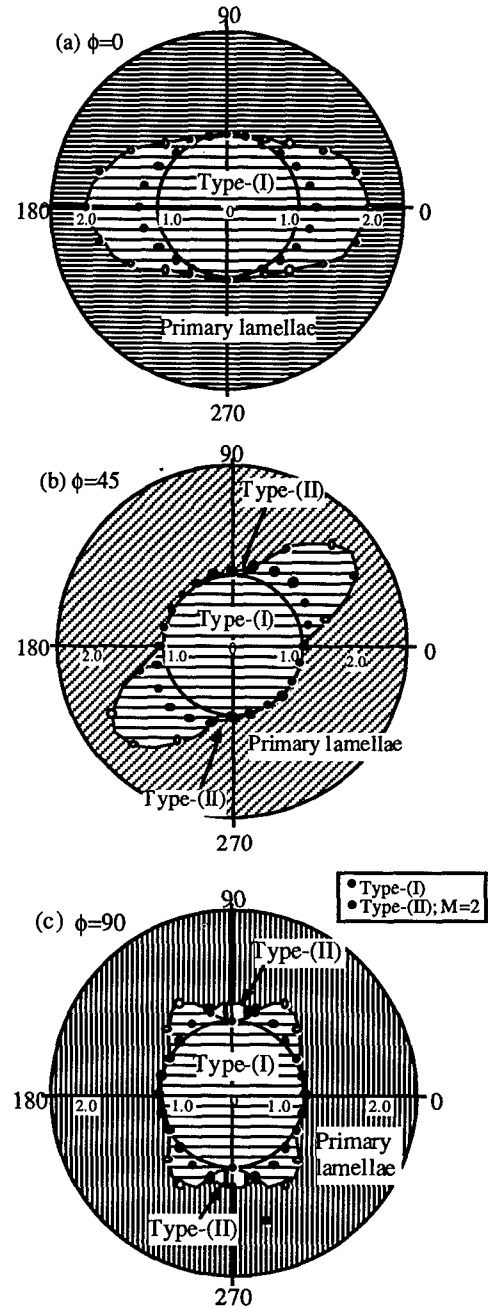


Figure 9: Polar plot of  $V_I$  and  $V_{II}$  as a function of  $\beta$ . (a)  $\phi=0$ , (b)  $\phi=45$  and (c)  $\phi=90$  degrees, respectively.  $M=2$  were taken for  $V_{II}$ .

The LCB energy ( $\sigma$ ) is assumed to be independent of  $\beta$ . The shape of the plot will be similar to the secondary cell shape (procedure similar to Wulff construction of the equilibrium shape of precipitates [18]). For  $\phi=0$  (the primary and Type-(I) secondary lamellar planes are parallel), the growth distance of Type-(I) lamellae in the direction nearly parallel to the lamellar planes is the greatest (Fig.9(a)). However, the growth distance of Type-(II) lamellae becomes greater than that of Type-(I) in directions nearly perpendicular to the Type-(I) lamellar plane in larger  $\phi$  (Fig.9(c)). It is noted that the secondary cell shape is strongly influenced by the primary lamellae, and becomes elongated along the

primary lamellar orientation. This is consistent with the observation of blocky shape of secondary cells.

For the formation of Type-(II) lamellae, nucleation of the  $\alpha_2$  phase on the LCB is not always necessary, and Type-(II) lamellae can be formed continuously from Type-(I) by simple bending of  $\alpha_2$ -plates as typically seen in middle of the secondary cell in Fig.3. On the contrary, in the formation process of Type-(III) lamellae, reprecipitation of  $\alpha_2$  plates having the habit plane with a different  $\{111\}_\gamma$  plane has to take place during DC. Therefore, the nucleation frequency should be taken into account for the formation of Type-(III) lamellae. This is considered to be the reason why Type-(II) lamellae are typically observed near  $\phi=\beta=90^\circ$  conditions in the earlier stage of DC. However, once Type-(III) lamellae are formed, the growth velocity of Type-(III) for the direction ( $\phi\sim\beta\sim90^\circ$ ) will be comparable to that of Type-(I) for  $\phi\sim\beta\sim0^\circ$  conditions. Type-(III) lamellae will be typically observed in the later stage.

### Conclusions

(1) Three types of the secondary lamellae were observed.

Type-(I) : The lamellar orientation is parallel to the original primary lamellae. Crystallographic orientation of the  $\alpha_2$  plates is the same as that of the original primary lamellae, and lamellar interfaces are the low energy habit plane.

Type-(II) : Although the crystallographic orientation of the  $\alpha_2$  plates is the same as that of the original primary lamellae, the lamellar orientation is not parallel to the original primary lamellae but rather normal to the LCB. The lamellar interfaces are not the low energy habit plane but high energy faceted ones. This type of lamellae was typically observed where the lamellar colony boundaries were nearly parallel to the secondary lamellae and the adjacent primary lamellae were nearly perpendicular to the boundaries.

Type-(III) : The lamellar orientation is not parallel to the original primary lamellae, and the crystallographic orientation of the  $\alpha_2$  plates is different from that in the original primary lamellae. Lamellar interfaces consist of the low energy habit plane. This type of lamellae is considered to be formed by reprecipitation of the  $\alpha_2$  plates having different variants with respect to  $\{111\}_\gamma$  planes.

(2) The secondary cells showed a tendency to be elongated along the penetrated primary lamellar orientation.

(3) Rate equations of DC were developed based on the Livingston and Cahn's treatment [4] in order to analyze the geometric effect for Type-(I) and (II) growth. The calculated results were consistent with the experimentally observed characteristics, such as the existence of Type-

(II) lamellae where the adjacent primary lamellae were nearly perpendicular to the Type-(I) secondary lamellae ( $\phi\sim90^\circ$ ) and the lamellar colony boundaries were nearly parallel to the Type-(I) secondary lamellae ( $\beta\sim90^\circ$ ), and the tendency of secondary cell shape to be elongated along the penetrated primary lamellar orientation.

### Acknowledgments

The authors gratefully acknowledge F. S. Biancianiello, M. E. Williams and L. C. Smith for experimental assistance. Numerous discussions with Dr. J.W. Cahn are also gratefully acknowledged.

### References

1. Y-W. Kim and D. M. Dimiduk, *JOM*, 43 (1991), 40.
2. Y-W. Kim and D. M. Dimiduk, *Proc. of JIMIS-7 on "Aspects of High Temperature Deformation and Fracture in Crystalline Materials"*, Japan Inst. of Metals, (1993), 373.
3. Y-W. Kim, *JOM*, 46 (1994), 30.
4. J. D. Livingston and J. W. Cahn, *Acta Metall.*, 22 (1974), 495.
5. R. Gronsky and G. Thomas, *Acta Metall.*, 23 (1975), 1163.
6. R. A. Fournelle, *Acta Metall.*, 27 (1979), 1135.
7. W. Gust, *Phase Transformations*, vol.1, Institution of Metallurgists, London, (1979), II-27.
8. D. B. Williams and E. P. Butler, *Int'l Metals Rev.*, 3 (1981), 153.
9. D. S. Shong and Y-W. Kim, *Scripta Metall.*, 23 (1989), 257.
10. Y. Yamabe, N. Honjo and M. Kikuchi, *Proc. of JIMIS-6 on "Intermetallic Compound - Structure and Mechanical Properties -"*, Japan Inst. of Metals, (1991), 821.
11. J. K. Park, Y. C. Lee, J. Y. Jung and Y. T. Lee, *Proc. of 3rd Japan Int'l SAMPE Symp.*, The Japan Chapter of SAMPE, (1993), 1359.
12. R. V. Ramanujan, *Acta Metall. Mater.*, 42 (1994), 2775.
13. S. Mitao and L. A. Bendersky, *Gamma Titanium Aluminides*, TMS, (1995), 181.
14. R. A. Fournelle, *Acta Metall.*, 27 (1979), 1147.
15. M. Hillert, *Jernkont. Ann.*, 141 (1957), 757.
16. M. P. Puls and J. S. Kirkaldy, *Metall. Trans.*, 3 (1972), 2777.
17. B. E. Sundquist, *Metall. Trans.*, 4 (1973), 1919.
18. J. W. Christian, *The Theory of Transformations in Metals and Alloys*, Second Edition, Part.I, Pergamon Press, (1975), 153.

## STRUCTURAL EVOLUTION OF TITANIUM DI-BORIDES IN WROUGHT Ti-47at%Al-2at%Mo-0.2at%B

Marc De Graef<sup>1</sup>, Dallis A. Hardwick<sup>2</sup> and Patrick L. Martin<sup>2</sup>

<sup>1</sup> Department of Materials Science and Engineering,  
Carnegie Mellon University, Pittsburgh PA 15213

<sup>2</sup> Rockwell International Science Center, Thousand Oaks, CA 91305

### Abstract

In this paper we report microstructural observations for a wrought Ti-47at%Al-2at%Mo-0.2at%B alloy in the as-cast, homogenized, forged and forged + heat treated states. This alloy contains flaky micron-sized boride particles, mostly of the TiB<sub>2</sub> type, which break down into smaller segments upon forging. The boride type and morphology are analyzed by means of transmission electron microscopy. We present evidence that small boride particles (50 nm size) are effective in retarding colony growth for a heat treatment above the  $\alpha$ -transus; colony sizes of 80-100  $\mu$ m can be obtained and diboride particles decorate the colony boundaries.

### Introduction

A consensus has developed in the aerospace industry that in the near future, the  $\gamma$ -TiAl-base alloys will replace heavier nickel-base alloys for some applications [1, 2]. Although many concerns remain, recent results indicate that  $\gamma$ -TiAl has sufficient ductility to survive normal manufacturing, assembly and engine operations [1, 3]. The initial applications will probably involve as-cast materials. Grain refinement is a critical issue in as-cast components and this is no less true for the titanium aluminides. Very large grains can have a detrimental effect on the strength and the toughness of cast near-gamma alloys.

It is well established that boron additions are a very potent inoculant for refining the grain size of cast  $\gamma$  titanium aluminide alloys [4, 5]. Boron additions of at least 0.5at% are required to produce grain refinement in as-cast titanium aluminide alloys [5]. Even at such low levels, <1at%, boron additions produce a dispersion of boride particles throughout the microstructure [6, 7, 8].

In binary alloys, the Ti/Al ratio helps to determine the morphology of the boride phase [6, 7, 8] while the amount of boron added is the prime determinant of the identity of the boride, TiB or TiB<sub>2</sub> [6, 7]. Refractory metal additions can also have an effect;

Ta and Nb additions can be incorporated into the borides or lead to the precipitation of TaB or NbB [9, 10].

The control of grain size is also very important in wrought materials including  $\gamma$  titanium aluminide alloys. Grain size control must be maintained during processing operations and particularly during final heat treatment operations.

The most desirable microstructural condition in these alloys remains to be determined, but as the debate about the virtues of duplex versus fully lamellar microstructures continues, it is obvious that the microstructure will ultimately be dictated by the application conditions [11]. In certain cases, a fine, fully lamellar colony microstructure will be most advantageous. The addition of low levels of boron to wrought near-gamma alloys has been gaining acceptance, as it has been shown to retard elevated temperature grain growth in the single phase alpha regime [12]. There has, however, been some concern about the ability to obtain the "optimum" microstructure in B-stabilized materials.

This study was undertaken in an effort to understand the role of borides during the wrought processing and subsequent heat treatment of near-gamma titanium aluminides. A hyper-peritectic alloy containing Mo was selected for this study; high Al alloys exhibit a greater degree of peritectic segregation than their low Al counterparts and the Mo addition highlights this segregation. In addition, the simultaneous addition of Mo and B to near-gamma titanium aluminide alloys has not been studied.

### Experimental Methods

A 100mm diameter ingot was produced by Duriron, Dayton, OH, with the aim composition: Ti-47at%Al-2at%Mo-0.2at%B. The ingot was prepared using an induction skull melting technique, and the melt was subsequently poured into a graphite mold. The analyzed composition of the 4" diameter ingot was Ti-47.5at%Al-1.8at%Mo-0.21at%B; the oxygen and carbon impurity levels were 790wppm and 0.03at%, respectively.

A series of heat treatments were performed to determine the microstructural response to homogenization. We began with a heat treatment of 4 hours at 1250°C and increased the temperature by 50°C increments. Specimens for heat treatment were wrapped in Ta foil and encapsulated in quartz tubes backfilled with a partial pressure of argon. All heat treatments were finished with an air-cool, during which the samples remained in their glass capsules. Following an homogenization heat treatment of 4 hours at 1400°C, a forging preform, ~150mm tall×100mm in diameter, was EDM machined from the ingot. This preform was forged, on the research press at Wyman Gordon, Houston, to a 60% upset at 1150°C at an initial strain rate of  $10^{-3}\text{s}^{-1}$ ; the final height was ~60mm for an average true strain of 0.9. Post-forging heat treatments were performed in a similar fashion to the homogenization screening studies.

The initial microstructural characterization method used was backscatter image SEM, performed on unetched electropolished surfaces. This method provides both chemical and microstructural information as the image is formed through a combination of atomic number (Z) contrast and orientation due to electron channeling.

All TEM observations were performed on a Philips CM30 operated at 300 kV. TEM Observations were carried out in the as-cast state, after 60% forging at 1150° and a strain rate of  $10^{-3}/\text{s}$ , and after forging + heat treatment (1380° for 2 hours followed by air-cool). Electron transparent thin foils were prepared by cutting thin slices along or perpendicular to the forging direction. These slices were then ground to roughly 200  $\mu\text{m}$  before 3 mm discs were punched out. Subsequent thinning was carried out in an electropolishing unit, using a methanol-4%  $\text{H}_2\text{SO}_4$  electrolyte, kept at -10°, with a current of 95 mA. All electron negatives were digitized at 600 dpi on a flatbed scanner with transparency attachment. Image processing was carried out with Adobe Photoshop and final prints were made on a Codonics photographic quality dye-sublimation printer.

Samples were also examined in a JEOL 4000EX high resolution TEM, equipped with a Gatan Imaging Filter (GIF) for energy filtered observations and a grade B 1024×1024 CCD camera.

## Experimental Observations

### Metallography

As shown in Figure 1a, the microstructure of the cast material is not fully lamellar. There is evidence of interdendritic equiaxed gamma phase, while beta phase is present in the dendrite core regions. A higher magnification view, Figure 1b, provides a good view of both the Mo-stabilized beta phase, the very bright lacy phase in the dendrite core, and the dark flakes of the intragranular boride phase.

The microstructures resulting from heat treatment of the cast alloy at a series of temperatures ranging from 1250°C up to 1400°C were examined (Figure 2a-d). With increasing heat treatment temperature, the Al-rich equiaxed gamma regions, initially expand and then shrink. During these heat treatments, the Ti-rich lamellar regions will be single phase  $\alpha$ , facilitating diffusional rearrangement within these regions while the interdendritic regions will remain as ordered  $\gamma$  phase. Following heat treatment at 1350°C (Figure 2c), this process has almost reached its conclusion but the continued existence of the interdendritic  $\gamma$  regions impedes homogenization until the  $\alpha$ -transus is exceeded in the range 1350°-1400°C. The  $\beta$  phase, present in the dendrite core regions, remains virtually unaffected by heat treatments at 1250°C (Figure 2a) and 1300°C (Figure 2b). After 4 hours at 1350°C (Figure 2c), the bright lacy phase is no longer present indicating that the Mo has dispersed sufficiently to allow the  $\beta$  phase to be taken into solution in the disordered  $\alpha$  phase. After 4 hours at 1400°C (Figure 2d), the microstructure is fully lamellar microstructure and it is quite easy to see the boride flakes, which appear to be unaffected by the time at temperature.

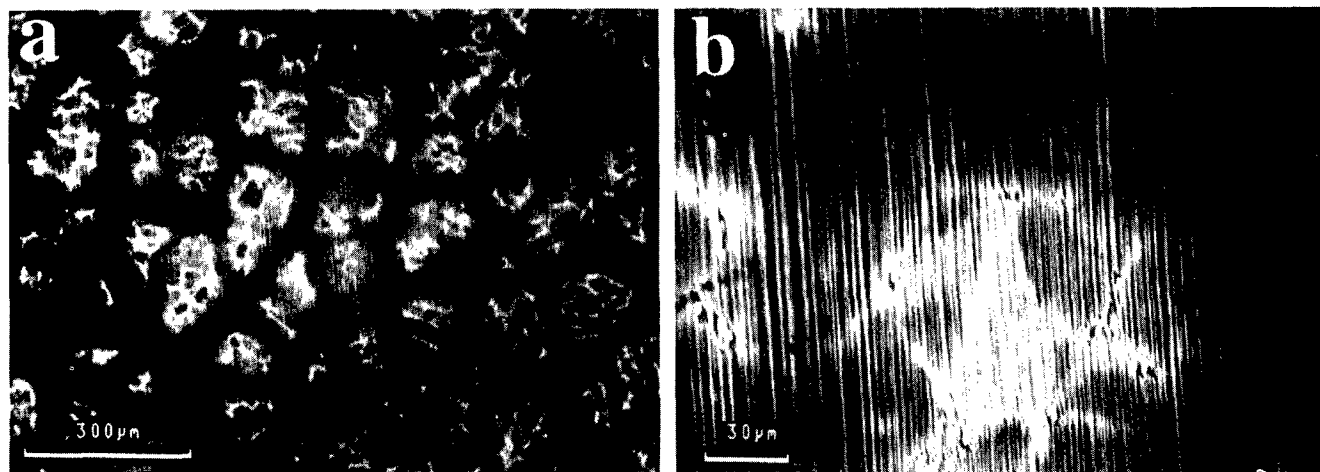


Figure 1. a) Back-scattered SEM picture of the as-cast microstructure; b) higher magnification view showing Mo-stabilized beta phase (white lacy phase) and dark intragranular flaky boride phase.



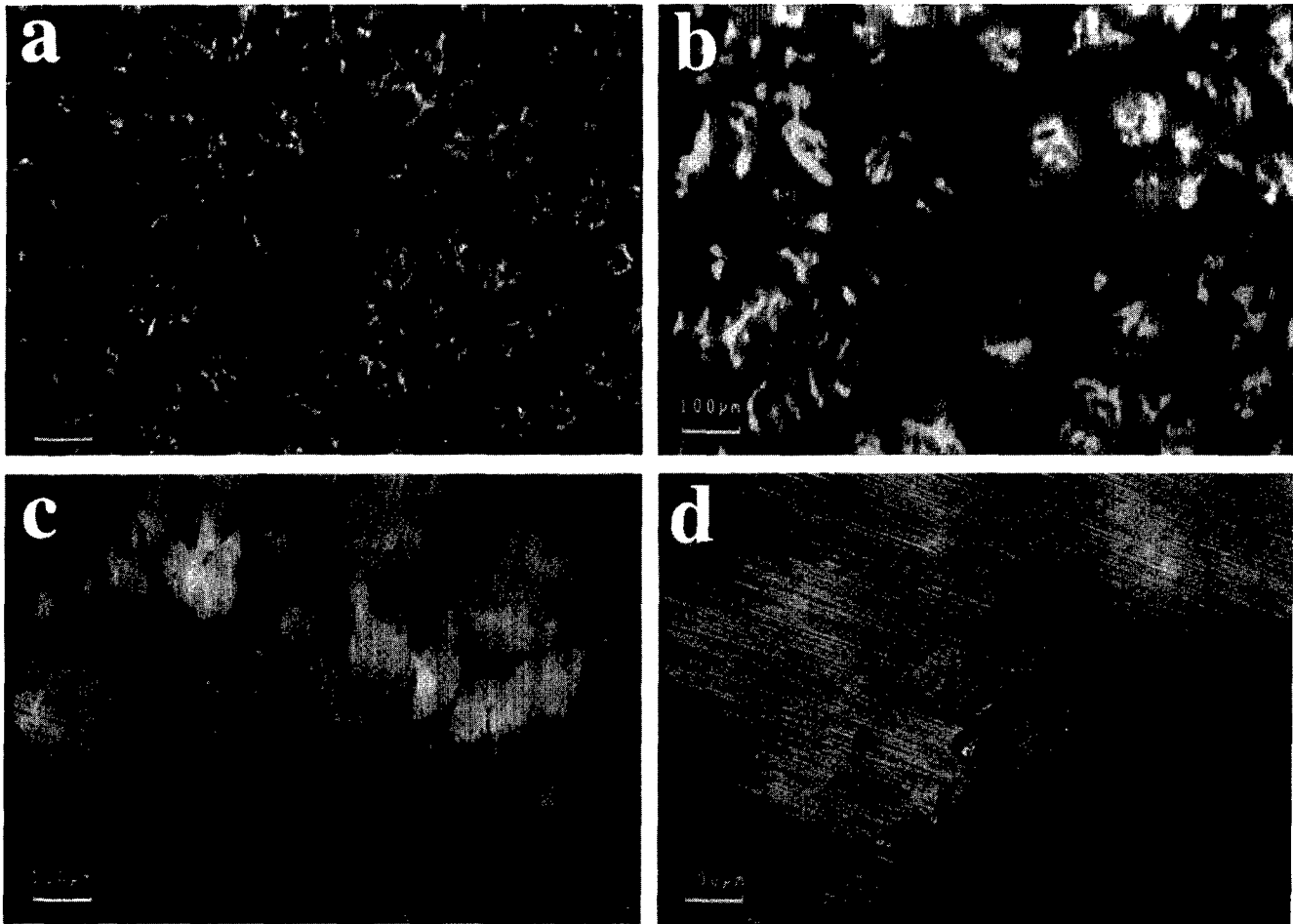


Figure 2. Back-scattered SEM micrographs of the heat treated microstructure after 4 hours at a) 1250°C, b) 1300°C, c) 1350°C, and d) 1400°C.

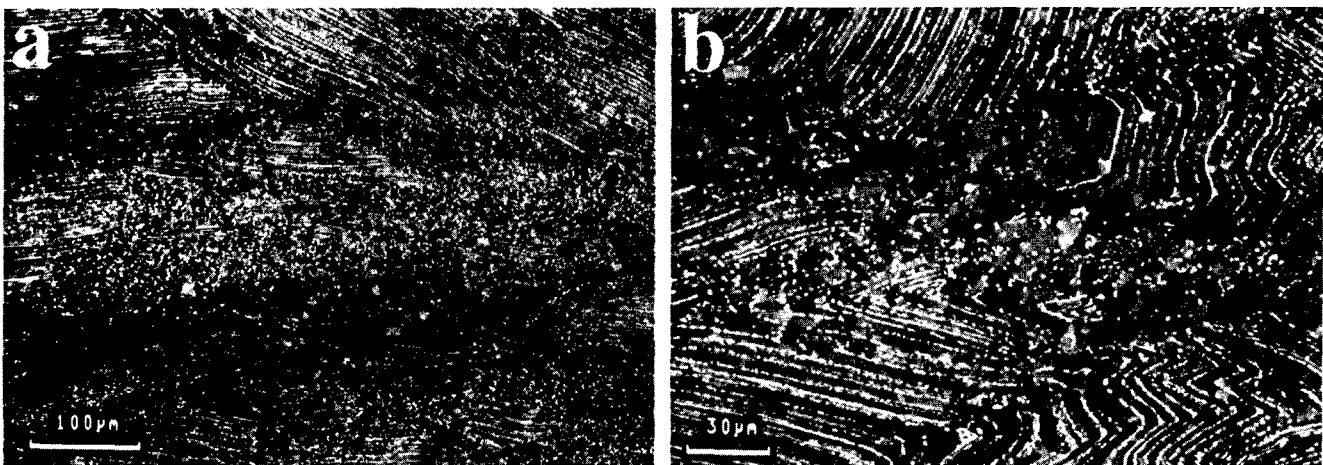


Figure 3. Back-scattered SEM micrograph of the microstructure of a highly worked region at half-radius of the forged pancake. Note regions with equiaxed grains interspersed with bent lamellae. b) shows a higher magnification view of the same area as a).

The macrostructure of a complete longitudinal cross-section through the forging revealed that, as would be expected, the most intensely worked zone was across the central region of the forged pancake, extending out to about half of the radius. The microstructure of specimens taken from this highly worked region contained large regions of fine equiaxed grains interspersed with regions containing bent lamellae, as shown in Figure 3a. Closer examination of the lamellar regions revealed that the  $\gamma$  phase had assumed a fine equiaxed structure with a grain size approximating the interlamellar spacing, while the thinner bands of  $\alpha_2$  phase had also begun to break up into individual very fine grains, as shown in Figure 3b.

The response of the forged microstructure to heat treatment is illustrated in Figure 4. Heat treatment at temperatures up to 1200°C did not produce any significant changes. In fact, little change was observed in material heat treated at 1200°C for 2 hours but 8 hours at this temperature resulted in significant changes. As shown in Figure 4a, there has been significant growth of the equiaxed gamma grains and the  $\alpha_2$  lamellae have pinched off and begun to spheroidize. Raising the heat treatment temperature to 1300°C results in the microstructure shown in Figure 4b.

After just 2 hours at this temperature there has not been sufficient time for much microstructural rearrangement. At temperature, the microstructure will contain a high fraction of ordered gamma phase and this will impede diffusional rearrangement. Coarsening of both the lamellar and the equiaxed microstructural units has occurred but they have retained their identities. Longer times at temperature would be needed in order to accomplish significant microstructural rearrangement. Figure 4c indicates that 1360°C is just below the  $\alpha$ -transus for this alloy. On cooling, the alloy has assumed an almost fully lamellar microstructure; there are still some residual gamma grains, most notably at the lamellar colony boundaries. At the highest annealing temperature, 1380°C, the alloy was obviously single phase, disordered alpha phase which, on cooling, has assumed a fully lamellar configuration. The grain size of this lamellar microstructure is significantly finer than that observed in the cast+homogenized material following heat treatment under similar conditions. This can be seen by comparing Figure 4d and Figure 2d. In Figure 4d it can also be seen that the original large lacy boride particles have been fragmented by the forging operation. Some of the borides reside at lamellar colony boundaries while others are intragranular.

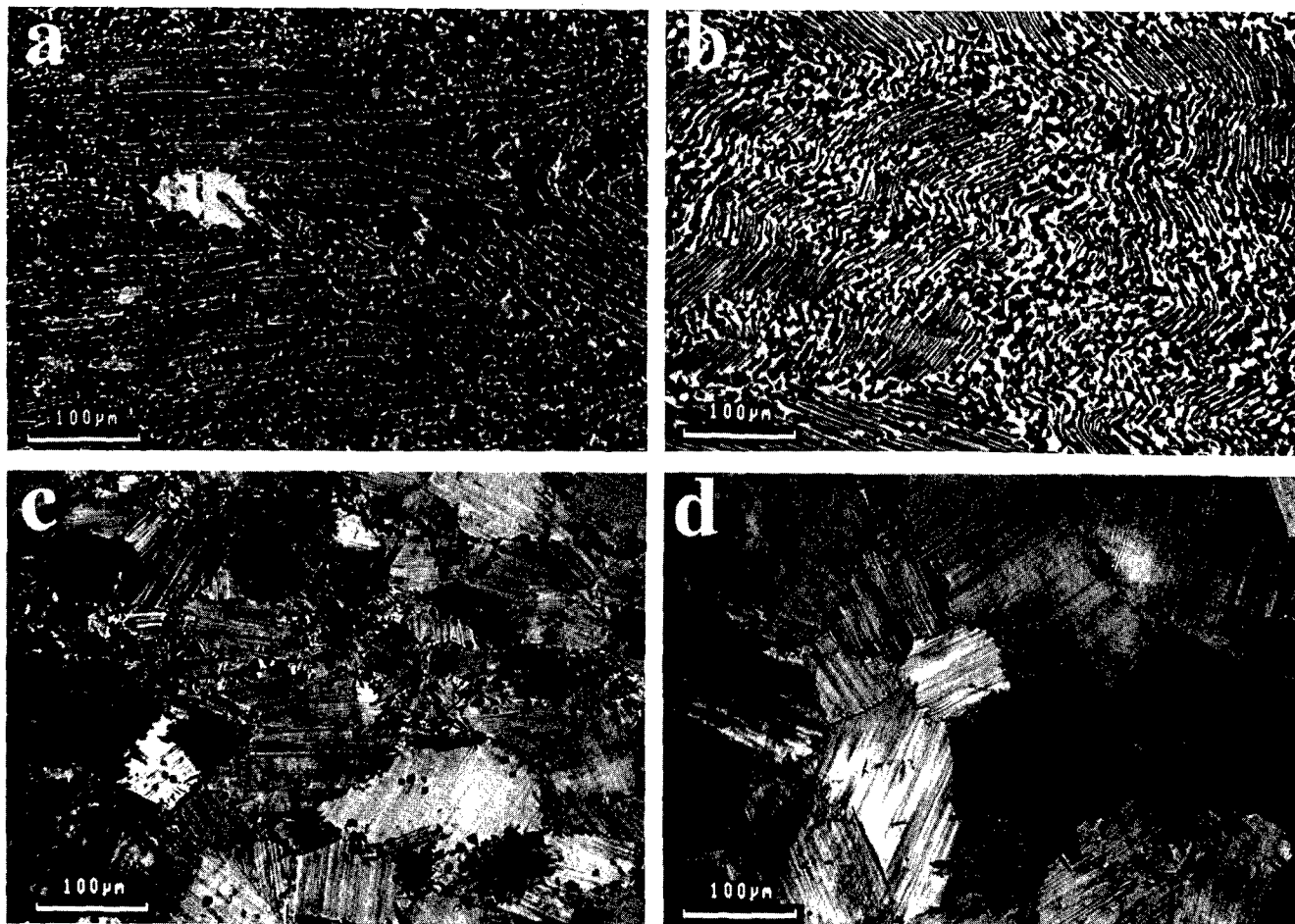


Figure 4. Back-scattered SEM micrograph of the forged and heat treated microstructure. a) 8 hrs @ 1200°C, b) 2 hrs. @ 1300°C, c) 2 hrs. @ 1360°C, and d) 2 hrs. @ 1380°C, all followed by an air cool.

Table I: Structure type, space group, lattice parameters and fractional coordinates for the most important stable and metastable titanium borides.

Structure Type	Space Group	Lattice Parameters (nm)	Wyckoff position	fractional atom coordinates		
TiB (B27)	Pnma (62)	a=0.611	Ti(4c)	0.177	0.250	0.123
		b=0.305	B(4c)	0.029	0.250	0.603
		c=0.456				
TiB (B <sub>f</sub> )	Cmcm (63)	a=0.323	Ti(4c)	0.000	0.146	0.250
		b=0.856	B(4c)	0.000	0.440	0.250
		c=0.305				
TiB (B <sub>g</sub> )	I4 <sub>1</sub> /amd (141)	a=0.311	Ti(8e)	0.000	0.000	0.196
		c=1.695	B(8e)	0.000	0.000	0.352
Ti <sub>3</sub> B <sub>4</sub> (D7 <sub>b</sub> )	Immm (71)	a=0.326	Ti(2c)	0.500	0.500	0.000
		b=1.373	Ti(4g)	0.000	0.180	0.000
		c=0.304	B(4g)	0.000	0.375	0.000
			B(4h)	0.000	0.444	0.500
TiB <sub>2</sub> (C32)	P6/mmm (191)	a=0.303	Ti(1a)	0.000	0.000	0.000
		c=0.323	B(2d)	0.333	0.666	0.500

Table II: Orientation relationships for coherent intergrowths between the five possible titanium borides.

$[100]_{B_f} \parallel [100]_{D7_b}$	$[100]_{B_f} \parallel [0001]_{C32}$	$[001]_{B_f} \parallel [010]_{B27}$	$[010]_{B_f} \parallel [001]_{B_g}$
$(010)_{B_f} \parallel (010)_{D7_b}$	$(010)_{B_f} \parallel (10.0)_{C32}$	$(110)_{B_f} \parallel (100)_{B27}$	$(001)_{B_f} \parallel (100)_{B_g}$

#### Transmission Electron Microscopy

The effect of B on the microstructure and properties of this and other Ti-Al based alloys can only be understood after a careful analysis of the crystal structures of all relevant boride phases. Earlier work has shown that there are three important equilibrium crystal structures for Ti-borides : (1) orthorhombic TiB (B27), (2) body-centered orthorhombic Ti<sub>3</sub>B<sub>4</sub> (D7<sub>b</sub>), and (3) hexagonal TiB<sub>2</sub> (C32). In addition there exists a metastable orthorhombic monoboride B<sub>f</sub>, isomorphous with TaB, and a metastable tetragonal boride B<sub>g</sub>, isomorphous with α-MoB. The crystallographic parameters for all five boride types are shown in Table I [13].

It has been shown [8] by electron diffraction and high resolution transmission electron microscopy that B<sub>f</sub>, D7<sub>b</sub>, and C32 can form complex, fully coherent intergrowths and that it is not always straightforward to distinguish between these structures by means of electron diffraction alone. The close relationship between the boride structures is a consequence of the presence of a common building block, a trigonal prismatic array of six Ti atoms with B at the center (Figure 5a). The base edge length of this trigonal prism is about 0.305 nm, and one can easily recognize this distance in the lattice parameters of all five borides. Boron-boron bonds stabilize columns of face-sharing trigonal prisms [8], as shown in Figure 5b and by edge or face-sharing of these columns one can build all five crystal structures. As shown in [8] several of these borides can form intergrowths while maintaining integrity of the prismatic building blocks. This ability of the various phases to grow coherently on top of each other has important consequences for the phase selection during solidification (see Discussion section).

An example of a complex intergrowth between various boride structures is shown in Figure 6a which shows a boride particle in the as-cast alloy. The corresponding electron diffraction pattern shown in Figure 6b indicates that the structure is a mixture of C32, D7<sub>b</sub> and B<sub>f</sub>. Detailed identification of the various reflections is shown in Figure 6c. In many boride flakes we observed a

center-line defect, indicating that the particle first nucleated as a thin sheet, and then coarsened into a thicker flake. Depending on the local boron concentration in the melt, a variety of defects, parallel to the center-line, are formed. The observed orientation relations between the borides ( $[101]_{D7_b} \parallel [101]_{B_f} \parallel [2\bar{1}.1]_{C32}$ ) are in agreement with the relations listed in Table II.

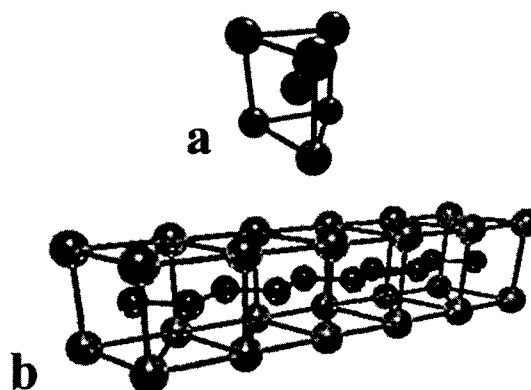


Figure 5. a) Trigonal prismatic building block with metal atoms at the corners and boron at the center; b) column formed by face-sharing of the prismatic blocks.

Boride particles were often found to intersect lamellar colonies at large oblique angles, sometimes perpendicular to the lamellar planes. Although in some cases interfacial dislocations were observed between borides and the surrounding γ plates, we did not find a simple orientation relation between the borides and the surrounding phases. Particle thicknesses varied from less than 100 nm to about 400 nm, with aspect ratios as high 70:1 (see Figure 7).

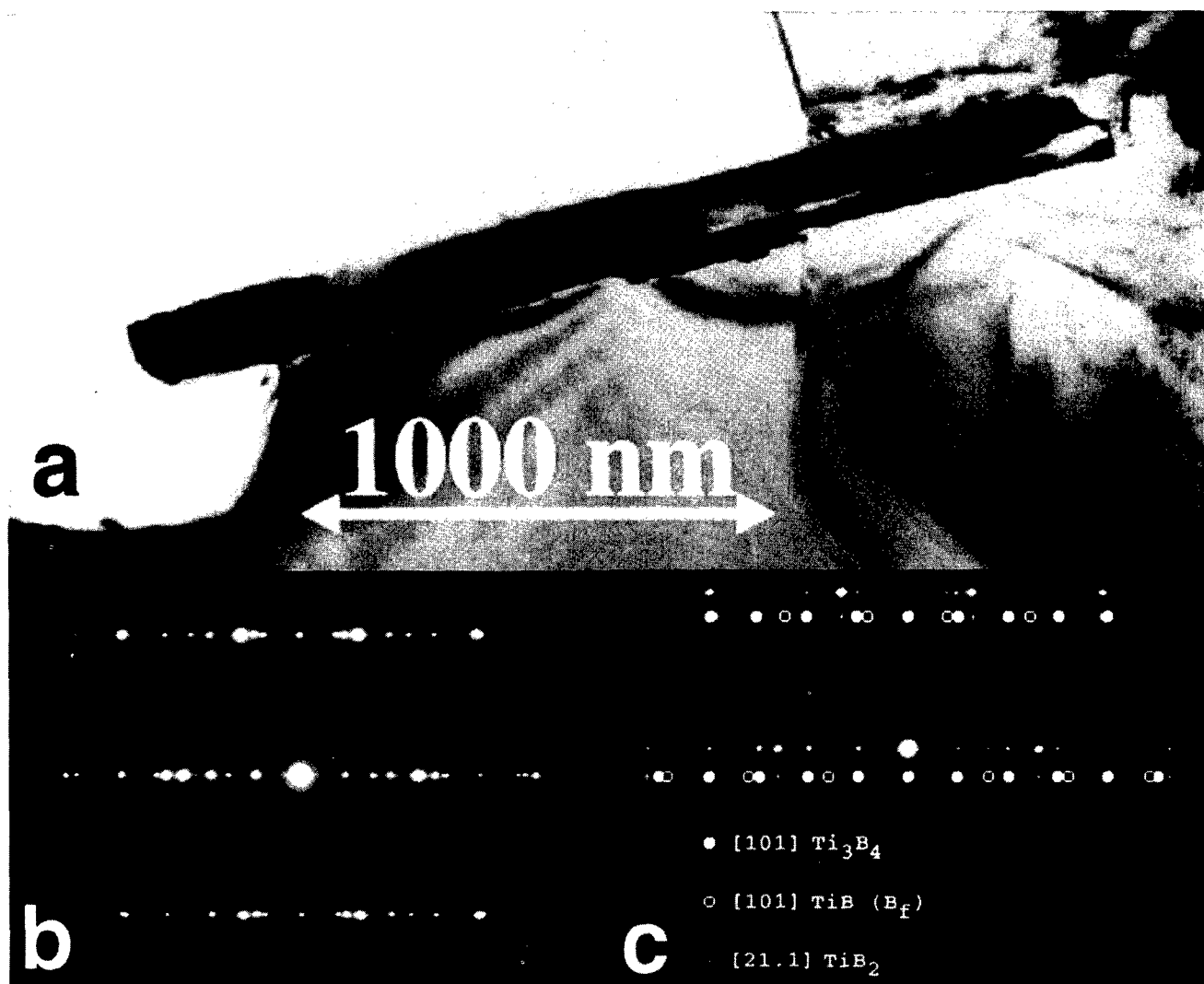


Figure 6. a) Boride flake in the as-cast alloy. The particle is heavily faulted and has poorly developed facets. b) zone axis electron diffraction pattern of a), indicating that the particle consists of a coherent intergrowth of three different boride phases. c) shows the detailed identification of the diffraction spots.



Figure 7. Boride flake with high aspect ratio (70:1) in the as-cast alloy.

After forging at 1150° the boride flakes break up into smaller micron-sized segments. The partial removal of the intergrowth defects indicates that there may be some boron redistribution. This evolution becomes even more pronounced after a 2 hour heat treatment at 1380° followed by an air-cool. As shown in Figure 8 the defect density has decreased to the point where well defined bend contours can be observed. The boride particles now measure in the micron to sub-micron range and show increased faceting, another sign of boron redistribution. Most boride particles still show a center-line defect and some are surrounded by  $\gamma$  grains, indicating a residual inhomogeneity of Al (see Figure 9). Since the thin foil preparation method used for this work causes some

preferential thinning of the  $\gamma$  phase, and most boride particles are found near or inside  $\gamma$ -phase grains, it is rather straightforward to locate the borides in a low magnification observation mode. After the heat treatment step the microstructure consists of lamellar colonies with a colony size of about 80-100  $\mu\text{m}$  and sub-micron lamellar spacings; a low magnification overview of a set of colonies is shown in Figure 10 (this figure combines eight micrographs; the gray rectangles correspond to either the negative counter region or to regions which were not captured in the montage). Colony boundaries are often decorated with  $\gamma$  grains, and several boride flakes can be observed, surrounded by  $\gamma$  phase material.

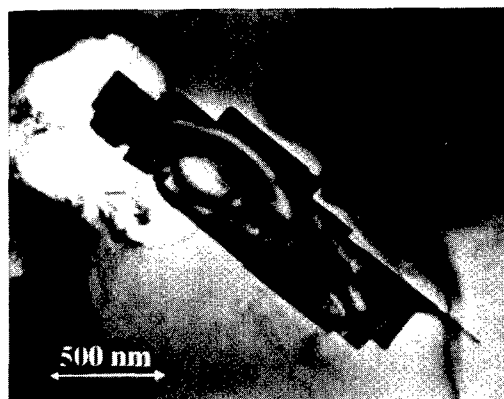


Figure 8. Boride morphology in the forged + heat treated alloy (2 hrs. @ 1380°C). Note the well developed bend contours, indicating a low fault density, and pronounced faceting.

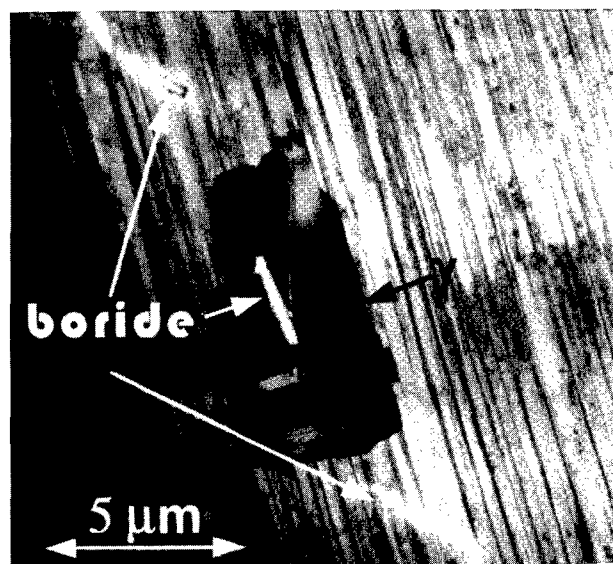


Figure 9. Boride particles inside a single lamellar colony. The dark region surrounding the center boride is a gamma grain, indicating a residual inhomogeneity of Al.



Figure 10. Montage of eight low magnification micrographs showing multiple colonies with irregular boundaries. The average colony size is 80-100 microns. Several boride particles can be observed inside the colonies and near the colony boundaries.

Detailed analysis of the colony boundaries has revealed that they are also decorated with fine boride particles (50-100 nm long), such as the ones indicated by dark arrows in Figure 11 and in the enlarged view in Figure 12. Electron diffraction has shown that these fine borides are of the C32 di-boride type. The curvature of the colony boundaries close to where they intersect the boride particles suggests that the borides are indeed effective in retarding colony and grain growth. Another example of a boride particle anchoring a colony boundary is shown in Figure 13; this

particle measures about 500 nm in length and the colony boundary clearly attaches to it.

Preliminary observations using a Gatan Imaging Filter (GIF) on a JEOL 4000EX HRTEM indicate that there may be boron distributed along the colony boundary. We observed a strong boron electron energy loss signal from the boride particles at the colony boundary, and a rather weak signal from the boundary itself. More detailed investigations are underway to confirm these observations.

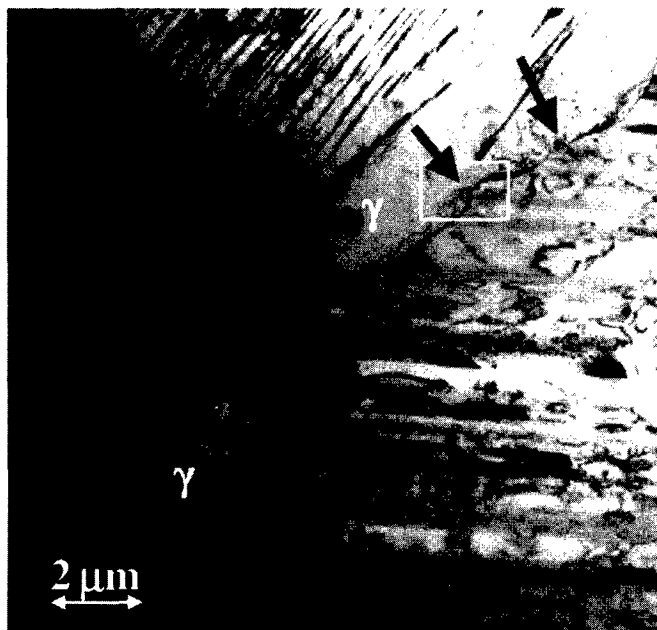


Figure 11. Colony boundary decorated with boride particles in the forged and heat treated alloy (1380°C). Arrows indicate the locations of the borides.



Figure 13. Diboride particle at another colony boundary.



Figure 12. Magnified view of the outlined region in Figure 11. The colony boundary is clearly pinned by the diboride particle.

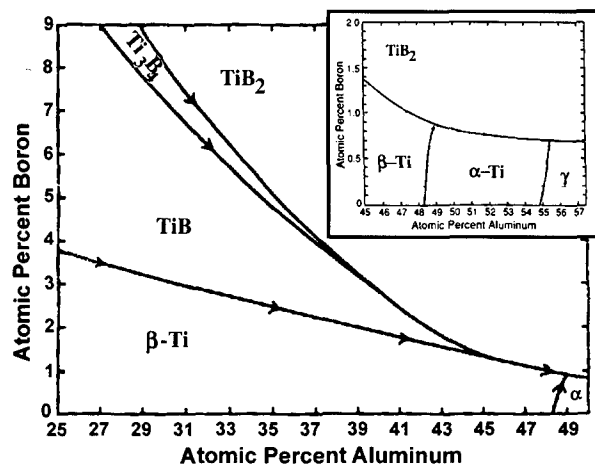


Figure 14. Liquidus projection of the ternary Ti-Al-B system, taken from ref. [7]. The inset shows the higher aluminum content part of the projection, and the dashed line indicates the boron level for the alloy in this paper.

### Discussion and Conclusions

To understand why a certain (stable or metastable) boride appears after cooling from the liquid, one must carefully consider the liquidus projection of the Ti-Al-B system, first proposed by Hyman et al. [7]. The relevant section of this diagram is reproduced in Figure 14. The alloy under consideration, with a B concentration of 0.2 at% (dashed line in inset), undergoes a double peritectic cascade, first forming primary  $\beta$  dendrites surrounded by  $\alpha$  and eventually by  $\gamma$  in the interdendritic spaces. The addition of Mo shifts the  $\beta$ - $\alpha$  line towards a higher aluminum content. The composition of the liquid becomes gradually richer in Al and B, until  $\gamma$  and borides are formed in the interdendritic spaces. For the Al content of the present alloy, the secondary boride will be the di-boride  $\text{TiB}_2$ . In agreement with the work by Hyman et al. [7] we find that the boride morphology in as-cast Ti-47at%Al-2at%Mo + 0.2at% B is mostly flaky. For boron contents above the monovariant line in the liquidus projection, the primary solidification morphology would be blocky while close to the monovariant line flakes, plates and needles have been reported.

Upon continued solidification the liquid becomes more dilute in boron and this is accommodated by the formation of coherent intergrowths between the di-boride and the  $D7_b$  and  $B_f$  structures which have a lower boron content. These metastable borides thus form in response to a change in the chemistry of the melt during solidification, which in the absence of kinetic constraints should produce the di-boride  $\text{TiB}_2$  [8]. The close orientation relationships between the various borides, listed in Table II, allow for the accommodation of changes of the local chemistry of the melt and result in complex, fully coherent intergrowths. The boride flakes grow fastest along their length axis and often show a centerline defect, which is presumably related to the solidification nucleus. The TEM observations presented in this paper provide strong evidence that borides are indeed effective in retarding grain growth at temperatures above the  $\alpha$ -transus. In an alloy with similar composition but without boron additions, the average colony size would easily be an order of magnitude larger than that observed for the boron containing alloy. We report here for the first time that the colony boundaries forged and heat treated Ti-47at%Al-2at%Mo + 0.2at% B are effectively pinned by diboride particles with sizes in the 50-500 nm range. In addition, there is preliminary evidence of the presence of atomic boron along the colony boundaries.

### Acknowledgements

This research was carried out under AFOSR Contract No. F49620-94-C-0023. MDG would like to thank the Rockwell International Science Center for partial financial support.

### References

- [1] C.M. Austin and T.J. Kelly, "Gas Turbine Engine Implementation of Gamma Titanium Aluminide", Superalloys 1996, ed. R.D. Kissinger, D.J. Deye, D.L. Anton, A.D. Cetel, M.V. Nathal, T.M. Pollock and D.A. Woodford, TMS, Warrendale PA, 1996, 539-543.
- [2] D.E. Davidson, "Designing with Gamma Titanium: CAESAR Program Titanium Aluminide Component Applications," Superalloys 1996, ed. R.D. Kissinger, D.J. Deye, D.L. Anton, A.D. Cetel, M.V. Nathal, T.M. Pollock and D.A. Woodford, TMS, Warrendale PA, 1996, 545-553.
- [3] C.M. Austen and T.J. Kelly, Structural Intermetallics, ed. R. Darolia, TMS, Warrendale PA 1993, 21-32.
- [4] S-C. Huang and E.L. Hall, "Structures and Properties of Gamma TiAl Alloys Containing interstitial Alloys," High Temperature Ordered Intermetallic Alloys IV, ed. L.A. Johnson, D.P. Pope and J.O. Steigler, *Mat. Res. Soc. Proc.* 213, Pittsburgh PA, 1991, 827-832.
- [5] D.E. Larsen, Jr., "Effects of XD  $\text{TiB}_2$  Volume Fraction on the Microstructure and Mechanical Properties of a Cast XD Near-gamma Alloy" in Microstructure/Property Relationships in Titanium Aluminides and Alloys, ed. Y-W. Kim and R.R. Boyer, TMS, Warrendale PA 1993, 345-352.
- [6] M.E. Hyman, C. McCullough, J.J. Valencia, C.G. Levi and R. Mehrabian, "Microstructure evolution in TiAl alloys with B additions: conventional solidification," *Metall. Trans.* 20A (1989) 1847.
- [7] M.E. Hyman, C. McCullough, C.G. Levi, and R. Mehrabian, "Evolution of boride morphologies in TiAl-B alloys," *Metall. Trans.*, 22A (1991) 1647-1662.
- [8] M. De Graef, J.P.A. Löfvander, C. McCullough, and C.G. Levi, "The evolution of metastable  $B_f$  borides in a Ti-Al-B alloy," *Acta Metall. Mater.*, 40 (1992) 3395-3406.
- [9] M. De Graef, J.P.A. Löfvander and C.G. Levi, "The structure of complex monoborides in  $\gamma$ -TiAl alloys with Ta and B additions," *Acta Metall. Mater.* 39 (1991) 2381-2391.
- [10] J.J. Valencia, J.P.A. Löfvander, C. McCullough, C.G. Levi and R. Mehrabian, "In-situ grown reinforcements for titanium aluminides," *Mat. Sci. Eng. A144*, (1991) 25-36.
- [11] D.M. Dimiduk, "Gamma Titanium - An Emerging Materials Technology," Gamma Titanium Aluminides, ed. Y-W. Kim, R. Wagner and M. Yamaguchi, TMS, Warrendale PA, 1995, 3-20.
- [12] P.L. Martin, "Effect of Boron on the Microstructure and Properties of Ti-47Al-2Nb-2Cr-1Mo," paper presented at the 124th TMS meeting, Las Vegas, Nevada, USA, 12-16 Feb. 1995.
- [13] Pearson, in *Handbook of Crystallographic Data for Intermetallic Phases* (edited by P. Villars and L.D. Calvert), American Society for Metals (1985)

## DEFECT SUB-STRUCTURES IN LAMELLAR Ti48Al AFTER 'HARD' ORIENTATION LOADING AT ROOM AND ELEVATED TEMPERATURES

Jörg M.K. Wiezorek, Xiao-Dong Zhang and Hamish L. Fraser  
The Ohio State University, Department of Materials Science and Engineering,  
2041 College Road, Columbus, OH-43210-1179, USA.

### Abstract

Binary ( $\gamma$ - $\alpha_2$ )-Ti-48at.%Al intermetallics with polycrystalline (with mixed lamellar and equiaxed microstructures) and poly-synthetically twinned (*PST*) microstructures have been deformed in tension and in compression at room temperature and at 800° to strain levels up to fracture. The deformation modes active in these lamellar TiAl compounds during loading along 'hard' directions, such as  $[111]$ ,  $[1\bar{1}0]$ ,  $[\bar{1}\bar{1}2]$  and approximately  $[\bar{1}01]$  for instance, have been determined by transmission electron microscopy (TEM). In particular, the deformation mechanisms in the  $\alpha_2$  phase have been studied, particularly those that provide shears normal to the lamellae. The role of deformation in the phase  $\alpha_2$  on the general deformation behavior of TiAl alloys has been assessed.

### Introduction

Most of the technologically relevant TiAl alloys have off-stoichiometric compositions deficient in Al, e.g. based on compositions such as Ti-44-49at.%Al, and microstructures containing significant volume fractions of morphologically lamellar grains [1]. Lamellar grains consist of a majority of  $\gamma$ -TiAl lamellae and a smaller fraction of  $\alpha_2$ -Ti<sub>3</sub>Al lamellae conforming to a crystallographic orientation relationship which can be expressed as  $(111)_\gamma // (0001)_{\alpha_2}$  and  $[1\bar{1}0]_\gamma // [\bar{1}1\bar{2}0]_{\alpha_2}$  [2]. The mechanical properties associated with the lamellar form of TiAl have been studied from a fundamental point of view using directionally solidified TiAl alloys comprising only a single lamellar grain, so-called poly-synthetically twinned (*PST*) crystals and have been shown to be markedly anisotropic [3-7]. For *soft* orientation loading, where shear components parallel to the lamellar interfaces are required for strain accommodation, elongations in excess of 20% have been reported at room temperature [4]. However, for some *hard* orientations, such as  $[111]$  and  $[1\bar{1}0]$ , which require significant contributions from shear

components perpendicular to the lamellar interfaces, much smaller elongations to failure have been observed [3]. Notably, for loading perpendicular to the lamellar interface plane, i.e. along  $[111]_\gamma // [0001]_{\alpha_2}$ , tensile ductility has been reported to more or less vanish [3, 6]. The deformation modes activated in the  $\gamma$ -lamellae of the *PST* TiAl during room temperature deformation after moderate strains of about  $\epsilon=1-3\%$  depend on their orientation relative to the load axis and involve ordered twinning of the type  $1/2\langle 112 \rangle \{111\}$  and slip of ordinary dislocations, i.e. systems of the type  $1/2\langle 110 \rangle \{111\}$  and superdislocations, systems such as  $\langle 101 \rangle \{111\}$  and  $1/2\langle 112 \rangle \{111\}$  [3, 5, 6]. As far as the deformation modes active in the  $\alpha_2$ -lamellae of *PST* TiAl are concerned, the current understanding is not as well developed as for the  $\gamma$ -lamellae. Independent reports agree that after loading *PST* TiAl parallel to the lamellar interfaces even at moderate levels of strain,  $\epsilon \approx 2-3\%$ , shear deformation occurred in the  $\alpha_2$ -lamellae which has been attributed to prism plane slip of  $\langle a \rangle$  dislocations (i.e. those with Burgers vectors,  $\mathbf{b}$ , given by  $\mathbf{b} = 1/3\langle 11\bar{2}0 \rangle$ ) [e.g. 5-7]. However, when *PST* TiAl has been loaded normal to the lamellar interface, reports regarding the deformation behavior of the minority phase have presented disparate conclusions. On the one hand, the absence of plasticity in the  $\alpha_2$ -lamellae has been reported which was attributed to the very high critical resolved shear stress (CRSS) required for the activation of pyramidal slip of  $\langle 2\mathbf{c}+\mathbf{a} \rangle$  dislocations with  $\mathbf{b} = 1/3\langle 11\bar{2}6 \rangle$ ; such slip systems are operative in similarly oriented single crystals of monolithic  $\alpha_2$ -Ti<sub>3</sub>Al [5, 6, 8]. On the other hand, clear evidence has been detected for the activation of pyramidal plane slip in the  $\alpha_2$ -phase in the form of surface traces on compressed coupons [7]. The CRSS for pyramidal slip of  $\langle 2\mathbf{c}+\mathbf{a} \rangle$  dislocations in Ti<sub>3</sub>Al with an off-stoichiometric composition, such as the  $\alpha_2$ -phase present in *PST* TiAl, has been reported to be 911 MPa [8]. On the basis of this CRSS value and the high Schmid factor for  $\langle 11\bar{2}6 \rangle \{11\bar{2}1\}$ , 0.45, for loading along  $[0001]$ , normal to the lamellar interfaces, an applied stress of about 2,025 MPa would be required to exceed the CRSS for



activation of  $\langle 11\bar{2}6 \rangle \{11\bar{2}1\}$  in the  $\alpha_2$ -phase. Despite the activity of  $\langle 11\bar{2}6 \rangle \{11\bar{2}1\}$  in  $\alpha_2$ -lamellae of *PST* crystals compressed at room temperature, such high levels of applied stress have not been reported [7].

In contrast to the large elongations realized for certain *soft* orientations of *PST* crystals [3, 4], the ductility of polycrystalline ( $\gamma$ - $\alpha_2$ )-TiAl aggregates is typically limited to less than 2-3% at room temperature (RT) [1]. A general shape change of such polycrystalline ( $\gamma$ - $\alpha_2$ )-TiAl aggregates requires the accommodation of strains with components perpendicular to the lamellar ( $\gamma/\alpha_2$ )-interfaces. This would involve *hard* modes of deformation in the  $\gamma$ - and  $\alpha_2$ -lamellae, e.g. for the latter this necessitates the activation of  $\langle c \rangle$ -component dislocations with  $\mathbf{b}=[0001]$  ( $=\langle c \rangle$ ) or  $\mathbf{b}=1/3\langle 11\bar{2}6 \rangle$  ( $=\langle 2c+a \rangle$ ). However, the activation of such *hard* deformation modes in Ti<sub>3</sub>Al requires critical resolved shear stresses (CRSS) very much higher than those required for plasticity of the  $\gamma$ -phase over a wide range of temperatures [5, 8, 9]. Recent studies reported that even in the presence of translamellar deformation in the  $\gamma$ -lamellae adjacent to  $\alpha_2$ -lamellae,  $\langle c \rangle$ -component slip has not been observed in the latter after room temperature loading to failure [10, 11]. Moreover, fracture processes in lamellar TiAl compounds have been shown to be associated often with failure along  $\gamma$ - $\alpha_2$  phase boundaries [e.g. 6, 7, 12]. These observations indicate that the plastic incompatibility between different variants of  $\gamma$ -TiAl and the  $\alpha_2$ -Ti<sub>3</sub>Al lamellae produces heterogeneous strain distributions, which may result in fracture, and it appears that the plastic behavior of the minority phase critically affects the mechanical behavior of technologically relevant polycrystalline ( $\gamma$ - $\alpha_2$ )-TiAl. Thus, in order to develop a better understanding of the plasticity and the strength of lamellar TiAl alloys it appears to be necessary to investigate carefully the deformation mechanisms active in both the  $\gamma$ - and the  $\alpha_2$ -phase during *hard* orientation loading.

In the present study polycrystalline aggregates of lamellar Ti-48at.%Al have been deformed in tension up to failure at room temperature and 800°C. Furthermore, *PST* Ti-48at.%Al material has been compressed to various degrees of strain at room temperature in *hard* orientations along the directions  $[111]$ ,  $[1\bar{1}0]$  and  $[\bar{1}\bar{1}2]$  respectively. The deformation mechanisms activated in these TiAl specimens have been identified by diffraction contrast experiments using transmission electron microscopy (TEM), where particular attention has been paid to the deformation in the  $\alpha_2$ -lamellae. The TEM observations typical of *hard* mode oriented grains in the polycrystalline material are compared with those observed in the *PST* crystals loaded in the three different *hard* orientations. These findings are discussed with respect to the fracture

and plasticity of lamellar TiAl alloys on the basis of resolved shear stress components, local stress levels and dislocation based models.

### Experimental procedures

A portion of a cylindrical ingot of Ti-48at.%Al, obtained from the Howmet Corporation, was placed in a stainless steel can prior to hot extrusion at 1250°C. Sections cut from the extruded bar of Ti-48at.%Al by electro-discharge machining were wrapped into Ti foil and encapsulated in silica quartz tubes under a partial pressure of Ar. Heat treatment for 3,600s at 1360°C, furnace cooling (FC), 21,600s at 900°C and a final FC of the encapsulated sections produced a polycrystalline intermetallic TiAl alloy with duplex microstructure containing a volume fraction of about 65% of lamellar grains between 100-150µm in diameter [12]. The remaining volume fraction exhibited an equiaxed morphology comprising mainly of  $\gamma$ -grains, 30-50 µm in diameter, and some intergranular  $\alpha_2$ -phase, 5-15 µm in size [12]. Rods of *PST* TiAl 12.5 mm in diameter and up to about 175.0 mm long have been obtained from the Materials Directorate, Wright Laboratories, Wright-Patterson Air Force Base. After crystallographic alignment of sections from the *PST* rods using a combination of the Laue Backscattering technique and diffraction analysis in the TEM coupons with 4.0x4.0 mm<sup>2</sup> square cross sections and 6.0 mm high have been cut with a low speed diamond saw. Thus compression coupons for loading perpendicular to the lamellar interfaces, i.e. along the  $[111]$  direction with  $(1\bar{1}0)$  and  $(\bar{1}\bar{1}2)$  side faces (from here on orientation N), and parallel to the lamellar interfaces, namely along both  $[1\bar{1}0]$  with  $(111)$  and  $(\bar{1}\bar{1}2)$  side faces (from here on orientation A1), and  $[\bar{1}\bar{1}2]$  with  $(111)$  and  $(1\bar{1}0)$  side faces (from here on orientation A2), have been obtained. Constant strain rate tensile tests to failure have been performed for the round bar specimens of the polycrystalline Ti-48at.%Al alloy in air at room temperature (RT) and at 800°C at a strain rate of  $1 \times 10^{-4} \text{ s}^{-1}$ . The *PST* coupons for the orientations N, A1 and A2 have been compressed at room temperature in air at a constant rate of  $1 \times 10^{-4} \text{ s}^{-1}$  producing strains up to about 7.0%. Some of the data collected during the mechanical tests is summarized in table 1. Thin disks have been obtained from the polycrystalline tensile test specimens and the *PST* TiAl compression coupons by sectioning both parallel and perpendicular to the loading axis. In order to analyze the activated deformation modes in terms of approximate local Schmid factors and resolved shear stresses TEM foils prepared from the perpendicularly cut disks have been used by approximating the foil normal, obtained by TEM with goniometer tilts set to zero, to the macroscopic loading axis [10]. Electron transparent foils have been prepared from these disks by twin-jet electropolishing using a solution of 6vol.% perchloric acid and 34vol.% butoxyethanol in methanol at a temperature of about -35°C, and by liquid nitrogen cooled ion-beam milling of ground and dimpled disks in a Gatan Dual Ion Mill using argon. A Philips CM200 TEM has been used for characterization of the defect substructures.

### Results

#### Mechanical Test Data

The mechanical test data pertinent to the current study is presented in table 1. At room temperature (RT) the polycrystalline Ti-48at.%Al

**Table 1:** Tensile and compression test data for Ti-48at.%Al.

specimen type & test condition	yield stress [MPa]	strains $\epsilon$ and $\epsilon_f$ ( failure)	max. stress [MPa]
poly, tension, RT	376.1	$\epsilon_f=2.5\%$	480.9
poly, tension, 800°C	367.1	$\epsilon_f=12.5\%$	680.3
A1 <i>PST</i> , comp., RT	521.1	$\epsilon=7.0\%$	653.7
A2 <i>PST</i> , comp., RT	513.3	$\epsilon=7.2\%$	632.1
N <i>PST</i> , comp., RT	810.2	$\epsilon=3.0\%$	944.8

failed after 2.5% elongation and yielded at a stress of 376.1 MPa. At 800°C much larger elongations to failure, 12.5%, have been realized without a significant decrease in yield strength, 367.1 MPa, whereas the maximum tensile stress prior to failure exhibited a significant increase to 680.3 MPa over that at RT, i.e. 480.9 MPa. The *PST* Ti-48at.%Al yielded during room temperature compression at stresses of 521.1 MPa and 513.3 MPa and reached maximum stresses at termination of the tests of 653.7 MPa and 632.1 MPa for the orientations A1 and A2 respectively. The stress-strain curves for N orientation loading exhibited very steep slopes. The yield stress shown in table 1 has been determined as the stress at 0.2% off-set strain. Small slope changes in the stress-strain behavior have been discerned for the N orientation loaded specimens in the stress range of about 800-850 MPa which appeared to be indicative of macroscopic yielding. Maximum stresses as high as 944.8 MPa have been reached at test termination for compression along [111].

#### TEM observations of defect substructures

##### Tensile deformation at RT

The bright field (BF) TEM micrograph of fig. 1a presents an overview of the deformation substructure typical of the lamellar colonies with a *hard* orientation with respect to the load axis after tensile fracture of the polycrystalline Ti-48at.%Al at room temperature (RT). The  $\gamma$ -

lamellae are heavily defected with both dislocations and a high density of *hard* mode deformation twins visible (e.g. figs. 1a-c), whereas the  $\alpha_2$ -lamellae are largely free of deformation induced defects (fig. 1a, b). TEM experiments confirmed that the  $\gamma$ -phase deformed by slip of both superdislocations and ordinary dislocations with Burgers vectors such as  $b=\langle 011 \rangle$  and  $1/2\langle 110 \rangle$  respectively, and by profuse deformation twinning of the ordered type  $1/2\langle 112 \rangle\{111\}$ . This is in agreement with previous work [5, 11, 12], and for brevity our detailed observations relating to the analysis of the  $\gamma$ -lamellae are not shown here [9, 10]. The lack of defect contrast within the  $\alpha_2$ -lamellae in fig. 1b demonstrates the absence of defects with  $\langle c \rangle$ -component Burgers vectors, whereas the dislocation visibility in fig. 1c clearly identifies the activation of  $\langle a \rangle$  dislocation slip. The lack of slip involving  $\langle c \rangle$ -component dislocations is consistent with the high CRSS required for activation of pyramidal slip systems involving these dislocations [8, 9] which remained in excess of the applied stresses during the tensile tests (table 1). Similar to earlier reports [10, 11] the  $\langle a \rangle$  dislocations have been observed in the  $\alpha_2$ -lamellae only in the vicinity of dense *hard* mode deformation twins in the adjacent  $\gamma$ -lamellae (e.g. fig. 1, 2). This suggests that pile-up stresses may have locally assisted the activation of sources in the  $\gamma/\alpha_2$  interface and/or that slip transmission from the  $\gamma$ -phase to the  $\alpha_2$ -phase occurred in these incidences [e.g. 10, 13]. As indicated in the micrograph of fig. 1c the traces of the slip planes associated with the  $\langle a \rangle$  dislocation activated locally in the  $\alpha_2$ -lamellae were consistent in some cases with prism planes,  $\{10\bar{1}0\}$ , which are

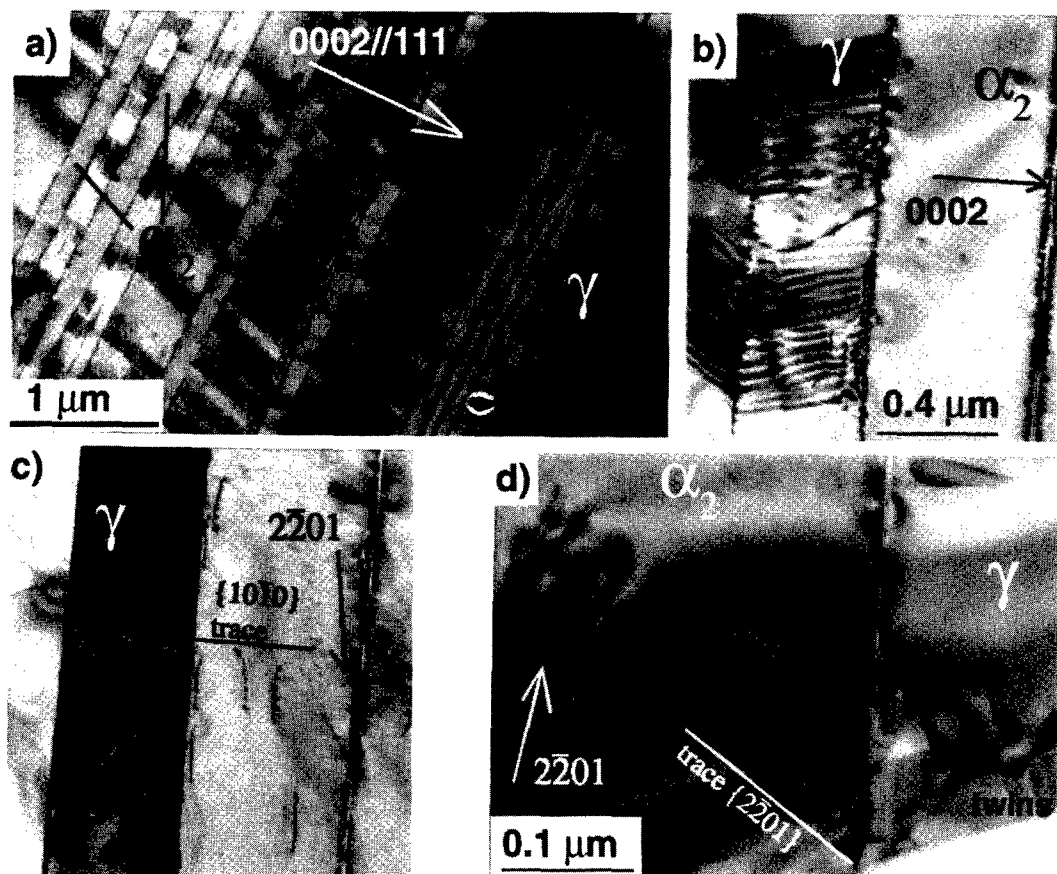


Fig. 1: Defect substructures typical of the RT fractured lamellar TiAl, a) overview,  $g=0002/111$ , b) detail from  $\alpha_2$ -lamella, 0002, c)  $g=2\bar{2}01$  (002 excited in  $\gamma$ ), and d)  $g=2\bar{2}01$ ; beam direction near  $[11\bar{2}0]$  for all micrographs.

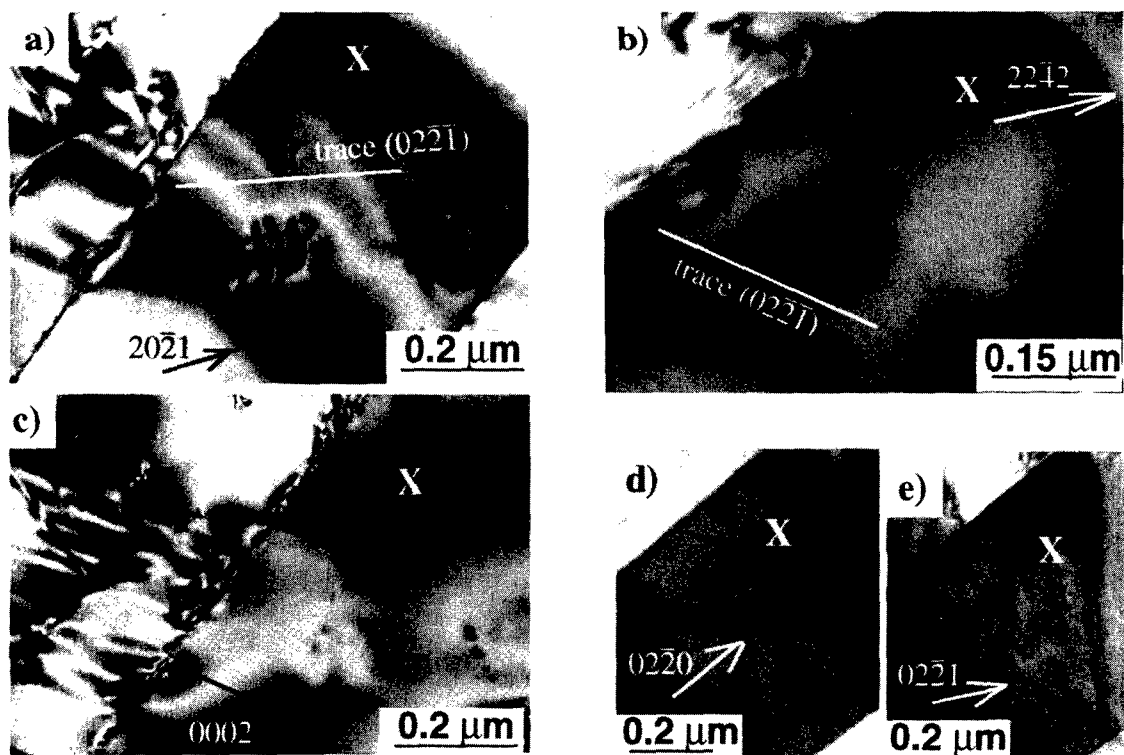


Fig. 2:  $\langle a \rangle$  dislocations in  $\alpha_2$ -lamellae after RT fracture in vicinity of *hard mode* twins impinging on  $(\alpha_2/\gamma)$ -interface, a) and c) for beam near  $[12\bar{1}0]$ ,  $\bar{2}110$ , and b) for beam off  $[\bar{2}113]$  to  $[\bar{1}100]$ , and d) and e) near  $[\bar{2}110]$ ; the arrows indicate the directions of  $\mathbf{g}$ .

commonly reported as the preferred planes for  $\langle a \rangle$  dislocation slip in monolithic  $\alpha_2$ -Ti<sub>3</sub>Al [e.g. 14-16]. However, quite frequently the traces of the slip planes of these locally activated  $\langle a \rangle$  dislocations were not consistent with prism slip (fig. 1d). Additional tilting experiments and stereographic analysis have been conducted on foils cut perpendicular to the tensile axis from the polycrystalline Ti-48at.%Al specimens in order to study slip systems involving planes other than  $\{10\bar{1}0\}$ . The foil normal at zero goniometer tilts for the particular  $\gamma$ -lamella shown in the micrographs of fig. 2 has been determined to be nearly parallel to  $[\bar{1}01]$ , i.e. approximately parallel to  $[\bar{1}2\bar{1}0]$  in the  $\alpha_2$ -lamella [e.g. 10]. The *hard mode* twinning system observed and labeled in the  $\gamma$ -lamella (fig. 2c) has been identified as  $1/2[1\bar{1}2](\bar{1}11)$  [10]. Assuming that the macroscopic load axis is parallel to the foil normal, a relatively high approximate local Schmid factor of 0.32 has been determined for the  $1/2[1\bar{1}2](\bar{1}11)$  twinning system. The contrast behavior of the dislocations in the  $\alpha_2$ -lamella shown in fig. 2, namely being visible in figs. 2a and b but out of contrast in figs. 2c, d and e, is consistent with a Burgers vector  $\mathbf{b} = 1/3[\bar{2}110]$ . Stereographic analysis determined that the slip plane traces associated with these  $\langle a \rangle$  dislocations (labeled in figs. 2a and b) are consistent with the pyramidal plane  $\{02\bar{2}1\}$  which contains the experimentally determined Burgers vector. Thus slip of  $\langle a \rangle$  dislocations on first order pyramidal planes,  $\{02\bar{2}1\}$ , has been observed in  $\alpha_2$ -lamellae of the Ti-48at.%Al alloy after RT tensile loading. The activation of  $1/3\langle 11\bar{2}0 \rangle \langle 10\bar{1}0 \rangle$  and  $1/3\langle 11\bar{2}0 \rangle \langle 20\bar{2}1 \rangle$  in the  $\alpha_2$ -lamella loaded approximately along  $[\bar{1}2\bar{1}0]$ , as depicted in fig. 2, is consistent with large values of approximate local Schmid factors (0.43 for  $1/3[\bar{2}110](01\bar{1}0)$ , 0.40 for  $1/3[\bar{2}110](02\bar{2}1)$  and 0.37 for  $[\bar{2}110](02\bar{2}1)$ ).

From TEM observations of the RT deformed polycrystalline material, it is clear that a much higher density of deformation induced defects exists in the  $\gamma$ -phase than in the  $\alpha_2$ -phase. Thus, it appears reasonable to conclude that the  $\gamma$ -phase accommodated most of the strain during RT deformation by dislocation slip and profuse ordered twinning, whereas the  $\alpha_2$ -phase exhibited plasticity only locally by prism and pyramidal slip of  $\langle a \rangle$  dislocations on systems with high resolved shear stresses in the vicinity of translamellar twinning deformation in the adjacent  $\gamma$ -lamellae. Activation of  $\langle c \rangle$ -component dislocations has not been observed [11-13].

#### Tensile deformation at 800°C

The defect densities observed for the 800°C fractured specimen were higher than for the RT deformed samples which may be ascribed to the higher strain to failure (table 1 and figs. 1a and 3a). Detailed TEM analysis of the deformation substructures in the  $\gamma$ -TiAl phase confirmed that the same deformation modes as at RT have been activated at 800°C with some evidence for climb assisted motion of dislocations confirming earlier investigations [11-13]. The deformation substructure characteristic of the  $\alpha_2$ -phase after fracture at 800°C comprised significant densities of  $\langle c \rangle$ -component dislocations visible in the micrograph of fig. 3b. The defects not visible in fig. 3b but giving rise to contrast in fig. 3c, namely  $\langle a \rangle$  dislocations, was very high after fracture at 800°C, preventing a detailed defect characterization in this case. An additional example of  $\langle c \rangle$ -component dislocations in the  $\alpha_2$ -lamellae of the 800°C fractured specimens is presented in fig. 4. The hairpin shaped dislocation loops visible in figs. 4a-d but invisible in

fig. 4e exhibited contrast characteristics consistent with dislocation loops with a Burgers vector  $\mathbf{b}=\frac{1}{3}[11\bar{2}6]$ , and their curved segments (C) and straight segments (A and B) being contained in first order pyramidal planes,  $\{20\bar{2}1\}$ , and the basal plane, (0001), respectively, as summarized below. For instance, visibility of the segment labeled C for  $g=0002$ ,  $22\bar{4}0$  and  $\bar{2}202$  (figs. 4a-d), and invisibility for  $\bar{2}200$  (fig. 4e) rules out dislocations with  $\mathbf{b}=\frac{1}{3}\langle 11\bar{2}0 \rangle$  and  $\mathbf{b}=[0001]$ , but is consistent with contrast expected from dislocations with  $\mathbf{b}=\pm\frac{1}{3}[11\bar{2}6]$  and  $\pm\frac{1}{3}[11\bar{2}\bar{6}]$ . The line directions of the straight segments, labelled A and B in the figure, and the curved segment, labelled C, of these dislocations have been determined from stereographic trace analyses to be approximately parallel to  $\mathbf{u}_A=\mathbf{u}_B=[\bar{1}100]$  and  $\mathbf{u}_C=[10\bar{1}4]$ . The former line direction is consistent with the rectilinear morphology of the straight segments and the change in line length along segment B between the kinks marked  $\Delta L$  and  $\cos(30^\circ)\Delta L$  in figs. 4a and b respectively. Tilting the crystal about the  $[\bar{2}202]$ -tilt axis resulted in a curved line morphology for those segments (e.g. fig. 4d). This indicates that the basal plane, (0001), contains the segments A and B. The direction  $\mathbf{u}_C=[10\bar{1}4]$  is contained in  $\{20\bar{2}1\}$  but not in any of the other potential slip planes for the two possible Burgers vectors of these dislocation loops, and would be a suitable slip plane for dislocations with Burgers vector  $\mathbf{b}=\pm\frac{1}{3}[11\bar{2}6]$  but not for those with  $\mathbf{b}=\pm\frac{1}{3}[11\bar{2}\bar{6}]$ . Thus, it appears reasonable to conclude that the dislocation loops shown in fig. 4 have  $\mathbf{b}=\pm\frac{1}{3}[11\bar{2}6]$ . The curved segments indicate slip activity, whereas the basal plane habit of the straight segments would be consistent only with non-conservative motion of these  $\langle 2c+a \rangle$  dislocations observed in the  $\alpha_2$ -lamellae of the 800°C fractured specimens. This is in concert with similar reports of the slip and climb activity of  $\langle c \rangle$ -component dislocations in the  $\alpha_2$ -phase of lamellar TiAl after tensile deformation to 2.5% strain at 800°C [11]. It appears that at 800°C, there is a marked increase in dislocation activity in the  $\alpha_2$  lamellae. Most significant is the observation of a reasonable density of  $\langle c \rangle$ -component dislocations, the majority of which have been identified to be  $\langle 2c+a \rangle$  dislocations. Hence, there are considerable contributions to strain accommodation of the minority phase during the elevated temperature tensile tests by dislocation climb and slip. It appears reasonable to conclude that the mechanical incompatibility of the  $\gamma$ - and  $\alpha_2$ -phases decreased at elevated temperature.

#### Hard orientation compression of PST Ti-48at.%Al

The deformation modes activated in the  $\gamma$ -lamellae after room temperature compression tests of the PST Ti-48at.%Al loaded parallel to the lamellar interface along the *hard* orientations A2,  $[\bar{1}1\bar{2}2]$ , and A1,  $[1\bar{1}0]$ , and normal to the lamellar interface, *hard* orientation N,  $[111]$ , have been found to depend on the orientation of the  $\gamma$ -domains with respect to the load axis. These translamellar deformation systems in the  $\gamma$ -phase involved ordered twinning and octahedral plane slip of both ordinary and superdislocations. The findings of the present work relating to the deformation of the  $\gamma$ -phase were entirely consistent with the extensive and detailed observations reported in a number of earlier studies [e.g. 3-6]. Furthermore, similar to the observations reported in the preceding two sections, the  $\gamma$ -phase has been found to be generally much more heavily deformed than the  $\alpha_2$ -phase, which indicated that the former accommodated most of the strain during the compression

tests, resulting in strain incompatibility between the two phases. Hence, for brevity the following two sections focus on the plasticity exhibited by the  $\alpha_2$ -phase during the *hard* orientation compressive loading of the PST specimens at room temperature.

#### Compression parallel to the lamellar interface

The micrographs presented in figs. 5 and 6 depict deformation substructures typical of the PST material after compression to about 7.0% strain in orientations A1 and A2 respectively. The defects visible in the  $\alpha_2$ -lamellae shown in figs. 5 and 6 have been identified to be dislocations with  $\mathbf{b}=\frac{1}{3}[\bar{2}110]$  as follows. For the specimen with orientation A1, the dislocations in the bands near the labels X and A in fig. 5 were in contrast for  $g=2\bar{2}00$  and  $2\bar{2}01$  (fig. 5b, d) but exhibited only residual contrast for  $g=0002$  and  $0\bar{2}21$  (figs. 5a, c) so that their Burgers vector lies parallel to  $[\bar{2}110]$ . Similarly, in fig. 6 for the orientation A2 specimen, the defects visible near the label X in the

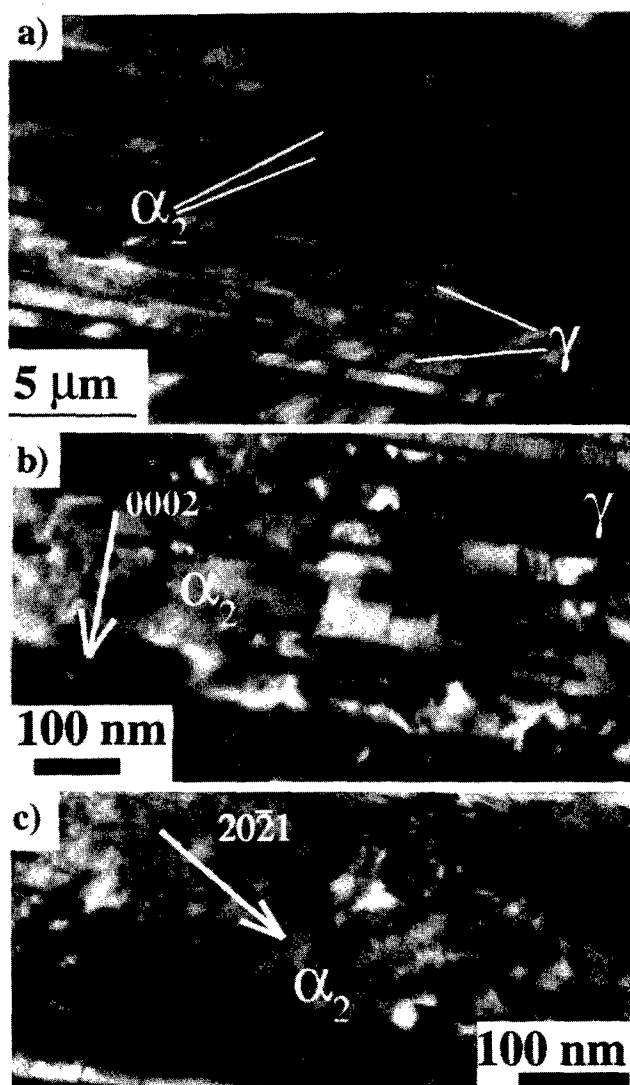


Fig. 3: Defect substructures typical of TiAl after fracture at 800°C, a) multiple  $g$  overview, detail of  $\alpha_2$ -lamella from central region of a) in b)  $g=0002$ , beam near  $[1\bar{1}210]$  and c)  $20\bar{2}1$ , near  $[0\bar{1}1\bar{2}]$ .

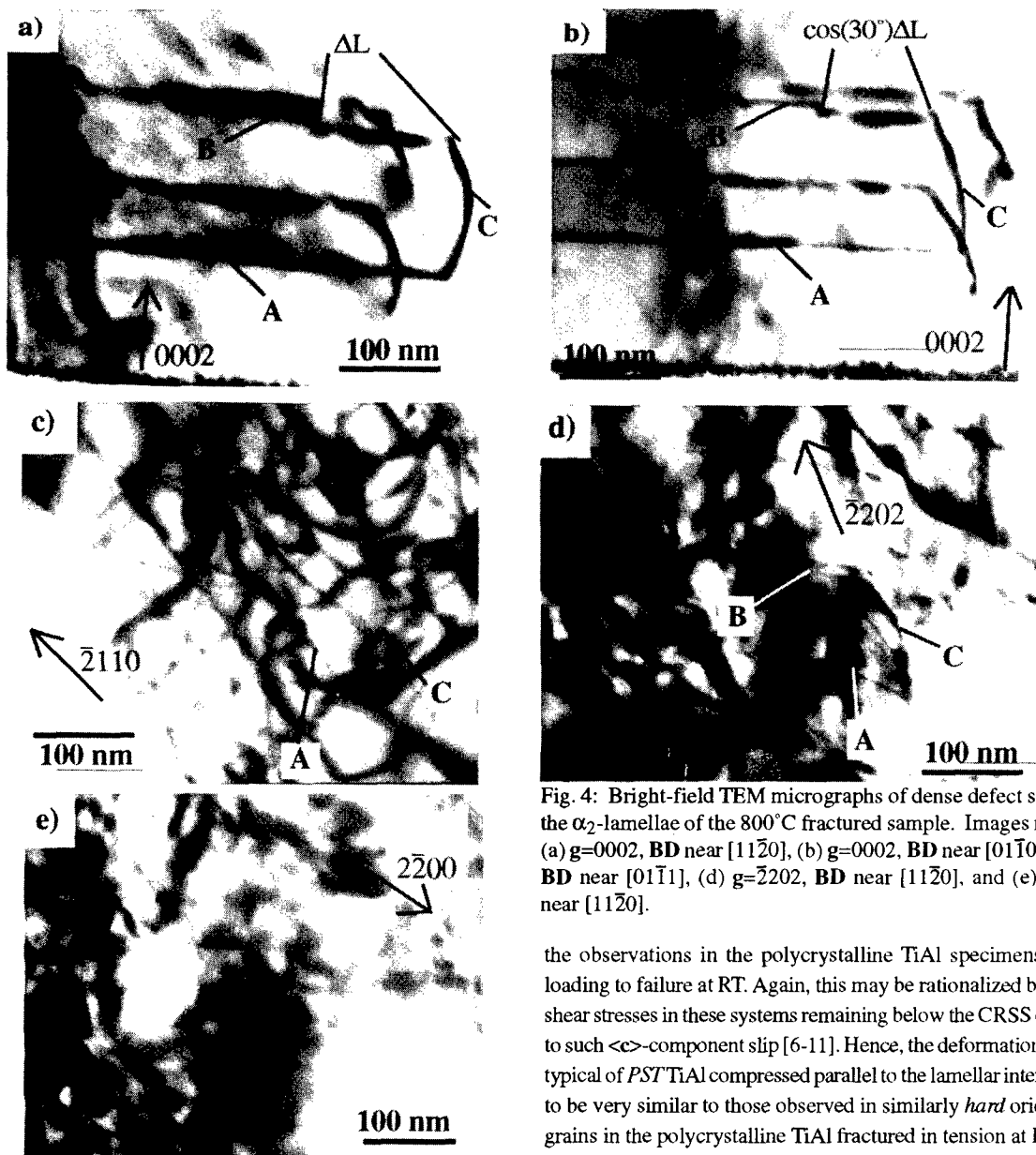


Fig. 4: Bright-field TEM micrographs of dense defect substructures in the  $\alpha_2$ -lamellae of the 800°C fractured sample. Images recorded with (a)  $g=0002$ , BD near  $[11\bar{2}0]$ , (b)  $g=0002$ , BD near  $[01\bar{1}0]$ , (c)  $g=2\bar{1}10$ , BD near  $[01\bar{1}1]$ , (d)  $g=2\bar{2}02$ , BD near  $[11\bar{2}0]$ , and (e)  $g=2\bar{2}00$ , BD near  $[11\bar{2}0]$ .

the observations in the polycrystalline TiAl specimens after tensile loading to failure at RT. Again, this may be rationalized by the resolved shear stresses in these systems remaining below the CRSS corresponding to such  $\langle c \rangle$ -component slip [6-11]. Hence, the deformation substructures typical of *PST* TiAl compressed parallel to the lamellar interface appeared to be very similar to those observed in similarly *hard* oriented lamellar grains in the polycrystalline TiAl fractured in tension at RT.

#### Compression normal to the lamellar interface

The micrographs shown in figs. 7 and 8 depict deformation substructures typical of the *PST* material deformed at RT in orientation N, along  $[111]$  perpendicular to the lamellar interface, to about 3.0% compressive strain. It may be noted that for this loading direction the resolved shear stresses vanish for slip and twinning systems involving Burgers vectors contained in the lamellar interface. The highly stressed deformation systems in each of the various variants of  $\gamma$ -lamellae involve one twinning system with a Schmid factor of 0.33, four superdislocation slip systems, and one slip system of ordinary dislocations, all with Schmid factor of 0.28. Accordingly, deformation twinning involving a single set of twins per lamella has been the most prominent deformation mode in the various variants of  $\gamma$ -lamellae after RT loading in orientation N, whereas the  $\alpha_2$ -lamellae exhibited only very moderate defect densities (fig. 7a). Hence, also in this orientation the  $\gamma$ -phase accommodated much more

bright field (BF) and weak beam (WB) micrographs of fig. 6c and d,  $g=22\bar{4}0$ , were invisible for  $g=0002$  (fig. 6a) and  $02\bar{2}0$  (fig. 6b) which is consistent only with  $b=\pm 1/3[\bar{2}110]$ . Assuming loading of the  $\alpha_2$ -phase along the directions  $[11\bar{2}0]$  for the A1 and along  $[1\bar{1}00]$  for the A2 specimens respectively, Schmid factors for slip systems involving dislocations with  $b=1/3[\bar{2}110]$  have been computed. The largest values of these Schmid factors are obtained for  $1/3[\bar{2}110]/(01\bar{1}0)$ , with a value of 0.43 (A1, A2), and  $1/3[\bar{2}110]/(02\bar{2}\pm 1)$ , with a value of 0.39 (A2) and 0.38 (A1). Traces of these highly stressed potential prism and first order pyramidal slip planes for the  $\langle a \rangle$  dislocations have been marked on some of the micrographs of figs. 5 and 6. In addition to the most easily activated prism plane  $\langle a \rangle$  slip [7, 14-16], e.g. fig. 6d, evidence for pyramidal slip of  $\langle a \rangle$  dislocations has been observed as marked in fig. 5b and also in fig. 6d. The absence of any significant defect contrast in the micrographs obtained for  $g=000\pm 2$  (figs. 5a and 6a) indicates the lack of activation of slip of  $\langle c \rangle$ -component dislocations, which is similar to

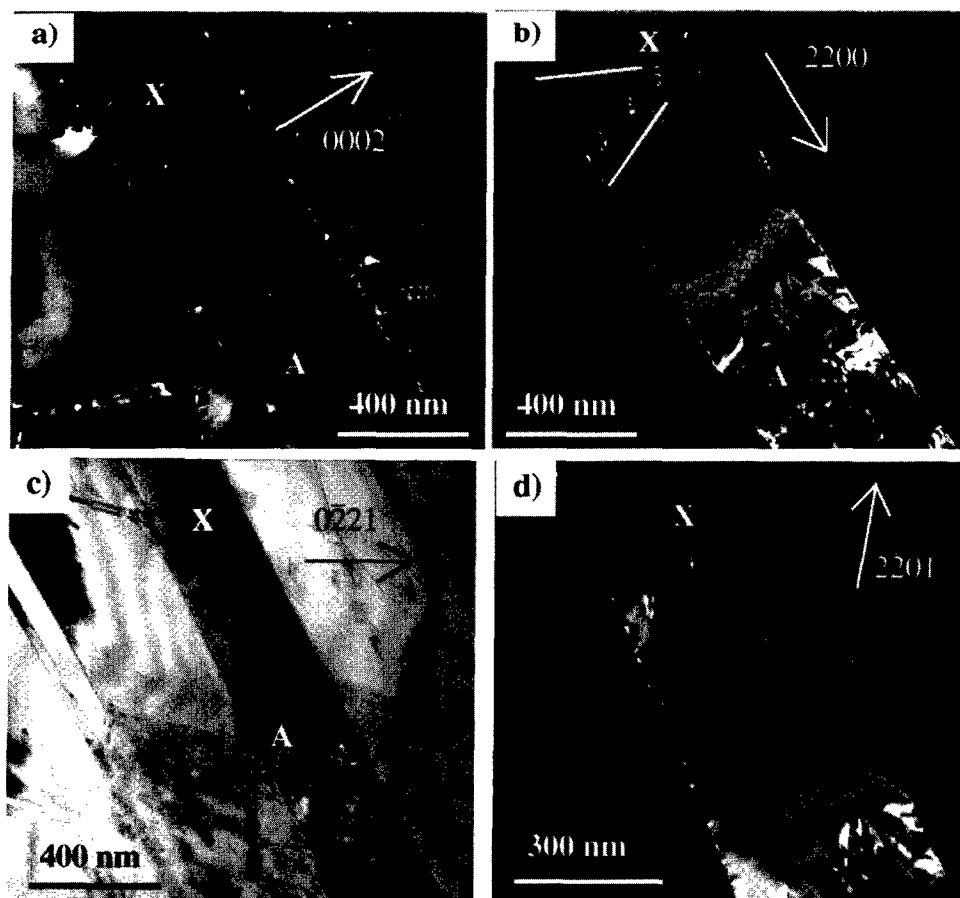


Fig 5: Typical deformation substructure observed in the PST TiAl after compression at RT in the  $[1\bar{1}0]$  orientation showing  $\langle a \rangle$ -dislocations with  $b=1/3[2\bar{1}10]$ , a)  $g=0002$  and b)  $g=2\bar{2}00$ , both weak beam (WB) near  $[11\bar{2}0]$ , c) BF  $g=0\bar{2}21$  near  $[11\bar{2}6]$ , and d) WB with  $g=2\bar{2}01$  near  $[11\bar{2}0]$ . The letters X and A indicate the same position in each micrograph and traces of  $\{20\bar{2}1\}$  type pyramidal planes are marked in b).

strain than the  $\alpha_2$ -phase resulting in strain incompatibility similar to the other cases presented here. However, the observation of defect contrast in the  $\alpha_2$ -phase is significant since in this orientation the only slip systems with non-zero Schmid factors involve  $\langle 2c+a \rangle$  dislocations on pyramidal planes. Indeed, the defects visible in the  $\alpha_2$ -lamella for  $g=0002$  (fig. 7a) and fig. 7b,  $g=2\bar{2}00$ , can be identified as  $\langle 2c+a \rangle$  dislocations. The WB image of fig. 7b has been obtained for an approximate beam direction (BD) close to  $[11\bar{2}0]\alpha_2$ . Stereographic analysis showed that the  $55^\circ$  angles between the traces of the slip bands associated with the  $\langle 2c+a \rangle$  dislocations and the trace of the basal plane are consistent only with second order pyramidal planes, such as  $(2\bar{1}\bar{1}1)$ ,  $(\bar{1}2\bar{1}1)$ ,  $(2\bar{1}\bar{1}\bar{1})$  and  $(\bar{1}2\bar{1}\bar{1})$  respectively. Additional tilting experiments have been performed in order to identify the Burgers vector of the dislocations involved in the accommodation of strain in the  $\alpha_2$ -lamellae during RT compression of the N orientation specimens.

Fig. 8 presents micrographs obtained near the  $[11\bar{2}0]$  and the  $[10\bar{1}2]$  zones respectively. The defect labeled [c] in the BF and WB images of fig. 8 has been identified to have  $b=\pm[0001]$  as it was invisible for  $g=2\bar{2}00$  (fig. 8c) and visible for all the other imaging conditions in fig. 8. This defect exhibited fringe contrast consistent with a stacking fault. The faulted area increased in projected width for increasing tilt angles towards  $[0001]$  indicating that the fault is contained in the basal plane (fig. 8c-e). Thus it appeared reasonable to conclude that the defect [c] was unlikely to be a product of N orientation loading at RT, because of zero resolved shear stress on basal plane systems. The defects labeled A and B were clearly visible in figs. 8a, b, d and e, and exhibited somewhat weaker contrast in fig. 8c. This contrast behavior is consistent

only with a Burgers vector parallel to  $\pm[2\bar{1}16]$ . This Burgers vector is contained in  $(2\bar{1}\bar{1}1)$ , the traces of which would be consistent with those observed experimentally (fig. 8). Thus, slip of  $\langle 2c+a \rangle$  dislocations on second order pyramidal planes,  $\{11\bar{2}1\}$ , has been identified as the mode of strain accommodation in the  $\alpha_2$ -lamellae during N orientation compression at RT. These observations are consistent with  $\langle 1\bar{2}16 \rangle \{11\bar{2}1\}$  being the most highly stressed slip systems in the  $\alpha_2$ -phase with Schmid factors of 0.45 and the deformation behavior reported for single crystals of  $\alpha_2$ -Ti<sub>3</sub>Al [16]. Furthermore, the applied stress levels reached a maximum of 944.8 MPa during RT loading in orientation N (table 1) which would give rise to resolved shear stresses in the  $\langle 1\bar{2}16 \rangle \{11\bar{2}1\}$  systems of 425.3 MPa. This resolved stress is of the order of the CRSS determined for  $\langle 2c+a \rangle$  slip in stoichiometric single crystals of  $\alpha_2$ -Ti<sub>3</sub>Al, 470 MPa [9, 16], but compares only to about 50% of the CRSS reported for off-stoichiometric  $\alpha_2$ -Ti-36.5at.%Al, 911 MPa [8].

### Discussion

The TEM observations of the defect substructures in the lamellar grains of polycrystalline and PST TiAl showed consistently higher defect densities in the  $\gamma$ -lamellae than in the  $\alpha_2$ -lamellae (figs. 1a, 3a, 5-7). Thus, it has been concluded that the former accommodated most of the strain under all loading conditions investigated here. The deformation modes activated in the  $\gamma$ -lamellae involved primarily twinning, and some slip of ordinary dislocations and superdislocations depending on the exact orientation of the various  $\gamma$ -domains with respect

to the local state of stress, for both the polycrystalline and the *PST* material. At 800°C, evidence for non-conservative motion of dislocations, especially for ordinary dislocations, has been detected in addition to the mechanisms active in the  $\gamma$ -phase during RT deformation. These observations further support previous reports relating to the deformation behavior of the lamellar  $\gamma$ -phase [e.g. 3-7, 11,12]. A comparison of the deformation substructures observed in the lamellar grains of the *PST* with those of the polycrystalline TiAl for RT loading parallel to the interfaces showed that the  $\alpha_2$ -lamellae behaved similarly in both materials. For example, in the case of RT loading parallel to the lamellar interfaces, i.e. tensile axis approximately at  $[\bar{1}01]/[\bar{1}2\bar{1}0]$  in the polycrystalline material (figs. 1, 2) and compression orientations

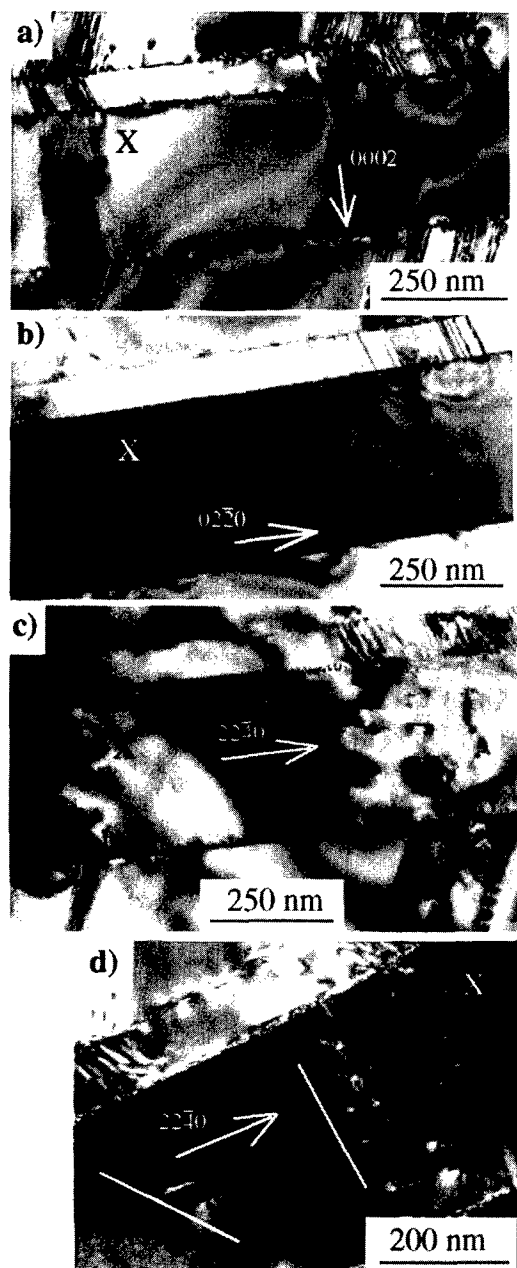


Fig. 6: Defect substructure typical of *PST* RT compressed in orientation  $[\bar{1}12]$ , a)  $g=0002$  and b)  $g=02\bar{2}0$ , both near  $[\bar{2}110]$ , and c) BF and d) WB with  $g=2240$  near  $[\bar{1}100]$ .

A1 and A2 for the *PST* TiAl (figs. 5, 6), the  $\alpha_2$ -lamellae exhibited limited plasticity solely by slip of  $\langle a \rangle$  dislocations on prism,  $\{10\bar{1}0\}$ , and first order pyramidal planes,  $\{20\bar{2}1\}$ . Although  $\langle a \rangle$  dislocations gliding on pyramidal planes have been considered previously as a possible deformation mode [e.g. 15], as far as the authors are aware, the experimental observation of such slip has not been reported for the ordered  $\alpha_2$ -Ti<sub>3</sub>Al phase to date. The particular prism and pyramidal  $\langle a \rangle$  dislocation slip systems observed after loading parallel to the lamellar interface experienced high resolved shear stresses in excess of the CRSS predicted for prism plane slip in Ti<sub>3</sub>Al, 65-110 MPa depending on composition [8, 9, 16]. For instance, at the yield stress of 376.1 MPa of the RT fractured Ti-48at.%Al polycrystals and loading along approximately  $[\bar{1}2\bar{1}0]$  resolved shear stresses of about 162 MPa and 150 MPa can be derived for  $1/3[\bar{2}110](01\bar{1}0)$  and  $1/3[\bar{2}110](02\bar{2}1)$  respectively (table 1 and fig. 2). Evidence for the activity of  $\langle c \rangle$ -component deformation modes has not been observed in the  $\alpha_2$ -phase for RT loading parallel to the interfaces, despite high Schmid factors for some slip systems involving  $\langle 2c+a \rangle$  dislocations. The lack of  $\langle c \rangle$ -component dislocation slip may be understood on the basis of the very high CRSS for these dislocations, i.e. 470-911 MPa, depending on composition [8, 9, 16], which remained in excess of the resolved shear stresses during loading parallel to the interfaces (table 1). The localized planar deformation behavior exhibited by the  $\alpha_2$ -phase is insufficient for the accommodation of the shears associated with the translamellar deformation modes activated in the more easily deforming  $\gamma$ -phase during RT loading parallel to the interfaces. Accordingly, stress concentrations are generated locally where translamellar *hard* deformation modes encountered the  $(\gamma/\alpha_2)$ -interface. Interestingly, the localized planar slip of  $\langle a \rangle$  dislocations in the  $\alpha_2$ -lamellae has generally been activated in the vicinity of the stress concentrations associated with translamellar twins impinging on the  $(\gamma/\alpha_2)$ -interface (figs. 1, 2, 5 and 6). In analogy to reports of sources in the  $(\gamma/\gamma)$ -interfaces [17], it is tempting to propose that the pile-up stresses associated with the *hard* mode twins resulted in the activation of interfacial sources leading to localized slip in the  $\alpha_2$ -phase. Alternatively, the shear associated with certain types of *hard* mode ordered twinning in the  $\gamma$ -lamellae could have been transmitted in part into the  $\alpha_2$ -phase resulting in localized  $\langle a \rangle$  dislocation slip following a decomposition reaction at the lamellar interface as described previously [10]. For both of these scenarios the easier deformation in the  $\gamma$ -phase and the constraint due to the lamellar morphology are required in order to generate local stress concentrations which would initiate the localized  $\langle a \rangle$  slip in the  $\alpha_2$ -lamellae. An additional effect of the limited width of the  $\alpha_2$ -lamellae would be considerable hardening of the locally activated prism and pyramidal plane slip systems. As a result, the local stress levels required for continued operation of these deformation modes are predicted to increase.

For loading normal to the lamellar interface a comparison between the behavior of *PST* and the polycrystalline TiAl was not possible due to the failure of observing lamellar grains of such orientation with respect to the load axis in TEM foils obtained from the latter. The TEM observations of the defect substructures in the *PST* TiAl compressed at RT normal to the interface demonstrated clearly the activation of significant amounts of slip of  $\langle 2c+a \rangle$  dislocations on second order pyramidal planes,  $\{11\bar{2}1\}$ , and strongly support the earlier conclusions



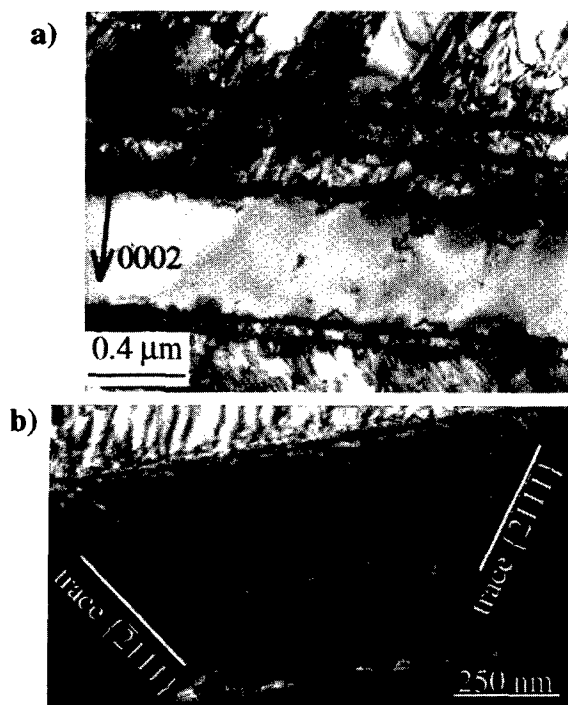


Fig 7: Deformation substructures typical of the PST TiAl after compression at RT in the N orientation a) 0002 and b)  $\bar{2}200$ , both near  $[11\bar{2}0]$ ; traces of  $\{2111\}$  pyramidal planes are marked.

which were based on surface traces on RT N orientation compressed PST TiAl coupons [7]. The same deformation mode has been observed for single crystals of  $\text{Ti}_3\text{Al}$  loaded normal to the basal plane and the CRSS have been determined as 470 MPa for stoichiometric and 911 MPa for Al-rich off-stoichiometric compositions [8, 9, 16]. However, despite the high Schmid factors for the observed pyramidal slip systems, 0.45, the resolved shear stresses due to the externally applied maximum stress, 944.8 MPa, in the N orientation compression tests reached only about 425 MPa. Hence, it appears that the macroscopically applied stress was insufficient for the activation of slip systems with  $\langle 2c+a \rangle$  dislocations. This implies that either additional local stress concentrations have assisted the activation of pyramidal  $\langle 2c+a \rangle$  slip or that the abundant number of dislocation sources in the  $(\gamma/\alpha_2)$ -interface permits activity of this slip system at lower stresses than those in monolithic crystals where, for example, shortage of sources might present a problem. Further studies are necessary to ascertain the reason for this apparent discrepancy. Nevertheless, the very high applied stresses required to generate the observed motion of  $\langle 2c+a \rangle$  dislocations on pyramidal planes in the  $\alpha_2$ -phase during RT deformation, even in the most favourably oriented N type specimens, suggests, that the general activation of this deformation mode in polycrystalline lamellar TiAl is highly improbable. Unlike the behavior at RT, during elevated temperature loading a significant amount of strain has been accommodated by the  $\alpha_2$ -lamellae by the more general activation of  $\langle a \rangle$  dislocation motion and  $\langle c \rangle$ -component defects in both conservative and non-conservative modes. This more ductile behavior of the  $\alpha_2$ -lamellae is predicted to reduce the strain incompatibility between the two phases. The extended elongations to failure and somewhat lowered strength of the lamellar

TiAl studied here are in concert with this conclusion. Both the climb and slip of  $\langle 2c+a \rangle$  dislocations has been observed for the 800°C fractured specimens [11]. Interestingly, in the  $\alpha_2$ -lamellae of the polycrystalline Ti-48at.%Al specimens deformed in tension at 800°C  $\langle 2c+a \rangle$  slip occurred on first order pyramidal planes of the type  $\{2\bar{2}01\}$  rather than on the second order pyramidal planes,  $\{1\bar{2}11\}$ , as in the  $\alpha_2$ -lamellae of the N orientation RT compressed PST TiAl. As pointed out above, the latter  $\langle 2c+a \rangle \{1\bar{2}11\}$  system has generally been associated with  $\langle c \rangle$ -component dislocation slip activity in single phase  $\text{Ti}_3\text{Al}$  [14-16]. However, first order pyramidal slip of  $\langle 2c+a \rangle$  dislocations,  $2c+a \{2\bar{2}01\}$ , has been observed previously in thin TEM foils of monolithic  $\text{Ti}_3\text{Al}$  during in-situ tensile straining experiments [18]. The reason for the discrepancy regarding the choice of the preferred slip system reported here can not be due to alloying effects, as both alloys are binaries, and is currently not completely understood. However, it may be proposed that the underlying reason for the choice of pyramidal slip plane for the  $\langle 2c+a \rangle$  dislocations in the lamellar  $\alpha_2$ -phase is related to either the deformation temperature or a tension-compression anisotropy due to the lamellar constraint.

The localized slip typical of the  $\alpha_2$ -lamellae during RT deformation parallel to the lamellar interfaces and also the observed significant activation of  $\langle 2c+a \rangle$  dislocations in samples deformed in the N orientation implied that local stress concentrations are generated during RT deformation of lamellar TiAl. Furthermore, heterogeneous dislocation distributions have been detected for all the *hard* orientation loaded TiAl alloys investigated here. Therefore, it can be concluded that the strain incompatibility between the two phases present in the lamellar TiAl grains would finally lead to failure because of the difficulty in accommodating shear components perpendicular to the lamellar interfaces even for loading in orientations A1 and A2. Local stress concentrations, which have been proposed to play a significant role in the initiation of fracture during RT deformation, may be predicted to be less significant during elevated temperature deformation, as they can be dissipated more easily by the higher mobility of both  $\langle a \rangle$  and  $\langle c \rangle$ -component dislocations in the  $\alpha_2$ -phase. Finally, the experimental TEM observations presented here are largely in agreement with computational models which predicted that failure of polycrystalline aggregates would most likely result from the large strain incompatibilities between lamellar grains oriented for *soft* mode and *hardest* mode deformation [19].

### Conclusions

The  $\gamma$ -lamellae accommodated most of the strain during *hard* orientation loading of lamellar Ti-48at.%Al alloys by slip of both ordinary dislocations and superdislocations, and by twinning. At RT the  $\alpha_2$ -lamellae deform only locally by activation of highly stressed  $\langle a \rangle$  dislocation slip systems on prism and pyramidal planes, such as  $1/3\langle 11\bar{2}0 \rangle \{01\bar{1}0\}$  and  $1/3\langle 11\bar{2}0 \rangle \{02\bar{2}1\}$ . This planar slip behavior and the general difficulty of the  $\alpha_2$ -phase to accommodate  $\langle c \rangle$ -component shears associated with the translamellar deformation in the softer  $\gamma$ -phase generated significant local stress concentration at the  $(\gamma/\alpha_2)$ -interface. The initiation of fracture and final failure of both PST and polycrystalline lamellar TiAl have been associated with these stress



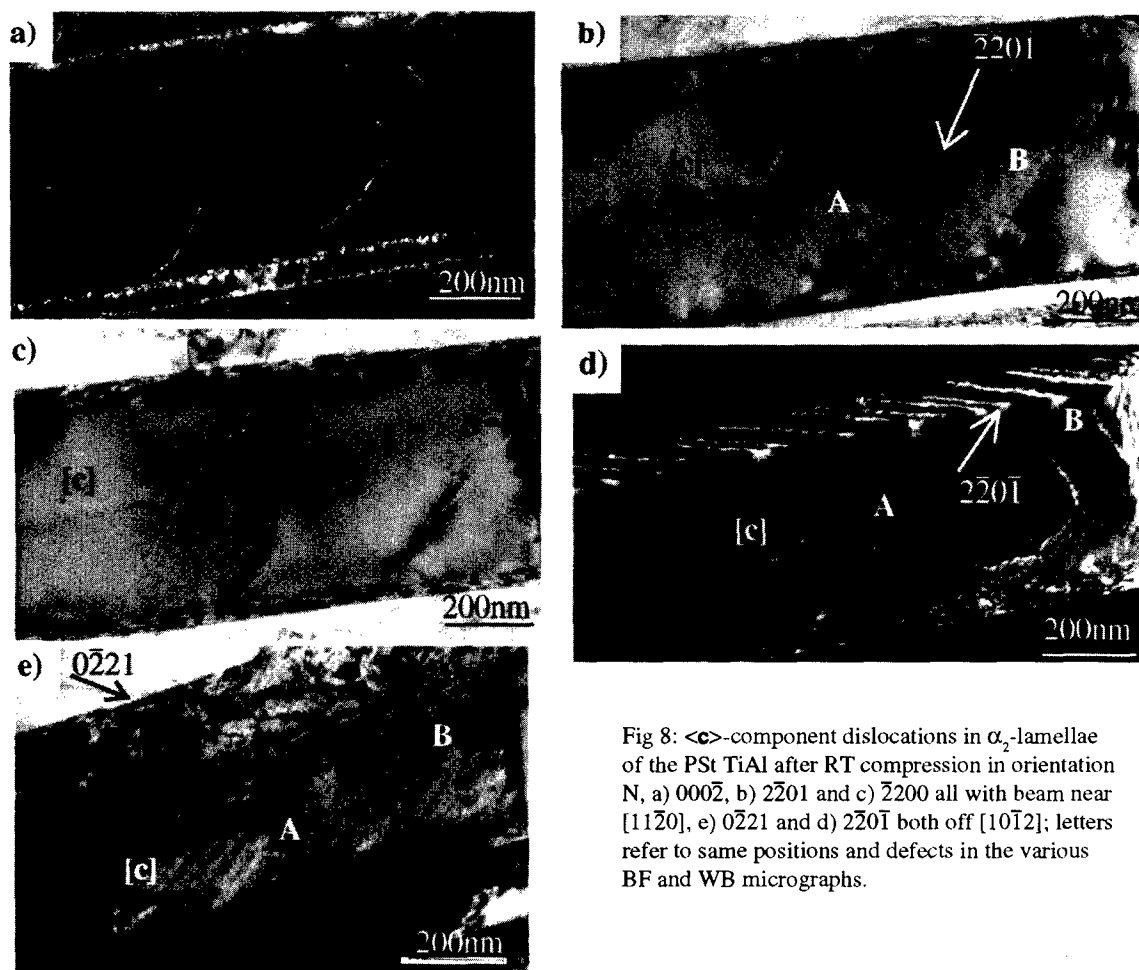


Fig 8:  $\langle c \rangle$ -component dislocations in  $\alpha_2$ -lamellae of the PST TiAl after RT compression in orientation N, a) 0002, b) 2201 and c) 2200 all with beam near [1120], e) 0221 and d) 2201 both off [1012]; letters refer to same positions and defects in the various BF and WB micrographs.

concentrations and the considerably heterogeneous strain distributions observed at room temperature. At 800°C, the more general activation of  $\langle a \rangle$  dislocations in the  $\alpha_2$ -lamellae, which was accompanied by the climb and slip motion of both  $\langle 2c+a \rangle$  dislocations and  $[c]$  dislocations, has been concluded to reduce the plastic incompatibility between the two phases.

#### Acknowledgments

Financial support from the National Science Foundation under grant DMR-96-22497 with Dr. Bruce MacDonald as program manager is gratefully acknowledged together with the kind assistance of Dr. Lee Semiatin in extruding the cast ingots and of Dr. Dennis Dimiduk in providing rods of PST Ti-48at.%Al.

#### References

- 1 Y.-W. Kim and D.M. Dimiduk, *J. Metals*, **43** (1991) 40.
- 2 H. Inui et al., *Phil. Mag. A*, **66** (1992) 539.
- 3 H. Inui et al., *Phil. Mag. A*, **66** (1992) 557.
- 4 T. Fujiwara et al., *Phil. Mag. A*, **61** (1990) 591.
- 5 M. Yamaguchi and H. Inui, *Structural Intermetallics*, ed. Darolia et al. (Warrendale, PA: TMS) 127.
- 6 H. Inui et al., *Phil. Mag. A*, **72** (1995) 1609.
- 7 Y. Umakoshi and T. Nakano, *Acta metall. mater.*, **41** (1993) 1155.
- 8 H. Inui, Y. Toda and M. Yamaguchi, *Phil. Mag. A*, **67** (1993) 1315.
- 9 Y. Umakoshi et al., *Acta metall. mater.*, **41** (1993) 1149.
- 10 J.M.K. Wiezorek et al., *Mat. Res. Soc. Symp. Proc.*, **High - Temperature Ordered Intermetallic Alloys VII** (Pittsburgh, PA: MRS) (1997) in press.
- 11 J.M.K. Wiezorek et al., *Phil. Mag. Lett.*, **75** (1997) 271.
- 12 J.M.K. Wiezorek, P. M. DeLuca and H.L. Fraser, *Proc. 8th World Conference on Titanium, Titanium'95* (Cambridge, UK: Cambridge University Press) **1** (1996) 144.
- 13 J.M.K. Wiezorek, X.D. Zhang and H.L. Fraser, *Deformation and Fracture of Ordered Intermetallic Materials III*, (TMS, Warrendale PA) (1996) 77.
- 14 H.A. Lipsitt, D. Shechtman and R.E. Schafrik, *Met. Trans.*, **6** (1980) 1369.
- 15 S.A. Court et al., *Phil. Mag. A*, **61** (1990) 109.
- 16 Y. Minonishi, *Phil. Mag. A*, **63** (1991) 1085.
- 17 F. Appel, H. Clemens and R. Wagner, *Deformation and Fracture of Ordered Intermetallic Materials III*, (TMS, Warrendale PA) (1996) 123.
- 18 M. Legros, Ph.D. thesis, (1994) *Paul Sabatier* University of Toulouse, France.
- 19 M. Dao, B.K. Kad and R.J. Asaro, *Phil. Mag. A*, **74** (1996) 569.

## ATOMIC MOBILITY AND POINT DEFECTS IN GAMMA TITANIUM ALUMINIDES

Gaël Sattonnay, Colette Dimitrov and Omourtague Dimitrov

CECM-CNRS, 15 rue Georges Urbain, F-94407 Vitry-sur-Seine Cedex, France

### Abstract

After a brief review of the available data concerning self-diffusion, interdiffusion and high-temperature creep of single-phase gamma titanium aluminides, the first part of the paper reports experimental results on the composition dependence of atomic mobility in high-purity TiAl compounds with 50.0 to 54.5 at% Al. Atomic mobility data were obtained by studying the changes in long-range order, as evidenced by residual electrical resistivity measurements, during thermal treatments in the range 720-1140 K. Atomic mobility is found to increase significantly with the aluminium content.

In the second part, the properties of lattice vacancies, which are the vehicles of atomic mobility, are considered. The recovery of excess point defects introduced by 2.5 MeV electron irradiation in the same high-purity TiAl compounds was investigated by means of electrical resistivity and of positron lifetime measurements. The results of both methods show a large recovery stage around 440 K in stoichiometric TiAl, which is assigned to vacancy migration and annihilation. A value of  $1.55 \pm 0.16$  eV was estimated for the vacancy migration enthalpy. The mobility of vacancies decreases with deviations from stoichiometry on the Al-rich side. The conjunction of this observation with the above-mentioned composition dependence of atomic mobility suggests that the equilibrium concentration of vacancies increases strongly with the aluminium content. This supports published theoretical predictions.

### Introduction

Titanium aluminides around 50 at% Al are potential high-temperature engineering materials for advanced aerospace and automotive applications, due to a number of

advantages over the presently used nickel-base and titanium-base alloys. An improved understanding of high temperature characteristics (structural stability, creep resistance) which imply an atomic transport, requires information on self-diffusion and on point defects. Although two-phase TiAl aluminides are the most promising candidates, up to now the few diffusion and defect property investigations have been performed essentially in the simpler single-phase  $\gamma$ -TiAl compounds.

$\gamma$ -TiAl is long-range ordered up to the melting temperature (1736 K), with a L1<sub>0</sub> structure (CuAu I type) characterized by a slight tetragonality ( $c/a$  ratio = 1.02) which increases in off-stoichiometric compounds on the Al-rich composition side [1,2]. The atomic arrangement, perpendicularly to the [001] direction, consists of alternate layers of titanium and aluminium atoms. The phase diagram is now relatively well established [3] and the off-stoichiometric single-phase  $\gamma$ -TiAl can accommodate up to 56 at% Al. On the Ti-rich side, two-phase  $\gamma/\alpha_2$  alloys are observed at room temperature, where  $\alpha_2$  is a long-range ordered hexagonal DO<sub>19</sub> phase.

The present paper first briefly reviews the available data on self-diffusion and interdiffusion, in connection with some creep results; it then reports a characterization of atomic mobility, as deduced from the changes in long-range order during thermal treatments. Finally, published data on thermal equilibrium or supersaturated point defects are reviewed and new results on self-interstitial and vacancy mobility, determined from the recovery of radiation-induced point defects, are reported. The concentration dependence of these characteristics will be emphasized.

### Self-diffusion, interdiffusion, creep

In single phase  $\gamma$ -TiAl binary alloys, self-diffusion implies the diffusion of two atomic species in the lattice and requires to have separately information on the self-diffusion of titanium and of aluminium. Ti self-diffusion experiments have been performed with the radiotracer  $^{44}\text{Ti}$  in a Ti-54at%Al intermetallic compound (noted TiAl<sub>54</sub>), and have led to an activation enthalpy of 3.02 eV [4] with a pre-exponential factor  $1.53 \cdot 10^{-4} \text{ m}^2 \text{ s}^{-1}$ . It thus turns out that Ti self-diffusion obeys the empirical rules valid for fcc metals, and should occur via a thermal vacancy mechanism. Up to now, the composition dependence of Ti self-diffusion has not been investigated. No Al self-diffusion data are available due to the very low activity of the  $^{26}\text{Al}$  radiotracer. Only an indirect estimation of the Al diffusivity  $D^*_{\text{Al}}$  has been proposed [5] from a data set of single phase TiAl interdiffusion coefficient  $\tilde{D}$  and of Ti self-diffusion coefficient  $D^*_{\text{Ti}}$ , by using Manning's generalization of Darken's equation:

$$\tilde{D} = (N_{\text{Ti}} \cdot D^*_{\text{Al}} + N_{\text{Al}} \cdot D^*_{\text{Ti}}) \Phi \cdot S \quad (1)$$

where  $N_{\text{Ti}}$  and  $N_{\text{Al}}$  are the atomic concentrations of the components,  $\Phi$  and  $S$  the thermodynamic and so-called "vacancy wind" factors. The Al diffusivity deduced in this way appears to be of the same order as the Ti diffusivity or, at most, one and a half order of magnitude smaller.

Interdiffusivity was investigated in single phase TiAl<sub>50</sub> / TiAl<sub>54</sub> [5] and in multi-phase [6, 7] couples; the results are somewhat different. In single phase couples, the values obtained for the activation enthalpy and the pre-exponential factor were similar to those of Ti self-diffusion; no effect of composition was detected in the considered Al concentration range. In multi-phase couples [6, 7], the diffusivity coefficient was found higher than in single phase experiments, especially at low temperatures, with smaller activation enthalpies ranging from 1.71 eV to 1.33 eV (when the Al content varied from 47.8 to 54.1 at%). The interdiffusion coefficient was found to increase with increasing Al content; however, it is not clear whether these data are representative of a volume interdiffusion mechanism.

Creep, in particular power-law creep, should also be related to self-diffusion. Oikawa [8] has investigated single phase  $\gamma$ -TiAl alloys of different compositions (50 to 53.4 Al at%). For a fixed grain size, at high stresses, the minimum creep rate increased with increasing Al content. This composition dependence is in agreement with the interdiffusion data of Hirano et al [6] and with the atomic mobility results to be reported in the next section. As for the temperature dependence of the creep rate, a comparison with diffusion data gives rise to two questions concerning, on the one hand, the conditions in which the creep rates are determined and, on the other hand, the type of diffusion data to which they should be compared. When minimum creep rates are considered [8], the apparent activation enthalpies are significantly larger (3.63 - 4.15 eV) than the one obtained in Ti self-diffusion experiments. For creep

rates in the high-strain plateau of the creep rate versus strain curves, lower activation enthalpy values were obtained [9]. In the same high-strain regime, Dlouhy [10], for a TiAl<sub>52</sub> alloy, reported apparent creep activation enthalpies (2.6 - 3.2 eV) close to the ones found for Ti self-diffusion. A second point to be considered concerns the definition of a pertinent diffusion coefficient since, in a binary material, matter transport involves the mobility of two atomic species. An experimental investigation of this problem has been performed by Some et al. [11] in the case of A<sub>3</sub>B-type intermetallic compounds with a D<sub>03</sub> structure, in the Cu-Sn system. They identified, among possible combinations of the diffusivities of the two components, the one which gave the best correlation with the activation enthalpies for power-law creep. Such a determination is not presently possible in TiAl since no  $D^*_{\text{Al}}$  data are available.

### Atomic mobility in $\gamma$ -TiAl

Since  $\gamma$ -TiAl intermetallic compounds are long-range ordered (LRO), the investigation of the kinetics of atomic order relaxation can be used to obtain characteristic time-constants and the corresponding activation enthalpies. These parameters are related to the overall atomic mobility in the material. Such determinations are useful to supplement tracer diffusion measurements, e.g. when no suitable radioactive isotopes are available. Also, this average atomic mobility may be directly used for modelling phenomena such as creep controlled by dislocation climb. In order to obtain information on atomic mobility, the variations of the state of LRO of the materials during thermal treatments were determined by means of residual electrical resistivity measurements.

A qualitative characterization of the atomic mobility was first performed by investigating the ordering and disordering processes during isochronal anneals. The atomic mobility was related to the threshold temperature above which changes in the degree of order can be detected.

Quantitative information (kinetics of approach to equilibrium, characteristic time-constants, activation enthalpies for the order changes) can be obtained by analysing the LRO relaxation from near-equilibrium states during isothermal heat treatments (see e.g. [12] for Ni<sub>3</sub>Al compounds). This involves very small LRO changes, which can nevertheless be investigated by high-resolution residual electrical resistivity measurements.

### Materials

Pure binary TiAl<sub>50</sub>, TiAl<sub>51.5</sub>, TiAl<sub>53</sub> and TiAl<sub>54.5</sub> alloys were investigated. They were prepared from high-purity metals by RF levitation melting, followed by directional solidification, then homogenized for 24 h at 1400 K. The titanium had a very low oxygen content (27 wt.ppm) and the main metallic impurities were iron and zirconium ( $\approx 100$  wt.ppm each). The aluminium was a zone-refined material with a total impurity content lower than 1 wt.ppm. The composition of the alloys was determined by Inductively Coupled Plasma-Atomic Emission Spectrometry (ICP-AES) chemical analysis. The relative

deviations from the nominal concentrations were usually lower than 1 %. The homogeneity of the alloys was evaluated by scanning electron microscopy with energy-dispersive X-ray spectrometry [13]. X-ray diffraction and transmission electron microscopy showed that the materials had a single phase L1<sub>0</sub> structure, except for some samples of the stoichiometric TiAl<sub>50</sub> alloy which contained a small volume fraction (a few per cent) of  $\alpha_2$ -Ti<sub>3</sub>Al phase. Rod-shaped samples (1 x 1 x 10 mm<sup>3</sup>) were machined from the ingots by diamond sawing. Before the kinetics studies, they were annealed for 10 h at 1223 or 1293 K and furnace cooled.

#### Isochronal anneals

Isochronal anneals were performed at temperatures increasing up to 1140 K then decreasing, either under a reduced pressure of pure helium gas up to 800 K or, at higher temperatures, under a vacuum of 10<sup>-4</sup> Pa. The samples were rapidly cooled at the end of each anneal in order to retain the achieved structural state. Residual electrical resistivity values, used for characterizing the order states, were deduced from the sample resistances measured at 4.2 K by a standard four probe d.c. technique, by applying geometrical shape factors. The uncertainty on resistivity variations was 1x10<sup>-9</sup>  $\Omega$ cm.

The evolution of residual resistivity for increasing annealing temperatures may be divided into three parts (figure 1):

i) At low temperatures, no significant change was detected. In this range, atomic mobility is too low to allow any evolution to occur during the time of annealing, and the resistivity value is entirely determined by the previous thermal history of the sample.

ii) At higher temperatures, after a small resistivity minimum, a large resistivity increase was observed; this variation is found to be reversible. It corresponds to thermal variations of the LRO parameter: the increase in resistivity reflects a decrease in atomic order.

iii) Beyond this domain, resistivity levels off and goes through a flat maximum. In this temperature range, atomic mobility is very high and the quenching at the end of the anneal is not fast enough to retain the high-temperature degree of order.

The reversible residual electrical resistivity variations, observed between 820 K and 1020 K in the stoichiometric TiAl<sub>50</sub> alloy, were assigned to changes of the equilibrium LRO parameter [14]. The curves obtained with the different alloys are strongly composition dependent [14, 15]:

- The amplitudes of the resistivity variations, in the range where they are reversible, decreases with increasing aluminium contents up to 53 at.%, then increases again (table I).

- The temperature at which atomic mobility begins to be appreciable was shifted to lower values when the aluminium concentration increased from 50 to 54.5 at.% (figure 1, table I). This indicates that atomic mobility increases with the aluminium content.

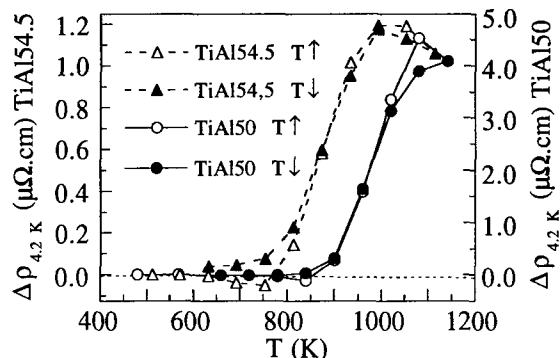


Figure 1: Residual electrical resistivity changes  $\Delta\rho(T) = \rho(T) - \rho_0$  in TiAl<sub>50</sub> and TiAl<sub>54.5</sub> alloys during isochronal anneals ( $\Delta T = 60$  K,  $\Delta t = 40$  min).

Table I. Atomic mobility threshold temperatures and total amplitudes of the variations of residual electrical resistivity  $\Delta\rho(T)$  in TiAl intermetallic compounds, during isochronal anneals.

Al concentration (at%)	50	51.5	53	54.5
Threshold temperature (K)	820	795	755	720
$\Delta\rho$ ( $\mu\Omega$ cm)	4.660	4.069	0.706	1.236

#### Isothermal evolution

The kinetics of ordering (or disordering) were investigated after introducing a deviation from an equilibrium structural state, by a small temperature change. The thermal treatments were carried out as described above and were followed by fast cooling. They typically consisted of isothermal anneals performed successively on the same samples at decreasing then increasing temperatures: starting from the equilibrium order achieved at a temperature  $T_q$ , the samples were annealed during cumulative time sequences at a temperature  $T_a = T_q + \Delta T$ , with  $\Delta T = \pm 25$  K, until a new equilibrium was achieved. Only preliminary results are presently available for this type of experiments.

During isothermal order relaxation after down-quenching ( $T_q > T_a$ ), the intermetallic compounds are expected to exhibit a decrease in residual resistivity, corresponding to an increase in LRO, and to reach an equilibrium value for long annealing times; the reverse should occur for up-quenching experiments ( $T_q < T_a$ ). The analysis of the approach to equilibrium yields information on the kinetics of changes in the state of order, and allows the determination of the relaxation time constants which characterize the kinetics of order change at the temperature of anneal.

**General behaviour.** The variations of residual resistivity during isothermal anneals of the TiAl alloys were found to depend on composition [30]:

(i) The TiAl<sub>50</sub> and TiAl<sub>51.5</sub> compounds displayed the expected electrical resistivity relaxation, to eventually reach a stationary value (figure 2). However, for anneals at the lower

temperatures, the resistivity relaxation was followed by a slow, steady drift to lower values.

(ii) In the TiAl<sub>53</sub> alloy, the resistivity relaxation was followed by a negative drift during down-quenching, but not during up-quenching (figure 3).

(iii) In the TiAl<sub>54.5</sub> alloy, important resistivity drifts were observed both for decreasing and for increasing annealing temperatures. The isothermal variations thus consist of two parts (figure 4): - First, a resistivity relaxation, the sign of which is reversed when going from down-quenching to up-quenching experiments. This phenomenon can be assigned to order relaxation. - Then a quasi-linear drift of resistivity, which always decreases irrespective of the sign of  $\Delta T$ .

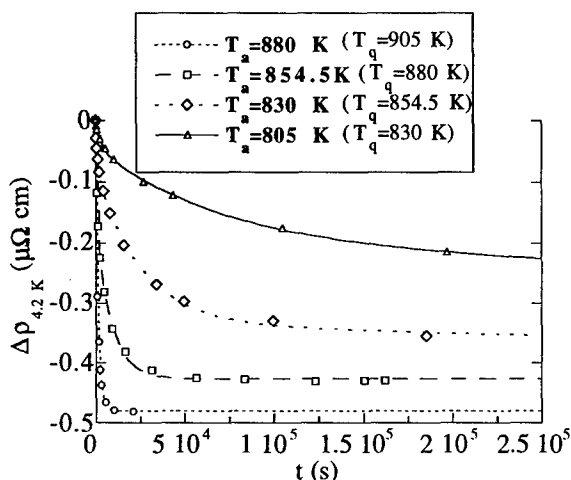


Figure 2: Variations of residual electrical resistivity during isothermal anneals in the TiAl<sub>50</sub> alloy.

**Long-term drift.** The downward drift is clearly composition dependent: it is present in TiAl<sub>50</sub> and TiAl<sub>51.5</sub> but only at lower temperatures, and it is much weaker than in the high-Al compounds. Moreover, it is much slower in TiAl<sub>53</sub> than in TiAl<sub>54.5</sub>. This drift is probably not caused by an oxidation of the samples, since its rate is the same under high vacuum and under a reduced pressure of helium. It might possibly be related to the precipitation of a second phase, due to the crossing of the boundary of a two-phase domain. This should occur at different temperatures for the different TiAl compositions. A comparable drift phenomenon was observed by Meisterle and Pfeiler [16] in a study of short-range ordering kinetics in Ag-Al alloys, and was assigned to precipitation. It should be noted that the Ti-Al phase diagram in the composition range 53-63 at.% Al has not been investigated in detail at low temperatures. The precipitation of a number of phases might be considered: TiAl<sub>2</sub> [17], Ti<sub>3</sub>Al<sub>5</sub> [18,19], Ti<sub>2</sub>AlN [20]. On the other hand, since deviations from stoichiometry are compensated in Al-rich off-stoichiometric TiAl alloys by antisite aluminium atoms (see next section), another possibility for this downward drift could be the ordering of the excess aluminium atoms present on the titanium sublattice, during long-term isothermal anneals. To

test the hypothesis of the formation of a second phase, transmission electron microscopy (TEM) observations on samples treated in the same conditions as the resistivity samples are in progress.

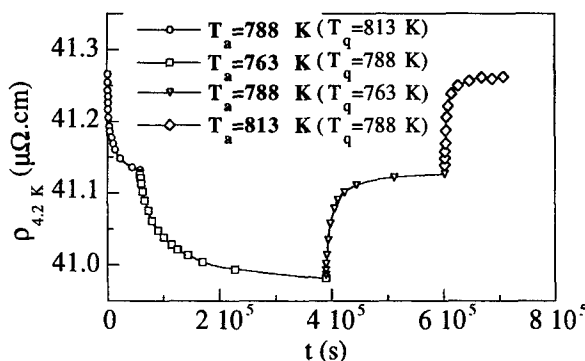


Figure 3: Evolution of residual electrical resistivity during successive isothermal anneals in the TiAl<sub>53</sub> alloy.

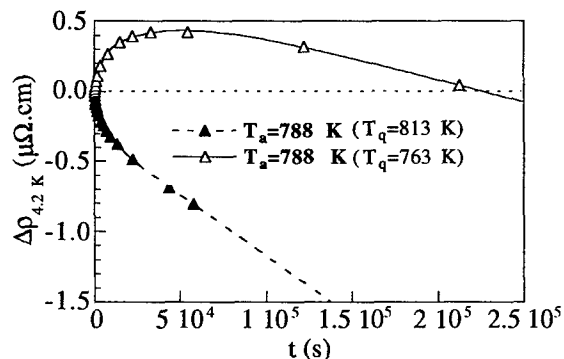


Figure 4: Isothermal 788 K variations of the residual resistivity in the TiAl<sub>54.5</sub> alloy, after down-quenching from 813 K, or after up-quenching from 763 K, fitted by two exponentials plus a straight line (see text):

- down-quenching:  
 $\tau_1 = 0.61 \text{ ks}$ ,  $\tau_2 = 7.5 \text{ ks}$ ,  $a = -8.7 \cdot 10^{-6} \mu\Omega \cdot \text{cm} \cdot \text{s}^{-1}$ .
- up-quenching:  
 $\tau_1 = 4.0 \text{ ks}$ ,  $\tau_2 = 40 \text{ ks}$ ,  $a = -3.2 \cdot 10^{-6} \mu\Omega \cdot \text{cm} \cdot \text{s}^{-1}$ .

**Analysis of relaxation kinetics.** Concerning the resistivity relaxation phenomenon, its kinetics have been up to now investigated at a few temperatures only. Nevertheless, a pure exponential relaxation law was found not to be consistent with the experimental data, even in the final part of the relaxation, close to the equilibrium.

The observed kinetics could be formally represented by a sum of two exponentials:

$$\Delta\rho(t) = \Delta\rho_1 \exp(-t/\tau_1) + \Delta\rho_2 \exp(-t/\tau_2) \quad (2)$$

where  $\Delta\rho_1$  and  $\Delta\rho_2$  are the amplitudes of the two relaxation processes,  $\tau_1$  and  $\tau_2$  the time constants; or, when a long-term drift was present, by the same kinetics with the addition of a linear term

$$\Delta\rho(t) = \Delta\rho_1 \exp(-t/\tau_1) + \Delta\rho_2 \exp(-t/\tau_2) + a \cdot t \quad (3)$$

where  $a_t$  represents the contribution of the drift to the resistivity variations.

The experimental data could also be satisfactorily adjusted by a stretched exponential:

$$\Delta\rho(t) = (\rho_{eq} - \rho_0) [1 - \exp(-(t/\tau)^n)] \quad (4)$$

where  $\rho_0$  is the initial resistivity and  $\rho_{eq}$  the final equilibrium value. A linear contribution was similarly added when a drift was present in the data.

In the  $\text{TiAl}_{54.5}$  and  $\text{TiAl}_{53}$  compounds, we observed an asymmetry in the relaxation rates when reversing the sign of the temperature jump: the rate was larger during down-quenching than during up-quenching experiments. Investigations are in progress to determine the origin of this asymmetry, and to identify the law which describes adequately the observed kinetics and should be used to derive the characteristic time constants.

The aluminium concentration has an important effect on the resistivity relaxation phenomenon: it is much faster in the  $\text{TiAl}_{53}$  and  $\text{TiAl}_{54.5}$  alloys since, in the same temperature range, the relaxation rates are larger than those of the  $\text{TiAl}_{50}$  and  $\text{TiAl}_{51.5}$  compounds. This means that atomic mobility increases with deviations from stoichiometry on the Al-rich side, in agreement with the conclusion of the isochronal investigation presented above.

#### Point defects at thermal equilibrium

In  $\gamma$ -TiAl intermetallics, no structural vacancies have been evidenced, even when the composition deviates from stoichiometry. Antisite defects are produced in order to adjust the composition. This conclusion is based on experimental results of X-ray diffraction [1, 21], density [1] and positron lifetime measurements [22, 23]; it is supported by calculations based on the local-density functional (LDF) theory [24], or performed in the framework of a nearest neighbour bond model [25].

The equilibrium concentration of thermal vacancies has been investigated as a function of temperature by positron lifetime spectrometry up to 1400 K in a  $\text{TiAl}_{51.5}$  compound [22]. A vacancy concentration of  $1.5 \cdot 10^{-4}$  near the peritectic temperature was estimated, very similar to the vacancy concentration in fcc metals near the melting point. A much higher concentration ( $\approx 4 \cdot 10^{-2}$  at the same temperature) results from the vacancy formation parameters reported by Fan and Collins [26] on the basis of perturbed angular correlation of  $\gamma$  rays (PAC) measurements in equi-atomic TiAl; however, such a concentration was considered unrealistic by the authors. By difference between the Ti self-diffusion enthalpy (3.02 eV) and the vacancy formation enthalpy ( $1.41 \pm 0.06$  eV) determined from their positron spectroscopy measurements, Brossmann et al. [22] estimated an activation enthalpy for vacancy migration of 1.6 eV. This value is in very good agreement with the one ( $1.55 \pm 0.16$  eV) deduced from the recovery of point defects

induced by low-temperature electron irradiation (see next section).

The equilibrium concentrations of Ti and Al vacancies and of antisite atoms on each sublattice have been theoretically estimated as a function of temperature and composition in the above-mentioned calculations [24,25]. At stoichiometry, the concentrations of  $\text{Al}_{\text{Ti}}$  and  $\text{Ti}_{\text{Al}}$  antisite atoms are several orders of magnitude larger than the Ti and Al vacancy concentrations and they increase with temperature (figure 5). Vacancies were found to be mainly located on the Ti sublattice. Their concentration is composition dependent: with increasing aluminium content, the concentration of Ti and Al vacancies increases; the same variation was found for the  $\text{Al}_{\text{Ti}}$  antisite atoms whereas the concentration of  $\text{Ti}_{\text{Al}}$  antisite atoms decreases (figure 6). The strong enhancement of the equilibrium vacancy concentration for higher aluminium contents is supported by the experimentally-based conclusions to be reported below, which were deduced by comparing the composition dependence of the atomic mobility [15] with the mobility of vacancies in  $\gamma$ -TiAl alloys [27].

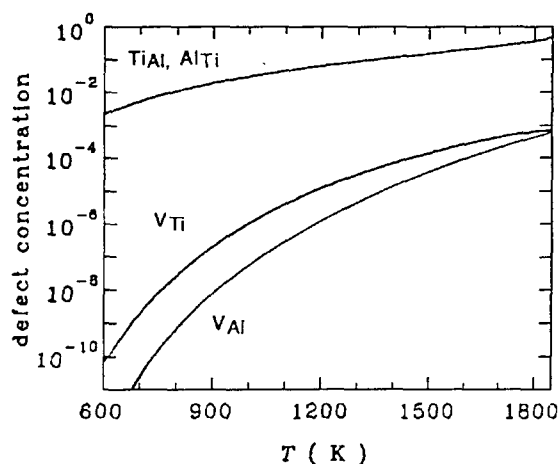


Figure 5: Temperature dependence of the vacancy concentration on the Ti ( $V_{\text{Ti}}$ ) and Al ( $V_{\text{Al}}$ ) sublattices and of the two types of antisites ( $\text{Ti}_{\text{Al}}$ ,  $\text{Al}_{\text{Ti}}$ ) in stoichiometric  $\gamma$ -TiAl, after [25].

The formation enthalpy of vacancies on the Ti and Al sublattices and of the two types of antisite atoms, evaluated by Fu and Yoo [24] are significantly larger than the values proposed by Badura and Schaefer [25]. The discrepancy between the two estimations (table II), leads to a difference of  $\approx 2$ -3 orders of magnitude between the two evaluations of defect concentrations; however the temperature and composition dependences are similar. In a  $\text{TiAl}_{51.5}$  alloy, the theoretically estimated values of 1.80 eV [24] and 1.25 eV [25] for the effective vacancy formation enthalpy on the Ti sublattice are respectively larger and smaller than the experimental vacancy formation enthalpy ( $1.41 \pm 0.06$  eV), determined by positron lifetime spectroscopy [22], which should be mainly

representative of the concentration of the dominant Ti vacancies.

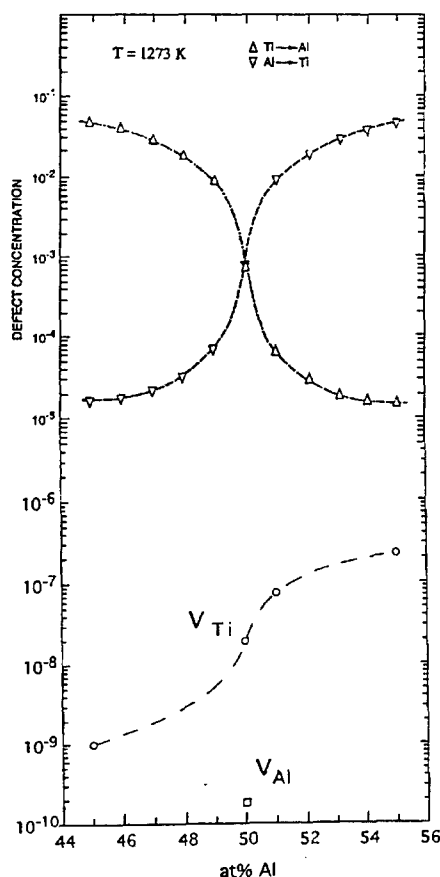


Figure 6: Composition dependence of point defect concentrations in  $\gamma$ -TiAl at 1273 K, after [24].

Table II. Calculated formation enthalpies, in stoichiometric TiAl of Ti ( $H_{V(Ti)}^F$ ) or Al ( $H_{V(Al)}^F$ ) vacancies and of antisite defects  $H_{TiAl}^F$ ,  $H_{AlTi}^F$  from Fu and Yoo [24], and Badura and Schaefer [25].

Formation enthalpy (eV)	$H_{V(Ti)}^F$	$H_{V(Al)}^F$	$H_{TiAl}^F$	$H_{AlTi}^F$
[24]	1.95	2.46	0.72	0.72
[25]	1.27	1.50	0.32	0.32
	(at 1300 K)	(at 1300 K)		

#### Irradiation induced defects in $\gamma$ -TiAl

The investigation of irradiation effects in  $\gamma$ -TiAl alloys is important for two main reasons. On the one hand, titanium aluminides have been considered for nuclear applications, due to their low induced radioactivity by comparison with conventional materials. On the other hand the investigation of irradiation-induced excess point defects yields direct information on the mobility of vacancies. Such investigations have been previously performed in  $\gamma$ -TiAl alloys by recovery experiments of positron lifetime, after low-temperature

irradiation by electrons of 10 MeV [23], 2.5 MeV or 0.55 MeV [28] and by protons of 2 MeV [23].

In the work reported here, low temperature electron irradiation was used to introduce self-interstitial/vacancy Frenkel pairs. The production of point defects and the disordering taking place during irradiation were investigated by means of residual electrical resistivity measurements. Next, the recovery during isochronal annealing experiments was determined both by electrical resistivity measurements and positron lifetime spectroscopy, thus yielding information on the mobility of self-interstitials and vacancies.

#### Experimental procedure

The same alloys as those used in the atomic mobility study (50, 51.5, 53 and 54.5 at.% Al) were investigated. Specimens were prepared by cutting, from the ingots, slices  $\approx 800 \mu\text{m}$  in thickness, then thinning them by mechanical polishing down to 200 - 300  $\mu\text{m}$  for the resistivity investigations and down to 700  $\mu\text{m}$  for the positron lifetime spectroscopy. After subsequent chemical or electrochemical etching, the samples were annealed in a vacuum of  $10^{-6}$  Pa for 10 hours at 1223 K or 1323 K and slowly cooled.

The irradiation experiments were performed with 2.5 MeV electrons at 21 K, in the liquid hydrogen cryostat of the Van de Graaf electron accelerator at the SESI, Ecole Polytechnique, Palaiseau (France). Radiation damage was investigated by electrical resistivity determinations performed at 21 K, with an uncertainty of  $1 \times 10^{-9} \Omega \cdot \text{cm}$ . The shape factors of the samples  $k = \rho_{4.2\text{K}} / R_{4.2\text{K}}$  were deduced from their 4.2 K electrical resistances before irradiation, by using resistivity values determined on separate specimens of suitable shape ( $\approx 1 \text{ mm}^2$  in section). The recovery behaviour was investigated on samples irradiated to  $3 \times 10^{18} - 1 \times 10^{19} \text{ e}^- \cdot \text{cm}^{-2}$  and isochronally pulse-annealed with a mean rate of temperature increase of  $1.5 \text{ K} \cdot \text{min}^{-1}$  [27]. The anneals were carried out, between 21 and 300 K, in a furnace located inside the cryostat, above the liquid hydrogen bath. At higher temperatures, the annealing conditions were the same as in the investigation of atomic mobility. Electrical resistivity measurements were performed at 21 K after anneals up to 300 K and at 4.2 K above this temperature. All the resistivity values measured at 21 K were corrected and reduced to 4.2 K values.

For the positron lifetime measurements, samples of  $5 \times 5 \times 0.7 \text{ mm}^3$  were used. After electron irradiation at 21 K to a fluence of  $5 \times 10^{18} \text{ e}^- \cdot \text{cm}^{-2}$ , the samples were rapidly transferred in liquid nitrogen. They were mounted on a sample holder, with a  $^{22}\text{Na}$  positron emitter source deposited on a 5  $\mu\text{m}$  thick aluminium foil sandwiched between two identical TiAl samples. Isochronal anneals were carried out with the same mean rate of temperature increase ( $1.5 \text{ K} \cdot \text{min}^{-1}$ ) as for the resistivity studies. The heat treatments were carried out in the lifetime measurement cryostat between 77 and 395 K. At higher temperatures, the samples were annealed as described above, after removing the positron source. After each anneal, positron

lifetime spectra were recorded at 77 K with  $2 \times 10^6$  coincidence counts by means of a fast-fast time spectrometer, yielding a time resolution full width at half maximum (FWHM) of  $228 \pm 4$  ps.

#### Radiation damage.

During irradiation the resistivity increased with the fluence. The excess resistivity at a given fluence was maximum for the alloy with 50 at.% aluminium and minimum for a concentration of 53 at.% aluminium (table III). This may be related to atomic order effects, which depend on composition [15]. The analysis of the initial resistivity damage-rate ( $\rho_0^{\text{exp}}$ ) data showed that the disordering contribution represents 8 to 15% of the damage-rate, for the stoichiometric alloy [27]. Thus, this contribution is not negligible, but the dominant effect of electron irradiation is the production of Frenkel defects. The obtained Frenkel-pair resistivities ( $\rho_F$ ) were very little composition dependent, and were close to  $60 \mu\Omega \text{ cm} \%$ .

Table III. Residual resistivity of unirradiated materials  $\rho_0$ , excess resistivity  $\Delta\rho_i$  induced by electron irradiation at 21K ( $\Phi = 8 \times 10^{18} \text{ e}^- \text{ cm}^{-2}$ ), and initial experimental damage rates  $\rho_0^{\text{exp}} = (d\rho/d\Phi)_0^{\text{exp}}$ .

Alloy composition (at.% Al)	50	51.5	53	54.5
$\rho_0$ ( $\mu\Omega \text{ cm}$ )	6.67 $\pm 0.15$	17.4 $\pm 0.4$	41.3 $\pm 0.9$	63.4 $\pm 1.4$
$\Delta\rho_i$ ( $\mu\Omega \text{ cm}$ )	1.573 $\pm 0.006$	1.531 $\pm 0.005$	1.465 $\pm 0.008$	1.525 $\pm 0.009$
$\rho_0^{\text{exp}}$ ( $10^{-25} \Omega \text{ cm}^3$ )	2.01 $\pm 0.03$	1.94 $\pm 0.03$	1.84 $\pm 0.03$	1.93 $\pm 0.03$

#### Recovery of electron-irradiated alloys

During post-irradiation isochronal anneals, two major stages of resistivity recovery (noted I and III in figures 7a and 7b) were observed. The first important stage is found to occur around 80 K and the second at 444 K in the stoichiometric alloy.

Composition has no effect on the temperature of stage I, but it has an important influence on the position of stage III. For a fluence  $\Phi = 8 \times 10^{18} \text{ e}^- \text{ cm}^{-2}$  it was shifted to higher temperatures, from 444 to 504 K, when the aluminium concentration increased from 50 to 54.5 at.% (table IV).

Table IV. Temperatures  $T_M$  (K) of maximum recovery rate for TiAl alloys irradiated to a fluence  $\Phi$ .

Alloys	$\Phi (10^{18} \text{ e}^- \text{ cm}^{-2})$	$T_M$ (K)	
		stage I	stage III
TiAl <sub>50</sub>	10	78	443
	8	81	444
TiAl <sub>51.5</sub>	8	81	449
	8	81	480
TiAl <sub>53</sub>	3	84	516
	8	81	504

The effect of the irradiation fluence on the recovery spectrum was determined in the TiAl<sub>53</sub> alloy. A lower fluence,

corresponding to a lower concentration of irradiation-induced defects, results in a slight shift of the position of stage I, and in an important shift of stage III to higher temperatures (table IV).

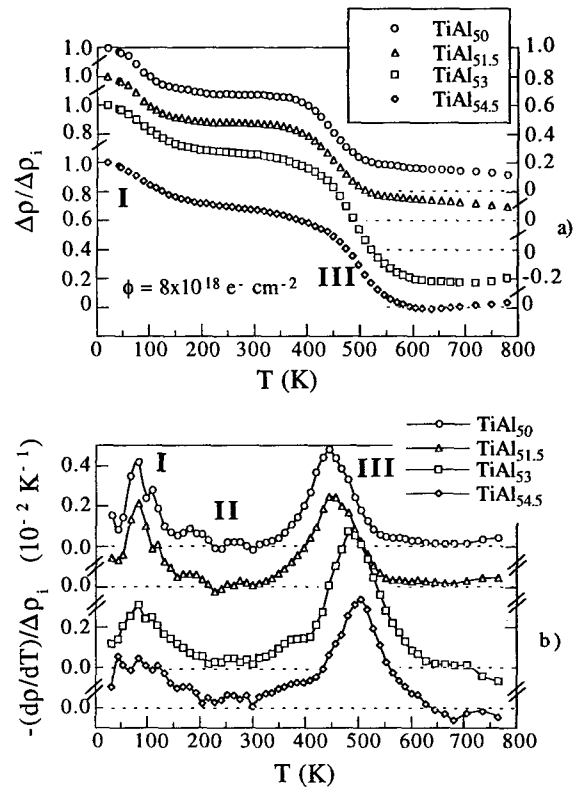


Figure 7: a) Isochronal resistivity recovery curves of the  $\gamma$ -TiAl compounds irradiated to  $8 \times 10^{18} \text{ e}^- \text{ cm}^{-2}$ . b) differential curves.

By analogy with the recovery of electron-irradiated pure metals or of Ni<sub>3</sub>Al intermetallic compounds [29], it seems reasonable to assign stage I to close-pair recovery followed by self-interstitial migration. Stage III has a temperature of maximum recovery rate which clearly depends on the fluence, a feature consistent with the free migration of point defects.

Positron lifetime measurements yield information about vacancy mobility, since positrons are mainly sensitive to vacancy-type defects. Before irradiation, the lifetime in TiAl<sub>50</sub> and TiAl<sub>54.5</sub> samples was  $154 \pm 1$  ps. After electron-irradiation, we measured a single positron lifetime equal to  $225 \pm 1$  ps in both alloys, which indicates that a large majority of positrons are trapped before their annihilation by an excess vacancy concentration. This value should be close to the characteristic lifetime of positron annihilation in single vacancies in TiAl compounds. It is equal to the one obtained in TiAl<sub>51.5</sub>, irradiated at 90 K ( $225 \pm 3$  ps) with 2.5 MeV electrons to a fluence of  $5.6 \times 10^{18} \text{ e}^- \text{ cm}^{-2}$  [22]. However, these values are larger than the one ( $200 \pm 3$  ps) reported by Shirai et al. [23] for the long lifetime component representative of the vacancy-trapped positrons in a TiAl<sub>56</sub> compound, after low-fluence 10 MeV electron irradiation.



During isochronal anneals of the stoichiometric compound at increasing temperatures, a slight decrease of mean positron lifetime can be seen first, particularly around 200 K, then a large drop in the positron lifetime is observed between 400 and 665 K (figure 8). This strong decrease can be associated with the elimination of vacancy-type traps, and occurs in the same temperature range as the recovery stage III of residual electrical resistivity. This suggests that stage III corresponds to the migration and elimination of radiation-induced vacancies. The slight positron lifetime variation before stage III might be connected with a small decrease of the vacancy concentration by recombination with mobile interstitial-type defects.

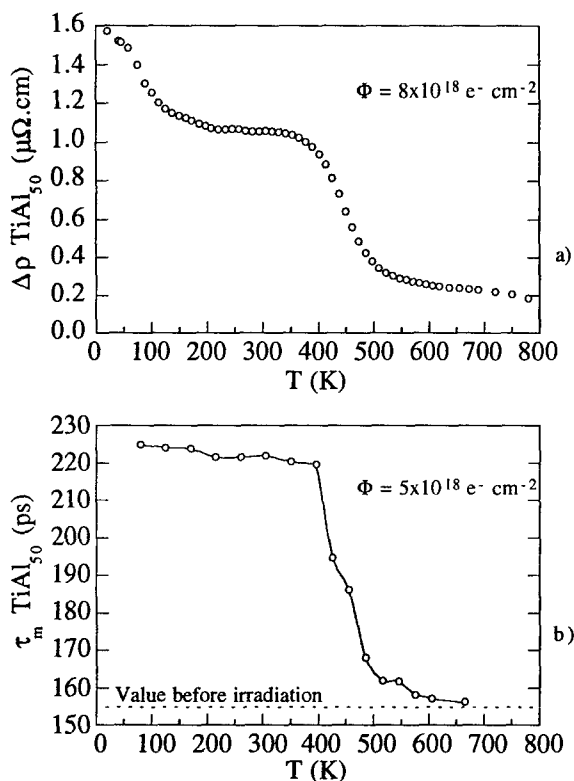


Figure 8: Isochronal recovery curves of TiAl<sub>50</sub> a) resistivity variations;  $\Phi = 8 \times 10^{18} \text{ e}^- \text{ cm}^{-2}$ . b) variations of the mean positron lifetime ( $\tau_m$ );  $\Phi = 5 \times 10^{18} \text{ e}^- \text{ cm}^{-2}$ .

The effective enthalpy of vacancy migration ( $H_V^M$ ) in stoichiometric  $\gamma$ -TiAl can be estimated from the temperature (444 K) of stage III of resistivity recovery, by comparison with the data (temperature and vacancy migration enthalpy) obtained for stage III in stoichiometric Ni<sub>3</sub>Al [29]. This estimation leads to  $H_V^M = 1.55 \pm 0.16 \text{ eV}$  for stoichiometric  $\gamma$ -TiAl, in excellent agreement with the estimation  $H_V^M = 1.6 \text{ eV}$  proposed by Brossmann et al. [22] for a TiAl<sub>51.5</sub> alloy.

#### Composition dependence of vacancy mobility and of vacancy equilibrium concentration

The above results show that stage III is shifted to higher temperatures with increasing Al content. Such a shift means that vacancy mobility (i.e. vacancy jump frequency  $\nu_V$ )

decreases when the aluminium concentration increases. This conclusion is not in contradiction with the variations of creep rate and of atomic mobility, which were found to increase with the aluminium content: atomic diffusion depends not only on the vacancy mobility but also on the vacancy concentration. Actually, since atomic jump frequency ( $\nu_{at}$ ) and vacancy jump frequency ( $\nu_V$ ) are related to the equilibrium vacancy concentration  $C_V(T)$  at temperature  $T$  by the expression:

$$\nu_{at} = \nu_V C_V(T) \quad (5)$$

we can deduce a composition dependence of the vacancy concentration. From (5), it turns out that the vacancy concentration at a given temperature increases with the aluminium content; therefore, the vacancy formation enthalpy ( $H_V^F$ ) decreases, according to the relation between  $C_V$  and  $H_V^F$ :

$$C_V(T) \propto \exp(-H_V^F/kT) \quad (6)$$

This experimental conclusion supports the theoretical predictions of Badura and Schaefer [25] and of Fu and Yoo [24] about the composition dependence of the vacancy formation enthalpy in  $\gamma$ -TiAl intermetallic compounds.

#### Conclusion

Although the diffusional and point defect properties of  $\gamma$ -TiAl intermetallic compounds are far from being fully characterized and understood, some new results have become recently available, particularly with respect to the influence of composition. Table V summarizes the present situation.

In single-phase  $\gamma$ -TiAl compounds, we have shown, from the kinetics of atomic order change, that the atomic mobility increases with the deviations from stoichiometry on the Al-rich side. This trend is similar to the one found for the creep rate. On the other hand, the vacancy mobility decreases at higher aluminium concentrations. These two sets of data imply that the equilibrium concentration of thermal vacancies strongly increases with the aluminium concentration, in agreement with theoretical predictions.

Table V points out a number of questions which are still open, and which should be addressed in future work. In particular, it would be interesting to:

- investigate the composition dependence of Ti self-diffusion, which has been determined at one concentration only, and measure directly the Al self-diffusion coefficient.
- consider whether the observed composition dependence of the atomic mobility and the apparent absence of such a dependence for the interdiffusion coefficient in single-phase couples can be reconciled, and compare the activation enthalpies for order relaxation (the determination of which is in progress) with that of interdiffusion.
- determine the effect of composition on the high-strain creep rates and on the associated activation enthalpy.
- measure the equilibrium concentration of thermal vacancies (and their formation enthalpies) in a range of alloy compositions.
- perform direct determinations of the activation enthalpy for

the migration of vacancies introduced by irradiation (such determinations are in progress).  
- investigate the elementary atomic jump processes in the L10

structure of  $\gamma$ -TiAl, in connection with macroscopic diffusion-related properties (e.g. by Molecular Dynamics calculations, local probe experimental methods, Monte-Carlo simulations).

Table V. Composition and temperature dependences of self-diffusion, interdiffusion, atomic mobility, creep rate, vacancy concentration and vacancy migration in  $\gamma$ -TiAl compounds. ( $c_{Al}$  is the Al concentration;  $D^*_{Ti}$  and  $\tilde{D}$ , the Ti tracer diffusion and the interdiffusion coefficients;  $v_{at}$  and  $v_V$ , the atomic and vacancy jump frequencies;  $\dot{\epsilon}_{\text{minimum}}$  and  $\dot{\epsilon}_{\text{high strain}}$ , the minimum and high strain creep rates;  $Q_{SD}$  and  $Q$ , the activation enthalpies for Ti self-diffusion and for interdiffusion;  $H^F_V$  and  $H^M_V$ , the formation and migration enthalpies of vacancies).

Property	Materials [References]	Temperature dependence	Concentration dependence
Ti self-diffusion	TiAl <sub>54</sub> [4]	$Q_{SD} = 3.02 \text{ eV}$	no data
Al self-diffusion (estimated from $\tilde{D}$ and $D^*_{Ti}$ )	TiAl <sub>54</sub> [4] and single phase (TiAl <sub>50</sub> /TiAl <sub>54</sub> ) [5]	no data	no data
Interdiffusion	single phase (TiAl <sub>50</sub> /TiAl <sub>54</sub> ) [5] multiphase TiAl <sub>47.8-54.1</sub> [7]	$Q = 3.02 \text{ eV}$  $Q = 1.71\text{-}1.33 \text{ eV}$	not seen  $\tilde{D}$ increases with $c_{Al}$
Atomic mobility	TiAl <sub>50-54.5</sub> [15, present results]	in progress	$v_{at}$ increases with $c_{Al}$
Creep			
$\dot{\epsilon}_{\text{minimum}}$	TiAl <sub>50-53.5</sub> [8]	$Q = 3.63\text{-}4.15 \text{ eV}$	$\dot{\epsilon}_{\text{minimum}}$ increases with $c_{Al}$
$\dot{\epsilon}_{\text{high strain}}$	TiAl <sub>50-53.5</sub> [9] TiAl <sub>52</sub> [10]	$Q = 3.42\text{-}3.94 \text{ eV}$ $Q = 2.6\text{-}3.2 \text{ eV}$	no data
Vacancy concentration	TiAl <sub>51.5</sub> [22]  TiAl <sub>50-54.5</sub> [27 and present results]	$H^F_V = 1.41 \pm 0.06 \text{ eV}$  $H^F_V(Ti), H^F_V(Al)$ decrease when $c_{Al}$ increases (theor.) [24,25]	no data  $c_V$ increases with $c_{Al}$ (from $c_V = v_{at}/v_V$ )  $c_{V_{Ti}}$ increases with $c_{Al}$ (theor.) [24,25]
Vacancy migration	TiAl <sub>51.5</sub> [22]  TiAl <sub>50-54.5</sub> [27]	$H^M_V = 1.6 \text{ eV}$ (from $Q_{SD} - H^F_V$ )  $H^M_V = 1.55 \pm 0.16 \text{ eV}$ (estimated in TiAl <sub>50</sub> )	  $v_V$ decreases when $c_{Al}$ increases

#### Acknowledgements

The authors would like to thank Dr F. Albenque (SESI) for the possibility to use the electron irradiation facility and M. J. Ardonneau (SESI) for his help during the irradiations. They are grateful to Dr C. Corbel (INSTN-CEA Saclay) for giving access to her positron lifetime spectroscopy device and for helpful discussions.

#### References

1. D. Vujic, Z. Li and S. H. Whang, *Metall. Trans. A*, 19 (1988), 2445-2455.
2. J. Braun, M. Ellner and B. Predel, *Z. Metallkd.*, 86 (1995), 870-876.
3. H. Okamoto, *J. of Phase Equil.*, 14 (1993), 120-121.

4. S. Kroll et al., Z. Metallkd., 83 (1992), 591-595.
- H. Mehrer, W. Sprengel and M. Denking, Diffusion in Ordered Alloys, eds B. Fultz, R.W. Cahn, D. Gupta, (TMS, Warrendale, 1993) 51-67.
5. W. Sprengel, N. Oikawa and H. Nakajima, Intermetallics, 4 (1996), 185-189.
6. K. Hirano and Y. Iijima, Diffusion in solids: Recent developments, eds. M. A. Dayananda and G. E. Murch, (The Metallurgical Society of AIME, 1984) 141-166.
7. K. O. Ouchi, Y. Iijima and K. Hirano, in Titanium' 80, Science and Technology, 4th Int. Conf. on Titanium Proceedings, eds. H. Kimura and O. Izumi, (Kyoto, May 19-22 1980), 559-568
8. H. Oikawa, Mater. Sci. Eng., A153 (1992), 427-432.
9. H. Oikawa: High Temperature Aluminides and Intermetallics, eds. S. H. Whang, C. T. Liu, D. P. Pope and J. O. Stiegler, (The Minerals, Metals and Materials Society, 1990), 353-373.
10. A. Dlouhy, Communication to COST 513 Technical Meeting (Neuchâtel, Switzerland, June 28, 1996)
11. G. Some, J. Bernardini and C. L'excellent, Acta Metall. Mater., 40 (1992), 761-769
12. C. Dimitrov, X. Zhang and O. Dimitrov, Acta Mater., 44 (1996), 1691-1699.
13. C. Dimitrov et al., J. de Physique IV, Coll. C7, 3 (1993), 481-484.
14. C. Dimitrov et al., Ann. de Phys., Coll. C3, 20 (1995), 65-72.
15. C. Dimitrov et al., Scripta Mater., 34 (1996), 1405-1409.
16. P. Meisterle and W. Pfeiler, Phys. Stat. Sol. a, 80 (1983), K37-K40.
17. U. R. Kattner, J.-C. Lin and Y. A. Chang, Metall. Trans. A, 23 (1992), 2081-2090.
18. R. Miida, S. Hashimoto and D. Watanabe, Jpn. J. Appl. Phys., 21 (1982), L59-L61.
19. A. Loiseau et al., Acta Cryst. B, 41 (1985), 411-418.
20. M. J. Kaufman et al., Scripta Metall., 20 (1986), 103-108.
21. R. P. Elliott and W. Rostoker, Acta Metall., 2 (1954), 884.
22. U. Brossmann et al., Phys. Rev. B, 49 (1994), 6457-6461.
23. Y. Shirai and M. Yamaguchi, Mater. Sci. Eng. A, 152 (1993), 173-181.
24. C. L. Fu and M. H. Yoo, Intermetallics, 1 (1993), 59-63.
25. K. A. Badura and H.-E. Schaefer, Z. Metallkd., 84 (1993), 405-409.
26. J. Fan and G. S. Collins, Hyperfine Inter., 79 (1993), 745-748.
27. G. Sattonnay et al., J. Phys.:Condensed Matter, 9 (1997) in press.
28. R. Würschum et al., Phys. Rev. B, 54 (1996), 849-856.
29. C. Dimitrov et al., J. Phys.:Condensed Matter, 4 (1992), 10211-10226.
30. G. Sattonnay et al., Defect and Diffusion Forum, 143-147 (1997), 377-382. Proc. Intl. Conf. "DIMAT-96", eds. H. Mehrer, Chr. Herzig, N. A. Stolwijk and H. Bracht, (Nordkirchen, Germany, August 1996).

## THE EFFECT OF COOLING RATE DURING CASTING ON MICROSTRUCTURAL DEVELOPMENT IN Ti-48Al-2Cr-2Nb TYPE ALLOYS

K. Muraleedharan, L. L. Rishel, M. De Graef, A. W. Cramb, T. M. Pollock and G. T. Gray III\*

Department of Materials Science and Engineering  
Carnegie Mellon University, Pittsburgh, PA 15213, USA.

\* Los Alamos National Laboratory  
MST-5, MS G755, Los Alamos, NM 87545, USA.

### Abstract

Microstructure development as a function of cooling rate during investment casting was studied in Ti-48Al-2Cr-2Nb alloys. Solidification times and subsequent solid state cooling rates were varied by influencing heat extraction from the investment mold. Solidification times ranged from approximately 5 to 25 seconds and cooling rates through the  $\alpha+\gamma$  phase region ranged from approximately 0.25 to 40 °C/second. Variations in cooling rate dramatically influenced the as-cast macro- and micro-structure and the subsequent development of microstructure and texture. Columnar macrostructures were observed in all as-cast samples. Fine lamellar-type secondary grains within the original columnar grains resulted from phase transformations during cooling to room temperature. TEM analyses of the as-cast microstructures revealed that cooling rate strongly influenced the character and orientation of the lamellar microstructure. The slowest cooling rate produced an  $\alpha_2+\gamma$  lamellar structure identical to that produced by heat treatment in the  $\alpha$  phase field followed by slow cooling. Faster cooling rates resulted in lamellar-like structures which were fully  $\gamma$  in character and exhibited significant deviations from the standard orientation relationships between adjacent lamellae. The slow cooled  $\alpha_2+\gamma$  lamellar structure remained lamellar after heat treatment in the  $\alpha+\gamma$  phase field; however, as-cast lamellar-like structures which were fully  $\gamma$  in character decomposed to form a near  $\gamma$  duplex microstructure.

### Introduction

Alloys based on the intermetallic compound  $\gamma$  (L1<sub>2</sub>, P4/mmm) in the Ti-Al system, and more recently Ti-48Al-2Cr-2Nb, are being considered for elevated temperature structural

components [1 - 4]. Among the several processing routes available, investment casting offers considerable flexibility in producing intricate 'near net shape' components, such as turbine blades [3, 5]. The investment casting process for gamma titanium aluminides typically includes either vacuum induction skull melting (ISM) or vacuum arc remelting (VAR) procedures [5]. In both melting processes, containment of the reactive titanium alloy in a water-cooled vessel is required for control of alloy chemistry. This presents a number of challenges with regard to control of microstructure and the minimization of casting defects during solidification.

Recent experiments on titanium aluminide alloys [6] have shown that casting defects such as porosity, cracking and mold metal reaction are sensitive to the casting process parameters that alter heat extraction from the casting, suggesting that cooling rate in the casting plays an important role in the quality of a casting. Castings of components with variations in section thickness, such as turbine blades and exhaust valves, are likely to be subject to a wide range of cooling rates during solidification. Yet, to date, there have been no detailed studies of the influence of casting parameters, and in particular variations in cooling rates, on the development of the solidification structure and the subsequent solid state phase transformations, even though these factors have the potential to dramatically affect mechanical properties. Variations in cooling rate during casting have the potential to alter solidification paths and influence the development of macrostructure, texture and segregation. Furthermore, subsequent solid state transformations that determine the final as-cast microstructure will also be sensitive to cooling rate. In this paper we present results of a study of these aspects of structure development as a function of variations in cooling rate during investment casting of Ti-48Al-2Cr-2Nb type alloys.

Table I - Chemical Compositions of As-cast Plates

Heat	Ti at. %	Al at. %	Nb at. %	Cr at. %	Fe at. %	O at. ppm
I- 1	Bal.	47.9	2.00	2.00	0.007	1390
II- 1	Bal.	48.2	2.02	2.02	0.016	1750
II- 2	Bal.	48.0	2.03	2.04	0.013	1690
II- 3	Bal.	48.0	2.02	2.03	0.017	1830
II- 4	Bal.	47.8	2.04	2.03	0.013	1940
II- 5	Bal.	48.0	2.05	2.04	0.017	1790

Table II - Casting Conditions and Calculated Solidification Times, Cooling Times and Rates for Alloy II Plate Centers

Heat	Aim Mold Preheat Temperature, °C	Mold Insulation	Local Solidification Time, sec	Time Spent above Eutectoid Temperature, sec	Average Cooling Rate through the $\alpha+\gamma$ Phase Region, °C/sec
II- 1	315	full wrap	5.0	13.5	37.0
II- 2	315	partial wrap	5.9	15.5	33.0
II- 3	815	no wrap	6.1	18.2	26.0
II- 4	1204	partial wrap	7.6	26.4	16.0
II- 5	1204	full wrap	23.0	1115.0	0.25

#### Experimental Materials and Procedures

For this study, ingots with a nominal composition of Ti-48Al-2Cr-2Nb (at%), were sectioned and vacuum arc remelted for investment casting of plates in six separate casting trials conducted at Howmet Corporation's Operhall Research Center. Chemical compositions of the subsequent castings are presented in Table I. Two different master ingots very close in nominal composition were utilized; these are designated by I and II, respectively. The plate from the first ingot, designated I-1 in Table I, was cast with dimensions of 150 x 100 x 12mm.

The five plates from the second master ingot (II-1 through II-5) were cast with dimensions of 102 x 102 x 3.8 mm into investment molds with varying mold preheat temperatures and mold insulating conditions in order to achieve variations in cooling rate during solidification and subsequent cooling of the casting [6]. Three aim mold preheat temperatures at the time of pour were considered: 315, 815, and 1204°C. Three mold insulating conditions were used: 1) no wrap; 2) Kaowool between the plates only, for a partial wrap; and 3) Kaowool between the plates and a double layer around the plate cluster, for a full wrap. Mold surfaces were instrumented with thermocouples to verify mold preheat temperatures and to measure mold cooling rates during casting. Solidification times and subsequent cooling rates in the solid were estimated using the UES ProCAST simulation package. Information on casting procedures for plates II-1 through II-5 is provided in greater detail elsewhere [6].

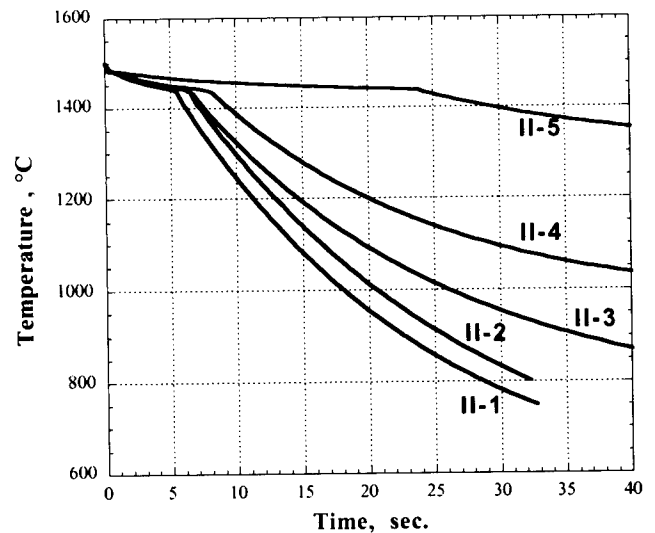


Figure 1. Calculated cooling curves for the centers of cast plates II-1 through II-5

Sections taken from each plate were ground to a 600 grit finish, and macroetched with a modification of Kroll's etchant containing 100 ml  $H_2O$ , 35 ml  $H_2O_2$ , 5 ml  $HNO_3$ , and 10 ml  $HF$ <sup>†</sup>. A stain remover consisting of 50% macroetch and 50%  $H_2O_2$  was used after macroetching. Specimens for microscopic examination were prepared by standard metallographic

<sup>†</sup> Modified Kroll's reagent for macro/micro etching of TiAl alloys developed at CMU by one of the authors (KM).

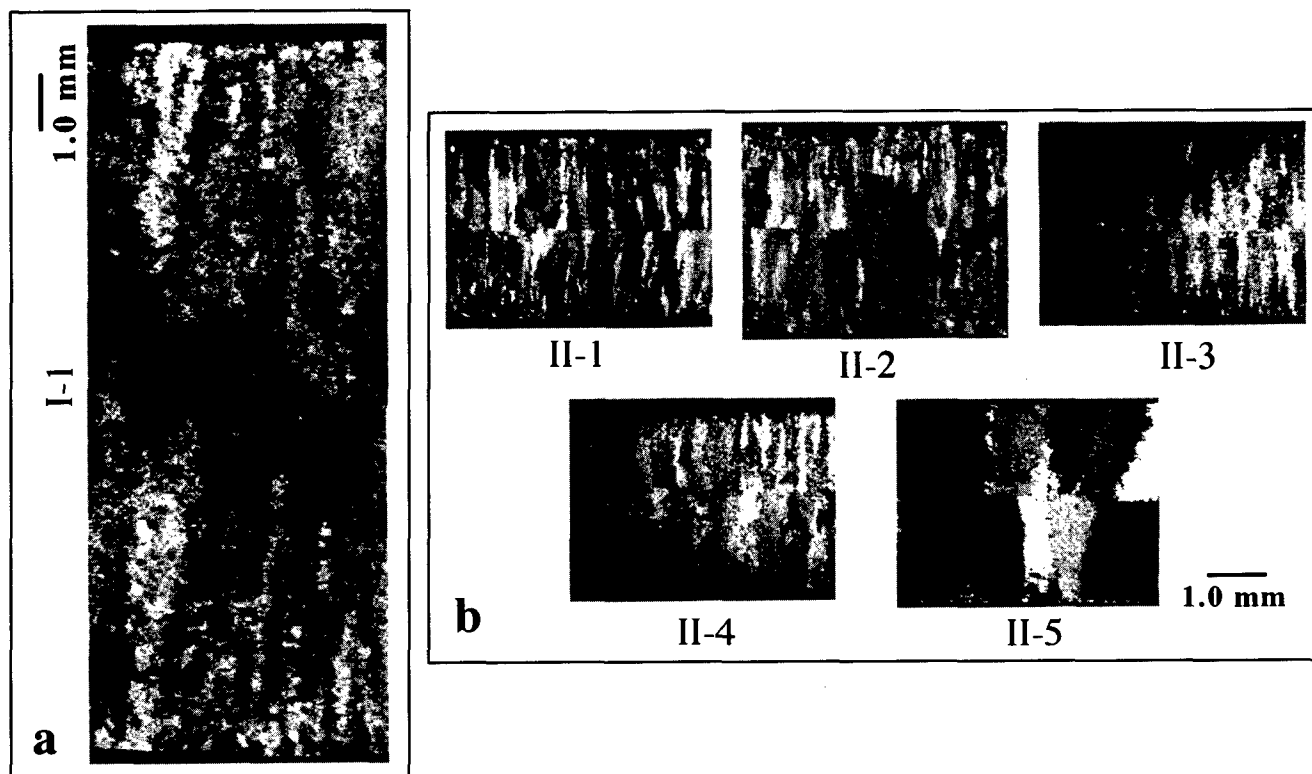


Figure 2. Macrostructures of the cast plates taken across the plate thicknesses for : (a) I-1; (b) II-1, II-2, II-3, II-4, and II-5. [Note, entire plate thicknesses are shown and the magnifications are the same in all micrographs.]

polishing procedures or by electropolishing in a solution containing 300 ml methanol, 175 ml n-butanol and 30 ml perchloric acid maintained at  $-50^{\circ}\text{C}$  [7]. Thin foils for transmission electron microscopy (TEM) were prepared using the same solution employing a twin jet electropolishing technique.

Microstructural analyses were conducted with the use of optical microscopy, scanning electron microscopy (SEM) employing the back scattered electron (BSE) imaging mode in a Camscan SEM operated at 25kV, and transmission electron microscopy (TEM) in a Philips EM420T machine operating at 120kV. The modified Kroll's etchant described above or an etchant consisting of 33 ml glycerol, 33 ml  $\text{HNO}_3$ , 33 ml acetic acid, and 1 ml HF were used for etching specimens for optical microscopy. Segregation in the dendritic microstructure was characterized by electron microprobe analysis using a JEOL 733 microprobe equipped with WDS spectrometers. X-ray texture analysis was performed at Los Alamos National Laboratory and the data was analyzed using the popLA software package [8].

## Results

### Estimates of Cooling Rates

A one-dimensional analysis of the heat transfer during solidification and subsequent solid state cooling of castings II-1 through II-5 was performed using the UES ProCAST

simulation package in conjunction with measured shell temperatures as boundary conditions. Measured plate and shell thicknesses were used to establish the problem geometry. Due to the unavailability of thermal data for the Ti-48Al-2Cr-2Nb alloy, thermal properties for Ti-45Al-2Nb-2Cr+0.9at.%B (XD<sup>TM</sup>) were utilized in the analysis. A liquidus temperature of  $1483^{\circ}\text{C}$  obtained from the binary TiAl phase diagram [9] and a non-equilibrium solidus temperature of  $1438^{\circ}\text{C}$  estimated using a modified Scheil analysis were used for casting simulations. Investment shell properties were provided by Howmet Corporation. Measured shell temperatures at the outer shell surfaces on both sides of the cast plate were input as a function of time for use as temperature boundary conditions on the mold surfaces. A variable interface heat transfer coefficient between the metal and the mold was assumed and this same interface condition was used for all castings.

Table II lists the casting conditions for plates II-1 through II-5 along with calculated local solidification times, estimated times the castings spent above the eutectoid temperature ( $1125^{\circ}\text{C}$ ), and average cooling rates through the  $\alpha+\gamma$  region of the TiAl binary phase diagram as defined by the nominal Al level. Calculated cooling curves for the centers of cast plates II-1 through II-5 are shown in Figure 1. Table II and Figure 1 clearly show that a range of cooling rates were achieved. Solidification times ranged from approximately 5 to 25 seconds and cooling rates through the  $\alpha+\gamma$  phase region ranged from approximately 0.25 to  $40^{\circ}\text{C/s}$ . Note that the kinetics of solidification and subsequent solid state cooling rates for

casting II-5 were markedly slower than those for castings II-1 through II-4.

### Macrostructural Examination

As-cast macrostructures for each of the plates (I-1 and II-1 through II-5) are presented in Figure 2, showing sections through the entire plate thicknesses. Grain morphologies were columnar over the range of cooling rates which were achieved. Moreover, cooling rate influenced the scale of the columnar macrostructure both at the surface and in the interior of the cast plates, with faster cooling conditions producing finer columnar grains. Mold preheat influenced the size of surface grains, with low mold preheats producing fine surface grains and high mold preheats producing large surface grains. Mold insulation influenced internal grain size, and to a lesser extent surface grain size. With the exception of the slowest cooled plate (II-5), all plates exhibited pronounced center-line macroporosity.

Columnar grain widths were measured for different distances from the cast surfaces using a linear intercept method. Columnar grain widths, plotted as a function of the normalized distance across the plate thickness are shown in Figure 3. [Note: the normalized distances 0, 0.5 and 1 represent the surface, center and opposite surface of the casting, respectively.] The plate thickness for I-1 was approximately three times that of plates II-1 through II-5. Qualitatively, the morphology of the chill zone and subsequent development of the columnar zone in I-1 resembles that of II-3 (See Figure 3). The wider range of columnar grain widths in I-1 is attributed to

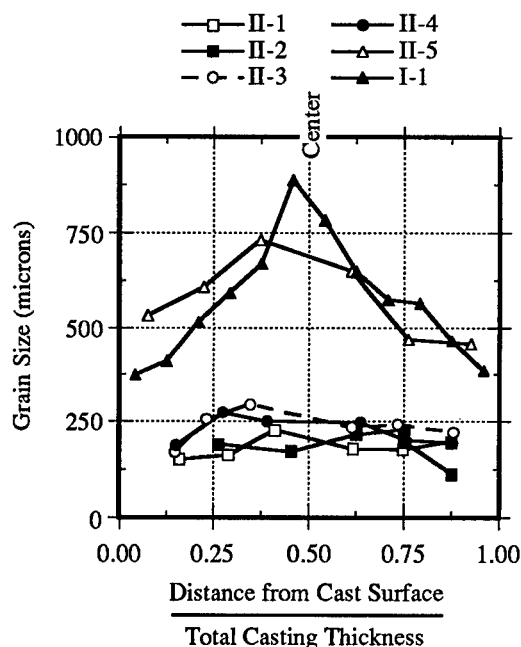


Figure 3. Columnar grain width as a function of normalized plate thickness for casting I-1 and II-1 through II-5.

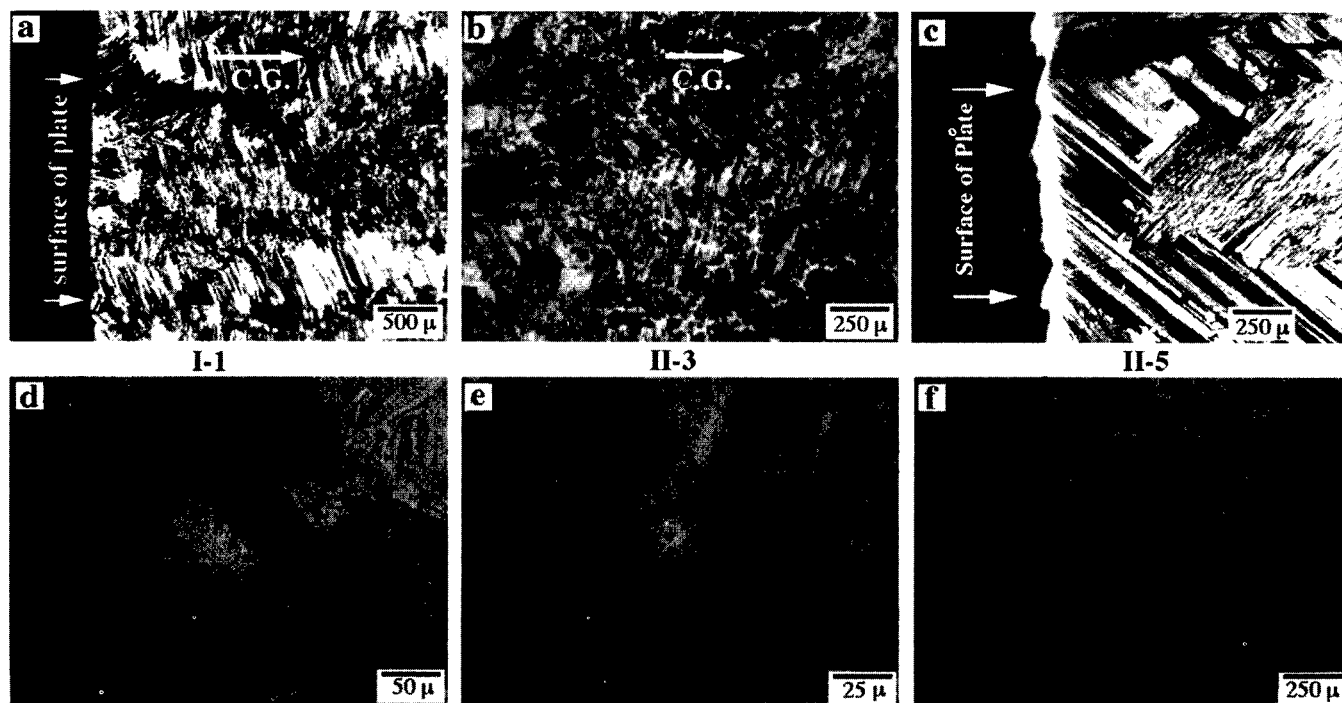


Figure 4. Optical micrographs from plates I-1, II-3 and II-5: (a, b, c) sections taken parallel to the columnar growth directions of I-1, II-3, and II-5, respectively and (d, e, f) sections taken perpendicular to the columnar growth directions of I-1, II-3, and II-5, respectively. Columnar growth directions (C.G.) and plate surface normals are indicated. [Note the different magnifications on the photomicrographs.]

the larger section thickness which presumably takes longer to solidify, providing more time for competitive growth between grains and a corresponding increase in columnar grain width with distance from the mold wall.

#### Optical Microscopy

Optical micrographs from castings I-1, II-3, and II-5 are presented in Figure 4. Figure 4(a) - 4(c) show sections taken parallel to the columnar growth directions in castings I-1, II-3, and II-5, respectively. Figures 4(d) - 4(f) show sections taken perpendicular to the columnar growth direction in the same castings, respectively.

Lamellar grains were observed within the original columnar grains for all cooling rates examined. The secondary lamellar grains appeared to be elongated in the columnar growth direction. Photomicrographs of the most slowly cooled plate (II-5), Figures 4(c) and 4(f), when compared with the columnar grain width measurements for the most slowly cooled plate presented in Figure 3, show approximately equal lamellar and columnar grain widths. However, the lamellar grain widths in the faster cooled plates (I-1 and II-3), Figures 4(a) and 4(d) and 4(b) and 4(e), were much smaller than the corresponding columnar grain widths.

Lamellar orientations with respect to the cast surface appeared to be influenced by the cooling rate. Lamellar orientations in the slowest cooled plate, II-5, tended to be inclined at large angles to the cast surface, often near  $45^\circ$  (Figure 4c); whereas lamellar orientations in the faster cooled plates tended to be oriented approximately parallel to the cast surface and perpendicular to the columnar growth direction (Figures 4a and 4b). Preliminary texture analyses were conducted to explore the observed differences in lamellar orientations.

Texture measurements were conducted on samples of the as-cast and HIP'ed plates. The  $\{111\}\gamma$  pole figures from I-1 as-cast, I-1 HIP'ed and II-5 as-cast specimens are shown in Figure 5. The overall textures are somewhat spotty in nature, apparently due to the relatively coarse columnar grain sizes. As shown in Figure 5(a), the faster cooled I-1 plate exhibits a  $\{111\}\gamma$  texture parallel to the plane of the plate which is the plane perpendicular to the columnar growth direction. This texture showed a tendency to weaken slightly with the HIP'ing treatment. Conversely, the slow cooled plate II-5 exhibited no indication of a  $\{111\}$  texture, albeit with a coarser prior columnar grain size.

#### SEM, EPMA and Microsegregation

SEM-BSE micrographs from plates I-1, II-3 and II-5, taken approximately 1 mm from the cast surface in a plane parallel to the growth direction, are shown in Figure 6. Light regions in the micrographs represent dendrite cores. Although the dendrite morphologies could not always be clearly categorized, 4-fold dendrites were observed near the surface and interior of the plates, indicating that the BCC ( $\beta$ ) phase is likely to

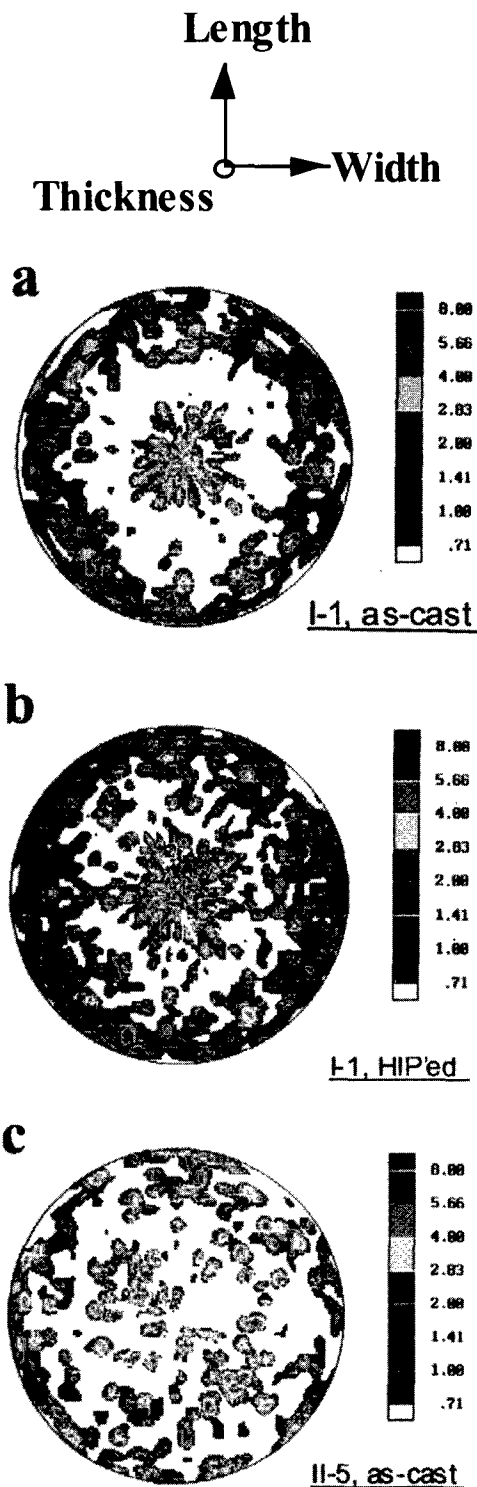


Figure 5.  $\{111\}$  texture maps for (a) I-1 as-cast, (b) I-1 HIP'ed [Pre-HIP @  $1093^\circ\text{C}$  / 5 hours; HIP @  $1205^\circ\text{C}$  / 170 MPa / 4 hours; Post-HIP @  $1205^\circ\text{C}$  / 2 hours / Fast Cool], and (c) II-5 as-cast



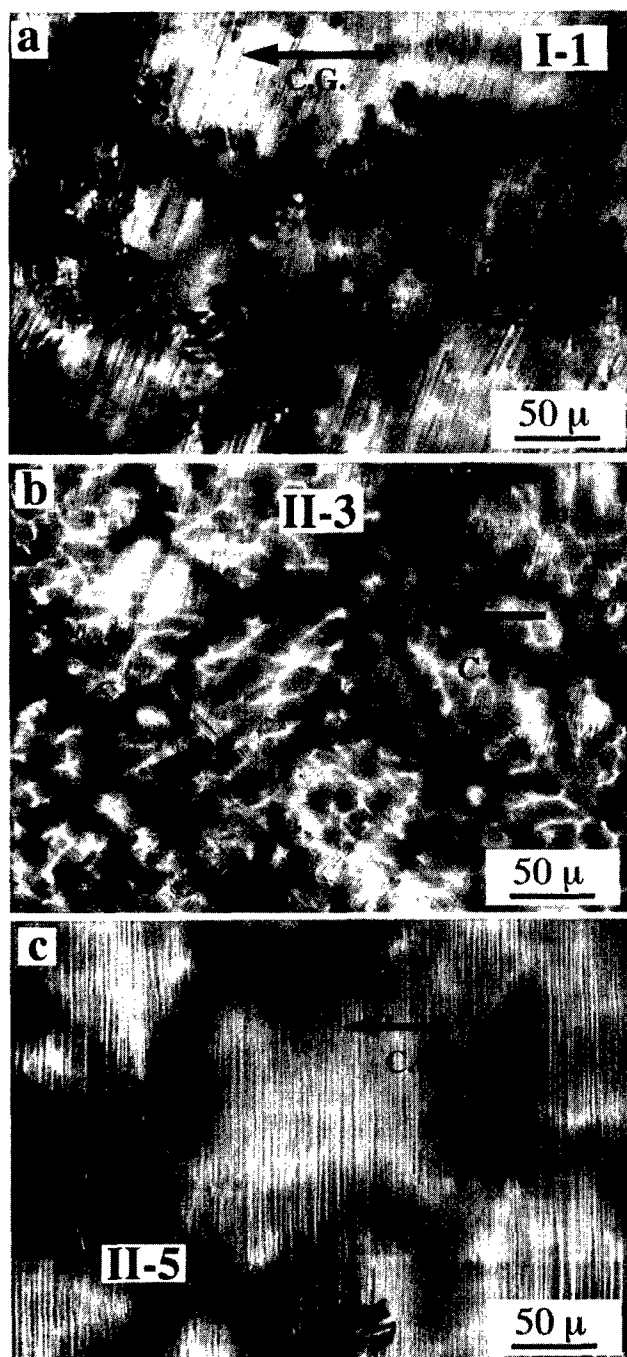


Figure 6. SEM-BSE micrographs from plates (a) I-1, (b) II-3, and (c) II-5.

solidify first. As expected, the scale of the dendrites varied with solidification time, with the longest solidification time, plate II-5, producing markedly coarsened dendrites.

Electron microprobe results from a near-surface section taken from plate I-1 are shown in Figure 7. This section was taken parallel to the cast surface to clearly reveal secondary dendrite arms. Scanned points traversing a secondary dendrite arm are shown in Figure 7a, and corresponding Ti and Al probe measurements are shown in Figure 7b. Electron microprobe

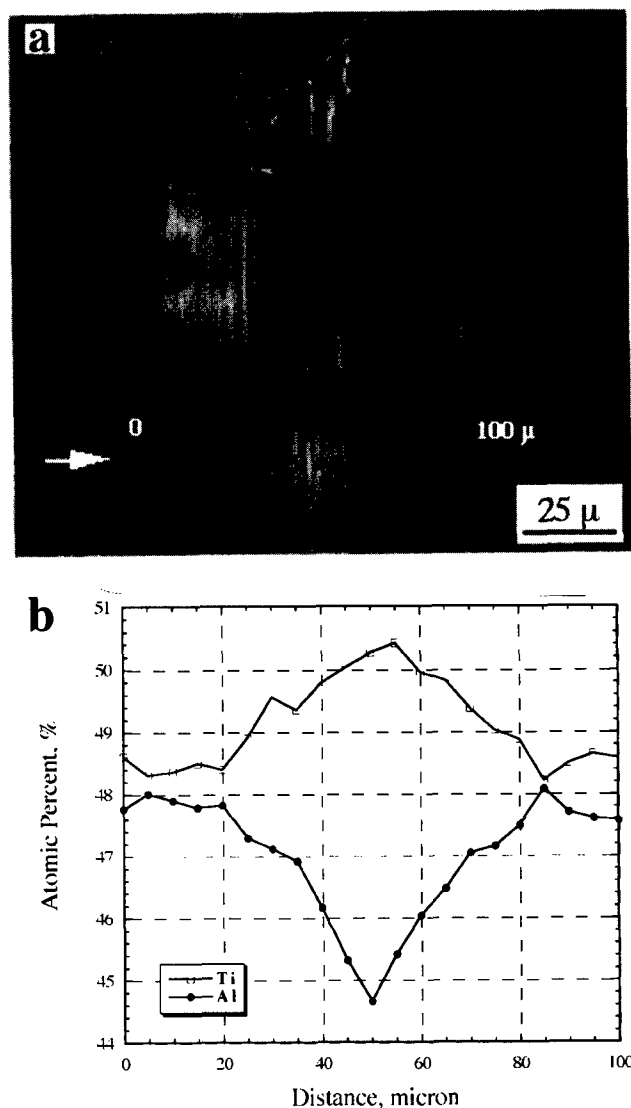


Figure 7. Electron microprobe results for I-1 showing (a) a backscattered image of the probed region (b) measured Ti and Al levels

results verified that the dendrite cores, light contrast regions, were enriched in Ti and depleted in Al. In this "faster" cooled sample, Al levels ranged from  $44.7 \pm 0.5$  at.% in the dendrite core to  $48.9 \pm 0.5$  at.% in the interdendritic regions. The Al levels in the dendrite cores agree with those reported by Larsen and Govern [10] for castings poured into molds with a 20°C mold preheat; however, Larsen and Govern reported higher Al levels in the interdendritic region than observed in this work. Based on the TiAl binary phase diagram, the minimum observed Al level of 44.7 at. % is not inconsistent with primary BCC ( $\beta$ )

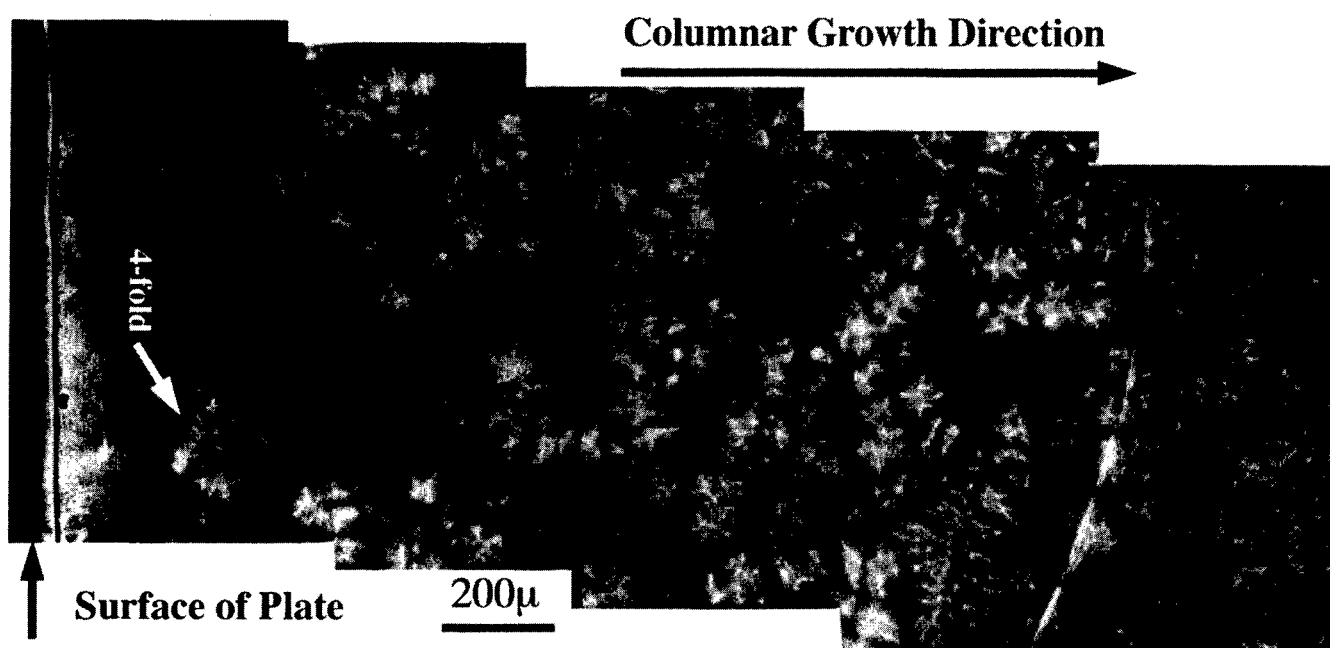


Figure 8. A montage of micrographs of plate I-1 showing a section parallel to the columnar growth direction

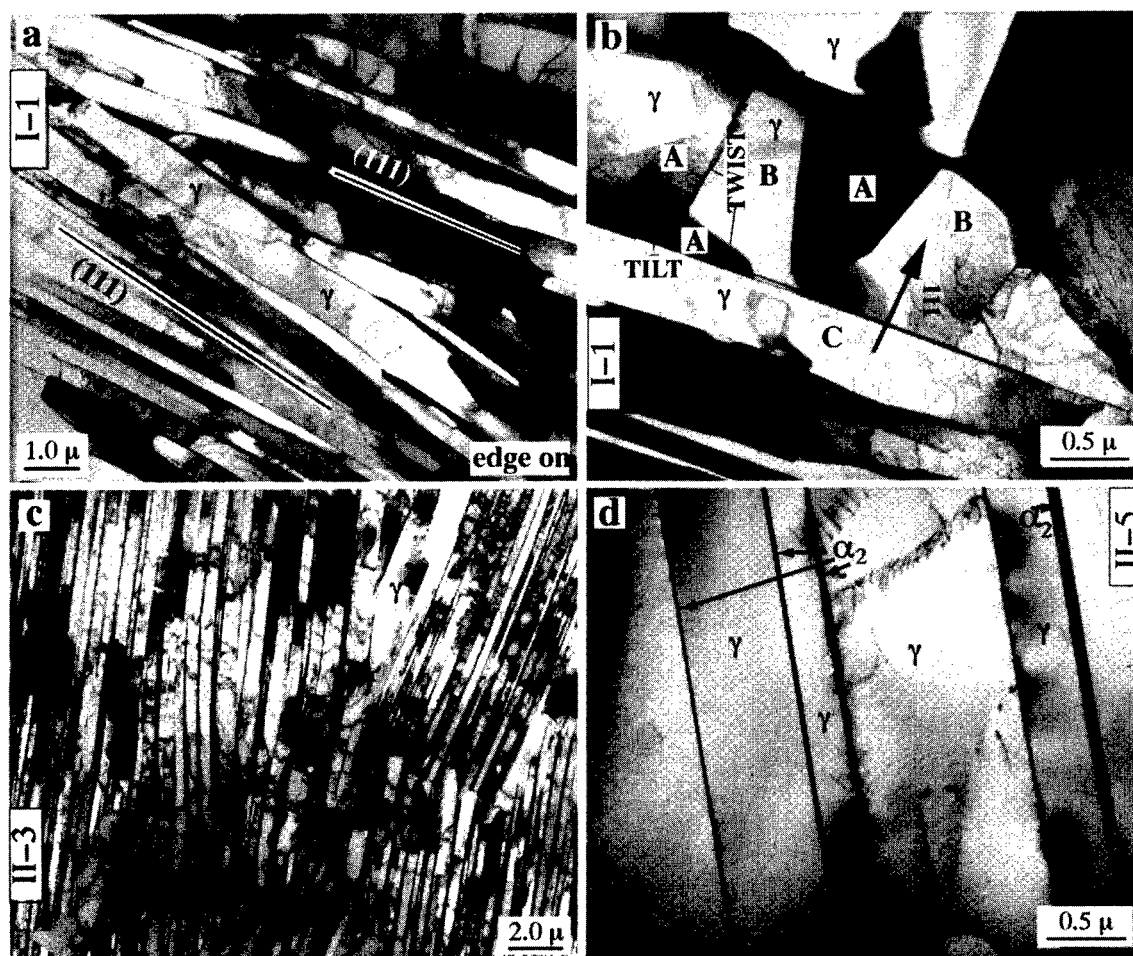


Figure 9. TEM bright field images from castings I-1, II-2, and II-5

phase solidification, and the addition of Cr and Nb should serve to further stabilize the BCC ( $\beta$ ) phase. Furthermore, an enrichment of Al in the interdendritic region is consistent with the partition coefficients of the binary TiAl phase diagram [9].

A montage of micrographs taken from casting I-1, which spans from the surface of the casting to a distance of approximately 3 mm into the casting along a longitudinal section taken parallel to the columnar growth direction, is shown in Figure 8. This micrograph approximately encompasses the width of a single columnar grain. In spite of the fact that columnar grains were observed across the range of cooling rates achieved, dendrites were not aligned with the columnar grains in this or any other section examined.

#### TEM Observations

Figure 9 presents TEM bright field (TEM-BF) micrographs from castings I-1, II-3 and II-5. The microstructure of the secondary grains in II-5, Figure 9(d), is composed of alternating lamellae of  $\alpha_2$  and  $\gamma$  phases, as is observed in a variety of Ti-Al alloys subjected to heat treatments in the  $\alpha$  phase field [1, 11 - 13]. However, the microstructures of plates I-1 and II-3, Figures 9(a) - 9(c), do not correspond to typical two phase  $\alpha_2 + \gamma$  microstructures. First, in most regions the microstructure consists of only  $\gamma$  phase plates without any  $\alpha_2$  phase separating the alternate lamellae. Secondly, the gamma variants do not develop with the commonly observed twin orientations, but are largely related by  $120^\circ$  rotational boundaries. Additionally, tilt and twist boundaries are frequently observed inside gamma plates, indicative of a sub-domain structure, Figure 9(b). The  $120^\circ$  rotational variants are identical to the  $90^\circ$  (about 'c' or 'a' axes of the  $L1_0$  structure) variants reported by Zhang *et al.* [14]. Furthermore, detailed electron diffraction observations have shown that the interface plane between the neighboring  $\gamma$  variants is slightly misoriented to the common (111) plane, Figure 9(a). The orientation of the average interfacial plane was determined to be  $3.5^\circ$  away from (111), by measuring the direction of the separation of diffraction spots, employing a technique due to Dahmen [15].

The angular misorientation between two groups of lamellae was determined (see Figure 9(a)) to be close to  $13^\circ$ . In this micrograph only one set of lamellar interfaces is in edge-on orientation (the bottom set). For the standard lamellar microstructure the sequence of phase transformations expected from the binary phase diagram cannot give rise to a misorientation angle of  $13^\circ$  between groups of lamellae. Thus the microstructure observed in plate I-1 represents a significant departure from the standard lamellar microstructure reported for many different TiAl alloys.

#### HIP'ed Microstructures

The microstructures of selected plates following HIP treatments are shown in Figures 10. Plate I-1 underwent a 5 hour pre-HIP treatment at  $1093^\circ\text{C}$ , a HIP treatment at  $1205^\circ\text{C}$  and 170 MPa for 4 hours, and a post-HIP treatment at  $1205^\circ\text{C}$  for 2 hours

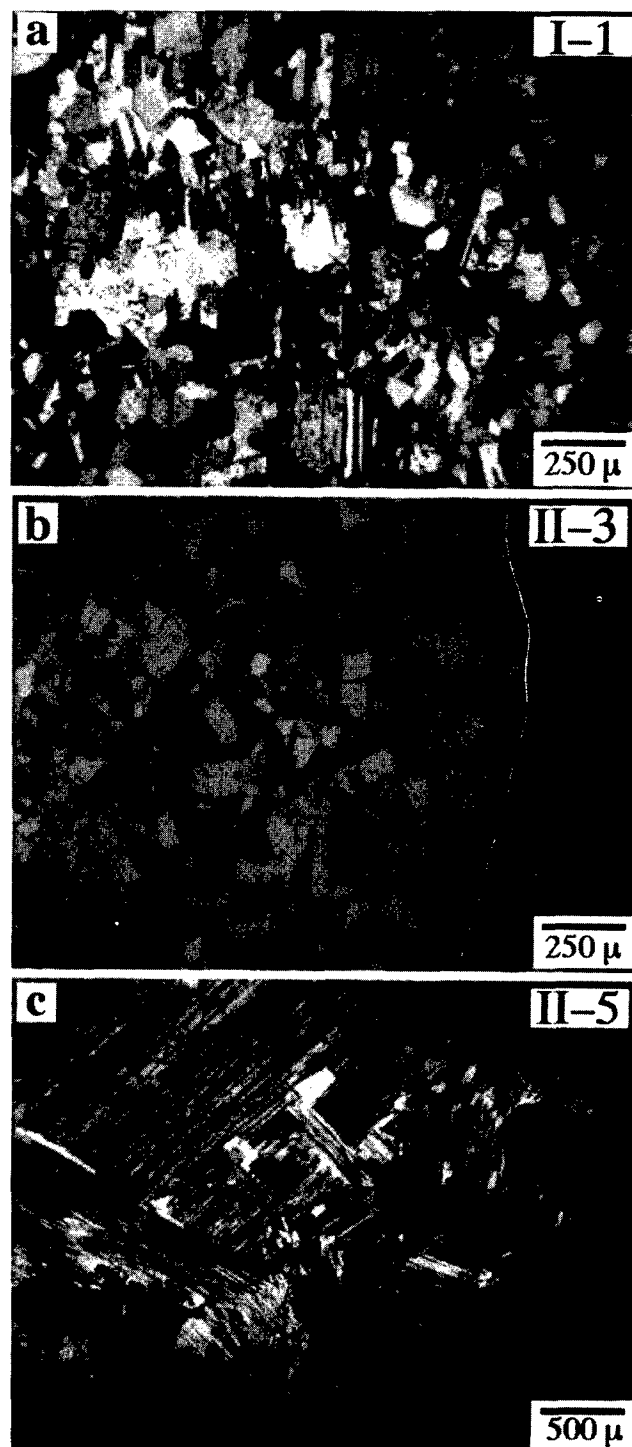


Figure 10. HIP'ed Microstructures: (a) I-1 following Pre-HIP @  $1093^\circ\text{C}$  / 5 hours; HIP @  $1205^\circ\text{C}$  / 170 MPa / 4 hours; Post-HIP @  $1205^\circ\text{C}$  / 2 hours / Fast Cool (b) II-3 following HIP @  $1260^\circ\text{C}$  / 170 MPa / 4 hours (c) II-5 following HIP @  $1260^\circ\text{C}$  / 170 MPa / 4 hours

followed by a fast cool. Plates II-3 and II-5 were given a HIP treatment at 1260°C and 170 MPa for 4 hours. For the rapidly cooled plates which contain no  $\alpha_2$  in the as-cast structure, the initial microstructures have decomposed to become equiaxed near- $\gamma$  in character, Figures 10(a) and 10(b). Conversely, the slower cooled material (from the same heat) subjected to the same HIP cycle retained its  $\gamma$  -  $\alpha_2$  lamellar character through the HIP cycle, Figure 10(c).

### Discussion

It is well known that  $\gamma$  -  $\alpha_2$  microstructures and corresponding mechanical properties of gamma titanium aluminide alloys are very sensitive to small variations in Al for a fixed heat treatment [1-3]. However, this study has shown that even for a fixed composition, profound differences in the evolution of microstructure result from variations in cooling rate during casting. Thus, considerable inhomogeneity in the as-cast and subsequently HIP'ed and heat treated structure of more complex-shaped castings could be expected if variations in cross-section result in significant variations in cooling rate.

Cooling rate influences the cast structure in two ways: through variations in the primary solidification structure and in subsequent solid state transformations that occur during cooling to room temperature. Several issues regarding the development of cast structure are discussed in more detail below.

### Cooling Rates and Macrostructure

Over the range of experimental conditions investigated, all castings solidified with columnar grain structures. It was not possible to directly measure melt superheat in the present (VAR) experiments, however, measurements of superheats for casting of TiAl alloys by other cold-crucible type processes suggest relatively low superheats [16]. Given the limited melt superheat in most cold crucible casting processes, the temptation exists to increase the mold preheat temperature to retain as much melt superheat as possible by minimizing the loss of melt superheat to the mold during filling. For this reason, the initial thermal conditions of the investment mold strongly influence the subsequent local solidification times, thermal gradients, solidification rates, and subsequent cooling rates of the solid. Even at low superheats and relatively high cooling rates, nucleation and growth of a substantial fraction of equiaxed grains does not occur during pouring and in subsequent solidification. This may suggest a reasonably high thermal gradient at the solidification front and/or an absence of a significant number of nucleants in the melt.

The variations in the scale of the dendritic structures are consistent with the variations in local solidification times (Figure 4). Sections normal to the columnar grain growth direction do show some indications of Ti-rich dendrites with four-fold symmetry that would seem to be indicative of primary  $\beta$  solidification. The expected growth direction of the cubic  $\beta$  phase would be  $\langle 001 \rangle$  parallel to the primary columnar grain

growth direction. However, no clear connection between the primary dendrite morphology and the columnar grain orientation could be established in this study.

### Development and Evolution of As-Cast Microstructure

Variations in cooling rate not only influenced the scale of the initial as-cast columnar structure, but also had a strong effect on the subsequent development of the final as-cast and HIP'ed microstructures.

For castings cooled at the slowest rate, the secondary lamellar grains were approximately of the same size and aspect ratio as the original columnar grains, suggesting that entire grains transformed to produce one set of parallel lamellae, independent of the microsegregation which existed on a finer scale. Under these conditions the lamellae were inclined at an angle of approximately 45° to the as-cast surface. As suggested by Kishida et. al [17], this lamellar orientation is consistent with the growth of  $\langle 001 \rangle$  oriented primary  $\beta$  grains and with the observation of 4-fold dendrites.

At the slowest cooling rate, the as-cast structure consisted of alternating lamellae of  $\alpha_2$  and  $\gamma$  phases, as is observed in a variety of Ti-Al alloys subjected to heat treatments in the  $\alpha$  phase field. According to the modeling estimate, the slow cooled plate experienced a total time of approximately 20 minutes above the eutectoid temperature. This slowly cooled lamellar structure had sufficient time to equilibrate during cooling of the casting, and consequently, the as-cast microstructure is largely unaffected by subsequent heat treatment in the  $\alpha$  +  $\gamma$  phase field. This finding is similar to that reported by Larsen and Govern [10]. It would appear then that in order to avoid relatively large lamellar colonies in cast and HIP'ed gamma, moderately high cooling rates during casting are required.

The lamellar structures that developed within the materials cooled at higher rates were markedly different than those observed in the most slowly cooled experiment. Multiple lamellar grains developed within the original columnar grains, and the lamellae within these grains were predominantly oriented parallel to the surfaces of the cast plates. The frequency with which this parallel orientation of the lamellae was encountered suggests that it is not likely to be produced by nucleation and growth of  $\langle 001 \rangle$  oriented columnar grains. In the faster cooled material the as-cast lamellar structure consisted predominantly of 120° rotational variants of the  $\gamma$  phase without any  $\alpha_2$  phase separating the alternate lamellae. Detailed electron diffraction observations also showed that the interface plane between the neighboring  $\gamma$  variants was not exactly equal to the common (111) plane, but misoriented by about 3.5°. The presence of a (111) texture in the faster cooled material was consistent with the observed orientations of the lamellae. These observations collectively suggest significant differences in the path by which these faster cooled microstructures developed, compared to the slower cooled material.

The development of the fast-cooled lamellar structure with {111} lamellar interfaces oriented normal to the columnar growth direction could occur if this structure evolved from [0001] alpha grains growing from either  $L \rightarrow \alpha$  or  $\beta + L \rightarrow \alpha$  transformations [17]. It is certainly possible that primary  $\alpha$  solidification is favored at higher solidification rates for the 47.9 at. % Al level of interest. However, the observed 4-fold dendritic morphologies indicate primary  $\langle 001 \rangle$  BCC  $\beta$  solidification. If  $\beta$  solidifies first, the  $\beta + L \rightarrow \alpha$  peritectic reaction may inhibit the growth of, and ultimately consume, the primary BCC ( $\beta$ ) phase. In this case, (111) gamma lamellae oriented normal to the columnar growth direction could only result if the peritectic  $\alpha$  phase grew in the [0001] direction. However, to date, there is insufficient experimental data to differentiate among these possible solidification and transformation paths. Further study of the development of as-cast microstructure in these faster cooled structures is in progress.

### Conclusions

1. During investment casting of Ti-48Al-2Cr-2Nb alloys, local solidification times and casting cooling rates are strongly influenced by the initial thermal conditions of the investment mold.
2. In as-cast Ti-48Al-2Cr-2Nb, columnar grain macrostructures develop for local solidification times that vary from approximately 5 to 25 seconds. Columnar grain width decreases with increasing cooling rate.
3. For the highest degree of mold preheat and insulation, corresponding to as-cast dwell times above the eutectoid temperature on the order of 20 minutes, secondary grains in the as-cast structure possess conventional  $\gamma$ - $\alpha_2$  lamellar structures due to slow cooling rates through the  $\alpha$  and  $\alpha+\gamma$  phase fields. These fully lamellar structures are very stable and persist through HIP treatments in the temperature range of 1200 - 1260°C.
4. For faster cooling rates during casting, secondary lamellar grains possess an unusual fully gamma lamellar structure, with significant deviations in orientation relationships between adjacent lamellae. During HIP treatments in the temperature range of 1200 - 1260°C, these decompose to conventional near  $\gamma$  duplex structures.
5. In order to avoid relatively large lamellar colonies in cast and HIP'ed gamma, moderately high cooling rates during casting are required.

### Acknowledgments

This research was funded by the AFOSR/PRET Program on Gamma Titanium Aluminides under Grant F49620-95-1-0359. The authors would like to acknowledge D. Larsen, K. Foran, S. Salter and M. Szczerbinski of the Howmet Corporation for providing access to casting facilities and chemical analyses of specimens, modeling property data, and assistance with casting experiments. We also wish to acknowledge S. McLeod of Pratt & Whitney Aircraft for providing thermophysical property data, D. Banerjee of UES for supplying a copy of ProCAST

software, and J. Bingert of Los Alamos National Laboratory for his assistance with texture measurements. C. Austin and M. Cannon of GE Aircraft Engines, are gratefully acknowledged for providing master ingots and for conducting EPMA analyses.

### References

1. Y-W. Kim, *JOM*, 46 (1994) 30.
2. S-C. Huang and J.C. Chesnut, 'Intermetallic Compounds Principles and Practice Vol: 2', ed. J.H. Westbrook and R.L. Fleischer, John Wiley & Sons, NY, 1995, 73-90.
3. C.M. Austin and T.J. Kelly, 'Gamma Titanium Aluminides', ed. Y-W. Kim, R. Wagner and M. Yamaguchi, TMS, Warrendale, PA, 1996, 21-32.
4. D. Davidson, 'Superalloys 1996', R.D. Kissinger, D.J. Deye, D.L. Anton, A.D. Cetel, M.V. Nathal, T.M. Pollock and D.A. Woodford, eds., TMS, Warrendale, PA, 1996, 545-553.
5. D.E. Larsen D.A. Wheeler and B. London, 'Processing and Fabrication of Advanced Materials III', ed. V.A. Ravi, T. Srivatsan and J.J. Moore, TMS, Warrendale, PA, 1994, 631-641.
6. L.L. Rishel, T. M. Pollock, A. W. Cramb and D.E. Larsen, 'Proc. of the International Symposium on Liquid Metal Processing and Casting', ed. A. Mitchell and P. Auburtin, Vacuum Metallurgy Division of AVS, 1997, 214-225.
7. M.J. Blackburn and J.C. Williams, *Trans. TMS-AIME*, 239 (1967) 287.
8. J.S. Kallend, U.F. Kocks, A.D. Rollett and H.R. Wenk, *Mater. Sci. Eng.*, A132 (1991) 1-11.
9. U. Kattner, J.C. Lin and Y.A. Chang, *Metall. Trans. A*, 23A (1992) 2081.
10. D.E. Larsen and C. Govern, 'Gamma Titanium Aluminides', ed. Y-W. Kim, R. Wagner and M. Yamaguchi, TMS, Warrendale, PA, 1995, 405-414.
11. M. Takeyama, T. Kumugai, M. Nakamura and M. Kikuchi, 'Structural Intermetallics I', ed. R. Darolia, J.J. Lewandowski, C.T. Liu, P.L. Martin, D.B. Miracle and M.V. Nathal, TMS-AIME, Warrendale, PA, 1993, 167-176.
12. M. Yamaguchi and Y. Umakoshi, *Progress in Materials Science*, 34 (1990) 1.
13. S.A. Jones and M.J. Kaufman, *Acta Metall. Mater.*, 41 (1993) 387.
14. X.D. Zhang, Y.G. Li, M.J. Kaufman and M.H. Loretto, *Acta Mater.*, 44 (1996) 3735.
15. U. Dahmen, 'Microstructure of Materials', ed. K.M. Krishnan, San Francisco Press, San Francisco, CA, 1993, 24.
16. A. Choudhury, M. Blum, H. Scholz and P. Busse, 'Proc. of the International Symposium on Liquid Metal Processing and Casting', ed. A. Mitchell and P. Auburtin, Vacuum Metallurgy Division of AVS, 1997, 226-236.
17. K. Kishida, D.R. Johnson, Y. Shimada, H. Inui, Y. Shirai and M. Yamaguchi, 'Gamma Titanium Aluminides', ed. Y-W. Kim, R. Wagner and M. Yamaguchi, TMS, Warrendale, PA, 1995, 219-229.

MECHANICAL BEHAVIOR AND MICROCRACK FORMATION  
IN  $\gamma$ -TiAl ALLOYS AS A FUNCTION OF STRAIN RATE AND TEMPERATURE

Zhe Jin<sup>1</sup>, George T. Gray III<sup>1</sup>, Young-Won Kim<sup>2</sup>, and Masaharu Yamaguchi<sup>3</sup>

<sup>1</sup> Los Alamos National Laboratory, Los Alamos, New Mexico 87545, U.S.A.

<sup>2</sup> UES Inc., Dayton, Ohio 45432, U.S.A.

<sup>3</sup> Kyoto University, Sakyo-ku, Kyoto 606, Japan

Abstract

The mechanical behavior and microcrack formation of a polysynthetically twinned (PST) TiAl crystal and a fine-grained duplex  $\gamma$ -TiAl alloy were studied as a function of strain rate, ranging from  $0.001 \text{ s}^{-1}$  to  $2500 \text{ s}^{-1}$ , and temperature, from  $-196^\circ\text{C}$  to  $1200^\circ\text{C}$ . The yield stress of the PST-TiAl crystal was found to exhibit a positive-concave-up dependence upon the lamellar interface tilting angle ( $\Phi$ ) with a minimum at  $\Phi=45^\circ$  at high-strain rates. The yield stress of the duplex  $\gamma$ -TiAl alloy showed two distinct yield stress-temperature dependencies at temperatures  $>600^\circ\text{C}$ : an anomalous temperature dependence for strain rates  $>1 \text{ s}^{-1}$  and a negative temperature dependence for strain rates  $<1 \text{ s}^{-1}$ . Three temperature regimes of plastic flow behavior were identified for the duplex  $\gamma$ -TiAl alloy. Translamellar microcracks in the PST-TiAl crystals were identified to be mode-I cracks while the interlamellar microcracks were seen to be a mixture of mode-II and mode-III. Grain interior microcracks observed in duplex  $\gamma$ -TiAl alloy are formed by shear displacement while grain boundary microcracks are formed by the strain mismatch between grains and grain boundary deformation.

Introduction

Gamma-TiAl alloys have received tremendous attention in the past decade for high temperature and high performance structural applications, primarily due to their low density, high strength to weight ratio, and good creep and oxidation resistance. Studies of PST-TiAl crystals under monotonic

tensile or compressive loading at quasi-static strain rates [1-8] have shown that the yield stress of PST-TiAl crystals exhibits a positive-concave-up dependence upon the lamellar interface tilting angle ( $\Phi$ ) with a minimum at  $\Phi=45^\circ$  [1,2,4]. Similar dependence of yield and flow stresses upon the tilting angle  $\Phi$  has been observed under cyclic loading [9]. The mechanical response of polycrystalline  $\gamma$ -TiAl alloys has been studied by numerous researchers [10-18]. The anomalous temperature dependence of the yield stress has been found to depend on grain size for single-phase  $\gamma$ -TiAl alloys [10-12,17], i.e., only the large-grained alloys exhibit the anomalous yield stress-temperature dependence [12,17]. The anomalous temperature dependence of the yield strength is ascribed to the Kear-Wilsdorf type blocking mechanisms of superdislocations [19]. While the anomalous temperature dependence of the yield stress in Ti-rich ( $\gamma+\alpha_2$ ) two-phase TiAl alloys is ascribed to twin intersections and dislocation jog pinning mechanisms [14,20]. However, a limited number of studies have probed the dynamic stress-strain behavior of  $\gamma$ -TiAl alloys to date [21-24].

The fracture behavior and toughening mechanisms of  $\gamma$ -TiAl alloys have been intensively studied including fracture behavior of PST-TiAl crystals under both monotonic and cyclic loading conditions [2,9,25-27], fracture behavior and toughening mechanisms of two-phase  $\gamma$ -TiAl alloys under various microstructures, strain rates, temperatures and environments [23,28]. However, the details of microcrack nucleation and propagation mechanisms in  $\gamma$ -TiAl alloys remain unclear. The object of this study is to systematically

examine the mechanical behavior and microcrack formation mechanisms in  $\gamma$ -TiAl alloys. Coincident examination of PST-TiAl and a fine-grained polycrystalline  $\gamma$ -TiAl alloy allows direct comparisons to probe the influence of grain structure and lamellar orientation on mechanical response.

### Experimental Procedure

Two  $\gamma$ -TiAl alloys, a polysynthetically twinned (PST) TiAl crystal and a fine-grained duplex  $\gamma$ -TiAl alloy, were used in this study. A PST-TiAl crystal was grown at Kyoto University, Japan, using an optical floating zone furnace. The nominal composition of the PST crystal was Ti-49.3Al (at.%). The fine-grained duplex  $\gamma$ -TiAl alloy with a nominal composition of Ti-46.5Al-2Cr-3Nb-0.2W (at.%) was made by the induction scull melting (ISM) and casting method at Duriron Co., Dayton, Ohio. The 25 kg ingot having a 7.1 cm diameter was HIP'ed in argon atmosphere at 1260°C/172MPa for 4 hrs. The fine-grained duplex microstructure was obtained by a two step forging process to a total reduction of 91% followed by annealing at 1270 °C for 3 hrs plus furnace-cooling to 900 °C and then air-cooling to room temperature at UES, Inc., Dayton, Ohio. The average grain size was  $\sim 10 \mu\text{m}$ .

Rectangular specimens,  $3 \times 3 \times 5 \text{ mm}^3$  in dimension, were cut from the as-grown PST-TiAl crystals in  $\Phi < \bar{1}10 >$  orientations such that the lamellar interfaces of the PST crystals were tilted  $\Phi$  degrees to the loading axis about the  $< \bar{1}10 >$  direction in the lamellar interface. The lamellar interface tilting angle  $\Phi$  was selected to be  $0^\circ$ ,  $22.5^\circ$ ,  $45^\circ$ ,  $67.5^\circ$  and  $90^\circ$ . Cylindrical specimens 5 mm in diameter by 6 mm in height were made from the duplex  $\gamma$ -TiAl alloys. Compressive mechanical tests were performed at a strain rate of  $2500 \text{ s}^{-1}$  and temperatures of  $25^\circ\text{C}$  and  $800^\circ\text{C}$  for the PST-TiAl crystals and at strain rates of  $0.001 \text{ s}^{-1}$ ,  $0.1 \text{ s}^{-1}$ ,  $35 \text{ s}^{-1}$ ,  $2000 \text{ s}^{-1}$  and temperatures from  $-196^\circ\text{C}$  to  $1200^\circ\text{C}$  for the duplex  $\gamma$ -TiAl alloy. High strain rate ( $2000 \text{ s}^{-1}$  to  $2500 \text{ s}^{-1}$ ) tests were conducted using a Split-Hopkinson Pressure Bar [29]. For microcrack observations, deformed specimens were mechanically polished and examined, with and without etching the polished sample surfaces, using optical microscopy.

### Results

#### Stress-Strain Curves

Compressive true stress-true strain curves for the PST-TiAl crystal at  $2500 \text{ s}^{-1}$  are shown in Fig. 1 (a) for  $25^\circ\text{C}$  and (b) for  $800^\circ\text{C}$ . The oscillating stress-strain curves are a result of elastic wave dispersion in the pressure bars. Taking an average of each stress-strain curve, we can see that the flow stress increases linearly with strain. The stress-strain curves are more or less parallel to each other for each temperature. The work hardening rate at  $800^\circ\text{C}$  is seen to be twice the work hardening rate at  $25^\circ\text{C}$ , i.e., 3000 MPa for  $800^\circ\text{C}$  and 1500 MPa for  $25^\circ\text{C}$ , respectively. As the strain increases, the difference in the flow stress between these two temperatures decreases due to the higher work hardening rate at  $800^\circ\text{C}$ .

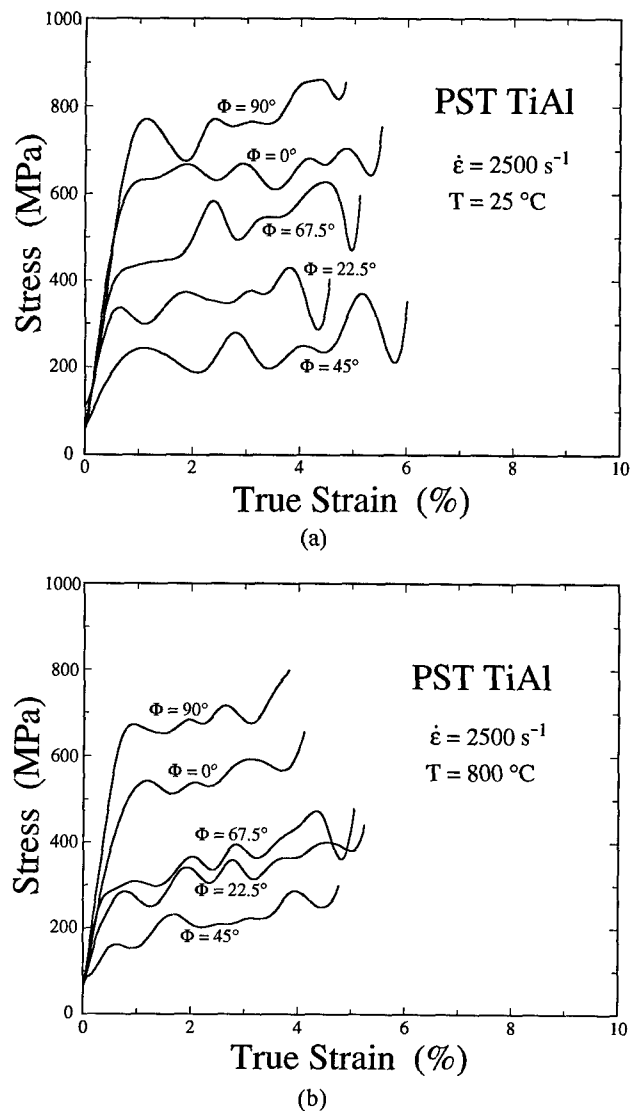


Fig. 1 True stress-true strain curves of PST-TiAl crystal at  $2500 \text{ s}^{-1}$  (a) for  $25^\circ\text{C}$  and (b) for  $800^\circ\text{C}$ .

The stress-strain curves of the fine-grained duplex  $\gamma$ -TiAl at  $0.001 \text{ s}^{-1}$  for temperatures from  $-196^\circ\text{C}$  to  $1200^\circ\text{C}$  are shown in Fig. 2 (a). Three distinctive temperature regimes are identified in terms of the stress-strain behavior in Fig. 2 (a): 1) The low temperature regime at temperatures below  $800^\circ\text{C}$ , where the flow stress exhibits a nearly-linear increment with strain up to the fracture point; 2) The intermediate temperature regime at temperatures between  $800^\circ\text{C}$  and  $<1100^\circ\text{C}$ , where the flow stress quickly reaches the saturation stage with increasing strain; 3) The high temperature regime at temperatures  $\geq 1100^\circ\text{C}$ , where the stress-strain curves are completely flat, following the initial softening stage after yield. The stress-strain behavior at temperatures from  $25^\circ\text{C}$  to  $600^\circ\text{C}$  is seen to be nearly insensitive to temperature. Similarly, three temperature regimes are observed at the intermediate strain rates of  $0.1 \text{ s}^{-1}$  and  $35 \text{ s}^{-1}$ . The low temperature regime, however, is extended to a higher

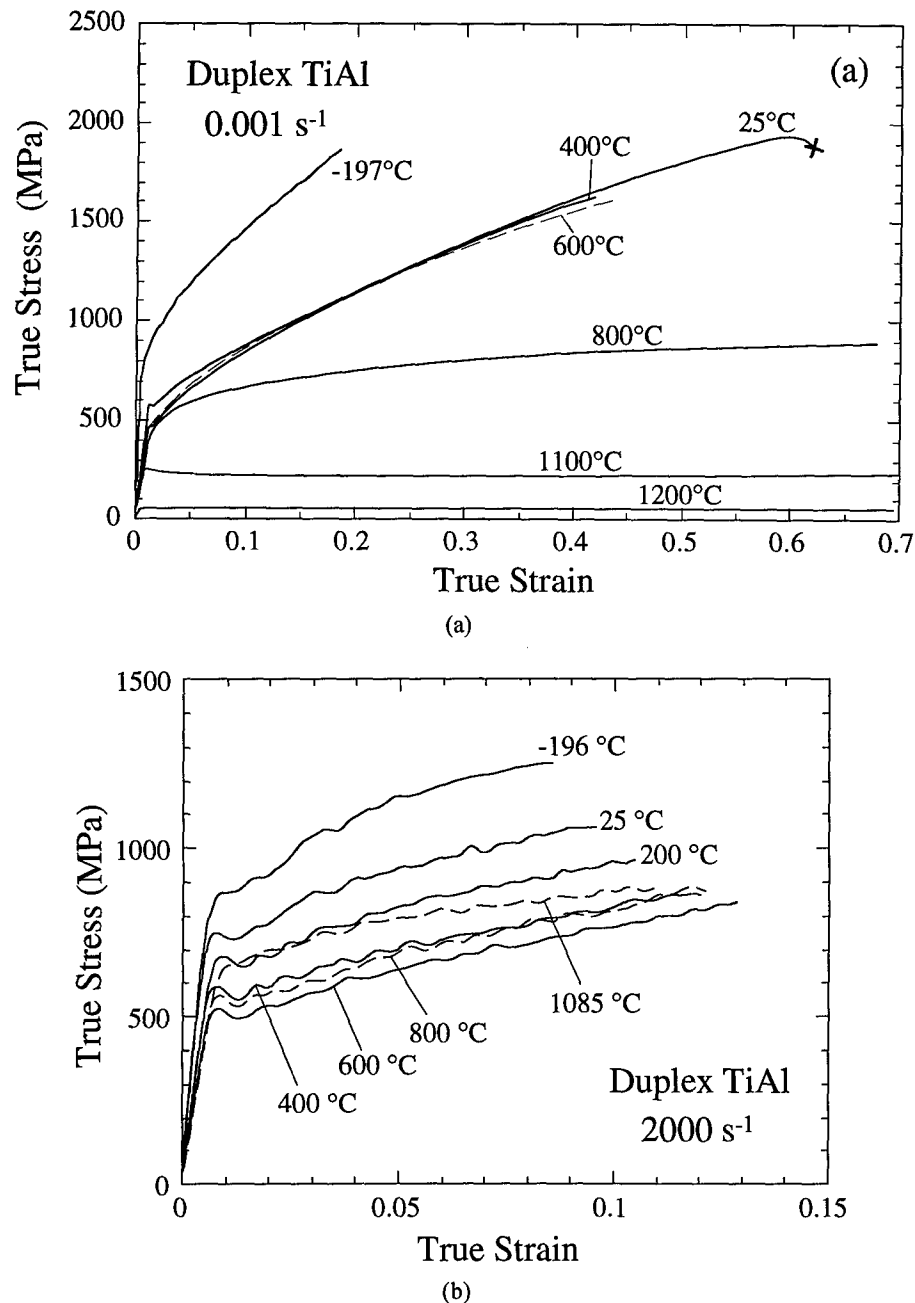


Fig. 2 True stress-true strain curves of a fine-grained duplex  $\gamma$ -TiAl (a) at  $0.001 \text{ s}^{-1}$  and (b) at  $2000 \text{ s}^{-1}$ .

temperature of  $900^\circ\text{C}$ ; Consequently, the intermediate and high temperature regimes in stress-strain behavior are shifted to temperatures between  $1000^\circ\text{C}$  and  $1100^\circ\text{C}$  and temperatures  $\geq 1200^\circ\text{C}$ , respectively. Due to the limitation of the length of this manuscript, the stress-strain curves for  $0.1 \text{ s}^{-1}$  and  $35 \text{ s}^{-1}$  are given elsewhere [30]. At  $2000 \text{ s}^{-1}$ , all the stress-strain curves are more or less parallel to each other except for the  $1085^\circ\text{C}$  curve which is slightly separate from the others (Fig. 2 (b)). Since the maximum temperature tested was  $1085^\circ\text{C}$  at  $2000 \text{ s}^{-1}$ , the intermediate and high

temperature regimes observed at strain rates  $\leq 35 \text{ s}^{-1}$  are not seen in Fig. 2 (b).

#### Yield and Flow Stresses

The yield stress of the PST-TiAl crystal exhibits a strong dependence upon the lamellar interface tilting angle  $\Phi$  at  $2500 \text{ s}^{-1}$  for both  $25^\circ\text{C}$  and  $800^\circ\text{C}$  (Fig. 3). Because of the inaccuracies in the stress-strain curves at the yield point at high strain rate (see Fig. 1), the flow stresses at 1.5% strain are used in Fig. 3. The yield stress of the PST-TiAl crystal shows



a positive-concave-up dependence upon the angle  $\Phi$ , i.e., the yield stress is large at  $\Phi=0^\circ$  and  $90^\circ$  and minimum at  $\Phi=45^\circ$ . The yield stress at  $25^\circ\text{C}$  is slightly larger than that at  $800^\circ\text{C}$ , which is independent of the  $\Phi$  angle (Fig. 3).

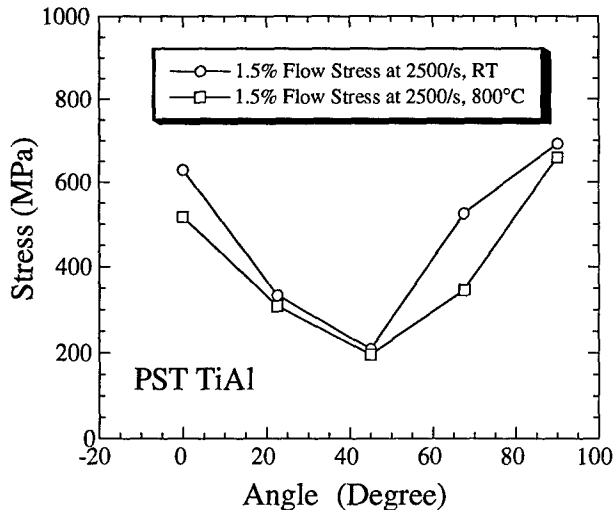


Fig. 3 Yield stress of a PST-TiAl crystal as a function of lamellar interface tilting angle.

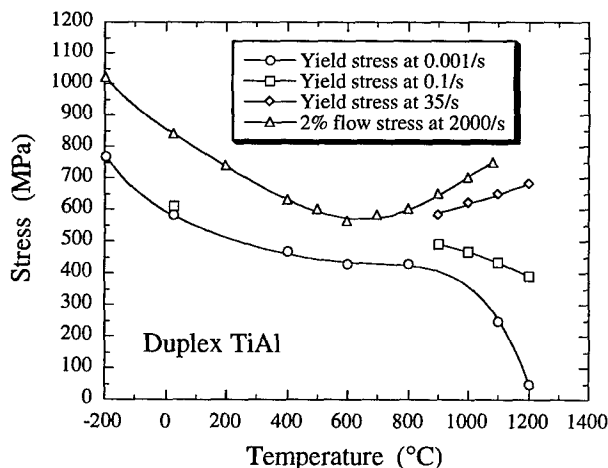


Fig. 4 Yield stress of fine-grained  $\gamma$ -TiAl alloy as a function of temperature.

The temperature dependence of the yield stress ( $\sigma_{0.2}$ ) of the fine-grained  $\gamma$ -TiAl alloy at different strain rates is shown in Fig. 4, where the flow stress at 2% true strain is used at  $2000\text{ s}^{-1}$  due to the same reasons described above. The yield stress of this fine-grained  $\gamma$ -TiAl alloy exhibits two distinctive temperature dependencies at temperatures above  $600^\circ\text{C}$ : At strain rates of  $35\text{ s}^{-1}$  and  $2000\text{ s}^{-1}$ , the yield stress exhibits a strong positive (anomalous) temperature dependence, while at strain rates of  $0.001\text{ s}^{-1}$  and  $0.1\text{ s}^{-1}$ , the yield stress shows a negative (normal) temperature dependence. At temperatures below  $600^\circ\text{C}$ , the yield stress decreases continuously with temperature for all strain rates

(Fig. 4), suggesting that the strain rate dependence of the yield stress is similar at temperatures below  $600^\circ\text{C}$ . At temperatures above  $600^\circ\text{C}$ , the strain rate dependence of the yield stress becomes significant, particularly at high temperatures.

The temperature dependence of the flow stress at low temperatures is found to be similar to that of the yield stress for the fine-grained  $\gamma$ -TiAl alloy: the flow stress decreases with increasing temperature. The temperature dependence of the flow stress at 10% true strain at high temperatures is different for the different strain rates (Fig. 5). The significant anomaly in the yield stress-temperature dependence at high strain rates (Fig. 4) no longer exists in the flow stress-temperature dependence (Fig. 5). At  $35\text{ s}^{-1}$ , the flow stress even decreases with temperature for temperatures above  $900^\circ\text{C}$ .

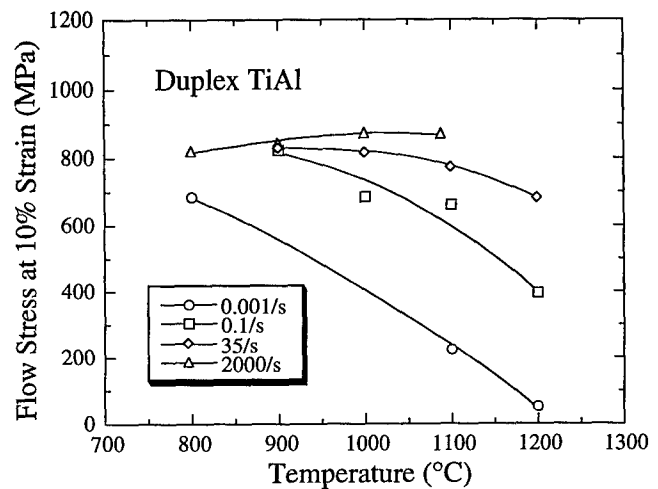


Fig. 5 Flow stress of fine-grained  $\gamma$ -TiAl alloy as a function of temperature.

#### Microcracking Behavior

Two types of microcracks are observed in PST crystals which were deformed at  $25^\circ\text{C}$ : translamellar microcracks formed within lamellar laths with certain angles to the lamellar interfaces and interlamellar microcracks formed along lamellar interfaces. Fig. 6 (a) shows these two types of microcracks observed on a sample surface perpendicular to the lamellar interface tilting axis for the  $45^\circ < \bar{1}10 >$  oriented specimen deformed at  $25^\circ\text{C}$  and  $2500\text{ s}^{-1}$ . The translamellar microcracks in Fig. 6 (a) are  $45^\circ$  to the lamellar interface, which does not change with tilting angle  $\Phi$  from  $22.5^\circ$  to  $67.5^\circ$ . Fig. 6 (b) shows the sample surface parallel to both the interface tilting axis and the loading axis, where both translamellar and interlamellar microcracks are parallel to the lamellar interfaces. Microcracks were found to start to form at a relatively small strain, for instance, microcracks were seen in the  $45^\circ < \bar{1}10 >$  oriented PST-TiAl specimen deformed to 2% true strain at  $2500\text{ s}^{-1}$  and  $25^\circ\text{C}$ . The number of microcracks was observed to increase with strain, however, no propagation or very little propagation of existing microcracks was observed with increasing strain to 20% in this  $45^\circ < \bar{1}10 >$  oriented PST-TiAl specimen. Fracture of the specimens was found to occur

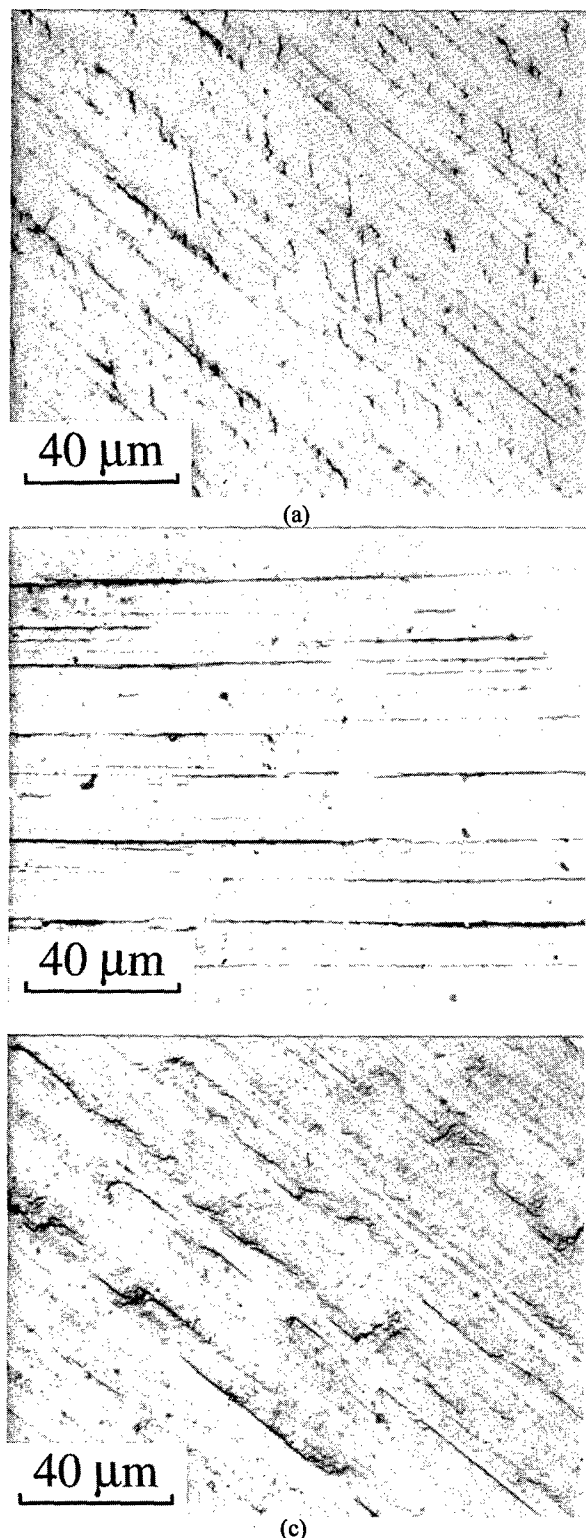


Fig. 6 Microcracks observed in PST-TiAl crystals deformed at  $2500 \text{ s}^{-1}$  (a) and (b) for  $25^\circ\text{C}$  and (c) for  $800^\circ\text{C}$ . (a) and (c) are sample surfaces perpendicular to the interface tilting axis, (b) the sample surface parallel to both the interface tilting and loading axes.

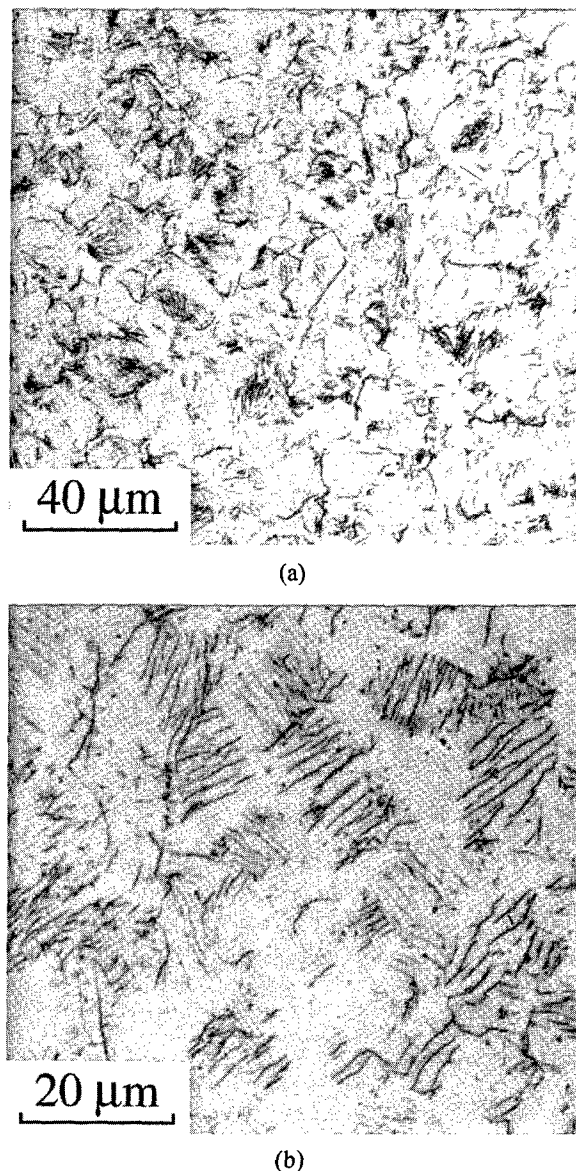


Fig. 7 Microcracks observed in fine-grained duplex  $\gamma$ -TiAl alloy deformed (a) at  $0.001 \text{ s}^{-1}$  and  $600^\circ\text{C}$  and (b) at  $2000 \text{ s}^{-1}$  and  $-196^\circ\text{C}$ . (a) is a cross section and (b) a longitudinal section of specimens.

by propagation of one or two major (or macroscopic) cracks which were formed during the last few percents of total strain to failure. The morphology of translamellar microcracks observed at  $800^\circ\text{C}$  and  $2500 \text{ s}^{-1}$  is completely different from that observed at  $25^\circ\text{C}$ , see Fig. 6 (c). Translamellar microcracks at  $800^\circ\text{C}$  formed either within a lamellar lath or near a lamellar interface. Most translamellar microcracks are located at/near domain boundaries (Fig. 6 (c)).

For the duplex  $\gamma$ -TiAl alloy, similar to the PST-TiAl crystals, two types of microcracking behavior were found following deformation (Fig. 7 (a)): grain interior microcracks and grain boundary microcracks. The grain interior microcracks are

normally parallel to each other and restricted within individual grains, i.e., none of the grain interior microcracks are seen to cross grain boundaries even at relatively large strains (for instance, 70%). The number of microcracks and the ratio of grain interior microcracks to grain boundary microcracks changes with strain, strain rate and temperature. The grain interior microcracks are found to be dominant at low temperatures. As the temperature increases grain boundary microcracks become significant. The distribution of both types of microcracks becomes more uniform at higher strain rates and/or higher temperatures. Although grain boundary microcracks exhibit no specific orientation relationships to the external loading axis, grain interior microcracks were most frequently observed on planes  $45^\circ$  to the loading axis (Fig. 7(b)). Grain boundary microcracks are also seen to preferentially form at grain boundaries of grains having no grain interior microcracks (Fig. 7(a)).

### Analysis and Discussion

#### Mechanical Behavior

Work hardening rate ( $\theta = \partial\sigma/\partial\epsilon$ ) calculations for the fine-grained duplex  $\gamma$ -TiAl alloy indicate the same three temperature regimes as seen from the stress-strain curves in Fig. 2 are operative. The ratio,  $M^2G/\theta$  (where  $G$  is the shear modulus  $G = (70390 - 0.0141T)$  MPa [31],  $M$  is the Taylor factor and  $\theta$  is the work hardening rate) ranges from 130 MPa to 390 MPa for the low temperature regime, from 1800 MPa to 3000 MPa for the intermediate temperature regime, and essentially infinity for the high temperature regime for the fine-grained  $\gamma$ -TiAl. This result indicates that the stress-strain response of this fine-grained duplex  $\gamma$ -TiAl alloy corresponds to approximately stage-II work hardening for FCC metals in the low temperature regime and stage-III work hardening in the intermediate temperature regime, respectively. The PST-TiAl crystals are considered to reflect material response between single crystals and polycrystals with respect to their Taylor factor since PST-TiAl crystals have six variant domains and lamellar interfaces. Thus the shear modulus normalized work hardening rate for the PST-TiAl crystals at  $2500 \text{ s}^{-1}$  should be between 47 MPa and 440 MPa at  $25^\circ\text{C}$  and between 24 MPa and 225 MPa for  $800^\circ\text{C}$ , respectively. These values are similar to those for the fine-grained duplex  $\gamma$ -TiAl alloy in the low temperature regime, where the stress-strain responses are dominated by stage-II work hardening. This finding supports the utility of comparing PST-TiAl and polycrystalline  $\gamma$ -TiAl behavior on a normalized Taylor factor basis to determine dominant  $\gamma$  deformation behavior in contrast to that dominated via geometrical reasons.

The strain rate sensitivity for the fine-grained duplex  $\gamma$ -TiAl alloy was calculated to be  $>0.3$  at  $1100^\circ\text{C}$  and  $1200^\circ\text{C}$  for deformation at  $0.001 \text{ s}^{-1}$ . This suggests that deformation of this fine-grained  $\gamma$ -TiAl alloy at high temperatures and  $0.001 \text{ s}^{-1}$  is most likely dominated by grain boundary sliding (GBS) [32] due to the small grain size ( $\sim 10 \mu\text{m}$  in diameter) and the high deformation temperatures;  $>0.75T_m$  ( $T_m = 1450^\circ\text{C}$ ). This argument is consistent with superplasticity studies on duplex  $\gamma$ -TiAl alloys reported in

the literature [33-37] where GBS was the dominant deformation mode. However, the zero work hardening for the  $0.1 \text{ s}^{-1}$  and  $35 \text{ s}^{-1}$  strain rates can not be interpreted in terms of a GBS argument since the strain rate sensitivity is  $<0.1$  at  $1200^\circ\text{C}$  for these two strain rates. The zero work hardening at  $0.1 \text{ s}^{-1}$  and  $35 \text{ s}^{-1}$  and high temperatures can be ascribed to grain boundary weakening and grain boundary deformation. At  $1200^\circ\text{C}$ , the grain boundary strength is weakened such that deformation occurs dominantly at and/or near the grain boundaries. Grain boundary diffusion is fast at high temperatures such that it can quickly recover the accumulated dislocations at grain boundaries during deformation. As the strain rate decreases, grain boundary diffusion plays a more and more important role during deformation such that diffusion controlled GBS dominates deformation at  $0.001 \text{ s}^{-1}$  and temperatures  $\geq 1100^\circ\text{C}$ . The grain size of this alloy is found to remain unchanged following deformation at all temperatures. This indicates that no appreciable dynamic recrystallization occurred during deformation at any strain rates and temperatures. Accordingly, mechanisms controlling the plastic flow behavior in this fine-grained  $\gamma$ -TiAl alloy are summarized in Fig. 8.

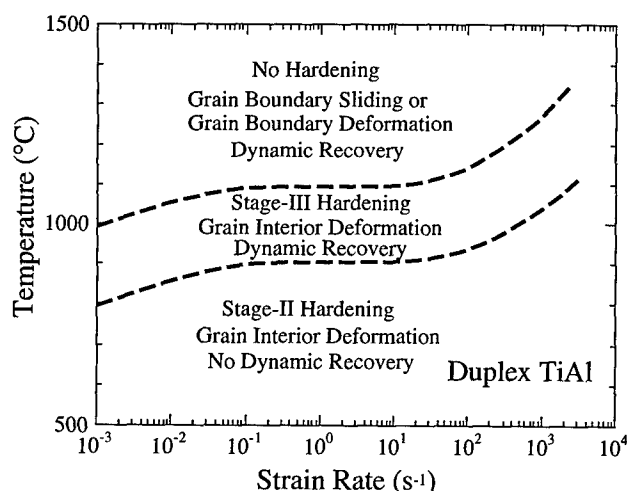


Fig. 8 Mechanisms of plastic flow behavior for a fine-grained duplex  $\gamma$ -TiAl alloy.

The negative temperature dependence of the yield stress in the fine-grained  $\gamma$ -TiAl alloy shown in Fig. 4 is ascribed to an increase in thermally activated dislocation slip with increasing temperature. The increment in the yield stress with temperature above  $600^\circ\text{C}$  at strain rates of  $35 \text{ s}^{-1}$  and  $2000 \text{ s}^{-1}$  can be interpreted using a dislocation-jog pinning mechanism proposed in  $\gamma$ -TiAl [20]. At high temperatures, some  $\frac{1}{2}\langle 111 \rangle$  screw dislocation line segments lying in the primary  $\{111\}$  slip plane can be thermally activated to cross-slip onto a conjugate  $\{111\}$  slip plane. Under external loading, the dislocation lines in the conjugate  $\{111\}$  slip plane will glide on the primary  $\{111\}$  slip plane with a certain planar spacing to the primary slip plane where the uncross-slipped dislocation lines glide. Jogs are thereby formed between the uncross-slipped and cross-slipped dislocation lines. The jogs are edge dislocations which are able to slip on conjugate slip planes. The jog-pinned dislocation configurations along

screw dislocations have been found to be common deformation microstructures in  $\gamma$ -TiAl alloys tested at high strain rates [22,24]. As temperature increases, the propensity for dislocation cross-slip onto conjugate slip planes increases and thus the probability of jogs formed along dislocation lines increases. Dislocation slip accordingly becomes more difficult at higher temperatures, resulting in a rising yield strength with temperature beyond 600 °C at 35 s<sup>-1</sup> and 2000 s<sup>-1</sup> in this fine-grained  $\gamma$ -TiAl.

The jog-pinning effect on dislocation slip becomes weaker as strain rate decreases, because edge dislocations are able to climb with the assistance of diffusion in the lattice and along grain boundaries at low strain rates. Because grain boundary diffusion is much larger than lattice diffusion and the grain size of the current alloy is small (~10  $\mu$ m), grain boundary diffusion should be an effective contributor to dislocation climb, in particular, at/near grain boundaries. In addition, grain boundaries become weaker at high temperatures such that deformation will more likely occur at/near grain boundaries at high temperatures. Thus the yield strength of this fine-grained  $\gamma$ -TiAl alloy is determined by a competition between two processes as temperature increases at low strain rates: One is a jog formation process which increases with increasing temperature such that it should strengthen the alloy; the second is a jog-dislocation climb process which also increases with increasing temperature but which should weaken the alloy. Whether the yield stress increases or not with increasing temperature thus depends on which process dominates. The strain rates of 35 s<sup>-1</sup> and 2000 s<sup>-1</sup> are so fast that there is no time for climb to take place. Thus the yield strength of this alloy at 35 s<sup>-1</sup> and 2000 s<sup>-1</sup> is controlled by the jog pinning process, resulting in an increase in the yield stress with increasing temperature (Fig. 4). At 0.001 s<sup>-1</sup> and 0.1 s<sup>-1</sup>, however, jog climb increasingly plays a role during deformation as the temperature increases because of diffusion; particularly grain boundary diffusion at high temperatures. Thus the yield stress increment due to dislocation pinning is compensated or depressed by jog climb at high temperatures and low strain rates. The yield stress plateau observed at temperatures between 600 °C and 800 °C at 0.001 s<sup>-1</sup> indicates that these two processes are balanced at intermediate temperatures. When the temperature is higher than 800 °C, jog climb is fast enough that dislocation pinning no longer plays a dominant role in the deformation. Similarly, the reduction in the anomaly of the stress-temperature dependence with increasing strain (compare Fig. 5 with Fig. 4) is ascribed to adiabatic heating during the high-rate deformation. This is consistent with the flow softening observed in Ti-48Al-2.5Nb-0.3Ta and Ti-48Al-2Nb-2Cr two  $\gamma$ -TiAl alloys when the alloys were deformed in the two-phase  $\alpha$ + $\gamma$  phase field [38].

The positive-concave-up dependence of the yield stress upon the lamellar tilting angle is similar to that observed at quasi-static strain rates [1,2]. The yield stress at high strain rates, however, is ~200 MPa greater than that at quasi-static strain rates. The strong  $\Phi$  angle dependence of the yield stress in this study is ascribed to the strong blocking effect of the lamellar interfaces on the strain transition across the lamellar

interface and the difference in the resolved shear stress on the dominant twin variants at different  $\Phi$  angles [2,24].

### Microcrack Formation

Translamellar microcracks have been found to form 45° to the lamellar interface on the sample surface perpendicular to lamellar interface tilting axis (Fig. 6 (a)) and parallel to the lamellar interface on the sample surface parallel to both the interface tilting axis and the loading axis (Fig. 6 (b)). According to the known crystallographic orientations of these two sample surfaces, the habit plane for translamellar microcracks is determined to be {44  $\bar{1}$ } for domains having a [ $\bar{1}$  10], or [0  $\bar{1}$  1] or [10  $\bar{1}$ ] tilting axis and {811} for domains having a [1  $\bar{1}$  0], or [01  $\bar{1}$ ] or [ $\bar{1}$  01] tilting axis. Since the orientations of domains where microcracks are formed are not determined in this study, an unambiguous determination of habit planes for individual translamellar microcracks shown in Fig. 6 (a) is impossible. However, a recent study of high-rate deformation microstructure in PST-TiAl crystals [24,39] has shown that domains with a [ $\bar{1}$  10] tilting axis are minimally deformed following 7% strain at 3000 s<sup>-1</sup>. This suggests that the deformation of PST-TiAl crystals is heterogeneous even within the same lamellar lath such that the translamellar microcracks observed in this study might be preferentially formed in domains having a [ $\bar{1}$  10] tilting axis, due to the lack of strain accommodation in these domains. It is well known that the deformation of a soft-mode-oriented PST-TiAl crystal is primarily carried out by a shear strain parallel to the lamellar interface. Thus the internal stress built-up by the strain mismatch between domains in the soft-mode-oriented PST-TiAl crystals should be a shear stress parallel to the lamellar interface. Accordingly, the formation of translamellar microcracks observed in this study can be speculated to be due to the tensile stress resolved from this internal strain-mismatch-induced shear stress since habit plans for these translamellar microcracks are coincident with the tensile principal plan of the shear stress. In addition, habit plans of these translamellar microcracks are also consistent with the tensile principal plan of the external loading for  $\Phi=45^\circ$ . Thus, translamellar microcracks observed in this study are most probably formed by the tensile stress, i.e., translamellar microcracks in this study are mode-I type cracks. For crystals oriented away from  $\Phi=45^\circ$ , it can still be speculated that translamellar microcracks are formed by the same strain-mismatch-induced shear stress with an assistance of external loading since the tensile principal plan of the external loading is not coincident with the microcrack habit plans in these crystal orientations. Accordingly, we can make an argument that translamellar microcracks observed in this study are formed primarily by the internal strain-mismatch-induced shear stress although a more systematic study is needed to further support this hypothesis.

When a PST-TiAl crystal is deformed in the  $45^\circ < \bar{3}21 >$  orientation where the tilting axis is  $< \bar{3}21 >$ , two different translamellar microcracks are observed [40]. However, one of these two translamellar microcracks is observed to form 45° to the lamellar interface on the sample surface perpendicular to lamellar interface tilting axis of  $< \bar{3}21 >$  and parallel to the lamellar interface on the sample surface parallel to both the interface tilting axis and the loading axis which is exactly the

same as those observed in this study. Thus the formation of this translamellar microcrack in the  $45^\circ\langle\bar{3}21\rangle$  oriented PST-TiAl crystals can be also ascribed to the principal tensile stress resulting from the internal strain-mismatch between domains. However, the habit planes for the translamellar microcracks in the  $45^\circ\langle\bar{3}21\rangle$  oriented PST-TiAl crystals are different from those determined in this study where the tilting axis is  $\langle\bar{1}10\rangle$ . Thus the indexes of habit planes of translamellar microcracks depend on the lamellar interface tilting axis but the geometric relation of crack habit planes to the lamellar interface is independent of the tilting axis. This indicates that the habit planes of the translamellar microcracks observed in this study depend on the local stress state rather than the energetic preference of individual crystallographic planes, thus habit planes of translamellar microcracks in the soft-mode-oriented PST-TiAl crystals depend on the PST crystal orientation.

According to the similar analysis above, the formation of interlamellar microcracks is ascribed to the shear stress resulting from the strain mismatch between domains across lamellar interfaces plus a shear stress resolved from the external loading.

At 800 °C, most translamellar microcracks are formed at/near domain boundaries (Fig. 6). This indicates that translamellar microcracks at 800 °C are formed due to strain mismatch between domains within the lath. The absence of completely cleavage type translamellar microcracks at 800 °C indicates that PST-TiAl crystals are less brittle at 800 °C for dynamic loading. The interlamellar microcracks observed at 800 °C are similar to those observed at 25 °C, indicating they are formed by a similar mechanism.

Fig. 7 (b) shows that grain interior microcracks in the fine-grained  $\gamma$ -TiAl occurs mostly on planes  $45^\circ$  to the loading axis. This indicates that the grain interior microcracks observed in this study are most likely formed by shear displacement on particular crystallographic planes having a maximum resolved shear stress. The parallelism of grain interior microcracks within each grain also indicates that grain interior microcracks are formed by shear displacement on a single microscopic crystallographic plane in each grain. Thus the formation of grain interior microcracks for polycrystalline TiAl is more likely controlled by the external loading, which is similar to the interlamellar microcracks in PST-TiAl crystals. However, grain boundary microcracks exhibit no specific orientation relationships to the external loading axis. Grain boundary microcracks are also seen to preferentially form at grain boundaries of grains having no grain interior microcracks (Fig. 7 (a)). Thus the grain boundary microcracks are most likely formed due to the lack of strain accommodation across the grain boundaries where the grains are heavily deformed. At least one of the grains on a grain boundary should be oriented in such a direction that this grain is able to deform to a large strain without nucleation of grain interior microcracks. Grain boundary microcracks should also be formed due to large grain-boundary deformations at high temperatures.

### Conclusions

1. The yield stress of PST-TiAl crystals shows a positive concave-up dependency upon the lamellar interface tilting

angle  $\Phi$  at both 25 °C and 800 °C for dynamic loading. The yield stress of a fine-grained duplex  $\gamma$ -TiAl exhibits two distinct temperature dependencies at temperatures  $>600$  °C: the strong anomalous (positive) temperature dependency of the yield stress for strain rates  $>1\text{ s}^{-1}$  and the normal (negative) temperature dependency of the yield stress for strain rates  $<1\text{ s}^{-1}$ . At temperatures  $<600$  °C, the yield stress decreases with temperature for all strain rates.

2. The plastic flow behavior of fine-grained duplex  $\gamma$ -TiAl is characterized into three regimes: 1) stage-II work hardening in the low temperature regime, 2) stage-III work hardening in the intermediate temperature regime and 3) zero work hardening with GBS or grain boundary deformation in the high temperature regime. The mechanical behavior of PST-TiAl is found to be controlled by stage-II work hardening under the strain rates and temperatures applied in this study. This is consistent with that observed in fine-grained duplex  $\gamma$ -TiAl. No occurrence of dynamic recrystallization was observed in both PST-TiAl and fine-grained duplex  $\gamma$ -TiAl under any of the testing conditions.

3. Translamellar and interlamellar microcracks were observed in the soft-mode-oriented ( $\Phi=22.5^\circ\text{--}67.5^\circ$ ) PST-TiAl crystals at 25 °C under dynamic loading. Translamellar microcracks were seen to be mode-I type and interlamellar microcracks a mixture of mode-II and mode-III. A similar microcracking behavior was observed in fine-grained duplex  $\gamma$ -TiAl under all deformation conditions: grain interior microcracks and grain boundary microcracks. However, the formation of microcracks in fine-grained duplex  $\gamma$ -TiAl seems to be dominated by shear displacement for both grain interior microcracks and grain boundary microcracks.

4. The habit plane for translamellar microcracks in the  $22.5^\circ\text{--}67.5^\circ\langle\bar{1}10\rangle$  oriented PST-TiAl crystals was determined to be  $\{44\bar{1}\}$  for domains having a  $[\bar{1}10]$ , or  $[0\bar{1}1]$  or  $[10\bar{1}]$  tilting axis and  $\{811\}$  for domains having a  $[1\bar{1}0]$ , or  $[01\bar{1}]$  or  $[\bar{1}01]$  tilting axis. The habit plane for grain interior microcracks in fine-grained duplex  $\gamma$ -TiAl was not determined due to the lack of individual grain orientation information. However, grain interior microcracks were seen to be normally parallel to each other within individual grains and inclined  $\sim 45^\circ$  to the external loading axis. No any specific orientation relationships between grain boundary microcracks and external loading axis were observed. However, grain boundary microcracks were seen to preferentially form at grain boundaries of grains having no grain interior microcracks. Grain interior microcracks dominate at low temperatures while grain boundary microcracks become significant at high temperatures.

### Acknowledgments

The authors acknowledge R.W. Carpenter II and M. Lopez for their help with the mechanical tests. This work was performed under the auspices of the U.S. Department of Energy. One of the authors (YWK) acknowledges support from the U.S. Air Force Wright-Laboratory Materials Directorate under contract No. F33615-91-C-5663.

## References

1. T. Fujiwara, A. Nakamura, M. Hosomi, S.R. Nishitani, Y. Shirai, and M. Yamaguchi, Phil. Mag. A, 61 (1990), 591.
2. H. Inui, M.H. Oh, A. Nakamura, and M. Yamaguchi, Acta Metall., 40 (1992), 3095.
3. P.A. Beaven, F. Appel, B. Dogan, and R. Wagner, Ordered Intermetallics-Physical Metallurgy and Mechanical Behavior, ed. C.T. Liu, R.W. Cahn and G. Sauthoff (Dordrecht: Kluwer Academic Publishers, 1992), 413.
4. Y. Umakoshi, T. Nakano, and T. Yamane, Mater. Sci. Eng., A152 (1992), 81.
5. Y. Umakoshi, and T. Nakano, Acta Metall., 41 (1993), 1155.
6. F. Appel, and R. Wagner, Defect-Interface Interactions, ed. E.P. Kvam, A.H. King, M.J. Mills, T.D. Sands and V. Vitek (Pittsburgh, PA: MRS, 1994), 279.
7. H. Inui, K. Kishid, M. Misaki, M. Kobayashi, Y. Shirai, and M. Yamaguchi, Phil. Mag. A, 72 (1995), 1609.
8. K.-F. Yao, H. Inui, K. Kishida, and M. Yamaguchi, Acta Metall., 43 (1995), 1075.
9. H.Y. Yasuda, T. Nakano, and Y. Umakoshi, Phil. Mag. A, 71 (1995), 127; 73 (1996), 1035; 73 (1996), 1053.
10. H.A. Lipsitt, D. Shechtman, and R.E. Schafrik, Metall. Trans. A, 6A (1975), 1991-1996.
11. S.C. Huang, Scripta Metall., 22 (1988), 1885-1888.
12. P.P. Rao, and K. Tangri, Mat. Sci. & Eng., A132 (1991), 49-59.
13. Y-W Kim, Acta Metall., 40 (1992), 1121-1134.
14. M.A. Morris, Phil. Mag. A, 69 (1994), 129-150.
15. D.G. Morris, S. Gunter, and M. Leboeuf, Phil. Mag. A, 69 (1994), 527-550.
16. B. Viguier, K.J. Hemker, J. Bonneville, F. Louchet, and J.-L. Martin, Phil. Mag. A, 71 (1995), 1295-1312.
17. S. Sriram, V.K. Vasudevan, and D.M. Dimiduk, Mat. Sci. & Eng., A192/193 (1995), 217-225.
18. A. Bartels, C. Koeppe, T. Zhang, and H. Mecking, Gamma Titanium Aluminides, ed. Y-W Kim, R. Wagner and M. Yamaguchi (Warrendale, PA: TMS, 1995), 655-663.
19. B.A. Greenberg, O.V. Antonova, V.N. Indenbaum, L.E. Karkina, A.B. Notkin, M.V. Ponomarev, and L.V. Smirnov, Acta Metall., 39 (1991), 233-242.
20. B. Viguier, M. Cieslar, K.J. Hemker, and J.L. Martin, High-Temperature Ordered Intermetallic Alloys VI, ed. J.A. Horton, I. Baker, S. Hanada, R.D. Noebe and D.S. Schwartz (Pittsburgh, PA: MRS, 1995), 653-658.
21. G.T. Gray III, Microstructure/Property Relationships in Titanium Aluminides and Alloys, ed. Y-W Kim and R.R. Boyer (Warrendale, PA: TMS, 1991), 263-274.
22. S.A. Maloy, and G.T. Gray III, Acta Metall., 44 (1996), 1741-1756.
23. Z. Jin, C. Cady, G.T. Gray III, and Y-W Kim, Deformation and Fracture of Ordered Intermetallic Materials, ed. W.O. Soboyejo, T.S. Srivatsan and H.L. Fraser (Warrendale, PA: TMS, 1996), in press.
24. Z. Jin, G.T. Gray III, and M. Yamaguchi, Phil. Mag. A, submitted, (1997).
25. M.H. Oh, H. Inui, M. Misaki, and M. Yamaguchi, Acta Metall., 41 (1993), 1939-1949.
26. Y. Umakoshi, H.Y. Yasuda, and T. Nakano, Mater. Sci. Eng., A192/193 (1995), 511-517.
27. S. Yokoshima, and M. Yamaguchi, Acta Metall., 44 (1993), 873-883.
28. K.S. Chan, and Y-W Kim, Metall. Trans. A, 23A (1992), 1663-1677; 24A (1993), 113-125; 25A (1994), 1217-1228.
29. P.S. Follansbee, The Metals Handbook, vol. 8 (Metals Park, OH: American Society for Metals, 1985), 198.
30. Z. Jin, C. Cady, G.T. Gray III, and Y-W Kim, Metall. Trans. A, submitted (1997).
31. R.E. Schafrik, Metall. Trans. A, 8A (1977), 1003-1006.
32. J.W. Edington, K.N. Melton, and C.P. Cutler, Prog. in Mater. Sci., 21 (1976), 61-158.
33. R.M. Imayev, O.A. Kaybyshev, and G.A. Salishchev, Phys. Met. Metallogr., 70 (1990), 179-186.
34. S.C. Cheng, J. Wolfenstine, and O.D. Sherby, Metall. Trans. A, 23A (1992), 1509-1513.
35. R.M. Imayev, V.M. Imayev, and G.A. Salishchev, J. Mater. Sci., 27 (1992), 4465-4471.
36. T. Tsuzuku, and H. Sato, J. Phys., IV, 3 (1993), 389-395.
37. H.S. Yang, W.B. Lee, and A.K. Mukherjee, Structural Intermetallics, ed. R. Darolia, J.J. Lewandowski, C.T. Liu, P.L. Martin, D.B. Miracle and M.V. Nathal (Warrendale, PA: TMS, 1993), 69-76.
38. S.L. Semiatin, N. Frey, S.M. El-Soudani, and J.D. Bryant, Metall. Trans. A, 23A (1992), 1719-1735.
39. Z. Jin, G.T. Gray III, and M. Yamaguchi, High-Temperature Ordered Intermetallic Alloys VII, ed. C.C. Koch, C.T. Liu, N.S. Stoloff and A. Wanner (Pittsburgh, PA: MRS, 1995), in press.
40. Z. Jin, and G.T. Gray III, unpublished research.

## MICROSTRUCTURE EVOLUTION IN GAMMA TITANIUM ALUMINIDES CONTAINING BETA-PHASE STABILIZERS AND BORON ADDITIONS

Madangopal Krishnan,<sup>1</sup> Bharath Natarajan,<sup>1</sup> Vijay K. Vasudevan<sup>1</sup> and Dennis M. Dimiduk<sup>2</sup>

<sup>1</sup>Dept. of Materials Science and Engineering, University of Cincinnati, Cincinnati, OH 45221-0012

<sup>2</sup>Wright Laboratories, Materials Directorate, WPAFB, Dayton, OH 45433

### Abstract

Phase transformations and microstructure evolution in Ti-47Al-2Cr-2Nb-1Mo-(0-0.2)B (in at.%) alloys were studied. The microstructures of the alloys in the as-cast, as-forged and heat treated conditions were characterized by optical, scanning and transmission electron microscopy. Analysis of the as-cast microstructures of the alloys indicates that the solidification and solid-state transformation pathway was:  $L \rightarrow L+\beta \rightarrow \alpha + \beta$  cores  $\rightarrow$  lamellar ( $\alpha+\gamma$ ) +  $\beta$  cores  $\rightarrow$  lamellar ( $\alpha_2+\gamma$ ) + B2 cores. In the alloys with boron, ribbon-like borides that have formed directly in the liquid are also present. The presence of the  $\beta$  phase and additions of boron are found to have complex, but somewhat different effects on transformations and microstructure development during cooling from the high temperature  $\alpha+\beta$  or  $\alpha$  regions. Boron has the dramatic effect of restricting  $\alpha$  grain growth, of promoting the lamellar  $\gamma$  morphology and lamellar growth rate and of suppressing the non-lamellar/feathery/massive  $\gamma$  mode of transformation. On the other hand, in the boron-free alloy, the feathery/massive  $\gamma$  morphologies are favored over the lamellar morphology. In addition, the  $\beta$  phase forms as a thick continuous film along the prior  $\alpha$  grain boundaries and is in association with several orientational variants of the  $\gamma$  phase. The  $\beta$  is found to be enriched in Cr and Mo and to transform to B2. With boron additions, the amount of the  $\beta$ /B2 phase reduces to where it is mainly present as particles enriched in Cr and Mo along prior  $\alpha$  grain boundaries. In all cases the borides were determined to be  $TiB_2$  and found to contain thin, interleaving layers of the B2 phase which have the following orientation relationship: (100) B2 // (10 $\bar{1}$ 0)  $TiB_2$ , [001]B2 // [0001]  $TiB_2$ . Based on the results obtained, the effects of the alloying additions on transformation pathways, modes, kinetics and microstructure are discussed.

### Introduction

Gamma ( $\gamma$ )-TiAl based alloys are considered as promising materials for high temperature aerospace applications because of their unique combination of properties. Significant improvements in the room temperature ductility and fracture toughness of these alloys have been achieved by the addition of beta phase ( $\beta$ ) stabilizing elements like Cr, Nb, Mo and V. On the other hand, the addition of small amounts of boron to these alloys produces a remarkable grain refining effect. [1,2]. Though it is known that both  $\beta$  stabilising elements and boron additions alter the microstructure, the combined effect of these elements on phase transformations and microstructure evolution during cooling from the high temperature  $\alpha+\beta$  and  $\alpha$  phase fields are not fully understood. In the present work, microstructure evolution in Ti-47Al-2Cr-2Nb-1Mo-(0-0.2B) alloys have been studied. The microstructures of these alloys in the cast, forged and heat treated conditions were characterized and the nature of the phases present and their crystallographic relationships determined.

### Experimental Details

The chemical compositions of the four alloys which were studied in this work are presented in Table I. While all four alloys have almost the same overall composition, two of them additionally contain 0.2 at.% boron. Consequently, the microstructures of each set are expected to be similar in all conditions. Boron was added during alloy preparation in the form of  $AlB_2$ . The alloy ingots were processed by extrusion and double forging in one case, and only double forging in the other. The forged ingots were subjected to intermediate recrystallization anneals at 1300°C for 2h between the forging steps and the final forging was conducted at 1100°C. Samples



Table I: Chemical Compositions of Alloys Studied.

Ingot Name	Composition (in at.%)
<b>a. Without Boron</b>	
Ti-25	Ti-47.5Al-1.8Cr-1.8Nb-1.0Mo (430 wt ppm Oxygen)
Ti-1126	Ti-46.6Al-1.8Cr-1.8Nb-0.9Mo (420 wt ppm Oxygen)
<b>b. With Boron</b>	
Ti-43	Ti-47.9Al-1.9Cr-1.8Nb-0.9Mo-0.2B (430 wt ppm Oxygen)
Ti-35	Ti-47.8Al-1.8Cr-1.8Nb-0.8Mo-0.2B (330 wt ppm Oxygen)

obtained from the hot worked ingots were heat treated at 1400°C and 1360°C for 1-2h and then either furnace-cooled (FC), air-cooled (AC) or water-quenched (WQ). Thin foils for TEM were prepared by twin-jet electropolishing using a solution composed of 60% methanol, 35% 1-butanol and 5% perchloric acid, at -30°C, 50V and 50 mA. The microstructures of the alloys in the as-cast, hot-worked and heat treated conditions were characterized by optical microscopy (OM), back scattered electron imaging in scanning electron microscopy (BSEI-SEM), transmission electron microscopy (TEM), selected area diffraction (SAD) and x-ray microanalysis (EDS); the latter three were conducted in a Philips CM20 200 kV TEM attached with an EDAX NX-2 ultra-thin window EDS system for chemical composition analysis of phases.

### Results

In what follows, the two sets of alloys are referred to as those without boron and those with boron. Using resistivity measurements as a function of temperature [3], the  $\alpha$ -transus,  $\alpha$ - $\beta$  transition and  $\beta$ -transus temperatures were determined to be near 1330, 1340 and >1420°C, respectively, for alloys with and without boron.

#### As-Cast and As-Forged Microstructures

The as-cast microstructure of the alloys without and with boron, Figs. 1a-b, is observed to consist of large fully lamellar grains (>500  $\mu$ m), with evidence of a fine-scale structure within the grains. Under BSE imaging, Fig. 1c, a dendritic structure was clearly revealed, consisting of bright cores (the fine structure) surrounded by greyish regions and a dark network of the interdendritic regions. These observations suggest that the cores are depleted in Al and enriched in Ti, Cr, Nb and Mo and therefore possibly contain the  $\beta$ /B2 phase, whereas the interdendritic regions, where the last liquid solidifies, are enriched in Al, but depleted in the other elements. EDS spectra acquired from the center to the periphery of the dendrites essentially confirmed this. In the alloy with boron, Fig. 1b, thin ribbon-like structures, presumably borides, similar to those reported by others [4,5], were also present within the lamellar grains. TEM examination, Figs. 2a-b, established the microstructure in the dendrite cores to be composed of alternate bands of B2

and  $\gamma$  phases. The B2 showed the standard orientation relation with the  $\gamma$  associated with it in these regions and the surrounding  $\alpha_2$ - $\gamma$  lamellae, viz.,  $\{011\}B2 // \{0001\}\alpha_2 // \{111\}\gamma$  (Fig. 2b). It should be noted that there is a random distribution of the borides and the grain size looks unaffected, i.e., it is still large and comparable to the alloy without boron. This is related to the fact that the boride ribbons seem to be mostly located within the lamellar grains. These ribbons, Fig. 2c, were established to be  $TiB_2$ , and appear to be much thinner in dimensions than those observed in other studies [4,5]. This may be due to the much lower amount of boron in the present alloys. Through SAD and dark field imaging, it was established that the boride morphology consisted of a composite structure of layers of  $TiB_2$  interleaved with the B2 phase.

The microstructures of the alloys with and without boron in the as-forged condition appear, in the BSE micrographs, Figs. 3a-b, to be generally similar, consisting of small equiaxed  $\gamma$  grains and white particles at the grain boundaries. TEM and electron diffraction examination, Fig. 3c, revealed these particles to have the B2 structure ( $a_0 = 0.316$  nm) and to be predominantly present at the triple junctions of the  $\gamma$  grains. The boride ribbons in the boron containing alloys had been broken down by the hot-working operation into smaller fragments and these were mostly present at the  $\gamma$  grain boundaries (Fig. 3d). Presumably, these boride fragments, in association with the non-homogeneous concentration of plastic deformation in the surrounding regions, serve as sites for the nucleation of recrystallised  $\gamma$  grains. As before, the boride fragments were established to be  $TiB_2$ , with thin interleaving layers of the B2 phase present within them.

#### Microstructures After Heat Treatment

The microstructures of the alloys with and without boron after heat treatment at 1360 or 1400°C ( $\alpha$ + $\beta$  phase field) for 1-2h followed by cooling are dramatically different. The microstructure of the boron-free alloy heat treated at 1360°C, Fig. 4a, is fairly coarse-grained with both lamellar and non-lamellar (massive/feathery)  $\gamma$  products and coarse and fine  $\beta$ /B2 particles (bright). In acute contrast, the boron containing alloy heat treated under the same conditions is fine-grained, fully lamellar, with a dispersion of fine, bright



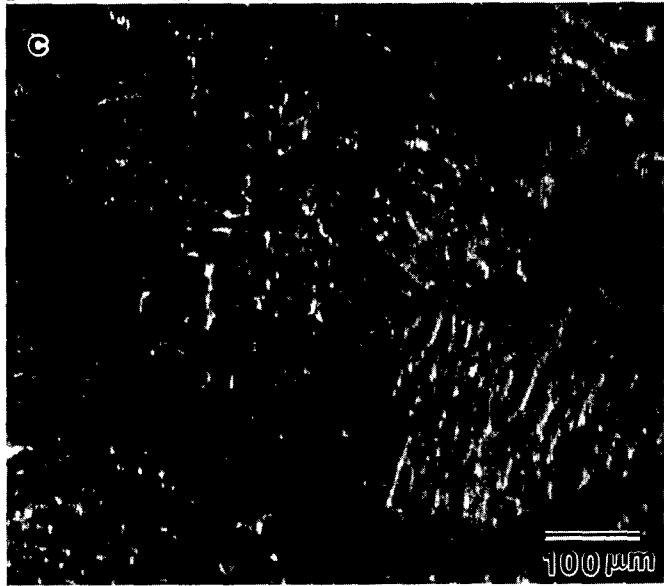
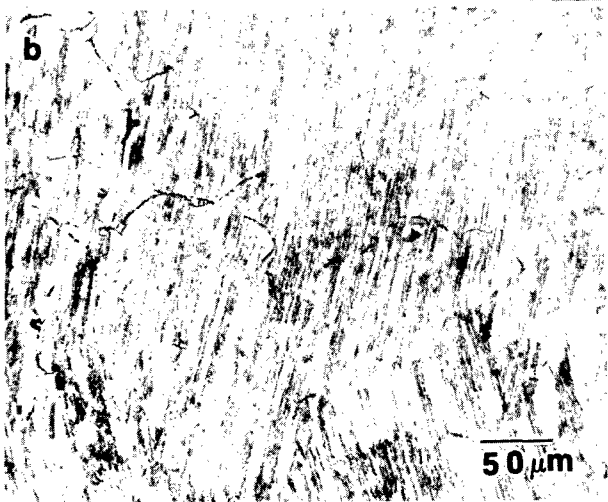
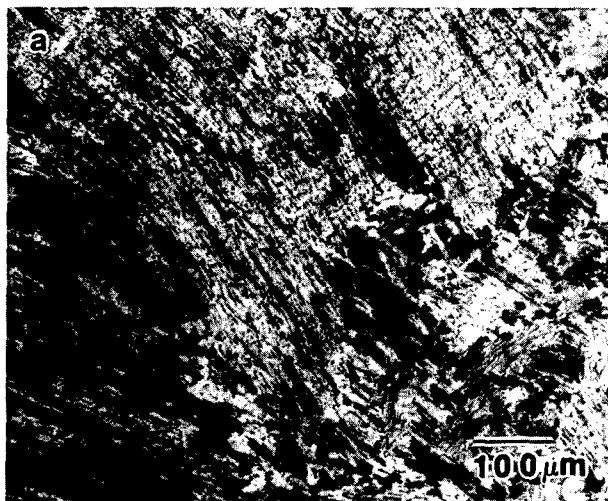


Figure 1: Micrographs showing as-cast microstructure of alloys. (a) 0.0B, OM; (b) 0.2B, OM; and (c) 0.2B, BSEI.

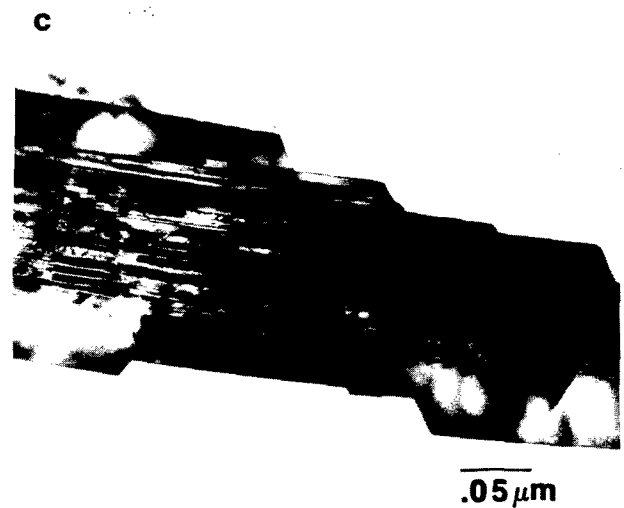
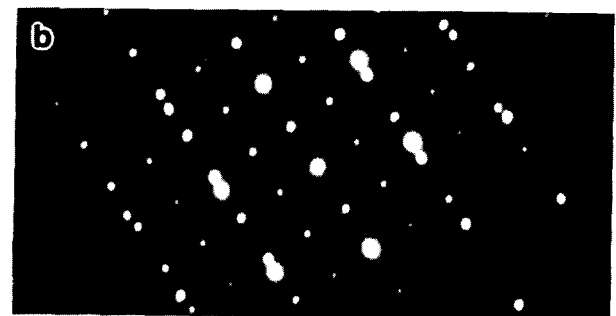
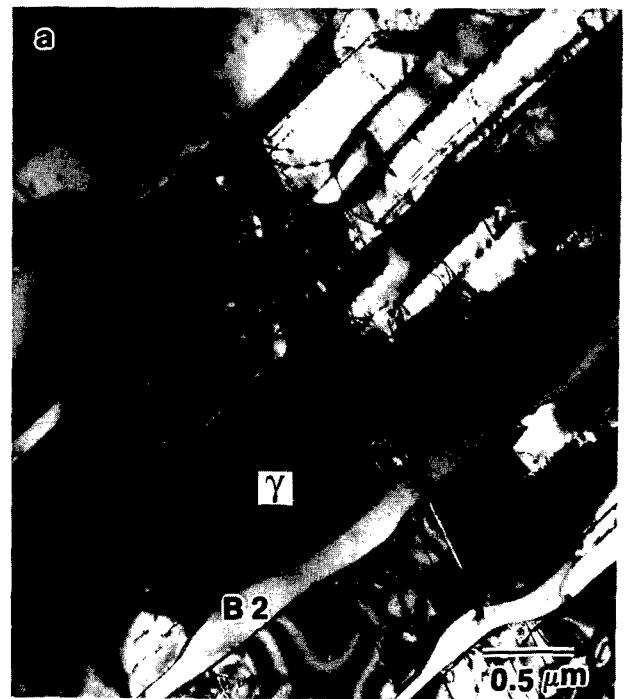


Figure 2: As-cast microstructure of 0.2B alloy. (a) TEM micrograph showing B2 cores with  $\gamma$ - $\alpha_2$  lamellae; (b)  $[111] \text{ B2} // [011] \gamma // [11\bar{2}0] \alpha_2$  SAD pattern; and (c) TEM micrograph showing boride morphology.

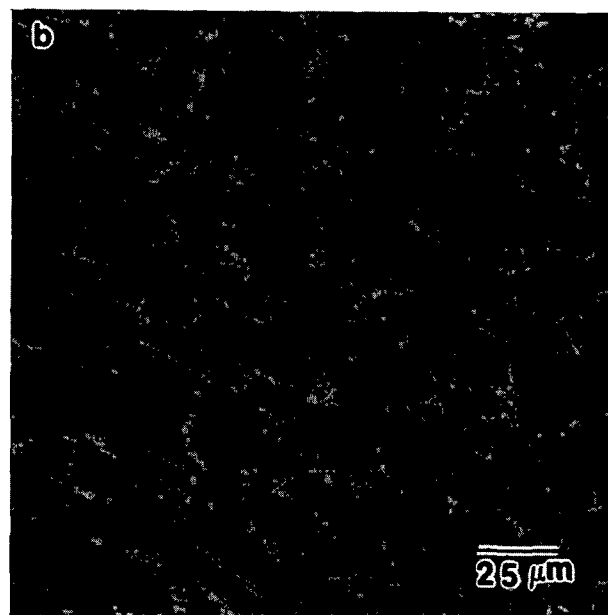
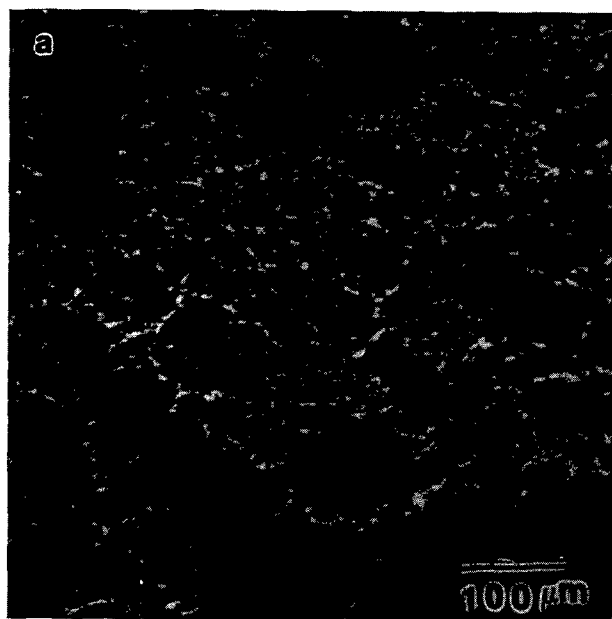


Figure 3: Microstructure of as-forged alloys. (a) 0.0B, BSEI; (b) 0.2B, BSEI; (c) 0.0B, TEM micrograph showing B2 particles with equiaxed  $\gamma$  grains (inset [001] B2 SAD pattern); and (d) 0.2B, TEM micrograph showing borides at  $\gamma$  grain boundaries.

particles mostly along the prior  $\alpha$  grain boundaries (Fig. 4b). Additionally,  $\alpha$ -grain growth appears to be significantly restricted in this alloy. The microstructure of the boron-free alloy air-cooled from 1400°C consists of a higher volume fraction of  $\beta$ /B2, which appears as almost-contiguous bright films in Fig. 4c, together with non-lamellar, feathery/massive  $\gamma$  (dark regions showing little or no contrast variations). The prior- $\alpha$  grain size is finer after this heat treatment compared with the one at 1360°C.

Thus, the films of  $\beta$  that form at the higher temperature appear to be effective in restricting  $\alpha$  grain growth, especially when continuous. TEM and electron diffraction examination of the same samples revealed that the thick layers of  $\beta$  at the grain boundaries have a B2 structure, and are associated with several different orientational variants of the  $\gamma$  phase (Fig. 5a). Interestingly, two different crystallographic orientation relationships, namely:

(0T1) B2 // (T11)  $\gamma$ , [111] B2 // [101]  $\gamma$ ; and (0T1) B2 // (T11)  $\gamma$ , [100] B2 // [101]  $\gamma$  // [110]  $\gamma$ , Figs. 5b-e, were seen to relate the  $\gamma$  and the B2 phases in these regions. These observations suggest that this  $\gamma$  has formed directly from the high-temperature  $\beta$  on cooling. Another observation is that the lamellae of the  $\gamma$  phase present in this region appear to be twin related orientation variants as seen from the SAD patterns in Figs. 5d-e.

The microstructure of the boron-containing alloy which was air-cooled from 1400°C appears practically similar to that cooled from 1360°C, i.e., it is fine-grained, fully lamellar and with the same dispersion of fine, bright particles along the prior  $\alpha$  grain boundaries (Fig. 4d). TEM examination of these samples revealed a near-lamellar structure with equiaxed  $\gamma$  grains in between the lamellar grains and few particles of B2 at the  $\gamma$  grain

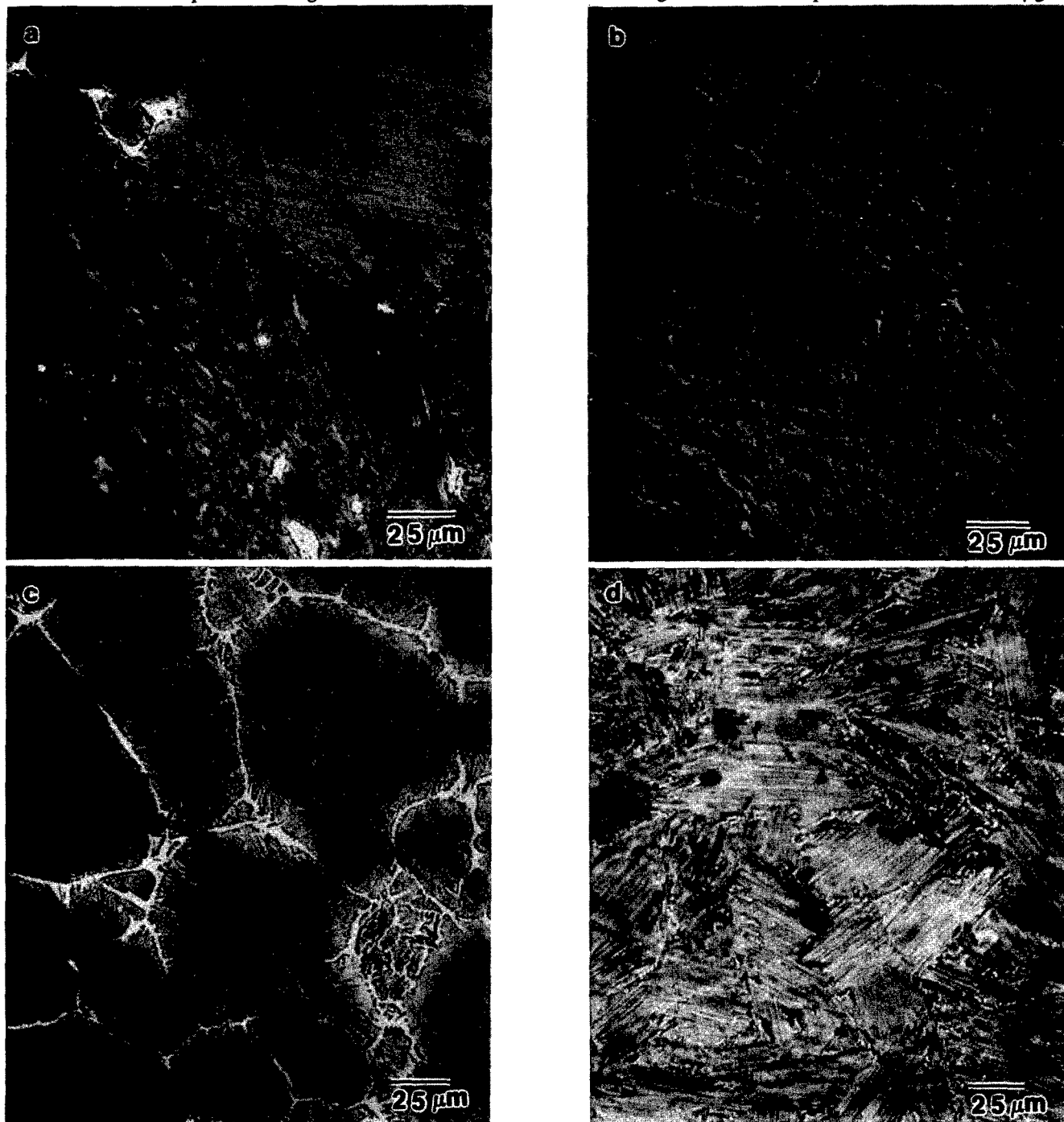


Figure 4: BSEI of 0.0B and 0.2B alloys, respectively, heat treated at 1360°C/2h/AC (a,b) and 1400°C/1h/AC (c,d).

boundaries (Fig. 6a). Interestingly, the volume fraction of the B2 is much lower in this alloy as compared with the similarly heat treated boron-free alloy (Fig. 5a). In addition, boride fragments were present, mostly at grain

boundaries and on occasion at continuous intervals within the lamellar grains. As before, the borides, Fig. 6b, were established by SAD, Figs. 6c-d, to be  $\text{TiB}_2$  and to contain a few intervening layers of B2 within them. The

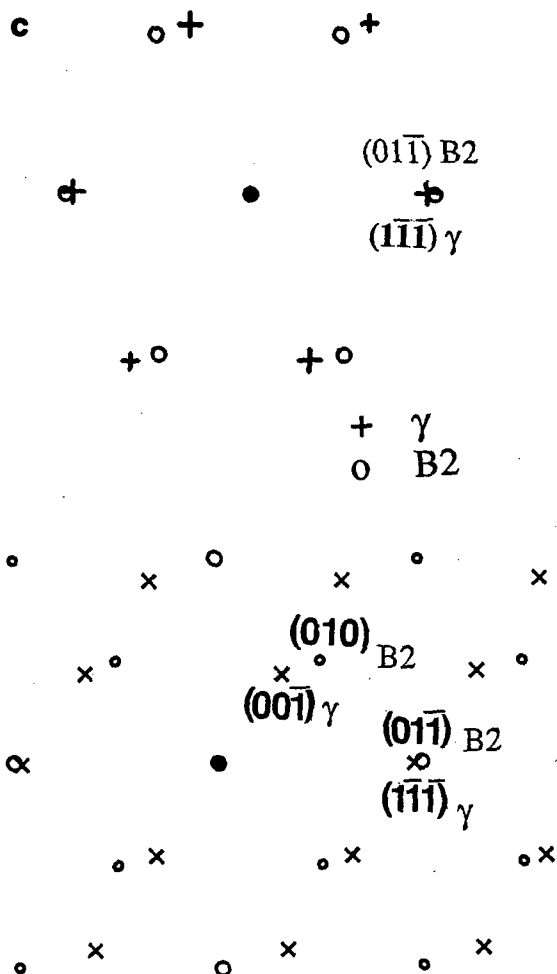
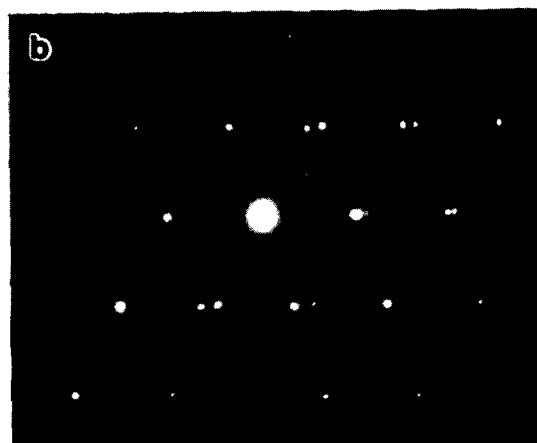
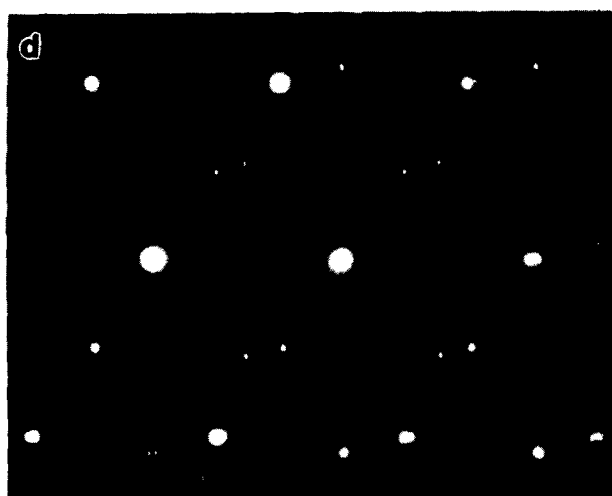


Figure 5: TEM micrographs of 0.0B alloy heat treated at  $1400^{\circ}\text{C}/2\text{h}/\text{AC}$ . (a) Grain boundary B2 films containing  $\gamma$  plates in several orientations; two orientation relationships between B2 and  $\gamma$  are depicted by (b,c)  $[111]\text{B}_2 // [101]\gamma$  and (d,e)  $[100]\text{B}_2 // [101]\gamma // [110]\gamma$  SAD patterns.

orientation relationship between the  $\text{TiB}_2$  and B2 phases was determined to be:  $(100) \text{ B2} // (10\bar{1}0) \text{ TiB}_2$ ,  $[001] \text{ B2} // [0001] \text{ TiB}_2$ , Figs. 6c-d, which is the same as the one reported in previous studies [4,5]. EDS analysis indicated that in all cases— as-cast, forged and heat treated—Ti and B were the major components in the borides, with the other elements being present in very small amounts.

The lamellar  $\gamma$  morphology persisted in the boron-containing alloy even on water quenching from  $1400^\circ\text{C}$ , Figs. 7a-b, as compared with the boron-free material, which was a mixture of lamellar, feathery and massive  $\gamma$  (with B2 along the prior  $\alpha$  grain boundaries), Figs. 7c-d. Furnace cooling from  $1400^\circ\text{C}$  lead to a fully lamellar structure in both boron-free and boron-bearing

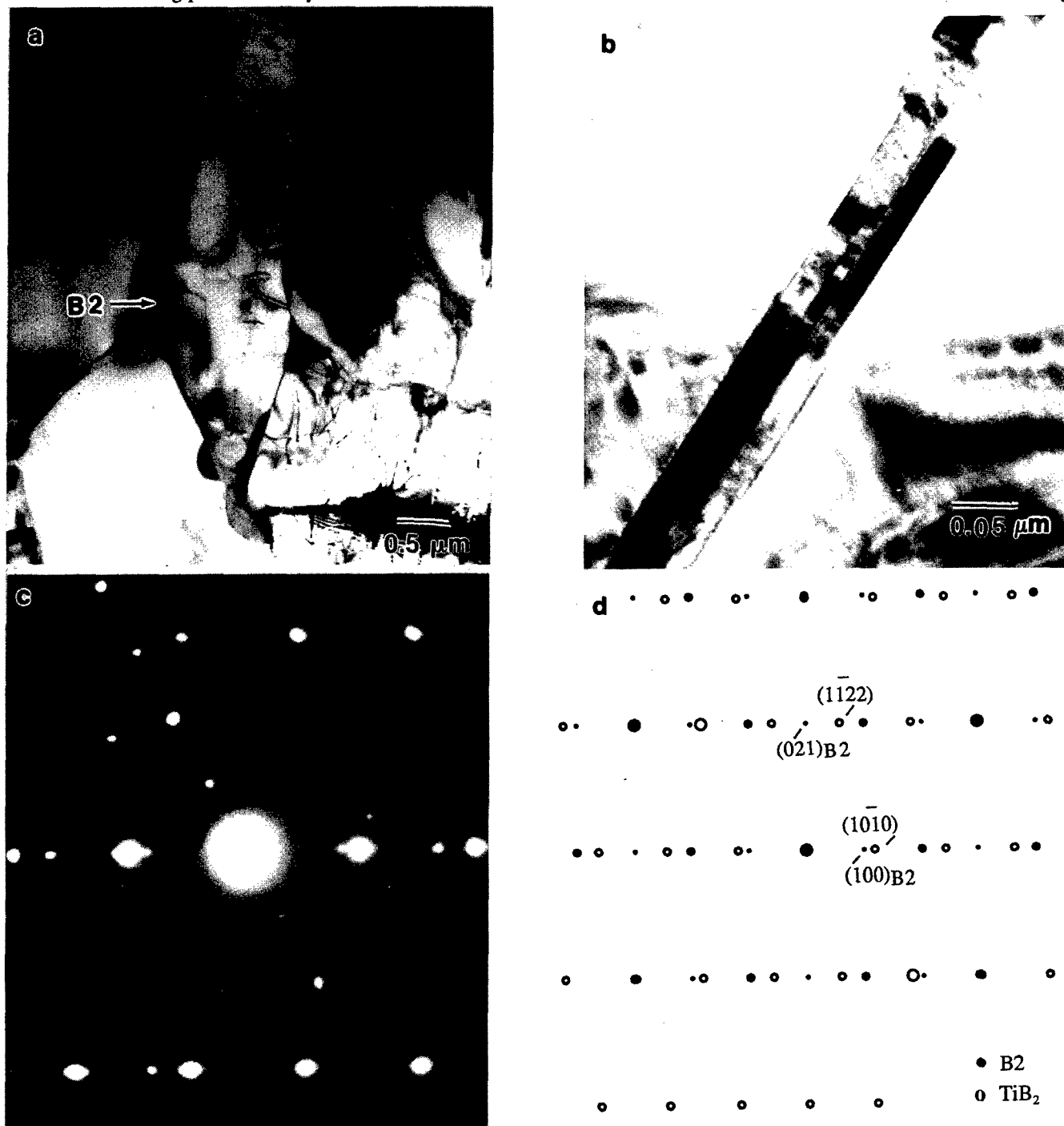


Figure 6: TEM micrographs of 0.2B alloy heat treated at  $1400^\circ\text{C}/2\text{h}/\text{AC}$ . (a) Grain boundary B2 particles; (b) a boride ( $\text{TiB}_2$ ) plate containing thin layers of B2; (c) experimental and (d) simulated  $[2\bar{4}23] \text{ TiB}_2 // [0\bar{1}2] \text{ B2}$  SAD pattern from composite boride plate in (b).

alloys, though the grain size of the latter was much finer and the lamellae somewhat coarser. In this case, the B2 phase in the boron-free alloy was present either as thin wavy structures or as triangular shaped particles at grain boundaries of large  $\gamma$  grains. As seen in the AC sample, these  $\gamma$  grains adjacent to B2 particles were also twin related. In Table II, the results of EDS analysis of the

composition of the B2 phase in the different samples of the Ti-46.6Al-1.8Cr-1.8Nb-0.9Mo alloy are presented. As can be seen, in all cases the B2 phase is enriched in Cr and Mo to a greater extent and Nb to a lesser extent. However, the Cr and Mo enrichment is more pronounced in the as-forged and FC samples than in the AC or WQ samples.



Figure 7: OM and TEM micrographs showing microstructure of 0.2B (a,b) and 0.0B (c,d) alloys heat treated at 1400°C/0.5h/WQ.

TABLE II: Composition (in at.%) of the B2 Phase in the Ti-46.6Al-1.8Cr-1.8Nb-0.9Mo Alloy

Condition	Ti	Al	Nb	Cr	Mo
As-forged	46.36	38.68	2.55	6.01	6.40
1400°C/1h/FC	49.46	33.36	2.45	8.26	6.46
1400°C/2h/AC	49.45	40.24	2.68	4.79	2.81
1400°C/1h/WQ	50.16	40.35	3.25	3.94	2.29

### Discussion

The symmetry of the dendrite arms in the as-cast samples of the alloys with and without boron could not be clearly discerned in the present study, so that it is difficult to state definitively whether  $\beta$  or  $\alpha$  is the primary solidification phase. However, a comparison of the microstructures of the cast samples with binary alloys of similar Al content [6] suggests that  $\beta$  is the primary solidification phase. This conclusion is the same as the one reached by Inkson *et al.* [4] in an Ti-45.5Al-1.6Fe-1.1V-0.7B alloy, but in contrast with that of Godfrey and Loretto [5] who studied Ti-47Al-2Cr-2Nb-(0.1-1)B alloys and proposed  $\alpha$  to be the primary solidification phase. The observation of the B2 phase at the dendrite cores (Figs. 1c, 2a) further supports the idea that  $\beta$  is the primary solidification phase. The enrichment of Mo and Cr in the  $\beta$  phase promotes ordering of this phase to B2 at lower temperatures. The solidification and solid-state transformation pathway for the ensuing as-cast microstructure is deduced to be:  $L \rightarrow L+\beta \rightarrow \alpha+\beta$  cores  $\rightarrow$  lamellar ( $\alpha + \gamma$ ) +  $\beta$  cores  $\rightarrow$  lamellar ( $\alpha_2 + \gamma$ ) + B2 cores. However, since  $\alpha_2/\gamma$ /B2 lamellae with a single orientation are observed, it is difficult to exclude the possibility that the  $L+\beta \rightarrow \alpha$  peritectic reaction above goes to completion and that the B2 phase is stabilized at lower temperatures in those regions of the  $\alpha$  that were the cores of the prior  $\beta$  dendrites, or that a double peritectic reaction of the type  $L \rightarrow L+\beta \rightarrow L+\beta+\alpha$  occurs, followed by transformation of the  $\beta$  cores to B2 and of  $\alpha$  to the lamellar structure. More work is required to fully establish this. The occurrence of the borides mostly within the lamellar grains in the alloys with boron, and the ribbon-like morphology suggests that these borides have formed directly in the liquid, a conclusion also reached by Inkson *et al.* [4]. In agreement with their work, the borides are found to be  $TiB_2$  interleaved with thin platelets of B2. This morphology, in which  $TiB_2$  and B2 occur as alternating layers, suggests a mechanism such as a eutectic reaction to be responsible for its creation. It is imagined that formation of  $TiB_2$  would result in the enrichment of the adjacent liquid layers with Cr, Mo and Nb, where the  $\beta$  phase would form.

The results presented have also shown that the presence of the  $\beta$  phase and boron additions have somewhat different effects on transformations and microstructure development during cooling from the high temperature  $\alpha+\beta$  or  $\alpha$  regions. Boron has the dramatic effect of restricting  $\alpha$  grain growth, of promoting

the lamellar  $\gamma$  morphology and of suppressing the non-lamellar, massive  $\gamma$  mode of transformation. On the other hand, in the boron-free alloys, the feathery/massive  $\gamma$  morphologies are favored over the lamellar morphology.

The  $\beta$  phase in the boron-free alloys cooled from 1400°C ( $\alpha+\beta$  phase field) occurs as thick layers at the grain boundaries of the  $\alpha$  grains and becomes enriched in Cr and Mo, which, in turn, leads to the stabilization of the B2 phase at lower temperatures. In these alloys,  $\alpha$  grain size is reduced only with a continuous or near-continuous layer of  $\beta$  around the grain boundaries. The  $\beta$  phase affects phase transformations only within it and the regions adjacent to. The occurrence of  $\gamma$  plates within the  $\beta$ /B2 regions with two different orientation relationships suggests that these  $\gamma$  plates form directly from the  $\beta$  phase on cooling. The transformation behavior of the  $\alpha$  grains surrounding the  $\beta$ , on cooling, is similar to that of binary alloys of similar Al content [3,7,8], with the lamellar  $\gamma$  morphology dominating at low (FC) cooling rates and the feathery/massive and fully massive morphologies appearing in sequence at high (AC, WQ) cooling rates. However, lamellar  $\gamma$  nucleation appears to be inhibited by the presence of  $\beta$  phase. The lower volume fraction and particle-like distribution of the  $\beta$ /B2 phase in the alloys with boron is likely to be related to the smaller prior  $\alpha$  grain size. The smaller the prior  $\alpha$  grain size, the thinner the  $\beta$  films that form at the solutionizing temperature around the grain boundaries and the more complete it's transformation to  $\gamma$  on cooling.

The mechanisms by which boron additions bring about prior  $\alpha$  grain refinement and promotion of the lamellar structure over the feathery and massive  $\gamma$  structures even on rapid cooling require consideration. At the level of 0.2 at.%B addition, there is little or no refinement of the as-cast grain size, but subsequent hot working and heat treatment do lead to considerable grain refinement. The evidence obtained to date in the present alloys, as well as those reported in other studies of similar alloys [4,5,9], indicates that all the added boron is present as  $TiB_2$  primarily and to a very limited extent in solid solution. This implies that there is probably no free boron available that might have segregated to the prior  $\alpha$  grain boundaries and restricted their growth. On the other hand, in the forged material, and in those heat treated at high temperatures (1360-1400°C),  $TiB_2$  particles were commonly observed at the  $\gamma$ - $\gamma$  grain boundaries in the former and the lamellar grain boundaries in the latter. Thus, the refinement of the lamellar grain size is most likely due to the pinning of the primary  $\alpha$  grain boundaries by the  $TiB_2$  particles. The plate-like shape of these particles is probably quite effective in exerting strong restraining forces against grain boundary migration, so that very few particles need be present along the grain boundaries. However, the presence of some  $TiB_2$  particles within the lamellar grains in heat treated specimens, in contrast with the situation in forged specimens, where

they are located entirely at the grain boundaries, suggests that in some cases the grain boundaries are able to unpin and migrate. Other factors that are probably influential in restricting grain growth are the layers of  $\gamma$  grains that are often observed to be present at the lamellar grain boundaries, together with small  $\beta$ /B2 particles at the  $\gamma$ - $\gamma$  grain boundaries. More work is required to ascertain whether these constituents play a significant role in  $\alpha$  grain growth and the subsequent transformations.

Perhaps the most intriguing effect of boron is the promotion of the lamellar  $\gamma$  structure over the feathery and massive morphologies, even at high cooling rates, unlike the situation observed in the boron-free alloys, as well as in binary alloys of similar Al content [3,7,8]. One might speculate that this change is related to the refinement of the prior  $\alpha$  grain size brought about by the  $\text{TiB}_2$  particles. In this regard, the finer grain size may be expected to enhance the nucleation frequency of the lamellar  $\gamma$  in  $\alpha$ , such that this transformation can begin at smaller undercoolings and go to completion before the samples have cooled sufficiently below the  $\alpha/\gamma$   $T_0$  temperature, where the driving force for the massive transformation becomes substantial enough for this morphology to appear. More experimental work on the determination of the reaction kinetics and temperature dependence (i.e. start and finish temperatures) of the different modes of transformation, using in situ electrical resistivity techniques [3], is underway to verify these ideas.

### Conclusions

The microstructures of Ti-47Al-2Cr-2Nb-1Mo-(0-0.2)B alloys have been studied in the as-cast, forged and heat treated conditions and the following are the significant results. The microstructure of the cast alloys show evidence of:  $L \rightarrow L + \beta \rightarrow \alpha + \beta$  cores  $\rightarrow$  lamellar ( $\alpha + \gamma$ ) +  $\beta$  cores  $\rightarrow$  lamellar ( $\alpha_2 + \gamma$ ) + B2 cores, solidification and transformation pathway; and in the alloys with boron, ribbon-like borides that have formed directly in the liquid are also present. The borides were determined to be  $\text{TiB}_2$  and found to contain thin, interleaving layers of B2 phase with the orientation relationship: (100) B2 // (10 $\bar{1}$ 0)  $\text{TiB}_2$ , [001]B2 // [0001]  $\text{TiB}_2$ . In the boron-free alloys heat treated above 1360°C, the  $\beta$  phase is present as a thick continuous film along the prior  $\alpha$  grain boundaries along with several variants of the  $\gamma$  phase. With boron additions, the volume fraction of the  $\beta$ /B2 phase reduces such that it is mainly found as small particles at the prior  $\alpha$  grain boundaries. In the boron-free alloy, the feathery/massive  $\gamma$  morphologies are favored over the lamellar morphology as the transformation product of the  $\alpha$  phase. In contrast, boron addition to this alloy has the dramatic effect of restricting  $\alpha$  grain growth, of promoting the lamellar  $\gamma$  morphology and lamellar growth and of suppressing the non-lamellar/feathery/massive  $\gamma$  mode of transformation. It is perceived that due to the finer grain size of the prior  $\alpha$  grains the lamellar

transformation can begin at smaller undercoolings and go to completion before the samples have cooled sufficiently below the  $\alpha/\gamma$   $T_0$  temperature to allow non-lamellar morphologies to appear.

### References

1. M. E. Hyman, C. McCullough, C. G. Levi and R. Mehrabian, "Evolution of Boride Morphologies in TiAl-B Alloys," *Metall. Trans.*, **22A**, 1647 (1991).
2. M. E. Hyman, C. McCullough, J. J. Valencia, C. G. Levi and R. Mehrabian, "Microstructure Evolution in TiAl alloys with B additions: Conventional Solidification," *Metall. Trans.*, **20A**, 1847 (1989).
3. D. Veeraraghavan and V. K. Vasudevan, "Phase Transformations in Two-Phase TiAl/Ti<sub>3</sub>Al Alloys During Continuous Heating and Cooling Studied by Electrical Resistivity Measurements," *Mater. Sci. Engg.*, **A192/193**, 950 (1995).
4. B. J. Inkson, C. B. Boothroyd and C. J. Humphreys, "Boride Morphology in a (Fe,V,B) Ti-Al Alloy," *Acta Mater.*, **43**, 1429 (1995).
5. A. B. Godfrey and M. H. Loretto, "The Nature of Complex Precipitates Associated with the Addition of Boron to a  $\gamma$ -based Titanium Aluminide," *Intermetallics*, **4**, 47 (1995).
6. C. McCullough, J. J. Valencia, C. G. Levi and R. Mehrabian, "Phase Equilibria and Solidification in Ti-Al alloys," *Acta Metall.*, **37**, 1321 (1989).
7. P. Wang, G. B. Viswanathan and V. K. Vasudevan, "Observation of a Massive Transformation in Quenched Ti-48Al Alloys," *Metall. Trans.*, **23A**, 792 (1992).
8. P. Wang and V. K. Vasudevan, "The Effect of Cooling Rate on Decomposition of the  $\alpha$  Phase in Ti-(43-50) At.% Al Alloys," *Mat. Res. Soc. Symp. Proc.*, **288**, 229 (1993).
9. B. J. Inkson, C. B. Boothroyd and C. J. Humphreys, "Boron Segregation in a (Fe,V,B) TiAl Based Alloy," *J. de Physique IV*, **3**, 397 (1993).

### Acknowledgements

Financial support for this research from AFOSR (Grant# F49620-95-1-0116), Dr. Charles H. Ward, Program Monitor, is deeply appreciated. The authors also wish to thank Dr. Patrick L. Martin of Rockwell International Science Center for supplying the materials used in this work.



# STABILITY OF ULTRAFINE LAMELLAR STRUCTURES DURING AGING IN TWO-PHASE $\gamma$ -TiAl ALLOYS

P.J. Maziasz, C.T. Liu, and J.L. Wright  
Oak Ridge National Laboratory,  
P.O. Box 2008  
Oak Ridge, TN 37831-6115

## Abstract

Two-phase  $\gamma$ -TiAl alloys such as powder-metallurgy (P/M) Ti-47Al-2Cr-2Nb or Ti-47Al-2Cr-1Nb-Ta hot-extruded above the  $\alpha$ -transus temperature ( $T_c$ ) have unique refined-colony/ultrafine lamellar structures. These lamellar microstructures consist of very fine laths of the  $\gamma$  and  $\alpha_2$  phases, with average interlamellar spacings ( $\lambda_c$ ) of 100 nm and  $\alpha_2$ - $\alpha_2$  spacings ( $\lambda_a$ ) of 200 nm, and are dominated by  $\gamma/\alpha_2$  interfaces. This ultrafine lamellar structure remains stable during heat-treatment at 900°C for 2 h, but becomes unstable after 4 h at 982°C. The ultrafine lamellar structure remains relatively stable in both alloys after aging for >5000 h at 800°C, but disappears completely at 1000°C. Continuous coarsening of the lamellar structure begins with the dissolution of fine  $\alpha_2$  lamellae. The aged Ta-modified alloy shows similar lamellar coarsening behavior within the colonies, but has more discontinuous coarsening of the intercolony  $\gamma$  with new precipitation of coarse  $\alpha_2$  and  $\beta$  phase particles. Analytical electron microscopy (AEM) microcompositional data shows that changes in composition of the  $\alpha_2$  phase correlate with microstructural instability.

## Introduction

Two-phase  $\gamma$ -TiAl alloys based on Ti-(46-48)Al-2Cr-2Nb (at.%) are being developed and tested for high-temperature structural applications. The properties driving new applications include low density (4 gm/cm<sup>3</sup>), and good elevated-temperature strength, stiffness and oxidation-resistance compared to current Ni-based superalloys or titanium alloys [1-9]. However, the mechanical properties of  $\gamma$ -TiAl alloys are extremely sensitive to microstructure, which in turn is also very sensitive to changes in minor alloying elements or in processing parameters. The paradox to date has been trying to achieve a good balance between both room-temperature and high-temperature mechanical properties. Generally, fully-lamellar, coarse-grained alloys have good high-temperature strength and creep-resistance at up to 800°C, but lack room-temperature tensile ductility. By comparison, fine-grained duplex alloys often have better tensile ductility, but have poorer fracture-toughness at room-temperature and lack high-temperature creep-resistance. In 1995, Kim indicated that refined-grained fully-lamellar structures (300  $\mu$ m grain size, 500 nm lamellar spacing) in an alloy with a composition of Ti-46.5Al-2Cr-3Nb-0.2W (K5) had a significantly better balance of both high-temperature and room-temperature properties [2,10].

In 1995, Liu et al. [11] reported very high levels of room-temperature and high-temperature yield strength (YS) (970 and 850 MPa at 800°C, respectively) in a fully-lamellar powder-metallurgy (P/M) Ti-47Al-2Cr-2Nb alloy with a unique refined colony and ultrafine lamellar structure. This alloy also had 1.4% tensile elongation and 22 MPa<sup>1/2</sup> fracture toughness at room-temperature. Wang et al. [12] showed that these same unique P/M TiAl alloys also had outstanding creep-resistance at 760°C. Furthermore, in 1996, Liu et al. [13] showed that ingot-metallurgy (I/M) Ti-(46-47)Cr-2Cr-2Nb alloys modified with W and B additions and with somewhat similar fully-lamellar microstructures had YS of 800 MPa with 3-5% tensile ductility and about 30 MPa<sup>1/2</sup> fracture toughness at room-temperature. Clearly these data indicate that with proper microstructural

control, it is possible to have  $\gamma$ -TiAl alloys with balanced good properties.

The purpose of this work is to present more detailed quantitative microstructural and microcompositional data on the fine  $\gamma$  and  $\alpha_2$  components of the ultrafine lamellar structure that initially forms in a P/M Ti-47Al-2Cr-2Nb alloy. The emphasis is on the overall average interlamellar and  $\alpha_2$ - $\alpha_2$  spacings ( $\lambda_c$  and  $\lambda_a$ , respectively), and on how those parameters change during heat-treatments or long-time aging. High spacial resolution analytical electron microscopy (AEM) data on the compositions of individual phase lamellae or particles are included, to clearly identify phases and to better determine the nature of the processing-induced microstructure. New data on a similar ultrafine lamellar P/M Ti-47Al-2Cr-1Nb-1Ta alloy are also included.

## Experimental

The Ti-47Al-2Cr-2Nb (73-1) and Ti-47Al-2Cr-1Nb-1Ta (74-1) - 325 mesh alloy powders were produced by Pratt&Whitney (West Palm Beach, FL) using their rotary atomization facility with a helium atmosphere. Wet chemical analysis showed that the powder contained 800 wt. ppm oxygen, 270 wt. ppm carbon and 35 wt. ppm nitrogen. Titanium cans with 15 Kg of powder were extruded at  $T_c$  (below the  $\alpha$ -transus temperature) and at  $T_c$  (above the  $\alpha$ -transus temperature), and then air cooled. Differential scanning calorimetry data (20°C/min heating, Ar atmosphere) determined the  $\alpha$ -transus temperature to be 1320°C. Pieces of the 20 mm diam. extruded rod were heat-treated in vacuum for 1-4 h at 900 to 1350°C and then furnace cooled. Some specimens were then also aged for 72-5020 h at 800 and 1000°C in vacuum. Button-head tensile specimens were electro-discharge machined (EDM) and surface-ground, with the gage axis parallel to the extrusion direction.

Wafers 0.25 mm thick were cut from either the shoulders of tested tensile specimens, or from extruded stock, perpendicular to the extrusion direction. Disks 3 mm diam. were then cut by EDM for transmission electron microscopy (TEM) analysis. TEM specimens were electropolished in a twin-jet unit using a solution of 6% perchloric acid, 60% methanol, 33.5% butyl cellosolve, and 0.5% glycerin at -20°C and 32 V. Conventional TEM was performed on a Philips CM30 (300 KV) microscope. Some electropolished TEM disks were also examined in a Hitachi S4100/FEG scanning electron microscope (SEM).

Lamellar microstructural parameters were measured for most specimens by examining up to three different, representative colonies, and tilting each grain so that the lamellar interfaces were parallel to the electron beam direction ( $Z$ ) with  $g$  at or near  $\langle 111 \rangle$ . Strong diffracting conditions ( $s \geq 0$ ) were used to image all the lamellar interfaces, while weaker diffracting conditions ( $s \gg 0$ ) were used to better distinguish the  $\alpha_2$  phase lamellae. Average lamellar spacing ( $\lambda_c$ , including both  $\gamma$  and  $\alpha_2$  lamellae) and  $\alpha_2$ - $\alpha_2$  spacing ( $\lambda_a$ ) were measured using a line-intercept method with >100 lamellae in the field of view. Several of the largest and smallest of each lamellar phase constituent in each analyzed area/colony were also measured to establish the maximum representative size range.

## Structural Intermetallics 1997

Edited by M.V. Nathal, R. Darolia, C.T. Liu, P.L. Martin,  
D.B. Miracle, R. Wagner, and M. Yamaguchi  
The Minerals, Metals & Materials Society, 1997

Microcompositional analysis of individual phase lamellae within colonies of selected specimens was performed using X-ray energy dispersive spectroscopy (XEDS) on either a Philips 400T (100 KV) or a CM200 (200 KV) analytical electron microscope (AEM) equipped with a field-emission gun (FEG, probe-size: 2-5 nm). XEDS analysis of coarser intercolony phase constituents was done on a Philips CM12 (LaB<sub>6</sub>, 120KV). XEDS were quantified using a standardless method, but *k*-factors for aluminum were checked against a known standard, as recommended by Ramanujan et al. [14,15].

## Results

### As-Extruded Ultrafine Lamellar Microstructures

P/M 73-1 alloy consolidated by hot-extrusion at temperature  $T_1$  well below the  $\alpha$ -transus temperature ( $T_\alpha$ ) had a very fine-grained (<1  $\mu\text{m}$ ), duplex structure, but poor mechanical properties at elevated temperatures [11], so further analysis was not done. The same P/M alloy consolidated by extrusion at  $T_2$  above  $T_\alpha$  was fully-dense with a near-fully lamellar structure (Fig. 1). The lamellar structure consists of a unique combination of refined colony size (70  $\mu\text{m}$ ) with very little intercolony  $\gamma$  (1-3  $\mu\text{m}$  thick, <5 vol.%) [11], and an ultrafine lamellar structure within the colonies. The P/M 74-1 alloy extruded at  $T_2$  had a similar microstructure, but with a slightly smaller colony size and even less intercolony  $\gamma$ . Quantitative lamellar microstructural data are given in Table 1.

The as-extruded ultrafine lamellar structure of P/M 73-1 alloy consists of very uniformly spaced, alternating lamellae of the  $\gamma$  and  $\alpha_2$  phases (Figs. 1-3). The overall  $\lambda_c$  is about 100 nm and  $\lambda_a$  is 220 nm. The  $\gamma$  lamellae are typically 100-200 nm wide (Fig. 2a), but a few can be as wide as 500 nm and contain twin subboundaries. The  $\alpha_2$  lamellae are much thinner (20-76 nm). This ultrafine lamellar structure is dominated by  $\gamma/\alpha_2$  boundaries with few  $\gamma/\gamma$  twins. The ultrafine  $\gamma$  and  $\alpha_2$  lamellae all have the same characteristic  $(111)\gamma // (0001)\alpha_2$  and  $\langle 110 \rangle \gamma // \langle 1120 \rangle \alpha_2$  crystallographic habit relationship between close-packed planes and directions in those respective phases seen by others in coarser lamellar structures [9]. It is particularly noteworthy that these ultrafine lamellae are very straight across the length of the colonies, and free of the common structural imperfections (kinks, jogs, subboundaries, etc.) found in lamellar structures by others [15].

The Ta-modified 74-1 alloy has a slightly finer initial lamellar structure with smaller  $\lambda_c$  (Table 1), which is due to a few more  $\gamma/\gamma$  twins within the wider  $\gamma$  lamellae. The  $\lambda_a$  remains 220 nm. All other features and characteristics are the same as found in the unmodified P/M Ti-47Al-2Cr-2Nb alloy.

### Heat-Treatment Affects on the Ultrafine Lamellar Structure

Heat-treatments of 4 h at 982°C with or without an additional 8 h at 704°C (to stabilize and stress-relieve the material, respectively) were found to slightly degrade the as-extruded microstructure of the 73-1 alloy. The ultrafine lamellar showed subtle signs of the early stages of continuous lamellar coarsening, including measureable increases in both  $\lambda_c$  and  $\lambda_a$  (Table 1), as well as partial dissolution of the initially continuous  $\alpha_2$  lamellae. Consistently, the colony boundaries also show evidence of discontinuous coarsening, which increases the amount of intercolony  $\gamma$  and causes coarse  $\alpha_2$  precipitation at the expense of the adjacent lamellar structure (Fig. 4). By contrast, heat-treatment for 2 h at 900°C produces no discernable changes in the as-extruded intercolony  $\gamma$  or ultrafine lamellar structures (Table 1). This heat-treatment appeared to optimize room-temperature tensile properties for both P/M 73-1 and 74-1 alloys [11,16] and was therefore chosen as the "standard" stress-relief treatment for subsequent mechanical properties studies of P/M and I/M ultrafine lamellar TiAl alloys [13,16,18].

To complete studies on the formation and stability of these refined-colony/ultrafine-lamellar alloys, as-extruded P/M 73-1 material was heat-treated for 2 h at up to 1350°C [11]. Heat-treatment at 1320°C (almost exactly at  $T_\alpha$ ) did not change the colony size, but dramatically coarsened the lamellar structure (both  $\lambda_c$  and  $\lambda_a$  increase by a factor of 4) (Table 1 and Fig. 5). Conversely, heat-treatment at 1350°C (above  $T_\alpha$ ) greatly increases the colony size, but has only a small effect on the

ultrafine lamellar structure (Table 1). The P/M 74-1 alloy showed very similar behavior.

### Aging Affects on the Ultrafine Lamellar Structure

Specimens of the as-extruded P/M Ti-47Al-2Cr-2Nb alloy (+2 h at 900°C) were aged at 800 and 1000°C for times ranging from 72 to 5040 h. Aging at 800°C for <2160 h produced no noticeable changes in the initial lamellar structure detectable by optical and TEM microstructural examination [16]. Aging for 5040 h at 800°C still shows very little change optically (Fig. 6a and 6b), but SEM (Fig. 7a) and TEM (Figs 2,3, and 8a) analyses do reveal subtle changes in both the intercolony and lamellar components of the structure. Discontinuous coarsening slightly increases the thickness of the intercolony  $\gamma$  and causes some new, coarse intercolony  $\alpha_2$  particles to form (compare Figs 1 and 7a and 8a). The lamellar structure also shows subtle changes which indicate that the very early stages of continuous lamellar coarsening are occurring. While there is very little change in  $\lambda_c$  (Table 1 and Fig. 2), there is a measureable change in  $\lambda_a$  and observable fragmenting and thinning of the  $\alpha_2$  lamellae that is consistent with dissolution (Fig. 3). Other work on aging and coarsening of similar ultrafine lamellar structures has shown that dissolution of the  $\alpha_2$  lamellae is the first step in the continuous coarsening of the overall lamellar structure [17].

The effects of aging for 5040 h at 800 and 1000°C on the ultrafine lamellar structure of the P/M Ti-47Al-2Cr-1Nb-Ta alloy are similar to those seen in the Ta-free alloy, but there are minor differences. At 800°C, the 74-1 alloy has slightly more discontinuous coarsening of the intercolony boundary regions, with considerably more precipitation of coarse  $\alpha_2$  particles along the interfaces between the intercolony  $\gamma$  and the lamellar structures (Figs. 7b and 8b). Within the lamellar colonies, the increases in both  $\lambda_c$  and  $\lambda_a$  in the Ta-modified 74-1 alloy are similar to those observed in the 73-1 base alloy (Table 1).

### XEDS Microcompositional Phase Analysis in As-Extruded, Heat-Treated or Aged Ultrafine Lamellar Structures

XEDS analysis of the composition of coarser individual phase particles within the intercolony  $\gamma$  regions were performed using a Philips CM12 (120KV, LaB<sub>6</sub>, 100-200 nm probe) AEM. High-spatial resolution XEDS of individual  $\gamma$  and  $\alpha_2$  lamellae were measured using a Philips EM400T (100KV, FEG, <5 nm probe) or a CM200 (200KV, FEG, <2 nm probe) AEMs. Average values of individual measurements of the two phases in various alloys are given in Table 2.

The initial microstructure (as-extruded + heat-treated 2 h at 900°C) of the 73-1 alloy shows about 39 at.% Al and more Cr (1.5-2.0 enrichment) in both lamellar and intercolony  $\alpha_2$  relative to adjacent  $\gamma$ . AEM results on the initial structure of the 74-1 alloy are similar. Partitioning of Nb and/or Ta is also fairly even between the two phases.

AEM was performed on specimens of both 73-1 and 74-1 heat-treated for 4 h at 982°C to clearly identify the new coarse precipitate particles that formed in the intercolony region of the microstructure. In both cases, the new precipitate particles were all  $\alpha_2$  phase (no  $\beta$ ), but there is a significant difference in composition between these new precipitates that form during discontinuous coarsening and those found in the initial microstructure. The  $\alpha_2$  particles produced during heat-treatment have less aluminum than those found in the initial microstructure (34-35 at.% compared to 39-40%), and no longer show any chromium enrichment.

Finally, AEM measurements of both intercolony and lamellar phase constituents in the 73-1 alloy aged 5040 h at 800°C show even larger composition differences between the  $\gamma$  and  $\alpha_2$  phases relative to the initial microstructure (Table 2). Both lamellar and intercolony  $\alpha_2$  have even less Al (31-32 at.%) after long-term aging, and now also have less Cr and Nb than the  $\gamma$ .

## Discussion

These unique refined-colony/ultrafine lamellar microstructures are new and interesting, but they are important because they produce an outstanding balance of mechanical properties in these two-phase  $\gamma$ -TiAl alloys at room- and elevated-temperatures

Table 1 - Quantitative Lamellar Microstructural Data on Hot-Extruded Above  $T_\alpha$  and Heat-Treated P/M Ti-47Al-2Cr-2Nb and P/M Ti-47Al-2Cr-1Nb-1Ta Alloys

Heat-Treatment	Interlamellar spacing (nm)	$\alpha_2$ - $\alpha_2$ spacing (nm)	$\gamma$ -width (nm)	$\alpha_2$ -width (nm)
<u>P/M Ti-47Al-2Cr-2Nb</u>				
none	100	220	100-500	20-76
2 h at 900°C	similar to above			
4 h at 982°C	180	325	60-600	20-60
2 h at 1320°C	390 ( $\pm 75$ )	900 ( $\pm 300$ )	80-2000	70-400
2 h at 1350°C	140	300	50-300	70-430
2 h at 900°C + aged >5000 h at 800°C	120	285	70-630	15-45
<u>P/M Ti-47Al-2Cr-1Nb-1Ta</u>				
none	86	220	40-480	13-76
2 h at 900°C	similar to above			
2 h at 900°C + aged >5000 h at 800°C	114	275	80-480	14-72

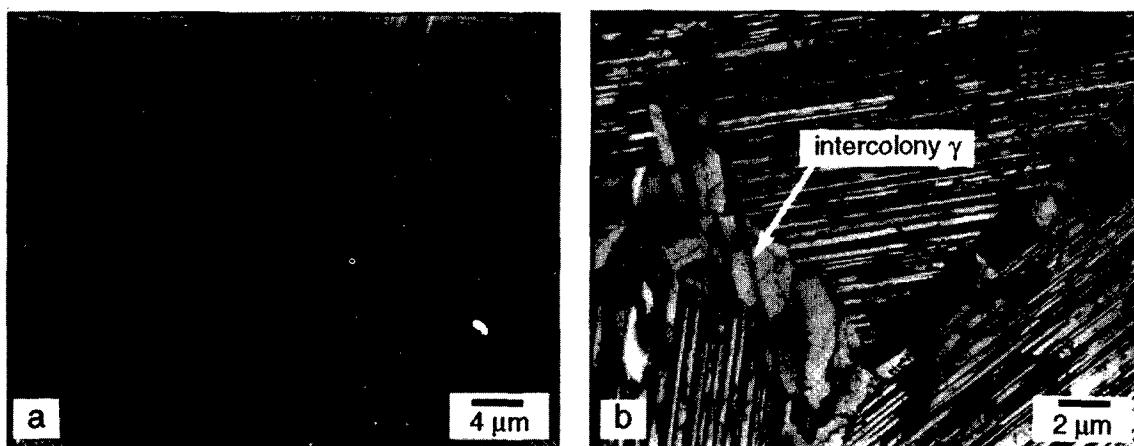


Fig. 1 - a.) SEM (electropolished surface) and b.) TEM of P/M Ti-47Al-2Cr-2Nb (73-1) hot-extruded at  $T_2$  above  $T_\alpha$  to produce a refined-colony, ultrafine lamellar structure.

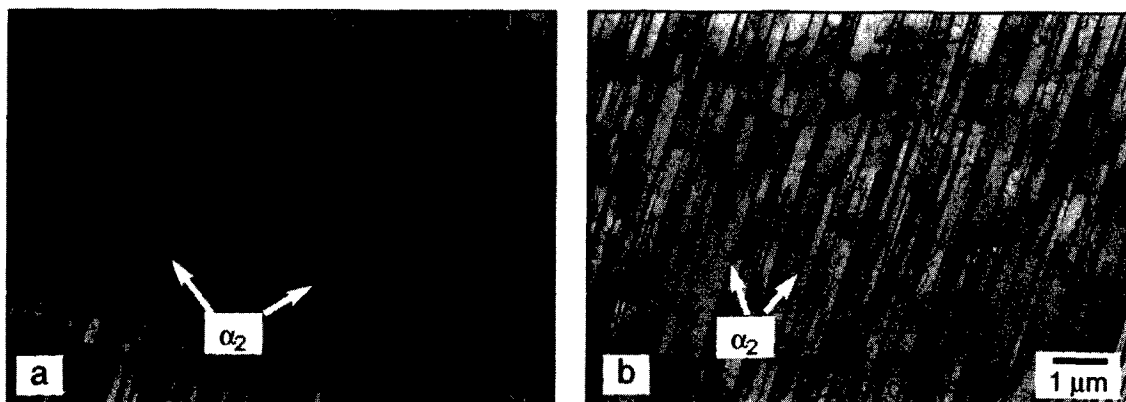


Fig. 2 - TEM of P/M Ti-47Al-2Cr-2Nb (73-1) a.) as-hot-extruded ( $T_2$ ) and heat-treated for 2 h at 900°C, and b.) aged for 5040 h at 800°C at lower magnification, showing the typical very straight and evenly spaced ultrafine lamellar structure found within each colony.

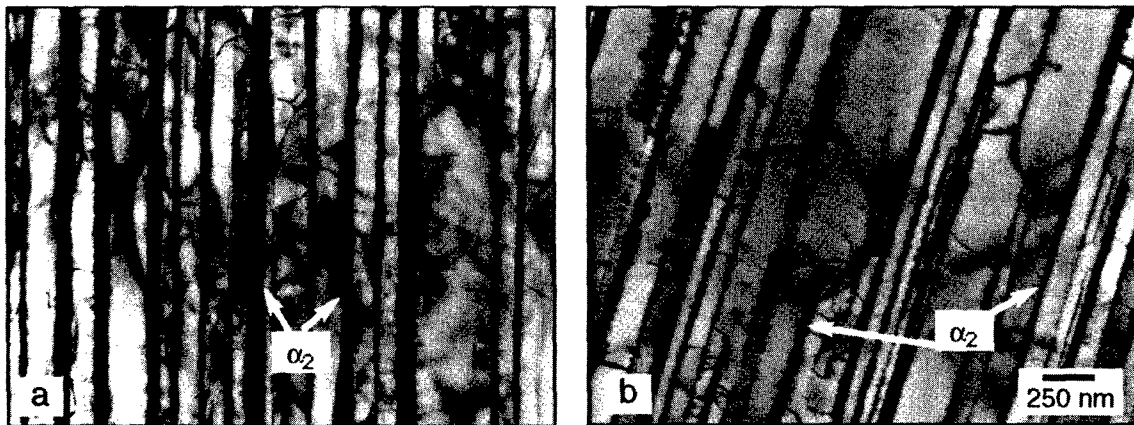


Fig. 3 - TEM of P/M Ti-47Al-2Cr-2Nb (73-1) a.) as-hot-extruded ( $T_2$ ) and heat-treated for 2 h at 900°C, and b.) aged for 5040 h at 800°C at higher magnification, showing the finer  $\alpha_2$  lamellae found uniformly distributed between most larger  $\gamma$  lamellae. b.) shows dissolution of the  $\alpha_2$  lamellae that is the first step in continuous coarsening of the such lamellar structures.



Fig. 4 - TEM showing the discontinuous coarsening that occurs along the intercolony boundaries during heat-treatment at 982°C for 4 h of P/M Ti-47Al-2Cr-2Nb (73-1) hot-extruded at  $T_2$ .



Fig. 5 - SEM (electropolished surface) showing the effects of heat-treatments of a.) 2h at 1320°C and b.) 2h at 1350°C on the lamellar and colony structures of P/M Ti-47Al-2Cr-2Nb (73-1) hot-extruded at  $T_2$ .

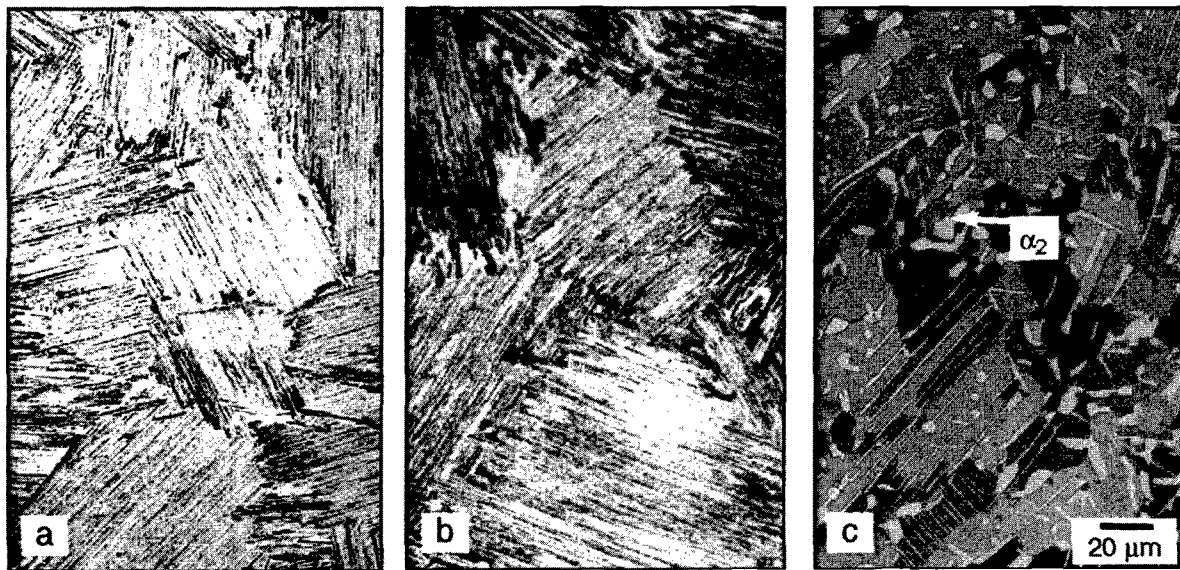


Fig. 6 - Optical (polished and etched) micrographs of P/M Ti-47Al-2Cr-2Nb (73-1) hot-extruded at  $T_x$ , showing a.) initial microstructure (with heat-treatment of 2 h at 900°C), b.) aged 5040 h at 800°C, and c.) aged 5040 h at 1000°C. Continuous and discontinuous coarsening complete remove the ultrafine lamellar structure during aging at 1000°C.

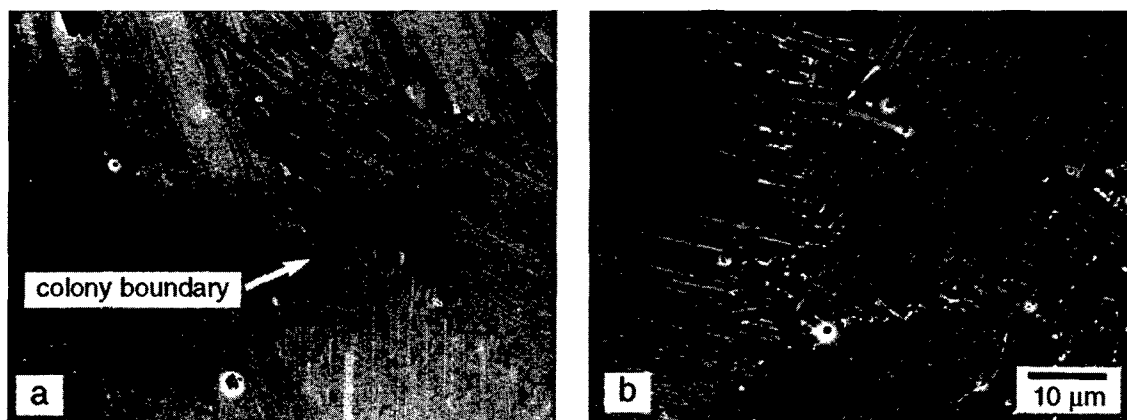


Fig. 7 - SEM (electropolished surface) of TEM disks showing the difference in discontinuous coarsening at intercolony boundaries of a.) P/M Ti-47Al-2Cr-2Nb (73-1) and b.) P/M Ti-47Al-2Cr-1Nb-1Ta (74-1) alloys aged for 5040 h at 800°C.

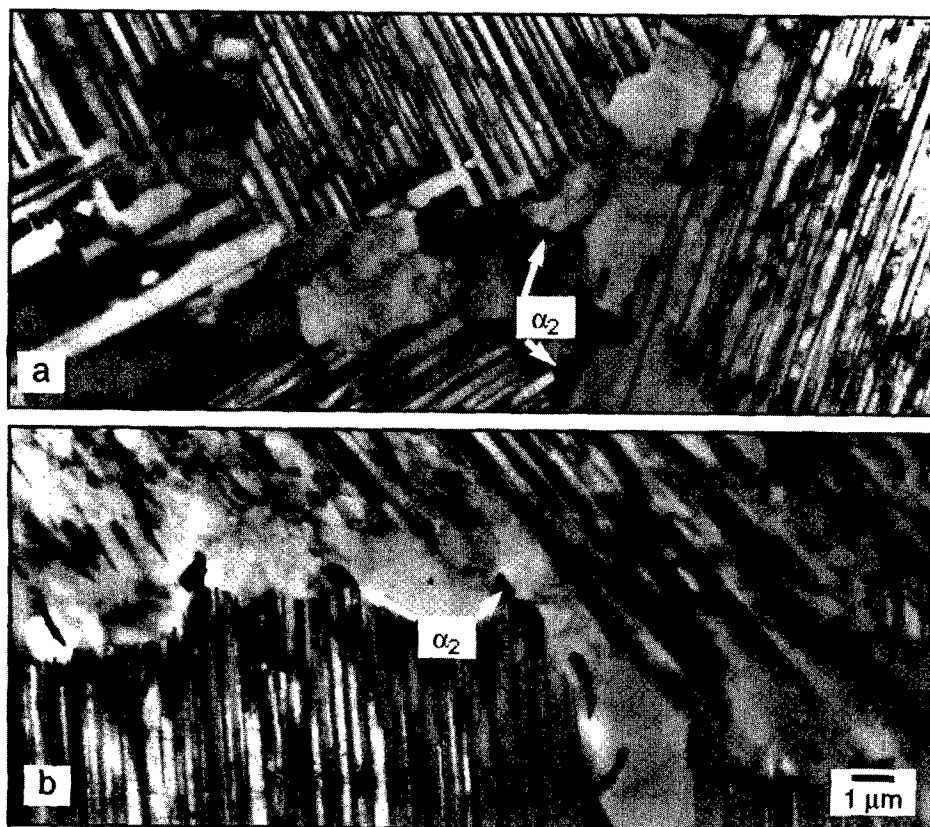


Fig. 8 - TEM showing the difference in discontinuous coarsening at intercolony boundaries of a.) P/M Ti-47Al-2Cr-2Nb (73-1) and b.) P/M Ti-47Al-2Cr-1Nb-1Ta (74-1) alloys aged for 5040 h at 800°C.

Table 2 - Quantitative Microcompositional Analysis of Phases in P/M Ti-47Al-2Cr-2Nb and P/M Ti-47Al-2Cr-1Nb-1Ta Alloys

Extrusion/Heat-Treatment	Phase	Composition (at.%)				
		Al	Ti	Cr	Nb	Ta
<u>P/M Ti-47Al-2Cr-2Nb</u>						
$T_2$ / 2 h at 900°C	lamellar $\gamma$ (8) <sup>a</sup>	47.4	49.2	1.6	1.8	
	lamellar $\alpha_2$ (4)	39	56	3	1.7	
	equiaxed $\gamma$ (1)	46.4	50	1.6	2.0	
	intercolony $\gamma$ (9)	49	47.3	1.4	2.3	
	intercolony $\alpha_2$ (1)	40.5	55	2.3	2.2	
$T_2$ / 4 h at 982°C	intercolony $\gamma$ (3)	47.7	48.4	1.5	2.4	
	intercolony $\alpha_2$ (4)	35 <sup>b</sup>	61	1.7	2.3	
$T_2$ / 2 h at 900°C + aged 5040 h at 800°C	lamellar $\gamma$ (6) <sup>a</sup>	47	48.3	1.7	3.0	
	lamellar $\alpha_2$ (6)	31.7	64.5	1.5	2.3	
	intercolony $\gamma$ (4)	47.6	47.7	1.8	3.0	
	intercolony $\alpha_2$ (4)	31.3	65	1.5	2.2	
<u>P/M Ti-47Al-2Cr-1Nb-1Ta</u>						
$T_2$ / 2 h at 900°C	lamellar $\gamma$ (4) <sup>a</sup>	51.6	45.1	1.3	0.8	1.2
	lamellar $\alpha_2$ (4)	39.5	55.4	2.5	0.8	1.8
	intercolony $\gamma$ (2)	48.7	47.4	1.3	1.1	1.6
	intercolony $\alpha_2$ (2)	38.6	56.5	2.3	1.1	1.7
$T_2$ / 4 h at 982°C	intercolony $\gamma$ (2)	48.4	47.5	1.4	1.1	1.6
	intercolony $\alpha_2$ (2)	33.6	61.2	1.5	0.8	1.9

a - number of individual measurements included in average

b -  $\pm 3.6$ , which is a typical variation for individual measurements

[11,13,16,17]. The P/M Ti-47Al-2Cr-2Nb alloy (extruded at  $T_x$  and heat-treated at 900°C) has 1.4% total tensile elongation, YS of 970 MPa, and a fracture toughness of 22 MPa $m^{1/2}$ , all at room-temperature [11]. Heat-treatment of the P/M alloy at 1320°C increases the elongation to 3.6%, but lowers the YS to 650 MPa [16]. Liu et al. [16,17] attributes the improved ductility in these P/M  $\gamma$ -TiAl alloys mainly to their refined colony size. Kim [2] noted a similar relationship between colony size and ductility for the FL I/M K5 (Ti-46.5Al-2Cr-3Nb-0.2W) alloy, with colony sizes in the 100-300  $\mu$ m range and elongations in the 2-4% range. Liu et al. [11] explains the very high strength of this P/M material on the basis of the ultrafine lamellar structure, comparing strengthening by the ultrafine and regularly alternating  $\gamma$  and  $\alpha_2$  platelets as similar to a micro-laminate. Even more important than the room-temperature strength is the strength that these ultrafine lamellar alloys retain at high temperatures. These P/M Ti-47Al-2Cr-2Nb alloys have a YS of over 800 MPa at 800°C [11].

In terms of their formation, these P/M Ti-47Al-2Cr-2Nb and Ti-47Al-2Cr-1Nb-1Ta alloys appear to fall into the category of Type I fully-lamellar microstructures described by Kim [18]. Such microstructures are formed by heating or processing the TiAl alloy above  $T_\alpha$ , and then the  $\gamma$  lamellae nucleate in the  $\alpha$ -grains as the alloy is undercooled. Generally, increasing the cooling rate (larger undercooling) decreases  $\lambda_c$  until a massive transformation of  $\alpha$  to  $\gamma$  occurs, which prevents the formation of the fully-lamellar structure [18-20]. The residual disordered  $\alpha$  phase trapped between the  $\gamma$  lamellae then transforms to  $\alpha_2$  below the eutectoid temperature to produce the final lamellar microstructure. For binary TiAl alloys, such fully-lamellar structures form more readily in Ti-47Al alloys than in alloys with less Al, and are also more resistant to discontinuous coarsening during aging [21]. Generally, slow furnace cooling rates produce  $\lambda_c$  of 1  $\mu$ m or more in binary TiAl alloys, and polysynthetically twinned TiAl crystals have lamellar structures with  $\lambda_c$  slightly less than 1-2  $\mu$ m and  $\lambda_\alpha$  of 5-10  $\mu$ m, dominated by  $\gamma/\gamma$  interfaces [8, 19-22]. Kim [19] has reported an ultrafine lamellar structure with  $\lambda_c$  of 0.03-0.2  $\mu$ m in a Ti-47Al-1Cr-1V-2.5Mo alloy heat-treated above  $T_\alpha$ , and Soe et al. [24] report  $\lambda_c$  of 0.3  $\mu$ m and  $\lambda_\alpha$  of about 1  $\mu$ m in investment-cast Ti-47Al-2Nb-2Mn with 0.8% TiB $_2$ , but generally there are no systematic studies of comparable alloys with fully-lamellar structures consistently as fine as reported here.

The ultrafine lamellar microstructure forms easily in the P/M Ti-47Al-2Cr-2Nb alloy processed above  $T_\alpha$ . At the same processing conditions (extrusion temperature and cooling rate), alloying changes of reduced Nb and added Ta slightly refine  $\lambda_c$  and almost eliminate the intercolony  $\gamma$ . Maziasz et al. [18,25] have found that additions of B+W to I/M Ti-47Al or Ti-47Al-2Cr-2Nb alloys also refine both  $\lambda_c$  and  $\lambda_\alpha$ . Rejection of W by the  $\gamma$  lamellae as they form, which retards their growth, has been suggested as the reason for this effect [14,18,25]. Such segregation is consistent with the  $\gamma/\alpha$  interfacial W segregation observed by Larson et al. [26], and with the W partitioning to the  $\alpha_2$  lamellae observed by XEDS [27]. A comparison of the  $\alpha_2$  phase composition in the initial and in the heat-treated or the aged specimens of the Ti-47Al-2Cr-2Nb alloy would suggest that Cr and Nb behave analogous to W, and also are dissolved by the metastable  $\alpha$  phase as they are rejected by growing  $\gamma$  lamellae.

The ultrafine lamellar structure that forms during cooling of the as-processed material must also remain stable during subsequent heat-treatment and thermal aging to provide technologically relevant improvements in high-temperature strength. In fact it is somewhat of a paradox for finer lamellar structures to also be more stable, because reducing the surface area of the structure is one of the driving forces for continuous lamellar coarsening [22]. The most important factors governing the stability and coarsening resistance of these ultrafine lamellar structures at high-temperatures appear to be the resistance of the original fine  $\alpha_2$  lamellae to dissolution and their metastable composition. Clearly, this structure is unstable in the P/M Ti-47Al-2Cr-2Nb alloy during heat-treatment or aging near or at 1000°C. The compositional change in the intercolony  $\alpha_2$  that precipitates after 4 h at 982°C is consistent with the equilibrium  $\alpha_2$  phase composition at that temperature (less Al). Aging for 5040 h at 800°C produces only subtle microstructural changes, consistent with the kinetics of diffusion being much more sluggish at the lower aging temperature, and with the equilibrium  $\alpha_2$  phase composition being even lower in aluminum (approaching Ti-

25Al). However, despite such small degree of microstructural coarsening, there is a much larger change in the composition of the  $\alpha_2$  phase, which is the same in the thin, lamellae that are dissolving from the original structure and the new  $\alpha_2$  particles that have formed during aging in the intercolony  $\gamma$  (Table 2). These data clearly indicate that diffusion is moving the originally metastable  $\alpha_2$  lamellae toward their equilibrium phase composition, and that such changes, include repartitioning of Cr and Nb back into the  $\gamma$  phase, precede dissolution.

Similar arguments have been offered to explain the improved aging resistance of the W+B modified simpler Ti-47Al alloys. Tungsten is also forced into the metastable  $\alpha_2$  lamellae when they form, and apparently is repartitioning much more slowly during aging at 1000°C than the Al [14,18]. Segregation of elements like W, Cr, Nb and Ta to the fine, metastable  $\alpha_2$  lamellae would then explain how those elements enable the ultrafine lamellar structure to form in the first place. The need for those elements to diffuse out of the metastable  $\alpha_2$  lamellae before they can dissolve at lower temperatures would then explain why those particular elements increase the coarsening resistance (at least relative to binary alloys) of such structures during aging. The reason for Cr and Nb dissolving in the metastable  $\alpha_2$  lamellae at higher temperatures initially but then being rejected at lower temperatures is not as clear; it may reflect solubility differences between disordered  $\alpha$  and ordered  $\alpha_2$  for those elements. However, it is clear that the longer the  $\alpha_2$  lamellae resists dissolution during aging, the longer the ultrafine lamellar structure remains stable and resists continuous coarsening. While  $\lambda_c$  may be the primary strength-controlling factor at any point in time, the role of the  $\alpha_2$  lamellae seems to be to act as the "glue" that holds these ultrafine lamellae together at high temperatures.

In summary, achieving a refined-colony/ultrafine-lamellar structure produces a combination of ductility and strength at room-temperature, and strength at high-temperatures, that has not been achieved previously in fully-lamellar two-phase  $\gamma$ -TiAl alloys. The refined colony size makes these alloys ductile, while the ultrafine  $\lambda_c$  makes them strong. Data presented here showing lamellar stability and microcompositional evolution during heat-treatment or aging, demonstrate that controlling and stabilizing the lamellar structure in general, and the fine  $\alpha_2$  component in particular, is a very important part of any alloy design strategy aimed at improving the properties of  $\gamma$ -TiAl alloys.

## Conclusions

1. Hot-extrusion of P/M Ti-47Al-2Cr-2Nb and Ti-47Al-2Cr-1Nb-1Ta alloys at  $T_x$  above  $T_\alpha$  produces ultrafine lamellar structures ( $\lambda_c \leq 100$  nm and  $\lambda_\alpha \leq 220$  nm) with a refined colony size  $\leq 70$  nm.
2. Such microstructures do not change after a heat-treatment of 2h at 900°C, but do show early stages of continuous lamellar coarsening after 4 h at 982°C. Heat-treatment for 2 h at 1320°C coarsens  $\lambda_c$  and  $\lambda_\alpha$  considerably with little change in colony size, while 2 h at 1350°C dramatically increases the colony size with little change in  $\lambda_c$  and  $\lambda_\alpha$ .
3. Aging for 5040 h at 1000°C totally coarsens the initial ultrafine lamellar structure in both 73-1 and 74-1 alloys, whereas similar aging at 800°C produces little change. Both alloys show the very earliest stages ( $\alpha_2$  dissolution) of continuous lamellar coarsening. The Ta-modified 74-1 alloy appears to show more discontinuous coarsening at intercolony boundaries, with more precipitation of coarse  $\alpha_2$  particles.
4. AEM studies of microcomposition of individual lamellae and phase particles show that  $\alpha_2$  phase in the initial microstructure contains about 40 at.% Al and more Cr than adjacent  $\gamma$  lamellae. Both heat-treatments near 1000°C and long-term aging at 800°C show compositional changes in the  $\alpha_2$  lamellae (much less Al, and less Cr and Nb), which indicate that the initial lamellae form with a metastable composition, and diffusion toward the equilibrium phase composition precedes dissolution of those lamellae.



### Acknowledgements

Thanks to D.S. Easton and L. Heatherly for alloy preparation and fabrication. Thanks to J.W. Jones for preparing specimens for electron microscopy. Thanks to D. Clemens at Pratt&Whitney, Advanced Engineering Operations, West Palm Beach, FL, for producing TiAl powders and support of the CRADA work. Thanks to P. Angelini for program management support for both the DP-CRADA and the Advanced Industrial Materials (AIM) work. Thanks to L. Heatherly and D.S. Easton for reviewing the manuscript. Research sponsored by the U.S. Department of Energy, Assistant Secretary for Energy Efficiency and Renewable Energy, Office of Industrial Technologies, AIM Program, and Assistant Secretary of Defense Programs (DP), Technology Management Group, Technology Transfer Initiative, under contract DE-AC05-96OR22464 with Lockheed-Martin Energy Research Corp.

### References

1. Y-W. Kim, *JOM*, 46 (1994) 30-40.
2. Y-W. Kim, in *Gamma Titanium Aluminides*, eds. Y-W. Kim, R. Wagner, M. Yamaguchi (Warrendale, PA: TMS, 1995) 637-654.
3. Y-W. Kim, in *High-Temperature Ordered Intermetallics Alloys IV*, vol. 213, eds. L.A. Johnson, D.P. Pope and J.O. Stiegler (Pittsburgh, PA: MRS, 1991) 777-794.
4. D.M. Dimiduk, in *Gamma Titanium Aluminides*, eds. Y-W. Kim, R. Wagner, M. Yamaguchi (Warrendale, PA: TMS, 1995) 3-20.
5. C.M. Austin and T.J. Kelly, in *Gamma Titanium Aluminides*, eds. Y-W. Kim, R. Wagner, M. Yamaguchi (Warrendale, PA: TMS, 1995) 21-40.
6. R. Wagner, et al., in *Gamma Titanium Aluminides*, eds. Y-W. Kim, R. Wagner, M. Yamaguchi (Warrendale, PA: TMS, 1995) 387-404.
7. S. Huang, in *Structural Intermetallics*, eds. R. Darolia, et al. (Warrendale, PA: TMS, 1993) 299-307.
8. M. Yamaguchi and H. Inui, in *Structural Intermetallics*, eds. R. Darolia, et al. (Warrendale, PA: TMS, 1993) 127-142.
9. M. Yamaguchi and Y. Umakoshi, *Prog. Mater. Sci. Eng.*, 34 (1) (1990) 1-148.
10. J. Kumpfert, Y-W. Kim and D.M. Dimiduk, *Mater. Sci. and Engin.*, A192/193 (1995) 465-473.
11. C.T. Liu, et al., in *Gamma Titanium Aluminides*, eds. Y-W. Kim, R. Wagner, M. Yamaguchi (Warrendale, PA: TMS, 1995), 679-688.
12. J.N. Wang, et al., in *Gamma Titanium Aluminides*, eds. Y-W. Kim, R. Wagner, M. Yamaguchi (Warrendale, PA: TMS, 1995), 949-957.
13. C.T. Liu, et al., *Intermetallics*, 4 (1996) 429-440.
14. R.V. Ramanujan, P.J. Maziasz and C.T. Liu, *Acta Mater.*, 44 (7) (1996) 2611-2642.
15. R.V. Ramanujan and P.J. Maziasz, *Met. and Mater. Trans. A*, 27A (1996) 1661-1673.
16. C.T. Liu and P.J. Maziasz, unpublished data, ORNL, 1995, presented at Symposium on Intermetallic Compounds at the JIM '95 Meeting, December 13-15, 1995 in Honolulu, HA.
17. C.T. Liu, P.J. Maziasz and J.L. Wright, "Key Microstructures Controlling the Mechanical Properties of Two-Phase TiAl Alloys With Lamellar Structures," to be published in Proc. Symp. *High-Temperature Ordered Intermetallic Alloys VII*, MRS, Pittsburgh, PA in 1997.
18. P.J. Maziasz, et al., *Intermetallics*, 5 (1997) 83-95.
19. Y-W. Kim, *Acta Metall. et Mater.*, 40 (1992) 1121-1134.
20. M. Takeyama, T. Kumagai, N. Nakamura, M. Kikuchi; in *Structural Intermetallics*, eds. R. Darolia, J. Lewandowski, C.T. Liu, P. Martin, D. Miracle and M. Nathal (Warrendale, PA: TMS, 1993) 167-176.
21. P. Wang and V.J. Vasudevan; *High Temperature Ordered Intermetallics V*, ed. I. Baker, R. Darolia, J.D. Wittenberger, and M.H. Yoo, vol. 288 (Pittsburgh, PA: MRS, 1993) 229-236.
22. J.D. Livingston and J.W. Cahn; *Acta Met.* 22 (1974) 495-503.
23. Y. Umakoshi, T. Nakano, and T. Yamane; *Matls. Sci. and Engin.* A152 (1992) 81-88.
24. D.Y. Seo, T.R. Bieler and D.E. Larson, "Effect of Interstitial Concentration and Heat Treatment on Microstructure and Primary Creep of Investment Cast Ti-47Al-2Nb-2Mn with 0.8 v.% TiB<sub>2</sub>," to be published in Proc. Symp. *High-Temperature Ordered Intermetallic Alloys VII*, MRS, Pittsburgh, PA in 1997.
25. P.J. Maziasz and C.T. Liu, "Ultrafine Fully-Lamellar Structures in Two-Phase  $\gamma$ -TiAl Alloys," to be published in Proc. Symp. *High-Temperature Ordered Intermetallic Alloys VII*, (Pittsburgh, PA: MRS) in 1997.
26. D.J. Larson, C.T. Liu and M.K. Miller, "Microstructural Characterization of Segregation and Precipitation in  $\alpha_2+\gamma$  Titanium Aluminides," submitted to *Matls. Sci. and Engin.* in 1997.
27. P.J. Maziasz and C.T. Liu, "Development of Ultrafine Lamellar Structures in Two-Phase  $\gamma$ -TiAl Alloys," submitted to *Met. and Matls. Trans. A* in 1997.



## A PRELIMINARY STUDY ON THE DECOMPOSITION OF THE BETA PHASE IN

### Ti-44Al-8Nb AND Ti-44Al-4Ta-4Zr-0.2Si ALLOYS

T.T. Cheng and M.H. Loretto

IRC in Materials for High Performance Applications  
The University of Birmingham, Birmingham B15 2TT, U.K.

#### Abstract

The decomposition of the beta phase has been studied in Ti-44Al-8Nb and Ti-44Al-4Ta-4Zr-0.2Si alloys cooled from the ( $\alpha+\beta$ ) phase field using TEM and SEM. The morphology of the transformation products is shown to be sensitive to cooling rate and the results of the microstructural observations are used to construct a schematic continuous cooling transformation (CCT) diagram for these alloys. It is shown that under slow cooling, the beta phase is mainly consumed by the neighbouring alpha grains via  $\alpha/\beta$  interfacial migration. During the subsequent  $\alpha \rightarrow \alpha + \gamma$  transformation which occurs at lower temperatures and produces a lamellar microstructure, the retained beta phase can transform partially to  $\gamma$  by a process analogous to the discontinuous coarsening of  $\gamma$  lamellae. It has also been shown that at higher cooling rates, the beta phase can decompose to alpha via secondary lath formation and/or a Widmanstätten transformation. The decomposition of beta directly to faceted gamma has also been observed in rapidly cooled materials. Possible mechanisms for each of these transformations are discussed.

#### Introduction

There has been significant interest in recent years in materials based on titanium aluminides as candidates for high temperature structural applications. Alloys based on  $\gamma$ -TiAl have been the focus of particularly intense activity since they offer a combination of low density and useful mechanical properties at temperatures higher than those possible with more conventional titanium alloys. There remains, however, significant room for improvement in properties such as ductility and fracture toughness. Much work has been devoted to studying the effects of thermomechanical processing and alloying in  $\gamma$ -TiAl based alloys. The general consensus is, however, that where thermomechanical processing results in the improvement of one specific property, it is often at the expense of another. The

evidence suggests that major overall improvements in the properties cannot be achieved with modest levels of alloying additions (say <5% in total)<sup>1,2</sup>. Much of the recent work has, therefore, been focused on alloying additions at much higher levels. Currently there are many different alloying elements which are being considered, many of which are known to be "beta stabilising". At significant levels of these additions, the beta phase becomes stable at temperatures where conventional thermomechanical processing takes place. Furthermore, the  $\alpha+\beta$  phase field has been considered beneficial for thermal processing since alpha grain growth is restricted, particularly when the volume fraction of the beta phase is high<sup>1</sup>. Thus, the decomposition of the beta phase during post-processing cooling could be important in determining the final microstructure.

In this study, we have examined the microstructures in Ti-44Al-8Nb and Ti-44Al-4Ta-4Zr-0.2Si alloys when annealed in the ( $\alpha+\beta$ ) phase field followed by cooling under a variety of different conditions. Special attention has been paid to the microstructural evolution in the prior beta region and the results are used to construct a schematic CCT diagram which is built upon that developed by Jones and Kaufman<sup>3</sup>.

#### Experimental Procedures

The alloys used for this study were Ti-44Al-8Nb and Ti-44Al-4Ta-4Zr-0.2Si (in at.%). They were prepared as 0.8kg buttons using transferred-arc plasma melting in a water-cooled copper hearth under argon. The ingots were remelted five times to ensure homogeneity. The actual compositions of the buttons were analysed by EPMA using elemental or compound standards and were found to be 44.2Al-8.0Nb and 43.4-4.5Zr-4.3Ta (the Si content was not assessed due to Si K peaks overlap with Ta M peaks). The interstitial contents were determined by Timet U.K. using inert gas fusion techniques and the O<sub>2</sub> and N<sub>2</sub> contents were 500-800 and 40-80 ppm (in wt.), respectively.

The ingots were HIPped at 1250°C for 4 hours at 150MPa followed by isothermal forging at 1150°C to a reduction in height of 70% at a strain rate of  $5 \times 10^{-3}$ /s. The forged materials were then heat treated at various temperatures in the ( $\alpha + \beta$ ) phase field and subsequently furnace cooled at 10°C/min or water quenched to room temperature. After heat treatment, the samples were examined using SEM and TEM. TEM specimens were prepared by electropolishing to perforation in a solution of 6% perchloric acid, 34% butane-1-ol, and 60% methanol followed by  $\text{Ar}^+$  ion beam thinning. TEM was performed using a Philips CM20 microscope operated at 200kV.

In addition to the heat treatments described above, the transus temperatures were determined for the two alloys by heat treating forged specimens at various temperatures followed by water quenching. The temperature at which the lamellar structure starts to form during cooling was determined for the 44-8 alloy by heat treating at 1350°C, furnace cooling at 10°C/min to various temperatures and then water quenching. (It should be noted, however, that this temperature does not necessarily correspond to  $T_0$  for the composition.) These samples were sectioned, polished, and examined metallographically to determine the phases present. These results are mentioned only briefly in the present paper but a full description of the detailed observations and their interpretation will be presented elsewhere.

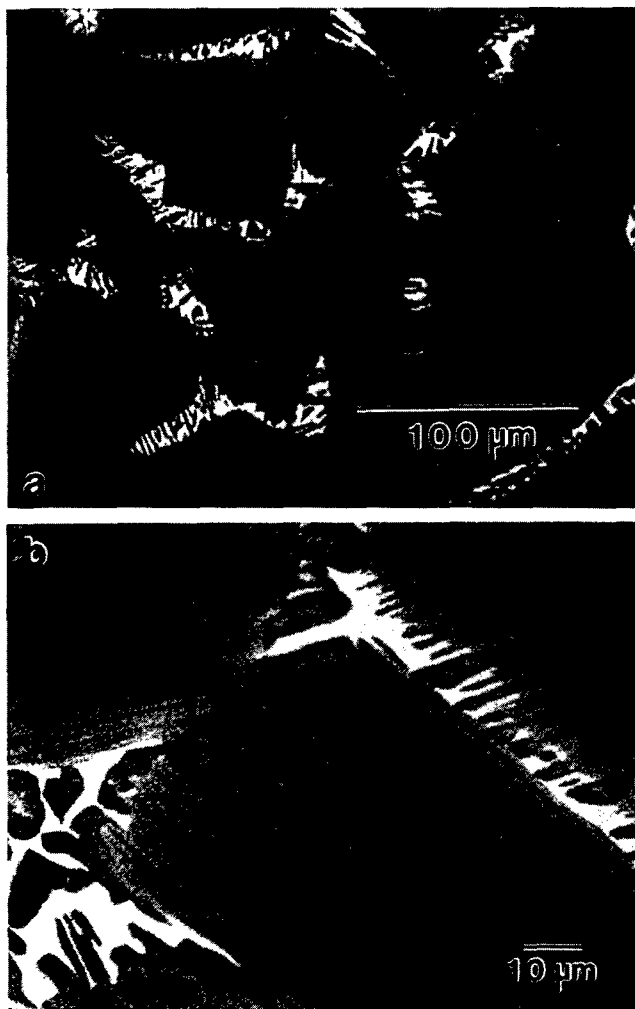


Figure 1(a)&(b) - Back scattered SEM images of the 44-8 alloy furnace cooled from 1350°C. (bright-beta, grey-alpha, dark-gamma)

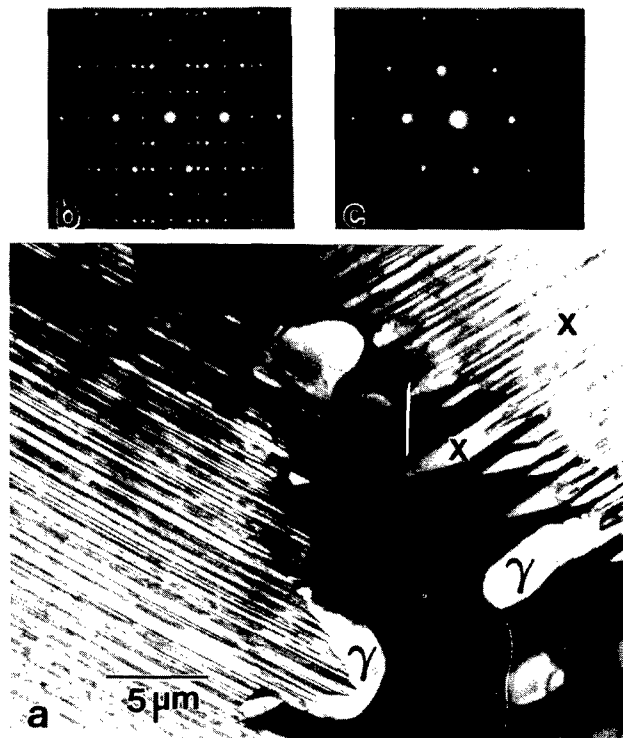


Figure 2(a) - TEM image of the 44-8 alloy furnace cooled from 1350°C (b) and (c) - selected area diffraction patterns of the lamellar region (marked) and coarsened  $\gamma$  grain (marked), respectively. ( $B = \langle 11\bar{2}0 \rangle_{\alpha 2} // \langle 011 \rangle_{\gamma}$ ); (d) - SAD pattern of the "retained beta",  $B = \langle 110 \rangle_{\beta 2}$ ).

## Results

Despite the differences in the compositions of the two alloys, the decomposition of the beta phase was nearly identical. In the following sections we consider the final microstructures obtained by the different heat treatment/cooling routes in turn.

### Transus temperatures

Two transus temperatures were determined for the alloys:  $T_{\gamma}$ , the highest temperature at which the gamma phase is stable, and  $T_{\beta}$ , the lowest temperature at which the beta phase is stable. We note that no disordered b.c.c phase or anti-phase boundaries (APB's) in the B2 have been observed and therefore no information on the b.c.c to B2 transformation temperature can be deduced. In what follows, the term 'beta' phase is used to describe regions which probably had the b.c.c. structure but then underwent ordering to give the B2 and/or  $\omega$  phases. The transus temperatures obtained were:

	$T_{\gamma}$	$T_{\beta}$
Ti-44Al-8Nb	1260°C	1290°C
Ti-44Al-4Ta-4Zr-0.2Si	1300°C	1290°C

These temperatures show that the equilibrium phase transformation for the 44-8 alloy is  $\beta + \alpha \rightarrow \alpha \rightarrow \alpha + \gamma$ , i.e. similar to those for Ti-Al binary alloys. For the alloy 44-4-4, the

sequence is  $\beta + \alpha \rightarrow \beta + \alpha + \gamma \rightarrow \alpha + \gamma$ , i.e. there is no single phase alpha regime.

#### Furnace-cooled from 1350°C

When annealed at 1350°C (i.e.  $\alpha + \beta$  field) followed by furnace cooling, the 44-8 alloy exhibited mainly a lamellar structure with retained beta present at colony boundaries and triple junctions. Figure 1(a) is an SEM image using back scattered electrons (BSE) showing the lamellar colonies ( $\approx 50\text{-}100\mu\text{m}$  in size) and the presence of retained beta. Higher magnification images such as Figure 1(b) suggest that some  $\gamma$  lamellae have grown into the beta region and coarsened. This can be readily confirmed using TEM. Figure 2(a) is a TEM image taken from this material showing that the beta region has been penetrated by various coarsened  $\gamma$  lamellae. These coarsened  $\gamma$  grains have the same orientation as their thinner counterparts which is demonstrated by the diffraction patterns obtained from one such  $\gamma$  and the lamellar region from where such  $\gamma$  grains are originating (Figs. 2(b) and (c)). Electron diffraction on the "retained beta" indicates that it has decomposed into small  $\omega$  domains and this is shown in Fig. 2(d). All spots which correspond to the  $\omega$  phase are sharp with no apparent streaking, suggesting that the transformation is nearly complete.

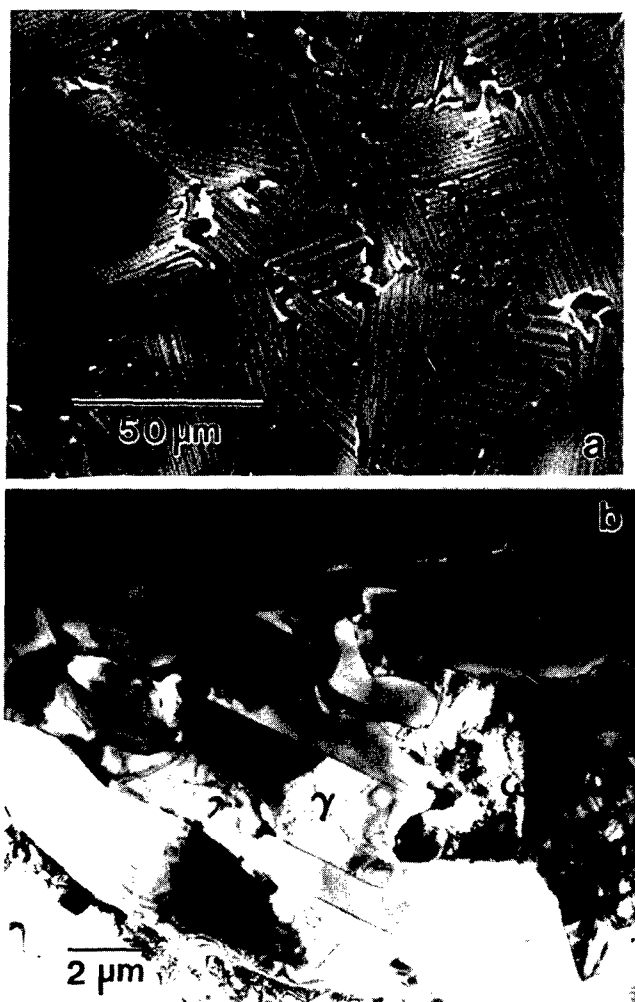


Figure 3(a)&(b) - Back scattered SEM and TEM images of 44-4 alloy furnace cooled from 1350°C.

The microstructure in the 44-4 alloy after furnace cooling from 1350°C (i.e. within the  $\alpha + \beta$  phase field) is similar to that in the 44-8 alloy. Figure 3(a) is a BSE image showing that the material also consists mainly of regions with a lamellar structure, but with a higher fraction of  $\gamma$  at the colony boundaries than in the 44-8 alloy (many colonies are surrounded by coarsened  $\gamma$ ). TEM observations also confirmed that the decomposition was more extensive with little  $\beta$  remaining (Figure 3(b)). Furthermore, higher magnification TEM images of the retained beta (e.g. Figure 4(a)) showed domain-like features which are  $\approx 1\mu\text{m}$  in size. Selected area diffraction patterns obtained from these domains indicate that they are  $\omega$  grains. Figures 4(b) and (c) are patterns obtained from two different domains. Other than the coarsened  $\gamma$  lamellae, there are large gamma grains present inside the prior beta regions, and these are often faceted. Figure 5(a) is a TEM image showing two such faceted  $\gamma$  grains surrounded by retained beta (i.e.  $\omega$ ). Analyses of selected area diffraction patterns from these large  $\gamma$  grain showed that they have an orientation relationship with the beta whereby:

$$\{111\}_{\gamma} // \{110\}_{\beta} \text{ and } \langle T01 \rangle_{\gamma} // \langle 1\bar{1}1 \rangle_{\beta}$$

Figure 5(b) and (c) are diffraction patterns obtained from the faceted  $\gamma$  and the surrounding "retained" beta (i.e.  $\omega$ ), respectively demonstrating their orientation relationship.

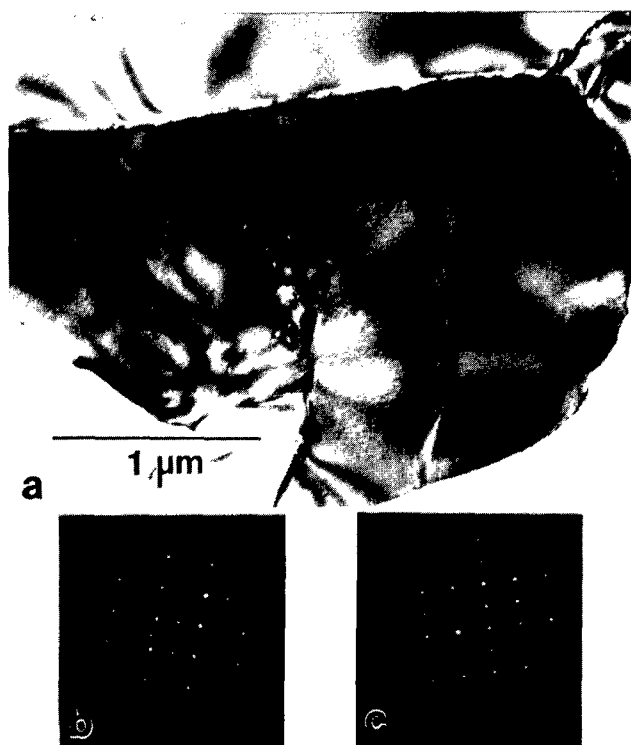


Figure 4(a) - TEM image obtained from the 44-4 alloy furnace cooled from 1350°C showing  $\omega$  domain structure in the "retained" beta; (b)&(c) diffraction patterns obtained from different  $\omega$  domains

#### Water quenched from 1350°C

After water quenching from 1350°C (i.e. within the  $\alpha + \beta$  phase field) the 44-8 and 44-4 alloys exhibited identical microstructures in the transformed beta regions - in both cases the beta had decomposed partially into thick secondary alpha laths. Figure 6(a) is a TEM image taken from the 44-4 alloy

showing such irregular alpha laths forming within a prior  $\beta$  grain. Analyses of selected area diffraction patterns indicated that these alpha laths exhibit the Burgers orientation relationship (Figures 6(b)&(c)),

$$(0001)_\alpha // \{110\}_\beta \text{ and } \langle 11\bar{2}0 \rangle_\alpha // \langle 1\bar{1}1 \rangle_\beta.$$

The decomposition of the alpha phase into  $\alpha+\gamma$  lamellae is entirely suppressed both in these  $\alpha$  laths and in the primary  $\alpha$ . It was also found that the  $\omega$  formation in these materials has been partially suppressed; this is indicated by the weaker and more diffuse features corresponding to the  $\omega$  phase in the diffraction patterns obtained from the retained  $\beta$  (Figure 6(c)). In addition to the formation of coarse secondary alpha laths, beta appeared to be consumed by neighbouring alpha grains as in the furnace-cooled material, however, this was only evident in the 44-4-4 alloy since this contains a small amount of silicides which act as pinning particles during the transformation. Figure 7 is a TEM image showing some retained beta phase sandwiched by two alpha grains in the 44-4-4 material. It is concluded, based on diffraction analysis, that the interface on the right is semi-coherent and appears flat. The interface on the left is, however, less coherent. In addition, silicide particles at the  $\alpha/\beta$  interface and bowing of the less coherent interface can be observed readily

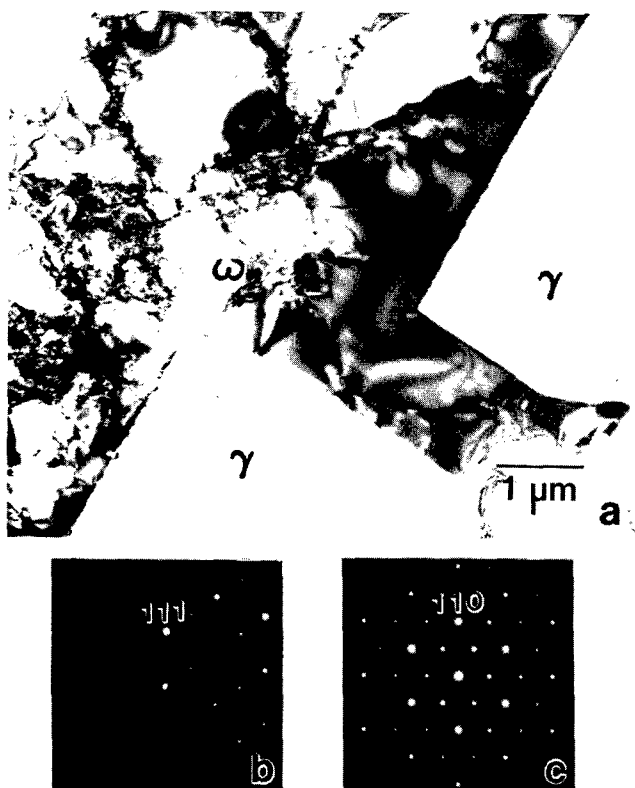


Figure 5(a) - TEM image obtained from the 44-4-4 alloy furnace cooled from 1350°C showing faceted  $\gamma$  grains; (b)&(c) diffraction patterns obtained from  $\gamma$  and the surrounding "retained" beta (i.e.  $\omega$ ), respectively. ( $B=\langle 110 \rangle_\gamma // \langle 1\bar{1}1 \rangle_{\beta 2}$ )

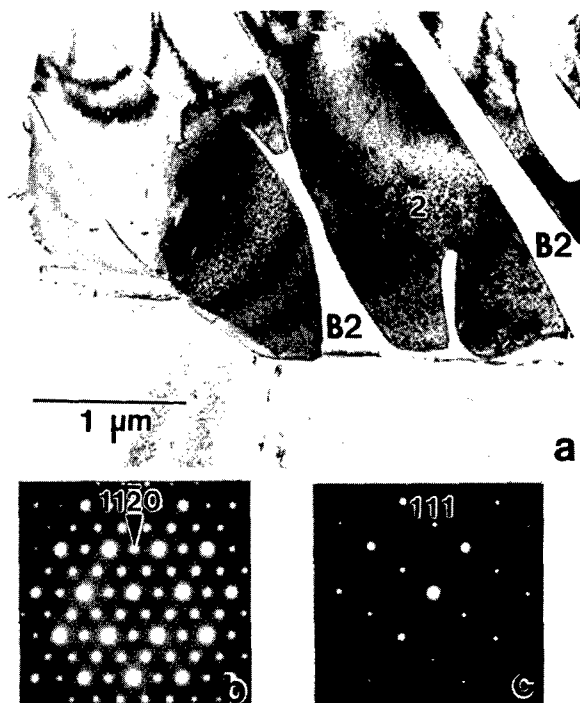


Figure 6(a) - TEM image obtained from the 44-4-4 alloy water quenched from 1350°C showing irregular secondary alpha laths forming within a prior beta grain; (b)&(c) - diffraction patterns taken from alpha and the surrounding retained beta, respectively. ( $B=\langle 0001 \rangle_{\alpha 2} // \langle 110 \rangle_{\beta 2}$ )

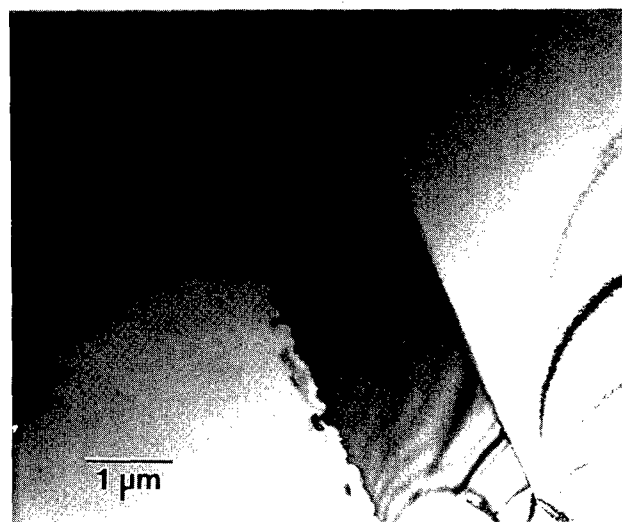


Figure 7 - TEM image obtained from the 44-4-4 alloy water quenched from 1350°C showing a narrow retained beta sandwiched by two alpha grains.

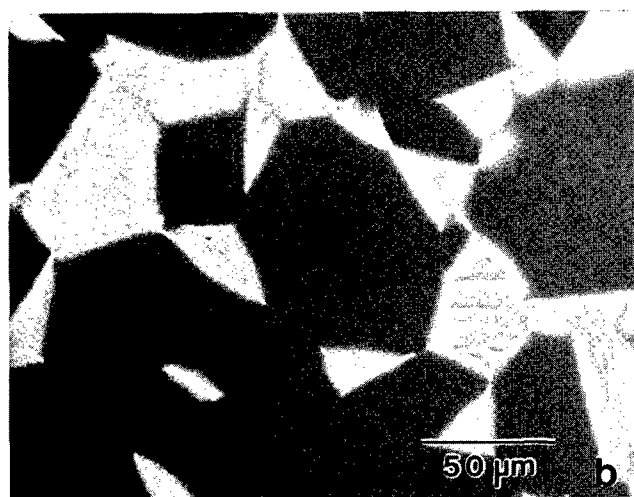
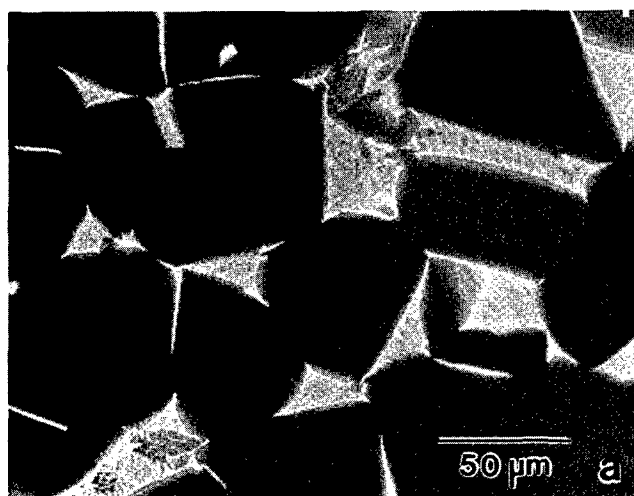


Figure 8(a) & (b) - BSE images obtained from the 44-8 and 44-4-4, respectively, after water quenching from 1310°C.

#### Water quenched from 1310°C

The microstructures produced by quenching from 1310°C (again from  $\alpha+\beta$  phase field) in alloys 44-8 and 44-4-4 are shown in Figures 8(a) and (b). Some of the beta grains exhibit a much finer contrast than those in samples quenched from 1350°C. TEM studies were performed on these materials and images of the transformed beta grains in 44-8 and 44-4-4 are shown in Figure 9(a) and (b), respectively. There are lenticular alpha laths present in a retained beta matrix. Higher magnification images of these lenticular laths indicate that they are heavily faulted. Figure 10(a) and (b) are a TEM image and a diffraction pattern, respectively, of an alpha lath observed in the 44-8 alloy. Analyses of selected area diffraction patterns suggest that these alpha laths also exhibit the Burgers orientation relationship with respect to the parent beta phase. Energy dispersive X-ray spectrometry (EDX) analyses on these alpha laths show that they have a different composition from the beta matrix (Table 1). In addition to the alpha laths, occasional  $\gamma$  grains have been observed embedded in the retained beta matrix. Figure 11 shows one such example. Here again, EDX analyses on these gamma grains show that they have a different composition from their parent beta phase. It should be noted that the lenticular alpha laths and faceted  $\gamma$  grains are not observed in the narrower retained beta regions - only  $\alpha/\beta$  interface migration is evident in

such regions. Both  $\alpha/\beta$  interface migration and alpha laths have been observed in intermediate-sized beta grains.



Figure 9(a) & (b) - TEM images of 44-8 and 44-4-4, respectively, showing the decomposed prior beta after water quenching from 1310°C.

Table 1 - Chemical composition of the 44-8 alloy quenched from 1310°C.

		Al	Nb
primary	$\alpha$	45.1 $\pm$ 0.5	7.5 $\pm$ 0.5
	$\beta$	40.0 $\pm$ 2.0	9.3 $\pm$ 0.5
transformed $\beta$ :	$\alpha$	43.9 $\pm$ 1.0	7.3 $\pm$ 0.5
	$\beta$	36.6 $\pm$ 4.0	9.2 $\pm$ 0.5
	$\gamma$	46.4 $\pm$ 0.5	7.2 $\pm$ 0.5

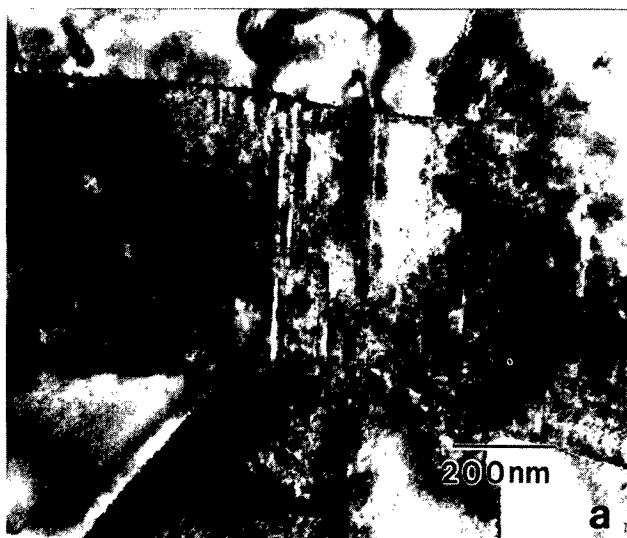
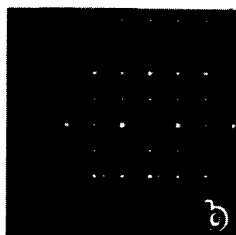


Figure 10(a) - TEM image showing a lenticular alpha plate in the 44-8 alloy after water quenching from 1310°C; (b) SAD pattern. ( $B = \langle 11\bar{2}0 \rangle_{\alpha_2}$ )



### Discussion

#### Furnace cooling

In furnace-cooled materials, the lamellar microstructure has been shown to be predominant. The lamellae appear to have advanced with no interruption which suggests that the prior  $\alpha/\beta$  interfaces have migrated during furnace cooling. Schematic diagrams which illustrate a plausible sequence for the decomposition in the prior beta regions are shown in Figure 12. Firstly, the  $\alpha/\beta$  interfaces migrate to reduce the volume fraction of beta. The migration rate of a specific interface would presumably depend on the nature of the boundary, i.e. factors such as coherency etc., and the presence of precipitates. As illustrated in Figure 7, coherent interfaces are less mobile and less likely to advance. Boundary precipitates can act as pinning points and reduce the effect of this mechanism. At lower temperatures, the lamellar microstructure is formed inside alpha grains and at the prior  $\alpha/\beta$  interfaces gamma lamellae would come into direct contact with beta phase. Some of the gamma lamellae have a favourable orientation with respect to the prior beta and can undergo a rapid expansion similar to that involved in discontinuous coarsening commonly observed in many fully lamellar TiAl-based alloys. The difference in the present case is that the gamma lamellae are advancing into neighbouring beta rather than into alpha. Furthermore, the driving force for such coarsening is usually attributed to interfacial energy. Such an argument could not be valid in the present case as the interfacial area is increasing. If we consider the compositional changes involved, the transformation from beta to alpha would require a smaller

adjustment than that for the beta to gamma transformation. Nevertheless, gamma formation appears to be more favourable than alpha. Gamma grains can also nucleate directly from the beta phase, particularly for the 44-4-4 alloy where there is no single  $\alpha$  phase field, i.e. a  $(\alpha+\beta+\gamma)$  phase field is directly below the  $(\alpha+\beta)$  field. The transformation from beta to gamma by direct nucleation could result in large gamma grains with the orientation relationship

$$\{111\}_{\gamma} // \{110\}_{\beta} \text{ and } \langle T01 \rangle_{\gamma} // \langle 1T1 \rangle_{\beta}$$

which was observed in the furnace cooled 44-4-4 alloy.

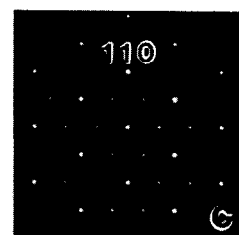
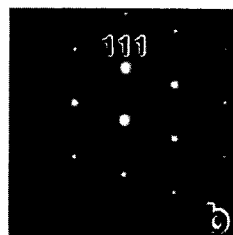
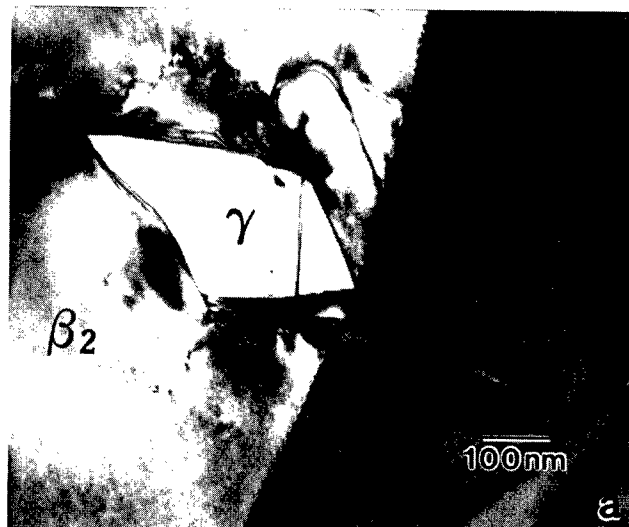


Figure 11(a) - TEM image showing a faceted  $\gamma$  grain in the 44-8 alloy after quenching from 1310°C; (b)&(c) SAD patterns of  $\gamma$  and the parent beta, respectively ( $B = \langle T01 \rangle_{\gamma} // \langle 1T1 \rangle_{\beta_2}$ )

#### Quenching from 1350°C

On water quenching from 1350°C, two different decomposition mechanisms can operate - boundary migration and secondary alpha lath formation. The former is evidenced by the presence of silicides inside the primary alpha grain and by the bowing of  $\alpha/\beta$  interfaces. Presumably, decomposition via this mechanism is sluggish due to the significant amount of diffusion involved through very limited areas of interface. The large driving force during rapid cooling is therefore released via another nucleation-growth mechanism which is the secondary alpha lath formation within the prior beta. These alpha laths have an irregular morphology and exhibit the Burgers orientation relationship (Fig. 6(a))<sup>4,5</sup>.

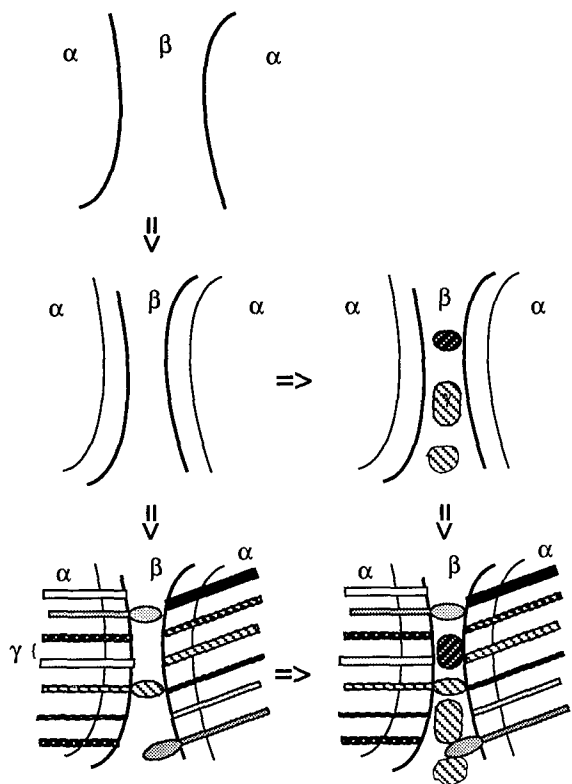


Figure 12 - Schematic diagrams illustrating the evolution of  $\gamma$  by discontinuous coarsening and direct nucleation within prior beta.

#### Quenching from 1310°C

On quenching from 1310°C, beta transforms to alpha by boundary migration, secondary alpha lath transformation, formation of lenticular alpha laths (Figs. 9(a) & (b)) and faceted  $\gamma$  formation (Fig. 11). It was shown that the lenticular laths are heavily faulted (Fig. 10(a)) and these resemble the Widmanstätten morphology observed in conventional  $\alpha$  and  $\beta$  titanium alloys. The occurrence of this mechanism is presumably due to the driving force for decomposition resulting from rapid cooling from 1310°C which is so great that it cannot be accommodated fully by boundary migration and secondary alpha lath formation. The remainder of the decomposition therefore occurs by a Widmanstätten transformation which results in alpha laths with a high aspect ratio, i.e. large interface area to accommodate the large driving force. Presumably, the point at which this transformation occurs will vary locally depending on the composition, grain size etc. and the compositions of the transformed products would, therefore, depend on the temperature at which the transformation occurs. This could account for the large variation in the measured compositions for the transformed products (Table 1).

In these materials, faceted  $\gamma$  grains with the orientation relationship

$$\{111\}_{\gamma} // \{110\}_{\beta} \text{ and } \langle T01 \rangle_{\gamma} // \langle 1T1 \rangle_{\beta}$$

are also observed. It is not clear that these arise from the same mechanism as the large  $\gamma$  grains observed in the furnace-cooled

materials, i.e. by direct nucleation, although they exhibit the same orientation relationship. We speculate that since the lenticular Widmanstätten laths are heavily faulted, the planar faults can lead to instantaneous  $\alpha \rightarrow \alpha + \gamma$  lamellar formation. As observed previously in the furnace-cooled materials, some of the  $\gamma$  lamellae can have a favourable orientation with respect to the parent beta phase and grow out rapidly in the same fashion as in discontinuous coarsening. The Widmanstätten alpha laths adopt the Burgers orientation relationship with respect to the parent beta phase and in the lamellar microstructure, the alpha and gamma exhibit the Blackburn orientation relationship<sup>6</sup>. There would, therefore, be a well defined orientation relationship between the discontinuously coarsened  $\gamma$  and the retained beta into which they grow given by:

$$\begin{aligned} (0001)_{\alpha} // \{110\}_{\beta} \text{ and } \langle 11\bar{2}0 \rangle_{\alpha} // \langle 1T1 \rangle_{\beta} \\ + \\ \{111\}_{\gamma} // (0001)_{\alpha} \text{ and } \langle T01 \rangle_{\gamma} // \langle 11\bar{2}0 \rangle_{\alpha} \\ \Downarrow \\ \{111\}_{\gamma} // \{110\}_{\beta} \text{ and } \langle T01 \rangle_{\gamma} // \langle 1T1 \rangle_{\beta} \end{aligned}$$

as observed experimentally. This could, therefore, account for the faceted  $\gamma$  grains found embedded in the "retained" beta matrix.

#### CCT diagram

Based on the microstructural observations, a schematic CCT diagram can be constructed to illustrate the decomposition of beta phase under various cooling conditions. This is shown in Figure 13. Firstly, the decomposition of beta to alpha via interface migration can occur most readily since no nucleation would be required and therefore negligible undercooling is necessary. When the cooling rate is increased, secondary alpha lath formation can become more important since this requires nucleation of the alpha inside prior beta or at  $\alpha/\beta$  interfaces. Quenching from lower temperatures can effectively correspond to higher cooling rates. This then leads to the formation of Widmanstätten alpha plates. The large density of "grown in" planar faults in these lenticular laths can presumably act as nucleation sites for  $\gamma$  lamellae. This is indicated by the thinner curve next to the Widmanstätten alpha curve. Occasionally, gamma grains are formed inside beta. It is possible that these  $\gamma$  grains are the results of discontinuously coarsened  $\gamma$  lamellae from Widmanstätten alpha laths.

The decomposition of beta to  $\gamma$  directly is also plausible. This is represented by the curve  $\beta \rightarrow \gamma$  by direct nucleation in contrast to the  $\beta \rightarrow \gamma$  by discontinuous coarsening. The position of this curve would therefore depend on the  $T_{\gamma}$  in that for 44-8 it would be near the  $\beta \rightarrow \gamma$  via discontinuous coarsening curve whereas for 44-4-4, there is a  $\alpha + \beta + \gamma$  phase region (and that  $T_{\gamma}$  is 40°C higher) which could push this curve towards higher temperatures and left of the diagram.

At lower temperatures and under slow cooling, the lamellar structure can form inside alpha grains. Some of the  $\gamma$  lamellae can grow into the neighbouring beta phase and undergo discontinuous coarsening. This is represented by the curve adjacent to the lamellar  $\alpha \rightarrow \alpha + \gamma$ .

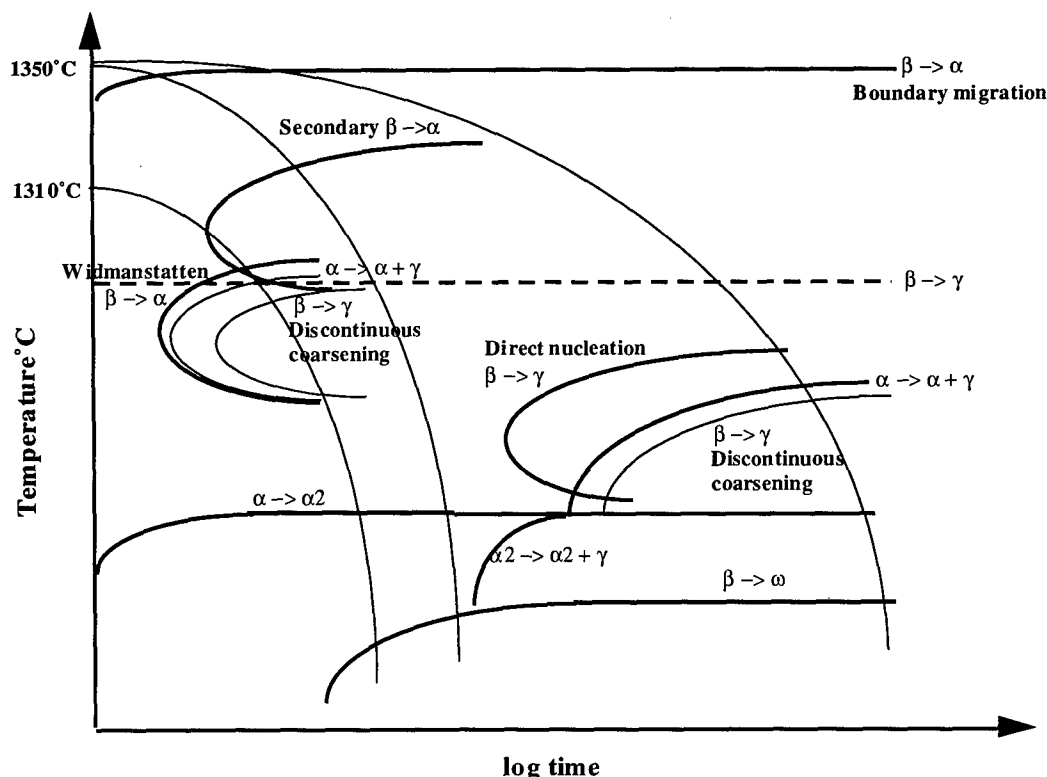


Figure 13 - A schematic CCT diagram for the alloys 44-8 and 44-4-4 simulating the decomposition of the beta phase when cooling from the ( $\alpha+\beta$ ) phase field.

#### $\omega$ ordering

Strong  $\omega$  ordering has been observed in both of the alloys and under all cooling conditions. Although this ordering reaction has been partially suppressed by water quenching, the domain size could reach a few microns (Fig. 4(a)) in diameter on furnace cooling which suggests that  $\beta \rightarrow \omega$  is a first order transformation, i.e. nucleation and growth. This is acknowledged by the  $\beta \rightarrow \omega$  curve in the CCT diagram although the exact position of the curve is still unknown.

#### Summary

A study has been performed on the transformed beta microstructures produced on cooling in two TiAl-based alloys heat treated in the ( $\alpha+\beta$ ) phase field. The morphology of the transformed products is sensitive to cooling rate. Under slow cooling, the beta phase is mainly consumed by the neighbouring alpha grains via  $\alpha/\beta$  interfacial migration. During the subsequent  $\alpha \rightarrow \alpha+\gamma$  lamellar transformation, the retained beta phase can transform partially to  $\gamma$  by a process analogous to the discontinuous coarsening of  $\gamma$  lamellae. At higher cooling rates, the beta phase can decompose to alpha via secondary lath formation and/or a Widmanstätten transformation. These mechanisms are introduced to accommodate the large driving force for decomposition which cannot be met by interfacial migration alone due to the significant diffusion which is required.

#### Acknowledgement

This work was supported by EPSRC through the IRC core funding. The authors are grateful to Prof. I.P. Jones, Dr. M.

Strangwood and Dr. M. Aindow for useful discussions and commenting on the manuscript. The use of facilities in the School of Metallurgy and Materials is also gratefully acknowledged.

#### Reference

1. Y-W. Kim, "Gamma Alloy Technology: Fundamentals and Development", IRC Workshop on TiAl, 1-3 May 1996, Birmingham UK.
2. S-C Huang, "Alloying Considerations in Gamma-Based Alloys", *Structural Intermetallics*, (ed. Darolia et al, The Minerals, Metals & Materials Society, 1993), 299-307.
3. S.A. Jones and M.J. Kaufman, "Phase Equilibria and Transformations in Intermediate Titanium-Aluminum Alloys", *Acta Met. Mat.*, 41(2)(1993), 387-398.
4. R.W. Cahn and P. Haasen, *Physical Metallurgy*, (Elsevier Science Publishers B.V., 1983).
5. D.A. Porter and K.E. Easterling, *Phase Transformations in Metals and Alloys*, (Van Nostrand Reinhold, UK, 1986).
6. M.J. Blackburn, *The Science, Technology and Application of Titanium*, (ed. R.I. Jaffee and N.E. Promisel, Pergamon Press, Oxford, 1970) 633.



## **PROCESSING OF TIAL**

## PROCESSING OF INTERMETALLIC ALLOYS

by S.L. Semiatin,\* J.C. Chesnutt,† C. Austin,‡ and V. Seetharaman§

\* Materials Directorate, Wright Laboratory, WL/MLLM, Wright-Patterson AFB, OH 45433

† General Electric Aircraft Engines, Cincinnati, OH 45215

§ UES, Inc., Dayton, OH 45432

### Abstract

The state of the art of processing of structural intermetallic alloys including various aluminides and silicides is reviewed. Special emphasis is placed on the manufacture of gamma titanium aluminide alloys for which a variety of deformation, solidification, powder, and heat treatment processes have been developed. Current understanding of microstructure evolution and fracture behavior during processing of the gamma aluminides is summarized with particular reference to production scaleable techniques. These methods include vacuum arc and plasma, cold-hearth melting, isothermal forging, conventional hot forging and extrusion, pack rolling, and superplastic sheet forming for ingot metallurgy (wrought) products; investment and permanent mold casting; and hot isostatic pressing (HIP) or HIP plus forging of powder. The selection and design of manufacturing methods in the context of processing-cost tradeoffs for gamma titanium aluminide alloys are also discussed.

### Introduction

Intermetallic alloys offer tremendous potential for structural applications requiring outstanding high temperature properties such as strength, toughness, creep resistance, and oxidation resistance. For this reason, research efforts to develop these materials have increased significantly in the last decade. Most of this work has been spurred by the needs of the aerospace industry, but interest has also been shown by others as evidenced by a variety of automotive, petrochemical, and other applications.

As for many advanced materials, the properties of structural intermetallics are heavily dependent on composition and microstructure. Thus, synthesis and subsequent processing methods play an important role in the control and optimization of properties and service performance. Synthesis techniques utilized to date have covered a broad spectrum of vapor, liquid, and solid state approaches. Vapor methods include those based on physical vapor deposition (PVD) techniques such as electron beam evaporation and magnetron sputtering. Liquid phase techniques range from conventional ingot-metallurgy/ingot casting (e.g., consumable and non-consumable arc melting) to spray forming and the production of pre-alloyed powders from the melt via gas atomization or the plasma rotating electrode process (PREP™). Solid state techniques include reactive sintering of elemental powders and mechanical alloying. Feest and Tweed (1) summarized some of the more common synthesis techniques and the intermetallic alloys for which they have been used (Table I). Post synthesis processing is most often applied for powder consolidation (e.g., die compaction, extrusion) or the working of ingot-metallurgy products (e.g., extrusion, forging, rolling, sheet forming).

In the present paper, the current status of processing experience for some of the more common aluminide and silicide intermetallic

alloys is reviewed. Special attention is focused on the gamma titanium aluminide alloys as a prototypical system for which a number of processing alternatives have been developed and for which technical and economic feasibility may both enter into final process selection.

### Background

In this section, the status of the processing of some of the more common aluminide and silicide systems is reviewed. These materials include those based on the compounds  $\text{Fe}_3\text{Al}$ ,  $\text{FeAl}$ ,  $\text{Ni}_3\text{Al}$ ,  $\text{NiAl}$ ,  $\text{Nb}_3\text{Si}$ ,  $\text{Nb}_3\text{Al}$ , and  $\text{MoSi}_2$ .

#### $\text{Fe}_3\text{Al}$

Iron aluminide alloys based on the  $\text{Fe}_3\text{Al}$  compound are probably the structural intermetallic materials which have been produced in the largest quantity to date.  $\text{Fe}_3\text{Al}$  has an ordered  $\text{DO}_{19}$  cubic structure below  $550^\circ\text{C}$ , and an imperfectly ordered B2 cubic structure above this temperature. The  $\text{Fe}_3\text{Al}$ -base alloys usually contain chromium, zirconium, carbon, boron, as well as other elements to reduce environmental embrittlement and refine grain structure, among other reasons (2). These materials exhibit excellent oxidation and sulfidation resistance and potentially lower cost than the stainless steels with which they compete. As such, a number of potential applications for these iron aluminides have been identified (2). These include metalworking dies, heat shields, furnace fixtures and heating elements, and a variety of automotive components.

The primary synthesis techniques for  $\text{Fe}_3\text{Al}$  alloys have been based on melting. The materials have been prepared by air induction melting, vacuum induction melting (VIM), argon induction melting (AIM), non-consumable and consumable arc melting, and electroslag remelting. VIM and AIM are the most common methods; these processes also offer an advantage relative to air melting in that they minimize moisture pickup which can lead to porosity caused by rejection of hydrogen from solution during the solidification of ingots or castings.

Table I. Synthesis Techniques Used to Manufacture Intermetallic Alloys (1)

Synthesis Technique	Alloys Synthesized
Electron Beam PVD	$\text{Ti}_3\text{Al}$ , $\text{Ti}_2\text{AlNb}$ , $\text{TiAl}$
Arc Melting	$\text{Fe}_3\text{Al}$ , $\text{NbAl}_3$ , $\text{Ni}_3\text{Al}$ , $\text{Ti}_3\text{Al}$ , $\text{TiAl}$
Induction Melting	$\text{Ni}_3\text{Al}$
Spray Forming	$\text{Ni}_3\text{Al}$
Pre-Alloyed Powder	$\text{FeAl}$ , $\text{Ni}_3\text{Al}$ , $\text{NiAl}$ , $\text{Ti}_3\text{Al}$ , $\text{TiAl}$
Reaction Synthesis	$\text{Ni}_3\text{Al}$

Structural Intermetallics 1997

Edited by M.V. Nathal, R. Darolia, C.T. Liu, P.L. Martin,  
D.B. Miracle, R. Wagner, and M. Yamaguchi  
The Minerals, Metals & Materials Society, 1997

Sikka and his coworkers at Oak Ridge National Laboratory (ORNL) have developed a rather simple technique to enable the melting of large heats (~2500 kg) of Fe<sub>3</sub>Al alloys while avoiding problems associated with the melting of alloys with both low-melting point (e.g., Al) and high-melting point (e.g. Fe) elements (3). The method makes use of induction melting and a special furnace loading scheme, whose design is based on knowledge of the nature of the exothermic reaction that occurs when Fe<sub>3</sub>Al is formed from iron and aluminum. In brief, the furnace load comprises three regions, i.e., a region at the top containing the aluminum and a portion of the iron, a middle region containing ternary, quaternary, etc. alloying elements, and a bottom region with the remainder of the iron. When the induction power is turned on, the charge heats uniformly until the aluminum at the top reaches 660°C, melts, and reacts exothermically with the iron. This hot liquid runs through the middle and bottom layers thereby dissolving the remainder of the charge.

The ORNL team has also been successful in demonstrating casting of Fe<sub>3</sub>Al using gravity or centrifugal casting into sand or ceramic molds. Alternatively, large ingot castings have been easily extruded, forged, or rolled at temperatures in the range of 900°C to 1200°C. The wrought structure thus produced can be warm rolled to plate or sheet at temperatures between 500 and 600°C to manufacture product with room temperature tensile ductility of 15 to 20 percent (3,4). However, wrought Fe<sub>3</sub>Al alloys do not possess adequate workability for cold rolling or cold drawing.

Sikka, *et al.* (5) have also demonstrated the manufacture of Fe<sub>3</sub>Al containing 2 to 5 percent chromium from gas atomized powder. The powder was consolidated by hot extrusion at 1000°C, after which hot forging and hot rolling, also at 1000°C, and warm rolling at 650°C were carried out successfully.

#### FeAl

The FeAl-base alloys have an ordered cubic B2 crystal structure for aluminum contents between 35 and 50 atomic percent; FeAl remains ordered B2 to the melting point. Compared to Fe<sub>3</sub>Al, FeAl is much more difficult to process and rather far from becoming a commercially feasible product.

Gaydosch and Crimp (6) successfully conducted canned hot extrusion of small castings to produce a recrystallized structure. However, hot rolling has been unsuccessful. Canned hot extrusion of FeAl powders at 900°C using extrusion ratios of 8:1 to 12:1 has also been found to be an effective method for obtaining fully dense material with fine equiaxed, recrystallized grains (7). Stout and Crimp (8) measured the crystallographic textures developed during hot extrusion of FeAl. The powder precursor material developed a <111> texture which, in conjunction with oxide inclusions, was found to give rise to abnormal grain growth during high temperature annealing. By contrast, cast-and-extruded material was found to develop primarily a <110> texture with a weaker <111> component, but was not susceptible to abnormal grain growth during subsequent high temperature heat treatment.

Vacuum hot pressing and hot isostatic pressing have also been used to consolidate FeAl powders, but these operations provide insufficient deformation to breakup oxides at prior particle boundaries.

#### Ni<sub>3</sub>Al

The nickel aluminide Ni<sub>3</sub>Al is probably the intermetallic closest to full-scale commercialization after Fe<sub>3</sub>Al. Ni<sub>3</sub>Al is ordered up to its melting point (~1395°C) and has a L1<sub>2</sub> crystal structure analogous to face-centered cubic crystals with an ABC stacking arrangement; its unit cell comprises nickel atoms at face-centered positions and aluminum atoms at the corner positions. Furthermore, Ni<sub>3</sub>Al is the strengthening constituent ('gamma prime') in many commercial nickel-base superalloys and as such exhibits excellent high temperature strength and creep properties. The Ni<sub>3</sub>Al-base alloys typically contain boron and chromium for ductilization at ambient and intermediate temperatures (600-800°C) and zirconium for solid solution strengthening. Principal applications include turbochargers for heavy-duty diesel engines; automotive valves, valve seats, and pistons; high

temperature dies and molds; cutting tools; and jet engine blades and vanes (in the directionally solidified condition) (9,10,11).

The processing of Ni<sub>3</sub>Al has been most commonly done via ingot metallurgy routes and less commonly by powder metallurgy processing and reaction synthesis. Typical melting methods include induction melting in air or vacuum, vacuum arc melting, and electron beam melting. Experience has shown that the preferred route is vacuum induction melting (using the furnace-loading scheme mentioned above for Fe<sub>3</sub>Al) followed by electroslag remelting (ESR) (11,12). By this means relatively porosity-free ingots with good surface quality can be made. The electroslag remelt produces an equiaxed grain structure that is much finer, and hence workable, than that produced via vacuum induction melting alone (11). Ingots as large as 2500 kg have been melted. Melted material has also been direct cast into sheet (thickness ≤ 3 mm), bar, and complex-shape castings. Problems associated with hot-cracking, porosity, and interaction with shell materials in the production of investment castings can be alleviated by controlling casting parameters and adjusting alloy composition and mold material (10).

The primary breakdown of Ni<sub>3</sub>Al ingots is dependent on alloy composition, grain size, and processing temperature and strain rate. In general, the hot workability in forging increases with decreasing zirconium concentration and finer grain sizes (10). For example, alloys containing less than 0.3 atomic percent zirconium can be successfully hot forged at temperatures between 1050 and 1200°C. Conventional hot extrusion and hot rolling of these alloys is possible at comparable temperatures, but the material must be encapsulated, typically using mild steel cans (12). Some of the alloys are also cold workable in the as-cast condition (3,12). For example, direct cast sheets of an alloy containing 21.7 aluminum and 0.35 zirconium (atomic percent) were cold rollable to 60 percent reduction without an intermediate anneal (12). Another alloy with 15.9 aluminum, 8.0 chromium, 1.7 molybdenum, and 0.50 zirconium (atomic percent) was found to be capable of being cold worked with intermediate anneals at 1100°C to produce 2-mm diameter welding wire. Furthermore, the fine wrought structures developed in the Ni<sub>3</sub>Al alloys lead to substantial improvements in room temperature tensile properties (13) and make them superplastic; superplastic material has been isothermally forged into jet engine turbine disks at 1100°C and a nominal strain rate of 8.3 x 10<sup>-3</sup> s<sup>-1</sup> (12).

A number of investigations have also examined the feasibility of processing of Ni<sub>3</sub>Al using gas atomized pre alloyed powders. As-HIP'ed powder has been found to have inferior tensile elongations compared to cast-plus-extruded material (14). This behavior has been attributed to easy failure along the prior particle boundaries in the HIP'ed powder product. For this reason, some form of hot work is advantageous in breaking up the oxides at the particle boundaries. To this end, hot extrusion in steel cans at temperatures between 1100 and 1200°C using reductions of approximately 8:1 or greater is often used (13). The hot extruded material has a fine-grain structure (10 to 20 μm) and contains a very small amount of microporosity. Alternate working methods include isothermal forging and rapid omnidirectional compaction (13).

Reaction synthesis of elemental powders has also been utilized to make Ni<sub>3</sub>Al (15,16). Alloys with a density up to 97 percent of the theoretical value have been produced by optimizing the reaction synthesis parameters (e.g., particle size, heating rate, atmosphere). Nishimura and Liu (17) have shown that Ni<sub>3</sub>Al with somewhat higher density (>99 percent) can be produced by reaction synthesis under compressive stresses.

#### NiAl

The nickel aluminide alloy NiAl has been under investigation for several decades. However, interest in the processing and properties of the alloy has accelerated over the last 10 to 15 years. NiAl has a B2 crystal structure comprising two interpenetrating simple cubic lattices, one each of nickel atoms and aluminum atoms. It melts congruently at 1638°C. The principal intended use of NiAl alloys has been as a replacement for nickel-base superalloy jet engine turbine blades. Processing approaches have focused on the solidification processing of single crystals and the powder metallurgy processing of fine-grained

polycrystalline material. Single crystal alloys usually have microalloying additions of iron, gallium, or molybdenum to improve low temperature ductility.

NiAl single crystals can be produced by techniques such as those based on growth from the melt (e.g. Czochralski; edge-defined, film-growth), the float zone method, pedestal growth, and the Bridgman process (18). A modified Bridgman process, comprising the slow withdrawal from a casting furnace of a ceramic mold holding the molten metal and utilizing a grain selector to produce a single crystal of desired orientation, has received the most attention. One of the greatest challenges in using the technique has been the selection of mold material to contain the molten NiAl alloy. Important considerations in this selection have been reactivity and thermal expansion mismatch between the metal and the ceramic mold. If the thermal expansion coefficient of NiAl is greater than that of the mold material, the casting will shrink more during cooldown and thus be subjected to tensile stresses which could crack it. The problems of reactivity and thermal expansion have been attacked by using molds of alumina and silica as well as more advanced (proprietary) compositions which have less tendency to sinter or produce volatile compounds at the melting temperature (18,19).

Because most single crystal blades are hollow, they are typically cast using ceramic cores. These cores may shift, sag, or break during the casting operation, however. Hence, an alternative process has been developed to make hollow blades (20,21). This process consists of casting a solid blade, wire EDM sectioning, plunge (electrode) EDM to produce the internal cooling cavities, activated diffusion bonding to re-join the two halves, and final machining of airfoil contours, cooling holes, etc. This so-called fabricated blade approach can result in improved dimensional tolerances and improved inspectability while allowing the freedom to incorporate advanced cooling designs.

Single-phase, single crystal NiAl alloys have good creep strength but poor toughness. One method of overcoming this shortcoming is the use of directional solidification of a eutectic system in which the NiAl phase is toughened by phases such as alpha-chromium, alpha molybdenum, or a chromium-molybdenum solid solution (21).

Efforts to ductilize NiAl alloys have also used approaches based on powder metallurgy processing. HIP, hot pressing, extrusion, and swaging have all been applied to NiAl. For example, Vedula (22) consolidated powder by canned, hot extrusion at temperatures of 1125 to 1175°C. The extruded grain size decreased with decreasing extrusion temperature. Related work by Schulson and Barker (23) showed that grain sizes as small as approximately 10  $\mu\text{m}$  could be obtained by the use of microalloying and a two-step extrusion operation, the first at 1000°C and the second at 500°C. However, even with such a fine grain size, room temperature ductility was almost nil. However, calculations using Chan's model for the dependence of ductility on grain size for semibrittle materials suggests that grain sizes of the order of 0.1  $\mu\text{m}$  are needed to ductilize polycrystalline NiAl (24,25). Even if such fine grain sizes were achievable, it is unclear whether the microstructure would be stable during service or subsequent processing.

#### Niobium-Base Intermetallic Alloys

The last decade has seen a very large amount of research on niobium-base intermetallic alloys. The principal alloy systems have been based on the ordered B2, Nb<sub>5</sub>Si<sub>3</sub>, and Nb<sub>3</sub>Al phases. Jackson and his coworkers (26,27) have investigated a series of ordered and disordered beta alloys in the composition range Nb-(35-60)Ti - (7-15)Al (atomic percent). Later alloys in this class also contained chromium or hafnium additions to obtain improved environmental resistance and mechanical properties. Processing of the materials comprised vacuum arc melting followed by heat treatment and/or hot rolling.

Mendiratta and Dimiduk (28-33) have been instrumental in the development of in-situ composites containing solid-solution-strengthened (disordered) Nb plus the line compound Nb<sub>5</sub>Si<sub>3</sub>. The wide Nb/Nb<sub>5</sub>Si<sub>3</sub> two phase field of the Nb-Si phase diagram (viz., 0.6 to 37.5 atomic percent silicon) permits great flexibility in obtaining composites with a wide range of volume fractions of the phases. However, research has suggested that the best blend of properties is

obtained for compositions between 6 and 18.7 atomic percent silicon, the latter being the eutectic composition. After initial alloy development using nonconsumable arc melting of buttons, larger quantities of the Nb/Nb<sub>5</sub>Si<sub>3</sub> alloys were prepared by vacuum arc melting using consumable electrodes prepared from strips of Nb and Nb-Si master alloys. Canned, hot extrusion of the cast ingots was conducted at temperatures between 1480 and 1650°C to reductions between 4:1 and 10:1. The alloys have also been synthesized using a powder metallurgy technique. In this approach, mixtures of niobium and crushed Nb<sub>5</sub>Si<sub>3</sub> particles were consolidated by vacuum skull pressing with or without subsequent hot extrusion. A number of other refractory metal-silicide, in-situ composites have been studied to a limited degree. By and large, these materials have been synthesized on a small, laboratory scale using techniques such as cold-crucible directional solidification (34).

Another niobium-base intermetallic that has received attention, albeit still on a laboratory scale, is Nb<sub>3</sub>Al with an A15 crystal structure. Single phase Nb<sub>3</sub>Al can be produced for aluminum levels between approximately 21 and 23 atomic percent (35,36). Alloys leaner in aluminum contain Nb<sub>3</sub>Al plus beta; those richer in aluminum contain Nb<sub>3</sub>Al plus Nb<sub>2</sub>Al. Kamata, *et al.* (36) have used both induction skull melting (ISM) and vacuum arc melting to make Nb<sub>3</sub>Al. ISM was found to provide better homogeneity and control of alloy composition. Kamata, *et al.* also investigated ceramic mold materials for casting of Nb<sub>3</sub>Al alloys. They found that yttria, hafnia, and calcia provided the least reaction with the molten niobium-aluminum alloys. Molds of magnesia and zirconia reacted much more with the molten alloys.

#### MoSi<sub>2</sub>

Because of its excellent high temperature oxidation resistance, molybdenum disilicide alloys have received considerable attention as candidates for structural applications (37). The majority of the processing work for this material has focused on vacuum hot pressing or HIP of commercial powder produced by reacting Mo and Si in elemental powder form (38). Unfortunately, such powders contain undesirably high levels of oxygen and hence grain boundary silica. At temperatures below the glass transition, the silica particles crack easily and offer fracture nucleation sites, whereas above this temperature, the silica becomes viscous and detracts from creep properties.

Two alternate methods to producing MoSi<sub>2</sub> material are discussed by Hardwick, *et al.* in reference 39. The first of these is reaction synthesis (or reaction-HIP synthesis). Molybdenum and silicon powders are mixed in stoichiometric proportions. When the powders are reacted in vacuum or an inert gas environment, the synthesis is a self-purifying operation. The resulting product can be crushed to form a coarse powder and consolidated via hot pressing or HIP. The second technique comprises the application of mechanical alloying in an inert atmosphere to produce MoSi<sub>2</sub> from elemental powders.

Other synthesis approaches to eliminate the detrimental silica compound have focused on the addition of elements that have a greater affinity for oxygen than silicon or that form crystalline rather than amorphous/glassy second phases (40,41). For example, the addition of carbon to MoSi<sub>2</sub> powder leads to a reaction that forms silicon carbide and (volatile) CO during hot pressing (40).

Powder metallurgy approaches have also been used extensively in efforts to improve the low-temperature fracture resistance and high-temperature strength and creep properties. Typically, these methods make use of the addition of ductile refractory metals in particulate or fiber form (e.g. niobium, molybdenum, tungsten, or tantalum) or ceramics in whisker or particulate form (e.g. silicon carbide, titanium carbide). All of the toughening/strengthening approaches lead to high-temperature reaction between the molybdenum disilicide and the second phase to various degrees, however.

#### Processing of Gamma Titanium Aluminide Alloys

Of all the structural intermetallic alloys that are titanium base, the titanium aluminides are the most mature with respect to the development cycle and closest to being produced commercially. Orthorhombic titanium aluminide alloys, based on the Ti<sub>2</sub>AlNb phase,

are being developed for a range of jet engine applications in both monolithic form and as the matrix for continuous fiber, metal matrix composites (42). The gamma titanium aluminide alloys, based on the face-centered tetragonal TiAl phase, are under development primarily in monolithic form as a lightweight replacement for nickel-base superalloys in jet engines and several non-aerospace applications such as automobile engine valves. Because of the improved ability to control microstructure in two-phase materials as well as their more attractive properties (43), most current attention is being focused on near-gamma alloys which contain a small amount of second-phase alpha-two ( $Ti_3Al$ ) or ordered beta. The near-gamma alloys typically contain between 45 and 48 atomic percent aluminum as well as 0.1 to 2.5 atomic percent of secondary alloying elements such as niobium, chromium, manganese, vanadium, tantalum, and tungsten. In the sections that follow, the processing of near-gamma titanium aluminide alloys via ingot metallurgy/wrought, casting, and powder metallurgy routes is described. All alloy compositions are quoted in atomic percent.

#### Ingot Metallurgy Processing of Near-Gamma Titanium Aluminide Alloys

In broad terms, the ingot metallurgy processing of near-gamma titanium aluminide alloys bears a number of similarities to the processing of conventional alpha/beta titanium alloys. A high temperature second phase (alpha) is used as a structure control phase for the near-gamma alloys in much the same manner as the beta phase for alpha/beta alloys. Hence, the choice of working temperature relative to the alpha transus  $T_\alpha$  (temperature at which  $\alpha + \gamma \rightarrow \alpha$ ) for near-gamma alloys plays an equally important role vis-à-vis processing relative to the beta transus for alpha/beta alloys. For most near-gamma alloys, however, the alpha transus temperature is only 100 to 150°C below the solidus temperature. Thus, alpha-phase-field working is done to a much less degree than beta working in alpha/beta alloys because of rapid grain growth and the accompanying loss in microstructure control and workability.

The typical ingot metallurgy approach for processing near-gamma titanium aluminide alloys usually comprises (i) ingot production, (ii) ingot breakdown with or without intermediate and final heat treatment, and (iii) secondary processing.

**Ingot Production and Ingot Structure.** Three principal methods have been used successfully to melt near-gamma titanium aluminide ingots; these are induction skull melting, vacuum arc melting, and plasma (cold-hearth) melting. The first of these, induction skull melting, has been used primarily to produce small diameter (approx. 75 to 125 mm) ingots for laboratory research. Larger ingots (up to approx. 350 mm diameter) have been made by the other two techniques (44). Thermal stresses developed by nonuniform temperature fields during arc or plasma melting and casting may be quite large, especially for larger diameter ingots, and thus give rise to cracking of the low-ductility gamma titanium aluminide alloys (Figure 1) (45). One method of alleviating the thermal cracking tendency to a small extent involves a modified consumable arc melting process in which the electrode is melted using high power input to keep the entire charge molten after which the heat is poured into a metal mold.

For a given alloy composition, the cast structure is at least qualitatively similar irrespective of melting method and ingot size (46,47,48). The broad features of cast structure development are most easily understood with reference to the binary titanium-aluminum phase diagram in the region of the equiatomic composition (Figure 2). The most important feature of the phase diagram with regard to solidification structure is the occurrence of a double cascading peritectic reaction. The reaction gives rise to dendritic regions of alpha-two and gamma lamellae (which have evolved from the high temperature beta and alpha phases) and interdendritic regions of nominally single-phase gamma which are last to solidify from the melt (Figure 3).

The size of the lamellar grains in as-cast near-gamma alloys with 46 to 48 atomic percent aluminum is typically 100 to 300  $\mu m$ . A much wider range of grain sizes may be found in near-gamma alloys with less than 46 atomic percent aluminum, or materials that freeze without an interdendritic gamma phase which can pin the alpha grain

boundaries. In these alloys, it appears as though cooling rate below the solidus temperature plays an important role. For example, a 75-mm diameter induction skull melted ingot of Ti-45.5Al-2Cr-2Nb exhibited an alpha grain size of 150  $\mu m$ , whereas a 200-mm diameter, vacuum arc remelted ingot of the same alloy had a grain size of approximately 700  $\mu m$  (50).

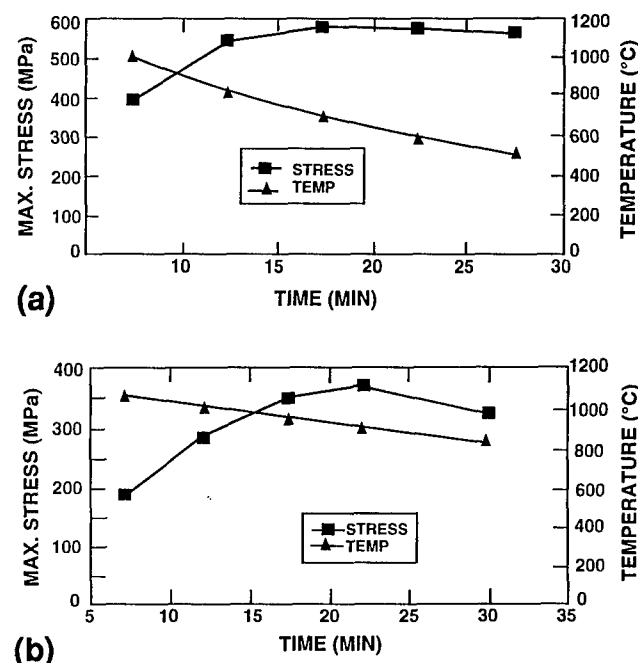


Figure 1. Predicted maximum tensile stresses (as functions of time) generated in a 350 mm diameter near-gamma titanium aluminide ingot produced via (a) vacuum arc remelting or (b) melting followed by casting in a steel mold. (45)

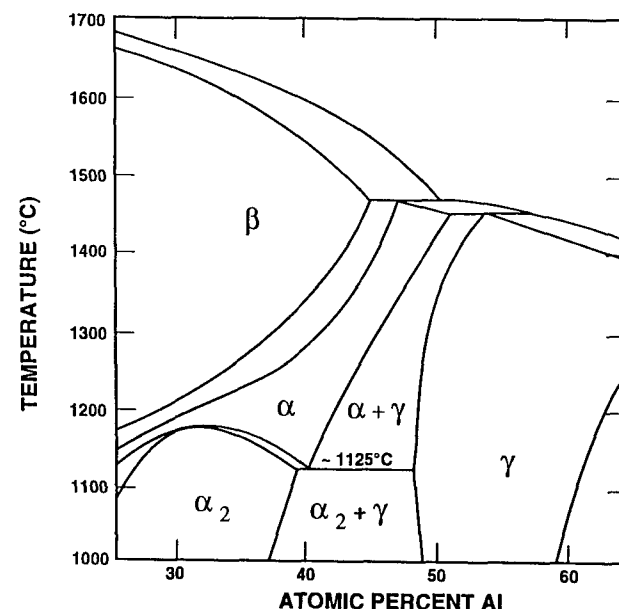


Figure 2. Portion of the binary titanium-aluminum phase diagram of interest in the processing of near-gamma and single-phase gamma titanium aluminide alloys. (49)

Extensive research has been conducted on the near-gamma alloys to develop homogenization treatments to eliminate the microsegregation characterized predominantly by the interdendritic phase. Not surprisingly, the majority of this work has shown that processes conducted solely in the alpha plus gamma phase field are insufficient to dissolve the interdendritic gamma fully to produce a completely homogeneous structure (Figure 3b); these processes have included various heat treatments, hot isostatic pressing (e.g. 1260°C/175 MPa/4h), and metalworking operations. Thus, attention has been focused on homogenization heat treatments in the single-phase alpha field (47,51) or in the alpha plus beta phase field (52). Most applicable to alloys with aluminum content less than approximately 46 atomic percent, treatment in the alpha plus beta phase field minimizes grain growth and hence concomitant losses in workability.

**Ingot Breakdown Techniques.** Three production-scaleable processes have been successfully utilized to breakdown the cast structure of gamma titanium aluminide alloys: isothermal forging, conventional (canned) forging, and conventional (canned) extrusion. For each approach, the ingot is usually HIP'ed or given a homogenization heat treatment prior to working. HIP'ing is usually done at 1260°C and a pressure of approximately 175 MPa; near-gamma alloys with an aluminum content less than approximately 46 atomic percent may be HIP'ed at a slightly lower temperature to avoid an incursion into the single-phase alpha field and a large amount of alpha grain growth during the long thermal exposure typical of the process.

Isothermal forging to breakdown the coarse ingot structure typically consists of pancaking cylindrical preforms to reductions between 4:1 and 6:1 at temperatures between 1065 and 1175°C and nominal strain rates between  $10^{-3}$  and  $10^{-2} \text{ s}^{-1}$ . Under these conditions, the ductility is usually fairly high, and sufficient hot work is imparted to globularize the lamellar structure in near-gamma alloys at least partially (percent spheroidization  $\approx 50$ ). Seetharaman and Semiatin (53) investigated the kinetics of globularization during isothermal hot

compression deformation of Ti-45.5Al-2Cr-2Nb samples which had been heat treated to provide lamellar microstructures with various alpha grain sizes. Examination of the as-compressed microstructures revealed that dynamic globularization initiated at and proceeded inward from the prior-alpha grain boundaries (Figure 4). The grain interiors showed evidence of moderate-to-extensive kinking of the lamellae, depending on the orientation of the lamellae relative to the applied load. However, there was no evidence of the kinking giving rise to globularization unlike the behavior commonly observed for the deformation of alpha/beta titanium alloys with Widmanstätten alpha microstructures. With regard to the rate of breakdown of the lamellar microstructure, globularization kinetics were found to increase as the strain rate decreased, for a given alpha grain size, and to decrease with increasing alpha grain size for a given strain rate (Figure 5). In most cases, the dependence of percent globularization on strain followed an Avrami (sigmoidal) behavior, at least approximately.

Several novel isothermal forging practices have been developed to enhance the rate of globularization or otherwise refine the microstructure during breakdown of near-gamma titanium aluminide ingots. These include the utilization of a short dwell period ( $\sim 15$  minutes) on the dies midway through the forging stroke in order to effect an increment of static globularization (Figures 6a,b) as well as the use of a two step forging process with an off-line, intermediate furnace heat treatment in the alpha plus gamma phase field (54,55). Although more expensive from a production standpoint, the latter of these two modified practices permits higher overall reductions through the ability to relubricate after the intermediate heat treatment. Another novel practice for near-gamma alloys, known as alpha forging, has evolved from thermomechanical processing principles developed originally for enhancing the properties of high-strength steels. To be specific, alpha forging is analogous to ausforming of steels in which refined microstructures and higher strengths are obtained by deformation of a metastable (high temperature) austenite phase. The corresponding practice for breakdown of near-gamma titanium aluminide ingots comprises billet preheating high in the alpha plus gamma phase field, cooling as rapidly as possible to an isothermal forging temperature substantially lower in this two-phase field, and then forging immediately (55). Success of the process depends, of course, on the ability to retain a large percentage of the metastable alpha phase during cooling. Therefore, the technique is most well-suited for small ingot melts which can be cooled rapidly. A demonstration of the process for the breakdown of cast plus HIP'ed Ti-45.5Al-2Cr-2Nb was described in reference 55. In this example, the preform was preheated at 1260°C (40°C below the alpha transus), cooled to 1150°C within 60s, and then isothermally forged to a 6:1 reduction using a standard, constant ram speed corresponding to a nominal strain rate of  $0.0015 \text{ s}^{-1}$ . The as-forged pancake in this case exhibited an almost totally globularized microstructure (Figure 6d), which contrasts sharply to the partially broken down microstructure obtained in the same material via standard isothermal forging practice (Figure 6a).

Conventional hot pancake forging of cast plus HIP'ed near-gamma titanium aluminide alloys such as Ti-45.5Al-2Cr-2Nb and Ti-48Al-2Cr has been successfully demonstrated (55-58). In this process, the dies are usually at ambient or slightly higher ( $\sim 200^\circ\text{C}$ ) temperatures. To minimize die chilling and thus the tendency for fracture, strain rates typical of conventional hot working processes (i.e.,  $\sim 1 \text{ s}^{-1}$ ) are used. However, even with these strain rates, the workpiece must be canned to produce a sound forging. Because of can-workpiece flow stress differences and heat transfer effects, uniform flow of typical can materials (e.g., type 304 stainless steel) and gamma titanium aluminide preforms can be difficult to achieve. To remedy this problem, Jain, *et al.* (56) applied FEM techniques to design cans and select process variables. It was shown that moderately uniform gamma pancake thicknesses can be achieved through a judicious choice of can geometry and can-workpiece insulation.

Because of the higher strain rates involved in conventional hot forging, as compared to those in isothermal forging, more hot work is imparted by the conventional process conducted at the same nominal workpiece temperature and to the same level of reduction. Thus, the as-forged microstructure from conventional hot forging of near-gamma alloys is typically finer, more uniform, and contains very little if

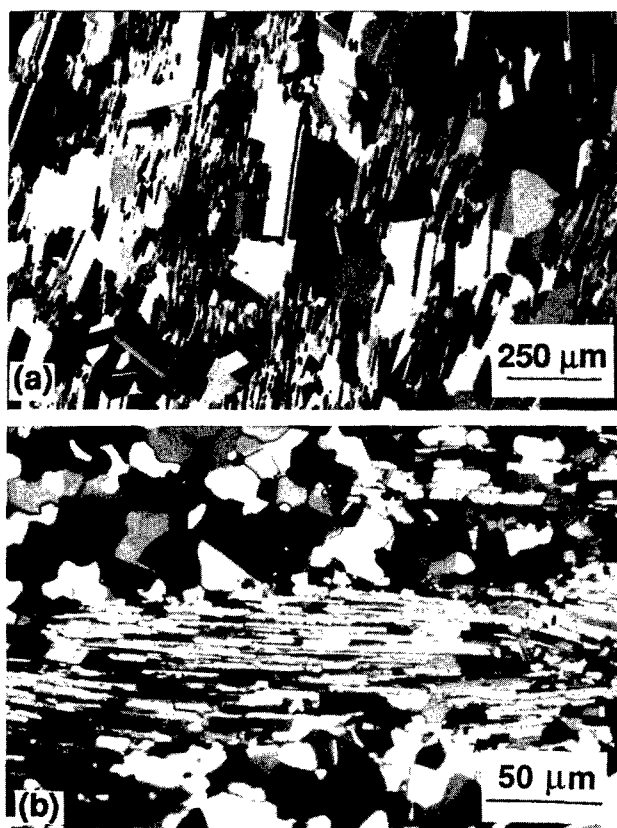


Figure 3. Polarized light optical micrographs of microsegregation in (a) cast plus HIP'ed Ti-47.3Al-2.0Nb-1.7Mn and (b) cast plus HIP'ed plus isothermally forged Ti-48Al-2.5Nb-0.3Ta. (47,51)



Figure 4. Polarized light optical microstructures developed in Ti-45.5Al-2Cr-2Nb samples isothermally upset to a 75 percent reduction at 1093°C and  $\dot{\epsilon} = 0.1 \text{ s}^{-1}$ . Prior to compression testing, the samples had been processed to yield lamellar microstructures with prior-alpha grain sizes of (a) 80  $\mu\text{m}$ , (b) 200  $\mu\text{m}$ , (c) 600  $\mu\text{m}$ , or (d) 900  $\mu\text{m}$ . The compression axis is vertical in all micrographs. (53)

any remnant lamellar colonies (Figure 6c). In addition, with optimal can design and insulation, temperature and deformation nonuniformities within the gamma preform can be minimized during conventional forging, and relatively uniform macrostructure and microstructure throughout wrought pancakes are obtained (55).

Considerable effort has been expended to develop conventional (canned) hot extrusion techniques for the breakdown of a variety of near-gamma ingot materials. As with conventional hot forging, the selection of can materials and geometry, can-workpiece insulation, and process variables is extremely important with regard to obtaining sound wrought products with attractive microstructures (59,60). Typical process variables for conventional hot extrusion to breakdown the cast structure of gamma titanium aluminide alloys include ram speeds of 15 to 50 mm/s, reductions between 4:1 and 12:1, and preheat temperatures ranging from 1050°C to 1450°C. Dies with streamline or conical geometry have been used with equal success in round-to-round extrusion. Streamline dies have also been employed in producing round-to-rectangle extrusions to make sheet bar having a width-to-thickness ratio as large as 6:1.

Can materials for conventional hot extrusion are usually type 304 stainless steel (for preheat temperatures of 1250°C or lower) or either Ti-6Al-4V or commercial purity titanium (for preheat temperatures higher than 1250°C). Even with canning, however, substantial temperature (and hence microstructural) nonuniformities may develop during extrusion due to the complex interaction of heat transfer and deformation heating effects. The temperature nonuniformities are most marked for the extrusion of billets of small diameter, i.e., O(75 mm) (Figure 7). These temperature nonuniformities can be decreased, but not eliminated, by the use of insulation between the billet and can. One of the best materials for reducing heat losses has been found to be woven silica fabric (62), although other materials such as various foil alloys are also effective. Nevertheless, even with such measures, the temperature gradients are sufficiently large to produce noticeable

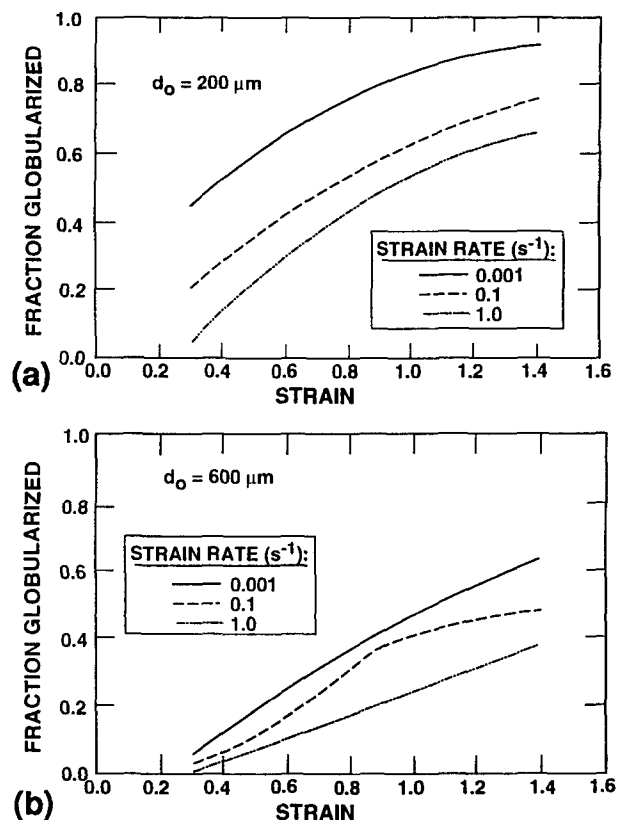


Figure 5. Fraction globularized microstructure as a function of height strain for samples of Ti-45.5Al-2Cr-2Nb isothermally upset at 1093°C and various constant strain rates. Prior to compression testing, the samples had been processed to yield lamellar microstructures with prior-alpha grain sizes of either (a) 200  $\mu\text{m}$  or (b) 600  $\mu\text{m}$ . (53)



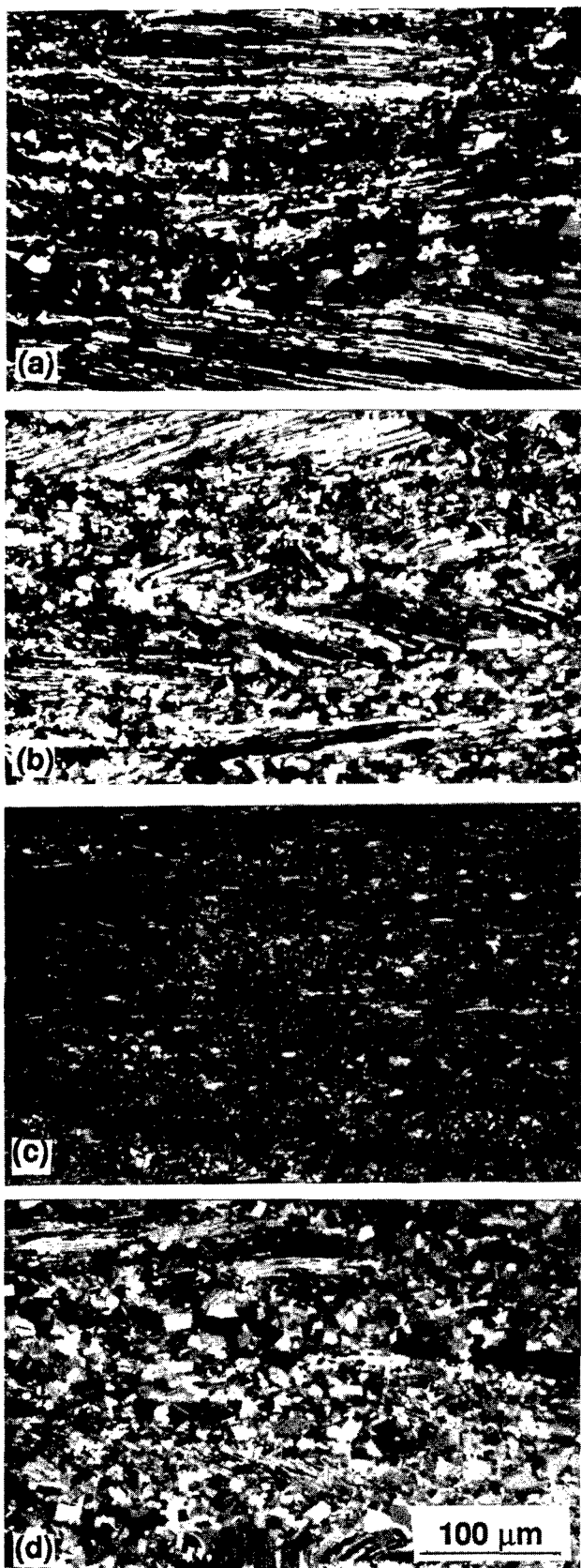


Figure 6. Polarized light optical microstructure developed in Ti-45Al-2Cr-2Nb pancakes upset at 1150°C to a 6:1 reduction using (a) "standard isothermal forging practice, (b) isothermal forging with a 15 minute dwell after the first 2:1 reduction, (c) conventional forging ( $\dot{\epsilon} \sim 1 \text{ s}^{-1}$ ), and (d) alpha forging. (55)

radial microstructure variations in the extrudate. For example, Seetharaman, *et al.* (59) found that the gamma grain size varied from 6  $\mu\text{m}$  to 14  $\mu\text{m}$  from the surface to the center of a Ti-49.5Al-2.5Nb-1.1Mn workpiece extruded at 1050°C to a 6:1 reduction. A similar effect is seen in the "TMP extrusion" (63,64) of near-gamma alloys to obtain fully-lamellar microstructures. This extrusion technique involves billet preheating at or just below the alpha transus temperature. Deformation heating raises the workpiece temperature well into the alpha phase field, thereby promoting recrystallization of single-phase alpha which then transforms to the lamellar structure during cooldown. A typical variation in alpha grain size from the surface to the center of a Ti-45Al-2Cr-2Nb extrusion hot worked by the "TMP extrusion" technique is shown in Figure 8 (61).

Two novel conventional (canned) hot extrusion processes have been developed and applied to breakdown gamma titanium aluminide alloys. These are referred to as "controlled-dwell" extrusion and "equal channel angular extrusion". The controlled-dwell extrusion process (65) is a technique aimed at overcoming difficulties associated with the extrusion of a harder workpiece material such as a gamma titanium aluminide alloy in a softer, inexpensive can material such as a stainless steel. At a given temperature, the flow stress mismatch may be so great that the relative flow of the workpiece and can during extrusion may become nonuniform, sometimes leading to can thinning and failure and then gross fracture of the workpiece when it contacts the cold tooling. This problem of the flow stress mismatch is overcome to a large extent by preheating the canned workpiece in a furnace (or induction heater), removing the assembly from the furnace, and allowing it to air cool for a prespecified, or controlled, dwell period prior to extrusion. The purpose of the controlled dwell is to set up a temperature differential between the can and the workpiece in order to make their respective flow stresses more nearly equal and thus to enhance the uniformity of metal flow during the deformation process. Such a practice contrasts sharply with standard techniques in which efforts are usually made to *minimize* the transfer time.

Developed in the former Soviet Union, the equal channel angular extrusion (ECAE) process (66) offers an attractive alternative for the primary breakdown of conventional and advanced alloys. In the process, an ingot (or prior-worked billet) is extruded through a channel consisting of two continuous sections situated at an angle  $2\phi$  to each other. The imposed strain per pass is a function of the channel angle. Much larger strains can also be imposed in a given set of tooling through the use of multi-pass extrusion which is possible because the

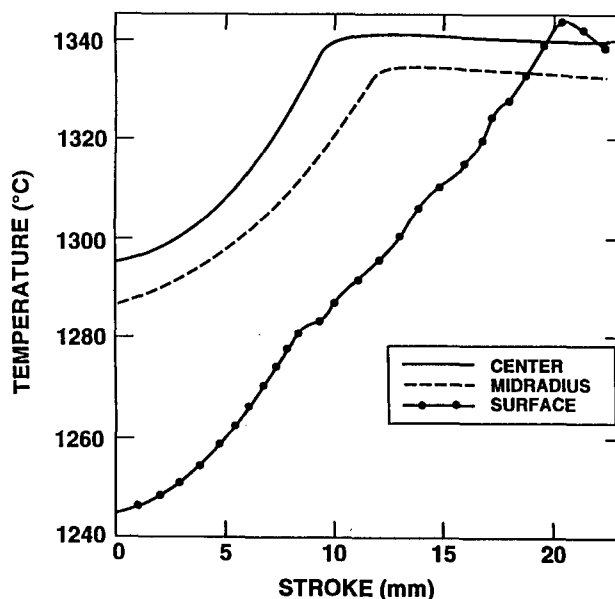


Figure 7. FEM-predicted temperature-versus-time curves at the center, midradius, and outer diameter of a Ti-45Al-2Cr-2Nb billet encapsulated in a Ti-6Al-4V can, preheated at 1300°C, and extruded to a 6:1 reduction. (61)



cross-sectional area of the workpiece is not changed. The ability to impart large deformations without a change in cross-section permits smaller ingots to be melted to obtain a given size of semi-finished product. Hence, the process is especially useful for materials prone to macrosegregation during the casting of large ingots. The broad feasibility of using ECAE for breakdown of canned gamma titanium aluminide ingot materials was demonstrated recently (67).

**Secondary Processing.** The development of uniform, fine microstructures during breakdown of ingot-cast gamma titanium aluminide alloys leads to improved workability with regard to both fracture resistance and reduced flow stresses. These improvements are useful in secondary processes such as sheet rolling, superplastic forming of sheet, and isothermal, closed-die forging.

Two major techniques for rolling of sheet have evolved from the early work on near-isothermal, hot pack rolling conducted by Hoffmann, *et al.* (68). These methods are conventional hot pack rolling and bare isothermal rolling. With regard to the former process, pack design (e.g., cover thickness, use of parting agents, etc.) and the selection of rolling parameters have been aided by the development of models which quantify the temperature transients and hence the stresses during rolling (69,70) as well as information on the hot

workability of gamma titanium aluminide alloys (71). For the near-gamma titanium aluminide alloys, rolling is usually most easily conducted in the alpha plus gamma phase field at temperatures approximately 40 to 150°C below the alpha transus using reductions per pass of 10 to 15 percent and rolling speeds that produce effective strain rates of the order of  $1 \text{ s}^{-1}$ . Using these parameters, sheets as large as 400 mm x 700 mm and ranging in thickness from 0.2 to 2.0 mm have been produced (72). In addition, a variety of microstructures have been developed in rolled sheet products, some with gamma grain sizes as small as  $2 \mu\text{m}$  (70). Sheets rolled and then "direct" heat treated have exhibited an even wider range of microstructures (73).

An alternate sheet fabrication technique, involving rolling of *uncanned* gamma titanium aluminide preforms under isothermal conditions, has been developed and demonstrated (on a laboratory scale) by Kobe Steel, Ltd. (74,75). The rolling equipment includes a mill with 300-mm wide, 60-mm diameter, ceramic work rolls and 150-mm diameter TZM molybdenum backup rolls. The rolls and gamma workpiece are enclosed in a vacuum chamber and heated under an argon atmosphere. To date, Ti-46Al and Ti-51Al binary alloys have been rolled to 0.75 to 1.0 mm-thick, 150 mm-wide sheet from 3.0 mm-thick preforms using this equipment. Typical processing parameters include a preform/roll temperature between 1000 and 1100°C, rolling speed between 2 and 6 mm/minute, and reduction per pass between 5 and 15 percent. For the reduction per pass and rolling speed utilized, the effective strain rate of the preform as it is rolled is approximately  $10^{-3} \text{ s}^{-1}$ , or a rate at which the workability of gamma alloys is good in both the as-cast and wrought forms. Unfortunately, these very low strain rates lead to relatively long processing times. However, the microstructures produced by isothermal rolling (75) are similar to those produced by conventional, hot pack rolling conducted under higher temperature/higher strain rate conditions.

The fact that fine-grained microstructures can be developed in two-phase (alpha - two + gamma) or three-phase (alpha - two + gamma + beta) near-gamma titanium aluminide alloys during ingot breakdown and/or rolling suggests that these materials might be prime candidates for superplastic forming. With this possibility in mind, Lombard (76) reviewed a number of the phenomenological observations for these materials in the literature. The alloys investigated had a wide range of aluminum contents, microstructures, and degrees of microstructural refinement. In addition, the materials were tested over a wide range of temperatures and strain rates. For most of the test conditions, the *m* values generally ranged from 0.4 to 0.8, or conditions under which tensile ductilities in the range of approximately 800 to 8000 percent might be expected (77). In the vast majority of the cases, however, the observed tensile ductilities were much less (i.e., ~200 to 500 percent), thus suggesting the influence of fracture processes such as cavitation in controlling formability. A noteworthy exception to this general trend was the achievement of an elongation of approximately 1000 percent at  $T = 1200^\circ\text{C}$  and a nominal strain rate of  $10^{-3} \text{ s}^{-1}$  in rolled, fine-gamma grain samples of Ti-45.5Al-2Cr-2Nb (78). Under these test conditions, the *m* value was estimated to be between 0.4 and 0.5.

In isothermal, closed-die forging, the high *m* values developed in fine-grained gamma titanium aluminide alloys deformed at low strain rates have been utilized to make parts such as jet-engine blades (64). Forging results obtained thus far have shown excellent die-filling capability even in complex areas such as blade root sections. The enhanced metal flow of the fine-grained titanium aluminide alloys has also spurred efforts to develop higher rate, conventional forging processes (using unheated tooling) for parts such as automotive engine valves (64).

The fine equiaxed gamma grain microstructures that enable the forming of intricate parts during superplastic sheet forming or isothermal closed-die forging provide good ductility and strength, but inferior fracture toughness and creep resistance. On the other hand, near-gamma titanium aluminide alloys containing a fully lamellar microstructure with a moderately small (~50 to 200  $\mu\text{m}$ ) alpha grain size have been found to provide a better property mix (79). Several processing techniques have been developed to obtain such microstructures. These include the supertransus heat treatment of alloys containing grain-growth inhibiting elements, such as boron, in

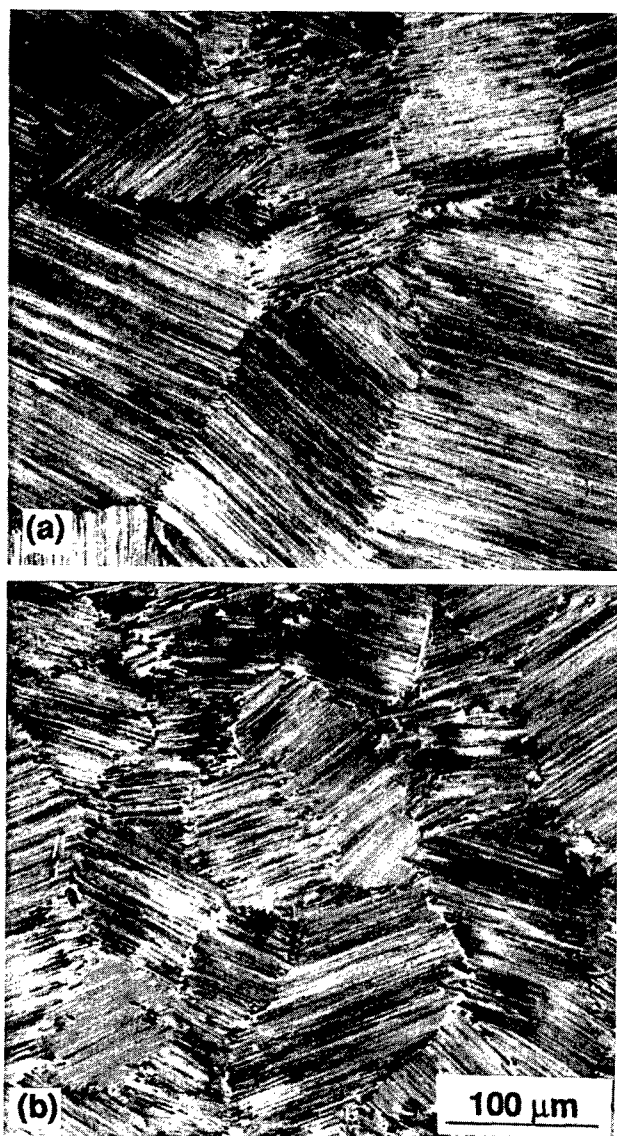


Figure 8. Polarized light optical microstructures developed in a canned Ti-45Al-2Cr-2Nb billet preheated at the alpha transus temperature and extruded to a 6:1 reduction: (a) center of extrudate, (b) outer diameter of extrudate. (61)

solid solution or in the form of precipitates (80,81) or controlled, transient heating into the alpha phase field, a method suitable for parts of thin cross-section (82).

**Workability Considerations.** As for conventional titanium alloys, failures during deformation processing of near-gamma titanium aluminide alloys are usually one of two types: fracture controlled and flow-localization-controlled. The phenomena of wedge crack and cavity formation play an important role with respect to fracture. Research now suggests that two major regimes can be defined with regard to overall fracture behavior. One is a low-temperature, high-strain rate regime in which wedge crack initiation occurs at very low deformation levels and leads to very brittle, intergranular type failures. Such fracture behavior is of utmost importance in the design of conventional, high-rate working operations such as forging, rolling, and extrusion. The other regime comprises higher-temperature, low-strain rate deformation in which cavity formation, growth, and coalescence occurs and is a gradual process, thereby giving rise to moderate-to-high hot ductility. An understanding of this type of fracture response is important with regard to the design of processes such as isothermal forging and superplastic sheet forming.

The work of Seetharaman, Semiatin, and their coworkers (71,83,84) has sought to provide a first step toward quantifying the factors that control the brittle, intergranular mode of fracture during hot working of gamma titanium aluminide alloys. In the former work, the hot tension behavior of Ti-49.5-2.5Nb-1.1Mn in both the cast plus HIP'ed condition and the wrought condition was established. Both material conditions exhibited a complex relationship between reduction in area, test temperature, and strain rate (Figure 9). However, in broad terms, the data revealed transitions from brittle behavior (with extensive wedge cracking) to ductile behavior characterized by somewhat stable cavity growth over a rather narrow temperature. For each material condition, the brittle-to-ductile transition temperature increased with increasing strain rate (Figure 10). Furthermore, the transition temperatures for a given strain rate were higher for the coarse-grained, cast material than for the finer-grain, wrought material. An Arrhenius-type of analysis of the transition-temperature data yielded values of activation energy comparable to those that describe the dynamic recrystallization of gamma titanium aluminide alloys during hot compression testing (85). From this analysis, it was thus concluded that the onset of dynamic recrystallization was the mechanism by which brittle fracture was suppressed.

The observations of wedge crack formation in isothermal, hot-compression testing of wrought Ti-48Al-2.5Nb-0.3Ta also showed a strong effect of strain rate and temperature on fracture behavior (86). However, a simple analysis suggested that a fracture criterion in terms of the product of the applied stress and square root of the grain size, much like the Griffith criterion, may be useful in predicting brittle failures due to wedge cracking (Figure 11).

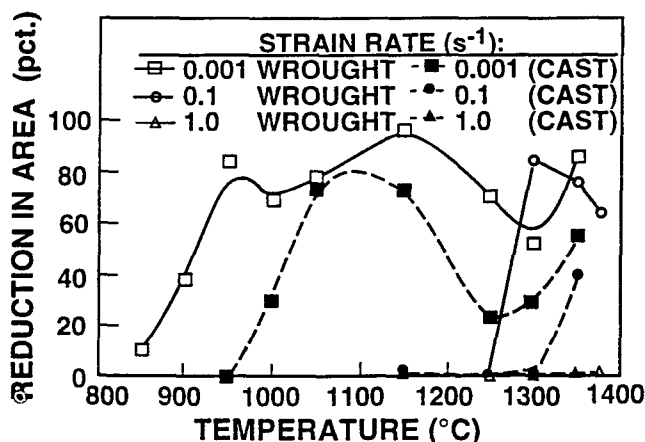


Figure 9. Dependence of reduction in area on test temperature and strain rate for hot tension tests on cast or wrought (extruded + recrystallization heat treated) samples of Ti-49.5Al-2.5Nb-1.1Mn. (83)

The work of Semiatin, *et al.* (71) has also revealed that the occurrence of wedge cracking during hot compression testing could be used to predict gross fracture during pack rolling of gamma titanium aluminide alloys. In this operation, secondary (rolling direction) tensile stresses are generated when a relatively high flow stress material (the titanium aluminide) is packed and rolled within a material with a lower flow stress. These tensile stresses cause microscopic wedge cracks to propagate giving rise to fractures that lie transverse to the rolling direction.

Secondary tensile stresses also play an important role in the more ductile failures that result from cavity formation (at grain edges or triple points), growth, and coalescence which occur under low strain rate deformation conditions. One example of such failures is the cracking that develops at the bulged free surfaces of gamma titanium aluminide alloys during open-die forging processes. The kinetics of

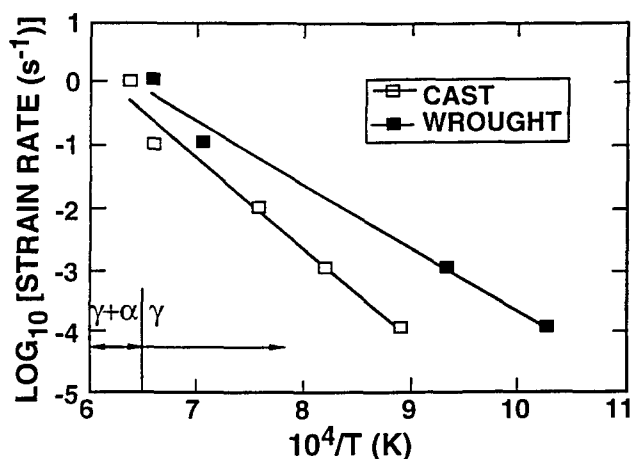


Figure 10. Relationship between strain rate and inverse of the ductile-to-brittle transition temperature for the hot tension behavior of cast and wrought (extruded + recrystallization heat treated) Ti-49.5Al-2.5Nb-1.1Mn. (83)

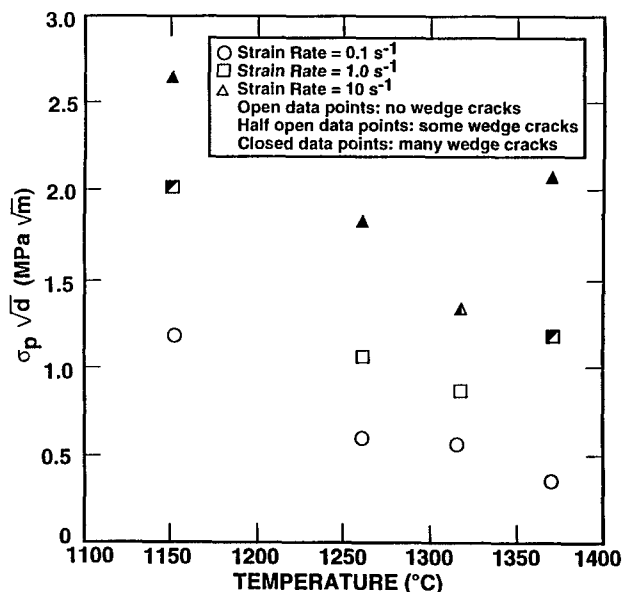


Figure 11. Plot of the product of the applied peak stress  $\sigma_p$  and the square root of the grain size  $d$  versus temperature indicating the occurrence of wedge cracking during hot compression testing of Ti-48Al-2.5Nb-0.3Ta. (86)

this type of failure were analyzed by Seetharaman, *et al.* (87) who investigated free surface cracking of Ti-49.5Al-2.5Nb-1.1Mn during pancake forging of cylindrical mults. The degree of bulge during pancake forging, and thus the level of the tensile stresses, is a function of the instantaneous aspect ratio of the workpiece and the die-workpiece interface friction conditions. For the specific geometry and interface friction involved in the experiments of Seetharaman, *et al.*, it was found that the free-surface fracture could be predicted using the maximum tensile work criterion first proposed by Cockcroft and Latham (88) (for ductile fracture under cold-working conditions).

As mentioned above, the work of Lombard, *et al.* (76,78,89) indicates that failure during superplastic sheet forming is also cavitation/fracture controlled rather than flow localization controlled. The kinetics of the cavitation process are readily described using the approach developed by Nicolaou, *et al.* (90).

Shear localization and shear fracture during hot working of gamma titanium aluminide alloys are most common in deformation modes that are plane strain or simple shear in nature. For example, the workability of the near-gamma alloy Ti-45.5Al-2Cr-2Nb during equal channel angular extrusion (ECAE) was shown to be limited by shear localization (67). A relatively sound product was produced by extrusion at 1250°C of cast plus HIP'ed material of this composition canned in type 304 stainless steel, but shear bands and gross shear cracks were developed when extrusion was attempted at 1150°C (Figure 12). These observations were explained in terms of the effect of extrusion temperature on the magnitude of the flow localization, or 'alpha', parameter in simple shear, defined as the ratio of the normalized flow softening rate (from stress-strain curves not corrected for deformation heating effects) to the strain rate sensitivity exponent (i.e., *m* value).

#### Casting of Near-Gamma Titanium Aluminide Alloys

In the last several years, melting and casting of discrete gamma titanium aluminide parts has been actively pursued as an alternative to ingot metallurgy, wrought processing. Many of these efforts have focused on minor modifications of investment casting practices used for conventional titanium alloys. Typically, feed stock is melted via vacuum arc remelting (VAR) and cast into special ceramic shell materials/facecoats designed to minimize mold-metal reactions and casting defects (91,92,93). Following casting, parts are usually HIP'ed to seal casting porosity, heat treated, chemical milled, and straightened. General Electric has developed a number of novel heat treatments to obtain various equiaxed gamma or duplex (equiaxed gamma/lamellar) microstructures (94). Chem milling is usually carried out to a depth of approximately 0.5 to 1.5 mm to remove surface reaction zones and/or layers depleted in aluminum during HIP or heat treatment. Parts made by such methods include low pressure turbine blades, transition duct supports, and compressor cases for jet engines and valves for automobile engines (91,92,95-97). Similar practices using vacuum induction melting (instead of VAR) and a counter-gravity low-pressure

casting technique have been used to make automotive turbocharger rotors of gamma titanium aluminide alloys (98).

Several approaches besides the special heat treatment techniques mentioned above have been utilized to control microstructure in gamma titanium aluminide castings. These include chemistry modifications and different casting practices. Noticeable changes in microstructure are possible through the utilization of grain-refining agents such as titanium diboride introduced as boride particles or elemental boron (93). Casting practices to develop single-crystal or multi-crystal like directionally solidified (DS) structures or highly refined structures have also been examined. For example, London, *et al.* (93) used a RAM-DS furnace and ceramic molds to produce DS structures, while minimizing oxygen pickup to a certain extent. In similar work, Takeyama, *et al.* (99) used a float-zone technique to produce DS microstructures comprising alpha-two and gamma lamellae. As the growth rate was increased, the structure was found to change from one comprising essentially a single colony to one characterized as a columnar grain structure.

Jones and Eylon (100) established the effect of various casting practices on microstructure refinement. These practices included "slow cool" and "fast cool" investment casting in ceramic molds and static (gravity feed) and pressure injection casting into steel permanent molds. The "fast cool" investment castings were made by pouring molten metal into a colder-than-usual ceramic mold. The fineness of the microstructures so produced was quantified by measuring the "characteristic segregation length" (CSL), or the spacing between adjacent low-aluminum dendrites or cell cores. The CSL measurements were used to estimate the solidification rate relative to that for the "slow cool" investment castings by application of the classical relationship between dendrite arm spacing and local solidification time. The results (Table II) revealed that the solidification rate and degree of microstructure refinement in "fast cool" investment castings can approach those achievable in permanent mold casting. Furthermore, it was found that pressure injected permanent mold castings may develop lamellar microstructures whose colony size is comparable to or smaller than that achievable in investment castings of near-gamma alloys containing titanium diboride grain refining agents. It is also of interest to note that the range of colony sizes found in permanent mold castings is comparable to that observed in spray-formed near-gamma titanium aluminide alloys, i.e., ~100  $\mu$ m (101).

Table II. Microstructure Features in Ti-48Al-2Cr-2Nb (a/o) Cast By Various Means (100)

Casting Process	Characteristic Segregation Length ( $\mu$ m): Avg. Range	Colony Size Range ( $\mu$ m)	Local Solidification Time Ratio*
"Slow Cool" Investment Casting	193	135-280	100-500
"Fast Cool" Investment Casting	23	17-35	55-78
"Static" Permanent Mold	33	27-40	100-250
Injection Permanent Mold			
- Coarse Region	30	15-57	28-39
- Fine Region	6	3-9	28-39
Investment Cast (with Boron Addition)	50	37-57	55-78

\* Solidification time ratio relative to that for "slow cool" investment casting

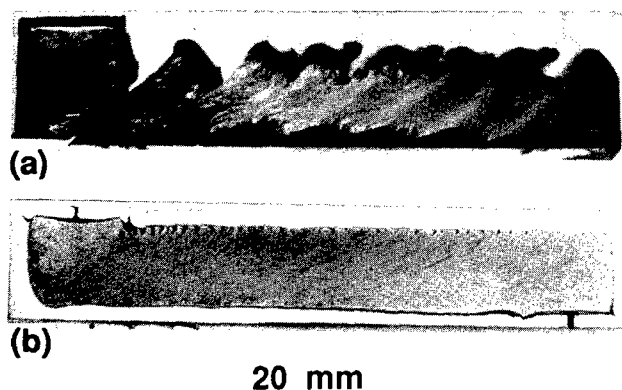


Figure 12. Micrographs of sections of canned samples of cast + HIP'ed Ti-45.5Al-2Cr-2Nb deformed via equal channel angular extrusion at (a) 1150°C or (b) 1250°C. (67)

A number of rapid solidification techniques have been utilized over the past twenty-five years to synthesize powders of various near-gamma and single-phase gamma titanium aluminide alloys (102). Perhaps the first process to be used, the Pratt and Whitney rapid solidification rate (RSR) method involved the pouring of a molten stream of liquid onto a rapidly spinning disk thereby producing fine droplets that solidified in flight. More recently, the plasma rotating electrode process (PREP), developed by Nuclear Metals, and gas atomization, developed by Pratt and Whitney and Crucible Materials Corporation, have been used to make powders of these materials.

Powder consolidation has been performed primarily by HIP (in metal or ceramic cans) or canned hot extrusion. HIP has been used to make finished parts as well as preforms for subsequent sheet rolling, forging, etc. (102-105). HIP at temperatures of 1050 to 1150°C has been found to be capable of transforming the dendritic solidification structure of as-produced powders into a fine equiaxed gamma structure while bringing about consolidation to full or nearly-full theoretical density (103). As-HIP'ed compacts or HIP'ed + rolled/forged powder products have exhibited mechanical properties comparable to or exceeding those in wrought ingot metallurgy near-gamma titanium aluminide products (104,105,106).

Other powder metallurgy techniques for gamma titanium aluminide alloys that have been investigated in less detail include powder production via reaction of elemental powders, mechanical alloying, and magnetron sputtering (107,108), and the manufacture of components with microstructure/property gradients (109).

#### Processing-Cost Tradeoffs for Gamma Titanium Aluminide Alloys

In the context of ever-increasing economic competition, cost as well as technical considerations enter into the selection of production processes. Hence, the development of "technical cost models" (110) during process design is becoming common. Such modeling usually involves determination of broad process alternatives, the manufacturing details of each process flow path, the properties attainable by each route, and some sort of detailed cost analysis. It is not atypical that system designers are involved at an early stage because different production techniques may involve different final microstructures and properties which in turn affect the final product design. For example, if the design requirement for a specific near-gamma titanium aluminide part is primarily stiffness limited, the selection of a casting, metalworking, or powder metallurgy approach can probably be based solely on cost because the modulus of these alloys does not appear to be heavily-microstructure dependent. On the other hand, if the design is for a load-bearing structural part, the strength, toughness, creep resistance, etc. of the microstructures attainable by different processing methods become important because these attributes affect required section thicknesses, inertial loading in rotating parts, as well as the design of other system components. In turn, such part design and performance characteristics affect operational (life-cycle) cost as well as production cost.

In this section, a simple "bottom-up" cost analysis approach for a specific near-gamma titanium aluminide jet-engine part is described to illustrate a methodology that can be used to assess cost tradeoffs. To a first order, it is assumed that identical properties can be achieved in finish machined-and-heat treated parts made via the different processing techniques. The analysis is easily modified when properties are different (by adjusting final part geometry and thus input material weights, etc.), or part geometry complexity is greater or less. The analysis involves outlining the processing steps followed by estimating the cost of each.

#### Process Flow Charts

The "bottom-up" method is applied here to a near-gamma titanium aluminide jet engine component whose specific shape is proprietary in nature but which consists essentially of an axisymmetric hub-flange geometry with a hollow center (111). The inner and outer diameters of

the part are approximately 140 and 250 mm, respectively. The hub height, flange thickness, and flange width are approximately 40, 3, and 40 mm, respectively. Four prototypical processing approaches were considered:

- (i) Wrought process: extrude + hot-die pancake forge + closed-die isothermal forge
- (ii) Wrought process: two-step isothermal pancake forge + hog-out
- (iii) 'Standard' investment casting process
- (iv) Net shape, HIP-powder process

The manufacturing steps for each scenario are shown in Figure 13. In broad terms, each process comprises input material synthesis, mult/die/mold manufacture, one (or several) actual part making processes, and a final series of operations comprising heat treatment, rough/finish machining, and inspection. The extrude + forge and two-step isothermal forge processes both make use of triple-melted ingot; in the former case, ingot HIP prior to metalworking is included as a processing step to close solidification porosity. The melt stock for the investment casting approach is double-melted material, whereas the powder for the PM route is made by atomizing a heat of liquid metal made from various readily available conventional/master alloys and/or elemental metal additions. Special dies/molds that are required include TZM molybdenum tooling for closed-die isothermal forging and flat-die pancake forging and mild steel/low alloy steel dies for wax-injection tooling.

#### Cost Estimates

Cost estimates for starting materials, tooling, canning, processing, finishing operations, etc. are summarized in Table III for the four manufacturing scenarios. Because tooling represents a major cost item, the cost per part is estimated based on lot sizes of either 250 or 500 parts to amortize the tooling investment; these calculations assume therefore that tool life is at least 500 parts. Moreover, the cost estimates for input material requirements incorporate typical "buy-to-fly" ratios for the various processes. These ratios are dependent of course on the degree of net-shape processing achievable and material losses due to cropping, machining, gating, etc. in the various scenarios. In addition, because of the sensitive nature of any cost modeling exercise to competing vendors in the aerospace area, the costs in Table III are quoted in terms of processing cost units (PCUs) rather than dollars. By this means, only the relative competitiveness of the various approaches is quantified.

The results in Table III reveal that by and large all four manufacturing approaches are cost competitive to a first order. The extrude + forge sequence is the most costly, leading to a 30 percent cost penalty relative to the other three scenarios. However, such a

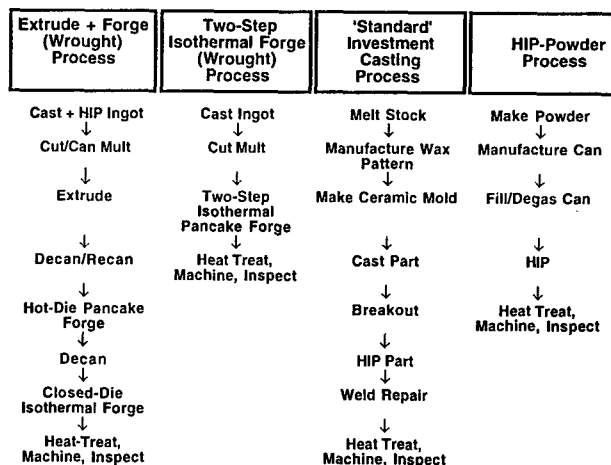


Figure 13. Flow charts for four processing scenarios for a near-gamma titanium aluminide hub-flange part.

Table III. Cost Analysis for Processing Alternatives for a Near-Gamma Titanium Aluminide Part\*

Cost Element:	Extrude + Forge		Two-Step Isothermal Forge		Investment Casting		HIP Powder	
	250 Pts.	500 Pts.	250 Pts.	500 Pts.	250 Pts.	500 Pts.	250 Pts.	500 Pts.
Input Material <sup>†</sup>	22.6	22.6	15.0	15.0	8.8	8.8	13.4	13.4
Tooling	10.0	5.0	10.0	5.0	4.0	2.0	----	----
Canning	2.5	2.5	----	----	----	----	40.0	40.0
Wax Pattern/Mold Mfg	----	----	----	----	4.3	4.3	----	----
Extrusion	5.8	5.8	----	----	----	----	----	----
Isothermal/Hot Die Forging	20.0	20.0	20.0	20.0	----	----	----	----
Casting/Breakout/Weld Repair	----	----	----	----	28.3	28.3	----	----
HIP	----	----	----	----	3.8	3.8	6.3	6.3
Heat Treat/Machine/Inspect	36.6	36.6	31.5	31.5	24.4	24.4	16.3	16.3
Total Cost (PCUs):	97.5	92.5	76.5	71.5	73.6	71.6	76.0	76.0

\* Costs are in terms of 'processing cost units' (PCUs), not dollars

<sup>†</sup> Input material includes HIP of cast ingots for extrude + forge scenario; the 'buy-to-fly' material ratio for the various processing approaches was as follows: extrude + forge - 5.7, two-step isothermal forge - 4.6, investment casting - 3.4, and HIP powder - 1.4.

manufacturing technique may be justified on the grounds of optimal control over final microstructure, optimal properties, etc. Several other observations can also be made. For instance, two-step isothermal pancake forging is most competitive with investment casting for situations in which forging and machining costs can be minimized. This suggests that parts of simple geometry and few details may be the best candidates for the forging process. Table III results also show that the net-shape, HIP-powder approach can be competitive with investment casting. Besides the ability to obtain desirable properties via HIP alone, the powder process appears to be most attractive when the input material and canning costs can be minimized. These requirements translate into the need for net- or near-net-shape processing and the design and manufacture of easily produced cans. As for similar powder metallurgy technologies, the most obvious applications for net-shape PM technology for the gamma titanium aluminide alloys appear to be axisymmetric parts, especially those with large internal holes.

#### Summary and Future Outlook

The processing of structural intermetallic alloys has seen tremendous advances in the last decade and especially in the last five years. Although very few parts of these materials are being commercially manufactured and sold at present, production size quantities of Fe<sub>3</sub>Al and Ni<sub>3</sub>Al have been made, and scaleup of the gamma titanium aluminide alloys is approaching these levels. These strides have been facilitated by the development of detailed information on phase equilibria, phase transformation behavior, microstructure evolution, and workability as well as by the design and implementation of novel processes, many of which can be done using existing manufacturing equipment. The development of this technical understanding is essential in establishing economic feasibility and hence the cost drivers for the introduction of structural intermetallic alloys. Future activities which will enhance the transitioning of these materials into service include the following:

- Further development of material behavior and process models for specific alloys.
- Definition of processing windows and demonstration of process robustness in real manufacturing environments.
- Rethinking of part design methodologies, taking into proper consideration the attractive as well as limiting attributes of specific alloy classes.

- Increased activity in assessing production and life cycle costs in determining the suitability of structural intermetallic alloys as substitutes for existing materials or in totally new systems.

#### Acknowledgements

The authors gratefully acknowledge the enthusiastic and longstanding support and encouragement of the management of the Air Force Office of Scientific Research and the Wright Laboratory Materials Directorate in the discovery and development of much of the current knowledge on structural intermetallic alloys. The work discussed in this review has resulted from the patient efforts of a large number of the authors' colleagues, who are too numerous to mention, but to whom a heartfelt thanks is extended. The expert assistance of J.A. Martus and M.A. Schobert in performing the cost analysis and L. Farmer and J. Paine in preparing the manuscript is graciously acknowledged.

#### References

1. E.A. Feest and J.H. Tweed, *Materials Science and Technology*, 8 (1992), 308-316.
2. V.K. Sikka, S. Viswanathan, and C.G. McKamey, in R. Darolia, et al., eds., *Structural Intermetallics* (Warrendale, PA: TMS, 1993), 483-491.
3. V.K. Sikka, in J. Horton, et al., eds., *High Temperature Ordered Intermetallic Alloys VI* (Pittsburgh, PA: MRS, 1995), 873-878.
4. Z.Q. Sun, Y.D. Huang, W.Y. Yang, and G.L. Chen, in I. Baker, et al., eds., *High Temperature Ordered Intermetallic Alloys V* (Pittsburgh, PA: MRS, 1993), 885-890.
5. V.K. Sikka, B.G. Gieseke, and R.H. Baldwin, in K. Natesan and D.J. Tillack, eds., *Heat-Resistant Materials* (Materials Park, OH: ASM International, 1991), 363-371.
6. D.J. Gaydosch and M.A. Crimp, in C.C. Koch, et al., eds., *High-Temperature Ordered Intermetallic Alloys* (Pittsburgh, PA: MRS, 1985), 429-436.
7. K. Vedula, in J.H. Westbrook and R.L. Fleischer, eds., *Intermetallic Compounds: Volume 2, Practice* (Chichester, England: John Wiley and Sons Ltd., 1994), 199-209.
8. J.J. Stout and M.A. Crimp, *Mat. Sci. Eng.*, A152 (1992), 335-340.
9. J.W. Patten, in S.H. Whang, et al., eds., *High Temperature Aluminides and Intermetallics* (Warrendale, PA: TMS, 1990), 493-503.

10. C.T. Liu and D.P. Pope, in J.H. Westbrook and R.L. Fleischer, eds., *Intermetallic Compounds: Volume 2, Practice* (Chichester, England: John Wiley and Sons Ltd., 1994), 17-51.
11. V.K. Sikka, J.T. Mavity, and K. Anderson, *Mat. Sci. Eng.*, A153 (1992), 712-721.
12. V.K. Sikka, in S.H. Whang, et al., eds., *High Temperature Aluminides and Intermetallics* (Warrendale, PA: TMS, 1990), 505-520.
13. V.K. Sikka, *Mater. and Manuf. Processes*, 4 (1) (1989), 1-24.
14. R.N. Wright, B.H. Rabin, and J.R. Knibloe, *Mater. and Manuf. Processes*, 4 (1) (1989), 25-37.
15. A. Bose, B.H. Rabin, and R.M. German, *Powder Metall. Inter.*, 20 (1988), 25-30.
16. R.M. German, A. Bose, and N.S. Stoloff, in C.T. Liu, et al., eds., *High-Temperature Ordered Intermetallic Alloys III* (Pittsburgh, PA: MRS, 1989), 403-414.
17. C. Nishimura and C.T. Liu, *Acta Metall. et Mater.*, 41 (1993), 113-120.
18. E.H. Goldman, in I. Baker, et al., eds., *High-Temperature Ordered Intermetallic Alloys V* (Pittsburgh, PA: MRS, 1993), 83-94.
19. J.A. Oti and K.O. Yu, in R. Darolia, et al., eds., *Structural Intermetallics* (Warrendale, PA: TMS, 1993), 505-512.
20. R. Darolia, in R. Darolia, et al., eds., *Structural Intermetallics* (Warrendale, PA: TMS, 1993), 495-504.
21. R. Darolia, W.S. Walston, and M.V. Nathal, in R.D. Kissinger, et al., eds., *Superalloys 1996* (Warrendale, PA: TMS, 1996), 561-570.
22. K. Vedula, *Mater. and Manuf. Processes*, 4 (1) (1989), 39-59.
23. E.M. Schulson and D.R. Barker, *Scripta Metallurgica*, 17 (1983), 519-522.
24. K.S. Chan, *Scripta Metall. et Mater.*, 24 (1990), 1725-1730.
25. R.D. Noebe, R.R. Bowman, and M.V. Nathal, *Inter. Mater. Rev.*, 38 (4) (1993), 193-232.
26. M.R. Jackson and K.D. Jones, in K.C. Liddell, et al., eds., *Refractory Metals: Extraction, Processing, and Applications* (Warrendale, PA: TMS, 1990), 311-320.
27. K.D. Jones, M.R. Jackson, M. Larsen, E.L. Hall, and D.A. Woodford, in K.C. Liddell, et al., eds., *Refractory Metals: Extraction, Processing, and Applications* (Warrendale, PA: TMS, 1990), 321-333.
28. D.M. Dimiduk, M.G. Mendiratta, and P.R. Subramanian, in R. Darolia, et al., eds., *Structural Intermetallics* (Warrendale, PA: TMS, 1993), 619-630.
29. M.G. Mendiratta and D.M. Dimiduk, in C.T. Liu, et al., eds., *High Temperature Ordered Intermetallic Alloys III* (Pittsburgh, PA: MRS, 1989), 441-446.
30. M.G. Mendiratta and D.M. Dimiduk, *Scripta Metall. et Mater.*, 25 (1991), 237-242.
31. M.G. Mendiratta, J.J. Lewandowski, and D.M. Dimiduk, *Metall. Trans. A*, 22A (1991), 1573-1583.
32. M.G. Mendiratta and D.M. Dimiduk, *Metall. Trans. A*, 24A (1993), 501-504.
33. R.K. Nekkanti and D.M. Dimiduk, in D.L. Anton, et al., eds., *Intermetallic Matrix Composites* (Pittsburgh, PA: MRS, 1990), 175-182.
34. K-M. Chang, B.P. Bewlay, J.A. Sutliff, and M.R. Jackson, *JOM*, 44 (June, 1992), 59-63.
35. Y. Murayama, T. Kumagai, and S. Hanada, in I. Baker, et al., eds., *High-Temperature Ordered Intermetallic Alloys V* (Pittsburgh, PA: MRS, 1993), 95-106.
36. K. Kamata, T. Degawa, and Y. Nagashima, in R. Darolia, et al., eds., *Structural Intermetallics* (Warrendale, PA: TMS, 1993), 675-680.
37. J.J. Petrovic, *MRS Bulletin*, 18 (July 1993), 35-40.
38. S.M.L. Sastry, R. Suryanarayanan, and K.L. Jerina, *Mat. Sci. Eng.*, A192/193 (1995), 881-890.
39. D.A. Hardwick, P.L. Martin, S.N. Patankar, and J.J. Lewandowski, in R. Darolia, et al., eds., *Structural Intermetallics* (Warrendale, PA: TMS, 1993), 665-674.
40. N. Jacobson, K. Lee, S.A. Malloy, and A.H. Heuer, *J. Amer. Ceram. Soc.*, 76 (1993), 2005-2009.
41. R. Gibala, A.K. Ghosh, D.C. VanAken, D.J. Srolovitz, A. Basu, H. Chang, D.P. Mason, and W. Yang, *Mat. Sci. Eng.*, A155 (1992), 147-158.
42. R.G. Rowe, in S.H. Whang, et al., eds., *High Temperature Aluminides and Intermetallics* (Warrendale, PA: TMS, 1990), 375-401.
43. Y-W. Kim, *J. Metals*, 41 (July, 1989), 24-30.
44. D. Hardwick and P. Martin, unpublished research, Rockwell International Science Center, Thousand Oaks, CA, 1995.
45. M.K. Alam, S.L. Semiatin, and Z. Ali, submitted to *Trans. ASME, J. Eng. Ind.*, 1995.
46. J.D. Bryant and S.L. Semiatin, *Scripta Metall. et Mater.*, 25 (1991), 449-453.
47. S.L. Semiatin and P.A. McQuay, *Metall. Trans. A*, 23A (1992), 149-161.
48. B. Godfrey, A.L. Dowson, and M.H. Loretto, in P.A. Blenkinsop, et al., eds., *Titanium '95: Science and Technology* (London, England: Institute of Metals, 1996), 489-496.
49. C. McCullough, J.J. Valencia, C.G. Levi, and R. Mehrabian, *Acta Metall.*, 37 (1989), 1321-1336.
50. S.L. Semiatin and V. Seetharaman, unpublished research, Wright Laboratory Materials Directorate, Wright-Patterson AFB, OH, 1992.
51. S.L. Semiatin, R. Nekkanti, M.K. Alam, and P.A. McQuay, *Metall. Trans. A*, 24A (1993), 1295-1306.
52. P.L. Martin, unpublished research, Rockwell Science Center, Thousand Oaks, CA, 1992.
53. V. Seetharaman and S.L. Semiatin, unpublished research, Wright Laboratory Materials Directorate, Wright-Patterson AFB, OH, 1995.
54. P.L. Martin, C.G. Rhodes, and P.A. McQuay, in R. Darolia, et al., eds., *Structural Intermetallics* (Warrendale, PA: TMS, 1993), 177-186.
55. S.L. Semiatin, V. Seetharaman, and V.K. Jain, *Metall. and Mater. Trans. A*, 25A (1994), 2753-2768.
56. V.K. Jain, R.L. Goetz, and S.L. Semiatin, *Trans. ASME, J. Eng. Ind.*, 118 (1996), 155-160.
57. K. Wurzwallner, H. Clemens, P. Schretter, A. Bartels, and C. Koeppe, in I. Baker, et al., eds., *High-Temperature Ordered Intermetallic Alloys V* (Pittsburgh, PA: MRS, 1993), 867-872.
58. H. Clemens, P. Schretter, K. Wurzwallner, A. Bartels, and C. Koeppe, in R. Darolia, et al., eds., *Structural Intermetallics* (Warrendale, PA: TMS, 1993), 205-214.
59. V. Seetharaman, J.C. Malas, and C.M. Lombard, in L.A. Johnson, et al., eds., *High-Temperature Ordered Intermetallic Alloys IV* (Pittsburgh, PA: MRS, 1991), 889-894.
60. V. Seetharaman, L. Dewasurendra, A.B. Chaudhary, J.T. Morgan, and J.C. Malas, in N. Chandra and J.N. Reddy, eds., *Advances in Finite Deformation Problems in Materials Processing and Structures* (New York, NY: ASME, 1991), 97-109.
61. R.L. Goetz, S.L. Semiatin, and S-C. Huang, unpublished research, Wright Laboratory Materials Directorate, Wright-Patterson AFB, OH, 1994.
62. R.L. Goetz, V.K. Jain, and C.M. Lombard, *J. Mater. Proc. Techn.*, 35 (1992), 37-60.
63. Y-W. Kim and D.M. Dimiduk, U.S. Patent 5,226,985, July 13, 1993.
64. Y-W. Kim, *JOM*, 46 (7) (1994), 7, 30-40.
65. S.L. Semiatin, V. Seetharaman, R.L. Goetz, and V.K. Jain, U.S. Patent 5,361,477, November 8, 1994.
66. V.M. Segal, V.I. Reznikov, A.E. Drobyshevskiy, and V.I. Kopylov, *Russian Metallurgy*, 1 (1981), 99-105.
67. S.L. Semiatin, V.M. Segal, R.L. Goetz, R.E. Goforth, and T. Hartwig, *Scripta Metall. et Mater.*, 33 (1995), 535-540.
68. A.L. Hoffmann and D.D. Bhatt, unpublished research, Battelle Memorial Institute, Columbus, OH, 1977.
69. S.L. Semiatin, M. Ohls, and W.R. Kerr, *Scripta Metall. et Mater.*, 25 (1991), 1851-1856.
70. S.L. Semiatin and V. Seetharaman, *Metall. and Mater. Trans. A*, 26A (1995), 371-381.
71. S.L. Semiatin, D.C. Vollmer, S. El-Soudani, and C. Su, *Scripta Metall. et Mater.*, 24 (1990), 1409-1413.
72. S.L. Semiatin, N. Frey, C.R. Thompson, and D.C. Volmer, unpublished research, Battelle Memorial Institute, Columbus, OH, 1989.
73. V. Seetharaman and S.L. Semiatin, in Y-W. Kim, R. Wagner, and M. Yamaguchi, eds., *Gamma Titanium Aluminides* (Warrendale, PA: TMS, 1995), 753-760.

74. N. Fujitsuna, Y. Miyamoto, and Y. Ashida, in R. Darolia, *et al.*, eds., *Structural Intermetallics*, (Warrendale, PA: TMS, 1993), 187-194.
75. A. Morita, N. Fujitsuna, and H. Shigeo, *Symp. Proc. for Basic Technologies for Future Industries High-Performance Materials for Severe Environments 4th Meeting* (Tokyo, Japan: Japan Industrial Technology Association, 1993), 215-223.
76. C.M. Lombard, unpublished research, Wright Laboratory Materials Directorate, Wright-Patterson AFB, OH, 1995.
77. S.L. Semiatin and J.J. Jonas, *Formability and Workability of Metals* (Materials Park, OH: ASM International, 1984).
78. C.M. Lombard, A.K. Ghosh, and S.L. Semiatin, in Y-W. Kim, R. Wagner, and M. Yamaguchi, eds., *Gamma Titanium Aluminides* (Warrendale, PA: TMS, 1995), 579-586.
79. Y-W. Kim, *Mat. Sci. Eng.*, A192/193 (1995), 519-533.
80. C.T. Liu, J.H. Schneibel, P.J. Maziasz, J.L. Wright, and D.S. Easton, *Intermetallics*, 4 (1996), 429-440.
81. Y-W. Kim, unpublished research, Wright Laboratory Materials Directorate, Wright-Patterson Air Force Base, OH, 1996.
82. S.L. Semiatin, V. Seetharaman, D.M. Dimiduk, and K.H.G. Ashbee, submitted to *Metall. and Mater. Trans. A*, 1997.
83. V. Seetharaman, S.L. Semiatin, C.M. Lombard, and N.D. Frey, in I. Baker, *et al.*, eds., *High-Temperature Ordered Intermetallic Alloys V* (Pittsburgh, PA: MRS, 1993), 513-518.
84. V. Seetharaman and S.L. Semiatin, submitted to *Metall. and Mater. Trans. A*, 1996.
85. V. Seetharaman and C.M. Lombard, in Y-W. Kim and R.R. Boyer, eds., *Microstructure/Property Relationships in Titanium Aluminides and Alloys* (Warrendale, PA: TMS, 1991), 237-251.
86. S.L. Semiatin and V. Seetharaman, *Scripta Mater.*, 36 (1997), 291-297.
87. V. Seetharaman, R.L. Goetz, and S.L. Semiatin, in L.A. Johnson, *et al.*, eds., *High-Temperature Ordered Intermetallic Alloys IV* (Pittsburgh, PA: MRS, 1991), 895-900.
88. M.G. Cockcroft and D.J. Latham, N.E.L. Report No. 240, National Engineering Laboratory, East Kilbride, Glasgow, Scotland, 1966.
89. C.M. Lombard, A.K. Ghosh, and S.L. Semiatin, in I. Weiss, *et al.*, eds., *Advances in the Science and Technology of Titanium Alloy Processing* (Warrendale, PA: TMS, 1997), in press.
90. P.D. Nicolaou, S.L. Semiatin, and C.M. Lombard, *Metall. and Mater. Trans. A*, 27A (1996), 3112-3119.
91. S.V. Ram and J.R. Barrett, in P.A. Blenkinsop, *et al.*, eds., *Titanium '95: Science and Technology* (London, England: Institute of Metals, 1996), 88-96.
92. C.M. Austin and T.J. Kelley, in R. Darolia, *et al.*, eds., *Structural Intermetallics* (Warrendale, PA: TMS, 1993), 143-150.
93. B. London, D.E. Larsen, Jr., D.A. Wheeler, and P.R. Aimone, in R. Darolia, *et al.*, eds., *Structural Intermetallics* (Warrendale, PA: TMS, 1993), 151-157.
94. T.J. Kelly, C.M. Austin, and R.E. Allen, unpublished research, General Electric Aircraft Engines, Cincinnati, OH, 1995.
95. S. Hurta, H. Clemens, G. Frommeyer, H.-P. Nicolai, and H. Sibum, in P. Blenkinsop, *et al.*, eds., *Titanium '95: Science and Technology* (London, England: Institute of Metals, 1996), 97-104.
96. S.C. Huang and J.C. Chesnutt, in J.H. Westbrook and R.L. Fleischer, eds., *Intermetallic Compounds: Vol. 2, Practice* (Chichester, England: John Wiley and Sons Ltd., 1994), 73-93.
97. P.E. Jones, W.J. Porter III, D. Eylon, and G. Colvin, in Y-W. Kim, *et al.*, eds., *Gamma Titanium Aluminides* (Warrendale, PA: TMS, 1995), 53-62.
98. Y. Nishiyama, T. Miyashita, S. Isobe, and T. Noda, in S.H. Whang, *et al.*, eds., *High Temperature Aluminides and Intermetallics* (Warrendale, PA: TMS, 1990), 557-584.
99. M. Takeyama, T. Hirano, and T. Tsujimoto, in O. Izumi, ed., *Intermetallic Compounds - Structure and Mechanical Properties* (Sendai, Japan: Japan Institute of Metals, 1991), 507-511.
100. P.E. Jones and D. Eylon, in P. Blenkinsop, *et al.*, eds., *Titanium '95: Science and Technology* (London, England: Institute of Metals, 1996), 225-232.
101. B. Li, W. Cai, and E.J. Lavernia, *Mater. Synth. Proc.*, 4 (1996), 35-41.
102. J.H. Moll, C.F. Yoltan, and B.J. McTiernan, *Inter. J. of Powder Metallurgy*, 26 (2) (1990), 149-155.
103. M.A. Ohls, W.T. Nachtrab, and P.R. Roberts, in *Proc. P/M in Aerospace and Defense Technologies Symposium* (Tampa, FL: 1991).
104. D. Eylon, C.M. Cooke, C.F. Yoltan, W.T. Nachtrab, and D.U. Furrer, in H. Bildstein and R. Eck, eds., *Plansee Seminar '93* (Reutte, Austria: Plansee, 1993), 552-563.
105. H. Clemens, W. Glatz, P. Schretter, C.F. Yoltan, P.E. Jones, and D. Eylon, in Y-W. Kim, *et al.*, eds., *Gamma Titanium Aluminides* (Warrendale, PA: TMS, 1995), 555-562.
106. G.E. Fuchs, in I. Baker, *et al.*, eds., *High-Temperature Ordered Intermetallic Alloys V* (Pittsburgh, PA: MRS, 1993), 847-852.
107. G. Wang and M. Dahms, *JOM*, 45 (May 1993), 52-56.
108. F.H. Froes, C. Suryanarayana, G.-H. Chen, A. Frefer, and G.R. Hyde, *JOM*, 44 (May 1992), 26-29.
109. J. Rösler and C. Tönnies, in B. Ilschner and N. Cherradi, eds., *Proc. Third Inter. Symposium on Structural and Functional Gradient Materials* (Lausanne, Switzerland: Presses Polytechniques et Universitaires Romandes, 1995), 41-46.
110. J. Szekely, J. Busch, and G. Trapaga, *JOM*, 48 (December 1996), 43-47.
111. C.M. Austin, J.C. Chesnutt, J.A. Martus, and M.A. Schobert, unpublished research, General Electric Aircraft Engines, Cincinnati, OH, 1994-1996.



## PROCESSING AND PROPERTIES OF GAMMA TITANIUM ALUMINIDES

H.Clemens\*, N.Eberhardt\*\*, W.Glatz\*, H.-P.Martinz\*, W.Knabl\*, and N.Reheis\*

\* Plansee Aktiengesellschaft, A-6600 Reutte, Austria

\*\* Institut für Metallkunde und Werkstoffprüfung, Montanuniversität, A-8700 Leoben, Austria

### Abstract

This paper describes the progress in processing of  $\gamma$ -TiAl based alloys on industrial scale which has been achieved since the first ISSI conference. Employing an advanced hot-rolling process sheets with lengths >1000 mm have been rolled. Furthermore, results of recent foil rolling tests are presented. In addition, the first results of hot-extrusion and near-net shape processing are outlined. The mechanical properties of  $\gamma$ -TiAl sheet material with regard to processing route, alloy composition and microstructure are summarized and discussed. Sheet forming by means of superplastic forming and conventional metal forming techniques has successfully been conducted. Different joining techniques have been screened for  $\gamma$ -alloys including solid-state diffusion bonding, laser welding and brazing. The oxidation resistance of  $\gamma$ -alloys is higher than that of Ti-alloys, however, for long-term applications at temperatures >700°C the need for reliable oxidation protective coatings is anticipated. Recent results of oxidation tests conducted on coated  $\gamma$ -TiAl sheets are presented. Finally, the results of a structural stability test conducted on a  $\gamma$ -TiAl panel at 750°C are summarized.

### Introduction

$\gamma$ -TiAl based alloys exhibit numerous attractive properties for high-temperature structural applications in aerospace and automobile industries. These include high elastic modulus, low density, high resistance to hydrogen absorption, good oxidation and burn resistance, good creep properties and specific strength up to high temperatures [1]. Research and development on  $\gamma$ -alloys have progressed significantly within the last decade. This research has led to a better understanding of the fundamental correlations between alloy composition and microstructure, processing behaviour and mechanical properties. This paper summarizes our progress in processing of  $\gamma$ -alloys with emphasis on sheet rolling and subsequent sheet processing.

### Processing of $\gamma$ -TiAl Based Alloys

The processing routes utilized at Plansee AG are summarized in figure 1. In the following, the processing of sheets and foils by rolling is described in detail. In addition, hot-extrusion of  $\gamma$ -alloys and processing by near-net shape technology is outlined.

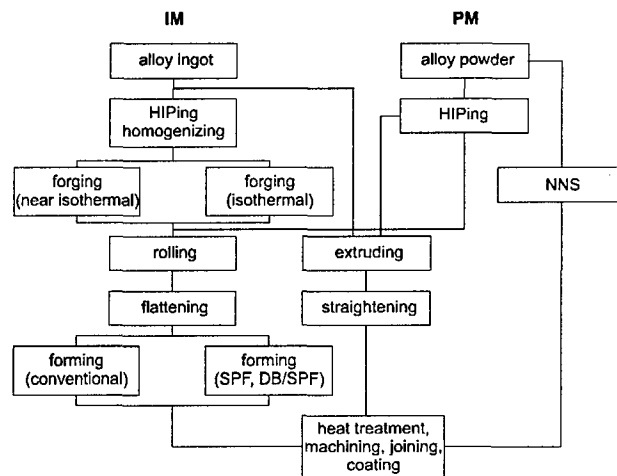


Figure 1: Processing routes utilized at Plansee AG (DB: diffusion bonding; SPF: superplastic forming; NNS: near-net shape).

### Rolling of $\gamma$ -TiAl Alloys

Rolling of  $\gamma$ -alloys to sheets and foils has been of interest since hypersonic and new turbine engines are under consideration. Two different sheet processing routes have been investigated. The ingot metallurgical (IM) route has been established in the framework of a German material research (Matfo) project [2]. Recent developments in clean powder production methods [3,4] and improved consolidation techniques, however, have increased the interest in powder metallurgical (PM) prematerials. Before the rolling process will be discussed the different prematerial production routes are outlined.

The Ingot Metallurgy Route uses a *Rotel* (rotating electrode) vacuum melting and skull casting unit to produce  $\gamma$ -alloy ingots [5]. Ti-48Al-2Cr and Ti-47Al-2Cr-0.2Si ingots (all compositions are stated in atomic percent, unless indicated otherwise) with diameters of 190 mm and weights up to 150 kg have been produced. Prior to forging the ingots are hot isostatically pressed to close cast porosity and then homogenized in the  $\alpha$ -phase region to minimize microsegregations which appear as a consequence of the peritectic solidification reactions. The ingots are cut into pieces of about 500 mm length and appropriately canned in order to obtain quasi-isothermal conditions during



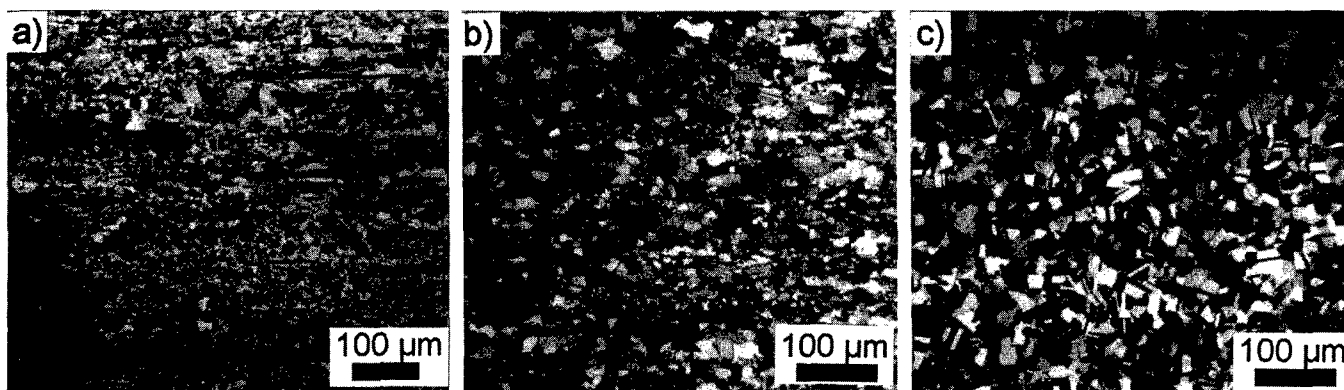


Figure 2: Microstructure of (a) single-step forged Ti-47Al-2Cr-0.2Si ingot, (b) isothermally forged Ti-47Al-2Cr ingot and (c) HIPed Ti-48Al-2Cr-2Nb prealloyed powder.

deformation on a hydraulic press. Single-step forging is conducted in the  $(\alpha + \gamma)$ -temperature range at the slowest strain rate which can be achieved (approx.  $1 \text{ s}^{-1}$ ). Pancakes with final diameters up to 570 mm have been forged (reduction in height of about 85%). A representative microstructure within a single-step forged Ti-47Al-2Cr-0.2Si pancake is shown in figure 2a. The microstructure is fine grained, however, striped zones of coarse  $\gamma$ -TiAl grains as well as isolated lamellar grains are still visible. It has been shown that distinct microstructural inhomogeneities (e.g. striped zones of coarse  $\gamma$ -TiAl grains) cannot be completely eliminated by the rolling process [5]. The homogeneity of the sheet microstructure, however, is extremely important with respect to the mechanical properties, in particular to the ductility below the brittle-to-ductile transition temperature. It should be pointed out that the microstructural quality of IM prematerial can be improved significantly by forging under isothermal conditions at low strain rates as demonstrated in figure 2b for a Ti-47Al-2Cr ingot. Especially in the USA many development programs have been accomplished in order to produce high-quality pancakes utilizing isothermal forging techniques [6].

The Powder Metallurgy Route is an alternative for the production of prematerial for sheet rolling, since  $\gamma$ -TiAl based alloy powder can be hot isostatically pressed (HIP) to a billet which can be rolled to sheets without prior homogenization heat treatments and forging. Due to the possibility of near-net shape HIPing the yield in the PM route is much higher than in the IM route, where a significant part of the pancake cannot be processed. Furthermore, the PM route enables the production of large  $\gamma$ -TiAl based alloy sheets because HIPing of prematerial in almost every dimension is possible. Normally, the powders are filled in a Ti-can, evacuated at elevated temperatures, sealed and then HIPed under proper conditions in order to obtain complete densification [7]. Figure 2c shows a typical microstructure of a PM Ti-48Al-2Cr-2Nb prematerial after HIPing for 2 hours at  $1300^\circ\text{C}$ . The powder was produced by means of high pressure argon gas atomization [3]. The microstructure is very homogeneous, and no pronounced irregularities as in the case of single-step forged IM prematerial (figure 2a) are visible.

The dimensions of the largest sheet which has been rolled so far are approximately  $1200 \times 400 \times 1.5 \text{ mm}$ . A further upscaling of the sheet dimensions with regard to length and width seems to be

feasible as far as the rolling process is concerned. Information on the rolling process is given in Refs.[2,5,8]. The present limiting factor in case of the IM route is the availability of high-quality forgings with good microstructural homogeneity over the entire cross section.

In order to qualify the rolling process as well as the homogeneity of the sheets it is important to note that in the as-rolled condition the  $\gamma$ -TiAl/ $\alpha_2$ -Ti<sub>3</sub>Al phase distribution, which very sensitively depends on the rolling temperature, is the same over the whole sheet area. Figure 3 shows the  $\gamma$ -TiAl/ $\alpha_2$ -Ti<sub>3</sub>Al phase distribution at different positions of a 1000 mm long  $\gamma$ -TiAl alloy sheet which was rolled at temperatures in the middle of the  $(\alpha + \gamma)$ -phase field. Note that there is no significant change in phase distribution between both ends. From this finding it is evident, that the utilized rolling process avoids temperature gradients and, therefore, provides quasi-isothermal rolling conditions. In addition, figure 3 shows the  $\gamma$ -TiAl/ $\alpha_2$ -Ti<sub>3</sub>Al phase distribution of a 700 mm long sheet which was rolled under non-optimized rolling conditions. It is obvious, that during rolling under non-isothermal conditions substantial heat loss takes place, which in turn limits the maximum sheet length.

For example, figure 4 shows the typical fine-grained microstructure of an IM Ti-47Al-2Cr-0.2Si sheet which has been rolled to a thickness of 1.5 mm. In the case of PM sheets isolated micropores in the range of 1-3  $\mu\text{m}$  were observed [2,7]. Investigations on powders, HIPed prematerials as well as sheets have revealed that the mechanism by which these pores are formed is related to thermally induced porosity due to Ar which is entrapped in hollow powder particles. These hollow powder particles are formed during the atomization process ("umbrella" effect). In contrast to Ar which is adsorbed on the powder surface, the entrapped Ar cannot be removed by the above mentioned outgassing process prior to HIPing. Although the portion of hollow particles in the atomized powders is rather low, their presence is reflected by a certain thermally induced microporosity within the sheets. It has been shown that these micropores are too small to have an influence on short-term tensile properties [2,7]. Recently, room temperature high-cycle fatigue tests at high frequencies have been conducted on PM  $\gamma$ -TiAl sheets. As in the case of static tensile tests no influence of the micropores on fatigue properties was found [9]. However, it might be speculated that these micropores may have a negative

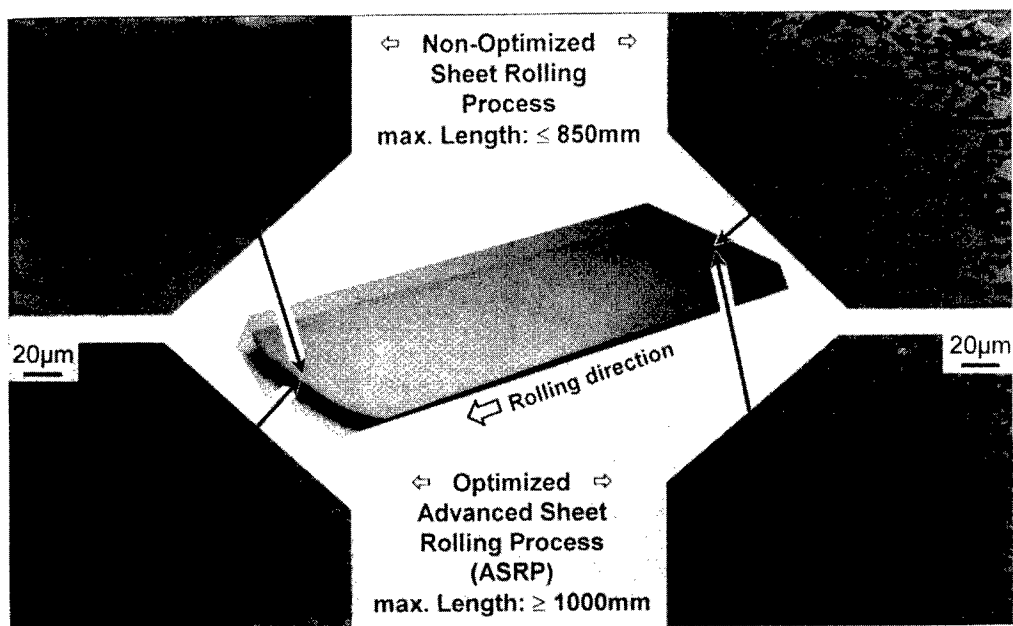


Figure 3:  $\gamma$ -TiAl/ $\alpha_2$ -Ti<sub>3</sub>Al phase distribution within  $\gamma$ -TiAl sheet material after processing under quasi-isothermal rolling conditions and non-isothermal rolling conditions. Note: the  $\alpha_2$ -Ti<sub>3</sub>Al phase appears brighter than the  $\gamma$ -TiAl phase.

impact on creep and superplastic properties. Current investigation activities are focused to clarify these open questions.



Figure 4: As-rolled microstructure of IM Ti-47Al-2Cr-0.2Si sheet (rolling direction is horizontal).

The texture of  $\gamma$ -TiAl sheets in as-rolled condition and after subsequent heat treatments has been investigated thoroughly [10]. For example, a sheet material which was rolled at a temperature within the ( $\alpha$  +  $\gamma$ )-phase field and subsequently annealed at 1000°C for 2 hours shows the following texture components: {011}<21 $\bar{1}$ > brass, {112}<11 $\bar{1}$ >-copper, {123}<634>-S, and {010}<100>-cube. A special feature of the cube component is that the c-axis of the  $\gamma$ -TiAl cell is aligned in the sheet plane perpendicular to the rolling direction.

The manufacturing of  $\gamma$ -TiAl alloy foils with a thickness of about 100  $\mu$ m is currently of interest. Recently, rolling tests have been

conducted with the intention of producing thin sheets with a thickness well below 1 mm. At present, small foils with a thickness down to 150  $\mu$ m have been rolled. For processing of  $\gamma$ -TiAl alloy foils in adequate dimensions, however, the requirements on the rolling process are more challenging as in the case of sheet processing. Beside other aspects a critical point is the surface quality which is developed during the rolling process. In the case of foils a sufficient surface quality, which does not need any final treatments, must be achieved during processing. Preliminary foil rolling tests have indicated that processing of foils with sufficient surface quality is feasible. However, before production of  $\gamma$ -TiAl alloy foils on industrial scale can be considered, additional efforts in research and development are needed to select suitable alloys, to define all processing parameters and to establish accompanying quality control regulations as well as to define appropriate test standards for  $\gamma$ -TiAl alloy foils.

#### Hot-extrusion of $\gamma$ -TiAl Alloys

Besides aerospace applications, world-wide interest is focused on automotive engine applications. Exhaust engine valves appear to be an ideal application for  $\gamma$ -alloys. Generally, there are three major benefits which could be exploited by the use of light-weight engine valves: (a) higher fuel economy, (b) better performance and (c) reduced noise and vibration [1,11-13]. So far, casting and reactive sintering are the two processing methods investigated most. However, the production of  $\gamma$ -TiAl valves from extruded rod material might be a potential alternative [1,12]. The extrusion behaviour of IM and PM billets was investigated in detail. Figure 5a shows the microstructure parallel to the extrusion direction for IM Ti-48Al-2Cr rod material. The extrusion was conducted at temperatures in the middle of the

( $\alpha + \gamma$ )-phase field. The extrusion ratio was about 12.5 : 1. A more homogeneous microstructure is obtained in the case of PM billets. For example, figure 5b shows the microstructure of PM Ti-48Al-2Cr-2Nb which was extruded under conditions comparable to those of the IM material. Further processing of the rods to valves includes upsetting of the valve disks. For this process step rod material with high straightness is required. Consequently, a method was developed which provides  $\gamma$ -TiAl rod material with lengths in the range of 200 - 500 mm exhibiting a straightness comparable to that specified for valve-steel rods.

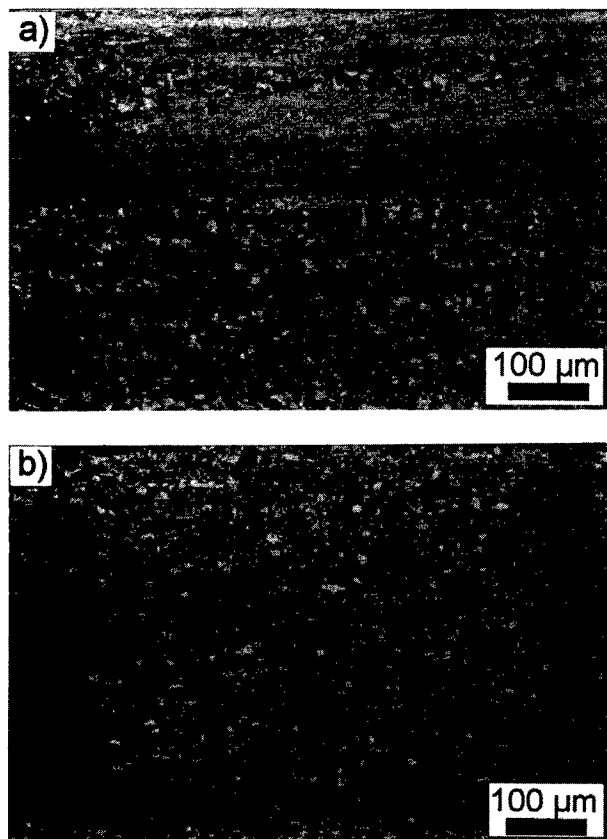


Figure 5: Microstructure of extruded (a) IM Ti-48Al-2Cr and (b) PM Ti-48Al-2Cr-2Nb parallel to the extrusion direction. Extrusion ratio: 12.5 : 1.

#### Near-net Shape Technology

Near-net shape (NNS) technology offers another attractive way of processing  $\gamma$ -alloys. Especially for simple geometries and small piece numbers this method has certain advantages over casting and wrought processing. Figure 6 shows preforms which have been produced from prealloyed  $\gamma$ -TiAl powders via HIPing.

#### Mechanical Properties

##### Tensile Properties

The variation of tensile properties of sheet material of various  $\gamma$ -TiAl based alloys with test temperature and microstructure is summarized in figure 7 [8]. The grain size of equiaxed primary

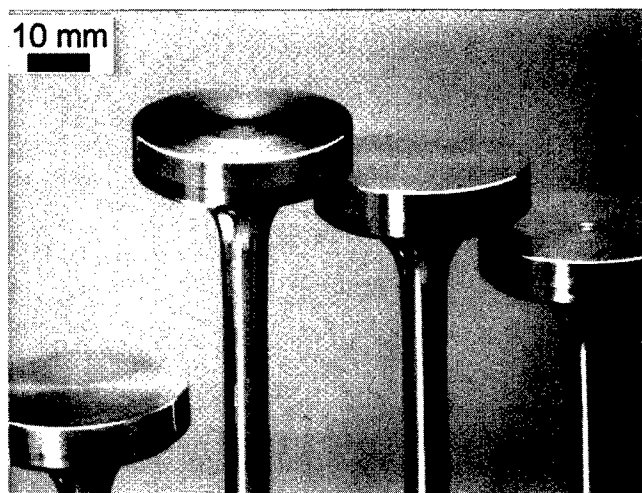


Figure 6:  $\gamma$ -TiAl preforms made via PM-NNS technology. The HIP-cans were removed by turning.

annealed, near gamma and duplex microstructures typically ranges between 10 - 40  $\mu\text{m}$ , whereby the primary annealed microstructure always represents the finest grain size. "Primary annealed" is referred to the microstructure which is developed during the annealing treatment used to flatten the sheets after rolling [2]. The grain size of coarse fully-lamellar microstructures is in the range of 500 - 1000  $\mu\text{m}$ . Tensile ductility is characterized by the brittle-to-ductile transition temperature (BDTT), which depends on alloy composition and microstructure, with fine-grained microstructures causing lower BDTTs and fully-lamellar microstructures causing higher BDTTs. Above the BDTT ductility increases considerably due to a significant increase in twinning as well as dislocation activity [10,14].

At room temperature, the highest plastic fracture strains are obtained for primary annealed materials. It must be noted that these high elongations were measured on specimens with electropolished gauge areas. For specimens with ground surfaces, however, the elongations are in the range of 1.5 - 2%. Again, at elevated temperatures the primary annealed microstructure shows the highest elongations, thus this microstructure is usually preferred for subsequent sheet forming operations. For more information concerning the tensile behaviour of  $\gamma$ -TiAl sheet materials, including strain rate sensitivity, deformation mechanisms and fracture behaviour see Refs.[2,10,14,15]. The influence of sheet texture on tensile properties has been published recently by Bartels et al. [16].

The temperature dependence of tensile properties of rod material of  $\gamma$ -alloys with compositions comparable to those used for sheet rolling is shown in figure 8. Tensile test specimens with turned gauge lengths have been used. The variation of tensile properties is due to differences in alloy composition, extrusion conditions and straightening temperatures which in sum control the microstructure as well as the texture within the rod. A detailed analysis will be given in a forthcoming paper. In general, as compared with sheet material (figure 7) extruded material shows higher strength properties.

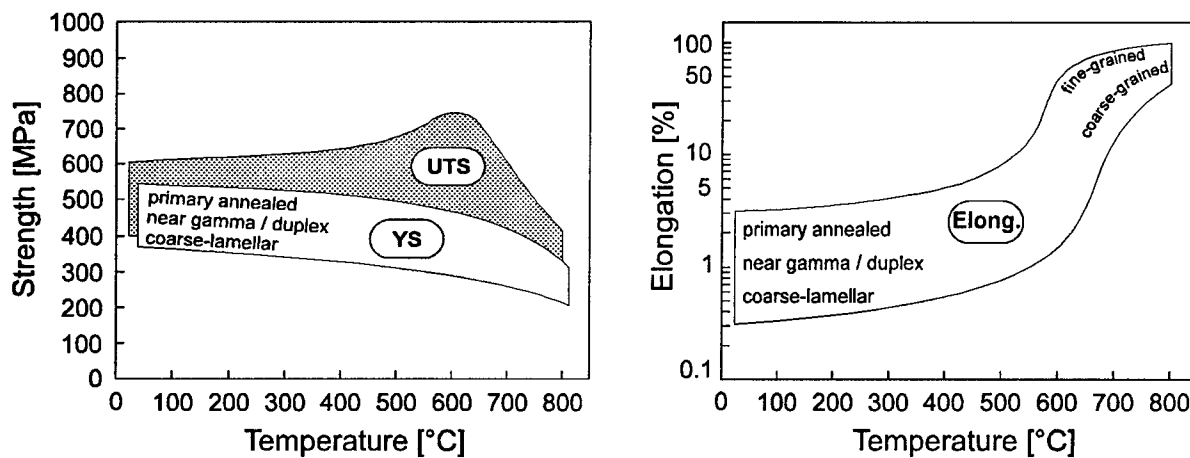


Figure 7. Variation of tensile properties of sheet material of various  $\gamma$ -TiAl based alloys with test temperature and microstructure. UTS: ultimate tensile strength; YS: 0.2%-yield strength.

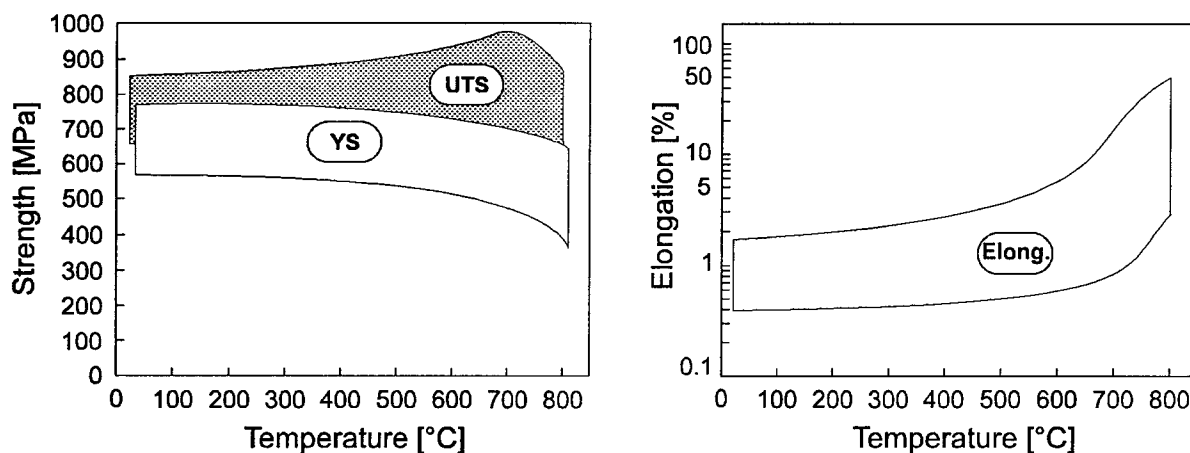


Figure 8. Variation of tensile properties of rod material of various  $\gamma$ -TiAl based alloys with test temperature. UTS: ultimate tensile strength; YS: 0.2%-yield strength.

#### Fracture Toughness

The room temperature fracture toughness of IM Ti-48Al-2Cr sheet material as well as the structural parameters of the different microstructures investigated are summarized in table 1.

Table 1: Effect of microstructure on room temperature fracture toughness of IM Ti-48Al-2Cr sheet material [18].

Microstructure	grain size [ $\mu\text{m}$ ]	lamellar volume fraction [%]	$K_{IC}$ [MPa $\sqrt{\text{m}}$ ]
near gamma	19	0	12
duplex	21	20	15
fully-lamellar	300	95	22

The test procedure is given in Ref. [18]. The major microstructural feature affecting fracture toughness is the volume fraction of lamellar grains. The transition from a microstructure dominated by equiaxed  $\gamma$ -grains to a fully-lamellar microstructure

results in an increase of the fracture toughness. The increased fracture toughness observed in fully-lamellar microstructures is explained in terms of crack deviation, crack bridging, crack propagation (surface tortuosity), and anisotropic composite-like fracture characteristics [17,18]

#### Fatigue Crack Growth Characteristics

Fatigue crack growth rates for fine-grained near gamma and duplex microstructures are found to be very high under constant-amplitude-loading conditions at room temperature and elevated temperatures, compared to those for superalloys, even after density adjustment [1]. The crack growth rates of coarse-grained fully-lamellar microstructures are considerably improved over those of fine-grained materials. In general, the fatigue crack growth characteristics of sheet material is similar to that of bulk material with similar microstructure. In the case of fully-lamellar sheet crack growth rate oscillations are observed because its grain size is coarse with respect to the sheet thickness, meaning only few lamellar colonies are involved and therefore the crack

## Fatigue Properties

The room temperature fatigue properties under bending mode conditions of Ti-48Al-2Cr sheet material with near-gamma microstructure is illustrated in figure 9. For the used test frequency of 25 Hz the endurance bending strength is 530 MPa which is approx. 35% higher than the 0.2%-yield strength obtained from tensile tests. Presently, the influence of test frequency on fatigue strength is under investigation.

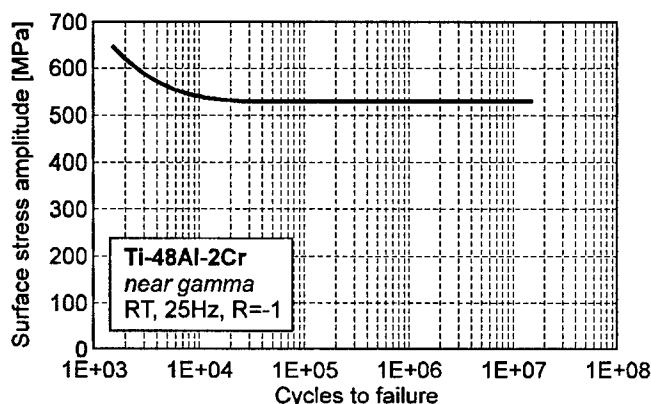


Figure 9: Room temperature fatigue behaviour under bending mode obtained for Ti-48Al-2Cr sheet material with near-gamma microstructure. Test conditions are given in the inset.

## Impact Toughness

Impact tests were conducted on a PM Ti-46.5Al-4(Cr,Nb,Ta,B) alloy at -196°C, 23°C, 545°C, 735°C, and 920°C, respectively. Two microstructures were investigated: a fine-grained equiaxed near gamma microstructure with an average grain diameter of about 10 µm and a fully-lamellar microstructure with a colony size of approximately 200 µm. Smooth specimens with a cross-section of 6 x 6 mm<sup>2</sup> were used. The speed of the hammer edge prior to impact was about 4.5 ms<sup>-1</sup>. At each temperature 5 specimens per microstructure have been tested. The results are summarized in figure 10. At -196°C and 23°C the impact toughness (= impact energy divided by cross-section) of the fine-grained specimens is higher than that obtained for the fully-lamellar specimens. At 545°C the situation is changed, i.e. the fully-lamellar microstructure shows a remarkably higher impact toughness than the fine-grained near gamma microstructure. At 735°C and 920°C, however, no significant difference between the two microstructures is found. The fracture surfaces were investigated by means of SEM. Irrespective of test temperature the fully-lamellar microstructure showed translamellar and interlamellar fracture mode. In the case of the fine-grained material a change in fracture mode was observed with increasing test temperature. At low temperatures (-196°C and 23°C) exclusively transcrystalline fracture took place. Specimens tested at 545°C showed predominantly intercrystalline, and to a small extent, transcrystalline fracture mode. At higher test temperatures the fracture mode was purely intercrystalline.

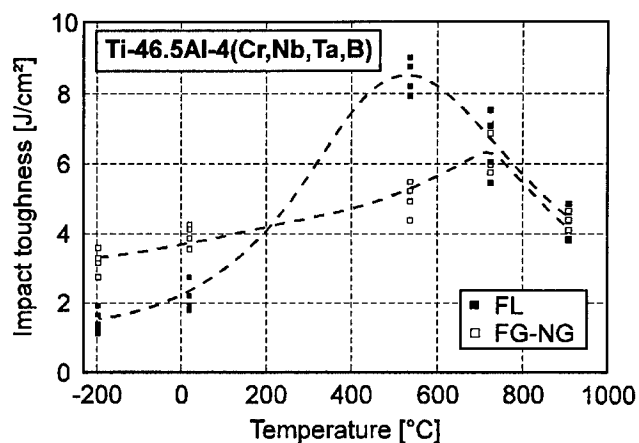


Figure 10: Impact toughness of PM Ti-46.5Al-4(Cr,Nb,Ta,B) as a function of temperature. FL: fully-lamellar microstructure; FG-NG: fine-grained near gamma.

At present, no full explanation of the behaviour shown in figure 10 can be given. Further investigations must be conducted to understand the marked maximum in case of the fully-lamellar microstructure. However, it might be speculated that the observed decrease at elevated temperature is correlated to decreasing material strength.

## "Foreign Object Damage"

Figure 11 shows the result of a "foreign object damage" (FOD) test conducted on an IM Ti-47Al-2Cr-0.2Si sheet with nearly-lamellar microstructure. The sheet was impacted at room temperature with a projectile of 7.8 mm in diameter (mass: 11.7 g; impact velocity: 890 ms<sup>-1</sup>). From figure 11 it is evident, that the sheet was penetrated without shattering. It must be emphasized that the observed benign failure mode is of great practical importance since large pieces of the sheet were not released which could increase the damage if application in gas turbines is considered.

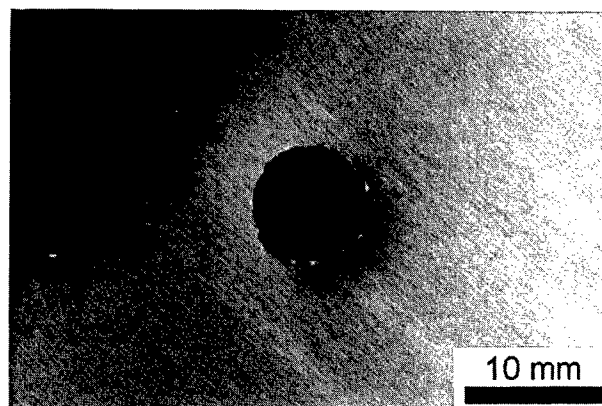


Figure 11: IM Ti-47Al-2Cr-0.2Si sheet impacted at room temperature shows penetration instead of brittle fracture.

### Oxidation Protective Coatings

It must be emphasized that the oxidation resistance might become a critical factor for  $\gamma$ -TiAl based alloys to be used for long durations at temperatures  $>700^{\circ}\text{C}$ , especially under cyclic thermal conditions and mechanical load. For jet engines typical service intervals are between 500 - 5000 hours depending on the type of engine (military or civil). In the case of stationary industrial gas turbines 8000 - 16000 hours are typical. That means that even with protective coatings (which might fail during service) a certain oxidation and hot corrosion resistance of the base material is demanded in order to ensure the integrity of components between inspection intervals [19]. In general, the oxidation resistance of  $\gamma$ -TiAl is higher than that of Ti-alloys, but it is still orders of magnitude lower than that of typical  $\text{Al}_2\text{O}_3$  formers, e.g. NiAl. The intrinsic oxidation resistance of the base material can be improved by alloying with Nb, Ta, and W which, however, reduces the ductility at low temperatures, whereas the alloying elements V, Cr, and Mn, which are used for increasing room temperature ductility, reduce the oxidation resistance [1].

Three different oxidation protective coatings have been investigated: (1) Al/Cr coatings deposited by pack cementation, (2) NiAl coatings prepared by Ni-electroplating and subsequent Al pack cementation and (3) a CoNiCrAlY coating deposited by atmospheric plasma spraying [20]. IM Ti-47Al-2Cr-0.2Si was selected as base material because this alloy exhibits a rather low oxidation resistance and shows strong spallation effects when submitted to cyclic oxidation [21].

Figure 12 summarizes the results of an isothermal oxidation test at  $800^{\circ}\text{C}$  for 672 hours in static air. For comparison the specific mass change obtained for uncoated IM Ti-47Al-2Cr-0.2Si is included.

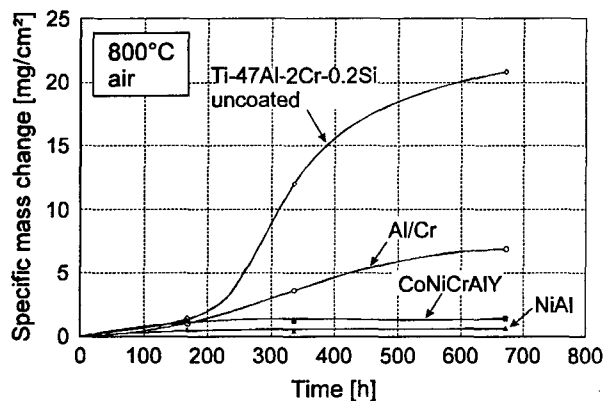


Figure 12: Isothermal oxidation behaviour of coated and uncoated IM Ti-47Al-2Cr-0.2Si at  $800^{\circ}\text{C}$  in static air.

From figure 12 it is evident, that especially the NiAl and CoNiCrAlY coatings improve the oxidation resistance significantly. Furthermore, a cyclic oxidation test at  $950^{\circ}\text{C}$  has led to similar results and no spallation effects were observed. Both isothermal and cyclic oxidation tests at  $950^{\circ}\text{C}$  have shown the best results for Al/Cr and NiAl coatings [20]. At this temperature where even more advanced  $\gamma$ -alloys exhibit high weight gain rates the two stated coatings show considerably

improved oxidation protection. For example, after 100 cycles (exposure time at  $950^{\circ}\text{C}$ : 30 minutes/cycle) the mass gain of uncoated PM Ti-48Al-2Cr-2Nb is approximately six times higher compared to that of the coated material [8,20].

Recently, the interaction between the different coatings and the IM Ti-47Al-2Cr-0.2Si base material has been investigated by 4-point-bending tests under static and cyclic conditions at room temperature. All coated samples have shown a significant decrease of bending strength and bending angle after the coating process. This behaviour is caused by the formation of brittle intermetallic phases and/or interdiffusion zones which may act as initiation sites for cracks upon loading. However, extended oxidation in air at  $800^{\circ}\text{C}$  show a strong embrittlement of the uncoated specimens at room temperature, whereas the coated specimens show only a slight decrease of the properties which have been measured after deposition. A detailed compilation of the observed results is given in Ref. [20].

### Superplasticity and Sheet Forming

The superplastic behaviour of sheet material processed via the IM and PM route was investigated thoroughly [2,8,22,23]. For example, figure 13 shows the strain rate sensitivity exponent ( $m$ ) as a function of strain rate and temperature for fine-grained IM Ti-47Al-2Cr-0.2Si sheet as determined from strain rate jump tests under tensile conditions. From figure 13 it is obvious that IM Ti-47Al-2Cr-0.2Si has a good potential for superplastic forming (SPF) even at temperatures below  $1100^{\circ}\text{C}$ . This is important because SPF facilities which are in use for Ti-alloys can also be used for SPF of  $\gamma$ -TiAl based alloy sheets. At  $1000^{\circ}\text{C}$  elongations up to 180% have been measured [23].

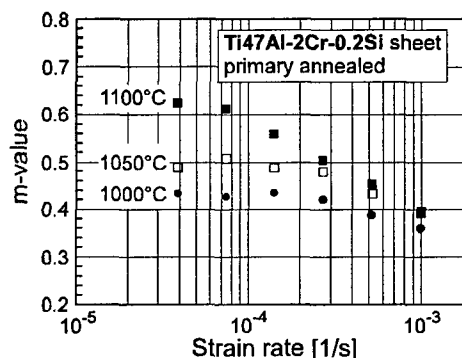


Figure 13: Dependence of the  $m$ -value on strain rate and temperature determined for IM Ti-47Al-2Cr-0.2Si sheet material (average grain size:  $12\text{ }\mu\text{m}$ ).

In the case of PM sheet material reduced superplastic properties have been observed. Although comparable  $m$ -values were determined, the fracture elongations at  $1000^{\circ}\text{C}$  were well below 100% [8]. Metallographic examinations have revealed that grain boundary separation takes place in the early stages of deformation which leads to the formation of massive voids during further deformation. Failure is then caused by subsequent growth of these voids. At present, no complete explanation for this degraded superplastic forming behaviour of PM sheet material can be given. However, it can be speculated that the presence of

thermally induced microporosity, fine dispersed oxides or, simply, the alloy composition are possible reasons.

SPF experiments on a laboratory scale have been performed to show the formability of  $\gamma$ -TiAl based alloy sheet materials [2,8,22]. For example, figure 14 shows the result of a gas-forming test conducted on IM Ti-47Al-2Cr-0.2Si sheet material at 1000°C. At present, such parts are used to investigate mechanical properties after SPF. In addition, tests on industrial SPF facilities have demonstrated that shaping of complex geometries is feasible [2].



Figure 14: IM Ti-47Al-2Cr-0.2Si part gas-formed under superplastic conditions at 1000°C.

Beside SPF conventional metal forming techniques can be applied to  $\gamma$ -TiAl based alloy sheets if the particular deformation characteristics (e.g. strain rate sensitivity) of these alloys are considered. For example, figure 15 shows 500 mm long stringer components which have been manufactured out of IM Ti-48Al-2Cr sheets by means of a modified bending technique. It must be emphasized that for forming techniques where no superplasticity is needed the forming capability of IM and PM sheet material was equally good, i.e. parts with geometries as shown in figure 15 have been formed.

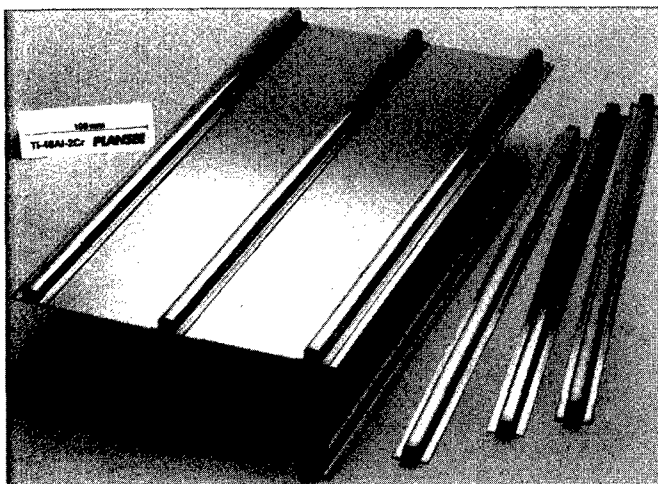


Figure 15: 500 mm long stringer components manufactured out of IM Ti-48Al-2Cr sheet material with near gamma microstructure (sheet thickness: 1 mm).

## Machining

$\gamma$ -TiAl based alloys in cast as well as wrought condition can be machined on conventional equipment, if appropriate precautions in regard to the low ductility of these materials are taken. In particular, problems have been experienced in: over-clamping (causing deformation, because at room temperature  $\gamma$ -TiAl based alloys are weaker than Ni- and Ti-based alloys); drilling (breakout); milling (splintering when approaching an edge); grinding (overheating) [24]. Machining of  $\gamma$ -TiAl sheets and rods of different compositions and microstructures was investigated thoroughly. All important machining methods were tested without major problems. For example, figure 16 shows parts which have been machined at Plansee AG using parameters similar to those used for refractory metals, e.g. Mo, and their alloys.

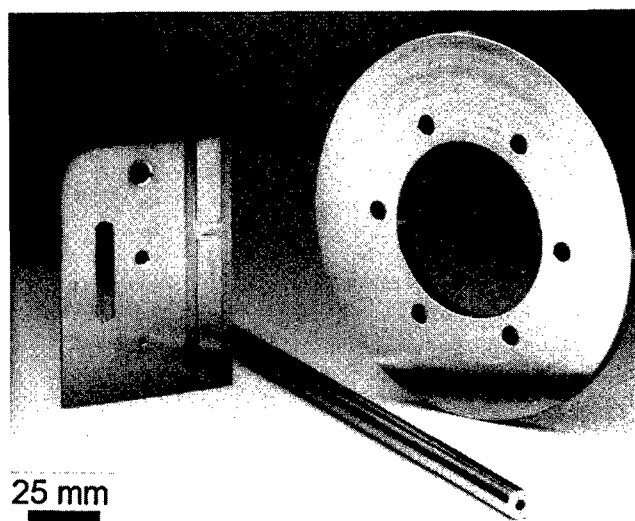


Figure 16: Machined  $\gamma$ -TiAl parts. For machining of these parts the following operations have been included: grinding, milling, drilling, turning, electro-discharge machining.

## Joining

For the future structural application of  $\gamma$ -TiAl alloys appropriate joining methods must be available which guarantee processing of reliable joints exhibiting good mechanical properties especially at temperatures below the brittle-to-ductile transition temperature. The feasibility of different welding techniques has been screened, e.g. electron-beam welding and laser-beam welding for sheet material [25] and rotary friction welding for rod material [12]. Due to the relatively low ductility of  $\gamma$ -TiAl based alloys at temperatures below the brittle-to-ductile transition temperature it is necessary to minimize local heat input and therefore also thermal stresses. However, due to the sensitivity to crack formation caused by electron-beam and laser-beam welding, preheating and/or subsequent heat-treatment are required to obtain crack-free welds. Especially for sheet material CO<sub>2</sub>-laser welding has been studied intensively [25,26]. With preheating above the brittle-to-ductile transition temperature it was possible to obtain crack-free weldments on different joining geometries like overlap, bead on plate, butt, and spot weldments with



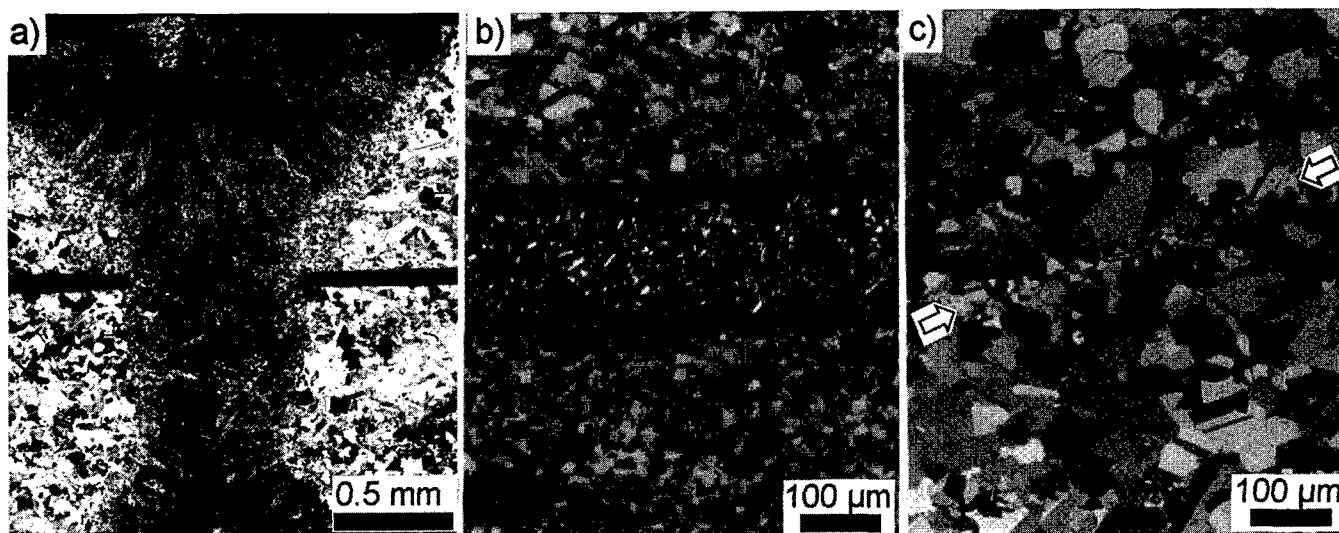


Figure 17: (a): Cross-sections of crack-free overlap weld obtained by CO<sub>2</sub> laser welding on IM Ti-48Al-2Cr sheet (preheating: 700°C, sheet thickness: 1 mm); (b) brazed joint (PM Ti-48Al-2Cr-2Nb sheet, Ni-based filler metal); (c) microstructure of diffusion bonded IM Ti-47Al-2Cr-0.2Si sheets (bonding zone is indicated by arrows).

different sample dimensions. Due to preheating the resulting thermal stresses are reduced by plastic deformation, and consequently crack formation after slow cooling to room temperature was avoided. In order to realize CO<sub>2</sub>-laser welding at elevated temperatures a special furnace was used to regulate the workpiece temperature during heating, welding and cooling [25]. For example, figure 17a shows a cross-section of an overlap weld obtained on IM Ti-48Al-2Cr sheet with near gamma microstructure.

High-temperature brazing has successfully been performed on  $\gamma$ -TiAl sheets and rods of various compositions. Brazed joints with good mechanical properties have been obtained using commercially available Ni-based brazing filler metals (figure 17b). Especially, for the manufacture of acoustic and non-acoustic  $\gamma$ -TiAl honeycomb sandwich structures for aerospace applications the use of advanced brazing technologies like liquid-interface diffusion (LID) bonding are under consideration [27].

Another joining method which is of particular interest in connection with superplastic forming is diffusion bonding. For example, superplastic forming in combination with diffusion bonding could be used for processing of stiff honeycomb structures. For IM Ti-47Al-2Cr-0.2Si sheet material diffusion bonding at temperatures of superplastic behaviour was intensively investigated [28]. The results of metallographic analysis of the bonding zone as well as tensile tests on bonded specimens have shown that excellent diffusion bonding quality can be obtained at 1000°C for bonding pressures in the range of 20 - 40 MPa and bonding times of 1 - 3 hours. However, from these results it is expected that sound joints could also be achieved applying lower bonding pressures. The microstructure of a diffusion bonded joint is illustrated in figure 17c.

#### Component Test

At the end of 1995, within the framework of a German hypersonic technology program, a stability test has been conducted on a  $\gamma$ -TiAl panel [26]. The entire panel was fabricated

out of IM Ti-48Al-2Cr sheet material with near gamma microstructure and consisted of a base sheet (500 x 250 x 1 mm) which was stiffened by three stringers as shown in figure 15. The assembling of the panel components was done by welding with a CO<sub>2</sub>-laser using a special furnace which allows preheating above the ductile-to-brittle transition temperature [25]. The test was conducted in air at 750°C and the test conditions combined both thermal and compressive loading. Both in-plane and out-of-plane deformation were measured by optical methods. The load was applied in direction of the stringers after the panel was in thermal equilibrium at the maximum test temperature of 750°C. The whole test consisted of 5 cycles. Cycle 1-5 comprised heating, thermalization, loading (except cycle 1), and subsequent cooling to at least 350°C (cycle 1-4). The displacement behaviour in direction of the stiffeners for the different test cycles is summarized in figure 18.

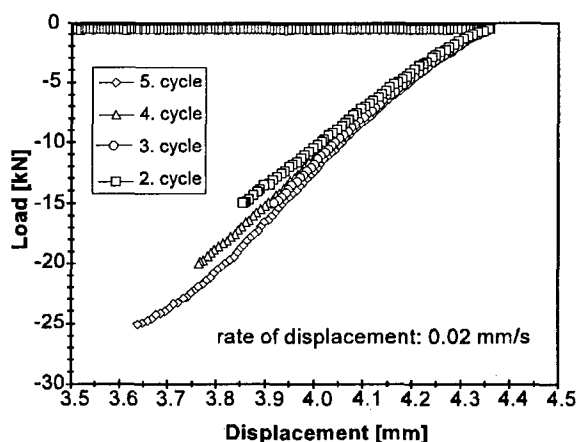


Figure 18: Displacement behaviour in direction of the stiffeners under compressive loading at 750°C.



After the maximum compressive load of -25 kN the test was stopped because a plastic deflection of the panel occurred. However, no onset of plastic buckling of the skin sheet and no detachment of the stiffeners were observed which proved the high stiffness and loading capacity as well as the good quality of the weldment joints. Nevertheless, forthcoming tests on  $\gamma$ -TiAl panels have to be conducted at temperatures below the ductile-to-brittle transition temperature where the material is more sensitive to deflectional effects and where the requirements on the quality of the welds are more stringent.

### Summary

Intermetallic  $\gamma$ -TiAl based alloys (" $\gamma$ -alloys") have a great potential to become one of the most important materials for advanced applications in aerospace, automotive and related industries. Research and development on  $\gamma$ -alloys have progressed significantly within the last decade. This research has led to a better understanding of the fundamental influence of alloy composition and microstructure on mechanical properties and processing behaviour of sheet and rod material.  $\gamma$ -TiAl based alloys can be processed using conventional metallurgical methods - a factor, which is necessary for these specific materials to be economically competitive with state-of-the-art materials. The processing of  $\gamma$ -alloys via ingot- and powder metallurgical routes has been successfully demonstrated. Also the feasibility of sheet forming by means of superplastic forming and other forming techniques has been shown on laboratory scale as well as on industrial facilities. Industry appears to be on the threshold of significant use of this new class of materials. In particular, all major aircraft and automotive engine manufacturers are advancing the qualification and introduction of  $\gamma$ -TiAl components. It is expected, that first implementation of  $\gamma$ -TiAl components will take place within the next five years. However, for widespread application of  $\gamma$ -alloys a further improved balance between room temperature ductility, fracture toughness, high-temperature strength, and oxidation resistance is required. Presently, next-generation  $\gamma$ -TiAl based alloys as well as oxidation resistant coatings are under development aiming to provide these improved properties.

### Acknowledgements

Part of this work was financially supported by the German Bundesministerium für Bildung, Wissenschaft, Forschung und Technologie within the framework of the following projects: Matfo 03M3029, Hyperschalltechnologie C12 - HT9401F and Matech 03N3034D.

### References

1. Y.-W. Kim, "Ordered Intermetallic Alloys, Part III: Gamma Titanium Aluminides," *JOM* 46(7)(1994), 30-39.
2. H. Clemens, "Intermetallic  $\gamma$ -TiAl Based Alloy Sheet Materials - Processing and Mechanical Properties," *Z. Metallkd.* 86(1995)814-822.
3. C.F. Yolton, *P/M in Aerospace and Defence Technologies* (Princeton, NJ: MPIF, 1989), 123.
4. R. Gerling, F.-P. Schimanski and R. Wagner, in *Advances in Powder Metallurgy & Particulate Materials* (Princeton, NJ: MPIF, 1992), 222.
5. H. Clemens et al., *Structural Intermetallics* (Warrendale, PA: TMS, 1993) 205.
6. S.L. Semiatin, *Gamma Titanium Aluminides* (Warrendale, PA: TMS, 1995) 509.
7. J.P. Beckman et al., *8th World Conference on Titanium: Titanium '95 - Science and Technology* (London, UK: The Institute of Metals, 1996) 217.
8. H. Clemens et al., *High-Temperature Ordered Intermetallic Alloys VII* (Pittsburgh, PA: MRS, 1997), in print.
9. W. Smarsly, private communication with author, MTU Munich, Germany, October 1996.
10. C. Koeppel et al., "Optimizing the Properties of TiAl Sheet Material for Application in Heat Protection Shields or Propulsion Systems," *Mater. Sci. Eng. A* 201(1995)182-193.
11. W.E. Dowling, W.T. Donlon and J.E. Allison, *High-Temperature Ordered Intermetallic Alloys VI* (Pittsburgh, PA: MRS, 1995), 757.
12. S. Hurta et al., in Ref.[7], p.97.
13. S.E. Hartfield-Wünsch et al., in Ref.[6], p.41.
14. F. Appel, H. Clemens and R. Wagner, *Deformation and Fracture of Ordered Intermetallic Materials III* (Warrendale, PA: TMS, 1996), 123.
15. H. Clemens, W. Glatz and F. Appel, "Tensile Properties and Strain Rate Sensitivity of Ti-47Al-2Cr-0.2Si Sheet Material with Different Microstructures," *Scripta metall. mater.* 35 (1996) 429-434.
16. A. Bartels et al., in Ref.[8].
17. K.S. Chan and Y.-W. Kim, "Influence of Microstructure on Crack-tip Micromechanics and Fracture Behaviour of a Two-phase TiAl Alloy," *Metall. Mater. Trans. A* 23(1992)1663-1677.
18. R. Behr et al., in Ref.[11], p.781.
19. W. Smarsly and L. Singheiser, *Materials for Advanced Power Engineering* (Dordrecht, The Netherlands: Kluwer Academic Publishers, 1994), 1731.
20. H.-P. Martinz, H. Clemens and W. Knabl, *14th International Plansee Seminar* (Tyrol, Austria: Plansee AG, 1997), in print.
21. R. Hofman et al., *4th European Conference on Advanced Materials and Processes - EUROMAT95* (Milano, Italy: Associazione Italiana di Metallurgia, 1995), pp. 91-96.
22. H. Clemens et al., "Characterization of Ti-48Al-2Cr Sheet Material," *Intermetallics* 2(1994)179-184.
23. N. Eberhardt, "Superplastische Eigenschaften von  $\gamma$ -TiAl Blechen" (Diploma thesis, Martin-Luther Universität, Halle-Wittenberg, Germany, 1995).
24. C.M. Austin and T.J. Kelly, in Ref.[6], p.143.
25. M. Klassen, E. Schubert and G. Sepold, *Laser Treatment of Materials* (Stuttgart, Germany: Arbeitsgemeinschaft Wärmebehandlung und Werkstofftechnik, 1996), p.193.
26. H. Clemens et al., *Spacecraft Structures, Materials and Mechanical Testing* (Noordwijk, The Netherlands: European Space Agency, SP-386, 1996), p.1297.
27. R. Leholm and M. Martinez, in Ref.[7], p.1617.
28. W. Glatz and H. Clemens, "Diffusion Bonding of Ti-47Al-2Cr-0.2Si Sheet Material," *Intermetallics* (1997), in print.

## Directional Solidification of TiAl-based Alloys

D. R. Johnson, Y. Masuda, Y. Shimada, H. Inui, and M. Yamaguchi

Department of Materials Science and Engineering  
Kyoto University, Sakyo-ku, Kyoto 606-01, Japan

### Abstract

Directional solidification of TiAl alloys was explored to discover if the gamma/alpha<sub>2</sub> lamellar boundaries could be aligned parallel to the growth direction. Ingots that solidified as the beta phase had a resultant lamellar orientation parallel and 45 degrees to the growth direction. Greater control of the lamellar orientation could be obtained by using a seed material from the TiAl-Si system. For the composition of the seed material, Ti-43Al-3Si, the original orientation of the lamellar microstructure was maintained after heating to and cooling from the single phase alpha region making seeding of the alpha phase possible. With the seed composition kept constant, the lamellar microstructure could be aligned in master alloys from the TiAl-Si, TiAl-Nb-Si, and Ti-Al systems at growth rates up to 40 mm/h.

### Introduction

Ordered intermetallics such as TiAl are considered as candidate materials for high temperature structural applications provided that the proper combination of room temperature toughness and elevated temperature strength can be developed. Improvements in these areas are generally found for multi-phase alloys such as those with the fully lamellar microstructure of TiAl (gamma) and Ti<sub>3</sub>Al (alpha<sub>2</sub>) [1-10]. Systematic studies on the deformation and fracture behavior of the lamellar microstructure have been conducted using polysynthetically twinned (PST) crystals where the entire ingot consists of only a single lamellar grain [3-5].

Results from these studies on PST crystals have shown that the mechanical properties of the lamellar microstructure are extremely anisotropic. For example, the optimum combination of strength, toughness, and ductility can be obtained if the lamellar microstructure is aligned parallel to the test axis [3-5]. However, if the lamellar boundaries are perpendicular to tensile axis, the material is extremely brittle [4,5]. Unfortunately, simple casting operations usually produce this case where the lamellar boundaries are all perpendicular to the dendritic growth direction [6,7]. For such an orientation, TiAl PST crystals show almost no tensile ductility even at 1000 °C [4].

However, by reducing the lamellar grain size, high strength materials with a balance of properties can be obtained and significant progress has been made in this area [7-9]. In addition, it may be possible to take advantage of the anisotropic nature of the lamellar microstructure by forming an appropriate texture. For example, very promising microstructures have recently been produced by forging TiAl-alloys within the alpha phase temperature range [10].

Another possibility, is to form a favorable texture directly upon solidification. Ceramic mold materials that are stable when in contact with molten TiAl for extended periods of time have been developed, and thus manufacture of component parts by directional solidification is possible [11]. Unfortunately, control of the lamellar orientation is difficult to achieve by directional solidification alone since the lamellar microstructure is formed from the solid state and not from the liquid. However, since many cast ingots often have only one lamellar orientation, it may be possible to change the lamellar arrangement with the appropriate processing technique.

The target microstructure for a directionally solidified ingot is one where the columnar grains have transformed to the fully lamellar microstructure upon cooling with all the gamma/alpha<sub>2</sub> boundaries parallel to the growth direction. In addition, each columnar lamellar grain should be rotated about its longitudinal axis to provide a reasonable off-axis fracture toughness. This paper will describe the recent progress in producing such microstructures by directional solidification techniques.

### Directional Solidification of binary Ti-Al ingots

#### Processing

Initially, the microstructure of binary alloys directionally solidified at different growth rates were characterized. Master ingots of Ti-45Al, Ti-46Al, Ti-48Al, and Ti-50Al (all compositions are given in atomic percentages) were directionally solidified at growth rates between 40 and 200 mm/h in an optical floating zone furnace using double halogen lamps as the heating source.

Structural Intermetallics 1997  
Edited by M.V. Nathal, R. Darolia, C.T. Liu, P.L. Martin,  
D.B. Miracle, R. Wagner, and M. Yamaguchi  
The Minerals, Metals & Materials Society, 1997

As-grown ingots, typically 10 mm in diameter and 80 mm in length, were sectioned and the distribution and orientation of lamellar grains were determined by optical microscopy on two perpendicular surfaces. For the Ti-45Al and Ti-48Al ingots, the as-processed microstructure was fully lamellar regardless of the growth rate. These ingots all contained columnar shaped lamellar grains with diameters in the range of 1 to 3 mm as shown in Fig. 1. As expected, the size of the columnar grains decreased with increasing growth rates but the overall size of each grain remained large even for those ingots processed at 200 mm/h. The microstructure of the Ti-50Al ingots consisted of a mixture of lamellar and equiaxed gamma grains due to the increased amount of interdendritic gamma. For this composition, the overall grain shape changed from columnar to equiaxed as the growth rate was increased above 100 mm/h.

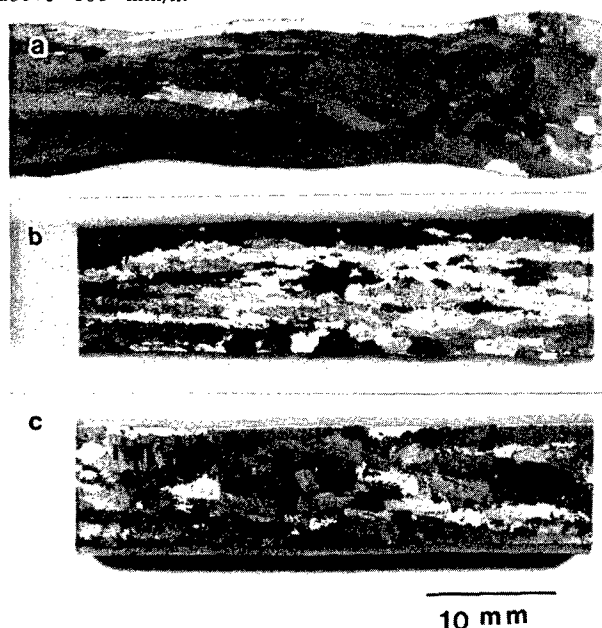


Figure 1: Longitudinal sections of directionally solidified ingots of (a) Ti-45Al, at 200 mm/h, (b) Ti-48Al at 200 mm/h, and (c) Ti-50Al at 100 mm/h.

#### Microstructure

The orientation of the lamellar grains, defined here as the angle between the lamellar boundaries and the growth direction, is shown in Fig. 2 for the Ti-45Al and Ti-48Al ingots. These results can be explained as follows. For the Ti-48Al ingots, the bulk of the solidification occurs through the hexagonal alpha phase which has a preferred growth direction parallel to the [0001] direction. Upon cooling, the lamellar microstructure is then formed from the parent alpha phase such that  $(0001)\alpha // (111)\gamma$  and  $\langle 11\bar{2}0 \rangle \alpha // \langle 110 \rangle \gamma$ . For this case, the lamellar boundaries would all be perpendicular to the growth direction. The difference in lamellar orientation for the Ti-48Al ingots processed at different growth rates (Fig. 2) can be attributed to two different growth morphologies. At low growth rates, a cellular morphology is favored where growth is parallel to the heat flow direction regardless of crystal orientation [12]. However, at high growth rates, a dendritic morphology is favored and by

competitive growth between differently oriented crystals, a preferred crystallographic orientation aligned closely with the heat flow direction will develop [12,13]. Thus, the well defined solidification texture observed at 200 mm/h (Fig. 2b) is due to the competitive growth of alpha phase dendrites.

For the Ti-45Al ingots, solidification occurs primarily through the Ti-based b.c.c. (beta) solid solution. For this case, the alpha phase would nucleate from the beta phase upon cooling following the Burgers orientation relationship. The lamellar microstructure would then form upon further cooling with the gamma/alpha orientation relationship previously mentioned. If the preferred growth of the beta phase dendrites is parallel to  $\langle 100 \rangle$ , then the final lamellar microstructure would be oriented between 0 and 45 degrees to the growth direction, Fig. 2(c)&(d). Also, one ingot of Ti-46Al was processed at 200 mm/h and the resultant microstructure consisted of very large lamellar grains, all with the lamellar boundaries parallel to the growth direction, indicating growth of beta phase dendrites.

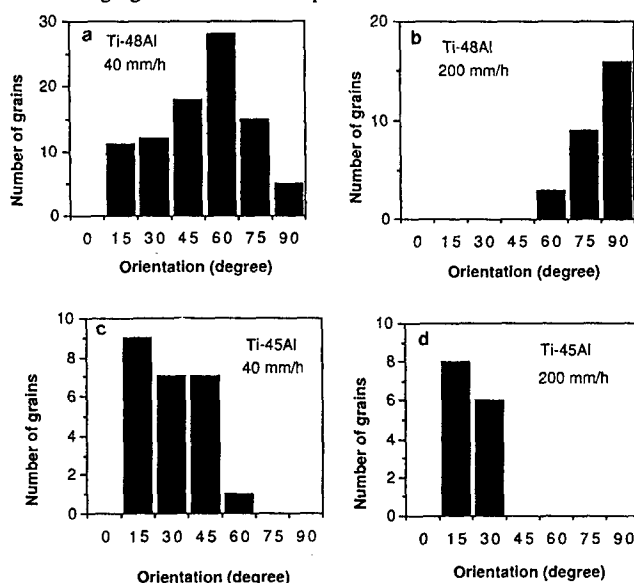


Figure 2: The measured angles between the lamellar boundaries and the growth direction in columnar grains of directionally solidified TiAl ingots.

#### Tensile properties

Table 1 lists the room temperature tensile properties measured from the directionally solidified ingots. Tensile specimens with a 20 mm gauge length and a square cross-section of 5 mm x 5 mm were tested at a strain of  $2 \times 10^{-4} \text{ s}^{-1}$  in air. The fracture surfaces of the Ti-48Al specimens were macroscopically flat while those of the Ti-45Al were slanted. From metallographic observations, fracture was found to occur parallel to the lamellar boundaries as expected. Thus, the shape of the fracture surfaces are consistent with the variation of lamellar orientation measured from each set of specimens shown in Fig. 2.

The tensile elongation was poor for all the specimens tested. A tensile elongation of 1% or more was only observed for specimens where the lamellar microstructure of all the grains was aligned parallel to the growth direction. Thus, for these large grain

specimens, the tensile ductility was more strongly dependent on the lamellar orientation than the  $\alpha_2$  volume fraction. Hence, if the mechanical properties are to be improved, the number of the columnar grains must be significantly increased and/or the lamellar boundaries in all the lamellar grains must be well aligned with the growth direction.

Table 1: Tensile properties of directionally solidified TiAl ingots.

Composition (at.%)	Growth rate (mm/h)	Yield Strength (MPa)	%Tensile elongation
Ti-45Al	70	381	0
	140	416	1.0 **
	140	260	0
	200	480	0
Ti-46Al	200	289	3.2 **
Ti-48Al	70	221	0.3
	140	261	0
Ti-50Al	40	206	0.6

\*\* lamellar orientation was parallel to growth direction for all the grains in the specimen

#### Directional Solidification of TiAl-Si Alloys

To better control the orientation of the lamellar microstructure, a seeding method was employed. For such an approach to work, the  $\alpha$  phase must be oriented directly from the liquid and hence must be the primary solidification phase. However, for most TiAl-based alloys of engineering importance, the Ti-based b.c.c. solid-solution is the first phase to solidify. Furthermore, even if  $\alpha$  is the primary solidification phase, the seed material must be stable upon heating. For example, a Ti-49.3Al PST crystal was initially used as a seed material. However, upon heating, recrystallization of the PST-seed occurred and the desired orientation was lost. Therefore, ternary systems were explored to locate an appropriate seed material.

The initial idea was to find a composition where  $\alpha$  was the primary solidification phase and where the  $\alpha$  (or  $\alpha_2$ ) phase was thermodynamically stable between the melting temperature and room temperature. Additions of Si were found to be a promising candidate. Initially, Si additions to TiAl were made to explore the silicide eutectic morphologies that form in these alloys as reported by a number of authors [14-17]. However, during the course of this investigation, silicon additions were found to shift the composition range where  $\alpha$  is the primary solidification phase towards a much lower Al content [18]. Hence, if recrystallization of the microstructure can be prevented during heating, then this may be a suitable system for a seed material. To determine this, a seed composition was chosen as shown in Fig. 3. Here, the liquidus surface is projected onto an estimate of the 1100 °C isothermal section. Manesh and Flower [16] have proposed a partial projection of the liquidus for the Ti-Al-Si system and this was combined with our data [18] for the primary  $\alpha$  region to produce the projection shown in Fig. 3. As can be seen in this figure, there is a small composition region where the primary  $\alpha$  region overlaps the TiAl+Ti<sub>3</sub>Al+Ti<sub>5</sub>Si<sub>3</sub> three phase region. Thus, this compositional region will satisfy the above requirements for a seed material and a composition of Ti-43Al-3Si was chosen for further study.

#### Growth from a TiAl-Si seed material

First an ingot with a composition Ti-43Al-3Si was directionally solidified by the floating zone method at 100 mm/h. The resulting  $\gamma/\alpha_2$  lamellar microstructure was oriented perpendicular to the growth direction as expected (Fig. 2b). A section of this ingot was then cut and rotated by 90 degrees for use as a seed. Directional solidification was carried out at 20 mm/h and seeding of the  $\alpha$  phase was successful as shown in Fig. 4 where the lamellar microstructure is aligned parallel to the growth direction for the complete ingot [18].

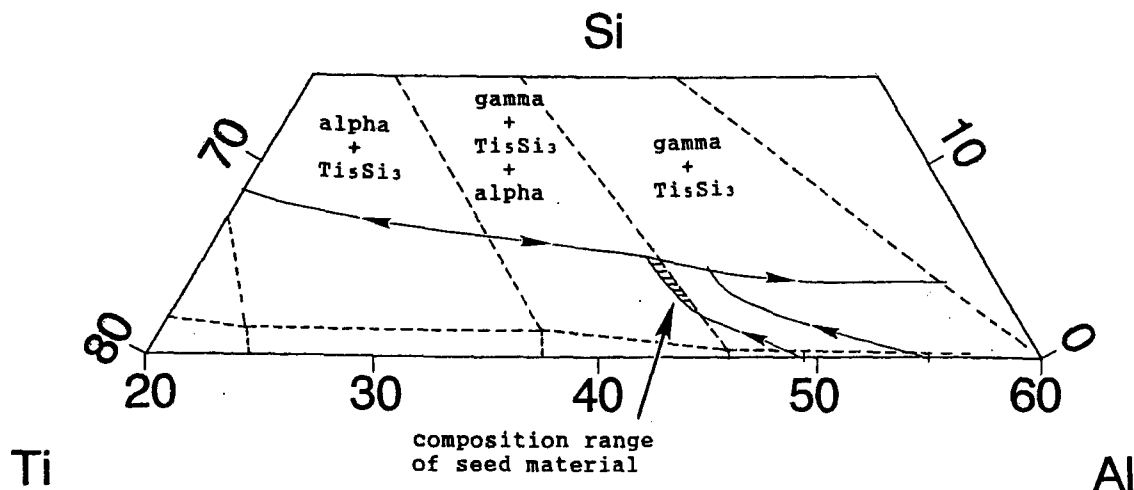


Figure 3: Liquidus surface projected onto the 1100 °C isothermal section showing the composition range where the seed material was chosen.



Figure 4: Microstructure of a directionally solidified Ti-43Al-3Si ingot grown from a seed with the silicide particles marked in each figure by arrows.

Numerous ingots with an aligned lamellar microstructure have been grown with the above composition from appropriately oriented seeds. For some ingots, the lamellar orientation of the seed was measured prior to processing by metallographic observation on two perpendicular surfaces. After processing, the original lamellar orientation of the seed was found to be restored. In addition, the lamellar microstructure was found to be continuous between that of the seed and the processed material. These results suggest that the volume fraction of the alpha phase must increase upon heating above the eutectoid temperature by a thickening of the alpha lamellae without nucleation of new alpha grains. Hence, once the alpha single phase field is entered, the basal plane has the same orientation as that of the alpha<sub>2</sub> phase in the original lamellar microstructure. Thus, by seeding the alpha phase, the processed ingot will have the same gamma/alpha<sub>2</sub> lamellar orientation upon cooling as that of the original seed.

#### Reducing the Si content

While the lamellar microstructure can be aligned for a composition of Ti-43Al-3Si, these alloys unfortunately contain a large volume fraction of the silicide phase Ti<sub>5</sub>Si<sub>3</sub> [18]. As can be seen in Fig. 4, the silicide particles can be very large and as such, the alloy would be unsuitable for engineering applications. Thus, alloys containing less silicon were processed to find if the volume fraction of the silicide phase could be reduced to acceptable levels while still maintaining the aligned lamellar microstructure. During these experiments, the seed composition was kept constant at Ti-43Al-3Si, but the composition of the master ingots was varied for alloys in the TiAl-Si, TiAl-Nb-Si and Ti-Al systems [19]. The compositions and results from the seeding experiments are shown in Table 2. From Table 2, the lamellar microstructure could be aligned for alloys containing approximately 47 at.% (Al+Si) for each alloy system investigated. However, when the composition of the master alloys contained an (Al+Si) content greater than 47 at.%, the lamellar microstructure could not be aligned by using the Ti-43Al-3Si seed. The reason for this is due to the mixing of the seed and master alloy compositions when the initial molten zone is made.

For the case where seeding was unsuccessful, the composition of the molten zone becomes too rich in both Si and Al causing the gamma phase to nucleate (see liquidus projection in Fig. 3). In contrast, steady state growth of the alpha phase develops for the successful case.

Table 2. Compositions of directionally solidified ingots and results of seeding experiments using a Ti-43Al-3Si seed [19].

Alloy composition (at.%)	Aligned lamellar microstructure?
<b>(TiAl-Si)</b>	
Ti-43Al-3Si	Yes
Ti-45Al-2Si	Yes
Ti-45.5Al-1.5Si	Yes
Ti-46Al-1Si	Yes
Ti-46.5Al-0.5Si	Yes
Ti-47Al-0.5Si	No
Ti-48.5Al-0.5Si	No
Ti-49Al-0.3Si	No
<b>(Binary TiAl)</b>	
Ti-50Al	No
Ti-49.5Al	No
Ti-48Al	No
Ti-47Al	Yes
<b>(TiAl-Nb-Si)</b>	
Ti-49Al-3Nb-0.5Si	No
Ti-48Al-3Nb-0.5Si	No
Ti-46.5Al-3Nb-0.5Si	Yes

For the successful seeding cases, the Si content could be reduced from 3 at.% to zero. The only major change in the microstructure between these alloys was the reduction of the silicide volume fraction. If silicide particles were found, their size was always very large. However, once the Si concentration was reduced to 0.5 at.%, the processed material was found to be free of silicide particles when observed by optical microscopy. Shown in Fig. 5 is a Ti-47Al ingot grown from a Ti-43Al-3Si seed. For this case, the lamellar microstructure is aligned parallel to the growth direction and is continuous with that of the seed (Fig. 5c). Silicide particles in this ingot were observed only for the first centimeter of processed material (Fig. 5b) with the rest of the ingot being free from such particles (Fig. 5a).



Figure 5: Microstructures taken from a directionally solidified binary Ti-47Al ingot grown from a Ti-43Al-3Si seed showing an aligned lamellar microstructure. (a) Silicide free material after 15 mm of growth; (b) reduced number of silicide particles in the first 10 mm of growth; and (c) large silicide particles in the seed material (GD=growth direction. SEM back scattered electron images) [19].

#### Effect of growth rate

The range of alloys listed in Table 2 were all grown at a slow growth rate of 5 mm/h. Faster growth rates are possible for the seed composition and for master alloys low in Si. For example, ingots of Ti-43Al-3Si, Ti-47Al, and Ti-46.5Al-3Nb-0.5Si have all been successfully processed at 40 mm/h with the as-grown microstructure consisting of a single lamellar orientation aligned parallel to the growth direction [19]. However, for Si concentrations near 1.5 at.%, processing becomes very difficult due to the large mushy zone that develops. Such alloys are difficult to process even at 5 mm/h and hence the growth rate could not be increased. Due to this reason, the growth rates for the low silicon alloys could not be increased until about 15 mm of material had been processed since the initial molten zone is a mixture between the Ti-43Al-3Si seed and the master alloy.

#### Mechanical properties

Results from tensile and compression tests for the TiAl-Si alloys that were successfully processed (Table 2) are shown in Fig. 6. Except for the seed material, these alloys all have a composition of Ti-(47-x)Al-xSi (x=0 to 2 at.%). Flat tensile specimens 20 mm in length with a gauge section of 5 mm x 2 mm x 0.5 mm were tested in air and in vacuum of  $5 \times 10^{-5}$  torr. Tensile testing was done at room temperature using a strain rate of  $2 \times 10^{-4} \text{ s}^{-1}$ . Compression specimens with dimensions of 5 mm x 2.5 mm x 2.5 mm were tested in vacuum of  $2 \times 10^{-4}$  torr at room temperature and 1000 °C using a strain rate of  $2 \times 10^{-4} \text{ s}^{-1}$ . In all tests, the lamellar boundaries were parallel to the loading axis.

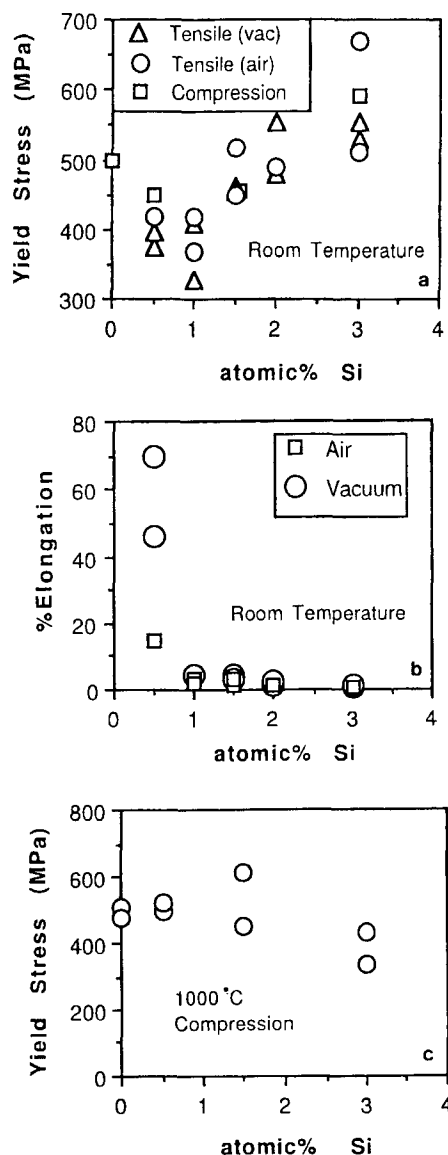


Figure 6: Results for tensile and compression tests of TiAl-Si alloys showing (a) room temperature yield stress, (b) room temperature tensile elongation, and (c) compressive yield stress at 1000 °C.

From Fig. 6a, the room temperature yield stress generally increases with increasing Si content while the tensile elongation (Fig. 6b) dramatically improves as the Si concentration is decreased. The increase in tensile ductility is clearly due to the reduced volume fraction of silicide particles since no such particles were observed for the Ti-46.5Al-0.5Si alloy while large elongated ones were found in the alloy containing 1 at.% Si [19].

Somewhat surprising was decrease in strength at 1000 °C for alloys containing greater percentages of Si as shown in Fig. 6c. The decrease in strength was found to be due to a coarsening of the lamellar microstructure when compared to the Ti-47Al binary case. The  $\alpha_2$  spacing before and after compression tests at 1000 °C are shown in Fig. 7 for the Ti-47Al and Ti-43Al-3Si specimens. These specimens were held at 1000 °C for approximately 30 minutes. During that time, the Ti-47Al specimens showed little coarsening with respect to the  $\alpha_2$  spacing while significant coarsening was observed the Ti-43Al-3Si specimen. The coarsening appears to occur by dissolution of some  $\alpha_2$  lamellae while others merge together to form a wide bundle. The rapid coarsening of lamellar microstructure with respect to the binary case may be one of the reasons why the Ti-43Al-3Si alloy can be used a seed material without recrystallization occurring.

## Discussion

### Ti-Al binary case

Recent compilations of the Ti-Al phase diagram show that beta is the primary solidification phase for alloys containing less than approximately 49 at.% Al [20]. However, from the directional solidification results, an alloy composition of less than 46 at.% Al was needed for the ingot to solidify as the beta phase. These results can be understood in terms of the peritectic reaction of liquid + beta = alpha as shown in Fig. 8. The general argument is that once a planar solid/liquid interface cools below the peritectic temperature, the alpha phase will nucleate, covering the beta phase and effectively stopping the peritectic reaction [21]. After this, steady state growth of the alpha phase may then be possible [22]. Also, for dendritic growth, the phase selection processes for peritectic alloys has recently been addressed by Umeda et al. [23] who have shown that at faster solidification velocities, growth of the metastable phase (in this case alpha) will be kinetically preferred due to the its smaller solute rejection with respect to the stable phase (beta).

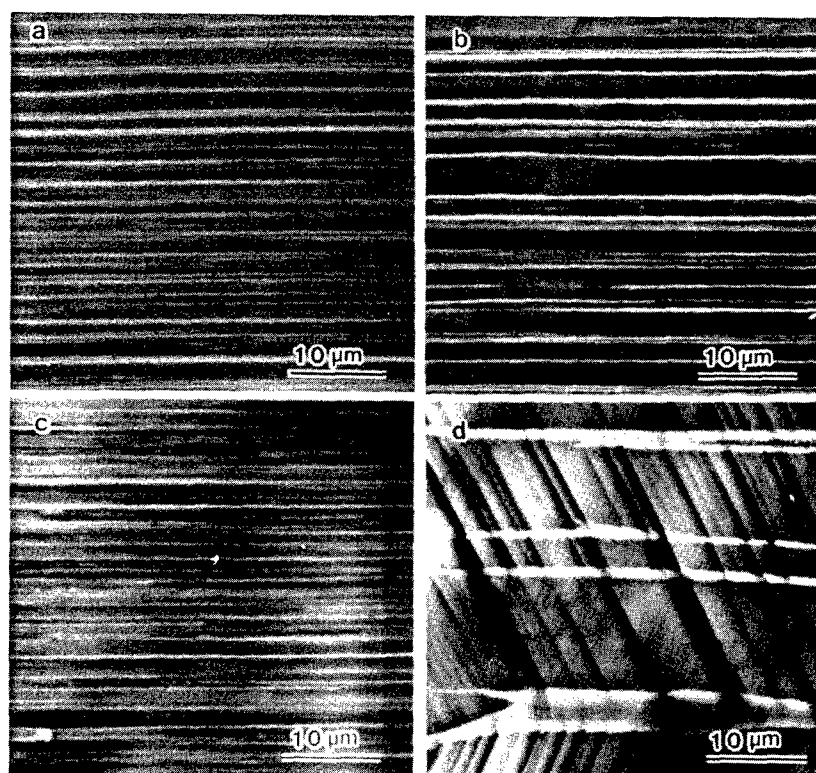


Figure 7: Side view of compression specimens showing the change in the lamellar spacing for (a)&(b) Ti-47Al specimen and (c)&(d) Ti-43Al-3Si specimen before and after the testing at 1000 °C. Deformation markings can be seen running across the lamellar boundaries in (d) and faintly in (b) (SEM back scattered electron images).

Ingots produced by beta phase solidification in this study had a very large grain size in addition to a low Al content (less than the optimum of 47 at.% [2]). Additions of refractory metals can significantly reduce the dendrite arm spacing [2,24] and may be one method for refining the columnar grain size. Furthermore, such additions tend to promote beta solidification allowing the Al concentration to be increased. However, the segregation of such heavy elements will tend to be pronounced [24] and this effect must be considered.

### Seeding procedure

Seeding of the alpha phase can provide a method for aligning all the lamellar boundaries parallel to the growth direction. Two types of microstructure have been observed for Ti-43Al-3Si ingots grown from a seed material. One case is where the processed ingot consists of a single lamellar grain (PST). The other case is shown in Fig. 9a where each grain has a similar lamellar orientation. The seed material for the latter case was cut from an ingot where each lamellar grain was oriented perpendicular to the growth direction (for example the seed material in Fig. 4). Therefore, growth occurred from several of the columnar grains in the seed material.

However, for the target microstructure, each grain should be rotated about its longitudinal axis as shown in Fig. 9b. Such a microstructure has been produced for the Ti-43Al-3Si alloy by placing four differently oriented seed crystals in the bottom of a  $Y_2O_3$  crucible and then directionally solidifying the alloy at 25 mm/h. Such a simple approach is not possible for the case where the composition of the seed and master alloy are different due to the large mushy zone that develops as previously discussed. Therefore, to produce silicide free ingots with the desired microstructure, the composition of the seed and master alloy should be more closely matched.

### Other possible seed compositions

By using the Ti-43Al-3Si seed material, the lamellar microstructure could successfully be aligned in alloys where beta is normally the primary solidification phase (Table 2). This result suggests that alpha may not necessarily have to be the primary solidification phase for the seed composition and hence some of the compositional requirements can be relaxed. To test this hypothesis, a Ti-47Al PST crystal was used as the seed and a master ingot of the same composition was directionally solidified at 5 mm/h by the floating zone method. The lamellar orientation of the PST seed was initially aligned parallel to the growth direction, but upon heating, recrystallization occurred as indicated by a number of new large lamellar grains shown in Fig. 10. These lamellar grains correspond to recrystallized alpha grains that transformed upon cooling. What is important is that the recrystallized grains in the unmelted portion of the seed are continuous with the processed material, indicating growth of only the alpha phase.

Since the beta phase did not nucleate, the alpha phase must be a poor catalyst for beta nucleation. Therefore, the undercooling required to nucleate beta from the liquid is great enough that the metastable alpha liquidus (dotted line in Fig. 8) can be met allowing continued growth of the alpha phase from the seed. This result is also consistent with a proposed model by Trivedi [22] for the formation of banded structures in peritectic systems. In this model, a banded structure will not form (no such structure has been observed for the alpha and beta phases in the Ti-Al system) if the nucleation undercooling for one of the phases is large [22].

When considering other compositions for the seed material, preventing recrystallization upon heating is the major problem that must be solved. For example, boron (as does Si [25]) has a stabilizing effect on the lamellar microstructure [7,26,27], but additions of up to 0.2 at.% to Ti-47Al have failed to prevent recrystallization upon heating close to the melting temperature. However, small additions of both boron and tungsten together have shown a greater stabilizing effect than boron alone [26,27] and such a quaternary approach may be required.

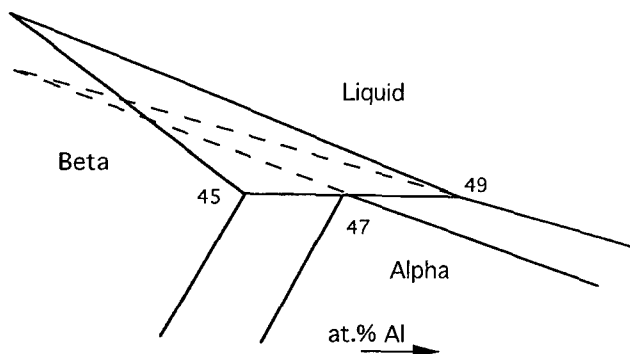


Figure 8: A schematic of the TiAl phase diagram near the liquid+beta=alpha peritectic reaction.

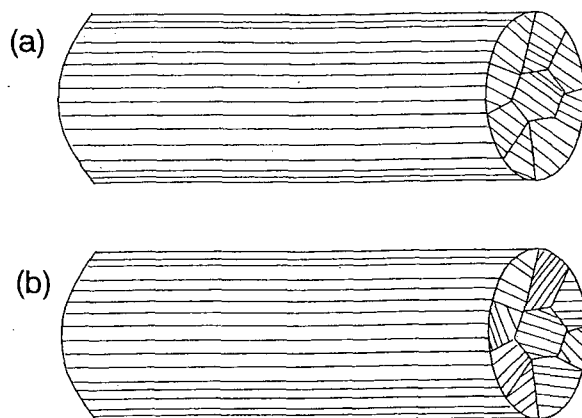


Figure 9: Schematic representation of directionally solidified TiAl ingots with (a) one orientation of columnar grains and (b) with a rotation about the longitudinal axis.



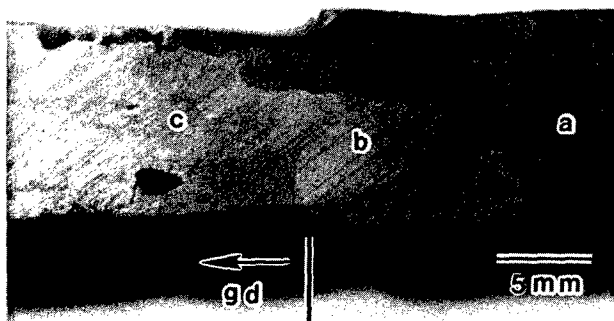


Figure 10: Photograph showing a Ti-47Al ingot grown from a Ti-47Al PST seed. (a) The original seed with an aligned lamellar microstructure; (b) a new grain in the recrystallized region; and (c) a grain in the processed material that is continuous with the unmelted material (gd=growth direction).

As with the TiAl-Si system, the composition of the seed and master alloy can be slightly different as long as a large mushy zone can be avoided. By using this approach, the seed material can be designed to prevent recrystallization while the master alloy can be designed to promote steady state of the alpha phase.

### Summary

The orientation of gamma/alpha<sub>2</sub> lamellar microstructure can be controlled directly from the liquid by using a seed crystal from the TiAl-Si system. By using such a seed material, the lamellar microstructure can be aligned parallel to the growth direction at growth rates up to 40 mm/h. Thus, with further alloy development, directional solidification appears to be a promising technique for producing high performance TiAl-based materials.

### Acknowledgments

This work was supported by "Research for the Future" Program (JSPS-RFTF 96R12301), The Japan Society for the Promotion of Science, and in part by a research grant from the Research and Development Institute of Metals and Composites for Future Industries. DRJ would like to thank the Japan Society for the Promotion of Science (JSPS) and the National Science Foundation (NSF) for a research fellowship.

### References

1. Y-W. Kim, *JOM*, 46 (1994) 30.
2. S.C. Huang, *Structural Intermetallics*, edited by R. Darolia, J.J. Lewandowski, C. T. Liu, P. L. Martin, D. B. Miracle and M. V. Nathal (Warrendale, PA: TMS, 1995), 299.
3. M. Yamaguchi and H. Inui, *Structural Intermetallics*, edited by R. Darolia, J.J. Lewandowski, C. T. Liu, P. L. Martin, D. B. Miracle and M. V. Nathal (Warrendale, PA: TMS, 1995), 127.
4. H. Inui, K. Kishida, M. Misaki, M. Kobayashi, Y. Shirai and M. Yamaguchi, *Phil. Mag. A*, 72 (1995), 1609.
5. S. Yokoshima and M. Yamaguchi, *Acta Mater.* 44 (1996), 873.
6. H. Mecking, Ch. Hartig, *Gamma Titanium Aluminides*, edited by Y-W. Kim, R. Wagner, and M. Yamaguchi (Warrendale, PA: TMS, 1995), 525.
7. R. Wagner, F. Appel, B. Dogan, P.J. Ennis, U. Lorenz, J. Mullauer, H.P. Nicolai, W. Quadakkers, L. Singheiser, W. Smarsly, W. Vaidya, and K. Wurzwallner, *Gamma Titanium Aluminides*, edited by Y-W. Kim, R. Wagner, and M. Yamaguchi (Warrendale, PA: TMS, 1995), 387.
8. Y-W. Kim, *Gamma Titanium Aluminides*, edited by Y-W. Kim, R. Wagner, and M. Yamaguchi (Warrendale, PA: TMS, 1995), 637.
9. C. T. Liu, J. H. Schneibel, P. J. Maziasz, J. L. Wright and D. S. Easton, *Intermetallics* 4 (1996), 429.
10. Y-W. Kim, "Fatigue deformation and failure in TiAl alloys" (Paper presented at 117 Meeting of JIM, Honolulu, 13-15 Dec. 1995).
11. Blair London, D. E. Larsen, Jr., D. A. Wheeler, and P. R. Aimone, *Structural Intermetallics*, edited by R. Darolia, J.J. Lewandowski, C. T. Liu, P. L. Martin, D. B. Miracle and M. V. Nathal (Warrendale, PA: TMS, 1995), 151.
12. W. Kurz and D. J. Fisher, *Fundamentals of Solidification*, (Aedermannsdorf, Switzerland: Trans Tech Pub., 1984) 70.
13. M. Rappaz, and Ch.-A. Gandin, *Acta Metall. Mater.* 41 (1993) 345.
14. J. S. Wu, P. A. Beaven and R. Wagner, *Scripta Metall. Mater.*, 24 (1990), 207.
15. L. Zhang, G. Qiu, and J. Wu, *Scripta Metall. Mater.*, 32 (1995) 1683.
16. S. H. Manesh and H. M. Flower, *Mater. Sci. Technol.*, 10 (1994), 674.
17. G. Frommeyer, R. Rosenkranz, and C. Ludecke, *Z. Metallkde.*, 81 (1990) 307.
18. D. R. Johnson, H. Inui, and M. Yamaguchi, *Acta Mater.*, 44 (1996), 2523.
19. D. R. Johnson, Y. Masuda, H. Inui and M. Yamaguchi, *Acta Mater* (1997) in press.
20. H. Okamoto, *J. Phase Equilib.*, 14 (1993), 120.
21. J. S. Shah, *Crystal Growth*, ed B. R. Pamplin (Oxford: Pergamon Press, 1989) 301.
22. R. Trivedi, *Met. Trans A*, 26A (1995) 1583.
23. T. Umeda, T. Okane, and W. Kurz, *Acta Mater.*, 44 (1996) 4209.
24. C. M. Austin and T. J. Kelly, *Structural Intermetallics*, edited by R. Darolia, J.J. Lewandowski, C. T. Liu, P. L. Martin, D. B. Miracle and M. V. Nathal (Warrendale, PA: TMS, 1995), 143.
25. M. Es-Souni, A. Bartels, R. Wagner, *Mater. Sci. and Engr.*, A192/193 (1995), 698.
26. R. V. Ramanujan, P. J. Maziasz, and C. T. Liu, *Acta Mater.*, 44 (1996), 2611.
27. P. J. Maziasz, R. V. Ramanujan, C. T. Liu and J. L. Wright, *Intermetallics* 5 (1997) 83.

# MULTILAYER COATING FOR PROTECTION OF TITANIUM ALUMINIDES FROM OXIDATION AND HYDROGEN EMBRITTLEMENT®

Beesabathina D. Prasad, Sankara N Sankaran, Karl E. Wiedemann, and David E. Glass

Analytical Services & Materials, Inc., 107 Research Drive, Hampton, VA 23666

## ABSTRACT

Significant research is underway to bring gamma-TiAl alloys to the final stage of development because of their attractive properties such as low density, high-temperature strength, high fracture toughness, and good creep resistance. To assist in this effort, a multilayer coating consisting of a sol-gel two-phase-glass (TPG) overlayer and a reaction-barrier layer was investigated using Ti-48Al-2Cr-2Nb alloy as the substrate material. Three reaction barriers were investigated: Sol-gel  $\text{Al}_2\text{O}_3$ ; Sol-gel  $\text{Y}_2\text{O}_3$ -stabilized  $\text{ZrO}_2$ ; and  $\text{TiAl}_3$  formed by pack-aluminizing. Isothermal oxidation and cyclic oxidation tests were performed in laboratory air at  $900^\circ\text{C}$  for 200 hours. Oxidation performance was evaluated by weight-gain measurements and post-exposure metallography. Hydrogen embrittlement susceptibility was evaluated through hydrogen analysis and room-temperature tensile testing of specimens subjected to 24 hour-exposure to moist air between  $200^\circ\text{C}$  and  $800^\circ\text{C}$ . For comparison, tensile specimens were tested after exposure to the same temperature and duration in argon. TPG overlayers on  $\text{TiAl}_3$  offered the best oxidation protection. No significant hydrogen pick-up was observed.

## INTRODUCTION

Intermetallic alloys based on the compound TiAl (or gamma titanium-aluminide) are potential candidates for high-temperature regions of gas turbine engines. These alloys display attractive properties such as low density and high-temperature strength. However, intermetallic aluminide alloys suffer from poor room-temperature ductility. In recent years, a second-generation of gamma titanium-aluminide alloys with tertiary and quaternary additions (for example Ti-48Al-2[Cr or Mn]-2Nb) have been developed which show improved room-temperature ductility [1-3]. In spite of the compositional improvements to enhance their properties, gamma titanium-aluminides suffer from two forms of environmental degradation: (1) oxidation, and (2) hydrogen embrittlement [4, 5].

The main objective of this study was to develop a low-cost multilayer coating for gamma titanium aluminides that will help retain the low-temperature ductility even after prolonged exposure to oxygen and hydrogen containing environments. During these studies, feasibility for a multilayer coating consisting of an alumina layer with a sol-gel two-phase-glass (TPG) overlayer has been demonstrated. The coating performance was evaluated by

® This work was supported by the Department of the Air Force under contract number F33615-95-C-5824. Approved as amended by Wright-Patterson Air Force Base, OH, U.S.A., Case No. ASC 97-0348.

measuring the tensile properties after exposure to moist air and by conducting both isothermal and cyclic oxidation tests at 900°C for 200 hours. The coating integrity was also assessed by microstructural examination of the exposed specimens.

## EXPERIMENTAL DETAILS

### Materials

The  $\gamma$ -titanium aluminide for this work was furnished by General Electric (GE) Company and the material was originally designed to correspond to Ti-48Al-2Cr-2Nb composition. This alloy was chosen since previous studies have indicated susceptibility of this alloy to hydrogen embrittlement [4]. However, the actual composition indicated a high amount of Al as seen in Table I. According to the information furnished by GE, the material was processed as follows. The cast blocks were hot isostatically pressed and heat treated at 1260°C/170 Mpa/3h HIP, plus 1300°C/20 h in argon with flowing helium quench. The structure of this alloy in as received condition contained both single-phase grains and grains with fine laths (duplex structure). The grains were essentially equiaxed and ~50  $\mu$ m in diameter. The grain size in this alloy is relatively larger than that observed in typical duplex structures.

### Coatings

Four types of coatings were evaluated: for comparison, uncoated specimens were also included for each of the tests. The specimens were prepared in the following categories:

- Uncoated
- Sol-gel Two Phase Glass(TPG) Coated [6]
- Sol-gel TPG overlayer on sol-gel  $\text{Al}_2\text{O}_3$  (TAO)
- Sol-gel TPG overlayer on sol-gel yttria-stabilized  $\text{ZrO}_2$  (TAZ)
- Sol-gel TPG overlayer on pack-aluminized coating (TAL)

Pack-aluminizing was done by Howmet Corporation, Whitehall, MI. The aluminizing treatment was followed by a diffusion anneal at 620°C for 8 hr to form  $\text{TiAl}_3$ . The aluminide coating was applied both on the test coupons and pre-machined tensile specimens.

The sol-gel coatings were applied by a dipping method. After each dip, the specimens were withdrawn from the sol under a nitrogen purge. The coating was then dried in an oven maintained at 75°C and then cured in a horizontal tube furnace at 650°C. All the fabrication steps were carried out at atmospheric pressure. Coating thickness's were calculated from the weights and specific densities of the coatings and the surface areas of the specimens. The estimated thickness' of the various coatings are summarized in Table II.

### Oxidation Exposures

Oxidation tests were performed to evaluate the protectiveness of the coatings in an oxidizing environment. These exposures were performed on coated and uncoated coupon specimens. Two types of tests were performed: a) isothermal oxidation, and b) cyclic oxidation.

Isothermal oxidation of the samples was conducted in a horizontal tube furnace at 900°C in laboratory air. At the end of every 20 hours of exposure,

**Table I: Chemical Composition of the Gamma Titanium-Aluminide Plate**

Element	Ti	Al	Cr	Nb	Fe	Si	O	H
Atom percent	46.9	49.3	2.1	2	0.006	0.03	0.14	4 wppm

**Table II: Estimated Coating Thickness**

Description of Coating	Reaction Barrier Type and Thickness, $\mu$ m	TPG Overlayer Thickness, $\mu$ m
TAO	Sol-gel $\text{Al}_2\text{O}_3$ : 0.5-1.0	2.5
TAZ	$\text{Y}_2\text{O}_3$ + $\text{ZrO}_2$ : 0.5-1.0	2.5
TAL	Titanium aluminide: ~ 20.0	2.0

**Table III: Sample Exposure Matrix**

Type of Tests	Exposure Conditions			
	200°C, 24 hr	500°C, 24 hr	800°C, 24 hr	900°C, 200 h Isothermal & Cyclic
Weight-gain				Laboratory air
Metallography				Laboratory air
Room Temperature Tensile Tests			Moist air, Argon	
Hydrogen Analysis	Moist air, Argon	Moist air, Argon	Moist air, Argon	

the furnace was shut off and the samples were allowed to cool in the furnace. The samples were then removed and weighed to an accuracy of 0.1 mg. Isothermal tests were continued for a cumulative exposure of 200 hours. The mass change data for the coated specimens were used as a qualitative indication of the coating effectiveness under these test conditions.

Cyclic oxidation tests were carried out at 900°C in laboratory air for 200 cycles. Each cycle consisted of a 1 hr hold at 900°C followed by 20 minutes cool down of fracture stress in the furnace in ambient air. Specific weight changes were determined at regular intervals of every 20 cycles.

#### **Moist-Air Exposures**

Moist air exposures were carried out in a horizontal tube furnace. The furnace was fitted with a reaction tube containing inlet and outlet ports for circulating air. Bottled air was bubbled through distilled water maintained at room temperature to provide humidity in the air. The air was flown at the rate of 150 sccm, and the relative humidity was measured to be ~ 90 % at 25°C.

The coupon specimens (coated and uncoated) were exposed in the moist air at 200°C, 500°C and 800°C for a duration of 24 hours. After exposure, the specimens were evaluated for hydrogen pick-up. Using the same set-up, tensile specimens were exposed to moist air and dry argon at 800°C for 24 hours. For each coating and test condition, two tensile specimens were exposed to provide duplicate specimens for the tests.

#### **Coating Evaluation**

Our testing scheme is summarized in the form of a matrix of tests as shown in Table III. Test specimens were in the form of coupons or tensile specimens. The entries in

the table cells indicate the exposure environment for each of the listed exposure temperatures and duration. The first column lists the tests that were performed for the selected exposure conditions.

### **RESULTS AND DISCUSSION**

The performance of multilayer coatings for the protection of gamma titanium-aluminides from oxidation and hydrogen embrittlement was evaluated through oxidation tests and moist-air exposure studies. Oxidation performance was evaluated using weight-gain and microscopy as primary techniques. Hydrogen analysis and mechanical tests were used to evaluate hydrogen embrittlement effect. The results of these studies are discussed in this section.

#### **Oxidation Performance**

The oxidation resistance of the coatings was evaluated using specific weight gain as the criteria. This parameter was monitored periodically in both isothermal and cyclic oxidation tests. The specimens at the end of the test were examined metallographically. The results of isothermal and cyclic oxidation tests are summarized in Figure 1. The data are presented as plots of the specific weight change as a function of time for the TAO, TZO, TAL coated, as well as the uncoated specimens. The samples coated with TPG alone showed extensive oxidation even after short-term exposures, and were therefore discontinued from the test-matrix after the early tests.

The TAL coated specimens showed very little weight change under both isothermal and cyclic conditions. The TAO coated specimens showed fairly good performance even though it showed some weight gain. Overall, the TAL and TAO coated specimens after 200 hours air-exposure at 900°C showed that the weight-gain

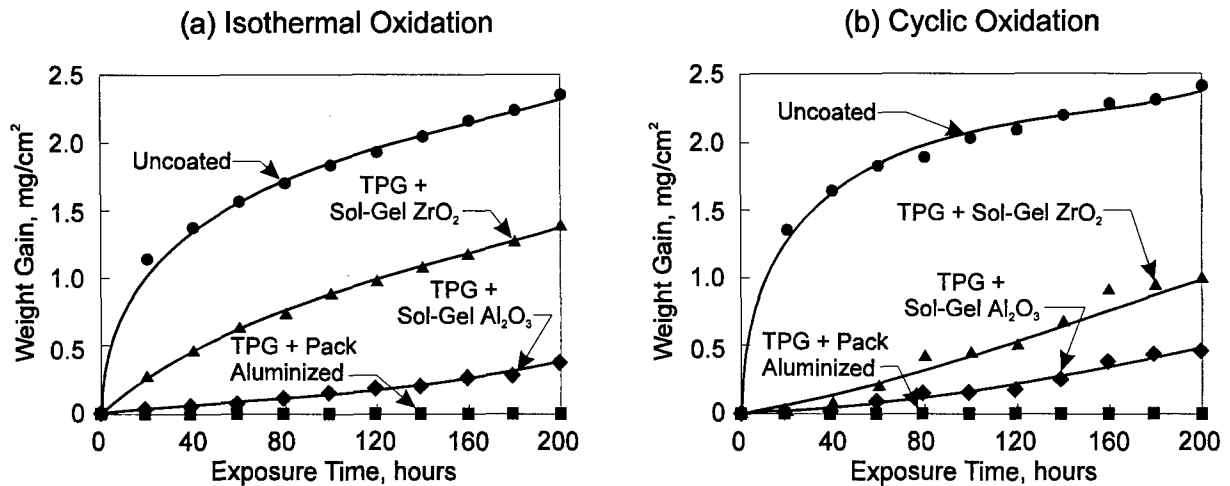


Figure 1: Weight Gain Behavior of Gamma Titanium-Aluminide After Oxidation in Air at 900°C.

after oxidation can be reduced by factors corresponding to ~ 23 and ~ 6 compared to the uncoated gamma titanium-aluminide. The weight-gain data indicates that the TPG overlayer served as an effective oxygen diffusion barrier on

the pack-aluminized specimens and the sol-gel Al<sub>2</sub>O<sub>3</sub> coated specimens. The superior oxidation resistance of these coatings are attributed to the low oxygen diffusivities of the TPG coating.

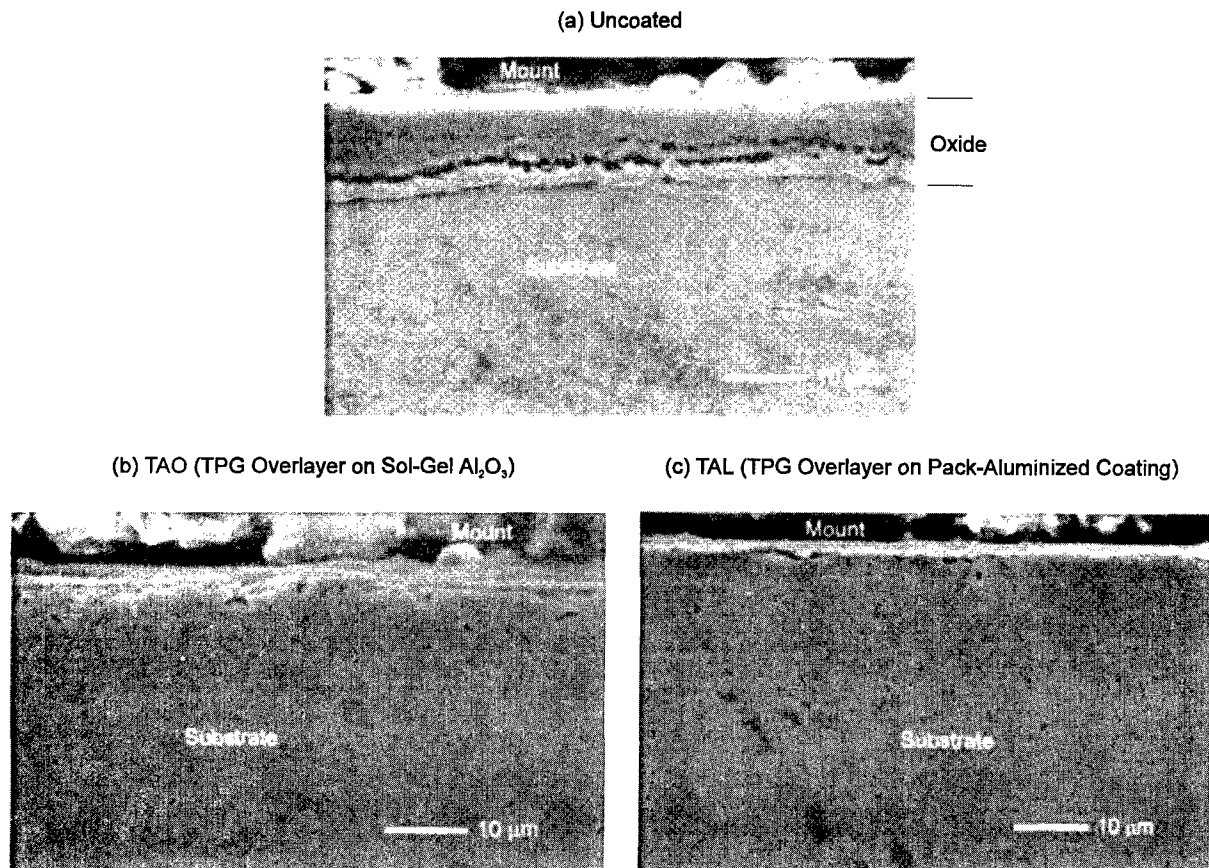


Figure 2: Cross-Sectional SEM Images of Gamma Titanium-Aluminide After Oxidation.

Figure 2 compares the cross-sections of the (a) uncoated, (b) TAO coated, and (c) TAL coated specimens. The uncoated specimen shows a fairly thick oxide scale (on the order of 10  $\mu\text{m}$  in thickness). The layers seen on the TAO coated and TAL coated specimens correspond to the coating. Considering that the TAO coating itself accounts for about 5  $\mu\text{m}$  of the layers seen in the photograph, the oxide layers on this specimen are too small to be identified in the SEM image. The TAL coated specimens show a continuous barrier layer between the TPG and the substrate, but the TAO coated specimen shows discontinuity in the alumina layer.

#### Oxidation Behavior of Uncoated Gamma Titanium-Aluminide

Figure 3 shows X-ray elemental maps of Ti, Al, Nb, O and Si after oxidation exposure of the uncoated specimen at 900°C for 200 hours. SEM has shown that the total oxide scale thickness is ~ 10  $\mu\text{m}$ , and that the oxide growth is layered with abundant porosity in the scale.

The X-ray maps indicate that the oxide sublayers contained both  $\text{TiO}_2$  and  $\text{Al}_2\text{O}_3$  in various proportions and as heterogeneous mixtures: the regions showing strong titanium signals show weak aluminum, and vice versa. Significant presence of  $\text{TiO}_2$  in the oxide shows the non-protective oxidation characteristics of the alloy. Niobium in the oxide layer is mostly associated with titanium, confirming the doping of the  $\text{TiO}_2$  with Nb ions [7, 8]. The surface regions of the alloy at the interface show niobium enrichment consistent with the depletion of both aluminum

and titanium through oxidation.

#### Oxidation Behavior of TAL (TPG Coating on Pack-Aluminized Alloy) Coating

At the outset, the pack-aluminized coating with the TPG overlayer shows the least oxidation damage as evidenced by the thickness of the various layers on the specimen surface after oxidation. The total thickness of these layers is ~ 3  $\mu\text{m}$ , which is about the same order of thickness as the coatings applied (Table II), i.e., there is no evidence of any oxidation. The weight-gain data (Figure 1), and the X-ray elemental maps (Figure 4) confirm this observation. A comparison of the elemental maps of Si, Ti and Al shows that the TPG overlayer remains intact even after exposure to air at 900°C for 200 hours. The oxygen maps do not show any indication of oxygen penetration into the alloy confirming the protectiveness of this coating. A significant observation is the occurrence of a thin surface layer of ~ 1  $\mu\text{m}$  in thickness below the TPG layer that shows a slight enrichment of aluminum. EDS spectrum from this layer, shown in Figure 5, indicates a Ti/Al ratio of 1/3, suggesting the formation of a  $\text{TiAl}_3$  layer. This layer is nearly continuous across the entire specimen surface.

The pack-aluminizing conditions furnished by Howmet Corporation indicated a coating thickness of ~ 20  $\mu\text{m}$ . Except for the thin  $\text{TiAl}_3$  layer, the cross-sectional images did not indicate any outer layers corresponding to this thickness. Therefore, X-ray elemental line scans of Ti, Al and Nb were acquired with a spacing of 1  $\mu\text{m}$  between points to understand the Al distribution, and the results are

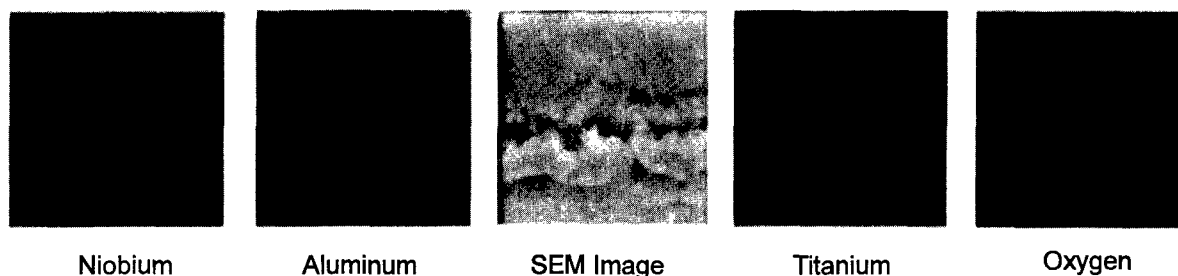


Figure 3: X-ray map of Gamma Titanium-Aluminide After Oxidation at 900°C for 200 Hours.

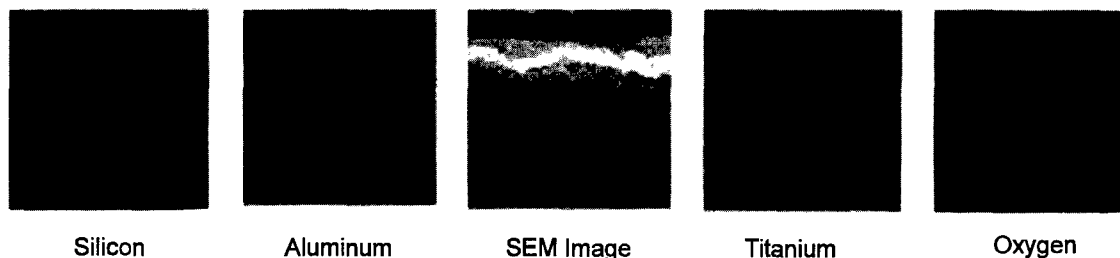


Figure 4: X-ray map of TAL Coated Specimen After Oxidation at 900°C for 200 Hours.

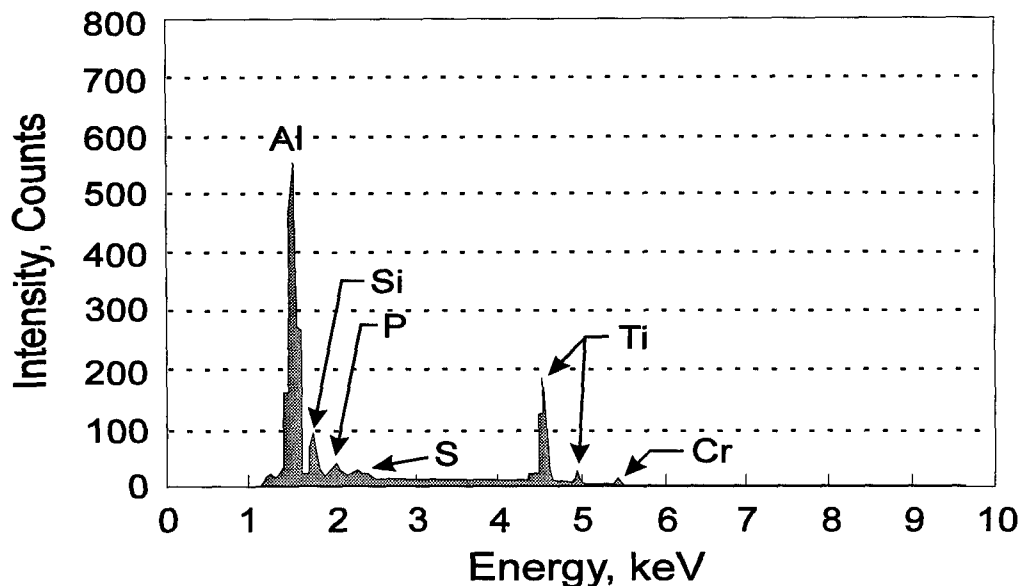


Figure 5: EDS Spectrum of the  $\text{TiAl}_3$  Layer on TAL Coated Specimen.

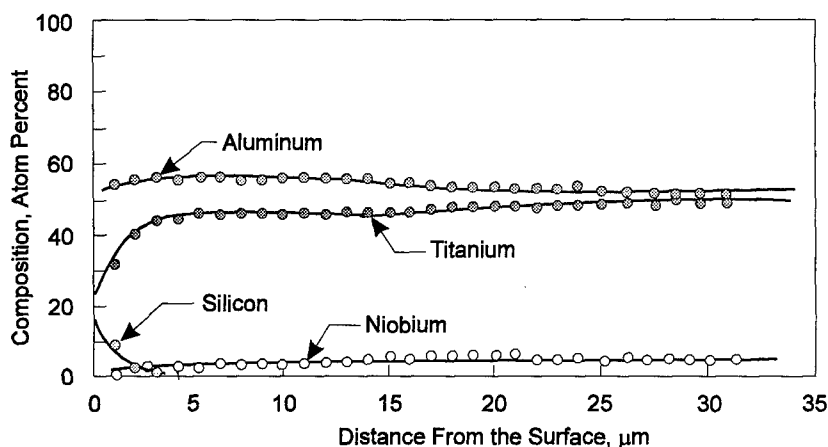


Figure 6: Elemental Scans Across TAL Coated Specimen After Oxidation at 900°C for 200 Hours.

summarized in Figure 6. The line-scans show that there is an enrichment of Al content with a corresponding decrease in the Ti content to a depth of  $\sim 16 \mu\text{m}$  from the surface. The lack of a distinct boundary between the aluminized layer and the substrate alloy shows that the aluminizing process led to a gradual diffusion and incorporation of aluminum into the gamma titanium-aluminide with no obvious microstructural changes.

The superior oxidation resistance of the pack-aluminized coating with the TPG overlayer suggests the high stability of the  $\text{TiAl}_3$  phase from oxygen embrittlement. The TPG overlayer helped to prevent the consumption of this layer through oxidation by acting as an oxygen barrier.

#### Moist-Air Exposure Performance

Performance of the coatings in a moist-air environment was evaluated through hydrogen analysis and residual mechanical properties after exposure. For the hydrogen analysis, coupon specimens were used, and for the mechanical tests, cylindrical specimens with a 4 mm gage diameter were used.

#### Hydrogen Analysis Results

Hydrogen analysis of the gamma titanium-aluminide samples using a hot vacuum extraction technique are presented in Table IV; the measurement accuracy in this technique is  $\pm 1 \text{ ppm}$ . Taking this error range into account, the hydrogen levels in most of the specimens after exposure

**Table IV. Hydrogen Analysis Results**

Specimen Type	Hydrogen Content in wppm After Exposure at			
	No Exposure	200°C, 24 hr	500°C, 24 hr	800°C, 24 hr
Uncoated	3	3	2	4
TAO	2	3	7	6
TAL	2	3	3	2

is about the same as that of the as-received material. Neither the exposure temperature, nor the coating type made a significant difference in the bulk alloy hydrogen content except the specimens coated with the sol-gel alumina.

Based on the hydrogen analysis, the differences in the hydrogen levels between the coated and uncoated specimens after moisture-exposures between 200°C and 800°C are too small to draw any conclusions on the hydrogen uptake behavior of the alloy. It may be necessary to perform hydrogen uptake measurements under pure hydrogen gas environment to characterize the effectiveness of the coatings against hydrogen absorption.

#### Residual Mechanical Properties

The sensitivity of gamma titanium-aluminide to hydrogen embrittlement caused by high-temperature moist air exposure was evaluated through the measurement of residual mechanical properties. For comparison, specimens were also tested after exposure to pure argon under the same temperature conditions to discriminate the thermal and environmental effects. Also, the tensile data of the alloy

were evaluated in the as-received condition to isolate all the effects. The tensile test results are summarized in Table V: at each condition, two tests were performed for repeatability. The test exposure was limited to only one temperature, 800°C.

A striking feature from the test results is that the ductility values for all conditions, including the as-received condition, are on the order of 0.5 %. Because of such a poor ductility of the starting alloy, the performance of the coatings could not be evaluated using this criteria.

The data in Table V also shows that the fracture stress is a function of the coating. Because of the difficulty in using ductility values as a discriminator, the fracture stress values were used as a criteria for evaluation of the coating performance. The fracture stress of the alloy in the as-received condition was 428 MPa; this value is about 10 % lower than that reported by Kelly et al [4]. Both uncoated and coated specimens showed a significant reduction in the fracture stress after exposure to argon or moist air at 800°C for 24 hours. The reduction in the fracture stress for the moist-air-exposed uncoated, TAO coated, and TAL coated samples correspond to 32%, 33%,

**Table V. Room Temperature Tensile Test Results**

Specimen Condition	Exposure Conditions	Fracture Stress, MPa	Elongation, %
Uncoated	None	431, 425	0.4, 0.2
Uncoated	Moist Air, 800°C, 24 hr	346, 305	0.3, 0.3
Uncoated	Argon, 800°C, 24 hr	340, 333	0.8, 0.2
TAO	Moist Air, 800°C, 24 hr	304, 341	0.2, 0.3
TAO	Argon, 800°C, 24 hr	347, 349	0.2, 0.3
TAL	Moist Air, 800°C, 24 hr	270, 258	0.5, 0.5
TAL	Argon, 800°C, 24 hr	252, 268	0.3, 0.4



and 62%. An equivalent comparison for the argon-exposed specimens yield 27%, 23%, and 65% corresponding to the same coating conditions. These results seem to indicate that the coatings are susceptible to environmental embrittlement. However, the tests need to be performed on an alloy with better ductility in the as-received condition to characterize the performance of the coatings in combating environmental (oxygen and/or hydrogen) embrittlement. The fracture stress loss is most significant for the specimens that were pack-aluminized, and this aspect is perhaps related to the chemical modification of the alloy.

#### Alloy Chemistry and Microstructure Effects on Mechanical Properties

The alloy investigated in this work (Table I) contained a slightly higher concentration of aluminum, 49.3 at. % Al, compared to the nominal value of 48 at. % Al. This alloy displayed a room-temperature elongation of only 0.3 % in the as-received condition, compared to ~ 2 % for Ti-48Al-2Cr-2Nb[4]. The structure of the alloy used in this study contained both single-phase grains and grains with fine laths (duplex structure) in as received condition. The grain are essentially equiaxed and ~50  $\mu\text{m}$  in diameter. The grain size in this alloy is relatively larger than that observed in typical duplex structures. The large grain size of the Ti-49.3Al-2.1Cr-2Nb alloy microstructure may be responsible for its poor tensile behavior.

If percent elongation is used as a criteria for evaluating room-temperature ductility of gamma titanium-aluminides, no appreciable change is evident among all the samples that were studied (unexposed and exposed, coated and uncoated), as seen from the data in Table V. This behavior indicates that the intrinsic brittleness of the alloy is overwhelming any environmental effects, and therefore, measurement of ductility does not establish the effectiveness of the coatings.

On the other hand, degradation in fracture stress (Table V) appears to provide some indication of the coating effectiveness. The uncoated samples and those coated with TAO display reduction in the fracture stress values that are more significant for moist-air exposures compared to the argon-atmosphere exposure. It is unclear at this stage if these differences are environment-induced or caused by the scatter due to the intrinsic low ductility of the alloy.

The specimens coated with TAL display the largest reduction in fracture stress values, and are independent of the exposure environment. The TAL coating results in the formation of a highly oxidation-protective, but brittle  $\text{TiAl}_3$  layer on the surface. From Figure 2(c), it can be noted that this layer is only ~ 1  $\mu\text{m}$  thick. However, inspite of good oxidation resistance, the fracture stress is significantly affected by the TAL coating possibly due to the enhancement of Al in the alloy after the coating process. A

close examination of the Al distribution in the alloy after TAL coating (Figure 6) shows that there is a significant enhancement of aluminum in the alloy after TAL processing, and this enhancement extends to a depth of ~ 20  $\mu\text{m}$ . The high sensitivity of the room-temperature ductility of gamma-titanium alloy to the aluminum content in the alloy implies that the ductility and strength loss may be caused by the aluminum enhancement due to the pack-aluminizing process. This data indicates that aluminum-enhancement in the alloy-interior may be a serious concern in using pack-aluminizing as a protection process for gamma titanium-aluminides. The reduction in fracture stress values with TAL coated specimens needs to be investigated in the as-coated condition to determine the stage (coating process or thermal exposure) at which loss in fracture stress occurs.

#### CONCLUDING REMARKS

Feasibility for a multilayer coating, consisting of a two-phase-glass (TPG) overlayer and a reaction-barrier layer, for protection of gamma titanium-aluminides from oxidation and hydrogen embrittlement was evaluated. The following observations are drawn from this work.

1. Gamma titanium-aluminides are susceptible to non-protective oxidation. Thick oxide scales readily form on the alloy surface when exposed to air at high temperatures (900°C).
2. TPG overlayers were effective in reducing the permeation of oxygen from the environment, but only a reactively-formed  $\text{TiAl}_3$  layer was an effective reaction barrier. Consequently, the best oxidation resistance (no discernible oxygen pick-up after 200 hours at 900°C) was offered by the coating consisting of TPG overlayer on the pack-aluminized alloy.
3. TPG overlayers on sol-gel based alumina reaction-barrier layer offered good oxidation resistance.
4. No discernible hydrogen pick-up was observed after the moist-air exposures based on bulk hydrogen analysis using the hot-extraction technique.
5. The alloy investigated was supplied with an inherent low ductility due to a slightly higher aluminum content. As a result, ductility-loss could not be used as an effective criterion to assess hydrogen embrittlement.
6. Fracture stress provided some insight on the coating performance. Specifically, the pack-aluminized coating led to substantial aluminum diffusion and enhancement in the alloy causing ductility loss as well as loss in strength in spite of superior oxidation performance.

## **ACKNOWLEDGMENTS**

The authors thank the Department of the Air Force for funding this work under a Phase I SBIR Contract No. F33615-95-C-5824 and express their sincere appreciation and thanks to Ms. Monica Stucke, USAF Wright Laboratory Materials Directorate, Wright-Patterson AFB, OH, for her encouragement and support during the work. The contributions of Ms. Dorinda Humphries in the microscopy work and Ms. Anna Sample, both of AS&M, in the sol-gel coating work, is greatly appreciated.

## **REFERENCES**

1. Kim, J. of Metals, vol. 41, 1989, pp. 24-30.
2. Kim, Acta Met., vol. 40, 1992, pp. 1121-1134.
3. Huang and E.L. Hall, in "High Temperature Ordered Intermetallic Alloys III", Materials Research Society, Pittsburgh, PA, 1989, pp. 373-383.
4. Kelly, C.M. et. al., Scripta Metall., vol. 30, 1994, pp. 1105-1110.
5. Liu, Young-Won (Y-W.) Kim, Scripta Metall., vol. 27, 1992, pp. 599-603.
6. Wiedemann, R. K. Clark, and P. J. Taylor: Light Weight Protective Coatings. NASA Case No. LAR14448-1, patent pending, S. No. 071912, 960, filed July 10, 1992.
7. Huang, and D.S. Shih, in "Microstructure/Property Relationships in Titanium Aluminides and Alloys", Y-M Kim and R.R. Boyer, eds., TMS, Warrendale, PA, 1990, pp. 105-122.
8. Tsuyama, S. Mitao, and K. Minakawa, in "Microstructure/Property Relationships in Titanium Aluminides and Alloys", Y-M Kim and R.R. Boyer, eds., TMS, Warrendale, PA, 1990, pp. 213-226.

## MEASUREMENT OF DEFORMATION-INDUCED RESIDUAL STRAINS AND STRESSES IN

### PST-CRYSTALS OF THE INTERMETALLIC ALLOY TiAl

Martin Riemer, Horst Biermann, Ralf Kowalewski and Haël Mughrabi

Institut für Werkstoffwissenschaften, Lehrstuhl I, Universität Erlangen-Nürnberg

Martensstr. 5, D-91058 Erlangen, Fed. Rep. Germany

#### Abstract

Some  $\gamma$ -based titanium aluminides have a microstructure with lamellar grains of alternating  $\gamma$ -TiAl and  $\alpha_2$ -Ti<sub>3</sub>Al lamellae. Due to the tetragonal crystal structure of the  $\gamma$  phase and the lattice misfit between  $\gamma$  and the  $\alpha_2$  phase, the lamellar microstructure of undeformed material contains internal coherency stresses, which are partly reduced by interfacial dislocation networks. In the present work, the evolution of internal strains related to deformation-induced residual long-range internal stresses after room-temperature compressive deformation of PST-crystals was investigated. X-ray measurements of the peak profiles were performed with a special high-resolution double-crystal diffractometer, which revealed the dependence of the internal stress evolution on the orientation of the lamellar microstructure with respect to the axis of deformation. Residual internal strains were measured in specimens with different orientations of the lamellae with respect to the stress axis. Deformation parallel to the lamellae induces internal strains, which indicate differences in the deformation behaviour of differently oriented  $\gamma$  domains. Deformation perpendicular to the lamellae and with the lamellae inclined to the deformation axis shows a uniform behaviour of the  $\gamma$  domains. The measured residual strains are a result of deformation incompatibility in the lamellar structure, in particular of the undeformable  $\alpha_2$  phase. Complementary microstructural investigations were performed to correlate the results of the X-ray experiments with deformation-induced changes in the microstructure.

#### Introduction

The intermetallic compound TiAl is the base for a growing number of low-density high-temperature alloys with interesting properties. According to Austin and Kelly [1], some of these alloys will be introduced into commercial service in gas turbines during 1997. The alloys consist of the two ordered intermetallic phases  $\gamma$ -TiAl with tetragonal L1<sub>0</sub> structure and  $\alpha_2$ -Ti<sub>3</sub>Al with hexagonal D0<sub>19</sub> structure. The tetragonality of the  $\gamma$  phase leads to slip systems on {111} lattice planes that do not disturb the ordered structure of the crystal lattice, namely slip in  $\langle 110 \rangle$  directions<sup>1</sup>. In the case of slip in the directions  $\langle 011 \rangle$ , the ordered crystal structure is disturbed [3].

Depending on processing and heat-treatments, the microstructure of technical alloys often shows a so-called duplex structure with lamellar grains of alternating  $\gamma$  and  $\alpha_2$  lamellae and globular  $\gamma$  grains. Size and distribution of the lamellar grains are, among others, controlling the mechanical properties of the  $\gamma$  alloys [4]. The lamellar boundaries are always parallel to (111) planes in  $\gamma$  and (0001) planes in  $\alpha_2$ , respectively. In the lamellar boundaries, the  $\langle 1\bar{1}0 \rangle$  directions in  $\gamma$  are parallel to  $\langle 11\bar{2}0 \rangle$  in  $\alpha_2$ . The tetragonality of the  $\gamma$  phase gives rise to the occurrence of different kinds of orientation relationships between adjacent  $\gamma$  lamellae. Besides a true twin relationship there can be a pseudotwin relationship as well as a rotational-fault boundary between two  $\gamma$  lamellae [5,6]. Within the single lamellae, domains of different orientations are present. In the lamellae, however, the stacking sequence remains constant over the domain boundaries, see e.g. [5]. Due to the tetragonal crystal lattice of the  $\gamma$  phase, the lattice of adjacent  $\gamma$  lamellae does not fit exactly in any case, except for a true twinning relationship of neighbouring lamellae. For this reason, internal coherency stresses are present, which are reduced by dislocation networks on the lamellar boundaries to a certain fraction [7-9]. In addition, different chemical compositions are found in the  $\gamma$  lamellae which result from the solid state reaction during manufacturing [10,11]. In so-called polysynthetically twinned (PST) crystals, the lamellae have a uniform orientation over the entire length of the crystal. Therefore, the influence of the lamellar orientation on the deformation behaviour can be studied in detail [3,12].

In the present work, the nature and sign of deformation-induced residual internal strains are examined. In particular, the dependence of the orientation of the lamellar boundaries with respect to the deformation axis on the deformation-induced long-range internal strains is investigated. The measurements were performed on PST-crystals of the intermetallic alloy Ti-49.1Al after deformation in compression at room temperature. A special high-resolution X-ray method was applied. The positions of the X-ray peaks and their deformation-induced shifts, which reflect the internal stress states in the investigated lamellae, are evaluated.

1. The notation  $\langle hkl \rangle$  indicates the tetragonality of the L1<sub>0</sub> lattice, where the c axis is not equivalent to the a and b axes. The notation was introduced by Hug et al. [2].

## Experimental

### Specimens

The material was provided by Prof. Y. Umakoshi from Osaka University, Japan. The PST-crystals have a nominal composition of Ti-49.1Al and were produced by a special zone-floating technique [13]. The volume fraction of the  $\alpha_2$  phase is about 8 % [14]. From the PST-crystals with a length of 90 mm and a diameter of 12.5 mm, cuboidal specimens for compression tests were machined with an edge length of 3 mm. The samples were prepared with three different orientations of the lamellae with respect to the compressive axis (see Fig. 1). In orientations A and N, the lamellar boundaries are parallel and perpendicular to the stress axis in the  $\{101\}$  and  $\{111\}$  directions of  $\gamma$ , respectively, see Figure 1 (the nomenclature A, N and B follows ref. [15]). It has to be noted that the orientations of the faces indicated in Figure 1 include all respective possible types of domain orientations, e.g. the investigation of the face  $\{101\}$  of Figure 1a includes information on all domains which have their directions  $[1\bar{1}0]$ ,  $[101]$  and  $[0\bar{1}1]$  perpendicular to the surface denoted  $\{101\}$  in Figure 1a. The latter two, however, are crystallographically equivalent.

Regarding the mechanical properties of the material, in the following, orientations N and A are called "hard" orientations and orientation B is called "soft" orientation, characterized by lamellar boundaries inclined under an angle of about  $45^\circ$  with respect to the deformation axis. The surfaces of the samples correspond to low indexed crystallographic planes as indicated in Figure 1. The specimens were deformed in compression at room temperature to plastic strains of about 5% at a strain rate of about  $2 \times 10^{-4} \text{ s}^{-1}$ .

### X-Ray Diffraction

Deformation-induced residual strains in the two phases  $\gamma$  and  $\alpha_2$  were investigated by means of a special X-ray double-crystal diffractometer which permits the measurement of X-ray profiles with negligible instrumental peak broadening and high angular resolution [16]. The primary X-ray beam of a Cu tube (operated at 40 kV and 30 mA) was monochromatized by a plane Ge monochromator, using a (444) reflection. The  $\text{CuK}\alpha_2$  radiation was stopped by a slit aperture and only the  $\text{CuK}\alpha_1$  was used for the measurements. The wavelength dispersion of the  $\text{CuK}\alpha_1$  radiation was compensated up to an angle of  $2\theta \approx 100^\circ$  ( $\theta$ : Bragg angle). Therefore, the obtained X-ray profiles depend only on the lattice parameter distribution of the investigated samples. The scattered radiation was registered by a

linear position-sensitive X-ray detector with a linear resolution of about 85  $\mu\text{m}$  and a nominal distance between two adjacent channels of 28.5  $\mu\text{m}$ . The sample-to-detector distance was set to 532 mm. In order to integrate the full intensity distribution of the Bragg reflections, the samples were rocked during the X-ray measurements around the maximal intensity in most cases.

The diffractometer is built up in such a way, that the X-ray tube and the Ge-monochromator are fixed to a special turn table and can thus be turned with respect to the unaffected direction between sample and detector. With this set-up, different Bragg peaks can be investigated without extensive adjustment. The exact scattering angles of the different fundamental reflections were determined by calibrating the respective set-ups by measurements of the diffraction peak-positions of Al single crystals with different orientations. Bragg reflections of both phases  $\gamma$  and  $\alpha_2$  can be investigated together in several cases due to the small lattice parameter mismatches and the fixed orientation relationships between the phases  $\gamma$  and  $\alpha_2$  mentioned above. All measurements were repeated at least four times on each surface and the peak positions were averaged for evaluation.

### Microstructural investigations

The microstructure of the deformed samples was observed by different microscopical techniques. The surfaces of the cuboidal specimens were mechanically and electrolytically polished as well as etched with hydrofluoric acid and investigated with an optical microscope using interference contrast. In order to reveal the traces of deformation at higher magnifications, a scanning electron microscope (SEM) with a backscattered electron (BSE) detector was used. Additional investigations were performed with a transmission electron microscope (TEM, Philips CM200) at 200 kV. The TEM foils were thinned either electrolytically or by ion milling.

## Results

### Macroscopic deformation behaviour

Measuring the macroscopic dimensions of the PST-specimens after compression shows an interesting observation, which was already reported by Kishida et al. [12]. Specimens deformed with the lamellar boundaries parallel to the stress axis (orientation A) show no change of the width of the samples in the  $[111]$  direction perpendicular to the deformation axis. In the direction parallel to the lamellae, however, the width of the samples increases in accordance with the expectations due to transverse strain. The specimens deformed in orientations N and B show regular transverse strain.

### X-Ray Profiles

Fig. 2 shows a plot of the normalized intensity versus the glancing angle  $\theta$  of the  $\{002\}\gamma$  Bragg-peak of an undeformed PST-sample. The figure indicates clearly the tetragonality of the TiAl  $\gamma$  phase. Two different types of

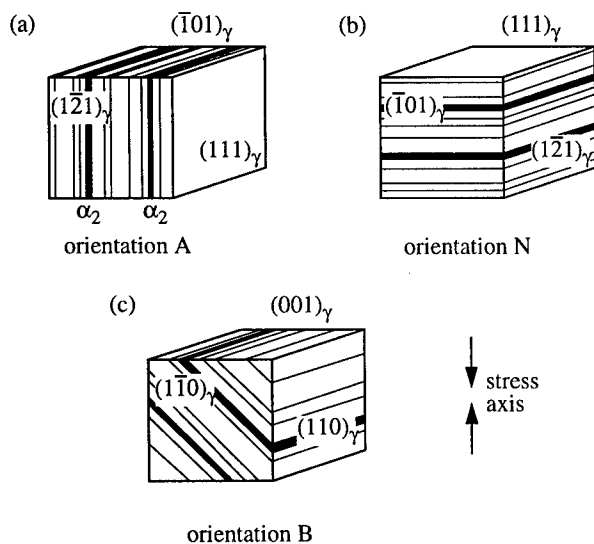


Figure 1: Schematic drawing of the specimens with different orientations of the lamellae with respect to the axis of deformation and the respective crystallographic orientations of the surfaces. The lamellar boundaries are (a) parallel (called A) and (b) perpendicular (called N) to the stress axis, respectively. (c) In orientation B, the lamellae are inclined under an angle of about  $45^\circ$  with respect to the deformation axis. The  $\alpha_2$  lamellae are drawn in black.

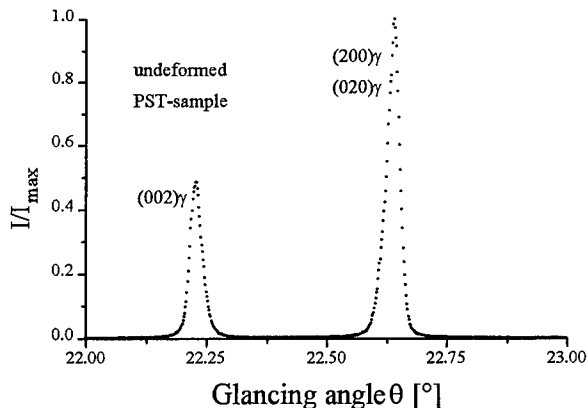


Figure 2: Plot of the normalized intensity vs. the glancing angle  $\theta$  of the  $\{002\}\gamma$  as well as the  $\{200\}\gamma/\{020\}\gamma$  Bragg-peaks of an undeformed PST-sample. The separation of the peaks indicates the tetragonality of  $\gamma$ .

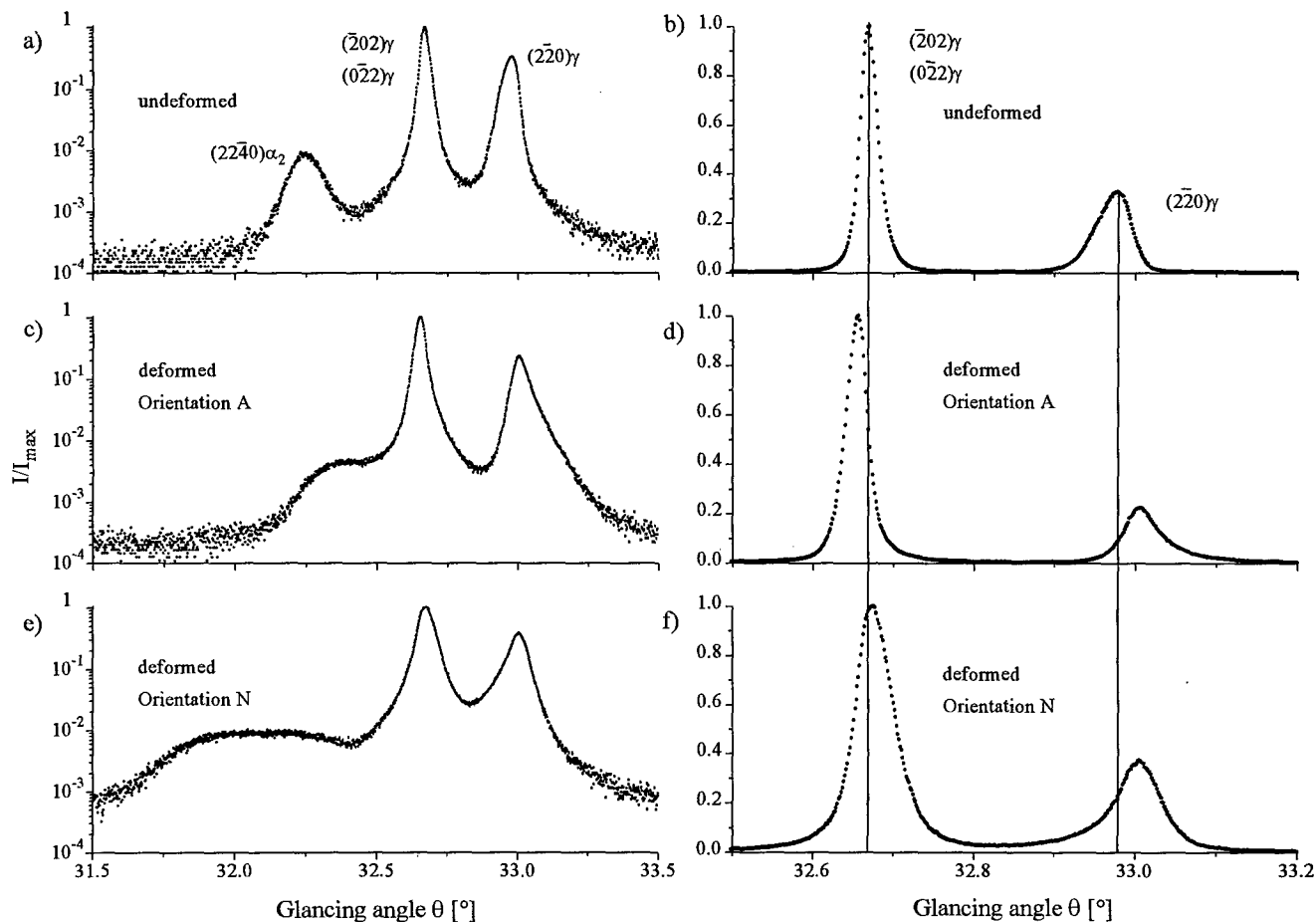


Figure 3: X-ray peak profiles of the reflections  $(2240)\alpha_2$ ,  $(\bar{2}02)\gamma/(\bar{0}2\bar{2})\gamma$  and  $(\bar{2}\bar{2}0)\gamma$  of an undeformed sample and for specimens deformed to plastic strains of about 5% in the hard orientations A and N. The intensity scales are plotted in a logarithmic and in a linear way in Figs. (a), (c) and (e) and Figs. (b), (d) and (f), respectively.

lamellae contribute to the scattered intensity in this case: (i) one peak arises from scattering on  $(002)$  lattice planes and (ii) one peak from scattering on crystallographically equivalent  $(200)$  and  $(020)$  lattice planes, respectively. The higher intensity of the right-hand peak compared to the left-hand peak is a consequence of the ratio of domains of orientations  $[100]$  and  $[010]$  with respect to domains of orientation  $[001]$  (i.e. a ratio of 2:1) and is within some scatter the same for all  $\{200\}$ -type Bragg reflections. From these measurements, the ratio of the lattice parameters  $c$  and  $a$  of the  $\gamma$  phase is determined to  $c/a = 1.0173$ .

In Figure 3,  $(\bar{2}\bar{2}0)\gamma$ ,  $(\bar{2}02)\gamma/(\bar{0}2\bar{2})\gamma$  and  $(2240)\alpha_2$  X-ray profiles are shown in a plot of the intensity vs. the glancing angle  $\theta$  for an undeformed sample (Figs. 3a,b) that serves as a reference as well as for specimens that were deformed in the hard orientations A (Figs. 3c,d) and N (Figs. 3e,f). Figs. 3a,c,e have a logarithmic intensity scale in order to reveal the weak intensity scattered by the  $\alpha_2$  phase. Figs. 3b,d,f show a detail with normalized linear intensity scale to reveal the deformation-induced shift of the  $\gamma$  peaks.

From the  $(\bar{2}\bar{2}0)\gamma$  and the  $(\bar{2}02)\gamma/(\bar{0}2\bar{2})\gamma$  peaks in Fig. 3b, a  $c/a$  ratio was calculated. The obtained value of  $c/a = 1.0171$  is in good agreement with the value obtained by evaluation of the  $\{002\}$ -type  $\gamma$  peaks. The evaluation of the separation of the  $(2240)\alpha_2$  peak and the  $(\bar{2}02)\gamma/(\bar{0}2\bar{2})\gamma$  peak (Fig. 3a) yields a value of 1.023 for the relative difference of lattice spacings of the  $(11\bar{2}0)\alpha_2$  and  $\{\bar{1}01\}\gamma$  lattice planes.

In case of the deformed samples A and N, the measurements of the  $\{220\}$ -type  $\gamma$  peaks were performed on surfaces perpendicular and parallel to the stress axis, respectively. Figure 3c shows a shift of the  $(2240)\alpha_2$  peak towards a larger glancing angle  $\theta$  for orientation A, Figure 3e reveals a shift of this peak to smaller glancing angle for orientation N. Figure 3e indicates strong broadening of the  $(2240)\alpha_2$  peak. Figures 3d and 3f give the shifts of the  $(\bar{2}\bar{2}0)\gamma$  and the  $(\bar{2}02)\gamma/(\bar{0}2\bar{2})\gamma$  peaks for the two hard orientations A and N, respectively. In case of orientation A, the  $(\bar{2}\bar{2}0)\gamma$  peak is shifted towards a larger glancing angle, whilst the  $(\bar{2}02)\gamma/(\bar{0}2\bar{2})\gamma$  peak is shifted into the direction of a smaller angle. The deformation-induced peak shift is uniform towards larger glancing angles for both  $\gamma$  peaks of orientation N, as shown in Figure 3f.

The peaks  $(111)\gamma$  and  $(0002)\alpha_2$  are shown in a logarithmic plot of the normalized intensity versus the glancing angle  $\theta$  in Figure 4. In the case of orientation A, this plane is oriented parallel to the stress axis, and in case of orientation N, the  $(111)\gamma$  plane is oriented perpendicular to the axis of deformation, respectively (see Figure 1). Figure 4a shows the profiles for an undeformed sample as reference material. The peaks of the two phases are separated due to the different lattice spacings. In Figure 4b, a shift of the  $(0002)\alpha_2$  peak to a smaller glancing angle is observed. The  $(111)\gamma$  peak, however, remains unaltered in position and shows strong broadening compared to the undeformed state. Regarding the profiles measured on samples deformed in orientation N given in Figure 4c, it is noticed that no  $(0002)\alpha_2$  peak is visible. The  $(111)\gamma$  peak is slightly shifted towards a larger glancing angle.

Some  $\{220\}$ -type X-ray profiles of the sample deformed in the soft orientation (B) are presented in Fig. 5 together with profiles of the undeformed material. The investigated side face of the PST-specimen was normal to the direction  $[1\bar{1}0]$  and parallel to the compression axis. Therefore, the lattice spacings were sampled perpendicular to the deformation axis  $[001]$  and parallel to the lamellae (see Figure 1c). Profiles of the undeformed and deformed material are shown in Figs. 5a,c in a logarithmic plot of the normalized intensity versus the glancing angle and in more detail in Figs. 5b,d in a linear plot of the intensity. The  $(2240)\alpha_2$  peak is slightly shifted to a larger glancing angle (cf. Figs. 5a,c) and the  $(\bar{2}20)\gamma$  and the  $(\bar{2}02)\gamma/(0\bar{2}2)\gamma$  peak profiles to a smaller glancing angle (Figs. 5b,d).

### Microstructure

Optical microscopy reveals traces of deformation in specimens deformed in the different orientations. Fig. 6 shows an optical micrograph of the  $(\bar{1}01)$  plane (perpendicular to the deformation direction) of a PST-sample deformed in orientation A (see Fig. 1a). The surface of the specimen was etched and the micrograph was taken using interference contrast. Obviously, some domains remain undeformed after compression, while in the majority of the lamellae traces of deformation are visible.

Scanning electron micrographs of samples deformed in orientations N and B taken in BSE contrast are given in Fig. 7. Fig. 7a shows the  $(\bar{1}01)$  side-plane of a specimen deformed in orientation N. Numerous deformation traces are visible in all domains of the different lamellae. The  $\alpha_2$  lamellae, which appear in bright contrast, show cracks due to an insufficient deformation accommodation. In Fig. 7b, a SEM picture of a PST-specimen deformed in orientation B is given. The regarded  $(\bar{1}10)$  side plane of the sample was parallel to the stress axis. Bright lines, representing  $\alpha_2$  lamellae, can be observed. The lamellae are inclined under an angle of approximately  $40^\circ$  to the stress axis. In the  $\gamma$  domains (grey), there are fine lines visible, lying parallel to the lamellar boundaries. These structures seem to be deformation traces.

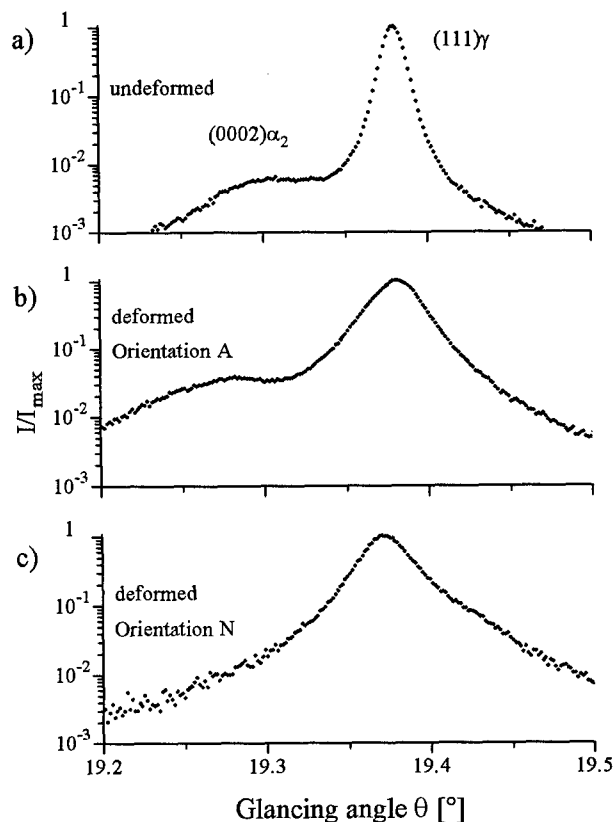


Figure 4: Logarithmic plot of the normalized intensity versus the glancing angle  $\theta$  for (a) an undeformed sample and for specimens deformed in (b) orientation A and (c) orientation N, respectively. The  $(0002)\alpha_2$  peak is visible as well as the  $(111)\gamma$  peak.

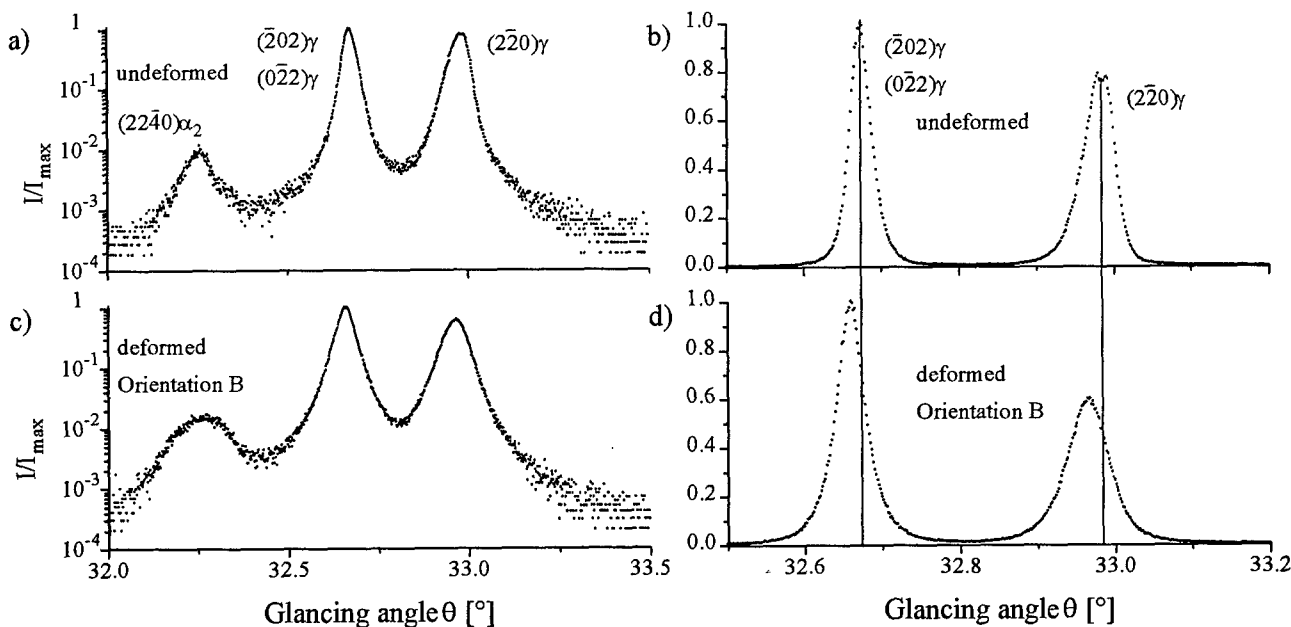


Figure 5: X-ray profiles of the reflections  $(2240)\alpha_2$  and  $(\bar{2}02)\gamma/(\bar{0}22)\gamma$  and  $(\bar{2}20)\gamma$  of an undeformed sample and for a specimen deformed to a plastic strain of about 5% in the soft orientation B. The intensity scales are plotted in a logarithmic and in a linear way in Figs. (a) and (c) and Figs. (b) and (d), respectively.

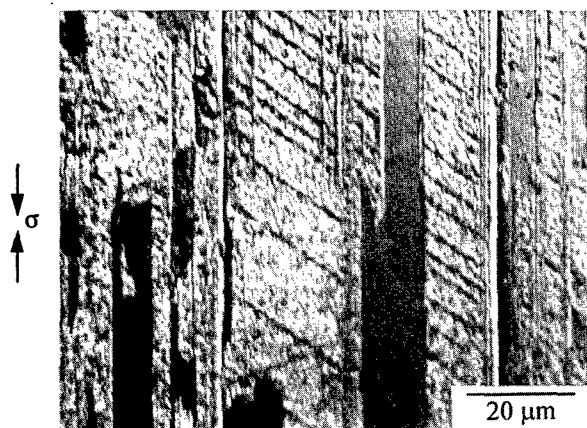


Figure 6: Optical micrograph of the  $(\bar{1}01)$  plane of a PST-specimen deformed in orientation A (perpendicular to the stress axis).

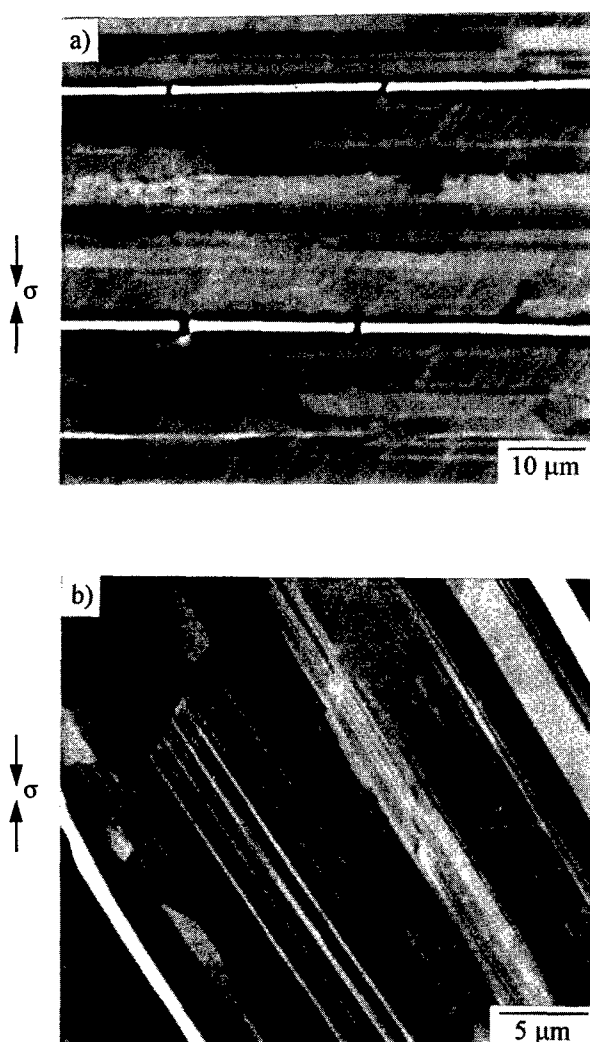


Figure 7: SEM micrographs taken in BSE contrast of samples deformed in (a) orientation N and (b) orientation B, respectively. The  $\alpha_2$  lamellae appear in bright contrast. Deformation traces are visible in the different  $\gamma$  domains.

TEM investigations of the microstructure of the deformed samples were performed in order to support the interpretation of the X-ray measurements. Fig. 8 shows TEM micrographs of PST-samples deformed in orientations A and N, respectively. Fig. 8a represents a typical deformation structure of the PST-sample deformed in orientation A. Deformation by twinning and dislocation activity is observed. In addition, the TEM-investigations have shown that some  $\gamma$  lamellae remain nearly undeformed after compression.

In Fig. 8b, a dark-field-image of the microstructure of the sample deformed in orientation N is given. The twin reflection used for the image is marked in the inlaid diffraction pattern. The  $\gamma$  lamellae show a large number of deformation twins. All lamellae seem to contribute to deformation.

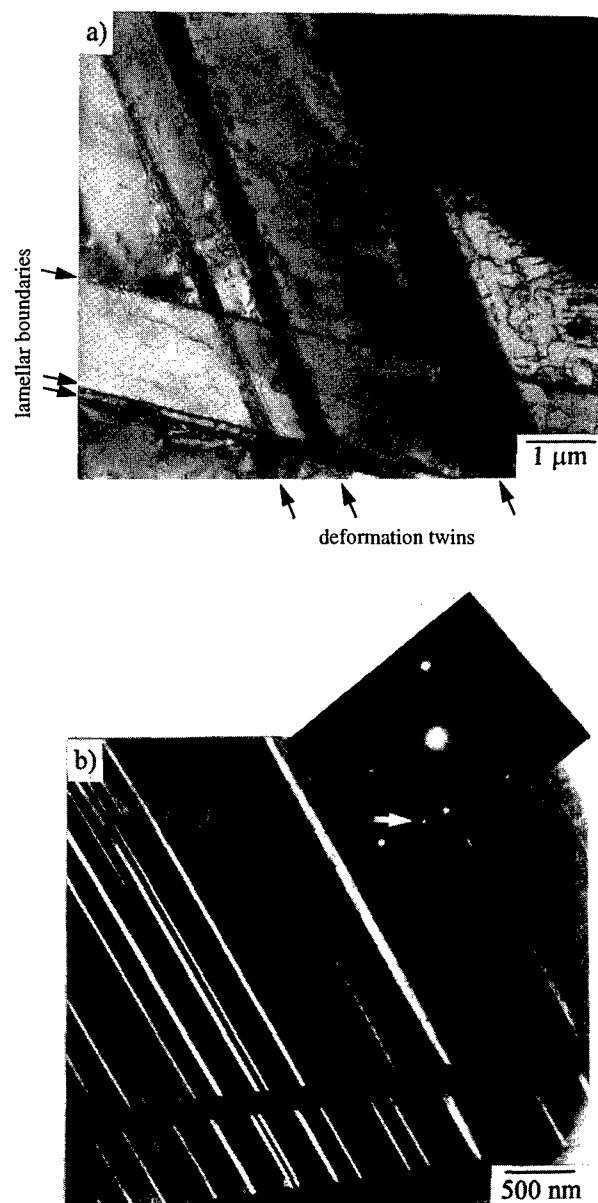


Figure 8: TEM micrographs of PST samples deformed in the hard orientations (a) A and (b) N, respectively. In the case of orientation A, the bright field image given in (a) shows deformation twinning as well as dislocation activity (zone axis  $\langle 110 \rangle$ ). (b) The dark field image of a sample deformed in orientation N shows numerous deformation twins. In the inlaid diffraction pattern (zone axis  $\langle 110 \rangle$ ), the twin reflection used for the dark-field image is marked.

## Discussion

The peak profiles measured on the undeformed PST sample yield values of the tetragonality of the  $\gamma$  phase. These values may not coincide with the tetragonality of homogeneous material without a lamellar microstructure due to coherency. The coherency stresses, however, are known to be reduced to a small fraction by dislocation networks located on the lamellar boundaries [7-9]. A second origin of internal stresses in the undeformed material are the coherency stresses acting between  $\gamma$  and  $\alpha_2$ . The widths of the peaks are not only a result of the lattice parameter variation due to lattice distortions, but also a result of the variation of the chemical composition in the different  $\gamma$  lamellae [10,11].

The X-ray investigations of the deformed samples yield peak shifts of individual phases or groups of domains with common orientation as well as peak broadening. The peak shifts, which are always related to the undeformed material, are a measure of long-range internal strains, which are a result of the superposition of originally present coherency stresses with deformation-induced internal stresses. In the sense of the present discussion, adjacent lamellae of  $\gamma$  and  $\alpha_2$  and adjacent lamellae of  $\gamma$  with different orientations to the deformation axis are interpreted as soft regions and hard regions with incompatible deformation. The deformation-induced internal stresses arising from the deformation incompatibility have ranges in the order of the microstructural dimensions, i.e. of the lamellar widths or domain sizes. The microstructural sources of the deformation-induced internal stresses are i) extra dislocations at the lamellar interfaces, which are held up by the interfaces during deformation and which have a preferred sign due to the deformability of individual domains with respect to domains in the adjacent lamellae as well as ii) deformation twins, which have the same effect as the extra interfacial dislocations. The deformation-induced stresses are considered in a first approximation to be biaxial in the plane of the lamellae without a restriction of the transverse strain in the direction perpendicular to the lamellae (i.e. in the  $[111]$  direction). In the following, the peak shifts of the samples deformed in the different orientations are discussed qualitatively in order to show the effects of deformation on the individual domains of common orientation.

Peak broadening can be interpreted in terms of lattice distortions due to increased dislocation and/or twin densities. A further possible source of peak broadening is the variation of the residual microstrains due to the variation of the local plastic deformation in differently oriented domains leading to a splitting of one X-ray peak into a number of peaks of small separation. The shape of the profiles, i.e. the appearance of asymmetries, which is an indication of heterogeneous plasticity, is not discussed in the present work in detail.

Another method to investigate long-range internal stresses is the analysis of the curvature of dislocation segments applied on undeformed and deformed TiAl by Appel and Wagner [17]. This method provides information on local residual stresses in the glide planes of the observed dislocations. The coherency shear stresses in an undeformed specimen were shown to range from 20 to 220 MPa. After deformation, an increase of the internal stresses to a range between 70 and 290 MPa was determined. Therefore, the TEM analysis of the curvature of individual dislocations yields information on local internal stresses. These observations, however, are restricted to shear stresses on the glide planes in contrast to the X-ray investigation of different Bragg peaks, which yields average spatial values.

### Deformation Axis Parallel to the Lamellae (Orientation A)

In the case of orientation A, the  $\{220\}$ -type Bragg profiles shown in Figs. 3c and 3d were measured at a section perpendicular to the stress axis, i.e. the lattice spacings are measured parallel to the deformation axis. The peak shift of the  $(2240)$  profile of the hard  $\alpha_2$  phase towards a larger glancing angle (Fig. 3c) indicates compressive axial forward stresses in this phase. Deformation of  $\alpha_2$  by activation of prismatic slip systems on glide planes of the type  $\{11\bar{2}1\}$  is possible in this orientation [13], but not sufficient to follow the plastic compression of the  $\gamma$  phase. For this reason, residual stresses remain in both phases after unloading. The compressive forward stresses in  $\alpha_2$  must be compensated by tensile back-stresses in the  $\gamma$  phase.

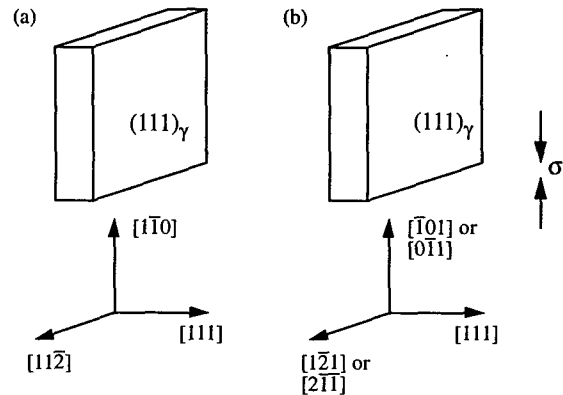


Figure 9: Schematic drawing of  $\gamma$  domains of different orientation in the case of a sample deformed in orientation A.

Fig. 3d shows the deformation-induced shifts of the  $\gamma$  peaks. The interesting observation is that the two  $\gamma$  peaks behave differently. The shift of the  $(202)\gamma/(022)\gamma$  peak indicates residual tensile back-stresses, whereas the  $(220)\gamma$  peak is shifted towards larger glancing angles (i.e. smaller lattice spacings), showing the same behaviour as the hard  $\alpha_2$  phase. Considering the possible glide systems in different kinds of domains shows a possible explanation for this behaviour. In Fig. 9, the possible orientations of different  $\gamma$  domains for the deformation of PST-samples in orientation A are drawn schematically. It is easily noticed that the Schmid factor for all glide systems in the  $(111)$  plane is zero in any case. For the case of the domains with the  $[1\bar{1}0]$  direction oriented along the compressive axis (Fig. 9a), the  $[001]$  direction is perpendicular to the stress axis. From this unique crystallographic relationship it follows that the Schmid factor in the remaining easy-glide systems along the slip directions  $[1\bar{1}0]$  and  $[110]$  is essentially zero, because the directions  $[1\bar{1}0]$  and  $[110]$  are parallel and perpendicular to the stress axis, respectively. For this reason, in all domains, which contribute to the  $(220)\gamma$  Bragg peak, only slip systems that disturb the ordered crystal lattice can be activated. In the other domains, which contribute to the  $(202)\gamma/(022)\gamma$  Bragg peak, it is possible to activate the regular glide systems, which do not disturb the ordered crystal lattice of the  $\gamma$  phase, see e.g. [15]. Fig. 9b presents the case of a domain with the  $[101]$  direction parallel to the axis of deformation. Now, the ordinary glide systems can be activated, since the slip directions  $[110]$  and  $[1\bar{1}0]$  as well as the respective glide planes are no longer perpendicular or parallel to the compression axis. From our results it is obvious that the domains contributing to the  $(220)\gamma$  Bragg peak are not deformable by activation of the ordinary slip systems in the case of orientation A. Therefore, in this type of domains compressive axial stresses are induced as in the case of the  $\alpha_2$  phase. Previous microstructural investigations on related materials [15,18-20] showed the activity of  $\{111\}\{112\}$  twinning systems as well as dislocation gliding on  $\{111\}\{110\}$  slip systems which preserve the ordered structure of the crystal lattice. Our microstructural TEM-investigations show the activity of dislocation gliding and deformation twinning for the given orientation. In some domains, significant deformation can neither be found in TEM nor in optical micrographs (cf. Fig. 6). These observations are in accordance with the results of the X-ray investigations performed in this study.

The X-ray investigations on the  $(111)$  plane have shown the shift of the  $(0002)\alpha_2$  peak to larger lattice spacings (Fig. 4b), indicating tensile strains in the hard  $\alpha_2$  phase. This is due to transverse strains induced by the residual elastic stresses in the direction of deformation mentioned above. The  $(111)\gamma$  peak does not significantly change its position with regard to the undeformed material but strong broadening can be recognized. The divergent behaviour of differently orientated domains, which generates strains of complementary sign, is responsible for this observation. In some domains, transverse compressive strains are induced, in others transverse tensile strains are caused by the residual internal stresses. In total, the  $(111)\gamma$  peak is not shifted in its position, but broadened and a slight asymmetry can be observed in the given logarithmic scaling.



### Deformation Axis Perpendicular to the Lamellae (Orientation N)

In the case of the  $(2\bar{2}0)\gamma$ ,  $(\bar{2}02)\gamma/(0\bar{2}2)\gamma$  and  $(2\bar{2}40)\alpha_2$  profiles (Figs. 3e,f), a surface parallel to the deformation axis was investigated. The plastic deformation of the  $\gamma$  phase induces transverse tensile residual strains in  $\alpha_2$  in the investigated direction perpendicular to the stress axis, indicated by the shift of the  $(2\bar{2}40)\alpha_2$  peak towards higher lattice spacings (see Figure 3e). In this orientation, the only glide systems of the  $\alpha_2$  phase with a Schmid factor not equal to zero are the pyramidal glide systems [13]. The critical resolved shear stress for this process, however, is too high [21]. In fact, the  $\alpha_2$  lamellae are practically undeformable for the given orientation, and plastic deformation of the adjacent  $\gamma$  phase causes cracking of the  $\alpha_2$  lamellae (see Fig. 7a). The large broadening of the  $(2\bar{2}40)\alpha_2$  peak arises from the variation of tensile residual stresses in the broken  $\alpha_2$  lamellae of different size and width.

The  $(2\bar{2}0)\gamma$  and  $(\bar{2}02)\gamma/(0\bar{2}2)\gamma$  profiles presented in Figure 3f are both shifted towards lower lattice spacings, which indicates transverse compressive stresses. These stresses are thus balancing the tensile transverse stresses of the hard  $\alpha_2$  phase, which is undeformable for the given orientation. The possible glide and twin systems are identical for all types of  $\gamma$  domains in this case, i.e. glide and twinning systems, which preserve the ordered structure, can be activated in each type of  $\gamma$  domains. The deformation of the lamellae induces transverse strains (in this case, the transverse strains act in the direction of deformation). They were measured by the investigation of a section of the specimen that is perpendicular to the deformation axis, in this case the  $(111)$  plane, see Fig. 4c. The shift of the  $(111)\gamma$  peak towards larger lattice spacings indicates the existence of tensile strains in the  $\gamma$  lamellae. This observation is in accordance with the measured compressive strains for the  $(\bar{1}01)$  side plane. The  $(0002)\alpha_2$  peak is not observed for the given orientation. This is probably due to the fact that the expected shift towards smaller lattice spacings resulting from compressive stresses in the  $\alpha_2$  lamellae, lets vanish the peak under the more intense  $(111)\gamma$  reflection.

The microstructural investigations showed deformation activity in all domains of the  $\gamma$  phase, mainly by twinning on  $\{111\}\{112\}$  systems (see also e.g. [13,15]). The observation of deformation in all types of lamellae is in agreement with the X-ray measurements.

### Deformation Axis inclined under $45^\circ$ to Lamellae (Orientation B)

In the case of the sample deformed in orientation B, X-ray profiles were measured on a surface parallel to the axis of deformation, more exactly, on the  $(1\bar{1}0)$  side plane given in Figure 1c, on which the traces of the lamellar boundaries lie under an angle of about  $45^\circ$  to the deformation axis. The slight shift of the  $(2\bar{2}40)\alpha_2$  peak towards smaller lattice spacings, shown in Fig. 5c, indicates the existence of compressive stresses in the hard  $\alpha_2$  phase. Figure 5d shows the corresponding behaviour of the different  $\gamma$  lamellae. Tensile stresses in all types of lamellae are indicated by the shift of the  $(2\bar{2}0)\gamma$  and  $(\bar{2}02)\gamma/(0\bar{2}2)\gamma$  peaks to larger lattice spacings. The compressive deformation of the PST-specimens in this orientation leads to plastic elongation of the  $\gamma$  lamellae along their boundaries. Therefore, residual back-stresses develop after unloading in  $\gamma$  in the direction of deformation and residual forward-stresses in  $\alpha_2$ , respectively. This leads to transverse strains in the direction perpendicular to deformation, i.e. in the investigated  $[1\bar{1}0]$  direction, which are indicated by the peak shifts shown in Fig. 5. In the microstructure, no indications of this interpretation of the X-ray measurements can be expected, since deformation is easily performed parallel to the lamellae in the  $(111)$  glide plane [10,15,18]. No deformation twinning was observed by SEM, see Figure 7b.

### Macroscopic Shape Change

The change of the shape of PST specimens in orientation A shows a strange effect reported earlier [12]. There is no macroscopical transverse strain in the direction perpendicular to the lamellae. This effect is discussed in [12] to be related to the different deformation behaviour of different  $\gamma$  lamellae taking into account the transformation matrices of the possible deformation systems (dislocation glide and deformation twinning). In the PST samples, this effect is just an interesting result. In polycrystalline material, however, it seems to induce large microstresses acting between grains of different orientations, since single grains may have the

respective orientation of the lamellae parallel to the deformation axis. Therefore, this effect should be, among others, responsible for the limited plasticity of polycrystalline TiAl.

### Summary

Samples of polysynthetically twinned TiAl were deformed in compression at room temperature. Different orientations of the lamellae with regard to the stress axis were examined. X-ray peak profiles of several Bragg reflections were investigated by a special high-resolution double-crystal diffractometer. The deformation-induced shift and broadening of the X-ray profiles was discussed in terms of residual long-range internal stresses.

The following observations were made:

1. Deformation parallel to the lamellar boundaries induced forward stresses in the hard  $\alpha_2$  phase in the direction of deformation. In the soft  $\gamma$  phase, differently oriented domains are under the action of forward and back stresses in this direction depending on the crystallographic orientations of the domains and the possible slip systems.
2. Deformation perpendicular to the lamellar boundaries resulted in large residual stresses in the  $\alpha_2$  phase, which is undeformable in this orientation. The  $\alpha_2$  phase was found to be under the action of tensile residual stresses perpendicular to the compression deformation axis, which are balanced by compressive residual stresses in the  $\gamma$  phase. In this case, no fundamental differences in the deformation behaviour of differently oriented  $\gamma$  domains were measured.
3. Deformation under an inclination of about  $45^\circ$  of the lamellae induced only small residual strains as expected from the easy deformability of the  $\gamma$  lamellae in this orientation. Nevertheless, a certain amount of residual stresses arose due to accommodation processes between  $\gamma$  and  $\alpha_2$ , which led to the measured transverse strains.

The results were discussed in terms of plastic deformation incompatibilities between the hard  $\alpha_2$  phase and the soft  $\gamma$  phase as well as the differently oriented  $\gamma$  domains. The deformation-induced long-range internal stresses have to be taken into account in future considerations of the local shear stress states during plastic deformation.

### Acknowledgments

The authors are very grateful to Prof. Y. Umakoshi and Dr. T. Nakano from Osaka University, Japan, for providing the PST-crystals and to Dr. P. M. Hazzledine, Dayton, OH for useful discussions. This work was supported financially by Deutsche Forschungsgemeinschaft (DFG Bi 418/2).

### Literature

1. C. M. Austin and T. J. Kelly, "Gas Turbine Engine Implementation of Gamma Titanium Aluminide", in *Superalloys 1996*, ed. R. D. Kissinger et al. (Warrendale, PA: TMS, 1996), 539-543.
2. G. Hug, A. Loiseau and P. Veyssiere, "Weak-beam Observation of a Dissociation Transition in TiAl", *Phil. Mag. A*, 57 (1988), 499-523.
3. Y. Umakoshi, "Deformation of Intermetallic Compounds", in *Materials Science and Technology*, eds. R. W. Cahn, P. Haasen and E. J. Kramer, Vol. 6: Plastic Deformation and Fracture of Materials, ed. H. Mughrabi (Weinheim: VCH, 1993), 280-291.
4. Y.-W. Kim, "Ordered Intermetallic Alloys, Part III: Gamma Titanium Aluminides", *JOM*, 46(7) (1994), 30-39.
5. H. Inui, M. H. Oh, A. Nakaura and M. Yamaguchi, "Ordered Domains in TiAl Coexisting with  $Ti_3Al$  in the Lamellar Structure of Ti-rich TiAl compounds", *Phil. Mag. A*, 66 (1992), 539-555.
6. D. M. Dimiduk, Y. Sun and P. M. Hazzledine, "Interfacial Structure and Lattice Mismatch in Lamellar TiAl Alloys", in *High-Temperature Ordered Intermetallic Alloys VI*, ed. J. Horton et al., (Mater. Res. Soc. Symp. Proc. 364, Pittsburgh, PA, 1995), 599-604.

7. L. Zhao and K. Tangri, "Transmission Electron Microscopy Characterization of Interfacial Boundaries in Heat-treated Ti<sub>3</sub>Al Two-phase Alloy", Phil. Mag. A, 64 (1991), 361-386.
8. P. M. Hazzledine, B. K. Kad, H. L. Fraser and D. M. Dimiduk, "Internal Stresses in TiAl Based Lamellar Composites", in Intermetallic Matrix Composites, ed. D. B. Miracle et al. (Mater. Res. Soc. Symp. Proc. 273, Pittsburgh, PA, 1992), 81-86.
9. F. Appel, U. Christoph and R. Wagner, "The Structure and Stress State of Lamellar Interfaces in Two-Phase Titanium Aluminides", in Interface Control of Electrical, Chemical and Mechanical Properties, ed. S. P. Murarka et al. (Mater. Res. Soc. Symp. Proc. 318, Pittsburgh, PA, 1994), 691-696.
10. T. Fujiwara, A. Nakamura, M. Hosomi, S. R. Nishitani, Y. Shirai and M. Yamaguchi, "Deformation of Polysynthetically Twinned Crystals of TiAl with a Nearly Stoichiometric Composition", Phil. Mag. A, 61 (1990), 591-606.
11. T. Pfullman and P. A. Beaven, "On the Relationship Between Lattice Parameters and Composition of the  $\gamma$ -TiAl Phase", Scripta Metall. Mater., 28 (1993), 275-280.
12. K. Kishida, D. R. Johnson, Y. Shimada, H. Inui, Y. Shirai and M. Yamaguchi, "Characteristics, Benefits and Applications of PST TiAl Crystal", in Gamma Titanium Aluminides, ed. Y.-W. Kim, R. Wagner and M. Yamaguchi (Warrendale, PA: TMS, 1996), 219-229.
13. Y. Umakoshi and T. Nakano, "Plastic Behaviour of TiAl Crystals Containing a Single Set of Lamellae at High Temperatures", ISIJ International, 32 (1992), 1339-1347.
14. Y. Umakoshi, private communication, 1994
15. H. Inui, A. Nakamura, M. H. Oh and M. Yamaguchi, "Deformation Structures in Ti-rich TiAl Polysynthetically Twinned Crystals", Phil. Mag. A, 66 (1992), 557-573.
16. M. Wilkens and K. Eckert, "Röntgenographische Untersuchungen über die Versetzungsanordnung in plastisch verformten Kupferkristallen", Zeitschrift für Naturforschung, 19a (1964), 459-470.
17. F. Appel and R. Wagner, "Slip-Twin Interactions in  $\gamma$ -Titanium Alloys", in Twinning in Advanced Materials, ed. M. H. Yoo and M. Wuttig (Warrendale, PA: TMS, 1994), 317-330.
18. K.-F. Yao, H. Inui, K. Kishida and M. Yamaguchi, "Plastic Deformation of V- and Zr-Alloyed PST TiAl in Tension and Compression at Room Temperature", Acta Metall. Mater., 43 (1995), 1075-1086.
19. H. Inui, K. Kishida, M. Misaki, M. Kobayashi, Y. Shirai and M. Yamaguchi, "Temperature Dependence of Yield Stress, Tensile Elongation and Deformation Structures in Polysynthetically Twinned Crystals of Ti-Al", Phil. Mag. A, 72 (1995), 1609-1631.
20. F. Appel and R. Wagner, "Interactions of Dislocations and Deformation Twins with Interfacial Boundaries in Titanium Aluminides", in Defect-Interface Interactions, ed. E. P. Kvam et al. (Mater. Res. Soc. Symp. Proc. 319, Pittsburgh, PA, 1994), 279-284.
21. Y. Umakoshi, T. Nakano, T. Takenaka, K. Sumimoto and T. Yamane, "Orientation and Temperature Dependence of Yield Stress and Slip Geometry of Ti<sub>3</sub>Al and Ti<sub>3</sub>Al-V Single Crystals", Acta Metall. Mater., 41 (1993), 1149-1154.

## DEVELOPMENT OF THIRD GENERATION CASTABLE GAMMA TITANIUM ALUMINIDES: ROLE OF SOLIDIFICATION PATHS

S. Naka, M. Thomas, C. Sanchez and T. Khan

Office National d'Etudes et de Recherches Aéronautiques

29, Av. de la Division Leclerc, 92322 Châtillon CEDEX, France

### Abstract

This paper deals with new (third generation) cast gamma titanium aluminide alloys developed at ONERA, based on detailed examinations of the role of solidification paths. While most of the alloys previously identified solidify through the  $\alpha$  phase showing an as-cast microstructure characterized by the presence of columnar  $\alpha$  grains in which all the  $\gamma$  lamellae are formed perpendicularly to the axis of these grains, the alloys developed in the present investigation solidify through  $\beta$ , the initial  $\beta$  grains being divided into differently oriented colonies of  $\alpha$  laths (or platelets) in which  $\gamma$  lamellae are subsequently formed. Although both categories of alloys show a  $\gamma+\alpha_2$  lamellar structure, the new  $\beta$ -solidification alloys exhibit much weaker texture and smaller grain size than the  $\alpha$ -solidification alloys such as Ti-48Al-2Cr-2Nb introduced by General Electric. Preliminary mechanical tests conducted on the new alloys such as Ti-46.6Al-2Re-0.8Si, without any specific optimization of heat treatments, indicate that they show a reasonable room-temperature tensile ductility, together with an excellent high temperature creep strength. Small quantities of silicon, present in most of these alloys, provide an additional strengthening effect in creep, although the origin of such a hardening effect has not yet totally been elucidated. Finally, advantages of  $\beta$ -solidification, when alloyed with silicon, are discussed; it is postulated that silicon is probably more soluble in  $\beta$  than in  $\alpha$ , and therefore, this alloying element can be more homogeneously incorporated in the  $\beta$ -solidification alloys than in the  $\alpha$ -solidification alloys.

### Introduction

Gamma titanium aluminides are now recognized as an

emerging class of low density alloys for intermediate temperature applications because of their unique properties (specific strength and oxidation resistance) up to almost 800°C. Considerable efforts made by General Electric over the last ten years toward developing gamma alloy technology for turbine-engine applications have led to the introduction of the now well-known GE alloy (Ti-(47-48)Al-2Cr-2Nb) [1, 2], typical of the first and second generation alloys [3]. Further development of new alloy compositions is being pursued in several countries. However, such alloy developments are, up to now, mostly conducted by "trial and error". Establishment of a sound physical metallurgy base for TiAl alloys seems to be essential in order to identify suitable compositions for each of the processing routes [4].

Among the various processing routes, casting is very attractive since it is cost-effective and it imparts high temperature creep strength to cast materials owing to the sufficiently large grain size. One of the key issues in this processing route is to obtain metallurgically sound cast products and to ensure reproducible mechanical properties in order to guarantee minimum values. However, numerous gamma alloys, developed until now especially in order to optimize various in-service properties, seem to show a significant difference in the castability which determines the soundness of cast thin components. There is no clear information in the open literature as to the solidification behaviour of such alloys or regarding the influence of alloy composition on the castability. In order to identify castable alloy compositions, a systematic investigation of the effect of various refractory alloying elements on the solidification behaviour was undertaken at ONERA for the past several years.

The aim of the present paper is thus to report a novel approach

for identifying gamma alloys suitable for casting by using results of various microstructural characterizations. The paper also reports the results of some preliminary mechanical tests conducted on our "third generation" alloys, more extensive mechanical characterization being now underway.

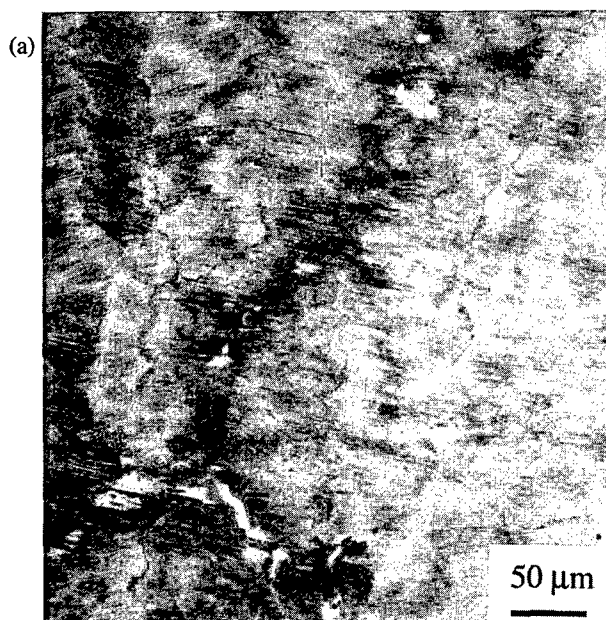
#### Effect of alloying elements

The first step of the present investigation was to classify various alloying elements such as Nb, Ta, Cr, Mo, W, Re and Fe according to their capability of stabilizing either  $\alpha_2$  or  $\gamma$  phase. For doing so, numerous ternary and more complex alloys were prepared by keeping the Ti/Al ratio equal to 52/48 with addition of 2-10 at.% of the above elements, and their microstructures both in the as-cast state and after subsequent heat treatments were examined by using optical and transmission electron microscopy (TEM).

Table 1: Alloying effects of various elements.

$\alpha_2$ stabilizing	Nb, Ta
neutral or slightly $\gamma$ stabilizing	Cr
moderately $\gamma$ stabilizing	Mo
Strongly $\gamma$ stabilizing (and highly $\beta$ stabilizing)	W, Re, Fe

These experiments led us to consider that there are quite roughly four types of tendencies, as indicated in Table 1. It should be emphasized that the classification given in this table is only a first approximation, because no quantitative analyses (for example, determination of volume fraction for each of the phases) were performed in this study. The aim was to use such a classification as a guide for our alloy development activities. It is therefore not surprising that slight differences of appreciation can be found between the present classification and the information reported in the literature [e.g., 5].



Strictly speaking, however, for establishing a more precise classification, it is necessary to investigate the phase diagram for each of the ternary systems in detail, in a composition range near TiAl and at various temperatures. It is worth mentioning here the recent atom-probe experiments on some of the above ternary alloys conducted by Menand's group [6] of Rouen University in France, which indicate the occurrence of complex situations. Based on the work of this group, niobium which is an  $\alpha_2$  stabilizer (i.e. increases the amount of the  $\alpha_2$  phase) partitions preferentially to the  $\gamma$  phase; on the contrary, chromium, a  $\gamma$  stabilizer, partitions preferentially to the  $\alpha_2$  phase. These situations result from the shape of the field of existence of the two phases  $\gamma$  and  $\alpha_2$  in the corresponding ternary phase diagrams.

The most important finding during this first step of the present investigation is however that there is a strong difference in the as-cast microstructure of the various alloys on the optical microscopy scale, as illustrated in Figure 1. While the well-known lamellar structure was observed for example in Ti-47Al-2Ta (Figure 1(a)), the microstructure observed for example in Ti-47Al-2W (Figure 1(b)) was, at first sight, difficult to understand. Examinations with TEM conducted on this alloy suggested, however, a stabilization of the b.c.c.  $\beta$  (or ordered  $\beta$  which is B2); as indicated on Table 1, such a stabilization also occurs easily with Re or Fe addition.

A thorough understanding of the as-cast microstructures shown in Figure 1 was at the origin of the development of our new alloys. The difference between them was found to result from two distinct solidification paths, and we realized that gaining insight into the solidification paths is one of the key factors for obtaining good castable alloys. Indeed, the alloys examined in the present study can be classified into two categories: the alloys solidifying through the h.c.p.  $\alpha$  phase and those solidifying through the b.c.c.  $\beta$  phase. In the following section, we will describe these solidification paths and their influence on the quality and soundness of cast products.

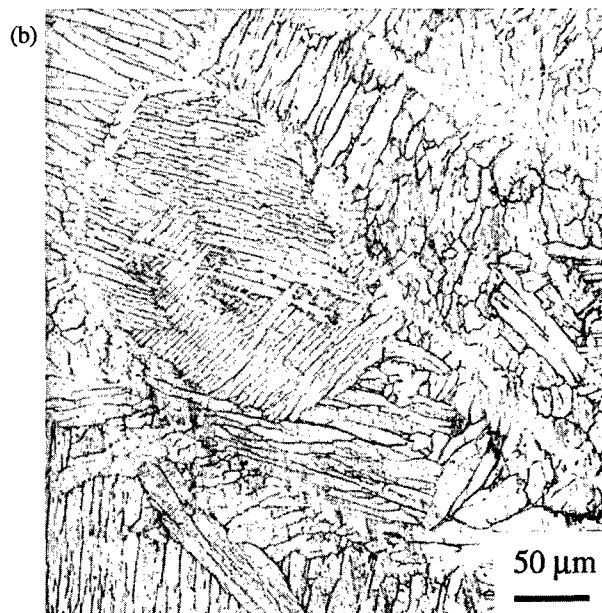


Figure 1: As-cast microstructures observed in (a) Ti-47Al-2Ta and in (b) Ti-47Al-2W.

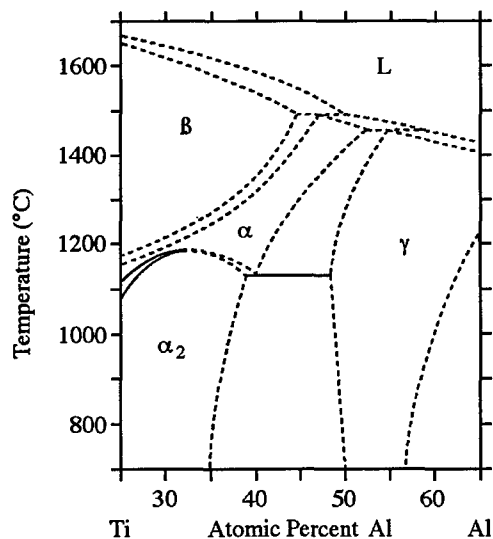


Figure 2: Binary Ti-Al phase diagram established by McCullough *et al.* [7].

#### Solidification through $\alpha$

##### Phase transition sequence and resulting microstructure

In the case of alloys solidifying through the  $\alpha$  phase, the binary phase diagram (Figure 2) proposed by McCullough *et al.* [7] is useful in understanding the corresponding microstructure formation during casting. In this case, the first solidified  $\alpha$  crystals tend to form columnar grains, as schematically depicted in Figure 3. Note that such a regular and simple as-cast microstructure was observed in a 50kg ingot of the GE alloy made by Böhler (Austrian company) using a rotating electrode vacuum arc melting furnace. As shown in Figure 4, the columnar nature is indeed extremely pronounced due to the preferential crystal growth direction parallel to the  $c$  axis which is unique in the h.c.p.  $\alpha$  phase. Moreover, during cooling

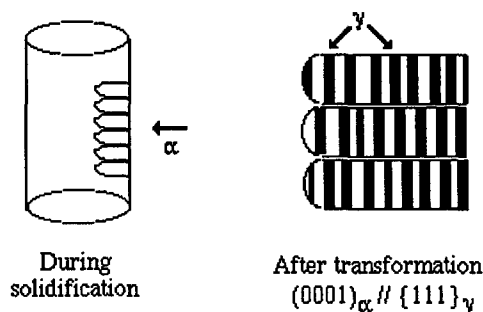


Figure 3: Schematic representation of an ingot solidified through  $\alpha$ , exhibiting a very strong texture.

subsequent to solidification, all the  $\gamma$  lamellae precipitating in each of columnar grains to form the well-known  $\gamma$ - $\alpha_2$  lamellar structure (Figure 4(b)) are oriented perpendicularly to the hexagonal  $c$  axis because of the orientation relationship  $(0001)_\alpha // \{111\}_\gamma$  and  $\langle 11\bar{2}0 \rangle_\alpha // \langle 11\bar{1}0 \rangle_\gamma$  inherent in the transformation mechanism involved.

#### Difficulties arising from this solidification path

As a consequence of such a phase transition sequence, it is not surprising that casting of gamma alloys of this category is prone to some serious difficulties: various defects such as microporosities, introduced in the interdendritic (or intercolumnar) zone, and a strongly anisotropic (or textured) character of the cast products which may be harmful to their mechanical performance. Indeed, if the shape of these products is simple such as the rod part of exhaust valves of car engine, the columnar structure may be quite regular and axisymmetric. In this case, the orientation of lamellae (parallel to the axis of the rod part) is quite favorable with regard to a notch effect, as was recently shown by Yamaguchi's group of Kyoto University using differently oriented PST crystals [8]. However, in most of the components of gas turbine engines that generally have complex shapes, the solidification texture after casting is still

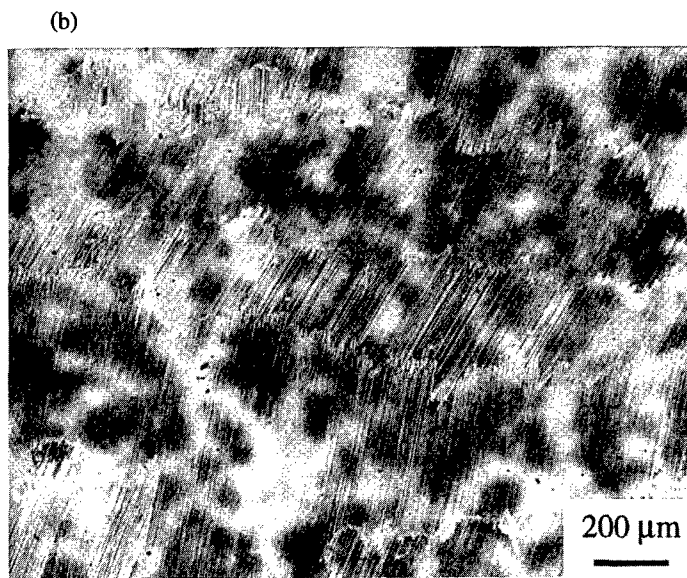
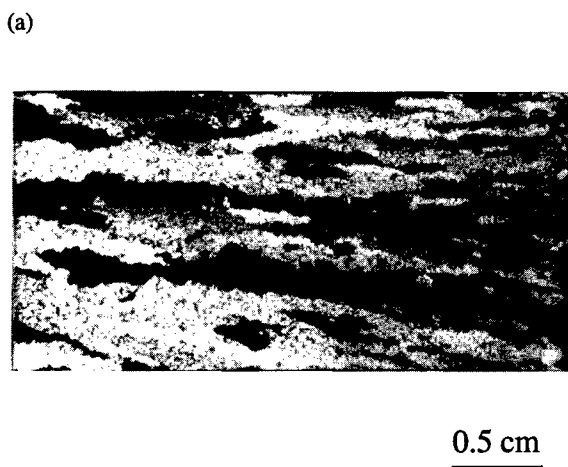


Fig. 4 (a) Columnar grains observed on a longitudinal section of the rod cut following its radial direction from a 50kg ingot of the GE alloy produced by Böhler and (b) lamellar structure where the lamellae are oriented nearly perpendicularly to the columnar grains' axis.

strong but may not be so simple. In this case, the mechanical response may strongly vary within a given component, whereas, for a jet engine manufacturer, the major concern is to guarantee a minimum value of mechanical properties for every component.

Most of the gamma alloys of first and second generations, however, belong to the category solidifying essentially through  $\alpha$ . Therefore, when these alloys are used for casting, it is necessary to resort to some specific casting techniques in order to reduce the columnar nature of the solidification and the associated texture.

**Role of post-casting processings** No systematic investigation seems to have been made regarding the influence of post-casting processings on the mechanical properties of cast products. As far as hot isostatic pressing (HIP) is concerned, this technique, in principle, reduces or suppresses porosities and may lead to an increase in ductility. However, since the use of HIP implies a higher cost, it is essential to get in the near future a more serious answer to the question whether this processing is absolutely necessary or not.

As for the post-cast heat treatments, it is worth mentioning a recent investigation of texture on the above mentioned GE alloy ingot, conducted by Penelle's group [9] of Orsay University in France. The main results of the work of this group are as follows. Combining neutron diffraction and electron back scattering pattern analyses, it has been shown that the solidification texture cannot be reduced through any heat treatment in the whole temperature range from 1000 to 1400°C. The as-cast  $\langle 111 \rangle$  texture, parallel to the axis of the rod cut from the ingot (Figure 3) following its radial direction, becomes more pronounced with increasing temperature, even at 1400°C which is beyond  $\alpha$  transus. This means that the dissolution and subsequent reprecipitation of the  $\gamma$  phase involved in the solutioning in the single-phase  $\alpha$  phase field at 1400°C do not modify the orientation of the matrix  $\alpha_2$  grains. Moreover, the reinforcement of the  $\langle 111 \rangle$  texture, together with the experimental fact that the volume fraction of monolithic  $\gamma$  grains increases during heat treatment at intermediate temperatures (1150 to 1250°C), indicates that the orientation of monolithic  $\gamma$  grains formed is not at random.

Based on the above-mentioned texture evolution upon heat treatments, it is most likely that HIP does not reduce the solidification texture. Accordingly, the alloys of the first and second generation should rather be considered as wrought alloys, since reduction of the solidification texture may be achieved only through appropriate thermomechanical treatments such as isothermal forging. Although any treatment of this sort is of course totally ruled out for cast components, it is interesting here to mention some difficulties arising during high temperature deformation (hot working) of these alloys. Figure 5 shows the results of tensile tests conducted at 1200°C on the strongly textured GE alloy ingot made by Böhler. These tensile tests were conducted on two types of specimens: parallel and perpendicular to columnar grains. The results indicate that deformability is higher for the tensile axis parallel to columnar grains than perpendicular to them. Such an anisotropy in deformability results in a heterogeneous deformation during isothermal forging (80% of reduction in thickness at 1150°C) of a small rectangular block cut from the same alloy ingot (Figure 6). Columnar grains were strongly deformed and elongated parallel to their axis, rendering the specimen of

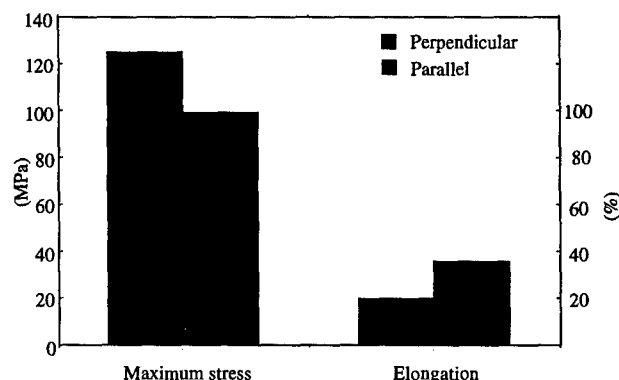
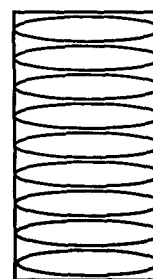


Figure 5: Tensile tests conducted on the textured GE alloy ingot at 1200°C with strain rate of  $5 \times 10^{-4} \text{ s}^{-1}$ .

rectangular shape to a forged product of a rounded shape. Finally, it is worth mentioning that the forged product exhibited, on the metallographical scale, a banded structure characterized by recrystallized grains alternating with non recrystallized lamellar zones, suggesting that the forging cannot

(a)



(b)

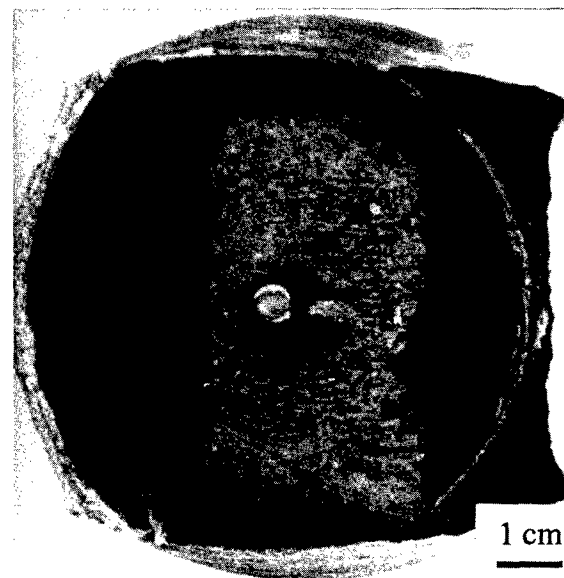


Figure 6: Isothermal forging of the textured GE alloy, (a) schematic representation of a small rectangular shape specimen where the orientation of columnar grains is depicted, (b) forged product where the trace of the initial rectangular shape is visible because of a lesser straining of the specimen surface region due to a friction stress.

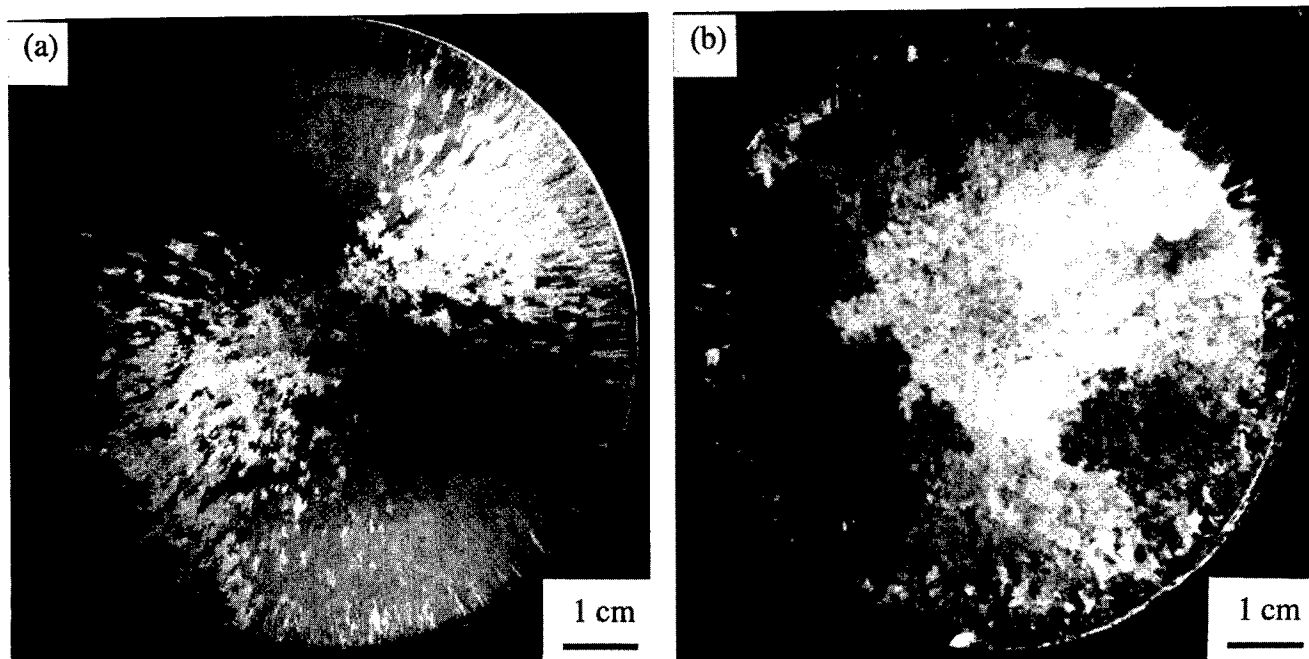


Fig. 7: As-cast ingots: (a) GE alloy solidifying through  $\alpha$  and (b) Ti-47Al-2Re alloy solidifying through  $\beta$ .

totally suppress the texture.

#### Solidification through $\beta$

##### Phase transition sequence and resulting microstructure

Contrary to the case of  $\alpha$ -solidification, the alloys that solidify through the  $\beta$  phase show a columnar character much less

pronounced (Figure 7) even though the  $\langle 100 \rangle$  axis of the  $\beta$  phase is the preferential direction of crystal growth during solidification; it is worth noting here that there are three equivalent directions for  $\langle 100 \rangle$ , namely  $[100]$ ,  $[010]$  and  $[001]$ . During cooling after solidification,  $\beta$  crystals are transformed into  $\alpha$ . This transformation, that most likely takes place by following the so-called Burgers orientation relationship  $\{1\bar{1}0\}_{\beta} // \{0001\}_{\alpha}$  and  $\langle 111 \rangle_{\beta} // \langle 11\bar{2}0 \rangle_{\alpha}$ , should, in theory, lead to

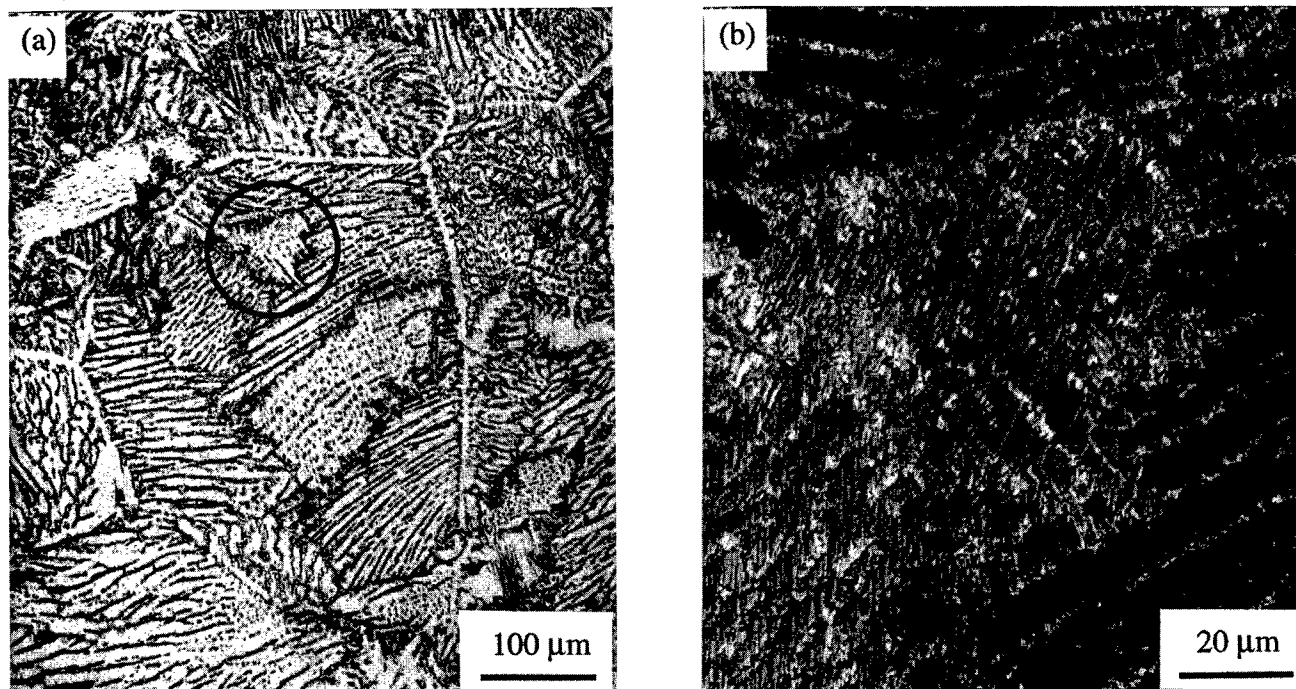


Fig. 8: Typical  $\beta$  solidification microstructure. At a low magnification (a), the microstructure is similar to that of conventional titanium alloys, while at a higher magnification (b), the well-known  $\gamma + \alpha_2$  lamellar microstructure becomes visible. Note that (b) corresponds to an enlarged image of the zone encircled in (a).



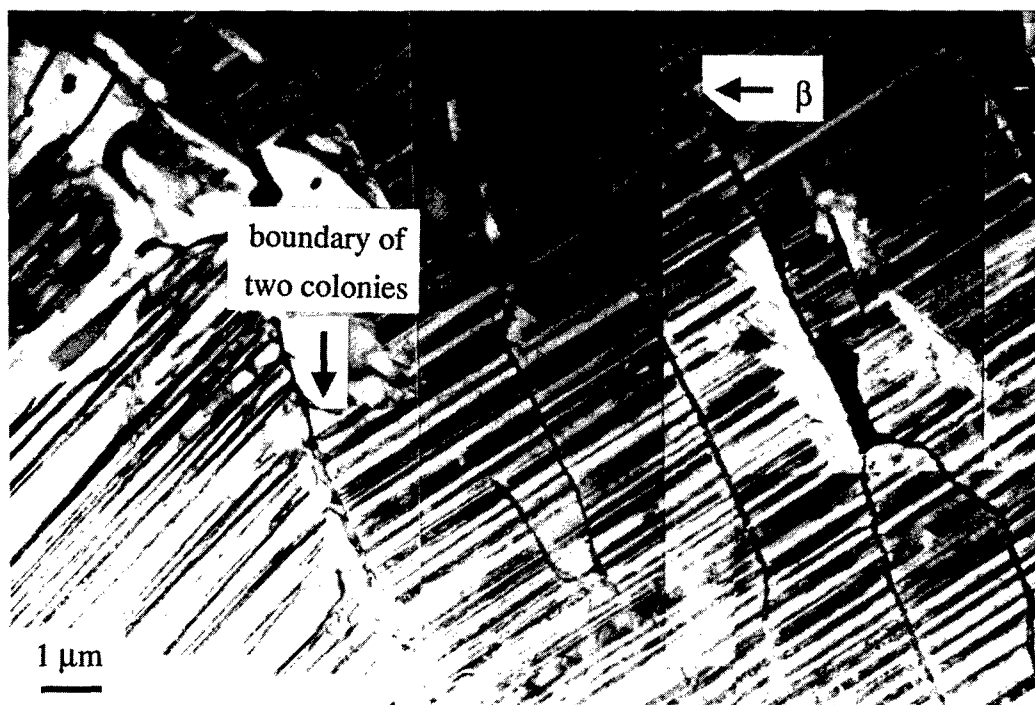


Figure 9: Microstructure observed by TEM in a  $\beta$ -solidification alloy (Ti-47Al-2Re). Note here the presence of two colonies of platelets (laths), which can be distinguished from each other by the difference of lamellae orientation.

the formation of twelve orientation variants of  $\alpha$ . During subsequent cooling, the  $\gamma$  phase precipitates in the lamellar form in each  $\alpha$  variant. The resultant microstructure (Figure 8(a)) is characterized by the presence, inside each initial  $\beta$  grain, of numerous colonies corresponding to the orientation variants. Moreover, each of these colonies comprises numerous  $\alpha$  platelets (or laths) and these platelets are often surrounded by some residual  $\beta$  phase (Figure 9). Finally, inside each platelet, one can observe the  $\gamma+\alpha_2$  lamellar structure (Figures 8(b) and 9).

#### Comments on the observed microstructure

The microstructure (Figure 8(a)) observed at a low magnification in TiAl alloys of this category shows a striking similarity to that generally observed in conventional titanium alloys. According to the physical metallurgy established for these titanium alloys [10], such a microstructure results from the phase transformation during cooling at a moderate rate from the high-temperature b.c.c.  $\beta$  phase to the low-temperature h.c.p.  $\alpha$  phase. Note also that the casting of titanium alloys occurs by solidification through  $\beta$ .

The  $\beta$  phase cannot be retained during cooling even with high-rate quenching in the case of titanium alloys devoid of  $\beta$ -stabilizing elements. With the addition of these elements, the  $\beta$  phase can be retained at room temperature; the retained  $\beta$  phase may either be metastable or in equilibrium depending on the degree of stabilization as a function of the nature and amount of alloying elements. When the  $\beta$  phase is retained, the previously-mentioned Burgers orientation relationship can be easily verified between the two phases.

Based on all these considerations, the low-magnification image

(Figure 8(a)) can be regarded as signature of the solidification through  $\beta$  which the alloy has undergone and a subsequent decomposition of this  $\beta$  phase in  $\alpha$ , whereas the higher magnification micrograph (Figure 8 (b)) can easily be represented as "overlapping" of conventional titanium alloy type microstructure on that of the lamellar structure typical of gamma titanium aluminides.

**Nature of the  $\beta$  phase** In the composition range of the binary Ti-Al phase diagram (see Figure 2), the  $\beta$  phase is present at high temperatures, and this phase is most likely a solid solution extension form of  $\beta$ -titanium. In this case, such a  $\beta$  phase cannot be retained at room temperature, as already mentioned for the case of conventional titanium alloys. Moreover, according to TEM analyses, the retained  $\beta$  phase observed in  $\beta$ -solidification alloys corresponds to an ordered form (B2), quite often accompanied with the presence of anti-phase domain boundaries (APBs), indicating the occurrence of ordering reaction  $\beta \Rightarrow B2$  at a certain temperature. Note that the B2 phase does not exist in the binary phase diagram.

Therefore, the retained ordered- $\beta$  B2 phase observed in  $\beta$ -solidification alloys is certainly due to a combined alloying effect of Al and  $\beta$  stabilizing elements. In this connection, our previous investigation conducted on various ternary Ti-Al-X (X = transition element) systems [11] should be mentioned; this work demonstrated a large field of existence of  $\beta$  and B2 starting from the composition  $Ti_2AlX$  ( $= Ti_{50}Al_{25}X_{25}$ ) and extending very often deeply toward both Ti and X corners but also toward TiAl region. The same study also showed that the  $\beta \Rightarrow B2$  ordering should correspond to a second-order reaction and the ordering temperature depended both on the nature of the element X and on the alloy composition.



### Implications of the $\beta$ -solidification and some future issues in the understanding of resulting microstructure

The phase transition sequence described above results in a kind of "crystal partitioning" effect, which should be effective in minimizing the difficulties encountered with the  $\alpha$  solidification, i.e. reduction of solidification defects, less pronounced texture and small grain (platelets colony) size. This strongly suggests that the category of alloys solidified through  $\beta$  will be much less prone to a scatter in mechanical properties, thereby guaranteeing consistent minimum values to the designers.

Based on some preliminary examinations of microstructures after heat treatments of various alloys of this category, the retained  $\beta$  (more exactly B2) phase appears to be metastable or in equilibrium, as in the case of the  $\beta$  phase of conventional titanium alloys. Indeed, in some of the alloys examined, the as-cast  $\beta$  phase totally dissolved when heat-treated in some temperature range, while in some others, the same phase remained during heat treatments, independent of the temperature. Further careful investigation is important, since the presence of  $\beta$  phase is not indispensable from the alloy development viewpoint. What is important is to solidify these alloys through  $\beta$  for achieving the crystal partitioning, as already mentioned. In view of a possible precipitation of the so-called  $\omega$  phase [12] in the metastable B2 phase at relatively low temperatures, it is even desirable to have alloy compositions where this phase can completely decompose into  $\alpha$  (and then  $\gamma + \alpha_2$ ) during cooling after solidification or where the same phase, if retained after casting, can totally be dissolved by subsequent heat treatments. It is recognized that the presence of  $\omega$  phase leads to a strong embrittlement of conventional titanium alloys [10]. Note however that a small volume fraction (most probably less than 5%) of the B2 phase present in our  $\beta$ -solidification alloys may not at all be harmful even if the  $\omega$  precipitation takes place within this B2 phase. In any case, the work is now underway in order to get a clearer insight into the behavior of the  $\beta$  phase during heat treatments.

Table 2: Rough estimation of alloying addition necessary to promote the  $\beta$ -solidification.

$\beta$ stabilizing elements	minimum content (at.%)
Fe, Re, W	$\approx 2\%$
Mo, Cr	$\approx 5\%$
Nb, Ta	$>> 5\%$

### Development of new alloys solidifying through $\beta$

#### Choice of chemical compositions and target of the alloy development effort

In our effort of developing third generation castable alloys, the prime concern was to preserve their light weight character and keep the Ti/Al ratio close to 52/48. The  $\beta$  solidification occurs even in binary alloys, if they are sufficiently rich in Ti, for example  $\text{Ti}_{60}\text{Al}_{40}$  (see Figure 2), which is quite off stoichiometry. Such Ti-rich alloys are not acceptable, since they are too brittle due to a very high volume fraction of the  $\alpha$  phase, as predicted by the phase diagram, and they have most probably poor oxidation resistance. Based on our various experiments conducted on ternary alloys, the elements such as Fe, Re and W were most potent for promoting the  $\beta$  solidification, followed by Mo, Cr, Nb and Ta in decreasing order. In ternary systems, there is a minimum content necessary for each of these alloying elements (Table 2), and these elements can roughly be divided into three groups. It is however worth noting that such an alloying effect on the  $\beta$  solidification is cumulative in more complex alloys. This means that combinations such as 1% of Re with 1% of W and 1% of W with 2.5% of Cr are satisfactory for promoting the  $\beta$ -solidification.

Based on the above consideration, we have favored the use of the first group of alloying elements, except Fe. Addition of this last element was excluded from our alloy development effort. Indeed, iron is known as quite detrimental to creep behavior of

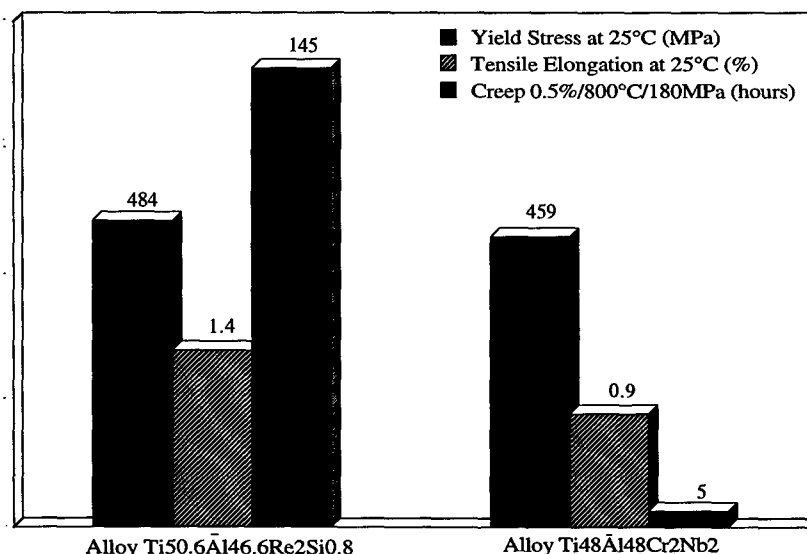


Fig. 10: Comparison of mechanical properties between one of our new alloys and the GE alloy. Mechanical tests were conducted after HIP at 1250°C/200 MPa followed by heat treatments of 1250°C/4 hours + furnace cool + 900°C/4 hours.

conventional titanium alloys [13], partly because of its expected propensity for fast diffusion in titanium alloys related to the small atomic size of this element compared with that of titanium. In the case of gamma titanium aluminides, such an effect has not yet been clearly verified, but the presence of iron does not seem to be desirable according to some results of our creep tests conducted in a TiAl-Fe-V-B alloy developed by IHI [14]. Note that this IHI alloy solidifies through  $\beta$ .

Major target of our alloy development effort was to obtain alloys having a good high temperature creep resistance. In this context, addition of silicon has been tested, since some information from the literature [15] suggests a beneficial effect of Si addition on the creep resistance of gamma titanium aluminides. Silicon content in the present investigation was limited to less than 0.8 at.% in order to maintain the  $\beta$  solidification.

#### Mechanical properties

Characterization of mechanical properties has been conducted up to now only on alloys of three systems TiAl-Re-Si, TiAl-Re-W and TiAl-Re-W-Si. All the mechanical tests were conducted after HIP at 1250°C/200 MPa followed by heat treatments of 1250°C/4 hours + furnace cool + 900°C/4 hours. The typical microstructure after these treatments is characterized by a slight globulizing of the  $\beta$  phase which was present between platelets (laths) in the as-cast state, while the  $\beta$ -solidification microstructure (presence of colonies of platelets) is preserved. Note that the above post-cast treatments are frequently applied to the GE alloy in order to enhance room-temperature ductility at the expense of creep resistance.

As illustrated in Figure 10, mechanical properties of these alloys were found in general to be excellent. Indeed, while the room-temperature tensile properties (yield stress and elongation) of one of them (Ti-46.6Al-2Re-0.8Si alloy) are quite similar to those of the GE alloy supplied by Howmet, our alloy is superior in terms of creep resistance. Therefore, it can be concluded that the high temperature creep/low temperature ductility compromise of this alloy is satisfactory.

Further examination of creep properties of the same alloy

(Table 3) confirms its excellent overall creep resistance. Note that the primary creep deformation is limited to less than 0.3% and the secondary creep rate fairly low ( $10^{-8}$ - $10^{-9}$  s $^{-1}$ ).

Another alloy of the present study (Ti-46Al-1Re-1W-0.2Si), that is based on a combination of Re with W together with a reduction of Si content, is even better in creep properties (table 4) than the former alloy (740 hours vs. 625 hours for 0.5% creep under 200MPa et 750°C). According to some of our most recent creep experiments under the same test conditions, the duration of 740 hours is about 20% longer than that of the Ti-46Al-2W-0.8Si alloy similar to the Ti-47Al-2W-0.5Si alloy developed by ABB [see 3] and about 10 times longer than that of the Alloy 7 (Ti-46Al-5Nb-1W) developed by Allison [see also 3]. Note that both ABB and Allison alloys solidify through the  $\beta$  phase.

It should finally be emphasized that further improvement of mechanical properties can be expected for our alloys through an optimization of heat treatment conditions.

**Strengthening through Si addition in creep** A comparison of creep properties under 200MPa at 750°C between the Ti-46Al-1Re-1W-0.2Si alloy with its silicon-free version can be made in Table 4. The results show quite a significant effect of Si addition on the creep resistance (740 hours vs. 212 hours for 0.5% creep). Note however that the duration of 212 hours of the silicon-free alloy is still excellent, compared to the GE alloy, based on our unpublished creep data on this alloy [16]. Although the GE alloy ingot supplied by Howmet has not yet been tested under the same test conditions, this ingot cannot compete with the silicon-free alloy (Ti-46Al-1Re-1W), in view of the weak performance of the former alloy under 180MPa/800°C (Figure 10). The creep properties of the already-mentioned as-cast GE alloy ingot supplied by Böhler may be comparable to those of the silicon-free Ti-46Al-1Re-1W alloy, because of a strong texture effect of this GE alloy ingot; this ingot does not show, however, any room-temperature ductility. Under these circumstances, it can be argued that alloying with heavy elements such as Re and W is beneficial to creep resistance of gamma alloys with their presumable solid solution hardening effect, while silicon gives an additional strengthening effect which is remarkable,

Table 3: Creep properties of the Ti-46.6Al-2Re-0.8Si alloy.

Test conditions	Time at 0.5% elongation (hours)	Primary creep elongation (%) duration (hours)	Secondary creep rate (s $^{-1}$ )
700°C/300MPa	525	0.27 45	8.4x10 $^{-9}$
750°C/200MPa	625	0.07 3	1.3x10 $^{-9}$
750°C/300MPa	100	0.22 0.39	5.5x10 $^{-9}$
800°C/180MPa	145	0.24 14	4.6x10 $^{-9}$

Table 4: Influence of Si addition on the creep properties (test conditions: 750°C/200MPa)

Alloy	Time at 0.5% elongation (hours)	Primary creep elongation (%) duration (hours)	Secondary creep rate (s $^{-1}$ )
Ti-46Al-1Re-1W	212	0.27 30	2.3x10 $^{-9}$
Ti-46Al-1Re-1W-0.2Si	740	0.18 18	9.2x10 $^{-10}$

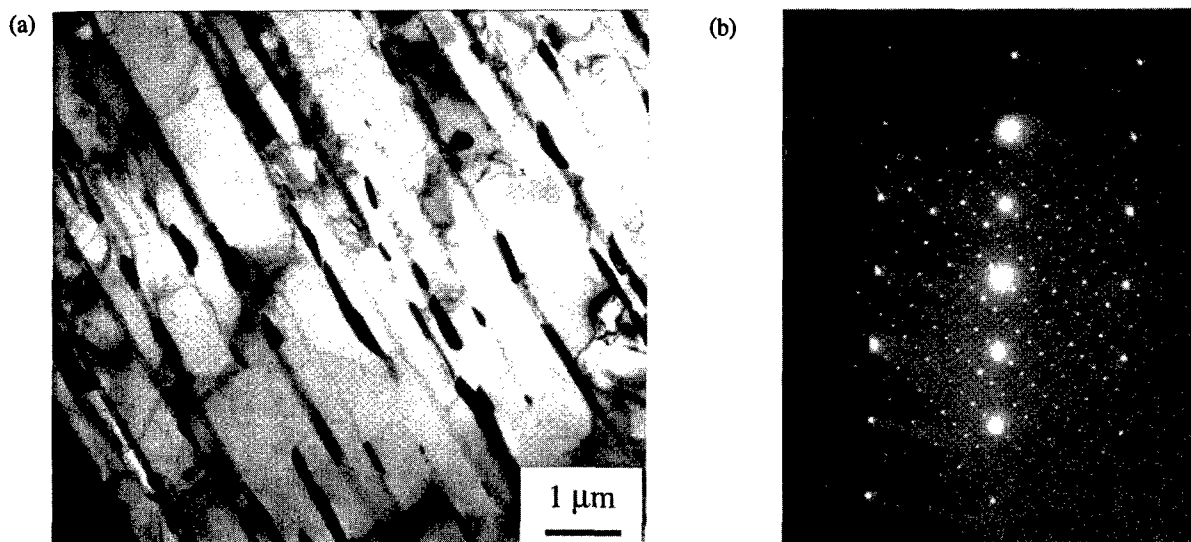


Fig. 11: Secondary silicide precipitation observed in the Ti-46.6Al-2Re-0.8Si alloy, most often in the inter-lamellar zones; (a) TEM image, (b)  $[0001]_{\text{Ti}_5\text{Si}_3}$  zone axis parallel to  $\langle 111 \rangle_\gamma$  axis. Due to a strong diffraction of  $\gamma$  matrix (spots of high intensity), many double diffraction spots are present in this diffraction pattern. Hexagonal character ( $[0001]_{\text{Ti}_5\text{Si}_3}$  zone axis) formed by  $(10\bar{1}0)$  spots can be found in the upper-left corner of the diffraction pattern due to the weakness of their neighboring double diffraction spots. Note also that the epitaxial relation is observed here between  $(0001)_{\text{Ti}_5\text{Si}_3}$  plane and one of the four  $\{111\}_\gamma$  planes that does not correspond to the lamellar interface; this interface is parallel to the  $(0001)$  plane of the  $\alpha_2$  phase from which  $\gamma$  lamellae are formed.

considering its low concentration (as low as 0.2 at.%).

Microstructural analyses conducted on both Ti-46.6Al-2Re-0.8Si and Ti-46Al-1Re-1W-0.2Si alloys indicated that the difference in Si content gave rise to a significant difference in its behavior between the two alloys. In the case of 0.8% addition precipitation of silicides (hexagonal D8 $\gamma$   $\text{Ti}_5\text{Si}_3$ ) is quite abundant. This precipitation seems to take place in two distinct stages: primary reaction (on the metallographic scale) of eutectic type induced by interdendritic segregation during solidification and secondary reaction (on the TEM scale) corresponding to a solid state precipitation like that shown in Figure 11. Primary silicides tend to dissolve during heat treatments at high temperatures (for example at 1250°C) but cannot totally disappear at least with a short time treatment (4 hours). The behavior of secondary silicides is much less clear, but they at least do not seem to dissolve during heat treatments. Note that the epitaxial character demonstrated in Figure 11(b) suggests a direct precipitation from the  $\gamma$  phase supersaturated in Si. In the case of 0.2% addition, on the contrary, a small number of primary silicides can be found in the as-cast state but tend to completely dissolve during heat treatments even at as low as 1250°C. Moreover, secondary silicides are apparently absent or at least very difficult to detect. Based on these microstructural examinations, it is most likely that the creep strengthening effect of Si addition is primarily due to an interaction of moving dislocations with silicon in the form of solid solution. The silicide dispersion hardening effect, suggested by Noda et al. [15] in their study on the Ti-48Al-1.5Cr alloy both silicon-free and with addition of 0.26-0.65 at.%Si, seems to be not so important in the case of our alloys.

**Advantages of  $\beta$ -solidification when alloyed with silicon** The last point which should be emphasized deals with the advantages of  $\beta$ -solidification when silicon is added. Indeed, by referring once again to the physical metallurgy of conventional titanium alloys [10], one can understand that the  $\beta$  phase

exhibits a stronger affinity with Si in comparison with the  $\alpha$  phase. This suggests that the tendency to interdendritic segregation of Si, consequently formation of primary silicides, during casting is less strong for  $\beta$ -solidification alloys than for  $\alpha$ -solidification alloys. Although no detailed investigation has yet been made about the influence of the presence of primary silicides on mechanical behavior of gamma alloys, it is quite reasonable to assume a detrimental effect on their damage tolerance. Further investigation is therefore necessary to identify the minimum Si content for obtaining silicide-free alloys with a good creep resistance. A first step of such an investigation is now underway in order to determine the solubility of Si in each of the three constituent phases :  $\gamma$ ,  $\alpha_2$  and  $\beta$  (or B2).

#### Concluding remarks

In this paper, we have reported a novel approach for developing new cast gamma titanium aluminide alloys. Several remarks can be made regarding the above approach both in terms of present achievement and future research directions:

- The basic idea for identification of the new alloys has been to promote the solidification path through  $\beta$  (b.c.c.) instead of that through  $\alpha$  (h.c.p.). The  $\beta$ -solidification leads to a sort of "crystal partitioning" effect because of the possibility of producing numerous orientation variants (laths' colonies) during  $\beta \Rightarrow \alpha$  transition during cooling after solidification.
- Since residual  $\beta$  (or B2) phase should be minimized from the in-service mechanical properties' viewpoint due to its possibly harmful decomposition, it is very important to get a deeper understanding on the field of existence of the  $\beta$  (or B2) phase both in the chemical composition and in the temperature within corresponding phase diagrams. In this context, the work recently conducted by some research groups [e.g., 17, 18] is certainly very useful.
- Further improvement may be expected for  $\beta$ -solidification alloys both through a more accurate and suitable adjustment of

chemical compositions and by optimization of post-cast heat treatments. One of the targets of our work now underway is to obtain a creep strength of more than 1000 hours for 0.5% elongation under 200MPa at 750°C together with a room-temperature ductility of at least 1.5%. It is also important to minimize the scattering of test data for these properties.

- It is worth emphasizing once again that the role of Si in creep should be elucidated in detail, since its strengthening effect is quite remarkable. For doing so, examination of the solubility of Si in various gamma alloys seems to be essential.

- As far as first and second generation alloys solidifying through  $\alpha$  such as the GE alloy are concerned, these alloys should be considered, in our opinion, as more appropriate for wrought alloy applications. The use of prealloyed powder metallurgy route should also be taken into account in order to reduce the texture effect.

- Finally, we hope that the present work significantly contributes to the establishment of a stronger and sound physical metallurgy base for gamma alloys, which will help identify reliable manufacturing routes and enable the use of these materials in the aerospace industry.

#### Acknowledgments

This work was conducted with a financial support of the French Ministry of Defense (DGA). The authors express our sincere thanks to Mr. P. Chéreau, an officer of the DGA, for his constant encouragement to our work. We are also grateful to Dr. A. Menand and Dr. A. Nérac-Partaix of Rouen University as well as Dr. R. Penelle, Dr. T. Baudin and Mrs. M.L. Dupont-Hosotte of Orsay University for allowing us to communicate in this paper their most recent results of our collaborative investigations. Thanks are also addressed to Dr. P. Thévenin, Mr. G. Marcon, Mrs. A. Bachelier-Locq, Mr. C. Verstraete, Mr. T. Renaud and Mr. D. Jacob for their helpful contribution.

#### References

1. S.C. Huang, D.W. McKee, D.S. Shih and J.C. Chesnutt, "TiAl Alloys Containing Cr and Nb", Intermetallic Compounds: Structure and Mechanical Properties, ed. O. Izumi (Sendai, Japan: The Japan Institute of Metals, 1991) 363-370.
2. C.M. Austin and T.J. Kelly, "Development and Implementation Status of Cast Gamma Titanium Aluminide", 1st ISSI: Structural Intermetallics, ed. R. Darolia, J.J. Lewandowski, C.T. Liu, P.L. Martin, D.B. Miracle and M.V. Nathal (Warrendale, Pennsylvania, U.S.A.: TMS, 1993) 143-150.
3. Y.W. Kim, "Ordered Intermetallic Alloys, Part III: Gamma Titanium Aluminides", JOM, 46 (7) (1994) 30-40.
4. S. Naka, "Advanced Titanium-Based Alloys", Current Opinion in Solid State & Materials Science, 1 (1996) 333-339.
5. Y.W. Kim and D.M. Dimiduk, "Progress in the Understanding of Gamma Titanium Aluminides", JOM, 43 (8) (1991) 40-47.
6. A. Menand and A. Nérac-Partaix, "Atom-Probe Analysis of TiAl Alloys", Extended abstract of the paper presented in International Symposium on Titanium Aluminides and Other Intermetallic Compounds, (Fall meeting of the French Society of Metallurgy and Materials, October 1996) 83.
7. C. McCullough, J.J. Valencia, C.G. Levi and R. Mehrabian, "Phase Equilibria and Solidification in Ti-Al Alloys", Acta Metall., 37 (1989) 1321-1336.
8. S. Yokoshima and M. Yamaguchi, "Fracture Behavior and Toughness of PST Crystals of TiAl", Acta Mater., 44 (1996) 873-883.
9. M.L. Dupont-Hosotte, T. Baudin, R. Penelle, S. Naka and M. Thomas, "Texture Analysis of TiAl Based Alloys", Extended abstract of the paper presented in International Symposium on Titanium Aluminides and Other Intermetallic Compounds, (Fall meeting of the French Society of Metallurgy and Materials, October 1996) 96.
10. I.J. Polmear, "Titanium Alloys", Light Alloys: Metallurgy of the Light Metals, ed. I.J. Polmear (London, U.K.: Edward Arnold, 1981) 162-209.
11. S. Naka, M. Thomas, M. Marty, G. Lapasset and T. Khan, "Complex B2 Aluminides of Refractory Metals: an Attempt to Explore Novel Alloy Systems", 1st ISSI: Structural Intermetallics, ed. R. Darolia, J.J. Lewandowski, C.T. Liu, P.L. Martin, D.B. Miracle and M.V. Nathal (Warrendale, Pennsylvania, U.S.A.: TMS, 1993) 647-656.
12. L.A. Bendersky, W.J. Boettinger, B.P. Burton, F.S. Biancaniello and C.B. Shoemaker, "The Formation of Ordered  $\omega$ -related Phases in Alloys of Composition  $Ti_4Al_3Nb$ ", Acta Metall. Mater., 38 (1990) 931-943.
13. S. Ankem and S.R. Seagle, "The Detrimental Effects of Iron on Creep of Ti-6242S Alloys" Titanium: Science and Technology, ed. G. Lütjering, U. Zwicker and W. Bunk (Oberursel, Germany: Deutsche Gesellschaft für Metallkunde, 1985) 2411-2418.
14. Y.G. Nakagawa, K. Matsuda, S. Masaki, R. Imamura and M. Arai, "Analysis of Cast TiAl Properties for Engine Materials", Gamma Titanium Aluminides, ed. Y.W. Kim, R. Wagner and M. Yamaguchi Warrendale, Pennsylvania, U.S.A.: TMS, 1995) 415-424.
15. T. Noda, M. Okabe, S. Isobe and M. Sayashi, "Silicide precipitation Strengthened TiAl", Mater. Sci. Eng., A192/193 (1995) 774-779.
16. M. Thomas, A. Morel and S. Naka, "Study of Creep in Intermetallic Alloys Based on TiAl" (Report ONERA N°19/3728MY (in French), ONERA, 1995).
17. K. Hashimoto and M. Kimura, "Effects of Third Element Additions on Mechanical Properties of TiAl", 1st ISSI: Structural Intermetallics, ed. R. Darolia, J.J. Lewandowski, C.T. Liu, P.L. Martin, D.B. Miracle and M.V. Nathal (Warrendale, Pennsylvania, U.S.A.: TMS, 1993) 309-318.
18. M. Takeyama and M. Kikuchi, "Phase Equilibria and Microstructure Evolution of Gamma Titanium Aluminides: Effect of Third Alloying Element on Binary Ti-Al alloys", Bulletin Japan Inst. Met. (in Japanese), 35 (1996) 1058-1064.

## DIFFUSION BRAZING OF A Ti-45Al-2Nb-2Mn+0.8vol.%TiB<sub>2</sub> XD ALLOY

Q. Xu, M. C. Chaturvedi, N. L. Richards\* and N. Goel\*

*Department of Mechanical and Industrial Engineering,  
The University of Manitoba, Winnipeg, Manitoba, Canada R3T 2N2  
\* Bristol Aerospace Limited, Winnipeg, Manitoba, Canada*

### Abstract

The feasibility of using diffusion brazing to join a Ti-45Al-2Nb-2Mn+0.8vol.%TiB<sub>2</sub> alloy to itself and to a Ti-6Al-4V alloy has been assessed. Suitable filler alloys for diffusion brazing of the TiAl based alloy have been found and the optimum brazing conditions have been established. It has been observed that a large number of intermetallic particles, which are hard and brittle, are formed in the as-brazed TiAl/TiAl joint. In order to eliminate these intermetallic particles, a prolonged homogenization treatment is required. A further post-brazing heat treatment is also needed to obtain a desired microstructure in the joint. Evaluation of mechanical properties has demonstrated that the bend strength of the joint is comparable to that of the base material. The Ti-45Al-2Nb-2Mn+0.8vol.%TiB<sub>2</sub> alloy has also been successfully joined to a Ti-6Al-4V alloy by diffusion brazing with a Cu-Ni transient liquid phase filler alloy.

### Introduction

TiAl alloys have a great potential for high temperature applications in aerospace and automotive fields because of their high strength, low density, high modulus, good resistance to creep and high-temperature oxidation [1 - 3]. There has been a significant progress in developing these alloys, in particular in addressing the vital problem of low-temperature ductility, and the alloys have matured to a level that designers can incorporate them into complex structures [2, 3]. Therefore, the ability of joining these alloys to themselves and to other materials is the key to making them industrially more attractive.

Joining of TiAl alloys by fusion welding processes and linear friction welding presents some difficulties [4, 5] and it has been consistently noted that very careful control of the process is needed to avoid cracking. It is believed [4, 5] that the low ductility of the alloys, combined with high residual welding stresses and rapid cooling rate is the main cause of cracking that occurred during autogenous fusion welding. Processing which does not impose severe stresses on the weld, such as diffusion bonding and brazing, is likely to prove less problematic. It has been well demonstrated that diffusion bonding can be successfully used to join these materials [5 - 8], but as yet little is known about brazing of these alloys. Blue et al. [9] studied reaction between a Ti-48at.%Al alloy and a Ti-15Cu-15Ni (wt.%) alloy and microstructural evolution of the reaction

zone during infrared processing. The results provided useful microstructural information for joining TiAl based alloys. Yan and Wallach [6] reported that joints with good properties were obtained in a Ti-48at.%Al alloy using a Ti-Cu or a Ti-Ni filler alloy.

This paper reviews current work on the diffusion brazing of a Ti-45at.%Al-2at.%Nb-2at.%Mn+0.8vol.%TiB<sub>2</sub> XD alloy, in particular, reports the microstructural evolution during diffusion brazing and post-brazing heat treatment. Suitable filler alloys and brazing conditions for joining the TiAl alloy to itself and to a Ti-6Al-4V alloy have been established.

### Experimental

#### Materials and Filler Alloys

The Ti-45Al-2Nb-2Mn+0.8vol.%TiB<sub>2</sub> alloy was made by XD process and hot isostatic pressed at 1250°C/172MPa/4hrs by Howmet Corporation. The microstructure of the as-received alloy is fully lamellar with TiB<sub>2</sub> particles dispersed in the lamellar matrix, as shown in Figure 1. No specific orientation relationship was observed between the TiB<sub>2</sub> particles and the lamellar structure. The filler alloys used in this research were a Ti-15wt.%Cu-15wt.%Ni alloy, a Cu-Ni transient liquid phase (TLP) alloy and the Cu-Ni alloy/Ti foil/Cu-Ni alloy. All the filler alloys were in a form of thin foil and in one case the Ti-Cu-Ni alloy was also sputter-coated on the surfaces of samples to be joined.



Figure 1 (To be continued on next page)

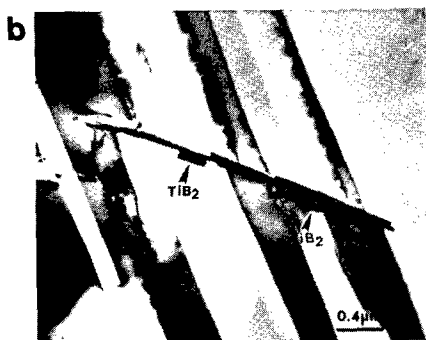


Figure 1 (a) SEM backscattered electron (BSE) image showing fine-grained fully lamellar structure of a Ti-45Al-2Nb-2Mn+0.8vol.%TiB<sub>2</sub> XD alloy; (b) TEM bright field image illustrating TiB<sub>2</sub> particles in the lamellar matrix.

#### Sample Preparation and Joint Fabrication

Samples with a faying surface area of 15×25 mm were cut by a diamond wheel from plates of the Ti-45Al-2Nb-2Mn+0.8TiB<sub>2</sub> alloy and mechanically grounded with emery paper of up to Grit No. 600. The surfaces of samples to be sputter-coated with the Ti-Cu-Ni alloy were further polished with 6 μm diamond polishing compound and finally cleaned by degreasing in acetone in an ultrasonic bath. The brazing was performed in a furnace with a vacuum of 10<sup>-4</sup> Torr or better. The samples and brazing filler metals, which were assembled with a little pressure to the assembly, were heated to temperatures ranging from 990°C to 1100°C at a rate of 2°C/minute and were held at the brazing temperatures for 5 ~ 30 minutes. They were cooled to 540°C at a rate of 2 ~ 10°C/minute and subsequently argon quenched. The as-brazed samples were subsequently homogenized at temperatures ranging from 1000 to 1100°C for two days to one week, and then further heat treated at 1310°C for 30 minutes followed by controlled cooling.

#### Microstructural Characterization of Joints

Samples, both as-brazed and post-brazing heat treated, were cut by a spark machine. Cross-sections of the samples were examined with an optical microscope and a JEOL 840 scanning transmission microscope. Chemical analysis was performed by energy dispersive X-ray spectrometry (EDS). The thin foils for transmission electron microscopy (TEM) examination were prepared either by ion milling or by electrochemical polishing. The microstructures in the joints were intensively investigated by a JEOL-2000 FX transmission electron microscope operating at an accelerating voltage of 200kV.

#### Mechanical Property Testing of Joints

Microhardness profiles of the joints were determined by a microhardness tester. Specimens of 3×5×35 (mm) for bend testing were spark cut from the brazed samples. The bend strength of joints was evaluated on an Instron using three point bending with a spacing of 25.4 mm at a displacement rate of 0.5 mm/minute at room temperature.

### Results and Discussion

#### Filler Alloys

Possible filler alloys to be used for diffusion brazing of the TiAl based alloys were selected by the consideration of two critical aspects: (1) a liquid filler alloy must form and become active in the joint area and (2) extensive diffusion of filler alloy elements into the base TiAl alloys must occur. In addition, filler alloys being chosen should have melting points lower than 1125°C because the TiAl alloy will undergo an eutectoid reaction at this temperature. A variety of filler alloys were tested in this research and performance of some of them is presented below.

Figure 2 (a) shows a cross-section of a sample brazed with 50μm thick Ti-Cu-Ni filler alloy at 990°C for 10 minutes and Figure 2 (b) gives more details in the joint. A large reaction zone was observed and the solidified melt contained essentially no porosity. It appears that the brazed sample exhibits excellent wetting between the Ti-Cu-Ni alloy and the base TiAl alloy, as observed by Blue et al. [9]. The EDS analysis, which is summarised in Table 1, demonstrates that extensive diffusion between the filler metal and the base TiAl alloy took place. As seen in Figure 2, a large bright zone formed in the solidified melt. It will be shown in the following section that this zone is very hard and brittle, and should, therefore, be eliminated. Figure 3 shows a cross section of as-brazed sample which is fabricated with 25μm thick Ti-Cu-Ni filler alloy at 1050°C for 30 minutes. It was observed that the thinner filler alloy, a higher brazing temperature and a longer holding time significantly reduced the size and volume fraction of the bright zone.

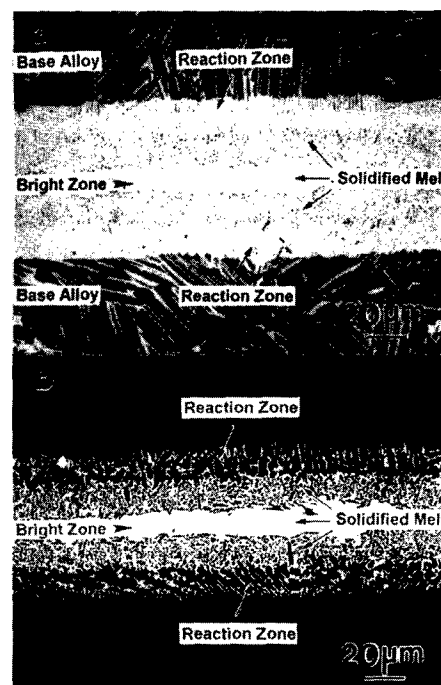


Figure 2 SEM backscattered electron (BSE) images (a, b) showing excellent wetting between the Ti-Cu-Ni filler alloy (50 μm thick) and Ti-45Al-2Nb-2Mn+0.8vol.%TiB<sub>2</sub> XD alloy (Brazed at 990°C for 10 minutes).

Table 1 EDS analysis of a Ti-45Al-2Nb-2Mn+0.8TiB<sub>2</sub> sample brazed at 990°C for 10 minutes with a 50μm thick Ti-Cu-Ni filler alloy (in unit of at.%).

	Ti	Al	Cu	Ni	Nb	Mn
BZ in SM	52.3	17.8	12.1	16.5	0.5	0.8
SM (G)	66.2	18.4	7.3	6.3	0.8	1.0
RZ	64.1	25.4	4.0	3.6	1.8	1.1
Base metal	51.3	44.7	---	---	2.0	2.0

Note: BZ - Bright zone; SM - Solidified melt; SM (G) - Solidified melt excluding the BZ; RZ - Reaction zone.

It was found that the Cu-Ni TLP alloy is not a suitable filler material for joining the TiAl alloy to itself. As-brazed samples fell apart during spark-cutting. Figure 4 provides images of cross-section of the failed sample brazed at 990°C for 30 minutes. It appears that extensive diffusion between the Cu-Ni TLP alloy and the TiAl alloy did not occur.



Figure 3 Optical micrograph (a) and SEM BSE image (b), showing a sample brazed at 1050°C for 30 minutes using 25 μm thick Ti-Cu-Ni filler alloy.

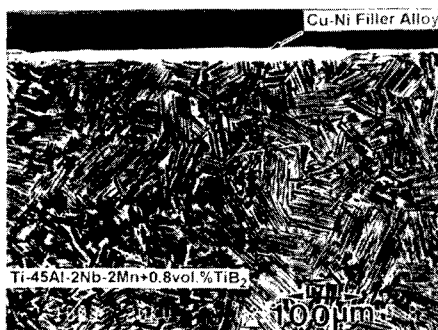


Figure 4 SEM BSE image showing poor wetting between the Cu-Ni TLP filler alloy and the Ti-45Al-2Nb-2Mn+0.8TiB<sub>2</sub> XD alloy (Brazed at 990°C for 30 minutes).

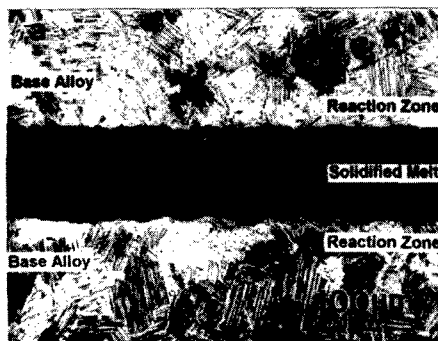


Figure 5 (To be continued)

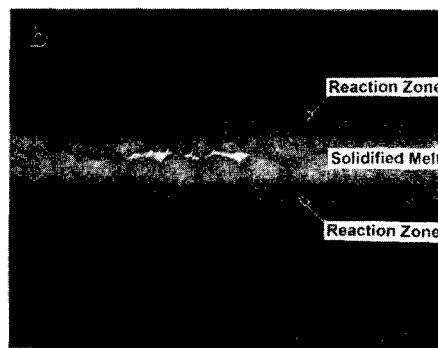


Figure 5 Optical micrograph (a) and SEM BSE image (b), showing excellent wetting between a combined filler material of the Cu-Ni alloy/Ti foil/Cu-Ni alloy and the Ti-45Al-2Nb-2Mn+0.8TiB<sub>2</sub> XD alloy (Brazed at 990°C for 30 minutes).

However, the combined filler metal of the Cu-Ni TLP alloy and Ti foils in the form of Cu-Ni alloy/Ti foil/Cu-Ni alloy led to an excellent wetting between the filler metal and the base alloy as shown in Figure 5. It was observed to act in the same fashion as the Ti-Cu-Ni alloy.

It has been well established [10] that Ti and Al atoms in excess of stoichiometric composition of titanium aluminides occupy antisites without creating vacancies, i.e., Ti atoms can readily be accommodated on Al sites and vice versa. Since Ti atoms have a strong affinity to Cu and Ni atoms, the Cu and Ni atoms can readily diffuse into the base alloy together with Ti atoms and occupy antisites in the TiAl alloy. The excellent wetting between the Ti-Cu-Ni alloy and TiAl alloy was thus observed. But because of the low solubility of Cu and Ni in titanium aluminides and since no extra Ti atoms are available in the TiAl alloy to react with Cu or Ni, a poor wetting between the Cu-Ni alloy and the TiAl alloy would be expected. Nevertheless, when the Cu-Ni alloy, along with Ti foil, is used as a filler material, they react first with each other and thus, cause an excellent wetting between the filler material and the base TiAl alloy.

#### Microstructural Evolution During Diffusion Brazing

Because of the similarity of the Ti-Cu-Ni and the Cu-Ni /Ti/Cu-Ni filler alloys, the diffusion brazing with the Ti-Cu-Ni filler alloy will mainly be presented in the following sections. The microstructures of the sample brazed with the Ti-Cu-Ni filler alloy was investigated in detail by cross-sectional TEM. It was found that "A" in the solidified melt (Figure 3b) is mainly composed of α<sub>2</sub> phase (C) dispersed with a large number of intermetallic particles (D), as shown in Figure 6. Figure 7 is a bright field TEM image of bright zone "B" in the solidified melt (Figure 3b), and it



Figure 6 TEM bright field image to show microstructure of region A in the solidified melt observed in Figure 3.

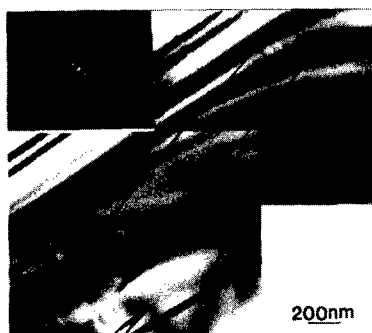


Figure 7 TEM bright field image of region B in the solidified melt observed in Figure 3.

was found that this phase has the same structure as the intermetallic particles (D). Figure 8 provides selected area diffraction (SAD) patterns and convergent beam electron diffraction (CBED) patterns of  $[0001]$  and  $[11\bar{2}0]$  zones taken from C. The  $[0001]$  and  $[11\bar{2}0]$  zones show 6mm and 2mm symmetry, respectively. Further examination of diffraction patterns has confirmed that C is  $\alpha_2$  phase. The intermetallic particles have been identified by CBED and SAD patterns to have an mmm point group. SAD and CBED patterns of the  $[001]$  and  $[100]$  zones are shown in Figure 9, revealing 2mm symmetry along both zones and  $a \neq b \neq c$ . No effort was made to determine the space group of these intermetallic particles.

#### Mechanical Properties of As-Brazed Samples

Figure 10 shows a microhardness traverse across the joint brazed with 50  $\mu\text{m}$  thick Ti-Cu-Ni filler alloy at 990°C for 10 minutes. An increase in joint centre was apparently associated with the bright zone in the

hardness was observed in the solidified melt, and the peak hardness at the solidified melt, indicating that this intermetallic phase is very hard and brittle. Bend strength of the joint was measured to be only about 100 MPa as compared to about 680 MPa of the base material. Cross sectional examination of the fractured brazement demonstrated that the brazement failed along the interface between the reaction zone and the solidified melt and cracks initiated in the bright zone, as shown in Figure 11. Even if the bright zone in the solidified melt was largely removed by reducing the thickness of the filler alloy, increasing the brazing temperature and the holding time, the as-brazed sample did not exhibit much improvement in bend strength. It is thus concluded that post-brazing heat treatment is required to remove the intermetallic phase from the joint.

#### Post-Brazing Heat Treatments

The intermetallic particles can dissolve into the base material by a post-brazing homogenization as a result of an extensive dissolution of base material, which, in turn, would dilute both Ni and Cu in the melt, and diffusion of Ti, Ni and Cu into the undissolved TiAl alloy [9]. It was found [6] that homogenization at temperatures at 1200°C or above resulted in remelting of the intermetallic particles and consequently the formation of many voids in the joint, probably due to volume contraction on solidification and loss of materials by dissolution and diffusion into the TiAl alloy. However, homogenization at an inappropriately low temperature would not be effective in removing the intermetallic phase which is formed during brazing. Therefore, it was decided to conduct the post-brazing homogenization treatment between 1000°C and 1200°C for an extended period of time. Figure 12 shows optical micrographs of the joint after this post-brazing homogenization at 1020°C for one week. TEM examination of the joint revealed that the intermetallic phase formed during brazing was completely eliminated and the joint contained  $\gamma$ ,  $\alpha_2$  and a large number of disordered  $\alpha$  particles, as seen in Figure 13. Figure 14 is SAD and CBED patterns of the  $[0001]$  and  $[11\bar{2}0]$  zones of the particles, verifying that the particles are disordered  $\alpha$  phases.

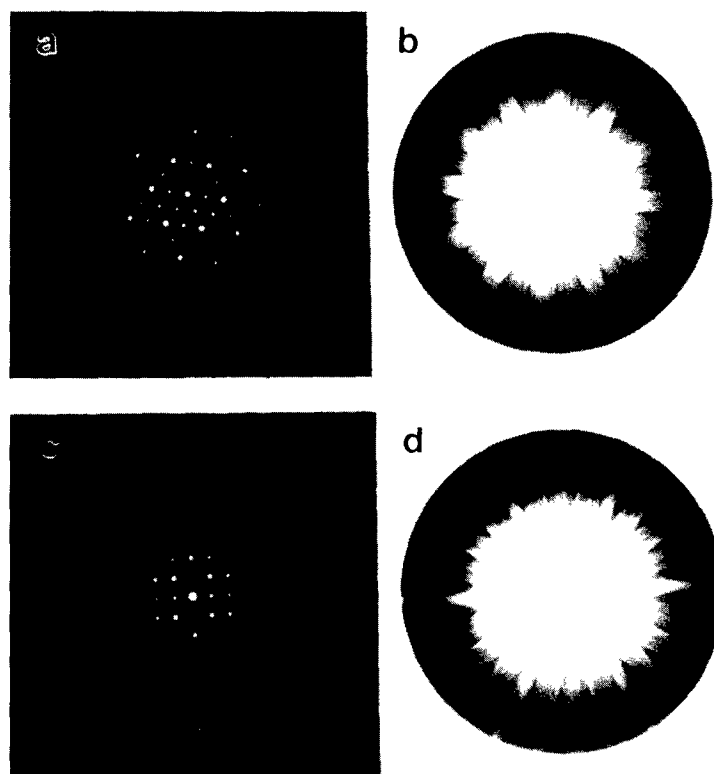


Figure 8 SAD and CBED patterns of the  $[0001]$  (a, b) and  $[11\bar{2}0]$  (c, d) zones taken from C in Figure 6, identifying that C is the  $\alpha_2$  phase.



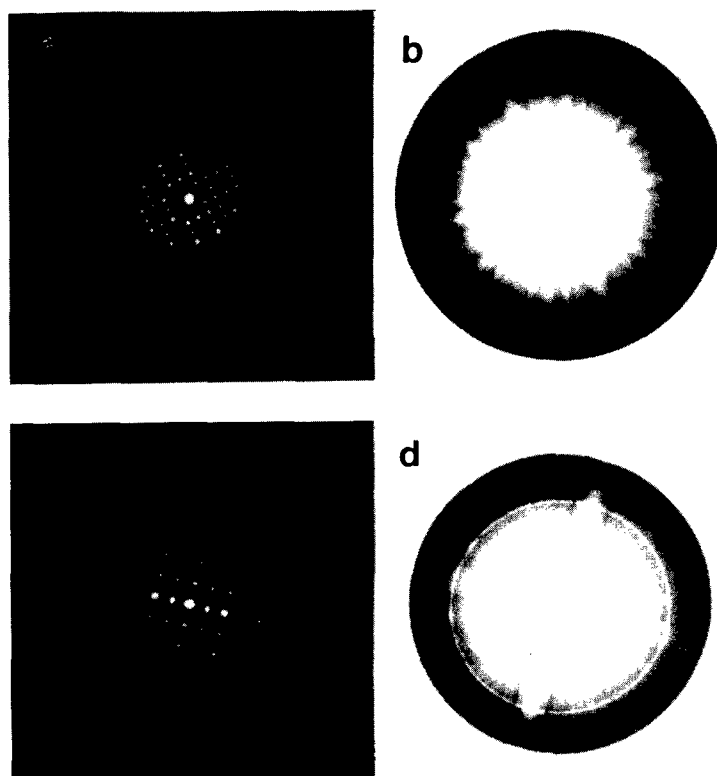


Figure 9 SAD and CBED patterns of the [001] (a, b) and [100] (c, d) zones taken from D in Figure 6, identifying that the particle is an intermetallic compound having an mmm point group.

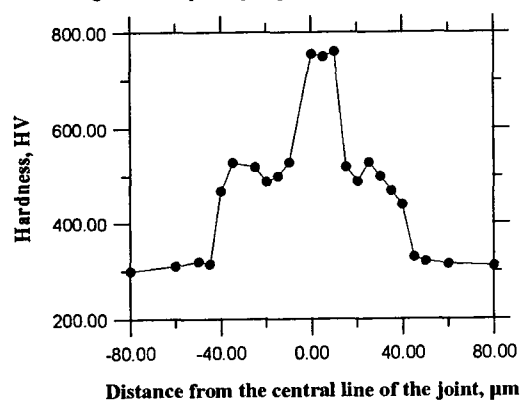


Figure 10 Hardness traverse across a joint shown in Figure 4.

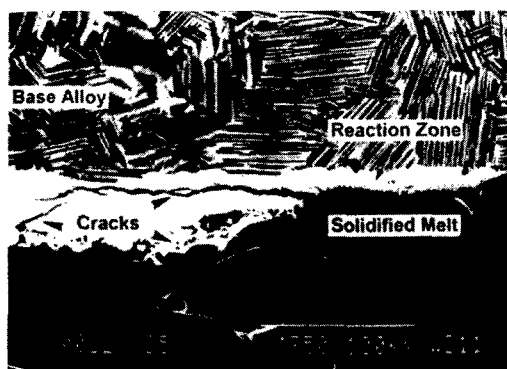


Figure 11 SEM BSE image showing a fractured sample brazed at 990°C for 30 minutes using 50  $\mu\text{m}$  thick Ti-Cu-Ni filler alloy.

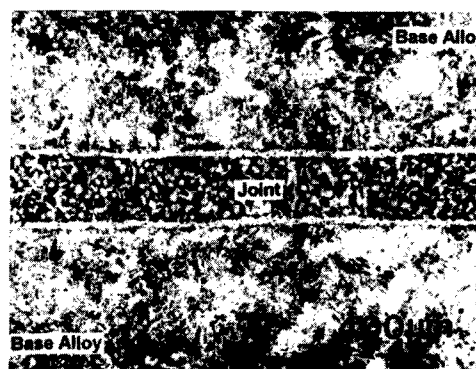


Figure 12 Optical micrographs of a brazed sample which was homogenized at 1020°C for one week.



Figure 13 TEM bright field image showing the microstructure in the homogenized joint.

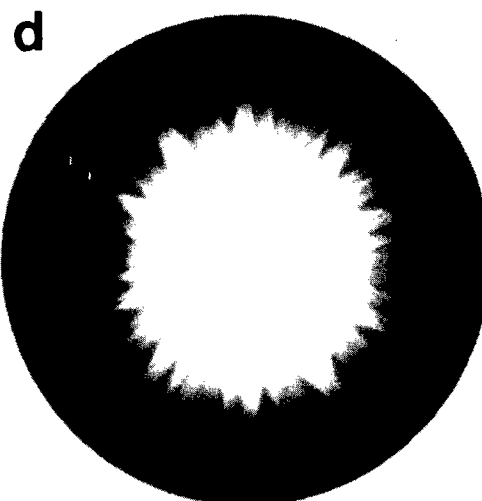
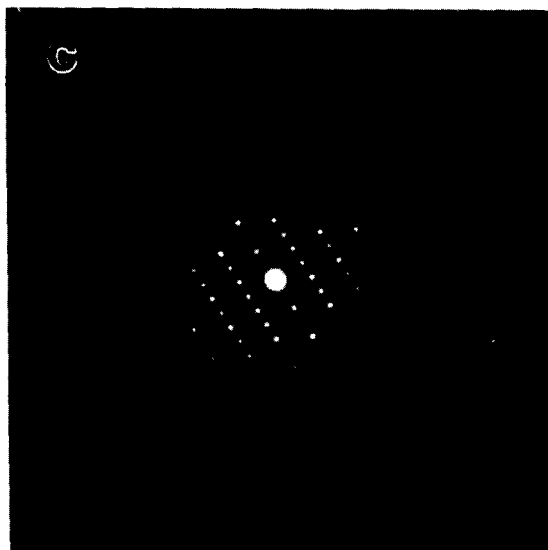
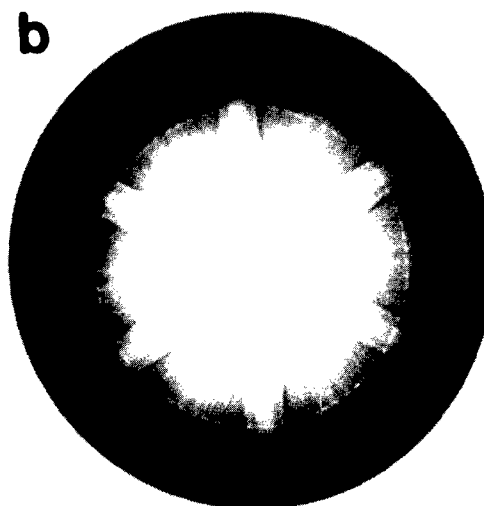
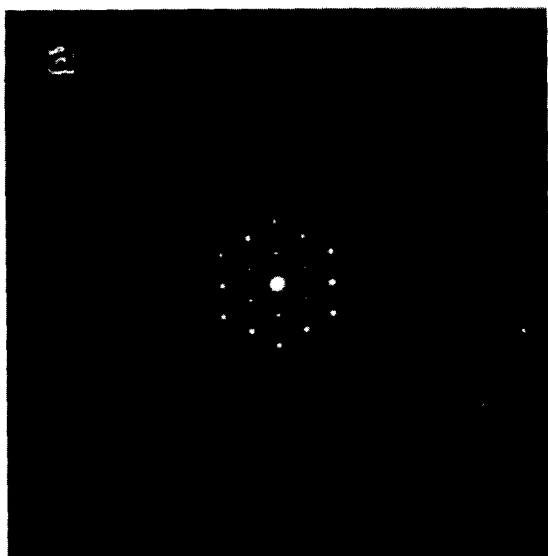


Figure 14 SAD and CBED patterns of the  $[0001]$  (a, b) and  $[11\bar{2}0]$  (c, d) zones taken from the particles in Figure 13, identifying the particles are disordered  $\alpha$  phases.

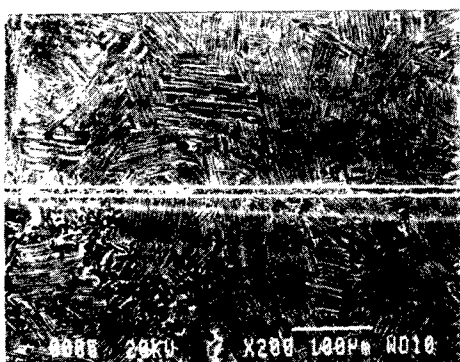


Figure 15 SEM BSE image of cross section of a joint brazed with sputter coated Ti-Cu-Ni filler alloy.

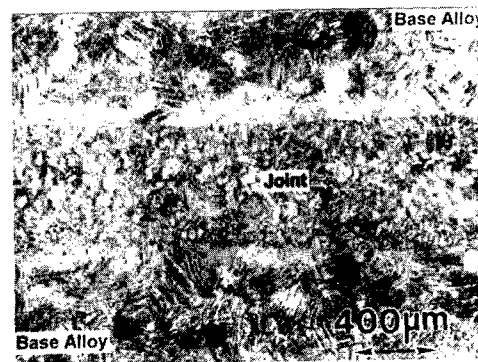


Figure 16 Optical micrographs of a brazed sample which was further heat treated at  $1310^{\circ}\text{C}$  for 30 minutes.

Obviously, the presence of disordered  $\alpha$  phases in the joint will adversely affect high temperature properties of the joint. Formation of the disordered  $\alpha$  particles should be attributed to the introduction of an excessive amount of Ti from the filler alloy. Therefore, it is evident that thickness of the filler alloy should be greatly reduced and the optimum thickness of the Ti-Cu-Ni filler alloy was estimated to be 5 ~ 10  $\mu\text{m}$ . In order to obtain such a thin filler layer, sputter coating technique was used to put the filler alloy on the faying surface of samples to be joined. Figure 15 shows a cross section of a joint brazed with sputter coated filler alloy.

A further heat treatment was also required to remove the disordered  $\alpha$  particles and produce a desired microstructure in the joints. The heat treatment scheme depended on the desired final microstructure. In this research the homogenized sample was heated to 1310°C for 30 minutes followed by slow cooling. Figure 16 shows a cross section image of the further heat treated sample.

#### Mechanical Properties of Joints After Post-Brazing Heat Treatments

Microhardness traverse across the heat-treated joint is shown in Figure 17. It is found that the microhardness is higher in the joint region than the base material and this should be attributed to solute strengthening by Cu and Ni. The bend testing showed a bend strength of 610 MPa, comparable to that of base material. Evaluation of ductility and high temperature properties of the joint is continuing. But it is anticipated that these properties would be adversely affected by presence of Cu, Ni and extra Ti in the joint introduced by the filler alloy.

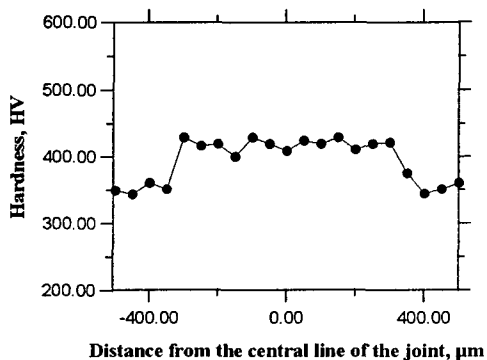


Figure 17 Microhardness traverse across the joint which has experienced homogenization at 1020°C for one week and further heat treated at 1310°C for 30 minutes.



Figure 18 Optical micrograph showing the feasibility of diffusion brazing to join the Ti-45Al-2Nb-2Mn+0.8TiB<sub>2</sub> XD alloy to a Ti-6Al-4V alloy by using the Cu-Ni TLP filler alloy.

#### Joining of the TiAl Alloy to a Ti Alloy

In some instances, the TiAl alloy may have to be joined to other materials. An effort was, therefore, made to join the Ti-45Al-2Nb-

2Mn+0.8vol.%TiB<sub>2</sub> XD alloy to a Ti-6Al-4V alloy by diffusion brazing. It was found that 10 $\mu\text{m}$  thick Cu-Ni TLP alloy is an ideal filler material for this purpose. An excellent joint of the  $\gamma$ -TiAl alloy with the Ti alloy was obtained by brazing them at 990°C for 10 ~ 30 minutes, as shown in Figure 18.

#### Conclusions

1. Ti-15wt.%Cu-15wt.%Ni alloy is a suitable filler material for brazing of a Ti-45Al-2Nb-2Mn+ 0.8vol.%TiB<sub>2</sub> XD alloy. The Cu-Ni transient liquid phase alloy alone can not be used as a filler material to braze the TiAl based alloy, but when combined with Ti foil, it works well as does the Ti-Cu-Ni alloy. The optimum thickness of the filler alloy is suggested to be 5 ~ 10  $\mu\text{m}$ .
2. The solidified melt of samples brazed with the Ti-Cu-Ni filler alloy was mainly composed of  $\alpha_2$  phases dispersed with intermetallic particles which were identified to have an mmm point group. The formation of the intermetallic particles was found to be detrimental to the joint properties.
3. It is suggested that the post-brazing heat treatment be conducted at 1000 ~ 1100°C for an extended time to dissolve the intermetallic phase formed during brazing. A large number of disordered  $\alpha$  particles were observed in the homogenized joint. A further heat treatment was also needed to remove the  $\alpha$  particles and to obtain a desired microstructure in the joint.
4. The Ti-45Al-2Nb-2Mn+0.8vol.%TiB<sub>2</sub> XD alloy can be successfully joined to a Ti-6Al-4V alloy by diffusion brazing with the Cu-Ni TLP filler metal.

#### Acknowledgments

The authors would like to thank the Consortium of Manitoba Aerospace Industries and Natural Science and Engineering Research Council of Canada for financial support. Q. Xu would like to thank the University of Manitoba for the award of a fellowship. They would like to acknowledge the technical assistance of Mr. Don Mardise and John Van Dorp. Thanks are also due to Howmet Corporation for providing the material.

#### References

1. H. A. Lipsitt, High temperature Ordered Intermetallic Alloys, MRS Symp. Proc., 39 (1985)351.
2. D. M. Dimiduk, Gamma Titanium Aluminides, Y. W. Kim, R. Wagner and M. Yamaguchi, eds., 1995, p. 3.
3. Y. W. Kim, JOM, 46, 7(1994)30.
4. R. A. Patterson, P. L. Martin, B. K. Damkroger and L. Christodoulou, Welding Journal, January 1990, 39s-44s.
5. P. L. Threadgill, Materials Science and Engineering, A192/193 (1995) 640.
6. P. Yan and E. R. Wallach, Intermetallics, 1(1993) 83.
7. Y. Nakao, K. Shinozake and M. Hamada, in International Trends in Welding Science and Technology, ed. S. A. David and J. M. Vitek, 1 - 5 June 1992, Gatlinburg, USA, p. 1057.
8. G. Çam, K. -H. Bohm, J. Müllauer and M. Koçak, JOM, (November 1996) 66.
9. C. A. Blue, R. A. Blue and R. Y. Lin, Scripta metall. mater., 32, 1(1995) 127.
10. R. P. Elliot and W. Rostoker, Acta metall., 2(1954)884.

## SPRAY PROCESSING AND MECHANICAL BEHAVIOR OF $\gamma$ -TiAl

B. Li and E.J. Lavernia

*Department of Chemical and Biochemical Engineering and Materials Science,  
University of California at Irvine, Irvine, California, 92697-2575, U.S.A*

### Abstract

Spray processing of gamma titanium aluminides had been investigated experimentally and numerically. Five different nominal compositions, including three monolithic alloys and two composites, had been successfully spray processed, either by spray forming or by spray forming+co-injection. The microstructure of spray formed Ti-47Al consisted of fine, equiaxed fully lamellar  $\alpha_2$ + $\gamma$  structures, with an average linear grain size of 60  $\mu\text{m}$  and an average interlamellar spacing of 0.3  $\mu\text{m}$ . These microstructural characteristics led to a higher creep resistance, in a temperature-stress regime of 780 to 850  $^{\circ}\text{C}$  and 180 to 320 MPa, relative to fully lamellar  $\gamma$ -TiAl obtained through conventional casting + heat treatment processes. The microstructure of the Ti-47Al/TiB<sub>2</sub> composite fabricated by spray forming+co-injection technique was characterized by fine grained, equiaxed fully lamellar structures, with an average linear grain size of approximately 40  $\mu\text{m}$ , and a volume percentage of TiB<sub>2</sub> of approximately 35%. The distribution of TiB<sub>2</sub> in the composite exhibited a layered morphology. Experimental observations on TiB<sub>2</sub> distribution in oversprayed powders as well as related numerical analysis revealed that this phenomenon originated from the segregation of TiB<sub>2</sub> particles to the exterior region of the droplets and the subsequent deformation of the droplets along the direction normal to the substrate during impingement. Numerical analysis on penetration also suggested that the most likely approach to improve the homogeneity of TiB<sub>2</sub> distribution in the deposit is to decrease the co-injector/atomizer distance. A two dimensional model of the momentum and thermal behavior of atomized droplets of  $\gamma$ -TiAl predicted that the two dimensional droplet size distribution in the spray cone changes from being heterogeneous to being almost homogeneous as axial flight distance increases. The modeling results also indicated that the two dimensional distribution of the fraction solidified in the spray cone is heterogeneous. The fraction solidified in the spray cone at any given axial distance increases with increasing radial distance from the spray axis.

### 1. Introduction

Due to their excellent combinations of density (3.76 g/cm<sup>3</sup>), creep/stress rupture and fatigue resistance, and elevated temperature strength [1, 2],  $\gamma$ -TiAl based intermetallic alloys, both monolithic [1-3] and composite [4-7], are being actively investigated as potential candidate materials for high temperature applications. It is also evident, however, that existing processing methods should be optimized and novel processing methods should be explored, before  $\gamma$ -TiAl can be successfully exploited as a structural material.

The present research efforts are aimed at using a novel synthesis approach, namely spray atomization and deposition, to eliminate macrosegregation and minimize microsegregation, to achieve grain refinement and compositional homogeneity, and to ultimately improve the mechanical properties of  $\gamma$ -TiAl. In spray atomization and deposition, a molten stream of metal is disintegrated into a fine dispersion of droplets using high velocity inert gas jets. The resulting semi-solidified droplets are directed towards a substrate where they impinge and collect as fine grained, chemically homogeneous, thin splats. The first high velocity droplets impact directly against the substrate surface, and then themselves act as a quenching substrate for their successors. Relatively high rates of solidification are imposed during processing as a result of the thinness of the

splats, and the rapid heat extraction during flight by the cold atomization gas. Spray atomization and deposition inherently avoids microstructural coarsening and extensive macrosegregation, which are normally associated with casting processes. To that effect it is documented that spray atomization and deposition has been successfully applied to improve the physical and mechanical characteristics of: Al and Mg alloys; Ni, Fe and Ni<sub>3</sub>Al intermetallics; and more recently, discontinuous metal matrix composites (MMCs) [8].

Spray forming of titanium aluminide alloys was attempted by several researchers [9-11], with preliminary results indicating that spray deposition processing may lead to low interstitial levels, low porosity, and fine grained structures. However, further research is required to detail the microstructural characteristics and the mechanical properties, and to establish the relationship between processing parameters and microstructure/mechanical properties during spray forming of titanium aluminide alloys. The objectives of this study were to spray process  $\gamma$ -TiAl alloys either by spray forming or by spray forming+co-injection, to characterize the microstructure of spray processed  $\gamma$ -TiAl, to investigate the creep behavior of spray formed  $\gamma$ -TiAl, and to explore the fundamental mechanisms associated with spray processing techniques using numerical analysis.

## 2. Experimental Procedures

Two closely related but distinct types of spray processing were employed in the present study: spray forming; and spray forming@co-injection. The induction skull melting/spray atomization and deposition facility utilized to spray process gamma TiAl alloys is schematically shown in Figure 1. The experimental procedure in spray forming may be described as follows. The skull crucible was charged with as-received  $\gamma$ -TiAl alloys. The cooling system in the skull crucible assured the formation of a  $\gamma$ -TiAl skull on the inside wall of the crucible when the molten Ti-Al alloys contact the cold crucible wall. The formation of the  $\gamma$ -TiAl skull prevented the reaction between the chemically reactive molten Ti-Al alloys and the crucible. Once the central part of the charge was completely melted, the skull crucible was tilted down, and Ti-Al melt was poured into a synchronously heated tundish. The Ti-Al melt was then delivered through a nozzle to an 18-jets atomizer, where it was atomized by high pressure Argon gas (dynamic atomization pressure ranges from 1 to 2 MPa). The atomized micro-sized droplets were subsequently deposited on a water cooled stationary planar Cu substrate.

The experimental procedure in spray forming@co-injection is very similar to that in spray forming, except that at certain distance below the atomizer, two injectors ejected ceramic particles into the spray cone. The ceramic particle penetrated into the monolithic droplets, forming composite droplets. The micro-sized composite droplets experienced cooling and solidification, and were finally collected on a water cooled substrate as a highly dense composite preform.

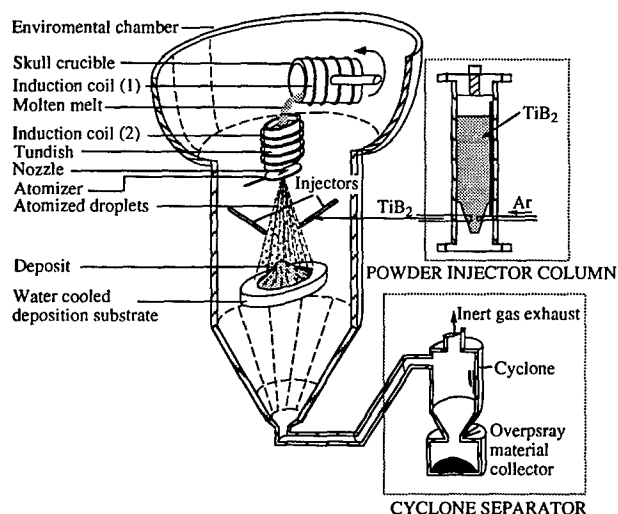


**Figure 1:** Schematic representation of the induction skull melting/spray forming and co-injection facility.

In either spray forming or spray forming@co-injection, powders not incorporated into the deposit, which are generally referred to as oversprayed powders, were carried by the gas flow into the cyclone and collected in the container attached to the cyclone. To prevent extensive oxidation of the materials during processing, all experiments were conducted in an environmental chamber, which was generally evacuated to a pressure of 133 Pa (1 torr) or lower, and back filled with argon gas to a pressure of  $1 \times 10^5$  Pa prior to melting and atomization.

Gamma titanium aluminides with five different alloy compositions were successfully spray formed as summarized in Table I. The spray formed  $\gamma$ -TiAl deposits generally exhibited Gaussian profiles, as shown in Figure 2 for a spray formed Ti-47Al. The thickness of the central region ranges from 10 to 15 mm depending on processing parameters, while the diameter of the bottom ranges from 10 to 15 cm.



**Figure 2:** Gaussian profile of spray formed Ti-47Al.

## 3. Monolithic Alloys

### 3.1. Microstructure Characterization

The spray formed Ti-47Al alloys generally exhibited fine, equiaxed fully lamellar  $\alpha_2 + \gamma$  structures. Figure 3 shows a typical microstructure of the spray formed Ti-47Al, with an average linear grain size of 60  $\mu\text{m}$  and an average interlamellar spacing about 0.3  $\mu\text{m}$ , in contrast with the coarse grains (which are normally 250 to 1800  $\mu\text{m}$  [1, 12], although grains as fine as 150  $\mu\text{m}$  were observed [13]) of  $\gamma$ -TiAl with fully lamellar microstructures which were produced from conventional cast or cast + heat treatment processes. This is important, since it has been reported that, for  $\gamma$ -TiAl with fully lamellar microstructures, a decrease in lamellar grain size increases both strength and ductility [1]. It is anticipated that a fully lamellar  $\gamma$ -TiAl with a fine grain size will lead to a good combination of ductility, strength, fracture toughness, and creep resistance.

**Table I.** Spray formed  $\gamma$ -TiAl alloys

Compositions (at.%)	Suppliers	Techniques
Ti-47.2Al Ti-46.9Al	The Duriron Company, Inc., Titanium Casting Operations, Dayton, OH	Spray forming
Ti-37.4Al-1.5Nb-1.5Cr	Dr. Don Larsen, Howmet Corporation, Operhall Research Center, Whitehall, MI	Spray forming
Ti-42.0Al-2.0Nb-2.0Cr	Dr. Shyh-Chin Huang, General Electric Research and Development Center, Schenectady, NY	Spray forming
Ti-44.8Al-1.9Nb + 1.2wt.%TiB <sub>2</sub>	Dr. Don Larsen, Howmet Corporation, Operhall Research Center, Whitehall, MI	Spray forming
Ti-46.9Al/TiB <sub>2</sub>	TiAl: The Duriron Company Inc., Titanium Casting Operations, Dayton, OH TiB <sub>2</sub> : CERAC Inc., Milwaukee, WI	Spray forming and co-injection



**Figure 3:** Optical microstructure of spray formed Ti-47Al.

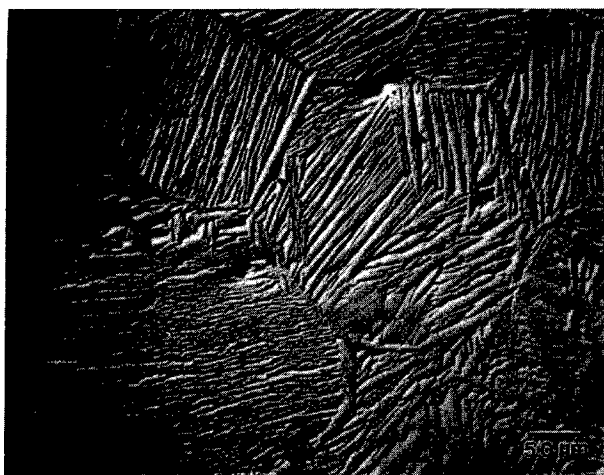


**Figure 4:** Optical microstructure of spray formed Ti-37.4Al-1.5Nb-1.5Cr.



**Figure 5:** Optical microstructure of spray formed Ti-37.4Al-1.5Nb-1.5Cr after heat treatment at 900 °C for 24 hours followed by air cooling

The spray formed Ti-37.4Al-1.5Nb-1.5Cr exhibited an equiaxed morphology, with an average linear grain size of approximately 142 μm, as shown in Figure 4. The acicular α phase precipitated from the elevated temperature β phase, forming a Widmanstatten structure. The grain refinement of Ti-37.4Al-1.5Nb-1.5Cr through spray forming processes is significant, since the grain size of the as-received material is larger than 1000 μm. Upon heat treatment (900 °C/24 hrs./air-cooling), the acicular α grains transformed into lamellar α₂+γ (Figure 5).

The spray formed Ti-42Al-2Nb-2Cr exhibited a fully lamellar α₂+γ microstructure, with an average grain size of approximately 130 μm (Figure 6). It is worth noting that, in each grain, there are several nearly parallel lines across the α₂+γ lamellae, as indicated by an arrow for one of the grains in Figure 6. Based on the results of heat treatment on spray formed Ti-37.4Al-1.5Nb-1.5Cr (Figure 5), it is believed that these lines are the traces of acicular α phase grain boundaries, i.e., lamellar α₂+γ were precipitated from the prior acicular α grains.

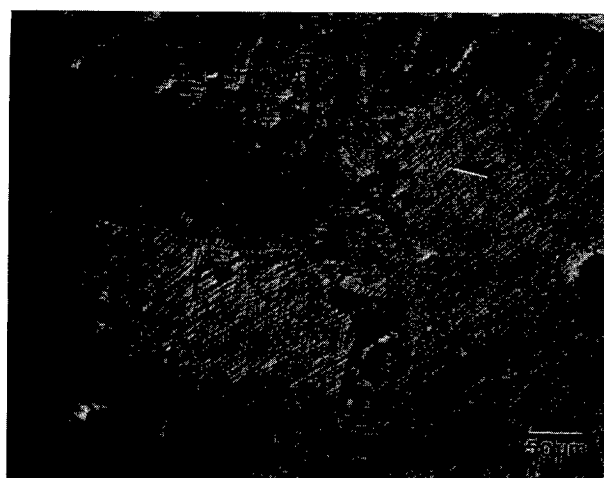


**Figure 6:** Optical microstructure of spray formed Ti-42Al-2Nb-2Cr.

### 3.2. Compressive Creep Behavior of Spray Formed Ti-47Al

The creep behavior of spray formed Ti-47Al with a fine, equiaxed fully lamellar microstructure was studied in a temperature-stress regime of 780 to 850 °C and 180 to 320 MPa, with the total strain ranging from 2 to 20 % as the temperature/stress increases. An apparent stress exponent of 4.3 and an activation energy of 342 kJ/mol were observed in the high-temperature high-stress regime. A stress exponent in the range from 4 to 5 suggests that the creep behavior is controlled by dislocation climb. This is further supported by the fact that the activation energy for creep (342 kJ/mol) is close to the activation energy for self-diffusion of Ti in single phase (γ) Ti-54Al (291 kJ/mol) [14]. The stress exponent and the activation energy for creep observed in the present study are close to those observed by several other authors [15-17], where the γ-TiAl materials with fully lamellar microstructures used in their study were fabricated from the conventional casting and heat treatment techniques. Using an average stress exponent obtained by different authors and an average activation energy, the creep data obtained by different authors were plotted in Figure 7. As evident from Figure 7, compared with the fully lamellar γ-TiAl which was obtained through conventional

casting + heat treatment processes [15-17], the spray formed  $\gamma$ -TiAl exhibited higher creep resistance. The fundamental mechanisms responsible for the higher creep resistance observed in the present study are still being explored.

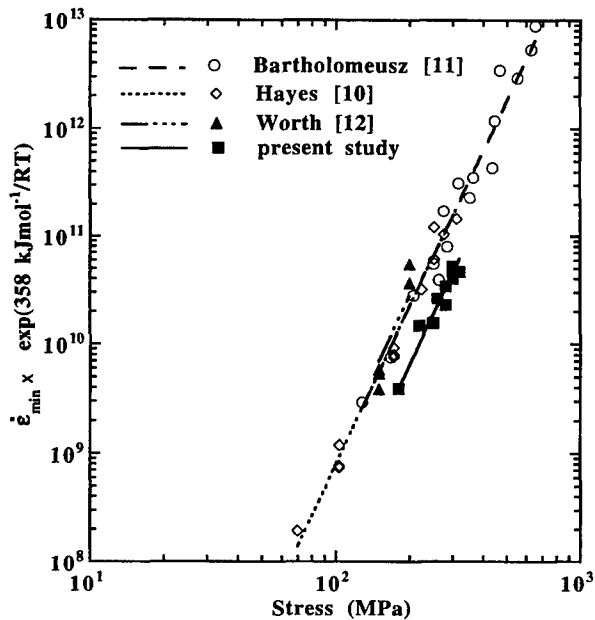


**Figure 7:** Comparison of temperature compensated minimum creep rates as a function of stress.

#### 4. Ti-47Al/TiB<sub>2</sub> Composite

##### 4.1. Characterization of Bulk Materials

The Ti-47Al/TiB<sub>2</sub> composite was fabricated by spray forming ⊕ co-injection technique. The volume fraction of reinforced TiB<sub>2</sub> particulate was determined by the Image Analysis to be approximately 35%. The porosity percentage in the spray formed composite was also evaluated from the metallographically polished/unetched specimens, with determined value of approximately 0.47 %. This is highly dense compared with the TiAl based particulate reinforced composites fabricated by other techniques, such as combustion reaction synthesis (~30% of pores) [18]. The distribution of TiB<sub>2</sub> in the reinforced region exhibited layered characteristic, as can be seen from Figures 8. Finally, the microstructure of spray formed TiAl/TiB<sub>2</sub> composite was characterized by fine grained equiaxed fully lamellar structures, with an average linear grain size of approximately 40  $\mu$ m.

In an effort to understand the layered characteristic observed in the deposit, experimental observation on TiB<sub>2</sub> distribution in the oversprayed powders, as well as related numerical analysis on the penetration of TiB<sub>2</sub> particles into liquid droplets at liquidus temperatures, were carried out.

##### 4.2. Oversprayed Powders

Since the spray forming ⊕ co-injection inherently involves interaction/penetration between the reinforcement particulates and the atomized droplets, knowledge on the distribution of TiB<sub>2</sub> in the oversprayed powders is of great significance in providing insight into the understanding of the fundamental

mechanisms for incorporation of reinforcement particulate into the metallic/intermetallic matrix during spray forming and co-injection.



**Figure 8:** Layered characteristic of TiB<sub>2</sub> distribution in the TiAl/TiB<sub>2</sub> composite bulk materials fabricated by spray forming ⊕ co-injection.

Three distinct cases of TiB<sub>2</sub> distribution in the oversprayed powders were observed: i). powders free of TiB<sub>2</sub>; ii). powders with exterior penetrated by TiB<sub>2</sub> and interior free of TiB<sub>2</sub> (Figure 9); and iii). powders with TiB<sub>2</sub> uniformly distributed in the exterior and interior of the droplets. Quantitatively, it was found that the presence of the first case (i.e., powders devoid of TiB<sub>2</sub>) decreases with increasing powder size range. In other words, the combined probability of presence of cases 2 and 3 increases with increasing size ranges. It was somewhat difficult, however, to separate quantitatively the effect of the powder size on the presence of case 2 from that of case 3. Qualitatively, there was no other distinctive general trend observed except that case 3 was much more frequently observed in all size ranges studied.

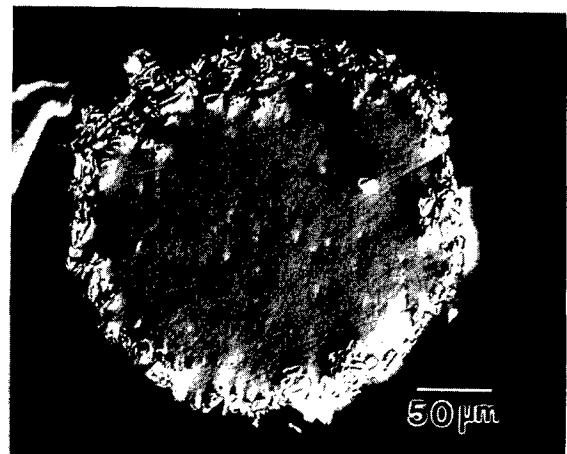


**Figure 9:** Oversprayed TiAl/TiB<sub>2</sub> composite powders with exterior region penetrated by TiB<sub>2</sub> and the interior free of TiB<sub>2</sub>.

##### 4.3. Numerical Analysis on Penetration

The incorporation of the reinforcements into the droplets, and the deformation of the droplets upon arrival onto the top

surface of the deposit, strongly depend on the velocity, temperature, and fraction of solid in the droplets. In the following sections, penetration of TiB<sub>2</sub> into liquid droplets at liquidus temperature was first numerically investigated. The effect of the actual thermal condition of various droplets at the penetration point were taken into account. Finally, the numerical results were correlated to the experimental observations.

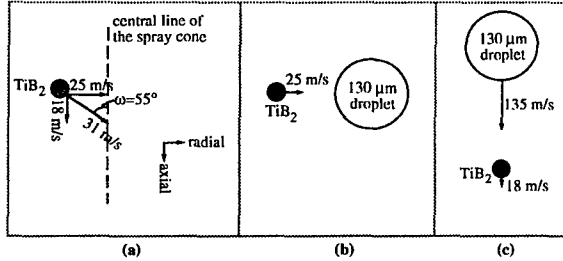


**Figure 10:** Schematic representation of the penetration direction of TiB<sub>2</sub> particle into Ti-47Al droplets: (a). decomposition of penetration direction; (b). radial penetration; (c). axial penetration (upwards).

#### 4.3.1. Penetration into a liquid droplets with $T=T_L$

In general, penetration of a ceramic particle into a moving liquid droplet involves the competition between, and finally the balance of, the driving and the resistance forces. The origin and accordingly the explicit forms of these forces, however, depend on the direction of penetration. In the present study, the penetration of the TiB<sub>2</sub> particles in Ti-47Al droplets is divided into two terms: radial penetration and axial penetration, as schematically illustrated in Figure 10. These two terms were evaluated individually in the following sections. It is worth noting that, in order to maintain the problem tractable, the geometry of the TiB<sub>2</sub> particles was assumed to be spherical in Figure 10 and the following sections.

##### (A). Radial penetration

As a one dimensional analysis, the velocity of the droplet in the radial direction was assumed to be zero. Accordingly, the driving force for penetration of a ceramic particle into a liquid droplet originates from its kinetic energy ( $E_k$ ) imparted by the co-injection gas, which is:

$$E_k = 0.5 \rho_p V_p (v_{pc} \sin \omega)^2 \quad (1)$$

where  $\rho_p$  is the density of the ceramic particle (TiB<sub>2</sub>),  $V_p$  is the volume of the particle, and  $v_{pc}$  is the velocity of the particle at the injector exit.

The resistance force for penetration are the surface energy change of the droplet caused by the interaction with the particle ( $\Delta E_s$ ), and the drag force exerted on the particle by the viscous melt in the droplet. The explicit form of  $\Delta E_s$  may be described as follows:

$$\Delta E_s = -A_p \sigma_m \cos \theta \quad (2)$$

where  $A_p$  is the surface of the particle,  $\sigma_m$  is the surface tension of the liquid droplet, and  $\theta$  is the wetting angle between TiB<sub>2</sub> and Ti-47Al. Due to the unavailability of the wetting angle between TiB<sub>2</sub> and Ti-47Al in the literature, two extreme cases were considered: no wetting ( $\theta=180^\circ$ ) and complete wetting ( $\theta=0^\circ$ ).

The penetration problem was evaluated through two closely related steps in the present study. First, the kinetic energy,

$E_k$ , was compared with the surface energy change,  $\Delta E_s$ . If  $E_k$  is smaller than  $\Delta E_s$ , which suggests that the kinetic energy of the particle is not large enough to circumvent the required surface energy changes, the penetration would be considered to be incomplete; and for simplicity, a penetration depth of zero would be assigned. If  $E_k$  is larger than  $\Delta E_s$ , the penetration would be considered to be complete. Its further penetration into the droplet, which is defined as the penetration depth, would be determined by taking into account the drag force exerted on the particle by the viscous melt in the droplet. With the drag force exerted on it, the particle would be decelerated to being stagnant in the droplet as follows:

$$\rho_p V_p \frac{dv_p}{dt} = -(A_p / 8) C_{drag} \rho_d v_p^2 \quad (3)$$

where  $v_p$  is the velocity of the particle in the droplet, and  $C_{drag}$  is the drag coefficient, which may be evaluated as [19]:

$$C_{drag} = \begin{cases} 24 / N_{Re} & 0 < N_{Re} < 1 \\ 24 / N_{Re}^{0.646} & 1 \leq N_{Re} < 400 \\ 0.5 & 400 \leq N_{Re} < 3 \times 10^5 \end{cases} \quad (4)$$

with the Reynolds number,  $N_{Re} = D_p \rho_d |v_p - v_d| / \mu_d$ , where  $D_p$  is the particle size,  $\mu_d$  is the Ti-47Al melt viscosity, and  $v_d$  is the droplet velocity. In the penetration problem, the droplet is a stagnant reference system; hence  $v_d$  is always zero in calculation of the Reynolds number,  $N_{Re}$ .

The initial condition in solving equation (3) is the velocity of the particle immediately following its completion of penetration,  $v_{p0}$ :

$$0.5 \rho_p V_p v_{p0}^2 = E_k - \Delta E_s \quad (5)$$

The penetration depth may be accordingly calculated as:

$$L = \int_{t=0}^{t=t_1} v_p dt \quad (6)$$

where  $t=0$  corresponds to the moment  $v_p = v_{p0}$ , and  $t_1$  the moment that  $v_p$  decayed to zero.

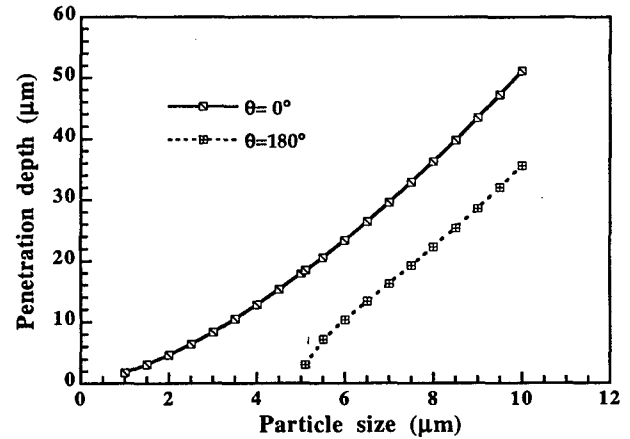


**Figure 11:** Calculated radial penetration depth as a function of the particle size for  $\theta=180^\circ$  and  $0^\circ$ .

Using equations (1)-(6), the radial penetration depth was calculated as a function of the particle size for the two extreme wetting behavior ( $\theta=0^\circ$  and  $180^\circ$ ), as summarized in Figure 11. An important result which may be inferred from Figure 11 is that, if the particles are penetrating coarse droplets, such as 333 and 500 μm droplets (their radii are 166.5 and 250 μm, respectively), the particles cannot reach the center of the droplets, since the maximum penetration depth in Figure 11 is 35.6 μm for a 10 μm particles when  $\theta=180^\circ$ . Noticing the fact



that the  $\text{TiB}_2$  particle size used in the present study is typically 10  $\mu\text{m}$  or less, segregation of particles to the exterior region of the droplets will occur in 333 and 500  $\mu\text{m}$  droplets. If the particles are penetrating fine droplets, such as 20, 54  $\mu\text{m}$  droplets (the radii are 10 and 27  $\mu\text{m}$ , respectively), most of the particles may reach the center of the droplets. It should be noted, however, the conclusions made here are only applicable for  $\text{TiB}_2$  particles penetrating liquid droplets at liquidus temperature. Whether it is the case still depends on the thermal condition of the droplets at the penetration point. Using the processing parameters used in the present study, the thermal behavior for the different droplets were calculated. The results indicated that at the penetration point, 20  $\mu\text{m}$  droplet is completely solidified; 130  $\mu\text{m}$  droplet partially solidified; and 54  $\mu\text{m}$  droplet in liquid state but highly undercooled. In an undercooled melt, the surface tension,  $\sigma_m$ , in equation (2), and the viscosity,  $\mu_d$ , in equation (4) are expected to increase dramatically [20, 21], making the penetration of a particle into droplets much more difficult. The presence of solid in the droplet would also increase the surface tension and the viscosity [22]. Moreover, presence of solid provides an additional resistance force for penetration: the strength of a solid. To that effect, it has been demonstrated that the penetration depth of a particle into a solid droplet is generally much less than the diameter of the particle, even though the penetration depth in the liquid droplet is more than ten times larger than the droplet diameter [23]. Although the analysis there [23] was somewhat simplified in the sense that it did not take into account the effect of temperature on the yield strength of the solid droplet, it did illustrate the difficulty encountered in penetrating a solid droplet compared with that in a liquid droplet.

#### (B). Axial penetration

The penetration problem in the axial direction may be addressed essentially the same way as that in the radial direction, except for some modifications on equation (1) and (3) as follows:

$$E_k = 0.5\rho_p V_p (v_{pe} \cos \omega - v_{dp})^2 \quad (1a)$$

and

$$\rho_p V_p \frac{dv_p}{dt} = -(A_p / 8) C_{drag} \rho_d v_p^2 - \rho_p V_p g + \rho_d V_p g \quad (3a)$$

where  $v_{dp}$  is the velocity of the droplet at the penetration point. Equation (1a) incorporated the fact that the droplets are moving along the axial direction; hence the kinetic energy contributing to the driving force of the particle penetration should be evaluated using the relative velocity between the droplet and the particle in the axial direction. Equation (3a) incorporated the effect of the gravitational force and the buoyant force. Since the velocities of the 20–500  $\mu\text{m}$  droplets are larger than the particle velocity in the axial direction at the penetration point, the penetration into all these droplets would be upwards. In this case, the gravitational force acts as a resistant force, while the buoyant force a driving force.

The droplet velocities at the penetration point for different droplet sizes were first calculated. Subsequently, the axial penetration depth as a function of the particle size was determined using equations (1a), (2), (3a), (4) and (5) with  $\theta=180^\circ$ . The axial penetration depth in a liquid droplet was found to be dependent on the droplet size, originating from the dependence of the relative velocity between particle and the droplet on the droplet velocity in the axial direction, which in turn is a function of the droplet size. In order to evaluate the

spatial distribution of the  $\text{TiB}_2$  particles in the droplets, the penetration depth was normalized by the droplet radius, as shown in Figure 12. As the droplet size increases from 20, 54 to 130  $\mu\text{m}$ , the minimum particle size required for it to penetrate into the center of the droplet increases from 1.6, 3.5 to 7.3  $\mu\text{m}$ . For 333 and 500  $\mu\text{m}$  droplets, particles with size not exceeding 10  $\mu\text{m}$  cannot reach the center of the droplets. The maximum penetration depth, which correspond to a 10  $\mu\text{m}$  particle size, are 40% and 20% of the droplet radii for 333 and 500  $\mu\text{m}$  droplets, respectively. The penetration depth for different particles with  $\theta=0^\circ$  were also calculated. However, since the surface energy changes are relatively small compared with the kinetic energy in the axial direction, the change of penetration depth resulting from the change of the wetting angle,  $\theta$ , from  $180^\circ$  to  $0^\circ$  were found to be negligible.

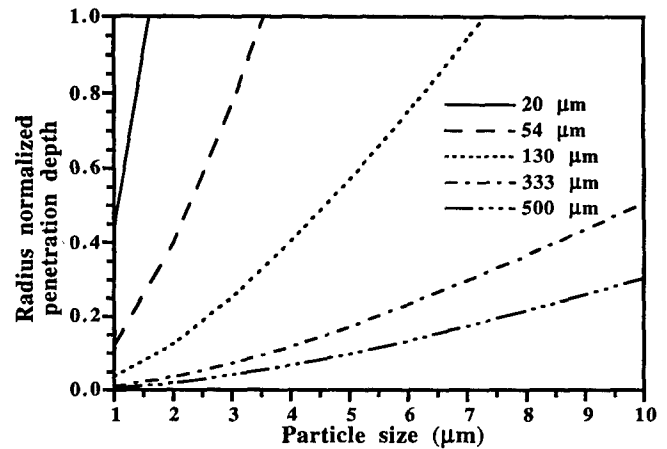


**Figure 12:** Calculated axial penetration depth (normalized by the radii of Ti-47Al droplets) as a function of the particle size when  $\theta=180^\circ$ .

#### 4.3.2. Correlation of the numerical results with the experimental observations

Figures 11 and 12 indicate that, for droplets in the liquid state with temperatures above the liquidus (333 and 500  $\mu\text{m}$ ), the  $\text{TiB}_2$  reinforcement particles are unable to reach the center of the droplets, since the droplets are coarse. This limits the  $\text{TiB}_2$  particles to the exterior region of the droplet. This is consistent with the experimental observations that a large proportion of  $\text{TiB}_2$  particles are segregated to the exterior regions of the droplets. However, the consistency of the numerical results with the experimental observations is limited to qualitative level in the sense that the experimentally observed segregated exterior regions in the droplets (15–20% of the droplet radius) are much less than the numerical results (~51% and 31% of the droplet radius for 333 and 500  $\mu\text{m}$  droplets, respectively). Numerical prediction of the penetration behavior may be improved by extending the entire problem from one dimension to two dimensions. Two dimensional modeling of the momentum exchange and heat transfer between the droplets and the atomization gas indicated that the fraction of solid in the spray cone at any axial distance increases from the center to the edge of the cone (see section 5), which will further limit the penetration of the particles into the center of the droplets.

The observed  $\text{TiB}_2$  particle segregation to the exterior region of the droplets may be associated with the layered structure

observed in the TiAl/TiB<sub>2</sub> composite bulk material. Numerical analysis on the solidification of droplets indicates that there are significant proportions of liquid phase in the 333 and 500  $\mu\text{m}$  droplets when they reach the substrate. This allows significant deformation of these droplets along the direction normal to the surface of the substrate, resulting in disc like splats in the deposit [24]. Under optical microscopy, the two dimensional nature of the metallographic technique will reveal these disc like splats as plates if the cross section of the specimen under examination is parallel to the axial direction (from the atomizer to the substrate), which is the case for Figure 8. Furthermore, if the exterior region of the droplets are decorated with the TiB<sub>2</sub> particles, as revealed from the numerical results and the observation of the oversprayed powders, the TiB<sub>2</sub> particles will be preferentially distributed along the direction parallel to the substrate surface, leading to the formation of layered structures.

In order to improve the homogeneity of the distribution of TiB<sub>2</sub> particles in the droplet and the deposit, the following methods may be considered in the order of priority:

i). Move the injector closer to the atomizer. This adjustment enables fine droplets to remain at higher temperature and contain more liquid at the penetration point, increasing the penetration depth of particles into fine droplets. As evident from Figures 11 and 12, when the fine (20, 54 and 130  $\mu\text{m}$ ) droplets are in liquid state with temperature above the liquidus, coarser (>5  $\mu\text{m}$ ) TiB<sub>2</sub> particles are able to reach the center of the droplets, improving the homogeneity of TiB<sub>2</sub> distribution in the droplet and consequently in the deposit.

ii). Increase the atomization pressure, which will increase the droplet velocity; hence increase the relative droplet/particle velocity, which in turn increases the particle penetration depth. Moreover, this adjustment will decrease the average droplet size, reducing the presence of coarse droplets. As has been discussed above, it is more difficult for a TiB<sub>2</sub> particle to reach the center of a coarse liquid droplet than a fine liquid droplet ( $T=T_L$ ). It is worth noting changes in atomization pressure also influence the thermal history of the droplets in a complex manner.

iii). Increase the co-injection pressure. This will increase the radial velocity of the particles; hence increase the radial penetration depth.

iv). Increase the particle size. It is evident from Figures 11 and 12 that coarser particles may penetrate deeper onto the droplets; hence increasing the particle size may increase the chance for particles to reach the center of the droplet. However, large particle size may adversely affect the mechanical behavior of the final product: the spray formed and co-injected composite.

## 5. Two Dimensional Modeling of Momentum and Thermal Behavior during Spray Atomization of Ti-48Al

The two-dimensional model was formulated based on the following assumptions:

(1). The alloy melt is atomized instantaneously in a small atomization zone, whose magnitude is approximately 3~4 times the inside diameter (~0.001 m) of a metal delivery tube.

(2). Following atomization, the concentration of the droplets in the gas environment is sufficiently dilute, so that the droplet-droplet interactions may be neglected.

(3). The flow of the atomization gas is axisymmetric. As a result, the droplets do not experience rotation around the spray cone axis. The motion of the droplets is then assumed to be two dimensional. Accordingly, a radial coordinate system, ( $r, Z$ ), is selected for the present problem, where  $r$  represents the radial distance and  $Z$  represents the axial distance. The coordinate system is shown schematically in Figure 13.

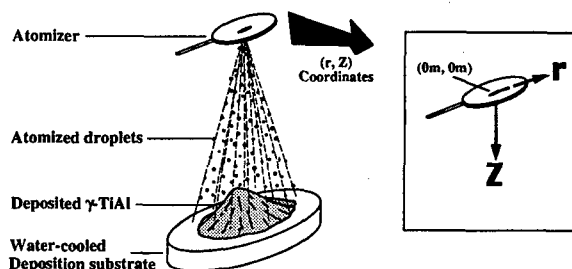


Figure 13: Schematic representation of radial coordinate system, ( $r, Z$ ), used in the two dimensional modeling.

(4). The ( $r, Z$ ) coordinates at the center of the atomization zone are selected to correspond to (0m, 0m), where the radial droplet velocity is zero, and the axial droplet velocity has a relatively small value (for example, 1 m/s) as a result of the initial free fall of the alloy melt. Consistent with assumption (1), the initial positions, ( $Z_0, r_0$ ), of atomized droplets will be in the range from (0m, 0m) to (0m, 0.004m). In addition, it is assumed that droplets are randomly distributed in the atomization zone once they are formed.

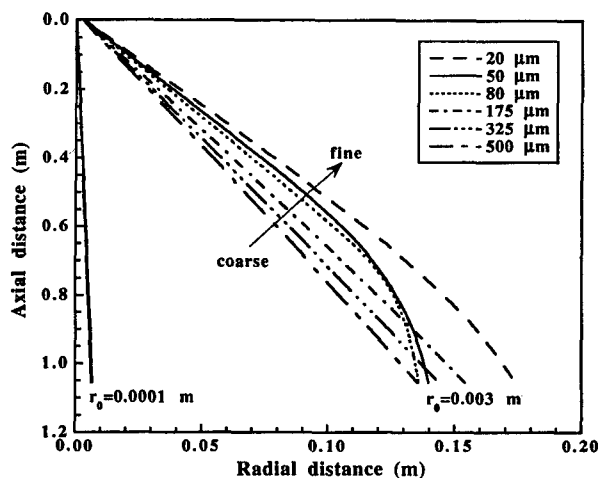


Figure 14: Trajectories of droplet of different sizes for  $r_0=0.0001$  m and  $r_0=0.003$  m. Droplet diameters are 20, 50, 80, 175, 325 and 500  $\mu\text{m}$ .

Using the formulated two-dimensional model, the velocity, temperature, cooling rate, flight time and solidification behavior of atomized droplets in the spray cone were investigated. It was found that the velocity, temperature, cooling rate, flight time and solidification behavior of atomized droplets in the spray cone strongly depend on the initial position,  $r_0$ , and the diameter,  $D$ , of the droplets. In addition, the velocity profiles, temperature histories, cooling rates, flight times and solidification behavior of droplets are also closely

related to each other. For identical  $r_0$ , i) fine droplets are more readily accelerated or decelerated relative to coarse droplets along both axial and radial directions, ii) fine droplets cool at a higher cooling rate than coarse ones, and iii) fine droplets also solidify at a faster rate relative to coarse ones. For identical  $D$ , i) the maximum value of the axial component of droplet velocity decreases with increasing  $r_0$ , while the maximum value of the radial component of droplet velocity initially increases and then decreases with increasing  $r_0$ , ii) flight time increases with increasing  $r_0$  and iii) the solid fraction at any given axial distance increases with increasing  $r_0$  resulting from the longer flight time for larger  $r_0$ .

The numerical model was also utilized to investigate the two dimensional droplet size distribution in the spray cone. Figure 14 shows the trajectories of droplets of various diameters with  $r_0=0.0001$  m and 0.003 m. The general trends observed for  $r_0=0.003$  m may be summarized as follows. First, for a given axial distance which is smaller than some critical value (say, 0.75 m), the radial distance traveled by a droplet increases with decreasing droplet diameter. Second, for a given axial distance which is larger than the critical value, the radial location of droplets becomes random. The results obtained herein for all other initial conditions ( $r_0=0, 0.00001, 0.0001, 0.001$  and  $0.002$  m) are qualitatively similar to those obtained with  $r_0=0.003$  m. It is worth noting, however, that the radial distance range,  $\Delta r$ , at a given axial distance decreases with decreasing  $r_0$ . For example, when  $r_0=0.0001$  m, the radial distance range  $\Delta r$  corresponding to any axial distance is so small that the trajectories of different droplets are almost indistinguishable in Figure 14. In addition, for the same droplet size, droplets initially located at a larger  $r_0$  will go farther in radial direction from the spray cone axis than those at a smaller  $r_0$ .

It may be envisioned that, if all the results calculated for different values of  $r_0$  were to be shown in Figure 14, the trajectory bands for different values of  $r_0$  will overlap with each other and a complete perspective of the spatial distribution of droplets with different diameters in the spray cone will be obtained. As a result, when the axial distance is smaller than some critical value (say 0.75 m), coarse droplets tend to concentrate in the central region of the spray cone, whereas fine droplets populate the periphery; when the axial distance is larger than the critical value, the two dimensional droplet size distribution in the spray cone will be homogeneous. These calculated results are qualitatively consistent with the experimental results reported on atomization of water with air [25]. In the atomization of water with air [10], it was found that coarse droplets concentrated in the central region of the spray cone at an axial distance of 0.025 m. When the axial distance increased from 0.025 m to 0.28 m, however, the two dimensional droplet size distribution became relatively insensitive to the radial position, i.e., from heterogeneous to almost homogeneous. The quantitative discrepancy between the numerical and the experimental results may be attributed to the difference in material properties and processing parameters.

The numerical model was also utilized to study the two dimensional distribution of the fraction solidified in the spray cone. This was accomplished through calculations of the average solid fraction,  $f_{avg}$ , for a collection of droplets which is initially located at an identical position,  $r_0$ . The calculated  $f_{avg}$  as a function of axial distance is summarized in Figure 15 for  $r_0=0, 0.001$  and  $0.003$  m. The effect of changing  $r_0$  on the solidification behavior is evident there: the larger the value of  $r_0$ , the higher the solid fraction at a given axial distance. As

illustrated above, for identical droplet size ( $D$ ), the radial distance traveled by a droplet at any given axial distance increases with increasing  $r_0$ , i.e., if a substrate is inserted across the spray cone, droplets with smaller  $r_0$  will concentrate in the central region of the substrate whereas droplets with larger  $r_0$  will populate the periphery of the substrate. Therefore, if a substrate were to be inserted across the spray cone, the solid fraction contained in the droplets arriving on the substrate would become higher with increasing radial distance from the center of the substrate. Although there is no direct experimental support to the two dimensional solidification behavior calculated herein, it was experimentally found that in spray deposited materials, such as: Al-Cu-Li-Ag-Mg-Zr alloy Weldalite™ 049 [26], 6061 aluminum alloy [27] and more recently for spray formed Ti-47Al [28], the peripheral region generally contained a higher volume fraction of porosity relative to the central region. Moreover, experimental evidences and numerical analyses suggest that porosity present in spray deposited material develops from interstices formed as droplets impinge on one another: micro-sized, irregular cavities are left behind as droplets overlap [24]. On the basis of this mechanism of porosity formation in spray deposited materials, a high solid fraction in the spray will result in a high volume fraction of porosity in the deposit, since insufficient molten material is available to flow over the deposit to fill pores and interstices. Therefore, the experimental observation that the peripheral region contains a higher volume fraction of porosity relative to the central region implies, to some extent, that the fraction solidified in the periphery is higher than that in the central region.

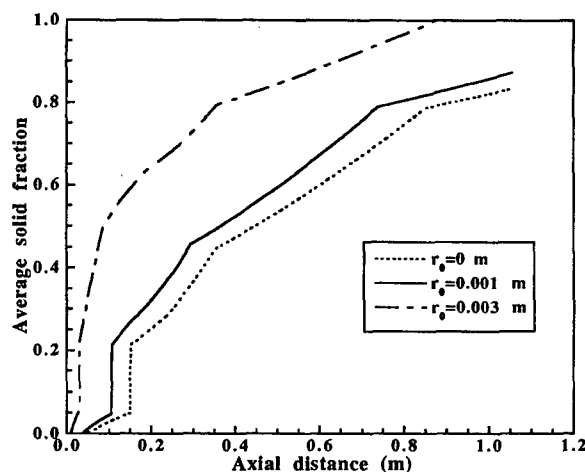


Figure 15. The average solid fraction contained in droplets which are initially located at: (a)  $r_0=0$  m; (b)  $r_0=0.001$  m and (c)  $r_0=0.003$  m.

## 6. Summary

The primary conclusions which may be drawn from this study are:

- (1). Gamma  $\gamma$ -TiAl alloys with five different nominal compositions were successfully spray processed, either by spray forming or by spray forming  $\oplus$  co-injection.
- (2). The microstructure of spray formed Ti-47Al consisted of fine, equiaxed fully lamellar  $\alpha_2+\gamma$  structure, with an average linear grain size of 60  $\mu\text{m}$  and an average interlamellar spacing of 0.3  $\mu\text{m}$ . These microstructural characteristics led to a higher

creep resistance, in a temperature-stress regime of 780 to 850 °C and 180 to 320 MPa, relative to fully lamellar  $\gamma$ -TiAl obtained through conventional casting + heat treatment processes.

(3). The microstructure of the Ti-47Al/TiB<sub>2</sub> composite fabricated by spray forming + co-injection technique was characterized by fine grained, equiaxed fully lamellar structures, with an average linear grain size of approximately 40  $\mu$ m and a volume percentage of TiB<sub>2</sub> of approximately 35%. The distribution of TiB<sub>2</sub> in the composite exhibited a layered morphology.

(4). Experimental observations of TiB<sub>2</sub> distribution in oversprayed powders and related numerical analysis revealed that this phenomenon originated from the segregation of TiB<sub>2</sub> particles to the exterior region of the droplets and the subsequent deformation of the droplets along the direction normal to the substrate during impingement. Numerical analysis on penetration also suggested that the most likely approach to improve the homogeneity of the distribution of TiB<sub>2</sub> in the deposit is to decrease the co-injector/atomizer distance.

(5). A two dimensional model of the momentum and thermal behavior of atomized droplets of  $\gamma$ -TiAl predicted that the two dimensional droplet size distribution in the spray cone changes from being heterogeneous to being almost homogeneous as axial flight distance increases. The modeling results also indicated that the two dimensional distribution of the fraction solidified in the spray cone is heterogeneous. The fraction solidified in the spray at any given axial distance increases with increasing radial distance from the spray axis. Those predictions are qualitatively consistent with the experimental results.

#### Acknowledgments

The authors would like to acknowledge the Air Force Office of Scientific Research for financial support, Grant No. F49620-94-1-0137, of this study.

#### References

1. Y.W. Kim, "Ordered Intermetallic Alloys, Part III: Gamma Titanium Aluminides" *JOM*, 46 (1994), 30-39.
2. K.S. Chan, "Understanding Fracture Toughness in Gamma TiAl" *JOM*, 44 (1992), 30-38.
3. H. Deve, A.G. Evans and D.S. Shih, "A High-Toughness Gamma Titanium Aluminide" *Acta Metall. Mater.*, 40 (1992), 1259-1265.
4. S.L. Kampe, P. Sadler, L. Christodoulou and D.E. Larson, "Room Temperature Strength and Deformation of TiB<sub>2</sub> Reinforced Near Gamma Titanium Aluminides" *Metall. & Mater. Trans.*, 25A (1994), 2181-2197.
5. K.S. Kumar and M.S. DiPietro, "Ballistic Penetration Response of Intermetallic Matrix Composites" *Scripta Metall. Mater.*, 32 (1995), 793-798.
6. Q. Ma, L.C. Liang, D.R. Clarke and J.W. Hutchinson, "Mechanics of the Push-out Process from in situ Measurement of the Stress Distribution along Embedded Sapphire Fibers" *Acta Metall. Mater.*, 42 (1994), 3299-3308.
7. S.M. Jeng and J.-M. Yang, "Effect of Fiber Coating on the Mechanical Behavior of SiC Fiber-Reinforced Titanium Aluminide Composites" *J. Mater. Res.*, 8 (1993), 905-916.
8. E.J. Lavernia and Y. Wu, *Spray Atomization and Deposition* (John Wiley & Sons, Chichester, UK, 1996)
9. J.W. Sears, "Titanium Spray Formed Structures" in *1992 Powder Metallurgy World Congress*, eds., J.M. Capus and R.M. German, MPIF/APMI, 1992, pp. 281-290.
10. D.G. Morris, M.A. Morris, S. Gunter, M. Leboeuf and G. Hollrigl, "Spray Deposition of Intermetallics based on Al<sub>3</sub>Ti and TiAl" *Scripta Metall. Mater.*, 27 (1992), 1645-1650.
11. T.P. Johnson, M.H. Jacobs, R.M. Ward and J.M. Young, "Spray Forming of Alloys for High Performance Applications" in *2nd International Conference on Spray Forming*, eds., J.V. Wood, Woodhead Publishing Lt., 1993, pp. 183-190.
12. S.C. Huang, "Microstructures and Property Tradeoffs in Wrought TiAl-Base Alloys" *Metall. Trans.*, 23A (1992), 375-377.
13. K.S. Chan and D.S. Shih, "Fatigue and Fracture Behavior of a Fine-Grained Lamellar TiAl Alloy" *Metall. & Mater. Trans.*, 28A (1997), 79-90.
14. S. Kroll, H. Mehrer, N. Stolwijk and C. Herzig, "Titanium Self-Diffusion in the Intermetallic Compound  $\gamma$ -TiAl" *Zeitschrift Fur Metallkunde*, 83 (1992), 591-595.
15. R.W. Hayes and P.A. McQuay, "A First Report on the Creep Deformation and Damage Behavior of a Fine Grained Fully Transformed Lamellar Gamma TiAl Alloy" *Scripta Metall. Mater.*, 30 (1994), 259-264.
16. M.F. Bartholomeusz, Q. Yang and J.A. Wert, "Creep Deformation of a Two-Phase TiAl/Ti<sub>3</sub>Al Lamellar Alloy and the Individual TiAl and Ti<sub>3</sub>Al Constituent Phases" *Scripta Metall. Mater.*, 29 (1993), 389-394.
17. B.D. Worth, J.W. Jones and J.E. Allison, "Creep Deformation in Near- $\gamma$  TiAl: Part I. The Influence of Microstructure on Creep Deformation in Ti-49Al-1V" *Metall. Mater. Trans.*, 26A (1995), 2947-2959.
18. H. Mabuchi, H. Tsuda and Y. Nakayama, "Combustion Synthesis of TiAl-Matrix Composites in the Ti-Al-BN System" *Scripta Metall. Mater.*, 32 (1995), 253-257.
19. H. Liu, R.H. Rangel and E.J. Lavernia, "Modeling of Droplet Gas Interactions in Spray Atomization of Ta-2.5W Alloy" *Mater. Sci. & Eng.*, 191A (1995), 171-184.
20. P. Ramachandrarao, "Heat of Crystallisation and Viscous Behavior of Metallic Glasses" *Trans. JIM*, 21 (1980), 248-251.
21. H.S. Chen, "A Method for Evaluating Viscosities of Metallic Glasses from the Rates of Thermal Transformations" *J. Non-Crystalline Solids*, 27 (1978), 257-263.
22. T.Z. Kattamis and T.J. Piccone, "Rheology of Semisolid Al-4.5%Cu-1.5%Mg Alloy" *Mater. Sci. & Eng.*, 131A (1991), 265-272.

23. Y. Wu and E.J. Lavernia, "Interaction Mechanisms between Ceramic Particles and Atomized Metallic Droplets" Metall. Trans., 23A (1992), 2923-2937.
24. H. Liu, E.J. Lavernia and R.H. Rangel, "Numerical Investigation of Micropore Formation During Substrate Impact of Molten Droplets in Plasma Spray Processes" Atomiz. & Sprays, 4 (1994), 369-384.
25. V.G. McDonell, E.J. Lavernia and G.S. Samuelsen, "Simultaneous Measurement of Metal Atomizer Particle Size and Velocity Using Phase Doppler Interferometry" in Synthesis and Analysis in Materials Processing: Advances in Characterization and Diagnostics of Ceramics and Metal Particulate Processing, eds., E.J. Lavernia, H. Henein and I. Anderson, The Minerals, Metals & Materials Society, 1989, pp. 13-37.
26. J.M. Marinkovich, F.A. Mohamed, J.R. Pickens and E.J. Lavernia, "The Spray Atomization and Deposition of Widalite 049" JOM, 41 (1989), 36-41.
27. J. Zhang, M.N. Gungor and E.J. Lavernia, "The Effect of Porosity on the Microstructural Damping Response of 6061 Aluminium Alloy" J. Mater. Sci., 28 (1993), 1515-1524.
28. B. Li, W. Cai and E.J. Lavernia, "Spray Forming of  $\gamma$ -Titanium Aluminide" J. Mater. Synth. Proc., 4 (1995), 35-41.

## IMPROVEMENT ON OXIDATION RESISTANCE OF TITANIUM ALUMINIDE INTERMETALLICS BY COATINGS

Zhaolin Tang, Fuhui Wang, and Weitao Wu  
State key Laboratory for Corrosion and Protection  
Institute of Corrosion and Protection of Metals  
Academia Sinica, Shenyang 110015, China

### Abstract

TiAl intermetallics are emerging as a revolutionary engineering material for high temperature structural applications. However, its poor oxidation resistance must be overcome before it may be used in practice above 800°C. In this paper, the effect of MCrAlY overlay coatings, reactively-sputtered  $\text{Al}_2\text{O}_3$  films and TiAlCr coatings on the oxidation resistance of TiAl alloy was investigated. CoCrAlY and NiCrAlY coatings could remarkably decrease the oxidation rate of TiAl. However, due to the inward diffusion of Co and Ni into the substrate, two brittle and hard diffusion layers formed at the coating/substrate interface. Reactively-sputtered  $\text{Al}_2\text{O}_3$  films were very effective to improve the isothermal oxidation resistance of TiAl at 900°C. However, the thermal expansion mismatch resulted in the poor cyclic oxidation resistance. TiAlCr coatings not only effectively improved the isothermal and cyclic oxidation resistance of TiAl due to the formation of adherent  $\text{Al}_2\text{O}_3$  scale, but also exhibited a good compatibility with the substrate. This coating may become a realistic protective coating for engineering  $\gamma$ -TiAl.

### Introduction

TiAl based intermetallics have received more and more attention as a potentially high temperature structural materials because they have many properties beneficial to high temperature applications, including low density, good high temperature strength, and high stiffness especially at

high temperature<sup>1,2</sup>. However, to develop these materials for real applications at elevated temperatures, their oxidation resistance must be improved.  $\gamma$ -TiAl possesses insufficient oxidation resistance as a result of the formation of  $\text{TiO}_2$  based scales rather than  $\text{Al}_2\text{O}_3$  on the surface<sup>3,4</sup>. Therefore some kinds of coatings may be needed for TiAl alloy before it can be put into practice.

In this paper, the effect of MCrAlY overlay coating, reactively-sputtered  $\text{Al}_2\text{O}_3$  film and TiAlCr coating on the oxidation resistance of TiAl was investigated.

### Experimental procedures

#### Alloy and coatings preparation

The TiAl (nominal composition Ti-36Al, wt%) was melted by using a vacuum-induction furnace with a CaO crucible. The coatings were produced by magnetron-sputtering technique. The nominal compositions of three metal coatings were Co-30Cr-6Al-0.5Y, Ni-30Cr-6Al-0.5Y, Ti-37Al-14Cr (wt%) respectively. Before sputtering, the TiAl ingot was cut into 20 × 10 × 3 mm specimens and ground down to 600-SiC paper, peened, and ultrasonically cleaned in ethanol. Sputtering parameters were as follows: argon pressure 0.2Pa; power about 2.3KW; substrate temperature 250-300°C and coating thickness about 30  $\mu\text{m}$ . The  $\text{Al}_2\text{O}_3$  film with thickness about 5  $\mu\text{m}$  was produced by reactively sputtering technique<sup>5</sup>.

## Oxidation tests

Isothermal oxidation tests were carried in static air. For the TiAl, an electronic thermal-balance was used to measure the weight change continuously, because the severe spallation of scales formed on this alloy occurred during cooling. For TiAl with coatings, the specimens were placed in alumina crucibles oxidized at the desired temperatures and cooled down to room temperature at regular intervals of 20 h for weight measurements. For cyclic oxidation tests, the specimens were kept at the desired temperature for 1 h and cooled down to room temperature for 10 min as a cycle.

## Specimen analysis

After oxidation, the specimens were analyzed using optical metallography(OP), X-ray diffraction(XRD) and scanning electron microscopy(SEM) with energy dispersive X-ray analysis(EDX).

## RESULTS AND DISCUSSIONS

### Oxidation of TiAl

Figure 1 shows the isothermal oxidation kinetics of TiAl and K38G alloy(a kind of Ni-based superalloy). TiAl alloy shows a higher mass gains than K38G alloy. Figure 2 shows their cyclic oxidation kinetics, TiAl exhibited more severe mass loss than K38G alloy. It is seen that TiAl shows much poorer oxidation resistance than K38G alloy and exhibits insufficient oxidation resistance. Therefore some kinds of measures may be needed to improve the oxidation resistance of TiAl before it may be used as high-temperature structural materials.

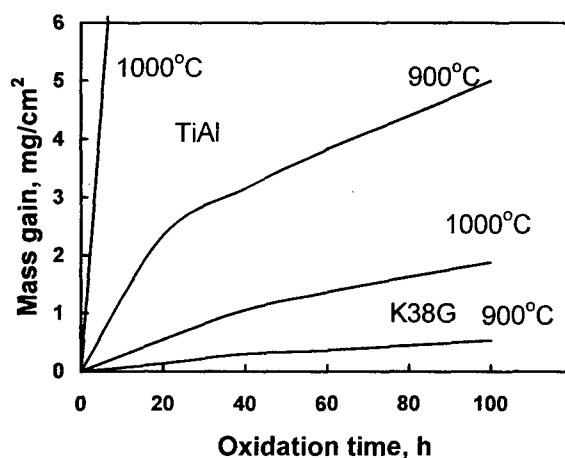


Figure 1: Isothermal oxidation kinetics of TiAl and K38G alloy in air

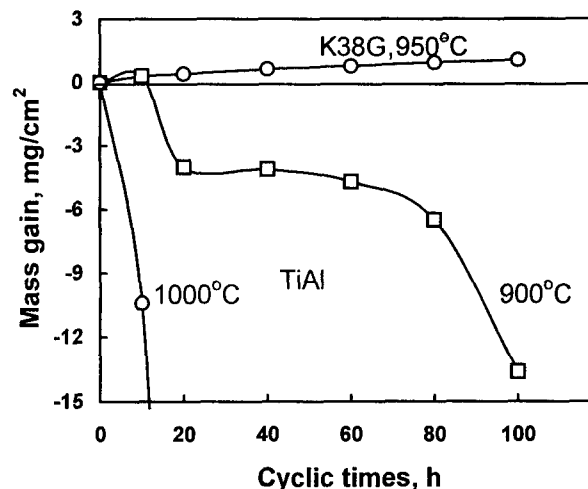


Figure 2: Cyclic oxidation kinetics of TiAl and K38G alloy in air

Conventional aluminizing can improve the oxidation resistance of TiAl significantly due to the formation of  $\text{TiAl}_3$ . However  $\text{TiAl}_3$  is very brittle and cracks normal to the surface may occur during cooling after aluminizing. This will have a detrimental effect on the long-term and cyclic-oxidation resistance<sup>6,7</sup>.

### MCrAlY coatings

Figure 3 shows the isothermal and cyclic oxidation kinetics of TiAl with CoCrAlY coatings at 900°C. It can be seen that CoCrAlY can remarkably improve the oxidation resistance of TiAl. The protection results from the adherent  $\text{Al}_2\text{O}_3$ .

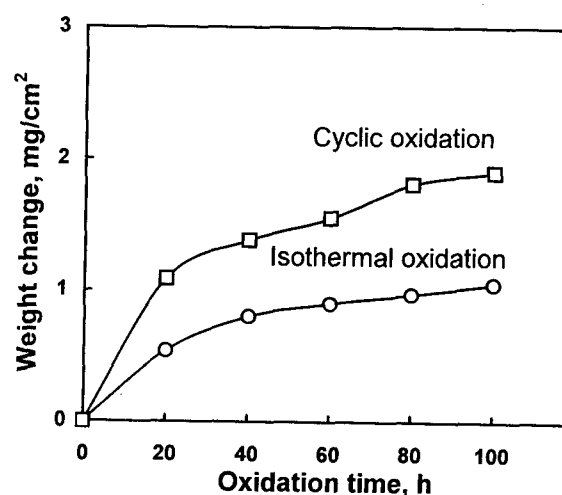


Figure 3: Isothermal and cyclic oxidation kinetics of TiAl with CoCrAlY coatings at 900°C

scale formed on the surface of CoCrAlY coatings (figure 4a). From the cross sectional microstructure (figure 4b), it can be seen that two diffusion layers and some voids formed between coating and substrate. The outer diffusion layers mainly consist of  $\text{AlCo}_2\text{Ti}$  ternary intermetallics which is brittle and hard. At  $1000^\circ\text{C}$ , the interdiffusion became severer and some void accumulated into cracks. The severe interdiffusion would influence the long-term oxidation resistance and the mechanical properties of TiAl alloy. NiCrAlY coating have the similar interdiffusion with TiAl substrate. So MCrAlY coatings, ever successfully used to protect Ni-, Fe-, and Co- based superalloys, may need further study to limit the interdiffusion for the protection of TiAl alloy.

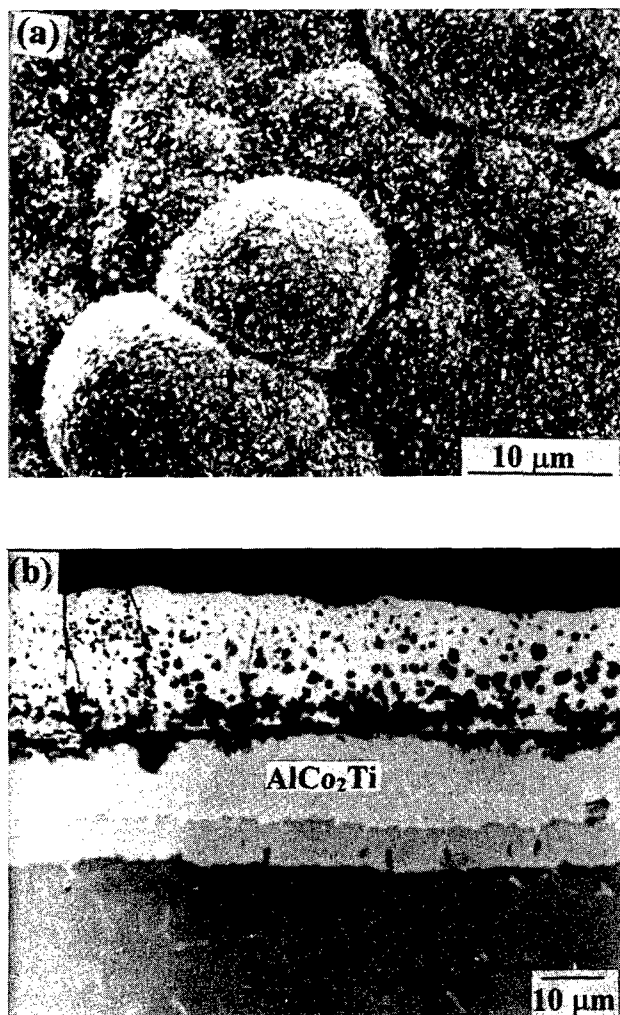


Figure 4: Surface morphology(a) and cross section(b) of TiAl with CoCrAlY coatings after 100h oxidation at  $900^\circ\text{C}$

#### Reactively sputtered $\text{Al}_2\text{O}_3$ film

Figure 5 shows the isothermal and cyclic oxidation kinetics of TiAl with  $\text{Al}_2\text{O}_3$  films at  $900^\circ\text{C}$ . It is seen that the  $\text{Al}_2\text{O}_3$  film is very effective in decreasing the isothermal oxidation rate of TiAl at  $900^\circ\text{C}$ ; however the effect is limited during

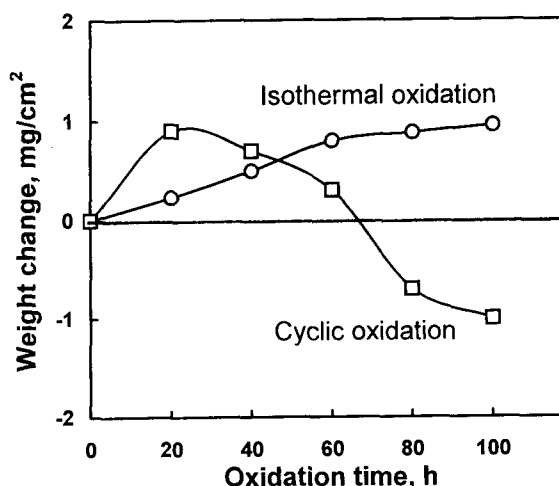


Figure 5: Isothermal and cyclic oxidation kinetics of TiAl with sputtered  $\text{Al}_2\text{O}_3$  films at  $900^\circ\text{C}$

the cyclic oxidation situation. Figure 6 shows the surface morphology and cross section of TiAl with  $\text{Al}_2\text{O}_3$  coating after 100h isothermal oxidation at  $900^\circ\text{C}$ .  $\text{Al}_2\text{O}_3$  film is very adherent to the substrate and the film has thickened compared to the original film. It is suggested that the preferential formation of  $\text{Al}_2\text{O}_3$  results in the thickening of the  $\text{Al}_2\text{O}_3$  film and blocking of microcracks because a low oxygen partial pressure was obtained beneath the  $\text{Al}_2\text{O}_3$  film<sup>8</sup>. However the  $\text{Al}_2\text{O}_3$  film is not very effective in improving the cyclic oxidation resistance of TiAl, mass loss is found for  $\text{Al}_2\text{O}_3$  coated TiAl, which is due to the cracks and spallation of the  $\text{Al}_2\text{O}_3$  scale (figure 7). The limited improvement may result from the mismatch of thermal expansion coefficient between TiAl and  $\text{Al}_2\text{O}_3$  (the thermal expansion coefficient for TiAl and  $\text{Al}_2\text{O}_3$  are  $14.4 \times 10^{-6}$  and  $8.3 \times 10^{-6} \text{ } ^\circ\text{C}^{-1}$  respectively) and the brittleness of the ceramic film.

#### TiAlCr coating

The ideal coating for TiAl intermetallics should form an adherent  $\text{Al}_2\text{O}_3$  scale and exhibit excellent compatibility with the substrate. Aluminide coating<sup>6,7</sup>, MCrAlY overlay coatings, ceramic coatings such as  $\text{Si}_3\text{N}_4$ <sup>9</sup> and  $\text{Al}_2\text{O}_3$ <sup>8,10</sup>, were effective in decreasing the oxidation rate of TiAl alloy. However, some problems existed mainly due to the incompatibility between substrate and coating. Recently, a new class of Ti-Al-Cr coatings has been proposed for the protection of TiAl intermetallics<sup>11,12</sup>. In this study, the effect



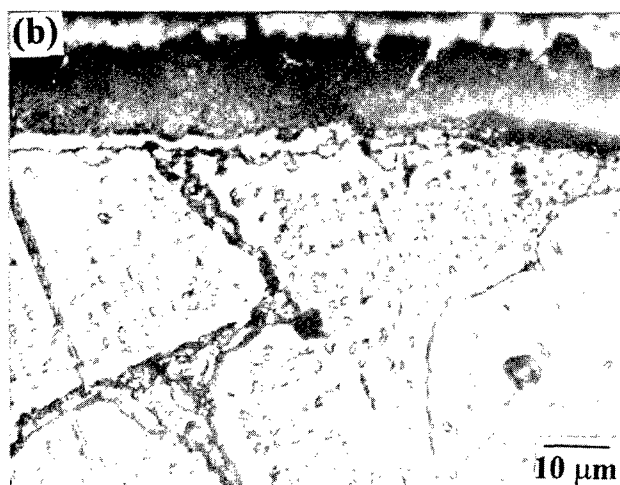
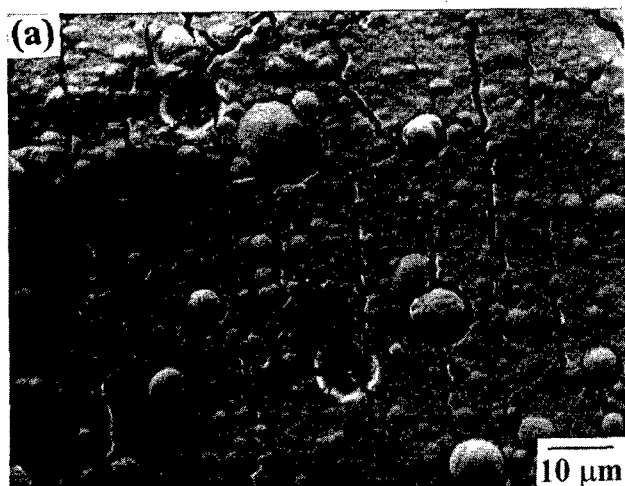


Figure 6: Surface morphology(a) and cross section(b) of TiAl with sputtered  $\text{Al}_2\text{O}_3$  after 100h oxidation at  $900^\circ\text{C}$

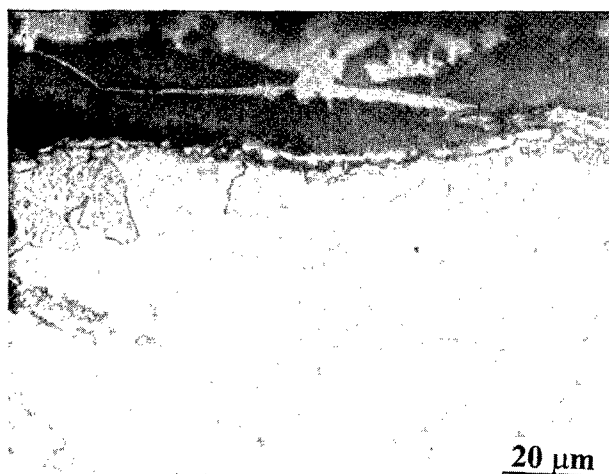


Figure 7: Cross section of TiAl with sputtered  $\text{Al}_2\text{O}_3$  after 100-cycle oxidation at  $900^\circ\text{C}$

of a TiAlCr coating (Ti-37Al-14Cr) on oxidation resistance of TiAl alloy was investigated.

Figure 8 shows the isothermal and cyclic oxidation kinetics of TiAl with TiAlCr coatings at  $900^\circ\text{C}$ . TiAlCr coatings remarkably improve the oxidation resistance of TiAl. The improvement results from the formation of a uniform and adherent  $\text{Al}_2\text{O}_3$  scale on this TiAlCr coating (Figure 9).

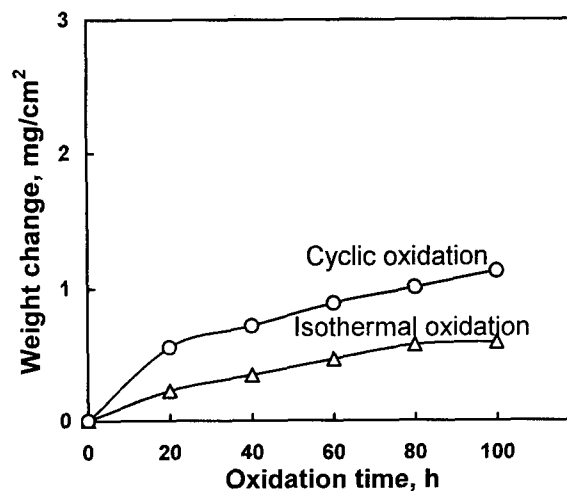


Figure 8: Isothermal and cyclic oxidation kinetics of TiAl with TiAlCr coatings at  $900^\circ\text{C}$

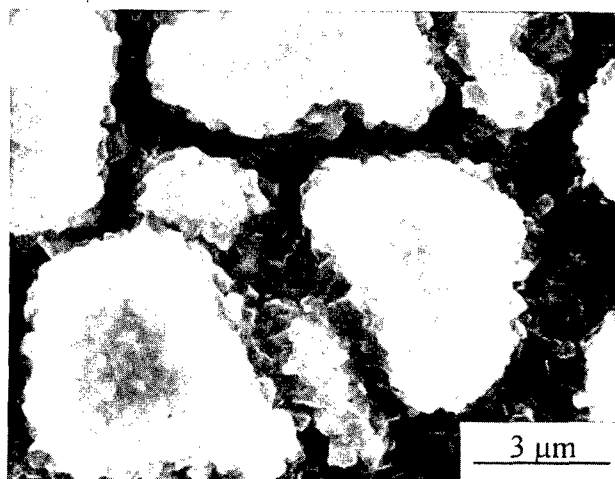


Figure 9: Surface morphology of TiAl with TiAlCr coating after 100h oxidation at  $900^\circ\text{C}$

After long term (1000h) oxidation at  $900^\circ\text{C}$ , TiAlCr coating still provides good protection for TiAl (Figure 10). The  $\text{Al}_2\text{O}_3$  scale is also adherent and protective. The TiAlCr coating is adherent to the substrate and no Kirkendall voids

appear in the coating/ substrate interface. EDAX analysis indicated that just a little Cr diffusion is found. The width of interdiffusion zone after 1000h at 900 °C would be only 12 $\mu$ m .

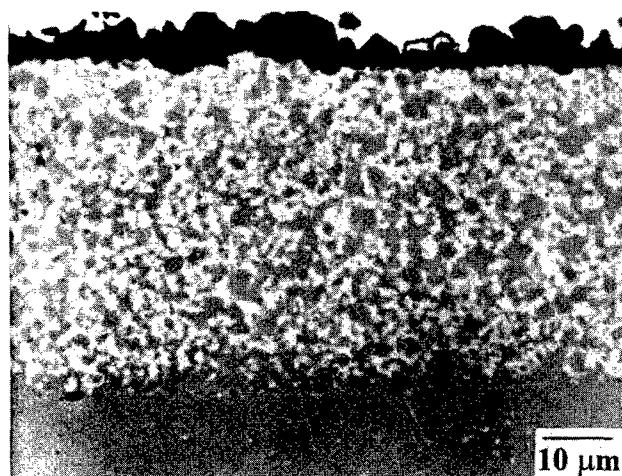


Figure 10: Cross section microstructure of TiAl with TiAlCr coating after 1000h oxidation at 900°C

It is seen that the TiAlCr coating not only remarkably improved the oxidation resistance of TiAl intermetallics, but also exhibited a better compatibility to the substrate than any other conventional aluminide and MCrAlY Coatings. Moreover The coating alloy is based on  $\gamma$ -TiAl and TiAlCr laves phases and the TiAlCr laves phase is surrounded by the continuous  $\gamma$ -TiAl. Therefore the TiAlCr coating can offer necessary mechanical properties so no cracks were found after cyclic oxidation or around microhardness indent. This coating may become a realistic protective coating for TiAl alloy. Future research should evaluate the effect of TiAlCr coatings on the mechanical properties of engineering  $\gamma$ -TiAl alloys .

#### CONCLUSIONS

1. TiAl alloy exhibits insufficient isothermal and cyclic oxidation resistance ,so some kinds of measures may be needed to improve its oxidation resistance.
2. MCrAlY (M=Co,Ni)coatings were effective in decreasing the oxidation rate of TiAl alloy. However Two diffusion layers formed between MCrAlY coatings and their substrate due to the inward diffusion of Co and Ni.
3. A reactively-sputtered  $Al_2O_3$  film was very effective to improve the isothermal oxidation resistance of TiAl alloy at 900°C. However, the thermal expansion mismatch resulted in poor cyclic oxidation resistance.
4. TiAlCr coatings not only effectively improve the isothermal and cyclic oxidation resistance of TiAl alloy due to the formation of adherent  $Al_2O_3$  scale , but also exhibit a better compatibility to the substrate than any other conventional aluminide, MCrAlY Coatings and ceramic coatings. This coating may become a realistic protective coating for engineering  $\gamma$ -TiAl.

#### ACKNOWLEDGEMENT

This work was supported by the National Natural Sciences Foundation of China(NSFC) for Outstanding Young Scientists.

#### REFERENCES

1. Y. M. Kim, "Gamma Titanium Aluminide: Their Status and Future," J. Met, 42(1989), 24-27
2. Y. M. Kim, "Alloy Design of Gamma (TiAl) alloys," Acta Metall. Sinica(English Letters), 8(1995), 319-339.
3. S.Becker, A.Rhamel, M.Schorr, and M.Schuetze, "Mechanism of Isothermal Oxidation of the Intermetallic TiAl and TiAl Alloys," Oxid.Met. 38(1992), 425-464.
4. K. L. Luthra, "Stability of Protective Oxide Films on Ti-based Alloys," Oxid.Met. 36 (1991) , 475-490.
5. H Lou, S. Zhu, F. Wang and W. Wu, "Amorphous Films of Alumina Prepared by Reactive Sputtering," Acta Metall. Sinica. 27 (1991) , B210-215.
6. J. Shen, Z. Teng, Z. Jiang, L. Zhou, and T. Li, "Aluminide Coatings on  $Ti_3Al$  Alloy by Pack Cementation ,"J. Uni. Sci. Technol. Beijing S13 (1991) , 624-627.
7. A. Takei, and A. Ishida, "Oxidation Resistance Coatings on Titanium Alloys and TiAl Intermetallic Compounds," 7th APCCC, Inter Academic Publ., China, 2 (1991), 718-723.
8. Z. Tang, F.Wang, and W. Wu, "The Effect of Reactively-sputtered  $Al_2O_3$  film on Oxidation Resistance of TiAl Intermetallics," Chin.J.Mater.Res. accepted to be published.
9. D. Xu, Z. Zheng, X. Liu, S. Zou, S. Taniguchi, T. Shibada, and T. Yamada, "Improvement of Oxidation

Resistance of TiAl by Ion-beam-enhanced Coatings," Surf. Coat. Technol. 66(1994), 486-494.

10. S. Taniguchi, T. Shibada, and K. Takeuchi, "Protectivness of a CVD- $\text{Al}_2\text{O}_3$  Film on TiAl Intermetallic Compound against High Temperature Oxidation," Mater. Trans. JIM, 32 (1991), 299-301.

11. L. McCarron, J. C. Schaeffer, G. H. Meier, D. Berztiss, R. A. Perkins, and J. Cullinan, "Protective Coatings for Titanium Aluminide Intermetallics," Titanium'92, Edited by F. H. Froes and I. Caplan (Warrendale, PA: TMS, 1993), 1971-1978

12. M. P. Brady, J. L. Smialek, W. J. Brindley, submitted to U. S. patent office(1996)

# NUMERICAL SIMULATION OF THERMAL STRESS FORMATION IN INVESTMENT CAST $\gamma$ -TiAl

L. Würker, M. Fackeldey, P.R. Sahm  
Giesserei-Institut RWTH Aachen  
Intzestr.5, D-52072 Aachen  
Germany

## Abstract

Numerical simulation was used to evaluate the formation of thermal stresses and cracks in  $\gamma$ -TiAl investment cast parts. The simulation is based on a coupled thermo-mechanical model which describes the transient three dimensional stresses and strains depending on the state of solidification and cooling. Casting experiments were carried out in order to validate the results of the numerical simulation. An experimental setup is introduced which allows the monitoring of crack formation in the casting during cooling. Initial experiments confirm that the results of the numerical simulations which predict the dependence of the build up of residual stresses in the casting. In addition to the investigations on the formation of thermal stresses, residual stresses have been measured by means of the hole drilling strain gage method.

## Introduction

Intermetallic  $\gamma$ -TiAl alloys represent a new material for high temperature applications in turbine and motor construction. A suitable near-net-shape manufacturing method for  $\gamma$ -TiAl alloys is the investment casting process. Investment cast parts show an excellent surface quality and high dimensional accuracy. However, the remarkable cracking sensitivity during cooling is a major

obstacle for casting titanium aluminides [1-3].

Due to hindered contraction and non-uniform cooling of the casting in the rigid ceramic mold, stresses are built up which cannot only cause cracking, but also remain in the casting and may cause distortions and dimensional deviations. The basic link between casting, solidification and cooling conditions and their effect on the formation of thermal stresses is widely unknown for  $\gamma$ -TiAl based alloys.

In order to avoid such casting defects and to predict cracking sensitivity in complex shaped  $\gamma$ -TiAl cast parts, it is necessary to determine quantitatively the formation of thermal stresses and their dependence on the casting parameters. Therefore, a three dimensional, finite element (FEM) program has been used to carry out investigations on the formation of stresses and to determine the cracking sensitivity of  $\gamma$ -TiAl based castings. A coupled thermo-mechanical model has been developed to calculate the distribution of strains and stresses in castings during cooling.

## Method of Simulation

### Temperature Simulation

The temperature simulation was carried out with the 3D FEM (finite element method) program CASTS, which was developed at the Giesserei-Institut. The program

takes the temperature dependent physical and mechanical properties and different thermal boundary conditions into account, figure 1.

The program is based on the Fourier equation of heat conduction which describes the thermal conditions in a casting. By solving this equation for every node of an enmeshed geometry, the three dimensional heat flow can be calculated. Interface elements are implemented to take into account the local heat transfer between different materials, e.g. casting and mold.

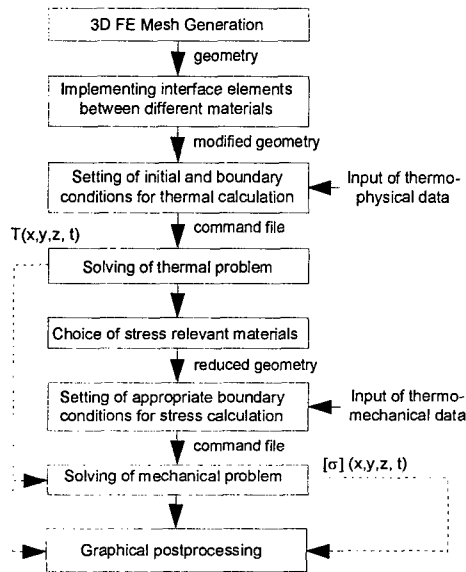


**Figure 1:** Flow chart of the coupled temperature-stress simulation.

The thermal calculation is performed considering the material specific thermophysical data (i.e. thermal conductivity, heat capacity, density, and latent heat) [4] and the casting system specific boundary conditions (casting temperature, mold preheating, radiation, insulation). A more detailed description of the method of temperature simulation can be found in [5-10].

In order to determine the unknown heat transfer coefficient between mold and casting, which is strongly influenced by for example air gap formation, cooling rates in  $\gamma$ -TiAl castings were measured for different mold preheating temperatures. The results of the experiments were used to fit the heat transfer coefficient in the numerical simulation. Figure 2 reveals a satisfying agreement between measured and calculated cooling rates.

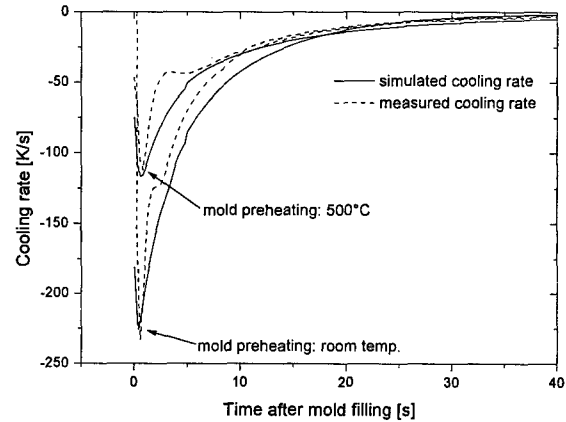


**Figure 2:** Comparison of simulated and measured cooling rates in the castings.

### Stress Simulation

Thermal stresses in a casting can be built up during cooling in a rigid mold by hindered shrinkage or by inhomogeneous cooling conditions. Depending on the thermomechanical behavior of the material during cooling, the amount of stress varies. For the calculation of thermal stresses the following temperature dependent mechanical data is taken into account:

- yield stress [11-13]
- thermal expansion [4],[12]
- Young's Modulus [14]
- Poisson's Ratio [14]

Based on the calculated time dependent temperature field in the casting the total stress is calculated incrementally according to an elastic-plastic constitutive model [15],[16].

$$\{\Delta\sigma\}_{x,y,z} = D \cdot \left( \{\Delta\epsilon\}_{x,y,z} - \{\Delta\epsilon_{th}\}_{x,y,z} \right) + \{\Delta\sigma_0\}_{x,y,z} \quad (1)$$

where  $D$  is the elastic-plastic stress-strain matrix,  $\Delta\epsilon$  and  $\Delta\epsilon_{th}$  are respectively total and thermal strain increments. The fictitious stress  $\Delta\sigma_0$  takes into account the temperature dependence of the yield condition. The total stress  $\sigma$  for each time increment can be obtained from:

$$\{\sigma\}_{x,y,z}^{t+\Delta t} = \{\sigma\}_{x,y,z}^t + \{\Delta\sigma\}_{x,y,z}^t \quad (2)$$

The results of the simulation are displayed and analyzed with the help of a graphical postprocessing tool, see figure 1.

## Experimental Procedure

### Casting Experiments

For the investigations on the cracking sensitivity of investment cast  $\gamma$ -TiAl a sample geometry was designed, figure 3. It consists of six segments of different diameters. Each segment is provided with a sharp notch, representing a predetermined cracking point. The enlarged diameters, which separate the segments from each other, guarantee a hindered shrinkage of the casting.

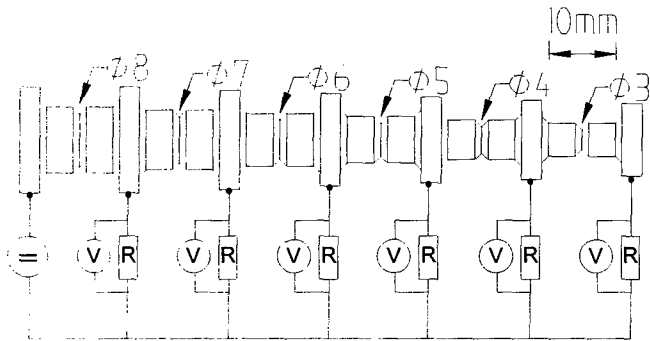


**Figure 3:** Sample geometry for the characterization of cracking sensitivity of  $\gamma$ -TiAl based alloys.

Hence, stresses in the casting are built up in the longitudinal direction during cooling. If the stresses exceed the ultimate tensile strength, the segments may crack. In order to monitor the formation of cracks in the segments, each of the enlarged diameters is supplied with an electric contact. By measuring a direct voltage, crack formation and growth during cooling can be observed either as a slow decrease (crack initiation) or a sharp drop of voltage (complete separation). The casting experiments were carried out in a centrifugal casting device using Yttria coated ceramic crucibles for melting.

Such experiments allow the validation of the results of the numerical simulation. Figure 4 shows a perspective view of the mesh of the sample geometry. Due to the symmetry of the casting the mesh is reduced to a quarter of the original shape in order to reduce computing time. The whole geometry, casting and ceramic shell mold, is described by 8984 nodes, 6560 volume elements, and 1405 interface elements. The stress calculation was only performed for the casting since the ceramic shell mold can be assumed as rigid.

In order to reproduce the mechanical resistance of the rigid mold and to rule out a rigid body movement of the calculated geometry, suitable displacement boundary conditions for all directions have to be chosen, figure 5.

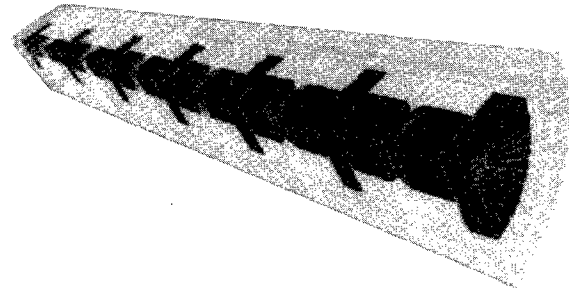


**Figure 4:** Enmeshment of the sample geometry.

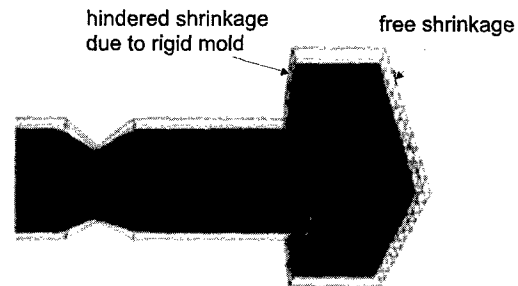


**Figure 5:** Example of a displacement boundary condition, considering the rigid mold in the end segment ( $\phi 3$ mm) of the sample geometry, see figure 3. The outer hull represents the original shape of the casting.

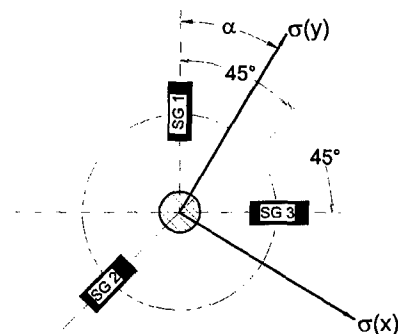
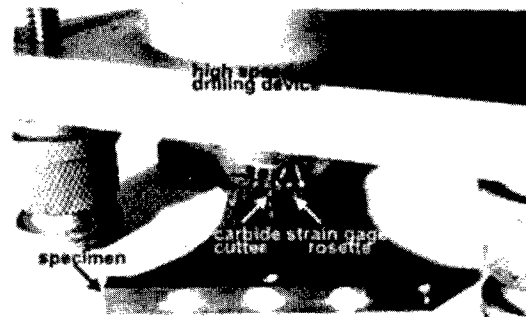


**Figure 6:** Measurement of residual stresses in a test piece by means of the hole drilling method.

The setting of these boundary conditions strongly influences the calculation of strains and stresses and is difficult especially for complex shaped castings.

### Hole Drilling Method

In addition to monitoring crack formation and growth, residual stresses were measured by means of the hole drilling strain gage method. The measuring of residual stresses was performed using a simple sample geometry as described in figures 6 and 9.

Drilling a blind hole into a specimen eliminates the stresses perpendicular to the surface and the corresponding changes in strains in the immediately surrounding region can be measured. By arranging three strain gages on a strain gage rosette at a defined distance around the hole, figure 6, the amount and direction of residual stresses can be calculated from the strain data[17-19].

### Results and Discussion

The temperature and stress distribution in the sample geometry was calculated for different cooling rates. The simulation reveals the positive effect of low cooling rates and homogeneous cooling on the formation of residual stresses, figure 7.

The maximum stresses can be found around the notches. They reach or even exceed the ultimate tensile strength of investment cast  $\gamma$ -TiAl [12],[13]. The occurrence of cracks as predicted by the simulation was confirmed by casting experiments. As described, electric contacts allowed the monitoring of crack formation and growth in the sample geometry during cooling. Figure 8 shows the result of casting experiments. As expected, higher cooling rates promote crack formation. Figure 8a reveals a complete separation of the  $\varnothing 3\text{mm}$  segment and a partial crack in the  $\varnothing 4\text{mm}$  segment for the mold preheated at  $500^\circ\text{C}$ . However, the non preheated mold causes all segments up to  $\varnothing 6\text{mm}$  to crack completely, figure 8b.

The results of measuring residual stresses in  $\gamma$ -TiAl castings confirm the tendency of decreasing residual stresses with decreasing cooling rate, figure 9. However, the total level of stress has to be questioned. Due to the high hardness of the alloys investigated the required shape of the blind hole was not exactly achieved. In cases of a non uniform stress distribution with increasing depth, this may lead to significant errors in the amount of stress determined [19].

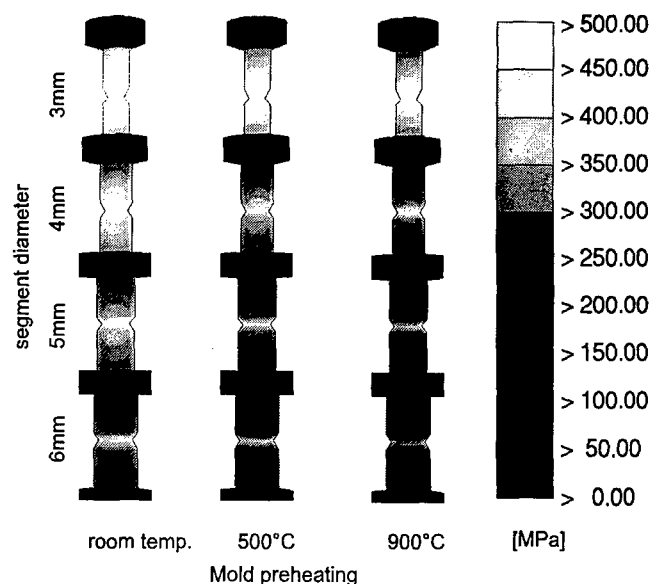


Figure 7: Simulated formation of residual stresses in dependence on the mold preheating temperature.

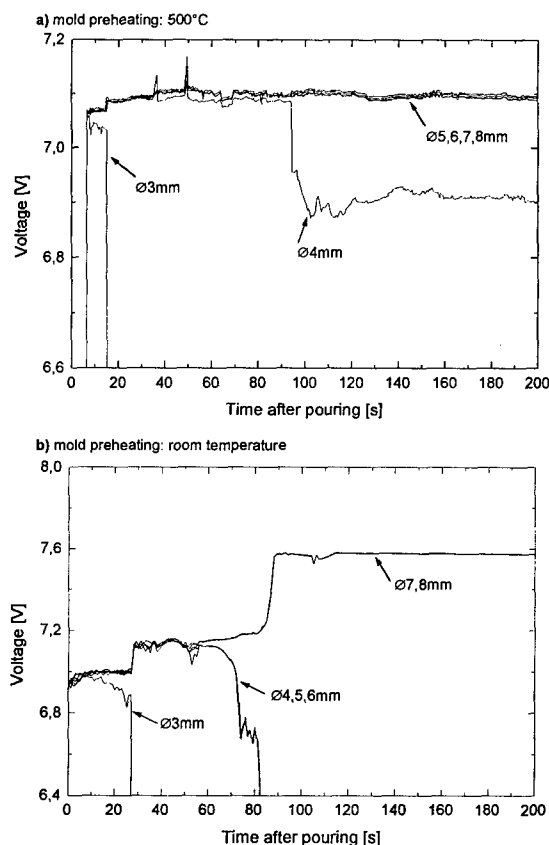
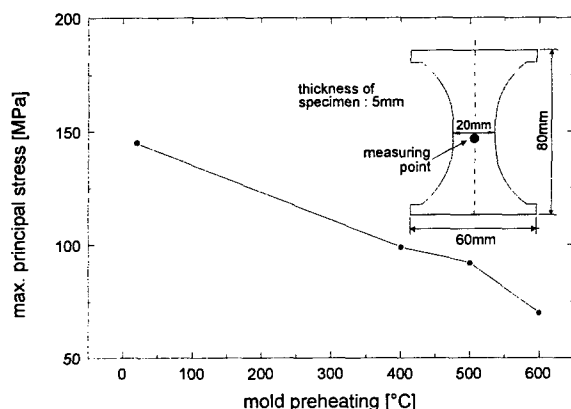


Figure 8: Monitoring of crack formation in the castings during cooling.



**Figure 9:** Dependence of residual stress on the mold preheating temperature for investment cast TiAl48Cr2Nb2 (at.-%) [20] alloy specimens.

### Conclusions

The results presented generally confirm that numerical simulation represents a useful tool for predicting temperature and thermal stress distributions in  $\gamma$ -TiAl castings during cooling. Yet, the quantitative reliability of the calculated results has to be improved. The predicted stresses may be overestimated since the formation of cracks is neglected within the calculation. Reliable thermomechanical and thermophysical data for elevated temperatures up to the solidus can rarely be found in the literature. Since the behavior of the material at high temperatures strongly influences the whole calculation, such data needs to be extended.

### Acknowledgments

Parts of this work are funded by the Deutsche Forschungsgemeinschaft (DFG). The authors would like to thank U. Hofmann and Prof. W. Blum (University Erlangen-Nürnberg) for supplying thermomechanical data.

### References

- [1] D.E. Larsen, C. Goven, "Advanced Investment Cast Processing", in: "Gamma Titanium Aluminides", Ed.: Y.W. Kim et al., TMS(1995), 405-14.
- [2] C.M. Austin et al., "Development and implementation status of  $\gamma$ -TiAl", in: "Structural Intermetallics", Ed.: R. Darolia et al., TMS, (1993), 143-50.
- [3] P.E. Jones et al., "Microstructure, process, and tensile property relationships in an investment cast near  $\gamma$ -TiAl alloy", 3rd International SAMPE Metals Conference, October 20-22nd, (1992).
- [4] J.B. Penkawa, "Untersuchung der pulvermetallurgischen Bildung und der Eigenschaften der intermetallischen Phasen LiAl und TiAl", (Ph.D. thesis Technical University Clausthal, Germany, 1988).
- [5] M. Meyer terVehn, M. Fackeldey, M. Diemer, P.R. Sahm, "Measurement and simulation of temperature stress fields during single crystal solidification of turbine blades", in: "Proceedings of Local Strain and Temperature Measurements in Non-Uniform Fields at Elevated Temperatures, Berlin 1996", Ed.: J. Ziebs, J. Bressers et al., Woodhead Publishing Ltd, Cambridge, England (1996), 243-52.
- [6] W. Schäfer, F. Hediger, A. Bührig-Polaczek, in: "Proceedings of the first European Conference on Materials and Processes Euromat 89", DGM Informationsgesellschaft, Oberursel, Germany (1990), 121-7.
- [7] P.R. Sahm, W. Richter, F. Hediger, "Mathematical simulation and modeling of solidification processes of castings", *Giesserei-Forschung*, 35(2)(1983), 35-42.
- [8] P.R. Sahm, P.N. Hansen, "Numerical Simulation and Modeling of Casting and Solidification Processes for Foundry and Cast-house", International Committee of Foundry Technical Associations CIATF, Zürich, Switzerland (1984).
- [9] J.C. Sturm, P.R. Sahm, "Solidification Simulation of an Integrated Aircraft Structure Component", in: "Modeling and Control of Casting and Welding Processes IV", TMS (1988), 69-78.
- [10] N. Hofmann, U. Reske, H. Vor, P.R. Sahm, "Numerical simulation of directional solidification using the Bridgman process", *Giesserei-Forschung*, 43(3) (1991), 101-6.
- [11] W. Wunderlich, T. Kremser, G. Frommeyer, "Enhanced Plasticity by Deformation twinning of TiAl-Base Alloys with Cr and Si", *Z. Metallkunde*, 81(1990), 802-8.
- [12] R. Wagner, F. Appel et al., "Investment casting of  $\gamma$ -TiAl-based Alloys: Microstructure and Data Base for Gas Turbine Applications", in: "Gamma Titanium Aluminides", Ed.: Y.W. Kim et al., TMS (1995), 387-404.
- [13] B. London et al., "Investment Cast Gamma Titanium Aluminide Alloys: Processing, Properties, and Promise", in: "Structural Intermetallics", Ed.: R. Darolia et al., TMS, (1993), 151-7.



- [14] R.E. Schafrik, "Dynamic Elastic Moduli of the Titanium Aluminides", Metallurgical Transactions A, 8A(1977), 1003-6.
- [15] J. Guan, P.R. Sahm, "Estimation of residual stresses in cooling down castings by the finite element method", Giesserei-Forschung, 43(1991), 10-7.
- [16] J. Guan, G.W. Dieckhues, P.R. Sahm, "Analysis of residual stresses and cracking of  $\gamma$ -TiAl castings", Intermetallics 2(1994), 89-94.
- [17] J. Mathar, "Determination of Initial Stresses by Measuring the Deformation Around Drilled Holes", Transactions of the ASME, 4(1934), 249-54.
- [18] S. Timoshenko, J.M. Goodier, Theory of Elasticity, (New York, McGraw-Hill, 1951).
- [19] G.S. Schajer, "Measurement of Non-Uniform Residual Stresses Using the Hole-Drilling Method", Journal of Engineering Materials and Technology, 110(4)(1988), 338-49.
- [20] G.S. Schajer, E. Altus, "Stress Calculation Error Analysis for Incremental Hole-Drilling Residual Stress Measurements", Journal of Engineering Materials and Technology, 118(1996), 120-6.
- [21] S.C. Huang, United States Patent 4.879.092 (1989).

## THE INFLUENCE OF ION IMPLANTATION UPON HIGH TEMPERATURE OXIDATION BEHAVIOR OF Ti-48at.%Al ALLOY

Y.G. Zhang, X.Y. Li, C.Q. Chen, X.J. Zhang\*, T.H. Zhang\* and H.X. Zhang\*

Department of Materials Science and Engineering  
Beijing University of Aeronautics and Astronautics, Beijing, 100083, P.R.China

\*Radiation Beams & Material Engineering Laboratory  
The Institute of Low Energy Nuclear Physics  
Beijing Normal University, Beijing, 100875, P.R.China

### Abstract

The isothermal oxidation resistance of Ti-48at.%Al alloy at 900°C and 950°C in an atmospheric environment could be significantly improved by Nb ion implantation with a dose of  $3 \times 10^{17} \text{ ions/cm}^2$ . Ta, W and Al self-implantation also have beneficial effect; but Cr, V and rare earth Y, Ce implantation have detrimental effect. Improvement of the oxidation resistance was enhanced with the increase of Nb ion implantation dose from  $3 \times 10^{15} \text{ ions/cm}^2$  to  $3 \times 10^{17} \text{ ions/cm}^2$ . Nb-implantation followed by post-implantation annealing at 800°C for 5h could further improve the oxidation resistance of the alloy, and the annealing temperature is a key parameter in such a treatment. The different influence of implanted elements upon the oxidation resistance of Ti-48at.%Al is attributable to the change of the oxidation mechanism, especially, modification of the oxidation scale and the diffusion rate during oxidation process.

### Introduction

Gamma Titanium Aluminide is one of the most widely investigated candidates for new alternative structural materials useful in high temperature applications because of its low density and high strength-to-density ratio at elevated temperatures[1]. However, the materials exhibits brittleness at ambient temperatures, and at the intended service temperature of about 700°C the oxidation resistance is relatively poor, particularly above 830°C. Therefore, improvement of oxidation resistance in the materials is a matter of concern in its application. Although the oxidation resistance can be improved to some extent by the addition of ternary elements[2-10], surface treatments are thought to be more effective [11-12].

It is well known that metal ion implantation is the process of altering surface properties and thus improving corrosion resistance by bombarding with high-energy metal ions. Because the process does not produce a coating, dimension and bulk properties of the part remain unchanged, and implanted surfaces have no problems with adhesion, residual stress or poor microstructure[13]. It also can be acted as a vehicle to study the effect of surface doping on the oxidation behavior which can be considered as a reference for bulk alloying additions.

The present work deals with the influence of ion implantation upon high temperature oxidation behavior of Ti-48at.%Al alloy.

### Experimental Procedures

#### Substrate Alloy and Specimens

The alloy used in present study was produced by a non-consumable argon arc furnace, using titanium sponge granular(99.9%) and pure aluminum plate(99.99%). The ingot was melted two times and followed by homogenizing treatment at 1000°C for 7 days. Isothermal forging was performed at 1150°C with the compression ratio of 59.82%, the ingot was subsequently heat treated at 1330°C/2hAC+980°C/8hAC in order to obtain similar duplex microstructure for the specimens used in ion implantation and isothermal oxidation test. The nominal composition of the ingot was Ti-48at.%Al(hereafter referred to as 48Al). Specimens measuring about  $2 \times 5 \times 9 \text{ mm}^3$  were machined from the ingot, and polished with up to 800# SiC paper and cleaned with acetone and ethanol before ion implantation and isothermal oxidation test.

### Ion Implantation

Ion implantation was carried out in MEVVA Source Ion Implanter. The element selected and the ion implantation conditions are listed in Table I.

Some of the Nb-implanted samples with a dose of  $3 \times 10^{17} \text{ ions/cm}^2$  were sealed in quartz tubes under  $1 \times 10^{-6}$  torr vacuum and post-implantation annealed at 300°C, 500°C, 800°C/5h and 500°C/1, 5, 10h, respectively.

**TABLE I Implant Species and Conditions of Ion Implantation**

Implant species	Dose(ions/cm <sup>2</sup> )	Energy(keV)	Current(mA)
V	$3 \times 10^{17}$	40×2.1	3
Nb	$3 \times 10^{15}, 3 \times 10^{16}, 3 \times 10^{17}$	40×3	1, 1, 3
Ta	$3 \times 10^{17}$	40×2.9	3
W	$3 \times 10^{17}$	40×3.1	3
Cr	$3 \times 10^{17}$	40×2.1	3
Al	$3 \times 10^{17}$	40×1.7	3
Y	$3 \times 10^{17}$	40×2.3	3
Ce	$3 \times 10^{17}$	40×3	3

### Isothermal Oxidation

The isothermal oxidation was performed at 900°C and 950°C for 100h under an atmospheric environment in a vertical furnace. The weight change of the specimens being oxidized was continuously recorded by a balance which has a resolution of 0.01mg. Two specimens were used for each isothermal oxidation test.

### Metallographic Examinations

The specimens after ion implantation and isothermal oxidation were examined by Auger Electron Spectroscopy(AES) and X-ray Diffraction(XRD). Outer surfaces and cross-sections of the oxidation scale were observed by Scanning Electron Microscopy(SEM).

## **Results**

### Isothermal Oxidation Kinetics

As only two sides ( $5 \times 9 \text{ mm}^2$ ) of a specimen was implanted, the kinetics of oxidation of the implanted surfaces was obtained by comparing the kinetics of oxidation of an implanted specimen with those of unimplanted specimens prepared in the same conditions. Then, weight change of the implanted region  $\Delta W_1$  is given as:

$$\Delta W_1 = \frac{W - \Delta W_2 S_2}{S_1}$$

Where

$\Delta W_1$  (mg/cm<sup>2</sup>) is weight gain of the implanted region.

$W$  (mg) is total weight gain of the implanted specimen.

$\Delta W_2$  (mg/cm<sup>2</sup>) is weight gain of the unimplanted specimen after the same exposure period.

$S_1$  (cm<sup>2</sup>) is the area of implanted surface on the implanted specimen.

$S_2$  (cm<sup>2</sup>) is the area of unimplanted surface on the implanted specimen

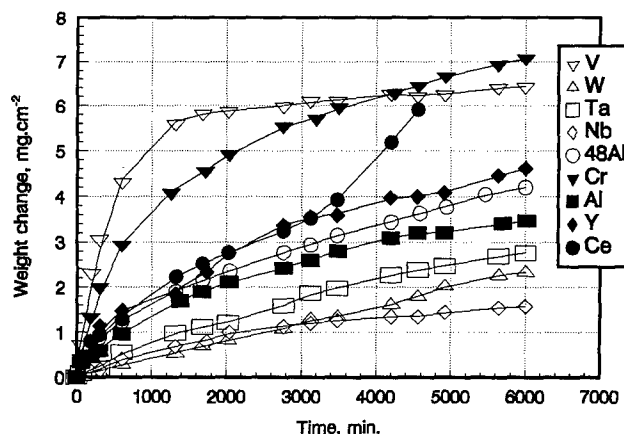


**Fig.1 The oxidation kinetics of 48Al and 48Al implanted with different elements to a dose of  $3 \times 10^{17} \text{ ions/cm}^2$ , oxidized at 900°C for 100h**

The isothermal oxidation kinetics of 48Al and 48Al implanted with different elements to a dose of  $3 \times 10^{17} \text{ ions/cm}^2$  oxidized at 900°C for 100h is shown in fig.1. It can be seen that for implanted elements V, Nb, Ta, W all have beneficial effects except V. In particular, Nb-implanted alloy shows the best oxidation resistance, and self-implanted with Al also has a noticeable improvement. However, rare earth Y, Ce and Cr which can form cations with valence lower than +4 have detrimental effect. The oxidation kinetics curves mainly are near parabola, and the oxidation resistance of Nb-implanted alloy with a dose of  $3 \times 10^{17} \text{ ions/cm}^2$  maintained considerable promotion even oxidized at 950°C for 100h (fig.2).

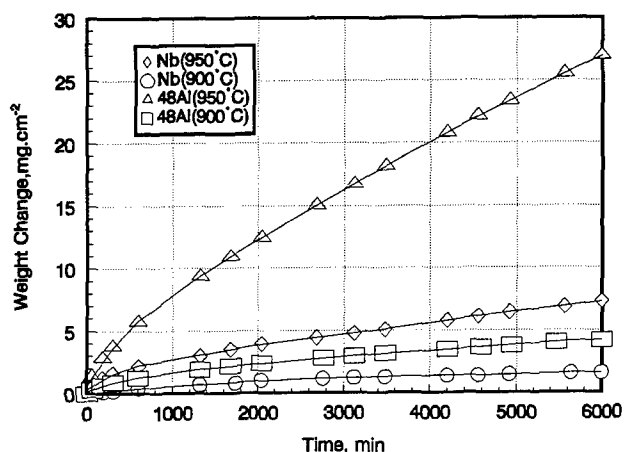


Fig. 2 The oxidation kinetics of 48Al and Nb-implanted 48Al with a dose of  $3 \times 10^{17} \text{ ions/cm}^2$ , oxidized at 900°C and 950°C for 100h

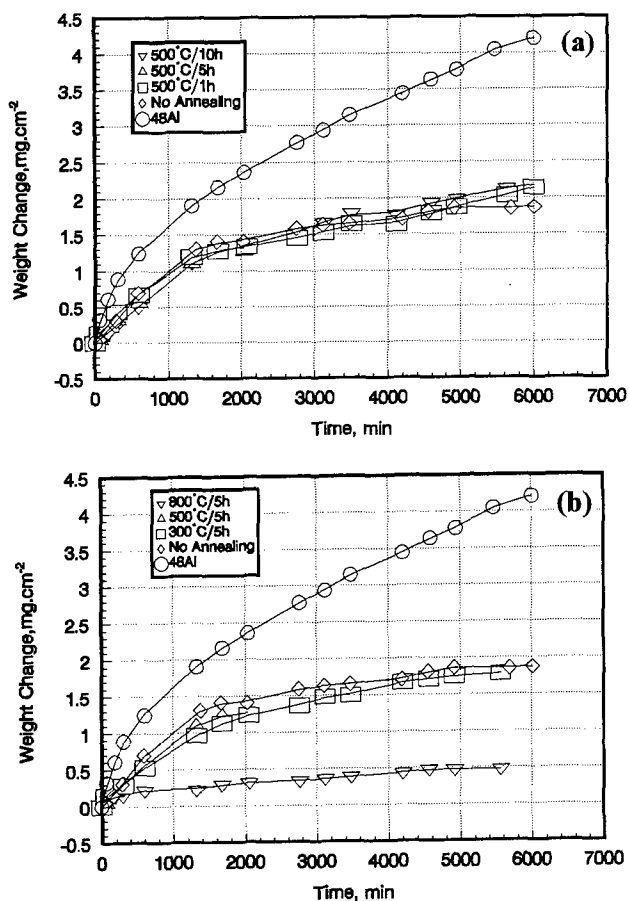


Fig. 3 Influence of different post-implantation annealing processes on the oxidation kinetics of Nb-implanted 48Al ( $3 \times 10^{17} \text{ ions/cm}^2$ ) oxidized at 900°C for 100h in air.

In comparison with the samples implanted with Nb without annealing, the post-implantation annealing at 500°C for 1, 5,

10h did not have obviously effects and this is also true for the samples with the annealing treatment at 300°C for 5h (fig. 3a and b). However, the annealing at 800°C for 5h dramatically lower the oxidation rate (fig. 3b), which indicated that annealing temperature is a key parameter in such a treatment.

#### Dose Dependence

The effect of dose on the oxidation kinetics of Nb-implanted alloy with a dose from  $3 \times 10^{15} \text{ ions/cm}^2$  to  $3 \times 10^{17} \text{ ions/cm}^2$  oxidized at 900°C for 100h is presented in fig. 4. The result shows that the oxidation rate of Nb-implanted samples decreased with the increase of the dose and, therefore, heavy dose is more effective for the Nb ion implantation to be used to modify the oxidation properties of the alloy.

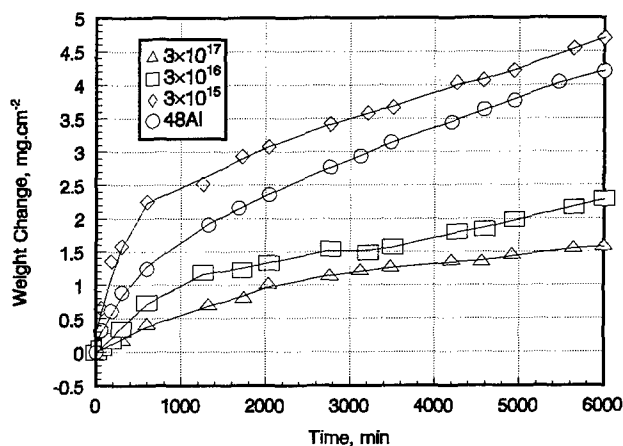


Fig. 4 The effect of dose on the oxidation kinetics of Nb-implanted alloy with a dose from  $3 \times 10^{15} \text{ ions/cm}^2$  to  $3 \times 10^{17} \text{ ions/cm}^2$  oxidized at 900°C for 100h

#### Distribution of Implanted Elements

Fig. 5 shows the element concentration distribution in Nb-implanted 48Al alloy analyzed by AES with a sputtering rate of about 5.5nm/min. The elemental concentration is a function of sputtering time, and follows near Gaussian curve, and there appears a peak concentration of Nb beneath the surface of the specimen at the depth of about 16.5nm of Nb-implanted alloy.

#### Oxidation Products

Representative XRD pattern of 48Al after isothermal oxidation at 900°C for 100h is presented in fig. 6a. In this case, TiO<sub>2</sub> and Al<sub>2</sub>O<sub>3</sub> were detected, with the strongest peak being TiO<sub>2</sub>.

XRD pattern of Nb-implanted 48Al followed by post-implantation annealing treatment at 800°C for 5h oxidized at 900°C for 100h is presented in fig. 6b. The strongest peak is TiAl followed by Ti<sub>3</sub>Al and then Al<sub>2</sub>O<sub>3</sub>, and no TiO<sub>2</sub> peak is detected. In addition, Nb<sub>2</sub>O<sub>5</sub> peak appears although it is relatively weak, which indicates that the implanted element also took part in the oxidation reaction.

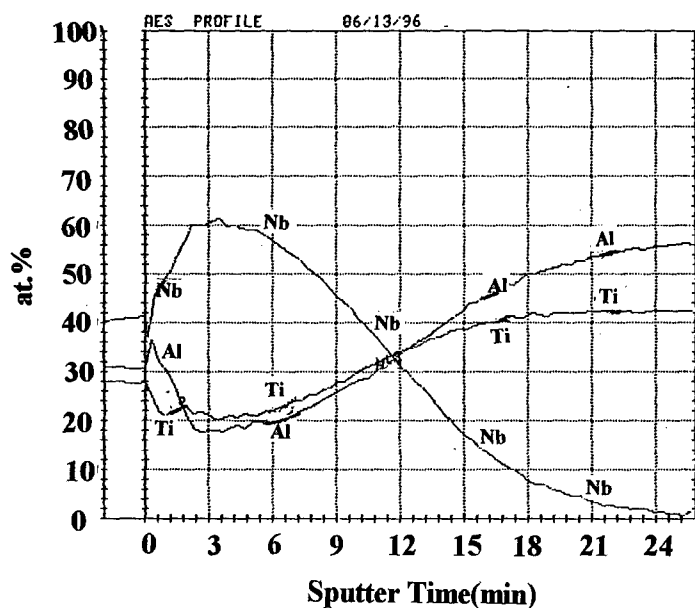


Fig. 5 AES analysis of elemental concentration distribution in Nb-implanted 48Al alloy versus sputtering time

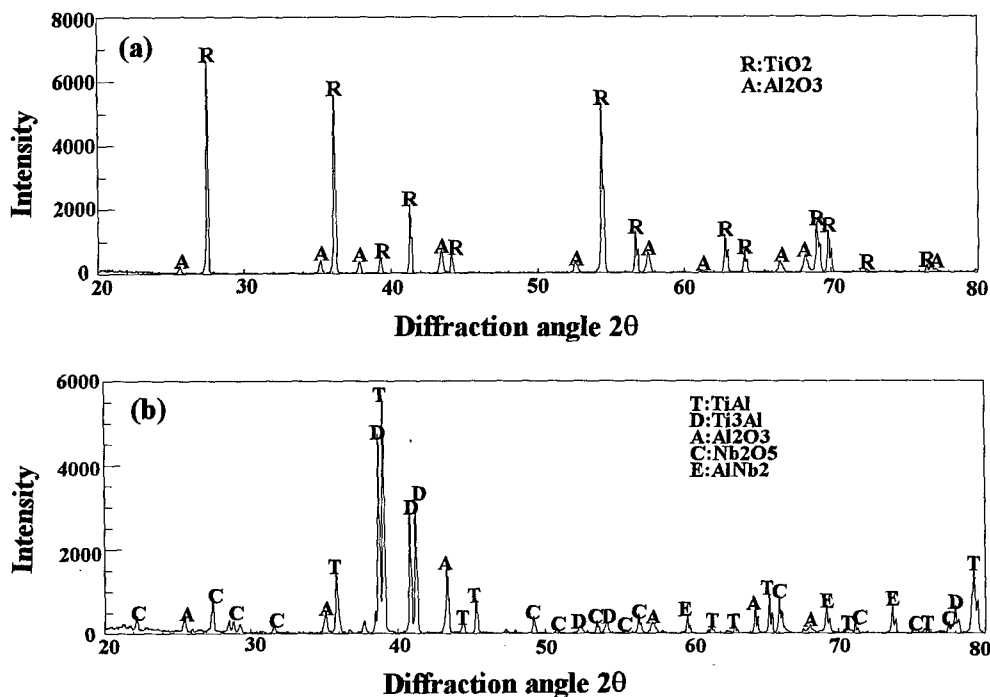


Fig. 6 XRD patterns of 48Al(a) and Nb-implanted 48Al followed by post-implantation annealing at 800°C for 5h(b) after oxidation at 900°C for 100h

#### Outer Surface Morphology of Oxidation Scale

The morphology of outer surfaces of the specimens implanted and unimplanted, oxidized at 900°C for different times, is shown in fig. 7. It is noteworthy that the shape and grain size of

the oxides developed on the surfaces of W and Ta implanted 48Al and unimplanted 48Al after oxidation at 900°C for 10h (fig. 7a, b, c) are significantly different with each other, which clearly exhibit that at the beginning of the oxidation reaction, the oxidation products and mechanism changed owing to the

influence of ion implantation. The grain size on the W-implanted surface with a dose of  $3 \times 10^{17} \text{ ions/cm}^2$  is sharply smaller than that of the unimplanted surfaces (fig.7a, c). A layer of dense TiO<sub>2</sub> grains appeared on the surface of unimplanted 48Al, and the oxide has regular shape (fig.7c). Shape of the oxides formed on the surface of Ta-implanted 48Al alloy is quite different from TiO<sub>2</sub> particles formed on unimplanted 48Al (fig.7b, c), which indicates that Ta might affect the oxidation process. After a much longer oxidation period, e.g. oxidized at 900°C for 100h, the oxides in the outer surface of

the oxidation scale in every cases almost have the same shape with the grain size increasing with exposure time, but to different extents. The average grain size of the oxides developed on the Nb-implanted surface with a dose of  $3 \times 10^{17} \text{ ions/cm}^2$  and  $3 \times 10^{16} \text{ ions/cm}^2$  is smaller than that on unimplanted 48Al alloy, especially with the dose of  $3 \times 10^{17} \text{ ions/cm}^2$  (fig.7d, f), but when the dose decrease to  $3 \times 10^{15} \text{ ions/cm}^2$ , the grain size becomes even larger than that on unimplanted one (fig.7d, e).

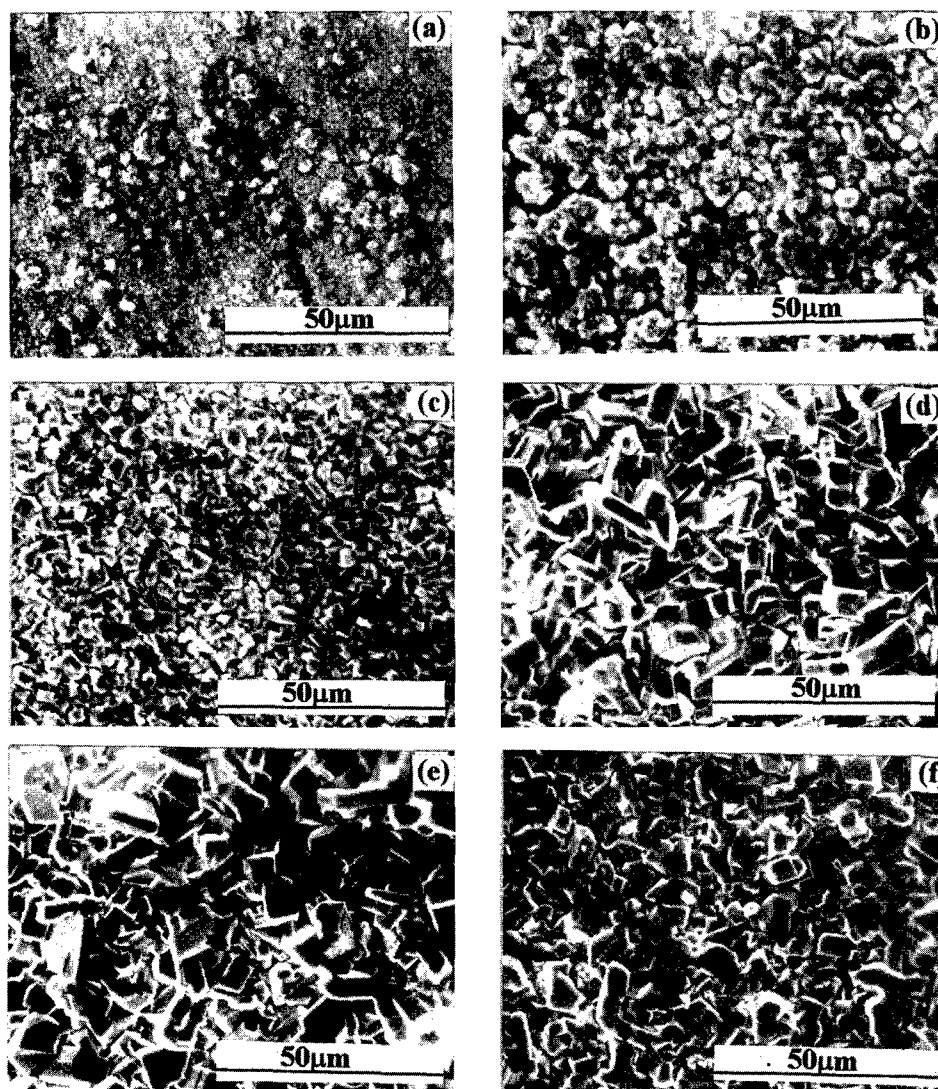


Fig.7 SEM morphology of the implanted and unimplanted 48Al oxidized at 900°C for different time

- (a) W-implanted( $3 \times 10^{17} \text{ ions/cm}^2$ ), 900°C/10h (b) Ta-implanted( $3 \times 10^{17} \text{ ions/cm}^2$ ), 900°C/10h  
(c) unimplanted 48Al, 900°C/10h (d) unimplanted 48Al, 900°C/100h  
(e) Nb-implanted( $3 \times 10^{15} \text{ ions/cm}^2$ ), 900°C/100h (f) Nb-implanted( $3 \times 10^{17} \text{ ions/cm}^2$ ), 900°C/100h

In fig.8a, b, it can be seen that the oxide grain size of Nb-implanted 48Al followed by the post-implantation annealing at 800°C for 5h is smaller than that of Nb-implanted 48Al with

the same dose of  $3 \times 10^{17} \text{ ions/cm}^2$  without the annealing treatment. The annealing treated alloy showed the best oxidation resistance.

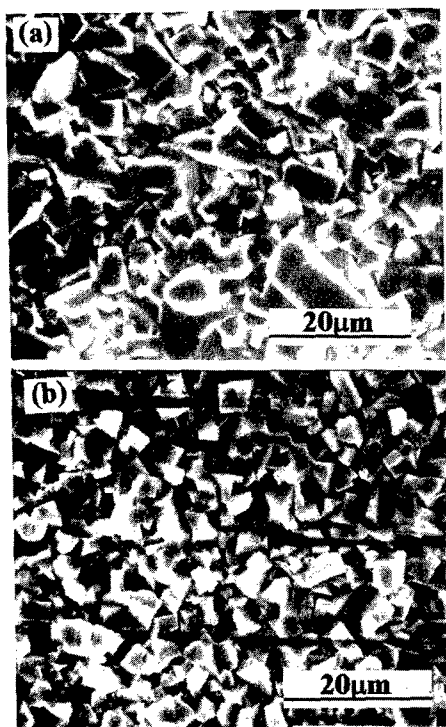


Fig.8 SEM morphology of Nb-implanted 48Al( $3 \times 10^{17}$  ions /  $cm^2$ )(a) followed by post-implantation annealing at 800°C for 5h(b) after oxidation at 900°C for 100h

#### Cross-Section Morphology of Oxidation Scale

Fig.9 shows the morphology of the cross-section of oxidation scales formed on unimplanted 48Al alloy and those implanted with Nb. The typical cross-section structure of the oxidation scale of 48Al oxidized at 900°C for 100h was multi-layer oxides, which is in agreement with other reports[14 -16]. It is noted that the  $Al_2O_3$  formed in the outer part of the oxidation scale was like islands and discontinuously dispersed in the  $TiO_2$  layer(fig.9a, c); a layer of almost pure  $TiO_2$  appears next to this part. The internal region is uniformly and loosely dispersed with mixture of  $TiO_2$  and  $Al_2O_3$ . There did not exist a layer of continuous and compact  $Al_2O_3$  to act as a barrier inhibiting the outward and inward fluxes of elements and oxygen during oxidation process. However, it can be seen that two layers of almost continuously  $Al_2O_3$  had been formed in the oxidation scale of Nb-implanted alloy with a dose of  $3 \times 10^{17}$  ions /  $cm^2$  oxidized at 900°C for 100h(fig.9b), and the oxidation scale is relatively thinner than that of unimplanted one. In the case of oxidized at 950°C for 100h, in addition to the outer continuously  $Al_2O_3$  layer, the  $Al_2O_3$  particles in the internal region almost completely linked each other (fig.9d) and look like a network. This kind of structure of  $Al_2O_3$  could retard and even block the diffusion process and effectively reduce the oxide growing rate. Hence, this result demonstrates that Nb-implanted alloy with a dose of  $3 \times 10^{17}$  ions /  $cm^2$  could enhance the formation of  $Al_2O_3$  to act as a barrier against the diffusion process and slow down the oxidation rate.

Fig.10 shows AES analysis of element concentration distributions with sputtering time in Nb-implanted alloy after post-implantation annealing at 800°C/5h and then oxidized at 900°C for 100h. In comparison with the Nb implanted 48Al without post-implantation annealing, Nb is more uniformly distributed in a wider region with a small concentration peak of about 8at.% beneath the surface, but Al has much higher concentration at the outer layer. It may be inferred that there is formation of a almost continuous  $Al_2O_3$  layer at the external part of the oxidation scale in this case. The results confirm that redistribution of the implanted Nb during the post-implantation annealing is responsible, at least partly, for the remarkable promotion of the oxidation resistance of the implanted alloy.

### Discussion

#### Influence of Different Implanted Elements

The oxidation kinetics of different element-implanted 48Al exhibit that the implanted species play different role in modifying the oxidation behavior of 48Al substrate alloy. Classically, the growth of the scale on 48Al alloy should follow Wanger mechanism, where by cations diffuse outward through the oxidation scale is a control-step to the oxidation reaction, therefore the factor which can slow the diffusion will lower the oxidation rate. It should be noted that  $TiO_2$  and  $Al_2O_3$ , which are major oxidation products of 48Al, are all N-type semiconductors. Additions of elements which forms cations with valence more than +4 will substitute the Ti and Al sites in the  $TiO_2$  and  $Al_2O_3$  space lattices and thus reduces the number of interstitial and oxygen ion vacancies in the oxides. This effect can decrease the diffusion rate in the oxidation scale. The implanted elements selected from VB group such as Nb, Ta and W may have this kind of influence, and Cr also follows this valent-control rule, but V is a exception. The reason may be due to the low melting point of  $V_2O_5$ . In addition to the valent-control rule, implanted elements may incorporate with the oxidation reaction of the base alloy and modify the structure of the oxidation scale as we discussed above.

The self-implanted with Al will form a higher Al content region in the surface of base alloy and, therefore, it is expected to enhance the formation of  $Al_2O_3$  layer against oxygen flux, and thus improve the oxidation resistance. However, the result shows that the improvement is not so effective. The reason should be investigated in the future.

Previous reference[17] reported that additions of rare earth elements Y and Ce could improve the adhesion between the interface of oxidation scale and substrate, but in this study, Y and Ce implantation with a dose of  $3 \times 10^{17}$  ions /  $cm^2$  did not have any beneficial effect on the oxidation resistance of 48Al. This may be due to the heavy dose we used, because Y and Ce have high affinity for oxygen and, as a result, they might easily react with oxygen at the beginning of the oxidation. There might have an optimum concentration for implantation of rare earth Y and Ce which may have good effects on the oxidation resistance of 48Al alloy.

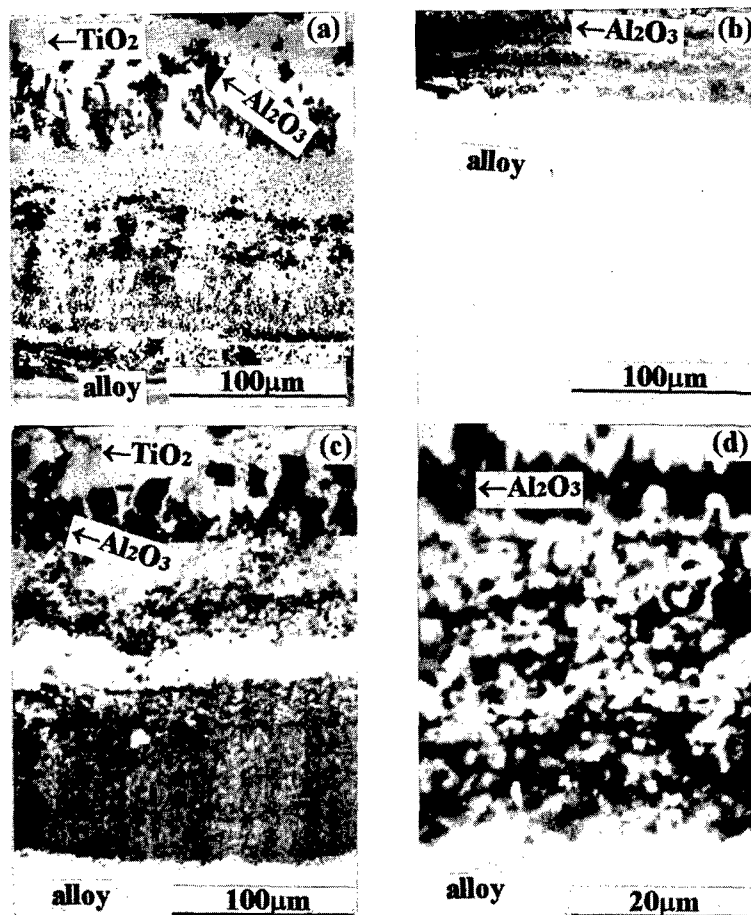


Fig.9 Cross-sections of the oxidation scale formed on Nb implanted and unimplanted 48Al alloy  
 (a) unimplanted 48Al, 900°C/100h (b) Nb-implanted( $3 \times 10^{17}$  ions /  $cm^2$ ), 900°C/100h  
 (c) unimplanted 48Al, 950°C/100h (d) Nb-implanted( $3 \times 10^{17}$  ions /  $cm^2$ ), 950°C/100h

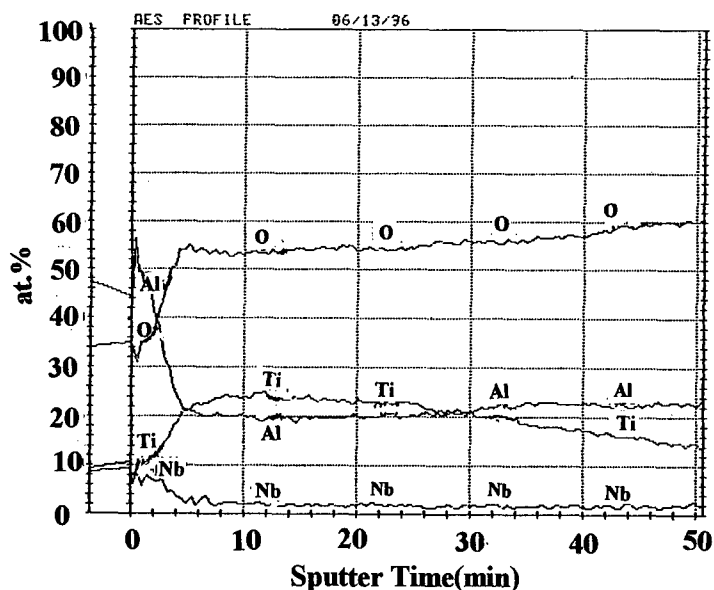


Fig.10 AES analysis of elemental concentration distribution versus sputtering time in Nb-implanted 48Al( $3 \times 10^{17}$  ions /  $cm^2$ ) alloy after post-implantation annealing(800°C/5h) and oxidized at 900°C for 100h in air.(sputtering rate:5.5nm/min)



### Influence of Dose and Post-implantation Annealing

The oxidation kinetics of Nb-implanted 48Al with different doses shows that the oxidation rate decreases with the increase of the dose from  $3 \times 10^{15} \text{ ions/cm}^2$  to  $3 \times 10^{17} \text{ ions/cm}^2$ . This may be explained by understanding the ion implantation process. Ion implantation is a very complex process, in addition to doping, a primary process of implantation, many secondary processes such as lattice damage and surface sputtering etc. can take place in the implanted region. The primary and secondary changes can play opposite roles in the oxidation behavior of 48Al alloy, therefore, when the dose is as low as  $3 \times 10^{15} \text{ ions/cm}^2$ , its oxidation resistance even poorer than unimplanted one. Because in this case, the secondary effect caused by ion implantation might exceed the beneficial effect of primary doping. Hence, it will be very important to annihilate the secondary effect using proper post-implantation annealing measure, this has been verified by our experiment results.

### Conclusions

- 1) The oxidation resistance of 48Al alloy implanted with Nb, W and Ta respectively and self-implanted with Al with a dose of  $3 \times 10^{17} \text{ ions/cm}^2$  has been significantly promoted in comparison with that unimplanted; in particular, Nb-implanted one has the best oxidation resistance among them; Y, Ce, Cr and V-implanted have detrimental effect.
- 2) The oxidation rate of Nb-implanted 48Al decrease with increasing of dose from  $3 \times 10^{15} \text{ ions/cm}^2$  to  $3 \times 10^{17} \text{ ions/cm}^2$ .
- 3) 48Al alloy implanted with Nb with proper dose can enhance the formation of a layer of continuous and compact  $\text{Al}_2\text{O}_3$  to act as a barrier of diffusion process during long-term oxidation; the other elements may influence the beginning of oxidation reaction and change the oxidation mechanism of the alloy.
- 4) Nb-implantation followed by post-implantation annealing at 800°C for 5h can further improve the oxidation resistance of the alloy, and the annealing temperature is a key parameter in such a treatment.
- 5) The post-implantation annealing effect is probably due to both the diminishing of the lattice damage induced by the implantation and redistribution of the implanted Nb, which may favor the formation of a continuous  $\text{Al}_2\text{O}_3$  layer as a barrier of diffusion.

### Acknowledgments

The authors would like to thank Aeronautical Science Foundation of China for the financial support.

### References

1. Young-Won Kim, JOM, July (1989) 24-30
2. Meier, G.H: Oxidation of high temperature intermetallics, ed. by T.Grobstein and J.Doychak, The Minerals, Metals and Materials Soc., (1989) 1-16
3. T.Shimizu, T.Iikubo and S.Isobe: Report of 123rd committee on heat resisting metals and alloys, Japan Soc. for the promotion of science, 31 (1990) 309
4. D.N.McKee and S.C.Huang: Corros. Sci., 33 (1992) 1989
5. S.Taniguchi, T.Shibata and H.Juso: Oxid. Met., 42 (1994) 205
6. R.A.Perkins, K.T.Chiang, G.H.Meier and R.Miller: Oxidation of high temperature intermetallics, ed. by T.Grobstein and J.Doychak, The Minerals, Metals and Materials Soc., (1989) 157-169
7. K.Shibue, M.Kumagw and H.Kim: J. Japan Inst. Metals, 56 (1992) 1457
8. K.Maki, M.Shioda, M.Sayashi, Shimuzu, et al Mater. Sci. Eng., A153 (1992) 591-6
9. R.A.Perkins, K.T.Chiang and G.H.Meier, Scripta Metall., 21 (1987) 1505
10. J.B. M.Couarew and H.D.Kessler, J. Met., 8 (1956) 1348
11. S.Taniguchi, T.Shibata and K.Takeuchi, Mater. Trans., JIM, 32 (1991) 299
12. S.Taniguchi, T.Shibata, T.Yamada, X.-H Liu and S.C.Zou, ISIJ International, 33 (1993) 869
13. James R.Treglio Anthony J.Peny and Robert J.Stinner, Advanced Mater. & Process, 5 (1995) 29
14. G.Welsh and A.I.Kahreei, in Oxidation of high temperature intermetallics (ed. T.Grobstein and J.Doychak). TMS, Warrendale, PA., (1989) 207
15. M.Yoshihara and R.Tanaka, Bulletin Japan Inst. Metals, 30 (1991) 61
16. Y.Shida and H.Anada, J. Japan Inst. Metals, 55 (1991) 690
17. M.J.Beunett, G.Dearnaley, M.R.Houlton and R.W.M.Hawes, Proc. of the 3rd Int. Conf. on modification of surface properties of metals by ion implantation, ed. by V.Ashworth, W.A.Grant and R.P.M.Procter, UMIST, Manchester, UK, 23-26, June (1981) 245

## STUDY ON SUPERPLASTICITY OF DEFORMED $\text{Ti}_3\text{Al}$ AND $\text{TiAl}$ BASE ALLOYS

Shiqiong Li, Jianmin Zhang, Bin Wang, Jianwei Zhang,  
Dunxu Zou, Tiancong Jia, and Zengyong Gong  
Dept. of Superalloys, Central Iron & Steel Research Institute (CISRI),  
Beijing, 100081, P. R. China

### Abstract

The superplasticity behaviour of a  $\text{Ti}_3\text{Al}$  base alloy, Ti-24Al-14Nb-3V-(0-0.5)Mo (at.%), and  $\text{TiAl}$  base alloys, Ti-46.5Al-2.5V-1Cr (at.%) and Ti-46.5Al-1Cr-0.3Si (at.%), developed in CISRI, Beijing, China, was studied. Experimental results indicate that the alloy, Ti-24Al-14Nb-3V-0.5Mo(at%), has excellent superplasticity. The tensile elongation of a cylindrical specimen tested at 960°C in air under an initial strain rate of  $1.5 \times 10^{-3}/\text{sec}$  has reached a value up to 1240% as a result of very fine  $\alpha_2$  and  $\beta_0$  grains ( $<1\mu\text{m}$ ) and their random distribution. The strain rate sensitivity parameter ( $m$ -value) of the alloy at 960°C being 0.76 has also been evaluated. Both total elongation and yield stress strongly depend on the strain rates and the grain sizes of the alloy. Metallographic observation on sections of fracture surfaces of the tested specimens shows that grain growth and recrystallization occurred during deformation but no cavities were observed. Some aerospace components made of this  $\text{Ti}_3\text{Al}$  base alloy have been fabricated by means of the superplastic forming techniques. A value of 164% of elongation has been obtained for the isothermally forged Ti-46.5Al-2.5V-1Cr (at%) alloy tested at 1000°C in air. Microstructure examination suggests that the superplastic deformation in this alloy is possibly related to the fine and equiaxed  $\beta$  grains around the boundaries of lump-shaped  $\gamma$  phase, as well as to recrystallization. Effect of coating of pure aluminum on the superplasticity of the isothermally forged Ti-46.5Al-1Cr-0.3Si(at%) alloy was also investigated by tension tests of sheet specimens at elevated temperatures. The superplasticity of the alloy increases for the specimens coated with pure aluminum. The superplastic elongation value has reached up to 250% for a coated specimen tested at 1100°C as a result of the coating of pure aluminum, which protects a specimen from oxidizing and releases

the location stress on the surface of the specimen, delaying formation and expansion of cavities.

### Introduction

Titanium aluminide intermetallic alloys based on  $\text{Ti}_3\text{Al}$  and  $\text{TiAl}$  have been received a great attention in the past two decades because of their strong potential for high-temperature applications(1). These materials, however, suffer from low ductility at room temperature, which places a great limit on their engineering applications. Development efforts have been active particularly in the areas of alloying and thermomechanical processing (TMP) design for the modification of microstructure to improve plasticity(2). Some success has been achieved and a series of  $\text{Ti}_3\text{Al}$  and  $\text{TiAl}$  base alloys with engineering significance have been developed(3). However, the difficulty in shaping these two types of titanium aluminides into structural parts is another important limitation to their engineering applications. In particular, hot working of  $\gamma$  titanium aluminide base alloys is a fundamental option for the preparation of sheets and parts. Therefore, improvement of superplasticity of  $\text{Ti}_3\text{Al}$  base and  $\text{TiAl}$  base alloys must be an important way to promote their applications. More research works have shown that the superplasticity of  $\text{Ti}_3\text{Al}$  and  $\text{TiAl}$  base alloys can be improved by microstructural control with extensive application of TMP(4-7).

A  $\text{Ti}_3\text{Al}$  base alloy, Ti-24Al-14Nb-3V-(0-0.5)Mo (at.%), named as TAC-1, and  $\text{TiAl}$  base alloys, Ti-46.5Al-2.5V-1Cr (at.%) and Ti-46.5Al-1Cr-0.3Si (at.%) were developed in CISRI, Beijing, China(8-10). These two types of  $\alpha_2$  and  $\gamma$  titanium aluminides base alloys exhibit not only good combinations of strength and ductility at room and elevated temperatures, but also good superplasticity

as result of modification in alloying and in TMP sequences performed(8-10). The objective of this paper is to mainly report recent results obtained in studying superplasticity behaviour of

these alloys and their engineering applications in fabricating aerospace components.

Table I Chemical Analysis of the Ti-24Al-14Nb-3V-0.5Mo (at%) Alloy

Ti	Al	Nb	V	Mo	O	N	H
		at%				ppm	
59.23	24.05	13.48	2.74	0.48	1110	54.0	40.5

Table II Mechanical Properties of the Ti-24Al-14Nb-3V-0.5Mo(at%) Alloy

Temperature, °C	$\sigma_b$ , MPa	$\sigma_{0.2}$ , MPa	$\delta_5$ , %
20	1010	799	9.07
	1058	795	9.73
700	680	550	25.85
	668	540	16.85

#### Material and Experimental

The TAC-1 alloy material used for this work was prepared by consumable electrode arc-melting furnace in vacuum environment. Three cycles of melting steps were performed to insure homogeneity and suitable size of ingot (25-50 kg). The composition of the alloy is given in Table I. In order to obtain a microstructure with finer primary  $\alpha_2$  and  $\beta_0$  grains, two TMP sequences were employed for the alloy which were used for the superplasticity tests. In sequence 1 the ingot obtained was first forged in the  $\beta$  field to 30 mm diameter billets and then forged at a lower temperature in the  $(\alpha_2 + \beta)$  field to 8.5 mm diameter bars followed by air cooling (AC). In sequence 2 the ingot was first extruded in the  $\beta$  field to 100 mm diameter billet, then forged in the  $(\alpha_2 + \beta)$  field to 20x50x200 mm billets, and then hot rolled at the lower temperature in the  $(\alpha_2 + \beta)$  field to plates with 2-3 mm of thickness followed by air cooling. The composition of the alloy used in sequence 2 was slightly modified, as it contained no Mo and the interstitial elements of O, H and N were very low. Table II gives the mechanical properties of tensile specimens prepared from the bars which first were subjected to the TMP sequence 1, and then to  $(\alpha_2 + \beta)$  solution treatment (ST) followed by water quenching (WQ) plus 850°Cx24h air-cooling aging. The tensile direction for the cylindrical shaped specimens(3mm in diameter) is parallel to longitudinal direction of the bars, and for the sheet specimens(1.5mm in thickness) is parallel to rolling direction.

The Ti-46.5Al-2.5V-1Cr(at%) and Ti-46.5Al-1.0Cr-0.3Si(at%) alloys used for superplasticity studies in the present work were produced by consumable electrode arc-melting in an evacuated and Ar-filled environment to cylindrical ingots having 130mm diameter and 240 mm height. The ingots were firstly subjected to homogenization heat treatment at 1000°C for 48h, then isothermally forged at 1050°C with about 80% height reduction. Specimens for superplastic testing were taken from the region with uniform structure in the forged disks and prepared by electric discharge machining followed by surface finishing with emery

polishing. The surfaces of some specimens of Ti-46.5Al-1.0Cr-0.3Si alloy were coated with pure aluminum by a plasma coating technique for examining the coating effect on superplastic deformation behaviour of the TiAl base alloy.

Strain rate sensitivity factors of the TAC-1 alloy,  $m$ -values, were evaluated on a Gleeble-1500 testing machine from tensile velocity jump tests of specimens at 940°C, 960°C and 980°C. High temperature tensile tests were performed in air in the range from 920 to 980°C for the TAC-1 Ti<sub>3</sub>Al base alloy and 900 to 1000°C for the Ti-46.5Al-2.5V-1Cr alloy as well as 900-1200°C for the Ti-46.5Al-1Cr-0.3Si alloy on SR-2 type tensile machine at a constant cross head speed with an initial strain rate ranging from  $8 \times 10^{-3}$  to  $3 \times 10^{-4} \text{ s}^{-1}$ . Before tensile testing, a pre-treatment process was given to specimens, which had been either in a forged or in a rolled state, by annealing the specimens for 15 minutes at the same temperature as that of the tensile testing performed in order to obtain a relatively stable recrystallization microstructure.

Metallographic observations with optical and scanning electron microscopy (SEM) equipped with image analysis system were performed at various stages of the processing. Specimens for microstructure examination were made by grinding and diamond polishing techniques and were etched with a solution containing 3% HF + 5% HNO<sub>3</sub> in H<sub>2</sub>O. Particularly, the microstructure details and phase distribution of the alloys were also characterized with transmission electron microscopy (TEM).

#### Results and Discussion

##### Microstructure Prior to High Temperature Tensile Testing

Figure 1(a) and 1(b) show characteristics of the recrystallization microstructure of TAC-1 alloy specimen which was subjected to TMP of sequence 1, and then to annealing at 960°C for 15 minutes followed by water quenching. The microstructure showed in the figures reveals a two phase microstructure of  $\alpha_2$  grains distributed

within a  $\beta_0$  matrix. The  $\alpha_2$  grains (dark phase) are very fine ( $<1\mu\text{m}$ ) and relatively equiaxed with an about 40% volume fraction. Such microstructure of TAC-1 alloy is recognized as that prior to high temperature tensile testing.

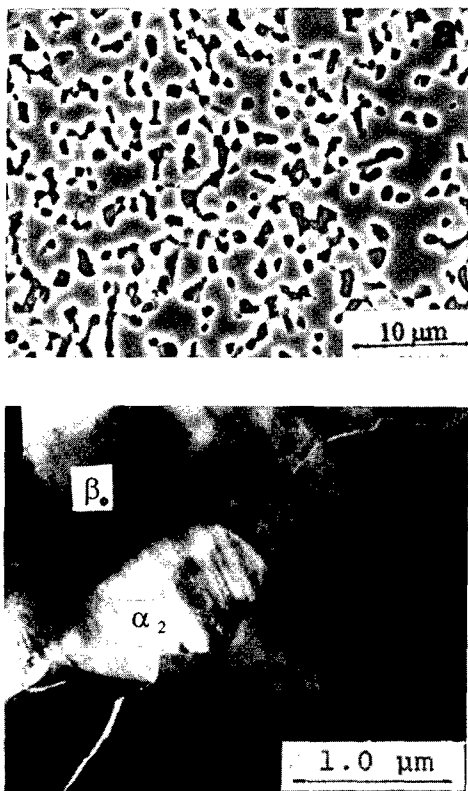


Figure 1: Microstructure prior to high temperature tensile testing of TAC-1 alloy: (a) Scanning electron micrograph (BSE); (b) TEM micrograph.

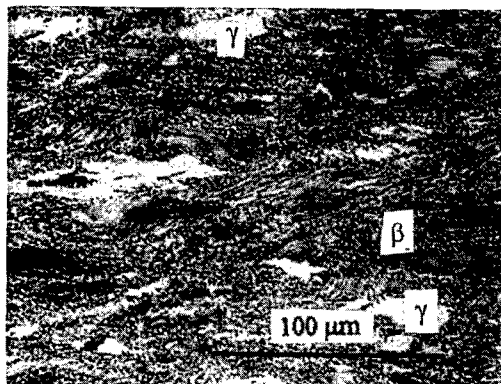


Figure 2. Optical micrograph of the Ti-46.5Al-2.5V-1Cr(at%) alloy after isothermal forging.

An optical micrograph of the Ti-46.5Al-2.5V-1Cr(at%) alloy after an isothermal forging at  $1050^\circ\text{C}$  with about 80% reduction in height is shown in figure 2. A relatively large amount of fine and equiaxed grains is observed around the boundaries of lump-shaped  $\gamma$  phase. These fine grains have been identified as  $\beta$  phase of a body

centred cubic structure by crystallographic analyses with X-ray and electron diffraction. The microstructure characteristics observed in the present work is consistent with the results of Naoya Masahashi (6) in studying a high-purity gamma titanium-aluminide ternary alloy, Ti-47Al-3Cr(at%). The authors (6) suggested that the fine  $\beta$  grains around the  $\gamma$  phase were produced by means of a recrystallization process during isothermal forging.

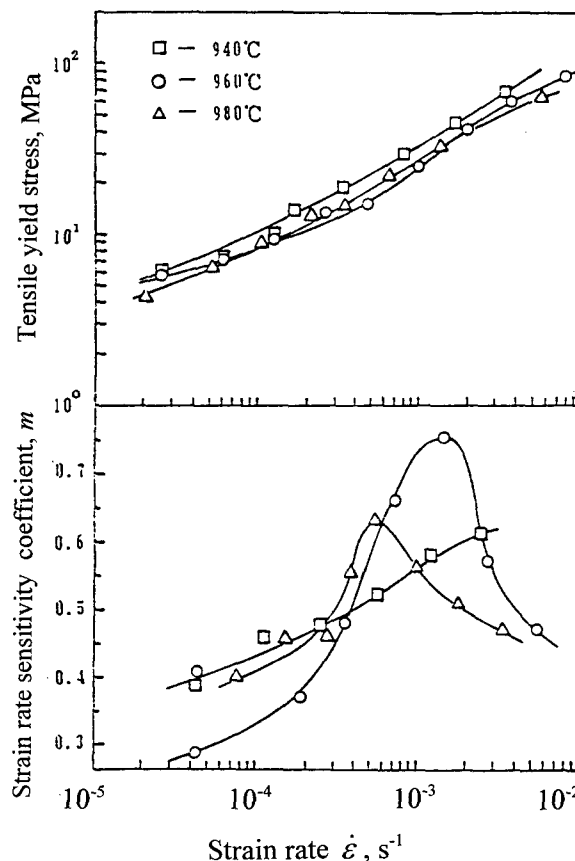


Figure 3: The variation of tensile yield stress and strain-rate sensitivity coefficient as a function of strain rate and testing temperature for the TAC-1 alloy treated by sequence 1 of TMP.

#### Superplasticity of the TAC-1 Alloy

Figure 3 shows the variation of tensile yield stress and strain-rate sensitivity coefficient ( $m$ -value) as a function of strain rate obtained for the TAC-1 alloy processed with sequence 1 TMP. The yield stresses vary slightly with testing temperatures in the range of 940 to  $980^\circ\text{C}$ . The  $m$ -values however are strongly dependent on testing temperature. A maximum  $m$ -value of 0.76 was assessed at  $960^\circ\text{C}$  at a strain rate of  $1.5 \times 10^{-3}/\text{sec}$ . Tensile elongation of a cylindrical specimen tested at  $960^\circ\text{C}$  in air under an initial strain rate of  $1.5 \times 10^{-3}/\text{sec}$  reaches a value up to 1240% (figure 4c) because of very fine  $\alpha_2$  and  $\beta_0$  grains ( $<1\mu\text{m}$ ) and their random distribution. The superplastic elongation of the alloy decreases greatly with increasing grain size of the  $\alpha_2$  and  $\beta_0$  grain. A maximum elongation of 818% was obtained for the specimen containing  $\alpha_2$  and  $\beta_0$  grains (Fig. 4b), the sizes of which were about  $2\mu\text{m}$ . Nevertheless, it was also noticed the fact that a higher elongation value of 1129% was obtained for the sheet sample treated in sequence 2 of TMP, and tested at  $960^\circ\text{C}$  under an initial strain rate of  $5 \times 10^{-3}/\text{sec}$  (figure

4g), even though the sizes of the grains had been relatively large (1-3 $\mu$ m). The origin for such high superplasticity deformation obtained in this case is probably associated with the very low contents of interstitial elements of O, H and N in the alloy treated according to sequence 2 of TMP. These effects have also been identified to improve RT ductility and formability of alloy TAC-1(3,10).

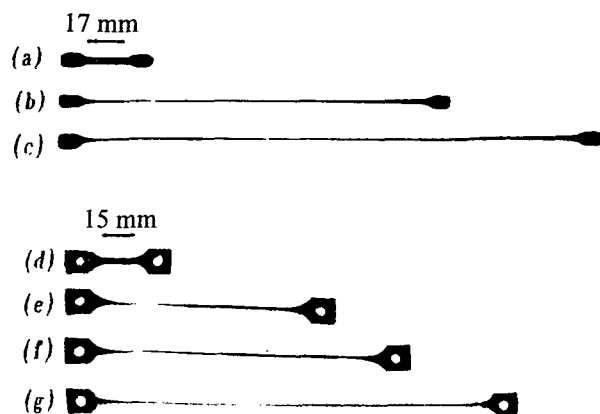


Figure 4: Profile of alloy TAC-1 specimens showing superplastic elongation obtained

- (a) undeformed cylindrical shaped specimen;
  - (b)  $\delta=818\%$ , at  $980^{\circ}\text{C}$ ,  $3.5 \times 10^{-4}/\text{sec}$ , grain size  $<2\mu\text{m}$ ;
  - (c)  $\delta=1240\%$ , at  $960^{\circ}\text{C}$ ,  $1.5 \times 10^{-3}/\text{sec}$ , grain size  $<1\mu\text{m}$ ;
  - (d) undeformed sheet specimen;
  - (e)  $\delta=413\%$ , at  $920^{\circ}\text{C}$ ,
  - (f)  $\delta=776\%$ , at  $940^{\circ}\text{C}$ ;
  - (g)  $\delta=1129\%$ , at  $960^{\circ}\text{C}$ ,
- for (e) (f) and (g) the initial strain rate  $5 \times 10^{-4}/\text{sec}$ .

Metallographic observation on the sections of fracture tips of deformed specimens showed that grain growth and recrystallization occurred during deformation but no cavities were observed. Figure 5 shows the variation in microstructure with increasing deformation, indicating that the growth of  $\alpha_2$  grains increases obviously near the fracture tip region, but the deformed specimen still features an equiaxed microstructure even at relatively large deformations. This facilitates grain boundary sliding and rotation mechanisms that are believed to play an important role in micrograin superplasticity(4-6).

The  $\alpha_2$  base alloy, TAC-1, remains free from cavitation after large superplastic tensile elongation ( $>1000\%$ ), although dynamic grain growth occurred. The alloy is therefore suitable for stretch forming without the need to impose back pressure to inhibit cavitation. The micrographs in figure 6 show two testing components with complicated shape fabricated by means of superplastic forming techniques. They represent a shroud and a corrugated plate, both of which will be applied for aerospace industry in China. Results of tensile testing performed on specimens which were machined from a position with 66% deformation of the shroud component indicated that the alloy still shows sufficient strength( $\sigma_b=850\text{MPa}$ ,  $\sigma_{0.2}=730\text{MPa}$ ) and ductility ( $\delta=7\%$  at room temperature) to satisfy the working conditions of this component.

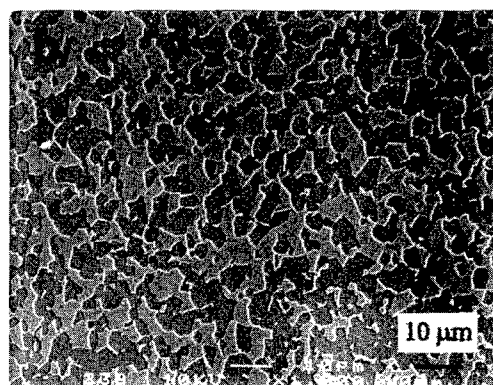
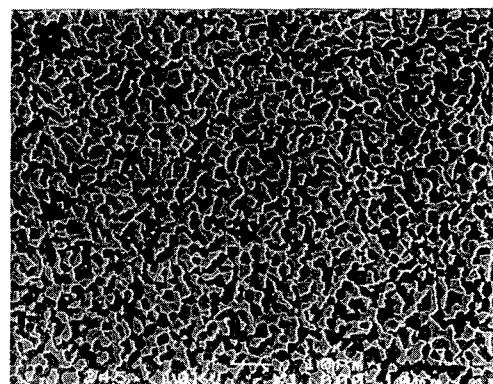


Figure 5: SEM micrographs showing microstructure on the two positions of the section of the fracture tip surface taken from the right part of the specimen shown in figure 4(f): (a) 10mm apart from tip, (b) vicinity of the fracture tip.

#### Superplasticity of the TiAl Base Alloys

An elongation of 164% was obtained for the specimen of Ti-46.5Al-2.5V-1Cr (at%) alloy tested at  $1000^{\circ}\text{C}$  in air at an initial strain rate of  $5 \times 10^{-4}/\text{sec}$ . The microstructures of the specimens prior and after deformation are shown in figure 2 and figure 7 respectively, suggesting that superplastic deformation in the alloy is possibly related to the fine and equiaxed  $\beta$  grains distributed around boundaries of lump-shaped  $\gamma$  phase (figure 2), as well as to recrystallization which occurred at high temperature deformation (figure 7). This is consistent with observation of Naoya Masahashi(6) on elevated temperature deformation behaviour in a high-purity gamma titanium-aluminide based ternary alloy: Ti-47Al-3Cr (at%). As has been concluded by the authors, the superplastic behaviour of this ternary alloy arises from grain boundary sliding promoted by the presence of the beta phase on grain boundaries. As mentioned before, the fine  $\beta$  grains around the  $\gamma$  phase in the Ti-46.5Al-2.5V-1Cr(at%) were produced by means of recrystallization during the isothermal forging process. The oxidation at high temperatures strongly affects the superplastic elongation obtainable in the Ti-46.5Al-2.5V-1Cr(at%) alloy.

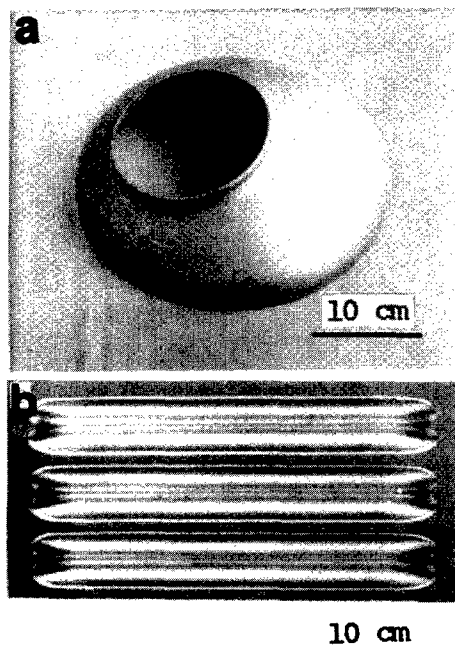


Figure 6: Photographs of a shroud (a) and corrugated plate (b) made from TAC-1 ( $\text{Ti}_3\text{Al}$  base alloy) by superplastic forming technique.

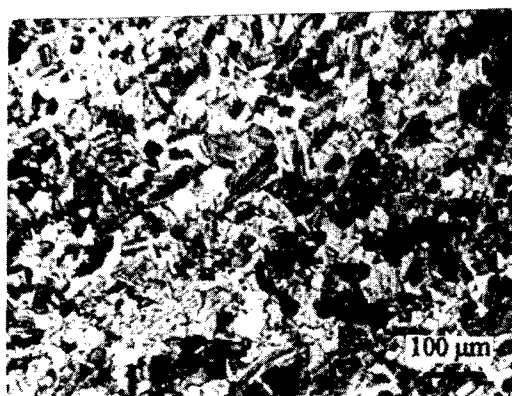


Figure 7: Optical micrograph of recrystallization microstructure observed on the surface of a deformed specimen of Ti-46.5Al-2.5V-1Cr(at%) alloy.

A relatively low elongation of 102% was the test at  $1100^\circ\text{C}$  when tested under the same conditions as at  $1000^\circ\text{C}$ . Formation and coalescence of cavities were observed on the surfaces of the deformed specimens (figure 8), which possibly determines the limit of superplastic elongation of the alloy.

Evaluation of the superplastic behaviour of the isothermally forged Ti-46.5Al-1Cr-0.3Si(at%) alloy showed that the superplastic elongation increases with the testing temperatures. A value of

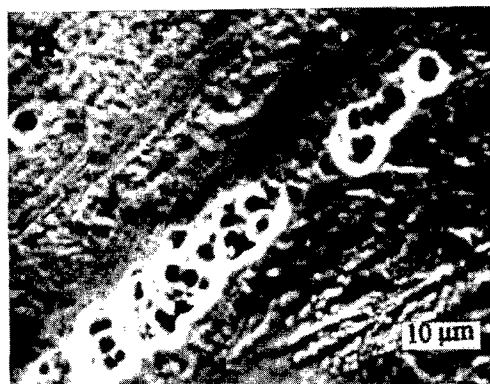


Figure 8: (a) SEM micrograph of cavities formed on surfaces of deformed specimens; (b) SEM fractograph showing cavities on the fracture surfaces of the Ti-46.5Al-2.5V-1Cr(at%) alloy.

158% of elongation (figure 9c) was obtained for the test at  $1100^\circ\text{C}$  in air at an initial strain rate of  $5 \times 10^{-4}/\text{sec}$ . Investigating the effect of coating of pure aluminum on the superplastic elongation of the Ti-46.5Al-1Cr-0.3Si(at%) alloy showed that the elongation of the alloy increases greatly for the specimens coated with pure aluminum, especially when the tensile testing temperatures were chosen at  $1000^\circ\text{C}$  and  $1100^\circ\text{C}$ , rather than  $900^\circ\text{C}$ . The superplastic elongation reached up to 250% (Figure 9f) for the sheet specimen tested at  $1100^\circ\text{C}$  in air at the same initial strain rate as that for the uncoated specimen. Metallographic and fractographic observations indicate that the coating protects specimen from oxidation and possibly releases the localized stress by forming a longitudinal crack between coating and TiAl alloy (as shown in Figure 10). These two effects delay the formation and expansion of cavities on the surfaces, resulting therefore in an increased superplastic elongation. Three regions can be clearly recognized: the coating of pure aluminium, the transition layer and the base TiAl alloy. Figure 10 shows an example of cracks occurred between the coating and the base alloy in a deformed specimen tested at  $1100^\circ\text{C}$ .

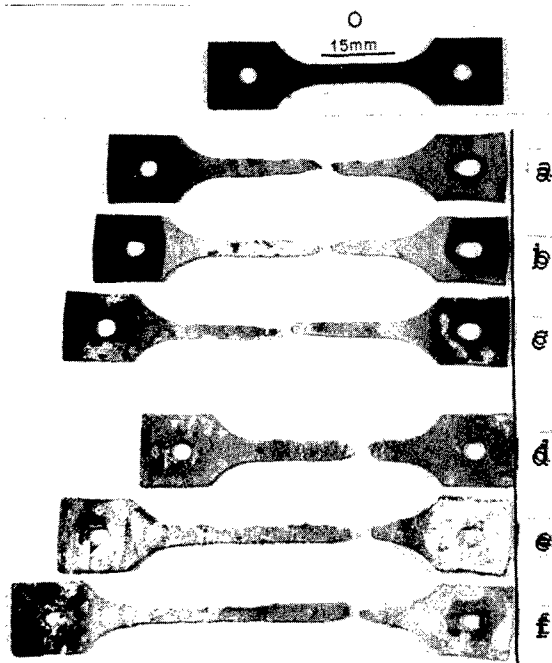


Figure 9: Profile of testing specimens of Ti-46.5Al-1Cr-0.3Si(at%) under an initial strain rate of  $5 \times 10^{-4}$ /sec, showing the superplastic elongation obtained:

- (a) unformed sheet specimen;
- (a)  $\delta=122\%$  at  $900^\circ\text{C}$ , uncoated;
- (b)  $\delta=145\%$ , at  $1000^\circ\text{C}$ , uncoated;
- (c)  $\delta=158\%$  at  $1100^\circ\text{C}$ , uncoated;
- (d)  $\delta=78\%$ , at  $900^\circ\text{C}$ , coated;
- (e)  $\delta=183\%$ , at  $1000^\circ\text{C}$ , coated;
- (f)  $\delta=250\%$ , at  $1100^\circ\text{C}$ , coated.

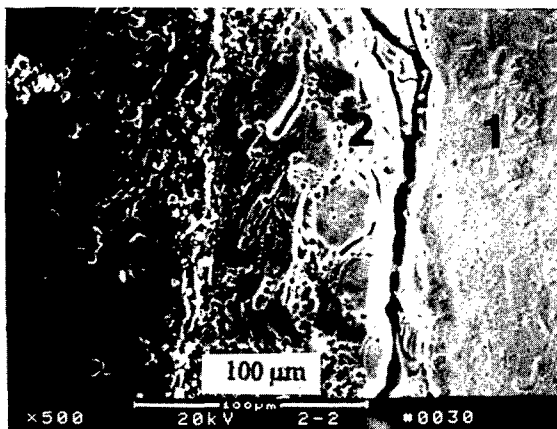


Figure 10: SEM micrograph of a section of coating on the surface of the specimen of Ti-46.5Al-1Cr-0.3Si(at%) alloy: Region 1--the TiAl alloy; Region 2--Transition layer; Region 3--Coating of pure aluminum

## Conclusions

1. A  $\text{Ti}_3\text{Al}$  base alloy, Ti-24Al-14Nb-3V-(0-0.5)Mo (at%), undergoes superplastic deformation when tested at temperatures from  $920\text{--}980^\circ\text{C}$ . Maximum elongation of 1240% has been obtained at an initial strain rate of  $1.5 \times 10^{-3}$ /sec in air. The very fine  $\alpha_2$  and  $\beta_0$  grains ( $<1\mu\text{m}$ ) and their random distribution are believed to enhance the superplastic properties of the alloy.
2. Maximum strain rate sensitivity parameters ( $m$ -value) of 0.76 for the Ti-24Al-14Nb-3V-0.5Mo(at%) alloy at  $960^\circ\text{C}$  have been evaluated. Both total elongation and yield stress strongly depend on strain rates and grain sizes of the alloy.
3. The fact that grain growth and recrystallization occurred, but no cavities or voids were observed after large superplastic deformation of the  $\text{Ti}_3\text{Al}$  alloy indicates that the alloy is suitable for applying superplastic forming techniques in fabricating aerospace components.
4. A value of 164% of elongation has been obtained for the isothermally forged Ti-46.5Al-2.5V-1Cr(at%) alloy tested at  $1000^\circ\text{C}$  in air. This superplastic deformation in the alloy is possible related to the fine and equiaxed  $\beta$  grains around the boundaries of lump-shaped  $\gamma$  phase, as well as to recrystallization. Oxidation of the surfaces of specimens at high temperatures strongly affects the superplastic properties of this alloy.
5. The elongation of the Ti-46.5Al-1Cr-0.3Si(at%) alloy increases significantly for the specimens coated with pure aluminium. A superplastic elongation of 250% was reached for a coated specimen tested at  $1100^\circ\text{C}$  in air at an initial strain rate of  $5 \times 10^{-4}$ /sec.

## Acknowledgement

Acknowledgement financial support under National Nature Science Foundation, High Technique "863" Program, and Ministry of Personnel in China.

## References

1. J. C. Beddoes et al., "The Technology of Titanium Aluminides for Aerospace Applications", Materials & Manufacturing Processes, 7(4)(1992), 527-559.
2. Y-W. Kim, and F. H. Froes, "Physical Metallurgy of Titanium Aluminides", High Temperature Aluminides and Intermetallics, ed. S.H. Whang, C.T. Liu and D. Pope (Warrendale, PA, TMS 1990) 465.
3. N. S. Stoloff and K.S. Sikka, ed., Physical Metallurgy and Processing of Intermetallic Compounds (Chapman & Hall 1996), 297-350.
4. R. M. Imayev, O. A. Kaibyshev and G.A. Salishchev, "Mechanical Behaviour of Fine Grained TiAl Intermetallic Compound-I. Superplasticity," Acta metall. mater., 40(3)(1992) 581-587.
5. T. G. Nieh, and J. Wadsworth, "Recent Advance in Superplastic Intermetallics," ACTA Metallurgica Sinica, (English Letters) 8(1995) 405-417.

6. Naoya MASAHASHI, et. al., "High Temperature Deformation Behavior of Titanium-Aluminide Based Gamma Plus Beta Microduplex Alloy," ISIJ International 31(7)(1991) 728-737.

7. Y. Rosenberg, and A.K. Mukherjee, "The Superplastic Properties of a  $Ti_3Al$ -Nb Alloy," Mater. Sci. Eng., A192/193(1995) 788-792.

8. Jia Tiancong, et al., "Microstructure and Properties of  $Ti_3Al$ -Nb-Mo-V Alloy," Mater. Sci. Eng., A152(1992) 318-322.

9. Pu ZhongJie, et al., "Effect of Microstructure on Tensile Properties of  $TiAl$  Based Alloy", J. Iron and Steel Research, International, 3(1)(1996) 29-32.

10. Zengyong Zhong, Dunxu Zou, and Shiqiong Li, "Advance in  $Ti_3Al$  and  $TiAl$  Intermetallics Research in CISRI," ACTA Metallurgica Sinica (English Letters) 8(1995),531-541.



## MICROSTRUCTURAL EVOLUTION DURING THERMOMECHANICAL PROCESSING OF TiAl

D.L. Anton  
United Technologies Research Center  
411 Silver Lane  
E. Hartford, CT 06108

### Abstract

In an attempt to obtain an intermediate colony size in a fully lamellar structure, a series of forging and post forge heat treatments has been conducted on plasma arc melted ingots of a Ti-46.5Al-2Cr-2Nb-0.8Mo-0.2W-0.2Si (atomic per cent) alloy. Forging was conducted to 80% deformation at temperatures ranging from 1175 through 1400°C under an inert atmosphere. True stress vs. true strain plots resulting from forging showed strong strain softening due to grain size breakdown and dynamic recrystallization events. Subsequent thermal treatments were given to the forged ingots to obtain a near fully lamellar microstructure while minimizing grain growth. Microstructural evaluations were performed utilizing optical as well as scanning electron microscopy and electron microprobe for quantitative chemical analysis. The single pass forgability of this alloy was observed to be marginal at temperatures below 1300°C and extraordinarily good above this temperature. The predominant microstructure consisted of a combination of lamellar colonies surrounded by a coarse intergranular  $\beta+\gamma$  phase. The coarse  $\beta+\gamma$  residing in the prior  $\alpha$  grain boundaries slowed their growth considerably, allowing for the attainment of relatively fine grains of lath  $\alpha_2/\gamma$ . The cooling rate from the heat treatment temperature was found to be crucial in obtaining lamellar structures with too rapid cooling resulting in Widmannstätten or acicular  $\alpha_2/\gamma$  colonies and too slow a cooling rate yielding large  $\beta+\gamma$  volume fractions. A time temperature transformation, TTT, curve has been generated for this alloy utilizing cooling rates from 12 to 460 °C/sec. obtained by controlled furnace cool down.

### Introduction

A balance of strength, ductility and fracture toughness is required for the introduction of TiAl into advanced gas turbine components. To obtain these properties, a theoretical microstructure composed of a fully lamellar structure having a grain size ranging between 100 and 250  $\mu\text{m}$  is desirable [1].

Fine grained fully lamellar microstructures are not easily obtained in either cast or wrought condition. Castings not containing boron typically result in fully lamellar grains having a size exceeding 800 $\mu\text{m}$ , while alloys which contain boron, can be readily cast with a grain size of 400 $\mu\text{m}$  [2]. Extruded ingot alloys can easily be produced in the duplex microstructure to grain sizes as small as 20 $\mu\text{m}$  [3], while extruded powder alloys have produced grain sizes as low as 1 $\mu\text{m}$  [4]. This is usually accomplished through deformation above the eutectoid temperature,  $T_e$ , within the  $\alpha+\gamma$  phase field. To transform the duplex to the fully lamellar structure, solutioning near or above the alpha transus,  $T_\alpha$ , is required. During solutioning, however, the alpha grains grow rapidly to very large sizes,

exceeding 1mm in many cases. Under these conditions, precipitates such as borides have been found to be effective in reducing  $\gamma$  grain growth, but one is still limited to the as cast alpha grain size of 400 $\mu\text{m}$ . In this regard, forging of the boron containing alloy 47XD, has been successful in achieving 100 $\mu\text{m}$  fully lamellar structures [5].

Hot working of  $\gamma$ -TiAl has not been as extensively explored as cast processing, however, interest in both extrusion and forge processing has increased greatly over the past few years. Extruded articles can be designed which take advantage of microstructures resulting from high deformation rates at high temperature. These articles are of course limited to long slender shapes. Forgings, which can be made into a wider variety of forms by use of shaped dies, are limited by conventional commercial equipment to lower temperatures, slower deformation rates and lower true deformation strains.

The mechanisms of forge deformation and resultant microstructures in  $\gamma$ -TiAl alloys have been studied at temperatures ranging from 650 to 1250°C at strain rates between  $10^{-3}$  and 20  $\text{sec}^{-1}$  [6-12]. The deformation mechanisms described have been found to be a strong function of starting microstructure, deformation temperature and strain rate. In starting from a nearly fully lamellar structure, these results can be summarized as: (i) at forging temperatures ( $T_F$ ) below  $T_e$ , significant strain hardening is observed resulting in highly distorted lamellar colonies, (ii) for  $T_e < T_F < T_\alpha$  strain softening is apparent with the development of the banded duplex plus near gamma microstructure and (iii) for  $T_e < T_F < T_\alpha$  strain softening decreases and a uniform duplex microstructure results. If the strain rate is too high to accommodate the controlling thermal process, either cracking or non-uniform deformation localization occurs.

In an attempt to obtain the desired intermediate grain size in a fully lamellar structure, a series of forging and post forge heat treatments has been conducted in the temperature range  $T_e < T < T_\alpha$  (where  $T_s$  = solidus temperature). An alloy selected specifically for forging, containing Si as a grain size stabilizer and W and Mo for creep strengthening, was utilized. Through metallographic examination of the resultant microstructures, an understanding of the physical metallurgical factors controlling colony size and constituent phases has been obtained.

### Experimental Procedures

A plasma arc melted, PAM, ingot of Ti-46.5Al-2Cr-2Nb-0.8Mo-0.2W-0.2Si (atomic per cent) was cast into a 300 mm diameter by 900mm water cooled hearth. One mid length radial slice 25 mm thick of this ingot was

\* All compositions given in atomic per cent unless otherwise indicated.

cut for this set of experiments. Pins, 15 mm in diameter and 25 mm in length were EDM cut from the resultant slab. The alloy pins were solution heat treated for eight hours at 1400°C and furnace cooled under an argon atmosphere. Forging was conducted to 80% reduction in height at temperatures ranging from 1175 through 1400 °C under an inert atmosphere. The specimen were soaked at temperature prior to forging for only fifteen minutes, to minimize coarsening of the lamellar colonies. Constant engineering strain rate was maintained at 0.0016 sec.<sup>-1</sup>. Load vs. displacement traces were recorded during the forging experiments and subsequently recalculated into true stress vs. true strain plots.

The resulting forged specimens were cooled at 24°C/sec. Subsequent one hour inert gas thermal treatments were given to the forged ingots to obtain a near fully lamellar microstructure while minimizing grain growth. Heating and cooling rates were microprocessor controlled and recorded. A series of controlled cooling experiments were performed on 1325 and 1375°C forged specimens. The most rapid cooling rates were achieved by turning the furnace off instantaneously. In these cases, specimen temperature was recorded and cooling rates estimated by averaging the measured cooling rates between the peak temperature and 800°C. Microstructural analyses were performed utilizing optical as well as scanning electron microscopy and electron microprobe for quantitative chemical analysis. Phase volume fraction determinations were made visually utilizing optical microscopy.

### Results

The alloy microstructure prior to forging was composed of large lamellar colonies, >1000µm, containing both discrete and accicular  $\beta$ . (The term  $\beta$ , representing the body centered cubic phase, is used advisedly since the crystallography and degree of order of this phase have not been.)

#### As Forged Structures

Table I gives the forging temperatures, post forge heat treatment temperature and resultant microstructures. The microstructural results are summarized under the heading *Grain Structure*, a general term describing the total microstructure. The term Bi-Modal is used where one microstructural type is not dominant, defined to be at <80% volume fraction. A short hand nomenclature is used and described at the bottom of this table. The microstructures observed were typically composed of two morphological types, lamellar colonies and  $\beta+\gamma$  regions, with lesser amounts of duplex ( $\alpha_2+\gamma$ ) and Widmannstätten structures also observed. The *Grain Structure* column is followed by descriptions of *Majority Type* and *Minority Type* structures their volume fraction and average size. The last column shows a qualitative term describing the *Single Pass Forgability* of the alloy based on uniformity of deformation, with the numeral designation one characterizing very inhomogenous deformation and five indicating totally uniform deformation.

The single pass forgability of this alloy was observed to be marginal at temperatures below 1300°C and extraordinarily good above this temperature. At 1175°C, deformation and the resultant microstructure were quite inhomogenous, consisting of large as cast lamellar colonies surrounded by regions of duplex microstructure. A typical intercolony region showing both the large lamellar grains as well as the duplex structure between these colonies is given in Fig. 1. The lathes of the large grains are seen to be distorted considerably from the forging action. The predominant lathe orientation was perpendicular to the stress axis, indicating that those colonies with lathe orientations deviating from this preferentially broke down into the duplex structure.

Low magnification observations showed that the duplex structure resulted in high deformation strains while the lamellar colonies deformed minimally. Some regions of the sample were fully duplex in nature and showed uniform deformation.

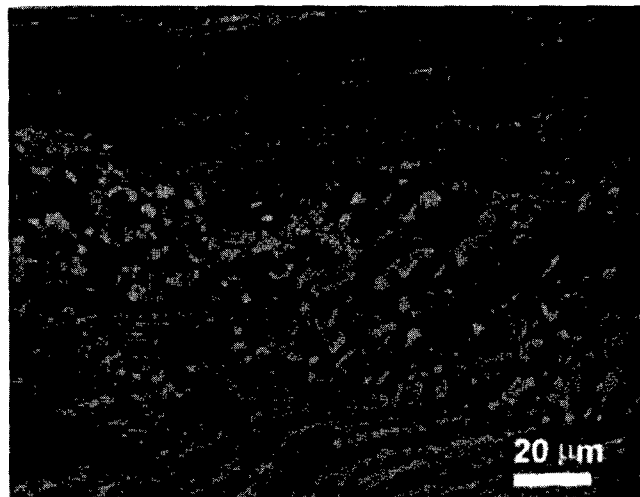


**Figure 1** Microstructure after forging at 1175°C showing inter colony duplex structure and misshapen lathes.

As the forging temperature was increased to 1225 to 1275°C, the volume fraction of the specimen composed of the duplex  $\alpha_2/\gamma$  increased to the point where at 1275°C the resultant structure was 95% duplex. At this point the lamellar grains remaining were only in the lathe orientation described above and elongated perpendicular to the compression axis (see Fig. 2).

At forging temperatures of 1325°C and above, a bi-modal microstructure resulted from forging which consisted of lamellar ( $\alpha_2+\gamma$ ) grains and a combination of  $\beta$  and  $\gamma$  grains. Details of the later structure are shown in Fig. 4. This backscatter electron image from an electron microprobe shows the fine lathe colony structure to hold a mixture of dark and light contrasting phases. The quantitative chemical analysis, resulting from wavelength dispersive spectroscopy, for these phases along with that of the lathe colony structure, is given in Table II. The  $\beta$  phase is seen to be enriched in Ti, Si, and all of the refractory elements with the notable exception of Nb. The refractory elements are known to be  $\beta$  stabilizers, while the darker  $\gamma$  phase is depleted in refractory elements.

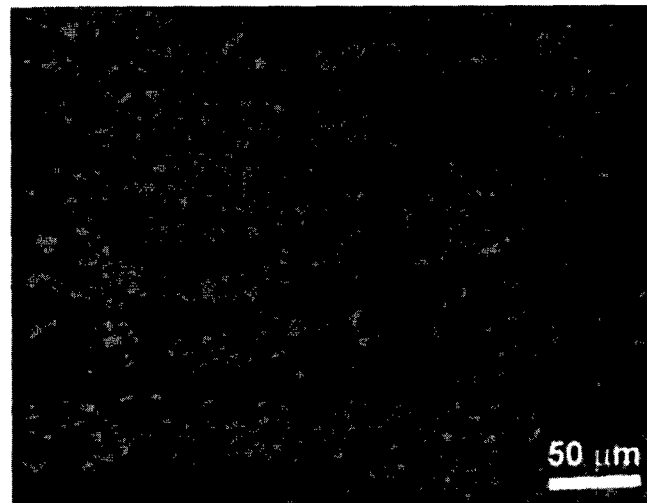


**Figure 2** Microstructure after forging at 1275°C showing predominantly duplex microstructure with remnant lathe colonies present.

**Table I Results of Microstructural Characterization of Forging and Post Forge Heat Treatments**

Forge Temp. (°C)	Heat Treat. Temp. (°C)	Cooling Rate (°C/min.)	Grain Structure	Majority Type	vol. %	size (μm)	Minority Type	vol. %	size (μm)	Single Pass Forgeability
1175	AF	24	Bi-Modal	NFL	80%	1500	Duplex	20%	6	1
1225	AF	24	Bi-Modal	Duplex	80%	10	Lamellar	20%	200x50	2
	1325	466	NFW	W	95%	50	β+γ	5%	10	
	1350	327	NFW	W	95%	50	β+γ	5%	10	
	1375	288	NFW	L+W+β	100%	100				
	1400	12	Bi-Modal	L	60%	50	β+γ	40%	15	
1275	AF	24	Duplex	Duplex	95%	20	Lamellar	5%	200x50	3
	1325	466	NFW	W	98%	40	β	2%	10	
	1350	327	NFL+W	L+W	98%	40	β	2%	10	
	1375	288	NFL+W	L+W	98%	40	β	2%	10	
	1400	12	NFL	L+β	100%	2000				
1325	AF	24	Bi-Modal	L	50%	50	β+γ	50%	50	5
	1325	12	Bi-Modal	L	60%	600	β+γ	40%	100	
	1325	48	Bi-Modal	L	60%	100	β+γ	40%	50	
	1325	466	NFW	W	98%	100	β	2%	10	
	1350	12	Bi-Modal	L	60%	300	β+γ	40%	150	
	1350	327	NFL+W	L+W	99%	150	β	1%	5	
	1375	12	Bi-Modal	β+γ	80%	100	L	20%	150	
	1375	288	NFL	L	98%	100	β	2%	5	
	1400	48	NFL	L+β	95%	100	β	5%	5	
1375	AF	24	Bi-Modal	L	60%	75	β+γ	40%	50	5
	1325	48	Bi-Modal	L	70%	75	β+γ	30%	100	
	1325	466	NFW	W	98%	150	β	2%	5	
	1350	48	NFL	L	95%	100	β+γ	5%	30	
	1350	327	NFL+W	L+W	98%	150	β	2%	5	
	1375	48	NFL	L	90%	300	β+γ	10%	125	
	1375	288	NFL+W	L+W	98%	150	β	2%	5	
	1400	12	NFL	L	90%	125	β+γ	10%	25	
1400	AF	24	Bi-Modal	L	80%	200	β+γ	20%	75	5
	1325	48	Bi-Modal	L	80%	400	β+γ	20%	75	
	1350	48	NFL	L	95%	400	β+γ	5%	30	
	1375	48	NFL	L	95%	400	β+γ	5%	25	
	1400	48	NFL	L	98%	400	β+γ	2%	25	

NFL Nearly Fully Lamellar  
 NFW Nearly Fully Widmannstatten  
 NFL+W Nearly Fully Lamellar + Widmannstatten  
 L Lamellar  
 W Widmannstatten  
 Duplex discrete α<sub>2</sub> + γ grains

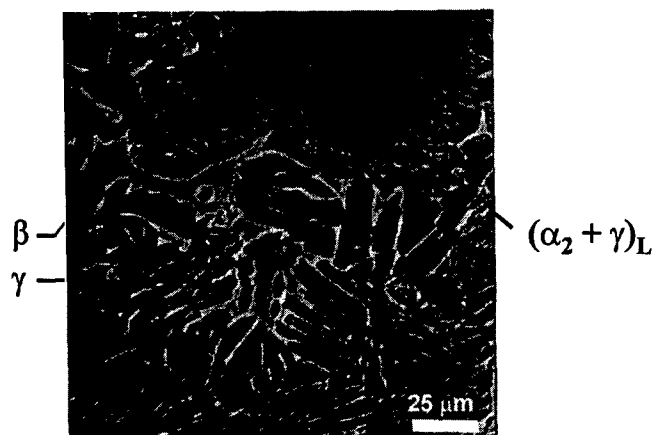


Figure 3 Backscatter electron image of material forged at 1275°C showing morphology of intercolony  $\beta + \gamma$

As the forging temperature was raised from 1325 through 1400°C the volume fraction of lamellar colonies increased significantly from 50% to 80%, while the average colony size increased from 50 to 200 $\mu\text{m}$ . From this evidence it can be hypothesized that the coarse  $\beta + \gamma$  stabilized the finer lamellar colony size.

The true stress vs. true strain plots for the forgings reported here are given in Fig. 4. The degree of microstructural uniformity is evident in this plot. The forging conducted at 1175°C, which displayed nonuniform deformation, underwent strong strain softening during forging. This softening was caused by the breakdown of the lamellar colonies into the duplex structure. The specimen forged at 1225°C showed slight softening upon initial straining, indicating that lamellar colony breakdown occurred rapidly at this temperature. Above the  $\alpha$ -transus temperature,  $T_\alpha$ , the alloy is quite soft and ductile, showing only a slight increase in stress

which probably results from increased frictional forces with the die material.

#### Post Forge Heat Treatment & Cooling Rate

The forged specimens were initially cooled from their heat treatment temperature via furnace shut off, which resulted in rapid cooling on the order of 300 to 400°C min.<sup>-1</sup> in order to maintain as fine a colony size as possible. This was found to result in Widmannstätten type  $\gamma$  formation as presented in Table I. A typical Nearly Fully Widmannstätten, NFW, structure is given in Fig. 5.

Table II Chemical composition for constituent phases in Fig. 3

Phase	Ti	Al	Cr	Nb	Mo	W	Si
$\beta$	56.0	32.8	5.7	2.2	2.3	0.4	0.6
$\gamma$	49.0	46.3	1.2	2.3	0.6	0.2	0.2
$\alpha_2 + \gamma$	50.9	44.7	1.6	1.9	0.6	0.1	0.2

This micrograph shows a relatively fine grain size of 20-30 $\mu\text{m}$ , but the internal structure consists of a mixture of deformed platelets and irregularly sized particles. This structure is typical of Widmannstätten phases observed in TiAl alloys rapidly cooled [3] and nickel base superalloys. A number of larger precipitates are also clearly visible between the grains. These particles, stemming from their general morphology, are likely  $\beta$  precipitates as shown in Fig. 3.

In order to understand these kinetics, a series of experiments were performed on 1325°C forged material in which samples were aged at 1325, 1350 and 1375°C and rapidly cooled via furnace shut off, or control cooled at 12°C/min. Additionally, a sample heat treated at 1325°C was cooled at a higher cooling rate of 48°C/min.

The microstructural summary given in Table I clearly indicates that heat treating at 1325 and 1350°C followed by rapid cooling results in the

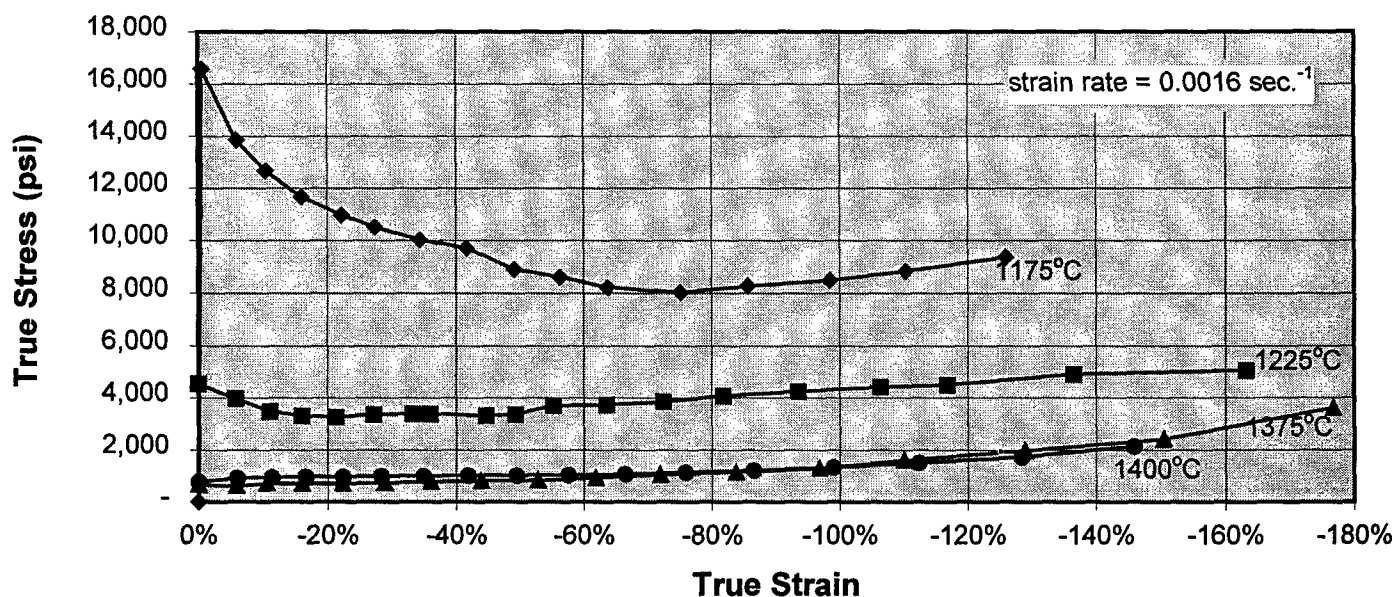
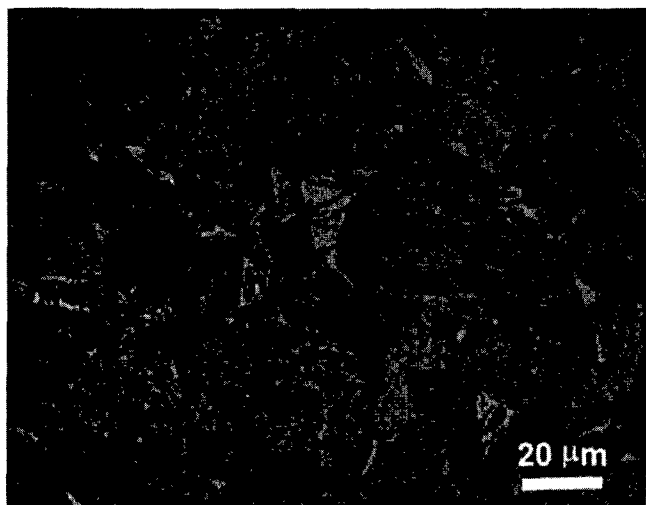


Figure 4 True stress vs. true strain plot for forgings reported in this report.

nearly fully lamellar plus Widmannstätten microstructures, similar to that shown in Fig. 5. Rapid cooling at 327°C/min. from the 1350°C heat treatment yielded a microstructure between the Widmannstätten and fully lamellar. An example of this microstructure is given in Fig. 6 where well defined lathes are clearly visible, but they are distorted and broken in places. This indicates that the transition from Widmannstätten to lamellar precipitation is not precipitous, but occurs over cooling a broad band of cooling rates ranging from 500 to 300°C/min.



**Figure 5** Optical image of a Nearly Fully Widmannstätten, NFW, microstructure resulting from 1325°C heat treatment cooled at 466°C/min. after forging at 1275°C.

Heat treatment at 1375°C followed by 288°C/min. cooling resulted in a fine NFL structure having a 100μm colony size (see Fig. 7a). This rapid cooling rate, not too dissimilar from the 327°C/min. described in Fig. 6 above, resulted in a decidedly finer lath structure. Those specimens cooled at 12°C/min. resulted in a bi-modal microstructure consisting of coarse β+γ and lamellar colonies. Comparison of Fig. 7a with Fig. 7b illustrates that increasing the heat treatment temperature to 1375°C increased the volume fraction of β+γ and decreased the average size of the lamellar colonies.

A comparison of the 1325°C heat treated specimens cooled at 12 and 48°C/min. respectively resulted in a similar overall microstructure with the higher cooling rate giving a lower lamellar colony size. Overall, these two cooling rates are expected to result in the same general microstructure.

A similar experimental plan was established for specimens forged at 1375°C in which comparison was made between the rapid cooling rate and controlled cooling at 48°C/min. subsequent to one hour thermal aging. The results were in accord with those given above, with rapid cooling giving the NFW and NFL+W structures after heat treatment at 1325 and ≥1350°C respectively. This combination of high cooling rate and higher forging temperature resulted in reduced volume fractions of lamellar phase and somewhat larger lamellar colonies, than for material forged at 1325°C.

Aging at 1375°C after forging at 1375°C notably, did not result similar structures to those obtained after a similar aging treatment of material forged at 1325°C. Rapid cooling at 288°C/min. resulted in a NFL+W structure while slower cooling at 48°C/min. gave the NFL (see Fig. 8a, compared to the Bi-Modal structure of Fig. 7a) structure (see Fig. 8b, compared to the NFL structure of Fig. 7b).

Forging at 1400°C, yielded nearly fully lamellar microstructures after heat treating at temperatures ≥ 1350°C, utilizing a slow cooling rate of 48°C/min. The grain sizes were somewhat greater than described above, typically 400μm, while maintaining lamellar colony volume fractions of 95% and greater.

## Discussion

### High Temperature Deformation

The alpha transus,  $T_{\alpha}$ , of this alloy has been determined to be approximately 1325°C by differential thermal analysis techniques. Strain softening occurs at forge temperatures below 1225°C as indicated in the true stress-true strain plot given in Fig. 4. Since the initial microstructure is coarse grain fully lamellar, and the dissolution of lamellar colonies into the single phase α is known to be sluggish, [6], we will presume the microstructure just prior to forge deformation to be essentially identical to the input material. This position is supported by the evidence that large distorted lamellar grains are present, indicative of lamellae that have been forged.

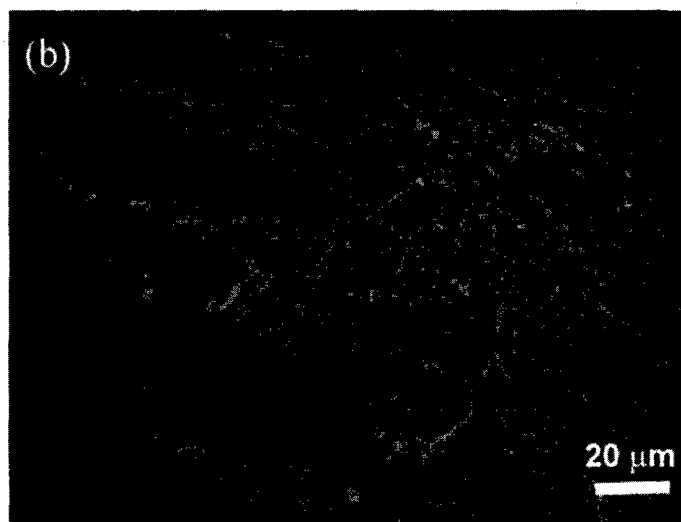
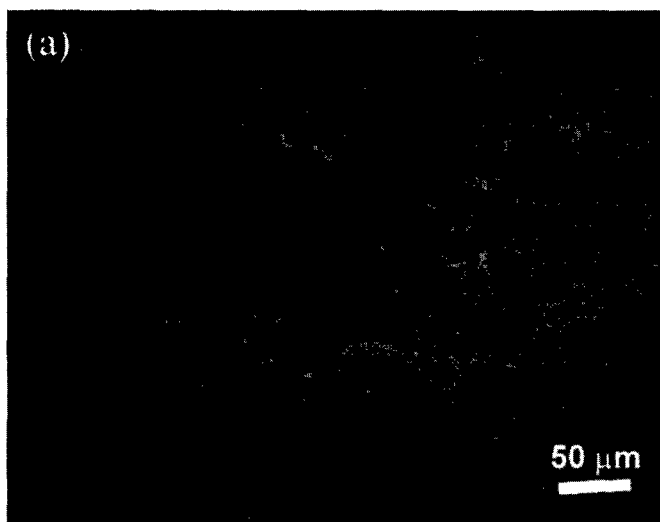


**Figure 6** Optical images of a Nearly Fully Lamellar + Widmannstätten, NFL+W, microstructure resulting from 1350°C heat treatment cooled at 327°C/min. following forging at 1325°C. (a) shows colony size overall structure and (b) shows detail of Widmannstätten morphology.

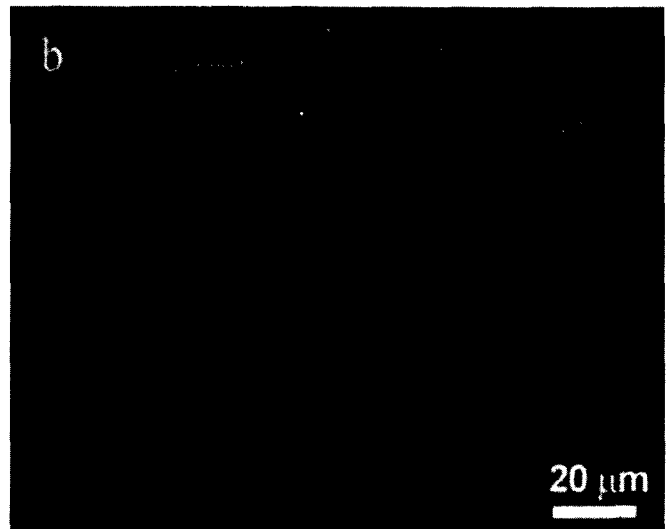
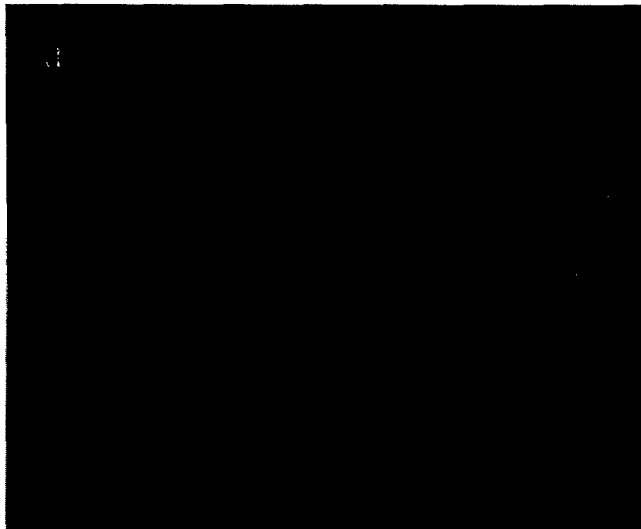
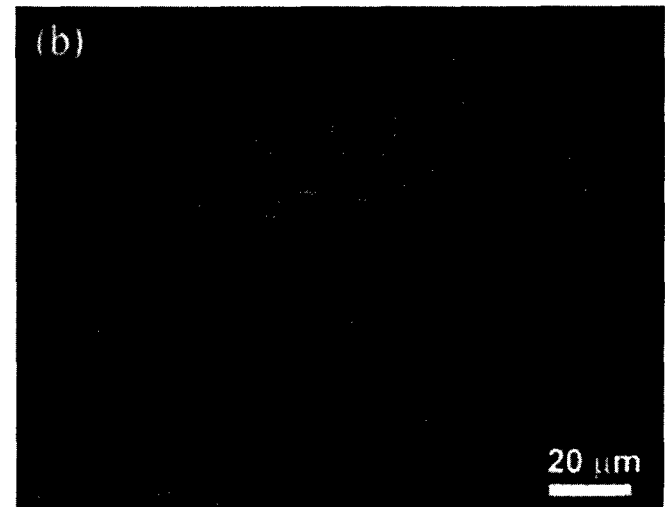
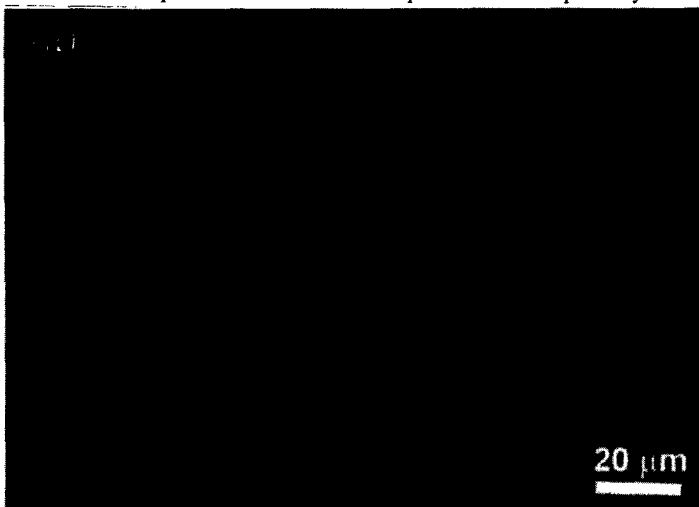


**Figure 7** Optical micrographs comparing the microstructures obtained after forging at 1375°C and heat treating at 1375°C and cooled at (a) 288°C/min. illustrating NFL+W and (b) 48°C/min showing NFL.

At forge temperatures below  $T_{\alpha}$ , both  $\alpha$  and  $\gamma$  grains are thermodynamically stable. As forging begins, the large lamellar grains begin to slide over one another to accommodate the imposed strains. At intercolony boundaries, the duplex structure forms, accelerated by the high strain energy concentrated at these boundaries. Within the lathe colonies, the lamellae slide over each other. This sliding, accelerates the formation of the duplex structures in grains oriented to promote sliding. These lamellar grains are consumed preferentially by the advancing duplex structure as strain energy imparted into the structure increases. Those lamellar colonies with lathes oriented either perpendicular or parallel to the stress axis are less susceptible to lamellar sliding and are the last to be consumed. This process of transformation to the duplex structure is accelerated by thermal activation, thus forging at temperatures nearer the  $T_{\alpha}$  leads to more rapid consumption of the lamellar grains. The change in morphology during forging can be represented by the following equation:



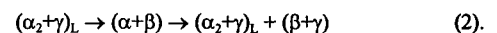
where L and D represent the Lamellar and Duplex structures respectively.



**Figure 8** Optical micrographs comparing the microstructures obtained after forging at 1325°C and heat treating at 1375°C and cooled at (a) 288°C/min. and (b) 12°C/min.

The rapid formation of the duplex structure is essential for uniform forging deformation. At lower temperatures, 1175°C in this set of experiments, the duplex structure is limited to intercolony regions, resulting in very non-uniform deformation. This non-uniformity manifests itself as gross irregular deformation of the ingot. As the forging temperature is raised, the entire specimen is consumed by the duplex structure and very large strains can be accommodated. In fact superplasticity has been reported in duplex microstructures of other TiAl alloys [14].

Forging at temperatures in excess of  $T_{\alpha}$ , begins with the large lamellar colonies breaking down rapidly and uniformly into  $\alpha$  grains and  $\beta$  particles. The  $\beta$  particles act to stabilize the  $\alpha$  grain size. Lathe  $\alpha_2 + \gamma$  and intercolony  $\beta + \gamma$  structures result during cooling from the forging temperature. This process is summarized by the following equation:



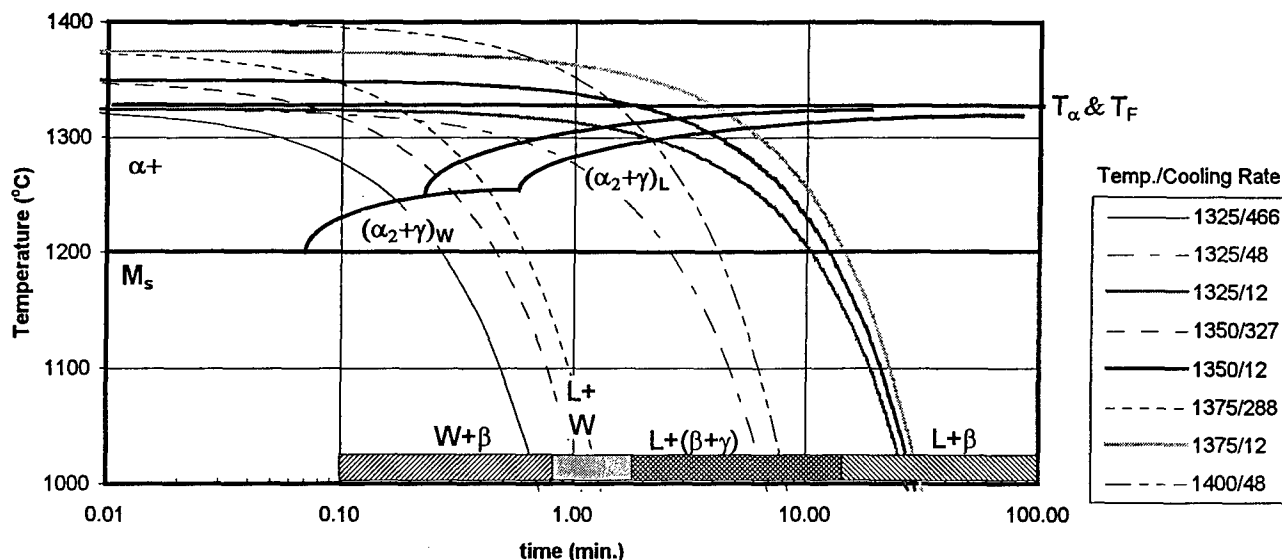


Figure 9 Time Temperature Transformation diagram derived from controlled cooling rate experiments showing resultant microstructures.

#### Kinetics

##### $\beta$ Precipitation

The  $\beta$  phase reported on here, was not observed until the alloy had been exposed to temperatures of 1325°C or greater, either during forging or through subsequent heat treatment. Once present through forging, it could not be totally eliminated. It is considered that the  $\beta$  phase is stable in this alloy at 1325°C, most probably the result of the relatively high five atomic per cent refractory metal content. This would explain the presence  $(\beta+\gamma)$  at enhanced levels in materials forged and heat treated at this temperature. The  $\beta$  phase was observed in 1-2% quantities in rapidly cooled samples. Cooling at rates slower than 100°C/min. resulted in significantly higher volumes. This indicates that the precipitation of  $(\beta+\gamma)$  continues to occur during cooling through 1325°C.

##### Cooling Rate

The cooling rate experiments performed here have shown the wide degree of microstructural morphologies that can occur in this alloy. The best method of describing these kinetics is through the use of Time-Temperature-Transformation, TTT, diagrams. Fig. 9 illustrates the data obtained from the 1325°C forged controlled cooling rate experiments. This figure shows the cooling paths taken for each of the specimens reported on. At the bottom of this plot is given a description of the resulting microstructure. From these microstructures, the phase fields can be inferred. Since this is not a rigorous determination of the location of these fields with respect to temperature, their locations should be used descriptively, and for reference to other literature data. Their actual positions and extents would require a rigorous series of salt bath quenching experiments. The TTT diagram given in Fig. 9 is plotted with the onset of cooling defined as time=0. Phase transformations do not begin until the temperature cools to below  $T_{\alpha}$ . By using the onset of cooling rather than the time of  $T_{\alpha}$  as time=0, these TTT diagrams can be used more readily in microstructural studies of cooling from above the alpha transus.

Three critical points are observed in microstructural alteration with cooling rate; Widmannstätten to Lamellar plus Widmannstätten,  $W \rightarrow L+W$ ; Lamellar plus Widmannstätten to Lamellar plus Beta and Gamma,  $L+W \rightarrow L+(\beta+\gamma)$  and Lamellar plus Beta and Gamma to Lamellar plus Beta,  $L+(\beta+\gamma) \rightarrow L+\beta$ . From these cooling rate dependent morphological changes, the Widmannstätten and Lamellar fields are projected onto this plot. Since regions of  $L+W+\beta$  can be differentiated from  $L+(\beta+\gamma)$ , lamellar start and finish lines have been included. When

specimens were cooled from 1325°C and above at 12°C min.<sup>-1</sup> lamellar colonies begin to form, but nucleation in the Widmannstätten morphology precludes a fully lamellar structure from resulting. The most technologically important aspect of this diagram is that in order to achieve the nearly fully lamellar microstructure, the cooling rate must be maintained below 100°C/min. One also notes that as the cooling time increases, approaching 100 minutes, the morphology of the lamellar structure changes from lamellar colonies with coarse  $\beta+\gamma$  in the inter-colony regions to lamellar colonies interspersed with  $\beta$  particles (referred to here as  $L+\beta$ ). During the slower cooling rates, aluminum may be allowed sufficient time to partition and allow lamellar colony growth into the coarse  $\gamma$  which has formed inhomogeneously around the  $\beta$  particles.

The results presented here are in general agreement with conclusions reached in two previous studies of precipitation kinetics in  $\gamma$ -TiAl alloys. Takeyama et. al. [15] depicted the TTT diagram as consisting of massive, lamellar and  $\gamma$  grains precipitation events, with no clear destination between Widmannstätten and lamellar  $\alpha_2+\gamma$  precipitation. Cooling rates of 30°C/min. could be extrapolated to result in  $W+L$  structures from their work. This is considerably slower than the 288 and 327°C/min. rates shown here. This was explained by the significant slowing of the precipitation kinetics described by McQuay et. al. [13] with Cr additions. The present results are in agreement with those given in [13], with special note of the inclusion of the Widmannstätten precipitation field underlying the lamellar region with a critical point residing at approximately 0.2 min., 1250°C.

#### Conclusions

Forging at temperatures well below the alpha-transus temperature resulted in localized deformation being accommodated fully within veins of fine duplex grains. At temperatures approaching  $T_{\alpha}$ , the deformation became very uniform, with the entire volume of the sample consumed by the duplex structure.

At forging temperatures of 1325°C and greater, acicular  $\beta$  precipitation was observed with coarse  $\gamma$  encapsulating it. This two phase morphology was most voluminous at 1325°C and decreased with increasing forging temperature. The  $\beta$  phase was found to be enriched in Mo, Si, W and Cr, typical  $\beta$  stabilizers in titanium alloys.

The prior  $\alpha$  phase is seen to precipitate into a Widmannstätten morphology  $\alpha_2 + \gamma$  at cooling rates in excess of 100°C/min. at cooling rates between 100 and 20 °C/min., the lamellar structure dominated, with coarse  $\beta + \gamma$  in the inter-colony boundaries. At cooling rates below 20°C/min., elemental redistribution is possible, and the  $\beta$  particles are found distributed within the lamellar colonies.

The nearly fully lamellar microstructure was obtained having colony sized less than 200  $\mu\text{m}$  through super alpha transus forging followed by post forge heat treatment at or above 1350°C followed by cooling at rates less than 100°C/min.

#### Acknowledgments

This work was performed under funding by Pratt & Whitney, a United Technologies Company along with provision of all materials used. The many helpful and guiding discussions with Messrs. D.R. Clemens and D.D. Davidson are acknowledged, along with those with Dr. P.L. Martin of Rockwell Science Center. The efficient conduct of the experimental work by Mr. R. J. Brown is also gratefully acknowledged.

#### References

1. Y-W. Kim, JOM, July, (1995) pp. 39-41.
2. D. Larsen, Mater. Sci. and Eng., A213 (1996) 128-133.
3. T. Tsuzukz and H. Sato, J. de Physique IV, vol. 3, Nov. (1993), pp.233-237.
4. L. Hsiung, T. Nieh and D. Clemens, Scripta Met., vol. 36, no. 2, (1997) pp. 233-238.
5. M. Jezioro, S. Moorhouse, M. Cope and P. Postans, *Titanium '92 Science and Technology*, F. H. Froes and I. Caplan eds., TMS, Warrendale, PA, USA (1993) pp.1033-1040.
6. V. Seetharaman, and S.L. Semiatin, Met. Trans., 27A (1996) pp.1987-2004.
7. Y-W. Kim, Acta Metall. Mater., 40 (1992) pp.1121-1134.
8. P. Martin, C. Rhodes and P. McQuay, *Structural Intermetallics*, R. Darolia et. al., eds., TMS, Warrendale, OH, USA (1993) pp.177-186.
9. N. Fujitsuna, Y. Miyamoto and Y. Ashida, *Structural Intermetallics*, R. Darolia et. al., eds., TMS, Warrendale, OH, USA (1993) pp.187-194.
10. H. Clemens, P. Schretter, K. Wurzwallner, A. Bartels and C. Koeppel, *Structural Intermetallics*, R. Darolia et. al., eds., TMS, Warrendale, OH, USA (1993) pp.205-214.
11. R. Srinivasan, J. Singh, E. Tuval and I. Weiss, Scripta Mat., vol. 34, no. 8 (1996) pp.1295-1301.
12. C. Sabinash, S. Sastry and K. Jerina, Mat. Sci. and Eng., A192/193, (1995) pp. 837-847.
13. P. McQuay, D. Dimiduk, H. Lipsitt and S. Semiatin, , *Titanium '92 Science and Technology*, F. H. Froes and I. Caplan eds., TMS, Warrendale, PA, USA (1993) pp.1041-1048.
14. T. Tsuzulu and H. Sato, J. de Physique IV, 3 (1993) pp.389-395.
15. M. Takeyama, T. Kumagai, M. Nakamura and M. Kikuchi, *Structural Intermetallics*, R. Darolia et. al., eds., TMS, Warrendale, OH, USA (1993) pp.167-176.



## New Surface Treatment Using a Fluidized Bed Furnace for Improving Oxidation Resistance of TiAl-Base Alloys

Hiroyuki Kawaura, Kazuaki Nishino and Takashi Saito

Toyota Central Research & Development Laboratories, Inc.  
41-1 Yokomichi, Nagakute, Aichi, 480-11 Japan

### Abstract

A new surface treatment using a fluidized bed with  $\text{WO}_3$  powder has been developed. The cyclic oxidation resistance of TiAl-base alloys in air and an exhaust gas atmosphere up to 1223K has been significantly improved. The excellent oxidation resistance obtained is attributable to a continuous and sound  $\text{Al}_2\text{O}_3$  surface layer formed during the treatment. This protective layer acts as a barrier against the formation of a complex oxide scale consisting of a  $\text{TiO}_2$  layer and a porous inner layer of  $\text{TiO}_2$  and  $\text{Al}_2\text{O}_3$ . The developed surface treatment gives a superior oxidation resistance to the Ni-base superalloy Inconel 713C up to 1223K.

### Introduction

The weight reduction of engine parts is an efficient approach to the improvement of the engine performance and fuel economy of automobiles. TiAl-base alloys are expected to be substitutes for conventional heat resistant materials for exhaust parts of automotive engines because of their attractive specific strength at elevated temperatures (1-3). However, their oxidation resistance at high temperatures is considerably inferior to that of heat resistant steels and Ni-base superalloys.

In recent years, as the combustion temperatures of automotive engines has increased year by year due to increasing engine output and better fuel economy, application temperatures above 1223K are now required for exhausts parts. Therefore, the improvement in oxidation

resistance and the understanding of the oxidation mechanism are important for practical application of TiAl-base alloys.

In general, the scales of TiAl-base alloys formed during oxidation in air are well known for being composed of a  $\text{TiO}_2$  layer and a porous inner layer consisting of a mixture of  $\text{TiO}_2$  and  $\text{Al}_2\text{O}_3$ , as shown in Figure 1. The reasons for the poor oxidation resistance of TiAl-base alloys at high temperatures are that  $\text{TiO}_2$  has a much higher rate of growth than  $\text{Al}_2\text{O}_3$  and that the intermixed  $\text{TiO}_2/\text{Al}_2\text{O}_3$  scale is less protective above approximately 1050K in air (4, 5). Therefore, how to suppress the growth of  $\text{TiO}_2$ , or how to form a continuous and sound  $\text{Al}_2\text{O}_3$  layer in the early stage of oxidation is most important in improving the oxidation resistance.

It has been revealed that the oxidation resistance of TiAl-base alloys is improved by the additions of ternary elements such as Mo, Nb, Si, Hf, Zr and W (4, 6-8). However, the alloying additions are less effective for the oxidation resistance above 1100K and additions of large amounts of these elements are harmful since they reduce the ductility. Therefore, surface treatments are thought to be more attractive than alloying additions.

Recently, several surface treatments, such as the pack-cementation with powders (a mixture of  $\text{Cr}_2\text{O}_3$  and metallic Cr (9),  $\text{SiO}_2$  (10), or  $\text{WO}_3$  (11)), the combination of heat treatment under a low partial pressure oxygen atmosphere and aluminum diffusion coating (12) and electrolytic chromium plating (13) have been proposed for improving the oxidation resistance of TiAl-base alloys. Besides these surface treatments, oxidation-resistant coatings have been

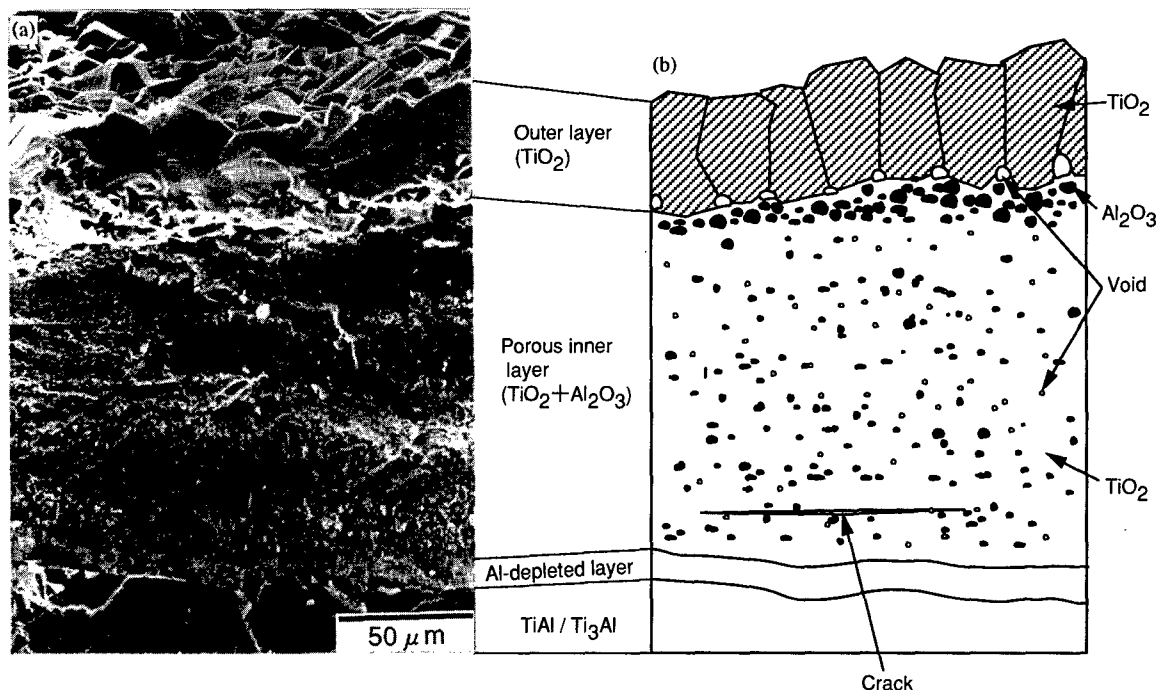


Figure 1 SEM of a fractured specimen (a) and schematic drawing of the surface structure (b) of a Ti-47Al specimen oxidized at 1173K for 100 hours.

recommended. For example, a representative  $\gamma$  + Laves coating alloy, Ti-51Al-12Cr, which was coated by low-pressure plasma spraying (14) was reported to successfully protect a TiAl-base alloy from oxidation at 1273K in air. However, the performance of the former surface treatments has been confirmed only under limited conditions such as static oxidation, and/or at temperatures below 1173K. In the case of the latter coatings, several problems still remain, their performance and reliability under cyclic oxidation, their applicability to complex shape parts, and their cost-performance, which are very important especially in the automotive industry.

A new surface treatment using a fluidized bed widely used for heat treatment of metallic materials has been developed. In the present study, the effectiveness of this surface treatment was investigated to find an efficient method for improving the oxidation resistance of TiAl-base alloys at high temperatures. The oxidation resistance was determined by cyclic oxidation tests up to 1273K.

### Experimental

#### Materials

The materials used in this study are a Ti-47Al (mol%) binary alloy and a Ti-47Al-2Nb ternary alloy with the chemical compositions shown in Table I. The ingots of the materials were prepared by induction melting in a CaO crucible and casting into a metal mold. A Ni-base superalloy of the same composition as Inconel 713C (Table II) was also prepared for comparison.

Specimens of 3 mm x 10 mm x 15 mm were cut out of the ingots and polished with SiC polishing papers up to #1500. All specimens were washed in acetone to remove contaminations before the surface treatment.

Table I Chemical Composition of the Ti-47Al and Ti-47Al-2Nb Specimens

Specimens	Al	Nb (mol%)	Ti	O	Si (mass%)	Ca
Ti-47Al	47.4	—	Balance	0.16	0.01	0.04
Ti-47Al-2Nb	47.2	1.88	Balance	0.22	0.02	0.02

Table II Chemical Composition of the Inconel 713C Specimens (mass%)

Cr	Mo	Al	Nb	Ti	Zr	C	B	Ni
12.5	4.2	6.1	2.0	0.8	0.1	0.12	0.012	Balance

#### Surface treatment

The schematic diagram of the equipment used for the surface treatment is given in Figure 2. The fluidized bed consisted of mixtures of 60 mass%  $\text{Al}_2\text{O}_3$  powder with a particle size of nominal 80 mesh and 40 mass% additional powder ( $\text{Cr}_2\text{O}_3$ ,  $\text{Nb}_2\text{O}_5$  or  $\text{WO}_3$  with a particle size of 100-200 mesh) and was fluidized by an argon gas flow. The specimens were treated in the fluidized bed at 973-1323K for 2 hours in an electric resistance furnace. This treatment will hereafter be referred to as **FB treatment**. For comparison, the pack-cementation treatment (11) was carried out. A specimen was packed with  $\text{WO}_3$  powder in an  $\text{Al}_2\text{O}_3$  crucible and then heated at 1273K for 2 hours in an argon atmosphere.

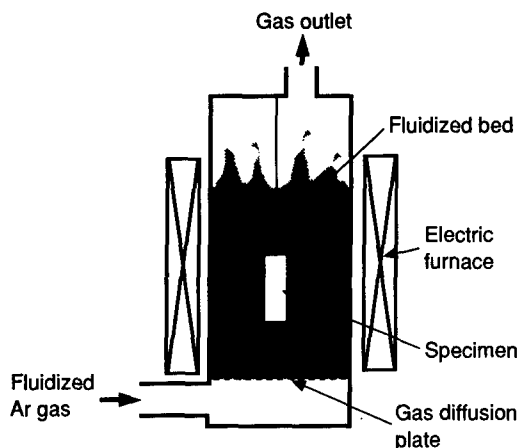


Figure 2 Schematic drawing of the surface treatment facility using a fluidized bed.

### Oxidation tests

Cyclic oxidation tests were carried out in air. Specimens were heated to 1173K, 1223K, or 1273K in an electric furnace, and cooled to room temperature. The holding time at the temperatures varied with the oxidation tests: In the case of the long-term cyclic test, it was 25 hours in the first and the second cycle, and 50 hours in the following cycles. In the case of the short-term cyclic test, it was 0.5 hour in each cycle as shown in Figure 3.

Cyclic oxidation tests were also carried out in a gas of the composition shown in Table III, which is a typical atmosphere of the diesel engine exhaust gas. In this case, specimens were heated to 1223K, and the holding time was 5 hours for each cycle.

The oxidation resistance was evaluated by measuring the mass gain of the specimens together with the spalled scales and by visual inspection.

The specimens were examined before and after the oxidation tests by X-ray diffraction (XRD) using Cu-K $\alpha$  radiation at 30 kV and 30 mA. After oxidation the specimens were fractured and the oxidized surfaces and the oxidized outer layers of the fracture surfaces were examined by scanning electron microscopy (SEM). Elemental analysis was also performed by Auger electron spectroscopy (AES). The sputtering depth was evaluated from the sputter velocity of SiO $_2$ /Si.

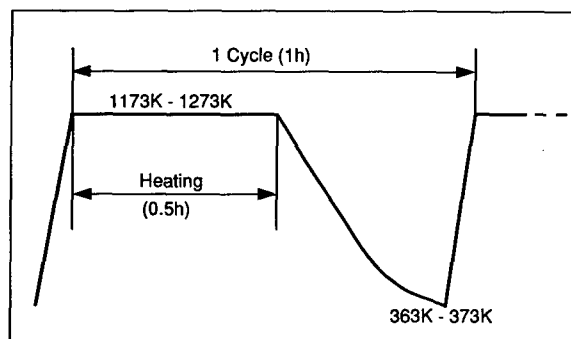


Figure 3 Temperature versus time curve of short-term cyclic test.

Table III Compositions of the Model Exhaust Gas

O $_2$	11.2 vol.%
CO $_2$	7.4 vol.%
NO	1000 ppm
CO	760 ppm
C $_3$ H $_6$	600 ppm
SO $_2$	300 ppm
H $_2$ O	3.5 vol.%
N $_2$	Balance

### Results and Discussion

#### Oxidation resistance of untreated materials

The oxidation behavior of the untreated specimens of Ti-47Al and Ti-47Al-2Nb tested in static air at 1173-1273K is shown in Figure 4 and Figure 5, respectively. For both specimens, the mass gain due to the oxidation at each temperature increased more rapidly in the short-term cyclic oxidation than in the long-term one. It is obvious that the niobium-containing alloy shows much smaller mass gain, about one twentieth, than the binary alloy. Thus, niobium addition is effective for improving the oxidation resistance. However, its effect is limited below 1173K, because the spalling of the scales has already occurred until 100 hours in the short-term cyclic test at 1173K.

#### Improvement of oxidation resistance by fluidized bed treatment

**Effect of treating conditions** Ti-47Al specimens were treated at 1273K for 2 hours in the fluidized bed with various additional powders. The oxidation curves of the long-term cyclic test of the specimens at 1173K are summarized in Figure 6, which also includes the curve for untreated specimen for comparison. The FB-treated specimens show mass gains extremely small compared with the untreated specimen,

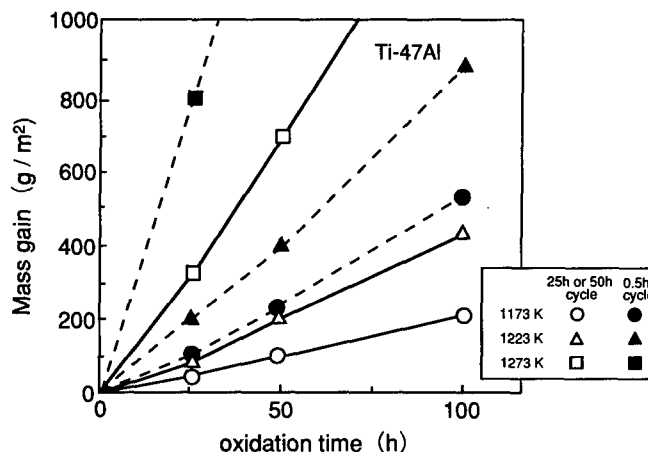


Figure 4 Comparison of oxidation behaviors of Ti-47Al specimens at 1173-1273K in air, during short-term (0.5h) and long-term (25 or 50h) cyclic tests.

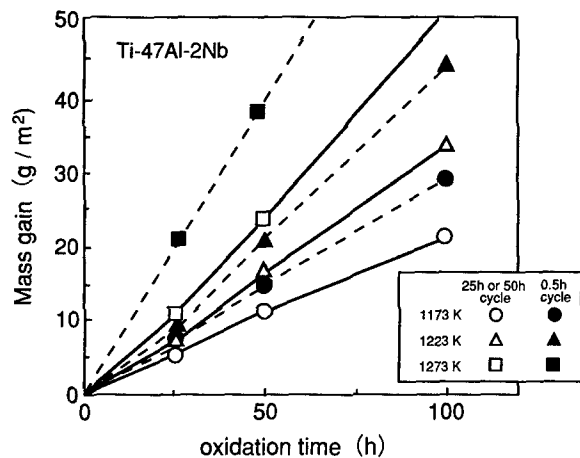


Figure 5 Comparison of oxidation behaviors of Ti-47Al-2Nb specimens at 1173-1273K in air, during short-term (0.5h) and long-term (25 or 50h) cyclic tests.

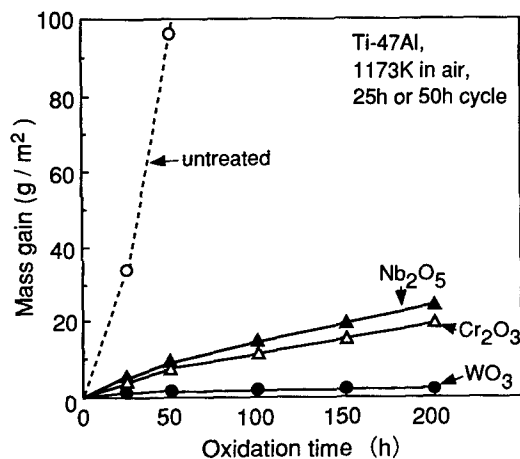


Figure 6 Mass gain at 1173K under cyclic oxidation of FB-treated Ti-47Al specimens with  $\text{Cr}_2\text{O}_3$ ,  $\text{Nb}_2\text{O}_5$  or  $\text{WO}_3$  powder.

regardless of the kind of additional powders. Particularly, the  $\text{WO}_3$  powder provides the best oxidation resistance among the three oxide powders.

Figure 7 shows the change in the mass gain with the treating temperature of the FB treatment with  $\text{WO}_3$  powder. The oxidation tests were performed at 1223K for 100 hours by long-term cycling. The mass gain remarkably decreased with increasing treating temperature. However, when treated at 1323K, the mass gain sharply increased in comparison to 1273K.

Considering the above results, the effectiveness of the FB treatment at 1273K using  $\text{WO}_3$  powder ( $\text{WO}_3$ -FB treatment) was investigated in detail.

**Effectiveness of  $\text{WO}_3$ -FB treatment** The results of the short-term cyclic tests at 1173K and 1223K of the binary alloys  $\text{WO}_3$ -FB treated at 1273K are summarized in Figure 8 and Figure 9, respectively. The results of the pack-cementation with  $\text{WO}_3$  powder and the results obtained on Inconel 713C are also shown in the figures for comparison. At 1173K, the mass gain of the FB-treated specimen is similar to that of the pack-cementation treated specimen, and is smaller than that of

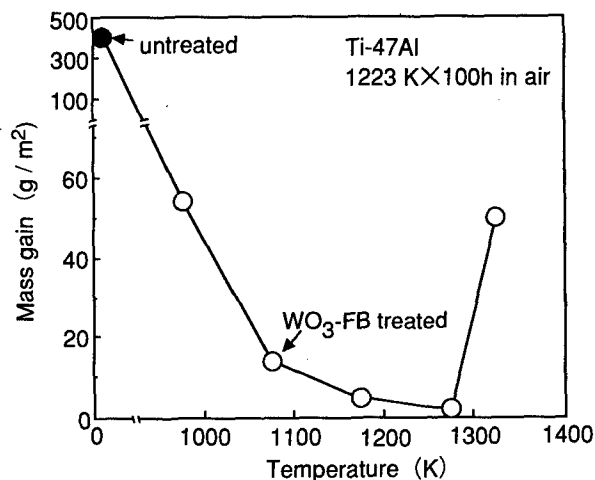


Figure 7 Relation between  $\text{WO}_3$ -FB treating temperature and mass gain of the  $\text{WO}_3$ -FB treated Ti-47Al alloys oxidized at 1223K for 100h in air.

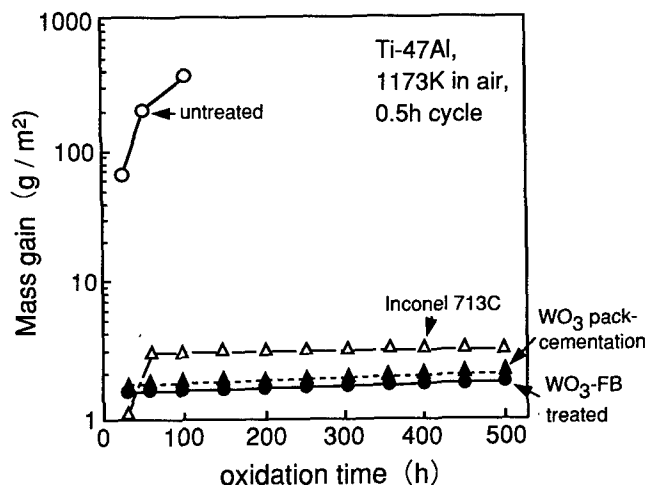


Figure 8 Mass gain under cyclic oxidation of Ti-47Al alloys at 1173K.

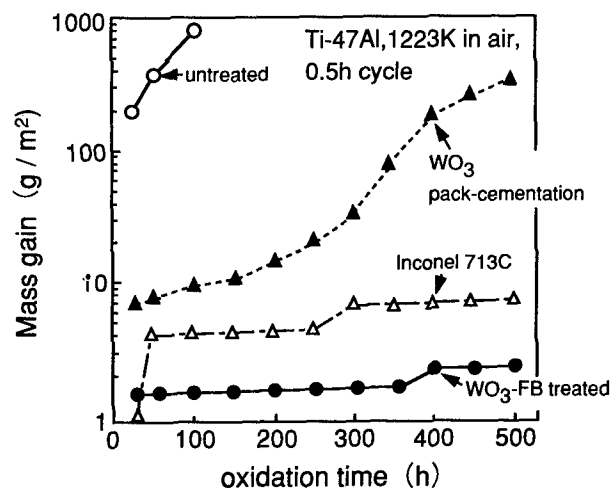


Figure 9 Mass gain under cyclic oxidation of Ti-47Al alloys at 1223K.

Inconel 713C even after 500 hours (1000 cycles). At 1223K, the pack-cementation treated specimen shows much larger mass gain than at 1173K. On the other hand, the mass gain of the FB-treated specimen still remains much smaller than that of Inconel 713C. Figure 10 shows the appearance of the specimens tested at 1223K. Spalling of the oxide scales has occurred after an extremely short period on the untreated specimen and after about 200 hours on the specimen treated by the pack-cementation. In the  $\text{WO}_3$ -FB treated specimen, however, spalling is not realized at all even after 500 hours.

Figure 11 shows the results of the short-term and long-term cyclic tests at 1273K of the  $\text{WO}_3$ -FB treated specimens and Inconel 713C. At this temperature, the oxidation resistance of the FB-treated binary alloy is not good even in the long-term cyclic test, and that of the niobium-containing alloy is also poor in the short-term cyclic test. However, the oxidation resistance of the FB-treated niobium-containing alloy is as good as that of Inconel 713C in the long-term cyclic test.

Considering all results mentioned above, it is concluded that the  $\text{WO}_3$ -FB treatment will be a promising process for giving TiAl-base alloys as well as such Ni-base superalloys as Inconel 713C an excellent oxidation resistance below 1223K. A satisfactory oxidation resistance at 1273K will be obtained through further investigations on both of the optimum condition of the FB treatment and a superior oxidation-resistant base alloy.

#### Surface structure

An XRD chart of the  $\text{WO}_3$ -FB treated specimen is shown in Figure 12, in which  $\text{WO}_3$ ,  $\text{WO}_2$ , tungsten and  $\text{Al}_2\text{O}_3$  were identified. An AES depth profile near the surface of the  $\text{WO}_3$ -FB treated specimen is shown in Figure 13. Tungsten oxides ( $\text{WO}_3$  and  $\text{WO}_2$ ) were formed on

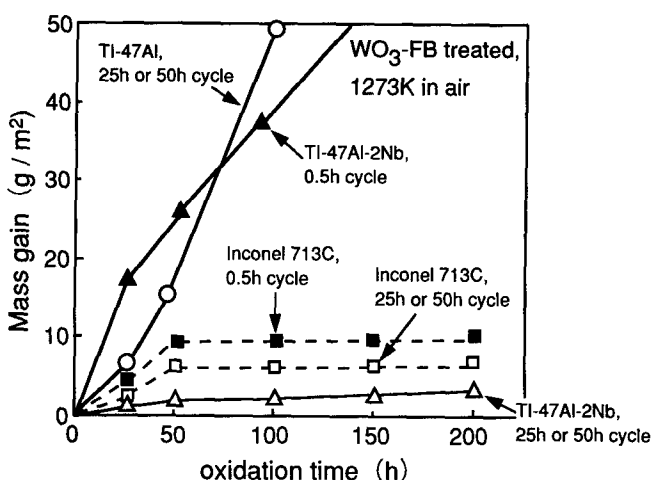


Figure 11 Mass gain under cyclic oxidation of Ti-47Al and Ti-47Al-2Nb alloys at 1273K.

the outer surface as indicated by the high concentration of both tungsten and oxygen. As the sputtering proceeds in the depth direction, the concentration of oxygen rapidly decreases, implying the formation of a tungsten-rich layer. In addition, an  $\text{Al}_2\text{O}_3$  layer was formed under the tungsten-rich layer. An AES depth profile of the specimen subsequently oxidized at 1223K for 200 hours is shown in Figure 14. The amount of tungsten decreased to be negligible. The  $\text{Al}_2\text{O}_3$  layer is thicker than that before the oxidation.

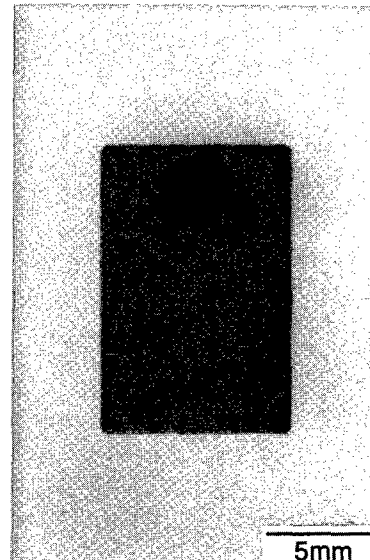
Figure 15 compares the outer surface and the fracture surface of the  $\text{WO}_3$ -FB treated specimen with the specimen subsequently oxidized at 1223K for 200 hours. After the  $\text{WO}_3$ -FB treatment, rod-shaped



(a) untreated  
(after 50h)



(b) pack-cementation treated  
with  $\text{WO}_3$  powder (after 500h)



(c)  $\text{WO}_3$ -FB treated  
(after 500h)

Figure 10 Appearance of untreated (a), pack-cementation treated with  $\text{WO}_3$  powder (b) and  $\text{WO}_3$ -FB treated (c) Ti-47Al specimens oxidized at 1223K in air after the short-term cyclic oxidation tests.

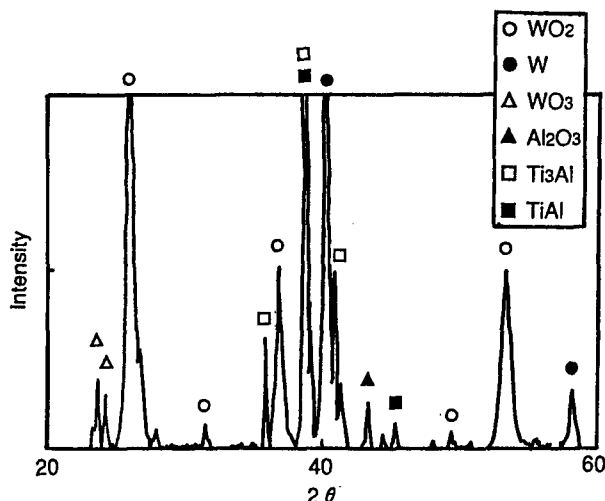


Figure 12 XRD chart of the  $\text{WO}_3$ -FB treated Ti-47Al specimen.

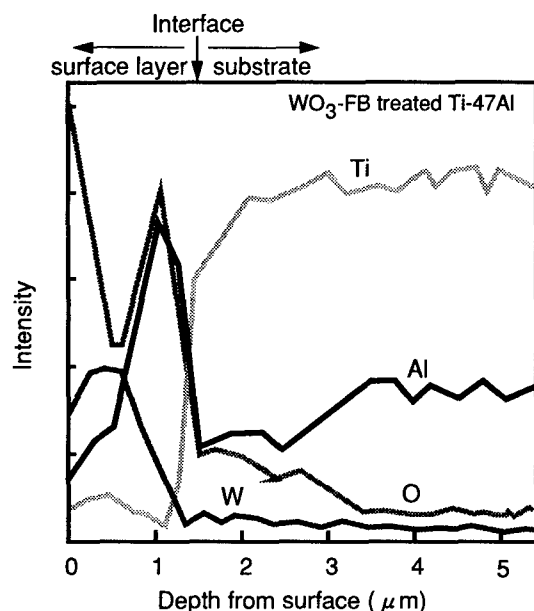


Figure 13 An AES depth profile near the surface of the  $\text{WO}_3$ -FB treated Ti-47Al specimen.

tungsten oxides were formed on the outer surface (Fig. 15(a)). Beneath the outer scales, a continuous layer of about  $1\text{ }\mu\text{m}$  in thickness was formed, as indicated by the arrows in Fig. 15(b). The layer is uniform in thickness and adheres well to the substrate. After the oxidation tests, the rod-shaped scales formed by FB treatment disappeared and granular scales were then observed (Fig. 15(c)). The oxide scales are far thinner than the complex oxide layer of the untreated specimen shown in Fig. 1. The structure of the scales consists of granular scales and a continuous layer. As shown by the arrows in Fig. 15(d), the inner layers are sound and there is no void near its interface with the substrate. On the other hand, an aluminum-depleted layer after the oxidation test is thicker than before. It is assumed that aluminum in the substrate is depleted because of the increase in the thickness of the  $\text{Al}_2\text{O}_3$  layer during the oxidation.

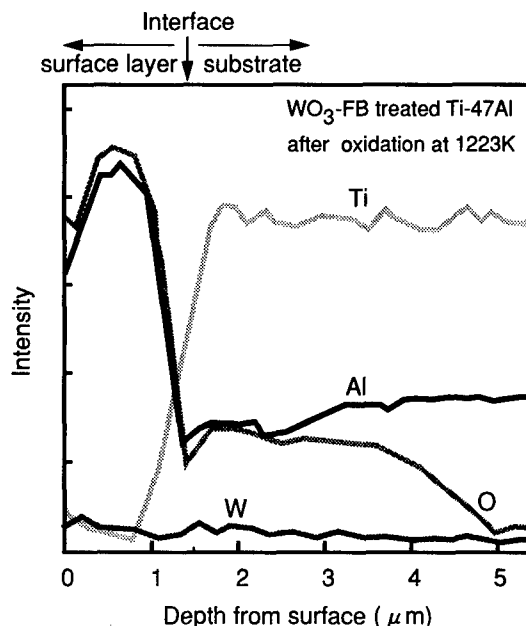


Figure 14 An AES depth profile near the surface of the  $\text{WO}_3$ -FB treated Ti-47Al specimen after oxidation at 1223K for 200h.

From the above results, the surface structures of the  $\text{WO}_3$ -FB treated and the specimens subsequently oxidized are illustrated in Figure 16. The surface structures are summarized as follows: After  $\text{WO}_3$ -FB treatment, rod-shaped  $\text{WO}_2$  particles have been formed on the surface. Beneath the scales, continuous layers (a tungsten-rich layer and beneath that an  $\text{Al}_2\text{O}_3$  layer) were formed. After oxidation test, the  $\text{WO}_2$  scales and the tungsten-rich layer was disappeared and the  $\text{Al}_2\text{O}_3$  layer is thicker than that before the oxidation. In addition,  $\text{TiO}_2$  scales were scarcely formed on the  $\text{Al}_2\text{O}_3$  layer, indicating that the  $\text{Al}_2\text{O}_3$  layer acts as a barrier against the formation of  $\text{TiO}_2$  scales.

The effectiveness of the present  $\text{WO}_3$ -FB treatment is compared with that of the pack-cementation with  $\text{WO}_3$  powder. XRD showed that, on the pack-cementation treated specimen,  $\text{TiO}_2$  scales were formed in addition to scales which also were identified for the FB-treated specimen. The fracture surface of the binary TiAl specimen treated by pack-cementation is shown in Figure 17. The most distinctive structures in comparison to that of the FB-treated specimen are as follows: Granular  $\text{TiO}_2$  scales were formed beneath the outer  $\text{WO}_2$  and  $\text{WO}_3$  scales, and voids were numerous observed near the interface between the  $\text{Al}_2\text{O}_3$  layer and the substrate. From these observations, it may be assumed that the spalling of the protective  $\text{Al}_2\text{O}_3$  layer easily occurred during the oxidation. Thus, the oxidation resistance of the TiAl-base alloys treated by pack-cementation is considered to be inferior to that of the FB-treated TiAl alloys, as shown in Fig. 9.

The main characteristics of the surface structure of the  $\text{WO}_3$ -FB treated specimens is the continuous and sound  $\text{Al}_2\text{O}_3$  layer, which is supposed to be formed as follows: Tungsten oxide is reduced to tungsten during the FB treatment, which causes the preferential oxidation of

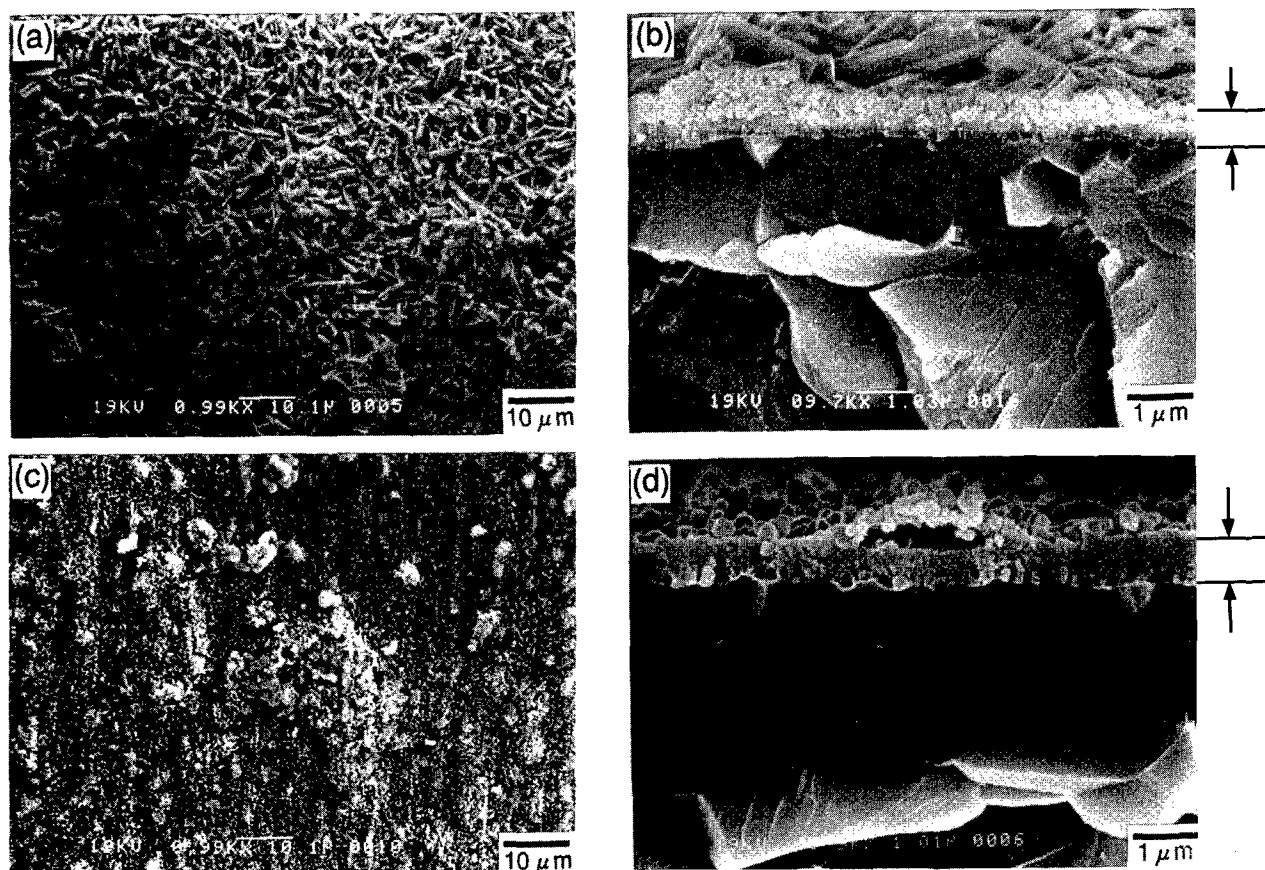


Figure 15 SEMs of outer surface (a and c) and fractured section (b and d) of  $\text{WO}_3$ -FB treated Ti-47Al specimens, before (a and b) and after oxidation at 1223K for 200h (c and d).

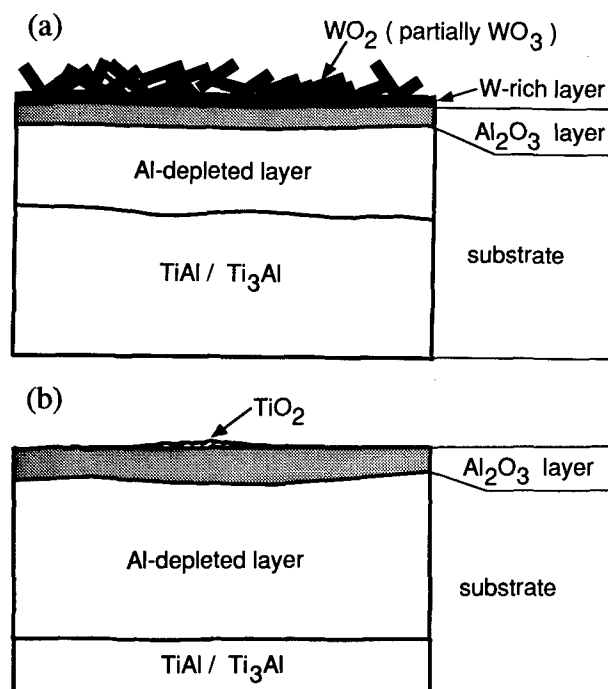


Figure 16 Schematic drawings of the  $\text{WO}_3$ -FB treated Ti-47Al alloy, before (a) and after the cyclic oxidation at 1223K for 200h (b).

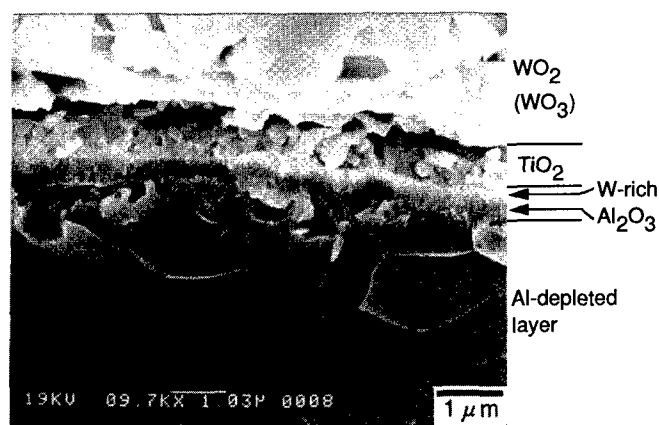


Figure 17 SEM of fractured section of Ti-47Al alloy after pack-cementation treatment with  $\text{WO}_3$  powder.

aluminum. In other words, the formation of the  $\text{Al}_2\text{O}_3$  layer is attributable to the reduction-oxidation reaction of the tungsten oxide and aluminum. In addition, as  $\text{WO}_3$  reagents are stirred in the fluidized bed and then activated contacting the specimen, the  $\text{Al}_2\text{O}_3$  layer may be continuously and soundly formed. Thus, the protective  $\text{Al}_2\text{O}_3$  layer is effectively obtained by the developed-FB treatment using the  $\text{WO}_3$  reagents, resulting in the excellent cyclic oxidation resistance.

### Comparison with other surface treatments

Several surface treatments have been reported for improving the oxidation resistance of TiAl-base alloys. Their performances have not been evaluated under a wide range of oxidation conditions, such as temperature, atmosphere and cycle time. Comparing with Inconel 713C for 200 hours in air, the oxidation resistance of the other surface treatments and the present WO<sub>3</sub>-FB treatment are summarized as shown in Table IV. It is revealed that the developed WO<sub>3</sub>-FB treatment must be one of the most effective processes for improving the oxidation resistance above 1223K. Among the previous treatments, the coating Ti-51Al-12Cr alloy by low-pressure plasma spray was reported to successfully protect the substrate from the oxidation at 1273K. However, its reliability has not yet been evaluated in severe cyclic oxidation, and it seems to be costly in respect of equipment and raw powders for the coating. We suppose that the WO<sub>3</sub>-FB treatment is advantageous in simplicity, productivity and cost efficiency because the fluidized bed furnace is widely used for the heat treatment.

### Possibility of application for automotive parts

For practical application of the present surface treatment to automotive parts, it is necessary to evaluate the oxidation resistance in an actual atmosphere, because the oxidation behavior strongly depends on the atmosphere. Therefore, the effectiveness of the WO<sub>3</sub>-FB treatment was examined in a typical model exhaust gas of the automotive diesel engine. The results of cyclic oxidation tests at 1223K in the model exhaust gas of the untreated and WO<sub>3</sub>-FB treated binary alloy are shown in Figure 18, which includes the results obtained on Inconel 713C for comparison. The mass gain of the treated specimen is extremely small compared with that of the untreated one, and smaller than that of Inconel 713C. Although the data is insufficient at present, the WO<sub>3</sub>-FB treatment significantly improves the oxidation resistance in an exhaust gas as well as in air.

There are two other performances to be evaluated for practical applications. One is the uniformity of the treatment, especially important in the case of the application to complex-shape parts. Another is

Table IV Summary of Oxidation Resistance in Air by the Developed Surface Treatment in Comparison to Other Surface Treatments

Surface treatment (substrate composition ,mol%)	Temperature, condition of oxidation test								Reference
	1173K			1223K			1273K		
	25h (50h ) cyclic	5h cyclic	0.5h (1h) cyclic	25h (50h ) cyclic	5h cyclic	0.5h (1h) cyclic	25h (50h ) cyclic	0.5h (1h) cyclic	
WO <sub>3</sub> -FB treatment (Ti-47Al)	S	S	S	S	S	S	I	I	this study
WO <sub>3</sub> - FB treatment (Ti-47Al-2Nb)	S	S	S	S	S	S	S	I	this study
WO <sub>3</sub> -pack cementation (Ti-47Al)	S	S	S	I	I	I	I	I	this study
WO <sub>3</sub> - pack cementation (Ti-47Al-2Nb)	S	S	S	I	I	I	I	I	this study
WO <sub>3</sub> -pack cementation (Ti-48Al)	S	S	S	—	—	—	—	—	(11)
Heat treatment under a low partial pressure oxygen atmosphere [※1] (Ti-50Al)	I	I	—	I	I	—	—	—	(12)
Al diffusion coating [※2] (Ti-50Al)	S	S	—	—	I	—	—	—	(12)
Cobination treatment of ※1 and ※2 (Ti-50Al)	S	S	—	—	S	—	—	—	(12)
Cr plating (Ti-47Al)	—	—	I	—	—	—	—	—	(13)
CoNiCrAlY coating by air plasma spray (Ti-47Al)	—	—	I	—	—	—	—	—	(13)
Ti-51Al-12Cr coating by low-pressure plasma spray (Ti-48Al-2Cr-2Nb)	S	—	—	S	—	—	S	—	(14)

The oxidation resistance for 200h in air is superior or equal (S), inferior (I) to Inconel 713C. unknown : —



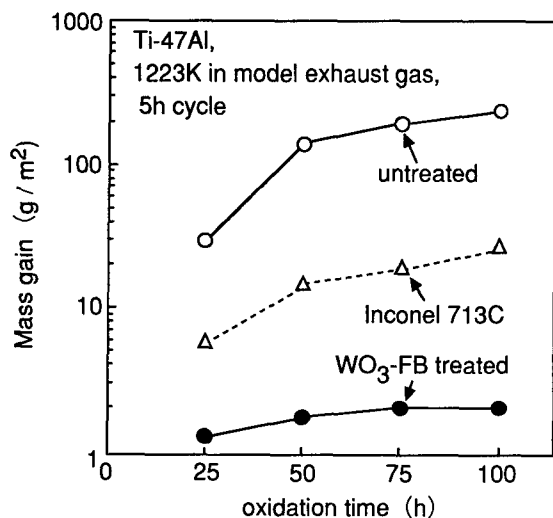


Figure 18 Mass gain under cyclic oxidation in model exhaust gas of Ti-47Al specimens at 1173K.

whether the treatment is effective or not even on the as-cast skin, because the TiAl-base alloy is likely used as castings with thin reactive surface layers formed by the chemical reaction with the mold. From this point of view, the WO<sub>3</sub>-FB treatment was applied to automotive turbocharger wheels, precision castings of Ti-47Al alloy, and the oxidation resistance of the wheels was evaluated. Figure 19 shows the appearance of the untreated and WO<sub>3</sub>-FB treated wheels after the cyclic oxidation test at 1223K. In the untreated wheel, spalling has already occurred until 50 hours: however, spalling could not be realized in the treated wheel until 200 hours. Thus, it was confirmed that the WO<sub>3</sub>-FB treatment will be applicable for complex-shape parts with the as-cast skin surface.

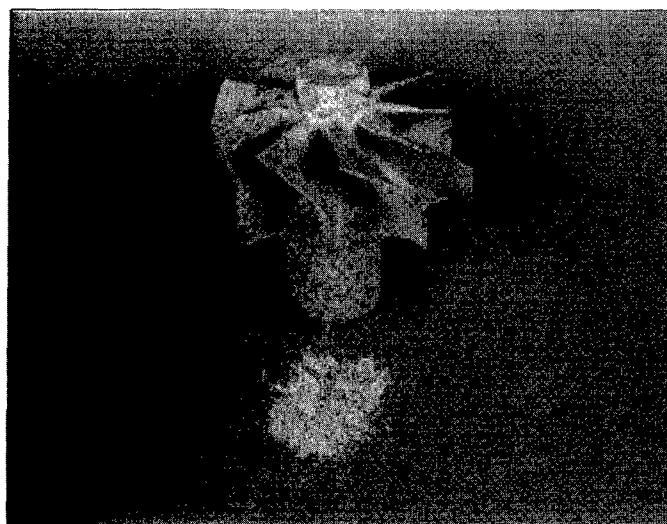
## Conclusion

A new surface treatment using a fluidized bed (FB treatment) was investigated in order to improve the oxidation resistance of TiAl-base alloys at higher temperatures. The effectiveness of the developed treatment was evaluated by long-term and short-term cyclic oxidation tests at 1173-1273K in air and model exhaust gas atmosphere. The results obtained are summarized as follows:

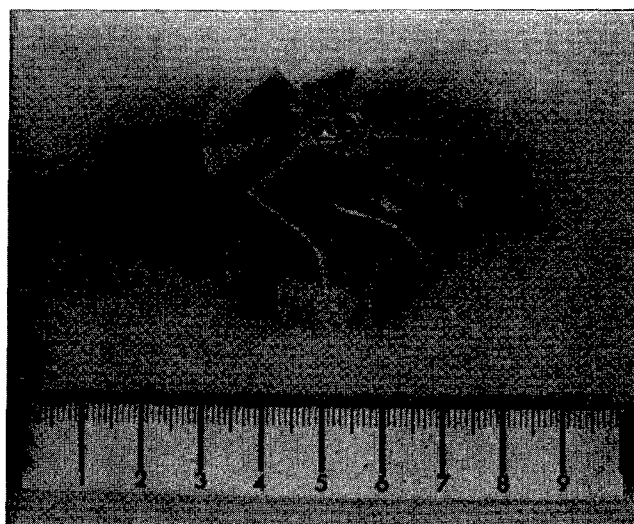
- (1) The FB treatment, regardless of the kind of additional powders (Cr<sub>2</sub>O<sub>3</sub>, Nb<sub>2</sub>O<sub>5</sub> or WO<sub>3</sub>), was very effective in improving the oxidation resistance of TiAl-base alloys. Particularly the WO<sub>3</sub> powder provided the best oxidation resistance among three powders.
- (2) The WO<sub>3</sub>-FB treated binary Ti-47Al alloy showed an oxidation resistance superior to Inconel 713C at 1223K both in air and in a model exhaust gas atmosphere. The oxidation resistance of the treated niobium-containing Ti-47Al-2Nb alloy was excellent in the long-term cyclic test at 1273K, although it was insufficient in the short-term cyclic test.
- (3) The remarkable improvement due to the WO<sub>3</sub>-FB treatment was attributable to the formation of a continuous and sound Al<sub>2</sub>O<sub>3</sub> layer formed by this treatment.
- (4) The WO<sub>3</sub>-FB treatment is extremely effective in its application to as-cast automotive engine parts, such as turbocharger wheels.

## Reference

1. Y. Nishiyama, T. Miyashita, S. Isobe and T. Noda, *High Temperature Aluminides and Intermetallics*, Edited by S. H. Whang, C. T. Liu, D. P. Pope and J. O. Stiegler (The Minerals, Metals & Materials Society, 1990), 557-584.



(a) untreated (after 50h)



(b) WO<sub>3</sub>-FB treated (after 200h)

Figure 19 Appearances of untreated (a) and WO<sub>3</sub>-FB treated (b) Ti-47Al turbine wheels after the cyclic oxidation tests at 1223K.

2. W. E. Dowling, Jr., J. E. Allison, L. R. Swank and A. M. Sherman, SAE paper 930620.
3. K. Maki, A. Ehira, M. Sayashi, T. Sasaki, T. Noda, M. Okabe and S. Isobe, SAE paper 960303.
4. S. Taniguchi and T. Shibata, Intermetallics, 4(1996), S85-S93.
5. S. A. Kekare, D.K. Shelton and P. B. Aswath, Structural Intermetallics, Edited by R. Darolia, J. J. Lewandowski, C. T. Liu, P. L. Martin, D. B. Miracle and M. V. Nathal, (The Minerals, Metals & Materials Society, 1993), 325-334.
6. Y. Shida and H. Anada, J. Japan Inst. Metals, 58(1994), 746-753.
7. Y. Shida and H. Anada, J. Japan Inst. Metals, 58(1994), 754-762.
8. H. Anada and Y. Shida, J. Japan Inst. Metals, 58(1994), 1036-1043.
9. S. Taniguchi, T. Shibata and S. Sakon, Mater. Sci. and Eng., A198 (1995), 85-90.
10. S. Taniguchi, T. Shibata and A. Murakami, Oxid. Met., 41(1994), 103-113.
11. H. Anada and Y. Shida, Proceeding of the 115th Meeting of JIM, (1994), 443.
12. M. Yoshihara, T. Suzuki and R. Tanaka, ISIJ International, 31(1991), 1201-1206.
13. T. Shimizu, T. Iikubo and S. Isobe, Mater. Sci. and Eng., A153(1992), 602-607.
14. M. P. Brady, W. J. Brindley, J. L. Smialek and I. E. Locci, JOM, 48(12), 46-50.

## Scale-up of Ingot Metallurgy Wrought $\gamma$ -TiAl

P.L. Martin, D.A. Hardwick, D.R. Clemens\*, W.A. Konkel<sup>§</sup> and M.A. Stucke<sup>¶</sup>

Rockwell Science Center, 1049 Camino Dos Rios, Thousand Oaks, CA 91360

\* Pratt & Whitney, 17900 Beeline Hwy, Jupiter, FL 33478

<sup>§</sup> Wyman-Gordon Forgings, 10825 Telge Rd, Houston, TX 77095

<sup>¶</sup> Wright Laboratories/MLLN, Wright Patterson Airforce Base, Dayton, OH 45433

### Abstract

One of the main obstacles to the implementation of wrought  $\gamma$ -TiAl in engineering systems has been the limited scale of ingot available using conventional casting techniques. Standard vacuum arc remelting (VAR) practice leads to significant cracking in ingots larger than approximately 280 mm (11") in diameter. Improvements in VAR melt shop techniques have allowed ingots as large as 355 mm (14") in diameter weighing over 270 kg (600lbs) to be made with reduced cracking. Alternative melting techniques, such as plasma arc melting (PAM) or skull melting (SM), have been used to make ingot this size and larger. To date, the largest ingot produced was 430 mm (17") in diameter and weighs over 700 kg (1500lbs); it was made using SM technology. Several alloy compositions have been made at this scale. Gross chemical inhomogeneity between the top and bottom of the ingots was not observed. Breakdown to billet was accomplished using commercial-scale hot extrusion equipment and standard superalloy handling procedures. Production of large ingots and their handling in a mill environment without debilitating precautions are significant milestones on the road to commercial reality for  $\gamma$ -TiAl alloys. In addition, the availability of large-

scale billet allows more extensive hot working to be accomplished during secondary processing operations. Microstructural refinement is facilitated during subsequent processing by forging, potting or extrusion. Results from these studies will be presented for two alloys: Ti-47Al-2Nb-2Cr-1Mo±B and Ti-47Al-5Nb-1W. Implications for the future of wrought ingot based  $\gamma$ -TiAl in engineering systems will be discussed.

### Introduction

A growing database demonstrates the benefits to be gained through the replacement of medium strength superalloys by near- $\gamma$  TiAl compositions in moderate temperature applications [1]. Various techniques used to make this intermetallic include casting (investment casting, permanent mold casting, conventional ingot casting), vapor deposition, powder metallurgy and reactive synthesis [2]. In material destined for wrought processing, ingot casting techniques, such as induction skull melting and vacuum arc remelting, as well as powder methods have been used to prepare forging or extrusion preforms [3-6]. Of these techniques, the ingot methods are potentially the most economical option, if the scale of the products can be increased to utilize

conventional "full-size" equipment and normal handling procedures [7]. The fundamental difficulties involved in converting the cast structures formed during the cooling of  $\gamma$ -TiAl alloys to wrought structures have been documented [5-8]. Assuming crack-free ingot can be produced, the major pitfalls revolve around elimination of both the segregation from peritectic solidification and the lamellar microstructure characteristic of lower Al regions. As ingots are made larger, the segregation distances become larger and homogenization issues are expected to become more critical.

This paper presents a preliminary report on attempts to expand the scale of available ingots and to demonstrate that they can be processed using conventional superalloy handling procedures during primary ingot breakdown. Two typical alloy compositions have been evaluated using three different casting methods. This should enable us to begin defining the casting limitations caused by both compositional and process variations. Non-isothermal hot extrusion, potting and isothermal forging have been evaluated for their ability to convert the ingots to standard mill product.

### Experimental Procedures

Large-scale ingots were produced using three processing methods: vacuum arc remelting (VAR), plasma arc melting (PAM) and skull melting (SM). The first two methods are commonly used to produce Ti ingots while the SM technique involves arc melting of a consumable electrode into a hearth followed by tilt pouring into a suitable mold. All of the techniques accomplish the melting and ingot solidification with the molten metal contained in water-cooled copper or other materials that do not contaminate the ingot. VAR of 355 mm diameter ingots weighing 270 kg was done at Timet, Henderson Technical Laboratory. Controlled cooling techniques were used to limit stress-induced cracks during ingot solidification. PAM of 355 mm diameter ingots weighing 290 kg was done at Pratt & Whitney Aircraft, Hartford in a multiple torch system described elsewhere [9,10]. SM of 430 mm diameter ingots weighing 690 kg was done at Ormet, Albany using full-scale commercial melting equipment and handling techniques.

Homogenization heat treatments of the ingots were conducted in a vacuum of  $10^{-2}$  Pa or better at a temperature of 1400°C for 2-4 hours. Heating and cooling rates were controlled in order to limit thermal stress-induced cracking of the ingots. Conversion of the ingots to billets was accomplished by hot extrusion using the commercial scale facility at Wyman-Gordon, Houston. This press has a capacity of over 300 MN of force and tooling that extends to over 1350 mm in ingot or can diameter. All primary breakdown extrusions were conducted at temperatures in the  $\alpha$ - $\gamma$  phase field using a maximum reduction ratio of 6:1.

Secondary processing of the billet was by either isothermal forging or further hot extrusion. The 88 MN press at Ladish was used for the isothermal forging which was accomplished at conventional temperatures and strain rates [6,8]. The 22 MN R&D press at Wyman-Gordon was used for the continued diameter reduction by extrusion. A range of preheat temperatures were utilized in order to achieve a variety of dynamically recrystallized microstructures in the extruded billet.

Microstructural characterization was performed principally by SEM metallography due to the ability of backscattered electron images (BEI) to highlight both regions of high average atomic number ('Z' contrast) and orientation changes (channeling contrast). Slowly varying concentration gradients, e.g. casting segregation patterns around dendrites, can be observed at low magnifications since heavy elements concentrate in the dendrite cores and Al is rejected to the interdendritic regions. All BEI micrographs were taken from electropolished surfaces, effectively eliminating artifacts due to etching or deformed surfaces.

### Results and Discussion

#### Ingot Casting

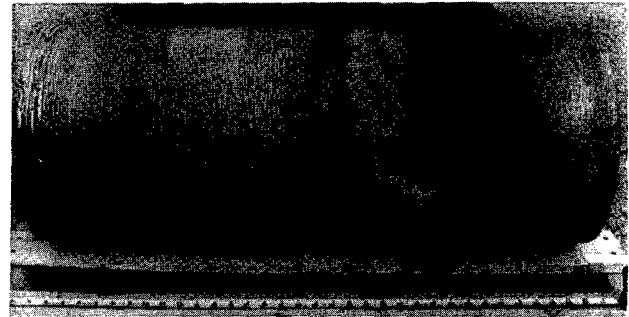
A large number of ingots have been melted in the course of this program. To date, a total of over 2500 kg of the base alloy, Ti-47Al-2Nb-2Cr-1Mo, has been produced in various size ingots using the three melting methods. In addition, an ingot of Alloy 7, Ti-46Al-5Nb-1W, has been made using skull melting (SM). The chemical compositions of the ingots to be discussed in this

Table I. Chemical composition of ingots produced; average of all ingot locations and multiple analysis providers (atomic %; wppm oxygen).

ID	Al	Nb	Cr	Mo	W	Fe	Si	C	B	O
VAR: 7852	46.7	1.9	1.9	0.9	-	0.025	0.045	0.046	-	620
PAM: 5-95	47.1	2.0	2.0	1.0	-	0.029	0.043	0.035	-	420
PAM: 3-95	46.2	2.0	2.0	1.0	-	0.027	0.042	0.085	0.2	395
SM: 525	46.5	2.0	2.1	1.1	-	0.049	0.043	0.056	0.016	720
SM: 980	47.3	5.0	-	-	1.0	0.075	0.073	0.054	-	720

manuscript are shown in Table 1. The VAR and PAM ingots weighed approximately 290 kg each while the SM ingots weighed approximately 690 kg each. Several of the ingots contained small, but intentional, additions of B to restrict high temperature grain growth [7, 11].

Typical 290 and 690 kg ingots are shown in Figure 1. The 290 kg ingots were all produced without cracks. The SM-980 ingot was crack-free on the bottom but contained a small crack extending from the solidification shrinkage pipe. This was observed prior to the homogenization heat treatment. Figure 2 shows the faces of this ingot following the homogenization at 1400°C; the crack has grown slightly compared with the as-cast condition. It is postulated that this crack extends only to the depth of the shrinkage pipe and not into the bulk of the ingot. Ultrasonic inspection was inconclusive in defining the depth of the shrinkage porosity due to the noisy signal caused by the large grains. This coarse macrostructure is shown in Figure 3 where a quadrant of SM-525 has been etched to reveal several distinct regions. The outer grains grow in a columnar fashion for several centimeters. Large equiaxed grains extend across the majority of the ingot. They are truncated by another region of columnar grains growing outward from the shrinkage pipe. These columnar grains nucleate on this inner surface and would not be expected in the center of the ingot where the steady state solidification front would be traveling up the ingot.



(a) 290 kg, 355 mm diameter PAM



(b) 690 kg, 430 mm diameter SM

Figure 1. Photographs of the larger ingots produced.

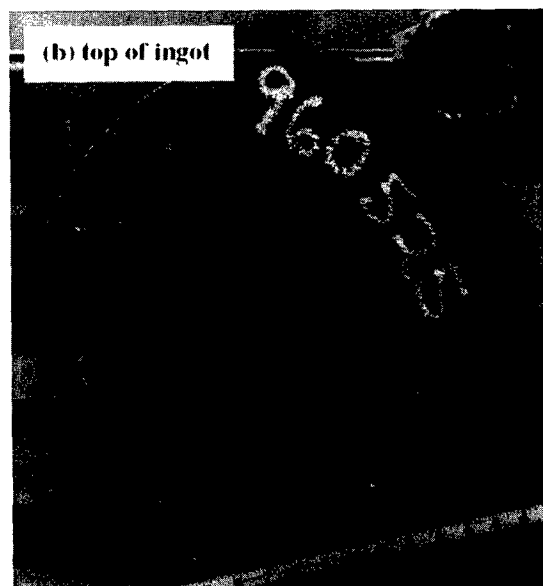
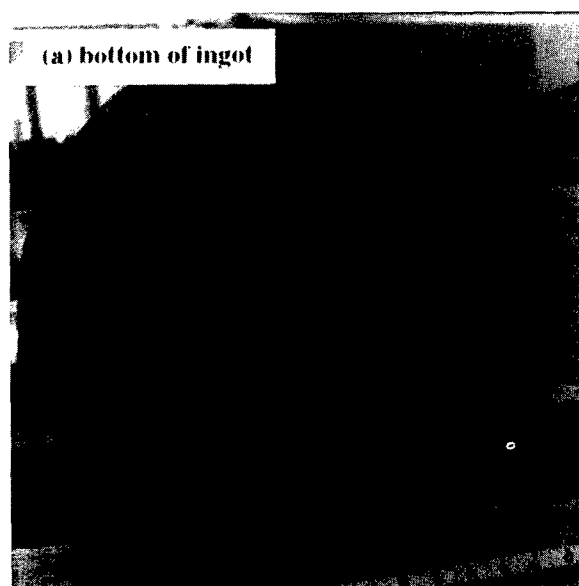


Figure 2. Photographs of the SM-980 ingot following homogenization heat treatment.

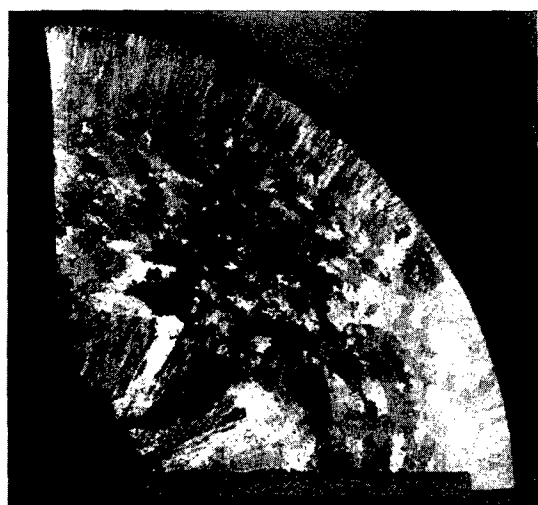


Figure 3. Macroetched quadrant from the top section of SM-525 showing the coarse grain structure.

Static homogenization of the ingots was used to lessen the segregation caused by peritectic solidification. Figure 4 illustrates the changes caused by a hold of 2 hours at  $1400^{\circ}\text{C}$  in the microstructure of SM-525. These images were taken from samples cut from the top of the ingot at approximately the mid-radius location. The dendritic segregation is maximized at this location and is easily seen in Figure 4(a). Some diffuse contrast from this dendritic structure can be seen after the homogenization in Figure 4(b). However, the decrease in Z contrast indicates a significant increase in chemical homogeneity. The alloy 7 ingot, SM-980, was not homogenized prior to extrusion.

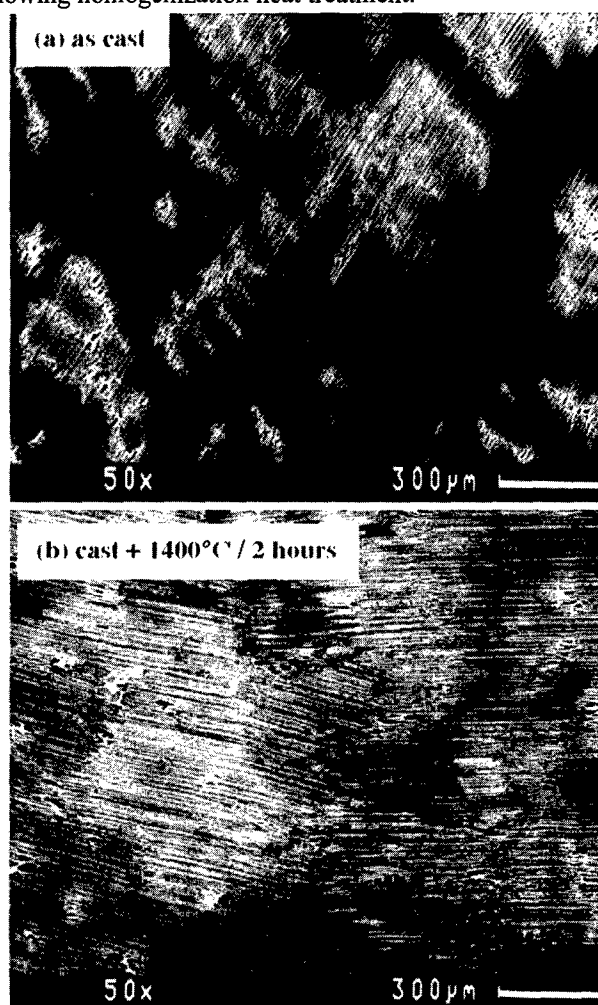


Figure 4. BEI micrographs from the top of SM-525 at approximately the mid-radius of the ingot.

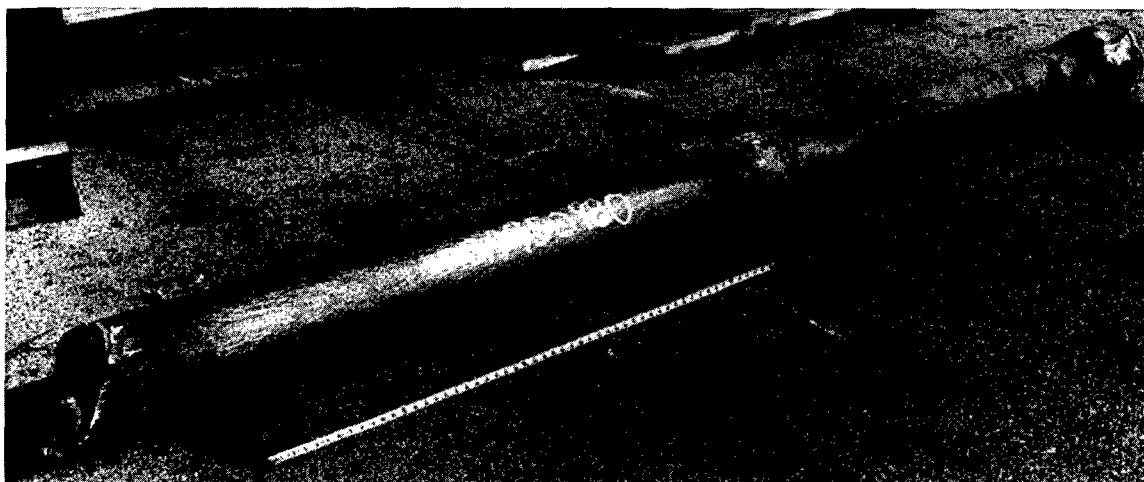


Figure 5. Decanned billet of SM-980 extruded 6:1.

The lamellar colonies following this very high temperature homogenization treatment are  $\approx 700\text{-}1200\mu\text{m}$  in size. The presence of some refractory metal stabilized  $\beta$  phase, seen in Figure 4(b) as small bright particles, can limit the extent of grain growth. However, this effect is quite sensitive to the exact chemistry of the ingot. This can shift the phase boundaries so that the  $\alpha+\beta$  field may not be accessible until the temperature approaches the liquidus. The B concentration in these alloys is insufficient to pin the colony boundaries. The borides are present as thin "strings", easily visible at higher magnification [12].

#### Primary Ingot Breakdown

While the large grain size in the homogenized material would be considered deleterious to wrought processing by forging, the flow conditions associated with hot extrusion allow uniform deformation to occur without creating macroscopic fracture or internal wedge cracks. The canned ingot is soaked at the working temperature long enough to ensure a uniform temperature prior to extrusion with a reduction in area of 5 or 6:1. Mechanical manipulators transfer the hot can assembly to the 35,000 ton press using the same practices as for superalloys. The loads involved do not approach the press capacity indicating that further scale increases are possible. Figure 5 shows the decanned billet of ingot SM-980 after extrusion. Following machining, the billet measures  $\approx 190$  mm in diameter. Work is continuing to increase the yield of billet and to minimize nose, tail and clean-up losses.

The longitudinal microstructures of extruded billet are considerably refined compared to the starting material. Figure 6 illustrates the microstructure of PAM 3-95 and SM-980 following extrusion. The large lamellar colonies, present in the ingot prior to extrusion, for example Figure 4(b), have been converted to a mixture of dynamically recrystallized gamma grains with a minor fraction of "strung out" lamellae. The elongation of the dark interdendritic regions in SM-980 is most noticeable, Figure 6(b); recall that this ingot was not homogenized before extrusion. No equivalent inhomogeneity was seen in any of the statically homogenized alloys, e.g. Figure 6(a). When viewed at higher magnifications this long range segregation cannot be seen, Figure 6(c) and (d). However, a difference in the scale of the microstructure is quite evident; the grain size of the PAM 3-95 billet is significantly coarser than that of SM-980. Both consist of  $\gamma+\beta$  phases with frequent annealing twins in the  $\gamma$  phase. The microstructural unit size is less than  $50\mu\text{m}$  for PAM 3-95 and well below  $20\mu\text{m}$  for SM-980.

If the purpose of homogenization and primary ingot breakdown is to minimize casting segregation, refine the as-cast grains and provide a relatively equiaxed microstructure for subsequent processing, then single step hot extrusion has accomplished this goal. Larger reductions in area and lower temperatures for the extrusion may be possible. While these may lead to greater refinement of the microstructure, the risks involved may overcome the benefits. Furthermore, large billet is desirable for secondary forging applications for the fabrication of large diameter components.

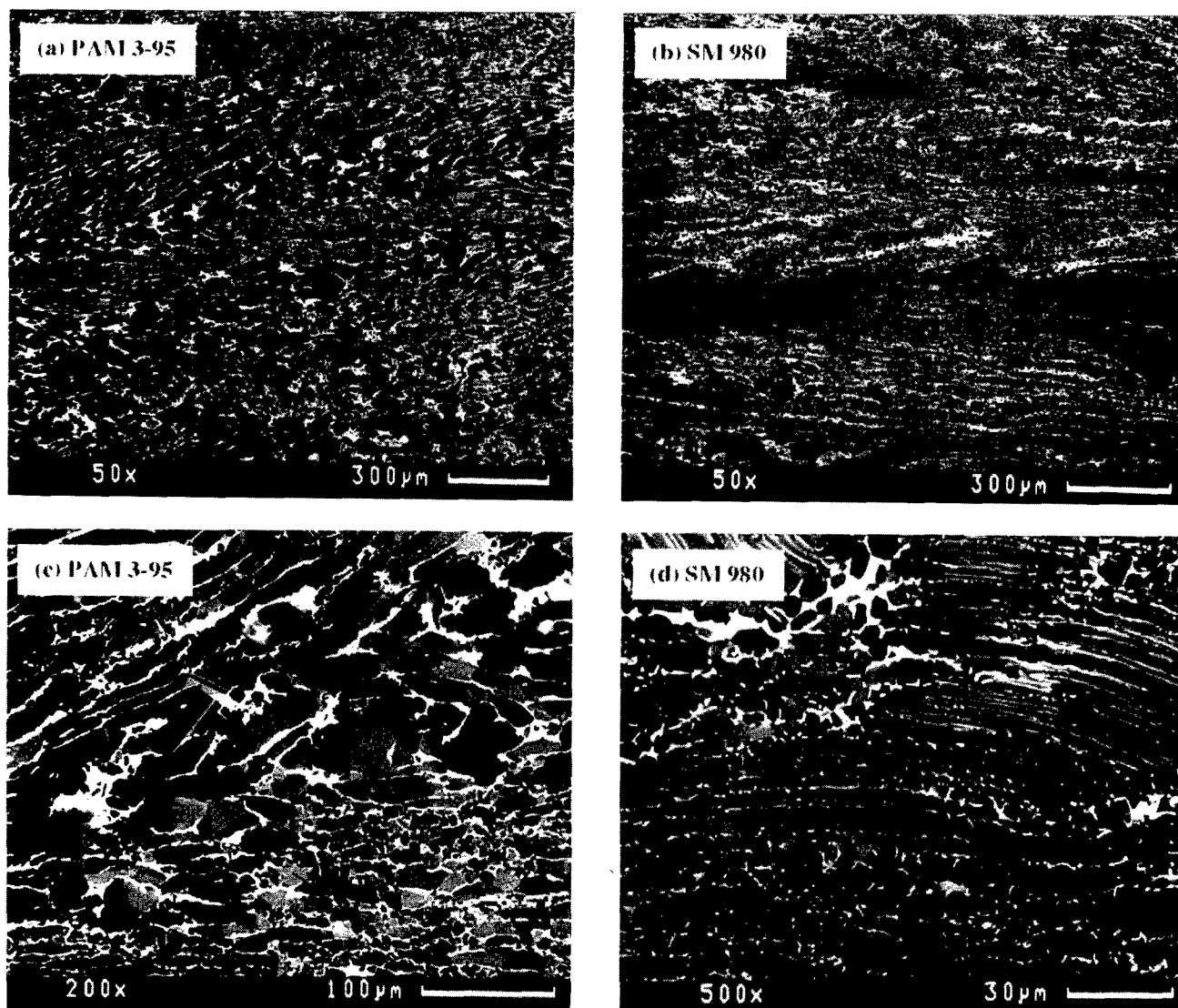


Figure 6. BEI micrographs from the longitudinal sections of as-extruded billet, specimens taken at  $\approx 0.5$  radius.

#### Secondary Wrought Microstructures

Isothermal forging is the normal method of continuing wrought processing of near- $\gamma$  alloys. The extruded billet described above can be upset forged at significantly lower temperatures than is normally used for cast starting material. Large strain deformation leads to uniform microstructures where the grains are  $\approx 10 \mu\text{m}$  in diameter, Figure 7. Some evidence of remnant lamellar colonies can still be seen as regions of finer grains, Figure 7(a).

Additional reduction by hot extrusion can also be used to attain a variety of microstructures of potential interest. Recanning and extruding billet from the 290 kg ingots at a

range of temperatures led to the structures in Figure 8. At low temperatures, Figure 8(a), the additional work further refines the grain dimensions. Observation of some elongated segregation implies that even after static homogenization and two hot working operations (in the same direction), diffusion has been insufficient to eliminate peritectic coring. As the extrusion temperature is increased, the volume fraction of  $\gamma$  decreases. Remnant segregation leads to "lines" of  $\gamma$  grains marking the interdendritic regions in the longitudinal section, Figure 8(b). Above the  $\alpha$  transus, single phase  $\alpha$  grains dynamically recrystallize during/following extrusion and lead to relatively equiaxed colonies of transformed  $\alpha$ . At still higher temperatures, the  $\beta$  phase again co-exists with the  $\alpha$  and is elongated during the extrusion, Figure 8(d).



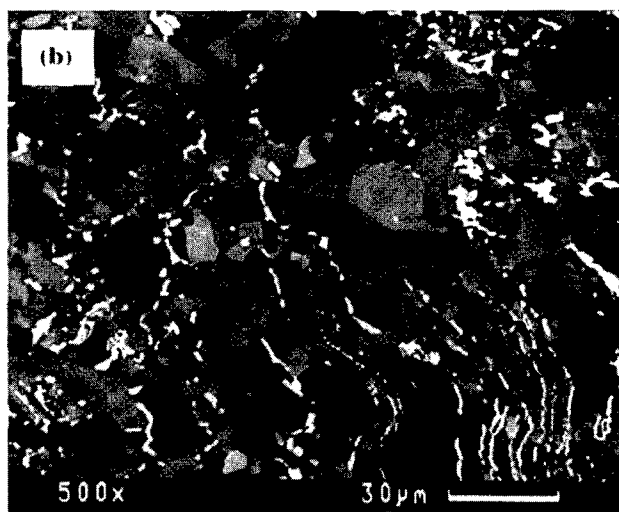
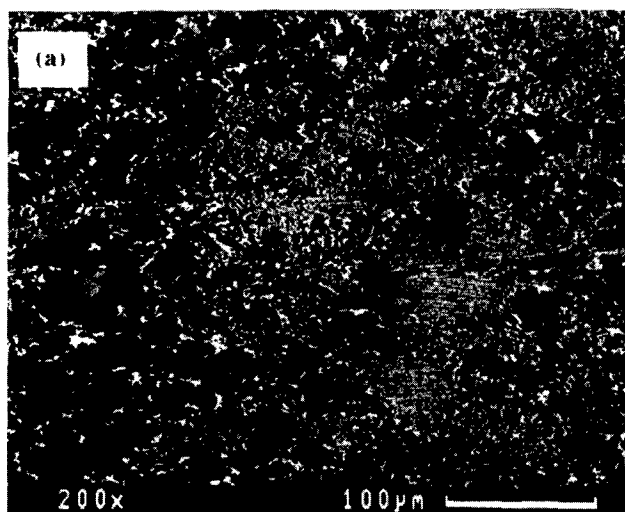


Figure 7. Through-thickness BEI micrographs from material forged at  $1100^{\circ}\text{C} / 73\% / 10^{-3} \text{ sec}^{-1}$ ; forging axis vertical.

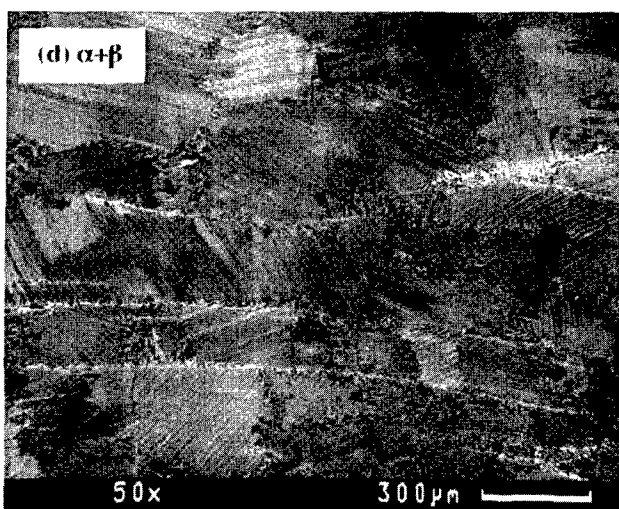
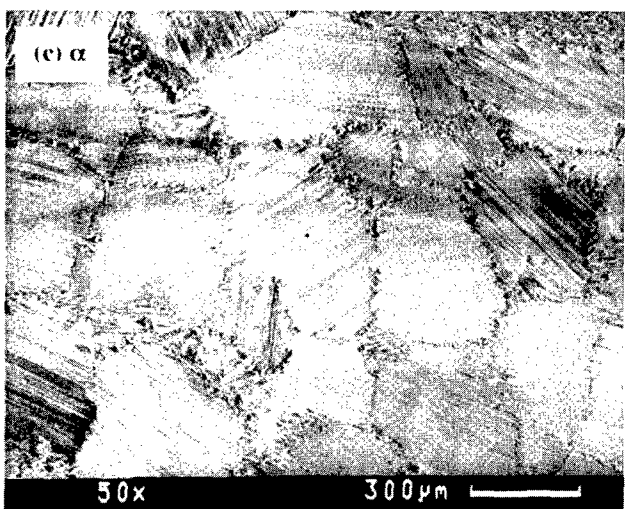
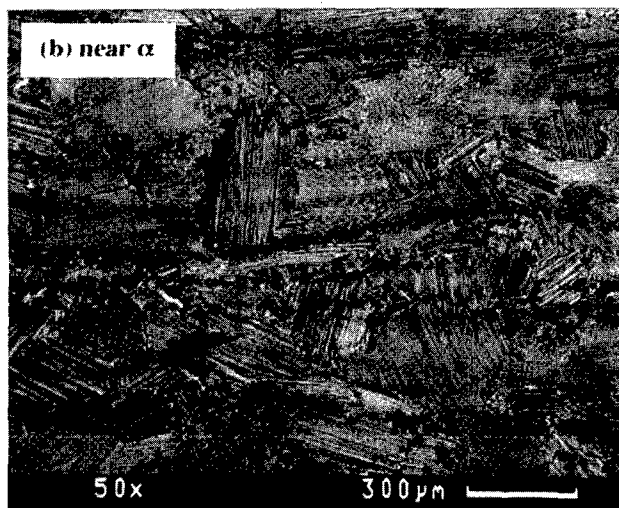
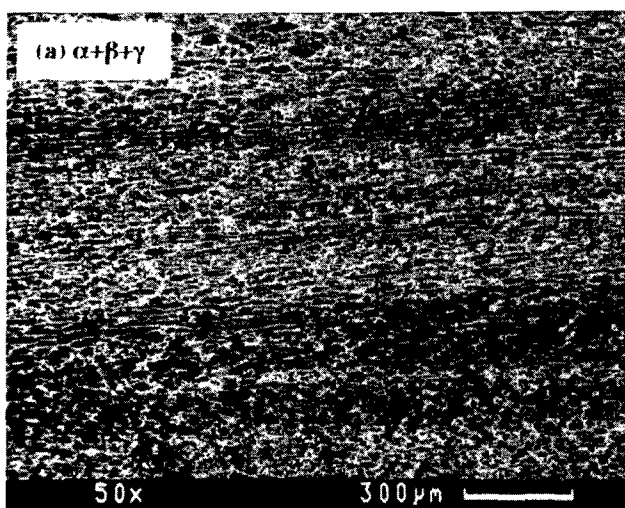


Figure 8. BEI micrographs from VAR 7852 extruded a second time from the indicated phase equilibrium regimes; longitudinal section,  $\approx$  mid-radius.

Each of these microstructures would be expected to have its own combination of properties; maximized strength for microstructure 8(a); maximum ductility for microstructures 8(a) or 8(b); a combination of good fracture toughness and creep resistance for microstructure 8(c) and, possibly, 8(d). Ongoing studies will elucidate these trade-offs. This will enable doubly extruded bar stock to be tailored for specific components and applications.

### Conclusions

This study has demonstrated that that scale-up of near- $\gamma$  alloy to produce commercial-scale mill product is feasible. As we learn more about controlling the stresses that occur during cooling of large ingots, ever larger lots will be produced with the attendant increasing economies of scale in conversion to wrought billet and bar. Handling experience for these alloys in the mill environment using standard practices has increased the confidence level to the point where they are no longer considered "experimental" at Wyman-Gordon. However, further reduction of the risks associated with large ingot melting and conversion are still required before full-scale production of wrought  $\gamma$  product will become commonplace. Component-driven demand for larger forgings with wrought properties will drive this development.

### Acknowledgement

Sponsorship of this program by the U.S. Air Force Wright Laboratories under contract F33615-93-C-5370 is gratefully acknowledged. The experimental assistance of Bob Spurling and Mike Calabrese is greatly appreciated.

### References

- [1]. See, for example, Gamma Titanium Aluminides, eds. Y-W. Kim, R. Wagner and M. Yamaguchi, TMS, Warrendale, 1995.
- [2]. P.L. Martin and D.A. Hardwick, "Synthesis and Processing Techniques", in Intermetallic Compounds: Principles and Practice, Chapter 27, eds J.H. Westbrook and R.L. Fleischer, John Wiley, 1995, pp. 637-660.
- [3]. D.M. Dimiduk, "Gamma Titanium Aluminides - An Emerging Materials Technology", in Gamma Titanium Aluminides, eds. Y-W. Kim, R. Wagner and M. Yamaguchi, TMS, Warrendale, 1995, pp. 3-20.
- [4]. S. Reed, "Gamma Titanium Aluminide Production Using the Induction Skull Melting (ISM) Process" in Gamma Titanium Aluminides, eds. Y-W. Kim, R. Wagner and M. Yamaguchi, TMS, Warrendale, 1995, pp. 475-482.
- [5]. G.E. Fuchs, "Thermo-Mechanical Processing (TMP) of Ti-48Al-2Nb-2Cr Based Alloys", in Gamma Titanium Aluminides, eds. Y-W. Kim, R. Wagner and M. Yamaguchi, TMS, Warrendale, 1995, pp. 563-570.
- [6]. P.L. Martin, C.G. Rhodes and P.A. McQuay, "Thermomechanical Processing Effects on Microstructures in Alloys Based on  $\gamma$ -TiAl", in Structural Intermetallics, eds. R. Darolia, J.J. Lewandowski, C.T. Liu, P.L. Martin, D.B. Miracle, M.V. Nathal, TMS, Warrendale, 1993, pp. 177-186.
- [7]. P.L. Martin and D.A. Hardwick, "Microstructure and Properties of Near- $\gamma$  Alloys Based on Ti-47Al-2Nb-2Cr-1Mo", in Titanium '95: Science and Technology, eds. P.A. Blankinsop, W.J. Evans and H.M. Flower, Inst. of Materials, London, 1996, pp. 168-175.
- [8]. S.L. Semiatin, V. Seetharaman and I. Weiss, "Hot Working of Titanium Alloys - An Overview", to appear in Advances in the Science and Technology of Titanium Processing, eds. I. Weiss et al., TMS, Warrendale, 1997.
- [9]. D.R. Malley, R.C. Eschenbach, M.E. Schlienger, "Control of Plasma Hearth Melted Ingot Surfaces", in Proceedings of 10<sup>th</sup> International Conference on Vacuum Metallurgy, Vol. 1, Metallurgical Industry Press, Beijing, China, 1991, pp. 178-188.
- [10]. M.J. Blackburn and D.R. Malley, in The Processing, Properties and Applications of Metallic and Ceramic Materials, Vol 1, eds M.H. Loretto and C.J. Beevers, MCE Publications Ltd., 1992, pp. 99-118.
- [11]. Y-W. Kim and D.M. Dimiduk, "Designing Gamma TiAl Alloys: Fundamentals, Strategy and Production", this proceedings.
- [12]. M. De Graef, D.A. Hardwick and P.L. Martin, "Structural Evolution of Titanium Di-Borides in Wrought Ti-47at%Al-2at%Mo-0.2at%B", this proceedings.

## Infrared Brazing of a TiAl-Base Alloy Using Ti and Al Foils and the Joint Microstructural Evolution

Sunil Annaji and Ray Y Lin

Dept. Of Materials Science And Engineering  
University of Cincinnati, M. L. 12  
OH 45221-0012

### Abstract

Joining of TiAl based alloy (Ti-48Al-2Nb-2Cr) with a novel infrared processing technique was investigated at 1200 °C and 1275 °C in a flowing argon environment for times varying between 15 seconds to 60 seconds. The joining filler materials were foils of aluminium and titanium. This joining process is closely related to the brazing process except that only Al was melted during joining. In the as-joined condition, various forms of titanium aluminide phases were observed in the joint. Cross sectional studies on the joined samples have shown different degrees of reaction depending on the temperature and time of holding. The joint microstructure evolution appears to be diffusion controlled, with Al being

the dominant moving species. To improve high temperature joint strength, heat treatments of the joined specimens at 1200 and 1300 °C for up to 4hrs in vacuum were performed. It was observed that the heat treatment resulted in homogenization and formation of a lamellar structure throughout the joint. Shear-in-compression tests of single lap specimens showed that the room temperature shear strength determined for these specimen, was better than that of the base metal. This was evidenced by the fracture path being through the base alloy instead of the joint. TEM studies have been employed to examine the phases in the joint.

## Introduction

Joining of titanium aluminides by welding using various conventional techniques has been studied by many researchers[1-4]. It was concluded from all these studies that the optimum weld structure can be obtained through proper control of cooling rates. In recent years solid phase welding (e.g. diffusion bonding and friction welding) of titanium aluminides has become increasingly popular. Studies on diffusion bonding of TiAl, using solid-state and transient liquid phase (TLP) processes, have been done in detail [5-8]. By use of interlayers in the solid state process, bonds have been fabricated at relatively low bonding temperatures and pressures. Such bonds were reported to have properties compatible with the base material after post heat treatment of the joint.

Scientists have reported work on joining of TiAl by using Al and Ti filler materials. TLP bonding of TiAl using Al was done at 900 °C [9, 10], which is determined by the melting point of the Al and its fluidity. Formation of TiAl<sub>3</sub> and TiAl<sub>2</sub> at the joint was reported. The joints were heat treated at 1300 °C and a single phase gamma was obtained in the joint. The tensile strength of the joints obtained at room temperature was found to be almost the same as that of the base material (220MPa). Joints were also obtained using Ti and Al powders as the filler materials. Self-propagating high temperature synthesis reaction yielded an inhomogeneous joint consisting of TiAl<sub>3</sub> and Ti<sub>3</sub>Al. TiAl<sub>3</sub> was formed at the bonding interface between the basemetal and the filler material. Subsequent heat treatment of the joint resulted in a fine lamellar phase in the joint and a single phase gamma at the interface. Joint strength at room temperature was found to be 220MPa which is about the same as the base materials strength.

Over the past few years, researchers at the University of Cincinnati have investigated joining of advanced materials with infrared.[11-13] Although infrared joining of TiAl with TiCuNi foils provides a fast and cost effective technique for obtaining strong joints, due to the low melting nature of TiCuNi the joint cannot survive high temperature application. To promote the temperature capability of the joint it has been suggested that Al and Ti be used as the filler materials. The objectives of this study are to establish a joining procedure for TiAl using Al and Ti foils, to study the microstructural evolution in the joint and to ultimately obtain joints that can perform as well as the base material at high temperatures.

## Experimental Procedure

Titanium aluminide used in this study was provided by GE Aircraft Engines, Cincinnati, OH. The nominal composition of this material was Ti-33.3Al-

4.8Nb-2.7Cr in wt% (Ti-48Al-2Cr-2Nb at%). This material was produced through isothermal forging at 1160 °C under a strain rate of 0.002-0.005 mm/mm/s, annealing at 1300 °C for 4hrs, and furnace cooling to 870 °C in 8hrs under flowing argon.

Since the focus of the study was on the microstructural evolution in the joint and its mechanical strength, the base material was cut into coupons of two different sizes: one for cross sectional examinations after joining and the other for joint shear strength measurements. The coupon size for cross-sectional examinations was 5mm × 5mm × 3mm and that for the strength specimen was 15mm × 6mm × 3mm. The strength testing sample size was chosen in accordance with the specifications used in our laboratory previously[11-13].

Before joining, the assembly was carefully loaded into the infrared furnace. The furnace was argon (Pre-purified, 99.95%) purged at a rate of 250 ml/min for approximately 120 seconds prior to the heating cycle. During the entire joining process, argon was purged through the heating chamber at the same rate to minimize sample oxidation. The processing temperature was monitored with a W-5%Re/W-26%Re (C-type) thermocouple held in contact with the specimen near the joint. Typically, the temperature of the specimen was brought to a preset temperature in 50 to 60 seconds and held at that temperature for various lengths of time before the furnace is switched off. The joining times ranged from 60 to 150 seconds. Time of joining at any particular temperature was varied to study its effect on the joint microstructure evolution (extent of reaction) and on mechanical properties. After joining, the samples cooled naturally in argon. The cooling rate was rapid since the furnace was water-cooled. The samples typically cooled to below 1000 °C in less than 15 seconds and reached the ambient temperature in approximately seven minutes.

Specimens removed from the furnace were tested room temperature for the shear strength of the joint. A shear-in-compression jig was utilized in this study. This technique has been successfully employed in a variety of other systems, such as SiC, TiAl, FeAl, etc., for determining the shear strengths of these joints [11-13]. The crosshead speed used for the strength test of TiAl was kept at 0.254 mm/min.

As-joined samples were also heat-treated in order to study its effect on the joint properties as well as the microstructural changes that occur during the process. The heat treatment was carried out between 1200-1325 °C for varied lengths of time, ranging between 1 and 4hrs. The furnace used for the purpose was a 110V, 2.2 kVA resistance furnace from Norton Vacuum Products. The heat treatment was carried out in vacuum (5Torr) maintained with a mechanical pump.

Joint microstructures were characterized with optical microscopy, scanning electron microscope (SEM), microhardness testing, transmission electron microscope (TEM) with cross section analysis using selected area diffraction (SAD), and energy dispersive x-ray (EDX) analysis. Cross section specimens for SEM, optical and microhardness analysis were cut with a slow speed diamond saw and mounted in epoxy. Polishing was performed down to a 1  $\mu\text{m}$  diamond paste finish. After polishing, the samples were cleaned with ethanol and rinsed in deionized water to remove any debris left on the surface. The surface was then etched by the Kroll's reagent (90 vol%  $\text{H}_2\text{O}$ , 5 vol%  $\text{HNO}_3$ , 5 vol%  $\text{HF}$ ).

The cross-sectional examination of the joints and the EDX analysis were done in the ultra high vacuum Hitachi 4000-S with a FEG source and an OXFORD Link Isis EDX system. The other characterization techniques used to evaluate the joint were optical microscopy and microhardness testing. TEM analysis was done on Phillips EM-400 and CM20 model microscopes to identify phases present in the joint.

An intermetallic phase, which is brittle at room temperature, is expected to form at the joint. Thus, it is probable that during the initial mechanical thinning of the specimen, for TEM sample preparation, the joint fractures easily. Also, jet polishing of the pre-thinned samples using perchloric acid (6-8%)-methanol-butanol mixture often resulted in the separation of the specimen along the joint or preferential polishing of the base metal. To alleviate this problem the specimen was carefully ground to a size so that it just fit into a 3mm steel tube [14]. This specimen was inserted into the steel tube and held in place by G1 epoxy made by Gatan, Inc. The epoxy was allowed to set at 100 °C for an hour. From this assembly, a number of TEM specimens were cut by a diamond blade on a low speed Buehler saw and subsequently thinned mechanically. After thinning to about 200  $\mu\text{m}$  the specimen was further thinned to 50 $\mu$  in the region of interest, using a dimpler. Jet polishing was then done using the methanol, butanol and a higher amount of (15%) perchloric acid electrolytic solution. The polishing was carried out at -40 °C at 90-110 mA current and 5-6 kV voltage. The higher amount of the acid in the electrolyte decreases the preferential polishing observed earlier and produces a uniformly polished joint. If further thinning was required, it was done by ion milling at a low angle (13-15°) and 4kV voltage. With the steel tube confinement, the TEM thin sections in the joint were successfully prepared.

#### Results and Observations

Joining of TiAl in this study was done using Ti and Al foils in the attempt to form TiAl in the joint for high temperature applications. The joining temperatures were 1200 °C and 1275 °C and joining time was varied

from 0 to 60 seconds. Heat treatment of the joints were carried out at temperatures of 1200 °C and 1300 °C for times varying between 1-4hrs.

#### Microstructural Observations

Figures 1 and 2 show two sets of optical micrographs of the joints obtained through the use of Ti (50 $\mu\text{m}$ ) - Al (60 $\mu\text{m}$ ) filler material for different times at 1200 °C and 1275 °C, respectively. At the basemetal-joint interface an Al rich region with a high void content grows with increasing time and processing temperature (Figure 1). This phase is formed due to the dissolution of the base material and the Ti foil in the Al melt. At 1200 °C, 0 second holding time, the wide dark region in the center of the joint is pure Ti or low Al containing solid solution of Ti. This region of the joint is found to progressively diminish in size, until it disappears after 60 seconds at 1200 °C. This change is observed to be much faster at higher processing temperatures 1275 °C. Just outside the initial dark region there is another layer which grows into the joint with increasing processing time and temperature at the expense of the dark region towards the center. This growing layer has higher Al content and could possibly be  $\alpha$ -Ti or the  $\alpha_2$  phase. The Al % in this phase decreases towards the joint center. Within the central phase a random orientation of grains is also observed. The surface relief features observed are similar to that of martensite.

To homogenize the joint, heat treatments were carried out at different temperatures and time. Heat treatment at 1200 °C and 1300 °C resulted in the formation of lamellar structures in the joint (Figure 3). It was also found that the heat treatment at a higher temperature resulted in the lamellar structure in a shorter time. Almost no voids are observed after heat treatment.

#### SEM/EDX Examination

The line scans of the joint cross-section obtained from the SEM are shown in Figure 4, 5 & 6. With increasing time the Al concentration at the center of the joint increases, thus indicating the diffusion of Al into the originally pure Ti. The increase was more pronounced at higher processing temperatures. Line scan across the heat treated samples confirmed the complete homogenization of the joints (Figure 6).

#### Joint Microhardness and Strength

The microhardness found in the various regions of the joints was listed in Table I. A load of 25g was applied for 15second dwell time in order to accommodate the indentations within the regions. The hardness across the joint was found to have reached a single value as the time of holding increased. In the heat treated joints, the hardness found in the central grains was higher than that in the peripheral grains. The Room temperature strength

testing was done on as-joined as well as the heat treated samples. It was found that the joint strengths were very low in the case of as-joined specimen (Table II). Heat treatment

drastically increased the strength by almost five folds. It was also observed that, in most cases, the fracture path was diverted into the base metal in the heat treated specimen.

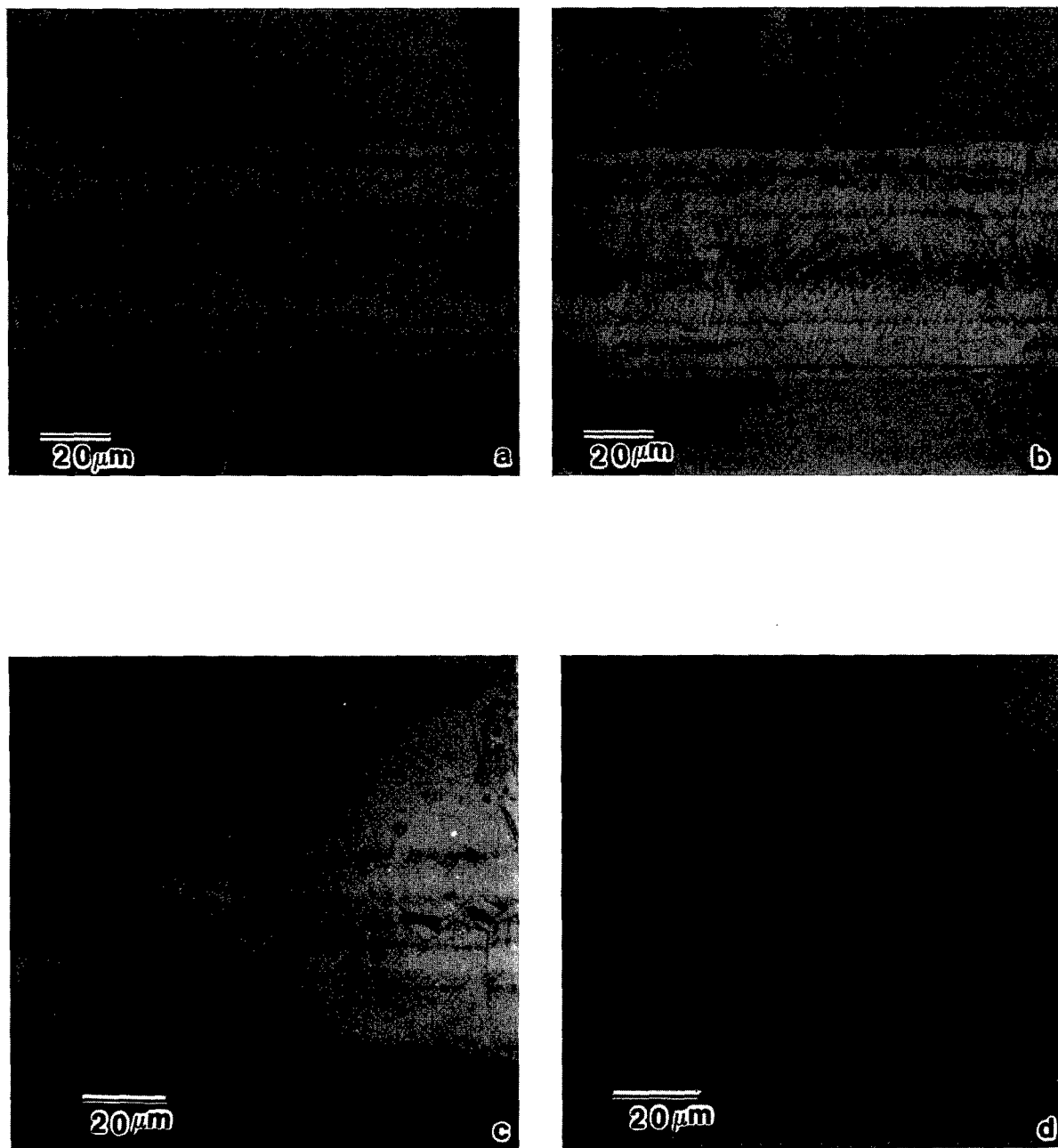


Figure 1: Optical micrographs of Al-Ti filler joints, joining temperature- 1200 °C, held for (a) 0 sec ; (b) 30 sec; (c) 60 sec; (d) 90 sec.

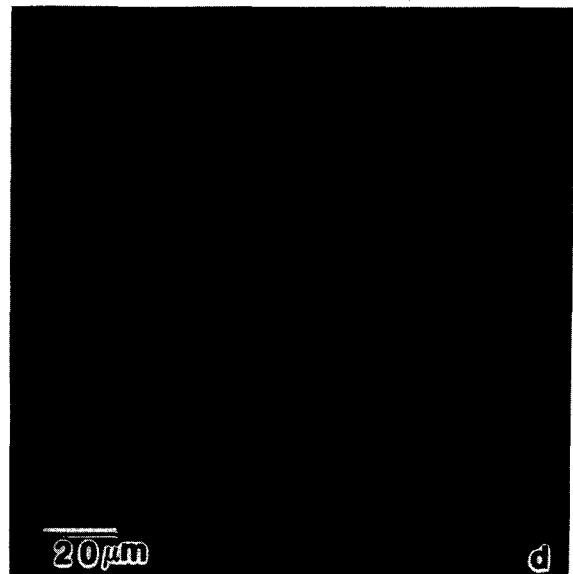
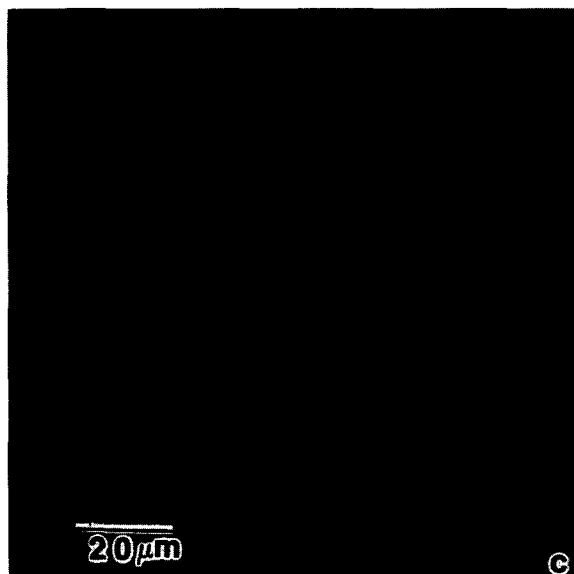
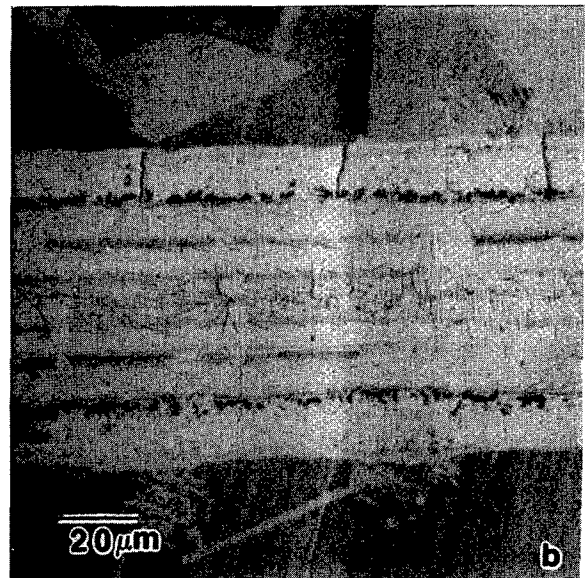
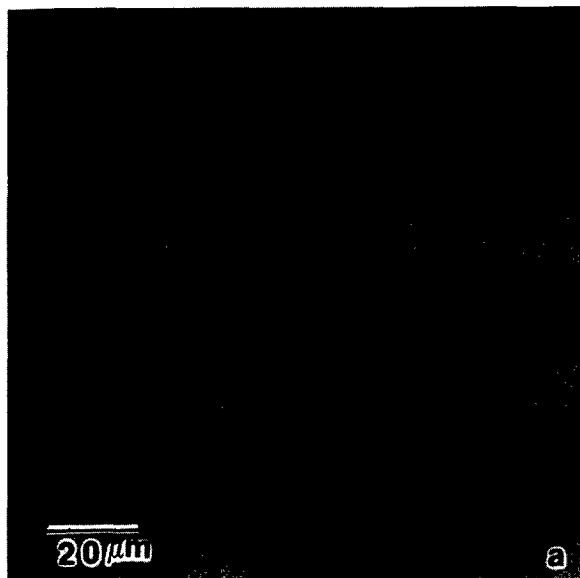


Figure 2: Optical micrographs of Al-Ti filler joints, joining temperature- 1275 °C, held for (a) 0 sec ; (b) 30 sec; (c) 60 sec; (d) 90 sec.

#### TEM Analysis

TEM samples were obtained from the joint processed at 1275 °C for 60seconds. The micrographs obtained are shown in Figure 7. A colony of platelets were observed in the joint center (figure 7a). The EDAX analysis done in the region gave a composition between

16-20 at% Al. Adjacent regions containing a higher Al % revealed a phase with a different morphology (Figure 7b).

#### Discussion

At the processing temperature, the Al alone is in liquid state. On one side of the melt the basemetal dissolves and the diffusion of Ti into Al shifts the composition of the liquid near the interface to that of



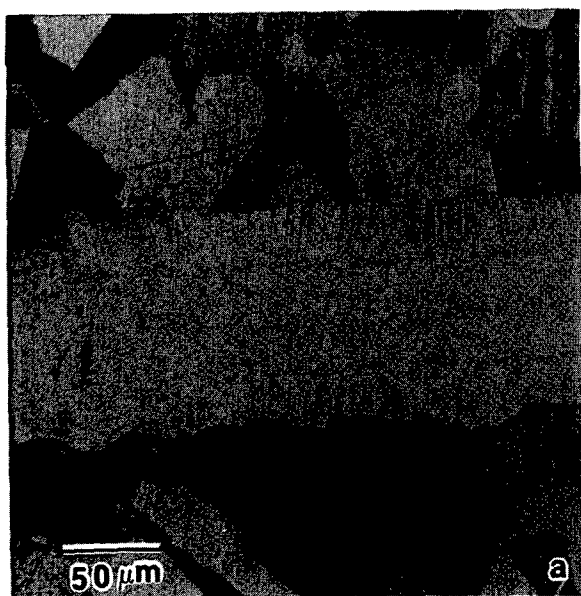


Figure 3: Optical micrographs of Al-Ti filler joints, joining temperature - 1200 °C, (a) held for 0 sec, heat treatment- 1200 °C, 4hr; (b) held for 60 sec, heat treatment 1200 °C, 4hrs.

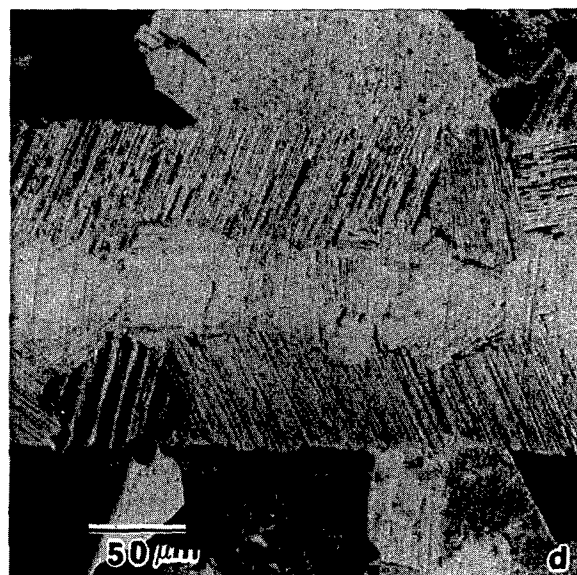


Figure 3: Optical micrographs of Al-Ti filler joints, joining temperature - 1200 °C, (c) held for 0 sec, heat treatment 1300 °C, 2hrs; (d) held for 60 sec, heat treatment 1300 °C, 2hrs.

$\text{TiAl}_3$ . This phase is expected to be present at the joint interface. The amount of  $\text{TiAl}_3$  formation, however, depended on how well the filler material wets the surface on melting and the pressure applied. On the other side of the melt, Al dissolves some Ti. Apart from the dissolution it is also believed that aluminium diffusion into the Ti foil occurs rapidly. Joints obtained through processing at 1275 °C for 60 sec have about 20 at% Al in the center of the joint.

#### Dissolution

In the processing condition of this study, Al dissolved the basemetal on one side and pure Ti on the other side. Results obtained from the line scan across the joint clearly showed that dissolution of the base metal is significant as compared to Ti dissolution from the foil. This was supported by the fact that the Ti foil thickness to begin with was 50μm and the high Al peaks corresponding to the  $\text{TiAl}_3$  phase were also separated approximately by



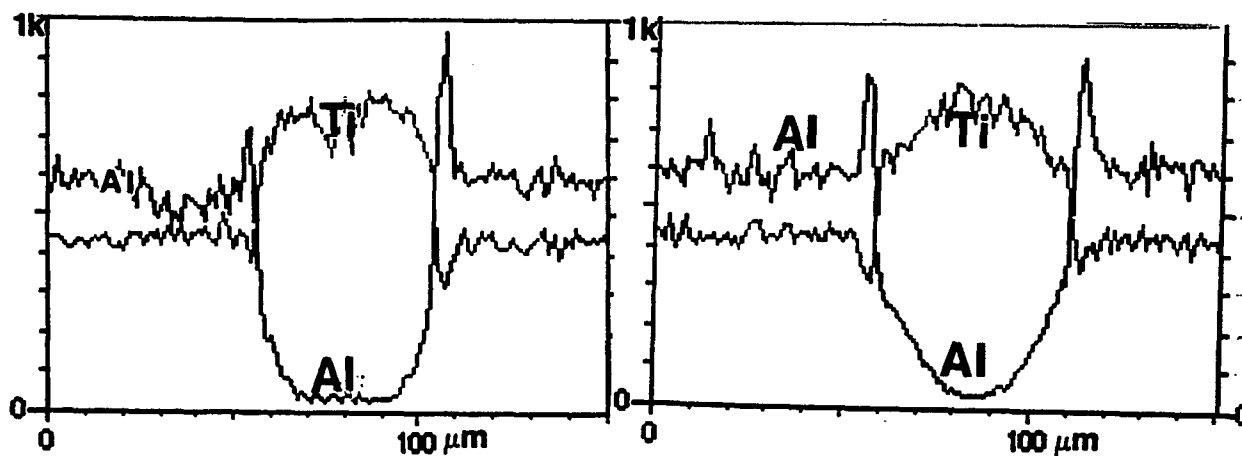


Figure 4: Line scan data obtained from the TiAl joints with Al-Ti filler material, processed at 1200 °C for holding times (a) 0 sec; (b) 30 sec.

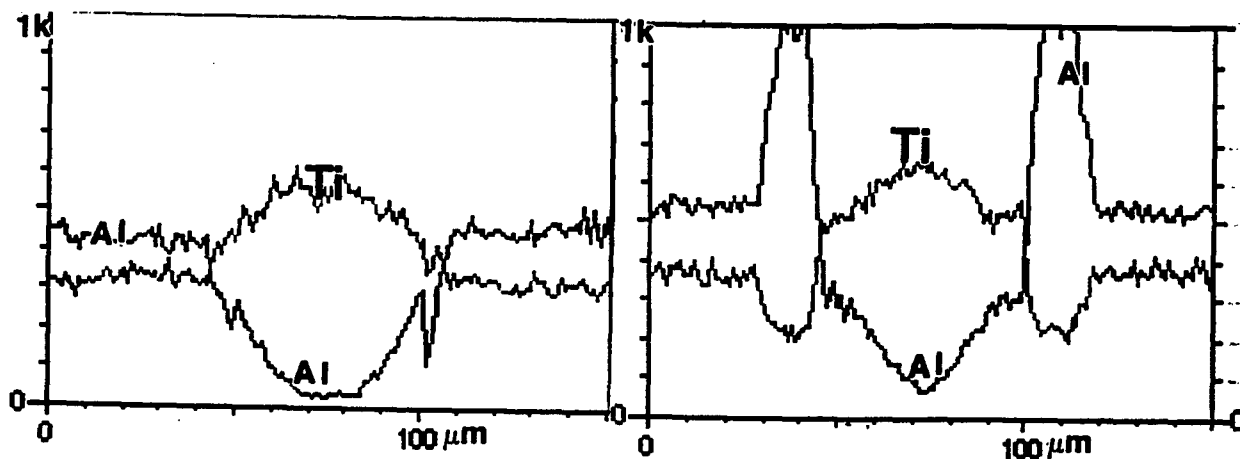


Figure 5: Line scan data obtained from the TiAl joints with Al-Ti filler material, processed at 1275 °C for holding times (a) 0 sec; (b) 30 sec.

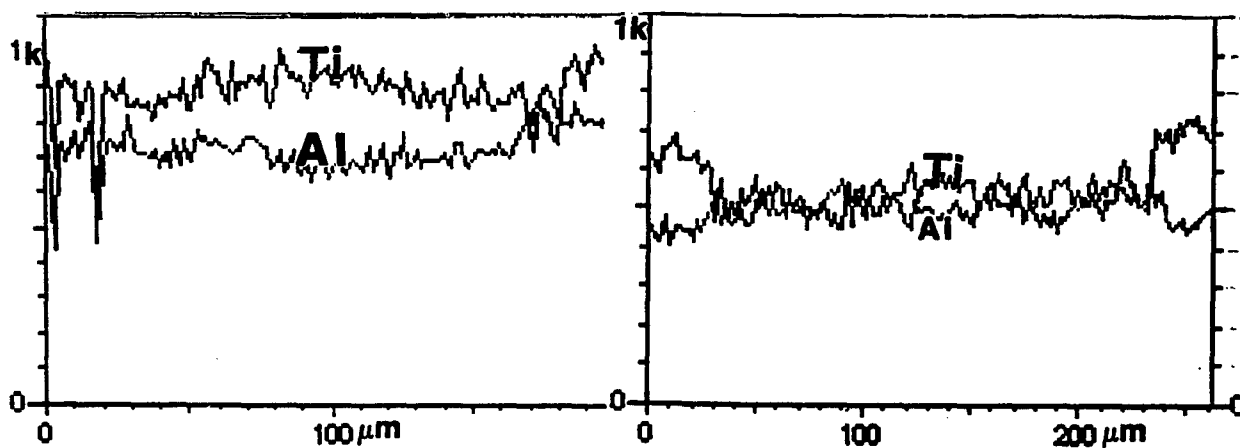


Figure 6: Line scan data obtained from the TiAl joint with Al + Ti filler material, processed at 1200 °C for holding time of 60 sec; (a) heat treatment 1200°C, 4hrs; (b) heat treatment 1300 °C, 2hrs.

Table I Microhardness measured in the joint with Al-Ti filler material.

Temperature, °C	Holding Time, s	Locations of analysis*	Hardness**, DPH	Load, gm
1200, as-joined	0	1	149 ± 3	25
		2	169 ± 5	
		3	216 ± 9	
1200, as-joined	60	1	220 ± 6	25
		2	247 ± 4	
		3	260 ± 7	
1275, as-joined	0	1	190 ± 4	25
		2	215 ± 13	
		3	289 ± 13	
1275, as-joined	45	1	252 ± 14	25
		2	240 ± 110	
		3	255 ± 8	
1275, as-joined	60	1	240 ± 10	25
		2	245 ± 8	
		3	251 ± 10	
1300, heat treated	7200	center grain	366 ± 12	100
		peripheral grain	325 ± 15	

\*(1) The center of the joint.(2) The region between the center and the periphery of the joint.. (3) The periphery of the joint.

\*\* Average of five hardness measurements taken in each region.

Table II Joint Strengths obtained for specimen processed at different conditions and tested at room temperature in air.

Heat Treatment	Time of holding, ( sec)	Temperature, (°C)	Average Strength, (MPa)*	Fracture Path
as-joined	60	1200	30 ± 8	Interface
as-joined	45	1275	35 ± 10	Interface
as-joined	60	1275	39 ± 3	Interface
1200/2hrs/fc	60	1200	110 ± 8	basemetal
1200/2hrs/fc	45	1275	144 ± 12	basemetal
1200/4hrs/fc	60	1200	139 ± 10	base metal

\*The strength values listed are an average of strengths obtained from three strength samples.

fc stands for furnace cooling

50µm indicating that TiAl<sub>3</sub> formed rapidly and the Ti was not severely attacked by the molten Al. From our studies using pure Al we already know that dissolution played an more important role during the joint formation than did diffusion. In this case however diffusion of Al into Ti was also significant. Dissolution was mostly confined to the interface between the Al and the basemetal, where we found the TiAl<sub>3</sub> phase.

#### Diffusion

Figures 5 and 6 show line scans for two sets of joints with varying holding times and temperatures. A gradual increase in the Al concentration in the Ti foil with increasing holding time was observed. Along with the microstructural changes observed in the micrograph, it indicated that diffusion of Al into the Ti foil occurred during joining. The net movement of the interface (cross-

over point of the Al-Ti curves) was also observed to be into the base metal which indicated that Al diffusion into the foil was significant as compared to Ti diffusion out of the foil. In general, the diffusion coefficient of Al in β-Ti is three orders in magnitude higher than that in α-Ti [15, 16]. At the joining temperature β-Ti phase is stable and thus diffusion of Al into Ti occurs at a fast rate. At low processing temperature and holding time, Al diffusion into the center of the joint is low. In this region the Al concentration was less than 10 at.%. Thus, the center of the joint would remain as a single phase α Ti. As the processing time increased, sufficient Al diffused in for microstructural changes to occur.

At the joining temperatures of this study, the β Ti phase is stable until the Al concentration reaches about 35-36at%. The cooling rate obtained in the infrared (IR)

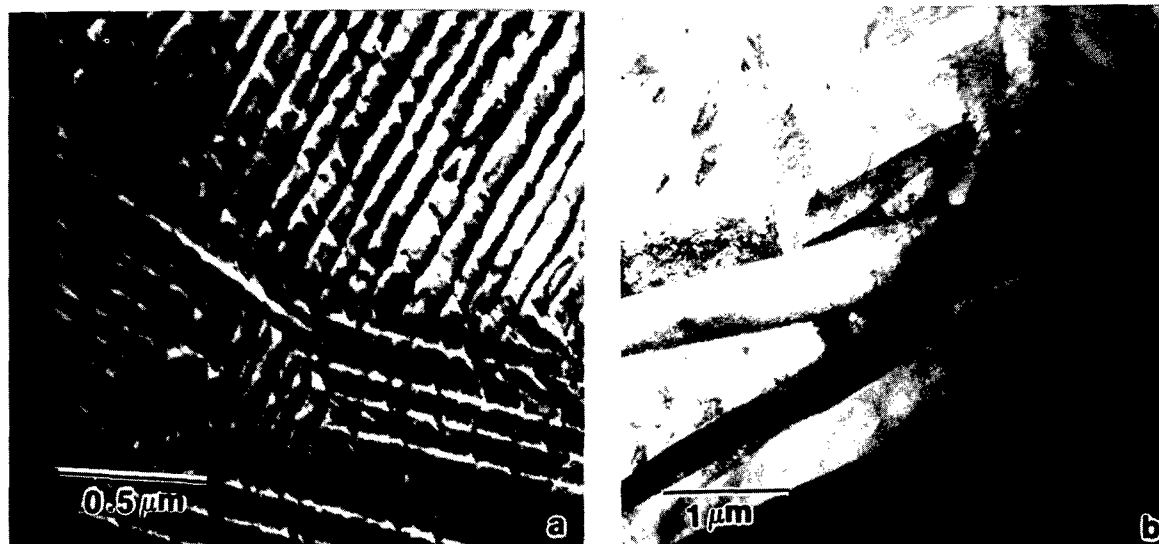


Figure 7: (a), (b) Martensitic  $\alpha_2$  phase with two different morphologies (lath and acicular), found in the joint.

furnace is rapid. Initial cooling from 1200 °C or 1275 °C (the joining temperature) to around 700 °C occurred within 45-60 seconds. Cooling below 700 °C was relatively slow. With the initial cooling rates, the formation of a martensite phase was favorable.  $\alpha_2$  martensite forms in the joint upon cooling, as verified with TEM examination.

The TEM micrograph in Figure 7 (a, b) show two martensite morphologies, the lath/massive type and the acicular type. The two were found within the joint in adjacent regions where the compositions were found to be 16-18 at.% Al and 24-26 at.% Al respectively (for sample processed at 1275 °C, 60sec).

Depending on the holding time, the Al concentration at the center of the joint varies. After joining for 60 seconds at 1275 °C the Al concentration at the center of the joint reached about 20 at%. The main constituent phases of the joint were  $\text{TiAl}_3$  at the joint/basemetal interface, a high Al containing  $\gamma$  phase next to it, and the  $\alpha_2$  ( $\text{Ti}_3\text{Al}$ ) with varying composition in the joint.

The hardness data for the joints obtained from the Al-Ti filler are listed in Table I. The hardness in the center of the joint was found to increase with increased holding time. At a higher joining temperature, the hardness value reached a constant value after 45 seconds holding time. There was no significant change in the joint hardness after 45 seconds of holding. Diffusion of Al into the foil resulted in an increase in the hardness value. The formation of the  $\alpha_2$  phase eventually led to a constant hardness value throughout the joint.

#### Heat treated joints

Since the as-joined samples had low joint strength, unwanted phases and voids, heat treatment was done to homogenize and improve the joint properties. During the treatment, diffusion of Al into the joint remained dominant till the concentration gradient was low and the concentrations of Al and Ti in the joint became almost constant throughout the joint. The SEM EDX

analysis in the joint showed that the concentration of Al in the joint varied between 39-41at%. Towards the interface the Al concentration was however around that of the base metal. Optical micrographs of the heat treated joints showed the growth of a lamellar structure in the joint.

Heat treatment of the joint resulted in the formation of a lamellar structure. The formation of a new microstructure and the increase in the Al content increased the hardness of the joint. It was also observed that the lamellar grains in the center having lesser Al % and smaller grain size register a higher hardness value than similar grains at the periphery.

The strengths obtained from the heat treated joints were found to be high. The fracture path was found to be through the base metal indicating a stronger joint. The presence of the lamellar structure in the joint might have reinforced the joint in a manner similar to fibers in a metal matrix composite [17] thus making it stronger than the base metal. The lamellar grain boundaries influence the toughness in that interlocked grain boundaries appeared to be more fracture tolerant than well defined, smooth boundaries [18].

#### Conclusions

Infrared joining of TiAl using Ti and Al foils as the filler material was investigated in this study. The high cooling rates at the end of infrared joining resulted in the formation of martensite in the joint.  $\alpha_2$  martensite with a lath morphology was obtained in the center of the joint while an acicular morphology was observed in joint regions away from the center where the aluminum content is higher than that in the joint center.  $\text{TiAl}_3$  was identified at the interface.

The use of Al +Ti filler material to join TiAl resulted in joints with low strengths in the as-joined condition. The reason for this is attributed to the high void content and the presence of the brittle  $\text{TiAl}_3$  phase at the interface.

Heat treatment of the joints resolved the problem by reducing the void content in the joint to almost a negligible amount and homogenizing the joint to form a lamellar phase throughout. The lamellar phase is known to impart toughness to the joint. Based on the phases formed and the morphology obtained it was concluded that the joints were suitable for high temperature applications.

#### References

1. W. A. Baeslack, III; M. J. Cieslack; T. J. Headley; "Structure, Properties and Fracture of Pulsed Nd: YAG Laser Welded Ti-14.8 Al-21.3 Nb (wt%) Titanium Aluminide"; Scripta Metallurgica, v22, n7, 1988; p 1155-1160.
2. G. S. Martin; C. E. Albright; T. A. Jones; "Evaluation of CO<sub>2</sub> Laser Beam Welding on a Ti<sub>3</sub> Al-Nb alloy"; Welding Journal, v74, n2, 1995; p 77s-82s.
3. M. J. Cieslack; T. J. Headley; W. A. Baeslack, III; "Effect of Thermal Processing on the Microstructure of Ti-26Al-11Nb. Applications to Fusion Welding"; Metallurgical Transactions A(Physical Metallurgy and Materials Science); v21A, n5 May 1990; p 1273-1286.
4. R. A. Patterson; P. L. Martin; B. K. Damkroger; L. Christodoulou; "Titanium Aluminide: Electron Beam Weldability"; Welding Research Supplement; Jan 1990; p 39-s - 44-s.
5. Hirose Akio; Arita Yoshihiro; Kobayashi Kojiro F.; "Microstructural Change of TiAl Intermetallic Compound during Laser Fusion Processing and Mechanical Properties of the Fusion Zone"; Zairya/Journal of the Society of Materials Science; Japan V44 n504; Sept. 1995; pp. 1145-1150.
6. Y. Nakao; K. Shinozaki; M. Hamada; "Diffusion Bonding of Intermetallic Compound TiAl"; Conference Proceedings; International Trends in Welding Science and Technology; ASMI, Materials Park, OH, USA, June 1993; p 1057-1067.
7. S. P. Godfrey; P. L. Threadgill; M. Strangwood; "Diffusion Bonding of Ti-48Al-2Mn-2Nb (at%)"; MRS Symposium, v364, 1995, MRS, p 793-798.
8. P. Yan; R. E. Somekh; E. R. Wallach; "Solid-State Bonding of TiAl with Interlayers"; Conference: International Trends in Welding Science and Technology; Gatlingburg, TN, 1-5 June 1992; ASMI, Materials Park, Ohio, 1993; pp. 1063- 1067.
9. Uenishi Keisuke; Sumi Hiroyuki; F. Kobayashi Kijiro; "Joining of Intermetallic Compound TiAl using Al Filler Material"; Z. Für metalKunde; v86 n4; 1995, pp. 270-274.

#### Acknowledgments

The authors would like to thank G. E. Aircraft Engines, Cincinnati for providing the base alloy. Acknowledgments are also due to Mahendra Pakala, John Spring, Dr. J. Lian for their support in the research work.

10. Uenishi Keisuke; Sumi Hiroyuki; F. Kobayashi Kijiro; "Joining of Intermetallic Compound TiAl using Self-Propagating High Temperature Synthesis Reaction"; Zeitschrift Für Metalkunde; V86 n1; 1995; pp. 64-68.
11. C. A. Blue, R. A. Blue, R.Y. Lin, Jih-Fen Lei and W. D. Williams; "Joining of SCS-6Beta 21S Titanium Composites," Processing of Advanced Materials, vol. 4, 1994, pp. 105-110.
12. C. A. Blue, R. A. Blue and R. Y. Lin, "Microstructural Evolution in Joining of TiAl with a Liquid Ti Alloy," Scripta Metallurgica, vol. 32 (1), 1995, pp.127-132.
13. C. A. Blue, R. A. Blue, R. Y. Lin, Jih-Fen Lei and W. D. Williams, "Joining of Hastelloy X to Inconel 718 Using an Infrared Process," J. Mat. Proc. Tech., Vol. 58, 1996, pp. 32-38.
14. Kim Ostereicher and Changmo Sung, "Advanced Preparation of Hard Materials for Cross Sectional TEM", Specimen Preparation for Transmission Electron Microscopy of Materials - III, Ed. R. Anderson, et al., MRS Proceedings, Dec. 5-6, 1991, Boston, MA, U.S.A, vol. 254, 1992,193-199.
15. Hideki Araki; Toshimi Yamane; Yoritoshi Minamino; Shigeoki Saji; Yoshitake Hana; and Seung Boo Jung; "Anomalous Diffusion of Aluminium in  $\beta$ - Titanium", Metallurgical and Material Transactions A; vol.25A, 1994, pp.874-877.
16. Z. Liu; G. Welsch; "literature survey on Diffusivities of Oxygen, Al, and Vanadium in Alpha Titanium, Beta Titanium and in Rutile.", Communications, Met. Trans.; Vol.19A, 1988, pp. 1121-1125.
17. Young-Won Kim; "Intermetallic Alloys Based on  $\gamma$  Titanium Aluminides"; JOM; July, 1989; pp. 24-30.
18. Young-Won Kim; F. H. Froes; "Physical Metallurgy of Titanium Aluminides"; High Temperature Aluminides and Intermetallics; Edited by Whang, S., H.; Liu, C., T.; Pope, D., P.; Stiegler, J., O.; TMS, Warrendale, PA, 1990, pp. 465-490.

## Oxidation behaviour of highly alloyed $\gamma$ -TiAl alloys

A. Partridge\* and M.R. Winstone

\*IRC for Advanced Materials, Birmingham University, Edgbaston, Birmingham, B15 2TT  
Structural Materials Centre, Defence Research Agency, Farnborough, GU14 0LX

### Abstract

$\gamma$ -TiAl alloys are candidate materials for use in future gas turbine aero-engines. Currently the maximum operating temperature of  $\gamma$ -TiAl based alloys is defined by mechanical property considerations and the rapid deterioration in oxidation resistance above 750°C. Recently a series of alloys have been developed which contain up to 8 at.% alloying additions. These alloys exhibit much higher tensile and creep strengths than many currently available alloys, and hold out the prospect of utilisation at higher operational temperatures. However, the full potential of these alloys will not be realised unless these alloys possess adequate oxidation resistance.

Therefore, the oxidation behaviour of 5 high alloying addition  $\gamma$ -TiAl alloys at a temperature of 850°C has been investigated. This analysis shows that all the high alloying addition alloys have much better oxidation resistance than conventional  $\gamma$ -TiAl alloys containing lower alloying additions. However, it is observed that three of the alloys, containing lower Nb contents and small Si additions, show breakaway behaviour after 100-300h of exposure. In contrast the alloys with a high Nb content and containing no Si show the best oxidation resistance and no breakaway behaviour.

The improvement in the oxidation rate of the high alloying addition alloys is discussed in term of the influence of the alloying elements on cation/anion diffusion and the effect of alloying on the activities of Ti and Al. The influence of nitrogen and nitride formation is also considered. The breakaway behaviour is attributed to the formation of oxide nodules on the surface of the alloy and the consequent breakdown of the thin outer  $\text{Al}_2\text{O}_3$  scale. In many cases this breakdown can be correlated with the presence of second phase silicide precipitates.

### 1. Introduction

$\gamma$ -TiAl intermetallic alloys are candidate materials for use in future gas turbine aero-engines as a result of their low density, high specific strength and high stiffness<sup>1,2</sup>. At the anticipated maximum use temperature of 700-750°C, the current generation of alloys exhibit marginal oxidation resistance<sup>3,4</sup>. However, continual efforts are being made to develop new alloys and process routes to produce alloys exhibiting improved mechanical properties with the potential to operate at higher temperatures.

Over the last few years an alloy development programme has been in progress within the IRC for Advanced Materials at Birmingham University aimed at producing high strength creep resistant alloys which offer the potential for use at temperatures above 750°C. These alloys are based on

a Ti-44Al base alloy with up to 8 at.% of alloying additions. A preliminary mechanical property assessment of these alloys indicate that they have ultimate tensile strengths between 700-900MPa combined with good creep resistance. However, the utilisation of these alloys at temperatures above 750°C require these high alloying addition (HAA) alloys to exhibit much improved environmental resistance compared to currently available alloys. From previous studies it is well known that the addition of ternary and quaternary alloying additions can have a very large effect on the oxidation behaviour of  $\gamma$ -TiAl based alloys<sup>3-9</sup>. Therefore a detailed investigation of the oxidation behaviour of five selected alloys at 850°C in air has been carried out to assess their environmental stability at elevated temperatures.

### 2. Experimental details

A series of 5 high alloying addition (HAA) alloys were produced by Plasma Arc Cold Hearth (PACH) melting to produce 1kg buttons. The alloying elements in each of the five alloys are given in Table I. The buttons were isothermally forged (70% reduction) at 1150°C using a strain rate of  $5 \times 10^{-3} \text{ s}^{-1}$  and furnace cooled. Sections of these forgings were then heat treated at 1200°C for 48h to recrystallise the heavily worked "as-forged" microstructure. Most of the alloys exhibited an irregular  $\alpha_2 + \gamma$  microstructure with occasional lamellar colony formation, as shown in Figure 1. None of the alloys, with the exception of Alloy 15, exhibit  $\beta$  phase formation. In the case of Alloy 15 localised  $\beta$  phase formation was observed to occur along the  $\alpha$  and  $\gamma$  grain boundaries.

Alloy number	Alloying additions*
13	Ti-44Al-Nb
14	Ti-44Al-(Nb,Ta)
15	Ti-44Al-(Nb,Zr,Si)
16	Ti-44Al-(Ta,Zr,Si)
17	Ti-44Al-(Hf,Nb,Si)

\*Exact alloy compositions are currently subject to patent application.

Table I: Composition of high alloying addition alloys

A series of oxidation coupons (15x15x1mm) were cut from the heat treated sections and ground and polished to an 800 grit SiC finish. The coupons were cleaned in acetone prior to isothermal oxidation at 850°C for periods up to 500h. A Ti-48Al and a Ti-48Al-2Mn-2Nb alloy (designated low alloying addition (LAA) alloys) were oxidised in the same manner for comparison. Following oxidation the weight gain of the samples was determined using a Mettler HK60 balance and a detailed analysis of the oxide scale was carried out.



Figure 1: Typical microstructure of HAA alloys following heat treatment at 1200°C/48h. A fine dispersion of silicides can be seen in this alloy.

The morphology of the outer scale was examined using a Cambridge 100 SEM, while the crystallography of the overlying oxide was determined using a Philips X-ray diffractometer. In addition cross-sections of the oxides were taken and a detailed analysis of the oxide scale was performed using a high spatial resolution Camscan FEG-SEM, incorporating a windowless LINK-EDX unit. The composition of the scales were determined using the internal standards and a fully ZAF corrected energy dispersive spectroscopy (EDS) routine. Additional quantitative analyses from the scales were obtained using a JEOL 840A microprobe equipped with Tracor wavelength dispersive spectroscopy (WDS) facilities. The elemental composition of the scales were determined using elemental standards and a fully corrected quantification routine; with the exception of oxygen which was determined by difference.

### 3. Results

#### 3.1 Isothermal oxidation

The oxidation behaviour of the five HAA alloys and the two comparator materials is shown in Figure 2. As can be clearly seen from this figure all of the HAA alloys initially exhibit much better oxidation resistance than either the Ti-48Al alloy or the Ti-48Al-2Mn-2Nb alloy. The HAA alloys all exhibit continuous, adherent blue-grey scales. In contrast, the Ti-48Al alloy exhibits a white/grey scale which tends to spall on cooling, while the Ti-48Al-2Mn-2Nb alloy exhibits a brown scale which remains partially adherent on cooling.

On initial oxidation all of the HAA alloys exhibit similar oxidation behaviour, although there are some differences apparent in the rate of weight gain with time. However after 100-300h it is apparent that several of the alloys exhibit breakaway oxidation behaviour, exhibiting a rapid weight gain with time. The two exceptions to this are the two high Nb alloys, alloys 13 and 14. In the case of these two alloys no breakaway behaviour is observed up to 500h. Analysis of the weight gain curves of alloys 13 and 14 indicates that the weight gain closely approximates a cubic behaviour.

#### 3.2 XRD analysis

XRD analyses of the oxidised samples were performed after 100h exposure to air (Figure 3). All of the samples showed strong diffraction peaks which were attributable to  $\text{Al}_2\text{O}_3$  and  $\text{TiO}_2$ , originating from the scale, and  $\gamma$  and  $\alpha_2$ , originating from the substrate. In addition all of the samples showed diffraction peaks which were attributed to  $\text{TiN}$  and  $\text{Ti}_2\text{AlN}$ . The XRD spectra from the two alloys with the highest Nb contents (Alloys 13 and 14) showed strong  $\text{TiN}$  peaks, whereas the spectra from alloys 15, 16 and 17 displayed predominantly  $\text{Ti}_2\text{AlN}$  peaks.

#### 3.2 Outer scale morphology

SEM analysis of the outer oxide scales following 500h exposure showed that the high Nb alloys had a relatively flat and faceted outer scale (Fig. 4a), very similar to that observed in the LAA comparator alloys. In contrast the other alloys exhibited a very irregular surface topography, as a result of the formation of highly faceted oxide nodules on the surface of the underlying oxide scale (Fig. 4b).

#### 3.3 Composition and structure of the oxide scale

In an attempt to simplify the analysis of the oxide scales two alloys were

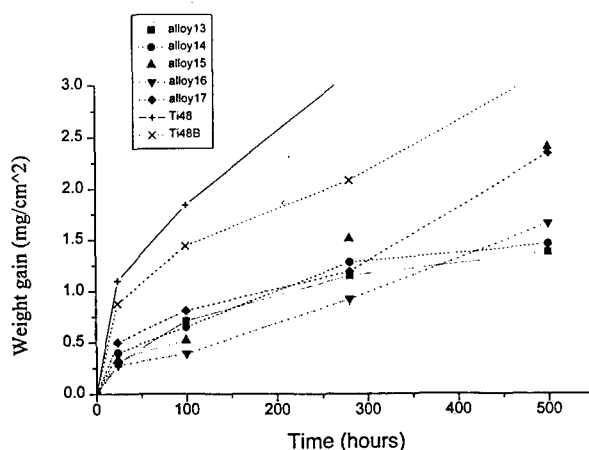


Figure 2: Isothermal weight gain curves of the 5 HAA alloys plus the 2 comparator alloys.

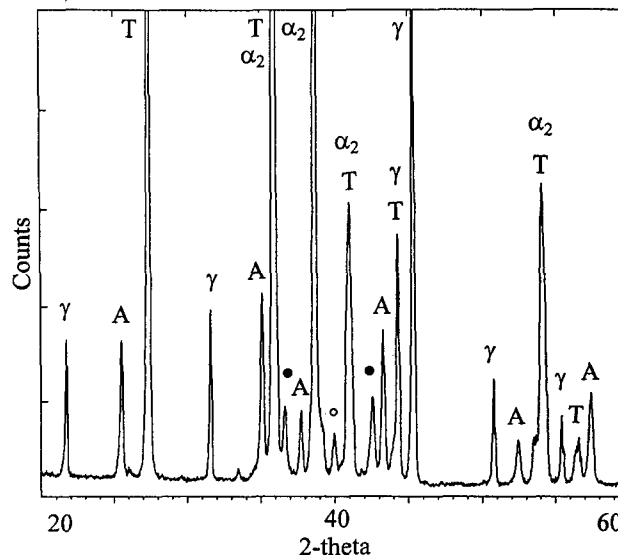


Figure 3: XRD spectra from Alloy 16, showing substrate peaks  $\gamma$  and  $\alpha_2$ , plus A ( $\text{Al}_2\text{O}_3$ ), T ( $\text{TiO}_2$ ),  $\circ$  ( $\text{Ti}_2\text{AlN}$ ) and  $\bullet$  ( $\text{TiN}$ ) peaks.

chosen for detailed investigation: Alloy 13, which shows good long term oxidation resistance, and Alloy 16, which exhibits breakaway oxidation after 300h exposure.

#### 3.3.1 Alloy 13: High Nb alloy

Figure 5a shows the oxide scale on Alloy 13 following 24h of exposure at 850°C. After 24h a 0.6  $\mu\text{m}$  thick, predominantly  $\text{Al}_2\text{O}_3$  surface scale has formed on the alloy. Beneath this surface scale a 1.0  $\mu\text{m}$  thick  $\text{TiO}_2$  scale, containing small isolated  $\text{Al}_2\text{O}_3$  precipitates, is present. Under these outer scales a thin Ti-rich layer has formed in which large discontinuous  $\text{Al}_2\text{O}_3$  particles have precipitated. EDS analysis of this Ti-rich layer, using windowless EDS, shows a strong N peak in the EDS spectra. The presence of this (Ti,N)-rich layer clearly correlates with the observation of peaks corresponding to  $\text{Ti}_2\text{AlN}$  and  $\text{TiN}$  in the XRD spectra. Subjacent to this nitride layer a series of Nb-rich particles have precipitated along the scale-metal interface, and the metal immediately beneath the scale/metal interface is enriched in Al and Nb.

After 100h of exposure the structure of the scale is very similar to that observed after 24h of exposure; with the exception that both the outer  $\text{Al}_2\text{O}_3$  and the subjacent  $\text{TiO}_2$  scales have coarsened considerably, and a significant degree of cracking and porosity is apparent near the centre of the  $\text{TiO}_2$  scale.

The morphology of the scale after 500h of exposure is shown in Figure 5b. On prolonged exposure the  $\text{Al}_2\text{O}_3$  and  $\text{TiO}_2$  scales have thickened significantly, and highly faceted Nb-free  $\text{TiO}_2$  crystallites have formed on the outer surface of the  $\text{Al}_2\text{O}_3$  scale. The underlying  $\text{TiO}_2$  scale is composed of two distinct layers. The upper layer is largely compact  $\text{TiO}_2$  with a low Al and Nb content, while the lower  $\text{TiO}_2$  is relatively porous and has a significantly higher Al and Nb content. A fine dispersion of  $\text{Al}_2\text{O}_3$  precipitates can be

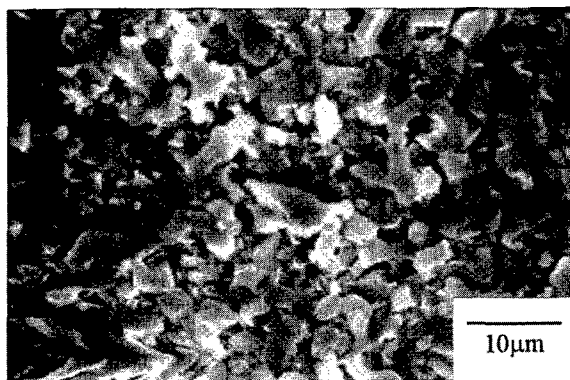


Figure 4a: SEM micrograph of outer scale on Alloy 13.

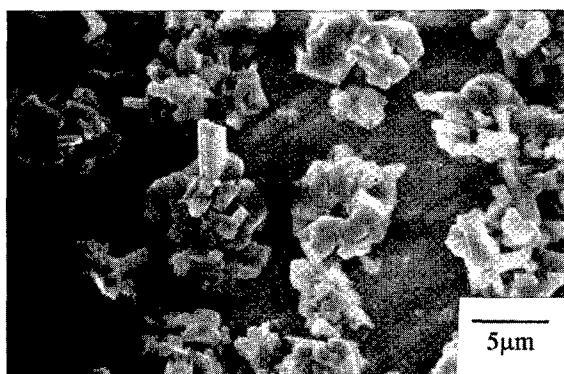


Figure 4b: SEM micrograph of outer scale on Alloy 16.

discerned within the lower half of the  $\text{TiO}_2$  scale. Another significant feature of the scale following 500h of exposure is the development of a complex double layer of  $\text{Al}_2\text{O}_3$  and Nb-rich precipitates near the scale/metal interface separated by a thin nitride layer. In many places a continuous  $\text{Al}_2\text{O}_3/\text{Nb}$ -precipitate layer has formed at the nitride/metal interface. Below this layer a 6-7µm region of fine equiaxed grains are present. EDS/WDS analysis of these grains indicate that are (Nb,Al)-rich  $\gamma$  grains.

### 3.3.2 Alloy 16: Ta-Zr bearing alloy

Following 24h of exposure at 850°C only a very thin oxide scale has formed on Alloy 16. This scale is composed of a 200nm  $\text{Al}_2\text{O}_3$  outer scale on top of a 350nm thick  $\text{TiO}_2$  sub-scale (Fig. 6a). Occasional Al-rich oxide outgrowths are present on the surface of the outer scale as well as a very fine dispersion of  $\text{TiO}_2$  crystallites. The composition of the Al-rich oxide outgrowths is consistent with them being  $\text{Al}_2\text{O}_3$ . Beneath the outer scale a layer of oxygen stabilised  $\alpha_2$  is present. This O-stabilised phase is low in Ta and Zr compared to the bulk alloy yet contains a fine distribution of Ta-rich precipitates. Along the edge of the oxygen stabilised  $\alpha_2$  regions very fine precipitates are observed with a composition close to that of the bulk  $\alpha_2$  phase. EDS analysis of the sample indicated the presence of nitrogen at the scale/ $\alpha_2$  interface.

After 100h of exposure the oxide scale morphology is similar to the scale after 24h of exposure. The outer  $\text{Al}_2\text{O}_3$  scale has not significantly increased in thickness, although the underlying  $\text{TiO}_2$  scale has doubled in thickness. A thin layer of oxygen stabilised  $\alpha_2$ , containing Ta rich precipitates, has also been retained along the scale/metal interface. A series of mixed  $\text{Al}_2\text{O}_3/\text{TiO}_2$  nodules were observed to have formed at irregular intervals on top of the oxide surface. These oxide nodules exhibit highly faceted, relatively pure  $\text{TiO}_2$  crystals on their outer surface, consistent with the images of the surface scale obtained by SEM (Fig. 4b).

On further exposure up to 500h the scale shows considerable variations of thickness and variations in the scale morphology along the length of the sample. Along much of the sample surface the outer oxide is composed of a thin (250nm) outer  $\text{Al}_2\text{O}_3$  scale on top of a 750nm thick  $\text{TiO}_2$  sub-scale, with occasional mixed  $\text{Al}_2\text{O}_3/\text{TiO}_2$  nodules present on the outer surface; very similar to what was observed after 100h exposure. However, in other areas it is clear that extensive oxidation of the sample surface has occurred, with a 5-10µm thick outer scale having been formed. These regions are characterised by extensive external nodule formation (Figure 6b). The formation of these mixed oxide

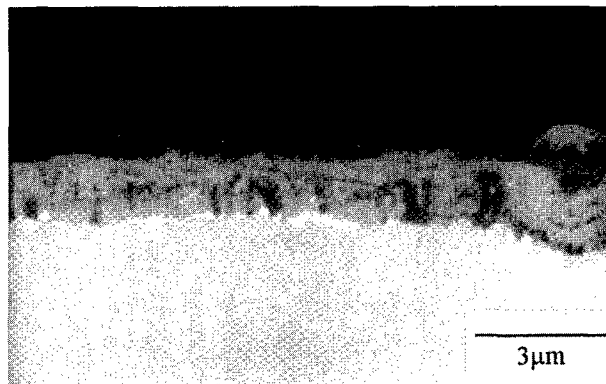


Figure 5a: BEI micrograph of oxide scale on Alloy 13 following exposure at 850°C for 24h.

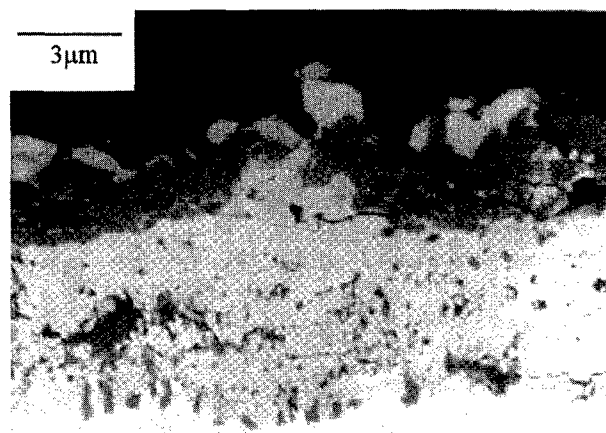


Figure 5b: BEI micrograph of oxide scale on Alloy 13 following exposure at 850°C for 500h.

nodules is associated with the breakdown of the thin continuous  $\text{Al}_2\text{O}_3$  scale into a mixed  $\text{Al}_2\text{O}_3/\text{TiO}_2$  scale; and are associated with the formation of a thicker region of internal oxidation. Careful examination of the oxide nodules reveals that many of them are associated with the presence of  $(\text{Ti,Zr})_3\text{Si}_3$  precipitates. EDS/WDS analysis of these precipitates clearly shows that they have been converted to oxide during the exposure to air at 850°C and that the oxidation of these particles leads to a breakdown in the continuity of the outer  $\text{Al}_2\text{O}_3$  scale (Fig. 7). As the alloy continues to oxidise an  $\text{Al}_2\text{O}_3/\text{TiO}_2$  scale forms on top of the  $(\text{Ti,Zr})_3\text{Si}_3$  particles creating outward growing oxide nodules. It is also apparent that the oxidised precipitates are a preferential path for oxygen ingress; leading to internal  $\text{Al}_2\text{O}_3$  formation and oxygen stabilised  $\alpha_2$  formation. However,  $(\text{Ti,Zr})_3\text{Si}_3$  precipitates were not observed to be present at the site of every oxide nodule. The  $\text{TiO}_2$  scale in the breakaway areas of Alloy 16 has a much higher Al concentration compared to the  $\text{TiO}_2$  scale in Alloy 13. However, as was observed in Alloy 13, the upper portion of the thick  $\text{TiO}_2$  scale appears to be primarily compact  $\text{TiO}_2$ , while the lower portion of the scale is composed of  $\text{Al}_2\text{O}_3$  and  $\text{TiO}_2$  crystallites, as well as a fine dispersion of  $\text{Ti}_2\text{AlN}$  precipitates. The presence of the  $\text{Al}_2\text{O}_3$  crystallites and  $\text{Ti}_2\text{AlN}$  precipitates accounts for the very high Al content detected in the lower  $\text{TiO}_2$  scale. Subjacent to the  $\text{TiO}_2$  scale an extensive oxygen stabilised  $\alpha_2$  layer is present, and (Ta,Zr,Si)-rich precipitates have precipitated out within the  $\alpha_2$  layer. Although the scales were observed to exhibit little porosity, fairly extensive cracking was observed parallel to the surface; both through the  $\text{TiO}_2$  scale and through the  $\alpha_2$  zone. However, it is thought that much of this cracking is produced during the preparation of the oxide cross-sections.

## 4. Discussion

From Figure 2 it is evident that the HAA alloys exhibit a much lower weight gain than either of the LAA alloys. In the case of the binary Ti-48Al alloy, which has very poor oxidation resistance, the rapid weight gain is attributable to the formation of a thick outer scale. On cooling the scale on the Ti-48Al tends to spall as a consequence of the large compressive stresses which

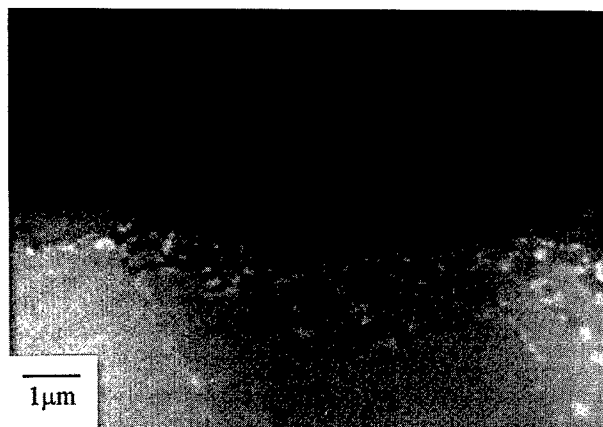


Figure 6a: BEI micrograph of oxide scale on Alloy 16 following exposure at 850°C for 24h.

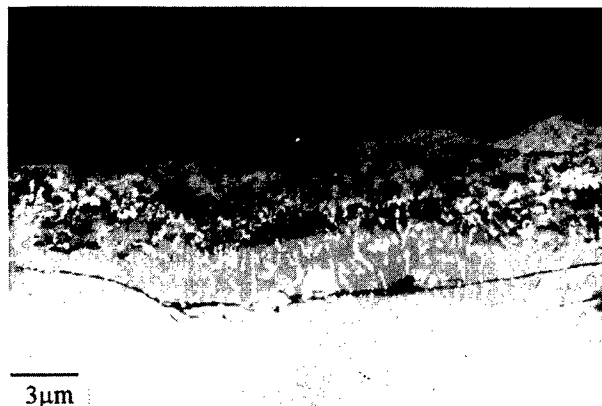


Figure 6b: BEI micrograph of oxide scale on Alloy 16 following exposure at 850°C for 500h.

build up in this thick scale. In the case of the Ti-48-2Nb-2Mn alloy, although the addition of Nb and Mn has produced a significant reduction in the oxidation rate, resulting in the formation of a thinner oxide scale, some spallation still occurs on cooling. However for the HAA alloys the weight gain behaviour and the oxide cross-sections indicate that the presence of the additional alloying elements has caused a significant reduction in the rate of oxide growth, which has the effect of reducing the compressive stresses which can build up within the scale. This is consistent with the fact that none of the HAA alloys exhibit spallation on cooling.

An analysis of the weight gain curves indicate that initially all of the scales follow an approximate cubic behaviour. This type of growth behaviour is indicative of an initially transient stage of oxidation followed by a second stage of

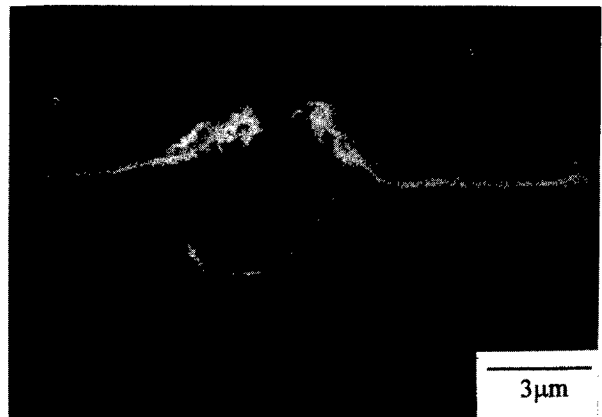


Figure 7: BEI micrograph of silicide particle interrupting the outer scale.

scale development which is dominated by diffusional transport. However, between 100 and 300h of exposure the low Nb scales show breakaway oxidation, while the high Nb alloys show a reduction in the rate of oxidation. The origin of the breakaway behaviour in the low Nb alloys and the reducing oxidation rate in the high Nb alloys can be explained by considering the development of the oxide scale with time.

#### 4.1 Scale development

It has been established previously that generally TiAl based alloys do not form protective outer  $\text{Al}_2\text{O}_3$  scales. This is a consequence of the fact that the oxygen equilibrium pressures of  $\text{Al}/\text{Al}_2\text{O}_3$  and  $\text{Ti}/\text{TiO}_2$  are very similar, which results in the formation of a non-protective mixed  $\text{Al}_2\text{O}_3/\text{TiO}_2$  scale; where  $\text{TiO}_2$  is formed rather than  $\text{TiO}$  due to the kinetics of titania formation<sup>3,4,10</sup>.

In the case of the high Nb alloy (Alloy 13) although a mixed  $\text{Al}_2\text{O}_3/\text{TiO}_2$  scale is formed, the outer scale is predominantly composed of  $\text{Al}_2\text{O}_3$ , with a  $\text{TiO}_2$  scale formed sub-jacent to it. As the  $\text{Al}_2\text{O}_3$  and  $\text{TiO}_2$  scales coarsen the partial pressure of oxygen at the scale/metal interface is reduced. This reduction in the partial pressure of oxygen can lead to the stabilisation of a  $\text{TiN}/\text{Ti}_2\text{AlN}$  layer beneath the outer scales; as has been proposed by Rakowski et al.<sup>11</sup>. Clearly this mechanism is consistent with the formation of the semi-coherent nitride layer beneath the oxide in Alloy 13 (Fig. 5a), and the formation of nitride precipitates in Alloy 16. WDS analysis of the nitride layer in Alloy 13 indicates that a relatively high Al concentration can be incorporated within it. However excess Al is expelled from the nitride phase leading to the formation of discrete  $\text{Al}_2\text{O}_3$  particles within the nitride layer. WDS analysis also reveals that only a low concentration of Nb is incorporated into the outer oxide scales and the underlying nitride layer. The expulsion of Nb from the growing oxide and nitride phases accounts for the precipitation of Nb-rich particles at the scale/metal interface, and in addition leads to the stabilisation of the fine  $\gamma$  grains<sup>12</sup>.

With continuing exposure time it is apparent that the  $\text{Al}_2\text{O}_3$  and  $\text{TiO}_2$  scales coarsen with time, and that the nitride interlayer is displaced further into the interior of the sample. As the nitride layer continues to move deeper into the alloy, the discontinuous  $\text{Al}_2\text{O}_3$  precipitates formerly in the nitride layer become incorporated into the growing  $\text{TiO}_2$  scale. However, on prolonged oxidation a reduction in the oxygen partial pressure in the lower part of the  $\text{TiO}_2$  scale leads the  $\text{Al}_2\text{O}_3$  particles to dissolve and re-precipitate in the outer scale where the oxygen partial pressure is higher<sup>8</sup>. The dissolution of the  $\text{Al}_2\text{O}_3$  precipitates and the associated outward diffusion of  $\text{Al}^{3+}$  cations results in the development of a thick continuous outer  $\text{Al}_2\text{O}_3$  scale. The dissolution of the  $\text{Al}_2\text{O}_3$  particles also leads to void formation in the lower portion of the  $\text{TiO}_2$  scale which can be observed in Figure 5b. It is also clear that  $\text{Ti}^{3+}$  and/or  $\text{Ti}^{4+}$  cations continue to diffuse outwards as is evidenced by the development of large rutile  $\text{TiO}_2$  facets on the surface of the  $\text{Al}_2\text{O}_3$  scale.

In contrast the Nb-rich precipitates located at the nitride/metal interface are not incorporated into the  $\text{TiO}_2$  scale; although an increasing concentration of Nb is incorporated into the  $\text{TiO}_2$  scale as the oxidation progresses. But most of the Nb is re-precipitated at the new nitride/metal interface and at the oxide/nitride interface, leading to the formation of a double Nb precipitate layer (Fig 5b). As the oxidation progresses an almost continuous layer of  $\text{Al}_2\text{O}_3$  and Nb-rich precipitates form at the nitride/metal interface. It is postulated that in the case of Alloy 13 the continuous growth of the outer  $\text{Al}_2\text{O}_3$  layer, as a result of outward  $\text{Al}^{3+}$  cation diffusion, and the formation over time of an  $\text{Al}_2\text{O}_3/\text{Nb}$ -precipitate barrier layer at the scale/metal interface is responsible for the reduction in the rate of weight gain with time observed on isothermal oxidation. Both the outer  $\text{Al}_2\text{O}_3$  layer and the inner  $\text{Al}_2\text{O}_3/\text{Nb}$ -precipitate layer providing a barrier to outward cation diffusion and further oxygen ingress.

In contrast to the development of the oxide scale on Alloy 13 the development of the scale on Alloy 16 reveals considerable differences. At the early stages of oxidation it is clear that a thin largely continuous outer  $\text{Al}_2\text{O}_3$  scale is formed on the alloy, with a slightly thicker  $\text{TiO}_2$  scale forming beneath it. This results in a much slower scale growth than observed on Alloy 13, consistent with the initially lower weight gain observed on this alloy (Fig. 2). In addition a continuous nitride layer is not observed to form under the scales in this alloy but an oxygen stabilised  $\alpha_2$  zone is observed to form. It appears that the greater incorporation of Al into the  $\text{TiO}_2$  scale, both in the outer compact  $\text{TiO}_2$  scale and in the underlying  $\text{TiO}_2$  scale, as nitride and  $\text{Al}_2\text{O}_3$  precipitates, leads to an enrichment of Ti at the scale/metal interface and to the stabilisation of the  $\alpha_2$  phase. Oxygen and Ta incorporation into this phase produces additional stabilisation of the  $\alpha_2$ . The changing alloy composition at the scale/metal interface due to the growth of the outer oxide overlayers and the expulsion



of Ta and Zr from the outer oxide scales leads to the formation of (Ta,Zr,Si)-rich second phase precipitates within the  $\alpha_2$ .

However, on prolonged exposure the outer  $\text{Al}_2\text{O}_3$  scale does not coarsen, while the underlying  $\text{TiO}_2$  coarsens steadily with time. The continual formation of the  $\text{TiO}_2$  sub-scale can be attributed to the preferential formation of  $\text{TiO}_2$  from the  $\alpha_2$ -stabilised metal phase. The fact that the outer  $\text{Al}_2\text{O}_3$  scale does not coarsen with time is attributed to the extensive incorporation of Al into the growing  $\text{TiO}_2$  sub-scale; as indicated by WDS analysis. The Al detected in the  $\text{TiO}_2$  is present as  $\text{Al}_2\text{O}_3$  and  $\text{Ti}_2\text{AlN}$  precipitates (Fig. 6b), and is possibly incorporated as elemental Al into the  $\text{TiO}_2$  lattice; as has been reported elsewhere<sup>8</sup>. The incorporation of Al in the growing sub-scale has the effect of reducing the outward migration of  $\text{Al}^{3+}$  cations and consequently inhibits the growth of a coarse outer  $\text{Al}_2\text{O}_3$  scale. An obvious exception to this case is where oxide nodule growth occurs on the surface. Where outward oxide nodule growth is observed, Ti and Al cations must continue to diffuse through the scale to the outer surface to form the mixed  $\text{Al}_2\text{O}_3/\text{TiO}_2$  oxide nodules. The formation of these oxide nodules were only observed on alloys 15, 16 and 17. Careful analysis of the oxide nodules and the underlying scales on Alloy 16 revealed that many of the oxide nodules were associated with the presence of  $(\text{Ti,Zr})_5(\text{Al,Si})_3$  precipitates. These precipitates were readily oxidised during exposure and caused local disruption of the outer  $\text{Al}_2\text{O}_3$  scale, as well as providing preferential paths for oxygen ingress into the alloy. With continuing exposure oxide nodules were observed to form on top of these near-surface silicide precipitates. The conclusion could be drawn that growth of the oxide nodules is solely related to the presence of the silicide particles. However, it has been shown previously that oxide nodules can form on non-silicon containing alloys<sup>11,13,14</sup>. Therefore, it is proposed that the oxide nodules form at defect sites in the outer  $\text{Al}_2\text{O}_3$  scale where outward cation migration is favourable. These defect sites could be cracks or second phase precipitates; such as silicides or nitrides, or areas where preferential  $\text{TiO}_2$  formation has occurred in the outer  $\text{Al}_2\text{O}_3$  film. Gil et al.<sup>14</sup> have argued that the formation of oxide nodules on the surface of  $(\alpha_2+\gamma)$ -TiAl alloys can be correlated with the composition of the underlying metal phase; such that the nodules preferentially form where the  $\alpha_2$  phase intersects the surface. However, although the HAA alloys had predominantly two phase microstructures no clear correlation between the underlying phase and the formation of oxide nodules could be established.

However, what is clear is that breakaway oxidation behaviour, which is the result of rapid internal oxidation, can be correlated with the formation of oxide nodules on the outer surface of the alloy and the breakdown of the protective  $\text{Al}_2\text{O}_3$  scale. The breakdown of this outer scale will lead to a significant reduction in the protective properties of the outer scale, and leads to rapid internal oxidation through the creation of preferential diffusion paths for cation and anion diffusion.

#### 4.2 Influence of alloying elements

From the above analysis it is clear that the difference in oxidation behaviour of the HAA alloys can be attributed to the differences in the development of the oxide scales with time, and that the break-away behaviour of Alloy 16 can be correlated with the dissolution of the thin outer  $\text{Al}_2\text{O}_3$  scale and the presence of second phase precipitates. However, the influence of the alloying additions on the scale development and oxidation kinetics has not been fully explained.

Possible explanations for the reduction in the rate of weight gain observed in the HAA alloys compared to the LAA alloys are oxide doping effects and/or a change in the Al/Ti activity ratio as a result of the addition of alloying elements. In terms of a doping effect it is quite clear that the incorporation of 5+ valency elements, such as  $\text{Ta}^{3+}$  and  $\text{Nb}^{3+}$ , into the n-type  $\text{TiO}_2$  scale could lead to a reduced defect concentration in the  $\text{TiO}_2$  which would reduce cation and anion transport through the oxide. However, it is quite clear that 4+ valency elements, such as  $\text{Hf}^{4+}$  and  $\text{Zr}^{4+}$ , have an equally large effect on the oxidation rate, which indicates that a valency effect is not responsible for the improved oxidation behaviour observed in these alloys. An alternative explanation is that the presence of the alloying elements effects the Al/Ti activity ratio. An increase in this ratio, as a result of alloying, would result in the preferential formation of an  $\text{Al}_2\text{O}_3$  oxide. The lower diffusivity of  $\text{Al}_2\text{O}_3$  compared to  $\text{TiO}_2$  would consequently result in a slower oxidation rate in these alloys. The formation alloys a predominantly  $\text{Al}_2\text{O}_3$  outer scale on the HAA alloys is consistent with this explanation. However, preliminary thermodynamic calculations indicate that alloying has a relatively small effect on the relative activities of Al and Ti<sup>12</sup>.

A third factor which is receiving considerable attention within the literature is the influence of nitrogen. The development of the oxide scales will clearly be effected by the formation of nitride phases. In the case of

Alloy 13 a semi-continuous predominantly TiN layer is formed at the oxide/metal interface. The formation and continual displacement of this layer further into the sample leads to the formation of an  $\text{Al}_2\text{O}_3/\text{Nb}$ -precipitate layer at the nitride/metal interface, and it has already been proposed that the formation of this layer could impede outward cation diffusion and oxygen ingress. In contrast, nitride particles in Alloy 16 are present as a fine dispersion of predominantly  $\text{Ti}_2\text{AlN}$  precipitates. It is thought that the incorporation of Al into these precipitates and into the  $\text{TiO}_2$  scale is one of the reasons why a thick  $\text{Al}_2\text{O}_3$  scale is not formed on this alloy. Similarly the expulsion and/or incorporation of alloying elements into the nitride phases will effect the stability of the metal phase in contact with the scale, which in turn effects the scale development. In Alloy 13 the expulsion of Nb from both the outer scale and the nitride phase results in the formation of Nb precipitates at the nitride/metal interface and the stabilisation of fine  $\gamma$  grains beneath the growing scale. In contrast, the expulsion of Ta and Zr from the oxide and nitride phases stabilises the  $\alpha_2$  phase. Clearly the stabilisation of  $\gamma$  or  $\alpha_2$  phases at the oxide/metal interface will have a significant effect on the subsequent scale development.

In summary the alloying additions clearly effect the relative stability of both the oxide and nitride phases. The preferential formation of certain phases, and the solubility of the alloy's elements in these phases, strongly effects the development of the scale and the overall oxidation resistance of the alloy. An improved understanding of the effects of alloying on phase stability can be aided by thermodynamic phase modelling. However, for the alloys examined in the present study the role of second phase precipitates in initiating breakaway needs to be clarified to enable the influence of the alloying elements to be assessed. Work is currently underway to establish the influence of second phase precipitates on oxidation.

#### 5. Conclusions

It has been established that the oxidation rate of  $(\alpha_2+\gamma)$ -TiAl based alloys at 850°C in air is significantly reduced by the addition of up to 8 at.% of Nb, Ta, Hf and Zr, compared to conventional Ti-48Al and Ti-48Al-2Nb-2Mn alloys.

The alloys with high Nb contents exhibited the best long term oxidation resistance. The oxidation kinetics of the high Nb containing alloys followed an approximately cubic behaviour, with a decreasing oxidation rate over time. The good oxidation resistance of these alloys was attributed to the formation of a thick continuous outer  $\text{Al}_2\text{O}_3$  scale and a thin  $\text{Al}_2\text{O}_3/\text{Nb}$ -precipitate layer at the scale/metal interface.

In contrast it was shown that those alloys with low Nb contents and which contained Si did not develop thick continuous  $\text{Al}_2\text{O}_3$  scales, and on prolonged exposure exhibited breakaway oxidation behaviour. The differences observed in the oxide scale development of the high and low Nb containing alloys is attributed to the effects of alloying on the stability of the metal phases in contact with the growing scale, and due to alloying induced changes in the formation and stability of nitride phases at the scale/metal interface.

A detailed study of one Si containing alloy showed that the breakaway behaviour was correlated with extensive internal oxidation, and the breakdown of the thin outer  $\text{Al}_2\text{O}_3$  scale. It is proposed that the breakdown of the outer  $\text{Al}_2\text{O}_3$  scale is the result of the formation and growth of oxide nodules on the surface of the oxide, where oxide nodule growth is favoured by the presence of defects in the  $\text{Al}_2\text{O}_3$  overlayer. In many cases the formation of oxide outgrowths could be correlated with the presence of second phase silicide precipitates, which act to interrupt the outer  $\text{Al}_2\text{O}_3$  scale and provide fast diffusion paths for anion and cation diffusion.

#### References

1. Y-W Kim, "Ordered Intermetallic alloys, Part III: Gamma titanium aluminides", *JOM*, (1994) 30.
2. D.M. Dimidak, "Gamma titanium aluminides - an emerging materials technology", in *Gamma titanium aluminides*, ed. Y-W Kim, R. Wagner and M. Yamaguchi, (TMS Pennsylvania, 1995), 3.
3. M.P. Brady, W.J. Brindley, J.L. Smialek and I.E. Locci, "The oxidation and protection of gamma titanium aluminides", *JOM*, (1996) 46.
4. A. Rahmel, W.J. Quaddackers and M. Schutze, "Oxidation of  $\gamma$ -TiAl based alloys: An overview" *Materials and Corrosion*, 46 (1995) 271

5. J.C. Schaeffer, C.M. Austin and F. Kaempf, Effect of alloying on the environmental resistance of cast gamma alloys", in Gamma titanium aluminides, ed.Y-W Kim, R. Wagner and M. Yamaguchi, (TMS Pennsylvania, 1995), 71.
6. K. Maki, M. Shioda, M. Sayashi, T. Shimizu and S. Isobe, "Effect of silicon and niobium on oxidation resistance of TiAl intermetallics", Mat. Sci. & Eng. A153 (1992) 591.
7. B.G. Kim, G.M. Kim and C.J. Kim, "Oxidation behaviour of TiAl-X (X=Cr,V,Si,Mo or Nb) intermetallics at elevated temperatures", Scripta Met., 33 (1995) 1117.
8. S. Becker, A. Rahmel, M. Schorr and M. Schutze, "Mechanism of isothermal oxidation of the intermetallic TiAl and of TiAl alloys", Oxidation of Metals, 38 (1992) 425.
9. S. Becker, M. Schutze and A. Rahmel, "Cyclic oxidation behaviour of TiAl and of TiAl alloys", Oxidation of Metals, 39 (1993) 93.
10. K.L. Luthra, "Stability of protective oxide films on Ti-base alloys", Oxidation of Metals, 36 (1991) 475.
11. J.M. Rakowski, F.S. Petit, G.H. Meier, F. Dettenwanger, E. Schumann and M. Ruhle, "The effect of nitrogen on the oxidation of  $\gamma$  - TiAl", Scripta Met. 33 (1995) 997.
12. N. Saunders, private communication.
13. A. Gil, E. Wallura, H. Grubmeier and W.J. Quadackers, "The influence of cooling rate during alloy casting on the oxidation behaviour of TiAl-based intermetallics", J. Mat. Sci. 28 (1993) 5869.
14. A. Gil, H. Hoven, E. Wallura and W.J. Quadackers, "The effect of microstructure on the oxidation behaviour of TiAl-based intermetallics", Corrosion Science 34 (1993) 615.

## **PROPERTIES AND APPLICATIONS OF TIAL**

# Aircraft Engine Applications for Gamma Titanium Aluminide

C. M. Austin, T. J. Kelly, K. G. McAllister and J. C. Chesnutt

GE Aircraft Engines

One Neumann Way, M89

Cincinnati, OH 45215

## ABSTRACT

Gamma titanium aluminide provides a unique set of properties that can lead to substantial payoffs in a range of aircraft engine applications. At least six components have been engine tested successfully. At least two specific engine components are the targets of serious introduction efforts at this time. Progress in implementation is being paced by the development of economical manufacturing processes and the accumulation of engineering experience.

## INTRODUCTION

Since the 1993 ISSI conference, extensive engine tests have been performed on a variety of components [1-4]. These tests have revealed no serious limitations and have prompted serious implementation efforts. Economical manufacturing processes are needed and behavior in service must be established by a progression of component, engine and field service evaluations. As is typical for any material, much research is required to establish a useful understanding of the process and physical metallurgy of gamma alloys.

This paper is largely oriented around specific components since it can be difficult to generalize about the requirements and issues of gamma applications. Through these "case studies", the reader will become more familiar with the payoffs, design principles, manufacturing issues, and limitations of gamma.

Our intent is to encourage the investigation and application of gamma, since understanding and cost reduction are best achieved by wide use in the industry. GE has selected a single alloy for implementation, Ti-48Al-2Cr-2Nb, and believes it suitable as a standard alloy for a wide range of gamma applications.

## PAYOFFS

The payoff for gamma is mostly in weight savings: gamma has half the density of superalloys and steel, and is about 10% lighter than titanium

alloys. Increased thrust-to-weight ratio translates into better range and greater payload. There are also opportunities to improve engine efficiency beyond those obtained from weight reductions.

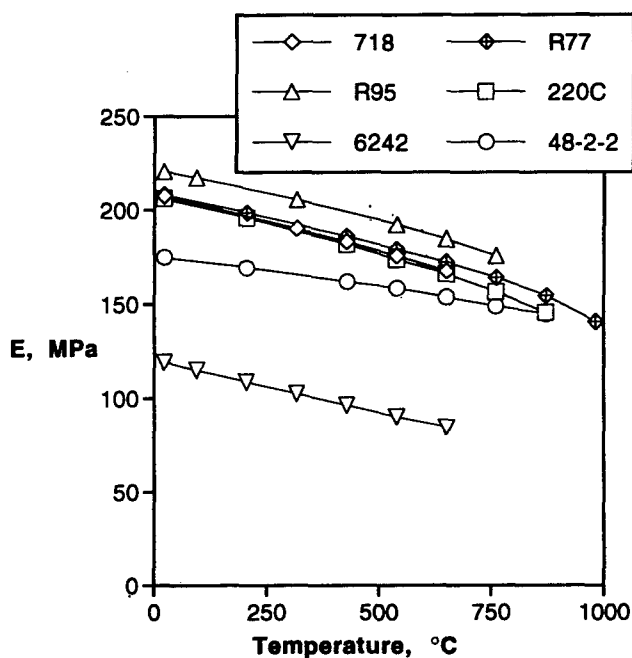


Figure 1: Modulus for gamma compared to a titanium alloy (6242) and a variety of nickel alloys used in aircraft engines [5].

The most unique property of gamma is its modulus, which approaches that of superalloys at operating temperature, while having half the density. Figure 1. Using specific modulus as a figure of merit may

understate the benefit since the increased component thickness allowed by the lower density of gamma also increases component stiffness. Component stiffness is of value in minimizing deflections that may cause interference between parts or increased leakage at seals. An important ramification of increased stiffness is an increase in vibration frequencies, since one of the most challenging aspects of engine design is avoiding the excitation of vibrations. Higher frequencies are usually better, but this is highly specific to the component and the surrounding system.

Is specific strength (yield or creep strength) a payoff area for gamma? The answer is usually no for two reasons, but within a limited context can sometimes be yes.

One can always find a conventional alloy that has greater specific tensile or creep strength than most forms of gamma. At a typical yield strength of 500 MPa, cast 48-2-2 cannot compete with 1) titanium alloys at low temperatures, 2) wrought superalloys at intermediate temperatures, and 3)  $\gamma'$ -strengthened cast superalloys at high temperatures, Figure 2.

The specific strength of gamma can exceed that of cast 718 and René 220. These  $\gamma''$ -strengthened alloys, formulated specifically for characteristics favorable to casting complex parts, lose strength rapidly at about 600°C, while gamma alloys remain strong for another 100°, Figure 3. Recently,  $\gamma'$  superalloys once considered unsuitable for large structural parts due to poor castability and weldability have become more accepted due to advances in casting and welding. For structural applications, the cost, performance and weight trade-offs will balance sensitively between gamma titanium aluminide and  $\gamma'$  superalloys.

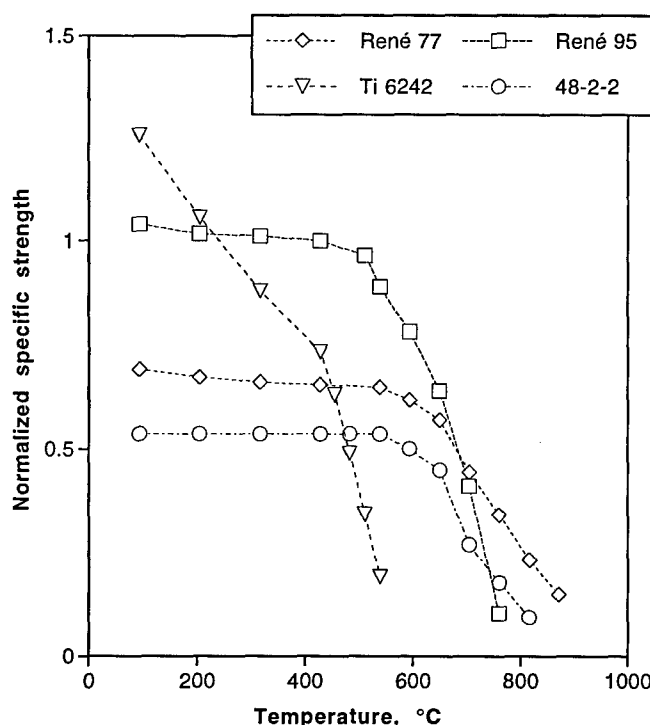


Figure 2: Graph of specific strength (YS or 0.2%/500h creep strength, whichever is lower) for gamma, titanium and superalloys [5].

Some recently developed forms of gamma [6] do have greater specific strength than conventional alloys. However, the steep slope of da/dN plots strongly suggests that fatigue crack growth threshold not be exceeded [7-10]. The plot in Figure 4 combines the limits on allowable maximum cyclic stress from S-N behavior and fatigue crack growth behavior for several hypothetical materials. The materials with high smooth-bar fatigue strength are limited by fatigue crack growth if a 375 $\mu$ m (0.015 inch) flaw is presumed. To increase allowable stress in most gamma components,  $\Delta K_{th}$  must be increased, not yield or LCF

strength. Full exploitation of gamma alloys will benefit from a detailed knowledge of defect types and their effective  $\Delta K$ , plus accurate measurements of minimum  $\Delta K_{th}$  under relevant situations.

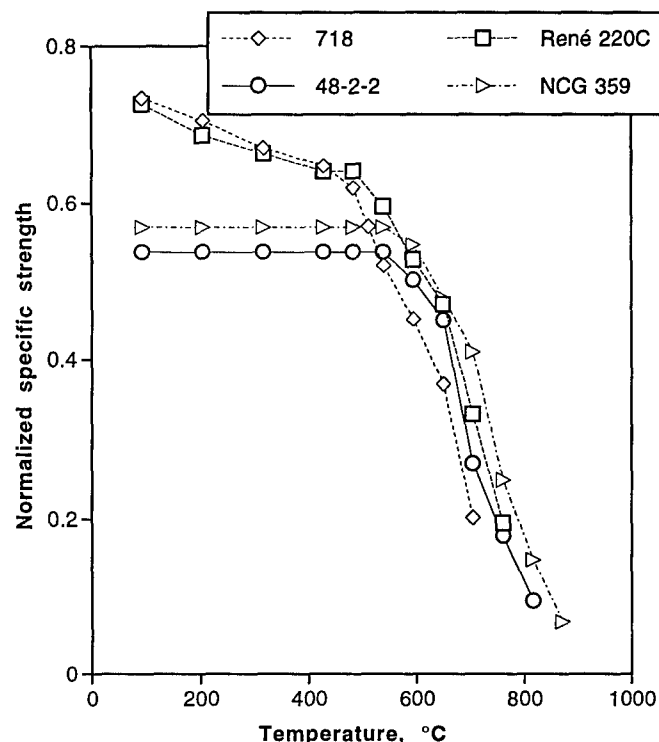


Figure 3: Specific strength comparisons (see Figure 2) between 48-2-2, NCG 359E, and two  $\gamma'$ -strengthened superalloys [5].

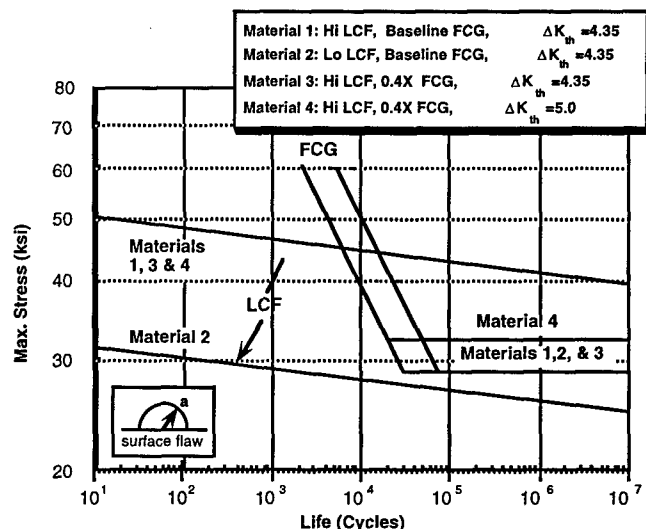


Figure 4: Plot of maximum stress versus life, taking fatigue crack growth behavior into account, for several hypothetical alloys and an assumed flaw size of 375 $\mu$ m (0.015 inch) [10].

The risk of fire restricts titanium alloys from certain applications. For example, the use of titanium airfoils within a titanium case is usually avoided in high pressure compressors. Gamma alloys are much more resistant to ignition than titanium alloys, Figure 5, though its ability to contain a titanium fire is not significantly greater than that of titanium, and much less than superalloys [5]. In other words, gamma airfoils in a titanium case may be an acceptable combination, but not vice versa. The ignition resistance of gamma is an important property for many candidate applications.

understate the benefit since the increased component thickness allowed by the lower density of gamma also increases component stiffness. Component stiffness is of value in minimizing deflections that may cause interference between parts or increased leakage at seals. An important ramification of increased stiffness is an increase in vibration frequencies, since one of the most challenging aspects of engine design is avoiding the excitation of vibrations. Higher frequencies are usually better, but this is highly specific to the component and the surrounding system.

Is specific strength (yield or creep strength) a payoff area for gamma? The answer is usually no for two reasons, but within a limited context can sometimes be yes.

One can always find a conventional alloy that has greater specific tensile or creep strength than most forms of gamma. At a typical yield strength of 500 MPa, cast 48-2-2 cannot compete with 1) titanium alloys at low temperatures, 2) wrought superalloys at intermediate temperatures, and 3)  $\gamma'$ -strengthened cast superalloys at high temperatures, Figure 2.

The specific strength of gamma can exceed that of cast 718 and René 220. These  $\gamma''$ -strengthened alloys, formulated specifically for characteristics favorable to casting complex parts, lose strength rapidly at about 600°C, while gamma alloys remain strong for another 100°. Recently,  $\gamma'$  superalloys that were once considered unsuitable for large structural parts due to poor castability and weldability have become more accepted due to advances in casting and welding. For structural applications, the cost, performance and weight trade-offs will balance sensitively between gamma titanium aluminide and  $\gamma'$  superalloys.

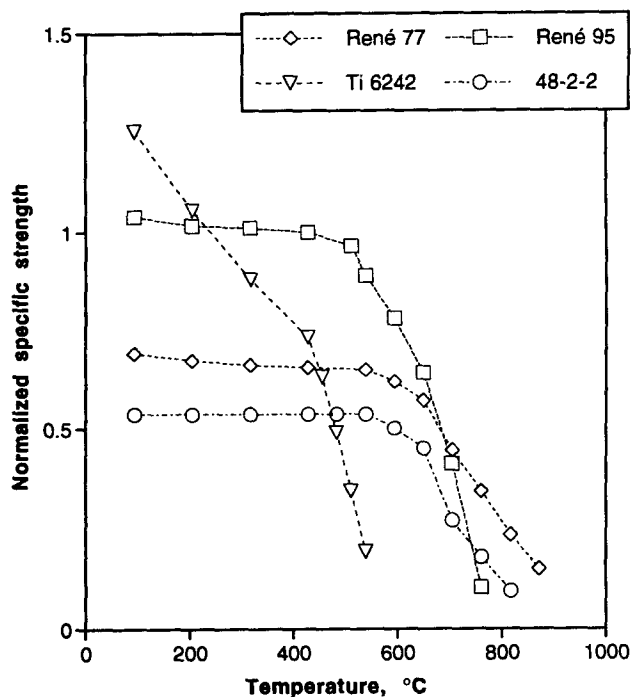


Figure 2: Graph of specific strength (YS or 0.2%/500h creep strength, whichever is lower) for gamma, titanium and superalloys [5].

Some recently developed forms of gamma [6] do have greater specific strength than conventional alloys. However, the steep slope of  $da/dN$  plots strongly suggests that fatigue crack growth threshold not be exceeded [7-10]. The plot in Figure 3 combines the limits on allowable maximum cyclic stress from S-N behavior and fatigue crack growth behavior for several hypothetical materials. The materials with high smooth-bar fatigue strength are limited by fatigue crack growth if a 375 $\mu$ m (0.015 inch) flaw is presumed. To increase allowable stress in most gamma components,  $\Delta K_{th}$  must be increased, not yield or LCF

strength. Full exploitation of gamma alloys will benefit from a detailed knowledge of defect types and their effective  $\Delta K$ , plus accurate measurements of minimum  $\Delta K_{th}$  under relevant situations.

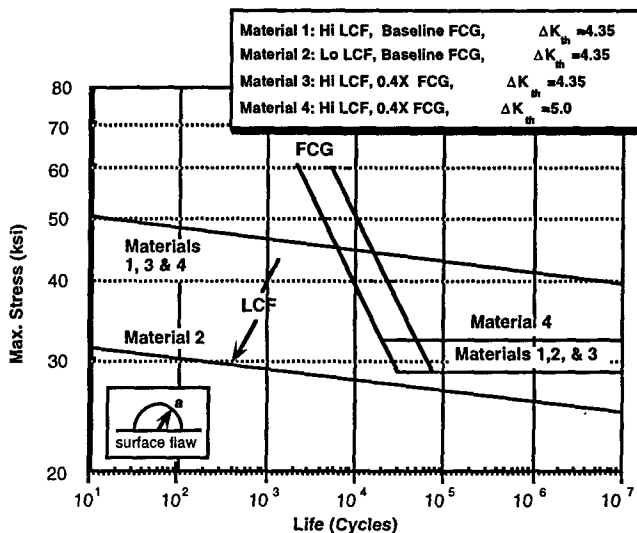


Figure 3: Plot of maximum stress versus life, taking fatigue crack growth behavior into account, for several hypothetical alloys and an assumed flaw size of 375 $\mu$ m (0.015 inch) [10].

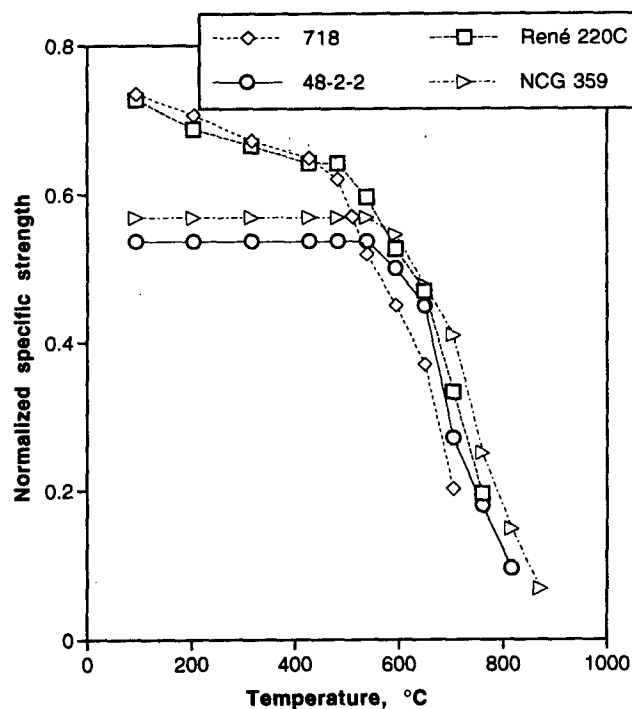


Figure 4: Specific creep strength comparisons between 48-2-2, NCG 359E, and two  $\gamma'$ -strengthened superalloys [5].

The risk of fire restricts titanium alloys from certain applications. For example, the use of titanium airfoils within a titanium case is usually avoided in high pressure compressors. Gamma alloys are much more resistant to ignition than titanium alloys, Figure 5, though its ability to contain a titanium fire is not significantly greater than that of titanium, and much less than superalloys [5]. In other words, gamma airfoils in a titanium case may be an acceptable combination, but not vice versa. The ignition resistance of gamma is an important property for many candidate applications.

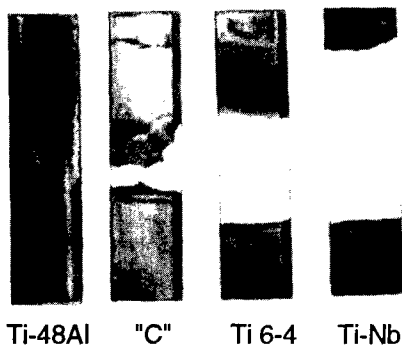


Figure 5: Ignition test results for various titanium-based materials ("C" is a so-called non-burning titanium alloy), 440°C, 1500 KPa, 0.5 Mach; white areas represent consumed material [5].

Finally, the low thermal expansion of gamma relative to superalloys, Figure 6, provides a potential advantage in efficiency by reducing leakage at seals and other structures that control clearances. (At joints between gamma and nickel components, however, the combination of low expansion with high modulus can lead to high thermal stresses.)

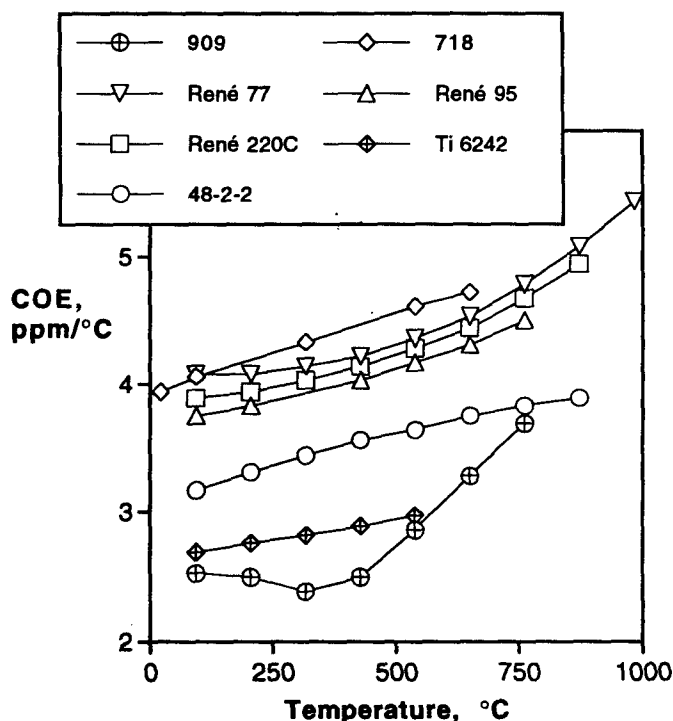


Figure 6: Thermal expansion coefficient for various materials including 909, an Invar-derived alloy with low thermal expansion [5].

## APPLICATIONS

A wide variety of materials and processes are used to produce aircraft engine components. For some components, the selection is straightforward. For others, a selection must be made among many competing choices. The best fit to cost and performance goals may require judgement and experience.

Gamma applications can be ranked according to payoff and risk, Figure 7. Overall risk is the sum of individual risks in cost, schedule and performance, including both the chance of failure and the consequence of failure. The first introduction of gamma should be for parts that are on the low-risk side; these will typically involve low payoffs as well. The design, manufacturing and service experience gained from these applications will greatly reduce the risk of subsequent applications.

Below are discussions of specific applications that have either been engine tested (in the first part) or are the subject of current development efforts (in the second part). We have attempted to include relevant discussion about choice of alloys, processes and designs for these components as well as the payoffs and results of the testing.

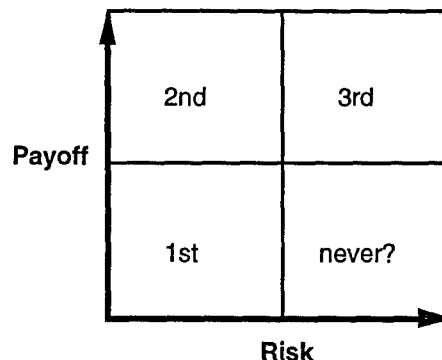


Figure 7: Applications can be plotted according to risk versus payoff; a prudent introduction plan will pursue applications in the order indicated to gradually build experience at minimum risk.

These pursuits are generally military in nature or, increasingly, related directly to commercial products; in both cases, the amount of information that can be made public is limited. All applications in which GE is involved are described, but attempts to incorporate the activities of other companies were not entirely successful.

## COMPLETED ENGINE TESTS

The first publicly disclosed engine test of gamma was conducted by GE Aircraft Engines in 1993. The authors are unaware of any earlier test.

### CF6-80C2 Stage 5 Low Pressure Turbine Blades

A full set of gamma LPT blades was prepared and subjected to 1000 simulated flight cycles during 1993 ground tests at GE's Peebles Test Operation [1-2]. The material normally used for this component is René 77, a  $\gamma'$  superalloy. Subsequently, the rotor was disassembled, inspected, reassembled and run for an additional 500 cycles the following summer. There was no "gamma-caused" distress from this testing, Figure 8. The qualification is necessary to distinguish factors directly relevant to future use of gamma in this type of application. For example, it was discovered after the first 1000 cycles that installation of blade retainers had cracked the mating feature on many blades. (That the cracks did not propagate was, of course, an encouraging sign of robustness.) The blade retention system was modified for the second run.

The design modifications for this test included several that are required for any blade. First, the airfoil section was re-oriented over the dovetail to balance centrifugal and aerodynamic loads; this reduces moments on the dovetail. Second, a single tang dovetail was implemented to avoid uneven loading across multiple tangs. Third, a vibration problem arising from the change in modulus-to-density ratio was prevented by use of mid-span damper pins. The aeromechanical design would normally be modified to avoid vibrations, but was outside the scope of this demonstration effort.

Low pressure turbine blades of high-bypass turbofan engines present the greatest weight savings potential for gamma. The last stage or two will generally involve temperatures suitable for gamma (this is not the case for the LPT of low-bypass engines for fighter aircraft). The strength requirements are modest, allowing the use of a material with lower specific strength. The requirements of aerodynamic efficiency, avoidance of vibrations, and manufacturing limitations jointly lead to thicker profiles in superalloy LPT blades than are otherwise required.

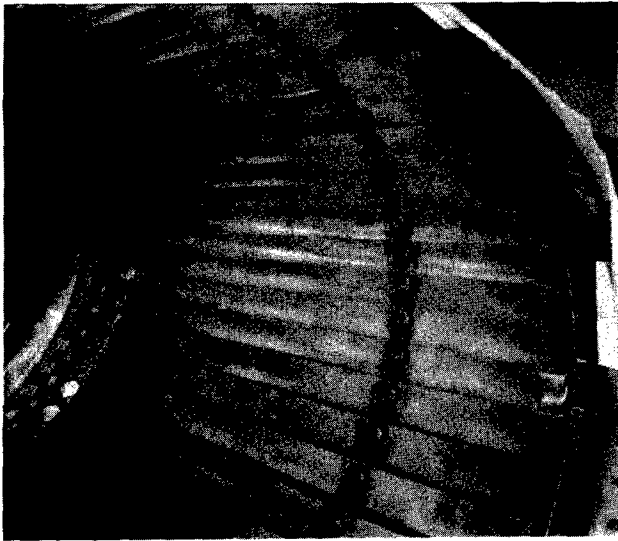


Figure 8: CF6-80C2 LPT stage 5 rotor with gamma blades after 1000 "C" cycles.

The risks involved in LP blades are under intense scrutiny at the present time, and are discussed in the section on current blade efforts below. Briefly, it is unlikely that a well-designed and manufactured gamma blade will fail other than through physical damage; such damage occurs rarely in normal service.

Nickel alloy LPT blades are always cast for two reasons, each sufficient: 1) only cast materials have the required creep strength, and 2) casting is the least expensive process. The same reasons justify cast gamma.

The standard titanium casting process was used to prepare the blades for the CF6-80C2 test. The process as applied to gamma was not sufficiently developed for production of net-shape airfoils, so over-sized castings were produced. Howmet Ti-Cast Division graciously provided most of the blade castings for the engine test. As might be expected at that time, casting defects were frequent and yields were low. The airfoil sections were electrochemically milled to size, while the dovetail, platform, and tip shroud were finished by EDM, milling and grinding.

The alloy used for most of the blades was the alloy known as "48-2-2", nominally Ti-48Al-2Cr-2Nb [11]. It provides greater toughness and ductility than any other alloy with the required creep strength. Toughness and ductility were thought to be especially important for the first demonstration of gamma.

Shop damage occurred when workers over-estimated the strength of the material; low ductility only made the damage more obvious. Workers should be allowed to get a feel for the strength and ductility of the material on coupons or scrap hardware.

The second test of this rotor included blades provided by IHI made of their Alloy 01A, an alloy developed specifically for casting that contains Fe, V and B [12]. These blades performed well.

From a manufacturing point of view, the most important property for an LPT blade material is castability. Ideally, a gamma alloy should be especially good for filling thin sections; extensive castability tests by GE have failed to show any significant compositional effects, but IHI has shown a benefit from alloying with Fe and B. High mold preheat temperatures are helpful for filling, but facecoat reactions and microshrinkage problems limit this approach. Howmet's approach is to use proprietary alloys inoculated with larger amounts of boron. Precision Castparts appears to employ more conventional casting approaches to promote proper filling and feeding of molds.

The chief quality issue with gamma castings has been and will likely continue to be surface-connected microshrinkage, which the HIP process cannot close. The low superheat of the Ti casting process together with the wide solidification range of gamma alloys conspire to

promote wicking of interdendritic liquid, forming extensive open channels of porosity.

### F414 carbon seal supports

These components are normally made from steel and place few demands on the material. They would be made of titanium if not for the possibility of fire. Laboratory testing of the areas of the seal that might rub with the shaft showed that ignition is far less likely with gamma. Several "No. 2" (Figure 9) and "No. 5" seals were machined from 48-2-2 castings and were successfully tested in a number of engines during the F414 qualification program.

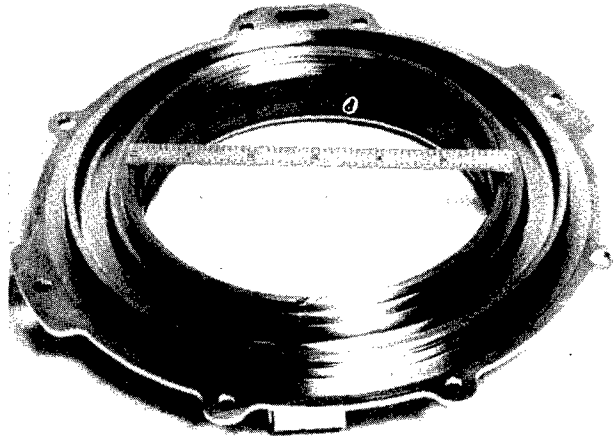


Figure 9: Carbon seal housing that underwent successful qualification testing in several factory test engines.

When it was time to decide if gamma should go into production for these seals, the engine program was well under its weight goal, and the added cost and remaining risk of gamma (over steel) could not be justified. However, a desire to reduce the weight of the aircraft has recently emerged and gamma seals are being reconsidered. Cost will be the principle issue.

A technical justification for choosing 48-2-2 exists: the highest toughness and ductility were desired. But the more significant factor is that once an engine company and its suppliers have acquired data and experience for a certain alloy, cost and risk can be reduced from standardization. Further cost and risk reductions can be realized if the industry were to standardize on 48-2-2. For this reason, GE has licensed 48-2-2 to several ingot makers.

The casting route was chosen because, at that time, castings were being acquired successfully while wrought processing was proving more difficult. Wrought processing has matured since that time and cost estimates place some forms of wrought processing in a competitive range with castings [13]. For undemanding applications such as these seals, cost is the only selection criteria.

### GE90 transition duct beams

At about the same time as the 80C2 blade program was initiated, it was realized that the first introduction of gamma should be in the form of a low-risk part. In terms of the risk-payoff plot in Figure 7, this meant pursuing the lower left corner first, rather than the upper middle. The entire process of design, development, manufacture and qualification of any component is a daunting task; introducing a simple gamma component would pay dividends at the time a more significant (and risky) component was introduced.

The transition duct beam in the GE90 engine was selected for this purpose. This component stiffens a flowpath panel between the high and low pressure turbine during engine surges/stalls, a rare event. They are currently made from cast René 77.



Beams were cast by PCC and IHI from 48-2-2 and 01A using the superalloy design, Figure 10. These beams were first tested in a rig that simulated stall conditions, with positive outcomes despite an apparent requirement for a degree of plasticity. Beams were then installed in two engines and completed more than 600h and 2200 cycles. Additional engine testing is ongoing.

Since that time, an inner beam has been designed for the properties and castability of gamma. Casting development is underway and gamma beams are on track for entry into service.

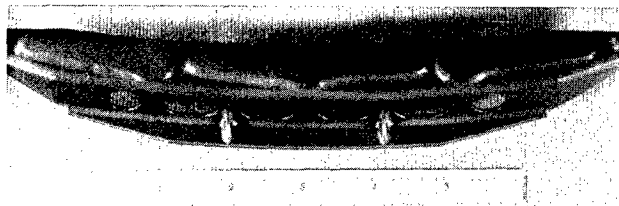


Figure 10: Transition duct beam castings; longest one is about 200mm long.

Since the point of the beam application is to gain experience for more significant applications, and 48-2-2 is the alloy for those applications, the alloy selected for the beams was, of course, 48-2-2. A similar statement may be made about the choice of casting as the manufacturing process. An independent selection process would also lead to the selection of cast 48-2-2 in order to provide the best toughness and ductility at the lowest cost.

### Volvo blade dampers

Volvo has engine tested a set of blade dampers produced by Howmet of an alloy consisting of Ti-47Al-2Nb-2Mn plus B to provide 0.8 volume percent  $\text{TiB}_2$  [3]. These components damp vibration in high pressure turbine blades by introducing a controlled amount of friction during blade movement. The gamma parts were successfully manufactured and performed their required function without appreciable wear. Excessive wear was observed on the turbine blades, however, perhaps due to the presence of  $\text{TiB}_2$  in the alloy.

### Allison 14th stage compressor blades

In very general terms, from forward to aft, compressor blades are made of titanium alloys, steel, and finally wrought superalloys. Higher temperatures in future engines may require cast superalloy compressor blades. In this context, gamma blades offer not only a weight payoff, but perhaps cost as well, depending on the relative costs of casting these thin components.

Allison has tested gamma compressor blades in a commercial turbofan development engine [14]. Though long-term durability testing has not yet been performed, basic feasibility for this sort of application was demonstrated. The blades were manufactured from extrusions by electrochemical machining (airfoil section) and grinding (dovetail). The material was Allison's "Alloy 7", a high strength alloy containing 5Nb and 1W and substituted for wrought alloy 718.

Some design engineers feel that compressor airfoils are in the high risk and low payoff corner of the risk/payoff diagram. The risk stems from the combination of high vibratory stresses and the possibility of foreign object damage. The low payoff stems from the low total weight of the airfoils compared to the "live" portion of the disk (the portion that adds rather than subtracts from the centrifugal loading on the disk bore); relatively little weight can be removed from a conventional disk by lightening HP compressor airfoils. However, for non-traditional systems such as a fiber-reinforced bladed ring, gamma blades are more or less required for compatibility with the reinforced Ti-based material and can contribute to a substantial overall payoff.

### PWA LP turbine side plates

These components fit on the aft face of the LP turbine disk of a military low-bypass turbofan. They serve both to retain the turbine blades and reduce leakage through the dovetail slots. Obviously, a very high payoff from reducing the weight of these plates can be obtained, whether used to lighten the disk, permit higher speed, or allow the use of advanced turbine blade alloys (which tend to be heavier).

The plates were manufactured by Howmet of the same  $\text{TiB}_2$ -containing alloy used by Volvo. According to PWA sources, the plates performed well. [4]

### Advanced Engine Radial Diffuser

This component, which controls the deceleration of compressor discharge air into the combustor, was prepared by wrought processing for an advanced demonstrator engine [15]. A 45% weight reduction was realized.

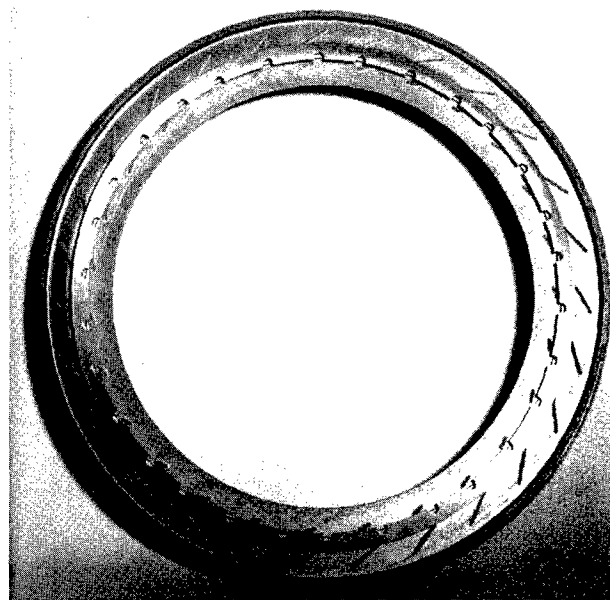


Figure 11: JTAGG radial diffuser assembled from isothermally forged forward and aft shrouds and aft flange, individual vanes, and forward spacer arm.

The production of this component began with VAR (vacuum-arc remelting) of three 280 mm dia. ingots needed for the component forgings. The ingots were HIP'd and machined into multiples for isothermal forging into pancake shapes from which the component pieces could be machined. The diffuser design required forgings with a minimum diameter of 560 mm. Initially, one-step forging of 635 mm diameter by 51 mm thick pieces was planned. Difficulty in obtaining these dimensions without exceeding press limits led to the use of a two-step forging sequence for the final forgings in the series.

These forgings, ranging from 635 mm to 735 mm in diameter, represented the largest forged up to that time. The forward and aft shrouds and the aft flange were machined from the isothermal forgings. The individual vanes were wire EDM'd from residual forging material. A Ti-6Al-2Sn-4Zr-2Mo forward spacer arm was machined from a conventional forging. These subelements were brazed together using Ti-15Cu-15Ni braze filler metal. The fabricated component passed static rig testing to 150% of the design stress.

Unfortunately, a different diffuser design was ultimately selected, preventing what otherwise would have been a successful engine test.

## CURRENT ENGINE TEST PROGRAMS

### CAESAR

High pressure compressor blades are the focus of the CAESAR (Component and Engine Structural Assessment Research) program in which four engine manufacturers have produced blades for engine test [16].

GE produced blades from extruded 48-2-2 barstock. At the beginning of the program, the extrusion process was limited to 25 mm bar from 75 mm diameter input material. Wyman-Gordon Houston scaled the process to 50 mm bar from 150 mm VAR ingots, which led the way to subsequent scale-up on production equipment to 350 mm bar [17].

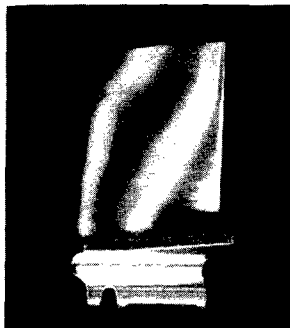


Figure 12: Gamma HPC blade for CAESAR program.

Heat treatment of bar for the compressor blades was intended to be at 25°C below the alpha transus, but coarse structures were produced in some of the extrusions, indicating inconsistent aluminum levels. This experience reinforces the need to control aluminum chemistry in wrought product as well as other forms.

The blades were machined from the bar stock by milling of the airfoils and grinding of the dovetails Figure 12. The blades are undergoing component and spin-pit testing prior to engine test which is scheduled for mid 1997. The manufacture of these components has resulted in greater confidence that wrought processing can be used to reliably produce gamma components.

### F119 components

Gamma is a candidate for several components for this engine [4]. Howmet's XD alloy is undergoing final manufacturing process development for introduction as 4th stage compressor ID shroud seals, substituting for a fiber-reinforced ceramic material [18].

### High Speed Civil Transport components

Under the High Speed Civil Transport (HSCT) project, NASA is funding a program on gamma in pursuit of stiff, lightweight and affordable nozzle structures [19]. The engine planned for the next generation of supersonic transports is very large and has a nozzle that must provide special features for performance and noise abatement. The large flaps and sidewalls of the nozzle are stiffness-limited when designed for superalloys. The high specific stiffness of gamma provides an opportunity for a substantial weight savings over superalloy construction.

The fabrication of such large components presents a great challenge. Since sheet processing and forming operations appear to involve high costs, a thin-wall casting approach is being pursued. No HIP chamber is large enough for the full component, so the components must be cast in sections and welded together. At the start of the program, only limited weldability had been demonstrated for gamma (e.g., weld repair of small casting defects).

Extensive cold-cracking occurs in long welds produced at room temperature (as for titanium, welding must always be performed in an inert environment). Welds made at elevated temperatures do not crack in the glovebox upon cooling, but will later crack when removed to normal atmospheric conditions; it is believed that the combination of residual

stresses and hydrogen in moist air is responsible. The solution to this problem is to perform a stress relief treatment prior to exposure to the atmosphere.

Special chambers have been constructed to implement this solution. A large chamber in which a full-size flap can be welded is being constructed and will be installed at PCC.

After extensive characterization and discussion, 48-2-2 was selected over the Howmet TiB<sub>2</sub>-containing alloy as the alloy for future efforts. The two alloys have opposite strengths and weaknesses in terms of the two prime issues of castability—cracking and shrinkage porosity. Since  $\Delta K_{\alpha}$  of the two alloys are similar, allowable stresses are similar. The decision was based on better weldability, greater ductility, wider availability and greater application experience.

The HSCT gamma program has made substantial contributions in other areas. Several challenging shapes have been cast, Figure 13. Mechanical behavior has been studied and design methods have been developed.

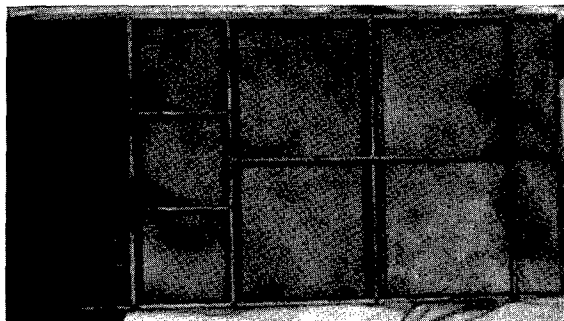


Figure 13: Small-scale demonstration of casting process for HSCT flap features; casting is about 1 meter long.

### GE90 Stage 5 & 6 low pressure turbine blades

This program is the most serious near-term gamma effort in the aerospace industry. A number of important results are reported here.

A NASA "AITP" program, which is intended to spur implementation efforts in not-quite-ready technologies, did exactly that when awarded in 1996 to a team composed of Chromolloy, GE Aircraft Engines, Howmet, NASA-LeRC and Precision Castparts. Substantial resources beyond that required by this program have been expended, including those of GE partners IHI and Fiat, aimed at implementing gamma as low pressure turbine blades in a future version of the GE90 commercial turbofan.

The weight reduction goal for this program is 80 kg. The system cost goal is parity with the current René 77 bladed disk, which can be achieved through somewhat higher-cost gamma blades coupled with a lighter, less-expensive disk. To meet customer expectations and match current hardware, a gamma rotor must be trouble-free for the life of the engine.

Many alloys are probably suitable for the last stage of high-bypass turbofan engines (which attempt to draw as much energy as possible from the HP exhaust to drive a large fan). The upstream gas temperatures rise nearly 100°C per stage, however, and immediately challenge all but the most creep resistant alloys. For this reason and others, 48-2-2 was selected.

Going into production with a new alloy forces engineers to more firmly define the alloy. A specification must be written that includes a number of details, not least of which are allowable impurities. A chemical analysis procedure must be developed, which has been a particularly troublesome aspect of gamma metallurgy. Heat treatment must be fixed. Extensive material property must be collected. Some success has been achieved in these areas and is discussed further below.

The AITP program initiated effort in several areas: 1) blade design and design data generation, 2) blade manufacturing development, and 3) evaluation of two specific performance concerns.

**Blade Design:** As mentioned above in the section on the CF6-80C2 test, design of a gamma low pressure turbine blade requires more lean than a blade made from a heavier alloys. Other design elements required a great deal of effort, especially those needed to facilitate producibility. "Net shape" casting is believed to be required to achieve cost goals; this actually means a shape that can be chemically-milled to the desired shape, or about 0.005" oversize. The current GE90 stage 5 & 6 LPT blades are the largest and thinnest blades in the business, too thin in fact for the gamma casting process. Changes desired for castability and other concerns (see below) initiate iterative mechanical, vibratory and aerodynamic analyses.

Every attempt was made to stay below yield strength in the blade, including at stress concentrations. (For many structural parts, this requirement would lead to a significant weight penalty; studies of behavior at various stress concentrations have been initiated to establish allowable concentrations. So far, these studies suggest that moderate levels of plasticity can sharply reduce concentrated stress.[20]) Another requirement, common to many but not all components, was that  $\Delta K$  (based on inspection limits) should not exceed minimum  $\Delta K_{th}$ .

After considerable effort by GE and PCC, a design was released and tooling ordered in late 1996 for the stage 6 blade.

**Design data:** For the design data program, cast slabs were prepared by Howmet and PCC. The castings were prepared from electrodes from six master ingots having a variety of aluminum levels. Three of the ingots were produced by Howmet and three by Oremet. As of this writing, extensive testing and analysis is ongoing. Preliminary results have shown the material and data to be unusually self-consistent and useful for a variety of purposes beyond design data. Where referenced elsewhere in this paper, this data is referred to as coming from the "six-ingot" program.

**Manufacturing development:** The GE90 Stage 6 blade is compared to the CF6-80C2 blade in Figure 14. Casting development began with both Howmet and PCC under the AITP program, but now involves only PCC. A number of casting parameters and configurations have been investigated extensively; at the time of this writing, it appears that a process should soon be established. Several sets of engine quality hardware are expected late in 1997.

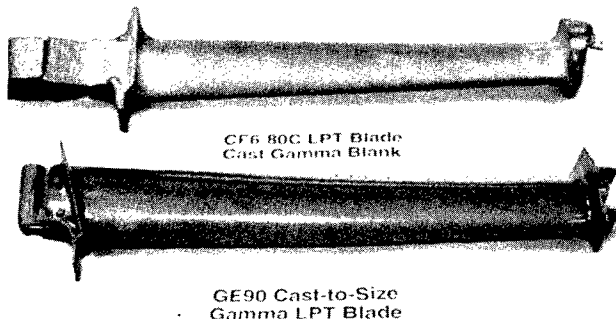


Figure 14: Comparison of oversized CF6-80C2 stage 5 LPT blade casting with recent near-net-shape casting of GE90 Stage 6 blade.

IHI, which is responsible for stage 5 of the GE90, has independently developed a design and is identifying a casting process. It is hoped that both stage 5 and 6 blades will be available for engine testing during 1998.

Significant processing technology and materials understanding has been developed as part of the AITP program and is discussed separately in the section on processing.

**Impact:** The impact resistance of gamma is substantially lower than superalloys, even after taking into account the latter's well-known embrittlement in service. Superalloy LPT blades do not fail from impact damage, however, and it is therefore difficult to establish an impact damage tolerance requirement. Thus far, examination of various engine test hardware and surveys of service shop personnel have not contradicted the statement "impact damage does not occur in LPT

blades, absent a significant upstream event". On this basis, gamma blades are moving forward despite the lower capability.

Nevertheless, it has been deemed prudent to establish the fatigue capability of gamma airfoils with impact damage. Analytical methods are not easily applied to this subject, so a direct approach is being taken. Fatigue tests are being conducted on simulated airfoil sections prepared by blade manufacturing processes, with damage inflicted under load at elevated temperature, with representative projectile velocities.

The specimen configuration is shown in Figure 15; the edges of this specimen have the exact profile of the selected leading edge configuration for the Stage 6 blade. Impact damage was imposed by NASA-LeRC using a precision gun tube mounted to a servo-hydraulic test machine equipped with a furnace.

NASA has completed an initial experiment to correlate impact conditions with damage appearance [21]. Related research is also being performed by a team of university researchers sponsored by the USAF [22]. The appearance of a typical dent is shown in Figure 16. A program is currently underway at NASA to establish the fatigue capability of these specimens with various impact damage. Among other uses, this will allow the translation of borescope observations to an allowable stress. A simple go/no go decision can then be made by comparing this stress to actual operating stresses.

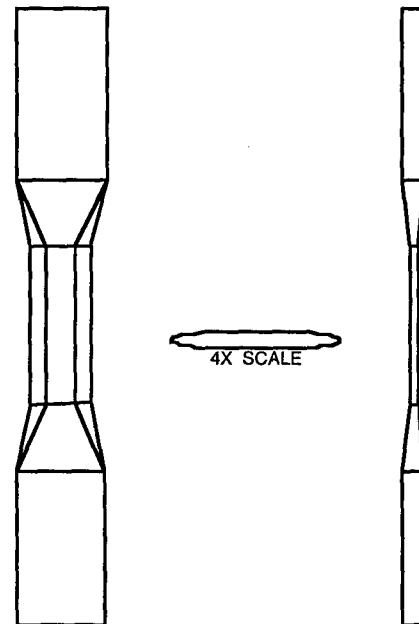


Figure 15: Cast-to-shape simulated airfoil specimen used for impact and other applied testing.

**Tip Rub:** The other serious performance issue evaluated in the AITP program is the behavior of gamma blades during tip rubs. To minimize leakage, clearances are set such that rubbing will occur during the factory green run (in a controlled manner) and also occasionally as part of normal operation. During these times, it is important that the tip seals of the blade wear away the honeycomb material of the surrounding case rather than vice versa.

There are also unusual situations when a heavy rub might occur. It was feared that high frictional heating might cause thermal cracking of gamma tip seals, or that the frictional force might cause outright failure of the blade itself.

These rubs can involve relative movement in both axial and radial directions between the tip and the turbine case. To better simulate severe rubs, an existing rig was modified to impose radial incursions as well as axial incursions, as shown in Figure 17. The drum was slotted and a collet mechanism was used to push the segments inward against the rotor. This

motion was combined with the normal axial motion to reproduce profiles representing normal and severe rubs.

The computer-controlled rig is instrumented with force and torque transducers plus a pyrometer that can monitor the temperature of the simulated tips near the area of rubbing.

A designed experiment included a range of test conditions, two tip profiles, both 48-2-2 and René 77 materials, and both bare and coated tips. The results showed no mechanical distress of the gamma tips and tolerable blade bending loads. While tip wear was comparable to René 77 under some conditions, wear was excessive in others, suggesting that an abrasive coating is desirable.



Figure 16: Typical morphology of backside impact damage observed on simulated airfoil specimen (inset shows impacted front side) [21].

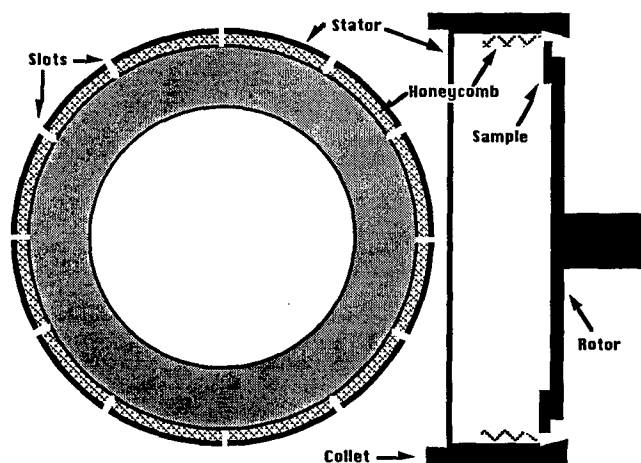


Figure 17: Schematic drawing of rub testing apparatus modified to simulate both radial as well as axial rubs by incorporating a collet mechanism.

## Advanced Engines

GE, Allison, Rolls-Royce and Pratt & Whitney are pursuing gamma components for various advanced engines. These include several structural components, such as the prototype diffuser casting shown in Figure 18 made of NCG 359E. This alloy has the nominal composition of Ti-47.3Al-1.7Cr-0.8Nb-1.7Ta [23] and promises to provide a substantial increase in temperature capability, Figure 19.

Wrought processing is being developed in US Air Force sponsored efforts directed at components requiring high integrity.

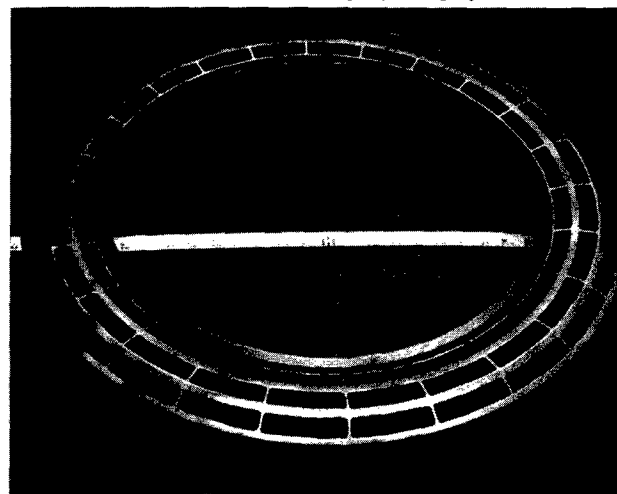


Figure 18: Prototype diffuser cast by PCC; alloy is NCG 359E, a developmental alloy containing Cr, Nb and Ta.

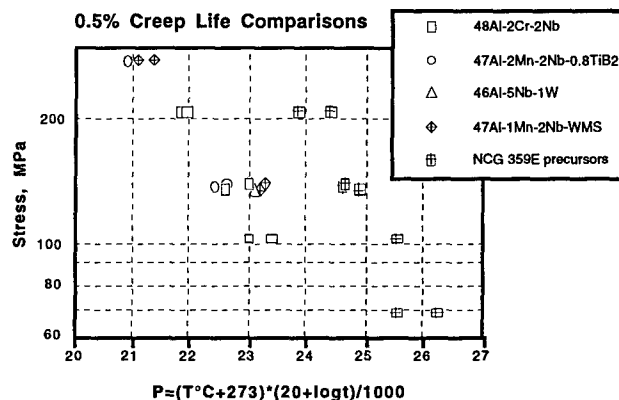


Figure 19: Larson-Miller plot for 0.5% strain for various gamma alloys [23, 24]

## PROCESSING

### Ingot making

Until recently, ingots often fell outside the Al specification range for 48-2-2, which is 32 to 33.5 wt. pct. Just how often could not be determined since the precision and reproducibility of chemical analysis procedures was poor. To some extent, both problems were due to inadequate mixing of Ti and Al, even after triple melting.

The raw material cost for gamma is low—lower than for common titanium alloys. But remelt electrodes for casting were much more expensive since each had to be separately formulated and qualified. (titanium alloy casting electrodes are prepared from large ingots that are forged to the required diameter.)

Howmet and Oremet reviewed their ingot processes, and each developed new procedures that simultaneously led to improved aluminum control and uniformity. At the same time, larger batch sizes became possible that will reduce qualification costs. However, further cost reductions are necessary to fully exploit the opportunity presented by gamma.

Both processes rely on an observation made in castings: no significant aluminum variations are evident within castings. The difference between

castings and ingots is that the VAR process for casting melts the entire charge in a crucible, while the withdrawal VAR ingot process does not.

## Chemical analysis

After a lengthy investigation of various chemical analysis procedures, a method has been implemented that uses x-ray fluorescence (XRF) and powder metallurgy standards covering high and low aluminum levels. The repeatability of analyses on P/M material within and across different laboratories is remarkable, but different samples from the same casting are repeatable only within  $\pm 0.2$  wt. pct. The source the variation within castings is not known.

## Microstructural Development

After a considerable effort, the gamma community has arrived at general consensus about the development of microstructure in the latter stages of processing, i.e., where alpha, gamma and alpha-two phases are predominant. There is little agreement on the events during and immediately after solidification, however.

GE Corporate Research and Development recently studied a range of 48-2-2 castings. The four-fold symmetry of dendrites, when observed, confirm that beta forms from the liquid. The random orientations of the dendrites suggest that the beta grains are equi-axed and possess no texture, Figure 20. This might be expected from the low superheat of the Ti casting process and the wide solidification range of 48-2-2.

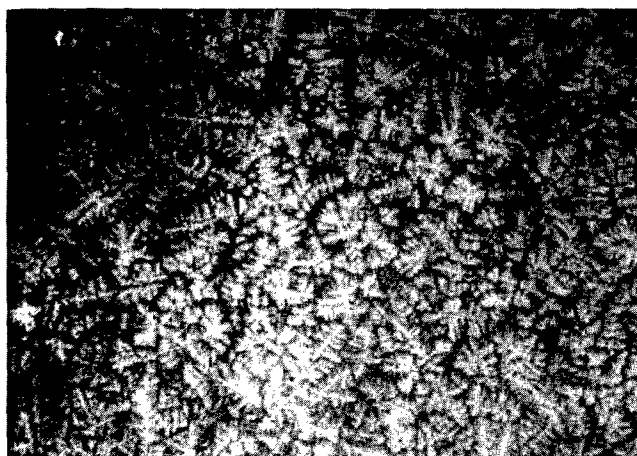


Figure 20: Dendritic segregation pattern in as-cast 48-2-2 observed in back-scattered electron contrast; macroscopic solidification direction is from bottom to top [27].

This observation is at odds with a clearly columnar macrostructure observed at room temperature, which varies in the expected manner with changes in solidification rate. Huang, et al. believes the columnar structure is produced by one of the two solid-state transformations that follow solidification [27]. The beta-to-alpha transformation is probably responsible, which follows closely behind the solidification front and is subject to the same G/R.

## HIP and heat treatment

The driving force for aluminum control and analysis is the variation in properties that occurs at otherwise fixed processing conditions. With the first heat treatment used extensively for cast 48-2-2, structure could vary from nearly equiaxed gamma to nearly lamellar. Toughness, strength and ductility were strongly affected by Al content. The nature of the toughness effect seemed obvious from the tortuous crack path evident in lamellar material. Ductility could not be firmly or unambiguously linked to any of the standard microstructural parameters (lamellar fraction and grain sizes) when working well within the duplex structure, though ductility loss could be attributed to microstructure when working at the limits. Strength seemed largely independent of those parameters, and in fact served as the best method for measuring Al.

Another issue that was addressed was the high cost of the HIP and heat treatment first used for cast gamma parts. The HIP cycle involved an unusually high temperature (1260°C) and pressures (175MPa), greatly reducing the number of vessels available. The heat treatment cycle was also long (20 hours) and hot (1300°C).

At the low end of the aluminum specification range, these treatments produced excessive lamellar fraction and low ductility. The change in the as-cast structure, which is a sort of metastable lamellar structure, appeared to occur during the first thermal exposure—the HIP cycle. It was clear that lower temperatures could promote the formation and growth of gamma grains, but the HIP temperature could only be reduced so far and still close porosity.

The thermal treatment that has been adopted takes the unusual step of applying a low temperature heat treatment cycle prior to HIP. This step, 1100°C for 5 hours, appears to age and coarsen the as-cast lamellar grains; the alpha-two in these grains is seen as a variety of irregular shapes, apparently from different coarsening mechanisms, see Figure 21.

HIP is then performed at about 1185°C for 4 hours. Since cooling rate from HIP is difficult to control, a final treatment at 1205°C for 2 hours is given. This treatment appears to form new lamellar grains, with a more conventional appearance, and may therefore increase toughness. Both heat treatments are short and relatively cool, and therefore less expensive.

The result of these steps, known as the PLL treatment [28], is a mixture of gamma grains, coarsened cast lamellar grains, and lamellar grains, Figure 21. While still dependent on aluminum level and casting solidification rate, structural variations are much reduced. The variations in most mechanical properties are also reduced, particularly ductility as shown in Figure 22, but yield strength remains strongly dependent on Al level, Figure 23.

## Factors influencing ductility

Though reduced by the PLL heat treatment, ductility variations are still seen in cast 48-2-2. The causal relationship with microstructure variations is not evident through normal metallographic evaluation. Since secondary cracks are rarely observed, and stable growth of a crack seems unlikely during tensile testing, it seems that failure originates at a single site. Therefore, a study of these sites should offer the most direct information about the causes of ductility variations.

The haphazard appearance of fracture surfaces in gamma has discouraged such studies, however. As a result, even basic questions have been left unanswered, such as whether fracture begins in gamma or lamellar grains.

Recent efforts have been successful and rewarding. Definite patterns emerged after examining initiation sites in a variety of 48-2-2 materials tested at room temperature, including cast slabs from the "six-ingot" program that provided information on the effect of aluminum and casting process. Other materials exhibiting large ductility variations were subsequently examined, providing further information on the effect of casting solidification rate. The major findings include:

- 1) Most fractures initiated internally.
- 2) Fracture initiation sites were mostly found to be associated with gamma grains, at or near interdendritic regions.
- 3) The type of initiation site could be correlated with aluminum and solidification rate, in a manner that suggests the cause of frequently observed ductility variations.

The types of sites found are discussed below.

**Interdendritic/transgranular**, Figure 24: These origins are located precisely at the point of maximum segregation in interdendritic regions. These points are high in Al, Cr, and presumably certain impurities, Figure 25. A particle of the Cr-rich B2 phase is sometimes located at this same spot, Figure 26. This type of origin was frequently seen in PCC slabs having high aluminum.

The dendritic segregation pattern is more visible in fractures of the Ta-bearing alloy NCG 359E, Figure 27 (all others shown are for 48-2-2).

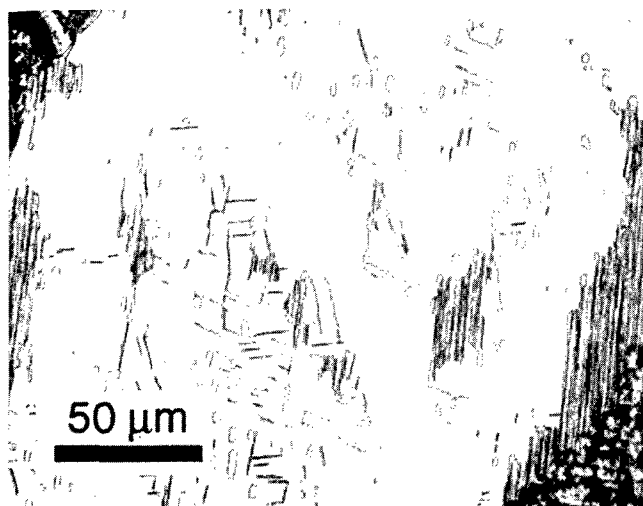
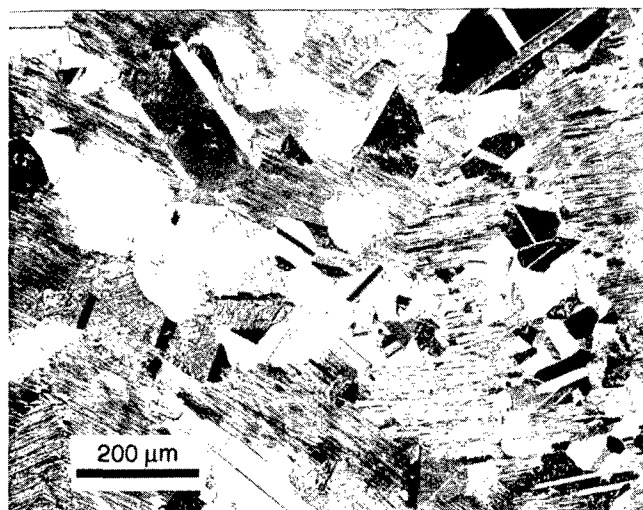


Figure 21: Examples of features present in cast 48-2-2 after PLL heat treatment; top photo shows general view, bottom photo shows morphologies of coarsened alpha-two.

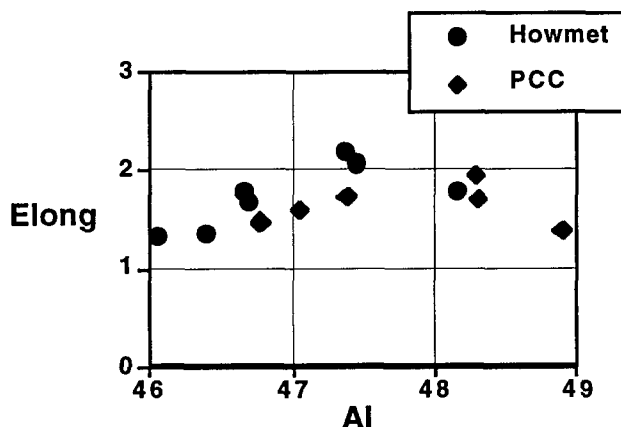


Figure 22: Effect of Al level on room temperature tensile plastic elongation, PLL heat treatment.

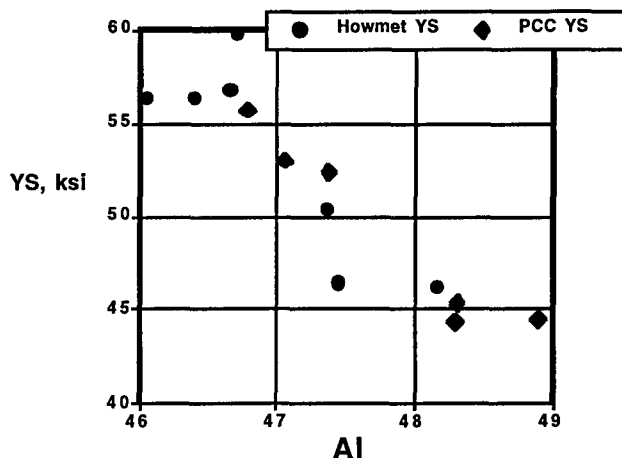


Figure 23: Effect of Al on room temperature yield strength, PLL heat treatment.

**Interdendritic/intergranular, Figure 28:** These origins are at failed boundaries among clusters of interdendritic gamma grains. The exact origin cannot be observed, but surrounding river patterns allow no other conclusion. This type of origin was frequently observed in Howmet slabs and may be associated with somewhat greater ductility than the transgranular type.

**Lamellar/intergranular, Figure 29:** This type of origin is at boundaries between lamellar grains and other grains. (This description is speculative; it is not possible to locate the origin within a lamellar grain.) This type of failure is bound to occur in fully lamellar material, of course. It has been observed only in material thought to have been cooled particularly slowly, which can exhibit very low ductility.

**Surface, Figure 30:** This origin location was only found in cast-to-size specimens that cool more quickly than the slabs from which all other observations were made. The microstructural feature at the surface may be any of the features noted above. This type for fracture is associated with very high ductility.



Figure 24: Interdendritic/transgranular fracture initiation site; top photo is of NCG 359E fracture that shows segregation clearly (all other fractures shown here are of 48-2-2).

A mapping of origin types consistent with these observations is presented in Figure 31. This is a conceptual view; solidification rate is not known quantitatively for any of the materials investigated.

This map applies to limited circumstances: room temperature fracture of ground, cylindrical tensile specimens. Elevated temperature test specimens have not been examined, but it is likely that even slightly elevated temperatures produce different behavior due to the low temperature ductility transition (about 200°C). Anything that disrupts the

residual stress from grinding (chemical milling, electropolishing, peening, exposure to high temperature, etc.) leads to surface initiation. There is evidence that rectangular specimens behave differently than round specimens, for reasons quite unknown at this time.

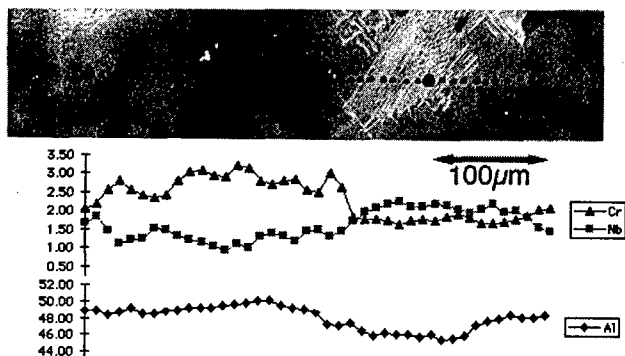


Figure 25: Microprobe analysis of segregation pattern in cast 48-2-2.

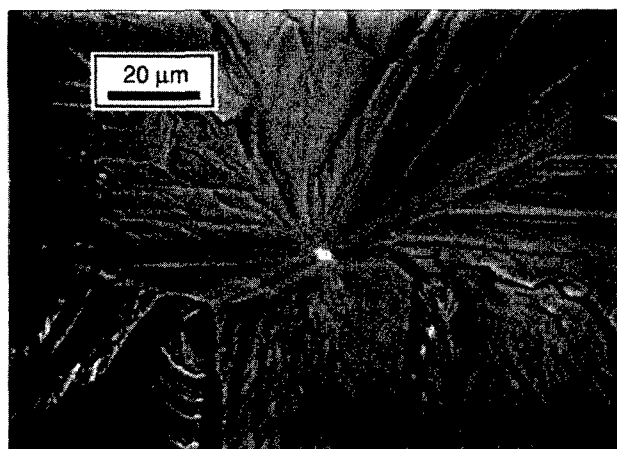


Figure 26: Interdendritic/transgranular fracture initiation site at a B2 particle.

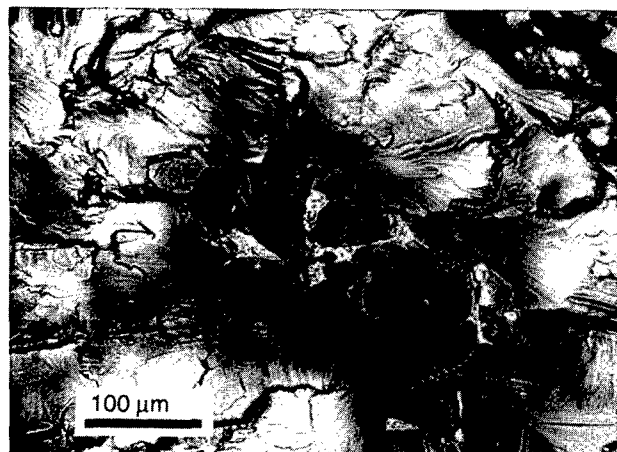


Figure 27: Interdendritic fracture initiation site associated with both B2 and a gamma grain boundary in NCG 359E; the Ta in this alloy produces a pronounced segregation pattern in BSE contrast.

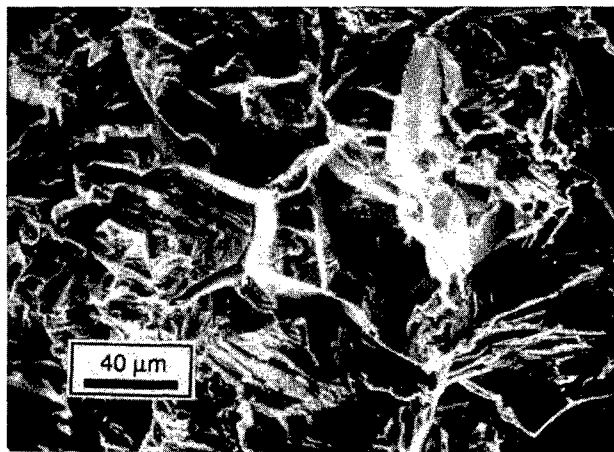


Figure 28: Interdendritic/intergranular fracture initiation site.

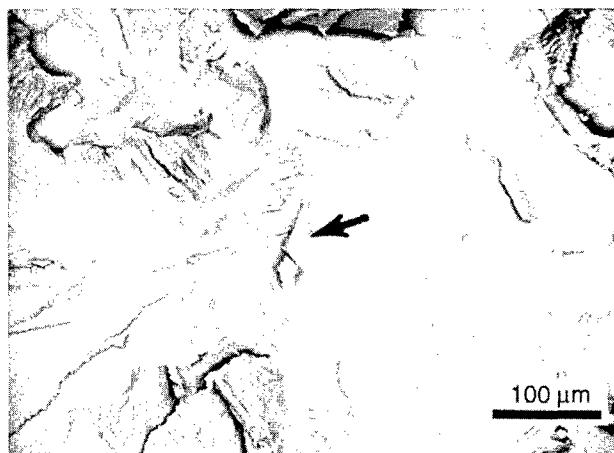


Figure 29: Lamellar/intergranular fracture initiation site (arrow indicates likely site).



## Summary

It has been a monumental task to identify the potential of a new alloy system, develop useful alloys, develop processing routes, design components, manufacture hardware and test it in engines. The entire



intermetallics community can take great pride in reaching the current state of engineering readiness of gamma.

Over the next few years, there must be a transition towards implementation, supporting fielded components, improving manufacturing processes, solving many remaining metallurgical mysteries—all the activities that keep technologists busy with conventional materials. Our goal should be to use all the new tools available to us, including communication tools, to strive for the most efficient and rapid progress in these areas.

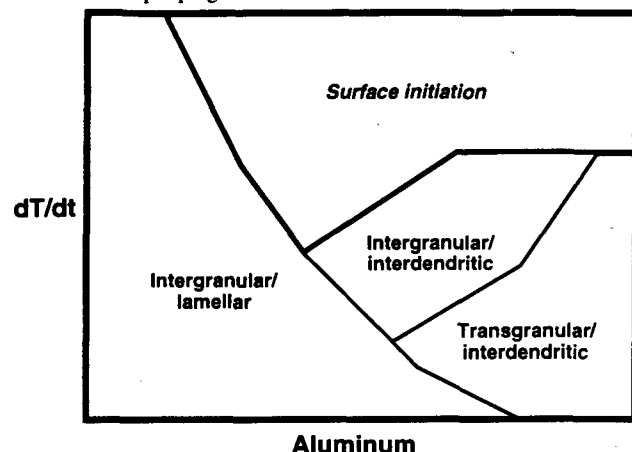


Figure 31: Conceptual mapping of fracture initiation site type in dimensions of solidification rate and aluminum level.

## Acknowledgements

The authors wish to acknowledge the contributions of PCC, Howmet, Oremet, Wyman-Gordon, and Chromalloy for process development; NASA-LeRC, M. V. Nathal, AITP program manager; Omer Erdmann, Kevin Kirkeng, Kevin Beacock and Mark Hostetler for design; John Sutcliffe, Scott Sitzman and S.C. Huang for microstructural development investigations; Paul Fink and Ken Wright for materials behavior evaluation; Susan Draper and Michael Pereira for impact testing; Tom Kauffung for technical support; and Jack Beuth, Peggy Jones, Tresa Pollock, Russell Smashey, Paul Steif, Michael Wiemer and Jim Williams for valuable technical discussions.

The financial and technical support of AFWL, NAWC-AD, AFOSR and NASA-LeRC is gratefully acknowledged.

This paper is dedicated to Robert E. Allen for his strong support of gamma implementation at GE Aircraft Engines.

## References

- C. M. Austin and T. J. Kelly, "Progress in Implementation of Cast Gamma Titanium Aluminide, Gamma Titanium Aluminides, ed. Y-W. Kim, et al., TMS, 1995, 21-32.
- Anonymous, Aviation Week and Space Technology, November 29, 1993, 37.
- B. Pettersson, et al., "Cast XD Gamma Titanium Aluminide Turbine Blade Dampers", Gamma Titanium Aluminides, ed. Y-W. Kim et al. (Warrendale, PA: TMS, 1995), 33-40.
- D. C. Stewart, "Application of Gamma Titanium Aluminides in Gas Turbine Engines", presented at Aeromat '94, Anaheim, CA, 6-9 June 1994.
- Unpublished data, GE Aircraft Engines.
- C. T. Liu, et al., "Room and Elevated Temperature Mechanical Properties of PM TiAl Alloy Ti-47-2Cr-2Nb", Gamma Titanium Aluminides, ed. Y-W. Kim, et al., TMS, 1995, 679-688.
- H. Kitagawa and S. Takahashi, Proceedings of the Second International Conference on Mechanical Behavior of Materials, Boston, MA (1976), 627-631.
- J. M. Larsen, B. D. Worth, S. J. Balsone, and A. H. Rosenberger, "Reliability Issues Affecting the Implementation of Gamma Titanium Aluminides in Turbine Engine Applications", Titanium '95 Science and Technology, Vol 1, Institute of Materials, 1996.
- C. M. Austin and T. J. Kelly, "Development and Implementation Status of Cast Gamma Titanium Aluminide", Structural Intermetallics, R. Darolia, et al., TMS, 143-150.
- P. K. Wright, personal communication, GE Aircraft Engines, March, 1997.
- S. C. Huang and M. F. X. Gigliotti, U. S. Patent 4,879,092, 1989.
- Y. G. Nakagawa et al., "Analysis of Cast TiAl Properties for Engine Materials, ed. Y-W Kim et al., Gamma Titanium Aluminides, TMS, Warrendale, PA, 1995, 415-424.
- S.L. Semiatin, et al., "Processing of Intermetallic Alloys", these proceedings, 1997.
- S. Jain, personal communication, Allison Engine Development Company, 1997.
- J.N. Fleck and M.P. Sousa, "Application of Emerging Cold Section Materials", Final Report for the Period Sep. 14, 1989 to Oct. 1, 1993, Contract No, DAAJ02-89-C-0030, Apr. 1994.
- D.E. Davidson, "Designing with Gamma Titanium - CAESAR Program Titanium Aluminide Component Applications", in R.D. Kissinger, et al., eds., Superalloys 1996 (Warrendale, PA: TMS, 1996), 545-553.
- Martin, et al., "Scale-up of Ingot Metallurgy for Wrought Gamma Titanium Aluminide", these proceedings, 1997.
- P. McQuay and D. E. Larsen, "A Case Study: Manufacturing - Performance - Cost Relationships in Gamma TiAl Castings, these proceedings, 1997.
- P. Barlotia, et al., "Cast Gamma Titanium Aluminide: Ti-48Al-2Cr-2Nb Production Ready", JOM, May 1997.
- J. Beuth, personal communication, Carnegie Mellon University, December, 1996.
- S. L. Draper, J. M. Pereira, and M. V. Nathal, HITEMP Review 1997, NASA CP-10192, Vol. II, 25.1-25.13.
- P. S. Steif et al., "Surface Damage Due to Impact and Fatigue Strength Reduction in Gamma Titanium Aluminides", these proceedings, 1997.
- C. M. Austin, T. J. Kelly and S. C. Huang, U.S. Patent 5,545,265, 1996.
- P. R. Bhowal et al., "Microstructure and Properties of a Creep Resistant Cast Gamma Titanium Aluminide", presented at ASM 3rd International Conference on High Temperature Intermetallics, San Diego, CA, 16-19 May 1994.
- P.E. Jones and D. Eylon, "Effects of Casting Conditions on Microstructure of Permanent Mold and Investment Cast Ti-47Al-2Nb-2Cr", Titanium '95 Science and Technology, Vol 1, Institute of Materials, 1996, 225-232.
- Muraleedharan, et al., "The Effect of Cooling Rate on Microstructural Development in Cast Ti-48Al-2Cr-2Nb Type Alloys", these proceedings, 1997.
- S. C. Huang, J. Sutcliffe and S. Sitzman, GE CRD, personal communication, 1996.
- T. J. Kelly et al., U. S. Patent 5,609,698, 1997.



## AUTOMOTIVE APPLICATION OF TiAl INTERMETALLICS

S.Isobe and T.Noda

Research & Development Division, Daido Steel Co., Ltd.  
2-30 Daido-cho, Minami-ku, Nagoya, Japan 457

### Abstract

As a castable TiAl for automobile components, an alloy, Ti-33.5Al-1Nb-0.5Si-0.5Cr(in wt%), has been designed to improve the oxidation resistance and the high temperature strength. Its cast structure is nearly fully-  $\gamma/\alpha_2$  lamellar and in the as-cast condition it possesses the excellent mechanical properties at RT and elevated temperatures. The near-net-shape investment castings are cast by CLV process in the ceramic molds. The exhaust engine valves are plasma carburized to enhance the wear resistance of the face and the stem. The turbocharger turbine rotors are brazed to the steel shafts. On the benches both of them have proven the higher performance attributed to the light weight and also the sufficient reliability ascribed to the higher strength. They are now being evaluated extensively in the field and also their mass production process is being substantiated.

### Introduction

An intermetallic compound, TiAl, has been highlighted as a promising heat resistant material since it possesses the higher strength and the lower density. Its specific stiffness and specific strength at elevated temperatures will exceed those of the conventional aerospace materials, Ti alloys and Ni-base superalloys, while it is free from the firing problem noticed in Ti alloys. Therefore, it is being applied to the

jet engine components(1).

The compound TiAl has also fascinated the automobile industries, who seek the exotic heat resistant materials for their engine members rotating or reciprocating at the higher speed(2 to 6). The major performance of TiAl is so attractive for them. For example the specific strength for tensile at RT and elevated temperatures and for high-cycle fatigue at elevated temperatures is superior to the conventional automobile materials, austenitic heat resistant steel and wrought Ni-base superalloys. The specific creep strength is equivalent to cast Ni-base superalloys(2). And besides the thermal fatigue life is longer than Type 304 austenitic stainless steel(7).

There have been explored the several routes to process the intrinsically brittle compound into the configuration of the various components. In the case of the ingot start, the hot working should be carried out at the lower strain rate by the isothermal forging or rolling, because its ductility is limited at the ordinary working rate even at the elevated temperatures beyond DBTT. The near-net-shape processes without the plastic deformation path are the sintering of prealloyed or elementary powders and the precision casting into the ceramic or permanent molds. The latter, especially the investment casting in the ceramic mold, is the simple and handy practice for TiAl. It can convert the TiAl molten metal directly into the complex NNS products with thin wall and full density. And the cast structure possesses the higher strength in the longitudinal direction generally

coincident with the loading axis. Both of the melting point and the reactivity of TiAl are relatively high, but its fluidity and shrinkage are equivalent to Ni-base alloys. Therefore, it is ready to cast TiAl into the similar castings through the minor modification of the well established investment casting technologies for Ni-base alloys.

Hereunder are the examples of the automotive engine components manufactured through the advanced investment casting by authors.

### TiAl for Casting

The castability is evaluated on the 2 indices, the molten metal fluidity to fill up the tip of the mold cavity labyrinth and the cracking resistance to withstand the shrinkage during solidification and cooling of the casings confined in the mold. The effect of the alloying elements was assessed in Ti- 48at% (34.2wt%) Al; the fluidity is improved by B and Zr and degraded by Si and Fe, while the cracking resistance is only impaired by B and Fe(8).

As for the castings no hot working is applicable to control nor modify the microstructure. The heat treatment should be performed in the vacuum or inert atmospheres at so high temperatures and for so long time that it will sacrifice the productivity and then push up the cost. So, authors had optimized the chemical composition of the binary TiAl to extract the inherent mechanical properties just in the as-cast condition. The obtained alloy is Ti- 33.5wt% (47.2at%) Al, which contains the slightly lower Al than the stoichiometric  $\gamma$  (TiAl), 50at% Al. Its cast structure consists of the lamellar colonies of  $\gamma$  and  $\alpha_2$  ( $\text{Ti}_3\text{Al}$ , about 20vol%) and the small amount of the equiaxed primary  $\gamma$ . The size of its colonies is smaller than the higher or the lower Al alloys. Around the equiaxed  $\gamma$  there was traced the branching of the crack propagating zigzag preferentially along the interface of  $\gamma$  and  $\alpha_2$  lamellae(9). Its elongation is 2% at RT tensile test. And the strength of the castings with 33.5wt%Al reaches maximum at all mechanical tests; tensile at RT and elevated temperatures, high-cycle fatigue at elevated temperatures and creep and creep-rupture(2). The significant anisotropy was observed for the yield stress and the tensile elongation in the poly-synthetically twinned (PST) single crystals of directional  $\gamma$  and  $\alpha_2$  lamellae(10). This anisotropy is rather beneficial in the columnar-grained conventional castings. During solidification the  $\beta$ -Ti columns grow from the rim to the core, which transform later into the  $\alpha$ -Ti through the peritectic reaction. After that the  $\gamma$  and  $\alpha_2$  lamellae develop perpendicularly to the axis of the columnar grains. In the direction parallel to the lamellae the yield stress is maximum while the tensile elongation is high enough (11). It is very convenient to design the TiAl castings, ex. the stem of the engine valves, with the well developed radial columnar structure, because the strength of the casting is the highest in the longitudinal and also loading direction.

Its near fully-lamellar structure retains the higher fracture toughness(12).

Among the several alloying elements reported to enhance the oxidation resistance(13), Nb and Si were synergistically added to the above system(14). The some portion of Si precipitates as  $\text{Ti}_5\text{Si}_3$ , which augments the creep strength. The Si treated alloy surpasses the conventional Ni-base cast superalloy, 713C, in the specific strength for 1073K-3.6Ms creep-rupture(15,16).

### Casting Technologies

In the melting of the alloy the contamination from the environments and the crucibles should be minimized as low as possible. From the point of view the alloy is generally melted in the water-cooled Cu crucible of vacuum arc, electron beam or Ar plasma skull furnaces. In the vacuum induction furnace the calcia ( $\text{CaO}$ ) crucible used to be applied, but recently the cold crucible is adopted, where the molten metal is sustained apart from the side wall of the bundle of the water-cooled Cu tubes(17). The avoidance of O pickup from the crucible refractory results in the increase of the mean value and the decrease of the scatter range in the tensile strength and consequently improves the reliability of the TiAl castings(18).

The ceramic molds are prepared in the oxide refractories. For the simple and small castings the zircon ( $\text{ZrSiO}_4$ ) face coat is serviceable, but it is prone to the interaction with the molten metal inducing the blow holes in the body and the Si-rich brittle layer on the surface. For the complex or large ones the zirconia ( $\text{ZrO}_2$ ) or the calcia ( $\text{CaO}$ ) coat is recommended(19). The molten metal is poured down by the gravity or the centrifugal force, or sucked up into the cavity of the mold.

### Processing after Casting

As mentioned before, no heat treatment is exercised to the castings. However, the HIP process is occasionally employed to squeeze down the x-ray detectable pores along the center shrinkage in the castings with the extremely high length/diameter ratio, ex. the stem of engine valves. For cutting or grinding the standard corundum (alumina) wheels are usable without the so-called grinder crack.

The ordinary WC-base cemented carbide tips are appropriate to turn or drill the casting, while the machining rate should be set lower than for Ti alloys in order to prevent the micro-chipping or cracking and then secure the integrity of the machined surface(20).

The various surface modification techniques have already been developed. The nitriding is effective to enhance the wear resistance of the face and the tip of the engine valves(6). The plasma carburizing generates the very hard  $\text{Ti}_3\text{AlC}$  surface layer, which significantly improves the wear resistance of the castings(21). If necessary the face of

the valves is overlaid by the hard- face alloy powders under Ar plasma flame, which is common for the valves in heat resistant steel.

The oxidation resistance is raised by the calorizing (Al diffusion coating)(2), the hard Cr plating, and the air or vacuum plasma spraying of MCrAlY(22).

### Heterogeneous Joining

The conventional fusion welding is not so easy to apply to the TiAl castings.

If the local service temperature is low enough, the brazing with Ag-base fillers is recommended to join the TiAl turbine rotor with the case-hardening steel shaft of the turbocharger. When they are joined by the friction welding the buffer plate of Ni-base superalloys, ex. Inconel 751, should be inserted between them(2). Onto the tip of the valve the thin chip of the high-C martensitic heat resistant steel is bonded by the induction-heating TLPDB(23). On cooling in the bonding cycle the chip is automatically hardened to HRC 60 and then it provides the tip with the excellent wear resistance.

### Examples of Automotive Components

The following 2 items were the examples of the trial products cast by the CLV (Counter Gravity Low- Pressure Vacuum Casting) process, in which the molten metal is sucked up into the cavity of the ceramic mold with the high permeability.

#### Exhaust Valves(18)

In order to increase the power output and to decrease the fuel consumption of the reciprocal automotive engines, it is vital to boost the rotation speed and to reduce the friction loss. The weight saving of the components is beneficial especially for the valves reciprocating at a high speed. The service temperature of the intake valves is under 770K, so the conventional martensitic heat resistant steel can be replaced with a Ti alloy, Ti-6Al-4V. However, as the metal temperature of the exhaust valves reaches 1070K or higher, the modern material is indispensable to trim the weight and to ensure the high temperature strength equivalent to the austenitic heat resistant steel or Ni-base superalloys.

Figure 1 shows the valves cast in an intermetallic compound TiAl, one of the promising candidate materials. The tailored alloy is designated RNT004, Ti-33.5Al-1Nb-0.5Si-0.5Cr (in wt%), where the combination of Nb and Si, additional Si and minor Cr are added to improve the oxidation resistance, creep strength and RT ductility, respectively.

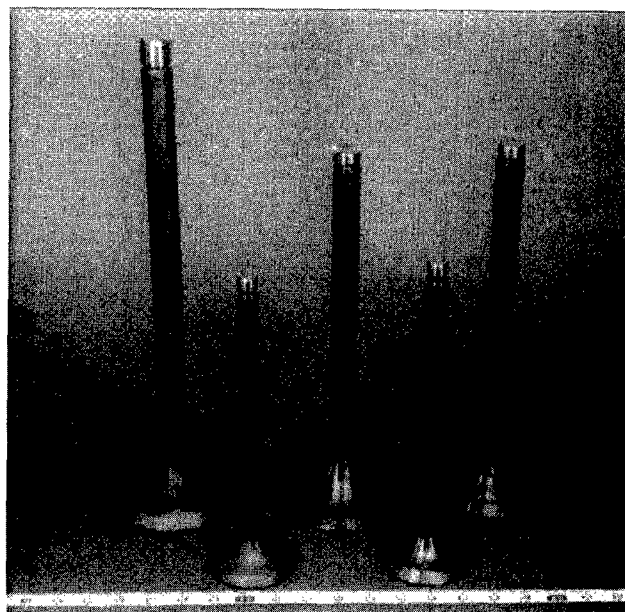


Fig.1 TiAl exhaust engine valves

Hereunder is the comparison of the primary properties between the RNT004 castings and the conventional wrought alloys for the exhaust valves, an austenitic heat resistant steel 21-4N (Fe-21Cr-4Ni-9Mn-0.5C-0.4N) and a Ni-base superalloy Inconel 751 (Ni-15.5Cr-7Fe-2.3Ti-1.2Al-0.9Nb). Table I shows the physical constants. It is attractive that the density of TiAl is less than half of the conventional austenitic alloys' and TiAl's thermal conductivity is so high.

Figures 2, 3 and 4 show the high temperature hardness, tensile properties and the high-cycle fatigue strength at elevated temperatures, respectively.

Table I Physical properties of exhaust valve materials

Properties	Temp. K	RNT004	21-4N	INCONEL 751
Density g/cm <sup>3</sup>	RT	3.9	7.9	8.1
Mean thermal expansion coefficient x10 <sup>-6</sup> /K	473	9.8	14.7	12.5
	673	10.8	16.7	13.6
	873	11.3	18.1	14.8
	1073	11.7	18.5	15.8
Thermal conductivity W/(m•K)	298	22.1	13.4	11.3
	673	24.5	20.1	13.7
	873	27.6	24.7	20.9
	1073	30.2	29.7	26.2
Young's modulus GPa	298	171	198	213
	673	160	168	191
	873	154	151	180
	1073	147	134	161

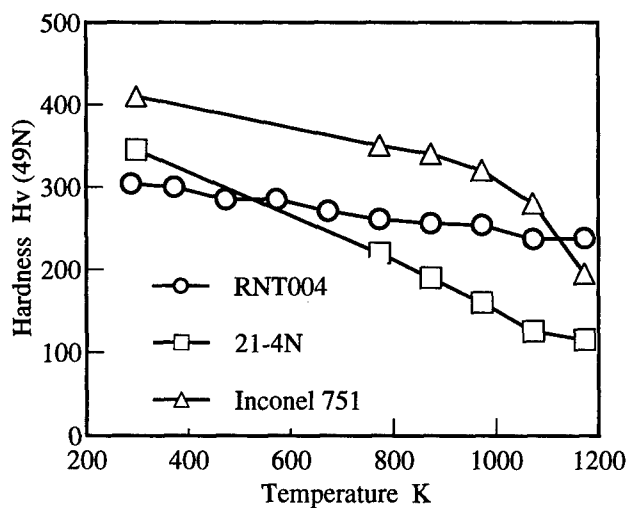


Fig.2 Hot hardness of exhaust valve materials

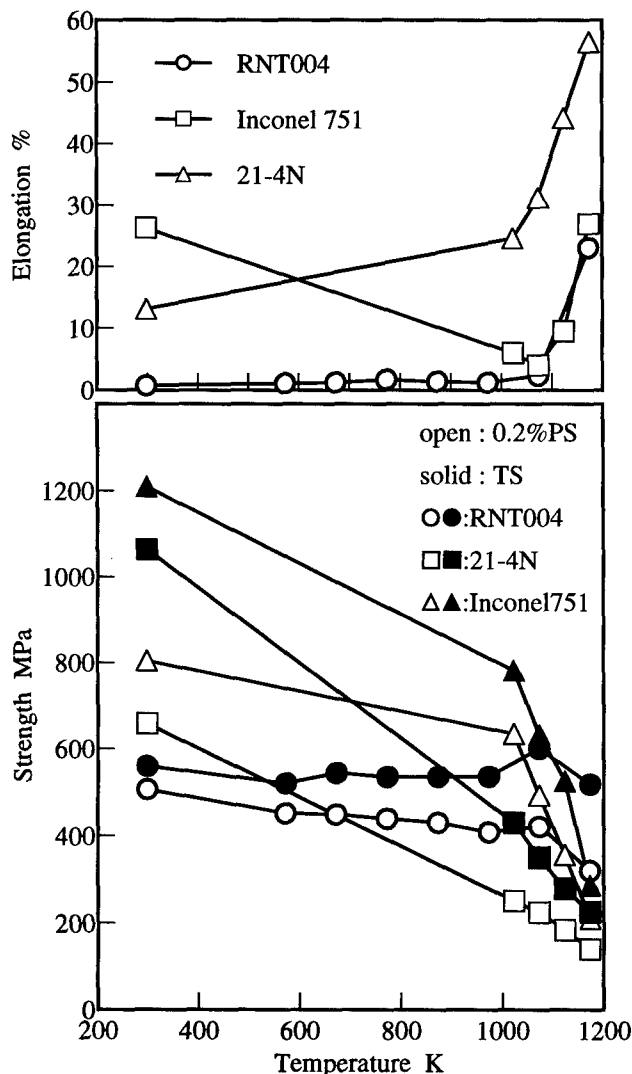


Fig.3 Tensile properties of exhaust valve materials

Commonly in all of them, with the test temperature going up, the decrement in the strength of TiAl is insignificant and at higher temperatures TiAl excels the conventional alloys. Fig. 5 shows the creep-rupture strength, which of TiAl is superior to a reference material Inconel 751 and also equivalent to Waspaloy for jet engine components.

The CLV investment cast valves were HIPped to press down the central shrinkage pores. In order to protect the face and the tip against the wear the surface of the valves was modified by the plasma carburization. Fig.6 shows the wear test results for the pins of TiAl on the disk of a hardened bearing steel, which proves that the surface thin layer of  $Ti_2AlC$  is so effective to enhance the wear resistance.

For the endurance test the above valves were mounted in a gasoline engine, 2.5l, L6, DOHC and twin-turbo. After running for 150hrs at 6,400rpm, the loss due to wear and

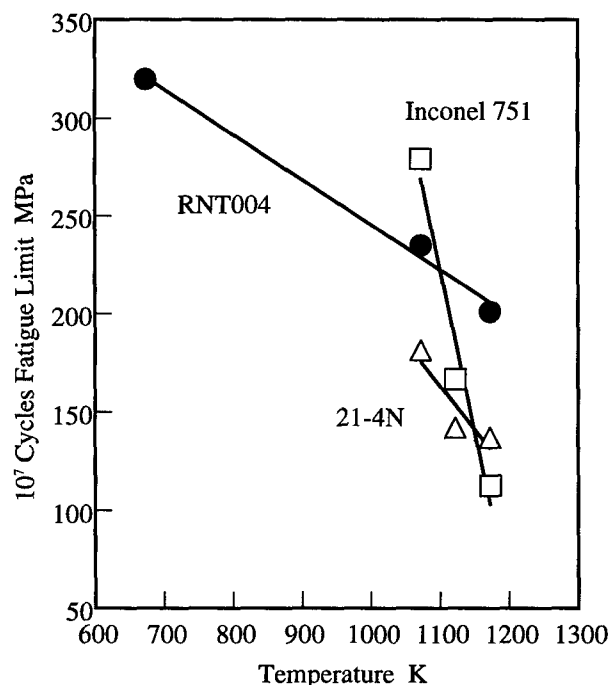


Fig.4 Rotating bending fatigue properties of exhaust valve materials

oxidation of the valves was confirmed negligible small, which demonstrates that the reliability of RNT004 cast valves is sufficient to be put into practical use.

And also the performance test was carried out for another engine, 3.5l, 12V, DOHC and natural aspiration. On a short run the rotation speed topped 13,000rpm. The reduction of the weight in the valvetrain is so advantageous to raise the critical speed for the surging that the maximum speed of the engine with the TiAl valves will be able to reach 14,000rpm.

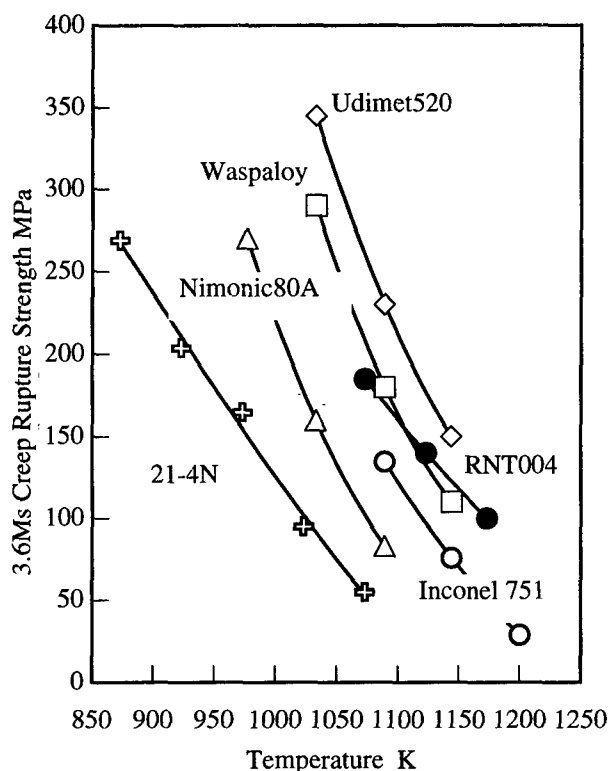


Fig.5 Creep rupture strength of exhaust valve materials and Ni base superalloys for jet engines

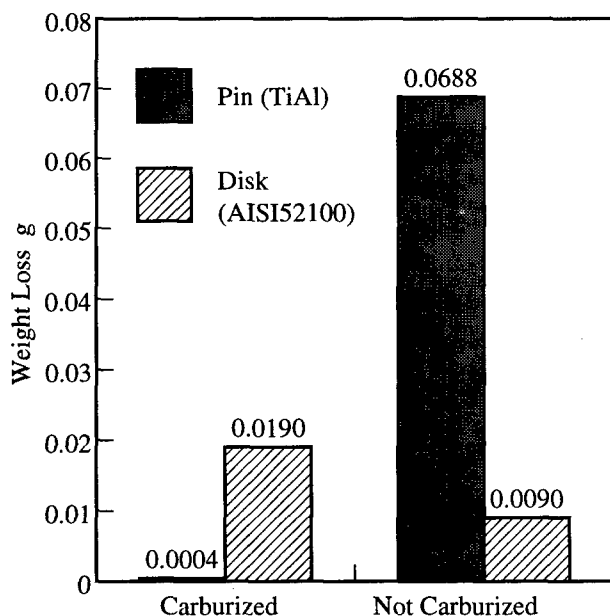


Fig.6 Wear resistance of plasma carburized TiAl

## Turbine Rotors of Turbochargers(2)

Figure 7 shows the some rotors for gasoline or diesel engines cast into the molds with the identical dimensions to Ni-base superalloy rotors. The minimum wall thickness is only 0.35mm for the small rotors.

The following is the hot-spin test results, where the high speed gas from the kerosene burner drove the turbochargers mounted with TiAl rotors. Their tip diameter, 47mm, and airfoil configuration were the dead copy of the conventional 713C rotors (Ni-12Cr-4Mo-2Nb-6Al-0.8Ti-0.1C). Comparing with the 713C rotors, the boost time from idling, 34,000rpm, was shortened by 16% to the transient speed, 100,000rpm and by 26% to the cruising speed, 170,000rpm, respectively. The reduction in the weight of the rotors contributes to lesson the so-called turbo-lag, and consequently to improve the accelerator response of gasoline engines and to diminish the particulate in the exhaust gas from diesel engines.

The speed to burst was over 210,000rpm for both of TiAl and 713C rotors, while it happened to be 170,000rpm for a ceramic  $\text{Si}_3\text{N}_4$  rotor.

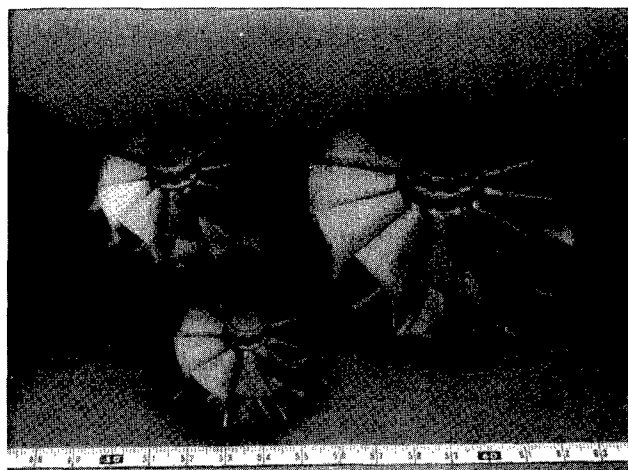


Fig.7 TiAl rotors for turbochargers

## Conclusions

The processing technologies for an intermetallic compound TiAl have already been developed to select the proper alloy, cast into NNS products, modify their surface and join the castings to the heterogeneous materials. And also the high performance of TiAl castings has already been proven as exhaust valves and turbine rotors.

In order to advance the marketing of them, it is essential to assess the durability of the components on the automobiles for a long term in the anticipated or unexpected environments(24). Besides it is inevitable to establish the production route in large quantities at the lower cost(25,26).

## References

1. M. Arai, R. Imamura, K. Matsuda, Y. Nakagawa, and T. Hosokawa, "Development of TiAl Blades for Large Low Pressure Turbine," Materia Japan, 36(1997), 394-396.
2. Y. Nishiyama, T. Miyashita, S. Isobe and T. Noda, "DEVELOPMENT OF TITANIUM ALUMINIDE TURBOCHARGER ROTORS," High Temperature Aluminides and Intermetallics, ed. S.H. Whang, C.T. Liu, D.P. Pope and J.O. Stiegler (Warrendale, PA : TMS,1990), 557-583.
3. B. Bondarev, N. Anoshkin, A. Molokov, A. Notkin and D. Elagin, "DEVELOPMENT OF PRODUCTION TECHNOLOGY FOR INTERMETALLIC TiAl-BASE ALLOY COMPONENTS AND EVALUATION OF POSSIBILITY OF THEIR APPLICATION," Intermetallic Compounds-Structure and Mechanical Properties JIMIS-6, ed. O. Izumi (Sendai : Japan Institute of metals, 1991), 1009-1014.
4. W.E. Dowling, Jr., J.E. Allison, L.R. Swank and M.A. Sherman, "TiAl-Base Alloys for Exhaust Valve Applications," SAE Technical Paper Series 930620, (1993), 31-38.
5. H. Shyamoto and T. Morikawa, "Application study of TiAl intermetallic compound for engine valves," Intermetallic Compounds - Their Potential as High Temperature Structural Materials, ed. O. Izumi, S. Hanada and M. Yamaguchi (Sendai : Japan Institute of Metals, 1996), 424-430.
6. S. Isobe, "Application of TiAl to Automobile Precision Casting," *ibid.*, 431-432.
7. T. Noda, T. Iikubo and S. Isobe, "Thermal Fatigue Properties of TiAl Intermetallic Compounds," Report of the 123rd Committee on Heat-Resisting Metals and Alloys, 31(2)(1990), 279-288.
8. S. Takagi, A. Kato and C. Oouchi, "The Factors Affecting Microstructure and Properties of  $\gamma$ -base Alloys in Investment-Cast Processing," Intermetallic Compounds - Their Potential as High Temperature Structural Materials, ed. O. Izumi, S. Hanada and M. Yamaguchi (Sendai : Japan Institute of Metals, 1996), 272-280.
9. S. Isobe, T. Iikubo and T. Noda, "The Optimum Al Content and Microstructure for Titanium Aluminide Castings," Titanium & Zirconium, 37(1989), 67-73.
10. H. Inui, "Plastic Anisotropy of TiAl/Ti<sub>3</sub>Al Two-Phase Lamellar Alloys in Relation to Their Crystal Structures and Microstructures," Intermetallic Compounds - Their Potential as High Temperature Structural Materials, ed. O. Izumi, S. Hanada and M. Yamaguchi (Sendai : Japan Institute of Metals, 1996), 83-92.
11. T. Noda, T. Iikubo, S. Isobe and N.S. Stoloff, "Effects of structural anisotropy of cast TiAl on mechanical properties," Preprint of the Spring Meeting of Japan Institute of Metals, 110(1992), 324.
12. S. Mitao, "Microstructural Effect on Fracture Toughness of  $\gamma$ -based Titanium Aluminides," Intermetallic Compounds - Their Potential as High Temperature Structural Materials, ed. O. Izumi, S. Hanada and M. Yamaguchi (Sendai : Japan Institute of Metals, 1996), 138-147.
13. K. Shibue, "Oxidation Properties of TiAl Intermetallic," *ibid.* 179-184.
14. K. Maki, M. Shioda, M. Sayashi, T. Shimizu and S. Isobe, "Effect of silicon and niobium on oxidation resistance of TiAl intermetallics," Material Science and Engineering, A153(1992), 591-596.
15. T. Noda, M. Okabe, S. Isobe and M. Sayashi, "Silicide Precipitation Strengthened TiAl," *ibid.*, A192(1995), 774-779.
16. T. Noda, M. Okabe and S. Isobe, "Creep Properties of Silicide-Precipitation Hardened  $\gamma$  TiAl Alloys," Intermetallic Compounds - Their Potential as High Temperature Structural Materials, ed. O. Izumi, S. Hanada and M. Yamaguchi (Sendai : Japan Institute of Metals, 1996), 214-218.
17. N. Demukai, "Present Status and Prospect of Titanium Precision Casting Technology," SOKEIZAI, 34(9)(1993), 7-13.
18. K. Maki, A. Ehira, M. Sayashi, T. Sasaki, T. Noda, M. Okabe and S. Isobe, "Development of a High-Performance TiAl Exhaust Valve," SAE Technical Paper Series 96030, (1996), 117-125.
19. T. Degawa, "Melting and Refining Technology of High Purity Metals and Alloys by Using Calcia," Bulletin of the Japan Institute of Metal, 27(6)(1988), 466-473.
20. S. Yamamoto, "Cutting Mechanism and Machined Surface Region in Intermetallic Compounds," Intermetallic Compounds - Their Potential as High Temperature Structural Materials, ed. O. Izumi, S. Hanada and M. Yamaguchi (Sendai : Japan Institute of Metals, 1996), 311-314.

21. T. Noda, M. Okabe and S. Isobe, "Hard surfacing of TiAl intermetallic compound by plasma carburization," Material Science and Engineering, A213(1994), 157-161.
22. T. Shimizu, T. Iikubo and S. Isobe, "Cyclic oxidation resistance of an intermetallic compound TiAl," Material Science and Engineering, A153(1992), 602-607.
23. T. Shimizu and M. Miyajima, "Liquid Phase Diffusion Bonding of Carbon Steel Bars for Machine Structural Use," Preprint of the National Meeting of Japan Welding Society, 53(1993), 372-373.
24. M. Nakamura, "Environment Embrittlement of TiAl Base Alloys," Intermetallic Compounds - Their Potential as High Temperature Structural Materials, ed. O. Izumi, S. Hanada and M. Yamaguchi (Sendai: Japan Institute of Metals, 1996), 169-178.
25. W.E. Dowling, Jr., W.T. Donlon and J.E. Allison, "Development of TiAl-Based Automotive Engine Valves," Materials Research Society Symposium Proceedings, ed. J. Horton, I. Baker, S. Hanada, R.D. Noebe, and D. Schwarz, (Pittsburgh, Pennsylvania : Material Research Society ,1993), 757-767.
26. P.E. Jones, W.J. Porter III, M.M. Leller and D. Eylon, "Microstructure/Property Studies Supporting Development of Low Cost Process for TiAl Automotive Valves," *ibid.*, 769-774.

## SURFACE DAMAGE DUE TO IMPACT AND FATIGUE STRENGTH REDUCTION IN GAMMA TITANIUM ALUMINIDES

P.S. Steif, J. W. Jones\*, T. Harding\*, M.P. Rubal, V.Z. Gandelsman, ‡N. Biery, ‡T.M. Pollock

Department of Mechanical Engineering,  
‡Department of Material Science and Engineering  
Carnegie Mellon University, Pittsburgh, PA 15213, USA.  
\* Department of Material Science and Engineering  
University of Michigan, Ann Arbor, MI 48109, USA.

### Abstract

The effect of surface damage on the subsequent performance of gamma TiAl is an issue of critical concern in contemplating its incorporation into aircraft engine components. This concern stems mainly from the relatively low ductility and low impact resistance of gamma alloys. Surface damage can be attributed to various sources, including small particle impacts during service and damage due to manufacturing or handling on the shop floor. Relatively little is known about the detrimental effects of surface damage, particularly on gamma alloys. This paper describes efforts to understand and quantify the damage so introduced and to assess the levels of such damage at which fatigue strength is impaired.

### Introduction

The ability to characterize and predict the dependence of low and high cycle fatigue (LCF and HCF) on damage is critical to the gas turbine engine industry. A recent study by Cowles [1] found that manufacturing induced damage and foreign object damage (FOD) make up a significant proportion of the causes of HCF failures in gas turbine engines. The same study found that of all failures caused by distress in the engine, the largest proportion resulted from HCF, and the majority of these were located in compressor blades.

Impact damage on blades in aircraft engines has received some attention in the literature [2]. An example of such an impact is depicted in Figure 1, which shows a superalloy blade removed from service. This blade had apparently received an impact on its leading edge; at least two other blades from the same set received similar impacts. Note that

the impact produced significant local plastic straining, resulting in a "dent" at the leading edge of the blade.



Figure 1. Superalloy blade damaged in service by small particle impact.

However, no obvious signs of cracking are present, presumably due to the reasonably high ductility of the superalloy. The nature of the damage that would be suffered in a similar event with a cast gamma TiAl alloy, given a uniaxial



tensile ductility typically less than 2%, is presently not well understood. Also, since a localized impact event such as that shown in Figure 1 is not likely to cause immediate failure, there is a need to understand how such damage would affect the subsequent fatigue response of the material.

This paper reports on several aspects of an investigation which has focused on the relations between impact events, damage and fatigue strength. Specifically, we consider two forms of surface damage: damage due to high speed impacts of small particles and damage due to low speed impacts associated, for example, with a tool dropped on a component during assembly. In the case of simulating the dropped tool, our choice of configuration is one of several that can be envisioned and is intended merely to be representative. In simulating the damage due to small particles, we are guided by a parallel study [3] in which small particles are fired at specimens that are shaped to resemble a turbine blade leading edge. This study has revealed several forms of damage: the dent on the impacted surface, a crack on the rear surface and cracks running through the dent on the impacted surface. We have chosen to focus here on the rear surface cracking and to study a simpler configuration which exhibits the same damage: impact of a particle perpendicular to a thin plate.

Finally, we note the importance of inter-relating each aspect of the potential failure process: the impact event, the extent of the physical damage incurred and the resultant degradation in fatigue strength. In the case of in-service damage due to high speed particles impacting blade leading edges, it is not possible to directly observe the damage. Therefore, it is important to be able to predict the stresses, strains and extent of damage associated with an impacting particle. Conversely, while the nature and geometry of "shop-floor" damage may be difficult to predict, the opportunity for visual inspection prior to service exists. In this case it is then most important to be able to predict the remaining fatigue life associated with the observed damage. For these reasons, this paper focuses on two related aspects of damage and fatigue: (i) prediction of the stresses and strains associated with high speed impacts on relatively thin plates and correlation with the resultant damage and (ii) characterization of the damage produced by the low-speed impact of a sharp wedge, and quantification of the associated reduction in fatigue strength. The extent of degradation of fatigue properties caused by high speed particles will be of interest in future studies. Currently, it is our assumption that the fatigue strength reduction associated with high speed particle damage will resemble, in some measure, the reduction induced by low speed impacts.

#### Materials and Experimental Procedures

##### Materials

Two different gamma TiAl alloys were utilized in this investigation. The first alloy, with composition Ti-47.3Al-2.2Nb-0.5Mn-0.4W-0.4Mo-0.23Si [4], will subsequently be referred to as Alloy WMS. This material was investment cast into plates measuring 3mm x 11mm x 75mm. Following casting the material was subjected to a HIP treatment consisting of 1260°C and 172 MPa for 4 h, followed by a heat treatment of 1010 °C for 50 h. The resulting microstructure, shown in the SEM-BSE image in Figure 2, was fully lamellar in character with significant

amounts of the  $B_2$  and  $\alpha_2$  phases, along with some degree of residual segregation. The second alloy was also investment cast with a final composition of Ti-47.9Al-2.0Cr-1.9Nb [5]; this alloy will be referred to as "48-2-2". Plates measuring 12.6mm x 100mm x 140mm were subjected to a pre-HIP treatment of 1093°C for 5 h, HIP'ed at 1205°C for 4 h at 172MPa and given a subsequent heat treatment of 1205°C for 2 h, followed by rapid cooling. The resultant microstructure, Figure 3, was near-gamma in character, with an average grain size of about 70  $\mu\text{m}$  and about 6 vol% of  $\gamma$ - $\alpha_2$  lamellar colonies. High speed impact studies have been conducted with the WMS alloy, while low speed wedge impacts and fatigue studies to date have focused on the 48-2-2 alloy.

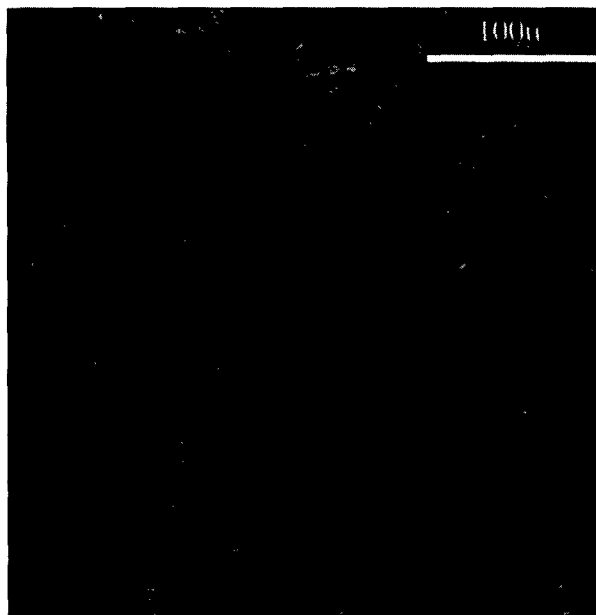


Figure 2. Microstructure of WMS alloy used for high speed particle impacts.



Figure 3. Microstructure of Alloy 48-2-2 used for wedge impacts and fatigue studies.

Rectangular flat plates of varying thicknesses for impact studies and dogbone-shaped specimens for fatigue studies were electro-discharge machined from the cast plates. The fatigue specimens had overall dimensions of 11mm x 3mm x 136mm and rectangular gage sections measuring 3mm x 6mm x 30mm. All samples were low stress ground, subjected to conventional mechanical polishing by hand with 600 grit paper and then electropolished in a solution containing 300ml methanol, 175ml n-butanol and 30ml perchloric acid maintained at -50°C.

#### Impact Procedures

High speed impact damage was produced using a ballistic impact facility at the NASA Lewis Research Center. Steel spherical projectiles were accelerated down a steel barrel by the release of compressed helium. The velocity of the projectile was measured at the end of the barrel by breaking two laser beams a known distance apart. The spheres were 1.587 mm in diameter and had velocities ranging from 152 m/s to 305 m/s. The particle impinged normal to the plate in the thickness direction and at its center.

Low speed impact tests were carried out using an instrumented, low speed drop weight impact apparatus (Dynatup Mini-Tower impactor and 930-I data acquisition system). A dynamic load cell measures the contact force as a function of time, with the contact time typically being on the order of  $10^{-3}$  s. For the experiments reported here, the impactor tip was a sharp, hardened steel wedge (60° included angle). Impacts of various energies were produced using a weight of 2.2 kg dropped from various heights. Each specimen was impacted twice within the gage section with the same impact energy. This was done in order to produce two potential sites for fatigue failure. Therefore, when the specimen fails at one impact site, the other site is still intact for further observation.

#### Damage Characterization

Optical and scanning electron microscopy (SEM) were used to characterize the damage incurred on the front and back surfaces of the rectangular plates subjected to the high speed impacts. The depth of the impact on the front face as well as the distribution and lengths of cracks on the front and back faces of the plate were measured. Finally, the use of electropolished specimens permitted variations in the intensity of slip within individual grains to be monitored.

Damage associated with low speed impacts of the 60° wedge-shaped indenter was characterized by scanning electron and optical microscopy surveys of the specimen surfaces. Damage is defined in terms of the depth and shape of the notch produced by the impact, by the extent of the plastic deformation zone produced and by the number, length and type of the cracks produced within the plastic deformation zone. Figure 4 shows a schematic representation of the damage zone and the primary types of damage produced; an SEM image of a typical damage zone from one of the impacts examined in this study is shown in Figure 5. Notch depth,  $D$ , and notch root radius,  $\rho$ , were measured for each impact. The size of the plastic zone was estimated by measuring the farthest extent of visible slip lines in gamma grains from the root of the notch using an optical microscope. All cracks were identified as either intergranular or transgranular and their location relative to the notch tip was noted. For the

range of impact energies examined, cracking always occurred at the root of the notches. We have defined an effective crack length,  $a_{eff}$  as the sum of the notch depth and the length of the crack connected to the notch tip; this is also illustrated in Figure 4.

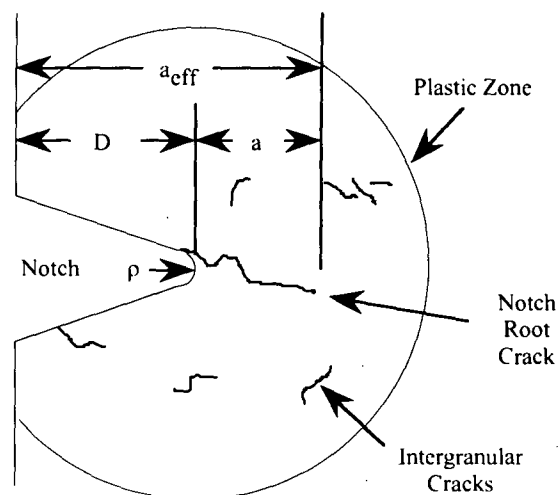


Figure 4: Schematic of a damage zone following low speed impact with a 60° wedge indenter.



Figure 5: Micrograph of a representative damage zone where notch root and incompatibility cracks are visible within the plastic zone.

## Fatigue Testing

To determine the effect of the damage due to low speed impact on fatigue strength, the step test method was used. This method involved testing a specimen at a particular stress level for a pre-determined number of cycles, or a block [6]. In these experiments the block consisted of  $10^5$  cycles. If the block ended and failure had not occurred, the stress was increased by an incremental amount, 10 MPa in this study. This procedure was continued until the specimen failed. Using this technique, fatigue strength, rather than fatigue life, is estimated. Denh and Amhof [7], working with smooth bar specimens of steam turbine steel, found that results of step tests with blocks greater than  $10^4$  cycles were within the scatter bands of conventional tests. In this study all tests were conducted on a servo-hydraulic fatigue test machine at room temperature in air. Tests were run at a frequency of 20 Hz and with a load ratio of  $R = 0.1$ .

## Finite Element Analysis

Finite element simulations of the high speed, small particle impact experiments were based on the idealized problem of a circular, simply supported plate impacted perpendicularly (without friction) by a rigid sphere with mass density  $7850 \text{ kg/m}^3$ . The mass density of the simulated gamma TiAl plate was set to  $3830 \text{ kg/m}^3$ . The calculations employed the commercial code ABAQUS EXPLICIT (Hibbit Karlsson and Sorenson, Inc.). Stress-strain behavior at high strain rates is necessary for the finite element simulations of high speed impacts. Accordingly, dynamic tests at strain rates from  $0.001 \text{ s}^{-1}$  to  $1300 \text{ s}^{-1}$  were conducted at Los Alamos National Laboratories utilizing a Split-Hopkinson Pressure Bar [8]; these tests were conducted on the 48-2-2 alloy. The results of these tests were then fit to a Zerilli-Armstrong model [9] which involves a logarithmic dependence on strain rate and a power law dependence on strain. For the WMS alloy, the static yield stress is approximately 200 MPa higher than that of the 48-2-2 alloy to which the fit was made. One coefficient in the Zerilli-Armstrong fit represents essentially the static yield stress. Therefore, we raised that coefficient by 200 MPa, and assumed the same hardening behavior and strain-rate sensitivity as was observed in the 48-2-2 material, yielding a stress-strain relation of the form:

$$\sigma = 470 + 660 \exp[-0.00350T + 0.0001750 T \ln(\dot{\epsilon})] + 3000 \epsilon_p^{0.960} \quad (1)$$

where the stress  $\sigma$  is in MPa,  $\dot{\epsilon}$  denotes the strain rate,  $\epsilon_p$  is the plastic strain, and  $T$  is temperature (taken to be 298K). This uniaxial behavior was generalized to multiaxial states through the Mises stress invariant. The elastic modulus and Poisson ratio were taken to be 192 GPa and 0.3, respectively, and the transition in the stress-strain curve from the elastic regime to the fully plastic regime was assumed to have the same shape as for the fit gamma alloy.

Besides accounting for the material strain-rate dependence, the response of the plate to these impacts is strongly affected

by the plate's inertia. In fact, the duration of the impact event is less than the time period for the fundamental plate bending mode; for this reason, the size of the plate and type of supports at its edge are unimportant. Accordingly, the dynamic terms in the equations of motion must be included. With its time integration method, ABAQUS EXPLICIT is suited to efficient calculations of problems in which inertia needs to be accounted for. Meshes of various types have been used to assess convergence; the results to be presented below are based on a mesh of 2304 elements.

## Results and Discussion

### High Speed Particle Impacts

High speed impacts on thin plates of gamma produce damage in the form of cracks on the rear surface. A typical damage pattern is shown in Figure 6; this impact corresponds to a particle with an initial velocity of 229 m/s impinging on a plate 2.25 mm thick. The pattern of crossing lines are associated with a grid from a strain mapping technique; results from such an analysis will be reported in the future.

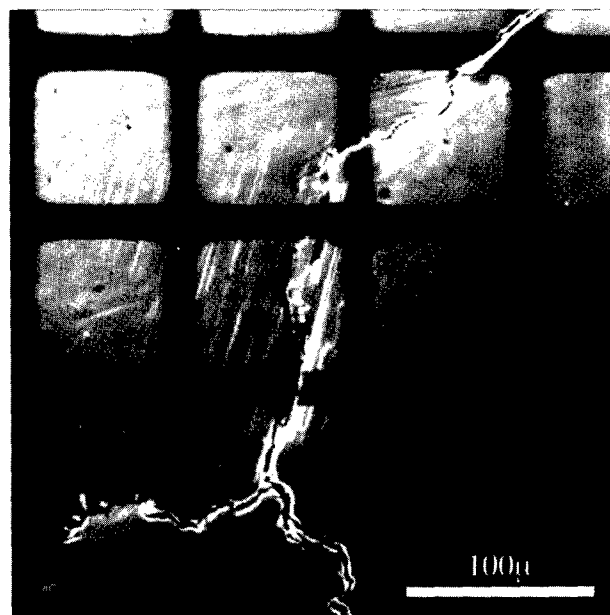


Figure 6. Typical damage on rear surface of plate subjected to high speed impact (plate thickness = 2.25 mm, particle speed 229 m/s).

The center of impact on the front face of the plate corresponds approximately to the point on the back face at which the three cracks branch away. The uniaxial ductility of a sample from this heat of the WMS alloy for a strain rate of  $8.3 \times 10^{-5} \text{ s}^{-1}$  was 0.5%. On the rear face beneath the center of the impact, observations of slip traces indicated intense but inhomogeneous local straining, suggesting that some grains suffer strains significantly higher than the uniaxial ductility. On the front face, the impact produces a very sharply defined

crater. Just outside the crater, intense plastic strains and occasional small intergranular cracks were detected.

A finite element analysis of this impact was performed. The impact event occurs over a time scale of approximately 1  $\mu$ s. Depicted in Figure 7 are the contact force, the indentation depth, the circumferential strain at the rear surface immediately below the point of impact, and the deflection at that point. To allow these quantities to be plotted on the same figure, each has been normalized by its peak value. There is a slight time delay between contact at the top and the development of strains at the rear surface; this is associated with the time for the stress wave to travel through the specimen thickness. Small oscillations in the rear surface deflection and strain towards the end of the impact event are associated with elastic vibrations. Extensive calculations for this set of problems, together with approximate analyses based on a sphere impacting a half space [10], have shed light on the dependence of the rear surface strain on the parameters of the impact event. These will be reported in the future.

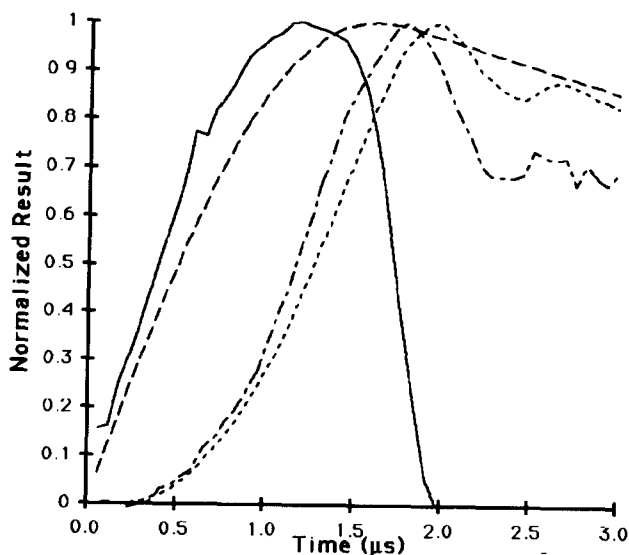


Figure 7. Results of impact analysis (force —: peak value = 3226 N; indentation — —: peak value = 0.22 mm; rear surface circumferential strain - · - ·: peak value = 0.83%; rear surface deflection · · ·: peak value = 0.018 mm).

Here, we focus on the results for the impacted plate shown in the Figure 6. From the finite element calculations, we extracted stresses and strains on the rear surface at the instant in time at which they reached their maximum values. The circumferential (hoop) strain exceeds the radial strain everywhere except at the center where they are equal. From these results, contours of constant hoop strain were extracted and superimposed on a micrograph of the cracking pattern (Figure 8). For purposes of drawing the contours, we assumed the center of the impact to be at the point where the cracks connect to each other. The strain at the center was predicted to be 0.83%. Besides the major cracking in the center, one can see that isolated cracks (indicated by arrows) have initiated away from the center. The three longer cracks were

mixed intergranular and transgranular in character, while the isolated cracks further away from the center were only observed along grain boundaries. The isolated transgranular cracking occurs approximately out to the radius corresponding to a strain of 0.7%.

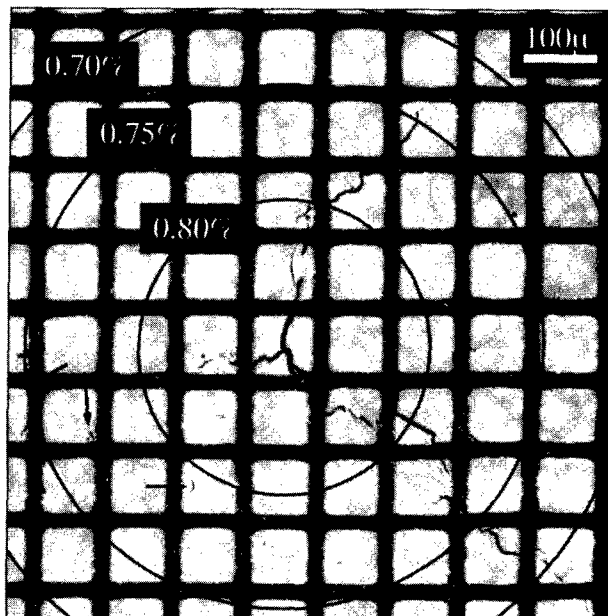


Figure 8. Contours of circumferential strain superposed on micrograph of rear surface damage for a plate impacted at high speed. The arrows indicate small intergranular cracks.

The evidence of high strains in a grain at the center of the impact and the rather sporadic appearance of cracks away from the center where the strains are less suggest the following picture. A given region of the material subjected to a macroscopically uniform strain would undergo a highly heterogeneous distribution of strains as one looks from grain to grain. This is not surprising given the anisotropy of the slip and twinning processes at the grain level in gamma TiAl. Thus, at a given macroscopic strain, individual grains will have a distribution of strains with mean equal to the macroscopic strain. If the strain in an individual grain happens to be sufficiently high - probably much higher than the uniaxial ductility of 0.5% - a crack might initiate at one of its grain boundaries. For a macroscopic strain of 0.7%, the statistical distribution of strains is such that relatively few grains would exhibit a strain sufficient to initiate a crack: hence, the sparseness of cracks at the radial position corresponding to a macroscopic strain of 0.7%.

The hoop and radial stresses on the rear surface were also extracted from the finite element analysis. It was found that the maximum tensile stress (the hoop stress) remained at a constant value of approximately 700 MPa from the center out to a radial distance of 0.8 mm (the radius of the impacting sphere). Of course, the radial stress decays in such a way as to be consistent with the hoop and radial strains. By contrast, the hoop strain decreases to a value of 0.48% at a radial distance of 0.8 mm. The rapidly diminishing cracking as one

moves outward tends to be more consistent with the strain variation than with the stress variation. Consistent with the picture described above, one is tempted to infer that crack initiation is more tied to strain conditions than to stress conditions, although more evidence is necessary to firmly establish this.

### Low-Speed Wedge Impacts

The nature and extent of damage produced by low speed wedge impact were correlated with impact energy and peak load produced during impact. Notch depth and effective crack length correlated well with peak impact load, but not as well with impact energy.

Cracks emanating from the notch were predominately transgranular and cracks remote from the notch were predominately intergranular, similar to the cracking patterns observed in the high speed particle impacts. The remote, intergranular cracks, generally ranged from 5 to 100  $\mu\text{m}$  in length. They appear to result from the stresses produced by strain incompatibilities across grain boundaries in the highly deformed regions. The number of these remote, intergranular cracks was moderately dependent on peak impact load.

As described subsequently, the critical damage parameters for fatigue strength were notch depth and effective crack length. The magnitude of these damage parameters correlated well with peak impact load, as shown in Figure 9. Figure 9 shows that the effective crack length increases at a faster rate than the notch depth, although both increase with the peak impact load. Examination of additional impactor geometries is necessary before the generality of these observations can be assessed.

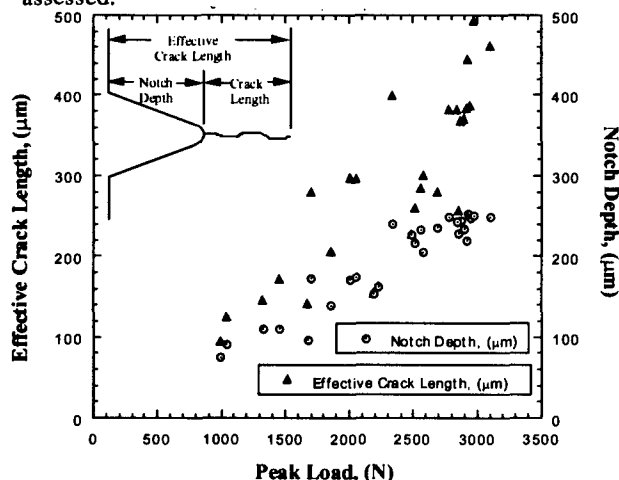


Figure 9: Correlation between peak impact load and damage parameters

The geometry of the notch following impact consists of a notch root with radius on the order of 10-30  $\mu\text{m}$ , and a notch depth of 80-250  $\mu\text{m}$  as indicated in Figure 9. From this geometry, the calculated stress concentration factor,  $k_t$ , would be in the range of 10-12 [11], which is inconsistent with the

experimental results of step tests. Smith and Miller [12] proposed that the notch produces an enhanced stress only within a radius,  $r$ , of the notch tip, where  $r$  is given by:

$$r = 0.13\sqrt{\rho D} \quad (2)$$

$\rho$  is the root radius, and  $D$  is the notch depth. Within this region, the stress concentration factor is employed in determining the stress intensity factor of a crack emanating from the notch root. However, beyond this region, the crack behaves as if its stress intensity were based upon the sum of the notch depth and the notch root crack length, that is, the effective crack length,  $a_{\text{eff}}$ . This is because as the notch root radius tends to zero, the notch can be treated as a crack with length,  $D$ . For the notches in this study,  $r$  was found to vary from 4 - 12  $\mu\text{m}$ , which is relatively small compared to the size of the majority of the notch root cracks. Therefore, it was presumed that the stress intensity factor,  $K_I$ , could be determined using the effective crack length according to:

$$K_I = 1.12 \sigma \sqrt{\pi(a+D)} = 1.12 \sigma \sqrt{\pi a_{\text{eff}}} \quad (3)$$

From this equation a threshold stress can be determined using long-crack fatigue crack growth data. This model assumes that the notch root crack is a through thickness crack. This approximation simplifies further examination of threshold-based life prediction models, work which is currently underway.

### Fatigue of Wedge-Impacted Specimens

Results of the step tests indicate that as the peak impact load increases, the fatigue failure strength decreases as seen in Figure 10. Step tests were also conducted on two undamaged specimens. At high impact loads there is nearly a 37% loss in fatigue strength relative to that of undamaged specimens. As the impact load decreases, the fatigue strength smoothly approaches that of the undamaged specimens. These results are also shown in Figure 10.

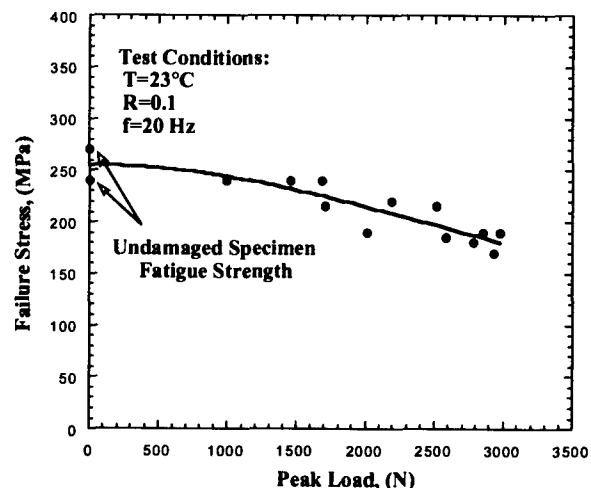


Figure 10: Effect of impact peak load on fatigue failure strength of gamma TiAl

Predictions of fatigue strength reductions or residual fatigue life will require an understanding of the role of critical damage in the fatigue failure process. One simplistic, yet practical approach to developing fatigue life models may be to use fatigue crack threshold  $\Delta K_{th}$  determined from standard fatigue crack growth tests as a measure of fatigue strength. In its simplest form such an approach would neglect short crack growth effects and residual stresses produced by impact.

We examine a threshold-based approach for the 48-2-2 alloy by comparing the fatigue strengths of impact-damaged TiAl to fatigue threshold stresses calculated from known long-crack fatigue crack growth thresholds. From Eq (3) and using the measured effective crack lengths,  $a_{eff}$ , produced by impact, the applied stress required to achieve threshold for each damage event can be calculated. The threshold values used are from a fatigue crack growth study conducted by Worth and Larsen [13] on the same 48-2-2 alloy. The results of these comparisons are shown in Figure 11 in a form modified somewhat from that popularized by Kitagawa and Takahashi in 1976 [14]. In this manner fatigue failure stress is plotted against effective crack length. The agreement between the data and the threshold-based calculation is quite good. This is not unreasonable, given the strong dependence of fatigue crack growth rate on  $\Delta K$  exhibited by 48-2-2 and similar TiAl alloys and implies that very little fatigue life is spent in crack propagation.

There are several assumptions in the approach used here that merit consideration. First, since most of the cracks produced by impact damage are shorter than 500  $\mu m$  it may not be possible to ignore small crack effects. Short cracks often propagate faster and have lower fatigue crack growth thresholds than long cracks. One explanation for this is that crack shielding effects, such as crack closure, are absent in short cracks [15]. As an approximation to short crack effects, threshold stresses have been calculated using Eq. (3) and closure-corrected fatigue crack growth thresholds measured for long cracks by Worth and Larsen [13]. These calculations are plotted as the dashed line in Fig. 11 to show the magnitude of the correction that might be expected. It is interesting to note that as crack size decreases, there is better agreement between the experimental data and the fatigue strengths predicted using the closure-corrected data.

Additional factors which will require future consideration are the role of the plastic deformation zone at the base of the notch produced by impact and the more accurate determination of crack sizes and shapes produced by impact. In the former case residual compressive stresses would be expected to increase fatigue strength, especially for cracks which were contained within the damage-induced plastic zone. This would lead to higher measured fatigue strengths for a given crack size. For the latter, approximations of surface cracks as through thickness cracks requires refinement. As described in the section on fractography, the presence of intergranular fracture in the specimen interiors indicates that impact damage is not limited to the surface region.

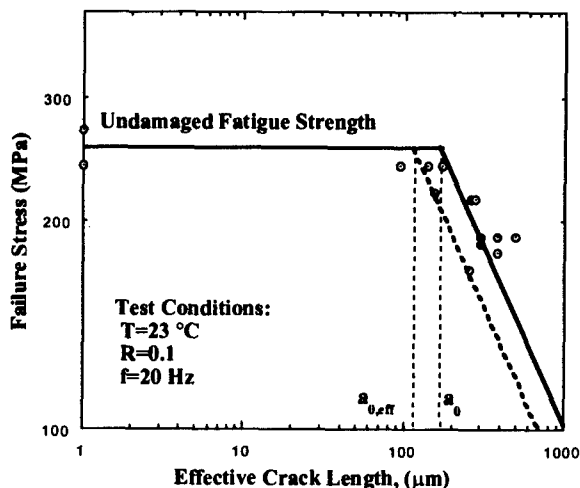


Figure 11: Kitagawa plot of damaged gamma TiAl assuming a through thickness crack ahead of a notch.

### Fractography of Fatigue Specimens

Figure 12 shows the fracture surface of a specimen subjected to a wedge impact followed by failure in a step test. This fractograph, taken near the notch root (seen on left), shows evidence of both transgranular cleavage and intergranular fracture.

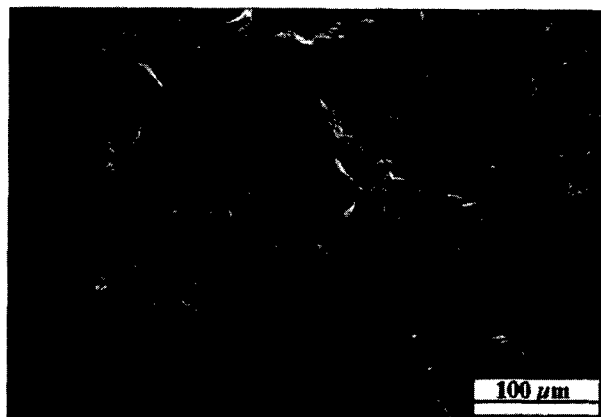


Figure 12: Fractograph of damaged specimen tested at room temperature showing evidence of intergranular fracture near the root of the notch, seen on left of image.

It is well known that at temperatures below the ductile-to-brittle-transition temperature (DBTT), duplex gamma microstructures tend to fracture in fatigue by means of transgranular cleavage across  $\gamma$  grains, and by either trans-, inter- or intra-lamellar fracture in lamellar regions [16,17]. Figure 13 shows a typical fatigue fracture surface from an undamaged specimen. The fracture surfaces of undamaged specimens reveal no evidence of intergranular fracture when tested at room temperature. The existence of intergranular fracture regions in damaged specimens suggests that these areas are generated by the impact event.

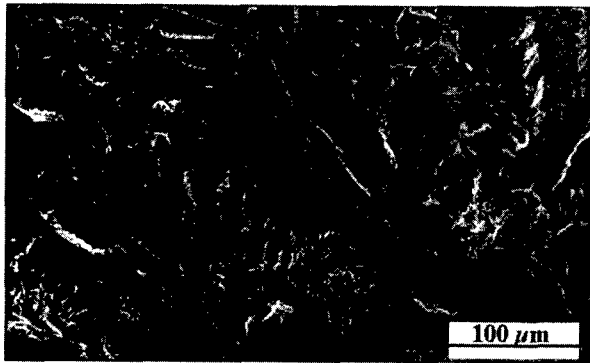


Figure 13: Fractograph of fatigue region of an undamaged specimen tested at room temperature showing transgranular cleavage as the primary mode of crack advance with no signs of intergranular fracture.

The existence of intergranular fracture regions on the fracture surface confirms the earlier statement that the cracks within the plastic zone away from the notch are generated by an incompatibility between the strains along the boundary between two unfavorably oriented grains. Furthermore, these regions may reveal some information regarding the shape and size of internal cracks created by the impact. The difficulty with this approach, however, is that the notch root crack is thought to be primarily transgranular in nature. This makes it difficult to make quantitative measurements of the notch root crack length, which tends to govern fatigue behavior in these specimens.

### Conclusions

1. A method of simulating the damage associated with high speed impact of small particles has been developed. Finite element calculations have been performed to estimate the strains prevailing during the dynamic impact event.
2. A method of simulating one possible form of shop-floor damage has been developed which allows for reliable control of damage parameters, such as notch depth and effective crack length.
3. For the high speed impacts, there is cracking in the regions of highest strain at the center of the impact, but only sporadic cracking outwards from the center. Strains in excess of the uniaxial ductility were necessary to initiate cracking locally.
4. Cracking due to high speed impacts appears to be more controlled by levels of strain than by levels of stress.
5. Fatigue strengths of wedge impacted specimens have been shown, through the use of step fatigue tests, to correlate well with an effective crack length defined as the sum of the notch depth and the longest crack connected to the notch.
6. Initial studies indicate that a fatigue crack growth threshold-based approach may be important in predicting the influence of damage on fatigue strength and fatigue life.

### Acknowledgments

The authors appreciate the assistance of several collaborators: G.T. Gray III who conducted the high strain rate tests, J. M. Pereira who conducted the high speed impact tests, and K. Muraleedharan who assisted with the microstructural observation. Useful discussions with C. M. Austin, J. L. Beuth, L. L. Rishel, S. L. Draper, M.V. Nathal, B. W. Worth, J. M. Larson, J. Lasalle and R. Bellows are gratefully acknowledged. This research has been supported by AFOSR/PRET Program on Gamma Titanium Alloys under Grant F49620-95-1-0359.

### References

- [1] B.A. Cowles, "High Cycle Fatigue in Aircraft Gas Turbines - an industry perspective," *Int. J. of Fracture*, 80, 1996, pp. 147-163.
- [2] T. Nicholas, J.P. Barber, R.S. Bertke, "Impact Damage on Titanium Leading Edges from Small Hard Objects," *Experimental Mechanics*, Vol. 20, No. 10, 1980, pp. 357-364.
- [3] S. L. Draper, J. M. Pereira, and M. V. Nathal, HITEMP Review 1997, NASA CP-10192, Vol. II, pp. 25-1 to 25-13.
- [4] P.R. Bhowal, H.F. Merrick and D.E. Larsen, Jr., *Mater. Sci. Eng. A192/193*, (1995), pp. 685 - 690.
- [5] S.C. Huang, U.S. Patent 5,076,858, (1991).
- [6] J.A. Collins, *Failure of Materials in Mechanical Design*, John Wiley and Sons, New York, 1993.
- [7] J. Denh and S. Amhof, "Determination of the High Cycle Fatigue Strength with a Load-Increasing Single-Specimen Technique," *Fatigue '96: Proc. of 6th Int. Fatigue Cong.*, Vol. III, G. Lütjering and H. Nowack, eds., Pergamon Press, 1996, pp. 1967-1972.
- [8] P.S. Follansbee, *High Strain Rate Compression Testing - The Hopkinson Bar*, 9th edn. Vol. 8, Am. Soc. Metals, Metals Park, Ohio, 1985, pp. 198-203.
- [9] F.J. Zerilli and R.W. Armstrong, "Dislocation-mechanics-based Constitutive Relations for Material Dynamics Calculations," *J. Appl. Phys.*, Vol. 61, 1987, pp. 1816-1825.
- [10] K.L. Johnson, *Contact Mechanics*, Cambridge University Press, Cambridge, 1985.
- [11] R.E. Peterson, *Stress Concentration Factors*, John Wiley and Sons, New York, 1974.
- [12] R.A. Smith and K.J. Miller, "Prediction of Fatigue Regimes in Notched Components," *Int. J. of Mech. Sci.*, Vol. 20, 1978, pp. 201-206.
- [13] B.D. Worth and J.M. Larsen, Personal Communication, 1-15-97.
- [14] H. Kitagawa and S. Takahashi, "Applicability of Fracture Mechanics to Very Small Cracks or the Cracks in the Early Stage," *Proc. of 2nd Int. Conf. on Mechanical Behavior of Metals*, Boston, MA, 1976, pp. 627-631.
- [15] J.C. Newman, Jr., "Modeling Small Fatigue Crack Behavior," *Fatigue '93*, Vol. I, J. Bailan and J. Dickson, eds., EMAS, 1993, pp. 33-44.
- [16] W.O. Sobojevo, J.E. Deffeyes and P.B. Aswath, "Investigation of Room- and Elevated-Temperature Fatigue Crack Growth in Ti-48Al," *Materials Science and Engineering*, A138, 1991, pp. 95-101.
- [17] S.J. Balsone, B.D. Worth, J.M. Larsen, and J.W. Jones, "Fractographic Study of Fatigue Crack Growth Processes in a Fully Lamellar  $\gamma$ -TiAl Alloy," *Scripta Metallurgica et Materialia*, Vol. 32, No. 10, 1995, pp. 1653-1658.

# EFFECTS OF ALLOYING ON THE MECHANICAL PROPERTIES OF GAMMA-BASED TITANIUM ALUMINIDES

W.O. Soboyejo, C. Mercer Y. Ni and A.B.O. Soboyejo

Department of Materials Science and Engineering, The Ohio State University,  
2041 College Road, Columbus, OH 43210

## Abstract

An overview of detailed studies of the effects of alloying and microstructure on the fatigue and fracture behavior of gamma-based titanium aluminides will be presented. Multiple linear regression expressions will be derived for the prediction of the combined effects of alloying/interstitial elements, microstructure and temperature on basic mechanical properties. The multiple regression expressions are analyzed within the context of linear superposition concepts.

## Introduction

Gamma-based titanium aluminides are currently being considered for near-term applications in the aerospace and automotive industries [1-3]. This is due largely to their attractive combinations of elevated-temperature strength retention and oxidation resistance in the intermediate temperature regime between ~ 650-815°C. Unfortunately, the risks associated with the structural applications of gamma alloys remain high due to their brittle fracture characteristics at temperatures below ~ 650-700°C [1-4]. Our current knowledge of microstructure/property relationships in gamma-based alloys is also limited [1, 2, 5-7]. There is, therefore, a need for the development probabilistic mechanics approaches for the prediction of risk/reliability in gamma-based alloys. There is also a need for the development of quantitative approaches for the prediction of the relationships between composition/microstructure/ temperature and fracture properties/reliability of gamma-based titanium aluminides.

The current paper presents the results of recent efforts to employ linear regression analysis and multiparameter models to study the effect of composition, microstructure and temperature on the basic mechanical properties (yield/ultimate tensile strength, ductility and fracture

toughness) of gamma-based titanium aluminide intermetallics. Simple Hall-Petch and modified Hall-Petch equations are then obtained for a range of experimental gamma alloys using multiple linear regression analysis. The paper highlights the need for employing multidisciplinary mechanics, materials and statistical approaches in ensuring the safe application of gamma-based titanium aluminide alloys.

## Experimental Procedures

The ingot metallurgy alloys employed in this study were supplied by Duriron, Dayton, OH. The 88mm diameter ingots were produced by triple vacuum-arc-remelting (VAR) techniques. The atomic compositions of the ingots are presented in Table I. The ~ 300mm long ingots were extruded at Wright Patterson Air-Force Base, Dayton, OH, using reduction ratios of 10:1 or 14:1. All the ingots were extruded at 1343°C. These extruded duplex gamma alloys were subjected to two sets of heat treatments designed to change the volume fractions of lamellar and equiaxed grains, as well as the grain/packet sizes [3]. The first set of heat treatments involved recrystallization at different temperatures above the eutectoid temperature (1150 or 1250°C), prior to annealing for 4 or 100h at 982°C (below the eutectoid temperature). The second set of heat treatments involved only annealing sequences below the eutectoid. These included: annealing at 982°C for 4h or 100h, and an empirical three-stage heat treatment, HTC = 982°C/4h/AC + 704°C/8h/FC + 815°C/24h/AC (AC = Air Cool and FC = Furnace Cool), which has been shown to result in attractive combinations of room- and elevated-temperature properties in a wide range of gamma alloys [3]. It is important to note here that the elevated-temperature properties of the different alloys were not determined in the as-extruded conditions due to inherent microstructural instabilities of the alloys at the test temperature (815°C). A detailed analysis of the microstructural features of these as-extruded and heat treated duplex gamma alloys is presented in Ref. 6.

Structural Intermetallics 1997

Edited by M.V. Nathal, R. Darolia, C.T. Liu, P.L. Martin,  
D.B. Miracle, R. Wagner, and M. Yamaguchi  
The Minerals, Metals & Materials Society, 1997



Smooth cylindrical tensile specimens (3mm diameter X 25mm gage length) and single edge notched (SEN) bend fracture toughness specimens (6mm X 6mm X 50mm blocks with central notches) were then fabricated from the extrusions. The specimens were fabricated using electro-discharge machining (EDM) techniques. The initial notch-to-width ratios, d/w, were ~ 45 in the SEN specimens. After machining, tensile tests were performed at 25 and 815°C under strain control. The tensile specimens were deformed continuously to failure at a strain rate of  $5 \times 10^{-4} \text{ s}^{-1}$ . The elevated-temperature specimens were allowed to "soak" for 30 minutes prior to tensile testing. The fracture toughness tests were conducted at room-temperature in accordance with ASTM-E399 specifications. The SEN bend specimens were loaded monotonically to failure at a loading rate that corresponded to a stress intensity factor increase rate of  $1 \text{ MPa}\sqrt{\text{m}} \cdot \text{s}^{-1}$ . Grain size measurements were carried out on optical micrographs obtained from polished samples of these alloys using the linear intercept method.

#### Multiparameter Model

A new multiparameter model is proposed for the prediction of the effects of multiple variables on mechanical properties in this section. The mathematical model will be used to predict mechanical properties, Y, of intermetallic compounds based on TiAl, as functions of known independent variables  $X_1, X_2, \dots, X_k$ , obtained from experimental mechanics data.

$$\left( \frac{Y}{Y_0} \right) = \prod_{i=1}^k \left( \frac{X_i}{X_{i0}} \right)^{\alpha_i} \quad (1)$$

In expression (1),  $X_{10}, X_{20}, \dots, X_{k0}$  are the reference independent variables, which correspond respectively to each of the independently random variables,  $X_1, X_2, \dots, X_k$ ; and each reference random variable has the same physical units as the corresponding independent random variable. Furthermore,  $Y_0$  is the reference variable which corresponds to the dependent random variable Y;  $Y_0$  also has the same physical units as the corresponding dependent variable, Y. In the statistical model for the regression analysis,  $Y_0 = \alpha_0$ ; and  $\alpha_1, \alpha_2, \dots, \alpha_k$  are the regression constants which will be determined from experimental mechanics data. For this particular work, the assumption is also made that

$$|X_{10}| = |X_{20}| = \dots = |X_{k0}| = 1.0 \quad (2)$$

Therefore, equation (1) reduces to

$$Y = \alpha_0 \prod_{i=1}^k X_i^{\alpha_i} \quad (3)$$

Linearizing equation (3), we have

$$\ln Y = \ln \alpha_0 + \sum_{i=1}^k \alpha_i \ln X_i \quad (4)$$

Equation (4) yields the expression which has been used in the multiple linear regression analysis. Experimental mechanics data give the results for the mechanical property, Y, of interest, and the corresponding values of the independent variables  $X_1, X_2, \dots, X_k$ .

#### Regression Analysis

Equation (4) can also be expressed in the following linearized form [8]:

$$Y = \alpha_0 + \sum_{i=1}^k \alpha_i X_i \quad (5)$$

where

$$Y = \ln y$$

$$\alpha_0 = \ln \bar{\alpha}_0$$

$$X_i = \ln x_i \text{ and } X_0 = 1$$

Equation (7) can now be used to determine the values of the constants  $\alpha_0, \alpha_1, \dots, \alpha_k$ ; from known experimental mechanics data for Y and the corresponding values of  $X_i$ s from a given set of data of size n. In order to achieve this, it is necessary to find a mathematical expression for the sum Q of the total squares of the errors of prediction from a given set of the n experimental mechanics data. This is given by:

$$Q = \sum_{i=1}^n \left( Y_i - \sum_{p=0}^k \hat{\alpha}_p X_{pi} \right)^2 \quad (6)$$

The desirable results for the estimated values of  $\hat{\alpha}_p$ s are those which give the least value for Q in equation (6). These can be obtained from the following equations [8]:

$$\frac{\partial Q}{\partial \alpha_p} = 0 \text{ for } p = 0, 1, 2, \dots, k \quad (7)$$

These give the (k+1) normal equations which are of the form:

$$\sum_{i=1}^n X_{qi} \left( Y_i - \sum_{p=0}^k \hat{\alpha}_p X_{pi} \right) = 0 \quad (8)$$

Let the matrix  $\sum_i X_{pi}X_{qi}$  be represented by

$$a_{pq} = \sum_i X_{pi}X_{qi} \quad (9)$$

and

$$Z_q = \sum_i Y_i X_{qi} \quad (10)$$

Then the normal equations can be expressed as

$$\sum_{p=0}^k a_{pq} \hat{\alpha}_p = Z_q \quad (11)$$

Inverting the matrix  $a_{pq}$ , we get  $a^{pq}$ , hence we have:

$$\hat{\alpha}_p = \sum_q a^{pq} Z_q \quad (12)$$

Hence, estimates of the unknown  $\hat{\alpha}_p$  values can be obtained. In view of the complexity involved in solving for the values of the constants  $\hat{\alpha}_p$ s, a standard computer program was used to estimate the constants from the experimental data.

Another important element of this statistical derivation is the quantity which is referred to as the coefficient of multiple correlation. This measures the combined importance of the several independent factors, as a means of explaining the difference in the dependent factor. A value of one indicates perfect correlation, while a value of zero indicates no correlation.

Furthermore, partial correlation coefficients measure the correlation between the dependent factor and each of the several independent factors. Thus, they eliminate the linear tendency of the remaining independent factors to obscure the relationship.

The exponents and coefficients obtained from the multiple regression analysis are summarized in Table II. It is important to note here that these are strictly valid only for the range of data that were used as inputs in the current study. Extrapolations beyond the current data field may therefore result in significant errors of predictions. In any case, some general trends may be discerned by careful analysis of the results presented in Table II.

First, it is important to note here that the relative magnitudes of the exponents provide a weighted measure of the relative contributions of the different variables to the different properties. In this case, the results shown in Table

II indicate that all of the above properties are most strongly affected by the Ti content when the Al nominal content is fixed at 48at%. However, it should be noted here that a different result could be obtained if the Al content is varied. The current results also indicate that the other alloying and the interstitial elements have only a small effect on mechanical properties in the range that was examined in this paper.

However, the effects of microstructure are somewhat more significant. The 0.2% offset yield strength exhibits a clear dependence on lamellar volume fraction,  $\theta_L$ , whilst the ultimate tensile strength and the plastic elongation to failure are apparently unaffected by lamellar volume fraction in the range of duplex alloys/microstructures that were examined. However, the properties were found to depend strongly on the average grain/lamellar packet size as discussed in the next section.

### Hall-Petch Behavior

The plots of yield/ultimate strength, fracture toughness and plastic elongation to failure versus the average equiaxed/lamellar packet size,  $d^{-1/2}$ , are presented in Figs. 1 to 5. These show clearly that a direct linear relationship exists between all measured mechanical properties and  $d^{-1/2}$ , indicating Hall-Petch behavior for yield strength, tensile strength, fracture toughness and ductility in gamma-based alloys with both fully lamellar and duplex microstructures. Hall-Petch behavior is also observed at 25 and 815°C (Figs. 1-5). These results, therefore, show that the average grain/lamellar colony size is a primary parameter that controls most of the important mechanical properties of gamma-based titanium aluminide intermetallics. This is contrary to results in the literature [1, 9] which suggest that the lamellar spacing is the primary microstructural parameter that controls the mechanical properties of duplex  $\alpha_2+\gamma$  gamma alloys.

The basic mechanical properties of the gamma alloys examined in this study may, therefore, be fitted to simple Hall-Petch equations. In the case of the yield strength,  $\sigma_y$ , the Hall-Petch equation is given by [10, 11]:

$$\sigma_y = \sigma_0 + k_y d^{-1/2} \quad (13)$$

where  $d$  is the average equiaxed/lamellar packet size,  $\sigma_0$  is a lattice friction strength and  $k_y$  is a measure of strengthening contributions from the underlying microstructural features. Similarly, an expression similar to that proposed by Stroh [12] can be used to describe the trends in the ultimate tensile stress,  $\sigma_u$ . This gives [12]:

$$\sigma_u = \sigma_u + k_u d^{-1/2} \quad (14)$$

where the constants  $\sigma_u$  and  $k_u$  are similar to the Hall-Petch constants presented earlier for the prediction of the yield

strength. Similarly, the Hall-Petch equation for the plastic strain to failure,  $\epsilon_p$ , is given by [13]:

$$\epsilon_p = \epsilon_0 + k_p d^{-1/2} \quad (15)$$

where  $\epsilon_0$  and  $k_p$  are the Hall-Petch constants obtained from Figs. 4 and 5. The fracture toughness is also given by a simple Hall-Petch type equation of the form [14]:

$$K_{Ic} = K_0 + k_f d^{-1/2} \quad (16)$$

where  $K_0$  is the intrinsic fracture toughness (does not include the effects of grain boundaries) and  $k_f$  represents the Hall-Petch slopes obtained from Fig. 3. It is thus apparent from the above discussion that all the basic mechanical properties examined in this study can be fitted to empirical equations of the form,  $Y = m d^{-1/2} + c$ . If we use subscript  $i$  to distinguish between the different mechanical properties, then  $i = 1$  corresponds to the yield stress,  $i = 2$  corresponds to the ultimate tensile stress,  $i = 3$  corresponds to the plastic elongation to failure and  $i = 4$  corresponds to the fracture toughness. The general Hall-Petch expression for the different mechanical properties is thus given by:

$$Y_i = m_i d_i^{-1/2} + c_i \quad (17)$$

The Hall-Petch lines obtained from the regression analysis of the experimental data are summarized in Table II. These show clearly that the Hall-Petch constants are different in the different alloys. The constants  $m_i$  and  $c_i$  are, therefore, strongly influenced by the effects of alloying.

The above behavior (Figs. 1 to 5) is consistent with previous studies [3, 11, 12, 15] that have shown the same type of Hall-Petch dependence in a wide range of polycrystalline materials. The results also suggest that the influence of lamellar spacing [1, 13] may be of secondary importance when compared to the effects of grain size, since the same Hall-Petch dependence was observed over a wide range of lamellar volume fractions [5]. The effects of these other microstructural parameters will be discussed later along with the effects of alloying. Nevertheless, it is practically important to note here that grain/lamellar colony size is easier to control (by careful processing and heat treatment) than the lamellar spacing which may vary widely (~10nm - 1mm) within any given microstructural condition.

All of the mechanical properties examined in this study exhibit simple Hall-Petch behavior. There are no inverse relationships between ductility, yield/ultimate strength and fracture toughness. Hall-Petch behavior is also observed at both room- and elevated- temperature (25 and 815°C). This suggests that further improvements in the mechanical properties of gamma alloys may be engineered by grain refinement strategies, e.g., nanocrystalline processing.

However, the grain refinement strategies must not neglect the possible degradation of creep resistance that can occur as a result of grain refinement. This is illustrated schematically in Fig. 6. It should be readily apparent from this figure that the engineering of balanced properties in gamma alloys may involve the optimization of creep resistance and the basic mechanical properties evaluated in this study. However, this possibility requires careful experimental verification.

Nevertheless, it is encouraging to note here that the best alloy examined in this study (Ti-48Al-1.5Cr extruded with a reduction ratio of 14:1 at 1343°C) has an attractive combination of basic mechanical properties (yield strength of ~ 660MPa, ultimate tensile strength of ~ 700MPa, ductility of ~ 2% and fracture toughness of ~ 34 MPa√m) after an optimizing heat treatment schedule (982°C/4h/AC+704°C/4h/AC+815°C/24h/AC). The Ti-48Al-1.5Cr alloy has an average grain size of ~ 100 μm in this condition. It should, therefore, be very exciting to explore the effects of grain refinement on the mechanical properties of this alloy. It may also be possible to further improve the mechanical properties of the gamma alloys by alloying strategies. However, such alloying efforts are typically empirical in nature, and there is a need for quantitative tools to reduce the number of iteration steps required for alloy optimization. The possible use of multiparameter regression approaches may be used to achieve this goal. These will be discussed in the next section.

### Multiple Linear Regression Equations

The coefficients,  $\alpha_0$ , and exponents,  $\alpha_i$ , obtained from the multiple linear regression analysis of the microstructural and compositional variables for these alloys are summarized in Table II. These can be used to determine the four basic mechanical properties  $Y_1$ ,  $Y_2$ ,  $Y_3$  and  $Y_4$ , by substitution of the appropriate exponents/coefficients and variables given in Table II into Equation (1). Missing exponents in Table II indicate that the relevant mechanical property has no dependence of that particular microstructural/ compositional variable. The resulting equations predict the basic mechanical properties of the gamma alloys examined in this study, as shown in Figs. 7a-7d, in which the room- and elevated-temperature properties are compared on single plots. Very good agreement is obtained between the predicted and measured yield/ultimate tensile strengths and the predicted and measured ductilities (Figs. 7a-7c). The agreement between the measured and predicted fracture toughness levels is not as good (Fig. 7d). Nevertheless, the agreement is still remarkable, given the simplicity of the above formulation. Correlation coefficients for the different equations for  $Y_i$  are summarized in Table II.

A cursory analysis of the equations presented in Table II also reveals that the exponent of  $d$  in the regression

Table I. Actual Compositions (Atomic %) of Cast Gamma Alloys

Alloy Composition	Ti	Al	C	O	N	H	Cr	Mn	S
Ti-48-Al	Bal	49.5	0.071	0.135	0.117	0.148	-	-	-
Ti-48Al-1.5Cr	Bal	49.1	0.034	0.104	0.011	0.075	1.79	-	0.011
Ti-48Al-1.4Mn	Bal	50.8	0.149	0.093	0.013	0.037	-	0.96	0.010
Ti-48Al-2Mn	Bal	48.2	0.041	0.099	0.086	0.075	-	1.98	0.010

Bal = Balance of composition

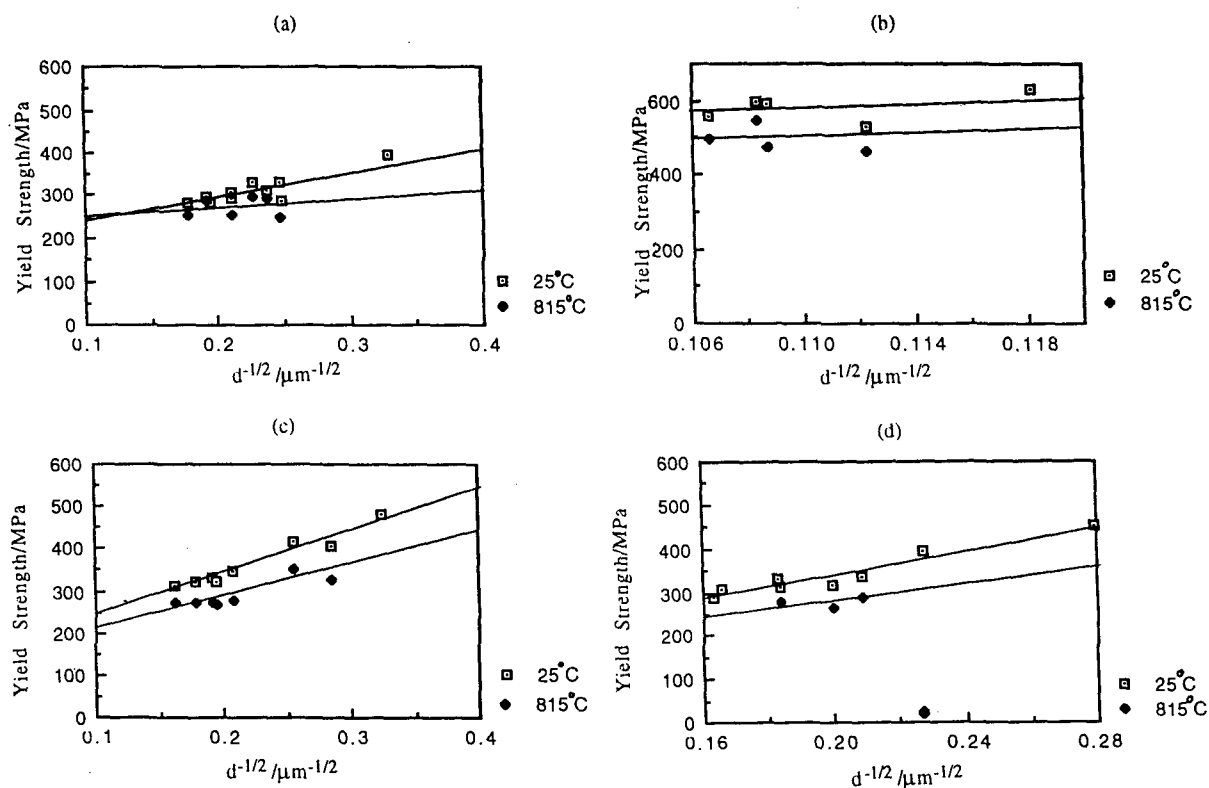


Figure 1. Plots of yield strength versus  $d^{-1/2}$  for (a) binary Ti-48Al; (b) Ti-48Al-1.5Cr; (c) Ti-48Al-1.4Mn and (d) Ti-48Al-2Mn.

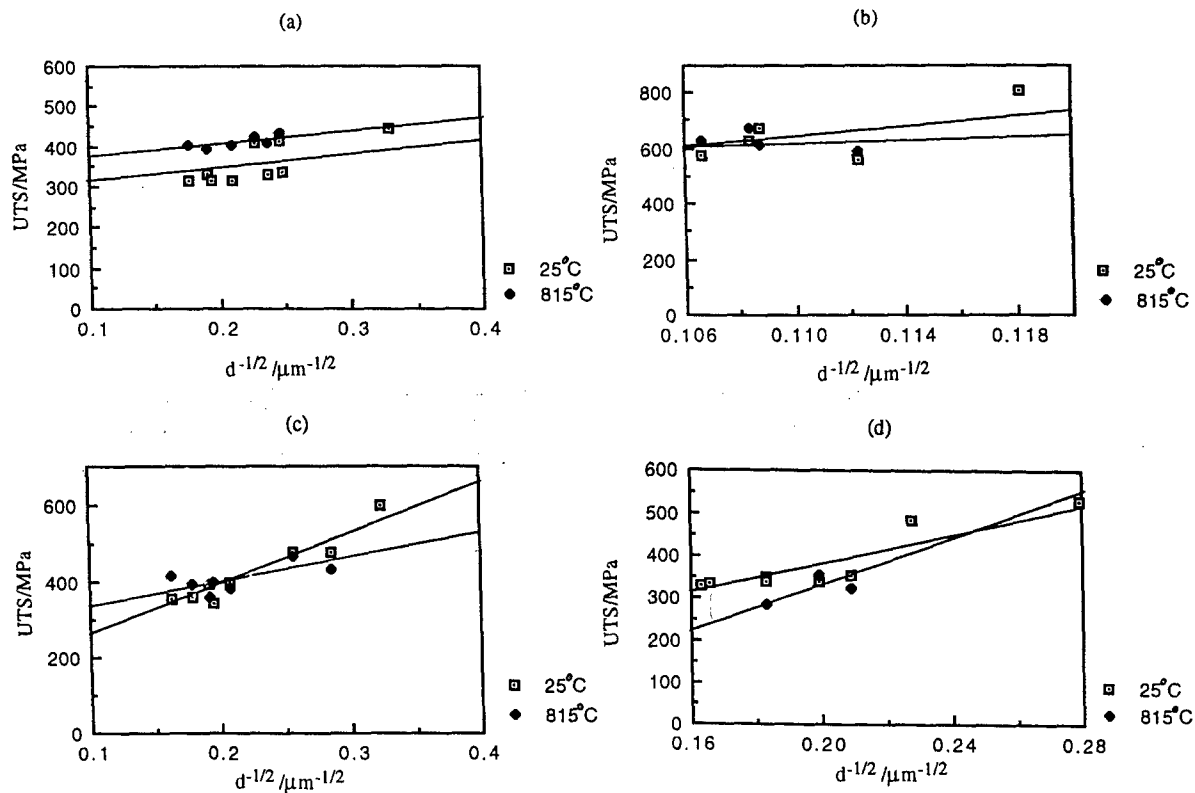


Figure 2. Plots of ultimate tensile strength versus  $d^{-1/2}$  for (a) binary Ti-48Al; (b) Ti-48Al-1.5Cr; (c) Ti-48Al-1.4Mn and (d) Ti-48Al-2Mn.

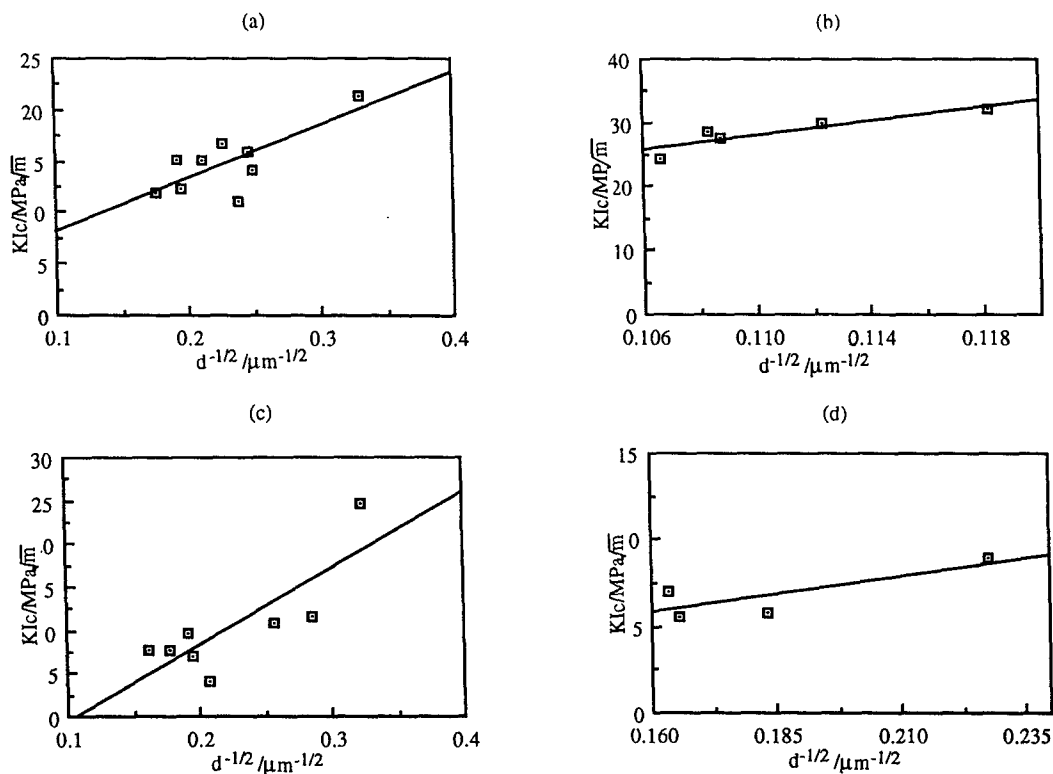


Figure 3. Plots of room temperature fracture toughness versus  $d^{-1/2}$  for (a) binary Ti-48Al; (b) Ti-48Al-1.5Cr; (c) Ti-48Al-1.4Mn and (d) Ti-48Al-2Mn.

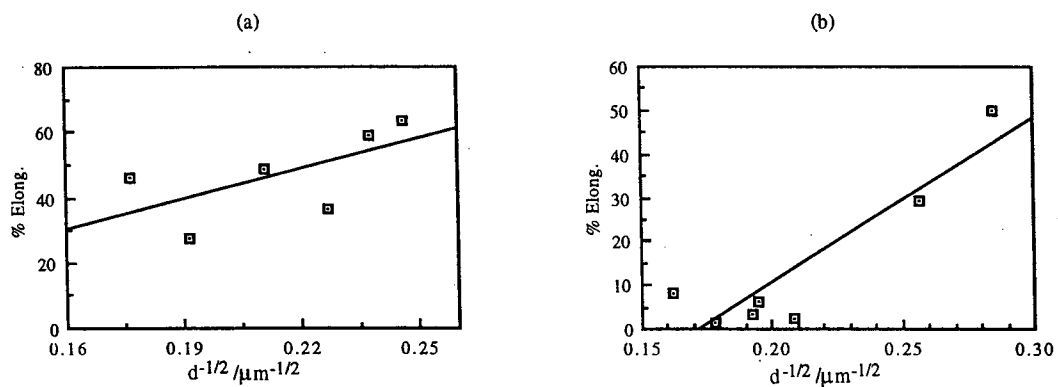


Figure 5. Plots of ductility at 815°C versus  $d^{-1/2}$  for (a) binary Ti-48Al and (b) Ti-48Al-1.4Mn.

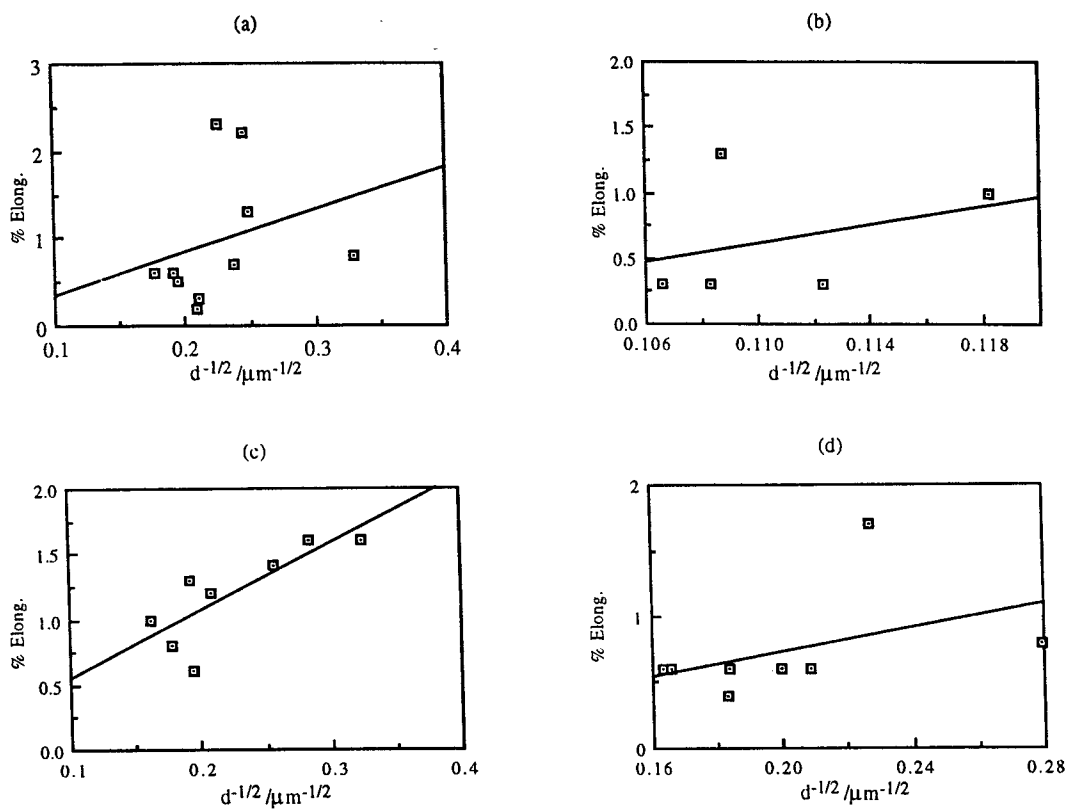


Figure 4. Plots of room temperature ductility versus  $d^{-1/2}$  for (a) binary Ti-48Al; (b) Ti-48Al-1.5Cr; (c) Ti-48Al-1.4Mn and (d) Ti-48Al-2Mn.

Table II. Multiparameter Regression Data

Property	Exponent of Variables $x_i$								$\ln(\alpha_0)^*$	Multiple Regression Coefficient R
	d	$\theta_L$	Ti	Al	C	Cr	Mn	T		
0.2 % Offset Yield Strength (MPa)	-0.247	0.519	-0.751	-	-0.041	0.041	-	-	8.13	0.972
Ultimate Tensile Stress (MPa)	-0.216	-	16.32	-	-0.273	-0.033	-	0.013	-57.86	0.909
Plastic Elongation to Failure (%)	-0.910	-	85.85	64.80	-	-	0.139	1.377	-588.17	0.645
Fracture Toughness (MPa $\sqrt{m}$ )	0.953	0.023	-13.76	-	0.450	0.002	0.003	-	53.98	0.608

\* Natural log values  $\alpha_0$  are presented in table since  $\alpha_0$  values are too small to show trends.

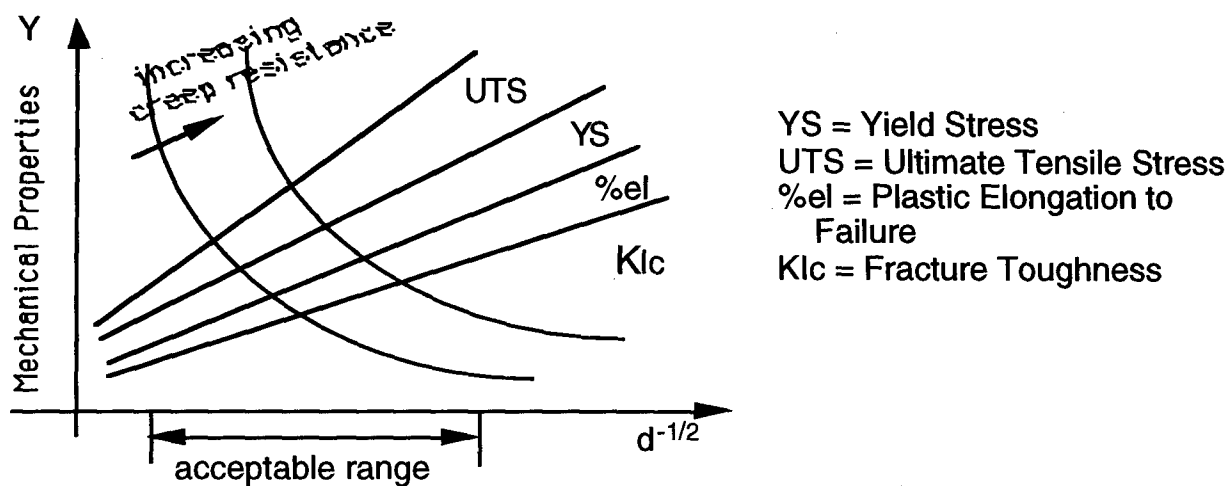


Figure 6. Schematic Illustration of Possible Approach to The Engineering of Balanced Properties in Gamma Titanium Aluminides

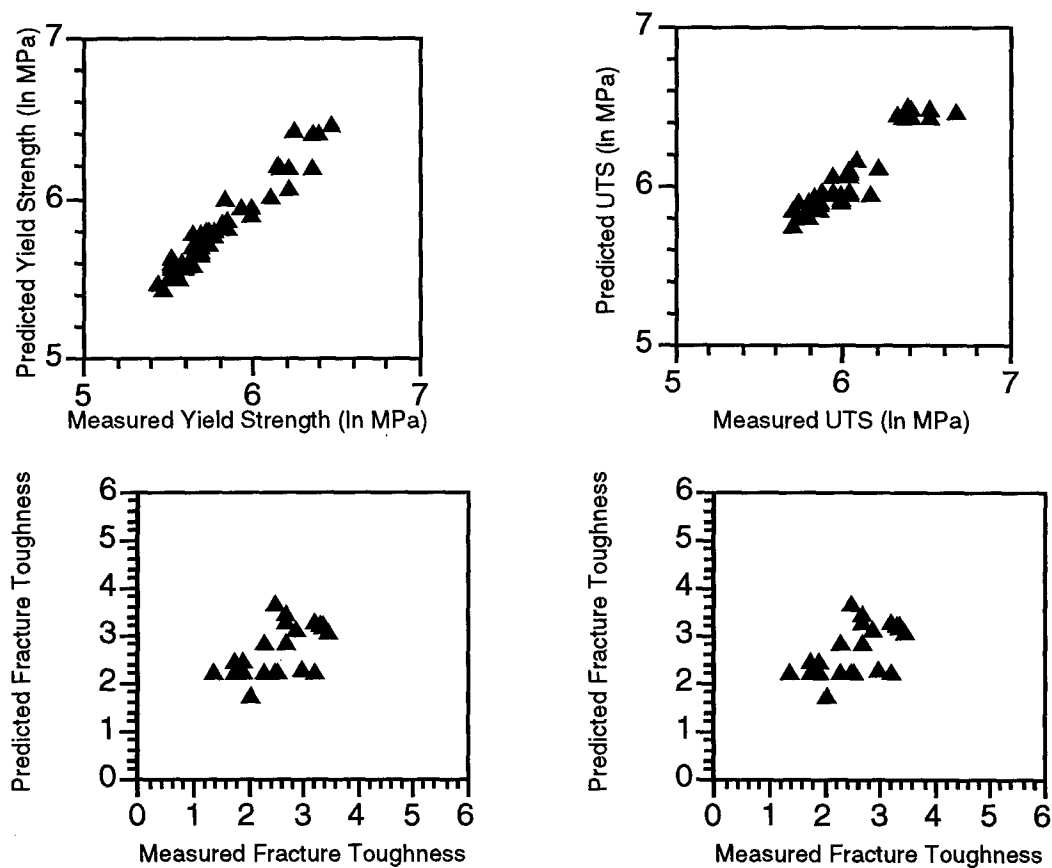


Figure 7. Plots of Predicted Versus Measured Mechanical Properties: (a) Yield Strength; (b) Ultimate Tensile Stress; (c) Plastic Strain to Failure and (d) Fracture Toughness.



equations is generally not equal to -0.5, as one might expect from the success of the Hall-Petch relationships presented earlier. In fact, the best correlations between the predicted and measured data were obtained typically with d exponents of : -0.24 for yield stress; -0.21 for ultimate tensile strength; -0.25 for tensile ductility, and 0.95 for fracture toughness. The differences are attributed to the complex nature of dislocation/microstructure interactions in duplex  $\alpha_2 + \gamma$  alloys. The modulus and Burgers vector mismatch (between  $\alpha_2$  and  $\gamma$  phases) may also explain some of the deviations in the Hall-Petch exponents.

### Summary

1. Simple Hall-Petch equations have been obtained for the prediction of the room- and elevated-temperature mechanical properties (yield/ultimate strength, ductility and fracture toughness) of gamma-based titanium aluminides at 25 and 815°C. The equations predict the mechanical properties of Ti-48Al, Ti-48Al-1.4Mn, Ti-48Al-2.0Mn and Ti-48Al-1.5Cr extrusions that were tested at 25 and 815°C.

2. Multiparameter expressions of the form:  $Y = \alpha_0 \prod X_i^{\alpha_i}$  have been obtained for the prediction of the basic mechanical properties of gamma alloys at 25 and 815°C. The equations predict the functional dependence of yield/ultimate tensile stress, ductility and fracture toughness on temperature, microstructure and composition. Single multiparameter equations have been obtained (by regression analysis) for the prediction of each property. The single equations predict the properties of each of the four alloys examined in this study. The errors in the predictions have also been computed.

3. The multiparameter expressions obtained via multiple linear regression analysis suggest that the average grain size and the titanium content are the key variables that have the strongest effects on the mechanical properties of gamma alloys at 25 and 815°C. The exponents of the average grain size, d, in the multiparameter expressions are also consistently different from the value of -0.5 expected from the Hall-Petch analysis.

### Acknowledgment

The research was supported by The Division of Materials Research of The National Science Foundation. The authors are grateful to the Program manager, Dr. Bruce MacDonald, for his encouragement and support. Appreciation is also extended to Prof. Ron Armstrong for useful discussions.

### References

1. Y.W. Kim and D.M. Dimiduk: J. Met., 43 (1991) 40-47.
2. Y.W. Kim: J. Met., 41 (1989), 24-30.

3. H.A. Lipsitt, "Titanium Aluminides - Future Turbine Materials", Advanced High Temperature Alloys Processing and Properties, S.M. Allen, R.M. Pelloux and R. Widner (Editors); ASM, Metals Park, Ohio, (1985), 57.

4. W.O. Soboyejo and C. Mercer, "The Effects of Alloying and Microstructure on the Fracture of Intermetallic Compounds Based on TiAl", Fatigue and Fracture of Ordered Intermetallic Materials I, Edited by W.O. Soboyejo; T.S. Srivatsan, and D.L. Davidson, 171-223 Published by The Minerals, Metals and Materials Society (TMS) Pennsylvania, USA (1993), 171-223.

5. W.O. Soboyejo and C. Mercer, Materials and Manufacturing processes, Parts I-IV, 11 (1996), 411.

6. W.O. Soboyejo, C. Mercer, K. Lou and S. Heath, Metall. Mater. Trans., 26A (1995), 2275.

7. C. Mercer and W. O. Soboyejo, Scripta Materialia, 35 (1) (1996), 17-22.

8. A.B.O. Soboyejo, "Plastic Flow in Reinforced Concrete", Technical Report No. 52; Dept. of Civil Engineering, Stanford University, Stanford, California (1965).

9. K.S. Chan and Y-W. Kim, Acta Metall. Mater., 43 (2) (1995), 439.

10. E. O. Hall, Proc. Phys. Soc., 64B (1951), 747.

11. N. J. Petch, Iron Steel Inst., 173 (1953), 25.

12. A.N. Stroh: Proc. R. Soc., A223 (1954), 404.

13. R.W. Armstrong, Proc. 7th Int. Conf. on The Strength of Metals and Alloys, Pergamon Press, New York, 1 (1985), 196.

14. R.W. Armstrong, MRS Symposium Proc., MRS, Pittsburgh, PA, 362 (1994), 40-47.

15. A.B.O. Soboyejo, "Propagation of Errors and Tolerance Analysis in Engineering Design and Stress Analysis Problems", Recent Advances in Stress Analysis, (New Concepts and Techniques and Their Practical Applications), The Joint Committee for Stress Analysis, Royal Aeronautical Society, London, England (1968), 1-7.

# Production of titanium aluminide valves for automotive engines by reactive sintering

D. Schneider<sup>a</sup>, T. Jewett<sup>b</sup>, C. Gente<sup>a</sup>, K. Segtrop<sup>c</sup>, M. Dahms<sup>d</sup>

a. GKSS Research Center GmbH, Max-Planck-Straße, D-21502 Geesthacht, Germany

b. Thermal Spray Laboratory, State Univ. NY-Stony Brook, Stony Brook, NY, USA

c. TRW Engine Components, D-30881 Barsinghausen, Germany

d. Flensburg Polytechnic Institute, Kanzleistraße 91-93, D-24943 Flensburg, Germany

## Abstract

Weight reduction of oscillating engine parts can help to enhance the fuel economy and the power of an automobile engine. Therefore, valves made of light weight metals for high temperature applications can be used to substitute for steel parts. Alloys based on the intermetallic compound  $\gamma$ -TiAl, having good mechanical properties combined with a low specific density, allow the design of valves with drastically reduced weight, compared to those made of more conventional materials. Obstacles for application as mass produced parts, such as workability problems and extreme production effort, can be avoided using powder metallurgical processing. Fully dense green valves were produced by extrusion of elemental powders and subsequent forging using aluminum technology. Upon reactive sintering in a following heat treatment, the desired intermetallic phases were formed. Caused by the different interdiffusion coefficients of the components, the material contains Kirkendall-pores, the amount depending on the sintering conditions and the refinement of the microstructure prior to sintering. With a refined microstructure and optimized annealing conditions, a porosity well below 0.5 % coupled with good mechanical properties (UTS>350 MPa) were achieved demonstrating a strong potential of HIP-free produced  $\gamma$ -TiAl for application in combustion engines.

## Introduction

Alloys based on the intermetallic compound  $\gamma$ -TiAl will become a new class of light weight materials for high temperature applications. The rising interest is generated by some attractive features of these alloys: good mechanical properties at high temperatures and a reasonable resistance to

oxidation, accompanied by a low specific density [1]. The use of this kind of material allows a decrease in the weight of a finished part greater than 40 %. A significant reduction of the mass of oscillating engine components such as valves leads to a substantially enhanced fuel economy and also to reduced noise pollution of the working engine [2, 3]. In addition, the dimensions of the reciprocating valve train parts can be reduced. However,  $\gamma$ -TiAl based alloys still suffer from a lack of actual applications, because their low ductility at ambient temperature and their difficult workability are major obstacles in producing parts from TiAl [4, 5, 6].

An elemental powder processing route has been developed to avoid the workability problems [7]. This route opens a reasonable pathway for economical production, which is in particular a basic condition for mass produced articles like motor components of automobiles such as exhaust valves. Fully dense near net shaped parts can easily be produced from elemental titanium and aluminum powders by extrusion and subsequent conventional shaping. In a following heat treatment, the desired intermetallic phases are formed by solid-state, or by liquid-solid reactions. However, pores develop in the material upon these reactions resulting in swelling [8] as well as in unacceptable mechanical properties.

Macro pores form, when pure aluminum is left in the material at 660 °C, the melting point of aluminum, in the heating cycle up to the desired annealing temperature of the heat treatment. Due to capillary forces the molten aluminum flows into Kirkendall pores and grain boundaries, leaving large pores behind, to form new reaction interfaces leading to a quicker reaction kinetics of the liquid-solid reaction [7, 9]. Therefore, it is essential to avoid melting of aluminum, i.e.

the total amount of pure aluminum has to be consumed by the transformation into the intermetallic  $\text{TiAl}_3$ -phase before the melting temperature of aluminum is exceeded. This can be achieved either with a reduction of the heating rate, which is not reasonable because of extremely increased processing duration, or with the refinement of microstructure prior to the reactive sintering step, resulting in strongly accelerated reaction kinetics of the solid-solid reaction due to shortened diffusion lengths.

A brief overview about further mechanisms that can have a significant influence on the pore structure of HIP-free annealed samples is given in the following. Possible mechanisms are:

- Pore formation upon transition into the intermetallic  $\alpha_2$ - $\gamma$ -composite [8, 10], caused by a density change and its corresponding volume reduction of the reacting material. When all elemental material is transformed, a further influence on the porosity can be excluded.
- Pore formation and increasing porosity due to the Kirkendall effect [11]. Because of the very different diffusion coefficients of aluminum- and titanium-atoms in the intermetallic product phases [12], vacancies are formed in the aluminum-regions that agglomerate to voids and small pores.
- Growth of pores by Ostwald ripening [13], that results in increased maximum pore sizes as well as in shifted integral pore area distributions towards larger pore areas without changes in the porosity.
- Reduction of porosity and pore sizes by classical sintering [14]. Since preferably small pores are affected by sintering mainly the population of small pores should be changed [15], and because Ostwald ripening is also present, the pore area distribution broadens. From dilatometric studies on extruded Ti-49Al rods it is known that relevant sintering activities are present above 1300 °C. [8]

For applications which are not very sensitive to extreme production cost, e.g. aerospace, the process-inherent formation of Kirkendall pores is usually suppressed by hot isostatic pressing (HIP) [1, 16, 17]. Due to the corresponding increase of production cost, HIP is unacceptable for industrial mass production. Therefore,  $\gamma$ -TiAl based alloys will only be attractive as material for mass produced engine valves, if a HIP-free, powder metallurgical production of the alloys with a very low porosity is possible, in order to keep the production costs low and to save the mechanical properties. Since the typical processing temperatures are in a range where classical sintering is effective, it seems to be reasonable to obtain a material with a sufficiently low porosity via a HIP-free powder processing.

However, it is unclear whether HIP-free processed material fulfill the mechanical requirements for an application such as an exhaust valve, as the influence of small amounts of small pores in  $\gamma$ -TiAl based materials is unknown at present. A quite complete overview on the physical and mechanical properties required for conventionally designed engine valves is given in [2]. Current standards require a tensile strength above 400 MPa and a ductility of more than 1 % for

valve material. Titanium-aluminide-valves with mechanical properties well above these limits were developed by powder metallurgical processing at Sumitomo Light Industries [18, 19] as well as with a special casting technique by Maki et al. [2]. Tensile strengths of 460 MPa and approximately 500 MPa with elongations of 1.5 % and 1 % respectively were observed. The Nissan valves were tested in high performance engines demonstrating a strong potential for the substitution of steel parts. However, to get these properties, the porosity of the material had to be minimized by HIP and hence, the observed results can be taken as upper limits for strength and ductility that are achievable with a HIP-free processing.

The required ductility of 1% seems to be of minor importance for good performance. Although ceramics are known to be brittle and thus to have a ductility quite close to zero, ceramic-valves made of high quality silicon nitride [3] have successfully been tested in automotive engines.

In the following, the results of a systematic study will be shown focusing on the dependence of pore formation and the corresponding pore area distribution with various annealing conditions and microstructures of extruded titanium-aluminum powder mixtures. In order to check the potential for industrial application, the mechanical properties of the material treated with the optimal annealing conditions are measured and discussed with respect to the above mentioned requirements.

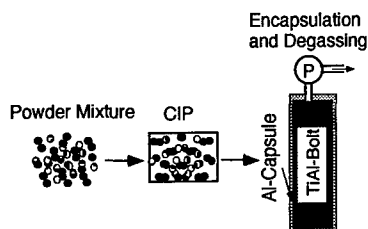
## Experimental

### Powder processing

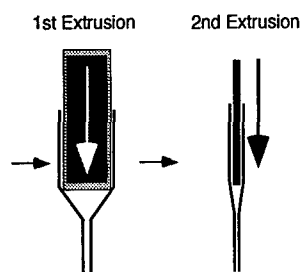
In Figure 1, a schematic of the whole powder processing procedure is shown, which starts with elemental powders and ends with finishing of the reactively sintered part. Elemental powders with purities of 99.8 % and particle sizes <150  $\mu\text{m}$  were mixed to the nominal composition of Ti-48at.% Al. The powder mixture was precompacted by cold isostatic pressing (CIP) to about 80 % of its theoretical bulk-density (Figure 1 a). Cylindrical green bodies of approximately 300 mm length and 160 mm diameter were encapsulated in aluminum tubes, degassed at 400 °C and subsequently extruded at 350 °C to a final diameter of 55 mm. Fully dense rods of 10 mm and 20 mm diameter were produced within a second extrusion at ambient temperature (Figure 1 b). The received total extrusion ratios  $R = d_x^2/d_0^2$ , where  $d_0$  is the initial- and  $d_x$  is the extruded diameter, are then  $R=60$  for the 20 mm rods and  $R=239$  for the 10 mm rods, considered that the coating, left from the aluminum capsules, was removed after the first extrusion. The 10 mm rods were left as is, so that different extrusion ratios for the quantitative estimation of the influence of different microstructures on the sintering behavior were available. For the production of green valves the 20 mm rods were cut into bolts of approximately 35 mm length. These bolts were partially extruded to a final diameter of 7 mm with an extrusion ratio  $R=487$  forming the stem. The undeformed part of the bolt was forged directly after the partial extrusion to a valve head in the same machine (Figure 1 c). Now the shape of the part is quite close to a

valve, and only a little grinding is necessary to get a near net shaped (NNS) green valve.

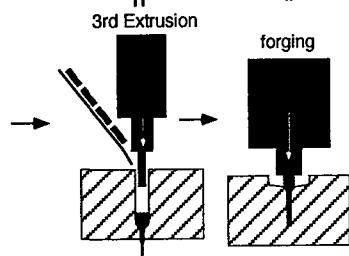
#### a. Powder Preparation



#### b. Refined Microstructure



#### c. NNS



#### d. Transform to Intermetallic Phase and finishing

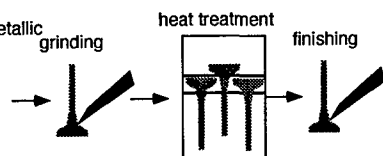


Figure 1: Schematic of the processing. After mixing, compaction, encapsulation, and degassing of the elemental powders (a.) the received bolts are extruded (b.) and forged (c.) before reactive sintering (d.) and finishing.

### Sintering

The NNS parts were pressureless sintered in order to obtain the desired intermetallic phases. From earlier work it is known that the best sintering activities of extruded TiAl rods were observed in the temperature range of 1300 °C to 1400 °C [8]. Therefore, the 10 mm rods and the valve shafts were heat treated under high vacuum ( $\approx 10^{-6}$  Pa) conditions at temperatures of 1300, 1350, and 1400 °C. The heating and the cooling rates were always set to 10 K/min. Since the temperatures are in the upper part of, and above the  $\alpha$ - $\gamma$  two phase field of the TiAl phase diagram [20], a duplex structure or a fully lamellar structure is expected to form upon annealing. Good mechanical properties of  $\gamma$ -based TiAl alloys were observed from samples with a duplex and with a fully lamellar microstructure [1]. The duplex structure is known to have a better room-temperature-ductility [1, 21] and tensile strength than the fully lamellar material. In order to avoid growth of pores to very large sizes due to Ostwald

ripening, the annealing time must be limited. For better long time stability of the material, the durations must be long enough to allow the system to approach the equilibrium concentrations.

### Characterization

For the microstructure characterization of the unreacted material, the chord lengths (from now on: sizes) of the aluminum regions were determined with computer aided image analysis of light optical micrographs. Using this method, a good quantitative description of the microstructure is obtained. The reliability of the method was checked using a comparison of the observed surface fractions of the aluminum regions with the volume fraction as calculated from the nominal composition. The determined relative aluminum areas, taken from micrographs prepared parallel as well as perpendicular to the extrusion direction, were 46.8 % and 45.7 %, and agree very well with the theoretically determined value of 46.5 %. No serious distortions of the results are present, caused by the preparation or the image analysis system.

The same combination of light microscopy and computer aided image analysis was used to determine the amount of pores and the pore size distribution of the heat treated material. After user-specific image transformations for the elimination of contrasts, which did not originate from pores, the relevant parameters of the pore structure, i.e. the area and diameter of every pore were measured. A resolution was chosen such that all pores with sizes between  $1 \mu\text{m}^2$  and  $1000 \mu\text{m}^2$  were detected.

Because of the radial symmetry of the extruded rods, the total volume fraction of all detected pores (from now on: porosity) is equal to the integral pore area fraction, as determined by the image analysis. Besides the porosity, the diameter of the largest pore (from now on: maximum pore size) was also taken from the results of the image analysis. Hence, with only one analysis this method allows the precise investigation of the most important parameters of the pore structure with respect to the mechanical properties

Scanning electron microscopy (SEM) was performed in order to investigate the type of microstructure (duplex, nearly- or fully-lamellar) and the volume fraction of its components, i.e. lamellar regions and globular grains. EDX-analyses were conducted in order to check the homogeneity of the phases formed upon annealing.

Tensile tests were performed at room temperature with samples prepared from the reactively sintered valve shafts, having a diameter of 4 mm and a testing length of 25 mm with an overall length of 80 mm. In addition to the strength of the alloy, the elongation of the tensile sample was measured using a contact extensometer.

## Results

### Unreacted material

As mentioned above, the influence of the extrusion ratio  $R$  on the reactive sintering process is strong since the pore formation strongly corresponds to the sizes of the aluminum-regions before annealing. Therefore a quantitative characterization of the aluminum-distribution in the cross sections after extrusion with different extrusion ratios is important for understanding the results of the heat treatments.

Figures 2a and 2b show light-optical micrographs perpendicular and parallel to the extrusion direction from the microstructure of the less deformed (LD) sample  $R=239$ . Elongated (dark) pure titanium particles are embedded in a (light) aluminum-matrix. Due to the irregular shape of the titanium-powder particles the phases mesh together with a large amount of interphase interfaces. This ensures rapid reaction kinetics upon annealing. The quantitative image analysis reveals that the distribution of the components is much finer in the highly deformed sample (HD) than in LD. The mean size of the HD aluminum regions is  $38\text{ }\mu\text{m}$ , for the LD aluminum regions it is  $60\text{ }\mu\text{m}$ .

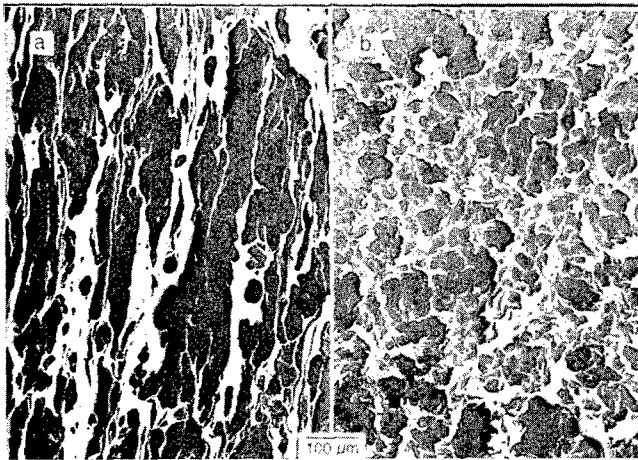


Figure 2: Microstructure of LD parallel (a.) and perpendicular (b.) to the extrusion direction

### Heat treated material

#### Porosity and pore sizes

Figures 3a and 3b show the development of the porosity of HD and LD depending on the annealing time at different temperatures. The porosity of LD is about 1 % after the shortest annealing at all temperatures, but the porosity increases rapidly at higher temperatures. At  $1400\text{ }^{\circ}\text{C}$ , a porosity maximum of 4.3 % is reached in LD after 1 h while at  $1350\text{ }^{\circ}\text{C}$  the porosity maximum of 6.1 % is reached after 4 h. Upon longer annealing the porosity decreases slightly in both cases. At the lowest temperature, the same tendency is observed, but a porosity maximum is not reached before the longest heat treatment of 9 h.

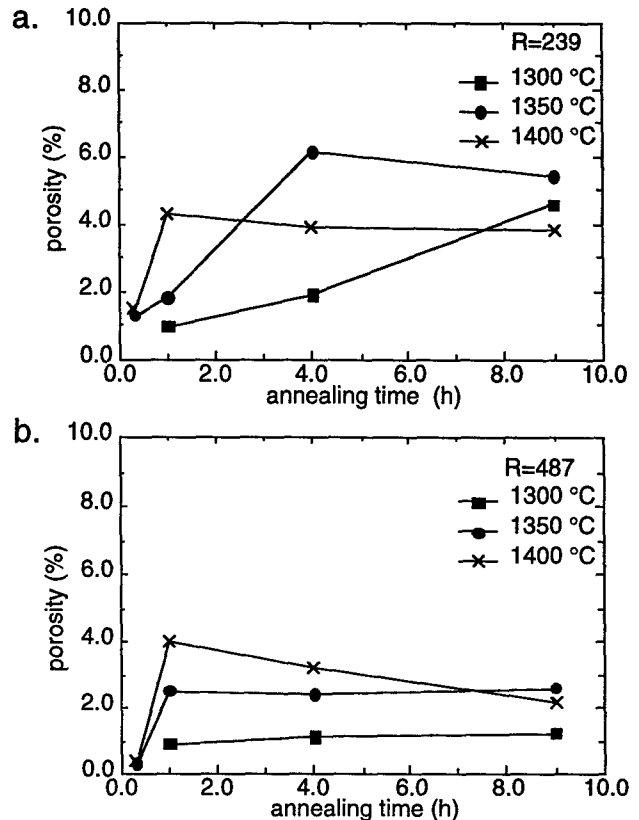


Figure 3: The porosities of LD (a) and HD (b) after heat treatments at different temperatures

The porosity of HD is significantly lower after annealing for 0.3 h and is about 0.3 %. Upon further annealing to 1 h, porosity maxima of 2.5 % and 4 % are found at  $1350\text{ }^{\circ}\text{C}$  and  $1400\text{ }^{\circ}\text{C}$ , respectively. At  $1300\text{ }^{\circ}\text{C}$  the porosity is about 1 % after 1 h and only slightly increases after longer heating times. Also at  $1350\text{ }^{\circ}\text{C}$  the porosity level does not change significantly upon further annealing, while at  $1400\text{ }^{\circ}\text{C}$ , a reduction of the pore fraction down to 2.5 % is found.

The evolution of the maximum pore sizes are plotted in Figure 4. In addition, the mean sizes of the former aluminum-regions prior to heat treatment are indicated in the figures by dashed lines. The maximum pore sizes of both materials clearly approach to these values of  $38\text{ }\mu\text{m}$  and  $60\text{ }\mu\text{m}$ , respectively.

The observed maximum pore sizes of LD (Figure 4a) quickly increase from  $43\text{ }\mu\text{m}$  after 0.3 h at  $1400\text{ }^{\circ}\text{C}$  up to  $60\text{ }\mu\text{m}$  after 1 h where a constant level is reached. A similar behavior, but on a different time scale, is observed for a LD sample treated at  $1350\text{ }^{\circ}\text{C}$ . The initial pore size of  $33\text{ }\mu\text{m}$  increases up to  $60\text{ }\mu\text{m}$  after annealing for 4 h and remains constant upon further annealing. At the lowest temperature the pore size development looks quite different. The pore size of  $27\text{ }\mu\text{m}$  first decreases in the time interval from 1 h to 4 h to  $20\text{ }\mu\text{m}$  before it slowly increases to the size of the former Al-regions after 9 h of heating.

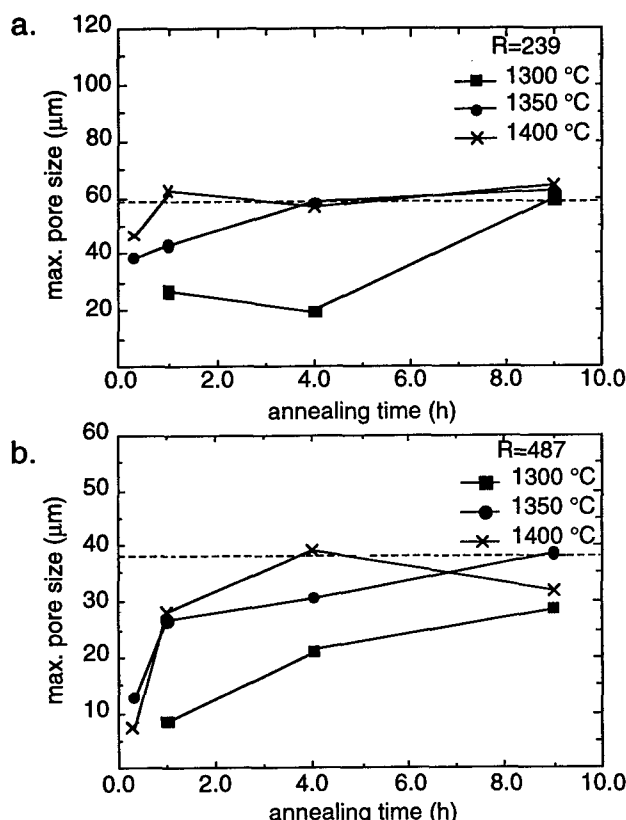


Figure 4: The maximum pore sizes of LD and HD after heat treatments at different temperatures. The sizes of the former aluminum regions prior to annealing are indicated by dashed lines.

At the higher extrusion ratio  $R=487$  HD, significantly smaller maximum pore sizes are observed (Figure 4b). The maximum pore sizes remain below  $10\text{ }\mu\text{m}$  after the first annealing step of  $0.3\text{ h}$  at  $1350\text{ }^{\circ}\text{C}$  and  $1400\text{ }^{\circ}\text{C}$ , and after  $1\text{ h}$  at  $1300\text{ }^{\circ}\text{C}$  respectively. From  $0.3$  to  $1\text{ h}$  the pore sizes grow up to  $26$  and  $28\text{ }\mu\text{m}$  at  $1350\text{ }^{\circ}\text{C}$  and  $1400\text{ }^{\circ}\text{C}$ , respectively. At  $1400\text{ }^{\circ}\text{C}$ , the size of the former Al-regions ( $\approx 38\text{ }\mu\text{m}$ ) is reached after  $4\text{ h}$  followed by a slight decrease of the pore size. At lower temperatures, the approximation of the pore sizes to the maximum level given by the size of the former aluminum-regions takes longer times. At  $1300\text{ }^{\circ}\text{C}$ , this level is not reached within  $9\text{ h}$ , but generally the same tendency as at the higher temperatures is observed.

#### Microstructure and mechanical properties after heat treatment

Figure 5 shows the cross sections of samples with both extrusion ratios annealed at  $1350\text{ }^{\circ}\text{C}$  for  $0.3\text{ h}$ . Here, the drastic influence of the deformation rate on the microstructure becomes obvious. In addition to the lower porosity and the smaller pore sizes, the  $\gamma$ -grain sizes as well as the lamellar grains of HD are typically half as large as those of LD. The  $\gamma$ -grain sizes of the LD-sample vary from  $17\text{ }\mu\text{m}$  to  $60\text{ }\mu\text{m}$  while the grain sizes of the HD sample range from  $10\text{ }\mu\text{m}$  to  $30\text{ }\mu\text{m}$ . The sizes of the lamellar regions exhibit variations in size similar to that observed for the  $\gamma$ -grains, varying from

$44$  to  $200\text{ }\mu\text{m}$  for the LD-sample and from  $20$  to  $147\text{ }\mu\text{m}$  for the HD-sample. All samples have a duplex structure with different lamellar fractions, increasing with time and temperature. Some annealing twins are observed after annealing times of  $9\text{ h}$ . The results of the characterization from the microstructure are summarized in tables 1 and 2.

Table 1:  $\gamma$ - and  $\alpha_2$ - $\gamma$ -lamellar grain sizes of heat treated HD after  $1\text{ h}$  and  $9\text{ h}$  heat treatment at  $1300\text{ }^{\circ}\text{C}$ , and after  $0.3\text{ h}$  and  $9\text{ h}$  at  $1350\text{ }^{\circ}\text{C}$  and  $1400\text{ }^{\circ}\text{C}$ .

Time	Grain size HD ( $\mu\text{m}$ )					
	1300 $^{\circ}\text{C}$		1350 $^{\circ}\text{C}$		1400 $^{\circ}\text{C}$	
	$\gamma$	lam.	$\gamma$	lam.	$\gamma$	lam.
0.3, 1	12	20	10	33	16	86
9	19	47	20	84	33	147

Table 2:  $\gamma$ - and  $\alpha_2$ - $\gamma$ -lamellar grain sizes of heat treated LD after  $1\text{ h}$  and  $9\text{ h}$  heat treatment at  $1300\text{ }^{\circ}\text{C}$ , and after  $0.3\text{ h}$  and  $9\text{ h}$  at  $1350\text{ }^{\circ}\text{C}$  and  $1400\text{ }^{\circ}\text{C}$ .

Time	Grain size LD ( $\mu\text{m}$ )					
	1300 $^{\circ}\text{C}$		1350 $^{\circ}\text{C}$		1400 $^{\circ}\text{C}$	
	$\gamma$	lam.	$\gamma$	lam.	$\gamma$	lam.
0.3, 1	17	44	17	49	21	78
9	27	100	34	109	62	191

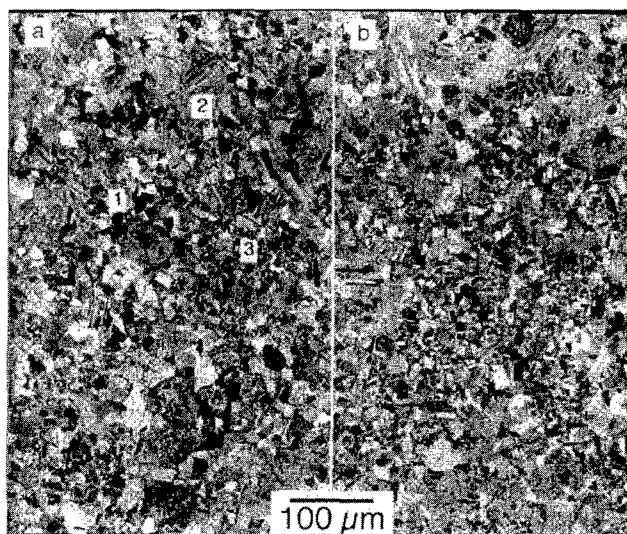


Figure 5: Microstructure of LD (a.) and HD (b.) heat treated at  $1350\text{ }^{\circ}\text{C}$  for  $0.3\text{ h}$ . Pores are black.

(1.): pore, (2.): lamellar grain, (3.): globular  $\gamma$ -grains

Although the highest evaluated temperature is in the single-phase  $\alpha$ -region of the phase diagram, no fully lamellar microstructure is observed. The amount of observed lamellar regions is always below that expected from the equilibrium phase diagram, and ranges from  $30$  to  $90\%$ . The chemical compositions of the  $\alpha_2$ -phase and  $\gamma$ -grains as the lamellae deviate from the equilibrium values after [20]. The observed aluminum-concentrations of the  $\alpha_2$ -lamellae are above, and of the  $\gamma$ -lamellae below the equilibrium concentrations. The

deviations increase with decreasing time and temperature. They are about 8 % in the  $\alpha_2$ -regions and 2-3 % in the  $\gamma$ -regions of LD, and up to 10 % or 3-4 % respectively, in HD- $\alpha$ -regions and HD- $\gamma$ -regions. In the globular  $\gamma$ -regions no significant concentration deviations were observed.

The deviations from the equilibrium concentrations, not suitable for the long term stability of the material, gave reason to develop a two step annealing program, in order to get a combination of optimized porosity with concentrations close to the equilibrium. The heat treatments were carried out as described before, but were then followed by a second annealing at 1100 °C for times ranging from 1 to 10 h. Best results are found for a combination of 0.3 h at 1400 °C followed by 1 h at 1100 °C yielding a porosity of 0.1 % and a maximum pore size of 10  $\mu\text{m}$ . The slightly decreased porosity combined with an increased maximum pore size show that sintering and Ostwald ripening are also present at the lower temperature. The grain sizes are not influenced by the second annealing step. Another suitable compromise, perhaps better for economical reasons, may be a combination of 0.3 h at 1350 °C followed by 4 h at 1100 °C. Here a slightly increased porosity of 0.4 % with a maximum pore size of 16  $\mu\text{m}$  is obtained.

Mechanical properties were investigated by tensile testing of samples processed with various two step heat treatments. A stress strain curve of the sample 1400 °C/0.3 h + 1100 °C/1 h is shown in Figure 6. In contrast to a sample heat treated for 9 h at 1400 °C and one treated at 1350 °C/1 h + 1100 °C/4 h, the material shows a distinct region of plastic deformation before cracking, after an initial region of elastic deformation. The sample with the highest annealing temperature, 1400 °C, in the first interval and an annealing time for 0.3 h exhibited the best plastic behavior. The tensile strength was 355 MPa after 0.65 % plastic strain and a total elongation of more than 0.8 %. The Young's modulus was determined to be 160 GPa.

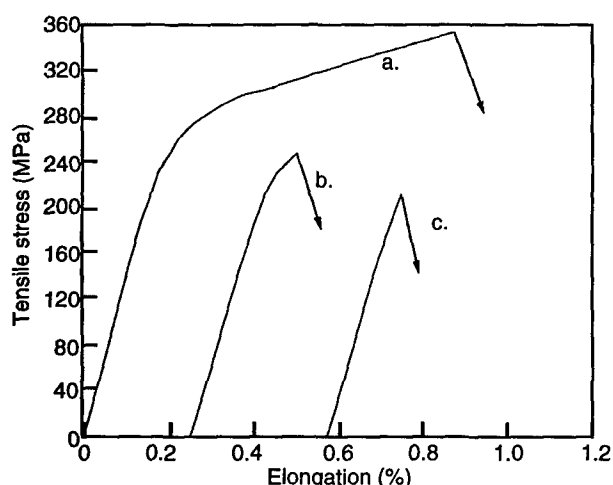


Figure 6: Stress-strain curves of reactively sintered valve shafts heat treated with different conditions.

- (a.): 1400 °C/0.3h + 1100 °C/1 h,
- (b.): 1350 °C/1 h + 1100 °C/4 h,
- (c.): 1400 °C/9 h

## Discussion

The above results clearly demonstrate that the porosity of reactively sintered Ti-48Al strongly depends on the heat treatment parameters as well as on the microstructure of the unreacted material. The density change upon the transition of the elemental titanium-aluminum mixture into the intermetallic phases may serve as a first source of pores. Since the transformation is almost complete after the first annealing interval, except for minor deviations from the equilibrium compositions, no further significant contribution to the materials overall porosity by this effect will be found in the following annealing intervals. The achievable porosity corresponding to the density changes must therefore be even smaller than the smallest porosity observed after the first annealing interval of 0.3 h, because the Kirkendall effect also influences the porosity directly from beginning of the transformation. Hence, it is reasonable to assume the actual pore-contribution of the density changes to be lower than 0.26 %.

Directly following the formation of the intermetallic phases, the pore structure is affected by sintering, Ostwald ripening, and the Kirkendall effect. An increase in porosity during a heat treatment step indicates that here the Kirkendall effect plays a dominant role for the pore structure development, while a decreasing porosity indicates that sintering is dominant. It should be kept in mind that when a large number of Kirkendall pores smaller than 1  $\mu\text{m}^2$  grow by Ostwald ripening to sizes which are then inside the detectable pore area range of the image analysis this may also cause an increase in porosity in absence of the Kirkendall effect. On the other hand, this effect only plays a role for the short time interval where the intensity of the Kirkendall effect decreases, as new pore formation ends. The Kirkendall effect may therefore have stopped a short time before the increase in the detected porosity ends.

At 1300 °C, an increasing porosity in both materials, LD and HD, over the entire heat treatment indicates that the Kirkendall effect is dominant for the duration of the process. At 1400 °C, the porosity increases only in the first hour, and subsequently decreases again upon further annealing, indicating a decreasing intensity of the Kirkendall effect after 1 h. Whereupon, the counteracting sintering overcomes the pore formation, leading to a decrease in the porosity. This point is reached after 4 h at 1350 °C, indicated by the decreasing porosity of LD, while a nearly constant porosity of HD points to a balance between sintering and the Kirkendall effect.

The differences in the time scales on which the Kirkendall effect decreases can mainly be attributed to the times needed by the system to level out concentration deviations, i.e. to attain equilibrium. Since the concentration deviations serve as driving force for aluminum diffusion, and in turn the formation of pores, a faster approach to equilibrium concentrations leads to a faster decrease of the Kirkendall effect. An additional effect on the time scales arises from faster sintering kinetics at higher temperatures, caused by the increased mobility of vacancies.

Finally, increasing pore sizes show that Ostwald ripening is present at all applied temperatures. The speed of pore growth again increases with increasing temperatures, again caused by the faster diffusion of vacancies. The maximum pore sizes of both materials are limited by the sizes of the former aluminum regions. A complete overview of the time regimes concerning the dominant processes is given in Figure 7a (LD) and Figure 7b (HD) summarizing the above discussed results.

Obviously, the combination of minimal porosity and the smallest pore sizes will only be achievable with sintering at 1350 °C or higher for 18 min. As reported above, a concentration deviation from the equilibrium must then be compensated with a second treatment at 1100 °C for 1 h to 4 h. For a small pore size, the total annealing time has to be limited. A combination of 0.3 h at 1400 °C with 1 h at 1100 °C results in a slightly increased pore size and a further reduced porosity. Acceptable results were also achieved at 1350 °C for 0.3 h followed by 4 h at 1100 °C, with a slightly higher porosity and a larger pore size. This shows that Ostwald ripening and Kirkendall effect are also present at 1100 °C, but slower than at higher temperatures.

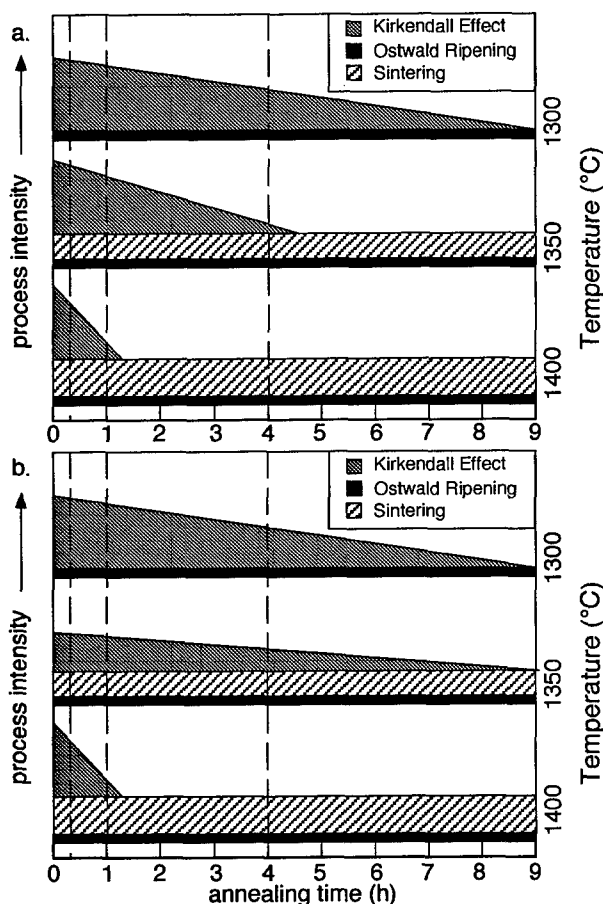


Figure 7: The intensity of processes effecting the pore structure at different temperatures after various annealing times. (a.) LD, (b.) HD

The achieved porosities are even better than those, obtained with pseudo HIP [22], but on the other hand, higher

temperatures have to be applied and the possible influence on the microstructure upon annealing is smaller.

Only the samples sintered at 1400 °C have satisfactory mechanical properties. Here, a ductility of 0.65 % and a yield strength of 355 MPa were measured, while all samples prepared with combinations of 1350 °C or 1300 °C annealings had almost no ductility and lower strengths. A fully lamellar structure with, perhaps, lower strength [1, 21] and ductility was not achieved with the annealing parameters applied in the present investigations. A higher annealing temperature or significantly longer annealings would be necessary to obtain this microstructure. However, from the economical point of view as well as with respect to the requirement of smallest pore sizes neither option is desirable. Hence, short two step heat treatments at 1400 °C + 1100 °C resulting in a duplex-structured material with a low porosity, small pores, and thus, a good deformation behavior appears to be the best compromise for the HIP-free production of  $\gamma$ -TiAl based materials for mass produced engine parts.

Nevertheless, the materials tensile properties are far lower than those of HIPed and forged cast materials, having the best properties recently reported [1]. As expected, the properties are also lower than those achieved by Sumitomo and Nissan [2]. In spite of the low porosity and the small maximum pore sizes, even the requirements given in [2] for an application as exhaust valve cannot be fulfilled with this processing. Since the materials have comparable microstructures, this must be attributed either to the residual pores in the HIP-free produced materials or to concentration deviations from the equilibrium state.

In order to improve the mechanical properties to the given requirements the pores must be further refined. These results clearly prove that the pore structure as well as the microstructure significantly change with the extrusion ratio. Hence, the pore sizes as well as the microstructure should easily be refined with a higher extrusion ratio. In addition, reduced deviations from the equilibrium concentrations of both phases are most likely due to shorter and therefore faster diffusion paths. On the other hand, this is coupled with the necessity of higher extrusion pressures, and the initial CIP-bolt diameter has to be enlarged to get the same final valve diameter. With respect to the tensile properties, a closer approximation to the results of Sumitomo and Nissan should then be possible. The deformation of the titanium-particles would be more effective if an aluminum-alloy instead of pure aluminum is extruded together with pure titanium, because of the increased strength of the prealloyed aluminum-powder. Chrome, known to improve the room temperature ductility, and silicon, forming silicides, and thus leading to particle hardening and reduced grain growth upon sintering [23, 2], are good alloying components. However, this modification also requires higher extrusion pressure.

### Conclusions

The results clearly demonstrate the potential of the reactive powder metallurgical method for the production of  $\gamma$ -based TiAl materials via reactive sintering of powder mixtures. The



material has a low porosity with small pore sizes when treated under optimized annealing conditions. The final pore structure is achievable without HIP, because a sufficiently fine distribution of the elemental components can be generated by extrusion prior to annealing.

The pore size as well as the porosity decrease significantly with higher extrusion ratios. Sintering also causes a reduction of the porosity, most effective at 1400 °C and after longer heat treatments when the pore forming Kirkendall effect has almost stopped. Due to Ostwald ripening, which is present at all temperatures with increasing speed at higher temperatures, the pores are much larger than after the shortest annealings. Therefore, the best annealing conditions were found to be a first treatment at 1400 °C for 0.3 h combined with a second treatment at 1100 °C for 1 h, in order to level out concentration deviations from the equilibrium compositions.

With the microstructure and the porosity achieved by this processing, a reasonable mechanical behavior of the present material as observed. However, both the tensile strength as well as the ductility are, as expected, lower than those of more advanced alloys prepared with HIP, and are still below the requirements for the target application. Nevertheless, with some modifications of the processing, i.e. a higher extrusion ratio and the addition of alloy components known to enhance the ductility and strength, it becomes reasonable to assume that these requirements will be fulfilled.

In spite of the lower mechanical properties, the HIP free powder metallurgical route is a reasonable alternative for the production of  $\gamma$ -based TiAl alloys with respect to the economical needs of industrial mass production. The near net shape potential of the extrusion technique and the opportunity to do most of the machining prior to annealing with well established methods the aluminum technology help to keep the production cost on a low level which is impossible to reach when HIP is utilized to avoid the porosity. Especially for the lower production costs, HIP-free processing is a better compromise for the production of TiAl valves on an industrial scale, and therefore has a strong potential to find a direct way to application.

#### Acknowledgement

We are grateful to Dr. R. Westerheide from Fraunhofer IWM Freiburg for the careful investigation of the mechanical properties of the heat treated valve shafts.

#### References

- [1] Y.W. Kim, *JOM* **46** (7), (1994), 30-39
- [2] K. Maki, A. Ehira, M. Sayashi, T. Sasaki, T. Noda, M. Okabe, S. Isobe, *SAE Technical Paper Series* No.: 960303, (1996), 117-125
- [3] E. Gugel, G. Wötting, P. Claeys, P. Woditsch, *VDI Berichte* **1235**, (1995), 209-219
- [4] G.Z. Sauthoff, *Z. Metallkunde* **77** (1986), 654
- [5] Y.W. Kim, D. M. Dimiduk, *JOM* **43**, (1991), 40
- [6] M. Yamaguchi, Y. Umakoshi, *Prog. Mater. Sci.* **34**, (1990), 1
- [7] G.-X. Wang, M. Dahms, *JOM* **45**, (1993), 52
- [8] M. Dahms, G. Leitner, W. Poeßnecker, S. Schultrich, F. Schmelzer, *Z. Metallkunde* **84**, (5), (1993), 351-357
- [9] G.-X. Wang, M. Dahms, G. Leitner, S. Schultrich, *J. Mater. Sci.* **29**, (1994), 1847-1853
- [10] A.P. Savitsky, N.N. Burtsev, *S. Powder Metallurgy and Metal Ceramics* **9**, (1981), 33-37
- [11] J.L. Bocquet, G. Brebec, Y. Limoge, *Physical Metallurgy*, 3rd.Edition, ed. by R.W. Cahn, and P. Haasen, (Netherlands,1983), 437-441
- [12] F.J.J. van Loo, G.D. Rieck, *Acta Met.* **21**, 1973, 61-71
- [13] H. Gleiter, *Physical Metallurgy*, 3rd.Edition, ed. by R.W. Cahn, and P. Haasen, (Netherlands, 1983), 684-690
- [14] H.E. Exner, E. Arzt, *Physical Metallurgy*, 3rd.Edition, ed. by R.W. Cahn, and P. Haasen, (Netherlands,1983), 1886-1911
- [15] W. Schatt, *Pulvermetallurgie Sinter- u. Verbundwerkstoffe*, VEB Deutscher Verlag f. Grundstoffindustrie, Leipzig, (1984)
- [16] R. Wagner, F. Appel, R. Bormann, R. Gerling, *Proc. 3rd. International SAMPE Symposium*, ed. by H. Fukotomi and M. Yamaguchi, (The Japan Chapter of SAMPE, 1993), 1886-1911
- [17] M. Dahms, H. Clemens, *Pulvermetallurgie in Wissenschaft und Praxis* **11**, (1995), 113-135
- [18] M.-S. Kim, K. Shibue, *Light Materials For Transportation Systems*, Center for advanced Aerospace Materials, ed. N.J. Kim, Korea, (1993), 295-303
- [19] K. Shibue, M.-S. Kim, M. Kumagi, *Intermetallic Compounds-Structure and Mechanical Properties*, The Japan Institute of Metals, Sendai, Japan, (1991), 833-838
- [20] M. Oehring, T. Klassen, R. Bormann, *J. Mater. Res.* **8**, (1993), 2819-2829
- [21] Y.W. Kim, D.M. Dimiduk, *The Processing, Properties, and Applications of Metallic and Ceramic Materials*, eds. M.H. Loretto, C.J. Beevers, (1992), 589
- [22] K. Taguchi, M. Ayada, K.N. Ishihara, P.H. Shingu, *Intermetallics* **3**, (1995), 91-98
- [23] G.-X. Wang, B. Dogan, F.-YHsu, H.-J. Klaar, M. Dahms, *Metallurgical and Materials Trans. A* **26**, (1995), 691-701

# Creep Behaviour of a Cast $\gamma$ -TiAl based alloy for Gas Turbine Applications

D. Lundström and B. Karlsson

Dept. of Engineering Metals  
Chalmers University of Technology  
SE-412 96 Göteborg, Sweden

## Abstract

The creep behaviour of the  $\gamma$ -TiAl based alloy Ti-48Al-2W-0.5Si (at.-%) has been investigated in the stress range 80 - 325 MPa at temperatures from 700 to 850°C. The material was produced by casting, followed by hot isostatic pressing and two successive heat treatments. Variations in the nominal compositions allowed both nearly lamellar ( $\gamma + \alpha_2$ ) as well as duplex ( $\gamma +$  lamellar) microstructures to develop. The nearly lamellar microstructure exhibits better creep resistance than the duplex material at lower temperatures/higher stresses, whereas both microstructures have similar creep behaviour at higher temperatures/lower stresses. For all conditions the creep rate in regime II passes a minimum at fairly small creep strains followed by gradually increasing creep rates until the onset of tertiary creep in regime III. The tertiary creep takes up a relatively large part of the whole creep life-time. The creep behaviour preceding final fracture depends on nucleation and growth of cavities as well as on microstructural instability.

## Introduction

During the last years, growing interests in the application of titanium aluminides have led to efforts for understanding the properties of this class of materials. Of primary concern is future replacement of mainly nickel-based super alloys and Ti-alloys in

gas turbines. Also, for automotive applications the aluminides are beginning to gain interest. The development so far has mainly been focused on  $\gamma$ -TiAl based alloys, where the phases  $\gamma$ -TiAl and  $\alpha_2$ -Ti<sub>3</sub>Al are contained in either lamellar/near lamellar or duplex microstructures. The  $\gamma$ -based TiAl has good mechanical properties up to about 700°C and can be cast, forged, machined and welded to components without sacrificing the properties too much. The highest competitiveness of aluminides is attained when the low density is taken into account. The cost of titanium aluminides is also fairly advantageous.

A serious drawback of titanium aluminides is the brittle behaviour at ambient and slightly elevated temperatures. Development of two-phase alloys, often alloyed with alloying elements such as e.g. Cr, Nb, W, Mn, V and Si [1], has led to improvement of the mechanical properties. It has been suggested that the most promising compositions should have a Al-content of about 48 at.-% [2], but the properties of these alloys are highly dependent upon the particular microstructure [3,4]. Thus fairly small shifts in chemical composition or heat treatments are very decisive for the emerging microstructure. The casting procedures are gradually recognised as being very important for the resulting properties.

( $\gamma$ -TiAl)-based alloys are often developed into duplex or nearly lamellar microstructures. The duplex structures often display better strength, toughness and low cycle fatigue properties than do nearly-lamellar microstructures [5]. Accompanying this situation

is the observation that duplex structures often exhibit less scatter in tensile, toughness and LCF data. Regarding creep properties it has been observed that lamellar or nearly lamellar structure exhibit better creep resistance than duplex materials [1,6,7]. The reason for this is not well understood [1], since the creep rate can not be easily related to the grain size or the volume fraction of present phases [1,7,8]. In technical situations the creep behaviour is of great importance for high temperature service.

In the present project, which is a part of a large European cooperation project (COST 501), characterization of creep behaviour of an ABB-patented two-phase ( $\gamma+\alpha_2$ ) alloy is made. The nominal composition of this alloy is Ti-48Al-2W-0.5Si (at.-%). Variations in chemical composition and heat treatment procedures lead to variations in microstructure and thereby in creep behaviour.

Comparisons of the present creep data with some other two-phase TiAl-alloys show that the material used in the present investigation exhibits comparable or even better creep resistance [6,9,10] than attained before in similar alloys.

### Experimental Procedures

#### Material and specimen fabrication

Four different materials have been investigated. The four materials are denoted 1, 1b, 2, and 3. Each material was cast, hot isostatically pressed (HIP) and later heat treated (HT) in two successive steps. All four materials were based on the newly patented ABB-alloy IMN-2 with a nominal composition of Ti-48Al-2W-0.5Si (at.-%) but with variations in chemistry and HIP-conditions. All materials were produced by investment casting at Precision Castparts Corp. (PCC) and at Howmet Corp. in USA. Table 1 shows the actual compositions, indicating lower Al-content and higher W-content for materials 1 and 1b. The subsequent HIP-treatment and successive heat treatments (HT 1 and HT 2) shown in Table 2 were virtually identical for all materials, apart from materials 1 and 1b, where a lower HIP-temperature was used.

Table 1 Chemical analysis and nominal composition (wt.-%)

Material	Ti	Al	W	Si	Fe	Cu	O	H	N
1	59.38	30.35	9.78	0.41	-	-	0.071	0.0012	0.005
1b	59.26	30.52	9.77	0.37	-	-	0.068	0.0014	0.006
2	59.36	31.32	8.98	0.20	0.031	0.04	0.0632	0.0012	0.0061
3	58.94	31.27	9.29	0.38	0.035	0.01	0.0653	0.0002	0.008
nominal	58.56	32.00	9.09	0.35	-	-	-	-	-

Table 2 HIP- and HT-conditions (°C, MPa and h)

Material	HIP			HT 1			HT 2		
	Temp	Pressure	Time	Temp	Time	Cooling	Temp	Time	Cooling
1	1185	172	3	1302	20	GFC	913	4	GFC
1b	1185	172	3	1302	20	GFC	913	4	GFC
2	1260	172	3	1302	20	GFC	899	4	GFC
3	1260	172	4	1302	20	GFC	899	4	GFC

GFC = gas fan cooling.

Materials 1-3 were produced to provide different microstructures and accordingly different creep behaviour. Series 1b, which essentially is a duplicate of material 1, was used to determine activation energies  $Q_c$  and the stress exponent  $n$ . The microstructures were characterized by optical microscopy (OM) and in some cases also by analytical electron microscopy (SEM, TEM, EDS). SEM was performed with CamScan S4-80 DV, and TEM analyses were carried out with a Zeiss EM 912 Omega instrument equipped with a Link EDS-system for quantitative elemental analysis.

#### Creep testing

The creep specimens were machined from cylindrical cast bars of diameters 15 mm. Two types of creep specimens were used, as required by the employed creep testing machines. The dimensions were as follows: (Overall length)/(gauge length)/(diameter) were 150/20/4 mm and 75/30/5 mm respectively.

The creep tests were performed with two different types of machines: a conventional creep machine (shorter specimen) and an equipment designed for ceramic materials, type NPL-K2 (longer specimen), respectively. All testing was conducted in air at constant applied load. Dead weight was used for the conventional creep machine, while the load in the NPL-K2 machine was controlled by a computerised step-motor. In both cases, the strain was measured by LVDT extensometers and sampled by a computer. The ranges of temperatures and initial stresses used were 700-850°C and 80-325 MPa respectively.

### Results

#### Microstructure of as received material

The lower HIP-ing temperature for materials 1 and 1b resulted in a remnant porosity of about 1 vol.-%, while materials 2 and 3 were fully dense. After final heat treatment materials 1 and 1b exhibited nearly lamellar ( $\gamma+\alpha_2$ ) colonies formed from the large dendritic grains developed during solidification (Figure 1), while material 2 and 3 had duplex microstructures consisting of lamellar ( $\gamma+\alpha_2$ )-colonies and single-phase  $\gamma$ -grains (Figure 2).

The *nearly lamellar* structure (Figure 1) consists of typically 80-90 vol.-% of large lamellar colonies with sizes up to about 1 mm. This dominance of the lamellar constituent emanates from the lower Al-content in material 1 [8]. In addition, single phase  $\gamma$  is present as small grains ( $\approx 20 \mu\text{m}$ ) separating the lamellar colonies. Moreover, large ( $\approx 100 \mu\text{m}$ )  $\gamma$ -grains are found with diffuse interfaces with the lamellar colonies (Figure 3). These  $\gamma$ -grains contain pores and small, spherical precipitates of diameter approximately  $2 \mu\text{m}$ . EDS-analyses of thin TEM-foils revealed these precipitates to be titanium silicides, presumably of type  $\text{Ti}_3\text{Si}_3$ . Such precipitation might be expected since the nominal Si-content for materials 1 and 1b is fairly high (Table 1), and the solubility limit for Si in the  $\gamma$ -phase is about 0.5 at.-% [11] ( $\approx 0.4$  wt.-%). Both the pores and the associated titanium silicides are mainly found in the last solidified regions towards to centre of the cast bars. Evidently Si is enriched in the melt during solidification causing silicides to be more frequent in the centre. Later HIP-ing diminishes the amount of pores while silicide precipitation is

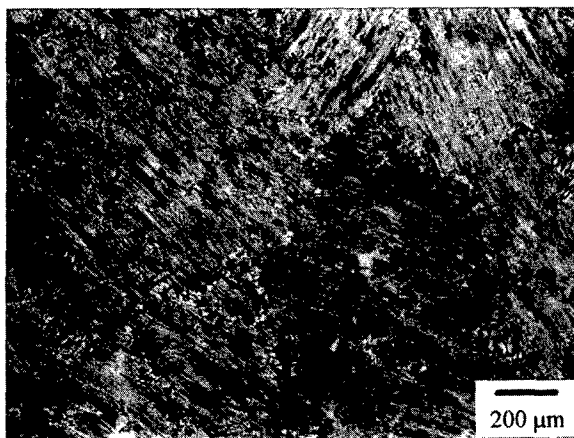


Figure 1: Optical micrograph showing the nearly lamellar structure of material 1.

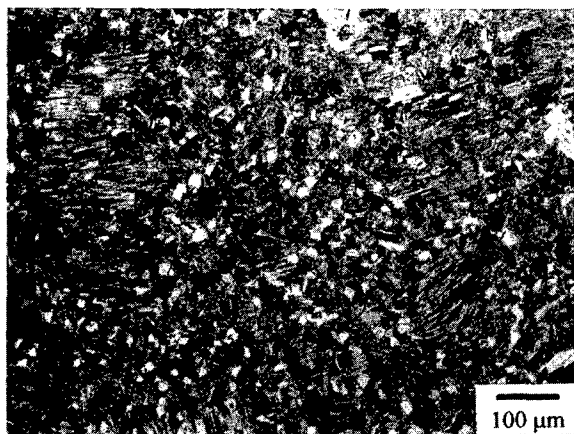


Figure 2: Optical micrograph showing the duplex structure from material 2.

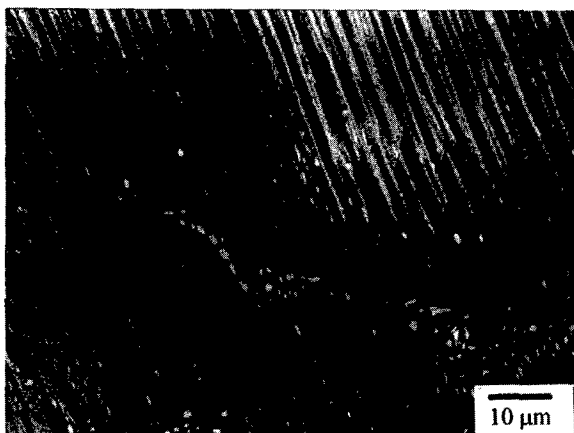


Figure 3: SEM (BSE imaging) micrograph showing pores and Si- and Ti-rich precipitates in nearly lamellar material, material 1.

further promoted. High local Si-contents decreases the amount of lamellar structures (Figure 3) [11]. Some coarser precipitates were also found in the nearly lamellar structure. EDS-analysis in TEM revealed these to be rich in W, indicating these precipitates to be  $\beta$ -phase. This phase also contained very fine, secondary precipitates, too tiny to allow EDS-analysis in TEM-foils.

Materials 2 and 3 consist of *duplex structures* (grain sizes about 50  $\mu\text{m}$ ) as a result of the higher Al-content. Some larger  $\gamma$ -grains and lamellar colonies grains were found. Precipitation of titanium silicide similar to material 1 was found in material 3 but only to a very limited degree in material 2 owing to its lower Si-content (Table 1). W-rich  $\beta$ -phase of the same kind as found in the nearly lamellar material, material 1, was observed in duplex materials (materials 2 and 3) as well.

A more detailed account of the microstructure will be presented elsewhere. An important observation is, however, that there exists a large variation in the microstructure in both the nearly lamellar and the duplex material. Typically, the volume fractions of lamellar regions and  $\gamma$ -phase could vary markedly both axially and longitudinally in the test bars. This is likely to cause variation in the creep behaviour of the material.

#### Microstructure of crept material

Studies of the microstructure of crept materials were also performed. Cavities in all materials were observed within the necked region preceding final fracture. Material 1 with its nearly lamellar microstructure showed preserved packages of bent lamellae close to the fracture surface. Some cracks along the lamellae within the colonies were seen close to the fracture surface. The duplex microstructures, materials 2 and 3 being more fine-grained, exhibited a more distorted structure with highly elongated  $\gamma$ -grains and lamellar colonies at high creep strains.

#### Creep behaviour

The results of the creep tests are summarised in Table 3, where the time to rupture ( $t_r$ ), tertiary creep time ( $t_t$ ), minimum creep rate in regime II ( $\dot{\epsilon}_{\text{min}}$ ), and strain to rupture ( $\epsilon_r$ ) are shown for the selected stresses and temperatures.

Figure 4 shows the recorded creep curves for the different test conditions. The creep starts with a pronounced primary creep period which extends up to about 1% creep strain at the lower temperatures/higher stress levels, but does not exceed 0.5% creep strain at the higher temperatures/lower stress levels employed. Although the strain-time curves in the secondary creep regime seem to exhibit linear parts (Figure 4), a more detailed analysis of the creep behaviour showed that the minimum in the creep rate after fairly limited strains is followed by increasing strain rates, indicating no extended steady state range. This observation is more clearly demonstrated by plotting creep strain rate vs. creep strain for some of the recorded creep curves (Figure 5), indicating a fairly gradual transition to the tertiary creep regime and making estimates of the secondary creep period approximate. The strain in the secondary creep regime is therefore rather limited. The period of succeeding accelerating creep rates in the tertiary regime was thus found to be large and corresponds to roughly 60 - 80% of the

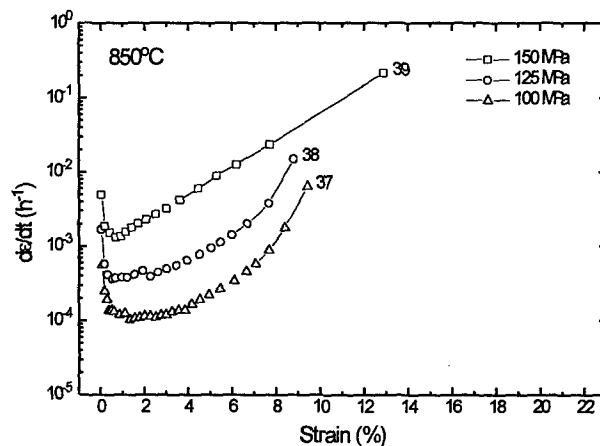
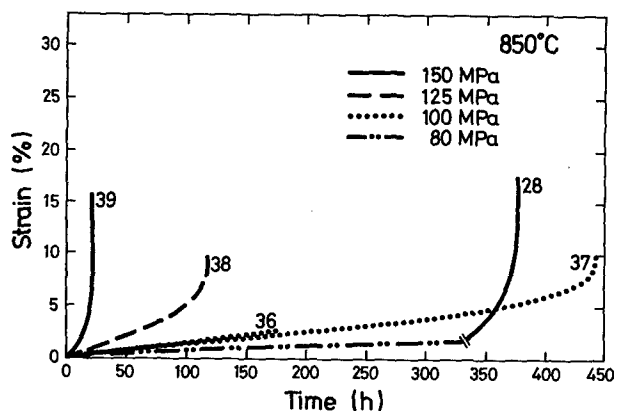
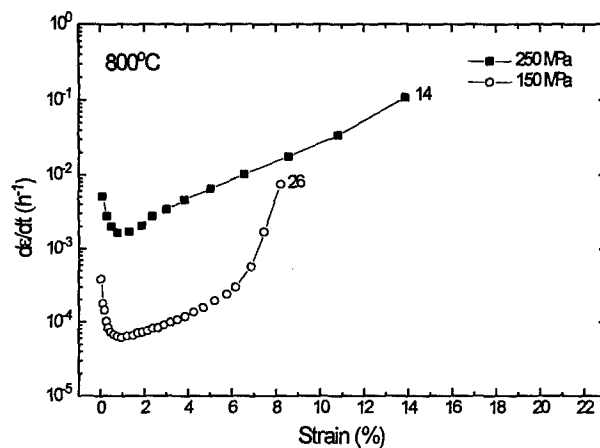
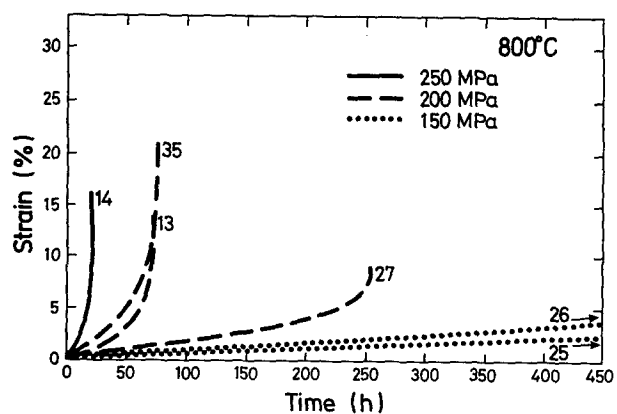
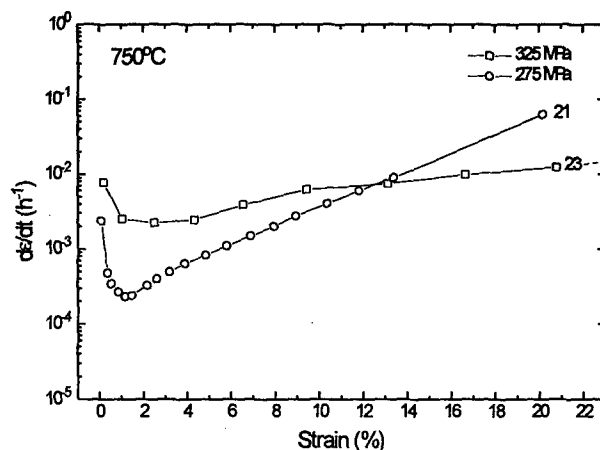
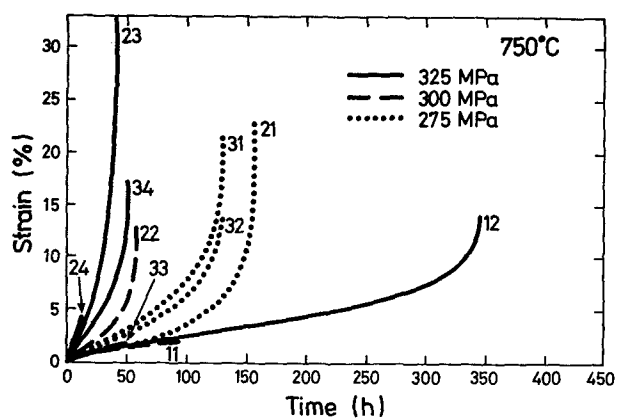


Figure 4: Creep strain vs. applied stress for 750°C, 800°C and 850°C. The number at each curve denotes the tested sample (cf. Table 3). It should be noticed that samples number 24, 33 and 36 are treated as "stopped within regime II" since they fractured outside the gauge length.

Figure 5: Strain rate vs. creep strain curves for 750°C, 800°C and 850°C. The number at each curve denotes the tested sample.

total creep strain to fracture. Although most of the tested specimens showed a creep strain to fracture ( $\epsilon_r$ ) of about 10 to 20%, as high creep strains to fracture as 33% were incidentally observed (Table 3). Considering times spent in the different regimes, Table 3 indicates a tertiary creep time  $t_t$  of about 25 - 50% of the total time to rupture  $t_r$ .

Table 3 Summary of creep data

Material Sample	Temp °C	$\sigma_{\text{applied}}$ MPa	$t_t$ h	$t_r$ h	$\dot{\epsilon}_{\text{min}}$ $10^{-5} \text{ h}^{-1}$	$\epsilon_r$ %	$\lambda$
1	11	750	300	-	13.0	-	-
1	12	750	325	-	349.8	13.6	2.2
1	13	800	200	25.0	74.9	13.5	5.1
1	14	800	250	11.1	23	15.7	4.2
2	21	750	275	82.8	160.9	22.4	5.6
2	22	750	300	22.8	60.3	12.4	2.9
2	23	750	325	24.8	48.5	32.9	3.0
2 <sup>1)</sup>	24	750	325	-	28.5	275	(>10.8)
2	25	800	150	438	961.4	4.4	2.3
2	26	800	150	373	622	6.2	8.5
2	27	800	200	114.3	257.3	13.8	9.2
2 <sup>2)</sup>	28	850	80	-	4.0	-	-
2 <sup>2)</sup>	28	850	150	-	(65)	104	17.8
3	31	750	275	77.0	134.2	55.7	21.1
3	32	750	275	58.0	133.2	44.0	13.4
3 <sup>1)</sup>	33	750	300	-	147.6	27.4	(>5.2)
3	34	750	325	22.0	53.8	134.9	16.5
3	35	800	200	42.1	78.3	74	21.1
3 <sup>1)</sup>	36	850	100	-	303.5	12	(>16.5)
3	37	850	100	112.7	447.7	11.1	10.1
3	38	850	125	45.0	120	38.0	9.7
3	39	850	150	12.6	23	130	15.1
1b <sup>3)</sup>	-	700	300	-	6.2	-	-
1b <sup>3)</sup>	-	750	300	-	87.6	-	-
1b <sup>3)</sup>	-	750	325	-	180	-	-

1) Fracture outside gauge length.

2) This sample has been tested at two stress levels, 80 and 150 MPa respectively. Time to rupture was estimated.

3) Material 1b was used mainly for calculation of activation energy for creep  $Q_c$ , stress exponent for creep  $n$ .

#### Minimum creep rate

To allow comparisons between samples crept at different temperatures and stress levels, Larson-Miller-plots [12] (LMP) were constructed. Such plots were evaluated for both the time to rupture ( $t_r$ ) - not shown here - and for the inverse of the minimum creep rate (approximately corresponding to the secondary creep rate), see Figure 6. The LMP parameter results in linear curves in both cases, over the stress and temperature intervals tested. The lamellar microstructures (material 1) exhibit somewhat larger creep life time (lower minimum creep rate), especially at lower temperatures and higher stresses. This is in agreement with results reported by others, namely that lamellar microstructures exhibit better creep resistance than duplex microstructures. However the coarse, nearly lamellar

microstructure and presence of pores in material 1 cause a larger scatter in the high stress (low temperature) region.

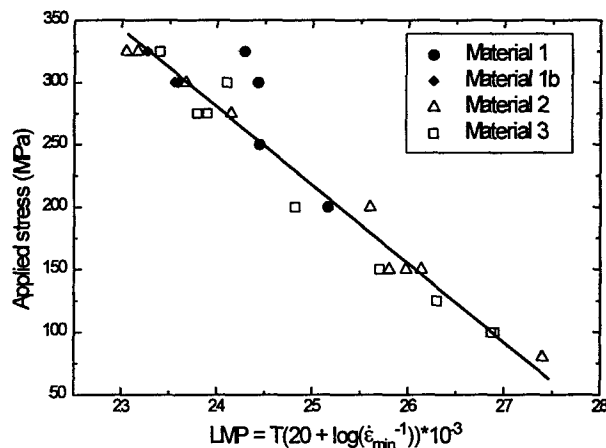


Figure 6: Applied stress vs. LMP-parameter using inverse of minimum creep rate.

#### Discussion

##### Minimum creep rate

As stated above, the creep rate steadily increases in regime II as demonstrated in Figure 5. Thus, once the creep strain rate has reached its minimum value  $\dot{\epsilon}_{\text{min}}$  at a strain level of approximately 1-2%, a continuously increasing strain rate ensues. This applies to all stress and temperature levels studied here. Such a pseudo-steady state creep regime existing only at creep rates close to the minimum has been observed before [10,13] for other types of aluminides. On the other hand, e.g. Kim, Cho and Hong [6] have reported extended steady state creep regimes for the aluminides Ti-47Al-2Mn, Ti-47Al-2Zr and Ti-48Al (at.-%). However, the use of short creep times and not evaluating creep strain rates vs. strain (as in Figure 5) make their conclusions doubtful.

The assumption that the creep rate is determined by the stress level (Norton's law) and by thermal activation allows a power creep law to be used to describe the minimum creep rate:

$$\dot{\epsilon}_{\text{min}} = K_1 \times (\sigma)^n \quad (1)$$

$$\dot{\epsilon}_{\text{min}} = K_2 \times (\sigma)^n \times \exp(-Q_c/RT) \quad (2)$$

where  $K_1$  and  $K_2$  are proportionality constants. To test this hypothesis, the minimum creep rates ( $\dot{\epsilon}_{\text{min}}$ ) as evaluated from the curves in Figure 5 were depicted vs. the applied stress in a log-log plot (Figure 7) for the different temperatures used here. With reasonably limited scatter the experimental data follow Norton's law (eq. 1) with stress exponents  $n$  of 6.6 and 5.3 at temperatures 800 and 850°C respectively for all three materials. At the lower temperature, 750°C, material 1 with its nearly lamellar structure shows a lower  $n$  value of 4.1; the latter value is, however, uncertain due to the availability of only two data points at close stress levels. These comparatively low  $n$  values ( $n \approx 4-6$ ) indicate that dislocation climb is the prevailing creep mechanism, i.e.

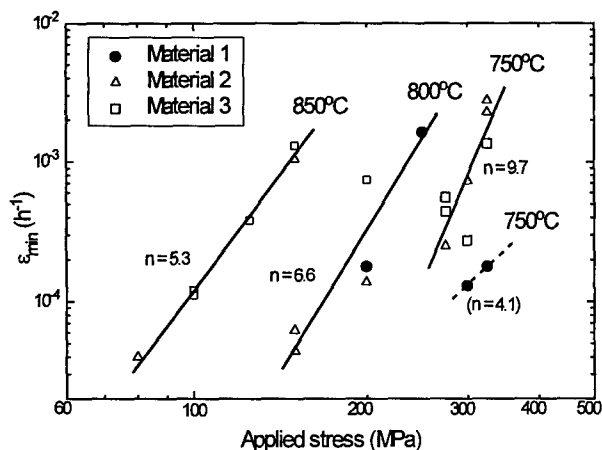


Figure 7: Minimum creep rate vs. applied stress.

power law creep. On the other hand, the duplex structures were observed to have an  $n$ -value of 9.7 at 750°C indicating a shift to dislocation glide as the dominating creep mechanism [1].

Figure 6 and Table 3 indicate that the nearly lamellar as well as the duplex microstructures exhibit similar creep resistance at 800°C for the fairly low creep stresses of relevance at this temperature. This observation can be compared with results obtained by Oikawa and Maruyama [14] showing that the lamellar ( $\gamma/\alpha_2$ ) structure at lower stresses displays a creep resistance between that of the two constituting phases  $\gamma$  and  $\alpha_2$ . At higher stresses, however, these phases have creep properties inferior to a lamellar microstructure.

Assuming that a similar behaviour applies to a duplex microstructure at lower stresses should indicate similar creep behaviour of lamellar and duplex microstructures under such conditions. On the hand, Figure 6 clearly indicates that the nearly lamellar microstructure offers better creep resistance than the duplex microstructure at the lower temperature 750°C.

The only sample available of material 1b was used for determination of the activation energy for creep  $Q_c$  and the stress exponent for creep  $n$  to represent the nearly lamellar microstructures. These values were obtained by changing temperature and stress respectively at the stage when minimum creep rate had been reached, Table 4. The minimum creep rates obtained during stress or temperature increment tests, though, should be interpreted with caution, since a slightly overestimated minimum creep rate could be obtained after the increased stress or temperature, due to the gradual increase in creep rate within the secondary creep regime.

Table 4 Activation energy and stress exponent for material 1b

Temp °C	Stress MPa	$Q_c$ kJ/mol	$n$	$K_1$ (MPa) $^{-n}$ s $^{-1}$	$K_2$ (MPa) $^{-n}$ s $^{-1}$	$\epsilon_{at shift}$ %
700→750	300	560	-	-	$4.2 \times 10^{-38}$	1.1
750	300→325	-	9.0	$1.2 \times 10^{-29}$	-	1.6

$\epsilon_{at shift}$  denotes creep strain at changed temperature or stress.

Table 4 shows the activation energy and stress exponent achieved on shifting temperature from 700 to 750°C and the stress from 300 to 325 MPa. It turns out that the activation energy  $Q_c$  here is higher than that found for other aluminides with a predominantly lamellar structure [1]. Also the stress exponent  $n$  is high, close to the value observed for the duplex structure at 750°C, which indicates power law break down creep. Since materials 1 and 1b have virtually identical chemical compositions and heat treatment conditions, it is expected that material 1b would have a creep behaviour similar to material 1.

Comparisons with similar alloys investigated in the literature indicate that the present material has similar or better creep resistance. A Ti-47Al-2Mn fully lamellar alloy, investigated by Kim, Cho, and Hong [6] exhibited about 5 times larger minimum creep rate than the present nearly lamellar microstructure in material 1 at 800°C/200MPa. However, a duplex Ti-47Al-2Zr alloy was shown [6] to have a creep resistance close to the present nearly lamellar structure at 800°C/200MPa. The stress exponent for their alloys was about 3.7-4.2, i.e. slightly lower than the stress exponent obtained in the present investigation. A Ti-48Al-2Cr fully lamellar alloy, investigated by Es-Souni, Bartels, and Wagner [10], also exhibited a comparable creep resistance in the region 800°C/150-260 MPa, but with a higher stress exponent, 7.6. These comparisons indicate that the material used in this investigation should be considered very competitive compared with alternative titanium aluminides.

#### Tertiary creep

The stress dependence of the time in tertiary creep stage,  $t_t$ , was used in order to analyse the tertiary creep behaviour. The time  $t_t$  was calculated as the time from onset of tertiary creep up to the time to rupture  $t_r$ .

The relation between applied stress and time spent in the tertiary creep regime was checked for all three materials by plotting the applied stress  $\sigma_{app}$  vs.  $t_t$  for the different temperatures in a log-log diagram, Figure 8. The straight lines found for each temperature indicate a relation of type

$$t_t = K_3 (\sigma_{app})^{-n} \quad (3)$$

where the stress exponent  $n$  is about 6 for all temperatures. As  $t_t$  is approximately inversely proportional to the creep rate at the onset of tertiary creep and the actual stress is close to  $\sigma_{app}$  (cf. Figure 4) it appears that eqns. (1) and (3) are formally equivalent indicating a similar kind of stress dependence of the creep rate in the tertiary creep as for the secondary creep. The temperature dependence of the tertiary creep behaviour thus resembles that for the secondary creep in regime II.

Dyson and Gibbons [15] have shown that the resistance to local strain concentrations in a material can be expressed by a damage tolerance parameter  $\lambda$

$$\lambda = \epsilon_f / (\dot{\epsilon}_{min} t_r) \quad (4)$$

where  $\epsilon_f$  is the creep strain to fracture,  $\dot{\epsilon}_{min}$  is the minimum creep rate and  $t_r$  the time to rupture. A material which fails predominantly by intergranular cavity nucleation and growth

would then always exhibit a  $\lambda$ -value between 1 and 2.5. The damage tolerance parameter  $\lambda$  for the present alloys was estimated from the creep tests and values are presented in Table 3, along with  $\epsilon_p$ ,  $\dot{\epsilon}_{min}$  and  $t_p$ . It is seen that the parameter  $\lambda$  falls between about 2 and 5. Investigations by Hayes and Martin [16] on single phase  $\gamma$ -TiAl indicate even higher  $\lambda$ -values. These evaluations thus indicate that formation and growth of cavities is not the only operative mechanism behind the accelerating creep rate in the tertiary creep regime. Instead it must be assumed that some kind of microstructural instability takes place which also might develop in regime II where the creep rate gradually increases. Still, the fairly high creep ductility found in the present materials indicates a slow development of microstructural break down. TEM-investigations of this process in the present material are in progress and will be published elsewhere:

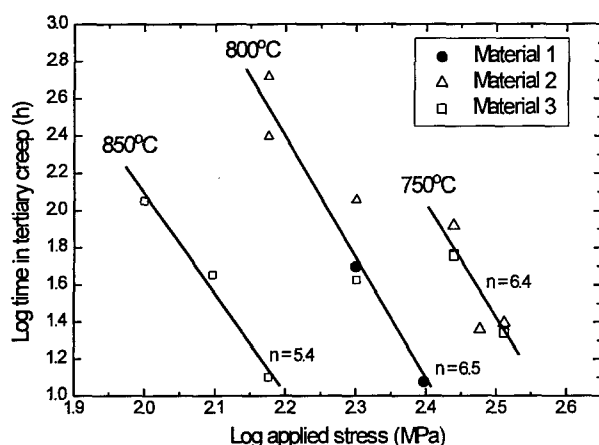


Figure 8: Time in tertiary creep regime vs. applied stress.

### Conclusions

$\gamma$ -TiAl based titanium aluminide of type Ti-48Al-2W-0.5Si (at.-%) has been studied regarding creep properties at temperatures between 700 and 850°C. Minor variations in the chemical composition allowed both nearly lamellar and duplex microstructures to be created. Following general conclusions can be drawn:

1. Nearly lamellar microstructures exhibit better creep resistance than duplex materials at lower temperatures/higher stresses. At higher temperatures/lower stresses the creep rates for both microstructures approach each other.
2. The creep rate in regime II exhibits a minimum rate at fairly low strains, followed by a gradual increase in creep rate until the onset of regime III.
3. The creep behaviour preceding final fracture depends on nucleation and growth of cavities as well as on microstructural instability.

### Acknowledgements

The Swedish National Board for Technical and Industrial Development has supported financially. The material was supplied by ABB Power Generation, Baden, within the European COST 501 programme. Dr. P. Sotkovszki provided assistance with metallography and Dr. M. Knutson-Wedel supported with electron microscopy work.

### References

1. J. Beddoes, W. Wallace, and L. Zhao, "Current understanding of creep behaviour of near  $\gamma$ -titanium aluminides," *International Materials Reviews*, 5 (1995), 197-217.
2. S. Mitao, S. Tsuyama, and K. Minakawa, "Effect of aluminum content on creep deformation behavior of  $\gamma$ -titanium aluminides," *Microstructure/Property relationships in titanium aluminides and alloys*, ed. Y.-W. Kim and R.R. Boyer, The minerals, metals and materials society, (1991) 297-311.
3. S.C. Huang and E.L. Hall, "Plastic deformation and fracture of binary TiAl-base alloys," *Metall. Trans.*, 22A, (1991) 427-439.
4. Y.-W. Kim, "Microstructural evolution and mechanical properties of a forged gamma titanium aluminide alloy," *Acta Metall. Mater.*, 40, (1992) 1121-1134.
5. V. Recina and B. Karlsson, "Tensile and low cycle fatigue properties of Ti-48Al-2W-0.5Si gamma titanium aluminide", This conference.
6. S. Kim, W. Cho, and C.-P. Hong, "Creep behaviour of cast TiAl based intermetallics," *Materials Science and Technology*, 11 (1995) 1147-1155.
7. D.I. Kimm and J. Wolfenstine, "Effect of grain size on the creep behavior of fully transformed  $\gamma$ -TiAl," *Scripta Metall. Mater.*, 30, (1994) 615-619.
8. S.-C. Huang, "Microstructures and property tradeoffs in wrought TiAl-base alloys," *Metall. Trans.*, 23A, (1992) 375-377.
9. G.B. Viswanathan and V.K. Vasudevan, "Tensile, creep properties and microstructural correlations in an extruded Ti-48Al alloy," *MRS Symp. Proc. on High temperature intermetallic alloys V*, ed. I. Baker et al., Pittsburgh, PA, Materials Research Society, 288, (1993) 787-792.
10. M. Es-Souni, A. Bartels, and R. Wagner, "Creep behaviour of a fully transformed near  $\gamma$ -TiAl alloy Ti-48Al-2Cr," *Acta Metall. Mater.*, 43, (1995) 153-161.
11. S. Tsuyama, S. Mitao, and K. Minakawa, "Alloy modification of  $\gamma$ -base titanium aluminide for improved oxidation resistance, creep strength and fracture toughness," *Materials Science and Engineering*, A153, (1992) 451-456.



12. F.R. Larson and J. Miller, "A time-temperature relationship for rupture and creep stresses," Trans. ASME, 14, (1952) 765-775.
13. T. Takahashi and H. Oikawa, "Influence of composition on the grain size dependence of compressive creep in single-phase TiAl intermetallics," Microstructure/Property relationships in titanium aluminides and alloys, ed. Y.-W. Kim and R.R. Boyer, The minerals, metals and materials society, (1991) 227-235
14. H. Oikawa and K. Maruyama, "Creep behavior of single-phase and two-phase Ti-Al binary alloys," Gamma Titanium Aluminides, ed. Y.-W. Kim, R Wagner and M. Yamaguchi, The minerals, metals and materials society, (1995) 919-930.
15. B.F. Dyson and T.B. Gibbons, "Tertiary creep in nickel-base superalloys: analysis of experimental data and theoretical synthesis," Acta Metall., 35, (1987) 2355-2369.
16. R.W. Hayes and P.L. Martin, "Tension creep of wrought single phase  $\gamma$  TiAl," Acta Metall. Mater., 43, (1995) 2761-2772.

**INFLUENCE OF MICROSTRUCTURE, ENVIRONMENT AND TEMPERATURE  
ON FATIGUE CRACK PROPAGATION IN TiAl ALLOYS.**

**Gilbert HÉNAFF, Catherine MABRU, Anne TONNEAU and Jean PETIT**

**Laboratoire de Mécanique et de Physique des Matériaux - UMR CNRS 6617**

**ENSMA - Téléport 2 - Avenue 1 - B. P.109 Chasseneuil du Poitou**

**F-86960 FUTUROSCOPE CEDEX**

**Abstract**

Titanium aluminides based on TiAl ( $\gamma$ , L1<sub>0</sub>) are currently holding great promise as elevated-temperature structural materials in place of the superalloys used at present. However, the damage tolerance assessment of these materials is key to their introduction in many applications. With this respect, the fatigue crack propagation behaviour of  $\gamma$ -based alloys has to be investigated. The present paper is addressing this issue with a special attention being paid to the role of intrinsic and extrinsic factors on crack growth. In particular the respective influence of microstructure on crack growth rates is examined in relationship with closure and other shielding mechanisms. Environmental effects are also investigated, mostly at room-temperature. For comparison purposes ancillary testings performed on an iron aluminide-based alloy are included. Finally the fatigue crack growth resistance of a  $\gamma$ -based alloy is evaluated at elevated temperature.

**Introduction**

Ordered intermetallic compounds have received considerable attention in recent years as viable candidates for structural applications in extreme conditions (high temperatures, hostile environments) (1). Among all the categories of intermetallic alloys which have monopolised attention, the TiAl based alloys are the most promising ones from an industrial processing point of view. Indeed, due to their low density, good oxidation and corrosion resistance, excellent modulus retention and quite reasonable strength at elevated temperatures, they are expected to replace the conventional alloys currently used in advanced gas turbine engine applications (2). However there are still some issues which need to be clarified before introduction in engineering structures. In particular the damage tolerance of these compounds is still under question. With this respect one has not only to consider the fracture toughness which

constitutes a main drawback, but also to get insights into the fatigue crack growth resistance.

The present study is addressing this issue. The fatigue crack growth resistance of two quaternary TiAl alloys, with two different microstructures, has been investigated under various environmental conditions. Indeed it is well recognised that the fatigue crack growth behaviour of conventional engineering alloys is more or less deeply affected by the influence of several extrinsic parameters. The question is then to determine to what extent the same mechanisms apply to the case of intermetallic compounds, especially under the brittle-ductile transition. In particular fatigue crack growth are generally higher in a moist environment than in an inert environment (3). Besides it has been shown that aluminides are prone to environmental embrittlement during tensile tests in similar moist environments (4-6). As a consequence environment is expected to play a detrimental role in the fatigue damage in these compounds. However when tackling the issue of environmentally-assisted fatigue crack propagation one has to clearly distinguish the specific role played by other extrinsic influence on the propagation, mostly crack closure effects. The methodology used here precisely aims to uncouple these effects, in a first step at room-temperature. Thus the fatigue crack growth behaviour of two characteristic microstructures, namely equiaxed and lamellar, has been examined in air and in vacuum by taking into account possible closure effects. Ancillary results related to environmentally-assisted fatigue crack propagation in an iron aluminide alloy are also included for comparison purposes. Finally, since  $\gamma$ -based alloys will operate at elevated temperature, it is essential to generate data in the same temperature range. This is the reason why fatigue crack growth rates have been performed in the range 600°C-800°C.

## Experimental details

### Materials

The main material investigated in this study is a quaternary alloy of nominal composition Ti-48Al-2Mn-2Nb. Table 1 gives its chemical composition.

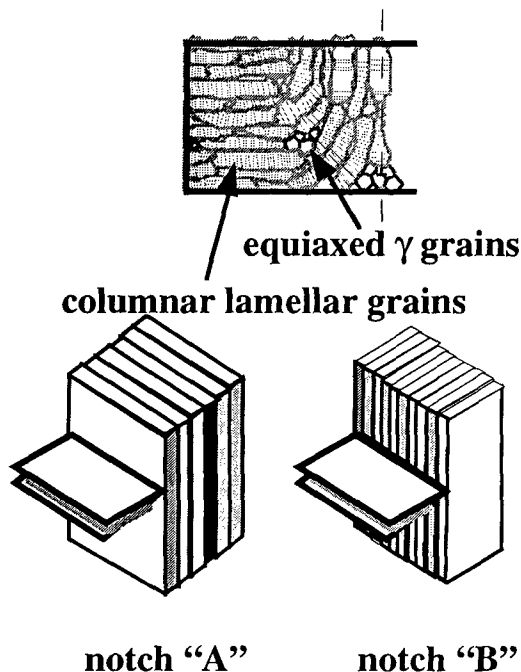


Figure 1 : Schematic representation of the ingot microstructure and the notch orientation of fatigue specimens.

The material was provided as a piece of ingot produced in a large-scale plasma furnace by the IRC (Interdisciplinary Research Centre) in Birmingham (UK). Further details are available elsewhere (7-9). In the

as-cast condition the microstructure is nearly fully lamellar, consisting of coarse alternating  $\gamma$  and  $\alpha_2$  plates grains with a grain size of approximately 300-400  $\mu\text{m}$  (figure 1). The preferential orientation of these plates is perpendicular to the longitudinal axis of the lamellar grains. The colonies elongation is longitudinal in the centre part of the ingot and becomes progressively radial for grains near the edge. Specimens were machined by taking into account the orientation of the crack plane with respect to the main lamellae orientation.

Two orientations were considered :

- notch "A" or crack arrester (10, 11);
- notch "B" or crack divider (10, 11).

Ancillary testings were also performed on some specimens previously heat-treated in order to get a randomised lamellae orientation which is of higher interest from an engineering point of view. The change in microstructural aspect is illustrated on figure 2.

In order to gain further insights into the role of microstructure, another quaternary alloy Ti-48Al-2Cr-2Nb provided by the CEA/CEREM/CE2M/LETRAM was also considered. The microstructure is equiaxed  $\gamma$  grains with a grain size of about 150  $\mu\text{m}$ . Details are available elsewhere (12, 13).

Table I Chemical composition of the Ti-48Al-2Mn-2Nb alloy (at. %).

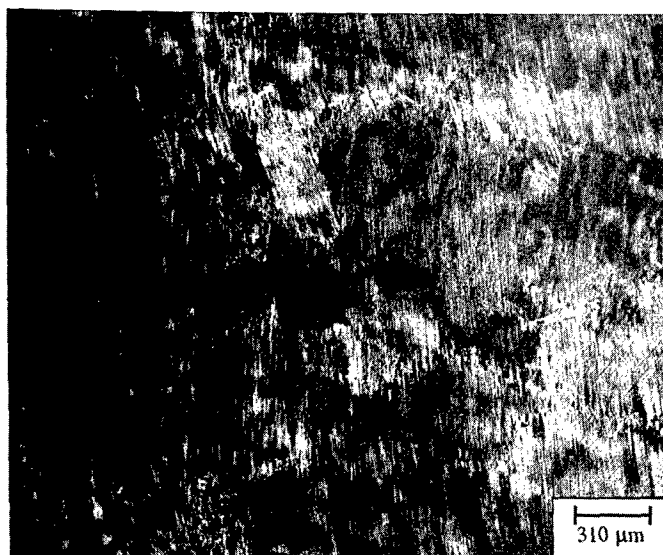
	Ti	Al	Mn	Nb	O
At. %	47.9	48	2	1.9	0.2

Table II Chemical composition of the Ti-48Al-2Cr-2Nb alloy (wt. %).

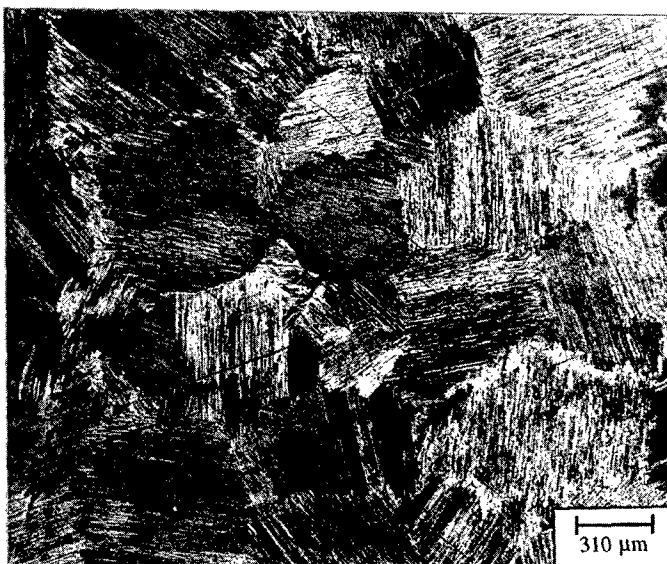
	Ti	Al	Cr	Nb	O
Wt. %	Bal.	32.7	2.62	4.7	0.002

Table III Nominal chemical composition of the FeAl40 grade 3 alloy (at. %).

	Fe	Al	Zr	B
At. %	Bal.	24	0.11	15 ppm.



(a)



(b)

Figure 2 : Microstructure of the Ti-48Al-2Mn-2Nb alloy a) as-cast - b) randomised.

Finally for comparison purposes ancillary testings were also performed on another kind of aluminide, namely a B<sub>2</sub> FeAl alloy. The composition is given in table III. This alloy, designed as FeAl 40 grade 3 was prepared by mechanical alloying and subsequently extruded at 1100°C by the CEA/CENG/CEREM in Grenoble France. Addition of B and Zr aims at strengthening grain boundaries and in improving creep resistance. Addition of nanometric dispersed Y<sub>2</sub>O<sub>3</sub> particles (1 wt. %) prevent grain coarsening during heat treatment and again to improve creep behaviour. The grain size is approximately 1µm. This processing route results in enhanced room temperature mechanical properties. More information about the material are available in reference (14).

### Testings

Fatigue crack growth experiments on TiAl were carried out using CT type specimens (W=22mm, B=5mm) taken with different orientations within the ingot (7). The conventional notch was prolonged by short slit ( $\approx 0.05$  mm) performed by electrodischarge machine. In the case of FeAl40 grade 3, due to the small diameter of extruded bars, small DCT specimens with W=9 mm and B=4 to 5 mm were used. Testings on a high strength steel on similar specimens have provided data very similar to those obtained with larger test pieces like CT specimens with W=75mm (15); this agreement validates the use of this particular geometry.

Fatigue crack propagation tests were carried out on servohydraulic machines. One of them is equipped respectively with an environmental cell permitting tests in vacuum ( $10^{-3}$  Pa) at ambient temperature and another one with a resistance furnace operating up to 1000°C. Tests were conducted at 35 Hz in tension-tension loading generally with a constant load ratio R=0.1. The crack length was determined by the use of a direct current potential difference technique. At room temperature it was also possible to optically measure the crack length on the polished side of the specimens by means of a travelling microscope. Crack closure measurements were performed at test frequency according to the unloading compliance method using, at room temperature, a back face gauge and, at elevated temperature, a sensor recording the rod displacement more precisely than the LVDT signal of the actuator. Additional fatigue tests were conducted in vacuum at 700°C at the IRC in Birmingham on a servohydraulic machine operating at 10Hz. In that case, crack closure measurements were not possible and different methods were used to indirectly estimate the crack closure effects or to operate under closure-free conditions (16).

### Results and discussion

Figure 3 presents the crack propagation rates obtained in air both on the lamellar Ti-48Al-2Mn-2Nb and the equiaxed Ti-48Al-2Cr-2Nb at room temperature. The salient feature of these curves resides in the rather high Paris law exponent exhibited by these curves, reflecting an intermediate behaviour between conventional metallic alloys and ceramics. Besides it appears on this plot that the lamellar microstructure exhibit an enhanced resistance with respect to the equiaxed alloy in the upper regime (above  $10^{-8}$  m/cycle).

This difference might be mainly attributed to the improved toughness of lamellar microstructure. It is generally admitted that this enhanced crack growth resistance results from different toughening mechanisms peculiar to the lamellar microstructure (17, 18):

- toughening by uncracked ligaments (19);
- toughening by crack tip debonding;
- toughening by diffuse microcracking.

Such mechanisms are less effective as the applied  $\Delta K$  value decreases and actually the nearly fully  $\gamma$  microstructure exhibits a slightly higher threshold value. However, as stressed in introduction, the behaviour presented on figure 1 results from a complex balance of both intrinsic fatigue damage and extrinsic influences. It is therefore difficult to conclude about the most relevant mechanisms. The next sections will aim to elucidate this aspect by investigating the specific role of various factors.

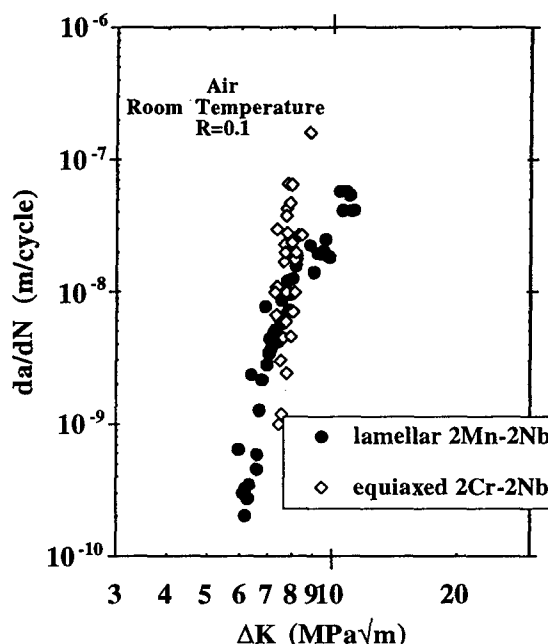


Figure 3 : Comparison of the fatigue crack growth behaviour a lamellar alloy and a equiaxed alloy in air at room temperature (R=0.1).

### Crack closure

Among the possible factors affecting the growth process, it is well established that especially at low R ratios, premature recontact of the crack walls under tensile loads might induce a significant crack tip shielding (20). This phenomenon is commonly designated under the generic name of "crack closure" although the operative mechanisms might differ from one case to another.

Figure 4 presents a set of data pertaining to the Ti-48Al-2Mn-2Nb lamellar alloy including crack-closure corrected data. The effective stress intensity factor amplitude  $\Delta K_{eff}$  is thus derived from the load-compliance diagrams as described elsewhere (7, 13). It can be seen that in the notch "A" orientation the effective curve is significantly shifted to the left. The shift is much less important in the notch "B" orientation. However there is a strong support to attribute such a difference in closure behaviour to an experimental artifact related to the test procedure rather than to a pure microstructural effect (7). In particular it has been shown that the initial load level has a significant influence on closure development in vacuum (7). Actually additional data obtained on another specimen with notch "A" orientation do not exhibit such high shielding effects as those shown here. It is believed that the influence of parameters such as load history, crack length or specimen geometry are at least as important lamellae orientation effects on closure behaviour. However since this influence is hardly predictable, nominal data, i. e. without closure corrections, are mostly representative of the test used to generate them.

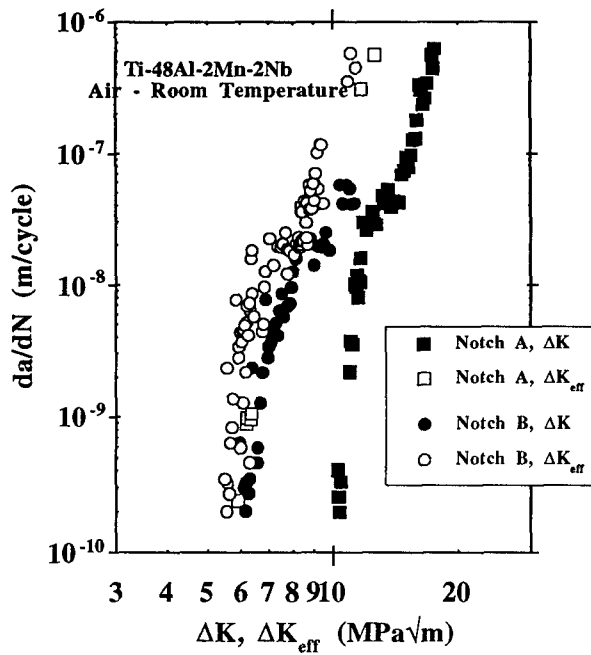


Figure 4 :  $da/dN$  vs.  $\Delta K$  and  $\Delta K_{eff}$  for the Ti-48Al-2Mn-2Nb alloy in the as-cast condition.

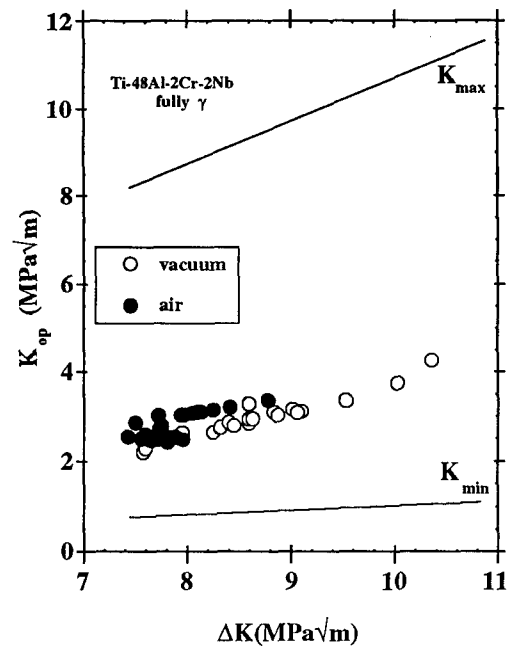


Figure 6 : Comparison of opening stress intensity factor  $K_{op}$  in air and in vacuum.

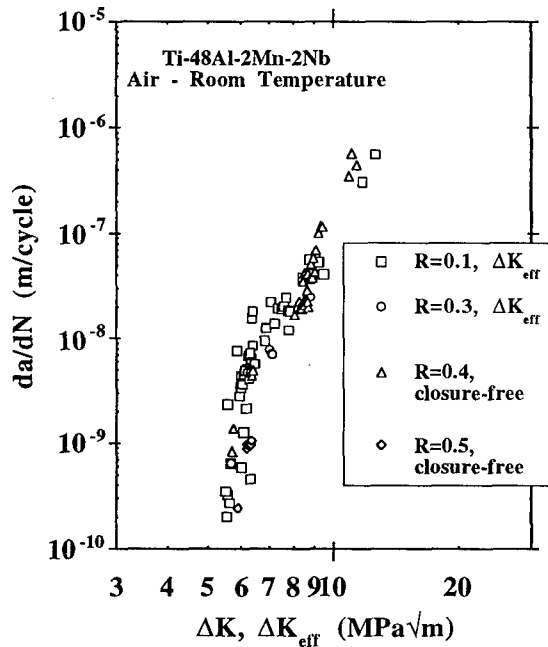


Figure 5 : Comparison of closure-free and crack closure-corrected generated at different R load ratio.

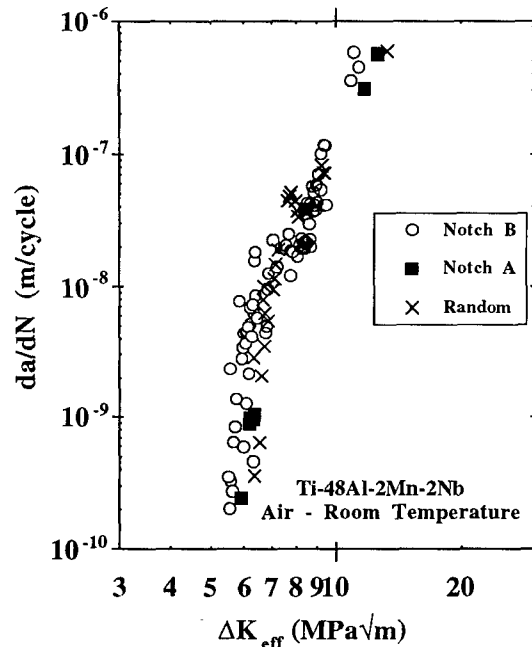


Figure 7 : Fatigue crack growth behaviour in crack arrester and crack divider orientations as compared to randomised microstructure.

The consequence of an enhanced-closure behaviour is that the  $\Delta K_{eff}$  range and the  $\Delta K$  range are in certain cases completely disjointed, resulting in a lower value of the effective threshold  $\Delta K_{eff,th}$ . Similarly for a same value of the applied  $\Delta K$  crack growth rate might vary over more than one order of magnitude, depending on the intensity of closure effects. This behaviour has also been observed the equiaxed microstructure (13). Therefore when dealing with nominal data, that is to say without taking into account possible closure effects, one has to be extremely careful about test procedure. This aspect has to be kept in mind in view of the development of a damage tolerance philosophy in  $\gamma$  titanium aluminides.

In order to definitively assess the relevance of closure in  $\gamma$ -based alloys, additional testings have been performed under higher load ratios, namely  $R=0.4$  and  $R=0.5$  providing closure-free conditions. The good agreement presented on figure 5 between closure-corrected data and those generated under closure-free conditions gives confidence in the experimental procedure and further validates the consistency of the  $\Delta K_{eff}$  concept for these compounds.

However the question of the source of closure is still on the table. Figure 6 compares the opening stress intensity factor measured in air and in vacuum nearly in the same  $\Delta K$  range for the 2Cr-2Nb equiaxed alloy. It is obvious that environmental effects only weakly interact with closure mechanisms. In particular oxide-induced closure (21) does not appear relevant to closure in these intermetallics at room-temperature. This conclusion is also valid for the lamellar alloy (22).

It is therefore strongly suggested that the roughness-induced closure mechanisms (23), in conjunction with a residual near-tip mode II displacement, would account for the shielding effects observed in these alloys (13).

#### Microstructural effects

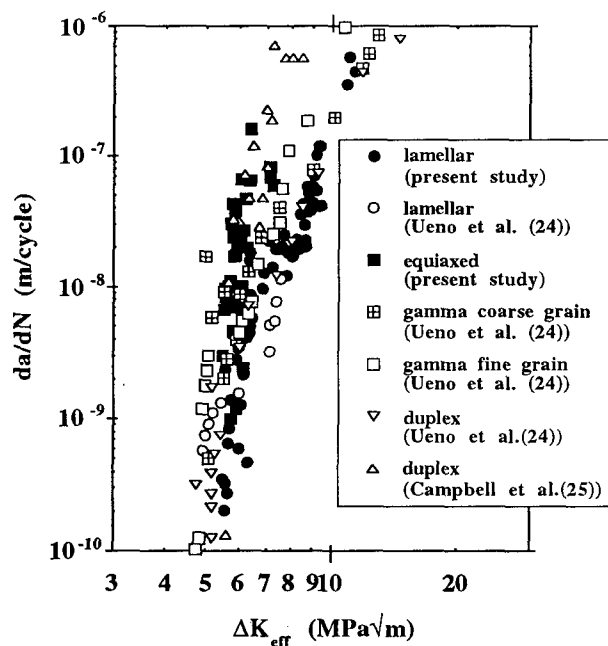


Figure 8 : Compendium of effective data in air at room-temperature (additional data from (12, 24, 25)).

Microstructural effects on fatigue damage have to be investigated on the basis of effective data. For instance the results presented on figure 7

clearly demonstrate by comparing effective data obtained for a crack arrester and a crack divider orientation and for a randomised microstructure that the lamellae orientation has little or no influence on the fatigue crack growth resistance. In a same way it has been shown that, for equiaxed microstructures, heat treatment and / or grain size do not affect this material property (12, 13).

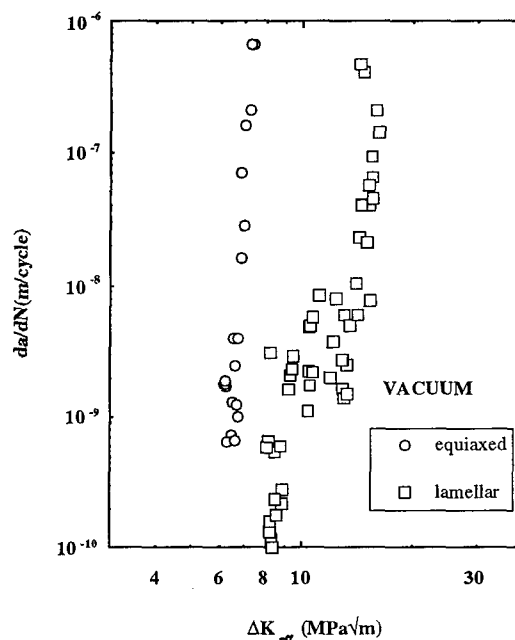


Figure 9 : comparison of the intrinsic behaviour of the lamellar and equiaxed microstructures.

Furthermore the compendium of data either generated in the present study or collected in literature and presented on figure 8 shows that as soon as closure effects are taken into account, no significant difference in crack growth behaviour is noticeable between the fatigue crack growth resistance of three characteristic microstructures, especially in the slow growth rate regime. Therefore most of the differences exhibited in fatigue crack growth behaviour by various microstructures results from differences in the magnitude of closure shielding in relationship with microstructural factors.

But once again this kind of comparison does not constitute a proper basis for the analysis of the mere role of microstructure since it also includes environmental effects. The problem encountered when tackling this issue resides in the lack of available effective data in inert environments. Figure 9 compares such data obtained in the present study for two characteristic microstructures in high vacuum. It turns out that the lamellar structure exhibits an improved fatigue crack growth resistance with respect to the equiaxed alloy. This improvement might be attributed to the previously evoked toughening mechanisms peculiar to this structure (18). However in the slow growth rate regime these mechanisms becomes less efficient. This degradation of extrinsic toughening mechanisms under cyclic loading has been thoroughly discussed by Ritchie (26). It is also noteworthy that the threshold measured for the  $\gamma$  alloy is extremely close to the final rupture, resulting in a very steep curve. This situation might also partly explain the difference between the two microstructures since a higher contribution of a quasi-static mode might be expected for the equiaxed alloy (8) and therefore the observed behaviour is not merely related to the fatigue damage. Conclusions are however limited due to the lack of extensive intrinsic data. However it is clear from the comparison between figure 8 and figure 9 that the possible improved intrinsic resistance in lamellar structures is annulled in presence of an active environment. In other

words the magnitude of environmental effects is so large that it tends to erase an improvement in intrinsic resistance if it does really exist. This aspect is more deeply discussed in the following.

#### Environmental enhancement

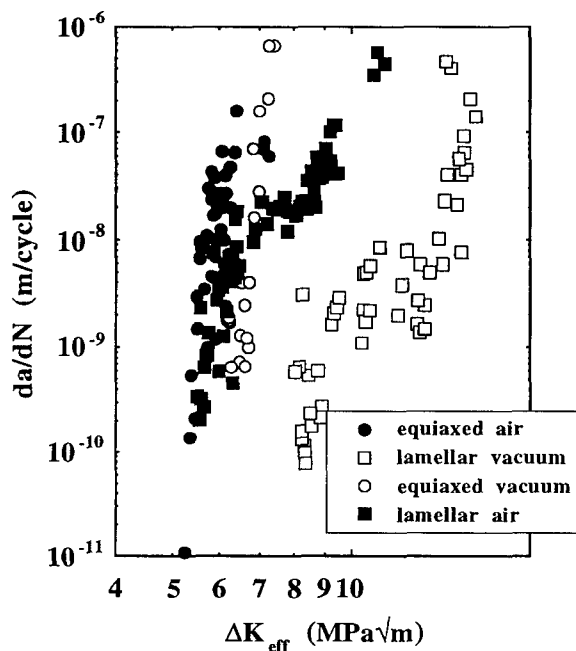


Figure 10 : Comparison of effective data in air and in vacuum.

The influence of environment is also investigated by taking into account crack tip shielding by closure. The results presented on figure 10 indicate a significant environmental enhancement of the crack growth whatever the microstructure. As for conventional alloys this deleterious effect might be attributed to the presence of moisture in this environment (3). Besides it has been shown that the ductility of aluminides is sensitive to the moisture content of the test environment (4, 27-30). This embrittlement would result from the following surface reaction (4, 28):



The hydrogen thus released would then diffuse into the bulk material and embrittle it. However oxygen might also compete with water vapour to adsorb on freshly cracked surfaces according to :



Such a competing adsorption process would explain the higher ductility observed by Liu and Kim (28) in oxygen atmosphere with respect to air and even vacuum in the case of a TiAl alloy.

The question is then to determine whether water vapour is the active species in terms of surface reactions in the particular case of a fatigue crack tip. In this aim additional testings have been conducted on the Ti-48Al-2Mn-2Nb alloy under two environmental conditions :

- low vacuum
- oxygen atmosphere with a residual moisture content of  $\approx 15$  ppm.

Thus the water vapour content in both conditions is roughly the same. The results are reported on figure 11.

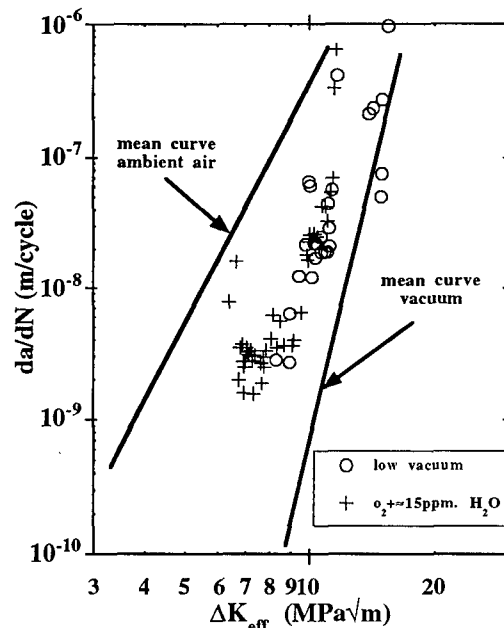


Figure 11: Fatigue crack growth rates measured in low vacuum and in oxygen.

First of all it can be easily seen that, as expected for these atmospheres with an intermediate moisture level, the crack growth rates are intermediate between those obtained in high vacuum and in ambient air. In addition the crack growth rates, for this intermediate moisture level, do not depend on the composition of the global atmosphere. It comes out from these observations that the environmental crack growth rate enhancement is essentially governed by the amount of water vapour present in the test atmosphere. In particular, oxygen even in much larger quantity is not efficient in preventing the moisture-related fatigue crack growth enhancement in  $\gamma$  titanium aluminides by blocking adsorption sites and therefore limiting the hydrogen release. This conclusion is somewhat contradictory with the results of Liu et Kim (28) quoted here above.

The same kind of experiments have been conducted on the FeAl40 grade 3 alloy under closure free conditions (15) and the picture is somewhat different as shown on figure 12. Indeed in this case oxygen is proved to be efficient in competing with water vapour since the crack growth rates obtained in the oxygen environment are nearly similar to those obtained under high vacuum and significantly lower than those obtained in low vacuum. Further work is required to elucidate this point, especially about the influence of the base alloy on competitive adsorption process. Nevertheless the present results support a high sensitivity of fatigue crack growth rates in aluminides to the water vapour content of the test environment. This parameter should therefore be rigorously controlled.

If we can now assume that water vapour is the active species, the detailed mechanism involved in the observed enhancement is still under question. The environmentally-assisted fatigue crack propagation of conventional alloys has been analysed according to two distinct mechanisms (31):

- a regime assisted by the adsorption of water vapour molecules which induces an enhancement of the crack propagation by lessening the energy required to extend the crack (32);

- a subsequent hydrogen regime assisted by the hydrogen released by the surface dissociation of adsorbed molecules; this hydrogen is presumably dragged by mobile dislocations into the strained material at the crack tip where it interacts with the fatigue damage (33).

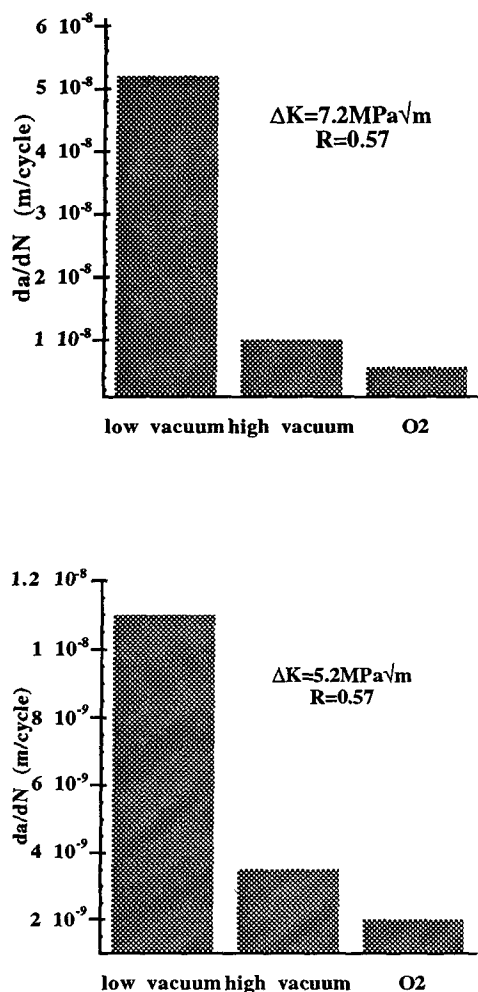


Figure 12 : Fatigue crack growth rates obtained under various environmental conditions in the FeAl40 grade 3 alloy.

The present results do not provide sufficient information to conclude the applicability of this analysis to the case of TiAl alloys. This is largely due to the poor understanding of the intrinsic behaviour of such compounds highlighted above. For instance it is not established whether the behaviour exhibited in intermediate atmospheres like low vacuum represents a saturating adsorption-assisted regime as observed under the same conditions in a high-strength steel (32). Results obtained by Aswath and Suresh (34) on a Ti<sub>3</sub>Al suggest that the environmentally enhanced crack growth rates are mainly governed by the exposure to water vapour, which is rather consistent with an adsorption process. Besides these results, as those obtained by Balsone et al. (35) further confirm that only traces of water vapour are sufficient to induce a significant enhancement of the growth process.

The level of exposure encountered in the intermediate environments considered here is sufficient to ensure the formation of an adsorbed monolayer. However it might also be high enough to induce a hydrogen-assisted fracture mechanism. This is actually the explanation proposed to account for the loss of ductility observed in TiAl in hydrogenous environments. However hydrogen-assisted fracture does not seem to be related to the formation of hydrides (30). The change in fracture mode observed in PST crystals when tested in hydrogen gas or in air with respect to vacuum suggests the bonding strength of lamellae boundaries

could be altered by hydrogen. The assumption of a hydrogen-assisted mechanism in the particular case of fatigue crack growth is supported by the results obtained by Castagna and Stoloff (36, 37) on a Fe<sub>3</sub>Al iron aluminide.

Finally the rupture surfaces obtained with fatigue specimens of similar lamellae orientation present only subtle differences with respect to test environment. In particular the fracture surface of the lamellar microstructure does not reveal a promoted interface decohesion when tested in air with respect to vacuum, conversely to what is observed with PST crystals (30). Besides the fracture surface morphology of an equiaxed Ti-48Al-2Cr-2Nb alloy also looks insensitive to test environment although environmental effects induce a fatigue crack growth enhancement of the same order of magnitude (12). Therefore the environmentally-induced interface weakness and subsequent enhanced-decohesion do not appear as the most relevant mechanisms in environmentally-assisted fatigue crack propagation. It is rather suggested that the environmental action does not deeply affect the basic fracture mode but rather promotes fatigue damage accumulation and thus enhances the crack growth in both equiaxed and lamellar microstructures.

Some scarce data generated in the case of the Ti-48Al-2Mn-2Nb at lower frequency, namely 0.35 Hz, present only slight differences with respect to results obtained at 35Hz. In particular a low test frequency does not induce higher growth rates. This lack of frequency effect in ambient air indicates that, as far as this exposure range is concerned, the overall enhancement process is not time-dependent but is mostly governed by the synergetic action of cyclic deformation at the crack tip and exposure to a moist atmosphere. This point is currently under more extensive investigation.

#### Fatigue crack propagation at elevated temperatures

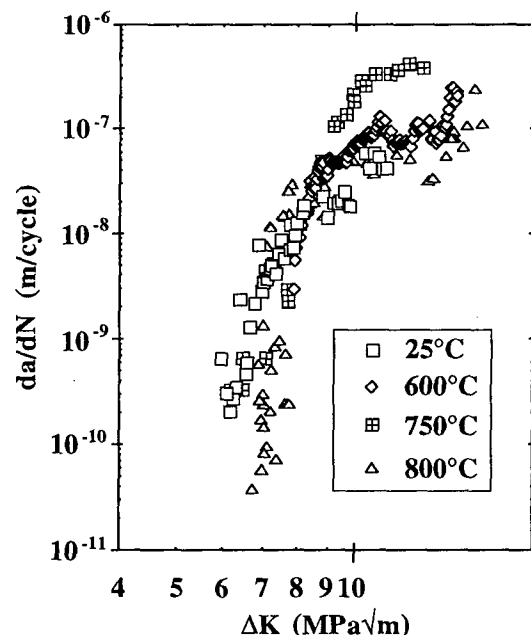


Figure 13: Elevated -temperature fatigue crack growth behaviour of the Ti-48Al-2Mn-2Nb alloy in the as-cast condition.

A short literature survey indicates that the influence of temperature on fatigue crack growth in TiAl alloys is controversial. For instance Balsone et al. noticed that in a duplex Ti-48Al-2Nb-2Mn alloy, the fatigue crack growth curves fall into a narrow band for temperatures ranging between room temperature and 954°C. According to Larsen et al. (38) and



McKelvey et al. (39) the worst situation would be encountered at elevated temperature but just below the ductile / brittle transition (DBT). Soboyejo et al.(40) observed an improved resistance at 700°C with respect to room temperature although James et al. (8) obtained an opposite conclusion in the same temperature range. According to Soboyejo and co-workers (40, 41), the improved resistance observed at elevated temperature would be related to a higher reversibility of deformation but the role of oxide-induced closure should also be examined.

In the present study the influence of temperature on fatigue crack growth resistance has been investigated in the case of the Ti-48Al-2Mn-2Nb alloy in the as-cast condition. The results are plotted on figure 13. At a first glance they are nearly consistent with the findings of Balsone et al.(42). One can hardly notice a weaker resistance at 750°C in the upper regime and conversely a slightly higher threshold value at 800°C. The question is then to determine whether the controversy indicated above could be related to a different balance in extrinsic factors, such as closure and environmental effects when temperature increases.

Actually once such shielding effect due to closure is taken into account, the data collapse into a narrow band as shown on figure 14. It should be noticed that on this figure the effect of elastic modulus variation is taken into account but does not substantially modify the tendencies. Furthermore it is shown that closure effects have almost the same magnitude whatever the temperature. As a consequence there is no enhanced contribution of oxide-induced closure as temperature increases up to 800°C (22).

This apparently temperature-independent behaviour might still result from a balance between a modification of the intrinsic behaviour and environmental effects. This assumption is examined in the following. Testings have been conducted at 700°C in vacuum using a load ratio of  $R=0.7$  in order to preclude closure effects (16). The results are included in figure 14. It can be seen that neither elastic modulus retention, nor closure effect can fully account for differences in the behaviour in such inert environment between 25°C and 700°C. As a result the intrinsic fatigue crack growth resistance at 700°C is slightly lower than at room temperature. It should be noticed that during testings at 700°C the water

vapour residual content was not fully controlled and higher crack growth rates could be partly considered to be a result of a moister atmosphere.

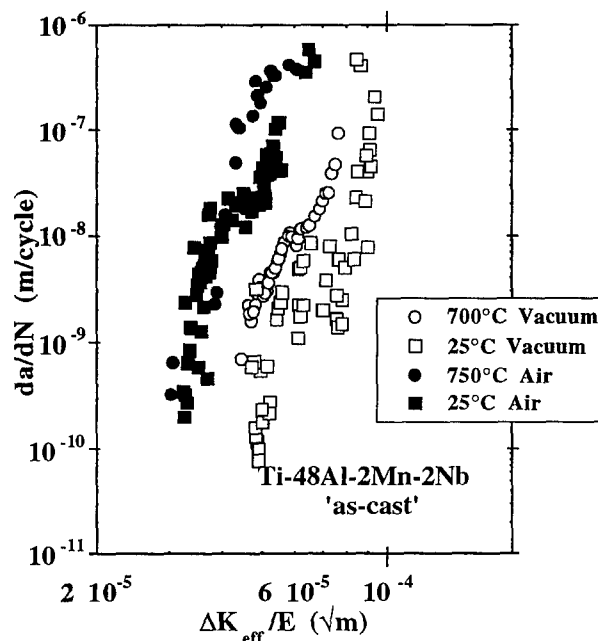
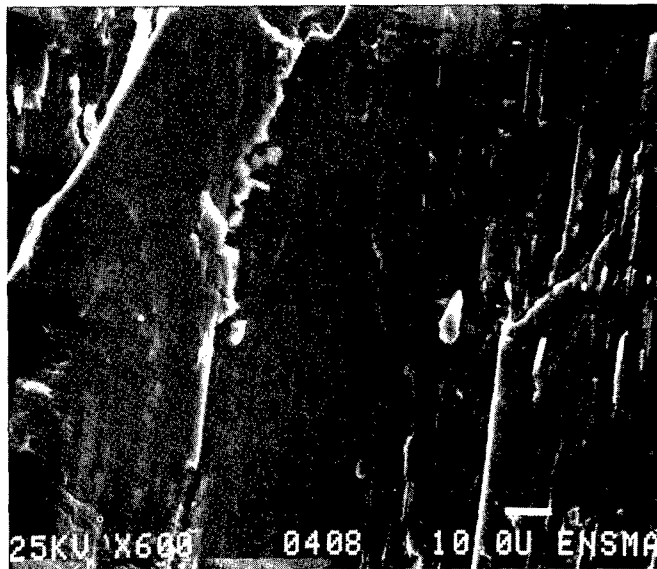


Figure 14 : Elevated-temperature fatigue crack growth in air and in vacuum.



(a)



(b)

Figure 15 : Fracture surfaces in air ( $\Delta K=10.7 \text{ Mpa}\sqrt{\text{m}}$ ;  $da/dN=3.10^{-7} \text{ m/cycle}$ ) at a) 25°C and b) 750°C.

Nevertheless these results are somewhat different from the results obtained by James and Bowen (8) on the same alloy in the same environmental conditions. One point worthy to note is that these authors did not take into account closure effects, which might explain the observed difference. However data generated in the present study at  $R=0.1$  and presented in reference (16) also present some discrepancy with their results. This might be due to the use of bending specimens by James and Bowen (8) which could induce different closure behaviour. The present findings are consistent with the trends presented by the results of Rosenberger et al. (43) on a Ti-46.5Al-1.5Cr-2Nb lamellar alloy in ultra-high vacuum. These authors found that the fatigue crack growth resistance at 600°C, although lower, was nearly similar to those obtained at room temperature. However a much more drastic decrease in resistance is observed at 800°C. The results obtained here would thus constitute an intermediate situation. This point is currently under more extensive investigation in our laboratory.

However, subject to further confirmation, this result suggests that the DBT would induce a deleterious effect on fatigue crack propagation resistance opposite to the expected improvement observed on other mechanical properties such as ductility. Larsen and co-workers reach almost the same conclusion (38). Such conclusions are somewhat controversial with the findings of Venkateswara Rao et al. (44). According to these authors an improved resistance is observed in air due to a beneficial effect of the DBT which would promote dissipation at the crack tip by blunting. However such mechanisms might also prevail in inert environment provided that the deformation and/or fracture mode at the crack tip is not fundamentally modified by a change in test environment. Such a change is not supported by fractographic observations. Indeed the main features are only poorly affected by change in temperature as shown on figure 15, suggesting that the basic propagation mode is not deeply modified. The same conclusion applies for the change from air to vacuum. In addition the diffuse damage processes of microcracking, crack branching and deflection, still retain their potency at elevated temperatures.

From the analysis developed above, it is also suggested that the intensity of environmentally-assisted fatigue crack propagation is slightly lessened as temperature is increased. Indeed, since on one hand the intrinsic resistance is affected and on another hand the behaviour observed in air is nearly temperature independent, the contribution of environment in the growth process is lower at 750°C or 800°C than at 25°C. However the change is so subtle that there is no reason to suspect a change in environmentally-assisted fatigue mechanisms. In particular water vapour might still be the active species. This is supported by the fact that water vapour has been proved to be the active species in environmentally-assisted fatigue crack propagation in titanium alloys up to 500°C (45).

Furthermore these conclusions are consistent with the analysis of environmental embrittlement in aluminides proposed by Li and Liu (46). According to these authors, an increase in temperature induces a shift in the equilibrium of equations (1) and (2). Thus the adsorption of oxygen is favoured while the amount of hydrogen generated by dissociation of adsorbed water vapour is lessened. The material is hence less embrittled despite the enhanced dissociation kinetics. Actually this assumption related to equilibrium effect is in agreement with the results presented here whatever the nature of mechanisms involved in environmentally-assisted fatigue crack propagation. That is to say surface adsorption or propagation assisted by hydrogen highly concentrated in the lattice at the crack tip. Future work will aim at getting more precise insights on this aspect.

Finally oxidation might also play a significant role. According to different authors (47, 48), an intermixed  $Al_2O_3/TiO_2$  scale is formed during oxidation of  $\gamma$  alloys instead of a protective  $Al_2O_3$  scale. Nitrogen appears to interfere in the oxidation process and to produce, by means of TiN, a barrier to continuous  $Al_2O_3$  scale formation. Furthermore alloying additions can modify the rate of oxidation. Actually oxidation mechanisms remains unclear and it would be valuable to determine whether the higher fatigue crack growth rates observed in air at elevated temperatures are associated with very near-surface interstitial oxygen/nitrogen embrittlement, TiN/TiAl<sub>2</sub> formation, or some other

environment-related mechanisms.

### Summary and conclusions

TiAl-based alloys exhibit a fatigue crack growth behaviour intermediate between conventional metallic alloys and ceramics. However, as for metallic alloys, the overall behaviour has been shown to result from a complex balance between the intrinsic resistance of these compounds and some extrinsic factors which might be either beneficial (shielding) or detrimental. On the basis of the present investigations, the following conclusions have been reached:

1. The intrinsic resistance of  $\gamma$ -based alloys is not strongly dependant on microstructural features. In particular toughening mechanisms are degraded under cyclic loading.
2. The present results highlight the prevailing role of crack closure as an extrinsic shielding source in these materials. In addition since closure behaviour appears tightly connected to test procedure the use of effective data is recommended when investigating the influence of a specific parameter.
3. The room temperature fatigue crack growth resistance of  $\gamma$ -based alloys is deeply altered in ambient air as compared to vacuum. This loss of resistance has been shown to be governed by the water vapour content. In particular oxygen adsorption is inefficient in preventing this embrittling effect, conversely to what is observed in iron aluminide. This environmental effect is all the more deleterious in that it is not balanced by the development of significant shielding by oxide-induced closure.
4. No marked influence of temperature is noticed on fatigue crack growth behaviour from 25°C up to 800°C. It seems however that there is a weak loss of intrinsic resistance as temperature increases but at the same time the environmental contribution could be lessened, resulting in an overall behaviour that is nearly temperature independent.

Future work on this subject will aim at more thoroughly understand these various aspects.

### Acknowledgements

The authors would like to sincerely thank Prof. Paul Bowen, from the University of Birmingham, for providing the Ti-48Al-2Mn-2Nb ingot and for his constant support during the course of this study. Supply of Ti-48Al-2Cr-2Nb alloy from CEA/CEREM/CE2M/LETRAM and FeAl40 grade 3 from CEA/CENG/CEREM by R. Baccino and F. Moret is also acknowledged. The authors also thank Peter Weidemann for technical assistance in elevated-temperature testings.

### References

1. Y. W. Kim, "Gamma titanium aluminides: Their status and future", *Jom - Journal of the Minerals Metals & Materials Society*, 47 (7) (1995), 39-41.
2. C. M. Austin and T. J. Kelly, "Development and implementation status of cast gamma titanium alloys", *Structural Intermetallics, first International Symposium on Structural Intermetallics*, Seven Spring Mountain, Champion, Pennsylvania, Editeurs R. Dariola, J. J. Lewandowski, C. T. Liu, P. L. Martin, D. B. Miracle and M. V. Nathal, TMS, Vol. 143-150 (1993).
3. J. Petit, J. De Fouquet and G. Hénaff, "Influence of ambient atmosphere on fatigue crack growth behaviour of metals", *Handbook of fatigue crack propagation in metallic structures*, Editeurs A. Carpinteri, Elsevier, 1159-1204 (1994).
4. C. T. Liu, E. H. Lee and C. G. McKamey, "An environmental effect as the major cause for room-temperature embrittlement in FeAl", *Scripta Metallurgica et Materialia*, 23 (6) (1989), 875-880.
5. C. T. Liu, "Recent advances in ordered intermetallics", *Materials Chemistry and Physics*, 42 (2) (1995), 77-86.
6. N. S. Stoloff and C. T. Liu, "Environmental Embrittlement of Iron Aluminides", *Intermetallics*, 2 (2) (1994), 75-87.
7. G. Hénaff, et al., "Fatigue crack propagation resistance of a Ti-48Al-

- 2Mn-2Nb alloy in the as-cast condition", *Materials Science & Engineering*, 219 (1-2 (Nov)) (1996), 212-220.
8. A. W. James and P. Bowen, "Elevated Temperature Crack Growth Resistance of TiAl under Monotonic and Cyclic Loading", *Materials Science and Engineering*, A153 (1992), 486-492.
  9. P. Bowen, R. A. Chave and A. W. James, "Cyclic crack growth in titanium aluminides", *Materials Science and Engineering A - Structural Materials Properties Microstructure and Processing*, 193 (1995), 443-456.
  10. S. Yokoshima and M. Yamaguchi, "Fracture behavior and toughness of PST crystals of TiAl", *Acta Materialia*, 44 (3) (1996), 873-883.
  11. K. S. Chan, "Understanding Fracture Toughness in Gamma TiAl", *Jom - Journal of the Minerals Metals & Materials Society*, (1992), 30-38.
  12. G. Hénaff, et al., "Fatigue Crack Propagation in TiAl-based Intermetallic Compounds", *Micromechanics of Advanced Materials, Materials Week'95, TMS fall meeting*, Cleveland, Ohio (October 29-November 2), Editeurs S. N. G. Chu, P. K. Liaw, R. J. Arsenault, K. Sadananda, K. S. Chan, W. W. Gerberich, C. C. Chau and T. M. Kung, TMS, Vol. 385-391 (1995).
  13. G. Hénaff, et al., "The role of crack-closure in fatigue crack propagation behaviour of a TiAl-based alloy", *Scripta Materialia*, 34 (9) (1996), 1449-1454.
  14. F. Moret, et al., "Propriétés et applications des alliages intermétalliques B2-FeAl", *Journal de Physique IV*, 6 (mars) (1996), C2-281-C2-289.
  15. G. Hénaff and A. Tonneau, "to be published.", (1997),
  16. C. Mabru, G. Hénaff and J. Petit, "Fatigue crack propagation behaviour of a lamellar TiAl Alloy", *ECF 11 (11th European Conference on Fracture)*, Futuroscope, France, Editeurs J. Petit, J. de Fouquet, G. Hénaff, P. Villechaise and A. Dragon, EMAS, West Midlands, Vol. II, 1187-1192 (1996).
  17. K. S. Chan and Y.-W. Kim, "Influence of Microstructure on Crack-Tip Micromechanics and Fracture Behaviors of a Two-Phase TiAl Alloy", *Metallurgical Transactions A*, 23A (June) (1992), 1663-1677.
  18. K. S. Chan, "Toughening Mechanisms in Titanium Aluminides", *Metallurgical Transactions A*, 24A (March) (1993), 569-583.
  19. K. S. Chan, "Evidence of shear ligament toughening in TiAl-base alloys", *Metallurgical and Materials Transactions A - Physical Metallurgy and Materials Science*, 26 (6) (1995), 1407-1418.
  20. W. Elber, "The Significance of Crack Closure", *Damage Tolerance in Aircraft Structures*, ASTM STP 486, Toronto, Ontario, Canada, Editeurs American Society for Testing and Materials, Philadelphia, Pa., Vol. 230-242 (1971).
  21. S. Suresh, Z. A. Zamiski and R. O. Ritchie, "oxide-induced closure closure: an explanation for near-threshold fatigue crack growth behavior", *Metallurgical Transactions*, 12A (1981), 1435-1443.
  22. C. Mabru, et al., "Fatigue Crack Growth Mechanisms at Room and Elevated Temperatures in a TiAl-based Alloy", *Engineering Against Fatigue (to be published)*, Sheffield, U. K., Editeurs Vol. (1997).
  23. S. Suresh and R. O. Ritchie, "Near-threshold fatigue crack propagation: a perspective on the role of crack closure", *Fatigue Crack Growth Thresholds Concepts*, Philadelphia, Pennsylvania, Editeurs D. L. Davidson and S. Suresh, The Metallurgical Society of AIME, Vol. 227-261 (1983).
  24. A. Ueno and H. Kishimoto, "Fatigue Crack Propagation in TiAl Intermetallic Compounds", *Fatigue'96*, Berlin, Germany, Editeurs G. Lutjering and H. Nowack, Pergamon, Vol. III, 1731-1735 (1996).
  25. J. P. Campbell, K. T. Venkateswara Rao and R. O. Ritchie, "Fatigue crack growth and fracture behavior in a  $\text{XD}^{\text{TM}}$   $\gamma$ -TiAl alloy with a fine lamellar microstructure", *Fatigue '96*, Berlin, Germany, Editeurs G. Lutjering and H. Nowack, Pergamon, Vol. III, 1779-1784 (1996).
  26. R. O. Ritchie and K. T. Venkateswara Rao, "Cyclic fatigue Crack Growth in Toughened Ceramics and Intermetallics at Ambient to Elevated Temperatures", *ECF 11, 11th European Conference on Fracture*, Poitiers-Futuroscope, France, Editeurs J. Petit, J. de Fouquet, G. Hénaff, P. Villechaise and A. Dragon, EMAS, Vol. I, 53-69 (1996).
  27. C. T. Liu, et al., "Environmental Embrittlement in FeAl Aluminides", *Isij International*, 31 (10) (1991), 1192-1200.
  28. C. T. Liu and Y. W. Kim, "Room-Temperature Environmental Embrittlement in a TiAl Alloy", *Scripta Metallurgica et Materialia*, 27 (1992), 599-603.
  29. S. Launois and A. Fraczkiewicz, "Effet de l'environnement sur le comportement mécanique d'un alliage FeAl (40 at. % Al) renforcé", *Journal de Physique IV*, 6 (mars) (1996), C2-223-C2-228.
  30. M. H. Oh, et al., "Environmental effects on the room-temperature ductility of polysynthetically twinned (PST) crystals of TiAl", *Acta Metallurgica et Materialia*, 41 (7) (1993), 1939-1949.
  31. G. Hénaff and J. Petit, "A logical framework for the analysis of fatigue crack propagation enhancement by ambient atmosphere", *Physicochemical mechanics of materials*, 32 (2) (1996), 69-88.
  32. G. Hénaff, K. Marchal and J. Petit, "On Fatigue Crack Propagation Enhancement by a Gaseous Atmosphere: Experimental and Theoretical Aspects", *Acta Metallurgica et Materialia*, 43 (8) (1995), 2931-2942.
  33. R. P. Wei and G. W. Simmons, "Recent progress in understanding environment-assisted fatigue crack growth", *International Journal of Fatigue*, 17 (2) (1981), 235-247.
  34. P. B. Aswath and S. Suresh, "Microstructural effects on ambient and elevated temperature fatigue Crack growth in titanium aluminide intermetallics", *Metallurgical Transactions*, 22A (April) (1991), 817-828.
  35. S. J. Balsone, et al., "Frequency, Temperature and Environmental Effects on Fatigue, Crack Growth in Ti3Al", *Fatigue'90*, Honolulu, Hawaii, Editeurs K. Kitagawa and T. Tanaka, MCEP, Birmingham, Vol. II, 1173-1178 (1990).
  36. A. Castagna and N. S. Stoloff, "The Influence of Environment on Fatigue Crack Growth of an  $\text{Fe}_3\text{Al}$ , Cr Alloy", *Scripta Metallurgica et Materialia*, 26 (1992), 673-678.
  37. A. Castagna and N. S. Stoloff, "Hydrogen embrittlement of Fe3Al alloys", *Materials Science and Engineering A - Structural Materials Properties Microstructure and Processing*, 193 (1995), 399-406.
  38. J. M. Larsen, et al., "Mechanisms and mechanics of fatigue crack initiation and growth in TiAl intermetallic alloys", *Fatigue'96*, Berlin, Germany, Editeurs G. Lutjering and H. Nowack, Pergamon, Vol. III, 1719-1730 (1996).
  39. A. L. McKelvey, et al., "High temperature fatigue crack growth behavior in an  $\text{XD}^{\text{TM}}$   $\gamma$ -TiAl intermetallic alloy", *Fatigue '96*, Berlin, Germany, Editeurs G. Lutjering and H. Nowack, Pergamon, Vol. III, 1743-1748 (1996).
  40. W. O. Soboyejo, P. B. Aswath and C. Mercer, "Mechanisms of fatigue crack growth in Ti-48Al at ambient and elevated temperature", *Scripta Metallurgica et Materialia*, 33 (7) (1995), 1169-1176.
  41. C. Mercer and W. O. Soboyejo, "Micromechanisms of fatigue and fracture in a forged powder metallurgy gamma-based titanium aluminide intermetallic", *Fatigue and Fracture of Ordered Intermetallic Materials: I*, Editeurs W. O. Soboyejo, T. S. Srivatsan and D. L. Davidson, TMS, 277-290 (1994).
  42. S. J. Balsone, J. Wayne Jones and D. C. Maxwell, "Fatigue crack growth in a cast gamma titanium aluminide between 25 and 954°C", *Fatigue and Fracture of Ordered Intermetallic Materials: I*, Editeurs W. O. Soboyejo, Srivatsan, T. S. and D. L. Davidson, TMS, 307-318 (1994).
  43. A. H. Rosenberger, B. D. Worth and S. J. Balsone, "Environmental effects on the fatigue crack growth of gamma titanium aluminides", *Fatigue'96*, Berlin, Germany, Editeurs G. Lutjering and H. Nowack, Pergamon, Vol. III, 1785-1790 (1996).
  44. K. T. Venkateswara Rao, Y. W. Kim and R. O. Ritchie, "high temperature fatigue crack growth behavior in a two phase ( $\gamma + \alpha_2$ ) TiAl intermetallic alloy", *Scripta metallurgica et materialia*, 33 (3) (1995), 459-465.
  45. S. Lesterlin, C. Sarrazinbaudoux and J. Petit, "Effects of temperature and environment interactions on fatigue crack propagation in a Ti alloy", *Scripta Materialia*, 34 (4) (1996), 651-657.
  46. J. C. M. Li and C. T. Liu, "Kinetic and equilibrium effects in the environmental embrittlement of ordered intermetallics", *Scripta Metallurgica et Materialia*, 33 (4) (1995), 661-668.
  47. C. Lang and M. Schutze, "TEM investigations of the early stages of TiAl oxidation", *Oxidation of Metals*, 46 (3-4) (1996), 255-285.
  48. M. P. Brady, et al., "The oxidation and protection of gamma titanium aluminides", *JOM - Journal of the Minerals Metals & Materials Society*, 48 (11) (1996), 46-50.

# TENSILE AND LOW CYCLE FATIGUE PROPERTIES OF Ti-48Al-2W-0.5Si GAMMA TITANIUM ALUMINIDE

V. Recina and B. Karlsson\*

Volvo Aero Corporation  
SE-461 81 Trollhättan, Sweden

\*Department of Engineering Metals  
Chalmers University of Technology  
SE-412 96 Göteborg, Sweden

## Abstract

Nine batches of the  $\gamma$ -TiAl alloy Ti-48Al-2W-0.5Si with a slightly varying composition have been examined through tensile and low cycle fatigue testing. The study has shown a large influence of the microstructure on the tensile and fatigue properties. A duplex fine grained microstructure has superior properties in comparison with a material low in aluminium with a coarse grained nearly lamellar structure. In addition, materials with the duplex structure show a much smaller scatter in test results. The brittle to ductile transition behaviour typical for  $\gamma$ -TiAl occurs between 700 and 800°C. The fracture mode of the equiaxed  $\gamma$ -grains is altered from a brittle inter- or transgranular mode to a ductile dimple-like fracture mode in this temperature range. The lamellar colonies sustain their brittle fracture behaviour. The low cycle properties can be described with the well-known Coffin-Manson equation. The strain controlled fatigue properties show a strong sensitivity to the strain range, an effect that can be attributed to the high Young's modulus and the relatively low yield strength of the material which leads to inelastic straining and fatigue damage at small strain ranges. The duplex material exhibits longer lives due to larger isotropic hardening and smaller Bauschinger effect, which lead to smaller inelastic strains and damage in each cycle. As in the tensile testing the scatter in results is smaller. The scatter in tensile and fatigue test results is explained by the anisotropic properties of the lamellar colonies. Fractography has shown that

initiation often occurs between the lamellas in large lamellar colonies at the surface of the gauge length. The probability to have a lamellar colony with the lamellas oriented perpendicular to the loading axis producing premature failure is increased as the content of this microconstituent is increased.

## Introduction

The development of advanced materials in the aircraft engine industry aims at lighter materials for improved strength to weight ratio and good fuel economy. The promising properties of  $\gamma$ -titanium aluminides make them interesting for replacing heavy Ni-based superalloys and Ti-alloys in future turbine engines. They exhibit retained mechanical properties up to 700-800°C, excellent creep and oxidation resistance, high stiffness, strength retention and burn resistance. Furthermore  $\gamma$ -TiAl can be cast, forged, machined and welded which makes component manufacturing fairly straightforward with the standard equipment of today. Many new advanced materials have failed implementation due to the cost. The increase in cost when replacing Ni-based superalloys or Ti-alloys with  $\gamma$ -TiAl should not be deterrent.

Large efforts have been focused on improving the poor ductility at ambient and slightly elevated temperatures. Increased understanding of the relationships between Al-content, additional

alloying elements in the alloys of today, microstructure and mechanical properties has led to a continuous improvement of the ductility [1-6]. Other problems in implementing  $\gamma$ -TiAl in gas turbines include the ability to control and reproduce the microstructure at casting since its influence on the mechanical properties is large. To achieve acceptable and predictable mechanical properties of  $\gamma$ -titanium aluminides requires a very close control of the chemical composition and processing techniques employed during manufacturing. Existing knowledge tells that a good combination of mechanical strength and ductility normally asks for duplex microstructures. On the other hand, relatively small variations in the chemical composition and actual casting and heat treatment procedures may cause considerable effect on the microstructure and, thereby, on the resulting properties. Successful alloy development, therefore, requires detailed studies of these variables to ensure reasonably low scatter in the mechanical properties.

The information in the existing literature is insufficient to allow a more complete description of the mechanical behaviour of the material in the present case. This study was undertaken to create an understanding of the tensile properties at temperatures from ambient up to 800°C and of the low cycle fatigue properties at 600°C of the  $\gamma$ -based alloy Ti-48Al-2W-0.5Si (atom-%). The relation between these properties and the underlying microstructure is demonstrated with emphasis on the reason behind the scatter in the mechanical data. Fractographic studies were also performed to elucidate the role of the microstructure on the fracture process.

## Experimental

### Materials and heat treatments

The alloy used in the study has the nominal composition of Ti-48Al-2W-0.5Si (atom-%) with the commercial name ABB IMN-2 alloy. The material was cast in nine different lots (named A-I) with slightly different chemical compositions. All variants were produced through investment casting at Precision Castparts Corporation (PCC) in USA, except for lot C which was made by Howmet Corporation, USA, with a similar technique. Table 1 shows the nominal as well as actual compositions of the received materials as used in the study. Subsequently the materials were hot isostatically pressed (HIP:ed) followed by heat treatment in two steps. Table 2 shows the HIP and heat treatment parameters employed.

### Testing and evaluation

A Material Testing System (MTS) servohydraulic test machine was used to perform the tensile testing at temperatures from RT up to 800°C and the Low Cycle Fatigue (LCF) testing at 600°C. All tests were performed in laboratory air. In all 32 tensile and 29 LCF tests were completed.

The tensile testing was carried out with a strain rate of  $1 \cdot 10^{-5} \text{ s}^{-1}$  applied in strain control up to an elongation of 3%, then in stroke control with the same strain rate until fracture. Cylindrical

specimens with a diameter of 4.5 mm and a gauge length of 40 mm were machined out from the centre of the cast cylindrical bars having a diameter of around 15 mm.

The LCF testing was performed in a fully reversed strain controlled push-pull mode ( $R = -1$ ). The strain rate was  $0.001 \text{ s}^{-1}$  applied in a triangular wave form. Cylindrical test pieces with a diameter of 6.35 mm and a gauge length of 14 mm were machined out from bars produced through the same route as the bars for the tensile testing but with a diameter of around 20 mm.

All test pieces were ground along the gauge length in the longitudinal direction with SiC-paper down to grit 1200 to prevent premature crack initiation at surface defects. Later inspection with fluorescent penetrants revealed absence of major surface cracks.

The microstructure of the present materials was characterised in detail in a previous study [4]. The volume percentage of the different phases in the material was determined through point counting on polished and etched specimens. These specimens were taken out from the gauge portion of tensile bars and examined in radial sections. Fractographic evaluation was performed on fractured surfaces in the SEM. Length sections through the fracture surface were also prepared and examined using optical microscopy. Energy Dispersive X-ray (EDS) spectrometry was used to analyse microconstituents in the fracture surfaces.

## Results

### Materials and microstructure

The composition, HIP and heat treatments of the materials in this study aimed at a duplex microstructure for balanced mechanical properties. The actual compositions of the lots, however, differed from the nominal one to various extents which led to different microstructures. This allowed the materials to be roughly distinguished as two groups, one with a nearly lamellar and one with a duplex microstructure [4].

The material from lots A to E shows a nearly lamellar microstructure where the large lamellar colonies consisting of alternating laths of  $\gamma$  and  $\alpha_2$  dominate, figure 1. The lamellar colonies have a size of about 2-3 mm, but occasionally colonies of up to 5 mm can be found. The volume percentage of the lamellar colonies ranges from about 70 vol.% up to 90 vol.% depending mainly on Al- but also W-content. Small equiaxed, approximately 30  $\mu\text{m}$  large,  $\gamma$ -grains are situated in the colony boundaries. W- and Ti-rich  $\beta$ -phase precipitates with an angular shape are often situated adjacent to these equiaxed  $\gamma$ -grains but can also be found in the interior of the lamellar colonies. Their size is around 30  $\mu\text{m}$ . Some of them have a stretched shape. The volume fraction of the  $\beta$ -phase is strongly affected by the W-content with higher amount of precipitates in lot A, B and C than in lot D and E. Small fractions of spherical Si-rich precipitates and some porosity are also found in the structure.

**Table 1. Nominal and real composition of the received material (weight%).**

LOT	Ti	Al	Si	W	H	O	N	STRUCTURE
nominal	58.65	32.00	0.35	9.00				
A	59.61	29.95	0.38	9.99	0.0005	0.068	0.0050	nearly lamellar
B	59.38	30.35	0.41	9.78	0.0012	0.071	0.0050	nearly lamellar
C	59.26	30.52	0.37	9.77	0.0014	0.068	0.0060	nearly lamellar
D	60.27	30.74	0.41	8.50	0.0009	0.076	0.0050	nearly lamellar
E	61.57	31.17	0.38	6.75	0.0010	0.120	0.0050	nearly lamellar
F	58.99	31.27	0.38	9.29	0.0002	0.0653	0.0080	duplex
G	58.86	31.32	0.20	8.98	0.0012	0.0632	0.0061	duplex
H	58.60	31.77	0.29	9.25	0.0017	0.0874	0.0049	duplex
I	59.20	32.06	0.29	8.36	0.0045	0.0783	0.0045	duplex

**Table 2. HIP and Heat Treatment parameters used**

LOT	HIP	HT #1	HT #2
A, B, C, D, E	1185°C / 172 MPa / 3h	1302°C / 20h (Ar) / GFC	913°C / 4h (Ar) / GFC
F and G	1260°C / 172MPa / 4h	1302°C / 20h (Ar) / GFC	913°C / 4h (Ar) / GFC
H	1185°C / 150 MPa / 4h	1300°C / 20h (Ar) / GFC	900°C / 4h (Ar) / GFC
I	1260°C / 172MPa / 4h	1300°C / 20h (Ar) / GFC	900°C / 4h (Ar) / GFC

GFC = Gas Fan Cooled

Ar = Argon

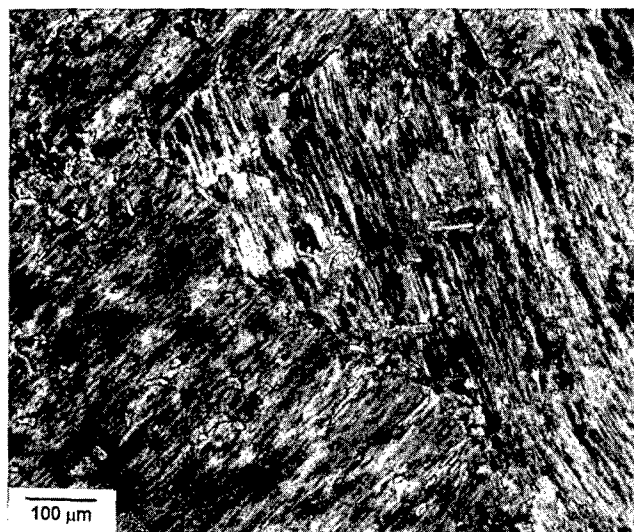


**Figure 1:** Optical micrograph of the nearly lamellar microstructure with alternating  $\alpha_2$ - and  $\gamma$ -plates.

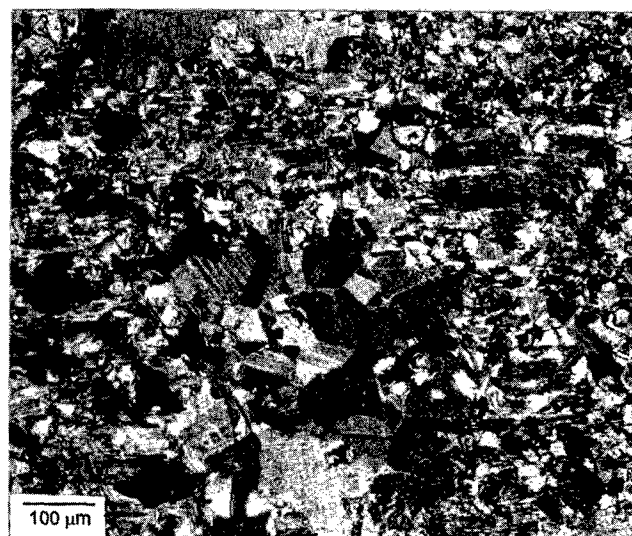


**Figure 2:** Optical micrograph of the duplex microstructure with equiaxed  $\gamma$ -grains of different sizes and lamellar colonies.

Higher Al-contents as found in lots F-I lead to duplex structures with a smaller volume percentage of lamellar colonies than found in the nearly lamellar structures, about 30 to 60 vol.%, figure 2. The colonies have a smaller size, around 500  $\mu\text{m}$ , and they are preferentially oriented with the lamellas in the direction of the cast bar. The content of  $\gamma$ -phase is much higher than in the nearly lamellar material. The  $\gamma$ -phase appears with different morphologies. Small equiaxed  $\gamma$ -grains with a size of around 20-30  $\mu\text{m}$  are situated in the boundaries between the lamellar colonies. In addition agglomerates of  $\gamma$ -grains with the same size as those in the colony boundaries can be found. In some samples these areas of small  $\gamma$ -grains are more frequent in the centre of the test bars than at the periphery. The variation in volume percentage

of these small  $\gamma$ -grains is large between the lots, but also within the cast bars showing a range of 10 to 50 vol.%. Larger  $\gamma$ -grains with volume percentage of 5-15 vol.%, a size of around 100  $\mu\text{m}$  and extending up to 350  $\mu\text{m}$ , some with annealing twins, are mostly situated at the periphery of the cast bars. Si-rich precipitates like those found in the nearly lamellar structures can also be seen. The duplex materials are completely free from porosity. Even when large variations in microstructure between but also within the cast bars of the duplex material are present, EDS-measurements did not indicate large alloy segregation. The complex process of nucleation and growth of the primary Ti-rich dendrites at solidification [4] leads to this variation in microstructure contributing to scatter in test results.

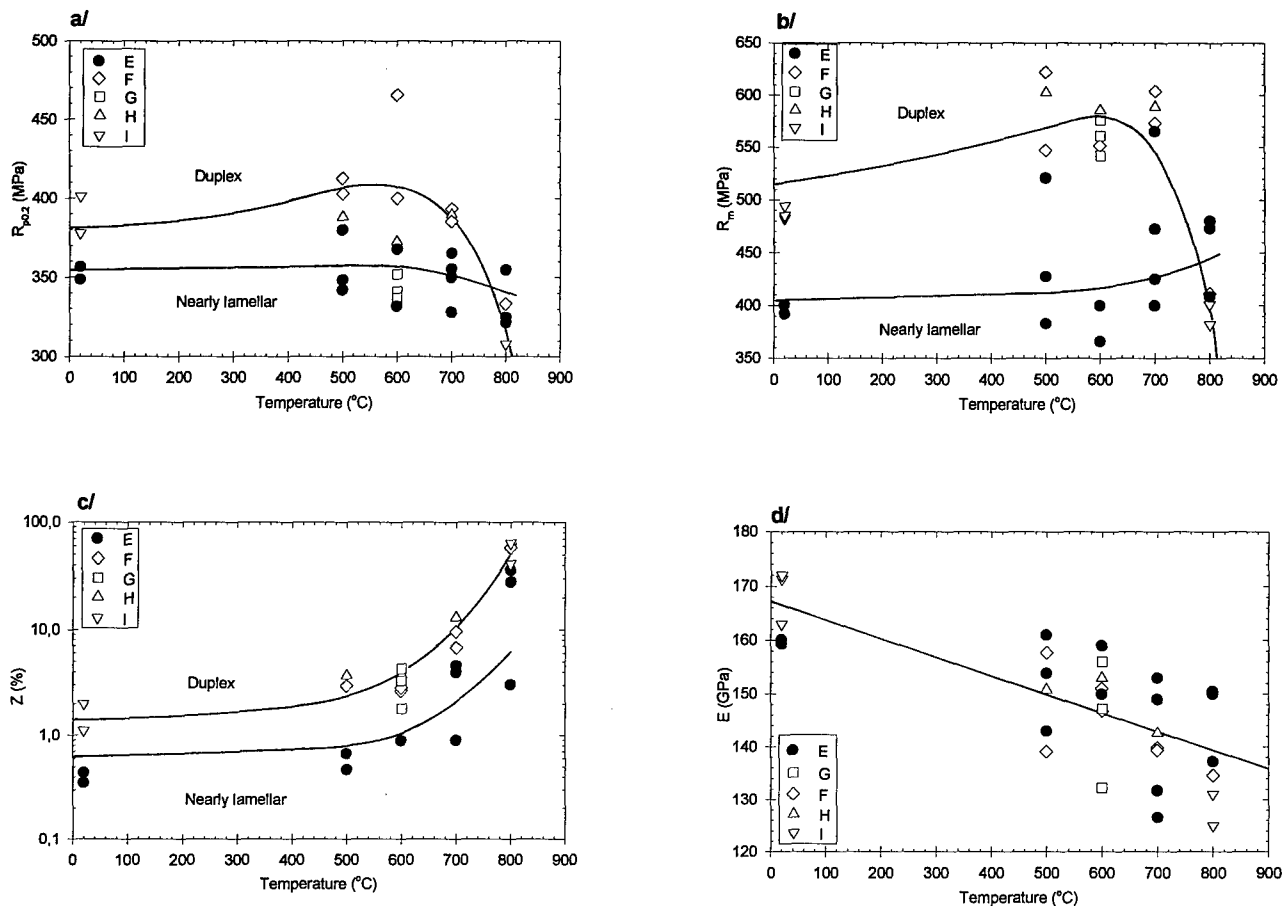


Figure 3: a/ Yield strength ( $R_{p0.2}$ ), b/ ultimate tensile strength ( $R_m$ ), c/ reduction in area (Z) and d/ Young's modulus (E) at temperatures between 20°C and 800°C. Nearly lamellar material is represented by filled symbols, duplex with open symbols.

### Tensile test results

The yield stress  $R_{p0.2}$  is fairly temperature independent up to about 700°C with duplex structures (lots F-I) having somewhat higher values, figure 3a. Above this temperature a gradual decrease in  $R_{p0.2}$  appears which is more marked for the duplex structures. Similar temperature dependence is found for the ultimate tensile strength  $R_m$  (figure 3b) but with considerably larger difference between the duplex and near lamellar structures. The softening occurring above 700°C leads to similar strength levels of the two groups. The ductility as measured by the reduction in area, Z, is low and fairly constant up to about 700°C (figure 3c), higher temperatures raise the ductility strongly. It is evident that the duplex structures exhibit markedly larger ductility, and this difference is more pronounced above 700°C.

The present materials show a brittle to ductile transition temperature (BDTT) behaviour as has been reported for many other  $\gamma$ -titanium aluminides [1,6-9]. Figure 3 indicates a BDTT lying between 700 and 800°C.

In contrast to the flow stresses, the Young's modulus E decreases gradually with increasing temperature, although with strong scatter between the different specimens, figure 3d. It should be

noted that the scatter at a given temperature largely exceeds the uncertainty in the evaluation. No significant difference in modulus could be seen between the two types of microstructures.

A number of randomly selected tensile specimens tested in the temperature range 500 - 700°C were microstructurally evaluated. The ultimate and yield strengths of these specimens are correlated to the volume fraction of lamellar colonies in figure 4. Virtual temperature independence of  $R_{p0.2}$  and  $R_m$  in this range allowed only the microstructural influence on these properties to be studied. As figure 4 indicates, increasing amounts of lamellar colonies only slightly decrease the yield stress, whereas the ultimate tensile strength obviously strongly decreases.

### Low Cycle Fatigue test results

#### Cyclic stress response

Figure 5 shows a typical example of the stress response during a test. All 29 tested specimens show a cyclic hardening behaviour during the entire life-time, with a decreasing rate towards the failure. The hardening behaviour is also illustrated in figure 6 where the tensile peak stress  $\sigma_{max}$  measured at tensile peak strain  $\epsilon_{max}$  from stabilised, half life hysteresis loops is compared with

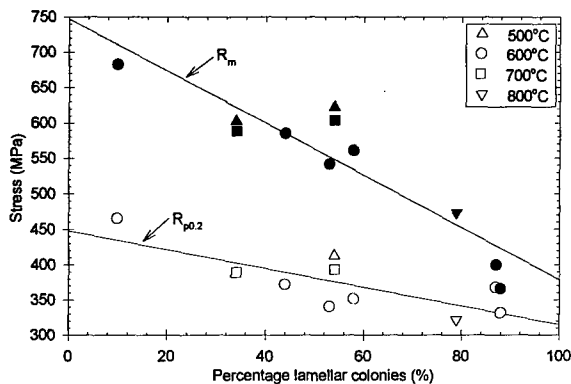


Figure 4:  $R_{p0.2}$  and  $R_m$  strengths vs. volume percentage of lamellar colonies at temperatures between 500°C and 800°C. The temperature dependence of the flow stresses is weak in this temperature range.

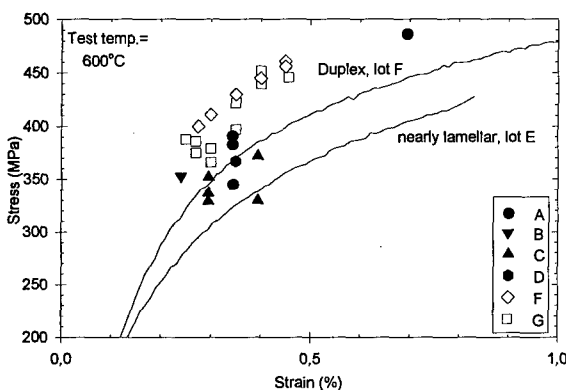


Figure 6: Monotonic and cyclic stress-strain behaviour at 600°C. nearly lamellar material is represented by filled symbols, duplex with open symbols.

two monotonic tensile test curves, one from material with duplex and one with nearly lamellar microstructure. As can be seen in figure 6 the material with duplex structure shows larger hardening with smaller scatter than the nearly lamellar material. As an example, the increase in stress at a strain range of 0.7% is on the average 75 MPa and 35 MPa respectively. During cycling, the compressive strain hardening component seems to be larger than the tensile leading to a negative mean stress. The duplex material shows a larger compressive mean stress than the nearly lamellar material, -25 MPa versus -5 MPa at a strain range of 0.7%.

Comparisons between stabilised half life hysteresis loops for the duplex and the nearly lamellar materials point out some important differences. Besides the large difference in stress response, the amount of inelastic deformation is much larger in the lamellar material since the elastic part at loading and unloading is smaller.

#### Strain life data

The fatigue strain-life plot in figure 7a illustrates the superior low cycle fatigue properties of the duplex material in lot F and G in comparison with the coarse grained nearly lamellar material in lot

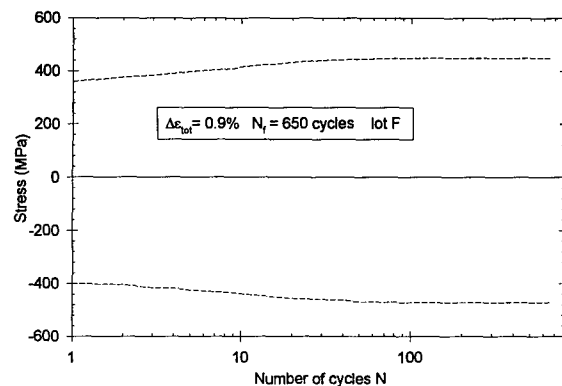


Figure 5: Cyclic stress response during life showing a continuous hardening behaviour. No decrease in load due to crack initiation can be detected.

A, B, C and D. In addition the duplex structure shows considerably less scatter in life times. The difference in lifetime between the two types of microstructures decreases when only the inelastic strain is studied, figure 7b. Still the scatter in results remains larger for the nearly lamellar structure.

Fatigue life-time in strain controlled design is often predicted with the Coffin-Manson model [ASTM, E606],

$$\Delta \epsilon_{tot} = (\sigma_f / E) * N_f^b + \epsilon_f * N_f^c$$

where

- $\Delta \epsilon_{tot}$  = total strain range
- $\sigma_f$  = fatigue strength coefficient
- $b$  = fatigue strength exponent
- $E$  = Young's modulus
- $N_f$  = number of cycles to failure
- $\epsilon_f$  = fatigue ductility coefficient
- $c$  = fatigue ductility exponent

The total strain life data for the duplex and nearly lamellar material can be represented by

$$\Delta \epsilon_{tot} = 0.0076 * N_f^{-0.040} + 0.019 * N_f^{-0.329} \quad (1)$$

$$\Delta \epsilon_{tot} = 0.0068 * N_f^{-0.045} + 0.011 * N_f^{-0.310} \quad (2)$$

where the constants have been determined by regression analysis. Strain-life time data represented by these two equations can be seen in figure 7a and 7b, elucidating the sensitivity in life time for the strain range at these large strains and the difference in life-time between the duplex and nearly lamellar material. The equation for the duplex structure fits better to the test results than the lamellar one. The larger scatter in the stress response of the lamellar material makes the estimation of the parameters in the equation uncertain.

#### Crack initiation and propagation

The crack propagation in  $\gamma$ -TiAl has been fairly well characterized in the literature [2,5,10]. The fractographic features of the specimens tested in monotonic loading and the fast fracture area



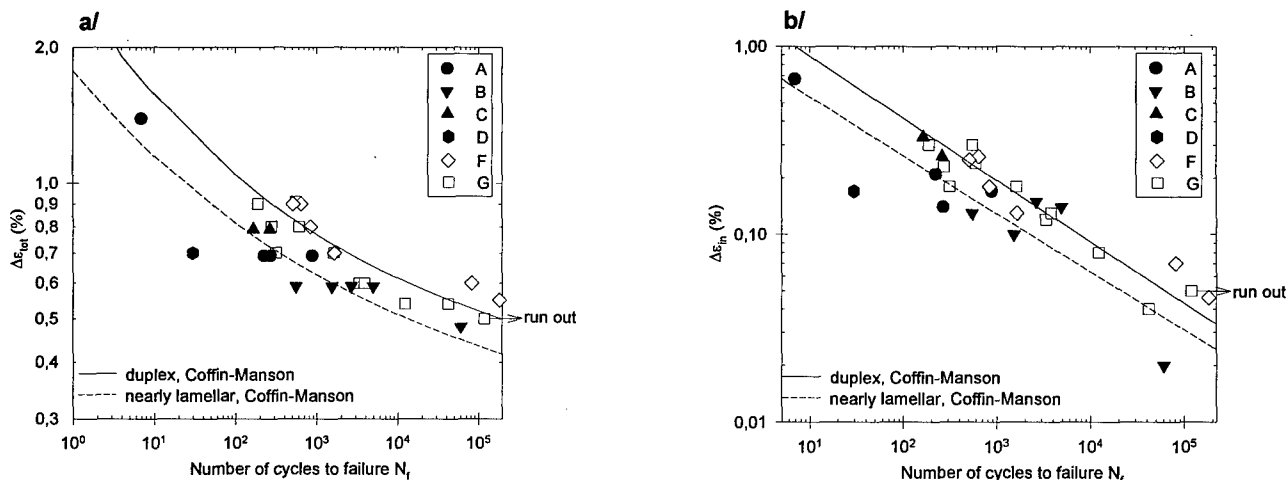


Figure 7: Low cycle fatigue test results. a/ Total strain range versus number of cycles to failure. b/ Inelastic strain range versus number of cycles to failure. Nearly lamellar material is represented by filled symbols, duplex with open symbols.

of the specimens tested in cyclic loading in the present case follow the behaviour of many other  $\gamma$ -TiAl alloys, i.e. brittle transgranular failure of the lamellar colonies, interlamellar when the lamellas are oriented perpendicular to the loading direction and translamellar at orientations parallel to this direction. The equiaxed  $\gamma$ -grains fail in a brittle transgranular cleavage mode or intergranular mode up to the brittle to ductile transition temperature of the material where the latter fracture type dominates at higher temperatures. The small equiaxed  $\gamma$ -grains fail in a ductile dimple-like fracture in samples tested at 800°C.

To determine the crack initiation sites through fractography in  $\gamma$ -TiAl alloys is often tricky, since the only microconstituent telling anything about the direction of the crack path is the  $\gamma$ -grains

fractured in cleavage mode with their characteristic river pattern. The amount of these grains found in a fracture surface is usually very low, since the volume fraction of equiaxed  $\gamma$ -grains often is low. In addition, many of these grains fail in a intergranular mode at elevated temperatures, especially at  $\gamma/\gamma$  grain boundaries.

Under monotonic loading initiation was found to occur 1) adjacent to larger  $\gamma$ -grains either in  $\gamma/\gamma$ - or  $\gamma$ /lamellar colony-boundaries, 2) transgranularly in  $\gamma$ -grains and 3) between lamellas in lamellar colonies. Initiation in or between  $\gamma$ -grains seems to dominate at room temperature. Interlamellar initiation becomes more common as the temperature and the fraction of lamellar colonies increase.

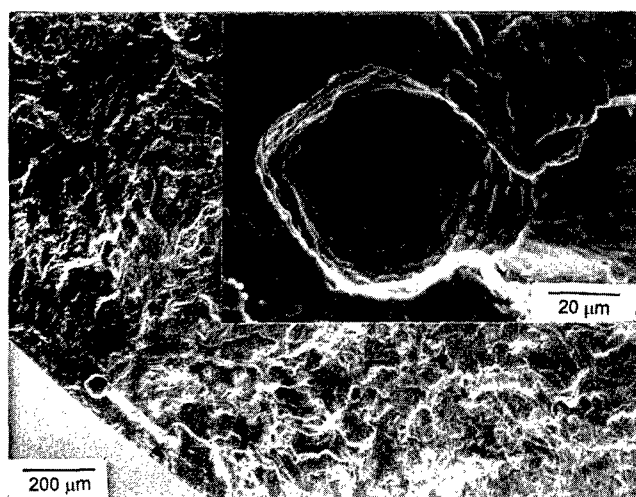


Figure 8: Crack initiation at a pore just below the surface in the nearly lamellar material. The precipitates in the pore are rich in Si. The crack has propagated in an interlamellar mode.

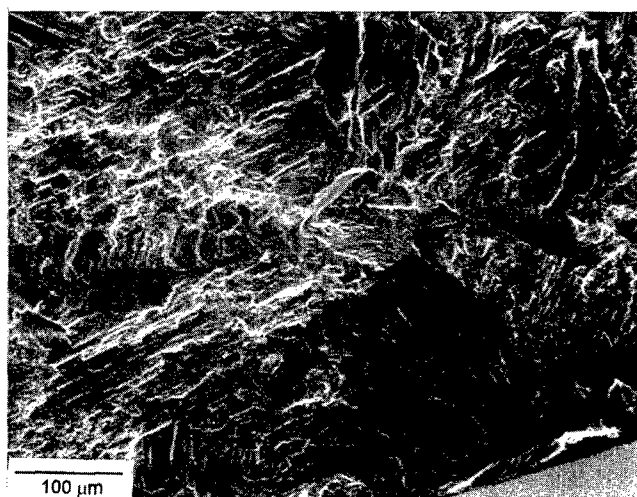


Figure 9: A smooth area in the fracture surface indicating stable crack growth in the duplex material.

Crack initiation at cyclic loading follows the same pattern as in monotonic loading. Interlamellar crack initiation dominates in the nearly lamellar material. In addition, crack initiation at pores can be found in specimens from lot A, figure 8. No evidence of stable crack growth can be found in the fracture surfaces. The duplex material on the other hand, shows some evidence of stable crack growth and multiple crack initiation sites. Smoother areas up to 500  $\mu\text{m}$  in length and 300  $\mu\text{m}$  in depth, presumably associated with the stable crack growth, can be seen near the surface of some specimens tested at lower strain ranges, figure 9.

## Discussion

### Tensile properties

#### *Strength and ductility of the material*

The strength of the present ABB IMN2  $\gamma$ -alloy is competitive with many Ni-based superalloys and Ti-alloys, especially when the low density of the material is considered. One drawback is the low ductility of the alloy. The room temperature ductility is lower than that of many other  $\gamma$ -based TiAl alloys such as the GE-patented Ti-48Al-2Cr-2Nb [6,8]. How much ductility is needed in service is still in dispute and also depends on the application. The room temperature ductility of the duplex material is below 2% which can lead to problems in handling and assembling of parts. An expected service temperature for this alloy is somewhere between 500°C and 700°C, where the reduction in area for the present duplex grade is above this ductility level.

The temperature dependence of the yield strength up to the BDTT is small, figure 3a. The slight decrease in strength and increase in ductility at higher temperatures comes from an increased activity of mechanical twinning on {111}-planes [9]. The ultimate tensile strength shows an anomalous strengthening behaviour with a peak strength at 700°C. The proposed origin of this effect is the enhanced mechanical twinning in the  $\gamma$ -phase at higher temperature which reduces the planar slip behaviour, increases the ductility and therefore the possible plastic strain accommodated in the material before fracture. Failure in weak spots in the microstructure is delayed.

The strength of the duplex material decreases substantially between 700°C and 800°C indicating the BDTT in this temperature range. The considerable increase in ductility is attributed to a substantial increase in mechanical twin activity and reduced planar deformation through cross twinning and dislocation climb in the  $\gamma$ -phase [9]. Fractography of the present material showed that the failure mode of the  $\gamma$ -phase changes from brittle at 700°C to ductile dimple-like at 800°C. The fracture mode of the lamellar structure is not affected between 700°C and 800°C and the nearly lamellar material has not yet reached the BDTT. The strength of the nearly lamellar material in lot E is in fact highest at 800°C. A more exact estimation of the BDTT requires testing between 700°C and 800°C. Another parameter for determining the position of the BDTT and the fracture behaviour is the strain rate [11].

### *Role of the microstructure for the tensile properties*

An example of the influence of the microstructure on the tensile properties is the dependence of the volume fraction of lamellar colonies on the strength of the material in figure 4. The influence is larger on the fracture strength than on the yield strength. Fractography has shown that failure can be initiated between the lamellas of large lamellar colonies. The probability of having a colony with an unfavourable orientation at the surface causing premature failure increases with the fraction of the colonies. On the other hand, the yield strength is reached before this failure and is therefore not affected.

The strength of materials is often correlated to the grain size. Many investigations in the literature points out the Hall-Petch relationship between yield strength and colony size of a lamellar microstructure and between strength and grain size of a single phase  $\gamma$  structure [12-14]. To gain any precision in statistics of the large colony size in this study is difficult. In addition, the colony size as well as the volume fractions of the phases, can differ quite a lot between test bars from the same melt and even between different areas in the same test sample [4]. This makes correlation to mechanical data uncertain with large scatter. The amount of lamellar colonies stands in close relationship to the colony size with larger colonies as the fraction increases [13]. The correlation between strength and fraction of lamellar microconstituent in figure 4 can also be an effect of the colony size. This is also confirmed by the fact that the  $\alpha_2$  phase is considered to be the strengthening phase in the lamellar structure. If there was no strength / colony size dependence, the relationship between the two should show an opposite slope of the curve, since the  $\alpha_2$  content increases with increased amount of lamellar constituent.

### Low Cycle Fatigue Properties

The total life of the samples showed a very strong sensitivity to the strain range, an effect that can be attributed to the high Young's modulus and the fairly low yield strength of the material which leads to inelastic straining and fatigue damage even at small strain ranges. The strong deformation hardening of the material, shown both in monotonic and cyclic loading, reduces this effect during life and the cyclic damage built into the material is decreased. If the cyclic saturation stress is below the ultimate tensile stress, the sample will show very long life [15]. The two run outs and the very flat high cycle fatigue curves found in the literature [15] point out this effect. On the other hand, a saturation stress above the ultimate tensile strength will lead to fracture and fatigue life will be strongly influenced by the inelastic strain [15].

The relationship between the plasticity, damage and fatigue performance is well documented for metallic materials. The difference between the duplex and the nearly lamellar material point out that this is also true for the intermetallic compound studied. Both structures show, as mentioned earlier, strain hardening, but the isotropic type of hardening is larger and the Bauschinger effect smaller in the duplex material. This difference leads to larger inelastic strains in each cycle causing irreversible damage in the nearly lamellar material leading to shorter fatigue lives.

The low cycle fatigue performance of the Ti-48Al-2W-0.5Si alloy is consistent with data for other types of  $\gamma$ -TiAl alloys found in the literature [16,17]. The low cycle fatigue properties of fully lamellar Ti 46Al-2Nb-2Cr in reference 16 are between the properties of the duplex and the nearly lamellar structure in this study.

The fatigue strength and the fatigue ductility coefficients for metallic materials are sometimes comparable to the monotonic ultimate tensile strength and fracture elongation. The fatigue strength coefficient ( $\sigma_f$ ) of the present duplex material is 1200 MPa, which is considerably higher than the monotonic tensile strength of around 570 MPa, while the fatigue ductility coefficient ( $\epsilon_f$ ) of 1.9% is slightly lower than the monotonic value of around 3% pointing out that estimation of fatigue lives out of monotonic test data give inadequate results.

#### Scatter in test results

Of large concern is the extensive scatter in test results, figures 3 and 7. This scatter can be explained by:

- Variations in chemical composition between the different lots of material. This variation leads to different microstructures and mechanical properties.
- Variations in HIP and heat treatments. The nearly lamellar material showed some porosity.
- The lamellar colony size in the nearly lamellar material is very large. This results in only 5-10 grains in the cross section of a tensile or a low cycle fatigue test bar. Measurements of bulk properties requires a considerably larger number of grains in the cross section. Test pieces with larger gauge diameters have to be used for mechanical testing of a coarse grained material as this.
- The mechanical properties of the lamellar colonies are anisotropic, i.e. strongly affected by the lamellar orientation. A grain oriented perpendicular to the loading axis will have a negative effect on crack initiation and propagation properties. This partly explains the larger scatter in ultimate strength than in yield strength for the nearly lamellar structure at tensile loading. The same effect can be attributed to the larger scatter in fatigue life in the nearly lamellar material.
- The fatigue life is mainly decided by the crack initiation stage. Failure is initiated at weak spots such as porosity, large lamellar colonies oriented perpendicular to the loading direction and large  $\gamma$ -grains near the surface of the test piece. The low fracture toughness and the fast cyclic crack growth make the lifetime very sensitive to such weak spots.
- Large precautions were taken to ensure that the alignment of the test piece was precise. Still, the low fracture toughness in combination with the large colony size could eventually cause premature fracture at testing.

The chemical composition, HIP and heat treatment of the material aims at a duplex microstructure. If the test results from the nearly lamellar material are omitted, i.e. only the material with a duplex microstructure are considered, the scatter in test results is reduced.

#### Summary and Conclusions

Material from nine different lots with a chemical composition that differed in various extent from the nominal Ti-48Al-2W-0.5Si has been evaluated through tensile and fatigue testing, microscopic evaluation of the microstructure and fractographic investigation of the fracture surfaces. This study has shown that:

1. Low aluminium content leads to a coarse grained lamellar microstructure with inferior tensile and low cycle fatigue properties.
2. The material shows good tensile strength up to 700°C. The brittle to ductile transition temperature occurs somewhere between 700°C and 800°C.
3. The scatter in test results is large. This scatter can be attributed to variations in composition and microstructure.
4. The monotonic tensile strength of the material is dependent on the volume fraction lamellar colonies. The strength is increased as the fraction is decreased.
5. A duplex fine grained structure shows superior low cycle fatigue properties with smaller scatter in life-time in comparison to a coarse grained nearly lamellar structure. The life-time can be attributed to the amount of inelastic strain in each cycle. The duplex material shows larger isotropic hardening and smaller Bauschinger effect leading to smaller inelastic strains and therefore longer life-times.

#### Acknowledgements

Co-operation with Dr. T. Hansson and Mr. B. Pettersson, Volvo Aero Corporation, Trollhättan, is greatly acknowledged. The present investigation is part of the European research programme COST 501/III WP 14 Project "Advanced Materials for Gas Turbines, subgroup 14.1 Intermetallics for Gas Turbine Applications". It has been financially supported by Volvo Aero Corporation and Swedish Council for Engineering Science.

#### References

1. S.-C. Huang, "Alloying Consideration in Gamma-Based Alloys", Proc. of First International Symposium of Structural Intermetallics, 26-30 sept. 1993, p.299-308.
2. S. Mitao, S. Tsuyama, K. Minakawa, "Effects of Microstructure on the Mechanical Properties and Fracture of  $\gamma$ -Base Titanium Aluminides", Material Science and Engineering, A143 (1993), p.51-62.
3. K. S. Chan, "Microstructural Effects on Fracture Resistance in TiAl-Base Alloys", Proc. of Symposium on  $\gamma$ -TiAl, Las Vegas 13-16 Feb. 1995, The Minerals, Metals & Materials Society, p.835-847.
4. V. Recina, J. Ahlström, B. Karlsson. "Sample Preparation and Microstructure Characterisation of Gamma Titanium Aluminides", Materials Characterization, 1997 in print.

5. V. Recina, B. Karlsson. "Tensile Properties of Ti-48Al-2W-0.5Si Gamma Titanium Aluminide at temperatures between RT and 800C", Submitted to Materials Science and Technology, Feb. 1997.
6. T.J. Kelly, C.M. Austin, "Effect of Aluminium and Heat Treatment on the Mechanical Properties of Cast Ti-48Al-2Cr-2Nb", Proc. of 8th Conf. on Titanium, Birmingham UK. 22-26 Oct. 1995, p.192-200.
7. Y.-W. Kim, "Ordered Intermetallic Alloys, part III: Gamma Titanium Aluminides", Journal of Metals, July 1994, p.30-39.
8. Shih D.S, et al., "The Microstructural Dependence of Mechanical Properties of Ti-48Al-2Cr-2Nb", The Minerals, Metals & Materials Society, 1991, p.135-148.
9. S.-C. Huang, E.L. Hall, "Plastic Deformation and Fracture of Binary TiAl-Base Alloys" Metallurgical Transactions Vol 22A, Feb 1991, p.427-439.
10. S. C. Kwai , "Understanding Fracture Toughness in Gamma TiAl" Journal of Metals, May 1992, p..30-38.
11. D. S. Shih, D. S. Schwartz, J.E. O'Neal, "Effects of Strain Rate and Prestraining on Tensile Behaviour of Duplex Gamma Titanium Aluminide." Mat. Res. Soc. Symp. Proc. vol. 288 1993 Material Research Society.
12. A.W. Thompson, W-Y. Chu, "Effect of Grain Size and Hydrides on Mechanical Properties of TiAl", Microstructure/Property relationships in Titanium Aluminides and Alloys. The Minerals, Metals and Materials Society, 1991.
13. J. D. Shi, Z. J. Pu, K. H. Wu, "Influence of Grain Size on Tensile and Fracture Toughness of TiAl Based Alloys", Proc. of Symposium on  $\gamma$ -TiAl, Las Vegas 13-16 Feb. 1995, The Minerals, Metals & Materials Society, p.709-716.
14. W.O. Soboyejo, C. Mercer, "The Effects of Alloying and Microstructure on the Fracture of Intermetallic Compounds Based on TiAl." Fatigue and Fracture of Ordered Intermetallic Materials 1994, The Minerals Metals & Materials Society, p.171-223.
15. W. E. Dowling, W. T. Donlon, J. E. Allison, "The Fatigue Behaviour of  $\gamma/\alpha_2$  Titanium Aluminides", Mat. Res. Soc. Symp. Proc. vol. 213, 1991 Material Research Society.
16. G. Malakondaiah, T. Nicholas, "High Temperature Low Cycle Fatigue of Gamma Titanium Aluminide Alloy Ti-46Al-2Nb-2Cr", Metallurgical and Materials Transactions, Vol 27A, June 1996, p.2239-2251.
17. M. C. Hardy, "Elevated Temperature Low Cycle Fatigue Behaviour of a Near- $\gamma$  Titanium Aluminide", Proc. of 8th Conf. on Titanium, Birmingham UK. 22-26Oct. 1995, p.256-263.

# Application of Cast Gamma Alloy for Turbochargers

T. Tetsui

Nagasaki Research and Development Center, Mitsubishi Heavy Industries Ltd.,

Nagasaki, Japan 851-03

## Abstract

The application of gamma TiAl alloy in the turbines of turbochargers was investigated. As cost reductions are imperative in order to realize practical utilization, as-cast precision castings were subjected to a number of tests. Although material evaluation indicated that high-temperature strength was not a problem, anti-oxidation properties were found to be insufficient. This led to consideration of application in diesel engines, which feature lower operating temperatures than gasoline engines. A gamma turbine was fabricated by means of a brazing method and subsequent processing, and was fitted to a turbocharger. The turbocharger in turn was attached to an actual diesel engine, and traditional response ability and engine endurance tests were conducted. As a result, it was found that response ability was superior to metal turbines currently in use, thereby confirming the effectiveness of turbine weight reduction. While endurance was confirmed within a set time period, it was also demonstrated that the anti-oxidation of the gamma alloy itself still requires improvement.

## Introduction

Lightweightness is the most significant characteristic of gamma alloy, having a specific gravity of 3.8 - 4.0. Accordingly, its most promising industrial application (i.e., as a substitute for metals in current use) is for rotating components such as turbine parts.(1)-(5) Lighter rotating components reduce centrifugal force, thereby allowing higher rotation speeds and improved response ability. In addition, the load on discs, bearings and other peripheral components is reduced, permitting structural simplification and highly increased reliability.

There is an extremely wide range of rotating components, depending on operating temperature and shape, in the heavy industrial products.

However, in ascending order of temperature, FRP, aluminum alloy, low alloy steel, titanium alloy, stainless steel and super alloy are selected and utilized with reference to required material characteristics.

The difficulty of manufacturing high quality large size components must be recognized in considering the practical application of gamma alloy, as well as the fact that its use is not advantageous in temperature regions where light weight titanium alloy can be used. Thus, the applications for high temperature small rotating components, where currently super alloy are used, offer the greatest possibilities for the use of gamma alloy. We have therefore been working to apply gamma alloy for use in turbocharger turbines, and this report provides an initial description of the results of the various considerations undertaken during the development process.

## Material Testing

### Cast Gamma Turbine Wheels

The gamma turbine wheel used for evaluation in this study was manufactured by means of the Levi-Cast method, a type of lost wax precision casting process, and was supplied by Daido Steel Co., Ltd. The alloy composition was Ti-33.5Al-0.5Si-1.0Nb-0.5Cr (wt%)(6), and the results of chemical analysis are shown in Table I. Because cost reduction is an essential factor for mass production, the material was used in an as-cast state, avoiding processes that would tend to increase cost (i.e., post-casting HIP or heat treatment). Figure 1 shows the external appearance of the cast gamma wheel, and Figure 2 shows its cross-sectional macrostructure. Because neither HIP nor heat treatment was undertaken, the macrostructure shows a columnar structure. Figure 3 shows the microstructure, which is the large grain size of fully lamellar structure, that generally seen in as-cast gamma

alloy, and proeutectic precipitate is observed. Both X-ray inspection for internal defects and visual inspection for misruns in blade tips were conducted.

Table I Chemical Composition of Gamma Alloy Used in this Study

(wt%)						
Al	Si	Cr	Nb	Ti	O	N
33.5	0.44	0.59	1.03	Bal.	0.074	0.014

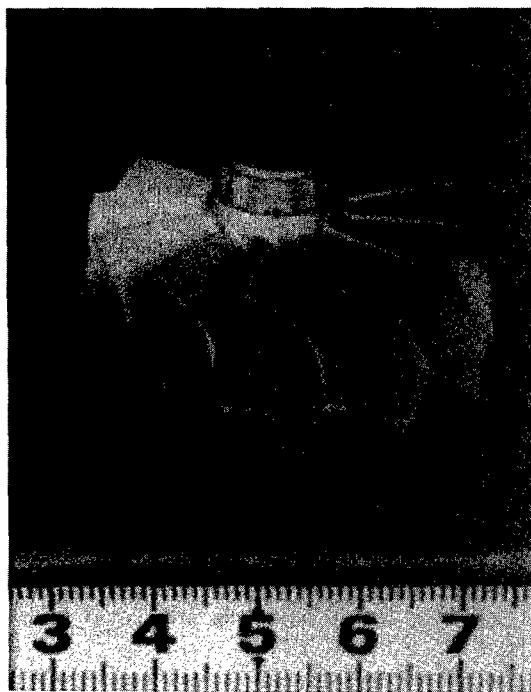


Figure 1 : A cast turbine wheel of gamma alloy.



Figure 2 : Macrostructure of cross section of a cast gamma turbine wheel.

## Tensile Testing

Specimens 4mm in diameter at the gage section were taken parallel to the turbine wheel central axis, and tensile testing was conducted both at room temperature and at 900°C. The tensile testing results appear in Table II. Because of the as-cast nature of the material, room temperature ductility is an extremely low 0.15%. High temperature ductility is greater, although there is only a small drop in strength.

## Oxidation Testing

Anti-oxidation is the most important characteristic required of gamma alloy in order to allow effective use for long periods at high temperatures. Cyclic oxidation testing was conducted on a 20×20×3mm. test piece cut from a cast gamma wheel. The test piece was held at 850°C in air for periods of 30 minutes and cooled, undergoing 200 cycles for cumulative oxidation time of 100 hours. Figure 4 indicates the relationship between the number of cycles and changes in weight; oxidation-induced weight gain was 16.6g/m<sup>2</sup> after 200 cycles. For Inconel 713C, currently used for turbine wheels, weight gain following 200 cycles of 30 minutes at 900°C is 1.3g/m<sup>2</sup>,<sup>(5)</sup> or , with constant exposure for 100 hours at a temperature of 950°C, 10g/m<sup>2</sup>.<sup>(7)</sup> This suggests that the applicable temperature of the current gamma alloy is at least 100°C lower than Inconel 713C.

A number of anti-oxidation surface treatment methods have already been proposed in order to improve the comparatively weak anti-oxidation properties of gamma alloy.<sup>(7)(8)(9)</sup> However, because surface treatment results in higher manufacturing costs, and because any conceivable surface treatment would only last a short time in comparison with the actual length of service envisioned, it is not practical for turbocharger application. Accordingly, future increases in the applicable temperature of gamma alloy will have to be effected through improvement of the anti-oxidation properties of the material itself.

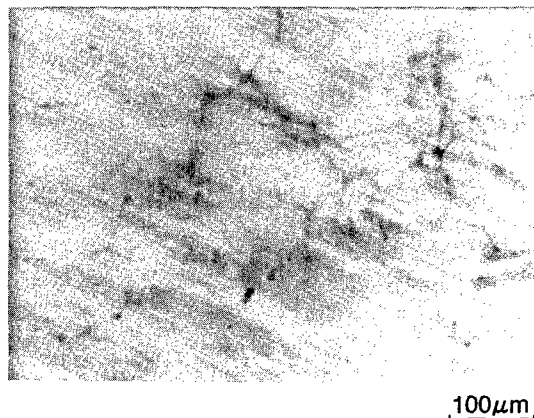


Figure 3 : Microstructure of a cast gamma turbine wheel.

Table II Tensile Properties of Cast Gamma Turbine Wheel

Temperature (°C)	Elongation (%)	Tensile Strength (MPa)
25	0.15	402
900	38.00	370

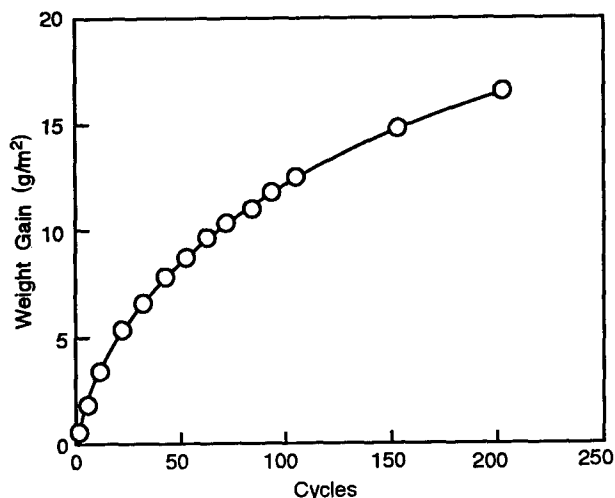


Figure 4 : Weight gain by cyclic oxidation at 850°C of a cast gamma turbine wheel.

From the standpoint of anti-oxidation, the gamma alloy considered in this study cannot be readily used in turbochargers for passenger vehicle gasoline engines (950°C and above), leading to consideration of its application for diesel engines (850°C and under).

### Turbine Manufacturing

#### Brazing Method

The turbine shaft is low alloy steel, and must be joined either directly or indirectly with the gamma wheel. Various methods have been proposed for the joining of gamma alloy,(5)(10) but vacuum brazing is the only acceptable method for industrial mass-production. In this study, the widely applicable silver brazing method was adopted, and the brazing filler metal utilized was BAg-8 (Ag-28Cu).

Although it is possible to form direct joints between gamma alloy and low alloy steel by brazing, the heat applied during the brazing process can cause softening of the shaft. Incoloy 909 was therefore used as an insert material; the Incoloy 909 and the gamma wheel were joined by means of brazing, and the Incoloy 909 and the shaft were joined by means of electron beam welding. Figure 5 is a schematic illustration of the joint. Given this configuration, and taking into account the high/low temperature heat expansion differential of Incoloy 909 ( $13.0 \times 10^{-6}/^{\circ}\text{C}$  at 850°C, and  $7.7 \times 10^{-6}/^{\circ}\text{C}$  at 100°C),(11) a shrinkage fit effect can be expected.

Figure 6 shows the microstructure and hardness distribution of a cross section of a brazed joint between the gamma alloy and the Incoloy 909. Compared with the initial gap, the joint section widened due to reaction with the base material. Hardness is greatest for the reaction phase nearest the gamma alloy. The results of EPMA quantitative analysis indicate that the composition of this phase is Ti: 24.5, Al: 22.1, Nb: 0.4, Si: 0.2, Cr: 0.3, Cu: 50.9, Ag: 0.7 (at%), suggesting that the phase is  $\text{AlCu}_2\text{Ti}$  with a B2 structure.(12)

Tensile test results for the brazed joint appear in Table III. At room temperature, the gamma alloy was broken, and satisfactory strength of 340MPa was obtained. At 350°C, however, the brazed joint was separated and tensile stress declined to 214MPa. This indicates that there is a definite limit on the temperature at which silver brazing filler can be used.

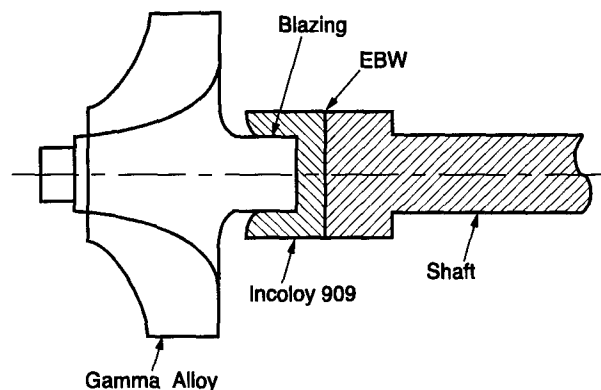


Figure 5 : Schematic illustration of joining method of a gamma turbine wheel to a steel shaft.

Incoloy 909 | Initial Gap | Gamma Alloy

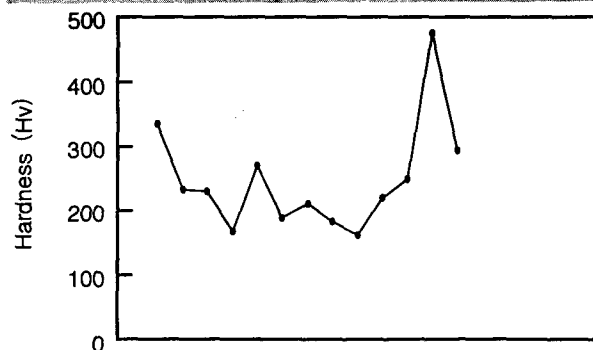
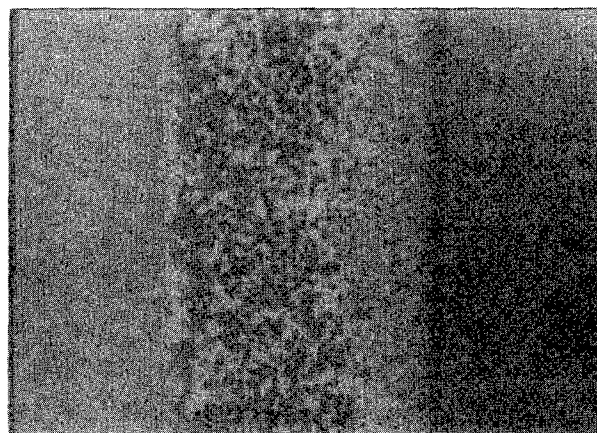


Figure 6 : Microstructure and hardness distribution of silver brazing joint of gamma turbine wheel to Incoloy 909.

Table III Tensile Strength of the Brazing Joint of Gamma Turbine Wheel to Incoloy 909

Temperature (°C)	Tensile Strength (MPa)
25	343
350	214

## Processing and Assembly

Figure 7 shows a gamma turbine after brazing, EBW, grinding of the edges of the blades, and balancing. The brittleness of gamma alloy at normal temperatures is most serious problem during these processes, and the failure most likely to be encountered during manufacturing is chipping of the blade tips. To avoid this, production workers must be aware of the extremely brittle nature of the material and handle it carefully. In operation, however, the only substances that come into contact with the blades are air and minute particles of fuel. This, together with the increased ductility of gamma alloy accompanying higher temperatures, means that brittleness is not an issue in terms of the application.

## Application Testing

### Engine Endurance Test

In order to evaluate the practical applicability of the gamma turbine, a turbocharger was built by adding a compressor and casing, and this was attached to the exhaust side of an actual diesel engine for endurance testing. Testing conditions were a turbine inlet temperature of 850-860°C, revolution speed of 400-420m/s, and a maximum load of 200 continuous hours.

Neither bursting of the gamma wheel nor breakage of the brazed joint was observed during endurance testing. Although the results of tensile testing of the brazed joint had shown a major reduction in strength at 350°C, this did not prove to be a problem during engine testing, suggesting that the temperature of the brazed portion during operation is much lower than that at the turbine inlet. Figure 8 shows the external appearance of the turbine following engine endurance testing. The color of the blade surfaces has changed to brown, except for the very tips, but this color change is not the result of oxidation scale (generally yellow/gray) on the gamma alloy. Rather, it comes from the adhesion of diesel fuel combustion residue.

Because the temperature is highest at the tips of the turbine blades, it was expected that oxidation would be most conspicuous at these points. The turbine was therefore sectioned following the endurance test, and the transformation of the blade tips was observed. Figure 9 provides cross-sectional back scattering electron images of the blade tips before and after testing. The side away from the adhesion of combustion residue shows wear at the tips, and the surface of the gamma alloy is exposed. The adhesion of oxidation scale was not observed here, but this is probably due to the spalling of scale as a result of centrifugal force.

The results of the engine test showed that the endurance of the gamma wheel was maintained during fixed-time maximum load conditions for a diesel engine. On the other hand, given the observation of wear at the blade tips, and given the necessity of preventing such wear in order to maintain sufficient aero-supercharging performance even after a long period of service, the anti-oxidation properties of the gamma alloy itself must be improved.

### Response Ability Test

A turbocharger with a gamma wheel was attached to a diesel engine, and a response ability test was conducted. For the purposes of comparison, a metal turbine of the same shape made of Inconel 713C was subjected to an identical test. Figure 10 shows the relation between time elapsed from the startup of the turbocharger and supercharging pressure. Compared with the metal turbine, the gamma

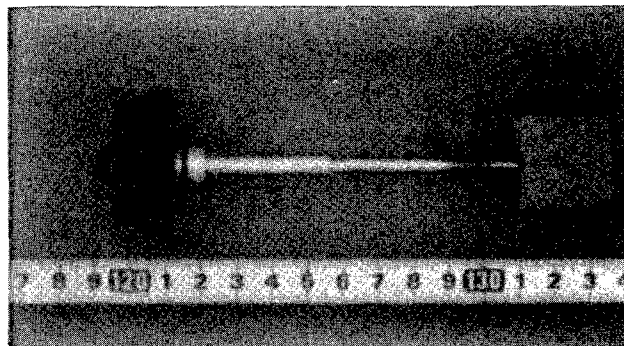


Figure 7 : A finished gamma turbine.

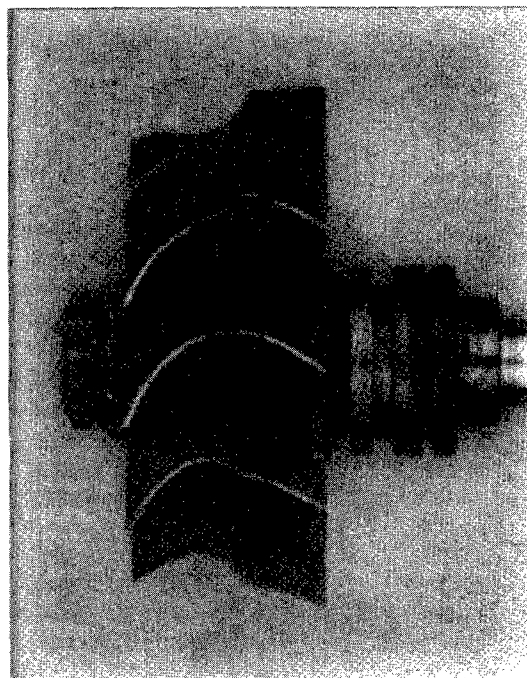


Figure 8 : A gamma turbine after engine endurance test at 850°C.

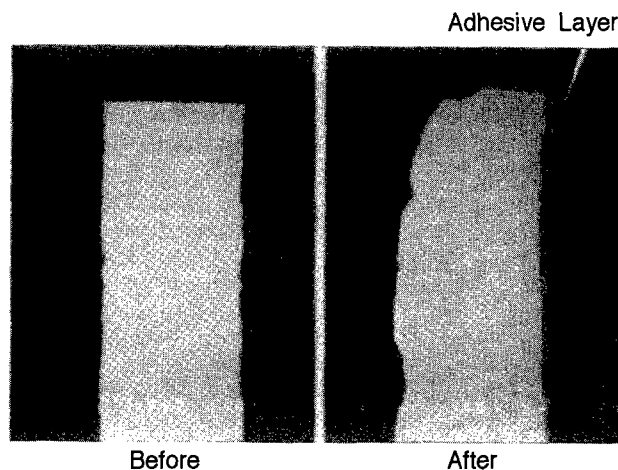


Figure 9 : Cross section of blade chip of gamma turbine before and after engine endurance test at 850°C.



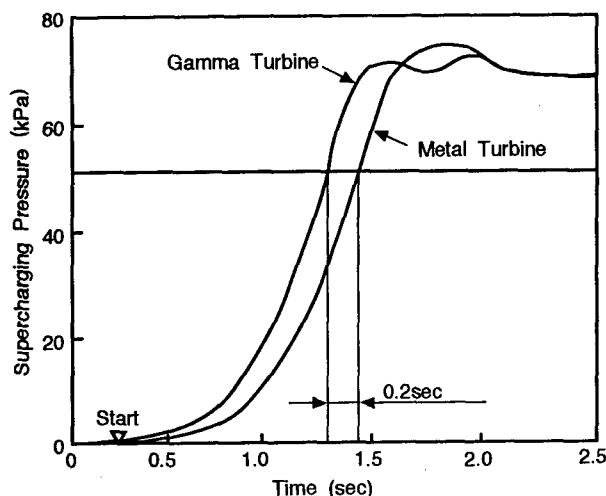


Figure 10 : Results of transition response ability test of gamma turbine and metal turbine.

turbine was 0.2 seconds faster in reaching a supercharging pressure of 50kPa, demonstrating the effect of the turbine's lighter weight. That is, it was shown that a lighter weight turbine (specific gravity of 3.9 as opposed to 7.9) reduces the moment of inertia of turbine rotation, thereby reducing the time required to reach the designated rotational speed.

#### Advantage of the Gamma Turbine

The primary advantage of the gamma turbine over currently used metal turbine is the improvement of response ability. If the time required to reach designated supercharging pressure can be cut, air required for combustion can be more quickly delivered to the engine, resulting in a lower level of incomplete combustion and a lower concentration of black smoke in exhaust gas. In addition, acceleration performance would improve, resulting in the lessening of so-called turbo-lag, and a higher level of drivability.

The performance of the turbocharger in a steady operating state (maximum supercharging pressure, etc.) is related not to the weight of the turbine but to the shape (aero-performance) of the blades. Gamma turbines can be manufactured using the same process as for metal turbines, yielding exactly the same shape, and performance during normal operation would be the same.

Ceramic turbines which are already being used in small scale, would be even lighter than gamma turbines, with corresponding better response ability. However, because the sintering process for the manufacture of ceramic turbines requires greater blade thickness and does not allow aerodynamically optimum shaping of the blades, the steady state performance of ceramic turbines would be inferior to that of metal or gamma turbines. In this respect, gamma turbines are superior to ceramic turbines.

#### Conclusion

The suitability of gamma alloy for turbocharger applications was considered using precision castings in an as-cast state. High-temperature strength was not a problem, but, because anti-oxidation

properties are insufficient, attention was directed to lower temperature diesel engine turbocharger applications. Application testing showed that response ability is superior to metal turbines, confirming the effect of lighter weight. Endurance was also confirmed within a set time period, although it was simultaneously demonstrated that further improvement in the anti-oxidation properties of gamma alloy itself is still required.

#### References

1. T. Tetsui, "Development of  $\gamma+\alpha_2+B2$  type Titanium Aluminide for forged turbine rotors," Gamma Titanium Aluminides, Y-W. Kim et al. eds., (TMS, Warrendale, PA, 1995), 603-610.
2. T. Tetsui, K. Takita, and H. Higuchi, "Development of TiAl Forged Alloy for High Temperature High Speed Rotating Components," Mitsubishi Technical Review, 34 (1997), 35-38.
3. T. Tetsui and S. Takahashi, "Manufacturing Process of a Forged TiAl Turbine Rotor Containing B2 Phase," Tetsu to Hagane, 81 (1995), 49-54.
4. C. M. Austin and T. J. Kelly, "Progress in Implantation of Cast Gamma Titanium Aluminides," Gamma Titanium Aluminides, Y-W. Kim et al. eds., (TMS, Warrendale, PA, 1995), 21-32.
5. Y. Nishiyama, T. Miyashita, S. Isobe and T. Noda, "Development of Titanium Aluminide Turbocharger Rotors," High Temperature Aluminides and Intermetallics, S. H. Whang et al. eds., (TMS, Warrendale, PA, 1990), 557-584.
6. K. Maki, A. Ehira, M. Sayashi, T. Sasaki, T. Noda, M. Okabe and S. Isobe, "Development of a High-Performance TiAl Exhaust Valve," SAE Technical Paper Series, No.960303, (SAE, Warrendale, PA, 1996), 117-125.
7. M. Yoshihara, T. Suzuki and R. Tanaka, "Improvement of Oxidation Resistance for TiAl by Surface Treatments under a Low Partial Pressure Oxygen Atmosphere and Aluminum Diffusion Coating," Tetsu to Hagane, 77 (1991), 88-95.
8. H. Mabuchi, H. Asai and T. Nakayama, "Aluminide Coatings on TiAl Compound," Scripta Metal., 23 (1989), 685-689.
9. S. Taniguchi, S. Shibata, T. Yamada and L. Zou, "High-Temperature Oxidation Resistance of TiAl Improved by IBED  $Si_3N_4$  Coating," ISIJ International, 33 (1993), 869-876.
10. K. Taguchi, M. Ayada, N. Ishihara and H. Shingu, "Near-Net Shape Processing of TiAl Intermetallic Compounds by Pseudo HIP-SHS," Gamma Titanium Aluminides, Y-W. Kim et al. eds., (TMS, Warrendale, PA, 1995), 619-626.
11. Inco Alloys International, Inc. Technical Data of Incoloy Alloy 909.
12. P. Villars and L. D. Calvert, Pearson's Handbook of Crystallographic Data for Intermetallic Phases, (ASM, Metals Park, OH, 1989), 958.

FATIGUE CRACK GROWTH IN TiAl INTERMETALLICS WITH EQUIAXED,  
DUPLEX AND LAMELLAR MICROSTRUCTURES AT ELEVATED TEMPERATURES

Y. Mutoh, S. Kurai, T. Hansson\*, T. Moriya, S.J. Zhu  
Nagaoka University of Technology, Nagaoka, 940-21, Japan  
\*Presently Volve Aero Corp., Trollhättan, Sweden

Y. Mizuhara  
Nippon Steel Corp., Nakahara-ku, Kawasaki, 211, Japan

Abstract

The fatigue crack growth behavior of Gamma titanium aluminides (TiAl) was investigated by scanning electron microscope (SEM) in situ observation in vacuum at 750 °C and room temperature. The results showed that the crack growth rates at 750 °C were higher than those at room temperature. If the stress intensity factor range was modified by Young's modulus, crack growth rates at 750 °C and room temperature could fall in the same data band. This indicated that the difference of crack growth rates between room temperature and 750 °C in vacuum primarily resulted from the difference of Young's modulus. The crack growth resistance of the duplex structure (TiAlCr) was higher than that of the equiaxed grain (Ti50Al) under the same grain size of 200  $\mu\text{m}$ . The fatigue crack growth resistance of Ti46Al with fine-grained (40  $\mu\text{m}$ ) lamellar structures was higher than that of TiAlCr with coarse-grained duplex structures at both room temperature and 750 °C. The small crack growth behavior appeared in all the materials when the half-crack length (a) is below about 0.6 mm.

Introduction

The Gamma titanium aluminides (TiAl) are emerging as important engineering materials due to their attractive performance [1]. The fatigue crack growth behavior of TiAl is one of the necessary properties for design, which is very sensitive to microstructures [2-14]. The research on microstructural effects on fatigue crack growth at room

temperature showed that the lamellar structures had the highest crack growth resistance and the duplex structures were better than the equiaxed-grain structures [7-14]. The fully lamellar structures normally have a grain size of about 1 mm. If fully lamellar microstructures were to be used in practice it was pointed out that these well aligned packets of lamellar plates should be limited to as small in size as possible and orientated randomly throughout the material to achieve acceptable crack growth resistance [9]. However, the too small grained lamellar structures may lose their high resistance to crack growth [10].

High temperature fatigue crack growth behavior of TiAl was recently studied in air or vacuum [9-18]. In air, fatigue crack growth rates at 800 °C were lower than at room temperature [10-14], but the reverse results were obtained in vacuum [11,12]. However, it was also reported that the fatigue crack growth rate at room temperature was 10 times faster in vacuum [17] and little slower than that at 800 °C in air [18]. Fatigue crack growth behavior at 600 °C was unusual in both vacuum and air, depending on the microstructures [10-14]. No difference in fatigue crack growth rate between 700 and 800 °C was found in air [9,16]. The limited research showed complicated results. The mechanism for fatigue crack growth in TiAl has not been clear.

Little research on small fatigue crack growth in TiAl was performed up to now [19]. The small fatigue crack growth in TiAl occurred at the stress intensity lower than the threshold value for long crack growth [19]. It was observed that the small crack growth rate decreased with increasing stress intensity and

finally crack growth stopped. The relation between the crack propagation rate and the effective stress intensity range for small cracks was identical to that for long cracks [19]. However, the detail of small crack growth behavior in TiAl has not been clear.

In this study, the effects of temperature and microstructure on fatigue crack growth in TiAl were investigated by SEM in situ observation during fatigue tests. The small fatigue crack growth process was studied to understand its mechanism and significance for engineering.

#### Experimental Procedure

Cast and heat-treated Ti-50 at.%Al (Ti-50Al), Ti-46 at.%Al (Ti-46Al) and Ti-47 at.%Al-3 at.%Cr (TiAlCr) were used. The high purity ingots were manufactured by plasma arc melting and homogenized for 96 h at 1050 °C in vacuum. The final microstructures, which are shown in Fig. 1, are fully equiaxed with an average grain diameter of 200  $\mu\text{m}$  for Ti-50Al and fully lamellar with a grain size of 40  $\mu\text{m}$  for Ti-46Al and duplex with grain size of 200  $\mu\text{m}$  for TiAlCr. The chemical composition, three-point bending strength and fracture toughness of the materials are shown in Table 1.

Fatigue crack growth experiments were carried out at both room temperature and 750 °C in the vacuum chamber of an SEM Servo-pulsar testing machine, which combined a servo-hydraulic fatigue machine with a scanning electron microscope for in situ observation. Tungsten wire was used to heat the specimens. The fluctuation of the testing temperature was within  $\pm 1$  °C. The testing specimens were in plate-shape with 1 mm thickness, 5 mm width and 20 mm gage length, as shown in Fig. 2. The surfaces of the specimens were polished by alumina powders of 5  $\mu\text{m}$  diameter. The central notch of about 1 mm length and 0.15 mm width was machined by an electric discharge machine. After the electric discharge machining, several cracks were formed around the notch due to rapid solidification.

The fatigue precracks were introduced by K-decreasing technique up to 0.5 mm from the notch root. After fatigue precracking, cyclic tensile loads were applied with initial K-values of about 3  $\text{MPam}^{1/2}$  and incremented by 0.3  $\text{MPam}^{1/2}$  until crack growth was observed. Then the load maintained constant. The crack length was measured directly by SEM and photographs. The sine wave form was used for both the fatigue precracking and fatigue crack growth tests at a frequency of 10 Hz and with a stress ratio of 0.1.

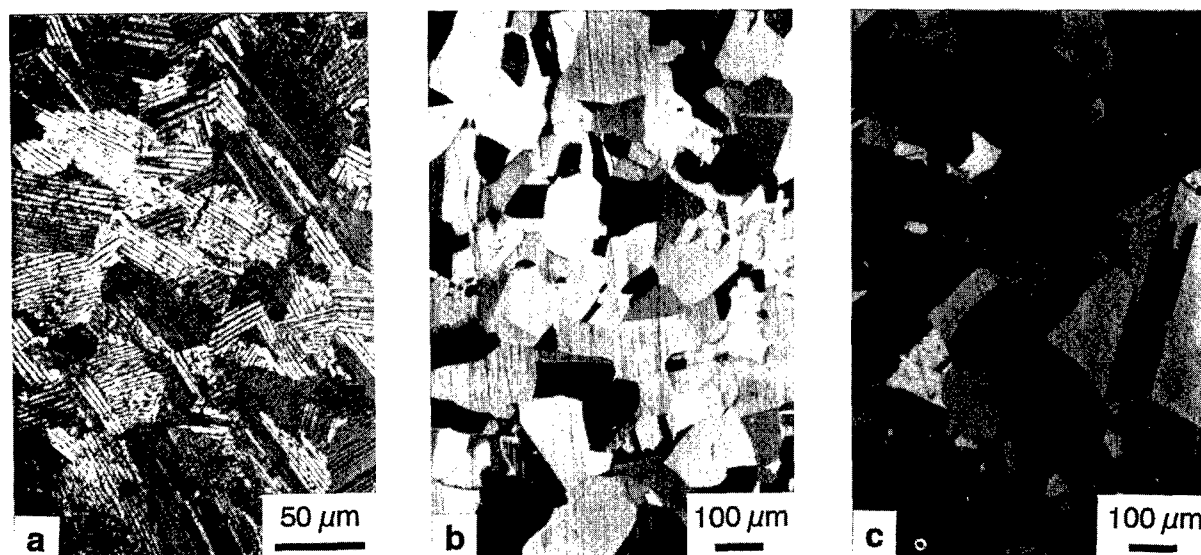


Figure 1: Microstructures of the testing materials. (a) Ti46Al; (b) Ti50Al; (c) TiAlCr.

Table I Chemical Composition, Bend Strength and Fracture Toughness of Materials

Material	Chemical Composition, at.%			Bend Strength MPa	K <sub>c</sub> MPam <sup>1/2</sup>
	Ti	Al	Cr		
Ti-46Al	55.3	44.7		836	34.3
Ti50Al	49.1	50.9		412	15.3
TiAlCr	50.7	46.4	2.8	713	32

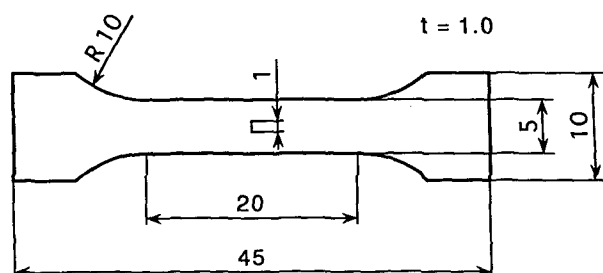


Figure 2: Geometry of the testing specimen.

The stress intensity factor for the center cracked tensile specimens was calculated by the expression [20]

$$K_I = \sigma \sqrt{\pi a} \cdot F_I(\alpha) \quad (1)$$

where  $\alpha = \frac{2a}{W}$  and

$$F_I(\alpha) = \left(1 - 0.025\alpha^2 + 0.06\alpha^4\right) \cdot \sqrt{\sec\left(\frac{\alpha\pi}{2}\right)} \quad (2)$$

$\sigma$  is the tensile stress,  $a$  is half of crack length and  $W$  is width of the specimen.

To estimate the effect of ligament bridging on fatigue crack growth, crack mouth opening was measured by laser sensor. Since it was impossible to use this method in SEM at high temperature, a four-point bending specimen (5x10x45 mm) was used and the fatigue tests were conducted at room temperature. Two copper sheets were fixed on the each side of the crack mouth. Thus, the laser passed through the gap between the two sheets.

## Results and Discussion

### Temperature Effects

Fatigue crack growth rates at 750 °C are higher than those at room temperature in all the three kinds of materials in SEM vacuum, although Fig. 3 only shows the data in TiAlCr. The fatigue crack growth rates in metals are normally described by the Paris relation as

$$\frac{da}{dN} = C(\Delta K)^m \quad (3)$$

The Paris law constant,  $m$  is presented in Table II. The fatigue crack growth curves are very steep, that is,  $m$  is very large

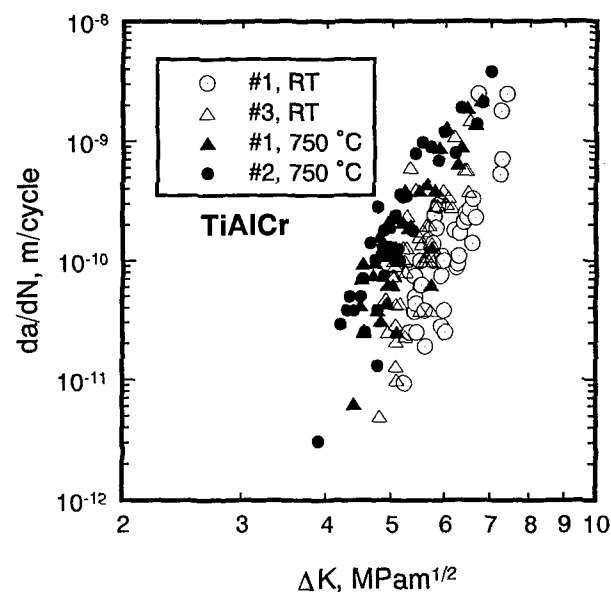


Figure 3: Fatigue crack growth rate as a function of stress intensity range in TiAlCr at room temperature and 750 °C in vacuum.

Table II Paris law constant

Material	m	
	RT	750 °C
Ti46Al	8	7
TiAlCr	11	10
Ti50Al	16	7

compared to the traditional metallic alloys. This means that the fraction of the total fatigue life resulting from crack propagation is small. As a result, damage-tolerant design for TiAl is questionable. The near-threshold fatigue crack growth and small crack growth are important for establishing a life prediction criterion. With an increase in temperature,  $m$  decreased.

The fatigue crack growth paths are mixtures of intergranular and transgranular in all the materials at room temperature and 750 °C. No large difference was observed between the room temperature and 750 °C besides the larger crack opening displacement at 750 °C.

For the lamellar structure, fatigue crack propagation prefers to be along the lamellar interfaces and grain boundaries (Fig. 4a,b). The translamellar cracks are about 45 ° to the lamellar direction (Fig. 4a). The three modes of fracture in Ti46Al: interlamellar, intralamellar [3,21] and translamellar can be seen in Fig. 4b. The ligament bridging mechanism operates in the lamellar structures (indicated by arrow in Fig. 4a).

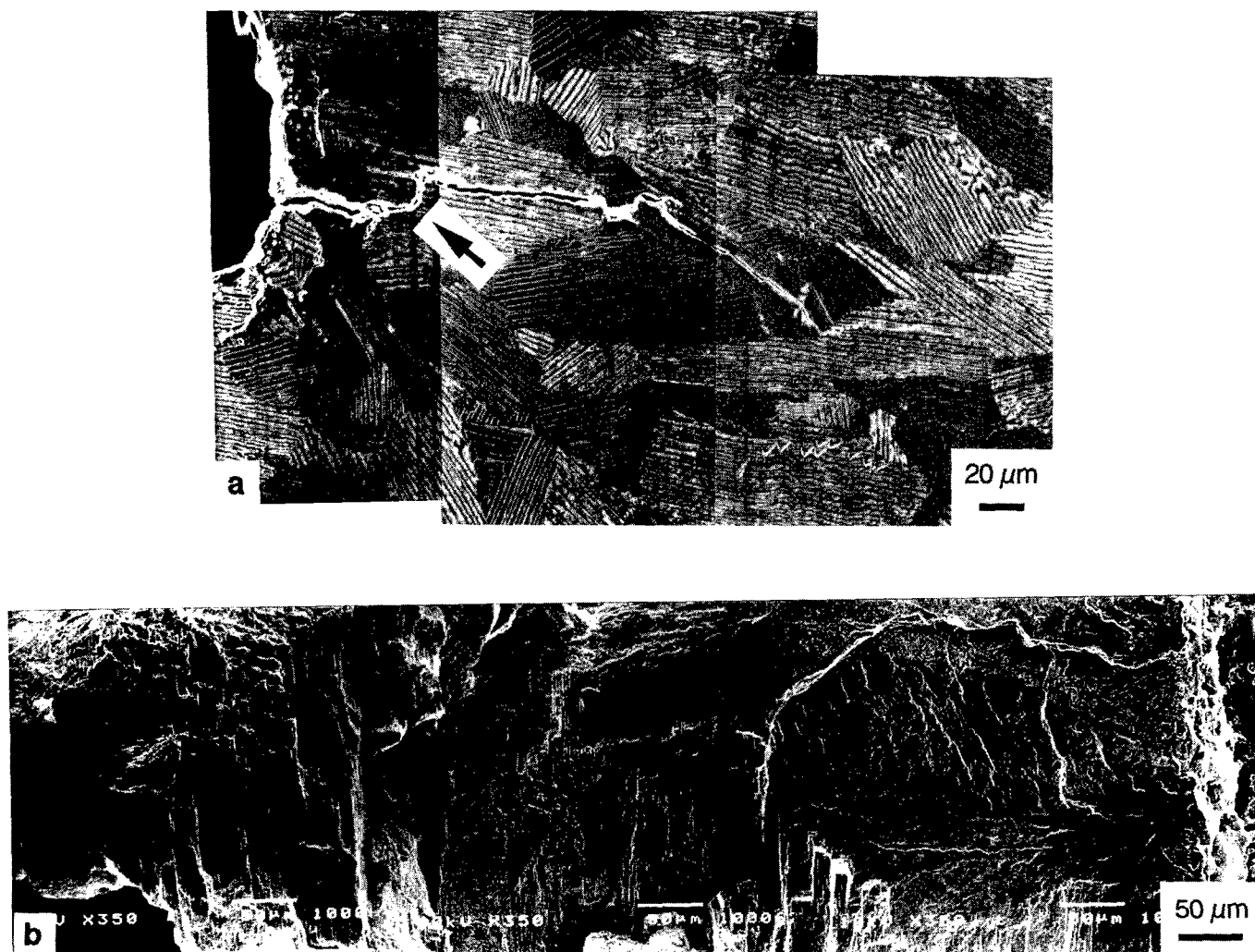


Figure 4: Fatigue crack growth paths (a) and fracture surface (b) in Ti46Al at 750 °C in vacuum.

In the duplex structure, the branching of the crack occurs and transgranular fracture is dominant (Fig. 5a). The debris by wear and the bridging ligament can be seen in Fig. 5. The cleavage pattern on the fracture surface in TiAlCr is shown in Fig. 5b.

In the equiaxed grain structure, the transgranular cleavage is also dominant (Fig. 6). The intergranular fracture predominates at high stress intensity region [13,14] and the fast fracture region in both the duplex and equiaxed structures.

From the in situ observations, microcracks were found to be formed near the crack tip. They coalesced to the main crack and some of them remained as the unbroken ligaments in the crack wake, which enhance the crack tip stress shielding effect. These basic crack growth processes were common in all microstructures and temperatures, although the site and size of microcracks strongly depended on the microstructure. These observations are well consistent with those reported in Reference [8].

The ductility and toughness of the present TiAl alloys are the highest in the temperature range between 700 and 800 °C, and the fracture morphology is also more ductile at elevated temperatures [22-24]. Therefore, it was expected at the beginning of this work that the fatigue crack growth mechanism at elevated temperature would change to one similar to common metallic materials, where crack blunting and resharping is the dominant mechanism. However, as mentioned above, the basic crack growth mechanism at elevated temperature coincided with that at room temperature [8]. The main reason for the non-altered crack growth mechanism at elevated temperature may be that microcracking occurs easily even at elevated temperature. Fig. 7 shows the development of microcracks, indicating that the fatigue damage (microcracking) is not confined to a small process zone at the crack tip, which is normally smaller than the yielding zone. Chan and Kim [25] also pointed out that the redistribution of the crack tip normal stress produced a diffuse damage zone where slip bands decohesion lead to the formation of microcracks.

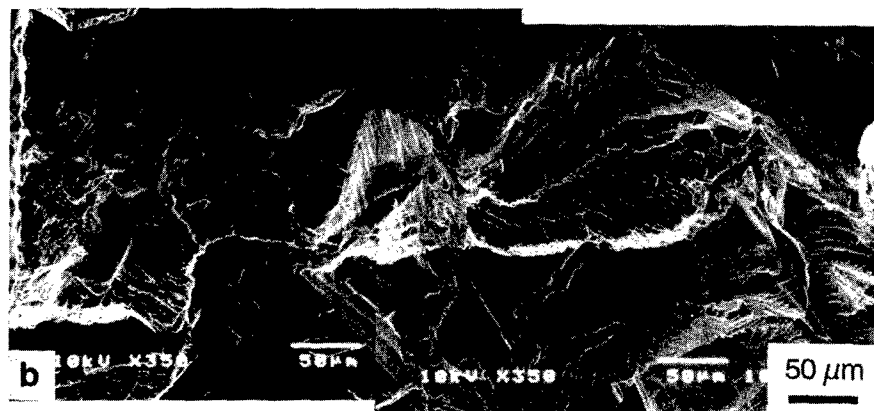
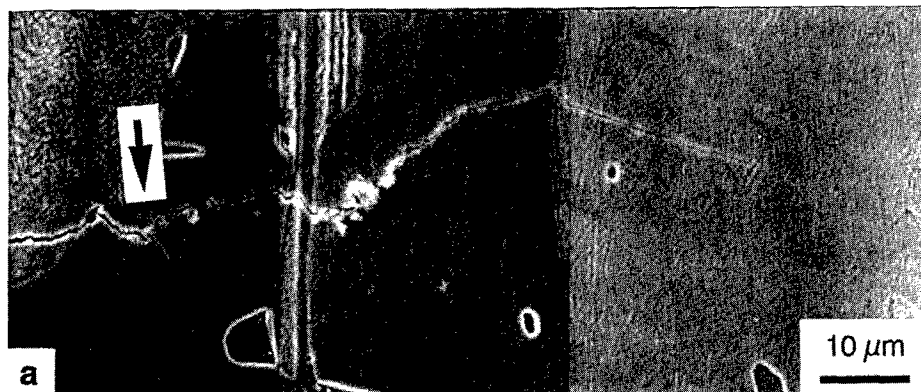


Figure 5: Fatigue crack growth paths (a) and fracture surface (b) in TiAlCr at room temperature in vacuum.

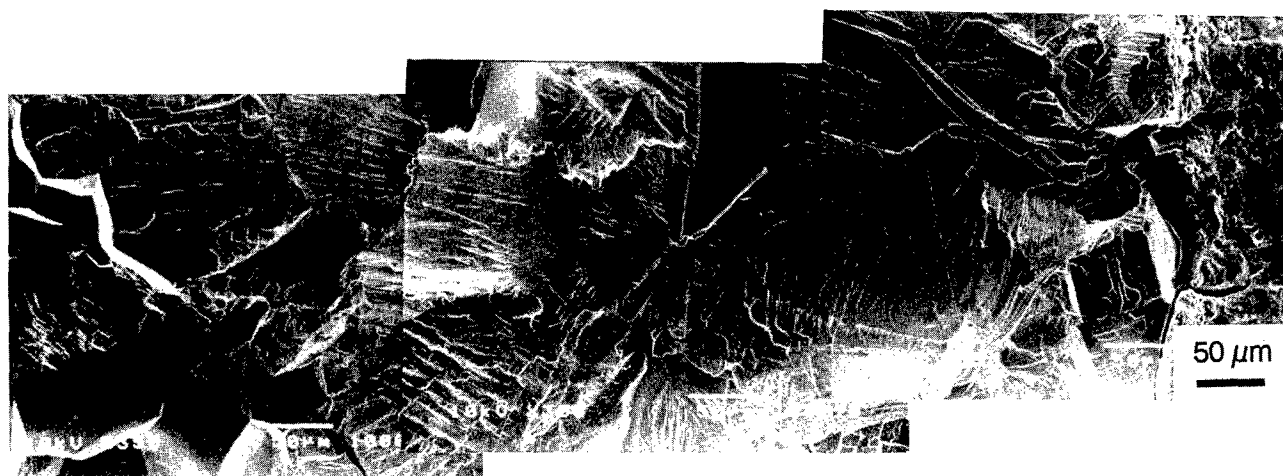


Figure 6: Fatigue fracture surface in Ti50Al at room temperature in vacuum.

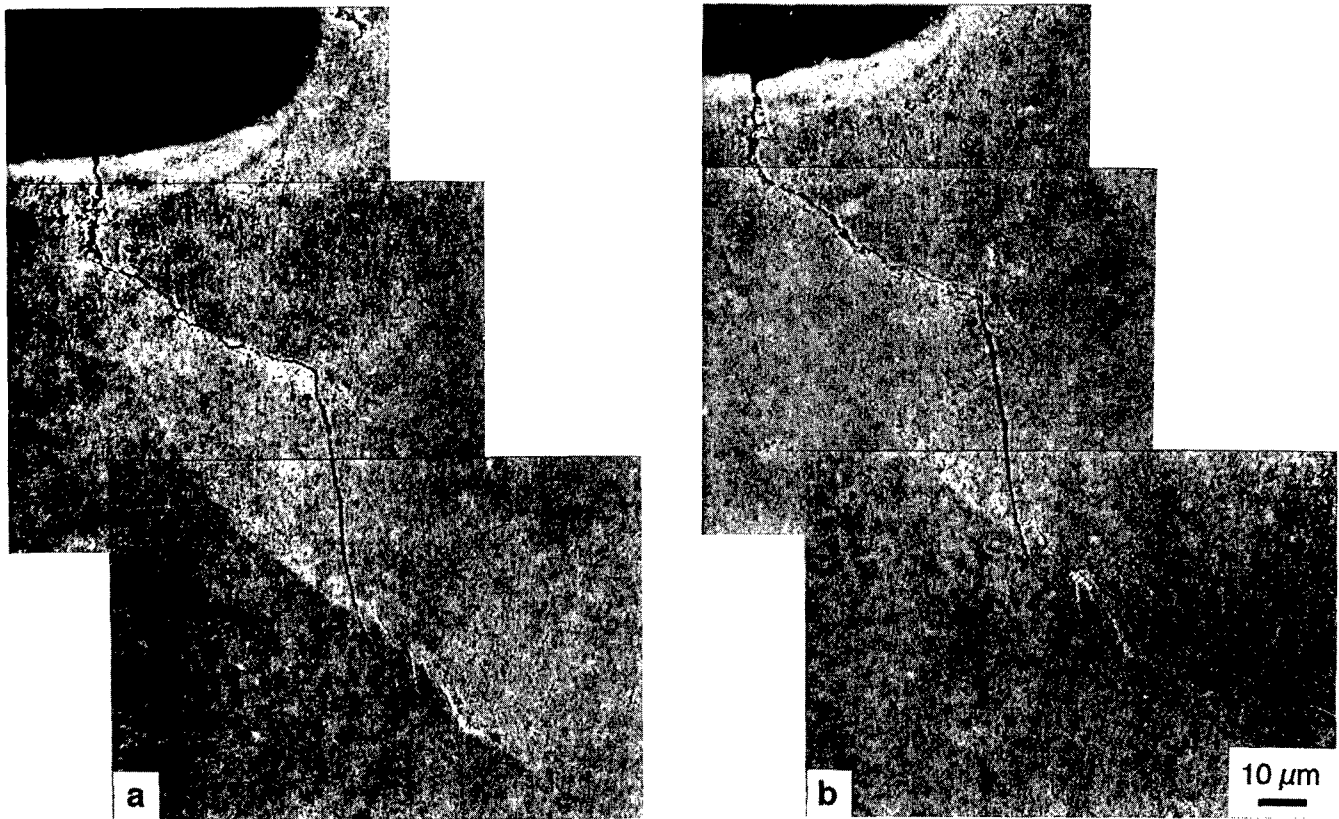


Figure 7: SEM in situ observation of cyclic fatigue growth in Ti46Al at 750 °C in vacuum.

(a)  $\Delta K = 4.77 \text{ MPam}^{1/2}$ ; (b)  $1.2 \times 10^5$  cycles after (a).

Although the basic mechanisms at room and elevated temperatures are similar, the fatigue crack growth resistance at 750 °C is lower compared to that at room temperature, as seen from Fig. 3. If the stress intensity factor range is normalized by Young's modulus, fatigue crack growth rates at 750 °C and room temperature can fall in the same data band (Fig. 8). This means that the difference of crack growth rates between room temperature and 750 °C in vacuum primarily results from the difference of Young's modulus.

#### Microstructural Effects

The fatigue crack growth curves for various microstructures at 750 °C are shown in Fig. 9. It is found that the crack growth resistance of duplex structure (TiAlCr) is higher than that of equiaxed grain (Ti50Al) under the same grain size of 200 μm. The fatigue crack growth resistance of Ti46Al with the fine-grained (40 μm) lamellar structures is higher than that of TiAlCr with the coarse-grained duplex structures at 750 °C.

The scatter of the crack growth rates of the lamellar structure are large, since the crack growth is fast when it is along the lamellar plates and slow when transverse to lamellar plates [17,26]. The larger colony size of the coarse lamellar structure had the lower crack growth rates than the smaller colony size of the coarse lamellar structure [8,10,27]. This may be why the

crack growth rates of the lamellar structure are not much lower than others (Fig. 9). It was found that the effect of lamellar structure on crack growth was originated from the crack shielding mechanism and not due to the crack closure mechanism [26]. When the crack plane was at an angle to the lamellar lath, the microcracking along the lamellar lath forms the bridging ligaments, which induce the stress shielding effect and consequently offers high resistance to crack growth.

It was pointed out that the bridging force reduce the stress intensity at the tip of the crack by superposing a compressive traction on the crack surfaces. Consequently the crack mouth opening for a bridged crack is smaller than for an unbridged crack and it was shown that the stress intensity at the crack tip,  $K_{tp}$ , could be successfully estimated by measuring the crack mouth opening [28,29].

The stress intensity experienced by the crack tip,  $K_{tp}$ , can be expressed in terms of the applied stress intensity,  $K_{app}$ , and the reduction in stress intensity by bridging,  $K_b$ , as:

$$K_{tp} = K_{app} - K_b \quad (4)$$

If the bridging zone is small compared to the crack length, it can be shown that the crack mouth opening follows a similar

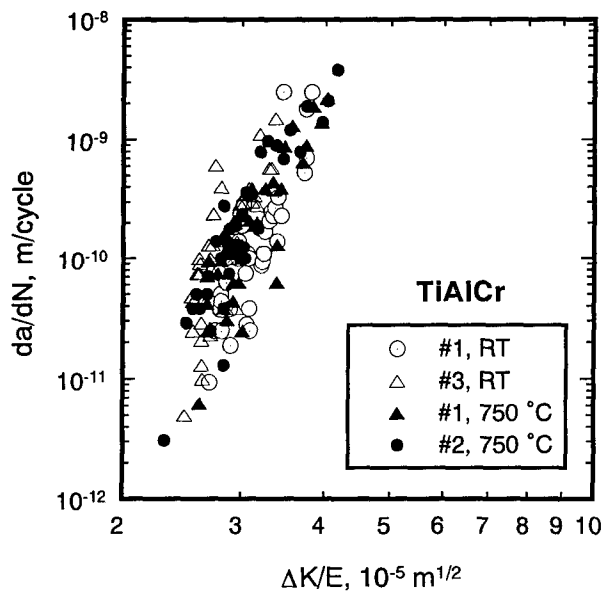


Figure 8: Fatigue crack growth rate as a function of stress intensity range modified by Young's modulus at room temperature and 750 °C in vacuum in TiAlCr.

relation to that for the stress intensity [28, 30, 31]. Figure 10 shows a schematic model for how the crack mouth opening is reduced by bridging forces behind the crack tip assuming that shielding mechanisms other than bridging can be neglected. As is seen from the model (see Fig. 10) the measured crack mouth opening,  $\delta_e$  is:

$$\delta_e = \delta_t - \delta_b \quad (5)$$

where  $\delta_t$  is the theoretically estimated crack mouth opening for unbridged crack and  $\delta_b$  is the negative crack mouth opening caused by bridging. Using the relationship of the crack mouth opening,  $\delta$ , with the stress for a bending specimen with a single edge precrack [32], a relation between the measured crack

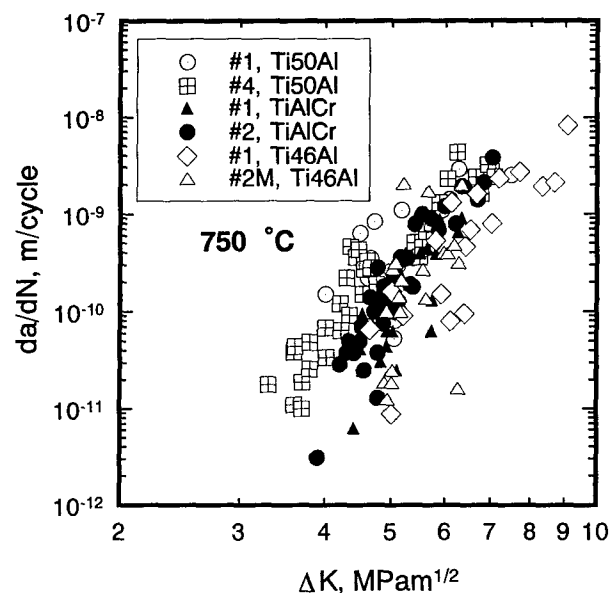


Figure 9: Effect of microstructure on fatigue crack growth rate at 750 °C in vacuum.

mouth opening,  $\delta_e$ , and the crack tip stress intensity was obtained as [28,30]:

$$K_{ap} = \frac{\delta_e \cdot E}{4a \cdot (1 - \nu)} \cdot \sqrt{\pi a} \cdot \frac{F(\frac{a}{W})}{V(\frac{a}{W})} \quad (6)$$

where

$$F(\frac{a}{W}) = 1.122 - 1.40(a/W) + 7.33(a/W)^2 - 13.08(a/W)^3 + 14.0(a/W)^4 \quad (7)$$

and

$$V(\frac{a}{W}) = 0.8 - 1.7(a/W) + 2.4(a/W)^2 + \frac{0.66}{(1 - a/W)^2} \quad (8)$$

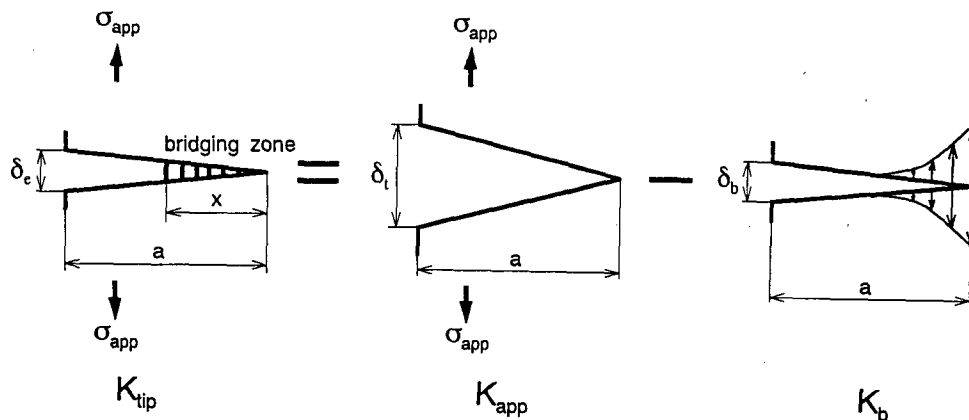


Figure 10: Schematic model for estimating the crack tip stress intensity factor



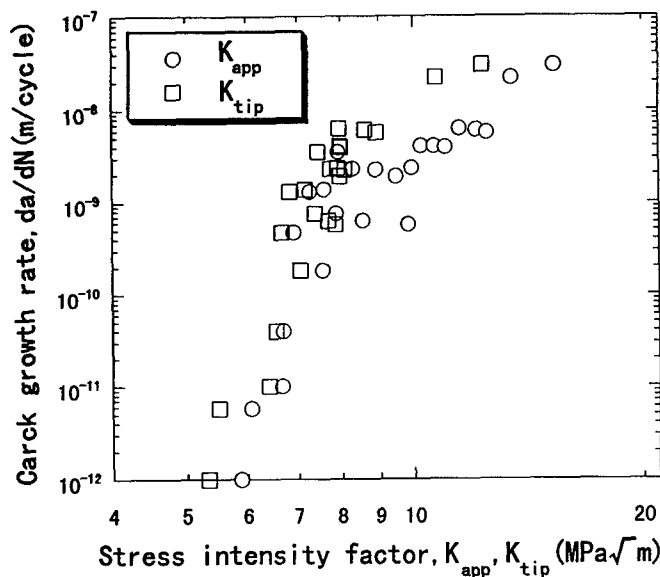


Figure 11: Crack growth rate versus applied stress intensity and crack-tip stress intensity in Ti46Al at room temperature.

It is to be noted that the presented approach is only an estimation of the  $K_{tp}$ -values since it requires that the bridging zone is small compared to the crack length and that the changes in crack tip geometry as a result of the bridging are small. However, Takahashi [30] showed that the error in  $K_{tp}$  was less than 10% even for test pieces with fully developed bridging zones.

Figure 11 shows the fatigue crack growth curves using  $K_{tp}$  and  $K_{app}$  for Ti46Al at room temperature. The shielding effect causes the decrease in  $K_{tp}$ , which is enough to result in the difference in crack growth rate (Fig. 9).

#### Small Crack Growth

Small crack growth behavior, i.e., the crack growth at stress intensity factors lower than threshold value for a long crack and the decrease of the growth rates with increasing stress intensity factor range, appears in all the materials when the half-crack length ( $a$ ) is below about 0.6 mm (Fig. 12). The small crack growth rates vary largely depending on specimens, that is microstructures at the crack tip, while the crack growth rates come into a narrow band when the half-crack length ( $a$ ) is above 0.6 mm, that is  $\Delta K > 4 \text{ MPa}\sqrt{\text{m}}^{1/2}$ . In the unnotched specimens, naturally formed fatigue crack growth also exhibited this kind of the small crack growth behavior up to the crack length of 150  $\mu\text{m}$  [33].

#### Conclusions

1. The fatigue crack growth rates at 750 °C were higher than those at room temperature in SEM vacuum. If the stress intensity factor range was modified by Young's modulus, crack

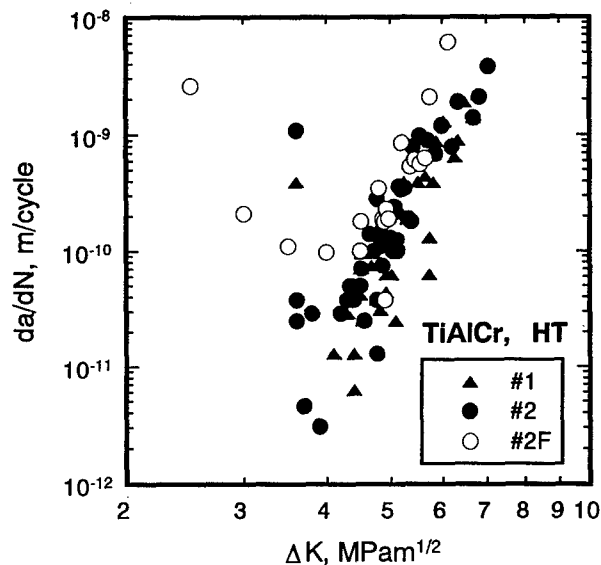


Figure 12: Small fatigue crack growth phenomena in TiAlCr at 750 °C in vacuum.

growth rates at 750 °C and room temperature could fall in the same data band. This indicated that the difference of crack growth rates between room temperature and 750 °C in vacuum primarily resulted from the difference of Young's modulus.

2. The crack growth resistance of Ti46Al with fine-grained (40  $\mu\text{m}$ ) lamellar structures was higher compared with that of the duplex structure (TiAlCr), which in turn was higher than that of the equiaxed grain (Ti50Al) under the same grain size of 200  $\mu\text{m}$  at both room temperature and 750 °C.

3. The small crack growth behavior appeared in all the TiAl alloys used when the half-crack length ( $a$ ) is below about 0.6 mm.

#### References

1. Y.-W. Kim, "Gamma Titanium Aluminides: Their Status and Future," *JOM*, 1995, July: 39-41.
2. K. T. Venkateswara Rao, Y.-W. Kim and R. O. Ritchie, "Fatigue-Crack Growth and Fracture Resistance of a Two-Phase ( $\gamma + \alpha_2$ ) TiAl Alloy in Duplex and Lamellar Microstructures," *Mater. Sci. Eng.*, A192/193 (1995), 474-482.
3. S. J. Balsone, B. D. Worth, J. M. Larson and J. W. Jones, "Fractographic Study of Fatigue Crack Growth Processes in a Fully Lamellar  $\gamma$ -TiAl Alloy," *Scr. Metall. Mater.*, 32 (1995) 1653-1658.
4. H. Shibata, K. Tokaji, T. Ogawa and H. Shiota, "Fatigue Strength and Fatigue Crack Propagation in Titanium Aluminide TiAl," *Trans. Mech. Soc. Japan*, 61 (1995) 1205-1211.
5. A. Ueno and H. Kishimoto, "Fatigue Crack Propagation Behavior in TiAl Intermetallic Compounds" (Paper presented at Fatigue '96, Berlin, Germany, 6-10 May 1996), 1731.

6. R. Gnanamoorthy, Y. Mutoh, N. Masahashi, Y. Mizuhara and M. Matsuo, "Flexural Strength, Fracture Toughness and Fatigue Crack Growth Behaviour of Chromium Alloyed  $\gamma$ -Based TiAl," *J. Mater. Sci.*, 29 (1994) 5199-5206.
7. R. Gnanamoorthy, Y. Mutoh, N. Masahashi and Y. Mizuhara, "Fracture Properties of  $\gamma$ -Base TiAl Alloys with Lamellar Microstructure at Room Temperature," *Mater. Sci. Eng.*, A184 (1994) 37-44.
8. R. Gnanamoorthy, Y. Mutoh, Y. Mizuhara, "Fatigue Crack Growth Behavior of Equiaxed, Duplex and Lamella Microstructure  $\gamma$ -Base Titanium Aluminides," *Intermetallics*, 4 (1996) 525-532.
9. P. Bowen, R. A. Chave, A. W. James, "Cyclic Crack Growth in Titanium Aluminides," *Mater. Sci. Eng.*, A192/193 (1995) 443-456.
10. A. L. McKelvey, J. P. Campbell, K. T. Venkateswara Rao, R. O. Ritchie, "High Temperature Fatigue Crack Growth Behavior in an XD<sup>TM</sup>  $\gamma$ -TiAl Intermetallic Alloy" (Paper presented at Fatigue '96, Berlin, Germany, 6-10 May 1996), 1743.
11. J. M. Larson, B. D. Worth, S. J. Balsone, A. H. Rosenberger and J. W. Jones, "Mechanisms and Mechanics of Fatigue Crack Initiation and Growth in TiAl Intermetallic Alloys" (Paper presented at Fatigue '96, Berlin, Germany, 6-10 May 1996), 1719.
12. A. H. Rosenberger, B. D. Worth, and S. J. Balsone, "Environmental Effects on the Fatigue Crack Growth of Gamma Titanium Aluminides" (Paper presented at Fatigue '96, Berlin, Germany, 6-10 May 1996), 1785.
13. S. J. Balsone, J. M. Larson, D. C. Maxwell and J. W. Jones, "Effects of Microstructure and Temperature on Fatigue Crack Growth in the TiAl Alloy Ti-46.5Al-3Nb-2Cr-0.2W," *Mater. Sci. Eng.*, A192/193 (1995) 457-464.
14. K. T. Venkateswara Rao, Y.-W. Kim and R. O. Ritchie, "High-Temperature Fatigue-Crack Growth Behavior in a Two-Phase ( $\gamma + \alpha_2$ ) TiAl Intermetallic Alloy," *Scr. Metall. Mater.*, 33 (1995) 459-465.
15. W. O. Soboyejo, J. E. Deffeyes, P. B. Aswath, "Investigation of Room- and Elevated-Temperature Fatigue Crack Growth in Ti-48Al," *Mater. Sci. Eng.*, A138 (1991) 95-101.
16. A. W. James and P. Bowen, "Elevated Temperature Crack Growth Resistance of TiAl under Monotonic and Cyclic Loading," *Mater. Sci. Eng.*, A153 (1992) 486-492.
17. D. L. Davidson and J. B. Campbell, "Fatigue Crack Growth through the Lamellar Microstructure of an Alloy Based on TiAl at 25 °C and 800 °C," *Metall. Trans. A*, 24A (1993) 1555-1574.
18. M. Tsutsumi, S. Takano, T. Kitamura and R. Ohtani, "Fatigue Crack Propagation in a Cast TiAl Intermetallic Compound at High Temperature," *Intermetallics*, 4 (1996) S77-S83.
19. Y. Akiwa, K. Tanaka, H. Kimura, "Propagation of Short Fatigue Cracks in Notched Specimens of Intermetallic Compound TiAl" (Paper presented at the 23rd Symp. on Fatigue, Kyoto, Japan, 25 November 1996), 298.
20. H. Tada, "A Note on the Finite Width Corrections to the Stress Intensity Factor," *Engng. Fract. Mech.*, 3 (1971) 345-347.
21. Z. W. Huang, S. Davey, P. A. Blenkinsop and P. Bowen, "Effects of Microstructure on Fatigue Crack Growth Behaviour in a PM Gamma Based TiAl Alloy" (Paper presented at Fatigue '96, Berlin, Germany, 6-10 May 1996), 1737.
22. R. Gnanamoorthy, Y. Mutoh, Y. Mizuhara, "Flexural Strength of Gamma Base Titanium Aluminides at Room and Elevated Temperatures," *Mater. Sci. Eng.*, A197 (1995) 69-77.
23. R. Gnanamoorthy, Doctor Thesis, "Fracture Behavior of Gamma Base Titanium Aluminides", Nagaoka University of Technology, 1994.
24. R. Gnanamoorthy, Y. Mutoh, N. Masahashi and Y. Mizuhara, "Fracture Toughness of Gamma Based Titanium Aluminides," *Metall. Mater. Trans. A*, 26A (1995) 305-313.
25. K. S. Chan and Y.-W. Kim, "Relationships of Slip Morphology, Microcracking, and Fracture Resistance in a Lamellar TiAl-Alloy," *Metall. Mater. Trans. A*, 25A (1994) 1217-1228.
26. R. Gnanamoorthy, Y. Mutoh, K. Hayashi and Y. Mizuhara, "Influence of Lamellar Lath Orientation on the Fatigue Crack Growth Behavior of Gamma Base Titanium Aluminides," *Scr. Metall. Mater.*, 33 (1995) 907-912.
27. J. P. Campbell, K. T. Venkateswara Rao and R. O. Ritchie, "Fatigue-Crack Growth and Fracture Behavior in a XD<sup>TM</sup>  $\gamma$ -TiAl Alloy with a Fine Lamellar Microstructure" (Paper presented at Fatigue '96, Berlin, Germany, 6-10 May 1996), 1779.
28. Y. Mutoh, M. Takahashi and M. Takeuchi, "Fatigue Crack Growth in Several Ceramic Materials," *Fatigue Fract. Engng. Mater. Struct.*, 16 (1993) 875.
29. Y. Mutoh, Y. Miyashita, T. Hansson and M. Takahashi, "Effect of Grain Size on Fatigue Crack Growth in Silicon Nitride and Alumina" (Paper presented at Plastic Deformation of Ceramics, 1995), 653.
30. M. Takahashi, "Basic Study on Fatigue Crack Growth Behavior in Ceramic Materials", Doctoral Thesis, Nagaoka University of Technology (1993).
31. D. S. Dugdale, "Yielding of Steel Sheets Containing Slits", *J. Mech. Phys.*, 8 (1960) 100.
32. H. Tada, P.C. Paris and G.R. Irwin, "The Stress Analysis of Cracks Handbook", Del Research Corporation, Hellertown (1973).
33. Y. Mutoh, S. Zhu, T. Moriya, Y. Mizuhara, "Fatigue Crack Initiation and Growth Mechanism in TiAl Intermetallics at High Temperature" (Paper presented at 46th National Conference on Materials, Nagano, Japan, 22-23 May, 1997), 223.

## AN APPROACH TO DUCTILITY IMPROVEMENT OF TiAl AND Ti<sub>3</sub>Al TITANIUM ALUMINIDES BASED ON MICROSTRUCTURE CONTROL

V.M. Imayev, G.A. Salishchev, R.M. Imayev, M.R. Shagiev,  
N.K. Gabdullin, and A.V. Kuznetsov  
Institute for Metals Superplasticity Problems, Russian Academy of Sciences,  
Khalturina 39, Ufa 450001, Russian Federation

### Abstract

The present investigation promotes two principal approaches to ductility improvement at room temperature of TiAl and Ti<sub>3</sub>Al titanium aluminides based on microstructure control. The first approach, realised in Ti<sub>3</sub>Al, consists in obtaining grain size at which the stress relaxation from pile ups becomes possible due to increasing the relaxation ability of grain boundaries. It is the most universal way for ductility improvement in intermetallics. The second approach, realised in TiAl, may be used for intermetallics prone to deformation twinning and it is connected with obtaining a certain length of pile up at which the relationship between basis deformation modes - slip and twinning - proves to be the most favorable for the development of steady plastic flow.

### Introduction

An extensive application of titanium aluminides as engineering materials is restricted because of low ductility caused by high energy of their ordering and by more complicated structure of crystal lattice, dislocations and grain boundaries than those in metals. As a result, the characteristic feature of plastic flow in titanium aluminides is their tendency to the localization of slip in the deformation bands that leads to the fast transgranular fracture both at room temperature (RT) and elevated ones [1,2]. The deformation character in titanium aluminides can be changed by alloying exerting influence on the crystallographic parameters and, thereby, on the deformation mechanisms [3]. However, this method has not brought an appreciable result. Another way is an adjustment of the pile up length to provide the stress relaxation by plastic flow and not by failure [4]. In order to control the pile up length, the most easy method is formation of microstructure with certain grain size and grain boundary structure.

The investigations of the effect of structural factors (the grain size, its

uniformity and grain boundary structure) on the deformation mechanisms and mechanical behavior in the stoichiometric TiAl and Ti<sub>3</sub>Al have given the following results.

### Experimental

Cast near-stoichiometric Ti-50.7 at.% Al and cast stoichiometric Ti-25 at.% Al (as model materials, hereafter TiAl and Ti<sub>3</sub>Al) were used as starting alloys. The fine equiaxed microstructures in the intermetallics were prepared by multistep forging the ingots at  $T=650-1050^{\circ}\text{C}$  followed by annealing at  $T=T_f \pm 70^{\circ}\text{C}$  in the air, where  $T_f$  is a temperature of last forging step. All microstructural conditions of both intermetallics were completely ordered. Flat samples with working dimensions of  $10 \times 5 \times 2 \text{ mm}^3$  were tensile strained at room and elevated temperatures at different strain rates. Instron (screw driven) and Schenck (hydraulic driven) machines were employed for tensile tests at strain rates not over  $8.3 \times 10^{-1} \text{ s}^{-1}$  and over  $8.3 \times 10^{-1} \text{ s}^{-1}$  respectively. The relative elongation to rupture at RT,  $\delta$ , was measured with an accuracy of  $\pm 0.1\%$ . The relative elongation to rupture at elevated temperatures, the yield strength,  $\sigma_{0.2}$ , the ultimate strength,  $\sigma_u$ , were determined by using the tensile stress-strain diagrams. The tensile axis of the samples was always perpendicular to the last forging direction of the intermetallics. The samples for tensile tests were polished prior to testing up to disappearance of surface scratches. The mean grain size,  $d$ , was measured by the linear intercept method. The content of  $\alpha_2$ -phase for TiAl was estimated with using the color etching. The structural investigations were conducted by transmission electron microscope JEM-2000EX. The fracture surfaces of failed samples were examined in a scanning electron microscope JSM-840. Density of dislocations was estimated taking into account 25 grains. The average number of twins per one grain,  $n$ , the volume fraction of twinned grains,  $\psi$ , and the fraction of grains twinned by 2 or 3 systems,  $\lambda$ , were counted by transmission electron microscope (TEM). In so doing for each case we made 3-5 foils and took into account 5 sets of grains. The

each set contained 20 grains chosen at random (i.e. in all, 100 grains were taken into consideration). The mean size of these grains was approximately the same as that in the investigated microstructural condition of the intermetallic. Credence probability of 0.5 was taken. In order to reveal deformation twins, varying the diffraction conditions was applied with respect to each grain. Mechanical compression tests of cylindrical samples  $\varnothing 10 \times 15$  mm were performed at an initial strain rate of  $8.3 \times 10^{-4} \text{ s}^{-1}$ . The deformation relief was studied after compression by  $\varepsilon = 5\%$  at RT. In order to investigate the interaction between lattice dislocations and grain boundaries, the cylindrical samples were compressed to  $\varepsilon = 1.5\%$  at 20 and 300–850°C for Ti<sub>3</sub>Al and TiAl respectively. For Ti<sub>3</sub>Al after compression the samples were annealed at 200–500°C during 60 min. Then the fraction of relaxed grain boundaries was estimated (by observation of the disappearance of trapped lattice dislocations (TLDs) contrast in grain boundaries) [5]. To do this, in each sample no less than 70 grain boundaries were taken into account.

## Results

### 1. Room temperature

#### 1.1. Investigation of TiAl

With multistep forging and subsequent heat treatment, the fine equiaxed microstructures with a mean grain size ranging from 0.4  $\mu\text{m}$  to 17  $\mu\text{m}$  were obtained in TiAl (Fig. 1). Some diversity of grain sizes is caused by line arrangement of the second  $\alpha_2$ -phase, its fraction being no more than 2–3% of the volume. The particles of the second  $\alpha_2$ -phase are commonly observed in volume of grains and sometimes on grain boundaries. The size of  $\alpha_2$ -phase particles depended on the temperature of last forging step and did not exceed 1  $\mu\text{m}$  for microstructures with  $d = 0.4$ –2  $\mu\text{m}$  and 3  $\mu\text{m}$  for microstructures with  $d = 6$ –17  $\mu\text{m}$ . Microstructural conditions with  $d = 0.4$ –8 and 14  $\mu\text{m}$  were obtained during dynamic recrystallization + annealing at  $T < T_f$  and contained a small quantity of twin grain boundaries (no more than 5% according to metallographic evaluation). Microstructural conditions with  $d = 12$ –17 (excepting  $d = 14 \mu\text{m}$ ) were obtained during dynamic recrystallization + annealing at  $T > T_f$  inducing multiple twinning and contained a large number of twin boundaries (about 50% according to metallographic evaluation). For conditions with  $d = 12$ –17  $\mu\text{m}$  the microstructure nonuniformity, caused by line arrangement of the second  $\alpha_2$ -phase, was expressed to a great extent than that for conditions with  $d = 0.4$ –8  $\mu\text{m}$ . TEM analysis showed that the nonuniform density of dislocations was observed in grains of structural conditions obtained. The density of dislocations in some grains appeared to be  $\sim 10^9 \text{ cm}^{-2}$ . So, for example,

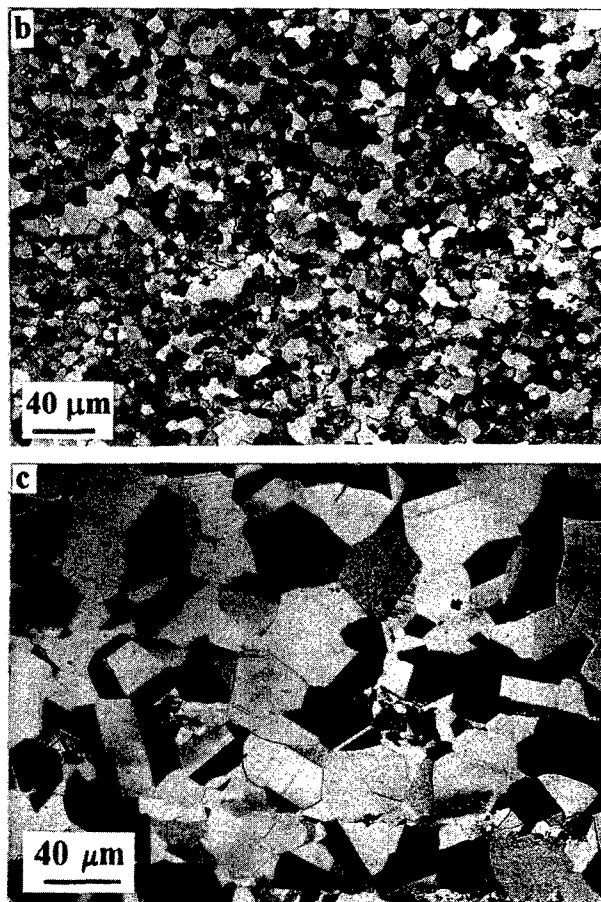


Figure 1: Some microstructures of TiAl,  $d = 0.4 \mu\text{m}$  (a),  $d = 8 \mu\text{m}$  (b),  $d = 17 \mu\text{m}$  (c).

for condition with  $d = 8 \mu\text{m}$  it changed from  $\rho = 1.7 \times 10^8 \text{ cm}^{-2}$  to  $\rho = 1.3 \times 10^9 \text{ cm}^{-2}$ , a mean dislocation density was  $\rho = 5.6 \times 10^8 \text{ cm}^{-2}$ . Deformation twins in all microstructures obtained were not observed.

Figure 2 shows true stress-strain curves for various grain sizes (at  $\dot{\varepsilon} = 3.3 \times 10^{-2} \text{ s}^{-1}$ ) and strain rates (for  $d = 8 \mu\text{m}$ ). With increasing the grain size the yield strength in the intermetallic changes in accordance with conventional Hall-Petch relationship. At the same time, with increasing

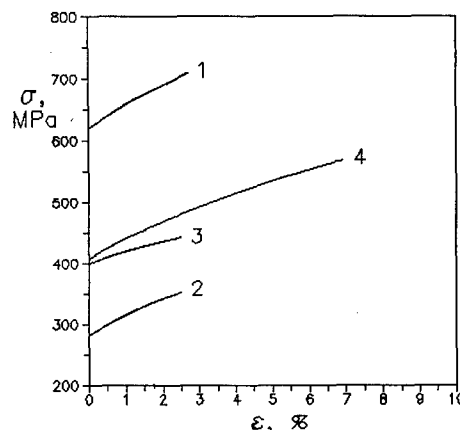


Figure 2: True stress-strain curves measured in tension of TiAl at RT: 1,2 -  $d = 2$  and  $16 \mu\text{m}$ ; 3,4 -  $\dot{\varepsilon} = 3.3 \times 10^{-4}$  and  $3.3 \times 10^{-2} \text{ s}^{-1}$  ( $d = 8 \mu\text{m}$ ).

the strain rate, the yield strength in the intermetallic is not practically changed: for example, for  $d=8\text{ }\mu\text{m}$  its value is about 400 MPa at  $\dot{\epsilon}=3.3\times 10^{-4}$  and  $3.3\times 10^{-2}\text{ s}^{-1}$ . However the increase of the strain rate leads to a more intensive strain hardening: for condition with  $d=8\text{ }\mu\text{m}$  the  $d\sigma/d\epsilon$  value increases by  $\approx 1.4$  times at transition from  $\dot{\epsilon}=3.3\times 10^{-4}\text{ s}^{-1}$  to  $3.3\times 10^{-2}\text{ s}^{-1}$ . The ultimate strength obeys the same tendency as the elongation: the maximum values of  $\sigma_u$  correspond to the maximum values of  $\delta$ .

Figure 3 presents the effect of grain size on the RT ductility of TiAl at different strain rates -  $\dot{\epsilon}=3.3\times 10^{-4}$ - $8.3\times 10^{-1}\text{ s}^{-1}$ .

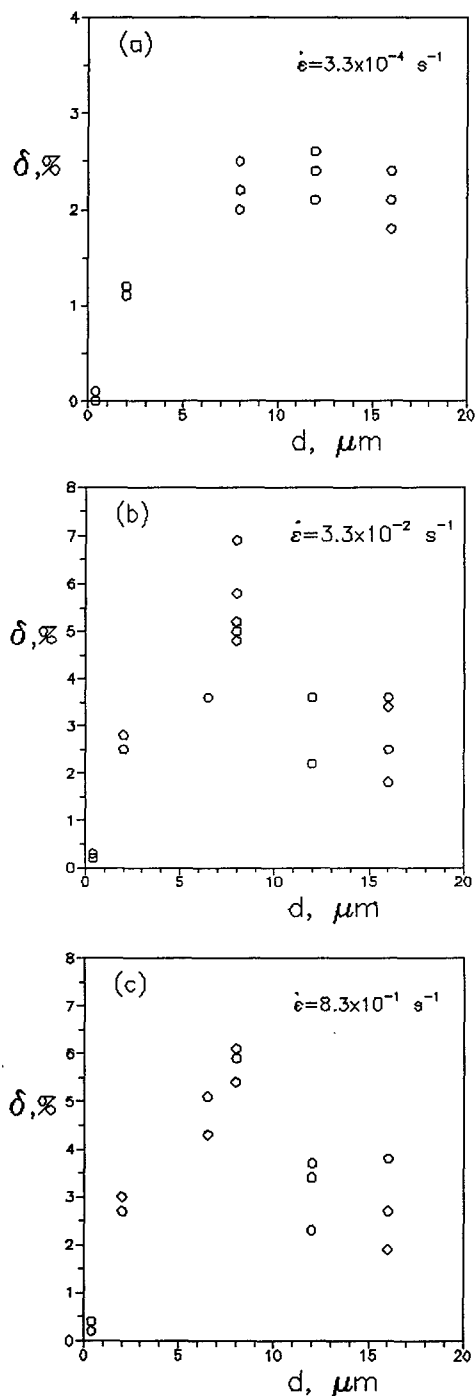


Figure 3: RT elongation vs. grain size at various strain rates of TiAl.

One can see that ductility of TiAl varies nonmonotonously depending on the grain size at all strain rates. As the strain rate increases, the grain size responsible for a maximum ductility decreases. The highest RT elongation  $\delta=4.6.9\%$  was obtained in TiAl with  $d=8\text{ }\mu\text{m}$  at the strain rates ranging from  $\dot{\epsilon}=3.3\times 10^{-2}$  to  $\dot{\epsilon}=8.3\times 10^{-1}\text{ s}^{-1}$ . Compression tests carried out at  $\dot{\epsilon}=8.3\times 10^{-4}\text{ s}^{-1}$  up to failure confirmed qualitatively the nonmonotonous character of the dependence of elongation on grain size (Fig.4).

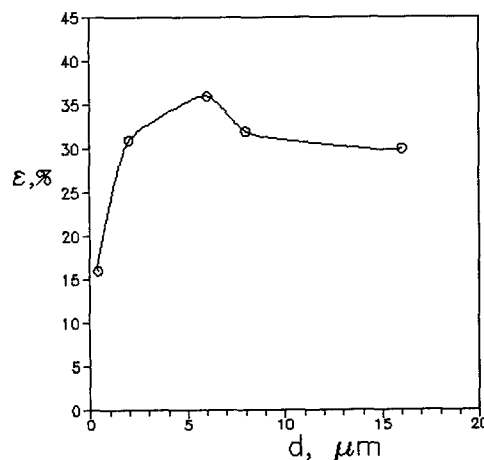


Figure 4: RT compression vs. grain size of TiAl ( $\dot{\epsilon}=8.3\times 10^{-4}\text{ s}^{-1}$ ).

To explain the dependencies of ductility on grain size obtained at various strain rates the investigation of slip pattern, TEM analysis of the dislocation structure of strained samples and examination of the fracture surfaces of tensile strained samples were conducted.

The investigation of slip pattern on an electropolished surface of compressed TiAl samples at RT indicates that it depends strongly on grain size. In structural conditions containing a small quantity of twin grain boundaries with  $d < 10 \mu\text{m}$ , practically no slip lines are observed on the surface (Fig.5a). This fact suggests that the slip is very fine and homogeneous. At the same time, as grain size increases up to  $d > 10 \mu\text{m}$ , planar slip lines are detected (Fig.5b). The planar slip lines are observed in the largest grains containing primarily twin boundaries and occupying about 50% of the sample surface. It can be seen (Fig.5b) that the grain-to-grain transfer of strain takes place predominantly through twin grain boundaries.

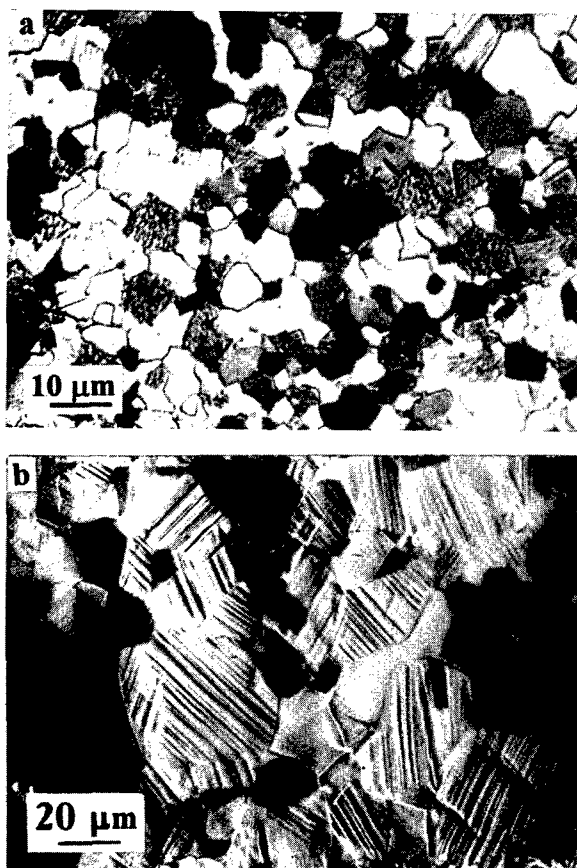


Figure 5: Slip pattern on an electropolished surface of compressed TiAl samples at RT: a -  $d < 10 \mu\text{m}$ , b -  $d > 10 \mu\text{m}$  ( $\dot{\epsilon} = 8.3 \times 10^{-4} \text{ s}^{-1}$ ).

TEM analysis revealed that with increasing the grain size the relationship between basic deformation modes in the grains of polycrystalline TiAl changes in favor of twinning (Fig.6 a,b). The similar change in deformation mechanisms takes place with increasing the strain rate (Fig.6 c-e). Quantitative analysis gave a more precise pattern of the twin structure change after deformation. Table 1 shows that for  $d = 8 \mu\text{m}$  the increase of the strain rate from  $3.3 \times 10^{-4} \text{ s}^{-1}$  to  $8.3 \times 10^1 \text{ s}^{-1}$  leads not only to increase of the twinning intensity but also to change of its character. At high strain rates the twinning by 2-3 systems is activated substantially. The density of dislocations with

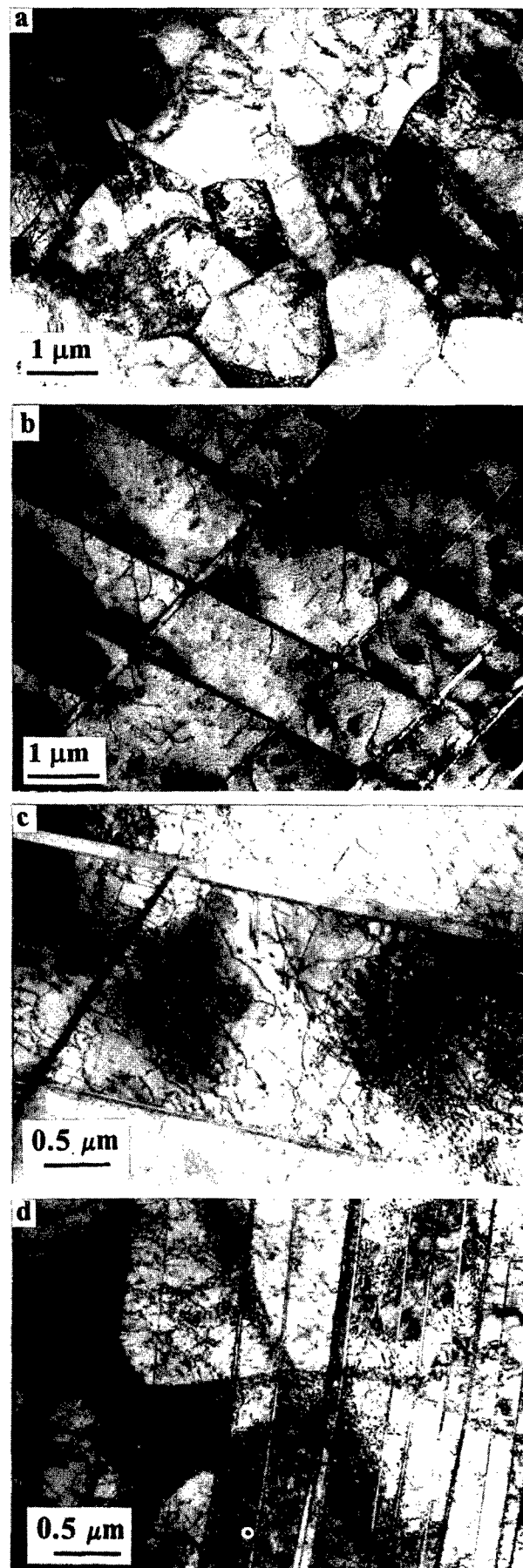




Figure 6: Typical microstructures of TiAl samples tensile strained up to failure at RT: a,b -  $d=2$  and  $16 \mu\text{m}$  respectively ( $\dot{\epsilon}=8.3 \times 10^1 \text{ s}^{-1}$ ); c,d,e -  $\dot{\epsilon}=3.3 \times 10^{-4} \text{ s}^{-1}$  ( $\delta=2.5\%$ ),  $3.3 \times 10^{-2} \text{ s}^{-1}$  ( $\delta=6.9\%$ ), and  $8.3 \times 10^1 \text{ s}^{-1}$  ( $\delta=2.6\%$ ) respectively ( $d=8 \mu\text{m}$ ).

increasing the strain rate changes slightly in this strain rate interval (Table 1). It should be noted that the nonuniformity of the initial dislocation density retains after RT deformation.

One can see (Table 1) that with increasing the grain size and the strain the volume fraction of twinned grains as well as the fraction of grains twinned by 2-3 systems increase substantially. In condition with  $d=0.4 \mu\text{m}$  twinning is practically suppressed, even at the highest strain rate ( $\dot{\epsilon}=8.3 \times 10^1 \text{ s}^{-1}$ ) the fraction of twinned grains does not exceed 4%. It should be also noted that in condition with  $d=2 \mu\text{m}$  at all strain rates the majority of grains is not covered by twinning and twinned grains, as a rule, are more than  $1.5\text{--}2 \mu\text{m}$ . For condition with  $d=8 \mu\text{m}$  the dependence of twinning on the strain rate reveals itself the most strongly: the twinning does not develop in the half of grains at the lowest strain rate, but with increasing the strain rate it develops in the majority of grains, at first predominantly by one system (at  $\dot{\epsilon}=3.3 \times 10^{-2} \text{ s}^{-1}$ ) and then by multiple way (at  $\dot{\epsilon}=8.3 \times 10^1 \text{ s}^{-1}$ ). At further increase of grain size - for  $d=16 \mu\text{m}$  the twinning depends slightly on the strain rate. At all strain rates the twinning develops in the majority of grains and in about half of them by 2-3 system. One can see that the revealed variations of twinning correlate with the variations of TiAl ductility.

Figure 7 shows the twinning evolution in the course of deformation of TiAl with  $d=8 \mu\text{m}$  at the optimum strain rate ( $\dot{\epsilon}=3.3 \times 10^{-2} \text{ s}^{-1}$ ) corresponding to a maximum ductility. It is important to note that, though the twinning embraces the majority of grains even at  $\epsilon=1.5\%$ , the growth of the twins number takes place in TiAl during deformation up to failure (Fig. 7a). The linear dependence of the twins number (per one grain) on the level of strain testifies to this (Fig. 7b). It is seen (Fig. 6d) that the fracture of the intermetallic (for  $\delta=6.9\%$ ) is preceded by so intensive twinning that the spacings between twins are less than  $1 \mu\text{m}$  almost in all the grains. Twinning leads to the fragmentation of microstructure during deformation. As a result, effective grain size decreases that affects the further development of twinning and slip. To estimate the effective grain size,  $d_{\text{eff}}$ , the relationship  $d_{\text{eff}} = d / n^{1/3}$  [6] was used. The effective grain size (Fig. 7b) changes nonlinearly during deformation: as the strain level increases, the rate of  $d_{\text{eff}}$  decreasing reduces and approaches to zero.

It is interesting that rather high density of dislocations and a great number of formed deformation boundaries (microbands) are observed at all the strain rates and the strain levels for condition with  $d=8 \mu\text{m}$  (Fig. 6d,e). It testifies to the origination of high elastic stresses in the intermetallic during deformation. It should be noted that the formation of such boundaries in metals demands considerably more high levels of strain than those in TiAl [7].

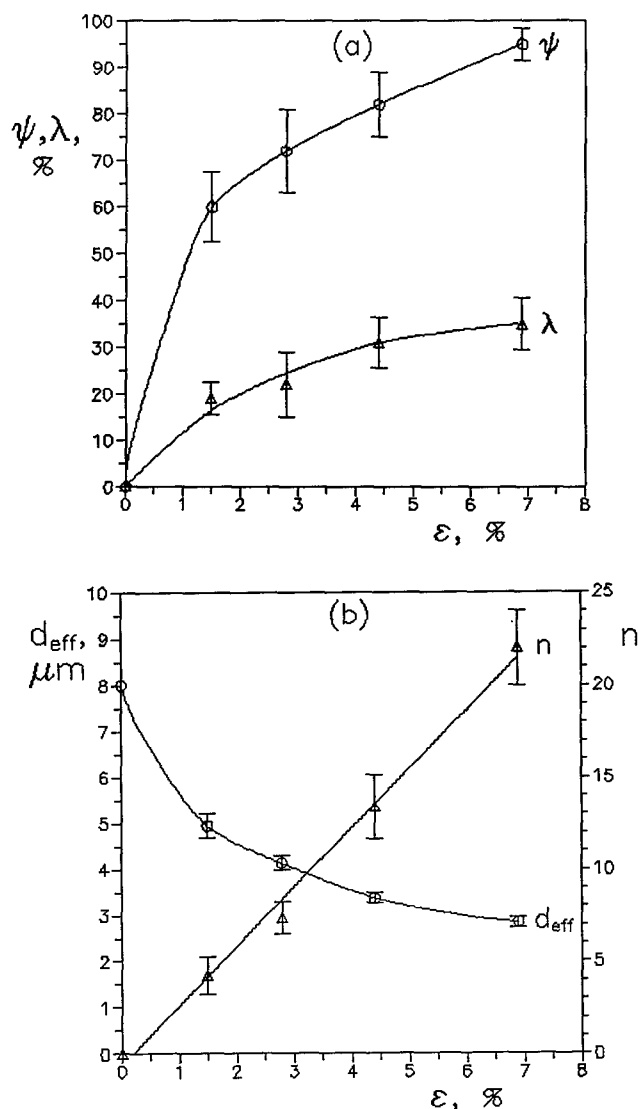


Figure 7: Dependencies of the twinned grains fraction,  $\psi$  (a), the fraction of grains twinned by 2 and 3 systems,  $\lambda$  (a), the average number of twins per one grain,  $n$  (b), and the effective grain size,  $d_{\text{eff}}$  (b), on the strain level  $\epsilon$  in microstructure of tensile strained TiAl samples ( $d=8 \mu\text{m}$ ,  $\dot{\epsilon}=3.3 \times 10^{-2} \text{ s}^{-1}$ ).

Examination of the fracture surfaces of tensile strained samples detected that as the grain size and the strain rate increase, the fracture mode changes appreciably: the fraction of transgranular component increases. For example, for  $d=8 \mu\text{m}$  - from 50% at  $\dot{\epsilon}=3.3 \times 10^{-4} \text{ s}^{-1}$  to 80% at  $\dot{\epsilon}=8.3 \times 10^1 \text{ s}^{-1}$ , for  $d=2$  and  $16 \mu\text{m}$  (at  $\dot{\epsilon}=3.3 \times 10^{-4} \text{ s}^{-1}$ ) - from 5% to 80% (see Table 2). It can be seen that the fraction of transgranular component in fracture mode is close to the fraction of grains embraced by twinning.

Table 1 Dependencies of the twinned grains fraction,  $\psi$ , the fraction of grains twinned by 2 and 3 systems,  $\lambda$ , the average number of twins per one grain,  $n$ , dislocation density,  $\rho$ , on grain size and strain rate in microstructure of tensile strained TiAl samples.

Strain rate, $s^{-1}$	Characteristics of deformation	$d=0.4 \mu m$	$d=2 \mu m$	$d=8 \mu m$	$d=16 \mu m$
$3.3 \times 10^{-4}$	$\delta$	$\delta=0.2\%$	$\delta=1.2\%$	$\delta=2.5\%$	$\delta=2.4\%$
	$\psi$	1.5	13 $\pm$ 2	52 $\pm$ 8.5	78 $\pm$ 6
	$\lambda$	-	4 $\pm$ 0.5	21 $\pm$ 6.5	45 $\pm$ 6
	$n$	-	0.5 $\pm$ 0.5	3.1 $\pm$ 0.7	12 $\pm$ 1.2
	$\rho$	-	-	3 $\times 10^9$ -2.2 $\times 10^{10}$	-
$3.3 \times 10^{-2}$	$\rho$	-	-	8.5 $\times 10^9$	-
	$\delta$	-	$\delta=2.5\%$	$\epsilon=2.8\%$ , without failure	$\delta=2.4\%$
	$\psi$	-	32 $\pm$ 4	72 $\pm$ 9	87 $\pm$ 6
	$\lambda$	-	11 $\pm$ 2.5	22 $\pm$ 7	51 $\pm$ 9
	$n$	-	1.3 $\pm$ 0.3	7.3 $\pm$ 0.8	14.7 $\pm$ 0.6
$8.3 \times 10^1$	$\delta$	$\delta=0.5\%$	$\delta=2.5\%$	$\delta=2.6\%$	$\delta=2.7\%$
	$\psi$	<4	43 $\pm$ 5	89 $\pm$ 6	91 $\pm$ 5
	$\lambda$	-	11 $\pm$ 2.2	56 $\pm$ 9	58 $\pm$ 6
	$n$	-	3.2 $\pm$ 0.8	12.8 $\pm$ 0.8	18.2 $\pm$ 1.2
	$\rho$	-	-	5 $\times 10^9$ -3.2 $\times 10^{10}$	-
	$\rho$	-	-	1.2 $\times 10^{10}$	-

Table 2 Fracture mode of TiAl at room temperature

Characteristic of fracture mode	$d \mu m$	$\dot{\epsilon}=3.3 \times 10^{-4} s^{-1}$	$\dot{\epsilon}=3.3 \times 10^{-2} s^{-1}$	$\dot{\epsilon}=8.3 \times 10^1 s^{-1}$
Fractions of inter-/transgranular components in fracture mode	2	95/5	20/80	95/5
	8	50/50		20/80
	16	20/80		10/90

### 1.2. Investigation of Ti<sub>3</sub>Al

With multistep forging and subsequent heat treatment, the fine equiaxed microstructures with a mean grain size ranging from 0.3  $\mu m$  to 27  $\mu m$  were obtained in Ti<sub>3</sub>Al (Fig 8).

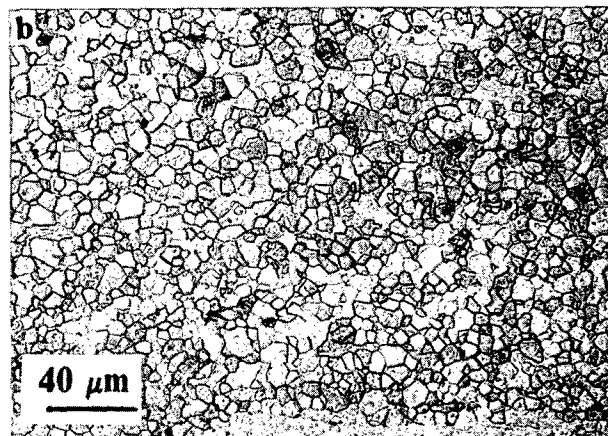


Figure 8: Some microstructures of Ti<sub>3</sub>Al,  $d=0.3 \mu m$  (a),  $d=5.5 \mu m$  (b).

The microstructures obtained were characterized by high uniformity of grain sizes, the dislocation density was about  $10^8$ -5 $\times 10^8 cm^{-2}$ .



Figure 9 shows true stress-strain curves for various grain sizes ( $\dot{\epsilon}=6.5 \times 10^{-4} \text{ s}^{-1}$ ). It is evident that the microstructure refinement leads to a significant strengthening of the intermetallic and to appearance of the appreciable steady flow in the range of submicrocrystalline grain sizes.

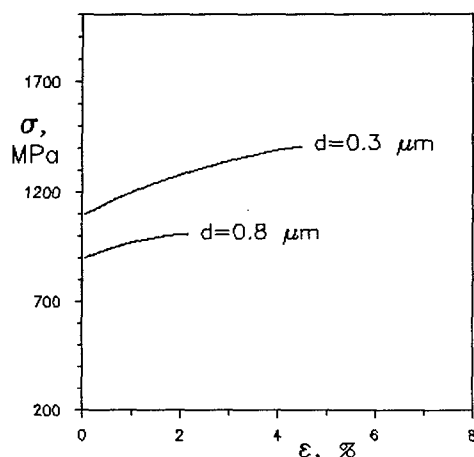


Figure 9: True stress-strain curves measured in tension of  $\text{Ti}_3\text{Al}$  at RT ( $\dot{\epsilon}=6.5 \times 10^{-4} \text{ s}^{-1}$ ).

Figure 10 presents the effect of grain size on the RT ductility of  $\text{Ti}_3\text{Al}$  at  $\dot{\epsilon}=6.5 \times 10^{-4} \text{ s}^{-1}$ . One can see that  $\text{Ti}_3\text{Al}$  is extremely brittle when  $d=5.5\text{--}27 \mu\text{m}$ , the failure occurs in elastic region. However at further decrease of grain size an appreciable ductility is observed. For  $d=0.3 \mu\text{m}$  elongation accounts for  $\delta=4.8 \%$ , i.e. the highest RT ductility in the intermetallic is observed when the grain size is minimum.

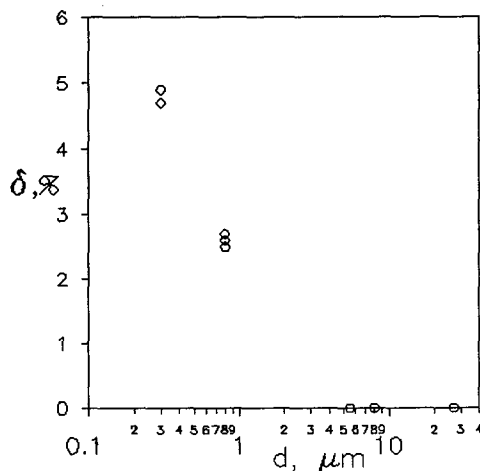


Figure 10: RT elongation vs. grain size ( $\dot{\epsilon}=6.5 \times 10^{-4} \text{ s}^{-1}$ ) of  $\text{Ti}_3\text{Al}$ .

To explain the obtained dependence of RT ductility on grain size the investigations of slip pattern and the fracture surface of tensile strained samples were conducted.

The investigation of slip pattern shows that the decrease of grain size from  $5\text{--}27 \mu\text{m}$  to submicrocrystalline values leads to the transition to fine and homogeneous slip, as it takes place in  $\text{TiAl}$  with decreasing the grain size from  $d > 10 \mu\text{m}$  to  $d < 10 \mu\text{m}$ .

Examination of the fracture surfaces of tensile strained samples detects that with decreasing the grain size, the fracture mode changes

appreciably: the fraction of intergranular component increases. For example, fractions of intergranular component for  $d=5.5$  and  $0.3 \mu\text{m}$  are about 5 and 90% respectively.

#### Elevated temperatures

##### 2.1. Investigation of $\text{TiAl}$

The relative elongation to rupture. Figure 11 demonstrates the temperature dependence of the relative elongation to rupture for structural conditions with different grain sizes. With increasing the temperature and decreasing the grain size and the twin boundaries fraction a growth of the elongation  $\delta$  takes place. As the grain size and the twin boundaries fraction increase, the brittle-to-ductile transition (BDT) is significantly shifted to higher temperatures. For example, in condition with  $d=17 \mu\text{m}$  the BDT range is shifted to higher temperatures approximately by 100 and  $200^\circ\text{C}$  as compared with  $d=14$  and  $0.4 \mu\text{m}$ .

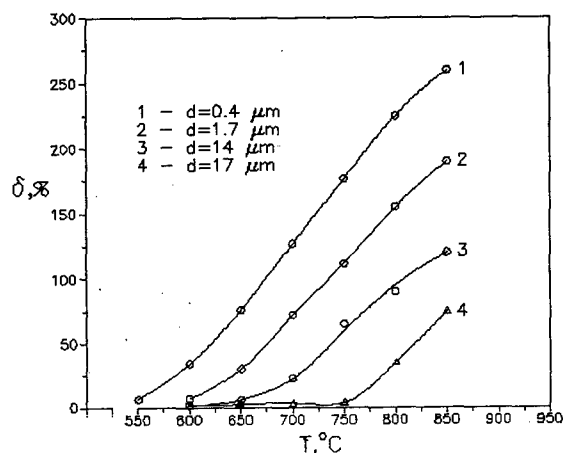


Figure 11: Elongation vs. strain temperature for different microstructural conditions of  $\text{TiAl}$  ( $\dot{\epsilon}=8.3 \times 10^{-4} \text{ s}^{-1}$ ).

Absorption properties of grain boundaries. To investigate the relaxation of lattice dislocations trapped by grain boundaries the conditions with  $d=1.7, 14$  and  $17 \mu\text{m}$  were chosen.

In initial conditions (before deformation), grain boundaries were free from TLDs and had conventional contrast. The presence of impurities in grain boundaries was not observed.

Figure 12 presents the dependence of the fraction of grain boundaries  $\psi$  in which TLDs relaxation occurred on the strain temperature. It is seen that the process of TLDs relaxation in grain boundaries occurs in a wide temperature range for all structural conditions studied. For conditions with  $d=1.7$  and  $14 \mu\text{m}$  the  $\psi$  value increases monotonously with increasing temperature and reaches a maximum of about 90% (curves 1 and 2). On the contrary, in condition with  $d=17 \mu\text{m}$  containing a large number of twin boundaries the  $\psi$  value varies slightly with the temperature change and reaches a maximum of only about 50% at  $850^\circ\text{C}$  (curve 3). With a further temperature increase no increase of the  $\psi$  value is observed. Other unrelaxed boundaries (about 50%) are probably special (predominantly twin type [8,9]) grain boundaries. Notice that for condition with  $d=1.7 \mu\text{m}$  the relaxation of TLDs does not occur at  $T=300^\circ\text{C}$  even in finest grains with  $d < 1 \mu\text{m}$ .

Comparing curves 1 and 2, one can see that the temperature range of

TLD<sub>s</sub> relaxation in grain boundaries for condition with  $d=14\text{ }\mu\text{m}$  is shifted to higher temperatures as compared to condition with  $d=1.7\text{ }\mu\text{m}$ . In this case, the shift value is 50-100°C. With increasing the fraction of twin boundaries (on retention of similar grain size -  $d=14$  and  $17\text{ }\mu\text{m}$ ), the TLD<sub>s</sub> relaxation temperature range is still greater shifted towards higher temperatures (curve 3) (Fig. 12). The value of this shift is about 100-200°C. Figure 12 b,c demonstrates grain boundaries with TLD<sub>s</sub> and without one's.

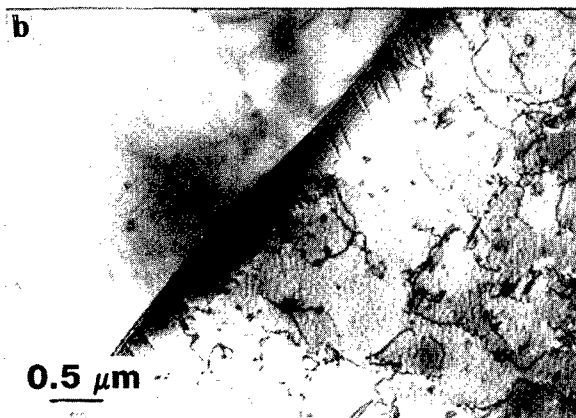
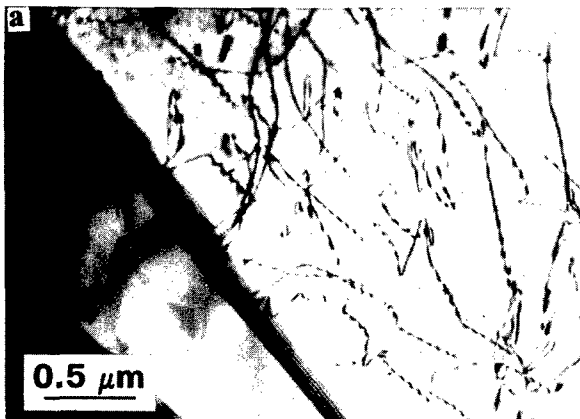
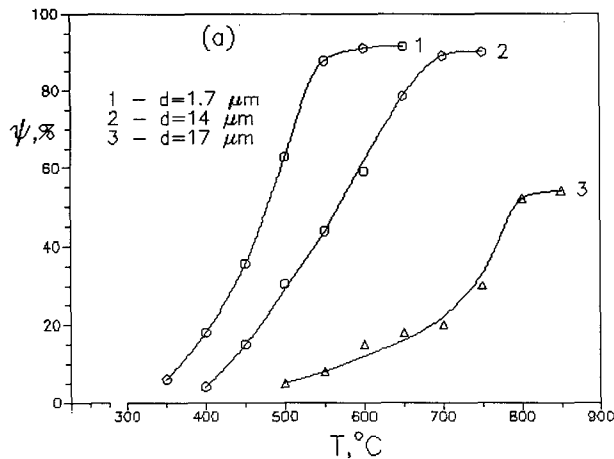


Figure 12: Fraction of grain boundaries free of trapped lattice dislocations  $\psi$  vs. compression temperature of TiAl (a). Relaxed (b) and unrelaxed (c) boundaries:  $d=17\text{ }\mu\text{m}$  ( $T=850^\circ\text{C}$ ).

**Dislocation structure.** Dependencies of dislocation and twin densities as functions of the deformation temperature have nonmonotonous character for all conditions (for condition with  $d=0.4\text{ }\mu\text{m}$  the left part of  $\rho(t)$  curve is apparently located at  $T<550^\circ\text{C}$ .) (Fig. 13). With increasing the testing temperature, the  $\rho$  and  $q$  values first increase reaching maximums, then drop. As the grain size and the twin boundaries fraction increase, the maximums of the  $\rho$  and  $q$  values are shifted to higher temperatures in all analyzed conditions. For conditions with  $d=0.4$  and  $17\text{ }\mu\text{m}$  the value of this shift is about 200-250°C.

From analysis of  $\delta(t)$ ,  $\rho(t)$ , and  $q(t)$  dependencies, it follows that the increase of TiAl ductility and the reduction of defects densities take place simultaneously beginning with a certain temperature, which decreases with decreasing the grain size and the twin boundaries fraction. For example, in conditions with  $d=0.4$ ,  $14$ , and  $17\text{ }\mu\text{m}$  this takes place beginning with  $600$ ,  $700$ , and  $850^\circ\text{C}$  respectively. It is explained by the fact that dynamic recovery, recrystallization and grain boundary sliding are occurred in the intermetallic beginning with a certain temperature in the BDT range, which decreases with decreasing the grain size and the twin boundaries fraction [8].

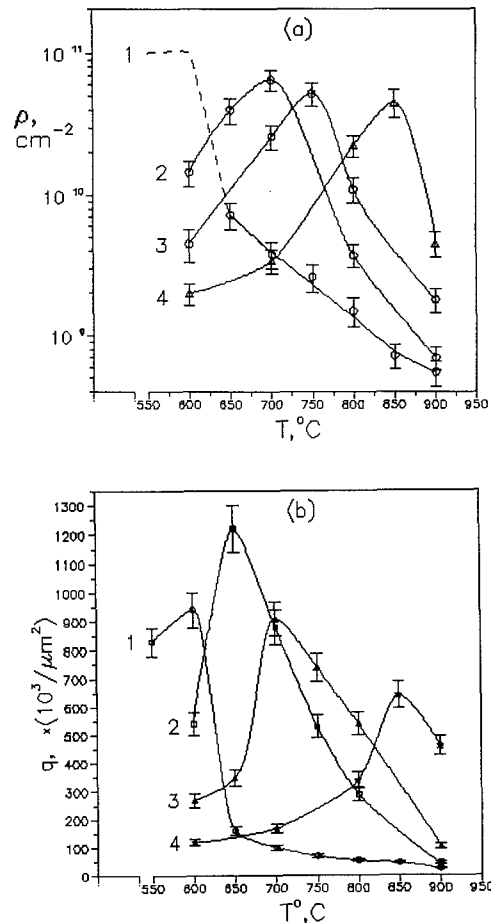


Figure 13: Dislocation (a) and twin (b) densities vs. strain temperature: 1 -  $d=0.4\text{ }\mu\text{m}$ , 2 -  $d=1.7\text{ }\mu\text{m}$ , 3 -  $d=14\text{ }\mu\text{m}$ , 4 -  $d=17\text{ }\mu\text{m}$ .

**Fracture mode.** With increasing the test temperature a tendency to the change of the fracture mode from transgranular to intergranular and then to viscous is observed. It is important that with increasing the test

temperature a growth of ductility begins at temperature being considerably lower than that of transition of the fracture mode from brittle type to viscous one. This feature was noted previously in [10].

## 2.2. Investigation of $\text{Ti}_3\text{Al}$

The relative elongation to rupture. Figure 14 demonstrates the temperature dependence of the relative elongation to rupture for structural conditions with different grain sizes. With increasing the temperature and decreasing the grain size a growth of the elongation  $\delta$  takes place. As the grain size decreases, the BDT is considerably shifted to lower temperatures. For example, in conditions with  $d=0.3$  and  $27 \mu\text{m}$  the elongation of about 25% is observed at  $T=300$  and  $700^\circ\text{C}$ , i.e. the BDT range is shifted to lower temperatures approximately by  $400^\circ\text{C}$ .

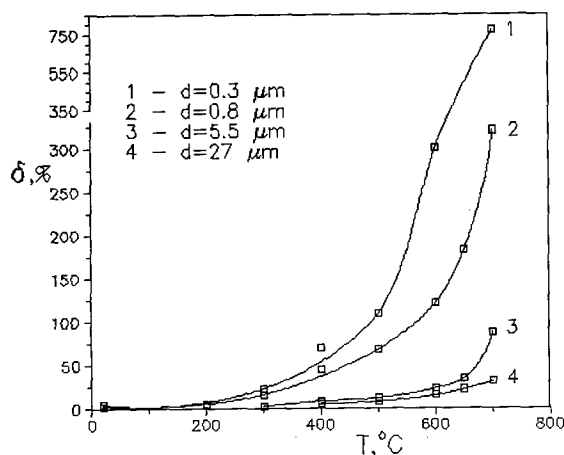


Figure 14: Elongation vs. strain temperature for different microstructural conditions of  $\text{Ti}_3\text{Al}$  ( $\dot{\epsilon}=6.5 \times 10^{-4} \text{ s}^{-1}$ ).

Absorption properties of grain boundaries. To investigate the relaxation of lattice dislocations trapped by grain boundaries the conditions with  $d=0.8$  and  $27 \mu\text{m}$  were chosen.

In initial conditions (before deformation), grain boundaries were free from TLDs and had conventional contrast. The presence of impurities in grain boundaries was not observed.

After RT compression and subsequent annealing the process of TLDs relaxation occurs for condition with  $d=0.8 \mu\text{m}$  at  $200^\circ\text{C}$  in a large number of grain boundaries, while for condition with  $d=27 \mu\text{m}$  this process is not observed even at  $500^\circ\text{C}$ . Notice that the relaxation properties of grain boundaries in the case of submicrocrystalline grain sizes are better significantly for  $\text{Ti}_3\text{Al}$  than for  $\text{TiAl}$ .

Fracture mode. Table 3 shows the change of the fracture mode depending on the grain size in the temperature interval of BDT. One can see that, as the temperature increases, the fracture mode in  $\text{Ti}_3\text{Al}$  changes from transgranular to intergranular and then to viscous fracture (for  $d \geq 5.5 \mu\text{m}$  viscous fracture takes place at  $T > 600^\circ\text{C}$ ). As the grain size decreases, this change of the fracture mode takes place at substantially lower temperatures. For example for  $d=27 \mu\text{m}$  predominantly transgranular fracture mode retains up to  $700^\circ\text{C}$  while for  $d=0.3 \mu\text{m}$  predominantly intergranular fracture mode is observed already at RT and viscous fracture occurs at  $400^\circ\text{C}$ . It should be noted that in  $\text{Ti}_3\text{Al}$  as well as in  $\text{TiAl}$  the transition to viscous type of fracture

takes place at temperature substantially higher than that for beginning of an increase of the intermetallic ductility. For example, for condition with  $d=0.3 \mu\text{m}$  the ductility begins to increase considerably from  $200^\circ\text{C}$  while the fracture type becomes viscous only at  $400^\circ\text{C}$  when  $\delta \approx 70\%$ .

Table 3 Fracture mode of  $\text{Ti}_3\text{Al}$  at room temperature

d, $\mu\text{m}$	Fractions of trans-/intergranular/viscous components in fracture mode, %		
	$20^\circ\text{C}$	$400^\circ\text{C}$	$600^\circ\text{C}$
0.3	10/90/- b	-/-/100 v	-/-/100 v
0.8	20/80/- b	-/57/43 (b+v)	-/-/100 v
5.5	92/8/- b	62/38/- b	50/50/- b
27	100/-/- b	100/-/- b	5/95/- b

b - brittle type of fracture, v - viscous type of fracture.

## Discussion

Thus, the investigations show that by varying the microstructure parameters - grain size and grain boundary structure, one can substantially improve the ductility of both considered intermetallics at room and elevated temperatures. Meanwhile the types of RT ductility dependence on the grain size differ considerably. For  $\text{TiAl}$  this dependence is of nonmonotonous character with maximum at a certain grain size (about  $8 \mu\text{m}$ ) and is affected strongly by the strain rate, while for  $\text{Ti}_3\text{Al}$  the ductility appears only at submicrocrystalline grain sizes and increases with decreasing the grain size. Difference in the plastic behavior of the intermetallics is observed also in the temperature range of BDT. Effect of the grain size on the temperature of BDT proves to be considerably stronger for  $\text{Ti}_3\text{Al}$  than for  $\text{TiAl}$ .

As follows from microstructural investigations, mechanical behavior of  $\text{TiAl}$  and  $\text{Ti}_3\text{Al}$  correlates with operated deformation mechanisms and fracture modes of the intermetallics at RT and at elevated temperatures. Let us consider these correlations.

$\text{TiAl}$ , unlike to  $\text{Ti}_3\text{Al}$ , is the intermetallic prone to deformation twinning. Therefore the deformation mechanisms responsible for change of RT ductility are different in these intermetallics. Meanwhile, as the grain size decreases, the slip character in  $\text{TiAl}$  and  $\text{Ti}_3\text{Al}$  changes by the same manner: from the planar slip to fine and homogeneous one that is accompanied with ductility improvement. However for  $\text{TiAl}$  the change of RT ductility is determined not only by the change of slip character but also by development of twinning. As it was found the twinning varies with the change of not only the grain size but also the strain rate. As the grain size and the strain rate decrease the twinning intensity decreases: the fraction of twinned grains and a number of twinning systems decrease. One can see (Table 1) that the twinning in the majority of grains and predominantly by one system is responsible for the highest RT ductility. It is explained by the fact that, as it is well known [6], the twinning plays a dual role in the course of deformation. On the one hand, taking into account the limited number of slip systems in  $\text{TiAl}$ , (according to Mizes criterion), the twinning improves the compatibility of deformation between grains. On the other hand, twinning is a "self-stopping" process owing to fragmentation of grains

and, consequently, to the decrease of the  $d_{\text{eff}}$  value. As a result  $d_{\text{eff}}$  becomes smaller than grain size,  $d_x$ , corresponding to the transition from deformation by slip to deformation by twinning [6] (Fig. 15).

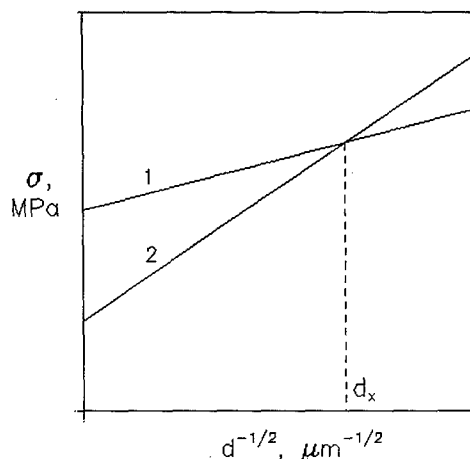


Figure 15: Schematic sketch of dependencies of critical stresses for slip (1) and twinning (2) on grain size<sup>-1/2</sup> ( $d^{-1/2}$ ).

As a result, the twinning development is stopped that may disturb the compatibility of deformation between the fragments and restrict the plastic flow of the intermetallic. For example, the negative role of twinning shows itself for condition with  $d=8 \mu\text{m}$  at the highest strain rate.

An increase of RT ductility in  $\text{Ti}_3\text{Al}$  begins only in the region of submicrocrystalline grain sizes. It is evident that the submicrocrystalline grain size proves to be less than the critical one which provides ductility improvement in the intermetallic as it was observed for  $\text{NiAl}$  [11]. This is caused, apparently, by change of the role of grain boundaries which become able for the relaxation of stresses arising from dislocation pile ups within grains. In this connection, it should be taken into account the behavior of both intermetallics in the range of BDT. Firstly, an increase of the deformation temperature leads to change of the fracture mode from transgranular to intergranular and then to viscous fracture. Transition from transgranular fracture mode to intergranular one is observed in intermetallics also with decreasing the grain size at RT. Secondly, a decrease of grain size results in substantial shift of BDT towards low temperatures. As follows from the investigations of absorption properties of grain boundaries, it is connected with improvement their relaxation ability. In this connection it is important to note that relaxation ability of grain boundaries for the finest grain sizes is higher considerably in  $\text{Ti}_3\text{Al}$  than in  $\text{TiAl}$  (when the grain sizes are similar). This circumstance explains a more strong shift of BDT to lower temperatures and abrupt improvement of RT ductility from zero to about 5% for  $\text{Ti}_3\text{Al}$  comparing to  $\text{TiAl}$  in the case of submicrocrystalline grain sizes. Meanwhile in  $\text{TiAl}$  the microstructural condition with  $d=0.4 \mu\text{m}$  does not allow to improve the RT ductility since for this grain size the relaxation ability of grain boundaries remains insufficient. Probably, one of the causes of this fact is the presence of the  $\alpha_2$ -phase particles in the grain boundaries. Change of fracture mode from transgranular to intergranular with decreasing the grain size at RT is the most likely accounted for difficulty of the twinning in  $\text{TiAl}$ . For  $d=0.4 \mu\text{m}$  this results in deterioration of the

deformation compatibility between grains and intergranular fracture without appreciable plastic deformation.

It should be noted the important contribution to the RT ductility improvement of titanium aluminides of other microstructural parameters: grain size uniformity and grain boundary structure. The experiment showed that both intermetallics demonstrated a strong sensitivity to changing the operated deformation mechanisms even at a small variation of grain size. Therefore the grain size nonuniformity may decrease significantly the intermetallic ductility because of it leads to localization of deformation promoting a fast failure. The presence of twin grain boundaries, apparently, plays a dual role from the point of view of RT ductility. On the one hand, they facilitate the transfer of strain from one grain to another. On the other hand, in so doing they, probably promote the development of planar slip and, consequently, localization of deformation.

Thus, the present investigations show two principal ways of ductility improvement in titanium aluminides at RT. The first way consists in obtaining such grain size at which the stress relaxation from pile ups becomes possible due to increasing the relaxation ability of grain boundaries. It is apparently the most universal way of ductility improvement in intermetallics. The second way may be used for intermetallics prone to deformation twinning and it is connected with obtaining a certain length of pile up at which the relationship between basis deformation modes - slip and twinning - proves to be the most favorable for the development of steady plastic flow. Thus, in both aluminides there are their own rigorously certain pile up length which provides the stress relaxation by making the deformation processes more active than the fracture processes.

#### References

1. H.A. Lipsitt, D. Shechtman, R.E. Schafrik, "The Deformation and Fracture of  $\text{TiAl}$  at Elevated Temperatures", *Met. Trans.*, 6A, N11 (1975), 1991-1996.
2. H.A. Lipsitt, D. Shechtman, and R.E. Schafrik, "The Deformation and Fracture of  $\text{Ti}_3\text{Al}$  at Elevated Temperatures", *Met. Trans.*, 11A (1980), 1369-1375.
3. C.T. Liu, F.H. Froes, and J.O. Stiegler, "Ordered Intermetallic Alloys", *Oak Ridge National Laboratory*, TN 37831, (1990), 69.
4. V.I. Vladimirov, *Physical Nature of Metals Fracture*, (Moscow: Metallurgia, 1984), 280 (in Russian).
5. O.A. Kaibyshev, and R.Z. Valiev, *Grain Boundaries and Properties of Metals*, (Moscow: Metallurgia, 1987), 216 (In Russian).
6. V.I. Trefilov, Yu.V. Milman, and S.A. Firstov, *Physical Aspects of the Strength of High Melting Point Metals*, (Kiev: Naukova Dumka, 1975), 316 (In Russian).
7. V.V. Rybin, *Large Plastic Deformations and Fracture of Metals*, (Moscow: Metallurgia, 1986), 224 (in Russian).
8. R.M. Imayev, O.A. Kaibyshev, and G.A. Salishchev, "Mechanical Behaviour of Fine Grained  $\text{TiAl}$  Intermetallic Compound - II. Ductile-Brittle Transition", *Acta Met.*, 40 (1992), 589-595.
9. V.Yu. Gertsman, R.M. Gayanov, A.B. Notkin, and R.Z. Valiev, "Investigation of Grain Boundaries in the  $\text{TiAl}$  Intermetallic Compound", *Scr. Met.*, 24 (1990), 1027-1032.
10. S-C. Huang, and E.L. Hall, "Plastic Deformation and Fracture of Binary  $\text{TiAl}$ -Base Alloys", *Metall. Trans.*, 22A (1991), 427-439.
11. E.M. Schulson, D.R. Barker, "Brittle to Ductile Transition in  $\text{NiAl}$  of a Critical Grain Size", *Scr. Met.*, 17 (1983), 519-522.

## HIGH TEMPERATURE MECHANICAL PROPERTIES EVALUATION OF A $\gamma$ -TiAl BASE INDUSTRIALLY DEVELOPED INTERMETALLIC ALLOY

V. Lupinc<sup>(\*)</sup>, M. Marchionni<sup>(\*)</sup>, M. Nazmy<sup>(o)</sup>, G. Onofrio<sup>(\*)</sup>, L. Rémy<sup>(x)</sup>, M. Staubli<sup>(o)</sup> and W.M. Yin<sup>(\*,+)</sup>

<sup>(\*)</sup> CNR -TEMPE, Via Cozzi 53, Milano, Italy

<sup>(o)</sup> ABB Power Generation Baden, Switzerland

<sup>(x)</sup> EMP, URA CNRS 866, Evry, France

<sup>(+)</sup> Institute of Metal Research, Chinese Academy of Sciences, Shenyang, China

### Abstract

A new  $\gamma$ -TiAl base cast alloy recently developed for creep properties maximization has been studied for evaluating high temperature mechanical properties.

Tensile and creep behaviour are very good when compared with that of density corrected IN738LC, except for tensile ductility. Variable load creep testing does not affect sensibly creep resistance. Low cycle fatigue resistance is not strongly dependent on temperature and hold time. Tests performed in vacuum at 700°C show a reduction of fatigue crack growth rate when frequency is reduced.

The observation of fatigue fracture surfaces has revealed the presence of lamellar propagation along crystallographic planes. Areas with intergranular zones are observed when hold time is introduced.

### Introduction

Gamma titanium aluminide base alloys are of great interest due to their low density, high stiffness and elevated temperature mechanical properties. Room temperature ductility and fracture toughness still remain the main problems of these alloys leading to poor fatigue resistance. Oxidation resistance is another strong limit for application of uncoated components at high temperature and creep behaviour is not completely satisfactory. However the alloys recently produced have shown a significant improvement of their performances and an encouraging possibility to be used for industrial applications.

A new cast alloy (Ti- 47Al- 2W- 0.5Si at%) has been recently developed by ABB for improving creep properties even if some ductility has been sacrificed [1, 2].

In order to evaluate the mechanical properties of the alloy tensile, creep and fatigue testing at different temperatures have been performed. For evaluating the influence of environment some fatigue tests have also been carried out in vacuum.

This activity is a part of the COST 501 European Concerted Action and the testing has been performed in three different laboratories TEMPE (formerly ITM), ABB and EMP.

### Material and experimental procedure

The cast bars used in the present investigation were HIP'ed at 1260°C / 172 MPa / 4 h and heat treated at 1300°C / 20 h / GFC (gas fan cooling) + 900°C / 4 h / GFC, and have the following chemical composition (wt.%):

Al	Si	W	Fe	O	H	N	Ti
31.27	0.38	9.29	0.035	0.0653	0.0002	0.008	Bal.

The metallographic observation by OM, SEM and TEM shows a duplex microstructure consisting of mainly lamellar  $\gamma/\alpha_2$  colonies and globular  $\gamma$  grains of 20  $\mu$ m average grain size. A smaller amount of Ti and W rich  $\beta$  phase and  $Ti_5Si_3$  primary silicides has been also observed (Fig. 1). On a smaller scale,  $Ti_5Si_3$  secondary silicides precipitate also within  $\gamma$ ,  $\alpha_2$  and  $\beta$  phases [3].

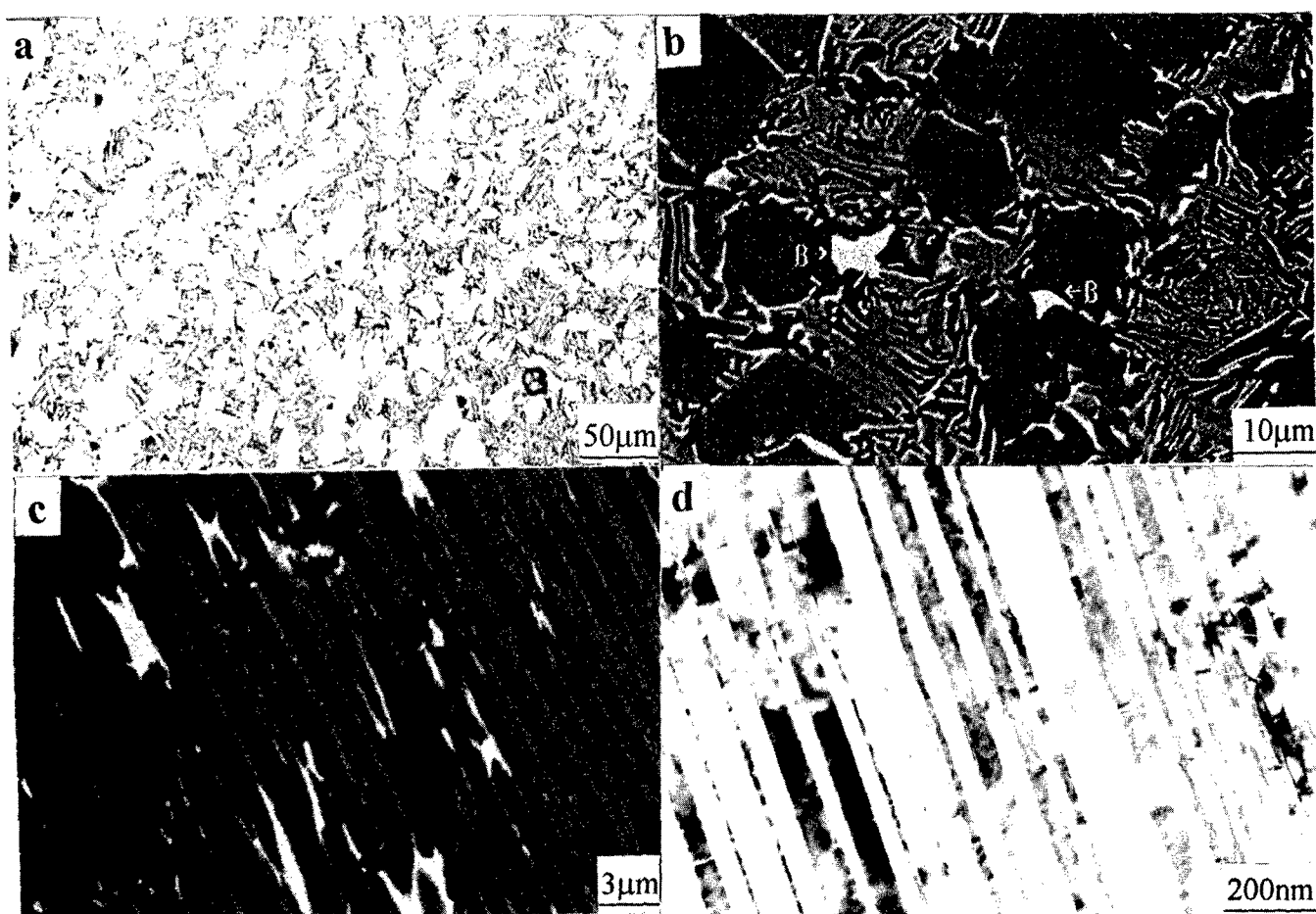


Fig. 1 - As received material: a) optical micrograph showing globular  $\gamma$  grains and lamellar colonies; b) SEM micrograph showing also  $\beta$  phase; c) SEM micrograph showing  $\gamma/\alpha_2$  lamellar and  $\beta$  particles; d) TEM micrograph showing details of lamellar microstructure.

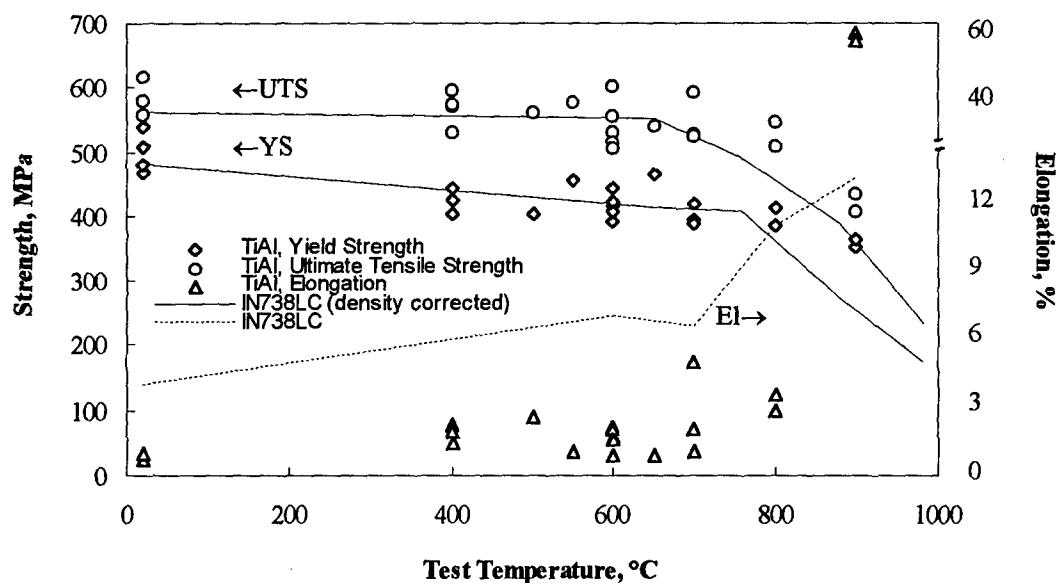


Fig. 2 - Tensile properties at  $7 \times 10^{-4} \text{ s}^{-1}$  strain rate as function of temperature show excellent strength behaviour compared to density corrected IN738LC alloy values and rather low elongation to rupture with a ductile to brittle transition between 800 and 900°C.

Tensile characterisation has been performed at a strain rate of  $7 \times 10^{-4} \text{ s}^{-1}$  from room temperature to 900°C.

Tensile creep tests at constant and variable load have been performed in the 600-750°C/490-250 MPa temperature and stress range with the longest creep test duration of about 14,500 h.

Low cycle fatigue tests have been performed in longitudinal strain controlled conditions with a triangular wave form ( $R = -1$ ) on cylindrical specimens having 8 mm minimum diameter and 12 mm gauge length. The strain rate applied has been  $10^{-3} \text{ s}^{-1}$ . The samples have been heated by induction coil at 600°C and by induction coil and lamp furnace at 700°C. The temperature has been controlled within  $\pm 3^\circ\text{C}$ . At 700°C a hold time of 300 seconds in tension has been superimposed. During the experiments the stress response and the hysteresis loop have been recorded at intervals.

Fatigue crack propagation tests have been carried out on single edge notch tension (SENT) specimens with a rectangular cross section of  $12 \times 4.5 \text{ mm}^2$  and a 1 mm deep starter notch. The fatigue crack propagation rate (FCPR) tests have been carried out in air and in vacuum ( $p_{\text{O}_2} < 10^{-3} \text{ Pa}$ ) in load control with triangular wave shape ( $R = 0.1$ ) at frequency ranging from 0.1 to 10 Hz and temperatures from 25 to 800°C. The specimens have been fatigue precracked at room temperature with a frequency of 10 Hz.

The samples have been heated by induction coil and temperature has been controlled within  $\pm 3^\circ\text{C}$ .

Crack lengths have been measured by the direct current potential drop technique. Crack rates have been calculated by the secant method according to ASTM specifications and correlated to the stress intensity factor range  $\Delta K = K_{\text{max}} - K_{\text{min}}$ . The stress intensity factor has been calculated as follows:

$$K = (P/BW) \sqrt{\pi a \{1.12 - 0.23(a/W) + 10.6(a/W)^2 - 21.7(a/W)^3 + 30.4(a/W)^4\}}$$

where  $P$  is the maximum load,  $W$  the specimen width,  $B$  the specimen thickness and  $a$  the crack length.

As far as the conditions of small scale yielding linear elastic fracture mechanics are respected for the examined conditions, the FCPR can be considered as a function of the stress intensity range.

### Experimental results and discussion

#### Tensile properties

Although this material has been designed for high creep resistance, it shows good tensile properties, that are comparable with the density corrected IN738LC yield stress and UTS values; they are even better at 800 and 900°C (Fig. 2). Elongation to rupture displays rather low values up to 700°C and shows a brittle to ductile transition behaviour between 800 and 900°C.

#### Creep properties

creep deformation is quite slow at 600°C/440 MPa (Fig. 3)

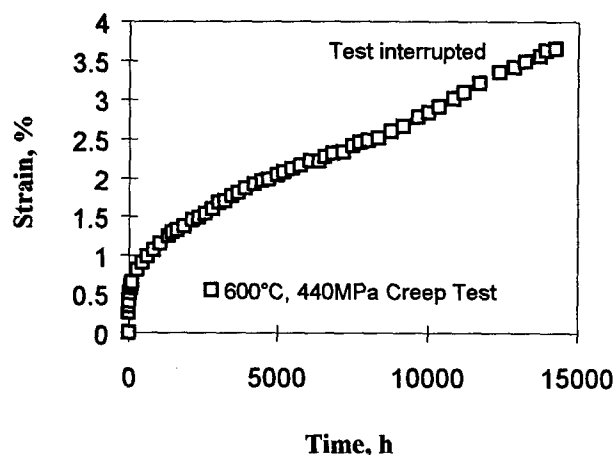


Fig. 3 - Long time creep behaviour at 600°C.

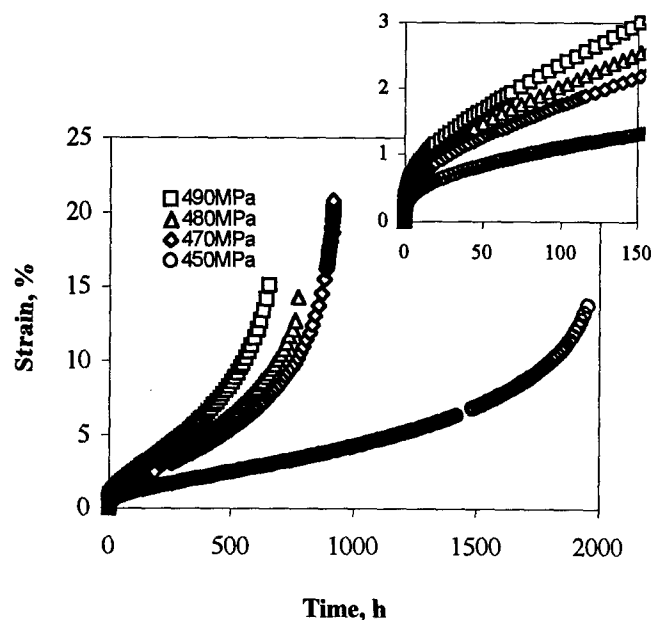


Fig. 4 - Constant load creep curves at 650°C.

and even at 650°C the material has to be loaded over its yield stress to produce rupture before 2000 h (Fig. 4). Stress rupture resistance remains good up to 750°C as shown in the Larson-Miller plot of Fig. 5 where data of this material show higher values than density corrected stress rupture data of IN738LC alloy. The variable load creep test results show that creep resistance does not change substantially after creep deformation in the 650-750°C temperature range, as shown in Fig. 6 where creep rate does not increase after 300 h of variable load creep at 700°C. On the contrary, it has been observed that ageing for 800 h at 800°C reduces creep life by a factor from 2 to 4, depending on creep testing parameters and microstructure.

In Fig. 7 minimum strain rate data are plotted as a function of true stress. Considering only the creep tests loaded below yield stress, the following equation has been used to describe the

minimum strain rate:

$$\dot{\epsilon}_m = A(\sigma/E)^n \exp(-Q/RT) \quad (1)$$

Stress sensitivity of minimum strain rate shows an average Norton exponent value  $n = 10$  and an apparent activation energy  $Q = 430$  kJ/mol in the  $650\text{--}750^\circ\text{C}/10^{-5}\text{--}10^{-4}\text{s}^{-1}$  temperature and strain rate range, respectively.

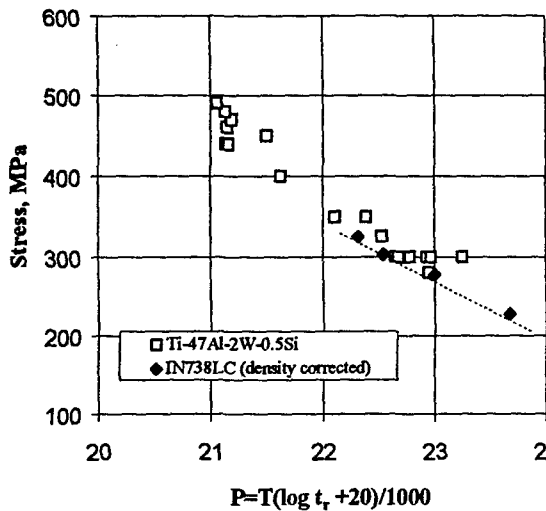


Fig. 5 - Stress rupture Larson-Miller graph comparing the alloy data with density corrected stress rupture data of IN738LC alloy.

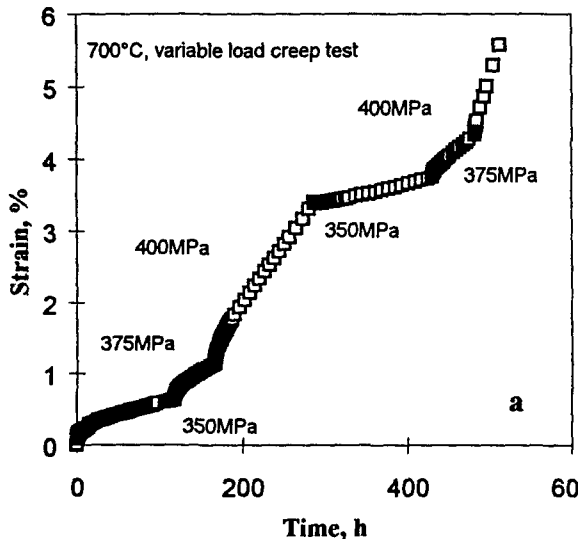


Fig. 6 - Variable load creep test at 700°C: a) strain vs. time; b) strain rate vs. strain showing irrelevant influence of previous creep at different loads on creep rate.

The TEM micrograph in Fig. 8 shows a typical example of twinned lamellae in creep fractured material at 650°C and 440 MPa.

#### Low cycle fatigue results

All the LCF, including the 300s hold time tests, are within a factor 2 scatter, as shown in Fig. 9. However, when temperature increases a small increase of fatigue life is observed. The hold time at 700°C does not reduce sensibly the number of cycles to failure.

The separation of the elastic and plastic components of the total strain ranges as a function of the number of cycles to failure is shown in Fig. 10. The low ductility of the alloy is confirmed by the small value of the plastic strain component (the transition point can be determined at about 20 cycles for tests at 600°C and 700°C and 400 cycles for tests with HT). The dispersion of the plots of the plastic components is higher than that of the elastic ones.

The fatigue results described in Fig. 10 have been analysed according to the following Basquin [4] and Coffin-Manson [5] relationships:

$$\Delta\epsilon_e = A \cdot N^{-\alpha} \quad (2)$$

$$\Delta\epsilon_p = B \cdot N^{-\beta} \quad (3)$$

in which  $\Delta\epsilon_e$  and  $\Delta\epsilon_p$  are respectively the elastic and plastic components of the total strain range,  $N$  the number of cycles to failure,  $A$ ,  $\alpha$ ,  $B$  and  $\beta$  constants of the material.

The parameter values of the equations (2) and (3) are reported in Table 1.



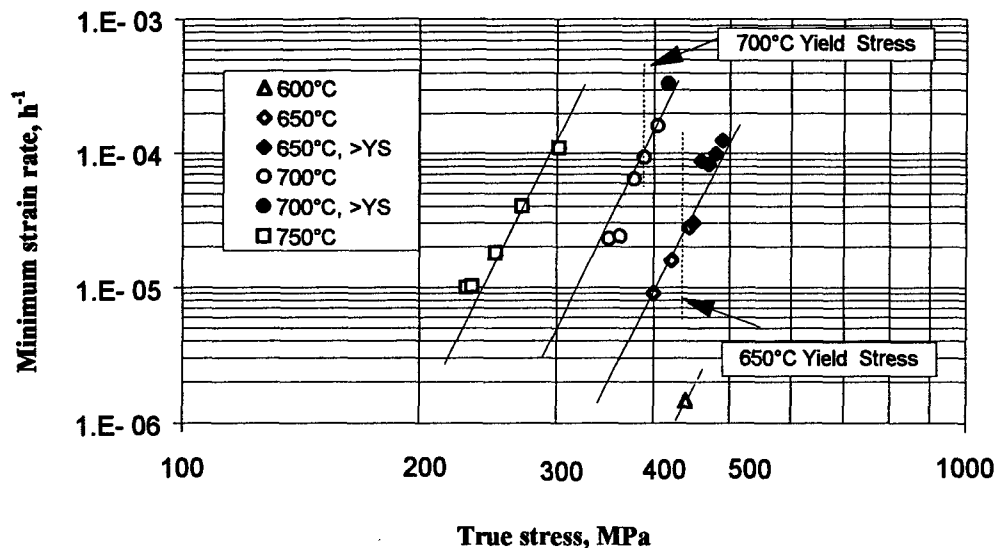


Fig. 7 - Minimum strain rate vs. true stress; solid points are representing creep tests loaded over yield stress.

Table 1 - Fatigue parameters from the equations (2) and (3).

Test Conditions	A	$\alpha$	B	$\beta$
600°C	0.019	0.152	0.012	0.25
700°C	0.006	0.028	0.010	0.21
700°C + HT	0.0073	0.073	0.025	0.28

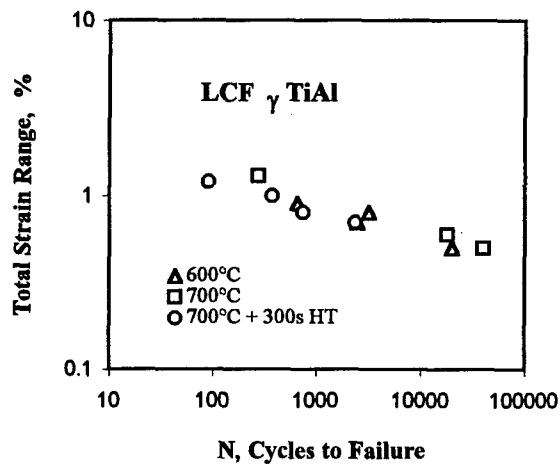


Fig. 9 - Total strain range vs. number of cycles to failure.



Fig. 8 - TEM micrograph showing twinned lamellae after creep rupture at 650°C and 440 MPa.

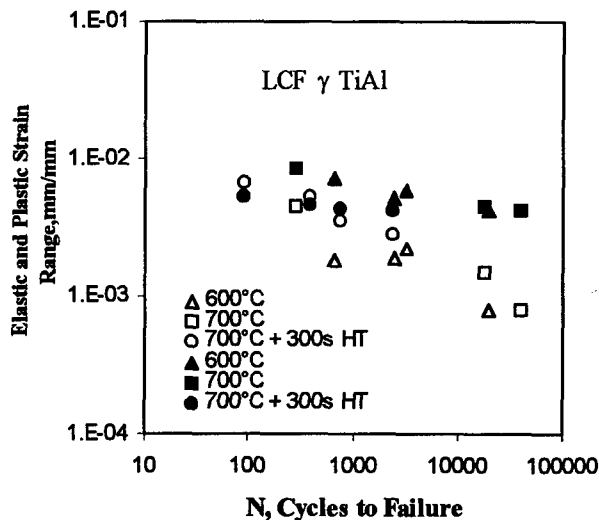


Fig. 10 - Elastic and plastic strain components of the total strain vs. number of cycles to fail

### Fatigue crack propagation results

The effect of temperature, in the 25 - 800°C range, on fatigue crack propagation rate is shown in Fig. 11. Very limited influence of temperature is observed from 500 to 700°C; steeper curves and consequently lower toughness come from the 25 and the 800°C tests that lead to a very similar FCPR behaviour.

The effect of R-ratio on FCPR, in the 0.1 - 0.5 range, appears in Fig. 12. The FCPR increases with increasing R-ratio. Since this effect is present at all the  $\Delta K$  values, no closure process could be involved, but the presence of a more effective static mode of fracture at higher R-ratio is apparent.

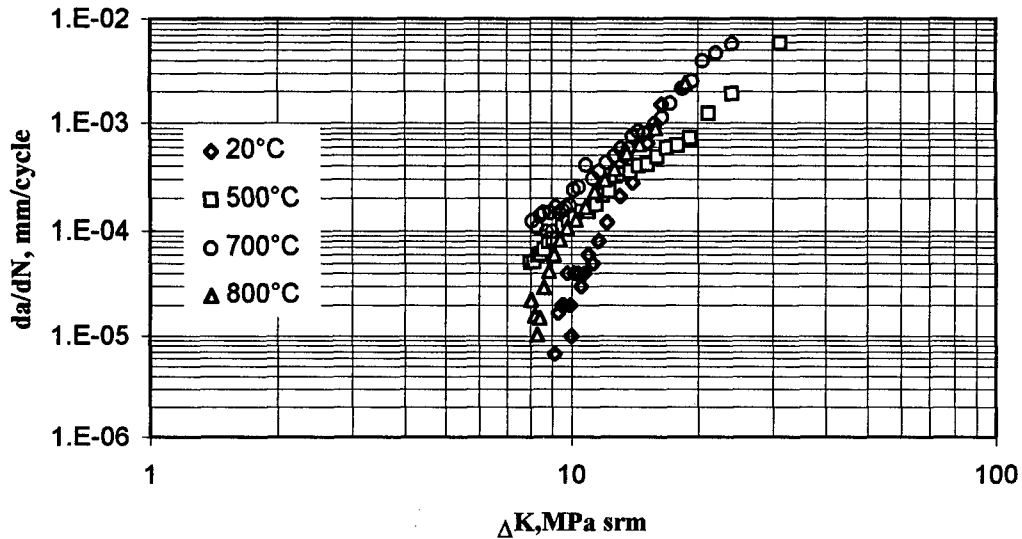


Fig. 11 - Influence of temperature on air FCPR at the frequency of 10 Hz.

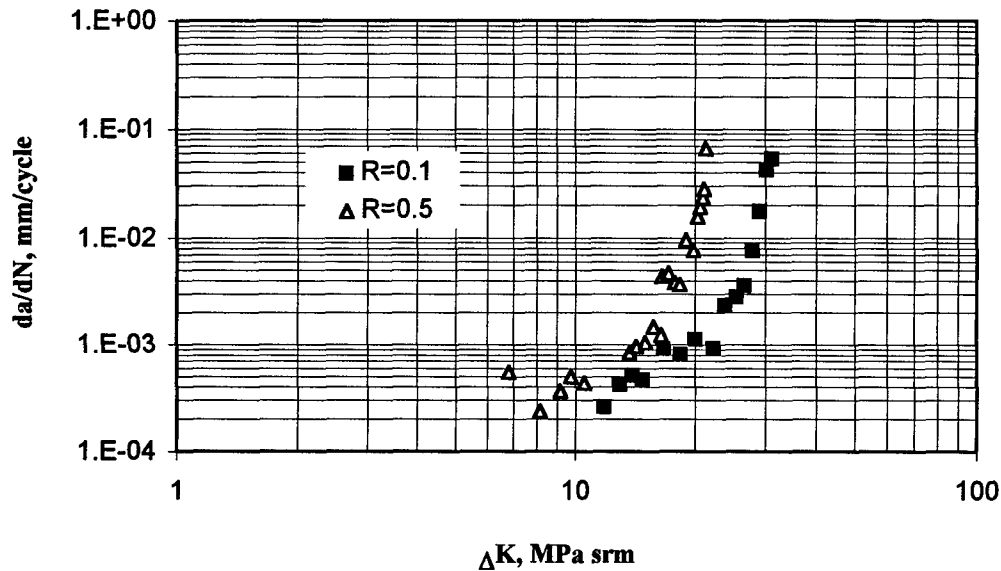


Fig. 12 - Influence of R-ratio on FCPR at 700°C and 0.1 Hz.

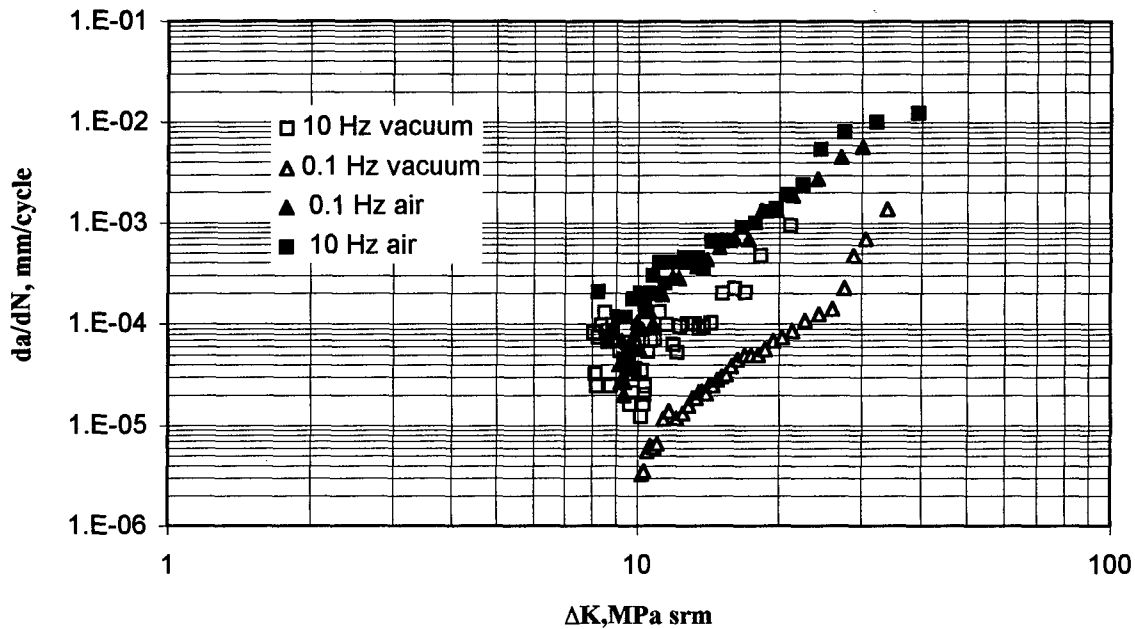


Fig. 13 - Influence of frequency and environment on FCPR at 700°C.

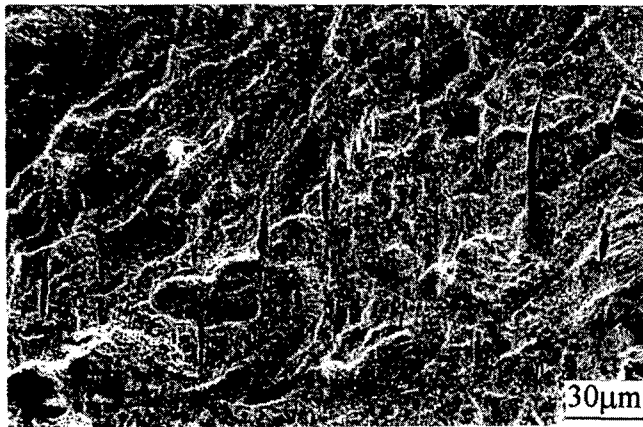


Fig. 14 - Fracture surface after fatigue crack growth test at 700°C, 0.1 Hz in vacuum.

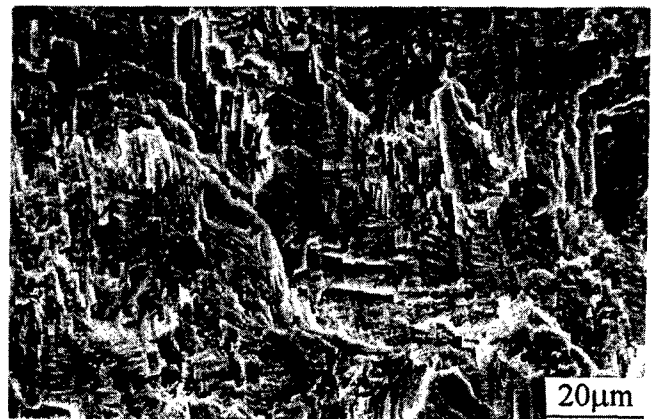


Fig. 15 - Fracture surface after fatigue crack growth at 700°C, 10 Hz in vacuum.

Fig. 13 shows the influence of test frequency, in the 0.1 - 10 Hz range, on FCPR at 700°C in air and in vacuum. The curves  $da/dN$  vs.  $\Delta K$  show the same threshold value; they diverge at intermediate  $\Delta K$  values where FCPRs in air are higher than in vacuum and tend to the same value at high  $\Delta K$ . Moreover in the examined frequency range the results obtained in air tests are not influenced by the test frequency; on the contrary in vacuum FCPRs increase when frequency increases from 0.1 to 10 Hz.

These results could be rationalised taking into account the overall

detrimental effect of oxidation at crack tip that explains the higher FCPRs in air tests and supposing a beneficial effect of creep under vacuum which should give rise to a stress relaxation at crack tip more effective at 0.1 Hz compared to 10 Hz test condition. This assumption is confirmed by the fracture surface analysis: at lower frequency (Fig. 14), due to stress relaxation, a more ductile fracture appears with the presence of secondary interlamellar cracks, that reduce the effective  $\Delta K$  for crack advance. A more brittle mode of fracture corresponding to a higher FCPR is apparent after the 10 Hz test in vacuum (Fig. 15).

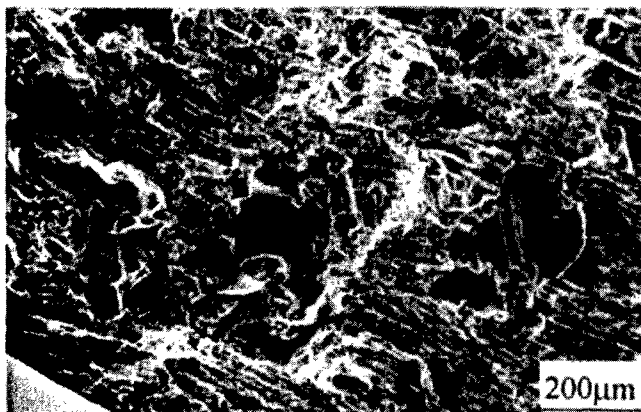


Fig. 16 - LCF test,  $T = 600^{\circ}\text{C}$ ,  $\Delta\epsilon_t = 0.90\%$ ,  $N = 660$ ; crack initiation zone and stage II crack propagation.

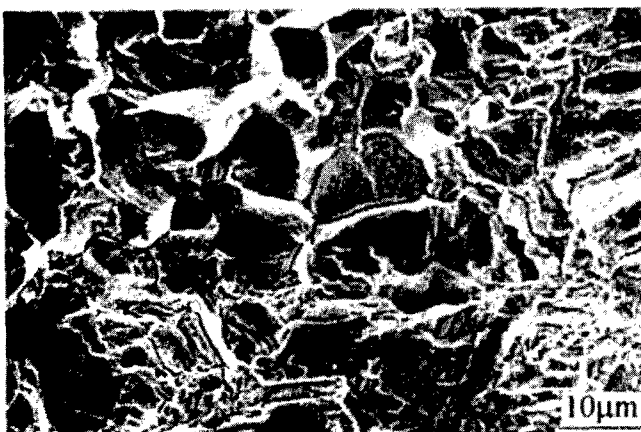


Fig. 17 - LCF test,  $T = 700^{\circ}\text{C}$ ,  $\text{HT} = 300 \text{ s}$ ,  $\Delta\epsilon_t = 0.80\%$ ,  $N = 758$ ; example of mixed intergranular and transgranular crack propagation zone.



Fig. 18 - Crack path on longitudinally sectioned specimen after fatigue crack growth test at  $800^{\circ}\text{C}$ , 10 Hz in air.

### Fracture surfaces examination

The aspect of the fracture surfaces confirms the low ductility of the alloy. In all LCF specimens, the crack starts at the external surface and propagates in transgranular mode without the presence of fatigue striations typically found in ductile alloys (Fig. 16). Some zones showing intergranular propagation were observed when a hold time is superimposed to the fatigue cycle (Fig. 17). Several areas indicate lamellar propagation along crystallographic planes.

The crack profile of the specimen tested in air at 10 Hz is shown in Fig. 18. The lamellar structure is predominantly oriented along the load axis, perpendicular to the direction of crack growth, but the propagation along lamellae appears favorite as shown by secondary crack growth. Apparently the crack does not cut  $\gamma$  phase.

### Conclusions

The new cast  $\gamma$ -TiAl base alloy examined in the present work has shown usable mechanical properties at elevated temperature. In particular, considering the density corrected results, the creep properties are better than those of IN738LC. The tensile parameters are not reduced sensibly from  $25^{\circ}\text{C}$  to  $800^{\circ}\text{C}$ . Also the fatigue properties are interesting, as the alloy does not appear to be sensibly affected by temperature changes and hold time in the temperature range studied. The fatigue crack propagation tests in vacuum at  $700^{\circ}\text{C}$  show a detrimental effect of air environment as well as a beneficial effect of creep that reduces FCPR when frequency decreases. The aspect of fracture surfaces after fatigue is typically that of a brittle alloy with lamellar propagation along crystallographic planes. The introduction of hold time produces intergranular propagation areas.

### Acknowledgements

This research work has been produced within COST 501/III/WP14 concerted European Action. The authors would like to thank Mrs. C. Béchemin, Mr. A. Bianchessi, Mr. D. Ranucci, Mr. E. Signorelli and Mr. G. Vimercati for their valuable contributions. One of the authors (W.M. Yin) would like to thank the ICTP Programme for Training and Research in Italian Laboratories, Trieste, Italy, which allowed his stay at CNR-TEMPE.

### References

1. M. Nazmy and M. Staubli, US Pat. Nrs. 5,286,443; 5,207,982 and 5,342,577. High Temperature Alloy For Machine Components Based on Doped TiAl.
2. D. E. Larsen Jr., "Status of Investment Cast Gamma Titanium Aluminides in the USA," Mat. Sci. Eng., A213(1996)128-133.
3. W. M. Yin and V. Lupinc, "Silicide Precipitation in A  $\gamma$ -based Ti-47Al-2W-0.5Si Alloy," Scripta Materialia, 36(1997).
4. O. H. Basquin, The Experimental Law of Endurance Tests, Proceedings ASTM 10, 610-625(1910).
5. L. F. Coffin Jr., Fatigue at High Temperature (New York: American Society For Testing and Materials, 1972). 5-34.

## Manufacturing - Performance - Cost Relationships in Gamma TiAl Castings

Paul McQuay and Don Larsen  
Howmet Research Corporation  
1500 So. Warner Street  
Whitehall, MI 49461

### Abstract

Product development efforts at Howmet for near-term aeroengine applications for cast gamma TiAl are focusing on process improvements and other cost reduction initiatives. This paper will focus on three major initiatives aimed at reducing the cost and improving the quality of gamma TiAl castings: gravity metal mold (GMM); low-cost alloy meltstock; and a simplified Hot Isostatic Pressing (HIP) and Heat Treatment (HT). The manufacturing-cost-performance relationships of the baseline process versus the proposed process will be discussed. These three initiatives together can provide a significant cost reduction in cast gamma TiAl components, while concomitantly providing an equivalent or improved balance of properties. Additional cost savings can be achieved by the reduction of scrap through other means encompassed within other Howmet process improvement initiatives, which are not discussed here.

### Introduction

Cast gamma TiAl alloys are presently under development, evaluation and testing for a number of near- and mid-term aerospace and automotive applications. These applications include static structural and rotating aerojet engine parts, and automotive turbocharger rotors and exhaust valves. While each of these potential components present unique manufacturing and product introduction challenges, a challenge they all share is the need to reduce manufacturing cost, while maintaining product performance and quality.

Two static structural aerospace applications are planned to complete testing and enter production in 1997 and 1998: the P&W F-119 HPC Variable Vane Shroud Seal produced by Howmet [1]; and the GE90 Transition Duct Beam produced by PCC [2]. Not surprisingly, the biggest threat to these and other potential material introductions is cost.

Gamma TiAl alloys are generally considered to represent a "revolutionary" advancement in aerospace materials technology [3], offering substantial weight reduction and performance benefits versus conventional materials for selected applications [1, 2]. One distinct advantage of gamma TiAl alloys over other "revolutionary" materials systems, such as ceramic or metal matrix composites, is that the production of cast gamma TiAl components requires no unique equipment or processes, and hence should require little or no capital investment [2].

In fact, gamma TiAl castings are being produced in conventional investment casting plants currently producing aerospace grade Ti and Ni components with very little requirement for new equipment or process changes. Additionally, gamma TiAl alloy raw material costs are cheaper than conventional Ti alloys. The apparent affordability of gamma TiAl alloys extends into the machining supplier base, where it has been demonstrated that with appropriate care, TiAl components can be machined with typical speeds and feeds, and that the machinability of gamma TiAl alloys is somewhere between Ti and Ni [1].

With this in mind, the current high costs associated with cast gamma TiAl components are not immediately apparent: they tend to arise from a lack of production experience and volume, not from inherent raw material or processing costs. Hence the age old materials introduction dilemma: it costs too much because the volume is low; and the corollary, the volume is low because it costs too much. This familiar dilemma is further exacerbated by the current cost consciousness of the aerospace community, which demands increased and even revolutionary performance at equal or lower cost.

This emphasis on cost for a revolutionary materials system has necessitated that cost be a main focus for each of the application development, testing and production programs. To illustrate some of the manufacturing and cost issues typical for cast gamma TiAl components, this presentation will discuss the HPC Variable Vane Shroud Seal development and production program. Although the configuration differs slightly from that for the proposed F-119 application, the Shroud Seal will undergo testing this year on a US Air Force (USAF) funded demonstration engine test bed [1]. A picture of a gravity metal mold (GMM) cast (also known as permanent mold cast) and investment cast Shroud Seal are shown in Figure 1.

### Cost Reduction Opportunities

In support of the Shroud Seal qualification program, Howmet has conducted a casting development study focusing on cost effective production of the component. The main emphasis to date has been the development of a low-cost facecoat/shell system, development of an efficient gating design and other casting variables in order to increase yield and decrease cost. The alloy selected for the Shroud Seal is the investment cast Ti-47Al-2Mn-2Nb + 0.8 vol% TiB<sub>2</sub> alloy (chemistries are given in atomic %, unless otherwise noted).

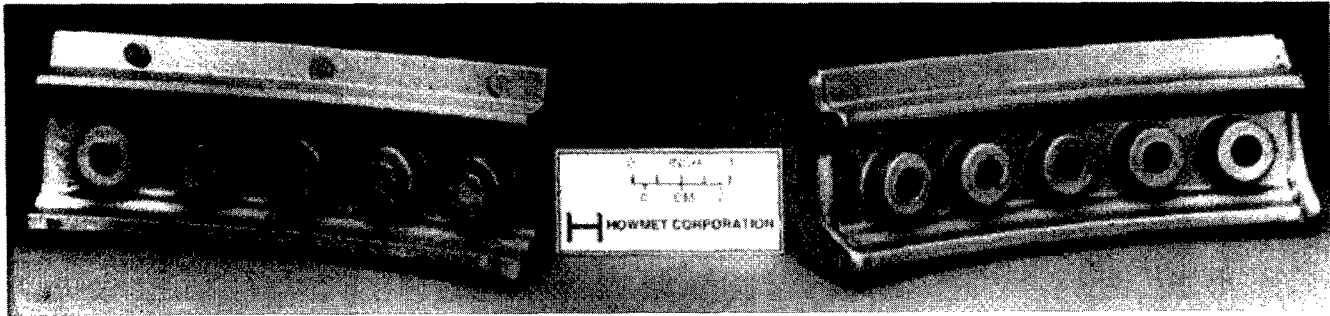


Figure 1. Picture of XD Gamma TiAl GMM Shroud Seal (left) and Investment Cast Shroud Seal (right)

Figure 2 presents a conceptual cost breakdown for a typical aerospace investment cast (IC) gamma TiAl component, such as the Shroud Seal. While there may be some variation from part to part, and alloy to alloy, this schematic provides an example of the various cost factors that currently determine component cost.

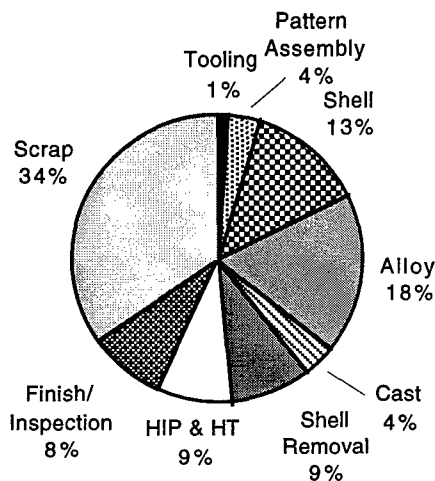


Figure 2. Cost Breakdown for Baseline Investment Cast Gamma TiAl Shroud Seal

Figure 2 illustrates that the cost contributions from scrap, alloy and shell make up a significant portion of the cast part cost, followed by shell/part removal, HIP and HT. Current developmental scrap

rates from wax through inspection are estimated to be approximately 35%. It is anticipated that as process improvements are continually made that the scrap rate will drop to the near-term target goal of 10%.

This paper will focus on three major initiatives aimed at reducing the cost of gamma TiAl castings: gravity metal mold (GMM); low-cost alloy meltstock; and a simplified HIP and HT. The three initiatives presented in this paper will provide an estimated 50% reduction in the cost of the Shroud Seal (see Figure 3). Efforts to reduce scrap are encompassed within other Howmet process improvement initiatives and are not discussed here.

#### Gravity Metal Mold Processing

The GMM process is a modification of the permanent mold casting process to cast alloys requiring a high vacuum, such as Ti or Ni-based alloys. This process has been described elsewhere [4]. This process has been demonstrated in gamma TiAl for a facsimile of the F-119 4th Stage Compressor ID Shroud Seal under a USAF funded R&D program, the Gamma Conversion Program (USAF contract number F33615-92-C-5900). Although funding for the GMM Shroud Seal was limited, and the schedule was very tight, sound Shroud Seal castings were produced (Figure 1), demonstrating the potential for cost reduction on the Shroud Seal.

Figure 3 provides a cost comparison for a cast gamma TiAl component, such as the Shroud Seal, produced by the current IC method versus the GMM manufacturing method, as well as the goals set for both of these methods. As can be seen from Figure 3, GMM offers a significant cost reduction for selected parts by reducing and/or simplifying process steps, and hence cost [4].

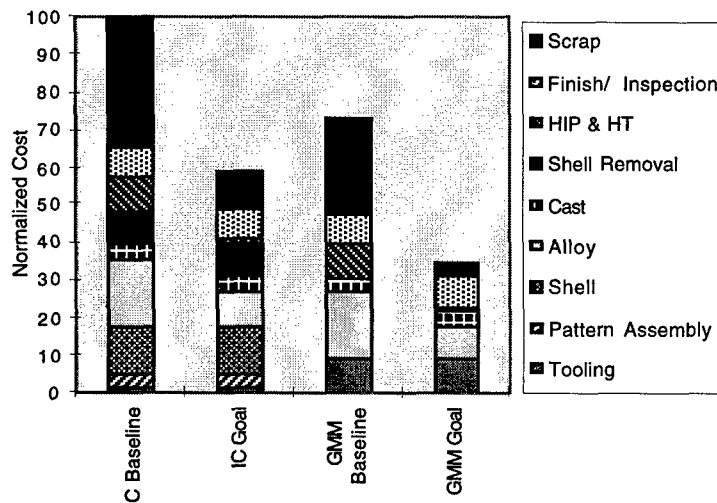
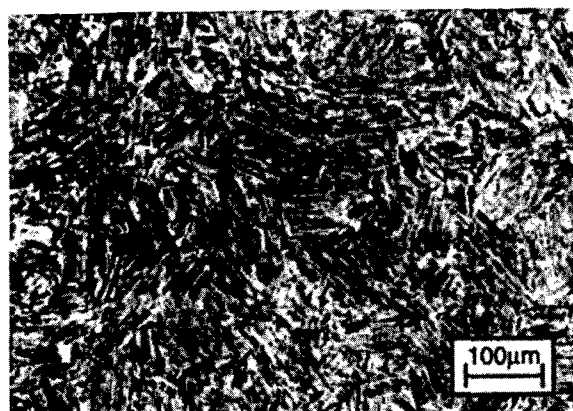


Figure 3. Normalized Cost Comparison for Various Cast Gamma TiAl Manufacturing Methods

While the permanent metallic mold is in fact not "permanent", using a reasonable projected life estimate for the metal mold based on accelerated testing and modeling, the cost of the mold amortized over the parts indicates that even for parts produced at a fairly low rate of production, such as that for the F-119 engine, GMM has cost savings potential. Overall, Howmet's cost model estimates that approximately 25% of the casting cost could be realized by utilizing GMM for this component.

The GMM process in gamma TiAl alloys has the added benefit of improved mechanical properties through microstructural refinement, as is demonstrated in Figure 4. Although investment cast XD alloys already exhibit a refined cast microstructure relative to monolithic alloys due to the demonstrated grain inoculation effect of the B addition during casting [5], GMM processing provides even further refinement due to the increased cooling rates due to the conductive metallic molds. This microstructural refinement, especially the interlamellar spacing, is expected to increase the room and elevated temperature strength and creep resistance of the GMM XD alloys over the IC XD alloys [6, 7].



(a)



(b)

Figure 4. Optical Micrographs of XD Gamma TiAl processed via (a) IC and (b) GMM. (Note the different magnifications).

Figure 4 illustrates that the colony size is refined from approximately 125  $\mu\text{m}$  for the IC XD, to approximately 50  $\mu\text{m}$  for the GMM XD alloy. Additionally, the lamellar spacing is also decreased from approximately 1  $\mu\text{m}$  to less than 0.5  $\mu\text{m}$  (not shown).

#### Alloy Meltstock

Alloy cost is approximately 15 -20% of the component cost for a typical gamma TiAl casting (Figure 2). Over the last 5 years, significant progress has been made in reducing the cost of large heats (> 450 kg) of 10 - 20 cm (4-8") diameter aerospace grade

meltstock, with the price falling from over \$88/kg to roughly \$44/kg - \$55/kg [8]. While this cost reduction is impressive, gamma TiAl alloy is still expensive compared to raw materials costs. In order to examine the opportunities to further reduce the cost of aerospace grade meltstock, traditional and alternative meltstock manufacturing processes have been evaluated.

An important consideration in selecting an appropriate meltstock production method is the requirement to produce a large heat, which can then be converted into meltstock of the appropriate size for use in the casting furnace. The need for large master ingot heats is driven by customer requirements that each heat of aerospace grade gamma TiAl alloy be certified to the alloy specification for chemistry, tensile and creep properties. The cost of this certification is included in the alloy cost, and hence, the larger the qualified heat, the lower the overall ingot cost.

The most common meltstock production methods used today are VAR + VAR pour, or induction skull melting (ISM). In the VAR + VAR pour method, a primary VAR electrode, usually in the 450 - 680 kg (1,000 - 1,500 lb) range, is produced either by single or double consumable-arc VAR melting of compacts. The electrode is then remelted in a consumable-arc cold-hearth VAR furnace, and tilt-poured into a tundish system which feeds pipes of the desired meltstock diameter. One advantage of this method is that it allows for the qualification of a large heat. One drawback is the relatively low efficiency of the process, around 80%, due to the loss of alloy in the skull and tundish systems.

In the ISM method, elemental or master alloy additions are melted in an induction skull furnace and directly poured into pipes of the appropriate size for the desired meltstock. The major disadvantage of this system is the small heat size, and higher overall cost, although it's efficiency is good for small heats (<45 kg.).

Alternative meltstock production methods show promise to provide low cost small diameter meltstock. These include Electron Beam (EB) and Plasma Arc Melting (PAM). Both of these methods employ a cold hearth and are considered flexible, as the input material can often be compacts, revert or ingot. Because the EB process requires a vacuum, the loss of volatile elements can be a problem due to the high surface area/energy configuration of the EB furnace. The PAM process, however, operates in an atmosphere of inert gas, such as Ar, dramatically reducing elemental losses during melting.

In order to evaluate the process capabilities, several heats of meltstock were produced from each of these four processes. A summary of the variation of measured versus aim chemistry for Al is provided in Figure 5.

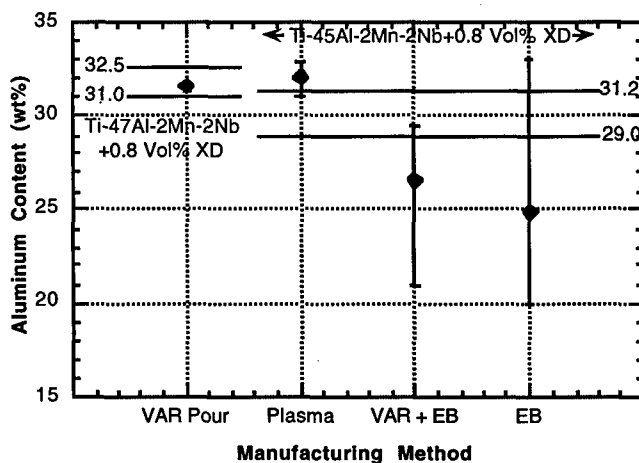


Figure 5. Measured Al Chemistry Versus Manufacturing Method for Cast Gamma TiAl Meltstock

The range of composition shown for each process is the average of chemistries measured from the top, middle and bottom of the ingots, from at least two different heats of alloy. Please note that the aim chemistry for the VAR Pour ingots was the Ti-47Al-2Mn-2Nb + 0.8 vol% XD alloy, while the remaining process aim chemistries were for the Ti-45Al-2Mn-2Nb + 0.8 vol% XD alloy.

It should be pointed out that of the three manufacturing methods examined, the VAR pour method is by far the most mature process for gamma TiAl alloys. While the EB processes may never be feasible due to the loss of Al and other volatile elements, the PAM process shows that with further development and experience it can be a low-cost manufacturing method for gamma TiAl alloy.

Another significant opportunity to reduce alloy cost is the introduction and qualification of revert material, which should potentially decrease the cost for all of these methods. Additionally, as the production volume of the gamma TiAl casting meltstock increases, and the vendor base achieves greater experience producing gamma TiAl alloys, prices for all the methods are projected to decrease with time. These projected cost improvements represent the potential for an additional 40-50% reduction in the alloy cost for gamma TiAl castings. A comparison of the projected cost, and benefits of each of these methods is summarized in Table 1.

#### Simplified HIP and HT

Current estimates indicate that HIP and HT contribute nearly 10% to the cost of a cast gamma component such as the Shroud Seal (Figure 2), and this percentage is likely to increase with part size. A long and often complicated HIP and HT process were developed in the past for cast gamma alloys, in an effort to optimize properties and to ensure complete closure of casting shrink.

The standard gamma TiAl HIP cycle is 1260 °C/175 MPa/4 hrs (2300° F/25ksi/4 hrs), compared with the standard Ni-based superalloy HIP cycle of 1185 °C/175 MPa/4 hrs (2165° F/25ksi/4 hrs). At Howmet, there is currently no difference in cost between these two HIP cycles. However, because the production volume of gamma alloys is currently low, the 1260° C HIP cycle is run relatively infrequently. In order to keep the HIP costs low as many parts as possible are batched together in a single run. This can sometimes cause delays of up to 2 weeks in processing.

Perhaps even more significant is the cost of the 50 hour 1010° C (1850° F) post-HIP "stabilization" HT currently applied to the XD, and other gamma alloys. This long HT was initially established

several years ago, based on the belief that the post-HIP'ed parts would require a long time HT near the eutectoid temperature in order to stabilize the microstructure. This HT is not only an additional processing step, but it requires at least 3 days to conduct, including the loading, cooling, and unloading operations.

In order to examine the effect of simplified HIP and HT processes on investment cast gamma TiAl alloys, 20 mm (0.75 ") diameter cylindrical test bars were cast from a single heat of the 47Al-XD alloy, with the exception of the room temperature tensile tests in the standard HIP/HT (2165°C HIP/1010° C for 50 hrs), where data was taken from earlier testing on different heats (hereafter referred to as "typical" data). Approximately half of the test bars were then given the standard gamma 1260° C HIP cycle, while the remaining test bars were given the lower temperature HIP cycle of 1185° C. The test bars were then given a HT at 1010° C for 0, 2, 4, 8 or 50 hours.

Test bars in each condition were then sectioned for metallography, and duplicate or triplicate tensile testing was conducted at room temperature and at 650° C (1200° F). Additionally, duplicate or triplicate tensile creep tests were conducted at 760° C/138 MPa (1400° F/20 ksi).

Representative optical and Scanning Electron Microscope Back-Scatter Electron (SEM BSE) micrographs for the high and low temperature HIP treated samples, respectively, are shown in Figures 6 and 7, with HT times of 0 (no HT) or 50 hours.

The optical micrographs from all HIP and HT combinations look similar, as one might expect. Unlike other cast gamma alloys, the cast 47Al XD alloy exhibits a relatively fine nearly lamellar microstructure. Both the fine equiaxed gamma grains and the lamellar colony size is quite stable and not easily adjusted unless the temperature of the thermal cycle approaches the alpha transus temperature.

However, the BSE images illustrate that the temperature of the HIP cycle does have an effect on the volume fraction and the width of the alpha-2 lamellar phase. This is expected due to the higher equilibrium volume fraction of the alpha phase predicted from the binary phase diagram at 1260° C, relative to the 1185° C HIP temperature [9]. An examination of the BSE images for the different HT for a given HIP cycle, however, indicates little or no effect of the HT on the volume fraction or morphology of the alpha-2 or gamma phases. These microstructural features are summarized in Table 2.

Table 1. Comparison of Meltstock Production Processes for Cast Gamma TiAl Alloy

Process	Current Cost (per lb)	Est. Prod. Cost (per lb)	Chemistry Control	Heat Size
ISM	\$30 - \$35	\$20 - \$25	Good	Small
VAR + VAR Pour	\$20 - \$25	\$12 - \$15	Excellent	Large
VAR + EB	NA	\$12 - \$15	Poor	Large
EB	NA	\$10 - \$15	Poor	Large
PAM	\$30 - \$35	\$10 - \$15	Very Good	Large

Table 2. Comparison of the Microstructure of the 47Al-XD alloy vs. HIP and HT.

HIP Temp (°C)	HT Time (Hrs)	Gamma Grain Size (µm)	Colony Size (µm)	Alpha-2 Vol %	Alpha-2 Lam. Width (µm)
1260	0	30 - 40	100 - 150	10 - 20%	0.5 - 1.0
1260	50	30 - 40	100 - 150	10 - 20%	0.5 - 1.0
1185	0	30 - 40	100 - 150	3 - 5%	0.1 - 0.5
1185	50	30 - 40	100 - 150	3 - 5%	0.1 - 0.5

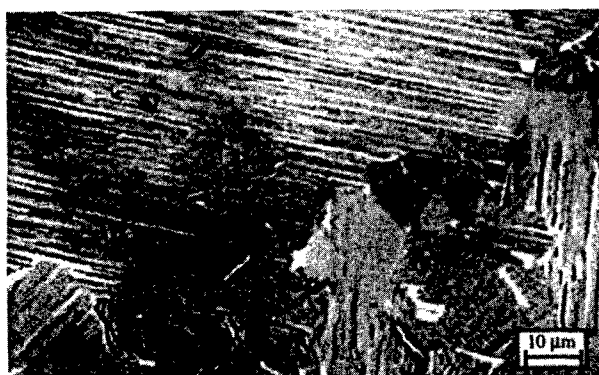




(a) 1260° C HIP/No HT



(b.) 1260°C HIP/1010° C 50 Hours



(c) 1260° C HIP/No HT



(d) 1260°C HIP/1010° C 50 Hours

Figure 6. Optical (a and b) and SEM BSE (c and d) Micrographs of XD Gamma Alloy with 1260°C HIP + various HT.



(a) 1165° C HIP/No HT



(b) 1165°C HIP/1010° C 50 Hours



(c.) 1165° C HIP/No HT



(d.) 1165°C HIP/1010° C 50 Hours

Figure 7. Optical (a and b) and SEM BSE (c and d) Micrographs of XD Gamma Alloy with 1165°C HIP + various HT.

Table 3. Typical Properties for Ti-47Al-2Mn-2Nb + 0.8 Vol% XD, 1260° C HIP/50 HT

Test Temp. - °C (°F) -	Tensile Test			Creep Test	
	YS - MPa (ksi) -	UTS - MPa (ksi) -	Plastic Elongation - % -	Applied Stress -MPa (ksi)-	Time to 0.5% Strain -Hrs-
20 (70)	402 (58)	482 (70)	1.2	--	--
650 (1200)	369 (54)	522(76)	3.6	276 (40)	460
760 (1400)	344 (50)	455 (66)	17.8	138 (20)	63

Typical tensile and creep data are given for the standard HIP/HT in Table 3. The pooled average tensile data for the 1260° C HIP cycle is higher than the typical standard HIP/HT data.

In comparison, the effect of HIP and HT on mechanical properties is illustrated in Figure 8, which shows the room temperature (RT) tensile yield stress versus the time at the HT temperature of 1010° C, for the low and high temperature HIP cycles. (This data is presented using a box plot, where the upper and lower lines represent the highest and lowest points in the data sample, and the middle line represents the average of the data sample.) It appears from the figure that there is an apparent difference in yield strength between the low and high temperature HIP treatments. However, with the exception of the 1260° C HIP/50 HT, all of the data within a given HIP cycle appear the same.

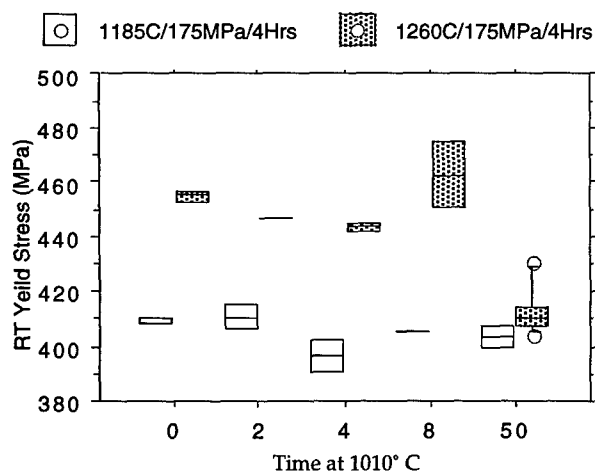


Figure 8. Box Plot of Room Temperature Yield Stress as a function of HIP and HT.

To test this hypothesis, an analysis of variance (ANOVA) statistical procedure was applied to the YS data. The ANOVA test indicated with a very high confidence interval (>99%) that there was no effect of HT on tensile YS for either HIP cycle, with the exclusion of the 1260° C HIP/50 HT data. This statistical test was also applied to the room and elevated tensile YS, UTS and elongation. While the 1260° C HIP/50 HT room temperature tensile data appear anomalous, there appears to be no change in properties as a function of HT for the elevated temperature tensile test data.

There was also an apparent effect of the HIP temperature on the tensile elongation at room and elevated temperature. The average plastic elongation for the standard 1260° C HIP specimens was approximately 1.1%, versus approximately 1.3% for the lower temperature 1185° C HIP specimens. A similar trend was seen for the 650° C tensile data, with the plastic elongation of 3.5% versus 4.0%, for the standard and lower HIP temperature specimens, respectively.

As mentioned earlier, because a database of room temperature tensile data already existed for the standard HIP/HT, the room temperature testing was not repeated for this study, whereas the

elevated temperature tensile and creep testing was repeated. ANOVA tests on all data, excluding the room temperature tensile data for the standard HIP/HT, indicates no effect of HT for a given HIP cycle. However, a similar ANOVA test comparing the YS of the "typical" data presented in Table 3, with the more recent data produced in this study does show a statistically significant difference between the two batches or heats of material (the "typical" data in fact represents material taken from many different heats, within several years time, but for simplicity is referred to here as a single heat).

This comparison implies that the apparent difference between the 50 hour HT and the pooled 1260° C HIP material is due a batch or heat effects, and not due to the HT. The chemistries of the different heats of material have been compared, and show no explicable trend. One potential effect may be that the "typical" data was produced via a VAR Pour casting furnace, whereas the data from this study was produced in a ISR casting furnace (the ISR casting furnace is now used for all castings less than 45 kg). Further testing may be required to confirm this conclusion.

The effect of HIP and HT on creep is summarized as a box plot Figure 9, as the time to 0.5% creep strain. It is apparent from the data that quite a bit of variability is seen in all conditions, and no discernible trends are apparent, as a function of HIP or HT. This has been again confirmed to a high confidence level with an ANOVA test. The reason for the high amount of variation in the time 0.5% strain analysis of the creep results is unknown.

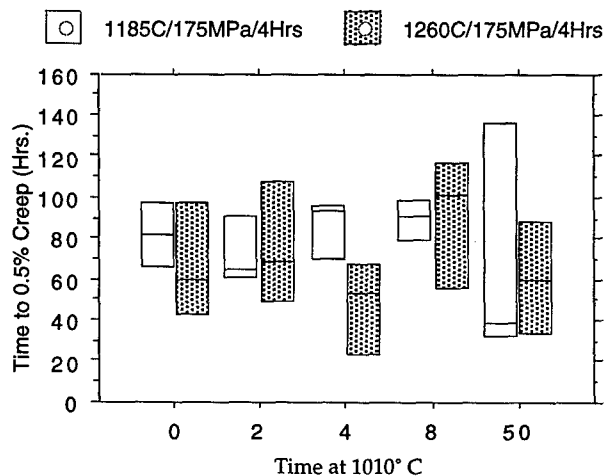


Figure 9. Summary of Time to 0.5% Creep Properties as a function of HIP and HT.

The effects of the HIP temperature on the room and elevated strength and ductility are likely due to the volume fraction of the alpha-2 phase, as summarized in Table 2. The higher volume fraction of alpha-2 present in the standard HIP treated material would be expected to provide higher strength, but lower ductility relative to the lower temperature HIP material. It is interesting to note that this difference in volume fraction of alpha-2 did not

apparently effect the creep data, at least not within the relatively short "Time to 0.5%" creep test.

The as-cast microstructure of the XD alloy is stable through HIP and HT, with only small variations in the volume fraction and thickness of alpha-2 lamellae observed. This preliminary study indicates that the HIP and HT can be dramatically simplified, and their cost reduced, without sacrificing mechanical properties or part integrity. Specifically, it appears that the standard "stabilization" HT can be eliminated with no detrimental effects on performance of the material. This preliminary conclusion will be confirmed by more in depth analysis and testing. Elimination of the HT would result in an estimated 6% cost savings on a part such as the Shroud Seal.

#### Summary

This paper has described three opportunities to reduce the cost of a small structural gamma TiAl casting with either positive or neutral effects on the performance of the cast component. These opportunities are: GMM processing; low-cost alloy meltstock; and a simplified, low-cost HIP and HT process.

GMM provides the opportunity to improve the component mechanical properties through microstructural refinement. Additionally, because of process simplification, GMM provides the opportunity to reduce the cost of the Shroud Seal an estimated 25% over current IC cost.

Several gamma TiAl alloy meltstock manufacturing methods have been evaluated for process capability and potential cost. The VAR + VAR Pour method is the current method of choice for large heats of meltstock, and has excellent chemistry control. An alternative meltstock manufacturing method is PAM, which provides greater flexibility in input material, and shows promise as a low-cost reliable process. The price of VAR + VAR Pour gamma meltstock has dropped by close to 50% over the last five years as industry has gained experience with the gamma TiAl alloys. Increased volume and manufacturing experience, coupled with the reversion of scrap alloy should offer the opportunity to cut the cost of gamma meltstock an additional 50% over the next several years.

Opportunities exist to dramatically reduce the cost and cycle-time of the standard HIP and HT processes for XD gamma alloy castings. The microstructural and mechanical properties of the standard gamma TiAl HIP cycle, 1260°C/175 MPa/4 hrs, have been compared with the lower temperature standard Ni-based superalloy HIP cycle, 1165°C/175 MPa/4 hrs. While the tensile strength of the standard HIP cycle is higher than that of the lower temperature Ni HIP cycle, a reduction in cost and cycle-time may be worth the trade-off in tensile properties. Additionally, a small improvement in ductility is observed in the lower temperature HIP treatment. No effect of HIP cycle on creep resistance has been seen. Metallography also indicates that the lower temperature HIP cycle is sufficient to close porosity in cast test bars, but further testing, such as fatigue testing, should be conducted to verify this conclusion.

Additionally, the preliminary evidence suggests that the "stabilization" HT applied after HIP has no effect on microstructure or properties of the XD gamma alloy studied. The as-HIP'ed microstructures are stable, and the mechanical properties, including creep are at least comparable to the material given the standard HT. Therefore, the XD alloy can be HIP processed at either 1260° C or 1165° C, and requires no HT, at least in the case of IC XD alloys. The appropriateness of this proposed processing change to GMM produced castings would also need to be verified. The elimination of the HT alone would provide a cost savings of approximately 85% of the HIP/HT cost or a reduction of approximately 6% of the investment cast component cost.

In total, if these three cost reduction opportunities were applied to a part such as the Shroud Seal, it would represent an estimated cost

savings of over 50%. Combined with other Howmet scrap reduction efforts, the estimated cost savings would increase to 65% of the current component cost.

#### References

1. D.E. Davidson, Proc. Of Superalloys 1996, Ed. R.D Kissenger et al, Seven Springs, PA, TMS (1996) 545.
2. C.M. Austin and T.J. Kelly, Proc. Of Superalloys 1996, Ed. R.D Kissenger et al, Seven Springs, PA, TMS (1996) 539.
3. M.J.Goulette, Proc. Of Superalloys 1996, Ed. R.D Kissenger et al, Seven Springs, PA, TMS (1996) 3.
4. G.N. Colvin, Proc. of Titanium '95: Science and Technology, Ed. P.A. Blenkinsop et al, Birmingham, UK, (1996) 691.
5. D.E. Larsen, S.L. Kampe, and L. Christodoulou, MRS Symposium Proceedings, 194 (1990).
6. M.M. Keller et al, The Journal of Metals, 49- 5, (1997) 42.
7. D.Y. Seo, T.R. Bieler, and D.E. Larsen, to be published in the Proc of Structural Intermetallics - 2, TMS, Warrendale, PA, (1997) in press.
8. P. Bartolotta et al, The Journal of Metals, 49- 5, (1997) 48.
9. C. McCullough et al, Acta Metall., 37 (1989), 1321.

#### Acknowledgments

The majority of this work was sponsored under the Howmet Research Corporation internally funded research and development program, with the exception of the GMM Shroud Seal casting, which was sponsored by the USAF contract entitled "The Gamma Conversion Program" (USAF contract number F33615-92-C-5900) through the UES Corp.

## DESIGNING GAMMA TiAl ALLOYS: Fundamentals, Strategy and Production

Young-Won Kim\* and Dennis M. Dimiduk

Wright Laboratory Materials Directorate  
WL/MLLM, Wright-Patterson AFB, OH 45433  
(\*UES, Dayton, OH 45432)

### Abstract

The properties of both fine-grained gamma and coarse-grained lamellar microstructures typically produced in engineering gamma TiAl alloys are discussed, along with recent efforts to improve their deficiencies. Empirical improvements made in cast alloys have led to gamma alloys which are a viable materials technology, and to the development of various applications (identified or being implemented) for gas-turbine engines, as well as automotive engines. For wrought alloys, over the last seven years extensive efforts to remove their deficiencies, and to achieve an improved balance of properties, have been made across three interrelated task areas at Wright Laboratory, Materials Directorate. The first effort was directed toward understanding fundamentals, such as phase relations and transformations, microstructure evolution through exploration of controlled processes and/or heat treatments, composition-structure-property relationships, and microalloying effects. The second task, which was later incorporated into the first task, was aimed at improving the balance of properties through designing refined lamellar microstructures and microalloying. The third task was to explore the methods to develop component-specific microstructures and compositions. This paper discusses the progress made from the ongoing efforts.

### Introduction

Since the first measurements of mechanical properties and oxidation resistance in a binary TiAl cast alloy in the early 1950's [1], ensuing reports [2-10] have confirmed various properties beneficial to high temperature structural applications including low density, excellent high-temperature strength retention, high stiffness especially at high temperatures, thermal expansion comparable to current alloys, good oxidation resistance, and hot-corrosion resistance comparable to, or better than, those of current alloys. The first generation alloy, Ti-47Al-1V-0.3C, developed on the basis of ductility and creep resistance had inadequate properties for the requirements set by many engine components [3,

11]. The second generation alloy, Ti-48Al-2(Cr or Mn)-2Nb, developed largely based on the previous knowledge is essentially a casting alloy (Table 1) and exhibits better oxidation resistance and a broader processing window [5, 9, 12].

Considerable empirical efforts have been made to control the cast lamellar structure through post-casting annealing treatments. These efforts aim to alter the microstructure into finer mixtures of gamma grains and alpha-2 plates and/or particles which are called "casting duplex" or "near-gamma" microstructures of about 100-200µm grain size [8]. The cast alloy Ti-48Al-2Cr-2Nb in these microstructural forms exhibits a reasonable balance of properties (though at relatively low levels), and was recently demonstrated as viable engineering materials through rigorous engine tests [9, 13]. Other extensive efforts were made to produce refined cast lamellar microstructures, resulting in the development of cast XD alloys containing boron additions for grain refinement [14, 15], Table 1. Data bases for the second-generation cast alloys are being established through extensive property evaluation, again for cast processing conditions. Most of the properties in the cast alloys measured at temperatures up to 760°C appear to be comparable to, or better than (when adjusted for density), those of many Ni-base superalloys for which they may be substituted [13, 14].

Clearly, current industry focus is on low cost implementation of cast gamma alloys in low risk applications. However, potential high-payoff higher-risk applications exist and are largely untapped. This is principally the result of the low strength of Ti-48Al-2Cr-2Nb, poorly developed design & life prediction methods, and the slow evolution of controlled wrought products on a large scale. For the higher-performance applications of gamma alloys, emphasis must be placed on lamellar microstructures. This manuscript reviews property-structure-synthesis relationships for gamma alloys to describe the state of development of these materials.

Wrought-processed gamma TiAl alloys typically yield two types of microstructures, coarse-grained fully-lamellar (FL) type and fine-grained duplex (DP) type. Through an understanding of the microstructure/property relationships, it has been demonstrated that these standard-type microstructures do not meet many of either the individual, or balance of, properties desired [14, 15]. Having recognized the importance and necessity of the properties pertinent to specific components, extensive efforts to develop materials through lamellar microstructure control and alloy modification have been underway since 1991. In this focused effort, the thrust has been to develop lamellar-based structures having grain sizes which are fine enough for enhanced room-temperature properties and coarse enough to retain desirable high-temperature properties, and toughness. Table I lists selected alloys for each generation; however, with a somewhat broad compositional range suggested for third generation alloys. The rationale behind the suggested compositions will be clearer as discussion proceeds.

In this paper, we will first briefly review the fundamentals of microstructure evolution, alloying effects, and microstructure-property relationships. From this understanding, a discussion is presented on optimizing microstructural features for a desirable balance of properties, along with selecting an appropriate alloy composition. Design fundamentals and production methods for various types of optimized microstructures will be introduced and discussed along with recently measured mechanical properties. Extensive efforts in further optimizing microstructures through development of innovative process control and alloy modification, as well as enhancing mechanical behavior by microalloying, are underway, and this progress will also be reported.

Table 1. Classification of Gamma TiAl Alloys (in at %)

*G	Compositions(at%)	Processing	Ref
1st	Ti-48Al-1V-0.3C	Exploratory	2, 3, 11
2nd	Ti-47Al-2(Cr, Mn)-2Nb	Cast	5
	Ti-(45-47)Al-2Nb-2Mn+0.8vol%TiB <sub>2</sub>	Cast XD	14, 15
	Ti-47Al-3.5(Nb, Cr, Mn)-0.8(B, Si)	Cast	10
	Ti-47Al-2W-0.5Si	Cast	18
	Alloy K5 (Ti-46.2Al-2Cr-3Nb-0.2W)	Wrought	8, 19
3rd	Ti-47Al-5(Cr, Nb, Ta)	Cast	13
	Ti-(45-47)Al-(1-2)Cr-(1-5)Nb	Wrought	48
	-(0-2)(W, Ta, Hf, Mo, Zr)-(0-0.2)B		
	-(0.03-0.3)C-(0.03-0.2)Si-(0.1-0.25)Ox		

\*G: Generation

### Fundamentals

Over the course of a decade a fundamental understanding of the intrinsic properties of the L1<sub>0</sub> gamma phase has advanced through various research methods. Both theoretical methods such as electronic structure modeling [20-22], atomistic simulations [23-25], and elasticity analysis [26-29], and detailed experimental methods such as transmission electron microscopy [30-33], atom-probe field ion microscopy [34], and single-crystal deformation experiments [35-37], contributed to this fundamental base. However, broad examination of this base also indicates that the

intrinsic properties of the gamma phase are globally fixed. The dislocation properties are common among the various alloys examined, and the material always exhibits limited ductility and a low cleavage strength. These fundamental findings support the common metallurgical view of most structural materials, that the balance of materials properties necessary for engineering use must be controlled through microstructural manipulation and processing. Further, just as for traditional structural alloys, one must command not only knowledge of the desired microstructural forms for a specific balance of properties, but also process control which is sufficient to mitigate defects in the final component geometries, and design methods which are sufficiently understood as to specify a particular component configuration and environment. Controlling microstructure requires both a careful selection of alloy chemistry and knowledge of the kinetics of microstructural evolution, thus providing the foundation for process control and an understanding of microstructure-property relationships. In these respects, gamma alloys are no different than any other structural alloy, and it is these aspects for fully-lamellar microstructures which are the focus of the present paper.

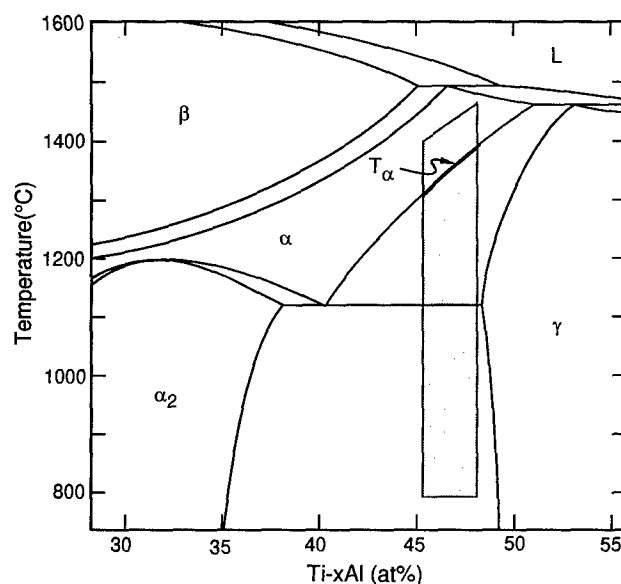


Figure 1. Central portion of the Ti-Al phase diagram [38]. The shaded area indicates the base for engineering gamma alloys.

The mid-section of the Ti-Al binary phase diagram has been established, Figure 1 [38], although ternary-diagram studies are more useful and have yet to be advanced. The sequence of phase transformations involving alpha ( $\alpha$ ) decomposition is fairly well documented, and the resulting microstructural classes are schematically depicted as a function of cooling rate and alpha grain size in Fig. 2. As shown, for the alloy compositions based on Ti-(45-48)Al, decomposition takes place via several possible paths yielding various types of structures: well-defined lamellar structure under relatively slow cooling ( $0.05-3^\circ\text{C/s}$ ) [38], Widmanstätten, "feathery" and/or acicular types under higher cooling rates [39, 40], and massive gamma structures when water-quenched [40, 41]. At the highest cooling rates or the largest undercoolings, the formation of decomposition products is suppressed in favor of ordering the alpha phase to the alpha-2 phase [38, 42]. Growing evidence indicates that the initial alpha-

grain size influences the cooling-rate dependency which, however, needs to be understood quantitatively.

### Forming Lamellar Microstructures

Among the microstructures in Figure 2, the investigation of lamellar structures has received the most attention for the reasons of their practical implications. Studies to date suggest that the lamellar structure is formed by a stacking-fault mechanism in which stacking faults are formed in the hexagonal matrix as the precursor to plate-type gamma precipitates. Their formation is completed through a short-range diffusion process taking place during subsequent cooling. Depending upon composition and/or cooling rate, gamma precipitation resulting in the lamellar structure derives from one of the two reaction sequences: (A)  $\alpha \rightarrow \alpha_2 \rightarrow L(\alpha_2 + \gamma)$  and (B)  $\alpha \rightarrow L(\alpha + \gamma) \rightarrow L(\alpha_2 + \gamma)$ , where L represents lamellar form [16, 38, 42, 43].

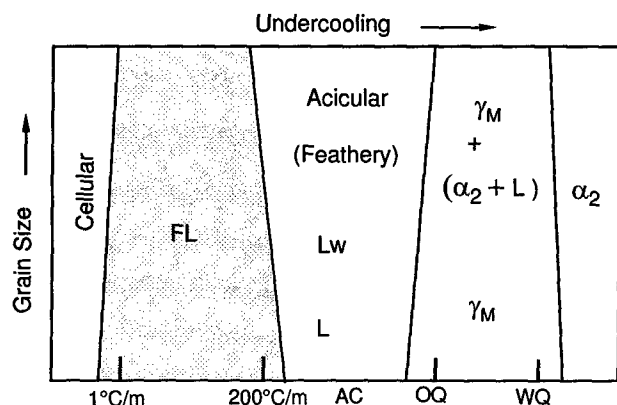


Figure 2. Schematic showing the effect of cooling rate and alpha grain size on the microstructural forms produced upon alpha decomposition

The undercoolings required for the formation (starting and finishing) of the lamellar structure have been measured recently as function of cooling rate and composition in binary TiAl [38]. Lamellar spacing ( $\lambda$ ) was found to depend on cooling rate ( $dT/dt$ ) and is expressed as  $\lambda = C(dT/dt)^{-1/2}$ , where C is a constant unique to a specific composition, Figure 3 [38]. The maximum cooling rate, above which the lamellar structure is disturbed by the formation of Widmanstätten structures, ranges from 1-4 °Cs<sup>-1</sup> [38, 40] depending on composition and grain size [38], Figure 2. Once the formation is complete, the lamellar spacing (or the gamma-plate thickness) coarsens during subsequent cooling which, however, can be minimized or suppressed by employing a rapid cooling such as air cooling or water quenching [19, 38].

Extensive investigations of the deformation behavior of the lamellar structure have been conducted in Japan with the major effort placed on establishing the extraordinary deformation anisotropy [7] intrinsic to the microstructures. Fine details and their influences on various mechanical properties are under continuous investigation worldwide. Advanced understanding of the lamellar structure, which is crucial for designing lamellar-based microstructural alloys, is far from being complete.

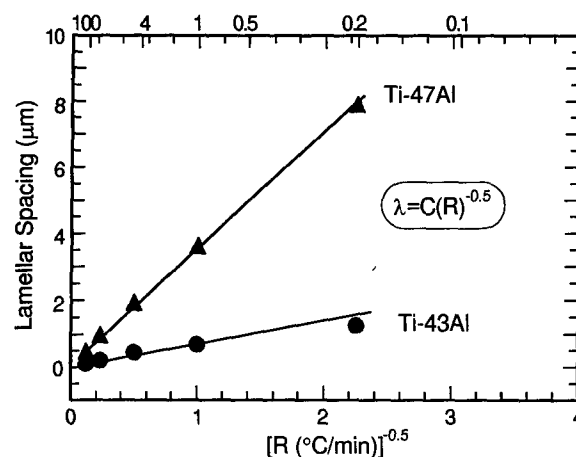


Figure 3. Cooling rate effect on lamellar spacing in Ti-Al binaries. The samples were alpha-treated and cooled at about 60°C/min [38]

### Composition Effects - Major Elements

In general, a reduction of Al content increases the strength level [2, 5, 12], while tending to decrease the ductility [2, 3, 5] and oxidation resistance [2, 4]. In binary alloys, the reduction to below 48 Al decreases toughness as well as creep resistance [12, 44]; however, the synergistic effects in multicomponent alloys on these properties have not been quantified. Influences of alloying elements such as Cr, Mn, V, Nb, Ta, and W on mechanical properties are known only qualitatively; nevertheless, some empirical rules for each element have been accepted in relating the effect and the amount to alloy behavior [4, 6]. Cr, Mn, and/or V additions, up to certain amounts (about 2 at% for each) have been shown to increase the ductility [2, 3, 5, 45] in two-phase alloys. Empirically, all these elements are known to be solution-strengtheners, although the relative effect for each element appears to differ. The upper limits for these additions were bounded by their solid solubilities as well as overall ductility considerations.

### Composition Effects - Minor Elements

Additions of C were shown to effectively lower the minimum creep rates in Ti-48Al-1V base alloys [2, 11, 46], and the effect has also been observed in other alloy compositions [47]. The mechanism(s) for these carbon effects has not been settled; however, both solid solution hardening and precipitation hardening are expected. Recently, creep tests on a wrought fully lamellar alloy (K5+0.1C) showed remarkable improvements in creep resistance at 760°C under a high applied stress [48]. TEM analysis showed fine Ti<sub>2</sub>AlC particles interacting with dislocations, suggesting the importance of precipitation hardening for the enhanced creep resistance [48]. The maximum allowable carbon content in a wrought duplex alloy (Ti-48Al-1V) was estimated to be 0.1wt% (about 0.3at%) set by ductility considerations [2, 3]. As more information has become available including the thermal and mechanical stability of the carbides, a revised estimate is that the upper limit for C may depend on Al content, with 0.2at% C limit for Ti-(47,48)Al base alloys and higher levels for lower Al-containing alloys [48].

A limited amount of investigation has recently shown that small amounts (0.2at%) of Si improve the creep resistance [47]. However, these effects have yet to be quantified and isolated. Some results, though unquantified, indicate that Si additions may embrittle alloys during ingot casting [48a] as well as after wrought processing [48]. Oxygen was known to increase both strength as well as creep resistance [2, 3], with the maximum content being 0.1 wt% (about 0.23 at%) in Ti-48Al-1V, again limited by ductility considerations in duplex microstructural forms [2]. Atom-probe investigations indicate that the oxygen solubility limit in the gamma TiAl phase is 300 atppm or less [34, 49], thus the oxide particles and/or oxygen partitioning to the  $\alpha_2$  phase may be responsible for the enhanced mechanical behavior.

#### Phase Boundary Information

The overriding aspects of chemical effects on alloy design and properties are contained in quantitative phase-diagram data, and the associated kinetic effects quantifiable through TTT diagrams. This information is crucial in determining and/or obtaining: 1) the exact composition for an alloy optimized for a given phase equilibria; 2) the growth kinetics and stability of constituent phases; and 3) the process route for controlling the microstructure in a given component. The only system for which the phase boundaries have been determined nearly completely, is the Ti-Al binary system (Figure 1), and even for this case, the very high-temperature phase boundaries are not clearly determined. For this reason, the binary system has been a frequently used guide for alloy design, and has proven to be reasonably adequate.

As indicated by these short discussions, our understanding of gamma TiAl is far from being complete. Nevertheless, there are indicators for alloy design and composition selection which evolved within this understanding, and yield a desirable microstructure and property set. Using this information, the alloy K5 (Table 1) was first formulated as a base composition which exhibits good microstructural controllability, reasonable strength levels in standard microstructural forms, and excellent oxidation resistance. For the last two years, extensive effort has been made in evaluating and refining the alloy. Collectively, this effort is leading us to the introduction of a 3rd-generation wrought alloy system, which is microalloyed with various elements including B, C, Si and O, Table 1.

#### Microstructure-Property Relationships

Based on knowledge of the phase relationships and transformations and the deformation anisotropy of lamellar microstructures, progress has been made in controlling and evaluating microstructures, primarily produced through wrought-processing in the alloy system Ti-(45-49)Al-(0-3)(Cr, Mn, V)-(0-5)Nb-(0-0.4)W-(0-0.5)B-(0.03-0.5)C-(0.05-0.3) Si [12, 16, 17, 19, 38, 48, 50-53]. Four different types of standard microstructures were: near-gamma (NG), duplex (DP), nearly-lamellar (NL) and fully-lamellar (FL) types [16]. DP and FL microstructures have been subjected to the most investigation, Figure 4. DP materials are fine-grained (5-30  $\mu\text{m}$ ) and were found to yield low toughness [16] and creep-resistance [17, 54]. FL microstructures consist of large lamellar grains (>600  $\mu\text{m}$ ) in general, resulting in poor ductility (<1%). Studies of these forms, however, indicated that a wide range of grain sizes (GS) could be obtained through various heat treatment cycles. The understanding of these aspects and

their influence on properties at RT is discussed below, although many detailed observations and quantitative analyses remain to be made. Systematic investigations of the elevated-temperature deformation and fracture processes have begun only recently.

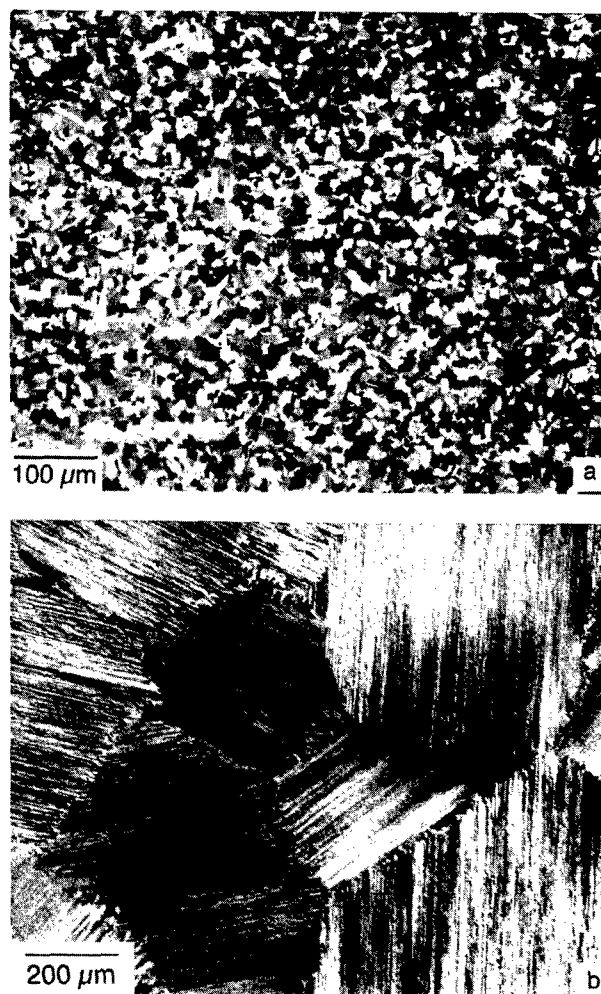


Figure 4. Duplex (a) and fully-lamellar (b) microstructures typically produced in wrought processed gamma alloys.

#### Tensile Behavior

At room temperature, DP materials exhibit reasonable strength levels and acceptable ductility (2-3%), while large-grained FL materials show low tensile properties [16]. Within each microstructural type, yield-strength (YS) and GS were found to be described by the Hall-Petch (HP) equation, with the HP constant being about 1  $\text{MPa}\sqrt{\text{m}}$  for DP materials [12, 55, 56] and initially measured as 4.5  $\text{MPa}\sqrt{\text{m}}$  [57, 58], and later corrected value of 2.3  $\text{MPa}\sqrt{\text{m}}$  [48] for FL material. The unusually large HP constant in FL material was measured for a GS (d) range of 250-2600  $\mu\text{m}$  and a constant lamellar spacing (l) of about 1  $\mu\text{m}$ , Figure 5. The HP relationship for FL material was proposed to be,  $\sigma_y = \sigma_0 + k_d \lambda d^{-1/2}$ , where  $\sigma_0 = f(\lambda)$  and  $k_d \lambda = f(d, \lambda)$  [48]. This empirical relation predicts: 1)  $\sigma_0$  increases with decreasing lamellar spacing; 2) the HP constant varies with both GS and lamellar spacing, approaching that for the DP material, for example, as spacing



coarsens; and 3) YS can be unusually high for fine grains and fine lamellar spacing, Figure 5 [48]. Recently, a more detailed analysis [59] confirmed that high yield-strength in FL materials [48, 52, 53, 60] may be accredited to the deformation anisotropy of the lamellar structure and lamellar refinement.

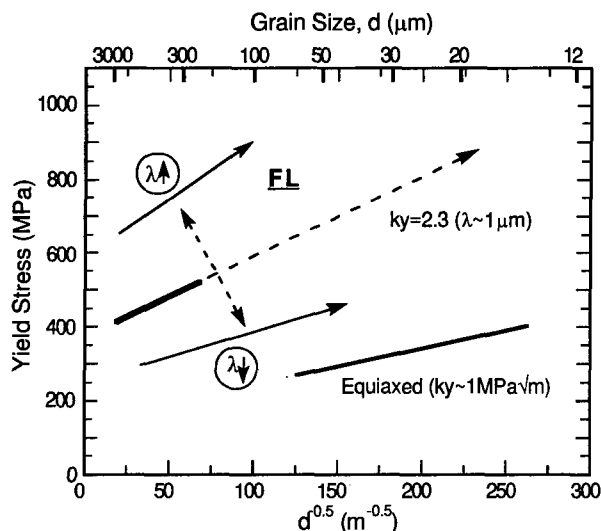


Figure 5. The relationship between grain size and yield strength in FL gamma materials, showing the HP constant for FL material may vary from that (1 MPa√m) for fine-grained duplex materials to large values (>2 MPa√m) with decreases in lamellar spacing [48, 57, 58].

In FL materials, an inverse relationship was observed between ductility/strength and GS [16, 61], and was rationalized on the basis of the deformation anisotropy, and the correlation between the crack-nucleation-process and GS [58, 61, 63]. Tensile ductility is characterized by the brittle-ductile transition temperature (BDTT) which varies depending on alloy composition and microstructure. Under strain rates between  $1 \times 10^{-4}$  to  $1 \times 10^{-3} \text{ s}^{-1}$ , it typically varies from about 650°C for fine duplex materials to about 820°C for large-grained FL materials [8, 58, 62, 64]. The BDTT is highly sensitive to strain rate; for example, it can rise above 1000°C for a duplex material when stretched at  $1 \text{ s}^{-1}$  [8, 48]. Though not quantified fully, the BDTT in FL materials appears to increase with grain size [48]. For a given grain size, the popular notion that a lower RT ductility is related to a higher BDTT, has yet to be substantiated.

High-temperature strength is closely correlated with strain-rate and the BDTT [48, 65]. Increases in strain rate lead to both higher strength retention and an increase in the BDTT, regardless of microstructure. Cleavage and transgranular cracking are the dominant fracture modes at RT for both microstructures, although the fine duplex material shows a mixture of transgranular and intergranular failure [16, 58, 62, 66]. At temperatures near the BDTT's, intergranular fracture prevails in DP microstructures and delamination and intergranular fracture become important for FL microstructures [58, 62]. The apparent grain-boundary (GB) and interface weakening with increasing temperature has yet to be understood as a function of GB morphology or alloy composition.

## Deformation and Fracture Resistance

Studies of local yielding of crack tips indicate that DP structures exhibit small plastic strain near the onset of crack extension and little resistance to crack propagation. Conversely, the FL structures show large crack-tip plastic strains and an increasing resistance to crack propagation [61]. This "R-curve" behavior was explained by the work expended in failing microstructural ligaments formed in the wake of the crack. The ligament failure often occurs by translamellar fracture, and recent quantitative analysis [67] has shown that the increased fracture resistance in FL material at 800°C under a standard loading rate may be related to increased translamellar fracture. The absence of crack-growth resistance behavior in duplex structures is due to a lack of such bridging ligaments.

The 'so-called' ductility-toughness inverse relationship is observed at temperatures below the BDT temperatures [16, 58, 61], Figure 6a. Fine-grain microstructures yield improved tensile properties but low fracture toughness, and the reverse is true for FL material. This relationship is explained by correlating GS, crack nucleation, and the plastic-zone size (PZS) [58, 62]; however, further increases in toughness appear to cease at a GS of 400 μm [16, 61] which is roughly the PZS,  $r_p$ , which was estimated by the relation,  $r_p = \alpha(K/\sigma_y)^2$  where  $\alpha \sim 0.16$ , and using available data [58]. Interestingly, both initiation and saturation toughness,  $K_{Ic}$  and  $K_{max}$ , were observed to increase with decreasing lamellar spacing (l) in FL materials having grains larger than the PZS, Figure 6b, and these are described by the HP type relation,  $K = K_0 + k_\lambda \lambda^{-1/2}$ , [58, 68], where  $K_0$  is the intrinsic toughness. This was explained by increased stresses required for translamellar slip/twinning [58, 68], assuming that changes in strain-to-failure are insignificant. When the GS is smaller than the PZS, however, some experimental results indicate the lamellar spacing effect on the toughness is relatively small, Figure 6b [58]. Nevertheless, the initiation toughness ( $K_{Ic}$ ) values of about 17 MPa√m measured for the small-grained FL materials are much higher than those ( $\sim 10 \text{ MPa}\sqrt{\text{m}}$ ) for DP materials [58].

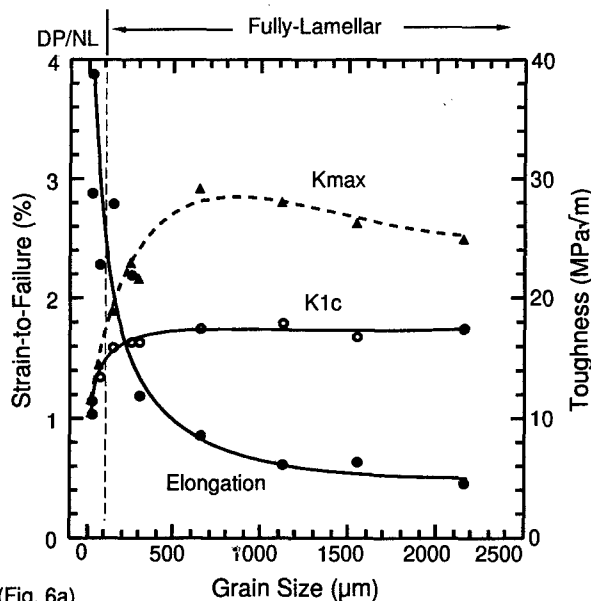


(Fig. 6a)



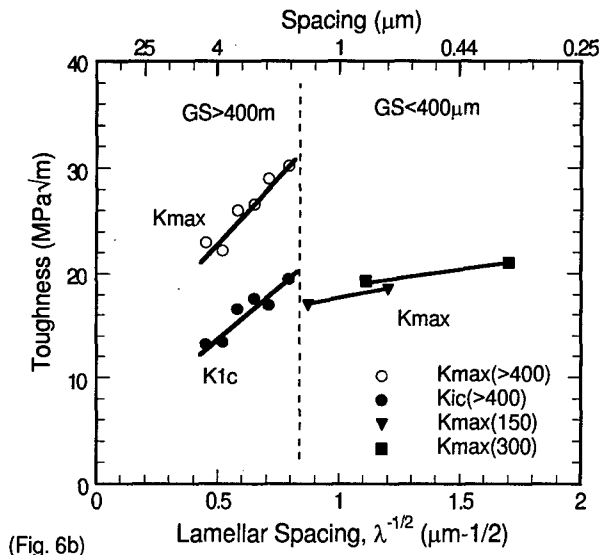


Figure 6. Effects of grain size and lamellar spacing in FL gamma materials: (a) GS vs. ductility and fracture toughness ( $K_{Ic}$  and  $K_{max}$ ) for a lamellar spacing [16, 58, 61]; and b) lamellar spacing vs. fracture toughness in two different GS regimes [58, 68].

Loading rate appears to have a significant effect on the fracture resistance in TiAl alloys. For example, decreases in loading rate were shown to result in increasing fracture resistance as temperature is raised [67]. On the other hand, the resistance decreases significantly at increasing loading rate even at RT [70]. The relative significance in the loading rate effect has not been quantified between DP and FL materials for the rates from  $10^{-5}$ –1 mm/s. Impact resistance has received minimal investigation and, naturally, is the least understood. Several measurements [10, 11, 48, 71] made on smooth impact specimens indicate that the energy associated with RT impact fracture ranges from 1–6 Joule, depending on microstructure and composition. In general, FL material exhibits higher resistance than fine-grained (FG) materials. However, a recent observation on standard-size smooth impact specimens of HIP'ed PM alloy material showed the resistance higher in FG near-gamma material than in FL material at temperatures at or below 200°C [71]. This observation has yet to be validated and explained.

#### Fatigue Resistance

High-cycle-fatigue (HCF) behavior in gamma alloys has been found to be a function of microstructure, defect size, and temperature. The S-N curves obtained on standard hourglass type specimens are fairly flat in general [10, 64] at least up to 600°C for both DP and FL microstructures, with the fatigue strength (FS) at  $10^7$  cycles approaching the ultimate tensile strength (UTS), as shown in Figure 7. At 800°C or higher, however, the fatigue resistance of FL material becomes higher than that of DP material at high cycles, yielding much higher FS, Fig. 7. The above trends are consistent with the greater strength retention at high temperature in FL material.

When tested on uniform-gage-section specimens [72, 73], the HCF responses were found to be of typical S-N curves showing continuous decreases in FS with cycles-to-failure (N) at all

temperatures. The specimen geometry effects indicate that microstructural inhomogeneity may play in reducing the FS, and that the crack-initiation sources active at lower temperatures become less effective as temperature increases. At 870°C, the fatigue life appears to be affected by oxidation [48, 60].

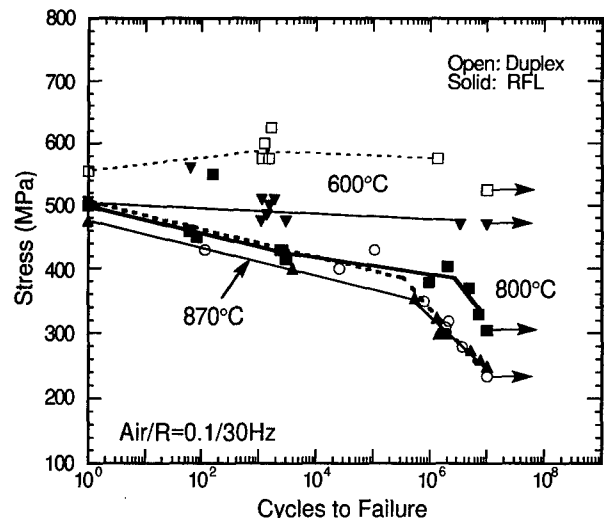


Figure 7. Load-controlled HCF behavior of alloy K5 in air at temperatures between 600° and 870°C measured on standard smooth hourglass fatigue specimens [48, 64].

The fatigue deformation in FL material was found to be planar and interlamellar at temperatures up to 800°C, and the failure modes are predominantly transgranular at RT and increasingly intergranular as temperature increases with lamellar splitting becoming important [64]. Crack initiation was observed to take place in general at the specimen surfaces for DP material and primarily in the interior (near the surface), especially, at elevated temperatures, for FL materials [48]. Unlike in DP material, the crack initiation in FL material was followed by an observable crack-growth stage. However, the relative significance of the crack-growth stage even in FL material with respect to fatigue lives was estimated to be insignificant [48]. Microstructural inhomogeneity (presence of coarse grains or features) often found in DP materials degrades the fatigue properties [73], as it does reduce tensile ductility [56].

The rapid increases in fatigue-crack-growth (FCG) rate with increasing stress intensity or crack length, as determined on precracked tension specimens, are characteristic of these alloys [10, 11, 72, 74–76] and are the greatest concern for structural applications where damage tolerance is the requirement. For crack propagation of existing cracks under cyclic loading conditions, the useful fatigue life is bounded by the FS (defined as the runout stress measured on smooth specimens at  $2 \times 10^8$  cycles) and the threshold values ( $\Delta K_{th}$ ) [72]. Useful fatigue life regions for alloy K5 in a duplex form (12  $\mu$ m GS) and a FL form (a 300  $\mu$ m GS) are compared at RT and 800°C in Figure 8, where the fatigue life for each microstructural form is bounded by its FS and  $\Delta K_{th}$ . From the fatigue behavior, it appears that large-grained material may fail more readily under a given applied stress because initiated cracks may grow rapidly to a size equal to the GS [61, 72]. Under this condition, it appears that finer FL materials may exhibit improved damage tolerance. Recently,

however, fatigue specimens from alloy K5 FL materials (280  $\mu\text{m}$  GS) were tested to show a runout stress of 337 MPa ( $10^7$  cycles) at RT in the presence of 80  $\mu\text{m}$  long defects (notches) which is compared to the FS of 380 MPa and the YS of 480 MPa of the material [77]. Although this result is cautioned by another observation [78] made on the behavior of short cracks in bend specimens of boride-containing FL (GS $\sim$ 200  $\mu\text{m}$ ) Ti-47Al-2Cr-2Nb-0.2B, it indicates that the useful FL GS in alloy K5 can be as large as 300  $\mu\text{m}$ . The relatively large GS may be more forgiving at elevated temperatures, as indicated in Figure 7 and 8, because at elevated temperature the FS value of FL materials becomes relatively higher than for duplex material.

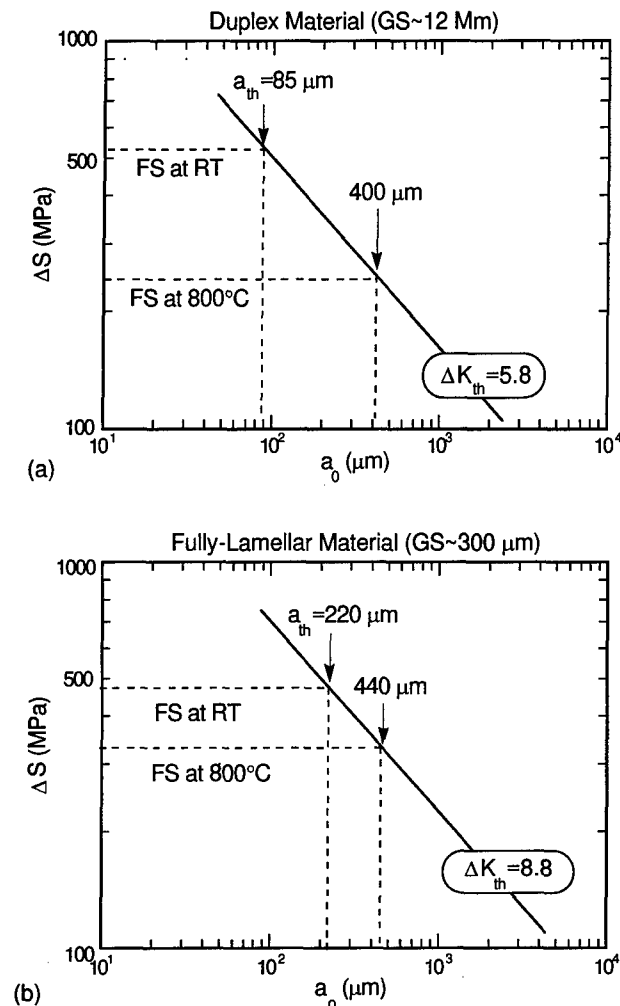


Figure 8. The damage tolerance for an initiated or existing crack of alloy K5 is shown as a function of applied fatigue stress (DS) at two different temperatures in two microstructural forms: (a) a duplex (12  $\mu\text{m}$  GS) and (b) a RFL (300  $\mu\text{m}$  GS). The useful life of the crack is bounded by FS and DTth. Published data on FS [48, 64] and DKth [72] was used.

The FCG rates in FL microstructures are considerably slower than those of DP microstructures at RT as well as elevated temperatures. The shear-ligament bridging, the main toughening mechanism, was found to be less effective under cyclic loading [74], especially, at low stress intensity levels, resulting in lowered

fracture-resistance under cyclic loading compared to monotonic loading. Nevertheless, the threshold ( $\Delta K_{th}$ ) value appears to be proportionally related to the initiation ( $K_{Ic}$ ) value for a given material; however, the relation has not been quantified in spite of its apparent significance.

### Creep Resistance

The creep resistance of TiAl alloys has usually been investigated for the secondary-stage behavior [78]. The secondary-creep resistance is higher for FL than for DP materials at all temperatures [47, 54, 79] and the difference appears to be wider as temperature is raised, Figure 9 [54]. The superior creep resistance for lamellar structures was originally explained in terms of composite-like strengthening [80]. In spite of extensive investigations, however, the fundamental mechanisms in FL material are basically unknown. Nevertheless, the creep behavior resembles that for elevated-temperature strength in the two materials, indicating that the deformation anisotropy in the lamellar structure may play an important role, although the larger grain size in FL may be additive. To date, the individual, or combined, effects of GS and lamellar-spacing have not been clarified, primarily because of poorly controlled microstructural features used in most investigations. The GS in FL material is expected to influence the creep resistance depending upon test condition (temperature and applied-stress) and lamellar spacing, although a recent analysis (made on reported data) predicts an insignificant GS effect [79]. The same report [79] evaluates that Si and W additions effectively enhance creep resistance; however, the individual role has not been isolated in the literature.

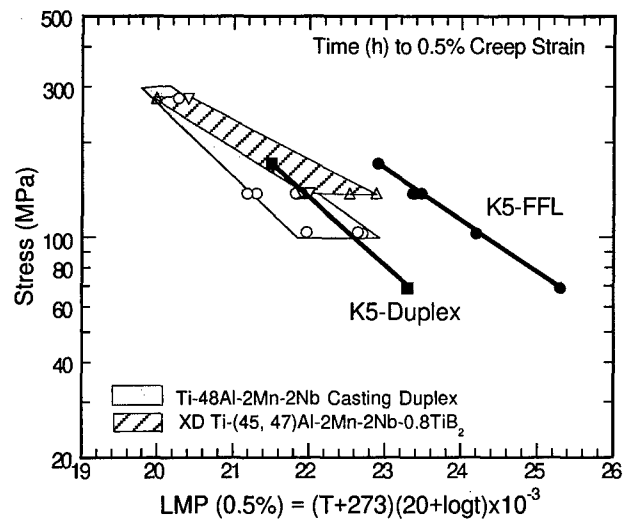


Figure 9. Larsen-Miller plot of time (h) to 0.5% creep strain for alloy K5 in duplex (12  $\mu\text{m}$  GS) and RFL (GS $\sim$ 300  $\mu\text{m}$ ) forms. LMP's for cast alloys [54] are compared. T is in  $^{\circ}\text{C}$ .

Primary-creep strains in TiAl alloys have been observed to be large in general, ranging from 0.2 to over 1 % depending on microstructure and creep condition [47, 48, 54]. In some cases, it can be greater in FL than in DP materials. This would cause serious problems for the structural application of the otherwise creep-resistant FL materials where small creep strains (typically,

0.3% or smaller) are required. Nevertheless, the least attention has been paid to the investigation of this early stage of creep behavior in TiAl alloys. Recent investigations indicate that the primary creep resistance appears to be significantly improved when small amounts of carbon are added and then aged properly [48] and that the thermal instability of the lamellae ( $\alpha_2$  plates) influences the primary creep behavior [81].

Creep-rupture strength in FL material is also higher than in DP material, and rupture life in FL structures is increased by having a serrated grain-boundary (GB) morphology [44]. Small grains (mostly  $\gamma$ ) frequently present in lamellar GB regions are known, though qualitatively, to increase creep rates. The effects of both the GB morphology and intergranular  $\gamma$  grains on the early stages of creep have not been investigated in any detail. The above comments indicate that our knowledge of the specifics of creep behavior in TiAl, particularly, in FL forms, is fragmentary at best.

### Summary of Microstructure-Property Relationships

Discussions made in this section lead to a general conclusion that in TiAl alloys, FL materials exhibit superior properties over DP materials, with possible exceptions of RT ductility and elevated-temperature impact resistance. Grain refinement in FL materials appears to help improve RT strength and ductility, and damage tolerance, especially under cyclic-loading conditions. These improvements, however, may be offset by possible decreases in creep resistance, fracture toughness, and high-temperature fatigue life. Further improvements in specific properties may be attained by alloy chemistry modification as well as microalloying. Most properties at low temperatures appear to be improved by a refined lamellar spacing, although an excessive refinement may weaken GB areas, thereby reducing ductility and creep resistance. A future challenge is to improve the interfacial bond strength (for either, or both, of grain and lamellar boundaries) at RT as well as high temperatures so that crack initiation/propagation is retarded, leading to enhanced damage tolerance.

### Designed Microstructures

#### Optimized Microstructural Features

Microstructural selection can be made by considering the fundamental understanding and the microstructure-property relationships discussed in previous sections. An optimum microstructure may be found within FL materials having the following microstructural features and ranges:

- Microstructure type: Fully-lamellar (FL)
- Average  $\alpha_2/\gamma$  volume ratio of 0.05 to 0.25 with minimum or absence of other phases
- Grain size range: 50-350  $\mu\text{m}$
- Lamellar spacing ( $\lambda$ ):  $\lambda_{\min} < \lambda < 1 \mu\text{m}$  ( $\lambda_{\min}$  is determined: 1) practically, by the maximum cooling rate above which the lamellar structures are disturbed; or 2) theoretically, by the lower limit below which the HP relationship may breakdown; and 3) also, by microstructural instability (coarsening) driven by internal surface energy.)

- Grain boundaries having serrated morphologies with a minimum number, or the absence, of small grains or cellular-type features.
- Textured lamellar structures when anisotropic properties are required.

The above descriptions, however, are rather qualitative, and thus need to be refined by further evaluating mechanical behavior in more detail. Furthermore, the exact magnitude or scales of a specific feature should be component-specific and may have to be determined and/or compromised considering not only the property requirements, but also component configurations and/or dimensions as well as selected processing routes. In the end, however, each feature should be combined to yield a synergistic balance of properties.

In the early stage of our effort in optimizing microstructures, it was realized that production of refined FL grains in Ti-48Al-2Cr-2Nb was not practically feasible and that XD alloys were not suitable as wrought alloys. In this effort, investigations were conducted to develop refined FL microstructures through these designated means [48, 53, 60]: TMTL and RFL by alloy modification, FFL using innovative heat-treatment cycles, TMPL by process control, and TMPAL by the development of a new processing route. Each of these categories is described below.

#### TMTL Microstructures

The thermomechanically treated lamellar (TMTL) microstructures are produced in hot-worked alloys through a short-time alpha treatment [51, 82], and more effectively, by alpha heat treating alloys containing small amounts (0.03-0.5 at%) of boron [48, 60, 83]. In the latter case, the boron is present as relatively fine Ti-borides whose distribution appears to exhaust alpha-grain growth during the alpha heat treatment [48]. Upon cooling, each alpha-grain transforms into a lamellar grain with ragged boundaries, resulting in the fine-grained TMTL microstructures [60, 83], Figure 10. For a given composition, the GS strongly depends on the boron content, Figure 11 [60, 83]; for example, grain refinement begins even with as little as 0.05 at% B and requires only 0.2at% B to obtain grains as fine as 100  $\mu\text{m}$ . The exact processes for the formation of the lamellae and the ragged GB morphology are not understood, although GB borides are likely to control those [48]. TMTL structures form at relatively small undercoolings [48, 83], causing the formation of coarse lamellar spacing, which lowers the strength levels [48]. This is a concern, and two ways to overcome the deficiency are under evaluation: these are further refining lamellar spacing by a faster cooling rate and strengthening by either reducing Al content and/or microalloying with interstitial elements [48]. On the contrary, very small amounts (140 at. ppm) of added boron appear to result in the reduction of lamellar spacing, as observed in cast Ti-47Al-0.014B [84]. This apparent effect of boron in solution needs further investigation.

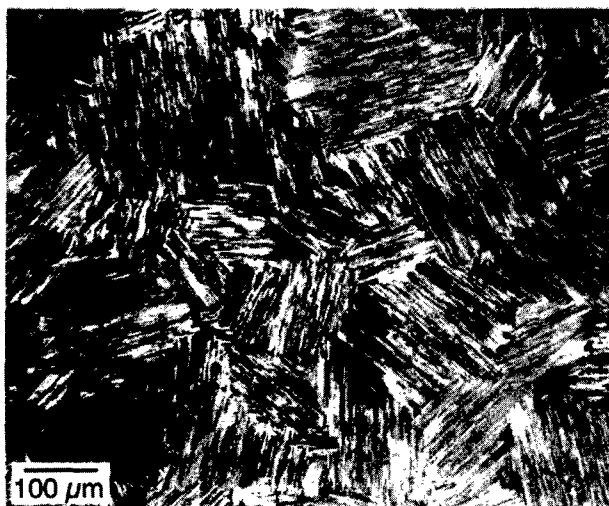


Figure 10. TMT lamellar microstructure in forged Ti-47Al-2Cr-3Nb-0.2W-0.2B produced through an alpha-treatment ( $T_\alpha + 10^\circ\text{C}$  for 1 h) followed by a two-step cooling [48, 60]

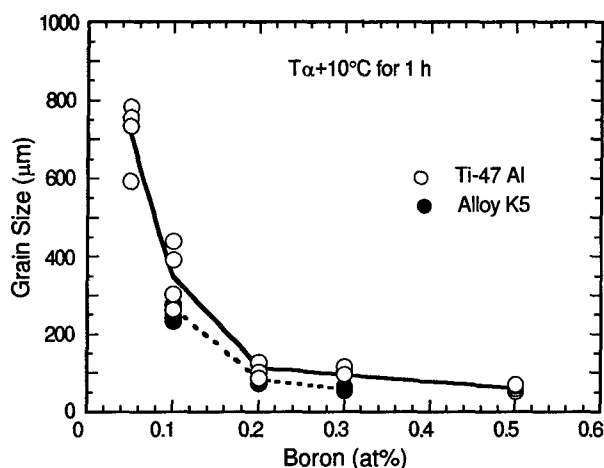


Figure 11. TMT lamellar grain size as a function of boron content in forged gamma TiAl alloys after alpha treatments for one hour [48, 60, 83]

#### RFL Microstructures

Refined fully-lamellar (RFL) microstructures are defined as the relatively fine-grained lamellar microstructures having well-defined grain boundaries produced by a unique cooling scheme. Refining the lamellae and GS has been achieved in two ways: one is to conduct heat treatments in the high-temperature  $\alpha + \beta$  field instead of the  $\alpha$  field [60, 85]; and the other is to conduct a short-time holding in the  $\alpha$  field through a two-step heating [53, 82], both followed by relatively fast (often two-step) cooling.

The first method can be achieved most effectively on a modified alloy which has a relatively lower  $T_\alpha$ , a narrowed  $\alpha$ -field and a wide  $\alpha + \beta$  field. For these RFL treatments, it is important to maintain minimal amounts of  $\beta$  phase in the two phase field in order to have compositional and microstructural uniformity and to

minimize grain boundary cellular reactions. One such example is alloy K5, Ti-46.5Al-2Cr-3Nb-0.2W (at%), with  $T_\alpha = 1320^\circ\text{C}$ ,  $T_{\alpha+\beta} \sim 1335^\circ\text{C}$  and  $T_{\beta} > 1400^\circ\text{C}$  [60, 85]. In this alloy, the volume fraction of  $\beta$  phase in the  $\alpha + \beta$  field increases gradually from near zero with increasing temperature, and thus the lamellar GS is controlled in the range of 100 to 500  $\mu\text{m}$  by increasing annealing temperature, Figure 12. A typical RFL microstructure with a 300  $\mu\text{m}$  GS and 0.5  $\mu\text{m}$  lamellar spacing is shown in Figure 13 where fine  $\gamma$  grains induced by the presence of the  $\beta$  phase exist along the lamellar GB's. The RFL K5 exhibited a considerably improved balances in mechanical properties over fine-grained DP, as well as coarse FL materials [54, 58, 60, 64, 83]. Nevertheless, more work is needed to optimize the RFL material by identifying the effect of alloying elements on the high-temperature phase relations, including phase boundaries and the formation and kinetics of the detrimental GB features shown in Figure 13.

For the second method, some innovative heat treatments involving step heating and/or controlled step cooling [53, 59, 82], were developed recently to refine lamellar grains and lamellae in on hot-worked alloy pieces with various thickness [53, 86]. In this effort made on various alpha-grain sizes (60-400  $\mu\text{m}$ ), the so-called "fine fully-lamellar (FFL)" microstructures consisting of finely-spaced (down to 0.02  $\mu\text{m}$ ) lamellae were obtained.

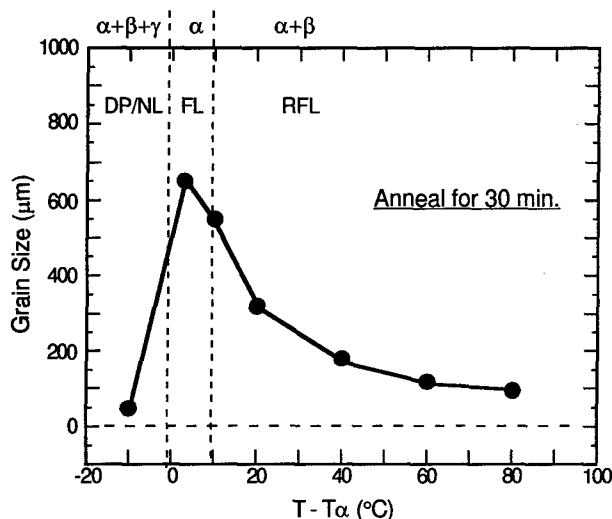


Figure 12. Relationship between phase field range, annealing temperature (with respect to  $T_\alpha$ ) and the resulting FL grain sizes in alloy K5 [60].

#### TMPL Microstructures

Thermomechanically processed lamellar (TMPL) microstructures are produced, when TiAl alloys are extruded at high temperatures [8, 19, 48, 50, 51, 52], resulting in various colony sizes (50-400  $\mu\text{m}$ ) and morphologies, Figure 14. When extrusion takes place at temperatures near the alpha transus ( $T_\alpha$ ), fine, morphologically random TMPL microstructures, with occasional dispersed gamma grains, are produced. Coarse lamellar grains, with a more definite texture, are formed when extruded at temperatures above the  $T_\alpha$  [48]. The formation process and growth kinetics of the TMPL structure and its texturing are not well understood. Compressive

yield stresses measured on TMPL materials ranged from 700-800 MPa for alloy K5 series, and they were thermally stable at 900°C at least up to 390 hrs [48]. However, a recent TEM observation revealed the lamellae morphology becoming unstable under higher-temperature aging conditions [87]. Further increases in strength are expected to be possible by modifying the extrusion parameters and conditions and also through controlled post-extrusion cooling rates. Excellent high-temperature-strength retention was observed as well, Figure 15, where yield strength variations with temperature are compared between TMPL and RFL materials [48]. Production of TMPL materials is also possible through extrusion of prealloyed-powder [52]: This PM/TMPL material exhibited extraordinarily high yield strength levels as high as 1000 MPa [52]. All TMPL materials show good tensile ductility in the range of about 2%. However, these responses have not been demonstrated for large product scales.



Figure 13. A RFL microstructure alloy K5 having a 300  $\mu\text{m}$  GS (see Figure 12) [60]

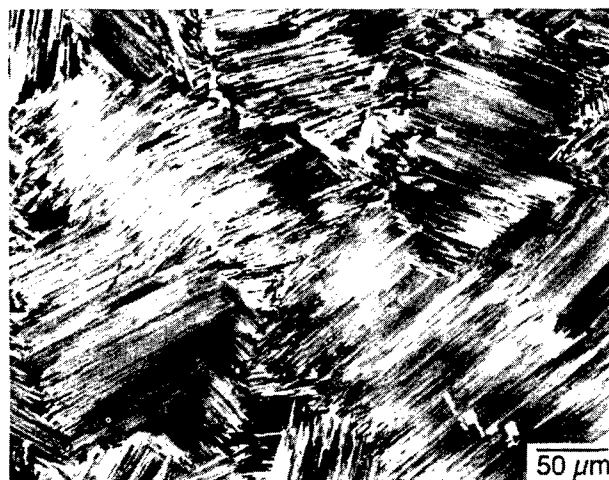


Figure 14. A typical TMPL microstructure in gamma alloys produced by extrusion at  $T \sim T_\alpha$  [48].

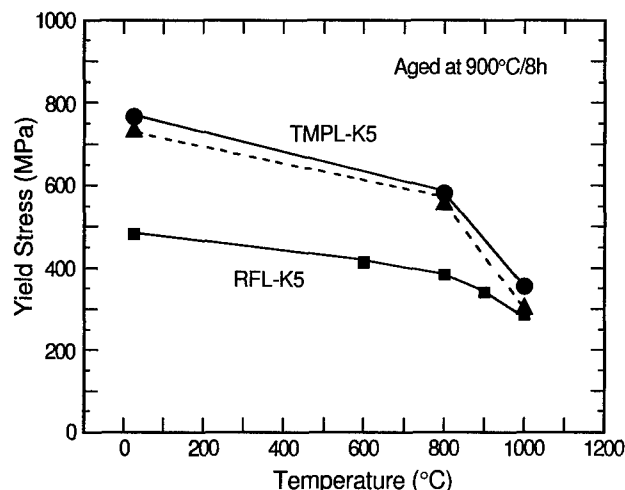


Figure 15. Yield strength variations as a function of temperature in alloy K5 in a TMPL and a RFL conditions [48]

A special group of TMPL microstructures was recently produced through the alpha forging process, wherein forging textures the alpha grains and the lamellar structure is formed in the stress-free alpha matrix during subsequent cooling [48, 88]. The resulting microstructure, called 'TMPAL' microstructure (Figure 16) was found to exhibit a [110] fiber texture with respect to the forging plane [48, 88]. Compression tests on TMPAL materials show that RT yield-strengths range from 620 to 950 MPa, depending upon the GS and composition, in both longitudinal as well as transverse directions. Their high-temperature strength retention is equally impressive with the yield strengths ranging from 500 to 670 MPa at 870°C and 320-600 MPa at 1000°C, Figure 17.

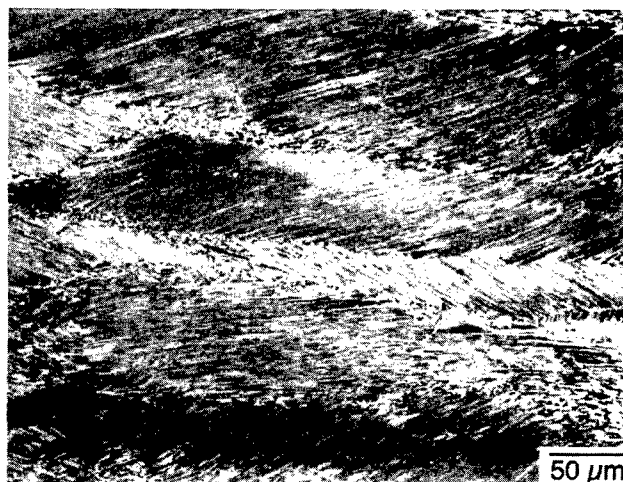


Figure 16. TMPAL microstructure (longitudinal) produced in alloy K5S (K5+ 0.15 at% Si) by a slow alpha-forging [48, 88].

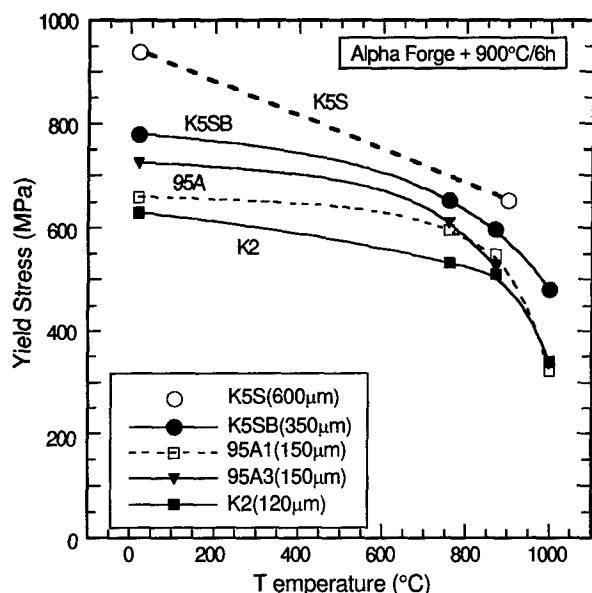


Figure 17. Compressive yield stress variations with temperature in alpha-forged TMPAL gamma alloys having various grain sizes [48, 88]

#### Comparative Evaluation of Designed Microstructures

Figure 18 collectively shows RT yield strength ranges for all designed microstructures against GS. TMTL materials with a GS range of 100-300  $\mu\text{m}$  show RT YS levels between 380 to 500 MPa and good tensile elongation (as high as 2.5 %). RFL materials with GS's ranging from 150-400  $\mu\text{m}$  exhibit yield strengths from 400-550 MPa, with a reasonable balance in mechanical properties; however, their relatively low ductility (0.5-1%) is a concern. By refining the lamellar spacing further, much higher YS levels are expected to be realized in RFL, and this was confirmed in recent compression tests on FFL materials which exhibit RT yield strengths as high as 1000 Mpa [53]. Impressive improvements were observed in TMPL materials, with YS levels reaching as high as 1000 MPa at RT and more than 450 MPa at 1000°C, both with tensile elongations of about 2%. Probably, the most significant property improvements in both strength and its high-temperature-retention were achieved in TMPAL materials produced in laboratory-scale disk forms by alpha-forging [88] experiments, although their ductility has yet to be tested.

#### Other Types of Microstructures

In addition to optimizing lamellar microstructures, it is very important to explore other possibilities of improving mechanical behavior such as ductility, fracture resistance, creep resistance, and the initiation toughness ( $K_{Ic}$ ) and thus  $DK_{th}$  values. Conceptually, this may be achieved through developing other types of microstructures, and by increasing cleavage and interface-bond strength. The effort to enhance the cleavage strength has been virtually nonexistent. With a given cleavage strength, certain types of microstructures may improve the initiation toughness, over current FL materials, by suppressing or retarding the formation of critical-size cracks. These microstructures may be produced through high-rate alpha-decomposition followed by innovative heat treatments [48].

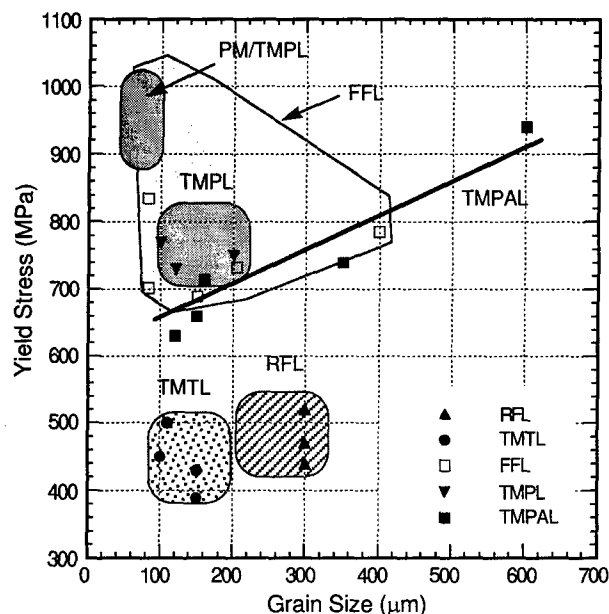


Figure 18. Room temperature yield stress ranges for controlled microstructures are collectively shown as a function of GS (and also lamellar spacing, though not shown here explicitly). The YS range for PM/TMPL materials [52] is also included.

Mounting evidence indicates that there are plenty of unexplored microstructures in gamma alloys that can be generated not only during cooling but also with choice of heating method and alloy chemistry modification. Widmanstätten-type lamellar structures, for example, which require faster cooling rates than for FL materials, are relatively unexplored. Preliminary experiments indicate that further specific-property improvements can be achieved from these microstructures [48]. It is important to realize that exploration of such designed microstructures described above is only just beginning. In order to further control and optimize the microstructures described above and to explore new ones, considerably more work has to be done in: 1) understanding fundamental aspects such as the formation mechanisms and thermal and mechanical stability of lamellar structures; 2) establishing process control, heat-treatment cycles and data bases; and 3) evaluating mechanical behavior including damage tolerance. It may also be important to explore the changes in properties by adding small amounts of Si, C, B, N or O. With the above described modifications, the alloys are expected to exhibit improved balances of properties and increased use temperatures by 50-100°C [8, 48, 60].

#### Component-Specific Alloy Design

##### Process Development

Investigations of workability, texture development and failure mechanisms during hot working have been extensively investigated worldwide for the last six years. On the basis of this fundamental understanding, and through use of concurrently developed process modeling, advances in process development have been realized for primary processing [89, 90, 91], secondary processing [90, 92], and component forming [93, 94]. Ingot

conversion through isothermal forging, extrusion and multistep processing has been commonly practiced, with and without homogenization treatments, on a small scale. Conversion of large ingots (over 250 kg) is now possible through multistep processing, although more details have yet to be understood before production-scale practices can be implemented. Ingot breakdown by non-isothermal forging has been shown to be feasible using a canned workpiece [90]. Pack-rolling technology has been advanced using both forged plates as well as prealloyed powder compacts, with sound sheet of 800x300x1.5 mm currently being produced [92]. The availability of large microstructurally homogeneous starting plates appears to limit production of larger sheet. In general, hot-worked gamma material is highly formable, isothermally, at temperatures as low as 1000°C. Prototype airfoils having 3D twisted geometries have been successfully demonstrated [6, 93], and rolled sheet has been superplastically formed into various complex-shape parts [94]. Forming by hot-die forging and high-rate extrusion, however, is a hurdle for gamma to overcome if wrought gamma components are to be produced more cost-effectively. Ingots having 30 cm diameter are routinely produced by the vacuum arc remelting (VAR) and plasma arc melting (PAM) techniques. Ingots having 35 cm diameter and weighing more than 250 kg have been produced using these techniques, and production of larger ingots by PAM appears to be feasible. The main concerns in scaling-up are ingot cracking, control of chemistry (especially, aluminum level), and compositional variations along the ingot length. In addition, methods to produce ingots having more refined and uniform cast structures are yet to be developed.

#### Component-Specific Microstructures and Properties

Fundamentally, however, the work discussed in this manuscript is just beginning to provide a sufficient understanding of the essential aspects of lamellar structures designed for the components produced through the above processing routes. The full spectrum of mechanical properties have not yet been tested for the materials. Considerably more work has to be done in various aspects such as understanding the lamellar formation mechanisms, thermal and mechanical stability, process control including heat treatment cycles, establishing data bases, property evaluation, and characterization of damage tolerance. By further optimizing the designed microstructures and controlled interstitial elemental additions, properly optimized wrought gamma alloys having enhanced properties are expected to emerge with significantly improved use temperatures (increased by 50-200°C).

#### Summary and Future

In summary, gamma alloys are emerging as important engineering materials. These alloys are a rare example of how the research community, developers, producers, and users can work closely to speed up and steer a materials technology in the right direction. The current casting alloys, basically cast alloys, developed under such remarkable collaborations meet property requirements of selected turbine, as well as automotive, engine parts. With the development of appropriate design methodologies and cost effective manufacturing methods, these alloys are certain to be implemented for selected applications in the near future. However, the research community still faces challenges: designing new and/or improved processing/microstructures for immediate, specific applications and development of new materials/alloys for higher performance and temperature applications.

#### Acknowledgment

The authors acknowledge technical discussions with many researchers, the metallographic assistance of Ms. Sonya Boone, and YWK acknowledges support from the U.S. Air Force Wright Laboratory Materials Directorate, Wright-Patterson AFB, OH under Contract Nos. F33615-91-C-5663 and F33615-96-C-5258.

#### References

1. J. B. McAndrew and H. D. Kessler, *J. Metals* (October, 1956) 1348.
2. M. J. Blackburn and M. P. Smith, *U.S. Air Force Report AFML-TR-79-4056* (1979).
3. M. J. Blackburn and M. P. Smith, *U.S. Air Force Report AFWAL-TR-82-4086* (1982).
4. Y-W. Kim, *JOM*, 41(7) (1989) 24-30.
5. S-C. Huang, *US Patent* 5,076,858 (31 Dec. 1991).
6. Y-W. Kim and D. M. Dimiduk, *JOM*, 43(8) (1991) 40-47.
7. M. Yamaguchi and H. Inui, *Structural Intermetallics*, eds., R. Darolia et al., TMS, PA, (1993), 127-142.
8. Y-W. Kim, *JOM*, 46(7) (1994) 30-39 and 7.
9. C. Austin, *Gamma Titanium Aluminides*, eds., Y-W. Kim, R. Wagner and M. Yamaguchi, TMS, PA, (1995), 21-32.
10. R. Wagner, F. Appel, B. Dogan et al., in *Ref. 9*, 387-404.
11. M. J. Blackburn and M. P. Smith, *US Patent* 4, 294, 615 (1981).
12. S-C. Huang and D. S. Shih, *Microstructure/Property Relationships in Titanium Aluminides and Alloys*, ed. Y-W. Kim and R. R. Boyer, TMS, PA (1990) 105-122.
13. C. Austin, General Electric, Private communication (1993).
14. B. London, et al., in *Ref. 7*, 151-157.
15. D. Larsen and C. Govern, in *Ref. 9*, 405-414.
16. Y-W. Kim, *Acta Metall. Mater.*, 40(1992), 1121-1134.
17. D. S. Shih, S-C. Huang, et al., in *Ref. 12*, 135-148.
18. M. Nazmy, ABB, Private Communication (1995).
19. Y-W. Kim and D. M. Dimiduk, *U.S. Patent*, No. 5,558,729 (17 April 1996).
20. C. Woodward, Y. Song, S. P. Tang, J. H. Xu, O. N. Mryasov, A. J. Freeman and D. M. Dimiduk, *Phil. Mag. B*, 70 (1994) 987-1002.
21. C. L. Fu and M. H. Man, *J. Intermetallics*, 1 (1993) 59.
22. C. Woodward, J. M. MacLaren and S. I. Rao, *J. Mater. Res.*, 7 (1992) 1735.
23. J. P. Simmons, S. I. Rao, and D. M. Dimiduk, *Phil. Mag. A*, (1997), In press.
24. A. Girshick and V. Vitek, *MRS Symp. Proc.*, 364 (1995) 145.
25. D. Farkas, C. G. Schon, and H. Goldenstein, *Acta Mater.*, 44 (1996) 409.
26. C. Woodward and J. M. MacLaren, *Phil. Mag. A*, 74 (1996) 337.
27. P. M. Hazzledine, B. Kad, H. L. Fraser and D. M. Dimiduk, *MRS Symp. Proc.*, 273 (1992) 81-86.
28. G. Hug, A. Loiseau, A. Lasalmonie, *Phil. Mag. A*, 54 (1986) 47.
29. Y. Q. Sun, *Phil. Mag. A*, (1997), In print.
30. S. Sriram, D. M. Dimiduk, P. M. Hazzledine, and V. K. Vasudevan, *Phil. Mag. A*, (1997), In print.
31. F. Appel, U. Sparka, and R. Wagner, 1995, *MRS Symp. Proc.*, 364 (1995) 623.

32. B. Viguier, K. J. Hemker, J. Bonneville, F. Louchet, and J. L. Martin, Phil. Mag. A, 71 (1995) 1295.
33. G. Hug, A. Loiseau, and P. Veyssiere, Phil. Mag. A 57 (1988) 499.
34. A. Huguier and A. Menand, Appl. Surf. Sci. 76/77 (1994) 191.
35. M. A. Stucke, D. M. Dimiduk, and P. M. Hazzledine, MRS Symp. Proc., 288 (1993) 471.
36. K. J. Hemker, B. Viguier, and M. J. Mills, Mater. Sci. & Eng., 164A (1993) 391.
37. N. Bird, G. Taylor, and Y. Q. Sun, MRS Symp. Proc., 364 (1995) 635.
38. Y-W. Kim, Metall. & Mater. Trans. A, (Submitted June 1997).
39. P. W. Wang and V. K. Vasudevan, MRS Symp. Proc., 288 (1993) 229-236.
40. M. Takeyama, T. Kumagai, M. Nakamura and M. Kikuchi, in Ref. 7, 167-176.
41. P. W. Wang, G. B. Viswanathan and V. K. Vasudevan, Metall. Trans. A, 24A (1992) 690-697.
42. Y-W. Kim, MRS Symp. Proc., 213 (1991) 777-793.
43. Y. Yamabe, M. Takeyama and M. Kikuchi, in Ref. 9, 111-129.
44. S. Tsuyama, S. Mitao and K. Minakawa, Mater. Sci. & Eng., A 153 (1992) 451-456.
45. T. Tsujimoto and K. Hashimoto, MRS Symp. Proc., 133 (1989) 391-396.
46. B. Worth, J. W. Worth, and J. E. Allison, Metall. & Mater. Trans. A 26A (1995) 2961-2972.
47. J. Beddoes, W. Wallace, and L. Zhao, International Materials Review, 40 (1995) 197-217.
48. Y-W. Kim, Research in Progress (1993-Present).
- 48a. D. Clemens, P&W, Private communication (1996).
49. A. Nerac-Partaix and A. Menand, Scripta Mater., 35 (1996) 199-203.
50. P. C. McQuay, Y-W. Kim and D. M. Dimiduk, U.S. Patent 5,417,781 (23 May 1995).
51. Y-W. Kim and D. M. Dimiduk, US Patent 5,226,985 (13 July 1993).
52. C. T. Liu et al., in Ref. 9, 679-688.
53. D. M. Dimiduk, Research in Progress (1995-Present).
54. S. Schwenker and Y-W. Kim, in Ref. 9, 985-992.
55. P. McQuay, M.S. Thesis, Wright State Univ. (1992).
56. C. Koeppe, A. Bartels, et al., Metall. Trans. A 24A (1993) 1795-1806.
57. Y-W. Kim, Intermetallic Compounds, eds. M. Yamaguchi and H. Fukutomi, 3rd Japan Int'l SAMPE Symp. (Chiba, Japan, Dec. 7-9, 1993) 1310-1317.
58. Y-W. Kim, Materials Sci. & Eng., A192/193 (1995) 519-533.
59. D. M. Dimiduk, P. M. Hazzledine, T. A. Parthasarathy, S. Seshagari, and M. Mendiratta, Metall. & Mater. Trans. A, (Submitted March 1997).
60. Y-W. Kim, in Ref. 9, 509-524.
61. K. S. Chan and Y-W. Kim, Metall. Trans. A, 23A (1992) 1663-77.
62. Y-W. Kim and D. M. Dimiduk, Proc. JIMIS-7 on High Temp. Deformation and Fracture, (JIM, Nagoya, Japan, 1993) 373-382.
63. P. M. Hazzledine and B. Kad, Mater. Sci. & Eng., A192 (1995) 340-346.
64. J. Kumpfert, Y-W. Kim and D. M. Dimiduk, Mater. Sci. & Eng., A192/193(1995) 465-473.
65. Z. Jin, G. T. Gray III, and Y-W. Kim, Metall. & Mater. Trans. A, (Submitted January 1997).
66. M. G. Mendiratta, Y-W. Kim, and D. M. Dimiduk, MRS Symp. Proc., 288 (1995) 543-548.
67. K. Jata and Y-W. Kim, Materials Sci. & Eng., (Submitted May 1997).
68. K. S. Chan and Y-W. Kim, Acta Metall. Mater., 43 (2) (1995) 439-451.
69. K. S. Chan and Y-W. Kim, Metall. Trans. A, 24A (1993) 113-125.
70. M. G. Mendiratta, R. L. Goetz, and D. M. Dimiduk, Metall. & Mater. Trans. A, 27A (1996) 3903-3912.
71. H. Clemens, These proceedings (1997).
72. J. Larsen, B. Worth, et al., in Ref. 9, 821-834.
73. E. Dolley, MS Thesis, Univ. of Dayton (1995).
74. K. T. V. Rao, Y-W. Kim and R. O. Ritchie, Mater. Sci. & Eng., A192/193 (1995) 474-482.
75. A. W. James and P. Bowen, Mater. Sci. and Eng., A153 (1992) 486-492.
76. P. Bowen, N. J. Rogers and A. W. James, in Ref. 9, 849-865.
77. B. Worth, Private Communication (1997).
78. J. P. Campbell, J. J. Kruzic, S. Lillibridge, K. T. V. Rao, and R. O. Ritchie, Scripta Mater., (Submitted January 1997).
79. T. A. Parthasarathy, M. Mendiratta, and D. M. Dimiduk, Scripta Mater., (Submitted Nov. 1996).
80. J. S. Huang and Y-W. Kim, Scripta Metall., 25 (1991) 1901-06.
81. J. Wang and T. G. Nieh, Acta Mater., (Submitted Nov. 1996).
82. S. L. Semiatin, D. S. Lee, and D. M. Dimiduk, US Letter Patent, S/N 08/437,858 (Filed 8 May 1995).
83. Y-W. Kim and D. M. Dimiduk, US Invention Disclosure (Filed 17 April 1996).
84. P. Maziasz, R. V. Ramanujan, and C. T. Liu, Intermetallics, 5 (1997) 83-95.
85. Y-W. Kim and D. M. Dimiduk, US Patent 5,558,729 (24 Sept. 1996).
86. S. L. Semiatin, V. Seetharaman, D. M. Dimiduk, and K. H. G. Ashbee, Metall. & Mater. Trans. A, (Submitted Dec. 1996).
87. R. V. Ramanujan, P. Z. Maziasz, and C. T. Liu, Acta Mater., 44 (1996) 2611-2642.
88. Y-W. Kim and R. Goetz, Materials Sci. & Eng., (Submitted April 1997).
89. Z. Jin, G. T. Gary III, and Y-W. Kim, Materials Sci. & Eng., (Submitted April 1997).
89. T. Tsujimoto, et al., Materials Transactions JIM, 33 (1992) 989-1003.
90. S. L. Semiatin, in Ref. 9, 509-524.
91. V. Seetharaman and S. L. Semiatin, Metall. & Mater. Trans. A, 27A (1996) 1987-2004.
92. H. Clemens, et al., in Ref. 7, (1993) 205-214.
93. D. U. Furrer, R. R. Hoffmann and Y-W. Kim, in Ref. 9, 611-618.
94. H. Clemens, W. Glatz, et al., in Ref. 9, 717-726.



## Alloying Effects and Deformation Processes in Duplex $\gamma$ -TiAl Alloys

C.T. Forwood, M.A. Gibson, P.R. Miller, C.J. Rossouw and A.J. Morton

CSIRO, Division of Materials Science and Technology,  
Private Bag 33, Clayton South MDC, Victoria 3169, Australia.

### Abstract

Quantitative methods for determining both the state of atomic order in intermetallics and the degree to which additional alloying elements partition between phases and occupy preferred atomic sublattice sites are applied to the  $\gamma$  and  $\alpha_2$  phases in duplex Ti-Al alloys containing small additions ( $\sim 1$  at. %) of different ternary and quaternary alloying elements. These analyses, which are based on quantum electron diffraction effects in high order Laue zones and statistical analysis of X-ray incoherent channelling patterns, are correlated with the effects of alloying elements on mechanical properties. The results are used to provide a preliminary test of a strategy for obtaining cast duplex Ti-Al alloys with improved deformation properties by seeking a balance in the plastic response between the  $\gamma$  and  $\alpha_2$  phases.

### Introduction

High values of stiffness to weight ratio and yield stress combined with good oxidation and creep resistance at elevated temperatures make  $\gamma$ -based Ti-Al alloys attractive as engineering materials for high temperature applications, such as in aerospace and automotive engine components. However, a major factor limiting their practical use is their very low ductility at room temperature.

It has been shown, [1-3], that improvements to mechanical properties can be achieved in alloys with titanium-rich compositions (eg.  $\text{Ti}_{52}\text{Al}_{48}$ ). Such alloys have a two-phase microstructure consisting of a mixture of a minority  $\alpha_2$ -phase, based on  $\text{Ti}_3\text{Al}$  with the ordered hexagonal  $\text{DO}_{19}$  crystal structure, together with a majority  $\gamma$ -phase, based on TiAl with the ordered tetragonal  $\text{L1}_0$  crystal structure. A range of differing morphologies can be established by appropriate heat treatment and optimum ductility is achieved with a duplex microstructure, which typically consists of lamellar ( $\gamma + \alpha_2$ ) grains interspersed with  $\gamma$  grains and a low density of faceted  $\alpha_2$  grains. The lamellar ( $\gamma + \alpha_2$ ) grains comprise alternate  $\gamma$  and  $\alpha_2$  lamellae ( $\sim 1 \mu\text{m}$  across) with interfaces

parallel to  $(111)_\gamma / (0001)_{\alpha_2}$ ; the orientation relationship being given by:  $(111)_\gamma \parallel (0001)_{\alpha_2}$  with  $\langle 1\bar{1}0 \rangle_\gamma \parallel \langle 11\bar{2}0 \rangle_{\alpha_2}$ . The improvement in ductility in these duplex alloys stems from the generation under stress of enhanced deformation twinning and slip dislocation activity in the majority  $\gamma$ -phase, which is considered to arise from the activation of dislocation sources associated with the  $\gamma/\alpha_2$  interfacial defect structure (see [4, 5]). However, ductility is still limited in these alloys and a possible factor contributing to this lack of ductility is that the deformation twins appear to be unable to penetrate the  $\alpha_2$  lamellae [4, 6, 7]. A means of overcoming this limitation on ductility would be to promote slip transfer across the  $\gamma/\alpha_2$  interfaces, thus enabling the transfer of plastic deformation across the  $\alpha_2$  lamellae so that deformation twins could propagate continuously from one  $\gamma$  lamella to the next across the  $\gamma$  matrix. A possible way to achieve this is by balancing the ease of deformation in the two phases i.e. by strengthening the  $\gamma$ -phase and softening the  $\alpha_2$ -phase. This paper describes an investigation into how such a balance may be obtained by modifying the  $\gamma$  and  $\alpha_2$  phases with minor additions of extra alloying elements.

That enhanced ductility can be achieved by alloying with ternary and quaternary elements in the range 1 to 5 at. % is well established, for example V, Cr and Mn have all been found to improve room temperature ductility (see [8-10]). The exact manner by which these extra alloying elements within the two alloy phases affect properties such as: electron bonding, phase equilibria, stacking fault energy, twin boundary energy, antiphase boundary energy and resistance to dislocation motion is at present unclear. However, such effects will depend strongly on: (a) the extent to which the atoms of each alloying element are partitioned between the  $\gamma$  and  $\alpha_2$  phases, (b) the type of crystal lattice sites that are occupied by the additional alloying atoms (i.e. the extent to which alloying elements favour Ti or Al sublattice sites in the  $\gamma$  and  $\alpha_2$  phases), and (c) the degree to which atomic ordering within the two phases is affected by the presence of the extra alloying elements; (see [11, 12]).

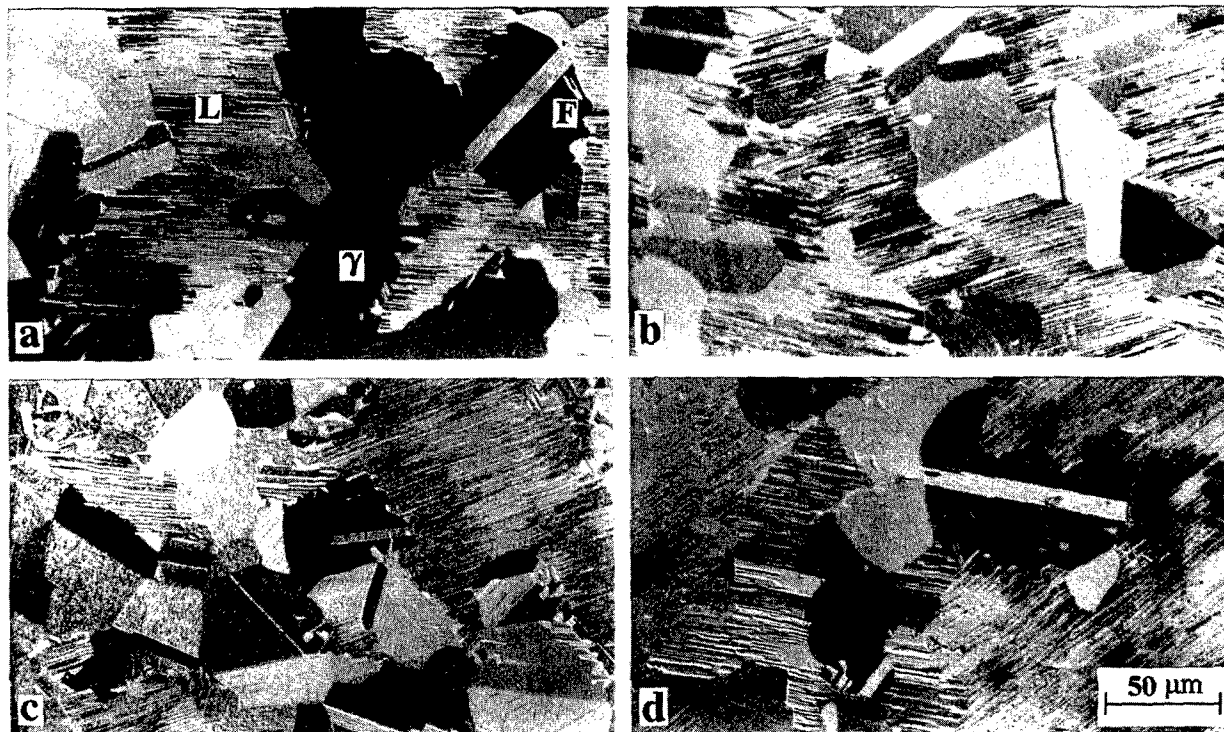


Figure 1. Optical micrographs of (a)  $\text{Ti}_{32}\text{Al}_{48}$ , (b)  $(\text{Ti}_{32}\text{Al}_{48})_{99}\text{Zr}_{1.0}$ , (c)  $(\text{Ti}_{32}\text{Al}_{48})_{99}\text{Cr}_{1.0}$  and (d)  $(\text{Ti}_{32}\text{Al}_{48})_{98}\text{Zr}_{1.0}\text{Cr}_{1.0}$  showing typical duplex microstructure of all alloys. Examples of  $\gamma/\alpha_2$  lamellar region are labelled L, equiaxed  $\gamma$  grains are labelled  $\gamma$ , and faceted  $\alpha_2$  grains are labelled F.

In the case of atomic site occupancy, Morinaga *et al* [11] argue that ductility is improved when alloying additions cause an enhancement of  $d$ - $d$  bonding at the expense of  $p$ - $d$  bonding, and have shown, using atomistic calculations, that this occurs only for certain atomic species (e.g. V, Cr and Mn) and only when they occupy Al sublattice sites rather than Ti sublattice sites. On the basis of this concept, a possible way of strengthening the  $\gamma$ -phase would be by the addition of an alloying element that (i) partitions preferentially into the  $\gamma$ -phase, (ii) preferentially occupies Ti sublattice sites so as not to reduce  $p$ - $d$  bonding and (iii) maintains atomic order within the  $\gamma$ -phase; and conversely a possible way of softening the  $\alpha_2$ -phase would be by the addition of an alloying element that (iv) partitions preferentially into the  $\alpha_2$ -phase, (v) preferentially occupies Al sublattice sites so as to enhance  $d$ - $d$  bonding at the expense of  $p$ - $d$  bonding and (vi) maintains atomic order within the  $\gamma$ -phase. The need to retain atomic order in the majority  $\gamma$ -phase is to ensure that the desirable properties of the  $\gamma$ -based alloys are not degraded. This paper describes preliminary results from a set of experiments aimed at examining whether the application of such an alloying strategy can lead to improved deformation properties in cast duplex alloys. This involved: determining the state of atomic order, interphase partitioning, and atomic site occupancy in duplex  $(\text{Ti}_{32}\text{Al}_{48})_{99}\text{X}_{1.0}$  alloys for a series of ternary additions  $\text{X} = \text{V}$ , Cr, Mn, Ga, Zr, Nb, Mo, Hf, Ta, and W; then selecting two alloying elements, one which satisfies (i) to (iii) above with the other satisfying (iv) to (vi); then preparing alloys with these elemental additions, mechanically testing them in tension to determine whether they exhibit enhanced ductility and finally examining sections from the tensile specimens by transmission electron microscopy to seek evidence for slip transfer across  $\gamma/\alpha_2$  interfaces and to characterise the process.

### Experimental

Titanium aluminides with nominal compositions  $(\text{Ti}_{32}\text{Al}_{48})_{99}\text{X}_{1.0}$ , containing a single ternary component from the series X (above) and selected quaternary alloys  $(\text{Ti}_{32}\text{Al}_{48})_{100-n}\text{Zr}_m\text{Cr}_n$  were prepared as 30 g

ingots by argon-arc melting followed by hot isostatic pressing under argon at 130 MPa for 2 hours at 1573 K. The ingots were then heat treated for 6 hours at 1473 K under argon at atmospheric pressure to establish a  $\gamma/\alpha_2$  duplex structure. Sections were cut from each ingot by electric discharge machining (EDM), mechanically polished and etched for examination by optical microscopy. This showed that in all the duplex alloys examined the microstructure was essentially the same, consisting of lamellar grains of fine alternate  $\gamma/\alpha_2$  lamellae ( $\sim 1 \mu\text{m}$  wide) separated by larger equiaxed  $\gamma$  grains ( $\leq 200 \mu\text{m}$  across) together with a relatively low density of ( $\leq 20 \mu\text{m}$ ) faceted  $\alpha_2$  grains, and typical examples are shown in Fig. 1. Electro-polished discs 3 mm in diameter were prepared for examination in a Philips CM30 analytical electron microscope operating at 200 kV. Tensile test specimens were cut from ingots of the quaternary and selected ternary alloys by EDM, mechanically polished to a  $1.5 \mu\text{m}$  finish and tested in tension to failure at a strain rate of  $10^{-3} \text{ s}^{-1}$  with an Instron 1115 using an extensometer to measure true plastic strain. Electro-polished discs 3 mm in diameter were prepared from the tensile specimens and examined by transmission electron microscopy (TEM) in a JEOL 2000EX microscope operating at 200 kV.

### Atomic Order

The state of atomic order in the  $\gamma$ -phase of each alloy was determined from convergent beam electron diffraction (CBED) patterns using the method recently developed by Rossouw *et al* [13]. The order parameter,  $P$ , is obtained from measurements of the relative separation of different branches of the dispersion surface as observed in quantum state rings present in diffracted electron beams of higher order Laue zones (HOLZ) when the crystal is orientated at an appropriate symmetrical zone axis orientation. Figure 2 shows  $n = 2$  HOLZ reflections from a  $[110]$  experimental CBED pattern of the  $\gamma$ -phase in the binary alloy  $\text{Ti}_{32}\text{Al}_{48}$  together with five calculated sets of reflections corresponding to five different degrees of atomic order  $P$ . Experimentally, three distinct rings of contrast are visible and the

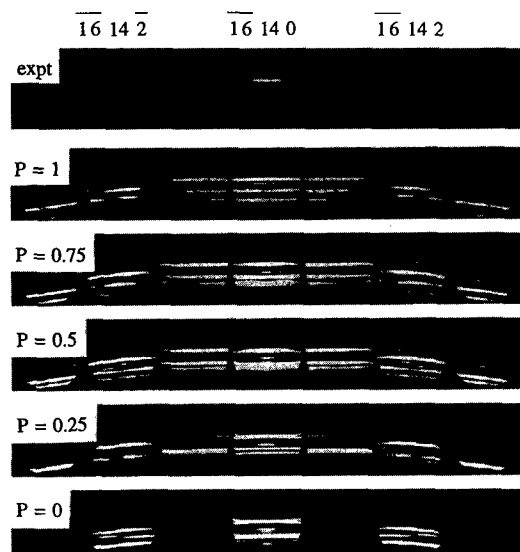


Figure 2.  $\text{Ti}_{32}\text{Al}_{48}$  [110]  $n = 2$  HOLZ beams compared with theory for order parameters as indicated.

calculations indicate that, although the position of the third (outer ring) is relatively insensitive to order, the first (inner) and second (middle) rings come together as the order parameter  $P$  decreases and merge completely when  $P = 0$ . The state of order of the alloy is simply determined by comparing calculated and experimentally measured values of the relative separation of the outer HOLZ ring from the middle and inner rings. It was found for all the ternary alloys, to an accuracy of  $\pm 10\%$ , that the  $\gamma$ -phase was fully ordered, within the constraint that excess Al atoms due to non-stoichiometry occupy antisite positions on available Ti sites. Thus conditions (iii) and (vi), that atomic order be maintained in the  $\gamma$ -phase, are satisfied for all the ternary elements.

### Interphase Partitioning

Although energy dispersive X-ray (EDX) analysis has limited reliability for determination of exact compositions (particularly for elements such as Al where low energy characteristic X-rays are generally quite strongly absorbed within the specimen), it can be applied with greater confidence to measure the relative partitioning of extra alloying elements between the  $\gamma$  and  $\alpha_2$  phases, since such measurements are not critically dependent on the absolute values of relative  $k$ -factors [14]. With absorption being fully taken into account [15] the results giving the relative partitioning of each ternary element  $X$  are shown in Fig. 3 as the ratio of the ternary element content in the  $\gamma$ -phase to that in the  $\alpha_2$ -phase. It can be seen that Ga (ratio 1.4), Zr (ratio 1.3) and Nb (ratio 1.1) partition preferentially into the  $\gamma$ -phase, whilst other ternary additions have a tendency to segregate preferentially into the  $\alpha_2$ -phase, with the  $\gamma/\alpha_2$  ratio reducing to 0.66 for Mo.

### Atomic Site Occupancy

Site occupancy of additional ternary elements in the  $\gamma$ -phase has been investigated by several workers using ratio techniques in conjunction with X-ray intensity measurements and atom location by channelling enhanced microanalysis (ALCHEMI), [8, 16-19]. However, the results obtained have not been entirely consistent, e.g. V additions have been shown in one case to strongly favour Al sublattice sites and in another case to strongly favour Ti sublattice sites. A likely reason for such discrepancies lies with the effects that interaction delocalisation can

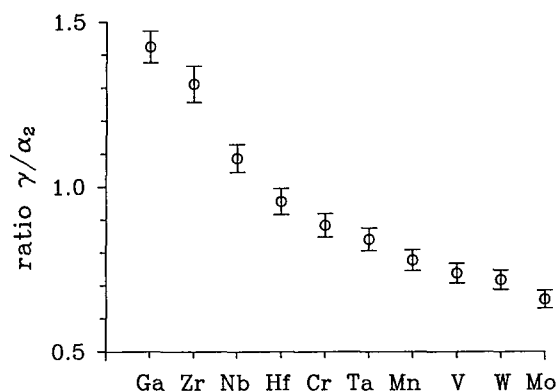


Figure 3. Composition ratio of ternary elements in  $\gamma$ -phase compared with  $\alpha_2$ -phase.

have on ALCHEMI when the ratio method is used, particularly for the case of relatively low energy characteristic X-rays from Al, and the inability of the ratio method to provide reliable estimates of the errors incurred which, in some situations can be exceptionally large [14]. It has, however, been demonstrated that the problem of determining site occupancies with realistic estimates of experimental error for ternary additions in both the  $\gamma$  and  $\alpha_2$  phases is readily overcome by using a statistical multivariate method for ALCHEMI [14, 19]. This method makes the single assumption that the measured X-ray counts,  $N_i^{(s)}$ , from additional substitutional atomic species,  $x$ , may be expressed as a linear combination of the host atom counts,  $N_i^{(h)}$ , for each channelling condition,  $s$ . For Ti-Al based alloys containing an added element,  $x$ , this is expressed as:

$$N_x^{(s)} = a_{Ti,x} N_{Ti}^{(s)} + a_{Al,x} N_{Al}^{(s)} + C_x \quad (1)$$

where  $a_{Ti,x}$ ,  $a_{Al,x}$  and  $C_x$  are coefficients to be determined and  $N_{Ti}^{(s)}$  and  $N_{Al}^{(s)}$  are the characteristic X-ray counts recorded from Ti and Al atoms respectively.  $C_x$  is a constant which is included to account for delocalisation effects, errors in background subtraction and to allow for the possibility of the added ternary atoms occupying interstitial sites. In the multivariate method the total number,  $S$ , of channelling conditions that is used is deliberately made large, so that eqn. (1) is satisfied with  $(S-3)$  degrees of freedom. The coefficients  $a_{Ti,x}$ ,  $a_{Al,x}$  and the constant  $C_x$  (together with their uncertainties  $\Delta a_{Ti,x}$ ,  $\Delta a_{Al,x}$  and  $\Delta C_x$ ) which best fit eqn. (1) for all  $S$  sets of experimental data are then obtained using standard multivariate analysis and chi-squared ( $\chi^2$ ) minimisation techniques, where

$$\chi(x)^2 = \sum_s \left| \frac{\sum_i a_{i,x} N_i^{(s)} + C_x - N_x^{(s)}}{\sigma_s(x)} \right|^2, \quad i = Ti, Al \quad (2)$$

and  $\sigma_s$  is the total noise contribution for each channelling condition which can be estimated from the measured X-ray counts recorded for the ternary atoms, each of the host atoms and background subtraction.

From the fitted values of  $a_{Ti,x}$ ,  $a_{Al,x}$  and  $C_x$  and the concomitant values of  $\Delta a_{Ti,x}$ ,  $\Delta a_{Al,x}$  and  $\Delta C_x$  the ternary atom concentration and the fractional distribution of ternary atoms on each host site can be readily determined together with reliable estimates of experimental error [14]. The reliability for each experimental case examined comes from testing the validity of the assumption made for the model in eqn. (1) in the following way: The model is adequate if the value of  $\chi_R^2$  ( $\chi^2$  divided by the number of degrees of freedom,  $S-3$ ) is close to unity; and inadequate if  $\chi_R^2$  is significantly different from unity, provided the number of degrees of freedom is large (ie. if  $S$  is large).

The experimental data is obtained using the Philips CM30 electron microscope with specimens mounted in a Gatan stage operating at 100 K. A 0.2  $\mu\text{m}$  electron beam with a 1.8 mrad total convergence angle is focussed onto the particular area of the  $\gamma$  or  $\alpha_2$ -phase required for analysis. With the beam set along a zone axis, it is rocked about two orthogonal axes through angles of  $\sim 160$  mrad by a beam rocking facility which is computer controlled with a pre-set number of pixels and with pre-set acquisition time. A full energy dispersive spectrum is recorded for each pixel from which the variation in characteristic X-ray emission from both types of host atoms, the additional alloying atoms (ternary or higher order) and background are selected within separate energy windows and displayed as 79 x 58 pixel X-ray incoherent channelling patterns (ICPs), each corresponding to a total of  $S = 4582$  channelling conditions which yields 4579 degrees of freedom for subsequent multivariate analysis.

#### $\gamma$ -Phase Analysis

Projected structures of the idealised stoichiometric  $\gamma$ -phase L1<sub>0</sub> tetragonal structure ( $a = 3.986$  Å,  $c/a = 1.02$  [21]) along different zone axes are shown in Fig. 4. It can be seen from the projections in Figs. 4(a) & 4(c) along  $[11\bar{2}]$  and  $[110]$  that these zone axes represent the most favourable incident electron beam directions for ICP analysis, because they distinguish best between Ti and Al host sites as well as between tetrahedral and octahedral interstitial sites; whereas the  $[11\bar{1}]$  and  $[100]$  projections of Figs. 4(b) & (d), project interstitial sites either totally or partially onto both Al and Ti sites. Figures 5(a) & (b) show examples of calculated and experimental ICPs obtained from Al and Ti counts and from the ratio of Al to Ti counts using the  $[110]$  zone axis, that are typical of all ternary alloys. Figure 5(c) shows similar ICPs for the ternary element counts obtained from the Ga, Hf and Mo

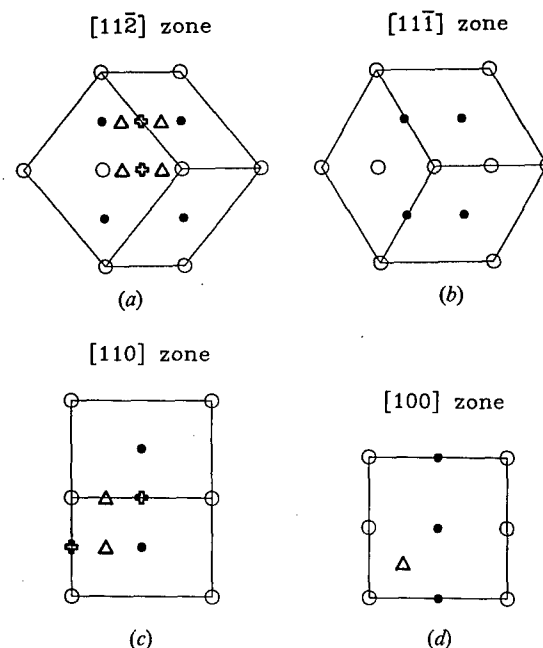


Figure 4. Projected atomic structures (Al large open circles, Ti small filled circles) of  $\gamma$ -phase for the following zone axes: (a)  $[11\bar{2}]$  (b)  $[11\bar{1}]$  (c)  $[110]$  and (d)  $[100]$ , where the edges of the tetragonal cell are shown, with the  $c$ -axis projected along the horizontal direction. Open triangles indicate tetrahedral interstitial sites, open crosses indicate octahedral sites.

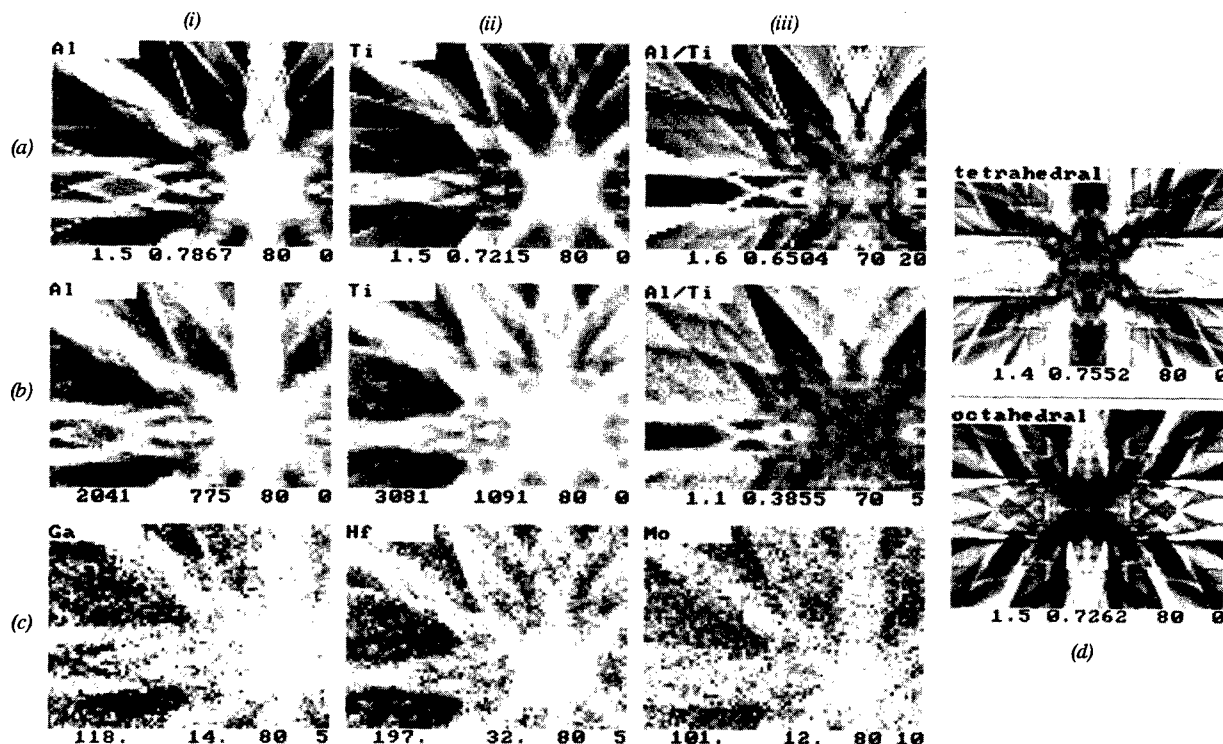


Figure 5. (a) Calculated and (b) experimental  $[110]$  ICPs for  $\gamma$ -phase (i) Al (ii) Ti and (iii) ratio Al/Ti. (c) Ternary atom ICPs showing (i) Ga (ii) Hf and (iii) Mo. (d) Calculated ICPs for tetrahedral and octahedral interstitial sites.

ternary alloys. From visual inspection of the ternary ICP contrast it is immediately evident that Ga occupies predominantly Al sites (i.e. the Ga pattern in Fig. 5(c) is similar to the calculated and experimental Al patterns in Figs. 5(a) and (b)), Hf occupies predominantly Ti sites (i.e. the Hf pattern in Fig. 5(c) is similar to the Ti patterns in Figs. 5(a) and (b)), whilst Mo occupies both Al and Ti sites (i.e. the Mo pattern of Fig. 5(c) is similar to a linear combination of Al and Ti ICPs in Figs. 5(a) and (b)).

The calculated octahedral site and tetrahedral site ICPs in Fig. 5(d) show no correlation with the experimental ICPs for the ternary additions and, since differences in ICP symmetries are related to differences in the local environment of the site of interaction within the unit cell [14], this provides a direct indication that the ternary atoms are accommodated substitutionally. In fact Figs. 5(d) illustrate a simple test for checking whether additional atoms are located on interstitial or substitutional sites i.e.: If the crystal is aligned down a zone axis where host sites are aligned and distinguished in projection from interstitial sites, then the X-ray emission rate for an interstitial atom will decrease as the crystal is tilted into the exact zone axis orientation, compared with an increase for a substitutional atom. From information obtained in this way it was concluded that the atoms of all the additional alloying elements were accommodated substitutionally.

The results obtained for atomic site occupancy in the  $\gamma$ -phase using full numerical analysis of the experimental data contained in ICPs for the different ternary alloys are summarised in Fig. 6. It can be seen from the combined results of Figs. 6 and 3 that the ternary alloying additions which satisfy conditions (i) to (iii) for strengthening the  $\gamma$ -phase (i.e. additions which preferentially both occupy Ti sublattice sites and partition into the  $\gamma$ -phase) are Hf, Zr and Nb. Of these Zr best satisfies the conditions and was therefore selected as a potential strengthener for the  $\gamma$ -phase.

### $\alpha_2$ -Phase Analysis

Projected structures of the idealised stoichiometric  $\alpha_2$ -phase  $\text{DO}_{19}$  hexagonal structure ( $a = 5.807 \text{ \AA}$ ,  $c/a = 0.83$ ) along different zone axes shows that, although Ti and Al sites are adequately resolved in

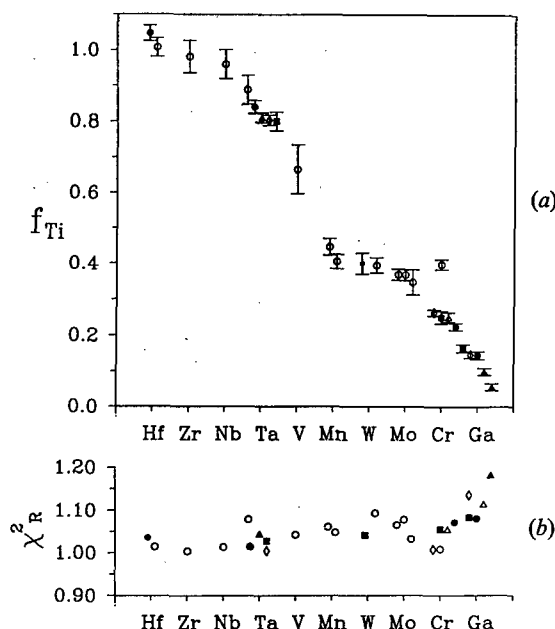


Figure 6. (a) Fraction of ternary atoms on Ti sites, for  $\gamma$ -phase. Error bars indicate one standard deviation. (b)  $\chi_R^2$  for analyses.

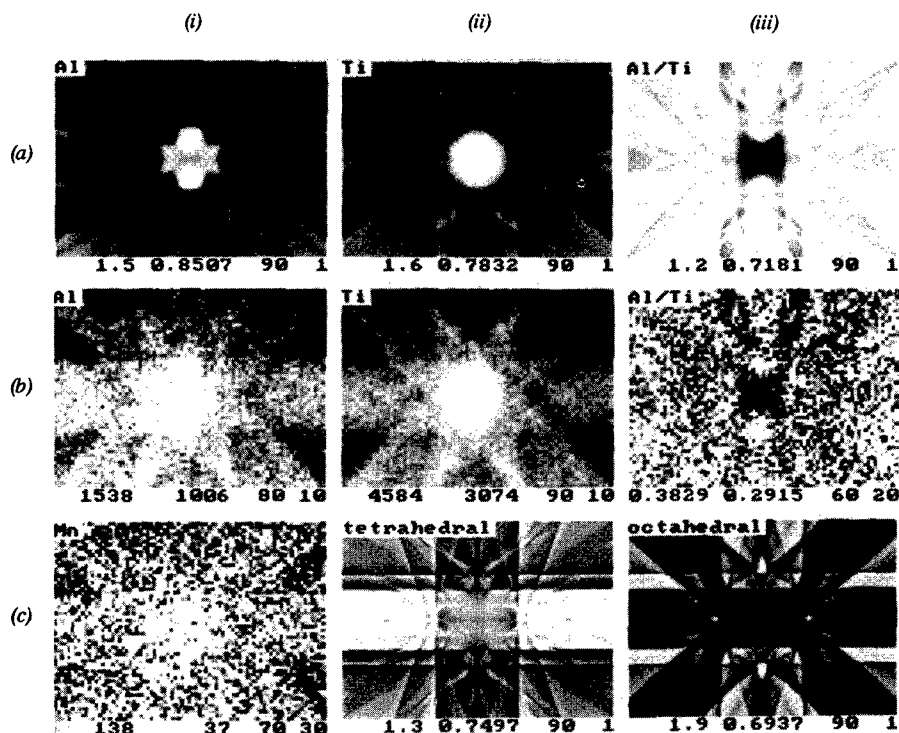


Figure 7. (a) Calculated  $[11\bar{2}3]$   $\alpha_2$ -phase ICPs for Al, Ti and ratio Al/Ti. (b) Experimental ICPs from Mn alloy, showing Al, Ti and ratio Al/Ti. (c) Mn ICP is shown in (i), compared with ICPs for (ii) tetrahedral and (iii) octahedral sites.

Table 1. Tensile Properties of  $Ti_{52}Al_{48}$  with Zr and Cr Additions

	$Ti_{52}Al_{48}$			+Zr <sub>1.0</sub>			+Zr <sub>2.0</sub>			+Zr <sub>3.0</sub>		
	Yield (MPa)	UTS (MPa)	$\epsilon_p$ %	Yield (MPa)	UTS (MPa)	$\epsilon_p$ %	Yield (MPa)	UTS (MPa)	$\epsilon_p$ %	Yield (MPa)	UTS (MPa)	$\epsilon_p$ %
$Ti_{52}Al_{48}$	377	404	0.51	472	520	0.78	524	582	0.81	531	501	0.26
+Cr <sub>1.0</sub>	384	448	0.94	511	572	0.87	586	659	1.15	601	612	0.45
+Cr <sub>2.0</sub>	516	573	0.81	531	662	1.88	583	669	1.13	560	621	0.68
+Cr <sub>3.0</sub>	687	612	0.25	481	543	0.66	522	556	0.46	542	544	0.32

Yield denotes 0.2% Proof Stress; UTS denotes Ultimate Tensile Stress;  $\epsilon_p$  % denotes true plastic strain.

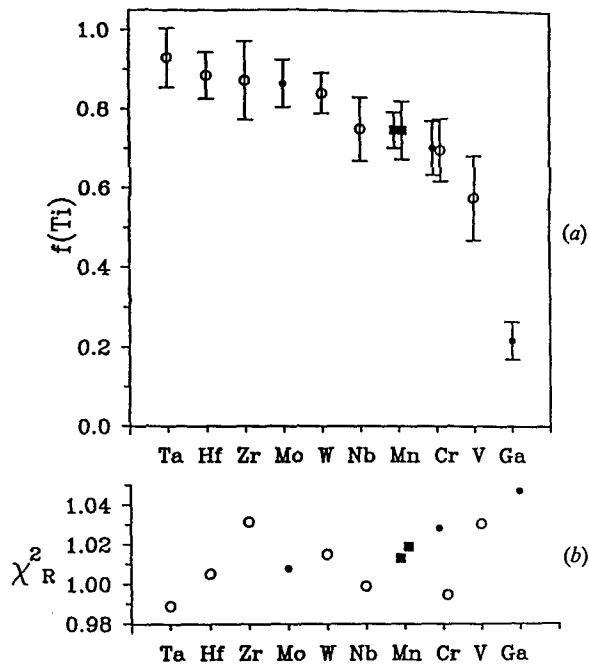


Figure 8. (a) Distribution of ternary atoms on Ti sites for  $\alpha_2$ -phase. Error bars indicate one standard deviation. (b)  $\chi_R^2$  values for each measurement.

[0001] and  $[11\bar{2}0]$  projections, octahedral and tetrahedral sites are not. This problem is overcome in the  $[1\bar{1}23]$  projection and this zone axis proved to be a favourable incident electron beam direction for ICP analysis. Figures 7(a) & (b) show examples, typical of all ternary alloys, of calculated and experimental ICPs obtained from Al, Ti and Al/Ti counts using the  $[1\bar{1}23]$  zone axis. Figure 7(c)(i) shows the ICP for the ternary element counts obtained from the Mn ternary alloy and, although this experimental ICP is very noisy, numerical ALCHEMI analysis of the data returns a value of  $75\% \pm 5\%$  for the Mn atoms on Ti sublattice sites. The calculated tetrahedral and

octahedral site ICPs in Fig. 7(c)(ii) & (iii) respectively show no correlation with the Mn ICP which indicates that the Mn atoms are accommodated substitutionally. As for the  $\gamma$ -phase, it was found that all the additional alloying elements were accommodated substitutionally in the  $\alpha_2$ -phase.

The results obtained for atomic site occupancy in the  $\alpha_2$ -phase using full numerical analysis of the experimental data contained in ICPs for the different ternary alloys are summarised in Fig. 8. It can be seen from the combined results of Figs. 8 and 3 that there are no ternary alloying additions which fully satisfy conditions (iv) to (vi) for softening the  $\alpha_2$ -phase (i.e. additions which preferentially both occupy Al sublattice sites and partition into the  $\alpha_2$ -phase), but V, Cr and Mn come close. Of these Cr was selected as a potential softener for the  $\alpha_2$ -phase.

#### Mechanical Testing

A series of alloys based on the binary composition  $Ti_{52}Al_{48}$  with additions (up to 3 at.%) of Zr, Cr and their combinations were prepared and tested to failure in tension, as described previously. The results are summarised in Table 1, where it can be seen: that the ternary addition of Zr up to 2 at.% acts as a strengthener (increasing both yield and ultimate tensile strength) and as a ductiliser but above 2 at.% mechanically degrades the alloy; that the ternary addition of Cr acts as a moderate strengthener and as a ductiliser up to 2 at.% (peaking between 1 and 2 at.%); and that the quaternary addition of Zr and Cr in combination results in even higher strength and ductility with the optimum occurring for the addition of Zr + Cr, each between 1 and 2 at.%. Thus the results are not inconsistent with that expected on the basis of satisfying conditions (i) to (vi). In this regard, for the alloys contained in Table 1, the microstructure observed by optical microscopy did not change appreciably from that shown in Fig. 1 for compositions with single or combined additions up to 4 at.%. However, for compositions with combined additions beyond 4 at.% a fine distribution of small particles ( $\leq 10 \mu m$ ) of  $\beta$ -phase appear in the microstructure.

When the interphase partitioning and the atomic site occupancy of Zr and Cr were measured for the Zr + Cr quaternary alloy, it was found that, within the limits of experimental error, the results for Zr and Cr were essentially unchanged from those found for the ternary alloys.

Thus in the quaternary Zr + Cr alloy, the ability of Zr and Cr to satisfy the conditions (i) to (vi) as a potential strengthener of the  $\gamma$ -phase and as a potential softener of the  $\alpha_2$ -phase is unchanged.

### Slip Transfer

Figure 9 is an electron micrograph from a section close to the fracture surface of a binary  $\text{Ti}_{52}\text{Al}_{48}$  tensile test specimen showing a typical example of deformation twinning in a  $\gamma$ - $\alpha_2$  lamellar region of this duplex alloy. It can be seen that a deformation twin, having propagated through a  $\gamma$  region, is arrested at the  $\gamma/\alpha_2$  interface being unable to penetrate the neighbouring  $\alpha_2$  grain, with the result that the twinning partials (identified as  $30^\circ 1/6 \langle 112 \rangle$  dislocations) pile up at the interface and generate a concentration of elastic strain ahead of the pile-up. This behaviour is contrasted with that shown in Fig. 10 which is a typical example of deformation twinning that occurs in the Zr ternary and Zr + Cr quaternary duplex alloys which exhibit enhanced strength and ductility. It can be seen that, in this case deformation twins are not held up at  $\gamma/\alpha_2$  interfaces but propagate across  $\alpha_2$  lamellae from one  $\gamma$  grain to the next. Although no statistical analysis has been made, it was concluded, from a survey of results of the type shown in Figs. 9 & 10 in alloys with the compositions of Table 1, that slip transfer across  $\gamma$ - $\alpha_2$  lamellar structures is noticeably more prevalent in those quaternary and ternary alloys which exhibit increased strength and ductility. Thus the slip transfer results are compatible with that expected from satisfying conditions (i) to (vi).

An example of slip transfer of  $30^\circ 1/6 \langle 112 \rangle$  twinning partial dislocations across a  $\gamma/\alpha_2$  interface, which enables the dislocation reactions that govern the process to be identified, is shown in Fig. 11. In this micrograph an  $\alpha_2$  lamella (viewed almost edge-on) separates two identically oriented  $\gamma$  grains. The upper  $\gamma$  grain contains several deformation twins of which that labelled *ab* will be considered first with reference to the schematic diagram of Fig. 12. In Fig. 12 the crystallography has been determined by stereographic analysis and the Burgers vectors have been determined in both sign and magnitude by the method of image matching [22], with the sense of motion being determined unambiguously by the sign that has been identified for the twinning dislocations. The crystallographic transformation relating the  $\gamma$  and  $\alpha_2$  phases was determined from the measured relationships between non-coplanar reciprocal lattice vectors in electron diffraction

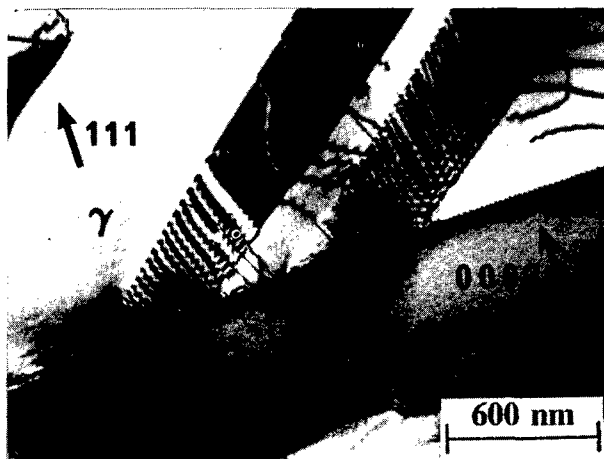


Figure 9. Electron micrograph of deformation twinning in a  $\gamma$ - $\alpha_2$  lamellar region of  $\text{Ti}_{52}\text{Al}_{48}$  alloy after tensile testing to failure; both grains are diffracting under "two-beam" conditions.

patterns (ie.  $(\bar{1}\bar{1}1)_\gamma = (0002)_{\alpha_2}$ ,  $(101)_\gamma = f(\bar{1}2\bar{1}0)_{\alpha_2}$  and  $(011)_\gamma = f(\bar{2}1\bar{1}0)_{\alpha_2}$  with  $f = 1.015$ , for a cubic approximation to the  $\text{L1}_0$   $\gamma$ -phase crystal structure) and is given by:

$$[uvw]_\gamma = \begin{pmatrix} 0 & +f & -f & -\frac{2}{3} \\ -f & 0 & +f & -\frac{2}{3} \\ -f & +f & 0 & +\frac{2}{3} \end{pmatrix} \begin{bmatrix} u \\ v \\ t \\ w_{\alpha_2} \end{bmatrix}; [uvw]_{\alpha_2} = \begin{pmatrix} 0 & -\frac{1}{3f} & -\frac{1}{3f} \\ +\frac{1}{3f} & 0 & +\frac{1}{3f} \\ -\frac{1}{3f} & +\frac{1}{3f} & 0 \\ -\frac{1}{2} & -\frac{1}{2} & +\frac{1}{2} \end{pmatrix} \begin{bmatrix} u \\ v \\ w_\gamma \end{bmatrix}$$

In Figs. 11 & 12 the deformation twin *ab* is formed by the movement  $1/6[112]_\gamma$  twinning dislocations which propagate in the direction *a*→*b* on their  $(\bar{1}\bar{1}1)_\gamma$  slip plane in groups of three. After intersecting the  $(\bar{1}\bar{1}1)_\gamma/(0001)_{\alpha_2}$   $\gamma/\alpha_2$  interface *XX'* along a  $[0\bar{1}\bar{1}]_\gamma/[2\bar{1}\bar{1}0]_{\alpha_2}$  direction, each group of three is transferred into the  $\alpha_2$  grain as a  $1/3[2\bar{1}\bar{1}0]_{\alpha_2}$  slip dislocation moving along *c*→*d* on a  $(01\bar{1}0)_{\alpha_2}$  plane, with a  $1/2[110]_\gamma$  slip dislocation being ejected back into the  $\gamma$  grain on



Figure 10. Mosaic of electron micrographs showing the propagation of deformation twinning across  $\gamma$ - $\alpha_2$  lamellae in a  $(\text{Ti}_{52}\text{Al}_{48})_{99}\text{Zr}_1$  alloy after tensile testing to failure;  $\gamma$  and  $\alpha_2$  grains are diffracting under "two-beam" conditions.

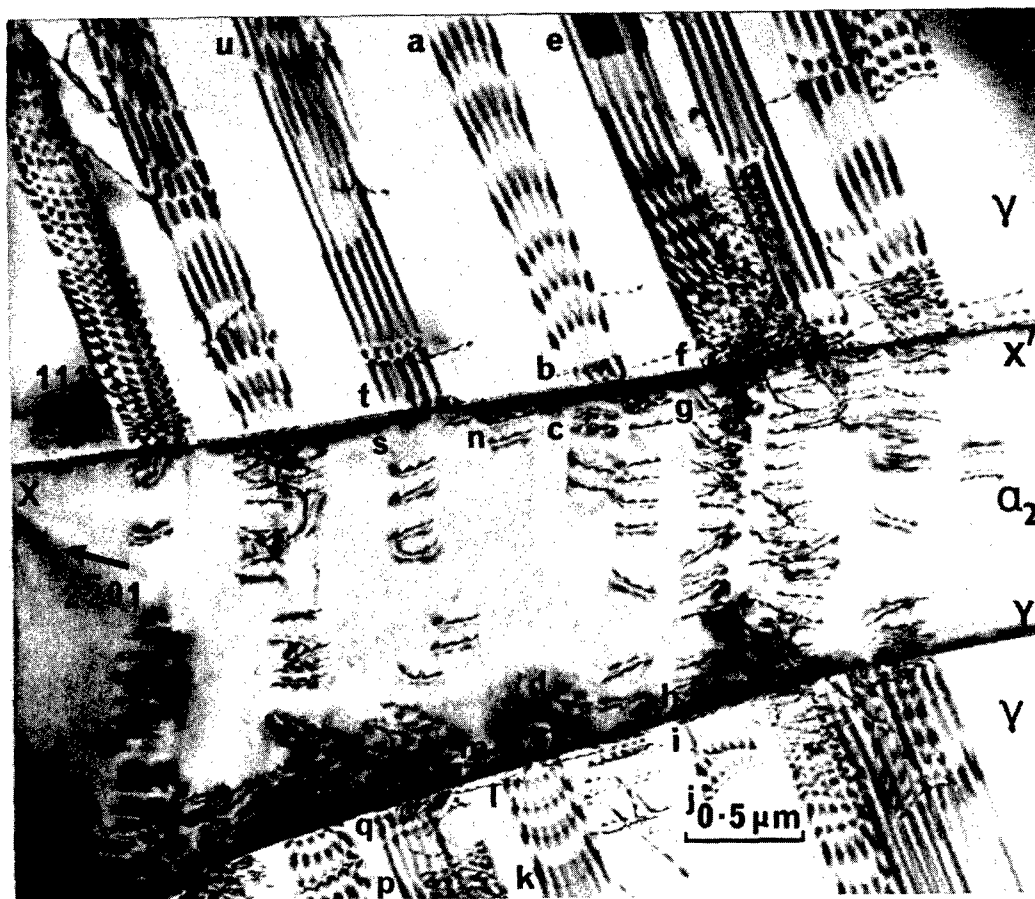
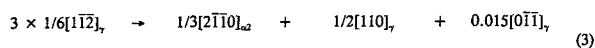


Figure 11. Simultaneous double two beam electron micrograph of slip transfer across  $\gamma/\alpha_2$  interfaces showing continuity of deformation twins from one  $\gamma$  grain to the next across an intermediate  $\alpha_2$  grain. The beam direction is close to  $[7\bar{8}1]_\gamma/[5\ 6\ \bar{1}\bar{1}\ 2]_{\alpha_2}$  and the diffracting vectors are indicated.

the same  $(1\bar{1}1)_\gamma$  slip plane as the incoming  $1/6[1\bar{1}2]_\gamma$  twinning dislocations. The dislocation reaction along the line of intersection at the interface that describes this slip transfer process is:



↓	↓	↓	↓
Incoming def <sup>n</sup> twin on $(1\bar{1}1)_\gamma$	Outgoing slip dislocation on $(01\bar{1})_{\alpha_2}$	Slip dislocation moving back on $(1\bar{1}1)_\gamma$	Residue left at interface along $[0\bar{1}\bar{1}]_\gamma$

which, on a  $b^2$  criterion, is energetically unfavourable and therefore, in order to proceed, requires the presence of an applied shear stress on the  $(1\bar{1}1)_\gamma$  plane operating in any direction within the  $90^\circ$  range from  $[1\bar{1}2]_\gamma$  to  $[0\bar{1}\bar{1}]_\gamma$ . It can be seen from eqn. (3) that a small residue in the form of a right-handed screw dislocation along the  $[0\bar{1}\bar{1}]_\gamma$  line of intersection remains in the interface. This will accumulate with the transfer of each group of three twinning dislocations from the upper  $\gamma$  grain until its Burgers vector exceeds that of a full  $[0\bar{1}\bar{1}]_\gamma$ , when it will transfer into the  $\alpha_2$  lamella according to the reaction:

$$[0\bar{1}\bar{1}]_\gamma = 1/3[2\bar{1}\bar{1}0]_{\alpha_2} + 0.015[0\bar{1}\bar{1}]_\gamma.$$

Another example of the reaction in eqn. (3) occurs in Fig. 11 along  $efgh$ , which then transfers from the  $\alpha_2$  lamella into the lower  $\gamma$  grain along  $ij$  as groups of three  $1/6[1\bar{1}2]_\gamma$  by the reverse reaction of eqn. (3). Examples of slip transfer from the lower  $\gamma$  grain, across the  $\alpha_2$  lamella, into the upper  $\gamma$  grain occur along  $klmn$  and  $pqrstu$ , each via a

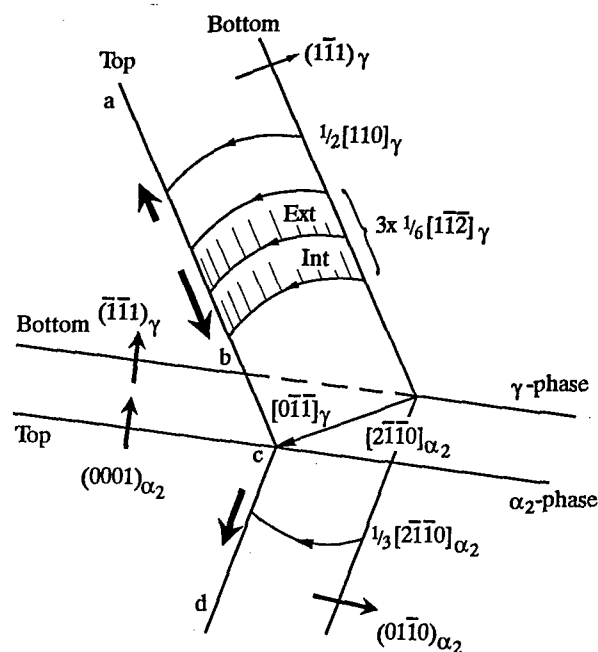


Figure 12. Schematic representation of slip transfer along  $abcd$  of Fig. 11. Bold arrows indicate direction of motion.



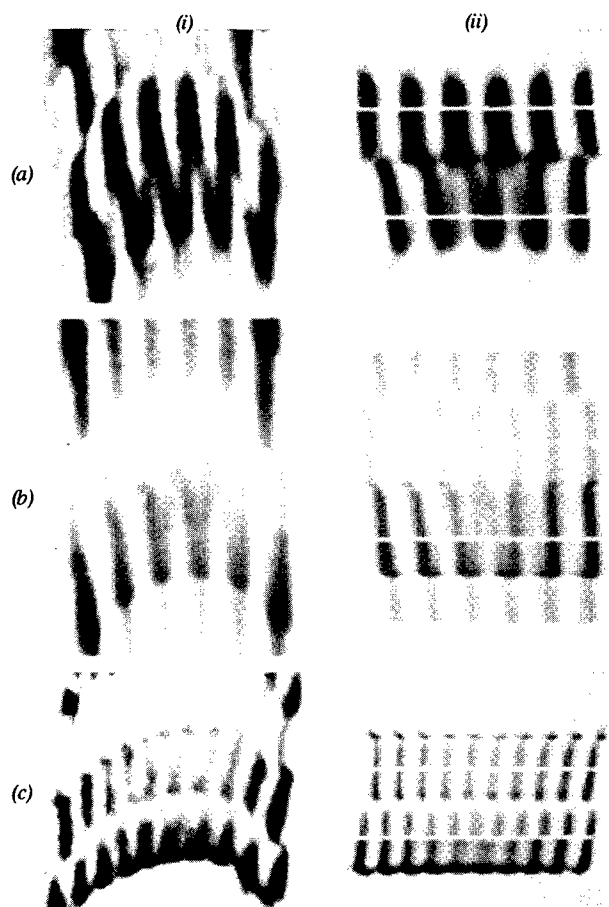


Figure 13. Comparison of (i) experimental and (ii) computed bright-field two beam electron micrographs of a group of three incoming twinning dislocations on the  $(1\bar{1}1)_\gamma$  plane labelled  $ab$  in Figs. 11 and 12, identifying each Burgers vector as  $1/6[1\bar{1}2]_\gamma$ . The beam direction and diffracting vector is:  $[5\bar{4}1]_\gamma$ ,  $\bar{1}\bar{1}1_\gamma$  in (a),  $[7\bar{8}1]_\gamma$ ,  $111_\gamma$  in (b) and  $[297]_\gamma$ ,  $\bar{1}\bar{1}1_\gamma$  in (c).

reaction given by negating the signs in eqn. (3) which proceed under the same conditions of applied shear stress.

The detailed description of slip transfer given above relies on the identification by image matching of the sense and magnitude of the Burgers vectors of the dislocations involved. Matching sets of experimental and computed images for the slip transfer  $abcd$  of Fig. 11 are given in Figs. 13 - 15, where the computed images were calculated using the appropriate tetragonal and hexagonal crystallography and anisotropic elasticity for the  $\gamma$  and  $\alpha_2$  phases respectively. Figure 13 identifies a group of three incoming  $1/6[1\bar{1}2]_\gamma$  dislocations in the upper  $\gamma$  grain, Fig. 14 an outgoing  $1/3[2\bar{1}\bar{1}0]_{\alpha_2}$  dislocation in the  $\alpha_2$  lamella and Fig. 15 a  $1/2[110]_\gamma$  dislocation that is moving back on the  $(\bar{1}\bar{1}1)_\gamma$  slip plane of the incoming  $1/6[1\bar{1}2]_\gamma$  dislocations (note: this dislocation is just above the field of view in Fig. 11).

#### Summary and Discussion

Improved ductility in duplex  $\gamma/\alpha_2$  titanium aluminide alloys is sought by adopting a strategy based on obtaining a more balanced plastic response within the two phases. This involves strengthening the  $\gamma$ -phase and softening the  $\alpha_2$ -phase. It is argued that it may be possible

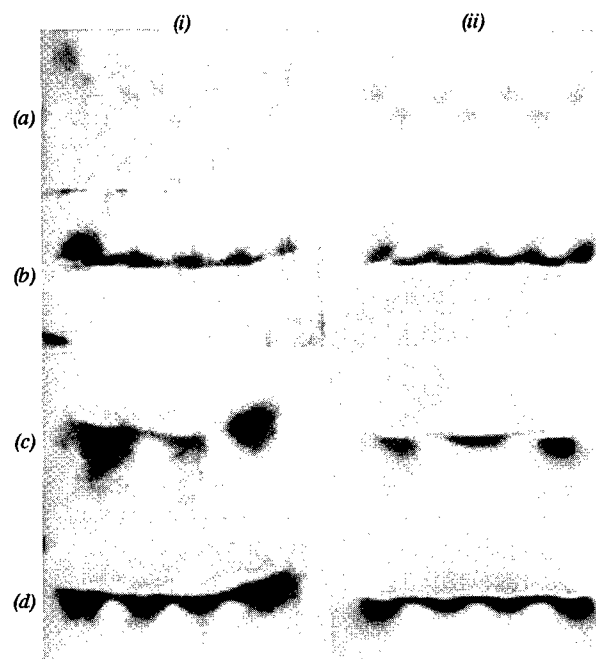


Figure 14. Comparison of (i) experimental and (ii) computed bright-field two beam electron micrographs of a transmitted slip dislocation in the  $\alpha_2$ -lamella on the  $(01\bar{1}0)_{\alpha_2}$  plane labelled  $cd$  in Figs. 11 and 12, identifying its Burgers vector as  $1/3[2\bar{1}\bar{1}0]_{\alpha_2}$ . Beam directions and diffracting vectors are:  $[12\bar{3}0]_{\alpha_2}$ ,  $0002_{\alpha_2}$  in (a),  $[1\ 7\ \bar{8}\ 18]_{\alpha_2}$ ,  $\bar{2}021_{\alpha_2}$  in (b),  $[2023]_{\alpha_2}$ ,  $\bar{2}\bar{2}40_{\alpha_2}$  in (c), and  $[5\ 6\ \bar{1}\bar{1}2]_{\alpha_2}$ ,  $\bar{2}\bar{2}01_{\alpha_2}$  in (d).

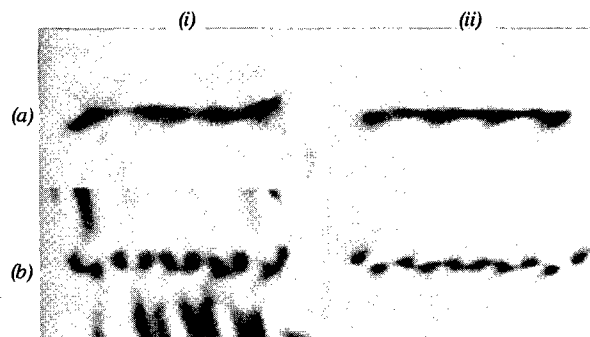


Figure 15. Comparison of (i) experimental and (ii) computed bright-field two beam electron micrographs of a group of a slip dislocation moving back on the  $(\bar{1}\bar{1}1)_\gamma$  plane labelled  $ba$  in Figs. 11 and 12, identifying its Burgers vector as  $1/2[110]_\gamma$ . Beam directions and diffracting vectors are:  $[196]_\gamma$ ,  $311_\gamma$  in (a) and  $[075]_\gamma$ ,  $\bar{2}00_\gamma$  in (b).

to achieve both these effects by the addition of extra alloying elements provided a particular set of constraints on atomic order, interphase partitioning and atomic site occupancy are satisfied. From a series of experiments, where these three atomic parameters are determined for a range of different ternary alloying elements, two particular elements are selected which best satisfy the constraints; Zr as a possible  $\gamma$ -phase strengthener and Cr as a possible  $\alpha_2$  softener. Although experiments to determine the relative strengthening and softening effects of Zr and Cr additions on the individual phases are still in progress, duplex alloys containing a range of Zr + Cr additions with an essentially similar

microstructure were prepared and mechanically tested to failure in tension. They were found to exhibit enhanced strength and ductility with optimum properties corresponding to additions of Zr and Cr each at the 1 to 2 at.% level. Examination of these deformed alloys by TEM confirmed that both  $\gamma$  and  $\alpha_2$  phases had deformed plastically with slip transfer having occurred across  $\gamma/\alpha_2$  interfaces allowing deformation twins to propagate from one  $\gamma$  grain to the next without the build-up of excessive strain at interfaces. The dislocation reactions involved in the slip transfer process have been identified by image matching for the case of  $30^\circ 1/6 < 112 \rangle_\gamma$  twinning dislocations at the head of a deformation twin in a  $\gamma$ -grain intersecting a  $\gamma/\alpha_2$  interface and transferring into the  $\alpha_2$  grain as a  $1/3 < 2\bar{1}\bar{1}0 >_{\alpha_2}$  slip dislocation on a  $\{01\bar{1}0\}_{\alpha_2}$  plane.

It is interesting to note from the combined results of Figs. 3 and 6 that Nb was also a possible candidate as a  $\gamma$  strengthener. Thus the well known  $\gamma/\alpha_2$  alloys containing Nb + Cr additions could also satisfy the proposed conditions for obtaining a more balanced plastic response between  $\gamma$  and  $\alpha_2$  phases.

Again in this case it was found that the atomic order parameter, interphase partitioning and atomic site occupancy for Nb and Cr in the Nb + Cr quaternary alloys were essentially unchanged from those obtained for the ternary alloys.

#### Acknowledgments

This effort was sponsored in part by the Air Force Office of Scientific Research, Air Force Material Command, USAF, under grant No. F49620-96-1-0024. The US Government is authorised to reproduce and distribute for Governmental purposes notwithstanding any copyright notation thereon.

The views and conclusions contained herein are those of the authors and should not be interpreted as necessarily representing the official policies or endorsements, either expressed or implied, of the Air Force Office of Scientific Research or the US Government.

The authors acknowledge the expert assistance of Darryl Jones in alloy preparation and mechanical testing.

#### References

1. Y.-W. Kim, "Intermetallic Alloys Based on Gamma Titanium Aluminide", *JOM*, 41, No.7 (1989), 24-30.
2. Y.-W. Kim, "Ordered Intermetallic Alloys, Part III: Gamma Titanium Aluminides", *JOM*, 46, No.7 (1994), 30-39.
3. Y.-W. Kim and D.M. Dimiduk, "Progress in the Understanding of Gamma Titanium Aluminides", *JOM*, 43, No.8 (1991), 40-47.
4. F. Appel, P.A. Beaven and R. Wagner, "Deformation Processes Related to Interfacial Boundaries in Two-Phase  $\gamma$ -Titanium Aluminides", *Acta metall. mater.*, 41 (1993), 1721-1732.
5. W. Wunderlich, Th. Kremser and G. Frommeyer, "Mobile Dislocations at the  $\alpha_2/\gamma$  Phase Boundaries in Intermetallic TiAl/Ti<sub>3</sub>Al-Alloys", *Acta metall. mater.*, 41 (1993), 1791-1799.
6. M.A. Morris, "Dislocation Configurations in Two Phase TiAl Alloys I. Annealed and Indented Structures", *Phil. Mag. A*, 68 (1993), 237-257.
7. M.A. Morris, "Dislocation Configurations in Two Phase TiAl Alloys II. Structures after Compression", *Phil. Mag. A*, 68 (1993), 259-278.
8. S.-C. Huang and E.L. Hall, "Characterisation of the Effect of Vanadium Additions to TiAl Base Alloys", *Acta metall. mater.*, 39 (1991), 1053-1060.
9. S.-C. Huang and E.L. Hall, "Effects of Cr Additions to Binary TiAl-Base Alloys", *Metall. Trans.*, 22A (1991), 2619-2627.
10. T. Hanamura, R. Uemori and M. Tanino, "Mechanism of Plastic Deformation of Mn-added TiAl L1<sub>0</sub>-Type Intermetallic Compound", *J. Mater. Res.*, 3 (1988), 656-664.
11. M. Morinaga, J. Saito, N. Yukawa and H. Adachi, "Electronic Effect on the Ductility of Alloyed TiAl Compound", *Acta metall. mater.*, 38 (1990), 25-29.
12. J.-h. Xu and A.J. Freeman, "Effects of Ternary Additions on the Twin Energy and Site Preference in  $\gamma$ -TiAl", *J. Mater. Res.*, 9 (1994), 1755-1760.
13. C.J. Rossouw, M.A. Gibson and C.T. Forwood, "Convergent Beam Electron Diffraction Zeroth Order Laue Zone and Higher Order Laue Zone Analysis of Order in TiAl Alloys", *Phil. Mag. A*, 73 (1996), 187-201.
14. C.J. Rossouw, C.T. Forwood, M.A. Gibson and P.R. Miller, "Zone-Axis Convergent-Beam Electron Diffraction and ALCHEMI Analysis of Ti-Al Alloys with Ternary Additions", *Phil. Mag. A*, 74 (1996), 77-102.
15. C.J. Rossouw, C.T. Forwood, M.A. Gibson and P.R. Miller, "Generation and Absorption of Characteristic X-Rays under Dynamical Electron Diffraction Conditions", *Micron*, (1997) in press.
16. H. Doi, K. Hashimoto, K. Kasahara and T. Tsujimoto, "Site Determination of Third Elements in TiAl Compound by X-Ray Diffractometry", *Mater. Trans. JIM*, 31 (1990), 975-982.
17. D. Shindo, M. Hirabayashi, T. Kawabata and M. Kikuchi, "A Channelling Enhanced Microanalysis on Niobium Atom Location in an Al-43%Ti-2%Nb Intermetallic Compound", *J. Electron Microsc.*, 35 (1986), 409-414.
18. D.G. Konitzer, I.P. Jones and H.L. Fraser, "Site Occupancy in Solid Solutions of Nb in the Intermetallic Compounds of TiAl and Ti<sub>3</sub>Al", *Scripta metall.*, 20 (1986), 265-268.
19. E. Mohandas and P.A. Beaven, "Site Occupation of Nb, V, Mn and Cr in  $\gamma$ -TiAl", *Scripta metall. mater.*, 25 (1991), 2023-2027.
20. C.J. Rossouw, C.T. Forwood, M.A. Gibson and P.R. Miller, "Statistical ALCHEMI: General Formulation and Method with Application to Ti-Al Ternary Alloys", *Phil. Mag. A*, 74 (1996), 57-76.
21. C.J. Rossouw, M.A. Gibson and C.T. Forwood, "Dynamical Electron Diffraction Analysis of Lattice Parameters, Debye-Waller Factors and Order in Ti-Al and Ti-Ga Alloys", *Ultramicroscopy* (1997) in press.
22. A.K. Head et al., *Computed Electron Micrographs and Defect Identification*, (North-Holland, Amsterdam, 1973).

## BEST PAPER AWARD (Co-Winner)

### EFFECTS OF MICROSTRUCTURE, TEMPERATURE AND ENVIRONMENTAL ON FATIGUE CRACK GROWTH IN Ti-46.5Al-3Nb-2Cr-0.2W $\gamma$ TITANIUM ALUMINIDE

A.H. Rosenberger<sup>1</sup>, B.D. Worth<sup>2</sup>, and J.M. Larsen<sup>1</sup>

<sup>1</sup>Air Force Research Laboratory – Materials Directorate  
Wright-Patterson Air Force Base, Ohio 45433-7817, USA

<sup>2</sup>The University of Dayton Research Institute  
Dayton, Ohio 45419-0128, USA

#### Abstract

The influence of environment on the fatigue crack growth in a gamma titanium aluminide alloy was examined through a comparison of crack growth behavior in laboratory air and ultra high vacuum (UHV). Specimens of wrought Ti-46.5Al-3Nb-2Cr-0.2W (at %) were tested in duplex, refined lamellar and coarse lamellar microstructures at temperatures ranging from ambient to 800°C. A pronounced environmental effect was observed at all temperatures, with crack growth rates more than an order of magnitude lower in vacuum than in air. The poorest crack growth resistance was observed in air at an intermediate temperature, however in a UHV environment, no anomalous temperature dependence on fatigue crack growth was observed. This temperature effect was shown to be the result of an environmental embrittlement that is mitigated by the increase in ductility at higher temperatures. A careful examination of crack closure levels supported this conclusion. Subtle fractographic differences in crack growth mode were observed in the two environments but were not sufficient to cause the dramatic changes in fatigue crack growth resistance.

#### Introduction

Gamma titanium aluminide alloys, which are based on the TiAl intermetallic phase, are candidates for use as structural materials in advanced gas turbine engines. Currently, however, there is a limited understanding of the influence of environment on mechanical properties of this class of alloys over the typical range of application temperatures. An effect of environment on the fatigue crack growth behavior of a cast gamma alloy was found by Mabru, et al., [1]. Here, near threshold, crack growth rates were two orders of magnitude slower in a vacuum and merged with the growth behavior in air at higher crack growth rates. Liu and Kim [2] also found an increase in ductility at 25°C in a duplex microstructure in vacuum and oxygen environments. Oh *et al.* [3] demonstrated a large, room temperature environmental effect on the tensile properties in polysynthetically twinned TiAl. Crystals oriented in a 'soft' orientation exhibited more translamellar fracture at low strain rates, but the orientation-dependent differences in fracture mode and ductility diminished at progressively higher strain rates. A decrease in fatigue crack growth rates was found in vacuum at 700°C in an "as cast"

TiAl material by James and Bowen [4]. However, these researchers found similar crack growth behavior in air and vacuum in duplex and near-gamma heat treated conditions. Balsone *et al.* [5] reported that the fatigue crack growth behavior of an alloy having a duplex microstructure was relatively insensitive to temperature over the range of 25 to 954°C. The highest crack growth rates, however, were found at the intermediate temperature of 425°C. This was attributed to environmentally-assisted crack growth that occurs at elevated temperatures below the ductile-to-brittle transition temperature. More recent work on a wrought gamma alloy in both fine duplex and fully lamellar microstructural conditions [6], and a fine lamellar XD alloy [7], have shown that the minimum in fatigue crack growth resistance occurred at a temperature of approximately 600°C. Generally, environmental effects on gamma materials have not been studied over a temperature range large enough to document the level of environmentally-assisted crack growth or to determine the cause of the poor crack growth resistance at intermediate temperatures.

The objective of this study was to perform fatigue crack growth experiments in an ultra high vacuum (UHV) environment and compare these results with those obtained in laboratory air [6] in order to characterize environmentally-assisted crack growth phenomena for temperatures ranging from ambient to 800°C. Levels of crack closure were measured and analyzed to help determine the relative influences of crack shielding and environmental attack on fatigue crack growth behavior as a function of temperature. This analysis was complemented by scanning electron microscopy of the fracture surfaces which was used to characterize the modes of crack advance.

#### Materials and Experimental Procedure

The gamma titanium aluminide alloy investigated in this study was a wrought material developed by Kim [8] of nominal composition Ti-46.5Al-3Nb-2Cr-0.2W (atomic %). This material, also designated as alloy K5, was tested in the three microstructural conditions: duplex, refined lamellar, and coarse lamellar (Fig. 1). Additional information on the processing, heat treatment, and microstructures of these materials may be found in [9].

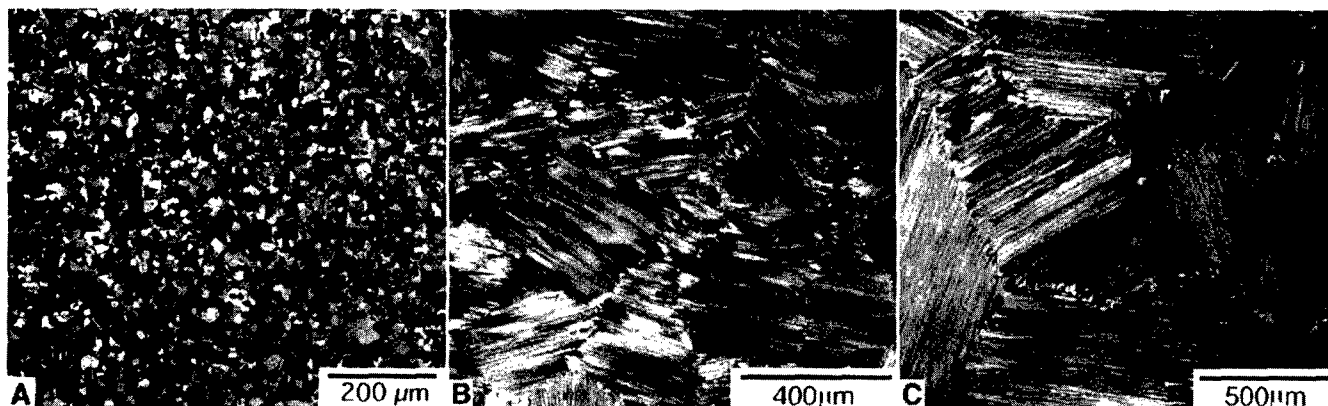


Fig. 1. Microstructures of the gamma titanium aluminides: a) duplex, b) refined lamellar, and c) coarse lamellar Ti-46.5Al-3Nb-2Cr-0.2W.

Fatigue crack growth tests were conducted on the three microstructures at temperatures of RT, 600, and 800°C in laboratory air and UHV. Compact tension specimens, C(T), of width equal to 20 mm and thickness of 5 mm, were tested under load-shedding (decreasing  $\Delta K$ ) and constant-load-amplitude (increasing  $\Delta K$ ) fatigue using a computer controlled servohydraulic test machine. A relatively high cyclic frequency of 10 or 20 Hz was used to minimize creep-fatigue interactions and thereby promote an examination of the effects of microstructure, temperature, and environment on the mechanisms of pure fatigue crack growth. A stress ratio ( $R = \sigma_{\min} / \sigma_{\max}$ ) of 0.1 was used on all tests. Crack lengths and crack closure loads were determined from measurements of crack mouth opening displacements. The level of crack closure was calculated from the load-displacement data using the slope-intercept method, which produced repeatable results on these low-R tests.

The refined lamellar material was subjected to an additional examination of the effects of temperature on crack growth behavior. Using a constant  $K_{\max} = 10 \text{ MPa}\sqrt{\text{m}}$  with  $R = 0.1$ , the crack growth rate in this material was measured in laboratory air over the temperature range from ambient to 800°C, in temperature increments of 100°C or less. During each increment, the crack was allowed to extend 0.5 mm or more before switching to a higher temperature. This allowed several increments of crack growth (several temperatures) to be examined on a single specimen. The crack growth threshold was also determined as a function of temperature in the refined lamellar microstructure by generating only the lower portion of the curve in a decreasing- $\Delta K$  test. A number of different, temperature-dependent threshold levels were determined from a single test specimen.

Ultra high vacuum crack growth tests were conducted on a servohydraulic test machine fitted with a vacuum chamber evacuated by a two-stage turbomolecular pumping system. This chamber is capable of maintaining a vacuum of  $3 \times 10^{-7} \text{ Pa}$ , with predominantly water vapor, nitrogen, and oxygen as the residual gasses, having partial pressures of approximately  $9 \times 10^{-8}$ ,  $1 \times 10^{-8}$  and  $3 \times 10^{-9} \text{ Pa}$ , respectively. Elevated temperature tests were conducted in UHV using a tungsten mesh hot zone which had no appreciable influence on the vacuum level or residual impurities. Fatigue crack growth rate curves were generated in UHV for the coarse lamellar and duplex microstructures only. Closure measurements were obtained using the same technique as used in the laboratory air experiments (quartz rod extensometer on the crack mouth).

## Results

### Fatigue Crack Growth

The fatigue crack growth behavior of the coarse lamellar and duplex microstructures tested at the temperatures of RT, 600, and 800°C are shown in the form of crack growth rate as a function of applied stress intensity factor range,  $\Delta K$ , in Figs. 2-3. In the laboratory air

environment, the minimum crack growth rates represent crack arrest, while no cessation of crack growth was found in the UHV environment.

Over the temperature range from RT to 800°C, there was a significant reduction of crack growth rates in the coarse lamellar microstructure material under the UHV conditions, Fig. 2. The crack growth rate behavior in UHV of the lamellar material at room temperature and 600°C was nearly identical, while faster fatigue crack growth rates were evident at 800°C. This behavior in vacuum is consistent with the decrease in strength and elastic modulus that occurs with increasing temperature. Notice that the increased crack growth rate observed in air at 600°C was not present in vacuum, which lends credibility to the argument of an environment-assisted crack growth at elevated temperatures that are still below the ductile to brittle transition temperature [6]. In the UHV environment, over the temperature range RT-600°C, the crack growth thresholds were higher than in air by approximately 5 MPa $\sqrt{\text{m}}$ , which is significant considering the apparent arrest of crack growth in air. At 800°C, the UHV threshold was lower than in air, due to the lack of crack arrest, but the growth rate at the same value of  $\Delta K$  was almost two orders of magnitude slower.

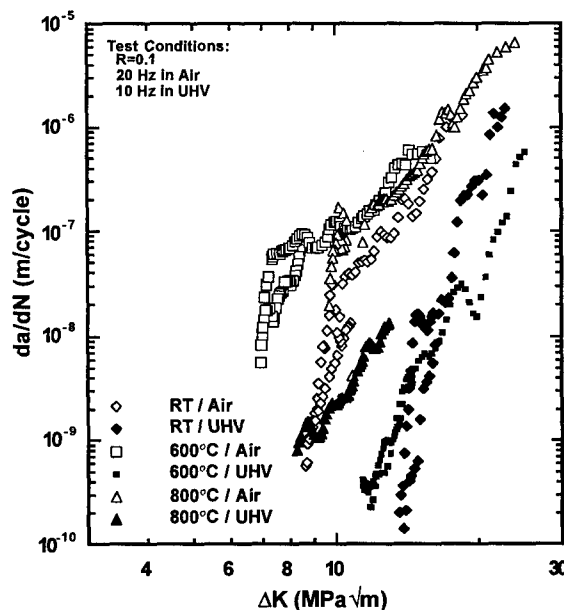


Fig. 2. Fatigue crack growth behavior of coarse lamellar K5 at RT, 600, and 800°C in air and UHV.

Crack growth rate curves for the duplex material, Fig 3, showed trends similar to those of the coarse lamellar material presented in Fig 2. There was, again, an obvious decrease in the crack growth rates by over an order of magnitude at all temperatures in the UHV compared to the air environment. The shift in  $\Delta K_{th}$  at the lower temperatures, RT and 600°C,

was less dramatic than in the lamellar material. However, the crack growth curves were over two orders of magnitude slower in UHV as compared to air. Notice, also that at RT and 600°C the apparent toughness,  $K_{IC}$ , was independent of environment. This resulted in steeper crack growth curves in UHV; for example, at room temperature, the exponent of a Paris equation fit was approximately 40! At 800°C, as in the lamellar material,  $\Delta K_{th}$  in UHV was lower than in air, but this was, again, a result of the arrest in air and the continued growth at low crack growth rates in UHV.

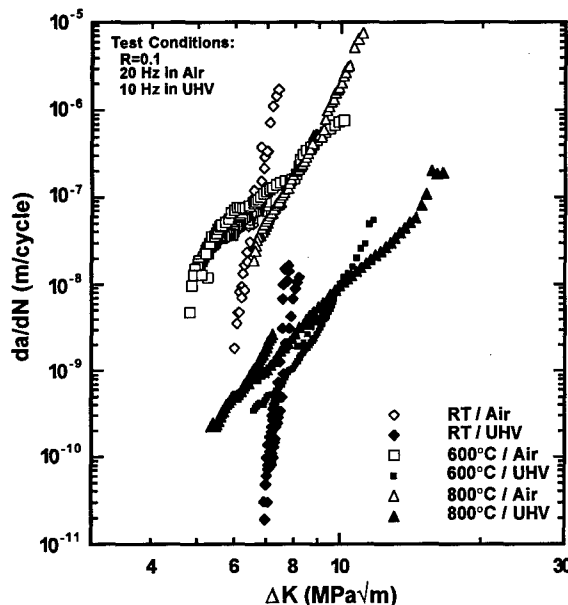


Fig. 3. Fatigue crack growth behavior of duplex K5 at RT, 600, and 800°C in air and UHV.

The crack growth behavior of the refined lamellar material in laboratory air was similar to that seen in the coarse lamellar material [9] and is not shown here. The decrease in the scale of the microstructure, apparent in Fig. 1, did not have a large influence on the fatigue crack growth resistance. It is expected that the refined lamellar microstructure would have an environmental influence on crack growth behavior similar to that of the duplex and coarse lamellar microstructures.

#### Crack Closure Corrected Crack Growth

It has been suggested that the anomalous temperature dependence on crack growth rate that has been observed in a number of gamma alloys [7, 6] is due to an extrinsic mechanism (i.e. oxide induced closure) [7] and not only a result of the changes in the deformation character and environmental attack that accompany the increase in temperature. This theory was investigated by a careful examination of the closure behavior of the coarse lamellar and duplex K5 materials, shown in Figs. 4 and 5, respectively. The level of closure may be represented by the  $U$  ratio,  $U = (P_{max} - P_{op}) / (P_{max} - P_{min}) = \Delta K_{eff} / \Delta K$  [10] and was described as a function of  $\Delta K$ . In the present results, closure was monitored during both the decreasing- $\Delta K$  and constant- $\Delta P$  portions of the test and appeared to follow the same dependence on  $\Delta K$  for both of these loading histories.

As shown in Fig. 4, closure in the coarse lamellar material displayed little variation with temperature in the air environment -  $U$  generally had a value of 0.8 to 0.9, though slightly lower at the lowest  $\Delta K$  levels at room temperature. However,  $U$  tended to be lower in UHV than in air at room temperature and higher in UHV than in air at the highest temperature. This suggests that closure was dominated by fracture surface roughness at low temperatures and included a contribution due to oxide wedging at higher temperatures. More discussion of these observations follows in later sections.

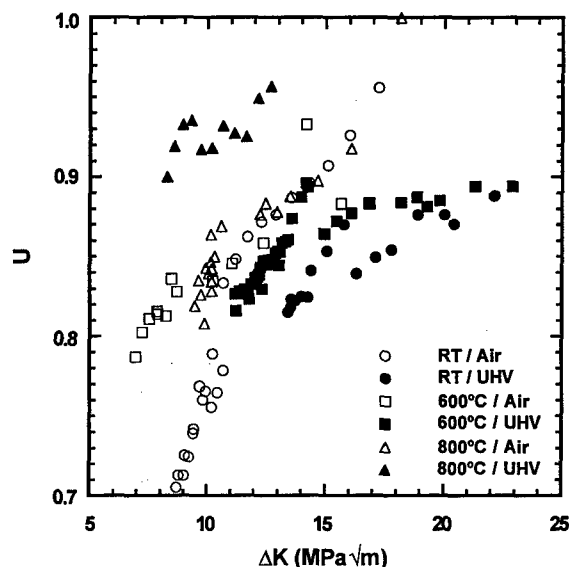


Fig. 4.  $U$  as a function of applied stress intensity factor range in coarse lamellar K5 at RT, 600, and 800°C in air and UHV.

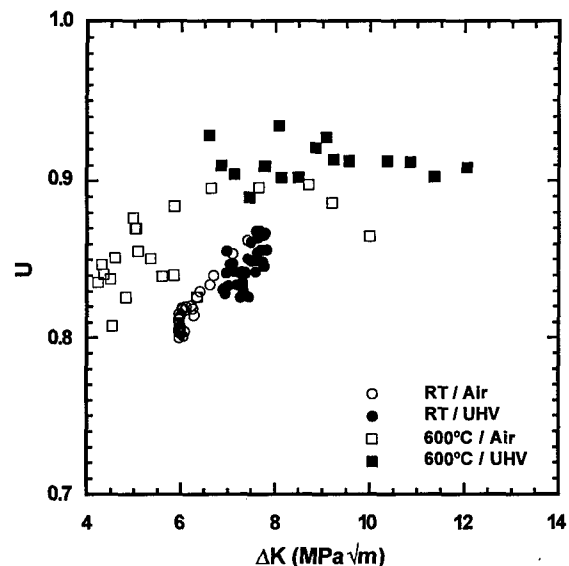


Fig. 5.  $U$  as a function of applied stress intensity factor range in duplex K5 at RT and 600°C in air and UHV. No closure was detected in either environment at 800°C.

In duplex K5, there was little influence of environment on the closure behavior. There was a general increase in  $U$  as the temperature increased. At 800°C (not shown in Fig. 5) the cracks were fully open over the full range of  $\Delta K$  (i.e.  $U=1$ ). The temperature dependence of closure is likely due to a decrease in roughness of the fracture surface at the lower temperatures and a lack of any closure at the highest temperature, due to creep and/or blunting at the crack tip. A comparison of the closure behavior in the coarse lamellar and duplex materials, Figs. 4 & 5 respectively, showed that  $U$  was generally higher in the duplex material. As discussed later (and in [11]), the main influence of microstructure on closure was probably due to differences in fracture surface morphology and roughness of the two materials. Especially notable was that at 800°C in air, no unusual increase in the level of crack closure was observed that could be linked to oxide wedge formation.

Closure corrected crack growth curves are shown in Figs. 6 and 7 for the coarse lamellar and duplex microstructural conditions, respectively. Here, the crack growth rate was correlated with  $\Delta K_{eff}$  where  $\Delta K_{eff} = K_{max} - K_{op}$ . The correction for closure generally shifted the crack growth rate curves to the left, however, the magnitude of the temperature-dependent layering and environmental influence of the data was unchanged.

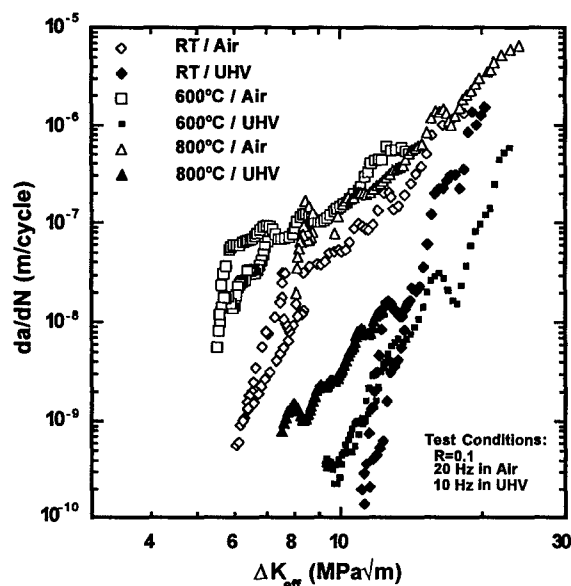


Fig. 6. Closure corrected fatigue crack growth behavior of coarse lamellar K5 at RT, 600, and 800°C in air and UHV.

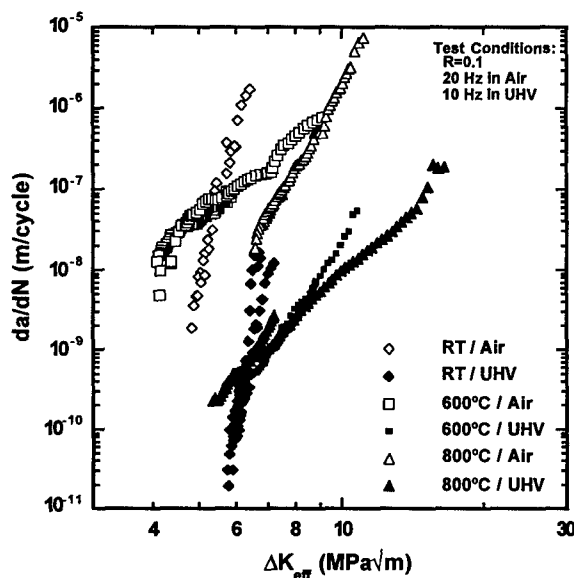


Fig. 7. Closure corrected fatigue crack growth behavior of duplex K5 at RT, 600, and 800°C in air and UHV.

#### Temperature Dependence of Fatigue Crack Growth

The fatigue crack growth behavior of the refined lamellar material was examined in more detail as a function of temperature. Using a small

number of specimens, the crack growth rate under constant- $\Delta K$  conditions was determined over the range of temperatures shown in Fig. 8. It is apparent that there was a gradual increase in growth rate as the temperature increased from 200 to 600°C, followed by a steep decline in growth rate at higher temperatures. No crack growth was measured at 800°C, which indicated that the growth rate was lower than  $10^{-10}$  m/cycle. Notice that the crack growth rates at the temperatures of RT, 600, and 800°C compare well with the curves for the coarse lamellar material presented in Fig. 2.

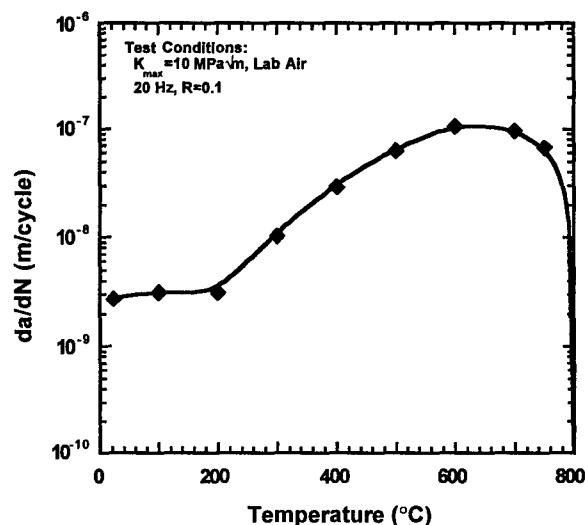


Fig. 8. Fatigue crack growth rate under constant- $\Delta K$  conditions plotted as a function of temperature for the refined lamellar material.

Closure measurements were obtained during each of the crack growth increments in Fig. 8. The closure levels were measured in the manner described earlier and are shown in terms of  $U$  as a function of temperature in Fig. 9. The trend of these closure measurements was similar to the associated crack growth rate behavior shown Fig. 8. That is, a peak in  $U$  was observed at approximately 650°C, followed by a steep drop at higher temperatures. This indicated that the variation in crack growth rate was influenced by crack closure, but the overall change in closure level at this value of  $\Delta K$  was only 10% (i.e.  $U$  changing from 0.8 to 0.9). This change in driving force would influence the room temperature crack growth behavior the most, as this test condition had the steepest crack growth rate curve. In this case a decrease in  $\Delta K$  of 10% would change the crack growth rate by a factor of 5, which is much less than the nearly 50x change in  $da/dN$  seen in Fig. 8. At the higher temperatures, where the crack growth curves are less steep, the variation in crack growth rate due to a 10% change in driving force would be even more limited.

Additional samples of the refined lamellar material were used to determine the crack growth thresholds and the influence of closure at threshold over the temperature range from 500 to 800°C. The variation in  $\Delta K_{th}$  and  $U$ , at threshold, are represented as a function of temperature in Fig. 10. The threshold levels in this figure do not represent growth at a fixed growth rate of, say,  $10^{-10}$  m/cycle, but represent the  $\Delta K$  at apparent crack growth arrest. This arrest occurred at growth rates between  $1 \times 10^{-8}$  and  $4 \times 10^{-8}$  m/cycle. The values of  $U$  in this figure are similar to, or lower than, the measurements of  $U$  obtained under constant- $\Delta K$  conditions (Fig. 9). This trend in  $U$  is consistent with the closure conditions that would be expected at the crack growth threshold (or arrest). It is interesting to note that the minimum  $\Delta K_{th}$  does not correspond to the maximum  $U$ . In fact, highest values of  $U$  occurred over the temperature interval from 650 to 750°C which showed a steep increase in threshold, indicating that closure was not the cause of the increase.

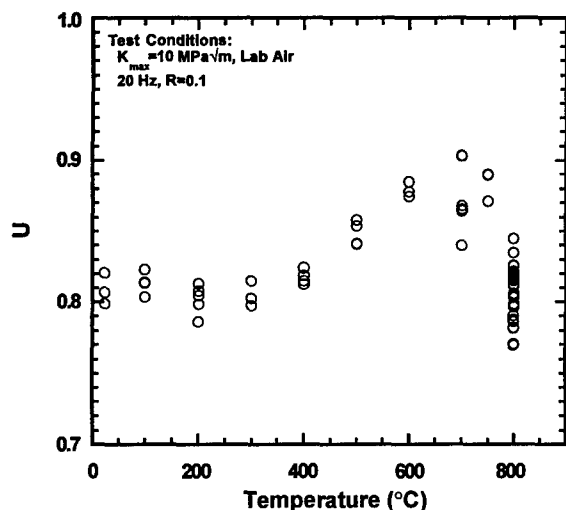


Fig. 9.  $U$  versus temperature corresponding to the constant- $\Delta K$  fatigue crack growth data presented in Fig. 8 for the refined lamellar material.

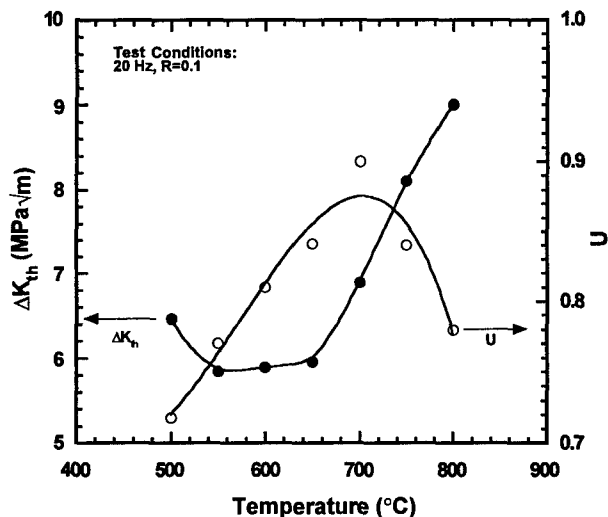


Fig. 10.  $\Delta K_{th}$  and  $U$  as a function of temperature in the refined lamellar material.

#### Fractography

Examinations of the fracture surfaces of the specimens revealed only subtle differences in the modes of fracture. However, the main fracture features were relatively unaffected by the test environment. The thick oxide layer on specimens tested at 800°C in air prevented observation of their fracture modes, but the specimens tested at 600°C in air had only a light surface oxide. The specimens tested in UHV retained their pristine condition, and no oxidation was apparent even at the highest temperature.

Crack advance in the coarse lamellar material was strongly dependent on the underlying microstructure and tended to produce a tortuous crack path. At room temperature, the specimen tested in air produced a predominantly translamellar fracture with occasional inter- and intralamellar facets, Fig. 11(a). Under UHV conditions, the fracture surface appeared rougher, with more interlamellar fracture facets and a mixture of inter- and translamellar fracture within a single colony, Fig. 11(b). These subtle differences were present at both the near-threshold and the mid- $10^{-8}$  m/cycle crack growth regimes. Preliminary measurements of the fracture surface roughness using scanning confocal laser microscopy indicated an appreciably greater asperity

height in UHV as compared to the surface produced in the air environment. This increase in roughness likely resulted in the lower values of  $U$  in the UHV environment, Fig. 4. Increasing the temperature to 600°C had little effect on the fracture behavior. The specimens tested in air and UHV had slightly flatter fracture surfaces that were less sensitive to the colony orientation. The specimen that was tested in UHV did, however, have more interlamellar fracture facets, similar to the room temperature specimen. At high levels of  $\Delta K$ , the specimen tested in UHV exhibited more secondary interlamellar splitting than the specimen tested in air. At 800°C, the air-tested specimen was too oxidized to examine, but the specimen tested in UHV exhibited evidence of ductile intralamellar and translamellar fracture and a macroscopically flatter fracture surface.

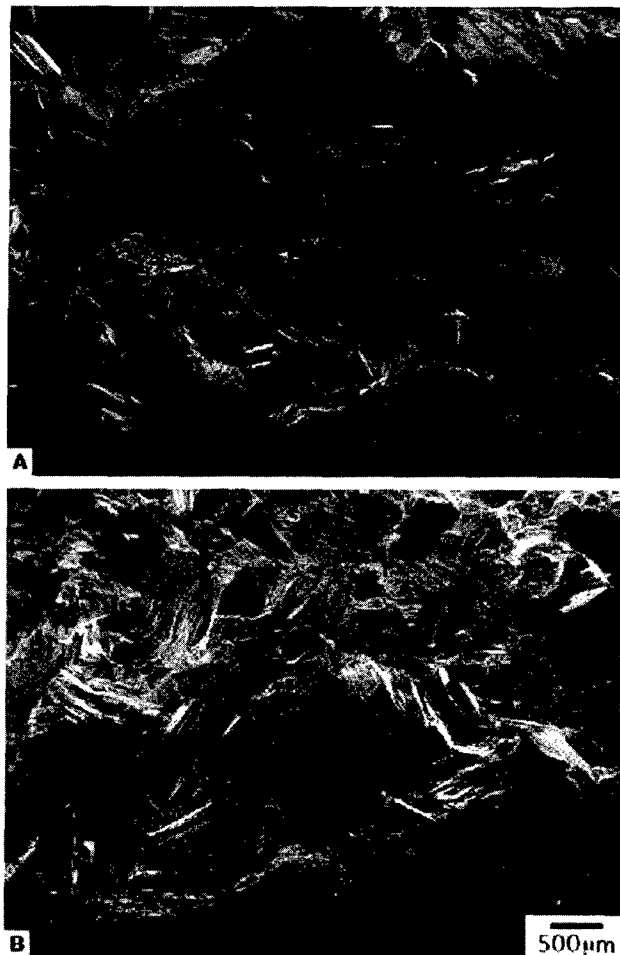


Fig. 11. Fracture behavior of lamellar Ti-46.5Al-3Nb-2Cr-0.2W at RT in: (a) air, and (b) UHV.

The fine grain size of the duplex material promoted a smooth fracture surface in both air and UHV. The dominant fracture mode at room temperature was transgranular cleavage or microcleavage. Here, no differences were observed between the specimen tested in air and UHV. At 600°C, however, the specimen tested in air exhibited a small amount of intergranular fracture at  $\Delta K_{th}$  that increased to approximately 20 percent of the total fracture at high growth rates near  $K_Q$ . In UHV, the fracture mode was completely transgranular cleavage in the threshold regime, but intergranular fracture accounted for approximately 10 percent of the fracture near  $K_Q$ . Overall, the differences in fracture behavior in air and UHV were small for the three materials tested and would not account for the large environmental influence on the crack growth behavior.

## Discussion

Over the entire temperature range examined in this study, crack growth rates were over an order of magnitude slower than in UHV as compared to lab air. This effect is believed to be due to a moisture-induced hydrogen embrittlement mechanism [2,3] at ambient temperatures. The likely mechanism of hydrogen generation by the reaction between moisture and an active metal, either aluminum or titanium in this case, was discussed by Liu and Kim [2]. However, the exact mechanism of the embrittlement is poorly understood. Hino and coworkers [12] measured a release of hydrogen at the moment of tensile fracture in a TiAl alloy indicating that hydrogen has some role in the failure of gamma alloys. The similarity in the  $K_{IC}$  values in UHV and air in this study and that of Mabru, et al. [1] indicated that the embrittlement was time dependent or was controlled by a diffusion process. Tensile tests at different strain rates by Oh, et al. [3] also support this.

The increase in fracture surface roughness observed in the UHV environment in the coarse lamellar gamma alloy indicates that a change in the deformation mode occurred, and this change may be due to an increase in ductility or slip length causing failure at strong boundaries within the microstructure. This would promote interlamellar fracture at lamella boundaries rather than the transgranular microcleavage observed in air. Confirmation of this interpretation was beyond the scope of this study and would require careful TEM work to study the slip character.

At elevated temperatures, the environmental effect is most likely caused by an oxygen embrittlement mechanism that is most virulent at temperatures high enough to cause oxygen diffusion but below the ductile to brittle transition temperature (DBTT). At temperatures above the DBTT, the crack growth rates are reduced, partly due to extrinsic oxide wedging, but mainly due to the intrinsic changes in the crack tip deformation that are brought about by the increase in ductility. The lack of an environmental influence on the fracture features at elevated temperatures, in both this study and that of James and Bowen [4], indicates that the deformation modes must be similar.

The measurements conducted in this study indicated that the only significant environmental influences on closure occurred in the lamellar microstructure at ambient and 800°C. At room temperature, the higher closure was consistent with the rougher fracture surface and the larger size of the facets. Given the low ductility of gamma alloys, it is unlikely that a mechanism other than roughness induced closure occurred at room temperature. At 800°C in the lamellar microstructure material, the higher level of closure in air compared to the UHV environment could signify an oxide contribution to closure, since the fracture surfaces of specimens tested in air had a oxide layer that was sufficiently thick to obscure most of the fracture features. However, the closure levels at 800°C in air were the same as those measured at 600°C. This indicated that any increase in closure at the higher temperature, due to oxide scale growth, was negated by the concomitant increase in crack tip opening due to creep and strength reductions. The duplex microstructure material did not exhibit closure at 800°C, indicating that creep and/or blunting increased the crack tip opening faster than the formation of an oxide layer would tend to decrease it. The UHV crack growth results, in general, showed that the fatigue crack resistance of the gamma alloys decreases with an increase in temperature. This, with the measured closure behavior, shows that the poorest, intermediate temperature, crack growth resistance in air is due to an environmental assist.

The examination of the crack growth rate as a function of temperature in the refined lamellar material showed (for  $K_{max} = 10 \text{ MPa}\sqrt{\text{m}}$ ) that the highest crack growth rates occurred at 600° to 650°C and were greater than could be expected based on closure corrections alone. The decrease in closure (increase in U, Fig. 9) that occurred over the 200° to 600°C temperature interval was most likely due to the decrease in fracture surface roughness that occurred over this temperature range. The variation in closure at  $\Delta K_{th}$ , Fig. 10, was greater than that observed at a higher  $K_{max}$ , Fig. 9, indicating that the arrest at the lower temperatures, 500°-600°C was likely associated with the high closure levels. However, the crack growth thresholds at these temperatures

were lower than those found at 700° and 750°C, where U was 10 to 20% higher. This temperature dependence on  $\Delta K_{th}$  was most likely caused by the similar environmental effect that was observed in the duplex and coarse lamellar materials and is not due to closure alone.

The increased  $\Delta K_{th}$  and crack growth resistance observed in vacuum indicated that failure of actual high-temperature components due to sub-surface defects should be extremely unlikely, since surface initiated cracks would propagate much faster than internally initiated cracks. This preference for surface cracks would facilitate damage detection and monitoring using conventional nondestructive techniques. Also, the decrease in crack growth rates in the UHV environment would have a significant effect on the integrated component life - if such a life prediction scheme is applicable to this intermetallic material.

The poorest crack growth resistance at intermediate temperatures below the ductile to brittle transition temperature may represent the most critical design hurdle for the implementation of gamma alloys in fracture critical applications. The mechanism of crack growth arrest that was observed in air but not in UHV raises questions whether the behavior of small cracks would be similar to that of the measured long crack thresholds, or would fundamentally differences in behavior exist? The pronounced environmental effect that was observed in crack growth rate also raises questions with regard to the fatigue and crack initiation performance of this class of alloys after prolonged, high-temperature service exposure.

## Conclusions

The crack growth behavior of three different variations of a gamma titanium aluminide were examined over a wide range of temperatures in aggressive and inert environments. Several conclusions can be drawn from this study.

- The environment has a major effect on the crack growth rates in gamma titanium aluminides at temperatures ranging from ambient to 800°C. Lower crack growth rates, by over an order of magnitude, were found in the UHV environment.
- The highest crack growth rates were observed in air at temperatures within the 600° to 700°C range. Crack growth at these temperatures in air was enhanced by environmental attack, which diminished as the temperature was increased above the ductile to brittle transition temperature.
- Crack closure had only a limited influence on the trends of crack growth behavior in air or UHV environments at any of the temperatures examined.
- Only minor changes in the mode of fracture occurred with changes in test environment.

## Acknowledgments

This research was performed in the Materials Directorate, Air Force Research Laboratory, Wright-Patterson Air Force Base, OH and was supported by the Air Force Office of Scientific Research under Task 2302BW. B.D. Worth gratefully acknowledges the support of Air Force contract F33615-94-C-5200. The authors would also like to thank Y.-W. Kim of UES, Dayton, OH for the K5 alloy.

## References

1. C. Mabru, G. Henaff, and J. Petit, "Fatigue Crack Propagation Behavior of a Lamellar Ti-Al Alloy in Air and Vacuum," in *Proceedings of the Sixth International Fatigue Congress Fatigue '96*, G. Lütjering and H. Nowack, eds, Pergamon, Oxford, (1996) 1749-1754.
2. T. Liu and Y.-W. Kim, "Room-Temperature Environmental Embrittlement in a TiAl Alloy," *Scr. Metall. Mater.*, 27, (1992) 599-603.
3. M.H. Oh, H. Inui, M. Misaki, and M. Yamaguchi, "Environmental Effects on the Room Temperature Ductility of Polysynthetically Twinned (PST) Crystals of TiAl," *Acta Metall. Mater.*, Vol. 41, No. 7, (1993) 1939-1949.



4. A.W. James and P. Bowen, "Elevated Temperature Crack Growth Resistance of TiAl Under Monotonic and Cyclic Loading," Mater. Sci. Eng., A153, (1992) 486-492.
5. S.J. Balsone, J.W. Jones, D.C. Maxwell, "Fatigue Crack Growth in a Cast Gamma Titanium Aluminide Between 25 and 954°C," in Fatigue and Fracture of Ordered Intermetallic Materials, W.O. Soboyejo and T.S. Srivatsan, eds., TMS, Warrendale, PA. (1994).
6. S.J. Balsone, J.M. Larsen, D.C. Maxwell, and J.W. Jones, "Effect of Microstructure and Temperature on Fatigue Crack Growth in the TiAl Alloy Ti-46.5Al-3Nb-2Cr-0.2W," Mater. Sci. Eng., A192/193, (1995) 457-464.
7. A.L. McKelvey, J.P. Campbell, K.T. Venkateswara Rao, and R.O. Ritchie "High Temperature Fatigue Crack Growth Behavior in an XD<sup>TM</sup>  $\gamma$ -TiAl Intermetallic Alloy," in Proceedings of the Sixth International Fatigue Congress Fatigue '96, G. Lütjering and H. Nowack, eds, Pergamon, Oxford, (1996) 1743-1748.
8. Y.-W. Kim, "Ordered Intermetallic Alloys, Part III: Gamma Titanium Aluminides," IOM, Vol. 46, No. 7, (1994) pp. 30-40.
9. B.D. Worth, J.M. Larsen, and A.H. Rosenberger, "Threshold Crack Growth Behavior of the Gamma Titanium Aluminide Alloy Ti-46.5Al-3Nb-2Cr-0.2W Under High Cycle Fatigue Conditions," in Second International Symposium on Structural Intermetallics, this proceedings, Seven Springs Resort, Champion, PA, (1997).
10. W. Elber, "The Significance of Crack Closure," in Damage Tolerance in Aircraft Structures ASTM STP 486, ASTM, PA, (1971) 230-242.
11. J.M. Larsen, B.D. Worth, S.J. Balsone, A.H. Rosenberger, and J.W. Jones, "Mechanisms and Mechanics of Fatigue Crack Initiation and Growth in TiAl Intermetallic Alloys," in Proceedings of the Sixth International Fatigue Congress Fatigue '96, G. Lütjering and H. Nowack, eds, Pergamon, Oxford, (1996) 1719-1730.
12. T.H. Hino, Okada, M. Kanno, "Analysis of Hydrogen Evolved from Fracture Surfaces of a TiAl Alloy," Scr. Metall. Mater., Vol. 29, (1993) 1029-1033.

THRESHOLD FATIGUE CRACK GROWTH BEHAVIOR  
OF THE GAMMA TITANIUM ALUMINIDE ALLOY Ti-46.5Al-3Nb-2Cr-0.2W  
UNDER HIGH CYCLE FATIGUE CONDITIONS

Brian D. Worth\*, James M. Larsen, and Andrew H. Rosenberger  
Air Force Research Laboratory – Materials Directorate  
Wright-Patterson Air Force Base, Ohio 45433, USA

\* The University of Dayton Research Institute  
Dayton, Ohio 45419, USA

Abstract

To date, there is a limited understanding of the mechanics of cyclic damage in gamma TiAl intermetallic alloys. The available studies indicate that the fatigue strength for this class of alloys typically exceeds 80 percent of the material's monotonic yield strength. Such data suggest the possibility of using a safe-life fatigue design at relatively high stresses. However, a safe-life design scheme does not account for the possible existence of intrinsic material defects or service-induced damage, both of which must be addressed in order to ensure reliability in fracture-critical applications. Previous results have shown that the long-crack growth rates in materials of both fully lamellar and duplex microstructures are highly sensitive to the level of applied loading. As a result, it appears likely that a fracture-mechanics-based approach to life prediction must assure that conditions for fatigue crack growth remain below the threshold stress intensity factor range,  $\Delta K_{th}$ . The current study examined the smooth and notched high cycle fatigue behavior of representative TiAl-based alloys to develop a better understanding of the events that lead to fatigue crack initiation and growth. The results of the study were used to identify key parameters that should be addressed in order to develop reliable life prediction models for this class of alloys in fracture critical applications in turbine engines.

Introduction

In the continuing effort to develop improved aerospace materials for turbine engine applications, considerable attention is being given to intermetallic alloys based on the ordered TiAl phase. These alloys, known as gamma titanium aluminides, have attractive mechanical properties that include high specific strength, specific modulus, and specific creep resistance, combined with good oxidation/hot-corrosion resistance [1-3]. Current gamma TiAl alloys appear to possess useful mechanical properties up to a temperature of approximately 760°C. This high temperature capability significantly exceeds the performance of conventional titanium-base materials and offers the potential to

replace nickel-base superalloys used in some turbine engine applications with a material of one-half the density. However, the attractive high temperature properties of gamma alloys are accompanied by relatively low levels of room temperature ductility, fracture toughness, fatigue crack growth resistance, and impact resistance.

The effective use of gamma TiAl alloys in the more aggressive turbine engine applications will require new approaches to structural design. Although gamma alloys exhibit smooth-bar fatigue limits approaching their monotonic yield strength, the tolerance of these materials to defects and service-induced damage is a key concern for fracture-critical components. In turbine engines, damage may result from high-velocity impacts by foreign objects in the gas flow path and from fretting fatigue in airfoil attachment regions. In addition, many turbine engine components experience combinations of low- and high-cycle fatigue, which may lead to the initiation and growth of cracks in otherwise undamaged material.

To predict the useful lifetime of gamma alloys used in many turbine engine applications requires consideration of damage tolerance. Fracture critical components in Air Force turbine engines are designed and life-managed under the Engine Structural Integrity Program (ENSIP) [4], which mandates the use of a damage tolerance approach wherein intrinsic or service-induced defects are assumed to exist. Moreover, the problem of high cycle fatigue (HCF) of turbine engine airfoils has recently gained considerable attention [5-7], and efforts are underway to extend the ENSIP requirement to address HCF.

It is clear that gamma alloys will need to satisfy any new high cycle fatigue requirements if these alloys are to replace the existing materials in engines. However, fatigue crack growth rate curves for gamma TiAl alloys exhibit a narrow interval between the threshold stress intensity factor range,  $\Delta K_{th}$ , and the apparent fracture toughness,  $K_Q$  [8-13], suggesting that the fraction of the total fatigue life associated with crack propagation is small.

Table I. Mechanical Properties of Alloy K5 (Ti-46.5Al-3Nb-2Cr-0.2W)

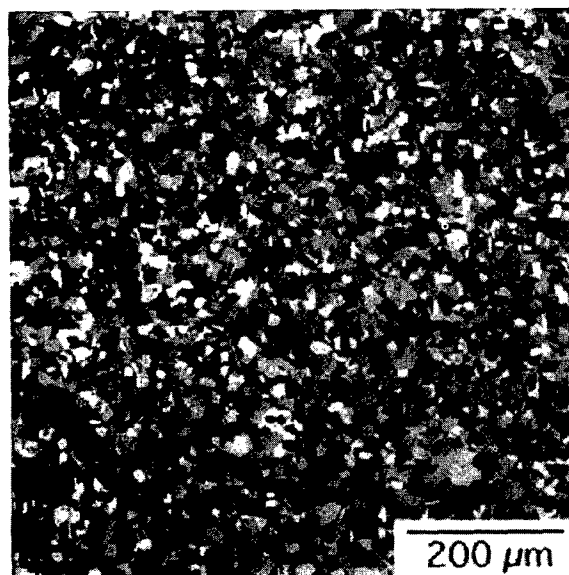
Microstructure	Processing	Y.S. (MPa)	U.T.S. (MPa)	Elongation (%)	Fracture Toughness (MPa√m)	Fatigue Strength (MPa) ( $\Delta\sigma$ ; R = 0.1, $10^7$ cycles)
Duplex	Forged + 1270°C/2 h/ FC to 900 °C + 900°C / 8 h/ AC	460	550	1.7	$K_{IC} = 11$	405
Refined Fully Lamellar (RFL)	Forged + 1260C/10 min/ to 1355 °C/ 4 min / to 1100 °C/ AC	479	547	1.0	—	392
Lamellar	Forged + 1340°C/0.6 h/ FC to 900 °C	375	450	0.9	$K_{IC} = 16.5$	331

FC: Furnace Cooled; AC: Air cooled

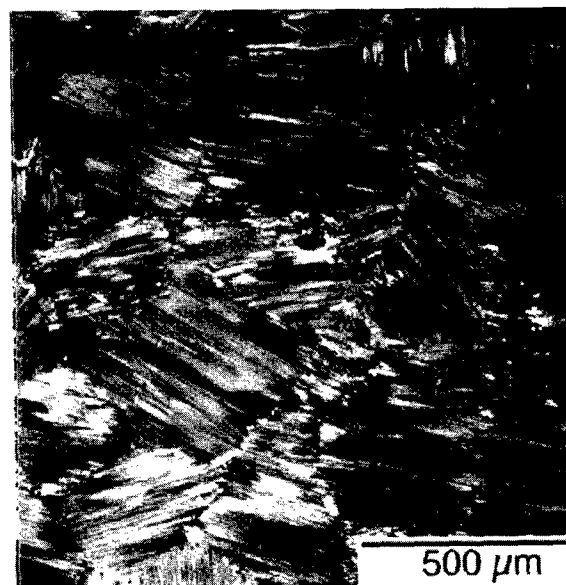
As a result, damage tolerant design of these materials is expected to require the use of  $\Delta K_{th}$  as a life-management criterion. This paper examines the damage tolerance fatigue capability of a representative gamma titanium aluminide alloy in three microstructural conditions. The role of the fatigue-crack-growth-rate threshold is examined for material usage conditions that are likely to be life-limiting for turbine engine components.

#### Material

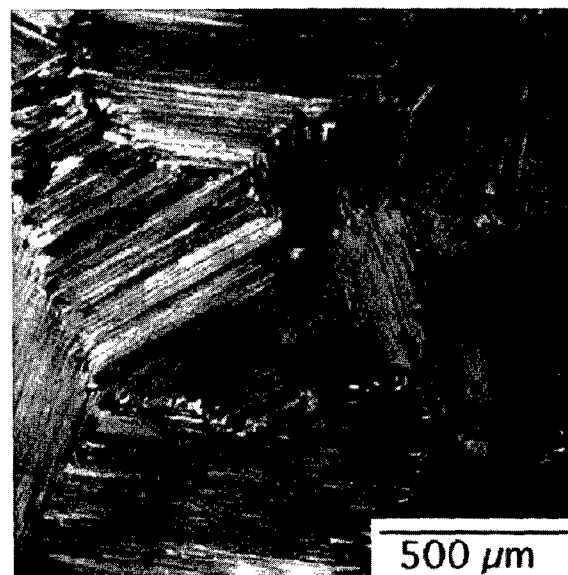
The experimental results to be presented are from an alloy developed by Kim [3], Ti-46.5Al-3Nb-2Cr-0.2W (atomic %), designated K5. This material was forged and heat treated to produce three microstructures: duplex, refined fully lamellar (RFL), and fully lamellar. The heat treatment conditions for the three microstructures are given in Table I, along with a summary of mechanical properties. Optical micrographs of the three microstructures are shown in Fig. 1. The duplex microstructure was composed of a mixture of equiaxed gamma grains ( $L1_0$  structure) and fine colonies of lamellar gamma plus alpha-2 phase ( $DO_{19}$  structure). The refined and coarse lamellar microstructures were composed of lamellar colonies of approximate diameters 280 and 700  $\mu\text{m}$ , respectively. The average lamellae thickness in the RFL microstructure was also less than that of the coarse lamellar material. As indicated in Table I, the coarse lamellar microstructure had a lower strength than either the RFL microstructure or duplex microstructure. Although the duplex microstructure exhibited a higher ductility than its lamellar counterparts, the duplex material also had a lower initiation fracture toughness than either of the lamellar microstructures.



(a)



(b)



(c)

Fig. 1 – Microstructures of the alloy Ti-46.5Al-3Nb-2Cr-0.2W: (a) duplex, (b) refined fully lamellar, and (c) coarse lamellar.

## Experimental Procedure

Fatigue and fatigue crack growth experiments were performed at room temperature on specimens of the three microstructures. The fatigue specimens were smooth bars, nominally 9.5 mm in diameter, having diametrically opposed flat sides that reduced the gage section to 25 mm<sup>2</sup>, producing a 25 mm-long uniform gage that was subsequently electropolished to remove surface residual stresses. The fatigue tests were performed in air at 40 Hz under a stress ratio ( $R = \sigma_{min}/\sigma_{max}$ ) of 0.1. In addition, to characterize sensitivity of the materials to small surface defects, fatigue tests were performed on smooth-bar specimens that had been fabricated with a series of equally spaced, semicircular, electro-discharge-machined surface notches. The details of this test method will be discussed later.

Fatigue crack growth experiments were performed on the three microstructures using standard procedures and compact type, C(T), specimens of width 20 mm and thickness 5 mm. These tests were conducted at 20 Hz in laboratory air at room temperature under a stress ratio of 0.1. The crack growth data were acquired under decreasing stress-intensity-factor-range,  $\Delta K$ , fatigue followed by constant-load-amplitude fatigue. For all of the data to be presented, crack arrest occurred at the minimum crack growth rate,  $da/dN$ , shown. Crack-opening-compliance measurements obtained using a crack-mouth extensometer provided measurements of crack length, and these data were analyzed to determine levels of crack closure,  $K_{cl}$ , which were used to calculate the effective stress intensity factor range  $\Delta K_{eff} = K_{max} - K_{cl}$ .

## Results

### Fatigue Crack Growth

Fatigue crack growth rate data for the three microstructures are plotted versus  $\Delta K$  in Fig. 2. The fine duplex microstructure offered the least resistance to fatigue crack growth. The slope of the  $da/dN$ - $\Delta K$  data for this microstructure was extremely steep, and this material had lowest value of threshold stress-intensity-factor range,  $\Delta K_{th}$ , and the lowest apparent toughness,  $K_{Qc}$ , of the three materials. In comparison to the duplex material, the two lamellar microstructures exhibited much greater crack growth resistance. Although the average colony sizes of the two lamellar microstructures differed by a factor of 2.5, their crack growth rate behavior was equivalent in all but the near-threshold region. The crack growth rate data from each of the materials were regressed with an equation of the form

$$\log(da/dN) = C_1[\arctanh(C_2[\log(\Delta K) + C_3])] + C_4 \quad (1)$$

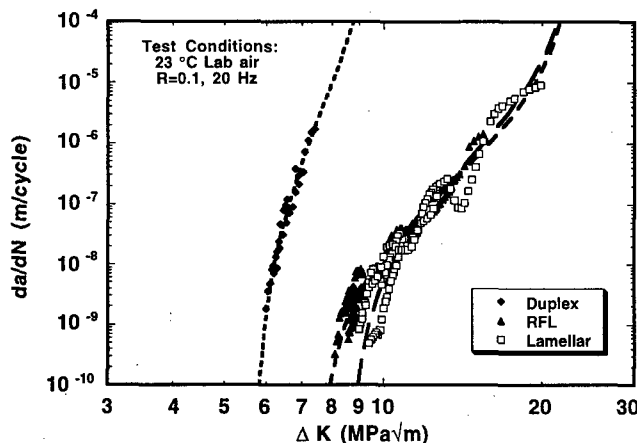


Fig. 2 - Fatigue crack growth behavior from tests of C(T) specimens tested in air at room temperature;  $R = 0.1$ .

which provided a good representation of the behavior over the full range of the data.

### Residual Crack Propagation Life

As noted earlier, the damage tolerance approach to life management requires that fracture critical components be assumed to contain initial defects or damage. Generally, the scale of the assumed damage is defined by the detection limit of some nondestructive inspection method. In this case the detection limit is the maximum crack size,  $a_i$ , that can be missed by the inspection. Damage tolerance life predictions are performed by calculating the number of cycles required to propagate a crack of initial size  $a_i$  to failure. This crack propagation lifetime is given by

$$N_p = \int_{a_i}^{a_c} \frac{da}{f(\Delta K)} \quad (2)$$

where  $a_c$  is the critical crack length corresponding to the material's effective fracture toughness in fatigue ( $K_{Qc}$ ),  $f(\Delta K)$  is a crack-growth-rate function such as Eq. 1, and  $\Delta K$  is defined for a specific crack geometry and loading history. In the example to follow, the crack was assumed to be a semicircular surface flaw of depth  $a$ , which is a crack geometry commonly observed in actual components.

To illustrate the effect of the assumed initial crack size on the calculated crack propagation lifetime, Eq. 2 was solved numerically to construct the remaining-life plot shown in Fig. 3. For a given initial crack size,  $a_i$ , the integrated remaining fatigue crack propagation life,  $N_p$ , is given by the ordinate of the plot. The lamellar microstructures clearly exhibit much more attractive damage tolerance than does the duplex material. For turbine engine components that are life-limited by low cycle fatigue, the maximum number of fatigue cycles is typically less than 10,000. Thus, for either of the lamellar materials, a cracked component could spend the majority of its fatigue life propagating a crack of initial depth equal to a millimeter, which is a crack size that is readily detectable by advanced methods of nondestructive evaluation. In the case of the duplex material, however, catastrophic failure would occur at a crack depth less than approximately 0.4 mm, making reliable, early crack detection extremely difficult or impossible.

As shown in the figure, each of the materials exhibits a critical crack depth, corresponding to  $\Delta K_{th}$ , below which the remaining crack propagation lifetime is effectively infinite. For the duplex,

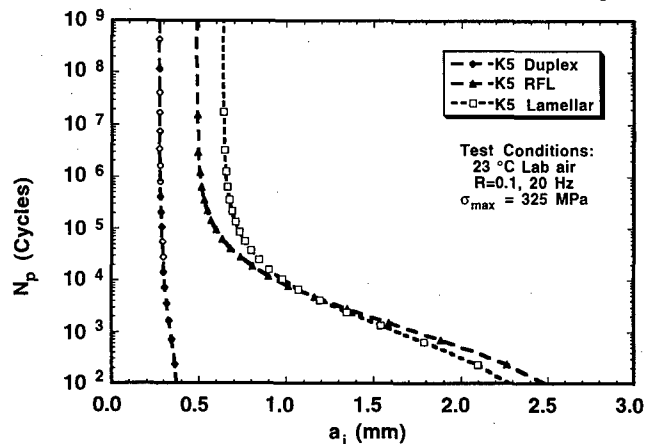


Fig. 3 - Remaining crack propagation lifetime,  $N_p$ , plotted versus initial crack size,  $a_i$ , for fatigue under conditions of  $R = 0.1$  and  $\sigma_{max} = 325$  MPa.

RFL, and lamellar materials, this crack size was 0.27, 0.49, and 0.64 mm, respectively. The general trends of the curves indicate that  $\Delta K_{th}$  is the dominate consideration for lifetimes exceeding approximately  $10^5$  cycles. Components that are subjected to high cycle fatigue may be expected to experience fatigue loadings greatly in excess of  $10^5$  cycles, highlighting the critical nature of the fatigue crack growth threshold,  $\Delta K_{th}$ , for life prediction under high cycle fatigue conditions.

Although it may be attractive to use the large-crack  $\Delta K_{th}$  as a life-management criterion, it is well known that data of large fatigue cracks may not accurately represent the behavior of small fatigue cracks in that occur actual structures [15,16]. One view of this issue follows from the original work of Kitagawa and Takahashi [17] who showed that threshold crack growth rate data display a dependence on crack size that is related to the material's fatigue strength,  $\Delta S_e$ , and  $\Delta K_{th}$ . As shown schematically in Fig. 4, a plot can be constructed that combines fatigue crack initiation and propagation concepts. Considering crack initiation, and disregarding the possibility of a preexisting crack, specimen failure should occur only if the applied stress range exceeds  $\Delta S_e$ , which is represented by the horizontal line in the figure. Alternatively, considering a fracture mechanics approach, crack growth should occur only if the applied  $\Delta K$  exceeded  $\Delta K_{th}$ , which is represented by the solid line of slope  $-1/2$  on the figure. Thus, the utility of  $\Delta K_{th}$  as a "material property" appears to be limited to cracks of approximate length greater than that given by the intersection of the two lines ( $a_0$ ). For many materials,  $a_0$  appears to provide a rough approximation of the crack size below which small-crack effects become potentially significant. If, as has been frequently suggested, a small crack has not yet developed the full level of crack closure that exists for large fatigue cracks, then the limiting small-crack threshold may be more accurately represented by a closure-free condition, defined as  $\Delta K_{eff,th} = \Delta K_{max,th} - \Delta K_{cl,th}$  corresponding to the threshold crack growth rate. In this situation, the solid line of slope  $-1/2$  in the Fig. 4 would be displaced to the left (assuming  $\Delta K_{eff,th} < \Delta K_{th}$ ).

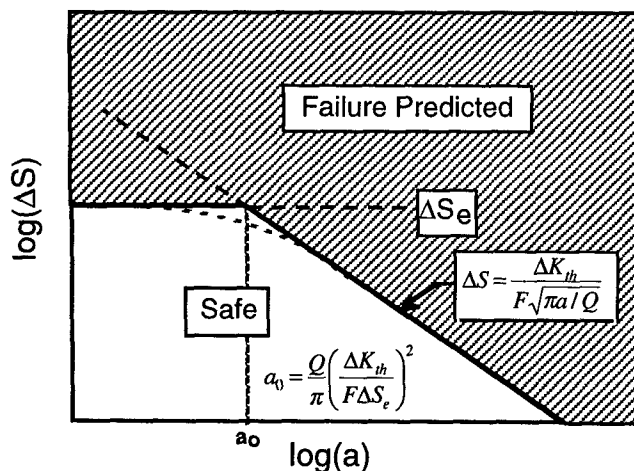


Fig. 4 - Schematic "Kitagawa plot" of threshold fatigue conditions in terms of crack size and stress range.

#### Notch Fatigue Behavior

To examine the feasibility of using a threshold crack growth approach to deal with occasional sources of damage, such as foreign object impacts, the influence of damage size on residual fatigue strength was examined. Previous research [18,13] had indicated that, in the coarse lamellar microstructure, the effective initial crack size was determined by the colony size. Thus, the

superior crack growth resistance of the lamellar, versus the duplex, microstructure can be misleading. The large initiation crack size in the coarse lamellar microstructure far outweighed the beneficial effects of the superior crack growth resistance and higher  $\Delta K_{th}$  of this material. For this reason, it was of interest to gain an understanding of the influence of notch size on residual fatigue strength in a lamellar microstructure having a refined colony size. Thus, the refined fully lamellar material was selected for study. As noted earlier, this microstructural condition also had more attractive monotonic properties than did a coarse lamellar microstructure.

In previous testing of materials with lamellar microstructures, it was found that when a single notch was machined into a specimen, fatigue failure to often occurred at a location away from the notch - a behavior that appeared to result from the coarse, anisotropic nature of the microstructure. To increase the chances of finding the 'weak link' of the structure, a series of equivalent notches were machined into each sample. The test method involved using electro-discharge machining (EDM) to produce twelve, well-separated semicircular notches of equal size on the surface of electropolished fatigue samples. Specimens were produced with three notch sizes, ranging in depth from 80  $\mu\text{m}$  to 400  $\mu\text{m}$ . The height of the notches was approximately 75  $\mu\text{m}$ . As noted earlier, the average colony size of the materials with the refined lamellar microstructure was 280  $\mu\text{m}$ , which meant that the notch depth ranged from 30 to 150 percent of the colony size. These specimens were then tested under constant-load-amplitude fatigue to determine the threshold stress range required to produce failure. Using this test method, failure always originated at a notch. A typical failure is pictured in Fig. 5, which shows a site of interlamellar fracture at the depth of the EDM notch.

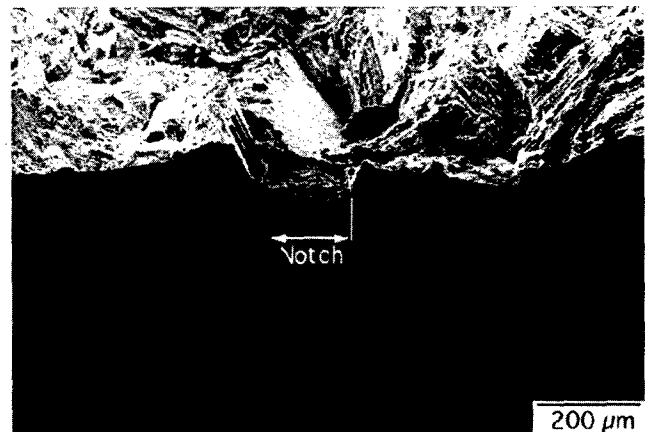


Fig. 5 - Fracture surface of a refined lamellar specimen showing the origin of the failure at a 200  $\mu\text{m}$  deep semicircular notch.

The  $10^7$ -cycle fatigue strengths for the three notch depths are listed in Table II. As shown in Fig. 6, when these results are plotted on a Kitagawa diagram, for all three notch sizes, the residual fatigue strength is below that predicted based on the large-crack  $\Delta K_{th}$ , and this disparity increased as the notch size is decreased. The data for the notched-threshold conditions fall near the line corresponding to  $\Delta K_{eff,th}$  but this large-crack parameter still overestimates the data from the 80  $\mu\text{m}$  deep notch. It should be noted that the latter notch size is well below the average colony diameter and that this threshold condition was probably controlled by the microstructural dimension rather than by the notch size, as was shown previously for the coarse lamellar material [18,13]. In a similar lamellar alloy, Campbell, et al [19] noted that the rapid growth of small fatigue cracks persisted up to a crack size approximately equal to the colony size. The trend in the notched-threshold data is also consistent with the smooth transition in

Table II. Notch Fatigue Results ( $R = 0.1$ )

Notch Depth ( $a$ ; $\mu\text{m}$ )	Stress Range, $\Delta\sigma$ (MPa)	$\sigma_{\text{max}}/\sigma_{\text{YS}}$ (MPa)
Smooth Bar	392	0.91
80	340	0.79
200	270	0.63
400	225	0.52

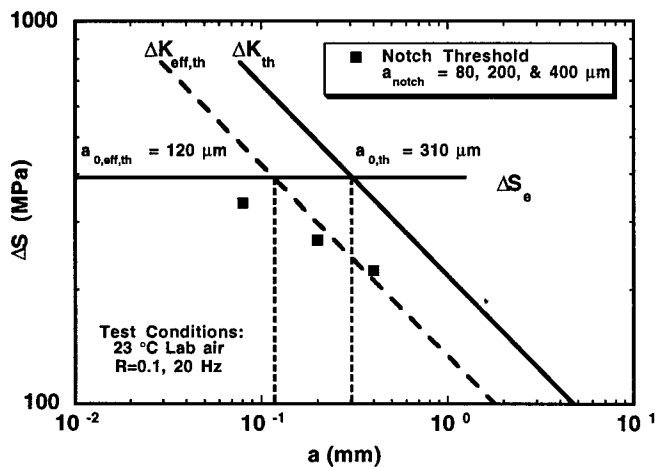


Fig. 6 – Plot of threshold fatigue conditions in terms of crack size and stress range for the RFL microstructure showing the threshold conditions for crack propagation from small semicircular notches.

threshold behavior depicted in Fig. 4 as the behavior becomes dominated by the fatigue-limit stress range,  $\Delta S_0$ .

An additional advantage of the multiple notch sample was that an indication of the fatigue crack propagation mechanisms could be

obtained by using periodic optical microscopy to examine the crack growth that occurred at unfailed notches. In several instances non-catastrophic cracks were observed from notches other than the notch from which failure occurred. As shown in Fig. 7 crack growth tended to occur preferentially along interfaces in the lamellar microstructure. It was also observed that crack growth was intermittent. Testing conducted at 400 MPa on samples with 80  $\mu\text{m}$  notches showed that cracks initiated from two notches after 25,000 cycles. One of these cracks continued to propagate for the next 50,000 cycles and then arrested at a colony boundary. The second crack arrested at a colony boundary after 30,000 cycles and showed no visible growth for the next 120,000 cycles (150,000 total cycles). Failure subsequently occurred from this second crack after a total of 165,000 cycles.

The subcritical crack shown in Fig. 7 gives a good indication of the strong influence that local microstructural orientation had on the growth of small cracks - in this case, small cracks growing from a notch. It appears that a ligament bridge formed between the crack that grew from the notch and the crack that formed in an adjacent colony. The actual crack morphology is probably more complicated than this two-dimensional image suggests, however, recognizing that the photograph shows two part-through surface cracks, which may eventually connect to form a single, shallow surface crack. While bridging may have contributed to the arrest of the crack in Fig. 7, the chronology of the cracking at the notch tip would have to be determined, as would the three dimensional nature of the cracking. In fatigue crack growth tests of a fine lamellar XD<sup>TM</sup> gamma alloy, Campbell [20] reported that ligament bridging reduced the crack-tip  $K$  by as much as 2 MPa $\sqrt{\text{m}}$ . However, other researchers [14] failed to find any indication of ligament bridging during fatigue crack growth in a coarse lamellar gamma alloy. The disparity in these findings indicates an obvious area for future work. In general, ligament bridging may be expected to be more significant in small cracks due to the generally lower crack tip opening displacements that occur at small crack lengths and the stronger influence of the microstructure.

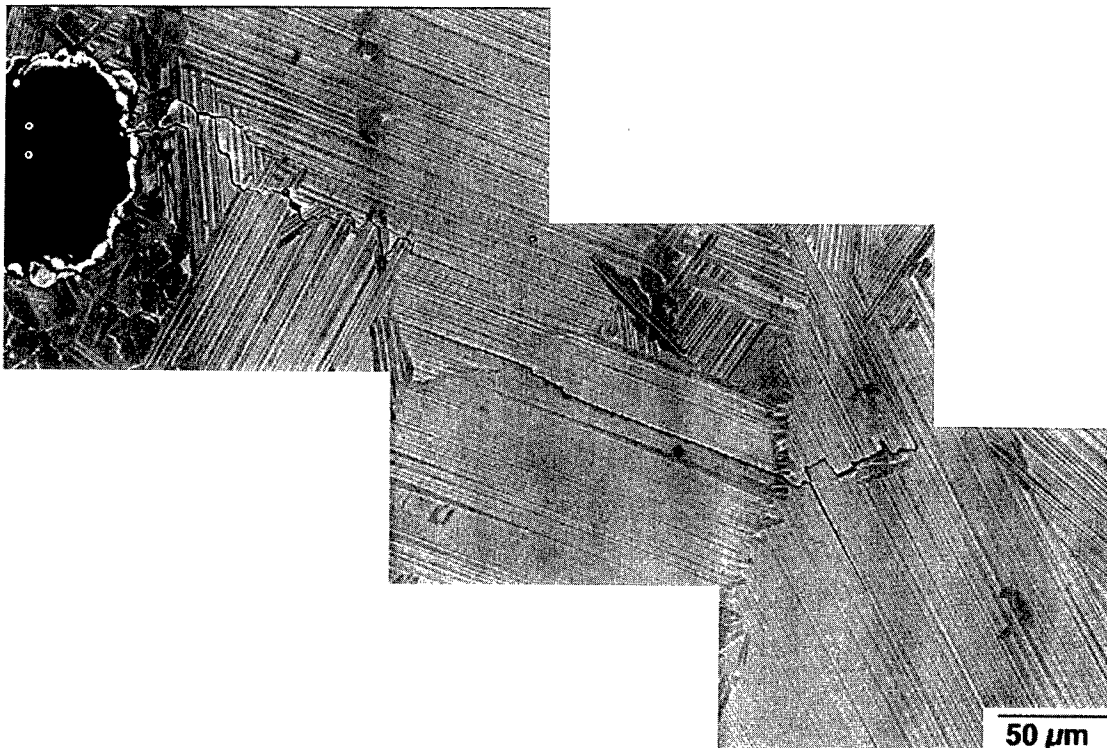


Fig. 7 Typical cracking from a notch tip showing the early states of ligament formation associated with multiple surface cracks.

### Discussion

Gamma titanium aluminide alloys have a variety of extremely attractive properties in demanding applications such as in gas turbine engines. The performance and fuel economy of turbine engines can be improved significantly by replacing existing alloys with less-dense, TiAl alloys in a number of components. Static components provide the opportunity to introduce these alloys into service with relatively low risk. However, the greatest payoff will occur when gamma alloys demonstrate capabilities suitable for fracture critical applications. Given their unusual balance of properties, it appears that the widespread use of these low-ductility materials will depend on (i) tailoring their properties to meet specific application needs and (ii) demonstrating reliability under actual service conditions.

A key aspect of a component's service requirements is defined by the imposed time-temperature-stress spectrum, which may contain significant levels of both low- and high-cycle fatigue. In addition, the material must be able to tolerate the occurrence of occasional intrinsic material defects and secondary damage from factors such as foreign object impacts and fretting fatigue. To ensure the long term reliability of TiAl alloy components in service, a life-prediction system capable of accurately predicting the effects of complex loading and secondary damage must be available.

Consistent with previous results, the current findings show that lamellar microstructures tend to be much more resistant to crack propagation than is material of a fine duplex microstructure. While the scale of the coarse and refined lamellar microstructures that were tested differed by a factor of 2.5, the fatigue crack growth behavior of these two materials was essentially equivalent in all but the near-threshold crack growth regime. Although  $\Delta K_{th}$  decreased with decreasing colony size, the overall fatigue resistance improved as colony size decreased. This behavior is believed to be associated with the reduced size of the initiated crack, which scaled with the colony size. The effect of this initiated crack size appears to far outweigh the benefits of improved crack growth resistance in the coarse lamellar microstructure. Further refinement in lamellar colony size should have a modest effect on overall crack growth resistance but may impart significant additional improvements in strength and resistance to fatigue crack initiation. Moreover, the evidence thus far suggests that a reduction in colony size would also reduce the minimum crack size for which the large-crack  $\Delta K_{th}$  may apply.

The data and analyses presented here show that a crack growth approach is useful for life management under low cycle fatigue, but that the typical crack propagation lifetimes are insufficient to permit crack growth under the number of cycles expected under high cycle fatigue. Recognizing that crack formation due to a variety of potential mechanisms cannot be avoided, it appears that an effective damage tolerance life prediction system must focus on the conditions necessary for threshold crack growth. This will require understanding the small-crack  $\Delta K_{th}$  as a function of residual stress, mode of crack formation, mission spectra, crack geometry, temperature, and material and microstructural characteristics.

### Summary and Conclusions

Based on the results presented on the alloy gamma titanium aluminide alloy Ti-46.5Al-3Nb-2Cr-0.2W, the following conclusions are drawn:

- The coarse and refined lamellar materials, having lamellar colony sizes equal to 700 and 280  $\mu\text{m}$ , respectively, had substantially greater crack growth resistance than did the fine duplex material (grain size approximately 20  $\mu\text{m}$ ).

- The crack growth resistance of the two lamellar materials was equivalent in all but the near-threshold region, where  $\Delta K_{th}$  in the refined lamellar microstructure was slightly below that of the coarse lamellar material.
- Analysis of the crack propagation behavior indicated that a crack growth approach to life prediction is feasible for low cycle fatigue but that the crack propagation lifetimes are insufficient to satisfy high cycle fatigue requirements. As a result, a fracture mechanics life prediction approach will probably require the use some form of a threshold criterion insure the non-propagation of small fatigue cracks.
- In tests of refined fully lamellar specimens containing small, semicircular surface notches, small cracks propagated at  $\Delta K$  levels less than the large-crack  $\Delta K_{th}$ . For notch depths of 200 and 400  $\mu\text{m}$ , the small-crack threshold condition was in reasonable agreement with the closure-free, large-crack threshold,  $\Delta K_{eff,th}$ . However, cracks growing from smaller, 80  $\mu\text{m}$ -deep, notches propagated under conditions below  $\Delta K_{eff,th}$ .
- Crack growth below  $\Delta K_{eff,th}$  appeared to occur when the surface crack length was less than the lamellar colony diameter in the refined fully lamellar material. This behavior was similar to findings reported earlier for the coarse lamellar material. In both materials, the lamellar colony size appears to control the size of the dominant initiated crack, leading to crack growth below  $\Delta K_{eff,th}$  for cracks of approximate surface length less than the colony diameter.
- Refinement of the lamellar colony size had a number of benefits (increased yield strength, increased fatigue strength, and improved resistance to propagation of small fatigue cracks), combined with modest detrimental effects (reduced tensile ductility and slightly reduced large-crack  $\Delta K_{th}$ ). Thus, further refinement of the lamellar colony size appears to be a valuable objective for the development of microstructures and alloys having an improved balance of properties.

### Acknowledgments

This research was performed in the Materials Directorate, Air Force Research Laboratory, Wright-Patterson Air Force Base, OH and was supported by the Air Force Office of Scientific Research under Task 2302BW. B. D. Worth gratefully acknowledges the support of Air Force contract F33615-94-C-5200. The authors would also like to thank Y.-W. Kim of Universal Energy Systems, Dayton, OH for his thoughtful discussions and for providing the K5 alloy.

### References

1. Y.-W. Kim, "Intermetallic Alloys Based on Gamma Titanium Aluminide," *IOM*, Vol. 41, No. 7, (1989) 24-30.
2. Y.-W. Kim and D. M. Dimiduk, "Progress in the Understanding of Gamma Titanium Aluminides," *IOM*, Vol. 43, No. 8, (1991) 40-47.
3. Y.-W. Kim, "Ordered Intermetallic Alloys, Part III: Gamma Titanium Aluminides," *IOM*, Vol. 46, No. 7, (1994) 30-40.
4. U.S. Air Force, Engine Structural Integrity Program. *Military Standard 1783*, Aeronautical Systems Division, Wright-Patterson Air Force Base, OH, (1984).
5. T. Nicholas and J. R. Zuiker, "On the Use of the Goodman Diagram for High Cycle Fatigue Design," *Int. J. Fract.*, 80, (1996) 219-235.
6. B. A. Cowles, "High Cycle Fatigue in Aircraft Gas Turbines - An Industry Perspective," *Int. J. Fract.*, Vol. 80., (1996) 147-163.

7. J. M. Larsen, B. D. Worth, C. G. Annis, Jr., and F. K. Haake, "An Assessment of the Role of Near-Threshold Crack Growth in High-Cycle-Fatigue Life Prediction of Aerospace Titanium Alloys Under Turbine Engine Spectra," Int. J. Fract., Vol. 80, (1996) 237-255.
8. S. J. Balsone, J. W. Jones, D. C. Maxwell, "Fatigue Crack Growth in a Cast Gamma Titanium Aluminide Between 25 and 954°C," in Fatigue and Fracture of Ordered Intermetallic Materials, W. O. Soboyejo and T. S. Srivatsan, eds., TMS, Warrendale, PA, (1994).
9. S. J. Balsone, J. M. Larsen, D. C. Maxwell, and J. W. Jones, "Effect of Microstructure and Temperature on Fatigue Crack Growth in the TiAl Alloy Ti-46.5Al-3Nb-2Cr-0.2W," Mater. Sci. Eng., A192/193, (1995) 457-464.
10. K. T. Venkateswara Rao, Y-W. Kim, and R. O. Ritchie, "High-Temperature Fatigue-Crack Growth Behavior in a Two-Phase ( $\gamma + \alpha_2$ ) TiAl Intermetallic Alloy," Scr. Metall. Mater., Vol. 33, No. 3, (1995) 459-464.
11. J. M. Larsen, B. D. Worth, S. J. Balsone, and J. W. Jones, "An Overview of the Structural Capability of Available Gamma Titanium Aluminide Alloys," in Gamma Titanium Aluminides, Y-W. Kim, R. Wagner, and M. Yamaguchi, eds., TMS/ASM International, Warrendale, PA, (1995) 821-834.
12. P. Bowen, R. A. Chave, and A. W. James, "Cyclic Crack Growth in Titanium Aluminides," Mater. Sci. Eng., A192/193, (1995) 443-456.
13. J. M. Larsen, B. D. Worth, S. J. Balsone, A. H. Rosenberger, and J. W. Jones, "Mechanisms and Mechanics of Fatigue Crack Initiation and Growth in TiAl Intermetallic Alloys," FATIGUE '96, Vol. III, Elsevier Science Ltd., Oxford, U.K., (1996) 1719-1730.
14. B. D. Worth, J. M. Larsen, S. J. Balsone, and J. W. Jones, "Mechanisms of Ambient Temperature Fatigue Crack Growth in Ti-46.5Al-3Nb-2Cr-0.2W," Met. Mat. Trans., Vol. 28A, (1996) 825-835.
15. R. O. Ritchie and J. Lankford, eds., Small Fatigue Cracks, The Minerals, Metals, and Materials Society, Warrendale, PA (1986).
16. K. J. Miller and E. R. de los Rios, Short Fatigue Cracks, Mechanical Engineering Publications Limited, London, UK, (1992).
17. H. Kitagawa and S. Takahashi, "Applicability of Fracture Mechanics to Very Small Cracks or the Cracks in the Early Stage," in Proceedings of the Second International Conference on Mechanical Behavior of Materials, Boston, MA, (1976) 627-631.
18. J. M. Larsen, B. D. Worth, S. J. Balsone, and A. H. Rosenberger, "Reliability Issues Affecting the Implementation of Gamma Titanium Aluminides in Turbine Engine Applications," in Titanium '95, Vol. I, The Institute of Materials, U. K., (1996) 113-120.
19. J. P. Campbell, J. J. Kruzic, S. Lillibridge, K. T. Venkateswara Rao, and R. O. Ritchie, "On the Growth of Small Fatigue Cracks in  $\gamma$ -Based Titanium Aluminides," Scr. Metall. Mater., submitted, (1997).
20. J. P. Campbell, M. S. Thesis, University of California, Berkeley, CA (1996).



## **NIAL ALLOYS**

## Prospects for the Development of Structural NiAl Alloys

R.D. Noebe and W.S. Walston\*  
NASA Lewis Research Center, Cleveland, OH 44135  
\*GE Aircraft Engines, Cincinnati, OH 45215

### **Abstract**

NiAl alloys continue to loom on the technological horizon as a potential high temperature replacement for Ni-base superalloys. To be competitive with superalloys, a balance of properties including reasonable fracture resistance, excellent creep strength, high thermal conductivity, and environmental durability is required. While conventional polycrystalline alloys do not meet these requirements and fiber reinforced composites have not lived up to their initial expectations for lack of a compatible fiber, there are still several classes of NiAl-based materials that have received significant attention. These are precipitation strengthened NiAl single crystals, directionally solidified NiAl-based eutectics, and dispersion strengthened NiAl alloys. The latest advancements, remaining problems, and lessons learned during the development of these systems will be discussed along with an assessment for the potential commercialization of NiAl and the most likely market niches.

### **Introduction**

As with most ordered intermetallic systems, NiAl was originally chosen for study as a potential structural material because of its high melting temperature, hardness, and chemical stability [1]. This initial work was followed soon thereafter by a concentrated effort in the 1960's to determine the effect of processing and other metallurgical variables on mechanical behavior [2]. By the mid 1960's, some of NiAl's other attributes, such as its outstanding oxidation resistance and high thermal conductivity were identified, leading to the first serious consideration of NiAl as a structural component in a gas turbine engine as the leading edge for a superalloy turbine vane [3]. However, no solution was found for the low temperature brittleness of this compound, and by the end of the 1960's government and industrial interest in NiAl faded. At this point, research on NiAl shifted to academic institutions and between 1970 and the mid 1980's there was a small but steady effort in the investigation of oxidation behavior, mechanical properties, and deformation mechanisms.

Then in the mid to late 1980's, the level of research on NiAl exploded along with a revival in ordered intermetallic research in general. The resurgence in NiAl was spurred in part by the renewed interest in ordered intermetallics and by generic government aer propulsion programs [4,5] and sustained by the relatively large effort by GE Aircraft Engines to develop NiAl single crystal alloys for turbine airfoil applications [6,7]. Unfortunately, we have now come full circle and government and industrial interest in NiAl has peaked, due once again to an inability to overcome the poor fracture toughness and impact resistance of this compound [8,9]. Therefore, at this stage in the development of NiAl, it is time to re-evaluate the present status and future potential of this material.

The driving force behind the development of alternative structural materials, particularly for aerospace applications, is the fact that Ni-base superalloys are used at temperatures exceeding 80% of their absolute melting temperature [10]. Consequently, the attainment of significantly higher operating temperatures, with the concomitant improvements in engine efficiency and thrust-to-weight ratio is very dependent on the development of new material systems. In regard to the development of new alloy systems, NiAl was an obvious choice for a number of reasons. First, was probably familiarity;  $\beta$ -NiAl is a much higher melting point compound in the same binary phase diagram that  $\gamma/\gamma'$  superalloys derive and NiAl has been used for years as an oxidation resistant coating for Ni-base superalloys. In addition to these advantages, NiAl has a density ( $5.9 \text{ g/cm}^3$ ) that is approximately 2/3 that of nickel-base superalloys, a thermal conductivity which is 4 to 8 times greater than superalloys, and it is relatively easy to process and machine by conventional techniques. An additional advantage is the ability to attain high temperature creep resistance in NiAl alloys, a benefit that has only been realized in the last several years and represents one of the greatest achievements in current alloy design programs. Unfortunately, poor fracture toughness and tensile ductility continue to be the main liabilities.

In polycrystalline form, conventional NiAl alloys do not possess adequate strength to be useful at the extremely high temperatures needed to compete with nickel-base superalloys [8,11], and there is little interest today in continuous fiber reinforced NiAl-based composites due to a number of presently unresolvable technical barriers including the lack of a compatible fiber [12,13]. However, there are still several NiAl-based material systems that have been actively investigated for potential utilization in niche high temperature applications: advanced NiAl single crystals, NiAl-based eutectics, and dispersion strengthened NiAl alloys. The property advantages, limitations, and present status of these systems are presented in the following sections.

#### Alloyed NiAl Single Crystals

Of the three NiAl-based systems covered in this paper, the most extensive development work has been performed on NiAl single crystals, with specific application as a high pressure turbine blade or vane. Through the efforts at General Electric Aircraft Engines (GEAE) and other supporting programs, significant improvements in material properties, processing, and design methodology have been attained. The greatest achievements in this area have been the development of a family of NiAl single crystal compositions with creep strengths competitive with the best Ni-based superalloys and the culmination of the processing and design studies with the successful engine test of a high pressure turbine vane.

NiAl single crystals can be made creep resistant by alloying with various combinations of group IVB and VB elements such as Ti, Hf, Zr, Nb, and Ta along with minor additions of Ga [14,15]. With typical total alloying additions of 5 - 6 at.%, NiAl single crystals can be made with creep strengths equivalent to René N4 (Fig. 1). However, on a density compensated basis, the same alloys would have strengths at least comparable to third generation single crystal superalloys such as René N6 [9]. It should be noted that the Larson Miller Parameter (LMP) used to compare creep-rupture lives in Fig. 1 (and subsequent figures) was calculated using the formula:  $LMP = T (C + \log t)$ , where  $T$  is the temperature in degrees Kelvin,  $t$  is the rupture life in hours, and a value of 20 was used for the constant "C".

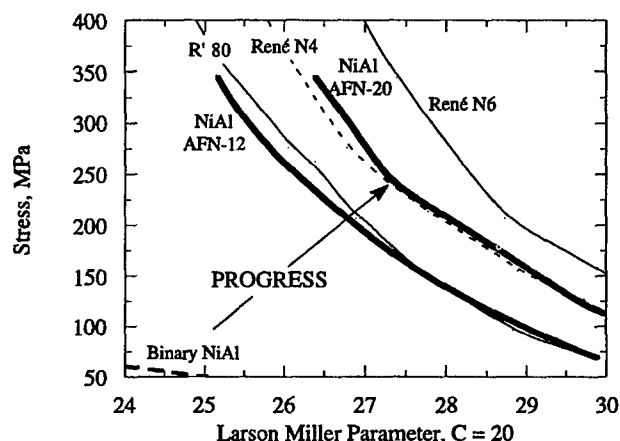


Figure 1. Progress made in the tensile rupture strength of NiAl single crystals.

Creep strength could be further optimized by an unambiguous determination of structure-property relationships in NiAl single crystals and a better understanding of the active strengthening mechanisms. While it is safe to assume that the most creep resistant materials are at least precipitate strengthened, there has been no systematic correlation between precipitate morphology, size,

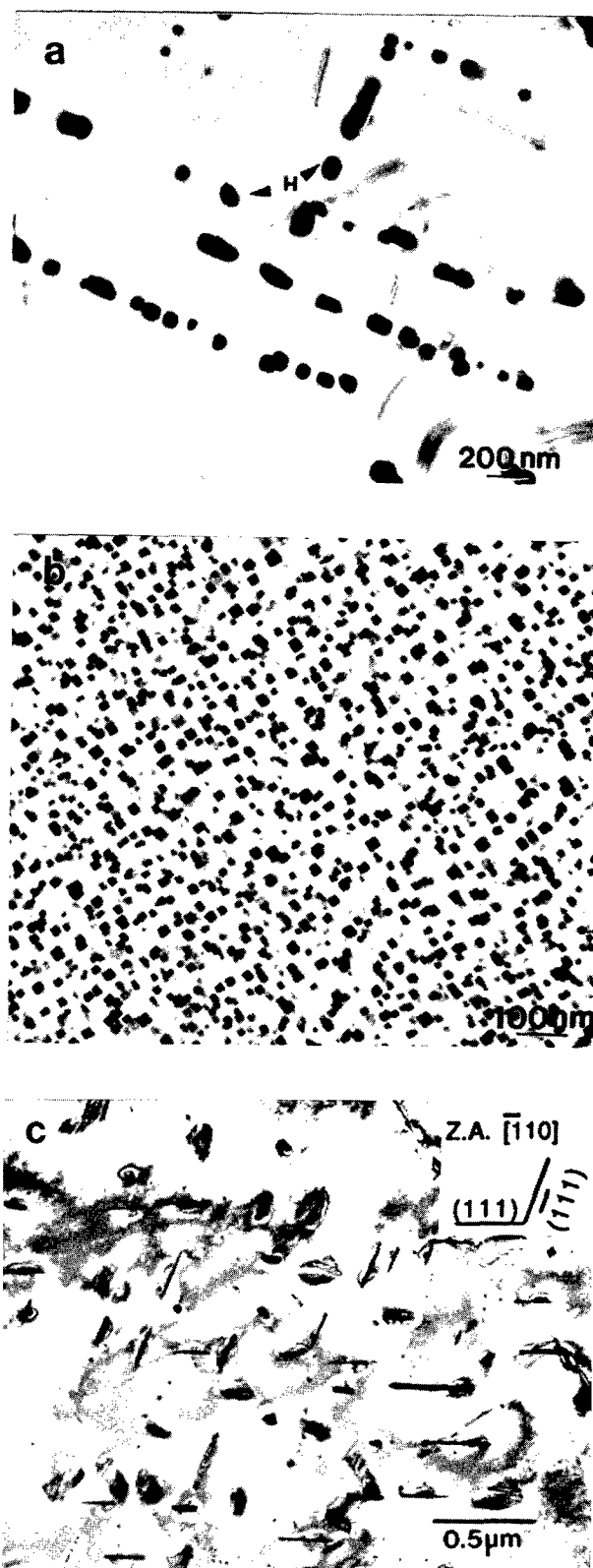


Figure 2. Microstructural variation in NiAl-Hf alloys due to the unintentional addition of Si. a.) high purity zone refined NiAl-1Hf alloy with Heusler ( $Ni_2AlHf$ ) precipitates, b.) G-phase ( $Ni_{10}Hf_6Si_2$ ) precipitates in a NiAl-1Hf alloy containing about 0.3 Si and c.) E-phase ( $NiHfSi$ ) precipitates in a NiAl-0.5Hf-0.3Si alloy.

distribution, structure, misfit, etc., and creep strength. In fact, the resulting precipitate phase is not always the anticipated one due to unintentional contamination of the NiAl melt with Si from reaction with the alumina-silicate mold materials during processing. This Si contamination, in turn, drastically alters the phase equilibria. For example, NiAl alloys doped with Hf at levels just above its solubility limit would be expected to contain Heusler ( $\text{Ni}_2\text{AlHf}$ ) precipitates (Fig. 2a), however, the presence of even trace additions of Si can result in alloys with completely different precipitate structures. These structures can include a fine dispersion of G-phase ( $\text{Ni}_6\text{Hf}_2\text{Si}_7$ ) [16] as shown in Fig. 2b, a structure consisting predominantly of E-phase ( $\text{NiHfSi}$ ) [17] as shown in Fig. 2c, or mixed structures composed of two or all three precipitate phases depending on the Hf:Si ratio in the alloy [18]. Zr-doped alloys exhibit the same diversity in structure due to additions of Si, intentional or otherwise [16,19]. One of the first attempts to determine the effect of these various phases on the high temperature strength of NiAl is presented in a companion paper in this proceedings [20]. The final conclusion of this study was that given a constant level of Hf, G-phase is a slightly preferred strengthening agent over Heusler and E-phase at temperatures at and below 1300 K. Above 1300 K, G-phase dissolves and therefore has no impact on strength, while Heusler is stable to about 1625 K, and the solvus for E-phase is unknown but greater than 1400 K. Similar results relating peak strengths to a fine dispersion of G-phase, compared to Heusler or E-phase, in Zr and Si co-doped NiAl alloys has been observed by Lim [19]. But those alloys which demonstrate the highest levels of strengthening such as AFN20\*, shown in Fig. 1, are much more highly alloyed than those materials studied in [19,20] and contain a very high density of Heusler precipitates.

We are far from understanding or even ranking the importance of the various mechanisms that contribute to the creep strength of these alloys, especially since solid-solution effects seem to play such an unusually large role. For example, Kitabjian et al. [21] found that the addition of 2.5% Ti to  $\langle 111 \rangle$  oriented single crystals decreased the creep rate by a factor of 5000 compared to binary NiAl at 1273 K (Fig. 3). This is an unusually high degree of strengthening compared to pure metals. For example, in what is considered a potent solid-solution strengthened alloy, Al-5.5Mg, creep rates are only 50 times slower than pure Al at the same homologous temperatures [22]. Furthermore, alloying additions such as Hf are even more effective strengthening agents than Ti. As Fig. 4 indicates, only 0.3% Hf has the same or a significantly greater strengthening effect on  $\langle 100 \rangle$  oriented

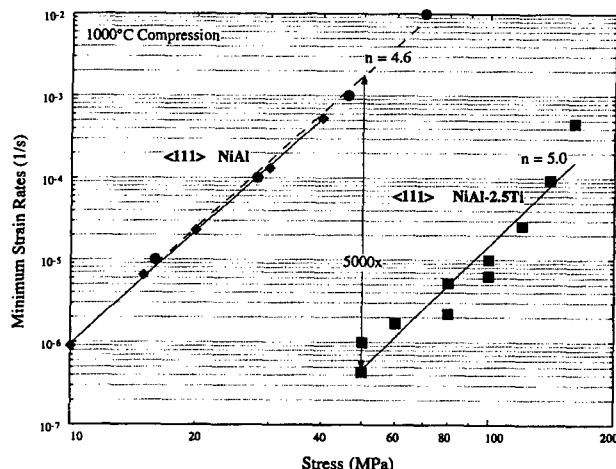


Figure 3. Creep strength of  $\langle 111 \rangle$  NiAl and  $\langle 111 \rangle$  NiAl-2.5Ti at 1273 K showing a 5000x reduction in creep rate for the solid solution NiAl-Ti alloy (from ref. 21).

\* The complete composition of all GE alloys can be found in Refs. 14 and 15.

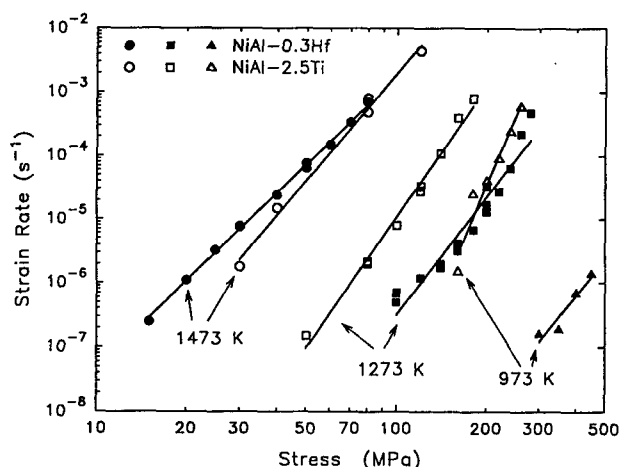


Figure 4. Comparison of the solid solution strengthening effect of Ti and Hf in  $\langle 001 \rangle$  oriented NiAl crystals (ref. 23).

crystals than 2.5% Ti, depending on the temperature [23]. Furthermore, the beneficial effect Ga on stress rupture strength has been clearly documented [14,15] but not at all understood. At this point, we can only speculate as to the mechanisms controlling these potent solid-solution effects. But given the complex dislocation core structures and their large elastic strain fields [24], it is reasonable to expect significant interactions between solute atoms and dislocations in NiAl.

While it is clear that the creep strength of NiAl single crystals could be improved further through optimization of the microstructure and a better understanding of the strengthening mechanisms, the properties generated to date are sufficient for most envisioned applications. In addition, issues concerning brittle fracture are limiting at this point. Inadequate ductility and toughness below the brittle-to-ductile transition temperature of NiAl and poor impact resistance at any temperature are problems that preclude near term production of structural components. There are conditions under which non- $\langle 100 \rangle$  NiAl single crystals can exhibit high room temperature tensile ductility, such as microalloying with Fe, Ga or Mo, [25], controlling the orientation and constraints due to gripping [26], and carefully preparing the specimen surface [27]. However, attaining a balance between creep strength and adequate room temperature tensile ductility is very difficult and the alloys designed for high temperature strength exhibit essentially zero plastic deformation below their BDTT (1100-1300 K) [9,28]. Furthermore, regardless of composition, the fracture toughness of NiAl is anisotropic and particularly low along  $\{011\}$  planes,  $\leq 5 \text{ MPa}\sqrt{\text{m}}$  [29,30], resulting in an extremely notch sensitive material. All of these problems are exacerbated in the creep resistant single crystals, since the same alloying additions which are good for reducing dislocation mobility at high temperatures preclude almost any dislocation motion at lower temperatures. Impact loading is also a serious issue at all temperatures, even above the BDTT. This is because the BDTT itself is essentially due to the operation of creep mechanisms, i.e., dislocation climb [28,31]. Therefore, when the loading rate is faster than what these rate sensitive deformation mechanisms can maintain, fracture reverts to a completely brittle mode. In subsequent agreement with this analysis, it was observed that NiAl panels did not survive impact conditions that could potentially be encountered by high pressure turbine blades at any temperature. But NiAl alloys behaved adequately at the lower impact velocities that would be encountered in turbine vane and combustor applications [9].

Based on the current limitations of NiAl single crystals, efforts [32,33] are now focused on developing testing and design methodologies that will account for this brittle behavior. Present engine experience and design is based on ductile metals. Therefore, the acceptance of new high temperature materials, such as NiAl, other

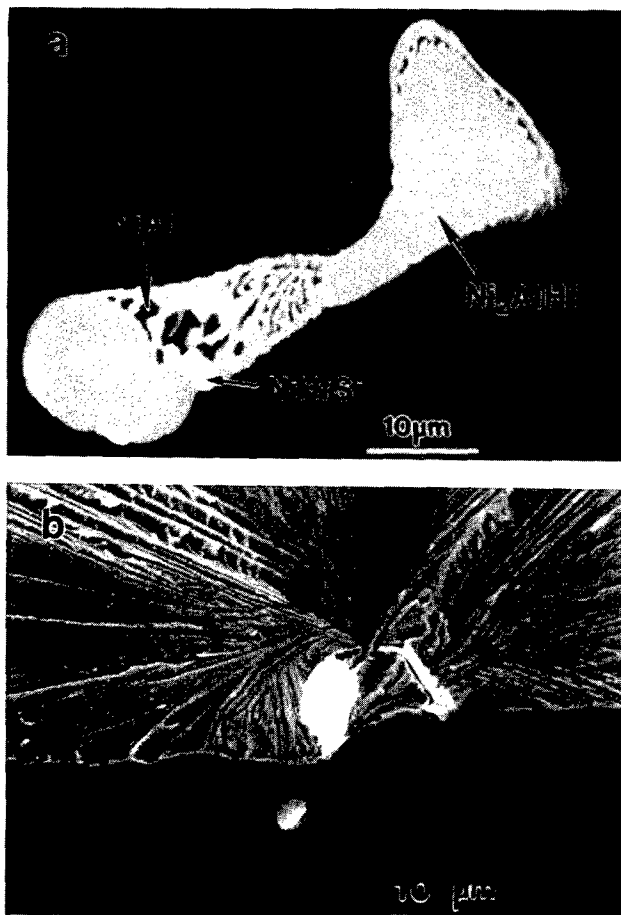


Figure 5. a.) An example of the characteristic interdendritic segregation that served as fracture initiation sites in AFN12 alloys prior to heat treatment optimization. b.) Once the heat treatment for these alloys was optimized, the flaw population shifted to smaller HfC particles as shown at the fracture origin of a NiAl AFN12 single crystal bend sample.

intermetallics or even ceramics, will require a complete rethinking in design methodology in order to enhance the introduction of these materials into advanced engines while minimizing the associated risks of failure. The approach to component design and validation with brittle materials involves the following steps; determination of the statistical nature and the source of fracture, measurement of the failure envelope for the material, coding of statistically based reliability models, and verification of the code and model using actual components that have undergone rig testing.

As part of this process, it was found that failure in the single crystal NiAl alloy, AFN12, originally initiated at unsolved interdendritic particles such as the one shown in Fig. 5a. This result led to further adjustment of the homogenization treatment. After the heat treatment was optimized to completely solution all interdendritic intermetallic phases, the average fracture strength of the alloy increased by over 40% and the flaw population shifted to either surface defects due to machining or HfC particles such as the one shown in Fig. 5b. Weibull statistics are presented in Table 1 for the flexural strength of this alloy when the flaw population was dominated by carbide particles [34]. From the data presented in Table 1, it is apparent that the characteristic strength of the NiAl alloy is actually quite high even compared to the best ceramics but is dependent on the material orientation. This dependence results simply because fracture toughness is also a function of orientation. However, no statistically significant

Table 1: Flexural Strength Weibull Statistics for Single Crystal NiAl Alloy AFN12 Tested at Room Temperature.

Orientation and Flexural Configuration	Characteristic Strength, $\sigma_0$ (MPa)	90% Confidence Bands, $\sigma_0$	Weibull Modulus, $m$	90% Confidence Bands, $m$
<100> 3-point	1350	1258 - 1475	6.1	4.4 - 8.5
<100> 4-point	1094	1032 - 1158	5.4	4.3 - 6.8
<110> 3-point	843	754 - 933	4.8	2.2 - 9.2
<110> 4-point	689	642 - 735	5.5	3.5 - 8.2

difference between <110> and <100> Weibull moduli could be detected at a 90% confidence. Analysis [35] indicates that this should be the case as long as the flaw population was the same in both orientations. But unfortunately the Weibull modulus, which is a measure of reliability, is quite low.

In spite of the relatively low Weibull modulus, many conventional and non-conventional low-stress material removal techniques (grinding, EDM, electrochemical machining, chemical milling, electrostream drilling, ultrasonic machining, and abrasive waterjet) have been successfully used on these NiAl single crystal alloys in the manufacture of high pressure turbine (HPT) vane airfoils. First, the airfoil shapes were rough machined from individual single crystal slabs, and the recrystallized layer generated by the EDM process was removed by subsequent chemical milling. Then using other low-stress machining techniques, details such as 350  $\mu$ m cooling holes, and trailing edge slots were generated. In addition, processes such as brazing and the application of thermal barrier coatings (TBC) were successfully developed for NiAl single crystals. Figure 6 is a picture of one of the high pressure turbine (HPT) vane airfoils demonstrating the machining detail that went into each turbine vane.

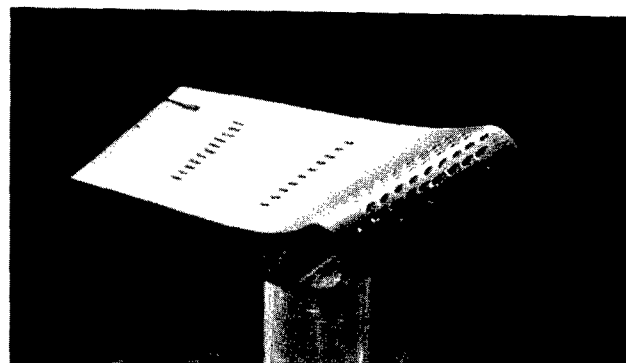


Figure 6. Typical single crystal NiAl HPT vane.

During the manufacturing stage, several component tests were performed on the NiAl HPT vanes in order to simulate engine thermal transient conditions as close as possible. These tests addressed concerns over thermal shock resistance because of the low ductility of the alloy. In addition, these tests served as 'proof tests' deemed necessary to weed out parts which might fail prematurely due to a manufacturing defect or handling damage. Component tests were also used to validate several new features utilized in the design of these vanes and their insertion into the combustor nozzle, including a rope seal technology developed at NASA LeRC, which allowed a floating vane arrangement in order to minimize thermal stresses. These component tests, including a full scale combustor rig test, were successfully carried out. Once confidence was demonstrated in the ability of the NiAl vanes to withstand sharp thermal transients, engine testing was approved. The fully assembled combustor nozzle containing several NiAl vanes that was used for the engine test is

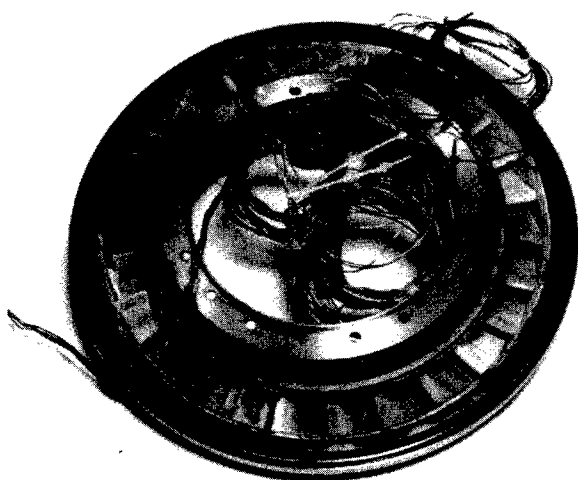


Figure 7. NiAl and superalloy high pressure turbine vanes assembled in a 1<sup>st</sup> stage HPT nozzle.

shown in Figure 7. In this assembly, the NiAl vanes were tested alongside single crystal superalloy vanes. Engine testing took place during the fall of 1995 with a number of cycles run between September and November. After the engine test, no cracking or distress of any kind was observed in the NiAl vanes while the superalloy vanes showed some spallation of the thermal barrier coating.

The successful engine test of HPT vanes has demonstrated that it is possible to design and manufacture complicated turbine engine components out of limited ductility intermetallic alloys for application in highly stressed and harsh environments. In essence, technical feasibility of such materials has been demonstrated. However, full scale production will still be a difficult challenge primarily due to the limited ductility and damage tolerance of this material.

#### Directionally Solidified NiAl-based Eutectic Alloys

An approach that is being considered in order to augment the intrinsically low damage tolerance and fracture toughness of single crystal NiAl alloys is to rely on extrinsic toughening mechanisms. This can be accomplished through the development of composite structures. Yet, artificial NiAl-based composites do not appear feasible at this time primarily due to the lack of a compatible fiber [12,13]. "Compatible" in this respect is meant much more generically to encompass not only chemical compatibility, but also thermal expansion compatibility, and a reasonable chance to process components without serious fiber degradation. However, NiAl can be conveniently reinforced "in-situ" with refractory phases by directional solidification of appropriate pseudo-binary and ternary eutectic systems. These materials are a natural and promising manifestation of artificial fiber reinforced composites, without many of the technical problems. While the combination of phases that can be incorporated in an eutectic system are limited by thermodynamics, there are a surprisingly large number of two- and even three-phase NiAl-based eutectic alloys. To date, over a dozen systems have been identified and evaluated jointly by the University of Tennessee and NASA LeRC [36,37,38], with a few promising systems undergoing further development at NASA and GE.

In general, these materials can be designed with a NiAl matrix reinforced with intermetallic phases for high temperature strength and bcc refractory metal phases for strength and enhanced fracture resistance. Typical microstructures for a common two- and three-phase eutectic are shown in Fig. 8 demonstrating the fine composite-like microstructure that can be generated by directional solidification. The range of properties exhibited by these types of eutectic alloys is demonstrated in Fig. 9, which compares the creep

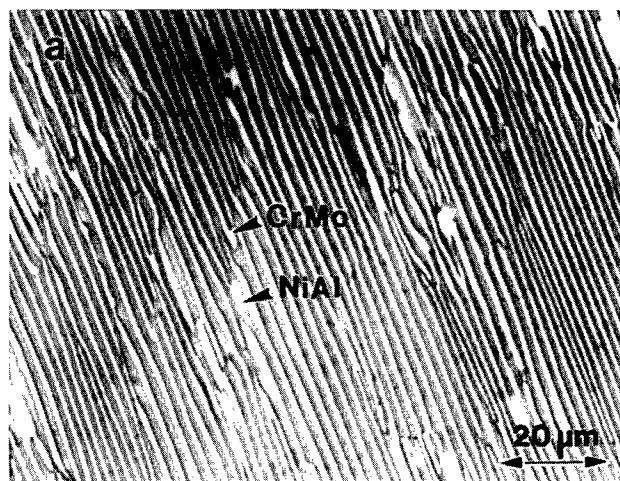


Figure 8. Microstructures of typical directionally solidified eutectic alloys, a.) two-phase (NiAl-Cr(Mo)) lamellar reinforced Ni-33Al-31Cr-3Mo alloy and b.) three-phase (NiAl-NiAlTa-Cr) Ni-30.5Al-6Ta-33Cr alloy.

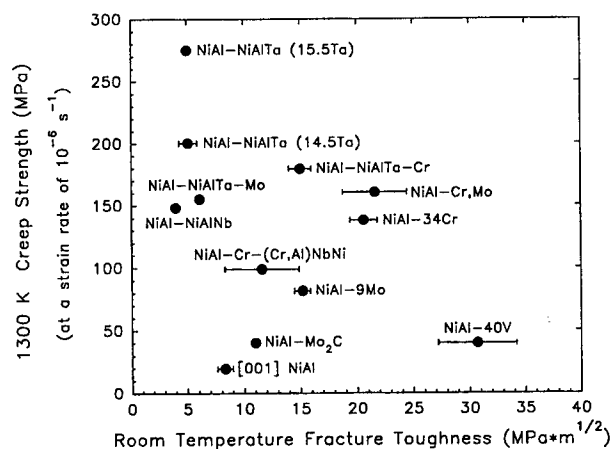


Figure 9. Comparison of various two- and three-phase NiAl-based eutectics taking into account both creep strength and room temperature fracture resistance.

strength and room temperature fracture toughness of various systems. This figure indicates that development of NiAl alloys with a more balanced set of properties is possible through *in-situ* reinforcement strategies.

High temperature strength is provided by continuous, creep-resistant second phases and the fine scale of the resulting microstructure [39]. Because of the continuous morphology of the reinforcing phases, there is a direct contribution of the refractory metal and other intermetallic phases on strengthening due to a typical rule of mixtures effect. However, the simple rule of mixtures does not take into account the quality or scale of the microstructure. It is evident from Fig. 8 that the scale of these microstructures is extremely fine, on the order of several tenths of microns to only several microns in spacing. Therefore, the dislocation mean free paths are very small and dislocation pileups between the phases lead to a Hall-Petch type of strengthening mechanism. Thus, any rule of mixtures strength rule would have to be modified to take into account Hall-Petch type strengthening of the matrix where the strength of the eutectic would be proportional to  $\sigma_f V_f + (\sigma_m + \alpha \lambda^{-1/2}) V_m$ , where  $\alpha$  is a constant and  $\lambda$  is the lamellar spacing. This concept carries over to creep deformation and when both the matrix and fiber can undergo creep (as in the case of NiAl-based eutectics),  $\log \dot{\epsilon} \propto 1/\lambda$  [40]. The significance of fiber spacing on longitudinal creep strength is borne out in Fig. 10, which shows the stress rupture properties of a NiAl-33Cr-1Mo eutectic with two different lamellar spacings and two typical Ni-based superalloys. The data indicates the marked effect of lamellar spacing on strength. The figure also indicates a trend that is pervasive for most NiAl-based systems: at low temperatures (lower Larson Miller numbers), advanced single crystal superalloys tend to be stronger and only at higher temperatures do the strength advantages of the NiAl systems become apparent.

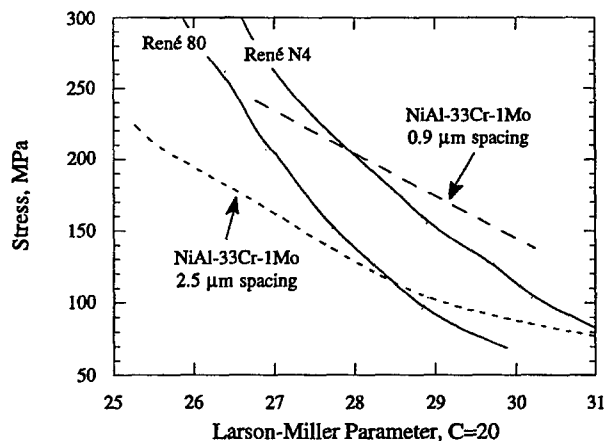


Figure 10. Effect of lamellar spacing on the longitudinal creep strength of NiAl-33Cr-1Mo eutectics.

The intermediate temperature (1300 K) creep properties of a number of different NiAl-based eutectic alloys are compared to a first generation single crystal superalloy in Fig. 11 [36-38,41]. It is apparent that the majority of the eutectic alloys, regardless of a wide variation in composition, have similar creep strengths, probably due to the similarity in eutectic spacing. And while the strengths are quite good compared to binary NiAl, except for the NiAl-15.5Ta alloy, all the eutectics fall short in strength compared to the single crystal superalloy. Thus intermediate temperature strength, as demonstrated in both Figs. 10 and 11, is one concern. Furthermore, alloying schemes to mitigate this problem have been unsuccessful. In fact, adding the type of alloying additions to the eutectics, that are successful in improving the creep strength of single crystals, can actually lessen the strength of the eutectic alloys as demonstrated in Fig. 12. This has been attributed to

the effect that these additions have on the microstructure of the eutectic. Apparently the alloying additions, even at these small levels, interfere with the eutectic solidification process resulting in a more globular and coarse structure [42]. Consequently, the loss in strength due to the increase in eutectic spacing and the disruption of reinforcement continuity is greater than any strengthening effect that the alloying additions may impart to the NiAl matrix. Therefore, further alloy development of the eutectic systems is problematic but still receiving some attention. Moreover, these future efforts may be significantly supplemented by computer-aided alloy design methods such as the BFS process described in another paper in this volume [43].

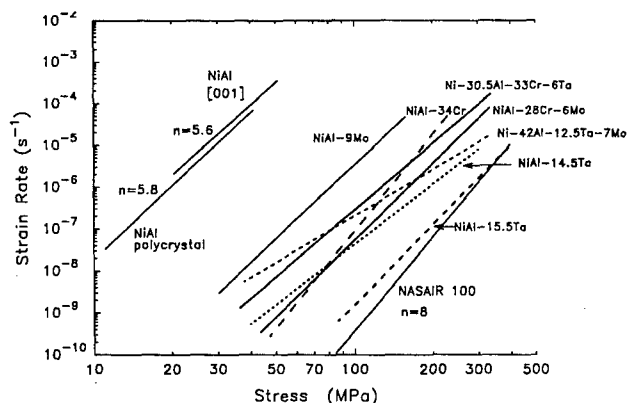


Figure 11. 1300 K creep behavior for various NiAl-based *in-situ* eutectic composites in the longitudinal direction compared to a first generation single crystal Ni-based superalloy.

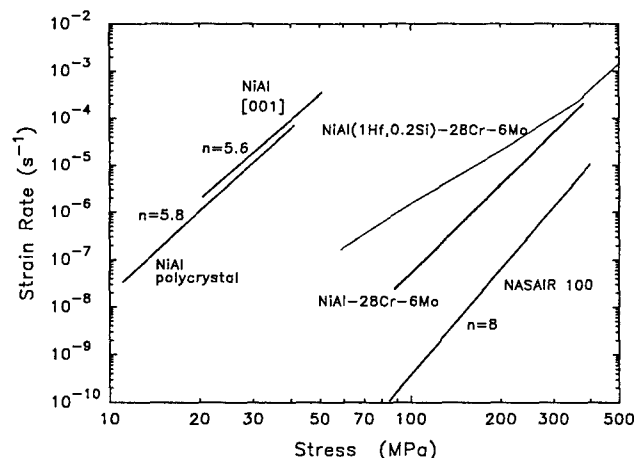


Figure 12. Effect of secondary alloying on the longitudinal creep strength of NiAl-based eutectics.

In addition to enhanced creep strength, the intent to use *in-situ* compositing methods is to develop toughened NiAl-based alloys. But NiAl eutectics are unique among brittle matrix composites in that toughness enhancements are achieved through both extrinsic and intrinsic mechanisms. The balance between these two mechanisms as they affect various NiAl-based materials is reviewed in Ref. [44]. Briefly, intrinsic mechanisms refer to toughening attributed to an augmentation in plasticity due to an increase in the nucleation and propagation of mobile dislocations. The typical example for this type of behavior is the B2/fcc Ni-20Al-30Fe eutectic, which exhibits easy slip transfer from the ductile  $\gamma$  phase to the brittle  $\beta$  matrix [45]. This

process serves as a continuous source of mobile  $\langle 100 \rangle$  dislocations in the  $\beta$  phase and permits compatible deformation of both phases. While in monolithic form the B2 Ni-30Al-20Fe matrix phase of this eutectic has essentially zero room temperature ductility, the two-phase Ni-20Al-30Fe composite exhibits 10-12% tensile ductility and a fracture toughness of  $\sim 30 \text{ MPa}\sqrt{\text{m}}$  [46]. The conditions which favor easy slip transfer are i.) a ductile reinforcing phase with lower yield stress than the NiAl, ii.) a crystallographic orientation relationship such that the slip planes for the reinforcing phase and NiAl are parallel or nearly so, and iii.) a strong interface so that slip transfer can occur before interface decohesion.

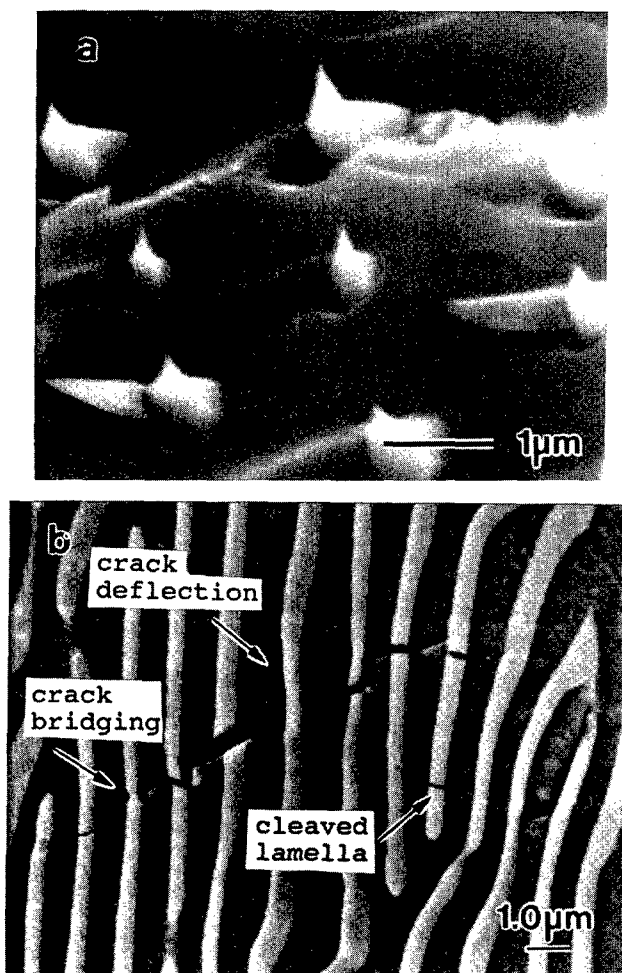


Figure 13. Experimental verification of extrinsic toughening mechanisms in NiAl/bcc-refractory metal composites: a.) evidence of crack bridging in NiAl-9Mo and b.) crack deflection and bridging in NiAl-34Cr.

Intrinsic toughening mechanisms are primarily responsible for delaying the initiation of fracture [47]. In contrast, extrinsic toughening mechanisms arise through the direct interaction of cracks in the brittle phase with a ductile second phase [48]. This is the basic contribution to the toughening of the NiAl/bcc-refractory metal composites such as the NiAl-Mo and NiAl-Cr(Mo) systems. Enhanced toughness results from various interactions, which include crack bridging (Fig. 13a,b), crack deflection (Fig. 13b), and crack blunting. In fiber reinforced eutectics, such as NiAl-9Mo with a toughness of around  $15 \text{ MPa}\sqrt{\text{m}}$  [49] and NiAl-34Cr with a toughness of nearly  $20 \text{ MPa}\sqrt{\text{m}}$  [36], crack bridging occurs through a crack trapping process. As the crack front is trapped by the higher toughness fibers, the crack will advance by bowing between the reinforcements leaving unfractured fibers in the crack wake that bridge the crack until they

plastically stretch and eventually rupture (Fig. 13). In lamellar reinforced eutectics, such as the NiAl-CrMo eutectics with a toughness of  $17\text{--}22 \text{ MPa}\sqrt{\text{m}}$  [50,51] and NiAl-V with a toughness of over  $30 \text{ MPa}\sqrt{\text{m}}$  [49], crack bridging is part of a crack renucleation process. In these alloys, as the  $\beta$  phase fractures, the crack may be blunted by the ductile reinforcing phase and then advance by renucleating in the adjacent  $\beta$  lamellae leaving a bridging ligament that plastically deforms in the crack wake. However, crack bridging can not account for the total increment in toughness observed in any of these systems [49,50,52]. While other mechanisms, such as crack deflection along inclined reinforcing phases, shear ligament formation, and a difference in cleavage plane that causes continuous minor deviations in the crack path have been proposed as additional mechanisms to account for this difference in toughness [53], it is clear from TEM observations [36,49,50] near the crack tip of NiAl/bcc-refractory metal eutectics that significant plasticity of the NiAl phase occurs (see for example Fig. 14). In other words, the plastic zone around the crack tip in these systems is quite large. Therefore, even in the NiAl/bcc refractory metal eutectics, extrinsic toughening occurs in combination with enhanced plasticity of the NiAl phase due to increased dislocation generation from the interfaces.

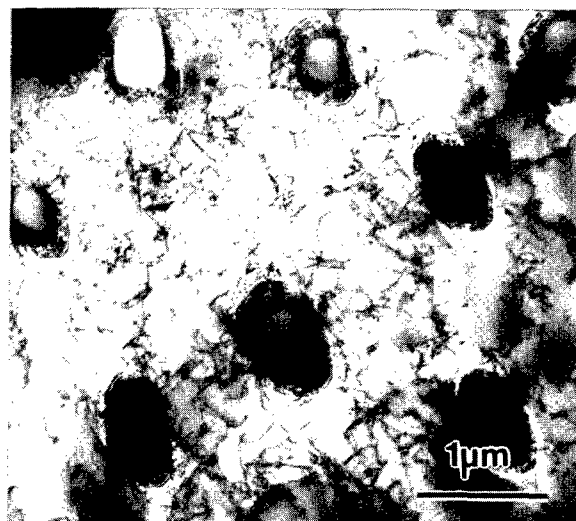


Figure 14. Evidence of enhanced plasticity of the NiAl phase near the crack tip of a NiAl-9Mo eutectic after fracture toughness testing.

While the NiAl-based eutectics have a considerable toughness advantage over the single crystal NiAl alloys, impact resistance is also better but still a concern. Fig. 15 is a comparison of the impact resistance of a NiAl-33Cr-1Mo eutectic and the single crystal alloy AFN12. Panels approximately 1 mm in thickness were impacted at several velocities with aluminum balls of various size and strength. Significant differences in impact resistance were observed between the eutectic and single crystal panels as indicated in Fig. 15 and the failure mode was also different with the eutectic panels tending to exhibit a more graceful failure than the AFN12 panels that either were undamaged during testing or shattered, with very little middle ground. While better than AFN12, the eutectic still has borderline impact resistance to be considered for use as a turbine blade material, though it has sufficient resistance for combustor and turbine vane applications.

More serious concerns with the eutectic materials include transverse properties, especially for the fiber reinforced morphologies such as exhibited by the NiAl-9Mo or the NiAl-34Cr alloys. In the case of fiber reinforced eutectics, the transverse fracture toughness is expected to be no better than binary NiAl. Transverse creep is also a significant problem with the fiber reinforced morphologies, but



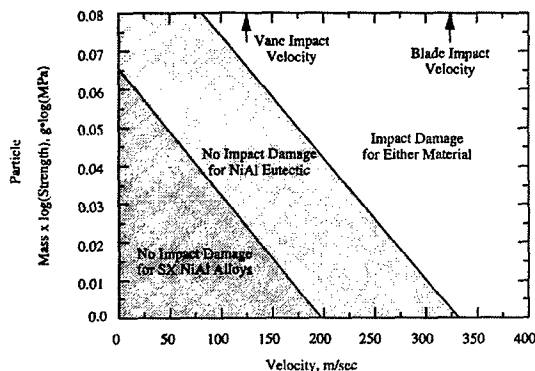


Figure 15. Ballistic impact map for single crystal NiAl alloys and NiAl-33Cr-1Mo indicating regions of safe operation.

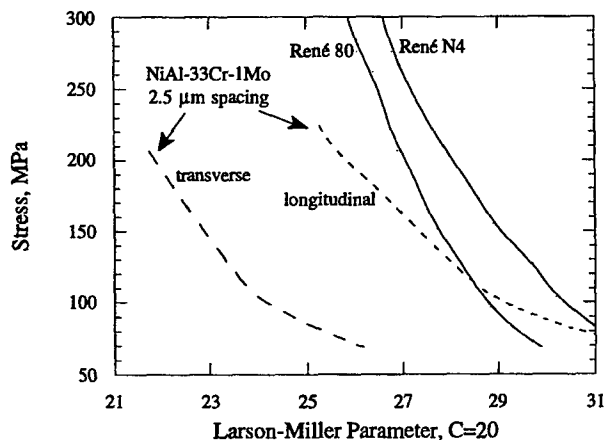


Figure 16. Effect of sample orientation on the stress rupture strength of a NiAl-33Cr-1Mo eutectic alloy.

lamellar reinforced alloys have been shown to have an advantage due to the two-dimensional nature of the reinforcement with no more than an order of magnitude difference in compressive creep rate reported for longitudinal versus transverse and 45° test orientations at 1273 K [54]. However, these initial results are quite misleading, and there is a much wider difference in strength as a function of orientation for stress rupture properties as shown in Fig. 16, indicating the need for more careful screening tests for these types of materials. Another concern is thermal stability of the microstructure. While there is no noticeable effect of heat treatment at 1300 K after 500 hours exposure on either the eutectic structure or fracture toughness for NiAl-34Cr and NiAl-CrMo eutectics [36], there is concern about exposure at higher temperatures (1673 K), which can result in complete spheroidization of the NiAl-34Cr eutectic after as little as 160 hrs. [55]. However, due to the faceted interface of the NiAl-Mo alloys, this eutectic was stable at 1673 K [55] providing hope that the lamellar NiAl-CrMo eutectics under development may also be stable. Thermal fatigue is also a potential problem that should be addressed in the future.

The final area of concern for NiAl eutectics is processing and manufacturability. GE Aircraft Engines has already demonstrated that the NiAl-CrMo eutectics can be manufactured into high pressure turbine vanes identical to the one shown in Fig. 6, by the same processes used on the single crystal alloys. However, for eutectic

alloys to be economically feasible, directional solidification rates of at least 1-3" per hr. will be necessary while still maintaining a well aligned microstructure. Presently, eutectics are grown at a rate of less than 1" per hr. in smaller laboratory scale furnaces. The prospects for achieving this goal with large commercial ingots does not look promising at this time due to the very high thermal gradients that would be necessary to maintain an aligned eutectic structure at these faster withdraw rates. Consequently, directionally solidified NiAl eutectics still need additional development work in the following areas: alloy design for better longitudinal and transverse creep strength while maintaining adequate fracture toughness, more economical processing, and more thorough characterization of their thermal stability.

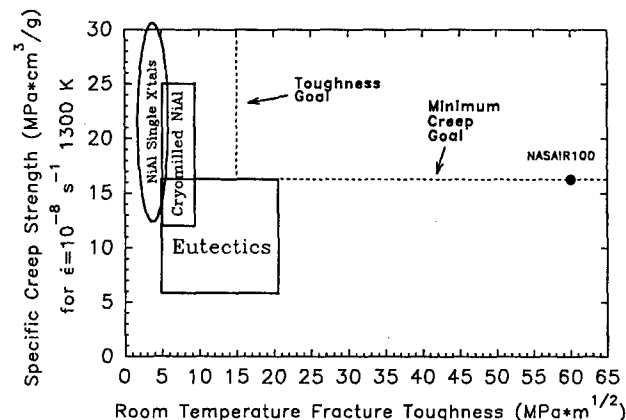


Figure 17. Relative comparison of the 1300 K creep strength and room temperature fracture toughness of various NiAl-based systems and a typical first generation single crystal superalloy. The goals for future alloy development are indicated.

#### Dispersion-Strengthened PM NiAl Alloys

Dispersion strengthened NiAl produced by powder metallurgical (PM) routes, while not quite as creep resistant as the best NiAl single crystals and not as tough as eutectics, may actually be better positioned to compete with superalloys (Fig. 17). Powder metallurgical NiAl alloys are being developed by two groups in particular. Arzt and his group at Max-Planck-Institut fuer Metallforschung [56,57] are developing oxide dispersion strengthened NiAl alloys by a conventional mechanical alloying (MA) approach followed by consolidation and a coarse-grain recrystallization treatment. The last processing step is necessary in order to minimize the detrimental effects of grain boundaries on high-temperature strength. Two wt.%  $Y_2O_3$  is added to these alloys as the oxide dispersion. However, after consolidation of the MA powders the microstructure consists of a fine-grain material containing nm size  $Y_3Al_5O_{12}$  dispersoids. This material is then rapidly deformed at 1323 K and given a recrystallization treatment at 1821 K. The final product consists of a coarse (~166 μm) equiaxed grain structure with a homogeneous dispersoid distribution, which gives the alloy good creep resistance up to 1673 K, or a homologous temperature of 0.9. The real benefit of these alloys is at temperatures above 1473 K, where instead of competing directly with superalloys they will find application at temperatures that exceed the capability of many conventional materials. The exceptional high-temperature strength of the ODS NiAl, as in ODS superalloys, is a consequence of precipitate-dislocation interactions, which in terms of deformation behavior results in very high stress exponents at all temperatures. This translates into good high temperature strength even at very slow strain rates and is a major advantage of these types of materials [58].

As with any NiAl-based material the obstacle that is preventing immediate widespread application of the ODS version is fracture behavior. The main approach being used to alleviate this

problem is to add ductile second phase particles. In essence to create an "artificial" eutectic, since eutectic alloys compared to other NiAl materials tend to show the most promise in the area of fracture resistance. To date, the ductile reinforcing phases investigated have been Nb, Cr, and Mo [56,59,60]. Of these, the Mo reinforced alloys have shown the most promise. The problem with Nb is that it reacts with NiAl to form a brittle intermetallic Laves phase, while Kirkendall porosity forms at the Cr-NiAl interfaces after elevated temperature annealing. For the NiAl-Mo alloys, the ductile particles are responsible for increasing the toughness by a factor of two and at the same time promotes pronounced R-curve behavior, though room temperature tensile ductility is still lacking. However, the fracture properties of the ODS NiAl after Mo reinforcement are now competitive with other hard metals such as WC-Co cermets.

Envisioned use of the ODS NiAl alloys would be as a replacement for common ODS Ni- and Fe-based superalloys in present applications where the added benefits of a much higher operating temperature, lighter weight, and better thermal conductivity would justify such a change in material. Representative applications include high temperature heat exchangers, dies for the production of steel wool, and certain automotive applications such as components for catalytic converters and preburning chambers in diesel truck engines.

A related program in the development of dispersion strengthened NiAl alloys has been ongoing at the NASA Lewis Research Center [61,62]. The dispersion strengthened alloy developed there is an AlN reinforced material produced by cryomilling. Cryomilling is an extension of the mechanical alloying process except performed at lower temperatures under a protective atmosphere with the goal of reducing the amount of oxygen contamination found in the milled product [63]. While there are a number of ways to achieve this, the most common is to use liquid nitrogen as both the coolant for the attritor vessel and as the protective atmosphere in the vessel. While the original intent with cryomilled NiAl was to create a yttria dispersed alloy, cryomilling of prealloyed NiAl powder in liquid nitrogen was found to have an entirely unexpected consequence [61,64]. During the grinding process the powder fragments, not surprising given the brittle nature of NiAl, but the new surfaces that are created react with the liquid  $N_2$  to form fine AlN particles in the near surface region of the powders [65]. Subsequent consolidation of the cryomilled powders (Fig. 18a) then results in a core and mantle type of microstructure, where the original prior powder surfaces contain an extremely high density of fine AlN particles surrounding a powder core that is mostly dispersoid free. Figure 18b is a TEM micrograph of extruded cryomilled NiAl powder which illustrates this structure [66].

Since the original observation of this phenomenon [61,64], cryomilling of NiAl powder has been shown to be a very reproducible technique [67] for generating NiAl alloys containing from 9 to 30 vol.% AlN [68,69]. The effect of volume percent reinforcement on the creep strength of NiAl composites is shown in Fig. 19. While small additions of AlN have a very dramatic effect on strength compared to binary NiAl, the 30 vol.% material has a creep strength just short of a first generation single crystal superalloy, (but would be much stronger than the superalloy on a density compensated basis, Fig. 17). In general, it was found that the creep strength of the cryomilled alloys was proportional to the square root of the volume percent AlN [69]. Therefore, achieving additional increments in strengthening by further increasing the AlN content is unrealistic. Instead, alternative strengthening techniques will need to be developed in order to compete more effectively with superalloys at intermediate temperatures. Alloying NiAl-AlN with Zr [70] or  $Y_2O_3$  [71] has not shown any marked improvements in strength of the cryomilled NiAl-AlN over unalloyed materials with similar AlN content. In fact, it is rather difficult to combine strengthening mechanisms in these alloys by trying to take advantage of the potent solid solution effects described previously in addition to dispersion strengthening. Most of the alloying additions that are so effective in increasing the strength of single crystals are strong nitride formers and therefore, will be taken out of solution. An alternative approach, based on recent results on a dilute  $N_2$ -doped NiAl alloy [72] and the work by Arzt et al. [56] that is

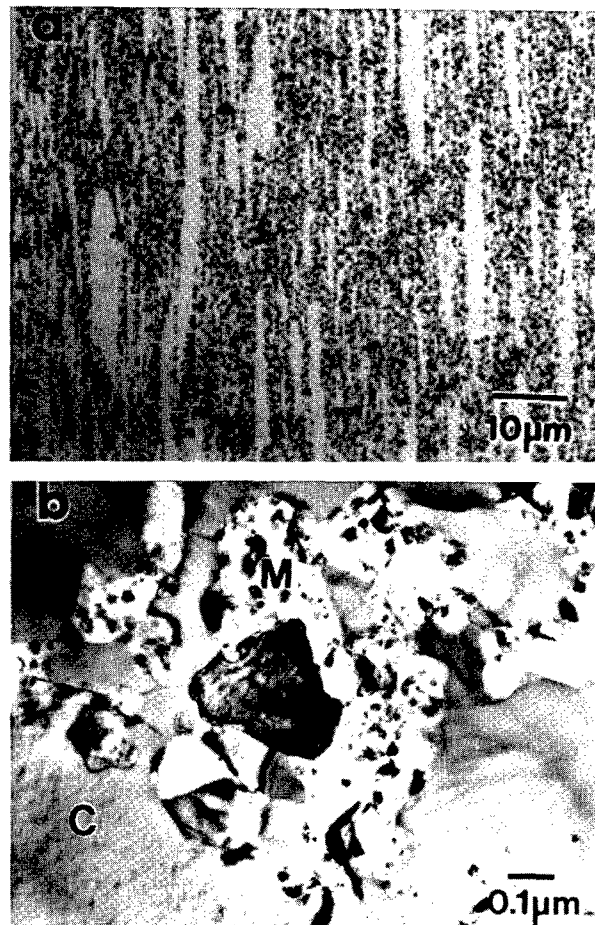


Figure 18. a.) Optical micrograph showing the overall structure of as-extruded cryomilled NiAl-10vol.%AlN, and b.) TEM micrograph showing particle-free NiAl cores "C" and AlN-enriched mantles "M".

illustrated in Fig. 18, would be to investigate grain coarsening strategies. Since most of the cryomilled NiAl produced and studied to date had grain sizes on the order of a few microns, the full potential of dispersion strengthening is probably not realized in these materials due to the offsetting effects of grain boundary sliding. This is evidently the case at low strain rates and high temperatures since the stress exponents are quite small at these test conditions [61,69,71]. However, it should once again be pointed out that competing head-to-head with superalloys is probably futile and the real niche for these alloys as with the ODS version is at temperatures exceeding 1400 K where most superalloys can no longer contend.

There has been significant progress in characterization of the fracture toughness of the cryomilled material as a function of AlN content, consolidation technique, and temperature [68,69]. In terms of room temperature properties, HIP consolidated NiAl-AlN composites have a fracture toughness roughly equivalent to that of binary NiAl ( $\sim 5$  MPa $\sqrt{m}$ ) and is independent of AlN content. Extrusion results in a slightly tougher material, on the order of 7-8 MPa $\sqrt{m}$ , which has been attributed to a higher dislocation density due to the thermomechanical processing. Fracture toughness as a function of temperature for the cryomilled material is compared to binary NiAl in Fig. 20. As can be seen in the figure, the BDTT for the cryomilled material, as defined by a change in slope of the toughness versus inverse temperature curve, is only about 175 K higher than that of binary polycrystalline material. In fact, at approximately 725 K, the BDTT for cryomilled NiAl is the lowest of any of the high strength materials reviewed in this paper.

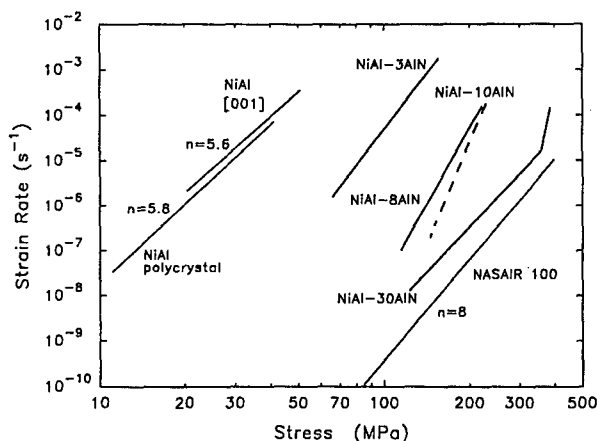


Figure 19. Creep strength of NiAl-AlN dispersion-strengthened alloys as a function of AlN content.

However, a room temperature toughness of 7 MPa $\sqrt{m}$ , while good compared to most other non-eutectic NiAl alloys, is still nothing to get overly excited about. Consequently, the course of action being pursued for toughening of cryomilled NiAl is essentially the same as that for the ODS alloys, i.e., ductile-phase toughening. Preliminary results for ductile-phase toughening of the cryomilled NiAl with Cr and Mo particulates have shown significant promise in toughness enhancement but at the expense of some creep strength [73]. But because these results are preliminary and the microstructure of the reinforcing phase was far from optimized, there is significant room for improvement in this area.

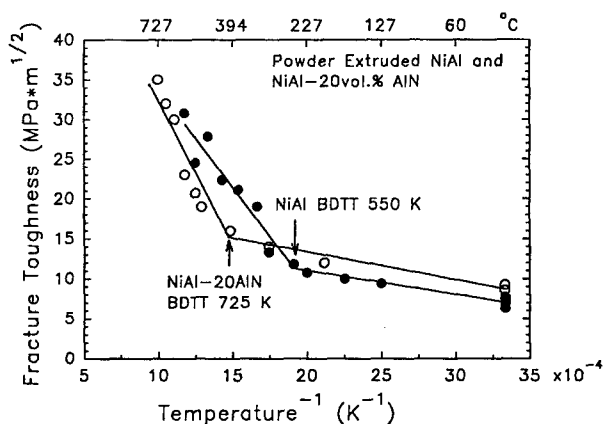


Figure 20. Fracture toughness as a function of temperature for extruded binary NiAl powder and a cryomilled NiAl-20vol.% AlN alloy.

Cryomilled NiAl is being developed specifically for potential aerospace related applications including jet turbine engine combustor components and first and second stage turbine vanes [68]. The same drawbacks effecting single crystal NiAl, poor fracture and impact resistance, precludes the development of cryomilled NiAl turbine blades unless successful ductile-phase reinforcement strategies can be developed. Nevertheless, the same applications identified for ODS NiAl alloys also apply for the cryomilled material.

### Current Status and Potential Applications

As with ceramics, a significant market for ordered intermetallics such as NiAl has been expected for many years due primarily to the initial promotion these materials received during their early developmental stages. Unfortunately, we have seen very little high tech application of ordered intermetallics with the recent exception of gamma titanium aluminides. It is true that NiAl has come a long way from the basic concept of using it simply as a leading edge for a turbine blade [3] to actual engine testing of single crystal NiAl vanes. And still, the low density, high thermal conductivity, and high temperature creep resistance make aluminides such as NiAl attractive in high temperature environments. However, the low toughness and lack of ductility make them less reliable than current superalloys.

Typical Ni-based superalloys, the material NiAl is meant to replace, at the very minimum have room temperature fracture toughnesses of at least 40 MPa $\sqrt{m}$  and tensile ductilities of 5%. This does not mean that structural NiAl alloys need to have equivalent properties; but an acceptable level of ductility and fracture toughness for a turbine airfoil material is difficult to define. It has become apparent that some ductility is necessary for the purpose of component assembly and greater reliability. In particular, plastic deformation, no matter how small, would be useful in relieving the high contact stresses that can arise between the airfoil root attachment and the turbine disk. Another problem is the generation of thermal stresses due to the joining of NiAl components to superalloys. In this case, up to 2% ductility is probably necessary based on the thermal expansion mismatch between NiAl and Ni-based superalloys at typical use temperatures [9]. In an attempt to gain a better understanding of ductility and toughness requirements, it is useful to look at another intermetallic,  $\gamma$ -TiAl, that has been successfully tested as a low pressure turbine blade and is being considered for several other engine applications. These alloys have room temperature tensile ductilities on the order of 1-2% and fracture toughness values starting around 15 MPa $\sqrt{m}$ . At this point, none of the three NiAl-based systems described in this paper meet these properties. Consequently, future research should be focused on developing a NiAl alloy with at least these properties as targets but still capable of competing with Ni-based superalloys on a creep strength level. Figure 17 indicates the progress that still needs to be made in order to meet such goals.

In the meantime, NiAl may still play a niche role in components which take specific advantage of its benefits such as high conductivity, good creep strength, and good TBC adherence, while also taking into account its limitations. Although the development of a NiAl turbine blade (probably the most demanding part in an engine) is not a current consideration, the possibility still exists for the development of high pressure turbine vanes, combustor liners, or other related components. The main competitors for these types of applications, however, are advanced ceramics and ceramic matrix composites (CMC's). Today there are ceramic systems that can readily achieve fracture toughness values of at least 10 MPa $\sqrt{m}$ , though tensile strength and tensile ductility are still limiting issues. In addition, while ceramics are not as amenable as NiAl to machining, some ceramics offer the advantage of even higher operating temperatures with reduced cooling requirements, and therefore simpler shapes are acceptable. Consequently, the choice of future turbine components, whether ceramic, CMC's, NiAl alloys or other intermetallics, may come down to a combination of functionality and manufacturability.

However, it is not a question of whether NiAl will find some commercial application but when and what applications. Ironically, most of these markets will probably be outside the gas turbine industry. Ones already alluded to in this paper include various automotive applications, dies for steel wool manufacture, and high temperature heat exchangers. Other potential applications include injection molds, and various furnace components. NiAl is also being widely investigated as a binder to replace Co or NiCr in WC-Co and Cr<sub>3</sub>C<sub>2</sub>-NiCr cermets [74,75] and Ni-rich alloys, due to their shape memory effect, are being considered as high temperature sensors and actuators.

[76]. And of course, the use of NiAl as a high temperature coating and bond coat alloy will continue for quite some time [77].

Finally, some of the same properties that have driven the development of NiAl as a high temperature structural material have made it extremely attractive to the electronics industry as a substrate, underlayer, or other thin film component in complex metal-semiconductor and magnetic devices [78]. NiAl is attractive in these types of applications because of its stability at high temperatures (required for overgrowth processes), its chemical stability, good electrical conductivity, and a stable native oxide (which allows patterning in air without destroying electrical continuity), along with a serendipitous lattice match to a number of semiconductor, superconducting, and magnetic materials. An extensive review of the use of NiAl in the electronics industry as a component in metallic/III-V semiconductor heterostructures such as enhanced-barrier Schottky contacts and semiconductor-clad metallic quantum wells can be found in reference [79]. The electronics industry is also gearing up for the production of high-end 10 Gb/in<sup>2</sup> hard disk storage devices that use NiAl as an underlayer material [80].

### Conclusions

Great strides have been made in improving the high temperature strength of NiAl alloys in single crystal and other forms. In addition, single crystal NiAl has been successfully manufactured and engine tested as a high pressure turbine vane. However, issues of limited ductility, low fracture toughness, and poor impact resistance continue to plague NiAl. Thus, while the technical feasibility of this material has been demonstrated via engine testing, widespread application remains elusive. Creep strength in many of the NiAl-based systems appears to be adequate for current high temperature applications, thus, future efforts should be concentrated on improving fracture-related properties. There are alternative processing and alloying approaches, such as NiAl eutectics and dispersion strengthened NiAl, that show promise in overcoming some of these limitations but these systems need significant development to overcome remaining obstacles.

### Acknowledgments

We would like to acknowledge the collaborators who have supported and nurtured this work over the years and whose data in many cases we have co-opted for this paper: R. Darolia of GE Aircraft Engines, Ben Oliver and his students D. Johnson and S. Joslin from the University of Tennessee, D. Whittenberger, A. Garg, M. Hebsur and I. Locci, of the NASA Lewis Research Center, and R. Gibala and A. Misra from The University of Michigan.

### References

1. E.M. Grala and W.A. Maxwell, "Cast Nickel Alloy of High Aluminum Content," Patent No. 2,910,356, Oct. 27, 1959.
2. D.L. Wood, et al., "Effect of Basic Physical Parameters on Engineering Properties of Intermetallic Compounds," WADD Technical Report 60-184, parts I-VII, (1960-1966).
3. R.H. Singleton, A.V. Wallace and D.G. Miller, "Nickel Aluminate Leading Edge for a Turbine Vane," in Summary of the Eleventh Refractory Composites Working Group Meeting, AFML-TR-179, (1966), pp. 717-738.
4. R.R. Bowman and R.D. Noebe, "Up-and-Coming IMCs," *Adv. Mater. Proc.*, 136(2), (1989), 35-40.
5. J. Doychak, "Metal- and Intermetallic-Matrix Composites for Aerospace Propulsion and Power Systems," *JOM*, 44(6), (1992), 46-51.
6. R. Darolia, "NiAl Alloys for High Temperature Structural Applications," *JOM*, 43(3), (1991), 44-49.
7. R. Darolia, "NiAl for Turbine Airfoil Applications," in *Structural Intermetallics*, R. Darolia et al., eds., The Minerals Metals & Materials Society, Warrendale, PA, (1993), pp. 495-504.
8. R.D. Noebe, M.G. Hebsur and J.D. Whittenberger, "Fracture Toughness Limits in Polycrystalline NiAl-Based Materials and Potential Directions for Developing Improved Alloy Systems," *HITEMP Review 1994: Advanced High Temperature Engine Materials Program*, NASA CP-10146, (1994), pp. 54-1 to 54-14.
9. R. Darolia, W.S. Walston and M.V. Nathal, "NiAl Alloys for Turbine Airfoils," in *Superalloys 1996*, R.D. Kissinger et al., eds., The Minerals Metals & Materials Society, Warrendale, PA, (1996), pp. 561-570.
10. D.P. Pope and R. Darolia, "High-Temperature Applications of Intermetallic Compounds," *MRS Bulletin*, 21(5), (1996), 30-36.
11. R.D. Noebe, R.R. Bowman, and M.V. Nathal, "Physical and Mechanical Properties of the B2 Compound NiAl," *Inter. Mater. Rev.*, 38, (1993), 193-232.
12. R. Bowman, A.K. Misra and I.E. Locci, "Unresolved Technical Barriers to the Development of a Structurally Viable Al<sub>2</sub>O<sub>3</sub>/NiAl Composite," *HITEMP Review 1993: Advanced High Temperature Engine Materials Program, Vol. II*, NASA CP-19117, (1993), pp. 57-1 to 57-12.
13. R.R. Bowman, A.K. Misra and S.M. Arnold, "Processing and Mechanical Properties of Al<sub>2</sub>O<sub>3</sub> Fiber-Reinforced NiAl Composites," *Metall. Mater. Trans. A*, 26A, (1994), 615-628.
14. R. Darolia, J.R. Dobbs, R.D. Field, E.H. Goldman, D.F. Lahrman, and W.S. Walston, "NiAl Intermetallic Alloy and Article with Improved High Temperature Strength," Patent No. 5,516,380, May 14, 1996.
15. R. Darolia and W.S. Walston, "Development of High Strength NiAl Single Crystal Alloys," in *Structural Intermetallics II*, M.V. Nathal et al., eds., The Metallurgical Society, Warrendale, PA, (1997).
16. I.E. Locci, R.M. Dickerson, A. Garg, R.D. Noebe, J.D. Whittenberger, M.V. Nathal, and R. Darolia, "Microstructure and Phase Stability of Single Crystal NiAl Alloyed with Hf and Zr," *J. Mater. Res.*, 11, (1996), 3024-3038.
17. A. Garg, R.D. Noebe and R. Darolia, "Crystallography of the NiHfSi Phase in a NiAl(0.5Hf) Single-Crystal Alloy," *Acta Mater.*, 44, (1996), 2809-2820.
18. A. Garg, R.D. Noebe and R. Darolia, "Characterization of the Microstructure of a Hf-Doped NiAl Single Crystal Alloy Containing Different Levels of Si Contaminant," *HITEMP Review 1995: Advanced High Temperature Engine Materials Program, Vol. II*, NASA CP-10178, (1995), Paper No. 28.
19. Y. Lim, "Microstructure, Phase Stability, and Mechanical Properties of NiAl Alloys Containing Zr and Si," Ph.D. Thesis, University of Florida, (1997).
20. J.D. Whittenberger, A. Garg, R.D. Noebe, W.S. Walston and R. Darolia, "Effect of Chemistry, Microstructure and Orientation on 1100-1400 K Plastic Flow Properties of Hf-doped NiAl Single Crystals," in *Structural Intermetallics II*, M.V. Nathal et al., eds., The Minerals Metals & Materials Society, Warrendale, PA, (1997).
21. P.H. Kitabjian, A. Garg, R.D. Noebe and W.D. Nix, "High-Temperature Creep Behavior of Single Crystals of the Solid Solution Strengthened Alloy NiAl-2.5Ti," to be published in *Creep and Fracture of Engineering Materials and Structures VII*, Pineridge Press, Swansea, England (1997).
22. M.J. Mills, J.C. Gibeling and W.D. Nix, "A Dislocation Loop Model for Creep of Solid Solutions Based on the Steady State and Transient Creep Properties of Al-5.5 at.% Mg," *Acta Metall.*, 33, (1985), 1503-1514.
23. P.H. Kitabjian, R.D. Noebe, A. Garg and W.D. Nix, unpublished research, 1996.
24. M.J. Mills and D.B. Miracle, "The Structure of  $a <100>$  and  $a <110>$  Dislocation Cores in NiAl," *Acta Metall. Mater.*, 41, (1993), 85-95.
25. R. Darolia, D. Lahrman and R. Field, "The Effect of Iron, Gallium and Molybdenum on the Room Temperature Tensile Ductility of NiAl," *Scripta Metall.*, 26, (1992), 1007-1012.
26. V. Levit, I.A. Bul, J. Hu and M.J. Kaufman, "High Tensile Elongation of  $\beta$ -NiAl Single Crystals at 293 K," *Scripta Mater.*, 34, (1996), 1925-1930.
27. R. Darolia and W.S. Walston, "Effect of Specimen Surface Preparation on Room Temperature Tensile Ductility of a Fe-Containing NiAl Single Crystal Alloy," *Intermetallics*, 4, (1996), 505-516.
28. R.D. Noebe and A. Garg, "Deformation Behavior of the Single Crystal NiAl Alloy D176," NASA TM 106981, 1995.
29. K.M. Chang, R. Darolia and H.A. Lipsitt, "Cleavage Fracture in B2 Aluminides," *Acta Metall.*, 40, (1992), 2727-2737.
30. H. Vehoff, "Fracture Toughness of Intermetallics," *High-Temperature Ordered Intermetallic Alloys V*, I. Baker et al. eds., MRS Symp. Proc. Vol. 288, (1993), pp. 71-82.
31. R.D. Noebe, C.L. Cullers and R.R. Bowman, "The Effect of Strain Rate and Temperature on the Tensile Properties of NiAl," *J. Mater. Res.*, 7, (1992), 605-612.
32. R. Darolia, W.S. Walston, R.D. Noebe and J. Salem, "Design Methodology of Intermetallics" Status Report No. 8, Contract Report F33615-94-C-2414, June 1996.

33. J. Palko, J. Salem, R.D. Noebe, S. Duffy, D.R. Wheeler and F. Holland: "Reliability Analysis of Single Crystal NiAl Turbine Blades" HITEMP Review 1994: Advanced High Temperature Engine Materials Technology Program, NASA CP-10146, pp. 56-1 to 56-11, 1994.
34. J. Salem, R.D. Noebe and R. Darolia, "Reliability Modeling of Brittle, Anisotropic Solids," HITEMP Review 1997: Advanced High Temperature Engine Materials Program, NASA CP-10192, (1997), Paper No. 27.
35. J. Salem, "Reliability Analysis of Brittle, Single Crystals for Turbine Applications," Ph.D. Thesis, University of Washington, (1998).
36. D.R. Johnson, X.F. Chen, B.F. Oliver, R.D. Noebe and J.D. Whittenberger, "Processing and Mechanical Properties of In-Situ Composites from the NiAl-Cr and the NiAl(Cr,Mo) Eutectic Systems," *Intermetallics*, **3**, (1995), 99-113.
37. D.R. Johnson, X.F. Chen, B.F. Oliver, R.D. Noebe and J.D. Whittenberger, "Directional Solidification and Mechanical Properties of NiAl-NiAlTa Alloys," *Intermetallics*, **3**, (1995), 141-152.
38. D.R. Johnson, B.F. Oliver, R.D. Noebe and J.D. Whittenberger, "NiAl-based Polyphase In-Situ Composites in the NiAl-Ta-X (X = Cr, Mo, or V) Systems," *Intermetallics*, **3**, (1995), 493-503.
39. M. McLean, Directionally Solidified Materials For High Temperature Service, The Metals Society, London, (1983), Chapter 6.
40. E. Bullock, P.N. Quested and M. McLean, "Creep Behavior of a Ni-Ni<sub>3</sub>Al-Cr<sub>2</sub>C<sub>2</sub> Eutectic Composite," *Acta Metall.*, **5**, (1977), 333-344.
41. J.D. Whittenberger, R.D. Noebe, D.R. Johnson and B.F. Oliver, "Compressive and Tensile Creep in Directionally Solidified NiAl-14.5(at.%Ta)," *Intermetallics*, **5**, (1997), 173-184.
42. R. Dickerson, R.D. Noebe and J.D. Whittenberger, to be published.
43. G. Bozzolo, R.D. Noebe, J. Ferrante and A. Garg, "Progress in the Modeling of NiAl-Based Alloys Using the BFS Method," in Structural Intermetallics II, M.V. Nathal et al., eds., The Minerals Metals & Materials Society, Warrendale, PA, (1997).
44. A. Misra, Z.L. Wu, R. Gibala, R.D. Noebe and B.F. Oliver, "Toughening Mechanisms in Directionally Solidified B2-NiAl-Based Eutectic Alloys," in Structural Intermetallics II, M.V. Nathal et al., eds., The Minerals Metals & Materials Society, Warrendale, PA, (1997).
45. A. Misra and R. Gibala, "Room Temperature Deformation Behavior of Directionally Solidified Multiphase Ni-Fe-Al Alloys," *Metall. Mater. Trans. A*, **28A**, (1997), in press.
46. A. Misra, R.D. Noebe and R. Gibala: "The Influence of Mobile Dislocation Density on the Fracture Toughness of B2-Based Alloys," Intermetallic Matrix Composites III, ed. J. Graves et al., MRS Symp. Proc. Vol. 350, (1994), pp. 243-248.
47. R.D. Noebe, A. Misra and R. Gibala, "Plastic Flow and Fracture of B2 NiAl-based Intermetallic Alloys Containing a Ductile Second Phase," *ISIJ International*, **31**, (1991), 1172-1185.
48. K.S. Chan, "Fracture and Toughening Mechanisms in an Alpha-2 Titanium Aluminide Alloy," *Metall. Trans. A*, **21A**, (1990), 2687-2699.
49. S.M. Joslin, X.F. Chen, B.F. Oliver and R.D. Noebe, "Fracture Behavior of Directionally Solidified NiAl-Mo and NiAl-V Eutectics," *Mater. Sci. Eng. A*, **196**, (1995), 9-18.
50. X.F. Chen, D.R. Johnson, R.D. Noebe and B.F. Oliver, "Deformation and Fracture of a Directionally Solidified NiAl-28Cr-6Mo Eutectic Alloy," *J. Mater. Res.*, **10**, (1995), 1159-1170.
51. J.-M. Yang, S.M. Jeng, K. Bain and R.A. Amato, "Microstructure and Mechanical Behavior of In-Situ Directional Solidified NiAl/Cr(Mo) Eutectic Composite," *Acta Mater.*, **45**, (1997), 295-305.
52. K.S. Ravichandran, "A Survey of Toughness in Ductile Phase Composites," *Scripta Metall. Mater.*, **26**, (1992), 1389-1393.
53. D.R. Johnson, "Processing and Mechanical Properties of NiAl-based In-Situ Composites" Ph.D. Thesis, The University of Tennessee, (1994).
54. T.M. Pollock and D. Kolluru, "Deformation of NiAl-Based Intermetallics," Micromechanics and Advanced Materials, S.N.G. Chu et al., eds., The Minerals Metals & Materials Society, Warrendale, PA, (1995), pp. 205-212.
55. J.L. Walter and H.E. Cline, "Stability of the Directionally Solidified Eutectics NiAl-Cr and NiAl-Mo," *Metall. Trans.*, **4**, (1973), 33-38.
56. E. Arzt and P. Grahle, "Creep of Particle-Reinforced NiAl Intermetallics: New Materials for Up to 1400 °C," High-Temperature Ordered Intermetallic Alloys VI, J.A. Horton et al., eds., MRS. Symp. Proc. Vol. 364, (1995), pp. 525-536.
57. P. Grahle and E. Arzt, "Microstructure Development In Dispersion Strengthened NiAl Produced by Mechanical Alloying and Secondary Recrystallization," *Acta Metall. Mater.*, **45**, (1997), 201-211.
58. E. Goehring, P. Grahle and E. Arzt, "Dislocation Structure and Creep Properties In Dispersion Strengthened Intermetallics," Proc. Of the 13<sup>th</sup> International Plansee Seminar, H. Bildstein and R. Eck, eds., Metallwerk Plansee, Reutte, vol. 3, (1993), pp. 501-513.
59. A. Wanner, P. Grahle, O. Lang, B. Schietinger, E. Arzt, I. Rumberg, P. Schretter and H. Clemens, "Processing and mechanical Properties of PM-NiAl Containing Nb and Cr As Coarse Second Phases," Proc. Of the 13<sup>th</sup> International Plansee Seminar, H. Bildstein and R. Eck, eds., Metallwerk Plansee, Reutte, vol. 3, (1993), pp. 514-527.
60. H. Clemens and H. Bildstein, "Investigations on the Ductilization of NiAl by Second Phases," *Z. Metallkd.*, **83**, (1992), 429-435.
61. J.D. Whittenberger, E. Arzt and M.J. Luton, "Preliminary Investigation of a NiAl Composite Prepared by Cryomilling," *J. Mater. Res.*, **5**, (1990), 271-277.
62. J.D. Whittenberger, "Characteristics of an Elevated Temperature AlN Particulate Reinforced NiAl," Structural Intermetallics, R. Darolia et al., eds., The Minerals, Metals & Materials Society, Warrendale, PA, (1993), pp. 819-828.
63. R.P. Luton and J. Vallone, "Method for Producing Dispersion Strengthened Metal Powders," US Patent No. 4,647,304, March 3, 1987.
64. J.D. Whittenberger, E. Arzt and M.J. Luton, "1300 K Compressive Properties of a Reaction Milled NiAl-AlN Composite," *J. Mater. Res.*, **5**, (1990), 2819-2827.
65. B.J.M. Aikin, R.M. Dickerson, D.T. Jayne, S. Farmer and J.D. Whittenberger, "Formation of Aluminum Nitride During Cryomilling of NiAl," *Scripta Metall. Mater.*, **30**, (1994), 119-122.
66. A. Garg, J.D. Whittenberger and B.J.M. Aikin, "Microstructural Characterization of Creep Tested Cryomilled NiAl-13vol.% AlN," Intermetallic Matrix Composites III, J.A. Graves et al., eds., MRS. Symp. Proc. Vol. 350, (1994), pp. 231-236.
67. B.J.M. Aikin, J.D. Whittenberger and M.G. Hebsur, "Reproducibility of NiAl Cryomilling," Proc. 2<sup>nd</sup> Int. Conf. on Mechanical Alloying for Structural Applications, ASM International, Metals Park, OH, (1993), pp. 283-290.
68. M.G. Hebsur, J.D. Whittenberger, C.E. Lowell and A. Garg, "NiAl-Base Composite Containing High Volume Fraction of AlN Particulate for Advanced Engines," High-Temperature Ordered Intermetallic Alloys VI, J.A. Horton et al., eds., MRS. Symp. Proc. Vol. 364, (1995), pp. 579-584.
69. M.G. Hebsur, J.D. Whittenberger and A. Garg, "The Effect of Volume Fraction Reinforcement and Annealing on the Strength of Cryomilled NiAl Containing AlN Particles," Structural Intermetallics II, M.V. Nathal et al., eds., The Minerals, Metals & Materials Society, Warrendale, PA, (1997).
70. J.D. Whittenberger and M.J. Luton, "Elevated Temperature Compressive Strength Properties of Reaction Milled NiAl-AlN and Zr-doped NiAl-AlN Composites," *J. Mater. Res.*, **7**, (1992), 2724-2732.
71. J.D. Whittenberger and M.J. Luton, "Elevated Temperature Creep Properties of NiAl Cryomilled With and Without Y<sub>2</sub>O<sub>3</sub>," *J. Mater. Res.*, **10**, (1995), 1171-1186.
72. J.D. Whittenberger, R.D. Noebe and A. Garg, "Elevated Temperature Compressive Properties of N-Doped NiAl," *Metall. Mater. Trans. A*, **27A**, (1996), 3170-3180.
73. B.J.M. Aikin, R.M. Dickerson and P.O. Dickerson, "Microstructure and Properties of Cryomilled Nickel-Aluminide Extruded with Chromium or Molybdenum," Advances in Powder Metallurgy & Particulate Materials - 1995, Metal Powders Industries Federation, Princeton, NJ, (1995), pp. 13-181 to 13-194.
74. K.G. Shaw, M.F. Gruninger and W.J. Jarosinski, "High Temperature Intermetallic Binders for HVOF Carbides," Thermal Spray Industrial Applications, C. Berndt and S. Sampath, eds., ASM International, Materials Park, OH, (1994), pp. 185-190.
75. V. Weihnacht, W.D. Fan, K. Jagannadham and J. Narayan and C.T. Liu, "A New Design of Tungsten Carbide Tools with Diamond Coatings," *J. Mater. Res.*, **11**, (1996), 2220-2230.
76. E.P. George, C.T. Liu, J.A. Horton, C.J. Sparks, M. Kao, H. Kunsmann and T. King, "Characterization, Processing, and Alloy Design of NiAl-Based Shape Memory Alloys," *Mater. Character.*, **32**, (1994), 139-160.
77. Karl. G. Shaw and J.H. Reinshagen, "Powder Production of Nickel and Iron Aluminides," Nickel and Iron Aluminides, S.C. Deevi and V. Sikka, eds., The Minerals, Metals & Materials Society, Warrendale, PA, (1997).
78. D.E. Laughlin, L.-L. Lee, L. Tang and D.N. Lambeth, "The Control and Characterization of the Crystallographic Texture of Longitudinal Thin Film Recording Media," *IEEE Trans. on Magnetics*, **32**, (1996), 3632-3637.
79. T. Sands, et al. "Stable and Epitaxial Metal/III-V Semiconductor Heterostructures," *Mater. Sci. Rep.*, **5**, (1990), 99-170.
80. D.N. Lambeth, E.M.T. Velu, G.H. Bellesis and D.E. Laughlin, "Media for 10 Gb/in<sup>2</sup> Hard Disk Storage: Issues and Status," *J. Appl. Phys.*, **79**, (1996), 4496-4501.

# Development and Characterization of High Strength NiAl Single Crystal Alloys

R. Darolia and W.S. Walston

GE Aircraft Engines, 1 Neumann Way, Cincinnati, OH 45215

## Abstract

The alloy development approach and characterization of high strength NiAl alloys are described. A large number of alloying elements were examined, and it was found that the Heusler-forming elements provided excellent precipitation strengthening capability. This approach was combined with the potent solid solution strengthening of Ti to produce alloys with good strength at all temperatures. In addition, it was found that small additions of Ga improved both the RT fracture strength and high temperature creep strength. This alloy development approach culminated in alloys with creep rupture strength equivalent to single crystal superalloys. The effect of precipitation morphology and distribution on the creep rupture strength will also be discussed. Two alloys, AFN-12 and AFN-20, represent a range of critical properties and were selected for extensive physical and mechanical property tests, as well as for component and engine testing.

## Introduction

NiAl has been one of the most studied intermetallics over the past 10 years, and many recent reviews cover the range of topics evaluated.<sup>1-5</sup> Several investigators have been successful in improving the ductility or strength of NiAl by using alloying additions. It is well known that small additions of Fe, Ga or Mo can improve the room temperature tensile ductility by several percent.<sup>1</sup> Likewise, many different alloying additions have been shown to improve high temperature strength.<sup>6</sup>

Elements such as Co, Fe, and Ti have a high solubility in NiAl, and can provide significant solid solution strengthening.<sup>6-8</sup> Solid solution strengthening can be significant even at a low level, especially with the addition of group IVB and VB elements such as Ti, Hf, Zr, Nb, V, and Ta.<sup>9,10</sup> For example, an addition of 0.2 at.% Hf to NiAl increases the room-temperature tensile strength of a <110>-oriented specimen from a typical value of 210 MPa for stoichiometric NiAl to 600 MPa.<sup>2</sup>

Four types of second phases have been shown to strengthen NiAl. These are: Heusler ( $\beta'$ )  $\text{Ni}_2\text{AlX}$  phase, where X is a Group IVB or VB element; NiAlX Laves phase, where X is Hf, Ta, Ti, Nb, V or Zr; silicide phases, such as  $\text{Ni}_{16}\text{X}_6\text{Si}_7$ ; G-phase, where X is Hf or Zr; NiHfSi; and  $\alpha$  elemental phases such as Mo, Cr, and Re. The Heusler phase ( $\beta'$ ) is a L2<sub>1</sub> structure and represents a further ordering of the B2 structure of the NiAl matrix, with the elemental addition ordering on the Al sublattice. The first report of precipitation strengthened NiAl was by Polvani, et al, using Ti-containing  $\beta'$  precipitates.<sup>11,12</sup> It was found that large amounts of Ti produced either a  $\beta$  matrix with  $\beta'$  precipitates or vice versa. The strongest of these alloys, containing 15-20 at.% Ti, had creep strength approaching first generation, single crystal Ni-base superalloys. Another study on Ti additions confirmed the potent strengthening capability of Ti-containing  $\beta'$  precipitates.<sup>13</sup> High temperature strengths of other alloys with Hf- or Ta-containing  $\beta'$  precipitates<sup>14-16</sup> have shown promise but did not equal the strength of the high Ti-containing alloys.

The NiAlNb Laves phase also has been utilized to strengthen NiAl,<sup>17-20</sup> however it was found that very large volume fractions of NiAlNb were necessary to approach the strength of Ni-base superalloys. The third type of precipitates observed in NiAl alloys are silicide phases, such as G-phase and NiHfSi. G-phase ( $\text{Ni}_{16}\text{X}_6\text{Si}_7$ ) generally appears as fine cuboidal-shaped, coherent precipitates.<sup>16</sup> It has been shown that G-phase provides precipitation strengthening and improves creep rupture properties.<sup>16,21,22</sup> Directional solidification has been used on alloys containing  $\alpha$ -forming elements such as Re, Cr and Mo. Directional solidification of eutectic compositions produces aligned  $\alpha$  fibers which can greatly improve strength.<sup>23</sup> The eutectic compositions of these ternary systems are 34 at.% Cr,<sup>24</sup> 1.5 at.% Re<sup>25</sup> and 9 at.% Mo.<sup>26</sup>

Other methods used to improve the high temperature strength of NiAl include the addition of dispersoids through rapid solidification or mechanical alloying and continuous and discontinuous composite reinforcements. The work in these areas will not be covered here, and the reader is referred to a review of these topics by Nathal.<sup>9</sup>

Research and development of NiAl alloys at GE Aircraft Engines for the last 10 years has led to improvements in both ductility and strength by utilizing alloying additions and the single crystal casting process. The effect of over 25 alloying elements on the physical and mechanical properties of NiAl has been studied. Many of these alloying elements were combined to study their additive effects as well as any synergistic effects. This paper describes the alloy development approach and characterization of high strength, single crystal NiAl alloys.

#### Experimental Procedures

Single crystals of the NiAl alloys were produced using a modified Bridgman technique.<sup>27</sup> These crystals measured approximately 2.5 cm x 4 cm x 10 cm. Excellent composition control was demonstrated with respect to major alloying elements. The typical values for O, N, C, P and S impurities were 40 to 60, 1 to 5, 40 to 80, 1 to 5 and 1 to 5 wppm, respectively. The values for Si were in the 600 to 1200 wppm range due to pick up from the mold material during single crystal processing. Most alloys received a solution and age heat treat cycle; the cycles used for individual alloys will be discussed later. Slabs were then oriented using the back reflection Laue technique, and specimen blanks were EDM wirecut in either the  $\langle 001 \rangle$  or  $\langle 110 \rangle$  orientation. Button head type tensile specimens with gauge diameters of 2.54 mm and gauge lengths of 19.05 mm were produced using low stress grinding techniques. The specimens were electropolished using a 7% perchloric-methanol solution at  $-30^\circ\text{C}$  to remove residual grinding marks and strains. Tensile, creep and stress rupture tests were performed in air using special grips to minimize misalignment. The Larson Miller Parameter (LMP) was used to rank the effectiveness of alloying additions on creep-rupture lives using the formula:

$$\text{LMP} = T(C + \log t)$$

where T is temperature in degrees Kelvin, C is a constant and t is rupture life in hours. A value of 20 was used for C, a value typical for Ni-base superalloys.

## Results

### Alloy Development Approach

Early alloy development work was primarily concentrated on the effects of single alloying additions on mechanical properties and microstructure. Typically, tensile and stress rupture testing was performed as part of the screening criteria for each alloy. Promising alloys were then tested at additional temperatures and evaluated for other properties, such as fracture toughness and thermal conductivity. In general, the levels of alloying additions were kept low to maintain thermal conductivity and density advantages of the NiAl alloys over Ni-base superalloys.

The vast majority of alloying additions were made by substituting for Al and leaving Ni at 50 at.%. Many of the site preferences were unknown at the early stages of this study. Several alloys were designed to evaluate the effect of site substitution and the Ni/Al ratio, such as alloys with Co, Cr or Fe additions.<sup>6</sup> However, no consistent effects were observed, and subsequent alloys were made with substitutions for Al which allowed for consistent comparisons. In later alloys with Heusler-forming elements, the substitution for Al corresponded to the site preference for these elements.<sup>28</sup>

It was initially hoped that an alloy could be developed that possessed both adequate room temperature tensile ductility ( $\sim 2\%$ ) and high temperature strength comparable to conventionally cast superalloys. It became apparent that alloying additions could be made to improve either ductility or strength, but it was difficult to develop alloys possessing both good ductility and strength. For example, binary NiAl has a RT ductility of about 2% and a yield strength of about 210 MPa in the  $\langle 110 \rangle$  orientation. Alloying additions that raised the yield strength to about 700 MPa always resulted in a loss of ductility and toughness. Thus, it was decided to pursue alloying additions that raised the tensile and creep rupture strength to values that could be used in a gas turbine application. The alloying strategy judiciously utilized strengthening effects such that the fracture toughness was not significantly affected, and the alloys could be fabricated into test specimens and engine hardware. Concurrently, design methodologies were developed to utilize materials with limited ductility and toughness.

Figure 1 summarizes the effect of many representative elements on room temperature  $\langle 110 \rangle$  tensile strength. This plot shows the maximum tensile strength obtained for an alloying addition for various levels evaluated. For instance, the maximum strength for a NiAl+Hf alloy occurred at 0.5 at.% Hf and for a NiAl+Cr ternary alloy at 2.0 at.% Cr. The maximum tensile strength value was subtracted from the single crystal binary NiAl  $\langle 110 \rangle$  value of 200 MPa and divided by the elemental addition level, i.e. 0.5 or 2.0. This is not a rigorous method because it only incorporates the alloys evaluated and perhaps not the ideal level of addition. This method also does not differentiate between solid solution and precipitation strengthening. Nonetheless, it was an effective means to determine potent strengtheners for NiAl. This plot shows that B, Hf and Ta were very effective strengtheners as single element additions to NiAl. Attempts to combine the strengthening effect of B with Hf or Ta did not produce higher strength alloys. These data,



along with other stress rupture data earlier reported,<sup>6</sup> suggested that the Heusler-forming elements were the most potent strengtheners for NiAl.

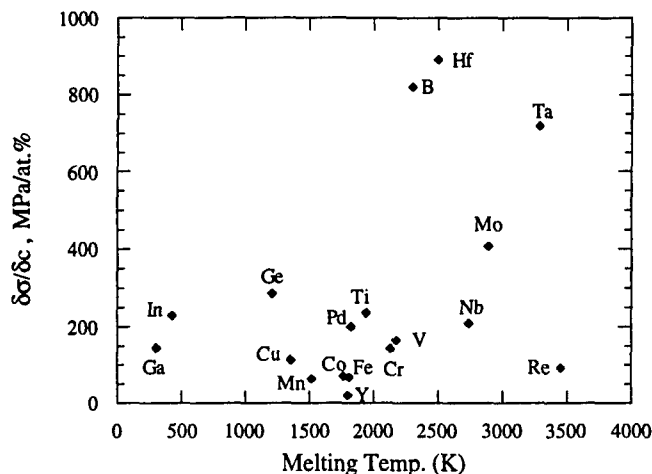


Figure 1. Room temperature strengthening potential ( $\delta\sigma/\delta c$ ) of various alloying additions versus their melting temperatures.

#### Heusler-forming Single Element Additions

Additions of group IVB or VB elements (Hf, Ta, Ti, Nb, V and Zr) beyond their solubility limits in NiAl produce several ternary intermetallic compounds, including the  $L2_1$  Heusler ( $\beta'$ ,  $Ni_2AlX$ ) phase. The close relationship between the B2 and  $L2_1$  crystal structures results in coherent or semi-coherent  $\beta'$  precipitates.<sup>29</sup> The solubilities of different  $\beta'$ -forming elements in NiAl vary widely. Microprobe data and analysis of precipitation reactions at various temperatures indicate that the solubility at 1000°C is about 0.5 at.% for Hf and < 0.5 at.% for Ta. It was previously shown that Ta containing alloys show precipitates at less than 0.5 at.% additions although very little characterization work has been performed.<sup>6</sup>

Other studies have shown that Zr has a very low solubility,<sup>29</sup> while V has at least 13 at.% solubility at 900°C.<sup>29</sup> Limited data exist on the solubility of Nb, but it is believed to be similar to that of Hf and Ta.<sup>15</sup> Ti has a solubility of about 6 at.% at 1000°C.<sup>30</sup> It has been found that Ti containing alloys do not have precipitates until greater than 5 at.% additions. At 7.5 at.%, a significant amount of fine  $\beta'$  precipitates are present at 871°C, however many coarsen and dissolve at 1093°C.<sup>6</sup>

Si pick up (600-1000 wppm) from the mold materials during single crystal processing also resulted in several different precipitate microstructures that are not implied from the ternary phase Ni-Al-X phase diagrams. Depending on the Si level and the heat treat cycle, both  $Ni_6X_6Si_7$  (G-phase) and  $NiXSi$  can form in addition to the expected Heusler and Laves phases. For instance, the microstructure of an alloy containing 0.5 at.% Hf is very dependent on the Si level.<sup>31</sup> Figure 2 shows a typical microstructure for an alloy containing an intentional addition of 0.5 at.% Hf and a Si impurity level of 0.2 at.%. These precipitates are nearly all G phase and provide significant precipitation strengthening at low and intermediate temperatures.

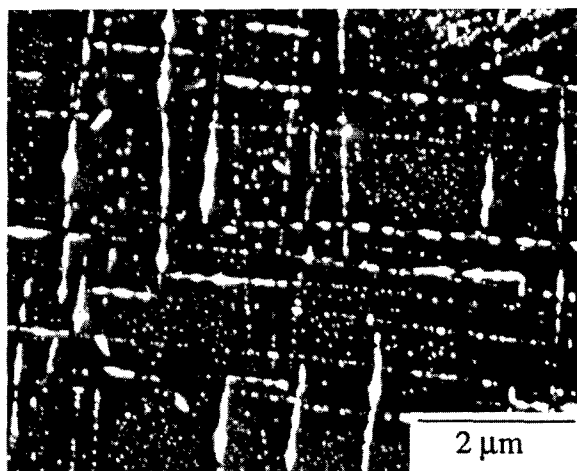


Figure 2. Microstructure of alloy D176 (50 Ni-49.45 Al-0.5 Hf-0.05 Ga at.%) showing presence of G phase as a result of the presence of 0.2 at.% Si impurity.

The room temperature tensile strength of <110> oriented alloys with different levels of single element additions is shown in Figure 3. This figure shows that Hf is the most potent strengthener among this group of elements. The four elements with low solubilities (Hf, Ta, Zr and Nb) show a peak in tensile strength at additions of less than 1 at.%. It is believed that the decrease in strength is due to the fact that the alloy becomes quite defect sensitive at higher alloying additions. Consequently, the specimen fractures at a much lower fraction of the true ultimate tensile strength. Consistent with these data, it was observed that some tensile failures occurred at unsolutioned, primary Heusler precipitates. Similar trends were observed for Hf and Ta containing alloys at 871°C. Figure 4 shows that the peak in strength at 871°C was now around 2 at.% alloying addition. This is likely due to the higher plasticity observed at 871°C compared to RT. Once again, Hf is the most potent strengthener at 871°C.

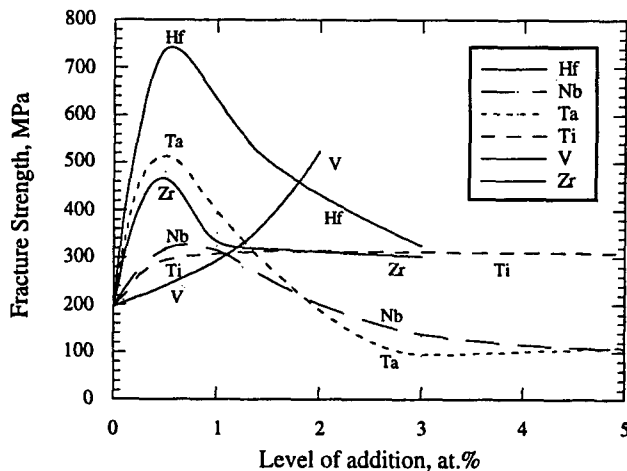


Figure 3. The effect of single element additions of  $\beta'$  formers on the <110> room temperature tensile strength of NiAl.



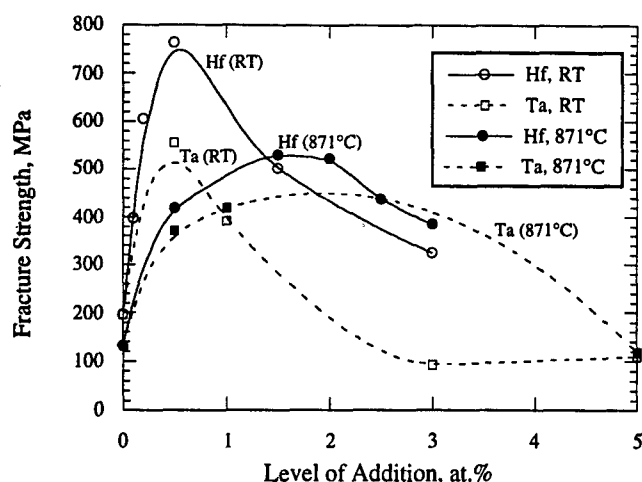


Figure 4. The effect of single element additions of  $\beta'$  formers on the  $\langle 110 \rangle$  871°C tensile strength of NiAl.

The effect of Heusler-forming elemental additions on stress rupture strength is shown in Figures 5-8. Figure 5 shows the effect of adding various levels of Hf to NiAl. There was a large increase in rupture strength simply by adding 0.5 at.% Hf, with much smaller improvements at larger levels of Hf. At many test conditions, the strongest alloy contained 1.5 at.% Hf with lower rupture data points at higher levels of Hf. A similar trend was seen with Ta additions (Figure 6). An 0.5 at.% addition of Ta provided substantial improvements in strength, while higher amounts of Ta resulted in marginal improvements or decreases in strength. All of the Hf and Ta alloys received a 1315°C/50 hr homogenization heat treatment with no subsequent aging cycle. It is likely that improved properties would result from optimizing the precipitate size and distribution. Modest improvements in strength were obtained by additions of either Nb, Zr or V, as shown in Figure 7. At the levels evaluated, there was little effect of the additional amounts of Zr or Nb and both elements produced similar strengths. Vanadium has a higher solubility than Zr or Nb, and there was a beneficial effect at the higher level of V addition. Even at 5 at.% V, no precipitates were observed, and strengthening was solely by solid solution strengthening. Titanium also has a high solid solubility in NiAl, and Figure 8 shows that high amounts of Ti were required to obtain good strengths. Additions of 7.5-10 at.% Ti resulted in the highest strengths obtained by single element additions.

As a result of the above findings, it was concluded that large improvements in stress rupture strength could be obtained by relatively small additions of Hf or Ta, while larger additions were required of the other Heusler-forming elements. These data, along with the tensile strength data, led to the use of 0.5 at.% Hf as the base for subsequent alloys.

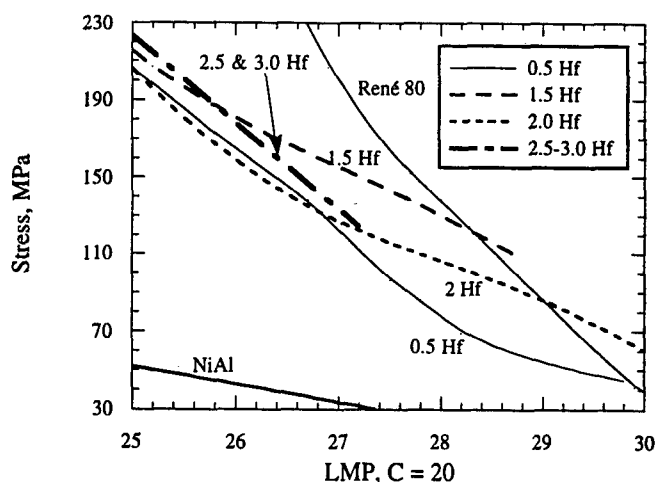


Figure 5. The effect of various levels of Hf on the stress rupture strength of NiAl.

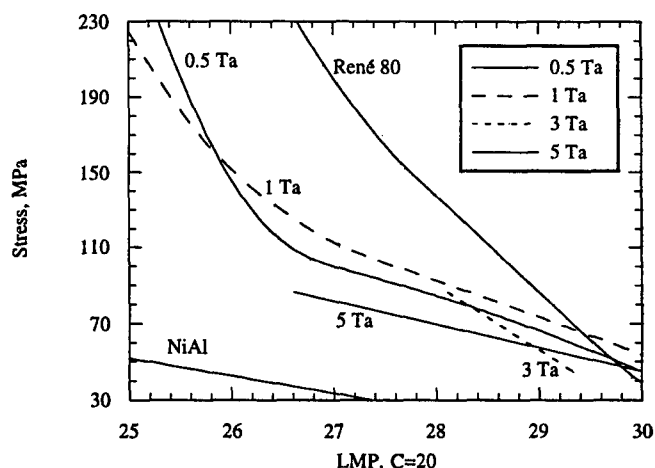


Figure 6. The effect of various levels of Ta on the stress rupture strength of NiAl.

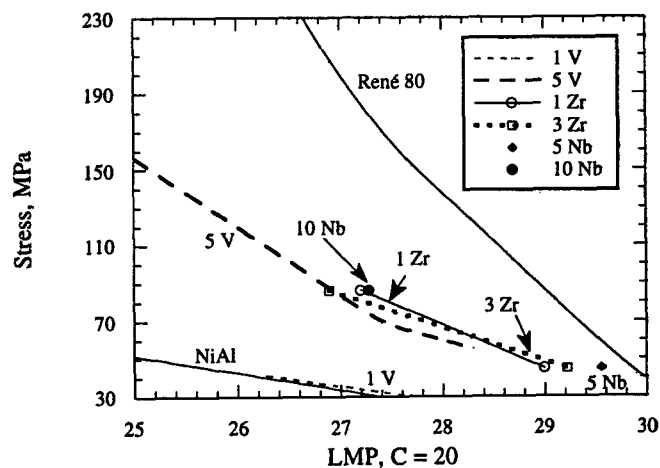


Figure 7. The effect of various levels of V, Zr or Nb on the stress rupture strength of NiAl.

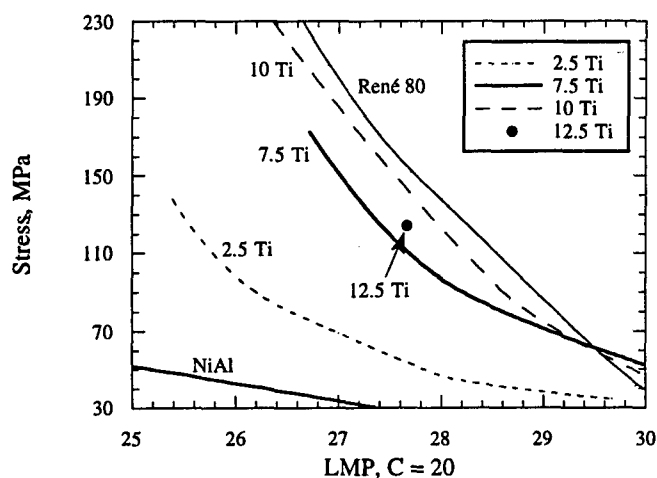


Figure 8. The effect of various levels of Ti on the stress rupture strength of NiAl.

#### Effect of Ga Additions on High Strength Alloys

Small additions of elements known to ductilize binary NiAl, such as Ga, Fe and Mo, were added to stronger alloys containing 0.5 at.% Hf. It was hoped that these elements would impart ductility to the stronger alloys or at least make them less defect sensitive. While measurable plastic strain was not obtained in RT tensile tests of these alloys, higher fracture strengths were obtained. Table 1 shows that additions of Ga improved the RT fracture strength up to 800 MPa. In addition, the machinability of these and other stronger alloys was found to improve with Ga additions. Small additions of Fe or In also had beneficial effects on RT fracture strength of Hf-containing alloys. It is believed that these elements reduce the defect sensitivity of strong NiAl alloys, although the exact mechanisms are not well understood.

Ga additions were also shown to improve the stress rupture properties of alloys containing Hf. Table 1 shows examples of improved rupture life with various levels of Ga additions. This table shows that in RT tensile and various stress rupture tests, there was a consistent increase in strength when Ga was added to a Hf-containing alloy. However, there does not seem to be much benefit to increasing the Ga content higher than 0.05 at.%, except in the 982°C/86 MPa stress rupture tests. These results led to the use of 0.5 at.% Hf with small additions of Ga as the baseline alloys for developing higher strength alloys.

Table 1. <110> Properties of NiAl+Hf Alloys with Ga Additions

Hf	Ga	RT Tensile Strength, MPa	Stress Rupture Life, hrs		
			871°C/ 241 MPa	982°C/ 86 MPa	982°C/ 124 MPa
0.5		620	4	97	0
0.5	0.05	772	34	600	46
0.5	0.2	800	41	1145	31
0.5	0.5	703	32	~1500 est.	69

#### Multiple Heusler-forming Additions

Several alloys were designed with combinations of Heusler-forming elements in an attempt to further increase rupture strength. Prior work showed that Hf and Ta were potent precipitation strengtheners and Ti was a potent solid solution strengthener. Many of these alloys were made with 53 at.% Ni to avoid Laves phase formation. However, in several direct comparisons, it was found that alloys with 50 at.% had superior rupture lives to those with 53 at.% Ni. In addition, with only small additions of Hf, Ti or Ta, the Laves phase was not observed at 50 at.% Ni. Figure 9 shows the beneficial effect of combining Hf, Ta and Ti in a single NiAl alloy. These alloys and subsequent high strength alloys received a solution heat treatment at 1371°C followed by an 982°C aging heat treatment.

Combining these elements, along with the addition of Ga, yielded beneficial synergistic effects that were not expected based on prior data on alloys with single element additions. Figures 10 and 11 show the effect of adding Hf, Ti and Ta to a baseline alloy containing 0.5 at.% Hf and 0.2 at.% Ga. Further additions of Hf or Ta improved the rupture strength slightly, however additions of Ti dramatically improved the rupture strength. Based on the rupture life effects of single element additions of Hf and Ti to NiAl, the combination of Hf and Ti was expected to be beneficial but not to the degree shown in Figures 10 and 11.

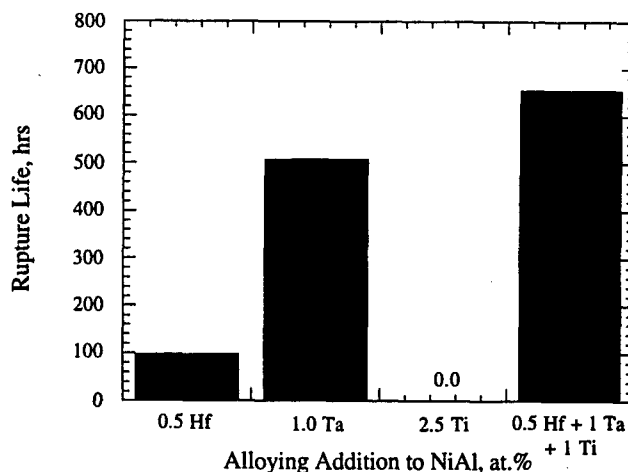


Figure 9. The beneficial effect of combining Heusler-forming elements on 982°C/86 MPa rupture strength of <110> specimens.

#### Effect of Cr and Zr Additions on High Strength Alloys

Various levels of Cr were added to high strength NiAl alloys in an attempt to improve environmental resistance. The effects on tensile and stress rupture properties were also evaluated. It was found that Cr additions to alloys containing Hf or Hf+Ti did not affect either the room temperature or elevated temperature tensile strength. However, there were consistent decreases in rupture strength when Cr was systematically added to two different alloy series. Figure 12 shows that increasing the Cr content to a baseline alloy containing Hf and Ga

reduced the stress rupture strength. A similar trend is shown in Figure 13 when Cr was added to stronger alloys containing Hf, Ti and Ga. The solubility of Cr in NiAl is believed to be about 3-4 at.% at 1000°C. In these high strength alloys, it is not known whether Cr is in solid solution or contributes to the precipitation reactions. A more detailed deformation mechanism study would need to be performed to understand why Cr additions decrease the rupture strength of these NiAl alloys.

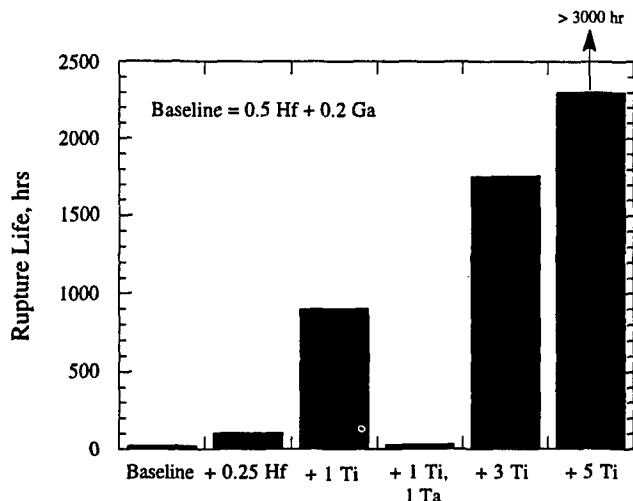


Figure 10. Synergistic effect of adding Ti to NiAl alloys containing Hf and Ga. 871°C/241 MPa rupture tests of <110> specimens.

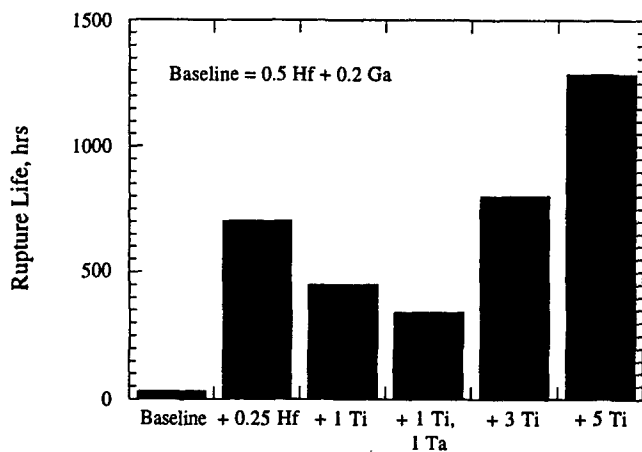


Figure 11. Synergistic effect of adding Ti to NiAl alloys containing Hf and Ga. 982°C/124 MPa rupture tests of <110> specimens.

In an attempt to reduce the number of internal defects in the high strength alloys and improve the low temperature fracture strength, Zr was substituted for Hf. It was hoped that Zr would not form detrimental oxides as readily as Hf. Unfortunately, the defect size and distribution was not greatly affected, and the RT tensile strengths of a series of alloys containing Zr and Hf were comparable. In addition, substitution of Zr for Hf decreased the rupture strength, as shown in Figure 13. This was to be expected since Hf was previously shown to be a more potent strengthener than Zr.

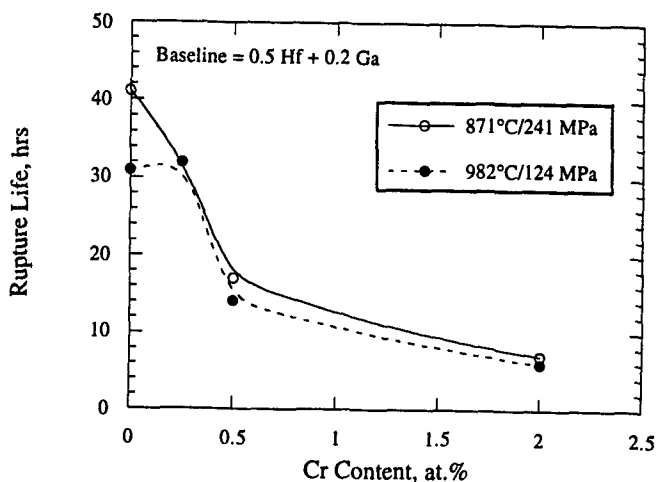


Figure 12. The effect of Cr additions to alloys containing Hf and Ga on the 871°C/241 MPa rupture strength of <001> specimens.

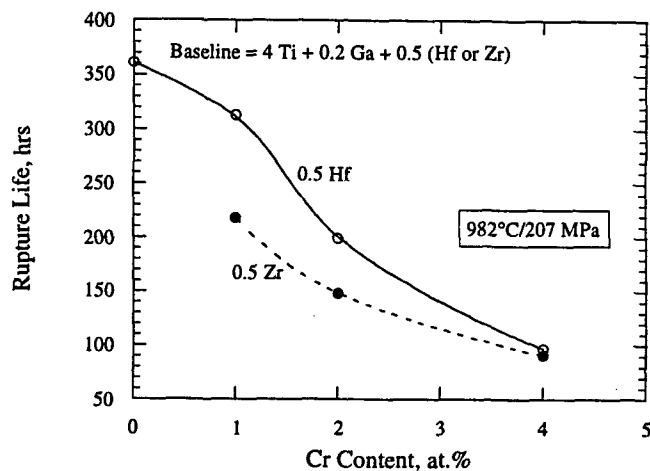


Figure 13. The effect of Cr additions to alloys containing Ti, Ga and either Hf or Zr on the 982°C/207 MPa stress rupture strength of <001> specimens.

#### Preferred Alloys

Based on this background alloy development work, two alloys, AFN-12 and AFN-20, were selected for extensive physical and mechanical property characterization, as well as for component and engine testing. The compositions and selected properties of these alloys are shown in Table 2. AFN-12 has stress rupture strength equal to René 80, and AFN-20 has stress rupture strength equal to René N4, as shown in Figure 14. On a specific strength basis, AFN-20 exceeds the strength of the latest single crystal superalloy, René N6, as shown in Figure 15. These two NiAl alloys contain Hf, Ti and Ga additions, and it was found that Ti played a large role in determining the critical properties of rupture strength and thermal conductivity. Figures 10 and 11 previously showed that the addition of 5 at.% Ti (AFN-20) gave rupture life increases of about 3X compared to an addition of 1 at.% Ti (AFN-12). However, increased Ti resulted in detrimental decreases in the thermal conductivity of the NiAl alloys.

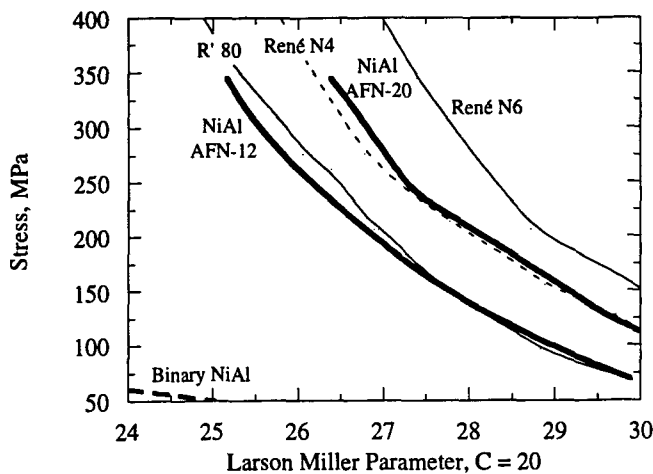


Figure 14. Stress rupture strength of NiAl alloys AFN-12 and AFN-20 compared to superalloys René 80 and René N4.

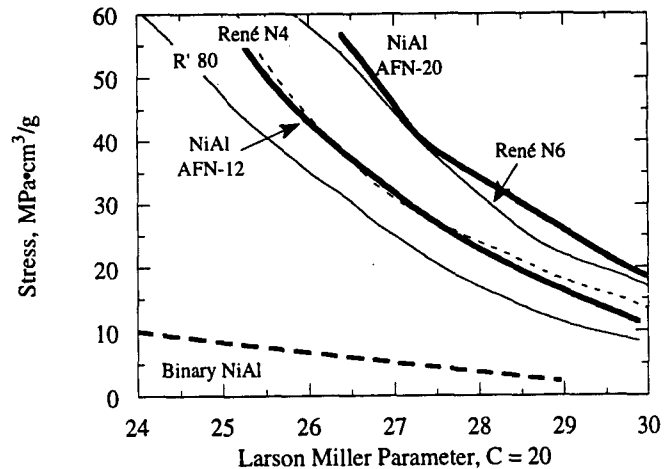


Figure 15. Specific stress rupture strength of NiAl alloys AFN-12 and AFN-20 compared to superalloys René 80 and René N4.

Table 2. Alloy Compositions and Representative Properties of Two Preferred NiAl Alloys

Property	AFN-12	AFN-20
Composition	50 Ni - 48.45 Al - 0.5 Hf - 1.0 Ti - 0.05 Ga at. %	50 Ni - 44.45 Al - 0.5 Hf - 5.0 Ti - 0.05 Ga at. %
Rupture Strength	Equal to René 80	Equal to René N4
Creep Strength	Slightly less than René 80	Slightly less than René N4
Fatigue Strength	Slightly less than René N4	Equal to René N4
High Temp. Tensile Strength	Equal to René N4	Equal to René N4
DBTT	<001> - 730°C, <110> - 925°C	<001> - 1150°C, <110> - 1150°C
RT Toughness	5 MPa√m	4 MPa√m
Density	6.00 g/cm³	6.12 g/cm³
Thermal Expansion	Similar to superalloys	Similar to superalloys
Thermal Conductivity	4X René N5	2X René N5
Machinability	Good	Good
Castability	Good	Excellent
Heat Treatment Response	Excellent	Good
Thermal Shock Response	Excellent	Very Good

Both alloys received an extended solution heat treatment at 1399°C followed by aging at 982°C. Typical fully heat treated microstructures of AFN-12 are shown in Figures 16 and 17. As previously shown with alloys containing Hf, the microstructure of AFN-12 is also dependent on the Si level. Although the level of Si was not measured in these specimens, it is believed that slab 2517 in Figure 16 contains higher Si levels than slab 2059 in Figure 17 based on prior observations on this alloy.<sup>31</sup> Figure 16 shows a microstructure consisting entirely of G phase, while Figure 17 shows G phase and some precipitation of  $\beta'$  phase. These figures also show the microstructures of stress rupture specimens from the same single crystal slabs following testing at 982°C. The G phase has nearly completely dissolved in Figure 16 and has completely

dissolved in Figure 17. Based on these types of microstructures, it is not believed that G phase is providing strength at this or higher temperatures, and most of the strengthening is from Hf and Ti in solid solution.

AFN-20 contains 4 at.% more Ti than AFN-12, which causes the microstructure to consist entirely of  $\beta'$  phase instead of mostly G phase. The microstructural changes in stress rupture bars are shown at different temperatures in Figure 18. These micrographs were taken in the unstressed grip section of the bar and show how the  $\beta'$  coarsens and dissolves at higher temperatures. Like AFN-12, precipitate strengthening is likely playing the dominant role at temperatures less

than 900°C with solid solution strengthening becoming significant at higher temperatures. Comparing Figure 18 with Figures 16 and 17 shows that AFN-20 has a significantly higher volume fraction of precipitates at all temperatures and more solid solution strengthening capability at high temperatures due to the 4 at.% higher Ti compared to AFN-12. The precipitation strengthening mechanism in AFN-20 is enhanced by the directional coarsening or "rafting" of the  $\beta'$  precipitates. Figure 19 shows the initial microstructure of AFN-20

compared to the microstructure following a 982°C stress rupture test. Analogous to Ni-base superalloys, the precipitates coalesce and form extended barriers to dislocation motion. In nearly all superalloys, rafts form perpendicular to the stress axis under tensile load, however Figure 20 shows that AFN-20 rafts parallel to the stress axis. This is likely due to the positive mismatch of the  $\beta'$  precipitate with the  $\beta$  matrix compared to the typically negative mismatch of the  $\gamma'$  precipitate with the  $\gamma$  matrix in superalloys.

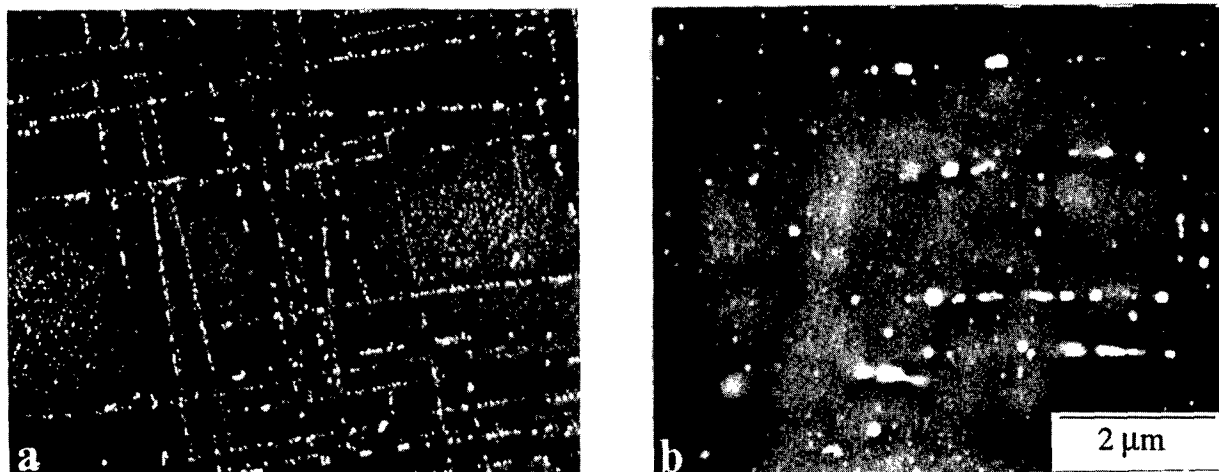


Figure 16. Microstructure of AFN-12 (slab 2517) in (a) as-HT condition and (b) following testing at 982°C/138 ksi/339 hrs. Only G phase present.

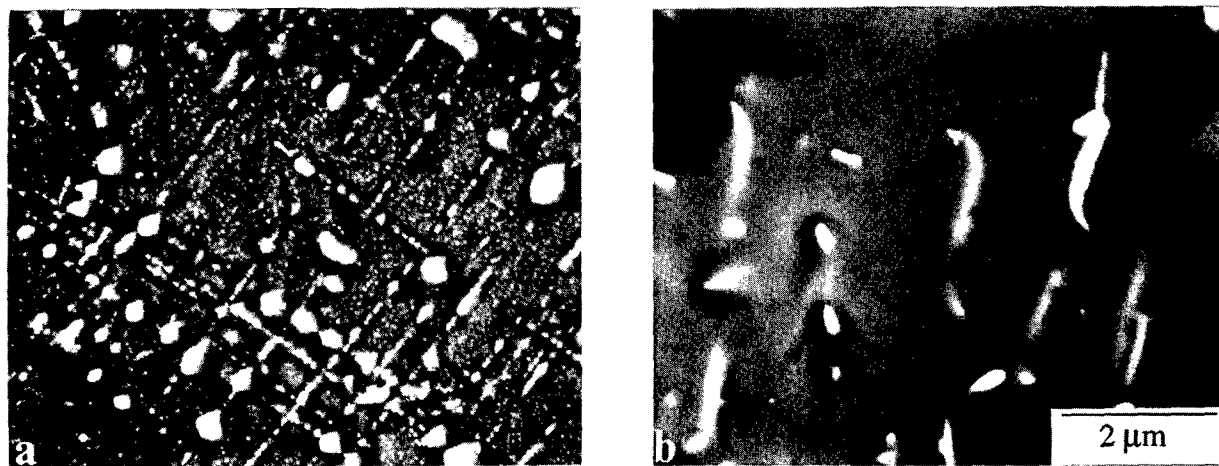


Figure 17. Microstructure of AFN-12 (slab 2059) in (a) as-HT condition (G phase and  $\beta'$ ) and (b) following testing at 982°C/124 ksi/304 hrs (only  $\beta'$ ).

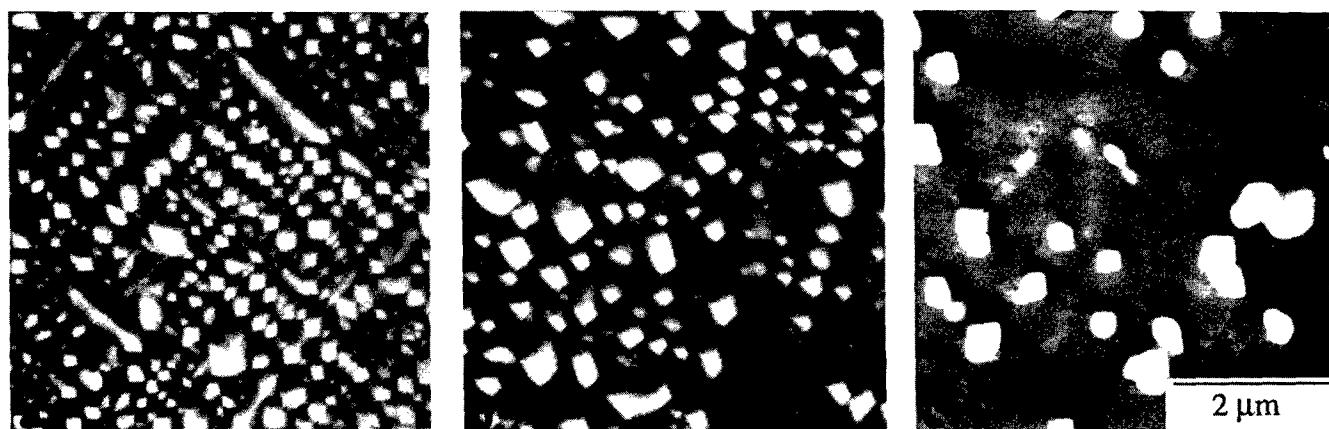


Figure 18. Microstructure of AFN-20 after stress rupture testing at (a) 871°C, (b) 982°C and (c) 1093°C. Note absence of G phase and coarsening of  $\beta'$ .

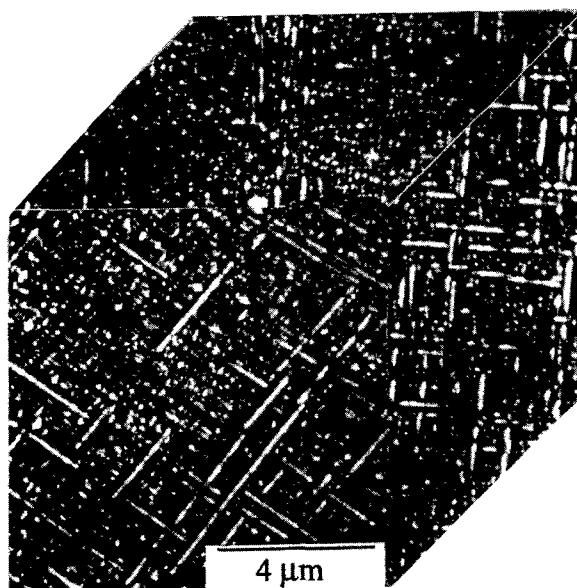


Figure 19. As heat treated microstructure of AFN-20.

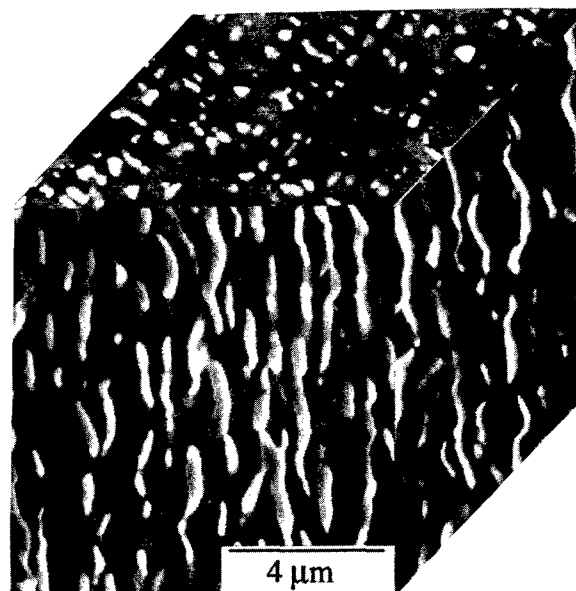


Figure 20. Microstructure of AFN-20 following stress rupture testing at 982°C/152 ksi/200 hrs. Stress axis is vertical.

#### Summary

Initial attempts to produce an alloy with a balance of ductility and high temperature strength resulted in alloys with improved strength but lower ductility and toughness. High strength alloys were pursued by adding Heusler-forming elements, and it was found that Hf was the most potent precipitation strengthener and Ti was a potent solid solution strengthener. It was also observed that small additions of Ga were beneficial to RT tensile strength and high temperature creep strength. Combinations of Hf, Ti and Ga resulted in creep rupture strengths equivalent to those of single crystal superalloys. The strengthening mechanism of these NiAl alloys is a combination of solid solution and precipitation strengthening.  $\beta'$  precipitates, along with G and NiHfSi phases are observed in these alloys. At low and intermediate temperatures, precipitation strengthening is dominant, and at higher temperatures solid solution strengthening becomes significant. Upon completion of the alloy development program, two alloys representing a range of critical properties were selected and have been successfully component and engine tested.

#### Acknowledgments

The authors would like to acknowledge the support of several sources including GE Aircraft Engines, and the U.S. Air Force and U.S. Navy under contract F33615-90-C-2006. Many individuals from these institutions have contributed to the content of this paper through their encouragement and discussions over the past several years. Helpful discussions and a collaborative effort with NASA-Lewis on understanding the strengthening mechanisms in NiAl are also acknowledged.

#### References

1. R. Darolia, *IOM*, Vol. 43, No. 3, 1991, pp. 44-49.
2. R. Darolia, *Structural Intermetallics*, R. Darolia, et al, eds., TMS, Warrendale PA, 1993, pp. 495-504.
3. D. B. Miracle, *Acta metall. mater.*, Vol. 41, No. 3, 1993, pp. 649-684.
4. R. D. Noebe, R. R. Bowman and M. V. Nathal, *Int. Materials Review*, Vol. 38, 1993, pp. 193-232.
5. R. Darolia, W.S. Walston and M.V. Nathal, *Superalloys 1996*, R.D. Kissinger, et al, eds., TMS, Warrendale PA, 1996, pp. 561-570.
6. W.S. Walston, R.D. Field, J.R. Dobbs, D.F. Lahrman and R. Darolia, *Structural Intermetallics*, R. Darolia, et al, eds., TMS, Warrendale PA, 1993, pp. 523-532.
7. M. Rudy and G. Sauthoff, *Mat. Sci. and Eng.*, Vol. 81, 1986, pp. 525-530.
8. M. Rudy and G. Sauthoff, *High Temperature Ordered Intermetallics*, C.C. Koch, et al, eds., Vol. 39, MRS, 1985, pp. 327-333.
9. M. V. Nathal, *Ordered Intermetallics - Physical Metallurgy and Mechanical Behaviour*, C. T. Liu, et al, eds., Vol. 213, Kluwer Academic Publishers, Netherlands, 1992, pp. 541-563.
10. V. M. Pathare, Case Western Reserve University, Ph.D. Thesis, NASA CR-182113, 1988.
11. R. S. Polvani, W. Tzeng and P. R. Strutt, *Metall. Trans.*, Vol. 7A, 1976, pp. 33-40.
12. R. S. Polvani, P. R. Strutt and W. Tzeng, *EMSA, 34th Annual Meeting*, Claitor's Publishing Div., Baton Rouge, LA, 1976, pp. 595.
13. J. D. Whittenberger, R. K. Viswanadham, S. K. Mannan and K. S. Kumar, *High Temperature Ordered Intermetallic Alloys III*, C. T. Liu, et al, eds., Vol. 133, MRS, 1989, pp. 621-626.

14. J. D. Whittenberger, M. V. Nathal, S. V. Raj and V. M. Pathare, Mater. Letters, Vol. 11, 1991, pp. 267-272.
15. K. Vedula, V. Pathare, I. Aslanidis and R. H. Titran, High Temperature Ordered Intermetallic Alloys, C. C. Koch, et al, eds., Vol. 39, MRS, 1985, pp. 411-421.
16. I. E. Locci, R. D. Noebe, R. R. Bowman, R. V. Minor, M. V. Nathal, and R. Darolia, High-Temperature Ordered Intermetallics Alloys IV, eds. L. Johnson, et al, MRS, Vol. 213, 1991, pp. 1013-1018.
17. G. Sauthoff, Intermetallic Compounds-Structure and Mechanical Properties, O. Izumi, eds., Japan Institute of Metals, 1991, pp. 371-378.
18. J. D. Whittenberger, L. J. Westfall and M. V. Nathal, Scr. Metall., Vol. 23, 1989, pp. 2127.
19. J. D. Whittenberger, R. Reviere, R. D. Noebe and B. F. Oliver, Scr. Metall., Vol. 26, 1992, pp. 987-992.
20. C.P. Reip and G. Sauthoff, Intermetallics, Vol. 4, No. 5, 1996, pp. 377-385.
21. I. E. Locci, R. Dickerson, R. R. Bowman, J. D. Whittenberger, M. V. Nathal and R. Darolia, High-Temperature Ordered Intermetallic Alloys V, eds. I. Baker, et al, MRS, Vol. 288, 1993, pp. 685-690.
22. A. Garg, R. D. Noebe and R. Darolia, Acta Mater., Vol. 44, 1996, pp. 2809-2820.
23. J. L. Walter and H. E. Cline, Metall. Trans., Vol. 1, 1970, pp. 1221-1228.
24. S. M. Merchant and M. R. Notis, Mat. Sci. Eng., Vol. 66, 1984, pp. 47-60.
25. D. P. Mason, D. C. V. Aken and J. G. Webber, Intermetallic Matrix Composites, D. L. Anton, et al, eds., Vol. 194, MRS, 1990, pp. 341-348.
26. P. R. Subramanian, M. Mendiratta, D. B. Miracle and D. M. Dimiduk, Intermetallic Matrix Composites, D. L. Anton, et al, eds., Vol. 194, MRS, 1990, pp. 147-154.
27. E. H. Goldman, High-Temperature Ordered Intermetallics V, I. Baker, et al, eds., MRS, 1992, pp. 83-94.
28. J. D. Cotton, R. D. Noebe and M. J. Kaufman, unpublished research, 1992.
29. M. Takeyama, C. T. Liu and J. C.J. Sparks, JIMIS 6, Sandai, Japan, 1991, pp. 871-875.
30. R. D. Field, R. Darolia and D. F. Lahrman, Scr. Metall., Vol. 23, 1989, pp. 1469-1474.
31. J.D. Whittenberger, A. Garg, R.D. Noebe, W.S. Walston and R. Darolia, Structural Intermetallics II, eds. M.V. Nathal, et al, 1997.

# CREEP DEFORMATION BEHAVIOR AND MICROSTRUCTURE EVOLUTION OF NiAl/Ni<sub>3</sub>Al MULTIPHASE ALLOYS

Hiroyuki Senba and Masaaki Igarashi\*

Corporate Research and Development  
Sumitomo Metal Industries, Ltd.  
1-8, Fuso-cho, Amagasaki, Hyogo, 660, JAPAN

\*Present address:  
Frontier Research Center for Structural Materials  
National Research Institute for Metals  
1-2-1, Sengen, Tsukuba, Ibaraki, 305, JAPAN

## Abstract

Microstructure evolution and creep deformation behavior in Ni-(10.5/13.5)Al-10Cr-0.005B(mass%) alloys consisting of  $\beta$ (B2-ordered) +  $\gamma'$ (L1<sub>2</sub>-ordered) +  $\gamma$  (disordered f.c.c.) have been studied in order to clarify their potential for high temperature structural applications. The  $\beta/\gamma'/\gamma$  alloy homogenized at 1473K consists of coarse  $\beta$  phase surrounded by  $\gamma'$  phase and a  $\gamma'/\gamma$  dual phase matrix. Spherical  $\alpha$ -Cr precipitates (disordered b.c.c.) have also been confirmed in the  $\beta$  phase. The solidification sequence examined using a thermodynamic software Thermo-Calc is:  $L \rightarrow L+\beta \rightarrow L+\beta+\gamma \rightarrow \beta+\gamma \rightarrow \beta+\gamma'+\gamma$ . Primary  $\gamma'$  phase precipitates in the  $\gamma$  phase matrix. In the  $\beta$  phase, excess Al diffuses toward the  $\gamma$  phase matrix and forms  $\gamma'$  during cooling and homogenization, resulting in a  $\beta$  phase surrounded by  $\gamma'$ . It is supposed that  $\alpha$ -Cr phase precipitates from the supersaturated  $\beta$  phase. Compressive creep strength of the  $\beta/\gamma'/\gamma$  alloys is much higher than that of  $\beta/\gamma'$  dual phase alloys. The stress exponents of the  $\beta/\gamma'/\gamma$  alloys with 10.5, 11.1, 12.5 and 13.5mass%Al are 4.0, 4.1, 3.3 and 3.4, respectively, while that of the  $\beta/\gamma'$  alloy (15mass%Al) is 2.9. It is, therefore, considered that the creep deformation of both  $\beta/\gamma'/\gamma$  and  $\beta/\gamma'$  alloys is basically dislocation creep.  $\beta/\gamma'$  interfacial sliding seems to be more operative with increasing the  $\beta$  phase fraction in the  $\beta/\gamma'/\gamma$  alloys with higher Al content (12.5 and 13.5mass%). The activation energy for creep of the  $\beta/\gamma'/\gamma$  alloy (11.1mass%Al) is estimated as 534kJ/mol, which is much higher than that for Ni diffusion in NiAl or Ni<sub>3</sub>Al. TEM observation of the deformation structure has clarified that the  $\gamma'/\gamma$  coherent interface contributes to creep resistance, while the  $\beta/\gamma'$  interface decreases creep

strength (but enhances ductility at high temperatures). The creep strength of the  $\beta/\gamma'/\gamma$  alloys decreases with increasing  $\beta$  phase fraction. It is, therefore, concluded that optimizing the volume fraction and morphology of  $\beta$  phase is a key to achieving both high creep strength and suitable hot workability.

## Introduction

NiAl ( $\beta$ : B2-ordered) and Ni<sub>3</sub>Al ( $\gamma'$ : L1<sub>2</sub>-ordered) are considered to be near-future candidates for advanced high temperature structural materials in aerospace applications. NiAl has excellent oxidation resistance and low density resulting from the high Al content and also exhibits high melting temperature and better thermal conductivity [1,2]. These properties are superior to those of ordinary superalloys. It is, however, noted that poor creep strength and low room temperature ductility are major drawbacks in NiAl [1,3]. Although creep strength has successfully been improved by precipitation strengthening [4,5,6], it is still necessary for practical applications to improve both creep resistance and room temperature ductility simultaneously. Ni<sub>3</sub>Al, showing positive temperature dependence of yield strength, is known as the most important strengthening constituent of commercial Ni-base superalloys [7,8]. It is, however, known that the creep strength of monolithic Ni<sub>3</sub>Al is lower than that of conventional superalloys having  $\gamma'/\gamma$  dual phase structure [9,10]. In fact, most of advanced Ni<sub>3</sub>Al-based alloys such as IC218 have  $\gamma'/\gamma$  dual phase structures in order to improve their creep strength. Although these Ni<sub>3</sub>Al-based alloys have superior properties, such as specific strength to weight and



oxidation resistance, to the conventional superalloys, they show only limited hot workability. This is considered one of the barriers for practical use.

Multiphase structures are often effective in improving strength while maintaining suitable ductility or toughness. Hence, in our previous study [11], high temperature strength and ductility of NiAl( $\beta$ ) + Ni<sub>3</sub>Al( $\gamma'$ ) + disordered  $\gamma$  three-phase alloys have been studied. It has been shown that the  $\beta/\gamma'/\gamma$  alloy with 12.2mass%Al has comparable high temperature compressive strength to IC218, and excellent tensile ductility, about 9% elongation at 1373K. This suggests that high temperature strength with enough hot workability can be achieved by controlling the microstructure of NiAl/Ni<sub>3</sub>Al multiphase alloys. This  $\beta/\gamma'/\gamma$  three-phase alloy also shows suitable room temperature ductility or toughness to be machined. In this paper, therefore, microstructure evolution and creep deformation behavior in Ni-(10.5/13.5)Al-10Cr-0.005B (mass%) alloys with  $\beta/\gamma'/\gamma$  three-phase structure have been studied in order to clarify their potential for high temperature structural applications.

#### Experimental Procedure

The chemical compositions of materials tested in this study are given in Table I. A ternary addition of Cr was chosen in order to achieve  $\beta/\gamma'/\gamma$  three-phase equilibrium in the Ni-Al-X system. Cr stabilizes  $\beta$  and also  $\gamma$  phases, but not the  $\gamma'$  phase [12,13]. Therefore  $\beta/\gamma$  equilibrium, which does not appear in the Ni-Al binary system, is obtained, resulting in  $\beta/\gamma'/\gamma$  equilibrium. 0.005mass%B, which is known as a grain boundary strengthener, and used as a dopant in the materials in the previous study [11], was added to all the alloys. They were prepared by vacuum induction melting (VIM). All the ingots melted by VIM were homogenized for 86.4ks at 1473K followed by cooling in air. The constituent phases of the alloys after heat treatment were determined by X-ray diffraction analysis. Alloys A through I have been identified as having a  $\beta/\gamma'/\gamma$  three-phase structure. It has also been confirmed that alloys J and K consist of a  $\beta/\gamma'$  dual phase structure. The microstructures of the alloys were examined by an optical microscope and a transmission electron microscope (TEM; JEOL 2000EX) operated at

200kV. Thin foils for TEM observation were prepared by a conventional twin-jet polishing technique using a 8 vol% perchloric acid and 92 vol% acetic acid bath at 286K. Electron probe micro analysis (EPMA) was also carried out in order to determine the compositions of the constituent phases.

Tensile creep test specimens, 6mm in diameter and 30mm in gage length after JIS Z2271, and compressive creep test specimens, 8mm in diameter and 12mm in height, were machined from the ingots. Constant load tensile creep tests were performed at 1373K in air using a lever type creep tester. Tensile creep strain was measured with a dial gage type extensometer attached to the specimen. Compressive creep tests were performed at 1323-1423K in air. Initial stresses of 5.9-68.6MPa were applied using an electro-mechanical type actuator (MTS 808). The displacement between compression platens made of SiC was measured with a strain gage type displacement meter and converted to compressive creep strain.

#### Results and Discussion

##### Microstructure evolution

Figure 1 shows representative microstructures of the  $\beta/\gamma'/\gamma$  three-phase and the  $\beta/\gamma'$  dual phase alloys after heat treatment at 1473K. These three and dual phase alloys have dendritic microstructures. It is seen that the dendrite arms become coarser with increasing Al content. Compositional measurements of the dendrite arms by EPMA have revealed that the dendrite arms are  $\beta$  phase, containing 13.7-14.1 mol% Cr in the  $\beta/\gamma'/\gamma$  three-phase alloys, and 5.4-5.8 mol% Cr in the  $\beta/\gamma'$  dual phase alloys. Figure 2 shows the detailed optical microstructure of a  $\beta/\gamma'/\gamma$  alloy (alloy F). It is noted that the  $\beta$  phase is surrounded by another phase, which has been identified as  $\gamma'$  phase containing 5.1-5.9 mol% Cr by TEM observation and EPMA. The matrix, which is a dark gray contrast region in Figure 2 around the  $\beta$  phase, has been identified as  $\gamma'+\gamma$  two-phase. In order to confirm the microstructure at the creep testing temperature, a dark field image has been taken in TEM from the matrix of alloy F reheated at 1373K, shown in Figure 3. It is noted that fine cuboidal  $\gamma'$  precipitates exist in the  $\gamma$  matrix as well as relatively coarse primary  $\gamma'$  phase.

Table I Chemical compositions\* and constituent phases of the alloys tested.

Alloys	Chemical composition : mass% (mol%)				Constituent phases	
	Al	Cr	B	Ni		
A	10.5 (20.1)	10.0 (9.9)	0.005 (0.02)	bal.		$\beta/\gamma'/\gamma$
B	11.0 (21.0)	10.0 (9.9)	0.005 (0.02)	bal.		$\beta/\gamma'/\gamma$
C	11.14 (21.18)	9.90 (9.77)	0.0052 (0.025)	bal.		$\beta/\gamma'/\gamma$
D	11.5 (21.8)	10.0 (9.8)	0.005 (0.02)	bal.		$\beta/\gamma'/\gamma$
E	12.0 (22.6)	10.0 (9.8)	0.005 (0.02)	bal.		$\beta/\gamma'/\gamma$
F	12.16 (22.89)	9.83 (9.60)	0.0051 (0.024)	bal.		$\beta/\gamma'/\gamma$
G	12.5 (23.4)	10.0 (9.7)	0.005 (0.02)	bal.		$\beta/\gamma'/\gamma$
H	13.0 (24.3)	10.0 (9.7)	0.005 (0.02)	bal.		$\beta/\gamma'/\gamma$
I	13.5 (25.1)	10.0 (9.7)	0.005 (0.02)	bal.		$\beta/\gamma'/\gamma$
J	15.0 (27.6)	5.0 (4.8)	0.005 (0.02)	bal.		$\beta/\gamma'$
K	16.0 (29.1)	5.0 (4.7)	0.005 (0.02)	bal.		$\beta/\gamma'$

\*Nominal composition except alloys C and F

Further detailed TEM observation of the  $\beta$  phase in the  $\beta/\gamma'/\gamma$  three-phase alloy (alloy F) reheated at 1373K has revealed spherical  $\alpha$ -Cr precipitates, which are approximately 20-100nm in diameter, in the ordered  $\beta$  phase regions (Figure 4). Although  $\alpha$ -Cr precipitation from the  $\beta$  phase has previously been reported in Ni-Al-Cr  $\beta$  single phase alloys [14,15,16], quaternary equilibrium of  $\alpha$ ,  $\beta$ ,  $\gamma'$  and  $\gamma$  phases is not possible in Ni-Al-Cr ternary system according to phase rule thermodynamic restrictions. Cr content in the  $\beta$  phase measured by EPMA after homogenization at 1473K is in a range between 13.7 and 14.1 mol%, exceeding the solubility limit of Cr in  $\beta$  phase estimated at approximately 6 mol% at 1423K from the Ni-Al-Cr ternary phase diagram [17]. It is, therefore, considered that the precipitation of  $\alpha$ -Cr phase from the  $\beta$  phase in the  $\beta/\gamma'/\gamma$  three-phase alloy occurs by a nonequilibrium reaction; i.e.  $\alpha$ -Cr phase precipitates from the supersaturated  $\beta$  phase.  $\alpha$ -Cr is a b.c.c. disordered phase and has a similar lattice constant of the  $\beta$  phase, a b.c.c. ordered. It is, thus, considered that the  $\alpha$ -Cr phase precipitates coherently or semi-coherently to the  $\beta$  phase with a specific

crystallographic orientation relationship. Nemoto et al. [15], in practice, have reported that the  $\alpha$ -Cr precipitate lattice has a perfect coherency with the  $\beta$  matrix lattice in Ni-42Al-8Cr(mol%) alloy by high resolution electron microscopy, and Field et al. [18] have estimated the lattice mismatch to be approximately 0.8% from the spacing of dislocation networks at the  $\alpha$ -Cr/matrix semi-coherent interface in Ni-49.1Al-5.75Cr(mol%) alloy.

To understand the microstructure evolution in the  $\beta/\gamma'/\gamma$  three-phase alloys it is necessary to analyze the Ni-Al-Cr ternary phase diagram. There is, however, only limited and unreliable information available at present. Therefore, Ni-Al binary and Ni-Al-Cr ternary phase diagrams have been calculated by Thermo-Calc [19], which is a general-purpose thermodynamics calculation software. Thermodynamics data used in the calculations were modified by Hasebe [20] and proved to be reliable in simulating various Ni-Al-X ternary systems in satisfactory agreement with experimental phase diagrams. Figure 5 shows a calculated Ni-rich phase diagram in the Ni-Al binary system. The diagram

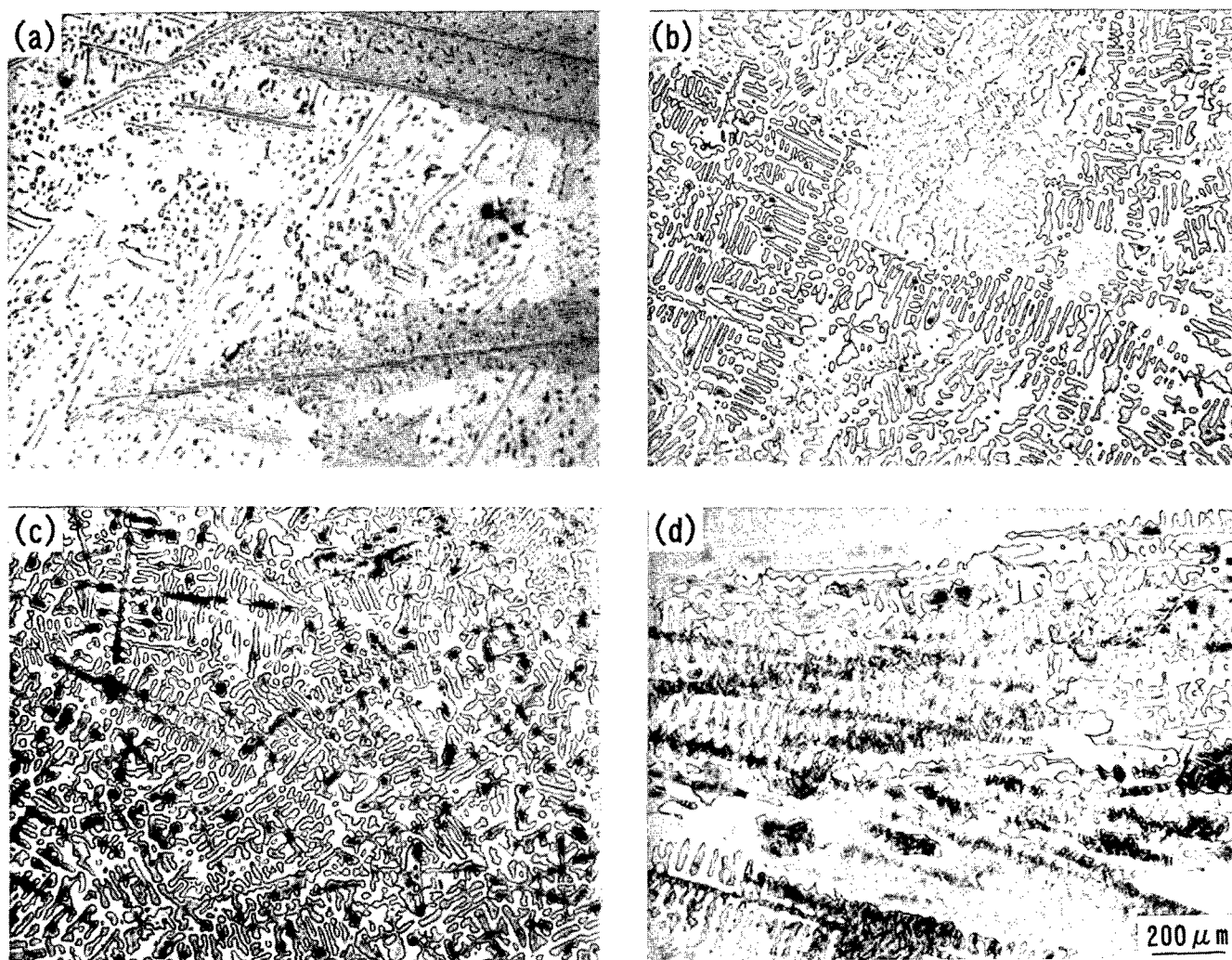


Figure 1: Optical micrographs of (a) alloy C, (b) alloy G, (c) alloy I and (d) alloy K homogenized at 1473K.

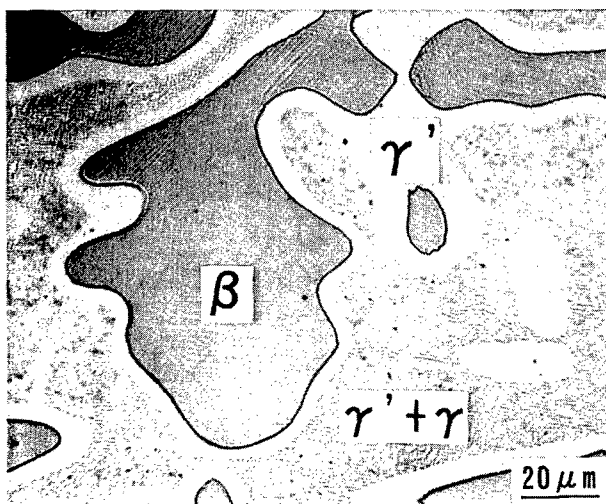


Figure 2: An optical micrograph of alloy F homogenized at 1473K.

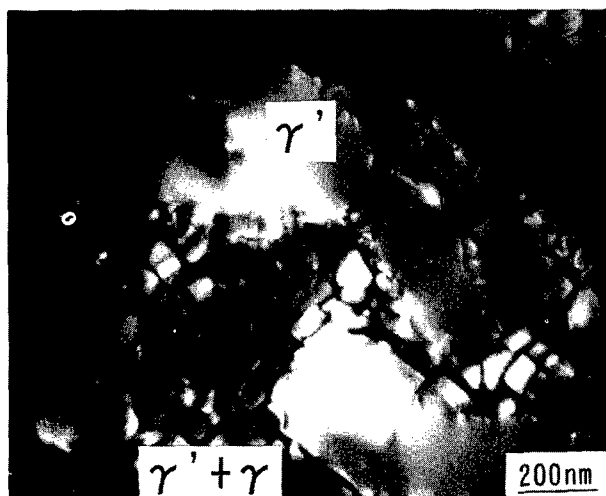


Figure 3: A dark field image obtained by TEM from the matrix of alloy F air-cooled after reheating at 1373K.

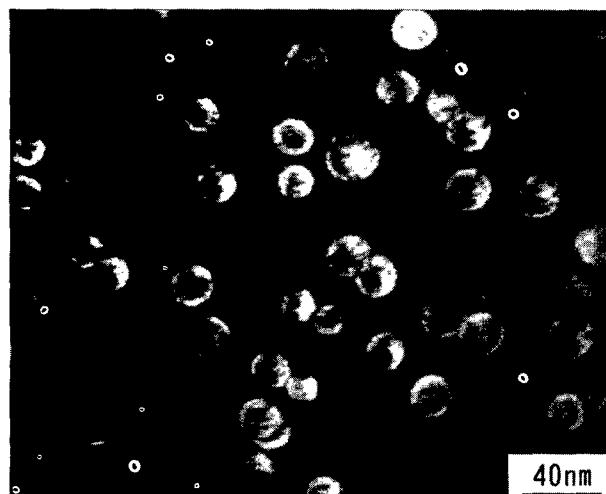


Figure 4: A dark field image obtained by TEM from the β phase of alloy F air-cooled after reheating at 1373K.

obtained is in good agreement with the experimental one [21]. Peritectic reaction of  $\gamma'$  phase appears as well as in the experimental phase diagram. The peritectic temperature calculated, 1663K, is very close to the experimental one, 1668K. Figures 6 and 7 show the Ni-rich isothermal section of the Ni-Al-Cr ternary system at 1573K and 1473K, respectively. The details of the calculated Ni-Al-Cr ternary phase diagrams (Figures 6 and 7) show some discrepancy, in particular the Cr-corner, compared to the experimental one [17]. Slight modification of the thermodynamic parameters may be necessary for better agreement with the entire experimental Ni-Al-Cr ternary phase diagram. It is, however, evident that these calculated phase diagrams are sufficient to study solidification behavior and microstructure evolution in the  $\beta/\gamma'/\gamma$  three-phase alloys.

Several isopleths (Cr is constant) in the Ni-Al-Cr ternary system have been calculated. B has not been considered for these calculation, since boride precipitation was not identified and such small amounts of B should not have a significant effect on the solidification process and phase equilibria. Figures 8 and 9 show calculated Ni-Al-2Cr and Ni-Al-5Cr (mol%) isopleths. The 2mol%Cr isopleth exhibits a complex phase equilibrium region. It is found that the peritectic temperature drops with the addition of 2mol%Cr, but the peritectic reaction still appears. On the other hand, it is noted that the peritectic reaction does not exist in the 5mol%Cr isopleth (Figure 9). Detailed calculations have revealed that the peritectic reaction disappears with the addition of more than 3mol%Cr and all the alloys having  $\beta/\gamma'/\gamma$  three-phase structure are formed through a  $\beta/\gamma$  dual phase region after solidification. Figure 10 shows the calculated Ni-Al-9.6Cr (mol%) isopleth. Although the general features in the higher temperature region is basically same with that of the 5mol%Cr isopleth,  $\beta+\gamma'$  dual phase and  $\gamma'$  single phase regions do not appear in the lower temperature region. The straight line in the figure indicates the composition of alloy F. The solidification sequence is:  $L \rightarrow L+\beta$  (1652K),  $L+\beta \rightarrow L+\beta+\gamma$  (1636K),  $L+\beta+\gamma \rightarrow \beta+\gamma$  (1632K) and  $\beta+\gamma \rightarrow \beta+\gamma'+\gamma$  (1503K). This can explain the solidification process and microstructure evolution of the  $\beta/\gamma'/\gamma$  alloys in this study.

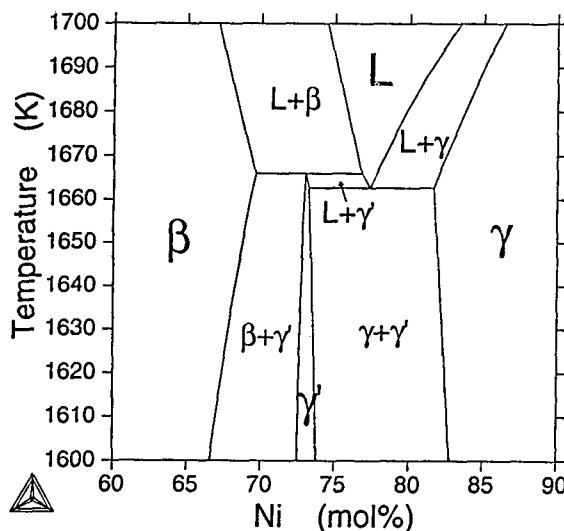


Figure 5: Calculated phase diagram in the Ni-Al binary system.

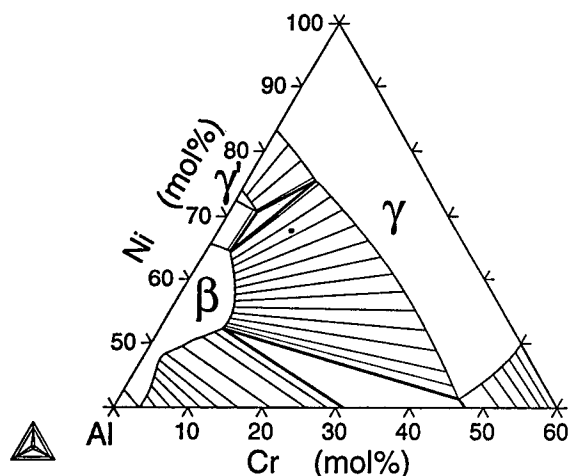


Figure 6: Calculated isothermal section in the Ni-Al-Cr ternary system at 1573K. • indicates the chemical composition of alloy F.

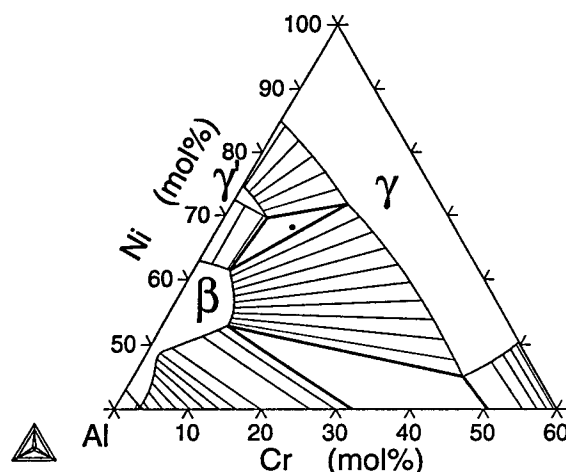


Figure 7: Calculated isothermal section in the Ni-Al-Cr ternary system at 1473K. • indicates the chemical composition of alloy F.

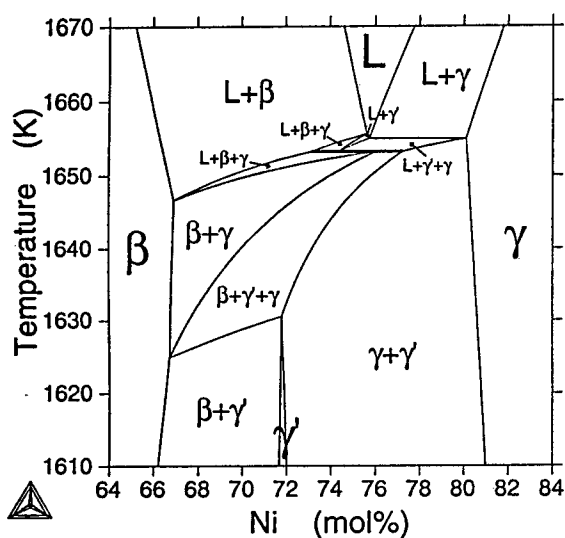


Figure 8: Calculated isopleth for Ni-Al-2mol%Cr.

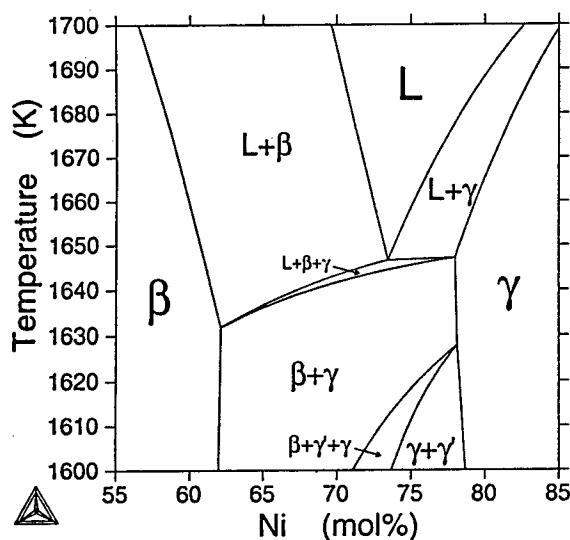


Figure 9: Calculated isopleth for Ni-Al-5mol%Cr.

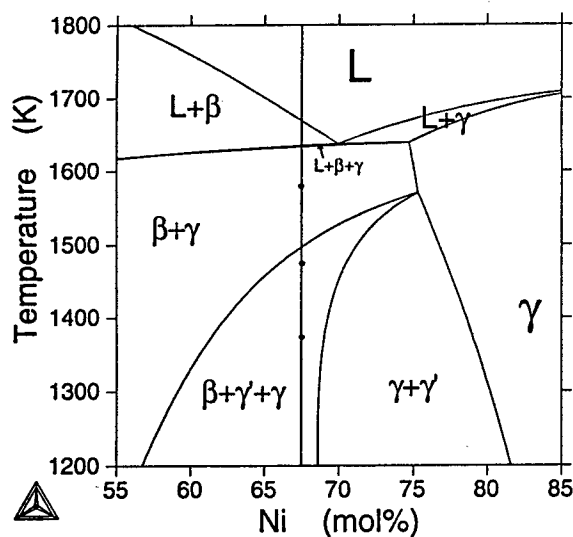


Figure 10: Calculated isopleth for Ni-Al-9.6mol%Cr.

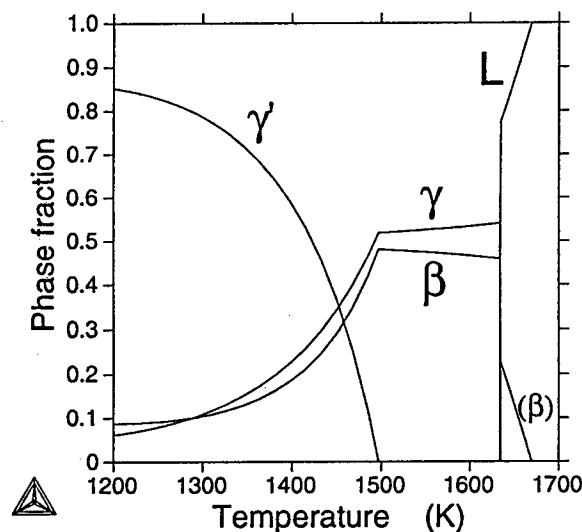


Figure 11: Calculated phase fraction for Ni-22.9Al-9.6mol%Cr (alloy F).

When alloy F reaches to the  $\beta/\gamma/\gamma$  region after passing through the  $\beta/\gamma$  field during cooling, primary  $\gamma'$  phase, which is coarse and denoted as  $\gamma'$  in Figure 3, starts to form in the  $\gamma$  phase. In the  $\beta$  phase, excess Al diffuses toward the  $\gamma$  phase and forms  $\gamma'$  during cooling and homogenization, resulting in the  $\beta$  phase surrounded by the  $\gamma'$  phase (see Figure 3). This means that the  $\beta$  phase fraction in the  $\beta/\gamma/\gamma$  region decreases compared with that in the  $\beta/\gamma$  region. Calculated phase fractions for Ni-22.9Al-9.6(mol%)Cr (alloy F) are shown in Figure 11. It is found that the calculated phase fraction of  $\beta$  decreases with decreasing temperature in the  $\beta/\gamma/\gamma$  region. These results support the above explanation of the formation of  $\gamma'$  surrounding the  $\beta$  phase. It is also noted that the fraction of  $\gamma'$  at 1373K is much larger than that at 1473K. It is, therefore, assumed that the fine cuboidal  $\gamma'$  in Figure 3 represents secondary  $\gamma'$  precipitation in the  $\gamma$  phase during reheating at 1373K.

### Creep deformation behavior

Figure 12 shows tensile creep curves for the  $\beta/\gamma/\gamma$  alloys (alloys C and F) crept at 1373K, 11.8MPa. Alloys C and F were ruptured at 102.6h and 61.5h, respectively. It is found that the creep curves under this condition are not an inverse type but a normal one as well as those of  $\text{Ni}_3\text{Al}(\gamma')$  in the higher temperature region; i.e., they clearly show primary, steady-state, and tertiary creep regions. Minimum creep rates appear in the secondary creep region. It is also noted that the secondary creep region accounts for 60-80% of the entire rupture life. Inverse creep has been reported for the  $\text{Ni}_3\text{Al}(\gamma')$  single crystals and polycrystals at intermediate temperatures [22,23], where the temperature dependence of yield stress is anomalous. Hemker et al. [23] have pointed out deformation during inverse creep in the  $\gamma'$  single phase alloys occurs by the activation of cross slip from  $[\bar{1}01](111)$  to  $[\bar{1}01](010)$  which enhances the stress anomaly. Creep strength of the  $\beta/\gamma/\gamma$  alloys is strongly controlled by  $\gamma'+\gamma$  dual phase region, where cross slip from  $[\bar{1}01](111)$  to  $[\bar{1}01](010)$  is in principle difficult due to the presence of  $\gamma$  [24]. It is, therefore, considered that inverse creep would not occur in the  $\beta/\gamma/\gamma$  alloys even at intermediate temperatures where inverse creep is observed for  $\text{Ni}_3\text{Al}(\gamma')$ . Figure 13 shows a strain-rate time curve for the  $\beta/\gamma/\gamma$  alloy (alloy F) crept at 1373K, 11.8MPa. It is seen that the minimum creep rate appears at about 10% of the rupture life.

Compressive creep curves for the  $\beta/\gamma/\gamma$  alloys show the same features as those of the tensile creep curves; that is, primary, steady-state and tertiary creep regions are clearly observed. The tertiary creep stage did not appear under some testing conditions such as at higher stresses or higher temperatures. This is caused by a decreasing true stress with increasing cross-sectional area of the compressive crept specimens, and the lack of tertiary creep is not intrinsic for compressive creep behavior. Figures 14 and 15 show the stress dependence of minimum creep rates for the  $\beta/\gamma/\gamma$  and  $\beta/\gamma'$  alloys at 1373K. It is noted that the creep strength of the  $\beta/\gamma/\gamma$  alloys (alloys A, C, G and I) is much higher than that of the  $\beta/\gamma'$  dual phase alloys (alloys J and K). A mathematical expression for creep deformation of crystalline materials is given by the Dorn equation

$$\dot{\epsilon} = A\sigma^n \exp(-Q/RT)$$

where  $\dot{\epsilon}$  is the steady-state creep rate,  $\sigma$  is the applied

stress,  $n$  is the stress exponent,  $Q$  is the activation energy for creep,  $R$  is the gas constant,  $T$  is the absolute temperature and  $A$  is a constant. The values for  $n$  and  $Q$  depend on the creep rate controlling process within a given temperature and stress range. In dislocation creep of disordered alloys, stress exponent would be 3-5 [25]. For  $\gamma'/\gamma$  dual phase alloys,  $n=4.5$  has been obtained in Ni-10Cr-10.2Al(mass%) ternary alloy at 1373K [10]. Higher stress exponents, 7 or more have been reported for  $\gamma'/\gamma$  conventional superalloys. In diffusional creep such as Nabarro-Herring or Coble creep, it would be around 1 [26]. For intermetallic compounds, the diffusional creep characterized by stress exponent of 1 has been revealed in B2 Ni-20Fe-50Al(mol%) alloy [27]. The stress exponent would be 1-2 in case of creep controlled by grain boundary sliding or interfacial sliding [28]. The stress exponent of 1.8 has been obtained for near-stoichiometric binary NiAl at 1200K in the low stress region where grain boundary sliding controls creep rates [29]. In this study, the determined stress exponents of the  $\beta/\gamma/\gamma$  alloys with 10.5, 11.1, 12.5 and 13.5mass%Al (alloys A, C, G and I) are 4.0, 4.1, 3.3 and 3.4, respectively, while those of the  $\beta/\gamma'$  alloys with 15.0 and 16.0mass%Al (alloys J and K) are 2.9 and 3.1, respectively, as shown in Figures 14 and 15. These stress exponents and deformation structure mentioned later strongly indicate that the creep deformation of the  $\beta/\gamma/\gamma$  and  $\beta/\gamma'$  alloys is dislocation creep. It is noted that the stress exponents of 12.5 and 13.5mass%Al  $\beta/\gamma/\gamma$  alloys, having higher  $\beta$  phase fraction, are lower than those of 10.5 and 11.1mass%Al alloys. In multiphase alloys, stress exponents are affected by creep mechanisms of constituent phases. In this temperature range, above 1300K, diffusional creep or grain boundary sliding is possible for polycrystalline NiAl [29, 30]. Deformation structure observations have clarified that  $\beta/\gamma'$  interfacial sliding operates in the  $\beta/\gamma/\gamma$  alloys. It is, therefore, considered that lower stress exponents of alloys G and I, 3.3 and 3.4, are due to increase in  $\beta$  phase and  $\beta/\gamma'$  interfaces, and  $\beta/\gamma'$  interfacial sliding would be more operative in high Al containing  $\beta/\gamma/\gamma$  alloys. Figure 16 shows the minimum creep rates of the  $\beta/\gamma/\gamma$  alloy (alloy C) plotted using an Arrhenius equation. The activation energy for creep is estimated as 534kJ/mol. It is noted that this value is much higher than that reported for atomic diffusion of Ni in  $\text{Ni}_3\text{Al}$ , 348kJ/mol [31], or in NiAl, 307kJ/mol [32], and close to the activation energy for creep in monocrystalline Udimet-700, 545kJ/mol [33], which is a conventional  $\gamma'/\gamma$  dual phase superalloy. This result and deformation structure shown in Figure 18 suggest that the creep rates for the  $\beta/\gamma/\gamma$  alloys are controlled by  $\gamma'+\gamma$  microstructure to a great extent.

Figure 17 shows a TEM micrograph of the  $\beta$  phase region of the  $\beta/\gamma/\gamma$  alloy in the steady-state creep regime. It is seen that dislocation density is low, and  $\langle 100 \rangle \langle 011 \rangle$  type dislocations have been observed as reported in polycrystalline binary NiAl deformed between 300 and 900K [34] and crept at 1200K [29]. It is seen that  $\alpha$ -Cr precipitates in the  $\beta$  phase interact with dislocations. Nemoto et al. [15] have reported that the  $\alpha$ -Cr phase precipitating coherently in the  $\beta$  phase increases the strength of NiAl especially at intermediate temperatures. They have, however, found that above 1100K the 0.2% flow stress of NiAl-Cr decreases gradually with increasing temperature and approaches to the strength level of monolithic NiAl. It is, therefore, probable that  $\alpha$ -Cr precipitates in the  $\beta$  phase have little effect on the overall

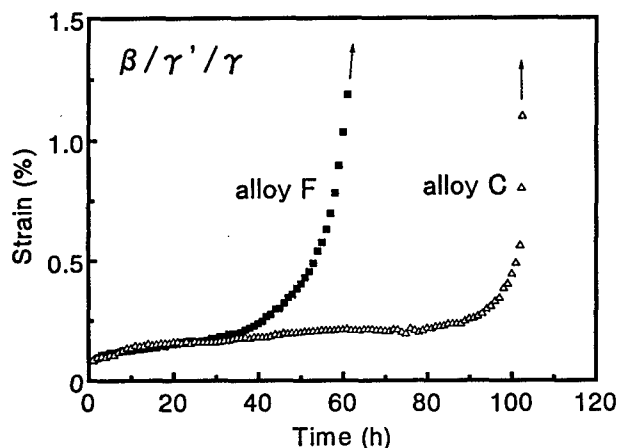


Figure 12: Tensile creep curves for the  $\beta/\gamma'/\gamma$  alloys (alloys C and F) crept at 1373K, 11.8MPa.

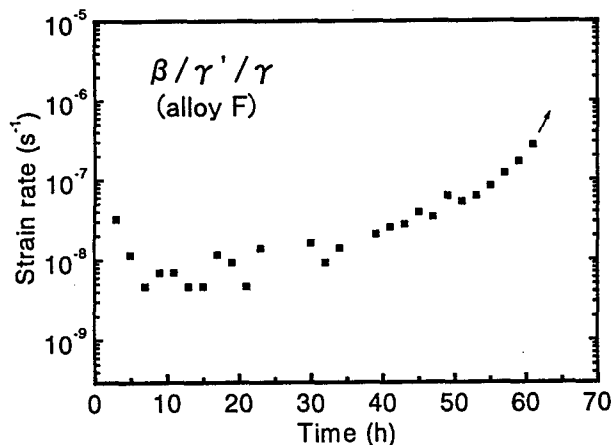


Figure 13: A strain-rate time curve for the  $\beta/\gamma'/\gamma$  alloy (alloy F) crept at 1373K, 11.8MPa.

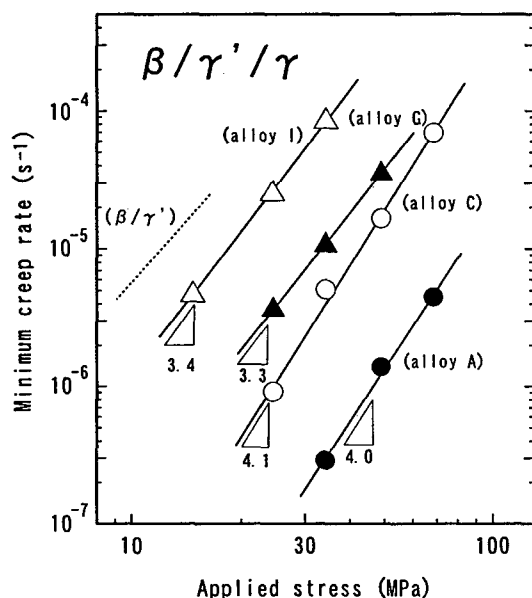


Figure 14: Stress dependence of minimum creep rates for the  $\beta/\gamma'/\gamma$  alloys (alloys A, C, G and I) at 1373K.

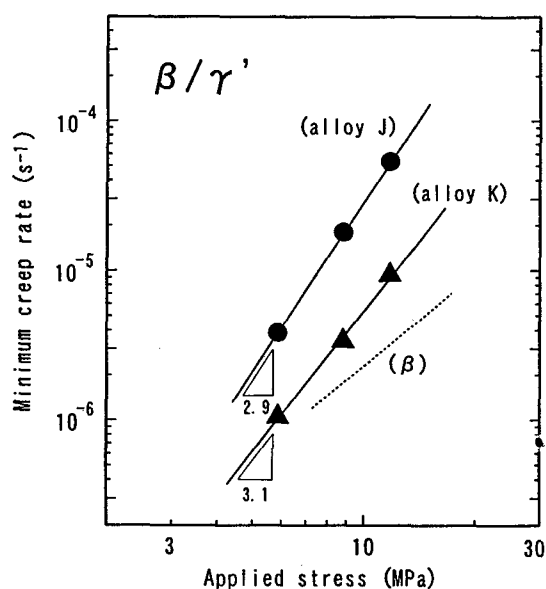


Figure 15: Stress dependence of minimum creep rates for the  $\beta/\gamma'$  alloys (alloys J and K) at 1373K.

creep strength of the  $\beta/\gamma'/\gamma$  alloys in the range of temperatures examined in this study. A dark field image obtained by TEM observation from the  $\gamma'/\gamma$  dual phase matrix in the  $\beta/\gamma'/\gamma$  alloy (alloy C) in the steady-state creep regime is shown in Figure 18. It is clearly seen that fine cellular networks are formed at the  $\gamma'/\gamma$  interface. The spacing of the network coincides with the size of the  $\gamma'$  phase. These networks would be formed by a dislocation climb mechanism or a slip process. The same deformation structure has also been observed in a CMSX-2,  $\gamma'/\gamma$  dual phase single crystal crept at 1323K, 120MPa [9]. This deformation structure seems to have a close relationship with the high activation energy for creep. This result suggests that the  $\gamma'/\gamma$  interfaces play an important role in creep resistance of the  $\beta/\gamma'/\gamma$  three-phase alloys. Figure

19 shows a TEM micrograph of the  $\beta/\gamma'$  interface in the same specimen (alloy C). It is found that dislocations pile-up at the  $\beta/\gamma'$  interface, and no direct evidence of dislocation transfer across the  $\beta/\gamma'$  interface has been obtained in this study. Noebe et al. [35] have reported that the nucleation of dislocations in the  $\beta$  phase due to dislocation pile-ups in the  $\gamma'/\gamma$  matrix can occur during room temperature deformation of Ni-20Al-30Fe(mol%)  $\beta/\gamma'/\gamma$  alloy. Yang et al. [36] have shown that dislocations are "injected" from the  $\gamma'$  phase into the  $\beta$  phase across the  $\beta/\gamma'$  interface in Ni-Al-Ti  $\beta/\beta'/\gamma'$  three-phase alloys. They suggest two ways to "inject" dislocations in the  $\beta$  phase. One is that dislocation pile-ups in a more ductile phase could activate a source of new dislocations. The other is that dislocations can glide out of the  $\gamma'$  into the

interface, becoming extrinsic grain boundary dislocations, and be converted into glissile dislocations in the  $\beta$  phase. It seems that a suitable orientation relationship between one phase and neighboring phase is necessary for the later case [35]. It is, therefore, believed that the pile-up process is relevant to the present alloy; i.e. dislocation pile-ups at the  $\beta/\gamma'$  interface enhances nucleation of dislocations in the  $\beta$  phase and interfacial slip between  $\beta$  and  $\gamma'$  phases without direct transfer of dislocations between the  $\beta$  and  $\gamma'$  phases.

In order to clarify the role of interfaces on the creep strength, the creep strength of  $\beta/\gamma'/\gamma$  three-phase alloy is shown in Figure 20, compared with those of each constituent phase ( $\beta$ ,  $\gamma'$  and  $\gamma$  [10,11]) and their composite phases ( $\gamma'/\gamma$  [10] and  $\beta/\gamma'$ ). The creep strength of the  $\gamma'/\gamma$  and  $\beta/\gamma'$  alloys does not satisfy the rule of strength mixture; that is, the creep strength levels of  $\gamma'/\gamma$  and  $\beta/\gamma'$  alloys are not in between those of  $\gamma'$  and  $\gamma$ , and between those of  $\beta$  and  $\gamma'$ , respectively. This means that the  $\gamma'/\gamma$  coherent interface increases creep strength and the  $\beta/\gamma'$  interface decreases it. The creep strength of the  $\beta/\gamma'/\gamma$  alloy is in between those of  $\gamma'/\gamma$  and  $\beta/\gamma'$  alloys. This is due to the fact that it includes  $\gamma'/\gamma$  and  $\beta/\gamma'$  interfaces and its creep strength is determined by some statistical average of the two. These results suggest that it is difficult for the creep strength of  $\beta/\gamma'/\gamma$  alloys to exceed that of  $\gamma'/\gamma$  alloys. It is, however, noted that a significant advantage for the  $\beta/\gamma'/\gamma$  alloys is a combination of high creep strength and high temperature ductility, which can not be obtained for the  $\gamma'/\gamma$  alloys [11].

The effect of  $\beta$  phase fraction on the creep strength of  $\beta/\gamma'/\gamma$  alloys has been investigated as shown in Figure 21. It is found that minimum creep rates of the  $\beta/\gamma'/\gamma$  alloys increase with increasing  $\beta$  phase fraction. This is due to the decrease in  $\gamma'/\gamma$  interfaces which contribute to creep strength and the increase in  $\beta/\gamma'$  interfaces which reduce creep resistance through interfacial slip. Previous study [11] has revealed that  $\beta/\gamma'$  interfaces contribute to high temperature ductility. It is, therefore, concluded that optimizing volume fraction and morphology of the  $\beta$  phase is a key to achieving both high creep strength and better hot workability.

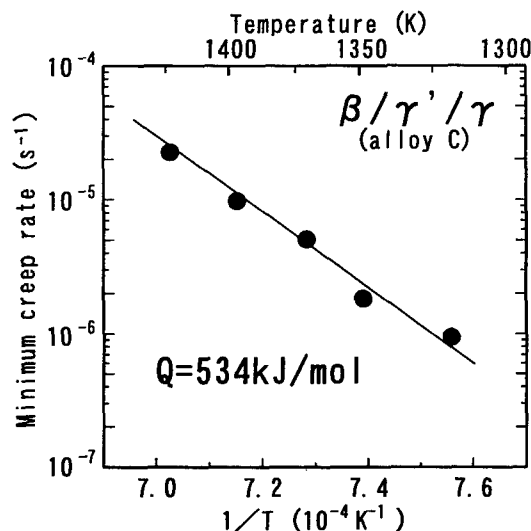


Figure 16: Minimum creep rates of the  $\beta/\gamma'/\gamma$  alloy (alloy C) under 34.3MPa using an Arrhenius equation.

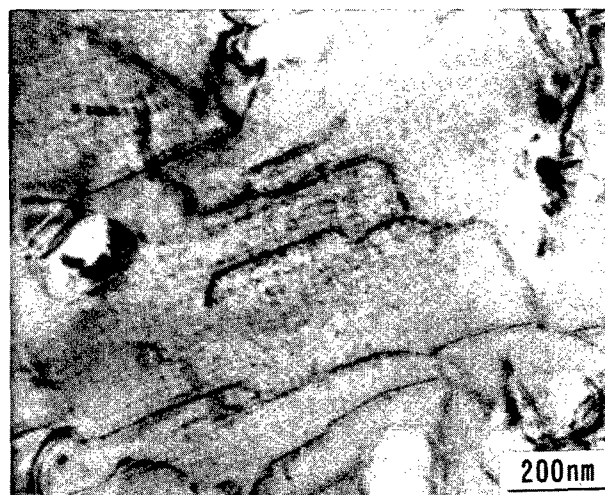


Figure 17: A TEM micrograph of the  $\beta$  phase region in the  $\beta/\gamma'/\gamma$  alloy (alloy C) crept at 1373K, 34.3MPa ( $\epsilon=3.8\%$ ).

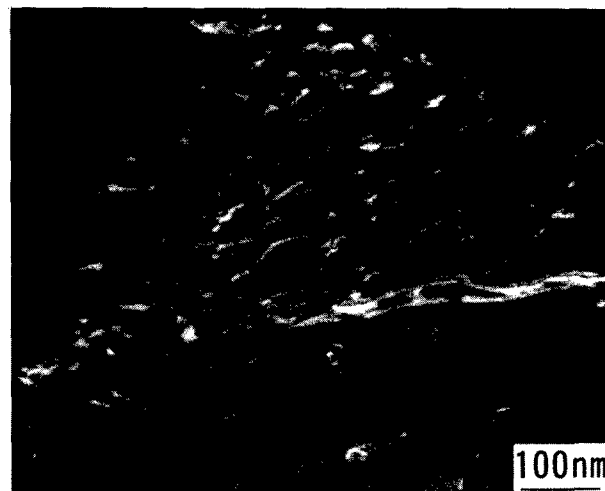


Figure 18: A TEM micrograph of the  $\gamma'/\gamma$  dual phase matrix in the  $\beta/\gamma'/\gamma$  alloy (alloy C) crept at 1373K, 34.3MPa ( $\epsilon=3.8\%$ ).

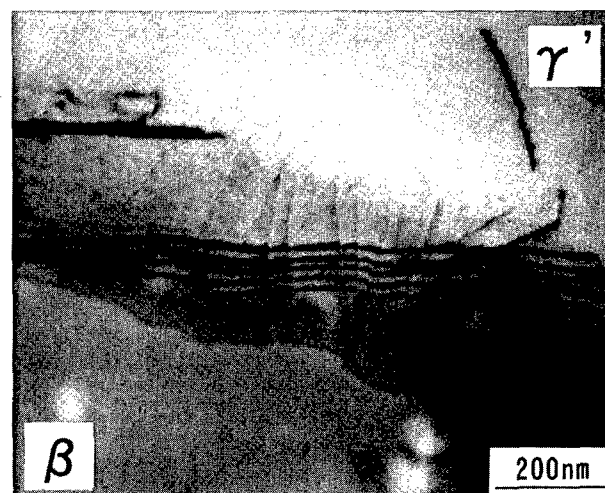


Figure 19: A TEM micrograph of the  $\beta/\gamma'$  interface in the  $\beta/\gamma'/\gamma$  alloy (alloy C) crept at 1373K, 34.3MPa ( $\epsilon=3.8\%$ ).

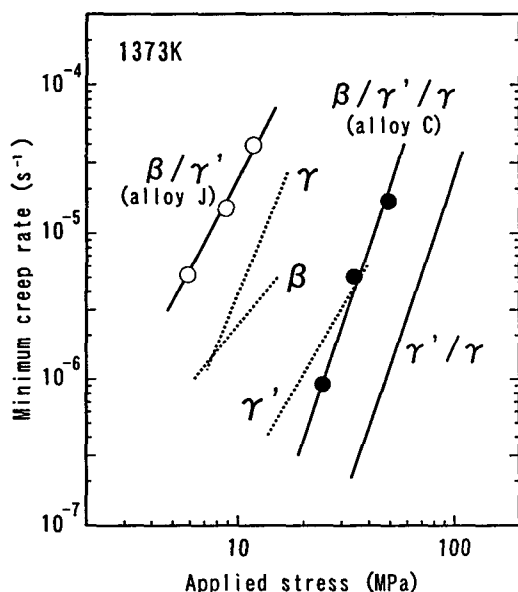


Figure 20: The compressive creep strength of  $\beta$ ,  $\gamma'$  and  $\gamma$  single phase,  $\beta/\gamma'$  and  $\gamma'/\gamma$  dual phase and  $\beta/\gamma'/\gamma$  three-phase alloys at 1373K [10,11].

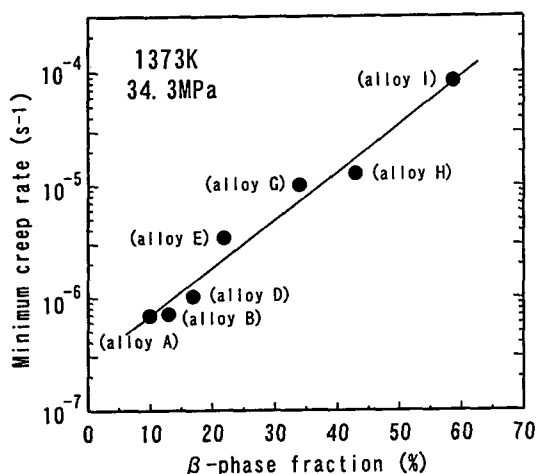


Figure 21:  $\beta$  phase dependence of minimum creep rates for the  $\beta/\gamma'/\gamma$  alloys at 1373K, 34.3MPa.

### Conclusions

Microstructure evolution and creep deformation behavior in Ni-(10.5/13.5)Al-10Cr-0.005B(mass%) alloys consisting of  $\beta$ (B2-ordered) +  $\gamma'$ (L1<sub>2</sub>-ordered) +  $\gamma$  (disordered f.c.c.) have been studied in comparison with  $\beta/\gamma'$  dual phase alloys. It has been shown that the  $\beta/\gamma'/\gamma$  alloy homogenized at 1473K consists of coarse  $\beta$  phase surrounded by  $\gamma'$  phase and a  $\gamma'/\gamma$  dual phase matrix. Spherical  $\alpha$ -Cr precipitates, b.c.c. disordered phase, have also been confirmed in the  $\beta$  phase. The solidification sequence examined by Thermo-Calc is:  $L \rightarrow L+\beta \rightarrow L+\beta+\gamma \rightarrow \beta+\gamma \rightarrow \beta+\gamma'+\gamma$ . Primary  $\gamma'$  phase precipitates in the  $\gamma$  phase matrix and excess Al in the  $\beta$  phase diffuses toward the  $\gamma$  phase matrix during cooling and homogenization,

resulting in the  $\beta$  phase surrounded by the  $\gamma'$  phase. It is considered that the  $\alpha$ -Cr phase precipitates from the supersaturated  $\beta$  phase. Compressive creep strength of the  $\beta/\gamma'/\gamma$  alloys is much higher than that of the  $\beta/\gamma'$  dual phase alloys. The stress exponents of the  $\beta/\gamma'/\gamma$  alloys with 10.5, 11.1, 12.5 and 13.5mass%Al are 4.0, 4.1, 3.3 and 3.4, respectively, while that of the  $\beta/\gamma'$  alloy (15mass%Al) is 2.9. It is, therefore, considered that the creep deformation of the  $\beta/\gamma'/\gamma$  and  $\beta/\gamma'$  alloys is basically dislocation creep.  $\beta/\gamma'$  interfacial sliding seems to be more operative with increasing the  $\beta$  phase fraction in the  $\beta/\gamma'/\gamma$  alloys with higher Al content (12.5 and 13.5mass%). The activation energy for creep of the  $\beta/\gamma'/\gamma$  alloy (11.1mass%Al) is estimated as 534kJ/mol, which is much higher than that for Ni diffusion in NiAl or Ni<sub>3</sub>Al. It has been revealed that  $\gamma'/\gamma$  coherent interfaces contribute to creep resistance and  $\beta/\gamma'$  interfaces decrease creep strength (but enhances ductility at high temperatures). The creep strength of the  $\beta/\gamma'/\gamma$  alloys decreases with increasing  $\beta$  phase fraction. It is, therefore, concluded that optimizing volume fraction and morphology of the  $\beta$  phase is a key to achieving both high creep strength and suitable hot workability.

### Acknowledgement

The authors are grateful to Professor M. Hasebe, Kyushu Institute of Technology for useful discussion and evaluation of the thermodynamic data in the Ni-Al-Cr system. Sincere appreciation is expressed to S. Tenokuchi for his assistance in experiments. The authors would like to thank Dr. S. Kobayashi, the General Manager of Corporate Research and Development, Sumitomo Metal Industries, Ltd., for permission to publish this paper.

### References

1. R. D. Noebe, R. R. Bowman and M. V. Nathal, "Physical and Mechanical Properties of B2 Compound NiAl," *Inter. Mater. Rev.*, 38(1993), 193-232.
2. R. Darolia, "NiAl alloys for High Temperature Structural Applications," *JOM*, 43(1993)No.3, 44-49.
3. M. V. Nathal, "Creep Deformation of B2 Aluminides," *Ordered Intermetallics-Physical Metallurgy and Mechanical Behavior*, C. T. Liu et al., eds., NATO ASI Series E, 213(1992), 541-563.
4. R. S. Polvani, W. S. Tzeng and P. R. Strutt, "High Temperature Creep in a Semi-Coherent NiAl-Ni<sub>2</sub>AlTi Alloy," *Metall. Trans. A*, 7A(1976), 33-40.
5. I. E. Locci, R. Dickerson, R. R. Bowman, M. V. Nathal and R. Darolia, "Microstructure and Mechanical Properties of Cast, Homogenized and Aged NiAl Single Crystal Containing Hf," *High Temperature Ordered Intermetallic Alloys V*, I. Baker et al., eds., (Materials Research Society), 288(1992), 685-690.
6. R. Darolia, "Structural Applications of NiAl," *J. Mater. Sci. Technol.*, 10(1994), 157-169.
7. N. S. Stoloff and C. T. Liu, *Physical Metallurgy and Processing of Intermetallic Compounds*, ed. by N. S.



Stoloff and V.K. Sikka, (Chapman & Hall, 1996), 159-211.

8. C. T. Liu and K. S. Kumar, "Ordered Intermetallic Alloys, Part I: Nickel and Iron Aluminides," JOM, 45(1993)No.5, 38-44.

9. T. Khan, P. Caron and S. Naka, "Mechanical Behavior of Ni<sub>3</sub>Al-based Intermetallics and the Need for Designing Multiphase Alloys," High Temperature Aluminides and Intermetallics, S. H. Whang et al., eds., (The Minerals, Metals & Materials Society, 1990), 219-241.

10. H. Senba and M. Igarashi, "Creep Behavior of  $\gamma'$  single and  $\gamma'/\gamma$  Dual Phase Alloys in Ni-Al Binary System," (Paper presented at the Japan Institute of Metals Annual Meeting, Chiba, Japan, April 1992), 338.

11. H. Senba and M. Igarashi, "High Temperature Strength and Ductility of  $\beta/\gamma'/\gamma$  Multiphase Alloys in Ni-Al-Cr system," Mater. Trans. JIM, 37(1996), 821-827.

12. K. Ishida, R. Kainuma, N. Ueno and T. Nishizawa, "Ductility Enhancement in NiAl(B2)-Base Alloys by Microstructural Control," Met. Trans., 22A(1991), 441-446.

13. J. D. Cotton, R. D. Noebe and M. J. Kaufman, "Ternary Alloying Effects in Polycrystalline  $\beta$ -NiAl," Structural Intermetallics, R. Darolia et al., eds., (The Minerals, Metals & Materials Society, 1993), 513-522.

14. D. Cotton, R. D. Noebe and M. J. Kaufman, "The effects of Chromium on NiAl Intermetallic Alloys: Part I. Microstructures and Mechanical Properties," Intermetallics, 1(1993), 3-20.

15. M. Nemoto, W. H. Tian, C. S. Han and T. Sano, "Dislocation-Particle Interactions in Precipitation Strengthened Ni<sub>3</sub>Al and NiAl," Structural Intermetallics, R. Darolia et al., eds., (The Minerals, Metals & Materials Society, 1993), 551-560.

16. P. Acleva, J. L. Gonzalez-Carrasco and M. Aballe, "Microstructure and Mechanical Properties of RS Ni-Al-Cr Melt-Spun Alloys," Acta Metall. Mater., 38(1990), 643-653.

17. N. C. Oforka and C. W. Haworth, "Phase Equilibria of Aluminum-Chromium-Nickel System at 1423K," Scand. J. Metallurgy, 16(1987), 184-188.

18. R. D. Field, D. F. Lahrman and R. Darolia, "The Effect of Alloying on Slip Systems in (001) oriented NiAl Single Crystals," Acta Metall. Mater., 39(1991), 2961-2969.

19. L. Höglund et al., Formation of Computational Thermodynamics, (Royal Institute of Technology, Stockholm, Sweden)

20. M. Hasebe, private communication with authors, Kyusyu Institute of Technology, February, 1997.

21. T. B. Massalski et al., eds., Binary Alloy Phase Diagrams (American Society for Metals, 1986), 142.

22. P. M. Hazzledine and J. H. Schneibel, "Inverse Creep in Ni<sub>3</sub>Al," Scripta Metall., 23(1989), 1887-1892.

23. K. J. Hemker and W. D. Nix, "An Investigation of the Creep of Ni<sub>3</sub>Al(B,Hf) Single Crystals at Intermediate Temperatures," High Temperature Ordered Intermetallic Alloys III, C. T. Liu et al., eds., (Materials Research Society), 133(1989), 481-486

24. W. H. Tian, T. Sano and M. Nemoto, "Orientation dependence of the Yield Stress in  $\gamma'$ -L1<sub>2</sub> Ordered Ni<sub>3</sub>(Al,Ti) Single Crystals Containing Disordered  $\gamma$  Precipitates," J. Japan Inst. Metals, 54(1990), 285-291.

25. O. D. Sherby and P. M. Burke, "Mechanical Behavior of Crystalline Solids at Elevated Temperature," Prog. Mater. Sci., 13(1967), 325-390.

26. H. Oikawa and T. G. Langdon, Creep Behavior of Crystalline Solids, ed. by B. Wilshire and R. W. Evans, (Pineridge Press, 1985), 33-82.

27. I. Jung, M. Rudy and G. Sauthoff, "Creep in Ternary B2 Aluminides and Other Intermetallic Phases," High Temperature Ordered Intermetallic Alloys II, N. S. Stoloff et al., eds., (Materials Research Society), 81(1987), 263-274.

28. T. G. Langdon, "A Unified Approach to Grain boundary Sliding in Creep and Superplasticity," Acta Metall. Mater., 42(1994), 2437-2443.

29. S. V. Raj and S. C. Farmer, "Observation of a New Creep Regime in Polycrystalline Ni-50(at%)Al Intermetallic Alloy," High Temperature Ordered Intermetallic Alloys V, I. Baker et al., eds., (Materials Research Society), 288(1992), 647-652.

30. J. D. Whittenberger, "Effect of Composition and Grain Size on Slow Plastic Flow Properties of NiAl between 1200 and 1400K," J. Mater. Sci., 22(1987), 394-402.

31. K. Hoshino, S. J. Rothman and R. S. Averback, "Tracer Diffusion in Pure and Boron-doped Ni<sub>3</sub>Al," Acta Metall., 36(1988), 1271-1279.

32. G. F. Hancock and B. R. McDonnell, "Diffusion in the Intermetallic Compound NiAl," Phys. Status Solidi(a), 4(1971), 143-150.

33. R. S. Polvani, A. W. Ruff and P. R. Strutt, "A Mechanism for Metalloid Strengthening of Udimet-700," J. Mat. Sci. Letters, 3(1984), 287-290.

34. R. R. Bowman, R. D. Noebe, S. V. Raj and I. E. Locci, "Correlation of Deformation Mechanisms with the Tensile and Compressive Behavior of NiAl and NiAl(Zr) Intermetallic Alloys," Metall. Trans. A, 23A(1992), 1493-1508.

35. R. D. Noebe, A. Misra and R. Gibala, "Plastic Flow and Fracture of B2 NiAl-based Intermetallic Alloys Containing a Ductile Second Phase," ISIJ International, 31(1991), 1172-1185.

36. R. Yang, J. A. Leake and R. W. Cahn, "Three Phase ( $\beta+\beta'+\gamma'$ ) Ni-Al-Ti-(Cr,Fe) Alloys for High Temperature Use," Mat. Sci. Eng., A152(1992), 227-236.

## MISFIT CONTROL IN NiTi/Ni<sub>2</sub>TiAl $\beta/\beta'$ ALLOYS

M A Peters and C J Humphreys

Department of Materials Science and Metallurgy,  
University of Cambridge, Pembroke Street,  
Cambridge, UK, CB2 3QZ

### Abstract

The crystallographic misfit between  $\beta$  NiTi and  $\beta'$  Ni<sub>2</sub>TiAl is -1.433% at ambient temperatures as measured by x-ray diffraction (XRD) techniques. Through cluster variation method (CVM) calculations, it is predicted that the addition of V or Cr will reduce this misfit by partitioning preferentially to the  $\beta$ -phase at temperatures above 900°C and reducing the lattice parameter of that phase. At temperatures below 900°C, Cr is predicted to preferentially partition to the  $\beta'$  phase and enlarge the misfit by reducing the lattice parameter of that phase. X-ray diffraction experiments confirm that V is useful in misfit reduction in these alloys, reducing the misfit at room temperature by 0.25% per atomic percent addition. In a 2 at.% V doped alloy, this is observed to take place by the reduction of the lattice parameter of the  $\beta$  phase by 0.012 Å and the slight enlargement of the lattice parameter of the  $\beta'$  phase. The effect of Cr doping is quite different, increasing the lattice parameter of the  $\beta'$  phase, and to a lesser degree, the  $\beta$  phase. EDS analysis using a STEM show that both V and Cr preferentially partition to the  $\beta$  phase.

The CVM technique with the phenomenological Lennard-Jones pair potentials correctly predicts V as an effective misfit reducing dopant element in NiTi/Ni<sub>2</sub>TiAl  $\beta/\beta'$  alloys. The observed partitioning behaviour of Cr at 800°C, to the  $\beta$  phase, is contrary to the CVM prediction. However, it is possible that the Cr partitions to the  $\beta$  phase during solidification and is slow to diffuse to the  $\beta'$  phase at lower temperatures, indicating that Cr has a higher activation energy of diffusion than Al in these alloys.

### Introduction

Stoichiometric polycrystalline NiTi has relatively high room-temperature ductility<sup>(1)</sup>, unlike other B2 intermetallics such as NiAl or FeAl. It is thought that an intermetallic alloy based on this phase will have sufficient ductility to be used in aero-engines, and could be used in that role if it could be significantly strengthened at higher temperatures. One attempt to strengthen these alloys at temperatures greater than 600°C involves age hardening with the precipitation of the Ni<sub>2</sub>TiAl ( $\beta'$ ) Heusler phase in Al-doped alloys with Al greater than 4 at.%<sup>(1,2,3)</sup>. Al-doped NiTi ( $\beta$ ) alloys with 7 at.% Al show better compressive specific yield strengths than Ni-based superalloys at temperatures lower than 600°C<sup>(3)</sup>. The high crystallographic misfit between the  $\beta$  and  $\beta'$  phases causes microstructural instability at high temperatures<sup>(4)</sup>, resulting in rapid precipitate growth and a loss of coherence between the matrix and precipitate phases. Thus, the reduction of misfit through quaternary elemental additions is being examined.

In the present study, the cluster variation method (CVM) is used to predict the partitioning of quaternary elemental additions of Cr and V between  $\beta$  and  $\beta'$  phases and the effect of these additions on the lattice misfit between the  $\beta'$  precipitates and the  $\beta$  matrix. The predictions made by the CVM are substantiated by XRD misfit measurements and the resultant aged microstructures are examined using transmission electron microscopy (TEM) techniques. The predicted phase partitioning behaviour of each dopant is confirmed through EDS techniques within a VG STEM.

### Method of Calculation

The CVM has been successfully used to predict quaternary element partitioning and the effect on misfit in  $\gamma/\gamma'$  Ni-based superalloys<sup>(5,6)</sup>. Recently, Enomoto and Kumeta<sup>(7)</sup> have demonstrated the CVM as an effective tool in phase diagram prediction and misfit calculation in ternary  $\beta/\beta'$  alloys. In the present study, using the tetrahedron cluster approximation<sup>(8)</sup>, the atomic arrangement and interatomic distances of Ni-Ti-Al-X alloys are optimised and thereby, the site occupancy, lattice misfit and equilibrium compositions of  $\beta$  and  $\beta'$  phases are calculated simultaneously. To perform this calculation, the first and second nearest neighbour atoms are considered in the determination of cluster energy using Lennard-Jones phenomenological potentials. The potentials are determined from lattice parameter and thermodynamic data where available and by empirical predictions when not available.

### The Free Energy

Using the method described by Sigli and Sanchez<sup>(8)</sup>, the free energy of a b.c.c. phase can be calculated from the internal energy and configurational entropy of the first and second nearest neighbours atoms as considered in a four atom cluster, shown in figure 1. The internal energy of the alloy is approximated by the sum of pair interactions arising from the phenomenological Lennard-Jones pair potentials:

$$e_{ij} = E_{ij}^0 \left[ \left( \frac{R_{ij}}{r} \right)^8 - 2 \left( \frac{R_{ij}}{r} \right)^4 \right] \quad (1)$$

where  $E_{ij}^0$  and  $R_{ij}$  are energy parameters and  $r$  is the distance between atoms  $i$  and  $j$ . Using this as the pair interaction energy, the average internal energy per lattice point, for the nearest and next-nearest neighbour configuration is given by:

$$\langle E \rangle = \frac{1}{2} \sum_{n=1}^2 \omega_n \left\{ \sum_{ij} e_{ij}(d_n) y_{ij}(d_n) \right\} \quad (2)$$

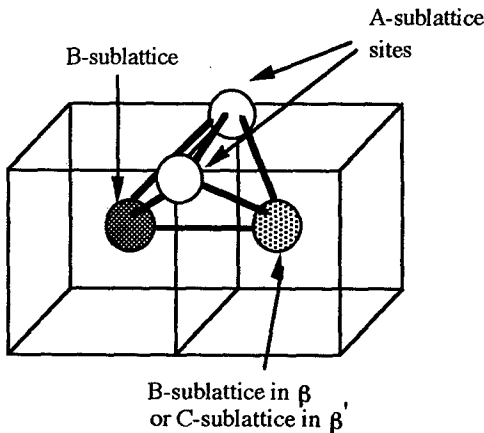


Figure 1 - Tetrahedron Approximation geometry for CVM calculation

where  $\omega_n$  is the co-ordination number and  $d_n$  is the distance between  $n$ th nearest neighbours.  $y_{ij}$  are the pair interaction probabilities. For ordered NiTi (B2) and Ni<sub>2</sub>TiAl (L2<sub>1</sub>) phases, the enthalpy can be expressed in terms of equations 3 and 4 respectively:

$$H_\beta = 4 \sum_{ij} e_{ij}(d_1) y_{ij}^{AB}(d_1) + \frac{3}{2} \sum_{ij} e_{ij}(d_2) \left( y_{ij}^{AA}(d_2) + y_{ij}^{BB}(d_2) \right) \quad (3)$$

$$H_{\beta'} = 2 \sum_{ij} e_{ij}(d_1) \left( y_{ij}^{AB}(d_1) + y_{ij}^{AC}(d_1) \right) + \frac{3}{2} \sum_{ij} e_{ij}(d_2) \left( y_{ij}^{AA}(d_2) + y_{ij}^{BC}(d_2) \right) \quad (4)$$

Where the superscripts A, B and C refer to the superlattice position in the tetrahedron approximation. With this approximation, the configurational entropy per lattice point of the  $\beta$  phase can be written as:

$$S_\beta = -k \left\{ \left[ 6 \sum_{ijkl} L(z_{ijkl}^{ABBA}) \right] - \left[ 6 \sum_{ijk} L(t_{ijk}^{ABB}) + L(t_{ijk}^{ABA}) \right] \right\} + \left[ \frac{3}{2} \sum_{ij} L(y_{ij}^{AA}(d_2)) + L(y_{ij}^{BB}(d_2)) \right] + \left[ 4 \sum_{ij} L(y_{ij}^{AB}(d_1)) \right] - \left[ \frac{1}{2} \sum_i L(x_i^A) + L(x_i^B) \right] \quad (5)$$

and for the  $\beta'$  phase as:

$$S_{\beta'} = -k \left\{ \left[ 6 \sum_{ijkl} L(z_{ijkl}^{ABCA}) \right] - \left[ \sum_{ijk} 6L(t_{ijk}^{ABB}) + 3L(t_{ijk}^{ABA}) + 3L(t_{ijk}^{ACA}) \right] \right\} + \left[ \frac{3}{2} \sum_{ij} L(y_{ij}^{AA}(d_2)) + L(y_{ij}^{BC}(d_2)) \right] + \left[ 2 \sum_{ij} L(y_{ij}^{AB}(d_1)) + L(y_{ij}^{AC}(d_1)) \right] - \left[ \frac{1}{2} \sum_i L(x_i^A) + L(x_i^B) \right] \quad (6)$$

Here,  $L(\phi)$  is equal to  $\phi \ln \phi$  and arises because of Stirling's approximation for factorials;  $k$  is Boltzmann's constant; and  $z_{ijkl}$ ,

$t_{ijk}$ ,  $y_{ij}$  and  $x_i$  are tetrahedron, triplet, pair and point probabilities. The subscripts  $i, j, k$  and  $l$  have the integer values 1, 2, 3 and 4 which correspond to the elements Ni, Ti, Al and X, the quaternary element, Cr or V. The superscripts A, B and C refer to the Ni, Ti and Al sublattices, respectively. The distance  $d_2$  is equal to the lattice parameter and  $d_1$  the nearest neighbour distance,  $r$ . Thus, for example,  $y_{12}^{AB}$  would be the probability of finding a Ni-Ti pair along an A-B side of the irregular tetrahedron.

The triplet, pair and point probabilities are given in terms of the  $z_{ijkl}$  by the following equations:

$$t_{ijk} = \sum_l z_{ijkl} \quad (7a)$$

$$y_{ij} = \sum_{kl} z_{ijkl} \quad (7b)$$

$$x_i = \sum_{jkl} z_{ijkl} \quad (7c)$$

To establish the most probable atomic configuration of the system at equilibrium, the grand potential

$$\Omega = H - TS + PV + \sum_i \mu_i x_i \quad (8)$$

is minimised with respect to both  $z_{ijkl}$  and the nearest neighbour distance (and thus the atomic volume) at constant temperature,  $T$ , pressure,  $P$ , and the chemical potential of the  $i$ th atom,  $\mu_i$ , using the normalisation condition:

$$\sum_{ijkl} z_{ijkl} = 1 \quad (9)$$

Using this condition, the most probable atomic configuration in the tetrahedron cluster for  $\beta$  and  $\beta'$  phases is given by the following equations:

$$z_{ijkl} = \frac{e^{\left(\frac{\beta\lambda}{6}\right)} e^{\left[\frac{-\beta}{6} \mu_{ijkl} \left(\frac{\mu_{il}\mu_{jk}\mu_{kl}}{4}\right)\right]}}{Y_1^{\frac{1}{6}} Y_2^{\frac{1}{4}}} T^{\frac{1}{2}} X^{\frac{1}{24}} \quad (10)$$

where  $\lambda$  is the Lagrange multiplier resulting from the normalisation condition,  $\beta$  is equal to  $1/kT$  and  $\mu_{ijkl}$  is given by:

$$\mu_{ijkl} = \frac{3}{2} [e_{il}(d_2) + e_{jk}(d_2)] + e_{ij}(d_1) + e_{ik}(d_1) + e_{jl}(d_1) + e_{kl}(d_1) \quad (11)$$

in which the function  $e$  is determined by equation 1 for the nearest and next-nearest neighbour distances  $d_1$  and  $d_2$ . The values  $T$ ,  $Y_1$ ,  $Y_2$  and  $X$  are given by

$$T = t_{ijk}^{ABB} t_{ijl}^{ABA} t_{ikl}^{ABA} t_{jkl}^{BBA} \quad (12a)$$

$$Y_1 = y_{ij}^{AB} y_{ik}^{AB} y_{jl}^{AB} y_{lk}^{AB} \quad (12b)$$

$$Y_2 = y_{il}^{AA} y_{jk}^{BB} \quad (12c)$$

$$X = x_i^A x_j^B x_k^B x_l^A \quad (12d)$$

for the  $\beta$  phase and

$$T = t_{ijk}^{ABB} t_{ijl}^{ABA} t_{ikl}^{ACA} t_{jkl}^{BCA} \quad (12e)$$

$$Y_1 = y_{ij}^{AB} y_{ik}^{AC} y_{jl}^{AB} y_{lk}^{AC} \quad (12f)$$

$$Y_2 = y_{il}^{AA} y_{jk}^{BC} \quad (12g)$$

$$X = x_i^A x_j^B x_k^C x_l^A \quad (12h)$$

for the  $\beta'$  phase. The nearest neighbour atomic distance is calculated by setting the first derivative of the grand potential with respect to  $r$  equal to zero and assuming that  $dP/dr$  and  $dS/dr$  are equal to zero.

#### Lennard-Jones Parameters

The values of the Lennard-Jones parameters are determined in the same manner as in the case for binary systems. By substituting eqn. (1) into eqn. (2), one has an equation relating the enthalpy of the cluster to the interatomic distance,  $r$ . For like elemental clusters (i.e. pure metals)  $y_{ij}=y_{ii}=y_{jj}=1$  for all atomic pairs. Finding the equilibrium condition with  $dH/dr=0$  enables one to derive a value for  $E_{ij}^0$  and  $R_{ij}$  which relates to the enthalpy of formation (sublimation) and lattice parameter of the b.c.c. phase, respectively. Values for the enthalpy of formation were obtained from Hultgren et al. (9) and lattice parameter data were obtained from Pearson (10). If the given species of the metal did not have a b.c.c. phase, the nearest neighbour atomic distance from the existent phase was converted into a b.c.c. parameter. For unlike elemental parameters, by assuming full ordering (for purposes of deriving parameters only),  $y_{11}^{AA}=1$ ,  $y_{22}^{BB}=0$ ,  $y_{12}^{AB}=1$  and other  $y_{ij}$ 's are 0. This enables one to derive expressions for the  $E_{ij}^0$  and  $R_{ij}$  values where  $i \neq j$  based on the energies of formation of B2 intermetallic compounds and their lattice parameters. Unfortunately, most elemental pairs (i.e. AlV) are not known to form a B2 intermetallic compound. In these cases, the mean lattice parameter of the constituent elements was used and the energy of formation was calculated by Miedema's approximation (11,12).

The values for potential parameters  $E_{ij}^0$  and  $R_{ij}$  at 800°C are given in table 1 below, where  $N$  is Avagadro's number.

Table 1- Lennard-Jones Potential Parameters  
Used in the Present Study at 800°C

Pair	$NE_{ij}^0$ (kJ/mol)	$R_{ij}$ (nm)
Ni-Ni	71.77	0.254
Ni-Ti	85.12	0.270
Ni-Al	78.15	0.265
Ni-Cr	67.48	0.249
Ni-V	77.43	0.256
Ti-Ti	79.35	0.297
Ti-Al	87.59	0.286
Ti-Cr	71.30	0.268
Ti-V	81.03	0.276
Al-Al	50.28	0.288
Al-Cr	56.43	0.265
Al-V	66.29	0.272
Cr-Cr	62.55	0.251
V-V	81.40	0.288

#### Determining Equilibrium:

Equilibrium is determined at the chemical potentials at which the grand potential of each phase is equal. This represents the tangential tie-line between free energy curves<sup>(13)</sup>. At the equilibrium condition, the value for the lattice parameter may be determined from the next-nearest neighbour distance for each phase. (In this paper the lattice parameter for the Heusler phase is indexed relative to the B2 phase for ease of comparison. For the true Heusler phase parameter, one must multiply by 2). Also, the partitioning coefficient,  $K_x$ , of the quaternary elemental dopant may be determined by:

$$K_x = \frac{X_\beta^4}{X_{\beta'}^4} \quad (13)$$

where,  $X^4$  is the equilibrium concentration of the quaternary dopant in each phase. The sublattice partitioning may also be examined by comparing  $X^A$ ,  $X^B$  and  $X^C$  for each element.

#### Experimental

Ni-Ti-Al alloys were prepared from 99.99% pure elemental pieces by standard arc-melting techniques within an Ar-atmosphere. Samples were cut from the ingot and solution treated at 1150°C for 4 hours and then aged at 800°C for 100 hours to achieve a semi-coherent state whereby XRD could easily resolve individual  $\beta$  and  $\beta'$  diffraction peaks. For microstructural evaluation, ageing times of 1, 10 and 100 hours were used. TEM samples were electropolished using a 10% perchloric acid - 90% acetic acid solution.

The lattice misfit was evaluated in a powder sample using a Philips  $\theta$ -2 $\theta$  x-ray diffractometer with a high temperature stage. The diffractometer was aligned using a Si standard prior to measurements. The diffractometer was operated at 40 kV and 40 mA using a Cu rotating anode assembly. The peak positions of

the (110), (200) and (211) peaks of both  $\beta$  and  $\beta'$  phases were determined by fitting a Pearson VII profile to the raw data; the lattice parameters were determined using the  $\cos\theta\cot\theta$  extrapolation function<sup>(14)</sup>. This resulted in accuracies in the lattice parameter measurement of  $\pm 0.0005$  Å at room temperature and  $\pm 0.001$  Å at higher temperatures due to poorer peak resolution. Microstructural analysis was performed using a Philips CM30 TEM operating at 300 kV. Energy dispersive x-ray analysis was carried out using a VG STEM operating at 100 kV. Composition was determined from the EDS measurements by applying sensitivity factors derived from standards. The overall accuracy of the composition is only  $\pm 0.5$  at %, but the precision of the measurement is better than  $\pm 0.01$  at %.

#### Results

##### Microstructure

The microstructure of a homogenised ternary Ni-Ti-Al alloy with 50 at.% Ni and 7.0 at.% Al following an ageing treatment of 10 hours at 800°C is shown in figure 2, with the beam direction close to [100] and  $g=011$ . The microstructure consists of arrays of coherent cuboidal  $\beta'$  ( $Ni_2TiAl$ ) precipitates aligned along  $\langle 001 \rangle$  directions within the matrix of  $\beta$  (NiTi). After heat treatments at 800°C for 100 hours, the precipitates have lost their coherency and the misfit is accommodated by arrays of  $a\beta\langle 001 \rangle$  type misfit dislocations. A typical DF WB TEM micrograph with  $g=002$  (and thus one set of the misfit dislocations made invisible as  $g \cdot b = 0$ ) is shown in figure 3. By examining the dislocation spacing of the misfit dislocations surrounding each precipitate, one can determine an approximate value for the misfit using:

$$\delta = \frac{N}{L} |b| = da_\beta \quad (14)$$

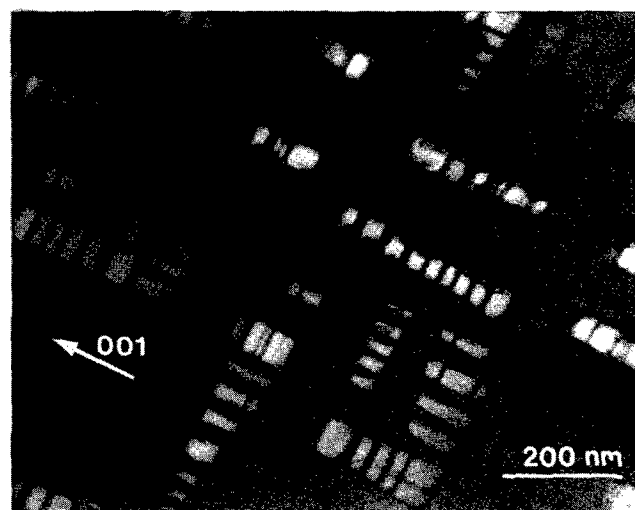


Fig. 2 - BF TEM Micrograph of (light grey)  $Ni_2TiAl$   $\beta'$  precipitates with (dark grey) NiTi  $\beta$  matrix.

where  $N$  is the number of dislocations across a unit length  $L$  of the precipitate, and  $d$  is the inter-dislocation spacing. The misfit

calculated in this way is listed below in table 2 for the ternary alloy,  $\text{Ni}_{50}\text{Ti}_{43}\text{Al}_7$ , a V-doped alloy,  $\text{Ni}_{50}\text{Ti}_{42}\text{Al}_6\text{V}_2$  and for a Cr-doped alloy,  $\text{Ni}_{50}\text{Ti}_{42}\text{Al}_6\text{Cr}_2$ . Each value is the mean derived from a measurement of at least ten precipitates; the error listed is the standard deviation of the values measured. It should be noted that care was taken to use those dislocations in the middle of precipitate faces, where the spacing was clearly defined for the purposes of determining misfit. In this table, one can see that V is clearly effective in reducing the misfit by 0.16% for 2 at.% or 0.08% per atomic percent, if we assume Vegard's Law. The effect of Cr on the misfit is not certain within the bounds of the statistical error.

Table 2 - Misfit at room temperature in undoped, V and Cr-doped alloys as measured by dislocation spacing

Alloy	Misfit (%)	error
Ternary	-1.33	$\pm 0.026$
V-doped	-1.17	$\pm 0.021$
Cr-doped	-1.31	$\pm 0.018$

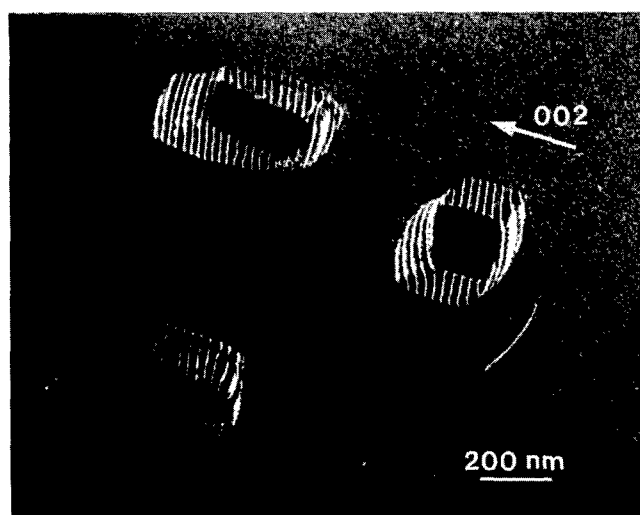


Figure 3 - DF TEM Micrograph showing the semi-coherent state of over-aged  $\beta'$  precipitates surrounded by a matrix of misfit dislocations ( $g=002$ )

#### Calculation Results

The CVM calculations predict preferential partitioning to the Ti-sublattice in the  $\beta$  phase of Ag, Co, Cu, Cr, Fe, and V for dopant amounts less than 0.25 atomic percent. However, the predicted partitioning behaviour at more meaningful dopant levels is highly complicated, and is dependant on temperature and composition; this will be treated in detail elsewhere. For Cr and V, the partitioning coefficients, as calculated by eqn. (13), are shown in figure 4 as a function of total dopant composition at 800°C. Here, we see that both dopant elements are predicted to strongly

partition to the Ti-sublattice in the  $\beta$  phase at low dopant amounts, though at concentrations greater than 0.9 at.%, Cr is predicted to preferentially partition to the Ni-sublattice of the  $\beta'$  phase. V is not predicted to preferentially partition to the  $\beta'$  phase; the limit of its solubility at 800°C occurs near 1.34 at.%. These partition coefficients are strongly affected by the temperature and by the deviation from stoichiometry in terms of Ni-concentration, thus for the purposes of these predictive calculations, the Ni-concentration was maintained at 50.0% in both phases. Both V and Cr additions are predicted to preferentially partition to the  $\beta$  phase above 800°C, with a greater degree the higher the temperature. At 800°C or below, and with a dopant concentration of 1 at.%, Cr is predicted to partition preferentially to the  $\beta'$  phase. This behaviour is seen in figure 5 which shows the predicted partitioning coefficient versus the temperature for 1 at.% of total added dopant. Two-phase  $\beta/\beta'$  equilibrium was usually not possible at dopant amounts much higher than 1 at.%. Values at temperatures lower than the data points shown in figure 5 were unobtainable because of the predicted lessening in the solubility of the dopant elements at these temperatures.

The predicted misfits of undoped, V and Cr-doped alloys are plotted as a function of temperature in figure 6, for 1 at.% of dopant addition. In this figure it can be seen that the predicted misfit for the ternary alloy increases in magnitude with increasing temperature from -1.1 % at 400°C to -1.6 % at 1000°C. The misfit in the V-doped alloy is less in magnitude, showing that V is an effective misfit reducer. At 800°C V-doping is predicted to reduce the misfit to -1.18% from -1.44%, in the ternary case. Cr-doping at the same conditions results in a predicted increase in the magnitude of the misfit to -1.61%. At temperatures above 900°C, Cr-doping results in Cr partitioning preferentially to the  $\beta$  phase (see fig. 5) and a reduction, rather than an increase in the magnitude of the misfit. There is a clear discontinuity in the partition coefficient behaviour with temperature between 900 and 1000°C in figure 5, which appears to be related to the large change in predicted equilibrium lattice parameters.

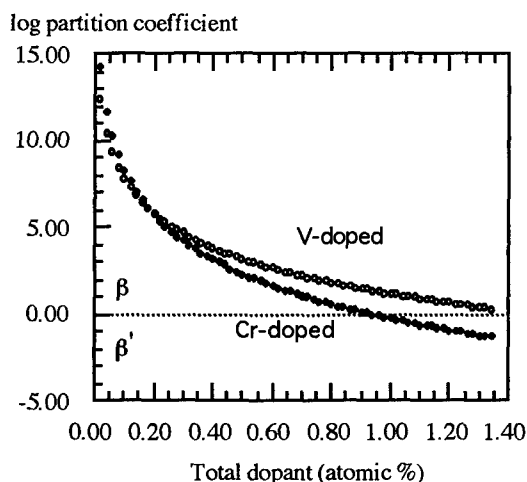


Figure 4 Predicted Partition coefficients of Cr and V-doped alloys at 800°C vs. dopant amount

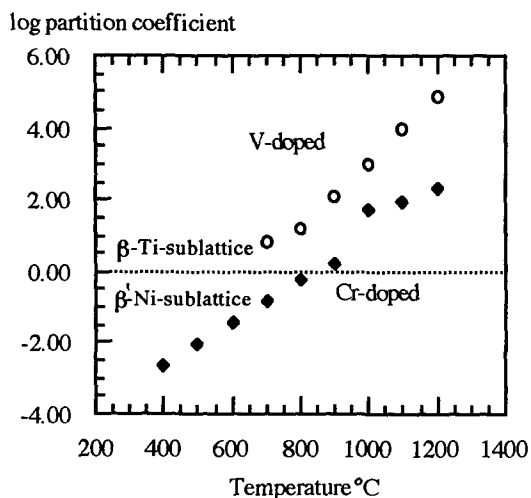


Figure 5 Partition coefficients of Cr and V doped alloys with 1 at. % total dopant vs. temperature

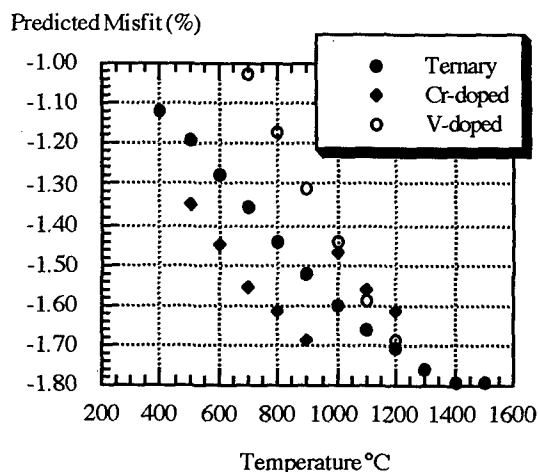


Figure 6 Predicted Misfit vs. Temperature for Ternary, Cr-doped and V-doped alloys by the CVM for 1 at.% doping.

#### X-ray Diffraction Results

It can be seen in figures 4 and 5 that V is expected to partition to the  $\beta$  phase. In figure 6, its addition is shown to decrease the misfit between the  $\beta$  and  $\beta'$  phases. Experimental XRD results verify these predictions. In figure 7 one can see that the lattice parameter, as measured by XRD techniques, of the  $\beta$  phase is reduced by V addition, especially at lower temperatures, while the  $\beta'$  remains nearly unchanged, indicating that V has partitioned preferentially to the  $\beta$  phase. In figure 7, it is clear that the misfit is reduced to a greater extent with the addition of V, the lower the temperature, which is the predicted behaviour of the CVM program shown in figure 6. This is seen more clearly in figure 8, which shows the misfit for Ternary, Cr-doped and V-doped alloys as determined by low and high temperature XRD. The misfits of both the ternary and V-doped alloys are shown to increase in magnitude with increasing temperature until about 700 degrees at

which point the misfit starts decreasing in magnitude with increasing temperature. This is almost certainly due to the increase of solubility of Al in the  $\beta$ -phase and increase of solubility of Ti in the  $\beta'$  making these phases more chemically alike. In the case of the Cr-doped alloy, the room-temperature lattice parameter of the  $\beta$ -phase is slightly decreased to  $2.942 \pm 0.0005 \text{ \AA}$  from the ternary parameter of  $2.944 \pm 0.0005 \text{ \AA}$ , whereas the parameter of the  $\beta'$ -phase is noticeably increased to  $2.909 \pm 0.0005$  from  $2.902 \pm 0.0005 \text{ \AA}$ , leading to a reduction of misfit of 0.16% per atomic percent dopant assuming Vegard's Law.

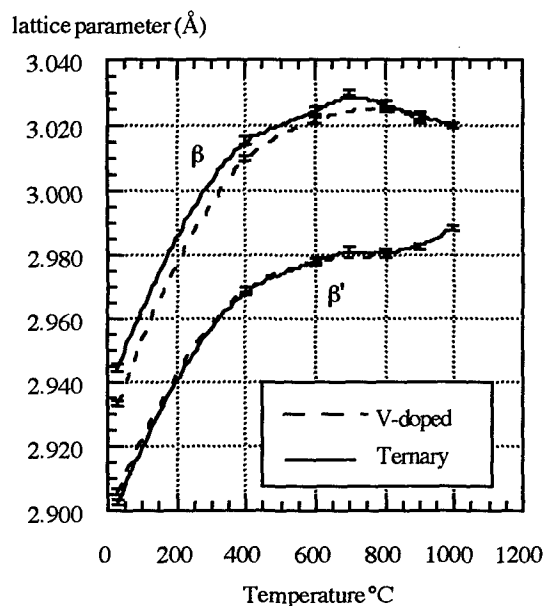


Figure 7 XRD determined lattice parameters for  $\beta$  and  $\beta'$  phases in Ternary and 2 at.% V-doped Alloy.

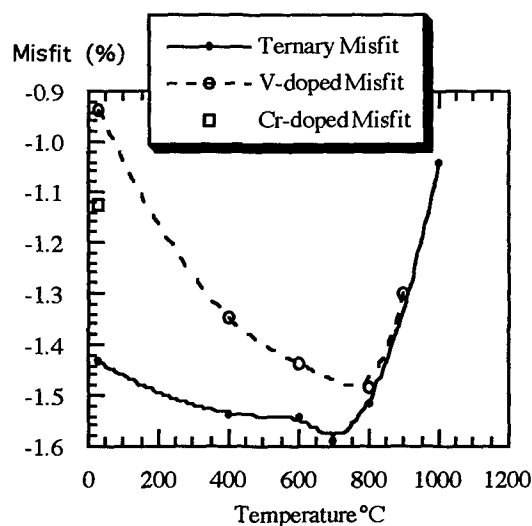


Figure 8 - XRD determined misfit between  $\beta$  and  $\beta'$  phases in Ternary, V-doped and Cr-doped alloys with 2 at.% dopant.

These observations can be readily shown if one examines the (011)  $\beta$  peak and (022)  $\beta'$  peak in the x-ray diffraction patterns of ternary and V-doped alloys. Such a pattern is shown in figure 9 in which the effect of the V-doping is to clearly reduce the distance (in 2-theta) between these peaks. Despite the slight apparent increase in the lattice parameter of the Cr-doped alloy (associated with a slight reduction in the 2-theta value), the actual parameter is slightly less and the deviation is due to systematic errors which diminish at higher values of 2-theta.

#### Partitioning Behaviour

From figures 4 and 5, both Cr and V are expected to partition preferentially to the  $\beta$  phase at high temperatures. In the STEM using EDS linescans across precipitates formed in samples aged at 800°C for 10 hours, this behaviour is seen to occur. Figure 10 shows the derived compositions of Ni, Ti, Cr and Al from EDS linescans using  $K\alpha$  x-rays. Figure 11 shows the same, but for the V-doped alloy. The value for the V counts was determined by subtracting the  $TiK\beta$  counts from the total  $TiK\beta + VK\alpha$  counts with the assumption that the  $TiK\beta/TiK\alpha$  ratio remained the same as for the Cr-doped case, i.e. 0.14. Calculating the partition coefficient of the quaternary dopant from the EDS scans yields values of 1.7 and 2.4 for Cr and V additions respectively.

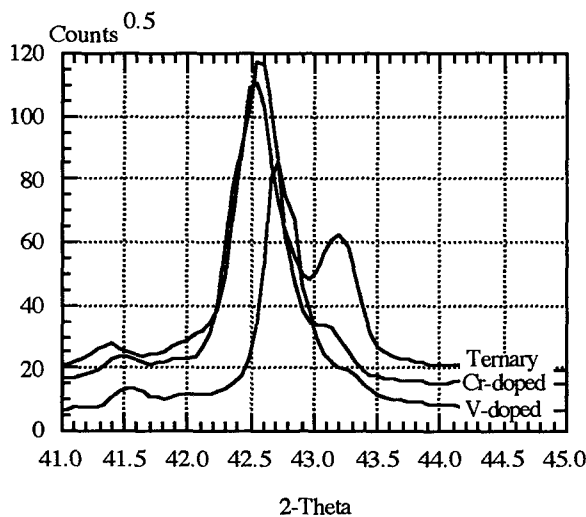


Figure 9 - XRD pattern for  $\beta$  (110) peak and  $\beta'$  (220) peak for ternary and Cr-doped alloys

#### Discussion:

We have shown that the CVM with Lennard-Jones Parameters has predicted the high temperature partitioning of Cr and V dopant elements to the  $\beta$  phase in the  $NiTi/Ni_2TiAl$   $\beta/\beta'$  alloy. EDS linescans within the STEM validate these predictions, although the measured partition values are substantially less than the predicted values. Also, at 800°C, the ageing temperature, Cr is predicted to partition to the  $\beta'$  phase at dopant levels greater than 1 at. %, yet it is observed to partition to the  $\beta$  phase preferentially. It is quite possible, however, that the CVM predicts correctly and the diffusion of Cr through NiTi is slow at 800°C, in which case, its diffusion from the  $\beta$ -phase into the

precipitates may take more time than the ageing treatments have allowed.

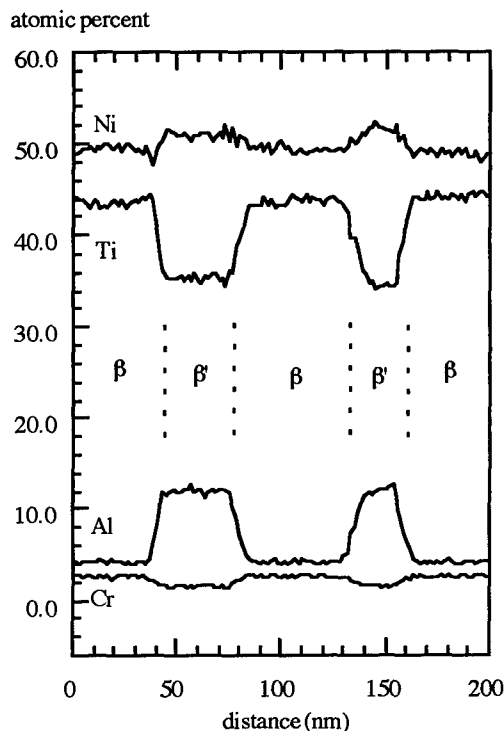


Figure 10 - EDS compositional linescans across two  $\beta'$  precipitates in a Cr-doped alloy.

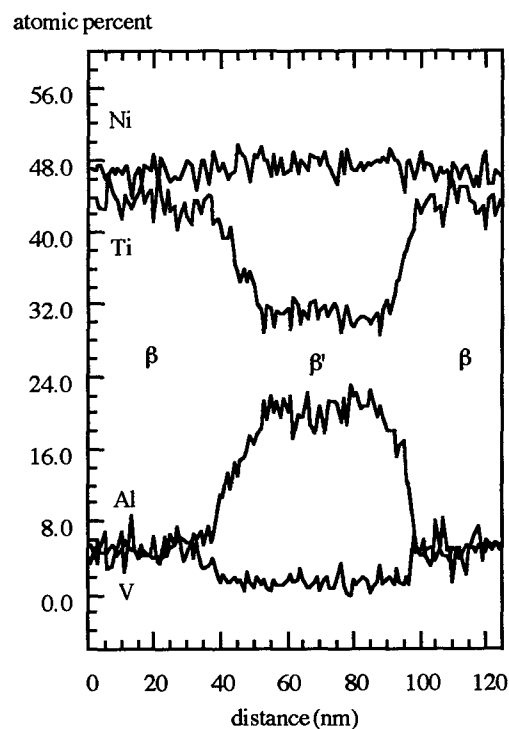


Figure 11 - EDS linescans across one  $\beta'$  precipitate in a V-doped alloy



### Summary

In conclusion, small additions (of 2 at.%) of Cr and V can be added to the two phase  $\beta/\beta'$  alloy to reduce the crystallographic misfit between the constituent phases. This was predicted by CVM calculations and verified using XRD and TEM techniques. It is hoped that the addition of these dopants as "misfit reducers" will slow the precipitate growth kinetics and improve the mechanical properties of these alloys at high temperature.

### Acknowledgements

The authors acknowledge the financial support of Rolls-Royce plc. M. Peters acknowledges useful discussions with H. Harada and M. Enomoto regarding the CVM method and the Cambridge Commonwealth Trust for further financial support.

### References:

1. Y. Koizumi et al., "NiTi-base Intermetallic Alloys Strengthened by Al Substitution" (Paper presented at the Symposium on Atomic Arrangement Design and Control for New Materials, NRIM, Tsukuba, Japan, 16 November, 1994), 36
2. K. Oh-ishi et al., "Phase Decomposition and Hardening in NiAl-NiTi Pseudo-binary Alloy System," J. Japan Inst. Metals, 60 (3) (1996), 239-246.
3. P. J. Warren et al., "Phase Decomposition in NiTi-Ni<sub>2</sub>TiAl Alloy System" (Paper presented at the 3rd Int. Charles Parson's Turbine Conference, Newcastle, UK, April 1995), 26
4. M. A. Peters, G. A. Botton and C. J. Humphreys, "The Precipitation of  $\beta'$  Ni<sub>2</sub>TiAl from Al-doped  $\beta$  Ni-Ti alloys," Inst. Phys. Conf. Ser., 147 (1995), 451-454
5. M. Enomoto and H. Harada, "Analysis of  $\gamma/\gamma'$  Equilibrium in Ni-Al-X Alloys by the Cluster Variation Method with the Lennard-Jones Potential," Metall. Trans. A, 20A, April (1989), 649-664
6. M. Enomoto, H. Harada and H. Murakami, "Calculation of Constitution of Ni-base Superalloys by Cluster Variation Method," Tetsu-to-Hagane-J. Iron and Steel Inst. of Japan, 80 (6) (1994), 487-492.
7. M. Enomoto and T. Kumeta, "Analysis of the  $\beta'$  Ni<sub>2</sub>TiAl/ $\beta$  NiTi equilibrium in Ni-Ti-Al alloys by the cluster variation method," Intermetallics, 5 (2) (1997), 103-109.
8. C. Sigli and J. M. Sanchez, "Calculation of Temperature-Concentration Diagrams by the CV Method With Lennard-Jones Pair Interactions," CALPHAD, 8 (3) (1984), 221-231
9. R. Hultgren et al., Selected Values of the Thermodynamic Properties of the Elements (Metals Park, OH: American Society for Metals, 1973).
10. W. B. Pearson, A Handbook of Lattice Spacing and Structure of Metals and Alloys (London UK: Pergamon Press, 1967)
11. A. R. Miedema, R. Boom and F.R. De Boer, "On the Heat of Formation of Solid Alloys," J. Less-Common Metals, 41 (1975), 283-298.
12. A. R. Miedema, "The Electronegativity Parameter for Transition Metals: Heat of Formation and Charge Transfer in Alloys," J. Less-Common Metals, 32, (1973), 117-136
13. R. Kikuchi and D. de Fontaine, "Theoretical Calculations of Phase Diagrams Using the Cluster Variation Method, NBS SP-496, (1977), 967-998
14. H. W. King and E.A. Payzant, "An Experimental Examination of Error Functions for Bragg-Bretano Powder Diffractometry", Advances in X-ray Analysis, 36 (1993), 663.

# Impact Resistance of NiAl Alloys

W. S. Walston and R. Darolia

GE Aircraft Engines, 1 Neumann Way, Cincinnati, OH 45215

## Abstract

Ballistic impact tests were conducted on NiAl alloys using conditions simulative of those in the turbine section of aircraft engines. Several parameters including velocity, impacting particle mass and thickness, target thickness and impact angle were varied in tests conducted at approximately 980°C. Impact damage of the single crystal NiAl alloy typically occurred due to high bending stresses on the backside of the impact panel resulting in complete failure of the specimen. Impact angle and target thickness were found to be important in determining the impact resistance of the specimens. It was found that single crystal NiAl alloys do not survive most impact conditions simulative of turbine blades, but demonstrated feasibility under impact conditions simulative of turbine vanes. The single crystal NiAl alloy results were similar to silicon nitride results reported in the literature, while a NiAl eutectic alloy evaluated in this study performed slightly better than both of these materials.

## Introduction

NiAl alloys are one of several candidate materials for advanced turbine airfoil applications. Almost all of these candidate material systems have low ductility and fracture toughness. Thus, one of the key properties which must be evaluated prior to service introduction is the ability to withstand impact events. Impact testing of ceramic material systems has been conducted for many years, however, there has been very little testing of intermetallic compounds.

Testing of ceramic material systems can be classified into two categories depending on the intended application. The first category is for use in armor applications.<sup>1,2</sup> Specimens in these tests

tend to be > 10 mm in thickness and impact velocities are over 1000 m/s. The second category is for use in gas turbine components or turbocharger rotors.<sup>3-6</sup> These ceramic specimens tend to be 1-5 mm in thickness and impact velocities range from 30 to 500 m/s. Ceramic specimens in both categories of applications typically use a metallic backing plate as part of the fixturing. The impacting particles are usually spheres of other ceramic materials, such as silicon nitride, silicon carbide or partially stabilized zirconia, although steel balls have been used in several tests.

Limited studies thus far on intermetallic materials have been confined to either dynamic fracture toughness testing<sup>7</sup> or ballistic impact testing for armor applications,<sup>2</sup> although impact testing of gamma TiAl has been initiated.<sup>8</sup> The only impact-type tests reported on NiAl have been Charpy impact tests on NiAl/superalloy composites.<sup>9,10</sup> In addition, limited high strain rate compression testing has been performed on NiAl,<sup>11,12</sup> however these studies did not assess impact resistance. The increasing focus on NiAl, TiAl and other intermetallics for gas turbine applications demonstrates the need for impact tests that simulate gas turbine service conditions.

In a gas turbine engine environment, the impacting particle will be at a high temperature (~1100°C) and will absorb significant energy by deforming upon impact due to its lower high temperature strength. Impacting particles in an engine are likely to be other engine components that are made from superalloys. An intermediate strength superalloy (HS188) at 1100°C has a yield strength of about 70 MPa, while a high strength superalloy (René N5) at 1100°C has a yield strength of about 345 MPa. The impacting particle in the simulated tests is at room temperature as it strikes the target. Thus, it was desired to use materials that had room temperature yield strengths equivalent to those of superalloys at elevated temperatures. Clearly, a ceramic or steel

sphere with a RT tensile strength of over 1000 MPa does not simulate an engine impact event. In tests described in this paper, aluminum spheres of varying strengths were used to simulate the strength of a superalloy impacting particle in an engine. The Al spheres were used in sizes ranging from 1.6 to 3.2 mm diameter. These particle sizes were judged to be realistic sizes for typical impact events that could occur in an engine. It was estimated that a typical velocity for an impact particle for a vane airfoil in an engine would be about 125 m/s and for a blade airfoil about 300-500 m/s.

In this study, ballistic impact tests were conducted on a NiAl single crystal alloy AFN-12 and a directionally solidified NiAl eutectic 33Cr-1Mo alloy using conditions to simulate turbine blade, turbine vane and combustor applications. The variables evaluated included impact velocity, impact angle, impact particle size (mass) and strength, specimen thickness, specimen coating and test temperature.

### Experimental Procedures

#### Impact Specimens

A high strength, NiAl single crystal alloy designated AFN-12 (50 Ni - 48.45 Al - 0.5 Hf - 1.0 Ti - 0.05 Ga at.%)<sup>13</sup> and a directionally solidified NiAl eutectic alloy (33 Ni - 33 Al - 33 Cr - 1 Mo at.%) were the two NiAl materials evaluated in ballistic impact testing. More information on these alloys can be found in another paper in these proceedings.<sup>14</sup> The NiAl panels were electro-discharge machined (EDM) wirecut from single crystal slab castings and chemically milled to remove the EDM re-cast layer. The typical impact panel dimension was 25 mm x 50 mm x 1 mm thick. Thicknesses of 1.5 and 2 mm were also tested. The long dimension of the specimen was parallel to the <001> orientation of the single crystal NiAl and parallel to the longitudinal direction of the Cr/Mo fibers in the NiAl eutectic. The spacing of the Cr/Mo fibers was approximately 2.5  $\mu$ m.

Selected panels were coated with thermal barrier coatings (TBC) to better simulate engine blades and vanes. TBC's were applied by either a physical vapor deposition (PVD) or an air plasma spray (APS) process. For the PVD TBC specimens, a 50  $\mu$ m aluminide (Codep) coating was applied as a bond coat for the NiAl eutectic specimens and no bond coat was used for AFN-12. The thickness of the PVD TBC was approximately 125  $\mu$ m. For the APS TBC specimens, a 75-125  $\mu$ m NiCrAlY bond coat was applied. The Plasma TBC thickness was 0.5 mm, although some panels were coated with 1 mm of TBC.

#### Impact Testing

Testing was conducted at the University of Dayton Research Institute using a compressed gas gun. Aluminum spheres were used as the projectiles in sizes ranging from 1.6 to 3.2 mm. The 2017 Al spheres were used in the T0 and T6 heat treat conditions, which resulted in yield strengths of approximately 70 and 345 MPa, respectively. Impact particles were loaded in a sabot, which was accelerated to velocities ranging from 45 to 300 m/sec using compressed helium gas. The test set-up is schematically shown in Figure 1. Impact particle velocity and test alignment measurements were conducted using a pair of He/Ne laser/photomultiplier stations. It was not possible to achieve the desired temperature of 1100°C because of the limited power of the induction heater and a less than optimum induction coil design. Temperatures of 980°C on bare specimens and 930°C on coated specimens were achieved. Impact angles were varied from 20 to 90° by rotating the specimen mounting fixture relative to the projectile trajectory. Specimens were heated by induction coils surrounding the specimen, and projectiles were shot such that their trajectory was between two loops of the induction coil. Temperatures were measured using a micro-optical pyrometer. The impact point was about 20 mm below the top of the 50 mm length specimen and centered along the 25 mm width. A high speed camera operating at 100,000 frames per second was used to document the impact location and any impact damage.

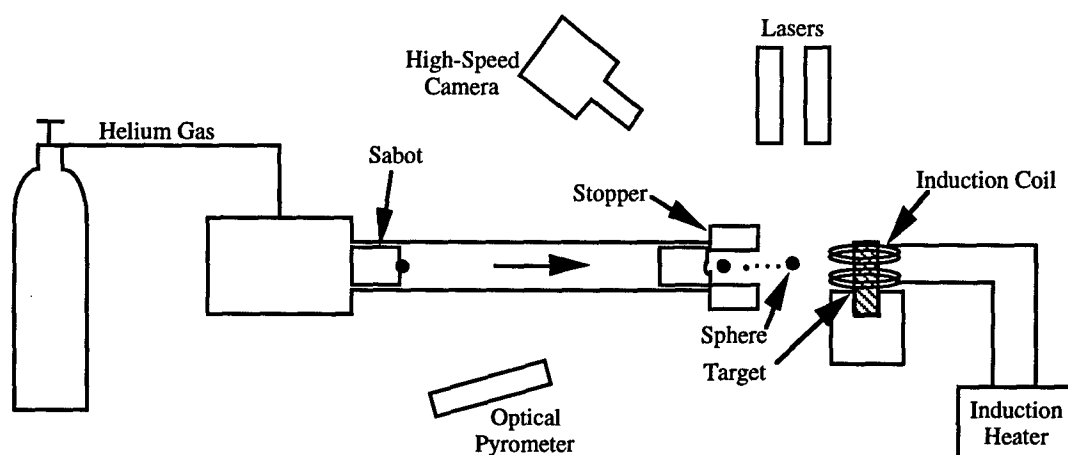


Figure 1. Schematic of the impact test setup for NiAl alloys.

## Results

### Impact Tests

For each of the material and coating combinations, it was attempted to determine the critical impact velocity for fracture of the specimen. The effect of impact angle, particle size and particle strength were also evaluated. It was found that the aluminum spheres deformed upon impact under many of the experimental conditions. As discussed in the introduction section, this was simulative of actual engine impact conditions. Figure 2 shows a typical high-speed photographic image showing the Al sphere contacting a NiAl panel with a thermal barrier coating. Impact locations could be pinpointed with the high-speed camera, but no propagating cracks were observed because the camera automatically turned off several frames after impact.

For the single crystal NiAl specimens, there was either complete failure or no damage. Several examples of fractured panels are shown in Figure 3 under increasingly severe conditions. At the least severe conditions that caused failure, typically a few cracks were

observed fanning out from the impact site. At intermediate conditions, the small pieces around the impact site were lost and several cracks propagated from this area. At very severe conditions, as shown in Figure 3c with a steel ball, a larger area of material near the impact site fractured into very small pieces with radial cracks propagating from this area. In some of the thicker coated specimens, the coating had a small dent only while the uncoated backside of the specimen fractured due to the imposed bending stresses, as shown in Figure 4.

In order to more easily assess the results, an impacting particle parameter that included impacting particle mass and strength was developed. Based on the analysis of the data, it was determined that the mass/size of the particle was a more important variable than the yield strength of the particle. The parameter that best fit the test data was mass times  $\log(\text{strength})$ , where mass is in grams and yield strength in MPa. For example, a 2.4 mm diameter sphere (0.02 g) in the T0 heat treat condition would equal  $0.02 \times \log(70) = 0.037$ , and a 2.4 mm diameter sphere (0.02 g) in the T6 heat treat condition would equal  $0.02 \times \log(345) = 0.051$ .

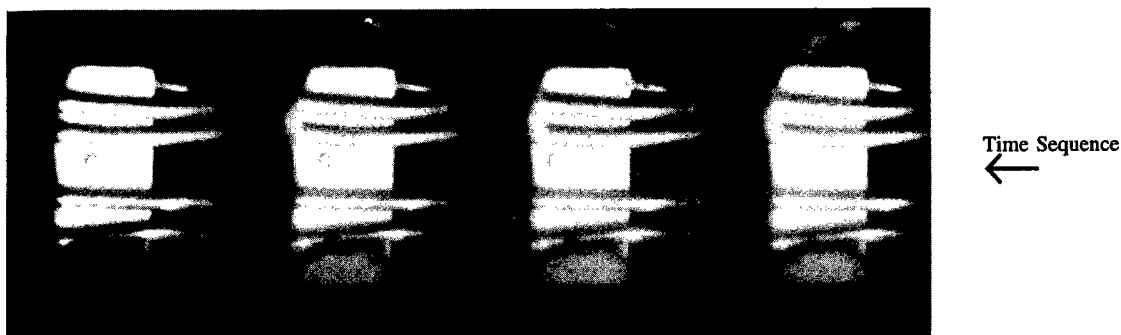


Figure 2. High-speed photographic image of the impacting particle traveling between the induction coils towards the NiAl panel. Photo on right is first in sequence.



Figure 3. Several examples of typical NiAl impact fractures for 1 mm thick panels under increasingly severe impact conditions. (a) velocity = 90 m/s, particle parameter = 0.04, (b)  $V = 135$  m/s, p.p. = 0.04 and (c)  $V = 90$  m/s, p.p. = 1.1 (steel ball).

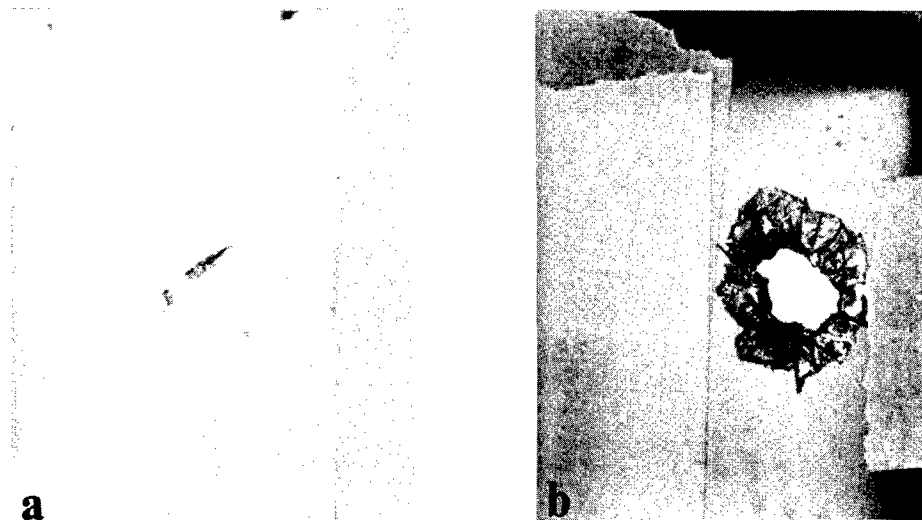


Figure 4. (a) Front of NiAl panel with 0.5 mm TBC showing no damage following impact and (b) back of same panel showing complete failure of NiAl.  $V = 135$  m/s, p.p. = 0.10.

#### Blade and Vane Conditions

A typical NiAl turbine blade or vane would have a wall thickness of approximately 1 mm and would likely have a thermal barrier coating. Figure 5 shows a summary of the data for NiAl alloy AFN-12 specimens that simulate the conditions for turbine airfoils. Critical lines were drawn that distinguished between no damage to the impact specimen and failure. Comparing bare and coated specimen results, it was found that there was essentially no effect of the 125  $\mu$ m PVD TBC on impact resistance. There was little difference in behavior between the 45° and 90° specimens, although the data were limited. There was noticeable improvement in the impact behavior when the impact angle was decreased to 20°. Figure 5 suggests that for impact velocities that might be encountered in a vane application (~125 m/sec), there are some conditions that would produce failure and some that would cause no damage. Failure would occur at nearly all

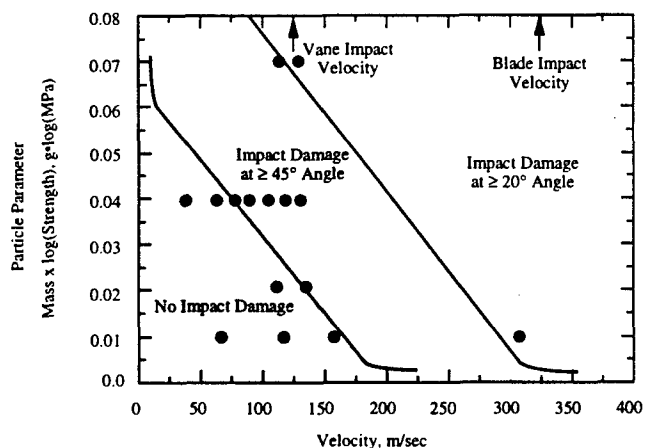


Figure 5. Schematic summary of the data for conditions simulating turbine airfoils. Single crystal NiAl alloy AFN-12 thickness was 1 mm. Circles show individual data points used to draw curves

conditions for blade applications (>300 m/sec) for the 1 mm thick specimens with and without TBC.

#### Effect of Thickness

It was observed that the TBC (PVD and APS) absorbed very little energy during the impact event. In some cases, a small dent was present, but it appeared that the coating did not absorb much energy. In fact, as shown previously in Figure 4, the front of one the plasma TBC specimens showed no damage, while the back of the specimen was severely cracked. Based on these observations, the coating was simply treated as additional thickness in plotting Figure 6. Again, critical lines between no damage and failure were drawn for each thickness. It can be seen that as the thickness of the specimen was increased, the benefit to impact resistance increased significantly.

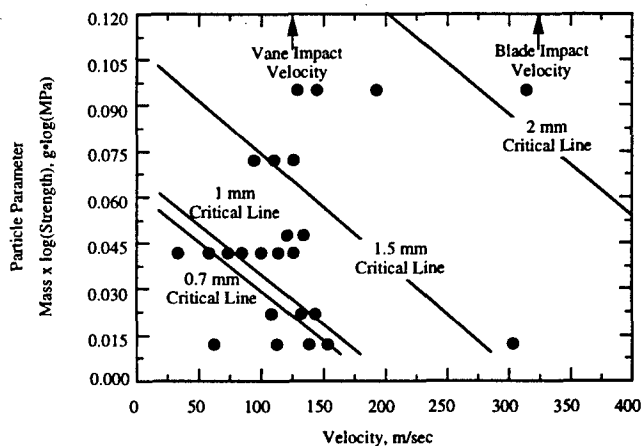


Figure 6. Effect of thickness on the impact resistance of single crystal NiAl alloy AFN-12. NiAl panels coated with TBC included in data summary. The region of no impact damage lies to the left of each curve. Circles show individual data points used to draw curves

### Combustor Conditions

A typical NiAl combustor liner application would involve a wall thickness of about 1 mm and an APS TBC of at least 0.5 mm thickness. In addition, impact events in a combustor would occur at more shallow angles and at lower gas path velocities. Thus, impact tests were conducted at 20° impact angles and at about 125 m/sec impact velocity. The 20° critical line shown previously in Figure 5 showed that there was significantly less impact damage from low angle impacts. The line drawn in that figure was for AFN-12 substrates that were either bare or had a thin, 125  $\mu$ m PVD TBC. Testing of 0.5 mm and 1.0 mm thick APS TBC coatings on AFN-12 showed that typical combustor impact events did not represent a problem. For a 0.5 mm APS TBC on an AFN-12 specimen, an impact at 127 m/sec and 20° angle produced no damage using the large, 3.2 mm diameter ball. A similar test at a 45° angle also produced no damage. The most severe condition was tested on a specimen with a 1.0 mm thick APS TBC at a velocity of 188 m/sec using the largest (3.2 mm) ball in the strongest T6 heat treatment condition. This test also showed no damage to either the TBC or AFN-12 substrate.

### Effect of Material Type

Two different NiAl materials were tested: NiAl single crystal alloy AFN-12 and directionally solidified NiAl eutectic 33 Cr - 1 Mo alloy. Figure 7 shows a relative comparison between the two materials. This figure summarizes the 45° data only; the 20° data behaved similarly. It was clear that the NiAl eutectic alloy had better impact resistance than the AFN-12 alloy. The failure mode was also much different between the two materials. While both materials failed by the formation of star cracks on the backside of the specimen, the NiAl eutectic specimens remained intact after most impact events. Many of the NiAl eutectic specimen failures consisted of hairline cracks on the backside of the specimen, which were difficult to observe. These cracks propagated along lamellar boundaries as expected. Crack propagation across the lamellae was probably more difficult, thus allowing the specimen to remain intact.

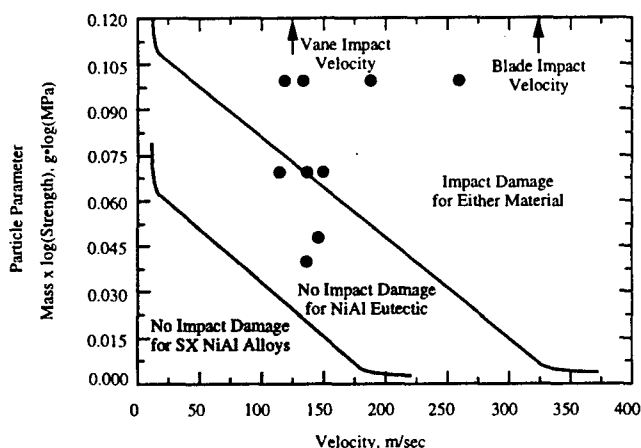


Figure 7. Relative comparison of impact resistance of single crystal NiAl alloy AFN-12 and NiAl eutectic 33 Cr - 1 Mo alloy. Circles show data points of eutectic alloy only.

### Discussion

In ceramic materials, damage in low intensity impact events occurs in the form of ring cracks surrounding the impact site. Radial cracks form at higher impact loads, which can result in complete fracture of the specimen. At the highest impact loads, star cracks form on the back side of the specimen resulting in complete fracture. The NiAl alloys tested in this study did not form ring cracks that are typically observed in impact testing of ceramic materials.

To better understand the differences between the behavior of the NiAl specimens relative to the literature data on impact testing of ceramics, the stress state of the NiAl plate specimen was analyzed. The stress state in the cantilevered, clamped plate specimens used in this study consisted of a contact stress on the front surface and bending stresses on the back surface. In a completely elastic impact event, the relationship between the kinetic energy of the projectile, the impact force, the impact area, and the resulting stress fields are all analytically defined by the elastic properties of the projectile and the target.<sup>15</sup> However, when the yield strength of the projectile is low enough such that plastic deformation occurs during impact, the impact force on the target will be reduced, and the impact contact area will increase. In both cases, Hertzian contact stresses and bending stresses will be induced in the target. By conducting both a purely elastic and a fully plastic projectile analysis, the results can be compared to the experimental results for NiAl. Since most of the aluminum projectiles used showed signs of plastic deformation after the impact event, it is expected that the plastic analysis should give more reasonable predictions of failure modes.

The above analysis showed that the bending stresses in thin plates exceeded the magnitude of the Hertzian contact stresses and sampled a larger area of surface flaws. Thus, the failure initiation on the back side of the specimen is expected. At larger thicknesses, it is expected that ring cracks would form in NiAl. Ring cracks and Hertzian cone cracks are typically observed in the ceramic specimens because the ceramic specimens are either much thicker than the 1 mm NiAl specimens used in this study or a metallic backing plate is used that significantly reduces the bending stresses in the ceramics.

It was found that under constant impact load conditions, specimen thickness was a very important variable. Figure 6 showed that significantly more severe impacts could be withstood simply by increasing the specimen thickness from 1 mm to 2 mm. By using the particle parameter previously described, it is possible to compare literature results on other materials using impact projectiles of different materials and sizes. Figure 8 shows a comparison of the thickness effect between NiAl and silicon nitride ( $\text{Si}_3\text{N}_4$ ) from two different studies at a constant particle parameter of 0.1.<sup>3,4</sup> NiAl and  $\text{Si}_3\text{N}_4$  appear to behave similarly in both the trend with thickness and the absolute values of critical velocity. It has been shown that thin plates of SiC and glass fracture in a manner similar to the NiAl in this study when the specimen thickness is less than 5 mm.<sup>16,17</sup>

The similarity between NiAl and  $\text{Si}_3\text{N}_4$  is not surprising based on their similar fracture toughness values.  $\text{Si}_3\text{N}_4$  has a room temperature fracture toughness value of about  $6 \text{ MPa}\sqrt{\text{m}}$ ,<sup>3,4</sup> which is similar to that of AFN-12 in the <001> orientation.<sup>18</sup> Dynamic fracture

toughness tests ( $K_{IC}$ ) may relate more meaningfully to impact tests, and in  $Si_3N_4$  the room temperature results were similar to the standard  $K_{IC}$  tests.<sup>19</sup>

The ductile-to-brittle-transition temperature (DBTT) for AFN-12 in tensile testing is 730°C and 930°C for the <001> and <110> orientations, respectively. In fracture toughness tests, the DBTT is 950°C and 1040°C for the <001> and <110> orientations, respectively. Thus, the impact tests were conducted above the tensile DBTT for the <001> orientation and in the vicinity of the DBTT for the <110> orientation. Based on tensile testing and fracture toughness testing, it was hoped that impact testing at high temperatures, such as 980°C, would provide some benefit to the impact resistance of NiAl. However, the impact test data did not show improved impact resistance at temperature above the tensile DBTT.

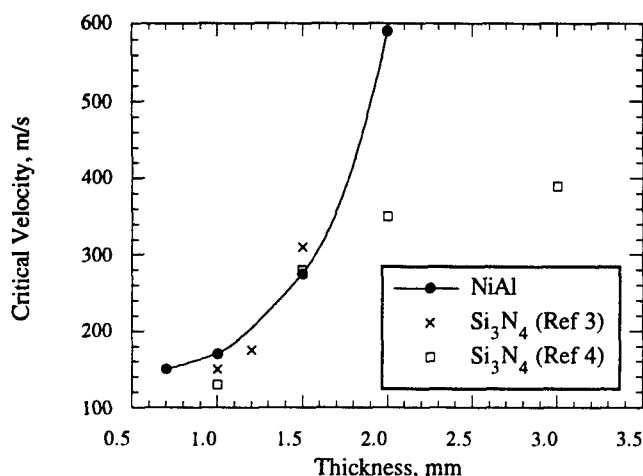


Figure 8. Comparison of particle velocity and plate thickness conditions to produce failure in and silicon nitride using a constant particle parameter of 0.1.

Strain rate is clearly a key parameter to consider. Strain rate effects on binary NiAl have been studied at moderate<sup>20</sup> and at very high strain rates.<sup>11,12</sup> The tensile DBTT of stoichiometric NiAl increased about 50-100°C in the <001> orientation when the strain rate was increased from  $8.3 \times 10^{-5}$  to  $8.3 \times 10^{-3}$ .<sup>20</sup> There was no effect on DBTT in the <110> orientation. At very high strain rates of 2000/s, NiAl had higher work hardening rates and a higher yield stress in the <001> orientation compared to strain rates of 0.001/s or 0.01/s.<sup>11,12</sup> These studies have indicated that at much higher strain rates typical of impact events in a gas turbine engine, one could expect the DBTT and yield strength to increase. Further, Gerberich, et al.,<sup>21</sup> have shown that the fracture toughness of NiAl decreases significantly at higher loading rates. Thus, using tensile and fracture toughness properties obtained under normal laboratory loading conditions to gauge impact resistance may be overly optimistic. Therefore, it is not surprising that even though the impact tests were conducted at temperatures above the tensile and fracture toughness DBTT, the material responded in a brittle nature.

One of the main objectives of this testing was to determine the sensitivity of NiAl to impact events when being considered for use in turbine blade, turbine vane or combustor applications. Design

estimates were made that the impact velocity for a blade would be 300-500 m/sec, while the velocity for vanes or combustor applications would be similar to the gas path velocity of about 125 m/sec. Another difference between these applications is the impact angle. For blades and vanes, impact angles of 45 to 90° are typical, while it is believed that only a shallow angle of less than 20° is typical for combustors. Finally, the type of coatings would differ between these applications; blades and vanes typically use a 125  $\mu$ m PVD TBC, and combustor applications use 0.5-1.0 mm of APS TBC.

Based on the numerous tests run at blade and vane conditions, it was concluded that it was unrealistic to assume that, using current design methodology, NiAl would survive an impact event that a turbine blade may experience. In all tests conducted near 300 m/sec, catastrophic failures were observed. Figure 7 showed that for either AFN-12 or NiAl eutectic, survival at 300 m/sec would occur only with very small particles.

For vane applications, it was concluded that AFN-12 and NiAl eutectic could withstand many impact events. However, there are still conditions where larger particles would likely cause crack initiation. For this reason, the design tradeoffs and risks should be carefully evaluated for future vane components. It was also shown that different materials (NiAl eutectics) and thicker walls or coatings could be used to increase impact resistance.

For combustor applications, it was concluded that NiAl can survive an impact event. More shallow impact angles and thicker coatings compared to blade and vane conditions resulted in much more favorable impact behavior. Impact conditions slightly higher than expected in a typical combustor application did not result in failure in either AFN-12 or NiAl eutectic.

## Summary

1. Impact conditions simulative to those in a gas turbine environment were used to test an advanced NiAl single crystal alloy and a directionally solidified NiAl eutectic alloy. Elevated temperature impact tests at 980°C showed that NiAl alloys are not good candidates for turbine blade applications using today's design methods. Application of NiAl alloys as a turbine vane is feasible based on the impact test results. Impact testing under conditions simulative of a combustor environment showed that NiAl could withstand impact conditions generally expected in a combustor application.
2. NiAl eutectic alloys have better impact resistance than high strength, single crystal NiAl alloys due to improved toughness provided by the lamellar structure.
3. The thin, 125  $\mu$ m PVD thermal barrier coating had little effect on the impact behavior of either NiAl alloy AFN-12 or NiAl eutectic. The thicker 0.5 and 1.0 mm APS thermal barrier coating on these materials absorbed very little energy during the impact event and essentially behaved in the same manner as equivalently thick NiAl specimens.
4. The impact resistance of NiAl was found to be similar to that reported for  $Si_3N_4$ , and the effect of thickness in NiAl was also similar to  $Si_3N_4$ . Increasing the specimen thickness from 1 mm to 2 mm significantly increased the impact resistance.

5. Ballistic impact testing using realistic conditions should be a required test, a critical tollgate, for any advanced turbine material with limited ductility or toughness.

#### Acknowledgments

Excellent testing resources and expertise was provided by Gary Abfalter and Bob Bertke at the University of Dayton Research Institute. This effort was supported by many individuals at GE Aircraft Engines including Gary McCabe, Jim Jackman and Bill Brausch who assisted in specimen preparation.

#### References

1. E. Lach, Ceramic Forum Int., Vol. 70, (1993), 486-490.
2. K.S. Kumar and M.S. DiPietro, Scr. Metall. Mater., Vol. 32, (1995), 793-798.
3. H. Tsuruta, M. Masuda, T. Soma and M. Matsu, J. Am. Cer. Soc., Vol. 73, (1990), 1714-1718.
4. Y. Akimune, T. Akiba, N. Hirotsaki and T. Ogasawara, J. Eur. Cer. Soc., Vol. 11, (1993), 425-429.
5. Y. Hara, S. Hamada, T. Minematsu, H. Takahashi and H. Abe, Proc. 3rd Int. Symp. of Ceramic Materials and Components for Engines, Las Vegas, Am. Cer. Soc., (1988), pp. 1179-1188.
6. J. Song, J. Cuccio and H. Fang, Proc. of Annual Automotive Technology Development Contractors' Coordination Meeting, Soc. Auto. Eng., (1994), pp. 53-60.
7. A. Kimura, A. Koya, T. Morimura and T. Misawa, Mat. Sci. Eng., Vol. A176, (1994), 425-430.
8. P.S. Steif, J.W. Jones, T. Harding, M.P. Rubal, V.Z. Gandelsman, N. Biery and T.M. Pollock, to be published in Structural Intermetallics 1997, TMS, Warrendale, PA, 1997.
9. V.C. Nardone, J.R. Strife and K.M. Prewo, Mat. Sci. Eng., Vol. A144, (1991), 267-275.
10. V.C. Nardone, Comp. Sci. Tech., Vol. 52, (1994), 151-161.
11. S.A. Maloy, G.T. Gray III and R. Darolia, Mat. Sci. Eng., Vol. A192/193, (1995), 249-254.
12. S.A. Maloy and G.T. Gray III, High Temp. Ordered Intermetallics VI, MRS Symp. Proc. Vol. 364, eds. J.A. Horton, et al, (1995), MRS, Pittsburgh, PA, pp. 549-554.
13. R. Darolia and W.S. Walston, to be published in Structural Intermetallics 1997, TMS, Warrendale, PA, 1997.
14. R. D. Noebe and W.S. Walston, to be published in Structural Intermetallics 1997, TMS, Warrendale, PA, 1997.
15. S.P. Timoshenko and J.N. Goodier, Theory of Elasticity, McGraw-Hill, New York, 1953.
16. A. Ball and H.W. McKenzie, J. De Physique IV, Vol. 4, (1994), pp. C8-783-C8-788.
17. P. Riou, L. Beylat, C. Cottenot and J.L. Derep, J. De Physique IV, Vol. 4, (1994), pp. C8-281-C8-287.
18. W.S. Walston and R. Darolia, Final Report, Contract F33615-90-C-2006, Wright Patterson AFB, (1996).
19. T. Kishi, Eng. Frac. Mech., Vol. 40, (1991), 785-790.
20. D.F. Lahrman, R.D. Field and R. Darolia, High Temp. Ordered Intermetallics IV, MRS Symp. Proc. Vol. 364, eds. L.A. Johnson, et al, (1991), MRS, Pittsburgh, PA, pp. 603-607.
21. W.W. Gerberich, S.K. Venkataraman, J.W. Hoehn and P.G. Marsh, Structural Intermetallics, eds. R. Darolia, et al, (1993), TMS, Warrendale, PA, pp. 569-576.



## THE EFFECT OF VOLUME FRACTION REINFORCEMENT AND ANNEALING ON THE STRENGTH OF CRYOMILLED NiAl CONTAINING AlN PARTICLES

Mohan G. Hebsur, \* J. D. Whittenberger, \*\* and A. Garg \*\*\*

\* NYMA Inc., LeRC Group, Brookpark OH 44142.

\*\* NASA-Lewis Research Center, Cleveland, OH 44135.

\*\*\* AYT Corp. at NASA-Lewis Research Center, Cleveland, OH 44135.

### Abstract

Cryomilling has been utilized to introduce several different volume fractions of particulate AlN in the B2 intermetallic NiAl. The resultant microstructures are inhomogeneous, where thin mantles of nanocrystalline AlN and NiAl grains surround micron size NiAl cores. Study of the 0.2 % compressive yield strength as a function of temperature and the 1200 to 1500 K slow compressive deformation properties indicate that the strength of as-cryomilled NiAl is essentially proportional to the square root of the AlN content. With one possible exception, factors such as AlN particle size and distribution, other second phases, Al content of the matrix, microstructure and elastic modulus do not appear to exert any significant influence on mechanical properties. Lower temperature yield strength (<800 K), however, suggests that densification techniques leading to a refinement of NiAl core dimensions can produce improvements in these properties. Post exposure testing of cryomilled NiAl after annealing at 1500 and 1600 K indicates that very high temperature heat treatments are detrimental; however the loss of mechanical strength is not catastrophic. As opposed to the strength properties, the fracture toughness of cryomilled NiAl is independent of amount of AlN.

### Introduction

With its high melting point, cubic B2 crystal structure, inherent oxidation resistance and relatively low density, NiAl has potential to be a replacement material for superalloys in elevated temperature gas turbine engine hardware. One major drawback to the use of NiAl-based materials has been their poor elevated temperature strength properties. Fortunately a number of different techniques have shown promise in strengthening NiAl. Darolia, et al. [1-4] have championed NiAl single crystal technology with small third element alloying additions and have produced materials with tensile creep strengths approaching Ni-based superalloys. Employing mechanical alloying methods in combination with secondary thermomechanical processing, Grahl and Arzt [5,6] have succeeded in the fabrication of oxide dispersion strengthened NiAl with useful strengths to 1673 K. Lastly, employing cryomilling which introduces small AlN particles in a polycrystalline NiAl matrix, Whittenberger and co-workers [7-10] have developed particulate strengthened aluminides with long term superalloy-like elevated temperature creep rupture strengths.

Because the strength of cryomilled NiAl is dependent on the AlN particles and not to any known feature of the cryomilling process [11], the amount of aluminum nitride in the composite should affect its properties. Indeed, Hebsur, et. al [9] have presented preliminary results which indicate that strength of cryomilled NiAl scales with the AlN content. The purpose of this paper is to document the influence of volume fraction of AlN on the compressive yield strength as a function of temperature and the elevated temperature compressive flow strength as a function of strain rate. Because the highest AlN content material possessed the best combination of properties, its elevated temperature plastic flow properties were examined in greater detail than the other compositions, and its fracture toughness was determined as a function of temperature. Additionally the elevated temperature deformation characteristics of one material were determined after it was heat treated at temperatures in excess of the proposed maximum use temperature for any AlN particulate reinforced NiAl.

### Experimental Procedures

The general principles of cryomilling of NiAl have been outlined in [7,12]. In brief all cryomilling was undertaken in a Union Process Model 01-HD attritor which was enclosed in a slightly positive nitrogen pressure environmental chamber. The attritor vessel was loaded in air with 200 to 500 g of prealloyed aluminide powder and ~2500 g of harden steel grinding media and then fixed in-place in the attritor. After closing the environmental chamber, flow of liquid nitrogen through the cooling jacket of the attritor vessel was initiated. Once the contents of the vessel reached cryogenic temperatures, it was filled with liquid nitrogen to create a nitrogen/grinding media/NiAl powder slurry, and milling was initiated. During milling liquid nitrogen was continuously circulated through the cooling jacket and was intermittently introduced into the vessel to maintain a constant slurry level. To produce NiAl-AlN alloys containing various amounts of AlN, the cryomilling parameters such as grinding media size, ball to charge ratio, milling speed and milling time were varied [13]. In addition several different forms and compositions of nickel aluminide were utilized as the starting material. These included gas atomized binary and Zr-doped -180 mesh NiAl powders as well as broken pieces of melt spun NiAl ribbon. Following cryomilling, the milled powders were allowed to warm to room temperature under a nitrogen cover gas and then separated from the grinding balls. All subsequent powder handling was then accomplished in laboratory

air. Two powder densification procedures were employed to produce material suitable for mechanical testing. Some powders were consolidated by initially vacuum hot pressing (HP) at 1423 K and 40 MPa for 2 h in graphite tooling. The resultant compacts, which were about 85 % dense, were then vacuum canned in stainless steel and hot isostatic pressed (HIP) at 1423 K and 210 MPa for 2 h to 100 % density. Other as-cryomilled powder was vacuum sealed in mild steel extrusion cans and extruded to full density at 1505K or 1300 K with a 7:1 reduction ratio. Mechanical property test specimens were prepared from the densified materials through electrodischarge machining (edm) and grinding techniques. Nominally three or four mm diameter cylindrical compression samples with 2:1 length to diameter ratios were wire edm'ed from the consolidated alloys with the sample lengths parallel to either the hot pressing or hot extrusion direction. After centerless grinding to remove the recast surface damaged layer, the ends of the cylindrical samples were ground flat and true. ASTM standard chevron notched four point bend bars (50 mm x 6 mm x 3 mm) for fracture toughness measurements were also electrodischarge machined from the HP + HIP and extruded materials with the long axis of the samples perpendicular to either the hot pressing direction or extrusion direction. All the surfaces were ground flat and parallel to reduce the surface defects.

Yield strengths of the consolidated materials were determined as a function of temperature by compressing samples between opposing SiC pushbars in an universal testing machine at an initial imposed strain rate of  $\sim 10^{-3} \text{ s}^{-1}$ . At lower test temperatures (<600 K) hardened steel pads were used to transmit the load from the samples to the push bars, while superalloy or ceramic pads were used at elevated temperatures. Yield strengths were determined from the autographically recorded load - time diagrams utilizing the 0.2 % offset method and the assumptions that all plastic deformation occurred in the specimen and that the volume of the sample remained constant. Elevated temperature slow plastic deformation properties were determined by compressing samples between SiC push bars under constant velocity conditions in an universal testing machine and constant load conditions in lever arm creep frames. The autographically recorded load - time charts from a universal test machine operating at speeds ranging from  $2.1 \times 10^{-3}$  to  $2.1 \times 10^{-6} \text{ mm/s}$  were converted to true compressive stresses, strains, and strain rates via the offset method and the assumptions that volume is conserved and that all plastic deformation occurred in the specimen. Creep deformation under constant load conditions was determined as a function of time by measuring the relative positions of ceramic push bars applying the load to the specimen. After normalizing the contraction - time results with respect to the final specimen length, the data were converted into true stresses and strains by assuming volume conservation. While most test samples were tested under a single load, a few specimens were subjected to multiple stress conditions.

The fracture toughness measurements were made on chevron notched specimens tested under four point bending in an universal test machine at room temperature on samples machined from materials containing various amounts of AlN. To estimate the effect of test temperature on the toughness of cryomilled NiAl, samples machined from extruded bar were tested between 300 K and 1000 K. All experiments were conducted at a crosshead speed of 0.00021mm/s which minimized the overload and creep effects. The fracture toughnesses,  $K_{Ic}$ , were calculated from the load - displacement curves utilizing the slice model of Blum [14]. The specimens were not pre-cracked before testing.

Light optical metallography and scanning electron microscopy (SEM) techniques were utilized to examine the microstructure of as consolidated NiAl-AlN alloys and selected samples after compression testing. Additionally a few samples were examined under a Phillips 400T transmission electron microscope (TEM). These specimens were prepared by electro-discharge machining 3 mm diameter cylinders from as-received and tested materials with the long axis of the cylinders parallel to the testing axis. Thin sectional slices were then cut from each cylinder, mechanically polished to  $\sim 150 \mu\text{m}$  thickness, dimpled and ion-milled to electron transparency.

## Results

### As-Consolidated Alloys

The consolidation method and overall chemical analyses of the various NiAl-AlN materials are given in Table 1(a) and estimates of the matrix composition and the second phase content for each alloy are presented in Table 1(b). The latter were calculated on the assumptions that the solubility of nitrogen and oxygen in the NiAl matrix was negligible and that all the nitrogen formed AlN and oxygen formed  $\text{ZrO}_2$  and/or  $\text{Al}_2\text{O}_3$ . The  $\sim 0.5 \text{ wt. \%}$  oxygen present in the cryomilled materials is due, in part, to oxygen in the initial aluminide powders, the unavoidable intrusion of some air into the environmental chamber during cryomilling and post-milling exposure to air. The presence of  $\sim 0.2 \text{ wt. \%}$  Fe in the cryomilled materials is a result of processing, where pieces of the steel grinding balls flaked off during milling.

Typical microstructures in the NiAl-AlN materials after densification are presented in Fig. 1. All the alloys possessed a core and mantle type structure where particle-rich mantles (dark gray particle rich regions in Figs. 1(a,b)) surrounded particle-free NiAl cores (light gray areas). The thickness and continuity of the mantle increased with the second phase content and the appearance of the cores depended on the densification technique. Hot pressed + HIP materials have nominally spherical shaped cores (Fig. 1(a)) while the hot extruded materials consisted of elongated cigar-shaped cores (Fig. 1(b)). Detailed structure of the mantle could be resolved through TEM, as illustrated in Figs. 1(c,d) for HP + HIP NiAl-30.4AlN. The bright field TEM image in Fig. 1(c) clearly shows a high density of small particles in the mantle (marked as "M") which essentially surround particle free NiAl cores (denoted as "C"). Selected area diffraction patterns from the mantle region (insert in Fig. 1(d)) showed ring patterns which could only be indexed to AlN or NiAl; thus revealing that the mantle consisted primarily of very fine AlN particles and NiAl grains. The existence of AlN particles in the mantle regions shown in Fig. 1(c) was also confirmed through TEM dark-field techniques utilizing a small section of the  $(1010)_{\text{AlN}}$  diffraction ring (Fig. 1(d)). Measurements of the sizes of visible phases within the mantle of NiAl-30.4AlN revealed that AlN particles ranged from 5 to 50 nm in diameter while NiAl grains varied from 25 to 250 nm.

### Mechanical Strength

**Compressive Yield Strength** - Fig. 2 shows the 0.2 % compressive yield strengths for several different AlN containing NiAl alloys as a function of temperature. For sake of comparison similar results obtained by Bowman et al. [16] for binary NiAl and NiAl+0.05Zr are included. Additionally, Fig. 2 includes the yield strength - temperature properties of the first lot of

Table 1. Consolidation Techniques and Compositions of Cryomilled Materials

Identification	(a) Densification and Chemistry							(b) Matrix Chemistry and Second Phase Content					
	Consolidation Technique	Al	Overall Composition*, wt. %					Matrix, at %			Second Phase, vol. %		
			C	Fe	N	O	Zr	Al	Fe	Ni	AlN	Al <sub>2</sub> O <sub>3</sub>	ZrO <sub>2</sub>
2.7	HP + HIP	29.2	0.02	0.1	0.5	0.35	0.1	47.4	0.1	Bal	2.7	1.0	0.1
8.4	Hot Extrusion	30.9	0.02	0.2	1.6	0.49	-	47.3	0.2	Bal	8.4	1.5	-
30.4	HP + HIP	37	0.03	0.2	6.61	0.52	0.08	48.0	0.2	Bal	30.4	1.3	0.1
10.3 [15]								47.3	-	Bal	10.3	1.3	*

\* Balance is Ni.

\*\* Alloy also contained about 0.5 vol. %  $\text{Y}_2\text{O}_3$ .

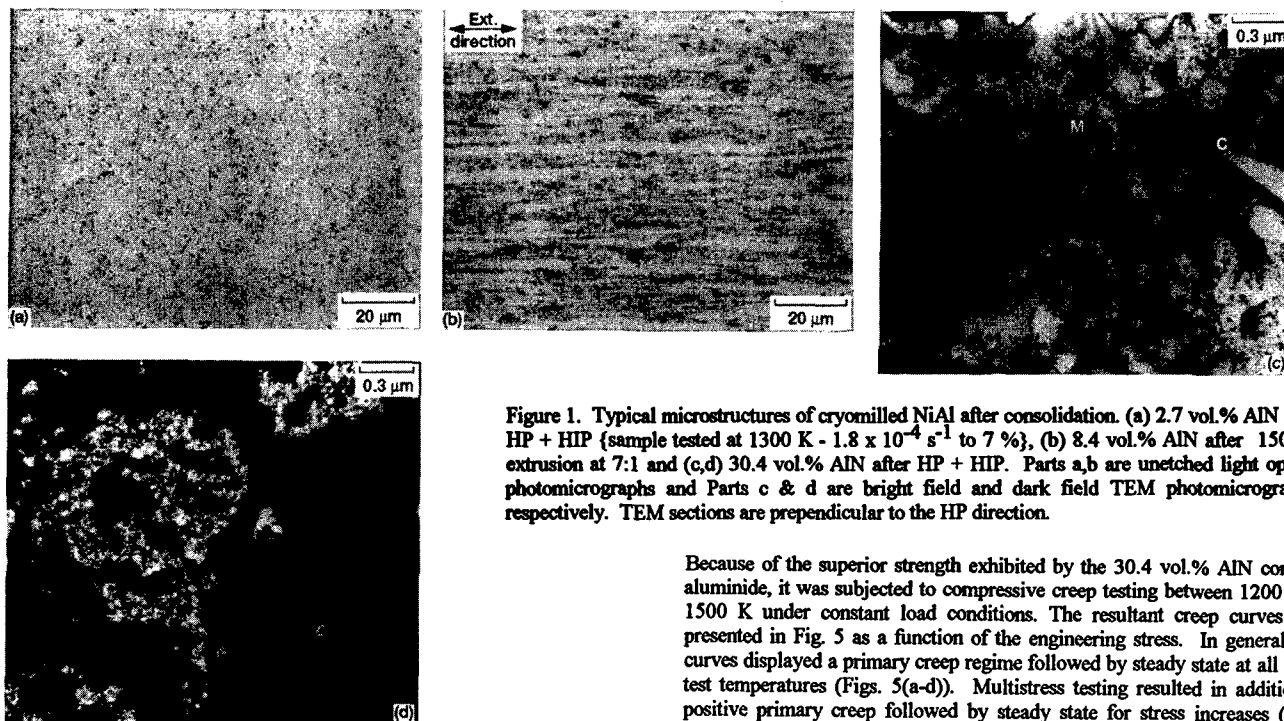


Figure 1. Typical microstructures of cryomilled NiAl after consolidation. (a) 2.7 vol.% AlN after HP + HIP {sample tested at 1300 K -  $1.8 \times 10^{-4} \text{ s}^{-1}$  to 7 %}, (b) 8.4 vol.% AlN after 1505 K extrusion at 7:1 and (c,d) 30.4 vol.% AlN after HP + HIP. Parts a,b are unetched light optical photomicrographs and Parts c & d are bright field and dark field TEM photomicrographs, respectively. TEM sections are perpendicular to the HP direction.

cryomilled NiAl [7,15] which contained 10.3 vol. % AlN (Table 1(b)) and had been hot extruded. The yield properties of this material were determined as part of this study following the procedures outlined above. Except for the near equivalence in strength for the 8.4 vol. % and the 10.3 vol. % materials above 750 K (Fig. 2), the yield strength at each temperature increased with the amount of AlN. Even a relatively small amount of aluminum nitride (2.7 vol. %, for example) was capable of doubling the yield strength of NiAl between room temperature and ~1100 K; however to significantly improve the elevated temperature properties, much greater amounts of AlN were needed (Fig. 2(b)).

#### Elevated Temperature Properties

**As-Densified Materials** – Typical stress - strain diagrams measured under constant velocity conditions are presented in Figs. 3 and 4. Regardless of the imposed nominal strain rates (Fig. 3) or test temperature (Fig. 4), strength was found to increase with increasing amounts of AlN. Additionally at each AlN level and temperature, strength decreased with decreasing strain rate (Fig. 4). In general terms the lowest AlN content material (2.7 AlN) exhibited very little work hardening which was then succeeded by continuous flow at a more or less constant stress (Fig. 3). The 8.4 and 30.4 vol.% AlN alloys, on the other hand, work hardened over the first few percent of deformation which either transitioned into a regime of very slow work hardening (Figs. 3 and 4(b)) or led to a maximum stress followed by strain softening (Figs. 3(a) and 4(a)).

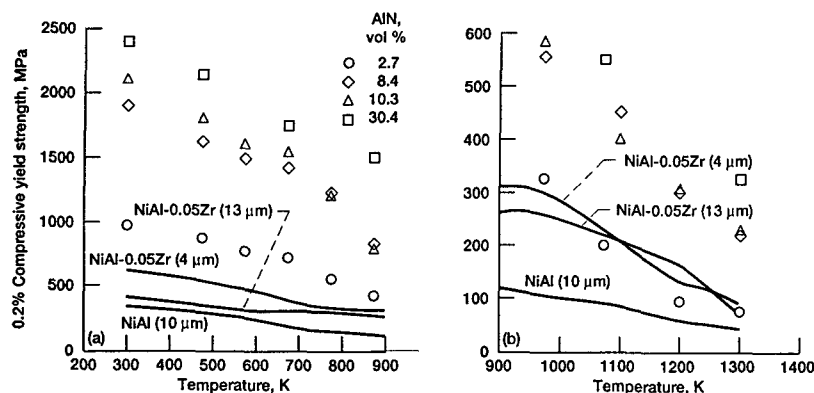


Figure 2. Temperature dependence of the 0.2 % compressive yield strength of cryomilled NiAl-based matrices containing various amount of AlN. (a) lower temperature behavior and (b) higher temperature behavior. Results for Ni-50.6Al and Ni-50.3Al-0.05Zr taken from [16].

Because of the superior strength exhibited by the 30.4 vol.% AlN content aluminide, it was subjected to compressive creep testing between 1200 and 1500 K under constant load conditions. The resultant creep curves are presented in Fig. 5 as a function of the engineering stress. In general the curves displayed a primary creep regime followed by steady state at all four test temperatures (Figs. 5(a-d)). Multistress testing resulted in additional positive primary creep followed by steady state for stress increases (Fig. 5(a)) and small contraction followed by apparent steady state for stress decreases (Fig. 5(d)).

True compressive flow stress ( $\sigma$ ) - strain rate ( $\dot{\epsilon}$ ) - temperature ( $T$ ) results for two alloys are given in Fig. 6, where constant velocity results are represented by values taken from the stress - strain diagrams at 3 % strain (for example Figs. 3 and 4) and the constant load creep results (Fig. 5) are portrayed by the steady state creep rate and average stress during steady state. In the case of the alloy containing 2.7 vol. % AlN (Fig. 6(a)) all the results could be described by a temperature compensated - power law (eqn (1));

$$\dot{\epsilon} = A \sigma^n \exp\left(\frac{-Q}{RT}\right) \quad (1)$$

where A is a constant, n is the stress exponent, Q is the activation energy and R is the universal gas constant. While the data for NiAl-30.4AlN at 1400 K and 1500 K (Fig. 6(b)) could also be well described by eqn (1), linear regression techniques suggested that a temperature compensated exponential law (eqn (2)) provided a better description of the lower temperature results for this alloy;

$$\dot{\epsilon} = A \exp(C\sigma) \exp\left(\frac{-Q}{RT}\right) \quad (2)$$

where C is a constant. Regardless of the mathematical description, the coincidence of the constant velocity and constant load data for the 30.4AlN

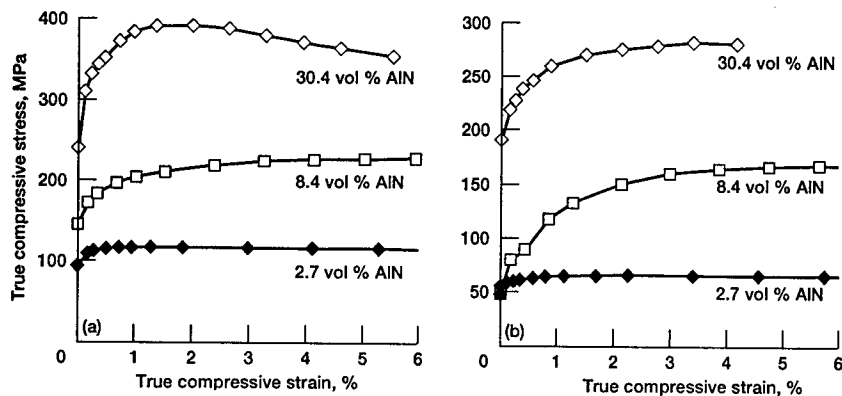


Figure 3. True compressive stress - strain curves obtained under constant velocity testing at 1300 K for cryomilled NiAl-based matrices containing various amount of AlN. Nominal strain rates of (a)  $2 \times 10^{-4} \text{ s}^{-1}$  and (b)  $2 \times 10^{-6} \text{ s}^{-1}$ .

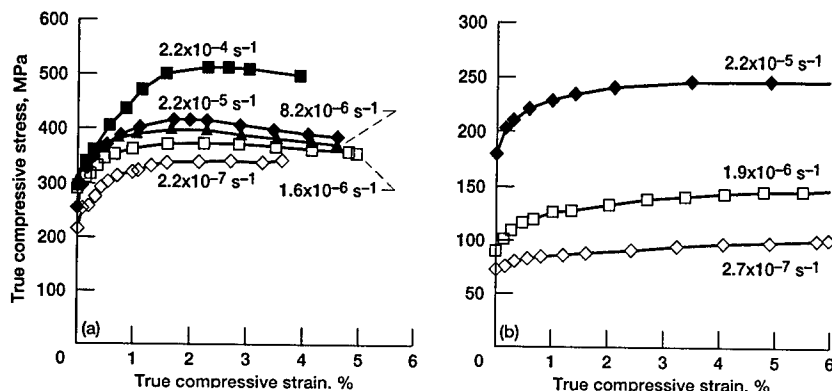


Figure 4. True compressive stress - strain curves for NiAl + 30.4AlN tested under constant velocity conditions at (a) 1200 K and (b) 1400 K as a function of nominal strain rate.

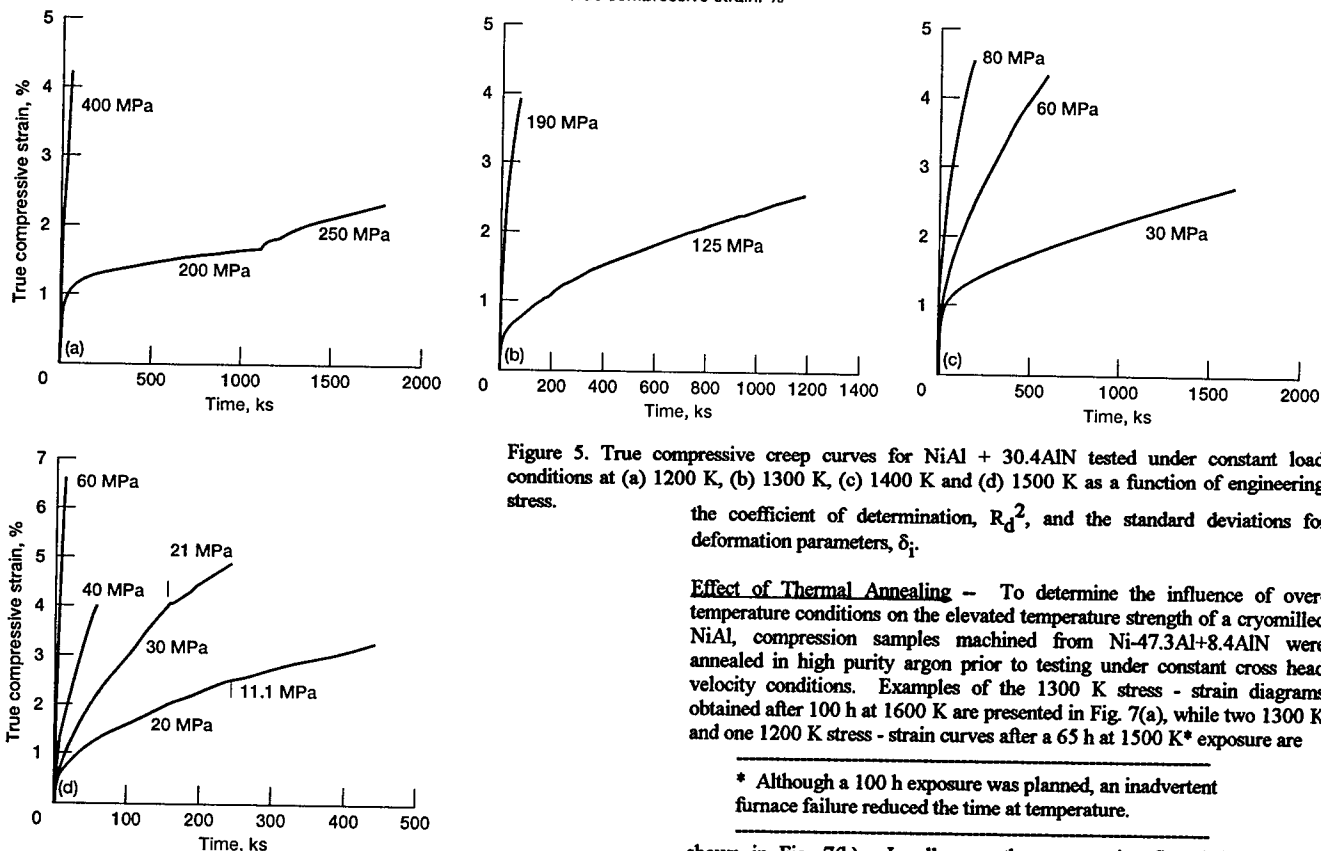


Figure 5. True compressive creep curves for NiAl + 30.4AlN tested under constant load conditions at (a) 1200 K, (b) 1300 K, (c) 1400 K and (d) 1500 K as a function of engineering stress.

the coefficient of determination,  $R_d^2$ , and the standard deviations for deformation parameters,  $\delta_i$ .

**Effect of Thermal Annealing** — To determine the influence of over-temperature conditions on the elevated temperature strength of a cryomilled NiAl, compression samples machined from Ni-47.3Al+8.4AlN were annealed in high purity argon prior to testing under constant cross head velocity conditions. Examples of the 1300 K stress - strain diagrams obtained after 100 h at 1600 K are presented in Fig. 7(a), while two 1300 K and one 1200 K stress - strain curves after a 65 h at 1500 K\* exposure are

\* Although a 100 h exposure was planned, an inadvertent furnace failure reduced the time at temperature.

shown in Fig. 7(b). In all cases the compressive flow behavior after annealing was essentially the same as that found in the as-consolidated material, where very minor work hardening or flow at an approximately constant stress occurred after the initial 1 to 2 % strain. Likewise in either the annealed or as-consolidated conditions, strength decreased with decreasing deformation rates and increasing temperature.

alloy at 1200, 1300 and 1400 K (Fig. 6(b)) suggests that both testing methods give the same response. This was statistically confirmed using a dummy variable in combination with linear regression techniques. Typical results of fits to eqns (1 and 2) are plotted in Fig. 6, and the deformation parameters for the three NiAl-AlN materials are given in Table 2 along with

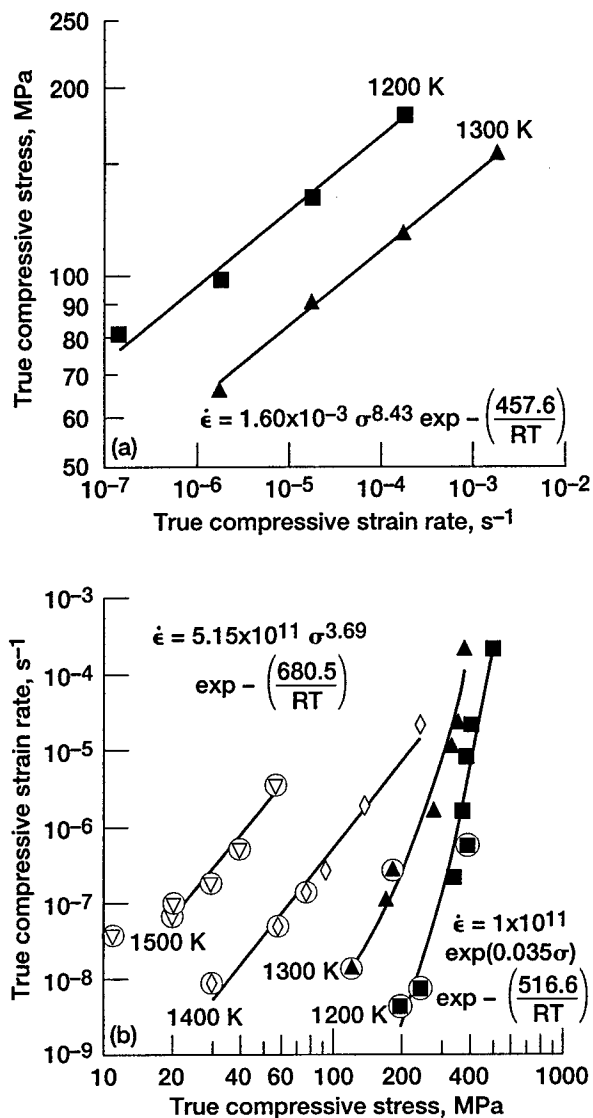


Figure 7. Behavior of as-extruded and heat treated NiAl + 8.4 AlN tested under constant velocity conditions. (a) True 1300 K compressive stress - strain curves for samples annealed 100 h at 1600 K; (b) true 1200 and 1300 K compressive stress - strain curves for samples annealed 65 h at 1500 K; and (c) true compressive flow stress - strain rate - temperature behavior for all three material conditions.

Although the general form of the stress - strain curves for the as-consolidated and annealed materials was similar, differences in strength levels were found. This is illustrated in Fig. 7(c) which presents the flow stress - strain rate - temperature data for the three different conditions. In this figure the solid symbols represent the data from 1300 K constant velocity tests while the open symbols report the 1200 K test results. Clearly prior heat treatment does reduce strength with exposure at 1600 K producing a more severe reduction than a 1500 K anneal. Use of a temperature compensated power law (eqn (1)) in combination with linear regression techniques and dummy variables revealed that heat treatments have no meaningful effect on either the stress exponent or the activation energy for deformation. This can be seen in (Tables 2(a,c)), where the deformation parameters  $n$  and  $Q$  for as-extruded Ni-47.3Al+8.4AlN are essentially the same for the joined results from the heat treated and as-extruded materials. The effect of prior elevated temperature exposure appears to simply produce an increase in the magnitude of the pre-exponential term  $A$  (Table 2(c)).

#### Microstructure Following Elevated Temperature Testing

Selected examples of the microstructures following constant velocity or

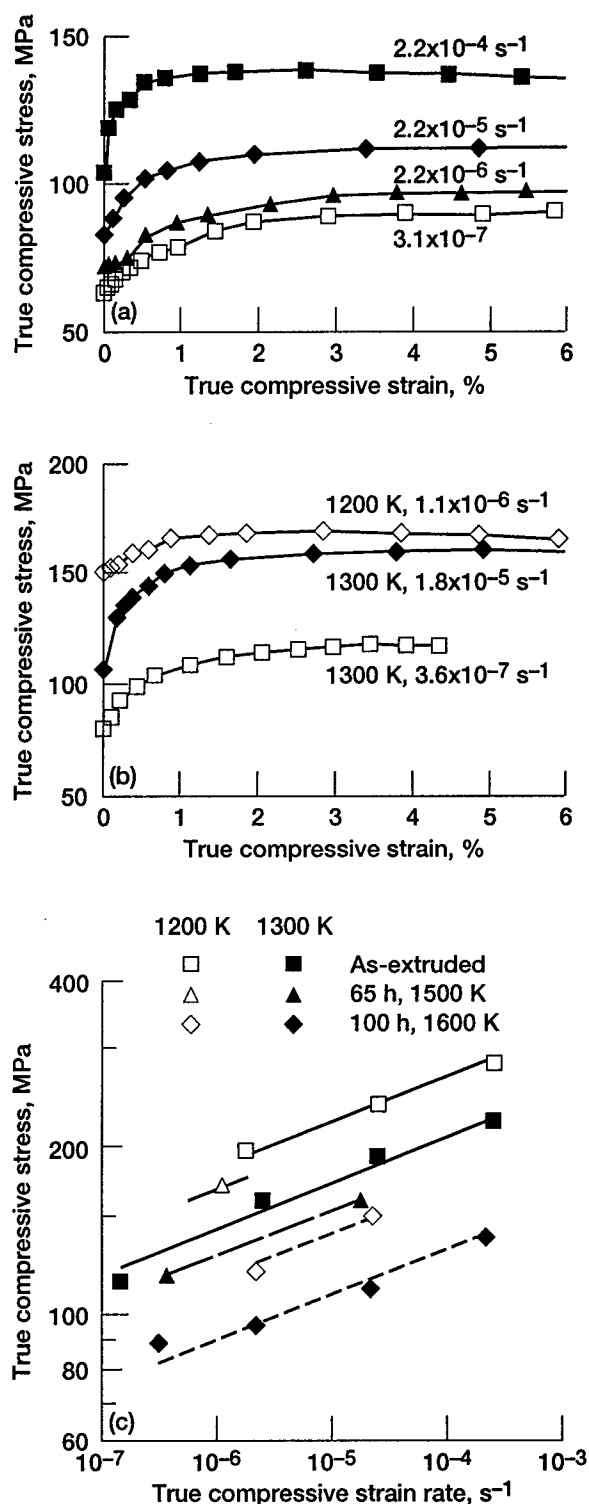


Figure 8. Light optical (a,b) and SEM (c) photomicrographs of NiAl + 30.4AlN compressed at elevated temperatures. (a) constant velocity testing at 1200 K -  $1.6 \times 10^{-6} \text{ s}^{-1}$  to 5.7 %, and (b,c) constant load creep testing at 1400 K and 30 MPa for 1.6 Ms to 2.7 %. Part (c) is an oxygen wave length dispersive map. The compression axis is horizontal.

Table 2. Temperature Compensated Power and Exponential Law Fits for Cryomilled NiAl Containing Various Amounts of AlN

(a) Power Law								(b) Exponential Law						
AlN, vol. %	Temperature Range, K	$A, s^{-1}$	$n$	$Q, kJ/mol$	$R_d^2$	$\delta_n$	$\delta_{Q_p}, kJ/mol$	Temperature Range, K	$A, s^{-1}$	$C$	$Q, kJ/mol$	$R_d^2$	$\delta_C$	$\delta_{Q_p}, kJ/mol$
2.7	1200 - 1300	$1.60 \times 10^{-3}$	8.43	457.6	0.98	0.36	29.8							
8.4	1200 - 1300	$6.40 \times 10^{-17}$	11.67	371.2	0.977	0.91	64.6							
30.4	1200 - 1300	$3.46 \times 10^{-8}$	9.05	495.7	0.87	1.0	101.2	1200 - 1300	$1.00 \times 10^{11}$	0.035	516.6	0.94	0.0026	69.5
30.4	1400 - 1500	$5.15 \times 10^{11}$	3.69	680.5	0.974	0.22	58.2	1400 - 1500	$7.87 \times 10^8$	0.0389	461.2	0.862	0.0051	113.2
10.3	1200 - 1400	$7.90 \times 10^{-10}$	13.1	640.4	-	-	-							

(c) Power Law for Ni-47.4Al + 8.4AlN Following Thermal Exposure									
Heat Treatment Condition	Temperature Range, K	$A, s^{-1}$	$n$	$Q, kJ/mol$	$R_d^2$	$\delta_n$	$\delta_{Q_p}, kJ/mol$		
As-extruded	1200 - 1300	$3.21 \times 10^{-17}$	12.3	398	0.968	0.71	42.5		
65 h at 1500 K	1200 - 1300	$1.2 \times 10^{-16}$							
100 h at 1600 K	1200 - 1300	$8.91 \times 10^{-15}$							

creep testing are presented in Figs. 8-10. Deformation at 1200 or 1300 K produced little change in the overall structure compared to the as-densified materials. Specifically the HP+HIP alloys (Figs. 8(a) and 9(a)) retained the nominally spherical particle-free NiAl cores surrounded by AlN enriched mantle, while the as-extruded material (Fig. 10(a)) displayed mantle covered elongated cigar shaped nitride-free cores. Compared to the as-densified state (Fig. 1(c)), TEM examination of 30.4AlN after creep testing for ~300 h at 1300 K (Fig. 9(a)), however, did indicate a slight coarsening of the AlN particles and NiAl grains within the mantle regions. Upon exposure to higher test temperatures a 'third' phase began to appear within the light optical microstructure of NiAl + 30.4AlN. This phase was just evident after overnight testing at 1400 K as an occasional small dark particle, but after 1500 K or extended 1400 K testing nodules of the third phase were quite pronounced under light optical conditions (Fig. 8(b)). SEM examination in the back scattered electron mode confirmed that the nodules were a second phase as opposed to voids or polishing artifacts. Energy dispersive spectroscopy (EDS) revealed that the nodules were composed of aluminum and oxygen, where this latter enrichment is illustrated by the oxygen X-ray map in Fig. 8(c). Because the EDS and wave length dispersive spectroscopy of the nodules failed to reveal measurable concentrations of elements other than Al and O, it is probable that the nodules are mainly alumina. In addition to the formation of the nodules, TEM study of 1400 K (Fig. 9(b)) and 1500 K (Fig. 9(c)) tested NiAl-30.4AlN samples indicated that the originally nanometer scale NiAl grains and AlN particles within the mantle coarsened to form submicron sized aluminide grains and nitrides.

Based on the light optical microstructures for 1200 K tested NiAl + 8.4AlN (Fig. 10), prior high temperature exposure can affect the mantle regions. Comparison of the as-extruded material (Fig. 1(b)) with that after 1200 K

testing (Fig. 10(a)) reveals that neither small amounts of deformation nor exposure at 1200 K affect the light optical microstructure of the consolidated alloy. On the other hand post test examination of a sample which had been heat treated for 65 h at 1500 K and then tested at 1200 K (Fig. 10(b)) indicates a changing microstructure. In particular the 1500 K anneal produced a definite decrease in the number of the small gray particles which are clearly part of the mantle in the as-extruded state (Figs. 1(b) and 10(a)). Furthermore after 100 h at 1600 K followed by 1200 K testing, the continuous distribution of fine gray particles has completely disappeared (Fig. 10(c)) and apparently has been replaced with linearly arrays of larger gray particles. This 1600 K heat treatment has also eliminated the elongated cigar shaped morphology of the NiAl cores which is clearly visible under less severe conditions (Figs. 1(b) and 10 (a,b)).

#### Fracture Toughness

The room temperature fracture toughnesses of cryomilled NiAl is presented in Fig. 11(a) as a function of the AlN content, where the 0, 2.7 and 30.4 vol.% AlN containing alloys were consolidated by hot pressing plus hot isostatic pressing while the 8.4 AlN material was hot extruded. These results reveal that toughness of cryomilled NiAl is essentially independent of the AlN content. Furthermore the fracture resistance of cryomilled NiAl is about the same as that of unreinforced NiAl, even when 30.4 vol. % AlN is present. Since none of the room temperature load - displacement curves generated during testing showed nonlinear behavior, little sub-critical crack growth occurred before fracture in these materials. Additionally SEM examination of fracture surfaces revealed that the predominant feature was transgranular cleavage.

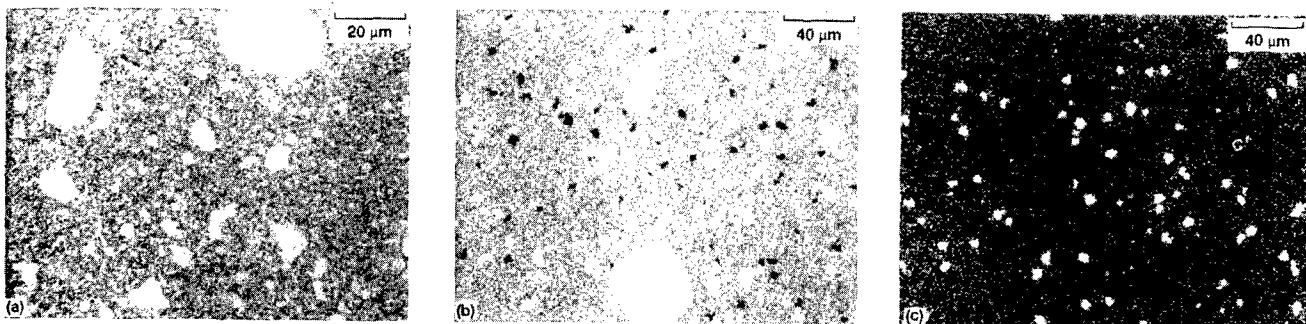


Figure 8. Light optical (a,b) and SEM (c,d) photomicrographs of NiAl + 30.4AlN compressed at elevated temperatures. (a) constant velocity testing at 1200 K and  $1.6 \times 10^{-6} s^{-1}$  to 5.7 %; (b-d) constant load creep testing at 1400 K and 30 MPa for 1.6 Ms to 2.7 %; Parts (c) and (d) illustrate the same region under back scattered electron imaging and oxygen wave length dispersive mapping, respectively. The compression axis is horizontal.



Figure 9. Transmission electron microscope photomicrographs of NiAl + 30.4AlN compressed at elevated temperatures. (a) constant load creep testing at 1300 K and 125 MPa for 1.2 Ms to 2.5 %; (b) constant load creep testing at 1400 K and 60 MPa for 0.6 Ms to 4.3 %, and (c) multistress constant load creep testing at 1500 K: 20 MPa for 44 ks to 2.5 % then 11 MPa for 198 ks for 0.7 % (total strain of 3.2 %). The compression axis is perpendicular to the plane of the photomicrographs.



Figure 10. Light optical photomicrographs of compressed NiAl + 8.4AlN. (a) as-extruded material after constant velocity testing at 1200 K and  $1.8 \times 10^{-6} \text{ s}^{-1}$  to 6.8 %; (b) heat treated at 1500 K for 65 h then subjected to constant velocity testing at 1200 K and  $1.1 \times 10^{-6} \text{ s}^{-1}$  to 6.3 %; and (c) heat treated at 1600 K for 100 h then subjected to constant velocity testing at 1200 K and  $2.2 \times 10^{-6} \text{ s}^{-1}$  to 9.5 %.

The toughnesses of an  $\sim 5 \mu\text{m}$  grain size, hot extruded (1200 K - 16:1) Ni-50Al [17] and a hot extruded (1300 K - 7:1) NiAl+30.4AlN are presented in Fig. 11(b) as a function of temperature. While neither material would be considered "tough" at room temperature; the data do demonstrate that extruded NiAl+30.4AlN is about 30 % tougher than extruded NiAl. Furthermore the 300 K toughness of the extruded NiAl+30.4AlN is about one and one half times that of the HP + HIP version of this material. Both extruded materials exhibit two regimes, where toughness is linearly dependent on temperature. Utilizing regression techniques the slopes of the lines were found to be about the same for both materials in each regime:  $\sim 0.062 \text{ MPa}\cdot\sqrt{\text{m}}/\text{K}$  at lower temperatures and  $\sim 0.2 \text{ MPa}\cdot\sqrt{\text{m}}/\text{K}$  at higher temperatures. Although the temperature dependencies are nominally the same, as can be visualized in Fig. 11(b), the transition temperatures were different for each alloy: about 510 K for NiAl and 725 K for NiAl+30.4AlN.

## Discussion

A number of factors should affect the mechanical strength of cryomilled NiAl-based materials: depending on the temperature and deformation rate, the composition and microstructure of the NiAl matrix as well as the size, distribution and amount of second phases (AlN,  $\text{Al}_2\text{O}_3$ , etc.) could all play a role.

### Lower Temperature/Faster Strain Rate Behavior

When considering quick deformation at lower temperature as exemplified by 0.2 % yield strengths (Fig.2), three factors can influence the strength of the matrix. Noebe et al.'s review [18] of binary, polycrystalline NiAl alloys indicates that the approximately 0.7 % absolute difference in Al content in the present four matrices (Table 1(b)) could result in a 80 MPa difference in lower temperature ( $T \leq 973 \text{ K}$ ) yield strengths. The very small amounts

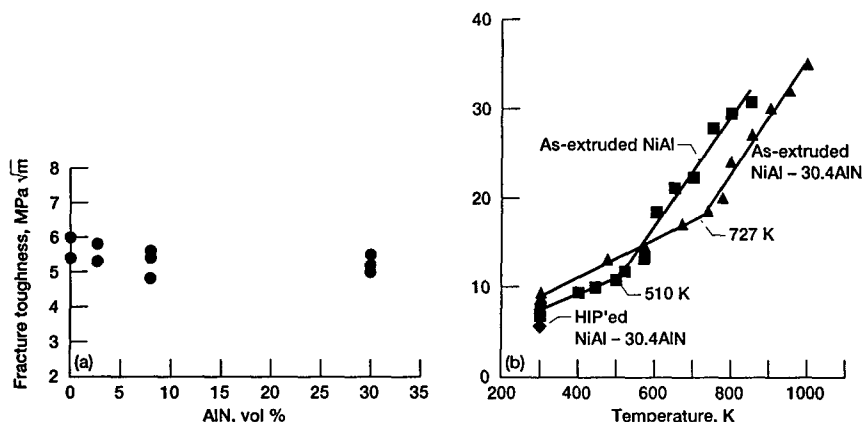


Figure 11. Fracture toughness and microstructure for cryomilled NiAl. Fracture toughness of (a) HP + HIP materials at room temperature as a function of the AlN content and (b) hot extruded NiAl + 30.4AlN and Ni-50Al [17] as a function of temperature.

( $\leq 0.1\%$ ) of Zr within some of the current materials (Table 1(a)) would also alter the mechanical properties, if Zr is in the form of a solid solution and/or an intermetallic second phase [16, 19, 20]. For example a 13  $\mu\text{m}$  grain size Ni-50.3Al-0.05Zr has compressive yield strengths ranging from 1.3 to 2.5 times greater than those for 10  $\mu\text{m}$  grain size binary Ni-50.6Al between room temperature and 1300 K, as is shown in Fig. 2. Lastly the small grain sizes of the matrix of the cryomilled materials, especially the nanocrystalline NiAl grains in the mantle regions, could vastly increase the lower temperature yield strengths. This factor can be readily visualized in Fig. 2, where the 4  $\mu\text{m}$  Ni-50.3Al-0.05Zr is much stronger than its 13  $\mu\text{m}$  version up to 1100 K.

In spite of the above precautions that the microstructure and composition of matrix could have a very large influence on the yield strength of cryomilled NiAl, the practical effect of the matrix properties, and for that matter the size/distribution of the ceramic phases, appears to be secondary to the amount of AlN. Since the yield strength is clearly dependent on the AlN content and temperature (Fig. 2), the data were fitted to the simple equation

$$\ln(\text{YS}) = \alpha \cdot T + \beta \cdot \ln(\% \text{ AlN}) \quad (3)$$

where YS is the yield strength in MPa, % AlN is the volume percentage of the aluminum nitride and  $\alpha$ ,  $\beta$  are constants. When viewed on a logarithmic scale, the yield strength data split into two temperature dependent regimes: above and below 800 K. Hence equation (3) was fitted to both regimes and the results are illustrated in Fig. 12, where the AlN volume fraction normalized yield strength is shown as a function of temperature along with the appropriate predictive equations and their coefficients of determination. Other attempts to fit the yield strength to more complicated relations involving, for example:  $1/T$ , the total second phase content of ceramics {volume % of  $(\text{AlN} + \text{Al}_2\text{O}_3 + \text{ZrO}_2)$ }, etc., resulted in descriptions of behavior which were no better or even worse than eqn (3).

Fig. 12 indicates that eqn (3) can reasonably predict the yield strength of cryomilled NiAl at any temperature solely on the amount of AlN, where the estimates are better above 800 K than below 800 K. Since the two Zr-free cryomilled alloys (8.4AlN and 10.3AlN, Table 1) are stronger in the lower temperature regime than either 2.7AlN or 30.4AlN which contained Zr (Table 1), one can conclude that the original assumption of Zr forming oxides (or possibly nitrides) in the cryomilled materials (Table 1(b)) is correct. Likewise the AlN volume fraction normalized results (Fig. 12) signify that the small differences in matrix Al content (Table 1(b)) play little role on yield strength. It is possible, however, that grain size, which is affected by the densification technique, might exert some influence on yield strength below 800 K since the extruded 8.4AlN and 10.3AlN alloys are generally stronger than either of the two HP + HIP materials (2.7AlN or

30.4AlN). While both densification methods do maintain nanocrystalline NiAl grains within the mantle (Figs. 1(c,d) for HP + HIP materials and [7, 8] for hot extruded alloys), extrusion refines the lateral dimensions of the AlN-free NiAl cores in comparison to those in hot isostatic pressed alloys. Such a refinement in the effective grain size could lead to an additional low temperature strengthening via Hall-Petch behavior.

It is also probable that extrusion could affect the toughness of cryomilled NiAl, where it can be seen (Fig. 11(b)) that the room temperature value for hot extruded 30.4AlN is approximately 50 % greater than that for HP + HIP material. The 7:1 reduction during 1300 K extrusion would introduce greater amounts of work into material than HP + HIP. Thus it is likely that some mobile dislocations remain after extrusion, and they should improve the toughness.

Comparison of the toughness results for NiAl and 30.4AlN in Fig. 11(b) indicates that both alloys have the same temperature dependency above and below their transition temperatures. This strongly suggests that cryomilled NiAl essentially behaved as pure NiAl except that the addition of a large amount of ceramic second phase increased the brittle to ductile transition temperature (BDTT). As the BDTT in polycrystalline NiAl [16,18] is related to the climb of  $\langle 001 \rangle$  dislocations, an increase in the transition temperature for cryomilled materials should be expected since these alloys are so much stronger than binary NiAl (Fig. 2 and [8]). Clearly the AlN particles in cryomilled NiAl must affect dislocation mobility and additional energy in the form of higher temperature would be required to overcome their pinning effects [18].

#### Higher Temperature/Slower Strain Rate Behavior

Like the lower temperature properties, third element alloying, Al content and microstructure can also affect the elevated temperature deformation behavior of the NiAl matrix. Although 0.12Zr would improve the creep strength of NiAl if this third element was in the form of a solid solution and/or an intermetallic second phase [20], the yield strength results (Fig. 12) strongly suggest that this is not the case. Additionally another high temperature deformation study [21] involving cryomilled NiAl+Zr alloys, did not reveal any strengthening effects which were attributable to Zr within the NiAl matrix. Thus the only possible chemistry effect in the current cryomilled materials (Table 1(b)) lies in the Al level of the matrix, but it has already been shown that NiAl containing from 50.6 to ~44Al have nearly identical elevated temperature plastic flow properties at and above 1100 K [22,23]. While matrix composition does not appear to influence strength, the NiAl grain size could be important. Examples of a decreasing grain size producing an increased creep strength or a reduced creep strength have been observed in NiAl [22-24]. These results suggest that the nanocrystalline NiAl would be very weak when grain boundary deformation can easily occur. If, however, grain boundary creep mechanisms are blocked, then a nanocrystalline NiAl could be very strong. Clearly the present results (Figs. 3-7) indicate that the AlN particles overcome any weakening tendency of grain boundaries and provide effective strengthening under creep conditions.

A number of other studies have shown that uniformly distributed "inert" second phase particles will increase the creep resistance of NiAl-based matrices. For example micron sized  $\text{TiB}_2$  particles were shown to act as barriers to dislocation motion and/or stabilize cold-work like dislocation structures [25], where elevated temperature strengthening scaled with the volume fraction of  $\text{TiB}_2$ . Dispersion strengthening through nanometer sized particles has also been found in a number of NiAl alloys [26,27]; however, such dispersion strengthening now appears to be the result of stabilization of a nonequilibrium subgrain size [24] rather than the result of a dislocation-particle attraction.

Following the example of eqn (3), the elevated temperature strain rate-flow stress results for the various cryomilled NiAl's were fitted to

$$\dot{\epsilon} = A \sigma^n (\% \text{ AlN})^p \exp\left(-\frac{Q}{RT}\right) \quad (4)$$

where  $p$  is an exponent describing the volume fraction dependency. Results, including appropriate mathematical descriptions and coefficients of determination, from the constant temperature form of eqn (4) are presented

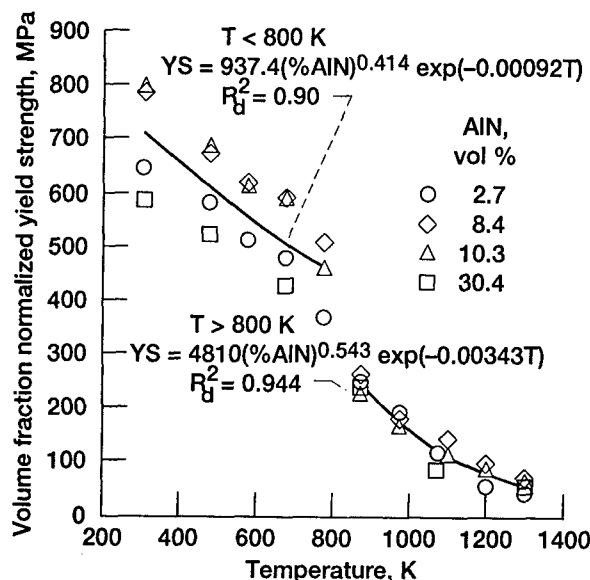


Figure 12. AlN volume fraction normalized yield strength for cryomilled NiAl as a function of temperature.



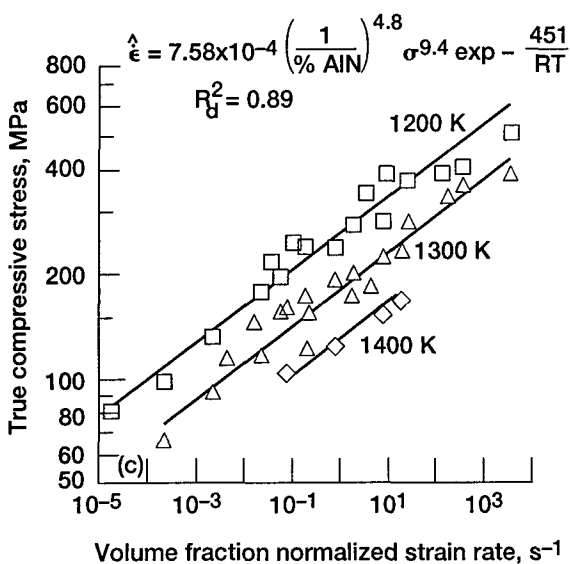
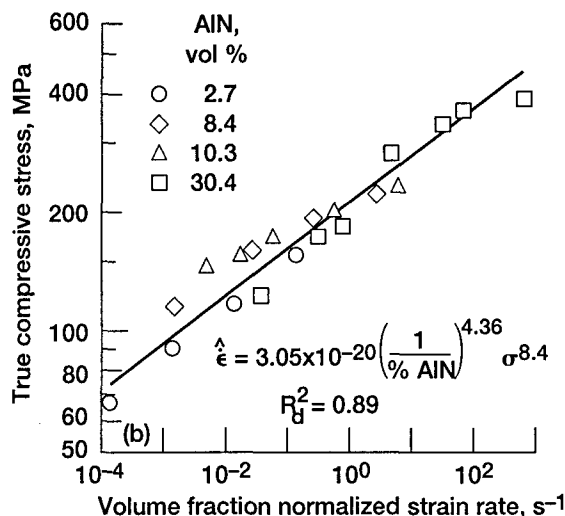
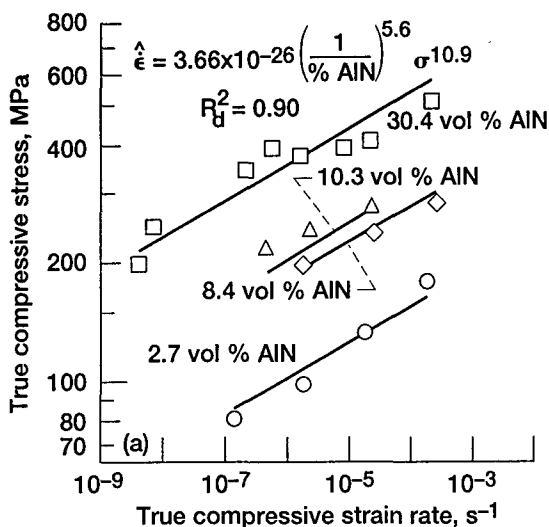


Figure 13. Effect of AlN volume fraction on the elevated temperature flow strength - strain rate behavior of cryomilled NiAl as a function of temperature. (a) 1200 K, (b) 1300 K and (c) 1200 - 1400 K.

$$\sigma = \frac{\epsilon^{1/n} \{A \exp(-Q/RT)\}^{-1/n} (\% \text{ AlN})^{-p/n}}{RT} \quad (5)$$

where  $-p/n$  is about 0.5 for testing between 1200 and 1400 K (Fig. 13). Therefore in spite of inhomogeneous microstructures, somewhat differing matrix compositions and small amounts of additional second phases, the compressive strength of cryomilled NiAl at any temperature is essentially proportional to the square root of the AlN content.

#### Effect of Temperature on Microstructure and Properties

The mechanical properties of 8.4 AlN in Fig. 7 reveal that prior exposure at 1500 or 1600 K will reduce the effective strength of cryomilled NiAl. Such reductions are due to changes in the AlN and matrix morphology within the mantle regions, where annealing produced growth from nanometer dimensions to submicron sizes in both phases [8]. Even on a light optical level (Fig. 10), it is clear that very high temperature exposure affects the microstructure of cryomilled NiAl. Although exposure does lessen the mechanical strength of cryomilled NiAl, Fig. 7 demonstrates that the losses are not catastrophic. Even after a prior exposure of 100 h at 1600 K, the effective strength is about 60 % of that measured for the as-extruded alloy. While such a degradation is not minimal, it should be noted that this exposure exceeds the expected maximum useful short term life under oxidizing conditions (100 h at 1573 K) and is far in excess of 1473 K which is the estimated maximum temperature for long term oxidative cyclic life [28]. Certainly a more reasonable exposure, as typified by 65 h at 1500 K (Fig. 7, Table 2), results in only a small reduction of strength (~10 %).

Although the appearance of 1400 and 1500 K tested 30.4AlN (Figs. 8(b,c) and Fig. 9(b,c)) indicates that very high temperature exposure under load can also significantly alter the microstructure, neither 1200 or 1300 K testing (Fig. 8(a) and Fig. 9(a)) produced large alterations from the as-consolidated structure (Fig. 1(c,d)). Microstructural changes in the AlN and NiAl within the mantle regions certainly should affect mechanical properties and probably are, at least partially, responsible for the change in deformation parameters and behavior in NiAl-30.4AlN (Table 2 and Fig. 6(b)) found when comparing 1200 - 1300 K results to those for 1400 - 1500 K. Extensive testing of NiAl-10.3AlN between 1200 and 1500 K [8,29] has yielded somewhat similar mechanical behavior. In this alloy two temperature compensated power law deformation regimes were found, where under lower temperature/fastest strain rate conditions the stress exponent was about 13 and approximately half this value (~6) after higher temperature/slower strain rate deformation. A similar separation into two power law regimes was observed by Aikin et al. [12] during 1300 K testing of cryomilled nominally Ni-45Al-13AlN-1Al<sub>2</sub>O<sub>3</sub>. While TEM [30] indicated that both the NiAl grains and AlN particles within the mantle grew

in Fig. 13 (a,b) and the fit of all the 1200 - 1400 K results to eqn (4) is shown in Fig. 13(c). The 1200 K strain rate - flow stress behavior shown in Fig. 13(a) directly demonstrates that creep strength increases with the AlN content, while Fig. 13(b) illustrates the ability of eqn (4) to collapse all the 1300 K data onto a single curve when flow stress is plotted as a function of volume fraction normalized strain rate. Fitting (Fig. 13(c)) of the 1200 - 1400 K results for the four different alloys to eqn (4) results in a stress exponent which is intermediate to those determined for either the 1200 or 1300 K fits (Fig. 13(a,b)) or power law fits for each composition (Table 2(a)). Likewise the activation energy given in Fig. 13(c) is intermediate to the activation energies for individual compositions (Table 2(a)). While the fits of the strain rate - flow stress - AlN volume fraction - temperature results in Fig. 13 are only reasonable with coefficients of determination on the order of 0.9, it must be considered that the current approach (eqn (4)) neglects other variables which should influence strength: such as the elastic modulus of the cryomilled NiAl's containing differing amounts of AlN, the inhomogeneity of the microstructure, and the AlN particle size/distribution parameters.

Comparison of the results in Fig. 12 to those in Fig. 13 reveals that measures of strength for cryomilled NiAl are, for all practical purposes, proportional to the square root of the AlN content. This behavior can be directly seen in mathematical descriptions for yield strength on Fig. 12, and through rearrangement of eqn (4) flow strength can be shown to be proportional to the AlN volume fraction raised to the power  $-p/n$ , or

significantly during long term testing but not during short term testing, basically the same dislocation structure (subgrains and/or networks within the NiAl cores) was observed irrespective of the value of the stress exponent. To date no unequivocal reasons for changes in deformation mechanism during the elevated temperature deformation of cryomilled NiAl have been obtained.

In addition to changes in the AlN and NiAl within the mantle regions after high temperature exposure, large nodules of  $Al_2O_3$  could be seen in 1400 and 1500 K tested 30.4AlN (Figs. 8(b,c)). Similar large alumina particles were found within Ni-47.3Al-10.3AlN by Lowell et. al [28] after 100 h - 1573 K cyclic oxidation testing, and they also appear to exist in 1500 & 1600 K exposed 8.4AlN (Figs. 10(b,c)). It is our belief that  $Al_2O_3$  is always present in cryomilled NiAl, but its generally low volume fraction and size make it difficult to identify in as-densified materials by X-ray or TEM methods. Most probably the large nodules of alumina are simply the product of Oswald ripening at elevated temperature, as Pyo et. al [31] have observed coarsening of  $Al_2O_3$  dispersoids in a NiAl matrix after short term (< 4 h) 1273 K densification processing.

Hebsur et. al [11] have produced an oxygen-rich NiAl by cryomilling with a gaseous air plus nitrogen atmosphere in the attritor vessel and a nitrogen-rich NiAl by cryomilling with liquid nitrogen in the attritor vessel. X-ray diffraction study of 1473K - 12:1 extruded alloys identified only NiAl and  $Al_2O_3$  in the oxygen-rich material and only NiAl and AlN in the nitrogen-rich material. These results were confirmed by TEM examination, where the oxygen-rich material contained ~0.5  $\mu$ m diameter alumina particles while the nitrogen-rich material possessed 5 to 100 nm AlN particles. In terms of overall chemistry, the matrix composition/second phase content of these two alloys were calculated to be respectively, Ni-48Al with 4.0 vol. %  $Al_2O_3$  + 0.5 vol. % AlN and Ni-47.3Al with 8.3 vol. % AlN + 1.1 vol. %  $Al_2O_3$ . Together the observations suggest that any oxygen pick-up during cryomilling will combine with Al to form alumina, but this oxide will not be detectable by X-ray or TEM unless the volume fraction is sufficiently large. Prolonged high temperature exposure of cryomilled NiAl simply allows the existing alumina to grow to sizes which can then be easily seen under light optical conditions.

#### Summary of Results

Study of the mechanical strength properties of as-cryomilled NiAl alloys containing various amounts of several second phases indicates that both the yield strength and elevated temperature creep strength are proportional to the square root of the AlN content. With the one possible exception, factors such as AlN particle size and distribution, other second phases, Al content of the matrix, the inhomogeneity of the microstructure and elastic modulus do not appear to exert any significant influence on mechanical properties. Lower temperature yield strength (<800 K) suggests that densification technique might be important through refinement of NiAl core dimensions. Post exposure testing of cryomilled NiAl after annealing at 1500 and 1600 K indicates that very high temperature heat treatments are detrimental; however the loss of mechanical strength is not catastrophic. As opposed to the strength properties, the fracture toughness of cryomilled NiAl is independent of amount of AlN

#### Acknowledgement

This work was supported under the HSCT/EPM and HITEMP programs at NASA-Lewis Research Center, Cleveland, Ohio. The authors would also like to acknowledge I.E. Locci for heat treating several alloys in Ar at elevated temperature.

#### References

1. R. Darolia. *JOM* 43(3) 44.
2. I.E. Locci, R.D. Noebe, R.R. Bowman, R.V. Miner, M.V. Nathal and R. Darolia. *High Temperature Ordered Intermetallic Alloys IV*, Vol. 213 (eds. L.A. Johnson, D.P. Pope and J.O. Stiegler) Materials Research Society, Pittsburgh, PA, 1991 pp. 1013-18.
3. I.E. Locci, R. Dickerson, R.R. Bowman, J.D. Whittenberger, M.V. Nathal and R. Darolia. *High-Temperature Ordered Intermetallic Alloys V*, Vol. 288, (eds. I. Baker, R. Darolia, J.D. Whittenberger and M.H. Yoo), Materials Research Society, Pittsburgh, PA, 1993, pp. 685-90.
4. W.S. Walston, R.D. Field, J.R. Dobbs, D.F. Lahrman and R. Darolia. *Structural Intermetallics*, eds. R. Darolia, J.J. Lewandowski, C.T. Liu, P.L. Martin, D.B. Miracle and M.V. Nathal, TMS, Warrendale, PA, 1993, pp. 523-32.
5. E. Arzt and P. Grahle. *High-Temperature Ordered Intermetallic Alloys VI*, Vol. 364, Part 1; (eds. J.A. Horton, I. Baker, S. Hanada, R.D. Noebe and D.S. Schwartz), Materials Research Society, Pittsburgh, PA, 1995, pp. 525-36.
6. P. Grahle. "Mechanisches Legieren, Gefüge und Kriechverhalten dispersiongehärtet NiAl- Werkstoffe" PhD. Thesis, University of Stuttgart and Max-Planck Institut für Metallforschung, Stuttgart, 1995.
7. J.D. Whittenberger, E. Arzt and M.J. Luton. *J. Mat. Res.* 5 (1990) 271-77.
8. J.D. Whittenberger. *Structural Intermetallics*, (eds. R. Darolia, J.J. Lewandowski, C.T. Liu, P.L. Martin, D.B. Miracle and M.V. Nathal) TMS, Warrendale, PA 1993, pp. 819-28.
9. M. G. Hebsur, J.D. Whittenberger, C.E. Lowell and A. Garg. *High-Temperature Ordered Intermetallic Alloys VI*, Vol. 364, Part 1; (eds. J.A. Horton, I. Baker, S. Hanada, R.D. Noebe and D.S. Schwartz), Materials Research Society, Pittsburgh, PA, 1995, pp. 279-84.
10. J.D. Whittenberger and M.J. Luton. *J. Mater. Res.* 10 (1995) 1171-1186.
11. M.G. Hebsur, J.D. Whittenberger, R.M. Dickerson and B.J.M. Aikin. *High Temperature Ordered Intermetallic Alloys -V*, (eds I. Baker, R. Darolia, J. D. Whittenberger, and M. H. Yoo), Vol. 288, Pittsburgh PA, Materials Research Society, 1993, pp 1111-16.
12. B.J.M. Aikin, J.D. Whittenberger, and M.G. Hebsur. *Proc. 2<sup>nd</sup> Internat. Conf. on Structural Applications of Mechanical Alloying*, (eds J.J. deBarbadillo and F.H. Froes), ASM International, Metals Park, OH, 1993, pp. 283-90.
13. M.G. Hebsur, J.D. Whittenberger, C.E. Lowell. U.S. Patent Application 238767, May 5, 1994.
14. J.I. Blum. *Eng. Frac. Mech.*, 7 (1975) 593-604.
15. J.D. Whittenberger. E. Arzt and M.J. Luton. *J. Mat. Res.* 5 (1990) 2819-27.
16. R.R. Bowman, R.D. Noebe, S.V. Raj and I.E. Locci. *Metall. Trans. A* 23A (1992) 1493-1508.
17. R.D. Noebe, M.G. Hebsur, J.D. Whittenberger, M.V. Nathal and B. Oliver. NASA CP-10146, 1994, pp. 54:1 - 54:14.
18. R.D. Noebe, R.R. Bowman and M.V. Nathal. *Inter. Mater. Rev.* 38 (1993) 193-232.
19. S.V. Raj, R.D. Noebe and R. Bowman. *Scripta Met.* 23 (1989) 2049-54.
20. J.D. Whittenberger and R.D. Noebe. *Metall. Mater. Trans. A* 27A (1996) 2628-41.
21. J.D. Whittenberger and M.J. Luton. *J. Mater. Res.* 7 (1992) 2724-32.
22. J.D. Whittenberger. *J. Mat. Sci.* 22 (1987) 394-402.
23. J.D. Whittenberger. *J. Mat. Sci.* 23 (1988) 235-40.
24. J.D. Whittenberger, R.D. Noebe and A. Garg. *Metall. Mater. Trans. A* 27A (1996) 3170-80.
25. J.D. Whittenberger, R. K. Viswanandham, S.K. Mannan and B. Sprissler. *J. Mat. Sci.* 35 (1990) 35-44.
26. J.D. Whittenberger, D.J. Gaydos and K.S. Kumar. *J. Mat. Sci.* 25 (1990) 2771-76.
27. J.D. Whittenberger, R. Ray and S.C. Jha. *Mat. Sci. Eng.* A151 (1992) 137-46.
28. Carl E. Lowell, Charles A. Barrett and J.D. Whittenberger. *Intermetallic Matrix Composites*, Vol. 194, (eds. D.L. Anton, P.L. Martin, D.B. Miracle and R. McMeeking), Materials Research Society, Pittsburgh, PA, 1990, pp. 355-60.
29. J.D. Whittenberger, Eduard Arzt and Michael J. Luton. *Scripta Metall. et Mater.* 26 (1992) 1925-30]
30. A. Garg, J.D. Whittenberger, and B.J.M. Aikin. *Intermetallic Composites III*, Vol. 350, (eds. J.A. Graves, R.R. Bowman, and J.J. Lewandowski), Materials Research Society, Pittsburgh, PA, 1994, pp. 231-36.
31. S.G. Pyo, N.J. Kim and P. Nash. *Mater. Sci. Eng.* A181/A182 (1994) 1169-73.

EFFECT OF CHEMISTRY, MICROSTRUCTURE AND ORIENTATION ON 1100 - 1400 K  
PLASTIC FLOW PROPERTIES OF Hf-DOPED NiAl SINGLE CRYSTALS

J. Daniel Whittenberger,<sup>1</sup> Anita Garg,<sup>2</sup> R.D. Noebe,<sup>1</sup> W. Scott Walston<sup>3</sup> and R. Darolia<sup>3</sup>

<sup>1</sup> NASA Lewis Research Center, Cleveland, OH

<sup>2</sup> AYT Corporation at NASA Lewis Research Center, Cleveland, OH

<sup>3</sup> General Electric Aircraft Engines, Cincinnati, OH

**Abstract**

A study of the 1100 -1400 K elevated temperature deformation properties of three NiAl-0.5Hf single crystal alloys containing differing amounts of Si and Ti has been conducted. This work indicates that higher Si contents in combination with a small amount of Ti leads to the precipitation of a high density of fine and coherent G-phase precipitates which maximize strength properties to at least 1300 K. Although prior thermal exposure can dissolve the G-phase precipitates in low Si-content alloys, such heat treatments only somewhat weaken the high temperature strength under faster deformation conditions. The <001> orientation appears to maintain a slight strength advantage over the <110> orientation under slower strain rate conditions.

**Introduction**

Although the B2 aluminide NiAl has potential for use as a high temperature structural material in advanced gas turbine engines, its lack of high temperature strength is a serious problem. One approach to improve the elevated temperature mechanical properties of NiAl has been the development of single crystal technology coupled with small alloying additions. Indeed results [1] have shown that the tensile creep rupture properties of <110> oriented NiAl crystals doped with 0.5 at. % Hf or Ta can approach those of Ni-based superalloys. Such strength levels are remarkable in view of the very low third element content, the "soft" non <001> testing direction, and the extreme weakness of binary NiAl crystals under similar test conditions. While it was speculated in [1] that the enhanced strength in the Hf or Ta-doped NiAl single crystals was the result of both solid solution and precipitation hardening, the influence of initial microstructure, second phase content, crystal orientation, impurity content, etc. was not well understood.

Recent elevated temperature results for NiAl-based single crystals containing multiple low alloying additions have been reported in a U.S. patent [2], and this work indicates that significant increases in strength over those produced by single element additions of Hf or Ta [1] can be achieved. Of the many compositions discussed in [2], <110> oriented single crystals of

alloy D218 with the approximate chemistry of 50Ni-0.2Ga-0.5Hf-1.0Ti-Al (at. %) produced the best combination of properties in terms of stress rupture life at 1155 K - 276 MPa and room temperature fracture strength. The elevated temperature strength in this alloy was thought to evolve from both the solid solution effects and second phase precipitates such as the Heusler phase Ni<sub>2</sub>AlHf within the NiAl matrix. Furthermore it was noted in [2] that essentially all the NiAl single crystals contained upwards of 1000 parts per million by weight (wppm) Si which derived from unintentional, and essentially unavoidable, reactions between the melt and mold materials. Such Si contributed to the formation of NiHfSi and G-phase (Ni<sub>16</sub>Hf<sub>6</sub>Si<sub>7</sub>) precipitates within the NiAl matrix [3] thereby directly lowering the volume fraction of the primary Ni<sub>2</sub>AlHf particles.

Since the amount of Si can not be strictly controlled, then batch to batch variations in mechanical properties are likely to result in spite of consistent single crystal growth parameters and heat treating conditions. Because of this uncertainty, <001> and <110> oriented D218 monocrystal samples possessing slightly different Si impurity levels and remarkably different initial distributions of second phases within the matrix were tested between 1100 and 1400 K. Additionally to probe the role of Ti as a strengthening agent, a few <110> oriented D176 single crystal samples, which contain the same amount of Hf but no Ti and slightly less Ga than D218, were tested at 1300 K and examined. This study documents the effects of chemistry, microstructure, and orientation on the elevated temperature plastic flow properties of Hf-doped NiAl single crystals and attempts to draw conclusions as to the operating strengthening and deformation mechanisms.

**Experimental Procedures**

NiAl-based D176 and D218 single crystal ingots, approximately 28 by 25 mm in cross section by 96 mm in length, were grown by a Bridgman technique [4] and given a 50 h - 1590 K homogenization heat treatment followed by furnace cooling. Nominal 8 mm long by 4 mm diameter cylindrical compression samples were then machined from the ingots by a combination of electrodischarge machining and centerless grinding. Specimens were oriented with either the <110> or <001> directions parallel

to the sample length. While the D176 and D218 <110> samples were only tested in the as-homogenized condition, D218 <001> specimens were tested in the as-homogenized condition and after homogenization plus a 100 h - 1300 K aging treatment. Compressive properties were determined between 1100 and 1400 K in air under constant velocity conditions in a universal testing machine operating from  $1.27 \times 10^{-2}$  to  $8.5 \times 10^{-7}$  mm/s. Load was autographically recorded as a function of time during each compression test, and the load - time charts were converted to true stress and true plastic strain via an offset method and the assumption of conservation of volume.

Alloy chemistry was determined by inductively coupled plasma techniques (Al, Ga, Hf, Ti, Ni), ultraviolet/visible spectrophotometry (Si) and combustion methods (C, N, O, S). The initial microstructures of as-homogenized D218 and D176 single crystals were characterized by transmission electron microscopy (TEM); in addition a number of compression tested samples were selected for in-depth TEM analysis to determine differences in second phase structure ascribable to alloy chemistry and the combined effects of heat treatment, deformation and temperature. Slices for TEM were sectioned from 3 mm diameter cylinders machined from the as-received and tested samples. These were mechanically ground and electropolished in a twin-jet Tenupol-3 polisher using a solution of 70% ethanol, 14% distilled water, 10% butylcellosolve, and 6% perchloric acid cooled to 263K. An applied potential of 20-25 V with a corresponding current of 10-15 mA produced electron transparent foils. Microstructural examination, trace analysis and energy dispersive X-ray spectroscopy (EDXS) were carried out in a Philips 400T TEM equipped with a double-tilt goniometer and a KEVEX Si/Li X-ray detector.

## Results

### As-Homogenized Materials

The compositions of the three single crystals examined in this study are given in Table 1. Because the single crystal growth process can never be exactly duplicated, chemical analysis of the ingots revealed slightly different compositions between the two D218 ingots (Table 1). With the exception of Al and Si contents, both D218-2000 and -2063 have essentially identical

compositions. Of these differences, the slight variation in Al level (0.3 at %) is well within the expected error for chemical analysis of high Al containing materials [5] and, even if real, should have little influence on the elevated temperature properties of NiAl-based single crystals [5,6]. On the other hand the observed difference in Si level, which is due to unintentional reactions between the melt and the alumina-silicate mold during Bridgman processing, is real and can be potentially important as it will affect the size, distribution and density of the Heusler particles as well as the Si-containing precipitates. Except for the absence of Ti and the lesser Ga content, Table 1 indicates that D176-1910 has almost the same chemistry as the D218 ingots.

Examination of the as-homogenized alloys in the TEM (Fig. 1) showed that, in general, three second phases can occur in these alloys: submicron size Heusler ( $\text{Ni}_2\text{AlHf}$ ) and  $\text{NiHfSi}$  particles and nanometer size G-phase ( $\text{Ni}_{16}\text{Hf}_6\text{Si}_7$ ) precipitates, which are denoted respectively as H, S and G on this figure. The lower Si content D218-2000 (Fig. 1(a)) with a Hf/Si of about 3.4 exhibited high densities of Heusler (avg. size  $\sim 300$  nm) and  $\text{NiHfSi}$  (avg. size  $\sim 300$  nm) particles along with the G-phase (avg. size  $\sim 25$  nm) precipitates. D218-2063 with a higher Si-content (Fig. 1(b)), and hence lower Hf/Si ratio ( $\sim 1.2$ ), had a significant distribution of G-phase precipitates (avg. size  $\sim 25$  nm) coupled with a few  $\text{NiHfSi}$  particles (avg. size  $\sim 130$  nm) and essentially no Heusler phase. Comparison of the second phases in these two as-homogenized D218 ingots suggests that high values of Hf/Si ratio lead to the formation  $\text{Ni}_2\text{AlHf}$  at the expense of  $\text{Ni}_{16}\text{Hf}_6\text{Si}_7$ . Secondary heat treatment (100 h - 1300 K) of D218-2000, which contained all three types of precipitates in the as-homogenized state (Fig. 1(a)), essentially dissolved all the G-phase and only slightly coarsened the  $\text{NiHfSi}$  and Heusler precipitates (Fig. 1(c)). Application of this heat treatment to D218-2063 did not significantly affect either the size or distribution of G phase; it simply coarsened the  $\text{NiHfSi}$  phase. The structure of as-homogenized D176-1910 with a Hf/Si ratio of about 2.3 consisted of a high density of fine G-phase (avg. size  $\sim 25$  nm) without any  $\text{Ni}_2\text{HfAl}$  or  $\text{NiHfSi}$  precipitates (Fig. 1(d)); thus its structure was similar to that of D218-2063 (Fig. 1(b)).

Detailed examination of as-homogenized D218 ingot 2000 (Fig. 1(a)) was undertaken to characterize the three different precipitates. G-phase particles

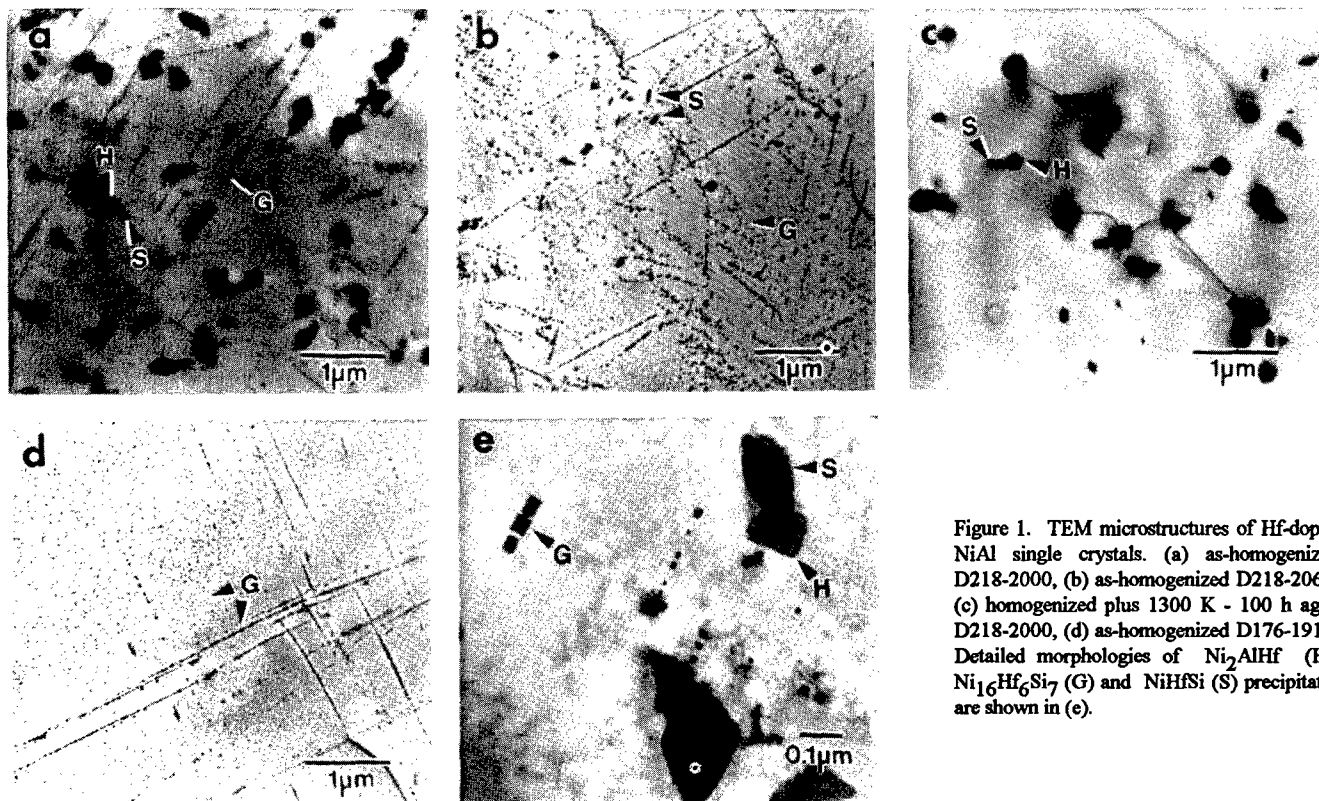


Figure 1. TEM microstructures of Hf-doped NiAl single crystals. (a) as-homogenized D218-2000, (b) as-homogenized D218-2063, (c) homogenized plus 1300 K - 100 h aged D218-2000, (d) as-homogenized D176-1910. Detailed morphologies of  $\text{Ni}_2\text{AlHf}$  (H),  $\text{Ni}_{16}\text{Hf}_6\text{Si}_7$  (G) and  $\text{NiHfSi}$  (S) precipitates are shown in (e).

Table 1. Chemical Composition (Atom %) and Hf/Si Ratio for D218 and D176 Single Crystals.

Alloy	Ingot	Al	Ga	Hf	Si	Ti	Ni	C	N	O	S	Hf/Si Ratio
D218	2000	49.2	0.19	0.51	0.15	0.90	50.0	0.0022	<0.0006	0.0054	<0.0007	3.4
D218	2063	48.9	0.19	0.53	0.46	0.91	50.0	0.013	<0.0006	0.0092	<0.0007	1.2
D176	1910	49.5	0.05	0.44	0.19	0.	49.8	-	-	-	-	2.3

generally nucleated as a high density of very fine (size  $\sim 5\text{-}50\text{nm}$ ) precipitates with a  $\{100\}_{\text{NiAl}}$  habit plane [3,7]. However dislocations on  $\{100\}_{\text{NiAl}}$  planes provided preferential nucleation sites resulting in a square grid type pattern with a uniform distribution of G-phase precipitates within the grids.  $\text{Ni}_{16}\text{Hf}_6\text{Si}_7$  has a FCC structure and a lattice parameter,  $a_0 = 1.14\text{ nm}$ , which is almost four times greater than that of NiAl ( $a_0 = 0.289\text{ nm}$ ) with its primitive cubic CsCl type structure (space group  $\text{Pm}\bar{3}\text{m}$ ). Therefore, the G-phase nucleates in the NiAl matrix with a cuboidal morphology and a cube-on-cube orientation-relationship (O.R.): i.e.  $(100)_{\text{G}} \parallel (100)_{\text{NiAl}}$  and  $[010]_{\text{G}} \parallel [010]_{\text{NiAl}}$ . The nucleation of a high density of G-phase is favored by its good coherency and a small lattice misfit (1.4%) in all the three  $\langle 001 \rangle_{\text{NiAl}}$  directions.

The silicide phase ( $\text{NiHfSi}$ ) [8] has an orthorhombic crystal structure with unit cell parameters,  $a = 0.639\text{ nm}$ ,  $b = 0.389\text{ nm}$ , and  $c = 0.72\text{ nm}$ , and forms as thin rectangular plates on  $\{111\}_{\text{NiAl}}$  planes with an O.R. that is given by  $(100)_{\text{NiHfSi}} \parallel (111)_{\text{NiAl}}$  and  $[010]_{\text{NiHfSi}} \parallel [101]_{\text{NiAl}}$  and  $[001]_{\text{NiHfSi}} \parallel [121]_{\text{NiAl}}$ . The  $\text{NiHfSi}$  phase is also semicoherent but has larger lattice misfits: i.e. 1.7%, 4.8% and 4.3%, respectively, along its three axes. Twelve variants of the  $\text{NiHfSi}$  phase exist in the NiAl-based single crystals, and the number of variants and rectangular morphology of  $\text{NiHfSi}$  plates are consistent with symmetry requirements. The nucleation of the  $\text{NiHfSi}$  phase is aided by the  $\langle 111 \rangle_{\text{NiAl}}$  vacancy loops that form on the  $\{111\}_{\text{NiAl}}$  planes in Hf-containing alloys. These loops act as preferential nucleation sites for the  $\text{NiHfSi}$  phase provided enough solute (both Si and Hf) is available for the nucleation.

Heusler phase has a FCC crystal structure ( $a_0 = 0.608\text{ nm}$ ) and a much larger lattice misfit (5.2%) with the NiAl matrix than the G-phase [3,7]. The  $\text{Ni}_2\text{AlHf}$  phase is semicoherent and nucleates with a cube-on-cube O.R. with the NiAl matrix. The large misfit between the precipitate and the matrix is accommodated by a square array of misfit dislocations at the particle-matrix interface which form on  $\{100\}$  faces of Heusler precipitates in a  $\langle 001 \rangle_{\text{NiAl}}$  orientation (Fig. 1(e)). Due to this large misfit, the Heusler phase generally nucleates heterogeneously in the alloy, and it is often found to nucleate adjacent to  $\text{NiHfSi}$  particles as illustrated in Figs. 1(a,c,e).

### Stress-Strain Behavior

The 1300 K stress - strain diagrams for as-homogenized  $\langle 110 \rangle$  oriented single crystal samples cut from both D218 ingots and the D176 ingot are illustrated in Fig. 2 as a function of nominal imposed strain rate. In general all three materials exhibited initial work hardening over about 1 % deformation followed by continuous flow at a more or less constant flow

stress at all the imposed strain rates through 4+ % strain. Such behavior was the rule for the D218 ingot 2000 ( $\text{Hf/Si} = 3.4$ ) except at  $\sim 10^{-7}\text{ s}^{-1}$  (Fig. 2(a)), where slow, but continuous work hardening occurred. Both D218-2063 ( $\text{Hf/Si} = 1.2$ ) and D176-1910 ( $\text{Hf/Si} = 2.3$ ) exhibit the opposite behavior (Fig. 2(b,c)) at the lowest strain rate ( $\sim 10^{-7}\text{ s}^{-1}$ ) with continuous, slowly decreasing flow taking place after the stress reached a maximum. These two materials additionally exhibited diffuse yield point behavior during the initial stages of deformation at the faster imposed strain rates ( $> 2 \times 10^{-4}\text{ s}^{-1}$ ); whereas the D218-2000 did not (Fig. 2(a)). In terms of strength the lower  $\text{Hf/Si}$  ratio D218-2063 (Fig. 2(b)) tended to exhibit a small advantage over the other two materials, particularly at the fastest and slowest rates of deformation.

The 1300 K stress-strain response for as-homogenized and aged  $\langle 001 \rangle$  oriented D218-2000 specimens are presented in Figs. 3(a) and (b), respectively. As was the case for the  $\langle 110 \rangle$  oriented crystals (Fig. 2(a)), the curves for both material conditions generally exhibited initial work hardening followed by more or less continuous flow. The aged material (Fig. 3(b)), however, continuously work harden at the slowest strain rate ( $\sim 10^{-7}\text{ s}^{-1}$ ) and also exhibited the unusual behavior, where deformation rates of  $1.5 \times 10^{-4}$  and  $1.6 \times 10^{-5}\text{ s}^{-1}$  produced nearly identical stress-strain curves. At deformation rates exceeding  $\sim 10^{-6}\text{ s}^{-1}$  as-homogenized  $\langle 001 \rangle$  D218-2000 oriented crystals (Fig. 3(a)) are stronger than similar samples given a post homogenization aging of 100 h at 1300 K (Fig. 3(b)). On the other hand no significant strength difference between these two heat treatment conditions is found at  $\sim 10^{-7}\text{ s}^{-1}$ . Furthermore at this latter, slow deformation rate, as-homogenized D218-2000  $\langle 110 \rangle$  (Fig. 2(a)) and  $\langle 001 \rangle$  (Fig. 3(a)) oriented specimens are equally as strong. Comparison of the flow behavior at faster rates, however, indicates that above  $1.5 \times 10^{-4}\text{ s}^{-1}$  the  $\langle 110 \rangle$  crystals have some strength advantage over the  $\langle 001 \rangle$  samples; whereas the opposite is true at intermediate rates: i.e.  $\sim 10^{-5}$  to  $10^{-6}\text{ s}^{-1}$ .

The stress-strain curves for different  $\text{Hf/Si}$  ratios, orientations and heat treatment conditions measured at 1400, 1200 and 1100 K are presented as a function of the imposed strain rate in Figs. 4-6, respectively. The general flow behavior at a higher test temperature (Fig. 4) and lower temperatures (Figs. 5 and 6) is identical to that seen at 1300 K (Figs. 2 and 3), where a small amount of initial work hardening is followed by continuous flow at a nominally constant stress. The major exception would be the apparent tendency toward a diffuse yield point in  $\langle 001 \rangle$  oriented D218-2000 ( $\text{Hf/Si} = 3.4$ ) at lower temperatures and faster strain rates (Figs. 5(b) and 6(b)). One deviation to the normal expectation that strength should decrease with a decreasing strain rate was found, where D218-2063 ( $\text{Hf/Si} = 1.2$ ) tested in the  $\langle 110 \rangle$  orientation at 1100 K was stronger at a deformation rate of  $\sim 10^{-7}$

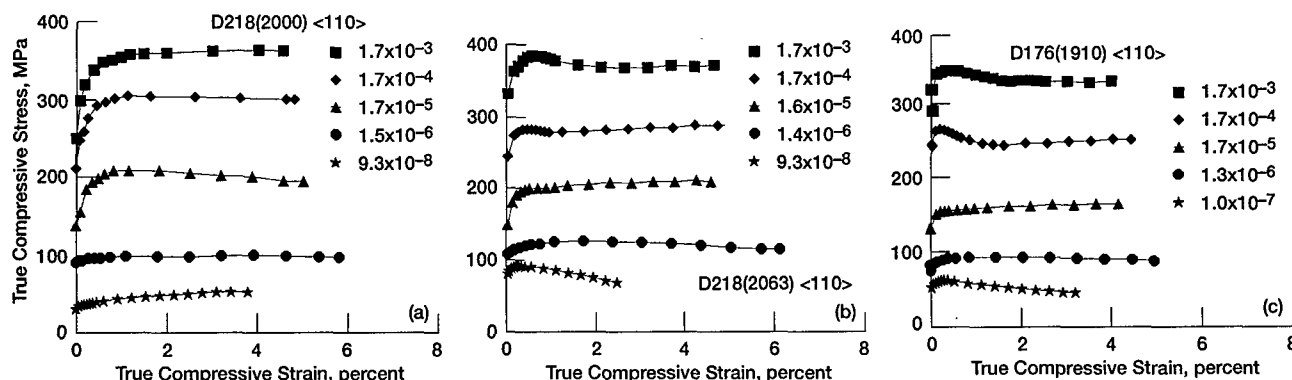


Figure 2. Stress-strain diagrams for as-homogenized  $\langle 110 \rangle$  oriented single crystals at 1300 K as a function of nominal imposed deformation rate. (a) D218 ingot 2000 with  $\text{Hf/Si} = 3.4$ , (b) D218 ingot 2063 with  $\text{Hf/Si} = 1.2$ , and (c) D176 ingot 1910 with  $\text{Hf/Si} = 2.3$ .

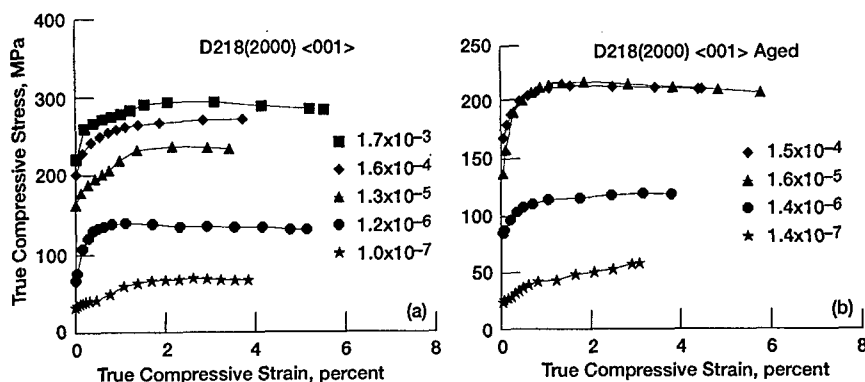


Figure 3. Stress-strain diagrams for <001> oriented D218-2000 (Hf/Si = 3.4) single crystals at 1300 K as a function of nominal imposed deformation rate. (a) as-homogenized, and (b) homogenized + 100 h at 1300 K.

$s^{-1}$  than at  $\sim 10^{-6} s^{-1}$  (Fig. 6(a)). In addition aged D218-2000 (Hf/Si = 3.4) tested in the <001> orientation at 1200 K had approximately the same strength at deformation rates of  $\sim 10^{-5} s^{-1}$  and  $\sim 10^{-6} s^{-1}$  (Fig. 5(c)); similar behavior was also observed for this material at 1300 K (Fig. 3(b)).

In terms of the overall strength of the D218 NiAl-based single crystals at each imposed strain rate, neither Hf/Si ratio (Figs. 4(a,b)), orientation (Figs. 4(a,c)) nor prior aging (Figs. 4(c,d)) appear to have a strong influence at 1400 K. While such detailed analyses are not possible at the lower test temperatures, it can be seen for ingot 2000 <001> oriented samples tested at 1200 K that prior 1300 K aging (Figs. 5(c)) does lower the strength at faster strain rates ( $> 10^{-6} s^{-1}$ ) in comparison to the as-homogenized state (Figs. 5(b)); however aging does not substantially affect strength at  $\sim 10^{-7} s^{-1}$ . Also at 1200 K the <110> oriented low Hf/Si ratio D218 ingot (Fig. 5(a)) is stronger than the high Hf/Si ratio <001> oriented D218 ingot (Fig. 5(b)) at the lowest and fastest strain rates; whereas there is little difference between these two material conditions at intermediate rates of  $10^{-6}$  to  $10^{-5} s^{-1}$ . At 1100 K and  $\sim 10^{-7} s^{-1}$  the high Hf/Si, <001> oriented ingot 2000 (Fig. 6(b)) is much weaker than its low Hf/Si, <110> oriented ingot 2000 (Fig. 6(a)), but at higher strain rates neither the ingot chemistry nor specific orientation affect the strength.

#### Flow Stress-Strain Rate-Temperature Properties

True compressive flow stress ( $\sigma$ ) - strain rate ( $\dot{\epsilon}$ ) - temperature (T) behavior for all tested Hf/Si ratios, orientations and heat treatment conditions is given in Fig. 7, where the  $\sigma$  and  $\dot{\epsilon}$  values were taken from the stress - strain diagrams at 1 % strain (Figs. 2-6). When appropriate, the data were fitted to a temperature compensated - power law (eqn. (1)) utilizing linear regression techniques;

$$\dot{\epsilon} = A \sigma^n \exp\left(\frac{-Q}{RT}\right), \quad (1)$$

where A is a constant, n is the stress exponent, Q is the activation energy, and R is the universal gas constant. While single temperature compensated - power laws could adequately describe the appropriate results for the two material conditions with limited data (Figs. 7(b,d)), multiple power law descriptions were required for the material states with more extensive data (Figs. 7(a,c)). Results of these fits are shown as solid lines in Fig. 7, and a listing of the appropriate parameters, the measure of fit as given by coefficient of determination,  $R_d^2$ , and the standard deviations for the deformation parameters,  $\delta_i$ , are given in Table 2.

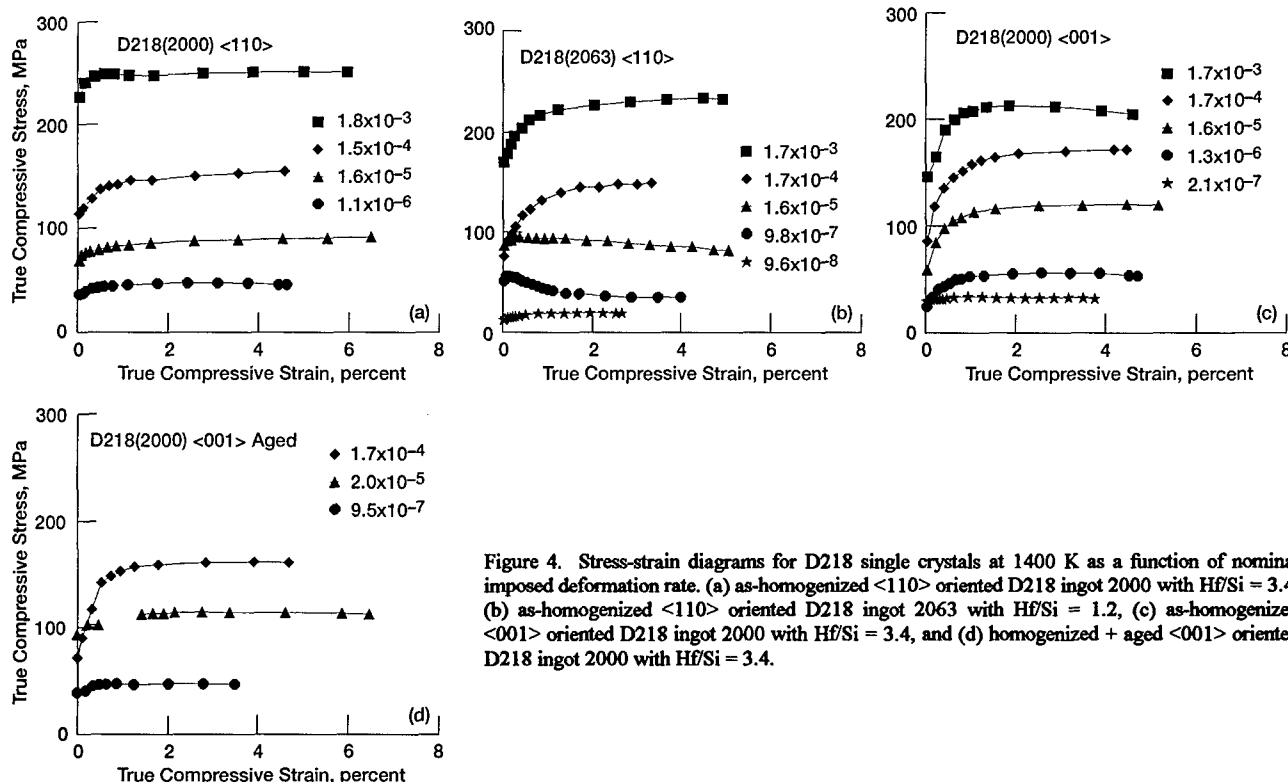


Figure 4. Stress-strain diagrams for D218 single crystals at 1400 K as a function of nominal imposed deformation rate. (a) as-homogenized <110> oriented D218 ingot 2000 with Hf/Si = 3.4, (b) as-homogenized <110> oriented D218 ingot 2063 with Hf/Si = 1.2, (c) as-homogenized <001> oriented D218 ingot 2000 with Hf/Si = 3.4, and (d) homogenized + aged <001> oriented D218 ingot 2000 with Hf/Si = 3.4.

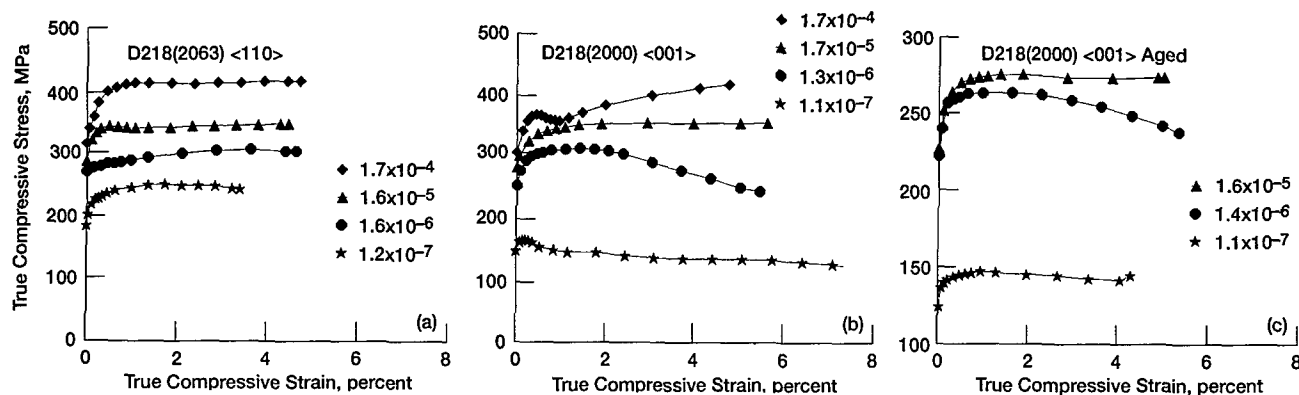


Figure 5. Stress-strain diagrams for D218 single crystals at 1200 K as a function of nominal imposed deformation rate. (a) as-homogenized  $\langle 110 \rangle$  oriented D218 ingot 2063 with  $\text{Hf/Si} = 1.2$ , (b) as-homogenized  $\langle 001 \rangle$  oriented D218 ingot 2000 with  $\text{Hf/Si} = 3.4$ , and (c) homogenized + aged  $\langle 001 \rangle$  oriented D218 ingot 2000 with  $\text{Hf/Si} = 3.4$ .

As can be seen by the curves in Fig. 7 and the coefficient of determinations in Table 2, temperature compensated - power laws are able to describe the majority of the results. Examination of the deformation parameters does reveal some commonality among the different material conditions regardless of the specific D218 ingot (i.e.  $\text{Hf/Si}$  ratio). For example, testing of as-homogenized D218  $\langle 110 \rangle$  and  $\langle 001 \rangle$  oriented samples from 1100 to 1400 K (Figs. 7(a,c), Table 2) indicates three distinct stress exponent regimes:  $\sim 14.5$ ,  $6-7$  and  $\sim 3.5$ . Furthermore the activation energy associated with both the  $n = 14.5$  and  $n = 6-7$  regimes might, in reality, be identical and equal to  $\sim 550$  kJ/mol, based on the large standard deviations for individual activation energies reported in Table 2. The  $n \sim 3.5$  regime exists in all the D218 results (i.e.:  $\text{Hf/Si}$  ratio, orientation or heat treatment) at the higher temperature, slower strain rate test conditions. In addition this low stress exponent regime appears to have an activation energy of about 400 kJ/mol predicated on the calculated  $Q$ 's and  $\delta Q$ 's reported in Table 2.

#### Post Test Microstructures

A group of deformed samples from each test temperature was chosen for TEM examination to characterize the post-test precipitate structures and the resulting dislocation structures. Most of these samples were selected after low strain rate testing ( $\sim 10^{-6}$  -  $10^{-7}$   $\text{s}^{-1}$ ), where differences in strengths were most pronounced. However, one set of samples tested under a faster strain rate ( $\sim 10^{-4}$   $\text{s}^{-1}$ ) at 1300 K was also chosen to correlate high strain rate deformation properties with those at lower rates.

**1400 K Results** - TEM microstructures of the D218-2063 and D218-2000  $\langle 110 \rangle$  samples tested at 1400 K -  $10^{-6}$   $\text{s}^{-1}$  are shown in Figs. 8(a,b), respectively. These microstructures are quite different from their as-homogenized counterparts shown in Figs. 1(b,a). The G-phase has completely dissolved in both of these alloys in favor of the more stable phases, e.g.  $\text{NiHfSi}$  in D218-2063 and  $\text{Ni}_2\text{AlHf}$  in D218-2000. The density of these precipitates is low in both alloys and their size ranges from 0.25 to 1.5  $\mu\text{m}$  for the  $\text{NiHfSi}$  phase and 0.25 to 0.5  $\mu\text{m}$  for the  $\text{Ni}_2\text{AlHf}$  phase. Occasional  $\text{NiHfSi}$  precipitates were also observed in the alloy D218-2000

(Fig. 8(b)), but judging from their small relative size ( $\sim 0.1 \mu\text{m}$ ) as compared to that in the as-homogenized alloy, it is clear that this phase is in the process of dissolving in favor of the  $\text{Ni}_2\text{AlHf}$  phase.

The microstructure of  $\langle 100 \rangle$  oriented D218-2000 sample after testing under the same conditions ( $1400 \text{ K} - 10^{-6} \text{ s}^{-1}$ ) in the as-homogenized state is shown in Fig. 8(c). Consistent with the  $\langle 110 \rangle$  sample (Fig. 8(b)), the G-phase has completely dissolved, and the microstructures in both conditions contain a low density of predominantly  $\text{Ni}_2\text{AlHf}$  particles. The presence of very fine  $\text{NiHfSi}$  precipitates (size  $\sim 0.05 \mu\text{m}$ ) with surrounding dislocation loops in the as-homogenized and tested material (arrows in Fig. 8(c)) indicate that these precipitates were not present at the test temperature but nucleated during the cool down cycle [8]. The microstructure of the homogenized + 1300 K aged  $\langle 100 \rangle$  oriented D218-2000 sample after  $1400 \text{ K} - 10^{-6} \text{ s}^{-1}$  testing was essentially identical to that shown in Fig. 8(c); except the average size of the  $\text{Ni}_2\text{AlHf}$  phase after testing the aged alloy was slightly larger ( $\sim 0.4 \mu\text{m}$ ) than that found after testing the as-homogenized alloy ( $\sim 0.25 \mu\text{m}$ ).

Dislocation pinning was observed at some of the  $\text{NiHfSi}$  precipitates in the D218-2063 alloy and at  $\text{Ni}_2\text{AlHf}$  precipitates in the D218-2000 material (Figs. 8(a-c)). However, due to the relatively low density of precipitates observed in the samples, this did not appear to be a very effective mechanism of impeding dislocation motion.

**1300 K Results** - TEM microstructures of  $\langle 110 \rangle$  tested samples from alloys D218-2063, D176-1910, and D218-2000 deformed at  $1300 \text{ K} - 10^{-7} \text{ s}^{-1}$  are shown in Figs. 9(a-d). These post-test microstructures are distinctly different from each other in terms of the sizes, density, and types of second-phase precipitates and in the propensity for dislocation-precipitate interactions. The precipitate structure of the deformed alloy D218-2063 (Fig. 9(a)) is very similar to that of the as-homogenized material (Figs. 1(b)) and consists of a high density of fine G-phase precipitates (average size  $\sim 25 \text{ nm}$ ) and some coarse  $\text{NiHfSi}$  particles (size ranging from 200 to 700 nm). When examined under weak-beam dark-field TEM conditions (Fig. 9(b)),

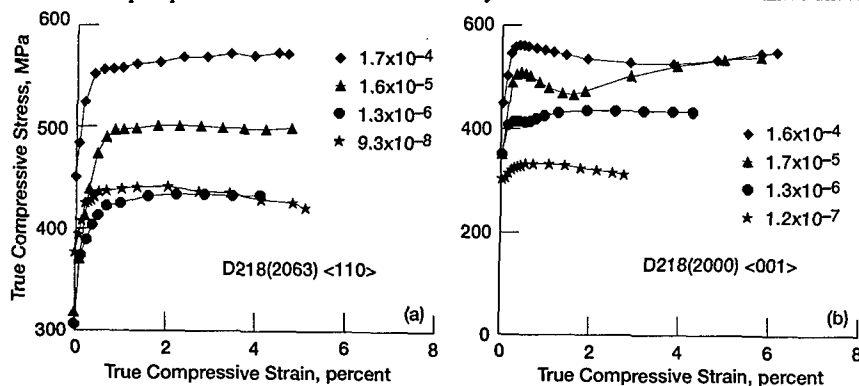


Figure 6. Stress-strain diagrams for D218 single crystals at 1100 K as a function of nominal imposed deformation rate. (a) as-homogenized  $\langle 110 \rangle$  oriented D218 ingot 2063 with  $\text{Hf/Si} = 1.2$ , and (b) as-homogenized  $\langle 001 \rangle$  oriented D218 ingot 2000 with  $\text{Hf/Si} = 3.4$ .



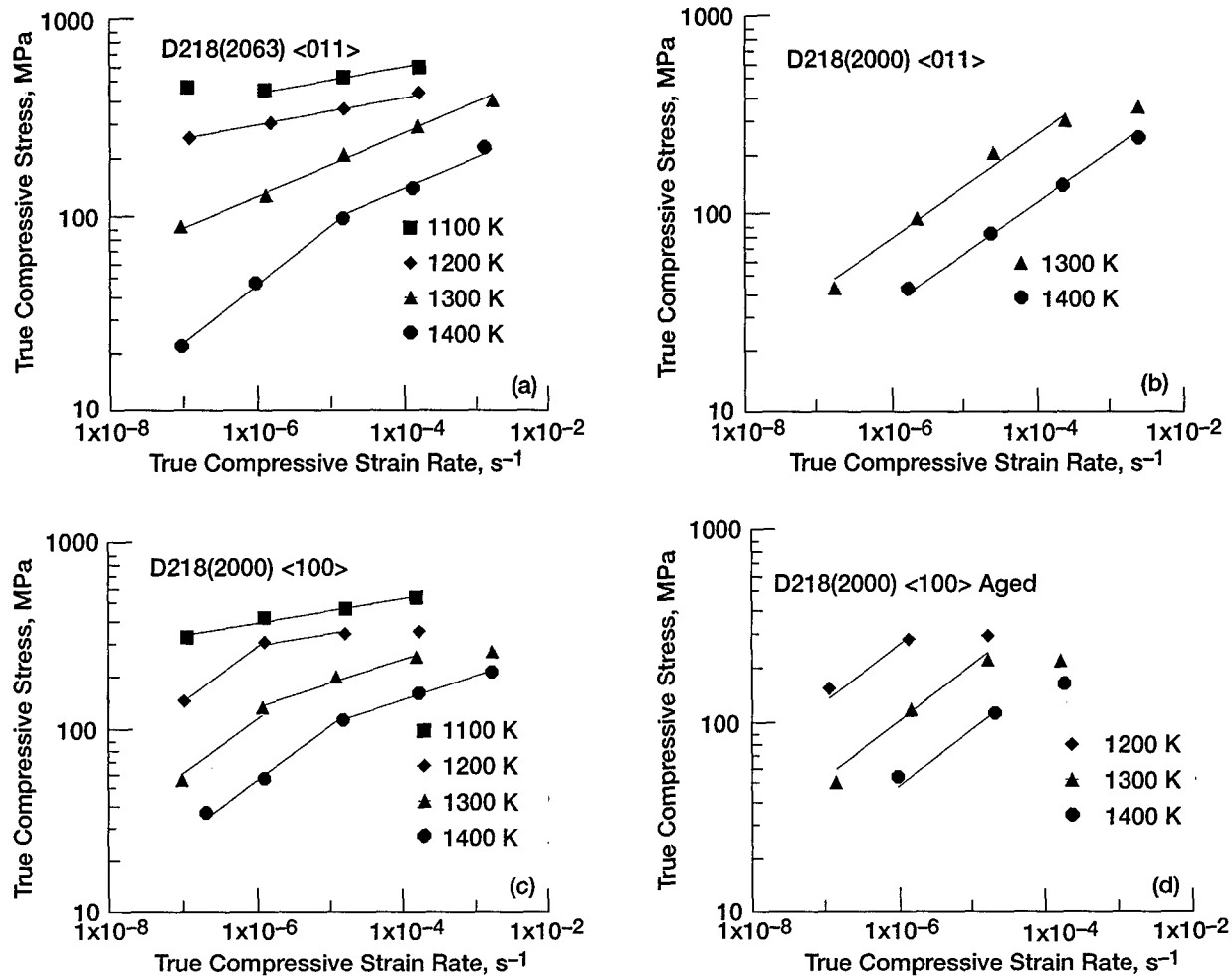


Figure 7. Flow stress - strain rate - temperature behavior for D218 single crystals. (a) as-homogenized ingot 2063 (Hf/Si = 1.2) tested in the  $\langle 110 \rangle$  orientation, (b) as-homogenized ingot 2000 (Hf/Si = 3.4) tested in the  $\langle 110 \rangle$  orientation, (c) as-homogenized ingot 2000 (Hf/Si = 3.4) tested in the  $\langle 001 \rangle$  orientation, and (d) homogenized and aged {100 h at 1300 K} ingot 2000 (Hf/Si = 3.4) tested in the  $\langle 001 \rangle$  orientation.

intense dislocation-precipitate interactions were visible in this material, as evidenced by extensive pinning and looping of dislocations on the G-phase. Under the same test conditions, bright-field imaging of D176-1910 (Fig. 9(c)) illustrated a non-uniform distribution of very fine (average size of 10 nm) G-phase precipitates and some coarse NiHfSi particles (size ranging from 200 to 900 nm). The density of G-phase was much lower in the vicinity of the NiHfSi precipitates suggesting that the G-phase was in the

process of dissolving at the expense of the more stable NiHfSi phase. Dislocation pinning by the G-phase was also observed in this alloy, but due to the small size of the precipitates, it was not as pronounced as in the D218-2063 sample (Fig. 9(a)). The microstructure of the 1300 K -  $10^{-7} \text{ s}^{-1}$  tested D218-2000 (Fig. 9(d)) was very different from either D218-2063 (Figs. 9(a,b)) or D176-1910 (Fig. 9(c)). In this case the G-phase had completely dissolved (Fig. 9(d)) and only a few coarse  $\text{Ni}_2\text{AlHf}$  (average size  $\sim 0.7 \mu\text{m}$ )

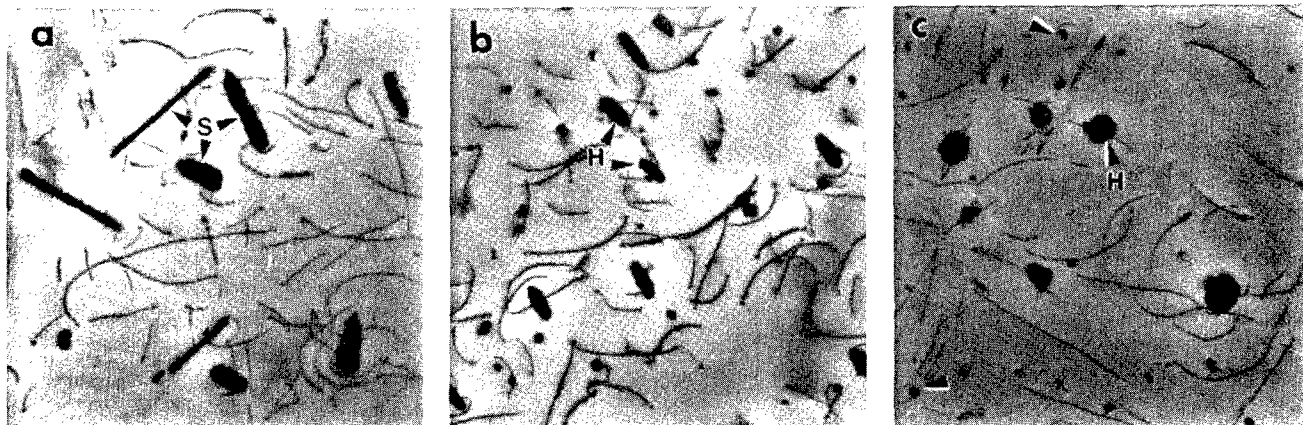


Figure 8. TEM microstructures of D218 single crystals tested at  $1400 \text{ K} - 10^{-6} \text{ s}^{-1}$ . (a) as-homogenized  $\langle 110 \rangle$  oriented 2063 to 4% strain, (b) as-homogenized  $\langle 110 \rangle$  oriented 2000 to 4.5% strain, (c) as-homogenized  $\langle 001 \rangle$  oriented 2000 to 4.6% strain.



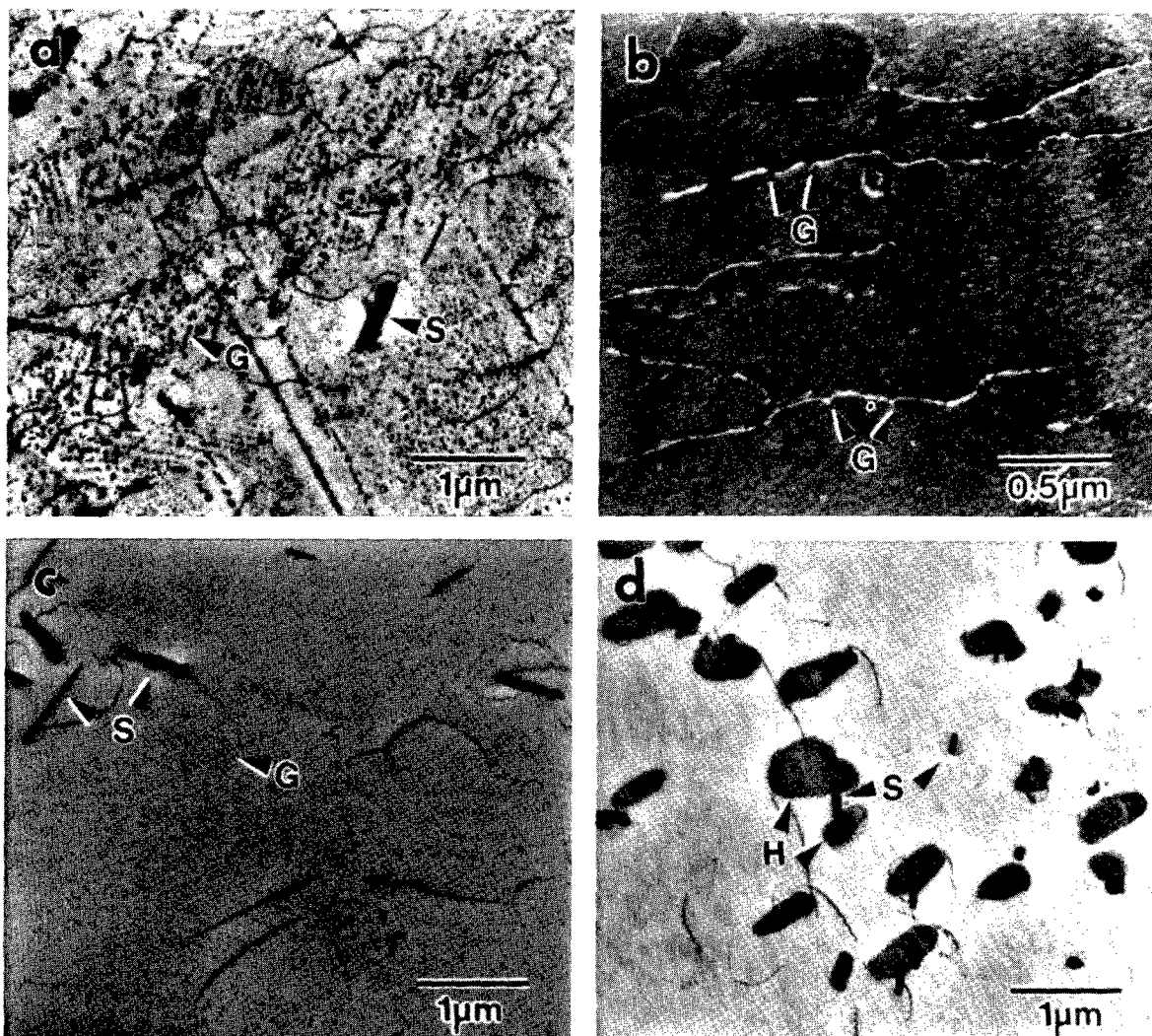


Figure 9. TEM microstructures of Hf-doped NiAl single crystals tested at  $1300\text{ K} \cdot 10^{-7}\text{ s}^{-1}$ . (a,b) as-homogenized  $\langle 110 \rangle$  oriented D218-2063 to 2.5 % strain, (c) as-homogenized  $\langle 110 \rangle$  oriented D176-1910 to 3.3 % strain and (d) as-homogenized  $\langle 110 \rangle$  oriented D218-2000 to 3.8 % strain. Parts (a,c,d) taken under bright-field conditions; part (b) taken under weak-beam conditions.

and NiHfSi precipitates (average size  $\sim 0.2\text{ }\mu\text{m}$ ) were present. Furthermore the dislocation density was low and the frequency of dislocation-precipitate interactions appeared to be diminished in this alloy as compared to the alloy D218-2063 (Fig. 9(a)). The microstructures of the  $1300\text{ K} \cdot 10^{-7}\text{ s}^{-1}$  tested  $\langle 100 \rangle$  samples for alloy D218-2000 in the as-homogenized as well as the aged condition were nearly identical. These structures contained a low density of  $\text{Ni}_2\text{AlHf}$  and NiHfSi precipitates with all the G-phase being completely dissolved, and they appeared very similar to that observed in the corresponding  $\langle 110 \rangle$  oriented sample (Fig. 9(d)).

TEM microstructures of the  $\langle 110 \rangle$  oriented as-homogenized samples from alloys D218-2063, D218-2000 and D176-1910 deformed at the faster strain rate of  $\sim 10^{-4}\text{ s}^{-1}$  at  $1300\text{ K}$  were examined. The structures, as exemplified by Figs. 10(a,b) were essentially the same as that of the corresponding as-homogenized alloys (Figs. 1(b,a)), except for the presence of a high density of dislocations. In particular a reasonably high density of G-phase precipitates is maintained in all the three alloys and D218-2000 (Fig. 10(b)) still possesses the  $\text{Ni}_2\text{AlHf}$  and NiHfSi precipitates that were originally present in the as-homogenized condition (Fig. 1(a)) prior to testing. Overall, there was no evidence of significant microstructural evolution in terms of precipitate dissolution and coarsening in any of the three alloys under  $1300\text{ K} \cdot 10^{-4}\text{ s}^{-1}$  test conditions.

TEM microstructures of the as-homogenized and the homogenized plus aged  $\langle 100 \rangle$  samples from alloy D218-2000 tested at a strain rate of  $\sim 10^{-4}\text{ s}^{-1}$  at  $1300\text{ K}$  were also examined, and a typical example is shown in Fig. 10(c). In both of these conditions, the G-phase has mostly dissolved and primarily  $\text{Ni}_2\text{AlHf}$  and the NiHfSi phases were present. Although the density of second phase precipitates did not appear to be too different for the two conditions, the average size of these precipitates was slightly larger in the aged alloy. Again, at this fast strain rate a high density of dislocations and some precipitate pinning are observed in both the conditions.

**1200 K results** – Only as-homogenized and the homogenized plus aged  $\langle 100 \rangle$  samples from ingot D218-2000 tested at  $1200\text{ K} \cdot 10^{-7}\text{ s}^{-1}$  were examined. The microstructure of this alloy in these two conditions was essentially the same and consisted of a coarse distribution of  $\text{Ni}_2\text{AlHf}$  and NiHfSi phases similar to Fig. 9(d); however, even at this low temperature, the G-phase originally present prior to testing (Fig. 1(a)) has completely dissolved in favor of the  $\text{Ni}_2\text{AlHf}$  and NiHfSi phases.

#### Discussion

Because it is difficult in Fig. 7 to compare the relative strengths of the Hf-modified single crystals measured in different orientations and after different heat treatments, the results have been replotted in Fig. 11, where true



Figure 10. TEM microstructures of Hf-doped NiAl single crystals tested at 1300 K -  $10^{-4}$  s $^{-1}$ . (a) as-homogenized <110> oriented D218-2063 to 5.1 % strain, (b) as-homogenized <110> oriented D218-2000 to 4.8 % strain, and (c) homogenized + aged <001> oriented 2000 to 4.4 % strain.

compressive flow stress - strain rate data for each material condition are presented as a function of temperature. For clarity, the results for <110> oriented samples are given by filled symbols, while the open symbols represent data from <001> oriented specimens. In this form, the data can be more easily examined to determine if the elevated temperature strength of D218 single crystals depends on chemistry, heat treatment, or orientation in any systematic manner.

#### Effect of chemistry on creep strength

**1400 K Testing** - At this temperature, creep strengths of the <110> specimens at each strain rate between  $\sim 10^{-3}$  and  $10^{-7}$  s $^{-1}$  are about the same irrespective of the Hf/Si ratio, as seen by comparing the results of D218-2063 (Hf/Si = 1.2) and D218-2000 (Hf/Si = 3.4) samples in Fig. 11(a). Examination of the TEM microstructures of the 1400 K -  $10^{-6}$  s $^{-1}$  deformed samples (Fig. 8(a,b)) indicated that the G-phase had completely dissolved in both of these alloys at the expense of the more stable NiHfSi and Ni $_2$ AlHf phases, and the distribution of NiHfSi phase in the alloy D218-2063 is about the same as the distribution of Heusler phase in the alloy D218-2000. Thus, any advantage at 1400 K due to G-phase precipitate hardening is lost, and both ingots have similar strengths which can mostly be ascribed to Hf and Ti solid solution strengthening.

**1300 K Testing** - Examination of 1300 K data in Fig. 11(b) reveals that the effect of alloy chemistry on the strength of D218 <110> crystals is most pronounced at slow strain rates where longer testing times are involved and hence coarsening and stability of different phases come into play. At a strain rate of  $\sim 10^{-7}$  s $^{-1}$  and a Hf/Si ratio of 1.2 (D218-2063), the microstructure of the creep tested samples consisted of a high density of predominantly fine G-phase precipitates, as shown in Fig. 9(a). Even after long term testing at this slow strain rate, the microstructure is very similar to that of the as-homogenized material (Fig. 1(b)). This suggests that in the alloy D218 with a low Hf/Si ratio, the G-phase is quite stable and has a low coarsening rate at 1300 K. On the other hand, the microstructure of the crept D218-2000 (Hf/Si = 3.4) samples tested under similar conditions consisted of only the coarse Heusler phase precipitates (Fig. 9(d)). Comparing this microstructure to that of the as-homogenized alloy D218-2000 (Fig. 1(a)), it is clear that in the alloy D218 with Hf/Si = 3.4, the G-phase is a metastable phase and dissolves at the expense of the more stable Heusler phase at 1300 K. Since precipitate hardening is a strong function of the particle size and interparticle spacing, a lower strength would be expected in the ingot D218-2000 as compared to that in D218-2063. This is in agreement with the creep strength data shown in Fig. 11(b), where at 1300 K -  $10^{-7}$  s $^{-1}$  the <110> alloy D218-2063 containing a high density of stable, fine G-phase is approximately 1.5 times stronger than the corresponding alloy D218-2000 containing only a coarse distribution of the Heusler phase.

At the higher strain rate of  $\sim 10^{-4}$  s $^{-1}$  the creep strength of all three <110> crystals is about the same (Fig. 11(b)), and TEM examination of the deformed samples (Figs. 10(a,b)) indicated that (1) deformation produced an

extensive amount of dislocation pinning by the G-phase and (2) the second phase morphology was similar to their as-homogenized counterparts (Figs. 1(a,b,d)). The retention of as-homogenized like microstructures is not surprising, since testing at the higher strain rate was of short term duration ( $\sim 600$  s). Whereas testing at the slower strain rate of  $\sim 10^{-7}$  s $^{-1}$  exposes the alloys to temperature for at least 350 ks which can provide sufficient time for phase transformations to occur.

Overall, the 1300 K slow strain rate results indicate that the primary influence of Si in D218 is related to precipitation hardening. G-phase containing alloys are stronger than G-phase free materials, and strength is proportional to the amount of G-phase present. The alloy with a lower Hf/Si ratio and a high density of stabilized G-phase precipitates is stronger than the alloy with a higher Hf/Si ratio containing only a low density of coarse Heusler phase precipitates. While alloy D176 was tested at 1300 K to determine the role of Ti/Ga on creep strength of Hf-doped NiAl single crystals, the current mechanical property and microstructural data are insufficient to draw any conclusions.

**1200 K and 1100 K Testing** - Extensive data for a direct comparison of Hf/Si ratio on creep strength were not obtained at 1200 and 1100 K; however, the limited amount of data shown in Figs. 11(c,d) suggests that trends similar to those observed at 1300 K (Fig. 11(b)) can be expected at lower temperatures. A comparison of the creep data for different Hf/Si ratio samples of the as-homogenized alloy D218 indicates that for faster strain rates ( $> 10^{-6}$  s $^{-1}$ ) creep strengths are not too different at these temperatures, but at a slow strain rate of  $\sim 10^{-7}$  s $^{-1}$ , creep strength of the alloy D218-2063 in the <110> orientation is at least 30-50 % higher than that of the D218-2000 alloy in the <100> orientation. TEM microstructure of the 1200K -  $10^{-7}$  s $^{-1}$  deformed samples for the <100> D218-2000 with Hf/Si = 3.4 indicated that even at this low temperature the G-phase had completely dissolved at the expense of Heusler and NiHfSi phases. The microstructure of the corresponding <110> D218-2063 tested sample was not examined, but having established the stability of G-phase in this alloy during the 1300 K -  $10^{-7}$  s $^{-1}$  test (e.g. see Fig. 9(a)), it is reasonable to expect that the second phase morphology after lower temperature -  $10^{-7}$  s $^{-1}$  testing would also contain a high density of fine G-phase precipitates similar to that found in the as-homogenized alloy (Fig. 1(b)). These observations suggest that the alloy D218 with a lower Hf/Si ratio and a corresponding high density of fine G-phase precipitates will be more creep resistant between 1100 and 1300K than D218 with a higher Hf/Si ratio and corresponding coarse Heusler phase distribution. Thus 1100 and 1200 K creep resistance will be maximized through G-phase precipitation strengthening in addition to the Hf solid solution effect.

#### Effect of prior aging treatment

The effect of prior heat treatment on the creep properties was studied utilizing <100> oriented D218-2000 samples, and the strength of the as-homogenized alloy are compared with that after a 1300 K - 100 h anneal

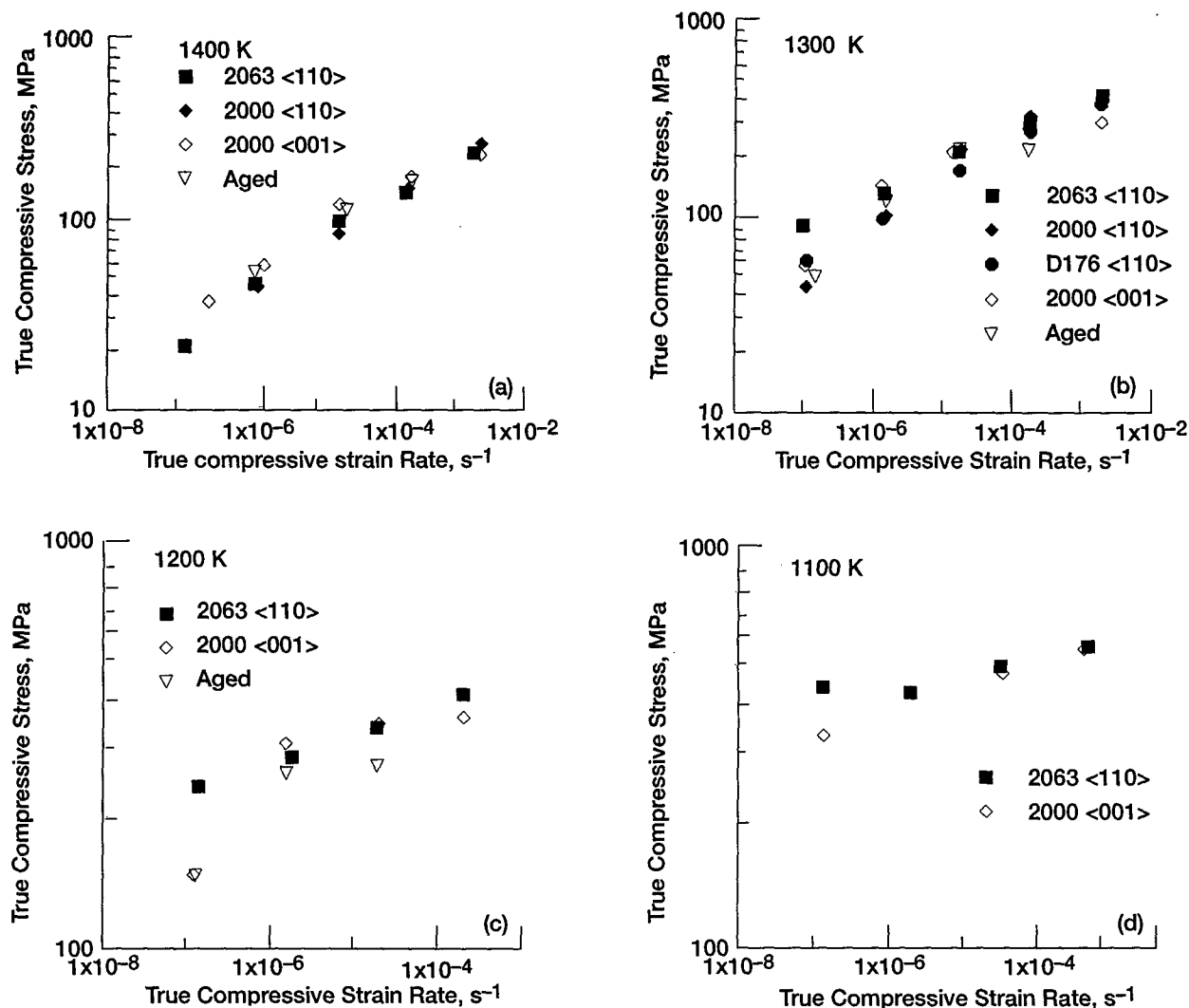


Figure 11. Flow stress - strain rate behavior of several D218 single crystals tested in different orientation and heat treatments. (a) 1400 K, (b) 1300 K, (c) 1200 K and (d) 1100 K. Data from <110> and <001> oriented crystals are represented by filled and open symbols, respectively. The results for D176 in Part (b) were taken at 1 % strain from Fig. 2(c)).

prior to testing between 1200 and 1400 K in Fig. 11(a-c). Examination of the 1400 and 1300 K results (Figs. 11 (a,b)) reveals that prior aging has very little effect at any imposed strain rate; likewise the strength of both heat treatment conditions is also the same after 1200 K -  $10^{-7}$  s<sup>-1</sup> testing (Fig. 11(c)). TEM examination of as-homogenized and aged samples which exhibited similar strength levels [i.e. 1400 K -  $10^{-6}$  s<sup>-1</sup> (Fig. 8(c)) & 1300 K -  $10^{-4}$  s<sup>-1</sup> (Fig. 10(c))] revealed similar microstructures. Consequently, whether the samples were or were not aged, testing under these conditions resulted in complete dissolution of the fine G-phase and produced a microstructure consisting of coarse Ni<sub>2</sub>AlHf phase and occasional NiHfSi precipitates. While prior aging does not affect either 1400 K, 1300 K or the slowest strain rate at 1200 K behavior (Figs. 11(a-c)), under higher strain rate - 1200 K conditions some degradation of the aged material in comparison to the as-homogenized alloy was apparent (Fig. 11(c)). This difference in strength is most likely due to the retention of some G-phase precipitates in the as-homogenized alloy during testing as opposed to the aged material, since the test times at the higher strain rates are relatively short. The initial distribution of G-phase precipitates in the as-homogenized alloy (Fig. 1(a)) compared to the aged alloy (Fig 1(c)) would suggest that some G-phase precipitate strengthening in the as-homogenized condition at 1200 K is probable.

#### Effect of orientation

The effect of orientation on the creep properties was studied for the alloy D218-2000 at 1400 and 1300 K (Figs. 11(a,b)). While the creep strength in both the <100> and the <110> orientations was not dramatically different at faster strain rates ( $>10^{-5}$  s<sup>-1</sup>), the <100> samples seem to be 10-20% stronger than the <110> samples at lower strain rates at both 1400 and 1300 K. This is consistent with the work of Kitabjian et al. [10] on NiAl-2.5Ti single crystals, where hard oriented <001> crystals exhibited a slight strength advantage at lower strain rates over the "softer" <111> orientation at 1473 K. Compared to binary NiAl single crystals, however, the results of the present work and that of Kitabjian et al. [10] are somewhat surprising, since a significant difference in creep strength exists between the hard and soft oriented binary NiAl crystals [11].

In both alloyed and unalloyed NiAl, non-<001> oriented crystals deform by the easy glide of  $b = \langle 001 \rangle$  dislocations, whereas <001> oriented crystals require the motion of  $b = \langle 110 \rangle$  dislocations [9-11]. Due to their decomposed core structure, the <110> dislocations have low mobility [12] which results in extensive dislocation interaction and subsequent decomposition into <100> dislocation networks [11]. This substructure formation imparts a much higher strength to the binary NiAl in the <100> orientation as compared to the non-<100> orientation. In the alloyed NiAl, neither the Ta/Hf-doped [1,2] single crystals follow this pattern since the

alloyed matrix and a high density of second phase precipitates impede the motion of dislocations irrespective of the specific type of dislocation, thus raising the strength levels in both orientations. The dislocation-precipitate interaction in the <100> oriented alloyed single crystals also prevents the dislocation reactions which lead to the widespread network formation which is mostly responsible for the higher strength of the <100> compared to <110> orientation. However, the inherent sluggish motion of <110> dislocations in the <100> orientation still exists in the alloyed single crystals and this is likely responsible for the small increase in the 1400 - 1300 K strength levels of the <100> versus <110> D218-2000 single crystal samples at slower strain rates, in spite of the fact that they exhibit similar precipitate structures.

#### Summary of Results

With the assumption that chemistry effects and orientation effects are independent variables, the present study suggests that low Hf/Si ratio, <001> oriented D218 single crystals would have better elevated temperature, slow strain rate deformation strength. First, a higher Si content in NiAl-0.5Hf single crystals leads to the precipitation of a high density of fine and coherent G-phase precipitates which are stable to at least 1300 K. Therefore, a relatively high Si content in the alloy D218 due to reactions between the melt and mold is not detrimental for the elevated temperature mechanical properties and, in fact, leads to somewhat better behavior. Second, the <001> orientation, which is generally accepted as the strongest orientation in binary NiAl, appears to maintain a slight advantage over the <110> orientation in D218 single crystals under slower strain rate conditions at both 1300 and 1400 K.

While both orientation and chemistry have some influence on the elevated temperature strength of NiAl-0.5Hf single crystals, in general the variables examined in this study do not significantly impact the creep behavior of D218. Therefore slight compositional differences from ingot to ingot will not greatly affect the properties of this single crystal NiAl-based alloy. Finally, although prior thermal exposure can dissolve the G-phase precipitates in D218 with a high Hf/Si ratio, such heat treatments should only somewhat weaken the high temperature strength under faster deformation conditions and leave the slow strain rate behavior unaffected.

#### Conclusion

Based on the study of three variants of NiAl-0.5Hf single crystals, future alloy development efforts on alloy D218 to develop elevated temperature creep resistance should concentrate on higher Si levels that lead to greater volume fractions of G-phase.

#### References

1. W.S. Walston, R.D. Field, J.R. Dobbs, D.F. Lahrman and R. Darolia. *Structural Intermetallics*, eds. R. Darolia, J.J. Lewandowski, C.T. Liu, P.L. Martin, D.B. Miracle and M.V. Nathal, TMS, Warrendale, PA, 1993, pp. 523-32.
2. R. Darolia, J.R. Dobbs, R.D. Fields, E. H. Goldman, D.F. Lahrman, W.S. Walston. U.S. Patent 5,516,380, May 14, 1996.
3. A. Garg, R.D. Noebe, and R. Darolia. NASA CP-10178, 1995 pp. 28:1 - 28:12.
4. E.H. Goldman. *High-Temperature Ordered Intermetallic Alloys V*, Vol. 288, (eds. I.Baker, R. Darolia, J.D. Whittenberger and M.H. Yoo), Materials Research Society, Pittsburgh, PA, 1993, pp. 83-94.
5. R.D. Noebe, R.R. Bowman and N.V. Nathal. *Physical Metallurgy and Processing of Intermetallic Compounds*, eds. N.S. Stoloff and V.K. Sikka, Chapman and Hall, New York, NY, 1996 pp. 212-296.
6. R.D. Noebe, R.R. Bowman and N.V. Nathal. *Inter. Mater. Rev.* 38 (1993) 193-232.
7. I.E. Locci, R. Dickerson, R. Bowman, J.D. Whittenberger, M.V. Nathal, and R. Darolia. *High-Temperature Ordered Intermetallic Alloys V*, Vol. 288, (eds. I.Baker, R. Darolia, J.D. Whittenberger and M.H. Yoo), Materials Research Society, Pittsburgh, PA, 1993, pp. 685-90.
8. A. Garg, R.D. Noebe and R. Darolia. *Acta mater.* 44 (1996) 2809-2820.
9. R.D. Noebe and A. Garg. NASA TM 106981, 1995.
10. P.H. Kitabjian, A. Garg, R.D. Noebe and W.D. Nix. *High-Temperature Ordered Intermetallic Alloys VII*, Vol. 460, (eds. C.T. Liu, N.S. Stoloff and C. Kock), Materials Research Society, Pittsburgh, PA, 1997.
11. K.R. Forbes, U. Glatzel, R. Darolia and W.D. Nix. *Metall. Mater. Trans. A* 27A (1996) 1229-1240.
12. M.J. Mills, J.E. Angelo, M.S. Daw, J.D. Weinberg and D.B. Miracle. *Mater. Sci. Eng. A192/193* (1995) 134-141.

Table 2. Temperature Compensated Power Law Fits of the Flow Stress - Strain Rate Data for Several D218 Single Crystals Tested as a Function of Orientation and Heat Treatment Condition.

Material ID	Orientation	Temperature Range, K	Strain Rate Range, s <sup>-1</sup>	A, s <sup>-1</sup>	n	Q, kJ/mol	R <sub>d</sub> <sup>2</sup>	δ <sub>n</sub>	δ <sub>Q</sub> , kJ/mol
D218-2063	<110>	1100 1200	10 <sup>-6</sup> - 10 <sup>-4</sup> 10 <sup>-7</sup> - 10 <sup>-4</sup>	4.53 x 10 <sup>-17</sup>	14.5	581.9	.984	0.95	57.8
D218-2063	<110>	1300 1400	10 <sup>-7</sup> - 10 <sup>-3</sup> 10 <sup>-5</sup> - 10 <sup>-3</sup>	5.30 x 10 <sup>5</sup>	6.19	613.0	.991	0.28	43.3
D218-2063	<110>	1400	10 <sup>-7</sup> - 10 <sup>-5</sup>	3.29 x 10 <sup>-12</sup>	3.37	-	.998	0.15	-
D218-2000	<110>	1300 1400	10 <sup>-7</sup> - 10 <sup>-4</sup> 10 <sup>-6</sup> - 10 <sup>-3</sup>	1.07 x 10 <sup>5</sup>	3.86	460.2	.990	0.19	41.4
D218-2000	<001>	1100 1200	10 <sup>-7</sup> - 10 <sup>-4</sup> 10 <sup>-6</sup> - 10 <sup>-5</sup>	8.87 x 10 <sup>-23</sup>	14.7	467.3	.958	1.8	84.8
D218-2000	<001>	1300 1400	10 <sup>-6</sup> - 10 <sup>-3</sup> 10 <sup>-5</sup> - 10 <sup>-3</sup>	3.92 x 10 <sup>1</sup>	7.48	586.2	.992	0.45	37.4
D218-2000	<001>	1200 1300 1400	10 <sup>-7</sup> - 10 <sup>-6</sup> 10 <sup>-7</sup> - 10 <sup>-6</sup> 10 <sup>-7</sup> - 10 <sup>-5</sup>	9.74 x 10 <sup>2</sup>	3.30	393.3	.987	0.21	24.1
D218-2000 + Aged	<001>	1200 1300 1400	10 <sup>-7</sup> - 10 <sup>-6</sup> 10 <sup>-7</sup> - 10 <sup>-5</sup> 10 <sup>-6</sup> - 10 <sup>-5</sup>	2.20 x 10 <sup>3</sup>	3.41	402.1	.971	0.34	37.6

MICROSCOPIC FRACTURE BEHAVIOR OF SINGLE  
CRYSTALLINE INTERMETALLICS

M. Göken, M. Maßmann, F. Thome and H. Vehoff  
University of Saarland  
Dept. of Material Science & Process Technology, Bldg. 43B  
PO Box 151150, D-66041 Saarbrücken, Germany  
email: m.goeken@matsci.uni-sb.de

Abstract

Local measurements of the fracture processes with an atomic force microscope (AFM) on NiAl single crystals in the so called soft orientation indicate stable quasi brittle crack growth in steps of some micrometers. The development of a plastic zone in front of the crack tip was observed *in-situ* with an AFM. From such measurements the burgers vector orientation as well as the dislocation distribution in front of the crack tip can be determined. The high resolution capability of the AFM, especially in the vertical direction, allowed observations of elastic displacements  $u_z$  at brittle crack tips for the first time. From these measurements the local stress intensity at the crack tip can be determined by comparison with calculations of the displacements  $u_z$ . An interpretation of these AFM measurements is done with three-dimensional anisotropic Finite Element calculations, since no analytic solution is available.

Introduction

The most challenging problem for structural applications of intermetallic materials like the cubic B2 alloys NiAl or FeAl is still the brittleness at room temperature. Therefore, investigations of the local fracture behavior is necessary under the aspect of improving the toughness for future high temperature applications. Recent results indicate strong influences of point defects and the degree of purity on the fracture toughness, which are not understood fully [1,2]. Observations of the fracture processes at the crack tip with very high magnifications, as achieved with an atomic force microscope (AFM), can give a considerable contri-

bution to an understanding of microscopic failure mechanisms.

In this work, an attempt is made to analyze the fracture processes at a very high magnification with an AFM. Three different processes are examined inside an AFM at the crack tip, crack tip blunting, dislocation emission - with burgers vector components vertical to the specimen surface - and elastic displacements  $u_z$  in the immediate crack tip region. The results are compared with anisotropic Finite Element Method (FEM) simulations in order to understand the fracture mechanism and brittleness of the intermetallics. Due to the strong anisotropy of NiAl the FEM calculations are performed for the anisotropic case and compared with an isotropic solution.

Measurements of dislocation distributions at the crack tip can be compared with dynamic computer simulations of the brittle to ductile transition [3]. These calculations are based on a dislocation mobility model, and take into account all forces and interactions between emitted dislocations in the crack tip field. Emission of dislocations is permitted in the model only directly at the crack tip. The simulations predict the observed dependencies of the fracture toughness on temperature and rate as described in reference [3]. But the interaction distance between cracks and interfaces and the plastic zone size are too small. Since dislocation multiplication occurs in the whole fracture process zone, experimental measurements of the distribution of dislocation sources are needed, to improve the simulations and interpretations of the fracture behavior.

For the measurements, an AFM with a so called

scanning tip design was used, with which large specimens can be investigated. A new device was built, that allows continuous loading of small four-point bending specimens inside this AFM. Preceding measurements [4] showed, that brittle crack growth alternate with plastic crack blunting through dislocation emission. The plastic crack opening displacement COD, which precedes an unstable crack jump was used to calculate the fracture toughness  $K_{IC}$ . A simple prediction could be given for the isotropic case by:

$$K_{IC} = \sqrt{COD \cdot E \cdot \sigma_Y} \quad (1)$$

Only small deviations are obtained if the exact formula for the anisotropic *soft* orientation is considered in this way. With a yield stress  $\sigma_Y$  of 150 MPa, an elastic modulus  $E$  of 188 GPa and a measured COD of 85 nm this led to a fracture toughness of  $1.5 \text{ MPam}^{1/2}$ . Even the results from this rather simple estimation are in good agreement with other experimental measurements on similar specimens from the same single crystals. The reported values for the fracture toughness of NiAl cover a range between 1.5 and  $15 \text{ MPam}^{1/2}$ , depending mainly on the heat treatment of the specimens. Theoretical calculations from the surface energy predicts a value of nearly  $1 \text{ MPam}^{1/2}$  [5]. However, a more precise analysis is in progress, which considers the measured dislocation distribution, as well.

#### AFM measurements

##### Experimental

Highly resolved measurements of surface displacements on in-situ deformed 4-point-bending specimens were performed with an AFM. This technique allows investigations of the surface topography

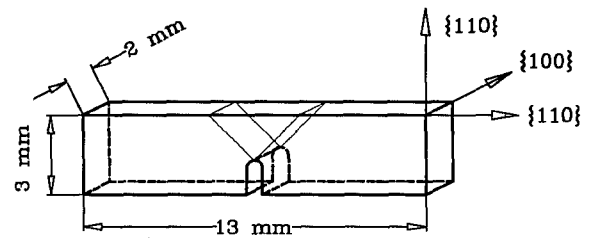


Figure 1: 4-point-bending specimen in a *soft* orientation.

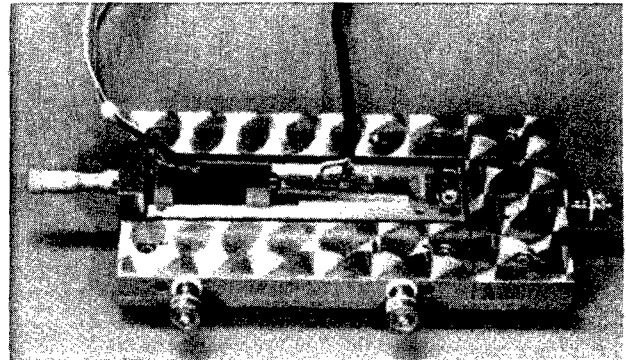


Figure 2: Loading device for the bending specimens. Loading is conducted with the piezostack on the left (black cylinder). The AFM head stands on top of the base plate with three micrometer screws as feet.

with a resolution limit of below  $1/10 \text{ nm}$  in the vertical direction and of  $1 \text{ nm}$  in the lateral direction (depending from the tip size radius). So, plastic and elastic deformations as low as one burgers vector length can be determined under laboratory air conditions routinely. Loading of

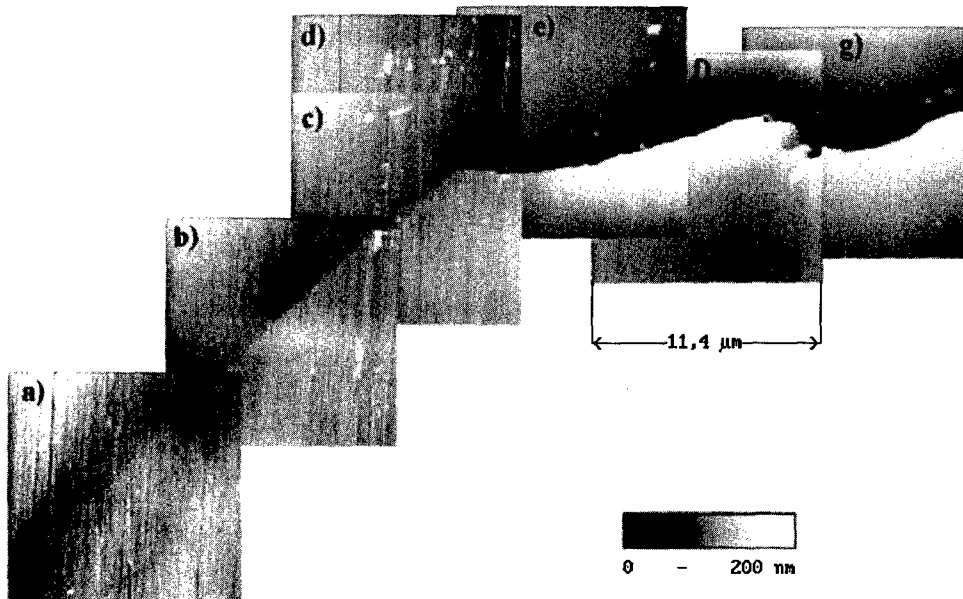


Figure 3: AFM image of a mode III crack in NiAl. 7 single images were combined to form a mosaic overview image along the crack line and a glide step. The crack tip is located in partial images c).



bending specimens (Fig. 1) has to be performed in a very rigid and compact device. The stiffness of this machine should be as high as possible to ensure imaging of quasi-stable crack growth in the brittle intermetallics. Since AFM is a vibration sensitive technique, the whole apparatus must be constructed small and compact. First measurements in this way were conducted with a miniaturized bending device described elsewhere [4]. This device fulfilled the above described requirements, but the possible deformation range was limited. Continuous loading of the bending specimens was only possible over a range of 4  $\mu\text{m}$ . The reason for this limit is based in the design of the AFM, which had been used there. Since scanning was performed by scanning the whole specimen and not the probe tip, the diameter of the loading device was restricted to 22 mm. Progress in the development of the scanning probe microscopy makes now reliable instruments with a scanning tip design available. Therefore, we developed a new loading device for such an AFM, that allows much larger deformations under the microscope. Figure 2 shows a photograph of the used loading device for the bending specimens. Loading is conducted under the AFM by a large piezostack with a maximum extension of 40  $\mu\text{m}$ . The piezo is extended by applying an electric voltage and the amount of extension is controlled simultaneously by strain gauges glued on the piezo, to exclude piezo hysteresis. Force control is performed by a second strain gauge fixed on a load beam between piezo stack and bending specimen. Since the fracture test is conducted in-situ in the AFM, the amount of bending can be evaluated directly from the AFM images.

#### Experimental AFM Results

As an example to demonstrate the high resolution of the AFM, Figure 3 gives an overview image of a precracked specimen. A crack with a large mode III opening component is visible, since a thin sheet

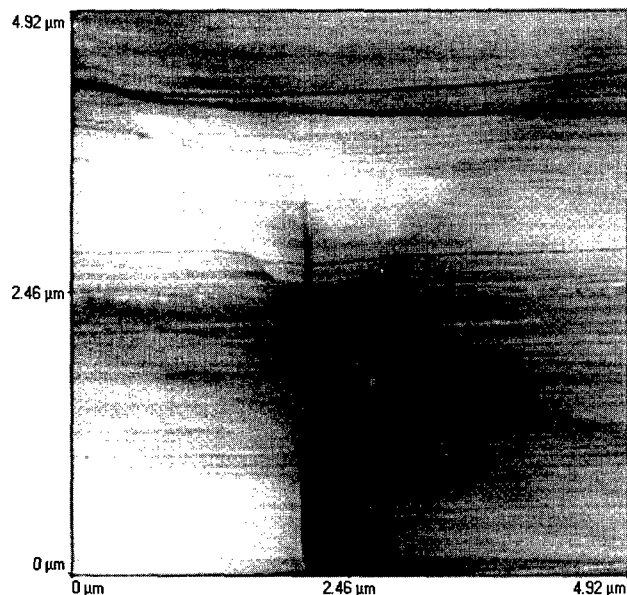


Figure 4: Mode I crack with glide traces. Dislocations were emitted on two (100) glide planes intersecting the crack tip. The gray scale covers 110 nm.

of a CT type specimen was used. At the end of the crack, a glide step emanates from the crack tip on a plane, which is inclined to the crack plane by an angle of 45°. These observations correspond with the known slip systems {100}<100> and cleavage plane (110) for NiAl. A description of a more detailed analysis of loaded mode III cracks, where the development of the plastic zone and the distribution of dislocations along the glide step were determined, is given in a reference [6].

In mode III loading no real blunting of the crack through dislocation emission occurs. All dislocations emitted from the crack must have at least a direction component vertical to the specimen surface, or have a pure screw character as in Fig. 3. For mode III loading the energy release rate  $G$  can be calculated from the shear deformation  $B$  by [7]:

$$G = \frac{2\sqrt{2}\sigma_y B}{(1+\nu)} = \frac{K_{III}^2}{E} \quad (2)$$

The shear mode deformation in Fig. 3 is 15 nm, which leads then to a stress intensity  $K_{III}$  of 0.95  $\text{MPa}\sqrt{\text{m}}$ .

Mode I cracks on the other hand, blunt through dislocations with burgers vectors parallel to the specimen surface, that create no slip steps vertical to the specimen surface. Figure 4 shows an AFM image of NiAl with a crack tip loaded in mode I. The crack flanks are V-shaped (blunted) through alternating slip on two perpendicular glide planes. The glide process is only visible, since remaining polishing traces or scratches are kinked on the surface. Figure 5 illustrates this kinking of polishing traces through dislocations. The amount of this scratch displacement given by the number of dislocations is relative high immediate at the crack tip and decreases at larger distances. The maximum scratch displacement amounts 110 nm, which is more or less constant in the crack tip region. From an absence of a gradient of

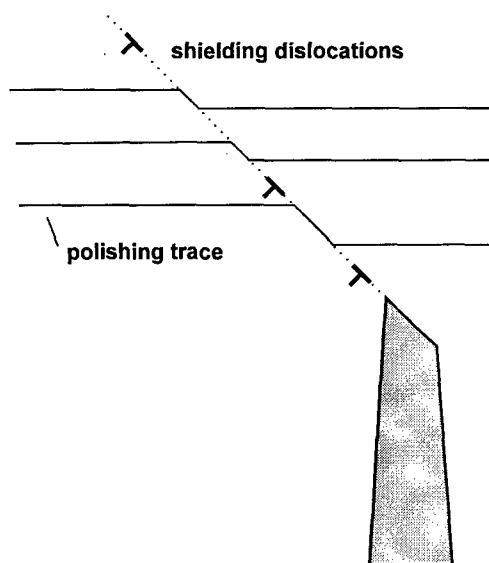


Figure 5: Schematic of kinking from polishing traces. Shielding dislocations are emitted by the crack tip on one glide plane.

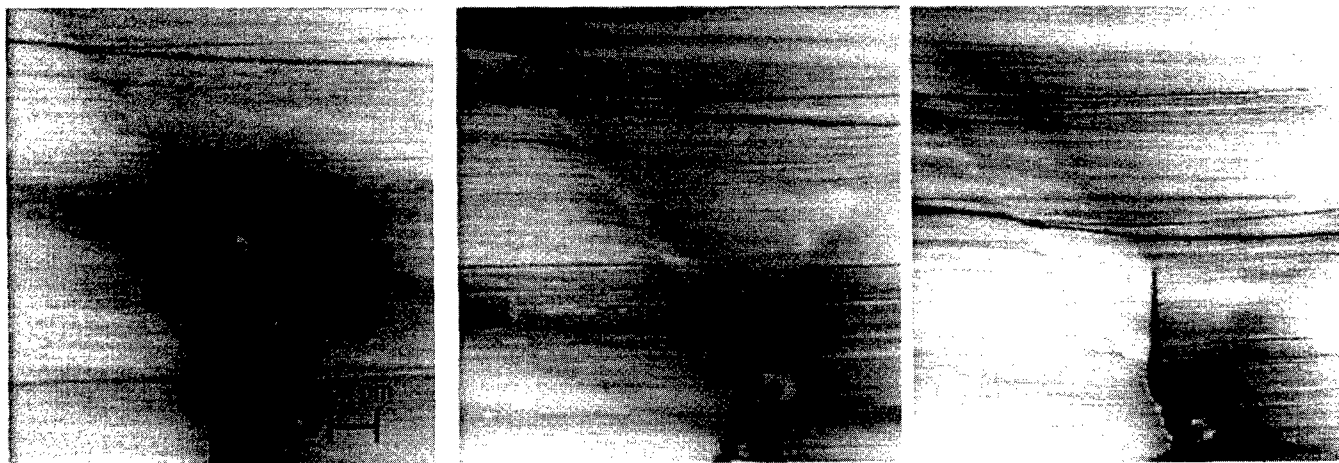


Figure 6: AFM images of the same crack at different applied loads with a scansize of  $4 \times 4 (\mu\text{m})^2$ . In the left image the nearly unloaded crack has emitted only dislocations on one glide plane. In the middle image, the second glide plane was activated and in the right image, the crack has propagated stable in a brittle manner (i.e. microcleavage). Compare also the image on the right with Fig. 4 where the same crack is shown after deloading.

the scratch displacement we conclude, that a region of at least  $1-2 \mu\text{m}$  around the crack tip is a dislocation free zone. No displacements vertical to the surface are found at the glide traces. From this observations it can be deduced that pure edge dislocations are emanated from the crack tip or a dislocation source at the crack tip, which contribute to a shielding of crack tip stresses. On the left side of the crack the dislocations are concentrated on a single glide plane, whereas on the right hand side *kinking* is blurred over nearly  $1 \mu\text{m}$  and therefore different parallel glide planes are activated.

In Figure 6, three images at different loads are given, where an opening of the crack tip combined with the evolution of a plastic zone and a discontinuous crack growth can be observed. *Kinking* of the scratches is related to the shape of the blunted crack (as illustrated in Fig. 5) and the orientation of the burgers vector could be determined from the direction of *kinking*. This is confirmed by the given series of AFM images. At the crack tip the scratch displacement must be equal

to the COD. Since this displacement can be examined with higher accuracy than the crack tip blunting, this value is used for the COD. The scratch displacement increases by loading, and is connected to the stress intensity factor by equation (1). From this, the local critical stress intensity factor of this NiAl specimen can be estimated to  $2.1 \text{ MPam}^{1/2}$ , with an assumed elastic modulus of  $188.1 \text{ GPa}$ , a yield strength of  $150 \text{ MPa}$  and a COD of  $155 \text{ nm}$ .

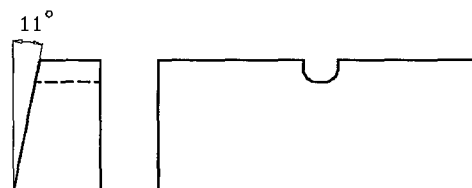


Figure 7: Specimen type with inclined surface.

In another experiment we inclined one surface of the specimens to emphasize the dislocation obser-

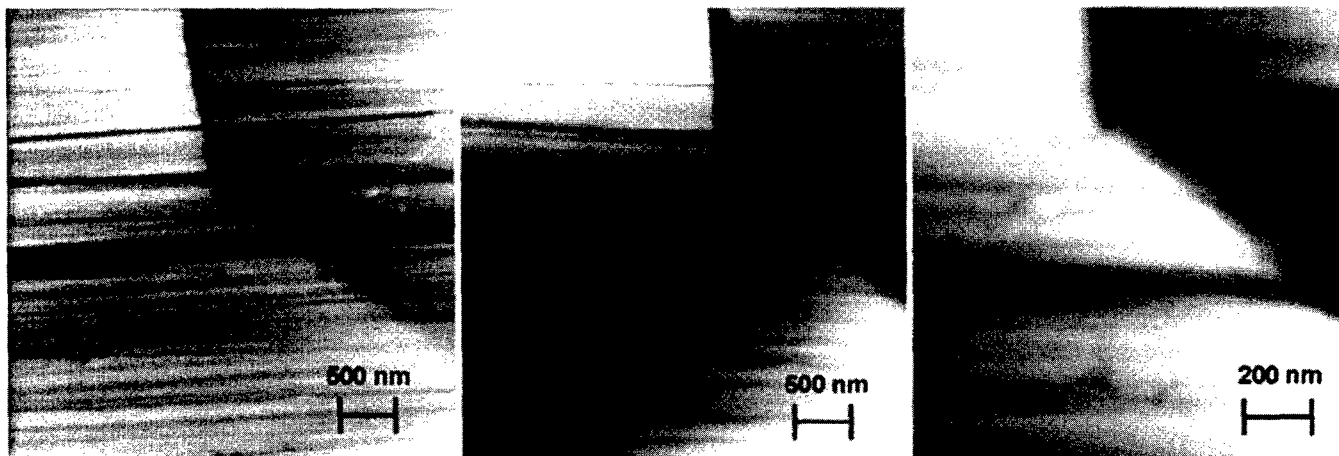


Figure 8: AFM images of slanted bending specimens. Now, the burgers vector of edge dislocations has a component vertical to the specimen surface.



vation as illustrated in Figure 7. In these prismatic specimens pure edge dislocations have a burgers vector component vertical to the specimen surface and therefore produce a glide step on the surface. This allows the observation of pure edge dislocations directly, that was, as described above, only detectable by kinking of polishing traces. The inclination of one surface plane amounts  $11^\circ$ , whereas the other orientation dependencies of Fig. 1 are retained.

One example of such measurement is given in Figure 8. The activation of mainly one glide system is obvious. Only a shallow glide step is visible in the first image. Loading of the specimen produces a relative large amount of dislocation movement, which in this specimen type is visible as a glide

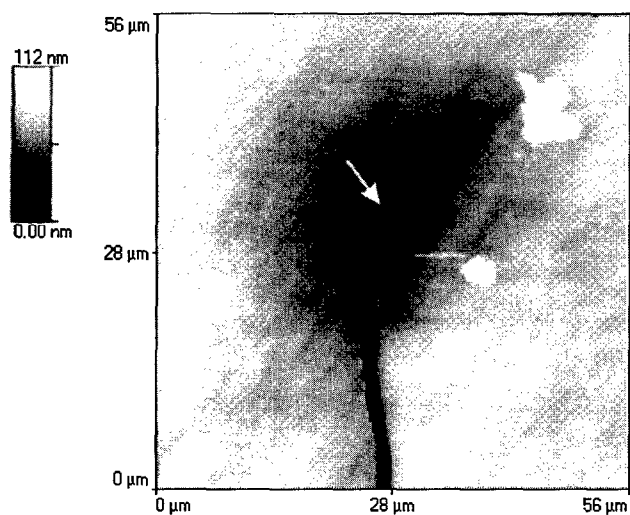


Figure 9a: Low magnification image of plastic and elastic crack tip displacements. An arrow indicates the elastic deformation zone.

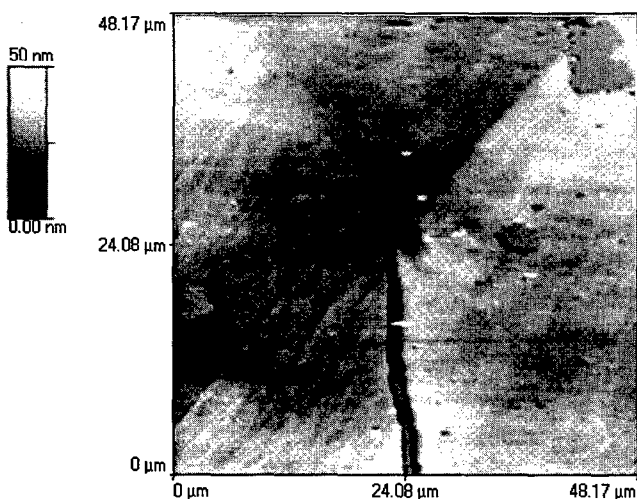


Figure 9b: Arithmetic subtraction of two AFM images with high and low applied load, respectively. The plastic deformations, i.e. the glide step on the right side and a shallow one on the left, prevail in the image.

step as well as kinking of scratches. This situation is enlarged in the right image, where the shape of the blunted crack tip is clearly visible, too.

In addition, next to plastic deformations at crack tips also pure elastic displacements of the specimen surface can be observed in the high stressed region of crack tips. In the following we will restrict ourselves mainly on observations of these elastic deformations at differently loaded mode I cracks. Elastic displacements of the specimen surface in the immediate crack tip region are imaged for the first time directly with AFM. Figure 9a is an example with relative low magnification where both deformation kinds are shown together. Around a small microcrack in front of the main crack an elastic deformation zone is visible at the upper right. A glide step emanates from this microcrack and stops at the upper right corner of the image. By mathematical subtracting pure elastic images from an elastic/plastic image of the same size, these different deformations could be separated and emphasized. The dust particles seen in Fig. 9a as bright spots and all other topographic patterns should disappear or at least be reduced by a large amount by this image processing. This is done in Figure 9b, where an image with a load of half maximum (not shown here) is subtracted from the image in Fig. 9a. Most topographic patterns including the crack diminish almost. Just the glide step remains and is emphasized in this representation, where the height scale is magnified from 112 nm to 50 nm. The two visible glide planes intersect the tip of the small microcrack.

A pure elastic deformation at another crack tip in NiAl is shown in Figure 10. Here a special representation is used, where discrete gray levels represent the height data. Thus, the borderline between two gray levels corresponds to a curve of constant altitude, i.e. constant elastic displacement  $u_z$ . A nearly radially symmetric displacement



Figure 10: AFM image, which shows elastic displacements  $u_z$  at a crack tip. The height differences between two gray levels amounts 7 nm, the scansize was  $11.4 \mu\text{m} \times 11.4 \mu\text{m}$ .

zone around the crack tip with a maximum depth of 46 nm can be seen. The pure elastic character of the displacements is confirmed by turning on and off the load repeatedly. The depth of this displacement fields depend on the local stress intensity factor  $K_I$  at the crack tip. But an evaluation of this local stress intensity factor from the observed elastic displacements requires calculating the elastic displacements from three-dimensional specimens. The measured elastic displacements  $u_z$  are far away from the plane stress solution, which is given by:

$$u_z = K_I \frac{\nu d}{E} \sqrt{\frac{2}{\pi r}} \cos\left(\frac{\phi}{2}\right) \quad (3)$$

This stress state is typically for thin sheets with thickness  $d$  and coordinates  $r, \phi$ , but is not valid at the surface of our bending specimens. Therefore, an evaluation of  $u_z$  can be done only by three-dimensional anisotropic FEM calculations.

#### FEM calculations

FEM calculations were performed with the commercially available software package Marc-Mentat on a HP-735 workstation [8]. The generated net geometry is depicted in Figure 11. A cylindrical net shape around the crack tip with a crack radius of  $1 \mu\text{m}$  and the other specimen dimensions as in Figure 1 was used. The density of nodes is increased radial to the crack front and vertical to the specimen surfaces by a large amount. The smallest distances between two nodes reach  $1 \mu\text{m}$  at the crack tip and at the specimen surface. The net geometry was adjusted as long as the stresses reproduce special cases of known analytical solutions. In the center plane of the specimen a plane strain case should prevail. For this special case analytical stress field solutions of the crack tip are known also for the anisotropic state [9, 10]. Comparisons of the stresses from FEM calculations and the ana-

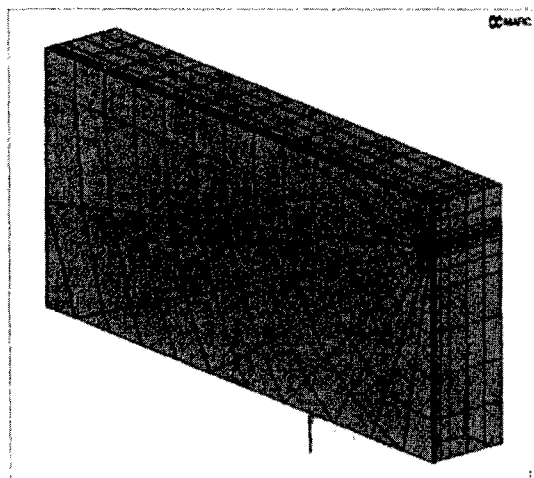


Figure 11: Net geometry of the FEM model. Only the calculated  $\frac{1}{4}$  part of the bending specimen is shown.

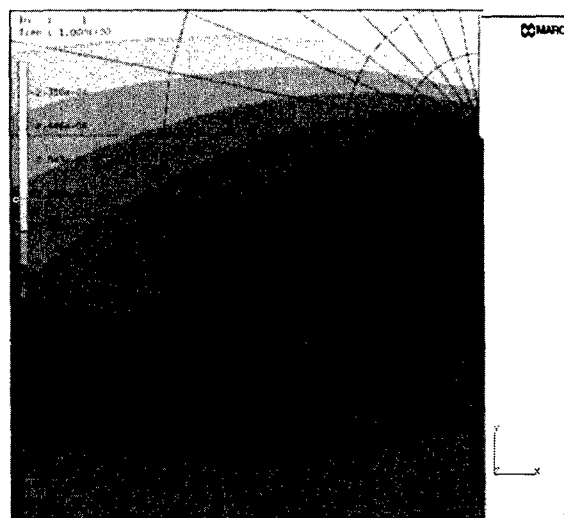


Figure 12: Displacements  $u_z$  at the crack tip calculated by three-dimensional FEM with a crack radius of  $1 \mu\text{m}$ .

lytical solution leads to deviations lower than 5% for the stresses in the crack tip region. At the surfaces of the specimens the stresses  $\sigma_{xx}$  and  $\sigma_{yy}$  must converge to a constant value whereas  $\sigma_{zz}$  has to diminish. Both requirements could be met by adjusting the net geometry.

The applied load was determined by adjusting the calculated displacement fields to the measured. From that the local fracture toughness can be determined. A value of  $3 \text{ MPam}^{1/2}$  was assumed for this specimen. The elastic constants of NiAl were taken from reference [11], i.e.  $C_{11}=199 \text{ GPa}$ ,  $C_{12}=137 \text{ GPa}$  and  $C_{14}=116 \text{ GPa}$ . Figure 12 shows a low magnification image of the calculated displacement field  $u_z$ , where only half of the symmetrical field is reproduced. In Figure 13 the size and height scaling was adjusted to the AFM image of Figure 10 and lines of constant displacements are repre-

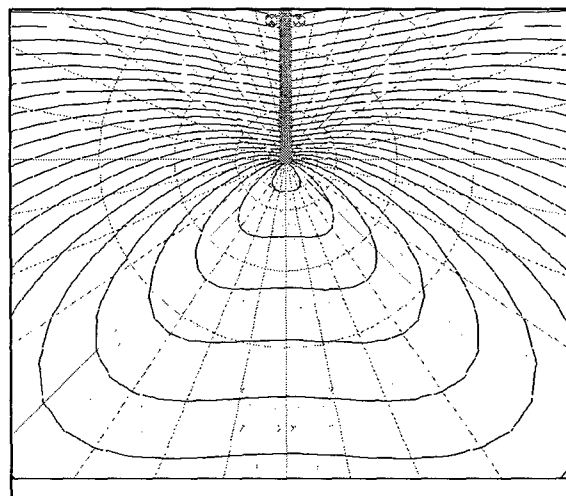


Figure 13: Lines of constant displacement  $u_z$  as calculated by FEM. The height difference between two lines amounts  $2.5 \text{ nm}$  at an applied load corresponding to a stress intensity of  $3 \text{ MPam}^{1/2}$ .

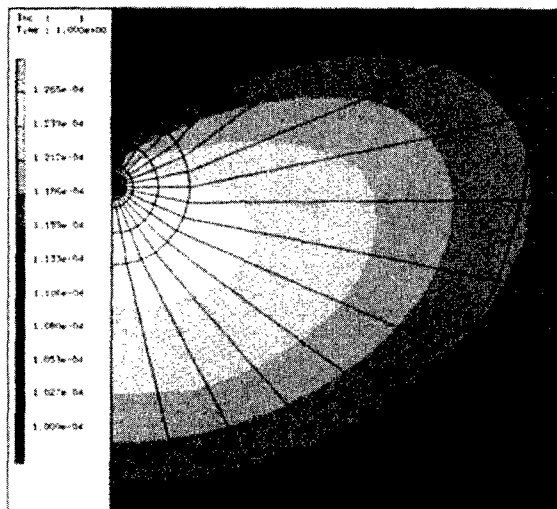


Figure 14a: FEM calculation of the displacements  $u_z$ . The crack front includes an angle of  $+ 26^\circ$  with the normal of the specimen surface (prerunning on the surface).

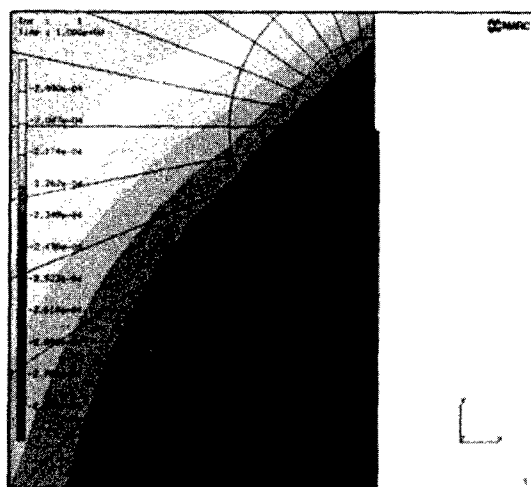


Figure 14b: FEM calculation of the displacements  $u_z$ . The crack front includes an angle of  $- 26^\circ$  with the normal of the specimen surface (prerunning in the specimen).

sented. A comparison of both images show that the calculated and measured displacements corresponds quantitatively. Only the shape of the fields show some differences.

So far, all FEM calculations are based on the assumption, that the crack front is straight and vertical to the specimen surface. The irregular fracture surfaces of NiAl indicate a high probability for nonvertical crack fronts at the surface. Therefore we tried to examine the effect of nonvertical crack front orientations on the elastic displacement fields around a crack tip. This examination is time consuming, because the net geometry has to be adopted for any crack front orientation. Here only the results for angles of  $\pm 25^\circ$  are presented. More details of the FEM analysis will be given in a forthcoming paper [12].

Figures 14a,b show the corresponding displacements fields, for the crack prerunning on the surface and delayed on the surface, respectively. The shape of the displacement fields from the prerunning crack are more radial symmetrically around the crack, whereas the other is stronger stretched in the crack propagation direction. So, the crack front orientation has a strong influence on the shape of the elastic displacement fields and a better agreement of calculated and measured images can be obtained.

### Discussion

AFM measurements clearly show plastic deformation behavior at room temperature in NiAl. The development of the size of the plastic zone can be observed by in-situ straining of standard fracture test specimens. Also, the burgers vector and the operating glide planes of moving dislocations are determinable. Next to these plastic behavior a quasi-stable brittle crack growth mode was observed on the specimen surface. Blunting through dislocation emission and brittle crack growth in steps of some micrometers seem to be concurrent processes before final fracture occurs. A model proposed by Roberts and Hirsch [13] suggests a mechanism for stable crack growth in semi-brittle materials such as Molybdenum. In their model local crack advance is associated with steps in the crack front, from which dislocation loops are emitted. This dislocation loops have either a shielding or antishielding effect on the crack tip stress fields. So the effective stress intensity factor  $K_{eff}$  is raised above the fracture toughness  $K_{IC}$  or lower than that value, which is necessary for quasi-stable crack growth. Computer simulations of such brittle to ductile transitions require information on possible dislocation sources [14]. Simulations of Ochmann et al. [3] assume, that emission of dislocations is allowed only on one glide plane with zero nucleation energy. They calculate all forces and interactions on emitted dislocations and introduce mobility by a velocity law for the dislocations. The results of these calculations led to a qualitative agreement with measured BDT's, but the interaction distance between cracks and interfaces and the plastic zone sizes are predicted too small, compared with the described AFM measurements. The AFM observations of the plastic zone as done by kinking of polishing traces indicate that dislocations are emitted direct at the crack tip or at most at a distance of less than some hundred nanometer. The dislocations travel through a zone of low dislocation density to distances of 4 - 20  $\mu\text{m}$ . Blunting of the crack tip has to be considered in the simulations and, as seen in the experiments, the dislocations often are emitted on parallel glide planes, which are separated up to 1  $\mu\text{m}$ . To get further details on the dislocation sources, also the preexisting dislocations (before loading takes place) must be known and the height resolution has to be increased to resolve single dislocations on the surface.

Measurements of the elastic displacements of the specimen surface at the crack tips should allow determinations of the local stress intensity, which may help understanding the fracture modes.

For this, comparisons with calculations of these displacements has to be performed. Only for isotropic materials and definite values of Poisson's ratio solutions are published in the literature [15, 16]. These solutions are mainly analytical but need some numerical integration.

Since no closed analytical solution for the anisotropic stress fields at a specimen surface are available, numerical calculations with the finite element method were done. The FEM results seem to correspond qualitatively with the AFM measurements (compare Fig. 10 and Fig. 13). The main difference which is obviously visible between AFM images and FEM images (with vertical crack front) is the shape of the displacements. The ideally elastic FEM calculations show displacement fields, which are strongly oriented and located ahead of the crack tip, whereas the shown AFM images nearly have radially symmetric displacement fields around the crack tip. Calculations with nonvertical crack fronts show an influence on the surface displacements by the direction of the crack front. A crack, prerunning on the specimen surface, shows a more radially symmetric displacements field at the surface. More refined experiments are underway, which allow a direct comparison between measured and calculated crack front orientations.

However, the combination of high resolution microscopy with FEM calculations can give a better understanding of the microcleavage behavior of intermetallics. In addition, it might be possible to find the dislocation sources on the specimen surface, if single dislocations can be identified. For this, the mean surface roughness after specimen preparation must be reduced to values in the range of a burgers vector length, to identify single dislocations on the surface.

#### Summary

In-situ loading experiments were carried out on single crystals of NiAl in a modified atomic force microscope. Sequences of dislocations emission, followed by discontinuous crack growth were evaluated on a submicron scale within the AFM. In addition, elastic deformations at the crack tip were observed, which are compared with FEM calculations. The FEM calculations of the elastic displacements are in good correspondence with the AFM measurements. In these FEM calculations also an inclination of the crack front orientation to the specimen normal was considered, which results in differently shaped elastic deformation fields.

The results proved that NiAl is inherently ductile, however, depending on purity, discontinuous crack growth occurred with local COD's of less than 100 nm and slip band length of nearly 10  $\mu\text{m}$ .

#### References

1. J.E. Hack, J.M. Brzeski, and R. Darolia, Scripta Mater., 27 (1992), 1259-1263
2. G. Bergmann, and H. Vehoff, Mater. Sci. Engng., A192/193 (1995), 309-315
3. P. Ochmann, and H. Vehoff, Mater. Sci. Engng. A, 192/193 (1995), 364-370
4. M. Göken, H. Vehoff, and P. Neumann, J. Vac. Sci. Technol. B, 14 (1996), 1157-1161
5. M. H. Yoo, and C.L. Fu, Mater. Sci. Eng. A, 153 (1992), 470-478
6. M. Göken, H. Vehoff and P. Neumann, Scripta Metall. Mater., 33 (1995), 1187-1192
7. J.F. Knott, Fundamentals of Fracture Mechanics (London: Butterworth & Co. Publishers, 1973), 117-119
8. M. Maßmann, Diploma thesis, University of Saarbrücken (1997)
9. G.C. Sih, P.C. Paris, G.R. Irvin, Int. J. Fracture Mechanics, 1 (1965), 189
10. T.L. Dragone, and W.D. Nix, Scripta Metall. 22 (1988), 431-435
11. N. Rusovic, and H. Warlimont, Phys. sta. sol. A, 44 (1977), 609-619
12. M. Göken, M. Maßmann, to be published
13. P.B. Hirsch, A.S. Booth, M. Ellis, S.G. Roberts, Scripta Metall. Mater., 27 (1992), 1723-1728
14. S.G. Roberts et al., Physica Scripta, T49 (1993), 420-426
15. J.P. Benthem, Int. J. Sol. Struct., 13 (1976), 479-492
16. J.P. Benthem, Int. J. Sol. Struct., 16 (1980), 119-130

# POINT DEFECT CONCENTRATIONS AND SOLID SOLUTION HARDENING IN NiAl WITH Fe ADDITIONS

L. M. Pike, C. T. Liu\*, and Y.A. Chang

Department of Materials Science and Engineering  
University of Wisconsin, Madison, WI 53706-1595

\*Metals and Ceramics Division, Oak Ridge National Laboratory  
Oak Ridge, TN 37831-6115

## Abstract

The solid solution hardening behavior exhibited when Fe is added to NiAl is investigated. This is an interesting problem to consider since the ternary Fe additions may choose to occupy either the Ni or the Al sublattice, affecting the hardness at differing rates. Moreover, the addition of Fe may affect the concentrations of other point defects such as vacancies and Ni anti-sites. As a result, unusual effects ranging from rapid hardening to solid solution softening are observed. Alloys with varying amounts of Fe were prepared in Ni-rich (40 at. % Al) and stoichiometric (50 at. % Al) compositions. Vacancy concentrations were measured using lattice parameter and density measurements. The site occupancy of Fe was determined using ALCHEMI. Using these two techniques the site occupancies of all species could be uniquely determined. Significant differences in the defect concentrations as well as the hardening behavior were encountered between the Ni-rich and stoichiometric regimes.

## 1.0 Introduction

Point defects, such as vacancies and anti-site defects, are known to strongly affect the properties of intermetallic compounds with the B2 crystal structure. For example, the off-stoichiometric hardening observed in NiAl has been attributed to the presence of constitutional defects (1). Thermally generated defects have also been reported to strongly affect the mechanical properties of such B2 compounds as FeAl, CoAl, and FeCo (2-4). In a

similar manner, the addition of ternary or higher order alloy additions can strongly affect the mechanical and physical properties of B2 compounds, e.g. NiAl (5,6). The addition of a ternary element to an ordered binary compound can drastically affect the concentrations of point defects. These defects are often directly responsible for the observed property changes. It is clear that any investigation of the effects of ternary alloying in this class of materials would benefit from a knowledge of the point defect concentration which result from this alloying. It will be the purpose of this investigation to examine the effect of substitutional ternary alloy additions on both the point defect structure and the resultant solid solution hardening behavior of an ordered B2 compound. The system chosen to investigate is NiAl with ternary Fe additions. This system is of interest since it has been reported that Fe additions affect the room temperature ductility (7) and high temperature creep properties (8) of NiAl.

## 2.0 Experimental

The experiments discussed in this paper are part of a larger study which will be presented elsewhere. For this reason only a brief review of the experimental details will be given here. Twelve alloys were prepared from high purity starting elements by arc melting. Alloys with up to 12 at. % Fe were made in two stoichiometric: Ni-rich (40 at. % Al) and stoichiometric (50 at. % Al). The compositions of the eight alloys are given in Table I. The as-cast alloys were then subjected to homogenizing heat

Table I. The Compositions and Properties of the Alloys in this Study, as Quenched from 700 and 1000°C

% Ni	% Fe	% Al	Lattice Parameter (Å)		Bulk Density (g/cm <sup>3</sup> )		Vacancy Concentration		Hardness (GPa)	
			700°C	1000°C	700°C	1000°C	700°C	1000°C	700°C	1000°C
60	0	40	2.8674	2.8663	6.494	6.476	-0.002	0.002	4.17	4.14
57.6	2.4	40	2.8710	2.8707	6.439	6.437	0.001	0.002	3.78	3.90
54	6	40	2.8770	2.8765	6.385	6.377	0.001	0.003	3.37	3.53
48	12	40	2.8836	2.8832	6.319	6.314	0.001	0.002	2.98	2.98
50	0	50	2.8876	2.8881	5.901	5.886	0.001	0.003	2.50	2.55
48	2	50	2.8881	2.8873	5.883	5.878	0.003	0.004	2.64	2.69
45	5	50	2.8878	2.8868	---	5.842	---	0.009	3.06	3.13
40	10	50	2.8878	2.8861	5.813	5.800	0.010	0.013	3.66	3.77

treatments. Fine powders were prepared from these ingots and given a heat treatment (in vacuum) of 5h/1000°C + water quench (WQ). The lattice parameters of these powders were measured using x-ray diffraction. The remaining portion of the ingots were given a heat treatment of 5h/1000°C + WQ. Sections of the ingots (approximate dimensions: 10 x 10 x 5 mm) were then taken for hardness measurements. The other sections of the ingots were crushed into a coarse powder for density measurements. The density measurements were made using the hydrostatic method. After the lattice parameter, density and hardness measurements, the samples were given a subsequent anneal for 3d/700°C + WQ. The measurements were then repeated. From the lattice parameter and density data, the vacancy concentration of the alloys could be calculated. One discussion of this type of calculation can be found in the review by Chang and Neumann (9).

Selected compositions from above were chosen for analysis with the TEM technique, ALCHEMI. Rods were prepared by arc melting followed by drop casting. These ingots were given homogenizing heat treatments followed by a treatment of 3d/700°C + WQ. TEM samples were prepared from the quenched rods. The details of the ALCHEMI technique will not be presented here, but follow the methods used by Anderson et. al. (10).

### 3.0 Results and Discussion

#### 3.1 Point Defect Hardening in Binary B2 Compounds

Before attempting to discuss solid solution hardening in a ternary B2 compound it is helpful to review the defect structure and point defect hardening in binary B2 compounds, especially for the NiAl system itself. It has been shown that the defect structure of NiAl can be approximated with the triple defect model (9,11). This model is based on the assumption that the majority of defects present are either vacancies on the Ni sublattice or Ni atoms on the Al sublattice (Ni anti-sites). Defects can be present either as constitutional or thermal defects. Constitutional defects consist of Ni anti-sites at Ni-rich compositions and vacancies at Al-rich compositions. Thermal defects consist of vacancies and Ni anti-sites occurring in a two to one ratio. This ratio maintains the site balance of the crystal. The concentrations of vacancies as well as Ni anti-site defects in NiAl as a function of composition are shown in Fig. 1. The lines in this figure are values estimated from the thermodynamic

model of Chang and Neumann (9). The data points are experimentally measured vacancy concentrations taken from Pike et. al. (4). Good agreement is seen between the model and the experimental values. Off-stoichiometric hardening occurs at both Ni-rich and Al-rich compositions. This hardening has been attributed to Ni anti-sites and vacancies, respectively (1). A recent study by Pike et. al. examined the point defect hardening in several B2 compounds including NiAl. It was found that the hardness could often be correlated to the square root of the hardening defect concentration, following the relationship derived for yield stresses in one solid solution hardening (SSH) theory (12). In Fig. 2 the off-stoichiometric hardening in NiAl is plotted vs. the square root of the hardening defect concentration for both Ni-rich and Al-rich compositions. The hardening rate of vacancies is seen to be significantly greater than that of the Ni anti-sites. For all of the B2 compounds considered by Pike et. al., the hardening rates ( $\gamma = dH/d\sqrt{c}$  where H is hardness and c is the hardening defect concentration) of defects fell into two distinct groups. Those of anti-site defects fell in the range G/9 to G/75 and could be linearly related to the term  $1/a|da/dc|$  which is a measure of the elastic dilation of the lattice (where G is the shear modulus and a is the lattice parameter). This suggests that the elastic "size effect" is at least partially responsible for the hardening caused by anti-site defects. The hardening rates of vacancies fell in the range G/3.1 to G/4.1. Thus, vacancies are considerably more effective hardeners than are anti-site defects. A correlation between the hardening rates of vacancies and the lattice dilation was not found. The hardening rate of vacancies may be affected by such factors as clustering or association with impurities.

#### 3.2 Point Defect Concentrations in Fe-doped NiAl

To understand the SSH which results from ternary alloying Fe to NiAl, it is important to first develop an understanding of the point defect concentrations which arise as a result of this alloying. Firstly, the Fe additions may occupy either the Ni or the Al sublattice (or both), affecting the hardness in significantly different fashions. Secondly, the addition of Fe may affect other point defect concentrations such as vacancies or Ni anti-site defects. For this reason the first step in our analysis will be to determine the defect concentrations which result from ternary alloying Fe to NiAl.

In a triple defect compound such as NiAl, it is assumed that the Al anti-site ( $Al^{Ni}$ ) and Al-site vacancy ( $\square^{Al}$ ) concentrations are negligible (we have introduced the notation  $A^b$  to indicate the

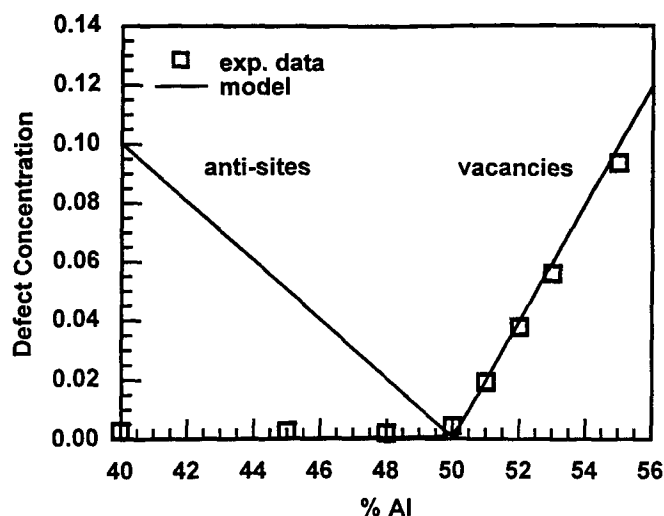


Figure 1: The vacancy and Ni anti-site concentrations in NiAl at 1000°C as calculated from the thermodynamic model along with experimentally determined vacancy concentrations of samples quenched from 1000°C (4).

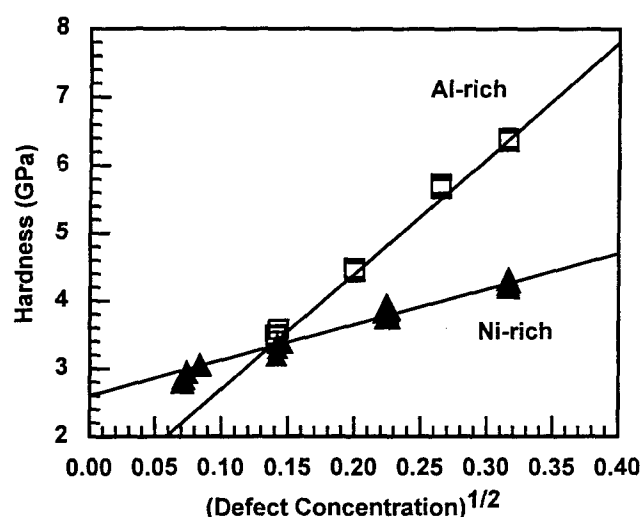


Figure 2: The hardness of Ni-rich and Al-rich NiAl vs. the square root of the Ni anti-site and vacancy concentrations, respectively (4).

species A located on the b sublattice; the symbol  $\square$  represents a vacancy). Therefore, there are six site occupancies which must be determined to fully characterize the point defect concentration of the crystal. These are the concentrations of  $\text{Ni}^{\text{Ni}}$ ,  $\text{Fe}^{\text{Ni}}$ ,  $\square^{\text{Ni}}$ ,  $\text{Ni}^{\text{Al}}$ ,  $\text{Fe}^{\text{Al}}$ , and  $\text{Al}^{\text{Al}}$ . Through mass and site balances the number of unknowns is reduced to two. Thus, there are two experimental variables which must be determined for any given composition and heat treatment in order to determine all point defect concentrations. The first variable we will measure is the vacancy concentration which can be determined by combining lattice parameter and bulk density measurements. This has been done for a number of binary B2 compounds (4, 9). A second experimental variable can be determined using the TEM technique ALCHEMI. Many

experimental difficulties which plagued the accuracy of early work using this technique have recently been overcome. Using this improved technique Anderson (13) was able to determine the site preference of several ternary additions to the FeAl system. In the present study ALCHEMI was used to determine the  $\text{Fe}^{\text{Ni}}/\text{Ni}^{\text{Ni}}$  ratio of several alloys. This information, combined with the vacancy concentration measurements was enough to fully determine the site occupancies resulting from Fe additions to NiAl.

**3.2.1 Fe added to Ni-rich NiAl.** First we will consider the case where Fe is added to replace Ni in Ni-40Al. Alloys were made from 0 to 12 at. % Fe, i.e.  $\text{Ni}_{60-x}\text{Fe}_x\text{Al}_{40}$  where  $x$  varies from 0 to 12. The lattice parameters of these alloys as quenched from 1000°C are shown in Fig. 3. The lattice parameter is seen to increase with increasing Fe concentration. The bulk densities of these alloys are listed in Table I. The vacancy concentrations as quenched from 1000°C, as calculated from the lattice parameter and bulk density, are shown in Fig. 4. Here the vacancy concentration is defined as the number of vacancies per the total number of atoms in the crystal. It can be seen that the vacancy concentration is around 0.002 (0.2 %) for all compositions. This is a relatively small value and approaches the threshold of detection. The vacancy concentration of these alloys as quenched from 700°C was also found to be very small. The  $\text{Fe}^{\text{Ni}}/\text{Ni}^{\text{Ni}}$  ratio of samples quenched from 700°C was determined using ALCHEMI. This data, combined with the vacancy concentration data, provided the information needed to determine the concentrations of Ni and Fe on the Al sublattice (which we will refer to as Ni and Fe anti-site defects, respectively). These are shown in Fig. 5. From this figure it is clear that as Fe is added to Ni-40Al, Fe anti-site defects begin to replace the Ni anti-site defects. This trend continues until around 10 at. % Fe where the anti-site concentrations begin to level off. At this point Fe begins to occupy the Ni sublattice in significant numbers. The  $\text{Fe}^{\text{Ni}}$  concentration is also shown in Fig. 5 and is significantly lower than the Fe anti-site ( $\text{Fe}^{\text{Al}}$ ) concentration for all of the alloys. These results clearly indicate that Fe atoms preferentially occupy the Al sublattice in Ni-rich NiAl. The above results are in qualitative agreement with predictions based on thermodynamic considerations (14).

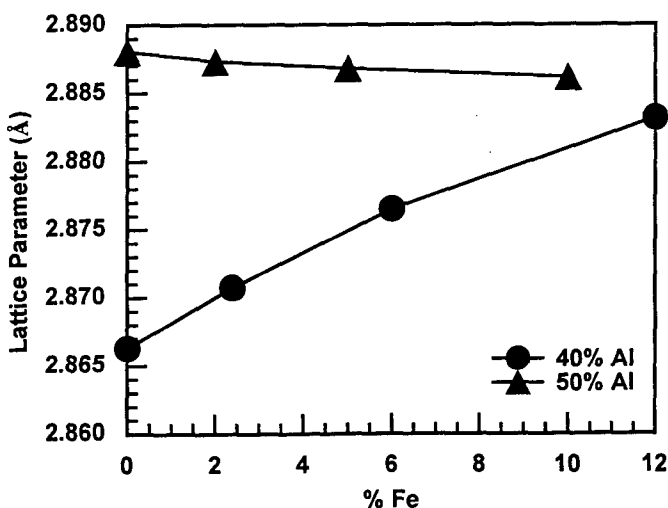


Figure 3: The lattice parameter vs. Fe concentration.

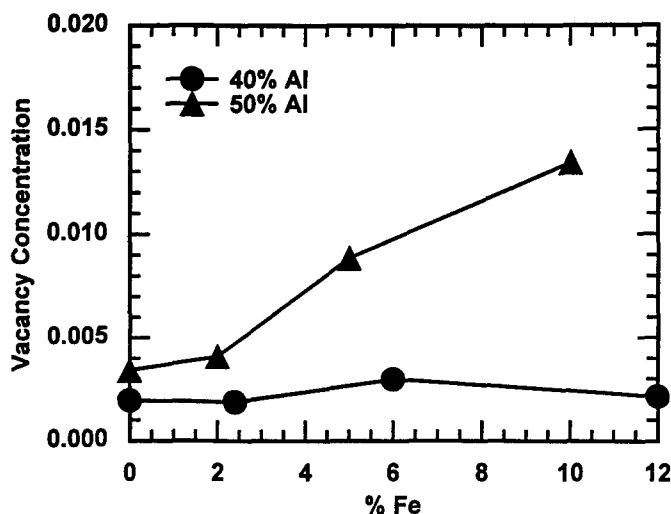


Figure 4: The vacancy concentration vs. Fe concentration.

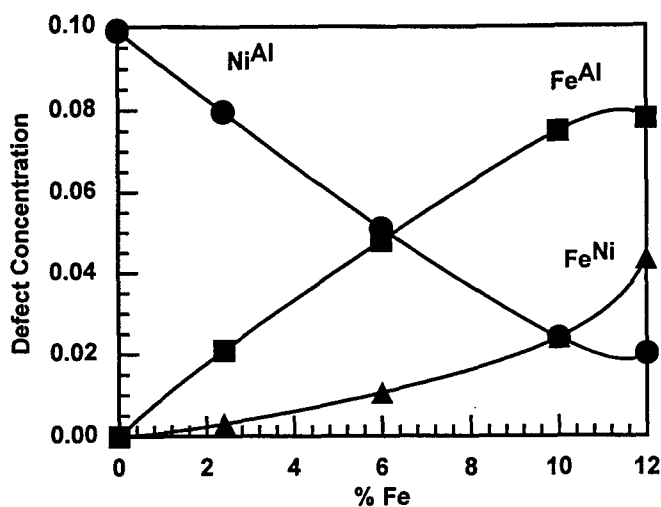


Figure 5: The concentrations of NiAl, FeAl, and FeNi defects vs. Fe concentration in the 40 at. % Al alloys.

**3.2.2 Fe added to Stoichiometric NiAl.** We next consider the case where Fe is added to replace Ni in Ni-50Al. Alloys were made from 0 to 10 at. % Fe, i.e.  $\text{Ni}_{50-x}\text{Fe}_x\text{Al}_{50}$  where  $x$  varies from 0 to 10. The lattice parameters of the alloys as quenched from 1000°C are shown in Fig. 3 and are seen to decrease slightly as the concentration of Fe is increased. The bulk densities are listed in Table I. The vacancy concentrations are shown in Fig. 4 for samples quenched from 1000°C. These are seen to monotonically increase from 0.003 to 0.013 (0.3 to 1.3%) as the Fe concentration increases from 0 to 10 at. %. A similar trend was observed in the samples quenched from 700°C. The Ni and Fe anti-site concentrations are shown in Fig 6. These were calculated using the vacancy concentration measurements of the present study combined with the ALCHEMI data from Duncan (15). For "stoichiometric" alloys such as these, any anti-site type defects are thermal defects. From this data it can be seen that the anti-site defect concentrations are small (relative to the number of FeNi defects), and that those anti-site defects that are present are primarily Fe anti-sites. The number of Fe anti-sites is seen to increase slightly as the concentration of Fe is increased. However, the

majority of the Fe is located on the Ni sublattice. The concentration of these FeNi defects are also shown in Fig 6. Thermodynamic calculations by Kao et. al. yielded estimates qualitatively similar to the above results (14,16).

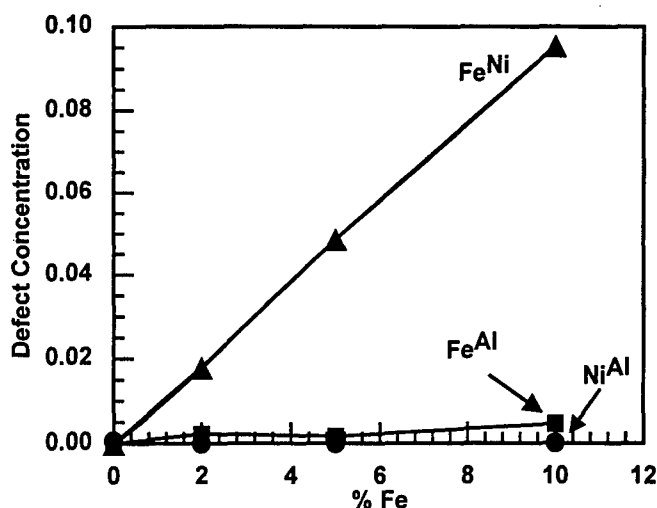


Figure 6: The concentrations of NiAl, FeAl, and FeNi defects vs. Fe concentration in the 50 at. % Al alloys. This data is calculated using the present vacancy concentration combined with the ALCHEMI data of Duncan (15).

### 3.3 Solid Solution Hardening in Fe doped NiAl

As discussed in section 3.2, the addition of Fe to NiAl can significantly affect the numbers and types of point defects. Each of these defect types will have a unique hardening rate. In addition, as was seen in the preceding section, there is often more than one type of defect present in significant numbers. Based on information garnered from SSH in binary B2 compounds, much useful qualitative information can be found for the SSH in Fe-doped NiAl. However, if a quantitative method of examining the solid solution hardening behavior is desired when there is more than one defect type present, a method of adding the two effects must be considered. Numerous methods for adding the effects of multiple hardening sources have been suggested (a list of these has been compiled by Gypen and Deruyttere (17)). One of these proposed by Koppelaar and Kuhlmann-Wilsdorf (18) is the "mean square law". This assumption suggests that the square of the total increase in the shear yield stress is equal to the sum of the squares of the changes in the shear yield stress if the two defects were considered separately. In a computer simulation, Foreman and Makin (19) found this rule to be applicable to a wide range of situations. Furthermore, using theoretical arguments Gypen and Deruyttere (17) found the mean square law to be expected when the individual defect hardening follows a square root relationship. If the shear yield stress is assumed to be roughly proportional to the hardness, the mean square law can be extended to the change in hardness:

$$\Delta H = \sqrt{(\gamma_1 c_1^{1/2})^2 + (\gamma_2 c_2^{1/2})^2 + \dots + (\gamma_n c_n^{1/2})^2} \quad [1]$$

where  $H$  is the hardness,  $\gamma_x$  and  $c_x$  are the hardening rate and defect concentration of the defect of type  $x$ , and  $n$  is the total number of different types of defects. The proportionality of the hardness to the yield stress is strictly valid only for perfectly plastic materials.



Unfortunately, the brittle nature of many of these compounds often makes direct measurement of the yield stress difficult. In the following sections we will investigate the SSH behavior of Fe-doped Ni-rich and stoichiometric NiAl.

**3.3.1 Fe added to Ni-rich NiAl.** The hardness of the  $\text{Ni}_{60-x}\text{Fe}_x\text{Al}_{40}$  alloys is shown in Fig. 7. The hardness is seen to decrease with increasing Fe concentration. That is, Fe actually causes solid solution softening in Ni-rich NiAl. A rational explanation for this unusual observation can be offered after consideration of the effect of Fe on the point defect concentrations in these alloys. As discussed in section 3.2.1, the two major defects in these alloys are Ni and Fe anti-site defects. The former being replaced by the latter as the concentration of Fe is increased. The Goldschmidt radii of Ni, Fe, and Al are 1.24, 1.27, and 1.43, respectively (20). A smaller Ni atom on the Al sublattice would obviously cause a contraction of the lattice and therefore be expected to harden the material. In a similar manner, an Fe atom on the Al sublattice would be expected to cause hardening. However, as the Fe atom is somewhat larger than the Ni atom, the Fe anti-site would be expected to be a less potent hardener than the Ni anti-site. Therefore, as Fe is added to Ni-40Al, Ni anti-sites (potent hardeners) are being replaced by Fe anti-sites (less potent hardeners). The net result would be a decrease in hardness. This decrease is most likely responsible for the solid solution softening observed in Fig. 7.

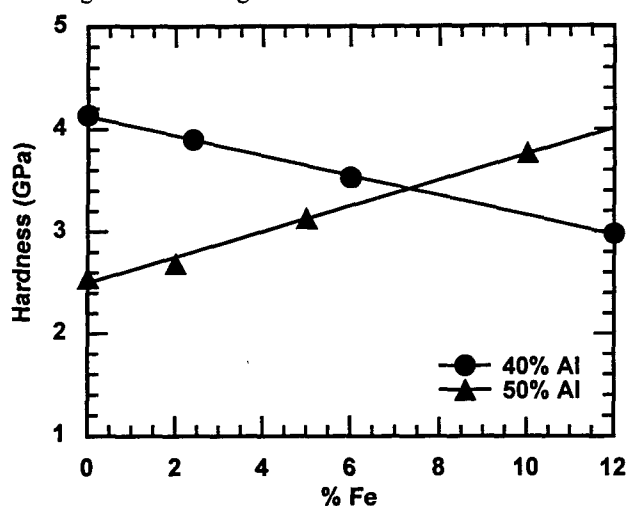


Figure 7: The hardness vs. Fe concentration.

Let us now consider whether the observed softening can be rationalized in a quantitative manner. From the study on binary B2 compounds the hardening rate of Ni anti-sites was around  $G/12$  (4). However, the hardening rate of Fe anti-sites in NiAl is not directly measurable due to the presence of more than one type of defect. Nevertheless, it is possible to estimate this hardening rate by recalling that the hardening rate of anti-site type defects has been shown to correlate to the lattice dilation of the hardening defect (4). Thus, it becomes necessary to determine the lattice dilation of Fe anti-site defects. From lattice parameter data of binary NiAl, the lattice dilation of Ni anti-sites was found to be  $-0.076$ . The increase in the lattice parameter with increasing Fe concentration seen in Fig. 3 represents the sum of the effects of removing Ni anti-sites while adding Fe anti-sites. If it is assumed that lattice dilations add linearly when there is more than one type of defect present (a

reasonable assumption considering most B2 compounds follow Vegard's law (9)), then the dilation of Fe anti-sites can be estimated from Fig. 3 to be  $-0.018$ . Thus, the lattice dilation of Fe anti-sites is considerably less than that of Ni anti-sites. With this dilation, an estimate for the hardening rate of Fe anti-sites can be made from the observed relationships between hardening rates and lattice dilations in binary B2 compounds (4). A value in the range of  $G/25$  to  $G/600$  is found, making the Fe anti-site a relatively weak hardener.

Taking the hardening rate of Ni anti-sites ( $G/12$ ) and the data of Fig. 7, Eq. 1 can be solved to estimate the hardening rate of Fe anti-sites. A value of  $G/35$  is found. This value lies well within the range estimated using the lattice dilation. The lattice dilations and hardening rates are summarized in Table II.

Table II The Lattice Dilations and Hardening Rates of Point Defects Important to this Study

Defect Type	Sub-lattice	Lattice Dilation $1/a(da/dc)$	Estimated Hardening Rate $\gamma$ (GPa)	Experimental Hardening Rate $\gamma$ (GPa)
vacancy	Ni	$-0.081$ (4)	—	$G/4.1$ (4)
Ni anti-site	Al	$-0.076$ (4)	—	$G/12$ (4)
Fe atom	Ni	$0.007$ (21)	$G/40$ to $0$ <sup>b</sup>	less than $G/60$ <sup>c</sup>
Fe atom	Al	$-0.018$	$G/25$ to $G/600$ <sup>b</sup>	$G/35$ <sup>d</sup>

<sup>a</sup> The shear modulus,  $G$ , of NiAl is 70 GPa (22).

<sup>b</sup> These estimates are based on the lattice dilation and the data available for the relationship between the lattice dilations and hardening rates of anti-site defects in binary B2 compounds (4).

<sup>c</sup> From applying Eq. [1] to the hardening data for the addition of Fe to stoichiometric NiAl.

<sup>d</sup> From applying Eq. [1] to the hardening data for the addition of Fe to Ni-rich NiAl.

**3.3.2 Fe added to Stoichiometric NiAl.** The hardness of the  $\text{Ni}_{50-x}\text{Fe}_x\text{Al}_{50}$  alloys is shown in Fig. 7 to increase as the concentration of Fe is increased. From the discussion in section 3.2.2, we must consider three types of point defects in the stoichiometric alloys: Fe anti-sites, Fe on the Ni sublattice ( $\text{Fe}^{\text{Ni}}$ ), and vacancies. All of these defects increase in number as the concentration of Fe increases. The question arises as to how do these different defect types contribute to the observed hardening. The hardening rate of vacancies in NiAl is around  $G/4.1$  (4), while the hardening rate of Fe anti-sites was found in the previous section to be around  $G/35$ . Thus, the only unknown hardening rate is that of the  $\text{Fe}^{\text{Ni}}$  defects. The lattice dilation of these defects has been estimated to be  $0.007$  using lattice parameter data of Al-rich NiAl (21). Following the relationship between hardening rates and lattice dilations in binary B2 compounds (4), a hardening rate of  $G/40$  to  $0$  can be estimated from this dilation. Solving Eq. [1] using the hardness data in Fig. 7, a hardening rate for  $\text{Fe}^{\text{Ni}}$  defects of less than  $G/60$  is calculated. This is well within the range estimated above. Consideration of the terms in Eq. [1] for this case reveals that the potent hardening rate of vacancies is responsible for making the vacancy term the dominant term in the equation. In effect, the observed hardening can be attributed solely to the increasing vacancy concentration. To

illustrate this point consider Fig. 8 where the hardness of the stoichiometric alloys is plotted against the square root of the vacancy concentration. The data is seen to fall along a line. The slope of this line is  $G/4.1$ , the same hardening rate found for vacancies in binary NiAl (4). The strong role vacancies play in hardening these stoichiometric alloys has also been explored by Duncan (15).

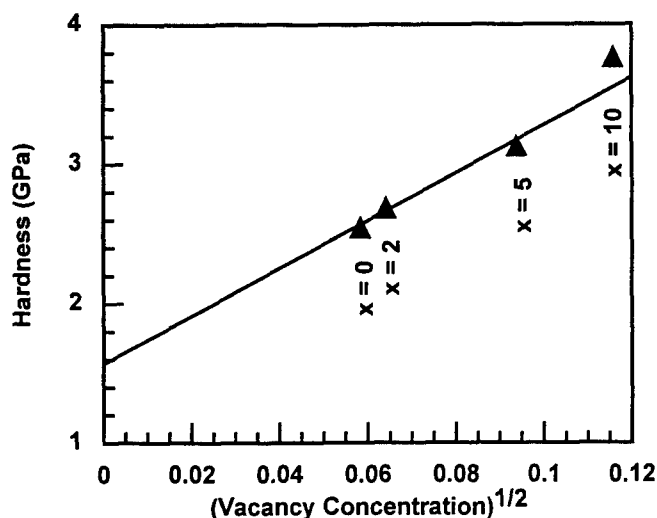


Figure 8: The hardness vs. the square root of the vacancy concentration in the  $\text{Ni}_{50-x}\text{Fe}_x\text{Al}_{50}$  alloys.

#### 4.0 Conclusions

The effects of Fe additions on the defect concentrations and the hardness of NiAl were investigated. Two compositional ranges were considered: Ni-rich and stoichiometric. It was found that there were significant differences in the hardening characteristics between the two regimes. An understanding of the site occupancy of the ternary Fe addition as well as the effect of this addition on the concentrations of other point defects, such as vacancies and Ni anti-site defects, was essential in rationalizing the observed hardening behaviors. To determine these defect concentrations, the vacancy concentration was experimentally determined on the Fe doped alloys. In addition, ALCHEMI was performed to determine the site occupancy of the Fe additions as well as the Ni anti-site concentrations. The lattice dilation of Fe defects on both the Ni and Al sublattices was estimated from lattice parameter data. Using the correlation between lattice dilation and hardening rates observed in binary B2 compounds (4), estimates were made of the hardening rates of these Fe defects.

Apparent solid solution softening by Fe was observed in the Ni-rich alloys. This softening was attributed to the replacing of Ni anti-site defects (potent hardeners) with Fe anti-sites (less potent hardeners). The net result being a decrease in hardness with increasing Fe concentration. In the stoichiometric alloys a strong increase in the hardness was observed with increasing Fe concentration. This hardening was found to be stronger than would be expected from the Fe defects alone. This hardening was attributed to the increase in the vacancy concentration which occurs with the addition of Fe.

#### Acknowledgments

The authors would like to acknowledge Dr. I. M. Anderson for integral assistance in obtaining the ALCHEMI data and Dr. J. H. Schneibel and Dr. A. J. Duncan for helpful discussions. This research was sponsored by the Division of Material Sciences of the Basic Energy Sciences, U. S. Department of Energy under contract DE-AC-05-96OR-22464 with Lockheed Martin Energy Research Corporation and subcontract SJ403-19 from Lockheed Martin Energy Research Corporation to the University of Wisconsin-Madison.

#### References

1. J. Westbrook, *J. Electrochem. Soc.*, **54** (1956), 103.
2. P. Nagpal and I. Baker, *Metall. Trans.*, **21A** (1990), 2281.
3. Y. A. Chang, L. M. Pike, C. T. Liu, A. R. Bilbrey, and D. S. Stone, *Intermetallics*, **1** (1993), 107.
4. L. M. Pike, Y. A. Chang, and C. T. Liu, *Acta Metall.*, in press.
5. R. D. Noebe, R. R. Bowman, and M. V. Nathal, *Inter. Mat. Reviews*, **38** (1993), 193.
6. D. B. Miracle, *Acta Metall.*, **41** (1993), 649.
7. R. Darolia, D. F. Lahrman, and R. D. Field, *Scr. Metall.*, **26** (1992), 220.
8. I. Jung, M. Rudy, and G. Sauthoff, *High Temperature Ordered Intermetallic Alloys II*, vol. **81**, ed. N. S. Stoloff, et al. (MRS Symp. Proc., Pittsburgh, PA 1987) pp. 263-74.
9. Y. A. Chang and J. P. Neumann, *Prog. Solid State Chem.*, **14** (1982), 221.
10. I. M. Anderson, A. J. Duncan, and J. Bentley, in *High Temperature Ordered Intermetallic Alloys VI*, vol. **364**, ed. J. A. Horton, et al. (MRS Symp. Proc., Pittsburgh, PA 1994) pp. 443-54.
11. A. J. Bradley and A. Taylor, *Proc. R. Soc. Lond.*, **A159** (1937), 56.
12. R. L. Fleischer, in *The Strengthening of Metals*, ed. by D. Peckner (Reinhold Publishing Corp., New York, 1964), pp. 93-140.
13. I. M. Anderson, *Acta Metall.*, in press.
14. C. R. Kao, L. M. Pike, S.-L. Chen and Y. A. Chang, *Intermetallics*, **2** (1994), 235.
15. A. J. Duncan, Ph.D. Thesis, University of Florida, 1995.
16. L. M. Pike, C. R. Kao, S. L. Chen, and Y. A. Chang, in *Design Fundamentals of High Temperature Composites, Intermetallics, and Metal-Ceramics Systems*, ed. R. Y. Lin et al. (TMS Publication, Warrendale, PA 1996) p. 171.
17. L. A. Gypen and A. Deruyttere, *J. Mater. Res.*, **12** (1977), 1028.
18. T. J. Koppenaal and D. Kuhlmann-Wilsdorf, *Appl. Phys. Letters*, **4** (1964), 59.
19. A. J. E. Foreman and M. J. Makin, *Phil. Mag.*, **22** (1966), 911.
20. F. Laves, in *Theory of Alloy Phases* (ASM Publication, Cleveland, OH, 1956).
21. L. M. Pike, unpublished data.
22. G. Simmons and H. Wang, *Single Crystal Elastic Constants and Calculated Aggregate Properties: A Handbook*, 2nd ed., (MIT Press, Cambridge, MA, 1971).

## PROGRESS IN THE MODELING OF NiAl-BASED ALLOYS USING THE BFS METHOD

Guillermo Bozzolo

Ohio Aerospace Institute, Cleveland, Ohio 44135

Ronald D. Noebe, John Ferrante

NASA Lewis Research Center, Cleveland, Ohio, 44135

Anita Garg

AYT Corporation, NASA Lewis Research Center, Cleveland, Ohio 44135

### Abstract

The BFS method has been applied to the study of NiAl-based materials to assess the effect of alloying additions on structure. Ternary, quaternary and even pent-alloys based on Ni-rich NiAl with additions of Ti, Cr and Cu were studied. Two approaches were used, Monte Carlo simulations to determine ground state structures and analytical calculations of high symmetry configurations which give physical insight into preferred bonding. Site occupancy energetics for ternary and the more complicated case of quaternary additions were determined, and solubility limits and precipitate formation with corresponding information concerning structure and lattice parameter were also 'observed' computationally. The method was also applied to determine the composition of alloy surfaces and interfaces. Overall, the results demonstrate that the BFS method for alloys is a powerful tool for alloy design and with its simplicity and obvious advantages can be used to complement any experimental alloy design program.

### Introduction

Development of new structural alloys and even small improvements to current alloys occur through extensive experimental trial and error, which is both costly and time consuming. However, there has been no other viable approach to alloy development, since computational methods for ternary and higher-order systems have been sorely inadequate. Although first-principles approaches are best suited for providing the most accurate and consistent framework for such studies, the complexity of the problems at hand and the overwhelming computational requirements for even simple systems, prevent these approaches from becoming useful

and economical predictive tools. To date, very few calculations exist that go beyond elementary binary alloys, and even in these cases, the results are limited in scope and accuracy.

Recent developments in the area of semiempirical methods created the hope of progress in the field of alloy structure analysis and design, however, most of the methods developed in the last two decades have been severely restricted in the type and complexity of systems amenable to such studies. The purpose of these methods is to provide an efficient and accurate way to compute the total energy of arbitrary atomic systems in terms of the geometrical configuration of the atoms. In most cases, the existing techniques are restricted to a few systems for which specific (and therefore nontransferrable) parameterizations are developed, thus limiting their predictive power and overall usefulness. Recently, a new semiempirical method was developed with the goal of avoiding these limitations of existing methods, and hopefully demonstrating the usefulness of such techniques. The BFS (Bozzolo-Ferrante-Smith) method for alloys (1) is particularly designed to deal with complex systems and geometries, as it has no constraints regarding the type and number of elements under consideration, or on the number or type of resulting phases. These are major obstacles for other techniques, which are usually limited to the treatment of a few elements, binary alloys and single phase components. Moreover, other techniques only provide reliable results for bulk properties, offering little confidence in applications such as extended defects of surfaces and interfaces (2).

The BFS method is based on quantum perturbation theory and the solution of simple transcendental equations for each atom in the sample, in order to compute its contribution to the total energy.

Table 1: LMTO and ECT parameters for the bcc structured versions of the various elements.

LMTO results					ECT parameters			
Atom	Lattice Parameter	Cohesive Energy	Bulk Modulus	Vacancy Energy	p	$\alpha$	$\lambda$	l
Ni	2.752	5.869	249.2	3.0	6	3.0670	0.763	0.2716
Al	3.192	3.942	77.3	1.8	4	1.8756	1.038	0.3695
Ti	3.213	6.270	121.0	2.0	6	2.6805	1.048	0.3728
Cr	2.837	4.981	286.0	4.9	6	2.8580	0.6460	0.2300
Cu	2.822	4.438	184.5	1.8	6	3.1082	0.7614	0.2710

Table 2: BFS parameters. The entry  $A_{ij}$  corresponds to the BFS parameter  $\Delta_{ij}$ 

$\begin{smallmatrix} i \\ j \end{smallmatrix}$	Ni	Al	Ti	Cr	Cu
Ni	0.00000	-0.05813	-0.06582	-0.02975	0.02085
Al	0.08220	0.00000	-0.06360	-0.01307	0.05887
Ti	0.45690	0.22830	0.00000	0.06579	0.21964
Cr	0.20480	-0.01637	-0.04691	0.00000	0.02664
Cu	-0.01489	-0.04793	-0.05555	-0.01016	0.00000

Thus, the computational requirements are trivial (a PC was used to perform all the calculations in this paper), favoring the use of BFS for large-scale simulations. In addition, the method relies on first-principles determined parameters with general transferrability to broad situations, as opposed to competing techniques that have the additional disadvantage that their parameters or potentials have to be determined and optimized for each specific application. Thus, the method provides a simple framework for large-scale simulations.

The predictive capabilities of the BFS method have been successfully tested in a number of systems (3), but most recently it has been used to predict and understand the effect of ternary alloying additions on the structure of NiAl-based alloys. Both experimental and theoretical studies were conducted in parallel, each in turn supporting the other. The experimental work was conducted in the normal course of evaluating these alloys and as a check on the modeling effort. Based on the performance of the BFS method to the basic binary and ternary systems, it has been applied to more complex systems and the modeling efforts have begun to lead the way for the alloy design program. In this paper, we will present an overview of recent results from BFS-based analyses of the structure of NiAl with ternary and quaternary additions (Ti, Cr, Cu), including a preliminary analysis of a 5-element alloy, together with conclusions drawn from extensive Monte Carlo/Metropolis large-scale computer simulations of these alloys. When appropriate, the modelling results have been compared to TEM and other experimental observations.

### The BFS Method

For a given distribution of atoms, the BFS method computes the configurational energy of formation by means of a perturbation theory-based approach. Ground state structures of alloys are there-

fore obtained by optimizing the atomic distribution via Monte Carlo simulations (3). The number of parameters necessary for this approach are four for each single element and two for each binary combination. These are generated from first-principles linear muffin tin orbital, full potential calculations (4). For the sake of brevity, we refer the reader to previous papers on the BFS method and its application to surface studies (5) and alloy characterization (6) for further details.

The method is based on the idea that the energy of formation of an alloy is the superposition of individual contributions  $\epsilon_i$  of atoms in the alloy  $\epsilon_i = \epsilon_i^S + g_i(\epsilon_i^C - \epsilon_i^0)$ .

The two main contributions to the energy are  $\epsilon_i^S$ , which is the strain energy computed with perturbation-theory based Equivalent Crystal Theory (ECT) (7) that accounts for the actual geometrical distribution of the surrounding atoms computed as if they were of the same atomic species, and a chemical energy  $\epsilon_i^C - \epsilon_i^0$ , which takes into account the different atomic species of each neighboring atom. We represent this defect (i.e. the change in composition with respect to a single-element crystal) by 'perturbing' the electronic density in the overlap region between dissimilar atoms while locating them at equilibrium lattice sites of atom  $i$ .  $\epsilon_i^0$  is a reference energy computed in the same fashion as  $\epsilon_i^C$ , but assuming that all surrounding neighbors are of the same atomic species as the reference atom. The coupling function  $g_i$  ensures the correct asymptotic behavior of the chemical energy term.

Ref. 5 provides details on the BFS method, its implementation, the operational procedure and the approach used in the Monte Carlo/Metropolis computer simulation. Table 1 lists the ECT parameters for the bcc variants of the pure elements. The BFS parameters for the binary combinations of these elements used in this work are listed in Table 2. More details on the determination of the BFS parameters can be found in Ref. 8. It should be emphasized that

the parameters listed in Tables 1 and 2 were used to generate all the results presented in this paper, demonstrating the robust nature of this approach.

### Binary Alloys - Defect Structure of B2 NiAl

A previous application of the BFS method to the analysis of the zero-temperature defect structure of NiAl alloys successfully reproduced the defect structure as a function of stoichiometry (8). This study raised confidence in the authenticity of the parameters used for the NiAl system, which once determined, remain the same for any further analysis based on this system.

Based on a 72-atom bcc cell, a few hundred atomic configurations were defined and then their energy computed using the BFS method. By creating this catalogue of possible defect structures, the lowest energy ground state configurations for each composition can be determined (if included in the catalogue) along with a series of possible metastable structures (those configurations with energies close to that of the ground state). Moreover, the site preference of the alloying additions as a function of their concentration, and as a result, information regarding the solubility limit and the possible formation of second phases, can also be obtained.

For the case of non-stoichiometric B2 NiAl, this approach indicates that Ni-rich NiAl alloys are essentially substitutional in

nature, whereas Al-rich alloys are characterized by the presence of vacancies primarily in Ni but also in Al sites (8). Both results are in excellent agreement with experiment (9). The calculated lattice parameter of the lowest energy configurations for each composition reproduced the experimental results quite accurately, particularly for Ni-rich NiAl alloys (10). A similar approach was successfully used to investigate the zero temperature defect structure of FeAl alloys (11)

### Ternary Alloys - Cr/Ti Addition to NiAl

The catalogue of individual atomic configurations mentioned in the previous section (see Ref. 12 for a detailed description of the 200 configurations used) can be extended to include an appropriately large number of atomic distributions of a 3-element alloy. The set of configurations used in this investigation includes several hundred states covering almost every possible substitutional scheme for a wide range of concentrations, including a large variety of possible short- and long-range ordering patterns. A subset of this catalog containing some simple configurations which correspond to possible site preference schemes is shown in Fig. 1. The energy of formation of these configurations, computed with the BFS method, is shown in Fig. 2 as an 'energy spectrum', helping to visualize the relative probability of each possible defect. From this set, it is seen that Ti preference for Al sites dominates,

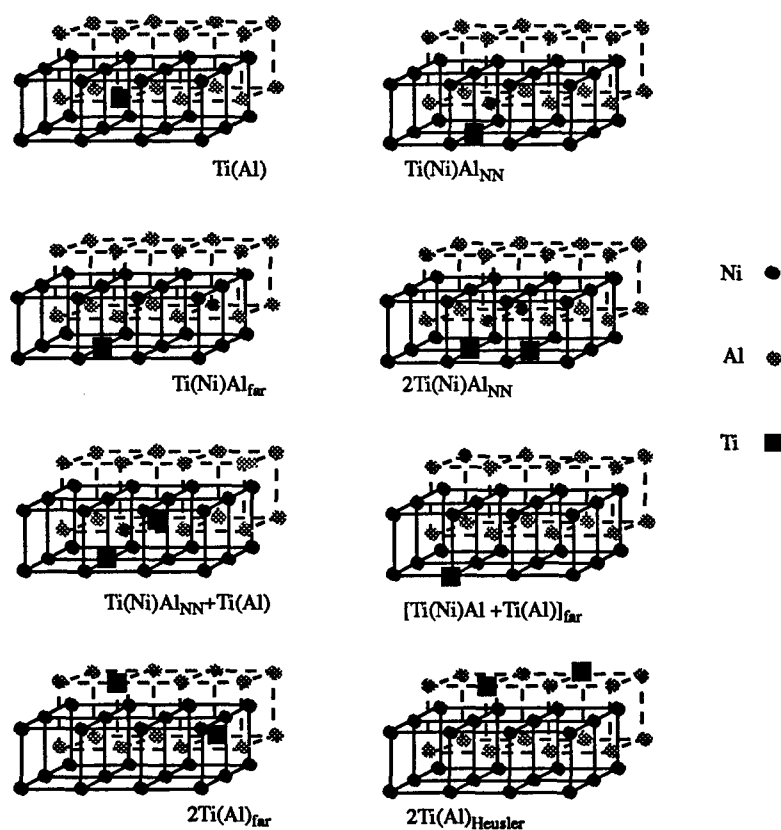


Fig. 1: Computational cells showing different substitutional schemes for Ti in NiAl. The corresponding energies of formation and lattice parameter are shown in Fig. 2 and Table 3. A(B) describes a configuration where an A atom occupies a site in the B-sublattice. A(B)C is the superposition of two substitutional defects: A(B)+(B)C. The subindices NN, far and Heusler indicates that the substitutional atoms are either at nearest-neighbor distance, at distances greater than nearest-neighbor distance or located following Heusler ordering (in opposite corners of the cube in the same sublattice)

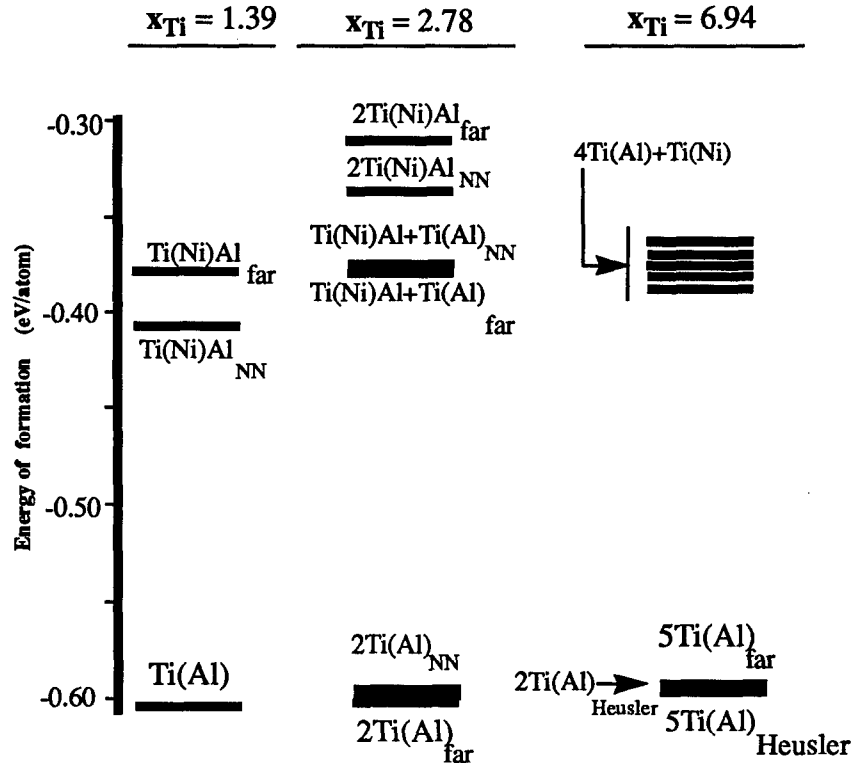


Fig. 2: Site preference energy spectrum for Ni-Al-Ti alloys. A(B) indicates an atom A in a B site and A(B)C indicates an A atom in a B site, with the B atom in a C site. See text for details.

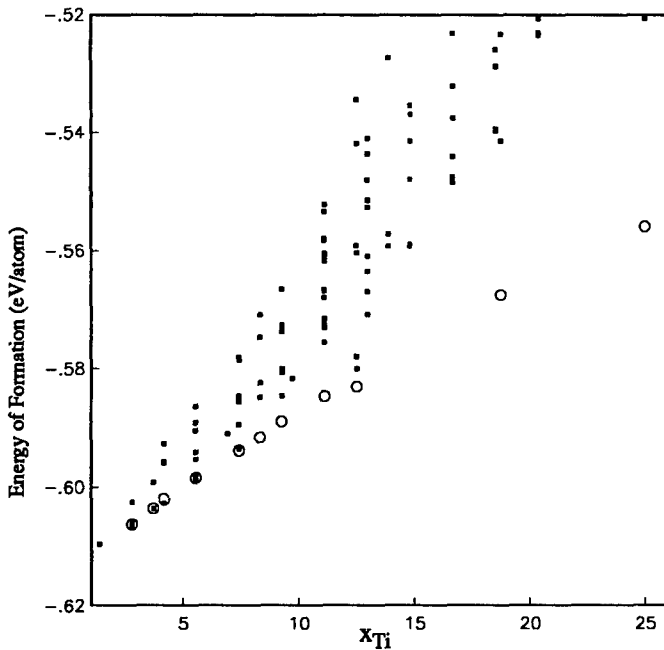


Fig. 3: Energy of formation of a large number of  $\text{Ni}_{50}(\text{Al}_{50-x}\text{Ti}_x)$  bcc-based configurations (defined in Appendix 2 of Ref. 12), displaying a variety of short-range order patterns as well as completely disordered states. Those configurations characterized by Heusler ordering are denoted with open circles, whereas the solid squares indicate any other arrangement,

$x_{\text{Ti}}$	Description of the configuration	Energy of Formation (eV/atom)	Lattice Parameter (Å)
1.39	$\text{Ti}(\text{Ni})\text{Al}_{\text{NN}}$	-0.41320	2.870
	$\text{Ti}(\text{Ni})\text{Al}_{\text{far}}$	-0.38052	2.870
	$\text{Ti}(\text{Al})$	-0.60839	2.853
2.78	$2\text{Ti}(\text{Ni})_{\text{NN}} + 2\text{Ni}(\text{Al})_{\text{NN}}$	-0.32607	2.881
	$2\text{Ti}(\text{Ni})\text{Al}_{\text{NN}}$	-0.32873	2.882
	$\text{Ti}(\text{Ni})\text{Al} + \text{Ti}(\text{Al})$	-0.36893	2.879
	$\text{Ti}(\text{Ni})\text{Al} + \text{Ti}(\text{Al})_{\text{far}}$	-0.37773	2.878
	$2\text{Ti}(\text{Al})_{\text{NN}}$	-0.59918	2.859
	$2\text{Ti}(\text{Al})_{\text{far}}$	-0.63500	2.858
	$2\text{Ti}(\text{Al})_{\text{Heusler}}$	-0.60350	2.858

Table 3: Energy of formation and lattice parameter for the defect structures shown in Fig. 1 for two Ti concentrations. The subindices indicate the distance between the two defects. For example,  $\text{Ti}(\text{Ni})\text{Al} + \text{Ti}(\text{Al})_{\text{NN}}$  indicates that the antistructure Ni atom and the Ti atom in the Al site are nearest-neighbors (NN)

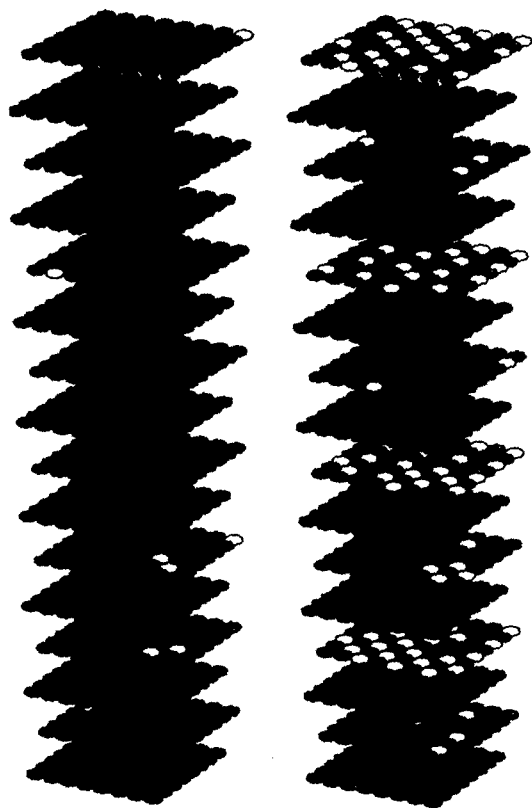


Fig. 4: Monte Carlo/BFS/Metropolis results of temperature cascade simulations of Ni-48Al-2Ti and Ni-40Al-10Ti alloys. The computational cell contains 1024 atoms and both simulations used a random placement of atoms to represent the initial, high temperature state (Ni:red; Al: blue; Ti: yellow).

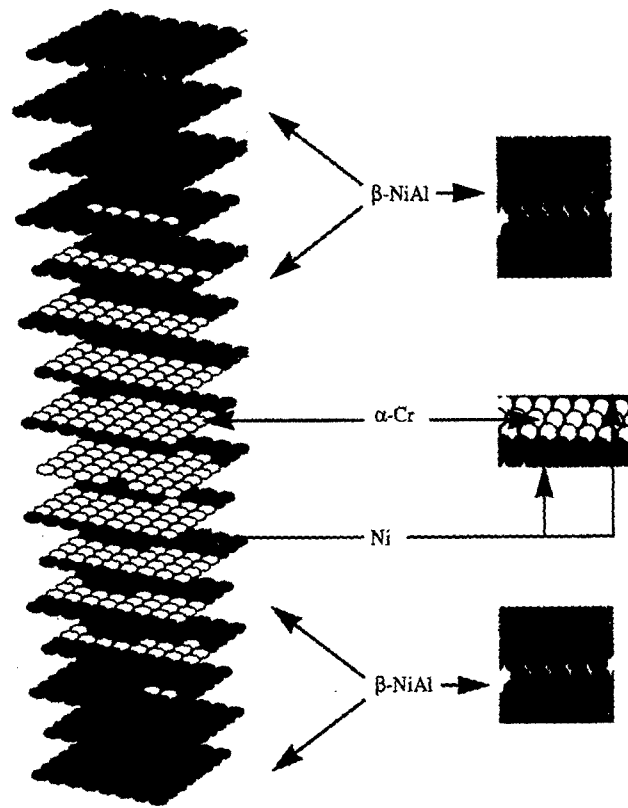


Fig. 5: Monte Carlo/BFS/Metropolis results of a temperature cascade simulation for a Ni-25Al-25Cr alloy (Ni:red,Al: blue,Cr:yellow circles). The computational cell contains 1024 atoms. The initial state corresponded to a completely random state, while the room temperature alloy consists of three phases: NiAl,  $\alpha$ -Cr, and a Ni-rich phase, consistent with the ternary phase diagram.

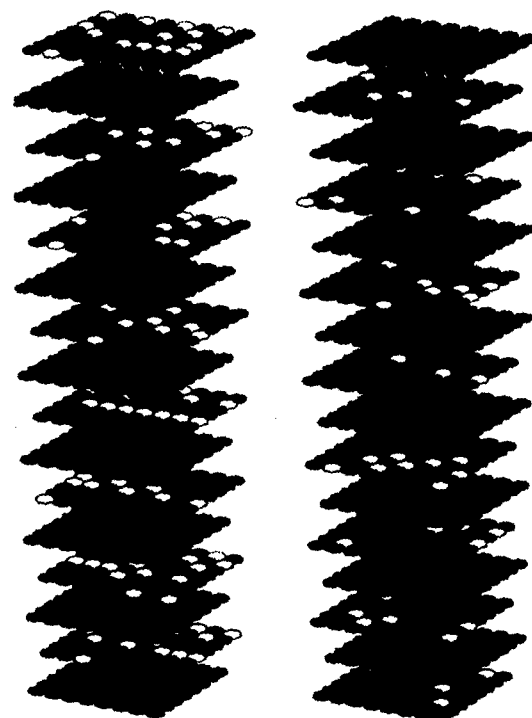


Fig. 6: Monte Carlo results of a temperature cascade on a Ni-23Al-10Ti-34Cr alloy (Ni:red, Al:blue,Ti:yellow,Cr: green)



Fig. 7: Monte Carlo results of a temperature cascade on a Ni-43Al-5Ti-2Cu alloy (Ni:red; Al:blue;Ti:yellow;Cu:green)

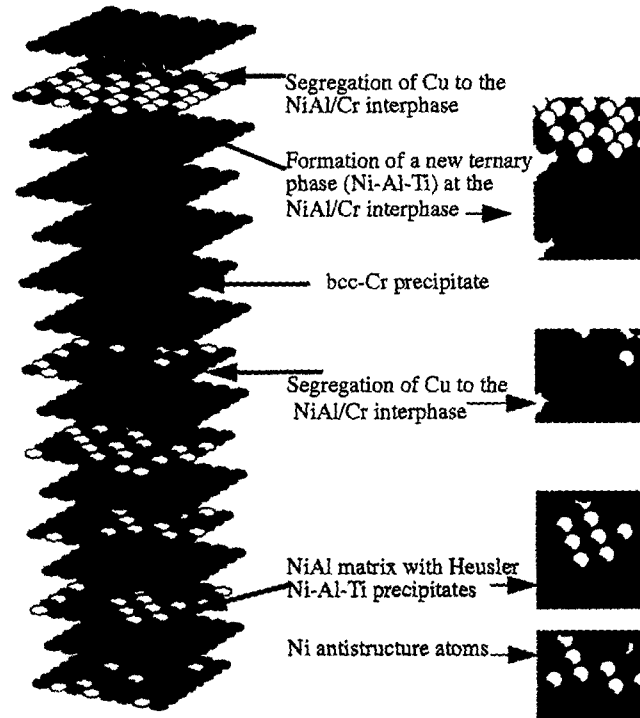


Fig. 8: Monte Carlo/BFS results of a temperature cascade on a Ni-22.56Al-9.47Ti-33.5Cr-1.95Cu alloy, showing the final state at 300 K. Ni,Al, Ti Cr and Cu are represented with red, blue, yellow, green and black circles, respectively.

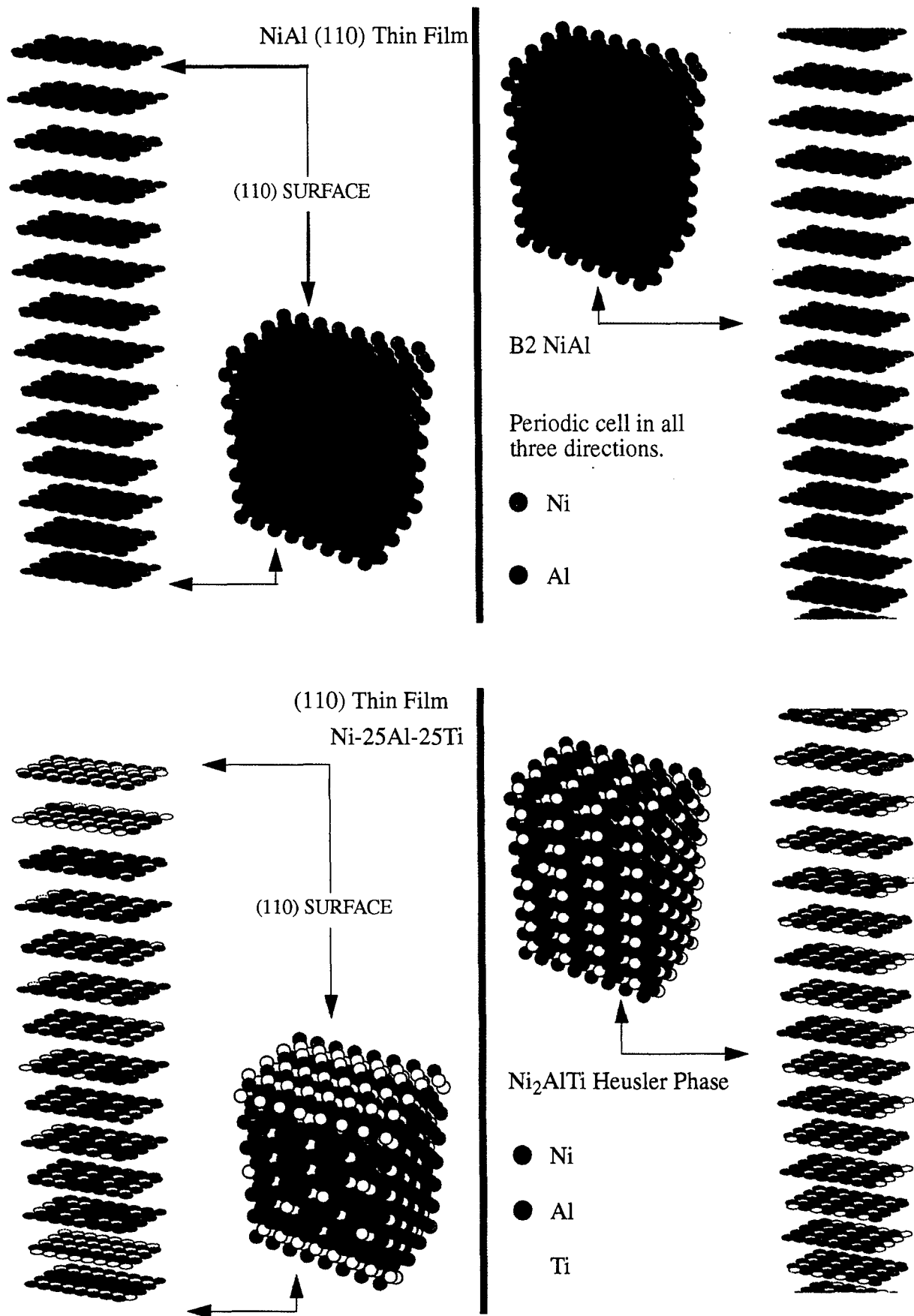


Fig 9: Comparison of bulk and thin film compositions for NiAl (top) and Ni<sub>2</sub>AlTi (bottom) alloys. The thin film cells are periodic in two directions, perpendicular to the top and bottom planes. The bulk cell is periodic in all three directions. The free-standing thin film terminates in two (110) surfaces.



as is clear from the energy of formation values in Table 3. It is precisely this marked preference for Al sites that explains the ordering pattern seen already at low Ti concentrations: Ti atoms tend to locate themselves at opposite corners of the cube in the Al-sublattice, so that they always have Al atoms as second neighbors. This local ordering of Ti is indicative of Heusler formation. This trend towards Heusler ordering can be more clearly seen in Fig. 3, where the energy of formation of the complete catalogue of configurations, computed with BFS, is plotted against their Ti concentration. Those states characterized by Heusler ordering (circles in Fig. 3) become energetically favored around 5 at. % Ti, with the energy gap between configurations with Heusler ordering and the next closest one in energy widening beyond that concentration. This information can be taken as an indirect way of determining the solubility limit of Ti (~5%) in NiAl. Beyond this value, Heusler precipitates form. The calculated lattice parameter of 0.5828 nm for the  $\text{Ni}_2\text{AlTi}$  phase from the  $x_{\text{Ti}}=25$  calculations is in excellent agreement with the reported experimental value of 0.5876 nm. Thus, based solely on BFS calculations, the lattice mismatch between NiAl and  $\text{Ni}_2\text{AlTi}$  is found to be 1.7 %, very close to the 1.5 % misfit obtained experimentally via TEM.

The results of several Monte Carlo/Metropolis simulations using BFS for the calculation of the energy are shown in Figs.4-9. In these simulations, the atoms are given the freedom to find their minimum

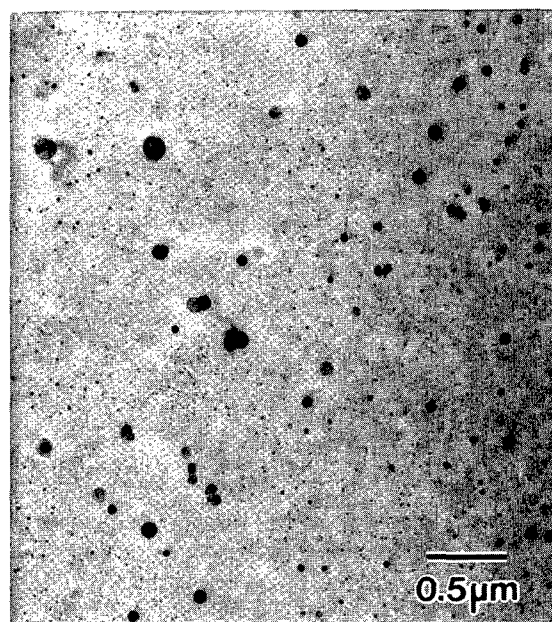


Fig. 11: TEM micrograph of Ni-45Al-5Cr showing  $\alpha$ -Cr precipitates in a  $\beta$ -NiAl matrix

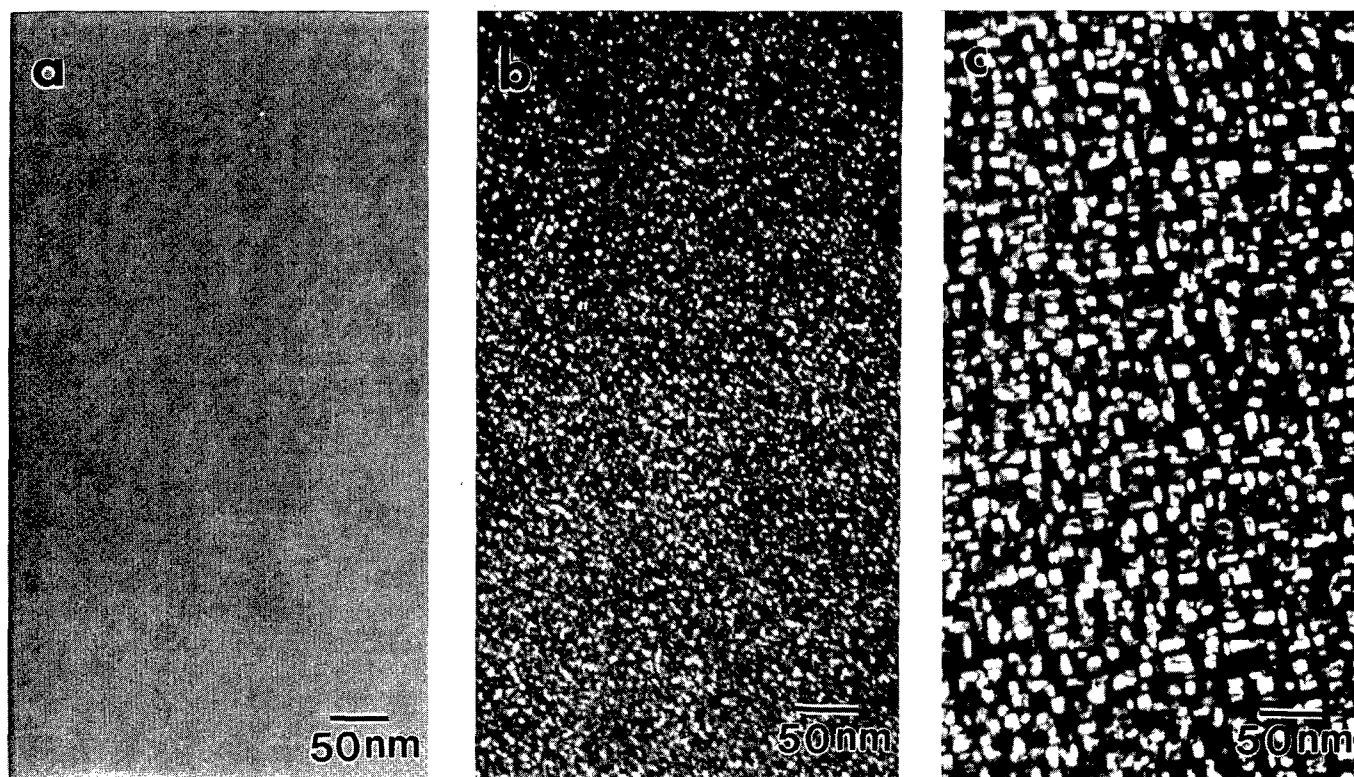


Fig. 10: TEM images of (a) a precipitate-free Ni-47Al-3Ti alloy, (b) precipitation of fine Heusler particles in a Ni-45Al-5Ti alloy and (c) dense precipitation of rectangular shaped Heusler particles in a Ni-43Al-7Ti alloy.

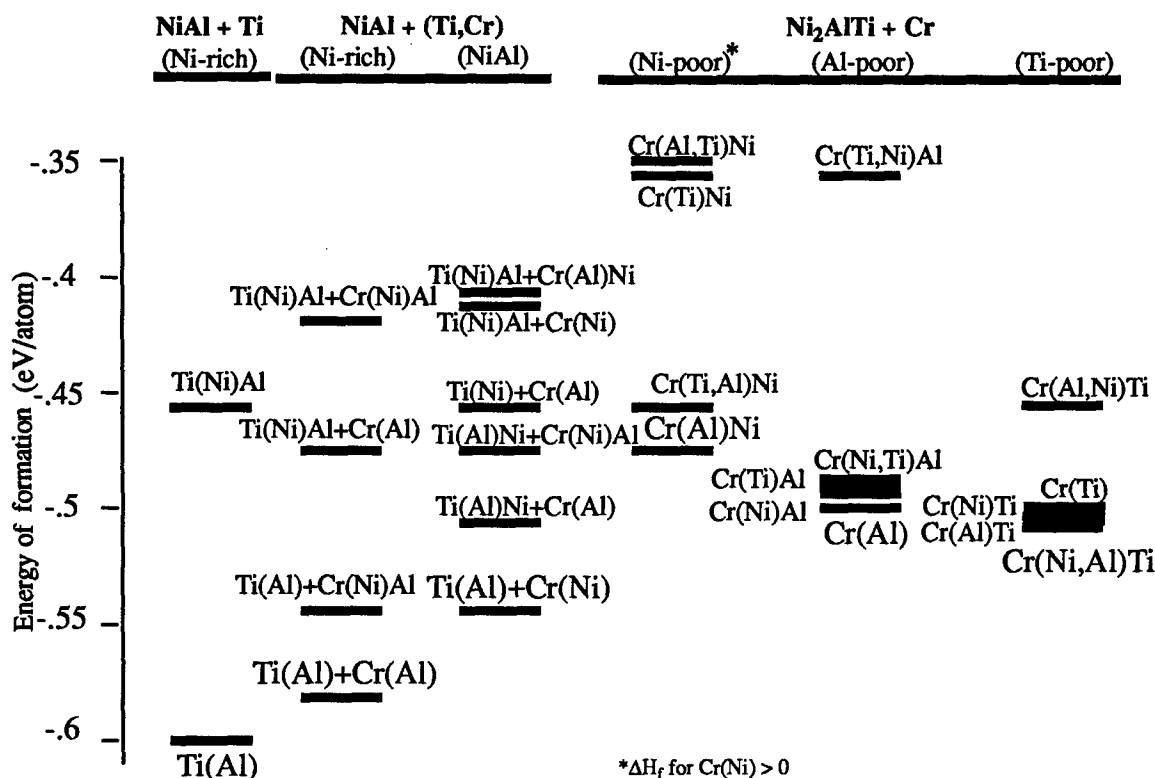


Fig. 12: Site preference 'energy spectrum'. Each line corresponds to the energy of formation of a given configuration characterized by the substitutional defect indicated. The different columns correspond to 1) Ti additions to Ni-rich NiAl alloys, 2) Ti and Cr additions to Ni-rich NiAl alloys and 3) stoichiometric NiAl alloys. Columns 4-6 correspond to Cr additions to Ni-, Al- and Ti-poor  $\text{Ni}_2\text{AlTi}$  alloys respectively.

energy positions at any given temperature, thus giving valuable information on the ground state structure and its dependence on temperature. Starting from random distributions, the atoms in the sample switch positions - the exchange is accepted or rejected depending on temperature-dependent probability factors computed with BFS- until the lowest energy configuration is found. Fig.4 shows the results of Monte Carlo simulations for Ni-48Al-2Ti and Ni-40Al-10Ti, clearly showing the formation of Heusler precipitates at  $x_{\text{Ti}} = 10$ . The Monte Carlo results were obtained by slowly cooling an initially random state, in 100 K temperature steps until equilibrium (i.e. no noticeable change in formation energy) is achieved at each step. Fig.10. shows experimental results for three alloys (Ni-47Al-3Ti, Ni-45Al-5Ti and Ni-43Al-7Ti) in agreement with the theoretical predictions: The TEM micrographs shown in Fig.10 clearly indicate the formation of Heusler precipitates beyond the solubility limit.

Cr additions affect the structure of NiAl somewhat differently than Ti: First of all, Cr preference for Al sites diminishes with increasing Cr concentration, instead it develops a tendency to segregate to bulk Al and Ni planes. This can be taken as a tendency towards the formation of Cr precipitates where Cr atoms occupy both types of sites in the bcc lattice. A similar analysis, using the same catalogue of atomic configurations as that used for Ti additions, shows that the solubility limit of Cr in NiAl is quite low, at 1-2 %, and that beyond that concentration  $\alpha$ -Cr precipitates form. The site preference scheme also indicates the tendency for displaced Ni atoms to form an interphase boundary between the NiAl matrix and the  $\alpha$ -Cr precipitate in some cases. Previous work by Cotton

et al. (13) has shown the low solubility of Cr in NiAl and Fig. 11 shows a TEM micrograph confirming the precipitation of Cr in a Ni-45Al-5Cr alloy. The ternary phase diagram confirms the BFS predictions of the formation of a three-phase alloy in the Ni-25Al-25Cr alloy, as shown in the results of a Monte Carlo/BFS simulation in Fig. 5. These results, together with the previous ones for Ti additions, raise the necessary confidence in the parameterization of Ni, Al, Cr and Ti to model more complicated systems. In what follows, we will investigate quaternary alloys composed of these elements concentrating on the effect of alloying interactions on site preference and their influence on the resulting microstructure of the alloy.

### Quaternary Alloys

Having established the reliability of the BFS calculations based on a successful comparison with experiment for the ternary alloys, we can now exploit the transferrability of the parameters determined for Ni, Al, Cr and Ti as well as the versatility of the BFS method and use them for similar studies of 4- and 5-element alloys. The first goal is to investigate the changes in behavior of each alloying addition due to the presence of the others. By defining a catalogue of configurations contemplating most of the possible distributions of the four atomic species, we can study the site preference energetics of each alloying addition, as shown in Fig. 12. This figure is an 'energy spectrum' which displays the results of the energy of formation of different configurations correspond to different site substitution alternatives in the catalogue.

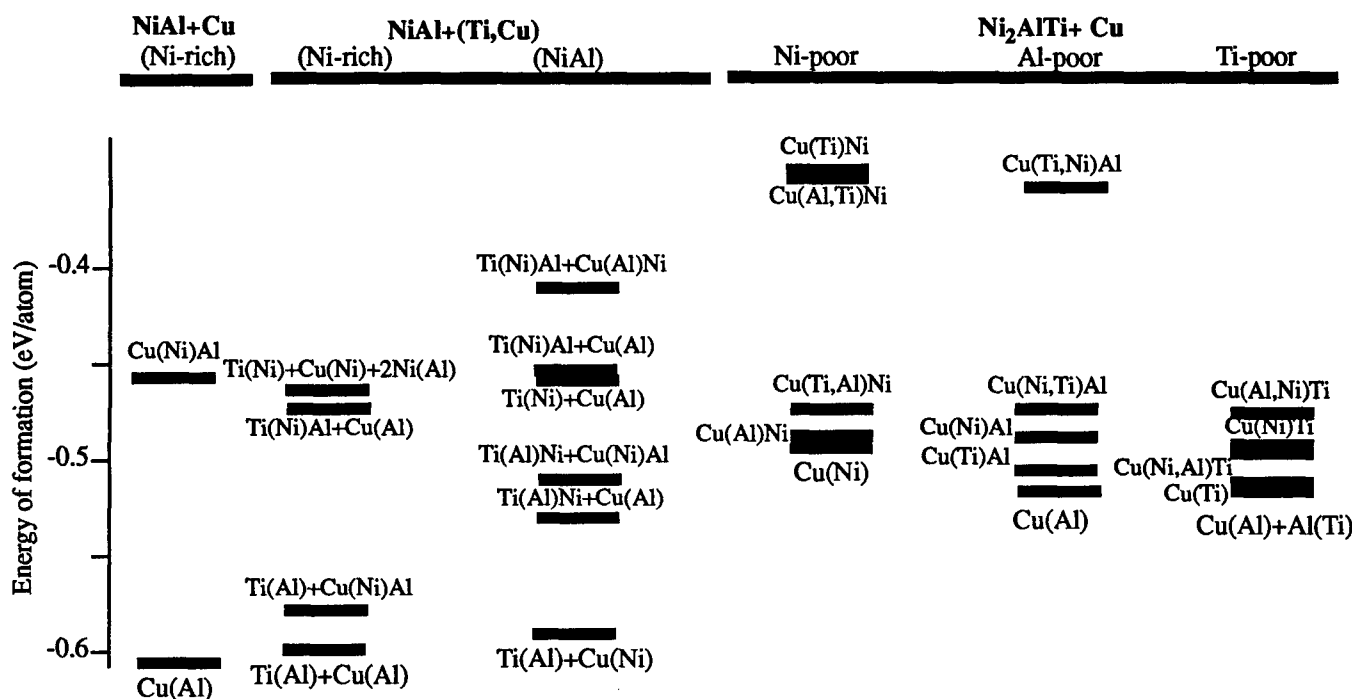


Fig. 13: Site preference 'energy spectrum' for Ni-Al-Ti-Cu alloys. Each line corresponds to the energy of formation of a given configuration characterized by the substitutional defect indicated. Several cases are considered: Ti additions to Ni-rich alloys (first column), Ti and Cu additions to Ni-rich (second column) and stoichiometric (third column) NiAl alloys. Several cases of Cu additions to Heusler  $\text{Ni}_2\text{AlTi}$  alloys are shown in the last three columns.

The site preference scheme shown in Fig. 12 for Cr additions to NiAl-Ti alloys shows that the preference of Ti for Al sites is still the dominant behavior. For stoichiometric NiAl+(Ti,Cr) alloys, Ti and Cr tend to substitute for Al and Ni respectively, emphasizing the weak preference of Cr for Al sites in the ternary case. The energy levels for Cr additions to Heusler ( $\text{Ni}_2\text{AlTi}$ ) alloys also indicates that Cr will have little influence in altering the individual behavior of Ti. As a result, it is reasonable to expect little interaction between Ti and Cr atoms. This translates into each element retaining its individual behavior as seen in the ternary case, with Ti (depending on its concentration) forming Heusler precipitates and Cr creating  $\alpha$ -Cr precipitates. However, the site substitution schemes also suggest some possible additional features: antistructure Ni atoms (in Al sites) and the possible creation of a Ni-rich phase due to the displaced Ni atoms. A Monte Carlo/BFS simulation of a temperature cascade for a Ni-Al-Ti-Cr alloy shown in Fig. 6 confirms the behavior extracted from the site preference calculations. Besides the expected formation of  $\alpha$ -Cr and Heusler ( $\text{Ni}_2\text{AlTi}$ ) precipitates, several antistructure Ni(Al) atoms and clustering of Ti atoms around these antistructure atoms is observed, as well as some indication for the formation of a Ni-film separating the NiAl phase from the Cr precipitate.

On the other hand, Cu additions to NiAl+Ti alloys display a quite different behavior. This can be seen from examining Fig. 13, where the site preference of Cu in NiAl and NiAl+Ti alloys is shown. Fig. 7 shows a Monte Carlo temperature cascade in a Ni-43Al-5Ti-2Cu alloy. The presence of Cu atoms does not alter the behavior of Ti in NiAl at low concentrations, consistent with the energy diagram shown in Figs. 12 and 13.

#### Pentalloys

While constraining the set of configurations to bcc-based structures proved to be sufficient in describing the NiAl based ternary and quaternary alloys discussed in previous sections, such a radical constraint (which, if lifted, would give information on the possible formation of additional ordered phases) might prove to be too restrictive when studying higher order systems. Any information obtained within this framework is therefore limited and should be interpreted and analyzed as such. In spite of this fact, it is still of interest to compare the behavior of alloys composed of all five elements, with respect to their behavior in the 3- and 4-element alloys. In the future, this constraint on structure will be lifted, since it is only a matter of computational efficiency and not an inherent problem with the BFS method itself.

The study of substitutional site preferences for 5-element alloys as a function of concentration is obviously much more involved than that for the simpler systems studied before, and it exceeds the scope of this paper. However, it should be noted that no additional input is required by BFS to tackle this task, as the parameters used in the 5-element alloy calculation are the same ones used in the previous examples and listed in Tables 1 and 2. Studying such fundamental issues as site preference in these higher order systems amounts to just a larger set of possible configurations with a slight increase in the computational effort involved. However, we have analyzed a 5-element alloy: Ni-22.56Al-9.47Ti-33.5Cr-1.95Cu. The concentrations were chosen so as to compare directly with the previous examples, i.e., Ti forms Heusler precipitates at that concentration, Cr forms  $\alpha$ -Cr precipitates, with the addition of a small amount of Cu in solid solution. The results of Monte Carlo/BFS simulations shown in Fig. 8, display a wealth of information

regarding the behavior of the five elements in such a reduced computational cell. A basic feature is the formation of a NiAl matrix, dotted with  $\text{Ni}_2\text{AlTi}$  precipitates as well as the presence of  $\alpha\text{-Cr}$ , a behavior that is not surprising in view of the results obtained for the quaternary case and the low concentration of Cu. However, something unusual is observed with the Cu atoms in the presence of Ti and Cr. In Ni-Al-Ti-Cu alloys Cu atoms favored the formation of short-range order patterns occupying Al sites in Ti-Al rich planes, but in the pentallloy, Cu tends to completely segregate to the NiAl/Cr interphase. in the 5-element alloy. In addition, there is evidence for the formation of a film of Al, Ti, Cu and Ni in the interface between the NiAl matrix and the Cr precipitate. This seems to be a natural consequence of the composition studied and not just the result of one isolated simulation since the same feature has showed up repeatedly in additional simulations. While the essential features (NiAl,  $\text{Ni}_2\text{AlTi}$ ,  $\alpha\text{-Cr}$ ) appear in all simulations, but in different parts of the computational cell, this new quaternary phase always forms along the interphase.

### Alloy Surfaces

The BFS method has been also applied to surfaces of the alloys studied in this work, with the main goal being to establish a comparison between the bulk structure and the surface composition. While the bulk results found some experimental validation as shown in this work, the surface analyses are of a pure predictive nature. These results are discussed in detail in Ref. 14. As an example, Fig. 9 shows a comparison between the bulk and surface composition of a Ni-25Al-25Ti alloy (Heusler phase). In contrast with the bulk cell, the results of a Monte Carlo/BFS simulation of a thin film with the same composition shows the segregation of Ti and Al to the surface planes and a mostly Ni-Ti second plane, at the expense of a depletion of Ti in the bulk. Similar features are found for quaternary alloys, including the formation of ordering patterns different from those found in the bulk. The simulations shown in Fig. 9 correspond to free-standing thin films, where no substrate is considered. Current work on surface structure of multicomponent systems includes details on the growth process, and segregation to the interface. It is expected that the ability of the method to deal with these situations will facilitate the study of grain boundaries.

### Conclusions

The results in this study represent a brief survey of the general effect of different alloying additions on the structure of NiAl. In doing so, we have subjected the BFS method to severe tests of its validity. Based on available experimental evidence, the method passed these tests both quantitatively and qualitatively. First, the correct solubility limit was predicted for both the NiAl+Ti and NiAl+Cr systems. The correct lattice parameter dependence on concentration was predicted for the NiAl+Ti system. The correct structure of the second phase particles was predicted for both cases, as well as the lattice mismatch between the alloy matrix and the precipitating phases. Site preference schemes were computed for the binary, ternary and quaternary systems studied. Based on these results, the study included predictions of the phase structure of quaternary and 5-element systems, both for their bulk and surface properties. Furthermore, we have shown that first-principles input can be used to generate needed parameters, thus removing the limitations of needing experimental data bases for input parameters.

These results show that most of the necessary parameters for a purely analytical alloy design approach are now within reach. The results also provide confidence in the BFS technique, the authenticity and transferrability of the parameters used, and the approach used for obtaining these parameters, thus the need to acquire experimental input parameters is completely eliminated by the use of the BFS method. Future applications will be focused towards integrating the role of techniques such as BFS in aiding the material design process.

### Acknowledgments

Fruitful discussions with Dr. N. Bozzolo are gratefully acknowledged. We would also like to thank Dr. B. Good for providing the code for performing the Monte Carlo simulations, and Dr. C. Amador for providing the input parameters for the BFS calculations.

### References

1. G. Bozzolo, J. Ferrante and J. R. Smith, 'Method for Calculating Alloy Energetics', *Phys. Rev. B* 45 (1992) 493.
2. A. Voter, 'Interatomic Potentials for Atomistic Simulations', *MRS Bulletin*, 21 (2) (1996) 21.
3. G. Bozzolo, B. Good and J. Ferrante, 'Cu-Au Alloys using Monte Carlo Simulations and the BFS Method for Alloys', *Mat. Res. Soc. Symp. Proc.*, Vol. 408, 1996.
4. O. K. Andersen, A. V. Postnikov and S. Y. Savrasov, *Mat. Res. Soc. Symp. Proc.* 253 (1992) 37.
5. G. Bozzolo, J. Ferrante and R. Kobistek, 'Modelling of Surfaces .2. Metallic Alloy Surfaces using the BFS Method', *J. Computer-Aided Mater. Design* 1 (1994) 305.
6. G. Bozzolo and J. Ferrante, 'Bulk Properties of  $\text{Ni}_3\text{Al}$  ( $\gamma$ ) with Cu and Au Additions', *J. Computer-Aided Mater. Design* 2 (1995) 113.
7. J. R. Smith, T. Perry, A. Banerjee, J. Ferrante and G. Bozzolo, 'Equivalent Crystal Theory of Metal and Semiconductor Surfaces and Defects', *Phys. Rev. B* 44 (1991) 6444.
8. G. Bozzolo, C. Amador, J. Ferrante and R. D. Noebe, 'Modelling of the Defect Structure of  $\beta\text{-NiAl}$ ', *Scripta Metall. Mater.* 25 (1995) 1907.
9. M. Kogachi, S. Minamigawa and K. Nakahigashi, *Acta Metall. Mater.* 40 (1992) 1113.
10. R. D. Noebe, R. R. Bowman and M. V. Nathal, 'Physical and Mechanical Properties of the B2 Compound NiAl', *Int. Mater. Rev.* 38 (1993) 193, and references therein.
11. G. Bozzolo, J. Ferrante, R. D. Noebe and C. Amador, 'Zero-Temperature Analysis of the Defect Structure of B2 FeAl Alloys', accepted, *Scripta Mater.*, 1997.
12. G. Bozzolo, R. D. Noebe, A. Garg, J. Ferrante and C. Amador, 'Atomistic Simulations and Experimental Analysis of the Effect of Ti Additions on the structure of NiAl', to be published.
13. J. D. Cotton, R. D. Noebe, M. J. Kaufman, *Structural Intermetallics*, R. Darolia et al. eds., The Minerals, Metals and Materials Society, 1993, 513-523.
14. G. Bozzolo, J. Ferrante and R. D. Noebe, 'Energetics of Ternary and Quaternary Alloy Surfaces', accepted, *Surf. Sci.*, 1997.

# DEFORMATION AND MICROSTRUCTURE OF Ni-RICH AND Hf-DOPED NiAl SINGLE CRYSTALS IN THE HARD ORIENTATION

R. Srinivasan, M.F. Savage, M.S. Daw<sup>#</sup>, R.D. Noebe<sup>\*</sup>, A. Garg<sup>\*</sup> and M.J. Mills

Department of Materials Science and Engineering, The Ohio State University, Columbus, OH 43210.

<sup>#</sup> Department of Physics and Astronomy, Clemson University, Clemson, SC 29634-1911.

<sup>\*</sup> NASA Lewis Research Center, Cleveland, OH 44135.

## Abstract

Ni-50Al, Ni-44Al and NiAl-0.3Hf single crystals have been tested in compression in the hard orientation over a range of temperatures. The mechanical behavior and dislocation microstructure of these three alloys are compared. While  $a\langle 111 \rangle$  dislocations dominate for all three alloys at lower temperatures, significant differences are observed at intermediate temperatures. In Ni-50Al, while  $a\langle 010 \rangle$  dislocations are prevalent above 600 K,  $a\langle 101 \rangle$  dislocations dominate at higher temperatures in both Ni-44Al (above 800 K) and NiAl-Hf (above 600 K). The mechanism of the slip transition from  $a\langle 111 \rangle$  to non- $a\langle 111 \rangle$  activity is discussed. Also, sessile  $a\langle 110 \rangle$  dislocations with no macroscopic resolved shear stress have been observed in the study of NiAl-0.3Hf samples deformed at 1000 K. The implications of the observed results on the macroscopic processes in both Ni-44Al and NiAl-0.3Hf is addressed.

## Introduction

NiAl has been extensively studied due to its potential for high temperature structural applications. Its many attractive properties include a relatively low density, excellent oxidation and corrosion resistance, and a high melting point. But lack of ductility at low temperatures and inadequate high temperature strength have been the main drawbacks limiting its application. Levit et al. [1] have demonstrated the importance of purity on ductility, indicating the intrinsic ductility of NiAl. Transition metal additions have shown potential for significant strengthening at higher temperatures [2]. In order to fully understand and exploit the possible alternatives to improving the low temperature ductility and high temperature strength in NiAl, in-depth analysis and understanding of the dislocation level processes are required.

Deviation from stoichiometry is known to increase the yield strength in poly-

crystalline NiAl. This effect has been attributed to the interaction of  $a\langle 010 \rangle$  dislocations with anti-site defects (for Ni-rich NiAl) or vacancies (for Al-rich NiAl) [3]. Deformation occurs primarily by  $\langle 010 \rangle$  slip in polycrystalline NiAl [4,5]. Consequently, single crystals of NiAl show some remarkable characteristics when deformed along the cube axes (also known as the "hard" orientation). At lower temperatures, the yield strengths are very high, with little softening as a function of temperature. The increased temperature dependence of the yield strength at intermediate temperatures appears to coincide with a dramatic increase in ductility, inferring a change in deformation mode [6-8]. Previous investigators have established a slip transition from  $\langle 111 \rangle$  to non- $\langle 111 \rangle$  type as the cause for the ductile-to-brittle transition [2,8,9]. The compression studies on hard-oriented Ni-44Al to be discussed below give further evidence for the occurrence of this slip transition. Deformation beyond the ductile-to-brittle-transition temperature (DBTT) has been reported to occur either through climb of  $a\langle 010 \rangle$  dislocations [10], or through glide of  $a\langle 101 \rangle$  dislocations [8,11]. There is presently no clear understanding as to which factors are responsible for the different dislocation activities.

Several studies have also attempted to improve the high temperature strength through solid solution alloying additions [12-14]. Alloying with Hf has been shown to improve high temperature strength considerably in single crystalline NiAl [2]. Whether this strengthening is related to a simple solute interaction or to more complex changes in dislocation activity is not presently known.

This paper examines the effects of deviation from stoichiometry and Hf alloying additions on the mechanical properties and dislocation structures in hard-oriented NiAl. Only deviations to the Ni-rich side have been explored thus far in these single crystals. Emphasis is placed upon the nature of the slip transition which occurs at intermediate temperatures, as well as upon the

mechanisms of deformation above the slip transition temperature. By studying the effects of these compositional changes, we hope to gain a better understanding of the complex dislocation processes which characterize deformation in the hard oriented NiAl single crystals.

### Experimental

Binary NiAl single crystals of varying stoichiometry were processed by a modified Bridgman technique and were kindly supplied by Dr. R. Darolia of General Electric Corporation. The NiAl-0.3Hf ingot was supplied by Dr. V. Levit, formerly of the University of Florida. Hard oriented cylindrical compression specimens were prepared and tested (strain rate =  $10^{-4}$ /s) at various temperatures (both above and below the DBTT for Ni-44Al) and various strain levels. The samples were unloaded and rapidly cooled after compression testing. Thin foils for transmission electron microscope (TEM) studies were prepared by cutting the specimens on a low speed saw, using 0.015" thick SiC abrasive wheels. Unless specified otherwise, all TEM specimens were prepared with near-[001] foil normals, where the [001] direction is the compression axis. Final electrojet polishing was performed at -40°C on a Tenupol-3 twin jet electropolisher, using an electrolyte of 10% perchloric acid in methanol. A current of 25-30 mA and a voltage of 6-10 V was used during polishing.

TEM studies were conducted on a Philips CM200 LaB<sub>6</sub> electron microscope operating at 200 kV, and a Philips EM400 electron microscope operating at 120 kV. The program CUFOUR developed by P. Stadelmann and R. Schaublin was used for performing diffraction contrast image simulations. Appropriate elastic constants were used to compensate for the deviation from stoichiometry [15]. Elastic constants for stoichiometric NiAl were used for NiAl-0.3Hf image simulations.

### Results and Discussion

Fig.1 shows the yield strength vs. temperature relationships for Ni-44Al, Ni-50Al and NiAl-0.3Hf. The remarkable effect of deviation from stoichiometry on the temperature of the "knee" (which is the transition from the region of low temperature dependence of the yield strength to that of increased temperature dependence) can be observed. Note the nearly athermal nature of the yield strength below the "knee" and the dramatic dependence on temperature above it. The "knee" in Ni-44Al occurs at a much higher temperature (~800 K) than in stoichiometric NiAl (~600 K). Below the "knee", Ni-44Al is slightly stronger than stoichiometric NiAl. The yield strength vs. temperature behavior resulting in the "knee" has been correlated with a transition from  $a\langle 111 \rangle$  to non- $a\langle 111 \rangle$  slip [8,16], and also corresponds to the

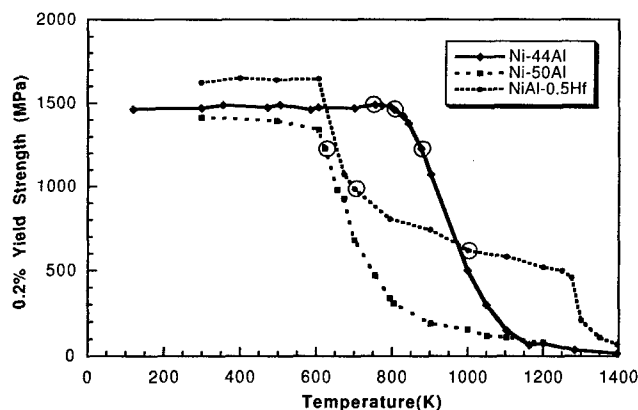


Fig.1: Variation of yield strength with temperature for Ni-50Al, Ni-44Al and NiAl-0.3Hf. Samples used for TEM study in this work are encircled.

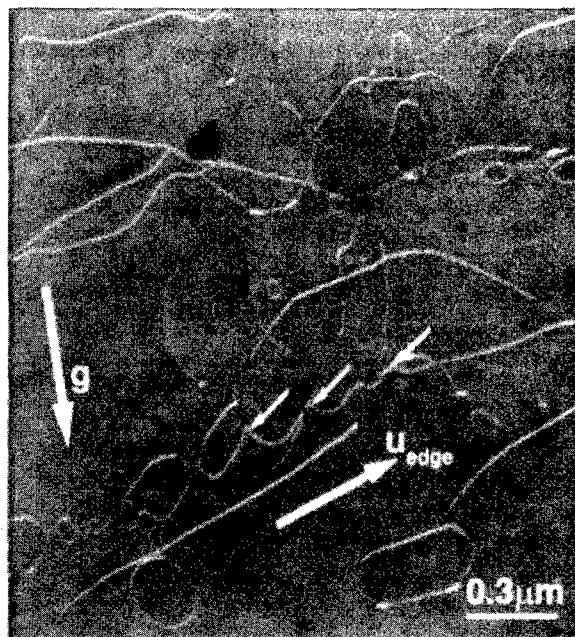


Fig. 2 :  $g(110)$  weak beam  $g\cdot 3g$  micrograph near the (001) zone in a Ni-44Al sample strained 0.7% at 750 K, showing cusp-like features (indicated by arrows) in near-edge  $a[111]$  segments. The cusps are possible local decomposition sites. The glide plane for the  $a[111]$  segments is  $(0\bar{1}1)$ , and the line direction uedge for the pure edge segments is  $[\bar{2}11]$ .

ductile-to-brittle transition temperature (DBTT) in binary NiAl [6,17].

Addition of Hf to NiAl has virtually no effect on the temperature of the "knee", but a profound increase in the yield strength is obtained at both low and high temperatures relative to Ni-50Al. There appears to be an additional deformation regime above 1250 K as compared to stoichiometric NiAl, where an increased temperature dependence is once again observed. In the case of the NiAl-Hf alloys, the DBTT actually corresponds to this second, high temperature "knee" [2]. This regime will not be considered in the present paper, but is currently the subject of investigation.

TEM studies have been performed on Ni-44Al within the temperature range 750 K to 900 K, NiAl-0.3Hf at 700 K and 1000 K and Ni-50Al between 530 K and 670 K. The primary objective was to study (a) the factors determining the slip transition and dislocation activity above the slip transition in Ni-50Al and Ni-44Al, and (b) the dislocation behavior and reason for the increased high temperature strength observed in NiAl-0.3Hf. To simplify the presentation, the binary alloy and NiAl-0.3Hf studies are discussed separately below.

#### Ni-44Al

(a) Mechanism of Slip Transition: Fig.2 shows the typical microstructure observed in Ni-44Al samples deformed just below the "knee". As discussed below, the observation of cusp-like features at 750 K indicates possible sites of local decomposition of  $a\langle 111 \rangle$  dislocations. The projected  $[\bar{2}11]$  edge line direction for the  $a[111]$  segments is indicated in the figure. The glide plane for the  $a[111]$  dislocations is  $(0\bar{1}1)$ . Based on anisotropic elasticity calculations, decomposition of  $a\langle 111 \rangle$  dislocations is favored near the edge orientation [18] according to:

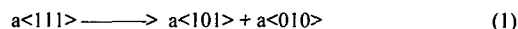


Fig.3(a) shows such the occurrence of a local decomposition of a near-edge



Fig. 3(a):  $g(101)$  bright field micrograph near the  $[T01]$  zone showing the local decomposition of an  $a[111]$  dislocation (indicated by A and B) occurring near the edge orientation. The sample is strained 0.4% at 800 K.

$a\langle 111 \rangle$  dislocation into  $a\langle 101 \rangle$  and  $a\langle 010 \rangle$  dislocations in Ni-44Al deformed 0.4% at 800 K. Fig.3(b) shows the microstructure for Ni-44Al deformed 1.7% at 800 K.  $a\langle 111 \rangle$  dislocations are no longer visible at this higher strain at 800 K; instead, a high density of both  $a\langle 011 \rangle$  and  $a\langle 001 \rangle$  dislocations are observed. The  $a[100]$  dislocations observed in Fig.3(b) are unlikely to be reaction products of gliding  $a[101]$  and  $a[10\bar{1}]$  dislocations, since no  $a[100]$  dislocations along  $[010]$  directions (the common line direction between the glide planes of the reacting  $a\langle 101 \rangle$  dislocations) are observed. Note that the constituent  $a\langle 100 \rangle$  and  $a\langle 011 \rangle$  dislocations that we observe here would add up to the respective parent  $a\langle 111 \rangle$  dislocations, once again indicating that these dislocations have been produced by the decomposition process indicated in Equation 1.

Significant strain softening is observed on deforming at 800 K, as shown in Fig.4. Assuming that the CRSS for  $\langle 101 \rangle$  glide is lower than that for  $\langle 111 \rangle$  glide in this temperature range, continual decomposition of  $a\langle 111 \rangle$  dislocations with increasing strain leads to a reduction in the flow stress for deformation. Note that there is no appreciable strain softening observed below the "knee".

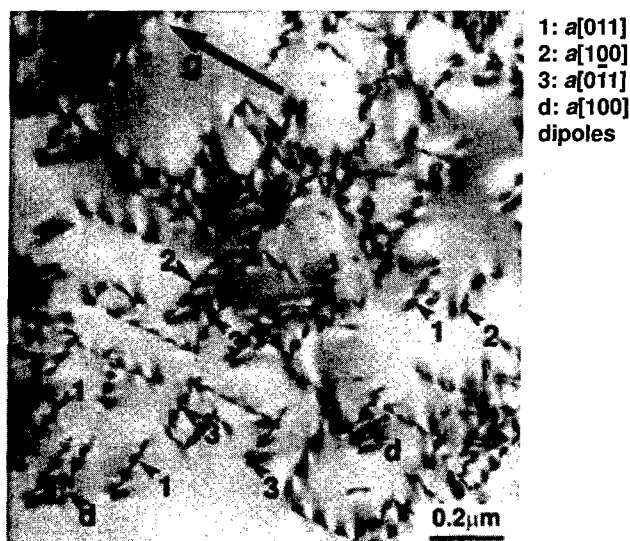


Fig. 3(b):  $g(110)$  bright field micrograph showing the dislocation structure in Ni-44Al strained 1.7% at 800 K. The beam direction is close to  $[001]$ .

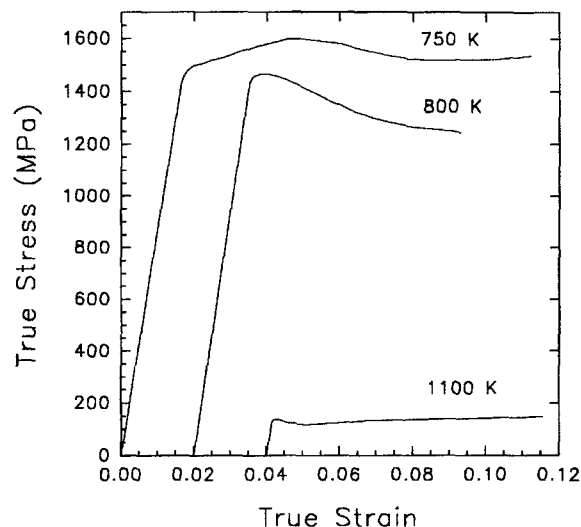


Fig. 4: True stress vs. true strain curves for Ni-44Al deformed at temperatures of 750 K, 800 K and 1100 K. The strain softening effect is clearly observed at temperatures near the "knee".

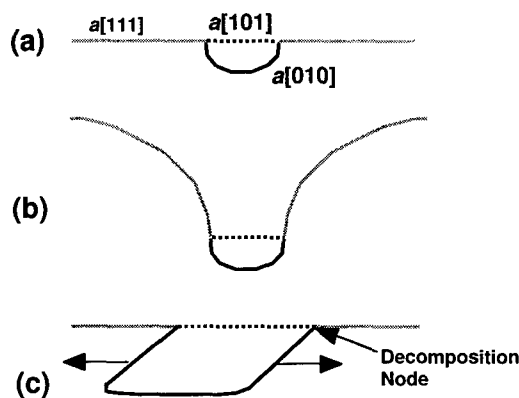


Fig. 5: Possible scenario for glide decomposition of  $a[111]$  dislocation near edge orientation. (a) Formation of local decomposed segment on  $(T01)$  glide plane. (b) If mobility of  $a[111]$  dislocation is greater than that for  $a[101]$ , former will move forward on glide plane and bow around slower decomposed segment. (c) If  $a[101]$  and  $a[111]$  dislocation mobilities are comparable, an  $a[010]$  dipole loop may be formed, and decomposition nodes may expand laterally.

A model has been proposed elsewhere [19] addressing the mechanism of decomposition and correlating it with the observed dislocation structures. This model is illustrated in Fig.5. If we presume that at temperatures below the "knee", the critical resolved shear stress (CRSS) for  $\langle 111 \rangle$  slip is lower than that for  $\langle 101 \rangle$  slip,  $a\langle 111 \rangle$  segments would be impeded by a local decomposition process producing  $a\langle 101 \rangle$  and  $a\langle 010 \rangle$  dislocations which are relatively immobile at this temperature, as indicated in Fig.5(b). The cusp-like features in Fig.2 and the decomposed segment in Fig.3(a) are possibly indicative of this premise. Our results indicate that above the temperature of the "knee", the CRSS for  $\langle 101 \rangle$  slip is lower than that for  $\langle 111 \rangle$  slip, making the  $a\langle 101 \rangle$  dislocations more mobile than the  $a\langle 111 \rangle$  dislocations. This would stabilize the decomposition process, enabling complete decomposition along the near-edge line length of the  $a\langle 111 \rangle$  dislocations (Fig.5(c)). The screw  $a\langle 111 \rangle$  dislocations observed in Fig.3(a) can annihilate by cross-slip. A complete anisotropic elastic analysis of this decomposition process



is in progress.

Note that in this proposed model for the slip transition, the decomposition of the  $a\langle 111 \rangle$  dislocation and the onset of  $a\langle 101 \rangle$  activity necessarily coincide since both occur when the CRSS for  $a\langle 101 \rangle$  motion is equal to or marginally less than the CRSS for  $a\langle 111 \rangle$  motion. The decomposition process also produces a large number of  $a\langle 101 \rangle$  segments which can subsequently act as sources. Evidence for intensive multiplication of  $a\langle 101 \rangle$  dislocations is discussed in the next section. Such a multiplication of relatively mobile  $a\langle 101 \rangle$  dislocations could contribute to the flow softening observed in Fig. 4. However, the large number of  $a\langle 010 \rangle$  dislocations also present just above the "knee" indicates that multiplication of  $a\langle 101 \rangle$  dislocations is not solely responsible for flow softening. Rather, the dislocation content present would add up to the parent  $a\langle 111 \rangle$  dislocations, suggesting that  $a\langle 111 \rangle$  dislocations were initially active (perhaps in the microstrain regime) prior to decomposition.

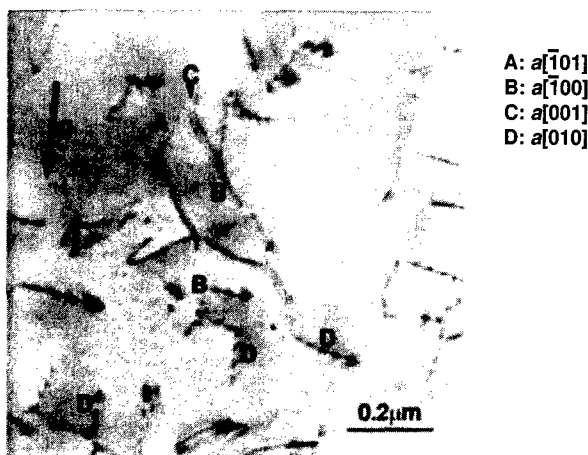
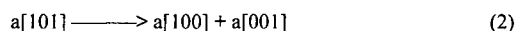


Fig. 6:  $g(110)$  bright field image showing the dislocation structure in stoichiometric NiAl deformed 1% at 650 K. The beam direction is close to  $[001]$ .  $a\langle 010 \rangle$  dislocations dominate the microstructure.

(b) **Deformation above the Slip Transition:** Fraser et al. [20], in studies on stoichiometric NiAl, have observed that  $a\langle 010 \rangle$  dislocations dominate the microstructure beyond the "knee". This is contrary to our observations in Ni-44Al, where  $a\langle 101 \rangle$  dislocations are abundant in the microstructure. This disparity can be explained when we consider that Mills et al. [21,22], in studies on stoichiometric NiAl, have shown that decomposition of  $a\langle 101 \rangle$  dislocations can occur along pure edge character according to:



Note that climb of  $a\langle 010 \rangle$  dislocations can also contribute to deformation in the temperature regime beyond the "knee" [20].

Forbes et al. [23] have demonstrated through creep studies that deformation in stoichiometric NiAl is indeed dominated by  $a\langle 101 \rangle\{101\}$  glide above the "knee". However, due to the decomposition of the  $a\langle 101 \rangle$  dislocations as in Equation 2, only  $a\langle 010 \rangle$  dislocations are left in the microstructure. Fig. 6 shows the typical dislocation structure obtained on deforming stoichiometric NiAl at 650 K, which is very close to the temperature of the "knee". The microstructure consists primarily of  $a\langle 010 \rangle$  dislocations; very limited  $a\langle 101 \rangle$  activity is actually observed. This agrees well with earlier studies, which also report the presence of  $a\langle 010 \rangle$  dislocations in the microstructure [20].

Studies on Ni-48Al [11,16] have indicated extensive  $a\langle 101 \rangle$  activity beyond the "knee" (note that the "knee" in Ni-48Al occurs at a higher temperature than for stoichiometric NiAl). This is similar to the observations in the Ni-44Al samples tested above the "knee", where a significant density of

$a\langle 101 \rangle$  dislocations is in fact obtained. This remarkable difference between the stoichiometric and non-stoichiometric, Ni-rich, compositions may arise for several reasons, as discussed further below.

Fig. 7 shows a different view of the dislocation structure obtained above the slip transition temperature in Ni-44Al. This TEM specimen was prepared with a  $[101]$  foil normal, providing a glide plane view on one particular slip system. The microstructure is dominated by  $a[\bar{1}01]$  dislocations. The significant difference between this microstructure and that obtained at lower temperatures (see Fig. 3b) is that the ratio of the dislocation densities of  $a\langle 101 \rangle$  to  $a\langle 010 \rangle$  segments is close to 1 in samples studied just above the "knee" (approximately 800 K) and it progressively increases with increasing temperature, suggesting that multiplication of  $a\langle 101 \rangle$  dislocations occurs in this temperature range.

Interestingly,  $a[\bar{1}01]$  dislocations are aligned along both  $\langle 111 \rangle$  directions in the glide plane, as evidenced by the long, rectilinear segments. Note that both the  $\langle 111 \rangle$  line directions would give equal screw character to the dislo-

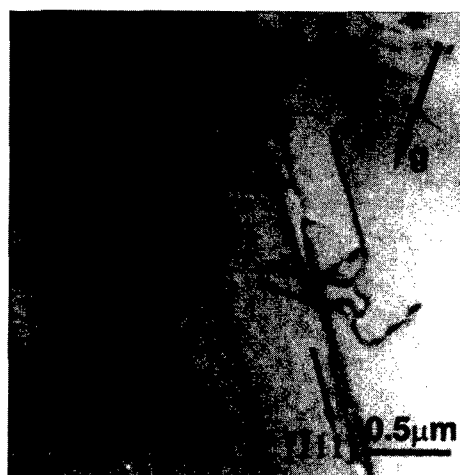
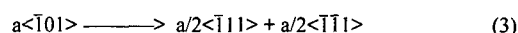


Fig. 7:  $g(101)$  bright field micrograph showing the deformation microstructure in Ni-44Al deformed 0.5% at 875 K.  $a[\bar{1}01]$  dislocations dominate the microstructure. The beam direction is near  $[101]$ .

cation segments, making them energetically equivalent.

The rectilinear shapes of the  $a\langle 101 \rangle$  dislocations seen in Fig. 7 deserves discussion. First consider the possibility that the preference for the  $\langle 111 \rangle$  line direction is due to a preferred line direction associated with  $a\langle 111 \rangle$  decomposition. As mentioned earlier, it is feasible, based on anisotropic elasticity calculations, for the near-edge  $a\langle 111 \rangle$  dislocations to undergo a decomposition process as indicated in Equation 1 [18]. The range of dislocation character through which this is favored is approximately  $60^\circ$  through pure edge. However, the decomposition force is not a maximum for dislocations aligned along  $\langle 111 \rangle$  directions, arguing against decomposition of  $a\langle 111 \rangle$  dislocations being solely responsible for the dislocation structure observed in Fig. 7. Likewise, line energy calculations using anisotropic elasticity [24] show that  $\langle 111 \rangle$  directions are not energetically favorable for the  $a\langle 101 \rangle$  dislocations. The line energy varies smoothly from edge (highest energy) to screw (lowest energy) character.

Another possible reason for the rectilinear shapes of the  $a\langle 101 \rangle$  dislocations is based instead on the dissociation of this dislocation according to the reaction below:



Anisotropic elasticity calculations indicate that dissociation is indeed energetically favorable for this line orientation. The dissociated superpartials



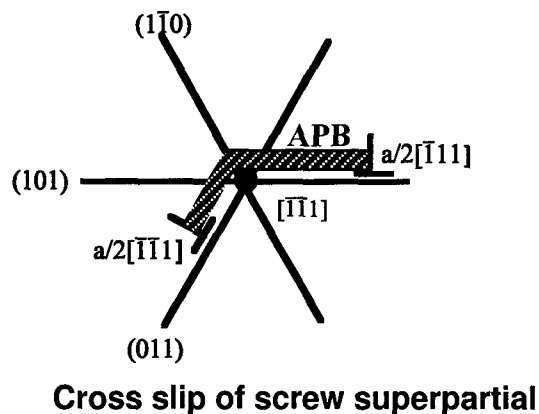
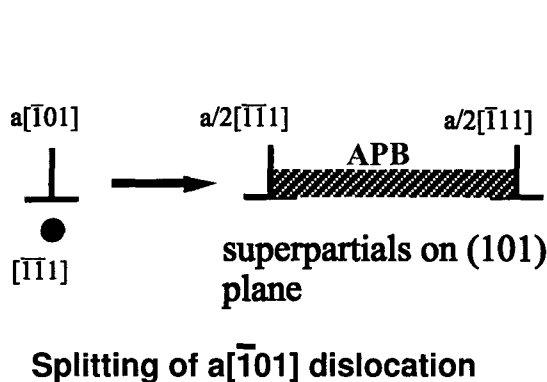


Fig. 8: Schematic representation of the dissociation process of an  $a[101]$  dislocation. The screw  $a/2[111]$  superpartial can cross slip onto equivalent  $\{110\}$  planes, causing a non-planar dissociated core.

would be joined by a ribbon of anti-phase boundary (APB), as shown in Fig. 8. The pure screw superpartial created as in Equation 3 can cross slip onto equivalent  $\{110\}$  planes. Interestingly, anisotropic elasticity calculations indicate that the planar configuration is metastable. The angular interaction force between the superpartials decreases upon a small perturbation from the planar dissociation, and is a minimum if the screw superpartial were to cross slip completely to one of the other two  $\{110\}$  planes in the  $\langle 111 \rangle$  zone. This cross-slip process, which is also illustrated in Fig. 8, would lead to the formation of a sessile lock, constraining an  $a[101]$  dislocation in the  $[111]$  direction. Similarly, the  $a/2[111]$  superpartial could cross slip along the  $[111]$  direction. Thus, this cross slip locking could explain the observation of rectilinear line lengths along both  $\langle 111 \rangle$  directions.

The above discussion concerning line direction preference assumes that the observed dislocations are in a configuration as after deformation. At the present time, unbowing of dislocations after unloading and during quenching cannot be ruled out. The effect of cooling of the compression specimens under load is being pursued to determine whether this results in any changes to these microstructures.

Above the "knee" for the Ni-44Al alloy, at least between 800 K and 900 K, we have found that glide of  $a\langle 101 \rangle$  dislocations is clearly the dominant mode of deformation. There is evidence to suggest that at least the initial sources

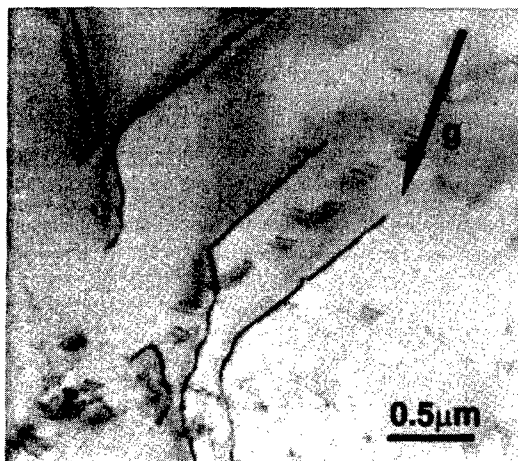


Fig. 9:  $g[101]$  bright field micrograph near the (101) zone showing kinks in rectilinear  $a[101]$  segments. The kinks are not aligned along  $\langle 111 \rangle$  directions.

of these  $a\langle 101 \rangle$  dislocations are still associated with  $a\langle 111 \rangle$  decomposition in the microstrain regime. This evidence is the presence of a small but significant density of  $a\langle 010 \rangle$  dislocations also present along with the  $a\langle 101 \rangle$  dislocations at 875 K. We point out that the remnant  $a\langle 010 \rangle$  dislocations present, if combined with a small fraction of the  $a\langle 101 \rangle$  dislocations, would yield parent  $a\langle 111 \rangle$  dislocations. The possibility that  $a\langle 111 \rangle$  decomposition might initiate deformation at this temperature is remarkable since the measured yield strength is significantly below the extrapolated yield strength values from below the "knee" (which presumably is associated with the CRSS for  $a\langle 111 \rangle$  slip), as can be seen in Fig. 1. It should be noted that these remnant  $a\langle 010 \rangle$  dislocations are unlikely to be grown-in defects since they lie along  $\langle 111 \rangle$  directions, which is not the configuration with the lowest line energy [24].

Fig. 9 shows an observation of kinks in a large number of  $a\langle 101 \rangle$  segments. This can be explained by considering either (a) glide of  $a\langle 101 \rangle$  dislocations through a kink-pair mechanism or (b) intersection of dislocation segments on two different slip planes. Intersection of dislocations would be expected to leave either a jog or a kink in a  $\langle 101 \rangle$  or  $\langle 010 \rangle$  direction. The lack of observation of any such features indicates a kink-pair mechanism for the glide of  $a\langle 101 \rangle$  dislocations. For deformation by  $a\langle 101 \rangle$  slip, thermal activation would be required to constrict the non-planar core of the  $a\langle 101 \rangle$  dislocation, which is postulated to exist along  $\langle 111 \rangle$  directions as discussed above. Thus, glide of  $a\langle 101 \rangle$  dislocations at higher temperatures may require a kink-pair mechanism. The kinks observed in Fig. 9 mostly appear to be along non- $\langle 111 \rangle$  directions, and hence, are expected to have a planar dissociated core, since the  $\langle 111 \rangle$  line directions are the only ones in which the proposed non-planar configuration could arise. Mobility of the kinks can thus be much faster than the remainder of the dislocation. The observation of long line lengths of  $a\langle 101 \rangle$  segments along  $\langle 111 \rangle$  directions also suggests that kink motion is easier than kink nucleation.

Finally, returning to the issue of why  $a\langle 100 \rangle$  dislocations dominate above the "knee" for Ni-50Al while  $a\langle 101 \rangle$  dislocations are dominant for Ni-44Al, the cross-slip locking model presented here may offer some additional insight. Earlier studies have provided evidence for the decomposition of  $a\langle 101 \rangle$  dislocations in stoichiometric NiAl [21,25] as in Equation 2. This decomposition requires that the  $a\langle 101 \rangle$  dislocations be *non-dissociated*. However, the APB energy can be reasoned to be lower for Ni-rich NiAl as compared to stoichiometric NiAl due to the presence of anti-site defects. The reduction in the APB energy may stabilize the dissociation process in Ni-44Al, as opposed to stoichiometric NiAl, where the high APB energy prevents any dissociation process. If the cross-slip locking mechanism does indeed occur, then for decomposition of  $a\langle 101 \rangle$  dislocations to occur in Ni-44Al, the split  $a\langle 101 \rangle$  core has to constrict. If this constriction is thermally activated, then higher temperatures would be required for the decomposition process, indicated in Equation 2, to occur. Decomposition is thus presumably more diffi-

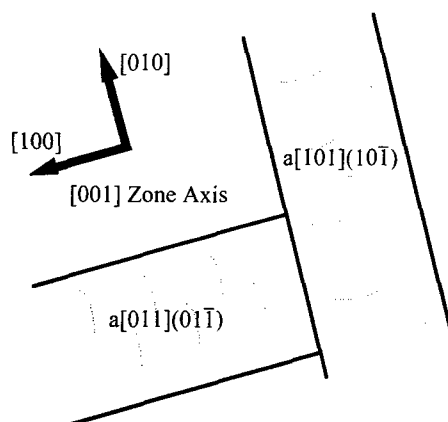
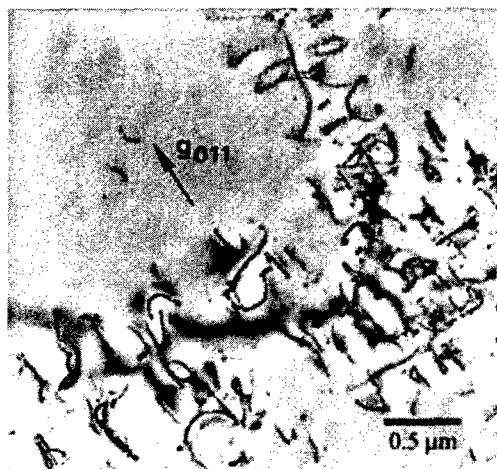


Fig. 10:  $g(011)$  bright field micrograph near the  $[11\bar{1}]$  zone of NiAl-0.3Hf deformed at 700 K showing bands of bowed  $a\langle 101 \rangle$  dislocations which dominate the microstructure. A schematic representation for a beam direction of  $[001]$  is shown.

cult to achieve in Ni-44Al than it is in Ni-50Al, on the assumption that there is no splitting of the  $a\langle 101 \rangle$  dislocation into  $a/2\langle 111 \rangle$  superpartials in the stoichiometric alloy in the temperature regime above the "knee". This reasoning may explain the disparity between the microstructure observations for stoichiometric NiAl and Ni-44Al deformed above the "knee".

It must be noted that the foregoing discussion requires that the  $a\langle 101 \rangle$  dislocations dissociate in the non-stoichiometric alloy. This has not been verified experimentally. Both weak beam and HRTEM investigations are presently underway to experimentally verify the postulated dissociation.

#### NiAl-0.3Hf

Fig. 10 shows the typical microstructure observed in NiAl with 0.3 at. % Hf addition deformed at 700K, which is above the "knee" for this alloy. Deformation occurs in localized bands of  $a\langle 101 \rangle$  dislocations on  $\{101\}$  planes. Thus, upon the addition of small amounts of Hf, a dramatic change in the deformation microstructure has occurred (in comparison to that found in stoichiometric NiAl). Note the kinked and bowed nature of these dislocations in contrast to the rectilinear dislocations observed in Ni-44Al. At least two  $a\langle 101 \rangle\{101\}$  slip systems appear active. At this temperature, the motion of  $a\langle 101 \rangle$  dislocations in NiAl-Hf appears easier than in Ni-44Al as evidenced by the lower yield strength (shown in Fig. 1) in the temperature range 800-1000 K. This occurs despite the probable strong solute interaction that should arise from the transition metal addition. This interaction contributes to the observed overall strengthening of NiAl-Hf as compared to stoichiometric NiAl, and the considerable advantage in strength that is observed at elevated temperatures. A higher mobility of the  $a\langle 101 \rangle$  dislocations may be responsible for the much lower "knee" temperature observed in Fig. 1 for NiAl-Hf as compared to Ni-44Al, making the  $a\langle 111 \rangle$  decomposition discussed previously more favorable at a lower temperature.

Fig. 11 shows the typical dislocation structure obtained on deforming NiAl-Hf to 0.9% at 1000 K. The microstructure consists primarily of  $a[1\bar{1}0]$  dislocations along  $[110]$  directions. A few  $a[110]$  dislocations are also observed. The  $a[1\bar{1}0]$  dislocations have neither a macroscopic resolved shear stress, nor an applied force for climb. It has been proposed that these are the reaction products between gliding  $a\langle 101 \rangle\{101\}$  dislocations [2]. The overall reaction can be represented as:



It is indeed remarkable that the  $a[110]$  dislocations in Fig. 11 choose to lie along the edge orientation, since the line energy is the lowest along the screw orientation, and highest along the edge orientation on the  $(001)$  planes [24].

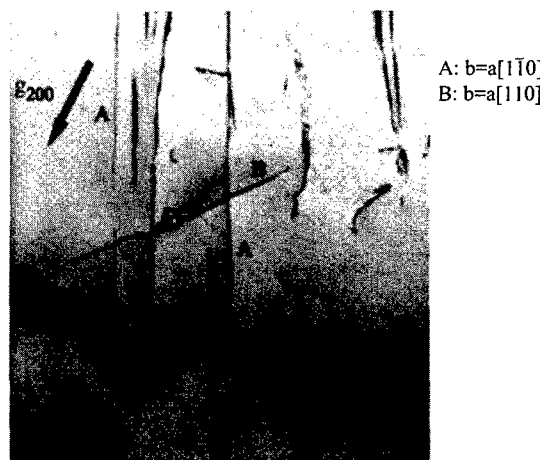


Fig. 11:  $g(200)$  bright field micrograph near the  $[001]$  zone of NiAl-0.3Hf deformed at 1000K. Long  $a[110]$  dislocations lying on  $(001)$  planes with no resolved shear stress or climb force dominate the microstructure.

The reason for this line direction preference is not presently known.

As a consequence of the reaction represented in Equation 4, the mobile  $a\langle 101 \rangle$  dislocation density could effectively be reduced. In addition, these  $a\langle 110 \rangle$  dislocations may act as sessile dislocation locks impeding the motion of subsequent  $a\langle 101 \rangle$  dislocations. Both of these factors probably contribute to the retention of significant strength levels even at quite high temperatures (up to 1300K), as seen in Fig. 1.

A remarkable feature is that essentially no  $a\langle 101 \rangle$  dislocations with resolved shear stresses have been observed in samples deformed at 1000 K, even after viewing multiple samples. Consequently, we do not presently know what dislocations are responsible for the production of strain. Observations of samples at larger strains are planned to address this issue.

#### Conclusions

At temperatures below the "knee" in the yield strength vs. temperature plots, slip in Ni-50Al, Ni-44Al and NiAl-0.3Hf is achieved through motion of

$a\langle 111 \rangle\{110\}$  dislocations. A slip transition which appears to be associated with the decomposition process of the  $a\langle 111 \rangle$  dislocations is postulated to occur when the mobilities of the  $a\langle 111 \rangle$  and  $a\langle 101 \rangle$  segments are comparable. At temperatures above the "knee" in Ni-44Al, deformation is achieved primarily through glide of  $a\langle 101 \rangle$  dislocations. The  $a\langle 101 \rangle$  dislocations are remarkably rectilinear along  $\langle 111 \rangle$  directions. It is energetically favorable for these  $a\langle 101 \rangle$  dislocations to undergo a dissociation process on  $\{011\}$  planes, creating two  $a/2\langle 111 \rangle$  superpartials. This dissociated configuration may be favored in the off-stoichiometric case, assuming that the APB energy is lower. Cross-slip of the screw superpartial results in an overall non-planar dissociated core for the  $a\langle 101 \rangle$  dislocation. Subsequent deformation will require constriction of this core. This can occur through a combination of applied stress and thermal activation. The observation of kinks in the  $a\langle 101 \rangle$  segments implies motion of the  $a\langle 101 \rangle$  dislocations through a kink-pair mechanism, which would require thermal activation and explain the strong temperature dependence in this regime.

The dissociation of  $a\langle 101 \rangle$  dislocations, and subsequent cross slip of the screw  $a/2\langle 111 \rangle$  superpartial explains the difference in observations between the Ni-rich and stoichiometric alloys. In the stoichiometric alloys, the higher APB energy would prevent any dissociation process from occurring. Instead, decomposition of  $a\langle 101 \rangle$  dislocations occurs at all temperatures above the "knee", leaving  $a\langle 010 \rangle$  dislocations in the microstructure. This model is offered without actual proof of the postulated dissociation. This is presently being sought with additional weak beam and HRTEM observations of  $a\langle 101 \rangle$  dislocations.

The increased strength in NiAl-0.3Hf at higher temperatures above the "knee" is believed to be achieved through the formation of sessile  $a\langle 110 \rangle\{001\}$  reaction products between gliding  $a\langle 101 \rangle$  dislocations. These dislocations can act as forest obstacles to gliding  $a\langle 101 \rangle$  dislocations, thus leading to enhanced yield strengths at higher temperatures relative to binary NiAl.

#### Acknowledgments

Support for this work was provided in part by the Department of Energy, Office of Basic Energy Sciences under DE-FG-02-96ER45550 (for MJM, SR and MFS), as well as the National Science Foundation under grant number 95-10259 (for MSD).

#### References

1. V. I. Levit, I. A. Bul, J. Hal, and M. J. Kaufman, *Scripta metall. mater.* **34**, 1925 (1996).
2. R. D. Noebe and A. Garg, NASA TM 106981, August 1995.
3. R. T. Pascoe and C. W. A. Newey, *Metal. Sci. J.* **2**, 138 (1968).
4. R. J. Wasilewski, S. R. Butler, and J. E. Hanlon, *Trans. metall. Soc. AIME* **239**, 1357 (1967).
5. A. Ball and R. E. Smallman, *Acta metall.* **14**, 1517 (1966).
6. R. R. Bowman, R. D. Noebe, and R. Darolia, 2nd Annual HITEMP Review, NASA CP-10039, 47-1 (1989).
7. R. D. Noebe, A. Misra, and R. Gibala, *Iron and Steel Institute of Japan International* **31**, 1172 (1991).
8. R. D. Field, D. F. Lahrman, and R. Darolia, *Acta metall. mater.* **39**, 2951 (1991).
9. R. D. Noebe, R. R. Bowman, and M. V. Nathal, *Physical Metallurgy and Processing of Intermetallic Compounds*, ed. N. S. Stoloff and V. K. Sikka (New York: Chapman and Hall), 212 (1995).
10. H. L. Fraser, R. E. Smallman, and M. H. Loretto, *Phil. Mag.* **28**, 651 (1973).
11. J. T. Kim and R. Gibala, *High Temperature Ordered Intermetallic Alloys IV*, ed. L.A. Johnson, D.P. Pope and J.O. Stiegler, *MRS Symp. Proc.* **213**, 261 (1991).
12. R. R. Bowman, R. D. Noebe, S. V. Raj, and I. E. Locci, *Metall. Trans. A* **23A**, 1493 (1992).
13. J. D. Whittenberger and R. D. Noebe, *Metall. Mater. Trans. A* **27A**, 2628 (1996).
14. P. H. Kitabjian, A. Garg, R. D. Noebe, and W. D. Nix, to be published in *MRS Symp. Proc.* **460**, (1997).
15. N. Rusovic and H. Warlimont, *Phys. Stat. Sol.(a)* **44**, 609 (1977).
16. J. T. Kim, Ph.D. Thesis, University of Michigan (1990).
17. R. D. Noebe, R. R. Bowman, and M. V. Nathal, *International Materials Review* **38**, 193 (1993).
18. C. L. Fu and M. H. Yoo, *Acta metall. mater.* **40**, 703 (1992).
19. R. Srinivasan, M. F. Savage, M. J. Mills, M. S. Daw, and R. D. Noebe, *Deformation, Fatigue and Fracture of Ordered Intermetallic Materials*, ed. W.O. Soboyejo, T.S. Srivatsan, and H.L. Fraser, TMS Publications, 325 (1996).
20. H. L. Fraser, M. H. Loretto, and R. E. Smallman, *Phil. Mag.* **28**, 667 (1973).
21. M. J. Mills and D. B. Miracle, *Acta metall. mater.* **41**, 85 (1993).
22. M. J. Mills, J. E. Angelo, M. S. Daw, J. D. Weinberg, and D. B. Miracle, *Mater.Sci.Eng. A* **192**, 134 (1995).
23. K. R. Forbes, U. Glatzel, R. Darolia, and W. D. Nix, *High Temperature Ordered Intermetallic Alloys V*, ed. I. Baker et al., *MRS Symp. Proc.* **288**, 45 (1993).
24. C. H. Lloyd and M. H. Loretto, *Phys. Stat. Sol.* **39**, 163 (1970).
25. M. J. Mills, M. S. Daw, S. M. Foiles, and D. B. Miracle, *High Temperature Ordered Intermetallic Alloys V*, ed. I. Baker et al., *MRS Symp. Proc.* **288**, 257 (1993).

## TOUGHENING MECHANISMS IN DIRECTIONALLY SOLIDIFIED B2-NiAl-BASED EUTECTIC ALLOYS

A. Misra\*, Z.L. Wu\*\* and R. Gibala,  
Department of Materials Science and Engineering, University of Michigan, Ann Arbor, MI 48109-2136

R.D. Noebe,  
NASA Lewis Research Center, Cleveland, OH 44135

B.F. Oliver,  
Department of Materials Science and Engineering, University of Tennessee, Knoxville, TN 37996-2200

\* Present address: Center for Materials Science, Los Alamos National Laboratory, MS K765, Los Alamos, NM 87545.

\*\* Present address: Electric and Fuel Handling Division, Ford Motor Company, Ypsilanti, MI 48197.

### Abstract

The room temperature mechanical behavior of two different types of directionally-solidified (DS) eutectic alloys is compared: (I) B2 Ni-Fe-Al matrix reinforced with a ductile fcc-based ( $\gamma$ ) second phase, and (II) B2 NiAl matrix reinforced with a bcc refractory metal second phase. The nominal composition of the type I alloy in atomic percent was Ni-30Fe-20Al. This alloy had room temperature tensile ductility of 10-12% and mode I fracture toughness of 30 MPa $\sqrt{m}$ . A substantial portion of the ductility was a result of slip transfer from the  $\{111\}<110>$  slip systems of the ductile  $\gamma$  phase to the  $\{011\}<100>$  slip systems of the brittle B2 matrix, which was facilitated by a Kurdjumov-Sachs orientation relationship. Extrinsic toughening mechanisms such as crack blunting and plastic stretching of the  $\gamma$  phase in the crack wake also contributed to the toughness. The tensile ductility of these alloys was found to be independent of the processing methods. In the type II alloys, the fracture toughness ranged from 14 to 15.7 MPa $\sqrt{m}$  for the NiAl-9Mo eutectic, and from 7 to 20 MPa $\sqrt{m}$  for the NiAl-34Cr eutectic with the higher values corresponding to materials with very low interstitial impurity contents. The toughening mechanisms observed were primarily extrinsic, although significant plasticity of the NiAl phase near the crack tip was observed, especially in the high purity alloys. The higher yield strength of the refractory metal phase as compared to the NiAl phase, weak interfaces (particularly in low purity alloys) and lack of favorable orientation relationships do not allow easy slip transfer and compatible plastic deformation of both phases in type II composites, resulting in lower toughness as compared to type I. However, type II alloys may offer a better balance of toughness and high temperature creep strength.

### Introduction

Although NiAl is still considered a potential high temperature structural material due to favorable properties such as a high melting point, low density, high thermal conductivity, and good oxidation resistance, the development of NiAl-based alloys possessing both adequate creep resistance and room temperature fracture toughness continues to be a challenge [1-3]. Generally, alloys can be developed optimizing one property, in particular high temperature strength but at the expense of the other property, which is usually fracture resistance [3]. Ductile phase reinforcement is a common way to produce intermetallic matrix composites possessing enhanced fracture toughness with respect to the monolithic ordered intermetallic materials [4-7]. However in such systems, the matrix is usually assumed to be an elastic medium and the

toughness of the composite is believed to result from plastic deformation only in the ductile reinforcement both at the crack tip process zone and in the crack wake [4-7]. Factors which maximize the plastic stretch of the ductile phase prior to failure tend to maximize the toughness achieved in the composite. Some of these factors are weak interfaces to allow limited interface debonding, and reinforcements possessing high ductility, high strength, high modulus and large diameters [4, 6]. In contrast, previous work on ductile phase toughened NiAl has revealed significant plasticity in the NiAl phase, afforded primarily by slip transfer from the ductile second phase [8]. Thus, the NiAl matrix phase cannot be assumed to be an elastic medium, especially since the classical ductile phase toughening approach seems to account for only part of the toughness in NiAl-based ductile-phase-toughened alloys [9]. Recent observations of inherent ductility in either high purity NiAl [10,11] or commercial purity NiAl single crystals heat treated to minimize static strain aging [12] indicate an effect of interstitial impurities on the room temperature mechanical behavior of NiAl and suggest a dislocation-density-limited behavior. These experiments support the view that it may be incorrect to ignore plasticity effects in NiAl, especially under conditions of constrained deformation in two-phase alloys [13]. Therefore, an in-depth understanding of the toughening mechanisms in NiAl-based ductile-phase-toughened alloys is needed to identify the alloying and microstructural modification schemes that would optimize room temperature toughness as well as high temperature creep strength.

In the present investigation, the toughening mechanisms operative in NiAl-based eutectic alloys containing a disordered fcc second phase are compared with NiAl/bcc refractory metal eutectics. The nominal compositions of the two types of alloys studied were: type (I) Ni-30at.%Fe-20at.%Al, and type (II) Ni-33at.%Al-34at.%Cr and Ni-45.5at.%Al-9at.%Mo. These are referred to as Ni-30Fe-20Al, NiAl-34Cr and NiAl-9Mo, respectively, throughout the remainder of this paper. The influence of second phase and interface properties on the toughness of the eutectics are discussed. We also considered factors which may limit toughness in the eutectics in order to identify conditions under which maximum toughness can be achieved.

### Experimental Procedures

All the eutectic alloys studied were processed by the DS route, but details of the actual processing methods varied. The Ni-30Fe-20Al alloy was prepared by a vertical Bridgman method at NASA Lewis Research Center. The details of the process are presented elsewhere [14]. The

NiAl-34Cr and NiAl-9Mo alloys were prepared by two different techniques. In one technique, arc-melted buttons of the final alloy composition were crushed and loaded into alumina crucibles coated with boron nitride and directionally solidified at ~11 mm/hr in a vertical Bridgman-type furnace under an argon atmosphere. Additional NiAl-34Cr and NiAl-9Mo alloys were prepared at the University of Tennessee by a containerless electromagnetically levitated zone (CELZ) DS process. The details of this process are presented elsewhere [15]. Fracture toughness data were obtained from either three-point or four-point notched bend tests. All mechanical testing details are presented elsewhere [14-16]. Scanning electron microscopy (SEM) investigations were performed either on a Philips XL30 or an ElectroScan microscope, and transmission electron microscopy (TEM) investigations were performed on a JEOL 2000FX microscope.

## Results

### Type I (B2/fcc) Eutectic Alloys

The composition of the type I eutectic alloy was Ni-30Fe-20Al. This alloy had a B2 matrix of nominal composition Ni-20at.%Fe-30at.%Al. Single phase B2 Ni-Fe-Al alloys are reported to have very limited tensile ductility and the same operative slip systems as NiAl at room temperature [17-19]. The ductile phase in this eutectic was  $\gamma$  (fcc) with nominal composition of Ni-38at.%Fe-13at.%Al and contained ~20-40 nm size precipitates of ordered  $\gamma'$  ( $L1_2$ ). This phase mixture of ( $\gamma+\gamma'$ ) is simply referred to as the  $\gamma$  phase in the remainder of the text. The orientation relationship between the  $\beta$  and the  $\gamma$  phases was a Kurdjumov-Sachs (KS) relationship with  $\{110\}\beta \parallel \{111\}\gamma$ ,  $\langle 111 \rangle\beta \parallel \langle 011 \rangle\gamma$ . The growth direction for the  $\beta$  phase was near  $\langle 001 \rangle$  and the microstructure was completely eutectic with a mixed lamellar/rod morphology and average inter-lamellar spacing of approximately 10  $\mu\text{m}$ .

The mechanical properties of the constituent matrix phase  $\beta$  Ni-20Fe-30Al and the multi-phase eutectic  $\beta+(\gamma+\gamma')$  Ni-30Fe-20Al alloys are summarized in Table I. Results from other investigations on these alloys are also included in Table I for comparison. The single phase  $\beta$  Ni-20Fe-30Al alloy has no tensile ductility in polycrystalline form. Under compressive deformation, the slip vector activated was  $a_0\langle 100 \rangle$  indicating that up to 20 at.% Fe was ineffective in promoting  $a_0\langle 111 \rangle$  slip in polycrystalline material [18]. No tensile data exist for single crystalline  $\beta$  Ni-20Fe-30Al but compressive deformation parallel to  $\langle 001 \rangle$  resulted in yield stresses slightly higher or equal to that of  $\langle 001 \rangle$  binary NiAl and slip on  $\{112\}\langle 111 \rangle$  slip systems [17]. No fracture toughness data are available for  $\langle 001 \rangle$  orientations of the  $\beta$  Ni-20Fe-30Al alloys, although they would be expected to be similar to  $\beta$  NiAl. The fracture toughness of mechanically alloyed  $\beta$  Ni-20Fe-35Al of 28  $\mu\text{m}$  grain size has been reported to be 9-10  $\text{MPa}\sqrt{\text{m}}$  [21]. As shown in Table I, the multi-phase Ni-30Fe-20Al alloy has fracture toughness of 30.4  $\text{MPa}\sqrt{\text{m}}$  in the DS condition and tensile ductility on the order of 10-12%, which happens to be independent of the processing method and scale and morphology of the microstructure. The significantly enhanced ductility and toughness of  $\beta/\gamma$  alloys as compared to single phase  $\beta$  may, therefore, be attributed to the effect of the ductile  $\gamma$  phase.

The deformation and fracture behavior of the Ni-30Fe-20Al alloy is shown in Fig. 1. Evidence of slip transfer from the ductile  $\gamma$  phase to the brittle  $\beta$  phase in a specimen deformed in compression is shown in Fig. 1(a). The slip planes in the two phases,  $\{011\}\beta$  and  $\{111\}\gamma$ , were parallel due to the KS orientation relationship and the slip vector activated in the  $\beta$  phase was  $a_0\langle 100 \rangle$ . Similar slip transfer at the crack tip of a notched bend specimen is shown in Fig. 1 (b). This behavior indicates that compatible plastic deformation in both phases provides crack tip shielding in these alloys. Fracture of the  $\beta$  phase was quasi-cleavage-like while the ductile  $\gamma$  phase failed by necking [22]. No evidence of pull-out of the  $\gamma$  phase or  $\beta/\gamma$  interface decohesion was seen and no large scale crack

bridging zone was detected. Observations of the side surfaces of fractured tensile specimens, (Fig. 1(c)), indicate that the  $\beta$  phase fractures first and crack blunting and plastic stretching of the ductile  $\gamma$  phase in the crack wake provide further enhancement in toughness and ductility. Again, no evidence of interface decohesion was observed.

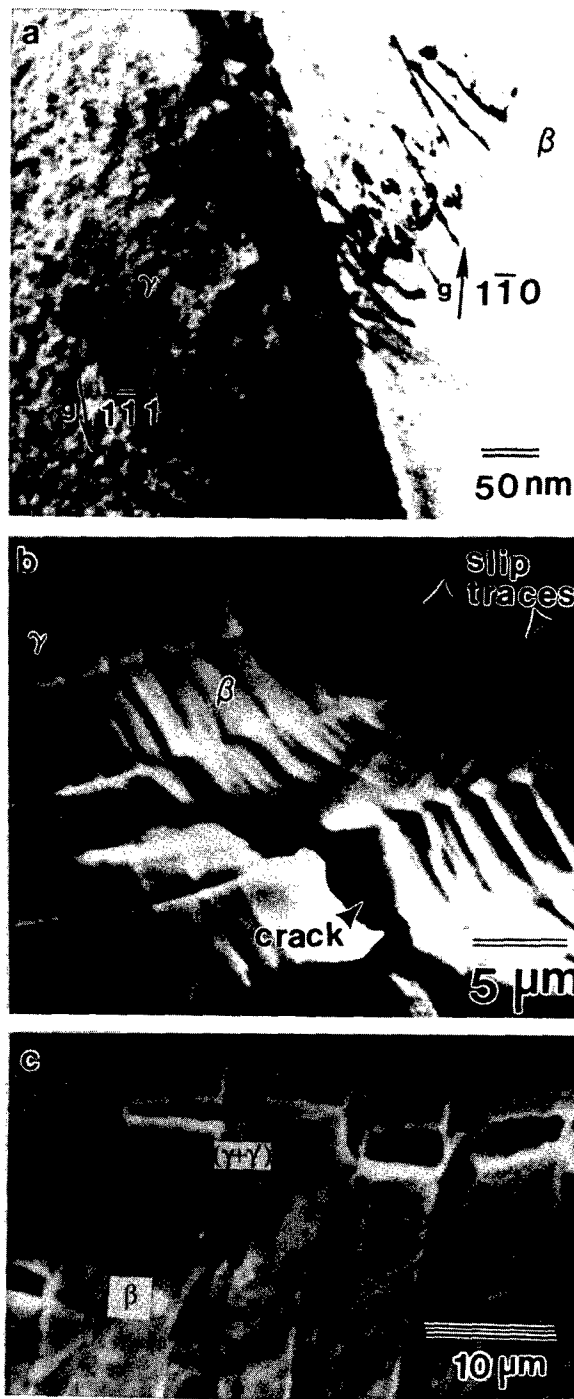


Fig. 1. Deformation and fracture behavior of the Ni-30Fe-20Al alloy; (a) TEM micrograph showing a  $\gamma$  phase dislocation pile-up activating slip in the  $\beta$  phase,  $B = [\bar{1}01]\gamma$  and  $[001]\beta$ . (b) Crack tip plastic zone in a notched bend specimen. Notice the evidence of slip transfer from the  $\gamma$  to  $\beta$  phases. (c) Side surface of a fractured tensile specimen showing crack blunting by the  $\gamma$  phase after  $\beta$  had fractured.

Table I Mechanical Properties of Single Phase  $\beta$   
Ni-20Fe-30Al and Multi-phase  $\beta+(\gamma+\gamma')$  Ni-30Fe-20Al Alloys

Alloy	Processing	Microstructure	Yield Stress (MPa)	Tensile Ductility %	$K_Q$ (MPa $\sqrt{m}$ )	Ref.
Ni-20Fe-30Al	DS	$\langle 001 \rangle \beta$ , Columnar Grain	1300	-	NR	[17]
Ni-20Fe-30Al	Extruded	Equiaxed $\beta$ , grain size 25 $\mu m$	770	0	NR	[18]
Ni-20Fe-30Al	Rapid Solidification	Columnar $\beta$ , grain size 1-2 $\mu m$	900	0	NR	[19]
Ni-30Fe-20Al	DS	Eutectic $\beta+(\gamma+\gamma')$ , inter-lamellar spacing ~ 10 $\mu m$	575	10-12	30.4	this study
Ni-30Fe-20Al	Extruded	Pro-eutectic $\beta$ (dia. ~50 $\mu m$ )+ eutectic $\beta+(\gamma+\gamma')$ inter-lamellar spacing ~ 1 $\mu m$	850	7	NR	[18]
Ni-30Fe-20Al	Rapid Solidification	Columnar $\beta+(\gamma+\gamma')$ grain size 1-2 $\mu m$	800	12	NR	[19]
Ni-30Fe-20Al	DS	eutectic $\beta+(\gamma+\gamma')$ inter-lamellar spacing ~ 10 $\mu m$	560	8	NR	[20]

NR : not reported

Table II. Typical Interstitial Levels in NiAl-Cr and NiAl-Mo and Binary NiAl Alloys

ALLOY	Carbon (wt.%)	Oxygen (wt.%)	Nitrogen (wt.%)	Sulphur (wt.%)
NiAl-34Cr *	0.0096 $\pm$ 0.0030	0.0081 $\pm$ 0.0050	0.0136 $\pm$ 0.0030	0.0015 $\pm$ 0.0005
NiAl-34Cr **	0.0036	0.0008	0.0016	<0.0010
NiAl-9Mo*	0.0047	0.0030	<0.0005	0.0013
NiAl-9Mo**	0.0051	0.0020	<0.0002	<0.0007
Containerless-processed NiAl [11]	<0.0005	0.0006- 0.0016	0.0001- 0.0005	<0.0005
Commercial purity single crystal NiAl [12]	0.0086 $\pm$ 0.0036	0.0058 $\pm$ 0.0012	0.0012 $\pm$ 0.0002	-

\* DS at University of Michigan using alumina crucibles.

\*\* DS at University of Tennessee by containerless float zone process [11,15]

#### Type II (B2/bcc) Eutectic Alloys

Microstructures of the two types of B2/bcc eutectic alloys studied are shown in Fig. 2. Both the NiAl-34Cr, (Fig. 2(a)), and NiAl-9Mo, (Fig. 2(b)), alloys had rod-type eutectic microstructures, with the former being non-faceted and the latter having faceted rods. The volume fractions of the rods were 0.34 and 0.11 for the NiAl-34Cr and NiAl-9Mo alloys, respectively. The orientation relationship between the bcc metal fibers

and the NiAl matrix was cube-on-cube and the growth direction close to  $\langle 001 \rangle$ , consistent with that reported by Cline *et al.* [23]. The interfaces are expected to be semi-coherent with misfit dislocation arrays accommodating the lattice mismatch. In the NiAl-34Cr alloy, the mismatch is only ~0.7% and the misfit dislocation arrays could be easily resolved [15,24]. However, in the NiAl-9Mo alloy, the mismatch is ~9% and the calculated misfit dislocation spacing of 3.2 nm could not be resolved by weak beam imaging and only the Moire type fringes were

observed at the interface of spacing very close to the calculated misfit dislocation spacing [16].

The results of combustion analyses using LECO Carbon/Sulfur and Nitrogen/Oxygen Determinators to determine the residual interstitial contents in these DS eutectics are shown in Table II. Note the low level of interstitials in the NiAl-34Cr alloy processed by the CELZ process as compared to the NiAl-34Cr alloy processed by the modified Bridgman method using alumina crucibles. Significant scatter was observed in the interstitial contents in the low purity NiAl-34Cr alloys and so the average values along with the deviation are reported. This table also shows the interstitial contents in binary NiAl of commercial purity and NiAl single crystals grown by the CELZ process. In the [001] orientation, high purity NiAl can have a fracture toughness of 10-11 MPa√m [11], as compared to 8 MPa√m observed in commercial purity NiAl [25]. The interstitial contents in the NiAl-9Mo alloy produced by either method were similar and about the same as that for commercial purity NiAl. The compositions of the constituent phases were determined by electron micro-probe analysis. In the NiAl-34Cr alloy, the Cr fibers contained ~ 2.5 at.% Ni and ~ 4 at.% Al in solid solution, while the NiAl matrix contained < 2 at.% Cr and no Cr precipitates were observed in the NiAl phase. In the NiAl-9Mo alloy, the Mo fibers contained ~ 4.2 at.% Ni and ~ 8.5 at.% Al in solid solution while the NiAl matrix contained < 0.06 at.% Mo. In both alloys, the NiAl matrix was Ni-rich since more Al partitioned to the fibers than Ni. The implications of these results are discussed later in this paper.

The fracture toughness values of these alloys are shown in Table III. For each alloy about 4-5 samples were tested. Note that for the NiAl-34Cr eutectics, the fracture toughness of the high purity alloys processed by the CELZ method is significantly higher than that of lower purity alloys. Fracture of both alloys occurred without stable crack growth. Therefore, the results indicate that the initiation toughness of the high purity material was much higher than the lower purity material. The fracture toughness of the high purity NiAl-34Cr alloys (~20 MPa√m) is double the toughness of comparably processed high purity NiAl (10-11 MPa√m [11]). The fracture toughness of commercial purity binary NiAl of <001> orientation is about 8 MPa√m [25]. Thus, the toughness of a low purity NiAl-34Cr eutectic is about the same or marginally higher than that of binary NiAl. The fracture behaviors of the NiAl-34Cr alloys are shown in Fig. 3. For the low purity alloy, brittle cleavage fracture was observed for both the NiAl and Cr phases. The mating fracture surfaces revealed the pulled-out fibers in one surface (Fig. 3 (a)) and holes in the matrix in the other surface (Fig. 3 (b)). In contrast, limited crack bridging and failure by necking of Cr fibers was observed in the higher purity alloys (Fig. 3 (c)). Interface decohesion and fiber pull-out were not observed in the high purity NiAl-34Cr alloys. In regions where Cr fibers appeared to have fractured by cleavage, mismatch of cleavage planes, {100} for Cr and {110} for NiAl, may result in additional toughening [15]. Trapping of matrix cracks by the higher toughness Cr fibers (due to their higher purity), and linkage of micro-cracks were also identified as operative toughening mechanisms, but only in the CELZ processed NiAl-34Cr alloy [15]. For the two NiAl-9Mo eutectics, no significant difference was noted in interstitial content. Nor was there any difference in the fracture toughness of alloys processed by the two different DS routes (Table III). Both alloys exhibited stable crack growth after crack initiation, although a large load drop occurred at initiation. Significant improvement in the fracture toughness as compared to monolithic NiAl was noted. The fracture behavior of the NiAl-9Mo alloy processed at the University of Michigan is shown in Fig. 4. The side-surface observations (Fig. 4(a)) indicate crack bridging by the necked Mo fibers. However, the length of the bridging zone with respect to the crack length is small. Also, the extent of the plastic stretch of the Mo fibers in the crack wake is small, indicating lower ductility of the Mo fibers as compared to the ductile  $\gamma$  phase in the type I eutectics. The fracture surface observations (Fig. 4(b) and (c)) indicate that fracture of

the NiAl phase is quasi-cleavage-like, while the Mo fibers fail by necking. Crack arrest lines on the fracture surface (Fig. 4(c)) indicate a crack trapping mechanism, where the crack growth is stopped by the fibers. Also, extensive interface debonding is noted for curved fibers near cell boundaries which are oriented at an angle to the crack path (Fig. 4(b)). The debonding is much less for the high-aspect-ratio fibers aligned normal to the crack path. A number of unbroken ligaments were observed along the length of the crack. These ligaments are expected to fracture in shear and provide some toughening. The fracture behavior of the NiAl-9Mo alloy processed by the CELZ method experienced similar toughness and the same set of toughening mechanisms [26].

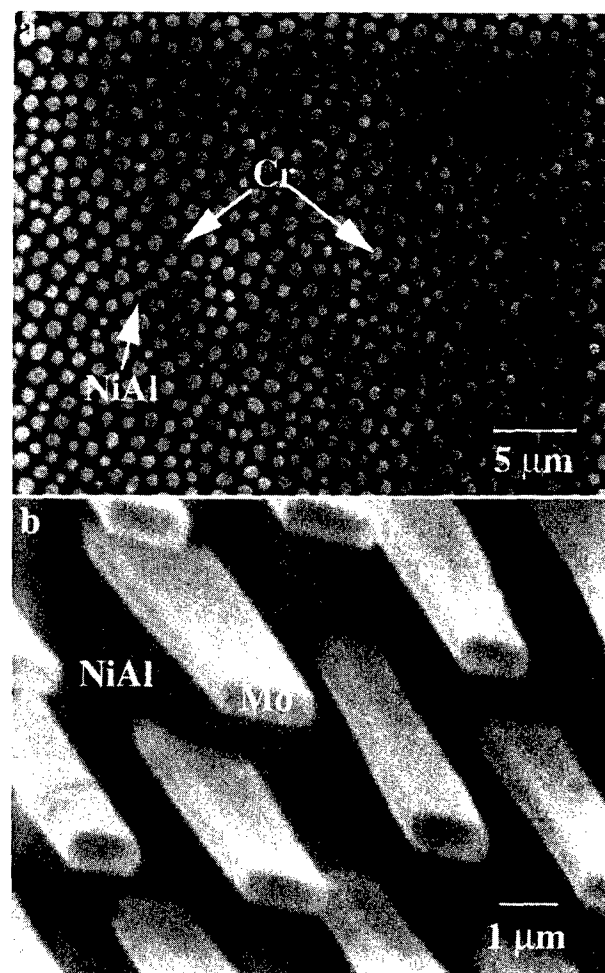


Fig. 2. SEM micrographs showing the rod-type eutectic microstructures of (a) a DS NiAl-34Cr alloy, transverse section; (b) a DS NiAl-9Mo alloy, inclined view with NiAl matrix selectively etched. Notice non-faceted fibers in (a) and faceted fibers in (b).

Table III Fracture Toughness of DS NiAl-34Cr and NiAl-9Mo Eutectic Alloys

Alloy	$K_{Ic}$ (MPa√m)
NiAl-34Cr*	7.6 - 12.5
NiAl-34Cr**	18.5 - 21.5
NiAl-9Mo*	14.4
NiAl-9Mo**	15.7

\* DS in alumina crucibles, (lower purity)

\*\* DS by CELZ method (high purity)

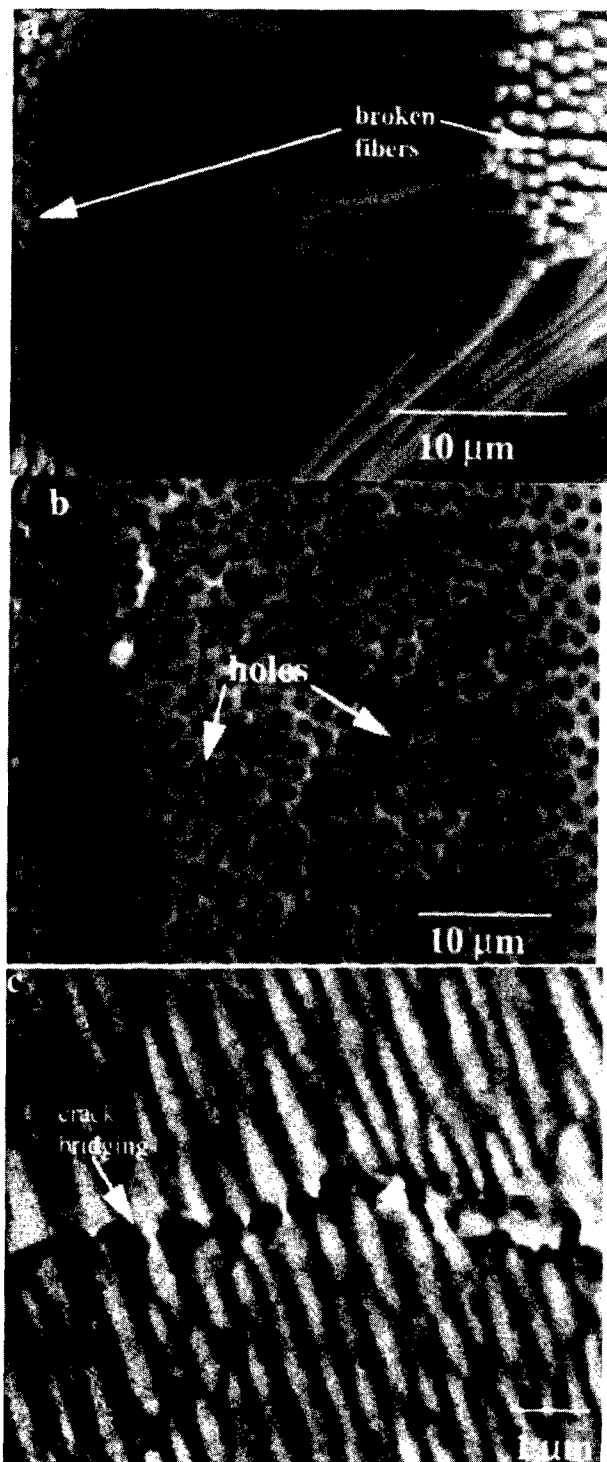


Fig. 3. Fracture behavior of DS NiAl-34Cr alloys: (a) and (b) low purity alloys exhibit brittle fracture of both phases and significant interface decohesion and fiber pull-out; (c) limited crack bridging and necking of Cr fibers in the high purity alloys.

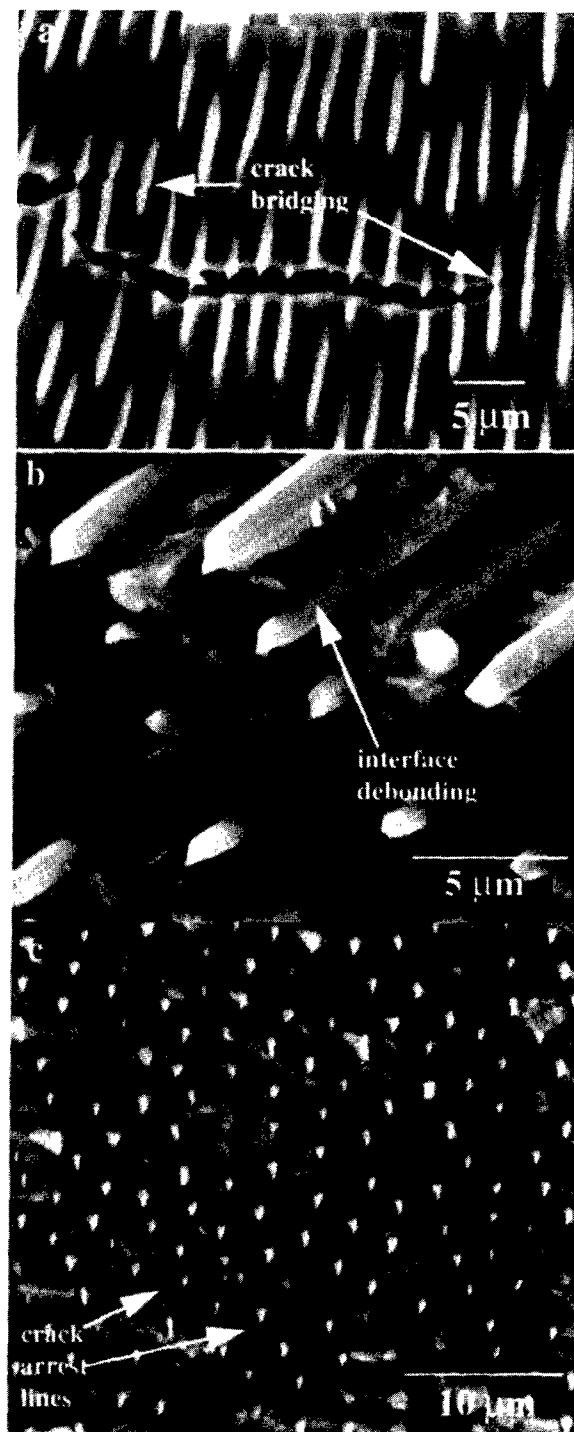


Fig. 4. Fracture behavior of DS NiAl-9Mo alloys: (a) side surface of a notched bend sample showing crack bridging and necking of Mo fibers, (b) fracture surface showing interface debonding for fibers inclined to the crack path; (c) crack arrest lines indicating crack trapping by Mo fibers.



Examination of TEM specimens from just below the fracture surfaces revealed a high density of dislocations only in the NiAl phase in the NiAl-9Mo [16], Fig. 5(a), and high purity NiAl-34Cr alloys [15], Fig. 5(b). In the low purity NiAl-34Cr eutectic, Fig. 5(c), no significant dislocation activity was discerned by TEM. Unlike the type I eutectic alloys, a direct slip transfer process from the disordered metallic phase to the NiAl phase was not observed. TEM results of the compressive deformation behavior of the various eutectics are shown in Fig. 6. In both NiAl-34Cr and NiAl-9Mo alloys, slip initiated in the NiAl phase (Fig. 6(a)). At higher strain levels (~2%), a very high density of dislocations was seen in the NiAl side of the interface (Fig. 6(b)), indicating the effectiveness of these interfaces in blocking slip. In the fibers, the dislocation density was much lower (Fig. 6(c)). The slip systems were  $\{011\}\langle 100 \rangle$  for NiAl and  $\{112\}\langle 111 \rangle$  for the bcc metal phases. Multiple slip along with evidence of cross-slip of  $a/2\langle 111 \rangle$  dislocations was observed in the bcc metal phase after several percent strain.

### Discussion

Room temperature tensile ductility, on the order of 10%, and mode I fracture toughness of 30 MPa $\sqrt{m}$  were observed in the type I eutectic alloys independent of the processing method and microstructural scale or morphology. In contrast, the fracture toughness of type II DS eutectics varied from 7 to 20 MPa $\sqrt{m}$  for the NiAl-34Cr alloy but was approximately 15 MPa $\sqrt{m}$  for the NiAl-9Mo eutectics regardless of the processing technique. The completely elastic behavior up to the point of crack initiation in notched bend tests and the large load drop at initiation suggest little or no tensile ductility in the type II eutectics. No tensile tests were performed on the CELZ-processed eutectics. The tensile samples of low purity NiAl-34Cr alloys fractured in the elastic regime, usually in the grip section. Furthermore, Yang *et al.* [27] have reported <0.6% tensile ductility in DS NiAl-Cr(Mo) alloys. The different behaviors of the NiAl-based eutectic alloys reinforced with either disordered fcc or bcc metal phases are discussed below in light of the toughening mechanisms observed.

### Intrinsic Toughening Mechanisms

These mechanisms refer to the enhancement of the toughness of NiAl due to increased nucleation and propagation of mobile  $a_0\langle 100 \rangle$  dislocations at the crack tip. For dislocation-density-limited behavior, the effect of crack tip dislocation density on the fracture toughness may be interpreted in terms of the Ashby-Embury model [28]. At higher dislocation densities, dislocations lie closer to the crack-tip. As shown in Fig. 7, up to a distance of  $r_c$  from the crack tip, the shear stress is higher than the critical resolved shear stress,  $\tau_c$ . If the mean spacing of the dislocations,  $1/\rho$  (where  $\rho$  is dislocation density), is less than the distance  $r_c$ , then the crack-tip stress field may cause significant dislocation motion and multiplication with the original dislocations acting as additional sources, which in turn will result in blunting of the crack [28]. In the type I alloys, easy slip transfer from the ductile  $\gamma$  phase to the brittle  $\beta$  phase served as a continuous source of mobile  $a_0\langle 100 \rangle$  dislocations in the  $\beta$  phase. This in turn relieved stress concentrations at the interface due to  $\gamma$  phase dislocation pile-ups which may otherwise result in crack initiation, and most importantly allowed compatible deformation of both phases even under tensile loading. The conditions which favored this easy slip transfer were i.) a ductile  $\gamma$  phase with a lower yield stress than  $\beta$  and which yielded first, ii.) a crystallographic orientation relationship such that  $\{011\}\beta$  and  $\{111\}\gamma$  slip planes were parallel, (Fig. 8(a)), and iii.) the interfaces were strong and showed no decohesion, thereby allowing slip transfer to occur instead of interfacial failure. In the type II alloys, dislocation generation from interfaces allow plasticity in the NiAl phase at a crack tip, but slip transfer across the interface resulting in general plasticity of the alloy is extremely difficult. This is due to several factors. First, the yield strength of the refractory metal phase was significantly

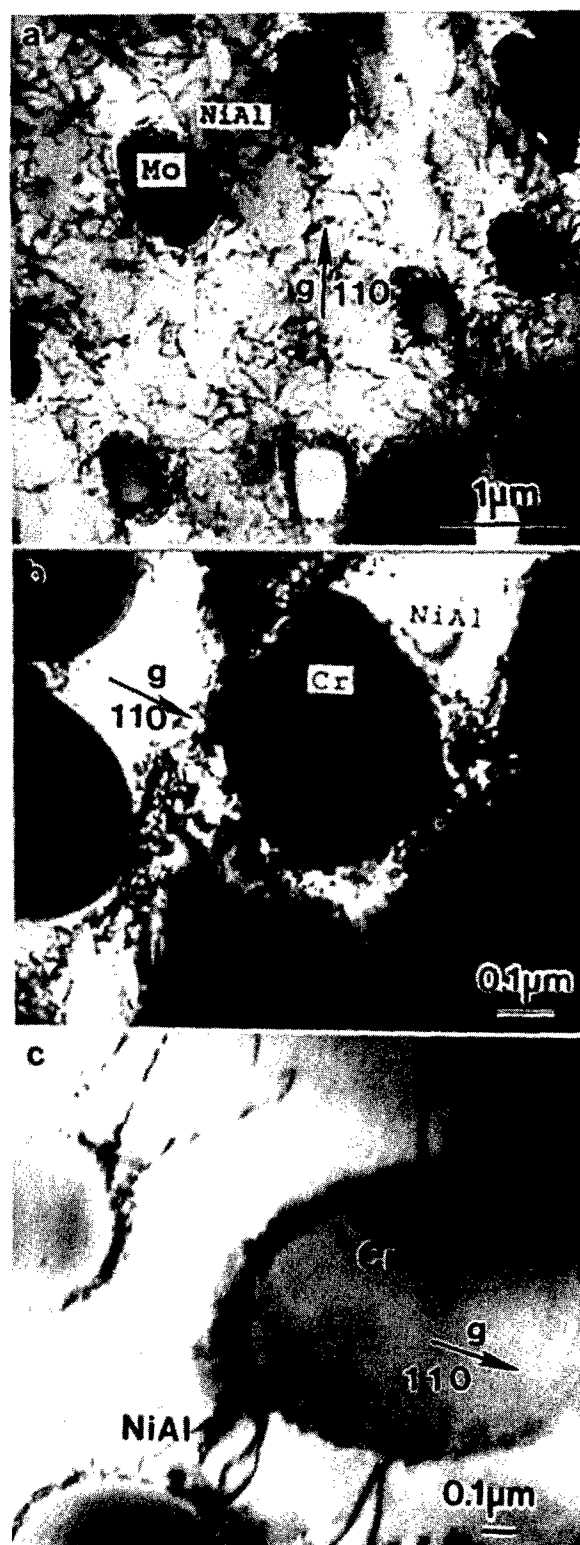


Fig. 5. TEM micrographs showing the plastic zone regions in the bend specimens of (a) NiAl-9Mo, (b) high purity NiAl-34Cr, and (c) low purity NiAl-34Cr alloy. Notice a high density of dislocations only in the NiAl phase in (a) and (b) and lack of significant crack tip plasticity in both phases in (c).  $B = [001]$  in all.

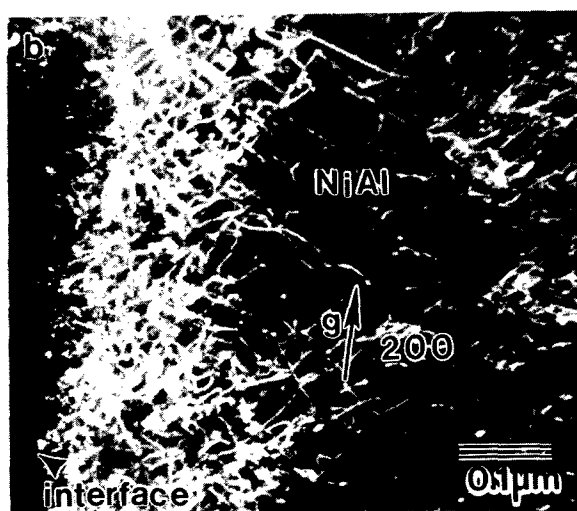
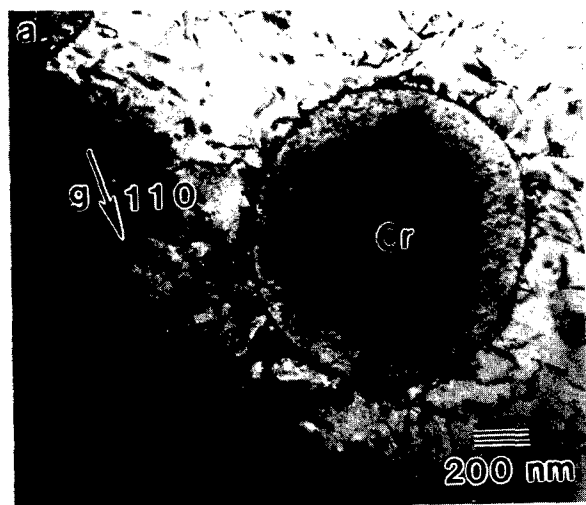


Fig. 6. TEM micrographs showing the compressive deformation behavior of NiAl/bcc-metal eutectics: (a) initiation of slip in the NiAl phase in NiAl-34Cr alloy,  $B=[001]$ ; (b) high density of  $a_0\langle 100 \rangle$  dislocations on the NiAl side of the NiAl/Mo interface,  $B=[011]$ ; (c) lower density of  $a/2\langle 111 \rangle$  dislocations in the Mo phase,  $B=[111]$ .

higher than that of the NiAl phase, primarily due to the partitioning of Ni and Al to the Cr or Mo phases [15]. Both Ni and Al are known to increase the yield strength and the ductile-to-brittle transition temperature of refractory metals like Cr and Mo [29]. Similarly, residual interstitial impurities, can embrittle both NiAl [10-12] and especially bcc refractory metals [29]. In NiAl/bcc-metal eutectics, slip initiates in the NiAl phase, while the fibers continue to deform elastically. For general ductility of NiAl the opposite of this process would be desired. Furthermore, transfer of slip is crystallographically unfavored in these systems due to the large angle of mismatch between the lines of intersection of slip planes with the interface and the large angle between slip plane normals [30] (Fig. 8(b)). During compressive deformation, slip in the bcc metal phase can be activated only when a significant density of NiAl dislocations piles-up at the interface (Fig. 6 (b)). However, during tensile or bend loading, the stress concentration due to piled-up slip bands results in crack initiation in the NiAl phase, similar to that observed in  $\alpha_2/\beta$  Ti-Al-Nb alloys [5]. Therefore, little or no macroscopic tensile ductility is observed in these alloys and the fracture toughness depends on the plasticity in the NiAl phase due to dislocations generated from the interfaces and the extrinsic mechanisms described below.

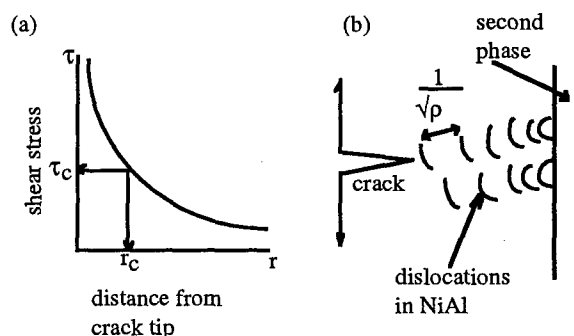


Fig. 7. Schematic diagram of (a) the crack tip stress field and (b) crack blunting by mobile  $a_0\langle 100 \rangle$  dislocations generated in the NiAl phase from interphase interface sources.

#### Extrinsic Toughening Mechanisms

In general, extrinsic toughening mechanisms in these systems arise from the interaction of cracks in the NiAl phase with the metallic second phase. Enhanced toughness of the composite then results from the dissipation of energy due to various interactions, which includes plastic deformation of the ductile reinforcement both at the crack tip process zone and in the crack wake [4-7].

In the type I alloys, after the  $\beta$  phase fractures, the crack may be blunted by slip in the ductile  $\gamma$  phase. In a predominantly lamellar microstructure, the crack will advance by renucleating in the adjoining  $\beta$  layer [8]. The bridging ductile phase can then plastically stretch in the crack wake as the crack front continues to move ahead by renucleating in the  $\beta$  layers. However, the amount of plastic stretch and the length of the bridging zone were found to be small. In the absence of interface decohesion, the contribution of the crack bridging mechanism would also be small [4] though a quantitative estimate of the toughening from extrinsic versus intrinsic mechanisms was not attempted. The various toughening mechanisms acting in the type I composites are summarized in Table IV.

In the NiAl-9Mo and CELZ-processed NiAl-34Cr alloys with fibrous microstructures, trapping of the crack front by the higher toughness fibers was observed. The crack front then had to advance by bowing

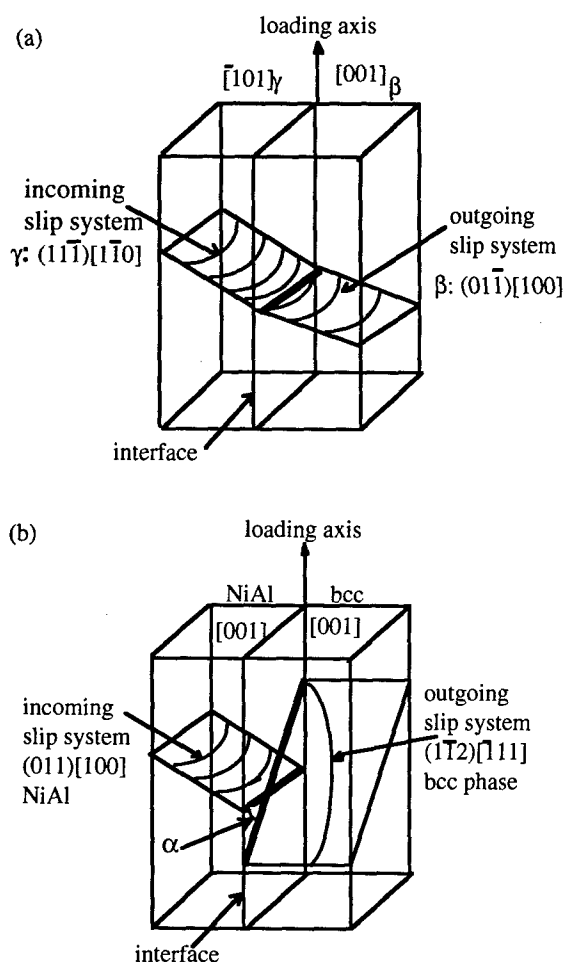


Fig. 8. Schematic illustration of the geometry of slip systems in the two types of alloys studied: (a) type I alloys in which slip planes are nearly parallel and have a common line of intersection at the interface due to the KS orientation relationship  $((110)_\beta // (111)_\gamma, [1\bar{1}1]_\beta // [0\bar{1}1]_\gamma)$ ; (b) type II alloys, which exhibited a cube-on-cube orientation relationship in which slip planes are not parallel and the angle  $\alpha$  between the lines of intersection of slip planes with the interface is large. Geometry favors slip transfer in (a) but not in (b).

between the fibers. Once the crack front moves ahead by bowing between the fibers, the uncracked fibers in the crack wake can bridge the crack. The toughness increment by this mechanism depends on the volume fraction of the fibers and a parameter which depends on the interface strength and reinforcement toughness [7], and is therefore difficult to estimate. Nevertheless, using a crack bridging model, Ravichandran [6] calculated the toughness of the NiAl-9Mo eutectic as 7.2 MPa $\sqrt{m}$  by assuming the matrix fracture toughness to be 6.5 MPa $\sqrt{m}$ . Similar calculations by Joslin *et al.* [26] and the present investigators also indicate a modest increment of  $\sim 1$  MPa $\sqrt{m}$  above the matrix fracture toughness. However, the experimentally observed toughening increment in the NiAl-Mo eutectics is actually 6-8 MPa $\sqrt{m}$  over that of conventionally pure NiAl. For the CELZ-processed NiAl-34Cr alloy, a toughness increase of only 4 MPa $\sqrt{m}$  was estimated using the crack bridging model, as opposed to the experimentally observed increment of 10-12 MPa $\sqrt{m}$  [15]. Since the volume fraction of the Cr fibers in the

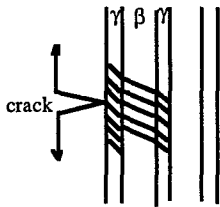
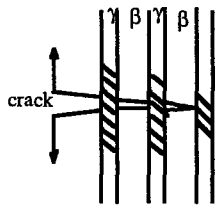
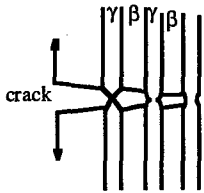
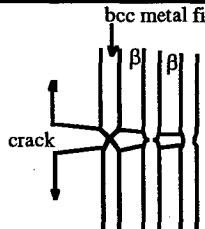
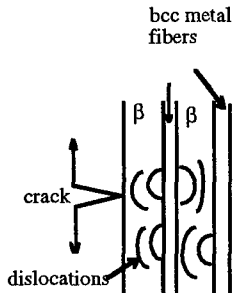
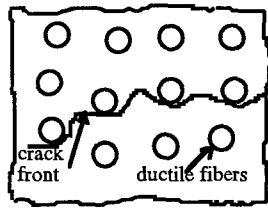
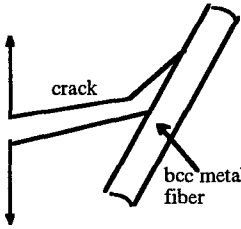
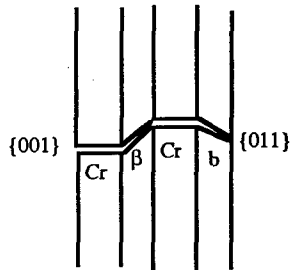
NiAl-34Cr eutectic was higher than the volume fraction of the Mo fibers in the NiAl-9Mo eutectic, the crack bridging model predicted higher toughness of the NiAl-34Cr eutectic. For the CELZ-processed NiAl-34Cr ( $K_I \sim 20$  MPa $\sqrt{m}$ ) and NiAl-9Mo ( $K_I \sim 15$  MPa $\sqrt{m}$ ) alloys, the higher toughness of the former may be related to the higher volume fraction of the Cr fibers. The calculations using a crack bridging model indicate that mechanisms other than crack bridging were operative as well. Extrinsic mechanisms observed in the type II alloys, other than crack trapping and crack bridging, were crack deflection to follow the weak interfaces when the fibers were inclined to the crack path. When the interface was strong, the difference in cleavage planes between the two phases also caused the crack to continuously deviate along its path [9,15]. These mechanisms are illustrated in Table IV. The easy debonding observed when the crack path was not perpendicular to the fiber axis could be due to the incompatible deformation of the two phases (particularly in the NiAl-9Mo alloys) or a result of reduced interface strength due to interstitial impurities (as seen in low purity NiAl-34Cr alloy). Whereas limited interface decohesion may be beneficial in allowing greater plastic stretch of the ductile phase and in deflecting the crack path, extensive decohesion as seen in low purity NiAl-34Cr, (Fig. 3(a) and (b)) only results in catastrophic fracture.

### Summary and Conclusions

The room temperature deformation and fracture behavior of DS NiAl-based eutectics containing either a fcc-based second phase or a bcc refractory metal second phase were studied. The findings may be summarized as follows:

- (i) Highest toughness ( $\sim 30$  MPa $\sqrt{m}$ ) and tensile ductility (10-12%) were observed in the B2 Ni-30Fe-20Al-based eutectic alloy containing a ductile  $\gamma$  (fcc)-based second phase when easy transfer of slip from  $\gamma$  to  $\beta$  allowed compatible deformation of both phases.
- (ii) Extrinsic mechanisms such as crack blunting and bridging probably had a smaller contribution to toughness relative to the intrinsic toughening of the B2 phase.
- (iii) In the NiAl-Cr and NiAl-Mo eutectic alloys, significant  $a_0 < 100 >$  dislocation activity was discerned in the NiAl phase in the crack tip plastic zone. However, the higher yield strength of the bcc metal phase as compared to the NiAl phase and the particular orientation relationship did not geometrically favor slip transfer. Incompatible deformation of the two phases due to difficulty of slip transfer across NiAl/bcc-metal interfaces lead to early crack initiation. As a result, little ( $< 0.5\%$ ) or no tensile ductility was observed.
- (iv) Fracture toughness of B2/bcc eutectics was controlled by extrinsic toughening mechanisms such as crack trapping, deflection, and bridging. A fracture toughness of  $\sim 20$  MPa $\sqrt{m}$  may be achieved in high purity NiAl-34Cr eutectic and  $\sim 15$  MPa $\sqrt{m}$  in the NiAl-9Mo alloy due to a combination of these extrinsic mechanisms. However, extrinsic mechanisms cannot account for the total increment in toughening observed in these systems. Therefore, extrinsic toughening occurs together with enhanced plasticity of the NiAl phase by dislocations generated from the interfaces.
- (v) Low purity alloys, especially as in the case of the Bridgman processed NiAl-34Cr, may have toughness as low as 7 MPa $\sqrt{m}$  due to embrittlement from interstitial impurities.
- (vi) Although the  $\beta/\gamma$  alloys have higher ductility and toughness, NiAl/bcc-metal alloys are presently being studied in greater detail since they possess a better combination of room temperature toughness and high temperature strength [31].

Table IV Summary of Toughening Mechanisms Observed in NiAl-based Eutectics

Alloy	Toughness (MPa√m)	Intrinsic Mechanisms	Extrinsic Mechanisms
Ni-30Fe-20Al	30	 <p>Slip Transfer</p>	 <p>Crack Renucleation, and Crack Blunting by Slip in <math>\gamma</math></p>  <p>Crack Bridging</p>
NiAl-9Mo	15		 <p>Crack Bridging</p>
NiAl-34Cr*	20	 <p>Plasticity in NiAl</p>  <p>Crack Trapping</p>  <p>Crack Deflection Along Interfaces</p>	 <p>Mismatch of Cleavage Planes **</p>

\* These toughening mechanisms were observed only in the high purity CELZ processed NiAl-34Cr material; In the low purity NiAl-34Cr alloy, catastrophic failure by cleavage in both phases and extensive fiber pull-out was observed,

\*\* This mechanism was observed only in NiAl-34Cr alloy. In the NiAl-9Mo alloys, the Mo fibers failed by necking.

#### Acknowledgements

Research at the University of Michigan was funded by the AFOSR-MURI Program, Grant No. DOD-F49620-93-1-0289, Dr. C. Ward, Program Manager. The authors also wish to acknowledge the efforts of Dave Johnson and Steve Joslin for their work in this area.

#### References

1. D.P. Pope and R. Darolia, *MRS Bulletin*, May (1996), 30-36.
2. R.D. Noebe, R.R. Bowman and M.V. Nathal, *International Materials Review*, 38 (1993), 193-232.
3. R. Darolia, *Superalloys 1996*, R.D. Kissinger et al. eds., (Warrendale, PA: The Minerals, Metals and Materials Society, 1996, 561-570).
4. M.F. Ashby, F.J. Blunt and M. Bannister, *Acta Metall.*, 37 (7) (1989), 1847-1857.
5. K.S. Chan, *Metall. Trans.*, 21A (10) (1990), 2687-2699.
6. K.S. Ravichandran, *Scripta Met.*, 26 (1992), 1389-1393.
7. F.E. Heredia, M.Y. He, G.E. Lucas, A.G. Evans, H.E. Deve and D. Konitzer, *Acta Metall. Mater.*, 41 (1993), 505-511.
8. R.D. Noebe, A. Misra and R. Gibala, *ISIJ International*, 31 (10) (1991), 1172-1185.
9. X.F. Chen, D.R. Johnson, R.D. Noebe and B.F. Oliver, *J. Mater. Res.*, 10(5) (1995), 1159-1170.
10. V.I. Levit, I.A. Bul, J. Hu and M.J. Kaufman, *Scripta Mat.*, 34 (12) (1996), 1925-1930.

11. D.R. Johnson, S.M. Joslin, B.F. Oliver, R.D. Noebe and J.D. Whittenberger, First International Conference on Processing Materials for Properties, ed. H. Henein and T. Oki (Warrendale, PA: The Minerals, Metals and Materials Society, 1990, 271-299).
12. J.M. Brzeski, J.E. Hack, R. Darolia and R.D. Field, Mat.Sci.Eng., 170A (1993), 11-18.
13. R.D. Noebe, R.R. Bowman, J.T. Kim, M. Larsen and R. Gibala, High Temperature Aluminides and Intermetallics, ed. S.H. Whang, C.T. Liu, D.P. Pope and J.O. Stiegler (Warrendale, PA: The Minerals, Metals and Materials Society, 1990, 271-299).
14. A. Misra, Ph.D. thesis, University of Michigan, Ann Arbor, MI, 1994.
15. D.R. Johnson, X.F. Chen, B.F. Oliver, R.D. Noebe and J.D. Whittenberger, Intermetallics, 3 (1995), 99-113.
16. A. Misra, Z.L. Wu and R. Gibala, High-Temperature Ordered Intermetallic Alloys VII, ed. C.C. Koch *et al.*, (MRS Sym. Proc., Fall 1996), in press.
17. A. Misra, J.T. Kim and R. Gibala, Metall. Mater. Trans., 28A (1997), 135-147.
18. S. Guha, P.R. Munroe and I. Baker, Mat. Sci. Eng., A131 (1991), 27-37.
19. S.C. Huang, R.D. Field and D.D. Krueger, Metall. Trans., 21A (1990), 959-970.
20. J.Chen, Q. Zheng, Y.A. Li, Y. Yu, Y.J. Tang and Z.Q. Hu, Scripta Metall. Mater., 33 (4) (1995), 675-680.
21. J. Kostrubanic, D.A. Koss, I.E. Locci and M. Nathal, High-Temperature Ordered Intermetallic Alloys IV, ed. L.A. Johnson, D.P. Pope and J.O. Stiegler, (MRS Sym. Proc., vol.213, 1991), 679-684.
22. A. Misra and R. Gibala, Metall. Mater. Trans., 28A (1997), 795-807.
23. H.E. Cline, J.L. Walter, E. Lifshin and R.R. Russell, Metall. Trans., 2 (1971), 189-194.
24. H.E. Cline, J.L. Walter, E.F. Koch and L.M. Osika, Acta Metall., 19 (1971), 405-414.
25. K.M. Chang, R. Darolia and H.A. Lipsitt, Acta Metall. Mater., 40 (1992), 2727-2737.
26. S.M. Joslin, X.F. Chen, B.F. Oliver and R.D. Noebe, Mat. Sci. Eng., 196A (1995), 9-18.
27. J.M. Yang, S.M. Jeng, K.Bain and R.A. Amato, Acta Mater., 45 (1997), 295-305.
28. M.F. Ashby and J.D. Embury, Scripta Metall., 19 (1986), 557-562.
29. G.T. Hahn, A. Gilbert and R.I. Jaffee, Refractory Metals and Alloys II, M. Semchyshen and I. Perlmuter, Interscience Publishers, 1963, 23-64.
30. Z. Shen, R.H. Wagoner and W.A.T. Clark, Acta Met., 36 (1988), 3231-3241.
31. R.D. Noebe and W.S. Walston, Structural Intermetallics II, M.V. Nathal *et al.*, eds. (Warrendale, PA: The Minerals, Metals and Materials Society, 1997).

## TENSILE BEHAVIOR OF $\beta$ -NiAl: INTRINSIC VS. EXTRINSIC PROPERTIES

V.I. Levit and M.J. Kaufman

Department of Materials Science and Engineering  
University of Florida  
Gainesville, FL 32611

### Abstract

The influences of such variables as specimen geometry (cylindrical vs. rectangular), orientation, purity, stoichiometry, thermal history, surface oxidation, surface damage and prestrain on the room temperature tensile properties of  $\beta$ -NiAl single crystals are described. The results indicate that  $\langle 001 \rangle \{110\}$  and  $\langle 001 \rangle \{100\}$  slip in high purity, stoichiometric NiAl occurs at similar, low stresses (CRSS  $\sim 50$  MPa) consistent with slip in pure metals. Furthermore, prestrain, surface oxides, alloying additions, impurities and thermal vacancies all harden NiAl in a manner similar to their effects in pure metals. Finally, it is shown that NiAl fractures by brittle cleavage even after elongations of up to 34% due to the lack of a sufficient number of slip systems. The implications of these results are described with respect to the potential of using this or other intermetallics with a limited number of slip systems in structural applications.

### Introduction

Although the compound  $\beta$ -NiAl has been promoted as one of the more promising potential structural intermetallics because of its high melting point, wide solubility range and oxidation resistance, its transition into application has been delayed by the fact that it is both soft and brittle in the unalloyed condition (1). While both of these properties can be enhanced somewhat via composition control, the enhancements tend to be offsetting in nature (2), i.e., alloying additions that enhance strength tend to increase brittleness whereas high purity crystals that are somewhat less brittle exhibit low strengths (3,4). In addition, the discrepancies in the literature concerning the effects of such extrinsic variables as surface films (5), impurities (6-10), thermal vacancies (6,9), prestrain (10-12), microalloying additions (13), surface finish (14,15), specimen and grip geometries (4,16,17), etc. have led to considerable confusion such that there has developed a definite need for a systematic study aimed at clarifying some or all of these issues. The AFOSR-sponsored University Research Initiative (URI) at the University of Florida and the Johns

Hopkins University was aimed at generating the necessary understanding of the microstructure-property-processing relationships in this compound. The purpose of this paper is to describe some of the more recent results, mostly at room temperature, and their relationship to previous reports.

### Experimental

Oriented single crystals of nominally stoichiometric NiAl and one silicon-doped alloy were prepared by Bridgman growth as described elsewhere [4], homogenized at 1573 K for 3h and furnace cooled (HFC). The compositions of the crystals used in the present study were measured using standard methods and are summarized in Table I. After homogenization, tensile specimens were cut using an electrical discharge machine (EDM). These specimens had rectangular cross sections with dimensions 1.6 mm wide (W) x 2.4 mm thick (T)<sup>1</sup> (approximately 1.3mm x 2.1mm after electropolishing to remove the recast layer and any surface roughness) and nominal gage lengths of 10 mm. The tests were performed in an Instron Model 1125 at a nominal strain rate of  $10^{-4}$ s<sup>-1</sup>. For the non- $\langle 001 \rangle$  specimens, the orientations of the sides of the rectangular sections were either random with respect to the preferred  $\langle 001 \rangle$  slip vector(s) or non-random, i.e., for tensile axes parallel to  $\langle 557 \rangle$  (single slip with Schmid factor,  $f_s$ , of 0.5) or  $\langle 011 \rangle$  (double slip with  $f_s = 0.5$ ), one of the sides was cut parallel to the plane containing the tensile axis, the Burgers vector(s), **b**, and the slip plane normal(s), **n**. Specifically, for the  $\langle 557 \rangle$  specimens, this was the parallel  $\{011\}$  plane while for the  $\langle 011 \rangle$  specimens, it was the parallel  $\{001\}$  plane (Fig. 1). Since the specimens are rectangular, the gage faces were cut such that this plane was parallel to either the thickness or the width of the specimens in order to determine the influence of the initial geometry, shape change and degree of constraint on the deformation and fracture behavior. Because of the nature of gripping such samples in the button-head grips, when the plane containing the tensile axis, **b**, and **n** is parallel to the width (Fig. 1a), there is greater constraint than when

<sup>1</sup> these dimensions were varied in one portion of the study in order to determine their influence on tensile properties.

parallel to the thickness (Fig. 1b). Consequently, these will be referred to as “constrained (C)” and “less constrained (LC)” geometries, respectively. It is noted that these special geometries correspond to plane strain conditions in the sense that the dimension orthogonal to this special plane does not change during plastic deformation whereas any dimension parallel to this plane does. For example, there is a change in the dimensions as shown in Fig. 1a where the plane OABC changes to OA'B'C' whereas the thickness, CD, does not change.

After spark cutting, the specimens were electropolished and, in some cases, given subsequent heat treatments in order to vary the vacancy concentration and/or the oxide thickness. These samples were cooled in one of the following ways: furnace cool (FC), air cool (AC) or water quench (WQ). A set of specimens were also notched to different depths in order to determine the notch sensitivity of the rectangular specimens. Most of the tests described here were performed at room temperature; the elevated temperature tests are described elsewhere [16].

Table I. Compositions of the NiAl single crystals used in this study.

Crystal ID	Ni at. %	Al at. %	Si ppm	Fe ppm	Cu ppm	C ppm	S ppm	O ppm	N ppm
SC-18	49.7	50.2	260	110	20	14	-	-	-
SC-64	50.6	49.3	240	-	-	180	n/d	81	<15
SC-36	49.7	50.2	300	50	-	53	-	-	-
SC-34	50.4	49.5	n/d	-	-	82	<5	106	<15
SC-31B*	50.0	49.9	136	-	-	50	7	90	12
SC-31T*	50.0	49.9	n/d	-	-	70	5	80	12
SC-60B*	49.2	50.7	170	27	-	18	-	-	-
SC-60T*	49.6	50.3	160	n/d	-	42	-	-	-
SC-76	50.1	49.8	107	-	-	93	-	73	-
SC-40	50.0	49.9	100	-	-	110	13	100	9
SC-93**	50.0	49.6	3400	-	-	180	<10	124	<15

\* B represents the bottom and T the top part of the crystal relative to the growth direction.

\*\* average composition of initial VIM rods used as feedstock for SC 93.

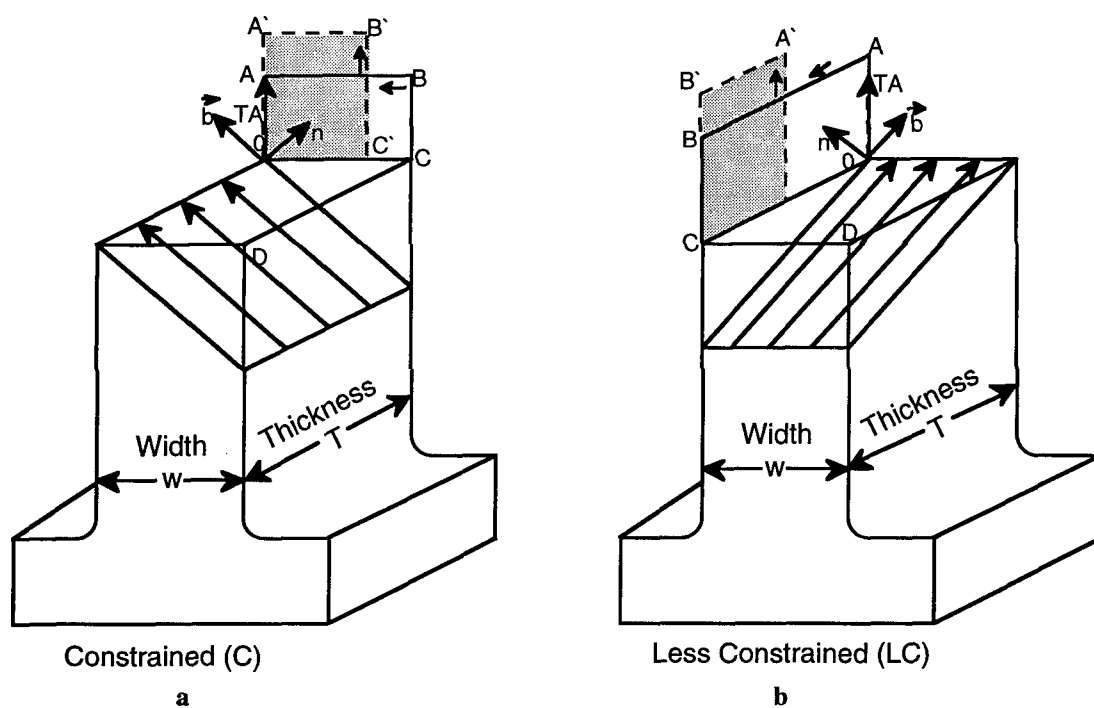


Figure 1. Schematics of the rectangular tensile specimens before and after deformation. Note the shape change (shaded) is consistent with “plane strain” in that there is no change in the thickness (T) in the constrained (C) specimens or the width (W) in the less constrained (LC) specimens.

## Results

The results are subdivided into sections that address such issues as the influence of purity, prestrain, thermal vacancies, surface oxidation and surface finish on the mechanical properties of NiAl. The first section addresses the importance of specimen geometry and constraints in the grips and justifies why the majority of the tests were performed on rectangular instead of the more commonly used cylindrical specimens.

### Specimen Geometry

When the literature concerning the tensile properties of NiAl is examined, it becomes apparent that the majority of the data were generated using cylindrical, button-head specimens whose gage sections were prepared by centerless grinding followed by electropolishing to a "shiny" surface finish. However, the present results generated using cylindrical and rectangular specimens cut from the same single crystal (SC-76) (Table II) provide important insight into the influence of geometry on tensile properties. While the CRSS values are not affected significantly by the specimen geometry and surface finish as might be expected, the elongations and fracture stresses depend strongly on these parameters. Clearly, the elongations are highest for the rectangular specimens, lowest for the cylindrical specimens that were lightly polished, and intermediate in the cylindrical specimens that were repolished after observing the low elongations characteristic of the samples given the light polish. This implies that the damage zone from centerless grinding exceeded the thickness of the material removed during the standard light polishing. These results are in agreement with the recent reports by Darolia and Walston (15). Considering the soft nature of the high purity NiAl crystals, it is not surprising that the extent of the damage that results from grinding may be considerably greater than that observed in stronger multiphase crystals or polycrystals.

The other important factor realized after these tests was that the rectangular geometry is superior to the cylindrical geometry in terms of achieving the highest elongations. This is presumably related to the greater constraints that exist when gripping cylindrical button-head specimens as described elsewhere (17). Consequently, the remaining tests were performed using rectangular specimens.

### "Plane Strain" Tests

As will be shown below, the highest elongations were achieved using the LC geometry sketched in Figure 1. In this part of the study, it was of interest to determine whether or not the high tensile elongations were related to the small specimen sizes which might allow the dislocations to slip out of the crystal more readily, thereby increasing the extent of Stage 1 deformation as happens in fcc metals such as copper (18). Small specimen sizes might also lead to higher elongations since the probability of the sample containing critical flaws decreases with decreasing cross-sectional area. Therefore, both LC and C specimens were tested with different cross-sectional areas. The results indicate that the elongation is not a strong function of specimen size. In fact, it appears that the elongation does not increase with decreasing cross-sectional

Table II. Tensile data for [135] specimens cut from SC-76 illustrating the influence of specimen geometry (R-rectangular, C-cylindrical) and surface finish (SP-standard polish, LP-lightly polished, RP-repolished).

Orient. Shape	Surface Finish	$\sigma_{0.2}$ MPa	$\sigma_f$ MPa	El. %
[135]R	SP	132	217	7.8
[135]R	SP	135	206	5.3
[135]C	LP	-	145	<0.1
[135]C	LP	-	142	<0.1
[135]C	RP	142	230	3.4
[135]C	RP	145	221	2.8

area; this may be related to the fact that the thinner specimens are more sensitive to surface damage or defects. It is noted that, for the single slip specimens, the rotation of the slip vector towards the tensile axis does not lead to conjugate slip as in fcc metals and, therefore, the slip can continue as long as the stress does not reach the fracture stress at some stress concentration. Consequently, the onset of Stage 2 deformation is not realized in these samples prior to fracture at room temperature.

It should be emphasized that the amount of scatter in the CRSS values for a given set of specimens is quite low whereas the scatter in the elongations and fracture stresses is high. This implies that the deformation of NiAl is similar to that of metals and is reasonably reproducible whereas the fracture stress and elongation vary considerably, consistent with the statistical nature of brittle fracture. As noted in ([1,2,4,17]), this is related to an insufficient number of slip systems to satisfy the von-Mises criterion and avoid the high stresses that develop at stress concentrations in the material.

Table III. Tensile properties (TA=[557]) of rectangular (C and LC) specimens cut from SC-34 with slightly different dimensions. The higher  $\sigma_{0.2}$  values for the 34T specimens are due to compositional differences.

ID	Geom.	Dimensions (W x T) mm	CSA* mm <sup>2</sup>	$\sigma_{0.2}$ MPa	$\sigma_f$ MPa	El. %
34B	LC	1.3 x 2.1	2.13	108	190	16
34B	"	1.2 x 1.3	1.56	137	317	13
34B	"	1.3 x 1.3	1.69	103	164	4
34B	"	1.3 x 0.8	1.04	100	206	10
34B	"	1.3 x 0.8	1.04	116	220	13
34B	"	1.1 x 1.0	1.10	87	225	8
34T	C	1.3 x 2.2	2.86	148	255	16
34T	"	1.4 x 1.0	1.40	142	242	15
34T	"	1.4 x 0.8	1.12	142	201	5
34T	"	1.3 x 0.8	1.04	155	249	15

\*CSA = cross-sectional area

### Notch Effects

In view of the higher elongations achieved in the rectangular specimens, an attempt was made to determine the effects of notches when the constraints were less than in the cylindrical (constrained) specimens where, as already shown,



any surface damage leads to negligible elongation. Consequently, standard rectangular specimens of both the LC and C geometries were notched using the wire EDM to different depths ranging from 50 to 1000  $\mu\text{m}$  on one of the faces. It is clear from Table IV that the specimens cut from the top of the crystal were stronger than those from the bottom as already described. More importantly, the influence of the notches resulted in a decrease in elongation. In all cases, the fracture originated at the notch as expected. It should be noted, however, that the elongations were still significant and considerably higher than those achieved with cylindrical specimens where the notch sensitivity appears to be enhanced presumably due to the constraining effects mentioned above.

Table IV. Effects of notch depth on the properties of [557] crystals of NiAl.

ID	Geom.	Notch Depth	$\sigma_{0.2}$ MPa	$\sigma_f$ MPa	El. %
34B	LC	Unnotched	108	190	16
"	"	1 mm	-	168	0
"	"	500 $\mu\text{m}$	-	136	<0.1
"	"	250 $\mu\text{m}$	110	117	0.2
"	"	100 $\mu\text{m}$	122	142	0.5
"	"	50 $\mu\text{m}$	111	156	3.4
"	"	75 $\mu\text{m}$	120	157	2
"	"	"	112	131	1.4
"	"	"	111	152	2.7
"	"	"	109	114	0.4
34T	C	Unnotched	148	255	16
"	"	75 $\mu\text{m}$	158	161	0.7
"	"	"	152	157	0.4
"	"	"	126	147	0.9
"	"	"	144	181	2.9
"	"	"	142	169	2.1

#### Orientation Effects

It is clear from Table V, that the samples tested along the hard  $\langle 001 \rangle$  orientation are considerably stronger than those tested along the softer orientations due to the negligible Schmid factor for cube slip. This leads to elastic deformation with no elongation and considerable scatter in the fracture stress as expected based on the above discussion.

For the soft orientations, it is important to realize the need to exercise caution when defining the CRSS based on a 0.2% offset value. Specifically, while easy glide (Stage 1) in fcc crystals assures that the CRSS at 0.2% strain is similar to that at the proportional limit,  $\sigma_p$ , where the dislocations first start to move, this is not necessarily the case in NiAl in spite of the fact that most reports of the CRSS in NiAl are calculated at 0.2% strain [1-3]. This is especially a concern in the higher purity crystals where there is no plateau in true stress - true strain curves as frequently observed for lower purity NiAl (see Fig. 2 and Table V).

In addition, it is necessary to distinguish between the behavior of specimens oriented for single slip (e.g.,  $\langle 557 \rangle$ )

and those oriented for double slip (e.g.,  $\langle 011 \rangle$ ). When a large sampling of test results from these samples are examined, the following conclusions become apparent. First of all, the CRSS for cube slip on  $\{001\}$  planes is essentially equal to that on  $\{011\}$  planes at room temperature and falls typically between 40 and 60 MPa. This variation is due mostly to purity or Ni/Al ratio as confirmed by noting that the CRSS for samples cut from the same region of the same crystal (e.g., the [011] and [557] specimens from 34T as well as the [233] and [557] specimens from 34B) exhibit similar  $\tau_p$  and  $\tau_{0.2}$  values.

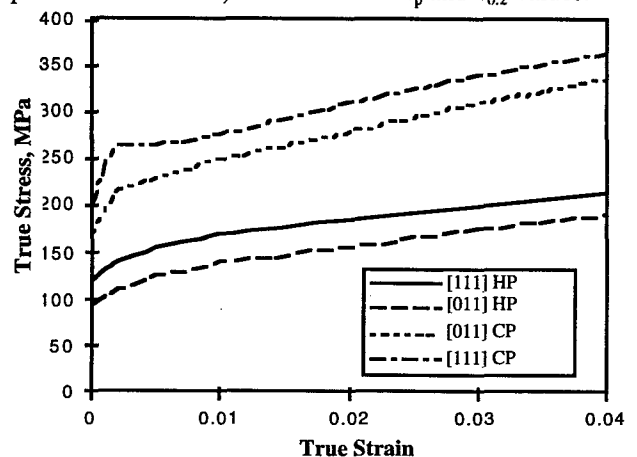


Figure 2. True stress vs. true strain for both high purity (HP) and commercial purity (CP) (19) NiAl along the [111] (single slip) and [011] (double slip) orientations.

In spite of their similar CRSS values, it is apparent that the work hardening rates (WHR) for the double slip orientations are considerably higher than those for single slip whereas the elongations tend to be lower. Clearly, this latter result is expected since the higher WHR, calculated from the shear stress - shear strain curves (Fig. 3) and compared with the  $\langle 001 \rangle$  shear modulus where  $\mu_{001} = 112 \text{ GPa}$  (20), leads to higher stresses for a given amount of elongation; these stresses, in turn, lead to fracture at lower total elongations.

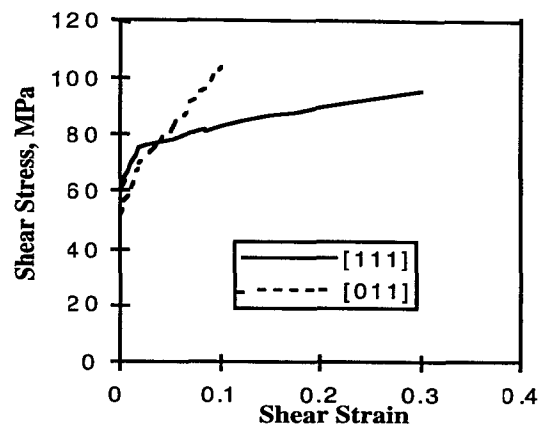


Figure 3. Shear stress vs. shear strain for high purity crystals tested along [111] (single slip) and [011] (double slip). Note the higher work hardening rate for the [011] as well as the comparable proportional limit.

Table V. Summary of tensile data for rectangular single crystal specimens of NiAl along different crystallographic directions.

Crystal ID	Orient.	$f_s$	$\sigma_p$ MPa	$\tau_p$ MPa	$\sigma_{0.2}$ MPa	$\tau_{0.2}$ MPa	WHR ( $\theta=d\tau/d\gamma$ ) MPa	$\sigma_f$ MPa	El. %
18	[100]	.5	1040	520	-	-	-	1040	0
18	[100]	.5	890	495	-	-	-	890	0
122	[100]	.5	1121	560	-	-	-	1121	0
122	[100]	.5	1120	560	1167	583	-	1167	0.2
36	[111]	.485	122	59	140	68		244	15
36	[111]	.485	134	65	156	76		213	6
36	[111]	.485	106	51.5	130	63		187	4
34B	[557]T	.5	104	52	114	57	62	266	34
34B	[557]T	.5	96	48	115	57.5		218	18
34B	[557]T	.5	98	49	109	54.5		190	16
34B	[233]	.485	98	47.5	117	56.5		186	5
34B	[233]	.485	97	47	119	57.5		202	4
34B	[233]	.485	110	53.5	127	61.5		169	3
34 T	[557]W	.5	114	57	137	68.5	102	239	15
34 T	[557]W	.5	121	60.5	134	67		221	13
34 T	[557]W	.5	107	53.5	127	63.5		196	10
34 T	[011]	.5	135	67.5	147	73.5		205	3
34 T	[011]	.5	95	47.5	133	66.5		180	3
34 T	[011]	.5	123	61.5	139	69.5		192	2
64	[011]T	.5	96	48	111	55.5	468	242	7
64	[011]T	.5	104	52	117	58.5	563	237	6
64	[011]T	.5	93	46.5	102	51		230	5
64	[011]W	.5	97	48.5	111	55.5	448	235	6
64	[011]W	.5	89	44.5	102	51	476	212	5
40	[123]	.454	98	44.5	116	52.5	110	306	19
40	[123]	.454	86	40	110	50	114	304	15
40	[123]	.454	102	46	124	56.5	109	318	14
60	[135]	.41	78	32	103	42	103	272	18
60	[135]	.41	98	40	112	46	100	241	16
60	[135]	.41	96	39.5	115	47	91	266	15

It has been noted that the [011] orientation is "stable" with respect to lattice rotation during deformation due to the offsetting nature of the equivalent slip systems ([001]/(010) and [010]/(001)). As pointed out previously [17], this appears to be the reason that the highest elongations in cylindrical specimens are achieved using  $\langle 011 \rangle$  specimens where there is little or no torque generated during deformation in contrast to the single slip orientations (e.g., TA=[557]; in this case, the crystal rotates in the classical sense with the slip plane normal rotating away from the tensile axis (i.e., the TA rotating toward the Burger's vector on the stereographic projection as shown in Fig. 4).

For the rectangular cross sections, higher elongations can be achieved due to (1) the lesser constraint in the grips and (2) the lower WHR associated with single slip. When these parameters were optimized, it was possible, using  $\langle 557 \rangle$ T specimens, to achieve elongations as high as 10% at 180K, 34% at room temperature (Table V) and 350% at 600K [17]. The cross-sections of these samples reveal the change in geometry and the fracture surfaces indicates that the fractures occur by brittle cleavage (Fig. 5a and 5b). Considering that the thin dimension gets thinner in the C samples as well as

their greater constraints in the grips, then it is not surprising that they experience lower elongations. It should also be noted that, for random specimens where the sides were not oriented parallel to the Burgers vector and the tensile axis was not coplanar with  $\mathbf{b}$  and  $\mathbf{n}$ , the shape change was more arbitrary (Fig. 5c) and the elongations

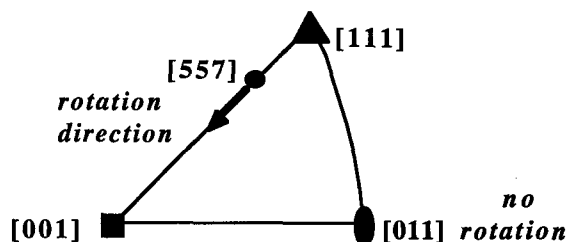


Figure 4. Orientations and nature of rotation during single (TA=[557]) and double (TA=[011]) slip. Note that no rotation is expected for the double slip geometry and that rotation in the single slip geometry which results in a drop in the Schmid factor.

tended to be somewhat lower. This may be due to the development of bending stresses and/or stress concentrations at the specimen corners during plastic deformation.

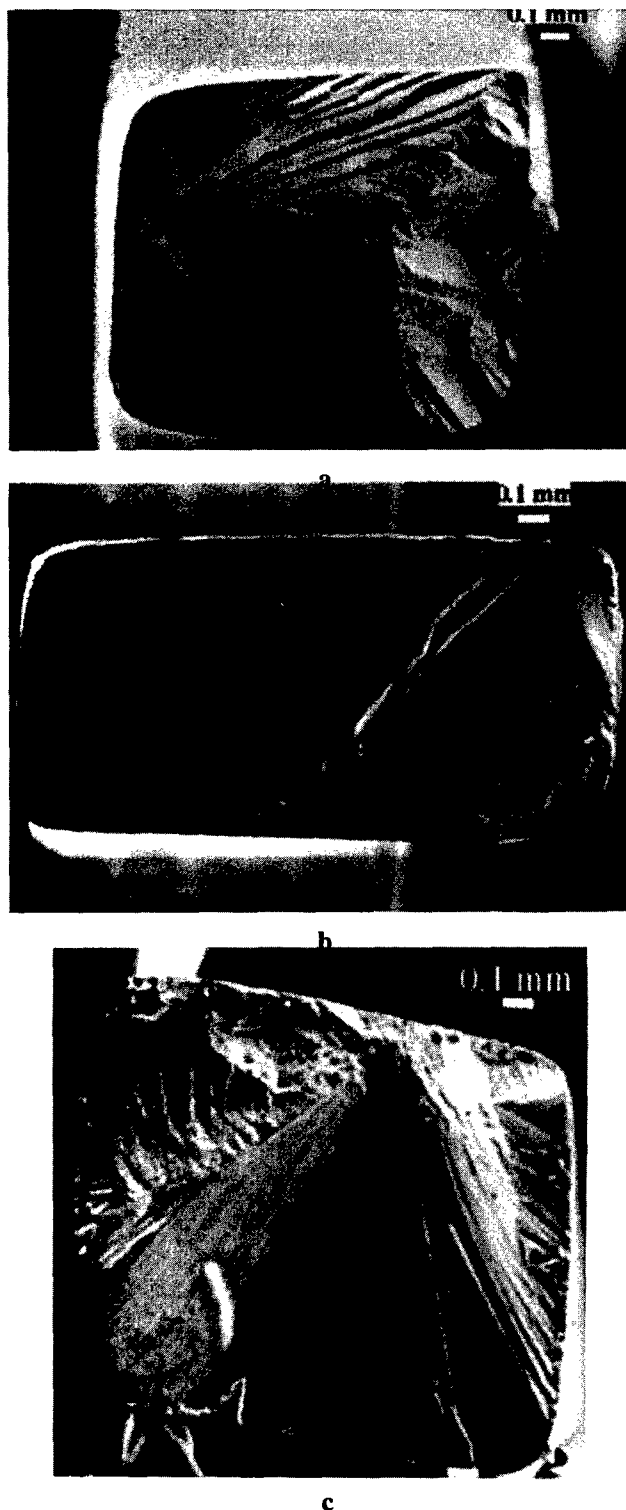


Figure 5. Scanning electron micrographs of the fracture surfaces of single crystal specimens after RT testing in tension. (a) LC geometry,  $TA = \langle 557 \rangle$ ; (b) C geometry; (c) random geometry.

#### Effects of Prestrain, Surface Oxides and Cooling Rate (Thermal Vacancies)

It has been proposed in the literature that the ductility and fracture toughness of NiAl can be enhanced by prestraining or by producing an appropriate surface film since both of these may produce mobile dislocations in a material that might normally have few such dislocations and few sources. In contrast, the influence of thermal vacancies has been reported to result in considerable hardening of NiAl which, in turn, leads to a decrease in elongation. Of interest in the present study was the examination of these effects as a function of specimen purity. Thus, both stoichiometric NiAl and NiAl doped with silicon were examined after various treatments designed to investigate these effects. As is apparent in Table VI, air cooling from 1000K leads to a slight reduction in ductility although there was little effect on the yield stress/CRSS. By prestraining 9% at 1000K and then air cooling, the specimen exhibited higher CRSS and elongations similar to those that were not prestrained. This suggests that the prestrain leads to hardening in NiAl much like in traditional metals and that NiAl does not suffer from a lack of dislocation sources.

For the silicon-doped crystal (SC-93), the properties depended somewhat on the thermal treatment and quench rate as indicated in Table VI. Although the elongation was not a strong function of these treatments and hovered around 2%, it appears that the 1000K treatment followed by WQ results in a decrease in yield stress suggesting that the silicon and/or interstitials may not have had time to segregate to dislocations and cause pinning.

As apparent in Table VII, water quenching from 1273 K results in a doubling of the yield stress and essentially eliminates the elongation compared to NiAl that was furnace cooled from 1273 K or given the original HFC treatment. It is noted that the fracture stress is not significantly different for the FC and WQ specimens consistent with the normal stress reaching some "critical" value in the material at which point a crack somewhere in the specimen becomes unstable. In addition, these results indicate that the vacancy concentration is considerably higher at 1273 K compared with that at 1000K and that the resulting thermal vacancies increase the CRSS considerably in high-purity NiAl. It should also be noted that the elongations are comparable to those achieved in commercial purity NiAl specimens tested after the HFC treatment.

The influence of surface oxides on tensile properties was established by comparing samples that had been heat treated in air with samples given equivalent heat treatments in argon. In addition, some of the specimens were repolished after the heat treatment in air in order to remove the surface oxide. The results are summarized in Table VIII where it is clear that the surface oxide results in higher  $\sigma_{0.2}$  values and considerably lower elongations. Furthermore, the data indicate that it is possible to reclaim the elongation levels somewhat by removing the oxide via repolishing. Again, this implies that high purity NiAl has sufficient mobile dislocations and, therefore, surface oxides may only enhance the "ductility" of lower purity NiAl. While it could be argued that the surface oxide was non-adherent in these studies, the heat treatment temperature used was sufficiently low to insure an adherent scale.

Table VI. Effect of prestraining and cooling rate on tensile properties of NiAl and NiAl-Si single crystals at room temperature. AC = air cool; FC = furnace cool; HFC = homogenized and furnace cooled.

ID	T.A.	Heat Treatment	$\sigma_p$ MPa	$\sigma_{0.2}$ MPa	$\sigma_f$ MPa	El. %
40	[123]	HFC	98	116	306	18.8
"	"	HFC	102	124	318	14.0
"	"	HFC	86	110	304	15.4
"	"	1000K, 0.5h, AC	95	103	188	4.3
"	"	1000K, 0.5h, AC	80	105	149	3.1
"	"	1000K, 0.5h, e=9%, AC	126	148	253	3.8
"	"	1000K, 0.5h, e=1.5%, AC	114	132	228	2.7
"	"	1000K, 0.5h, FC	79	116	237	6.5
"	"	1000K, 0.5h, e=1.5%, FC	82	117	229	3.4
93Si	[135]	HFC	168	187	232	1.6
"	"	HFC	144	211	240	1.1
"	"	1000K, 0.5h, FAC	127	161	231	2.4
"	"	1000K, 0.5h, e=1.5%, FAC	144	168	239	1.2
"	"	1000K, 0.5h, FC	174	206	259	2.4
"	"	1000K, 0.5h, e=1.5%, FC	189	220	278	2.6

Table VII. Influence of thermal treatment on the tensile properties of NiAl. All tests on SC-109 using the standard <557>LC geometry. FC = furnace cool; WQ = water quench.

Heat Treatment	$\sigma_{0.2}$ MPa	$\sigma_f$ MPa	El. %
HFC	118	183	9
HFC	126	212	12
1273K, FC	117	185	10
1273K, FC	112	173	7
1273K, FC	120	191	10
1273K, WQ	225	244	1.5
1273K, WQ	243	273	1
1273K, WQ	-	178	<0.1

### Discussion

The results of this study indicate that NiAl is a relatively well-behaved material and that much of the confusion in previous studies presumably stems from various extrinsic effects. For high purity NiAl, the results of this study and those of previous studies (6-10) indicate that (1) prestrain, (2) surface oxides, (3) interstitials, (4) substitutional solutes, (5) thermal vacancies and (6) deviations from stoichiometry (constitutional defects) all lead to increases in the CRSS of the cube dislocations from a very low value (~50 MPa) in "virgin" NiAl. This implies that the CRSS for cube slip in NiAl is similar to that in conventional metals and alloys in terms of its response to such extrinsic variables.

On the other hand, the fracture resistance of NiAl is quite different from typical metals and alloys. In fact, it is clear from these and other studies that fracture in NiAl tends to occur by brittle cleavage in spite of the ease of dislocation flow at room and elevated temperature. This implies that

Table VIII. Effect of surface oxidation on the tensile properties of NiAl. FC = furnace cool; AC = air cool; WQ = water quench.

ID	Heat Treatment	Surface condition	$\sigma_{0.2}$ MPa	$\sigma_f$ MPa	El. %
76	HFC	polished	128	211	7.5
76	HFC	polished	122	216	8.3
76	1273K, air, FC	oxidized	132	208	7
76	1273K, air, AC	oxidized	135	209	4.7
76	1273K, air, WQ	repolished*	141	207	2
76	1273K, AC	polished	149	252	11.8
76	1273K, AC	polished	142	237	6.7
60	HFC	polished	115	226	10.5
60	HFC	repolished	117	289	16
60	HFC	repolished	108	272	16.2
60	1273K, AC	oxidized	167	193	0.5
60	1273K, AC	oxidized	173	205	1
60	1273K, FC	oxidized	127	191	0.7
60	1273K, FC	oxidized	134	167	1.2

\*this sample although repolished, retained some surface cavities

certain intermetallics (or other compounds for that matter) may exhibit the characteristics of being both soft and brittle. This, in turn, seems to imply that NiAl is representative of a class of materials where the dislocations can move readily yet where the material fails in a brittle manner due to the simple fact that there is an insufficient number of active slip systems to satisfy the von-Mises criterion for general deformation and relieve the stress concentrations that develop during deformation. Whereas one might argue that this problem might not be as significant in single crystals, the present results suggest otherwise although it is clear that one can extend the elongation by careful selection of tensile axis and specimen geometry. Bearing this in mind, it is concluded that any

compound with fewer than five independent active deformation mechanisms will undergo brittle fracture regardless of the ease at which dislocations can move. It seems logical to extend this statement further and note that the significant amount of work on increasing the symmetry of a compound by alloying is only viable if the dislocations are mobile and the symmetry increase results in at least five independent slip systems.

#### Conclusions

It has been shown that many of the properties of pure NiAl respond to extrinsic variables in a manner very similar to those of pure metals. However, unlike pure metals, the fracture of NiAl single crystals tends to occur by brittle cleavage regardless the amount of tensile elongation. The effects of alloying additions, impurities, prestrain, surface films, etc. all tend to increase strength and decrease ductility much like in pure metals. Consequently, although NiAl can be strengthened using standard metallurgical approaches, it is not possible to overcome the brittleness problem without modifying the slip systems and this has not been possible to date. The implications are that all compounds that do not possess enough independent deformation mechanisms to satisfy the von-Mises criterion will be brittle in both the single and polycrystalline form, even when the dislocations can move readily.

#### Acknowledgments

This work is supported by The Air Force Office of Scientific Research (URI Grant F49620-93-0309) under the direction of Dr. Charles H. Ward. The discussions and technical assistance of Dr. R.D. Noebe of NASA-LeRC and I. Bul are greatly appreciated.

#### References

1. D.B. Miracle, *Acta Metall. Mater.*, **41**, 649 (1993).
2. R.D. Noebe, R.R. Bowman, and M.V. Nathal, Physical and Mechanical Metallurgy of NiAl, NASA Technical Paper 3398 (1994).
3. T. Takasugi, J. Kishino, and S. Hanada, *Acta Metall. Mater.*, **41**, 1009 (1993).
4. V.I. Levit, I.A. Bul, J. Hu and M.J. Kaufman, *Scripta Mater.* **34**, 1925 (1996).
5. R.D. Noebe and R. Gibala, *Scripta Metall.*, **20**, 1635 (1986).
6. J.E. Hack, J.M. Brzeski, and R. Darolia, *Scripta Metall.*, **27**, 1259 (1992).
7. M.L. Weaver, M.J. Kaufman, and R.N. Noebe, *Scripta Metall.*, **29**, 1113 (1993).
8. J.E. Hack, J.M. Brzeski, and R. Darolia, *Mater. Sci. Eng.*, **A170**, 11 (1993).
9. M.L. Weaver, R.D. Noebe, J.J. Lewandowski, B.F. Oliver and M.J. Kaufman, *Mater. Sci. Eng.*, **A192/193**, 179 (1995).
10. J.E. Hack, J.M. Brzeski, and R. Darolia, *Mater. Sci. Eng.*, **A192/193**, 268 (1995).
11. M.A. Morris, J.-F. Perez, and R. Darolia, *Phil. Mag.*, **69**, 507 (1994).
12. R.W. Margevicius, J.J. Lewandowski, and I. Locci, *Scripta Metall.*, **26**, 1733 (1992).
13. R. Darolia, D. Lahrman, and R.D. Field, *Scripta Metall. Mater.*, **26**, 1007 (1992).
14. J.H. Schneibel, S.R. Agnew, and C.A. Carmichael, *Met. Trans. A*, **24A**, 2593 (1993).
15. R. Darolia and W.S. Walston, *Intermetallics*, **4**, 505 (1996).
16. J.S. Winton, J. Hu, Yu.N. Gornostyrev, V.I. Levit and M.J. Kaufman, *Proceedings of the International Conference REX-96*, Monterey, CA, in press.
17. V.I. Levit, J. Hu, I.A. Bul, J.S. Winton and M.J. Kaufman, "Challenges in the Development and Application of  $\beta$ -NiAl as an Engineering Material" (Paper presented at the Engineering Foundation Meeting, Davos, Switzerland, May 19-24, 1996).
18. R.W.K. Honeycombe, *The Plastic Deformation of Metals*, E. Arnold (Publishers) Ltd, London 1968).
19. R.D. Field, D.F. Lahrman, and R. Darolia, in *High-Temperature Ordered Intermetallic Alloys IV*, Materials Research Society Symposium Proceedings, editors L. Johnson et al, MRS, Pittsburgh, PA, **213**, 255 (1991).
20. R.J. Wasilewski, *Trans. Metall. Soc. AIME*, **236**, 455 (1966).

# **NI<sub>3</sub>AL AND IRON ALUMINIDES**

## MECHANICAL PROPERTIES OF Ni<sub>3</sub>Al AND FeAl: RECENT DEVELOPMENTS

E. P. George and C. T. Liu  
Metals and Ceramics Division  
Oak Ridge National Laboratory  
Oak Ridge, TN 37831-6093

### Abstract

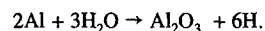
Recent developments in our understanding of the ductility and fracture behavior of Ni<sub>3</sub>Al and FeAl are reviewed. Both intrinsic factors (e.g., alloy stoichiometry), and extrinsic factors (e.g., environment) have been shown to affect their mechanical properties. Of all the recent developments, perhaps the most significant is the realization that Ni<sub>3</sub>Al and FeAl are intrinsically ductile (at least on the Al-deficient side of stoichiometry); their brittleness when tested in ambient air is due mainly to environmental embrittlement. Another intriguing discovery is that boron *embrittles* Ni<sub>3</sub>Al in gaseous hydrogen (until recently, B was thought to have only beneficial, or at most neutral, effects). We review these and other recent discoveries and discuss, wherever possible, the underlying physical mechanisms giving rise to the observed mechanical behavior.

### Introduction

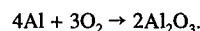
A major drawback of many otherwise attractive ordered intermetallics is their poor room-temperature ductility and tendency for brittle fracture. Often the brittleness is a consequence of their complex, non-cubic crystal structures, which do not provide the requisite 5 independent slip systems and in which dislocation motion is usually extremely difficult. But even intermetallics with relatively simple crystal structures are often brittle. For example, at room temperature, Ni<sub>3</sub>Al undergoes brittle intergranular fracture, and FeAl brittle intergranular fracture or transgranular cleavage depending on the Fe/Al ratio. Until recently, the behavior of these latter compounds was quite puzzling because there seemed to be no obvious reason for their brittleness. For example, slip occurs on {111}<110> in Ni<sub>3</sub>Al and {110}<111> in FeAl, providing both alloys with 5 independent slip systems. Additionally, neither is particularly strong at room temperature, suggesting that dislocation generation and motion are relatively easy. For lack of anything better, it was assumed that their ordered nature somehow made them *intrinsically* brittle.

Then, in 1989, Liu et al. [1] discovered that an *extrinsic* factor, the moisture in ambient air, was responsible for the brittleness of FeAl (36.5 at.% Al). They proposed that the water vapor in air reacted with the Al

atoms in FeAl, generating atomic hydrogen which embrittled the crack-tip regions:



When this "environmental embrittlement" was suppressed—by conducting the tests in dry oxygen—high tensile elongations were obtained, indicating that FeAl was intrinsically ductile. The following reaction between aluminum and oxygen to form protective aluminum oxide was proposed as an explanation for the high ductilities obtained in oxygen [1]:



The discovery of environmental effects in FeAl sparked widespread interest, not least because it offered the hope that other high-symmetry intermetallics may also be intrinsically ductile. Not long after the initial discovery in FeAl, environmental effects similar to those in FeAl were discovered in a whole host of other ordered intermetallics [2]. The basic reactions listed above (or their equivalents if other reactive elements are involved) have since been used to rationalize environmental effects in many different intermetallics.

The goal of the present paper is to review recent developments in our understanding of environmental effects by focusing on two model alloy systems, Ni<sub>3</sub>Al and FeAl. As we shall presently see, considerable progress has been made in elucidating the phenomenological aspects of environmental embrittlement; nevertheless, much remains to be done to uncover the detailed micromechanisms.

### Environmental Effects

#### H<sub>2</sub>O-Containing Environments

As mentioned earlier, it was in FeAl (36.5 at.% Al) that Liu et al. [1] first discovered environmental embrittlement. Table 1 summarizes the reported effects of environment on the room-temperature tensile properties of this alloy.

The ductility in air is 2.2%, which increases to 5.4% in vacuum and 17.6% in (dry) oxygen. In H<sub>2</sub>O vapor (at a pressure of 67 Pa, which is 5% of the water vapor pressure in ordinary ambient air), the ductility is similar to that obtained in air, indicating that moisture in air can severely embrittle FeAl. Interestingly, when environmental embrittlement was suppressed (by testing in oxygen), the fracture mode of FeAl (36.5% Al)

changed from transgranular to intergranular, suggesting that, in the absence of environmental effects, the grain boundaries, at least in this FeAl alloy, are weaker than the bulk. This intrinsic brittleness of the grain boundaries becomes more severe the closer one gets to the stoichiometric composition (more on this later).

TABLE 1. Effect of test environment on room-temperature tensile properties of Fe-36.5Al [1].

Environment (Pressure)	Elongation (%)	Yield strength (MPa)	Ultimate strength (MPa)
Air (1 atm)	2.2	360	412
Vacuum ( $<10^{-4}$ Pa)	5.4	352	501
Ar + 4% H <sub>2</sub> ( $6.7 \times 10^4$ Pa)	6.2	379	579
Oxygen ( $6.7 \times 10^4$ Pa)	17.6	360	805
H <sub>2</sub> O Vapor (67 Pa)	2.4	368	430

Shortly after environmental embrittlement was discovered in FeAl, several research groups decided to investigate whether a similar mechanism might be responsible also for the notorious brittleness of Ni<sub>3</sub>Al, another intermetallic whose brittleness had long stymied researchers. Unfortunately, polycrystalline Ni<sub>3</sub>Al is brittle at both low and high temperatures, making it extremely difficult to break down its cast structure and obtain equiaxed, recrystallized grains without introducing microcracks. Liu [3] attempted to minimize microcracking

by carefully cold forging conventionally cast Ni<sub>3</sub>Al alloys (Ni-23.5Al and Ni-24Al) which were then recrystallized to obtain equiaxed microstructures. However, room-temperature ductility increased from ~3% in air to only about 8% in (dry) oxygen, suggesting that moisture-induced embrittlement was not the sole reason for the poor ductility of Ni<sub>3</sub>Al [3], or that the specimens contained internal flaws which compromised the measured ductility despite the care taken during preparation [4].

TABLE 2. Effects of test environment, specimen orientation, and grain size on the room-temperature tensile properties of Ni-23.4Al.

Grain size ( $\mu\text{m}$ )	Specimen orientation <sup>a</sup>	Test environment (pressure)	Elongation to fracture (%)	Yield strength (MPa)	Ultimate strength (MPa)
13	0°	Air ( $10^5$ Pa)	3.1	308	392
	0°	Vacuum ( $1.3 \times 10^{-1}$ Pa)	7.9	323	519
	0°	Vacuum ( $3.8 \times 10^{-4}$ Pa)	12.8	301	602
	0°	Oxygen ( $6.7 \times 10^4$ Pa)	15.8	336	681
	0°	Vacuum ( $3.6 \times 10^{-8}$ Pa)	23.4	-- <sup>b</sup>	-- <sup>b</sup>
	45°	Air ( $10^5$ Pa)	4.8	327	401
	45°	Oxygen ( $6.7 \times 10^4$ Pa)	12.6	345	642
	0°	Oxygen ( $6.7 \times 10^4$ Pa)	15.9	248	630

<sup>a</sup>Relative to rolling direction.

<sup>b</sup>Not measured.

George et al. [4,5] realized that the way to obtain defect-free polycrystals of Ni<sub>3</sub>Al was to cold work and recrystallize *single crystals* of Ni<sub>3</sub>Al (because single crystals are ductile and can be deformed extensively without cracking). When polycrystalline specimens produced in this manner were tensile tested [6], it was found that their ductilities increased dramatically from around 3% in air, to more than 23% in ultrahigh ( $10^{-8}$  Pa) vacuum (Table 2). They concluded, therefore, that the *intrinsic* ductility of Ni<sub>3</sub>Al was quite high, and that (by analogy with the earlier work on iron aluminides [1,7]) moisture-induced embrittlement was what was responsible for the low ductilities commonly measured in air. With increasing amounts of air in the test environment, ductility dropped progressively, until in ordinary ambient air at atmospheric pressure it was only 3%—which is comparable to values commonly reported for the ductility of recrystallized fine-grained Ni<sub>3</sub>Al.

#### H<sub>2</sub>-Containing Environments

The reaction of H<sub>2</sub>O with Al is not the only way to generate atomic H; dissociative adsorption of H<sub>2</sub> on active metal surfaces can also produce it. In principle, therefore, some intermetallics may be embrittled by both H<sub>2</sub>O and H<sub>2</sub>. The degree to which each environment would produce embrittlement would depend on, among other factors, the relative efficiencies of H<sub>2</sub> and H<sub>2</sub>O dissociation.

In their 1989 study, Liu et al. [1] investigated the effect of H<sub>2</sub> by testing Fe-36.5Al in a gas mixture consisting of Ar + 4% H<sub>2</sub>. Their results, listed in Table 1, suggest that molecular hydrogen (at a partial pressure of  $2.7 \times 10^3$  Pa, which is about twice the partial pressure of the residual water vapor in atmospheric air) does, indeed, cause embrittlement, although not to the same degree as H<sub>2</sub>O. However, their experiments were conducted



in an unbaked, turbo-pumped vacuum chamber (base pressure,  $\sim 6 \times 10^{-4}$  Pa) in which trace amounts of water vapor were undoubtedly present as contamination. In order to measure the true effects of  $H_2$ , without the confounding effects of  $H_2O$ , experiments should be performed in very dry  $H_2$ .

Recently, Cohron and George [8] tensile tested Fe-37Al in an ultrahigh vacuum (UHV) chamber (base pressure,  $10^{-8}$  Pa) into which high-purity (99.9999%)  $H_2$  gas that had been dried by flowing through a liquid nitrogen cold trap was introduced at various pressures. Figure 1 shows the results of their study. In UHV, the ductility is around 16%, which is similar to the ductility measured by Liu et al. [1] in oxygen (see Table 1). With increasing hydrogen pressure, ductility decreases gradually, reaching a value of  $\sim 9\%$  at a hydrogen pressure of  $6.7 \times 10^3$  Pa. This decrease is somewhat less than that observed by Liu et al., indicating that part of Liu et al.'s decrease may have been due to moisture. Despite this minor difference, however, both studies clearly indicate that molecular hydrogen does embrittle FeAl. The embrittlement mechanism is expected to be similar to that discussed earlier except that the atomic H in this case is a result of the dissociative adsorption of  $H_2$  (rather than  $H_2O$ ). Interestingly, the embrittling effect of  $H_2$  is not as severe as that of  $H_2O$ . Another point to note is that over the entire pressure range tested, ductility is independent of whether the ion gage (a common device used to measure gas pressures) is turned on or off (Fig. 1). The significance of the ion gage is that, when it is turned on, its hot tungsten filament dissociates molecular  $H_2$  into atomic H. Since this external source of atomic H does not have any effect on the measured ductility, it must mean that the surfaces of FeAl are themselves effective in dissociating  $H_2$  into H. As discussed below, this behavior is quite different from that of  $Ni_3Al$ .

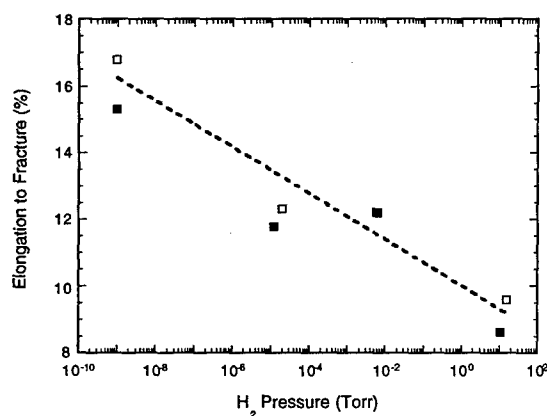


FIG. 1 Effect of  $H_2$  pressure on the room-temperature tensile ductility of Fe-37Al [8]. Open/filled symbols represent data obtained with gage on/off.

Unlike its effect on FeAl, molecular  $H_2$  does not embrittle otherwise ductile  $Ni_3Al$  (Fig. 2, "Gage OFF" data), at hydrogen pressures as high as  $1.3 \times 10^3$  Pa (which is roughly the partial pressure of  $H_2O$  responsible for the severe embrittlement caused by ambient air, Table 2). Since the partial pressure of hydrogen in atmospheric air is considerably lower,  $\sim 5 \times 10^{-2}$  Torr, it is clearly moisture and not hydrogen that is the cause of the observed embrittlement in air. Furthermore, since molecular  $H_2$  has to first dissociate into atomic H before it can enter the metal and cause embrittlement, the fact that gaseous hydrogen does not embrittle  $Ni_3Al$  must mean that the surfaces of  $Ni_3Al$  do not dissociate  $H_2$  into H very effectively. This inference needs to be verified in the future by experiments that directly measure  $H_2$  dissociation on  $Ni_3Al$  surfaces. So

far, such experiments have been performed only on  $NiAl$  surfaces, where it was shown that  $H_2$  does not in fact dissociate readily [10,11].

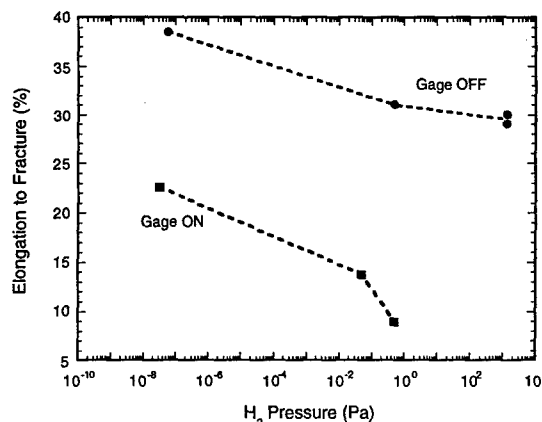


FIG. 2 Effect of  $H_2$  pressure on room-temperature tensile ductility of  $Ni_3Al$  (23.4% Al) [9]. Gage OFF and Gage ON refer to experiments conducted with the ionization gage turned off and on, respectively.

When the tensile tests were performed with the ion gage turned on (which produces atomic H), ductility dropped dramatically (Fig. 2), and the fracture mode changed from mostly transgranular to intergranular (Fig. 3). The "ion-gage effect" persists down to pressures in the UHV range (Fig. 2), indicating that even minute traces of atomic H in the test environment are deleterious to the ductility of  $Ni_3Al$ . When the availability of atomic H (from all sources, including  $H_2O$  and  $H_2$ ) is carefully limited, B-free  $Ni_3Al$  can be quite ductile, with elongations approaching 40% and mostly (>70%) transgranular fracture.

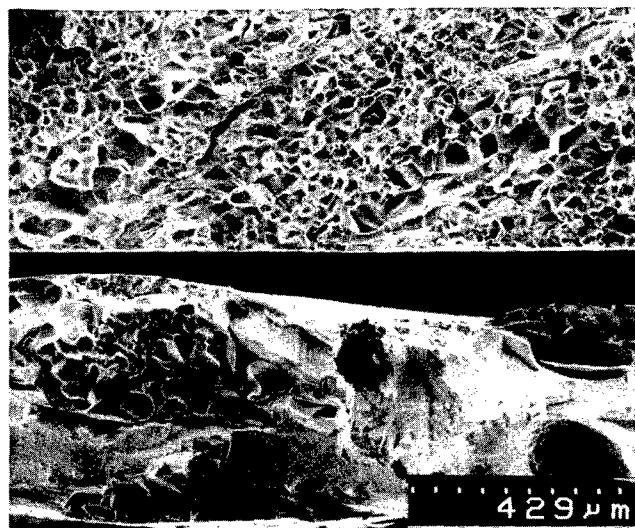


FIG. 3 Fracture surfaces of Ni-23.4Al tested in  $H_2$  with the gage on (top) and off (bottom) [9].

#### Mechanisms

Details of the atomic level interactions occurring during the dissociative adsorption of  $H_2O$  on aluminide surfaces were studied recently by Chia and Chung [12,13] and Gleason et al. [14] who performed thermal

desorption studies in conjunction with photoelectron and Auger electron spectroscopy on the surfaces of  $\text{Ni}_3(\text{Al,Ti})$  and  $\text{FeAl}$ , respectively. Their results confirm that Al is the active species responsible for the dissociation of water. When water is adsorbed at cryogenic temperatures on clean  $\text{Ni}_3(\text{Al,Ti})$  and  $\text{FeAl}$  surfaces, and the surfaces then slowly heated, molecular hydrogen (rather than water) is seen to desorb (Fig. 4). This indicates that the adsorbed water reacts with the Al-containing surfaces and dissociates into atomic H and O (or H and OH). Upon heating the atomic H recombines and desorbs as  $\text{H}_2$ .

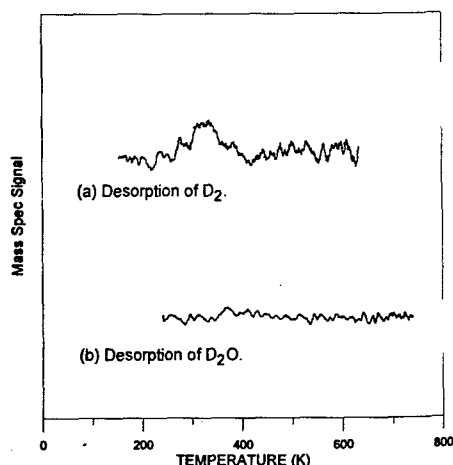


FIG. 4 Thermal desorption spectra [12] showing  $\text{D}_2$  evolution from (100) surfaces of  $\text{Ni}_3(\text{Al,Ti})$  exposed to 300 L  $\text{D}_2\text{O}$  at 200 K [ (a)  $m/e = 4$ ; (b)  $m/e = 20$ ].

Consistent with the above dissociation scheme, the oxygen 1s core level peak broadened and shifted to lower binding energies (relative to its position in water) [12]. Upon heating, the atomic H desorbed as  $\text{H}_2$ , and was detected in the thermal desorption experiments, whereas the oxygen stayed on the surface as a remnant of the water dissociation, and was detected by Auger electron spectroscopy performed after the desorption [12]. The oxygen produced during water dissociation appears to bind with the Al atoms because photoelectron spectroscopy [13,14] detected a component of the Al 2p peak at a higher binding energy than that normally associated with metallic Al (indicative of aluminum oxide formation). Hydrogen, on the other hand, resides on the transition metal atoms [14], but appears to be weakly bound because the Ni and Fe 2p peaks did not shift after the dissociation, remaining instead at the values corresponding to those of metallic Ni and Fe, respectively.

Interestingly, the reactivity of  $\text{Ni}_3(\text{Al,Ti})$  depended on which particular surface plane was examined [12]. The results noted above were for the (100) plane; on the (111) surface, in contrast, the adsorbed water remained unreacted, and desorbed upon heating as intact water molecules (i.e., no atomic H was generated), Fig. 5. Consistent with this desorption result, only the metallic Al 2p peak was observed on the (111) surface, indicating that the Al atoms on (111) do not react with water to form the oxide. The oxygen 1s binding energy also remained unchanged on (111), confirming that the adsorbed water molecules remained unreacted on this surface.

Since water dissociation is observed on the (100) planes of  $\text{Ni}_3(\text{Al,Ti})$  but not on (111), it suggests that the chemistry and/or structure of a grain boundary (or cleavage plane) may affect its susceptibility to moisture-induced embrittlement. In other words, some grain boundaries (and cleavage planes) may be more active than others for the dissociation of water. Consistent with this, Nishimura et al. [15] have shown that

stoichiometric  $\text{Ni}_3\text{Al}$  produced by a special directional solidification technique that results in mainly low-angle and  $\Sigma 3$  boundaries [16,17] is essentially immune to the harmful effects of  $\text{H}_2\text{O}$ : ductility remained high (Fig. 6), and the fracture mode predominantly transgranular, in vacuum, air, and water. In contrast,  $\text{Ni}_3\text{Al}$  alloys containing fewer special boundaries are severely embrittled by water vapor [18]. In the case of  $\text{FeAl}$ , while there is no direct evidence of certain planes being more active than others for the dissociation of water (the thermal desorption experiments discussed earlier were performed on polycrystals), fracture toughness studies have shown that the cleavage planes in  $\text{FeAl}$  change from {111} to {100} as a result of  $\text{H}_2\text{O}$ -induced embrittlement [19]. However, tensile tests of monocrystalline  $\text{Fe-40Al}$  resulted in {100} cleavage in both air and oxygen [20], suggesting that additional studies are needed to resolve this issue. Li and Liu [21] proposed that hydrogen may accelerate the formation of {100} edge dislocations from interacting {111} mixed dislocations (the so-called Cottrell mechanism), as well as their subsequent combination to form microcracks on the {100} plane, thus providing a mechanism for the observed {100} cleavage in hydrogen-containing environments.

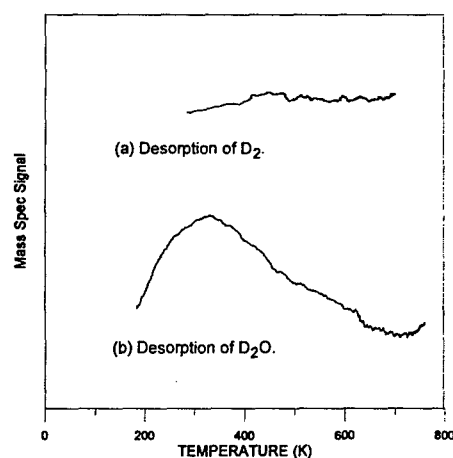


FIG. 5 Thermal desorption spectra [12] showing  $\text{D}_2\text{O}$  evolution from (111) surfaces of  $\text{Ni}_3(\text{Al,Ti})$  exposed to 300 L  $\text{D}_2\text{O}$  at 200 K [ (a)  $m/e = 4$ ; (b)  $m/e = 20$ ].

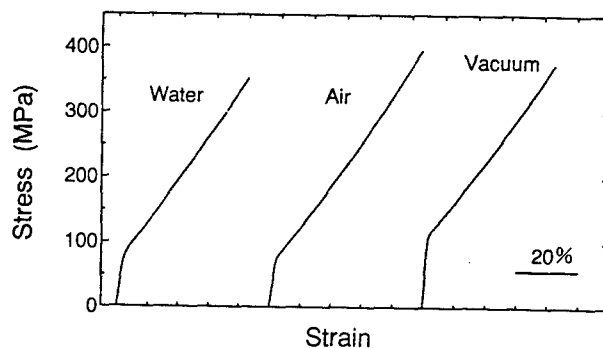


FIG. 6 Effect of environment on the room-temperature tensile properties of directionally solidified  $\text{Ni}_3\text{Al}$  [15].

As discussed above, there is considerable evidence to indicate that atomic H is generated on clean  $\text{Ni}_3\text{Al}$  and  $\text{FeAl}$  surfaces exposed to

water vapor. However, it is not clear *how* this hydrogen then causes embrittlement. Two of the mechanisms proposed for the hydrogen embrittlement of conventional metals are H-induced decohesion or H-enhanced local plasticity [see, e.g., 22]. These are candidate mechanisms also for the embrittlement of intermetallics. Unfortunately, there is insufficient evidence at present to discriminate between the two. Robertson and Birnbaum [23] performed in situ crack propagation experiments in a transmission electron microscope and found that both crack growth rate and dislocation activity in Fe<sub>3</sub>Al were higher in wet hydrogen (or helium) than in vacuum. Tests in dry hydrogen (or helium) did not show this acceleration relative to vacuum, suggesting that the atomic hydrogen generated in the reaction with moisture somehow enhanced local plasticity which in turn increased the crack growth rate. No such experimental results are available to support hydrogen-induced decohesion; however, first-principles quantum-mechanical calculations by Fu and Painter [24] showed that the ideal cleavage energy of FeAl can be reduced by 20-70%, depending on the dissolved hydrogen concentration (Fig. 7). Additional research is clearly needed, but given the lack of consensus in conventional metals despite decades of debate, it appears unlikely that this matter will be settled any time soon.

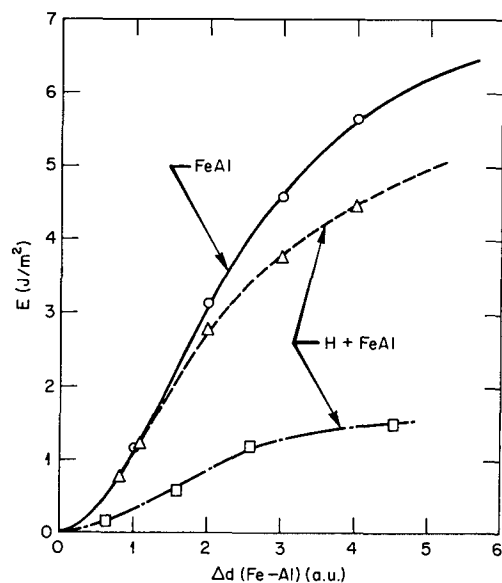


FIG. 7 Effect of interstitial H (low and high concentrations) on the ideal cleavage energy of FeAl as a function of distance between {100} planes [24].

#### Strain Rate Effects

The proposed mechanisms of environmental embrittlement in Ni<sub>3</sub>Al and FeAl involve many individual steps (e.g., surface adsorption of H<sub>2</sub>O / H<sub>2</sub>, their dissociation to form H, absorption of H into the metal, and transport of H to some critical location ahead of the crack tip) any of which may be rate limiting. Consequently, room-temperature ductility is expected to be a function of strain rate. Indeed, both FeAl (Fig. 8) and Ni<sub>3</sub>Al (Fig. 9) exhibit such a strain rate dependence, with ductility increasing as the strain rate increases. A common explanation for such strain rate dependencies is that, as the strain rate increases, it becomes increasingly difficult for the environmental reactions to keep up with the growing crack, and the ductility increases. If, instead of being limited by extrinsic environmental factors, ductility is limited by intrinsic factors (e.g., dislocation mobility and cross slip), strain rate usually has the opposite effect, i.e., ductility decreases with increasing strain rate.

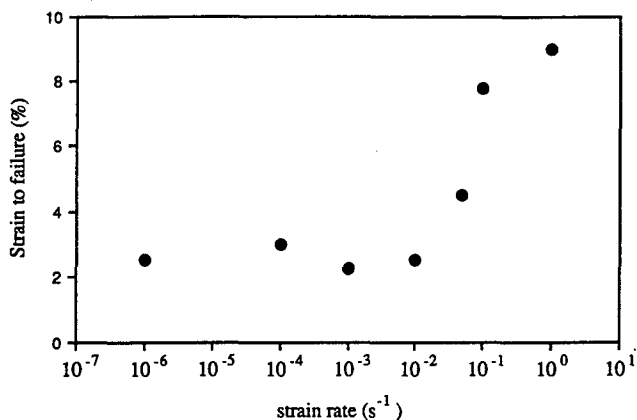


FIG. 8 Effect of strain rate on the room-temperature tensile ductility of Fe-45Al [25].

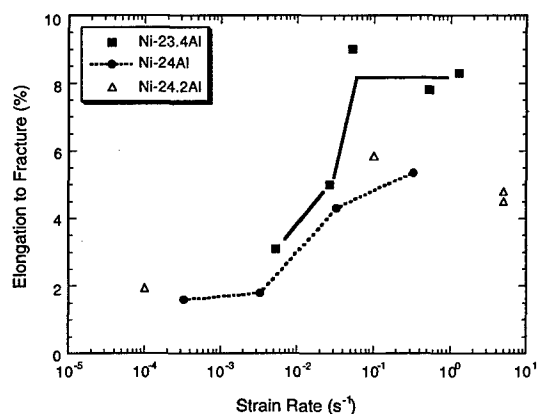


FIG. 9 Effect of strain rate on the room-temperature tensile ductility of Ni-23.4Al in air [26], Ni-24Al in moist Ar [27], and Ni-24.2Al in air [28].

#### Temperature Effects

The ductilities of alloys exhibiting environmental effects are expected to also show a temperature dependence. For example, with decreasing temperature, the free energies and kinetics of the various steps in the embrittlement process should decrease, whereas with increasing temperature, the sticking probability of the H<sub>2</sub>O (or H<sub>2</sub>) molecules on the intermetallic surfaces should decrease and the tendency for oxide formation should increase.

Consistent with this reasoning, the ductility of Ni<sub>3</sub>Al in air is seen to go through a local minimum at room temperature, with ductility increasing at both lower and higher temperatures [26]. In oxygen, the ductility is high at room temperature (because oxygen suppresses the embrittlement caused by H<sub>2</sub>O) but it decreases with increasing temperature because of the well-known embrittling effect of oxygen at elevated temperatures [29,30]. In vacuum, ductility remains high over the entire temperature range. Very high elongations to fracture were obtained recently by George et al. [31] when fine-grained (~15 μm) Ni<sub>3</sub>Al was tested in liquid nitrogen (77 K); Table 3 lists the tensile properties of two such

specimens. Consistent with these high ductilities, the fracture mode was found to change from intergranular at room temperature to >60% transgranular at 77 K, indicating that the grain boundaries in  $\text{Ni}_3\text{Al}$  are not necessarily weak (provided that environmental embrittlement is suppressed). Chiba et al. [32] also obtained high ductilities (approaching 50%) in liquid nitrogen, but their specimens were produced by a special strain-annealing technique and had very large grain sizes (670  $\mu\text{m}$ ). Lee and White [33], for reasons that are not entirely clear, obtained considerably lower ductilities in Ni-24Al specimens tensile tested in liquid nitrogen. Additional research is needed to better understand these differences. Nevertheless, it is clear that the ductility of  $\text{Ni}_3\text{Al}$  increases when it is tested at cryogenic temperatures—as it should, if environmental effects are responsible for its room-temperature brittleness.

TABLE 3 Tensile properties of polycrystalline Ni-23.4Al at 77 K [31].

Specimen	Elongation to fracture (%)	Yield strength (MPa)	Ultimate strength (MPa)
K-3	31.8	254	762
K-4	31.3	269	672

The behavior of FeAl is broadly similar to that of  $\text{Ni}_3\text{Al}$ . When tested in air, the ductility of FeAl (36.5% Al) goes through a minimum at around room temperature; in oxygen, on the other hand, its ductility remains relatively high over the entire temperature range (Fig. 10). Li and Liu [34] considered several thermodynamic and kinetic factors and produced a quantitative model of the effect of temperature on the ductility of FeAl that successfully reproduced the shape of the experimental curve (Fig. 10). They concluded that the dip in ductility due to environmental embrittlement was satisfactorily explained by a kinetic effect at low temperatures and an equilibrium effect at high temperatures.

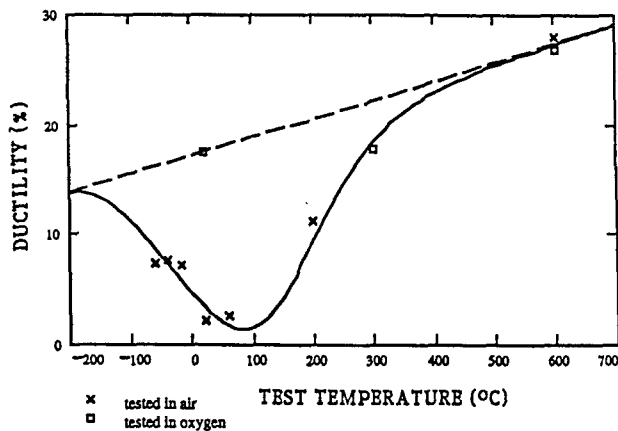


FIG. 10 Effect of temperature on the tensile ductility of FeAl (36.5% Al) in air and oxygen [34]. Curves calculated by Li and Liu [34] using a thermodynamic model.

#### Boron Effects

##### $\text{H}_2\text{O}$ -Containing Environments

Nearly two decades ago, Aoki and Izumi [35] discovered that microalloying with ppm levels of B suppressed grain boundary fracture and improved the ductility of  $\text{Ni}_3\text{Al}$  in ambient air. A few years later, Liu

et al. [36] showed that the beneficial effect of B resulted from its segregation to the grain boundaries, but that B improved ductility only on the Ni-rich side of stoichiometry. Until recently, B was believed to either increase grain boundary cohesion [36,37] or aid in slip transfer across grain boundaries [38,39]. However, more recent data indicate that the role of B is mainly to suppress environmental effects [40]. In general, if the amount of B is high enough, then  $\text{Ni}_3\text{Al}$  appears to be immune to embrittlement by water or its vapor [41]. If, however, there is a limited amount of B present,  $\text{Ni}_3\text{Al}$  is to some degree susceptible to  $\text{H}_2\text{O}$ -induced embrittlement [26,42].

Fig. 11 shows the effect of strain rate on the room-temperature tensile ductility of B-doped  $\text{Ni}_3\text{Al}$  (24% Al) in air and water [26]. The ductility of the 100 wppm B alloy is high and relatively insensitive to strain rate both in air and water, whereas the 50 wppm B alloy, while it is relatively ductile in air, undergoes a ductile-to-brittle transition in water as the strain rate is decreased. Except for the 100 wppm B alloy tested in air at the highest strain rate, which showed transgranular fracture with microvoid coalescence, all the other conditions resulted in some degree of intergranular fracture [26]. Taken together, these results suggest that, if the amount of B added to  $\text{Ni}_3\text{Al}$ , and therefore the amount segregated at the grain boundaries [43], is less than some "optimal" level, environmental embrittlement is only partially alleviated and, only when environmental effects are well and truly suppressed, do we get completely transgranular fracture. Additionally, a major role of boron appears to be the suppression of environmental embrittlement because virtually the same improvement in ductility can be obtained by increasing the strain rate, increasing the boron concentration, or decreasing the aggressiveness of the test environment.

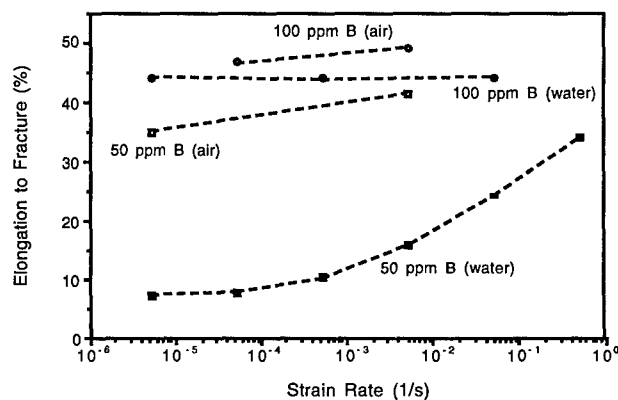


FIG. 11 Effect of strain rate, environment, and B doping on room-temperature ductility of Ni-24Al [26].

A possible mechanism [44] for the suppression of  $\text{H}_2\text{O}$ -induced embrittlement is that B inhibits the diffusion of H atoms along the grain boundaries of  $\text{Ni}_3\text{Al}$ . There is evidence to suggest that the apparent diffusivity of H along the grain boundaries of  $\text{Ni}_3\text{Al}$  is decreased in the presence of boron [45]. Other authors [46], have proposed that the role of B is to slow down the kinetics of the reaction of  $\text{H}_2\text{O}$  with the exposed grain boundaries of  $\text{Ni}_3\text{Al}$ , resulting in reduced hydrogen production. Fig. 12 shows Auger spectra taken from the grain boundaries of B-free and B-doped  $\text{Ni}_3\text{Al}$  alloys as a function of exposure (pressure  $\times$  time) to  $\text{H}_2\text{O}$  vapor. The build-up of oxygen (which is mostly the result of water dissociation into H and O) is greater on the B-free grain boundaries than on the B-doped grain boundaries, indicating that B enrichment at the grain boundaries slows down the reaction of water vapor with  $\text{Ni}_3\text{Al}$ , and therefore the production of atomic H.

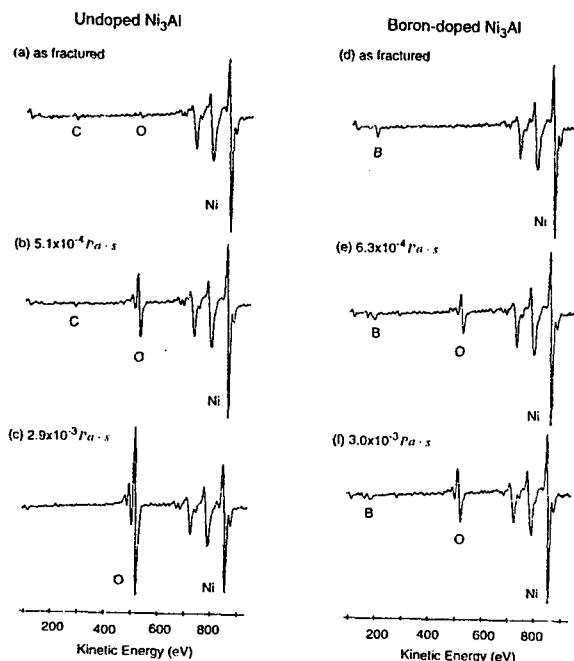


FIG. 12 Auger spectra from grain boundaries of B-free (left) and B-doped (right)  $\text{Ni}_3\text{Al}$  after exposure to  $\text{H}_2\text{O}$  [46]. (Exposures increasing from top to bottom.)

The behavior of B on FeAl surfaces appears to be somewhat different: Gleason et al. [14] using temperature-programmed desorption, in conjunction with Auger and photoelectron spectroscopy concluded that the amount of hydrogen product desorbing from boron-doped FeAl is very similar to that desorbing from clean FeAl surfaces after equivalent water exposures. They concluded, therefore, that B had little effect on the reactivity of FeAl surfaces to water dissociation.

#### $\text{H}_2$ -Containing Environments

Cohron et al. [47] recently investigated the effects of boron doping on the room-temperature ductility and fracture behavior of  $\text{Ni}_3\text{Al}$  (24 at.% Al) in dry  $\text{H}_2$  gas. As shown in Fig. 13, there is little change in ductility with increasing  $\text{H}_2$  pressure at first, until the pressure reaches a critical value, at which point the ductility drops precipitously. At all the  $\text{H}_2$  pressures employed, the higher the B concentration the higher the elongation to fracture. An important observation is that, over the entire pressure range tested, ductility is independent of whether or not the ion gage is on (unlike the case in B-free  $\text{Ni}_3\text{Al}$ , Fig. 2). Accompanying the dramatic drop in ductility with increasing  $\text{H}_2$  pressure is a change from predominantly (> 60%) transgranular fracture to predominantly (70%) intergranular fracture in all three alloys [47]. Consistent with the lack of dependence of ductility on the state of the ion gage, the fracture mode was also independent of whether the gage was on or off [47]. Together, these observations imply that the surfaces of B-doped  $\text{Ni}_3\text{Al}$ —unlike those in B-free  $\text{Ni}_3\text{Al}$ —are active for the dissociation of  $\text{H}_2$  into atomic H (the surfaces referred to here are the freshly created fracture surfaces which, prior to fracture, are the grain boundaries where the B atoms have segregated).

Transition metal surfaces are usually active for the dissociation of  $\text{H}_2$ . The mechanism is thought to involve the promotion of electrons from the partially filled  $d$ -band of the transition metal to the anti-bonding  $s$ -orbital of the  $\text{H}_2$  molecule, thereby destabilizing the H-H bond [e.g., 48]. It is not clear why the grain boundaries of B-free  $\text{Ni}_3\text{Al}$  are not as effective

as those of B-doped  $\text{Ni}_3\text{Al}$  in dissociating  $\text{H}_2$ . One possibility is that  $\text{Ni}_3\text{Al}$  is less able to make the charge transfer to the  $\text{H}_2$  molecule than, say, Ni. By extension, if B facilitated this charge transfer it might catalyze the hydrogen dissociation reaction and cause embrittlement. Both these possibilities need additional investigation.

A consequence of this difference in the surface reactions of the B-doped and B-free alloys is that, in dry  $\text{H}_2$  gas, at pressures in the range 1 to  $10^3$  Pa,  $\text{Ni}_3\text{Al}$  doped with 50 or 100 wppm B is significantly more brittle than B-free  $\text{Ni}_3\text{Al}$  (Fig. 14). Consistent with these elongation data, the two B-doped alloys exhibited predominantly grain boundary fracture at the higher  $\text{H}_2$  pressures, whereas B-free  $\text{Ni}_3\text{Al}$  exhibited a significant amount (~60%) of transgranular fracture [47]. This is an unexpected embrittling effect of B: until recently, B was thought to have exclusively beneficial effects in  $\text{Ni}_3\text{Al}$ .

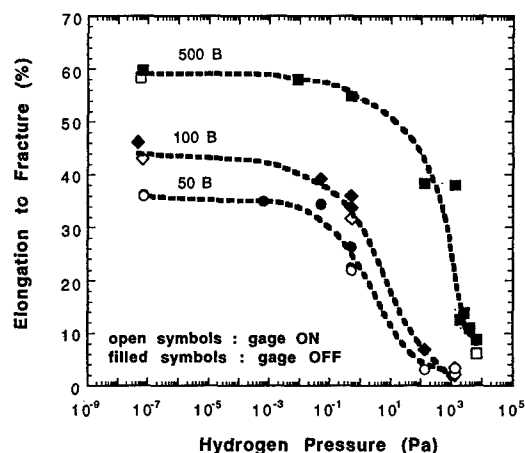


FIG. 13 Effect of hydrogen pressure on the room-temperature tensile ductilities of Ni-24Al alloys doped with 50, 100, and 500 ppm B [47].

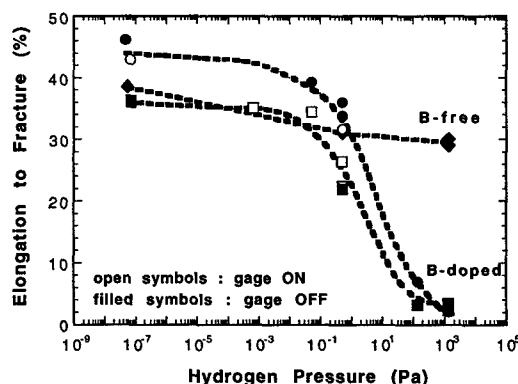


FIG. 14 Comparison of the room-temperature tensile ductilities of B-doped and B-free  $\text{Ni}_3\text{Al}$  in  $\text{H}_2$  [47]. Note that the doping with 50 or 100 ppm B severely embrittles  $\text{Ni}_3\text{Al}$  at the higher hydrogen pressures.

It is important to note, however, that B causes embrittlement over only a specific range of  $\text{H}_2$  pressures: at low pressures, B clearly improves ductility. Interestingly,  $\text{H}_2$  is more detrimental to the ductility of B-doped alloys than  $\text{H}_2\text{O}$ , whereas the opposite is true in the case of B-free  $\text{Ni}_3\text{Al}$ . This means that, although atomic H is the underlying cause of room-

temperature embrittlement, the kinetics of dissociation (from  $H_2O$  or  $H_2$ ) play an important role in determining the ductility and fracture mode of  $Ni_3Al$ . For example, the 50 wppm B alloy, which is fairly ductile (>20% elongation) when tested in water or in ordinary ambient air [26], is nevertheless severely embrittled (<5% elongation) in dry  $H_2$  environments. Even the 500 wppm B alloy, which has been considered to be immune to environmental effects [41], suffers embrittlement at  $H_2$  pressures above  $\sim 10^3$  Pa. These observations highlight the different roles of B in  $H_2O$ - and  $H_2$ -containing environments: in the former B suppresses embrittlement whereas in the latter it promotes embrittlement.

Choudhury et al. [43] have shown that the concentration of B on the grain boundaries of  $Ni_3Al$  increases as its concentration in the bulk increases. Consequently, the grain boundary concentration of B in the B-doped alloys is expected to increase (and eventually saturate) in the order 50, 100, 500 wppm. Therefore, the data in Fig. 13 imply that, as the amount of B on the grain boundaries increases, it becomes increasingly difficult for H to penetrate into the grain boundaries of  $Ni_3Al$ . That B hinders the uptake of hydrogen can also be seen by comparing the ductilities of the B-doped alloys with those of B-free  $Ni_3Al$  with the gage on (Fig. 15): when there is an external source of atomic H available, the ductilities of the B-doped alloys are always higher than those of the B-free alloy.

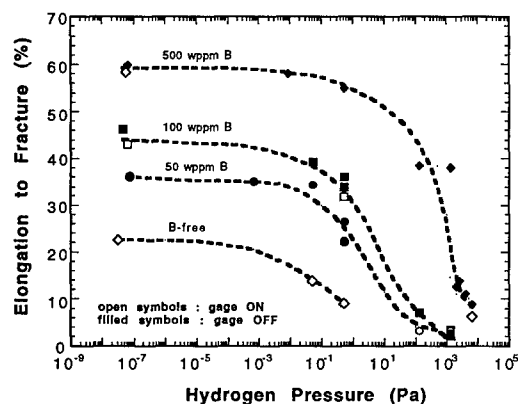


FIG. 15 Comparison of the room-temperature tensile ductilities of B-free  $Ni_3Al$  (gage on) with those of B-doped  $Ni_3Al$  (gage on or off) [47].

At pressures in the ultrahigh vacuum (UHV) range, B has a clear beneficial effect on the ductility of  $Ni_3Al$  (Fig. 13): ductility increases with increasing B concentration. If one assumes for the moment that extrinsic (i.e., environmental) effects are minimal in UHV when the ion gage is off, then the UHV results suggest that one effect of B is to strengthen the grain boundaries of  $Ni_3Al$ . Consistent with this, at a given level of ductility, the B-doped alloys tend to have greater amounts of transgranular fracture than the B-free alloy [47]. Thus, there appear to be three main effects of B in  $Ni_3Al$ , two of which are beneficial while the third is harmful: (i) boron enhances grain boundary cohesion (seen most clearly at low  $H_2$  pressures), (ii) it hinders the uptake of hydrogen (seen best at intermediate pressures), and (iii) it promotes the dissociation of  $H_2$  into H thereby embrittling  $Ni_3Al$  (at higher pressures).

Gleason et al. [14], showed that the amount of hydrogen product desorbing from B-doped FeAl surfaces was significantly less than that from clean FeAl surfaces after equivalent exposures to molecular hydrogen. They concluded, therefore, that B reduced the reactivity of FeAl toward  $H_2$  (recall that B has little effect on  $H_2O$  dissociation on FeAl). The different effects of B on the dissociation of  $H_2O$  and  $H_2$  on FeAl were ascribed by Gleason et al. [14] to the fact that the interaction

of B was primarily with the Fe site, which is also the site responsible for  $H_2$  dissociation. Water dissociation, on the other hand, takes place on the Al site, which is unaffected by B. Similar experiments have not yet been performed on  $Ni_3Al$ . If B is found to reduce the reactivity of  $Ni_3Al$  surfaces for  $H_2$  dissociation it would contradict the mechanism proposed [47] for the B-induced embrittlement of  $Ni_3Al$  (Fig. 14) and an alternative explanation would have to be proposed.

#### Alloy Stoichiometry Effects

##### FeAl

With increasing aluminum concentration, the grain boundaries in FeAl become increasingly more brittle [49-54]. In these high-aluminum alloys, therefore, there are *two* reasons for poor ductility and brittle fracture: (a) weak grain-boundary cohesion, and (b) environmental embrittlement (which may be inter- or trans-granular). Weak grain-boundary cohesion can be overcome by the addition of boron [49,55-57], which segregates to the grain boundaries [49] and suppresses intergranular fracture. Table 4 shows the effect of boron doping and test environment on the room-temperature ductility and fracture behavior of Fe-40Al.

TABLE 4. Effect of environment and B doping on the room-temperature tensile properties of Fe-40Al [49].

	Yield (MPa)	Ultimate (MPa)	Tensile Ductility (%)	Fracture mode
<u>No Boron</u>				
Air	390	405	1.2	GBF
Oxygen	402	537	3.2	GBF
<u>Doped with 300 wppm B</u>				
Air	391	577	4.3	TF
Oxygen	392	923	16.8	TF

GBF: grain boundary fracture

TF: transgranular fracture

Without boron the alloy fractures predominantly intergranularly regardless of test environment. Suppression of environmental embrittlement (by testing in dry oxygen) results in a small increase in tensile ductility (indicating an environmental effect on the grain boundaries), but the next brittle fracture mode (intrinsic grain boundary fracture) intervenes before significant plastic deformation can occur. If boron is added to the alloy, and it is tested in air, there is some improvement in ductility (suggesting that B counteracts intrinsic and/or extrinsic intergranular brittleness). However, the next brittle fracture mode (this time moisture-induced transgranular fracture) intervenes before significant plastic deformation can take place, and once again only limited ductility is obtained. Extensive ductility requires that all brittle fracture modes be suppressed, and when that is done (by testing B-doped FeAl in oxygen), it is seen that as much as 17% ductility is obtained. With further increases in aluminum concentration above 40 at.% Al, the grain boundaries become progressively more brittle, until in Fe-48Al they become so brittle that even boron segregation is unable to enhance grain boundary cohesion and suppress intergranular fracture [58]. Figure 16 shows the effect of test environment and aluminum concentration on the tensile ductility of B-doped and B-free FeAl alloys. In the low-aluminum alloys, boron doping overcomes grain-boundary brittleness, so a big improvement in ductility is seen when the test is conducted in oxygen instead of in air. As the aluminum concentration increases, however, boron becomes progressively less effective in overcoming grain-boundary brittleness, so there is progressively less difference in ductility between the air and oxygen tests. Note that the

fracture mode in alloys containing more than ~43% Al is predominantly intergranular, despite the fact that boron segregates just as strongly to the grain boundaries in these alloys as to those in the more Fe-rich alloys.

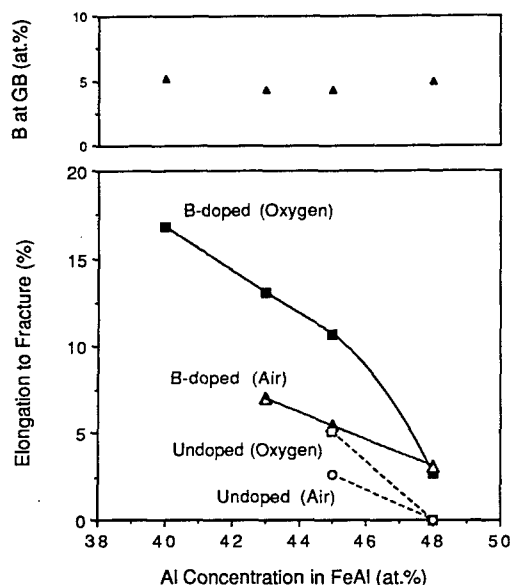


FIG. 16 Effect of environment, stoichiometry, and B doping on the room-temperature tensile ductility of FeAl (bottom), and grain boundary segregation levels of B as a function of Al concentration (top) [58].

## Ni<sub>3</sub>Al

As mentioned earlier in this review, B is effective in suppressing grain boundary fracture only on the Ni-rich side of stoichiometry [36]. In light of the discovery of environmental effects in Ni<sub>3</sub>Al, Liu and George [59] recently examined the effects of B concentration and alloy stoichiometry on the environmental susceptibility of Ni<sub>3</sub>Al. As shown in Table 5, Ni-24Al doped with 500 ppm B shows virtually no environmental embrittlement: ductility remains high (and fracture predominantly transgranular) independent of test environment and strain rate. This indicates that B at a level of 500 ppm is able to effectively suppress environmental embrittlement in Ni-24Al. At lower concentrations (50 ppm), B is unable to completely suppress environmental effects, as evidenced by the strain rate dependence of ductility in water (Fig. 8). This is due presumably to the decrease in grain boundary concentration of B with decreasing bulk concentration [43].

With increasing Al concentration in Ni<sub>3</sub>Al, the effectiveness of B in suppressing environmental embrittlement decreases (Table 5): the ductility in water is lower than that in air, which in turn is lower than that in oxygen. A possible reason for this behavior is that the amount of B that segregates to the grain boundaries of Ni<sub>3</sub>Al decreases with increasing Al concentration [36]. Consistent with this, an increase in the amount of bulk B from 500 to 1000 ppm (which presumably forces more B to segregate to the grain boundaries) increases the ductility of the 25.2% Al alloy significantly. Nevertheless, the best ductilities of the 24.8 and 25.2% Al alloys are substantially lower than those of the Ni-24Al alloy, suggesting that the *intrinsic* properties of the Ni<sub>3</sub>Al grain boundaries may be deteriorating with increasing Al concentration. As in FeAl (Fig. 16), even though B can be made to segregate to the grain boundaries, it is increasingly unable to overcome the intrinsic brittleness of the Ni<sub>3</sub>Al grain boundaries in the near-stoichiometric alloys.

## Concluding Remarks

We limited this review to ductility and fracture issues. Environmental embrittlement, a result of the atomic H generated during the dissociative adsorption of H<sub>2</sub>O or H<sub>2</sub> on fresh fracture surfaces, is now known to be the major factor limiting the ductility of several otherwise ductile intermetallics. However, the susceptibility of an intermetallic to environmental embrittlement is often determined by other intrinsic and extrinsic factors. The roles of some of these factors were discussed with the help of two examples: Ni<sub>3</sub>Al and FeAl of the L1<sub>2</sub> and B2 crystal structures, respectively.

Despite the considerable progress made in recent years much remains to be done. Among the issues still to be resolved are the following. How does H actually cause embrittlement? Are the grain boundaries in near stoichiometric and Al-rich Ni<sub>3</sub>Al intrinsically brittle? Why? What is the mechanism by which B suppresses environmental embrittlement in Ni<sub>3</sub>Al? Since environmental embrittlement affects the cleavage planes in FeAl, trace element additions (like B in Ni<sub>3</sub>Al) are not effective; what other mechanisms can one use to overcome environmental effects? Why is boron, even though it segregates, not effective in strengthening the grain boundaries of the near-stoichiometric FeAl alloys?

## Acknowledgments

The authors thank J. H. Schneibel and L. M. Pike for reviewing the paper. This research was sponsored by the Division of Materials Sciences, U.S. Department of Energy under contract DE-AC05-96OR22464 with Lockheed Martin Energy Research Corp.

## References

1. C. T. Liu, E. H. Lee, and C. G. McKamey, *Scripta Metall.*, **23**, 875 (1989).
2. C. T. Liu, *Proc. Intermetallic Compounds (JIMIS-6)* ed. O. Izumi, 703, JIM, 1991.
3. C. T. Liu, *Scripta Metall.* **27**, 25 (1992).
4. E. P. George, C. T. Liu, D. P. Pope, *Scripta Metall. Mater.* **27**, 365 (1992).
5. E. P. George, C. T. Liu, D. P. Pope, *Scripta Metall.* **28**, 857 (1993).
6. E. P. George, C. T. Liu, D. P. Pope, *Scripta Metall.* **30**, 37 (1994).
7. C. T. Liu, C. G. McKamey, and E. H. Lee, *Scripta Metall.* **24**, 385 (1990).
8. J. W. Cohron and E. P. George, Oak Ridge National Laboratory, unpublished results.
9. J. W. Cohron, E. P. George, L. Heatherly, C. T. Liu, and R. H. Zee, *Intermetallics*, **4**, 497 (1996).
10. A. T. Hambicki, A. P. Baddorf, E. W. Plummer, and B. Hammer, *Surface Science*, **331-333**, 811 (1995).
11. N. R. Gleason, S. Chaturvedi, and D. R. Strongin, *Surface Science*, **326**, 27 (1995).
12. W. J. Chia and Y. W. Chung, *Intermetallics*, **3**, 505 (1995).
13. W. J. Chia and Y. W. Chung, *J. Vac. Sci. Technol.* **A13**, 1687 (1995).
14. N. R. Gleason, C. A. Gerken, and D. R. Strongin, *Appl. Surf. Sci.* **72**, 215 (1993).
15. C. Nishimura, T. Hirano, and M. Amano, *Scripta Metall. Mater.* **29**, 1209 (1993).
16. T. Watanabe, T. Hirano, T. Ochiai, and H. Oikawa, *Mater. Sci. Forum*, **157-162**, 1103 (1994).
17. T. Watanabe, *Mater. Sci. Eng.* **A166**, 11 (1993).
18. E. P. George, C. T. Liu, H. Lin and D. P. Pope, *Mater. Sci. Eng.* **A192/193**, 277 (1995).

19. P. Specht, M. Brede, and P. Neumann, MRS Symp. Proc. **364**, 207 (1995).
20. M. V. Nathal and C. T. Liu, Intermetallics, **3**, 77 (1995).
21. J. C. M. Li and C. T. Liu, Scripta Metall. Mater. **27**, 1701 (1992).
22. J. Hirth, Metall. Trans. **11A**, 861 (1980).
23. I. M. Robertson and H. K. Birnbaum, University of Illinois, unpublished results.
24. C. L. Fu and G. S. Painter, J. Mater. Res. **6**, 719 (1991).
25. P. Nagpal and I. Baker, Scripta Metall. Mater. **25**, 2577 (1991).
26. E. P. George, C. T. Liu, and D. P. Pope, Acta Mater. **44**, 1757 (1996).
27. K. H. Lee and C. L. White, Scripta Mater. **33**, 129 (1995).
28. E. M. Schulson and Y. Xu, Acta Mater. (1997) in press.
29. C. T. Liu, C. L. White, and E. H. Lee, Scripta Metall. **19**, 1247 (1985).
30. A. I. Taub, K. -M. Chang, and C. T. Liu, Scripta Metall. **20**, 1613 (1986).
31. E. P. George and L. Heatherly, Oak Ridge National Laboratory, unpublished results.
32. A. Chiba, S. Hanada, S. Watanabe, T. Abe, and T. Obana, Acta Metall. Mater. **42**, 1733 (1994).
33. K. H. Lee and C. L. White, Scripta Metall. Mater. **32**, 1871 (1995).
34. J. C. M. Li and C. T. Liu, Scripta Metall. Mater. **33**, 661 (1995).
35. K. Aoki and O. Izumi, J. Jpn. Inst. Met. **43**, 1190 (1979).
36. C. T. Liu, C. L. White and J. A. Horton, Acta Metall. **33**, 213 (1985).
37. G. M. Bond, I. M. Robertson, and H. K. Birnbaum, J. Mater. Res. **2**, 436 (1987).
38. E. M. Schulson, T. P. Wiehs, D. V. Viens, and I. Baker, Acta Metall. **34**, 1395 (1986).
39. P. S. Khadkikar, K. Vedula, and B. S. Shabel, Metall. Trans. **18A**, 425 (1987).
40. E. P. George and C. T. Liu, MRS Symp. Proc. **364**, 1131 (1995).
41. C. T. Liu, MRS Symp. Proc. **288**, 3 (1993).
42. X. J. Wan, J. H. Zhu, and K. L. Jing, Scripta Metall. **26**, 473 (1992).
43. A. Choudhury, C. L. White, and C. R. Brooks, Scripta. Metall. **20**, 1061 (1986).
44. T. Takasugi, MRS Symp. Proc. **213**, 403 (1991).
45. X. J. Wan, J. H. Zhu, K. L. Jing, and C. T. Liu, Scripta Metall. Mater. **31**, 677 (1994).
46. K. H. Lee, J. T. Lukowski, and C. L. White, Scripta Mater. **35**, 1153 (1996).
47. J. W. Cohron, E. P. George, L. Heatherly, C. T. Liu, and R. H. Zee, Acta Mater. (1997), in press.
48. B. Hammer and J. K. Nørskov, Surf. Sci. **343**, 211 (1995).
49. C. T. Liu and E. P. George, Scripta Metall. **24**, 1285 (1990).
50. C. T. Liu and E. P. George, MRS Symp. Proc. **213**, 527 (1991).
51. D. J. Gaydos, S. L. Draper, and M. V. Nathal, Metall. Trans. **20A**, 1701 (1989).
52. M. A. Crimp and K. M. Vedula, Mater. Sci. Eng. **78**, 193 (1986).
53. I. Baker and D. J. Gaydos, Mater. Sci. Eng. **96**, 147 (1987).
54. W. R. Kerr, Metall. Trans. **17A**, 2298 (1986).
55. P. Morgund, P. Moururat, and G. Sainfort, Acta Metall. **16**, 867 (1968).
56. A. Causey and E. Teghtsoonian, Metall. Trans. **1**, 1177 (1970).
57. M. A. Crimp, K. M. Vedula, and D. J. Gaydos, MRS Symp. Proc. **81**, 499 (1987).
58. Y. Lin and E. P. George, Oak Ridge National Laboratory, unpublished results.
59. C. T. Liu and E. P. George, Oak Ridge National Laboratory, unpublished results.

TABLE 5. Effect of B doping and alloy stoichiometry on environmental embrittlement of Ni<sub>3</sub>Al alloys [59].

Strain rate (s <sup>-1</sup> )	Environment	Elongation (%)	Yield strength (MPa)	Ultimate strength (MPa)
<u>Ni-24Al + 500 ppm B</u>				
3.3 × 10 <sup>-3</sup>	oxygen	39.4	289	1316
	air	41.2	290	1261
3.3 × 10 <sup>-5</sup>	air	39.4	270	1223
	water	38.7	288	1200
<u>Ni-24.8Al + 500 ppm B</u>				
3.3 × 10 <sup>-3</sup>	oxygen	25.4	306	801
	air	18.1	290	671
	water	12.7	297	561
<u>Ni-25.2Al + 500 ppm B</u>				
3.3 × 10 <sup>-3</sup>	air	8.4	221	300
	water	4.7	219	270
<u>Ni-25.2Al + 1000 ppm B</u>				
3.3 × 10 <sup>-3</sup>	oxygen	18.6	301	566
	air	10.2	344	552
	water	6.1	304	398



# MICROSTRUCTURE AND MECHANICAL PROPERTIES OF Fe-40Al-0.6C

Lixin Pang and K.S. Kumar

Division of Engineering  
Brown University  
Providence, RI 02912

## Abstract

In this investigation, a cast, homogenized and hot-extruded Fe-40 at.%Al alloy containing 0.6 at.% C was characterized in terms of its microstructure and tensile properties. In the as-extruded condition, a three-phase microstructure consisting of B2 FeAl, a perovskite-type carbide ( $\text{Fe}_3\text{AlC}$ ) and graphite was present. The carbides were lath-shaped and present at grain boundaries and in the grain interior. A variety of heat treatments were undertaken to determine the stability of both, the graphite and the carbides in this alloy. Quenching and aging studies were performed to explore the potential for age-hardening. Tensile tests were performed as a function of temperature on the as-extruded material, and at room temperature on extruded and heat-treated alloys. Upon aging a quenched alloy, excess vacancies coalesce and precipitate as loops initially; this is followed by the precipitation of fine carbides at longer aging times, thereby relieving supersaturation. The resulting tensile properties are a consequence of the complicated interplay between point defect hardening and solid solution hardening in the early stages of aging that transition with aging time to work hardening from the dislocation loops and precipitation hardening. The resulting fracture surfaces were characterized. Intergranular failure dominated, emphasizing the role of environmental effects. The possible beneficial role of quenched-in vacancies acting as hydrogen traps in the grain and delaying the onset of intergranular fracture is discussed.

## Introduction

Iron aluminides based on FeAl (B2) have excellent oxidation and corrosion resistance because they are capable of forming protective oxide scales at elevated temperatures in hostile environments. For example, they have excellent oxidation resistance up to 1000°C. When tested in a sulfidizing environment at 800°C, these aluminides exhibit corrosion rates that are lower by a couple of orders of magnitude than those of promising iron-based alloys including coating materials. Further, iron aluminides offer relatively low material costs, possess high stiffness and are less dense (by ~25% for Fe-40Al) than steels. Thus, these materials are viewed as attractive alternatives to stainless steels. The major drawback of these iron aluminides is their poor strength and creep resistance above 600°C. Depending on their aluminum concentration, they also exhibit varying degrees of sensitivity to environmental embrittlement at room temperature.

Phase diagram information for the binary Fe-Al system [1] indicates that a large solid solution range exists for the B2 phase field, leading to flexibility in the chemical composition of the alloy. Of the various alloy compositions investigated to date, Fe-40Al appears to have a good combination of strength, creep resistance, low-temperature ductility and oxidation resistance. The Fe-40Al binary system undergoes an order-disorder transition at ~1200°C; at higher temperatures the compound has a bcc structure. The melting temperature for Fe-40Al is about 1400°C.

The microstructure-property relationships in FeAl have been discussed in detail in several recent reviews [2-5]. A number of investigators have examined the mechanical properties of single and polycrystalline FeAl in compression and tension at various temperatures [6-12]. Stoichiometric FeAl was found to be brittle by Mendiratta et al. [12], who noted pre-yield intergranular failure below 723K in fine grained Fe-50Al. Thermal vacancy retention by quenching is recognized as being responsible for hardening of the alloys at low temperatures. Contrary to this behavior, Fe-40Al retains strength to higher temperatures than stoichiometric FeAl and exhibits 2.5% elongation at room temperature. Recently, Liu et al [13], have shown that moisture-induced environmental embrittlement is a cause of limited room temperature ductility, especially in Fe-rich FeAl. Crimp et al. [14] found that B additions increased ductility and changed the fracture mode from intergranular to intragranular fracture at room temperature. In addition to the extrinsic brittleness, the grain boundaries in FeAl are known to become intrinsically weak with increasing Al concentration, with fracture becoming increasingly intergranular as the alloy approached the stoichiometric composition [4]. Thus, in general there are two major sources of brittleness in FeAl alloys: environmental (extrinsic) and weak grain boundaries (intrinsic). The relative dominance of each depends on the extent of deviation from stoichiometry.

In several studies in the Fe-Al system, carbon has been shown to play an important role either as a solid solution element or participating as a component in a second phase (carbide or graphite). Carbides were found in Fe-Al alloys either as intentional additions or as a result of contamination [15-19]. In most cases, they take the form of a perovskite carbide which has the formula  $\text{Fe}_3\text{AlC}_x$  [15-17, 19]. The presence of these carbides at grain boundaries is believed to have a deleterious effect on ductility and strength [19] and appropriate heat treatments can alleviate this effect. Morris et al [16] found that considerable strengthening can be achieved at ambient temperature by

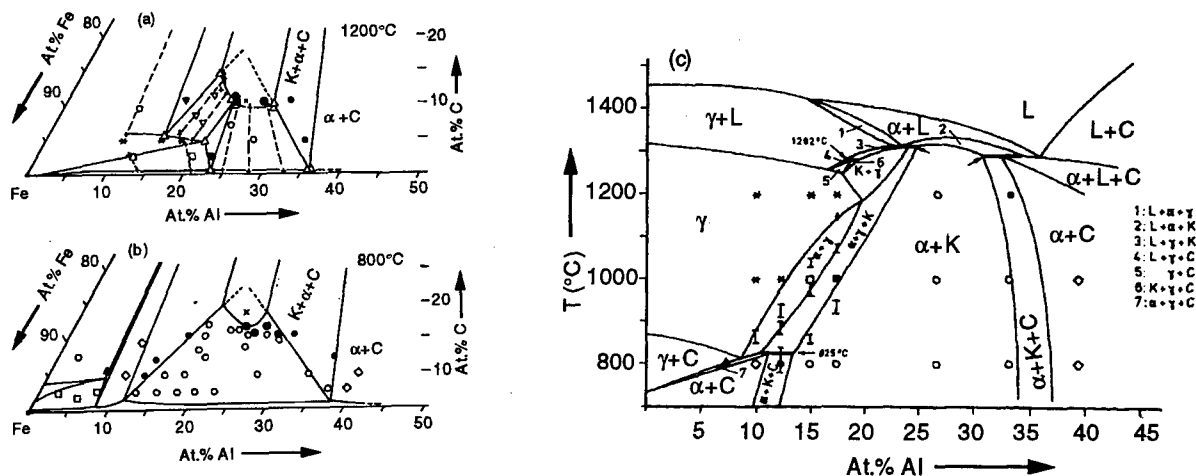


Figure 1: Phase equilibria at a) 1200°C, b) 800°C, and c) at a constant carbon concentration of 5 at.% in the Fe-Al-C system according to Palm and Inden [22].

the addition of carbon, if very fine carbides are distributed evenly in the FeAl matrix. Also, the addition of carbon has been shown to be important to the weldability of FeAl [4]. However, there have only been limited studies of the phase equilibria in the ternary Fe-Al-C system [20-22] and the influence of temperature on the size and shape of the phase fields associated with the binary FeAl and  $\text{Fe}_3\text{Al}$  compounds, particularly for low carbon levels ( $\leq 2$  wt.%) have not been well established.

According to the limited information on the ternary Fe-Al-C phase diagram, four phases can exist in the Fe-rich end depending on the exact levels of carbon present. They are:  $\alpha$ ,  $\gamma$ , K and free graphite. At low carbon concentrations, the bcc ( $\alpha$ ) phase exists in the disordered state A2, as well as in the long range ordered states of the type B2 and  $\text{DO}_{19}$ . At higher C-concentrations, the fcc solid solution ( $\gamma$ ) is stable, and a ternary intermetallic phase denoted as K-phase (based on the perovskite structure) is additionally present. It can be considered as an ordered fcc arrangement of Fe and Al of type  $\text{L}_{12}$ , with C atoms in the octahedral interstices. In several studies regarding the microstructure of FeAl alloy with C [15-17], the perovskite precipitates were identified as a sub-stoichiometric, carbon-deficient  $\text{Fe}_3\text{AlC}_x$ , or more specifically as  $\text{Fe}_3\text{AlC}_{0.5}$ . More recently, Palm and Inden [22] have referred to this compound as "an ordered solid solution stabilized by carbon" rather than regarding it as a carbide; this was accounted for by assigning it a compositional range of existence of the form  $\text{Fe}_{4-y}\text{Al}_y\text{C}_x$  where x can vary from 0.8 to 1.2 and y between 0.42 and 0.71.

Four invariant reactions are known to occur in the ternary Al-Fe-C system. These include  $U_1: L + \alpha \leftrightarrow K + \gamma$ ,  $U_2: L + K \leftrightarrow \alpha + C$ ,  $L + K \leftrightarrow \gamma + C$ , and  $U_4: K + \gamma \leftrightarrow \alpha + C$ . ( $\alpha$  is the bcc/B2/ $\text{DO}_{19}$  phase; K is the ternary carbide and C is the graphite) There has been some disagreement about the exact temperature at which each of these reactions occurs, although the recent work of Palm and Inden [22] reported these temperatures to be 1315°C, 1295°C, 1282°C, and 825°C respectively. In addition, Palm & Inden [22] used electron microprobe analyses of quenched samples and high temperature X-ray diffraction experiments to generate three isothermal sections at 800, 1000 and 1200°C and three vertical sections. According to Palm and Inden [22], no new phases formed below the invariant reaction  $U_4$  and, except for changes in solubility, the isotherm just below  $U_4$  reflected the situation that would be present at lower temperatures. Two isotherms, (1200°C and 800°C) and a vertical section at a constant carbon concentration of 5 at.% confirm that in the vicinity of Fe-40Al, the  $\alpha$ -carbide+ graphite phase field shifts to higher Al concentration with decreasing temperature (Figure 1). This implies that with increasing temperature, the carbides will completely dissolve in the matrix yielding a two-phase mixture; from the vertical section, it is also possible to infer that, on heating to higher temperatures, a liquid phase forms to generate a three-phase structure of  $\alpha+L+C$ . Thus, there exists a temperature range for the Fe-40Al alloy between the carbide solvus and the alloy solidus that consists of a two-phase mixture of  $\alpha+C$ . In principle, it should be possible to solutionize such an alloy in this temperature range and quench it to retain the carbon in supersaturation; subsequent aging should make the alloy amenable to precipitation hardening. It is also noted from Figure 1 that the compositions of the K-phase stretches over a wide composition range and the theoretical Fe/Al ratio of 3 : 1 is only a mean value.

In this investigation, the microstructure of an Fe-40 at.% Al alloy containing 0.6 at.% C (0.17 wt.% C) has been examined in detail in the as-extruded condition, and following a variety of heat treatments. The potential for precipitation hardening such an alloy has been explored. Tensile specimens were obtained from the extruded rods and tested as a function of temperature. Tensile tests were also conducted at room temperature as a function of heat treatment to understand the effect of microstructure on strength and ductility. Fracture surfaces were examined and observations were correlated with measured properties.

#### Experimental Procedure

Sections of 99.99% pure aluminum and an Al-Fe master alloy were melted in the appropriate proportion to produce an Fe-40 at.% Al alloy in a zirconia crucible by induction melting; an ingot of the alloy was obtained by tilt-pouring the melt into a graphite mold. The ingot was homogenized to eliminate coring, canned in a mild steel container and extruded into a cylindrical rod at 1000°C using an extrusion ratio of 16:1. The extrusion was performed at the NASA Lewis Research Center in Cleveland, OH.

Microstructures in the extruded, and in the extruded and subsequently annealed conditions were examined by optical microscopy using Kellers etching reagent. X-ray diffraction (XRD) was performed using Cu K $\alpha$  radiation (40KV, 35mA). Bulk X-ray diffraction was unsuccessful in revealing the presence of minor quantities of second phase that was observed by optical microscopy. Therefore, the second phase particles were electrolytically extracted from the matrix. The process involved an electrochemical cell made up of 7% HCl solution in methanol, a voltage of 15V and varying currents between 20mA and 80mA. A stainless steel cathode was employed, the anode being the Fe-40 at.% Al based alloys. The Fe-40Al matrix was dissolved under these conditions, leaving the second phase particles to settle at the surface of the specimen; the specimen was carefully dried and examined by X-ray diffraction. Differential thermal analysis (DTA) was performed using a DSC 2910 differential scanning calorimeter equipped with a DTA 1600 high temperature heating cell. Specimens were generally solid pieces weighing approximately 100 mg and were heated at 10°C/min. to the desired temperatures. From the results of DTA scans of the as-extruded material and the extruded+annealed material, endotherms and exotherms corresponding to phase dissolution and precipitation were recognized; the temperatures relating to these events were obtained.

A series of heat treatments were undertaken to understand the origin of each of the endotherms and exotherms in the DTA scans. Small specimens of the FeAl + 0.6 at.% C alloy were heated to temperatures in the range 850°C to 1200°C in 50 degree intervals, held at temperatures for 30 minutes and then quenched to room temperature. These specimens were carefully ground and polished, etched and examined using the optical and scanning electron microscope. Some of the quenched specimens were also subjected to DTA to verify their potential for age-hardening. These DTA scans were conducted in the temperature range 20°C to 600°C. In such scans, exotherms would correspond to precipitation, occurring to relieve the supersaturation

resulting from quenching. Temperatures at which such exotherms occur were identified so that subsequently, isothermal heat treatment could be performed as a function of time to understand the aging behavior.

The aging behavior of Fe-40 at.% Al with 0.6 at.% C was studied by optical and transmission electron microscopy. Transmission electron microscope foils were prepared by jet polishing 3-mm disks with an electrolyte of 20% HNO<sub>3</sub> in methanol at -26°C and 15V and subsequently further ion milling them to increase the electron-transparent areas. A Philips 420 transmission electron microscope (TEM) operating at 120 kV was used. Matrix stoichiometry and precipitate chemistry were determined by EDX attached to the Philips 420 transmission electron microscope. Selected area diffraction techniques were used to confirm the identity of the precipitated phases as well as to obtain the precipitate-matrix orientation relationships.

The variation in yield strength and ductility of the alloy in the as-extruded condition as a function of temperature was determined through a series of uniaxial tensile tests. A schematic of the tensile specimen used in the study together with its dimensions and a photograph of the actual specimen are all shown in Figure 2. Specimens were electro-discharge machined with the gauge length lying along the extrusion axis, ground and polished, and tested in tension using a nominal strain rate of  $4 \times 10^{-4}$ /s. The resulting fracture surfaces were examined using a scanning electron microscope (SEM). Tensile specimens were also quenched from 1000°C to dissolve the precipitates present in the extruded material; they were then ground, polished and carefully examined to ensure the absence of cracks or grain boundary melting. Such specimens were tested either in the as-quenched condition, or following low-temperature aging for various times. Fracture surfaces from such specimens were also characterized.

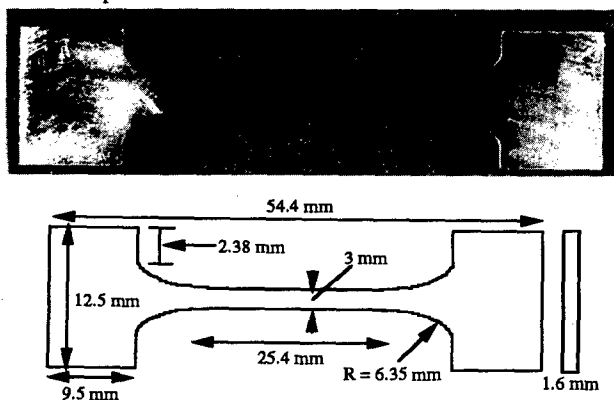


Figure 2: A schematic of the tensile specimen used and a photograph of the actual specimen.

## Results

### As-extruded microstructure:

Optical metallography of the transverse section in the as-extruded condition revealed a fine distribution of needle-like precipitates both at grain boundaries and in the grain interior; in addition, the presence of globules of a dark precipitate both at grain boundaries and in the grain interior can also be observed. A representative micrograph is shown in Figure 3. The average grain size in this as-extruded condition was ~80  $\mu$ m. Chemical analysis of the extruded specimen yielded a carbon level of 0.17 wt.% which translates to 0.6 at.%. The source of carbon in the alloy was either the graphite mold into which the molten metal was poured, or the Fe-Al master alloy. X-ray analysis of the as-extruded specimen showed the typical B2 structure of Fe-40Al. The intensity of the (111) superlattice peak was significantly higher than that reported by the JCPDS card file, suggesting a [111] texture along the extrusion direction. This is consistent with result from the literature [23]. No additional peaks corresponding to the precipitate phase(s) observed by optical microscopy were present. X-ray analysis of the surface-extracted sample however confirmed the presence of Fe<sub>3</sub>AlC<sub>0.5</sub> (note: in the rest of the paper, we refer to the perovskite carbide by this formula although we did not ascertain that this formula is correct). It is believed that the fine needle-like precipitates observed at the grain boundaries and in the grain interior are Fe<sub>3</sub>AlC<sub>0.5</sub>. X-ray analysis however didn't show any trace of the third phase corresponding to the dark globular

phase. In order to identify the crystal structure of the dark phase, TEM, SEM and TEM in conjunction with EDX capabilities were employed. A bright field TEM image of the dark phase (Figure 4) showed a completely different microstructure from the FeAl matrix and Fe<sub>3</sub>AlC<sub>0.5</sub> precipitates. The corresponding SAD pattern (inset-Figure 4) shows a very good fit with graphite. The result of the EDX analysis of the dark phase in TEM indicated that the primary element present in this area was C. EDX analysis of the dark phase using the SEM confirmed the result from TEM. Based on these observations, the dark precipitates were identified as free graphite.

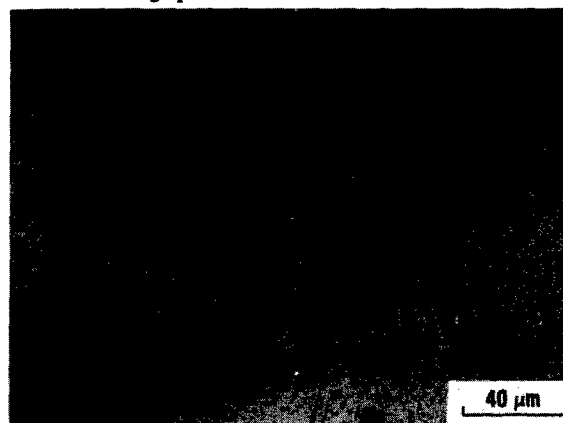


Figure 3: Optical micrograph of the transverse section of Fe-40Al+0.6C in the as-extruded condition.



Figure 4: A bright field TEM image and the associated SAD pattern of the graphite particle.

Differential thermal analysis of the Fe-40Al + 0.6 at.% C showed four endotherms on heating and the corresponding exotherms on cooling (Figures 5a,b). Two weak peaks occur at ~950°C and ~1050°C (Figure 5b). The third endothermal peak is strong and asymmetric, which is typical of an order-disorder transition. In Figure 5a, for the case of initially ordered Fe-40 at. % Al alloy, there is a gradual disordering on heating above 1200°C (at a heating rate of 10°C/min.), and rapid disordering on approaching  $T_c$  near 1280°C. By 1300°C, disordering is completed. On cooling at the same rate, reordering occurs rapidly just below 1280°C. From such profiles, the order-disorder transition temperature  $T_c$  is determined to be ~1280°C. Comparing this observation to the Fe-Al binary phase diagram, it is seen that the order-disorder transition temperature obtained is ~80°C higher. Similar trends were also recognized by Palm and Inden [see Table 2 and Figure 10 of ref. 22]. This implies that the introduction of carbon in FeAl stabilizes the ordered B2 structure with respect to the disordered A2 structure. The fourth endotherm (and the corresponding exotherm) is located at ~1380°C, which indicates the melting temperature of the alloy.

### Annealed microstructure:

The microstructure of Fe-40Al containing 0.6% C in the as-annealed condition is shown in Figure 6. A comparison of the microstructure to that observed in the as-extruded condition shows the shape of the precipitates in both cases to be lath-like. Precipitate free zones were observed in both conditions. It's worth noting that the size of the precipitates in the annealed condition were much larger than those from the as-extruded condition implying that significant coarsening of

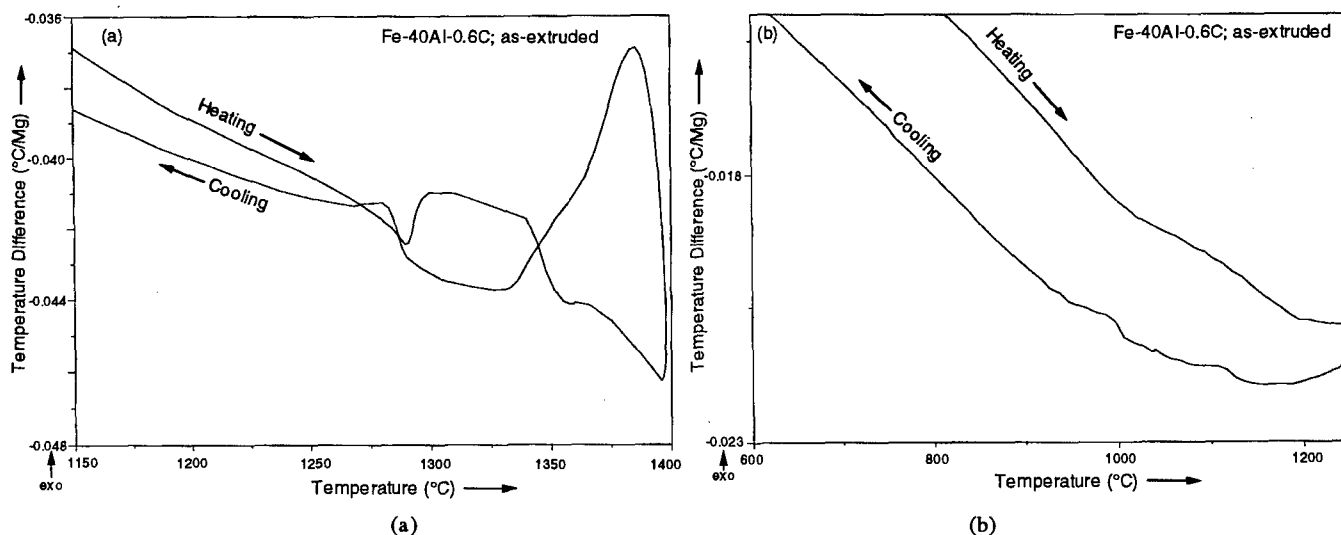


Figure 5: DTA scans in the temperature regime a) 1150 - 1450°C, and b) 600 - 1250°C for as-extruded Fe-40Al+0.6C.

the  $\text{Fe}_3\text{AlC}_{0.5}$  precipitates had occurred. Another important feature of the annealed microstructure is that instead of the globular shape observed in the as-extruded condition, the graphite in the annealed condition appeared to bear a flake/"star-shape" which is similar to one of the several basic shapes of graphite in cast iron.

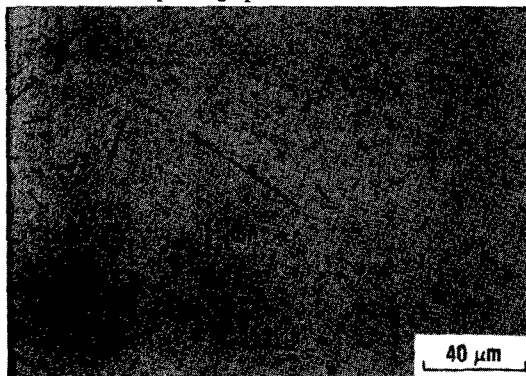


Figure 6: The microstructure of Fe-40Al+0.6C in the as-annealed condition.

#### Quenched microstructure:

Phase transformation in the Fe-40 at.% Al alloy was studied by differential thermal analysis (DTA), optical microscopy, X-ray diffraction, SEM and TEM. As previously mentioned, four endothermal peaks were observed upon heating the as-extruded material. The first endotherm at  $\sim 950^\circ\text{C}$  corresponds to the dissolution of the  $\text{Fe}_3\text{AlC}_{0.5}$  precipitates. This was supported by results from optical microscopy and X-ray analysis of quenched specimens. Selected microstructures of the Fe-40 at.% Al alloy quenched from  $850^\circ\text{C}$  to  $1150^\circ\text{C}$  in  $50^\circ\text{C}$  intervals are shown in Figures 7a-d. Below  $950^\circ\text{C}$ , the  $\text{Fe}_3\text{AlC}_{0.5}$  precipitates were stable but the amount decreased with increasing temperature. At  $1000^\circ\text{C}$ , there were no  $\text{Fe}_3\text{AlC}_{0.5}$  precipitates left in the microstructure, indicating that these precipitates had dissolved completely. The second endotherm was noted at  $\sim 1050^\circ\text{C}$  and this is believed to be a consequence of grain boundary melting. As shown in Figures 7a-d, below  $1000^\circ\text{C}$ , the dark phase, identified as free graphite, has a globular shape. At  $1100^\circ\text{C}$ , no graphite globules were observed on the grain boundaries, but a continuous thin layer of the dark phase was found instead. According to the phase equilibria of Palm and Inden [22], this is a consequence of the reaction  $\alpha + \text{C} \leftrightarrow \alpha + \text{L} + \text{C}$ . Above this temperature, the quenched material became noticeably brittle and significant quenching cracks were observed. Based on the experimental observations listed above, the phase equilibria of the Fe-40Al with 0.6 at.% C examined in this effort can be summarized as the following:

$$\begin{aligned} T < 950^\circ\text{C}: & \alpha + \text{K} + \text{C} \\ 950^\circ\text{C} < T < 1050^\circ\text{C}: & \alpha + \text{C} \\ 1050^\circ\text{C} < T < 1380^\circ\text{C}: & \alpha + \text{L} + \text{C} \end{aligned}$$

#### Aged microstructure:

A DTA scan of a specimen of Fe-40 at.% Al + 0.6 at.% C that had been previously quenched from  $1150^\circ\text{C}$  is shown in Figure 8a. Quenching from  $1150^\circ\text{C}$  to room temperature is anticipated to provide carbon supersaturation in the matrix. The purpose of performing a DTA experiment on the quenched specimen was to see if low-temperature precipitation occurred and whether the alloy demonstrated a potential for age-hardening. Two exothermal peaks were observed: one at  $\sim 260^\circ\text{C}$  and the other one at  $\sim 400^\circ\text{C}$ . Both peaks disappeared during the second and third cycle of DTA heating and cooling of the specimen, thereby giving the baseline for the two peaks (these second and third cycles are not shown in Figure 8a to keep it from looking crowded). In order to determine the origin of these two peaks, a substantially carbon-free Fe-40Al extruded specimen was obtained from Oak Ridge National Laboratory. Optical microscopy verified the absence of precipitates at grain boundaries and grain interior. A portion of the extruded specimen was heat treated and quenched from  $1200^\circ\text{C}$ . A DTA scan of this quenched specimen is shown in Figure 8b. An exothermic peak similar to the C-containing alloy, is noted at  $\sim 280^\circ\text{C}$  although the second larger peak at  $\sim 400^\circ\text{C}$ , evident in Figure 8a, is now absent. Subjecting the specimen to a second heating cycle in the DTA eliminates the  $260^\circ\text{C}$  peak, demonstrating the irreversible nature of the reaction responsible for the exotherm. It is thought that the exotherm observed at  $\sim 260^\circ\text{C}$  is a consequence of excess vacancy coalescence into dislocation loops.

Transmission electron microscopy analysis was performed on specimens aged at  $400^\circ\text{C}$  for 6 hours and  $520^\circ\text{C}$  for 140 hours. A bright field image of the specimen aged for 6 hours at  $400^\circ\text{C}$  (Figure 9a) shows the presence of fine precipitates that are uniformly distributed in the matrix. An SAD pattern using the matrix  $[001]$  zone axis shows streaking in addition to the matrix spots (Figure 9b). A computer-generated diffraction pattern verifies that these streaks corresponds to thin plates of  $\text{Fe}_3\text{AlC}_{0.5}$  precipitates. The following orientation relationship exists between the matrix and the precipitate:

$$[001]_m // [\bar{1}\bar{1}0]_p; (110)_m // (111)_p$$

A computer-generated diffraction pattern using the above orientation relationships and  $[112]$  as the thickness direction of the precipitates (Figure 9c) gives a good fit with the experimental SAD pattern obtained from TEM. Thus, the second exothermal peak at  $\sim 400^\circ\text{C}$  corresponds to the precipitation of  $\text{Fe}_3\text{AlC}_{0.5}$ . Above  $400^\circ\text{C}$ , the precipitates coarsen with increasing time. A bright field image of Fe-40Al quenched and aged for 140 hours at  $520^\circ\text{C}$  is shown in Figure 9d. In comparison to the specimen aged at  $400^\circ\text{C}$ , the precipitates are significantly coarser and appear to have a lath morphology. In addition, in the background dislocations are observed, some with the appearance of loops. Whether these dislocations are a consequence of excess vacancy coalescence or due to precipitate/matrix mismatch strain, or both remains to be ascertained. Aging at even higher temperature will increase the precipitate coarsening rate and this was verified by heat-treating a quenched specimen at  $720^\circ\text{C}$  for 48h where the precipitates could easily be resolved at the optical microscope level.

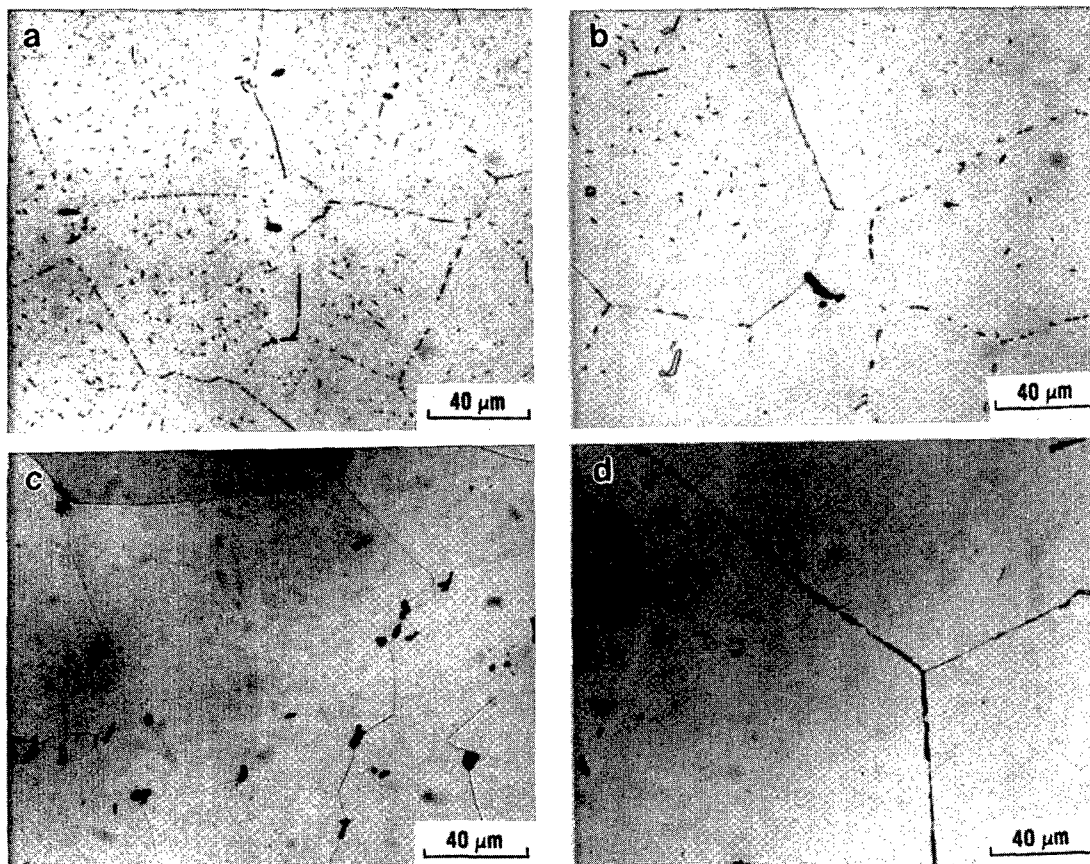


Figure 7: Microstructures of the Fe-40Al+0.6C alloy quenched from a) 850°C, b) 950°C, c) 1000°C, and d) 1100°C.

#### Mechanical Properties:

The effect of temperature on the yield strength, elongation and work-hardening rate in uniaxial tension for the *as-extruded* material (grain size  $\sim 80 \mu\text{m}$ ) is shown in Figures 10a-c. These tests were conducted in air at an initial strain rate of  $4 \times 10^{-4} \text{s}^{-1}$ . Yield strength decreases continuously with increasing temperature from 512 MPa at room temperature to 344 MPa at 600°C. Ductility at room temperature was 2.3% that increased gradually to 6.9% at 300°C; at the higher test temperatures of 450°C and 600°C, ductility increased sharply to  $\sim 30$  percent. This is suggestive of a ductile-brittle transition temperature in the vicinity of 350-400°C. It is interesting to note that there is not a discontinuous drop in yield strength however in this temperature range. An estimate of the work-hardening rate in the 0.2%-to-1.0% plastic strain regime was obtained from the load-displacement curves (Figure 10c). Attempts to accurately determine work-hardening rates from the load-displacement graphs at discrete strains such as 0.2% and 1.0% were not successful. Instead, the rate was obtained by using a linear fit between 0.2% and 1.0% plastic strain. The work hardening rate remains at  $\sim 8 \text{ GPa}$  ( $\sim 0.1$  Shear Modulus) in the temperature range 25°C-300°C before starting to decrease at higher temperatures. At 600°C, an initial work softening followed by steady-state flow was noted. An examination of the fracture surface of the specimen tested at room temperature revealed a predominantly intergranular failure mode (Figure 11a). An examination of the grain boundary surfaces however showed that these surfaces were not smooth and that crack propagation along these surfaces was often interrupted by the lath-shaped perovskite carbides at the boundaries (Figure 11b). These precipitates appear to deflect the crack into the grains, although the crack appears to return to the grain boundaries. This lends the fracture surface a rough appearance. The fracture surfaces of the specimens tested at 300°C and 450°C are shown in Figures 11c and 11d respectively. Whereas the 300°C specimen failed after  $\sim 7$  percent plastic strain, the 450°C specimen deformed to a strain of  $\sim 30$  percent. The 350°C specimen fails predominantly by intergranular fracture although there is occasional evidence of transgranular cleavage. As in the room-temperature-tested specimen, the fracture surface has a rough appearance indicative of

crack interruption by grain boundary precipitates. The 450°C specimen that failed following  $\sim 30\%$  tensile plastic strain exhibited a mixture of intergranular failure and transgranular cleavage. The grains are elongated and the boundaries continue to exhibit a rough surface, again reflecting the effect of the grain boundary precipitates.

Tensile tests were also conducted at room temperature on several specimens that had been subjected to a variety of heat treatments that included a water quench from high temperatures (1000°C or 1050°C) and subsequent low-temperature aging. The average grain size in these quenched and aged specimens was  $\sim 140 \mu\text{m}$ . The results obtained in terms of yield stress, fracture stress and ductility for these specimens are summarized in Table I. The as-quenched specimens (quenching temperatures of 1000°C and 1050°C) as well as the specimen quenched from 1000°C and aged at 300°C for 1h failed prior to macroscopic yielding; the fracture strength however was high, being as high as double the yield strength in the extruded material and significantly higher than the fracture stress recorded in the as-extruded condition as well. Approximately 80% of the fracture surface constituted intergranular failure while the rest was indicative of transgranular cleavage. A representative fracture surface from the specimen quenched from 1000°C and subsequently heat treated for 1h at 300°C (Figure 12a) shows smooth grain boundaries (unlike the as-extruded material) interspersed with transgranular cleavage.

A series of specimens were quenched from 1000°C and subsequently aged at 400°C for 1h, 2h, 6h and 24h and 168h. The results of tensile tests on these specimens indicate that the yield strength has dropped significantly relative to the as-quenched condition but is still higher than that measured in the as-extruded material. Some ductility was regained and was 0.6% for the specimen aged for 24h at 400°C and 1.2% for the specimen heat treated at this temperature for 1 week (168h). One specimen was heat treated at 500°C for 24 h and tested. A substantial drop in yield strength was noted, the strength being lower than that obtained for the extruded condition (this suggests the presence of a high vacancy concentration in the extruded condition); the ductility in the

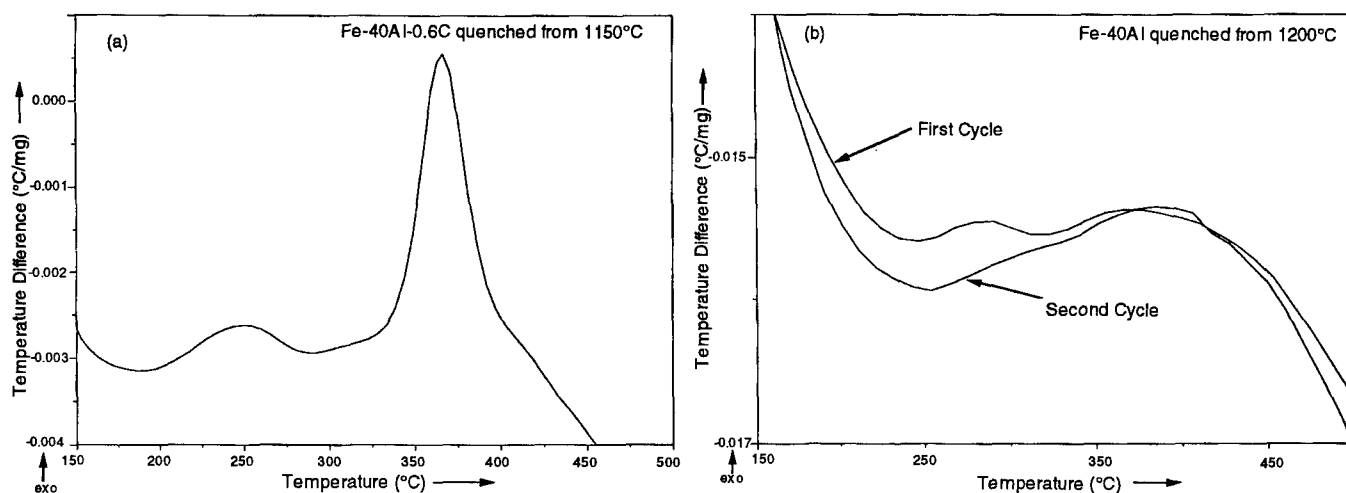


Figure 8: DTA scans of a) Fe-40Al+0.6C quenched from 1150°C, and b) Fe-40Al quenched from 1200°C.

material was 4.0%, being higher than that for the extruded material and similar to values reported previously for B-doped Fe-40Al [24].

Table I: Effect of Heat Treatment on the Tensile Properties\* of Extruded Fe-40Al-0.6C.

Condition	Yield Strength (MPa)	Fracture Strength (MPa)	Ductility (%)
As-Extruded	512	665	2.3
Extruded + annealed at 400°C/72h + 500°C/24h	316	584	4.4
Quenched from 1050°C	----	963	0
Quenched from 1000°C	----	824	0
Quenched from 1000°C + aged at 300°C/1h	1010	1010	≤0.2
Quenched from 1000°C + aged at 400°C/1h	735	763	0.5
Quenched from 1000°C + aged at 400°C/6h	752	757	0.3
Quenched from 1000°C + aged at 400°C/24h	684	720	0.6
Quenched from 1000°C + aged at 400°C/168h	614	679	1.2
Quenched from 1000°C + aged at 500°C/24h	323	579	4.0

\* all tests were conducted in air at an initial strain rate of  $\sim 4 \times 10^{-4} \text{ s}^{-1}$

Fracture surface of the tensile specimen heat treated at 400°C for 24h following the 1000°C quench was examined; fracture had occurred by intergranular crack propagation (Figure 12b). The grain boundaries were smooth with occasional interruptions from the graphite particles at these boundaries. Based on the smoothness of the fracture surface, it is concluded that if there was any grain boundary precipitation following the 24h exposure of the quenched material to 400°C, it had no substantial effect on crack propagation. The fracture surface of the specimen that was quenched and aged at 500°C for 1 h (Figure 12c) showed intergranular failure that was mixed with some transgranular rupture; the regions exhibiting transgranular failure showed a rough surface appearance that at higher magnifications (Figure 12d) is indicative of microvoid coalescence.

### Discussion

The presence of 0.6% carbon in this Fe-40Al alloy leads to the formation of the perovskite carbide  $\text{Fe}_3\text{AlC}_{0.5}$  and free graphite. These carbides are found, both in the interior of grains and at the grain

boundaries and exhibit a lath morphology. Likewise, the graphite is present as globules at grain boundaries and within the grains. The carbides are not stable in the FeAl matrix at elevated temperatures, and upon heating in excess of 900°C, they dissolve rapidly in the matrix; above 1000°C they are completely dissolved. Around 1100°C, the globular graphite particles participate in a reaction containing a liquid phase that causes the graphite to coat the grain boundaries as a continuous film, rendering the material brittle. Such an alloy provides an opportunity to dissolve the carbides via a solution treatment and re-precipitate the carbides in a fine uniform dispersion by aging. This could render the material stronger, and by dispersing slip, could perhaps render the material more ductile. Potential for such an aging response was verified by conducting a differential thermal analysis scan of the material in the quenched condition. In the previous section, it was speculated based on DTA observations upon heating the quenched material with and without carbon, that the weak endotherm observed at  $\sim 260^\circ\text{C}$  may have been a consequence of vacancy coalescence into loops. To confirm this possibility, TEM foils were prepared from the grip section of the as-quenched tensile specimen (1000°C quench), from a specimen that had been quenched and aged at 300°C for 1 hour and from the specimen that had been quenched and aged at 400°C for 1 h. Representative bright field images of the as-quenched material confirms the absence of any precipitates at grain boundaries and a low dislocation density in the grain interior (Figures 13a,b). It is also interesting to note that these dislocations are rather straight and there are no dislocation loops present. In general, following quenching, a non-equilibrium vacancy concentration is retained in an alloy and produces point defect hardening; during prolonged aging, these vacancies may be precipitated out as loops. If the free-vacancy concentration is low, due to a high vacancy-solute binding energy, dislocation helices rather than loops may result from vacancy interactions with matrix dislocations. The absence of loops and/or dislocation helices implies that the quenched-in vacancies are not mobile at room temperature or during the quench, and is indicative of a high vacancy binding energy. In the specimen that had been aged at 300°C for 1 hour however, a large number of small loops were recognized (Figure 13c) and this is consistent with the DTA observations of an exotherm around 260°C. Clearly, these vacancies are mobile at 300°C. The bright field image from the specimen aged at 400°C for one hour shows a high concentration of large loops (Figure 13d); in addition a loop-free zone is observed adjacent to the grain boundary and also a decrease in loop size as one moves into the interior of the grains.

In an early study of Fe-42Al single crystal, Fourdeux and Lesbats [25] performed TEM analysis on specimens quenched from 1000°C and subsequently annealed at 400°C and concluded that quenched-in vacancies did not precipitate as loops resulting from vacancy clusters but precipitated heterogeneously on existing matrix dislocations. They argued this to be a consequence of difficulties associated with the nucleation of loops. This is in contrast to the present

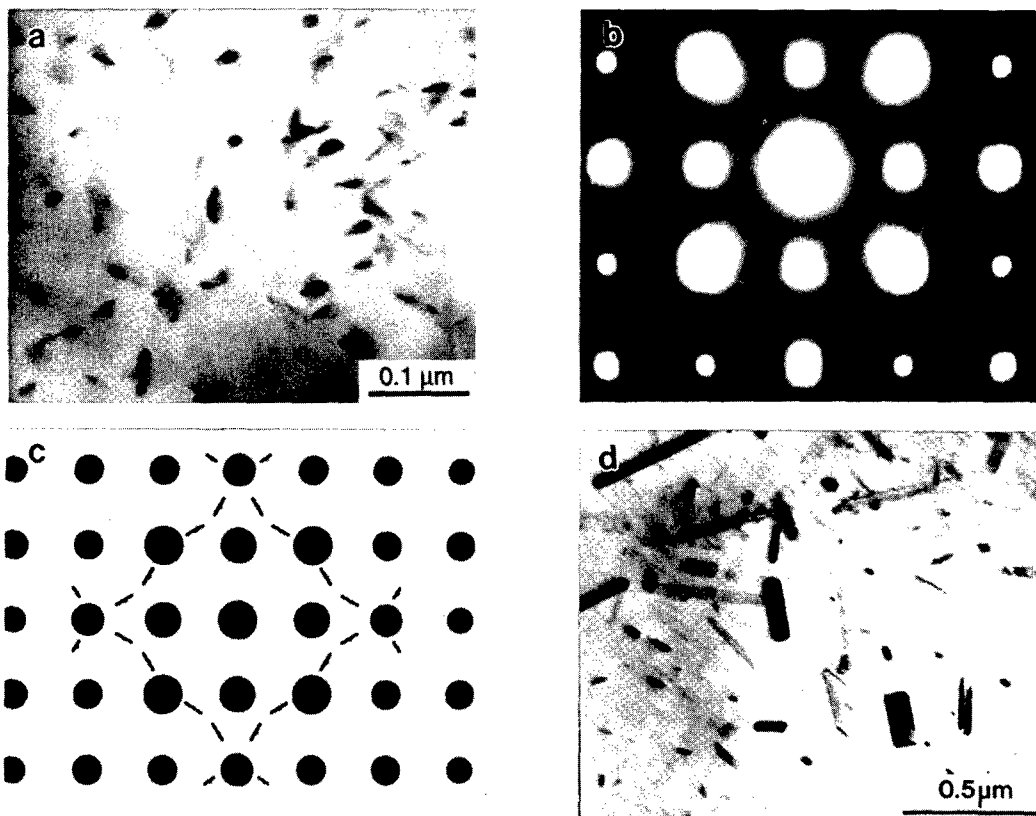


Figure 9: Transmission electron microscopy of Fe-40Al+0.6C quenched and aged at 400°C for 6 h: a) bright field image, b) SAD pattern using matrix [001] zone axis, and c) a computer-generated diffraction pattern. In d) a bright field image of a specimen aged at 520°C for 140 h is shown.

study where dislocation loops were clearly observed (Figures 13c and 13d). Junqua et al. [26] also reported the presence of loops and helices in Fe-40Al that had been quenched from the temperature range 600-1200°C and then aged in the temperature range 300-400°C, heat treatments that are similar to those used in the present study.

It is well known that FeAl retains a high vacancy concentration even if it is air-cooled from a high temperature, and typically, a low-temperature anneal (~400°C) for extended times is used prior to mechanical testing [27-29] to ensure that contributions from point defect hardening is minimized. In this investigation, the extruded material was not given a low-temperature anneal prior to mechanical testing as a function of temperature. The observed yield strength levels are somewhat higher than those typically reported for binary Fe-40Al alloys in the extruded and annealed condition suggesting a possible contribution from vacancy hardening, although the role of the carbides in providing some strengthening cannot be discounted.

In considering the work hardening rate and ductility of binary Fe-40Al alloys, it is now well established that the presence of excess vacancies not only increases the yield strength, but also decreases the ductility and the work hardening rate. When the vacancies are precipitated out as loops, ductility increases as does the work hardening rate [14, 30]. The grain sizes in the present study were ~80 μm in the as-extruded condition and ~140 μm in the quenched and heat treated conditions in contrast to the earlier studies [14, 30] where the grain sizes were 12 μm and 31 μm. More recently, Klein and Baker [28] have reported on the beneficial effects of a low-temperature, vacancy-relieving anneal on the ductility at room temperature of a binary Fe-45Al alloy when tested in air. In that study [28] the investigators have also examined the influence of grain size on these properties. An as-extruded specimen with a grain size of 80 μm (similar to the grain size of the extruded material in this study) had a fracture strength of 790 MPa and failed elastically, whereas when it was provided a suitable heat treatment that included a homogenizing anneal, furnace cooling and a low temperature vacancy anneal, the yield strength dropped to 320 MPa and a 2% ductility was recognized. It is also interesting to note from the

work of Klein and Baker [28] that while ductility is enhanced and yield strength is lowered by precipitating the vacancies out as loops, the fracture stress is lowered too, while the fracture mode remains unchanged. Further, these observations hold for both, coarse (~230 μm) and fine (80 μm) grain sizes. Similar trends were observed in the present study where the quenched material and the material aged for 1 hour at 300°C failed at fairly high stress levels without macroscopic yielding. Upon aging these alloys at 400°C for various times, there was a noticeable decrease in yield strength, recognizable macroscopic plastic deformation but failure occurred at significantly lower stresses than it did in the quenched material and the quenched + 300°C/1 hour specimen. In the specimens used by Klein and Baker [28], unlike those in the present study, carbon or other interstitials were not present in appreciable quantities. Thus, the significant differences in fracture stress between specimens that had experienced a low temperature anneal and those that had not, must be related to vacancies in the matrix versus their collapse into loops following the low temperature anneal. Note that all specimens failed intergranularly.

It is now known [24, 31, 32] that the B2 iron aluminides fail with low ductility at room temperature (in air) intergranularly as a consequence of hydrogen embrittlement resulting from the breakdown of moisture. It is also known that the addition of boron to Fe-Al somewhat enhances the ductility. It is believed that there is a minimum hydrogen concentration that is needed at the boundary, for a particular stress level, to advance the crack. If this level of hydrogen is not available in the vicinity of the crack tip, then one can anticipate that the boundary can cope with a higher stress level. Alternately, for a given hydrogen concentration, if the stress concentration at the boundary is lowered for an applied global stress level, then the boundary can withstand a higher global stress. Either, or both of these features will influence the fracture stress. In the situation where the vacancies are present in the matrix in supersaturation, the fracture stress is high. This may be a consequence of vacancies acting as moderately strong hydrogen traps [33-35]. The hydrogen-vacancy binding energy in bcc iron has been reported to be 46 kJ/mol compared to screw dislocation cores and elastic stress fields where  $E_b = 20-30$  kJ/mol. If a similar



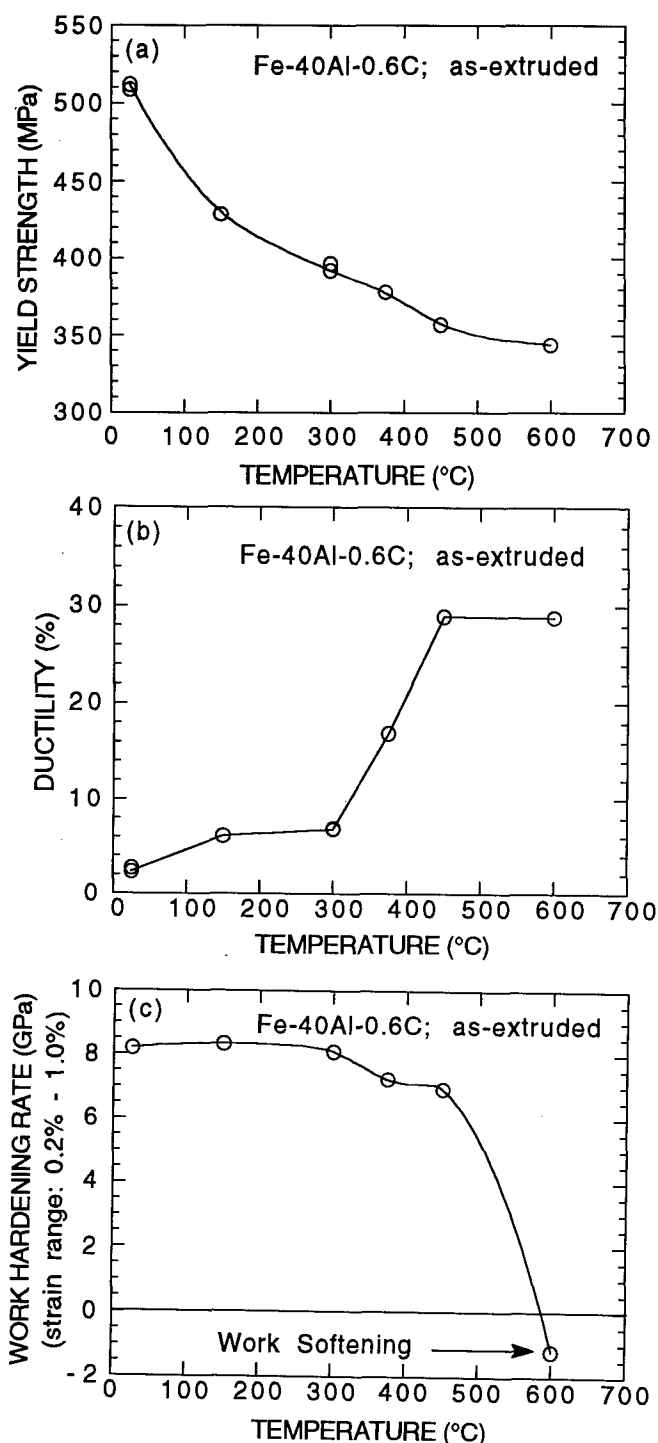


Figure 10: The effect of temperature on the a) yield strength, b) elongation and c) work-hardening rate in uniaxial tension for the as-extruded material (grain size  $\sim 80 \mu\text{m}$ ).

situation can be envisioned for the case of B2 Fe-40Al, then we can speculate that the formation of dislocation loops by vacancy coalescence during the low-temperature anneal reduces the density of these traps and promotes intergranular embrittlement at lower stresses by increasing the hydrogen concentration at the boundaries. A similar thinking has been provided by Takasugi and Hanada recently [36] in the case of  $\text{Ni}_3\text{Al}$  where they used pre-deformation to introduce lattice defects to trap hydrogen and suppress intergranular fracture. Alternately, the point defect strengthening from the vacancies can discourage dislocation motion and stress build-up at the grain boundaries, requiring higher fracture stresses. To verify if this latter mechanism indeed dominates, it

is necessary to conduct experiments that will suppress yielding without changing microstructure or test strain rate. This could perhaps be accomplished by performing biaxial tension tests on specimens containing a high vacancy concentration and comparing the fracture stress with that measured in uniaxial tension. A feature that requires emphasis is that although fracture occurs intergranularly as a consequence of environmental embrittlement, it is possible to influence the fracture stress by changing the microstructure within the grain.

With respect to mechanical properties in the aged material, it is at present difficult to isolate the microstructural features responsible for the observed mechanical behavior. In the early stages of aging, point defect hardening gives way to dislocation hardening by the coalescence of vacancies to loops. In this time frame, solid solution hardening is gradually displaced by precipitation hardening. Studies are underway to attempt isolate these contributions. Finally, the role of lath-shaped coarse carbides at grain boundaries in deflecting the crack into the grain repeatedly is viewed as being beneficial to the ductility and toughness of the as-extruded material. Likewise, it is anticipated that if intergranular failure is suppressed, say via boron addition to the alloy, the next easy fracture mode, namely transgranular cleavage could be deterred by heat treatments that encourage uniform matrix precipitation.

### Conclusions

A. The microstructure of an Fe-40Al-0.6C alloy has been characterized in detail in the as-extruded condition as well as after a variety of heat treatments. From this study, the following observations are made:

- In the as-extruded condition, the matrix is B2 FeAl containing lath-shaped perovskite carbides ( $\text{Fe}_3\text{AlC}_{0.5}$ ) and isolated globular graphite particles both at the grain boundaries and in the interior of the grains.
- Upon heating above  $950^\circ\text{C}$ , the carbides completely dissolve in the matrix; heating to  $1100^\circ\text{C}$  causes the formation of a liquid phase and involves a reaction that redistributes the graphite globules as a continuous film along grain boundaries. This makes the material excessively brittle.
- It is possible to heat treat this alloy in the temperature range  $950^\circ\text{C}$ - $1100^\circ\text{C}$  and then quench it to room temperature thereby producing a carbon-supersaturated matrix. Such a quench also incorporates a high vacancy supersaturation into the matrix.
- Upon low-temperature aging this quenched alloy, the vacancy supersaturation is relieved by the formation of dislocation loops. Longer aging times or higher aging temperatures lead to the precipitation of fine perovskite carbides in the grains.

B. From the results of tensile tests and fracture surface analysis, the following observations were made:

- In the as-extruded condition, at room temperature the yield strength was in excess of 500 MPa with an attendant 2.3% ductility. The initial work hardening rate of  $\sim 8 \text{ GPa}$  is in agreement with previous reports. This strength level, based on previous reports in the literature is indicative of some vacancy hardening. A low-temperature anneal of the extruded material produced  $\sim 4.5\%$  ductility and  $\sim 325 \text{ MPa}$  yield strength.
- A gradual loss in strength was noted with increasing temperature; the ductility however increased only gradually up to  $300^\circ\text{C}$  beyond which it increased rapidly to 30% at  $450^\circ\text{C}$ . This increase in ductility with temperature does not correlate well with either the strength or work-hardening rate variation with temperature.
- Fracture progresses intergranularly in all the specimens independent of test temperature. The lath-shaped carbide particles appear to deflect the crack into the grains although the crack prefers to return to the grain boundaries. This gives the intergranular fracture surface a rough appearance.
- The as-quenched specimens and the quenched specimen that was aged at  $300^\circ\text{C}/1\text{h}$  failed in the elastic regime at a high fracture stress. Aging at  $400^\circ\text{C}/1\text{h}$  provides some macroscopic plasticity; the yield strength was significantly lower than in the quenched condition, although still higher than in the as-extruded material. Fracture stress was also lower than that for the quenched specimens.
- Aging at  $400^\circ\text{C}/1\text{h}$  results in a high density of large vacancy loops. The elimination of vacancies is associated with a decrease in yield stress



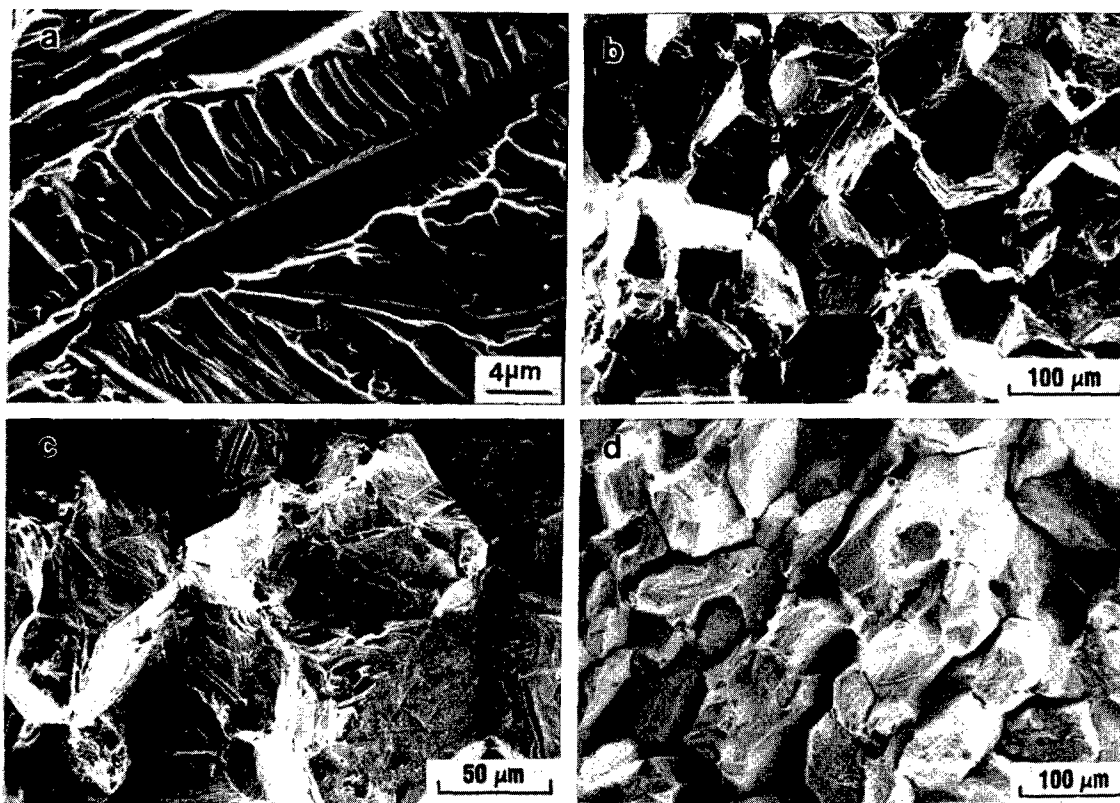


Figure 11: Fracture surfaces of the specimens tested at (a, b) room temperature, (c) 300°C, and (d) 450°C. The lath-shaped carbides at the grain boundaries appear to deflect the cracks into the grains repeatedly, as seen in (b).

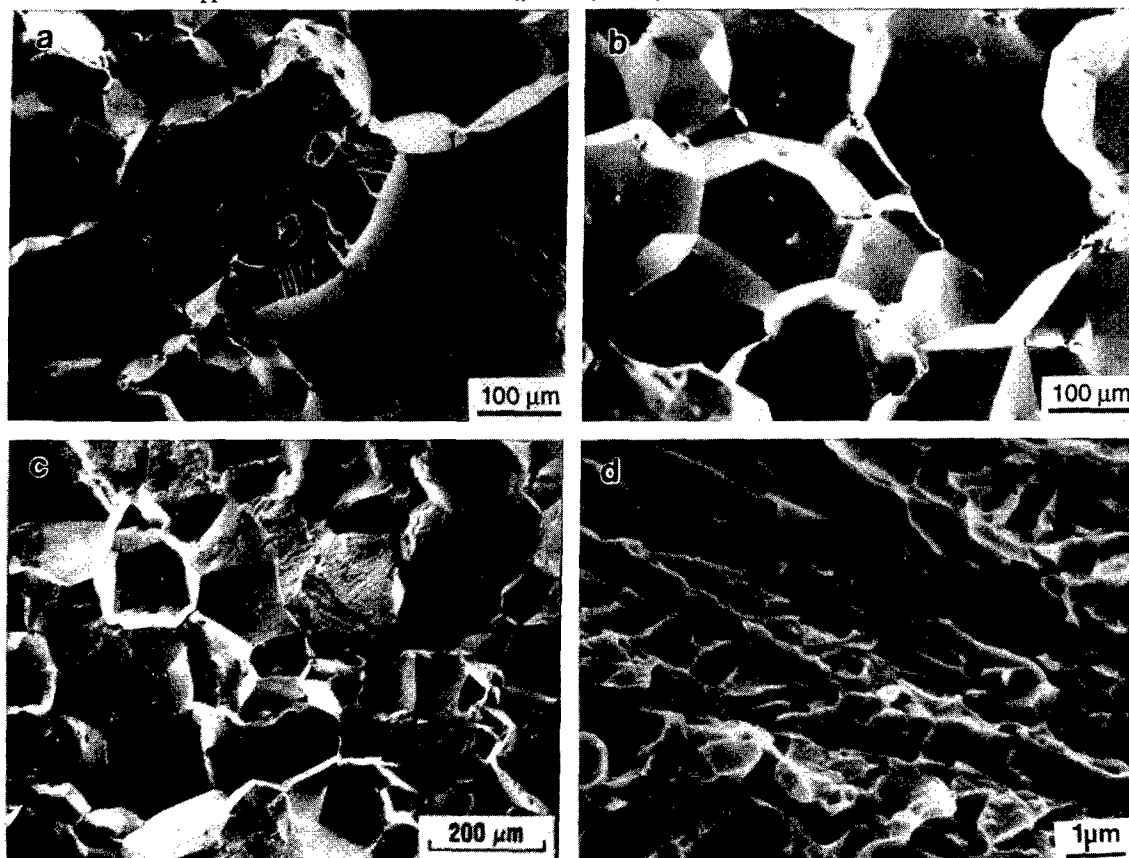


Figure 12: Fracture surfaces of the quenched and aged tensile specimens: a) 300°C/1h, b) 400°C/24h, and (c,d) 500°C/24h.

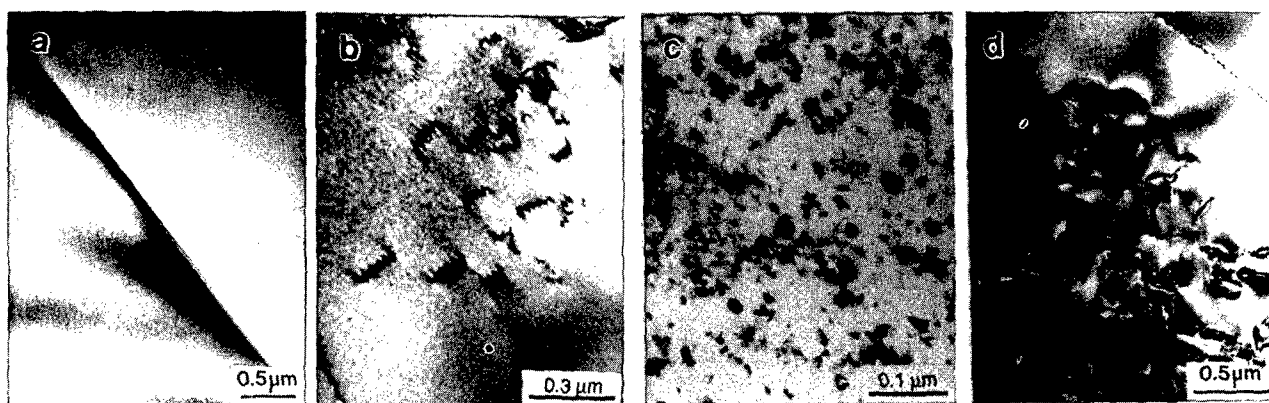


Figure 13: TEM bright-field images from (a,b) as-quenched condition, (c) quenched and aged at 300°C/1h, and (d) quenched and aged at 400°C/1h.

and enhancement in ductility. Long-term aging at 400°C (168 hours) produces 1.2% ductility and still a significantly high yield strength.

- Aging at 500°C/1h lowers the yield strength appreciably (323 MPa) and increases the ductility to 4%. While fracture is predominantly intergranular, there is evidence for some transgranular ductile tearing.

#### Acknowledgments

This research is sponsored by the Office of Naval Research under Contract # N00014-95-1-0564 with Dr. Steven Fishman as the Program Monitor. The authors would like to thank Dr. C.L. Briant for several valuable discussions.

#### References

1. *Binary Phase Diagrams*, ed: T. B. Massalski, ASM, Metals Park, OH., 1986, p. 112.
2. I. Baker and P. Nagpal, in *Structural Intermetallics*, ed: R. Darolia et al., TMS, Warrendale, PA. 1993, p. 463.
3. V.K. Sikka, S. Viswanathan and C.G. McKamey, in *Structural Intermetallics*, ed: R. Darolia et al., TMS, Warrendale, PA. 1993, p. 483.
4. C.G. McKamey, in *Physical Metallurgy and Processing of Intermetallic Compounds*, editors: N.S. Stoloff and V.K. Sikka, Chapman and Hall, New York, NY. 1996, p. 351.
5. I. Baker, in *Processing, Properties and Applications of Iron Aluminides*, ed: J.H. Schneibel and M.A. Crimp, TMS, Warrendale, PA. 1994, p. 101.
6. T. Yamagata and H. Yoshida, *Mater. Sci. Eng.*, **12**, 95 (1973).
7. Y. Umakoshi and M. Yamaguchi, *Phil. Mag.*, **41**, 573 (1980).
8. M. Yamaguchi, D. Pope, V. Vitek and Y. Umakoshi, *Phil. Mag.*, **43**, 1265 (1981).
9. J.D. Whittenberger, *Mater. Sci. Eng.*, **57**, 77 (1983).
10. J.D. Whittenberger, *Mater. Sci. Eng.*, **77**, 103 (1986).
11. K. Yoshimi, S. Hanada and M.H. Yoo, *Intermetallics*, **4**, 159 (1996).
12. M.G. Mendiratta, S.K. Ehlers, D.M. Dimuduk, W.R. Kerr, S. Mazdiyasi, and H. A. Lipsitt, in *High-Temperature Ordered Intermetallics II*, vol. 81, eds: N.S. Stoloff, C.C. Koch, C.T. Liu, and O. Izumi, Mater. Res. Soc., Pittsburgh, PA, 1987, p. 393.
13. C.T. Liu, E.H. Liu and C.G. McKamey, *Scripta Metall. Mater.*, **23**, 875 (1989).
14. M.A. Crimp, K.M. Vedula, and D.J. Gaydos, in *High-Temperature Ordered Intermetallics II*, vol. 81, eds: N.S. Stoloff et al, Mater. Res. Soc., Pittsburgh, PA, 1987, p. 499.
15. D.J. Gaydos, S.L. Draper, and M.V. Nathal, *Metall. Trans. A*, **20**, 1701 (1989).
16. D.G. Morris and M.A. Morris, *Acta metall. mater.*, **38**, 551 (1990).
17. R. Frattini, L. Schiffrini, G. Scipione, E. Bonetti and S. Enzo, *Processing, Properties and Applications of Iron Aluminides*, ed: J.H. Schneibel and M.A. Crimp, TMS, Warrendale, PA. 1994, p. 79.
18. P. Specht and P. Neumann, *Intermetallics*, **3**, 365 (1995).
19. J.E. Wittig, E. Vogt, R. Möller and G. Frommeyer, *Scripta Metall.*, **21**, 721 (1987).
20. V. Raghavan, *Phase diagrams of ternary iron alloys*, Part 1, ASM, Metals Park OH, USA, 1987, p. 89. -- updated in *J. Phase Equilibria*, **14** (1993) 615.
21. L. Oden, *Metall. Trans.*, **20(A)**, 2703, (1989).
22. M. Palm and G. Inden, *Intermetallics*, **3**, 443 (1995).
23. K. Vedula, in *Intermetallic Compounds, Principles and Practice*, Vol. 2, ed: J. H. Westbrook and R.L. Fleischer, John Wiley and Sons Ltd., New York, NY, 1995, p. 199.
24. C.T. Liu and E.P. George, *Scripta Metall. Mater.*, **24**, 1285 (1990).
25. A. Fourdeux and P. Lesbats, *Phil. Mag. A*, **45**, 81 (1982).
26. N. Junqua, J.C. Desoyer and P. Moine, *Phys. Stat. Sol. (a)*, **18**, 387 (1973).
27. P. Nagpal and I. Baker, *Metall. Trans.*, **21A**, 2281 (1990).
28. O. Klein and I. Baker, *Scripta Metall. Mater.*, **30**, 627 (1994).
29. C.H. Kong and P.R. Munroe, *Scripta Metall. Mater.*, **30**, 1079 (1994).
30. D.J. Gaydos, S.L. Draper, R.D. Noebe and M.V. Nathal, *Mater. Sci. Eng.*, **A150**, 7 (1992).
31. C.T. Liu, E.H. Lee and C.G. McKamey, *Scripta Metall.*, **23**, 875 (1989).
32. D.J. Gaydos and M.V. Nathal, *Scripta Metall. Mater.*, **24**, 1281 (1990).
33. R. Gibala and D.S. DeMiglio, in *Hydrogen Effects in Metals*, eds: I.M. Bernstein and A.W. Thompson, TMS-AIME, Warrendale, PA., 1981, p. 113.
34. S.M. Myers, S.T. Picraux, and R.E. Stoltz, in *Hydrogen Effects in Metals*, eds: I.M. Bernstein and A.W. Thompson, TMS-AIME, Warrendale, PA., 1981, p. 87.
35. J.P. Hirth, *Metall. Trans.*, **11A**, 861 (1980).
36. T. Takasugi and S. Hanada, *Intermetallics*, **5**, 127 (1997).

## DEVELOPMENT AND ENGINEERING APPLICATION OF A DS CAST Ni<sub>3</sub>Al ALLOY IC6

Y. F. Han, Z. P. Xing

Beijing Institute of Aeronautical Materials, Beijing 100095, P.R.China

M.C. Chaturvedi

Department of Mechanical and Industrial Engineering, University of Manitoba  
Winnipeg, Manitoba, Canada R3T 2N2

### Abstract

A directionally solidified casting Ni<sub>3</sub>Al base alloy, named Alloy IC6, has recently been developed at Beijing Institute of Aeronautical Materials. The alloy not only has high strength and ductility from room temperature to 1200 °C, excellent creep resistance over a wide temperature range of 700 °C to 1100 °C, but also shows very good thermal cycle fatigue resistance and high incipient melting point ( $T_m=1310-1320$  °C), which are very important for aero-engine turbine vanes. In order to improve its oxidation and corrosion resistance, a overlay NiCrAlYSi coating system was successfully developed for operating temperature up to 1100 °C. Alloy IC6 has been successfully applied for turbine vanes of an advanced aero-engine and passed 250h engine tests as well as 30 taking off/landing cycles and 15 flight hours.

### Introduction

As a matrix of high temperature structural materials Ni<sub>3</sub>Al has some inherent advantages<sup>[1-4]</sup>, such as high melting point, low density, high resistance to oxidation, low diffusion coefficient, high resistance to elevated temperature creep, and a yield strength that increases with increasing temperature up to 760 °C. A high performance cast Ni<sub>3</sub>Al base alloy has been recently developed in this Institute for turbine blades and vanes of advanced aero-engines and other high temperature structural components. This alloy is named Alloy IC6 which is a directionally solidified (DS) cast alloy. Alloy IC6 has some specific advantages as a high temperature structural material. For example, it has high yield strength and fairly good ductility from room temperature to 1200 °C, high creep resistance to 1100 °C, low density (7.90g/cm<sup>3</sup>) and a higher

incipient melting point ( $T_m=1310-1320$  °C) than most of the advanced nickel-base cast superalloys. It also has a lower production cost due to the absence of more expensive alloying elements, such as Ta, Hf and Re. The microstructure-mechanical properties relationship, microstructure stability during high temperature aging and creep and boron content effect on microstructure and mechanical properties of the alloy have been studied earlier<sup>[5-7]</sup>. In the present paper the alloy design, processing, microstructure, mechanical properties, high temperature protective coating, and engineering application of Alloy IC6 are reported.

### Alloy Development and Processing

Ni-Al-Mo system has been selected for the development of the present alloy since Mo has some inherent advantages, such as, high melting point, lower density than W, Ta, Hf, high solubility in both  $\gamma$  and  $\gamma'$  phases, lower production cost than Ta, Hf and it can form different strengthening phases in different temperature ranges. A small amount of boron was added to improve the strength at both grain boundaries and interdendritic areas. The optimum chemical composition of Alloy IC6 was determined mainly by the yield and ultimate strengths, ductility at room temperature and 870 °C as well as creep resistance at 1100 °C. The microstructural stability was also considered during the development of the alloy based on the experimental results and previous studies on Ni-Al-Mo phase equilibria<sup>[8,9]</sup>. The experimental results showed that the alloys within the composition range of Ni-(7.5-8.5)Al-(10-14)Mo-(0.02-0.15) B in wt.% exhibit best combination of mechanical properties. Some typical compositions of Alloy IC6 are listed in Table I.

Table I Typical compositions of Alloy IC6

Alloy No	Composition, wt%				Composition, at%			
	Ni	Al	Mo	B	Ni	Al	Mo	B
1	78.20	7.8	14.0	0.03	75.26	16.34	8.25	0.16
2	78.15	7.8	14.0	0.05	75.17	16.33	8.24	0.26
3	78.10	7.8	14.0	0.10	74.97	16.29	8.22	0.52
4	78.05	7.8	14.0	0.15	74.76	16.26	8.20	0.78
5	77.35	8.5	14.0	0.15	73.51	17.58	8.14	0.78

The master alloy was prepared by a vacuum induction furnace with a refining temperature of 1570 °C-1600 °C for 15-20 minutes. In order to improve the resistance of high temperature creep and thermal cycle fatigue, unidirectional solidification technique was used during the alloy development and components manufacture. The columnar grain specimens for physical, chemical and mechanical properties tests, and integrated DS turbine vanes were produced by the power reduction method in vacuum induction furnaces. The drawing rate of the  $Al_2O_3$  precision investment mold filled with molten alloys and connected to a water cooling copper plate was 6-8mm per minute.

In order to obtain the optimum mechanical properties, a homogenization treatment of 1250 °C  $\pm$  10 °C/6-10hrs. followed by rapid cooling in either oil or flowing Ar, is usually used for alloy specimens and components.

#### Microstructure

Typical microstructure of a specimen homogenized at 1260 °C for 10 hours and followed by oil quenching is shown in Fig.1 a-c, which are the back scattered electron (BSE) images of alloys 2 and 4 obtained by SEM microscopy. The results of x-ray energy dispersive spectroscopy (EDS) analysis indicate that three major phases,  $\gamma$ ,  $\gamma'$  and boride, are present. The white particles in area A are borides, the dark phase is  $\gamma' - Ni_3(Al, Mo)$  with a chemical composition of (74-75) Ni-(21-22) Al-(3.9-4.3) Mo at%, and the grey phase is  $\gamma$ -Ni solid solution. Area A is the interdendritic area consisting of fine ( $\sim 0.3\mu m$ ) cubic shaped  $\gamma'$  phase with skeletal network of  $\gamma$  phase around it and white particles of boride. Area B is the dendrite arm consisting of larger (1-2 $\mu m$ )  $\gamma'$  phase and ( $\gamma + \gamma'$ ) two phase area similar to area A. Area C, located in interdendritic region, is a single  $\gamma'$  phase 3 to 10 $\mu m$  in size. The volume fraction of  $\gamma'$  phase in the present alloy was in the range of 75-80% determined by quantitative analysis of electrolytical extraction method.

The lattice parameters of  $\gamma'$  and  $\gamma$  phase of alloy 2 have been determined to be 3.5859 Å and 3.6289 Å, respectively, by x-ray diffraction technique. Therefore, the lattice misfit between  $\gamma'$  and  $\gamma$

phases is about 1.185%, which is higher than the reported values of lattice misfit in other Ni base superalloys and  $Ni_3Al$  base alloys. This value of lattice misfit has been confirmed by the existence of high density misfit dislocations in the area of  $\gamma'/\gamma$  interfaces. The high density misfit dislocation network plays an important role in alloy strengthening<sup>[5]</sup>

TEM micrographs of this alloy as shown in Fig. 1 d-f, which were taken from the specimens of as-cast, homogenized at 1260 °C for 10 hrs, followed by oil quenching, and then were creep deformed. Misfit dislocation networks were found in all the above three conditions. The interface dislocations are observed to be primarily edge dislocations. The Burgers vectors of these interface dislocations have been determined to be mainly of  $a/2 \langle 110 \rangle$  type and a very few of them are of  $\langle 100 \rangle$  type<sup>[5]</sup>.

#### Mechanical Properties

##### Tensile properties

The tensile properties from room temperature to 1250 °C are listed in Table II. The results show that Alloy IC6 has high tensile strength and fairly good ductility over a wide temperature range. The tensile yield strengths at temperatures above 700 °C are higher than all present DS nickel base superalloys and single crystal alloys. The ductility at room temperature is between 8 to 16%, and at 760 °C, where a minimum ductility for most of the  $\gamma'/\gamma$  two-phase superalloys is observed, the ductility is greater than 4% which is acceptable for many engineering applications. The results in Table II also show that the yield strengths of the alloys increase with temperature up to about 760-800 °C and then decrease with increasing temperature, as has been observed in other  $\gamma'$  base alloys.

Table II Tensile properties of Alloy IC6 with the composition of 7.8 Al-14Mo-0.03 B-Ni balance wt.% after 1260 °C/10 hours followed by rapid quenching

Testing Temp.(°C)	R.T.	700	760	870	1000	1050	1100	1150	1200	1250
$\sigma_{UTS}$ (MPa)	1115	1040	1170	1075	705	585	465	310	178	68
	1225	1090	1165	1040	720		500			
$\sigma_{0.2}$ (MPa)	805	980	1105	975	565	520	385	278	163	61
	780	995	1110	950	640		395			
Elongation (%)	14.2	8.5	6.3	11.0	28.1	28.0	44.0	—	—	—
	15.7	8.7	4.2	10.3	25.0		32.4			

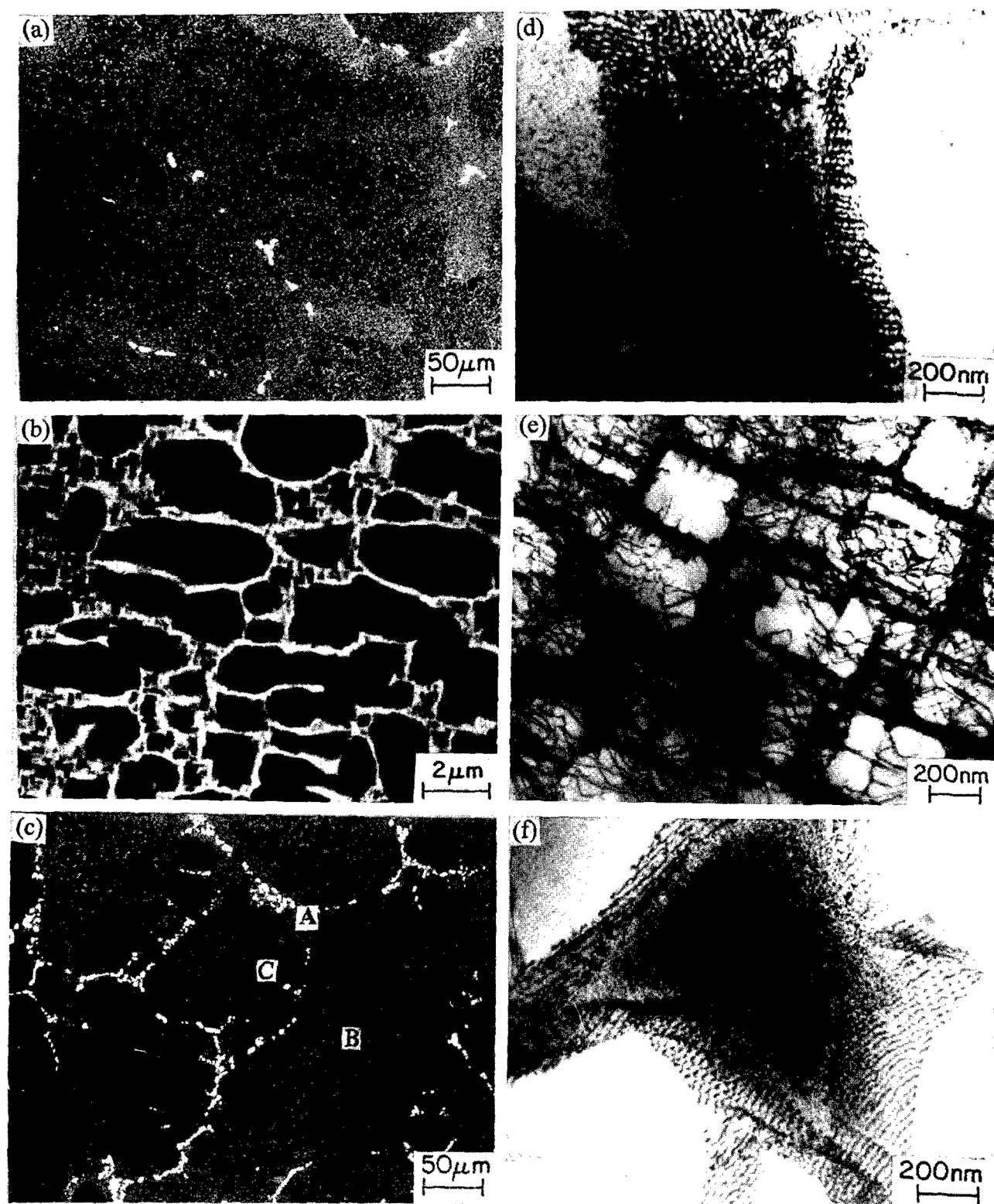


Fig.1 Microstructure of Alloy IC6 : BSE images of alloy 2 (a,b) and alloy 4 (c); and TEM micrographs of alloy 2, showing misfit dislocation networks, specimens of as-cast (d), 1260 °C/10h oil quenching (e) and 1100 °C/95MPa, 190 h (f).

## Stress-rupture resistance

The stress-rupture tests were carried out in the temperature range of 760 °C-1100 °C at various stress levels and the results are shown in Table III. For comparison, the stress rupture lives of some advanced casting DS nickel and Ni<sub>3</sub>Al base alloys are also listed in Table III. DS NX188 is an experimental  $\gamma'$  base alloy with a chemical composition of Ni-18Mo-8Al-0.05C wt.% which was developed by PW Company in the early 1970's for gas turbine vanes operating at 1100 °C; PWA 1422 is a recently developed DS nickel base superalloy (Ni-0.1C-9Cr-10Co-12W-5Al-2Ti-1Nb-2Hf-0.02B-0.05Zr) widely used as turbine blade materials for advanced aero-engines; DZ-3 is a high performance DS nickel base superalloy (Ni-0.1C-11Cr-5Co-5W-4.2Mo-5.6Al-2.7Ti) developed in the 1980's in Beijing Institute of Aeronautical Materials for use as gas turbine blades and vanes. The results in Table III show that the creep resistance of the present Ni<sub>3</sub>Al base alloy at an intermediate temperature of 760 °C and higher temperature of 1040 °C and 1100 °C are higher than those advanced experimental and commercial DS cast Ni and Ni<sub>3</sub>Al base superalloy. The creep resistance of the alloy in the temperature range of 1040 °C-1100 °C compares favorably with the advanced Ni base single crystal alloys CMSX-2(Ni-8Cr-4.6Co-7.9W-0.6Mo-5.6Al-0.9Ti-5.8Ta-0.1Hf) and NASIR100(Ni-9Cr-10.5W-1.0Mo-5.8Al-1.2Ti-3.3Ta). This is illustrated in Fig.2 which shows Larson-Miller parameter plots for 1038 °C and 1100 °C<sup>[9]</sup>. However, the density of the present alloy, 7.9g/cm<sup>3</sup>, is about 10% lower than that of CMSX-2 and NASAIR 100. Therefore, the density compensated strength of this alloy is higher than those advanced single crystal Ni base alloys, which suggests that the present alloy has good potential for application in the manufacture of gas turbine components in the temperature range 1000 °C-1100 °C.

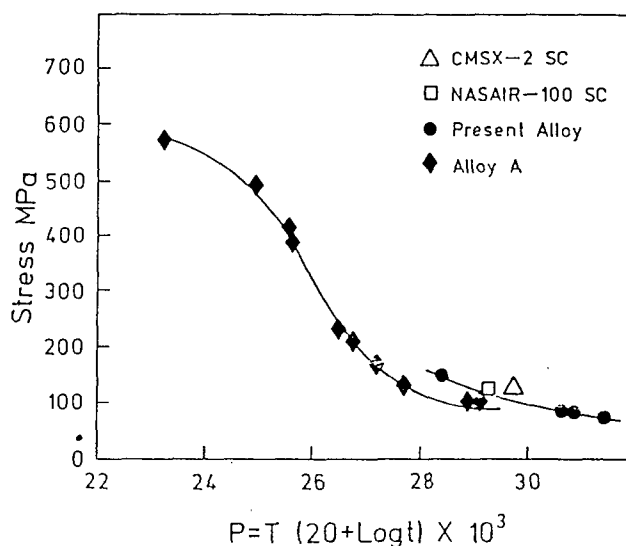


Fig.2 Larson-Miller parameter plot of Alloy IC6 (No.2) compared with some advanced Ni-base DS and single crystal (SC) alloy. Alloy A is a Ni-Al-Ti-X(Ta,Mo,Cr) DS eutectic  $\gamma'/\gamma$  experiment alloy.

Table III Comparison of stress-rupture lives of Alloy IC6 with some advanced DS  $\gamma'$  base alloy and Ni base superalloys

Testing Temp. (°C)	Stress (MPa)	Stress Rupture Lives (hours)			
		DS IC6 $\gamma'$ -base	DS NX188 $\gamma'$ -base	PWA1422 $\gamma'$ -base	DZ-3 $\gamma'$ -base
760	804	197, > 190		100	100
	765				
950	220	124, 122		100	100
	235				
	255				
980	180	161-172		100	100
	206				
1040	137	107-169		100	100
	140				
1100	78.5	> 500	30, 39	42, 44	100
	88.3				
	100				

## Thermal cycle fatigue resistance of Alloy IC6

For a turbine vane, failure often arises from thermal cycle fatigue cracking due to the rapid temperature cycle during service. Therefore thermal fatigue resistance is very important for turbine vane materials. The thermal cycle fatigue tests of Alloy IC6 were carried out under the conditions of 20 °C  $\leftrightarrow$  900 °C, 20 °C  $\leftrightarrow$  1000 °C and 20 °C  $\leftrightarrow$  1100 °C by induction heating and water quenching. The specimens used for the tests were 50  $\times$  20  $\times$  1.5mm plate specimens with a notch of  $\phi$  60 ° and R=0.1 mm. The results of the tests are listed in Table IV. For comparison, the thermal cycle fatigue tests of DZ-3, a popular turbine vane alloy mentioned above, were also carried out under the same condition, and the results are also listed in Table IV. The results show

that the thermal cycle fatigue resistance of Alloy IC6 is superior to alloy DZ-3.

Table IV Thermal cycle fatigue properties of Alloy IC6 compared with alloy DZ-3

Testing Condition	Alloy	Crack length, mm	
		longitudinal	Transversal
20 °C $\leftrightarrow$ 900 °C (200cycles)	IC 6	0.46, 0.45	0.26, 0.25
	DZ-3	2.32, 1.86	0.52, 0.46
20 °C $\leftrightarrow$ 1000 °C (100cycles)	IC 6	1.62, 2.61	0.18, 0.29
	DZ-3	5.16, 3.38	1.47, 0.95
20 °C $\leftrightarrow$ 1100 °C (50cycles)	IC 6	1.60, 0.92	0.18, 0.32
	DZ-3	3.98, 4.38	1.95, 1.70

### Coating of Alloy IC6

Alloy IC6 has some oxidation resistance. It has been found that the weight loss of the alloy after static oxidation test of 1100 °C/100h was 1.6-4.0 g/m<sup>2</sup> · h. However, for high temperature application over 950 °C, coating is necessary for Alloy IC6 as it is for most of the Ni base superalloys<sup>[10,11]</sup>.

For the present alloy and its components NiCrAlY and NiCrAlYSi overlay coatings were deposited using magnetron sputtering. Thickness of the coating was 20 ~ 50μm depending on the service condition of components. The composition ranges of the coatings used in this study are listed in Table V.

Table V Compositions of the coatings (wt.%)

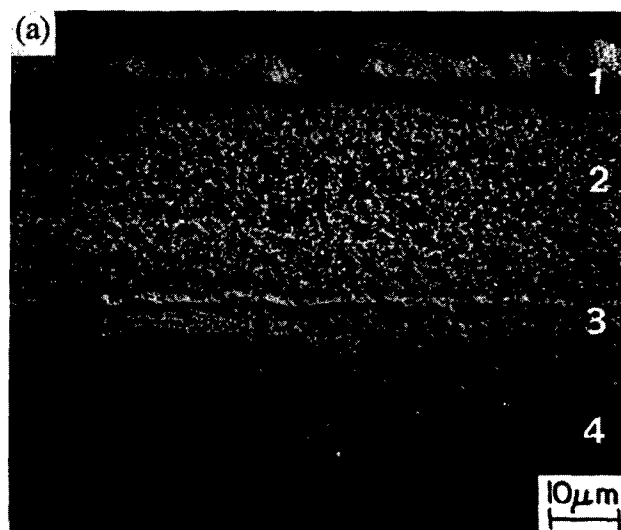
Coating	Ni	Al	Cr	Y	Si
NiCrAlY	Balance	8-12	20-40	≤0.5	-
NiCrAlYSi	Balance	10-14	20-30	≤0.3	≤0.3

After deposition the NiCrAlYSi coated samples were subjected to a diffusion anneal in vacuum at 950-1100 °C for 2h. Then the tensile properties at room temperature and stress rupture properties at high temperature of 1100 °C of uncoated and as-coated specimens were tested. Cyclic oxidation tests were carried out in an air furnace. The specimens were kept at 1100 °C for 1h and then cooled down to room temperature in a cycle. For studying the microstructure and metallurgical stability of the coating, a portion of samples were examined and analyzed by SEM using an X-ray energy dispersive spectroscopy (EDS).

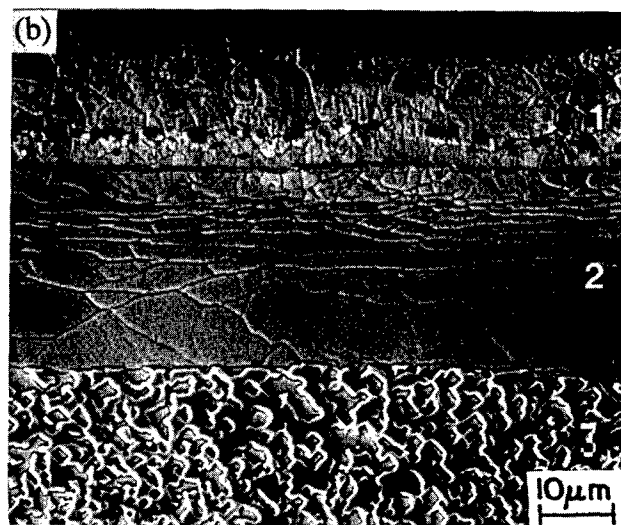
#### Microstructure stability of Coating

Fig.3a shows the microstructure of the NiCrAlYSi coated alloy after diffusion annealing. The coating consisted of three zones, that is, outer layer, deposition layer and diffusion layer. The average thickness of the outer layer, deposition layer and the diffusion layer was about 10μm, 25μm and 5μm, respectively. Limited interdiffusion of elements took place after the diffusion annealing.

Fig.3b shows the microstructure of the NiCrAlYSi coating after cyclic oxidation test for 180h. The coating consisted of three zones, different from that of the as-coated specimen, i. e., deposition layer, diffusion layer and the affected region, respectively. The thickness of the deposition layer was decreased to 12-15μm, and that of the diffusion layer was increased to 25-30μm. Significant interdiffusion of Mo, Cr and Al in the coating took place. However, the elemental diffusion did not result in the formation of brittle phases on the coating/substrate interface. No cracking and spallation in the coating were found. Therefore, it can be concluded that the NiCrAlYSi overlay coating was successful for protecting the alloy.



Area 1. Out layer, 2. Deposition Layer, 3. Affected Region, 4. Substrate



Area 1. Deposition Layer, 2. Affected Region, 3. Substrate

Fig.3 Cross-sectional SEM microstructure of the NiCrAlYSi coating. (a) after annealing at 900-1100 °C for 2h, (b) after cyclic oxidation for 180h.

# Effect of the coating on the mechanical properties of the alloy

Table VI and VII provides the tensile properties and high temperature stress rupture properties of the NiCrAlY(Si) coated alloy, respectively. The tensile strength (Table VI) and stress rupture strength (Table VII) of the coated alloy at testing temperature were about the same as that of the uncoated alloy, and the corresponding ductility is decreased in some degree. Therefore, the mechanical properties of Alloy IC6 were not influenced by the coating.

# Effect of NiCrAlY(Si) overlay coating on thermal fatigue resistance

In order to simulate the operating condition of the alloy used as an aero-engine turbine vane the specimens for the thermal cycle fatigue tests were cut from the air draining edge of the experimental turbine vane. The testing conditions were as follows: localized high frequency induction heating at the air draining edge up to 930 °C and 1000 °C, and then cooling by blasting with mixture of air and distilled water to 40 °C, as one cycle. The results of the tests are listed in Table VIII. The results in Table VIII show that both coatings improve the thermal fatigue resistance significantly.

Table VI Effect of the coatings on the tensile properties

processing condition		20 °C				870 °C			
		UTS	YS	El.	R.A.	UTS	YS	El.	R.A.
NiCrAlYSi + 1050 °C/2h	uncoated IC6 (A40#)	1101	747	17.0	19.5				
		1180	770	17.4	21.3				
	coated IC6 (A40#)	851	790	3.3	11.0				
		1191	763	8.7	14.3				
NiCrAlY as-coated	uncoated IC6 (52#)	1170	810	12.0	19.5	1040	940	14.7	17.0
	coated IC6 (52#)	1165	780	15.0	—				
		1150	770	15.0	—				
	uncoated IC6 (58#)	1115	805	14.2	14.2	1075	975	11.0	—
		1225	780	15.7	15.7	1040	950	10.3	—
	coated IC6 (58#)	1280	835	12.0	10.5	1090	970	11.0	21.0

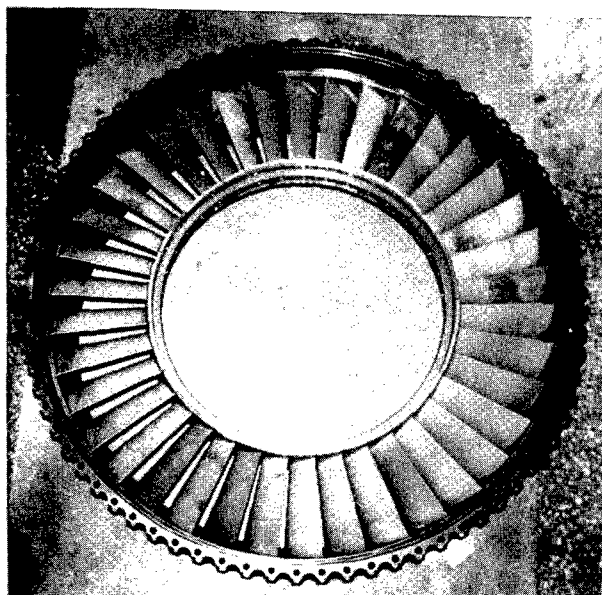
Table VII Effect of the coatings on the stress rupture properties

processing condition		1100 °C/100MPa			1100 °C/90MPa			900 °C/350MPa		
		hrs	El.	R.A.	hrs	El.	R.A.	hrs	El.	R.A.
NiCrAlYSi + 1050 °C/2h	uncoated IC6 (A40#)	81:15	11.60	36.26	92:25	22.8	26.34			
		50:10	8.16	27.8	159:50	20.4	28.87			
	coated IC6 (A40#)	60:05	14.64	45.57	106:00	8.8	26.67			
		76:25	20.72	42.49	318:30	8.4	25.14			
NiCrAlY as-coated	uncoated IC6 (58#)	70:30	14.8	34.97				114:55	16.0	26.04
		43:45	10.0	29.72				97:15	20.0	22.40
	coated IC6 (58#)	72:30	20.32	7.07				102:45	8.03	22.56
		72:40	9.84	41.63				99:20	19.04	27.41

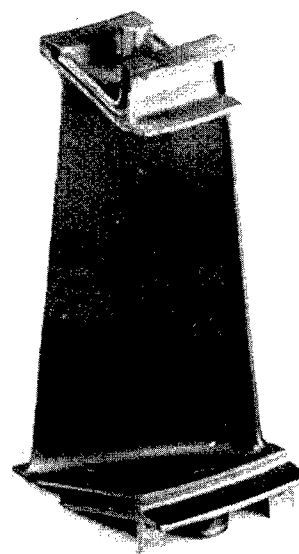
Table VIII Effect of NiCrAlY(Si) overlay coating on thermal fatigue resistance of Alloy IC6 (250 cycles)

Specimen condition	930 °C ↔ 40 °C		1000 °C ↔ 40 °C	
	crack length of longest crack, mm	number of Cracks	crack length of longest crack, mm	number of cracks
without coating	0.28	4		
	0.30	6		
			1.48	> 10
NiCrAlYSi + 1050 °C/2 hrs	0.10	1		
			0.50	4
NiCrAlY (as-coated)	0.09	1		
			0.47	4





(a)



(b)

Fig.4 DS casting turbine vanes made of Alloy IC6 with NiCrAlYSi coating in an advanced aero-engine. (a) 25 hrs engine test, 23 pieces of Alloy IC6 showing no any oxidation and damage (15pieces DS nickel base superalloy with Al-Si coating); (b) after 250 hrs engine test.

#### Engineering Application of the alloy

Alloy IC6 is a recently developed high performance DS cast Ni<sub>3</sub>Al base alloy, which can be used for gas engine turbine blades and vanes operating in the temperature range of 1000 °C – 1100 °C, and also for other high temperature structural parts. For engineering application, a great deal of study related to the alloy application, such as, high frequency fatigue resistance, thermal cycle fatigue resistance, oxidation and corrosion resistance, microstructural stability, weldability, castability, and machinability, has been done in both the research laboratory and the aero-engine manufacturing factory during the last five years besides the essential research of the alloy. Based on these results four whole sets (~ 150 pieces) of qualified integrated DS turbine vanes with NiCrAlY(Si) overlay coating have been manufactured. Among them one engine fitted with Alloy IC6 turbine vanes has successfully passed 250h engine tests, including 30h simulating flying test, as shown in Fig.4. Other two engines with Alloy IC6 turbine vanes have successfully passed 30 cycles of taking off/landing and accumulated 15 flight hours.

It is decided that the turbine vanes of Alloy IC6 are being produced in small batches in 1997 and production will be increased later on.

Alloy IC6 has been also selected as turbine vane material for two other more advanced aero-engines. These new type turbine vanes have complex cooling tunnels. It seems that Alloy IC6 will find wider application in aero-engine industry in China.

#### Conclusions

1. A high performance Ni-Al-Mo γ' base DS cast Alloy IC6 has been developed for high temperature structural components

operating in the temperature range up to 1200 °C, especially suitable for turbine vanes operating in the temperature range of 1000-1100 °C.

2. NiCrAlY(Si) overlay coating is suitable for Alloy IC6 and can operate in the temperature range up to 1100 °C.

#### Acknowledgments

The authors wish to acknowledge the Advanced Materials Committee of China and Natural Science and Engineering Research Council of Canada for their financial support.

#### References

1. D.H. Maxwell, *Metall. Eng. Quart.*, 10(1970), 42.
2. C.L.Coley, B. Lisowsky, *Trans AIME*, 239(1967), 239.
3. K. Aoki, O. Izumi, *J. Jpn. Met.*, 43(1979), 1190.
4. C. T. Sims, W.C. Hagel, *The Superalloys*, New York: Wiley, 1987, 551.
5. Y.F.Han, Y.M.Wang, M.C.Chaturvedi, *J. Mater. Eng. perf.*, 2(1993), 589.
6. Y.F.Han, S.H.Li, M.C.Chaturvedi, *Mater. Sci. Eng.*, A160(1993), 271.
7. Y.F.Han, S.H.Li, M.C.Chaturvedi, *Structural Intermetallics*, ed. T. Darolia, J. J. Lewandowski, C. T. Liu, et al, TMS, 1993, 453.
8. M.J.Kaufman et al, *Metall. Trans. A*, 14A(1983), 1561.
9. D.B Miracle et al, *Metall. Trans. A*, 15A(1984), 481.
10. P. Choquet, C. Indrigo and R. Mevrel, *Mater. Sci. Eng.* 88 (1987), 97.
11. S. R. J. Saunders, J. R. Nicholls, *Mater. Sci. Tech.*, 5 (1989), 780.

# DEFECT PROPERTIES AND DEFECT ANALYSIS IN IRON ALUMINIDES

J. Wolff, M. Franz, A. Broska, B. Köhler and Th. Hehenkamp

Institut für Metallphysik, Georg - August Universität  
Hospitalstraße 3-7, 37073 Göttingen, Germany

## Abstract

The applications and properties of ordered FeAl alloys may be strongly composition-dependent as well as temperature-dependent due to the different types of point defects and their concentrations. Positron annihilation experiments have been carried out to obtain various information about defect types in FeAl alloys. In the FeAl system the formation enthalpy decreases with Al content and is found to be constant in the B2 phase. The formation volume increases to the largest defect formation volume of  $1.42 \Omega$  in a Fe-40at%Al alloy. This formation volume in the B2 phase can only be described by double vacancies or triple defects. In quenching experiments the migration enthalpy is measured using the fast Doppler broadening technique and changes from 0.5 to 1.2 eV. Positron lifetime measurements at high temperatures show an increasing lifetime of positrons in defects and may be interpreted as formation of divacancies. The present results suggest that thermal defects in the B2 phase are mainly triple defects at low temperature and double vacancies at higher temperatures. In the A2 as well as in the D0<sub>3</sub> structure single vacancies are supposed to be the predominant defect types. This knowledge is important for the discussion about the diffusion and the thermomechanical properties of ordered intermetallic phases.

## Introduction

Ordered FeAl of the B2 type and other aluminides have been extensively studied as high temperature structural materials due to their mechanical properties, low mass density and good oxidation resistance [1]. The potential of technical application is restricted by poor ductility and low fracture toughness of such alloys [2, 3].

The applications and properties may be strongly connected with the composition of the alloy and defects and their concentration [4, 5]. For a basic physical understanding of the properties one requires the knowledge of the defect type and its concentration. Experimental techniques are needed to distinguish between single vacancies, anti-structure atoms, double vacancies and triple defects. The triple defects are composed of two vacancies on one sublattice and one anti-structure atom on the other sublattice [6]. Positron annihilation techniques are a sensitive, specific tool [7] to clarify the nature of atomic defects in intermetallic compounds.

It is established that vacancies are the predominant defect type in metals and alloys in thermal equilibrium. Their concentration is given by:

$$c_v = \exp\left\{-\left(E_v^f + pV_v^f - TS_v^f\right)/k_B T\right\} \quad (1)$$

where  $E_v^f$ ,  $V_v^f$  and  $S_v^f$  are the activation energy, volume and entropy of formation of a vacancy, respectively. Under common isobaric conditions Eq. 1 can be simplified and the vacancy formation enthalpy  $H_v^f$  can be determined from the slope of an Arrhenius graph. In isothermal experiments the pressure effect on the vacancy concentration directly yields the vacancy formation volume  $V_v^f$  [8]:

$$V_v^f = -k_B T \left( d \ln c_v / dp \right)_T \quad (2)$$

In the case of alloys the data have to be understood as effective values, because a mixing of several defects is to be considered. A model is required to relate the measured quantities to physically meaningful ones. The two state trapping model [e. g. 9] connects the measured  $S$  parameter, which is defined as the ratio of counts under the central 13 channels to the total counts under the 81 channels covering the entire 511 keV  $\gamma$  annihilation peak, with the vacancy concentration  $c_v$ :

$$\bar{S} = \frac{S - S_f}{S_v - S} = \mu \tau_f c_v \quad (3)$$

$S_f$  and  $S_v$  are the  $S$  parameter in the free and in the trapped positron state, respectively.

One can determine the vacancy formation volume from Doppler broadening measurements assuming that there is no pressure dependence of the trapping rate  $\mu$  and that the change of bulk lifetime  $\tau_f$  and vacancy lifetime  $\tau_v$  are equally small. These assumptions were verified [10, 11].

A positron lifetime measurement yields the product of vacancy concentration and positron trapping rate  $\mu$ , in terms of the trapping model:

$$\mu\tau_v = I_2(\lambda_1 - \lambda_2) \quad (4)$$

$\lambda_1$  and  $\lambda_2$  are the reciprocal measured lifetimes and  $I_2$  is the intensity of the lifetime  $\tau_2$ .

### Experimental

All samples were prepared by melting and remelting pure iron of 99.98% and aluminum of 99.9995% purity or blanks of Fe<sub>3</sub>Al and Fe<sub>52</sub>Al<sub>48</sub> polycrystalline rods (Institut für Eisenforschung, Düsseldorf) in Al<sub>2</sub>O<sub>3</sub> crucibles under an atmosphere of high purity Argon. Homogeneity and concentration was checked by electron probe microanalysis. The rods were spark-cut into cylinders with 7 or 5 mm diameter and 15 mm length. A 2 mm hole was spark cut into the sample, chemically polished and filled with 1.2 MBq <sup>22</sup>Na positron emitter. After drying the emitter the hole was closed with a rod of the same alloy and plasma welded. The samples were annealed at 3/4 absolute melting temperature for two days.

A fast lifetime spectrometer was employed. The equipment showed a time resolution (FWHM) of 215 ps using <sup>22</sup>Na source and a counting rate of 30 to 60 Hz. All electronic components were temperature controlled. A stability of  $\pm 1.5$  ps with a not measurable drift over a period of four weeks could be maintained. A typical spectrum contains  $1.5 \times 10^6$  counts at a peak to background ratio of about 2500 : 1. For the analysis of the spectra, the fit program PATFIT 88 [12] was employed.

The Doppler broadening measurements were carried out using a high purity germanium detector system with a resolution of 1.3 keV FWHM for the 511 keV  $\gamma$  annihilation line. All electronic components were temperature stabilized again. Continuous monitoring of the maximum channel of the 511 keV  $\gamma$ -line showed a drift less than 0.1 channel over 150 hours.

For Doppler broadening measurements a conventional high pressure autoclave (Nova Swiss) was used, which was placed in a furnace. The temperature of the furnace was controlled to better than  $\pm 1$  K. Argon gas with a purity of 99.98 % served as pressure medium up to a pressure of 700 MPa. The pressure was measured by means of a membrane gauge with an error of less than  $\pm 1$  MPa.

For the positron lifetime measurements a special high pressure autoclave was developed. The intention was to minimize the distance between scintillator and sample to avoid a drastic decrease of counted coincidences. The autoclave was machined from two layers of different steels, which were inserted into one another with pre-tension. The furnace was placed inside the autoclave (internal heater, 12.3 mm dia.). The temperature was controlled with two thermocouples, one on each side of the sample.

For details about the positron annihilation equipment as well as the high pressure autoclave see [13, 14].

### Results

Positron lifetime spectra and Doppler broadening spectra have been determined varying temperature and pressure as parameters.

#### Formation and migration of defects

Positron lifetime experiments at atmospheric pressure have been carried out to determine the vacancy formation enthalpy. The results are plotted in table 1. The effective formation enthalpy in the B2 phase seems to be constant at  $\sim 1$  eV. The higher values of Fe-43at%Al and Fe-48at%Al are explained in the next part of this paper. Mostly, a vacancy lifetime component was always detectable from spectra even at very low temperatures. This effect could not be removed with long term annealing close to phase transition temperatures. As one can see in the figure 1 the "frozen in" defect concentration depends strongly on Al content. With increasing Al content approaching the stoichiometric composition these samples contain more and more "frozen in" or possibly structural defects. There are some hints that in different parts of the B2 phase the behavior is different (upper and lower Al concentrations). In the range of 30 to 40 at%Al and at high temperatures no increasing positron lifetime was found in contrast to the range of 40 to 50 at%Al.

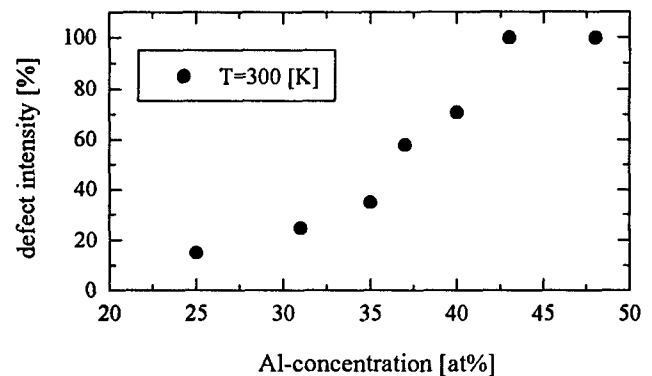


Figure 1. Intensity of the defect lifetime component against Al content of samples with 0.1 K/min. cooling rate.

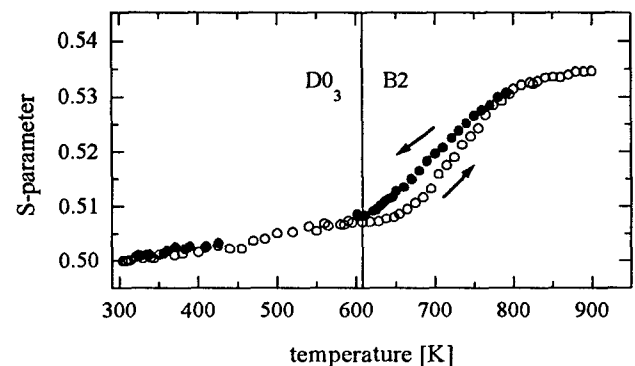


Figure 2. S-parameter against temperature of Fe-35at%Al during heating and cooling

TABLE 1. Effective defect formation enthalpy  $H_{v,eff}^f$  and migration enthalpy  $H_{v,eff}^m$  in FeAl alloys

Al content (at%)	$H_{v,eff}^f$ (eV)	$H_{v,eff}^m$ (eV)	method	reference
0 ( $\alpha$ -Fe)	$2.0 \pm 0.20$		DB	[15]
0 ( $\alpha$ -Fe)	$1.6 \pm 0.05$		DB	[16]
0 ( $\alpha$ -Fe)	$1.89 \pm 0.10$		life time	[17]
7	$1.41 \pm 0.06$		life time	[14]
23.7	$1.18 \pm 0.04$	1.4 - 1.6	life time	[18]
25	$1.08 \pm 0.08$	0.5	DB	[14]
25	$0.92 \pm 0.05$		life time	[14]
31	$0.96 \pm 0.07$		life time	this work
35	$1.04 \pm 0.06$		DB	[19]
37	$1.02 \pm 0.07$		life time	this work
37	$1.04 \pm 0.07$		life time	[20]
39	$0.98 \pm 0.07$	$1.7 \pm 0.2$	life time	[20]
40	$1.13 \pm 0.06$	$1.2 \pm 0.2$	DB	[14], this work
40	$0.98 \pm 0.06$		life time	[19]
40	0.91		resistance	[21]
43	$1.42 \pm 0.04$		lifetime	this work
48	$1.38 \pm 0.06$		lifetime	this work

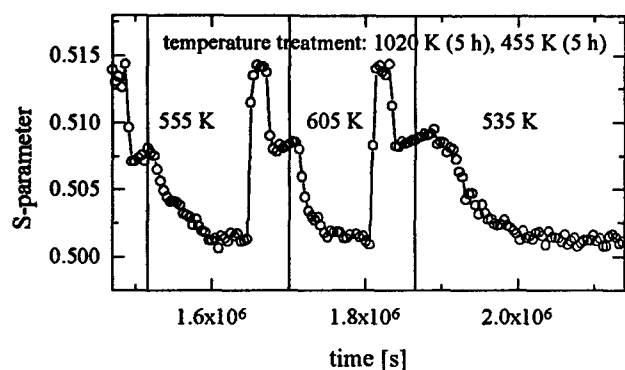


Figure 3. Plot of  $S$ -parameter from Doppler broadening of Fe-25at%Al against time.

DB measurements are influenced by the frozen in defects mentioned above. For example, if one takes an amount of  $I_2 = 15\%$  of such frozen in defects (Fe-25at%Al) at room temperature into account, the DB experiment yields a value which is reduced from  $H_{v,eff}^f = 1.08 \text{ eV}$  to  $H_{v,eff}^f = 0.97 \text{ eV}$  in good agreement with the lifetime experiment (see table 1). The effective formation value of  $1.13 \text{ eV}$  of the Fe-40at%Al sample is another example.

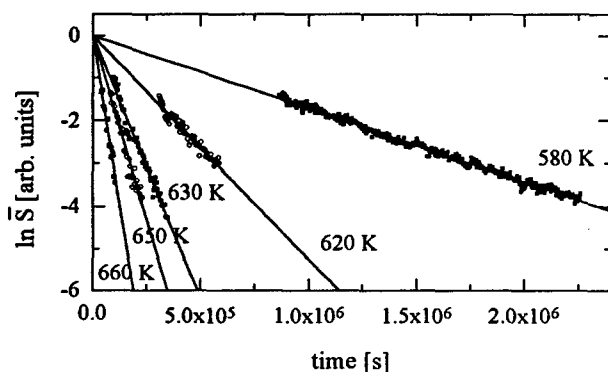


Figure 4. Plot of  $\ln \bar{S}$  from Doppler broadening of Fe-40at%Al at various temperatures against time. The rate constant was determined from the slope.

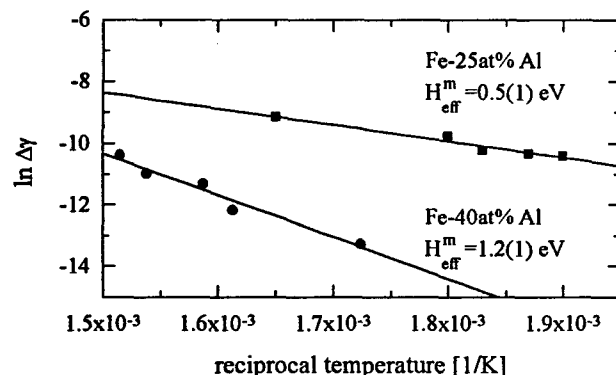


Figure 5. Arrhenius plot of the decay constants from two alloys

Furthermore, in some cases a hysteresis can be observed during heating and cooling of Fe-35at%Al alloy due to a nonequilibrium defect concentration (Figure 2). These experiments are reflecting a different dynamic behavior of the thermal created defects and their migration. For the sake of clear conditions quenching experiments are lead through. In figure 3 some examples of Fe-25at%Al of the measured  $S$ -parameter during quenching and annealing are depicted. The decay constants  $\Delta\gamma$  from various temperatures are determined from the slope of  $\ln \bar{S}$  versus time in figure 4. The slope of the fitted line in figure 5 of the variation of the decay constant with the reciprocal temperature leads to the effective migration enthalpy. The value in the case of Fe-25at%Al is surprisingly low in comparison to the literature data discussed below. However, the phase transition from B2 to the highly ordered D0<sub>3</sub> phase and the corresponding change of the defect type should be considered. Schaefer et al. [18] find a migration enthalpy for Fe<sub>3</sub>Al of  $1.4 - 1.6 \text{ eV}$  by combination of positron lifetime measurements and diffusion experiments of Larikov [22].

This result should be interpreted with caution, because the defect types in B2, where positron lifetime experiments have been performed and in A2, the region of the diffusion experiments are different. Recently, a comparable value to  $0.5 \pm 0.1 \text{ eV}$  was published [23] and explained with a dynamic lattice effect. In the B2 phase (Fe-40at%Al) a slower motion of the defects and in this case a higher effective migration enthalpy of  $1.2 \pm 0.2 \text{ eV}$  is found (Figure 5). Würschum et al [20] determined the migration enthalpy to  $1.7 \text{ eV}$  (Fe-39at%Al) with positron lifetime measurements. The difference is still unknown but one has to take into account that these experiments are difficult and the errors are large. In any case these measurements show that the migration of defects depend on the Al content and hence the different phases have to be considered. Nevertheless, this was one of the hints that in both phases different defect types are predominant.

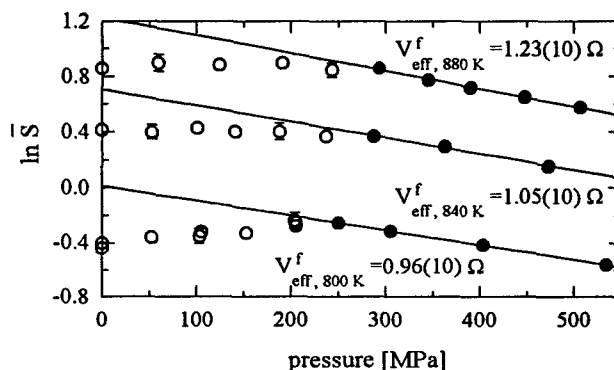


Figure 6. Plot of  $\ln \bar{S}$  from Doppler broadening in Fe-25at%Al at various temperatures against pressure. The effective defect formation volume was determined from the slope.

#### Formation volume of defects

Doppler broadening measurements at various pressures have been carried out. Results are plotted in Figures 6, 7 and 8. The slope of the lines fitted by least squares yields the effective formation volume  $V_{eff}^f$ . For the calculation of  $\Omega$  lattice parameters measured with a precise x-ray diffractometer at given temperatures [24] and published data [25] have been used. In a first approximation the volume of a created single vacancy is smaller than  $1.0 \Omega$  due to the relaxation of the surrounding atoms into the defect. In Fe-25at%Al (Fig. 6) a formation volume can be determined from pressures exceeding 250 MPa only. The low pressure part deviates from the linear dependence. This seems to be due to a pressure dependence of the two phase field A2 - D0<sub>3</sub> in the phase diagram [26]. However, it has to be pointed out, that in this alloy the effective formation volume appears to be temperature dependent, which could be due to fractions of B2 and D0<sub>3</sub> phases in the region of the B2 - D0<sub>3</sub> transition varying with temperature. This continuous phase transition changes the fraction of different defect types continuously too. The larger effective formation volume of  $1.2 \Omega$  in the B2 region (Fig. 7) gives evidence of an additional defect with apparently more than one single vacancy (single vacancy  $\leq 1.0 \Omega$ ). The Fe-40at%Al alloy

(Fig. 8) shows the largest defect formation volume of 1.42 Ω. No temperature dependence is observed.

This formation volume in the B2 phase can not be described by means of a single vacancy. Double vacancies or triple defects have to be considered. Single vacancies and triple defects do apparently not have measurably different positron lifetimes. This was to be expected, because in triple defects the two vacancies are not next neighbors. On the other hand, one can assume

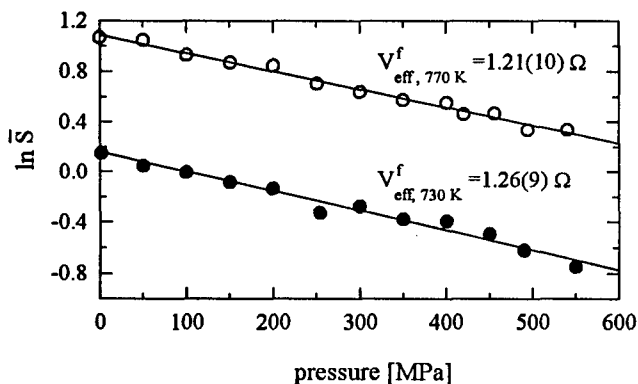


Figure 7. Plot of  $\ln \bar{S}$  from Doppler broadening in Fe-35at%Al at various temperatures against pressure. The effective defect formation volume was determined from the slope.

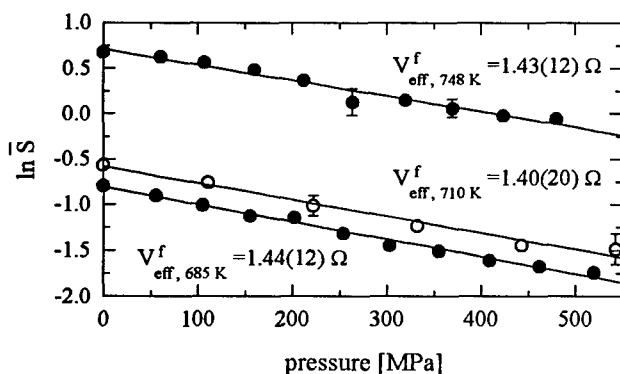


Figure 8. Plot of  $\ln \bar{S}$  from Doppler broadening in Fe-40at%Al at various temperatures against pressure. The effective defect formation volume was determined from the slope.

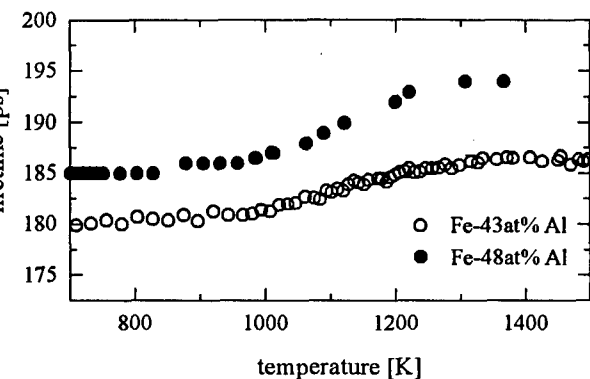
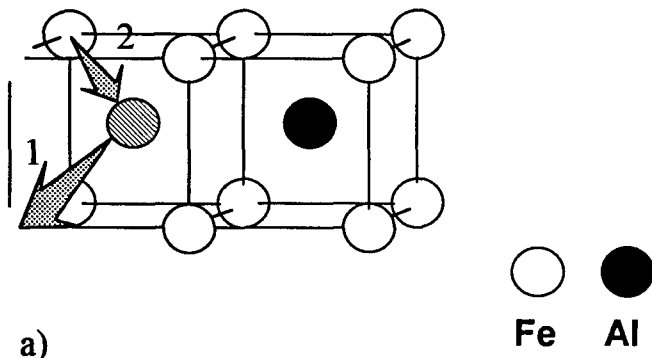


Figure 9 Plot of mean positron lifetime in Fe-43at%Al and Fe-48at%Al versus temperature.

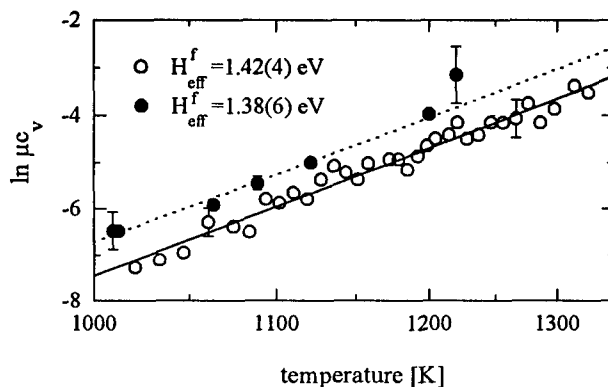


Figure 10. Plot of  $\ln \mu_v$  in Fe-43at%Al (open circle) and Fe-48at%Al (filled circle) versus temperature. The effective defect formation enthalpy was determined from the slope.

that the defect lifetime changes measurably if the main defect type switches from triple defect to double vacancies.

Results of additional lifetime experiments are depicted in Fig. 9. This experiment shows an increase of the defect lifetime  $\tau$  with rising temperature. This suggests, that the defect type may be changed. According to Puska and Nieminen [27] an increase by 9 ps can be interpreted as originating from double vacancies. In this case the two vacancies are located as next neighbors. A simple analysis with the two state trapping model would lead to an effective formation enthalpy of double vacancies in the order of  $1.4 \pm 0.1$  eV (Fig. 10). This analysis predicts in a very simple approach only

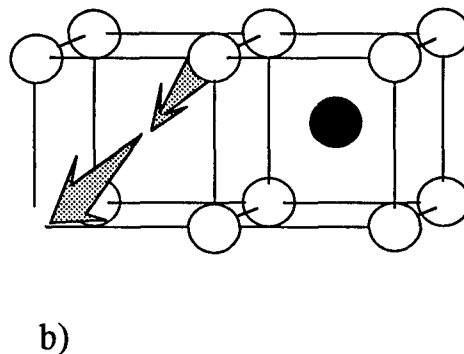


Figure 11. B2 structure of FeAl. The arrows marked the possible atom jumps of diffusion mechanism in the limited cases of stable triple defects (a) and double vacancies (b).

triple defects at lower temperatures and double vacancies at higher ones. With this approach the atomic diffusion process can be discussed. Two different diffusion mechanisms should result as limiting cases. At high temperature and with increasing Al content the diffusion process can be explained taking double vacancies (one vacancy on every sublattice and on next neighbor sites) into account (Fig. 11b). This is consistent with Mössbauer results [28, 29] on the elementary hopping process. In the case of the nearly stoichiometric composition the experimental results are in contradiction to the theoretical results of Mayer et al. [30] and Fu [31]. Their investigations predicts clearly that the formation of an Al vacancy should be impossible, but their predictions are limited to concentrations very close to the stoichiometric composition. No experimental evidence was found for this prediction. At low temperatures and increasing Fe content the diffusion process could be described via triple defects. If the anti-structure atom jumps into its own sublattice the next Fe atom uses the Al vacancy to form a new anti-structure atom. This first jump may be triggered by one or more next neighbor Fe atoms to push it from the anti-structure site to its own sublattice. In this case the stable defect is a triple defect (Fig. 11a). A complete double vacancy will be never formed because the jumps of two or more atoms are correlated. The diffusion process changes continuously between both cases depending on temperature and Al content and can easily be described as a change from one defect type to the other via a jump of one atom in a vacancy in to its nearest neighbor site. Then both types of defects are stable because the average time during which the different defects are present is in the same order of magnitude. In any case the defects are created in thermal equilibrium taking the binding energy of vacancies, the energy of order and the corresponding excess entropies of the defects into account.

#### Conclusions

In conclusion, the present results suggest that thermal defects in the A2 phase as well as in the D0<sub>3</sub> phase are mainly single vacancies. In the ordered B2 phase triple defects and double vacancies are supposed to be the predominant defect types. Diffusion mechanisms in the B2 phase which require single vacancies to operate do not fit our data. The diffusion process depends on temperature and Al content due to the change of stable defect types with these parameters. This knowledge is important for the discussion about the thermomechanical properties of ordered intermetallic phases.

#### Acknowledgements

The authors thank Prof. F. Faupel for various help. The support of this work by DFG under contract no. Wo 555 / 1 is gratefully acknowledged.

#### References

- [1] G. Sauthoff, *Intermetallics*, (Weinheim, Germany: VCH Verlag, 1995).
- [2] S. C. Deevi, V. K. Sikla, *Intermetallics*, 4 (1996), 357.
- [3] C. T. Liu, *Mat. Chem. and Phys.*, 42 (1995), 77.
- [4] J. P. Neumann, *Acta Metall*, 28 (1980) 1165.
- [5] Y. A. Chang, J. P. Neumann, *Prog. Solids St. Chem.*, 14 (1982), 221.
- [6] R. J. Wasilewski, *J. Phys. Chem. Solids*, 29 (1968), 39.
- [7] P. Hautojärvi, *Positrons in solids*, (Springer Verlag, Heidelberg, 1979).
- [8] H. Mehrer, N. Stolice ed., *Landolt-Börnstein III* 26, Springer Verlag, Berlin, (1990), 600.
- [9] B. Bergerson, M. J. Stott, *Solid State Commun.*, 7 (1963), 1023.
- [10] M. Franz, J. Wolff, Th. Hehenkamp, *Materials Science Forum*, 175-178 (1995), 355.
- [11] J. Wolff, M. Franz, Th. Hehenkamp, *J. Radioanalytical and Nucl. Chem.*, 210 (1996), 591.
- [12] P. Kirkegaard, N. J. Pedersen, M. Eldrup, *PATFIT 88: A Data-Processing System for Positron Annihilation Spectra on Mainframe and Personal Computers*, Risø National Laboratory Roskilde, Denmark (1989).
- [13] M. Franz, (Ph. D. thesis, Georg-August University, Göttingen, 1995), 8-38.
- [14] J. Wolff, M. Franz, Th. Hehenkamp, *Mikrochemica Acta*, 125 (1997), 263.
- [15] L. DeSchepper, D. Segers, L. Dorikens-Vanpraet, M. Dorikens, G. Knuyt, L. M. Stals, P. Moser, *Phys. Rev. B*, 27 (1983), 5257.
- [16] H.E. Schaefer, K. Meier, M. Weller, D. Herlach, A. Seeger, J. Diehl, *Ser. Metall.*, 11 (1977), 803.
- [17] Y. Shirai, H.E. Schaefer, A. Seeger, *Positron Annihilation*, Ed. M. Dorikens, L. Dorikens-Vanpraet, D. Segers, Gent, Belgium, (1988), 419.
- [19] J. Wolff, A. Broska, M. Franz, Th. Hehenkamp, Presented at DIMAT96, Nordkirchen, *Defects and Diffusion Forum*, to be published.
- [18] H. E. Schaefer, R. Würschum, M. Šob, T. Žák, W.Z. Yu, W. Eckert, F. Banhart, *Phys. Rev. B*, 41 (1990), 11869.
- [20] R. Würschum, C. Grupp, H.-E. Schaefer, *Phys. Rev. Letter*, 75 (1995), 97.
- [21] J. P. Rivièrè, J. Grilhè, *Phys. Stat. Sol. A*, 25 (1974), 429.
- [22] L.N. Larikov, V.V. Geichenko, V.M. Fal'chenko, *Diffusion Processes in Ordered Alloys*, (Oxonian Press, New Delhi, 1981).
- [23] E. Kentzinger, V. Pierron-Bohnes, M. C. Cadeville, W. Petry, B. Hennium, Presented at DIMAT96, Nordkirchen, *Defects and Diffusion Forum*, to be published.
- [24] Th. Hehenkamp, W. Berger, J.-E. Kluin, C. Lüdecke, J. Wolff, *Phys. Rev. B*, 45 (1992), 1998.
- [25] W. B. Pearson, *A Handbook of Lattice Spacings and Structures of Metals and Alloys* Bd.2, (Pergamon Press, Oxford, 1967).
- [26] O. Kubaschewski, *Iron-Binary Phase Diagrams*, (Springer Verlag, Berlin, 1982), 5.
- [27] M. J. Puska, R. M. Nieminen, *J. Phys. F*, 14 (1983), 333.
- [28] G. Vogl, B. Sepiol, *Acta metall. mater.*, 42 (1994), 3175.
- [29] R. Feldwisch, B. Sepiol, G. Vogl, *Acta metall. mater.*, 43 (1995), 2033.
- [30] J. Mayer, C. Elsässer, M. Fähnle, *Phys. Stat. Sol. (b)*, 191 (1995), 283.
- [31] C. L. Fu, *Phys. Rev. B*, 52 (1995), 3151.

## PROTECTIVE COATINGS BASED ON FeAl INTERMETALLIC OBTAINED BY A GAS DETONATION METHOD

Z. BOJAR<sup>1)</sup>, W. PRZETAKIEWICZ<sup>1)</sup>, R.A. VARIN<sup>2)</sup>, J. BYSTRZYCKI<sup>1,2)</sup>

<sup>1)</sup>Institute of Materials Technology and Applied Mechanics,  
MILITARY UNIVERSITY OF TECHNOLOGY

Kaliskiego 2, Warsaw 01-489, Poland

<sup>2)</sup>Department of Mechanical Engineering,  
UNIVERSITY OF WATERLOO  
Waterloo, Ontario, Canada N2L 3G1

### Abstract

The results of structure and selected properties investigations of protective coatings obtained by gas-detonation spraying of Fe-Al powder compositions with additions of chromium and boron are shown in this work. It was found that immediately after gas-detonation the coatings exhibit chemical, phase and microhardness nonuniformity. Significant improvement of fatigue life of 0.45% C structural steel and excellent wear resistance of the coatings on the AISi7 cast alloy were found.

### Introduction

In recent years, intermetallic materials have attracted considerable attention in view of their potential for elevated temperature structural applications [1,2]. In particular, an interest in these materials is related to their ability to retain high strength and resist environmental attack, e.g. oxidation at elevated and high temperature. Among the various intermetallics FeAl are the most interesting from the point of view of elevated-temperature mechanical properties and oxidation resistance. Additionally, FeAl is based on relatively inexpensive elemental metals. Moreover, one of the most persistent stumbling blocks in commercialisation of these intermetallics in a bulk form is their brittle fracture behaviour [3,4]. It is, therefore, much easier to utilize intermetallics in the form of protective coatings rather than in their bulk form [5]. Classical techniques of production of protective coatings are rather not useful for applying protective coatings based on FeAl intermetallic. The diffusion nickel aluminide coatings, applied to nickel-based superalloys, have been known since the early 1950's. The most common method of their production is the Pack Cementation Technology

(PCT) [4]. However, this technique has the following drawbacks: (a) coatings are solely dependent on solid state diffusion and since the process takes place at sufficiently high temperature, it can change the substrate (superalloy) microstructure; a post coating heat treatment may usually be required, (b) contamination of the component surface due to the pack mixture being in intimate contact with it may occur, and (c) there is a lack of flexibility in chemical composition of the coating produced. There is no known technique for applying protective coatings based on FeAl intermetallic. It seems [6-8], that an excellent method for applying protective coatings based on FeAl intermetallic is gas-detonation technique. The gas detonation coating process consists of four stages: (a) injection of the oxygen and fuel mixture into the combustion chamber, (b) injection of the powder and nitrogen, which separates the gas supply from the explosion area and prevents backfiring, (c) ignition of the mixture and powder acceleration by the detonation wave, (d) ventilation of the barrel by nitrogen gas [9]. The major advantages of this technique are as follows: easiness of obtaining a very high kinetic energy of metallic powders, no thermal effects on a substrate material, minimal porosity and very good adhesiveness of the coatings and possibility of coating with practically unlimited number of various materials with very different chemical composition.

The major idea of the present work is to replace high alloys steels and speciality alloys used in extreme service conditions by substantially less expensive structural materials coated with intermetallic alloys particularly those based on the Fe-Al system.

### Materials and methods

Commercially available elemental powders of iron, aluminium, chromium and boron were mixed in air to obtain composite powders, using

conventional ball milling. The obtained composite powders with the composition of FeAl (50/50 at. %) + 5wt.% Cr + 0.1wt.% B and FeAl (50/50 at. %) + 10wt.% Cr + 0.1wt.% B, and (60-120) $\mu$ m particle size were applied by a gas-detonation technique as a (0,2 $\pm$ 0,3)mm thick coatings on either a plain carbon steel (0,45wt.%C) or an AlSi7 cast alloy. The process of coating application was carried out at „normal detonation energy on steel substrate and either at „normal” or „enhanced” level of the detonation energy of the detonating mixture on AlSi7 substrate. The same compositions of powders were plasma sprayed on a steel substrate for a comparison. Conditions typical for plasma spraying of NiAl (50/50) powder were used. Plasma spraying method was not optimized for Fe+Al. powder mixture. However, to the best of our knowledge, no literature exists on the plasma spraying of Fe-Al.

Standard metallographic techniques (SEM, EDX, X-ray diffraction) were used to analyse the microstructure as well as phase and chemical homogeneity of coatings. The studies of the effects of composition of powders and the coating parameters on the microstructure and properties of coatings were also carried out. In particular, the studies of properties were focused on microhardness and residual stress distribution, mechanical fatigue and wear resistance of coatings.

### Results

X-ray and chemical analysis of the elemental powders after 20h ball milling did not reveal the presence of the intermetallic phases (Figure 1). Perceptible effect of prolonging a time of ball milling is the reduction of diffraction peaks intensity related to increase of residual stress level in particles of powder, especially in aluminium powder. As a result of ball milling the harder particles of iron, chromium and boron were coated by a softer aluminium metal leading to the formation of a composite powder (Figure 2, table I).

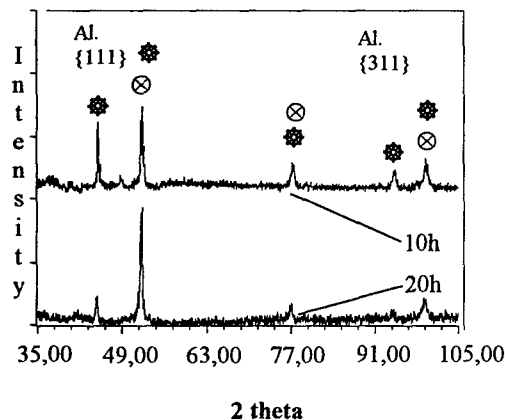


Figure 1. X-ray diffraction pattern of initial powder after different ball milling time; The symbols determine positions of probable phases:  $\odot$  - Fe;  $\star$  - Al.

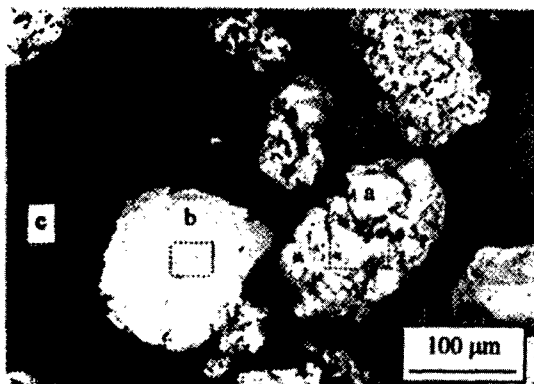


Figure 2. Morphology of powder particles after 20h ball milling.

Table I. Chemical composition of powder particles showed in the Figure 2

Place of analysis	Contents of elements (at.%)			
	Fe	Al	Cr	O
a	84.0	13.5	0.5	2.0
b	3.8	92.6	0.1	3.5
c	0.6	3.9	94.2	1.3

This powder exhibited a very suitable behaviour during a gas-detonation coating. Especially a danger of explosive combustion of pure aluminium was eliminated.

The results of X-ray phase analysis confirm a really different course of coating by using plasma spraying or gas-detonation method. X-ray diffraction patterns of coatings recorded directly after coating on a steel substrate, are put together in Figure 3. A fundamental difference

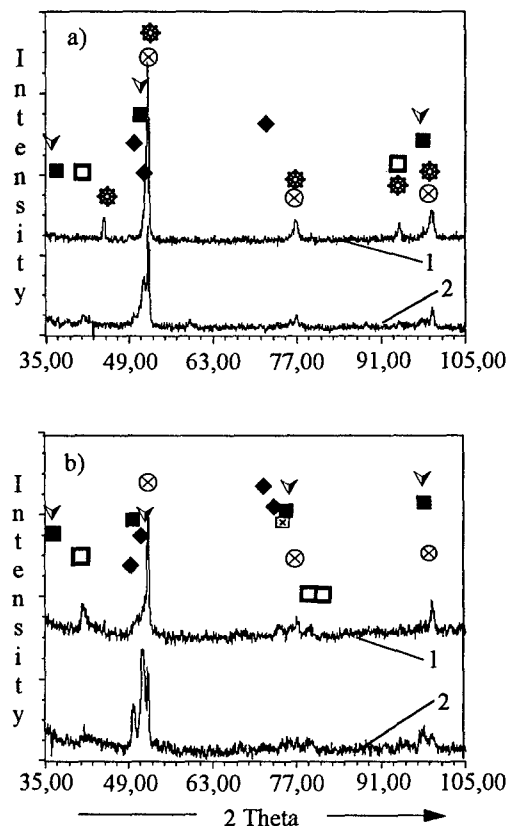


Figure 3. X-ray diffraction patterns of coatings applied on the steel substrate by plasma (a) and gas-detonation spraying (b); 1- after application, 2 - after additional heat-treatment (700°C/10h); The symbols determine positions of probable phases:  $\odot$  - Fe;  $\star$  - Al;  $\nabla$  - FeAl;  $\blacksquare$  - Fe<sub>3</sub>Al;  $\blacklozenge$  - Fe<sub>2</sub>Al<sub>3</sub>;  $\boxtimes$  - Fe<sub>2</sub>O<sub>3</sub>;  $\boxdot$  - Al<sub>2</sub>O<sub>3</sub>.

between plasma and gas-detonation coatings before their additional heat-treatment is a preservation of characteristic {111} and {311} reflexes of aluminium in a X-ray diffraction pattern of plasma sprayed coating (Fig.3a). This X-ray diffraction pattern is practically the same as an initial powder diffraction patterns (Fig.1), i.e. it does not include reflexes confirming that intermetallics phases have been obtained. On the X-ray diffraction pattern of gas-detonation coatings (Fig.3b) there are no {111} and {311} aluminium reflexes. In this case the diffraction effects resulting from formation of Al<sub>2</sub>O<sub>3</sub> and Fe<sub>2</sub>O<sub>3</sub> oxides during gas-detonation process have appeared. Moreover a strong asymmetric broadening of initial {110} iron reflex (Fig.3b, Fig.4) on this pattern can be attributed to the formation of Fe-Al intermetallic phases in due course of gas-detonation coating. The comparison of X-ray phase analysis results of gas-detonation coatings obtained on a steel substrate (Fig.3b) and AlSi7 substrate (Fig.5) confirms very important role of stiffness of the substrate. In gas-detonation coating obtained on a „soft” AlSi7



substrate a volume of cumulated energy is not enough to initiate a reaction of the Fe-Al phases formation and in X-ray diffraction patterns there are only very weak {111} and {311} aluminium reflexes and they do not show a characteristic broadening of {110} iron reflex (compare Fig.4 and Fig.6). A distinct phase transition in investigated coatings on a steel substrate appeared as an effect of an additional heat-treatment. The pair of the strongest {002} and {130} reflexes (in both cases 100% intensity) characteristic for  $\text{Fe}_2\text{Al}_5$  confirms that this phase exists on both: plasma sprayed and gas detonation coatings on a steel substrate.

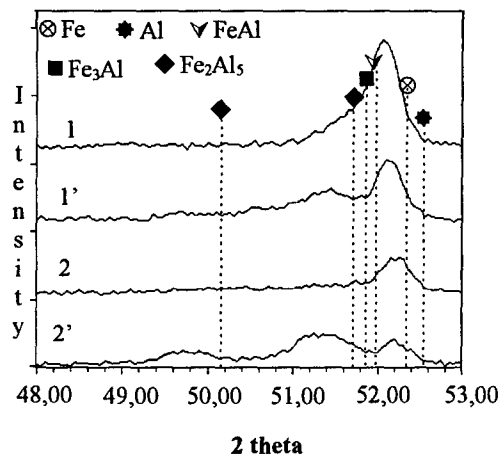


Figure 4. Broadening of the {110} iron diffraction reflex resulting from the Fe-Al phases forming in coatings on the steel substrate; 1 - plasma sprayed, 2 - gas-detonation sprayed, (') - after additional heat-treatment;

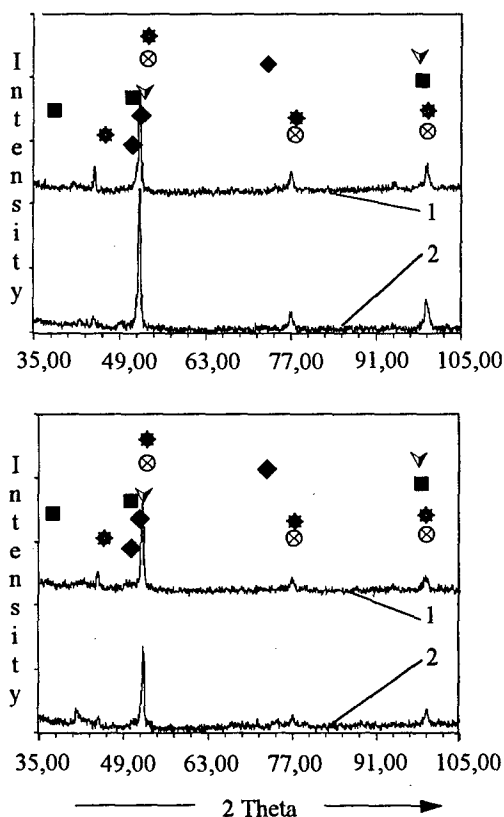


Figure 5. X-ray diffraction patterns of coatings applied on the AlSi7 substrate at „normal” (a) and „enhanced” (b) detonation energy; 1 - after spraying, 2 - after additional heat-treatment (600°C/4h); Descriptions of symbols as shown in Figure 3.

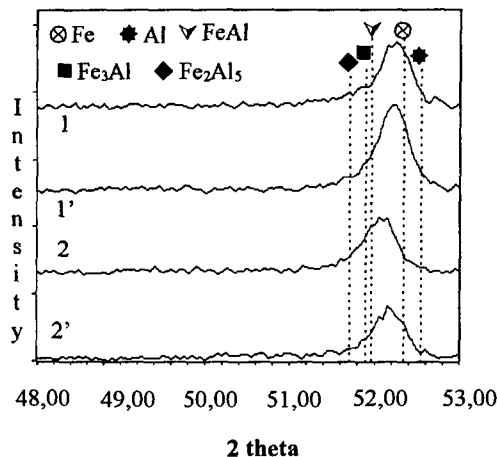


Figure 6. Section of diffraction patterns of gas-detonation sprayed coatings embracing the {110} iron reflex zone; 1 - „normal” energy, 2 - „enhanced” energy, (') - after additional heat-treatment;

Changes of the phase structure of gas-detonation coatings on the AlSi7 substrate caused by changes of level of detonation energy or as an effect of additional heat-treatment are less pronounced (Fig. 5). First of all the „enhanced” level of detonation energy decreases but does not eliminate a part of „pure” aluminium in coating. However the additional heat-treatment enhances this process and increases the content of oxide phases in coatings. In all cases of this phase analysis practically „pure” iron as a microconstituent of investigated coatings was confirmed.

The microstructure of the coatings immediately after gas-detonation (Fig. 7) exhibits the structural, chemical, phase and microhardness non-uniformity just like plasma sprayed coatings taken for comparison.

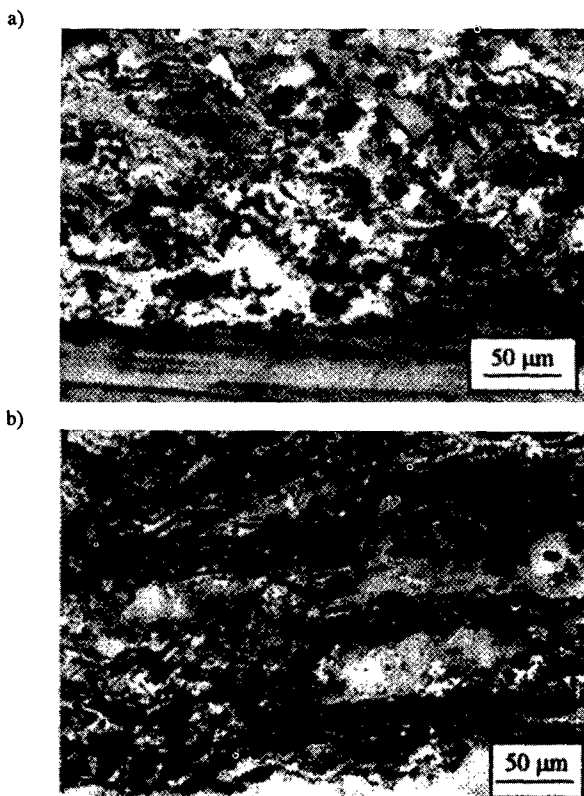


Figure 7. Typical microstructure of the FeAlCr5B0.1 gas-detonation coatings on a steel (a) and AlSi7 (b) substrate.

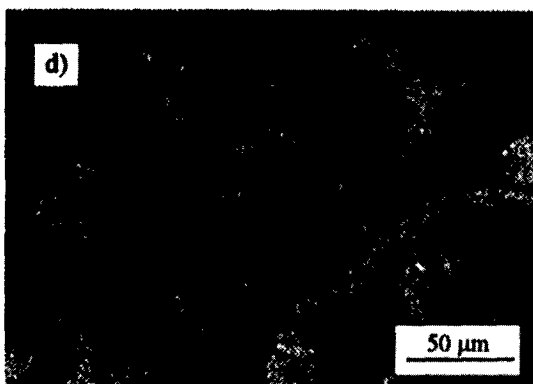
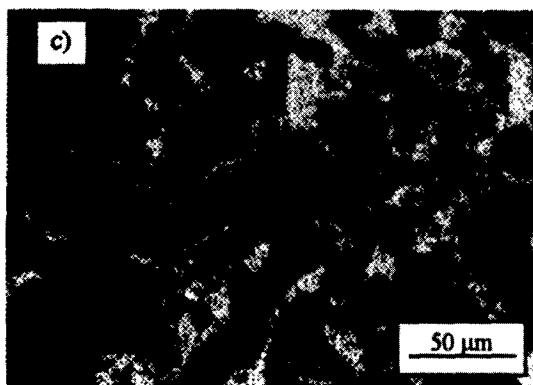
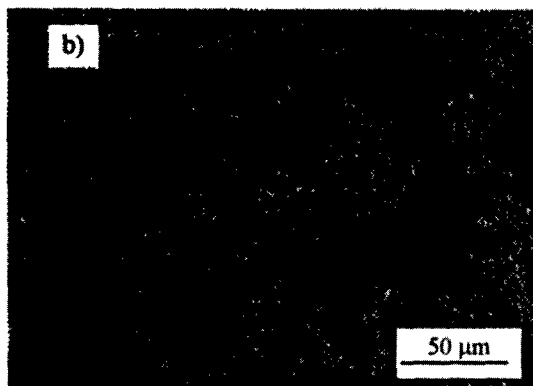
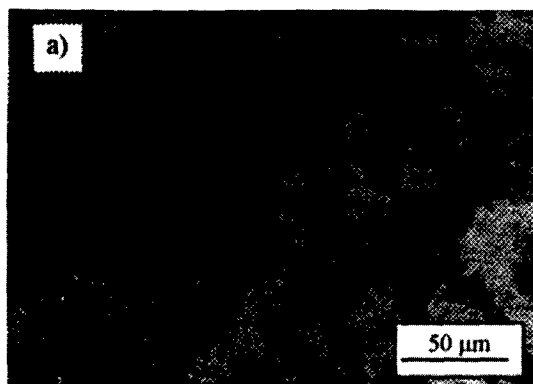


Figure 8. SEM microstructure (a) as well as iron (b), aluminium (c) and chromium (d) distribution in the FeAlCr5B0.1 plasma-sprayed coating on the steel substrate.

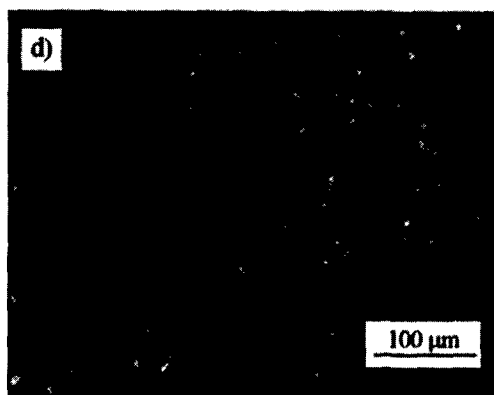
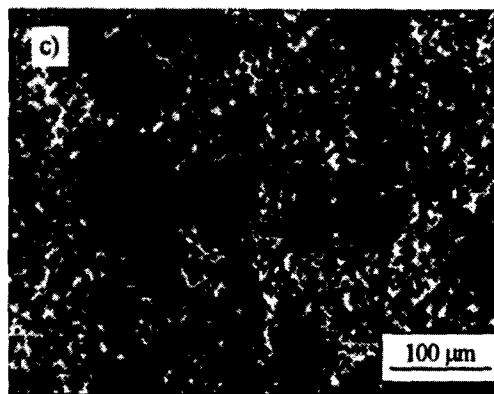
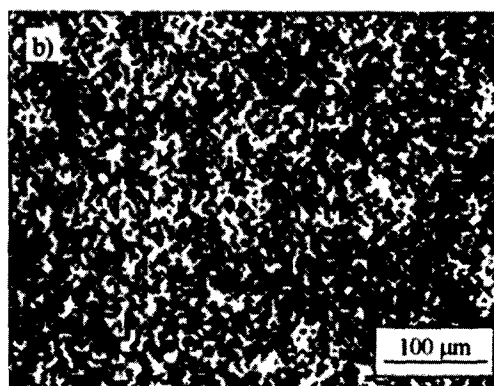
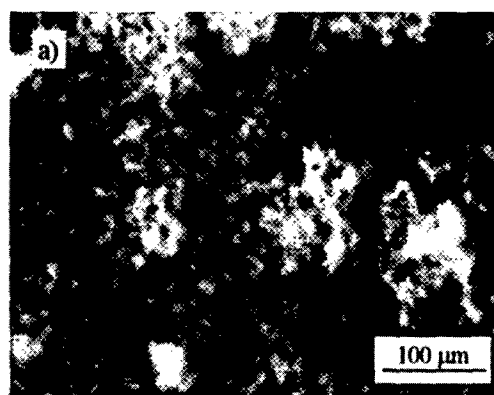


Figure 9. SEM microstructure (a) as well iron (b), aluminium (c) and chromium (d) distribution in the FeAlCr5B0.1 gas-detonation coating on the AISi7 substrate.

However the degree of chemical non-uniformity of plasma sprayed coatings is significantly higher (Fig.8). In spite of the higher temperature and intensive heating, plastifying or even melting of powder particles in plasma-sprayed method, a mapping of elements distribution shows that an initial geometry of powders is preserved. The mapping of elements distribution in gas-detonation coating (Fig.9) shows that in spite of localisation of individual chemical components of coating, the initial composite powders particle have been subjected to strong frittering and geometrical changes.

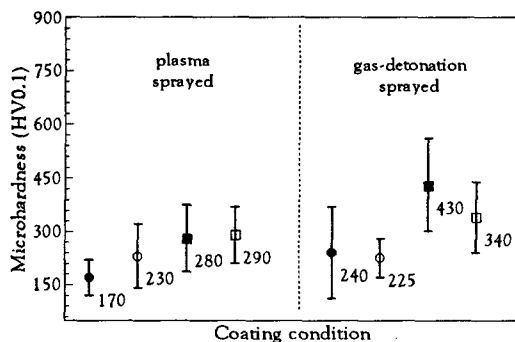


Figure 10. Microhardness of individual phases (circle - "pure" Fe, square - FeAl) in coatings on the steel substrate; solid symbols - after spraying; open symbols - after additional heat-treatment (700°C/10h).

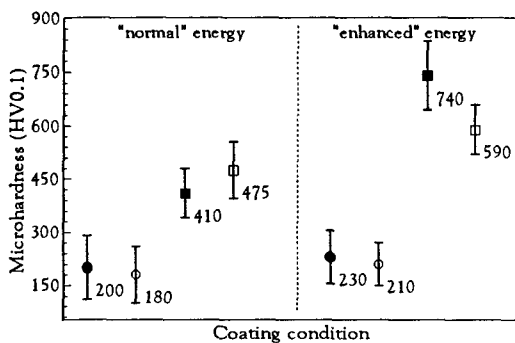


Figure 11. Microhardness of individual phases (circle - "pure" Fe, square - FeAl) in coatings on the AlSi7 substrate; solid symbols - after spraying; open symbols - after additional heat-treatment (600°C/4h).

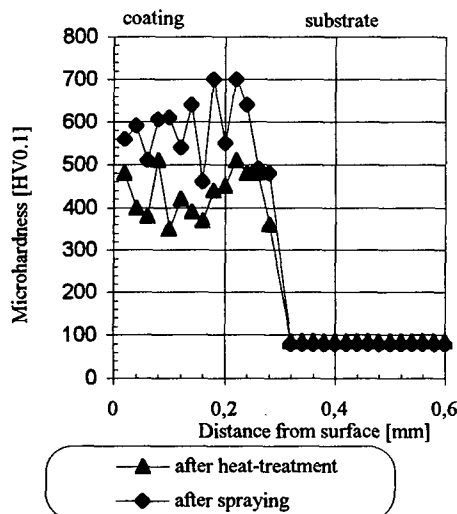


Figure 12. Microhardness distribution in FeAlCr10B0.1 coating on the AlSi7 substrate.

The results of supplementary microhardness measurements let us confirm that in the coating applied on the AlSi7 substrate, there is a minor volume fraction of oxides (microhardness 900÷1000 HV0.1kg) and approximately equal fractions of the FeAl phase (microhardness ~450HV for the „normal“ detonation energy and ~750HV for the „enhanced“ detonation energy) and grains of „pure“ iron (200HV) (Fig. 10). In the coating on the steel substrate besides the FeAl phase (430HV) there exist also highly deformed grains of „pure“ iron (240HV) (Fig. 11).

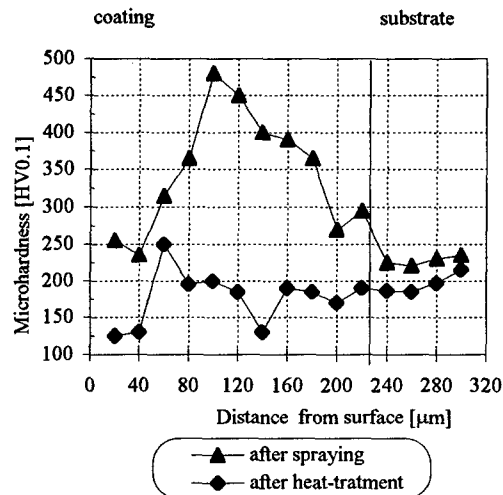


Figure 13. Microhardness distribution in FeAlCr10B0.1 coating on the steel

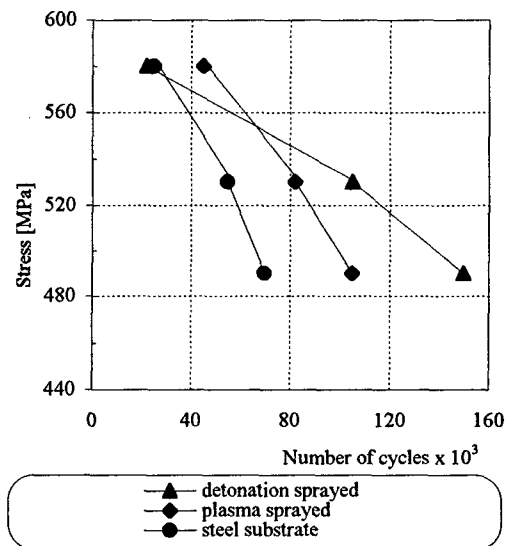


Figure 14. The influence of coating on a fatigue life of steel substrate in the range of limited number of cycles.

A substantial difference is observed in the microhardness distribution on both types of substrate. Coatings on the aluminium substrate (Fig. 12) exhibit a very uniform and constant microhardness distribution throughout the entire thickness with an abrupt drop at the coating/substrate interface. Coatings on steel (Fig. 13) exhibit a maximum microhardness at the half of the coatings thickness and the more gradual decrease of microhardness level of the steel substrate. Microhardness measurements were made along three traverses for each coating and the results shown in Fig.12 and Fig.13 were calculated as the averages, so they represent a real trend observed in investigated coatings.

Adhesiveness to both types of substrate is very good - no peeling is observed during static and dynamic mechanical testing. Gas-detonation coated steel specimens with FeAl based coatings are characterised by a

twofold increase of the fatigue resistance at the specified number of fatigue cycles with respect to the uncoated specimen. Their fatigue resistance is also higher than that of plasma coated specimen (Fig. 14).

In case when both: a substrate and (or) a coating with significant aluminium part are used, the problem of thermal stress resulting from a difference between their coefficients of the linear thermal expansion (Fig. 15) becomes more important. Using a measuring chamber as shown in Appendix (Fig. A-1a), the following cycle of experiments: determining Young's modulus  $E(T)$  for substrate and coating/substrate system (Fig. A-1b), also continuous measuring of deflection  $y(T)$  (Fig. A-1c) and force  $P(T)$  (Fig. A-1d) were carried out.

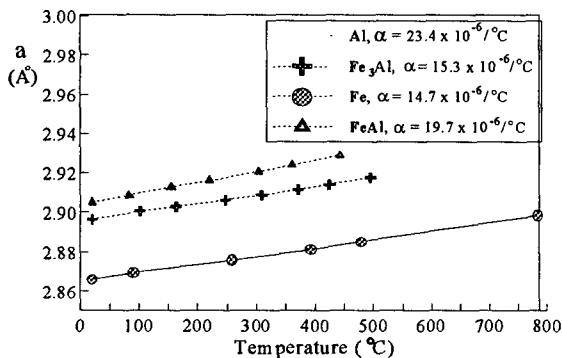


Figure 15. Temperature-dependence of the lattice parameter for selected phases [10].

For semi-beam (Fig. A-1b) loaded by constant concentrated force  $G=3N$ , a deflection  $y$  was registered and from equation:  $E = \frac{Pl^3}{3I} \cdot y$ , the Young's modulus  $E(T)$  of substrate and of coating/substrate system were determined (Fig. 16).

The detonation coating obtained at „normal” energy only negligibly „stiffens” the AlSi7 substrate but in the both cases: for substrate and for coating/substrate system the Young's modulus decreases above the temperature of 250°C.

The influence of the detonation mixture energy used during spraying of coatings on the thermo-mechanical properties of coating/substrate „bimetallic” system was evaluated by comparing (Fig. 17) the results of measurements according to the diagrams in Fig. A-1c and Fig. A-1d.

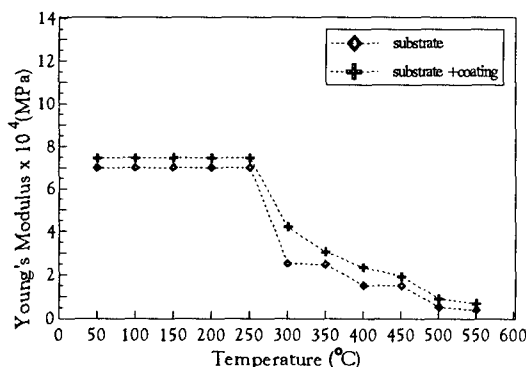


Figure 16. Young's modulus of AlSi7 substrate and „normal energy” coating/substrate system as a function of temperature.

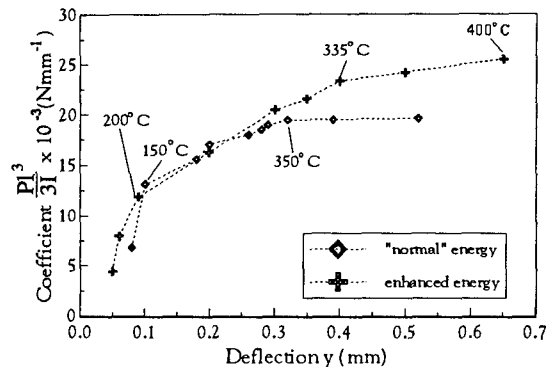


Figure 17. Measured force  $P(T)$  versus deflection  $y(T)$  of „bimetallic” samples during heating.

Bimetallic system with gas-detonation coating obtained at „normal” energy deforms above the temperature of 350°C without increment of the force. In a system obtained at „enhanced” detonation energy, the increase of force exists up to the temperature of 400°C.

Treating [11] bimetallic coating/substrate beam as a self-balanced load (see Appendix - Fig. A-2) the elastic modulus of the coating ( $E_2$  - for „separated” gas-detonation coating) can be estimated.

Knowing  $E_1(T)$  (Fig. 16),  $P(T)$  (Fig. 17) and geometrical parameters of the sample, as well making a simplified assumption (because of a non-uniform structure of coating and especially a fact that the coefficient of linear thermal expansion of aluminium alloys depends on temperature):  $\zeta = \frac{\alpha(FeAl) - \alpha(Al_{20-50})}{\alpha(Al)} = 0.17$ , the coefficient  $\kappa$  (from

equation 6) and also the elastic modulus  $E_2(T)$  of investigated coatings may be estimated (Fig. 18).

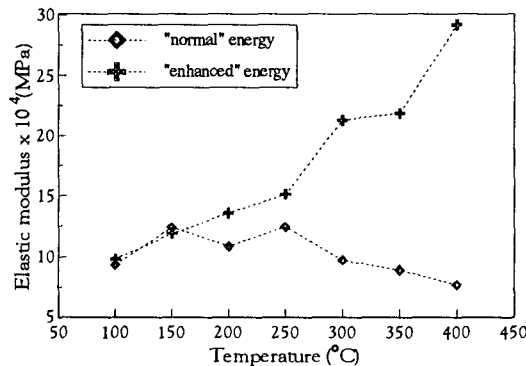


Figure 18. Calculated values of elastic modulus  $E_2$  of the gas-detonation coatings on AlSi7 substrate as a function of the heating temperature.

In both cases: „normal” and „enhanced” energy coatings the elastic modulus is higher than one of substrate. For the „normal” detonation energy coating the calculated elastic modulus averages about  $12 \times 10^4$  MPa up to the temperature of 250°C and then decreases slightly. For the „enhanced” energy detonation coating its elastic modulus gradually increases with increasing the heating temperature and reaches nearly  $30 \times 10^4$  MPa at the temperature of 400°C. These effects are probably connected with increasing the volume of intermetallic phases in investigated coatings.

X-ray studies of the coatings (an analysis of {211} iron peak was conducted) on the aluminium alloy substrate showed the existence of residual compressive stress (Fig. 19) at the half-thickness of the coating approaching the maximum value 350 to 380 MPa for the „normal” and 500 to 570 MPa for the „enhanced” detonation energy.

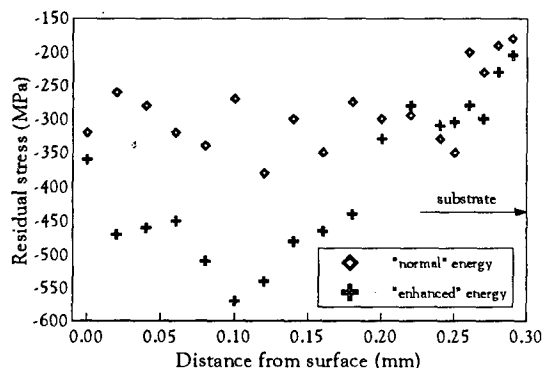


Figure 19. Distribution of compressive residual stress in the FeAlCr10B0.1 gas-detonation coating on AlSi7 substrate.

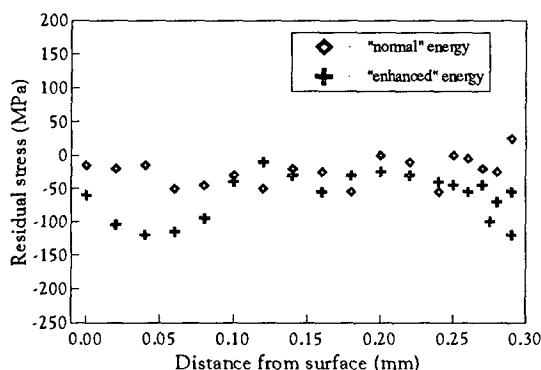


Figure 20. Distribution of compressive residual stress on the back-side of AlSi7 substrate plate coated by the gas-detonation sprayed FeAlCr10B0.1 coating.

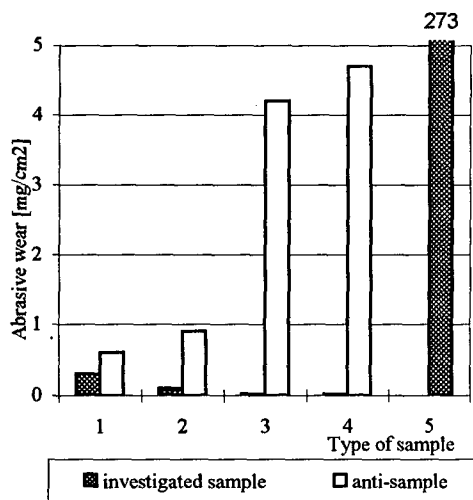


Figure 21. Abrasive wear of gas-detonation coating/AlSi7 sample and anti-sample under different condition:

1 - FeAlCr5B0.1 coating after spraying; 2 - FeAlCr5B0.1 coating after additional heat-treatment 600°C/4h; 3 - FeAlCr10B0.1 coating after spraying; 4 - FeAlCr10B0.1 coating after additional heat-treatment 600°C/4h; and tested for comparison: 5 - alloyed cast iron used as a classic material of cylinder barrel.

It is interesting that at the coating/substrate interface there also exists a compressive residual stress  $\approx 200\text{MPa}$ . The distribution of residual

stress at a back-side of substrate (Fig.20) shows that in this region the stress is compressive too. Such state of stress is a result of summation of stresses caused by the force and by the moment (Fig. A-2) (they form during gas-detonation spraying) and occurs after the coating process is completed.

An excellent wear resistance of the gas-detonation coatings on the AlSi7 substrate was found out by using the „float on float” tribology machine (Fig.21). On the comparative basis the gas-detonation coatings exhibit a fifteen-fold lower wear degradation than the as-cast Fe<sub>3</sub>Al and two hundred-fold lower wear degradation than the alloyed cast iron. The highest wear resistance is exhibited by the coatings with the increased content of chromium obtained by the „enhanced” detonation energy. This time the coatings containing 5wt.% of chromium exhibit a bit higher abrasive wear degradation but simultaneously they caused significantly lower attrition of anti-samples.

### Conclusions

Investigated metallic protective coatings obtained on the steel or aluminium alloy substrate by gas-detonation spraying of preliminary prepared Fe-Al-Cr-B powders manifest a number of interesting properties.

1. Using relatively inexpensive elemental metals and technology of coating, a very good compactness and adhesiveness to steel and AlSi alloy substrates was obtained.
2. A desirable state of residual compressive stress at the coating and at the coating/substrate interface, causing an increase of the fatigue life of coating/substrate system, and finally as well an excellent wear resistance of the coating were obtained.
3. Chemical, phase and microhardness non-uniformity, resulting in a relatively low elastic modulus (its value is near the value of aluminium alloys) and intermediate value (between Fe and Al) of the linear thermal expansion coefficient of the investigated coatings were found. Due to their low values the gas-detonation coatings exhibit a very good durability under mechanical and thermal load on both types of used substrate.
4. A significant part of secondary solid solutions based on Fe-Al intermetallic phases and existence of hard aluminium oxide particles besides the highly deformed (but relatively soft) grains of practically pure iron forms an excellent material for usage under sliding friction conditions.
5. Low wear degradation of coatings is related to low wear degradation of anti-samples which used during the test.

### Acknowledgement

This work was supported by grant from the Polish Committee for Scientific Research which is gratefully acknowledged.

### References

1. Proc. Third Int. Conference on High Temperature Intermetallics, eds., D.P.Pope, C.T.Liu and S.HWhang; published in Mater. Sci. Eng., A192/193 (1995).
2. Proc. Symp. on High Temperature Ordered Intermetallic Alloys VI, eds., J.A.Horton et al., MRS, Pittsburgh, PA, vol. 364, 1995.
3. R.D.Noebe, R.R.Bowman and M.V.Nathal, *Int. Mater. Rev.*, (38) (1993) 193.
4. N.S.Stoloff and C.T.Liu, *Intermetallics* (2) (1994) 75.
5. P.C.Patnaik, in „Advances in High Temperature Structural Materials and Protective Coatings, eds., A.K.Koul, V.P.Parneswaran, J.P.Immarigeon and W.Wallace, NRC, Ottawa, Canada (1994) 169.
5. T.Durejko, unpublished results, Military University of Technology, Warsaw, 1995.
6. J.Bystrzycki, R.A.Varin, Z.Bojar, „Last advances in investigations of intermetallic alloys with aluminium content”, *Inżynieria Materiałowa*, (in Polish) 5 (1996).

7. Z.Bojar et al., „Structure and properties of Ni-Al and Fe-Al protective coatings” (Paper presented at the meeting: Advanced Materials and Technologies in Surface Engineering of Corrosion and Wear Protective Layers Katowice, Poland, April 1996) (in Polish).

8. Z.Bojar, Z.Komorek, T.Durejko, „Structure and properties of protective intermetallic layers obtained by gas-detonation method” (Paper presented at the Symposium on „Solidification of metals and alloys” - Jawor, Poland, December 1996) (in Polish).

9. E. Kadyrov, V.Kadyrov, „Gas Detonation Gun for Thermal Spraying”, *Advanced Materials & Processes* 8 (1995), 21.

10. W.B.Pearson, *A Handbook of Lattice Spacings and Structures of Metals and Alloys*, vol.4, (Pergamon Press, 1958), 313-345.

11. M.Wieczorek, private communication with author, Military University of Technology, Warsaw, Febr. 1997.

## APPENDIX

Measurements of thermo-mechanical properties of coating/substrate system

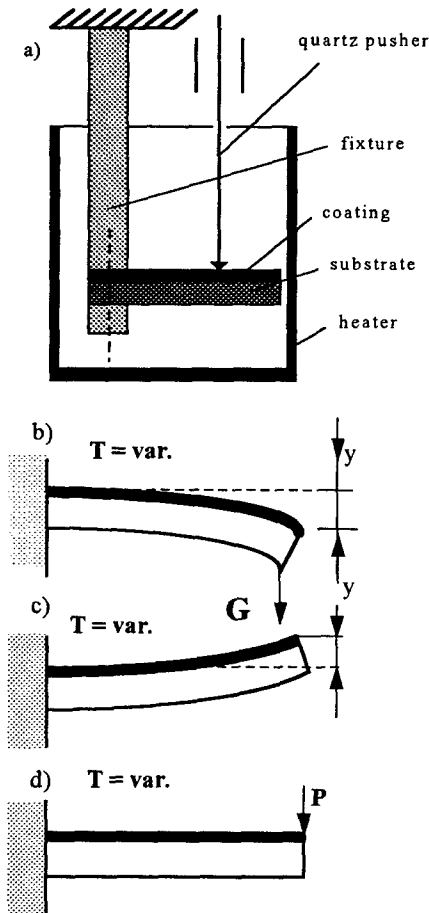


Figure A-1. Measuring chamber (a) and diagrams of experiments (b-d).

Estimating of the gas detonation coating elastic modulus

Designating:  $\alpha_1, \alpha_2$  - coefficient of the thermal linear expansion of substrate and coating, respectively;  $\Delta\alpha = \alpha_1 - \alpha_2$ ;  $q$  - load intensity;  $m$  - moment intensity;  $E_1, E_2$  - Young's modulus of substrate and coating, respectively;  $N$  - force (tensile for coating, compressive for substrate);  $I$  - moment of inertia;  $A$  - cross-section;  $H, h, l$  - geometrical parameters of sample as

shown in Fig. 19;  $T$  - temperature of heating;  $\Delta l(N)$  - linear strain caused by a force;  $\Delta l(M)$  - linear strain caused by a moment;  $\delta = h/H$ ;  $\kappa = E_1/E_2$ ;  $\xi = \Delta\alpha/\alpha_1$ ;

and making assumptions (in general case):

$$\Delta l(N) = \frac{Ndx}{EA}; \quad \Delta l(M) = \int_0^l \frac{Mh}{2EI} dx; \quad N = qx; \quad M = (q\frac{h}{2})x;$$

$$\Delta l = \Delta l(N) + \Delta l(M); \quad \Delta l = \Delta\alpha l; \quad \Delta\alpha l = \frac{Ndx}{EA} + \int_0^l \frac{Mh}{2EI} dx;$$

the following equations are obtained for the coating/substrate system:

$$\Delta\alpha l = \int_0^l (\frac{qxdx}{E_1 A_1} + \frac{qxdx}{E_2 A_2} + \frac{qh^2}{4} \frac{xdx}{E_2 I_2} + \frac{qh^2}{4} \frac{xdx}{E_1 I_1}) \quad (1)$$

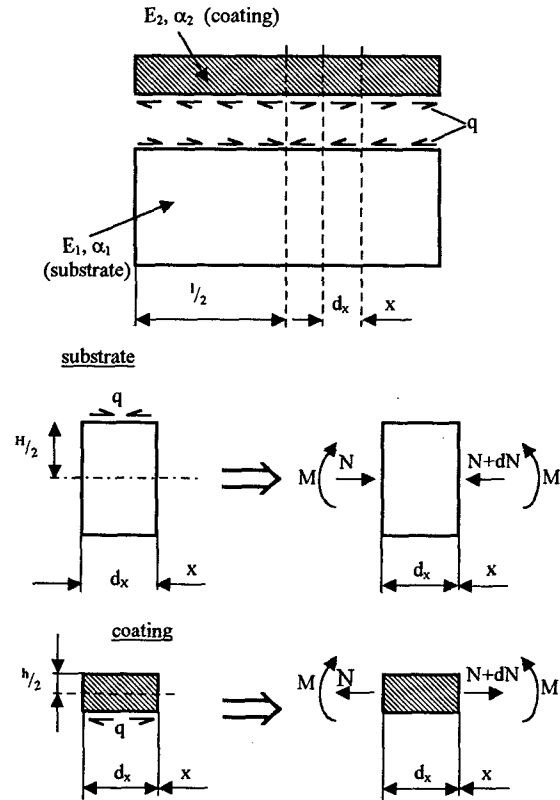


Figure A-2. Pictorial diagram of bimetallic coating/substrate system.

$$\Delta\alpha l = \frac{2ql^2}{2} (1 + \frac{1}{\delta\kappa}) \Rightarrow q = \frac{\Delta\alpha b H E_1 T}{2l(1 + \frac{1}{\delta\kappa})}; \quad (2)$$

$$\text{Because: } m = \frac{qH}{2} = \frac{\Delta\alpha b H^2 E_1 T}{4l(1 + \frac{1}{\delta\kappa})}; \quad (3)$$

the determined deflection (Maxwell-Mohr method) can be expressed as:

$$y = \frac{1}{EI} (\frac{ml^3}{8}) \quad (4)$$

By comparison:  $\frac{Pl^3}{3EI} = \frac{ml^3}{8EI}$ , a force  $P$  released in the bimetallic coating/substrate system may be determined as:

$$P = \frac{3}{8} m. \quad (5)$$

Consequently:

$$P(T) = \frac{3}{32} \frac{b H^2 E_1(T) \alpha_1 \xi T}{l[1 + \frac{1}{\delta\kappa(T)}} \quad (6)$$

HOW TO OBTAIN SOME ROOM TEMPERATURE DUCTILITY  
OF FeAl (B2) INTERMETALLIC ALLOYS

Anna FRACZKIEWICZ, Anne-Sophie GAY, Sebastien LAUNOIS, Michel BISCONDI

Ecole des Mines de Saint-Etienne, Centre SMS  
158 Cours Fauriel, 42-100 St-Etienne, FRANCE

Abstract

The fracture of B2 FeAl alloys, tested at room temperature, takes place in a brittle manner. This behaviour has two origins: intergranular (due to the intrinsic weakness of grain boundaries) and transgranular (extrinsic, due to an "environmental effect"). In this paper, both aspects of room temperature brittleness of FeAl alloys were studied, with the purpose to identify their reasons and to determine conditions to avoid them.

A small addition of boron, segregating to the grain boundaries in FeAl alloys, is a well-known manner to avoid their intrinsic brittleness. The mechanisms of the segregation of boron were studied in alloys containing 40 to 50 at.% Al, in a large domain of temperatures (300 - 700°C) and times (up to 120 h) of heat treatment. The double origin of this segregation has been identified. First, the very fast kinetics of boron segregation is due to a non-equilibrium mechanism, resulting from an interaction between boron atoms and migrating thermal vacancies. Still, a low-level equilibrium segregation is also stable; it is sufficient to change the fracture mode from intergranular (in B-free alloys) to transgranular by cleavage (in B-doped alloys). It is interesting to note that thanks to these two aspects of boron segregation, no specific "segregation heat treatment" is needed to reinforce the grain boundaries in FeAl.

The cleavage-like brittle fracture of B-doped alloys is due to the "environmental effect", an embrittlement by hydrogen in water-containing testing atmospheres. The embrittling hydrogen is introduced in the material before or during the test.

In the case of samples tested in the embrittling conditions, the fracture occurs by a two-stage process. If the fracture initiation occurs by cleavage, at a stress depending on the test conditions (strain rate, moisture content), then the final fracture has mechanical origin and occurs at a constant value of stress (1480 MPa).

To avoid the environmental embrittlement by hydrogen, an efficient protection of material from water vapour in the atmosphere, before and

during the test, is necessary. A heat treatment at 800°C, before the test, removes the hydrogen from the material and so, the embrittlement by pre-induced hydrogen is reduced. However, as the kinetics of re-introduction of hydrogen seems to be very fast, so a protection of the degassed material is also needed. This protection can be obtained, for example, by a thick oxide layer on the sample surface.

Introduction

Some properties of the B2 FeAl alloys (containing about 40 at. % of aluminium), such as their good specific mechanical properties at intermediate temperatures (up to 500°C /1/) and excellent corrosion resistance, would be very interesting for industrial applications, if some ductility was obtained at room temperature. Unfortunately, in these conditions, the FeAl alloys are brittle - as it is also the case for many other intermetallic alloys.

Two different origins of the room temperature brittleness of FeAl alloys were identified: intergranular and transgranular.

In pure FeAl alloys, the fracture is of brittle intergranular type: the intrinsic weakness of grain boundaries seems to be responsible for this behaviour of the material. As in the case of Ni<sub>3</sub>Al /2/, small boron additions (few hundreds of atomic ppm) permit a change of the fracture mode: with the presence of boron, the fracture of the alloys becomes mixed, mainly of transgranular type.

This beneficial effect of boron on fracture of intermetallic alloys was attributed to its presence at grain boundaries. There is no clear explanation of the elementary mechanism, responsible for the effect of the intergranular boron on the fracture mode. George /3/ suggests two possible hypotheses: an enhancing of the grain boundaries cohesion, or a modification of the conditions of the sliding transmission through the grain boundaries. Moreover, if the presence of intergranular boron is the assumed reason of the observed effect, there is no comprehension of its segregation mechanism. In fact, the only informa-

tion that we have is some AES grain boundaries analysis in intermetallic alloys, mostly in  $\text{Ni}_3\text{Al}$ , showing a boron peak, of relatively low intensity /2,4/.

If in B-doped FeAl alloys the fracture is no longer intergranularly brittle, then no ductility can generally be obtained, as the fracture occurs by cleavage. This phenomenon seems to have an extrinsic origin, identified by Liu as the "environmental effect" /6/, existing if a sample is tested in a water-containing atmosphere. As a result of  $\text{H}_2\text{O}$  particle reduction by Al atoms on the free surface of the sample, atomic hydrogen is produced; its diffusion into the material is easy thanks to its atomic (and not molecular) nature.

The ab initio calculations by Fu and Painter /7/ have shown that the hydrogen presence in the structure of B2 FeAl weakens the atomic bindings between Fe and Al atoms, which results in a possible fracture by cleavage on (100) planes, in accordance to experimental observations.

For a long time, the model of hydrogen embrittlement of FeAl alloys has been presented as a simple hypothesis; recently, this was clearly reinforced by experimental observations by Zhu et al. /8/ of the atomic hydrogen presence at the sample surface, when it was exposed to a chemical reaction with water.

In the present paper, both aspects of brittleness of FeAl alloys, intergranular and transgranular, are studied. The purpose of this work is to identify the causes of brittleness of FeAl alloys and to determine conditions to avoid them. Two different kinds of alloys were used in this work. The study of intergranular brittleness was performed on laboratory cast, large grain FeAl alloys, B-free or B-doped. The characterization of the environmental embrittlement was done on a semi-industrial alloy prepared by mechanical alloying, and called FeAl40 Grade 3 /1/. In this material, thanks to its very fine microstructure, which limits the cleavage propagation, some room temperature ductility was obtained.

#### Intergranular brittleness. Effect of boron

##### Experimental

Three FeAl alloys, containing 40, 46 or 50 at. % Al were studied. The alloys were laboratory cast; their grain size was of about 400  $\mu\text{m}$  in all the cases. The alloys were pure (B-free) or doped by small boron addition (40 to 800 at. ppm). A two-stage heat treatment was applied. The aim of the first treatment (1h at 950°C, followed by air quenching) was to create a large quantity of thermal vacancies. Hence, an annealing treatment was given to eliminate the excess of thermal vacancies and/or to enable the boron intergranular segregation. To characterize the boron segregation, a large domain of temperatures (300 to 700°C) and times of heat treatment (up to 120 h) was studied. The boron segregation was measured by Auger electron spectroscopy (AES) with direct acquisition of Auger peaks. The results were quantified by a method based on internal standards /9/. After the AES analysis, the samples were observed by SEM to verify the intergranular type of fracture of analysed surfaces.

In the study of kinetics of vacancies elimination, isothermal dilatometric experiments were performed at temperatures near 400°C. The samples contraction, or  $\Delta l$ , was measured; it permits the calculation of the excess vacancy concentration, or  $\Delta N$ , from the formula:

$$\Delta N = 3 \Delta l / l$$

##### Intergranular boron segregation

Two characteristic examples of fracture surfaces are shown on Fig. 1. In accordance with previous observations, the fracture of B-free alloys is completely brittle, independently of the Al content (40 to 50 at. %) of the alloy. On the contrary, it becomes mixed, with predomination of transgranular cleavage, in the case of boron-doped alloys.

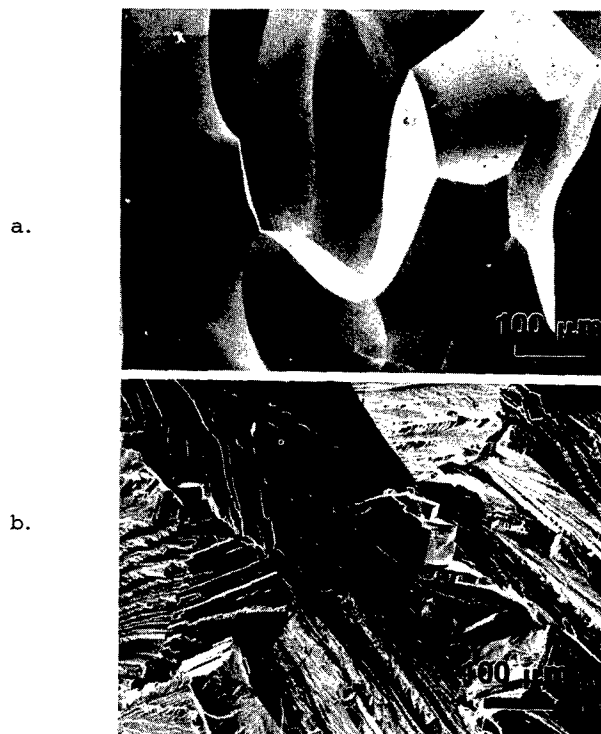


Figure 1: Fracture surfaces of Fe-Al (40 at. % Al) alloys: a/ pure alloy b/. B-doped (200 at. ppm) alloy

In the boron-doped alloys, a low level of intergranular segregation of boron is shown on intergranular fracture surfaces by AES. The effect of heat treatments on a level of intergranular boron segregation was studied in the case of Fe-46 at% Al alloy, containing 400 at. ppm of boron. The Fig. 2 shows the effect of the temperature of a 24h heat treatment on intergranular boron content. A very slight maximum of boron segregation could be observed in the sample annealed at 600°C; this temperature was then chosen for the study of the kinetics of boron segregation in isothermal conditions (Fig. 3).

No significant influence of thermal conditions on the boron segregation was observed. Only few atomic percents of intergranular boron are measured just after



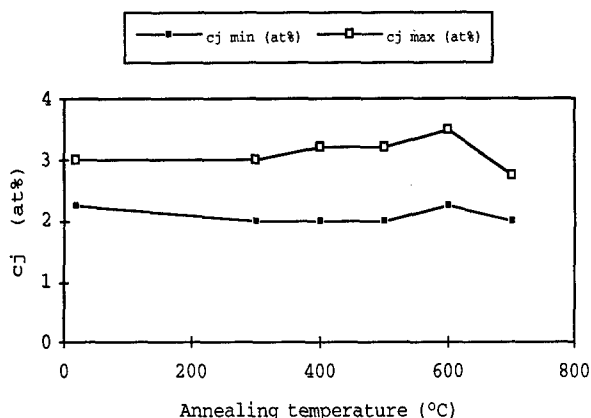


Figure 2: Effect of temperature of heat treatment during 24 hours on the intergranular boron segregation. Fe-46 at. % Al alloy, doped by 400 at. ppm of boron.

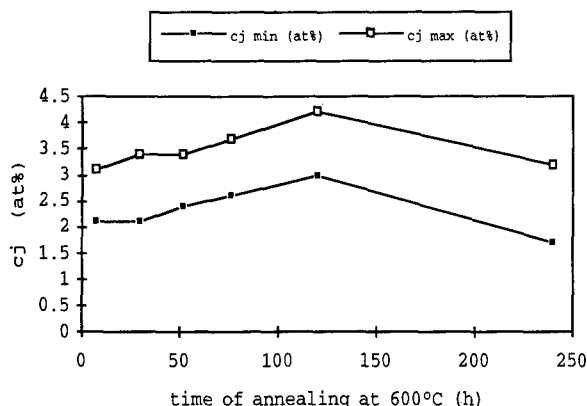


Figure 3: Effect of time of heat treatment at 600°C on the intergranular boron segregation. Fe-46 at. % alloy, doped by 400 at. ppm of boron.

quenching and in all the range of studied temperatures and times of heat treatment.

From the theoretical point of view, the intergranular segregation phenomena can have two different origins. The first one, corresponding to the equilibrium segregation, is well described by the McLean's model /10/ and is based on thermodynamic equilibrium of segregating atoms in the grain boundary structure. This kind of segregation presents a specific behaviour : it is characterized by a saturation value (in the simplest case, it can be considered as a monolayer of segregating atoms, present in the plane of grain boundary) and a strong exponential decreasing dependence of its level on temperature. In numerous cases, another type of intergranular segregation can take place, in presence of thermal vacancies. Those point defects, migrating to grain boundaries to annihilate there, can be accompanied by segregating atoms and thus, provoke some segregation. This kind of segregation is considered as a non-equilibrium one. The observed characteristics of boron intergranular segregation in FeAl (low level, very fast kinetics, no temperature dependence) hardly correspond to the

classic equilibrium segregation description. Moreover, the FeAl (B2) alloys are known to be able to retain large concentrations of thermal vacancies, up to 1 at. % in stoichiometric alloy /12/. As it is easy to think that an interaction between vacancies and boron atoms exists in B-doped FeAl alloys, the hypothesis of a non-equilibrium mechanism of the boron segregation has to be checked.

#### Kinetics of thermal vacancies migration

B-free and B-doped alloys, containing 40 or 50 at. % Al, were quenched from 950°C and isothermal dilatometric experiments were performed at temperatures near 400°C (fig. 4 and 5).

As previously noted by other authors /12/, a strong effect of Al content on excess vacancies concentration is observed : their concentration in Fe-50% Al is almost four times higher than in Fe-40% Al and attains 0.8 at. %. This value is slightly lower than that given by bibliographic data ; probably, the conditions of quench were not sufficiently violent and some vacancies were eliminated during the quench.

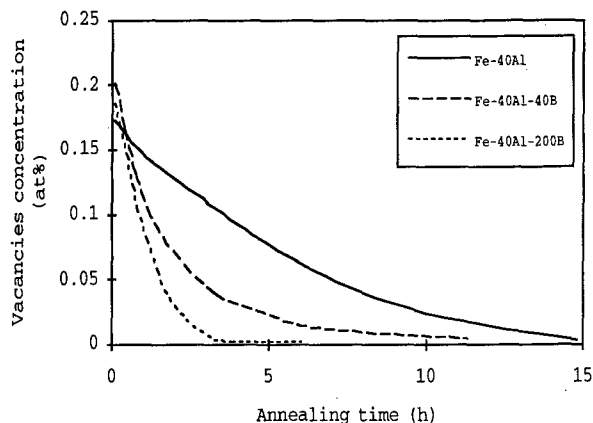


Figure 4: Kinetics of vacancies elimination at 380°C for Fe-40 % at. Al containing 0, 40 and 200 at. ppm of boron. Samples previously quenched from 950°C.

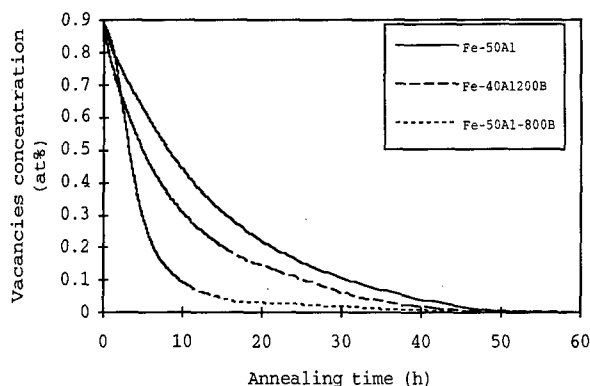


Figure 5: Kinetics of vacancies elimination at 380°C for Fe-50 % at. Al with boron content varying from 0, 200 and 800 at. ppm. Samples previously quenched from 950°C.

In both studied alloys, the boron addition strongly accelerates the vacancies migration kinetics. To quantify the boron effect, the decrease of the excess vacancy concentration with time  $t$ , in isothermal conditions, was described by an exponential function :

$$N = N_0 \exp(-Kt)$$

where  $K$  is the constant of the reaction of vacancies elimination. The values of  $K$  for the studied alloys are given in fig. 6, as a function of B content in the alloy, normalized by the corresponding vacancy concentration after quench. For both Al contents in the studied FeAl alloys, a strong modification of the reaction constant  $K$  in presence of boron is observed. In the case of Fe-40%Al alloy, as little as 40 ppm of boron are sufficient to double the value of  $K$ . It is interesting to note that in the case of the Fe-50 % Al alloy, the "boron efficiency" for modifying the vacancies migration kinetics (measured by the slope of the curve, Fig. 6) is much lower than in the other one.

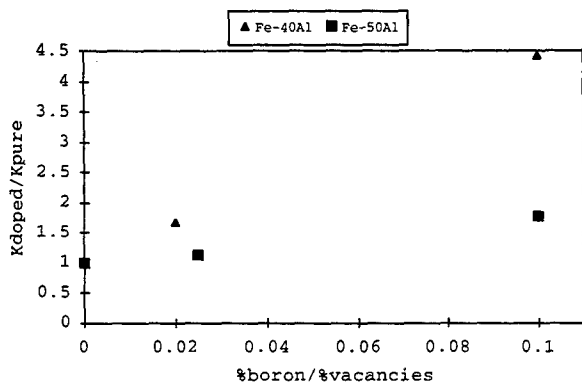


Figure 6: Constant of the reaction of vacancies elimination ( $K$ ) as a function of boron content, normalized by the after-quench vacancies concentration in the alloy.

To quantify the effect of boron on the kinetics of vacancies elimination in the Fe40at.% Al alloy, we first considered a simple model consisting in the creation of boron atom-vacancy complexes [13]. Thus, an interaction energy value of about 0.4 eV was calculated. However, our latest results clearly indicate that the energy of interaction strongly depends on the Al content in the alloy : in fact, in the Fe-50 at. % Al alloy, the boron effect is clearly slighter than in the Fe40at.% Al. Our previous model is probably not sufficient to describe the real interactions, which seem to be more complex. A more satisfactory model will need a better knowledge of point defects in FeAl for a large domain of Al content ; unfortunately, this kind of information is still hardly accessible.

## Transgranular brittleness Environmental effect

### Experimental

The studied alloy ( FeAl40 Grade 3, /1/) was prepared by mechanical alloying and hot extrusion. This alloy, containing 40 at. % Al, is doped by 40 at. ppm of B and reinforced by a fine  $Y_2O_3$  dispersion. It has a strong wire texture with the  $\langle 110 \rangle$  axis parallel to the tensile axis of machined specimens. The very fine grain size (1  $\mu m$ ) of the studied alloy leads to a high value of the yield stress (780 MPa) and some ductility at room temperature. A heat treatment at 1000°C for a 1h followed by furnace cooling was performed on the material before machining. The tensile tests were performed at two different strain rates :  $3 \cdot 10^{-4}$  and  $3 \cdot 10^{-6} s^{-1}$ , and in three different atmospheres (called : air, argon and dry argon), containing the estimated volumic concentration of water of 1,5 %, 400 ppm and 50 ppm, respectively.

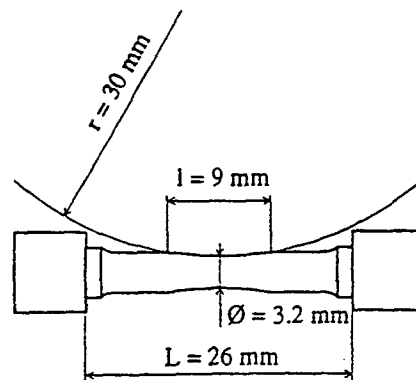


Figure 7: Tensile specimen. A local thinning was necessary to ensure its fracture into the central part of specimen

Dumbbell-shape specimens (Fig. 7) were machined and mechanically polished. Some specimens were then annealed at 800°C for a 1h and furnace cooled, in order to be oxidized enough to get a protective scale.

Because of a local thinning of tensile specimens (necessary to ensure their fracture into the central part of specimen), a strong localisation of deformation was observed. The values of relative elongation given below are the ratios of the measured elongation to the length of specimen,  $L$ . In the same testing conditions, a comparison of thinned and unthinned samples shows that the thinning reduces the relative elongation by a factor of 3. For this reason, it is not worth noting that the reported values of elongation are of only few percent, surprisingly low for the studied material.

### Effect of water vapour content in the atmosphere on the relative elongation

In dry argon, the relative elongation of samples is almost three times higher than that of the samples tested in air (Fig. 8). This ratio is conserved for the two used strain rates, but in the case of lower strain rate ( $10^{-6} s^{-1}$ ), the absolute values are

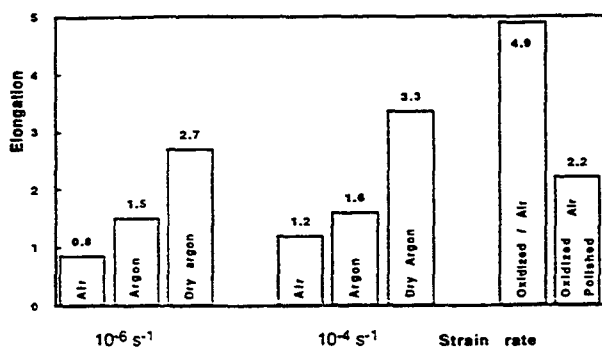


Figure 8: Relative elongation-to-fracture of FeAl 40 Grade 3 alloy at room temperature as a function of water vapour content in the testing atmosphere.

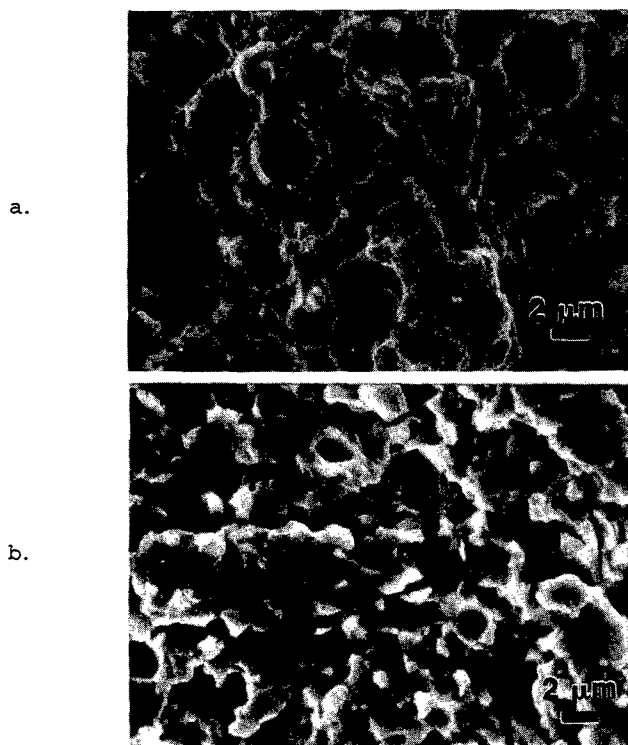


Figure 9: Fracture surface of FeAl Grade 3 alloy: a/. ductile fracture in the central part ; b/. cleavage-like fracture in the peripheral part of tensile specimen

slightly lower.

The two characteristic types of fracture, observed in the tested specimens, are shown on Fig. 9. In the central part of specimens, the fracture is always of a ductile type (Fig. 9a), independent of the testing atmosphere. On the contrary, in the peripheral part of specimens, some cleavage-like fracture (Fig. 9b) was observed locally. This last kind of fracture, cleavage-like, seems to be a result of environmental embrittlement. The observation of fracture surfaces and the analysis of stress-strain curves have allowed us to propose a model of two-stage fracture of the embrittled material [14]. According to this, the fracture nuclea-

tion takes place by cleavage fracture, at a stress depending on environmental conditions. Obviously, its value decreases with higher water vapour content in the atmosphere and with lower strain rate value. Only after the environment-induced nucleation of the fracture, and as a result of the reduction of the sample section, the final fracture can take place, if the real stress reaches the intrinsic strength of material. Its value was estimated as  $1480 \pm 40$  MPa. In all the cases, this final fracture is of ductile type.

It is of particular interest to note that both the constant value of the intrinsic fracture stress of material and the limitation of cleaved fracture to the embrittled, superficial region of samples, confirm intrinsic ductility of the FeAl40 Grade 3 alloy.

#### Origins of embrittling hydrogen

The embrittling element of FeAl alloys, according to the previous hypothesis and recent observations, should be atomic hydrogen. This element, of atomic nature, resulting from the oxidation of Al at the sample surface by a water molecule, can be introduced into the material before or during the test. In the present study, both cases were observed.

In samples tested with the higher strain rate,  $3 \cdot 10^{-4} \text{ s}^{-1}$ , the time of test is of about 3 min. It is much too short to get a significant hydrogen diffusion during the test. In this case, the cleavage fracture observed is due to the pre-existing hydrogen, introduced into the material in the static conditions, before the test. On the contrary, lower values of elongation obtained for samples tested with lower strain rate ( $3 \cdot 10^{-6} \text{ s}^{-1}$ ) can be explained by an additional effect of in-situ hydrogen, introduced during the test.

#### Role of oxidation heat treatment

This strong effect of pre-existing hydrogen was confirmed by some tests in air, performed on oxidized samples; one of them was polished after the oxidation treatment to remove the oxide layer. After the heat treatment and before the test, samples were stored for few days in laboratory air. The relative elongation of so-prepared samples, tested at  $3 \cdot 10^{-4} \text{ s}^{-1}$ , is given of Fig. 8.

Compared to just-polished samples, tested in the same conditions, both samples after the oxidation heat treatment show a higher value of relative elongation to fracture. Moreover, the elongation of the sample tested with the superficial oxide layer is even higher than that tested without this kind of protection in the least "dangerous" atmosphere: in dry argon (Fig. 8). However, the elongation of oxidized-and-polished sample is only a half of the value obtained for the oxidized one.

It seems that the main effect of oxidation heat treatment is an efficient degassing of material from the pre-existing hydrogen. Unfortunately, the kinetics of re-introduction of hydrogen into the material seems to be very fast; in fact, only a few days of storage before the test were sufficient to embrittle the oxidized-and-polished sample. On the contrary, the oxide layer on the sample surface was an efficient protection against the re-introduction of hydrogen. Thanks to this effect, a very high elongation value in air could be obtained.

### Conclusions

Some ductility of FeAl (B2) alloys can be obtained, if two conditions are fulfilled :

1° to avoid the intrinsic intergranular brittleness of FeAl (B2), an addition of small amount of boron is needed. A few atomic percents of intergranular boron are sufficient to strengthen grain boundaries by an intergranular segregation. This segregation has two different origins. Its very fast kinetics results from a non-equilibrium mechanism, due to an interaction with thermal vacancies migrating to grain boundaries. Nevertheless, a low-level equilibrium segregation is also stable in the studied alloys.

Thanks to these two origins of the boron segregation, no specific "segregation heat treatment" is needed to ensure the reinforcement of grain boundaries in FeAl alloys.

2° the environmental embrittlement by hydrogen can be avoided by an efficient protection of material from water vapour in the atmosphere, before and during the test. A heat treatment at 800°C before the test allows to reduce the embrittlement by pre-induced hydrogen. However, as the kinetics of re-introduction of hydrogen seems to be very fast, a protection for the degassed material is also necessary. This protection can be obtained, for example, by a thick oxide layer on the sample surface.

### References

1. F. Moret, R. Baccino, P. Martel, L. Guetaz, "Propriétés et applications des alliages intermétalliques B2-FeAl", J. Phys. 6, C2 (1996), 281
2. C.T. Liu, C.L. White, J.A. Horton, "Effect of Boron on Grain-Boundaries in Ni3Al", Acta Met., 33 (1985), 213
3. E.P. George, C.L. White, J.A. Horton, "Grain Boundary Cohesion and Fracture in Ordered Intermetallics", Scripta Met. 25 (1991), 1259
4. I. Baker, E.M. Schulson, J.R. Michael, R.A. Padgett, "Grain Boundary Chemistry in Ni3Al and Ni3Si", J. Phys. 1, C1 (1990), 77
5. C.T. Liu, E.H. Lee, C.G. McKamey, "An Environmental Effect as the Major Cause for Room-Temperature Embrittlement in FeAl", Scripta Met., 23 (1989), 875
6. C.L. Fu, G.S. Painter, J. Mater. Res., 6, (1991), 719
7. Y.F. Zhu, C.T. Liu; C.H. Chen, "Direct Evidence of Hydrogen Generation from the Reaction of Water with FeAl", Scripta Met. 35 (1997), 1435
8. M.-T. Perrot-Simonetta, C. Lorenzon, M. Biscondi, "Practical Interest of Multicomponent Standards for Quantitative AES", Surf. Interface Analysis, 21 (1994), 316
9. D. McLean, Grain Boundaries in Metals (Oxford : Clarendon Press, 1957)
10. D. Paris, P. Lesbats, "Vacancies in Fe-Al Alloys", J. Nuclear Mat., 69, (1978)
11. A.-S. Gay, A. Fraczkiwicz, M. Biscondi, "Ségrégation intergranulaire du bore dans Fe-40at. % Al (B2) : influence d'une interaction entre lacunes thermiques et atomes de bore", J. Phys. 6, C2 (1996), 153
12. S. Launois, A. Fraczkiwicz, " Effet de l'environnement sur le comportement mécanique d'un alliage FeAl (40 % at. Al) renforcé", J. Phys. 6, C2 (1996), 223

# HIGH TEMPERATURE MECHANICAL PROPERTIES AND MICROSTRUCTURE OF Fe<sub>3</sub>Al BASED INTERMETALLIC ALLOYS

Antonio Augusto Couto and Paulo Iris Ferreira

Instituto de Pesquisas Energéticas e Nucleares  
Comissão Nacional de Energia Nuclear  
P. O. Box 11049 -São Paulo, SP, 05422-970, Brazil

## Abstract

Four Fe<sub>3</sub>Al alloys with compositions 29Al-0.15Zr-0.2B-Fe, 29Al-1.6Cr-0.14Zr-0.2B-Fe, 30.5Al-2.4Cr-0.13Zr-0.2B-Fe, and 30.5Al-4.5Cr-0.13Zr-0.2B-Fe, were prepared by induction melting and casting in air, then homogenized at 1373 K / 24h and hot forged and rolled at 1273 K. Two conditions of heat treatment were used: HT1 - 1073 K / 1h ; and HT2 - 1073 K / 1h plus 773 K / 7days. The HT1 specimens were tensile tested in temperatures pertaining to the RT-1073 K interval, while the HT2 specimens were only tested at room temperature. Room temperature microhardness and yield stress of hot worked annealed samples are slightly dependent on Cr content in the alloy. The tensile tests performed on HT1 specimens in temperatures pertaining to RT-1073 K interval evidenced the presence of a peak in the yield stress around 873 K and a dramatic decrease above this temperature. The elongation to fracture of all compositions increases continuously with test temperature, reaching a value of 60 % at 1073 K. The fracture mode of all the alloys at room temperature is cleavage for HT1 and intergranular for HT2 conditions. The fracture mode of HT1 heat treated specimens changes from brittle cleavage at room temperature to ductile transgranular with dimples and microvoids at temperatures above 873 K. In the interval 873-1073 K the yield stress and maximum stress can be well correlated to temperature and strain rate according to the equation  $\sigma = A' \cdot \epsilon^m \cdot \exp(mQ/RT)$ , where m is the strain

rate sensitivity coefficient and Q is the apparent activation energy for the processes. Best fit of the experimental points to the equation allowed the determination of  $m = 0.20 \pm 0.01$  and  $Q = (306 \pm 25) \text{ kJ.mol}^{-1}$ . The values of these parameters are consistent with values obtained for equivalent parameters in high temperature creep studies in some Fe<sub>3</sub>Al alloys. The apparent activation energy for the process is of the same order of the activation energy for diffusion in these alloys.

## Introduction

Intermetallic alloys based on Fe<sub>3</sub>Al present a very good mechanical strength up to temperatures around 873 K and an excellent resistance to oxidation and sulfidation [1,2]. Furthermore, Fe<sub>3</sub>Al alloys are characterized by a low density and high specific strength, good hot workability and wear resistance properties, as well as, a relatively low cost. Use of these materials has been limited either by their low room temperature ductility or by the rapid decrease of mechanical strength at temperatures above 873 K [3,4].

Recent development efforts in alloying and thermomechanical processing have resulted in improved room temperature mechanical properties and an increased comprehension of these materials [2,5-9]. With the prospect of reasonably ductile ordered intermetallics becoming more broadly utilized, increased attention is being concentrated on their behavior during mechanical

processing at high temperatures. Variations on the alloy composition and addition of alloying elements has been seen to induce changes in the alloy mechanical properties. Addition of small amounts of niobium and molybdenum to Fe<sub>3</sub>Al alloys results in improved high temperature strength and creep behavior but is harmful to room temperature ductility [10-13]. In its turn, chromium additions do not seem to alter the creep properties of the alloy [14].

To our knowledge, no systematic studies have been conducted to investigate the effects of temperature and strain rate on the mechanical properties of iron aluminides. Therefore, the objective of this study is to investigate the mechanical behavior of four Fe-30Al based alloys containing additions of Cr, Zr and B in temperatures pertaining to the RT-1073 K interval.

### Experimental

Four Fe-30Al-(0 to 4)Cr at.% containing small amounts of zirconium and boron, were prepared by induction melting and casting in air, using commercial purity starting materials. Boron was added to the alloys via a master Fe-B alloy. The chemical composition of the alloys (major elements) determined by x-ray fluorescence is presented in table I with a identification code for each alloy. The 5 Kg cast ingots obtained were initially homogenized at 1373 K for 24h, then hot forged and rolled at 1273 K to plates with a final thickness of 1.5 mm and 120 mm wide.

Table I Chemical composition of the alloys (at.%)

Alloy	Nominal Composition					x-Ray Fluorescence Composition			
	Al	Cr	Zr	B	Fe	Al	Cr	Zr	Fe
M1	30	0	0.1	0.2	Bal	29	0	0.15	Bal
M2	30	1	0.1	0.2	Bal	29	1.6	0.14	Bal
M3	30	2	0.1	0.2	Bal	30.5	2.4	0.13	Bal
M4	30	4	0.1	0.2	Bal	30.5	4.5	0.13	Bal

Samples from the hot rolled plates were heat treated for one hour under argon atmosphere, in temperatures ranging from 773 to 1273 K. These specimens were used to perform room temperature microhardness measurements and optical metallography observations. Plate-type tensile test specimens with reduced section of 38.0mm X 6.0mm X 1.5mm were laser cut from the hot rolled plates. These tensile test specimens were submitted to two conditions of heat treatment: HT1 - 1073 K / 1h; and HT2 - 1073 K / 1h plus 773 K / 7days. The first heat treatment (HT1) established the grain size and promotes B2 ordering in the alloys. The second heat treatment (HT2) promotes D0<sub>3</sub> ordering in the alloys.

Optical metallography was used to determine the average grain size after the heat treatments. The average grain size was determined by the linear intercept method. The phases present in the specimens after the various heat treatments were determined from X-ray diffractograms obtained using Cu K<sub>α</sub> and Fe K<sub>α</sub> radiation.

The HT1 specimens were tensile tested in temperatures pertaining to the RT-1073 K interval, while the HT2 specimens were only tested at room temperature. The tensile tests were conducted in a universal test machine under a strain rate of  $2 \times 10^{-4} \text{ s}^{-1}$  and argon (commercial purity) atmosphere. The effect of strain rate on the yield stress and maximum stress of HT1 specimens was investigated in the temperature range 873 - 1073 K by performing tensile tests with strain rates in the range  $9 \times 10^{-5}$  -  $9 \times 10^{-3} \text{ s}^{-1}$ . The test temperature was measured using a NiCr-Ni thermocouple positioned at the central part of the tensile specimen gage length. The fracture surfaces of the tensile tested specimens were analyzed in a scanning electron microscope.

### Results and Discussion

Figure 1 shows the room temperature Vickers microhardness results plotted as a function of heat treatment temperature for samples of the hot worked material that were submitted to one hour heat treatment. The figure shows that the microhardness of the as hot worked material decreases with an increase in the amount of chromium in the alloy. Also, no change in microhardness is observed for all the specimens for heat treatment temperatures below 773 K; however, for higher heat treatment temperatures a small decrease in microhardness is observed for the chromium containing alloys. This decrease is higher the higher is the chromium content of the alloy.

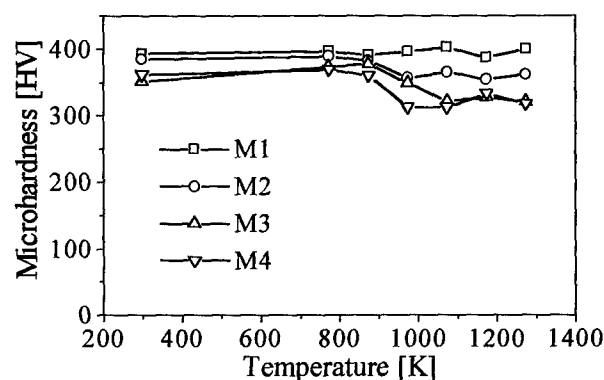


Figure 1: Vickers microhardness vs. heat treatment temperature (1 hour) for initially hot-rolled alloys.

Figure 2 shows a typical micrograph of the as hot rolled and one hour heat treated materials obtained for the M4 alloy. Similar behavior was observed for the other alloys. An average grain size of  $(80 \pm 10) \mu\text{m}$  was obtained for all the four alloys in the hot rolled condition. The average grain size of all the alloys did not show any significant variation with the heat treatment temperature, even after the 1273 K treatments. Microhardness and optical metallography results indicate that the addition of chromium to the alloy tends to induce softening. This softening could be associated with an incomplete recrystallization at the end of the hot rolling operation. Also, chromium seems to play a role in the mechanism responsible for the decrease in the room temperature microhardness for heat treatments at temperatures above 773 K.

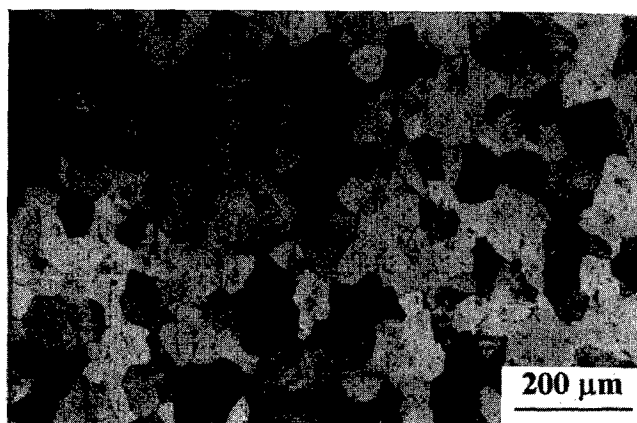


Figure 2: Optical photomicrograph showing typical microstructure of as-rolled and heat treated at 1273 K / 1 h - (alloy M4).

Table II shows the room temperature tensile test results obtained for the specimens in the as hot rolled, HT1 and HT2 conditions. To better illustrate what occurs with the mechanical strength, the yield stress plotted as a function of the chromium content in the alloy is presented in figure 3 for the three conditions investigated. Coherently with the microhardness results, the room temperature yield stress decreases slightly with an increase in the chromium content of the alloy. Furthermore, HT1 and HT2 heat treatments induce a decrease in the room temperature yield stress of the as hot rolled samples. This decrease is higher for the HT2 heat treatment. The room temperature ductility as given by the elongation to fracture of all the alloys in the three conditions is small ( $\sim 1\%$ ), probably related to the purity of the starting materials and the melting / casting procedure

utilized. The mode of fracture does not seem to depend on chromium content; it was transgranular cleavage for the as hot rolled and HT1 specimens, and changed to intergranular for the HT2 specimens, as can be deduced from the SEM micrographs of the fractured specimens of the alloy M4 presented in figure 4. For the other alloys a similar behavior was observed.

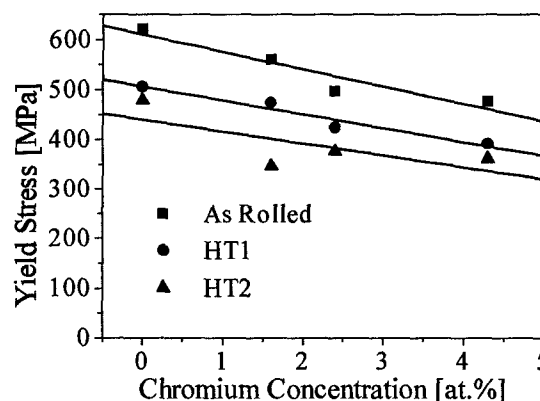


Figure 3: Room temperature yield stress vs. chromium content in the alloys for the conditions: as-rolled, HT1, and HT2.

Figure 5 shows the effect of the test temperature on the yield stress (a) and elongation to fracture (b) of the four alloys in condition HT1, tested under a strain rate of  $2 \times 10^{-4} \text{ s}^{-1}$ . In general, the yield stress of all the alloys decreases to a minimum value at a temperature in the range 523-673 K. For temperatures above this minimum, the yield stress increases to a peak value around 873 K, decreasing rapidly above this temperature. A distinct maximum in the yield stress at temperatures near the critical  $\text{D}_{03}$  - B2 transition has been reported for binary  $\text{Fe}_3\text{Al}$ , particularly for specimens with  $\text{D}_{03}$  structure [15 - 19]. Though the HT1 heat treated specimens submitted to high temperature tensile testing had primarily B2 ordering it is believed that the holding time at the temperature before testing could be sufficient to induce some transformation to  $\text{D}_{03}$  ordering structure. In fact, the presence of  $\text{D}_{03}$  diffraction lines is detectable in the x ray diffractograms for this condition.

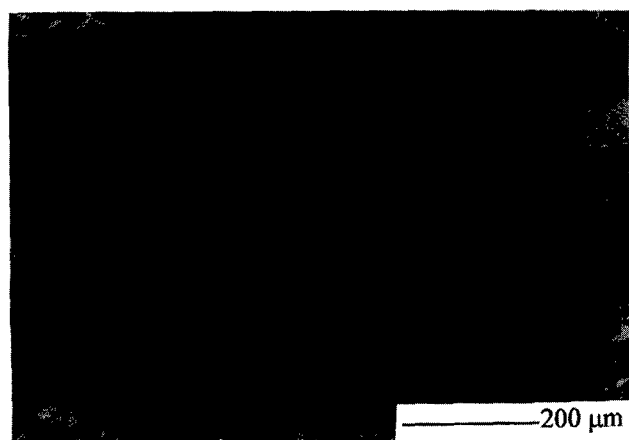
The elongation to fracture of the four alloys investigated, shown in figure 5(b), increases continuously with the increase in the test temperature. A significant ductility is only observed for temperatures above 773 K, reflecting the good workability of the alloys at high temperatures. The elongation to fracture observed for the alloys is inferior to the values reported by McKamey et al. for the Fe-30Al in tests performed on 12.7 mm gage length tensile specimens [20].

Table II Tensile test results at room temperature for the alloys in the as rolled, HT1 and HT2 conditions.

ALLOY	CONDITION	YIELD STRESS [MPa]	MAXIMUM STRESS [MPa]	ELONGATION [%]
M1	AS ROLLED	621	654	0.4
	HT1	506	606	0.9
	HT2	478	536	0.5
M2	AS ROLLED	560	614	0.5
	HT1	474	576	1.1
	HT2	346	457	1.3
M3	AS ROLLED	497	532	0.4
	HT1	424	424	0.2
	HT2	376	466	0.8
M4	AS ROLLED	476	476	0.1
	HT1	391	454	1.0
	HT2	361	410	0.8



(a)



(b)

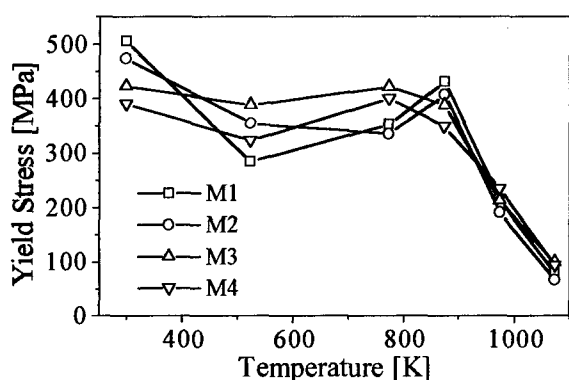
Figure 4: SEM micrographs illustrating typical room temperature fracture surfaces of M4 alloy after heat treatments: (a) HT1; (b) HT2.

The fracture surface of each alloy tensile tested specimen was analyzed; different alloys tested at a same temperature presented similar fracture behavior. Figure 6 shows typical SEM micrographs of the fracture surface for the alloy M4 in the HT1 condition. The examination of the fracture surfaces evidenced that at room temperature the fracture occurs mainly by a brittle cleavage fracture mode (fig.4a). The fracture surfaces from the specimens tested at temperature 973 K and above are entirely ductile evidencing the presence of dimples and microvoid coalescence. For temperatures in the range RT-973 K, the fracture has a mixed character with the operation of both mechanisms. These results are similar to those reported by Mendiratta et al. [17] and Knibloe et al. [14] for binary and chromium containing Fe<sub>3</sub>Al alloys, respectively.

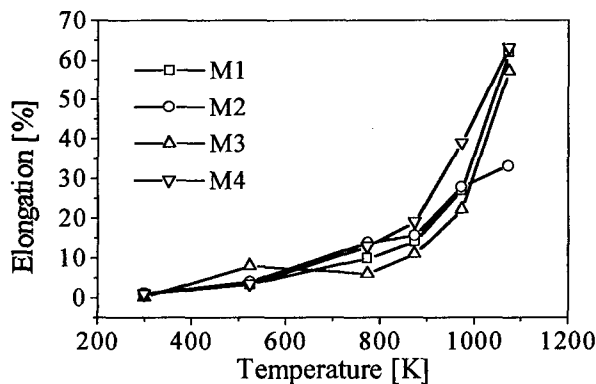
All the stress-strain curves determined by tensile tests above 873 K for all the four alloys investigated display the usual hot flow curve of metallic materials, a stress rising to a maximum value followed by a softening behavior at high strains, usually associated with dynamic recovery or recrystallization, depending on the test temperature. In general, the initial strain hardening behavior that occurs at stresses above the yield stress up to the maximum stress is, associated with the effects of unbalanced rates of dislocation multiplication and dislocation annihilation. At the maximum stress these rates are believed to equalize and dynamic recovery or recrystallization starts to take place, leading to a continuous decrease on the stress until a steady state value is finally reached, corresponding to continuous dynamic recrystallization [19]. This steady state behavior is usually observed at very large strains ( $\epsilon \approx 1.5$  % and above) in torsion and compression testing, where specimen instabilities are minimized. In tensile testing, however, necking occurs and the specimen fractures before a steady state behavior is reached.



In this study, the yield stress and the maximum stress are clearly present in all the tests performed. The maximum stress occurs at strains ranging from 1% to 3% depending on strain rate and test temperature. To eliminate the effect of the deformation on the analysis that follows, the yield stress (0.2% off-set) and the stress at a plastic strain of 2%, (maximum stress - noted  $\sigma_{2\%}$ ) were selected as representative stresses of each curve. It should be mentioned that this maximum stress differs only slightly from the ultimate tensile strength. The values of  $\sigma_y$  and  $\sigma_{2\%}$  determined from all experimental curves are presented in table III.



(a)



(b)

Figure 5: (a) Yield stress and (b) elongation to fracture vs. tensile test temperature for the four alloys investigated. Condition HT1.

In general, the isothermal true stress-true strain relation  $\sigma(\epsilon)$  in metallic materials depends upon strain rate and upon temperature through a general equation  $\sigma = \sigma(Z, \dot{\epsilon})$ , where  $Z$  is the Zener-Hollomon parameter ( $Z = \dot{\epsilon} \exp(Q/RT)$ ),  $Q$  is the apparent activation energy for the process,  $R$  is the gas constant ( $8.318 \text{ J.mol}^{-1}.\text{K}^{-1}$ ),  $T$  is the absolute temperature at which the deformation is

performed and  $\sigma$  the flow stress [19]. One generally accepted relation between stress and  $Z$ , usually applied to hot tensile testing and creep testing studies, is  $\dot{\epsilon} \exp(Q/RT) = A \cdot \sigma^n$  where  $A$  is a parameter which involves microstructural variables and  $n$  is the stress sensitivity parameter which is independent of the temperature. This equation can be rewritten as  $\sigma = A' \cdot \dot{\epsilon}^m \exp(mQ/RT)$ , where  $m = 1/n$ . Using this equation, the strain rate sensitivity,  $m$ , and the apparent activation energy  $Q$  can be determined from constant strain rate and constant temperature tensile tests.



(a)



(b)

Figure 6: SEM micrographs illustrating typical tensile fracture surfaces of M4 alloy in the HT1 condition at test temperatures (a) 873K and (b) 973K.

An attempt was initially made to correlate the yield stress and the maximum stress with the strain rate and test temperature for each alloy independently, through this equation. Though the correlation coefficients were high ( $\approx 0.99$ ), the values obtained for the adjusting parameters,  $m$  and  $Q$ , did not show any significant variation that could be confidently associated with changes in the alloy composition.

Table III The values of  $\sigma_y$  and  $\sigma_{2\%}$  determined from all experimental curves.

Test Temp.[K]	Alloy	$9 \times 10^{-5} \text{ s}^{-1}$		$2 \times 10^{-3} \text{ s}^{-1}$		$4 \times 10^{-3} \text{ s}^{-1}$		$9 \times 10^{-3} \text{ s}^{-1}$	
		$\sigma_y$	$\sigma_{2\%}$	$\sigma_y$	$\sigma_{2\%}$	$\sigma_y$	$\sigma_{2\%}$	$\sigma_y$	$\sigma_{2\%}$
873	M1	184	184	426	437	416	435	539	539
	M2	156	164	384	397	385	385	488	512
	M3	138	161	434	493	467	515	507	604
	M4	173	191	350	452	446	524	482	576
973	M1	125	140	152	152	257	270	310	329
	M2	85	90	142	145	155	155	269	286
	M3	71	86	232	244	226	241	246	277
	M4	143	143	235	273	249	258	340	370
1073	M1	34	36	70	74	78	80	82	104
	M2	28	30	65	66	64	64	95	102
	M3	33	40	94	104	85	89	97	104
	M4	39	45	94	99	107	91	152	171

Consequently, the  $\sigma_y$  and  $\sigma_{2\%}$  data obtained for all the four alloys investigated were utilized for the strain rate and temperature dependence analysis and the results are presented in figures 7-10. At constant temperature, the yield stress and maximum stress (figures 7 and 8) show a power law dependence on the strain rate imposed to the test, with the strain rate sensitivity parameter  $m = (0.20 \pm 0.01)$  in both situations. The dependence of the yield stress and of the maximum stress, at constant strain rate, on temperature is well correlated by the exponential function as indicated by the data presented in figures 9 and 10. From these data an apparent activation energy for the deformation process,  $Q = (306 \pm 25) \text{ kJ mol}^{-1}$ , is also determined in both cases.

The deformation process occurring for stresses between the yield stress and the maximum stress in a hot tensile test has its similarities with what occurs during a creep test. In the former, the strain rate is imposed to the specimen and the stress adjusts itself as the deformation continues. In the latter, the stress applied to the specimen is maintained constant and the strain rate adjusts itself as the deformation proceeds. An unique correlation between strain, strain rate, stress and temperature is expected from tensile and creep tests performed under the same experimental conditions (same sets of values of  $(\epsilon, \dot{\epsilon}, \sigma, T)$ ).

According to this, the strain rate sensitivity parameter,  $m$ , obtained in a hot tensile test can be related to the stress sensitivity exponent,  $n$ , usually obtained in creep test in the intermediate range of stresses (power law creep) by the relation  $m = 1/n$ . Also, an equal value for the apparent activation energy for the process is expected. The value obtained for the strain rate sensitivity parameter  $m$  in the present investigation is of the same order of the values 0.14 - 0.22 obtained by Knibloe et al [14] for  $\text{Fe}_3\text{Al}$  alloys containing 2% and 5% chromium obtained by

powder metallurgy, and by Rabin and Wright [21] on combustion synthesized  $\text{Fe}_3\text{Al}$  containing 5% chromium. However, the equivalent  $n = 5$  value deduced from the  $m$  value obtained in this work is comparable to  $n$  values 3.5 - 7.7 obtained by McKamey et al. [12] in creep studies performed for  $\text{Fe}_{28}\text{Al}$  at a lower temperature (923 K) in the same stress-strain rate interval. A  $n = 5$  value is usually associated with a dislocation climb mechanism in high temperature creep [22].

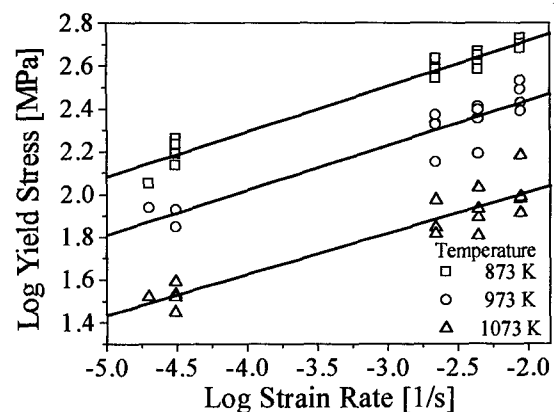


Figure 7: The dependence of yield stress ( $\sigma_y$ ) on strain rate at constant temperatures.

The apparent activation energy determined in this study,  $(306 \pm 25) \text{ kJ.mol}^{-1}$  is comparable to the values determined for the creep process by McKamey et al. [12] for  $\text{Fe}_{28}\text{Al}$  -  $(347 \text{ kJ.mol}^{-1})$  and for  $\text{Fe}_{28}\text{Al}_{12}\text{Mo}$  and  $\text{Fe}_{28}\text{Al}_{11}(\text{Zr/Nb})$  -  $(334 \text{ kJ.mol}^{-1})$ , by Davies [23] for the  $\text{Fe}_{20}\text{Al}$  alloy -  $(305 \text{ kJ.mol}^{-1})$ , and by Lawley et. al [24] for  $\text{Fe}_{27.8}\text{Al}$  -  $(275 \text{ to } 355 \text{ kJ.mol}^{-1})$ . Values for the activation energy for diffusion in ordered  $\text{Fe}_{30}\text{Al}$  alloys have been determined by a number of investigators [25] to

lie within the range 260 to 290 kJ.mol<sup>-1</sup>. The apparent activation energy determined in this investigation is consistent with these values, indicating the diffusion controlled character of high temperature mechanical behavior of these alloys.

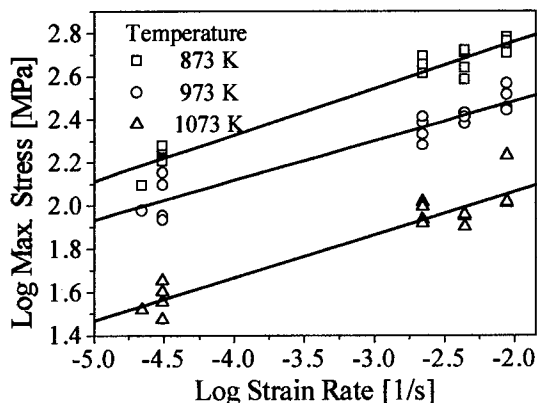


Figure 8: The dependence of the maximum stress ( $\sigma_{2\%}$ ) on the strain rate for several temperatures.

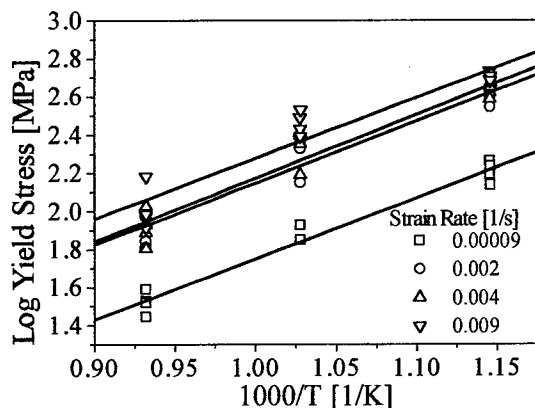


Figure 9: The dependence of yield stress ( $\sigma_y$ ) on the test temperature for various strain rates.

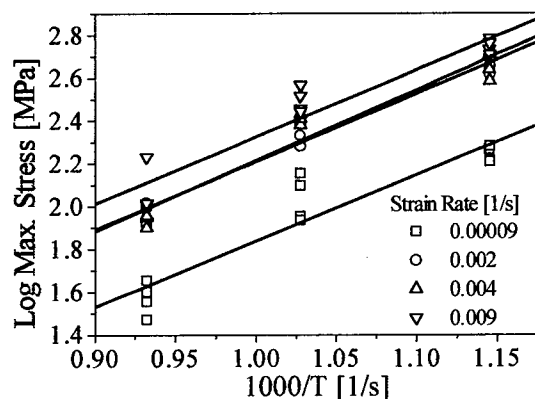


Figure 10: The dependence of maximum stress ( $\sigma_{2\%}$ ) on the test temperature at various strain rates.

## Conclusions

Room temperature microhardness, yield stress, and ultimate tensile strength of the four alloys investigated are slightly affected by the chromium content in the alloy. The fracture mechanism of room temperature tensile tested specimens changes from transgranular cleavage for B2 ordering (heat treatment HT1) to intergranular for D0<sub>3</sub> ordering (heat treatment HT2). An anomalous peak in the yield strength was observed in all four alloys around 873 K. The ductility of each alloy, heat treated according to HT1, increases continuously with the increase in test temperature. Fracture mode changes from brittle cleavage at low test temperatures to ductile transgranular at high temperature. At intermediate temperatures fracture has a mixed character. For temperatures above 873 K the yield stress and the maximum stress are dependent on test temperature and strain rate. A power law equation  $\sigma = A' \cdot \epsilon^m \cdot \exp(mQ/RT)$ , can be utilized to describe the behavior of the yield stress and maximum stress, where  $m$  is the strain rate sensitivity coefficient and  $Q$  is the apparent activation energy for the processes. Best fit of the experimental points to the equation allowed the determination of  $m = 0.20 \pm 0.01$  and  $Q = (306 \pm 25)$  kJ.mol<sup>-1</sup>. The values of these parameters are consistent with values obtained for equivalent parameters in high temperature creep studies in some Fe<sub>3</sub>Al alloys. The apparent activation energy for the process is of the same order of the activation energy for diffusion in these alloys.

## Acknowledgements

This work was supported by Conselho Nacional de Pesquisas (CNPq/Brazil), contract 521385/96-2 and Financiadora de Estudos e Projetos - Finep/Brazil contract 54.940003-00.

## References

1. J. H. DeVan, H. S. Hsu, and M. Howell, ORNL/TM-11176, (Oak Ridge National Laboratory, TN, 1989).
2. C. G. McKamey, J. A. Horton, and C. T. Liu, J. Mater. Res., 4(1989),1156.
3. M. Johnson, D. E. Mikkola, P. A. March, and R. N. Wright, Wear, 140(1990),279
4. C. G. McKamey, J. H. DeVan, P. F. Tortorelli, and V. K. Sikka, J. Mater. Res., 6(1991),1779.
5. I. Baker and E. M. Schulson, Scripta Metall., 23(1989),345.

6. C. T. Liu, C. L. White, and J. A. Horton, Acta Metall., 33(1985),213.
7. C. T. Liu, C. G. McKamey, and E. H. Lee, Scripta Metall., 24(1990),385.
8. D. B. Kasul and L. A. Heldt, Scripta Metall., 25(1991),1047.
9. R. Carleton, E. P. George, and R. H. Zee, Intermetallics, 3(1995),433.
10. R. S. Diehm and D. E Mikkola, Mater. Res. Soc. Symp. Proc., Materials Research Society, Pittsburgh, PA, 81(1987),329.
11. R. T. Fortnum and D.E Mikkola, Mater. Sci. Eng., 91(1987),223.
12. C. G. McKamey, P. J. Maziasz, and J. W. Jones, J. Mater. Res., 7(1992),2089.
13. V. K. Sikka, C. G. McKamey, C. R Howell, and R. H Baldwin, ORNL/TM-11465 (Oak Ridge National Laboratory, TN, 1990).
14. J. R. Knibloe, R. N. White, V. K. Sikka, R. H. Baldwin, and C. R. Howell, Mater. Sci. Eng., 153(1992),382.
15. N. S. Stoloff, and R. G. Davies, Acta Metall., 12(1964),473.
16. P. Morgand, P. Mouturat, and G. Sainfort, Acta Metall., 16(1968),867.
17. M. G. Mendiratta, S. K. Ehlers, D. K. Chatterjee, and H. A. Lipsitt, Metall. Trans.A, 18(1987),283.
18. D. G. Morris and S. Gunther, Mater. Sci. and Eng., A211(1996),23.
19. C. M. Sellars and W. J. M. Tegart, Mém. Scient. Métall., 63(1966)731.
20. C. G. McKamey, C. T. Liu, J. V. Cathcart, S. A. David, and E. H. Lee, ORNL/TM-10125 (Oak Ridge National Laboratory, TN, 1986).
21. B. H. Rabin and R. N. Wright, Metall. Trans., A23(1992)35.
22. O. D. Sherby and P. M. Burke, Progress Mater. Sci., 13(1968),325.
23. R. G. Davies, TMS AIME, 227(1963),665.
24. A. Lawley, J. A. Coll, and R. W. Cahn, TMS AIME, 218(1960),166.
25. C. J. Smithells, Smithells Metals Reference Book 6th ed., p 13-9, Butterworth, London (1983).

# HIGH TEMPERATURE YIELD STRENGTH OF BINARY STOICHIOMETRIC AND AL-RICH Ni<sub>3</sub>Al SINGLE CRYSTALS

D. Golberg, M. Demura, and T. Hirano

National Research Institute for Metals, 1-2-1 Sengen, Tsukuba, Ibaraki 305, Japan

## Abstract

Large stoichiometric (Ni-25Al) and Al-rich (Ni-26Al, Ni-27Al) Ni<sub>3</sub>Al single crystals that do not contain any ternary elements have been produced for the first time, by using unidirectional solidification floating zone method (FZ-UDS). The compressive mechanical properties of these crystals at 293-1273 K were evaluated for orientations close to [001] and [011]. The peak temperature of the yield stress anomaly decreased with increasing Al content. Compared to Al-rich crystals, stoichiometric Ni<sub>3</sub>Al exhibited higher yield strength at 1073-1273 K (above the peak temperature) and lower yield strength at lower temperatures. Stoichiometric Ni<sub>3</sub>Al single crystals with compression axis oriented close to [001] exhibited the highest yield strength at 1073-1273 K. The effect of Al content on the yield strength is discussed with respect to alloy stoichiometry and the NiAl second phase in Al-rich crystals.

## Introduction

Ni<sub>3</sub>Al, which shows positive temperature dependence of the yield stress, exists over a small composition range on both sides of the stoichiometric composition [1]. It can be expected that the mechanical properties depend on the alloy stoichiometry. There are few studies on the effect of stoichiometry on the mechanical properties at various temperatures [2-5], and they have been performed only on polycrystalline specimens because of difficulty in growing binary Ni<sub>3</sub>Al single crystals. This difficulty is caused by the peritectic reaction, liquid+NiAl→Ni<sub>3</sub>Al. Grains nucleate easily during the peritectic reaction and it is difficult to suppress the nucleation by a Bridgman technique. Thus, almost all the single crystals grown so far contain ternary additions or deviate from stoichiometry towards the Ni-rich side in order to avoid the peritectic reaction (see a comprehensive review by Suzuki et al. [6]). Therefore, the mechanical properties of binary stoichiometric Ni<sub>3</sub>Al single crystals have never been studied.

We have undertaken systematic work on unidirectional solidification of binary Ni<sub>3</sub>Al using a floating zone method (FZ-UDS) [7-14]. In most cases the stoichiometric alloys grown by FZ-UDS have columnar-grained structure with a high percentage of low angle and low

Σ boundaries [9, 15]. However, we have recently found that large single crystals of binary stoichiometric Ni<sub>3</sub>Al can be occasionally grown [16, 17]. The present work is the first attempt to evaluate the compressive yield strength between 293-1273 K of stoichiometric and Al-rich Ni<sub>3</sub>Al single crystals grown by FZ-UDS.

It is worth noting that Al-rich compositions of binary Ni<sub>3</sub>Al would be much more promising candidates for high temperature applications because of their better oxidation resistance and reduced density. However, there has been only one recent report on the mechanical properties of an Al-rich (Ni-25.9Al) single crystal, by Dimiduk et al. [18].

## Experimental

Stoichiometric (Ni-25Al, hereafter at.%) and Al-rich (Ni-26Al, Ni-27Al) alloys were arc-melted to prepare the feed rods for FZ-UDS using 99.9999% Al and 99.97% Ni. All ingots were remelted 8-10 times to achieve chemical homogeneity. The FZ-UDS procedure was the same as previously reported [7-14]. Crystal growth was carried out in a flowing argon atmosphere using infrared radiation from double halogen lamps as the heating source. During the process the seed rod and the feed rod were rotated at 24 rpm in opposite directions to reduce asymmetry of temperature distribution and achieve forced convection in the molten zone. The growth rate was fixed at 25 mm/h. Crystals of length 160-170 mm and diameter 10-12 mm were grown.

Longitudinal and transverse sections of the as-grown crystals were studied on the as-polished and etched surfaces with an optical microscope. Marble reagent was used for etching. An inhomogeneity in microstructure was observed on the periphery of the as-grown Al-rich crystals; therefore, the Al-content was confirmed by the wet chemical method excluding the periphery. The results agreed fairly well with the nominal compositions, within 0.3 at.%, as listed in Table 1.

Table 1. Chemical Composition of FZ-UDS Ni<sub>3</sub>Al Crystals Studied, at.%

No.	Nominal Composition	Analyzed Composition
1	Ni-25Al	Ni-25.2Al
2	Ni-26Al	Ni-25.7Al
3	Ni-27Al	Ni-27.0Al

Compression specimens with dimensions of 3.7x3.7x7.7 mm were cut with an electrical discharge machine from the center of the as-grown crystals. The long dimension of the specimens was oriented parallel to the desired crystallographic orientation by the Laue X-ray back reflection method. Before tests all specimens were mechanically polished on 600 grit SiC paper until an approximately 100  $\mu\text{m}$  thick layer had been removed from each surface, with subsequent  $\text{Al}_2\text{O}_3$  lapping for a final "mirror" finish. Compression tests were carried out with a Tensilon 5000 testing machine at 293-1273 K at a strain rate of  $2.3 \times 10^{-4}/\text{s}$  in air. Plastic strain was calibrated from the change in specimen length after the compression test by assuming constant strain rate.

## Results

### Characterization of the grown crystals

The transverse microstructures of the crystals are presented in Fig. 1a-c. They consist of single phase  $\text{L}_{12}$   $\text{Ni}_3\text{Al}$  for Ni-25Al (Fig. 1a), and duplex phase for other alloys (Fig. 1b and 1c). The second phase in the duplex structure is the  $\text{L}_{10}$  NiAl phase at room temperature, which is that observed in stoichiometric  $\text{Ni}_3\text{Al}$  FZ-UDS alloys

grown at growth rates higher than 50 mm/h [10]. The evolution of the two different microstructures can be explained based on the phase diagram. B2 NiAl forms from the melt during solidification and dissolves through the peritectic reaction,  $\text{liquid} + \text{B2 NiAl} \rightarrow \text{Ni}_3\text{Al}$ . The residual B2 NiAl martensitically transforms into  $\text{L}_{10}$  NiAl during cooling. The morphology and thermal stability of  $\text{L}_{10}$  NiAl depend on the alloy composition.

In the case of Ni-25Al, B2 NiAl grows in the form of rods simultaneously with  $\text{Ni}_3\text{Al}$  at the applied growth rate of 25 mm/h. Since NiAl is unstable below the solidification temperature, it starts to dissolve into the  $\text{Ni}_3\text{Al}$  phase during cooling. The dissolution of the rod-like NiAl is complete, resulting in the single  $\text{L}_{12}$   $\text{Ni}_3\text{Al}$  phase. It is noted that no grain boundaries are observed in Fig. 1a. So far, it has been impossible to grow single crystals of stoichiometric  $\text{Ni}_3\text{Al}$  by a Bridgman technique because of the precipitation of NiAl phase, that is, NiAl phase acts as a nucleation site for new  $\text{Ni}_3\text{Al}$  grains. This difficulty still exists in the floating zone method, which commonly produces a columnar-grained structure with high percentage of low angle and low  $\Sigma$  boundaries [12, 15]. However, large single crystals can be occasionally grown by strictly controlling the dimensions of the molten zone during the crystal growth [16, 17]. Figure 2a shows the X-ray Laue pattern of the as-grown Ni-25Al. The

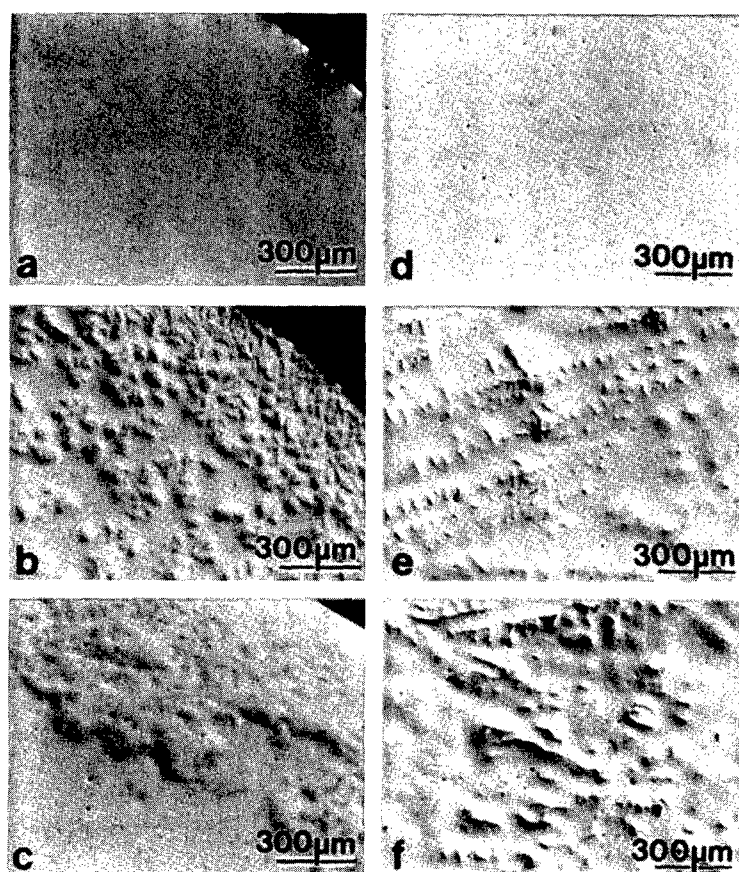


Figure 1: Optical micrographs of the binary  $\text{Ni}_3\text{Al}$  single crystals grown by FZ-UDS, in sections that are (a-c) perpendicular and (d-f) parallel to the growth direction. (a, d) Ni-25Al; (b-e) Ni-26Al; and (c, f) Ni-27Al.

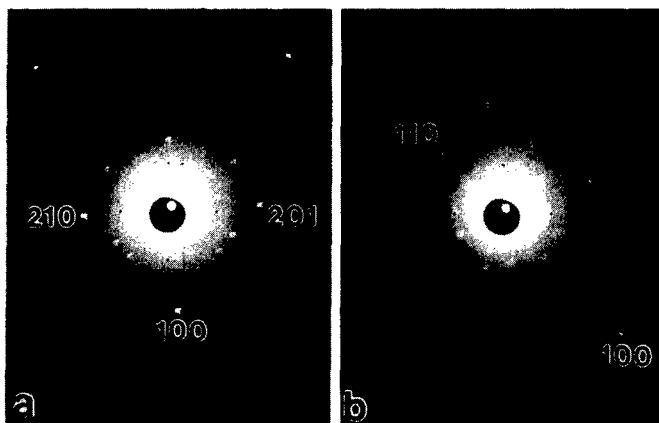


Figure 2: X-ray Laue back reflection patterns of (a) Ni-25Al, and (b) Ni-27Al.

X-ray spots are slightly split, implying the existence of small angle boundaries, but the maximum misorientation angle measured was about  $1^\circ$ . Thus, our crystals can be considered as single crystals for evaluation of the mechanical properties.

In case of Ni-26Al and Ni-27Al, B2 NiAl grows in the form of dendrites preceding the formation of  $\text{Ni}_3\text{Al}$ . This NiAl is thermodynamically stable, unlike that in the stoichiometric alloy, as reported by Dimiduk et al. [18]. Figure 3 shows the microstructure of Ni-27Al after heat treatment at 1573 K for 18 ks. This heat treatment temperature is about 100 K below the peritectic temperature. The NiAl phase remains after this heat treatment although there are some changes in its morphology. Ni-26Al showed the same microstructural changes, indicating that there is a  $\text{Ni}_3\text{Al}/\text{Ni}_3\text{Al}+\text{NiAl}$  boundary between 25.2 and 25.7 at.% Al on the phase diagram (see Table 1).

The volume fraction of NiAl sharply increased near the periphery of the as-grown crystals, as shown in Fig. 1b. The thickness of the peripheral layer is about 300  $\mu\text{m}$ .

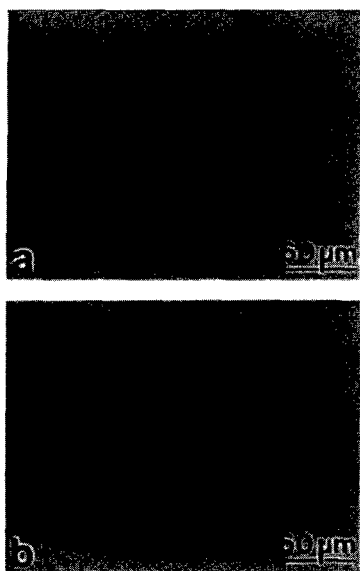


Figure 3: Optical micrographs of Ni-27Al. (a) as-grown; (b) heat-treated at 1573 K for 18 ks.

Although the microstructure is duplex in Fig. 1b (Ni-26Al) and Fig. 1c (Ni-27Al), it is noted again that no grain boundaries are seen in the  $\text{Ni}_3\text{Al}$  matrix except in the peripheral layer in Fig. 1c (Ni-27Al).

Longitudinal sections of the as-grown crystals cut from the central parts are shown in Fig. 1e-f. No grain boundaries are seen in  $\text{Ni}_3\text{Al}$  matrix in any of the crystals studied in spite of the presence of the NiAl second phase in Al-rich alloys. Figure 2b shows the X-ray Laue pattern taken from near the center of the as-grown Ni-27Al. This figure confirms that the  $\text{Ni}_3\text{Al}$  matrix possesses a single crystalline character with a similar crystallinity to that in Ni-25Al. It is amazing that the NiAl second phase does not hinder single crystal growth of the  $\text{Ni}_3\text{Al}$  matrix.

In summary, we could successfully grow single crystals or single crystal-like  $\text{Ni}_3\text{Al}$  over a wide range of Al contents, though it is still rather difficult to grow crystals to a desired orientation using oriented seeds.

### Compressive properties

The compression axes of the single crystalline specimens studied are plotted on the standard [001]-[ $\bar{1}11$ ]-[011] unit triangle in Fig. 4. Calculated Schmid factors and Schmid factor ratios are listed in Table 2. Hereafter the major crystal orientations are referred to orientation A (No's 1, 2, and 3), which is close to the [001] corner, and orientation B (No's 5, 6, and 7), which is close to the [011] corner. Orientation C (No.4) is between these two.

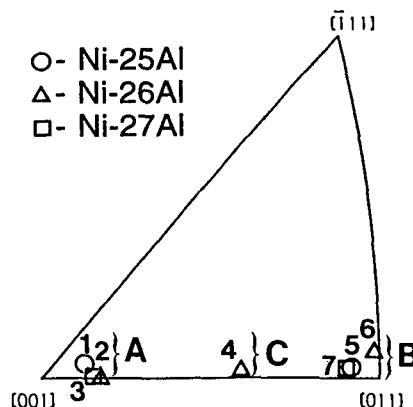


Figure 4: Orientation of the compression axes for the binary  $\text{Ni}_3\text{Al}$  single crystals studied.

Figure 5 shows the compressive stress-strain curves of the as-grown crystals for orientations A and B as a function of Al content and temperature. Stoichiometric Ni-25Al crystal exhibits a smooth yielding below 973 K. At 1073 K and above the stress-strain curves show a yield drop followed by a steady state deformation with almost zero or even negative work-hardening. This yield drop is believed to be due to rapid dislocation multiplication, i.e., Johnston-Gilman type yielding [6]. The yield drop is much larger for orientation A than for orientation B. This agrees well with that in alloyed crystals,  $\text{Ni}_3(\text{Al,Ti})$  [19, 20].

Table 2. Schmid Factors and Schmid Factor Ratios for Ni<sub>3</sub>Al Single Crystals Studied

No.	Orientation	Composition	(111)[ $\bar{1}$ 01]	(010)[ $\bar{1}$ 01]	(001)[ $\bar{1}$ 10]	N*	R*
1	A	Ni-25Al	0.46	0.08	0.08	0.17	0.17
2	A	Ni-26Al	0.45	0.10	0.10	0.22	0.22
3	A	Ni-27Al	0.46	0.10	0.08	0.22	0.17
4	C	Ni-26Al	0.49	0.29	0.28	0.59	0.57
5	B	Ni-25Al	0.44	0.35	0.35	0.80	0.80
6	B	Ni-26Al	0.43	0.38	0.40	0.88	0.93
7	B	Ni-27Al	0.44	0.35	0.35	0.80	0.80

\*N: Schmid factor ratio for cross-slip system (010)[ $\bar{1}$ 01] and octahedral slip system (111)[ $\bar{1}$ 01]; R: Schmid factor ratio for primary cube slip system (001)[ $\bar{1}$ 10] and octahedral slip system.

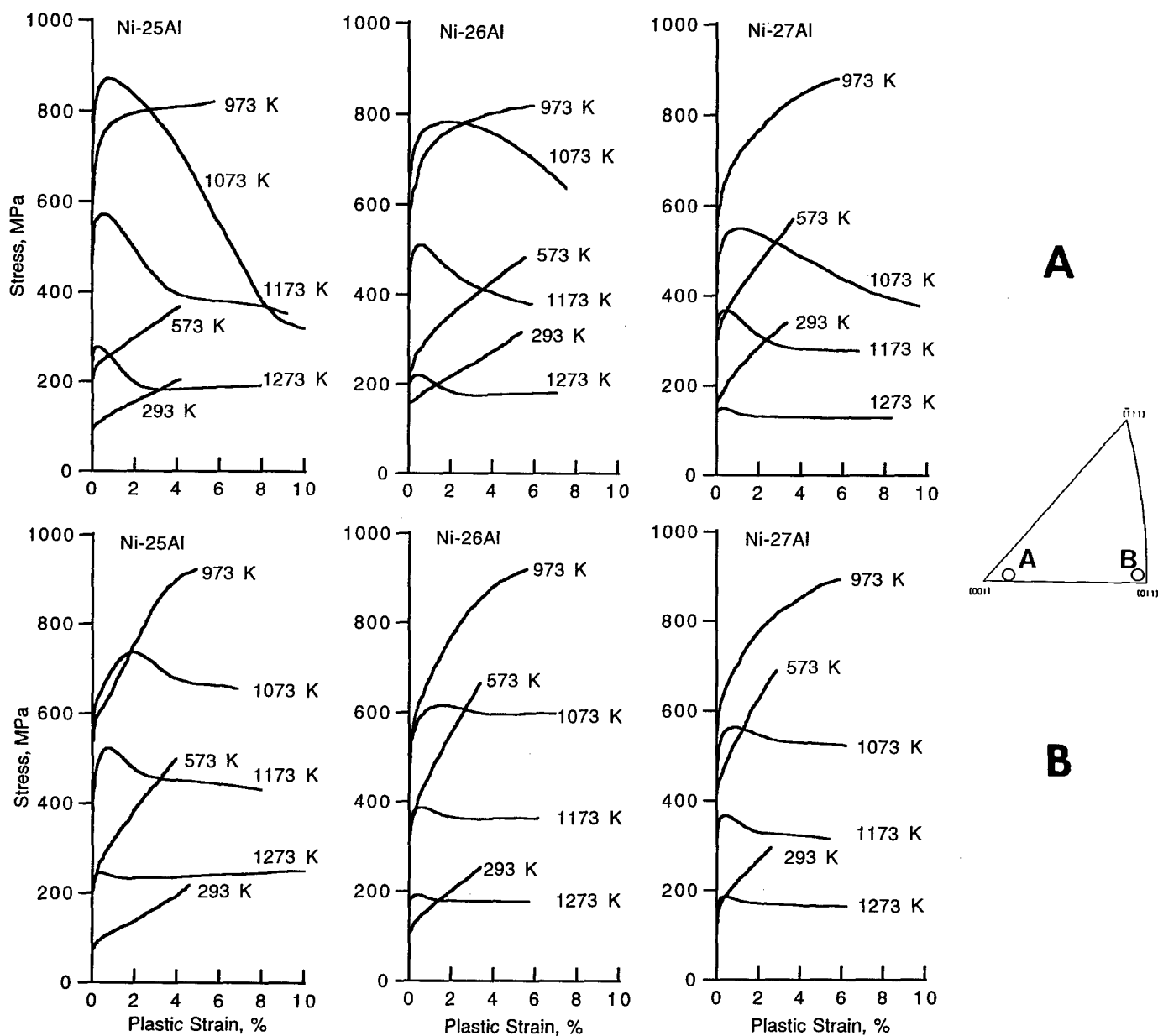


Figure 5: Stress-strain curves of the binary Ni<sub>3</sub>Al single crystals as a function of temperature.



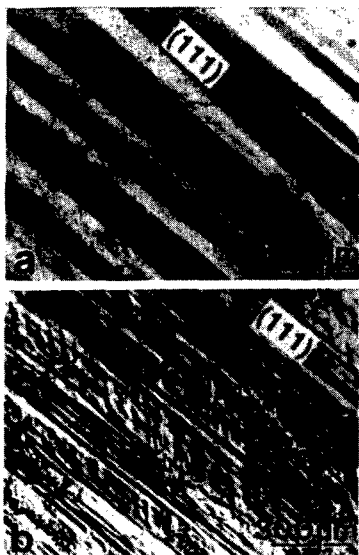


Figure 6: Optical micrographs of slip traces in  $\text{Ni}_3\text{Al}$  single crystals of orientation **B** compressed at 673 K. (a) Ni-25Al deformed to 2.7 % plastic strain; (b) Ni-26Al deformed to 4.4% plastic strain.

Ni-26Al and Ni-27Al exhibit almost similar stress-strain curves to those of Ni-25Al. The yield drop, which becomes less pronounced with increasing Al content, is larger for orientation **A** than for orientation **B**. The temperature where the yield drop is first observable, 1073 K, is the same as that for stoichiometric Ni-25Al. All these features indicate that Al-rich  $\text{Ni}_3\text{Al}$  crystals have a basically similar deformation character to stoichiometric  $\text{Ni}_3\text{Al}$ , though they contain the NiAl second phase.

Figure 6 shows optical slip traces on representative Ni-25Al and Ni-26Al specimen surfaces for orientation **B** after about 4 % plastic strain at 673 K. The slip lines in single phase Ni-25Al are straight and correspond to the primary octahedral slip. The same slip lines character can be observed in the matrix of Ni-26Al, implying that the  $\text{Ni}_3\text{Al}$  matrix in Al-rich alloys deforms in the same way as stoichiometric  $\text{Ni}_3\text{Al}$  single crystals. Thus, we can treat Al-rich crystals like single crystals for evaluation of the mechanical properties.

The 0.2% proof stress as a function of temperature and Al content for orientations **A** and **B** is shown in Fig. 7. All the crystals exhibit a positive temperature dependence of the proof stress at lower temperatures and a negative dependence at higher temperatures, exhibiting the peak temperature of the so-called yield stress anomaly. This feature is a familiar characteristic of  $\text{L}_{12} \text{Ni}_3\text{Al}$  [21, 22], which indicates that the yield stress in Al-rich  $\text{Ni}_3\text{Al}$  is mainly attributable to the  $\text{Ni}_3\text{Al}$  matrix and partly to the NiAl second phase. Among the crystals studied stoichiometric Ni-25Al shows the highest peak temperature, 1073 K, independent of change in compression axis from **A** to **B**. The peak temperature generally decreases with increasing Al content. This trend is more marked for orientation **B** compared to orientation **A**. These results disagree with the previous data for polycrystals by Noguchi et al. [3], who observed that the peak temperature, about 875 K, is independent of Al content. The peak temperatures of our

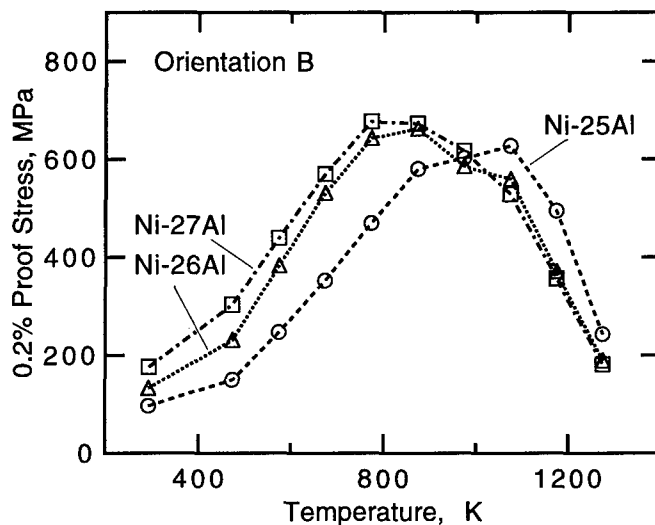
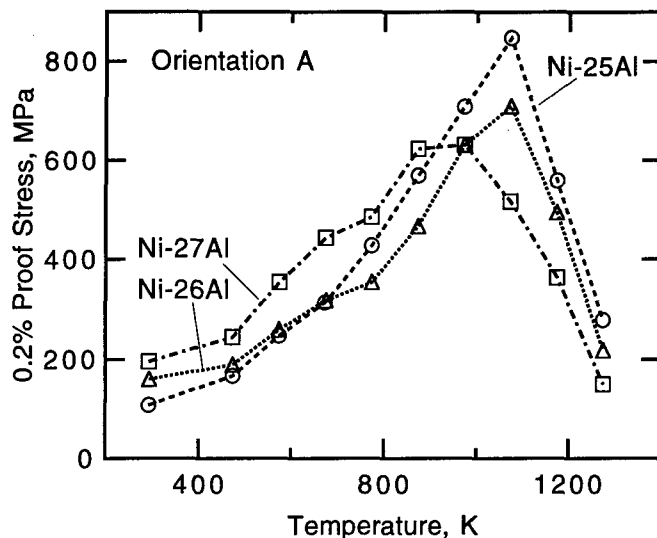


Figure 7: The 0.2% proof stress of the binary  $\text{Ni}_3\text{Al}$  single crystals as a function of temperature.

single crystals correspond to the onset temperature of yield drop in Fig. 5 for both orientations in Ni-25Al and for orientation **A** in Ni-26Al, but is lower than that for the other crystals.

Below the peak temperature of the yield stress anomaly there is a tendency for proof stress to be higher when the Al content is higher, whereas this tendency is reversed above the peak temperature. Thus, stoichiometric Ni-25Al crystal shows the lowest yield strength at lower temperatures but the highest yield strength at higher temperatures.

The peak temperature of Ni-25Al is generally in good agreement with that of Ni-rich [23], and alloyed  $\text{Ni}_3\text{Al}$  [6, 24-26] single crystals with the same orientation as ours. However, there is a marked scatter in the peak stress, depending on the ternary elements. It varies from 630 MPa in Ni-rich  $\text{Ni}_3\text{Al}$  [23] to 1200 MPa in  $\text{Ni}_3(\text{Al},\text{Nb})$  [24] with [001] compression axis. The corresponding value for the present Ni-25Al, 850 MPa, is close to those of  $\text{Ni}_3(\text{Al},\text{W})$  [25] and  $\text{Ni}_3(\text{Al},\text{Ta})$  [26] single crystals.

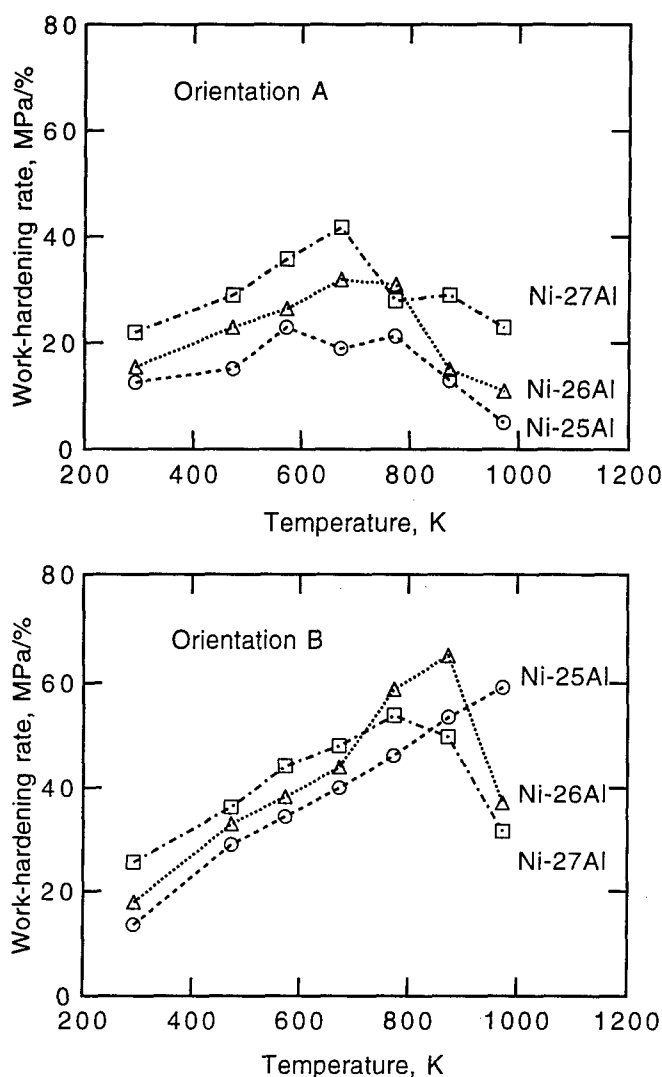


Figure 8: Work-hardening rate (measured at 3% plastic strain) of the binary  $\text{Ni}_3\text{Al}$  single crystals as a function of temperature.

Figure 8 shows the work-hardening rate (WHR) calculated at 3% plastic strain as a function of temperature and alloy composition for orientations A and B. WHR also exhibits a positive temperature dependence similar to the 0.2% proof stress for all the crystals and both orientations. At the lower temperatures WHR for orientation B is more highly dependent on temperature than that for orientation A. The absolute values of WHR are higher for orientation B compared to those for orientation A, supporting the cross-slip mechanism of hardening [6, 21, 22]. This orientation dependence of WHR is consistent with that in  $\text{Ni}_3(\text{Al,Ti})$  reported by Staton-Bevan [27].

#### Discussion

In this study we have grown single crystals of binary stoichiometric  $\text{Ni}_3\text{Al}$ . This is the first report on the high temperature mechanical properties of these crystals. In the course of this work a  $\text{Ni}_3\text{Al}/\text{Ni}_3\text{Al}+\text{NiAl}$  boundary was

found between 25.2 and 25.7 at.%Al on the Ni-Al phase diagram. Thus, it is impossible to grow single crystals of single phase  $\text{Ni}_3\text{Al}$  with higher Al content above this boundary. Instead, we have successfully grown duplex phase alloys of Al-rich  $\text{Ni}_3\text{Al}$ , which consist of single-crystalline  $\text{Ni}_3\text{Al}$  matrix and NiAl second phase. Therefore, we can systematically discuss the effect of Al content on the yield strength of binary  $\text{Ni}_3\text{Al}$  over a wide range of both the Ni-rich and Al-rich sides of stoichiometry.

Figure 9 plots the 0.2% proof stress as a function of Al content for orientations A and B. In Fig. 9 the values for Ni-23.4Al are from the data of Heredia and Pope [23]. The effect of Al content on the proof stress can be related to the stoichiometry of  $\text{Ni}_3\text{Al}$  matrix and the NiAl second phase as follows.

Within the single phase region the 0.2% proof stress increases with increasing deviation from stoichiometry towards the Ni-rich side at lower temperatures, whereas this trend is reversed above the peak temperature of the yield stress anomaly. The lower temperature behavior suggests defect hardening, as pointed out by Noguchi et al. [3]. That is, the deviations from stoichiometry produce Ni or Al anti-site defects, which increase the yield strength. Strictly speaking, we still do not know whether these stoichiometry effects hold for the very narrow region on the Al-rich side, although we expect so. The stoichiometry effect is often observed in other intermetallic compounds, e.g.,  $\text{L}_{12}\text{Ni}_3\text{Ga}$  [3], or B2  $\text{NiAl}$  [28]. On the other hand, the observed behavior above the peak temperature could be reasonably explained if deformation is controlled by diffusion rate, which normally has a minimum at the stoichiometric composition [29]. However, the stoichiometry effect at high temperatures has not yet been well understood in  $\text{Ni}_3\text{Al}$  and other intermetallic compounds, e.g., B2  $\text{NiAl}$  [28].

In the duplex phase region the effect of Al content is apparently similar to the stoichiometry effect in single phase  $\text{Ni}_3\text{Al}$ , i.e., the 0.2% proof stress increases with deviation from stoichiometry at lower temperatures, while this trend is reversed above the peak temperature. However, since Al-rich crystals consist of duplex phase  $\text{Ni}_3\text{Al}+\text{NiAl}$ , it is necessary to consider effect of the second phase on strength.

The NiAl phase is known to exhibit a strong temperature and orientation dependence of the yield stress [28]. Since Ni-rich NiAl possesses higher yield stress than stoichiometric  $\text{Ni}_3\text{Al}$  below 850 K [30], the  $\text{Ni}_3\text{Al}$  matrix can be strengthened by the NiAl second phase in this temperature range. On the other hand, the yield stress of Ni-rich NiAl starts to fall rapidly at about 850 K [30]. For instance, the compressive yield stress of directionally solidified Ni-30Al, which consisted of duplex phase  $\text{NiAl}+\text{Ni}_3\text{Al}$ , was reported to be higher at lower temperatures but lower at higher temperatures than that of binary Ni-23.4Al single crystals [30]. The same trend may be pointed out for polycrystals. The compressive yield stress of duplex phase Ni-37Al at a strain rate of  $10^{-4}/\text{s}$  was reported to be about 60 MPa and 30 MPa at 1200 K and 1300 K, respectively, [31], whereas polycrystalline  $\text{Ni}_3\text{Al}$  alloys exhibit a strength of 300-200 MPa at this strain rate in this temperature interval [21, 22]. Thus, the NiAl phase may cause the yield strength of the duplex alloys to increase at

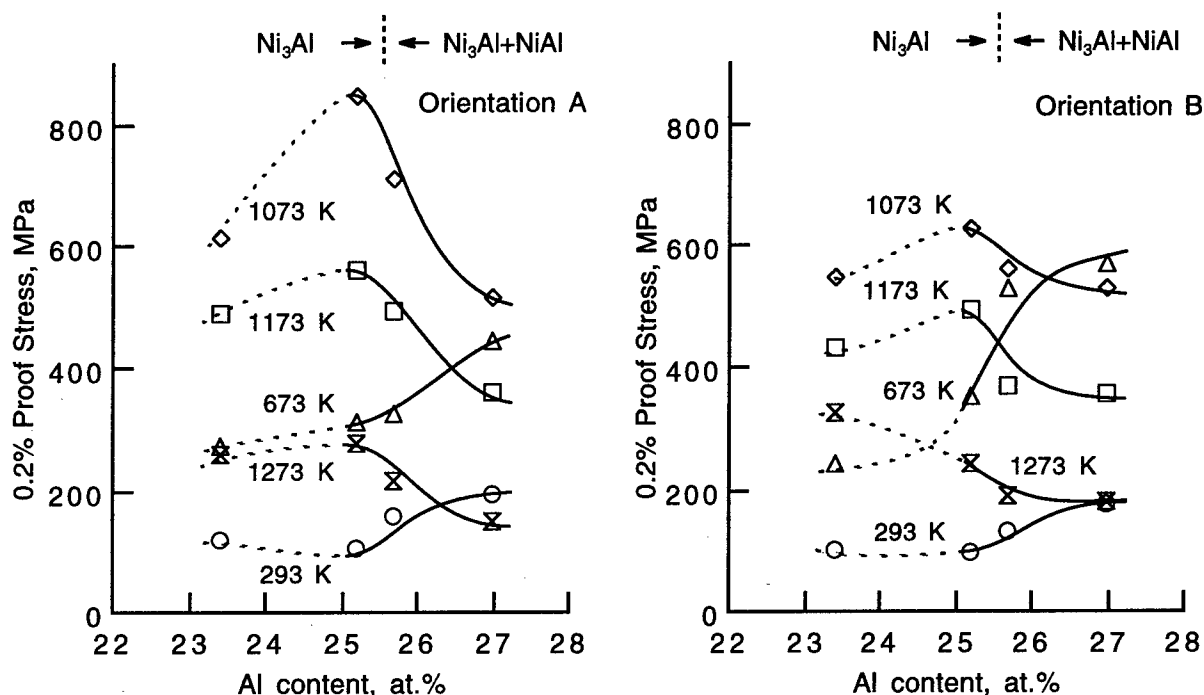


Figure 9: The 0.2% proof stress of the binary  $\text{Ni}_3\text{Al}$  single crystals as a function of Al content. The data for Ni-23.4Al are from Ref. [16].

lower temperatures and to decrease at higher temperatures compared to that of single phase  $\text{Ni}_3\text{Al}$ .

Consequently, the compositional dependence of the 0.2% proof stress shown in Fig. 9 can be considered to be the combined effect of stoichiometry in  $\text{Ni}_3\text{Al}$  and strengthening or weakening due to the Ni-rich  $\text{NiAl}$  second phase. As a result, the yield strength reveals a minimum at the stoichiometric composition at lower temperatures and a maximum above the peak temperature of the yield stress anomaly. This tendency is more marked for orientation A than for orientation B.

Until now the effect of Al content on the mechanical properties of  $\text{Ni}_3\text{Al}$  has been studied only for polycrystals [2-5]. According to these previous studies, compressive yield stress exhibits a similar Al content dependence to that of this study below the peak temperature. However, there is a marked disagreement above the peak temperature between this study and the data reported so far. Noguchi et al. [3] observed a gradual increase in compressive yield stress with increasing Al content even above the peak temperature (similar to the behavior at lower temperatures). Aoki and Izumi [4] also found a similar compositional dependence between 600 K and 1100 K. The strain rates applied in our study and their study are comparable,  $2.3 \times 10^{-4}/\text{s}$  and  $1.4 \times 10^{-4}/\text{s}$ , respectively. There are two possible reasons for this disagreement. First, these research groups used polycrystalline specimens, i.e., the anisotropy effect of the yield strength and the probability of grain boundary slip at high temperatures were not taken into account. Second, these authors did not consider the second phase effect in Al-rich crystals. It is worth noting that in early work by Guard and Westbrook [2] a minimum in hardness at 293 K, and a maximum at 1073 K, were found for the stoichiometric composition. Hardness markedly increased

at 293 K but decreased at 1073 K on both sides of stoichiometry. The latter results are consistent with the yield strength behavior in Fig. 9.

Recently, Dimiduk et al. [18] have reported the effect of Al content on the compressive yield strength using binary single crystals of Ni-rich and Al-rich  $\text{Ni}_3\text{Al}$  (Ni-22.9, Ni-24.2, and Ni-25.9 at.%Al). The Ni-25.9Al crystal consisted of duplex phase like the present Al-rich crystals. Their results are consistent with the above discussion on the Ni-rich side of  $\text{Ni}_3\text{Al}$  stoichiometry but different on the Al-rich side: the yield stress increases gradually with increasing Al content between room temperature and 1100 K. Since these authors did not report the yield stress for the stoichiometric composition, this disagreement cannot now be reasonably understood. One possible explanation is the difference in thermal history of the Al-rich crystals between their and our studies. The present study was carried out on the as-grown crystals, whereas that of Dimiduk et al. [7] on the heat-treated ones. Our preliminary results showed that the yield stress of Al-rich crystals, in particular above the peak temperature, can be increased by heat treatment just below the peritectic temperature. This may be due to the redistribution of Al content between  $\text{Ni}_3\text{Al}$  and  $\text{NiAl}$  phases.

In summary, we emphasize here that the highly ordered stoichiometric  $\text{Ni}_3\text{Al}$  single crystalline alloy has the highest yield strength at high temperature (above the peak temperature). The yield strength decreases on both sides of stoichiometry. Note that the yield strength at 1073 K in Ni-25Al (orientation A) is 230 MPa and 320 MPa higher compared to that of Ni-rich  $\text{Ni}_3\text{Al}$  single crystals oriented similarly [23] and the polycrystalline B-doped Ni-rich  $\text{Ni}_3\text{Al}$  developed by Liu [32], respectively. This demonstrates the

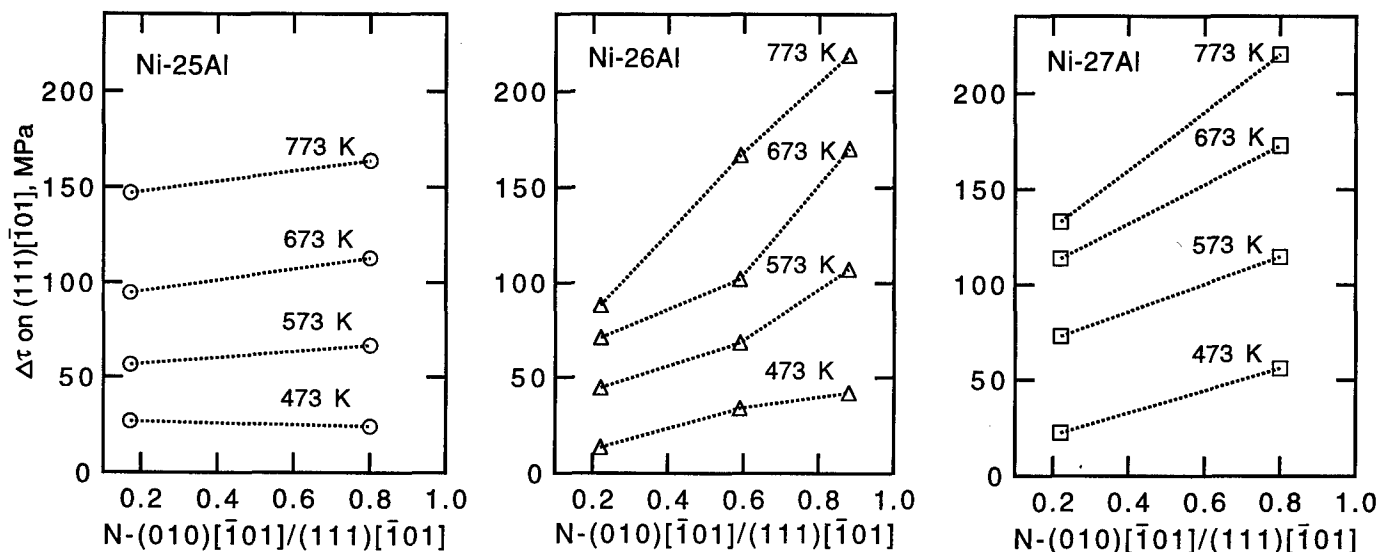


Figure 10: The change in critical resolved shear stress for (111)[ $\bar{1}$ 01] slip ( $\tau_T - \tau_{293K}$ ) for the binary  $Ni_3Al$  single crystals as a function of Schmid factor ratio  $N$ , as defined in Table 2.

advantage of using single crystalline stoichiometric  $Ni_3Al$  alloys for high temperature structural applications.

Finally, the orientation dependence of the critical resolved shear stress (CRSS) for (111)[ $\bar{1}$ 01] octahedral slip may be briefly discussed. Figure 10 shows the change in the CRSS ( $\Delta\tau = \tau_T - \tau_{293}$ ) as a function of the parameter  $N$ , defined in Table 2, in the yield stress anomaly regime for Ni-25Al single crystal together with Ni-26Al and Ni-27Al single crystal-like alloys.  $\Delta\tau$  generally increases with increasing  $N$ , indicating that the Takeuchi-Kuramoto model holds [33]. Heredia and Pope [23] reported the  $N$  dependence of  $\Delta\tau$  for Ni-rich  $Ni_3Al$  (Ni-23.4Al) single crystal in the same  $N$  range as ours. They observed that the  $\Delta\tau$  behavior is a complicated function of  $N$ , but overall it tended to have a negative dependence on  $N$ , implying that the Takeuchi-Kuramoto model does not hold. This disagreement may be due to Al content. Clearly, a variety of binary  $Ni_3Al$  single crystals should be studied to determine the orientation dependence of flow stress more in detail. This is the subject of a forthcoming paper.

### Conclusions

1. For the first time large single crystals of binary stoichiometric  $Ni_3Al$  and single crystal-like duplex phase alloys of Al-rich  $Ni_3Al$  that do not contain any ternary additions have been successfully produced. The Al-rich crystals consist of single crystalline  $Ni_3Al$  matrix and NiAl second phase.
2. A  $Ni_3Al/Ni_3Al+NiAl$  boundary was estimated between 25.2 and 25.7 at.%Al on the Ni-Al phase diagram.
3. All the crystals exhibited a positive temperature dependence of the compressive yield strength. The peak

temperature of the yield stress anomaly decreased with increasing Al content. It was independent of the change in compression axis from [001] to [011] in stoichiometric  $Ni_3Al$  single crystals, whereas it markedly decreased in Al-rich  $Ni_3Al$  crystals.

4. Compared to Al-rich crystals, stoichiometric  $Ni_3Al$  crystals for both [001] and [011] exhibited higher yield strength at 1073-1273 K (above the peak temperature), but lower yield strength below the peak temperature. It is proposed that a combination of alloy stoichiometry and strengthening at lower temperatures, and weakening at higher temperatures due to the NiAl phase explain the yield strength behavior.

5. Among the crystals studied stoichiometric  $Ni_3Al$  single crystals whose compression axis is close to the [001] crystallographic orientation showed the highest compressive yield strength at 1073-1273 K.

### Acknowledgments

This research has been carried out under the Japanese Science and Technology Agency (STA) Fellowship Program. D. Golberg expresses his gratitude for the award of an STA post-doctoral Fellowship, tenable at the National Research Institute for Metals, Tsukuba, Japan. The authors wish to thank E.P. George at Oak Ridge National Laboratory for many helpful discussions and J. Hester at the National Institute for Research in Inorganic Materials, Tsukuba, Japan, for reading the manuscript and providing useful suggestions.

## References

1. R.W. Cahn, P.A. Siemers, J.E. Geiger, and P. Bardhan, "The Order-disorder transformation in  $\text{Ni}_3\text{Al}$  and  $\text{Ni}_3\text{Al-Fe}$  Alloys-I. Determination of the Transition Temperatures and Their Relation to Ductility", Acta metall., 35 (1987), 2737-2751.
2. R.W. Guard and J.H. Westbrook, "Alloying Behavior of  $\text{Ni}_3\text{Al}$  ( $\gamma$  'phase)", Trans. Met. Soc. AIME, 215 (1959), 807-813.
3. O. Noguchi, Y. Oya, and T. Suzuki, "The Effect of Nonstoichiometry on the Positive Temperature Dependence of Strength of  $\text{Ni}_3\text{Al}$  and  $\text{Ni}_3\text{Ga}$ ", Metal. Trans., 12A (1981), 1647-1653.
4. K. Aoki and O. Izumi, "Influence of Substitutional Solute Elements on the Strength of Intermetallic Compound  $\text{Ni}_3\text{Al}$  at Elevated Temperatures", J. Jpn. Ins. of Metals, 12 (1975), 1282-89.
5. R.D. Rawlings and A.E. Staton-Bevan, "The alloying behaviour and Mechanical Properties of Polycrystalline  $\text{Ni}_3\text{Al}$  ( $\gamma$ -phase) with ternary additions", J. Mater. Science, 10 (1975), 505-514.
6. T. Suzuki, Y. Mishima, and S. Miura, "Plastic Behavior in  $\text{Ni}_3(\text{Al,X})$  Single Crystal-Temperature, Strain-rate, Orientation and Composition", ISIJ International, 29 (1989), 1-23.
7. T. Hirano, "Improvement of Room Temperature Ductility of Stoichiometric  $\text{Ni}_3\text{Al}$  by Unidirectional Solidification", Acta metall., 38 (1990), 2667-2671.
8. T. Hirano, "Tensile Ductility of Stoichiometric  $\text{Ni}_3\text{Al}$  Grown by Unidirectional Solidification", Scripta metall., 25 (1991), 1747-1750.
9. T. Hirano and T. Kainuma, "Improvement of Room Temperature Ductility of Stoichiometric  $\text{Ni}_3\text{Al}$  by Unidirectional Solidification", ISIJ International, 31 (1991), 1134-1138.
10. T. Hirano, Sea-Sung Chung, Y. Mishima, and T. Suzuki, "Improvement of Room Temperature Ductility of  $\text{Ni}_3\text{Al}$  by Unidirectional Solidification", Mat. Res. Symp. Proc., 213 (1991), 635-640.
11. T. Hirano and T. Mawari, "Unidirectional Solidification of  $\text{Ni}_3\text{Al}$  by a Floating Zone Method", Acta metall., 41 (1993), 1783-1789.
12. T. Hirano and T. Mawari, "Improvement of Room-Temperature Ductility of  $\text{Ni}_3\text{Al}$  by Unidirectional Solidification", in Structural Intermetallics, eds. R. Darolia et al. (The Minerals, Metals, and Materials Society, Seven Springs, 1993), 437-443.
13. T. Mawari and T. Hirano, "Effects of Unidirectional Solidification Conditions on the Microstructure and Tensile Properties of  $\text{Ni}_3\text{Al}$ ", Intermetallics, 3 (1995), 23-33.
14. T. Hirano and T. Mawari, "Ductility Improvement of Al-rich  $\text{Ni}_3\text{Al}$  by Unidirectional Solidification", in Proc. Int. Symp. Processing and Design Issues in High-Temperature Materials (Davos, Switzerland, 1996), in press.
15. T. Watanabe, T. Hirano, T. Ochiai, and H. Oikawa, "Texture and Grain Boundary Character Distribution (GBCD) in B-Free Ductile Polycrystalline  $\text{Ni}_3\text{Al}$ ", Mater. Sci. Forum, 157-162 (1994), 1103-1108.
16. M. Demura and T. Hirano, "Stress Response by the Strain-rate Change in Binary Stoichiometric  $\text{Ni}_3\text{Al}$  Single Crystal", Phil. Mag. Letters, 75 (1997), 143-148.
17. M. Demura and T. Hirano, "Stress Response by the Strain-rate Change in Binary Stoichiometric  $\text{Ni}_3\text{Al}$  Single Crystal", Mat. Res. Soc. Proc. (Boston, 2-6 Dec., 1996), in press.
18. D.M. Dimiduk, A.W. Thompson, and J.C. Williams, "The Compositional Dependence of Antiphase-Boundary Energies and the Mechanism of Anomalous Flow in  $\text{Ni}_3\text{Al}$  Alloys", Phil. Mag. A, 67 (1993), 675-698.
19. S. Ochiai, S. Miura, Y. Mishima, and T. Suzuki, "High Temperature Yielding of  $\text{Ni}_3(\text{Al, Ti})$  Single Crystals", J. Jpn. Ins. Metals, 51 (1987), 608-615.
20. M.S. Kim, S. Hanada, S. Watanabe, and O. Izumi, "Orientation Dependence of Deformation and Fracture Behavior in  $\text{Ni}_3(\text{Al,Ti})$  Single Crystals at 973 K", Acta metall., 36 (1988), 2967-2978.
21. N.S. Stoloff, "Physical and Mechanical Metallurgy of  $\text{Ni}_3\text{Al}$  and its Alloys", Inter. Mat. Rev., 34 (1989), 153-183.
22. D.P. Pope and S.S. Ezz, "Mechanical Properties of  $\text{Ni}_3\text{Al}$  and Nickel-base Alloys with High Volume fraction of  $\gamma$ ", Inter. Mater. Rev., 29 (1984), 136-167.
23. F.E. Heredia and D.P. Pope, "The Plastic Flow of Binary  $\text{Ni}_3\text{Al}$  Single Crystals", Acta metall., 39 (1991), 2027-2036.
24. C. Lall, S. Chin, and D.P. Pope, "The Orientation and Temperature Dependence of the Yield Stress of  $\text{Ni}_3(\text{Al,Nb})$  Single Crystals", Metal. Trans., 10A (1979), 1323-1332.
25. T. Saburi, T. Hamana, S. Nenno, and Han-ryong Pak, "Temperature and Orientation Dependence of the Yield Strength of  $\text{Ni}_3(\text{Al,W})$ ", Jpn. J. Appl. Phys., 16 (1977), 267-272.
26. Y. Umakoshi, D.P. Pope, and V. Vitek, "The Asymmetry of the Flow Stress in  $\text{Ni}_3(\text{Al,Ta})$  Single Crystals", Acta metall., 32 (1984), 449-456.
27. A.E. Staton-Bevan, "The Orientation and Temperature Dependence of the Work-hardening Rate of Single Crystal  $\text{Ni}_3(\text{Al,Ti})$ ", Phil. Mag. A, 47 (1983), 939-949.
28. R.D. Noebe, R.R. Bowman, and M.V. Nathal, "Physical and Mechanical Properties of the B2 Compound  $\text{NiAl}$ ", Inter. Mater. Rev., 38 (1993), 193-232.

29. G. Sauthoff, "Intermetallic Compounds: Principles and Practice", eds. J.H. Westbrook et al. (John Wiley & Sons, 1995), 911.
30. R.D. Noebe, A. Misra, and R. Gibala, "Plastic Flow and Fracture of B2 NiAl-based Intermetallic Alloys Containing a Ductile Second Phase", ISIJ International, 31 (1991), 1172-1185.
31. J.D. Whittenberger, K.S. Kumar, and S.K. Mannan, "1000 to 1300 K Slow Plastic Compression Properties of Al-deficient NiAl", J. Mater. Science, 26 (1991), 2015-2022.
32. C.T. Liu, "Ni<sub>3</sub>Al Aluminide Alloys", in Proc. 1st Int. Symp. on Structural Intermetallics, eds. R. Darolia et al. (Seven Springs, 1993), 365-377.
33. S. Takeuchi and E. Kuramoto, "Temperature and Orientation Dependence of the Yield Stress in Ni<sub>3</sub>Ga Single Crystals", Acta metall., 21 (1973), 415-425.

# ELASTICITY AND INTERNAL FRICTION OF $\text{Fe}_{70}\text{Al}_{30}$ -SINGLE CRYSTALS

W. Hermann, T. Ort and H.-G. Sockel

Institut für Werkstoffwissenschaften, Lehrstuhl I, Universität Erlangen-Nürnberg,  
Martensstrasse 5, D-91058 Erlangen, Fed. Rep. Germany

## Abstract

The purpose of this work was the investigation of the anelastic behavior of single crystals of the iron-aluminum alloy  $\text{Fe}_{70}\text{Al}_{30}$ , which crystallizes in several cubic crystal structures ( $\text{D}_{03}$ , B2 and A2), at elevated temperatures by a free-free beam resonance technique in the kHz-range. With this technique also the elastic moduli (Young's modulus and shear modulus) can be obtained as a function of the temperature from the measured resonant frequencies. Damping or internal friction is defined by the ratio of the dissipated and the stored energy in one cycle of elastic deformation. Using the dynamic resonance technique the damping can be determined from the free decay of vibrations or from the slope of the characteristic phase shift at resonance. The damping was investigated for five monocrystalline samples in the temperature range between 20°C and 1050°C using several flexural vibration modes in the frequency range from 5 kHz to 40 kHz. The results of the damping investigations lead to a very interesting spectrum exhibiting four internal friction peaks: one maximum at 300°C, the next at 520°C and two further strong peaks between 700°C and 800°C. These damping maxima are connected to discontinuous changes of the elastic moduli. The maximum at around 300°C was found to be due to the movement and breakaway of complete  $\text{D}_{03}$ -superdislocations, which is in agreement with a minimum in yield strength at about 310°C, observed by other authors. The peak at 520°C could be connected to the second order transformation from  $\text{D}_{03}$  to B2 structure and can also be recognized in the temperature dependence of the coefficient of thermal expansion. Both high temperature peaks were found to be due to thermally activated relaxation processes. One is a Zener peak due to stress-induced changes in order, while no exact predictions about the mechanism of the other one can be made so far.

## Introduction

Iron rich iron-aluminides with compositions around  $\text{Fe}_3\text{Al}$  have found great scientific and technical interest in material development because of their outstanding physical and mechanical properties [1, 2]. Particularly the variety of superlattices and the anomalous increase in yield strength with increasing temperature have been investigated intensively. Furthermore, these alloys have a great potential for structural high temperature applications, due to a high strength, a high corrosion resistance, a low density compared with steels, and low costs.

Exact elastic constants and their variation with temperature are of direct engineering use and are needed for the design of statically and dynamically loaded components as well as for the calculation of special properties, e.g. in the calculation of the strength of solids or in fracture mechanics. In a previous work [3] the elastic constants of  $\text{Fe}_{70}\text{Al}_{30}$  were determined from single crystal measurements between 20°C and 900°C as a function of temperature. During these investigations several discontinuities of the elastic moduli (Young's-modulus  $E$  and shear modulus  $G$ ) and elastic constants (compliances  $S_{ij}$  and stiffnesses  $C_{ij}$ ) were observed. These deviations from linearity in the temperature dependence of the elastic properties at about 300°C, 520°C and 700°C are related to an increase in damping. Hence, the purpose of this paper is the characterization of the damping or internal friction properties of  $\text{Fe}_{70}\text{Al}_{30}$ , which is defined by the ratio of the dissipated and the stored energy in one cycle of elastic deformation. Damping measurements supply information about internal relaxation processes like point defect relaxation, diffusion processes, phase transitions, dislocation movement or grain boundary sliding.

For that reason the investigation of internal friction behavior is an interesting tool to achieve a better understanding of internal material processes. Damping measurements on Fe-Al alloys so far were published in three papers [4, 5, 6]. The internal friction spectrum of Fe<sub>70</sub>Al<sub>30</sub> was investigated between 20 and 1050°C in the kHz frequency range (4 - 40 kHz), which partially corresponds with natural frequencies of turbine blades (2 - 8 kHz) [7].

### Material

According to the phase diagram of Kubaschewski [8] the iron-aluminum alloy Fe<sub>70</sub>Al<sub>30</sub> exhibits three different structures: disordered A2 structure ( $\alpha$ -Fe) at temperatures above 1000°C, long range ordered B2 structure (FeAl) between 520°C and 1000°C and also long range ordered D0<sub>3</sub> structure (Fe<sub>3</sub>Al) below 520°C. All three structures are bcc and can be described by a cubic unit cell containing 16 atoms. Beneath these second order phase transitions an additional ferromagnetic transition occurs at a temperature depending strongly on the aluminum content [8] (Curie temperature). In the case of Fe<sub>70</sub>Al<sub>30</sub> this transition should be approximately at 200°C.

An interesting effect of Fe<sub>70</sub>Al<sub>30</sub> with D0<sub>3</sub> structure is the yield strength anomaly with a minimum around 300°C and a maximum at around 480°C, which has been observed both in single crystals [9] and polycrystals [10]. The peak temperature of this anomalous increase in yield strength with increasing temperature is observed consistently below the critical temperature for loss of D0<sub>3</sub> ordering [9, 10, 11]. According to Schröer et al. [9] the yield strength anomaly is due to a complex temperature dependence in dislocation mobility.

Table I: Elemental composition of Fe<sub>70</sub>Al<sub>30</sub> [9].

element	Fe	Al	C	O	N
content (at. %)	69.71	30.22	0.047	0.015	0.003

Five monocrystalline samples of the alloy Fe<sub>70</sub>Al<sub>30</sub> were obtained from the Arbeitsbereich Werkstoffphysik und -technologie of the Technical University of Hamburg-Harburg. The single crystals were made by a modified Bridgman technique [9]. The resulting rods had a length of 42 to 49 mm and a diameter of 4 mm. In order to obtain D0<sub>3</sub>-ordered specimens the single crystals were annealed at 900°C for 1 hour and cooled down to room temperature with 1 K/min. The elemental composition according to [9] is given in Tab. I, the density is 6.42 g/cm<sup>3</sup>. The orientations were determined by the X-ray back-reflection Laue method.

### Internal Friction

A useful technique for the investigation of defect motion in crystalline solids is the internal friction or damping measurement, which is the determination of the time-dependence of elastic deformation. If a static load is applied to an ideal elastic solid the strain follows without any delay. In the case of a real, anelastic solid the elastic strain consists of a time independent elastic part  $\epsilon_{el}$  and a time dependent anelastic part  $\epsilon_{an}$  due to defect motion [12] (Fig. 1). This effect is known as elastic aftereffect.

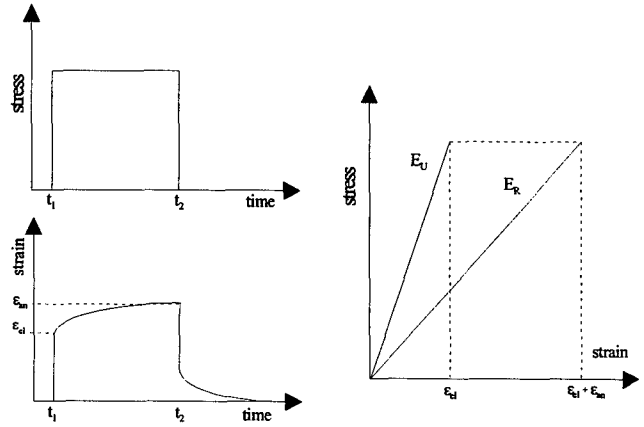


Figure 1: Anelastic deformation and time dependence of the elastic modulus.

The time dependence of anelastic behavior causes two different elastic moduli, the unrelaxed modulus  $E_U$  at time  $t_0$  and the lower relaxed modulus  $E_R$  at time  $t_{\infty}$ .

If a cyclic load  $\sigma = \sigma_0 \exp(i\omega t)$  is applied, the resulting strain is delayed by a phase shift  $\delta$ :  $\epsilon = \epsilon_0 \exp[i(\omega t - \delta)]$ . For cyclic loading internal friction  $Q^{-1}$  is defined by the ratio of the dissipated energy  $\Delta W_{diss}$  and the maximum stored elastic energy  $W_{max}$  in one cycle of elastic deformation [13]:

$$Q^{-1} = \frac{1}{2\pi} \frac{\Delta W_{diss}}{W_{max}} \quad (1)$$

The internal friction corresponds to the tangent of the loss angle and can be expressed as a function of the driving frequency  $\omega$  and the relaxation time  $\tau$  [13]:

$$Q^{-1} = \tan \delta \approx \frac{E_U - E_R}{\sqrt{E_U E_R}} \frac{\omega \tau}{1 + \omega^2 \tau^2} \quad (2)$$

Equation (2) describes a Debye peak with a maximum of  $Q^{-1}$  when  $\omega \tau = 1$ :

$$Q_{max}^{-1} = \frac{E_U - E_R}{2\sqrt{E_U E_R}} \quad (3)$$

The damping vanishes for very high and very low values of  $\omega \tau$ , while the elastic modulus  $E$  approximates  $E_R$  if  $\omega \tau \ll 1$  and  $E_U$  if  $\omega \tau \gg 1$ . For  $\omega \tau = 1$   $E$  takes the value of  $(E_R + E_U)/2$ .

According to Zener [12] the relaxation is characterized by the relaxation strength  $\Delta$ :

$$\Delta = \frac{E_U - E_R}{E_R} \quad (4)$$

If the responsible process is thermally activated the relaxation time is given by



$$\tau(T) = \tau_0 \exp(H / kT) \quad (5)$$

where  $\tau_0$  is the limit relaxation time,  $H$  the activation energy and  $k$  the Boltzmann's constant. The activation energy can be determined by an Arrhenius plot:

$$H = -k \left. \frac{d(\ln \omega)}{d(1/T)} \right|_{T=T_{max}} \quad (6)$$

### Experimental

The elastic properties and the internal friction were measured by a free-free beam resonance technique. Monocrystalline thin rods of  $\text{Fe}_{70}\text{Al}_{30}$  are excited to vibrations by a piezo-electrical driving transducer, which were detected also by a piezo-electrical pick-up transducer. These transducers are coupled to the specimen by suspension of the rod into carbon wire loops (Fig. 2). By the Gain-Phase Analyzer the amplitude and the phase angle are measured as a function of the applied frequency. In the case of resonance, a maximum in amplitude and a characteristic phase shift are measured. The measurements were carried out in vacuum in the 4 to 50 kHz frequency range between 20 and 1050°C. The temperature was controlled by a Pt/PtRh-thermocouple located 1 mm away from the middle of the specimen.

For the determination of the elastic properties three vibrational modes, the flexural, longitudinal and torsional, are excited in the fundamental and in several overtones. Flexural and longitudinal vibrations supply information about the Young's modulus  $E(T)$ , and the torsional vibrations about the shear modulus  $G(T)$ . From the measured resonant frequencies the Young's modulus and the shear modulus are calculated via the following theoretical relationships [14, 15, 16]:

$$E(T) = \frac{4 \cdot \pi^2 \cdot \rho(T) \cdot l^4(T) \cdot f_{n,flex}^2(T)}{\chi^2(T) \cdot m_n^2} \cdot K_f \quad (7)$$

$$G(T) = 4 \cdot \rho(T) \cdot l^2(T) \cdot \frac{f_{n,tors}^2(T)}{n^2} \cdot K_t \quad (8)$$

where  $\rho(T)$  is the density,  $l(T)$  the length,  $\chi(T)$  the radius of inertia,  $n$  the order of vibration, and  $f_n(T)$  the resonant frequency of the  $n$ -th mode of vibration of flexure or torsion.  $K_f$ ,  $K_t$ , and  $m_n$  are vibration mode dependent correction factors, tabulated in [14].

For measurements at temperatures above 20°C the specimen dimension and the density had to be corrected by the thermal expansion. The technical coefficient of thermal expansion was measured by a push-rod vertical dilatometer with a heating rate of 1K/min and is given by

$$\alpha_t(T_0, T_{mes}) = \frac{1}{l_0} \cdot \frac{l_{mes} - l_0}{T_{mes} - T_0} \quad (9)$$

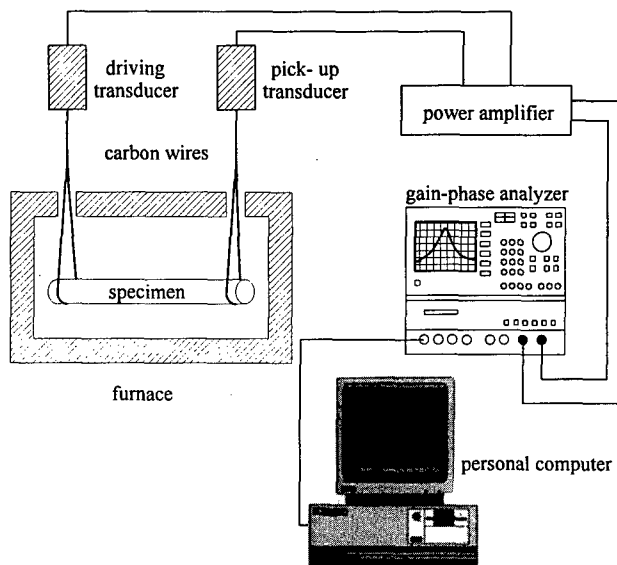


Figure 2: Schematic representation of the measurement technique.

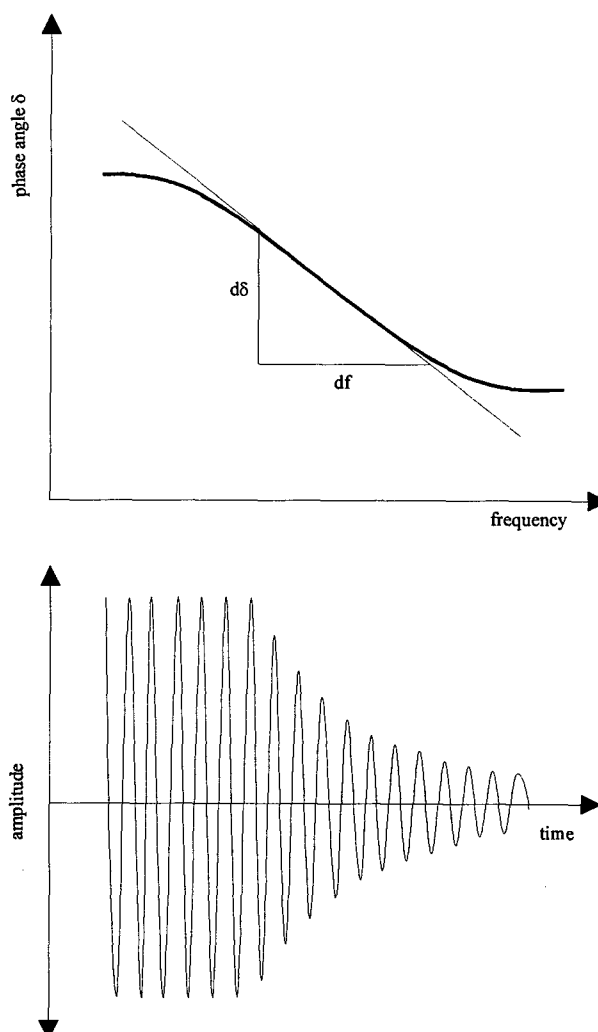


Figure 3: Determination of internal friction.

where  $T_0$ ,  $T_{mes}$ ,  $l_0$  and  $l_{mes}$  are the room and measurement temperature and the specimen length at room and measurement temperature, respectively.

For the determination of the damping values either the phase-angle method or the free decay of vibrations was used. In the phase-angle method the damping was detected from the slope of the tangent  $d\delta/df$  at the point of inflection of the phase curve at resonance by the following equation [17] (Fig. 3):

$$Q^{-1} = 2 / f_n \left( \frac{d\delta}{df} \right)_{f_n} \quad (10)$$

where  $\delta$  is the phase angle and  $f$  the driving frequency. With the free decay of vibrations the damping is measured via the number of vibrations  $n$  required for the amplitude  $A_n$  decrease to a value of  $A_0/e$  [18], where  $A_0$  is the initial forced amplitude (Fig. 3):

$$Q^{-1} = \frac{1}{n\pi} \ln \left( \frac{A_0}{A_n} \right). \quad (11)$$

## Results

### First Studies

In order to carry out the measurements in an almost equilibrium state of  $D0_3$  or  $B2$  order the samples must be held at test temperature for longer times. Schröder et al. [9] e.g. annealed for 1.5 hours ( $Fe_{70}Al_{30}$ ) at each temperature, Morris et al. [19] chose annealing times from 2 weeks at  $200^\circ C$  to 1 hour at  $550^\circ C$  ( $Fe_{72}Al_{28}$ ) or Köster et al. [20] annealed up to a half year at  $250^\circ C$  ( $Fe_{72}Al_{28}$ ).

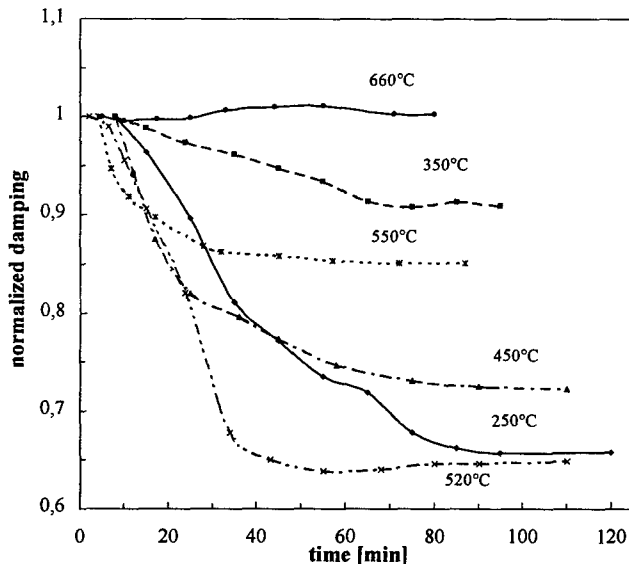


Figure 4: Annealing time dependence of the damping of  $Fe_{70}Al_{30}$  for different temperatures.

Hence, in situ damping measurements were performed at test temperature as a function of the annealing time in order to find a good compromise between equilibrium state and efficient measurement. The results of these investigations at 6 temperatures are shown in Fig. 4, where the measured damping values normalized by the damping of the first measurement are plotted versus the annealing time. For all temperatures except at  $600^\circ C$  we observed at first a strong decrease in damping with time and then an approach to a steady state. An exponential time law was not found. From these results the following annealing times at measurement temperature were chosen:  $20^\circ C - 500^\circ C$ : 2 hours; up to  $600^\circ C$ : 1 hour and above  $600^\circ C$ : 30 min.

### Thermal Expansion

The technical coefficient of thermal expansion is given in Fig. 5 as a function of the temperature. At about  $510^\circ C$  a change in the slope of the thermal expansion is clearly visible. This temperature is in perfect agreement with the  $D0_3 - B2$  transition temperature according to the phase diagram of Kubaschewski [8].

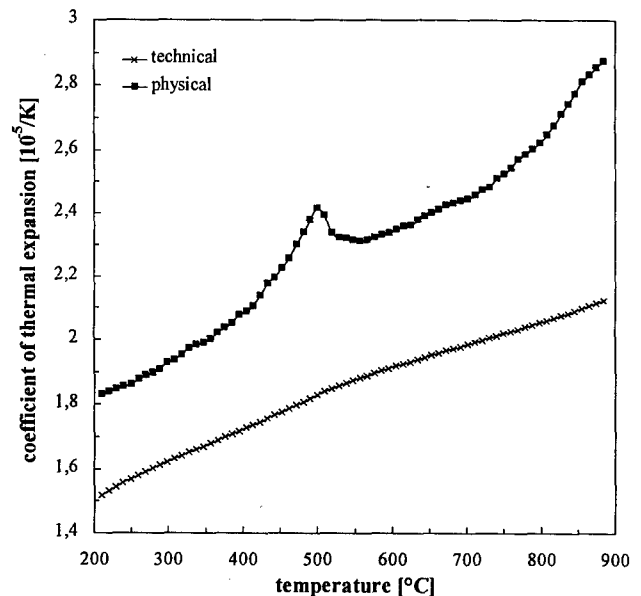


Figure 5: Coefficients of thermal expansion of  $Fe_{70}Al_{30}$ .

### Internal Friction

Fig. 6 is a plot of the room temperature normalized damping of  $Fe_{70}Al_{30}$  as a function of the temperature obtained from the fundamental flexural vibration. In addition the Young's modulus is also shown in Fig. 6. The main characteristic of the internal friction behavior are three clear maxima at around  $300^\circ C$  (peak A),  $520^\circ C$  (peak B) and  $700^\circ C$  (peak C). Beside this, for most of the samples and vibration modes a decrease in damping was observed between 20 and  $200^\circ C$ . At temperatures above  $1000^\circ C$  another increase of the internal friction is visible. The elastic moduli decrease with temperature and show several deviations from linearity at about  $300^\circ C$ ,  $520^\circ C$  and  $700^\circ C$  corresponding with the internal friction peaks.

A detailed investigation of the damping peak A at 300°C is presented in Fig. 7 and 8, where the measured values of damping  $Q^{-1}$  of three vibration modes and the corresponding Young's moduli of one sample are plotted versus the temperature. Independent of the vibration mode this peak appears always at 300 - 320°C. This was confirmed by several other measurements on the available samples, except  $\langle 111 \rangle$  single crystal (Fig. 8), which will be discussed later.

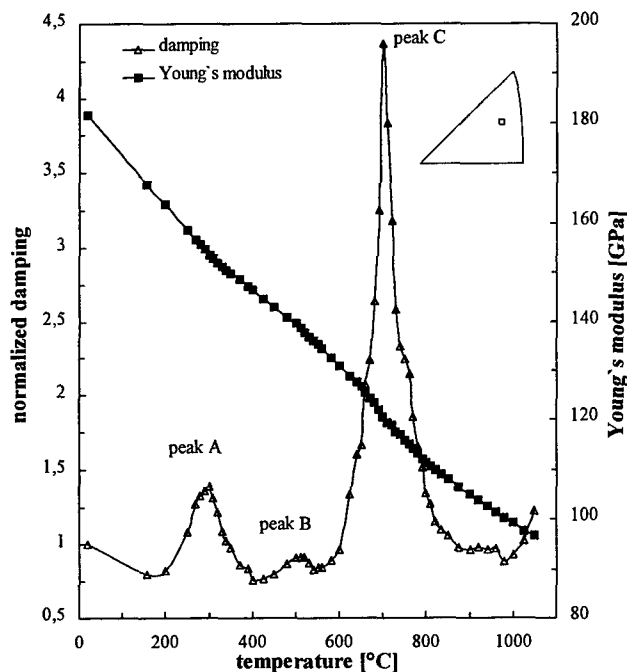


Figure 6: Normalized damping and corresponding Young's modulus of  $\text{Fe}_{70}\text{Al}_{30}$  between 20°C and 1050°C.

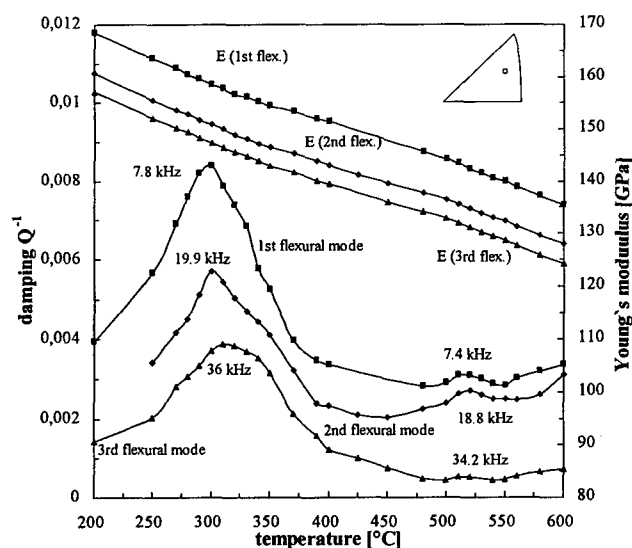


Figure 7: Measured damping and corresponding Young's moduli of three different vibration modes between 200°C and 600°C.

The temperature range of peak B, around 520°C, is also shown in Fig. 7 and 8 for different vibration modes. The investigation of this maximum is difficult because it is very small and was not observed for each measurement. Peak B seems to be frequency independent and agrees well with the predicted  $\text{D0}_3$  - B2 transition temperature.

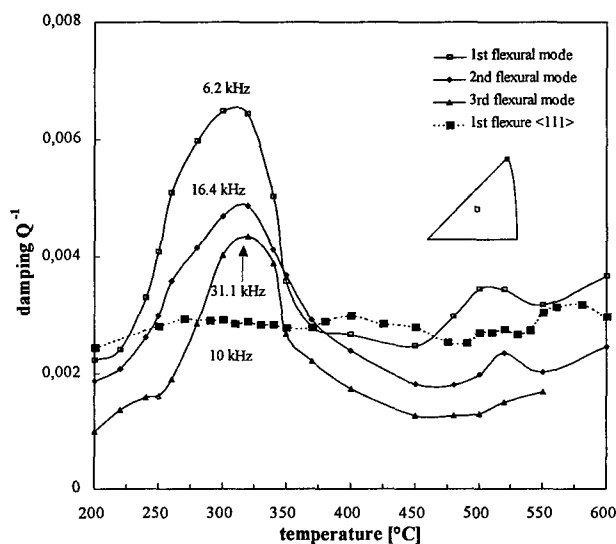


Figure 8: Measured damping of three different vibration modes including values of  $\langle 111 \rangle$  sample.

Further investigations of peak C for different vibration modes are shown in Fig. 9. These measurements reveal clearly two different maxima, C1 and C2, in the temperature range between 700°C and 800°C. Furthermore these peaks appear at higher temperatures for higher vibration modes. This frequency dependence of peaks C1 and C2 indicates that the accompanying damping process is thermally activated.

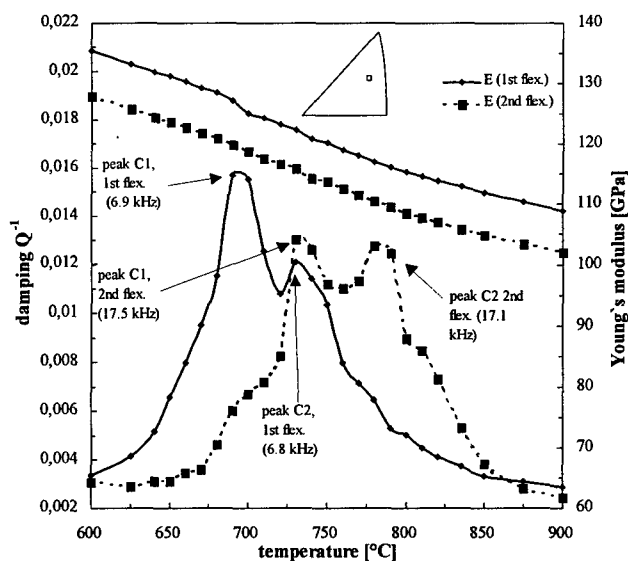


Figure 9: High-temperature damping and corresponding Young's moduli of  $\text{Fe}_{70}\text{Al}_{30}$ .

An Arrhenius plot of the natural logarithm of the frequency at the damping maximum versus the reciprocal absolute temperature is given in Fig. 10. The data yielded values of the activation energy  $H$  of 2.38 eV for peak C1 and 1.73 eV for peak C2, respectively. The relaxation times were determined to be  $1.16 \cdot 10^{-17}$  s (peak C1) and  $5.25 \cdot 10^{-11}$  s (peak C2).

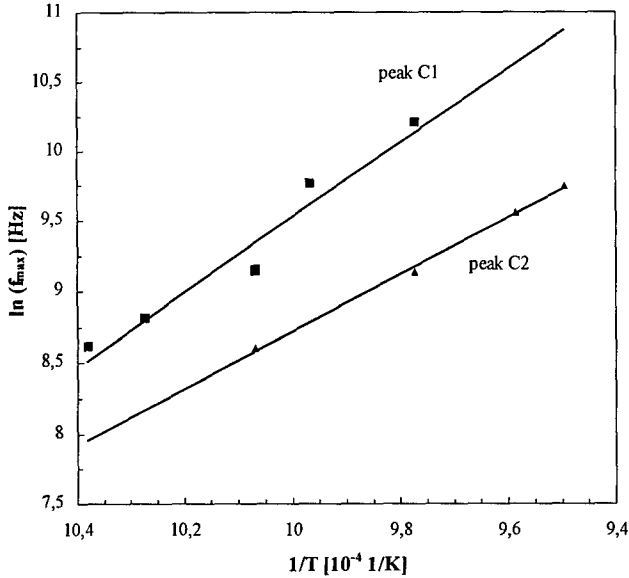


Figure 10: Arrhenius plot of peaks C1 and C2.

### Discussion

The elastic constants  $S_{ij}$  and  $C_{ij}$  determined by resonance technique are discussed in detail and compared with the results of other authors in [3]. In this work, however, we will focus on internal friction and related influence on the elastic properties, therefore both effects will be discussed together.

#### Thermal Expansion

The coefficient of thermal expansion in Fig. 5 shows a change in slope at around 500°C. This is more clearly visible from the physical coefficient of thermal expansion, given by  $\alpha_{phy} = 1/l_0 \cdot dl/dT$ , also shown in Fig. 5. These results are in good agreement with results in [20], where strong discontinuities in thermal expansion at the transition temperatures for several Fe-Al alloys were found. Hence, the change in thermal expansion at 500-510°C can be regarded as a proof for the  $DO_3$ -B2 transition and the validity of the phase diagram of Kubaschewski [8]. The shift of 10-20K is probably caused by measurement errors.

#### Internal Friction

Damping measurements on five monocrystalline  $Fe_{70}Al_{30}$  samples reveal several interesting characteristics. Investigations starting from 20°C show often a decrease in damping with a minimum at 200°C (Fig. 6). This is in good agreement with the predicted Curie temperature. Similar effects with a minimum in damping at the ferromagnetic-paramagnetic transition were observed in [21, 22, 23]. This probably could be explained by the loss of magnetoelastic background damping with in-

creasing temperature and is in agreement with the results of Wert [4] for a  $Fe_{72}Al_{28}$  alloy. Fischbach [6] found a clear magnetic damping due to magnetostrictive coupling for Fe-Al alloys with aluminum contents of 8-20 at.% at temperatures around 600°C measured in the Hz range. This peak disappears for alloys containing more than 21 at.% aluminum and was explained by the drop in Curie temperature or the appearance of long range order.

On the other hand some of the internal friction and elasticity measurements indicate a further maximum between 100°C and 200°C. This could be a Snoeck-relaxation due to interstitial impurities of carbon or nitrogen, also reported in [6]. Unfortunately, the lack of sufficient enough measurement data between 20°C and 200°C allows no exact predictions of damping processes in this low temperature range.

The internal friction peak A at around 310°C was investigated carefully for several samples and vibration modes by sufficient enough measurements. The main characteristic of this maximum is the frequency independence, indicating a hysteretic damping mechanism, which means that the energy loss of this process is most probably caused by the movement and breakaway of dislocations. This is supported by results of Schröer et al. [9], who found for  $Fe_{70}Al_{30}$  a minimum of the shear stress  $\tau_{0.2}(T)$  at about 300°C. It is correlated with the occurrence of complete  $DO_3$ -superdislocations. A pile-up effect within the  $DO_3$  quadruplet increase the shear stress exerted on the leading superpartial. Complete superdislocations therefore need lower stresses for their movement. This high superpartial mobility could also explain the higher damping at this temperature.

If damping peak A is really caused by dislocations, either by vibrating dislocation lines or irreversible motion, an orientation dependence should occur. This orientation dependence is due to different shear stress components in the slip systems of different monocrystalline samples and is taken into account by an orientation factor  $\Omega$  by Granato and Lüke [24, 25] in their theory about dislocation damping. Green and Hinton [26, 27] treated this problem in detail and derived a solution for the orientation factor in fcc crystals for standing waves. Applying this relation on bcc crystals we obtain a theoretical orientation dependence, which is compared with the measurement data.

The whole damping  $Q_{sum}^{-1}$  due to dislocations of a certain single crystal results from the sum of the damping of the different possible slip systems  $Q_i^{-1}$ , multiplied by the orientation factor  $\Omega_i$  [26, 27]:

$$Q_{sum}^{-1} = \sum \Omega_i Q_i^{-1} \quad (12)$$

A mean orientation factor  $\Omega$  is given by equation (13) taking into account simultaneous dislocation motion on several slip systems:

$$\Omega = \frac{E}{n} \cdot \sum_{i=1}^n \frac{m_i^2}{G_i} \quad (13)$$

where  $E$  is the orientation dependent Young's modulus of the investigated sample,  $n$  the number of slip systems,  $m_i$  the Schmid factor and  $G_i$  the shear constant of the  $i$ -th slip system. According to a paper of Calnan and Clews [28] the following slip systems are most favorable in a bcc

lattice and were therefore used for the calculation of the orientation factors:

- Sample A:  $\approx \langle 168 \rangle$ : (101)[11 $\bar{1}$ ]; (112)[11 $\bar{1}$ ]; (213)[11 $\bar{1}$ ];  
 Sample B:  $\approx \langle 6115 \rangle$ : (101)[11 $\bar{1}$ ]; (112)[11 $\bar{1}$ ]; (213)[11 $\bar{1}$ ];  
 Sample C:  $\approx \langle 3519 \rangle$ : (101)[11 $\bar{1}$ ]; (2 $\bar{1}$ 1)[111]; (3 $\bar{1}$ 2)[111];  
 Sample D:  $\approx \langle 5817 \rangle$ : (101)[11 $\bar{1}$ ]; (112)[11 $\bar{1}$ ]; (213)[11 $\bar{1}$ ];  
 Sample E:  $\approx \langle 168 \rangle$ :  $6 \times \{110\} \langle 111 \rangle$ ;  $3 \times \{112\} \langle 111 \rangle$ ;  
 $6 \times \{123\} \langle 111 \rangle$ ;

A plot of the calculated factors  $\Omega$  of the 5 samples representing the theoretical orientation dependence of the damping, normalized with the value of the  $\langle 111 \rangle$ -sample, is given in Fig. 11. In addition also the measured damping values at 310°C,  $\langle 111 \rangle$ -specimen normalized are given in Fig. 11. There is a rather good agreement between the predicted and the observed orientation dependence, which supports a dislocation damping mechanism. In order to get information about the active slip systems the orientation factors  $\Omega_i$  were separately calculated for  $\{110\}$  and  $\{112\}$  slip planes. Here the  $\Omega_i$  of all samples for  $\{110\} \langle 111 \rangle$  slip were found to be distinctly higher than for  $\{112\} \langle 111 \rangle$  slip, indicating that the observed damping is due to dislocation motion on  $\{110\} \langle 111 \rangle$  slip systems. This is in agreement with results in [9], where in the temperature range of the yield stress minimum only  $\{110\} \langle 111 \rangle$  slip systems were observed.

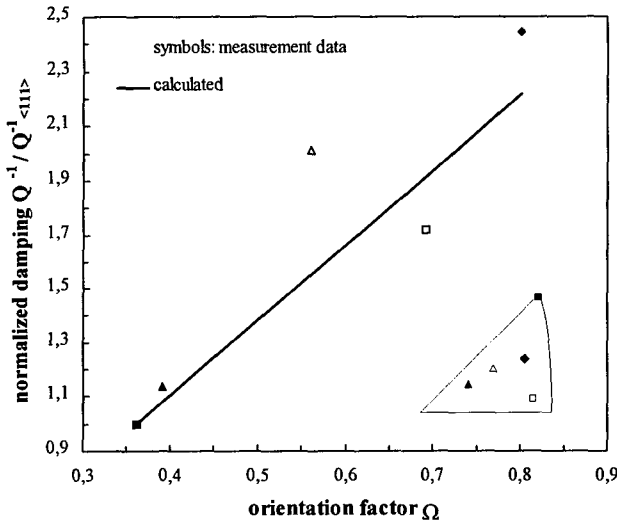


Figure 11: Plot of calculated and measured  $\langle 111 \rangle$ -normalized damping of all five samples versus the orientation factor  $\Omega$ .

In order to get more information about the mechanism of the dislocation damping (dislocation resonance or dislocation hysteresis) it was tried to describe the observed damping by the following equation given in [24] for the vibrating string model of dislocation resonance damping:

$$Q^{-1} = \frac{8 \cdot G \cdot b^2}{\pi^3 \cdot C} \cdot \Lambda \cdot l^2 \cdot \frac{\omega \tau}{1 + \omega^2 \tau^2} \quad \text{where } C = \frac{2 \cdot G \cdot b^2}{\pi(1 - \nu)} \quad (14)$$

where  $G$  is the shear modulus,  $b$  Burgers vector,  $\Lambda$  the dislocation density,  $l$  the dislocation free loop length and  $\nu$  Poisson's ratio.

The relaxation time  $\tau$  is given by

$$\tau = \frac{B \cdot l^2 \cdot (1 - \nu)}{2 \cdot \pi \cdot G \cdot b^2} \quad (15)$$

where  $B$  is the damping constant.

A calculation of the damping for a dislocation resonance mechanism over several magnitudes of frequency gives a maximum of damping between 7 and 8 MHz. In the frequency range used in our investigations (5-30 kHz) only a weak nearly linear increase of the background damping with frequency and temperature is expected. For that reason a dislocation resonance damping according to the vibrating string model in [24, 25] can be excluded and an irreversible dislocation motion is most likely.

In order to proof the predicted hysteretic dislocation damping the amplitude dependence ( $\epsilon_d$ ) can be checked by a so-called Granato-Lücke plot of  $\ln(Q^{-1} \epsilon_d^{1/2})$  versus  $1/\epsilon_d$  as shown in Fig. 12. According to the theory of Granato and Lücke this should yield a straight line, which in deed can be observed in Fig. 12. According to [29] for the hysteretic dislocation damping

$$Q^{-1} \cdot \pi = \Delta \quad (16)$$

is expected, where  $\Delta$  is the relaxation strength according to equation (6).  $\Delta$  was determined to be near to  $3.3 \cdot 10^{-3}$ , which is nearly one magnitude lower than the values calculated from the measured Young's moduli. This unexpected low modulus defect is most probably caused by a superimposition of a relative increase in Young's modulus due to a decrease of the  $D0_3$ -ordering parameter. This is visible from Fig. 6 and 7, where the decrease in Young's modulus exhibits a lower slope between 300°C and 500°C than in other temperature ranges.

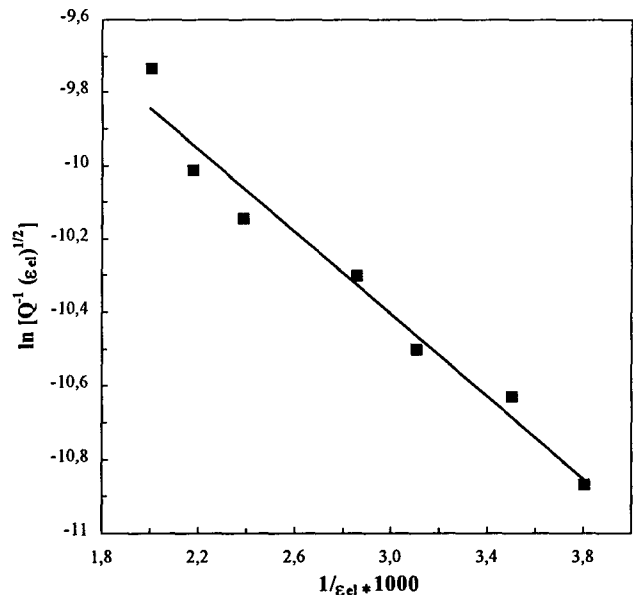


Figure 12: Granato-Lücke plot of the amplitude dependent damping of  $\text{Fe}_{70}\text{Al}_{30}$  at 310°C.

At around 520°C for all samples and several vibration modes the small internal friction peak B and a corresponding modulus defect were observed, as shown in Fig. 7 and 8. This maximum is in good agreement with the D0<sub>3</sub>-B2 transition temperature in Fe<sub>70</sub>Al<sub>30</sub>. Similar observations with an elevated damping were made by Artman [30] for CuZn and by Wolfenden et al. [21] for Cu<sub>3</sub>Au for second order transformations from the ordered into the disordered state. For Fe<sub>70</sub>Al<sub>30</sub> at nearly 520°C the ordered D0<sub>3</sub> structure is transformed into the partially disordered B2 phase. According to Schaefer et al. [31] this requires partial exchange of Fe and Al atoms within the central sublattice. Therefore [31] propose a vacancy jump mechanism between next-nearest neighbor sites in the central sublattice, which may cause the observed relaxation effect.

A mathematical model due to second order transformations was derived in [32, 33] and is briefly represented and discussed by Nowick and Berry [13]. According to this theory the damping can be described by the following relation

$$Q^{-1} \propto (T - T_c)^2, \quad (19)$$

independent if  $T < T_c$  or  $T > T_c$ , where  $T_c$  is the transition temperature. This variation of  $Q^{-1}$  with temperature is in contrast to the usual thermally activated relaxation processes, with  $\omega\tau \gg 1$  at temperatures below the damping maximum and  $\omega\tau \ll 1$  on the high temperature side. For the second order transition  $\omega\tau \ll 1$  on both sides of the peak. In addition the maximum occurs at  $T = T_c$  independent of the driving frequency, which is in agreement with the measurement data. In order to check the observed damping at 520°C according to the theory peak B was subtracted from the background as shown in Fig. 13 and the normalized damping was plotted versus  $(T - T_c)^2$  also given in Fig. 13. For temperatures not too far away from  $T_c$  ( $< 50^\circ\text{C}$ ) a reasonably linear dependence is observed.

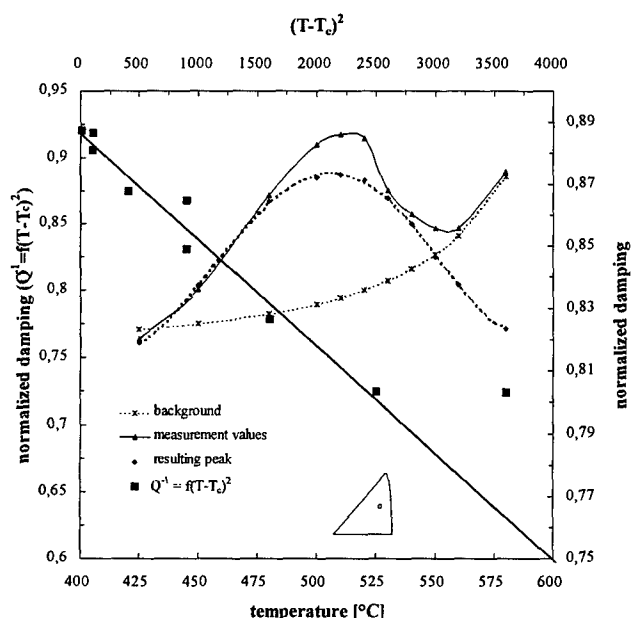


Figure 13: Measured damping around 520°C as a function of the temperature and  $(T - T_c)^2$ .

The main characteristics of the damping spectrum of Fe<sub>70</sub>Al<sub>30</sub> are the two sharp high temperature peaks, C1 and C2, between 700 and 800°C. The frequency dependence of the temperature at the maximum indicates a relaxation mechanism of both peaks. Previous measurements by other authors [4, 5, 6] in the Hz range reveals an internal friction maximum at about 500°C. A comparison of the evaluated damping parameters, activation energy  $H$  and limit relaxation time  $\tau_0$ , obtained in [5, 6] and in this work is given in Table II, where a good agreement between the data of other authors and peak C1 in this work is visible.

Table II: Relaxation parameters of the high temperature damping of Fe-Al alloys.

alloy	Fe <sub>87</sub> Al <sub>13</sub>	Fe <sub>73</sub> Al <sub>27</sub>	Fe <sub>83</sub> Al <sub>17</sub>	Fe <sub>78</sub> Al <sub>22</sub>	Fe <sub>70</sub> Al <sub>30</sub>
H [eV]	2.50	2.44	2.41	2.30	2.38
$\tau_0$ [sec]	$5.3 \cdot 10^{-17}$	$1.5 \cdot 10^{-17}$	$\approx 8 \cdot 10^{-17}$	$\approx 6 \cdot 10^{-17}$	$1.2 \cdot 10^{-17}$
ref.	[5]	[5]	[6]	[6]	peak C1

Shyne et al. [5] and Fischbach [6] predicted a Zener relaxation mechanism due to stress-induced changes in order. According to the theory of Zener [34] this requires the presence of defects with a lower symmetry than that of the crystal. In the case of the partially ordered B2 structure of Fe<sub>70</sub>Al<sub>30</sub> tetragonal defects with a distortion along  $\langle 100 \rangle$  or trigonal defects with distortions along  $\langle 110 \rangle$  are expected. These defects are most probably caused by Al-atom pairs, which is supported by the agreement between the determined damping activation energy and the activation energy of aluminum diffusion in iron (2.41 eV [35]). In the simplest approximation the Zener peak is then caused by atom jumps of either member of the pair that retains the pair.

In a perfectly ordered crystal no Zener relaxation is expected. Fe<sub>70</sub>Al<sub>30</sub>, however, exhibits only an imperfect ordering with a high density of thermal vacancies [31, 36] (700°C:  $C_v = 5 \cdot 10^{-5}$ ), therefore a Zener mechanism is possible. Neumann [37] and Ho [36] predicted triple defects in the B2 structure consisting of a Fe-atom on an Al-site and two accompanying vacancies in the Fe-sublattice. From this point of view enough vacancies should exist allowing the formation and stress-induced reorientation of Al-pairs of either tetragonal or trigonal defect symmetry. In order to predict a specific defect Nowick and Berry [13] gave selection rules for different crystal and defect symmetries. According to these rules in cubic lattices only the compliance  $S_{11}$ - $S_{12}$  will undergo relaxation for a tetragonal defect, while only the constant  $S_{44}$  may show relaxation in the case of a trigonal defect. In the present problem we observed relaxation only for the compliance  $S_{11}$ - $S_{12}$  around 700°C indicating a tetragonal defect. Unfortunately the elastic constants were determined only at a few points in the high-temperature range (550°C, 600°C, 700°C, 800°C). Hence, this result should not be overestimated, because the lack of sufficient enough data may lead to wrong conclusions. On the other hand a comparison of the calculated jump rates for Al-diffusion retaining the Al-pair and the applied driving frequencies fits best for second next-nearest-neighbor jumps of the tetragonal defect. For these calculations the diffusion data were taken from [31]. This is supported by [13], who predict for concentrated bcc alloys that the dominant relaxation mechanism is the reorientation of the next-nearest-neighbor pairs, rather than of nearest-neighbor pairs.

The original pair-reorientation model of Zener is only appropriate at low

solute concentrations, but cannot explain the relaxation effects in concentrated alloys. Le Clair and Lomer [38] introduced a theory of two components with no distinctions between solute and solvent. Instead of solute pairs short-range order parameters were considered. According to this model in the case of zero stress the short-range order parameters are the same for all nearest-neighbor directions. If a stress is applied the equilibrium value of the parameters in one direction relative to the other direction changes and an anelastic relaxation results. In other words, if a stress induces more bonds between near-neighbor atoms of one sort in one direction than in others an overall distortion of the lattice occurs. Extensions of this theory [39] takes also ordering parameters and energies between first and second next-nearest-neighbors into account. According to [13] the relaxation strength can be described by  $\Delta\alpha \propto 1/T$  and indeed for  $\text{Fe}_{70}\text{Al}_{30}$  we observed decreasing relaxation strength with increasing temperature.

The second high-temperature peak, C2, could not be identified in this work. The value of the activation energy of 1.73 eV lies in the range of the data observed for Zener relaxation, while the accompanying limit relaxation time of  $5.3 \cdot 10^{-11}$  s is very high. Unfortunately, only for a few vibration modes reliable data could be obtained from peak C2 for the determination of the relaxation parameters. For that reason the damping parameters of peak C2 must be regarded as approximate values. This second maximum was not observed by other authors [4, 5, 6].

Finally, we want point out the increase in damping in  $\text{Fe}_{70}\text{Al}_{30}$  at temperatures above 1000°C indicating probably a further maximum. The reason of this increase in internal friction is unknown, but probably related to the B2-A2 transition or diffusional processes. The investigation of this effect and of peak C2 should be subject of future measurements.

### Summary

The elastic and anelastic behavior of  $\text{Fe}_{70}\text{Al}_{30}$  single crystals was investigated by a free-free beam resonance technique in the temperature range between 20°C and 1050°C. The temperature dependent elastic moduli show several discontinuities at around 300°C, 520°C and 700°C, related to damping maxima. Peak A at nearly 300°C corresponds very well with the observed yield strength minimum and is caused by a frequency independent hysteresis damping due to irreversible dislocation motion, most probably on  $\{110\} \langle 111 \rangle$  slip systems. A further frequency independent internal friction maximum (peak B) at 520°C is related to the  $\text{DO}_3$ -B2 transition, which was also detected by thermal expansion measurements. In the high-temperature range between 700°C and 800°C two thermally activated maxima C1 and C2 were observed. Peak C1 is due to a Zener mechanism of stress-induced Al-pair-reorientation most probably via next-nearest-neighbor jumps. The damping parameters of this peak, activation energy  $H$  of 2.38 eV and limit relaxation time of  $1.16 \cdot 10^{-17}$  s, are in excellent agreement with the literature and correspond with the activation energy of Al-diffusion in Fe. Peak C2 could not be identified.

Beside these internal friction effects at low temperatures a decrease in damping due to the loss of magnetoelastic background damping with increasing temperature and a minimum at the predicted Curie temperature (200°C) was observed. Furtheron some of the internal friction and elasticity measurements indicate a Snoeck-relaxation peak due to intersti-

tial impurities of carbon or nitrogen between 100°C and 200°C. At temperatures above 1000°C an additional damping maximum is supposed. These effects should be subject of a further treatment of the internal friction behavior of  $\text{Fe}_{70}\text{Al}_{30}$  and other Fe-Al alloys.

### Acknowledgments

The authors wish to thank Prof. Mecking and Dr. Hartig from TUHH for supplying the samples and Mr. Langner for the performance of the thermal expansion measurements. The critical discussions with Dr. M.H. Yoo, Prof. Mecking and Dr. Hartig are gratefully acknowledged. We also thank Prof. Mughrabi for critical reading of the manuscript. This work was supported by the Deutsche Forschungsgemeinschaft DFG).

### References

1. H. Schneibel and M.A. Crim, Processing, Properties and Applications of Iron Aluminides, TMS Symp. Proc., TMS, Warrendale, PA, (1994).
2. C.G. McKamey, J.H. De Van and P.F. Tortorelli, J. Mater. Res., 6 (8) (1991) 1779.
3. M. Koeppel, M.H. Yoo, C. Hartig, H. Mecking, W. Hermann and H.-G. Sockel, Effect of temperature on Elastic Constants and Dislocation Properties of Fe-30% Al Single Crystals, submitted to Acta Metall.
4. C. Wert, J. Appl. Phys., 26 (1954) 640
5. J.C. Shyne and M.J. Sinnott, Trans. Amer. Inst. Min. (Metall.) Eng., 218 (1960) 861.
6. D.B. Fischbach, Acta Metall., 10 (1962) 319.
7. H.E. Miller and W.L. Chambers, in Superalloys II, C.T. Sims, N.S. Stoloff and W.C. Hagel, Eds., John Wiley and Sons, 1987, 27.
8. O. Kubashewski, Iron-Binary Phase Diagrams, Springer, Berlin, 1982.
9. W. Schröer, C. Hartig and H. Mecking, Z. Metallkd., 84 (1993) 294.
10. D.G. Morris and D. Perguiron, High-Temperature Ordered Intermetallic Alloys VI, eds. Horton, J.A., Baker, I., Hanada, I., Noebe, R.D. and Schwartz, D.F. (MRS Symp. Proc., MRS, Pittsburgh, PA, 1995).
11. S. Hanada et al., Scr. Metall., 15, (1981) 1345.
12. C. Zener, Elasticity and Anelasticity of Metals, University of Chicago Press, Chicago, Illinois, 1948.
13. A.S. Nowick and B.S. Berry, Anelastic Relaxation in Crystalline Solids, Academic Press, New York, 1972.

14. E. Goens, Annalen der Physik 11, 6 (1931) 649.
15. J. Spinner and W.E. Tefft, Proc. ASTM 61 (1961), 1229.
16. G. Pickett, Proc. ASTM 45 (1945) 846.
17. J.W. Pendered and R.E.D. Bishop, J. Mechanical Engineering Science, Vol. 5, No. 4 (1963) 345.
18. C.W. Bert, J. Sound and Vibration, Vol. 29, No. 2 (1973) 129.
19. D.G. Morris et al., Phil. Mag. A, 70, 6 (194) 1067.
20. W. Köster and T. Gödecke, Z. Metallk. 71 (1980) 765.
21. A. Wolfenden, L.S. Cook and J.M. Wolla, in M3D: Mechanics and Mechanisms of Material Damping, ASTM STP 1169 (1992) 124.
22. F. Förster and W. Köster, Z. Metallk. 29, 4 (1937) 116.
23. W. Schneider, P. Schrey, G. Hausch and E. Török, J. de Physique, C5, 42 (1981) 10, 635.
24. A.V. Granato and K. Lücke, J. Appl. Phys. 27 (1956) 583, 789.
25. A.V. Granato and K. Lücke, J. Appl. Phys. 52 (1981) 7136.
26. R.E.Jr. Green and T. Hinton, Trans. AIME 236 (1966) 435.
27. T. Hinton and R.E.Jr. Green, Trans. AIME 236 (1966) 439.
28. E.A. Calnan and C.J.B. Clews, Phil. Mag. 42 (1951) 616.
29. R. de Baptist, Internal Friction of Structural Defects in Crystalline Solids, North Holland Publishing Company, Amsterdam 1972.
30. R.A. Artman, J. Appl. Phys. 23 (1952) 475.
31. H.E. Schaefer et al., Phys. Rev. B, 41, 17 (1990) 11869.
32. L.D. Landau and I.M. Khalatnikov, Dokl. Akad. Nauk. USSR 96 (1954) 469.
33. I.A. Yakovlev and I.S. Velichkina, Sov. Phys. Usp. 63 (1957) 552.
34. C. Zener, Phys. Rev. 71 (1947) 34.
35. P. Gröbner, Hutnicke listy, 10 (1955) 200.
36. K. Ho and R.A. Dodd, Scripta Metall. 12 (1978) 1055.
37. J.P. Neumann, Y.A. Chang and C.M. Lee, Acta Metall., 24 (1976) 596.
38. A.D. Le Claire and W.M. Lomer, Acta Metall., 2 (1954) 731.
39. D.O. Welch and A.D. Le Claire, Phil. Mag. 16 (1967) 981.



# OBSERVATION OF QUENCHED-IN VACANCIES IN THE B2 INTERMETALLIC COMPOUNDS FeAl

T. Haraguchi and M. Kogachi

Department of Materials Science, College of Integrated Arts and Sciences,  
Osaka Prefecture University, Sakai 593, Japan

## **Abstract**

The concentrations of quenched-in vacancies retained in B2 Fe<sub>1-c</sub>Al<sub>c</sub> alloys were obtained as functions of composition ( $0.39 < c < 0.51$ ) and quenching temperature (773 to 1273K) from lattice constant and density measurements. Obtained vacancy concentration indicated a gradual increase with composition in the lower Al content region, while it increased rapidly when approaching stoichiometry. Slow-cooled (1K/min) samples showed that retained vacancy concentration is higher than that for samples annealed at and quenched from 773K. Relations of vacancy concentration to the lattice constant, quenching temperature and hardness were discussed. Present results well supported the hardening effect due to retained vacancy and further the proposed linear relation of hardness to the square root of vacancy concentration.

## **Introduction**

Because of its relatively high strength, excellent high oxidation resistance and low cost, the B2-type intermetallic compound FeAl is one of the potential materials for high temperature structural applications. The major difficulty in practical fabrications is in its poor ductility at ambient temperature. Much effort has been devoted to the improvement of ductility and also

to the understanding of mechanical properties in FeAl. Through these works, some topics have been presented to date [1], one of which is quenched-in vacancy hardening. It is well known that FeAl easily retains a high concentration of thermal vacancies by rapid quenching from high temperatures. Nagpal and Baker [2] found a strong dependence of hardness on heat treatment; it increased drastically with increasing cooling rate from furnace-cooling to water-quenching. Further, their noteworthy finding is that the minimum in hardness was attained on the samples annealed at low temperature (673K) not on the furnace-cooled samples, indicating that vacancies cannot be sufficiently eliminated even by the furnace-cooling. Successively, Chang et al. [3] examined a correlation between the hardness and the vacancy concentration by measuring the microhardness as functions of composition and quenching temperature. They found a definite relation between these quantities, i.e. the increase in hardness is proportional to the square root of vacancy concentration, and concluded that vacancies act as more effective strengtheners than anti-structure atoms. It was confirmed also in the successive studies [4,5].

B2 intermetallic compounds consisting of VIII transition metal (TM) atoms and IIb metal (M) atoms, such as NiAl, FeAl and CoGa, have a unique point defect structure with deviation of

composition from the stoichiometry. The defect structure first proposed by Bradley and Taylor [6] (the BT model) is characterized by constitutional defects, i.e. anti-structure defects by excess TM atoms (TM-rich side) and vacancies on the TM sublattice site (M-rich side). This model was later extended as the triple defect model (the TRD model) [7,8]. Point defect behavior is well recognized to sensitively affect physical and mechanical properties [9]. The hardening effect in the FeAl mentioned above is a good example. It is thus essential to clarify the detailed defect structure for understanding their properties. Some investigations focusing on the problem have been recently reported [5,10-15]. In the case of FeAl, however, detailed experimental studies of the defect structure are few. Chang et al. [3] used numerical results of vacancy concentrations based on the TRD model, in discussing their relation to the hardness. The present aim is to determine the concentrations of quenched-in vacancies in B2 FeAl alloys as functions of composition and temperature and is also to reexamine the proposed relation between vacancy and hardness [2,3].

## Experimental

For the measurements of density and lattice constant, eight alloys of  $\text{Fe}_{1-c}\text{Al}_c$  ( $0.40 \leq c \leq 0.51$ ) were prepared. Details of the sample preparation will be described elsewhere [16]. The density measurements were performed in the same way as described previously [13,14], using powdered samples with particle size of 60 to 160  $\mu\text{m}$ . They were given a heat treatment at 1173K for 10-20 min followed by slow-cooling at a rate of 1K/min. The lattice constants,  $a$ , were obtained from 222 reflections as done previously [10,12-14]. Subsequently, the powders were again given a heat treatment at a desired temperature followed by water-quenching. Quenching temperatures and holding times were 773K (13-15 days), 973K (5-6 h), 1073K (3h), 1173K (1h) and 1273K (20min). Total vacancy concentration,  $c_v$ , can be determined from the measurements of lattice constant and density by the relation as [9,13]

$$c_v = N_v / N_s = (\rho_x - \rho_{\text{obs}}) / \rho_x, \quad (1)$$

where  $N_v$  and  $N_s$  are the total number of vacancies and lattice sites and  $\rho_x$  and  $\rho_{\text{obs}}$  the X-ray density and observed density, respectively. Another definition of vacancy concentration is that [7-9]

$$Z = N_v / N_a = c_v / (1 - c_v), \quad (2)$$

where  $N_a$  is the total number of atoms.

We have also prepared other powder samples with different particle size (30 to 60  $\mu\text{m}$ ) in order to examine the dependencies of lattice constant on quenching temperature and cooling rate in more detail. Details of the former dependence will be reported elsewhere [16]. For the latter, the sample with composition of  $c=0.499$  was cooled from 1173K at various cooling rates (0.1, 1, 5, 10, 14 and 22 K/min), in addition to air-cooling and water-quenching.

## Results

Obtained results of lattice constant,  $a$ , are shown in Figure 1 for the samples water-quenched from various temperatures. Data for quenching temperature of 1273K are omitted from the figure for clarity since the difference with those for 1173K was small. The lattice constant for respective temperatures increases linearly with increasing composition until  $c \sim 0.5$ , beyond which it decreases or shows a gradual change. As the quenching temperature increases from 773K to 1173K,  $a$  decreases for any composition, except for the most Fe-rich sample where it shows no distinguishable change. Changes in vacancy concentration,  $c_v$ , with composition are shown in Figure 2 for water-quenched samples, together with slow-cooled samples. Data for quenching from 1273K are omitted from the same reason as above. The broken line indicates the change in  $c_v$  when defect structure obeys the BT model. A general trend in the vacancy concentration is found, i.e.,  $c_v$  indicates a rather gradual increase with composition in lower Al content region and a more rapid increase as the composition approaches stoichiometry. Further, the concentration of quenched-in vacancies becomes higher in higher quenching temperature as expected, except for the most Fe-rich sample. This trend corresponds well to the observed lattice constant change (Figure 1) and also the microhardness change observed by Chang et al. [6]. Pike et al. [17] recently determined the vacancy concentration from density measurements by using the coarse powder samples (about 200-400  $\mu\text{m}$ ) quenched from 773K or 1273K. The trend resembles the present observation although some deviations are found in lower Al content region for 1273K quenching case. Another noticeable fact is that the vacancy concentration for slow-cooled samples is higher than that for samples annealed at and water-quenched from 773K, in the region of  $c \geq 0.45$ . This is consistent with the observation of microhardness by Nagpal and Baker [2] mentioned in the introduction.

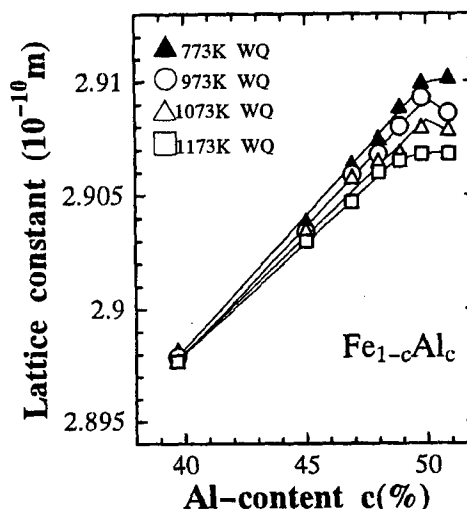


Figure 1: Changes in lattice constant  $a$  with composition  $c$  in  $\text{Fe}_{1-c}\text{Al}_c$  for quenching temperatures of 773K, 973K, 1073K and 1173K (e.g., 773K WQ means the water-quenching from 773K).

Figure 3 shows the lattice constant vs. vacancy concentration relation for the water-quenched (including 1273K quenching case) and slow-cooled samples. The vacancy

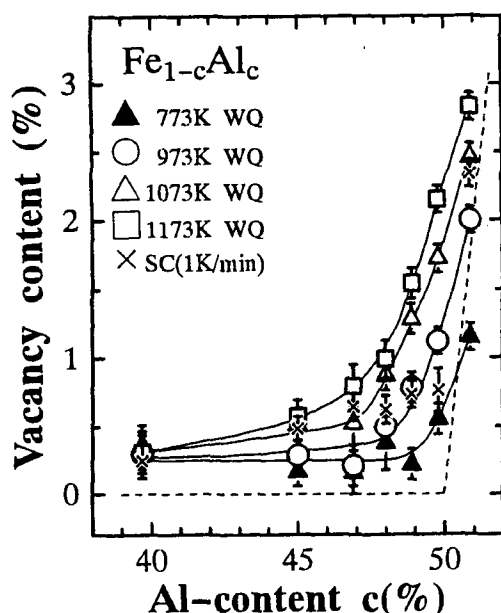


Figure 2: Changes in vacancy concentration  $c_v$  in  $\text{Fe}_{1-c}\text{Al}_c$  for samples water-quenched (WQ) from 773K, 973K, 1073K and 1173K, together with those slow-cooled (SC) at 1K/min from 1173K. The broken line represents the change in  $c_v$  when defect structure obeys the BT model.

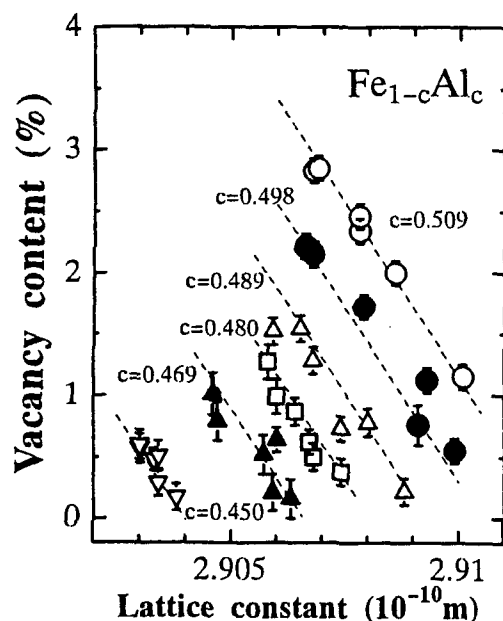


Figure 3: Relation between vacancy concentration  $c_v$  and lattice constant  $a$  for the water-quenched and slow-cooled samples of  $\text{Fe}_{1-c}\text{Al}_c$ . The broken lines represent the numerical results.

concentration decreases monotonically with increase in lattice constant for respective compositions, irrespective of heat treatment conditions. The reduction of lattice constant may be interpreted as volume relaxation in the B2 unit cell due to retained vacancies. Then, the observed change in  $a$  may be expressed as

$$a = \alpha \left( 1 + \frac{1}{3} \beta c + \frac{1}{3} \gamma c_v \right), \quad (3)$$

where

$$\alpha = (2V_{\text{Fe}})^{1/3}$$

$$\beta = (V_{\text{Al}} - V_{\text{Fe}}) / V_{\text{Fe}}$$

$$\gamma = (V_v - V_{\text{Fe}}) / V_{\text{Fe}}$$

$V_{\text{Fe}}$ ,  $V_{\text{Al}}$  and  $V_v$  represent the effective atomic volumes of Fe atom, Al atom and vacancy in B2 cell, respectively. By making the least squares fitting calculation for the data shown in Figure 3, they are obtained as

$$V_{\text{Fe}} = 11.485 \quad V_{\text{Al}} = 13.137 \quad V_v = 9.340$$

in  $10^{-30} \text{ m}^3$  units. Numerical results shown by the broken lines reproduce well the observations.

## Discussion

Present results revealed that B2  $\text{FeAl}$  easily retains a high concentration of thermal vacancies through quenching from temperatures higher than 773K in the region of  $c > 0.40$  (Figure 2). This is in contrast to the cases of  $\text{NiAl}$  and  $\text{CoAl}$  where they could not be detected even when quenched from temperatures higher than 1373K [12,14], suggesting a lower formation energy of

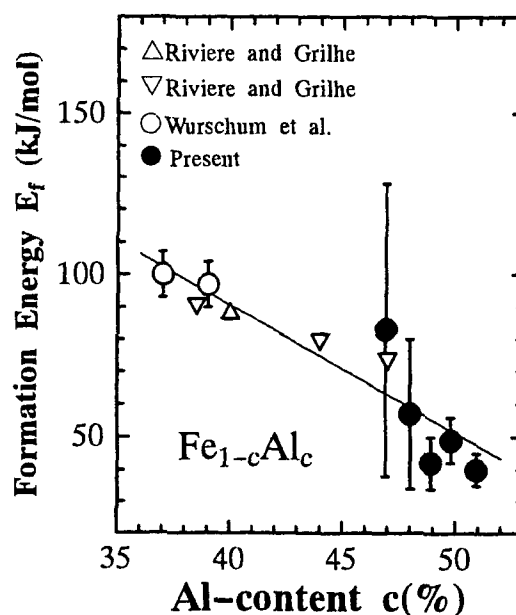


Figure 4: Apparent vacancy formation energies  $E_f$  (closed circles) estimated for the samples of  $\text{Fe}_{1-c}\text{Al}_c$  ( $c > 0.45$ ), together with published data (triangle [17], reversed triangles [19] and open circles [20]).

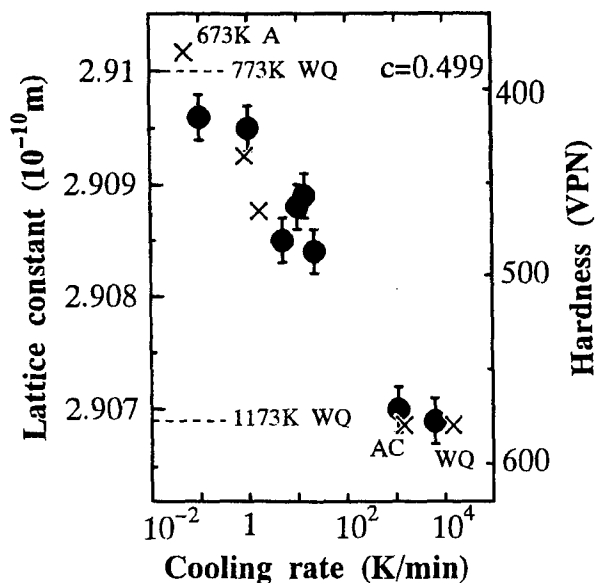


Figure 5: Relation between lattice constant  $a$  and cooling rate for the sample of  $c=0.499$  (closed circles) and that between microhardness [2] and cooling rate for the alloy of  $c=0.50$  (cross marks). Two broken lines represent the lattice constant values for the samples water-quenched from 773K (upper) and 1173K (lower). WQ, AC and 673K A mean the water-quenching, the air-cooling and the annealing at 673K.

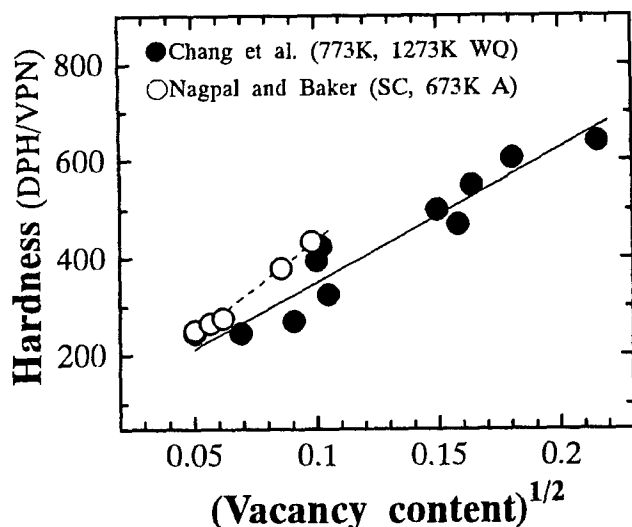


Figure 6: Relation between microhardness and square root of vacancy concentration  $c_V$  in  $\text{Fe}_{1-c}\text{Al}_c$ . Closed circles are for the data (in DPH units) for water-quenching (WQ) from 773K or 1273K [3]. Open circles are for the data (VPN units) for slow-cooling (SC) at 50K/h from 1273K or annealing at 673K (673K A) [2].

vacancies than in these alloys. We estimated apparent vacancy formation energy,  $E_f$ , for the alloys of  $c > 0.45$ , by adopting the following relation:

$$Z = Z_0 + A \exp(-E_f / k_B T_Q), \quad (4)$$

where  $Z$ ,  $k_B$  and  $T_Q$  are the vacancy concentration (equation (2)), Boltzmann constant and quenching temperature, respectively.  $Z_0$  and  $A$  are constant quantities independent of temperature. Since no appreciable change in lattice constant was observed for  $T_Q \leq 773\text{K}$  [16], we used observed value of  $Z$  at  $T_Q = 773\text{K}$  for  $Z_0$ . The numerical results are shown in Figure 4 by closed circles, together with published data determined from the measurements of electrical resistivity [18,19] and positron lifetime [20]. Estimated values are rather small compared with data for the NiAl [9] (e.g., 155kJ/mol in the stoichiometric NiAl [21]). Further, the tendency for  $E_f$  to decrease with increase in composition from  $c = 0.37$  to 0.509 is recognized, which also presents a contrast to the NiAl case where it increases rapidly in the Al-rich region [9].

We finally examine the relation between retained vacancy concentration and hardness. Closed circles in Figure 5 indicate the lattice constants obtained for various cooling rates in the sample of  $c=0.499$ , including those for air-cooling (AC) and water-quenching (WQ). WQ case shows the lowest value of lattice constant, while cooling with the slowest rate (0.1K/min) gives the highest value, close to that for 773K water-quenching. We can say that retained vacancy concentration strongly depends on cooling rate. The cross marks represent the microhardness data reported by Nagpal and Baker [2] for the sample of  $c = 0.50$ . The trend that the hardness increases with the increase in cooling rate corresponds well to the present results. In Figure 6, the microhardness data by Chang et al. [3] (closed circles) and Nagpal and Baker [2] (open circles) are plotted as a function of square root of vacancy concentration,  $c_V$ . Since the lattice constant data by Chang et al. [3] were given only for the quenching temperatures of 773K and 1273K, estimation of  $c_V$  through the equation (3) is impossible for other quenching temperatures and so only the data for these two are shown in the figure. Data points by Nagpal and Baker [2] are for the samples ( $c \geq 0.40$ ) slow-cooled at a rate of 50K/h or annealed at 673K, for which  $c_V$  was estimated from present data for the slow-cooling (1K/min) or the water-quenching from 773K (Figure 2). It appears that the hardness increases with the square root of vacancy concentration as revealed by Chang et al. [3].

Above arguments successfully confirmed the relation between vacancy concentration and hardness in B2 FeAl alloys. Nevertheless the following two points should be noted. First, even in much higher Fe content region ( $c \leq 0.4$ ) where the creation of large amount of thermal vacancies cannot be expected, rather strong dependency of hardness on heat treatment is recognized [2,3]. This suggests that the anti-structure defects by the Fe and Al atoms will act there as another strengthener. Second, as found from Figure 2, the retained vacancy after

annealed at low temperature (773K) has a lower concentration than in the BT model in the Al-rich region, as observed in the NiAl [13] and CoAl [14] alloys. This indicates a formation of the Al anti-structure defects that is neglected in the TRD model. Further precise determination of defect structure is necessary to clarify the problem.

### **Acknowledgment**

The authors wish to thank Professor M. Yamaguchi and Dr. H.Inui for their kind help in the sample preparation by the use of facilities at Kyoto University.

### **References**

1. Processing, Properties, and Applications of Iron Aluminides, eds J.H.Schneibel and M.A.Crimp, (TMS, Warrendale, 1994).
2. P.Nagpal and I.Baker, "Effect of Cooling Rate on Hardness of FeAl and NiAl," Metall. Trans., **A21** (1990) 2281-2282.
3. Y.A.Chang et al., "Correlation of the Hardness and Vacancy Concentration in FeAl," Intermetallics, **1** (1993) 107-115.
4. L.M.Pike, Y.A.Chang and C.T.Liu, High Temperature Ordered Intermetallic Alloys, MRS Symp. Proc., **364** (1995) 65-70.
5. H.Xiao and I.Baker, "The Relationship between Point Defects and Mechanical Properties in Fe-Al at Room Temperature," Acta Metall. et Mater., **43** (1995) 391-396.
6. A.J.Bradley and A.Taylor, "An X-ray Analysis of the Nickel-Aluminum System," Proc. Roy. Soc. London, **A159** (1937) 56-72.
7. J.P.Neumann, Y.A.Chang and C.M.Lee, "Thermodynamics of Intermetallic Phases with the Triple-Defect B2 Structure," Acta Metall., **24** (1976) 593-604.
8. J.P.Neumann, "On the Occurrence of Substitutional and Triple Defect in Intermetallic Phases with the B2 Structure," Acta Metall., **28** (1980) 1165-1170.
9. M.Kogachi, "The Long-Range Order and Defect Structures in B2 NiAl Type and L1<sub>2</sub> Ni<sub>3</sub>Al and Al<sub>3</sub>Ti-X Type Intermetallic Compounds," Defect Diff. Forum, **121-122** (1995) 15-40.
10. M.Kogachi, S.Minamigawa and K.Nakahigashi, "Determination of Long Range Order and Vacancy Content in the NiAl  $\beta$ -Phase Alloys by X-ray Diffraction," Acta Metall. et Mater., **40** (1992) 1113-1120.
11. H.Xiao and I.Baker, "Long Range Order and Defect Concentrations in NiAl and CoAl," Acta Metall. et Mater., **42** (1994) 1535-1540.
12. M.Kogachi, Y.Takeda and T.Tanahashi, "Defect Structure in Al-rich Composition Region in the  $\beta$ -NiAl Intermetallic Compound Phase," Intermetallics, **3** (1995) 129-136.
13. M.Kogachi et al., "Determination of Vacancy Concentration and Defect Structure in the B2 Type NiAl  $\beta$ -Phase Alloys," Scripta Mater., **34** (1996) 243-248.
14. M.Kogachi and T.Tanahashi, "Point Defect Behavior in the B2 Type Intermetallic Compounds CoAl," Scripta Mater., **35** (1996) 849-854.
15. S.M.Kim, Y.Takeda and M.Kogachi, "Observation of High Temperature Al Vacancies and Al Antistructure Atoms in B2 NiAl Alloys by In Situ Neutron Diffraction," Scripta Mater., **34** (1996) 1845-1850.
16. M.Kogachi and T.Haraguchi, "Quenched-in Vacancies in B2-Structured Intermetallic Compound FeAl," Mater. Sci. Engineer., A (1997) (accepted).
17. L.M.Pike, Y.A.Chang and C.T.Liu, Processing, Properties, and Applications of Iron Aluminides, eds J.H.Schneibel and M.A.Crimp, (TMS, Warrendale, 1994) 217-229.
18. J.P.Rivière and J.Grilhe, "Restauration de Defauts de Trempe dans un Alliage Fe-Al 40 at.% Ordonné," Acta Metall., **20** (1972) 1275-1280.
19. J.P.Rivière and J.Grilhe, "Energie de Formation des Lagunes dans les Alliages Fe-Al Ordonnés de Type B2," Scripta Metall., **9** (1975) 967-970.
20. R.Würschum, C.Grupp and H.E.Schaefer, "Simultaneous Study of Vacancy Formation and Migration at High Temperatures in B2-type Fe Aluminides," Phys. Rev. Lett., **75** (1995) 97-100.
21. R.J.Wasilewski, "Thermal Vacancies in NiAl," Acta Metall., **15** (1967) 1757-1759.

# **ADVANCED INTERMETALLICS AND COMPOSITES**

# THE MECHANICAL BEHAVIOUR OF THE INTERMETALLIC $\text{Ti}_2\text{AlNb}$

T.K.Nandy and D. Banerjee  
Defence Metallurgical Research Laboratory  
Hyderabad-500058, India

## Abstract

The ternary intermetallic  $\text{Ti}_2\text{AlNb}$  (the O phase) is an important constituent of several alloys currently under evaluation both as monolithic products and as matrix material for intermetallic matrix composites. We have therefore initiated a program to evaluate the mechanical behaviour of polycrystalline, single phase O alloys as a function of Nb content, grain size, interstitial content and substitutional alloying additions. In this paper we report results on the elastic moduli as a function of alloying content and temperature, yield stress as a function of temperature and strain rate, and steady state creep behaviour for several ternary alloys with varying levels of Nb.

The yield stress shows three regimes of behaviour as a function of temperature; a strong temperature dependence is observed at low temperatures followed by an intermediate, largely athermal region, and finally again a region over which the yield stress drops with temperature. Nb increases the yield stress in the low temperature regime for substoichiometric levels to the stoichiometric content. Examination of dislocation structures reveals that 'a' 'a\*' and 'c+a/2' dislocations are operative at low temperatures. The balance of the microstructural evidence suggests that the flow behaviour at low temperatures is controlled by the restricted mobility of either [100] or [102] dislocations.

The steady state creep behaviour of alloys with three different Nb contents has been investigated

over a temperature range between 973 - 1023 K, and a wide range of applied stresses. The Nb content of the alloy does not appear to influence the steady state creep rate. Stress exponents ranging from 7 at 973 K to 5 at 1023 K have been recorded and the apparent activation energy ranges from 290 to 330 kJ/mol. Dislocations are randomly arrayed after steady state creep has been attained. Attractive junctions between 'a' and 'a\*' dislocations and between 'a', 'a\*' and 'c' dislocations are observed, and it is suggested that the network coarsening model of creep may be applicable to the O phase, although it is not clear whether dislocation climb or the rate of escape from attractive junctions controls the steady state creep rate.

## Introduction

The ternary intermetallic O phase based on the stoichiometry,  $\text{Ti}_2\text{AlNb}$ , was discovered<sup>1</sup> while examining the influence of Nb on phase transformations in alloys based on  $\text{Ti}_3\text{Al}$  ( $\alpha_2$ ). It was simultaneously realised<sup>2</sup> that alloys with a high Nb content (15-30 at.% Nb) possess better combinations of strength, toughness and creep than those with lower Nb contents (10-15 at.% Nb). Figure 1a suggests that over the former range of composition, the microstructure consists primarily of the O phase while the lower Nb alloys contain mainly the  $\alpha_2$  phase. Figure 1a also indicates that the O phase exists over a wide range of Nb, and increasing the Nb content in the O+B2 region results in an increasing Nb content of the O phase at a nearly constant Al

level. Figure 1b shows a vertical section at 27.5 at.% Al indicating that the O phase is stable upto about 1273 K at this Al level but that it exists in 2 ordered forms, designated O1 and O2<sup>3</sup>. The site occupation in the former is similar to that in Ti<sub>3</sub>Al while in the latter, Nb atoms occupy a distinct sublattice (Figure 2 and Table 1).

We have initiated a study of the mechanical behaviour of polycrystalline O2 phase as a function of Nb content and several important quaternary additions including different interstitial levels. We report in this paper studies which evaluate the yield stress as a function of temperature and strain rate and creep in the temperature range 973K to 1023K at Nb levels ranging from 18% - 25%. The study is supported by exploratory investigations of dislocation arrangements generated under these conditions.

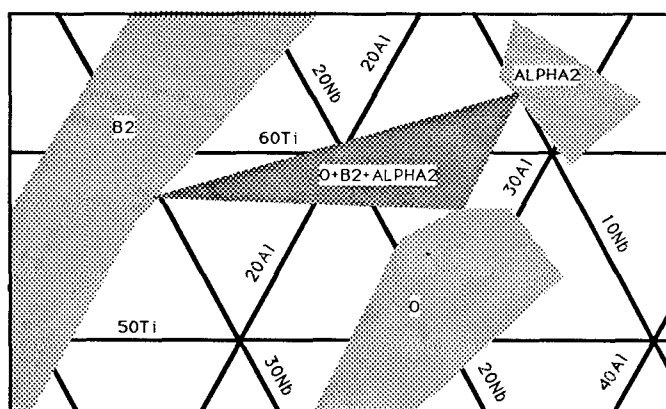


Figure 1a : 1173K Isothermal Section of the Ti-Al-Nb System<sup>4</sup>

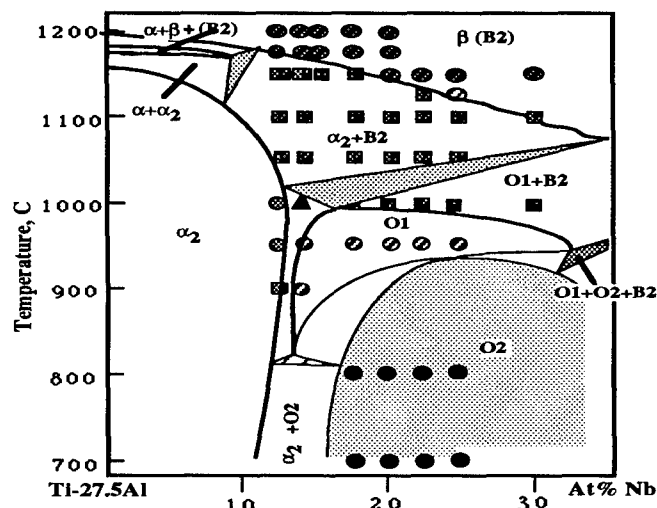


Figure 1b : Vertical Section of the Ti-Al-Nb System at 27.5 at.% Al<sup>3</sup>

Atom	Al	Ti	Nb	Ti/Nb
Layer A	●	⊙	⊙	⊙
Layer B c/2 above	●	⊙	⊙	⊙

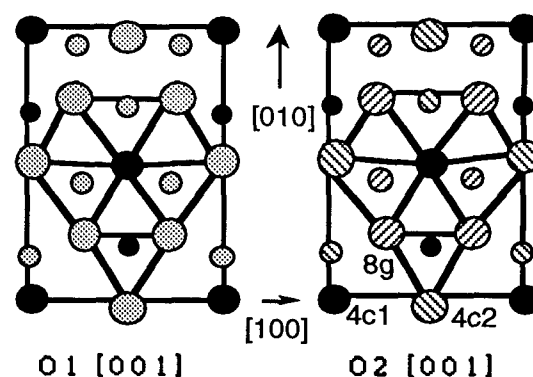


Figure 2 : Basal Plane Projections of the O1 and O2 Structures based on Ti<sub>2</sub>AlNb Stoichiometry

Table 1 : Crystallographic Parameters for the O2 Phase (From Reference 5)

Multiplicity Wyckoff Notation	Coordinates				Site Occupation			Conditions for reflection for fundamental reflections
		x	y	z	Ti	Al	Nb	
8g	x y 1/4; x y 1/4 x y 3/4; x y 3/4	0.2310	-0.0959	0.25	82	0	18	hkl h+k=2n okl k=2n hol h,l=2n hko h+k=2n hoo h=2n oko k=2n ool l=2n
4c <sub>1</sub>	0 y 1/4; 0 y 3/4	0	0.1633	0.25	0	100	0	
4c <sub>2</sub>	0 y 1/4; 0 y 3/4	0	-0.3643	0.25	35	0	65	



## Experimental

Alloy compositions listed in Table 2 were remelted several times in a non-consumable vacuum arc remelting unit, starting with Ti sponge, Aluminium and Al-Nb masteralloy. The as-melted pancakes were cut into rods, heat treated at 1473 K for 45 minutes in the single phase region, oil quenched, and then transformed into a polycrystalline O structure by heat-treatment at 1173 K for 100-200 hours. Alloy compositions are given in Table 2. Compression samples were machined from the fully heat-treated alloy rods. Transmission electron microscopy was carried on thin foils prepared from sections cut at 45° to the compression axis.

**Table 2 : Chemistry of O Phase Alloys**

Alloy Desgn.	Al at.%	Nb at.%	O ppm (wt.)	N ppm (wt.)	H ppm (wt.)
2718	27.1	18.5	690	130	30
2720	27.4	20.3	530	150	22
2722	27.3	22.3	705	155	39
2725	26.9	24.3	700	140	50

## Results

### Microstructure

The microstructure of a typical alloy in the fully heat-treated condition is shown in Figure 3. Equiaxed grains of the O2 phase form through a massive transformation to yield a polycrystalline structure, leaving behind a 'ghost' of the prior  $\beta$  grain boundaries formed after the high temperature treatment. A separate analysis of the elastic properties of these samples<sup>6</sup> indicated that no marked crystallographic texture was present. The density of dislocations in the transformed structure is very low and subgrain boundaries composed of 'c' component dislocations are frequently observed. Electron diffraction confirmed that the O2 phase was formed in all alloys. Table 3 indicates the grain size of the polycrystalline O2 structure after the transformation treatment.

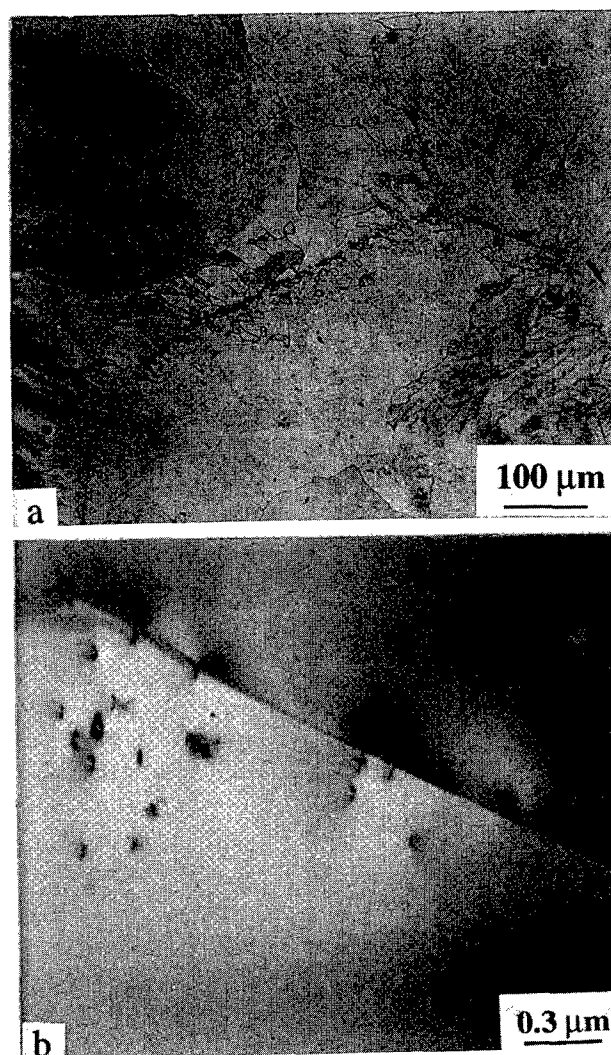


Figure 3 : (a) Optical micrograph of a Ti-27Al-20Nb alloy.  
(b) TEM micrograph showing isolated dislocations within grains.

**Table 3 : Grain Size of O Phase Alloys**

Alloy Designation	Grain size ( $\mu\text{m}$ )*
2718	157
2720	164
2722	166
2725	153

\* Grain size measured as a mean linear intercept

## Elastic Properties

Elastic properties of the alloys were evaluated in a separate study<sup>6</sup> both by a resonant ultrasound spectroscopy technique as well as from compression tests and are summarised here for the sake of completeness (Table 4 and Figure 4). Both the shear modulus and Young's modulus of the O2 phase increases with Nb content, while the Poisson's ratio is unaffected and has a value of 0.32 suggesting that the bonding is metallic in nature. The Young's modulus of the O2 phase is significantly lower than that of TiAl, but similar to that of Ti<sub>3</sub>Al alloyed with 5at.% Nb. The temperature dependence is similar to that of Ti<sub>3</sub>Al.

**Table 4 : The Elastic Properties of O2 Alloys Measured by Resonant Ultrasound Spectroscopy<sup>6</sup>**

Alloy	K (GPa)	E (GPa)	G (GPa)	$\nu$
Ti-27Al-20Nb	118.40	128.78	48.83	0.3187
Ti-27Al-24Nb	123.04	135.90	51.63	0.3159

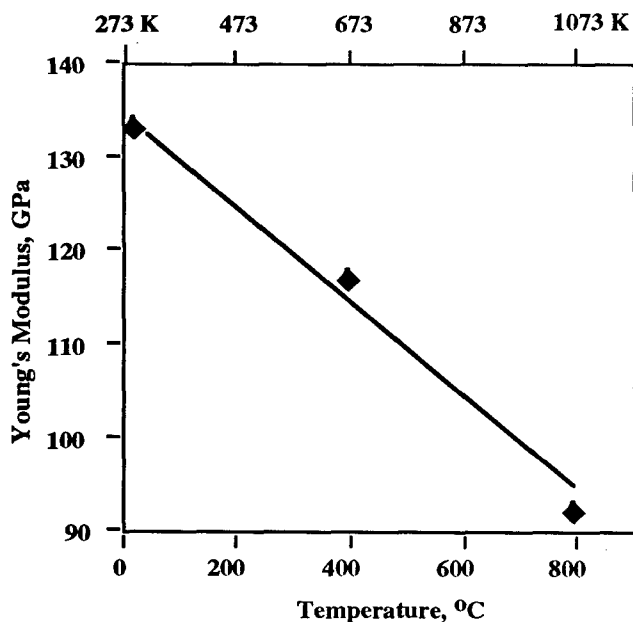


Figure 4 : Young's modulus as a function of temperature for Ti-27Al-18Nb and Ti-27Al-25Nb measured by compression tests<sup>6</sup>

## Yield Stress as a Function of Nb Content, Temperature and Strain Rate

The yield stress is shown in Figure 5 as a function of temperature for the four compositions for a strain rate of  $1.85 \times 10^{-2} \text{ sec}^{-1}$ . The yield stress is strongly, thermally activated in the low temperature regime. In this temperature range the yield stress increases with Nb content as shown in Figure 6.

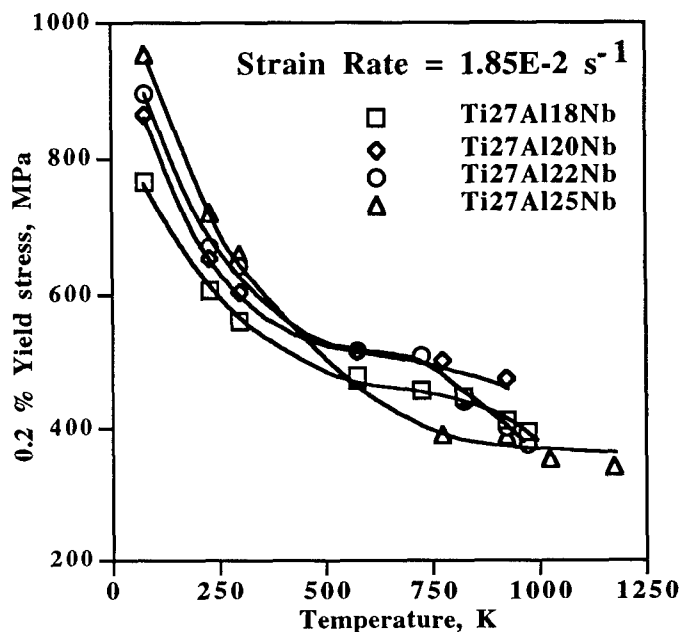


Figure 5 : Yield Stress as a function of temperature for the four ternary alloys

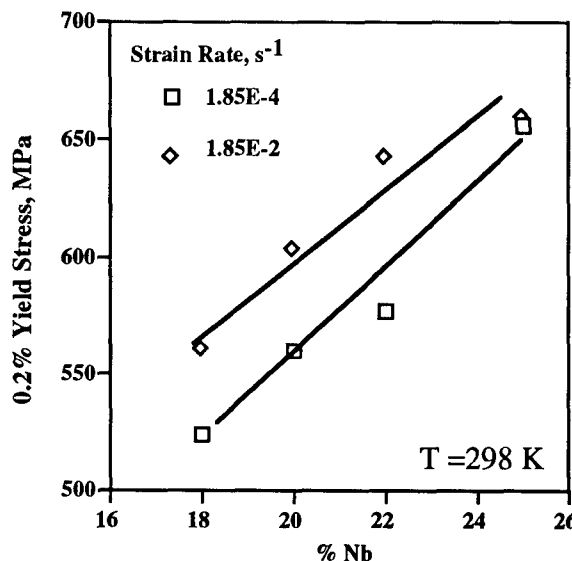


Figure 6 : Yield Stress as a Function of Niobium Content at 298K.

The temperature dependence of the yield stress decreases at intermediate temperatures so that an extended athermal region is observed for the Ti-27Al-18Nb, Ti-27Al-20Nb and Ti-27Al-22Nb alloys between about 500K and 750K, and above 750K in the Ti-27Al-25Nb alloy. Beyond the athermal region, the yield stress again decreases with temperature for the lower Nb alloys. Modulus compensated plots of yield stress versus temperature are shown in Figure 7. An increase in the modulus compensated yield stress is observed at around 750K. No consistent trends with Nb content are apparent at high temperatures.

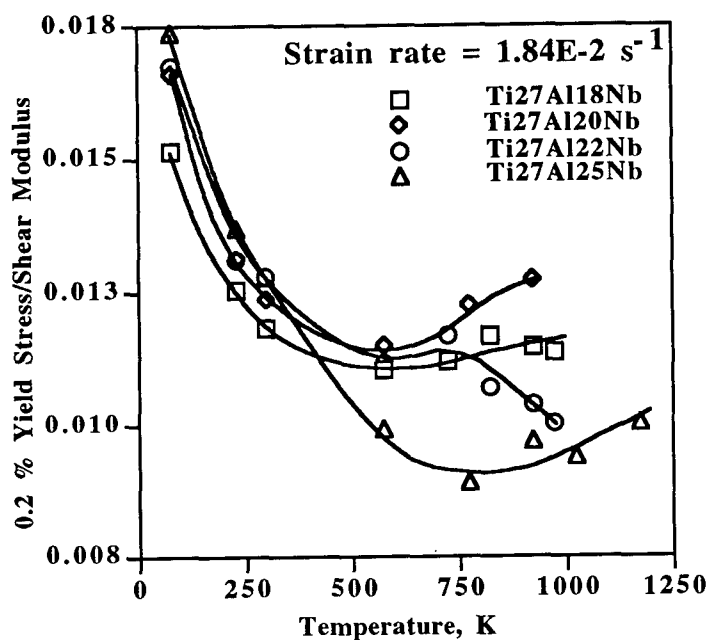


Figure 7 : Modulus Compensated Yield Stress as a Function of Temperature

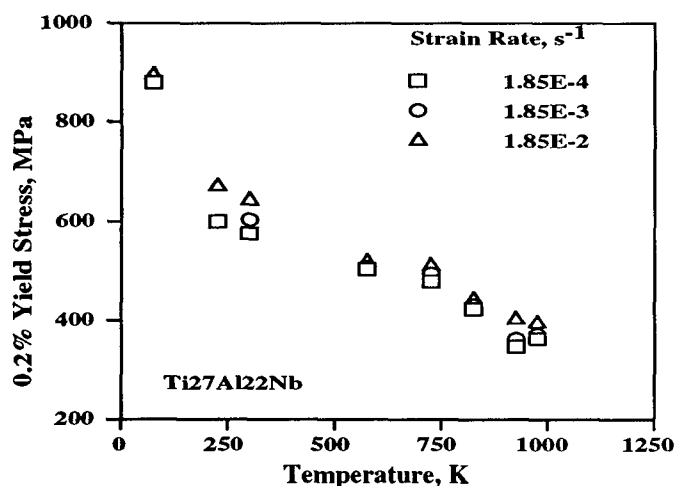


Figure 8 : The Effect of Strain Rate on Yield Stress in Ti-27Al-22Nb Alloy

Figure 8 shows the effect of strain rate on the yield stress for the Ti-27Al-22Nb alloy. The trend in the strain rate sensitivity with temperature is shown in Figure 9.

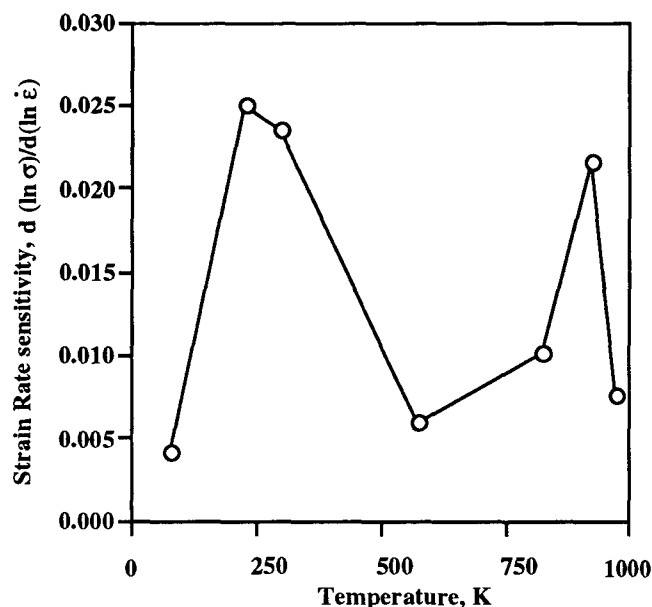


Figure 9 : Variation of Strain Rate Sensitivity with Temperature in Ti-27Al-22Nb

### Creep

The steady-state creep behaviour of the O2 alloys has been evaluated over a temperature range 973K to 1023K. Typical creep curves are shown in Figure 10. These indicate a normal primary creep behaviour with a well defined steady state. The steady state strain rate as a function of stress was evaluated through stress change experiments, and this dependence is shown in Figure 11 for the Ti-27Al-18Nb, Ti-27Al-20Nb and Ti-27Al-25Nb alloys. The Nb content has no significant influence on the creep strength of the alloys. The stress exponent shows a very mild temperature dependence decreasing from values about 7 at 1023K to 5 at 973K, and this behaviour is consistent for all the three alloys. While a conventional activation energy plot is inappropriate when the stress exponent varies with temperature, we nevertheless show such a plot in Figure 12 since the temperature dependence of the stress exponent is very small. The apparent activation energies vary from 294-327 kJ/mol.

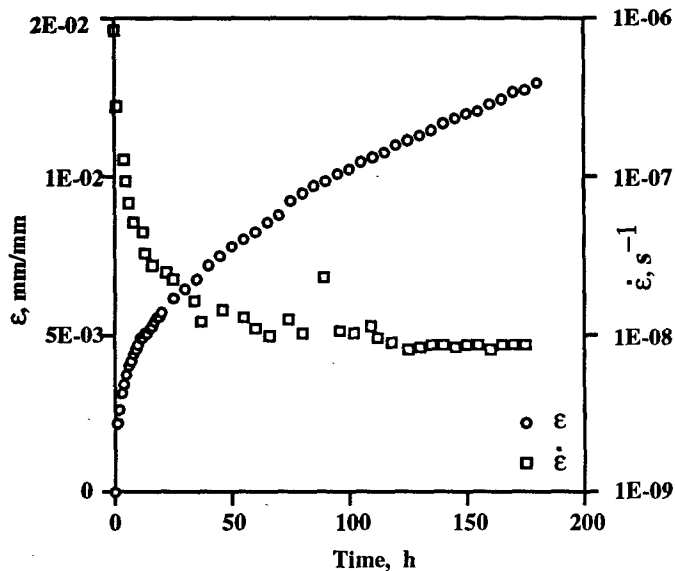


Figure 10 : Typical Creep Curve for a Ti-27Al-25Nb Alloy

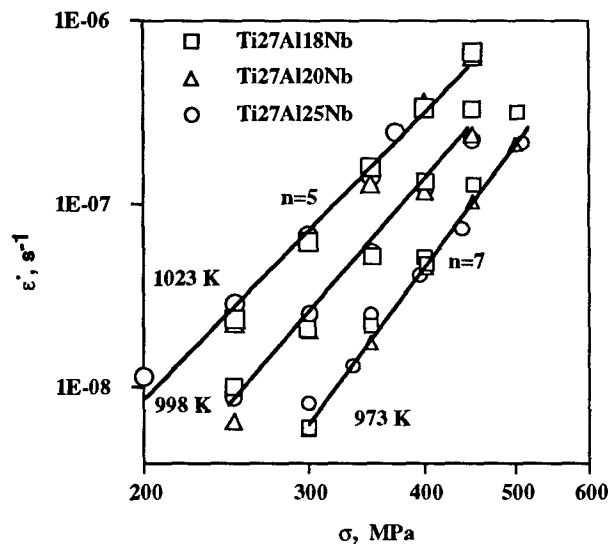


Figure 11 : Stress Dependence of Steady State Strain Rate of the Ternary Alloys

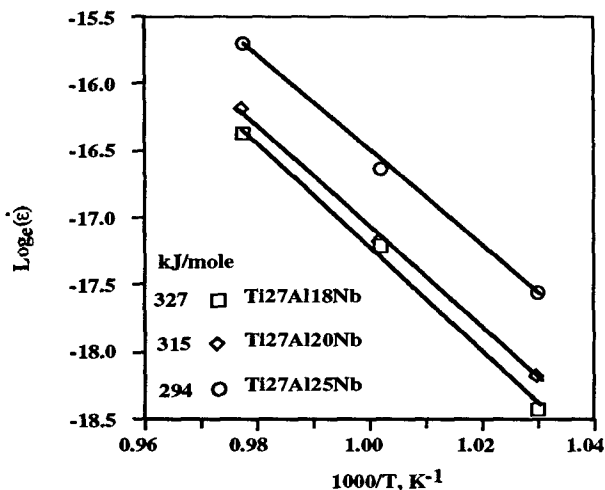


Figure 12 : Conventional Arrhenius Plots Showing the Apparent Activation Energy for Steady State Creep

## Dislocations and Planar Faults

Figure 13 shows possible slip vectors of the O2 phase and relates these to analogous slip vectors in the  $\text{Ti}_3\text{Al}$  phase which has a hcp,  $\text{DO}_{19}$  structure. Due to the lower symmetry of the O2 phase,  $1/3\langle 11\bar{2}0 \rangle$  dislocations in  $\text{Ti}_3\text{Al}$  are equivalent to the crystallographically distinct  $[100]$  ('a') and  $1/2\langle 110 \rangle$  ('a\*') dislocations in O2. Similarly,  $c+a/2$  dislocations in  $\text{Ti}_3\text{Al}$ ,  $1/3\langle 11\bar{2}6 \rangle$  are equivalent to  $[102]$  and  $1/2\langle 114 \rangle$  dislocations in O2. Figure 13 also shows possible dissociations on the (001) plane of the O2 structure. The bond distances in this structure depend on the  $c/a$  ratio and the  $b/a$  ratio, and for a given combination of these, on the specific atomic coordinate of the 8g and two 4c sites (Table 1). Formulations for antiphase boundary and complex stacking fault energies have been developed<sup>7</sup> in terms of pair-wise interactions upto seventh nearest neighbours ignoring the changes in bond distances which arise out of specific atomic coordinates.

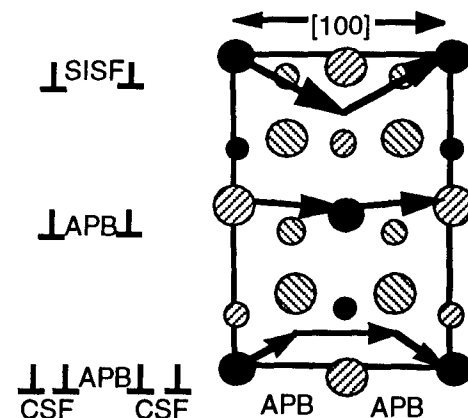
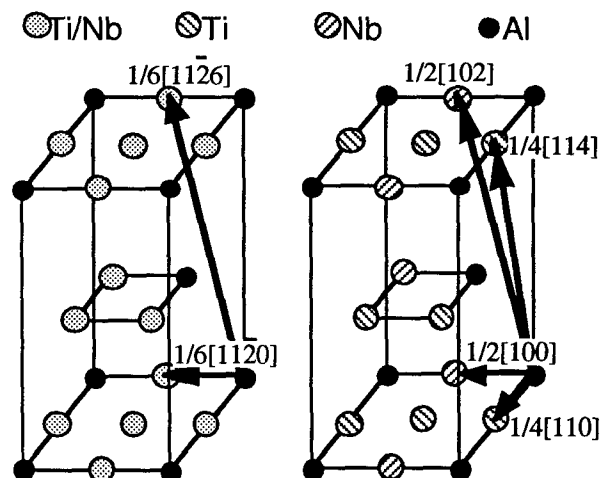


Figure 13 : Dislocations in the  $\alpha_2$  and O2 phases, and Planar Faults on the Basal Plane in the O2 Phase

### Dislocations arrangements in low temperature regime

An exhaustive study of dislocation structure has been carried out on a Ti-26Al-20Nb alloy in separate studies<sup>8-11</sup>. We describe here initial results on a Ti-27Al-25Nb alloy and compare previous work. Figure 14 shows low magnification micrographs obtained with the prismatic (110) plane, the (001) plane and the (010) plane parallel to the foil plane respectively.  $1/2$  [110] dislocation gliding in (110) are smoothly curved and show no anisotropy in the shape of the loops (Figure 14a). These are dissociated into APB coupled  $1/4$ [110] superpartials<sup>9</sup>. These dislocations appear straight when the (110) glide planes are edge-on to the beam direction in Figure 14b, and evidence of cross-slip to the basal plane is observed, consistent with previous results. We have not yet analysed [100] dislocations in the Ti-27Al-25Nb alloy. However, the previous study<sup>10</sup> suggests that [100] dislocations glide in the basal plane and are present as APB coupled  $1/2$ [100] superpartials in near-screw orientations.  $1/2$ [102] c+a/2 dislocations are found localised into slip bands on (010) planes and Figure 14c shows the arrangement of these dislocations within a slip band with the slip plane parallel to the foil plane. Extremely anisotropic loops extended along the screw direction are evident. This behaviour is distinct from that observed in the Ti-26Al-20Nb alloy of the previous study<sup>9</sup>, where the [102] dislocations were seen to lie in (221) slip bands and are strongly cusped as shown in Figure 15.

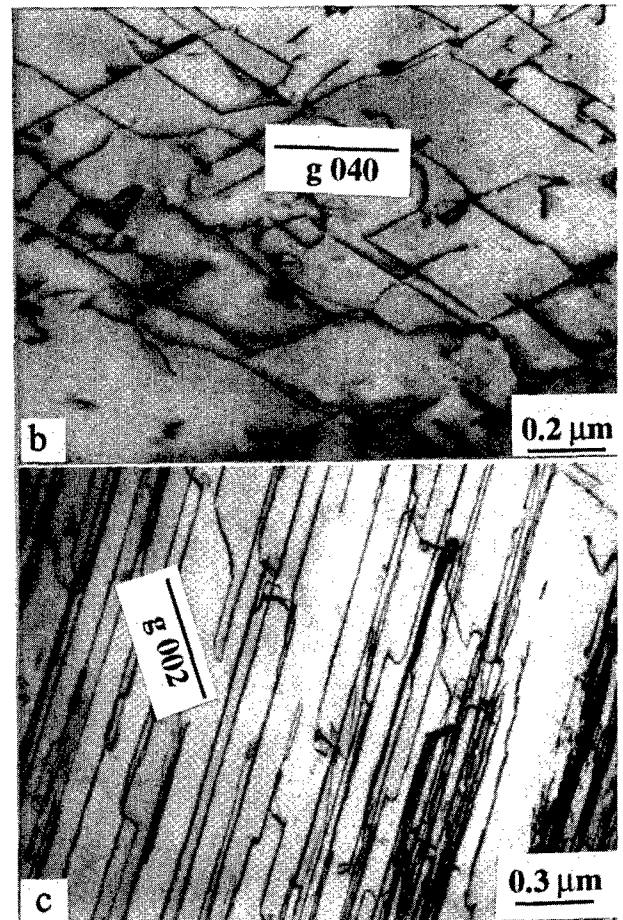
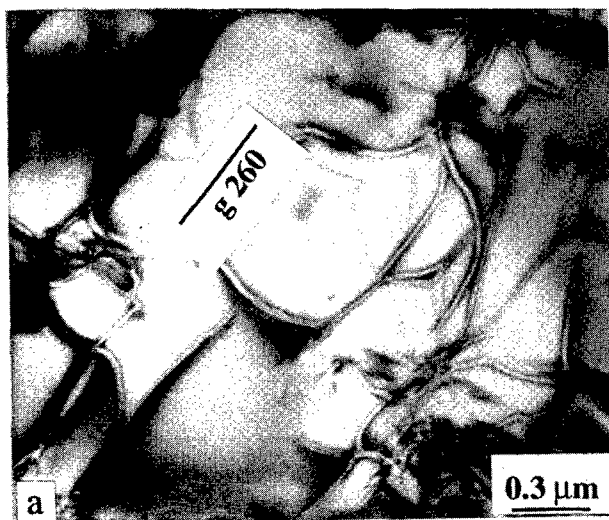


Figure 14 : Dislocation structures in a Ti-27Al-25Nb alloy deformed at 228 K. (a)  $1/2$ [110] dislocations in a (110) plane; (b)  $1/2$ [110] dislocations with foil plane parallel to (001). [100] dislocations are invisible with the operating reflection; (c) [102] dislocations with foil plane parallel to (010).

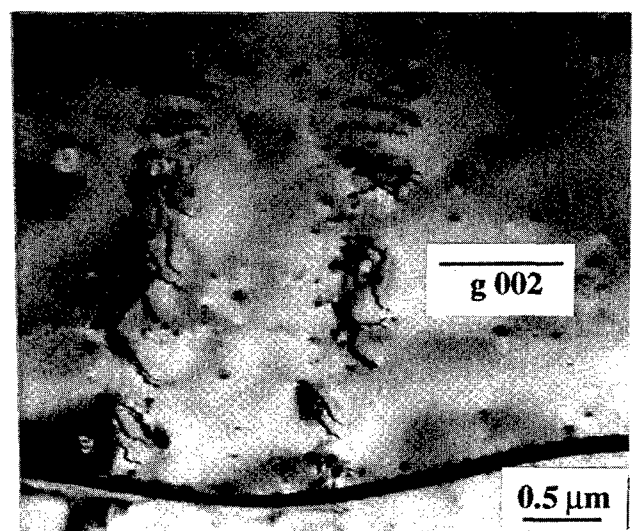


Figure 15 : c+a/2 Dislocations in a Ti-26Al-20Nb Alloy

As in the previous study, the microstructure was characterised by attractive junctions between the 'a' and 'a\*' dislocations. We have not yet examined the deformation structure in the intermediate and high temperature regimes in this study.

**Dislocations in Creep** : Figure 16 shows dislocations arrangements in creep in a Ti-27Al-25Nb alloy. No subgrain structures are observed despite these observations being recorded on samples crept well into the steady state region. All dislocations are arranged randomly.  $1/2[110]$  dislocations glide in primarily (110) planes (Figure 16a) while loops of  $[100]$  dislocations are observed in the basal plane (Figure 16b).  $[001]$  'c' dislocations are present in high densities primarily as elongated edge segments (Fig.16a) and typical loops are shown in Figure 16c. Attractive junctions between 'a' dislocations, 'a\*' dislocations, and between 'a' and 'c' dislocations are present.

### Discussion

The O2 phase is an interesting example of a relatively ductile intermetallic with a non-cubic symmetry. It is structurally very similar to the hexagonal  $Ti_3Al$  phase to which it is related by very small distortions<sup>3</sup>, but is a ternary intermetallic in the sense that each atomic species can be associated with a distinctive sublattice. Its yield stress behaviour at low temperature is very strongly temperature dependent. In this, its behaviour parallels that of pure polycrystalline Ti<sup>12</sup>, and that for basal and prismatic slip in  $Ti_3Al$ <sup>13</sup>. Deformation twinning or 'a' slip on pyramidal planes is observed in pure Ti, but not observed in the O2 phase, and in contrast to the behaviour of  $Ti_3Al$ , extensive  $c+a/2$  slip has been recorded. It has been found that the CRSS for  $c+a/2$  slip in  $Ti_3Al$  is much higher than that for basal or prismatic slip<sup>13</sup>. This apparently is not the case for the O2 phase. Our observations of the dislocation structure suggests that since no anisotropic behaviour is associated with the glide of  $1/2[110]$  dislocations, the flow stress may be primarily controlled by the motion of

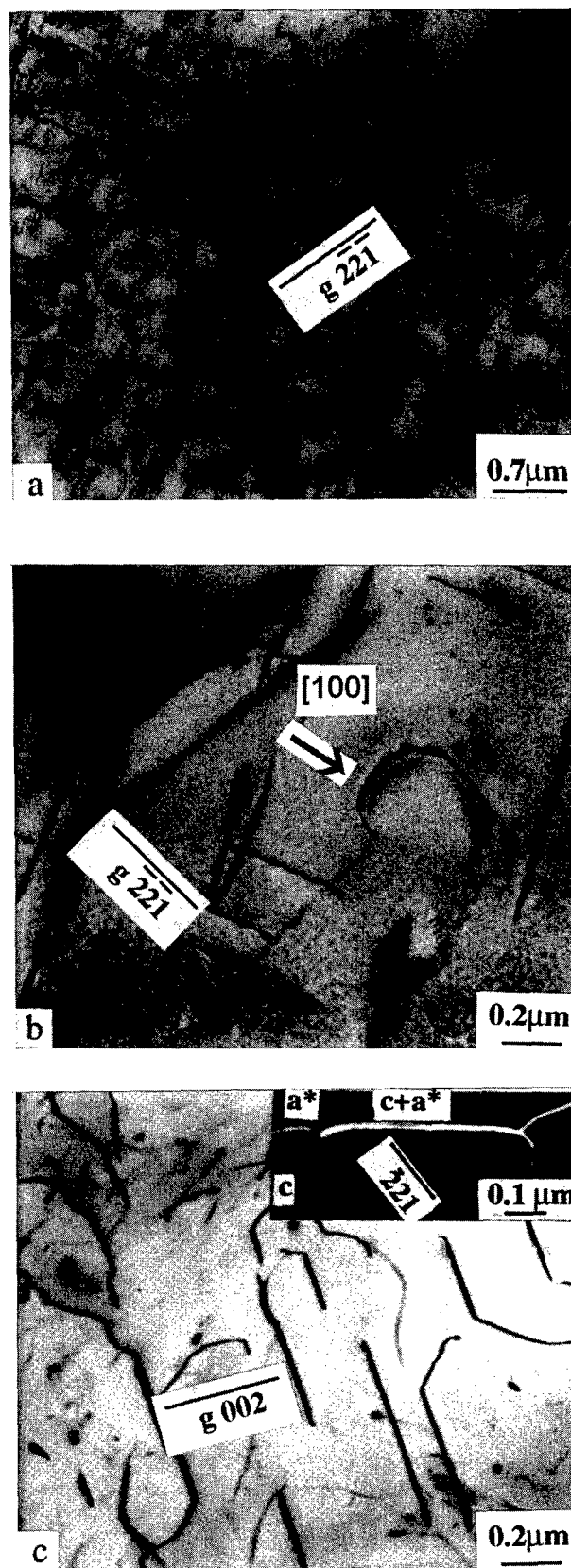


Figure 16 : Dislocation Structures of as-crept Ti-27Al-25Nb Alloy. (a) (110) dislocations, (110) plane; (b) (100) dislocations, (001) plane; (c) (001) dislocations. The inset shows an attractive junction between the different dislocations

[100] or [102] dislocations, both of which are observed to lie in less mobile screw or near-screw orientations. Activation analysis of low temperature deformation in pure titanium suggests that the strong thermal activation arises from interstitial interactions with the core structure of the dislocations<sup>12</sup>. This possibility remains to be explored in O2 phase.

The transition to an athermal regime is associated with the onset of dynamic strain aging in pure titanium<sup>12</sup>. Alternatively, it is possible that the attractive junctions present in the deformation structure in the O2 phase provide the athermal component of the flow stress. We are currently investigating alloys with different interstitial contents to explore these alternatives, and to arrive at a mechanistic explanation of the low and intermediate temperature behaviour.

The cause for the anomalous increase in the modulus compensated yield stress above 750K is also not understood. We note that the flow stress for c+a/2 slip in Ti<sub>3</sub>Al shows an anomalous increase with temperature over an identical temperature range, and it is possible that this may be so for the O2 phase as well and therefore result in the mild anomaly observed in this study. The lack of single crystal data for these alloys may preclude a complete understanding of this behaviour in the near future.

The stress exponents in the steady state creep behaviour of the O2 phase suggest that climb controlled creep is operative, as does the shape of the transient creep curves. Nevertheless, no subgrain structures are observed and, in terms of dislocation arrangements, it appears that network models of creep<sup>14-16</sup> (which essentially consider a 3-dimensionally linked network of dislocations in which the increase in dislocation density is realised by escape from attractive junctions and balanced by climb of the links to coarsen the network) may be applicable to the present case. No diffusion data is available for the O2 phase, but the apparent activation energies obtained are in broad agreement with the values of interdiffusion in Ti<sub>3</sub>Al<sup>17</sup>.

## Conclusions

We have investigated the yield stress of the O2 phase as a function of Nb content and strain rate over the temperature range 77K to 1173K, and the steady state creep behaviour as a function of the Nb content in the temperature range 973K to 1023K. A preliminary study of dislocation arrangements under these conditions has also been carried out. It is observed that

- 1) The yield stress is a strong function of temperature in the low temperature regime from 77K to about 500K, and in this regime the flow stress increases with Nb content.
- 2) An athermal regime is observed above 500K. Beyond this regime the yield stress again decreases with temperature.
- 3) Modulus compensated yield stress values show a mild increase with temperature above 750K.
- 4) Nb has no significant influence of the steady state creep behaviour of the O2 phase.
- 5) The stress exponents in creep are very weakly temperature dependent and decrease from 7 to 5 with increasing temperature.
- 6)  $1/2[110]$ , [100] and [102] dislocations are operative in the low temperature regime of deformation in the Ti-27Al-25Nb alloy.  $1/2[110]$  dislocations are randomly distributed and glide in an isotropic manner on (110) planes. [102] loops are extended in screw orientations in slip bands suggesting low mobility of such orientations.
- 7) [001] dislocations in edge orientation are observed in creep instead of [102] dislocations, while  $1/2[110]$  and [100] dislocations glide on (110) and (001) planes respectively. All dislocations are randomly distributed and form attractive junctions with each other.

### Acknowledgement

Funding by the Defence Research and Development Organisation, India and Indo-US Grant No. N00014-95-1-0132 through ONR, USA is gratefully acknowledged. Authors are grateful to Dr. Abhijit Datta, Mr. Venugopal Rao and Dr. Eswar Prasad of Defence Metallurgical Research Laboratory for help in experimentation. Authors are also grateful to Dr. A. K. Gogia (DMRL), Dr. P. Veyssiere (Onera, France) and Dr. R. G. Rowe (GE, USA) for many fruitful discussions.

### References

1. D. Banerjee, A. K. Gogia, T. K. Nandy and V. A. Joshi, Acta Metall., 36 (1988), 871-882.
2. Rowe R.G., US Patent No. 5,032,357 (1991).
3. K. Muraleedharan, T. K. Nandy, D. Banerjee and S. Lele, Intermetallics, 3 (1995), 187-199.
4. R.G. Rowe, D. Banerjee, K. Muraleedharan, M. Larsen, E.L. Hall, D.G. Konitzer and A.P. Woodfield, Titanium '92, Science and Technology (Warrendale, PA : TMS, 1993), 2, 1259-1266.
5. B. Mozer, L. A. Bendersky, W.J. Boettinger and G. Rowe, Scripta Metall., 24 (1990), 2363-2368.
6. F. Chu, T. E. Mitchell, B. Mazumdar, D. Miracle, T. K. Nandy and D. Banerjee, Intermetallics, 5 (1997), 147-156.
7. A.K. Singh, T. K. Nandy, D. Mukherjee and D. Banerjee, Phil. Mag. A, 69 (1994), 701-718.
8. D. Banerjee, R.G. Rowe, and E.L. Hall, High Temperature Ordered Intermetallic Alloys IV, (Pittsburgh, PA, USA: MRS, 1991), 285.
9. D. Banerjee and R.G. Rowe, Titanium '92, Science and Technology (Warrendale, PA : TMS, 1993), 1, 1147-1154.
10. D. Banerjee, Phil. Mag. A, 72 (1995), 1559-1587.
11. F. Popille and J. Douin, Phil. Mag. A, 73 (1996), 1401-1418.
12. H. Conrad, Progress in Materials Science, 26 (1981), 123-403.
13. Y. Minonishi, Phil. Mag. A, 63 (1991), 1085-1093.
14. D. McLean, Trans. AIME, 242 (1968), 1193-1203.
15. R. Lagneborg, Metal Sci. J., 6 (1972), 127-133.
16. B. Burton, Phil. Mag. A, 45 (1982), 657-675.
17. J. Rusing and Chr. Herzig, Intermetallics, 4 (1996), 647-657.



# ENVIRONMENTAL EFFECTS ON THE FRACTURE TOUGHNESS OF THE TERNARY CUBIC (L<sub>1</sub><sub>2</sub>) TITANIUM TRIALUMINIDE INTERMETALLICS

R.A. Varin and L. Zbroniec

Department of Mechanical Engineering, University of Waterloo, Waterloo, Ontario  
Canada N2L 3G1

## Abstract

To understand the effect of environment on the fracture toughness of cubic titanium trialuminide (based on Al<sub>3</sub>Ti) intermetallics a wide program of fracture toughness testing using the single-edge-precracked-beam (SEPB) and chevron-notched-beam (CNB) in three- and four-point bending was carried out in air, vacuum ( $\sim 1.3 \times 10^{-5}$  Pa), oxygen, argon, water and liquid nitrogen. The cubic titanium trialuminide (average composition 66at.% Al, 25at.% Ti and 9at.% Mn) modified with Mn, cast and HIP-ed at 1200°C for 2h under 170 MPa was used for testing. Testing in air, vacuum and argon was carried out up to 1000°C. It is shown that fracture toughness of cubic titanium trialuminides at ambient temperatures is not affected by the environments containing moisture (water vapour). It seems that at ambient temperatures these materials are completely immune to the water-vapour hydrogen embrittlement and their cause of brittleness is other than environment. At the intermediate temperature range of approx. 200- 600°C trialuminides tested in air and vacuum exhibit a mild but discernible peak of fracture toughness. However, testing in high-purity argon eliminates this peak and fracture toughness in argon is practically independent of temperature at the range from room temperature to 1000°C.

## Introduction

In the last several years it has been found that some ordered cubic (or near-cubic) intermetallics are prone to a very peculiar type of embrittlement caused by moisture-containing environments such as, for example, air. As reported in the literature, the moisture-induced embrittlement can result in both intergranular failure and transgranular cleavage. For example, under tensile or bending loading conditions a polycrystalline, ordered FCC (L<sub>1</sub><sub>2</sub>) Ni<sub>3</sub>Al fails by intergranular fracture [1] but a polycrystalline, ordered BCC (B2), Al-lean FeAl compound fails by transgranular cleavage [2]. The embrittlement mechanism is thought to involve reaction of a reactive metallic M, with water vapour in air, resulting in the generation of atomic hydrogen [1,2]:



Atomic hydrogen penetrates into crack tips causing embrittlement and a premature failure. However, the details of this water vapour-hydrogen embrittlement are still not completely understood.

A series of ternary cubic (L<sub>1</sub><sub>2</sub>) trialuminides based on a tetragonal Al<sub>3</sub>Ti has been shown to be formed by alloying with the elements such as Ni, Cu, Fe, Cr and Mn [3]. Despite having the prerequisite number of five independent slip systems (typical in FCC

structure) these cubic titanium trialuminides are still brittle in tension although they show quite a substantial apparent ductility in compression. Their yield strength and hardness are low, i.e. they are rather soft materials in this sense. This soft-brittle behaviour is the most peculiar phenomenon which makes the cubic titanium trialuminides extremely interesting from the scientific point of view. The exact causes of such a behaviour are not well understood. However, by analogy to what is said above, it could also be possible that the environment (e.g. water vapour) might somehow be responsible, if only partially, for the embrittlement of the ternary cubic (L<sub>1</sub><sub>2</sub>) titanium trialuminides. This is important in view of more recent findings that the room-temperature ductility of another titanium aluminide, namely duplex and PST TiAl, is mildly affected by water vapour-induced environmental embrittlement [4-5].

There is a lack of studies on the effects of environment on the fracture toughness and fracture behaviour of the ternary cubic (L<sub>1</sub><sub>2</sub>) titanium trialuminides. To understand the effect of environment on the fracture toughness of these intermetallics a testing of the L<sub>1</sub><sub>2</sub> Mn-modified Al<sub>3</sub>Ti in bending was carried out in air, vacuum, argon, water and liquid nitrogen. The results of these studies are reported and critically discussed in the present paper.

## Experimental

Rectangular ingots were induction melted from pure elements (Al- 99.99999%, Ti- 99.7% and Mn- 99.9%) under high purity argon and cast into a steel mold. Subsequently, the ingots were HIPed at 1250°C for 2h under 170 MPa pressure. Single-edge-precracked beam (SEPB) specimens having width W=4mm, thickness B=4mm, length L=19mm and the notch slot width N=110µm were electrodischarge machined from the ingots. These bending bars were polished with a 0.3 µm alumina powder and then pre-cracked at the notch tip by bridge method [6] (Fig.1). Pre-crack length was measured under optical microscope. At least 9 readings of the pre-crack length were made along the thickness of the specimen using Java software [7]. Subsequently, they were tested in three-point bending with a 16mm span. Cross-head speed was 0.05 mm/min which gives  $\dot{K}=0.03-0.15$  MPa<sup>0.5</sup>/s. Testing was carried out in air, approx.  $1.3 \times 10^{-5}$  Pa vacuum, high-purity argon (according to supplier specifications 99.998%, less than 20vppm impurities), oxygen (99.5%, less than 6vppm moisture) water and liquid nitrogen. Both argon and oxygen were admitted to the environmental chamber evacuated first to  $\approx 1.3 \times 10^{-5}$  Pa.

Structural Intermetallics 1997

Edited by M.V. Nathal, R. Darolia, C.T. Liu, P.L. Martin,  
D.B. Miracle, R. Wagner, and M. Yamaguchi  
The Minerals, Metals & Materials Society, 1997

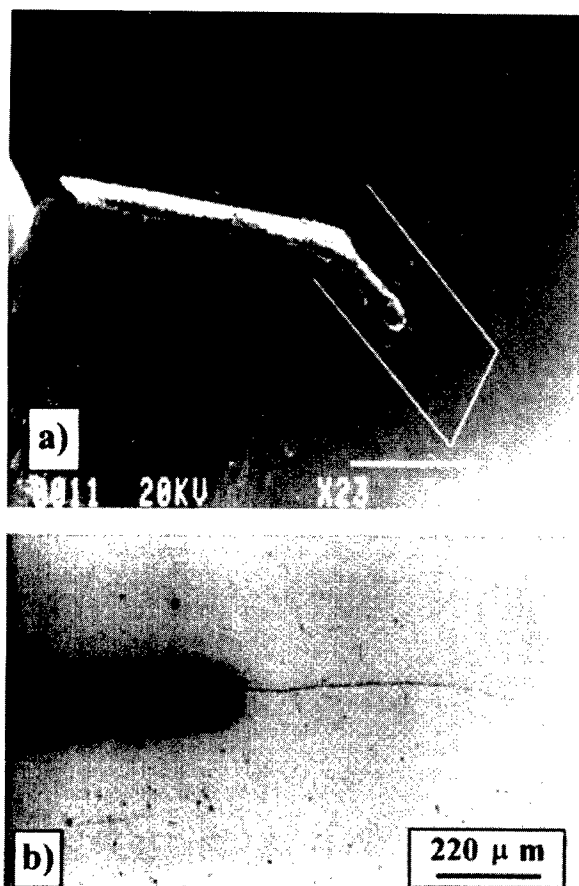


Figure 1. Single- Edge- Precracked- Beam (SEPB), a) overall view, b) machined notch and a sharp precrack introduced by bridge method [6].

After admitting gases the pressure in the environmental chamber was on the order of an atmospheric pressure. Compliance function and provisional fracture toughness values  $K_{Ic}$  for SEPB specimens were calculated from the maximum load on the load-load point displacement (LPD) curves using equations presented in the ASTM E 399-90 standard. Composition of the fracture toughness specimens was measured by a quantitative energy dispersive X-ray spectroscopy (EDX) using elemental standards and ZAF program. The microstructure and fracture surfaces were examined by optical and scanning electron microscopy.

## Results and Discussion

### Microstructure

Porosity after HIP- ing was  $\approx 1\%$  and the average compositions of the specimens tested in various environments are listed in Table I (the averages and standard deviations are from at least five readings).

Table I. Compositions of SEPB Specimens

SPECIMEN	Al (at.%)	Ti (at.%)	Mn(at.%)
air- series 1	65.70 $\pm$ 0.20	25.20 $\pm$ 0.09	9.20 $\pm$ 0.20
air- series 2	65.99 $\pm$ 0.13	24.86 $\pm$ 0.13	9.15 $\pm$ 0.13
argon	66.10 $\pm$ 0.25	24.90 $\pm$ 0.21	9.00 $\pm$ 0.16
vacuum, liq.N <sub>2</sub> ,water	67.10 $\pm$ 0.17	24.02 $\pm$ 0.21	8.90 $\pm$ 0.19

It is seen that the compositional scatter is minimal. All compositions fall into a single  $L_{12}$  phase field in the ternary Al-Mn- Ti system [8]. As reported earlier [9-10] the ingots exhibited an essentially single- phase  $L_{12}$  structure (neglecting a small volume fraction of unidentified needle- like particles) with the

equiaxed grains (0.2- 1mm) in the central portion and columnar grains (length  $\sim 2.5$ mm, diameter 0.15- 0.3mm) at the edges of the ingot (Fig.2). The fracture toughness specimens were cut from both equiaxed and columnar portions of the ingot.

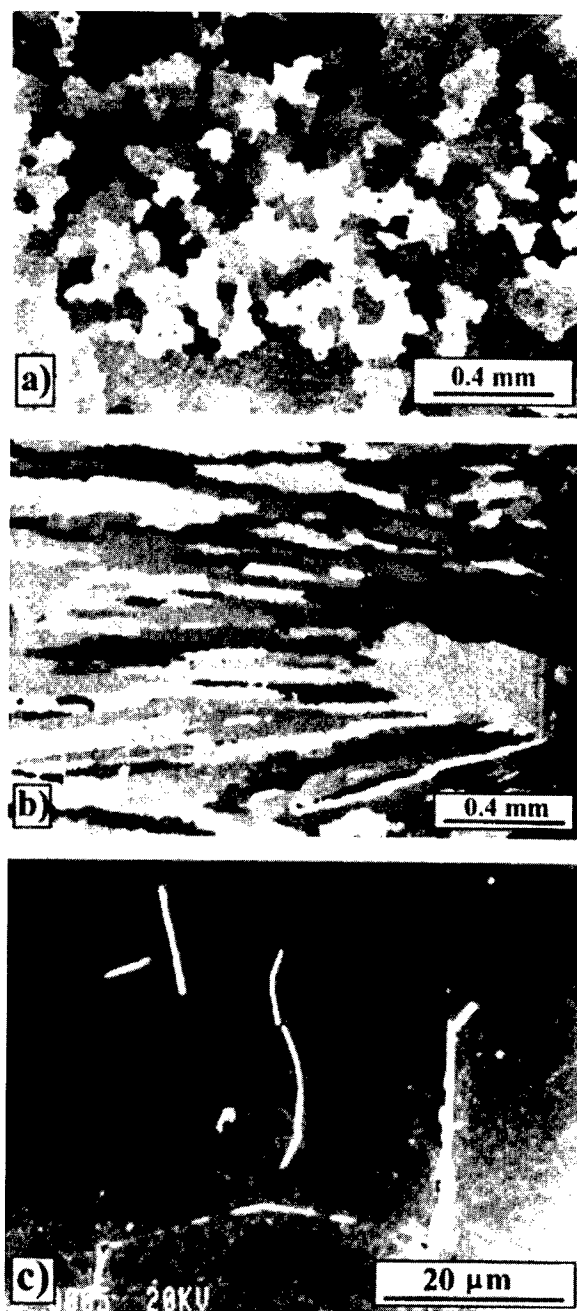


Figure 2. Microstructure after HIP-ing; (a) equiaxed grains, b) columnar grains, (c) unidentified needle- like particles.

### Fracture Behaviour and Toughness

Figure 3 shows the load- LPD curves for SEPB specimens tested in air and argon. The shape of the air and argon curve at each testing temperature is essentially very similar. It must be pointed out that the pre- crack lengths (remaining ligament lengths) are different for different specimens so a direct comparison of the maximum loads for the same testing temperature in air and argon (Figs. 3a,b) is not meaningful. At low testing temperatures ( $\leq 400^\circ\text{C}$ ) the load increases linearly with displacement until

unstable crack growth occurs. At higher temperatures the crack growth is rather stable resulting in a characteristic "tail" on the load- LPD curve after the maximum (peak) load. At 1000°C the peak load is preceded by a certain range of approximately stable crack growth in both air and argon (curve 6 in Figs.3a,b). Load displacement curves recorded in oxygen, vacuum, water and liquid nitrogen exhibit a very similar shape to these in Fig. 3.

Figure 4 shows the results of fracture toughness testing, i.e.  $K_Q$  vs. remaining ligament length at room temperature (Fig. 4a). Figure 4b shows the dependence of  $K_Q$  on temperature. The horizontal broken lines represent the plane strain thickness validity lines calculated from the ASTM E 399-90 standard equation  $B \geq 2.5 (K_Q/\sigma_{ys})^2$  (or alternatively  $K_{IC} \leq \sqrt{B\sigma_{ys}}/\sqrt{2.5}$ ), where  $\sigma_{ys} = 160 \text{ MPa}$  [11] and  $B \approx 4 \text{ mm}$ .

The vertical broken line in Fig. 4a represents a validity criterion for the remaining ligament:  $(W-a) \geq 2.5(K_Q/\sigma_{ys})^2$  which after substituting  $K_Q \approx 4 \text{ MPam}^{0.5}$ , gives  $(W-a) \geq 1560 \mu\text{m}$ , i.e. the valid  $K_Q$  data at room temperature are presumably those obtained for the ligament length greater than  $\approx 1500 \mu\text{m}$ . Figure 4a shows a strong dependence of fracture toughness,  $K_Q$ , on the remaining ligament length but no dependence on the environment at ambient temperatures. It seems that the  $\text{L}_{12}$  titanium trialuminides are completely immune to the water vapour- hydrogen embrittlement and their cause of brittleness at ambient temperatures is other than environment.

Figure 4b shows that when tested in air and vacuum the ternary cubic  $\text{L}_{12}$  titanium trialuminide  $\text{Al}_3\text{Ti}(\text{Mn})$  exhibits a broad peak of toughness at the 200- 600°C temperature range. Some  $K_Q$  values in this temperature range lie above the plane strain thickness validity line in Fig. 4b. However, other fracture toughness tests were also carried out in air using the chevron- notched beam (CNB) specimens ( $W=5.5 \text{ mm}$  and  $B=4 \text{ mm}$ ) in four- point bending with 26mm support and 10mm loading span [9,10] as well as 16mm support and 4mm loading span [12]. The latter CNB specimens with shorter span were machined from the broken halves of the longer CNB's (26 mm span) (exactly the same chemical composition of the material, i.e. air- series 1 in Table I). The results of testing of the CNB specimens are shown in Figure 5. Because the plane strain validity criterion for a CNB specimen is less stringent than that for a straight- through- notch SEPB specimens, all the  $K_{Qvm}$  values obtained in the room to 1000°C temperature range obeyed the plane strain thickness validity criterion for the CNB specimens. A horizontal broken line in Figure 5a indicates the plane strain validity criterion for thickness calculated for a CNB specimen from  $K_{Qvm} = K_{IVm} \leq \sqrt{B\sigma_{ys}}/\sqrt{1.25}$  where  $K_{Qvm}$  is a provisional fracture toughness value calculated from a maximum fracture load (ASTM E 1304- 89) and  $K_{IVm}$  is a valid chevron- notch plane strain fracture toughness. The CNB data in Figure 5 clearly exhibits a broad peak of fracture toughness in the same temperature range (200- 600°C) as observed for the SEPB specimens in Figure 4b.

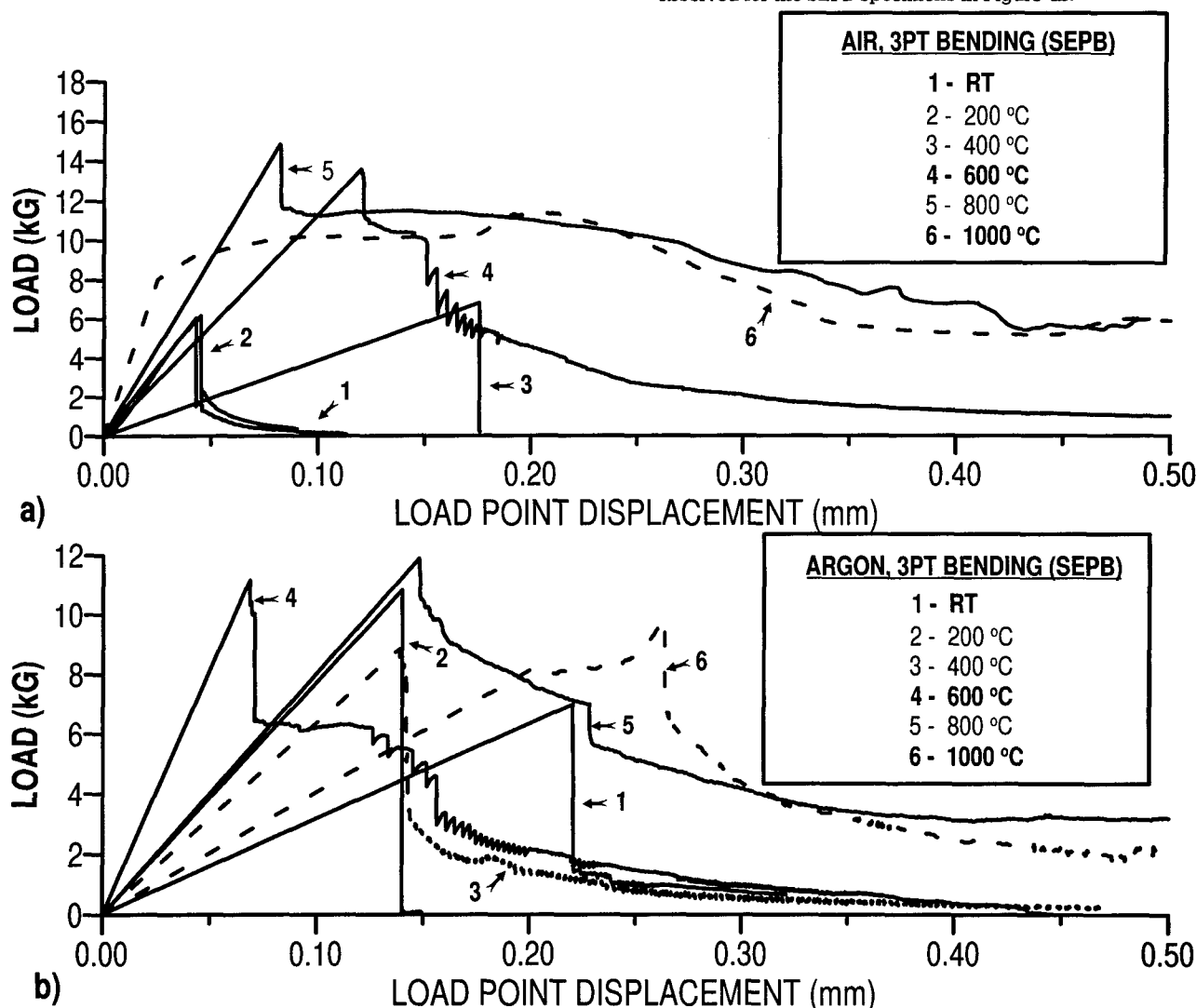


Figure 3. Load- LPD graphs at air and argon obtained at various testing temperatures.

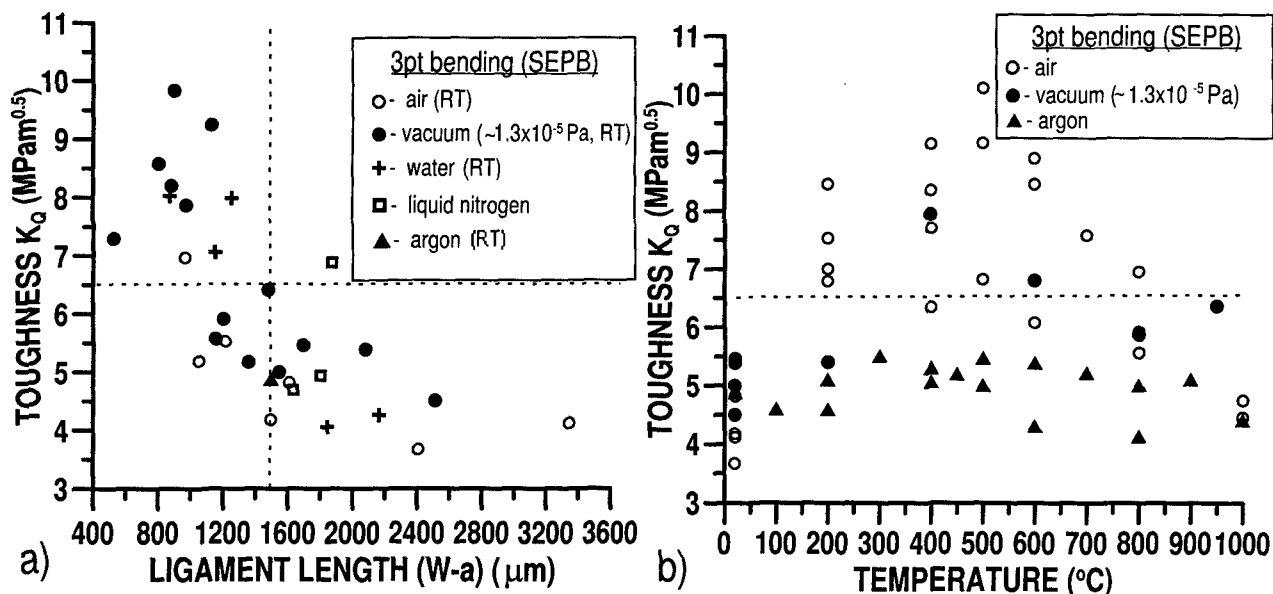


Figure 4. Fracture toughness,  $K_Q$ , as a function of (a) remaining ligament length,  $(W-a)$  at room temperature, where  $W$ - specimen's width and  $a$ - total crack length, and (b) temperature. RT- room temperature. One data point represents one specimen tested.

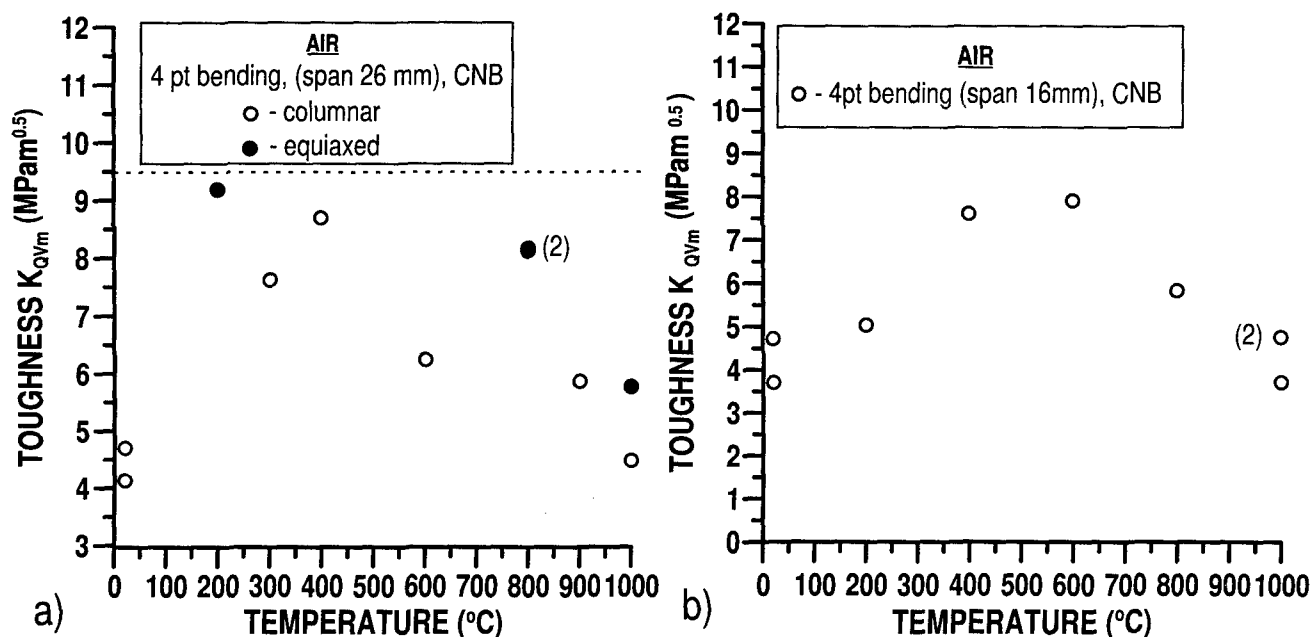


Figure 5. Results of fracture toughness testing of (a) long span (26 mm) [10] and (b) short span (16 mm) [12] CNB specimens of the L12 titanium trialuminide as a function of temperature.

It seems, therefore, that the observed toughness peak at intermediate temperatures is true and that the triaxial state of stress (plane strain) at the crack tip is still obeyed for the SEPB specimens tested at the 200 to 600 $^{\circ}C$  range despite that the thickness validity criterion ( $K_{IC} \leq \sqrt{B\sigma_{ys}}/\sqrt{2.5}$ ) would indicate to the contrary.

Another interesting and rather striking feature of the toughness results in Fig. 4b is that the peak of toughness is not observed in argon, i.e.  $K_Q$  in argon is essentially independent of temperature up to 1000 $^{\circ}C$ . The examination of the fracture surfaces using SEM of all the specimens tested in air and argon revealed a gradual transition from 100% transgranular cleavage at room temperature to almost 100% intergranular failure at 1000 $^{\circ}C$  (Figs 6 and 7).

Figure 8 shows the measured surface area of intergranular fracture for specimens tested in air and argon as a function of test temperature. The numbers beside each data point indicate  $K_Q$  value. A gradual increase in the fraction of intergranular fracture in both air and argon with increasing test temperature is clearly seen. This increase in the percentage of intergranular fracture observed on the SEPB specimens fractured in three-point bending is exactly the same as the one measured on the chevron-notched-beam (CNB) specimens tested in four-point bending [9,10]. It confirms that the transition from transgranular cleavage to intergranular failure with increasing temperature is indeed true and does not depend on the method of fracture toughness testing (SEPB vs. CNB). Moreover, fracture mode transition from cleavage to intergranular with increasing temperature observed here using

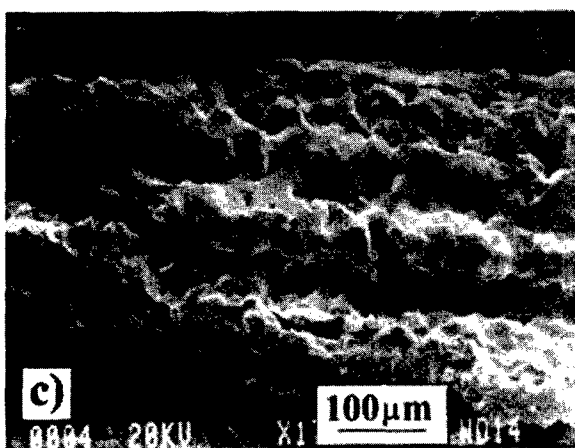
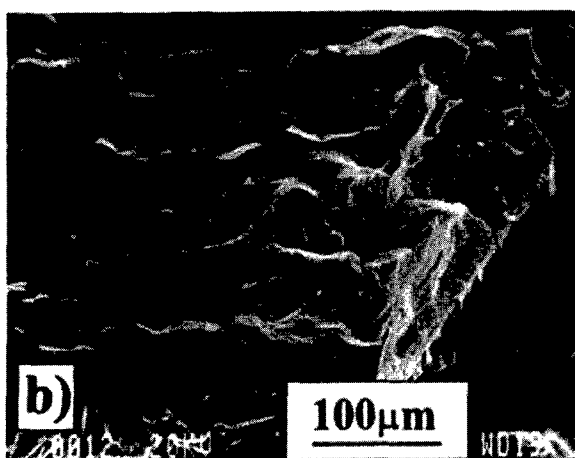
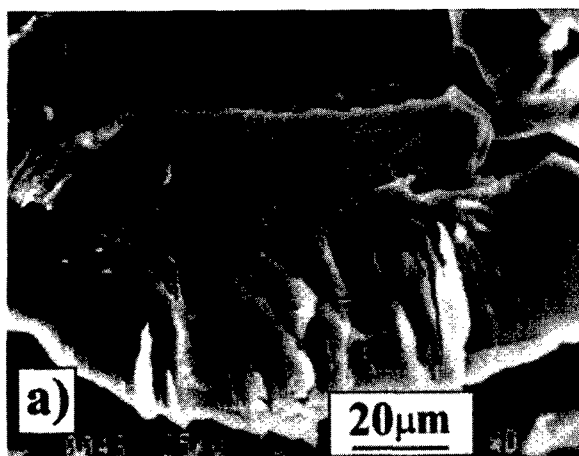


Figure 6. Fracture modes in air at temperatures. (a) RT (cleavage), (b) 600°C (mixed mode) and (c) 1000°C (intergranular) [9].

bend specimens is in good agreement with the results obtained in tension by Kumar and Brown [3,13]. The explanation of the origin of the fracture toughness peak observed in air and vacuum at intermediate temperatures (Fig. 4b) is not available at the present moment. It is rather difficult to correlate the occurrence of the peak with the transition from the transgranular cleavage to intergranular mode of fracture which is rather gradual and spreads over a wide temperature interval (Fig. 8) (also see Fig. 11 in Ref. 9 and Fig. 6 in Ref. 10 for the data from the CNB specimens).

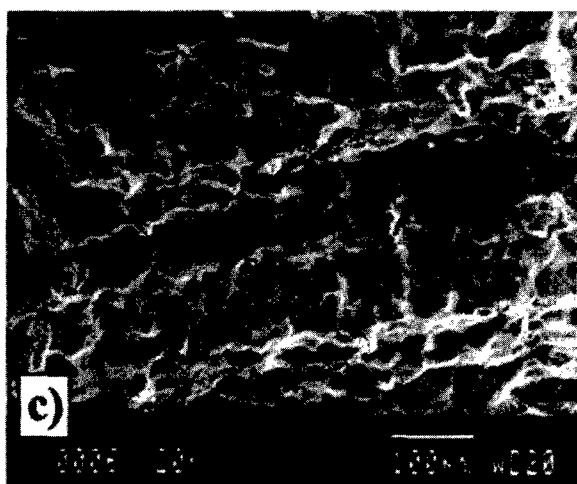
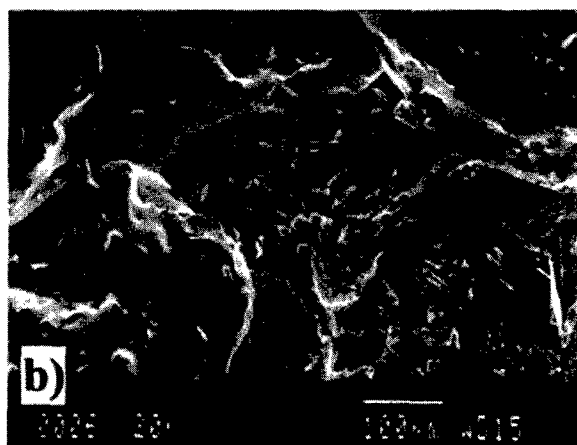
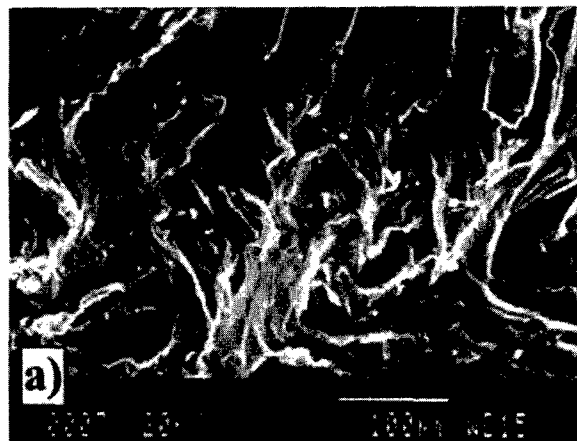


Figure 7. Fracture modes in argon at temperatures. (a) RT (cleavage), (b) 600°C (mixed mode) and (c) 1000°C (intergranular)

Since there is practically no difference in the mode of fracture vs. temperature in air and argon the disappearance of toughness peak in argon at the intermediate temperature range (Fig. 4b) cannot be explained by the change in the mode of fracture. The  $K_{IC}$  fracture toughness numbers indicated in Fig. 8 show that there is no dependence of fracture toughness on the fraction of intergranular (or cleavage) mode of fracture for specimens tested in air and argon. It must also be pointed out that the  $K_{IC}$  values obtained at higher temperatures in both air and argon do not exhibit any dependence on the remaining ligament length, (W-a)

(Fig. 9) as observed at room temperature (Fig. 4a). It is clearly seen that  $K_Q$  data obtained in argon are independent of the remaining ligament length in the 800- 2500  $\mu\text{m}$  range. The scatter of data obtained in air is the effect of the existence of a  $K_Q$  peak at intermediate temperatures (Fig. 4b). Figure 9 once again confirms that the testing in argon eliminates the appearance of a  $K_Q$  peak at intermediate temperatures. It has also been found that within the experimental scatter, in both air and argon the fracture toughness at various temperatures seems to be independent of whether the grains are equiaxed or columnar (Fig. 5a). Also, the orientation of columnar grains being either perpendicular or parallel to the direction of loading does not have any measurable influence on the obtained values of  $K_Q$ . This has been carefully checked for specimens tested in air and argon by either examining in SEM the fracture surfaces of those SEPB and CNB specimens which exhibited largely an intergranular failure or by

etching the sides of the specimens which failed by cleavage and noticing in both cases the orientation of columnar grains with respect to the loading axis. Also, the cleavage fracture areas on the fracture surfaces of specimens tested in air and argon at temperatures of 400, 500 and 600°C which correspond to the  $K_Q$  peak range in air (Fig. 4b), were carefully examined in SEM under various magnifications with the objective of revealing differences (if any) in the cleavage behaviour during testing in air and argon that could explain the disappearance of the  $K_Q$  peak during testing in argon (Fig. 4b). Typical examples of cleavage surface appearance after fracture toughness test at 500°C in both air and argon (two pictures for each environment) are shown in Figure 10.

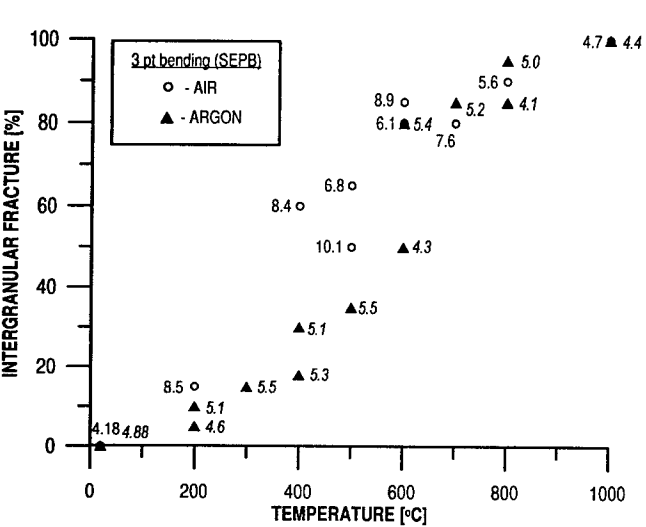


Figure 8. Surface area of intergranular fracture in air and argon for the SEPB specimens vs. temperature. The numbers indicate  $K_Q$  values. The italic numbers indicate  $K_Q$  obtained from testing in argon. Each data point corresponds to one specimen.

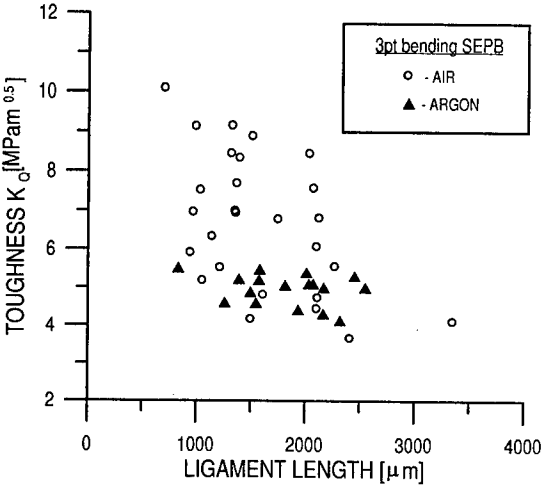
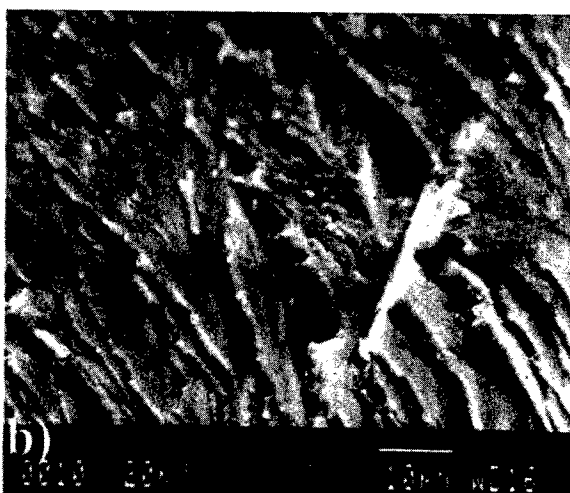
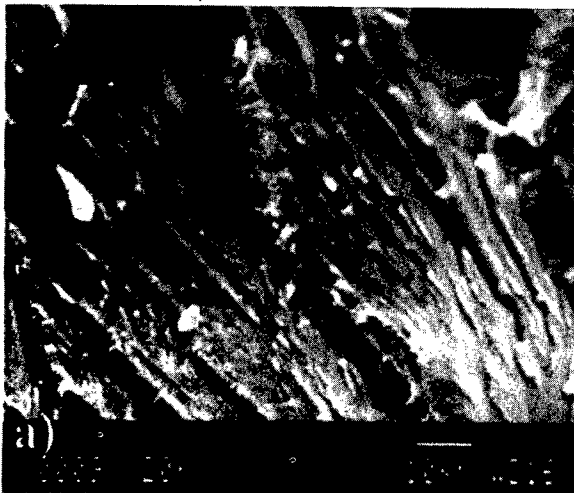


Figure 9. Dependence of fracture toughness,  $K_Q$ , on the remaining ligament length of the SEPB specimens tested in air and argon at various temperatures (room temperature to 1000°C). Temperature designation for each data point has been omitted for clarity.



(Figure caption see next page)

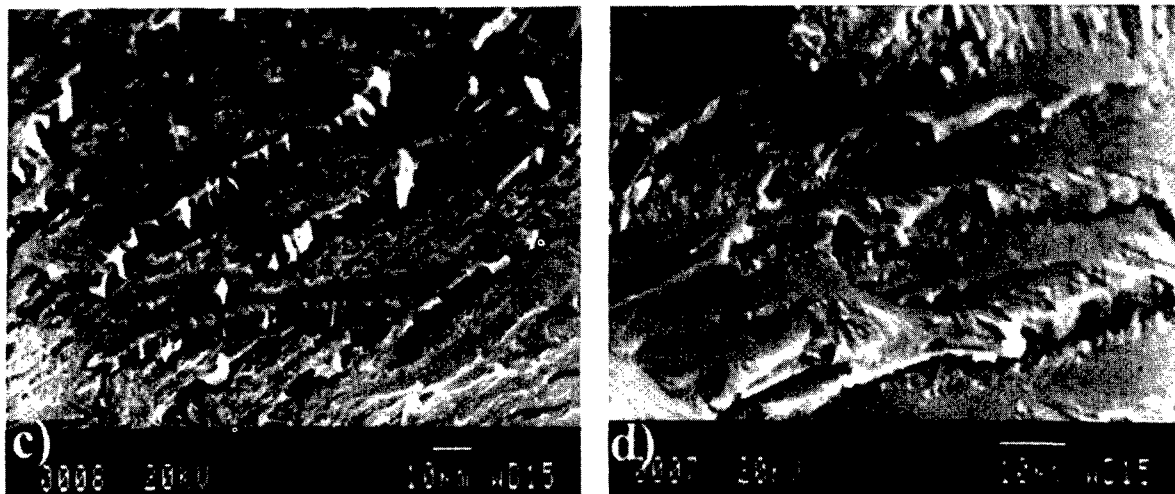


Figure 10. SEM fractographs of cleavage in the  $L_{12}$  titanium trialuminide tested at 500°C in (a,b) air and (c,d) argon.

The cleavage facets in Figure 10 look quite typical of cleavage in a coarse polycrystalline material. Each large cleavage facet (area) contains numerous parallel cleavage planes joined by tearing steps approximately perpendicular to the cleavage planes. The tearing step lines form the "river patterns" on the cleavage facet. Unfortunately, there is no discernible difference between cleavage facets obtained in air (Fig. 10a,b) and argon (Fig. 10c,d). They look quite alike. One might speculate that the elimination of the intermediate temperature fracture toughness peak in argon might be somehow related to the trapping of the argon gas at the crack tip. This might lead to a build up of a localized argon pressure at the crack tip and assisting in easier crack propagation. Unfortunately, the exact mechanism is unclear. Therefore, the origin of the fracture toughness peak in air at the intermediate temperature range and its elimination during testing in argon does not have any immediate explanation. For the sake of clarity, it must be mentioned that recent testing of boron-doped (0.2 at.%B) single-phase  $L_{12}$  trialuminide with the composition in Table I as well as higher-Mn (14 at.%) trialuminide showed a steady although modest increase of  $K_{IC}$  from  $\sim 4 \text{ MPam}^{0.5}$  at room temperature to  $\sim 8-10 \text{ MPam}^{0.5}$  at 1000°C [12]. Also, one large CNB specimen was tested at room temperature in pure oxygen and showed  $K_{IC} = 3.7 \text{ MPam}^{0.5}$  which is essentially the same as those obtained in other environments at room temperature.

### Conclusions

1. Fracture toughness of the cubic ( $L_{12}$ ) Mn- modified titanium trialuminide at room temperature is relatively low, on the order of  $4-5 \text{ MPam}^{0.5}$  but it is not affected by testing in various environments such as air, vacuum ( $\sim 1.3 \times 10^{-5} \text{ Pa}$ ), argon, oxygen, water and liquid nitrogen. It seems that this group of intermetallics is completely immune to the water-vapour hydrogen embrittlement.
2. Fracture toughness of specimens tested in air and vacuum at the room to 1000°C temperature range exhibits a broad peak at the intermediate 200- 600°C temperature range ( $K_{IC} \approx 8-10 \text{ MPam}^{0.5}$ ).
3. Testing in argon eliminates the appearance of the fracture toughness peak at the intermediate temperature range and the cubic ( $L_{12}$ ) Mn- modified titanium trialuminide exhibits approximately the same fracture toughness  $K_{IC} \approx 5 \text{ MPam}^{0.5}$ , in the entire room to 1000°C temperature range.
4. During testing in air, vacuum and argon there is a gradual transition in the mode of fracture with increasing temperature from completely transgranular cleavage at room temperature to completely intergranular failure at 1000°C.

### Acknowledgements

This work was supported by grant from the Natural Sciences and Engineering Research Council of Canada which is gratefully acknowledged.

### References

1. E.P. George, C.T. Liu, and D.P. Pope: *Acta Mater.*, 44(1996), 1757- 63.
2. N.S. Stoloff and C.T. Liu: *Intermetallics*, 2(1994), 75- 87.
3. K.S. Kumar: in *Structural Intermetallics*, R.Darolia, J.J. Lewandowski, C.T. Liu, P.L. Martin, D.B. Miracle and M.V. Nathal, eds., TMS, Warrendale, PA, 1993, pp.87- 96.
4. C.T. Liu and Y-W. Kim: *Scripta Metall. Mater.*, 27(1992), 599- 603.
5. M. Yamaguchi and H. Inui: in *Structural Intermetallics*, R. Darolia, J.J. Lewandowski, C.T. Liu, P.L. Martin, D.B. Miracle and M.V. Nathal, eds., TMS, Warrendale, PA, 1993, pp.127- 142.
6. T. Nose and T. Fuji: *J. Amer. Cer. Soc.*, 71(1988), 328-33.
7. G. Albiner, Java Jandel Video Analysis Software, Jandel Scientific, Corte Madera, CA, 1988.
8. S. Zhang and D.E. Mikkola: *Scripta Metall. Mater.*, 26(1992), 1315-20.
9. R.A. Varin, L. Zbroniec and Z. Witczak: in *Deformation and Fracture of Ordered Intermetallic Materials III*, W.O. Soboyejo, T.S. Srivatsan and H.L. Fraser, eds., TMS, Warendale, PA, 1996, pp.583-601.
10. R.A. Varin and L. Zbroniec: in *High- Temperature Ordered Intermetallic Alloys VIII*, MRS (in press).
11. M.B. Winnicka and R.A. Varin: *Metall. Trans. A*, 24A(1993), 935-46.
12. L. Zbroniec and R.A. Varin, University of Waterloo, unpublished results.
13. S.A. Brown and K.S. Kumar: *Phil. Mag. A*, 65(1992), 91-109.

PHASE EVOLUTION, STABILITY, AND  
MICROSTRUCTURE-CREEP RELATIONS IN  
AN ORTHORHOMBIC Ti-23Al-27Nb ALLOY

C. J. Boehlert<sup>1</sup>, B.S. Majumdar<sup>1</sup>, V. Seetharaman<sup>1</sup>, D.B. Miracle, and R. Wheeler<sup>1</sup>

USAF Wright Laboratory Materials Directorate, Wright-Patterson AFB, Ohio, 45433-7817

<sup>1</sup> UES, Inc., 4401 Dayton-Xenia Road, Dayton, Ohio 45432-1894

**Abstract**

The phase evolution and creep behavior were studied for an orthorhombic Ti-23Al-27Nb alloy. Monolithic sheet materials were produced through conventional thermomechanical processing techniques comprising nonisothermal forging and pack rolling. Phase evolution studies showed that, depending on the heat-treatment schedule, this alloy may contain several constituent phases including:  $\alpha_2$  (ordered hexagonal close-packed DO<sub>19</sub> structure), B2 (ordered body-centered-cubic (bcc)),  $\beta$  (disordered bcc), and O (ordered orthorhombic based on Ti<sub>2</sub>AlNb). DTA studies indicated that the B2 transus temperature was 1070°C. Heat treatment and TEM studies showed that the  $\alpha_2$ +B2 phase field extended between 1010°C and 1070°C. From 875 to 975°C, a two-phase O+B2, field existed. Sandwiched between these two-phase regimes was a narrow three-phase  $\alpha_2$ +B2+O field. Below 875°C an O+ $\beta$  field existed. All heat treatments at or above 875°C, followed by quenching, resulted in equiaxed microstructures. However, below 875°C, the B2 phase transformed into a mixture of O and bcc phases with lenticular morphologies. Cellular precipitation of O+ $\beta$  platelets at O/B2 and  $\alpha_2$ /B2 grain boundaries occurred depending on solutionizing and aging temperatures. The kinetics of this reaction at 650°C and its effect on creep were recorded. Unaged microstructures, which transformed during the creep experiments, exhibited larger creep strains than long-term aged microstructures. In terms of phase volumes, load did not appear to significantly effect the transformation behavior. Three microstructures were compared in the creep study including: supertransus B2,  $\alpha_2$ +B2, and O+B2 solutionized microstructures which were aged in the O+ $\beta$  region prior to the creep experiments. The measured creep exponents and activation energies suggested that the creep mechanisms are dependent on microstructure and stress. The power-law creep behavior indicated the presence of three regimes for the supertransus microstructure at 650°C. For low applied stresses a Coble creep mechanism was suggested as the creep exponent was close to unity and  $Q_{app} = 171$  kJ/mol. For intermediate stresses, the creep exponent was two and grain boundary sliding was suggested. For high stresses the stress exponent tended toward 3.7 and dislocation climb was suggested. The sub-transus microstructures contained much smaller grain sizes and based on the deformation behavior and measured creep parameters, grain boundary sliding was considered to be the dominant mechanism. Overall, those microstructures solution treated at higher temperatures

prior to aging exhibited larger grain sizes and greater creep resistance. For targeted low stress and intermediate temperature applications, grain size appears to be the dominant microstructural feature influencing the creep behavior of this alloy.

**Introduction**

Titanium alloys that contain the ordered orthorhombic (O) phase (Cmcm symmetry based on Ti<sub>2</sub>AlNb) have exhibited potential for intermediate temperature applications. Single-phase O alloys possess excellent creep resistance in the temperature range 650°C-750°C [1]. However, because single-phase O alloys have exhibited poor toughness and room-temperature (RT) ductility [2-4], the body centered-cubic (bcc) phase, which enhances the toughness and ductility of O alloys [2,4-7], is needed for practical engineering use. Creep-microstructure relations have been studied for first generation O alloys such as Ti-25Al-17Nb<sup>1</sup> [6] and Ti-22Al-23Nb [8], which contain the  $\alpha_2$ +B2+O phases. These studies showed a strong creep-microstructure correlation where the creep resistance increased with volume percent of the O phase and decreased with volume percent of the  $\alpha_2$  phase. This may be explained by the superior creep resistance of the O phase [1]. However, morphological effects may have played a role as the O phase was typically in a lenticular morphology, while the  $\alpha_2$  phase was equiaxed. In addition, grain size effects have also proved important [9]. A fourth possibility is that the nature of the bcc phase, which depends on alloy content and heat treatment, is important. In particular, the bcc phase chemistry determines ordering, where at lower Al and higher Nb contents the ordered B2 structure undergoes a composition induced disordering, which preferentially occurs during long aging times at low temperatures [10-12]. This is of practical importance in view of the substantially higher diffusivity expected for the disordered  $\beta$  phase compared with B2, as this may adversely effect the creep resistances of such alloys. Such a large number of possibilities make it difficult to determine the most significant microstructural aspect and a thorough understanding of the creep mechanisms is necessary. Some mechanistic work has been initiated over the stresses and temperatures of projected applications [13]. However, a more comprehensive understanding of creep mechanisms, especially for second generation O+bcc phase alloys such as Ti-22Al-27Nb, is necessary to fully understand microstructure-creep relationships.

<sup>1</sup> All alloy compositions are given in atomic percent.



In this paper, the phase evolution, which plays a significant role in terms of the thermodynamic stability of the microstructure, and creep behavior for a Ti-23Al-27Nb alloy are discussed in detail. Emphasis is placed on microstructural changes occurring at creep temperatures and its effects on the creep behavior. Three types of microstructures were chosen for the creep-microstructure investigation. These include super-transus B2,  $\alpha_2$ +B2, and O+B2 microstructures which were aged in the O+B region prior to the creep experiments. Stress exponents, activation energies, and deformation behavior were used to identify creep mechanisms and important microstructural features. In addition, this work describes the opportunities and limitations of using processing and heat-treatment schedules for obtaining stable microstructures that contain different grain sizes, phase volume fractions and morphologies.

### Experimental

A cast ingot with a nominal composition of Ti-23Al-27Nb was procured from Duriron Metals Inc., Dayton, Ohio. Forging preforms 60 mm in diameter and 150 mm in height, cut from this ingot by an electro-discharge machine (EDM), were sealed in a 6 mm thick stainless steel can and unidirectionally forged to a final height of 50 mm in air at a rate of 150 mm/min. Prior to forging, the can assembly was coated with a protective layer of glass and heat treated at 1000°C for 15 minutes followed by a 982°C soak for two minutes. After the initial forging, the piece was EDM cut to a height of 75 mm and forged to 25 mm in a direction perpendicular to that of the original under identical conditions. The re-canned pancake was then isothermally soaked at 815°C for one hour followed by a 982°C soak for 15 minutes prior to rolling. The unidirectional rolling steps consisted of several passes on a cold die each after a soak at 982°C for 5 minutes. The estimated reduction per pass was 5% with a total reduction of 80%. After the final pass, the sheet was reheated at 982°C for 3 minutes and then cooled slowly in vermiculite. All rolling and forging steps were performed below the B2 transus.

Threaded-grip creep specimens of 5 mm diameter and 30 mm gage length were machined along the rolling direction. Specimens and companion samples were wrapped in tantalum foils and encapsulated in quartz tubes backfilled at a low pressure of high purity argon gas. The capsules were subjected to solution treatments followed by controlled cooling or water quenching. Selected samples were then reheated at a lower temperature, followed by water quenching, for the transformation studies.

Constant-load tensile-creep experiments were performed on a vertical load frame in air between 650°C-760° and 50-450 MPa. In order to identify deformation behavior from surface observations, a finely polished rectangular specimen was tested in vacuum ( $9 \times 10^{-7}$  torr). The creep tests were performed such that the samples were soaked at the creep temperature for one hour prior to applying load, in order to minimize the thermal stresses. The extension was measured by two parallel linear variable differential transformers mounted on the specimens. Specimen temperatures were maintained within  $\pm 5^\circ\text{C}$ . After the creep had proceeded well into the steady-state regimes, either the load or temperature was increased or the creep tests were discontinued and specimens cooled under load to minimize recovery of the deformed structures. The phase compositions were measured for different regions of polished samples using a Japan Electron Optics Ltd (JEOL 733) electron microprobe. Grain size and phase volume fractions were

determined quantitatively using NIH image analysis software on digitized, high-contrast back-scattered-detector (BSD) images taken from a Leica 360 FE scanning electron microscope (SEM). Transmission electron microscopy (TEM), used for phase identification and deformation characterization, was performed on a JEOL JEM-2000FX electron microscope. TEM foils were produced by ion-milling mechanically dimpled samples. X-ray diffraction was used to confirm the presence of the different phases and differential thermal analysis (DTA) was performed to estimate the B2 transus.

### Results

#### Microstructure

The chemical composition of the as-rolled sheet is given in Table I. The Ti, Al, and Nb contents indicate good adherence to the target composition. The as-rolled sheet contained elongated B2 and O and/or  $\alpha_2$  grains, approximately 3  $\mu\text{m}$  in size, with fine O-phase precipitates within the B2 grains. This precipitation occurred during the gradual cool to RT.

Table I Chemical Analysis of the Sheet Material

atomic percent			weight parts per million		
Ti	Al	Nb	N	Fe	O
Bal	23.2	27.2	200	1100	1160

Table II describes the microstructures obtained after different heat treatments. The average grain size (GS), determined by the line-intercept method, was measured independent of phase. Phase volume percent (Vp) and chemical composition are also indicated for each microstructure. Measurement errors of  $\pm 5\%$  and  $\pm 1\%$  apply for the reported values of Vp and chemical composition, respectively. Note the wide variation in phase volume percents with heat treatments. In general, the chemistry of the O phase was close to the stoichiometric  $\text{Ti}_2\text{AlNb}$  composition. The chemistry of the  $\alpha_2$  phase was relatively constant at Ti-25Al-16Nb. The bcc phase composition changed considerably, depending on its volume percent. Solution treatments at temperatures higher than 875°C favored the B2 phase (bold data); however, the B2 phase disordered below 875°C, in agreement with previous work [12]. The chemical compositions and grain sizes of phases occurring in the extremely fine regions, obtained after 650°C aging treatments, were not measured (marked by \* in Table II). The structures of these phases will be described in more detail later in this section.

Selected solution-treated and quenched microstructures are illustrated in Figures 1a-d. In these BSD images, the light, gray, and dark regions correspond to the B2, O, and  $\alpha_2$  phases, respectively. Solution treatments above 1070°C resulted in large-grained microstructures, Figure 1a. X-ray diffraction data, containing the super-lattice (210) peak, confirmed the presence of B2. An analyzed DTA trace estimated the B2 transus to be 1070°C. This is in good agreement with the metallographic and X-ray results. Sub-transus solution treatments of 875°C and above produced equiaxed microstructures with the higher-temperature treatments generally resulting in larger average grain sizes (see Table II). This average grain size difference, which is primarily an effect of the increasing B2 grain size with temperature, plays an important role in determining mechanical properties.

Table II Heat Treatments and Measured Average Grain Sizes, Phase Compositions and Volume Percents

Heat Treatment	$\alpha_2$			bcc			O			GS $\mu\text{m}$
	Al	Nb	Vp	Al	Nb	Vp	Al	Nb	Vp	
875°C/100h/wq			0%	15.1	36.5	27%	24.8	24.2	73%	2.2
875°C/40h/wq/650°C/336h/wq			0%	*	*	14%	*	*	86%	*
950°C/45h/wq			0%	<b>20.1</b>	<b>30.7</b>	<b>52%</b>	25.2	23.6	48%	3.8
950°C/45h/wq/650°C/373h/wq			0%	*	*	15%	*	*	84%	*
1000°C/45h/wq	25.6	16.1	3%	<b>18.8</b>	<b>31.7</b>	<b>43%</b>	25.0	24.5	54%	2.9
1000°C/45h/wq/650°C/304h/wq	25.3	15.8	3%	*	*	16%	*	*	81%	*
1025°C/200h/wq	25.6	15.5	12%	<b>22.1</b>	<b>28.5</b>	<b>88%</b>			0%	5.0
1025°C/45h/wq/650°C/450h/wq	25.6	15.4	12%	*	*	14%	*	*	74%	*
1090°C/0.5h/wq			0%	<b>23.0</b>	<b>27.0</b>	<b>100%</b>			0%	100.0
1090°C/0.5h/wq/650°C/112h/wq			0%	*	*	20%	*	*	80%	*

wq: water quenched; \*data includes fine regions where compositions and grain sizes were not measured; bold data represents the ordered bcc, B2, structure

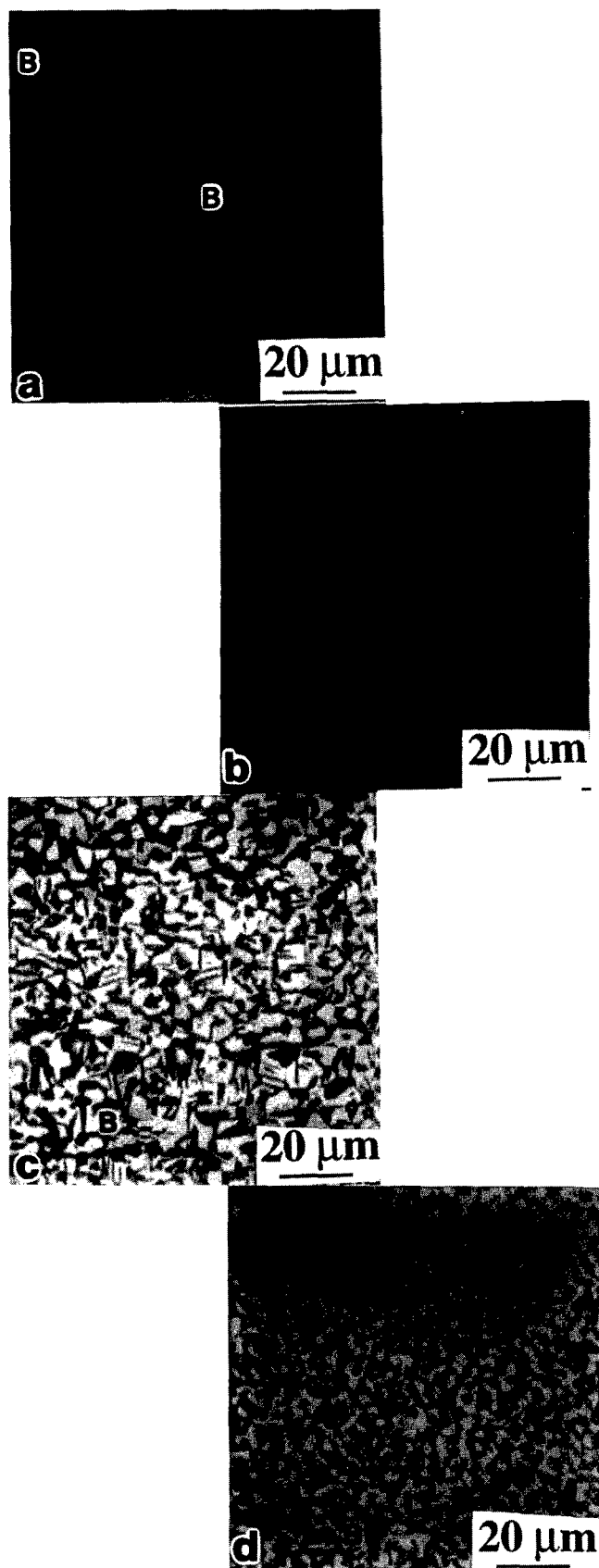


Figure 1: Microstructures of solution treated and water quenched specimens. Solution-treatment temperatures were (a) 1090°C, (b) 1025°C, (c) 1000°C, and (d) 900°C.

Solution treatments between 1010°C and 1070°C resulted in  $\alpha_2$ +B2 microstructures. A 1025°C treatment exhibited a majority of B2 phase, approximately 88% by volume, with the remainder as  $\alpha_2$ , Figure 1b. Orientation relations (ORs) between adjacent  $\alpha_2$  and B2 grains can be described as:  $[111]B2//[1120]\alpha_2$ ,  $(011)B2//(\bar{0}001)\alpha_2$ , which is the well known Burgers OR. Work by Sagar et al. [14] has shown that at 975°C, the  $\alpha_2$  phase undergoes dynamic recrystallization which destroys the Burgers OR. Assuming no  $\alpha_2$ /B2 OR exists in the as-rolled microstructure, the current OR was restored through the sub-transus 1025°C solution treatment, where both the  $\alpha_2$  and B2 phase volumes increased at the expense of the O phase volume. Solutionizing at 1000°C resulted in a three-phase  $\alpha_2$ +B2+O microstructure, Figure 1c, where the B2 phase was continuous. Because the O phase formed preferentially as a ring around the  $\alpha_2$  phase, some  $\alpha_2$  phase is expected to have been present in the as-rolled microstructure. This microstructure is similar to three-phase microstructures in other O alloys [6-8], except the O-ring is much thicker for the current case. The  $\alpha_2$  content was only 3% (see Table II), indicating that 1000°C is close to the two-phase O+B2 region. Solution treatments between 875°C and 975°C resulted in equiaxed O+B2 microstructures without any  $\alpha_2$  and lower temperatures corresponded to greater O volumes (see Table II). Figure 1d depicts a 900°C heat-treated microstructure which contained approximately 63% O by volume. The OR found between the O and B2 grains is common [15] i.e.:  $[111]B2//[110]O$  and  $(110)B2//(\bar{0}01)O$ , Figure 2a. For Figures 1b-d, the B2 phase was verified by super-lattice reflections in the  $[001]$  B2 selected area diffraction pattern (SADP), Figure 2b. Samples subjected to super-transus solution treatments which were either control cooled to RT, Figure 3, or quenched and then aged in the O+B2 region were devoid of equiaxed phases and retained large prior B2 grains containing fine precipitates of O and  $\alpha_2$ . Thus the fine equiaxed grains are only obtainable when hot work is performed below the transus.

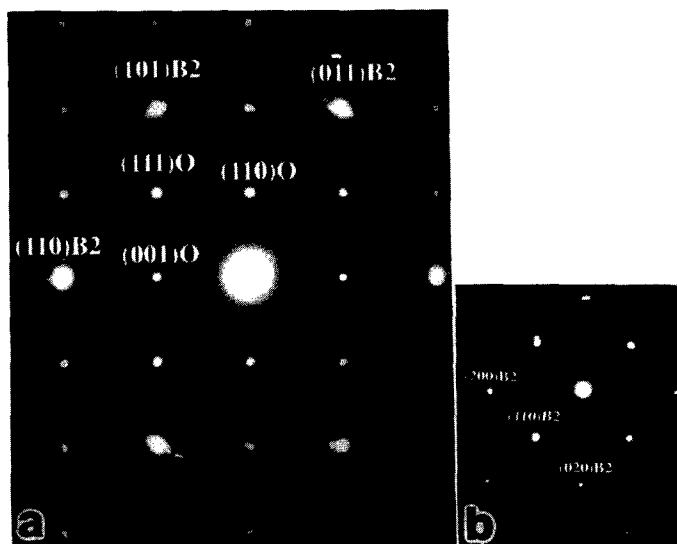


Figure 2: (a) SADP taken from neighboring O+B2 grains for a 900°C/45h/wq heat treatment. The OR is:  $[111]B2//[110]O$ ,  $(110)B2//(\bar{0}01)O$ . (b) Verification of the ordered B2 structure in the same sample depicting super-lattice reflections from a  $[001]$  zone axis.

In order to investigate microstructural stability, aging treatments were performed on selected solutionized and quenched samples. Figure 4a depicts a baseline microstructure solutionized at 950°C for 45 hours. Figures 4b-d illustrate the microstructure obtained after aging treatments between 650-850°C for 13 hours followed by water quenching. Each microstructure exhibited Widmanstätten precipitates of the O phase within B2 grains, where their size and volume depended on aging temperature. The largest precipitate size occurred at 850°C and the finest size was exhibited at 650°C. The primary O or  $\alpha_2$  grains (depending on solution-treatment temperature) remained relatively unchanged. This is important for the design of microstructures because the ratio of the primary phase volume to the precipitated phase volume will differ depending on the initial solution treatment. In addition,

the primary O or  $\alpha_2$  and prior B2 grain sizes were unaffected by aging as the precipitation only occurred within the B2 grains. Aged microstructures which were re-solution treated above and below 875°C reconfirmed the morphological transition; those microstructures re-solutionized below 875°C remained lenticular while those re-solutionized above 875°C contained only equiaxed grains.



Figure 3: Super-transus heat-treated microstructure (1150°C/0.5h/cooled at 15°C/min. to RT) containing large prior B2 grains with O and  $\alpha_2$  precipitates.

The microstructures obtained on aging at 650°C and 750°C depicted a small volume of discontinuous precipitation initiated at O/B2 interfaces, indicated by arrows in Figures 4c and d, resembling the initial stages of cellular reaction [16]. This phenomenon was investigated in detail using long-term aging treatments. Figures 5a-d depict the microstructural changes occurring after aging at 650°C for 24, 48, 96 and 304 hours. For long aging times, the discontinuous precipitation products coarsened and advanced into B2 grains. The migration of the discontinuous precipitation interface resulted in the consumption of the fine uniformly distributed precipitates. After 304 hours, some of the fine precipitates remained, indicative that the discontinuous precipitation was incomplete. This is evident in the 1025°C solution-treated case where after 610 hours at 650°C, Figure 6, a large volume of the discontinuous precipitation was present yet some of the finer precipitation remained. Convergent beam electron diffraction (CBED) patterns, Figures 7a and b, taken from the frontal regions, identified the alternating platelets as O and B. Therefore the discontinuous precipitation is characterized by both O-phase precipitation and disordering of the B2 phase. A high magnification dark field image of this region is depicted in Figure 8a and the corresponding OR between the platelets,  $[011]B/[001]O$ ,  $(211)B/(110)O$ , is depicted in Figure 8b. Considering the structural similarity between the O and  $\alpha_2$  phase, this is the same as the previously mentioned Burgers OR between bcc and hcp phases. The B phase was not solely associated with the discontinuously precipitated regions. It was also found within the homogeneously-precipitated regions. Interestingly, in some cases the ordered B2 phase was also retained in regions surrounding the fine-precipitated O phase. Super-transus solution-treated plus aged microstructures also exhibited discontinuous precipitation. Figures 9a and b depict the baseline microstructure of Figure 1a after aging times of 9 and 100 hours, respectively, at 650°C. The discontinuous precipitation migrated much farther in this case compared with the sub-transus solutionized samples. In addition, extremely fine bcc platelets were exhibited within the precipitating structures, Figure 9c. Discontinuous precipitation was exhibited in very small volumes for those microstructures solution treated below 950°C prior to aging. In those cases the majority of precipitation occurred homogeneously throughout the bulk.

The following summarizes the microstructural observations of aged samples. The O phase precipitated homogeneously within B2 grains for all solution-treated samples which were aged below 875°C. Discontinuous precipitation, characterized by alternating O+B platelets at O/B2 or  $\alpha_2$ /B2 grain boundaries, was exhibited for solution-treated and quenched samples which were subsequently aged at  $T \leq 750^\circ\text{C}$ . Samples solution-treated at higher temperatures and aged at lower temperatures exhibited greater volumes of discontinuous precipitation. Temperature dictates the bcc phase composition and the discontinuous precipitation appears to be driven by the compositional gradient within the bcc phases as will be described in the discussion.

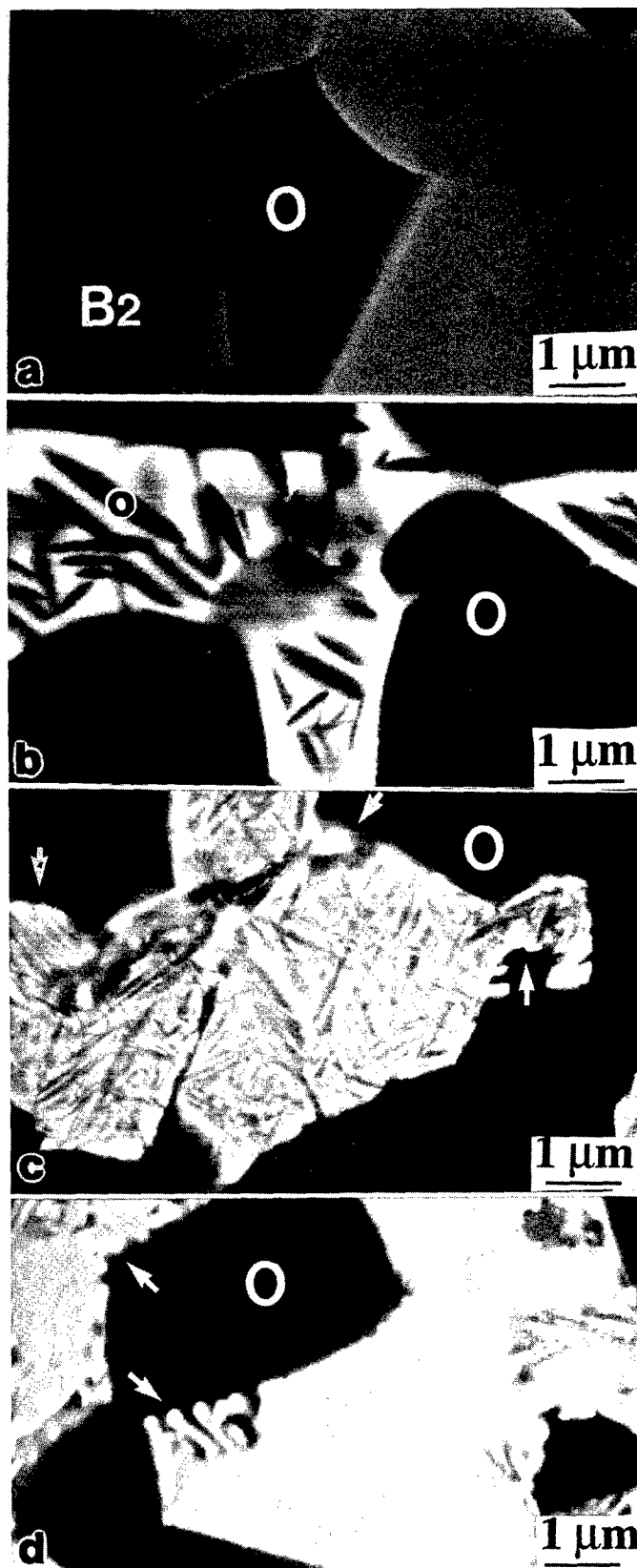


Figure 4: Comparison of a solution-treated (a) (950°C/45h/wq) microstructure with solution-treated and aged microstructures. The specimens were aged at (b) 850°C, (c) 750°C, and (d) 650°C for 13 hours followed by water quenching. The arrows indicated in (c) and (d) represent the initiation of discontinuous precipitation.

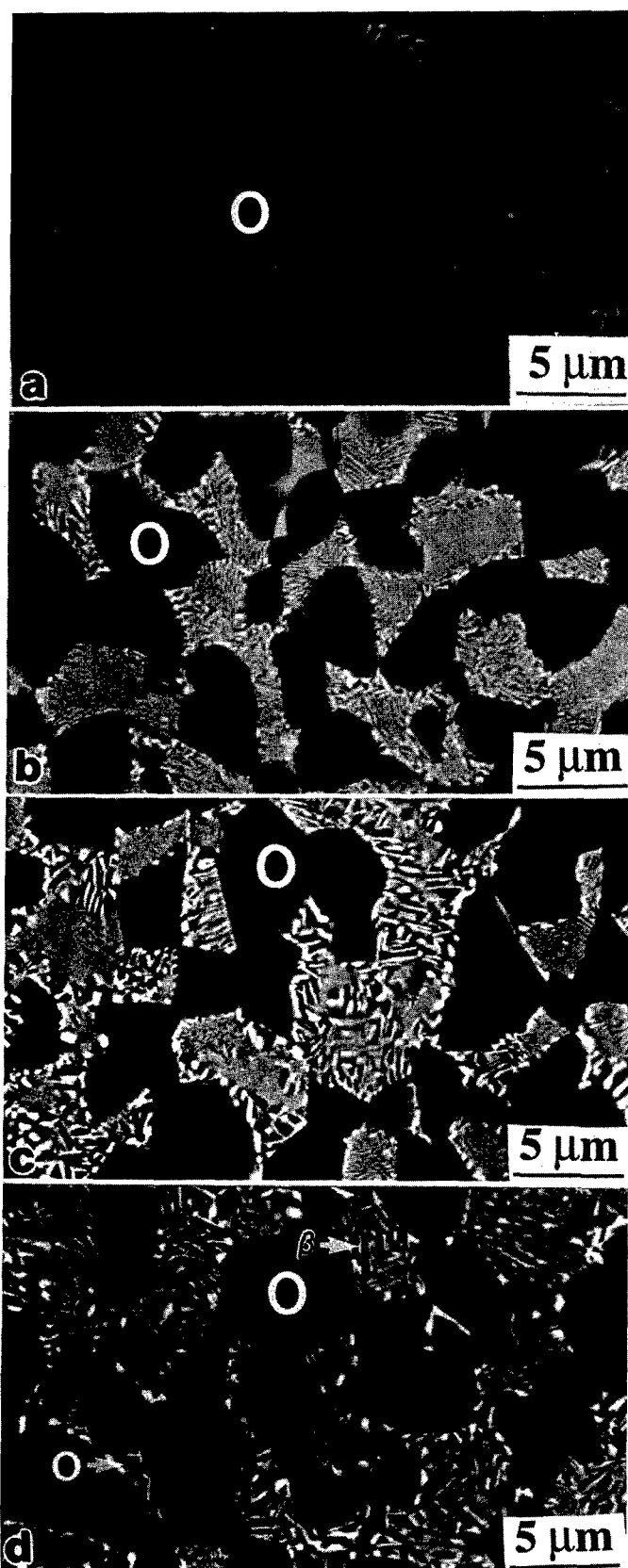


Figure 5: Effect of aging time on microstructure. These specimens were solution-treated at 950°C and then aged at 650°C for (a) 24 hours, (b) 48 hours (c) 100 hours and (d) 304 hours, followed by water quenching.

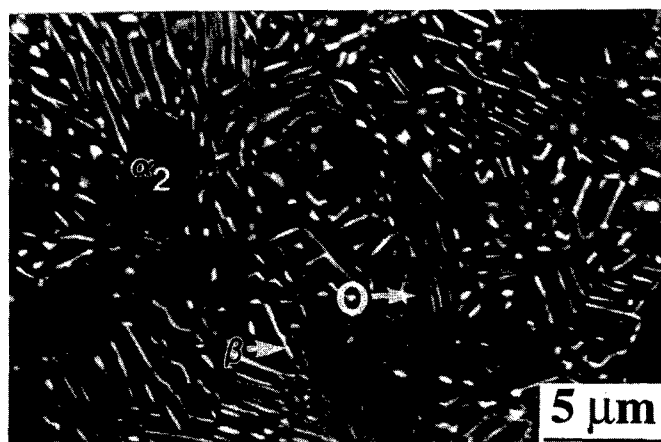


Figure 6: Microstructure obtained by solution treatment at 1025°C/45h/wq plus aging at 650°C/610h/wq. The majority of the B2 phase has undergone discontinuous precipitation.

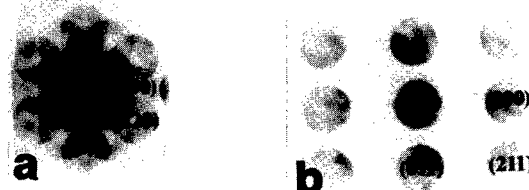


Figure 7: CBED patterns taken from a discontinuous precipitating region for a 950°C/45h/wq/650°C/373h/wq heat-treated sample. The patterns are identified as (a) [001]O and (b) [011]β.

#### Creep Behavior

In order to investigate the effect of microstructure on creep behavior, three types of microstructures were chosen. These included super-transus B2 (1090°C), sub-transus  $\alpha_2$ +B2 (1025°C), and sub-transus O+B2 (875 or 950°C) solutionized microstructures which were aged at 650°C. As described above, the aging treatment induced the precipitation of O and  $\beta$  platelets within equiaxed prior B2 grains. Henceforth, these microstructures will be referred to by their solution-treatment temperature. In addition, two specimens were solution-treated in the O+B2 region (950°C), without aging, to examine the effect of microstructural instability. Figure 10 compares creep strain versus time curves for aged and unaged specimens which underwent identical O+B2 (950°C) solution-treatments. Aging resulted in lower creep strains, where the solution-treated condition exhibited higher primary strains and minimum creep rates than the solution-treated and aged condition. However, the differences in both primary strain and minimum creep rate were within a factor of 1.5. The solution-treated only samples were unloaded after 44 and 66 hours of creep to identify the effect of load on instability. There was no significant difference, in terms of phase volumes or sizes, from heat-treated samples which were aged for similar exposure times without load. Creep strain rate versus time data indicate that strain rates reached a constant value within 10 hours of applying the load. Thus, the samples were unloaded well after the transient creep regime. As seen in the aging studies, the volume of discontinuous precipitation increased during creep deformation.

Table III lists the primary strain ( $\epsilon_p$ ), primary transient time ( $t_p$ ), and minimum creep rate ( $\dot{\epsilon}_{min}$ ) for all heat-treated specimens tested in creep. Primary creep was determined by the 'onset method' [17] and minimum creep rates were calculated after strain rates were determined to be constant with respect to time. The results indicate that for a given test condition higher temperature solution treatments, which correspond to larger equiaxed grain sizes, offer greater creep resistance. For example, a greater than two times decrease in primary creep strain and minimum creep rate was observed for samples solutionized at 950°C compared with 875°C. The best creep resistance was found for the super-transus microstructure, which contained a 100  $\mu$ m prior B2 grain size.

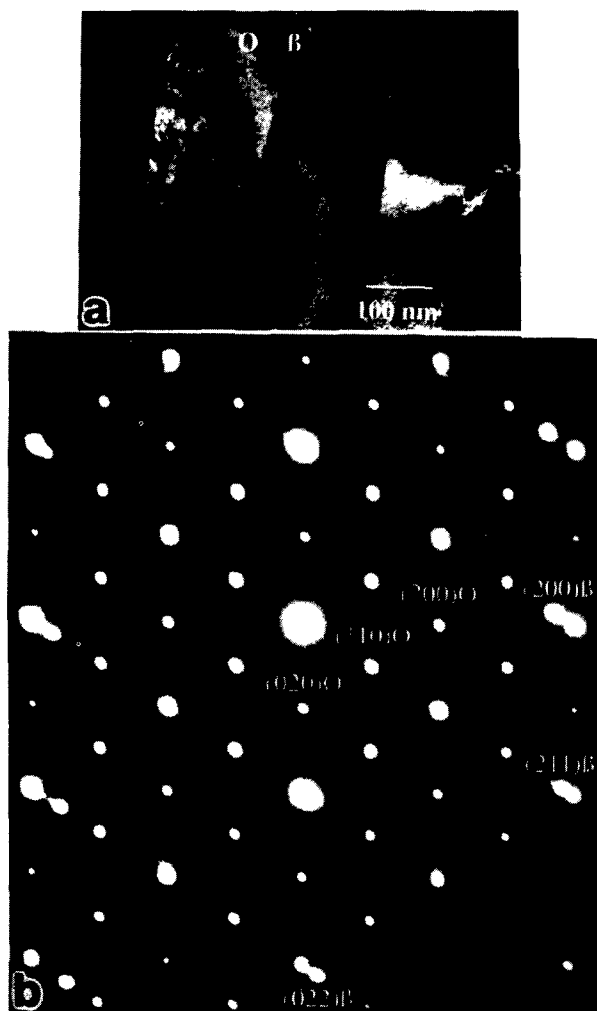


Figure 8: (a) A dark field image of the O+β phase platelets corresponding to the CBED patterns of Figure 7. (b) SADP taken from the same region depicting the OR: [011]β//[001]O, (211)β/(110)O.

Table IV lists the creep parameters for each microstructural condition which were calculated from the power-law creep equation for minimum creep rate:

$$\dot{\epsilon}_{\min} = A \sigma^n \exp(-Q_{\text{app}}/RT) \quad (1)$$

where  $A$  is a constant,  $\sigma$  is the applied stress,  $n$  is the creep exponent,  $Q_{\text{app}}$  is the apparent activation energy,  $R$  is the gas constant, and  $T$  is absolute temperature. Figures 11a and b show plots of  $\log \dot{\epsilon}_{\min}$  versus  $\log \sigma$  and  $\ln \dot{\epsilon}_{\min}$  versus  $(1/T)$ , respectively. The creep behavior of the super-transus solutionized then aged specimens<sup>2</sup> at 650°C (Figure 11a) exhibits the classic transition in creep exponents noticed for pure metals and alloys, where each transition typically corresponds to a change in deformation mechanism [18]. The creep behavior of sub-transus microstructures, which were examined over a smaller stress range, suggests they are confined to a region dominated by a single mechanism. Judging from the similar values of creep parameters, the deformation mechanism is the same for both microstructures.

<sup>2</sup> The data for the super-transus then aged microstructure at 650°C was taken from a single experiment where the load was increased after steady-state creep was achieved. The data for the super-transus then aged microstructure at 50MPa/705-760°C was also taken from a single experiment where the temperature was increased after steady-state creep was achieved.

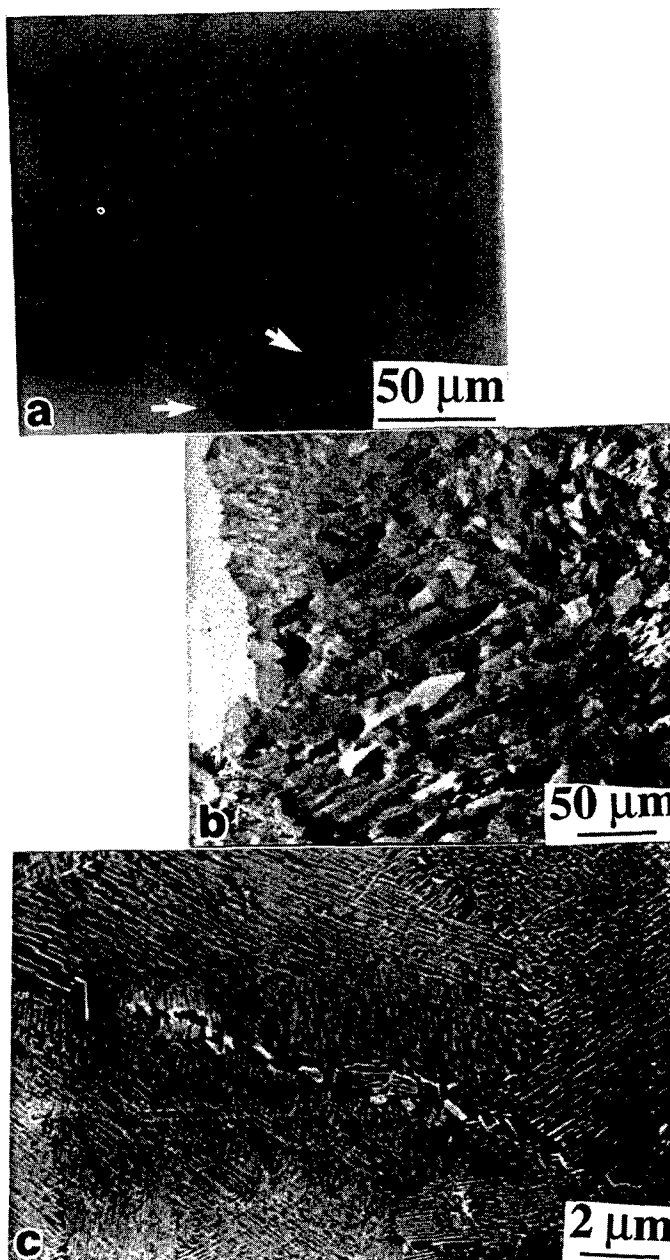


Figure 9: Super-transus solution-treated samples (1090°C/0.5h/wq) which were aged at 650°C for (a) 9 and (b) 100 hours, followed by water quenching. Precipitation initiated at B2/B2 boundaries (marked by arrows). (c) A higher magnification image of (b) depicts the very fine bcc platelets within the precipitating structures.

At the lowest applied stresses, both the activation energy,  $Q_{\text{app}} = 171$  kJ/mol, and the creep exponent,  $n=1.2$ , of the super-transus microstructure were smaller than those of the sub-transus microstructures. The creep exponent was close to unity, which corresponds to a mechanism involving the stress-directed diffusion of vacancies [18]. If the activation energy for lattice self-diffusion ranges between 340-376 kJ/mol [1,19], the activation energy for the super-transus microstructure can be considered as that of grain boundary diffusion; as the activation energy for grain boundary diffusion is typically half that for lattice self-diffusion [18]. Therefore based on the creep parameters of the super-transus microstructure a Coble creep mechanism is suggested over the stress range 50-172 MPa [18]. This may be related to the phase evolution of this microstructure as the precipitation at 650°C was also dominated by grain boundary diffusion.

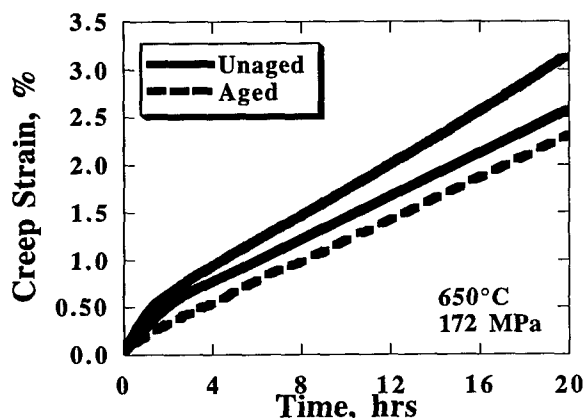


Figure 10: Creep strain vs time curves for solution treated (950/45/wq) and solution treated and aged (950°C/45h/wq/650°C/304h/wq) specimens.

Table III Creep Properties for Heat Treated Ti-23Al-27Nb Sheet

Heat Treatment	$\sigma/T$ (MPa/°C)	$\epsilon_p$ (%)	$t_p$ (h)	$\dot{\epsilon}_{min}$ (1/s)
875°C/45h/wq/650°C/304h/wq	250/650	na	na	1.50E-06
875°C/45h/wq/650°C/304h/wq	172/650	1.40	3.7	6.71E-07
875°C/45h/wq/650°C/304h/wq*	172/654	1.43	4.7	5.20E-07
875°C/45h/wq/650°C/304h/wq	100/650	na	na	3.00E-07
875°C/45h/wq/650°C/304h/wq	50/655	3.12	57.2	8.51E-08
875°C/45h/wq/650°C/304h/wq	50/709	na	na	3.15E-07
875°C/45h/wq/650°C/304h/wq	50/760	1.90	1.6	2.86E-06
950°C/45h/wq	172/650	0.79	4.3	2.94E-07
950°C/45h/wq	171/651	0.77	2.8	3.80E-07
950°C/45h/wq/650°C/304h/wq	172/650	0.68	5.1	2.90E-07
1025°C/45h/wq/650°C/288h/wq	172/650	0.69	10.8	9.93E-08
1025°C/45h/wq/650°C/288h/wq	100/650	1.30	67.0	3.61E-08
1025°C/45h/wq/650°C/288h/wq	50/650	0.79	172.0	8.83E-09
1025°C/45h/wq/650°C/288h/wq	50/707	na	na	5.27E-08
1025°C/45h/wq/650°C/288h/wq	50/764	0.80	4.0	3.96E-07
1090°C/0.5h/wq/650°C/112h/wq	442/650	na	na	4.90E-08
1090°C/0.5h/wq/650°C/112h/wq	394/650	na	na	3.17E-08
1090°C/0.5h/wq/650°C/112h/wq	360/650	na	na	2.32E-08
1090°C/0.5h/wq/650°C/112h/wq	318/650	na	na	1.43E-08
1090°C/0.5h/wq/650°C/112h/wq	246/650	na	na	9.58E-09
1090°C/0.5h/wq/650°C/112h/wq	172/650	na	na	4.27E-09
1090°C/0.5h/wq/650°C/112h/wq	97/650	na	na	2.71E-09
1090°C/0.5h/wq/650°C/112h/wq	50/650	0.13	115.0	1.00E-09
1090°C/0.5h/wq/650°C/112h/wq	50/705	0.14	113.8	1.32E-09
1090°C/0.5h/wq/650°C/112h/wq	50/730	na	na	2.10E-09
1090°C/0.5h/wq/650°C/112h/wq	50/760	na	na	4.03E-09

wq: water quenched; na: not available; \*tested in vacuum ( $9 \times 10^{-7}$  torr)

For the stress range 172-318 MPa, the creep exponent,  $n=2.0$ , of the super-transus microstructure is close to that of the sub-transus microstructures. Grain boundary sliding is suggested as the dominant mechanism when  $n$  is close to two [18,20]. Typically this mechanism is related to the build-up of dislocations near grain boundaries, where the activation energy for grain boundary sliding is close to that for lattice self-diffusion [20,21]. Therefore the activation energies of the sub-transus microstructures at 50 MPa are expected to be close to that of self-diffusion. The measured values,  $Q_{app} \sim 265$  kJ/mol, approach 80% of those found in other studies [1,19]. Data taken from the primary creep stage also suggest a grain boundary deformation mechanism as the stress exponent based on the power-law equation for transient time [13] is 1.8 for the 1025°C solutionized microstructure. For stresses greater than 318 MPa,  $n=3.7$  for the super-transus microstructure. Dislocation climb, suggested to be the rate-controlling process for O alloys under high stresses [1,19], is expected to dominate when  $n > 3.5$  [18]. High stress experiments have yet to be performed for the sub-transus microstructures.

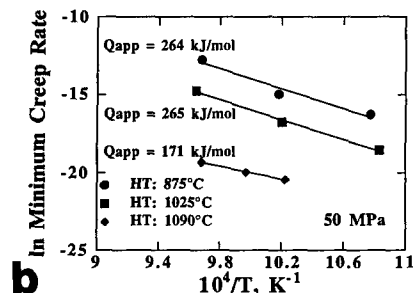
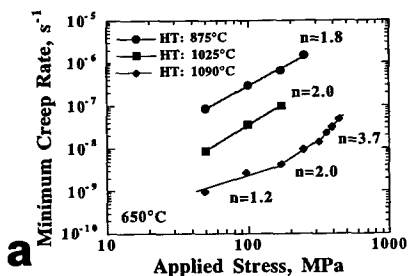


Figure 11: Creep plots for the three microstructures, represented by their solution-treatment temperature. (a) Log  $\dot{\epsilon}_{min}$  vs log  $\sigma$  curves at 650°C, where the data for the 1090°C microstructure indicated a transition in creep exponent at 172 and 318 MPa. (b) Arrhenius plot of  $\ln \dot{\epsilon}_{min}$  vs  $10^4/T$  for an applied stress of 50 MPa, where the 1090°C microstructure exhibited a lower  $Q_{app}$  than the sub-transus microstructures.

Table IV Measured Creep Exponents and Apparent Activation Energies for Heat Treated Ti-23Al-27Nb Sheet

Heat Treatment	$\Delta\sigma^*$ , (MPa)	$n$	$\Delta T^{**}$ , (°C)	$Q_{app}$ , kJ/mol.
875°C/45h/wq/650°C/304h/wq	50-250	1.8	655-760	264
1025°C/45h/wq/650°C/288h/wq	50-172	2.0	650-764	265
1090°C/0.5h/wq/650°C/112h/wq	50-172	1.2	705-760	171
1090°C/0.5h/wq/650°C/112h/wq	172-318	2.0	na	na
1090°C/0.5h/wq/650°C/112h/wq	318-450	3.7	na	na

wq: water quenched; na: not available; \* $T=650^\circ\text{C}$ ; \*\*  $\sigma=50\text{MPa}$

Microstructural evidence of specimens indicates that grain boundary sliding contributed to creep strains. Grain boundary offsets were observed for a sample which was unloaded after four percent creep strain, Figures 12a and b. Wedge cracks formed preferentially at grain boundaries aligned normal to the load axis (see Figure 12b), which would not be expected to slide due to the low shear stresses at such boundaries [22]. Surface slip traces have been observed for ambient and elevated temperature deformed O+B2 microstructures [4], yet no slip traces were found on this specimen. Instead the damage appeared to accumulate through grain boundary cracking. This was depicted for a specimen which exhibited more than 20% strain without failing, Figure 13. Throughout the specimen extensive cracking was found along the grain boundaries, especially at O/O grain boundaries. Except for near-surface locations, few cracks penetrated grains deeply. Environmentally assisted damage influenced the creep behavior as severe transgranular surface cracking, up to 500  $\mu\text{m}$ , was exhibited and this was expected to have been responsible for premature failure. Fracture surface observation of the super-transus microstructure revealed fracture occurred intergranularly, while a very limited amount of cracking was exhibited away from the fracture surface.

TEM investigations revealed relatively little evidence of deformation occurring at grain interiors for specimens crept below 250 MPa. Dislocations formed preferentially at O/B interfaces within transformed B2 regions; however, these were also found in the grip regions and probably resulted from transformation stresses as seen previously [12]. A large number of equiaxed O grains were examined for specimens which were unloaded in the secondary creep regime after at least 6% creep strain. Few grains exhibited a significant number of dislocations. After comparing the microstructures of gage regions and grip sections, it was concluded that the dislocation activity within the equiaxed O grains could not be responsible for the creep strains measured.

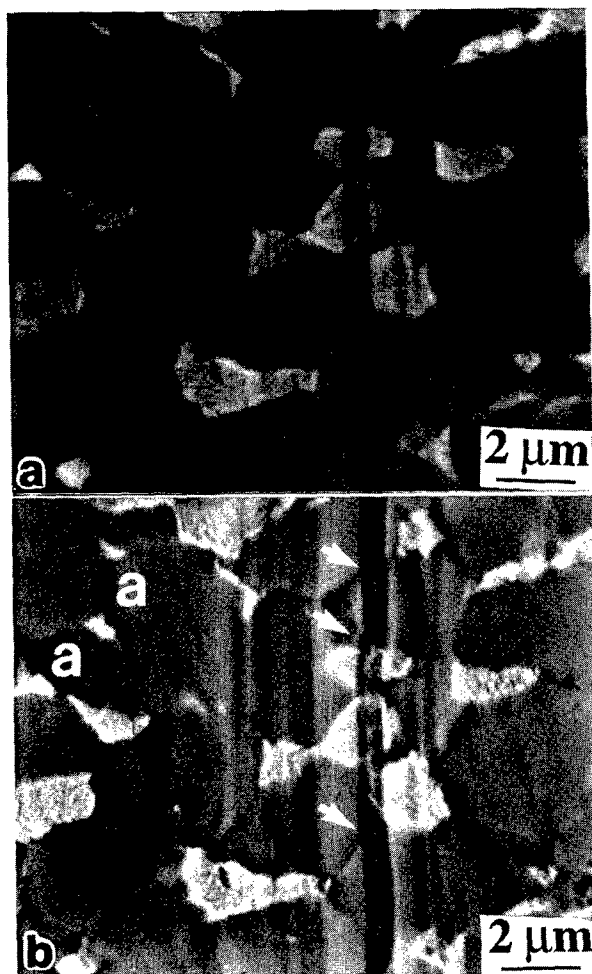


Figure 12: A 875°C heat-treated sample containing fiducial marks; (a) prior to creep and (b) post 4% creep at 650°C/172MPa. Arrows indicate displacement offsets at grain boundaries. Cracks were located at O/O boundaries, marked 'a', aligned normal to the loading axis (horizontal).

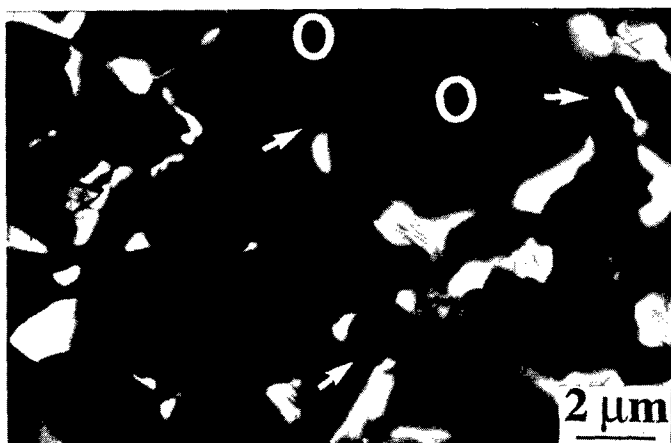


Figure 13: Severe grain boundary cracking (indicated by arrows) in the bulk for a 875°C/45h/wq/650°C/304h/wq heat-treated specimen which was crept to a strain higher than 20% at 650°C/100 MPa.

## Discussion

### Microstructure

The compositions of the  $\alpha_2$ , B2, and O phases (see Table II) in the Ti-23Al-27Nb alloy are in agreement with compositional data from similar

O alloys [4,11]; however, the Nb content of the  $\alpha_2$  phase was significantly higher than that found in a Ti-25Al-17Nb alloy [6,7]. Thus for Ti-23Al-27Nb, the Nb solubility in  $\alpha_2$  appears to have increased and Nb is expected to have substituted at Ti sites more frequently. This agrees with previously developed phase diagrams [14,23] depicting the  $\alpha_2$ +B2 and  $\alpha_2$ +B2+O fields extending with increased Nb concentrations. The Ti-22Al isopleth developed by Miracle and Rhodes [23] is provided in Figure 14, and the current data is overlaid. The current data agrees with the depicted phase boundaries. Although no attempt was made to characterize the order/disorder temperature of the bcc phases in the two-phase O+bcc region in Figure 14, the current O+B2 data agree well with published results [12].

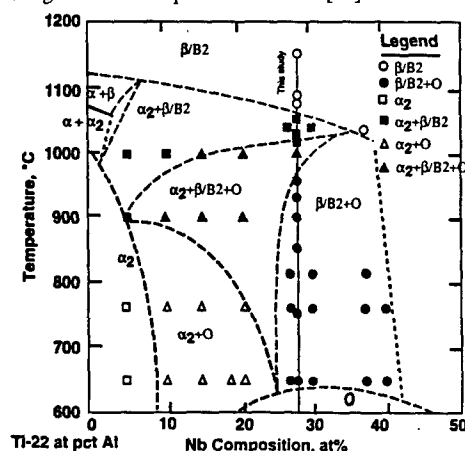


Figure 14: The Ti-22Al isopleth taken from Miracle and Rhodes [23], where the current data are overlaid for a Nb composition of 27 at.%.

The regime below the O+B2 field is poorly understood. In agreement with the current work, it has been shown that the  $\alpha_2$  phase formed by sub-transus heat treatment at high temperatures is extremely stable and cannot transform to the O phase at lower temperatures [5]. Though both the  $\alpha_2$  and B2 phases are not considered to be equilibrium phases at 650°C, the kinetics of  $\alpha_2$  transformation may be quite slow, whereas the decomposition of the B2 phase is relatively rapid. From the work of Bendersky et al. [12], the O+B2 to O+ $\beta$  transus is expected to lie between 700°C and 875°C. This transition window corresponds to a distinct morphological transformation within the B2 phase. Above 875°C, the equiaxed B2 phase coarsens at O/B2 grain boundaries, whereas below 875°C, O precipitates within B2 grains in a lenticular fashion (see Figure 4). The O+ $\beta$  equilibrium may be somewhat responsible for this morphological change, as it has been suggested that the nature of the precipitate shape is obtained through the minimization of elastic energy where the  $\beta$  phase preferentially forms as platelets [12]. In the current work, the order/disorder temperature is expected to lie close to 750°C, where the  $\beta$  phase precipitated discontinuously.

The discontinuous precipitation which migrated from grain boundaries is defined as cellular precipitation according to the reaction:



where B2 is the super-saturated matrix,  $\beta$  is of similar structure but with a lower thermodynamic excess of solute (Al), and O is the equilibrium precipitate. Similar transformations are found in several metallic alloy systems [16,24]. Thus it appears to be easier for the system to lower its total free energy by cellular transformation than by the coarsening of individual O platelets within the bulk. This is evidently related to the coherency of the O/B2 and  $\alpha_2$ /B2 phases as well as the composition of the B2 phase. The two factors which appear to have the greatest effect on cellular precipitation are the solutionizing and aging temperatures, where higher solutionizing temperatures and lower aging temperatures are more conducive to this type of reaction. This may be explained in terms of bcc phase chemistry and composition induced disordering [10].

Upon aging, the O phase precipitates uniformly within B2 grains and the chemistry of the O phase typically adheres to its  $\text{Ti}_2\text{AlNb}$  stoichiometry. As the volume fraction of O phase increases, the B2 phase volume fraction decreases and the B2 composition loses Al and



gains Nb. At some point the B2 structure will disorder due this chemistry difference. The B2 phase is thus considered to be super-saturated with respect to  $\beta$ . The degree of this super-saturation depends on the composition gradient between the bcc structures which is a function of the solutionizing and aging temperatures. As the composition gradient between the B2 phase and the  $\beta$  phase narrows, such as through lower temperature solutionizing and higher temperature aging or through slow-cooling treatments, the degree of super-saturation lessens. In this case only small chemistry changes are necessary for the transition of B2 to  $\beta$ , which may be accommodated by diffusion within the bulk of the B2 region. However, at higher solutionizing and lower aging temperatures, the degree of super-saturation of B2 with respect to  $\beta$  is increased, whereby a more severe compositional gradient exists. In such cases, the driving force for cellular precipitation is great and subsequent diffusion along grain boundaries appears to be the kinetically favorable route [16,24]. Thus the thermal activation processes which favor cellular precipitation appear to be enhanced by higher solution-treatment temperatures and lower aging temperatures which lead to larger bcc phase compositional gradients. Cellular precipitation was not exhibited for super-transus solutionized then slow cooled samples (see Figure 3). In addition, subsequent aging of these samples did not promote any cellular reaction. This is consistent with the above reasoning as the bcc phase gradually transforms to O upon cooling and therefore decreases its Al and increases its Nb concentrations along the way. Quenching treatments enhance the super-saturated nature of the bcc phase and should be avoided for producing stable intermediate temperature microstructures.

### Creep Behavior

Long term aging for O+B2 microstructures led to a reduction in primary creep strain and minimum creep rate. The difference in creep strain was more significant in the primary stage as within the first few hours after loading the strains of the unaged specimens had doubled compared to that of the aged specimens (see Figure 10). A similar result has been found by Rowe and Larsen [9]. Of course this is undesirable as primary creep strains are typically used to rank structural materials for design purposes. However, in terms of the secondary creep regime, the aging transformation had a relatively small effect, which may be explained by the steady-state creep mechanisms.

The stress dependence on minimum creep rate at high applied stresses (>318 MPa) suggests that dislocation climb is the likely mechanism, in agreement with the literature [1,19]. However at lower applied stresses, where relatively little work has been performed on creep mechanisms of O alloys, the stress dependence on minimum creep rate and transient time indicate the likely mechanism to be a grain boundary process. This is not unexpected as grain boundaries are the locus of damage for O alloys. It has been well established that  $\alpha_2/\alpha_2$  and O/O boundaries are preferred sites for crack nucleation from RT to 650°C, which has been explained by the limited number of slip systems in the  $\alpha_2$  and O structures and the high stress concentrations at grain boundaries [3-9]. The bcc phase helps blunt such cracks at elevated temperatures [4], however, the most convenient crack path appears to be intergranular. B2/B2 boundaries are also detrimental as the poor ductilities of super-transus microstructures have been attributed to cracking at prior B2 grain boundaries [4,7]. From the phase evolution studies, diffusion along B2 grain boundaries appears to be faster than in the grain interior. Thus such boundaries may also be effective in absorbing dislocations. The low density of dislocations within grains indicates that grain interiors are not contributing significantly to the relatively high creep rates measured. Grain interiors were also more resistant to cracking as cracks typically grew intergranularly (see Figures 12 and 13). Thus both the deformation and strain rate behavior suggest that grain boundaries are controlling creep for applied stresses less than 318 MPa.

The type of grain boundary process appeared to be dependent on microstructure and stress. A Coble creep mechanism is suggested for the large-grained super-transus microstructure at stresses less than 172 MPa. For applied stresses between 172 and 318 MPa, a grain boundary sliding mechanism is suggested. In agreement sliding has been reported for Ti-25Al-23Nb at 650°C/310 MPa [9]. However, the finer-grained (sub-transus) microstructures exhibited sliding even for stresses below 172 MPa and no transition in creep exponent was experienced (see

Figure 11a). Their measured activation energies at 50 MPa were significantly greater than that of the super-transus microstructures. Therefore, sub-transus microstructures are suggested to remain in the grain boundary sliding regime at the lowest applied stresses, and a Coble creep mechanism is not considered to be rate controlling.

In order to understand this behavior as well as the microstructural factors influencing the secondary creep rates, models based on grain boundary sliding were investigated. From the deformation observations, sliding did not appear to be accommodated by plasticity within the grains as suggested by Crossman and Ashby [21]. Assuming sliding occurs by the climb and glide of extrinsic lattice dislocations in grain boundary zones, where the rate of sliding is governed by the rate of climb, the rate of sliding has been equated by Langdon [20]. The accommodating process is considered to be the opening of grain boundary cavities and cracks. Similar to other grain boundary sliding models [18,21], this model predicts the grain boundary sliding rate is inversely proportional to grain size. (This is to be expected considering that if dislocation motion near the grain boundary contributes to grain boundary shear and promotes sliding, the sliding rate will be a function of grain size in that the grain boundary area per unit volume increases as the grain diameter decreases.) A similar relationship is found in the experimental data. Overall, the minimum creep rates of the microstructures within the grain boundary sliding regime obey a  $\sigma^2/d$  relationship, where  $d$  is taken to be the average equiaxed grain size, independent of phase, for the solution-treated microstructures. The size of the very fine grains precipitating within the equiaxed B2 grains was not considered as most of the damage appeared to accumulate at the larger equiaxed grain boundaries. A plot of measured minimum creep rate versus  $\sigma^2/d$  is given in Figure 15 for all data within the grain boundary sliding regime. The data is well represented using a curve of constant slope. Other microstructural features, including phase volume, composition, and morphology, did not appear to have as significant an effect as grain size. Thus grain size appears to be the dominant microstructural feature in the low-to-intermediate stress regime governed by grain boundary sliding.

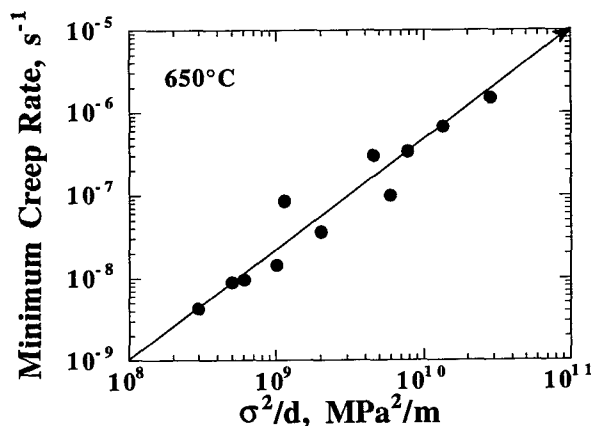


Figure 15: Minimum creep rate versus  $\sigma^2/d$  for the sub-transus solutionized plus aged microstructures. The 650°C/172-318 MPa data for the super-transus plus aged microstructures is also plotted.

Grain size may also be responsible for the change in creep behavior observed below 172 MPa for the super-transus microstructure. It has been suggested that for grain sizes smaller than 100  $\mu\text{m}$ , creep rates increase rapidly due to the importance of grain boundary sliding [25]. If smaller grain sizes promote higher strain rates and greater contributions from grain boundary sliding, the sub-transus microstructures would be expected to maintain a greater grain boundary sliding stress range. If grain boundary sliding is contributing less to the strain rates of the large-grained super-transus microstructures, a transition to another creep regime (in this case Coble creep) may occur at a higher stress level than for the sub-transus microstructures.

In addition grain size may explain the similar minimum creep rates for aged and unaged specimens. If a majority of the creep deformation is limited to grain boundary locations, transformations occurring at grain interiors would not be expected to have a significant



influence on the secondary stage. As concluded from the transformation study, the migrating front of the cellular precipitation continued to grow within the prior B2 grain, even after long aging times, while the platelets at grain boundary locations were relatively stable (see Figure 5). Thus the transformation occurring during the creep test for aged specimens is not likely to have significantly effected the creep behavior. However, for unaged specimens, cellular precipitation initiating at grain boundaries may increase measured strains due to grain boundary instability. This may explain the increase in primary-stage strains observed for unaged samples relative to long-term aged samples. A smaller effect on the secondary creep rates would be expected as the grain boundary locations, assumed to be controlling creep rates, stabilize with time.

This work suggests that the low stress, intermediate temperature creep behavior of Ti-23Al-27Nb is principally dictated by grain size. Sub-transus processing and heat treatment appear to degrade creep resistance due to the smaller resulting grain sizes compared to super-transus microstructures. However, super-transus microstructures have proved to be susceptible to grain boundary cracking in tension and show poor ductilities [4,6,7]. Thus a balance between grain size and ductility must be maintained through proper thermomechanical treatments which control grain size. Such treatments may be designed for desired structural applications.

### Summary

The phase evolution of O alloys plays an important role in terms of achievable microstructures. The temperature ranges for the  $\alpha_2$ +B2,  $\alpha_2$ +B2+O, B2+O, and O+ $\beta$  phase regions were estimated for Ti-23Al-27Nb sheet material, which was hot worked below the B2 transus. Orientation relations existed between sub-transus heat-treated equiaxed  $\alpha_2$ /B2 and O/B2 grains. Below 875°C, the B2 phase transformed into a mixture of O and bcc phases with lenticular morphologies. Aging studies showed that the kinetics of transformation for the  $\alpha_2$  phase is much more sluggish than for B2. At creep temperatures, the B2 phase undergoes a composition induced disordering and subsequently transforms both homogeneously and through cellular precipitation. The extent of cellular precipitation exhibited was related to the super-saturated nature of the B2 phase, which was determined by the solutionizing and aging temperatures. Higher solution-treatment temperatures and lower aging temperatures were more conducive to cellular precipitation. Overall, the cellular precipitation was sluggish and did not fully consume the prior B2 grains after over 600 hours at 650°C.

The phase evolution, including the aging-transformation behavior and elevated temperature grain growth, significantly influenced the creep response. Long term aging at 650°C resulted in lower primary creep strains compared to unaged microstructures. In terms of phase volumes and sizes, load did not appear to significantly affect the transformation behavior. For applied stresses greater than 318 MPa, dislocation climb is suggested to be the rate-controlling creep process. Microstructural evidence as well as the stress dependence suggest that grain boundary sliding is the dominant mechanism at lower stresses. In this regime, grain boundary cracks and displaced grains were characteristic of the deformation behavior and the minimum creep rates were proportional to  $\sigma^2/d$ . However, the large-grained super-transus microstructure did not follow this relationship at the lowest applied stresses and grain boundary sliding was thought to have contributed less. In such cases a behavior characteristic of Coble creep was observed and similar to the phase evolution behavior of this microstructure, grain boundary diffusion appeared to be the rate-controlling process. Overall, those microstructures solution treated to obtain greater initial grain sizes and then aged exhibited greater creep resistance. Thus the creep behavior of Ti-23Al-27Nb is quite sensitive to grain size, which appears to be more influential than phase volume fraction, composition, and morphology. This is important for the design of microstructures because processing and heat-treatment schedules can be tailored to control grain size which in turn dictates the creep behavior. Coarse-grained microstructures are recommended for creep-driven structural applications.

### Acknowledgments

This research was performed at the USAF Wright Laboratory Materials Directorate under Air Force contracts F33615-91-C-5663 and F33615-92-C-5900 to UES, Inc. We thank Drs M. Mendiratta and K.

Krishnamurthy for helpful discussions and Dr. A. Rosenberger, T. Brown J. Brown, M. Dodd, E. Fletcher, and J. Henry for technical assistance.

### References

1. T. K. Nandy, R. S. Mishra, and D. Banerjee, "Creep Behavior of an Orthorhombic Phase in a Ti-Al-Nb Alloy," *Scrip. Metall.*, 28 (1993), 569.
2. R.G. Rowe, "The Mechanical Properties of Titanium Aluminides Near Ti-25Al-25Nb," *Microstructure/Property Relationships in Titanium Aluminides and Alloys*, Y-W. Kim and R.R. Boyer, eds., (Warrendale, PA: TMS, 1991) 387-98.
3. F. Popille and J. Douin, "The Dislocation Microstructure in Orthorhombic O Ti<sub>2</sub>AlNb Deformed Between Room Temperature and 800°C," *Phil. Mag.*, 73 (1996) 1401-18.
4. C.J. Boehlert, B.S. Majumdar, and V. Seetharaman, "Processing and Heat Treatment Effects on the Phase Evolution, Tensile, and Creep Behavior of an Orthorhombic Ti-25Al-25Nb Alloy," *Deformation and Fracture of Ordered Intermetallic Materials*, W.O. Soboyejo, H.L. Fraser, and T.S. Srivatsan, eds., (Warrendale, PA: TMS, 1996) 565-82.
5. A.K. Gogia et al., "The Effect of Heat Treatment and Niobium Content on the Room Temperature Tensile Properties and Microstructure of Ti<sub>3</sub>Al-Nb Alloys," *Mater. Sci. and Engin.*, A159 (1992) 73-86.
6. B.S. Majumdar et al., "Structure-Property Relationships and Deformation Mechanisms in an Orthorhombic Based Ti-25Al-17Nb Alloy," *High Temperature Ordered Intermetallic Alloys-VI*, J. Horton et al., eds., (Pittsburgh, PA: MRS, 1995) vol. 364, 1259-65.
7. C.J. Boehlert et al., "Role of Matrix Microstructure on RT Tensile Properties and Fiber-Strength Utilization of an Orthorhombic Ti-alloy Based Composite," *Metall. Trans.*, 28A (1997) 309-23.
8. P.R. Smith, et al., "The Effect of a Post-Consolidation Heat Treatment on the Tensile and Creep Behavior of Neat Ti-22Al-23Nb," *Metal Matrix Composites* (Proc. Tenth International Conference on Composite Materials), A. Poursartip and K.N. Street, eds., 1995, vol. 2, pp. 731-38.
9. G. Rowe and M. Larsen, "The Effect of Microstructure and Composition on the Creep Behavior of O Phase Titanium Aluminide Alloys," *Titanium '95*, P.A. Blenkinsop, W.J. Evans, and H.M. Flower, eds., (Cambridge, UK: The University Press, 1996) vol. 1, 364-71.
10. H.T. Kestner-Weykamp et al., "Microstructures and Phase Relations in the Ti<sub>3</sub>Al + Nb System," *Scrip. Metall.*, 23 (1989) 1697-1702.
11. C.G. Rhodes, "Ti-Al-Nb Phase Equilibria Studies" (Advanced Ti-Based MMC Development Report, Rockwell Inter. Sci. Center, 1996).
12. L.A. Bendersky, W.J. Boettinger, and A. Roytburd, "Coherent Precipitates in the B.C.C./Orthorhombic Two-Phase Field of the Ti-Al-Nb System," *Acta Metall. Mater.*, 39, (1991), 1059-69.
13. R.W. Hayes, "Minimum Strain Rate and Primary Transient Creep Analysis of a Fine Structure Orthorhombic Titanium Aluminide," *Scrip. Metall.*, 34(6)(1996) 1005-12.
14. P.K. Sagar et al., "High Temperature Deformation Processing of Ti-24Al-20Nb," *Metall. Trans.*, 27A (1996) 2593-2604.
15. K. Muraliedharan et al., "Transformations in a Ti-24Al-15Nb Alloy: Part II. A Composition Invariant Bo-O Transformation," *Metall. Trans.*, 23A (1992) 417-31.
16. K.U. Tu, "The Cellular Reaction in Pb-Sn Alloys," *Metall. Trans.*, 3 (1972) 2769-76.
17. R.S. Mishra and D. Banerjee, "Transient Mechanisms in Diffusional Creep in a Titanium Aluminide," *Scrip. Metall.*, 31(11)(1994) 1555-60.
18. R.W. Evans and B. Wilshire, *Creep of Metals and Alloys*, ed. D. McLean (The Institute of Metals, 1985) 295-307.
19. T.K. Nandy et al., "The Effect of Aluminum on the Creep Behavior of Titanium Aluminide Alloys," *Scrip. Metall.*, 32(6)(1995) 851-6.
20. T.G. Langdon, "Grain Boundary Sliding as a Deformation Mechanism during Creep," *Phil. Mag.*, 22 (1970) 689-700.
21. F.W. Crossman and M.F. Ashby, "The Non-Uniform Flow of Polycrystals by Grain-Boundary Sliding Accommodated by Power-Law Creep," *Acta Metall.*, 23, (1975), 425-40.
22. C. Gandhi and R. Raj, "An Upper Bound on Strain Rate for Wedge Type Fracture in Ni During Creep," *Metall. Trans.*, 12A (1981) 515-20.
23. D.B. Miracle and C.G. Rhodes, unpublished research, 1997.
24. D.A. Porter and K.E. Easterling, *Phase Transformations in Metals and Alloys* (UK: Van Nostrand Reinhold Company Ltd, 1981) 322-30.
25. C.R. Barrett, J.L. Lytton, and O.D. Sherby, "Effect of Grain Size and Annealing Treatment on Steady-State Creep of Copper," *Trans. Metall. Soc. A.I.M.E.*, 239 (1967) 170-80.

## PLATINUM GROUP METALS-BASE REFRACTORY SUPERALLOYS FOR ULTRA-HIGH TEMPERATURE USE

Y. Yamabe-Mitarai, Y. Ro, T. Maruko\*, T. Yokokawa, and H. Harada

National Research Institute for Metals, 1-2-1 Sengen, Tsukuba, Ibaraki, 305, Japan

\*Furuya Metals Co. Ltd., 1915 Morizoeshima, Shimodate, Ibaraki, 308, Japan

### Abstract

The microstructure and compression strengths of Ir-X (X= Ti, Ta, Nb, Hf, Zr, or V) binary alloys and Rh-X (X= Ti, Ta, or Nb) at temperatures between room temperature and 1800 °C were investigated. The fcc and L1<sub>2</sub> two phase structures of these alloys were observed by transmission electron microscopy and scanning electron microscopy. The 0.2% flow stresses of the Rh-base alloys at 1500 °C and of the Ir alloys at 1800 °C were about 200 MPa, equivalent to those of the strongest W-base refractory alloys at these temperatures. We also found that the strengths of these alloys at temperatures at 1200 °C were far higher than those of the Ni-base superalloys. Lattice parameters of the fcc matrix and L1<sub>2</sub> precipitates in Ir-base and Rh-base alloys were measured up to 1200 °C using a high temperature X-ray diffractometer to understand lattice misfit dependence of the strength. The strength of these alloys increased with increasing the lattice misfit. The microstructure of the Ir-base alloys with large lattice misfit appeared to have a 3 dimensional maze structure. It was concluded that the 3 dimension maze structure prevent movement of dislocations. In Ir<sub>3</sub>Nb with the L1<sub>2</sub> single phase structure, strength was anomalous temperature dependent around 1200 °C.

### Introduction

An approach to develop new alloys, which can be used at higher temperature where Ni-base superalloys cannot be used, is being made with intermetallic compounds or refractory alloys, for example, NiAl-base alloys strengthened by coherent Ni<sub>3</sub>AlTi precipitates<sup>(1)</sup>, W-base HfC dispersion hardening alloys<sup>(2)</sup>, and Nb-base alloys precipitation hardened by Nb<sub>3</sub>Al<sup>(3)</sup>. However, problems remain with the poor room temperature ductilities of intermetallic compounds and the poor oxidation resistance of refractory alloys. As an alternative, platinum group metals are now being considered because of their high melting temperatures and superior oxidation resistance. The Ir-0.3%W alloy is used as the primary containment in space power systems or general purpose heat sources<sup>(4)</sup>. From the intermetallic compound's viewpoint, AlRu and RuSc with a B2 structure and IrNb and RuTa with an L1<sub>0</sub> structure<sup>(5)</sup> and Ir<sub>3</sub>Nb and Ir<sub>3</sub>Zr<sup>(6)</sup> with an L1<sub>2</sub> structure have been noted. However it is known that alloys with a single phase are less resistant to creep deformation at lower strain rate, e.g., <10<sup>-8</sup> sec<sup>-1</sup>, even though they show high strengths during tensile testing at higher strain rates, e.g., >10<sup>-4</sup> sec<sup>-1</sup>. For example, in Ni-base superalloys, the γ' single phase alloy with the L1<sub>2</sub> structure (ordered fcc structure) as

well as the γ single phase alloy with an fcc structure is less resistant to creep deformation compared with the γ/γ' two phase alloys<sup>(7)</sup>, because the precipitates with the L1<sub>2</sub> structure are formed in the fcc matrix with coherent interfaces and these coherent interfaces prevent movement of the dislocation and coarsening of the precipitates<sup>(8)</sup>.

We have proposed "refractory superalloys"<sup>(9-11)</sup> with the fcc and L1<sub>2</sub> two phase coherent structure using platinum group metals as ultra high temperature materials which are highly resistant to creep deformation. The melting temperatures of Ir and Rh (2447 and 1963, respectively) are higher than that of Ni (1455 °C<sup>(12)</sup>) and Ir and Rh were selected as base materials from among platinum group metals. In the Ir-Nb system, the fcc structure equilibrates with the L1<sub>2</sub> structure according to binary phase diagrams<sup>(12)</sup> (Fig. 1). We concluded that the Ir-base and Rh-base alloys have good potentials as materials for use at ultra-high temperatures which Ni-base superalloys can not reach. However strengthening mechanisms for the Ir-base and Rh-base alloys were not investigated in our previous studies.

In the present paper, we investigated effects of the lattice misfit on the microstructure and mechanical properties of the Ir-base and Rh-base alloys. The obtained result that the strength increased with increasing positive lattice misfit (the lattice parameter of the precipitates is larger than that of the matrix) in the Ir-base alloys was discussed in comparison with the case of single crystal Ni-base superalloys; the negative lattice misfit around -0.25 % (the lattice parameter of the precipitates is smaller than that of the matrix) was reported to improve the creep rupture life<sup>(13,14)</sup>. The mechanism of strengthening of the Ir-base and Rh-base alloys are discussed.

### Experimental Procedures

#### Material preparation

All the Ir and Rh binary alloys were prepared as 70 g button ingots by arc-melting in an argon atmosphere. V, Ti, Nb, Ta, Hf, or Zr were selected as alloying elements of the Ir and Rh binary alloys (nominal compositions and expected phases summarized in Table I). The Ir-17at% Ti, Ir-18at% Ta, Ir-17at% Nb, and Ir-12at% Zr alloys were prepared, since these are expected to have 50% volume fraction of the phase with the L1<sub>2</sub> structure at 1200 °C, according to the phase diagrams<sup>(12)</sup>. At Nb contents up to 10at%, the fcc single phase exists in the Ir-Nb alloys. The Ir-25at% Nb alloys have the L1<sub>2</sub> single phase.

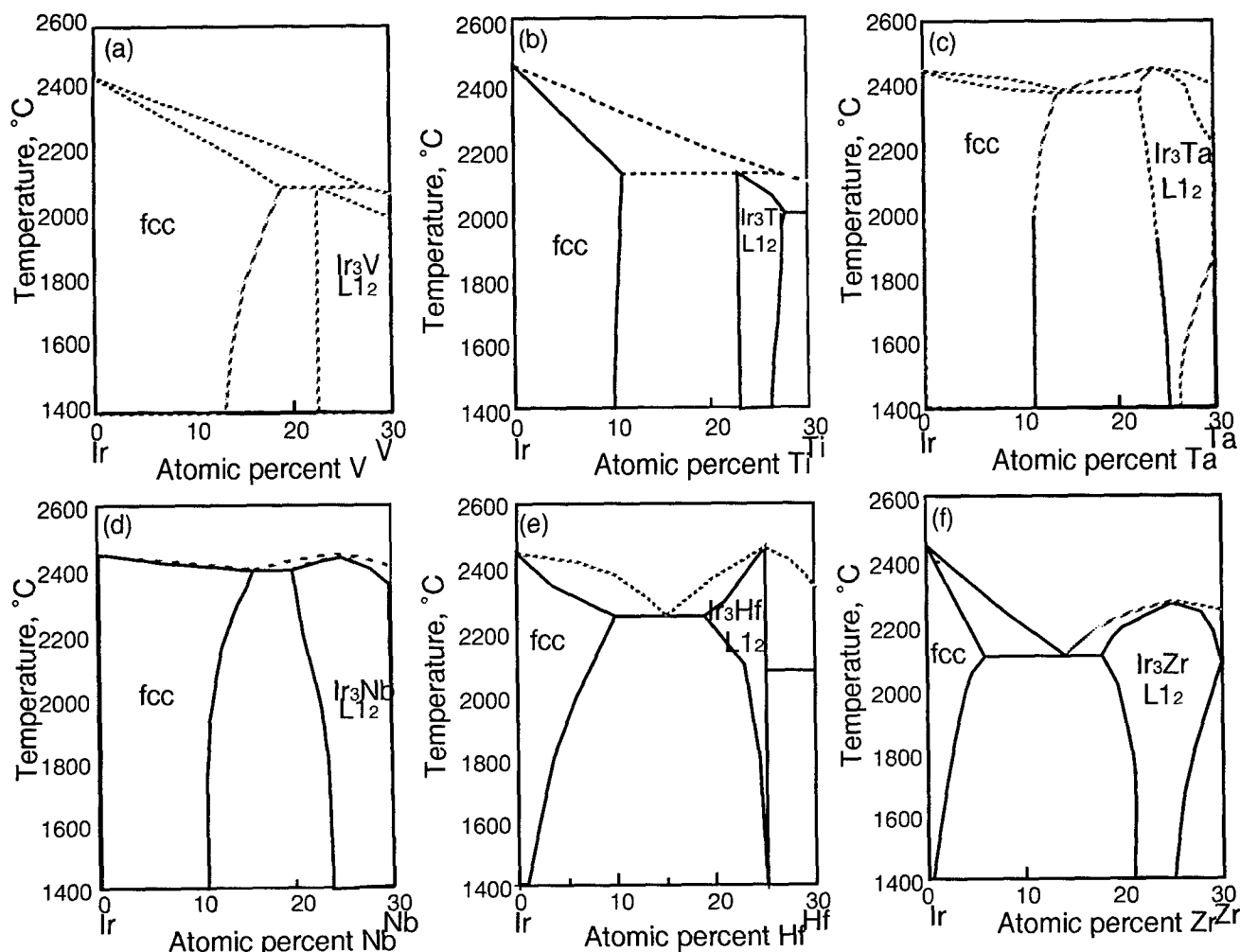


Fig. 1 The phase diagram for the Ir-: (a)V, (b)Ti, (c)Ta, (d)Nb, (e)Hf, and (f) Zr system<sup>(12)</sup>.

The pure Ir sample was cast by swaging, followed by annealing at 1200 °C for 1 hour.

#### Microstructural observation

To understand the microstructure of these binary alloys, cylindrical samples of 3 mm diameter were cut from the binary alloy ingots and heated at 1200 and 1500 °C for up to 1 week in an argon atmosphere. The heating at 1200 °C was carried out with these samples encapsulated in quartz tubes filled with argon gas, followed by water quenching. For the heat treatments at 1500 °C, the whole sequence of heating and cooling was carried out within a vacuum furnace. The microstructures of the as cast and heat treated samples were observed using a scanning electron microscope (SEM) after electrolytically etching in a ethyl alcohol solution of 5% HCl. Thin discs were cut from the as cast and heat treated samples and ion-milled for observation using a transmission electron microscope (TEM). All images were taken in the beam direction of [001]. All dark field images were taken with superlattice reflections ( $g=110$ ) from the  $L1_2$  phase.

#### Measurement of lattice parameters with a high temperature X-ray diffractometer

A high temperature diffractometer was used to determine the lattice parameters of the fcc and  $L1_2$  phases for the Ir-15at% X alloys ( $X = V, Ti, Nb, Ta, Hf$ , or  $Zr$ ) and Rh-15at% X alloys ( $X = Ti, Nb$ , and  $Ta$ ). The sample holder and a circumferential type platinum heater are located in the middle of a vacuum chamber with beryllium windows. The samples of the Ir-base alloys were heated at 1200 °C for 1 hour to

form precipitates. The heating was performed in quartz tubes filled with argon gas, followed by water quenching. These samples were powdered with a hammer. The intensities of the (220) fundamental peaks of the precipitates and the matrix were measured at room temperature, 800, 1000, 1100, and 1200 °C and analyzed by the Pearson-VII profile fitting method<sup>(15)</sup>.

Table I Phase composition of tested alloys.

Alloy composition	Phase
Ir-15at% V	fcc, $L1_2$
Ir-15at% Ti	fcc, $L1_2$
Ir-17at% Ti	fcc, $L1_2$
Ir-2at% Nb	fcc
Ir-5at% Nb	fcc
Ir-10at% Nb	fcc
Ir-15at% Nb	fcc, $L1_2$
Ir-17at% Nb	fcc, $L1_2$
Ir-20at% Nb	fcc, $L1_2$
Ir-25at% Nb	$L1_2$
Ir-15at% Ta	fcc, $L1_2$
Ir-18at% Ta	fcc, $L1_2$
Ir-15at% Hf	fcc, $L1_2$
Ir-12at% Zr	fcc, $L1_2$
Ir-15at% Zr	fcc, $L1_2$
Rh-15at% Ti	fcc, $L1_2$
Rh-15at% Ta	fcc, $L1_2$
Rh-15at% Nb	fcc, $L1_2$

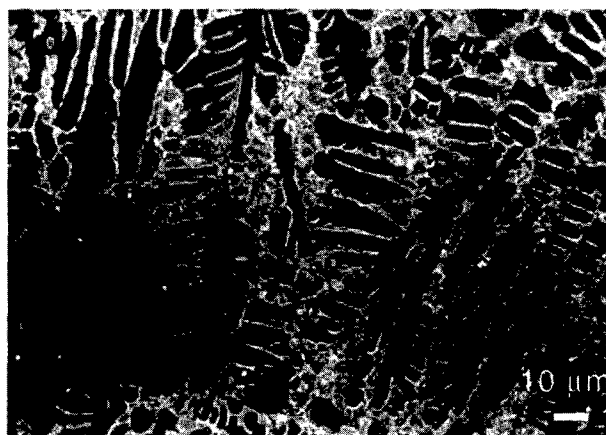
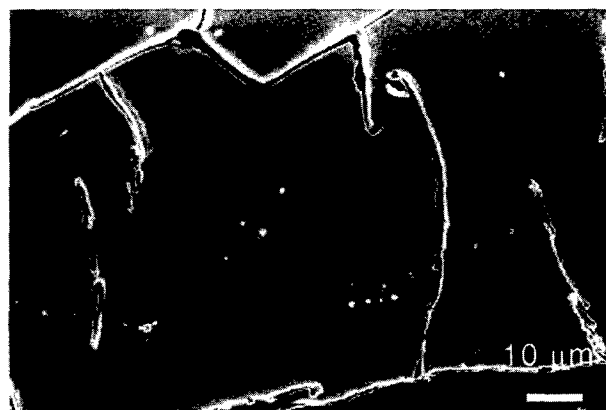
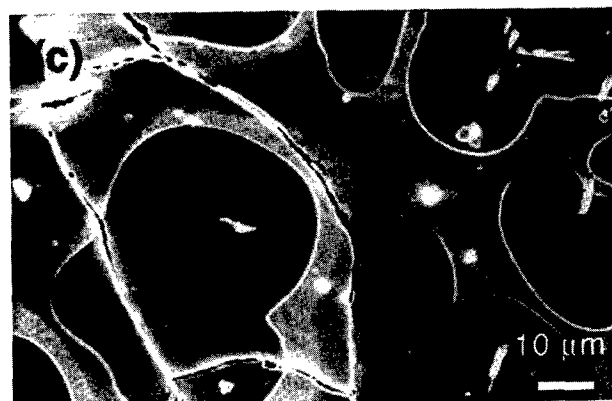
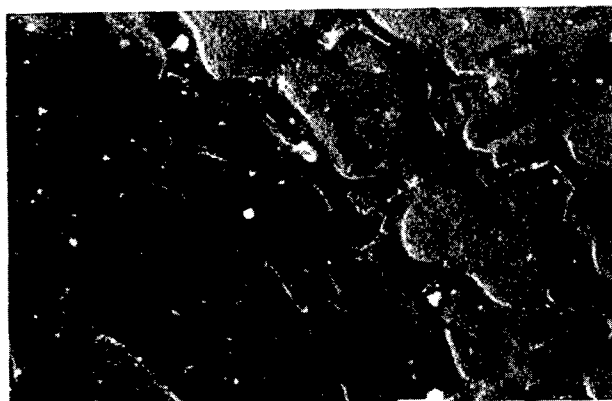


Fig. 2 Secondary electron images of as cast Ir-: (a)15at% Ti, (b)17at% Nb, (c)18at% Ta, (d)15at% Hf, and (e)15at% Zr alloys.

were observed in the interstices between dendrite arms instead of in dendrite arms in the Ir-18at% Ta alloy (see Fig. 2(c)). It is considered that these structures in as cast samples in the Ir-Ti and Ir-Ta alloys are the fcc and  $L1_2$  two phase structures according to their phase diagrams. Precipitates were not observed in the Ir-17at% Nb, Ir-15at% Hf, and Ir-15at% Zr alloys (see Figs. 2(b), (d), and (e)). A lamellar structure, rather than precipitates, was observed in the interstices between dendrite arms in the Ir-15at% Zr (Fig. 3(b)). Although the lamellar structure was not observed clearly in the Ir-15at% Hf alloy, some kind of contrast was observed in interstices between dendrite arms (Fig. 3 (a)). Cracks induced by mechanical polishing existed in the Ir-18at% Ta and Ir-17at% Nb alloys.

The samples of the Ir-15at% Nb and -15at% Zr alloys heat treated at 1200 °C for 1 hour were observed by TEM because it is difficult to prepare thin discs of brittle as cast samples. Precipitates with the  $L1_2$  structure were observed in these alloys showing that the Ir-Nb and -Zr alloys have the fcc and  $L1_2$  two phase structure. The shapes of the (220) X-ray diffractometer peaks of the Ir-Hf and Ir-V alloys showed that the fcc and  $L1_2$  two phase structure exists in these alloys after heat treatment at 1200 °C for 1 hour, although the as cast Ir-Hf and Ir-V alloys were not studied.

The Ir-15at% Nb, Ta, Hf, Zr, and V alloys were studied with TEM (Fig. 4) to observe precipitate shape after heat treatment at 1200 °C for 1 week. The phases with bright contrast were  $Ir_3Nb$ ,  $Ir_3Zr$ , and  $Ir_3V$  with the  $L1_2$  structure (see Figs. 4 (a), (d), and (e) respectively). Bright field images of the Ir-Ta and Ir-Hf alloys were taken (see Figs. 4(b) and (c)), since it is difficult to detect superlattice reflections from the  $L1_2$  structures of these alloys due to the closer atomic scattering factors of Ir, Ta, and Hf resulting in very small structure factors of the superlattices in the  $L1_2$  structures. Cuboidal precipitates between 100 and 200 nm in size were observed in the Ir-Nb and Ir-Ta alloys (see Figs. 4(a) and (b)). The cuboidal precipitates in the Ir-Nb alloy were surrounded by finer precipitates about 20 nm in size. Since finer precipitates were also observed in Ni-base superalloys during cooling, we conclude that the fine precipitates were formed in the matrix during cooling. Plate-like precipitates were formed in the Ir-Hf and Ir-Zr

#### Compression test

Cylindrical samples, 4 mm in diameter and 8 mm in height, were cut from each binary alloy ingot and 4 mm diameter swaged bar of pure Ir for compression testing. The compression test was carried out in air for tests at room temperature and 1200 °C and in an argon atmosphere for tests at 1500 and 1800 °C. In the tests at 1200, 1500, and 1800 °C, the samples were kept at the test temperature for 15 mins before loading. The initial compressive strain rate for every compression test was  $3.0 \times 10^{-4}/s$ .

#### Results

##### Microstructure

As cast samples of the Ir-base alloys with second elements contents between 15 and 18at% were observed by SEM (Fig. 2). A dendritic structure was observed within grains except for the Ir-15at% V alloy, although the microstructure of that alloy is not shown in Fig. 2. The microstructure of the Ir-15at% V alloy appeared to have a single phase with smooth grain boundaries. Fine precipitates were observed in the dendrite arms in the Ir-15at% Ti alloy (see Fig. 2(a)). Fine precipitates

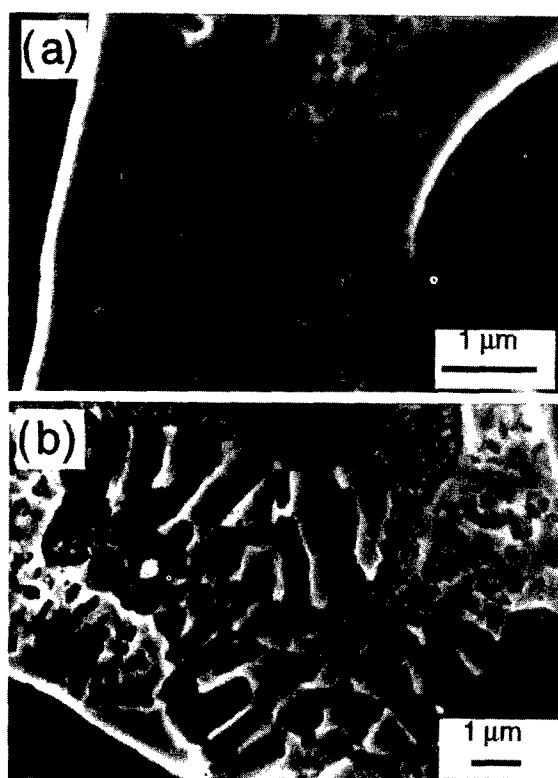


Fig. 3 Secondary electron images of as cast Ir-15at%: (a) Hf and (b) Zr alloys.

alloys (see Fig. 4(c) and (d)), although which phase has the  $L1_2$  structure in the Ir-Hf alloy is not clear. The habit planes in these Ir-base alloys were close to  $\{100\}$  planes independent of precipitate shape. In the Ir-V alloy, irregularly shaped precipitates, 10 nm in size, were observed (see Fig. 4(e)).

A dendritic structure with a small amount of interstice between the dendrite arms was observed in the Rh-15at% Ti, Nb, and Ta alloys in the as cast states and even after heat treatment at 1200 or 1500 °C. The  $L1_2$  precipitates expected to form within the dendrite were not clearly visible in the as cast and 1200 °C heat treated samples. During heat treatment at 1500 °C, precipitates grew large enough to be observed with SEM. In the Rh-Nb and Rh-Ta alloys, we observed well aligned precipitates, about 200 nm in size. The shape of the precipitate in the Rh-Ti alloy was not clear. From the above observations, the fcc and  $L1_2$  two phase structure was confirmed in the Ir-base and Rh-base alloys.

#### Determination of lattice parameters using a high temperature X-ray diffractometer

Lattice parameters of the fcc matrix and the  $L1_2$  precipitates of the Ir-base and Rh-base alloys increased with increasing temperature (Fig. 5). The rates of increase of the lattice parameters of the fcc matrix and the  $L1_2$  precipitates with temperature are equivalent among the Ir-base and Rh-base alloys. The lattice parameters of the fcc matrix in the Ir-V, -Hf, and -Zr alloys were smaller than that of pure Ir<sup>(16)</sup> (see Fig. 5(a)). The lattice parameters of the fcc matrix of other Ir-base and Rh-base alloys were larger than that of pure Ir. The lattice parameters we determined for the  $L1_2$  precipitates, Ir<sub>3</sub>V, Ir<sub>3</sub>Ti, and Rh<sub>3</sub>Ti, were larger than those determined by Dwight et al.<sup>(16)</sup>, the latter being shown as open symbols in Figs. 5(b) and (c). On the other hand, the lattice parameters we determined for Ir<sub>3</sub>Nb, Ir<sub>3</sub>Ta, Ir<sub>3</sub>Hf, Ir<sub>3</sub>Zr, Rh<sub>3</sub>Nb, and Rh<sub>3</sub>Ta were smaller than those determined by Dwight et al.<sup>(16)</sup> (see Figs. 5(b) and (c)).

The lattice misfits between the fcc matrix and the  $L1_2$  precipitates were estimated using the following equation:

$$\Delta a = \frac{a_{\text{precipitate}} - a_{\text{matrix}}}{a_{\text{matrix}}}$$

The lattice misfits of the Ir-base and Rh-base alloys were plotted in Fig. 6 together with the lattice misfits calculated using reference lattice parameters<sup>(16)</sup> at room temperature. The lattice parameter of the  $L1_2$  precipitates was smaller than that of the fcc matrix in the Ir-V alloy and the lattice misfit of this alloy was negative. All lattice misfits determined by high temperature X-ray diffractometry analysis were smaller than those estimated using reference lattice parameters<sup>(16)</sup>. The lattice misfits did not change with increasing temperature, although they decreased slightly at 1200 °C in the Ir-base alloys and varied widely in the Rh-base alloys.

#### Mechanical properties

The temperature dependence of the 0.2% flow stress in the Ir-15at% X (X= V, Ti, Nb, Ta, Hf, or Zr) alloys and Rh-15at% X (X= Ti, Nb, or Ta) alloys was investigated during compression testing at temperatures up to 1800 °C (Fig. 7). The 0.2% flow stresses of a Ni-Al-Cr alloy with 40%  $L1_2$  phase<sup>(17)</sup> (a base for development of Ni-base superalloys), a commercially available Ni-base superalloy, MarM247 (Ni-10Co-10W-8.5Cr-5.5Al-0.7Mo-3Ta-1.4Hf wt%)<sup>(2)</sup>, and the tensile yield stresses of a third generation single crystal Ni-base superalloy, CMSX-10 (Ni-2Cr-3Co-0.4Mo-5W-8Ta-6Re-0.1Nb-5.7Al-0.2Ti-0.03Hf wt%)<sup>(18)</sup> and of a W-base HfC dispersion hardening alloy (W-0.35wt%Hf-0.025wt%C)<sup>(2)</sup> are also plotted for reference. The strengths of Ni-base superalloys decreased drastically with increasing temperature above 800 °C. Although the strengths of the Ir-Nb, Ir-Ta, Ir-Hf, and Ir-Zr alloys also decreased with increasing test temperature, they were equivalent to or far higher than the strengths of MarM247 and CMSX-10 at room temperature and 1200 °C. The 0.2% flow stress of these 4 Ir-base alloys were above 800 MPa even at 1200 °C and much higher than that of MarM247 (50 MPa) at that temperature. At 1800 °C, the strengths of the 4 Ir-base alloys were about 200 MPa and they are equivalent to the strength of the W-HfC alloy (197 MPa), which had been the strongest known metallic material available at this temperature. The strengths of the Ir-Ti and Ir-V alloys were low at all testing temperatures. Note that among the Ir-base alloys tested here, only the Ir-V alloy has an fcc single phase at 1800 °C according to the phase diagram<sup>(12)</sup>. The strengths of the Rh-Ti, -Ta, and -Nb alloys were half of those of the Ir-Ti, -Ta, and -Nb alloys, respectively at any testing temperature (see Fig. 7). Despite the lower strength of the Rh-base alloys than those of the Ir-base alloys, the strengths of the Rh-Ta and Rh-Nb alloys were equivalent to those of Ni-base superalloys at temperatures under 800 °C. The strengths of the Rh-Nb and Rh-Ta alloys were 400 MPa at 1200 °C and 200 MPa at 1500 °C, equivalent to that of the W-base alloy.

The 0.2% flow stresses of the Ir-17at% Ti, Ir-18at% Ta, Ir-17at% Nb, and Ir-12at% Zr alloys with 50% volume fraction of precipitates were investigated by compression testing at 1200 °C (Fig. 8) as a function of lattice misfit determined by high temperature X-ray diffractometer. The strength of these Ir-base alloys increased with increasing lattice misfit. The volume fraction of the precipitates in the Rh-15at% Ti, -Ta, and -Nb alloys, as estimated from the phase diagrams<sup>(12)</sup> were 30.7, 37.5, and 25%, respectively. The strengths of the Rh-15at% Ta and -15at% Nb alloys with large lattice misfits are higher than that of the Rh-15at% Ti alloys with small lattice misfit at any testing temperature although we must consider the effect of volume fraction of precipitates.

We evaluated the temperature dependence of 0.2% flow stress in Ir-Nb alloys with Nb contents between 0 and 25at% (Fig. 9). The strength decreased with increasing temperature for all Ir-Nb alloys except for the Ir-25at% Nb alloy, which is Ir<sub>3</sub>Nb with the  $L1_2$  single phase. The strength of the Ir-25at% Nb alloy at 1200 °C was stronger than that at room temperature. The strength of the alloys increased with increasing Nb concentration up to 15at% at all tested temperatures. Over 15at% Nb, the strength decreased with increasing Nb concentration. For the Rh-base alloys, we investigated the Ta concentration dependence of strength. The strengths of the samples with the fcc and  $L1_2$  two phase structure were higher than those of the samples with the fcc single phase and the  $L1_2$  single phase.

#### Discussion

##### Microstructure of as cast samples

The difference between microstructures of as cast samples can be explained from phase diagrams<sup>(12)</sup>. A peritectic reaction occurs in the Ir-V and Ir-Ti alloys at up to 30at% alloying elements contents (see Figs. 1(a) and (b)). The microstructure appeared to have a single phase with smooth grain boundaries in the Ir-15at% V alloy, since a sample

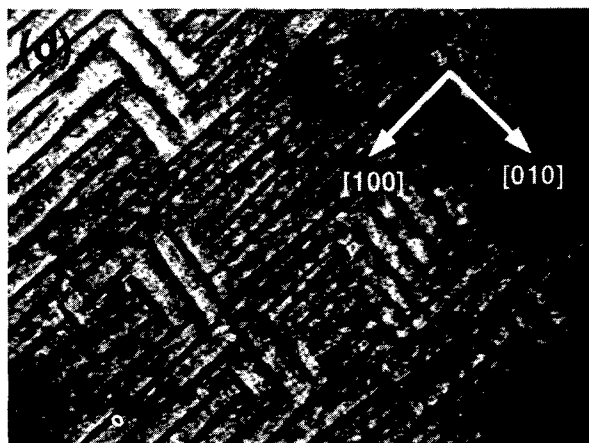
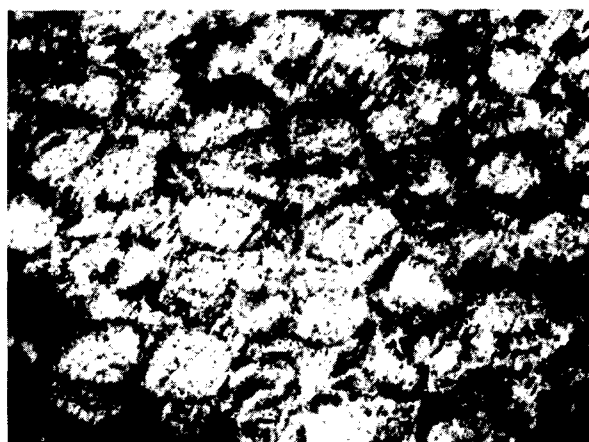
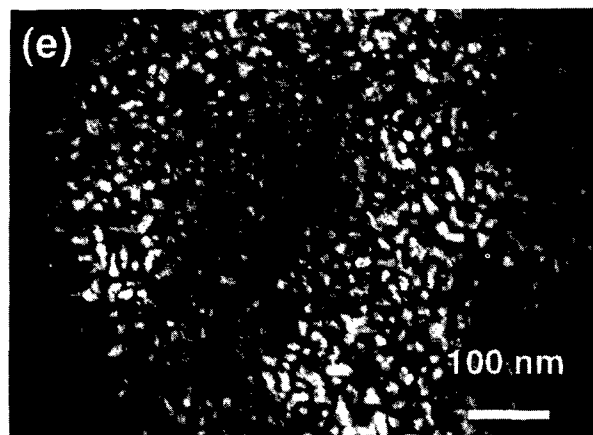
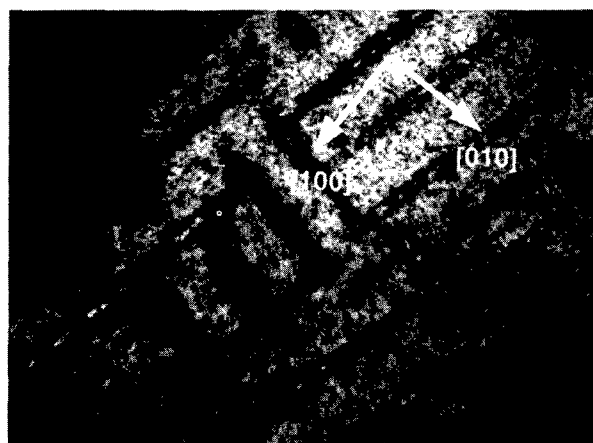
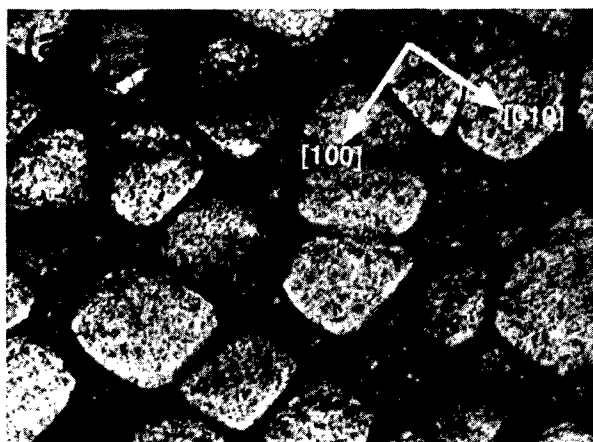


Fig. 4 Bright field images of (b) Ir-15at% Ta and (c) Ir-15at% Hf alloys. Dark field images of (a) Ir-15at% Nb, (d) Ir-15at% Zr, and (e) Ir-15at% V alloys taken from superlattice reflection ( $g=110$ ) from the  $L1_2$  phase. These Ir-base alloys were heat treated at 1200 °C for 1 week and observed in the beam direction of [001].

passed through the fcc single phase during solidification. Thus, the single phase with smooth grain boundaries has the fcc structure. A primary crystal of the Ir-15at% Ti alloy has the fcc structure according to the phase diagram<sup>(12)</sup> and primary crystal, dendrite, is surrounded by the  $L1_2$  phase at the peritectic temperature. During further cooling,  $L1_2$  precipitates form in the fcc dendrite. A eutectic reaction occurs in the Ir-18at% Ta, Ir-17at% Nb, Ir-15at% Hf, and Ir-15at% Zr alloys (see Figs. 1(c)–(e)). The primary crystal, dendrite, of the Ir-18at% Ta alloy has the  $L1_2$  structure, since the concentration is hyper-eutectic concentration. The  $L1_2$  precipitates form in the interstices between the dendrite arms with the fcc structure during further cooling. The 17at% Nb and 15at% Hf alloys are at close to the eutectic concentrations. Despite the 17at% Nb being at close to the eutectic concentration, the microstructure of the Ir-17at% Nb alloy appeared to have a single

phase structure. The sample must have passed through the fcc single phase during cooling since the solubility limit concentration of the fcc phase and the eutectic concentration differ by only about 0.5at%. The lamellar structure formed by the eutectic reaction can not be observed in the Ir-Hf alloy despite the concentration being close to the eutectic concentration. Instead of a lamellar structure, a primary crystal was observed because of concentration deviation of the alloy. The lamellar structure can not be observed even in interstices between the dendrite arms, where a lamellar structure can form at the eutectic temperature. Rapid quenching may prevent the eutectic reaction. The primary crystal of the Ir-15at% Zr alloy has the  $L1_2$  structure since 15at% Zr is the hyper-eutectic concentration. The lamellar structure was formed by the eutectic reaction in the interstices between the dendrite arms. Thus the Ir-15at% Zr alloy developed a typical eutectic microstructure.

#### Microstructure after heat treatment

The dendritic structure formed in as cast sample remained even after heat treatment at 1200 °C for 1 week. However precipitates were clearly formed in all Ir-base and Rh-base alloys after the heat treatment. The shape of these precipitates depends on the lattice misfit between the precipitates and the matrix in the Ir-base alloys. The photographs in Fig. 4 are aligned in order of increasing lattice misfit, that is: 0.33, 0.4, 1.89, and 2.19% for the Ir-Nb, -Ta, -Hf, and -Zr alloys, respectively, as determined by high temperature X-ray diffractometry analysis. Plate-like precipitates formed in the Ir-Hf and Ir-Zr alloys with large lattice misfits around 2%. Cuboidal precipitates were observed in the Ir-Nb and Ir-Ta alloys with lattice misfits between 0.3 and 0.4%. In Ni-base superalloys, cuboidal precipitates are often observed since the lattice misfit is less than 1%. Thompson et al.<sup>(19)</sup> showed, by calculation of the interfacial energy and the elastic energy which is related to lattice misfits, that the shape of precipitates

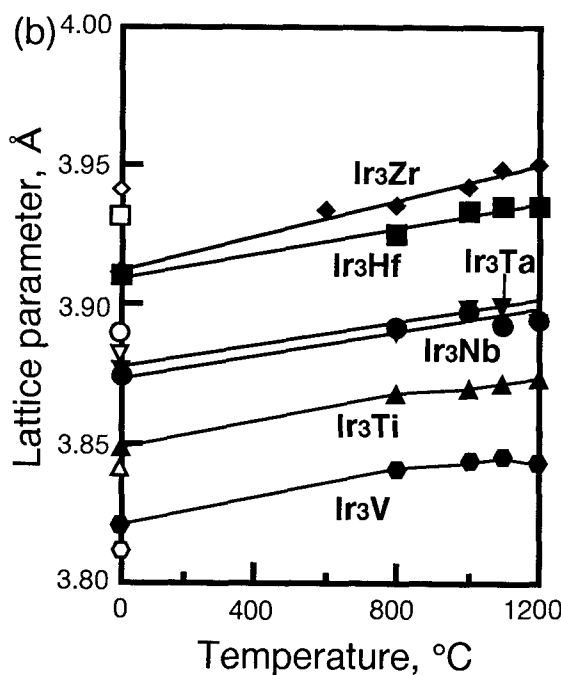
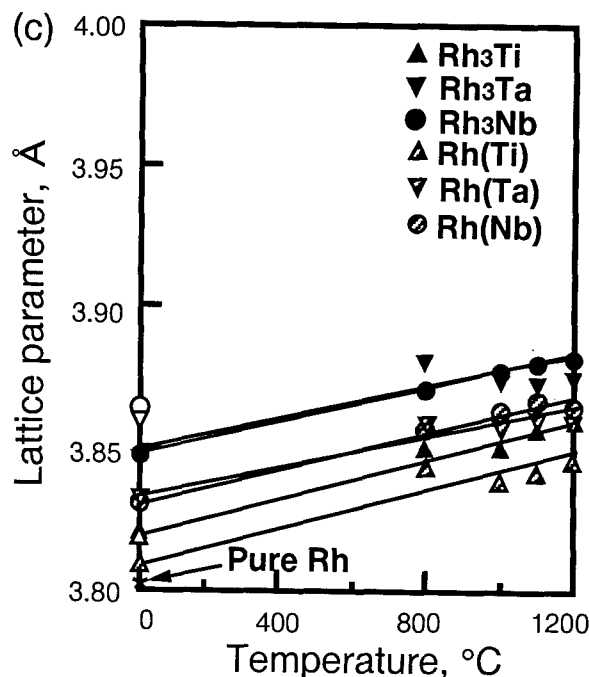
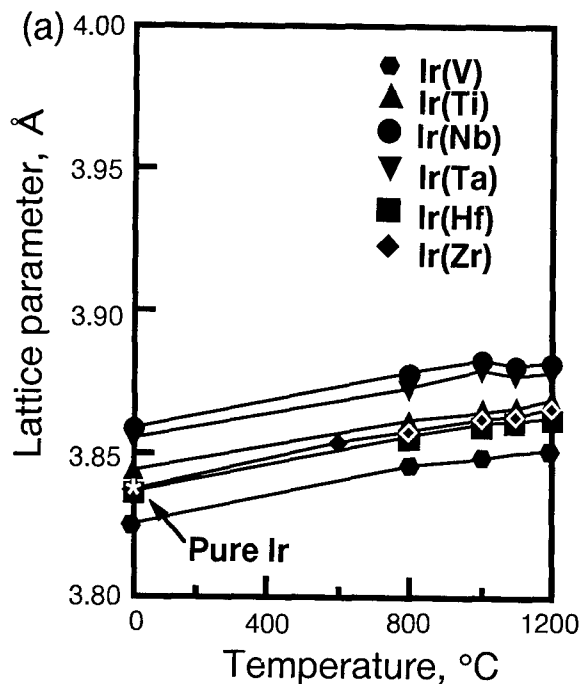


Fig. 5 Temperature dependence of the lattice parameters of (a) the fcc matrix and (b) the  $L_{12}$  precipitates in the Ir-base alloy and (c) the lattice parameters of both phases in the Rh-base alloys. Open symbols show the lattice parameters of the  $L_{12}$  precipitates estimated by Dwight<sup>(16)</sup>. Asterisks show the lattice parameters of pure Ir and Rh<sup>(16)</sup>.

large on the coherent interface between the matrix and precipitates, the strain energy on the interface becomes very high. Thus the precipitates coarsen discontinuously in order to reduce strain energy in Ni-base superalloys with large lattice misfits. In the Ir-base alloys, the lamellar structure at grain boundaries was observed in only the Ir-Hf and Ir-Zr alloys with large lattice misfits. We attribute the formation of the lamellar structures to discontinuous coarsening, as occurs in Ni-base superalloys.

#### Precipitate coherency

The most important aspect of the microstructure in the Ir-base alloys is the coherency of the interface between the matrix and precipitates since coherent interfaces strengthen by preventing the movement of dislocations. If the interface is semicoherent, misfit dislocations which reduce energy raised by strain on the interface can be observed on the interface. No dislocations were observed in any of the Ir alloys we studied. Our observations indicate that the interface is either perfectly coherent or incoherent. We conclude that the interface is coherent, since the precipitates were surrounded by {100} planes, like Ni-base superalloys in which the cuboidal precipitates are formed with coherent interfaces, {100} planes. When the precipitates are incoherent with the matrix, the lattice misfit has no significance. In this case, the shape of the precipitates depends on volume misfit, since the elastic strain energy is proportional to the square of the volume misfit<sup>(21)</sup>. Therefore the equilibrium shape of incoherent precipitates will be an oblate spheroid which balances the interfacial energy and the strain energy. In the Ir-base alloys, the habit planes were not correctly {100} planes. If the elasticity is anisotropic, then the habit plane may deviate from a {100} plane. Note that the precipitates in the Ir-V alloy have the coherent interface with a very small lattice misfit, because of their irregular shapes.

#### Lattice parameters of the fcc matrix and the $L_{12}$ precipitates

The atomic radius and solubility of alloying elements in pure Ir and pure Rh affect the lattice parameters of a solid solution with the fcc structure in the Ir and Rh binary alloys. The atomic radius and solubility of alloying elements at 1200 °C are summarized together with the lattice parameters of the fcc matrix and the  $L_{12}$  precipitates in Tables II and III. The atomic radii of Ti, Ta and Nb are larger than that of Ir

changes from 4-fold symmetric to 2-fold symmetric in 2 dimensions to reduce total energy when the precipitates grow large. It seems reasonable to suppose that when precipitates have large lattice misfits, then the precipitate shape becomes plate-like to reduce the strain energy of the interface according to the prediction from Thompson's results. The reason why the precipitate shape of the Ir-V alloy was irregular is probably due to the small lattice misfit around -0.2%. The precipitates formed in the Rh-Nb alloy were cubic as revealed by TEM observation. Although TEM observation was not performed for the Rh-Ti and Rh-Ta alloys, it is considered that the precipitates shapes of these Rh base alloys is also cubic because of their similar lattice misfits between 0.3 and 0.4.

In the Ir-Hf and Ir-Zr alloys with large lattice misfits, not only plate-like precipitates but also lamellar structures at grain boundaries were observed. It is known that discontinuous coarsening occurs in the Ni-base superalloys with large lattice misfits<sup>(20)</sup>. When the lattice misfit is

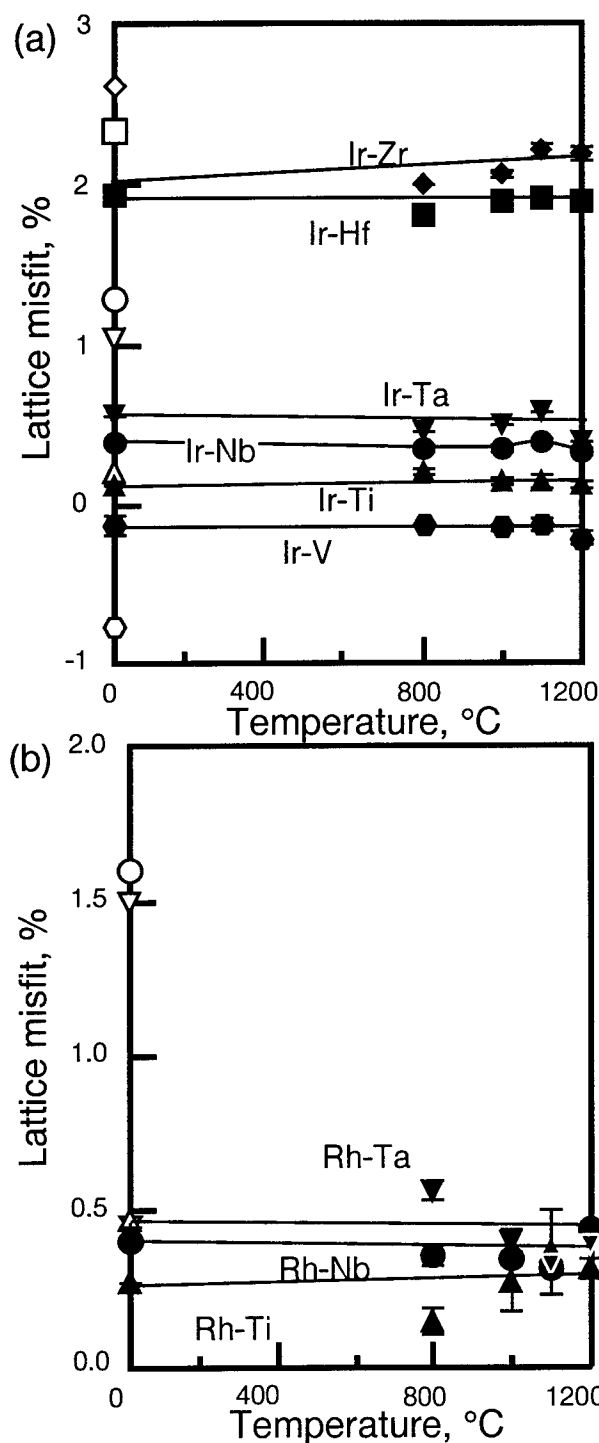


Fig. 6 Temperature dependence of lattice misfit of (a) the Ir-base and (b) Rh-base alloys. Open symbols show the lattice misfit estimated using the reference lattice parameters<sup>(16)</sup>.

(Table II). Thus the lattice parameters of the solid solution with Ti, Nb, or Ta are larger than that of the pure Ir. On the other hand, the lattice parameter of the solid solution with V is smaller than that of the pure Ir since the atomic radius of V is smaller than that of Ir. Similar to the case with Ir, the atomic radii of Ti, Nb, and Ta are larger than that of Rh. Thus the lattice parameters of the solid solutions with Ti, Nb, or Ta are larger than that of the pure Rh. In addition, the solubility limit which is different in each alloy system, affects the amount of change in the lattice parameters. The solubilities of Hf and Zr in Ir are about 2at%. The solubilities of the other alloying elements in both Ir and Rh are over 10at%. To compare the solubility effects of each alloying element,

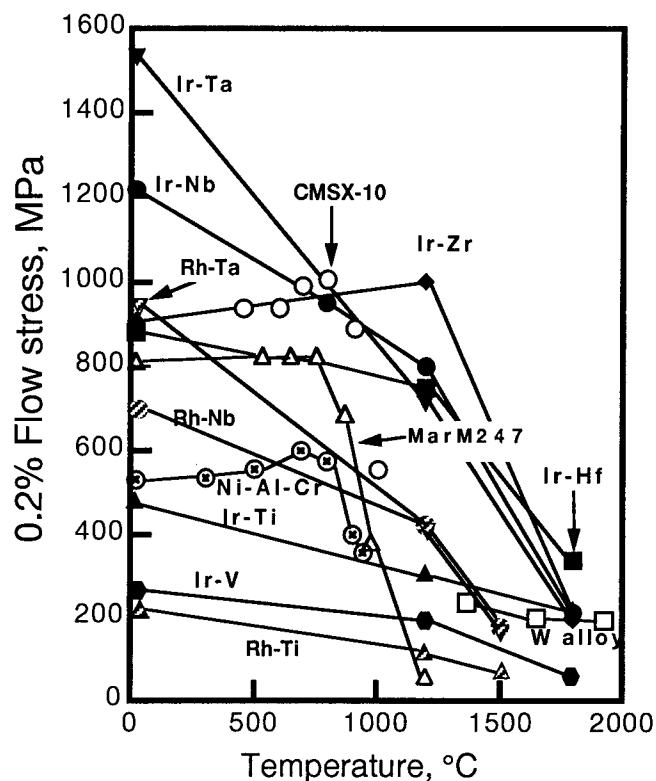


Fig. 7 Temperature dependence of the 0.2% flow stress during compression testing in as cast Ir-base and Rh-base alloys with 15at% second elements, Ni-base, and W-base alloys.

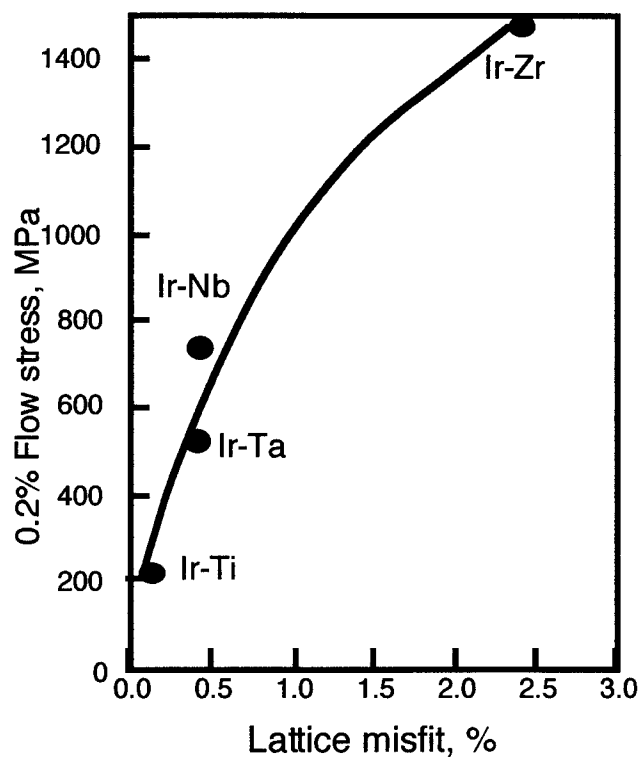


Fig. 8 Lattice misfit dependence of 0.2% flow stress during compression testing in the as cast Ir-base alloys with 50% precipitates in volume fraction.



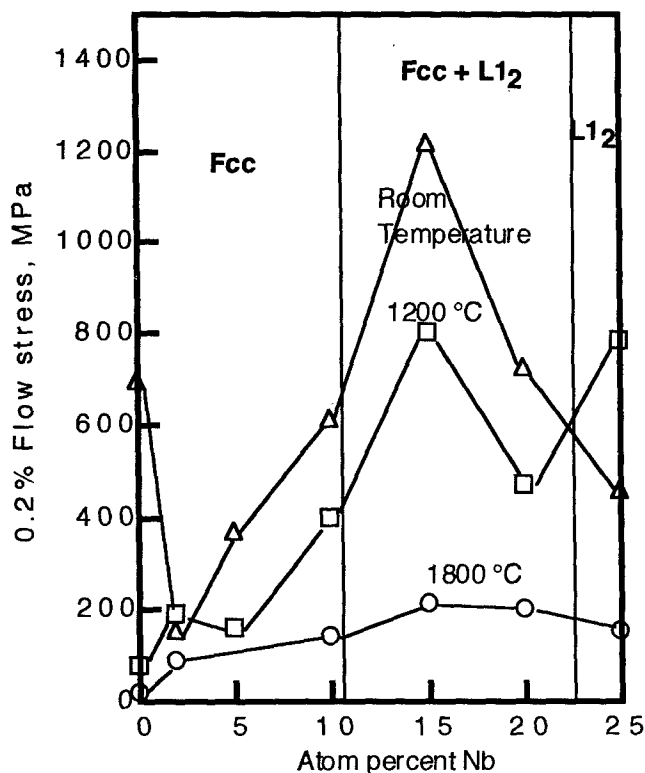


Fig. 9 Nb concentration dependence of 0.2% flow stress in as cast Ir-Nb alloys.

we calculated lattice parameter change per 1% solubility.  $\Delta d$  was defined as

$$\Delta d = \frac{a_s - a_{\text{pure}}}{S}$$

where  $a_s$  is the lattice parameter of the solid solution,  $a_{\text{pure}}$  is the lattice parameter of pure Ir or pure Rh, and  $S$  is the solubility estimated from the phase diagram for 1200 °C. The solubility effects are summarized in Tables II and III. The solubility effect of Nb was the greatest among Ti, Nb, and Ta which increased the lattice parameters of the solid solutions, showing that Nb is the most effective element to increase the lattice parameter of the solid solution. Despite the atomic radii of Ti, Ta, and Nb being almost the same, their solubility effects were different. Hf was the most effective element to decrease the lattice parameter among V, Hf, and Zr. Furthermore, despite the atomic radii of Hf and Zr being larger than those of Ti, Ta, and Nb, the lattice parameters of the solid solutions with the former elements were smaller than that of the pure Ir. The reason is not clear yet. For the Rh-base alloys, all alloying elements increase the lattice parameters of the solid solutions. Despite an atomic radius and solubility limit similar to those of the other tested elements, Ti was less effective at increasing the lattice parameter.

The differences between the lattice parameter of the  $L_{12}$  precipitates we determined and those determined by Dwight<sup>(16)</sup> arose because the  $L_{12}$  precipitates we studied do not have the stoichiometric concentration, 25at%, since the  $L_{12}$  precipitates formed in the fcc matrix with equilibrium concentration which is lower than 25at%. The lattice parameters of the  $L_{12}$  precipitates in the Ir-Nb, -Ta, -Zr, and -Hf alloys may increase with increasing alloying elements concentrations up to 25at% since the lattice parameters of the  $L_{12}$  precipitates in our result at room temperature are smaller than those of the  $L_{12}$  phases with 25at% alloying elements (see Fig. 5(b)). The lattice parameters we determined for the  $L_{12}$  precipitates in Ir-Ti, and -V alloys at room temperature were larger than those of the  $L_{12}$  phases with 25at% alloying elements (see Fig. 5(b)). In these alloys, the lattice parameter may decrease with increasing alloying elements concentration up to 25at%. The Rh-base alloys have similar tendency of the relationship between the lattice parameters and alloying element concentration. The lattice misfits calculated using the reference lattice parameters of pure Ir and Ir<sub>3</sub>X with 25at% alloying element<sup>(16)</sup> were larger than those we determined (see Fig. 6), because the difference of

the lattice parameters between the fcc matrix and the  $L_{12}$  precipitates decreases in our result by increasing the lattice parameters of the fcc matrix and decreasing the lattice parameters of the  $L_{12}$  precipitates. The lattice misfit is independent of temperature, since the lattice parameters of the fcc matrix and the  $L_{12}$  precipitates increase at the same rate probably due to that the thermal expansion coefficients of the phases are close to each other and that the change in equilibrium chemical compositions of the phases are small up to 1200 °C.

Table II Lattice parameters of the fcc matrix and  $L_{12}$  precipitates, solubility limit at 1200 °C, solubility effect, and atomic radius of pure Ir and Ir-base alloys.

	pure Ir	Ir-V	Ir-Ti	Ir-Nb	Ir-Ta	Ir-Hf	Ir-Zr
L.P. of fcc	3.84 <sup>(16)</sup>	3.83	3.84	3.86	3.85	3.84	3.84
L.P. of $L_{12}$ , <sup>(16)</sup>	-	3.81	3.84	3.90	3.88	3.93	3.94
L.P. of $L_{12}$	-	3.82	3.85	3.87	3.88	3.91	3.91
Solubility limit, at%	-	13	10	10	10	2	2
Solubility effect $\Delta d$ , $\times 10^{-3}$	-	-1.1	0.4	1.9	1.5	-1.5	-1.0
Atomic radius, $10 \times 10^{-10}$ m	1.35	1.32	1.47	1.43	1.43	1.60	1.62

L.P.: Lattice parameters

Table III Lattice parameters of the fcc matrix and  $L_{12}$  precipitates, solubility limit at 1200 °C, solubility effect, and atomic radius of pure Rh and Rh-base alloys.

	pure Rh	Rh-Ti	Rh-Nb	Rh-Ta
L.P. of fcc	3.803 <sup>(16)</sup>	3.810	3.830	3.820
L.P. of $L_{12}$ , <sup>(16)</sup>	-	3.821	3.870	3.860
L.P. of $L_{12}$	-	3.821	3.850	3.850
Solubility limit, at%	-	10	12	10
Solubility effect $\Delta d$ , $\times 10^{-3}$	-	0.69	2.79	2.04
Atomic radius, $10 \times 10^{-10}$ m	1.34	1.47	1.43	1.43

L.P.: Lattice parameters

#### Strengthening mechanisms in Ir-base alloys

We investigated dependence of Nb concentration on the strength in the Ir-Nb alloys (see Fig. 9). At concentrations up to 10 at% Nb, the alloys have the fcc single phase structure. The  $L_{12}$  single phase alone exists in the Ir-25 at% Nb alloy. The fcc and  $L_{12}$  two phase region exists in alloys with concentrations between 10 and 23 at% Nb. In the fcc single phase structure, strength increased gradually with increasing Nb concentration, suggesting that Nb in Ir acts not only as an  $L_{12}$  precipitate former, but also as a solid solution hardener. The solid solution hardening effect is larger at lower temperature. We attribute the further strengthening achieved by increasing the Nb content to 15 at% to precipitation hardening of the  $L_{12}$  phase or to the fcc and  $L_{12}$  coherent two phase structure preventing dislocation movement, as occurs in Ni-base superalloys<sup>(7, 22)</sup>. The precipitation hardening effect is also larger at lower temperature. The volume fractions of the  $L_{12}$  phase are about 0.3 and 0.8 in the Ir-15at% and -20at% Nb alloys, respectively, according to the phase diagram<sup>(12)</sup>. The strength of the Ir-20at% Nb alloy is lower than that of -15at% Nb alloy, demonstrating that the strength of Ir-Nb alloys reaches maximum value particular volume fraction of the  $L_{12}$  phase, as is true with Ni-base superalloys where volume fractions of the precipitates between 60 and 70% show maximum strength, but strength decreases drastically at 80% volume fraction<sup>(22)</sup>. The strength of our pure Ir at room temperature was high due to the work hardening effect, because the sample was not sufficiently annealed; the swaging samples were annealed at 1200 °C for 1 hour.

In Ir-base alloys with 50% volume fraction of the  $L_{12}$  precipitates, the 0.2% flow stress by compression test increased with increasing positive lattice misfit (see Fig. 8). The microstructure of the Ir-base alloys with large lattice misfit (Ir-Hf and Ir-Zr) appeared as a 3 dimensional maze structure. In the 3 dimensional maze structure, the  $L_{12}$  precipitates are surrounded by thin fcc phase. Width of the fcc phase in the 3 dimensional maze structure is thinner than that of the fcc matrix in the microstructure with cuboidal precipitates. We considered that the 3 dimensional maze structure can prevent movement of dislocations more than the microstructure with cuboidal precipitates.

The negative lattice misfit was effective in improving the creep rupture life<sup>(13,15)</sup> in single crystal Ni-base superalloys. For example, the experimental Ni-base superalloy TMS-63 with negative lattice misfit of around -0.25 % has a longer creep rupture life, 2657 hours under 137 MPa at 1040 °C than do CMSX-4 (800 hours between -0.1 and 0.1% lattice misfit) and TMS-19 (447 hours with positive lattice misfit between 0 and 0.25%). This is because the cuboidal precipitates form plates normal to the [001] stress axis, so-called rafted structure, if tensile stress is applied along the [001] axis of the single crystal Ni-base superalloys. The rafted structure is effective in improving the creep performance at high temperatures and low stresses when dislocations climb over the precipitates since the rafted structure increase length of the climb path<sup>(8)</sup>. The 3 dimensional maze structure is expected to act as the rafted structure does. Thus the 3 dimensional maze structure will be effective in improving the creep strength because its shape and fineness will oppose the dislocations climbing.

Not only the lattice misfit and the volume fraction of precipitates but also the solid solution hardening and the precipitation hardening effects strengthen the Ir-base alloys. The solubility of alloying elements depends on the alloy system (Table II). Differences in the strengths of the L1<sub>1</sub> precipitates themselves may affect strengths of the alloys with the fcc and L1<sub>2</sub> two phase structures. For example, fineness of the microstructure, and precipitates size also affect alloy strength because small precipitates can prevent movement of dislocations. Furthermore, the effects of precipitates shape on strength must be considered. In this study, as cast samples were used for compression testing. The precipitates size and shape were different in each alloys. Thus, differences in the solid solution hardening, precipitation hardening and microstructure effects must be investigated to understand which factor is effective in imparting strength.

#### Strength Behavior of Ir<sub>3</sub>Nb with L1<sub>2</sub> structure

The temperature dependence of the 0.2% flow stress in Ir<sub>3</sub>Nb with the L1<sub>2</sub> structure is anomalous; specifically, strength increases with increasing temperature around 1200 °C (see Fig. 9). This type of behavior has been observed in other L1<sub>2</sub> structures in Ni<sub>3</sub>Si and Co<sub>3</sub>Ti<sup>(23)</sup>, in Ni<sub>3</sub>Ga<sup>(24)</sup>, and in Zr<sub>3</sub>Al<sup>(25)</sup>, etc., since Guard and Westbrook first noted the anomalous increase of hardness of Ni<sub>3</sub>Al with increasing temperature<sup>(26)</sup>. In platinum alloys like Pt<sub>3</sub>Sn, Pt<sub>3</sub>Ga, Pt<sub>3</sub>In, and Pt<sub>3</sub>Al, weak and anomalous temperature dependence occurs at temperatures around 500 °C, with drastic decreases in strength with increasing temperatures less than room temperature<sup>(27)</sup>. For Ir alloys, Bruemmer et al.<sup>(28)</sup> showed that hot hardness of sputtered thin film Ir<sub>3</sub>Nb with 10 nm grains increased with increasing temperature and the temperature of peak hardness was 800 °C. However Gyurko et al.<sup>(6)</sup> showed that hardness and 0.2% yield stress during compression testing of Ir<sub>3</sub>Nb and Ir<sub>3</sub>Zr decreased with increasing temperature. They concluded that Ir<sub>3</sub>Nb, with higher ordering energy compared with that of Ni<sub>3</sub>Al, should exhibit normal yield behavior since such behavior is expected in systems with high ordering energy. However, Wee et al.<sup>(27)</sup> suggested that the temperature dependence of strength, positive or negative, is not controlled by antiphase boundary energy itself, which is correlated strongly with ordering energies. The strength behavior depends on the anisotropy of antiphase boundary energy instead of the amount of antiphase boundary energy. For example, Ni<sub>3</sub>Ge, with high antiphase boundary energy, exhibits anomalous temperature dependence. Thus it is possible to have anomalous temperature dependence of strength for the Ir<sub>3</sub>Nb. The difference between Gyurko's result and ours might be due to the difference in the strain rate of the compression tests. The strain rate used by Gyurko was 5.0 x 10<sup>-3</sup>/s, an order of magnitude faster than our strain rate, 3.0 x 10<sup>-4</sup>/s.

#### Conclusions

The lattice parameters of the L1<sub>1</sub> precipitates and the fcc matrix of Ir-base and Rh-base refractory superalloys -- defined as alloys with fcc and L1<sub>2</sub> coherent structures similar to those of Ni-base superalloys but with considerably higher melting temperatures -- at temperatures up to 1200 °C were investigated using a high temperature X-ray diffractometer. The lattice parameters of these two phases increased with increasing temperature in any alloy. The lattice misfits determined by these lattice parameters did not change with increasing temperature up to 1200 °C. The strength of the Ir-base alloys with 50% precipitates in volume fraction were compared as a function of the lattice misfit. The strength increased with increasing positive lattice misfit (the lattice parameter of the L1<sub>2</sub> precipitates is larger than that of the fcc matrix). The microstructures of the Ir-base alloys with large lattice misfits appeared to have a 3 dimensional maze structure. We conclude that the 3 dimensional maze structure improve the compression strength by impeding the movement of dislocations.

#### Acknowledgments

We are grateful to Mr. S. Nishikawa of Furuya Metal Co., Ltd. for preparing the Ir-base and Rh-base alloy ingots and to Mr. N. Sasaki and Mr. Y. Matsumoto of the Japan Ultra-high Temperature Materials Research Center for carrying out the compression testing at 1800 °C.

#### References

1. D. B. Miracle and R. Darolia, "NiAl and Its Alloys", *Intermetallic Compounds Principles and Practice*, J. H. Westbrook and R. L. Fleischer, eds., JOHN WILEY & SONS, U. S., 2(1995), 53-72.
2. W. F. Brown, Jr., H. Mindin, and C. Y. Ho, *Aerospace Structural Metals Handbook*, vol. 5, (CINDAS/Purdue University, 1992), p. 4218, 5502.
3. T. Yamagata, "Effect of Al Content and Third Elements on Structure and Properties of High Temperature Nb-Al systems", *Proc. Fifth. Symp. on High-Performance Materials for Severe Environments (in Japanese)*, RIMCOF, Tokyo, Japan, 1994, pp. 107-14.
4. D. E. Harasyn, R. L. Heestand, and C. T. Liu, "Deep drawing of Ir-0.3%W alloys", *Mat. Sci. Eng.*, A187(1994), 155-160.
5. R. L. Fleischer, "Intermetallic Compounds for High-Temperature Structural Use -Unique Iridium and Ruthenium Compounds-", *Platinum Metals Rev.*, 36(3)(1992), 138-145.
6. A. M. Gyurko and J. M. Sanchez, "Characterization of Mechanical Properties in The Ir-Nb-Zr Intermetallic System", *Mat. Sci. Eng.*, A170(1993), 169-175.
7. Y. Ro, Y. Koizumi, and H. Harada, "High Temperature Tensile Properties of a Series of Nickel-Base Superalloys on a  $\gamma/\gamma'$  Tie Line", *Materials Science Engineering A*, March (1997) in press.
8. D. D. Pearson, F. D. Lemkey, and B. H. Kear, "Stress Coarsening of  $\gamma'$  and Its Influence on Creep Properties of A Single Crystal Superalloy", *Superalloys 1980*, J. K. Tien, S. T. Wlodek, H. Morrow III, M. Gell, and G. E. Maurer eds., ASM, Seven Springs, (1980), 513-519.
9. Y. Yamabe, Y. Koizumi, H. Murakami, Y. Ro, T. Maruko, and H. Harada, "Development of Ir-base Refractory Superalloys", *Scripta Metall.*, 35(2)(1996), 211-215.
10. Y. Yamabe-Mitarai, Y. Koizumi, H. Murakami, Y. Ro, T. Maruko, and H. Harada, "Rh-base Refractory Superalloys for Ultra-high Temperature Use", *Scripta Metall.*, 36(4)(1997), 393-398.
11. Y. Yamabe-Mitarai, Y. Koizumi, H. Murakami, Y. Ro, T. Maruko, and H. Harada, "Platinum Group Metals Base Refractory Superalloys", *Mat. Res. Soc. Symp. Proc.*, (1996) in press.
12. T. B. Massalski et al., ed., *Binary Alloy Phase Diagrams*, (Materials Park, OH, ASM International, 1992), p. 2082, 2330, 2355, 2361, 2366.
13. H. Harada, K. Ohno, T. Yamagata, T. Yokokawa, and M. Yamazaki, "Phase Calculation and Its Use", *Superalloys 1988*, S. Reichman, D. N. Duhal, G. Maurer, S. Antolovich, and C. Lund, eds., The Metallurgical Society, Seven Springs, (1988), 733-742.
14. T. Yokokawa, K. Ohno, H. Murakami, T. Kobayashi, T. Yamagata, and H. Harada, "Accurate Measurement of lattice Misfit Between  $\gamma$  and  $\gamma'$  in Nickel-base Superalloys at High Temperatures", *Advanced in X-ray Analysis*, in press.
15. T. C. Huang, and W. Parrish, "Qualitative Analysis of Complicated Mixtures by Profile Fitting X-Ray Diffractometer Patterns", *Advanced in X-ray Analysis*, 21(1977), 275-288.
16. A. E. Dwight and P. A. Beck, *Trans. Am. Inst. Min. Eng.*, 215(1959), 976.
17. P. Beardmore, R. G. Davies, and T. L. Johnston, "On The Temperature Dependence of The Flow Stress of Nickel-Base Alloys", *TMS-AIME*, 245(1969), 1537-1545.
18. G. L. Elickson, "The Development of the CMSX-10", *Superalloys 1996*, R. D. Kissinger, D. J. Deye, D. L. Anton, A. D. Cetel, M. V. Nathal, T. M. Pollock, and D. A. Woodford, eds., TMS, Seven Springs, (1996), 35-44.
19. M. E. Thompson, C. S. Su and P. W. Voorhees, "The Equilibrium Shape of A Misfitting Precipitate", *Acta Metall. Mater.*, 42(6)(1994), 2107-2122.
20. H. Harada, T. Yamagata, T. Yokokawa, K. Ohno, and M. Yamazaki, "Computer Analysis on Microstructure and Property of Nickel-base Single Crystal Superalloys", *Proc. Fifth. Intern. Conf. on Creep and Fracture of Engineering Materials and*

- Structures, B. Wilshire, and R. W. Evans, eds., The Institute of Materials, Swansea, U. K., (1993), 255-264.
21. D. A. Porter and K. E. Easterling, Phase Transformations in Metals and Alloys, (London, CHAPMAN & HALL, 1992), 149-160.
  22. H. Harada, M. Yamazaki, Y. Koizumi, N. Sakuma, N. Fukuya, and H. Kamiya, "Alloy Design For Nickel-base Superalloys", Proc. of High Temperature Alloys for Gas Turbines, R. Brunetaud, D. Coutouradis, T. B. Gibbons, Y. Lindblom, D. B. Meadowcroft and R. Stickler, eds., D. REIDEL PUBLISHING COMPANY, Liege, Belgium, (1982), 721-735.
  23. P. H. Thornton and R. G. Davies, "The Temperature dependence of the Flow Stress of Gamma Prime Phases Having the  $L1_2$  Structure", Met. Trans., 1(1970), 549-550.
  24. S. Takeuchi and E. Kuramoto, "Anomalous Temperature Dependence of the Yield Stress in  $Ni_3Ga$ ", J. Phys. Soc. Japan, 31(1971), 1282.
  25. E. M. Schulman and J. A. Roy, "The Yield Strength of The  $L1_2$  Phase  $Zr_3Al$ ", Acta Met., 26(1978), 29-37.
  26. J. W. Guard and J. H. Westbrook, "Alloying Behavior of  $Ni_3Al$  ( $\gamma'$  Phase)", TMS-AIME, 215(1959), 807-814.
  27. D-M. Wee, O. Noguchi, Y. Oya, and T. Suzuki, "New  $L1_2$  Ordered Alloys Having the Positive Temperature Dependence of Strength", Trans. JIM, 21(1980), 237-247.
  28. S. M. Brummer, J. L. Birnhall, and C. H. Hengager, Jr., "Strength and Toughness of Single-Phase And Dual-Phase High-Temperature intermetallics", Mat. Res. Soc. Symp. Proc. 194(1990), 257-262.

## STRUCTURE-PROPERTY-APPLICATION RELATIONSHIPS IN RUTHENIUM ALUMINIDE RuAl

I.M. Wolff\*, G. Sauthoff†, L.A. Cornish\*, H. DeV. Steyn\* and R. Coetzee\*

\*Physical Metallurgy Division, Mintek, P. Bag X3015, Randburg, 2125 South Africa

†Max-Planck-Institut für Eisenforschung GmbH, Düsseldorf, D-40074 Germany

\*University of the Witwatersrand, Johannesburg, South Africa

### Abstract

Ternary alloying and microstructural control are key methodologies for further developing the high-temperature properties of intermetallics based on the B2 RuAl compound. Apart from modifying the physical and mechanical properties, substitutional alloying holds out the hope of reducing the cost of these alloys. However, partial replacement of the ruthenium is almost invariably accompanied by a loss of ductility in the monolithic phase. This can be greatly ameliorated by the provision of secondary phases. The incorporation of secondary phases allows the apparently conflicting requirements for high-temperature strength and room-temperature ductility to be addressed, namely by way of ductile phase toughening and dispersion strengthening. The tension between phase chemistry, and the dictates for high-temperature stability, resistance to chemical attack, and thermal shock resistance are exemplified in applications such as spark-plug electrodes based on RuAl.

### Introduction

The unusual combination of properties inherent to the B2 RuAl compound have made it the subject of a number of development studies. To wit:

- (1) Its intrinsic room-temperature toughness, first highlighted by Fleischer *et al.*<sup>(1)</sup>, in combination with high-temperature strength, oxidation resistance and high melting point, makes it a likely candidate for structural applications.
- (2) The occurrence of five independent slip systems has also targeted RuAl for research into providing clues to the behaviour of its less ductile NiAl and CoAl counterparts, and some convergence in their behaviour has been sought by substitutional alloying<sup>(2,3)</sup>.
- (3) The corrosion resistance of RuAl is impressive. Its virtual immunity to attack in hot, concentrated mineral acids, observed by Wopersnow and Raub<sup>(4)</sup>, has been found to apply over a much wider range of aqueous media, which makes it eminently suitable for development in corrosion resistant coatings and electrochemical applications<sup>(5)</sup>.
- (4) The difficulties inherent in producing RuAl by melt processing can be overcome by reactive powder processing or RHIP techniques. The successful production of bulk RuAl by these techniques<sup>(6)</sup> has catalysed wider research into its properties and the fabrication of some, albeit small, prototype components.
- (5) A more comprehensive investigation of the phase relationships has been undertaken to clarify the microstructural response<sup>(7-11)</sup>.

Cost is nevertheless a key determinant in exploiting RuAl, and in this regard substitutional alloying has assumed importance quite apart from the need to enhance the mechanical properties. Some ternary additions, such as Co, Ti and Ni, have been explored as a means of optimising high-temperature strength, oxidation resistance and alloy content. Alloying

usually implies a loss of room-temperature ductility and an increase in hardness, but this can be tempered by balancing the phase make-up. In the present paper, the efficacy of multi-phase systems in reconciling alloy content, high-temperature strength and room-temperature ductility, is highlighted. Attention is drawn to more recent development work, which exploits some of the structure-property relationships in novel spark-plug electrodes based on RuAl.

### Manufacture

The recently modified binary phase diagram for the Ru-Al system is shown for convenience in Fig. 1. Ternary alloys based on Ru-Al-X were manufactured by conventional melt processing of compacted high-purity (>99.9%) powders in a vacuum arc furnace, and also by reactive powder processing, or RHIP (Reactive Hot Isostatic Pressing), according to procedures established previously<sup>(6)</sup>. The melt-processed material was characterised in the as-cast condition, whereas the RHIP processed material existed in the homogenised state. (Homogenisation consisted of an anneal of up to 12 hours at 1500 °C to eliminate the non-equilibrium, multi-phase structure present after RHIP<sup>(6)</sup>. Hill *et al.*<sup>(12)</sup> have drawn attention to the existence of a heavily dislocated, partially polygonised dislocation substructure prevalent after this treatment. This is probably the result of dislocation formation to take up mismatch strain in the lattice, concurrent with dissolution of the intermediate phases (see for example Ref. 13). Thus considerably longer annealing times and/or higher temperatures are required to achieve full restoration. The residual substructure has implications for such parameters as the formability, diffusion, and electrical transport properties of the alloys).

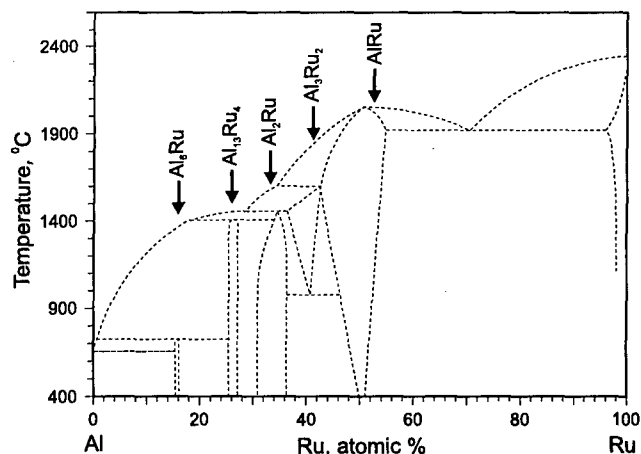


Figure 1: Binary equilibrium phase diagram for the Ru-Al system (after Boniface and Cornish<sup>(8)</sup>).

Structural Intermetallics 1997

Edited by M.V. Nathal, R. Darolia, C.T. Liu, P.L. Martin,  
D.B. Miracle, R. Wagner, and M. Yamaguchi  
The Minerals, Metals & Materials Society, 1997

In the Ru–Al system deviations from the RuAl composition in the Ru-rich direction give rise to a secondary intergranular (eutectic) phase at room temperature, thus minimising the constitutional defects associated with excess atoms in the B2 phase. Compositions slightly rich in Ru are therefore convenient, in theory, insofar as they allow spurious hardening from this source to be largely discounted in the binary systems. It is obviously not known to what extent this is true for the ternary alloys, as both CoAl and NiAl show extended superstoichiometric ranges of stability for the B2 phase. The melt-processed and powder-processed material differ primarily insofar as RHIP imparts a discontinuous dispersion of the secondary phase to Ru-rich compositions, as opposed to the continuous intergranular layers found in the former. As substoichiometric (i.e. Al-rich) compositions are characteristically more brittle<sup>(1)</sup>, both the melt and RHIP samples are generally selected to be slightly superstoichiometric for improved mechanical properties and handling.

#### Substitutional Alloying in the RuAl System

Based on the existence of B2 CoAl, NiAl and RuTi phases, Co and Ni would be expected to substitute for Ru, and Ti for Al. Ternary formulations in the pseudo-binary ranges RuAl–CoAl, RuAl–RuTi and RuAl–NiAl have been examined based on the pre-supposed existence of a continuous solid solubility range in the B2 phase. Such a solubility range has in fact been reported for the Ru–Al–Ti and Ru–Al–Co systems<sup>(14,15)</sup>, but it was previously contended that a miscibility gap existed between the isostructural RuAl and NiAl B2 phases, despite large degrees of solid solubility for Ni and Ru respectively<sup>(16)</sup>. This is unexpected, since the RuAl and NiAl phases show very small degrees of lattice mismatch. One argument advanced to account for this is the severe coring that occurs on solidification, with the high-melting point RuAl phase forming primary dendrites, leaving a Ni-rich phase to solidify afterwards<sup>(17)</sup> (Fig. 2). Low diffusion rates and/or relatively long diffusion paths in this system can mean that, even with extended homogenising practices, the cored structure in melt-processed material cannot be readily overcome.

From a consideration of size factors and enthalpies of formation listed below, the coring effect would have been expected to manifest itself in the RuAl–CoAl alloys as well. This does not appear to be the case, possibly in consequence of a narrower solidification range across the RuAl–CoAl series.

Enthalpy of formation: (kJ.mol <sup>-1</sup> )	CoAl = -110.9 NiAl = -118.5 RuAl = -124.1	Source (ref.) 18 18 19
Lattice parameter: (nm)	CoAl = 0.28611 RuTi = 0.307 NiAl = 0.28864 RuAl = 0.29916	20 20 21 22
Covalent radius: (nm)	Co = 0.116 Ti = 0.132 Ni = 0.115 Ru = 0.125	various
Atomic radius: (nm)	Co = 0.167 Ti = 0.200 Ni = 0.162 Ru = 0.189	various

Manufacture by RHIP appears to effectively take account of coring by either (i) reducing the microstructural scale of coring (assuming that the transient liquid state that accompanies the reaction process results in a more localised solidification area in the bulk<sup>(6)</sup>) and thereby reducing the diffusional distances, or (ii) eliminating coring altogether and ensuring homogeneous reaction to give rise to an apparently continuous single phase. Similar compositions prepared by melt processing (in a button arc furnace) and powder processing showed that the latter

were essentially single phase when viewed optically, bearing out the premise of a continuous solubility range. The existence of a continuous solubility range is also lent support by a recent study of Horner *et al.*<sup>(9)</sup>. No differences between the melt and powder-processed alloys were found in the Co system.

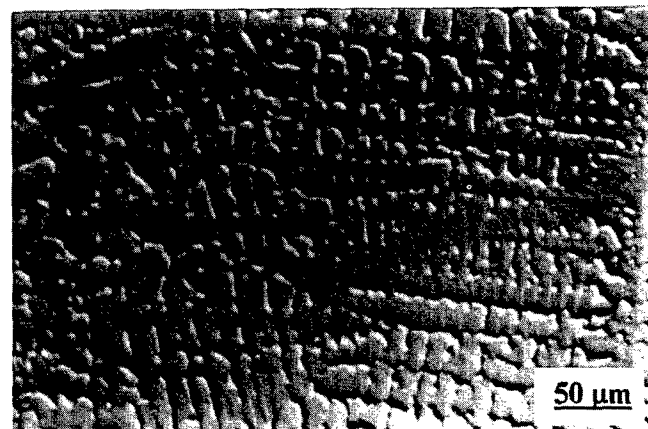


Figure 2: Cored structure of a melt-processed Ru<sub>25</sub>Ni<sub>25</sub>Al<sub>50</sub> alloy, shown with the aid of differential interference contrast.

#### Microstructural Parameters

RuAl exhibits disparate behaviour in its mechanical response to Co, Ti and Ni additions. Whereas substitutional alloying is found to result in an averaging effect between the hardnesses of RuAl, and CoAl and RuTi respectively, the RuAl–NiAl series evidences hardnesses considerably higher than those of the respective binary compounds. (Fig. 3). A logical explanation for this could be sought in the first analysis in the lattice misfit strain. However, as already noted, comparable dimensions for Co beg the question why similar effects are not observed in the Co alloys.

The variation in lattice constant with substitutional alloying is shown in Fig. 4 for Co and Ni additions, both of which are expected to substitute for the Ru. (As noted previously, slightly super-stoichiometric compositions were selected to improve toughness, although the dotted lines show extrapolation to the literature values for binary stoichiometric NiAl and CoAl). The alloys lie on an apparently straight line, as expected for a continuous range of mutual solubility. This corresponds to Vegard's law, indicating ideal miscibility. Although this linear variation in each case offers no explanation for the observed hardness, several points of interest emerge.

The first is the localised discontinuity in the lattice parameters of the RuAl–NiAl alloys, which also corresponds to a distinct maximum in hardness, roughly at the point where equiatomic amounts of Ru and Ni are alloyed. This suggests that formulations of nominal RuNiAl<sub>2</sub> stoichiometry may be subject to extraneous hardening effects, even when exhibiting an apparently single phase B2 microstructure.

One hypothesis to account for this is provided by the possibility of ternary ordering<sup>(23)</sup>. Although no ternary phase has been reported for the Ru–Ni–Al system, the Ru–Nb–Al<sup>(24)</sup> and Ru–Ti–Al<sup>(15)</sup> systems both exhibit examples of ternary ordering. In the former, a Heusler phase of the type NbRu<sub>2</sub>Al has been identified, whereas the Ru–Ti–Al system contains a G-phase close to the ideal composition of Ti<sub>6</sub>Al<sub>16</sub>Ru<sub>7</sub>. G-phases that are coherent with the B2 NiAl phase have also been reported<sup>(25)</sup>. Although resolvable X-ray spectra would only be expected for sufficiently high volume fractions, some evidence for a higher degree of ordering in the vicinity of the hardest alloys has in fact been found<sup>(10)</sup>.

Substitution with Co yielded a roughly linear variation of the lattice constant. It is worth observing that the addition of Co at the 13 at.% level led to a relatively small change in the lattice parameter, whereafter the lattice parameter decreased almost monotonically with higher additions. This can be explained in terms of a previous study<sup>(3)</sup> that found that the Co showed a high propensity to segregate to the hexagonal Ru-rich eutectic phase, leaving less Co to enter the matrix lattice. As the alloys were usually chosen to be slightly rich in Ru, yielding a small volume-fraction of the Ru-rich secondary phase into which the Co can enter, this can partially account for the smaller impact of the Co addition. This phenomenon is however overridden at greater alloying amounts.

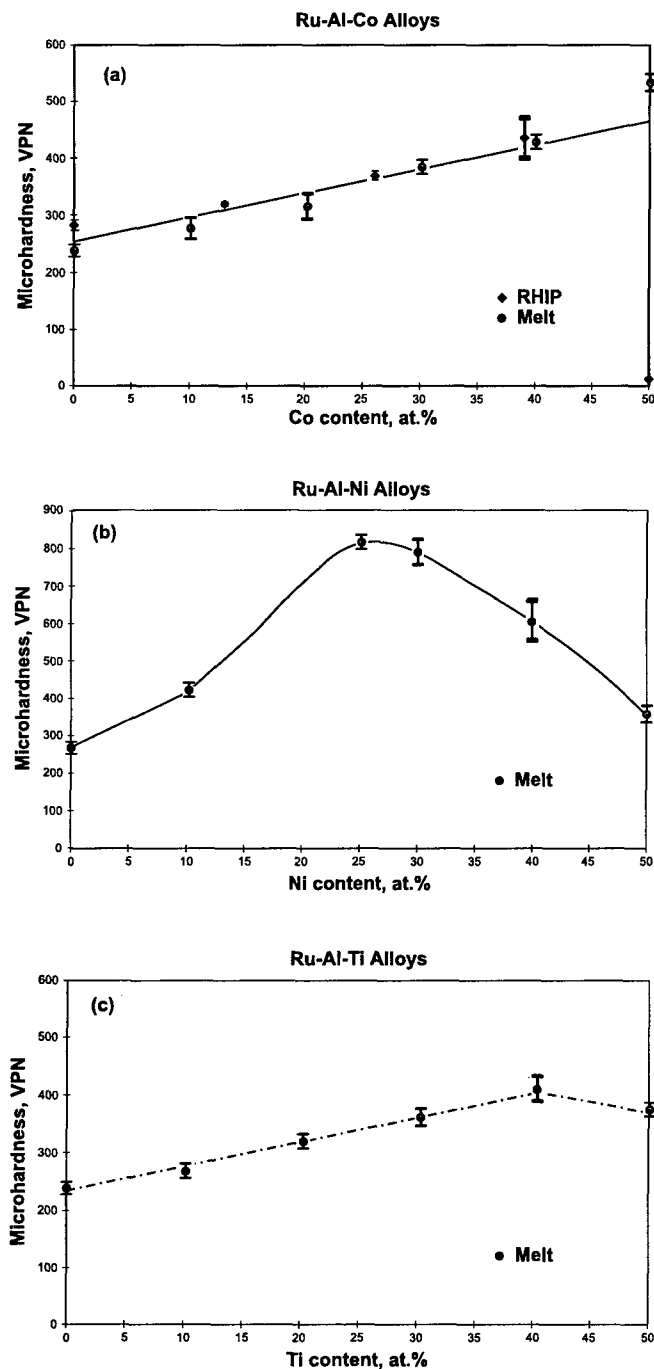


Figure 3: Hardness profiles of (a) the RuAl-CoAl, (b) RuAl-NiAl, and (c) RuAl-RuTi series.

#### Hardness Anomaly in Ru-Ni-Al

Although extraneous phase effects such as ordering would account for some hardening in the RuAl-NiAl series, other hardening mechanisms can play a role. It has been postulated elsewhere<sup>(2)</sup> that the widely disparate APB energies associated with the  $\langle 111 \rangle$  slip in NiAl and RuAl, and the covalent-like bonding in NiAl, can be directly responsible for the lack of  $\langle 111 \rangle$  dislocations in NiAl, and, by extension, reduced slip in RuAl substitutionally alloyed with Ni. However, this cannot completely account for the severe hardening in RuAl-NiAl since hardness governed primarily by a lack of  $\langle 111 \rangle$  slip would anticipate a much higher hardness in binary NiAl i.e. would lead to a monotonic increase in hardening with the approach to NiAl.

More recently Munroe and Kong<sup>(26-28)</sup> have pointed out that Ni also increased the hardness of B2-structured FeAl beyond that predicted by atomic misfit calculations, and furthermore reduced the softening that occurred on low-temperature annealing of this compound. This was attributed to the interaction of nickel atoms with the thermal vacancies that form on high-temperature heat treatment. Although the exact mechanism is unknown, they speculate that the larger atomic radius of nickel favours the formation of divacancies in the vicinity of the atom, which are then effectively restricted in mobility.

Munroe and Kong's observation of a defect hardening mechanism appears to be substantiated by other systems. For example, an examination of the B2 RuTi-NiTi system<sup>(29)</sup> reflects a similar hardness profile to RuAl-NiAl across the pseudo-binary (shown in Fig. 5), with a strong maximum, which suggests that the hardening effect might be intrinsic

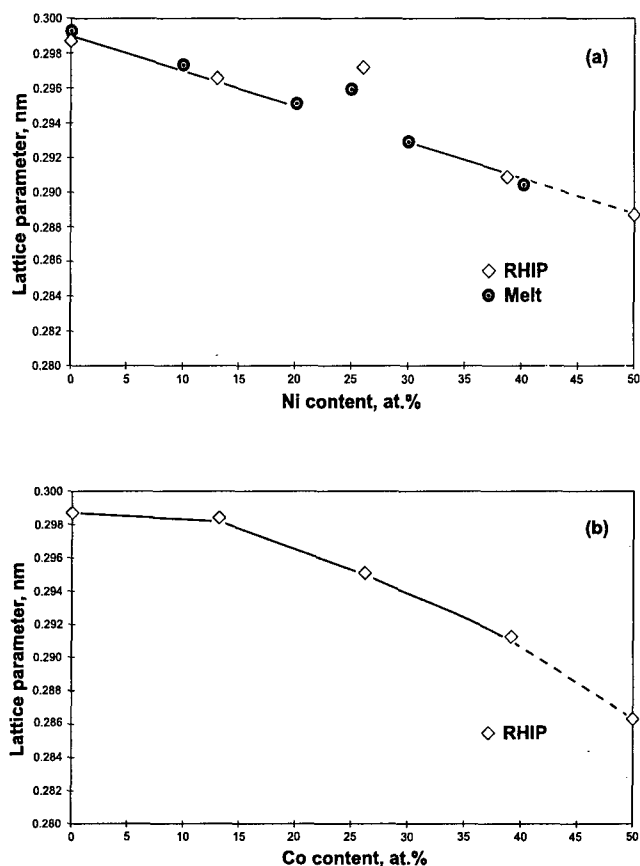


Figure 4: Variation in lattice parameter (a) with Ni content and (b) with Co content.

to nickel in the B2 structure rather than the B2 system itself. Interestingly, the RuTi-NiTi system also evidences severe coring during melt-processing. Re-evaluation of the system using higher homogenisation temperatures to eliminate segregation established that a continuous solubility range does in fact exist here too<sup>(29)</sup>.

To summarise, despite parameters that predict comparable substitutional misfit in the B2 lattice, the Ni, Co and Ti additions differ profoundly in their effect on the hardness. Even in the designated single-phase B2 regions, Ni alloying is accompanied by severe hardening, whereas the Co additions lead to a linear averaging effect between the RuAl and CoAl extremities. If any second phase effects could be excluded, one would be left to view Ni as a 'rapid hardener' in terms of Fleischer's definition<sup>(30)</sup>, i.e. an atom that not only produces large asymmetrical strains, and strong interactions with screw and edge dislocations, but also possibly strong vacancy-hardening effects. Further work is required to resolve this discrepant effect of Ni on hardening, although the evidence of other B2 systems, such as the FeAl-NiAl and RuTi-NiTi series, points to this probably being intrinsic to Ni.

### Secondary Phases in Ru-Rich Stoichiometries

As already noted, the RuAl phase field does not extend much beyond stoichiometry in the Ru-rich direction. (The recently revised phase diagram does, in fact, indicate that a Ru-rich RuAl nose protrudes at elevated temperature (Fig.1)). In consequence, slightly Ru-rich formulations lead to the formation of a secondary (solid state) phase when cooled to room temperature, which favours an intergranular distribution. Similarly, melt-processed RuAl typically takes on an intergranular 'necklace structure' with the formation of a Ru-rich (eutectic) phase forming around the primary RuAl dendrites. Significantly, these structures are associated with increased compressional ductility, and a higher incidence of transgranular fracture, which gives them attributes of a compliant layer<sup>(3)</sup>.

When this secondary phase is included in ternary formulations, superstoichiometric alloys in the pseudo-binary systems RuAl-RuTi and RuAl-CoAl have been found to tolerate significant replacement by Ti and Co, without undergoing the rapid falloff in room-temperature ductility as in the case of the stoichiometric alloys<sup>(3)</sup>.

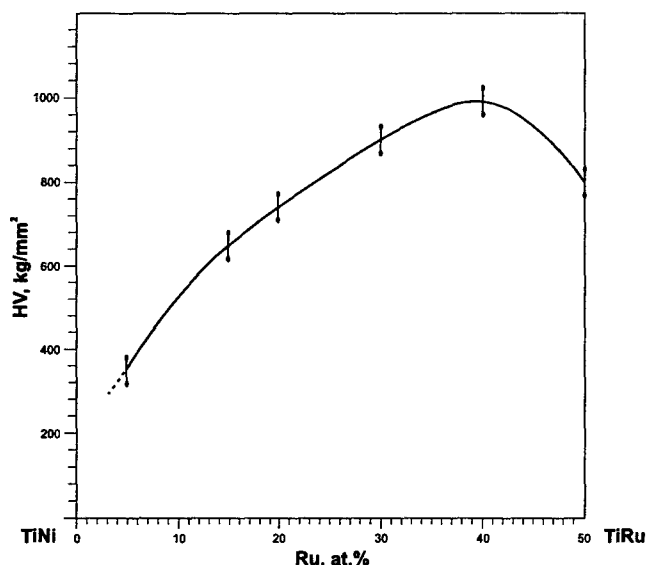


Figure 5: Hardness profile reported for the RuTi-NiTi system (after Semenova *et al.*<sup>(29)</sup>)

Moreover, room-temperature compressional ductility is retained despite an overall increase in the offset proof stress (the increase in strength is presumably due to constitutional defect hardening within an expanded B2 phase field). This is illustrated in Fig. 6. The RuAl-NiAl system is less susceptible to ductilization by the grain-boundary phase, obviously due to overriding hardening effects, but, as noted in the succeeding section, exhibits useful ductility in mixed eutectic composites.

### In Situ Composite Structures

The success of the nickel-base superalloys continues to attract the notion that a succeeding generation of high-temperature alloys might draw on related precepts, namely those of a finely dispersed and coherent (hard but deformable) secondary phase in a ductile matrix. Analogous  $\gamma/\gamma'$  systems based on coherent  $L1_2$  dispersoids in a fcc matrix have enjoyed some attention, and indeed those based on iridium have led to the suggestion of a class of alloys to be named 'refractory superalloys'<sup>(31)</sup>. The tenability of such composite structures based on RuAl are discussed elsewhere<sup>(32)</sup>.

Alongside the  $\gamma/\gamma'$  analogues are other so-called *in situ* composites, amongst which those suitable as vehicles for 'ductile phase toughening' concepts are particularly interesting. Ductile phase toughening methodologies stem from the recognition that 'ductile' secondary phases not only contribute to crack deflection processes in the normal way, but also contribute to strengthening (by acting as obstacles to dislocation motion at the phase interface). Moreover, if very finely distributed, these interface barriers can contribute more to overall hardening during deformation, for example during creep, than work-hardening within the phase<sup>(33)</sup>.

Eutectic systems lend themselves to the exploitation of inherently compatible phases in a finely divided mix, and are natural candidates for ductile phase composites. A recent study has examined some eutectics based on Ru-Al, Ir-Al, Ru-Nb, Ir-Nb and Ru-Al-Ni<sup>(34,35)</sup>. The systems are unusual in that, whereas the ductilities of Ru and Ir in elemental form are unprepossessing, some of the ordered phases are uniquely ductile within the context of intermetallics.

As discussed above, the incorporation of a thin layer of eutectic phase effectively improves the room-temperature mechanical response of the B2 phase. The benefits of the eutectic layer raises the possibility of enhancing extrinsic toughening by multiplying this compliant-layer effect on the micrometer level in a ductile phase composite. A similar premise has been explored in NiAl/Ni<sub>3</sub>Al lamellar composites<sup>(36)</sup>, and can be extended to the lamellar eutectic structure of the Ru-RuAl system. The synergy of the constituent phases of the Ru-RuAl eutectic in evolving strengths far greater than that anticipated from simple rules of mixture is demonstrated in Fig. 7. The salient finding is that this strength increase is accompanied by significant ductility at room temperature<sup>(34)</sup>, while at the same time reducing the scale of microfracture.

By way of further observation, ternary alloys, such as those based on Ru-Ni-Al, may be formulated to give mixed eutectic structures that evidence substantially higher strengths than the simple Ru-RuAl binary (Fig. 8), with little loss in room-temperature compressional ductility<sup>(23,34)</sup>. This is attributed largely to the strong hardening contributed by Ni to the B2 phase, noted above.

While useful strengths are maintained in the eutectic systems at temperatures up to the order of 1300 °C, interfacial effects may account for a rapid fall-off in strength above that<sup>1</sup>, seen in Fig. 8, and there is

<sup>1</sup> Both toughness and strength rely on a favourable lamellar orientation. This is often achieved by directional solidification or processing. Randomly oriented lamellar packets may be susceptible to interfacial sliding.

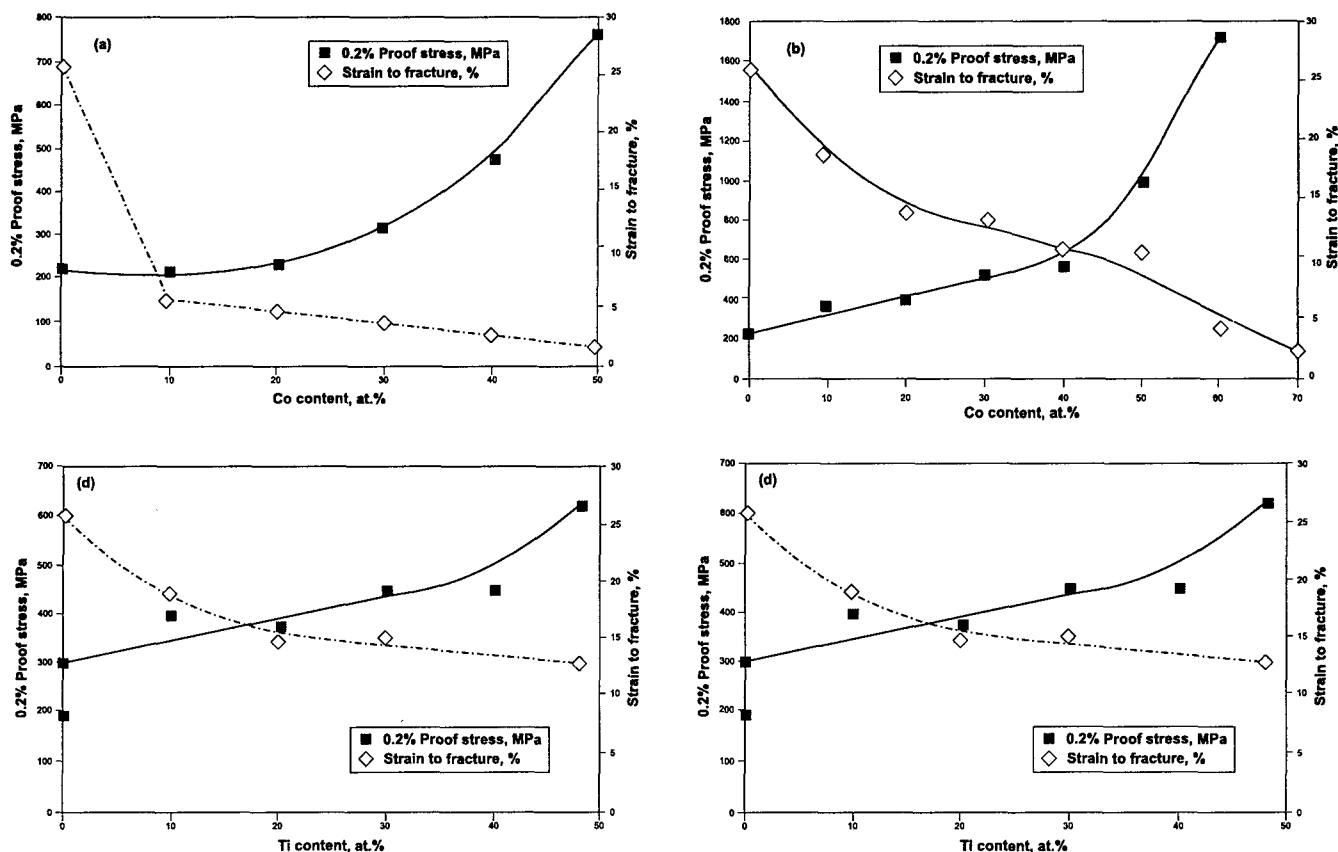


Figure 6: Mechanical properties of RuAl-CoAl and RuAl-RuTi alloys at room temperature obtained for melt-processed alloys (after Wolff and Sauthoff<sup>(3)</sup>).

- (a) Single-phase alloys lying on the RuAl-CoAl transus
- (b) Dual phase alloys lying on the RuAl-Co<sub>70</sub>Al<sub>30</sub> transus
- (c) Single phase alloys lying on the RuAl-RuTi transus
- (d) Dual-phase alloys lying on the Ru<sub>52</sub>Al<sub>48</sub>-Ru<sub>52</sub>Ti<sub>48</sub> transus

also some question as to the stability of the eutectic structure during prolonged exposure at these temperatures i.e. coarsening, leading to a loss of the fine lamellar morphology. For higher temperature service, a modified phase distribution is therefore indicated, one embodying discrete dispersoids of the secondary phase. This can be achieved via, *inter alia*, controlled precipitation (see for example the Ir-Nb system<sup>(31,34)</sup>) or processing. An example of the latter is provided by RHIP, which is particularly advantageous for engineering 'dispersion-strengthened' *in situ* Ru-RuAl structures, such as that shown in Fig. 9. At high volume fractions of the dispersed phase, composite structures reminiscent of the superalloys emerge.

#### RuAl as a Spark-Plug Electrode Material

A recent review<sup>(32)</sup> examines some potential applications for RuAl, which include its use as a corrosion protection coating, based on its excellent resistance to attack in hot mineral acids, exploitation of its electrochemical properties in the chlor-alkali industry, and as structural components in energy generation. One of the more onerous environments for which it has been targeted is that encountered by a spark plug. Specifically, it must comply with voltage demand, thermal and electrical conductivity, work function, arc-erosion resistance, oxidation resistance, chemical attack, extreme elevated temperatures, resistance to grain growth and thermal shock requirements, to name but a few.

A number of trends in automotive design have engendered a new generation of spark-plug materials. Key amongst these trends are the introduction of leaner burn engines, higher performance engines, and longer

service intervals. While carmakers in Europe and Japan have specified a service life of 60 000 km, manufacturers in the United States are presaging 100 000 km lifespans. To date, only the precious metals, notably alloys of Pt, and Au-Pd, have held out the hope of meeting these requirements.

An extensive test programme of prototype RuAl-based spark-plug electrodes (SPE) has found a remarkable convergence of all the physical and mechanical requisites in this intermetallic compound, and results have been detailed elsewhere<sup>(37)</sup>. The toughness of RuAl is sufficient to overcome the intense thermal shocks (associated with cycling between gas temperatures of 60 and 3000 °C). Its electrical conductivity has been found to be almost metallic in nature, and it has excellent work function attributes<sup>(38)</sup>. It has, moreover, the necessary thermal conductivity<sup>(39)</sup> to ensure rapid heat conduction away from the working face, preventing pre-ignition, even in high-performance engines. Endurance tests on prototype RuAl-base spark plugs have already indicated that they could meet the requirements for a 60 000 km service interval, and form the basis of patents sought world-wide<sup>(40)</sup>.

Several microstructural effects illustrate the importance of structure-property relationships in the RuAl electrodes. Optimum erosion resistance was found to be a function of the Ru content in the binary alloy, and also the fuel mixture<sup>(40)</sup>. Higher Ru contents favoured leaded fuels, in accordance with ruthenium's well-known resistance to lead attack<sup>(41)</sup>, and an optimum composition was found at around 68 at.% Ru (Fig. 10). The erosion mechanism was nevertheless found to be intimately linked to attack by the lead component, which left a Ru-rich skeleton



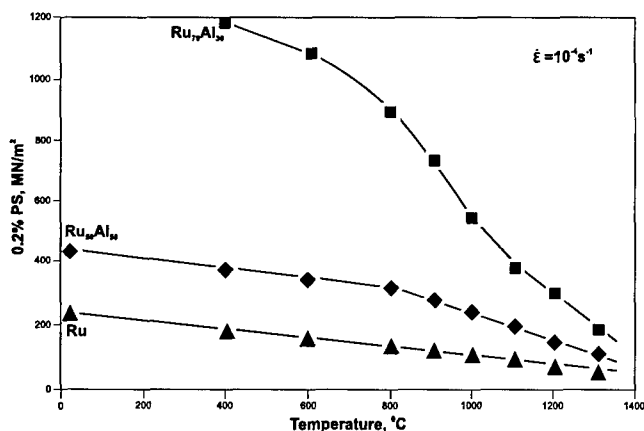


Figure 7: Strength of Ru-RuAl eutectic in relation to its constituent phases (after Wolff and Sauthoff<sup>(34)</sup>).

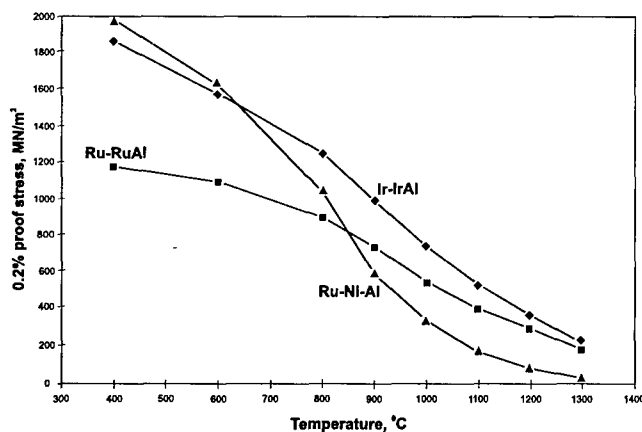


Figure 8: Comparison of flow behaviour in Ru-RuAl and the mixed Ru-Al-Ni eutectic (after Wolff and Sauthoff<sup>(23,34)</sup>).

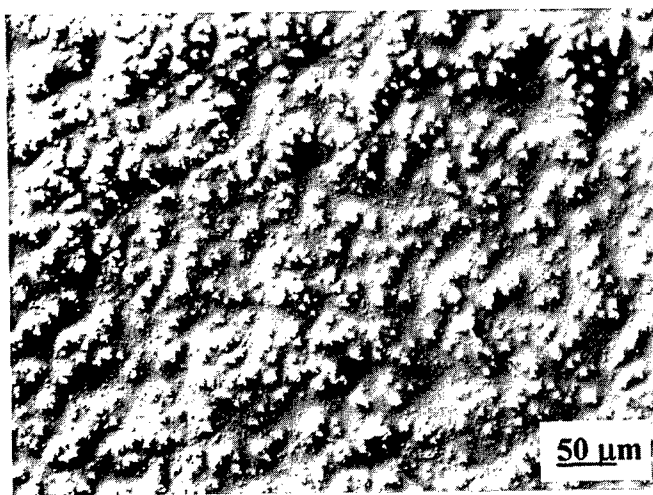


Figure 9: Dispersion of Ru-rich particles in a RuAl matrix, generated by RHIP

at the working surface (Fig. 11). The predominant erosion mechanism in unleaded fuels was found to be the volatilization of ruthenium oxides, and compositions close to stoichiometry were favoured, consistent with a maximum degree of order, conductivity, and a higher melting point. The performance advantage over conventional Ni-base electrodes is illustrated in Fig. 12.

Thermogravimetric analyses of near-stoichiometric RuAl yielded the following high-temperature oxidation characteristics. At 1100 °C initial surface oxidation and mass gain was followed by spalling, while at 1300 °C incipient internal oxidation became noticeable (Figs. 13 and 14). Microalloying with boron yielded comparable behaviour up to 1100 °C, but promoted catastrophic and uniform internal oxidation, with accompanying mass gains, at higher temperatures. This effect over similar time scales is emphasised in Fig. 13(b). The reason for this is not clear, and has, to the authors' knowledge, not been reported previously. Thus the good ductility achievable with boron<sup>(1)</sup>, which is desirable for cold forming, appears to be tempered by a debilitation of the high-temperature oxidation resistance.

To ensure good contact between the RuAl-based insert, and the nickel sheath, welding or cold crimping is required. With prolonged exposure at operating temperature, inter-diffusion at the interface can lead to the formation of secondary phases in the Ni-RuAl couple. This is desirable from the point of view of ensuring a good joint, but the nature of these phases in turn determine the resistivity and mechanical properties across the interface. In particular, reaction with the Ni can emulate the embrittling effects found above, necessitating a sound understanding of the operative phase relationships.

Finally, limitations on primary fabrication of RuAl waited on a means of manufacturing high-integrity bulk RuAl. The development of a RHIP process has allowed the production of homogeneous, near full-density RuAl of sufficient quantity for test-bed trials. RHIP processing remains, of necessity, a batch process, and subsequent machining is wasteful. It remains to anticipate the production of wire, coated, or sintered components for large-scale production.

## Conclusions

Compounds based on the B2 RuAl system have been the subject of a number of studies probing their exceptional room-temperature ductility, high-temperature stability, aqueous corrosion resistance, and amenability to substitutional alloying. Convergence in the properties of RuAl and its less ductile counterparts has been sought by substitutional alloying, with the additional objective of lowering the cost of bulk RuAl. In this regard

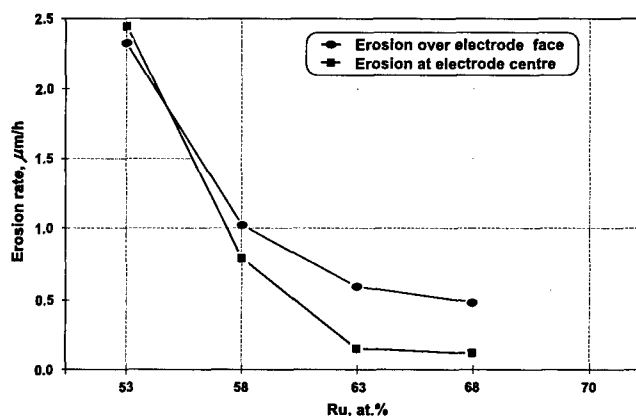


Figure 10: Wear-rate of Ru-RuAl based spark-plug electrodes after 72 hours (after Steyn *et al.*<sup>(37)</sup>).

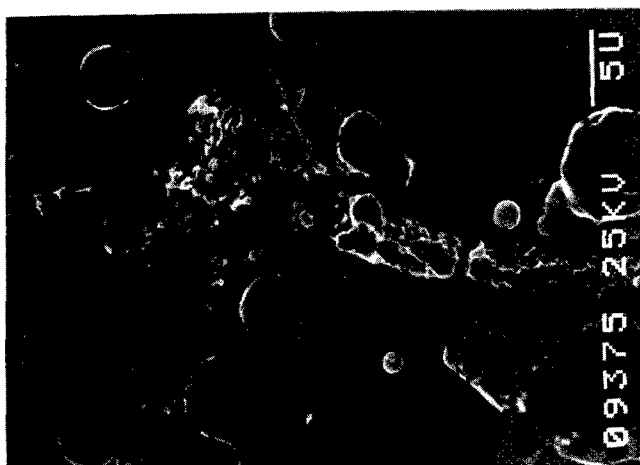


Figure 11: Preferential erosion of the RuAl phase at the working surface by the lead additives.

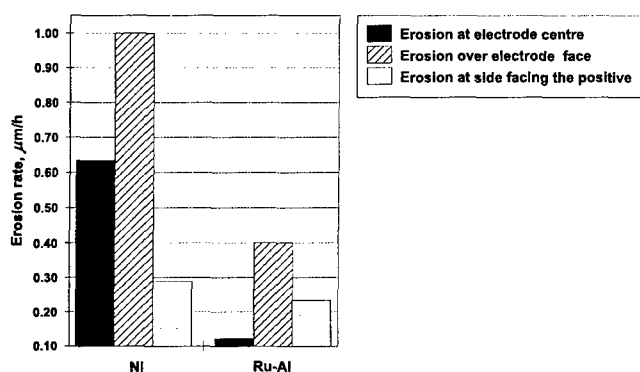


Figure 12: Relative performance of nickel- and RuAl-based electrodes after 60 hours (after Steyn *et al.*<sup>(37)</sup>).

the extent of the solid solubility range of the B2 phase with ternary additions, and the associated phase relationships and mechanical response, are of interest. Multi-phase approaches were shown to be effective means of addressing the requirements for room-temperature ductility, while concurrently increasing strength.

Recent work has found disparate behaviour in RuAl with different substitutional additions. Whereas relatively high levels of Ti and Co may be alloyed without significantly debilitating the room temperature ductility of dual-phase RuAl, Ni causes rapid hardening, leading to speculation that this may arise from vacancy interactions, as noted in other B2 systems containing Ni. The existence of a continuous solid solubility range across the RuAl-NiAl series was probed using X-ray diffraction and metallographic techniques. Reactive powder processing appeared to yield nominally single phase structures, as opposed to melt processing which yielded microstructures which were apparently dual-phase in nature. However, the existence of a hardness maximum within the designated pseudo-binary series supports the idea of extraneous hardening effects, which require additional work to clarify.

Prototype trials with RuAl-based spark-plug electrodes have demonstrated the viability of RuAl in near-term applications. Extremes in operational service, requiring thermal shock resistance, high thermal and electrical conductivity, and inertness to aggressive and high-temperature chemical environments have been successfully met with a combination of microstructural and alloy design. It is concluded that considerable scope remains to take these alloys still further up the performance ladder.

#### Acknowledgements

Results reported here are drawn from a wide-ranging research programme, and the authors are particularly indebted to Gencor and Gencor Process Research, South Africa, and Impala Platinum Limited, South Africa. This paper is published by permission of Mintek.

#### References

1. R.L. Fleischer, R.D. Field, and C.L. Briant, "Mechanical Properties of High Temperature Alloys of AlRu," *Metallurgical Transactions A*, 22A (1991), 404-414.
2. W. Lin, J-h. Xu, and A.J. Freeman, "Cohesive properties, electronic structure, and bonding characteristics of RuAl - A comparison to NiAl," *J. Mater. Res.*, 7(3)(1992), 592-604.
3. I.M. Wolff and G. Sauthoff, "Role of an Intergranular Phase in RuAl with Substitutional Additions," *Acta Materialia* (In Press: Ms No. A-0239-96-RW).
4. W. Wopersnow and Ch.J. Raub, "Eigenschaften einiger binärer intermetallischen Phasen des Palladiums und Rutheniums mit anderen Metallen," *Metall.*, 33(7)(1979), 736-740.
5. J.J. McEwan and T. Biggs, "Exploiting the Excellent Corrosion Resistance of a Precious Metal Aluminide," (Paper presented at the 13th International Corrosion Congress, Melbourne, Australia, 25-29 November, 1996), ACA Inc., Victoria, Paper 096, 6 pages.
6. I.M. Wolff, "Synthesis of RuAl by Reactive Powder Processing," *Metallurgical and Materials Transactions A*, 27A (1996), 3688-3699.
7. T.D. Boniface and L.A. Cornish, "Investigation of the high aluminium end of the aluminium-ruthenium phase diagram," *J. Alloys and Compounds*, 233 (1996), 241-245.
8. T.D. Boniface and L.A. Cornish, "Investigation of the aluminium-ruthenium diagram above 25 at.% ruthenium," *J. Alloys and Compounds*, 234 (1996), 275-279.
9. I.J. Horner, N. Hall, L.A. Cornish, M.J. Witcomb, M.B. Cortie, and T.D. Boniface, "An investigation of the B2 phase between AlRu and AlNi in the Al-Ni-Ru ternary system," *J. Alloys and Compounds* (In Press).
10. A.S. Harte, P.M. Hung, I. Horner, N. Hall, L.A. Cornish, and M.J. Witcomb, "Comparison of Modelled and Experimental Data for the  $Ni_xRu_{1-x}Al$  Intermetallic Compound in the Ni-Ru-Al Ternary System", *Advances in X-ray Analysis*, vol. 39, In press, Colorado Springs, USA.
11. I.J. Horner, L.A. Cornish, and M.J. Witcomb, "A study of the Al-Ni-Ru Ternary System above 50 at.% Aluminium," *J. Alloys and Compounds* (In Press).
12. P. Hill, L.A. Cornish, and M.J. Witcomb, University of the Witwatersrand, Johannesburg, Unpublished Research.
13. I.M. Wolff, "Development of a Sub-Structure in a Nickel-base Superalloy", *Z. Metallkd.*, 82 (10) (1991), 773-778.
14. V.F. Tsurikov, E.M. Sokolovskaya, and T.P. Loboda, "Examination of the Phase Diagram and Some Properties of Ru-Al-Co Alloys," *Russ. Met.*, 6 (1980), 201-204.

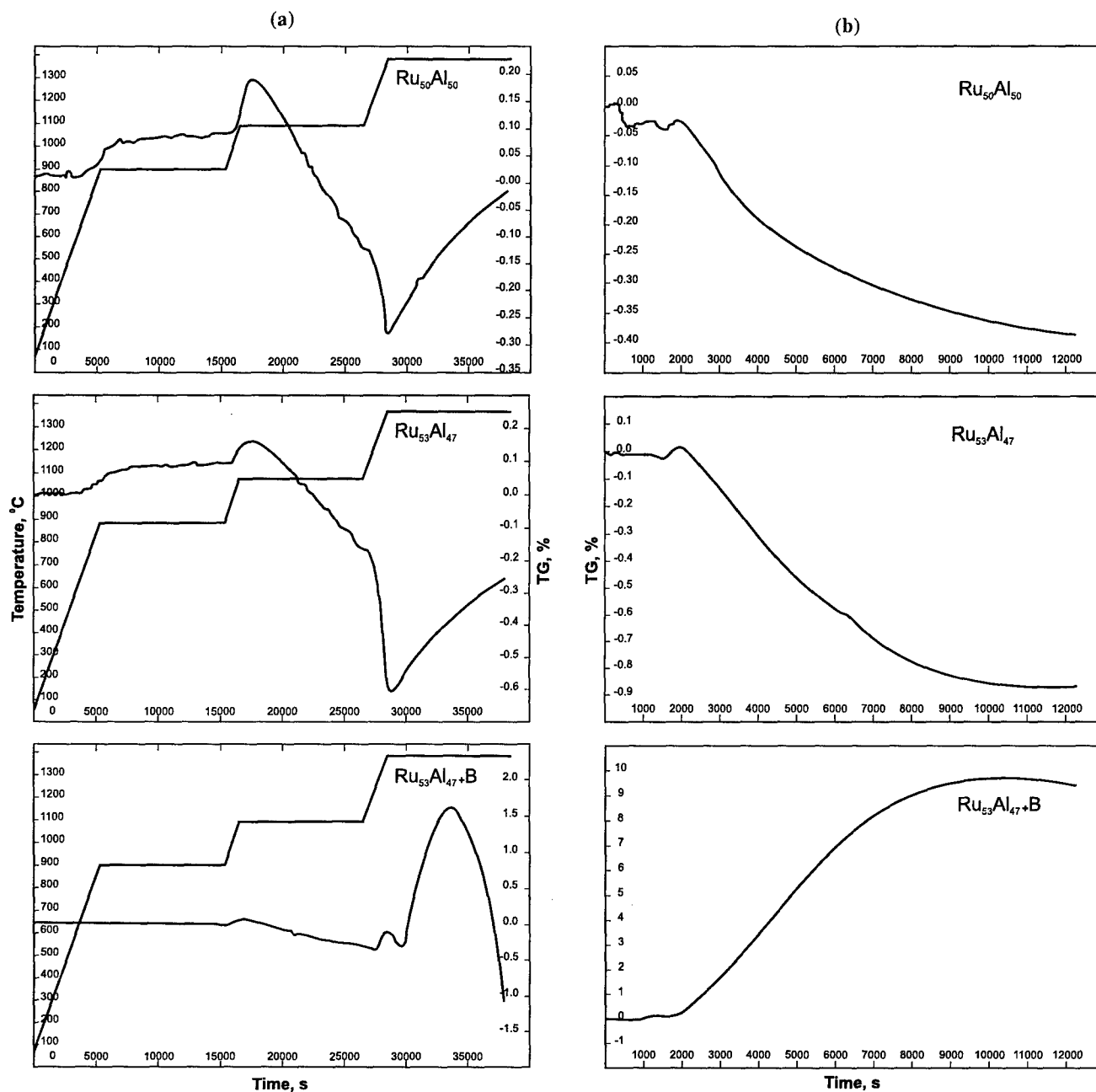


Figure 13: Thermogravimetric analyses of oxidation in air, showing

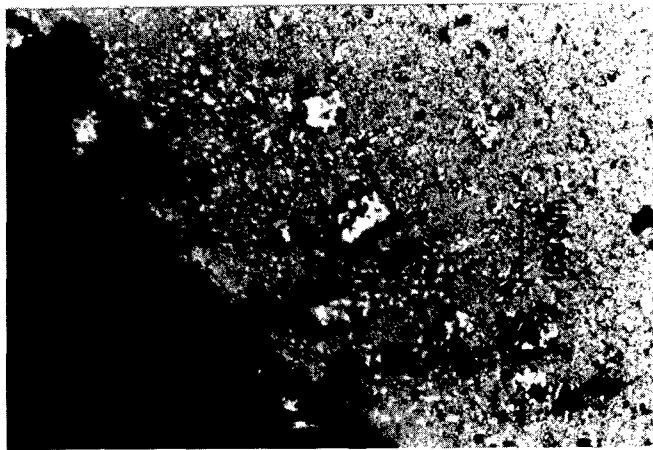
(a) Mass loss as a function of temperature

(b) Isothermal behaviour at 1300°C

15. A. Khataee, H.M. Flower, and D.R.F. West, "Constitution of Ti-Al-Ru System," *Materials Science and Technology*, 5 (1989), 632-643.
16. S. Chakravorty and D.R.F. West, "The Constitution of the Ni-Al-Ru System," *J. Materials Science*, 21 (1986), 2721-2730.
17. M.B. Cortie, Mintek, Private Communication.
18. C.J. Smithells, ed., *Metals Reference Book*, 5th Edition, (Butterworths, London 1976), 193-194.
19. W-G. Jung and O.J. Kleppa, "Standard Molar Enthalpies of Formation of MeAl (Me=Ru, Rh, Os, Ir)," *Metallurgical Transactions B*, 23B (1992), 53-56.
20. P. Villars and L.D. Calvert, *Pearson's Handbook of Crystallographic data for Intermetallic Phases*, (ASM, Ohio 1985), vol.2, 926 and vol.3, 3113.
21. R.D. Noebe, R.R. Bowman, and M.V. Nathal, "Physical and mechanical properties of the B2 compound NiAl," *International Materials Reviews*, 38 (4) (1993), 194.
22. R.L. Fleischer, "Boron and Off-Stoichiometry Effects on the Strength and Ductility of AlRu," *Metallurgical Transactions A*, 24A (1993), 227-230.
23. I.M. Wolff and G. Sauthoff, "Mechanical Properties of Ru-Ni-Al Alloys," *Metallurgical and Materials Transactions A*, 27A (1996), 1395-1400.



(a)



(b)

Figure 14. Oxidation behaviour at 1300 °C of (a) RuAl, showing incipient internal oxidation, and (b) an Ru<sub>53</sub>Al<sub>47</sub> alloy with B additions, with uniform internal oxidation

24. P. Cerba, M. Vilasi, B. Malaman, and J. Steinmetz, "Caracterisation de trois nouvelles phases ternaires, Nb(Pd,Al)<sub>2</sub> et Nb(Ru,Al)<sub>2</sub> de type MgZn<sub>2</sub>, et NbRu<sub>2</sub>Al de type BiF<sub>3</sub>, dans les systemes Nb-Pd-Al et Nb-Ru-Al," *J. Alloys and Compounds*, 201 (1993), 57-60.
25. D.B. Miracle and R. Darolia, R., in: *Intermetallic Compounds*, J.H. Westbrook and R.L. Fleischer, eds, (John Wiley and Sons, Chichester, England 1995), 61.
26. C.H. Kong and P.R. Munroe, "The effect of composition on defect structure associated with elimination of vacancies across the NiAl-FeAl pseudobinary," *Intermetallics*, 2 (1994), 333-341.
27. P.R. Munroe, "The effect of nickel on vacancy hardening in iron-rich FeAl," *Intermetallics*, 4 (1996), 5-11.
28. P.R. Munroe and C.H. Kong, "The effect of ternary additions on vacancy hardening in near stoichiometric FeAl," *Intermetallics*, 4 (1996), 403-415.
29. E.L. Semenova, N. Yu. Rusetskaya, and V.M. Petyukh, "The TiNi-TiRu System," *J. Phase Equilibria*, 16 (4) (1995), 297-299.
30. R.L. Fleischer, "Substitutional Solute in AlRu - I. Effects of Solute on Moduli, Lattice Parameters and Vacancy Production," *Acta metall. mater.*, 41 (3) (1993), 863-869.
31. Y. Yamabe, Y. Koizumi, H. Murakami, Y. Ro, T. Maruko, and H. Harada, "Development of Ir-Base Refractory Superalloys," *Scripta Materialia*, 35 (2) (1996), 211-215.
32. I.M. Wolff, "Toward a Better Understanding of Ruthenium Aluminide," *IOM* (Jan. 1997), 34-39.
33. J. Klöwer, and G. Sauthoff, "Creep Behaviour of Directionally Solidified Lamellar Nickel-Iron-Aluminium Alloys," Part I, *Z. Metallkd.*, 82 (7) (1991), 510-518, and Part II, *Z. Metallkd.*, 83 (9) (1992), 699-704.
34. I.M. Wolff and G. Sauthoff, "High Temperature Behaviour of Precious Metal Base Composites," *Metallurgical and Materials Transactions A*, 27A (1996), 2642-2652.
35. I.M. Wolff and G. Sauthoff, "Composite Structures in Intermetallics," (Paper presented at Minerals and Materials '96, Cape Town, 31 July - 2 Aug. 1996), S.A.I.M.M., vol. 2, 641-648.
36. I.M. Wolff and G. Sauthoff, "Evolution of Composite Plate and Lamellar Structures in Ni-rich NiAl," *Z. Metallkd.*, 87 (2) (1996), 111-119.
37. H. DeV. Steyn, I.M. Wolff, and R. Coetzee, Mintek, Unpublished research.
38. E.G. Smith and C.I. Lang, "High Temperature Resistivity and Thermo-Emf of RuAl," *Scripta Metallurgica et Materialia*, 33 (8) (1995), 1225-1229.
39. S.A. Anderson and C.I. Lang, "Thermal Conductivity of Ruthenium Aluminide (RuAl)," Submitted to: *Scripta Metallurgica et Materialia*.
40. H. DeV. Steyn, I.M. Wolff, and R. Coetzee, "Spark-Plug Electrodes Containing Intermetallic Phases and Spark Plugs Embodying Same," S.A. Patent 94/10180, (22 Dec. 1994).
41. A.S. Darling, "Some Properties and Applications of the Platinum-Group Metals," *International Metallurgical Reviews*, 18 (175) (1973), 91-122.

## EFFECTS OF Al ON $\omega$ FORMATION IN TRANSITION METAL INTERMETALLIC ALLOYS

G. Shao, E. Passa, P. Tsakirooulos and A. P. Miodownik  
Department of Materials Science and Engineering, University of Surrey,  
Guildford, Surrey GU2 5XH, UK

D. Nguyen Manh and D. G. Pettifor  
Department of Materials, University of Oxford, Parks Road,  
Oxford OX1 3PH, UK

### Abstract

Study of  $\omega$  phase stability has been experimentally extended into the metastable  $\beta$  phase in Nb-17Al-xMo alloys. The results support the hypothesis that addition of Al to later transition metals stabilises the  $\omega$ -type structures and promotes A2 $\rightarrow$ B2 ordering in the  $\beta$  phase. Theoretical predictions using the total energy FP-LMTO method are consistent with experimental results. The free electron density of the  $\beta$  phase is a controlling factor for  $\omega$  formation.

An ordered  $\omega$ -type structure,  $\omega^*$ , has been observed in Nb-17Al-xMo alloys heat treated at 973K. The lattice parameter of  $\omega^*$  is  $a_{\omega^*} = \sqrt{6}a_{B2}$  and  $c_{\omega^*} = \sqrt{3}a_{B2}$ . The orientation relationship between  $\omega^*$  and B2 is  $\langle 111 \rangle_{B2} // \langle 0001 \rangle_{\omega^*}$  and  $\{10\bar{1}\}_{B2} // \{10\bar{1}0\}_{\omega^*}$ . A disordered  $\omega$  phase has been observed in Fe-Al alloys produced by PVD.

### Introduction

Transition metal (such as Ti, Nb, Fe and Ni) based aluminides have attracted extensive attention recently due to their promising application as light, high strength and creep resistant alloys suitable for thermal engine components. The main hurdle for the application of such intermetallic alloys is their poor room temperature ductility. One way to overcome this is to introduce a bcc phase to composite the intermetallics, as the bcc structure is expected to have good ductility. However, the bcc phase would lose its ductility if the  $\omega$  phase were to form in it by a displacive transformation mechanism [1-3].

Since Frost et al encountered the  $\omega$  phase in some  $\beta$ -Ti (bcc) alloys which were unexpectedly brittle [4], this phase has been found in numerous alloys of the group IVB transition metal elements Ti, Zr and Hf with other  $\beta$ -stabilising (d-electron-rich) transition elements and has received extensive experimental as well as theoretical attention from materials scientists and physicists. The  $\omega$  phase formation in Ti-alloys has received the greatest attention due to their importance in industrial

applications [1,3].

There are two routes by which omega formation is usually avoided in conventional titanium alloys. The addition of  $\alpha$  (hcp) stabilisers such as Al and Sn leads to the preferential formation of alternative decomposition products such as martensitic  $\alpha$  [5]. Alternatively, large additions of  $\beta$  stabilisers such as V, Nb and Mo can be used to depress the  $\beta \rightarrow \omega$  transus sufficiently below room temperature so as to create an effectively stable  $\beta$  phase [1,6]. It has been shown that the deviation of diffuse  $\omega$  structure from the crystalline  $\omega$  lattice [6,7],  $|\Delta| = u/(k_{111}\beta/3) = 2u/(k_{222}\beta/3)$ , increases with increasing content of later transition metal (LTM: on the right of group IVB) elements in group IVB metal base alloys [2,5,6-10].

As an  $\alpha$ -stabilising element, Al was found to suppress the  $\omega$  phase formation in commercial  $\alpha+\beta$  Ti-alloys [5]. However, when large amount of Al together with large amount of  $\beta$ -stabilising elements such as Nb and V was introduced in Ti-alloys, ordered  $\omega$  phases were observed in the metastable ordered B2 phase [6,11]. It has been found that even in quenched-in binary V-Al alloys, the  $\omega$  phase is stabilised by introducing Al into V. This has shed new light on the role of Al on  $\omega$  formation, as both Al and V were expected to suppress the  $\omega$  formation. Correlation of  $|\Delta|$  to the free electron density of the  $\beta$ /B2 phase,  $\phi$  (free electrons per unit cell volume), has shown that both electron and size factors are important for the  $\omega$  phase formation [6]. By adding Al to V or Ti-V, the free electron density of the  $\beta$  phase approaches that of pure Ti, promoting  $\omega$  formation in these alloys [6]. It is therefore necessary to extend the investigation of the effect of Al on  $\omega$  phase formation in other LTMs such as Nb and Mo.

In this work,  $\omega$  formation in Nb-17Al-xMo alloys ( $x=20, 30, 40$  at%) has been studied. It will be shown that the  $|\Delta|$  values of the diffuse  $\omega$  phase in the metastable  $\beta$  phase of Nb-17Al-xMo alloys fall in the same trend of the  $|\Delta|-\phi$  plot of Ti-Al-V and other Ti-alloys, confirming that the stability of the  $\omega$  structure is controlled by the free electron density. Also the  $\omega$  phase stability has been theoretically modelled using the full potential linear muffin tin orbital (FP-LMTO) method, giving further physical insight on  $\omega$  formation. The structure of a new  $\omega$ -type phase formed by isothermal heat treatment is also reported.

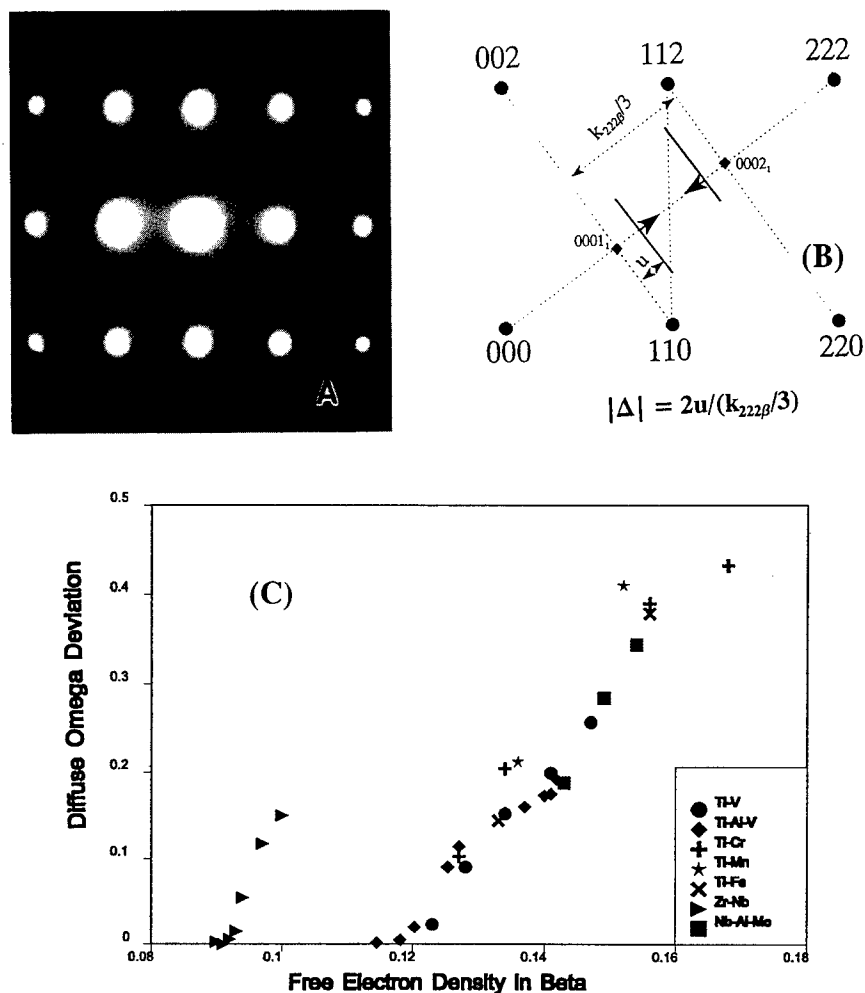


Fig. 1 (A) [110] SADP from the metastable  $\beta$  of the Nb-17Al-30Mo ingot, (B) definition of  $|\Delta|$ , and (C)  $|\Delta|$ – $\phi$  plot in different alloys and experimental data other than Nb-Al-Mo are from Ti-Al-V [6], Ti-Cr [7], Ti-V [8], Ti-Mn [9], Ti-Fe [5,10], and Zr-Nb [2].

### Experimental

Nb-17Al-xMo alloys were prepared by arc melting high purity Nb, Mo and Al in a modified Marko Materials melt-spinner. The ingots were re-melted four times in the water cooled copper hearth to promote homogeneity. The actual alloy compositions were Nb-17.3Al-20.3Mo, Nb-16.0Al-30.6Mo and Nb-16.6Al-41.3Mo. Special care was taken to limit the interstitials  $O_i < 200$  wppm,  $H_i < 10$  wppm (analysis by IMI Titanium Ltd.).

TEM specimens were prepared by ion beam thinning and TEM studies were carried out using Philips EM 400T and JEOL 2000fx microscopes. Energy dispersive X-ray (EDX) analyses were performed using the LINK AN10000 system attached on EM 400T for thin foils and a JEOL JXA8600 electron probe microanalysis (EPMA) system for bulk ingots. Thin foil EDX quantification was carried out using experimental profiles and Cliff-Lorimer factors.

### Results and Discussion

#### Diffuse $\omega$ in the as-solidified Metastable $\beta$

The equilibrium microstructure of the Nb-17Al-xMo alloys should contain Nb<sub>3</sub>Al (A15 structure) and the  $\beta$  phase (A2 structure). The formation of the Nb<sub>3</sub>Al phase was largely suppressed in the ingot

close to the water cooled copper hearth and in the melt spun ribbons of 60-150 $\mu$ m thickness. Detailed information on phase equilibria in the Nb-17Al-xMo alloys is published elsewhere [12]. The metastable  $\beta$  in the as-solidified ingots of the alloys with 20 and 30 Mo contained ordered B2 domains in an A2 matrix, while the metastable  $\beta$  in the ingot with 40at%Mo and the melt spun ribbons of all three alloys had the disordered A2 structure. There was diffuse streaking in the diffraction patterns from the metastable  $\beta$  phase. This streaking is typical of the presence of a diffuse  $\omega$  phase in the metastable  $\beta$  phase. A detailed description of the streaking due to the presence of the diffuse  $\omega$  phase can be found in [6]. The [011] $_{\beta}$  patterns from the metastable  $\beta$  phase in the as-solidified 30Mo ingot is shown in Fig. 1A as an example. The  $|\Delta|$  values of the diffuse  $\omega$  structure of Nb-17Al-xMo (Fig. 1B) are superimposed on Fig. 17 of [6] and shown in Fig. 1C.

#### Structure of an Ordered $\omega$ -type Phase in Heat Treated Ribbons

After heating the melt spun ribbons of the three alloys at 973K for 500h, A2 $\rightarrow$ B2 ordering occurred in the  $\beta$  phase and fine precipitates ( $< 30$ nm in size) were formed in some localised regions within the B2 grains. TEM images exhibiting the precipitates in the heat treated ribbons with 20 and 30 Mo are shown in Fig. 2. It was found that the amount and

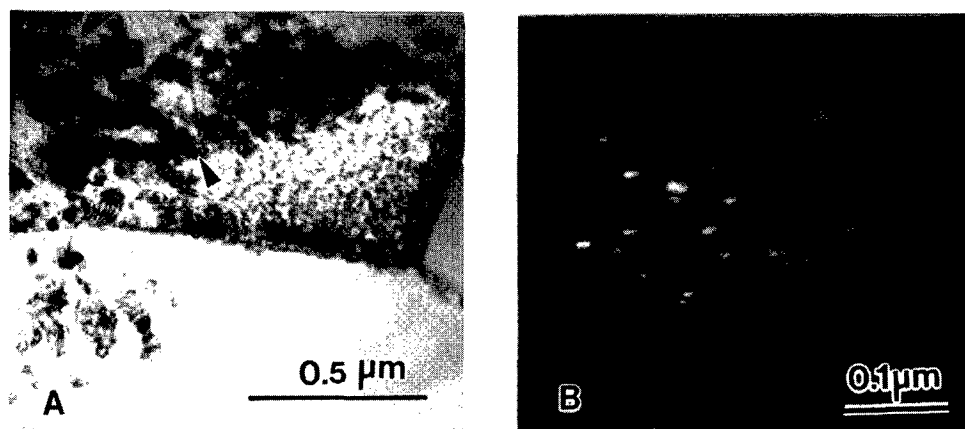


**Fig. 2** TEM images of Nb-17Al-20Mo (A: bright field) and Nb-17Al-30Mo (B: dark field) ribbons heat treated at 973K for 500h, showing fine precipitates in B2.

**Table 1** [T] matrices for the four OR variants of  $\omega^*$

Variants	$[111]_{B2}/[0001]_{\omega}$ $(10\bar{1})_{B2}/(10\bar{1}0)_{\omega}$	$[\bar{1}11]_{B2}/[0001]_{\omega}$ $(101)_{B2}/(10\bar{1}0)_{\omega}$	$[1\bar{1}1]_{B2}/[0001]_{\omega}$ $(10\bar{1})_{B2}/(10\bar{1}0)_{\omega}$	$[11\bar{1}]_{B2}/[0001]_{\omega}$ $(101)_{B2}/(10\bar{1}0)_{\omega}$
[T]	2 -1 -1 -1 2 -1 1 1 1	1 -1 2 1 2 -1 -1 1 1	1 -1 -2 1 2 1 1 -1 1	1 1 2 1 -2 -1 1 1 -1

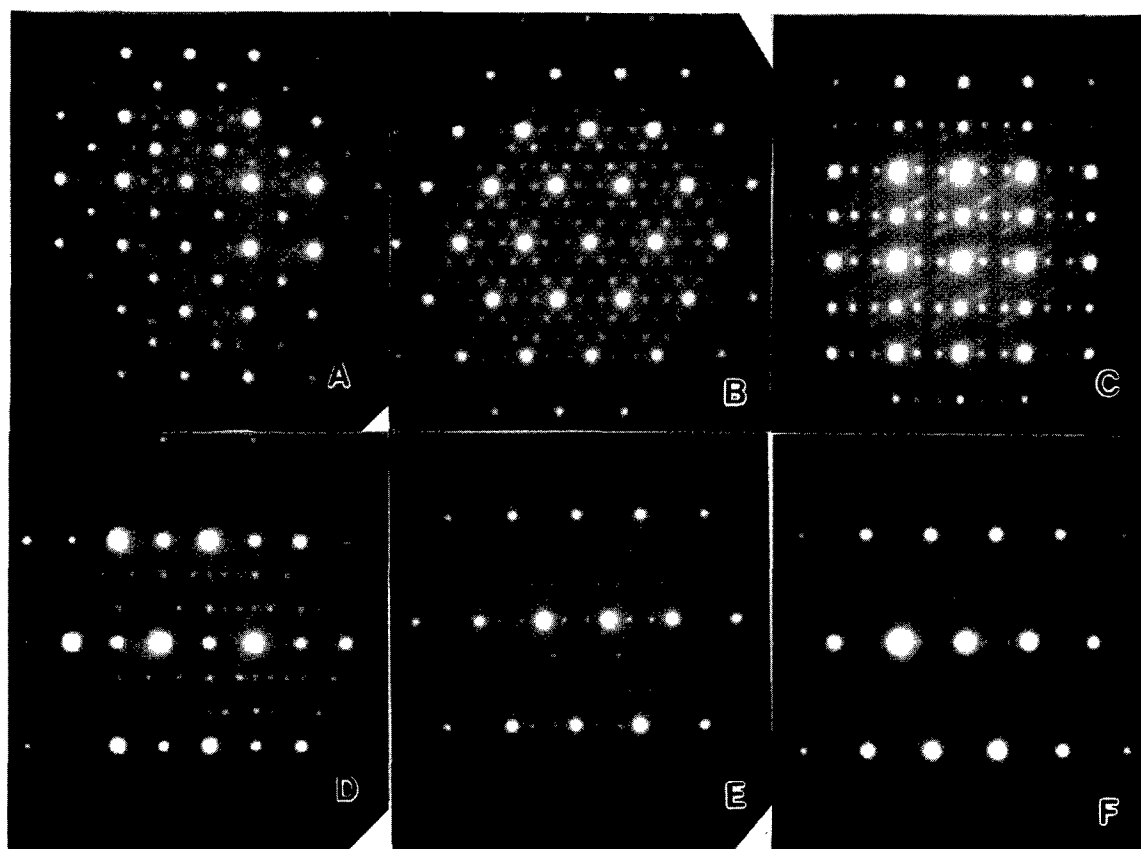


**Fig. 3** SADPs taken at (A)  $[001]_{B2}$ , (B)  $[111]_{B2}$ , (C)  $[110]_{B2}$ , (D)  $[012]_{B2}$  and (E)  $[113]_{B2}$  from the heat treated Nb-17Al-20Mo ribbon. (F) at  $[113]_{B2}$  from the heat treated Nb-17Al-30Mo ribbon.

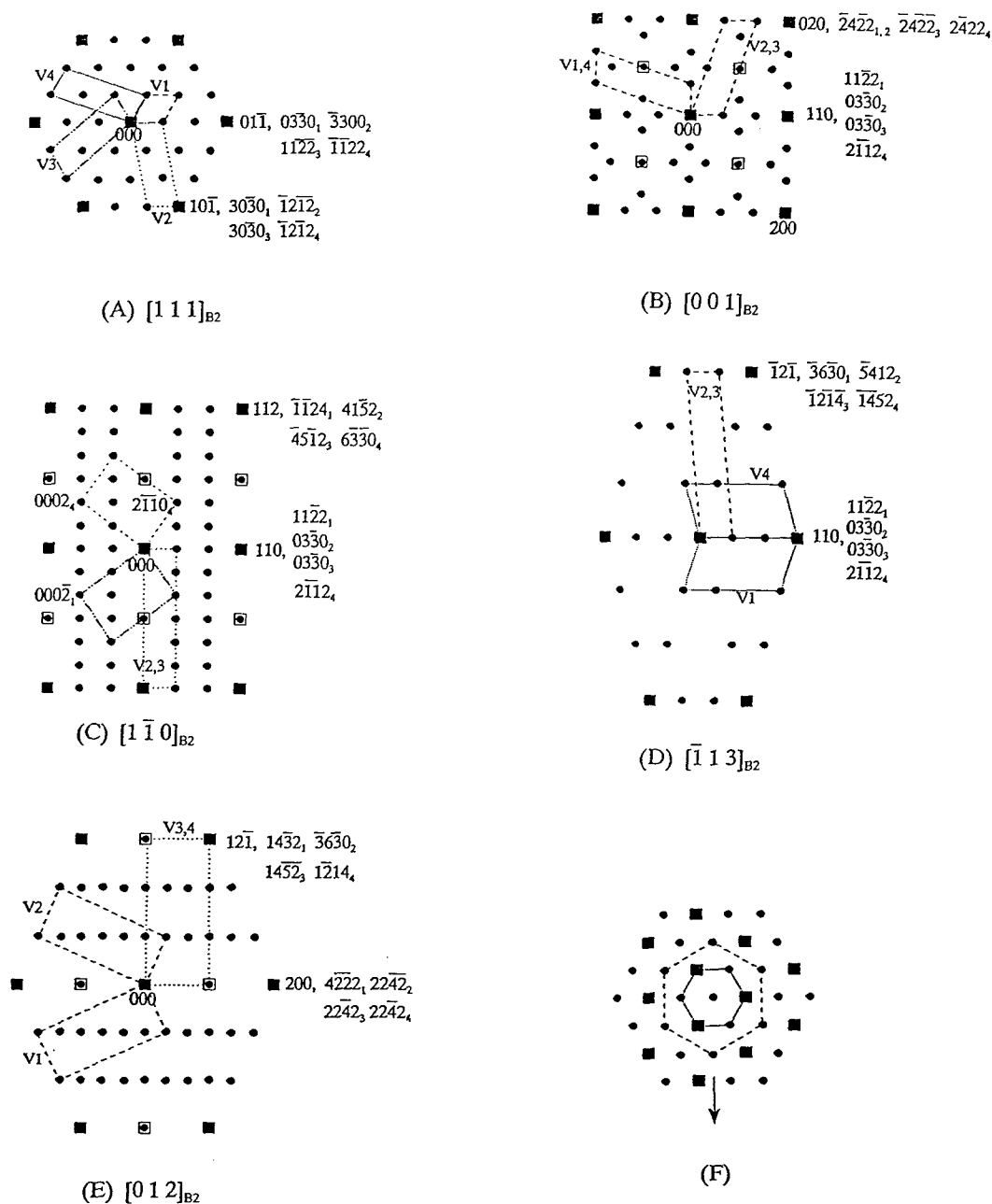


Fig. 4 Superimposed computer simulated electron diffraction patterns of B2 and four variants of  $\omega^*$  at (A)  $[001]_{B2}$ , (B)  $[111]_{B2}$ , (C)  $[110]_{B2}$ , (D)  $[012]_{B2}$  and (E)  $[113]_{B2}$ . (F) is a schematic diagram showing the atomic array of Al (squares) and Nb/Mo (circles) atoms on a  $(0001)_{\omega^*}$  plane. Note the difference between the sizes of  $\omega$  (dotted line) and  $\omega^*$  (dashed line). The arrow in (F) indicates  $[101]_{B2} // [1120]_{\omega} // [1010]_{\omega}$ .

size of the precipitates decreased significantly from the Nb-17Al-20Mo alloy ribbon to the ribbons with 30 and 40 Mo. EDX analysis showed that the region containing the precipitates was richer in Al than the precipitate free region (PFR). In the heat treated ribbon of Nb-17Al-20Mo, the PFR composition was Nb-21.9Mo-16.1Al, while the composition of the precipitate was Nb-16.6Mo-23.0Al (due to the small sizes of the precipitates, it was impossible to avoid the contribution of the B2 matrix to the EDX results).

Fig. 3(A-E) show a set of SADPs taken from the indicated region containing the precipitates in Fig. 2A, at various B2 zone axes. The patterns are complicated due to the presence of the precipitate spots and tilting experiment showed that all precipitate spots were not caused by

double diffraction. A hexagonal configuration was assigned to the precipitate phase ( $\omega^*$ ). The lattice parameters of  $\omega^*$  were  $a_{\omega^*} = \sqrt{6}a_{B2}$  and  $c_{\omega^*} = \sqrt{3}a_{B2}$ . There are four orientation relationship (OR) variants between B2 and  $\omega^*$  (see Table 1). The equivalent plane indices between  $\omega^*$  and B2 can be expressed mathematically by:  $[h]_{\omega^*} = [T][H]_{B2}$  (see Chapter 4 in [13] for details). The  $[T]$  matrices for the four OR variants are listed in Table 1. Superimposed electron diffraction patterns containing B2 and the above four  $\omega^*$  variants can then be calculated using the  $[T]$  matrices in Table 1. The calculated patterns at various B2 zone axes are shown in Figs. 4(A-E), showing excellent agreement with the experimental SADPs. Presence of  $(0001)_{\omega^*}$  spots in the electron diffraction patterns suggests



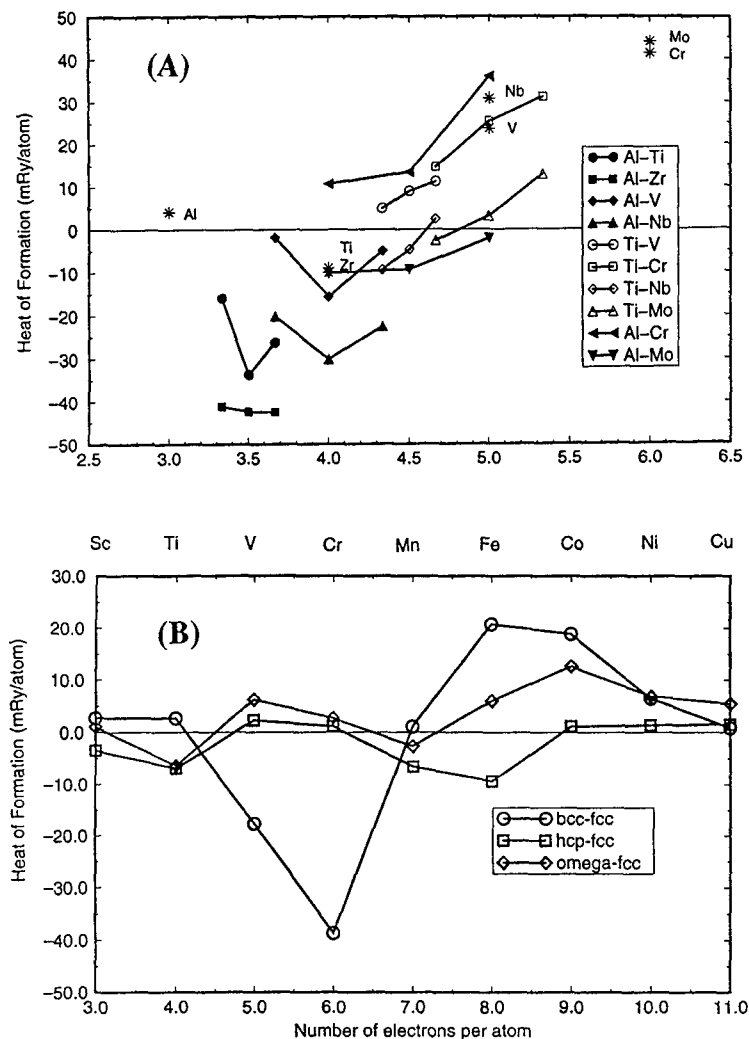


Fig. 5 Predicted heats of formation for  $\omega$  in binary alloys (A) and in pure elements (B).

that the space group of  $\omega^*$  is not the same as that of the  $B8_2$  structure ( $P6_3/mmc$ ). The probable space group of  $\omega^*$  is therefore suggested to be  $P\bar{3}m1$  [6,11]. The streaking contrast in Fig. 3D is due to the plate morphology of the  $\omega^*$  phase, with the  $\omega^*$  plate normal parallel to  $\langle 111 \rangle_{B2} // \langle 0001 \rangle_{\omega}$ . Comparison of  $\omega^*$  with the disordered  $\omega$  structure reported by Silcock ( $\omega$ , space group  $P6/mmm$ ) [14] shows that  $a_{\omega} = \sqrt{3}a_{\omega}$  and  $c_{\omega} = 2a_{\omega}$ . Therefore, the  $\omega^*$  phase can be considered as an ordered  $\omega$ -type structure. Bendersky et al [11] reported an ordered  $\omega$  structure in B2 ( $\omega$  space group  $P\bar{3}m1$ ) which has the same c-lattice parameter as  $\omega^*$ , but the OR between  $\omega$  and B2 is the same as the OR between  $\omega$  and A2, i.e.  $[111]_{B2} // [0001]_{\omega}$ , and  $(110)_{B2} // (1120)_{\omega}$ , as the atomic array of the  $\omega$  basal plane is the same as that of the  $(111)_{B2}$  plane.

It should be pointed out that only one type of atoms exists on the  $(0001)_{\omega}$  basal plane as the result of the inheritance of the atomic array of  $(111)_{B2}$ . The different OR plane pair between  $\omega^*$  and B2 here suggests that atomic reordering occurred in the  $(0001)_{\omega}$  basal plane. Fig. 4F shows tentatively the atomic array on  $(0001)_{\omega}$  where circles represent Nb/Mo atoms (type I atoms) and squares represent Al atoms (type II atoms). The projections of the unit cells of  $\omega$  and  $\omega^*$  are indicated on Fig. 3F. When the different atom types are not considered, the atom positions in  $\omega^*$  can be considered to be the same as those of  $\omega$ . The occurrence of atomic

reordering in the  $(0001)_{\omega}$  plane suggests that in addition to the displacive mechanism, diffusion is also important for  $\omega^*$  formation. This is consistent with the present experimental observation that a prolonged heat treatment was necessary for  $\omega^*$  formation. Only diffuse  $\omega$  ( $\omega_d$ ) streaking was observed in the B2 diffraction patterns when the heating time was short. Therefore, the decomposition of the  $\beta$  phase in the Nb-17Al-xMo ribbons heated continuously at 973K is suggested to be:  $A2 \rightarrow B2 \rightarrow (B2 + \omega_d) \rightarrow (B2 + \omega^*)$ .

The plate morphology of the  $\omega^*$  phase is attributed to the low  $(111)_{B2} // (0001)_{\omega}$  interface energy, as this pair consists of the most compact planes of the two phases. The growth rate of the  $\omega^*$  phase along the  $[0001]_{\omega}$  directions is thus lower than along other directions, leading to a plate morphology with  $[0001]_{\omega}$  as the plate normal.

#### The Stability of the $\omega$ -type Structures

The relative stability of the  $\omega$  structures with respect to the parent metastable  $\beta$  phase is closely correlated to the electron density  $\phi$  (which combines both size and electron factors) of  $\beta$  and hence also the  $|\Delta|$  parameter of  $\omega$  [6]. Thermodynamically,  $T_0^{\beta \rightarrow \omega}$  will decrease with increasing  $\phi$  [6,15]. Later transition metals have been found to destabilise the  $\omega$  phase in group IVB based alloys, as was summarised in [6]. Addition of Al will decrease  $\phi$  and  $|\Delta|$  values of later transition metals, so that the  $\omega$ -

type structures will be stabilised. This is supported by the results on  $\omega$  stability in Nb-17Al-xMo where the  $|\Delta|$  value of the  $\beta$  phase increases with increasing  $\phi$  (or rather, with increasing Mo content). The amount and size of the isothermal  $\omega^*$  phase decrease with increasing Mo content and the Al content of the  $\omega^*$  phase is evidently lower than that of the  $\beta$  matrix. Also, the  $\omega^*$  phase was more diffuse-like with higher Mo content in the  $\beta$  phase (compare Figs. 3E and 3F).

It is seen from Fig. 1C that (i) addition of later transition metals (with electron per atom ratio  $e/a \geq 5$ ) to group IVB elements would destabilise the  $\omega$  phase via increasing  $\phi$  of  $\beta$ , and (ii) introduction of Al into later transition metals would stabilise the  $\omega$  phase via decreasing  $\phi$  of  $\beta$ . Although the  $\omega$  phase would be destabilised with increasing  $\phi$  for all investigated transition metal alloys, summarised in Fig. 1C, it is the relative rather than the absolute  $\phi$  value that controls the  $\omega$  phase stability in different alloy systems. This can be seen by the fact that the  $|\Delta|$ - $\phi$  relationship of Zr-Nb is apparently away from the  $|\Delta|$ - $\phi$  relationship of other transition metal base alloys.

In order to understand the experimental results on  $\omega$  phase stability, we have calculated the binding energy curves of binary Al-LTM and Ti-LTM alloys, using the total energy full potential linear muffin-tin orbital (FP-LMTO) method. Details about the calculation have been described elsewhere [16]. The predicted heat of formation of the  $\omega$  structure with reference to the  $\beta$  phase is plotted in Fig. 5A against the electron per atom ratio ( $e/a$ ). The figure confirms that addition of LTMs to the group IVB element Ti does destabilise the  $\omega$  structure by increasing  $e/a$  of  $\beta$ . Addition of Al to a LTM (such as Nb, Mo and V) would stabilise the  $\omega$  structure, but too much addition of Al (such as  $> 50\text{at}\%$ ) would destabilise the  $\omega$  structure as  $\omega$  is unstable with reference to  $\beta$  in pure Al. Besides, the stabilising effect of Al on  $\omega$  stability in Nb, V and Mo is remarkably high, while  $\omega$  is unstable with reference to  $\beta$  in Cr-Al.

The  $\omega$  phase stability in pure transition metal elements is plotted in Fig. 5B against  $e/a$ . According to this figure,  $\omega$  is, with reference to  $\beta$ , stable in group IVB element Ti, unstable in group VB and VIB elements (such as V and Cr) and stable in VIIB and VIIIB elements (such as Fe, Co). This explains the experimental results that addition of LTMs (such as V, Cr, Nb, Mn, Mo, Fe) to Ti or Zr destabilises the  $\omega$  structure (Fig. 1C), as it shifts the  $e/a$  value from 4 toward 5. It is interesting to notice that  $\omega$  is again stable with reference to  $\beta$  for  $7 \leq e/a < 10$ .

Recently, disordered  $\omega$  grains of the classic P6/mmm space group were observed in Fe-Al alloys produced by physical vapour deposition (PVD) [17]. The Al contents of these  $\omega$  grains are in the range of 20-23at%, leading to an  $e/a$  value of  $\sim 7$ . The observation of the disordered  $\omega$  structure in PVD Fe-Al alloys is consistent with inheritance of structures of the parent  $\beta$  phase [6], as the Al content was not high enough to produce A2 $\rightarrow$ B2 ordering in the parent  $\beta$  phase and hence to lead to the formation of an ordered  $\omega$  structure.

Bouid, Servant and Lyon [18] observed  $\omega$  precipitation in a martensitic matrix of Fe-17.74Ni-8.83Co-3.01Mo (at%), which had an  $e/a \approx 8.7$ . The  $\omega$  phase in this alloy contained little Fe ( $C_{Fe} \approx 0$ ) and  $C_{Mo}/(C_{Ni} + C_{Co}) \approx 0.5$ . It is worth noting that the enrichment of Mo in the  $\omega$  phase in this alloy lowers  $e/a$  ( $\approx 8.4$ ), so one might expect stabilisation of the  $\omega$  phase (see Fig. 5B).

However, it should be pointed out that the formation of  $\omega$ -type phases is not only controlled by their stability with reference to the parent  $\beta$  phase, but also by the relative stability of other competing phases in the system. Thermodynamic assessment of all the competing phases in a system is critical for a reliable prediction of the probability of  $\omega$  formation. Such an assessment has been performed for the Ti-Al-V system by incorporating FP-LMTO heats of formation into the

CALPHAD method, which shows that  $\omega$  can be thermodynamically unstable in ( $\alpha_2 + \beta$ ) alloys but an ordered  $\omega$  is metastable in alloys containing the  $\gamma$  phase [15]. This explains why the  $\beta$  phase can be used to effectively ductilise the  $\alpha_2$ -base Ti-Al-LTM alloys (the so-called super- $\alpha_2$  alloys), but cannot be used to ductilise  $\gamma$ -base alloys as the  $\beta$  phase is even harder than  $\gamma$  [19] due to  $\omega$  formation in B2.

## Conclusions

Study of  $\omega$  phase stability has been experimentally extended into Nb-17Al-xMo alloys. The results support the previous hypothesis that addition of Al to later transition metals stabilises the  $\omega$ -type structures and promotes the A2 $\rightarrow$ B2 ordering in the  $\beta$  phase.

Calculation of binding energies using the total energy FP-LMTO method has given predictions of the  $\omega$  phase stability which is consistent with experimental results. Both electron and size factors are important to  $\omega$  phase stability. Al evidently stabilises  $\omega$  in Nb, V and Mo, but the stabilising effect of Al on  $\omega$  formation in Cr is not enough to make  $\omega$  a stable phase with reference to  $\beta$  in binary Cr-Al.

An ordered  $\omega$ -type structure,  $\omega^*$ , has been observed in Nb-17Al-xMo alloys heat treated at 973K. The lattice parameter of  $\omega^*$  is  $a_{\omega^*} = \sqrt{6}a_{\beta 2}$  and  $c_{\omega^*} = \sqrt{3}a_{\beta 2}$ . The orientation relationship between  $\omega^*$  and B2 is  $\langle 111 \rangle_{\beta 2} // \langle 0001 \rangle_{\omega^*}$ ,  $\{10\bar{1}\}_{\beta 2} // \{10\bar{1}0\}_{\omega^*}$ .

## References

1. B. S. Hickman, *J. Mater. Sci.*, **4**(1969), 544.
2. L. Sass, *J. Less-Common Metals*, **28**(1972), 157.
3. S. K. Sikka, Y. K. Vohra and R. Chidambaram, *Prog. Mater. Sci.*, **27**(1982), 245.
4. P. D. Frost, W. M. Parris, L. L. Hirsch, J. R. Doig, and C. M. Schwartz, *Trans. Am. Soc. Metals*, **46**(1954), 231.
5. J. C. Williams, B. S. Hickman and D. H. Leslie, *Met. Trans.*, **2**(1971), 477.
6. G. Shao, A. P. Miodownik and P. Tsakirooulos, *Phil. Mag. A*, **71**(1995) 1389.
7. W. Sinkler and D. E. Luzzi, *Acta Metall. Mater.*, **42**(1994), 1249.
8. K. K. McCabe and S. L. Sass, *Phil. Mag.*, **23**(1971), 957.
9. N. N. Aparov, I. V. Lyasotskiy and Y. D. Tyapkin, *Fiz Metall. Metalloved.*, **40**(1975), 1107.
10. N. B. D'yakonova and I. V. Lyasotskiy, *Fiz Metall. Metalloved.*, **52**(1981), 119.
11. L. A. Bendersky, W. J. Boettinger, P. B. Burton, F. S. Biancanello and C. B. Shoemaker, *Acta Metall. Mater.*, **38**(1990), 931.
12. E. Passa, G. Shao and P. Tsakirooulos, *Intermetallics*, **5**(1997), in press.
13. G. Shao, PhD thesis, University of Surrey (1995).
14. J. M. Silcock, M. H. Davies and H. K. Hardy, in *Proc. Symp. Mechanisms of Phase Transformations in Metals* (London: Institute of Metals, 1955), 93.
15. G. Shao, A. P. Miodownik, P. Tsakirooulos, D. Nguyen Manh and D. G. Pettifor, in *Titanium'95, Vol. 3*, eds. B. A. Blenkinsop, W. J. Evans and H. M. Flower, Institute of Materials (1996), 2281.
16. D. Nguyen Manh, D. G. Pettifor, G. Shao, A. P. Miodownik and A. Patsurel, *Phil. Mag. A*, **76**(1996), 1385.
17. G. Shao, P. Tsakirooulos, C. Loader, D. Dunford and M. C. Ward-Close, in *Synthesis of Light-Weight Intermetallic Materials II, TMS*(1997), in press.
18. N. Bouid, C. Servant and O. Lyon, *Phil. Mag. B*, **57**(1988), 343.
19. T. Ahmed and H. M. Flower, *Mater. Sci. Technol.*, **10**(1994), 272.

## PHASE STABILITY IN HIGH TEMPERATURE Mo-RICH Mo-B-Si ALLOYS

C.A. Nunes<sup>\*,\*\*</sup>, R. Sakidja<sup>\*</sup> and J.H. Perepezko<sup>\*</sup>

<sup>\*</sup> Department of Materials Science and Engineering  
University of Wisconsin - Madison  
1509 University Ave.  
Madison WI, 53706

<sup>\*\*</sup> Department of Materials Engineering - DEMAR  
Chemical Engineering College - FAENQUIL  
Polo Urbo-Industrial s/nº, Mondesir  
12600-000, Lorena (SP), Brazil

### Abstract

The phase stability in a new refractory metal silicide system based on Mo-rich alloys in the Mo-Si-B system has been examined with emphasis on the reported existence of a  $\text{Mo}_{\text{SS}} + \text{Mo}_3\text{SiB}_2$  ( $T_2$ ) two phase coexistence as the basis for multiphase microstructure design. Even at 1600°C the large scale solidification segregation and sluggish diffusion in the Mo-Si-B system required the use of annealing times of 150 hours to approach equilibrium in arc-melted samples. At 1200°C, the annealing of ingot samples was ineffective, but rapidly solidified foils with refined microstructural scale allowed for the attainment of equilibrium structures upon annealing. The results from 1600°C and 1200°C isothermal annealing experiments as well as the analysis of the solidification reactions confirm the stability of a  $\text{Mo}_{\text{SS}} + T_2$  two phase field. The  $T_2$  phase region at 1600°C has a composition range of existence of several atomic percent outside of the stoichiometric  $\text{Mo}_3\text{SiB}_2$  value and  $T_2$  is stable up to at least 2100°C. The phase stability analysis has been summarized in terms of a plethral section between  $\text{Mo}_{\text{SS}}$  and  $T_2$ . The accommodation of non-stoichiometric compositions in the ordered  $T_2$  lattice is likely to involve a defect structure and is reflected in the compositional variation of lattice parameters. There are several opportunities for the development of different microstructural morphologies in ( $\text{Mo}_{\text{SS}} + T_2$ ) phase mixture including the application of rapid solidification and the precipitation of Mo within a  $T_2$  matrix for strengthening and toughening.

### Introduction

The requirements of elevated temperature use limit the available materials to a few specific classes. There are a number of ceramic materials, intermetallic compounds and refractory metals with melting temperatures,  $T_m$ , above 1500° C [1]. At the same time, the successful application of high temperature structural materials is reflected in variety of mechanical properties: strength, ductility, toughness, creep resistance and oxidation resistance. As single components, ceramic materials and intermetallic phases are known to suffer from embrittlement problems at low temperature [2,3]. Similarly, refractory metals such as molybdenum and niobium have sufficient ductility, but are

sensitive to oxidation problems and poor creep resistance at high temperatures [4]. Since a single component is unlikely to satisfy all of the demanding and diverse requirements for structural integrity at high temperatures, multiphase designs are essential [5]. Such designs include composites as well as multiphase alloys [6]. There is a strong history of success which indicates that multiphase designs in a monolithic material are an effective approach for developing reliable components for structural applications [7-12]. With this in mind a multiphase design based on a refractory metal and an intermetallic is a useful starting point.

While a variety of various intermetallic phases have been examined in recent years, it is clear that of all of the intermetallics,  $\text{MoSi}_2$  has emerged as a leading candidate in terms of a vastly superior oxidation resistance at elevated temperatures [13,14]. Indeed,  $\text{MoSi}_2$  is a proven oxidation resistant material that finds wide application commercially in heating elements. As with other intermetallics,  $\text{MoSi}_2$  has ductility problems at low temperatures [15] which has motivated the development of toughening strategies [15,16]. Unfortunately,  $\text{MoSi}_2$  is not in equilibrium with other refractory metals [17,18] so that toughening strategies have for most part focused on controlling the most challenging interface reactions that occur between  $\text{MoSi}_2$  and refractory metal solid solutions [16,17]. There are other silicide phases such as  $\text{Me}_3\text{Si}_2$  (where  $\text{Me} \equiv$  refractory metal) but in all cases these have much lower oxidation resistance than that for the disilicides [13,14]. There are a few selected cases where a refractory metal is in equilibrium with a ternary intermetallic containing Si. Most notably  $\text{Me}_3\text{SiB}_2 + \text{Me}$  appear to coexist as reported in the literature where  $\text{Me}$  is Nb or Mo [20]. There is also a possibility of two phase equilibrium between Mo and a ternary  $\text{MoZrSi}$  phase [21] and between Mo and a ternary  $\lambda$  phase in the  $\text{MoSiNi}$  system [21]. However, in terms of oxidation resistance, it appears that an intermetallic containing both Si and B and in equilibrium with Mo or Nb is most attractive.

There is a reasonably complete database available for the phase equilibria in binary refractory metal silicides and borides [22], but the extension of this base to ternary systems is incomplete and the reported information is of uncertain reliability. The published information on the phase equilibria in Mo-Si-B and Nb-Si-B alloys especially for Mo and Nb rich compositions of interest is very limited. Estimated isothermal sections, at 1600°C, have been published [19,20]. However, the sample

preparation in the study involved the sintering of elemental powder compacts for only 12 hours so that the attainment of full equilibrium and the influence of impurities are uncertain. The isotherm does indicate a two-phase field between a Mo and Nb solid solution and a ternary  $T_2$  phase,  $Mo_5SiB_2$  or  $Nb_5SiB_2$  respectively.

The  $T_2$  phase has the  $D8_7$  structure which is represented by a body-centered tetragonal unit cell, space group  $I4/mcm$ , with lattice parameters  $a = 6.013 \text{ \AA}$ ,  $c = 11.03 \text{ \AA}$  [23-26]. An illustration of the  $T_2$  structure is shown in figure 1 together with two projections. From the perspective presented in figure 1, it is apparent that the  $T_2$  structure is formed by 3 different types of layers: layer 1 with Mo and B atoms in contact, layer 2 consisting of only Mo atoms and layer 3 consisting of only Si atoms. It is interesting to note that layer 1 and 3 are situated between layers of pure Mo so that the  $T_2$  phase is fully ordered at stoichiometry. The reported information in the Mo-Si-B and Nb-Si-B systems indicates that  $T_2$  phase occurs over a range of composition. This is of special importance in processing since it indicates that the two phase field between the refractory metal and  $T_2$  phase has some width to allow for a reasonable phase structure control during processing. There are also promising indications from initial studies that Mo-Si-B alloys offer good oxidation resistance [27-28] and high temperature creep resistance [29]. With this in mind, an examination of the high temperature phase stability in the Mo-Si-B system for Mo-rich compositions has been undertaken. One of the key objectives is the examination of multiphase microstructures that are possible in this system which also offers insight into some of the challenges that alloys with very high melting temperatures pose to materials processing.

#### Experimental Procedure

All alloys in this study were initially prepared by arc-melting pure materials, Mo (99.97%), B (99.5%) and Si (99.995%) in a cooled copper crucible under pure argon (99.998%). Multiple melting cycles were carried out for each alloy in an effort to obtain homogeneous ingots. Before each melting cycle the furnace was evacuated and back-filled with argon several times. A pure Ti sample was melted before each melting cycle to getter residual  $O_2$  and  $N_2$  present. No evidence of oxidation was noticed on the surface of the ingots.

The long-term heat-treatments were carried out at  $1200^\circ\text{C}$  and  $1600^\circ\text{C}$  for 150 h under flowing argon (99.998%) followed by furnace cooling. Samples from selected arc melted ingots were wrapped with Ta foils, placed in an  $Al_2O_3$ -crucible and heat treated in an horizontal tube furnace. Two crucibles containing Ti-sponge were placed surrounding the crucible containing the samples to getter residual oxygen and nitrogen.

After the heat-treatments there was no indication of either reaction between the samples and the Ta foil or external oxidation. In addition, no evidence of melting was noticed.

As will be shown later, the microstructural analysis of the samples heat-treated at  $1200^\circ\text{C}$  did not indicate any important modification compared to the as-cast structures. Thus, in order to reduce the segregation observed in the as-cast ingots and to allow for a faster approach to equilibrium at  $1200^\circ\text{C}$ , several samples were rapidly solidified via splat-quenching. The resulting splats were annealed at  $1200^\circ\text{C}$  for 150 h following the procedure described earlier. The splat-quenching process consisted of levitation and melting of samples from the arc-melted ingots in an evacuated and purged argon (99.998%) environment. After the sample was molten, the power to the radio frequency coil was stopped and as the droplet fell a photo-detector sensed the radiating sample, discharging two capacitors which accelerated two copper anvils together. The falling molten droplet was splat-quenched between the two anvils permitting rapid solidification ( $10^3$ - $10^4 \text{ K/s}$ ) in the resultant foil.

The microstructural characterization of the alloys was carried out via SEM (Scanning Electron Microscopy) / BSEI (Back-Scattered Electron Image), Electron Probe Microanalysis (EPMA) / Wavelength Dispersive Spectroscopy (WDS), X-Ray Diffraction (XRD) and Transmission Electron Microscopy (TEM). In addition, bulk chemical analysis was performed to determine the Si, B, O and N content of selected as-cast alloys. The B and Si content of selected as-cast alloys were measured by direct current plasma emission spectroscopy (ASTM E1097) using a Beckman SpectraSpan VI Spectrometer while the oxygen and nitrogen content were measured by inert gas fusion (ASTM E1019) using a LECO model TC 136 Analyzer.

For the experiments involving SEM/BSEI and EPMA/WDS, samples were hot-mounted in a conductive media, ground on silicon carbide paper (240  $\rightarrow$  600) and polished with diamond paste ( $6\mu\text{m} \rightarrow 0.25\mu\text{m}$ ). No coating was used. The SEM/BSEI analysis were carried out in a JEOL 35C and JEOL 6100 operated at 20/25kV. The EPMA/WDS experiments were carried out in a CAMECA SX50 microprobe. Further details of the EPMA/WDS experiments are given in the appendix.

The XRD experiments were carried out at room temperature using a STOE/Siemens diffractometer (Cu-K $\alpha$  radiation) operated at 40 kV / 25 mA in the reflection mode. Samples from the as-cast and heat-treated ( $1600^\circ\text{C}$  / 150h) alloys were used in a powder form (below 170 mesh) while the splats and heat-treated splats were examined without change. The phases present in the samples were identified via the JCPDS database and the lattice parameters calculated using the software TRIESTE.

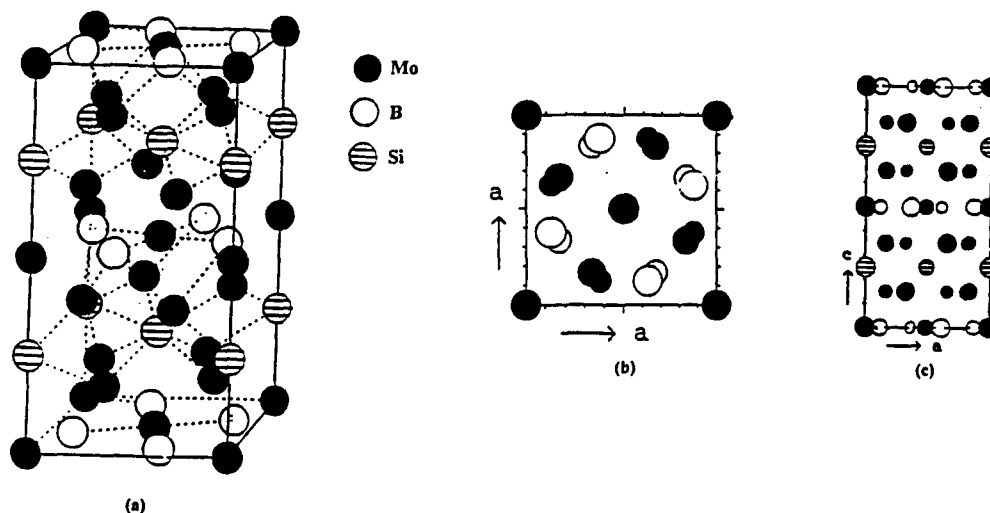


Figure 1.  
Crystal structure for  $T_2$  ( $Mo_5SiB_2$ ) phase  
(isomorphous with  $Cr_5B_2$  [26]).



The results of EPMA/WDS (appendix) have indicated a low solubility of silicon in both  $\text{Mo}_2\text{B}$  and  $\alpha\text{MoB}$  phases at  $1600^\circ\text{C}$  after extended annealing at  $1600^\circ\text{C}$ . The current values are smaller than those given by Nowotny [20]. In addition, the results of EPMA/WDS have also indicated a low solubility of B in both the  $\text{Mo}_3\text{Si}$  and the  $\text{Mo}_5\text{Si}_3$  phases. Additional information concerning extension of binary phase stability into ternary compositions as well as that on the range of solubility of the  $\text{T}_2$ -phase can be obtained through lattice parameter data. The lattice parameter values of the phases present in each of the five three-phase triangles surrounding the  $\text{T}_2$ -composition are given in Table 1 together with the JCPDS reported values.

From the lattice parameter trends in Table 1 and the phase relations indicated in figure 2, it is possible to identify additional features of the solubility behavior. For instance, the lattice parameter of the  $\text{Mo}_3\text{Si}$  and  $\text{Mo}_5\text{Si}_3$  phases present in the ternary alloys which are at their saturation values for B are very close to those of the binary  $\text{Mo}_3\text{Si}$  and  $\text{Mo}_5\text{Si}_3$  phases, confirming the low solubility of B in those phases. The same result is observed in the case of the solubility of silicon in both  $\text{Mo}_2\text{B}$  and  $\alpha\text{MoB}$  phases. The lattice parameter of the  $\text{T}_2$ -phase varies in the range of  $a = 6.0060 - 6.0413 \text{ \AA}$  and  $c = 11.0525 - 11.0948 \text{ \AA}$ . It can be observed that the  $a$  and  $c$  lattice parameter values of the  $\text{T}_2$ -phase are both minimum in the  $\text{Mo}_2\text{B}+\text{T}_2+\alpha\text{MoB}$  three-phase field and maximum in the  $\text{Mo}_3\text{Si}+\text{T}_2+\text{Mo}_5\text{Si}_3$  three-phase field. The results of EPMA/WDS experiments have shown that in the  $\text{Mo}_2\text{B}+\text{T}_2+\alpha\text{MoB}$  three-phase field the  $\text{T}_2$ -phase has the lowest Si and highest B content among the three-phase fields where this phase is present.

On the other hand, in the  $\text{Mo}_3\text{Si}+\text{T}_2+\text{Mo}_5\text{Si}_3$  three-phase field the  $\text{T}_2$ -phase presents the highest Si and lowest B content. A closer examination of this general behavior can be made by comparing the change in lattice parameter for the  $\text{T}_2$  phase in selected regions. For example, in the  $(\text{Mo}_3\text{Si} + \text{Mo}_5\text{Si}_3 + \text{T}_2)$  and  $(\text{Mo}_2\text{B} + \alpha\text{MoB} + \text{T}_2)$  three phase fields the Mo content of  $\text{T}_2$  is approximately constant. Between these two three-phase regions, the Si content of  $\text{T}_2$  decreases while the B content increases and both the  $a$  and  $c$  parameter values decrease.

An examination of figure 1 reveals that the lattice parameter behavior is consistent with a substitution behavior of B on Si sites and may also involve vacancies [12,30]. Furthermore, the overall results

Table 1

Lattice Parameter Measurements for Phases in Mo-Si-B System

THREE-PHASE FIELD		PHASES AND LATTICE PARAMETER (Å)	
		a	c
$\text{Mo}_{55}+\text{T}_2+\text{Mo}_3\text{Si}$	$\text{Mo}_3\text{Si}$	4.8977	
	$\text{Mo}_{55}$	3.1466	
	$\text{T}_2$	6.0265	11.0718
$\text{Mo}_{55}+\text{T}_2+\text{Mo}_2\text{B}$	$\text{Mo}_2\text{B}$	5.5556	4.7478
	$\text{Mo}_{55}$	3.1452	
	$\text{T}_2$	6.0177	11.0553
$\text{Mo}_5\text{Si}_3+\text{T}_2+\text{Mo}_3\text{Si}$	$\text{Mo}_5\text{Si}_3$	9.6424	4.9058
	$\text{T}_2$	6.0289	11.0948
	$\text{Mo}_3\text{Si}$	4.8960	
$\text{Mo}_2\text{B}+\text{T}_2+\alpha\text{MoB}$	$\text{Mo}_2\text{B}$	5.5651	4.7499
	$\text{T}_2$	6.0060	11.0525
	$\alpha\text{MoB}$	insufficient data	
$\text{Mo}_5\text{Si}_3+\text{T}_2+\alpha\text{MoB}$	$\text{Mo}_5\text{Si}_3$	9.6441	4.9058
	$\text{T}_2$	6.0225	11.0850
	$\alpha\text{MoB}$	3.1149	16.9907
JCPDS Data:	Mo	3.1472	
	$\text{Mo}_3\text{Si}$	4.890	
	$\text{Mo}_5\text{Si}_3$	9.6483	4.9135
	$\text{Mo}_2\text{B}$	5.547	4.739
	$\alpha\text{MoB}$	3.105	16.970
	$\text{T}_2$	6.013	11.034

indicate that the  $\text{T}_2$ -phase is not a line compound which is an important feature for the development of processing options for the  $\text{Mo}_{55}+\text{T}_2$  two-phase microstructure.

#### Two-Phase ( $\text{Mo}_{55} + \text{T}_2$ ) Microstructure

After confirming the existence of the  $\text{Mo}_{55}+\text{T}_2$  two-phase field in the Mo-rich region at  $1600^\circ\text{C}$  the  $\text{Mo}_{55}+\text{T}_2$  two-phase microstructure was examined in more detail. Based upon the  $\text{Mo}_3\text{SiB}_2$  stoichiometry ( $\text{Mo}_{62.5}\text{Si}_{12.5}\text{B}_{25}$ ) for the  $\text{T}_2$ -phase, two alloys of composition  $\text{Mo}_{79}\text{B}_{14}\text{Si}_7$  (# 10) and  $\text{Mo}_{70}\text{B}_{20}\text{Si}_{10}$  (# 18) were prepared via arc-melting and heat-treated at  $1600^\circ\text{C}$  for 150h. In alloy # 10, a microstructure consisting of the phases  $\text{Mo}_{55}$ ,  $\text{Mo}_2\text{B}$ ,  $\text{T}_2$  and  $\text{Mo}_3\text{Si}$  was observed in the as-cast condition. After the heat-treatment, a two-phase microstructure consisting of  $\text{Mo}_{55}$  and  $\text{T}_2$  developed indicating the dissolution of both  $\text{Mo}_2\text{B}$  and  $\text{Mo}_3\text{Si}$  phases during heat-treatment. In alloy # 18,  $\text{T}_2$ ,  $\text{Mo}_{55}$  and  $\text{Mo}_3\text{Si}$  were observed in the as-cast microstructure. A SEM/BSEI micrograph and XRD pattern of this alloy are shown respectively in figures 3a/b. As in the case of alloy # 10, after

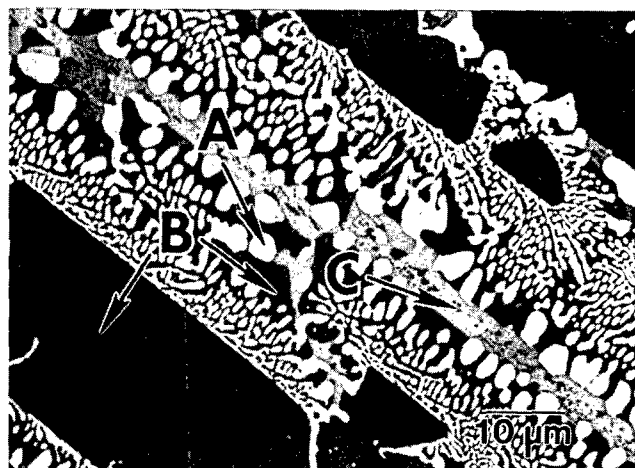


Figure 3a.  
SEM/BSEI micrograph of as-cast  $\text{Mo}_{70}\text{B}_{20}\text{Si}_{10}$  (# 18).  
A =  $\text{Mo}_{55}$ , B =  $\text{T}_2$ , C =  $\text{Mo}_3\text{Si}$

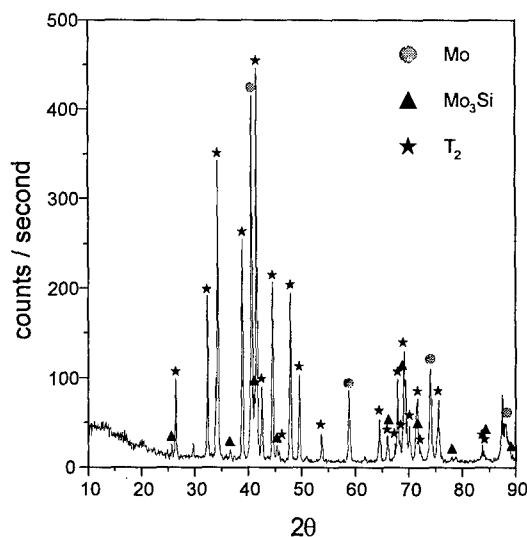


Figure 3b.  
XRD pattern for as-cast  $\text{Mo}_{70}\text{B}_{20}\text{Si}_{10}$  (# 18).

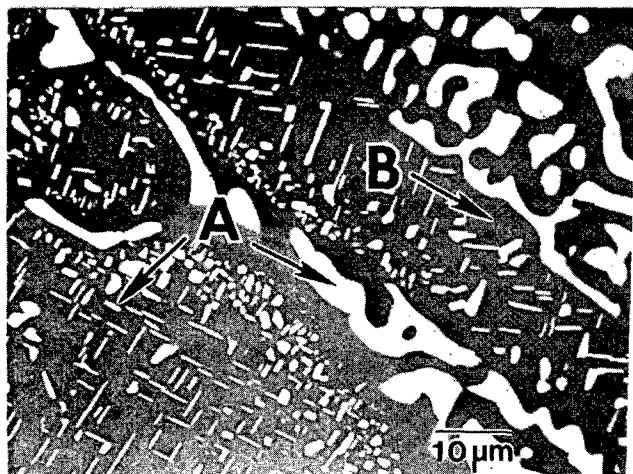


Figure 4a.  
SEM/BSEI micrograph of  $\text{Mo}_{70}\text{B}_{20}\text{Si}_{10}$  (# 18)  
(arc-melted + heat-treated at 1600 °C for 150 h).  
A =  $\text{Mo}_{\text{SS}}$ , B =  $\text{T}_2$

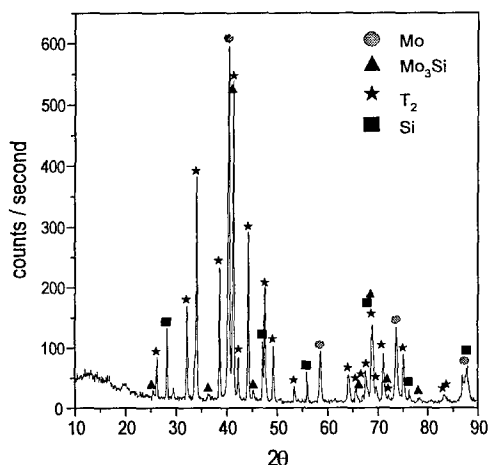


Figure 4b  
XRD pattern for  $\text{Mo}_{70}\text{B}_{20}\text{Si}_{10}$  (# 18)  
(arc-melted + heat-treated at 1600 °C for 150 h)

the heat-treatment a microstructure of essentially  $\text{Mo}_{\text{SS}}+\text{T}_2$  developed, however, minor regions of  $\text{Mo}_3\text{Si}$  are noticed suggesting that the bulk composition of this alloy should be slightly shifted into the  $\text{Mo}_{\text{SS}}+\text{T}_2+\text{Mo}_3\text{Si}$  three-phase field.

A SEM/BSEI micrograph and XRD pattern of alloy #18 after heat-treatment are shown respectively in figures 4a/b. In figure 4a the development of  $\text{Mo}_{\text{SS}}$  precipitates was observed in the former  $\text{T}_2$  dendrites. The precipitation occurred during the heat-treatment in the solid state since no precipitation was observed in the as-cast microstructure of this alloy (figure 3a). In addition, in figure 4a that the  $\text{Mo}_{\text{SS}}$  precipitates appear to display some crystallographic relationship with the  $\text{T}_2$ -phase [30]. The precipitation reaction is a very significant finding since it allows for the development of toughening strategy for the  $\text{Mo}_{\text{SS}}+\text{T}_2$  microstructure. Furthermore, it should be pointed out that in both #10 and #18 alloys the  $\text{T}_2$ -phase constituted the matrix in the microstructure and displayed excellent oxidation resistance [28]. Further experiments to examine the development of a  $\text{Mo}_{\text{SS}}$ -matrix two-phase microstructure are in progress.

#### Rapid Solidification Processing (RSP) and the Phase Relations at 1200°C

Arc-melted alloys were initially used to determine the phase relations in the Mo-rich side of the Mo-Si-B system at 1200°C. However, no significant modification of the as-cast microstructure could be observed even after 150h heat-treatment, which is related to the low diffusivity of the atomic species of this system. A SEM/BSEI of the  $\text{Mo}_{70}\text{B}_{20}\text{Si}_{10}$  alloy (#18) after heat-treatment at 1200°C for 150 h is shown in figure 5 and can be compared with the as-cast microstructure shown in figure 3a. In fact, a comparison of the observed change in microstructural scale of the interdendritic Mo-rich phase upon annealing at 1600°C (i.e. figure #3a and figure 4a) allows for an estimate of the interdiffusivity in the range of about  $10^{-18}$  to  $10^{-19}$   $\text{m}^2/\text{s}$  which is comparable to that reported for Mo [31]. This experience is a good example of a major challenge in the processing of high temperature materials. The desired attributes for high temperature service of low oxidation rate and creep resistance are related to diffusion rates which must be low for good performance. However, the same diffusion characteristics clearly govern the attainment of phase and microstructural equilibrium; thus these processes will also be slow.

In order to produce a shorter diffusion path for the establishment of equilibrium conditions, several arc-melted alloys were splat quenched and then heat-treated at 1200°C for 150h. It is well-known that RSP can suppress macrosegregation and generate a more homogeneous and a refined microstructure due to inherently large undercooling and solidification velocity [32]. In fact, for the  $\text{Mo}_{70}\text{B}_{14}\text{Si}_6$  Alloy (# 10), in which the  $\text{Mo}_3\text{Si}$  and  $\text{Mo}_2\text{B}$  phases were observed in addition to the Mo and  $\text{T}_2$  phases in the as-cast microstructure, only Mo and  $\text{T}_2$  were present after splat-quenching. A plan view TEM analysis indicated a very fine  $\text{Mo}+\text{T}_2$  lamella microstructure in the middle section of the splat with thickness from less than 50 nm to 150 nm. Upon heat-treatment at 1200°C for 150h the microstructure evolved into a homogeneous  $\text{Mo}+\text{T}_2$  duplex microstructure. As in the case of alloy # 10, the  $\text{Mo}_{70}\text{B}_{20}\text{Si}_{10}$  alloy (# 18) also exhibited a  $\text{Mo}+\text{T}_2$  two-phase microstructure after splat-quenching, indicating the suppression of the  $\text{Mo}_3\text{Si}$ -phase formation. A SEM/BSEI micrograph of this alloy after splat-quenching is shown in figure 6. Upon heat-treatment the cross-section SEM/BSEI and TEM indicate a homogeneous distribution of Mo grains in a  $\text{T}_2$ -matrix which is shown in figures 7a/b. In terms of phase stability, these results confirm clearly the existence of the  $\text{Mo}+\text{T}_2$  two-phase field at 1200°C. In addition, this experience also demonstrates the feasibility of producing a  $\text{Mo}_{\text{SS}}+\text{T}_2$  two-phase microstructure directly from the melt via an RSP technique.

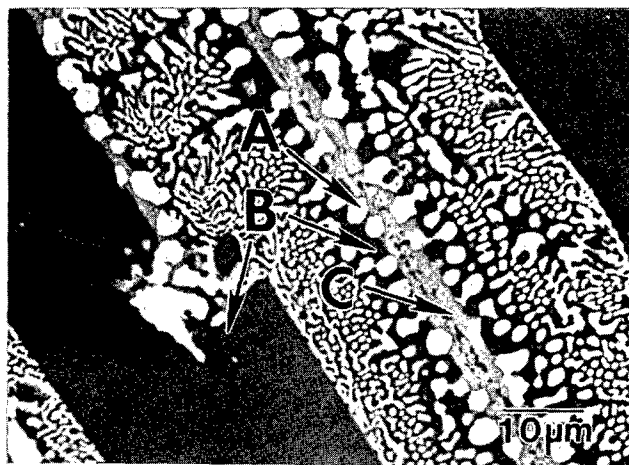


Figure 5.  
SEM/BSEI micrograph of  $\text{Mo}_{70}\text{B}_{20}\text{Si}_{10}$  (# 18)  
(arc-melted + heat treated at 1200 °C for 150 h).  
A =  $\text{Mo}_{\text{SS}}$ , B =  $\text{T}_2$ , C =  $\text{Mo}_3\text{Si}$



Figure 6.

SEM/BSEI micrograph of splat-quenched  $\text{Mo}_{70}\text{-B}_{20}\text{-Si}_{10}$  (# 18)  
The dark phase (matrix) is  $T_2$ , the bright phase is Mo.

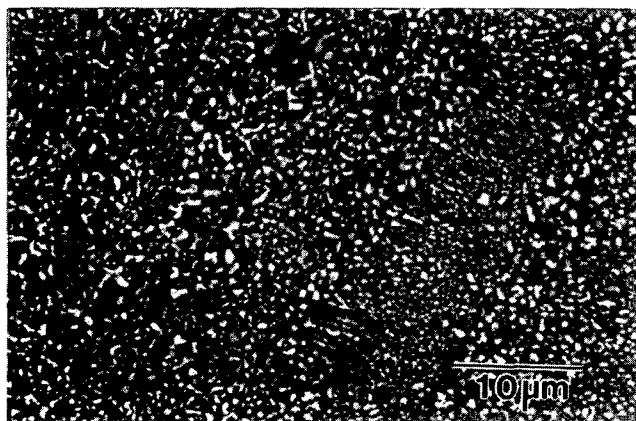


Figure 7a.

SEM/BSEI micrograph of  $\text{Mo}_{70}\text{-B}_{20}\text{-Si}_{10}$  (# 18)  
(splat-quenched + heat-treated at 1200 °C for 150 h)  
The dark phase (matrix) is  $T_2$ , the bright phase is Mo.

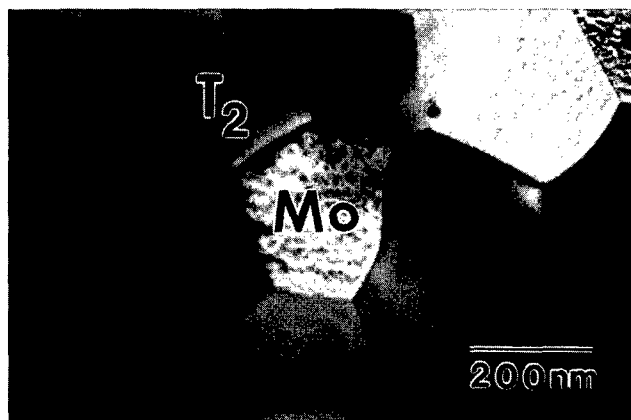


Figure 7b

TEM/BFI micrograph of  $\text{Mo}_{70}\text{-B}_{20}\text{-Si}_{10}$  (# 18).

Similar RSP treatments were also carried out with alloy compositions in four of the five three-phase fields neighboring the  $T_2$ -composition at 1600°C. After splat-quenching, all samples presented a three-phase microstructure following the phase relations established at 1600°C. Furthermore, the similar phases were observed in each alloy after the heat-treatment at 1200°C, indicating that in the Mo-rich region of the Mo-B-Si system similar phase relations exist at 1600°C and 1200°C.

#### Liquidus Projection

A complete analysis of the solidification reactions will be given elsewhere [32], but several results from the analysis relate to the solid state phase stability and are included in this context in the present discussion. The liquidus projection in the Mo-rich part of the Mo-B-Si system determined in this study is presented in figure 8. It was obtained from an analysis of 25 ternary and 7 binary alloys whose compositions are indicated on figure 8. The symbols  $p_1$ ,  $p_2$ ,  $e_1$ ,  $e_2$ ,  $e_3$ ,  $c_1$  and  $c_2$  on the figure represent the following invariant reactions (i.e.  $p$ = peritectic,  $e$ = eutectic and  $c$ = congruent melting) in the binary Mo-B and Mo-Si systems:

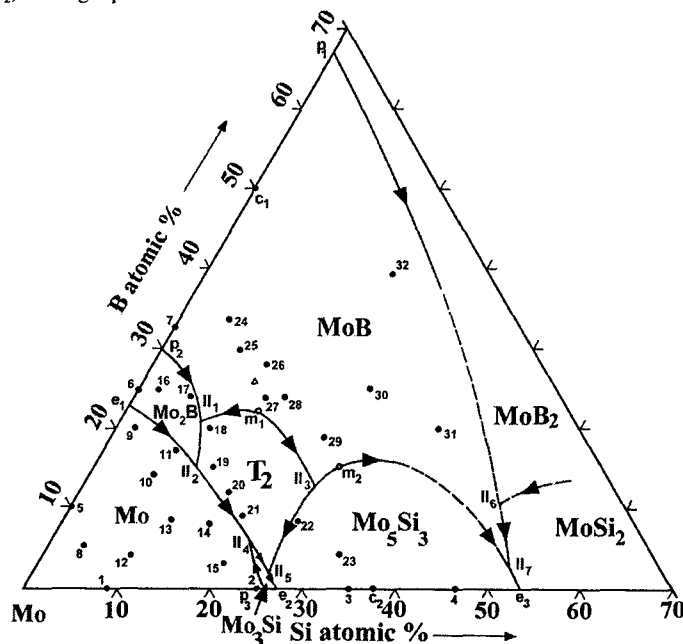


Figure 8.

Liquidus projection for Mo-rich side of the Mo-B-Si system



$p_1 > L + \beta\text{MoB} \rightleftharpoons \text{MoB}_2$  (T = 2375 ± 12°C)  
 $p_2 > L + \beta\text{MoB} \rightleftharpoons \text{Mo}_2\text{B}$  (T = 2280 ± 12°C)  
 $p_3 > L + (\text{Mo}) \rightleftharpoons \text{Mo}_3\text{Si}$  (T = 2025°C)  
 $e_1 > L \rightleftharpoons (\text{Mo}) + \text{Mo}_3\text{B}$  (T = 2175 ± 6°C)  
 $e_2 > L \rightleftharpoons \text{Mo}_3\text{Si} + \text{Mo}_5\text{Si}_3$  (T = 2020°C)  
 $e_3 > L \rightleftharpoons \text{MoSi}_2 + \text{Mo}_5\text{Si}_3$  (T = 1900°C)  
 $c_1 > L \rightleftharpoons \beta\text{MoB}$  (T = 2600 ± 6°C)  
 $c_2 > L \rightleftharpoons \text{Mo}_5\text{Si}_3$  (T = 2180°C)

The symbol  $\Delta$  corresponds to the approximate  $T_2$ -phase composition and  $m_1$  and  $m_2$  are points of maximum on the liquidus surface. As can be observed, the liquidus surfaces indicate the existence of seven primary liquidus regions which are:  $\beta\text{MoB}$ ,  $\text{Mo}_2\text{B}$ ,  $\text{Mo}_{55}$ ,  $T_2$ ,  $\text{Mo}_3\text{Si}$ ,  $\text{Mo}_5\text{Si}_3$  and  $\text{MoB}_2$ . The liquidus surfaces descend toward the Mo-Si binary side, which is primarily associated to the lower liquidus temperature in this system compared to that of the Mo-B system. The  $T_2$ -composition is located on the  $\beta\text{MoB}$  primary region, showing that the  $T_2$ -phase does not melt congruently. In fact, this phase is formed through the peritectic-type reaction  $L + \beta\text{MoB} \rightleftharpoons T_2$ . Some ternary reactions such as  $\text{II}_4$  and  $\text{II}_5$  are under further study. Due to the relatively small differences in composition and temperature for these reactions, variations in processing conditions can modify the solidification path and microstructure. In addition, it should be pointed out that arc-melted alloys with composition in the  $\text{Mo}_{55} + T_2$  two-phase field (1600°C) always exhibit the  $\text{Mo}_3\text{Si}$  phase in the last part to solidify. A SEM/BSEI and XRD pattern of alloy #13 are shown respectively in figures 9a/b. This alloy displays primary precipitation of the with composition in the  $\text{Mo} + T_2$  two-phase field (1600°C) always exhibit the  $\text{Mo}_3\text{Si}$ -phase in the last part to solidify.  $\text{Mo}_{55}$ -phase followed by the coupled precipitation of  $\text{Mo}_{55}$  and  $T_2$  and then coupled precipitation of  $\text{Mo}_3\text{Si} + T_2$  in the final solidification reaction

#### ( $\text{Mo}_{55}$ - $T_2$ ) Plethral Section

Based on the established phase relations at 1600°C (figure 2) and 1200°C and the liquidus projection (figure 8), an estimated  $\text{Mo}_{55}$ - $T_2$  plethral section was drawn which is shown in figure 10. This section has been constructed to include the  $\text{Mo}_{55}$  and  $T_2$  two-phase region so that it does not include pure Mo. The existence of four different primary liquidus regions:  $\text{Mo}_{55}$ ,  $\text{Mo}_2\text{B}$ ,  $T_2$  and  $\beta\text{MoB}$  is included in the diagram.

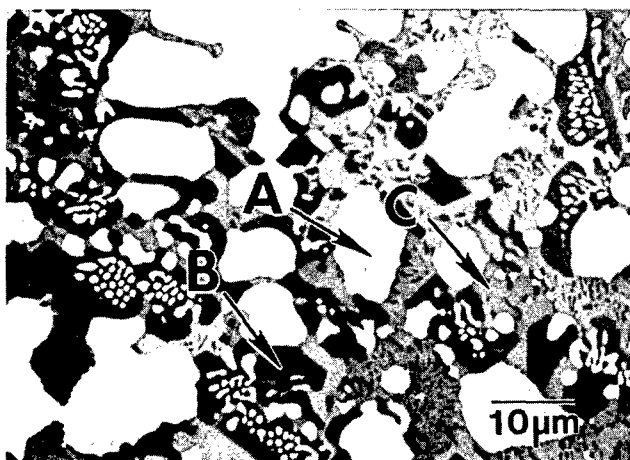


Figure 9a.  
SEM/BSEI micrograph of as-cast  $\text{Mo}_{80}\text{-B}_{8.2}\text{-Si}_{11.8}$  (# 13).  
A =  $\text{Mo}_{55}$ , B =  $T_2$ , C =  $\text{Mo}_3\text{Si}$

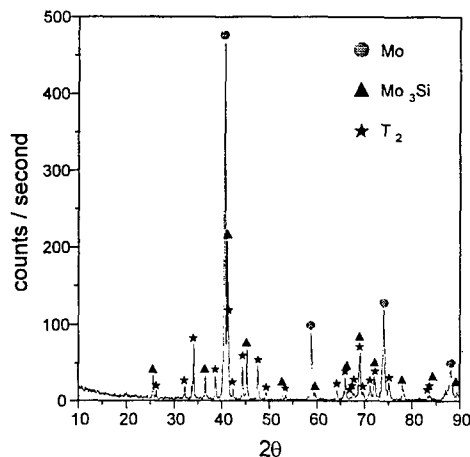


Figure 9b.  
XRD pattern for as-cast  $\text{Mo}_{80}\text{-B}_{8.2}\text{-Si}_{11.8}$  (# 13).

Thus, samples conventionally cast with composition in the  $\text{Mo} + T_2$  two-phase field may also exhibit the  $\beta\text{MoB}$  or the  $\text{Mo}_2\text{B}$  phase in addition to the  $\text{Mo}_{55}$ ,  $T_2$  and  $\text{Mo}_3\text{Si}$  phases. The section is not given as an isoplethal section so that the tie lines are not necessarily contained in the plane of the section. However, since the  $\text{Mo} + T_2$  two phase region is relatively narrow, the error involved in treating this portion of the section as isoplethal should not be large. The maximum temperature of existence of the  $\text{Mo} + T_2$  two-phase field is estimated to be about 2100°C based on the relative position of point  $\text{II}_2$  (figure 8) with respect to points  $e_1$  and  $e_2$  (figure 8) and the expected liquidus surface topology. It should be pointed out that point  $\text{II}_2$  in figure 8 corresponds to the four-phase invariant equilibria:  $L + \text{Mo}_2\text{B} \rightleftharpoons \text{Mo}_{55} + T_2$ . The maximum temperature of existence of the  $\text{Mo} + T_2$  two-phase field is a significant finding to support further evaluation of the  $\text{Mo} + T_2$  potential for high-temperature structural applications.

A number of features in the plethral section are not fully established, but have been included to reflect the observed solidification behavior and solid state phase stability. For example, Si and B are common additions

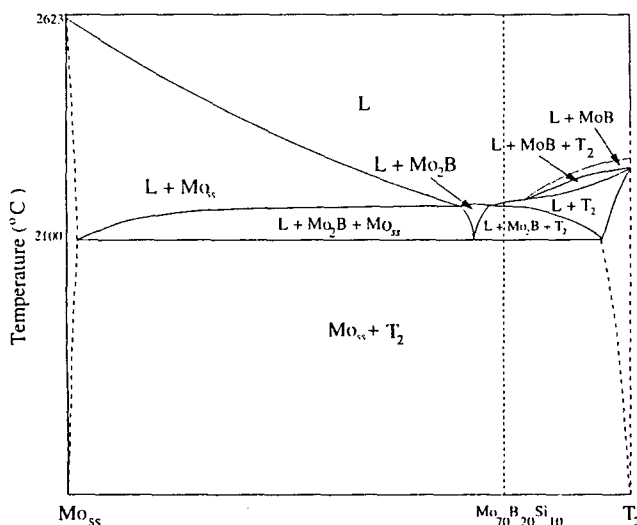


Figure 10.  
Estimated  $\text{Mo}_{55}\text{-}T_2$  plethral section  
(Temperatures for elevated T reactions are tentative).

to promote metallic glass formation due to their strong influence in depressing the alloy liquidus. In the ternary Mo-Si-B alloys glass formation was not observed after RSP which is a reflection of the high temperature stability of the  $T_2$  phase which also tends to yield a shallow liquidus in the plethal section. The shallow liquidus in the plane of the section and the fact that both  $Mo_2B$  and  $MoB$  can be suppressed during RSP suggests that the phase regions containing liquid and either  $Mo_2B$  or  $MoB$  exist over a relatively narrow temperature range. After RSP, a supersaturation of the  $T_2$  phase was observed which is further demonstrated by the formation of Mo precipitates in the  $T_2$  phase upon annealing of the arc-melted ingots. This behavior indicates that the  $T_2$  phase exhibits some solid solubility which increases at high temperature and is noted by the dashed boundaries in figure 10.

### Summary

Based upon an analysis of the phase stability in the Mo-Si-B system, it has been experimentally shown the  $Mo_{SS}+T_2$  two-phase field exists at 1600°C and 1200°C. From the estimated  $Mo_{SS}-T_2$  plethal section, it is expected that the two-phase field exists up to about 2100°C. Results of EPMA/WDS and lattice parameter data have indicated that the  $T_2$ -phase is not a line compound. The composition of the  $T_2$  phase is close to the stoichiometric  $Mo_3SiB_2$  value. In terms of the general phase equilibria in the Mo-rich region of the Mo-Si-B system, it has been shown that five three-phase fields surround the  $T_2$  phase at 1600°C and 1200°C which include the  $Mo_{SS}$ ,  $Mo_2B$ ,  $\alpha MoB$ ,  $Mo_3Si$ ,  $Mo_5Si_3$  and  $T_2$  phases. EPMA/WDS and lattice parameter data have indicated a very low solubility of B in both  $Mo_3Si$  and  $Mo_5Si_3$ , as well as that of Si in  $Mo_2B$  and  $\alpha MoB$ . As-cast alloys with composition in the  $(Mo_{SS}+T_2)$  two-phase field always present the  $Mo_3Si$ -phase in the last part to solidify. Depending on the particular alloy composition either the  $\beta MoB$ - or the  $Mo_2B$ -phase may also be present. However, results from RSP experiments (splat-quenching) have indicated the complete suppression of the phase segregation observed in the as-cast microstructures. In addition, RSP has allowed for the direct production of a  $Mo_{SS}+T_2$  two-phase microstructure from the melt. For alloys within the  $Mo_{SS}+T_2$  two phase region, it has been established that precipitation reactions occur during solid state annealing. The development of Mo precipitates within the  $T_2$  phase offers a valuable option to explore in designing strengthening or toughening strategies. The observed solubility behavior of the  $T_2$  phase also indicates other possibilities for alloying and the development of constitutional defects. A remarkable microstructural stability in the Mo-Si-B system is related to the sluggish diffusion kinetics which is both an attribute for elevated temperature service and a challenge to processing. Overall, the  $(Mo_{SS} + T_2)$  microstructures developed in the current work show good potential for structural applications.

### Acknowledgment

The support of AFOSR ( F49620-96-1-0286 ) and helpful discussions with D. Berczik and S. Chin are most gratefully acknowledged.

### Appendix

#### On the determination of the chemical composition of Mo-B-Si phases via EPMA/WDS

In order to fully assess the general phase equilibria it is also necessary to know the solubility of B and/or Si in the binary phases as well as the range of solubility of the ternary  $T_2$ -phase. To provide this information, measurements were performed via EPMA/WDS in a CAMECA SX50 microprobe. An accelerating voltage of 7 kV was chosen to decrease the absorption of B-K $\alpha$  X-Rays in the Mo-Si-B matrix. A current of 5 nA was used due to dead time correction issue upon the calibration from a pure Boron standard with a PC3 crystal ( $B_4C$ -Mo multilayer,  $2d=200\text{\AA}$ ). The crystals PET, PC3 and TAP were used to determine respectively the contents of Mo (L $\alpha$ ), B (K $\alpha$ ) and Si (K $\alpha$ ).

Pure Mo, B and Si were used as standards. The results reported are for the alloys heat-treated at 1600°C.

Major problems must be addressed to accurately determine the B content of the phases. The first is related to the serious interference between the Mo-M $\gamma$  line and the B-K $\alpha$  line, which is also reported by Bastin & Heijligers [34]. The differential mode of PHA (Pulse Height Analysis), commonly used to suppress multiple order lines, can not be used in this case because both lines, Mo-M $\gamma$  ( $\lambda=68.95718\text{\AA}$ ) and B-K $\alpha$  ( $\lambda=67.64049\text{\AA}$ ), are first order. This particular problem can be solved by using an on-line overlap correction program [34] which subtracts the Mo-M $\gamma$  line from the B-K $\alpha$  peak counts on the unknown based upon the empirically determined ratio of Mo-L $\alpha$  to Mo-M $\gamma$  on the Mo-standard. However, in addition, the highly non-symmetrical shape of the peaks obtained with PC3 makes the background correction difficult. The most commonly used method of background measurement with a wavelength-dispersive spectrometer is to detune to wavelengths above and below the characteristic peak and then establish the value of the background at the peak setting by linear interpolation [35, 36]. Thus, using this procedure, the following condition was initially used for background correction: Boron: +4000 / -4000 ( $\sin\theta \times 10^5$  units); Silicon: +500 / -500 ( $\sin\theta \times 10^5$  units); Molybdenum: +500 / -500 ( $\sin\theta \times 10^5$  units).

From an analysis using the conditions above, the following results were obtained relating to solubility. The solubility of Si in the  $\alpha MoB$  phase (0.02at% Si) is smaller than that in the  $Mo_2B$  phase (0.26-0.5 at% Si). These values are smaller than those given by Nowotny [20], who suggests respectively 2.4at% and 1.0at% Si solubility in the  $\alpha MoB$  and  $Mo_2B$  phases. The solubility of B in the  $Mo_{SS}$ -phase varied from 0.1 at% to 1.3 at% and that of Si from 1.0 at% to 2.1 at%. The results indicated negligible solubility of B in both  $Mo_3Si$  and  $Mo_5Si_3$  phases. The result for the  $Mo_3Si$  phase is in agreement with the value proposed by Nowotny, but disagrees with the value for the  $Mo_5Si_3$  phase where a solubility of approximately 4.3 at% is proposed. As a further test of the current EPMA/WDS analysis method, a  $Mo_{64}B_4Si_{32}$  alloy was prepared via arc-melting and heat-treated at 1600°C for 150h. If there were significant B solubility in the  $Mo_3Si$  and  $Mo_5Si_3$  phases, this alloy should develop a two-phase microstructure after heat-treatment. However, in fact, a significant amount of the  $T_2$ -phase was observed in the microstructure in addition to the  $Mo_3Si$  and  $Mo_5Si_3$  phases, which also confirms the low solubility of B in both binary phases. The B and Si content of the  $T_2$  phase are respectively a minimum and maximum for alloys with composition in the  $Mo_3Si+T_2+Mo_5Si_3$  three-phase field and for alloys with composition in the  $Mo_2B+T_2+\alpha MoB$  three-phase field. The results have indicated that the B content of the  $T_2$ -phase is larger than that expected from the stoichiometry  $Mo_3SiB_2$  (25.0 at% B). Furthermore, these results show a maximum change in solubility of the  $T_2$ -phase of about 4.3 at% B and 3.0 at% Si.

### References

- [1] R.L. Fleischer, J. Mater. Sci., **22**, 2281 (1987).
- [2] C.T. Sims, Advanced Materials & Processes, **6**, 32 (1991).
- [3] E.P. George, M. Yamaguchi, K.S. Kumar and C.T. Liu, Annu. Rev. Mater. Sci., **24**, 409 (1994).
- [4] S. Banerjee, High Temperature Materials and Processes, **11** (1-4), 1, (1993).
- [5] C.H. Ward, Int. Mat. Rev., **38**, 79 (1993).
- [6] D.M. Dimiduk, D.B. Miracle and C.H. Ward, Mater. Sci and Tech., **8**, 367 (1992).
- [7] N.A. Stoloff, Superalloys II, C.T. Sims ed., John Wiley, NY, p. 61 (1987).
- [8] E.R. Ross and C.T. Sims, ibid p. 97.
- [9] R.W. Cahn, Phil. Trans. R. Soc. London, **A351** 497 (1995).
- [10] Y.W. Kim and D. Diminuk, J. Metals, **43**, 40 (1991).
- [11] S. Naka, M. Thomas and T. Khan, Mat. Sci and Tech., **8**, 291 (1992).
- [12] J.H. Perepezko, C.A. Nunes, S.H. Yi and D.J. Thoma, Mat. Res. Soc. Symp. Proc. (in press).
- [13] G.H. Meier and F.S. Petit, Mater. Sci and Tech., **8**, 331 (1992).
- [14] C.E. Ramberg, P. Beatrice, K. Kurokawa and W.L. Worell,

- Mat.Res.Soc.Symp.Proc. , **322**, 243 (1994).
- [15] A.K. Vasudevan and J.J. Petrovic, Mater. Sci. Engr. , **A155**, 1 (1992).
  - [16] D.M.Shah, D. Berczik, D. Anton and R. Hecht, Mater.Sci. Engr. , **A155**, 45 (1992).
  - [17] W.J. Boettinger, J.H. Perepezko and P.S. Frankwicz, Mater. Sci. Engr. , **A155**, 33 (1992).
  - [18] S. Chin, D.L. Anton and A.F. Giamei, Mat.Res.Soc.Symp.Proc. , **322** , 423 (1994).
  - [19] H. Nowotny, F. Benesovsky, E. Rudy and A. Wittman, Mon. Chem., **91** , 975 (1960).
  - [20] H. Nowotny, R. Kieffer, F. Benesovsky, Planseeberichte Fuer Pulvermetallurgie, **5** , 86 (1957).
  - [21] K.S. Kumar. Intermetallic Compounds: v.2, Practice, Chapter 10, p. 211. J.H. Westbrook and R.L. Fleisher. Ed. , John Wiley & Sons Ltd. , NY ,(1994.)
  - [22] T.B. Massalski, Binary Alloy Phase Diagrams , American Society for Metals , Metals Park , Ohio. v. 1, p. 502,503; v.3, p.2664,2666, (1990).
  - [23] JCPDS. Powder Diffraction File. International Centre for Diffraction Data Swarthmore, PA. Card No. 9-292, (1987).
  - [24] B. Aronsson , Acta Chem. Scand. , **A4** , 1414 (1960).
  - [25] B. Aronsson , Acta Chem. Scand., **9** , 1107 (1955).
  - [26] J.L.C. Daams, P. Villars and J.H.N. Van Vucht . Atlas of Crystal Structures Types for Intermetallic Phases. ASM. Metals Park , Ohio. p. 4269-4299 (1991).
  - [27] M.K. Meyer and M. Akinc , J. Am. Ceram. Soc. , **79** 938 , 2763 (1996).
  - [28] C.A. Nunes, R. Sakidja and J.H. Perepezko, Univ. Of Wisconsin-Madison, unpublished research.
  - [29] M.K. Meyer, M.J. Kramer and M. Akinc, Intermetallics, **4** , 273 (1996).
  - [30] J.H. Perepezko, Intermetallic Compounds: v.1 , Principles, J.H. Westbrook and R.L. Fleisher ed. , John. Wiley, Ny , p. 849 , (1994).
  - [31] K. Meier, H. Mehrer and G. Rein , Z. Metallkde. , **70** , 271 (1979).
  - [32] S.K. Das and F.H. Froes., Rapidly Solidified Alloys, Howard H. Liebermann. Marcel Dekker, Inc. NY (1993) , pp. 339-377.
  - [33] C.A. Nunes and J.H. Perepezko , to be published.
  - [34] G.F. Bastin and H.J.M. Heijlingers. X-Ray Spetroscopy in Electron Beam Instruments , David Williams, J. Goldstein and D. Newbury ed. , Plenum Press, NY (1995).
  - [35] CAMECA. Quantiview 2.0 Reference Guide. Overlapping Correction Program (FILOVL Program): 16.1 - 16.6. Courbevoie Cedex, France (1992).
  - [36] Goldstein, J.I. et al. Scanning Electron Microscopy and X-ray Microanalysis. Second Edition. Plenum Press, New York. p. 376 (1994).

## A STUDY OF THE MICROSTRUCTURE AND MECHANICAL BEHAVIOUR OF DUCTILE Nb-Al-V ALLOYS

D.N. Horspool, D.K. Tappin, and M. Aindow

School of Metallurgy and Materials and IRC in Materials for High Performance Applications  
The University of Birmingham, Birmingham B15 2TT, UK

### Abstract

This paper describes a preliminary assessment of the microstructures and mechanical behaviour of Nb-10Al-20V and Nb-15Al-20V alloys. Both exhibited a single B2 phase in the as-cast state and they contained 5 and 45 vol.% A15, respectively, when heat treated. The B2 phase deformed in compression by martensitic pseudotwinning and dislocation glide and is inherently ductile. Both alloys show low work hardening rates and could be cold-rolled to >80% reduction in thickness with ease. Heat treatment of the cold-rolled structures resulted in a fine distribution of A15 precipitates which gave a significant increase in hardness. These observations indicate that a high strength, ductile, heat-treatable alloy for high temperature applications could be developed on the basis of these compositions.

### Introduction

The intermetallic compound  $\text{Nb}_3\text{Al}$  has considerable technological potential as the basis for high temperature structural materials since it exhibits the desirable properties of good creep resistance, low density and good high temperature strength [1]. This potential has yet to be realised, however, as like many other A15 intermetallics,  $\text{Nb}_3\text{Al}$  exhibits severe brittleness at low to intermediate temperatures (<900°C), and suffers from poor oxidation resistance at high temperatures [1, 2]. The ductility of  $\text{Nb}_3\text{Al}$  has been improved greatly by the retention of a non-equilibrium B2 structure in both rapidly cooled alloys [3] and in off-stoichiometric monolithic specimens [4]. In addition, Shyue *et al.* [5] have shown that it is possible to retain a stable B2 phase by ternary alloying with Ti. Unfortunately, Ti-modified alloys exhibit a number of other phases, including an orthorhombic phase and an omega

phase [6] which may adversely affect the mechanical properties of the alloy. Several alternative ternary additions have been examined including Mo [7], Cr, V and Zr [8] in an attempt to overcome this problem. Of these, V appears to be the most viable: it stabilises the B2 phase but does not promote the formation of omega or orthorhombic phases and, unlike Zr, it does not lead to catastrophic oxidation behaviour.

In recent work [9] we have examined the phase stability, mechanical properties and deformation mechanisms for a series of five V-modified alloys containing 10-25 at.% Al and 20-40 at.% V. These compositions were chosen on the basis of Pettifor structure maps using the method outlined in Smith *et al.* [10]. It was found that the volume fraction of the A15 and B2 phases varied linearly with the ratio of the Al and V contents for the alloys. For samples which had been heat-treated to produce the equilibrium phase distribution, alloys with Al/V  $\approx$  0.5 exhibited only the B2 phase whereas those with Al/V  $\approx$  1 were almost completely A15. The B2 phase was found to be V-rich and to have an Al concentration of  $\approx$  14 at.% except for those alloys which had a low nominal concentration of Al in the starting material: in an Nb-15Al-20V alloy the B2 phase contained 11 at.% Al and in a Nb-10Al-20V alloy it contained 7 at.% Al. The lower Al content in the B2 phase resulted in weaker B2 ordering in these alloys.

In this paper we present a study on the microstructures and mechanical behaviour of these two alloys. In the first part of the paper the key features of the phase stability and deformation mechanisms in these alloys are addressed. In the second part some preliminary data obtained from cold rolling trials and subsequent heat treatments are used to illustrate how thermomechanical processing might influence the microstructural development of the alloys.

## Experimental Procedure

The alloys were prepared by transferred-arc plasma melting of high purity (>99.8%) elemental Al, Nb and V in a Retech plasma melter on a water-cooled copper hearth under a positive pressure of Ar. Each 500g button was re-melted several times to ensure homogeneity. To combat the effect of vaporisation, the concentration of Al in the charge was increased by 10 % of the value that was required in the alloy. The buttons were weighed after melting, and were found to be within 2 at % of their nominal compositions if all the weight loss were attributed to Al vaporisation. This would represent the most severe change in composition since it is the constituent with the lowest atomic mass.

The alloys were examined in the as-cast, heat-treated and homogenised conditions. Portions of each of the alloys were heat treated at 1500°C for 50hrs in a sealed tube furnace under an argon atmosphere and with Ta foil as a getter for oxygen, and were then cooled in the furnace. Other portions were homogenised for 1hour at 1700°C in a high vacuum ( $10^{-7}$  torr) induction furnace and were then quenched by admitting air into the furnace chamber.

Compression tests were performed on the as-cast alloys at room temperature using strain rates of  $10^{-2}$  to  $10^{-4}$  s $^{-1}$  in a screw-driven INSTRON 1195 testing machine. Specimens were in the form of square bars 5mm across the faces, with an aspect ratio of 1.5. The majority of the tests were terminated at 3% engineering strain but, in a number of cases, tests were performed to higher total strains to examine the ductility of the alloys.

Preliminary cold-rolling trials were performed on specimens of the homogenised alloys, with a 10mm square cross-section and  $\approx 20$ mm in length. The apparatus used was a laboratory-scale mill with 120mm diameter rolls and paraffin was used as a lubricant. Portions of the cold-rolled specimens were heat treated at 1000°C and 1500°C for 50hrs in a sealed tube furnace under an argon atmosphere and with Ta foil as a getter for oxygen.

At each stage of processing the alloys were characterised by hardness testing, optical microscopy and transmission electron microscopy (TEM). Specimens for TEM were prepared by twin-jet electropolishing using a 10% solution of sulphuric acid in methanol at -40°C and 90mA. TEM experiments were performed in a Philips CM20 operating at 200kV.

## Results and Analysis

### As-Cast and Heat-Treated Microstructures

Both alloys exhibited a single phase microstructure with columnar and equiaxed zones of large (100-350 $\mu$ m) grains (e.g. Fig 1). Selected area diffraction patterns (SADPs) obtained from TEM specimens of these alloys have superlattice reflections which correspond to B2 order in a Nb solid solution (Fig. 2). This is consistent with that observed previously in TEM studies on Nb-Al-V alloys [11] but the reflections are weaker and more diffuse which may indicate that the ordering is weaker and experiments using ALCHEMI are underway to confirm this. The specimens homogenised at 1700°C also exhibited only the B2 phase in the form of larger equiaxed grains (350-1000 $\mu$ m).

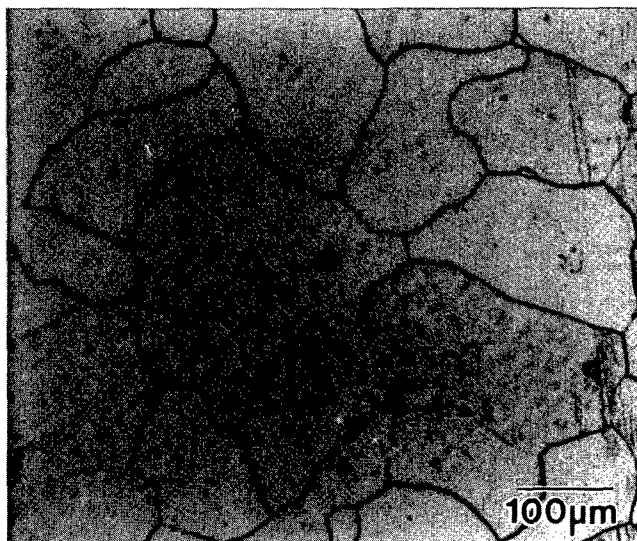


Figure 1: Photomicrograph of the single phase as-cast structure near the central equiaxed zone in the Nb-15Al-20V alloy.

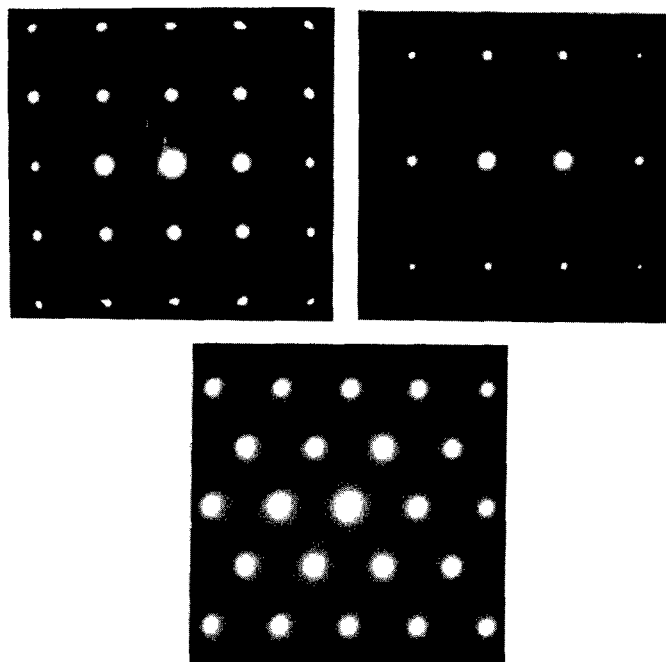


Figure 2: SADPs obtained from TEM specimens of the as-cast Nb-15Al-20V alloy showing B2 ordering.

After heat-treating at 1500°C, the Nb-10Al-20V alloy retained a similar microstructure with only  $\approx 5$  vol. % of a second phase in the form of occasional large grains: there was no precipitation within the matrix grains. SADPs showed that the matrix exhibits B2 order and that the second phase had the A15 structure as expected. There was no well-defined orientation relationship between the phases. Homogenisation of the Nb-15Al-20V alloy at 1500°C resulted in the formation of lenticular A15 precipitates within the B2 grains and at the grain boundaries (Fig. 3). Figure 4a is a bright field TEM image of a typical A15 precipitate and Figures 4b-d are characteristic selected area diffraction patterns (SADPs)

obtained from this phase. There was no consistent crystallographic orientation relationship exhibited between these precipitates and the matrix. The volume fraction of the A15 phase was  $\approx 45$  vol. % for the Nb-15Al-20V alloy as compared with  $< 5$  vol. % for the Nb-10Al-20V alloy. These volume fractions are consistent with the Al/V ratios of 0.75 and 0.5, respectively and illustrate that Al is a potent A15 stabiliser in this compositional range.



Figure 3: Photomicrograph of the two phase structure in the Nb-15Al-20V alloy heat-treated at 1500°C.

These data are largely consistent with the published phase diagrams (e.g. [12]). There is no precipitation of the A15 phase at 1700°C but this occurs extensively at 1500°C since the peritectic temperature lies between these values. The obvious discrepancy is that the B2 phase appears to be stable in this system despite the fact that it does not appear in any of the published Nb-Al-V phase diagrams. This is presumably due to the use of x-ray diffraction for phase diagram determination whereby the subtle superlattice diffraction peaks are not detected.

#### Compression Testing

Values of the offset yield strength (OYS) were measured at 2% plastic deformation for as-cast specimens of the alloys. In both cases the OYS values were  $\approx 1200 \pm 100$  MPa. The samples showed extensive ductility with plastic strains of well over 10% achieved for both alloys. Similar tests were performed on a specimen of the Nb-15Al-20V alloy heat-treated at 1500°C. The OYS for this specimen was  $\approx 1400$  MPa and the ductility was significantly lower with only 3% plastic strain being achieved before failure.

It is interesting to note that all of the specimens exhibited a transient serrated yielding regime in the stress-strain curves and, as the strain rate of the tests was increased, the range of stress and strain over which serrated yielding was observed decreased (e.g. Fig. 5). Serrated yielding was accompanied by the formation of linear features on the surfaces of the specimens (Fig. 6). This is consistent with twin formation in

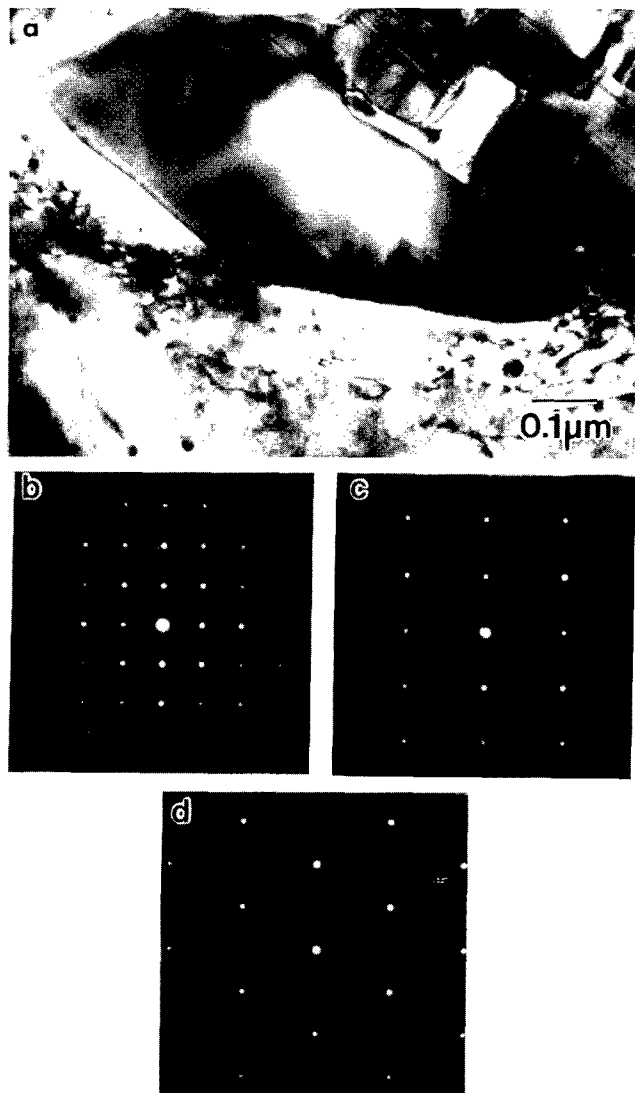


Figure 4: (a) Bright field many-beam TEM micrograph of an A15 precipitate in the Nb-15Al-20V alloy heat-treated at 1500°C. (b)-(d) SADPs obtained from the particle with the beam direction parallel to: (b) [100]; (c) [110]; and (d) [111].

the initial stages of plastic deformation. TEM analysis of these features (e.g. Fig. 7) was used to show that they are actually regions which had transformed to an orthorhombic crystal structure with the orientation relationship:

$$\begin{aligned} \{110\}_{\text{Ortho}} // \{100\}_{\text{B2}} \\ \langle 111 \rangle_{\text{Ortho}} // \langle 011 \rangle_{\text{B2}} \end{aligned}$$

This structure has a unit cell whose dimensions are  $a_o = b_o = \sqrt{2} a_{\text{B2}}$  and  $c_o = a_{\text{B2}}$  as shown in Fig. 8. Similar features have been identified previously in the Ti-modified Nb-Al alloys [13] and in other B2 compounds (e.g. [14]). They are thought to be formed by a stress-induced martensitic transformation referred to as pseudo-twinning. The proposed pseudo-twinning shear is the same as that for true twinning in BCC metals, that is  $1/6 \langle 111 \rangle \{112\}$ , but because of the ordered nature of the B2 structure it results in the formation of the orthorhombic phase [14]. It is interesting to note that this pseudotwinning is

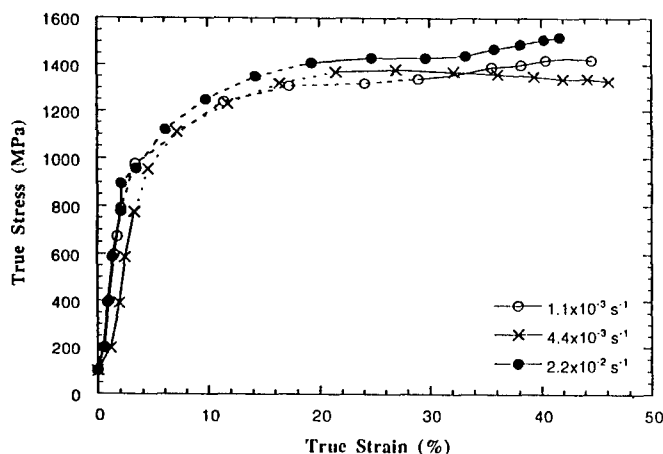


Figure 5: True stress vs. true strain compression curves for the as-cast Nb-15Al-20V alloy (room temperature). Serrated yielding was observed in the dashed portion of the curves.

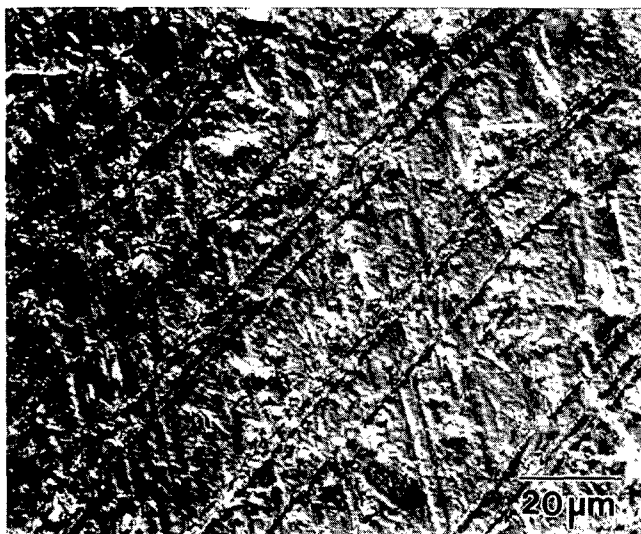


Figure 6: Photomicrograph of the Nb-10Al-20V alloy after compression testing showing linear features in the B2 phase.

not observed in the more strongly ordered Nb-Al-V alloys studied previously [9] and this is presumably because of a larger free energy difference between the B2 and orthorhombic structures for these latter compositions.

In addition to these "pseudo-twins", there was extensive dislocation activity (Fig. 7). Analysis of diffraction contrast images was used to show that these dislocations all had Burgers vectors,  $\mathbf{b}$ , parallel to the  $\langle 111 \rangle$  directions and tended to adopt screw orientations. In a phase with a B2 structure one would expect these defects to have  $\mathbf{b} = 1/2 \langle 111 \rangle$ , and to be paired with an antiphase boundary (APB) between them. Dark field images were obtained using 100-type superlattice reflections but no conclusive evidence for the presence of APBs was obtained. This may simply be due to the low structure factors for these reflections in such weakly ordered materials. The dislocations appeared to lie in bands on  $\{110\}$  and this is consistent both with our previous observations on the more strongly ordered alloys [9] and with the low APB energy that we expect for the alloys considered here [15].

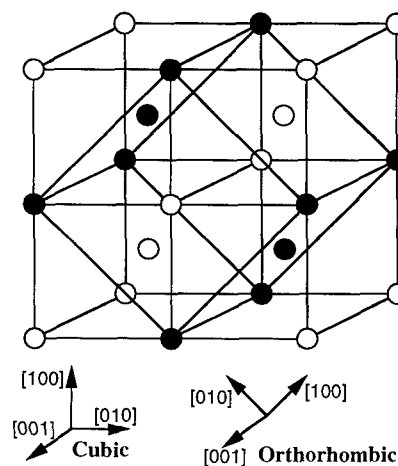


Figure 8: Schematic diagram of the relationship between the unit cells of the B2 and orthorhombic pseudotwin structures (after [14]). The filled and unfilled circles represent the two different sublattices in the prior "untwinned" B2 structure.

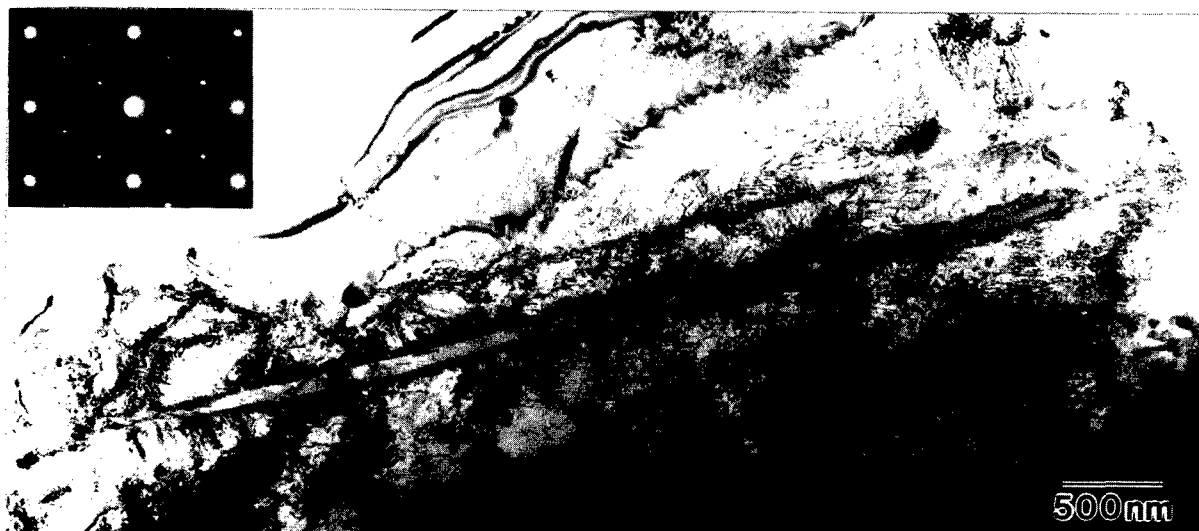


Figure 7: Bright field many-beam TEM micrograph of a martensitic pseudotwin in the compression-tested Nb-15Al-20V alloy. The inset SADP shows the orientation relationship.

### Cold-Rolling

Portions of each alloy in the homogenised state were rolled to a thickness of 1.25mm (i.e. a total reduction of 87%) in a series of ten passes with a similar incremental reduction at each pass. The strip produced was then cut in half and one half was given four further passes which reduced the thickness to 0.8mm. This was the maximum reduction which could be achieved for these alloys in the apparatus used. An unrolled specimen is shown together with the two strip halves for the Nb-15Al-20V in Fig. 9. Whilst there is some evidence of edge tearing on the rolled strips it is clear from such simple tests that the alloys exhibit extensive ductility even after deformation to high total plastic strains.

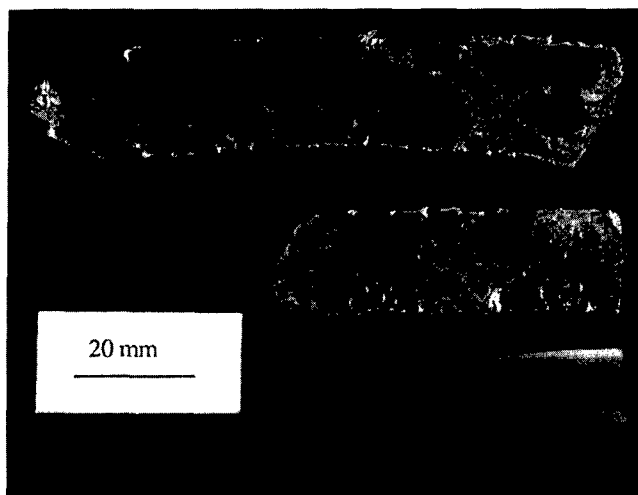


Figure 9: Cold-rolling of Nb-15Al-20V; bottom - initial specimen; middle - half strip reduced in thickness by 87% in 10 passes; top - half strip reduced by a further 36% (i.e. to 92% in total) in four passes.

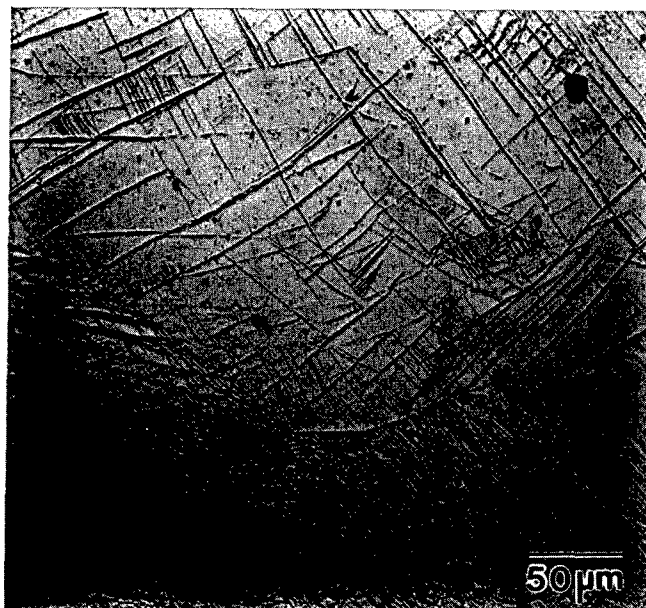


Figure 10: Photomicrograph of the structure viewed along the rolling plane normal after cold-rolling the Nb-15Al-20V alloy to 86% reduction in thickness.

The microstructures of the cold-rolled specimens (e.g. Fig. 10) exhibit similar linear features to those observed after compression testing and TEM data indicate that, here again, they are martensitic pseudotwins. In the cold-rolled specimens, however, these are present at much higher densities. At first this seems a surprising result since for twinning associated with transient serrated yielding one might expect only dislocation glide once a certain twin content had developed. Such arguments are, however applicable only to monotonic deformations and thus for the complex stress states experienced during rolling, and with the workpiece inevitably being introduced into the rolls in a slightly different orientation at each pass, much higher twin densities might develop as observed experimentally. It is an interesting feature of this material that the presence of such a high density of pseudotwins does not compromise the ductility. For  $1/6\langle 111 \rangle \{112\}$  twinning in BCC materials it has been proposed that cracks may be nucleated at the intersections of twins on different systems. There is no evidence of any such effect in these materials despite the very high density of twin intersections which are present. Moreover, it is clear from the curved appearance of the pseudotwins in many areas that they can accommodate extensive plastic deformation in the B2 matrix which surrounds them. This indicates that slip transmission must occur through the matrix/pseudotwin interfaces with great ease.

### Post-Rolling Heat Treatment

After heat-treating the cold-rolled Nb-10Al-20V alloy at 1000°C, the samples appeared to exhibit a very similar microstructure to those observed for the as-rolled samples (Fig 11(a)). On closer examination, however, it became clear that small lenticular precipitates ( $0.3 \times 2 \mu\text{m}$ ) had formed and that these were arranged in bands (Fig 11(b)). This is consistent with the A15 phase nucleating preferentially either within the pseudotwins or at the matrix/pseudotwin interfaces. TEM images and SADPs obtained from this material (e.g. Fig. 12) revealed that the precipitates have clean semicoherent interfaces with the matrix and exhibit the orientation relationship:

$$\begin{aligned} \{012\}_{A15} // \{110\}_{B2} \\ \langle 221 \rangle_{A15} // \langle 112 \rangle_{B2} \end{aligned}$$

Which is different to the orientation relationship observed previously between B2 and A15 phases in Ti-modified alloys [16]. This difference is probably due to the influence of the pseudotwins on the nucleation of the A15 phase in these materials. After heat-treating the cold-rolled Nb-10Al-20V alloy at 1500°C, however, a recrystallised microstructure was observed with well-defined equiaxed matrix grains ( $100\text{--}400 \mu\text{m}$ ) and larger ( $>8 \mu\text{m}$ ) blocky and lenticular A15 precipitates within the grains and straddling the boundaries (Fig. 13).

After heat-treating the cold-rolled Nb-15Al-20V alloy at 1000°C, the samples again exhibited a similar microstructure to those observed for the as-rolled samples (Fig 14(a)). For these samples, however, higher magnification images revealed that small lenticular precipitates ( $0.5 \times 3 \mu\text{m}$ ) had formed in the matrix between the pseudotwins (Fig 14(b)). Here again images and SADPs obtained from this material in the TEM





Figure 11: Photomicrographs of the structure in the Nb-10Al-20V alloy after cold rolling and heat-treating at 1000°C: (a) banded structure; (b) fine precipitates within the bands.



Figure 12: Bright field many-beam TEM micrograph of an A15 precipitate in the Nb-10Al-20V alloy after cold rolling and heat-treating at 1000°C. The inset SADP shows the orientation relationship.

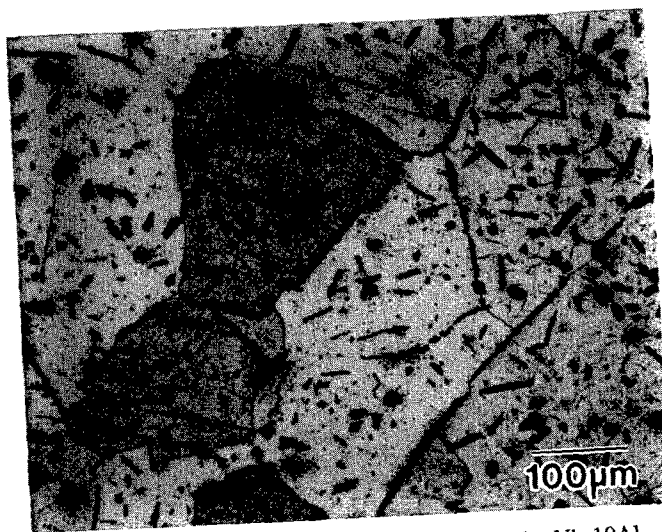


Figure 13: Photomicrograph of the structure in the Nb-10Al-20V alloy after cold rolling to 86% reduction in thickness and heat-treating at 1500°C.

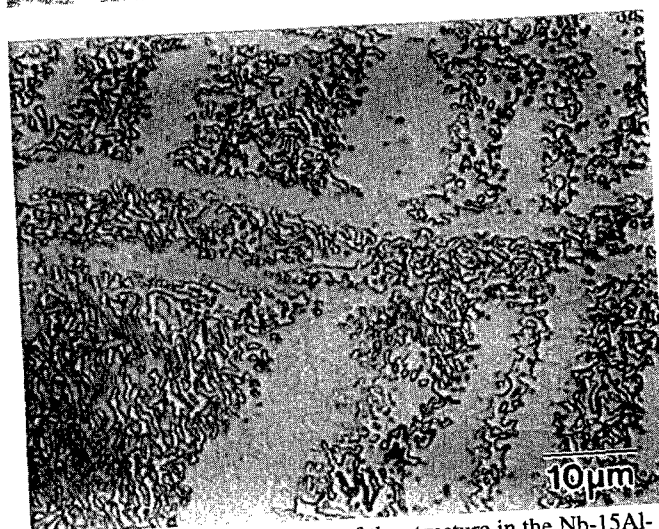
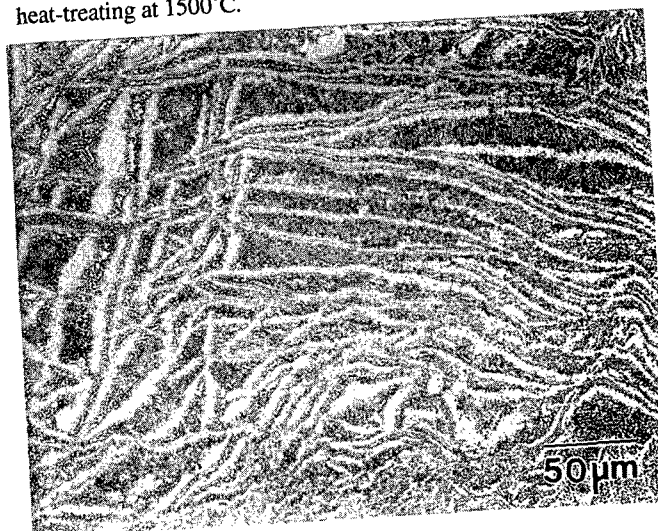


Figure 14: Photomicrographs of the structure in the Nb-15Al-20V alloy after cold rolling to 86% reduction in thickness and heat-treating at 1000°C: (a) banded structure; (b) fine A15 precipitates between the bands.

(Fig. 15) revealed clean semicoherent precipitate/matrix interfaces and a well defined orientation relationship of:

$$\begin{aligned} \{110\}_{A15} // \{100\}_{B2} \\ \langle 112 \rangle_{A15} // \langle 011 \rangle_{B2} \end{aligned}$$

which is also different from that observed previously. In this case the reason for the discrepancy is not clear since the precipitates have presumably nucleated in the bulk of the matrix. Here again, heat-treating at 1500°C gave a recrystallised microstructure with equiaxed larger (>8µm) A15 precipitates within the grains (Fig. 16).



Figure 15: Bright field many-beam TEM micrograph of an A15 precipitate in the Nb-15Al-20V alloy after cold rolling to 86% reduction in thickness and heat-treating at 1000°C. The inset SADP shows the orientation relationship.

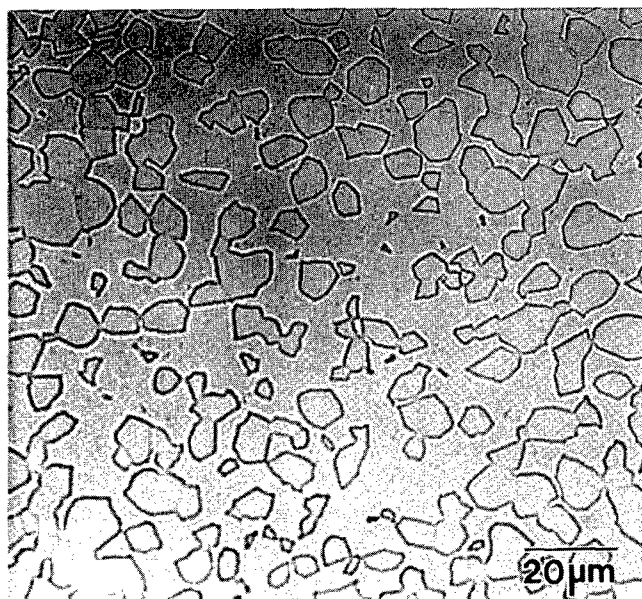


Figure 16: Photomicrograph of the structure in the Nb-15Al-20V alloy after cold rolling to 86% reduction in thickness and heat-treating at 1500°C.

### Hardness Data

Hardness testing was used to obtain a preliminary indication of the effect of cold-rolling and heat treatment on mechanical properties. Vickers hardness tests were performed with a standard pyramidal diamond indenter and a 10kg load. A minimum of 10 indentations were measured for each sample and the maximum standard deviation for the values presented is 20. The measured hardnesses for reference samples of pure Nb and stoichiometric Nb<sub>3</sub>Al were 107 and 824 kg/mm<sup>2</sup>, respectively, although in the latter case there was extensive cracking around the indentations. The values obtained from some of the samples considered in this work are presented in Table I below.

Table I: Vickers hardness data for some of the samples.

Sample	VHN (kg/mm <sup>2</sup> )
<b>Nb-10Al-20V</b>	
As-cast	357
Hom. & Rolled by 86%	406
Hom. Rolled + 1000°C/50h	440
Hom. Rolled + 1500°C/50h	367
<b>Nb-15Al-20V</b>	
As-cast	384
Heat-treated 1500°C/50h	528
homogenised 1700°C/1h	393
Hom. & Rolled by 86%	443
Hom. & Rolled by 92%	452
Hom. Rolled + 1000°C/50h	610
Hom. Rolled + 1500°C/50h	562

The values obtained from the as-cast specimens are roughly one third of the room-temperature compressive yield stress as expected for this indenter geometry. These hardnesses are three to four times that of pure Nb indicating the effect of ordering and solid solution strengthening in these alloys. For the Nb-15Al-20V alloy, homogenisation had little effect on the hardness but heat treatment at 1500°C gave a significant increase. This may have been at the cost of reducing fracture toughness since cracking occurred around the indentations in this sample. It is interesting to note that these alloys show only modest work hardening with an increase of ≈15% in the hardness for cold-rolling to 92% reduction in thickness for the Nb-15Al-20V alloy. Heat treatment of the cold-rolled specimens at 1000°C for 50 hours produced a modest increase in hardness for the Nb-10Al-20V alloy but a much more significant increase of over 50% for the Nb-15Al-20V alloy. These increases were not accompanied by any cracking around the indentations and this is consistent with the presence of the fine A15 precipitates. Thus the difference between the two alloys would be due to the volume fractions of the A15 phase in the final microstructure. Heat treatment of the cold-rolled specimens at 1500°C for 50 hours resulted in less hardening and this would thus correspond to an overaged microstructure.

## Discussion

The data presented here show that the B2 phase in these two alloys exhibits both high strength and extensive ductility at room temperature. These characteristics must be related to the deformation micromechanisms and a more detailed investigation of these is underway. What is clear is that glide on the systems  $\langle 111 \rangle \{110\}$  provides sufficient independent slip systems. The high OYS indicates that the Peierls barriers to the motion of the paired partial dislocations and their associated APB is high although there is no strong locking which prevents their motion. The magnitude of these barriers is presumably due to a combination of solid solution strengthening and ordering effects. These effects would also influence the balance between the pseudotwinning and dislocation glide contributions to the deformation with a high level of solid solution strengthening and a low degree of long range order tending to favour pseudotwin formation. The role of the pseudotwinning in the ductility of the alloys is less obvious. As noted above, pseudotwin intersections do not appear to act as crack nucleation sites and it seems that slip transmission through the matrix/pseudotwin boundaries must be particularly easy. Such behaviour would normally only be expected for systems in which cross-slip is particularly easy. This could lead to stresses at twin intersections being relieved more easily by the production of emissary dislocations and to slip propagating with ease onto inequivalent slip planes across matrix/pseudotwin interfaces but detailed TEM experiments would be required to test this hypothesis. The presence of slip bands on a variety of high index planes in the B2 phase of Ti-modified alloys [5] indicates that easy cross-slip can occur in such compounds, but slip bands were only observed on  $\{110\}$  in the V-modified alloys considered in this paper.

The extensive ductility of the B2 compound in conjunction with its very low work hardening rate make it amenable to processing via a wide variety of conventional forming routes. For high temperature applications, however, it seems unlikely that a single phase alloy would be appropriate. Although we have not yet performed elevated temperature mechanical tests on these two alloys, the probable behaviour can be deduced from our previous work on an Nb-25Al-40V alloy (i.e. Al/V = 0.625) which was also predominantly B2 in the as-cast state. The 2% OYS in compression for this latter alloy was  $\approx 1200$ MPa at room temperature but fell to  $\approx 500$ MPa at  $800^\circ\text{C}$ . If similar behaviour were exhibited by the B2 phase in the alloys considered here then additional strengthening would be required if such alloys were to be used for elevated temperature applications. One obvious possibility is the use of A15 precipitation. Whilst the heat-treated Nb-15Al-20V samples cracked during indentation testing indicating that the increase in hardness had been achieved at the expense of fracture toughness, the same was not true of the cold-rolled and heat-treated specimens which had even higher values of the hardness. Thus, as one might expect, a fine dispersion of the precipitate phase gives a more profound strengthening effect and is less likely to compromise the ductility than coarse A15 precipitates which often form at grain boundaries. To obtain such a microstructure, one would obviously require an appropriate density and distribution of dislocations, pseudotwins or other preferential nucleation sites for A15 precipitates. Further work is being performed on the exact nature of the nucleation sites and the way that these result in the new orientation relationships revealed in this study.

It would, therefore, appear that this system exhibits considerable potential for use as a high temperature structural material since even alloys with such simple compositions as those considered in this preliminary study have attractive properties. One could envisage an alloy with an Al/V ratio whereby the as-cast or homogenised material is single-phase B2 which can be shaped with relative ease and then aged to produce an appropriate density and distribution of strengthening A15 precipitates. Such alloys could be used as replacements for conventional Nb alloys or even for superalloys in certain elevated temperature applications although the stability of the microstructure would need to be assessed. The factor which may limit the use of such alloys is the oxidation behaviour which may include sub-surface transformations as seen for Ti-modified alloys [17] as well as scale formation.

## Conclusions

A preliminary study has been performed on the microstructure and mechanical behaviour of two V-modified Nb-Al alloys: Nb-10Al-20V and Nb-15Al-20V. The following points were established:

(a) Both alloys exhibited a single B2 phase in the as-cast state. On heat treatment, the A15 phase precipitated within the B2 matrix. The final volume fractions of A15 in the 10-20 and 15-20 alloys were 5% and 45%, respectively. Since the B2 phase is not present in published ternary phase diagrams, it must occupy a portion of the nominal A2 region.

(b) Compression tests on as-cast specimens gave an OYS of  $\approx 1200$ MPa for both alloys. Significant plastic strain ( $>10\%$ ) was obtained after serrated yielding in both cases and TEM was used to show that this was corresponded to the formation of martensitic pseudotwins plus glide of screw dislocations on  $\langle 111 \rangle \{110\}$ .

(c) Homogenised specimens of each alloy were cold-rolled with ease to reductions in thickness of  $>80\%$  with only modest work hardening. The as-rolled microstructures contained very high densities of distorted and intersecting pseudotwins which did not appear to compromise the ductility.

(d) Heat-treatment of the rolled specimens resulted in the formation of A15 precipitates which exhibited well-defined orientation relationships with respect to the B2 matrix. After heat treatment at  $1000^\circ\text{C}$  these precipitates were dispersed finely and gave significant increases in hardness whereas heat-treatment at  $1500^\circ\text{C}$  gave coarser precipitates and less hardening.

Such compositions could thus form the basis of ductile heat-treatable Nb alloys which could be worked in the partially metastable single phase B2 state and then aged to precipitate the A15 phase.

## Acknowledgements

The authors would like to thank Prof. H.L. Fraser, Prof. I.P. Jones and Dr. L.S. Smith for helpful discussions, Dr. P.S. Bate for assistance with the mechanical testing, and Professors J.F. Knott and M.H. Loretto for the provision of laboratory facilities. This work has been carried out with the financial support of the EPSRC and the Ministry of Defence. Technical

Monitor for the project was Dr. M.R. Winstone of the DRA Structural Materials Centre, Farnborough.

#### References

1. D. M. Shah and D. L. Anton, "Evaluation of Refractory Intermetallics with A15 Structure for High Temperature Structural Applications" Mat. Sci. Eng. A153 (1992), 402.
2. Y. Murayama, S. Hanada, K. Obara and K. Hiraga, "Dissociated Dislocations in Deformed Nb<sub>3</sub>Al Produced from Alloy Powder" Philos. Mag. A, 67 (1993), 251.
3. H. Kohmoto, J. Shyue, M. Aindow and H. L. Fraser, "Observation of a Metastable B2 Phase in Rapidly Solidified Ribbons of Nb-Al Alloys" Scripta Metall. 29 (1993), 1271.
4. S. S. Yang and V. K. Vasudevan, "Transformations, Microstructures and Properties of Nb-(10-16)At.% Al Alloys" Mat. Res. Soc. Symp. Proc., 288 (1993), 731.
5. J. Shyue, D-H. Hou, M. Aindow and H.L. Fraser, "Deformation Mechanisms in Intermetallic Compounds Based on Nb<sub>3</sub>Al" J. Mat. Sci. and Eng. 170 (1993), 1.
6. D.H. Hou, S.S. Yang, J. Shyue and H.L. Fraser, "Investigation of B2 and Related Phases in Ti-Modified Nb-Al Alloys" Mat. Res. Soc. Symp. Proc., 322 (1994), 437.
7. E. Passa and P. Tsakiroopoulos, "The Microstructure of Nb<sub>3</sub>Al -Mo Intermetallics" Mat. Res. Soc. Symp. Proc., 364 (1994), 1353.
8. D.K. Tappin, D.N. Horspool, M. Aindow and I.P. Jones, "The Development Of Ternary Alloys Based On Nb<sub>3</sub>Al" in preparation.
9. D.K. Tappin, L.S. Smith, D.N. Horspool and M. Aindow, "Microstructures and Deformation Behaviour In Nb/10-25at.%Al/20-40at.%V Alloys" Acta Mater. (accepted for publication, in press).
10. L.S. Smith, D.K. Tappin and M. Aindow, "The Application of Pettifor Structure Maps to Ternary Additions in Nb<sub>3</sub>Al -Based Alloys", Scripta Metall. et Mater. 34 (1996) 227.
11. L.S. Smith, M. Aindow and M.H. Loretto, "Microstructures, Defects and Deformation Mechanisms in Vanadium-Modified Nb<sub>3</sub>Al", Mat. Res. Soc. Symp. Proc., 322, (1994), 453.
12. G. Petzow and G. Effenberg eds. "Ternary Alloys: a Comprehensive Compendium of Evaluated Constitutional Data and Phase Diagrams" (Basel, Weinheim, 1991), 399.
13. S.S. Yang, D.H. Hou, J. Shyue, R. Wheeler and H.L. Fraser, "Pseudo-Twinning in a Deformed Nb-15Al-25Ti Alloy" Mat. Res. Soc. Symp. Proc., 364 (1994) 1359.
14. E. Goo, T. Duerig, K. Melton and R. Sinclair, "Mechanical Twinning in Ti<sub>50</sub>Ni<sub>47</sub>Fe<sub>3</sub> and Ti<sub>49</sub>Ni<sub>51</sub> Alloys" Acta Metall. 33, 1725 (1985).
15. M. Yamaguchi and Y. Umakoshi, "The Operative Slip Systems and Slip Line Morphology in  $\beta$ CuZn and  $\beta$ (CuNi)Zn Alloys" Acta Metall. 24, 1061 (1976).
16. J. Shyue, D.H. Hou, S.C. Johnson, M. Aindow and H.L. Fraser, "The Stability of B2 Compounds in Ti-Modified Nb-Al Alloys" Mat. Res. Soc. Symp. Proc., 288 (1993), 243.
17. B.V. Cockeram, H.J. Schmutzler, J. Shyue, S. Meng, R. Wheeler and H.L. Fraser, "The High Temperature Oxidation of Nb-40Ti-15Al and the Effect of Cr Alloying and Silicide Diffusion Coatings" Mat. Res. Soc. Symp. Proc., 364 (1994) 1327.

## ATOMIC STRUCTURE AND DEFORMATION OF Nb-Ti-Al ALLOYS

R. Wheeler, S. Perungulam, S. Banerjee†, D.-H. Hou, R.J. Grylls and H.L. Fraser

Department of Materials Science and Engineering, The Ohio State University

2041 College Road, Columbus, OH 43210, USA

† Bhabha Atomic Research Centre, Bombay, India 400 085

### Abstract

Alloys with compositions Nb-15Al-(10, 25 or 40)Ti exhibit the B2 crystal structure in the single-phase state, yet have compositions that deviate markedly from B2 stoichiometry. The degree of order of these alloys has been studied using ALCHEMI with the Ordering Tie Line (OTL) approach. It is shown that both the degree of ordering and the sublattice occupancies change markedly for the three alloys considered. The tensile behavior of the Nb-15Al-40Ti alloy has been evaluated at room- and intermediate-temperatures. This alloy shows extensive ductility at room-temperature despite its ordered structure. Several interesting phenomena have been seen, including both static and dynamic strain-aging, the latter being illustrated by serrated flow and negative strain-rate sensitivity at intermediate temperatures. It is proposed that these effects are caused by the pinning of dislocations by the precipitation of a second phase.

### Introduction

There has been growing interest in Nb-based systems for intermediate and elevated temperature applications. At the higher temperatures, the interest has been in the silicide systems [1] and at intermediate temperatures the aluminides are of interest [2]. In this paper, some aspects of the Nb aluminides containing Ti alloying additions are considered. The Nb aluminides of interest have the composition Nb-15Al-xTi, where x varies from 10-40% (all compositions being in atomic percent), and in the single phase condition have the B2 crystal structure. As has been reported, these compounds can show an interesting balance of properties which includes reasonable strength up to  $\approx 850^\circ\text{C}$ , good tensile ductility at room temperature (up to  $\approx 30\%$  in Nb-15Al-40Ti), and reasonable oxidation resistance (e.g. more than 250 cycles between room temperature and  $800^\circ\text{C}$  without oxide spallation in Nb-15Al-40Ti-4Cr-2Zr). Hence, given their densities, these compounds prove to be rather attractive for potential application.

In the present paper, two aspects of these aluminides will be considered: firstly the ordered state of the compounds will be addressed, as their compositions necessarily deviate markedly from B2 stoichiometry, and secondly their be-

havior during deformation in the temperature range between room temperature and  $700^\circ\text{C}$ , where discontinuous yielding is observed. In the first of these, the Ordering Tie Line (OTL) approach will be used to determine and describe the state of ordering in these compounds [3]. It will be shown that both the ordering schemes and degree of ordering vary quite markedly over the compositions studied, and an attempt will be made to relate this to the mechanical behavior of these materials. Regarding deformation behavior in the intermediate temperature range, serrated yielding effects are considered together with phase instabilities and also other characteristics of deformation such as slip localization, yield points and work softening.

### Experimental Procedure

Ingots of three compositions, namely Nb-15Al-xTi, where  $x=10\%$ ,  $25\%$ , and  $40\%$  were produced by plasma arc melting under an Argon/Helium atmosphere. After cold rolling ( $\approx 50\%$  reduction in thickness), flat plates were cut from the master ingot, and either small samples for the OTL experiments or tensile coupons were machined, all of which were subsequently recrystallized ( $1100^\circ\text{C}$  for 1 hour) in quartz tubes backfilled with Argon gas, followed by a water quench. This heat treatment yielded a fully recrystallized, essentially single-phase microstructure with a grain size of approximately  $200\mu\text{m}$ . Following grinding of the surfaces of tensile coupons of the 40Ti alloy, tensile tests were conducted at  $300^\circ\text{C}$  and  $400^\circ\text{C}$  with the furnace being slowly purged with high purity Argon gas. Strain aging heat treatments were performed at temperatures ranging from  $400^\circ\text{C}$  to  $700^\circ\text{C}$  for 10 minute intervals. The static tests were carried out at a constant strain rate of  $10^{-4}\text{s}^{-1}$ . Dynamic tests were performed over a wide range of strain rates. Dislocation microstructures were characterized using transmission electron microscopy (TEM), involving both a Philips CM200 and a CM200FEG, and these two instruments were utilized in the ALCHEMI experiments to provide the data necessary to construct the OTLs for the various compounds.

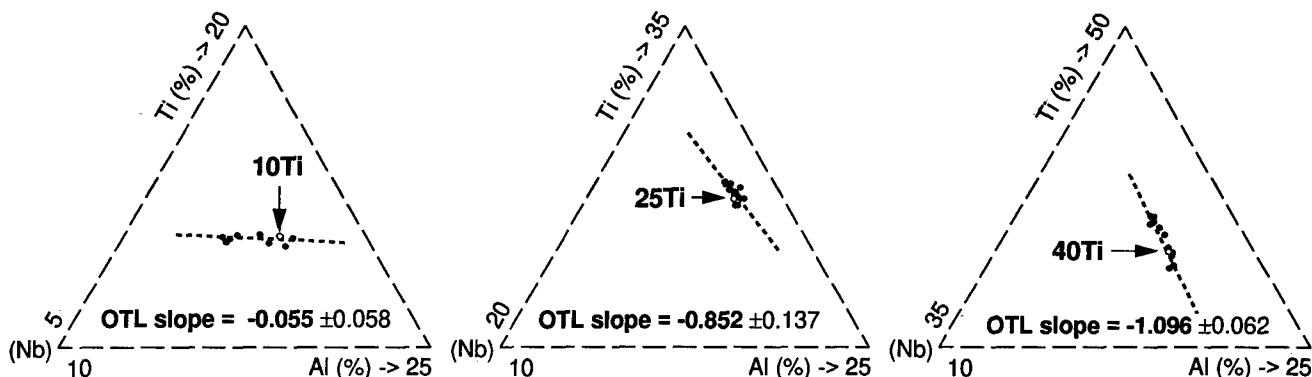


Figure 1. Apparent compositions measured at different tilt angles from samples of the three alloys (Nb-15Al-xTi, where x=10, 25, and 40). The OTL is plotted as the best straight line through the data points.

## Results and Discussion

### The Ordered State and Degree of Order

The slope of an OTL of a given compound is plotted by first conducting a series of ALCHEMI experiments, i.e. where x-ray spectra are recorded with positive and negative deviations from the Bragg condition for a given superlattice reflection. These x-ray spectra yield apparent compositions which differ from that of the actual compound because channeling effects result in an unequal distribution of the fast electrons over the various sublattices. It has been shown [3] that these apparent compositions lie on the given OTL, and so the various spectra are first converted to compositions (using an appropriate set of  $k$ -factors, for example), and then plotted on a composition diagram. Following this procedure, ALCHEMI experiments have been performed on thin foils made from homogenized samples of the three alloys (Nb-15Al-xTi, where x=10, 25, and 40). The apparent compositions determined from these experiments have been plotted on the composition diagrams shown in Fig. 1, and the best straight-line fit through the points has in each case yielded the slope of the given OTL.

The actual OTL requires not only a knowledge of the slope of the line but also the locations of the end-points of the line. This latter information is gained

from the degree of order of the given compound. If it is assumed that the compounds are in their *most ordered* state, then the lines will be extended from the alloy composition in both directions (for B2 stoichiometry and mass balance) along the line until a boundary of the composition diagram is intersected, as discussed in Hou, et al.[3]. Following this assumption, the resulting OTLs are plotted in the composition diagram shown in Fig. 2, where the shaded regions represent the statistical errors involved in the measurements of the slopes ( $\Delta C_{Ti}/\Delta C_{Al}$ ). It is important to establish whether the compounds are indeed in their most ordered state, or whether the long range order parameter,  $S$ , is in fact less than unity. If an OTL for a material with  $S < 1$  is known, the value of  $S$  is defined as the ratio of the length of the OTL to that if it were to be in its most ordered state [3]. Conversely, if the degree of order is known, then the end-points can be plotted using this relationship involving the ratio of lengths. In an attempt to determine the degree of order of the compounds studied here, the dynamical theory of electron diffraction (17 beams) has been used to calculate the estimated spread of measured apparent compositions as a function of long range order parameter which would be expected from ALCHEMI experiments. The results of these calculations are shown graphically in Fig. 3. Since the spread in apparent compositions is larger for negative deviations from Bragg, these values will be used for comparison between theory and experiment. In the case of the 40Ti alloy, this experimental spread is  $\approx 2\%$ , and as shown in Fig. 3, this

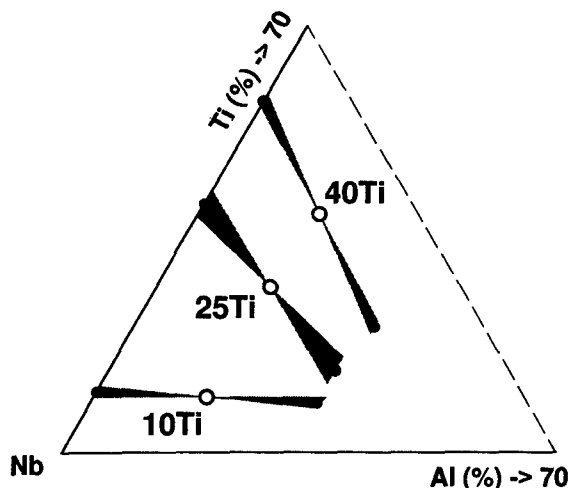


Figure 2. OTLs of the three alloys plotted on a composition diagram, with the end-points of the OTL taken to be at the boundary of the diagram.

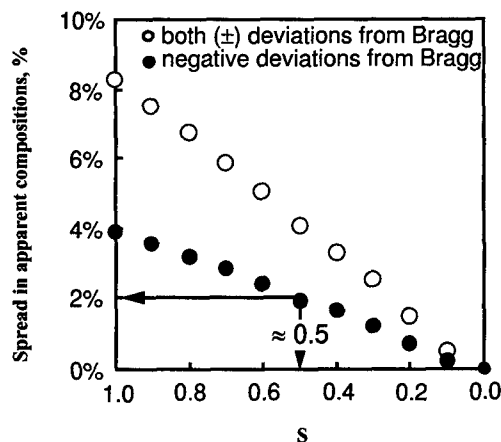


Figure 3. Plot showing the results of dynamical theory calculations which indicate that for the 40Ti alloy,  $S$  is approximately 0.5.

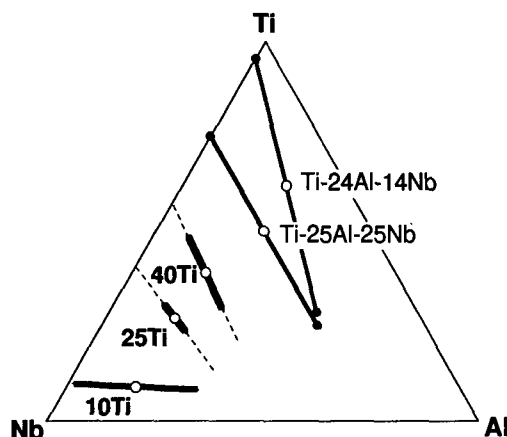


Figure 4. Calculated OTLs for the alloys considered here.

corresponds to  $S \approx 0.5$ . Similar analyses (i.e. simulation using the dynamical theory) for the case of alloys containing 10Ti and 25Ti yield  $S \approx 0.88$  and  $S \approx 0.25$ , respectively. The corresponding OTLs are shown in Fig. 4. From these analyses, it appears that the 10Ti alloy is close to being in its most ordered state, while the other two alloys are not so fully ordered. It should be noted that the results of these analyses give estimates of the end-points of the OTLs, but most confidence may be placed in the slope of the OTL.

It appears from the OTLs presented in both Figs 2 and 4, that the trend in ordering state varies from 10Ti to 40Ti, even though both these compounds have the B2 structure. The degree of ordering varies from highly ordered (i.e. the compound with 10Ti) to partially ordered with  $S \approx 0.5$  (the compound with 40Ti), with the compound containing 25Ti being only slightly ordered ( $S \approx 0.25$ ). Presumably, the compounds with 25Ti and 40Ti represent transitional states such that with increasing Ti content, the degree of ordering would increase as the slope of the OTL increases. Inspection of the OTLs for the three alloys studied, shown in Fig. 2, reveals that the significant factor in achieving the most ordered state is that all Al atoms remain on the one sublattice. This requirement for the Al atoms implies that the partitioning of Al atoms between the two sublattice sites is a critical factor for B2 ordering in these ternary Nb-Al-Ti alloys, as discussed elsewhere[4]. This suggestion can be further supported by the fact that phases with the B2 structure have been found in some Nb-Al alloys [5] but not in the Nb-Ti binary system.

Superdislocations, with Burgers vectors,  $\mathbf{b}$ , given by  $\mathbf{b} = \langle 111 \rangle$ , are observed in these B2 compounds, and an interesting observation concerns the separation of the superpartials, each with  $\mathbf{b} = 1/2 \langle 111 \rangle$ , as the Ti content is varied. For the 10Ti compound, the dissociation widths are typically 10nm, whereas for the 25Ti and 40Ti the widths can be extremely large, for example  $\approx 100\text{nm}$  [6]. Interestingly, the order-disorder transition temperature  $T_C$  of the 40Ti and 25Ti compounds is higher than that of the compound with 10Ti. It is often argued that the ordering energy is proportional to this transition temperature, and so here it might be assumed that the anti-phase boundary (apb) energy of the compound with 10Ti is lower than that of the other two compounds. However, if that were the case, the opposite trend in dissociation might be expected. Based on the results obtained here, it might be argued the degree of ordering determined using the OTL analysis gives a better reflection of the APB energy than does  $T_C$ . Also, changes in the slope of the OTL, as shown in Fig. 4, may have an effect via the change in atomic structure of the apb on changing the nature of the atomic ordering.

#### Deformation Behavior at Room and Intermediate Temperatures

Several interesting observations concerning the behavior of these compounds deformed at intermediate temperatures (e.g. 400°C) have been made. In the following, the deformation behavior of the compound containing 40Ti is considered, and its deformation behavior at room temperature and then at a range of intermediate temperatures is considered.

The phase diagram in figure 5 shows that all the alloys considered here lie outside the limit of B2 solid solubility at intermediate temperatures. In the case of the 40Ti alloy, aging the as-recrystallized and quenched material at 800°C and 900°C has been seen to result in the precipitation of the O-phase. As-quenched samples show no visible precipitation, however weak diffuse scattering is observed in diffraction patterns. The scattering is consistent with the precipitation of the O-phase or the  $\omega$ -phase, or both. It has not been possible to determine the actual origin of this diffuse intensity, or form interpretable images using the diffuse intensity in dark-field imaging.

#### Deformation at Room Temperature

There are two salient features of the stress-strain curves of these materials deformed at room temperature in the as-recrystallized condition, one being the presence of a yield point and the other being an absence of work hardening, often with evidence of work softening. These are shown in the curve marked A in Fig. 6 corresponding to a tensile test at room temperature with a strain rate of  $10^{-4}\text{s}^{-1}$ . After interrupting the test, the sample was aged at 400°C for 10 mins, and the test repeated again, with the result being the curve marked B in Fig. 6. As can be seen, following aging the yield point has become more significant. To determine the effect of the temperature of aging, these tests were repeated at 500°C and 700°C, each for ten minutes, and the results are shown as the curves D and E in Fig. 6. As can be seen, while aging at 500°C tends to promote the yield point, aging at 700°C results in a considerable reduction in its signifi-

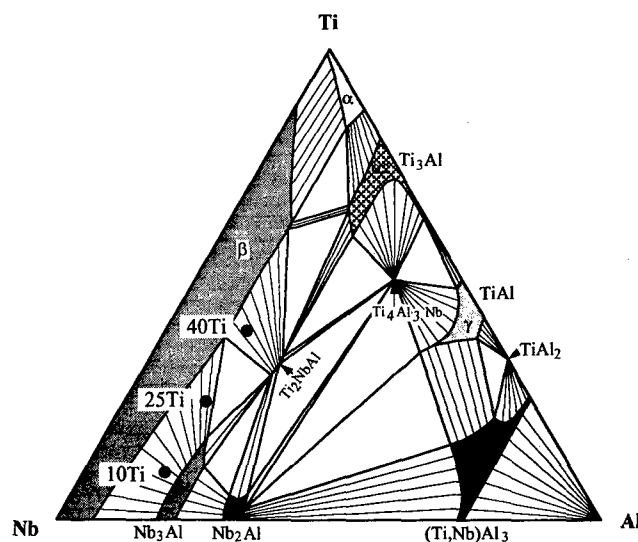


Figure 5. Schematic Nb-Ti-Al phase diagram at 800°C. (from U.R. Kattner and W.J. Boettinger, Mat. Sci. Eng., 152 (1992) 9)



cance. However, it can be seen that the flow stress of the alloy has increased after aging at 700°C. Aging at the lower temperatures had no effect on the flow stress. Interestingly, following multiple interruptions and aging treatments, the total strain in this sample was very much less than that achieved in a single tensile test at room temperature.

A typical microstructure of samples deformed at room temperature is shown in Fig. 7. Diffraction contrast experiments reveal that these dislocations have Burgers vectors parallel to  $\langle 111 \rangle$ , being superpartial dislocations with  $b = 1/2 \langle 111 \rangle$  as observed previously [6], and glide predominantly on  $\{110\}$  planes. Interestingly, the slip is localized in discrete bands. One cause of such slip localization might be due to the presence of a very fine distribution of a second phase, the particles of which are cut by the gliding dislocations [7]. It is common for such a process to be accompanied by a lack of work-hardening, or even work softening, as the resistance to dislocation motion offered by the second phase reduces the effective size of the obstacles as the particles are cut. As noted above, the stress-strain curves do indeed exhibit such an absence of work-hardening. This localization of slip does not lead to problems with ductility (the tensile elongation at room temperature being greater than 30%) and slip is apparently transmitted quite easily across grain boundaries as shown in Fig. 8, leaving significant slip steps on the grain boundaries.

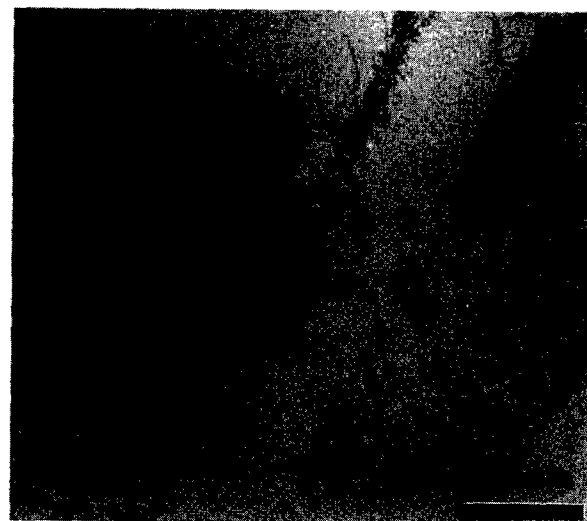


Figure 7. Slip bands in an unaged Nb-15Al-40Ti sample deformed at room temperature in tension.

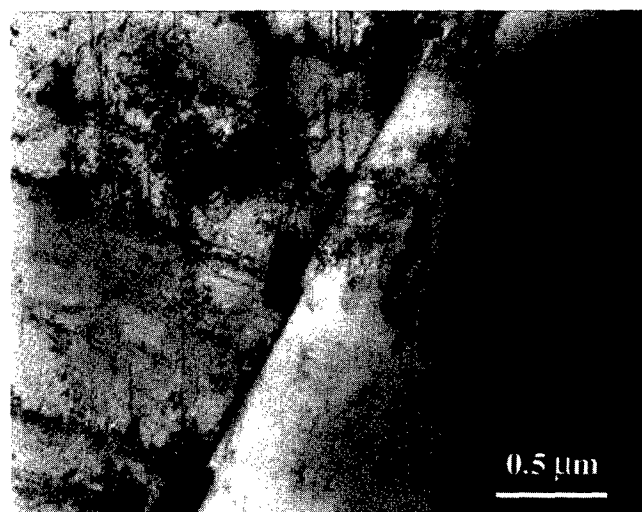


Figure 8. Inhomogeneous slip along bands of high dislocation activity leading to pronounced grain boundary steps.

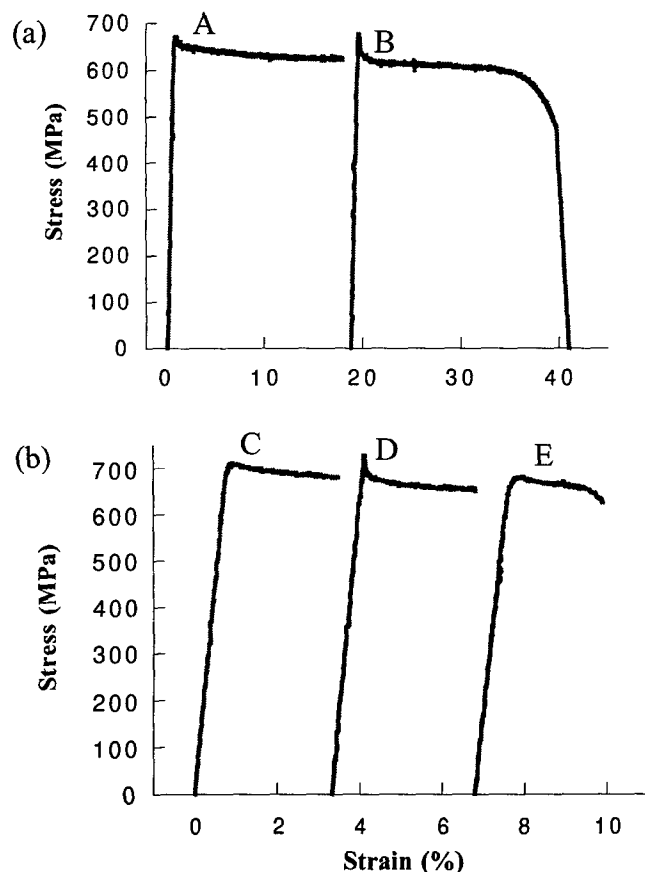


Figure 6. (a) Stress-strain curves for a sample initially deformed in the as-recrystallized condition, giving yield point A, and after unloading, aging for 10 minutes at 400°C and retesting, giving the sharp yield point at B. (b) Yield point behavior of as-recrystallized material indicated at C, after subsequent agings of 500°C/10 minutes at D and 700°C/10 minutes at E.

#### Deformation at Intermediate Temperatures

Recrystallized samples of the compound containing 40Ti have been tested in tension at 400°C at three different strain rates, namely  $3.3 \times 10^{-4} \text{ s}^{-1}$ ,  $6.7 \times 10^{-4} \text{ s}^{-1}$  and  $3.3 \times 10^{-3} \text{ s}^{-1}$ . The general characteristics of the stress-strain curves at this temperature are shown in Fig. 9, where in addition to a yield point, serrated yielding is observed. The amplitude and period of these serrations vary with strain rate, as shown in Fig. 10. Larger serrations are present at slower strain rates (e.g. Fig. 10a, where  $3.3 \times 10^{-5} \text{ s}^{-1}$ ). The serrations have both a decreased amplitude and period with  $3.3 \times 10^{-5} \text{ s}^{-1}$ , while discrete serrations are more or less absent at higher strain rates (e.g. Fig. 10c, where  $3.3 \times 10^{-3} \text{ s}^{-1}$ ). Since such serrated yielding and strain aging is often accompanied by a negative strain rate sensitivity, tensile tests were conducted at 400°C in which the strain rate was varied between  $6.6 \times 10^{-4} \text{ s}^{-1}$  and  $3.3 \times 10^{-5} \text{ s}^{-1}$ . The relevant part of the resulting stress-strain curve is shown in Fig. 11. From these curves, it may be seen that decreasing the strain rate leads to an increased average and peak stress, which corresponds to negative strain rate sensitivity.



Figure 9 shows that serrations begin at the very start of the plastic region of the stress-strain curve, and continue until fracture. Other specimens have been tested at 300°C and 250°C, and these also show serrations throughout the plastic region.

#### Microstructural Characterization

Since the precipitation of the O-phase during elevated-temperature deformation would be expected from the phase diagram, attempts have been made to determine whether a fine distribution of solute clusters or second phase particles exist in samples which have been recrystallized, deformed and subsequently aged at intermediate temperatures (e.g. 500°C), i.e. such as those used to produce the curves in Fig. 6. Weak diffuse scattering has been observed in diffraction patterns recorded from such samples, indicating the presence of a dispersion of some kind. It has not been possible to determine the actual origin of this diffuse intensity, or form interpretable images using the diffuse intensity in dark-field imaging. However, long-term annealing at 500°C has shown that diffuse intensities develop into those which are consistent with the formation of clusters and/or particles of the O-phase [8]. It seems reasonable to expect that the diffuse intensities seen in diffraction patterns taken from samples corresponding to Fig. 6a arise from incipient precipitation of the O-phase and/or the  $\omega$ -phase. A more exact identification of these dispersions is underway.

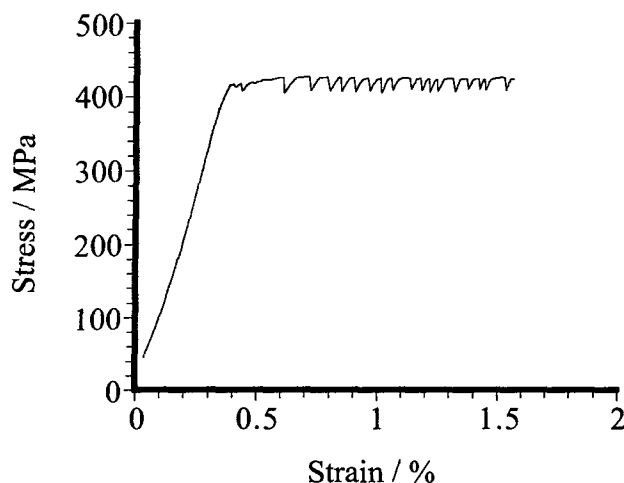


Figure 9. Tensile stress/strain curve for the 40Ti material deformed at 400°C. There is no significant incubation period before serrated flow begins.

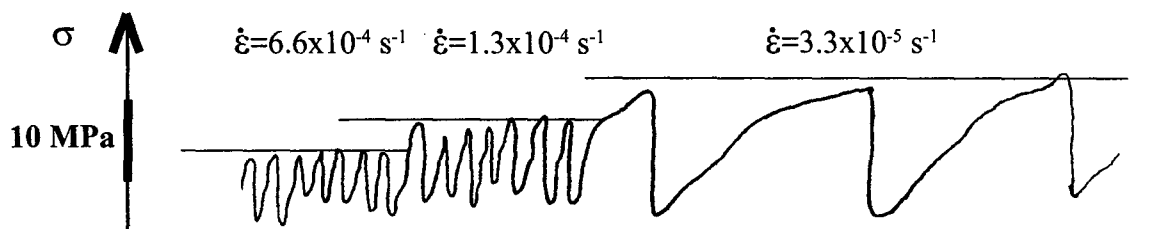


Figure 11. Plastic flow curve for the Nb-15Al-40Ti compound deformed at 400°C showing effect of strain rate changes giving rise to negative strain rate sensitivity factors.

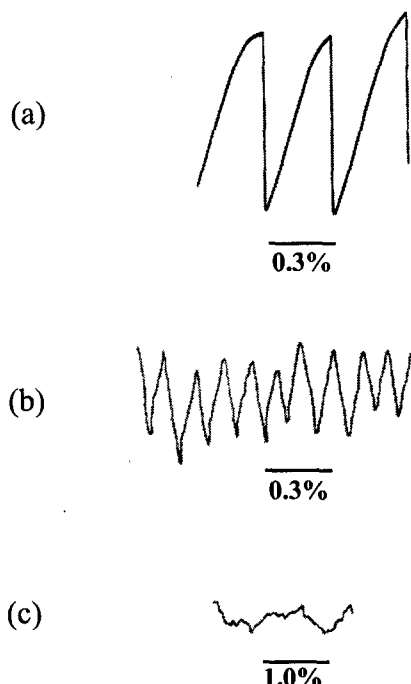


Figure 10. Serrations from the stress-strain curve of a Nb-15Al-40Ti alloy tested at 400°C at the strain rates of (a)  $3.3 \times 10^{-5} \text{ s}^{-1}$ , (b)  $6.7 \times 10^{-4} \text{ s}^{-1}$  and (c)  $3.3 \times 10^{-3} \text{ s}^{-1}$ .

Similar TEM analyses have been initiated on the sample given two aging treatments and presented in Fig. 6b. Electron diffraction patterns recorded from this sample contain extra intensity maxima which are not consistent with the matrix B2 crystal structure. For example, a selected area diffraction pattern is shown in Fig. 12a, where the reflections 220 and 04 $\bar{1}$  are from the O-phase. The positions of the streaked maxima are consistent with a single variant of the O phase. In Fig. 12b, a simulated [113] pattern from the B2 matrix is shown with the reflections corresponding to one variant of the O phase given by the orientation relationship:

$$\begin{array}{l} [011]_{\text{B2}} \parallel [001]_{\text{O}} \\ (2\bar{1}1)_{\text{B2}} \parallel (110)_{\text{O}} \end{array}$$

In this case, the [113] matrix orientation is parallel to the  $\bar{1}14$  orientation of the O phase.

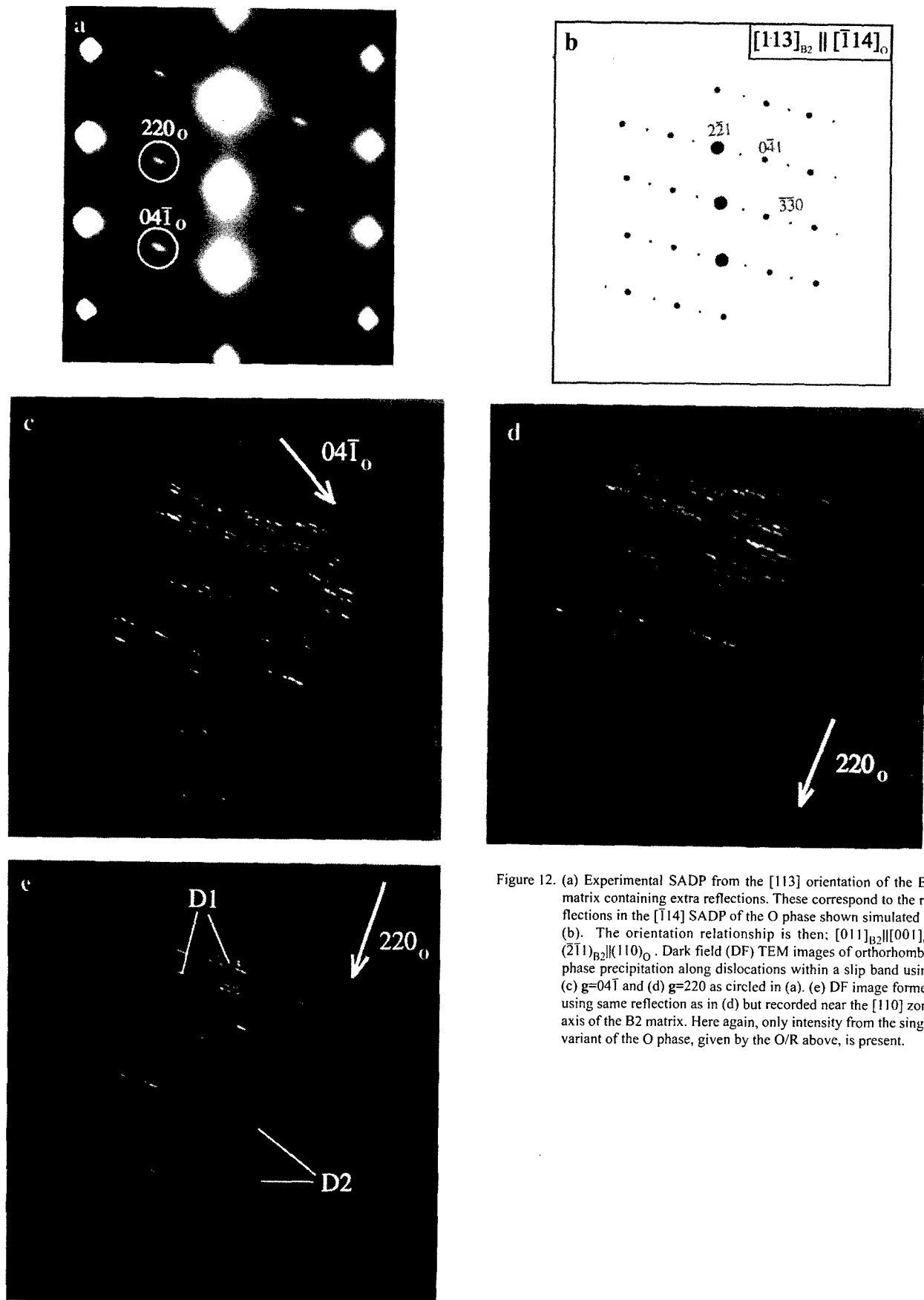


Figure 12. (a) Experimental SADP from the  $[113]$  orientation of the B2 matrix containing extra reflections. These correspond to the reflections in the  $[\bar{1}14]$  SADP of the O phase shown simulated in (b). The orientation relationship is then:  $[011]_{B2} \parallel [001]_O$ ,  $(\bar{2}\bar{1}1)_{B2} \parallel (110)_O$ . Dark field (DF) TEM images of orthorhombic phase precipitation along dislocations within a slip band using (c)  $g=04\bar{1}$  and (d)  $g=220$  as circled in (a). (e) DF image formed using same reflection as in (d) but recorded near the  $[110]$  zone axis of the B2 matrix. Here again, only intensity from the single variant of the O phase, given by the O/R above, is present.

Dark field (DF) TEM images of a slip band are shown in Fig. 12 c,d which have been formed using the reflections corresponding to  $g=04\bar{1}$  and  $g=220$ , respectively, in the O-phase. These two reflections are associated with the same particles in both images. If other variants existed in this region, additional reflections would be present or different particles would be imaged with the two reflections used. To confirm this conclusion, the image in Fig. 12e was recorded near the [011] matrix orientation using the same condition as in Fig. 12d, i.e.  $g=220$ . Again, only reflections associated with the previously determined variant were observed. The observation of only one variant of the O-phase in this region is important because there appear to be two distinct sets of defects present, one indicated by "D1" and the other by "D2". Only defects of the D1 type are decorated with the O-phase. Hence, dislocations associated with the O-phase particles will necessarily be locked while the other set may be glissile.

To examine the nature of the dislocation pinning taking place during elevated-temperature deformation, tensile tests at 250°C were interrupted after a number of serrations had occurred. The test bar was unloaded, and a TEM foil made from the deformed region of the sample. In these specimens there were no apparent microstructural differences from a specimen tested at room-temperature. The diffraction patterns obtained had a similar intensity of weak diffuse streaking as found in a sample deformed at room temperature.

### Discussion

In refractory alloys with bcc-type structures it has been determined that deformation at intermediate temperatures is often associated with serrated yielding [7]. In these materials the cause of such behavior has been attributed to the presence of a fine dispersion of the  $\omega$ -phase, and its re-precipitation following cutting by dislocations to give rise to the dynamic effects observed. If such a fine distribution of a second phase exists in the present intermetallic compound, then it is important to determine whether similar deformation characteristics are also observed in samples tested at intermediate temperatures.

The aim of this study has been to understand the factors causing slip localization and work softening in this ternary Nb aluminide compound, and also to determine the behavior of the material when deformed at intermediate temperatures. It has been shown that deformation at intermediate temperatures is indeed accompanied by serrated yielding, and that intermediate-temperature annealing gives rise to a yield point on subsequent deformation at room-temperature. Both these observations are consistent with a Portevin-Le Chatelier (PLC) effect. Since these various observations may be influenced by the presence of a refined dispersion of solute clusters or precipitate particles, it is important first to discuss the evidence for such a dispersion, and then consider these other factors in the light of this discussion.

In this compound, depending on temperature and aging times, it is possible to effect the formation of both the  $\omega$ - and O-phases [7]. In the present work, the intensities of the diffuse scattering observed in diffraction patterns from samples taken from the tensile coupons after heat-treatment at either 400°C or 500°C (corresponding to fig. 12) are too weak to permit a differentiation between either of these two phases. It is noted that on aging for extended times at these temperatures, (eg. for 200 hours at 400°C followed by 20 hours at 500°C) the O-phase certainly develops. In the case of aging at 700°C (Fig. 12), it is shown unambiguously that the O-phase does indeed form directly on some of the dislocations. At this temperature the  $\omega$ -phase would be unstable. It is tempting to

speculate that the dislocations which become decorated with the O-phase already were decorated, albeit to a much smaller extent, following aging at 500°C, and that the dislocations which are not decorated after this annealing treatment (marked D2 in fig. 12) were generated during room temperature deformation following annealing at 500°C.

In a diffusion-controlled pinning process, such as pinning by solute atoms, it is found that at lower temperatures serrations do not begin as soon as plastic deformation starts, but that there is some 'incubation period', possibly as much as 10% strain, before serrations are seen. This is due to slower diffusion at lower temperatures, such that serrations can only begin once sufficient vacancies have been generated by the deformation to assist in the diffusion process. The fact that in this case serrations are seen at the start of the plastic region of the stress-strain curve at temperatures as low as 250°C indicates that there is a strong possibility that the pinning process is *not* diffusion-controlled, and thus could *not* be due to the precipitation of the equilibrium O-phase, which has a different composition than the B2 matrix. It is tempting to speculate that pinning might be caused by precipitation of  $\omega$ -phase precipitates by some conservative mechanism, and that these precipitates constitute ideal nucleation sites for O-phase precipitates on higher-temperature annealing. Further tests will be performed below 250°C and above 400°C to see if an incubation period is ever seen in this material.

Further evidence that the O-phase is not responsible for the effects seen is found in the samples aged at 700°C and subsequently deformed. As was seen in figure 12, some dislocations are pinned after aging at 700°C by O-phase precipitates. Also, the flow stress is increased after aging at 700°C, indicating more general precipitation in the sample. However, no yield point is seen after this heat-treatment, indicating that the O-phase is not in general locking dislocations very efficiently. Also, during testing at 600°C no serrations are seen, whereas the O-phase would certainly be expected to precipitate to some extent during a tensile test at 600°C.

The origin of the slip localization and the work softening observed in samples of this compound deformed at room temperature may now be understood. From the presence of weak diffuse scattering, it appears that a dispersion of either or both of the O- and  $\omega$ -phases is present in recrystallized samples as well as those subsequently heat-treated at intermediate temperatures ( $\approx 400^\circ\text{--}600^\circ\text{C}$ ). It is expected that once deformation occurs at room temperature, slip will be concentrated on those systems activated initially since particles will be cut by dislocations gliding on the slip planes corresponding to those systems, and hence the dispersion of particles will offer increasingly less resistance to dislocation motion. Consequently, the slip will be localized, and the reduced resistance to dislocation motion will be manifested by reduced applied stresses, i.e. softening.

Serrated yielding has been observed, and a negative strain rate dependence has been determined. These are both consistent with a PLC effect. If this effect is caused by the precipitation of the  $\omega$ -phase, then at intermediate temperatures it would be necessary for particles which are cut by dislocations to dissolve and re-precipitate such that the resistance to dislocation motion is re-established (dynamically). This possibility is the subject of further work.

### Summary

This study can be summarized as follows:

1. A refined dispersion of the O-phase and/or the  $\omega$ -phase is present in samples of Nb-15Al-40Ti which have been recrystallized, and also in those which have been recrystallized and subsequently heat treated at intermediate temperatures. This refined dispersion of second phases is responsible for the slip localization and work softening observed in samples of this compound deformed at room temperature.
2. Static strain aging has been shown to occur in samples aged at intermediate temperatures. Sharp yield points occur when the aging is carried out in the temperature range 400°-500°C. These phenomena are attributed to a strong interaction between dislocations and the refined dispersion of particles that forms on such aging.
3. A PLC effect has been observed, involving serrated yielding and a negative strain rate dependence. This is also attributed to the dynamical interaction of dislocations with the refined dispersion of particles which form in this compound at intermediate temperatures.

### References

1. E.S.K. Menon, P.R. Subramanian and D.K. Dimiduk, *Met. and Mater. Trans.* **27A**, (1996) 1647.
2. R. Wheeler, S.S. Yang, D.-H. Hou and H.L. Fraser, to appear in *Proceedings of Processing and Design Issues in High Temperature Materials*, TMS (1996).
3. D-H Hou, I.P. Jones and H.L. Fraser. 1996, *Phil. Mag. A*, **74**, 741
4. D-H Hou and H.L. Fraser. 1997, *Scripta Mat.*, **36**, 617
5. H. Komoto, J. Shyue, M. Aindow, H.L. Fraser, *Scripta Mat.*, **29**, 1271
6. J. Shyue, D.-H. Hou, M. Aindow and H.L. Fraser, *Mater. Sci. Eng.*, **A170** (1993) 1.
7. S. Banerjee and U.M. Naik, *Met and Mater. Trans.* (1996), in press.
8. R. Wheeler, S. Perungulam, S. Banerjee and H.L. Fraser, submitted to *Acta Met. Matls.* (1996).

# MECHANICAL PROPERTIES AND OXIDATION RESISTANCE OF BINARY $\text{Al}_2\text{Ti}$ INTERMETALLIC COMPOUND

John E. Benci and John C. Ma\*  
Materials Science and Engineering  
Wayne State University  
Detroit, MI 48202

\*Research and Engineering  
Preformed Line Products Co.  
Cleveland, OH 44101

## Abstract

This paper provides an overview of the research on the intermetallic compound  $\text{Al}_2\text{Ti}$ . A review of the literature regarding the existence, stability, and crystal structure of this phase is first presented. This is followed by a summary of the work performed in this laboratory over the last five years on the processing and characterization of this compound. The two main processing routes used to produce the material are casting and powder processing. Various thermal and thermomechanical treatments were employed subsequent to casting.  $\text{Al}_2\text{Ti}$  powder was consolidated by either hot isostatic pressing or uniaxial hot pressing. A total of six material conditions were produced. The characterization performed includes: X-ray diffraction crystal structure analysis; phase transition determinations utilizing differential thermal analysis (DTA); microstructural analysis using optical microscopy and scanning electron microscopy (SEM)/energy dispersive spectroscopy (EDS); hardness and fracture toughness evaluations using Vickers microhardness indentation testing; compressive yield strength and plastic strain-to-failure determinations between room temperature and  $1000^\circ\text{C}$ ; coefficient of thermal expansion measurements between  $200$  and  $900^\circ\text{C}$  by thermal mechanical analysis (TMA); and isothermal oxidation testing at  $815^\circ\text{C}$  and  $982^\circ\text{C}$  in air using thermogravimetric analysis (TGA). The results from the characterization of  $\text{Al}_2\text{Ti}$  are compared to and contrasted with those of other Ti-Al intermetallic alloys.

## Introduction

A significant portion of the work on intermetallic alloys has concentrated on the Ti-Al system, particularly  $\text{Ti}_3\text{Al}$ - and TiAl-based alloys.  $\text{Al}_3\text{Ti}$  has also received considerable research attention more recently because of its lower density and superior oxidation resistance. Another intermetallic compound in the binary Ti-Al system, which has been essentially overlooked by researchers, is  $\text{Al}_2\text{Ti}$ . Until recently, the published work containing reference to  $\text{Al}_2\text{Ti}$  has been limited to phase equilibria and structure studies on the aluminum-rich half of the Ti-Al system.

The Ti-Al phase diagram from the widely used and referenced compilation of binary phase diagrams of Hansen and Aderko [1] published in 1958 is reproduced in Figure 1. This phase diagram does not indicate the existence of an intermetallic compound at or near the 67 at.% Al composition. The two supplements to Hansen and Aderko's work, published in 1965 [2] and 1969 [3], did not contain an updated Ti-Al phase diagram covering this Al concentration. This at least partially explains why  $\text{Al}_2\text{Ti}$  did not receive much attention through the 1970's and beyond.

The  $\text{Al}_2\text{Ti}$  phase was first identified by Potzschke and Schubert in 1962 [4]. They determined that  $\text{Al}_2\text{Ti}$  has the  $\text{HfGa}_2$  crystal structure, a tetragonal structure containing 24 atoms in its unit cell, with lattice parameters of  $a = 3.976 \text{ \AA}$

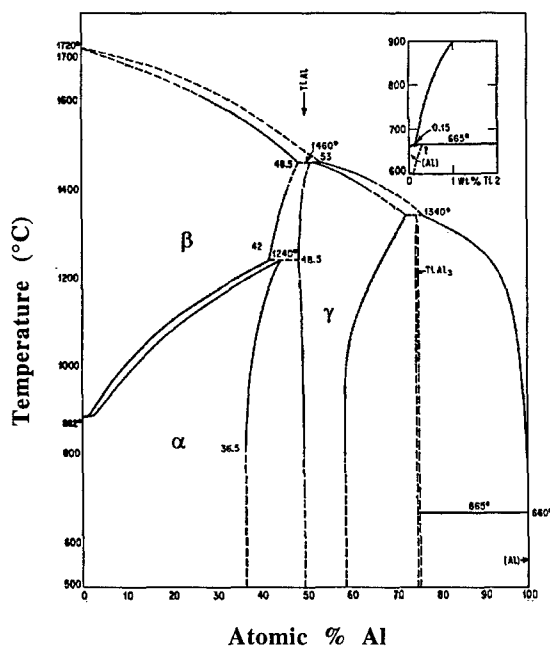


**Figure 1:** The binary Ti-Al phase diagram published by Hansen and Aderko [1].

and  $c = 24.360 \text{ \AA}$ , yielding a  $c/a$  ratio slightly greater than 6. The partial Ti-Al phase diagram covering the Al concentration range between 60 and 85 at.% published by Raman and Schubert in 1965 [5] was the first to include the  $\text{Al}_2\text{Ti}$  phase. The Ti-Al binary phase diagram constructed by Murray [6] and published in a 1986 compilation of binary phase diagrams [7] includes both the  $\text{Al}_2\text{Ti}$  phase and, at high temperatures, the  $\delta$  ( $\text{Ti}_2\text{Al}_5/\text{Ti}_9\text{Al}_{23}$ ) phase between TiAl and  $\text{Al}_3\text{Ti}$  based largely on the work of Raman and Schubert [5]. However, all of the boundaries associated with the  $\text{Al}_2\text{Ti}$  phase were drawn as dashed lines, indicating the lack of information and uncertainty associated with this phase. The aluminum-rich portion of Murray's phase diagram taken from ref. [8] is shown in Figure 2. Based on Murray's assessment: the  $\text{Al}_2\text{Ti}$  phase is stable below 1240°C; above this temperature it decomposes into the  $\gamma$ -TiAl and  $\delta$  ( $\text{Ti}_2\text{Al}_5/\text{Ti}_9\text{Al}_{23}$ ) phases via a peritectoid reaction; and on heating, the first liquid in an Al-33 at.% Ti alloy will form at about 1380°C.

Some more recent experimental work on the structure and phase stability of the intermetallic compounds in the Ti-Al system containing between 24 and 42 at.% Ti has been performed by Loiseau and Vannuffel [9], Kaltenbach et al. [10] and Schuster and Ipsen [11]. The results for the  $\text{Al}_2\text{Ti}$  phase field from these three studies are somewhat contradictory. Kaltenbach et al.'s proposed phase diagram [10] shown in Figure 3 is similar to that of Murray [6]. A single phase  $\text{Al}_2\text{Ti}$  region is shown to be stable up to 1175°C, at which temperature it decomposes into  $\gamma$ -TiAl and  $\xi$  ( $\text{Al}_{11}\text{Ti}_5$ ), with the first liquid forming at about 1415°C. Loiseau and Vannuffel [9] proposed a substantially different phase diagram, a portion of which centered around the  $\text{Al}_2\text{Ti}$  composition is reproduced in Figure 4. They claimed that  $\text{TiAl}_2$  is a reentrant phase, meaning it has the same structure at high and low temperatures, but a different structure at

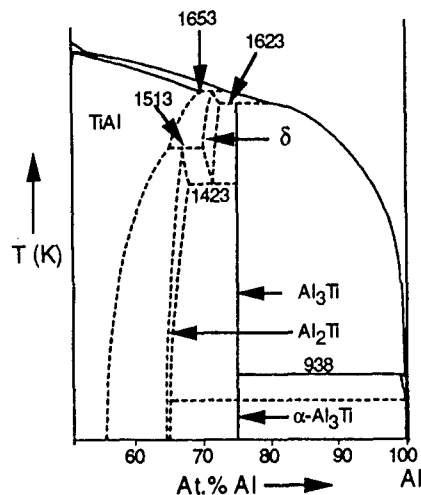


**Figure 2:** A portion of Murray's binary Ti-Al phase diagram [6] taken from ref. [8].

intermediate temperatures. They called the phase which is stable at intermediate temperatures  $\text{TiAl}_2^{\text{II}}$ , and determined its structure to be isotypic with  $\text{HfGa}_2$ . The low and high temperature phase,  $\text{TiAl}_2^{\text{I}}$ , was determined to have the  $\text{ZrGa}_2$  structure, an orthorhombic structure closely related to  $\text{HfGa}_2$ . Loiseau and Vannuffel [9] show the  $\text{TiAl}_2^{\text{II}}$  single phase field to have a solubility range of about 3 at.%, and, with increasing temperature, have  $\text{TiAl}_2^{\text{I}}$  transforming into  $\text{TiAl}_2^{\text{II}}$  at about 600°C,  $\text{TiAl}_2^{\text{II}}$  transforming into  $\text{TiAl}_2^{\text{I}}$  at about 1260°C, a peritectoid transformation of  $\text{TiAl}_2^{\text{I}}$  to TiAl and a long-period structure and have the first liquid phase appearing at about 1400°C. Perhaps the most complete research on the Ti-Al phase diagram between the compositions  $\text{Al}_3\text{Ti}$  and TiAl was performed by Schuster and Ipsen [11]. They also found two polymorphs for  $\text{Al}_2\text{Ti}$  but did not find any evidence that  $\text{Al}_2\text{Ti}$  is a reentrant phase. Figure 5 shows the Ti-Al phase diagram of Schuster and Ipsen [11] taken from ref. [8] which summarizes their results. The phase  $\gamma$ -TiAl<sub>2</sub> is stable at temperatures below 1215°C and has the  $\text{HfGa}_2$  crystal structure

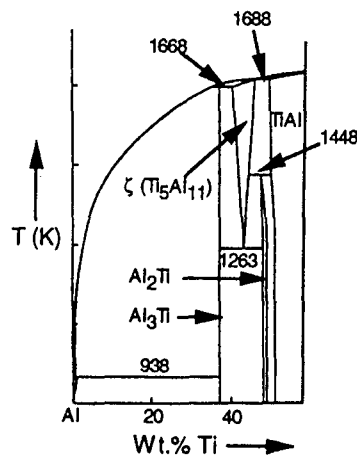


**Figure 3:** A region of the Ti-Al binary phase diagram proposed by Kaltenbach et al. [10] taken from ref. [8].

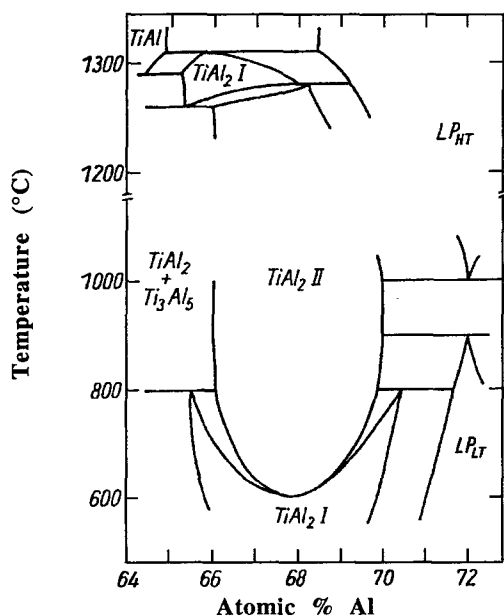


Figure 4: A region of the Ti-Al phase diagram of Loiseau and Vannuffel [9] centered around the composition  $\text{Al}_2\text{Ti}$ .

with lattice parameters  $a = 3.967\text{\AA}$  and  $c = 24.2968\text{\AA}$ . At temperatures above  $1216^\circ\text{C}$  the h- $\text{TiAl}_2$  phase is stable and has the  $\text{ZrGa}_2$  crystal structure. h- $\text{TiAl}_2$  melts incongruently at  $1433^\circ\text{C}$ .

One application where the properties of  $\text{Al}_2\text{Ti}$  may be very important is oxidation resistant coatings for  $\text{Ti}_3\text{Al}$  and  $\text{TiAl}$  structural components.  $\text{Al}_3\text{Ti}$  and  $\text{Al}_3\text{Ti}$ -based alloys are being considered as coating materials for these alloys. Mabuchi et al. [12] used the pack cementation technique to produce  $\text{Al}_3\text{Ti}$  coatings on  $\text{TiAl}$ . When these samples were diffusion annealed for 4 hours at  $1323\text{K}$ , an intermediate layer was found to form at the  $\text{Al}_3\text{Ti}$ - $\text{TiAl}$  interface. Mabuchi et al. [12] measured the composition of this intermediate layer to be  $\text{Al-33 at.}\%$  Ti and determined its crystal structure to be of the

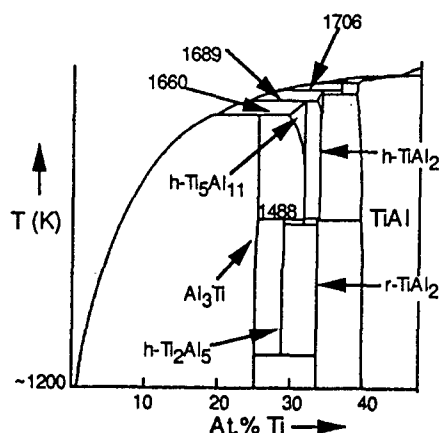


Figure 5: Schuster and Ipsier's [11] contribution to the Ti-Al binary phase diagram around the region of 33 at.% Ti [8].

$\text{HfGa}_2$  type, corresponding to the  $\text{Al}_2\text{Ti}$  phase. They calculated the  $\text{Al}_2\text{Ti}$  lattice parameters to be  $a = 3.971\text{\AA}$  and  $c = 24.32\text{\AA}$ . Several different methods were used by van Loo and Rieck [13] to obtain aluminum layers on substrate materials ranging in composition from 100% Ti to  $\text{TiAl}$ . They then subjected these diffusion couples to various annealing treatments and examined the reaction products. An  $\text{Al}_3\text{Ti}$  layer was formed under all conditions studied, however an intermediate  $\text{Al}_2\text{Ti}$  layer was also formed under certain conditions. van Loo and Rieck [14] conducted another study of interdiffusion in the Ti-Al system. They found that when an  $\text{Al}_3\text{Ti}$  layer was bonded to Ti,  $\text{Ti}_3\text{Al}$  or  $\text{TiAl}$ , and then annealed between  $700^\circ\text{C}$  and  $958^\circ\text{C}$ , an intermediate layer of  $\text{Al}_2\text{Ti}$  was always formed. The properties of  $\text{Al}_2\text{Ti}$  would therefore be extremely important in the performance of  $\text{Al}_3\text{Ti}$ -based oxidation resistant coatings on titanium and titanium aluminide components.

This lab embarked on a program to produce the  $\text{Al}_2\text{Ti}$  phase through a variety of processing methods and then characterize the mechanical, physical and oxidation properties of this phase in the various material conditions obtained. This paper is essentially a summary of the Ph.D. thesis research of one of the authors [15-18].

### Materials Processing

All of the material used in this study was processed by the authors starting from high purity elemental Al and Ti. Figure 6 is a flow chart of the processing utilized to produce the material for this study.

Aluminum and titanium in the appropriate mole ratios (2:1) were arc-melted in a water-cooled copper crucible under an Ar atmosphere producing approximately 300 g ingots. The cast ingots were melted several times in order to ensure chemical homogeneity. At this point in the processing, some of the ingots were used to produce powder while others were further processed in ingot form. Some of the ingots were left in the as-melted condition which is referred to as the as-cast (A-C) material condition. One ingot was annealed at  $1150^\circ\text{C}$  for 4 hr to produce the cast and annealed (C&A) material condition. Another ingot was hot isostatically pressed at  $1150^\circ\text{C}$  for 4 hr under 70 MPa (10 ksi) gas pressure to produce the cast and hot isostatically pressed (C&H) material condition.  $1150^\circ\text{C}$  was chosen as the temperature for both the annealing and HIP'ing treatments in order to remain in the  $\text{Al}_2\text{Ti}$  phase field, based on all of the proposed phase diagrams, and to compare the two conditions after the same thermal exposure. Some samples in the A-C condition underwent simulated hot forging treatment at  $1150^\circ\text{C}$  to a 50% reduction in height at an initial strain rate of  $6 \times 10^{-4} \text{ s}^{-1}$  to produce the cast and forged (C&F) material condition.

The ingots used to produce powder were arc-melted one more time and then rapidly solidified by melt spinning using the melt overflow technique yielding fine, needle-shaped ribbon. The rapidly solidified ribbon was ground and subsequently sieved to yield powder with particle sizes ranging between 5 and  $60 \mu\text{m}$ .  $\text{Al}_2\text{Ti}$  powder was consolidated by either hot isostatic pressing or uniaxial vacuum hot pressing. After the powder was encapsulated in a Ti can, hot isostatic pressing was conducted at  $1100^\circ\text{C}$  for 4 hr under a pressure of 175 MPa

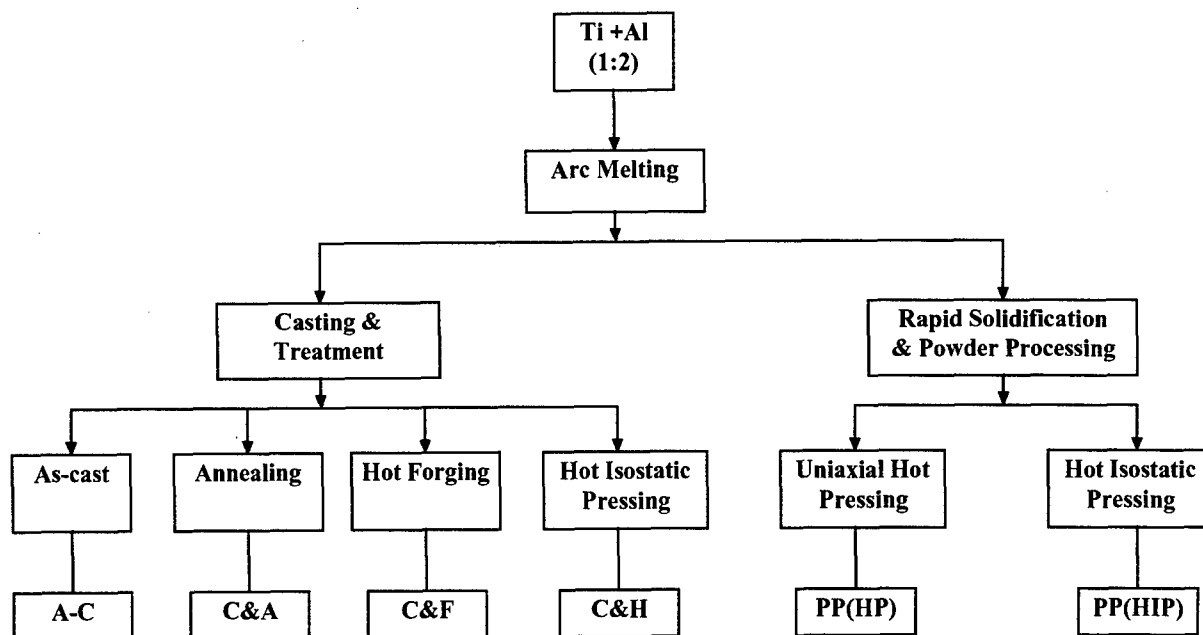


Figure 6: Schematic of the processing routes used to produce  $\text{Al}_2\text{Ti}$  in six material conditions for this study.

(25 ksi) to produce the powder processed/hot isostatically pressed (PP(HIP)) material condition. Consolidation by uniaxial hot pressing was performed in a graphite die at  $1175^\circ\text{C}$  for 3 hr with an applied pressure of 40 MPa (6 ksi). Material consolidated by hot pressing is referred to as the powder processed/hot pressed (PP(HP)) material condition.

Samples from these six material conditions were prepared for testing using electro-discharge machining (EDM) followed by the grinding and polishing of each face of the samples.

## Results and Discussion

### X-ray Diffraction

Powder X-ray diffractometry was performed on  $\text{Al}_2\text{Ti}$  samples in the following material conditions: as-cast; cast and subsequently annealed (either  $500^\circ\text{C}$  or  $700^\circ\text{C}$  in Ar for 4 hr); cast & hot isostatically pressed ( $1150^\circ\text{C}$  and 70 MPa for 4 hr); rapidly solidified ribbon; and annealed rapidly solidified ribbon (either  $1100^\circ\text{C}$  in Ar for 72 hr or  $600^\circ\text{C}$  in Ar for 4 hr).

The X-ray diffraction data obtained from the rapidly solidified ribbon which was annealed at  $1100^\circ\text{C}$  for 72 hr in Ar and then slowly cooled was used to determine the equilibrium crystal structure and lattice parameters for this composition. The experimentally obtained X-ray diffraction pattern has an excellent match with a calculated pattern for  $\text{Al}_2\text{Ti}$  with the  $\text{Ga}_2\text{Hf}$  crystal structure obtained using the FINAX [19] program. A version of the unit cell for the  $\text{Ga}_2\text{Hf}$  crystal structure is shown in figure 7. The lattice parameters obtained from a least squares refinement of the data using FINAX are  $a = 3.9705 \text{ \AA}$  and  $c = 24.322 \text{ \AA}$ , for a  $c/6a$  ratio of 1.02 and a theoretical density of  $3.530 \text{ g/cm}^3$ . These values are in very good agreement with those determined by Schuster and Ipser [11] and Mabuchi et al. [12]. The X-ray diffraction results from rapidly solidified ribbon which was not annealed

indicates that material in this condition has the  $\text{L1}_0$  crystal structure with lattice constants  $a = 3.950 \text{ \AA}$  and  $c = 4.115 \text{ \AA}$  and a theoretical density of  $3.51 \text{ g/cm}^3$ . Rapidly solidified  $\text{Al}_2\text{Ti}$  annealed at  $600^\circ\text{C}$  for 4 hr in Ar has the  $\text{Ga}_2\text{Hf}$  crystal structure indicating that  $\text{Ga}_2\text{Hf}$  is the stable structure for this composition at temperatures as low as  $600^\circ\text{C}$ , and potentially down to room temperature.

In addition to the major peaks corresponding to the  $\text{Ga}_2\text{Hf}$  crystal structure, the X-ray diffraction spectrum of as-cast  $\text{Al}_2\text{Ti}$  also contains several peaks which can be indexed to the  $\text{L1}_0$  structure. Diffraction peaks due to  $\text{L1}_0$  are still present after annealing at  $500^\circ\text{C}$  for 4 hr, however only  $\text{Ga}_2\text{Hf}$  peaks are present after annealing at  $700^\circ\text{C}$  for 4 hr. All of the peaks present in the X-ray diffraction pattern of cast & hot isostatically pressed  $\text{Al}_2\text{Ti}$  can be attributed to the  $\text{Ga}_2\text{Hf}$  crystal structure. These results indicate that there is a second phase present in as-cast  $\text{Al}_2\text{Ti}$  which has the  $\text{L1}_0$  crystal structure and which dissolves or transforms somewhere between  $500^\circ\text{C}$  and  $700^\circ\text{C}$  during annealing.

### Microstructure

As-cast  $\text{Al}_2\text{Ti}$  has a grain size of approximately 1 to 2 mm. Substantial cracking and a large amount of porosity are present in A-C material due to the rapid cooling rates during solidification in a water-cooled copper mold. Bright particles are evident in backscattered SEM images of this material condition. EDS compositional analysis performed on the second phase particles indicates they have a composition of approximately 51 at.% Al and 49% Ti. The density of A-C  $\text{Al}_2\text{Ti}$  was measured to be  $3.511 \text{ g/cm}^3$  by helium pycnometry.

The microstructure of C&A  $\text{Al}_2\text{Ti}$  is similar to that of the A-C material. The cracks and voids present in the A-C material remain. Additionally, the Ti-rich precipitates are still present in the microstructure of the C&A material. These results



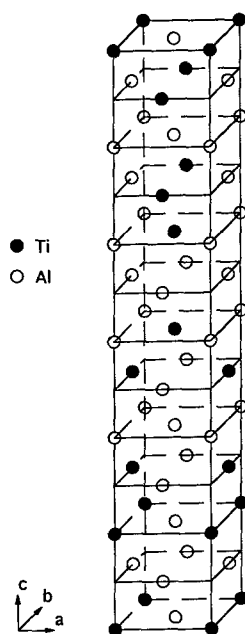


**Figure 7:** The unit cell for  $\text{Al}_2\text{Ti}$  with the  $\text{Ga}_2\text{Hf}$  crystal structure.

indicate that either the annealing time was not sufficient to dissolve the second phase particles or that the overall composition of the sample is in the two-phase field of the phase diagram.

The density of C&H  $\text{Al}_2\text{Ti}$  was measured to be  $3.536 \text{ g/cm}^3$  by helium pycnometry. This is slightly greater than the density measured for A-C material, probably as a result of the closure of some of the porosity and smaller cracks which were not connected to the surface of the sample. The microstructure of the C&H material condition is essentially identical to that of the C&A material condition as expected since both were subjected to the same thermal exposure.

Hot forging A-C material at  $1150^\circ\text{C}$  to a 50% reduction in height results in a refinement of the grain size due to recrystallization. C&F material also has a much lower density of porosity and cracks than the A-C material condition.

Several distinct morphologies were observed in the microstructure of rapidly solidified melt-spun ribbon including featureless regions, columnar grains, and equiaxed grains of 5 to  $20 \mu\text{m}$  diameter. No evidence of a second phase was found. Consolidating powder obtained from melt-spun ribbon by hot isostatic pressing for 4 hr at  $1150^\circ\text{C}$  and a pressure of 175 MPa yielded single phase material with a grain size of 5 to  $8 \mu\text{m}$ . A density of  $3.538 \text{ g/cm}^3$  was measured by helium pycnometry, about 100.2% of theoretical density, and no porosity is seen on polished surfaces of the PP(HIP) material.

Consolidating rapidly solidified powder by vacuum hot pressing in a graphite die at  $1075^\circ\text{C}$  and 40 MPa for 3 hr produced single phase material with a grain size of about 12 -  $13 \mu\text{m}$ . The density was measured to be between 98 and 99%

of theoretical and a small amount of porosity is visible on polished surfaces of this PP(HP) material condition.

#### Phase Transitions

A limited number of differential thermal analysis (DTA) experiments were run on rapidly solidified  $\text{Al}_2\text{Ti}$  between room temperature and  $1500^\circ\text{C}$  in order to identify the transition temperatures associated with this composition. A DTA curve shows a very shallow peak on heating starting at about  $640^\circ\text{C}$ . Upon further heating, much sharper peaks are observed starting at approximately  $1214^\circ\text{C}$  and  $1423^\circ\text{C}$ .

Evaluating the information from the DTA experiments in light of the X-ray diffraction results and proposed phase diagrams [5,6,9-11] we conclude that rapidly solidified  $\text{Al}_2\text{Ti}$  transforms from the nonequilibrium  $\text{L1}_0$  structure to the equilibrium  $\text{Ga}_2\text{Hf}$  structure at about  $640^\circ\text{C}$  to  $650^\circ\text{C}$  during the DTA run. X-ray studies indicate that the transition will occur at a lower temperature, between  $500$  and  $600^\circ\text{C}$ , when the sample is held at one temperature for several hours.  $\text{Al}_2\text{Ti}$  with the  $\text{Ga}_2\text{Hf}$  crystal structure undergoes another transition at approximately  $1214^\circ\text{C}$ . This is consistent with either a change in structure from  $\text{Ga}_2\text{Hf}$  to  $\text{Ga}_2\text{Zr}$  [9,11] or the peritectoid reaction of  $\text{Al}_2\text{Ti}$  decomposing into  $\gamma\text{-TiAl}$  and  $\text{Al}_{2.2-2.5}\text{Ti}$  [5,6,10] on heating. The temperature we measured for this transformation is close to those proposed by other researchers:  $1250^\circ\text{C}$  [5],  $1240^\circ\text{C}$  [6],  $1260^\circ\text{C}$  [9],  $1215^\circ\text{C}$  [11] and  $1175^\circ\text{C}$  [10]. Finally, the DTA peak observed at  $1423^\circ\text{C}$  is consistent with the onset of melting. This temperature is also close to those proposed by other researchers:  $1400^\circ\text{C}$  [5],  $1380^\circ\text{C}$  [6],  $1400^\circ\text{C}$  [9],  $1433^\circ\text{C}$  [11] and  $1415^\circ\text{C}$  [10].

#### Microhardness Testing

Microhardness testing was performed on samples of  $\text{Al}_2\text{Ti}$  in the six material conditions described in the materials processing section. The hardness of  $\text{Al}_2\text{Ti}$  as a function of material condition was determined using a Vickers indenter at a 200 g load, and the results are shown in Figure 8. The hardness for A-C  $\text{Al}_2\text{Ti}$  is approximately 4.3 GPa. Annealing and hot isostatic pressing both result in a decrease in the hardness to about 4.0 GPa since samples in both material conditions were subjected to the same thermal history. PP(HP) and PP(HIP)  $\text{Al}_2\text{Ti}$  both have a hardness of about 5.3 GPa, significantly higher than that of the A-C material condition. This large increase in hardness is most likely due to the two order of magnitude decrease in grain size compared to the A-C condition. The hardness of C&F  $\text{Al}_2\text{Ti}$  is 4.9 GPa. Again, a decrease in grain size due to hot forging is probably responsible for this hardness increase compared to the A-C material condition.

A fracture toughness value was also calculated for each material condition using the critical load necessary to initiate cracks around a Vickers indent. The crack initiation load was determined by increasing the indenter load through the following increments: 200, 300, 500, 1000, 1500, 2000, 2500 and 3000 g, until cracks were detected. The upper load limit, the load increment at which cracks first initiated, is plotted in Figure 8 along with the 200 g hardness value for each of the six material conditions. Cracks are present around 500 g indents in the A-C material condition. The lowest load increment at which cracks were detected increased to 1000 g in the C&A material condition due to the effects of annealing.

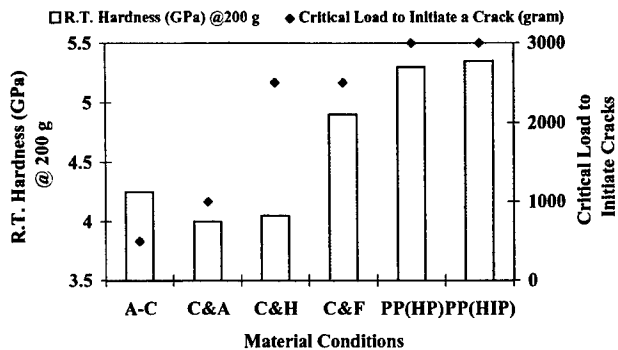


**Figure 8:** The room temperature microhardness and the upper limit crack initiation load for the six  $\text{Al}_2\text{Ti}$  material conditions investigated in this program.

The upper load limit for crack initiation jumped to 2500 g for the C&H material condition. Since the C&H material condition was exposed to the same thermal history as the C&A condition, the large increase in cracking load is due to the superimposed pressure which healed some of the casting defects. C&F  $\text{Al}_2\text{Ti}$  also has a 2500 g upper load limit since hot forging also heals many of the defects present in the A-C condition. PP(HP) and PP(HIP) material conditions have the highest crack initiation loads at 3000 g. Samples of both powder processed material conditions are crack and void free while PP(HP) has only a low volume fraction of small pores present.

Fracture toughness values were calculated from the following equation [20,21]:

$$K_{Ic} = C^{-1/4} [H^3 P_c]^{1/4} \quad (1)$$

where  $K_{Ic}$  is the fracture toughness,  $P_c$  is the critical load to initiate cracks,  $H$  is the hardness and  $C$  is a constant whose value is not well defined. The upper load limit and the lower load limit, the next lower load increment at which cracks did not form, were used to calculate an upper limit and lower limit fracture toughness value for each material condition. The average of the upper limit and lower limit fracture toughness values for the A-C material condition was arbitrarily set to 100 since the value of the constant  $C$  in eqn. 1 is not uniquely defined. The two limiting values of fracture toughness for each material condition normalized by the average A-C fracture toughness value are plotted in Figure 9. The average of the upper limit and lower limit fracture toughness values has, by definition, a value of 100 for the A-C material condition. This corresponds to a fracture toughness of  $4.2 \text{ MPa m}^{1/2}$  when the value of the constant  $C$  in eqn. 1 provided by Hagen [21] is used. The C&A material condition has an average fracture toughness about 20% greater than that of the A-C material condition. The fracture toughness of C&H  $\text{Al}_2\text{Ti}$  is about 50% greater than that of A-C. Powder processing results in a 90 - 95% increase in fracture toughness compared to A-C  $\text{Al}_2\text{Ti}$ . Hot forging cast material produces many of the benefits associated with powder processing including a 75% increase in fracture toughness.

#### Compression Testing

The yield strength and plastic strain-to-failure in compression between room temperature and 1000°C was measured for the

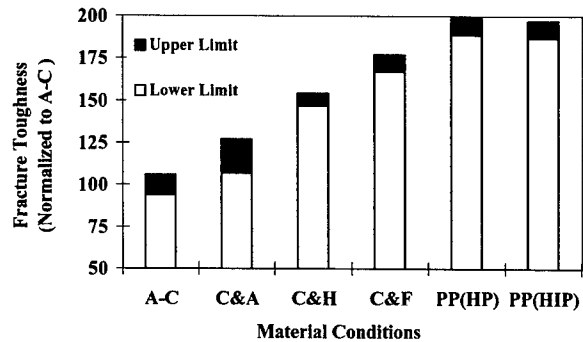


**Figure 9:** The relative fracture toughness values for the six  $\text{Al}_2\text{Ti}$  material conditions investigated in this program normalized by the toughness of the A-C material condition.

A-C, C&A, C&H, PP(HIP) and PP(HP) material conditions. Compression samples measuring 3 mm x 3 mm x 7 mm were cut using EDM. All of the surfaces of each sample were then ground and polished. Two types of compression tests were performed. In both cases the testing was performed under 1 atm of Ar at a constant displacement rate corresponding to an initial strain rate of  $5.7 \times 10^{-4} \text{ s}^{-1}$ . In the first type of testing, used to determine the yield strength as a function of temperature, a sample was heated to 1000°C, loaded to just past yielding and then unloaded. The temperature was then decreased to the next desired temperature, usually 100°C lower, and the procedure was repeated on the same sample at this new temperature. This process was continued down to room temperature. In the second type of testing, a sample was loaded to failure at a single temperature in order to determine the compressive plastic engineering strain-to-failure as a function of temperature. These tests were run at room temperature, 300°C, 500°C, and 850°C for all five material conditions. Tests to failure were conducted at additional temperatures for the powder processed material conditions. The yield strength was also determined for all of the tests run to failure in order to verify the yield strength results from interrupted testing. The yield strengths determined by the two methods are very close with no systematic deviations.

The 0.2% offset compressive yield strength of A-C, C&A and C&H  $\text{Al}_2\text{Ti}$  as a function of temperature is shown in Figure 10. The yield strength of the A-C material condition is about 700 MPa at room temperature and decreases steadily with increasing temperature. A-C  $\text{Al}_2\text{Ti}$  has a yield strength of 600 MPa at 300°C, 520 MPa at 500°C, 475 MPa at 700°C and 355 MPa at 900°C. This material retains a strength of 200 MPa at 1000°C. The yield strengths of the C&A and C&H material conditions are very close to each other over the entire temperature range and approximately 45 - 70 MPa lower than that of the A-C material condition between room temperature and 900°C. This is consistent with the identical thermal treatments C&A and C&H samples received. There is no apparent effect of the applied pressure during hot isostatic pressing on the compressive yield strength of this material. At 1000°C, all three ingot metallurgy material conditions have the same yield strength of 200 MPa.

Figure 10 also compares the compressive yield strength of cast  $\text{Al}_2\text{Ti}$  to that of cast  $\text{Al}_3\text{Ti}$  [22] as a function of temperature. The yield strength of A-C  $\text{Al}_2\text{Ti}$  is

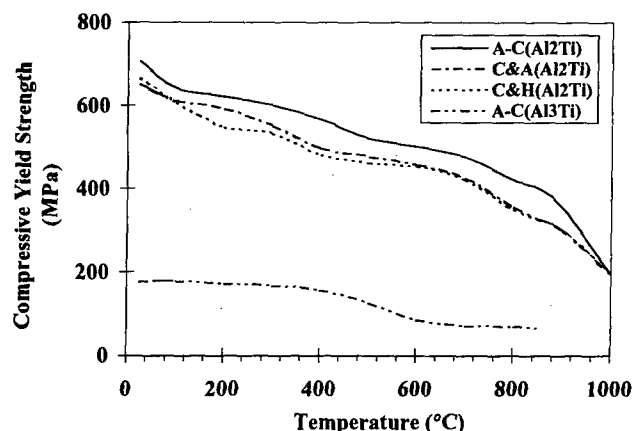


Figure 10: The compressive yield strengths of A-C, C&A and C&H  $\text{Al}_2\text{Ti}$ , and cast  $\text{Al}_3\text{Ti}$  [22].

approximately four times greater than that of cast  $\text{Al}_3\text{Ti}$  over the temperature range - room temperature to 850°C - for which the cast  $\text{Al}_3\text{Ti}$  results were reported.

Producing  $\text{Al}_2\text{Ti}$  through the powder processing route results in a dramatic increase in the compressive yield strength at room temperature, consistent with the large increase seen in the room temperature hardness. The 0.2% offset compressive yield strength of PP(HIP) and PP(HP)  $\text{Al}_2\text{Ti}$  as a function of test temperature between room temperature and 1000°C is shown in Figure 11. The two material conditions have very similar yield strengths over the whole temperature range with perhaps a statistically meaningful difference only between about 600 and 800°C. The yield strength is 1350 MPa at room temperature and decreases almost linearly with increasing temperature up to about 800°C. The yield strength decreases more rapidly between 850 and 900°C. The yield strengths for these two material conditions have values of approximately 1080 MPa at 300°C, 870 MPa at 500°C, 595 MPa for PP(HIP) and 685 MPa for PP(HP) at 700°C, 200 MPa for PP(HIP) and 225 MPa for PP(HP) at 900°C, and 95 MPa at 1000°C. The yield strength of powder processed  $\text{Al}_2\text{Ti}$  is approximately two times that of cast or cast & treated  $\text{Al}_2\text{Ti}$  at room temperature. At 500°C, the yield strength of powder

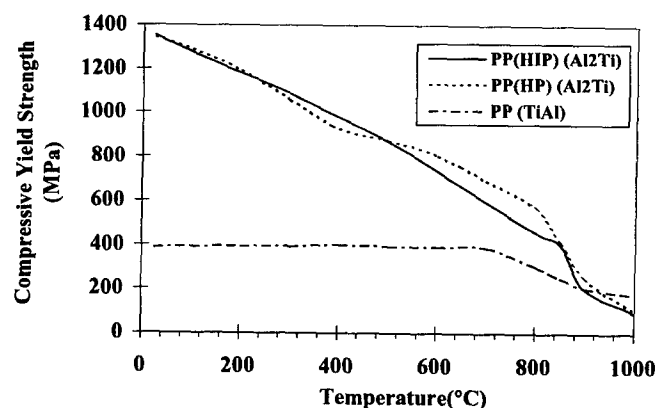


Figure 11: The compressive yield strength of PP(HP) and PP(HIP)  $\text{Al}_2\text{Ti}$  and similarly processed TiAl [23].

processed  $\text{Al}_2\text{Ti}$  is about 65% greater than that of the A-C material condition. The difference is between 25% (for PP(HIP)) and 45% (for PP(HP)) at 700°C. The yield strengths of all five material conditions are about the same somewhere between 800 and 850°C. Above this temperature range the powder processed material conditions have lower strength than the cast material conditions. The increased strength at room temperature and the decreased strength at high temperatures of the powder processed materials compared to the cast materials is consistent with the much smaller grain size in the powder processed material conditions.

The compressive yield strength of powder processed  $\text{Al}_2\text{Ti}$  is also compared to the results reported by Nakayama et al. [23] for powder processed TiAl in Figure 11. The yield strength of  $\text{Al}_2\text{Ti}$  has a much stronger temperature dependence, decreasing more rapidly with increasing temperature. At room temperature the yield strength of  $\text{Al}_2\text{Ti}$  is about 3.5 times greater than that of TiAl. The difference in strength decreases with increasing temperature until at about 900°C the two materials have the same strength. Above 900°C, powder processed TiAl has a slightly greater yield strength than powder processed  $\text{Al}_2\text{Ti}$ .

The second type of testing was used to determine the compressive plastic engineering strain-to-failure at select temperatures for the A-C, C&A, C&H, PP(HIP) and PP(HP) material conditions. The results for A-C, C&A and C&H  $\text{Al}_2\text{Ti}$  are shown in Figure 12. The plastic strain-to-failure of A-C  $\text{Al}_2\text{Ti}$  has a value of 0.3% at room temperature and it increases slowly with increasing temperature with values of 0.4% at 300°C, 1.1% at 500°C and 4% at 850°C. Annealing does not have any effect on the room temperature ductility, however it does slightly increase the ductility at 300, 500 and 850°C to values of approximately 2%, 3% and 5%, respectively. An additional small increase in the plastic strain-to-failure at 300 and 500°C can be achieved through hot isostatic pressing with values of 3.5% at 300°C and about 4% at 500°C. Hot isostatic pressing also does not improve the room temperature ductility of cast  $\text{Al}_2\text{Ti}$ , however it has a very large beneficial effect on the strain-to-failure at 850°C. The test run on C&H  $\text{Al}_2\text{Ti}$  at 850°C was interrupted before failure after accumulating a plastic strain of greater than 20%.

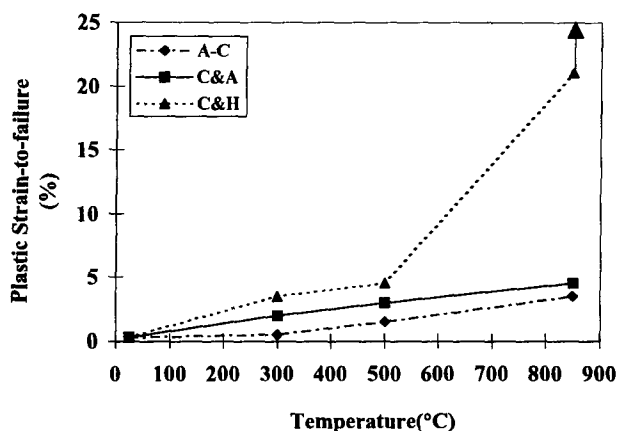
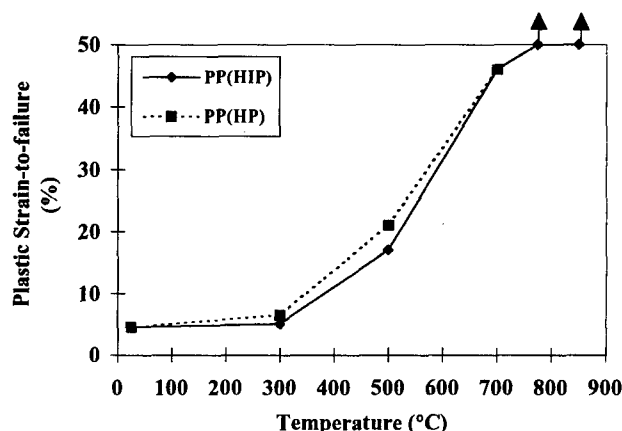


Figure 12: The compressive plastic strain-to-failure of A-C, C&A and C&H  $\text{Al}_2\text{Ti}$  at several temperatures.



**Figure 13:** The compressive plastic strain-to-failure of PP(HIP) and PP(HP)  $\text{Al}_2\text{Ti}$  at several temperatures.

The results from the compression tests run to failure on PP(HIP) and PP(HP)  $\text{Al}_2\text{Ti}$  are shown in Figure 13. Once again, the behavior of these two material conditions are similar to each other. The room temperature plastic engineering strains-to-failure for PP(HIP) and PP(HP)  $\text{Al}_2\text{Ti}$  are over an order of magnitude greater than those of the cast and cast & treated material conditions - 4.5 to 5% compared to about 0.3%. Additionally, samples of the PP(HIP) material condition from tests interrupted at 0.5% plastic strain increments do not show any signs of microcracking until a strain of 4.0% is reached. The plastic strain up to at least 3.5% must therefore be accommodated by plastic deformation of the bulk material. The ductility initially increases only slightly with increasing temperature, reaching values of approximately 6% and 7% for PP(HIP) and PP(HP), respectively, at 300°C. The ductility then increases rapidly with further increases in temperature. At 500°C, PP(HIP)  $\text{Al}_2\text{Ti}$  has a plastic strain-to-failure of 17% while the PP(HP) material condition has a value of 21% at this temperature. Both powder processed material conditions undergo about 46% plastic strain before failure at 700°C. The compression tests conducted at 775 and 850°C were interrupted prior to failure after the samples had been subjected to greater than 60% compressive plastic strains.

#### Oxidation Behavior

The oxidation behavior of A-C, C&H and PP(HIP)  $\text{Al}_2\text{Ti}$  was characterized at two temperatures. Thermogravimetric analysis (TGA) was used to monitor the weight gain for each of the three material conditions both at 815°C and 982°C in flowing laboratory air for a minimum of 100 hrs. Additionally, SEM/EDS was used to analyze both the surfaces and cross-sections of samples oxidized at the same two temperatures for various times up to 100 hrs.

The results for the weight gains measured by TGA after 100 hrs at 815°C and 982°C for the three material conditions are summarized in Figures 14 and 15. Also included in Figures 14 and 15 are the oxidation results for other Ti-Al intermetallic alloys obtained by other investigators [24-27]. As can be seen from these two figures, the processing method/material condition also has a significant effect on the oxidation behavior of  $\text{Al}_2\text{Ti}$ . The 100 hr weight gain for the A-C material condition is the largest of the three material

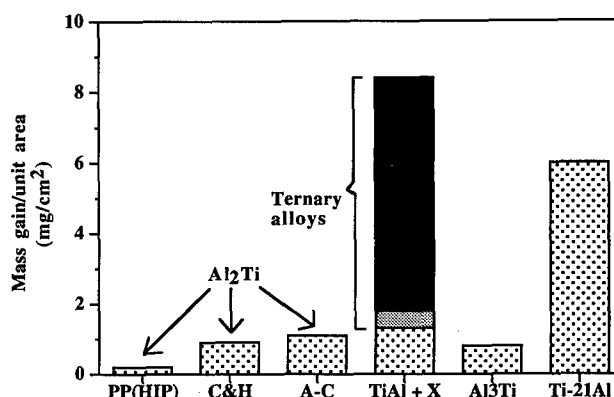


**Figure 14:** Comparison of the 100 hr weight gains for A-C, C&H and PP(HIP)  $\text{Al}_2\text{Ti}$ , binary  $\text{Al}_3\text{Ti}$  [24], TiAl [25,26] and  $\text{Ti}_3\text{Al}$  [27], and ternary TiAl alloys [25] oxidized in air at either 815°C or 800°C.

conditions at both temperatures. C&H  $\text{Al}_2\text{Ti}$  has a 20 - 30% lower weight gain after 100 hrs than the A-C material condition. The weight gain for PP(HIP)  $\text{Al}_2\text{Ti}$  is only about 15 to 35% that of A-C  $\text{Al}_2\text{Ti}$  after 100 hrs at the two temperatures. The weight gain values after 100 hrs at 815°C are 1.1 mg/cm² for A-C, 0.9 mg/cm² for C&H and 0.15 mg/cm² for PP(HIP)  $\text{Al}_2\text{Ti}$ . The 100 hr weight gain values at 982°C are 10.5 mg/cm² for A-C, 7.4 mg/cm² for C&H and 3.9 mg/cm² for PP(HIP)  $\text{Al}_2\text{Ti}$ .

The oxidation weight gain values for  $\text{Al}_2\text{Ti}$  compare favorably to published data on other Ti-Al alloys [24-27] as seen in Figures 14 and 15. The mass gain of  $\text{Al}_3\text{Ti}$  after 100 hrs at 800°C in flowing  $\text{O}_2$  is 0.8 mg/cm² [24]. Kekare et al. [25] studied a series of Ti-48Al + X ternary alloys and measured 100 hr mass gains at 815°C ranging from 1.3 to 8.4 mg/cm² depending on the ternary alloying element. For binary Ti-48Al they measured a 100 hr mass gain of 1.6 mg/cm². Murata et al. [25] measured the mass gain of a Ti-50Al alloy to

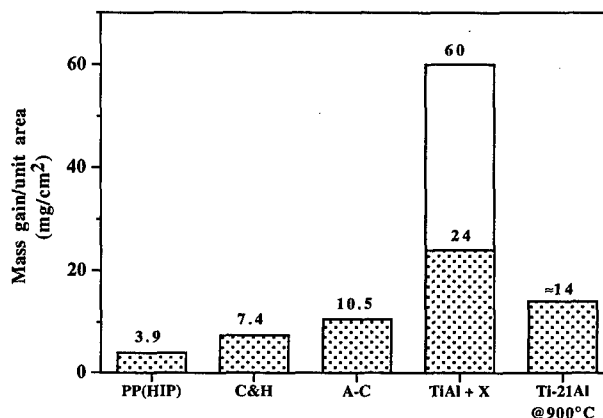


**Figure 15:** Comparison of the 100 hr weight gains for A-C, C&H and PP(HIP)  $\text{Al}_2\text{Ti}$ , binary TiAl [25,26] and  $\text{Ti}_3\text{Al}$  [27], and ternary TiAl alloys [25] oxidized in air at either 982°C or 900°C ( $\text{Ti}_3\text{Al}$ ).

be 1.6 mg/cm<sup>2</sup> after only 24 hrs at 815°C. A mass gain of approximately 6 mg/cm<sup>2</sup> was measured for a Ti-21Al alloy after 100 hrs at 800°C [27]. Kekare et al. [25] also measured the 100 hr oxidative weight gain for the same Ti-48Al + X ternary alloys at 982°C. Their measured values range from 24 to 60 mg/cm<sup>2</sup> depending on the ternary element used, with values of 29 and 52 mg/cm<sup>2</sup> for two binary alloys with different initial oxygen contents. The mass gain for a Ti-21Al alloy oxidized for 100 hrs at a lower temperature of 900°C is approximately 14 mg/cm<sup>2</sup> [27].

SEM/EDS was used to study the surfaces and cross-sections of oxidized A-C, C&H and PP(HIP) Al<sub>2</sub>Ti samples. PP(HIP) Al<sub>2</sub>Ti is chemically homogeneous and does not contain macroscopic defects such as voids or cracks. When samples of this material condition are oxidized in air at 815°C or 982°C, a thin aluminum-rich layer, presumably Al<sub>2</sub>O<sub>3</sub>, is formed on the surface and the mass gains are relatively low. This mechanism dominates the oxidation behavior of PP(HIP) Al<sub>2</sub>Ti at 815°C and at shorter times at 982°C. The higher concentration of cracks in A-C Al<sub>2</sub>Ti results in higher effective surface area for oxidation and therefore higher weight gains per nominal surface area compared to C&H Al<sub>2</sub>Ti. The initial oxide layer which forms on the surface of A-C and C&H samples is a predominantly (>95%) aluminum oxide. However, particularly at the higher temperature, large Ti-rich oxide nodules form and grow. In addition to the surface area effect, cracks appear to be preferred nucleation sites for these Ti-rich oxide nodules. The presence of Ti-rich precipitates in the A-C microstructure may also serve as nucleation sites for Ti-rich oxide nodules. Titanium oxide nodules also form on PP(HIP) Al<sub>2</sub>Ti samples oxidized at 982°C, however not as quickly as they do on the A-C samples. After 25 hrs at 982°C, titanium oxide nodules are coalescing and cover much of the surface of an A-C sample. The surface of a PP(HIP) sample exposed in air for 25 hrs at 982°C has only a low concentration of widely-spaced titanium oxide nodules present. However, once formed, these nodules expand until they cover most of the surface. The majority of the surface of a PP(HIP) Al<sub>2</sub>Ti sample oxidized at 982°C for slightly more than 100 hrs is covered with a titanium oxide scale. This oxidation sequence explains why the rate of weight gain for PP(HIP) Al<sub>2</sub>Ti at 982°C increases with increasing test time up to about 100 hrs instead of decreasing as was observed for all three material conditions at 815°C. If the weight gain measured for the PP(HIP) sample in the first 25 hrs at 982°C was linearly extrapolated to 100 hrs, the weight gain curve would have a value of slightly less than 1.0 mg/cm<sup>2</sup> at 100 hrs compared to the experimentally measured value of 3.9 mg/cm<sup>2</sup>.

A uniform aluminum oxide scale forms on chemically homogeneous, defect-free Al<sub>2</sub>Ti at temperatures up to at least 815°C. However, this alloy is susceptible to the formation of titanium oxide nodules at 982°C and the much larger mass gains associated with nodule formation and growth.

#### Thermal Expansion

The coefficient of thermal expansion (CTE) for A-C and PP(HIP) Al<sub>2</sub>Ti between 200°C and 900°C was measured by TMA [15,17]. The thermal expansion of these two material conditions is about the same over this temperature range. The CTE for the A-C and PP(HIP) Al<sub>2</sub>Ti has a value at 200°C of  $12 \times 10^{-6} \text{ }^{\circ}\text{C}^{-1}$  and increases almost linearly up to a value of

$16 \times 10^{-6} \text{ }^{\circ}\text{C}^{-1}$  at 900°C. These values are about 15-20% larger than those for TiAl [28] between 200°C and 800°C.

#### Summary

The X-ray diffraction and DTA results indicate that the Al<sub>2</sub>Ti phase with the Ga<sub>2</sub>Hf crystal structure is stable up to 1214°C. This phase has a theoretical density of 3.53 g/cm<sup>3</sup>. Upon heating, the onset of melting occurs at 1423°C for the Ti-67 at.% Al composition.

Cast Al<sub>2</sub>Ti has a small volume fraction of a Ti-rich second phase. Rapidly solidified and annealed Al<sub>2</sub>Ti is single phase as is material produced by consolidating rapidly solidified powder. Consolidating Al<sub>2</sub>Ti powder by hot isostatic pressing yields material which is essentially 100% dense. A density of 98 - 99% can be achieved through vacuum hot pressing.

As-cast Al<sub>2</sub>Ti has a room temperature hardness of 4.3 GPa and a compressive yield strength which is about four times greater than that of cast Al<sub>3</sub>Ti between room temperature and 850°C. This material condition has a compressive plastic strain-to-failure of only 0.3% at room temperature. If we choose the value for the constant C in equation 1 proposed by Hagen [21], the fracture toughness of this material condition is calculated to be 4.2 MPa m<sup>1/2</sup>.

Annealing cast Al<sub>2</sub>Ti results in a small decrease in room temperature hardness and yield strength between room temperature and 900°C. However, the fracture toughness is increased by about 20%. While annealing does not improve the room temperature ductility, it does increase the elevated temperature strain-to-failure by a small amount.

Hot isostatically pressing cast Al<sub>2</sub>Ti heals some of the casting defects so while hardness and strength values are similar to those for the C&A material condition, further improvements in the room temperature fracture toughness and elevated temperature ductility are obtained.

Powder processed Al<sub>2</sub>Ti has a higher room temperature hardness - 5.3 GPa, higher fracture toughness - by 90 to 95%, double the room temperature strength and an order of magnitude increase in the room temperature plastic strain-to-failure compared to A-C Al<sub>2</sub>Ti. Additionally, the elevated temperature plastic strain-to-failure increases much more rapidly with increasing temperature reaching values of greater than 60% at temperatures of 775°C and above. These property improvements are due to the much finer grain size and the absence of macroscopic defects in the PP(HIP) and PP(HP) material conditions.

The oxidation behavior of Al<sub>2</sub>Ti is strongly dependent on material condition. The 100 hr oxidative weight gain of PP(HIP) Al<sub>2</sub>Ti is about 15% and 35% that of the A-C material condition at 815°C and 982°C, respectively. An aluminum oxide scale forms on all material conditions at both temperatures. In addition, macroscopic defects such as cracks, and possibly the presence of Ti-rich precipitates, lead to the formation of titanium-rich oxide nodules on samples in the A-C material condition at both temperatures. These oxide nodules cover a large portion of the surface of A-C samples

oxidized at 982°C for only 25 hrs. There is no evidence of nodule formation on PP(HIP) samples oxidized for up to 100 hrs at 815°C. However, at 982°C a small number of Ti-rich nodules form on the surface of PP(HIP) Al<sub>2</sub>Ti within the first 25 hrs of testing. By 100 hrs, the nodules have grown to cover most of the surface. This nodule growth is probably responsible for the increasing rate of weight gain with time up to 100 hrs measured for the PP(HIP) material condition.

### Acknowledgements

The authors would like to thank W. Frazier of the Naval Air Warfare Center and A. Ghosh of the University of Michigan for their assistance with materials processing; T. Feist of General Electric, L. Harrison of Du Pont, and J. Obien and L. Wenger of Wayne State University for their assistance with the TGA, TMA and DTA measurements; and M. Brady of NASA LeReC and L. Bergeron, H. Plummer, Jr. and R. Baird of Ford Motor Company for their assistance with some of the SEM/EDS of oxidized samples. The authors would also like to acknowledge the assistance of M. Lukitsch in preparing this manuscript.

### References

1. M. Hansen and K. Aderko, eds., Constitution of Binary Alloys, (New York, NY: McGraw-Hill, 1958), 140.
2. R.P. Elliott, ed., Constitution of Binary Alloys. First Supplement, (New York, NY: McGraw-Hill, 1965), 58-61.
3. F.A. Shunk, Constitution of Binary Alloys. Second Supplement, (New York, NY: McGraw-Hill, 1969), 44-45.
4. M. Potzschke and K. Schubert, Z. Metallkde., 53 (1962), 548-561.
5. A. Raman and K. Schubert, Z. Metallkde., 56 (1965), 44-52.
6. J.L. Murray, in Binary Alloy Phase Diagrams, ed. T.B. Massalski, (Metals Park, OH: American Society for Metals, 1986).
7. T.B. Massalski, ed., Binary Alloy Phase Diagrams, (Metals Park, OH: American Society for Metals, 1986).
8. K.S. Kumar, in Structural Intermetallics, eds. R. Darolia, J.J. Lewandowski, C.T. Liu, P.L. Martin, D.B. Miracle and M.V. Nathal (Warrendale, PA: The Minerals, Metals & Materials Society, 1993) 87-96.
9. A. Loiseau and C. Vannuffel, Phys. Stat. Sol. A, 107 (1988), 655-671.
10. K. Kaltenbach, S. Gama, D.G. Pinatti, and K. Schulze, Z. Metallkde., 80 (1989), 511-514.
11. J.C. Schuster and H. Ipsier, Z. Metallkde., 81 (1990), 389-396.
12. H. Mabuchi, T. Asai and Y. Nakayama, Scripta Metall., 23 (1989), 685-689.
13. F.J.J. van Loo and G.D. Rieck, Acta Metall., 21 (1973), 61-71.
14. F.J.J. van Loo and G.D. Rieck, Acta Metall., 21 (1973), 73-84.
15. J.C. Ma, "A Study of Processing, Properties, and Deformation Mechanisms of the Binary Intermetallic Compound Al<sub>2</sub>Ti" (Ph.D. thesis, Wayne State University, 1996).
16. J.E. Benci, J.C. Ma, and T.P. Feist, Mater. Res. Soc. Proc., 288 (1993), 397-402.
17. J.E. Benci, J.C. Ma, and T.P. Feist, Mater. Sci. Eng., A192/193 (1995), 38-44.
18. J.C. Ma, J.E. Benci, and T.P. Feist, Mat. Res. Soc. Proc., 364 (1995), 1303-1308.
19. E.R. Hovestreydt, J. Appl. Cryst., 16 (1983), 651-653.
20. B.R. Lawn and A.G. Evans, J. Mater. Sci., 12 (1977), 2195-2196.
21. J.T. Hagen, J. Mater. Sci., 14 (1979), 2975-2976.
22. M. Yamaguchi, Y. Umakoshi and T. Yamane, Phil. Mag. A, 55 (1987), 301-315.
23. Y. Nakayama, H. Mabuchi, H. Tsuda, and K.-I. Hirukawa, Scripta Metall. Mater., 24 (1990), 505.
24. J.L. Smialek and D.L. Humphrey, Scripta Metall. Mater., 26 (1992) 1763.
25. S.A. Kekare, D.K. Shelton, and P.B. Aswath, Mater. Res. Soc. Proc., 288 (1992), 1025.
26. Y. Murata, M. Morinaga, Y. Shimamura, Y. Takeda and S. Miyazaki, in Structural Intermetallics, eds. R. Darolia, J.J. Lewandowski, C.T. Liu, P.L. Martin, D.B. Miracle and M.V. Nathal, (Warrendale, PA: The Mineral, Metals & Materials Society, 1993), 247-256.
27. J. Rakowski, D. Monceau, F.S. Pettit, G.H. Meier and R.A. Perkins, in Microscopy of Oxidation 2, eds. S.B. Newcomb and M.J. Bennett, (London, England: The Institute of Materials 1993), 476-487.
28. S. Krishnamurthy, in Interfaces in Metal-Ceramic Composites, eds. R.Y. Lin, R.J. Arsenault, G.T. Martins & S.G. Fishman, (Warrendale, PA: The Metallurgical Society, 1990), 75.

## Oxidation Studies on $\text{MoSi}_2\text{-X}$ ( $\text{X}=\text{Al}, \text{Ta}, \text{W}$ ) Alloys

A Stergiou and P Tsakiroopoulos  
Department of Materials Science and Engineering,  
University of Surrey, Guildford, Surrey GU2 5XH, England, UK

### ABSTRACT

The oxidation of  $\text{MoSi}_2$  alloyed with Al, Ta and W was studied. At low temperatures ( $T=773\text{K}$ ) pest oxidation was observed in the alloys with W and/or Ta addition. The pest oxidation temperature was shifted to slightly higher values in the Ta containing alloys. Mo and Si were detected in the oxides. Suppression of pest oxidation was achieved in alloys with Al addition where a mixed Al/Si oxide was formed with traces of Al/Mo oxide. In the former alloys a silica scale (2 to 7  $\mu\text{m}$  thick) was formed at high temperatures ( $T>1600\text{K}$ ) and there was no evidence of  $\text{Mo}_5\text{Si}_3$  formation beneath the silica scale. The scale thickness depended on alloy composition with the thinner scales formed on the Ta containing alloys. In the latter alloys an alumina scale (10 to 20  $\mu\text{m}$  thick) was formed at 1623K. Formation of  $\text{Mo}_5\text{Si}_3$  beneath the alumina scale depended on the Al content of the alloy.

### INTRODUCTION

The use of  $\text{MoSi}_2$  as a structural material for high-temperature ( $T\leq 2000\text{K}$ ) applications is restricted by pest oxidation at intermediate temperatures (573-873 K) and poor mechanical properties at low temperatures [1]. The excellent oxidation resistance of  $\text{MoSi}_2$  at high temperatures is due to the formation of a self-healing, glassy silica ( $\text{SiO}_2$ ) [2]. In the pest temperature regime  $\text{MoSi}_2$  loses its metallic structure and is converted into small particles of disilicide covered with a voluminous greenish-yellow powder. It has been suggested that for polycrystalline samples the pest of  $\text{MoSi}_2$  involves grain boundary diffusion of oxygen and that the grain boundaries undergo first the pest reaction leading to formation of  $\text{MoO}_3$  and  $\text{SiO}_2$  in the sample [3]. As a result internal stresses may arise due to: (1) volume expansion caused by the formation of  $\text{MoO}_3$  and  $\text{SiO}_2$  at grain/particle boundaries, (2) internal pressure build-up caused by the volatilization of  $\text{MoO}_3$  and (3) the uneven stress distribution resulting from the

formation of protruding  $\text{MoO}_3$  whiskers. Once the internal structure of a sample is opened up and more interfaces are produced and exposed to oxygen, pest reaction via volume diffusion of  $\text{O}_2$  readily proceeds.

$\text{WSi}_2$  is formed in the tetragonal  $\text{C11}_b$  structure and although it has been suggested as a potential addition to  $\text{MoSi}_2$  to improve its mechanical properties through solid solution strengthening, its oxidation behaviour is suggested to be identical to that of  $\text{MoSi}_2$ ; pest oxidation at intermediate temperatures, protective oxidation at high temperatures [4]. On the other hand,  $\text{TaSi}_2$  is formed in the hexagonal C40 structure. Combination of  $\text{TaSi}_2$  with  $\text{MoSi}_2$  therefore leads to formation of a two-phase microstructure, which has been considered promising. Nowotny et al showed that the phase with the C40 structure was the dominant second phase in alloys of  $\text{MoSi}_2$  with Ta [5]. The oxidation behaviour of  $\text{TaSi}_2$  has not been studied extensively as for  $\text{MoSi}_2$ . However, an earlier study by Lavandel et al reports pest oxidation of  $\text{TaSi}_2$  [6]. The high temperature oxidation of  $\text{TaSi}_2$  is poorer compared to  $\text{MoSi}_2$  [4]. This is attributed to the low free energy of  $\text{Ta}_2\text{O}_5$  oxide formation, which is stable even at high temperatures. As a result, exposure of  $\text{TaSi}_2$  at high temperatures results to the formation of a mixed  $\text{SiO}_2/\text{Ta}_2\text{O}_5$  scale. According to Yanagihara et al the oxidation of  $\text{MoSi}_2$  with addition of about 3.5 at% Ta did not show any significant change compared to  $\text{MoSi}_2$  [7]. They showed that pure  $\text{SiO}_2$  was formed after oxidation at 1958 K and only a small amount of  $\text{Ta}_2\text{O}_5$  was dissolved in the scale (less than 1 mol%). However, the oxidation rate of  $(\text{Mo}, \text{Ta})\text{Si}_2$  at 1773 K showed a higher weight gain in the initial stages of oxidation, suggesting a difficulty in forming a protective scale.

Aluminium addition has been reported to improve the oxidation

properties of  $\text{MoSi}_2$ . Early high temperature oxidation work by Brukl et al showed that alloys with low Al content containing the  $\text{Mo}(\text{Si},\text{Al})_2$  phase (hexagonal C40 structure) followed the well-known oxidation behaviour characteristic of pure  $\text{MoSi}_2$  [8]. In addition, these alloys seemed to develop an optimal oxidation resistance at temperatures above 1873 K. Recent work on the oxidation behaviour of  $\text{MoSi}_2$  alloys containing Al has again concentrated only on the high-temperature oxidation behaviour. The results were promising in terms of scale cracking and spalling. More specifically, it has been reported that the  $\text{SiO}_2$  scale formed on  $\text{MoSi}_2$  spalls off largely at high temperatures (2023 K) [7]. This problem arises from the degree of crystallization of the  $\text{SiO}_2$  scale to beta-cristobalite and becomes more intense at high temperatures.

In this paper we present results of our studies of the intermediate-temperature (pest-regime) and high temperature oxidation behaviour of  $\text{MoSi}_2$  alloys containing W, Ta and Al using DSC/TG, isothermal oxidation experiments and characterisation of the oxide scales formed. For comparison purposes, oxidation studies were also performed on  $\text{MoSi}_2$  at the same temperatures.  $\text{MoSi}_2$  was used as the reference material.

### EXPERIMENTAL

The alloys given in Table 1 were prepared by cold hearth clean melting high purity Mo, Si and Al elemental materials. Each ingot was melted four times to ensure homogenisation. Losses of Si and Al by evaporation were compensated by adding slightly larger amounts of these elements. Interstitial levels were  $\text{O}_2 < 200$  wppm and  $\text{H}_2 < 20$  wppm. The oxidation of the alloys was studied on 90mg specimens using a Rheometric Sciences thermobalance with maximum operating temperature 1773 K and a standard heating and cooling rate of 20 K/min. All experiments were conducted in air and DSC/TG curves were obtained during heating.

Isothermal oxidation experiments were carried out on 1 to 2 g cubes under still laboratory atmosphere for a standard period of 170 hours at 773, 1073, 1223 and 1673 K (selected on the basis of the results obtained from the DSC/TG study and the results reported in the literature), using a calibrated Stanton Redcroft thermal balance. The weight of the specimen was monitored continuously throughout the experiment. The surface area of each specimen was calculated by measuring its dimensions using a micrometer (0.001 mm accuracy). The initial and final weight of the specimen was also measured using a microbalance (0.0001 g accuracy). Specimens of each alloy were also oxidised in air at 1623 K for 72 hours in order to study the scale forming at this temperature. The oxidised surfaces were studied using energy-dispersive X-ray analysis on a JEOL JXA8600 electron probe microanalysis system to determine the bulk composition of the ingots and the oxide composition.

### RESULTS

The microstructures of the alloys are discussed in detail elsewhere [9,10]. Below, the essential features of their as-cast ingot microstructure are summarised. In alloy 1 the matrix consisted of  $\text{MoSi}_2$  of exact stoichiometry. A small amount of  $\text{Mo}_5\text{Si}_3$  was also observed; its formation was attributed to Si loss during melting which resulted to a shift towards the Mo-rich area in the Mo-Si phase diagram. Alloy 2 showed no significant change in microstructure as the major phase present was  $\text{MoSi}_2$  with W in solid solution. Traces of  $\text{Mo}_5\text{Si}_3$  with W in solid solution were also observed at the grain boundaries. In alloy 3 the matrix was  $\text{MoSi}_2$  (C11<sub>b</sub> structure), with W and a negligible amount of Ta in solid solution, while a second phase was formed in the C40 structure. The latter contained higher amount of Ta compared to the matrix. In alloy 4 phases with the C11<sub>b</sub> and C40 structures were present, although the amount of the latter was higher compared to alloy 3 due to higher amount of Ta present in

alloy 4. In addition, free Si was observed in the microstructure and was attributed to the excess Si added to alloy 4. In alloy 5 the main phase was  $\text{Mo}(\text{Si},\text{Al})_2$  (C40 structure). Minor amounts of other phases were present on the grain boundaries, such as  $\text{Mo}_5(\text{Si},\text{Al})_3$ ,  $\text{Mo}_3\text{Al}_8$  and the C54 orthorhombic structure (a modification of the C40 structure with higher amount of Al). In alloy 6 the major phase (C40) and the other minor phases (C54 and  $\text{Mo}_3\text{Al}_8$ ) were present together with free Al due to chemical segregation. The amount and size of the minor phases was increased in alloy 6 compared to alloy 5. Cracks were present in the microstructure of alloys 1 to 4. The intensity of cracking was associated with the presence of  $\text{Mo}_5\text{Si}_3$  and to a lesser degree with the presence of  $\text{TaSi}_2$ , and decreased significantly in alloy 4.

The DSC/TG data for  $\text{MoSi}_2$  (alloy 1) showed the first exothermic peak at 787 K, which was accompanied by weight gain in the TG curve, in agreement with reported results [11,12]. There was reduction in weight above 1000 K and a strong exothermic peak accompanied by weight gain at 1550 K, owing to the rapid formation of the protective silica layer (see below). The DSC/TG results for alloys 2, 3 and 4 were similar with an exothermic peak and weight gain occurring around 800 K followed by a reduction in weight similar to alloy 1 (figure 1). Only a small shift of the pest peak to higher temperatures was observed, suggesting that suppression of the pest phenomenon was not achieved through W and Ta addition. Alloys 2 and 3 exhibited similar behaviour to alloy 1 at  $T > 1200\text{K}$ . On the contrary, in alloy 4 the high temperature exothermic peak was suppressed. Furthermore an endothermic peak was observed at about 1600 K, which is attributed to melting of free Si present in the ingot microstructure.

The DSC/TG data of alloys 5 and 6 showed no evidence of "pest" oxidation, and no weight gain occurring at around 773 K, in contrast to the behaviour of alloys 1 to 4, suggesting that suppression of the pest phenomenon was achieved through Al addition (figure 2). A small exothermic peak was observed at 799 K in alloy 5, but compared to alloy 1 the weight gain was negligible. Minor exothermic peaks at 980 and 993 K were obtained for alloys 5 and 6 respectively and a small weight gain over this range was observed, in contrast to alloy 1. The drop in weight gain noticed at 1000 K for alloy 1 was absent in alloys 5 and 6. At  $T \sim 1170\text{K}$  a major exothermic peak and weight gain were observed for alloys 5 and 6. Reduction in weight was observed at  $T > 1280\text{K}$ . No other peak was observed on the DSC/TG curves of alloys 5 and 6 at temperatures up to 1773 K. No peaks were obtained for any of the alloys during cooling down to room temperature.

Isothermal oxidation at 773 K showed massive weight gain per unit surface area for alloys 1 to 4 (figure 3). All specimens were converted to powder covered by a greenish-yellow oxide. The powders of alloy 1 consisted of  $\text{MoO}_3$  whiskers and of intermetallic particles covered by an oxide layer containing Si and Mo, which is in agreement with reported results [11,12]. The powders of alloys 2 to 4 also consisted of intermetallic particles covered by oxide. Composition maps of the alloying elements in the oxide scale showed that the powder particles were covered by a mixed oxide of Si and Mo, while Ta and W contributed less in the oxide formation [13].

The above phenomena characteristic of pest oxidation were not observed for alloys 5 and 6 (figure 3). Negligible weight gain was observed and the oxidised specimens remained intact, covered only by a very thin blueish oxide film which was less than 0.1  $\mu\text{m}$  thick. Surface examination of this oxide using T-o-F SIMS gave spectra with a strong Al peak accompanied by a small Si peak [14]. The Mo and  $\text{MoO}_3$  peaks were negligible, suggesting that only a small amount of Mo was present in the surface layer. The compositional maps from the surface films suggested that a mixed Al/Si oxide was formed with traces of mixed Al/Mo oxide in some areas [14].



Table 1 Chemical compositions (at%) of the alloys

Alloy	Nominal Composition					EPMA (large area analysis)				
	Mo	Si	W	Ta	Al	Mo	Si	W	Ta	Al
1	33.3	66.7	-	-	-	34.1	65.9	-	-	-
2	31.2	66.7	2.1	-	-	32.6	65.2	2.2	-	-
3	29.1	66.7	2.1	2.1	-	27.8	67.6	2.4	2.2	-
4	24.8	66.7	2.1	6.4	-	23.6	68.1	2.2	6.1	-
5	33.3	44.1	-	-	22.6	32.8	45.4	-	-	21.8
6	33.3	36.7	-	-	30	31.2	39.5	-	-	29.3

Table 2 : Weight gain rates during isothermal oxidation at 773 K

Alloy	Incubation Period (hours)	Slope A (mg/cm <sup>2</sup> sec)	Slope B (mg/cm <sup>2</sup> sec)
1	8	$2.10 \times 10^{-5}$	$1.29 \times 10^{-4}$
2	6	$1.94 \times 10^{-5}$	$0.85 \times 10^{-4}$
3	10	$2.77 \times 10^{-5}$	$0.92 \times 10^{-4}$
4	16	$0.66 \times 10^{-4}$	

Table 3 : Oxide scales formed on ingots oxidised at 1623 K for 72 hours in still air

Alloy	EPMA	Oxide Scale Formed	Scale Thickness ( $\mu$ m)
1	32.5 at% Si	SiO <sub>2</sub>	~7.9
2	32.4 at% Si	SiO <sub>2</sub>	~7.6
3	33.7 at% Si	SiO <sub>2</sub>	~2.8
4	32.3 at% Si	SiO <sub>2</sub>	~2.3

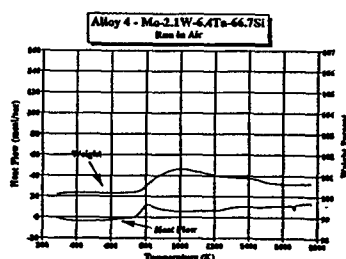
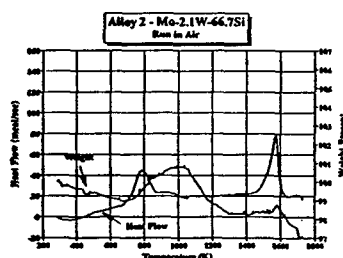
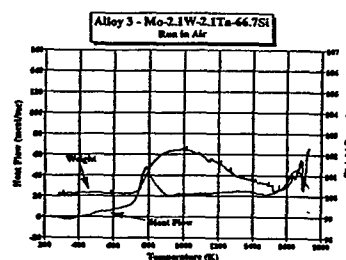
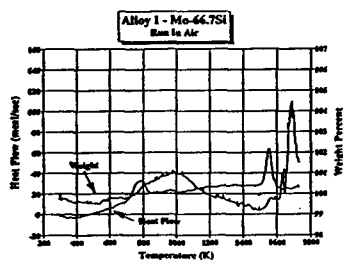


Figure 1: DSC/TG data for alloys 1 to 4

Alloys 1 to 4 exhibited an incubation period, where no weight gain was observed and then oxidised linearly (figure 3). This incubation period varied and alloy 4 exhibited the longer period as shown in Table 2. After the incubation period, rapid oxidation took place for all alloys. The major difference though, was the fact that alloys 1, 2 and 3 followed linear oxidation with a small rate at the beginning (slope A in Table 2), followed by an increase in the weight gain rate (slope B in Table 2), while alloy 4 followed the same weight gain rate during the whole period of the experiment. In addition, the time when the change in weight gain rate occurred was longer for alloy 1 than for alloys 2 to 4.

Isothermal oxidation at 1073 K showed no severe weight gain for alloys 1 to 4 with a small weight loss occurring for alloy 1 (figure 4). As time progressed weight gain was again observed. All alloys did not exhibit any sign of disintegration and a thin oxide layer was formed on their surfaces [13]. In alloy 5 an initial weight gain was followed by a weight loss. As time progressed weight gain was again observed. In alloy 6 a more controlled behaviour was observed with a small and continuous increase in weight for the whole period of 170 hours (figure 4).

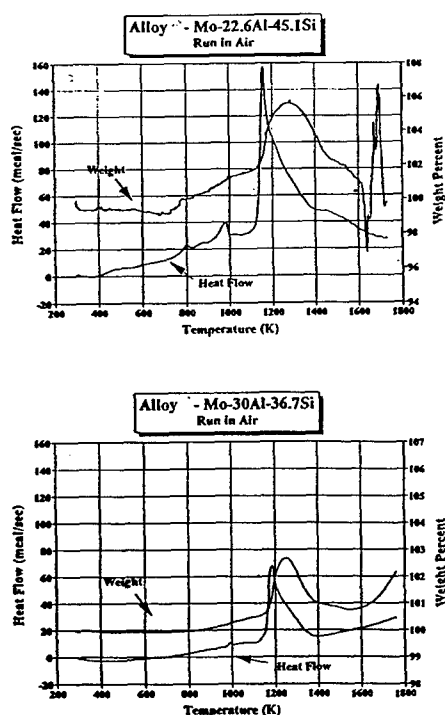


Figure 2: DSC/TG data for alloys 5 and 6

Isothermal oxidation of alloys 1, 5 and 6 at 1223 K showed no significant weight gain (figure 5). On alloys 5 and 6 the oxide thickness was less than  $0.1 \mu\text{m}$ . T-o-F SIMS revealed a massive Si peak and minor Mo peaks in the spectra of alloy 1, suggesting that pure silica was formed at this temperature [14]. Compositional maps supported these results. The silica layer was protective and no significant weight gain was observed after exposure for 170 hours. In the T-o-F SIMS spectra of alloys 5 and 6, a massive Al peak accompanied by a smaller Si peak was observed as for 773 K. However, in this case the relative intensity of the Si peak was significantly smaller compared to that obtained on specimens oxidised at 773 K, suggesting a possible

enrichment of the oxide in  $\text{Al}_2\text{O}_3$ . The Mo and  $\text{MoO}_3$  peaks were negligible suggesting that only small amount of Mo is present in the surface layer [14]. The compositional maps showed that a mixed Al/Si oxide was formed with traces of Al/Mo mixed oxide in some areas and that the amount of Al/Mo oxide was reduced compared to that formed on specimens oxidised at 773 K.

The oxidation behaviour of alloys 1 to 4 at 1673 K exhibited an initial period of rapid linear oxidation, a short intermediate period, when the rate of oxidation diminished with time, and a final period in which the oxidation rate increased again except for alloy 4, for which the weight gain rate decreased to zero after 55 hours (figure 6). EPMA of alloy 1 oxidised at 1623 K for 72 hours revealed the formation of pure silica of around  $8 \mu\text{m}$  thick. The  $\text{Mo}_5\text{Si}_3$  layer that was expected [15] to form adjacent to the scale, due to depletion in Si, was not observed. Alloys 2 to 4 also formed a  $\text{SiO}_2$  scale and no other layer was apparent. The thickness of the oxide scale in alloy 3 was around  $7 \mu\text{m}$ , similar to alloy 1. In contrast, the oxide scale thickness in alloys 3 and 4 was around 2 to  $3 \mu\text{m}$ . The compositions of the scales were determined by EPMA and are given in Table 3.

Alloys 5 and 6 exhibited a similar behaviour to alloy 1 at the early stages (Figure 6), the mass gain per unit area in alloy 5 during the first period of rapid oxidation being higher compared to alloys 1 and 6. The overall weight gain for alloy 5 was higher at 1673 K, the rate of weight gain of alloy 6 decreasing to zero after 40 hours at 1673 K. In alloys 5 and 6, a pure alumina scale (around  $20 \mu\text{m}$  thick) was formed on the surface, in agreement with other results [16]. In addition, in alloy 5 a layer of  $\text{Mo}_5\text{Si}_3$  was present beneath the oxide scale. No such layer was developed beneath the oxide scale in alloy 6 [14].

## DISCUSSION

The results for alloy 1 at 773K are in agreement with the literature. As shown in figure 1 pest was accompanied by weight gain which started at around 700 K and continued up to around 1000 K, where volatilization of  $\text{MoO}_3$  took place and led to a reduction in weight. Severe weight gain, accompanied by catastrophic failure of the material, was observed in the isothermal oxidation experiments at 773K (figure 3) and mixed Si/Mo oxides were formed on the surface of the produced powder [13,14]. The  $\text{MoO}_3$  whiskers formed under these conditions have also been reported by Chou et al [12].

In the weight gain data, an incubation period of about 8 hours was confirmed (Table 2). The main feature of pest oxidation is that the attack by oxygen is predominately intergranular. The incubation period can thus be attributed to the time required for boundary penetration by the diffusing gas. After the incubation period, rapid oxidation of the specimen took place. The oxidation in this stage was linear. However, in this study the linear pest oxidation behaviour of  $\text{MoSi}_2$  exhibited two distinct regions (Figure 3) with rates of  $2.10 \times 10^{-5}$  and  $1.29 \times 10^{-4} \text{mg/cm}^2\text{sec}$  respectively (Table 2). This can be explained as follows: Initially, after the incubation period, the specimen was oxidised and formation of  $\text{SiO}_2$  and  $\text{MoO}_3$  took place on the surface, in cracks, pores and grain boundaries. These oxides and especially  $\text{MoO}_3$  exhibit high molar volume differences compared to  $\text{MoSi}_2$ . Consequently the presence of these oxides led to shattering of the material with progression of time and additional free surfaces were formed. Oxidation of these surfaces can explain the steep increase in weight gain rate after about 100 hours. Such a behaviour has been reported for HIPed materials only [17] and not for as-cast  $\text{MoSi}_2$ . In the HIPed materials the result of oxidation at 773 K was the formation of a thick oxide scale which remained intact after prolonged periods of time. This behaviour was attributed to the lack of cracks in the HIPed materials [17]. However, similar behaviour was observed in this study, suggesting that the oxidation of cracks is not the major contributor in  $\text{MoSi}_2$  pest and that other mechanisms, such as

diffusion of oxygen to the grain-boundaries, are the main contributors to this phenomenon [12,18].

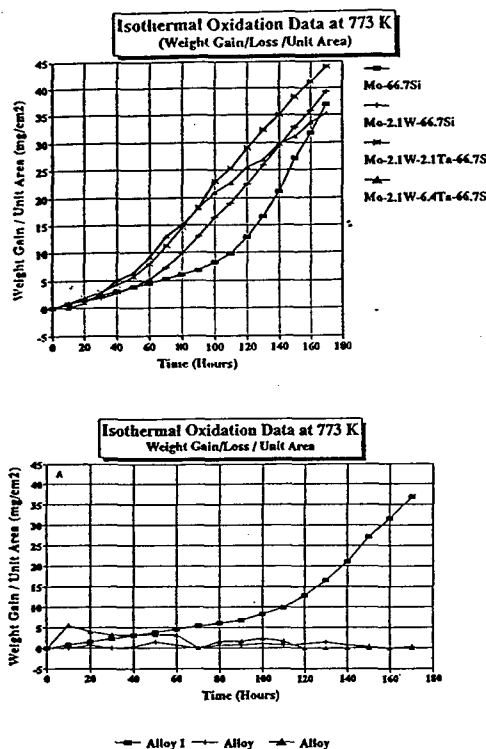


Figure 3: Isothermal oxidation data at 773K

Incubation period varied for the alloys, with the lowest values obtained for alloys 1 and 2 (Table 2). Berztiss et al [19] have shown that the surface condition could shorten or extend the incubation period. However, as all specimens were prepared in exactly the same way, the relatively small incubation period of alloys 1 and 2 can be attributed to the presence of  $\text{Mo}_5\text{Si}_3$ , which was absent in alloys 3 and 4.  $\text{Mo}_5\text{Si}_3$  is known to be preferentially oxidised to form  $\text{MoO}_3$  [3]. Grabke and Meier have reported that alloys with excess of Si show a clearer incubation period, which seems to be the case for alloy 4 [3].

The oxidation behaviour of alloys 2 and 3 at 773K was similar to alloy 1 with the change from one weight gain rate to the other occurring at different times for these alloys. This is also attributed to the factors discussed above. In alloy 4 however, no change in weight gain rate was observed after the incubation period. This is attributed to the higher amount of the phase with the C40 structure ( $\text{TaSi}_2$ ), which probably does not contribute to the pest phenomenon at 773 K. The presence of a negligible amount of Ta in the oxide suggests that only  $\text{MoSi}_2$  (matrix) was responsible for the pest of this alloy. Such a behaviour could also be attributed to the smaller amount of cracks present in this alloy. This would lead to a more even oxidation. Data on the oxidation behaviour of  $\text{TaSi}_2$  is still lacking. In any case, if  $\text{TaSi}_2$  were susceptible to pest oxidation, this would probably occur at a different temperature regime, as one of the key features of this phenomenon is that its temperature range is specific to a given compound [20]. It could be possible then, that  $\text{TaSi}_2$  could remain intact at 773 K but at a different temperature it could show an

accelerated oxidation behaviour. This is supported by the fact that a small shift of the pest peak was observed in the DSC trace of alloy 4.

In alloys 5 and 6 the addition of aluminium suppressed pest oxidation and TG showed a slight weight gain compared to alloy 1 (figures 1,2). Isothermal oxidation at 773 K confirmed the above results as the specimens remained intact. The oxide layer consisted mainly of Al and Si. Formation of Aluminium oxide is expected as  $\text{Al}_2\text{O}_3$  has a lower free energy of formation compared to  $\text{SiO}_2$ . Formation of this oxide and suppression of pesting are therefore attributed to the more rapid growth of the alumina scale, compared to the silica one in alloy 1. In this way extensive formation of  $\text{MoO}_3$  was prevented and consequently protective oxidation could be achieved.

Isothermal oxidation of alloy 1 at 1073 K suggested that this temperature is within the regime where protective oxidation occurs instead of catastrophic oxidation. A small weight loss was observed

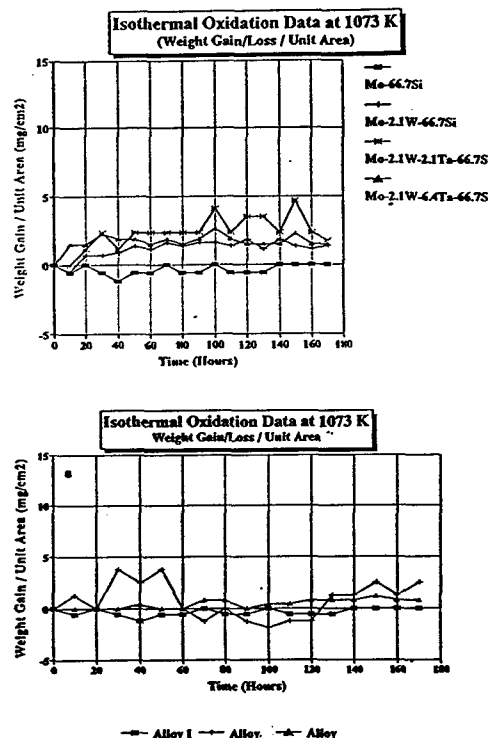


Figure 4: Isothermal oxidation data at 1073K

(Figure 4), and is attributed to volatilisation of  $\text{MoO}_3$ . This is in agreement with the DSC/TG results (Figure 1), as no peak was identified at this temperature regime, and weight loss was observed above 1000 K. As suggested in the literature [11], the upper limit for pesting is around 973 K as pesting is controlled by the vapour pressure of  $\text{MoO}_3$ . Even though pesting has been reported for  $\text{TaSi}_2$  at this temperature regime [4] no severe weight gain was noted in this study for alloys 3 and 4. This suggests that suppression of  $\text{TaSi}_2$  pesting was achieved and that the presence of  $\text{MoSi}_2$  enabled the formation of a continuous and protective silica layer. For alloys 5 and 6 slight

increase in weight was observed in the isothermal oxidation experiments at 1073 K (Figure 4), in agreement with the DSC/TG results (Figure 2).

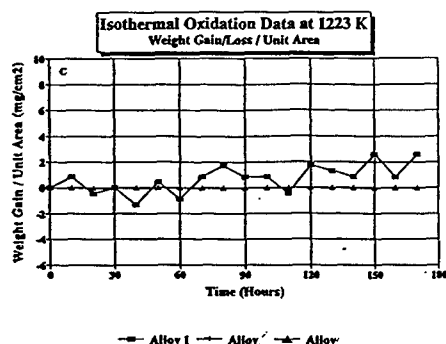


Figure 5: Isothermal oxidation data at 1223K for alloys 1,5,6

As the temperature increased,  $\text{MoSi}_2$  exhibited a controlled oxidation behaviour and at 1223 K a pure silica scale was formed on the surface. Isothermal oxidation at this temperature showed an initial increase in weight (Figure 5) which is attributed to the formation of silica and  $\text{MoO}_3$ . This increase was followed by a decrease in weight, attributed to volatilisation of  $\text{MoO}_3$ . As the time progressed, weight gain was observed due to oxygen consumption and formation of the silica layer. The results are in agreement with those obtained by the DSC/TG study as no significant weight gain was observed at this temperature (Figure 1). As the temperature increased, the scale of alloys 5 and 6 became enriched in  $\text{Al}_2\text{O}_3$  [14]. DSC/TG showed a major exothermic peak accompanied by significant weight gain at 1223 K (Figure 2). However, isothermal oxidation at 1223 K was accompanied by negligible weight gain (Figure 5) and the specimens remained intact after 170 hours. The observed DSC peak could be attributed to decomposition of the mixed Al/Si and Al/Mo oxides with subsequent volatilisation of  $\text{MoO}_3$ , which is responsible for the weight loss. The alumina formed on the surface is considered responsible for the controlled oxidation behaviour of alloys 5 and 6.

At higher temperatures, a silica layer was present on the surface of alloy 1 [13,14]. The absence of  $\text{Mo}_5\text{Si}_3$ , which is predicted to form as a result of depletion of Si from  $\text{MoSi}_2$  at the  $\text{MoSi}_2$ - $\text{SiO}_2$  interface [21], has been reported by many investigators [22,23]. Apparently the growth of such a layer is sluggish. An alternative is that  $\text{MoO}_3$  is also formed and migrates through the oxide layer and evaporates at the  $\text{SiO}_2$ /gas interface. Such a mechanism is probable and it is envisaged that it could contribute to the small thickness of the silica scale.

The scale obtained in both alloys 5 and 6 after oxidation at 1623 K for 72 hours was pure alumina and is in agreement with other results [16]. Diffusion of Al into the scale is expected to bring out a depletion in Al of the layer adjacent to the scale of the alloy. This was observed for alloy 5 but not for alloy 6 and is attributed to the lower Al content in alloy 5. In previously reported results [7,16] where a second layer of  $\text{Mo}_5\text{Si}_3$  was present after oxidation, the alloys did not contain more than 24 at% Al. Another reason could be that the composition of alloy 5 was close to the stoichiometric one. As a result any deviation from this composition would result to the formation of  $\text{Mo}_5(\text{Si}_{1-x}\text{Al}_x)_3$ . As formation of  $\text{SiO}_2$  and  $\text{MoO}_3$  is thermodynamically disadvantageous compared to the formation of alumina, formation of a Mo-Si layer is expected under the scale. On the contrary, in alloy 6 the Mo-content was lower than 33 at% (Table 1). According to the isothermal section at 1873 K of the Mo-Si-Al diagram [24], free Al is expected to be present in the microstructure of this alloy as was indeed observed [10]. These Al pockets could have acted as reservoirs for any losses of Al

during oxidation and preserved the stoichiometry of the matrix. Apparently, in case of  $\text{Mo}_5\text{Si}_3$  formation (as in alloy 5), the oxidation rate is controlled by diffusion of  $\text{Al}^{3+}$  through this layer, while in alloy 6, where no second layer is formed, the oxidation rate is controlled by diffusion of oxygen through the scale. The oxide coating formed on the surface is protective for temperatures up to 2000 K [25].

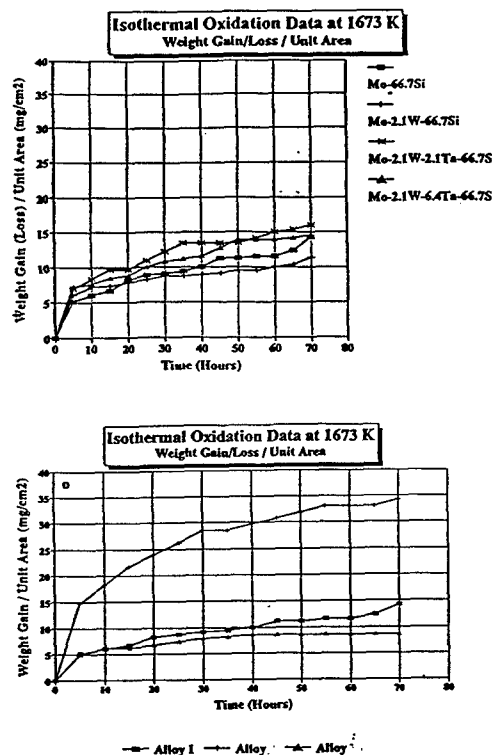


Figure 6: Isothermal oxidation data at 1673K

The oxidation behaviour of alloy 1 at 1673 K (Figure 6) can be explained as follows: In the initial period of rapid linear oxidation,  $\text{MoO}_3$  and  $\text{SiO}_2$  formed on the surface.  $\text{MoO}_3$  evaporated as rapidly as it formed, while  $\text{SiO}_2$  nucleated and grew on the silicidic surface. Growth of  $\text{SiO}_2$  decreased the surface area available for reaction with oxygen and thus weight gain diminished with time. Eventually, a continuous protective silica layer was formed, and subsequent oxidation continued only by diffusion of oxygen through the silica film barrier. As a result, very low weight gain rates were observed at exposures up to 70 hours.

Similar behaviour is suggested for alloys 5 and 6. However, instead of formation of silica as the protective barrier against oxygen, alumina was formed on the surface. The higher weight gain observed in alloy 5 compared to alloys 1 and 6 is attributed to the difficulty of forming a continuous alumina layer because of the presence of  $\text{Mo}_5\text{Si}_3$ . Such a layer would govern the oxidation rate as Al has to diffuse through this layer to the environment-scale interface where it oxidises to form alumina.

In isothermal oxidation at 1673K, alloys 3 and 4 exhibited higher initial weight gain, which is attributed to the difficulty in forming a stable silica scale due to the presence of Ta. After 72 hours at 1673 K, a silica oxide was present on the surface of alloy 1. The thickness of the scale did not vary in alloys 1 and 2 (Table 3) and was in the range of

7-8  $\mu\text{m}$ . In alloys 3 and 4 the silica layer was thinner (2 to 3  $\mu\text{m}$ ) compared to alloy 1 which suggests that the presence of  $\text{TaSi}_2$  in the matrix does affect the oxidation properties of the alloy. It is possible that Ta retards the formation of a continuous  $\text{SiO}_2$  layer as  $\text{Ta}_2\text{O}_5$  (which is the stable Ta-oxide forming) is less volatile at this temperature compared to  $\text{MoO}_3$ . A synergistic effect on oxidation behaviour seems to occur between  $\text{MoSi}_2$  and  $\text{TaSi}_2$ . The former probably encourages formation of protective silica at high temperatures [well above the limit of  $\text{TaSi}_2$  (1273 K) reported by Aitken et al [26], Goldschmidt [27] and Regan et al [28]]. Regan et al [28] have shown that addition of up to 10at%Ta to  $\text{MoSi}_2$  does not influence the oxidation resistance of the alloy at 1860 K and that significant weight gain at this temperature occurs only at Ta addition over 25 at%. Therefore, further investigation should be carried out to establish whether an optimum volume fraction of the two disilicides ( $\text{MoSi}_2$  and  $\text{TaSi}_2$ ) could lead to a material exhibiting the beneficial properties of the two compounds.

### CONCLUSIONS

In  $\text{MoSi}_2$  base alloys with W and/or Ta addition the destructive "pest" oxidation occurring at temperatures around 773 K was not suppressed. Ta addition increased slightly the temperature of pest oxidation. Mainly Mo and Si were detected on the oxides formed after exposure at this temperature. At temperatures higher than 1073 K all alloys exhibited very low oxidation rates. At temperatures higher than 1600 K a silica scale was formed in all alloys. The thickness of the scale depended on alloy composition, with the smaller thickness corresponding to alloys with Ta addition.  $\text{Mo}_5\text{Si}_3$  layer beneath the scale was not detected. Aluminium addition to  $\text{MoSi}_2$  suppressed "pest" oxidation. A mixed Al/Si oxide was formed at this temperature with traces of Al/Mo oxide. At higher temperatures the scale was enriched in Al. At 1623 K, pure alumina was formed on the surface.

### ACKNOWLEDGEMENTS

The authors would like to thank Prof. J.E. Castle for the provision of laboratory facilities and the EPSRC for supporting part of this research.

### REFERENCES

1. E. Fitzer, Plansee Proceedings, (1955) 56
2. C.E. Ramberg, P. Beatrice, K. Kurokawa and W.L. Worrel, High Temperature Silicides and Refractory Alloys, MRS Symp. Proc., 322 (1994) 243
3. H.J. Grabke and G.H. Meier, Oxidation of Metals, 44(1995) 147
4. D.A. Berztiss, R.R. Cechiara, E.A. Gulbransen, F.S. Pettit and G.H. Meier, Mater. Sci. Eng., A155 (1992), 165
5. H. Nowotny, H. Kudielka and E. Parthe, Proceedings Plansee Seminars, Metallwerk Plansee, REutte, (1965), 166
6. H.W. Lavandel, R.A. Perkins, A.G. Elliot and J. Ong, Investigations of Modified Silicide Coatings for Refractory Metal Alloys with Improved Low Pressure Oxidation Behaviour, Technical Report AFML TR 65 344, Air Force Laboratory, Lockheed Missiles & Space Co, Palo Alto, (1965).
7. K. Yanagihara, T. Maruyama and K. Nagata, Intermetallics 3(1995), 243
8. C. Brukl, F. Benesovsky and H. Nowotny, Planseeberichte für Pulvermetallurgie, (1963), 20
9. A. Stergiou and P. Tsakiroopoulos, in preparation
10. M. Whiting, A. Stergiou and P. Tsakiroopoulos, in preparation
11. J.B. Berkowitz-Mattuck, P.E. Blackburn and E.J. Felten, Trans. Met. Soc. AIME, 233(1965), 1093
12. T.C. Chou and T.G. Nieh, JOM, (1993), 15
13. A. Stergiou and P. Tsakiroopoulos, Intermetallics, 5(1997), 117
14. A. Stergiou, P. Tsakiroopoulos and A. Brown, Intermetallics, 5(1997), 69
15. G.H. Meier, N. Birks, F.S. Pettit, R.A. Perkins and H.J. Grabke, Structural Intermetallics, ed. R. Darolia et al, TMS, Warrendale, (1993), 861
16. T. Maruyama, X.F. Bi and K. Nagata, High Temperature Corrosion of Advance Materials and Protective Coatings, ed. Y. Saito et al, Elsevier Science Publishers, (1992), 291
17. G.H. Meier and F.S. Pettit, Mater. Sci. Eng., A153(1992), 548
18. J.H. Westbrook and D.L. Wood, J. Nucl. Mat., 12(1964), 208
19. D.A. Berztiss, F.S. Pettit and G.H. Meier, High Temperature Ordered Intermetallics VI, MRS Symp. Proc., 322(1995), 1285.
20. V.U. Kodash, P.S. Kisly and V.J. Shemet, High Temperature Science, 29(1990), 143
21. G.H. Meier, Oxidation of High-Temperature Intermetallics, ed. T. Grobstein and J. Doychak, TMS, Warrendale, (1989), 1
22. D.A. Berztiss, R.R. Cechiara, E.A. Gulbransen, F.S. Pettit and G.H. Meier, Mater. Sci. Eng., A155(1992) 165
23. J. Schlichting and S. Hofmann, High Temperatures - High Pressures 10(1978) 349
24. C. Brukl, H. Nowotny and F. Benesovsky, Monatshefte für Chemie 92(1961), 967
25. K. Yanagihara, T. Maruyama and K. Nagata, Mat. Trans. JIM, 34 (1993), 1200
26. E.A. Aitken, in "Intermetallic Compounds", Ed. J.H. Westbrook, (1967)
27. H.J. Goldschmidt, Interstitial Alloys, Butterworth, (1967)
28. R.E. Regan, W.A. Baginski and C.A. Krier, Ceramics Bulletin, 46(1967), 502

# MICROSTRUCTURAL CHARACTERIZATION OF NiTi-BASED $\beta_2$ / Ni<sub>2</sub>TiAl-BASED $\beta'$ TWO PHASE ALLOYS

H.Murakami, P.J.Warren\*, T.Kumeta\*\*, Y.Koizumi and H.Harada

National Research Institute for Metals, Advanced High Temperature Materials Research Group,  
1-2-1, Sengen, Tsukuba, 305, Japan

\* University of Oxford, Department of Materials, Parks Road, Oxford, OX1 3PH, U.K.

\*\* Department of Materials Science, Ibaraki University, 4-12-1, Nakanarusawa, Hitachi 316, Japan.

## Abstract

The microstructural evolution of  $\beta_2$  (NiTi-based) /  $\beta'$  (Ni<sub>2</sub>TiAl-based) two phase alloys as a function of ageing time has been investigated using transmission electron microscopy, atom probe field ion microscopy, and high-temperature X-ray diffractometry. The materials investigated were Ni<sub>49</sub>Ti<sub>41.7</sub>Al<sub>7.3</sub>Mo<sub>2</sub> and Ni<sub>49</sub>Ti<sub>41.7</sub>Al<sub>7.3</sub>Cr<sub>2</sub> quaternary alloys together with a Ni<sub>50</sub>Ti<sub>42.5</sub>Al<sub>7.5</sub> ternary alloy as a reference. These materials all showed supersaturated  $\beta_2$  single phase microstructures after homogenisation heat treatment at 1200°C for 2hrs, and coherent cuboidal precipitation of  $\beta'$  phase after the early stages of the ageing treatment at 800°C (0.2hrs). Further ageing caused precipitate coarsening and alignment followed by loss of coherence and coalescence (after 10hrs for Ni<sub>49</sub>Ti<sub>41.7</sub>Al<sub>7.3</sub>Mo<sub>2</sub> and 100hrs for Ni<sub>49</sub>Ti<sub>41.7</sub>Al<sub>7.3</sub>Cr<sub>2</sub> at 800°C). Atom probe analyses revealed that both Mo and Cr partition preferentially into the  $\beta_2$  phase matrices. The different rates of change in morphology between the alloys investigated is discussed in terms of the partitioning behaviour of the alloying additions and the resultant changes in lattice misfits.

## Introduction

Over the last decade, intermetallics such as nickel aluminides and titanium aluminides have been intensively investigated for high temperature applications. However, the combination of good strength and good ductility has generally been elusive in these intermetallics. Among intermetallics, the NiTi  $\beta_2$  phase with B2 ordering has reasonable ductility while the Ni<sub>2</sub>TiAl  $\beta'$  phase with additional L2<sub>1</sub> (Heusler) ordering has superior mechanical strength. As can be seen from the crystal structures in Fig.1, substitution of aluminium for a fraction of the titanium in a NiTi-based alloy causes additional ordering of the Ti/Al sublattice forming the quasi-binary phase diagram shown in Fig.2<sup>(1)</sup>. Therefore the  $\beta_2$  and  $\beta'$  phases might be expected to form a precipitation hardening system with both good mechanical strength and some ductility, which is similar to the conventional fcc  $\gamma$  / L1<sub>2</sub>  $\gamma'$  structure of Ni-base superalloys. In fact, preliminary investigations revealed that even the as-cast ternary  $\beta_2$  /  $\beta'$  phase alloys had good mechanical properties up to 600°C<sup>(2,3,5,6)</sup>. Appropriate heat treatment and alloying additions should further improve the mechanical properties of this alloy system, thus it is important to understand the effect of alloying additions and ageing treatments on the

microstructural evolution of this alloy system. The aim of this work is to investigate the microstructural evolution of NiTiAlMo and NiTiAlCr quaternary  $\beta_2$  /  $\beta'$  two phase alloy systems as a function of ageing time. Although several researchers have reported the phase determination and microstructural morphologies of  $\beta_2$  /  $\beta'$ <sup>(4,5,7-13)</sup>, or NiAl  $\beta$  / Ni<sub>2</sub>TiAl  $\beta'$ <sup>(10-16)</sup> alloy systems, there have been no reports investigating the effect of alloying additions on the morphological change.

In this paper, the different rates of change in morphology between the alloys investigated is discussed in terms of the partitioning behaviour of the alloying additions and the resultant changes in lattice misfits.

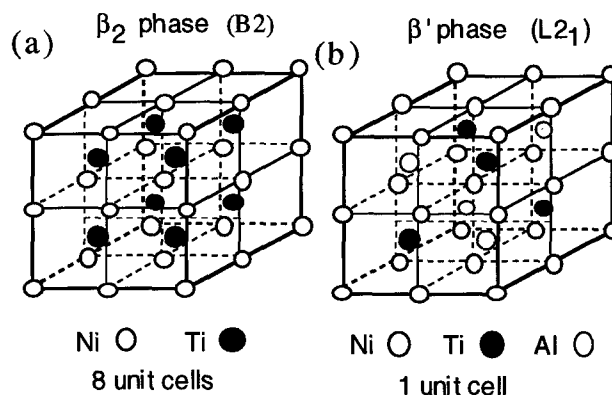


Figure 1: Schematic illustration of the crystal structure of (a)  $\beta_2$  and (b)  $\beta'$  phases.

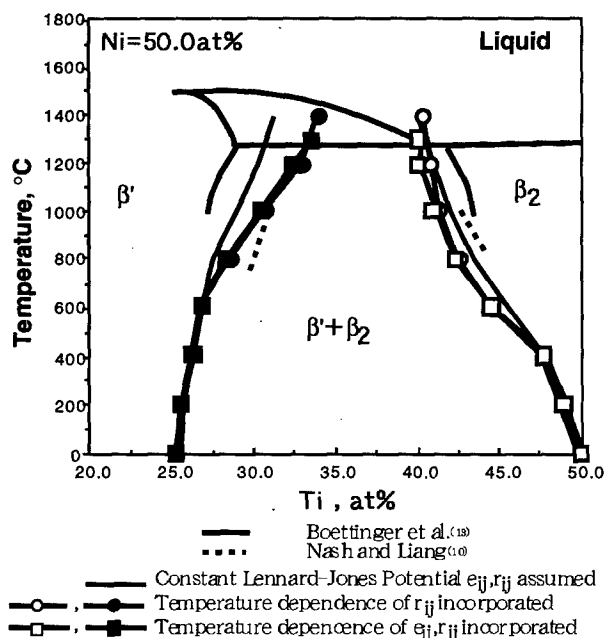


Figure 2: Calculated  $\beta_2/\beta'$  equilibrium phase boundaries in quasi-binary  $\text{Ni}_2\text{TiAl}$ - $\text{NiTi}$  section. Ni content is fixed at 50 at%. (Ref.1)

#### Experimental

The compositions of alloys investigated are listed in Table I. Hereafter, these alloys are denoted as  $\text{NiTiAl}$ ,  $\text{NiTiAlMo}$ , and  $\text{NiTiAlCr}$  respectively. These compositions were chosen so that they would have  $\text{NiTi}$ -based  $\beta_2$  /  $\text{Ni}_2\text{TiAl}$ -based  $\beta'$  two phase microstructure under equilibrium conditions<sup>(1,10-13)</sup>. The Al content was chosen on the basis of preliminary mechanical tests reported previously<sup>(2,3,5,6)</sup>: for ternary  $\text{Ni}_{50}\text{Ti}_{50-x}\text{Al}_x$  alloys,  $\text{Ni}_{50}\text{Ti}_{43}\text{Al}_7$  has a high yield stress yet still exhibits some ductility and is suitable for solution treatment and precipitation hardening.

TABLE I Composition of alloys investigated (in atomic %)

Alloy name	Ni	Ti	Al	Mo	Cr
$\text{NiTiAl}$	50	42.5	7.5	-	-
$\text{NiTiAlMo}$	49	41.65	7.35	2.0	-
$\text{NiTiAlCr}$	49	41.65	7.35	-	2.0

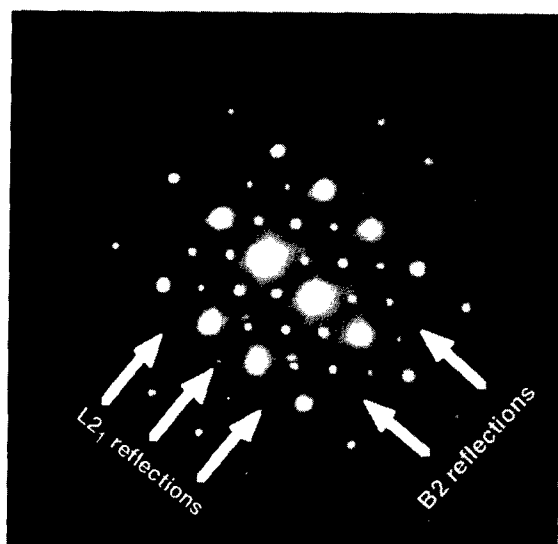


Figure 3: Typical electron diffraction pattern of the  $\beta'/\beta_2$  pseudo-binary  $\text{NiTiAlCr}$  alloy aged for 0.2 hrs. Foil normal is  $[110]$ .

Bulk samples were solution heat treated in Ar-sealed quartz tubes at  $1200^\circ\text{C}$  for 2hrs and then air cooled. These samples were then sectioned before further ageing in Ar-sealed quartz tubes at  $800^\circ\text{C}$  for 0.2hrs and 0.5hrs followed by water quenching, and for 1hr, 10hrs and 100hrs followed by air cooling in order to investigate the change in microstructure as a function of ageing time. These heat treated samples were then examined using transmission electron microscopy (TEM) for the observation of microstructures, atom probe field ion microscopy (APFIM) for the determination of phase compositions, and high-temperature X-ray diffractometry (HTXRD) for the determination of lattice misfits between the  $\beta_2$  and  $\beta'$  phases.

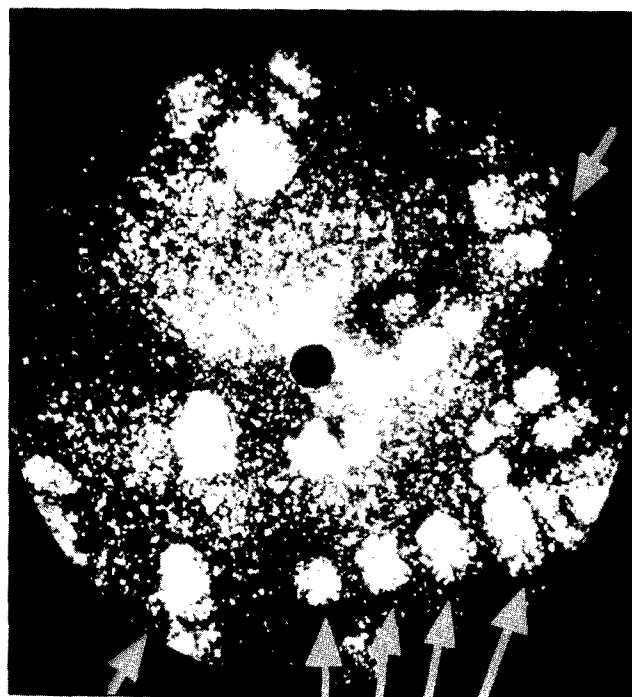


Figure 4: Field ion micrograph of the  $\text{NiTiAlCr}$  alloy aged for 10hrs at  $800^\circ\text{C}$ , where cuboidal precipitates are indicated by arrows. Tip temperature =  $-243^\circ\text{C}$  (30K), tip voltage = 17.5 kV.

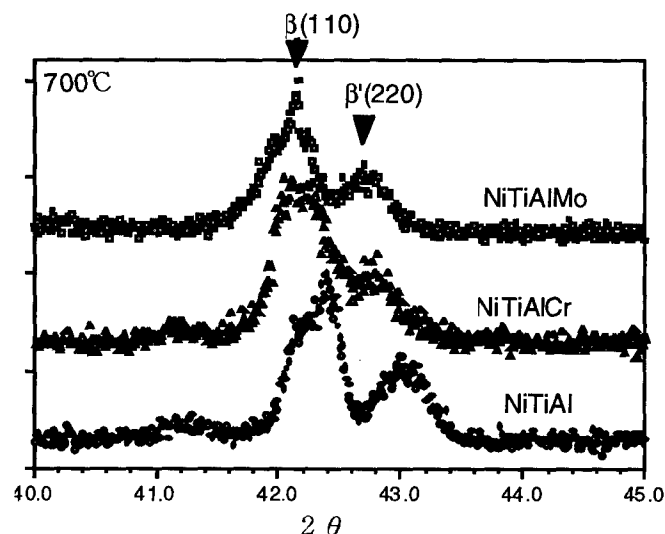


Figure 5: Typical X-ray diffraction profiles obtained at  $700^\circ\text{C}$  in which  $\beta_2(110)$  and  $\beta'(220)$  peaks are observed.

TEM samples were prepared by mechanical grinding and twin-jet standard electropolishing using a 10% perchloric acid and 90% acetic acid electrolyte at about 2°C with an applied voltage of around 30V. TEM studies were performed on a Philips CM200 microscope. For the observation of fine coherent precipitates at early stages, the dark field imaging technique was applied using the  $1/4(111)$   $L_2$  lattice reflection. A typical transmission electron diffraction (TED) pattern showing B2 and  $L_2$  spots is shown in Fig.3.

APFIM samples were prepared by standard two step electropolishing using a 25% nitric acid and 75% methanol first stage solution and a 3% perchloric acid 97% 2-butoxyethanol second stage solution.

APFIM analyses were carried out using an APFIM220 commercial instrument with a sample stage temperature of -243°C (30 K) and a pulse fraction of 20%. In field ion microscopy, the coherent precipitates can be imaged as bright rectangular regions as shown in

Fig.4. The phase composition analysis can be conducted either by selected area analysis on the basis of the field ion image such as Fig.4, or by random area analysis. In this study, the latter method was employed for ease of analysis.

For HTXRD analysis, solution treated bulk samples were mechanically crushed into powder. The powder was uniformly spread on an  $Al_2O_3$  powder bed set on a platinum sample holder, and was gradually heated up to 800°C in a vacuum goniometer chamber which was evacuated down to  $10^{-4}$ Pa. HTXRD analysis was conducted after the sample temperature was kept at 800°C for 0.2hrs. The lattice parameters were determined by using (110), (200), and (211) diffractions for B2 structure, and (220), (400), and (422) diffractions for  $L_2$  structure, respectively. Typical X-ray profiles at 800°C are shown in Fig.5, where the B2 and  $L_2$  diffraction peaks are clearly separated.

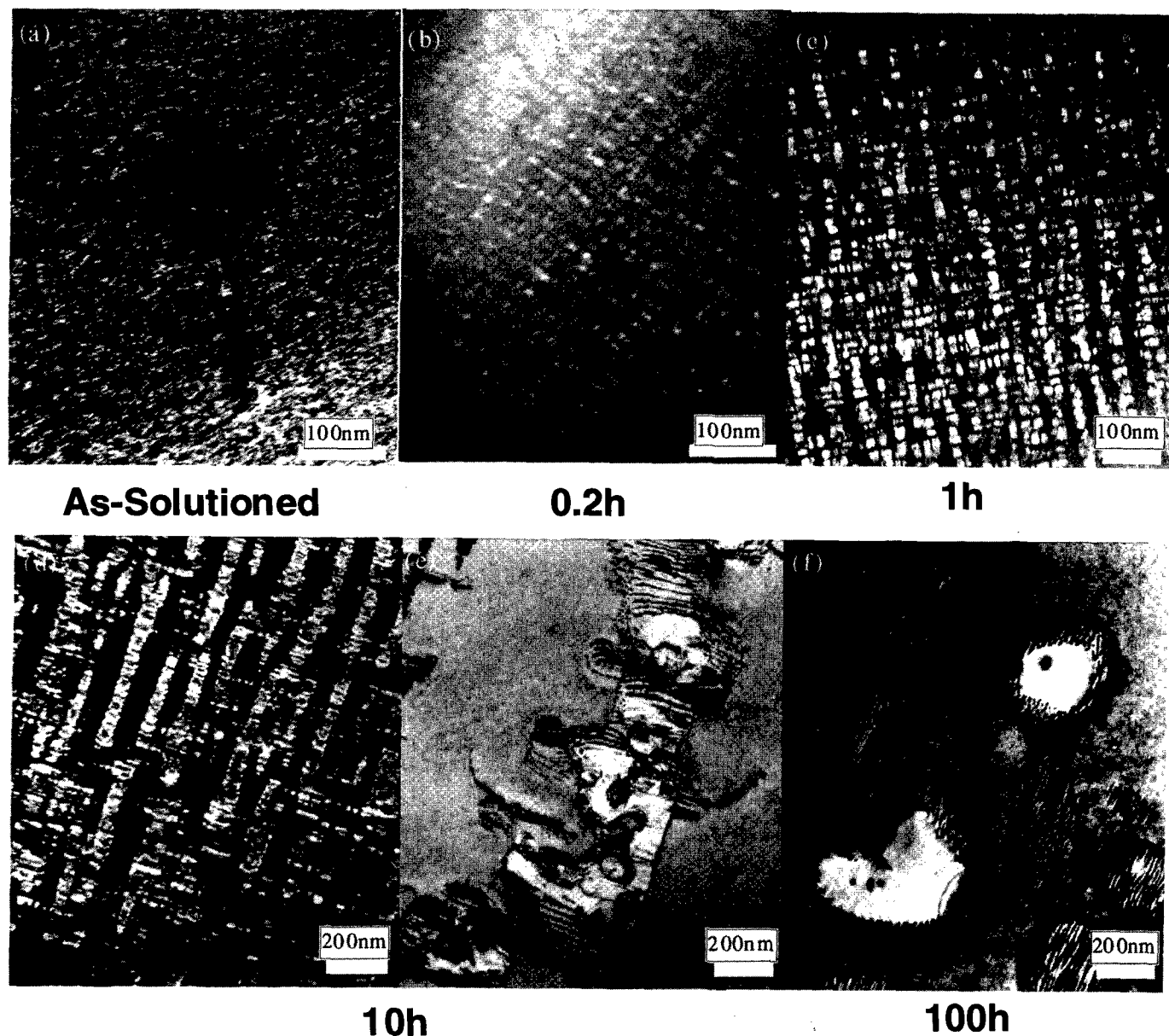


Figure 6: TEM photographs showing the microstructural change of the NiTiAlMo alloy during ageing at 800°C. a) A bright field image of the as-solution treated specimen; (b)-(d) dark field images showing coherent precipitates; (e),(f), bright field images showing semi-coherent coarsened precipitates. Coherency loss started from the 10hrs of ageing.



## Results

### Microstructural Change as a Function of Ageing Time

TEM micrographs of the morphology of phase decomposition during ageing in the case of the NiTiAlMo alloy and the NiTiAlCr alloy are shown in Fig.6 and Fig.7, respectively. The solution treated materials showed uniform fine scale mottling in bright field imaging (Fig.6a and Fig.7a). It should be noted that although the L2<sub>1</sub> reflection spots are observed in the TED pattern in solution treated materials (Fig.8), the dark field images do not show any precipitates.

Precipitation occurs after slight ageing for 0.2hrs at 800°C; the dark field images show fine cuboidal precipitates distributed throughout the matrix (Fig.6b and Fig.7b). The precipitate sizes at this ageing stage are 5–9 nm for the NiTiAlMo alloy and 3–7 nm for the NiTiAlCr alloy, respectively. After further ageing for 1hr, the dark field images (Fig.6c

and Fig.7c) show that the precipitates have coarsened and have aligned to form orthogonal platelets on the {100}. After this, the precipitates begin to coalesce and lose coherency. At this ageing stage, both coherent (Fig.6d and Fig.7e) and semi-coherent (Fig.6e and Fig.7f) precipitates are observed in the same specimen. This loss of coherency has started after 10hrs of ageing in the NiTiAlMo alloy and after 100hrs in the NiTiAlCr alloy. After further ageing (100hrs for NiTiAlMo alloy as shown in Fig.6f, and 1000hrs for NiTiAlCr alloy), all the precipitates have become semi-coherent surrounded by networks of orthogonal dislocations.

The average precipitate size roughly determined from the TEM micrographs is shown as a function of ageing time in Fig.9. This shows that the NiTiAlCr alloy has a lower rate of coarsening of coherent precipitates and a larger critical size above which precipitates lose coherency compared to the NiTiAlMo alloy.

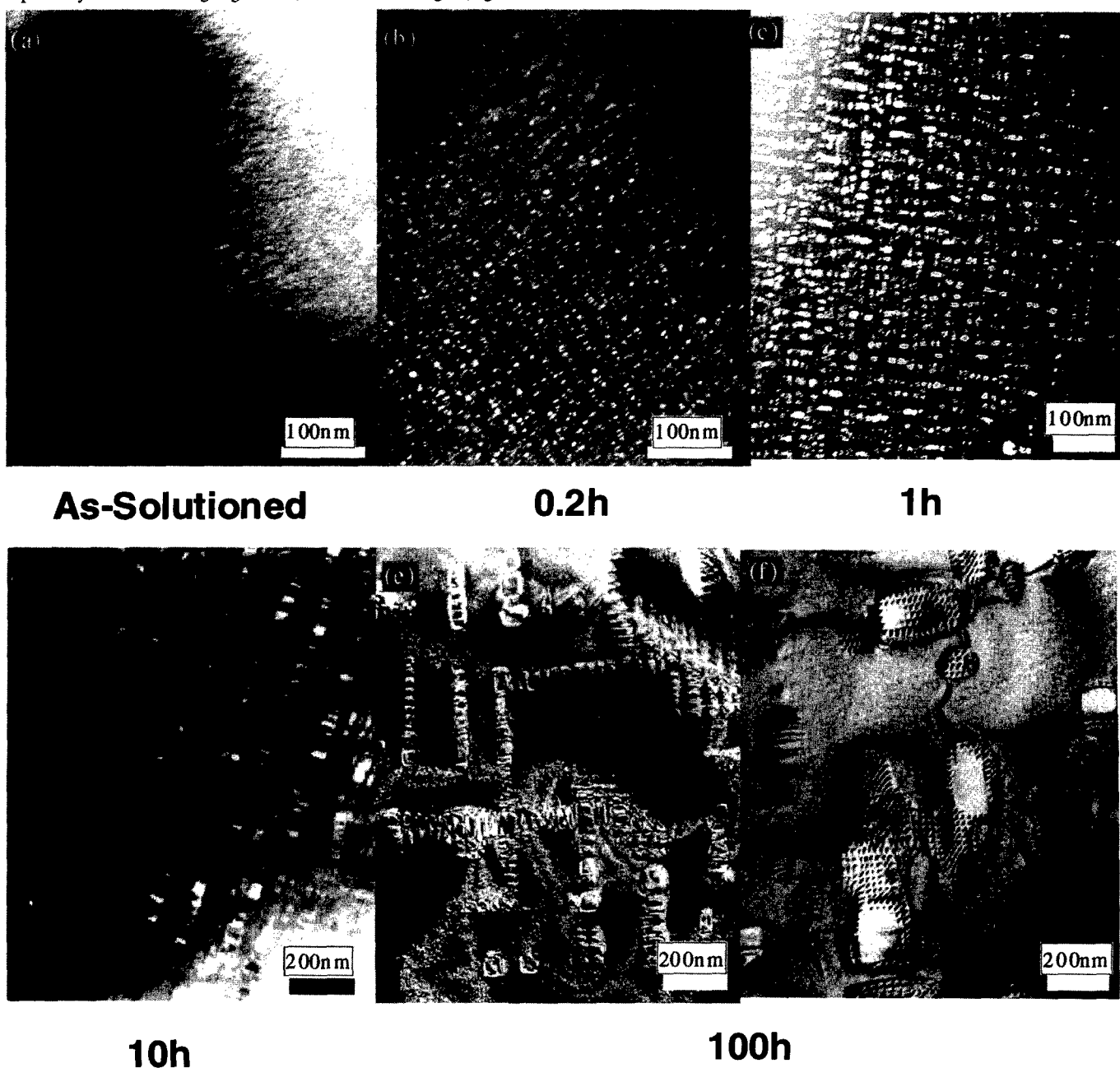


Figure 7: TEM photographs showing the microstructural change of the NiTiAlCr alloy during ageing at 800°C. a) A bright field image of as-solution treated specimen; (b)-(d) dark field images showing coherent precipitates; (e) bright field images which indicates that coherent precipitates are still observed even after 100hrs of ageing; (f) bright field images showing semi-coherent coarsened precipitates.

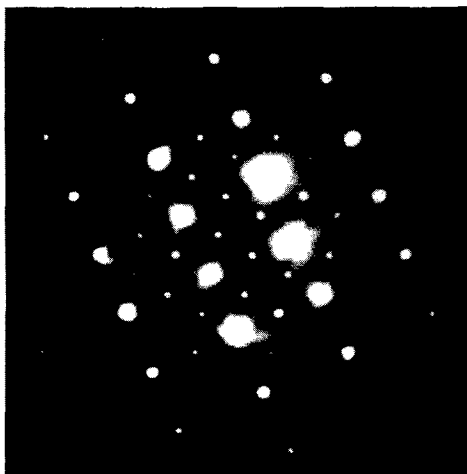


Figure 8: Typical electron diffraction pattern of a  $\beta_2/\beta'$  pseudo-binary alloy taken from the solution treated NiTiAlMo specimen. Foil normal is [110].

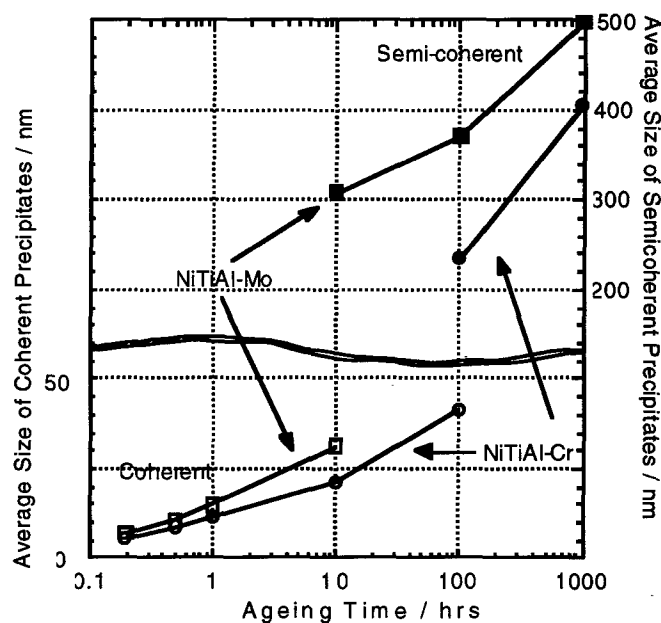


Figure 9: Change in precipitate size and morphology as a function of ageing time.

#### $\beta_2/\beta'$ Composition Analysis

APFIM random area analysis was employed to determine the compositions of the precipitates and matrices as a function of ageing time. For the solution treated materials, no compositional variations were observed (Fig.10), indicating that precipitation does not occur during solution treatment process. This result is consistent with the TEM observation that precipitates were not observed in the solution treated specimens.

After heat treatment at 800°C, precipitates were clearly observed as distinct increases in the concentration of Al and resultant decreases in the concentration of Ti as shown in Fig.11. The compositions of precipitates and matrices for the NiTiAl, NiTiAlMo and NiTiAlCr alloys aged for 1hr and 10hrs at 800°C are given in Table II and Table III, respectively. The errors are calculated from the binomial distribution as

$$e_A = \pm 2\sigma = \pm 2\sqrt{C(1-C)/N}$$

where C is the concentration of element A calculated over a total number of N atoms detected. It should be noted that APFIM analyses

can have additional errors such as preferential evaporation of specific elements etc. Comparing precipitate and matrix compositions shows clearly that Mo and Cr both partition into the matrix.

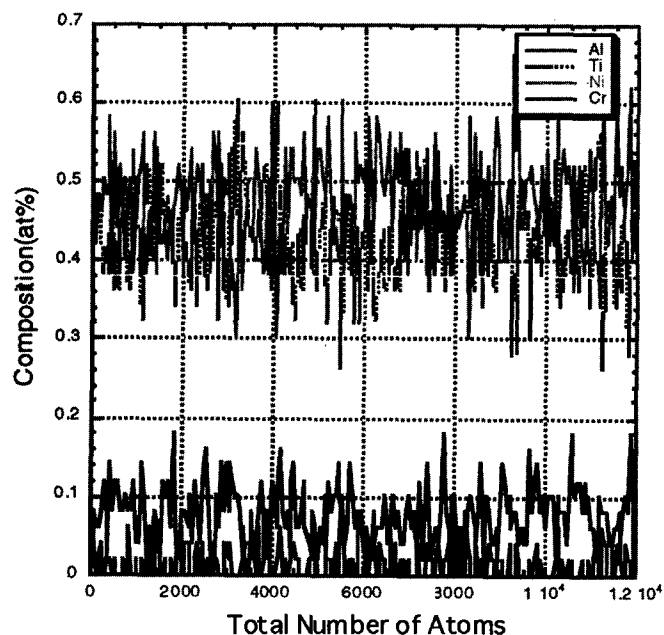


Figure 10: Composition profile of the as-solution treated NiTiAlCr alloy in which no clear composition change are observed.

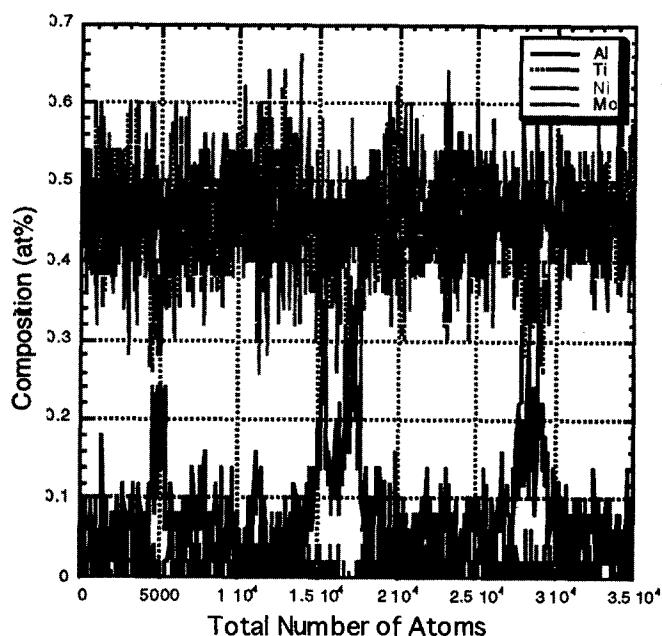


Figure 11: Composition profile of the NiTiAlMo alloy aged for 0.2hrs at 800°C showing the existence of precipitates.

The change in precipitate composition with ageing time is plotted in Fig.12. Although some fluctuations in composition are observed, this figure suggests that the composition of the precipitates does not change significantly after the earliest stages of precipitation (0.2hrs for 800°C in this study).

TABLE II Averages of atom probe analyses of phase compositions after 1h at 800°C

Alloy name	Phase	Ni	Ti	Al	Mo	Cr
NiTiAl <sup>(a)</sup>	$\beta_2$	50.2±1.0	43.4±1.0	6.3±0.5	-	-
NiTiAl <sup>(a)</sup>	$\beta_2'$	48.9±2.4	31.1±2.1	20.0±1.9	-	-
NiTiAlMo	$\beta_2$	49.1±1.2	42.0±1.2	6.5±0.6	2.4±0.4	-
NiTiAlMo	$\beta_2'$	47.2±2.2	32.4±1.5	22.1±1.3	0.7±0.4	-
NiTiAlCr	$\beta_2$	49.4±1.0	41.9±0.9	7.0±0.5	-	1.7±0.2
NiTiAlCr	$\beta_2'$	47.4±1.6	31.8±1.5	20.2±1.3	-	0.6±0.2

TABLE III Averages of atom probe analyses of phase compositions after 10h at 800°C

Alloy name	Phase	Ni	Ti	Al	Mo	Cr
NiTiAl <sup>(a)</sup>	$\beta_2$	50.9±0.8	43.1±0.7	6.0±0.4	-	-
NiTiAl <sup>(a)</sup>	$\beta_2'$	48.4±1.2	30.2±1.2	21.4±0.8	-	-
NiTiAlMo	$\beta_2$	49.8±0.5	42.5±0.5	5.8±0.2	1.8±0.1	-
NiTiAlMo	$\beta_2'$	45.3±1.4	31.3±1.3	22.7±1.2	0.6±0.2	-
NiTiAlCr	$\beta_2$	48.7±0.5	43.7±0.5	5.6±0.2	-	2.0±0.2
NiTiAlCr	$\beta_2'$	46.5±1.3	29.8±1.2	23.1±1.1	-	0.7±0.2

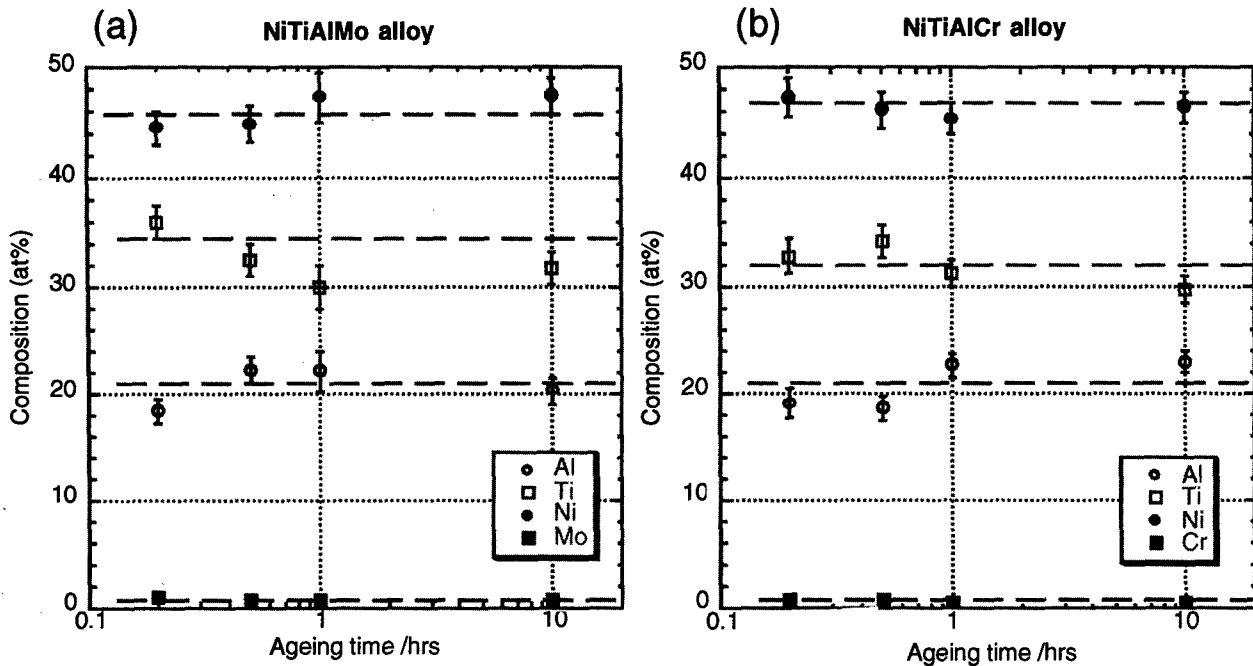


Figure 12: Change in precipitate composition as a function of ageing time for (a) NiTiAlMo and (b) NiTiAlCr.

### $\beta_2/\beta'$ Lattice Misfit

The lattice misfit between the two phases affects the microstructural evolution during ageing since the lattice misfit strain is a major contribution to the interface energy. The lattice misfit,  $\delta$ , is defined here as

$$\delta = \frac{a_{\text{precipitate}} - a_{\text{matrix}}}{a_{\text{matrix}}}$$

Since the lattice misfit is a strong function of temperature, HTXRD analysis was employed to determine the lattice misfit at the ageing temperature of 800°C. The results are shown in Table IV.

TABLE IV Lattice parameters and lattice misfits derived by HTXRD analysis at 800°C

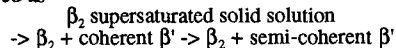
Alloy name	$a_{\text{matrix}}$	$a_{\text{precipitates}}$	Lattice misfit (%)
NiTiAl	3.0331	5.9715(2.9858)	-1.561
NiTiAlMo	3.0227	5.9569(2.9784)	-1.465
NiTiAlCr	3.0177	5.9657(2.9828)	-1.157

It is also possible to measure the lattice misfit from the spacing of interfacial dislocations round the semi-coherent precipitates. Since the  $\beta_2/\beta'$  interface dislocations are determined to be of pure edge type with Burgers vector,  $b$ , which is parallel to [010] and is  $\frac{1}{2}a_{\text{precipitate}} = a_{\text{matrix}}$  in size<sup>(9,12)</sup>, the lattice misfit can be determined from the measurements of the separation of misfit dislocations using the relation  $\delta = |b|/d$ , where  $d$  is the average spacing of the misfit dislocations. From the TEM observations at room temperature of the dislocation networks around precipitates in materials aged for 100hrs, the lattice misfits of the NiTiAl, NiTiAlMo, and NiTiAlCr alloys were calculated as -1.65<sup>(4)</sup>, -1.5 and -1.4%, respectively. Overall the HTXRD analysis and TEM observations showed good quantitative agreement. It is concluded that the lattice misfit at 800°C is smallest in the NiTiAlCr alloy and largest in the NiTiAl ternary alloy.

## Discussions

### Precipitation Sequence

From the the TEM and APFIM observations, the sequence in the development of morphology of the precipitates at 800°C of ageing can be summarised as



The sequence is the same in each alloy, except for the difference in ageing time at which the precipitates started to lose coherency (10hrs for NiTiAlMo and 100hrs for NiTiAlCr).

For the as-solution treated alloys, TED patterns showed L2<sub>1</sub> spots while the dark-field image of these alloys did not show any discrete precipitates (Fig.8). In addition, APFIM analysis did not show any compositional fluctuations (Fig.10). This may be explained by the presence of short-range ordered L2<sub>1</sub> nanodomains, or by disorder of the B2 lattice resulting in structure factor contrast due to the different scattering efficiencies of Al and Ti atoms on the Ti sublattice. These results, in addition to the streaks observed in the TED patterns, should be discussed elsewhere.

The precipitation starts after slight ageing for 0.2hrs at 800°C. Initially, the precipitates are fully coherent with the matrix. As ageing progresses, the precipitates grow maintaining coherency and the precipitates align into orthogonal platelets due to the elastic strain fields generated by the precipitate-matrix misfit<sup>(9)</sup>. Further development occurs by loss of interfacial coherence to form a semicoherent interface between precipitate and matrix where the lattice misfit is accommodated by an array of orthogonal interfacial dislocations. After loss of coherency with the matrix, further growth occurs rapidly at the expense of surrounding coherent precipitates. The critical size for loss of coherency is thus strongly dependent on the magnitude of the lattice misfit.

### Precipitation Mechanism

To understand the precipitation mechanism in the NiAl-Ni<sub>2</sub>AlTi or NiTi-Ni<sub>2</sub>TiAl pseudo-binary alloy system is of particular interest. There are several reports investigating the transformation mechanism of this alloy system.

Peters et al. suggested a possibility of spinodal decomposition in a Ni<sub>50</sub>Ti<sub>42.9</sub>Al<sub>7.1</sub> alloy since both the precipitates and the spaces between precipitate arrays increase, while the spacing between precipitates within a single array remained fixed during the ageing process<sup>(8)</sup>. Bendersky et al. investigated the rapidly solidified a Ni<sub>50</sub>Ti<sub>37.5</sub>Al<sub>12.5</sub> alloy and reported the chemical spinodal decomposition of the supersaturated Heusler phase into Al-rich regions and Ti-rich regions<sup>(9)</sup>. There have been several attempts to determine the NiAl-NiTi equilibrium phase diagram and consider the phase separation mechanism<sup>(1,9,11,13,15)</sup>. Boettinger et al. proposed a NiAl-NiTi quasi-binary phase diagram with metastable extensions and a B2  $\rightarrow$  L2<sub>1</sub> continuous ordering curve and concluded that the decomposition of  $\beta$  phase must occur by nucleation and growth of  $\beta'$  precipitates for Ni<sub>50</sub>Ti<sub>37.5</sub>Al<sub>12.5</sub> melt-span alloy, because the composition of the alloy lies outside the ordering curve after quenching<sup>(13)</sup>. It is difficult to elucidate the precipitation mechanism from the limited experimental data, since it may vary in terms of both composition and ageing temperature. However, from the following results the precipitation mechanism at 800°C for all the alloys investigated in this study was found to be nucleation and growth, rather than chemical spinodal:

- All the alloys examined exhibited almost identical precipitation morphologies.
- The precipitate compositions did not drastically change from the earliest stage of precipitation (Fig.12), which is typical of the nucleation and growth mechanism
- Provided that the quasi-binary phase diagram shown in Fig.2<sup>(1)</sup> is correct, it is more likely that the composition of the ternary NiTiAl alloy lies outside the ordering curve at 800°C. This is also supported by extrapolating Boettinger's proposed quasi-binary phase diagram<sup>(10)</sup> down to 800°C.

However, in order to fully elucidate the mechanism, further investigation will be required by changing the composition of the alloys, changing the ageing temperature etc.

## Effects of Alloying Additions

### i) Morphological Evolution

In this study, the alloying additions of Mo or Cr did not change the morphological sequence during progressive ageing, but additions of Mo or Cr did change the coarsening rate of precipitates and critical ageing time at which precipitates have started to lose coherency as described in the results part. This is mainly caused by the difference in lattice misfits between the two alloys. It can be explained that in the NiTiAlMo alloy, having the larger lattice misfit, the precipitates are coarsened and become semicoherent more rapidly than in the NiTiAlCr alloy due to the larger coherency strains at the precipitate / matrix interfaces. However, in the NiTiAlMo alloy some unidentified precipitates 0.1-1 $\mu$ m in size were observed even in the as-solution-treated sample, suggesting that the Mo additions might have exceeded the solubility limit of the  $\beta_2$  -  $\beta'$  two phase region. Therefore it is possible that these additional precipitates might have enhanced the coarsening of the  $\beta'$  precipitates in the NiTiAlMo alloy.

### ii) Lattice Misfit

It is found from the HTXRD results that the change in lattice misfit is mainly caused by the change in the  $\beta_2$  lattice parameter, i.e. the smaller lattice misfit is obtained by the decrease in lattice parameter of the  $\beta_2$  matrix during precipitation. Since the Cr atoms have preference to partition into the  $\beta_2$  phase, the addition of Cr atoms is expected to decrease the lattice parameter of the  $\beta_2$  phase. Accordingly, the negative lattice misfit is decreased. To reduce the lattice parameter of the  $\beta_2$  phase, Cr atoms should substitute for the Ti sublattice in the B2 crystal structure since Cr has smaller atomic radius than Ti and has larger atomic radius than Ni. Mo has similar but less pronounced effect in reducing the lattice misfit due to the larger atomic radius compared to Cr (Ni < Cr < Mo < Ti). To verify this discussion, the ALCHEMI method is expected to be conducted in future. The change in lattice misfit as a function of temperature is also of particular interest, which will be discussed in detail elsewhere.

The small discrepancies of lattice misfits obtained by TEM and HTXRD may be attributed to the fact that the lattice misfit may change during the progressive ageing, because as the volume fraction of precipitates increases with increasing ageing time, the composition of the matrix changes as shown in Table II and Table III. It should also be noted that the composition of the coherent precipitates may be different from that of the semi-coherent precipitates, which accordingly suggests that the lattice misfits of coherent and semi-coherent precipitates should not be the same. Since the lattice misfit derived from the HTXRD analysis can be regarded as that aged between 1hr and 10hrs at 800°C taking the experimental procedure into account, it is thus reasonable that lattice misfit values derived from TEM and HTXRD are slightly different. However, we can conclude that the difference in lattice misfit obtained by TEM and HTXRD is not critical, and investigations in this study proved that the lattice misfit of the NiTiAlCr alloy is always smaller than that of the NiTiAlMo during the progressive ageing.

To summarise our investigations, Cr additions are more effective in stabilizing the  $\beta'$  precipitates. However, the lattice misfit of approximately -1.2 ~ -1.4% in the NiTiAlCr alloy is still too large compared with that of  $\gamma / \gamma'$  Ni-base superalloys which usually have lattice misfits whose absolute values are less than 0.5%. Increased amounts of Cr additions together with alloying additions of other elements should be attempted in order to reduce the lattice misfit further.

## Conclusions

The microstructural evolution of these  $\beta_2 / \beta'$  two phase alloys was investigated and the following results were obtained.

- The sequence of precipitation is in the following order:  $\beta_2$  supersaturated solid solution  $\rightarrow$  cuboidal coherent precipitation of  $\beta'$  phase  $\rightarrow$  equiaxed semi-coherent precipitation of  $\beta'$  phase.
- Both Mo and Cr have preference to partition into the  $\beta_2$  matrices in this study.
- The lattice misfit is smallest in the Ni<sub>49</sub>Ti<sub>41.7</sub>Al<sub>7.3</sub>Cr<sub>2</sub> alloy followed by the Ni<sub>49</sub>Ti<sub>41.7</sub>Al<sub>7.3</sub>Mo<sub>2</sub> and the Ni<sub>50</sub>Ti<sub>42.5</sub>Al<sub>7.5</sub> ternary alloy has the largest lattice misfit.
- The Ni<sub>49</sub>Ti<sub>41.7</sub>Al<sub>7.3</sub>Mo<sub>2</sub> alloy started losing coherency after 10hrs ageing at 800°C whereas the Ni<sub>49</sub>Ti<sub>41.7</sub>Al<sub>7.3</sub>Cr<sub>2</sub> alloy still maintained coherency. This is partly caused by the larger lattice misfit of the Mo alloy and partly caused by addition of excess Mo above the solubility

limit. It is thus expected that Cr additions are more effective in improving the mechanical properties of this alloy system.

5. The composition of precipitates doesn't change after the early stages of precipitation until semi-coherent coarsening, which suggests that precipitation may be occurring by a nucleation and growth mechanism rather than spinodal decomposition.

#### Acknowledgments

The authors would like to thank Mr. T. Yokokawa for all his assistance in determining the lattice misfits.

#### References

1. M. Enomoto and T. Kumeta, "Analysis of the  $\beta'$ -Ni<sub>3</sub>TiAl /  $\beta$ -NiTi Equilibrium in Ni-Ti-Al Alloys by the Cluster Variation Method," *Intermetallics*, 5(1997), 103-109.
2. Y. Koizumi, Y. Ro, S. Nakazawa and H. Harada, "A Method to Improve High Temperature Mechanical Properties of NiTi-base Alloys," (Paper presented at the 114th Japan Institute of Metals Spring Meeting, Tokyo, 1 April 1994), 270.
3. Y. Koizumi, Y. Ro, S. Nakazawa and H. Harada, "Development of New High-Temperature Alloys Based on NiTi Intermetallic Compound," (Report of the 123rd Committee on Heat-Resistant Metals and Alloys, Vol. 35., No. 2 Japan Society for the Promotion of Science, 1994), 195-201.
4. P. Warren, H. Murakami, Y. Koizumi and H. Harada, "Phase Separation in NiTi-Ni<sub>2</sub>TiAl Alloy system," (Report of the ISIJ Meeting, Vol. 8. No. 3, Paper presented at the 129th ISIJ Meeting, Tokyo, 6th April 1995), 737.
5. P. J. Warren, Y. Koizumi, H. Murakami and H. Harada, "Phase Decomposition in NiTi- Ni<sub>2</sub>TiAl Alloy System," *Proceedings of the Third International Charles Parsons Turbine Conference*, Newcastle upon Tyne, U.K., (1995) 211-216.
6. Y. Koizumi, Y. Ro, S. Nakazawa and H. Harada, "NiTi-base Intermetallic Alloys Strengthened by Al Substitution," accepted for publication in the *Mat. Sci. Eng. A*, (1997).
7. P. J. Warren, H. Murakami, and H. Harada, "Microstructural Evolution in NiTiAl alloy," to be published.
8. M. A. Peters, G. A. Botton and C. J. Humphreys, "The Precipitation of  $\beta'$  Ni<sub>2</sub>TiAl from Al-doped  $\beta$  Ni-Ti Alloys," *Inst. Phys. Conf. Ser.*, No147:Section II(1995), 451-454.
9. L. A. Bendersky et al., "The Role of Elastic Energy in The Morphological Development of a Ni-Ti-Al Alloy," *Scripta Metall.*, 22(1988), 1029-1034.
10. P. Nash and W. W. Liang, "Phase Equilibria in the Ni-Al-Ti System at 1173 K," *Metall. Trans.*, 16A(1985), 319-322.
11. K. Oh-ishi et al., "Phase Decomposition and Hardening in NiAl-NiTi Pseudo-binary Alloy System," *J. Japan Inst. Metals.*, 60(1996), 239-246 (in Japanese).
12. K. Oh-ishi, Z. Horita and M. Nemoto, "Phase Separation and Lattice Misfit in NiAl( $\beta_1$ )-Ni<sub>2</sub>TiAl(H)-NiTi( $\beta_2$ ) System," *Mat. Trans. JIM*, 38(1997), 99-106.
13. W. J. Boettinger et al., "Rapid Solidification and Ordering of B2 and L2<sub>1</sub> Phases in the NiAl-NiTi System," *Mat. Sci. Eng.*, 98(1988), 273-276.
14. R. S. Polvani, Wen-Shian Tzeng, and P. R. Strutt, "High Temperature Creep in a Semi-Coherent NiAl- Ni<sub>2</sub>TiAl alloy," *Metall. Trans.*, 7A(1976), 33-40.
15. R. D. Field, R. Darolia, and D. F. Lahrman, "Precipitation in NiAl/Ni<sub>2</sub>TiAl Alloys," *Scripta Metall.*, 23(1989), 1469-1474.
16. A. W. Wilson et al., "HRTEM and Chemical Analysis of NiAl-5Ti," *Proceedings of Microscopy and Microanalysis*, 1996, 230-231.

STRUCTURE AND MECHANICAL PROPERTIES OF Ti-AL-Fe ALLOYS  
AT AMBIENT AND HIGH TEMPERATURES

M. Palm, A. Gorzel, D. Letzig, and G. Sauthoff

Max-Planck-Institut für Eisenforschung GmbH  
D-40237 Düsseldorf, Germany

Abstract

The constitution and the mechanical behaviour of TiAl-Fe alloys have been investigated and compared to a reference TiAl-V alloy. Phase equilibria in the Fe-Al-Ti system in the temperature range of interest were established. Therefore an isothermal section at 900°C was determined from metallography, X-ray diffraction and electron probe microanalyses. Compression and four-point-bending tests on five selected TiAl-Fe alloys have shown that they have a lower brittle-to-ductile transition temperature (BDTT  $\approx$  800°C) compared with the TiAl-V alloy and thus appear to be more promising for high-temperature applications. Heat treatments strongly influence the distribution of second phases, in particular the B2-ordered FeTi phase occurred at 1000°C in three near- $\gamma$  alloys. At 800°C and 900°C, particles of the  $\alpha_2$ - (Ti<sub>3</sub>Al) and  $\tau_2$  phase form instead. The microstructure strongly affects the mechanical behaviour which is most evident in creep. At 900°C, creep rates varied by a factor of 10 with variation of microstructure (under applied stresses between 10 and 100 MPa).

Introduction

Intermetallic  $\gamma$ -TiAl based alloys are of interest as potential aerospace structural materials because of their low density ( $\rho = 3.75 \text{ g/cm}^3$ ) and relatively good high-temperature mechanical properties. The problems of these TiAl alloys are their poor ductility and fracture toughness at ambient temperatures. The ductility can be improved by alloy modification with formation of Ti<sub>3</sub>Al ( $\alpha_2$ ) as second phase and microstructural control [1]. Two-phase ( $\gamma + \alpha_2$ )-TiAl alloys (ordered  $\gamma$  phase, with L1<sub>0</sub>-structure and  $\alpha_2$  phase with D0<sub>19</sub>-structure) with a duplex microstructure have shown tensile plastic elongation up to 2.2% in binary Ti-

48Al and 4% in ternary Ti-48Al + (1-2 at% Mn, Cr or V) alloys [2]. The microstructure can be varied by heat treatments and thermomechanical processing. Maximum tensile ductility was obtained with a two-phase TiAl alloy containing about 10 vol.% of  $\alpha_2$  phase. The state of development has been reviewed recently [3].

There still exists insufficient knowledge of the effects of other alloying additions that could open further possibilities for property optimization by making use of appropriate alloying and processing. In particular, the microstructure and mechanical properties of TiAl-Fe alloys at various temperatures are still unknown. Phase diagrams of the Fe-Al-Ti system for 800°C and 1000°C have been established [4]. The aim of this work is to study the constitution and mechanical behaviour of two-phase  $\gamma$ -TiAl-base alloys with Fe for checking the development potential of such alloys. As reference material, a TiAl-V alloy was used.

Experimental

Investigations of one Ti-Al-V alloy and five Ti-Al-Fe alloys were made to study the ductility and the proof stress as a function of temperature. Alloys Nos. 1 and 3 were arc melted. All other alloys including those listed in Table II were produced by levitation melting. From pure iron (99.97%), titanium (99.77%), and aluminum (99.99%) ingots of at least 200 g were produced. All alloys were in the as cast state prior to the heat treatments, i.e. no mechanical pre-treatment was performed. The alloy compositions are shown in Table I.

Specimens for 4-point bending tests (18 mm x 6 mm x 3 mm) and for compression tests (10 mm x 5 mm x 5 mm) were cut by spark erosion. The compressive 0.2% proof stress was determined by means of isothermal compression tests with a constant strain rate of  $\dot{\epsilon} = 10^{-4} \text{ 1/s}$  in the temperature range 23°C - 1200°C.

Table I: Compositions of the tested Ti-Al-V and Ti-Al-Fe alloys (in at.%).

Alloy	Ti	Al	V	Heat treatment
1	49.5	50.0	0.5	as cast

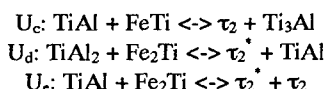
  

Alloy	Ti	Al	Fe	Heat treatment
2	51.0	36.5	12.5	1000°C/Vac/100h→H <sub>2</sub> O
3	48.0	50.0	2.0	1000°C / 12h/ furnace
4	54.0	42.5	3.5	1000°C / 100h / H <sub>2</sub> O
5	55.5	39.5	5.0	1000°C / 100h / H <sub>2</sub> O
6	57.0	36.5	6.5	1000°C / 100h / H <sub>2</sub> O

## Results

### Constitution

A preceding investigation of phase relationships in the Al-Fe-Ti system [4] revealed that in the temperature range between 800°C and 1000°C five invariant reactions are expected. Three of those five invariant reactions concern the phase  $\gamma$ -TiAl (L1<sub>0</sub>):



( $\tau_2$  is a cubic phase with complex fcc structure of D8<sub>8</sub>-type;  $\tau_2^*$  is a tetragonal polymorph of this phase which becomes stable at high Al contents. This phase has also been assigned as FeTiAl<sub>2</sub>. Because of its extended homogeneity range and incomplete determination of its structure the designation  $\tau_2$  is preferred in favour of a stoichiometric formula.)

All three reactions are expected to occur within a comparatively small temperature interval of 50°C at about 900°C. As these reactions will result in varying multi-phase equilibria with the phase  $\gamma$ -TiAl and no information exists on phase equilibria between 800°C and 1000°C, it appeared desirable to obtain some information about phase equilibria of the phase  $\gamma$ -TiAl at 900°C (For isothermal sections at 800°C and 1000°C see also [5]).

### Isothermal section at 900°C

Alloys of 30 different compositions were employed to establish a partial isothermal section at 900°C. Two slices of each alloy of about 5 mm thickness and 10 mm diameter were encapsulated in quartz ampoules back-filled with argon. After annealing at 900°C for 500 hours the specimens were quenched in water. All alloys were examined metallographically and the structures of all phases were identified by X-ray diffraction (XRD). Compositions of coexisting phases were determined by electron probe microanalysis (EPMA).

Table II: Compositions, XRD and EPMA results of alloys annealed at 900°C. Compositions are given in at.%. Phases given in brackets [] are supposed to have formed during quenching. Compositions of alloys marked by an asterisk (\*) have been obtained by analysis whereas all others are nominal compositions.

Composition of alloy	Phase 1	Composition of phase 1			Phase 2	Composition of phase 2			Phase 3	Composition of phase 3		
		Fe	Al	Ti		Fe	Al	Ti		Fe	Al	Ti
*35.4 40.3 24.3	FeAl	48.4(0.7)	29.2(0.2)	22.4(0.2)	Al <sub>2</sub> FeTi	26.0(0.6)	46.6(0.5)	27.4(0.2)	Fe <sub>2</sub> Ti FeAl FeAl	35.5(0.1) 35.2(0.1) 29.3(0.1) particles too small for analysis 48.8(0.2) 28.5(0.2) 22.7(0.3)  		

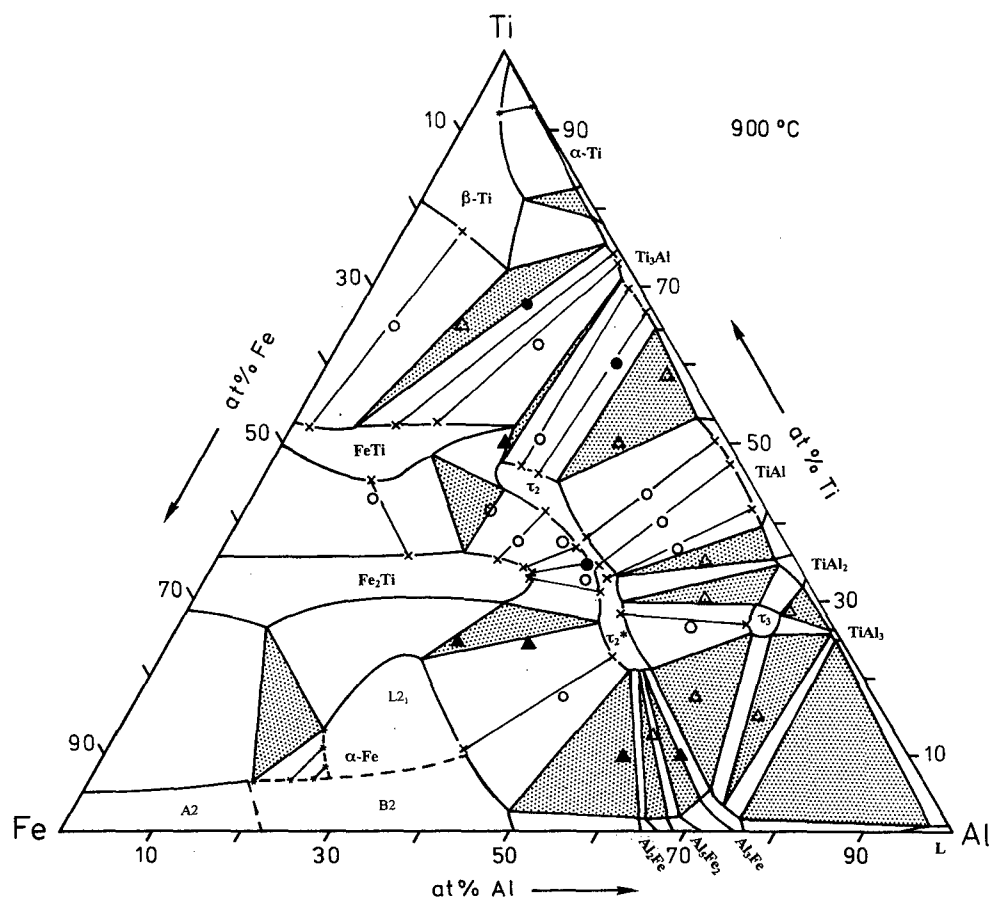


Figure 1: Isothermal section of the Fe-Al-Ti system at 900°C. The symbols denote two-phase (●) and three-phase alloys (▲). Filled symbols represent analyzed bulk compositions, while open symbols are given for nominal compositions. For the two-phase alloys, the results of the microprobe analyses are given as tie lines (X—X). Composition ranges for the three polymorphs of  $\alpha$ -Fe (A2, B2, L2<sub>1</sub>) as well as tie lines between B2 and L2<sub>1</sub> (\*—\*) are taken from Ohnuma et al. [6]. The tie line between  $\alpha$ -Ti and  $\beta$ -Ti (\*—\*) is taken from [7].

Table III: Compositions and EPMA results of alloys annealed at 1000°C. Compositions are given in at.% as in Table II.

No.	Composition			Phase 1	Composition			Phase 2	Composition			Phase 3	Composition		
	Fe	Al	Ti		Fe	Al	Ti		Fe	Al	Ti		Fe	Al	Ti
4	3.5	42.5	54.0	FeTi	7.5(0.2)	33.3(0.2)	59.2(0.3)	TiAl	1.76(0.06)	45.2(0.2)	53.0(0.2)	Ti <sub>3</sub> Al	1.14(0.04)	34.7(0.2)	64.1(0.2)
5	5.0	39.5	55.5	FeTi	7.8(0.1)	33.1(0.1)	59.0(0.2)	TiAl	1.81(0.04)	45.2(0.2)	53.0(0.2)				
6	6.5	36.5	57.0	FeTi	8.8(0.3)	32.5(0.2)	58.7(0.3)	TiAl	1.99(0.04)	45.4(0.1)	52.6(0.1)				

The results obtained from XRD and EPMA investigations are summarized in Table II. On the basis of those results the partial isothermal section at 900°C in Fig. 1 is established. The solubility for iron in  $\gamma$ -TiAl is between 1.5 and 2.5 at.% at this temperature.  $\gamma$ -TiAl is in equilibrium with the phase  $\tau_2$ . The three-phase equilibria, which limit the stability range of  $\gamma$ -TiAl, are TiAl + Ti<sub>3</sub>Al +  $\tau_2$  on the Ti-rich side and TiAl + TiAl<sub>2</sub> +  $\tau_2$  on the Al-rich side. Those multi-phase equilibria are the same as for 800°C. This means that the invariant reactions involving the phase  $\gamma$ -TiAl occur at somewhat higher temperatures.

#### Phase equilibria between TiAl and FeTi at 1000°C

The aim of this investigation was to study the mechanical properties of two-phase alloys containing  $\gamma$ -TiAl and B2-ordered FeTi. From the preceding study of phase equilibria in the Al-Fe-Ti system [4] it is clear that those two phases are in equilibrium with each other at 1000°C. The exact extent of the respective two-phase field had not been established in that study. Three alloys with different compositions were prepared in a levitation furnace (Nos. 4 - 6 in Table I). Slices of each alloy were prepared as before and equilibrated at 900°C. After a heat treatment for 100 hours at 1000°C the samples were quenched to



room temperature. Metallographic sections were prepared and the compositions of coexisting phases were determined by EPMA. The intended compositions of the alloys and the EPMA results are given in Table III.

In Fig. 2 an enlarged part of the isothermal section at 1000°C is shown. The intended compositions of the alloys are marked by black stars. The compositions were chosen in such a way that they lie on a common tie line and that the phase fractions of TiAl : FeTi are about 2:1 (alloy No. 4), 1:1 (5) and 1:2 (6) at 1000°C. The tie line for alloy No. 6 determined by EPMA is given in Fig. 2. The tie lines for the other two alloys, which are nearly identical with the one given, have been omitted for reasons of clarity. The EPMA results show that the solubility of iron in  $\gamma$ -TiAl in equilibrium with FeTi is about 2 at.% at 1000°C and the width of the two-phase field  $\gamma$ -TiAl + FeTi is about 3 at.% Fe at this temperature. In Figs. 3, 4 and 5 the microstructures of these three alloys are presented. The phase equilibria in the temperature range 800°C to 1000°C are listed in Table IV for all studied alloys.

Table IV: Phase equilibria in the studied alloys at 800°C, 900°C, and 1000°C.

Alloy	800°C	900°C	1000°C
1	TiAl	TiAl	TiAl
2	TiAl + $\tau_2$ + Ti <sub>3</sub> Al	TiAl + $\tau_2$ + Ti <sub>3</sub> Al	TiAl + $\tau_2$ + Ti <sub>3</sub> Al
3	TiAl + $\tau_2$	TiAl + $\tau_2$	TiAl + Fe <sub>2</sub> Ti
4	TiAl + $\tau_2$ + (Ti <sub>3</sub> Al)	TiAl + $\tau_2$ + Ti <sub>3</sub> Al	TiAl + FeTi
5	TiAl + $\tau_2$ + Ti <sub>3</sub> Al	TiAl + $\tau_2$ + Ti <sub>3</sub> Al	TiAl + FeTi
6	TiAl + $\tau_2$ + Ti <sub>3</sub> Al	TiAl + $\tau_2$ + Ti <sub>3</sub> Al	TiAl + FeTi

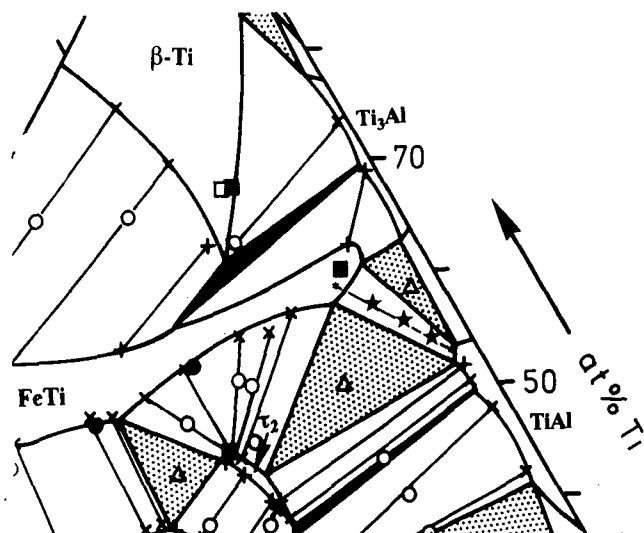


Figure 2: Partial isothermal section of the Fe-Al-Ti system at 1000°C according to [4]. The nominal compositions of alloys Nos. 4 - 6 are given as filled stars (★). Analyzed compositions of TiAl and FeTi are given as tie line for alloy No. 6 (\*—\*). The tie lines for the other two alloys, which are nearly identical with the one given, have been omitted for reasons of clarity. The symbols are the same as in Fig. 1 with (■) indicating single-phase alloys.

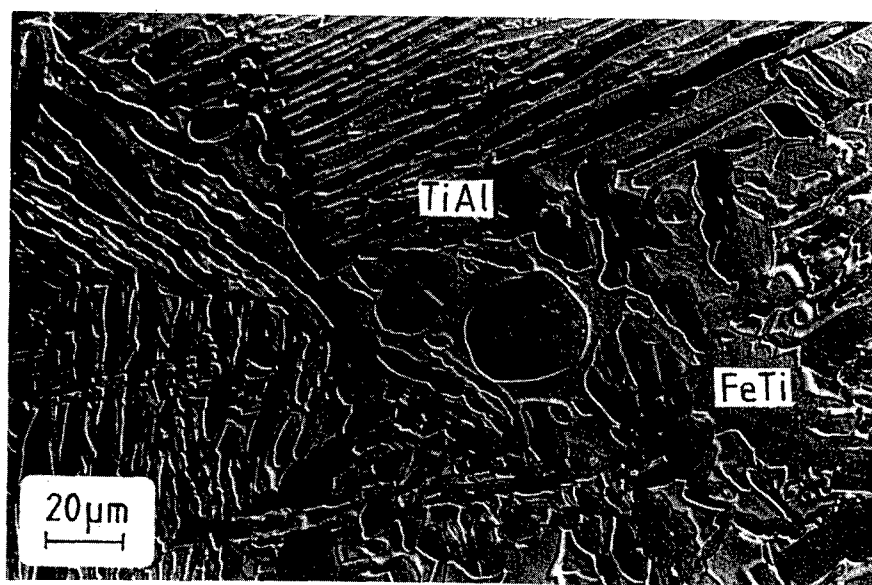


Figure 3: Optical micrograph (differential interference contrast) of alloy No. 4 with heat treatment 1000°C/Ar/100h → H<sub>2</sub>O.

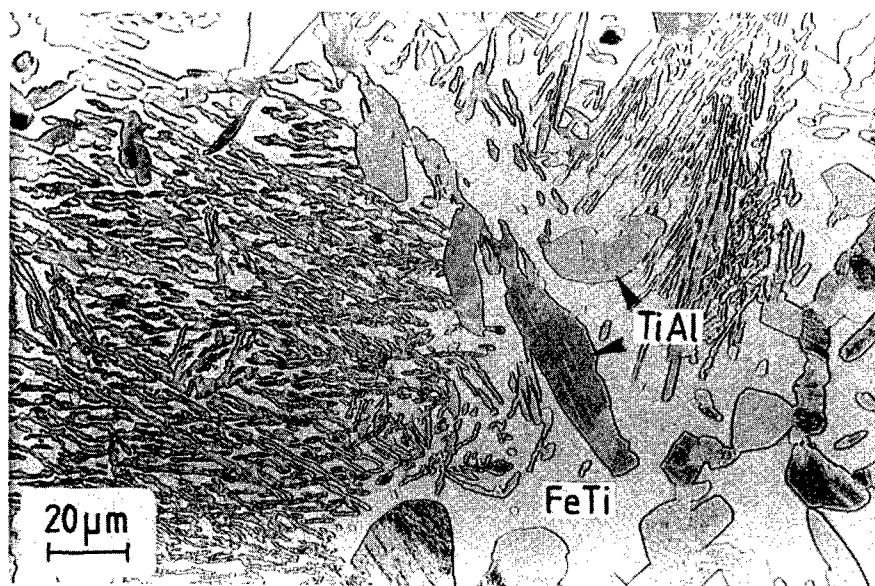


Figure 4: Optical micrograph of alloy No. 5 with heat treatment 1000°C/Ar/100h → H<sub>2</sub>O. The light matrix is identified as FeTi, grey particles are TiAl.

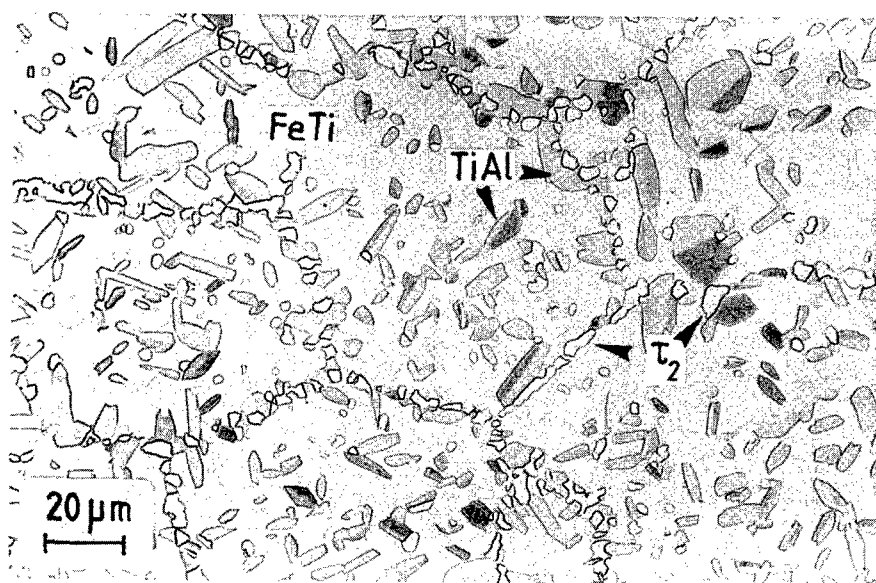


Figure 5: Optical micrograph of alloy No. 6 with heat treatment 1000°C/Ar/100h → H<sub>2</sub>O. The grey matrix is identified as FeTi, black particles are TiAl. The grey particles were identified as Ti<sub>3</sub>Al and small light particles, precipitated at grain boundaries, are τ<sub>2</sub>. Both phases formed during cooling.

## Mechanical Behaviour

### Ti-Al-V

The microstructure of the Ti-Al-V alloy is partially duplex and lamellar. The result of the compression tests for this alloy is shown in Figure 6. There is a steep decrease of the compressive yield stress at temperatures above 800°C. At 1100°C the yield stress of the Ti-Al-V alloy is about 100 MPa which compares favourably with respect to literature [8].

The plastic elongation of this material was determined by 4-point-bending tests. The results of these tests are shown in Figure 7. It can be seen that the alloy has limited ductility with about 1-2% strain to fracture between room temperature and 800°C. All the specimens broke during testing in this temperature range. Microstructure investigations have shown that cracking occurs intergranularly. Above 800°C abundant plastic deformation was observed.

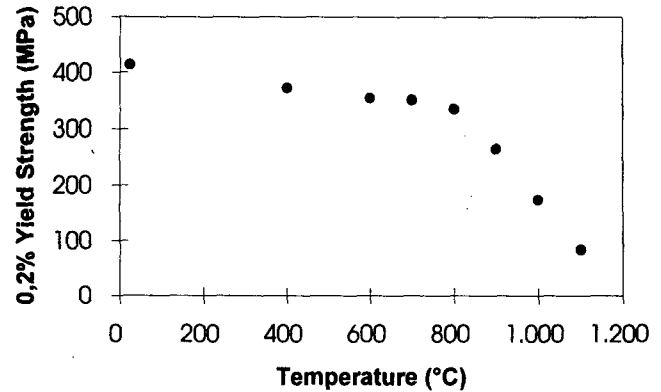


Figure 6: Compressive yield stress as a function of temperature with constant strain rate of  $\dot{\epsilon} = 10^{-4}$  1/s for the Ti-Al-V alloy.

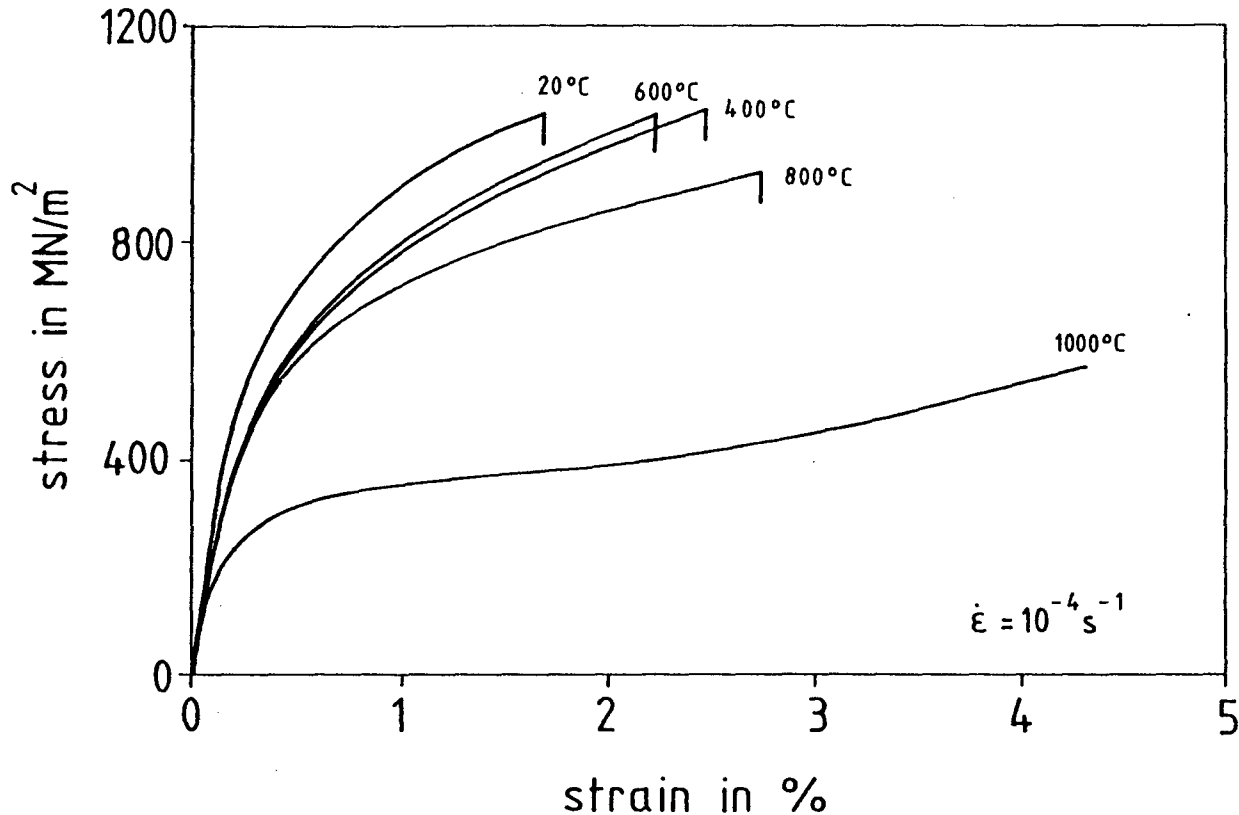


Figure 7: Stress-strain curves in 4-point-bending tests for the Ti-Al-V alloy at various temperatures with constant strain rate  $\dot{\epsilon} = 10^{-4}$  1/s.

### Ti-Al-Fe

For alloy No. 2 ( $\text{Ti}_{51}\text{Al}_{36.5}\text{Fe}_{12.5}$ ) the compressive yield stress versus true strain rate was determined in the temperature range 23°C - 1100°C. The deformation rate was again  $\dot{\epsilon} = 10^{-4}$  1/s. The results are shown in Figure 8. It can be seen that alloy No. 2

has limited ductility in compression with about 1 - 2 % strain to fracture between room temperature and 400 °C. The specimens broke during testing in the temperature range up to 600 °C. Above 600 °C abundant plastic deformation was observed. The compressive yield stress of alloy No. 2 is much higher than that of the Ti-Al-V alloy.

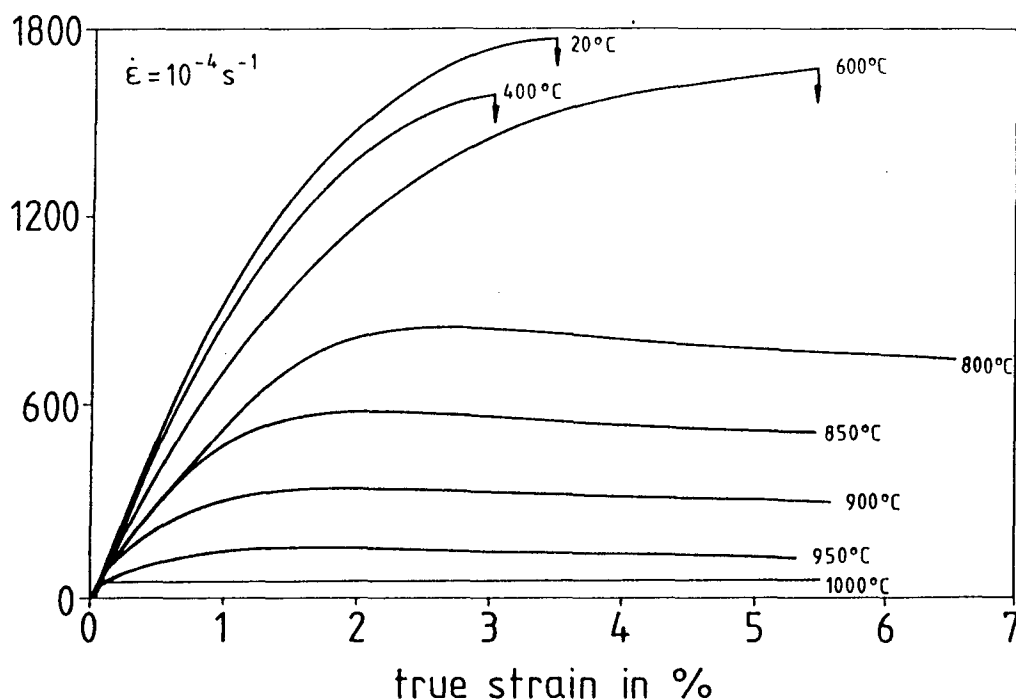


Figure 8: Stress-strain curves in compression for the multiphase Ti-Al-Fe alloy No. 2 at various temperatures with constant strain rate  $\dot{\epsilon} = 10^{-4} \text{ 1/s}$ .

#### Near- $\gamma$ Fe-Al-Ti alloys

For four near- $\gamma$  Fe-Al-Ti alloys (Nos. 3-6) the brittle-to-ductile transition was studied by isothermal compression tests with constant strain rate of  $\dot{\epsilon} = 10^{-4} \text{ 1/s}$ . Figure 9 shows the results for the as-cast alloys, in Figure 10 the alloys have been heat treated for 100 h at 1000°C under argon. In both diagrams, there is a steep decrease of the compressive yield stress with increasing

temperature. Compared to alloy No. 3 ( $\text{Ti}_{48}\text{Al}_{50}\text{Fe}_2$ ), the other three TiAl-Fe alloys have lower proof stresses with plastic deformability in the high temperature range between 800 and 1000°C, whereas at lower temperatures they are stronger and brittle. There is no significant change in the behaviour by the used heat treatment.

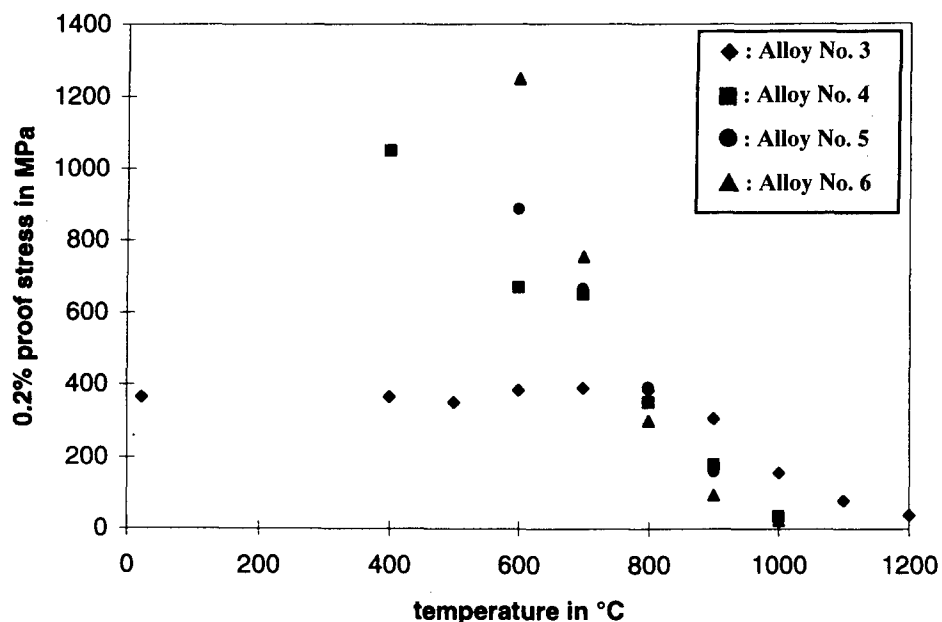


Figure 9: Compressive 0.2% proof stress as a function of temperature with constant strain rate of  $\dot{\epsilon} = 10^{-4} \text{ 1/s}$  for four near- $\gamma$  alloys (Nos. 3-6), as cast.

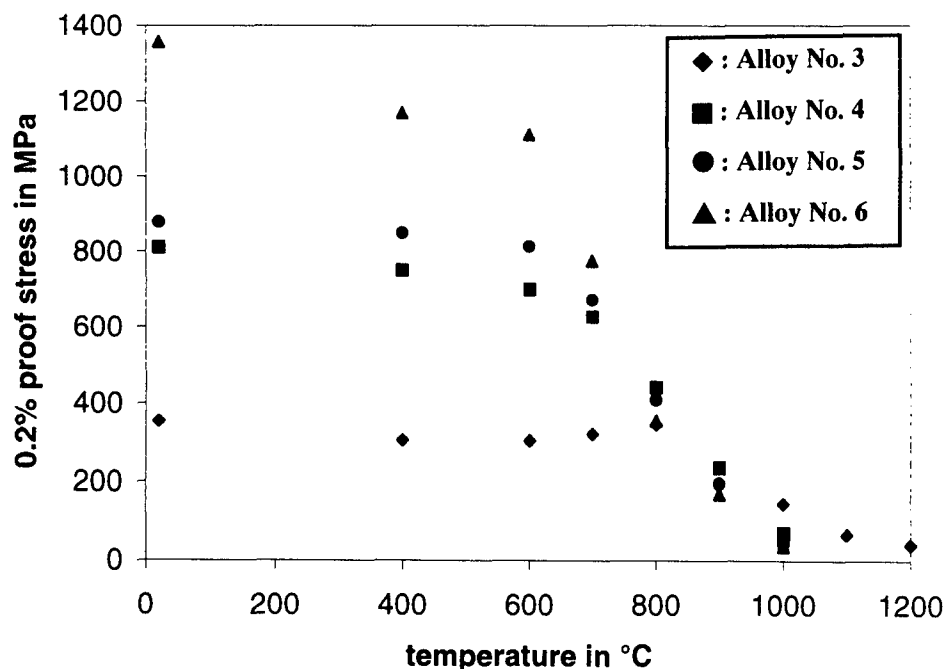


Figure 10: Compressive 0.2% proof stress as a function of temperature with constant strain rate of  $\dot{\epsilon} = 10^{-4}$  1/s for four near- $\gamma$  alloys (Nos. 3 - 6), heat treatment: 1000°C, 100 h, argon.

The fracture strain of the three alloys was determined by 4-point-bending tests. The results of these tests are shown in Table V. As in the compression tests, the high-temperature properties of the TiAl-Fe alloys with higher deformability are superior to those of alloy No. 3 ( $\text{Ti}_{48}\text{Al}_{50}\text{Fe}_2$ ) with a brittle-to-ductile-transition temperature between 1000 and 1100°C, depending on deformation rate.

Table V: Strain to fracture  $\epsilon$  in 4-point-bending for three near- $\gamma$  alloys at various temperatures and deformation rates  $\dot{\epsilon}$  (referred to the outer fibre).

Alloy 4:  $\text{Ti}_{54.0}\text{Al}_{42.5}\text{Fe}_{3.5}$  (as-cast)

Temperature in °C	$\dot{\epsilon} = 10^{-4}\text{s}^{-1}$	$\dot{\epsilon} = 10^{-3}\text{s}^{-1}$
23	$\epsilon < 0.3\%$	
200	$\epsilon < 0.3\%$	
400	$\epsilon < 0.3\%$	
700	$\epsilon > 3\%$	
750	$\epsilon > 3\%$	$\epsilon > 3\%$

Alloy 6:  $\text{Ti}_{57.0}\text{Al}_{36.5}\text{Fe}_{6.5}$  (as-cast)

Temperature in °C	$\dot{\epsilon} = 10^{-4}\text{s}^{-1}$	$\dot{\epsilon} = 10^{-3}\text{s}^{-1}$
23	$\epsilon < 0.3\%$	
200	$\epsilon < 0.3\%$	
400	$\epsilon < 0.3\%$	
700	$\epsilon < 0.3\%$	
750	$\epsilon = 0.63\%$	
800	$\epsilon > 3\%$	

Alloy 3:  $\text{Ti}_{48.0}\text{Al}_{50.0}\text{Fe}_{12.5}$  (heat treatment: 1000°C/12h/ furnace cooled)

Temperature in °C	$\dot{\epsilon} = 10^{-4}\text{s}^{-1}$	$\dot{\epsilon} = 10^{-3}\text{s}^{-1}$
23	$\epsilon < 0.3\%$	
700	$\epsilon < 0.3\%$	
800	$\epsilon < 0.3\%$	
900	$\epsilon < 0.3\%$	$\epsilon < 0.3\%$
1000	$\epsilon > 3\%$	$\epsilon < 0.3\%$
1100	$\epsilon > 3\%$	$\epsilon > 3\%$

#### Creep Tests

The alloys Nos. 4 - 6 have shown the best high temperature properties and thus are the most promising ones. For this reason, the alloys have been subjected to creep tests to get more information in the high-temperature range. Figure 11 shows the secondary creep behaviour of the alloys Nos. 4 - 6 under stresses between 10 and 100 MPa at 900°C. The heat treatment was 1000°C for 100 h under argon. Alloys No. 5 and 6 show nearly the same creep behaviour, whereas No. 4 exhibits a much higher creep resistance. The stress exponent, given by the slope in a double-logarithmic plot, is about  $n = 3$ . This indicates that under these stress and temperature conditions viscous dislocation glide is the dominating deformation mechanism. Creep tests at 1000°C revealed a high oxidation rate for all tested specimens and thus lead to unreliable results.

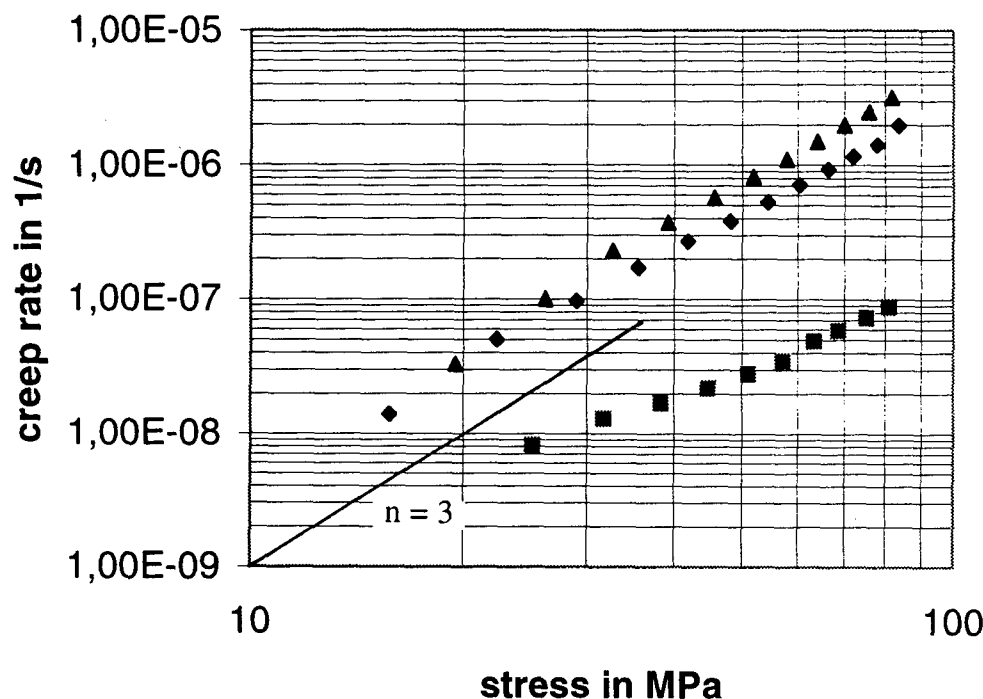


Figure 11: Secondary creep rate of the alloys Nos. 4 - 6 at 900°C (double-logarithmic plot; ■: alloy No. 4, ◆: No. 5, ▲: No. 6) as a function of compressive stress, heat treatment: 1000°C, 100 h, Argon.

### Conclusions

The  $\gamma$ -TiAl-base alloys with Fe may offer some potential for developing high strength TiAl alloys with limited ductility at low temperatures for applications at 900°C. The properties depend sensitively on the amount and distribution of second phases. All five TiAl-Fe alloys showed better mechanical properties than the reference material TiAl-V, in particular the three alloys in the two-phase-field TiAl - FeTi (Nos. 4 - 6) are the most promising ones for high temperature applications. More work is necessary for optimizing the microstructure by appropriate processing and characterizing the development potential in detail.

### References

- [1] K.S. Chan and Y.-W. Kim, "Influence of Microstructure on Crack-Tip Micromechanics and Fracture Behaviors of a Two-Phase TiAl Alloy," *Metall. Trans.*, 23A (1992), 1663-1677.
- [2] Y.-W. Kim, *Microstructure / Property Relationships in Titanium Aluminides and Alloys*, eds. Y.-W. Kim and R.R. Boyer (Warrendale, PA: TMS, 1991), 91-103.

- [3] Y.-W. Kim, "Ordered Intermetallic Alloys, Part III: Gamma Titanium Aluminides," *JOM*, 46 (1994), 30-39.

- [4] M. Palm, G. Inden, and N. Thomas, "The Fe-Al-Ti System," *J. Phase Equilibria*, 16 (1995), 209-222.

- [5] M. Palm and G. Inden, "Constitution of Ternary Aluminide Systems as Basis for Materials Development," *ISSI-2* (1997).

- [6] I. Ohnuma, R. Kainuma, G. Inden, and K. Ishida, "Ordering and Phase Separation in the  $\alpha$ -Fe Phase of Fe-Al-Ti System," in preparation for publication in *Acta Mat.*

- [7] U. Zwicker, "Metallkundliche Untersuchungen an der Implantatlegierung TiAl5Fe2,5," *Z. Metallkd.*, 77 (1986), 714-720.

- [8] Y.-W. Kim and D.M. Dimiduk, "Progress in the Understanding of Gamma Titanium Aluminides," *JOM*, 43 (1991), 40-47.

### Acknowledgements

The authors thank A. Stern and M. Talianker, Ben-Gurion University, for providing the Ti-Al-V reference alloy. This research was carried out in the framework of the European Community Research Programme. Financial support by the European Commission is gratefully acknowledged.

# MICROSTRUCTURE EVOLUTION, PHASE TRANSFORMATIONS AND OXIDATION OF AN ORTHORHOMBIC TITANIUM ALUMINIDE ALLOY

J. Kumpfert, C. Leyens  
DLR - German Aerospace Research Establishment  
Institute of Materials Research  
51140 Köln, Germany

## Abstract

The  $\text{Ti}_2\text{AlNb}$  based alloy Ti-22Al-25Nb was processed via swaging to investigate the microstructure evolution during hot working depending on the deformation ratio. The starting material was a hot isostatically pressed ingot with a lamellar microstructure. Subtransus processing led to an equiaxed microstructure. However, depending on the deformation ratio a wavy contrast was observed instead of the classical homogeneous structure. In addition a continuous grain boundary phase seems to hinder the recrystallization of the  $\beta_0$  phase up to high deformation ratios. In order to study the phase transformations in Ti-22Al-25Nb X-ray diffraction, scanning electron microscopy, and TEM analysis were performed. A preliminary time-temperature-transformation (TTT) diagram is proposed for isothermal transformations from retained  $\beta_0$  phase. Age hardening experiments demonstrated the influence of the phase transformations on the mechanical properties. A rapid transformation of the  $\beta_0$  phase to the orthorhombic phase leads to very high strength material. Slower cooling rates than quenching after solution heat treatment followed by aging appeared to yield higher strength material.

The oxidation behavior of Ti-22Al-25Nb was analyzed between 650°C and 1000°C. In comparison to near- $\alpha$ ,  $\text{Ti}_3\text{Al}$ , or TiAl-based alloys the relative oxidation resistance of this  $\text{Ti}_2\text{AlNb}$  based alloy depends less on the temperature regime. At low temperatures oxidation kinetics are close to near- $\alpha$  and  $\text{Ti}_3\text{Al}$ -based titanium alloys. However, at high temperatures oxidation resistance of Ti-22Al-25Nb is in the order of magnitude of TiAl-based alloys. The oxide scale consists of different portions of  $\text{TiO}_2$ ,  $\text{AlNbO}_4$ , and  $\alpha\text{-Al}_2\text{O}_3$  depending on the test temperature. Oxygen

diffusion into the subsurface zone beneath the oxide scale leads to severe embrittlement as detected by microhardness measurements.

## Introduction

The class of orthorhombic titanium aluminide alloys currently appears to offer the best approach as matrix material in titanium matrix composites (TMCs) designed for elevated temperature aircraft engine applications [1, 2, 3]. Various approaches in the past with different matrix materials exhibited severe limitations with respect to specific properties [4]. TMCs with matrices out of the group of near- $\alpha$  titanium alloys suffer primarily from their low oxidation resistance. Thus maximum service temperature of TMCs employing near- $\alpha$  titanium alloys as matrix are restricted to temperatures below ~530°C.  $\text{Ti}_3\text{Al}$  based alloys offer distinctly better oxidation behavior, however, this approach was confined by the strong environmental embrittlement of this class of alloys. TiAl based alloys are known for their excellent oxidation resistance. However, as a matrix material in TMCs employing SiC fibers their high coefficients of thermal expansion in combination with their low room temperature ductility indicate the limited viability of such a combination of matrix material and reinforcing phase. The recently emerged class of alloys based on the orthorhombic phase  $\text{Ti}_2\text{AlNb}$  seems to be more appropriate as matrix material in TMCs for elevated temperature applications.

To be considered for true engine applications TMCs must offer a significant benefit over nickel-based superalloys. Titanium matrix composites are known for their high specific strength potential and creep resistance parallel to the fiber axis. However, these excellent properties in the direction of fiber orientation can only taken advantage of if the

lower transverse properties of TMCs do not fall below design requirements [5]. Especially off-axis properties, as transverse tensile strength and creep resistance are mainly determined by the matrix performance. Under such loading conditions the fiber contributes very little to strengthening due to a weak fiber matrix interfacial bond. Since the mechanical properties of titanium aluminides can be varied in a wide range depending on microstructural modifications, fundamental microstructure/property relationships need to be known for new matrix materials in order to estimate their potential for application in TMCs. Other matrix-influenced TMC properties include environmental degradation during elevated temperature applications. This behavior is influenced by the oxidation behavior of the matrix and the oxygen embrittlement of the subsurface zone.

In the present study, the influence of hot working and subsequent heat treatments on phase transformations and microstructure evolution has been investigated for the  $\text{Ti}_2\text{AlNb}$  base alloy Ti-22Al-25Nb. In addition, the isothermal oxidation behavior of this alloy has been analyzed between 650°C and 1000°C, including investigations of oxide scale formation and oxygen embrittlement.

#### Material and Procedures

The alloy with the nominal composition Ti-22Al-25Nb (all compositions are in atom percent) was produced by GfE - Gesellschaft für Elektrometallurgie, Germany, in cooperation with the DLR - German

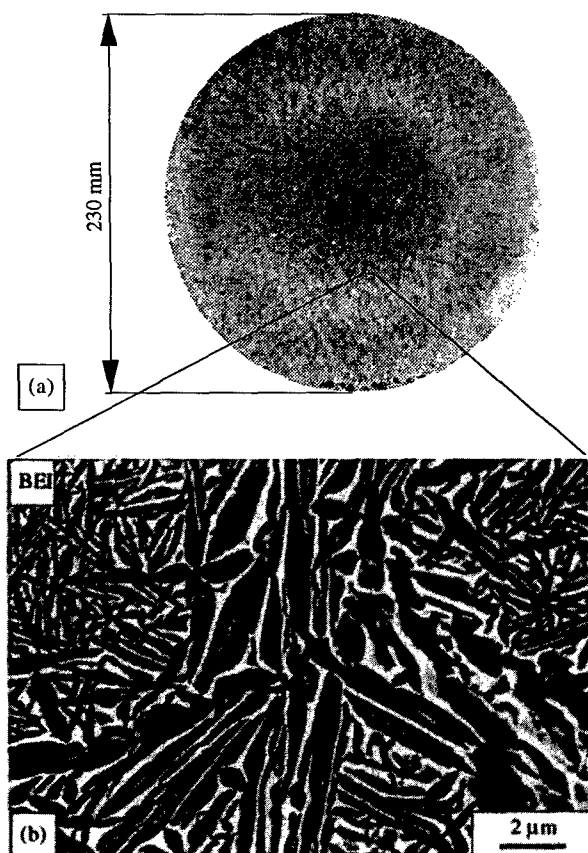


Figure 1: Ti-22Al-25Nb in the as-cast condition; (a) ingot (b) BEI of the as-cast microstructure.

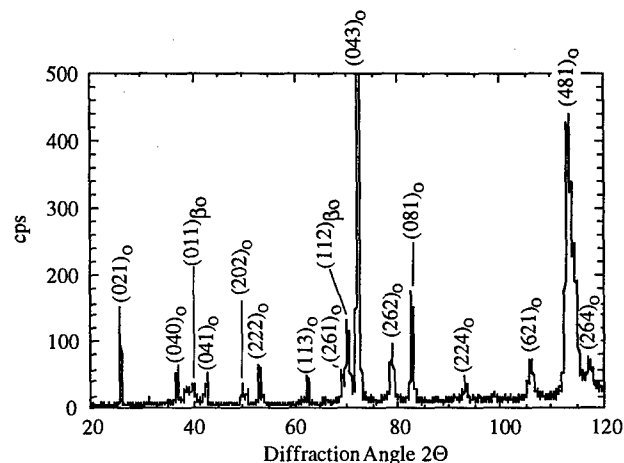


Figure 2: XRD spectrum of the as-cast material. Peaks corresponding to the O and  $\beta_o$  phases are labeled.

Aerospace Research Establishment, by employing vacuum induction melting. The alloy was produced as a 60 kg ingot, which was triple-melted (Figure 1a).

Samples for chemical analysis taken from the top and the bottom of the ingot exhibited a chemical composition very close to the nominal composition, i.e. average being Ti-21.8Al-24.9Nb (designated hereafter as Ti-22-25). The oxygen content was determined to be as low as 500 ppm. The microstructure of the as-cast material is shown in Figure 1b as an backscattered electron image (BEI). Within the former  $\beta_o$  grains relatively fine Widmanstätten morphology can be obtained, while near the prior  $\beta_o$  grain boundaries lamellae width reaches values close to 1  $\mu\text{m}$ . The XRD spectrum taken from the as-cast material revealed the ordered orthorhombic (O) phase and the ordered  $\beta_o$  phase (Figure 2). To remove any porosity, the ingot was given a hot isostatic pressing (HIP) treatment at 1200°C for 3h under an argon pressure of 190 MPa. This treatment did not change the as-cast microstructure significantly.

Billets were cut from the ingot and subsequently hot worked via swaging. For a total reduction in area of 95% the material was swaged in 14 passes with an intermediate annealing of 5 minutes at 960°C. The average reduction per pass was 20%. Solution heat treatments were performed between 1100°C and 960°C for 30 minutes, then cooled to room temperature at different cooling rates. The average cooling rates were determined to be 120 K/s during water quenching (WQ), 9 K/s during air cooling (AC), and 1 K/s during controlled furnace cooling (FC) between the solution heat treatment (SHT) temperature and 600°C.

The  $\beta$  transus temperature ( $T_\beta$ ) was determined by metallographic methods, X-ray diffraction and dilatometric measurements. The resulting microstructures after different heat treatments were investigated using optical microscopy (OM), backscattered electron imaging (BEI) in scanning electron microscope (SEM), image analysis techniques, and transmission electron microscopy (TEM). Metallographic samples were ground and polished through 3 $\mu\text{m}$  diamond paste to prepare surfaces for SEM and XRD. Chemical etching and polishing was not used, as this has been found previously to stabilize the orthorhombic phase [6]. All SEM images were obtained from the center of each sample to avoid phases associated with surface reactions. XRD was conducted on polished samples using a standard diffractometer. Most diffraction scans were



collected between  $32^\circ$  and  $44^\circ$  and some between  $20^\circ$  and  $120^\circ$  for  $2\theta$  using  $\text{Cu K}\alpha$  radiation. To analyze the X-ray diffraction spectra and selected area diffraction patterns the software program 'Desktop Microscopist' was used. Due to known artifacts related to hydrogen charging all TEM foils were prepared by ion milling. Age hardening response was determined using a Vickers indenter with a load of 98.1 N.

For oxidation tests flat samples were used, the geometry of which was  $11 \times 9 \times 1 \text{ mm}^3$  for the as-cast condition and  $6 \text{ mm } \phi \times 1 \text{ mm}$  for the as-swaged condition. Sample front sides were ground with SiC polishing paper up to 1200 grit and edges were slightly rounded. Before testing samples were ultrasonically cleaned in acetone and alcohol. Isothermal oxidation was performed between  $650^\circ\text{C}$  and  $1000^\circ\text{C}$  using a Setaram thermobalance which furnace chamber was flown through by dry compressed air with  $2000 \text{ cm}^3\text{h}^{-1}$ . The heating rates were  $50 \text{ Kmin}^{-1}$  and deviation from rated maximum temperature was determined to be smaller than  $\pm 0.7^\circ\text{C}$ . Average cooling rates achieved by furnace cooling were  $20 \text{ Kmin}^{-1}$ . Microhardness was measured using a Vickers indenter with a load of 0.49 N.

### Results and Discussion

Processing TMCs via coating fibers with matrix material by magnetron sputtering and subsequent consolidation by hot isostatic pressing results in fine grained, equiaxed microstructures within the matrix [7]. Similar microstructures can also be produced in titanium aluminides by multi-step hot working. Fine equiaxed microstructures are well suited for composite

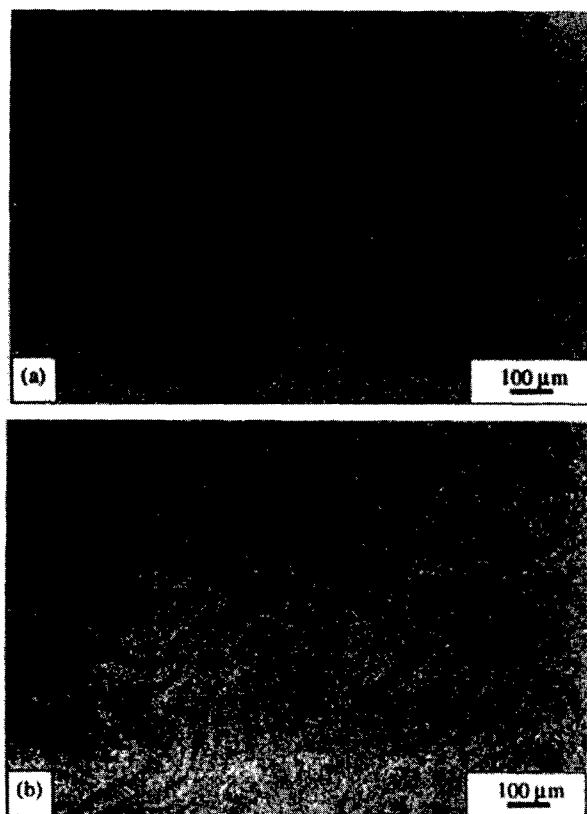


Figure 3: Optical microstructure of as swaged Ti-22-25 material in the cross section. Total reduction in area are 68% in (a) and 95% in (b).

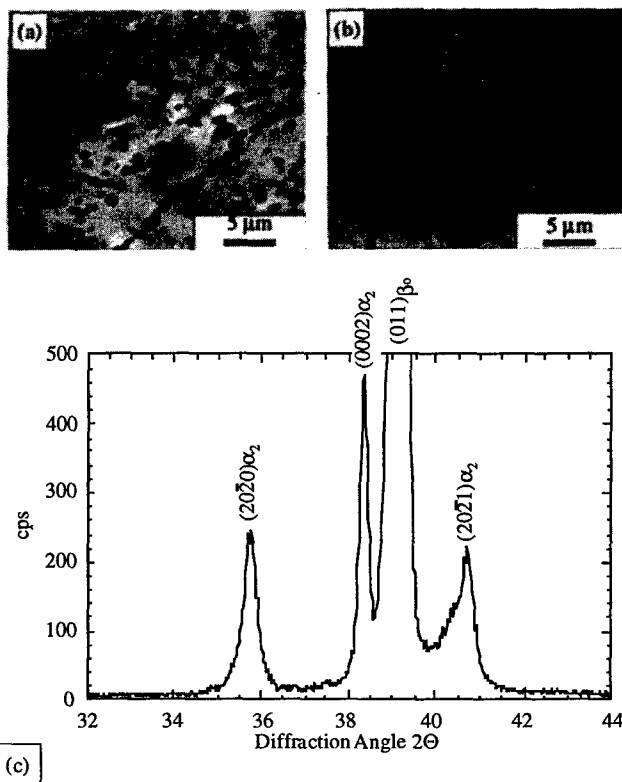


Figure 4: BEI of the as swaged bar (a), (b) and XRD spectrum of the as swaged material. Total reduction in area are 89% in (a) and 95% in (b).

consolidation, but lead to poor creep characteristics [8]. Modifying the microstructure by subsequent controlled heat treatments can improve the mechanical properties and therefore demonstrate the potential of orthorhombic alloys as matrix material in TMCs.

### Microstructural Evolution during Swaging

To obtain homogeneous equiaxed fine grained microstructures thermomechanical treatments are required in order to recrystallize the coarse as-cast material. The parameters which control the quality of equiaxed structures are the deformation conditions (deformation rate and temperature), the recrystallization conditions (time and temperature), and the initial microstructure before deformation.

Hot working was performed by swaging imparting deformation ratios up to 95% in several steps with an intermediate annealing. Two different trends have been obtained with increasing deformation ratio. On the one hand the highest deformation ratios applied led macroscopically to a wavy contrast instead of the classical homogeneous equiaxed recrystallized microstructure (Figure 3a, 3b). On the other hand increasing the total deformation ratio tends to decrease the occurrence of grain boundary phase (Figure 4a, 4b).

Thomas et al. found a similar wavy morphology after extrusion in the single phase  $\beta_0$  field and designated it as VGS microstructure [9]. The VGS contrast was related to local variation in chemistry due to dendritic segregation of the ingot leading to variation in deformability within individual  $\beta_0$  grains. Rowe et al. found strongly aligned O phase lath structure after extrusion an O phase alloy just below the  $\beta$  transus [10]. The source of the aligned O lath appeared to be due to slip banding within

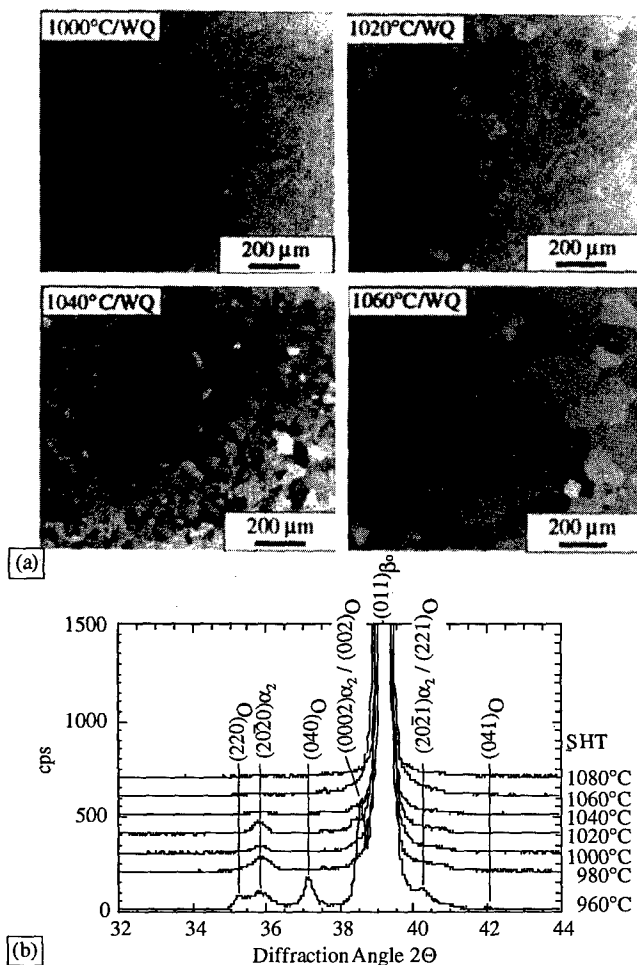


Figure 5: (a) Microstructure of Ti-22-25 after different SHT temperatures and quenching (BEI), (b) XRD spectra of water quenched specimens after SHT for 30 minutes.

the  $\beta_0$  phase. The strongly anisotropic microstructure in this case was noticeable even at a high magnification and was found to lead to zero ductility. However, the VGS microstructure exhibited very high room temperature ductility. Also the alloy Ti-22-25 with the microstructure shown in Figure 3b exhibited room temperature tensile ductility of 16% [11]. High deformation ratios seem to promote inhomogeneous deformation of the  $\beta_0$  phase leading to inhomogeneous precipitation of the  $\alpha_2$  or O phase depending on the hot working temperature. Under the deformation conditions studied here, the material showed macroscopically a wavy contrast, while microscopically a fairly homogeneous microstructure was formed (Figure 3b, 4b). Hot working conditions (temperature & deformation ratio) yielding strongly aligned O phase lath structure are therefore not obtained for Ti-22-25 deformed at  $T_\beta$ -80°C with deformation ratios ranging from 61% to 95%.

A relative sluggishness of recrystallization of the  $\beta_0$  phase could also contribute to a microstructural texture. Semiatin et al. found that the  $\beta_0$  phase did not recrystallize during subtransus hot rolling [12]. They attributed this behavior to grain boundary precipitates which were present during rolling. Such precipitates could also be obtained in this study (Figure 4a). Since the material had a two phase microstructure after swaging at 970°C the BEI image clearly shows grain boundary  $\alpha_2$  phase at the prior  $\beta_0$  boundaries (Figure 4b). The coarse prior  $\beta_0$  grain

boundaries, however, appear to be pinned by the grain boundary  $\alpha_2$  phase. This effect was noticeable up to deformation ratios of 89%. Higher deformation ratios of up to 95% (4 more passes) tend to form less pronounced grain boundary  $\alpha_2$  phase and hence fewer pinned prior  $\beta_0$  grain boundaries.

The interior of the prior  $\beta_0$  phase, however, was fully recrystallized with a fine homogeneous equiaxed microstructure after total reduction in area of 95% as shown in Figure 4b. Deformation ratios down to 61% did provide still a high enough amount of hot work to recrystallize the interior of the prior  $\beta_0$  grains. The grain size within the recrystallized regions is in the order of 3-5 μm (Figure 4b). Such a morphology, rather than the platelet form in Figure 1b, can be attributed to an increased nucleation rate and lower amounts of growth due to the large amount of hot work.

#### Beta Transus Temperature and Phase Transformations

A necessary precaution of processing titanium alloys is the knowledge of the beta transus temperature ( $T_\beta$ ). Figure 5a shows the respective microstructures after solution heat treatment between 980°C and 1060°C followed by water quenching.

Rapid grain growth can be obtained after solution heat treatment above 1040°C indicating the dissolution of the second phase (Figure 5a). In addition XRD patterns exhibit the  $\beta_0$  phase only after quenching from above 1040°C (Figure 5b). From these results the  $\beta$  transus can be estimated to be close to 1050°C in this alloy containing 500 ppm of oxygen. However, significant inhomogeneous coarsening of some  $\beta_0$  grains could also be obtained after solution heat treatment at 1020°C for 30 minutes. This indicates a relatively flat  $\beta$  approach curve, i.e. the primary  $\alpha_2$  phase content is low already 30°C below the  $\beta$  transus. The sluggish grain growth of the  $\beta_0$  grains during solution heat treatment close to the  $\beta$  transus could be of importance to form refined fully transformed microstructures.

The order-disorder temperature  $T_c$  had been determined employing

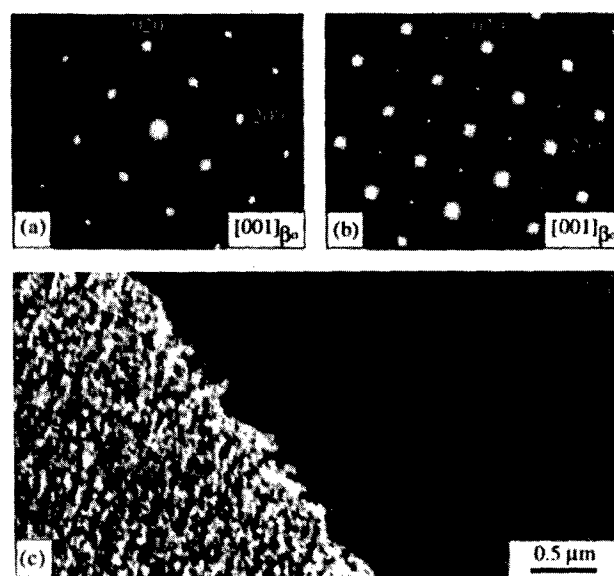


Figure 6: Selected area diffraction patterns obtained after (a) 1080°C/30'/WQ and (b) 1080°C/30'/AC; (c) 'Tweed'-like contrast observed in the air cooled specimen from (b).

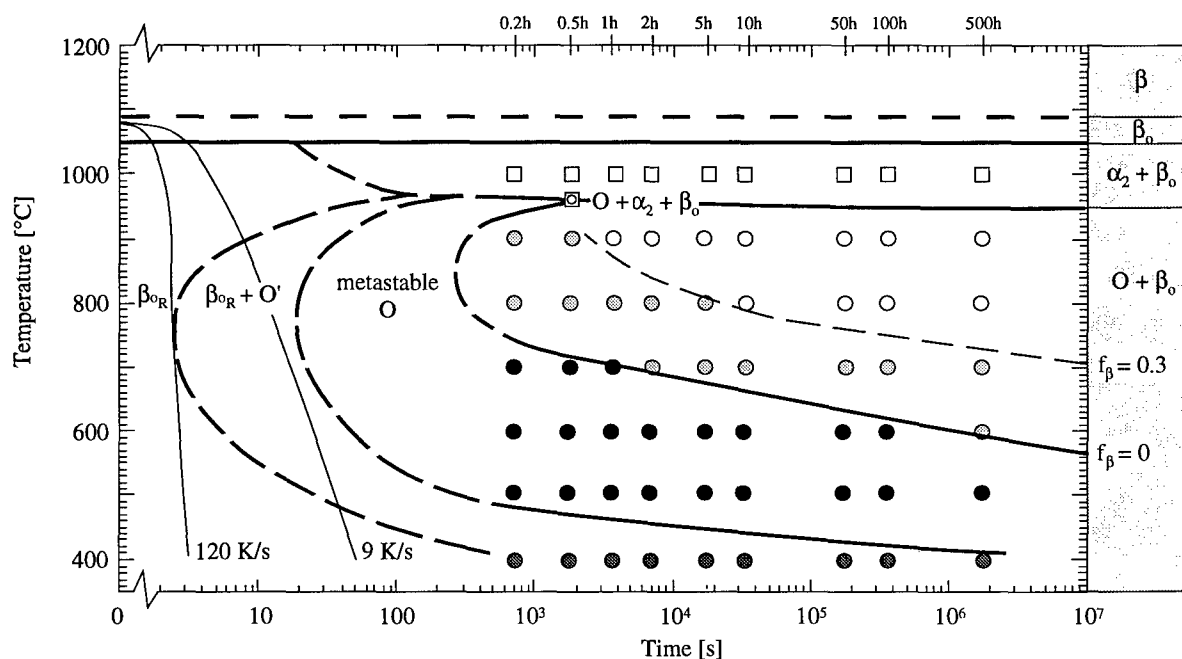
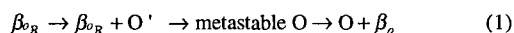


Figure 7: Preliminary TTT diagram of Ti-22Al-25Nb estimated from analytical electron microscopy and X-ray diffraction analysis ( $\beta_{0R}$ : retained  $\beta_0$  phase).

differential scanning calorimetric (DSC) measurements. Since ordering of the disordered B phase (A2) takes place in a narrow temperature range a reproducible peak during the heating and cooling cycle indicated the temperature  $T_c$  to be close to 1090°C.

A series of isothermal heat treatments was performed with quenched-in single  $\beta_0$  phase material. Aging temperatures varied between 600°C and 1000°C and aging times ranged from 0.2 to 500 hours in order to study the phase transformations in Ti-22-25. In addition TEM analysis was conducted on continuous cooled specimens to observe the initial fast phase transformations. A summary of the results obtained on super-transus quenching and aging the Ti-22-25 alloy is shown in Figure 7. Below about 950°C the following transformation path was obtained, which will be discussed below:



where  $\beta_{0R}$  is the retained  $\beta_0$  phase after quenching. The ordered nature of the  $\beta_0$  phase was confirmed by TEM after water quenching from 1080°C. The presence of super-lattice spots in Figure 6a indicates that the crystal structure corresponds to  $\beta_0$ . In addition some weak diffuse  $\langle 110 \rangle$  streaking can be obtained in the diffraction pattern. More pronounced streaking can be observed after air cooling from 1080°C (Figure 6b). Streaks as found here are often accompanied by a 'tweed'-like contrast in dark field TEM images formed by  $\beta_0$  super-lattice spots. Such a diffraction condition is given for one grain in Figure 6c. Both diffuse streaks in diffraction pattern and the tweed-like image contrast had been identified to be the result of displacive shearings during the decomposition of the  $\beta_0$  phase [13]. The O phase is structurally related to the  $\beta_0$  phase through an intermediate orthorhombic phase with a B19 structure (AuCd-type,  $Pnma$  space group). [14]. The B19 structure has only two Wyckoff

sites with occupancies similar to the  $\beta_0$  phase, i.e. mixed occupancies of Al and Nb atoms on one site and Ti atoms on another. However, the O phase is a ternary ordered  $A_2BC$ -type phase with distinct sublattices for Ti, Al, and Nb, respectively. Ordering via diffusion between Al and Nb on the mixed sites of the B19 phase is therefore required to form the O phase via the B19 structure out of the retained  $\beta_0$  phase after quenching from above the  $\beta$  transus. The pre-precipitation stage of the O phase will be designated here as O'.

The partitionless transformation of the retained  $\beta_0$  phase to the metastable O' phase followed by short range diffusion leads to extremely fine microstructures consisting of orthorhombic plates. Figure 8 shows such a fine microstructure of Ti-22-25 after quenching and aging at 700°C for 12 minutes. The XRD spectrum of this specimen indicates a single phase

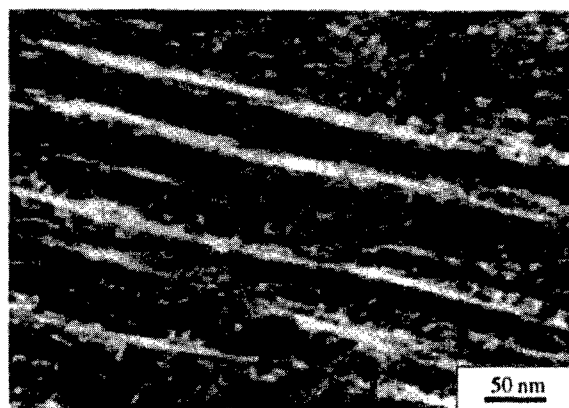


Figure 8: Bright field TEM microstructure of Ti-22Al-25Nb after quenching from above the  $\beta$  transus and aging at 700°C for 12 minutes. The substructure of the orthorhombic plates exhibits a high density of interfaces.

Table I: Phases in Ti-22Al-25Nb.

	Space-group	Strukturbericht	Pearson	Lattice parameters
$\beta_0$ phase	Pm $\bar{3}$ m	B2	cP2	a=0.328 nm
O phase	Cmcm	A <sub>2</sub> BC	oC16	a=0.604 nm b=0.962 nm c=0.467 nm
$\alpha_2$ phase	P6 <sub>3</sub> /mmc	D0 <sub>19</sub>	hP8	a=0.580 nm c=0.470 nm

material, with peak positions close to O phase peaks in stable microstructures. After aging for 1h at 700°C weak  $\beta_0$  phase peaks become apparent. The intensity of the  $\beta_0$  peaks is continuously increasing up to aging times of 500h. At an aging temperature of 800°C a stable situation appears to be reached after aging for 10h. Analysis of respective backscattered electron images with an image analysis system did confirm that the  $\beta_0$  phase reached its final volume fraction at each temperature. The aging time to produce 30 vol.% of  $\beta_0$  phase ( $f_\beta=0.3$ ) is marked in Figure 7 as a dashed line. Therefore aging treatments up to 500 hours and 700°C or at 900°C for 0.5 hours produce microstructures with  $f_\beta$  below 0.3. After aging at 960°C for 0.5 hours a three phase mixture -  $\alpha_2+\beta_0+O$  - was obtained. Within a narrow temperature range between 950°C and 1000°C all three phases might be in equilibrium. Recent results on equilibrium phases in orthorhombic alloys with a constant 22 at.% Al indicate the existence of such a three phase field [15].

The lattice parameters of the phases obtained in Ti-22-25 in near equilibrium microstructures after slow cooling (FC) are shown in Table I. In comparison to the lattice parameters of the respective phases in the Ti<sub>3</sub>Al based alloy Ti-25Al-10Nb-3V-1Mo most of the parameters are increased by 1-2% [8]. This can be attributed to the high content of the large Nb atoms in Ti<sub>2</sub>AlNb alloys. Another obvious effect of increasing the Nb content is the stabilization of the O phase. In Ti-25Al-10Nb-3V-1Mo with an Nb-equivalent of 18 at.% the O phase is not stable above 800°C and a  $\alpha_2+\beta_0$  phase mixture is formed after prolonged aging at this temperature. However, in Ti-22-25 the  $\alpha_2$  phase is not formed below 950°C starting with quenched material and aging times up to 500h.

#### Age Hardening Response

To study the influence of phase transformations due to thermomechanical

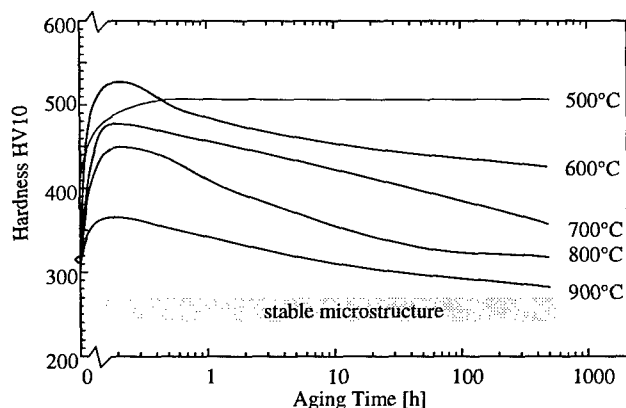


Figure 9: Age hardening response of Ti-22-25 at different aging temperatures. The material was initially solution heat treated at  $T_\beta+30^\circ\text{C}$  and water quenched.

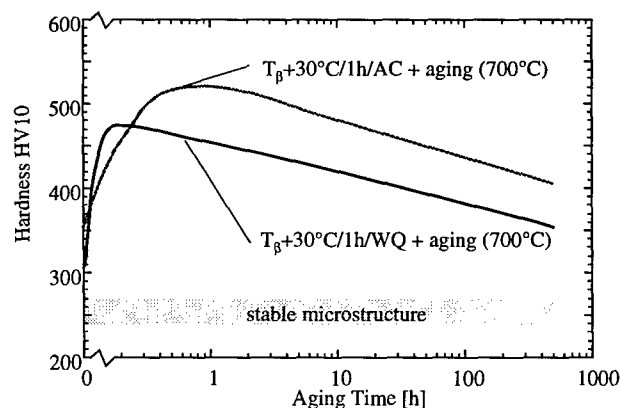


Figure 10: Age hardening response at 700°C after SHT and air cooling and water quenching, respectively.

processing on mechanical properties the age hardening behavior of the material was determined.

The age hardening response of Ti-22-25 is shown in Figure 9. The material was initially solution heat treated at  $T_\beta+30^\circ\text{C}$  followed by water quenching. Depending on the aging temperature the material exhibits a very pronounced age hardening response. Hardness values above 500 HV10 can be obtained after low temperature aging, i.e. below 700°C. During aging between 900 and 600°C peak hardness is reached very rapid and a continuous decrease in hardness with aging was observed. However, during aging at 500°C and below the developing microstructure seems to be at least kinetically stable for the aging times studied.

The high hardness values obtained at peak hardness after aging at 700°C result from the very fine microstructure during decomposition of the retained  $\beta_0$  phase (Figure 8). The partitionless transformation of the retained  $\beta_0$  phase to the O phase involving only fast short range diffusion leads to extremely fine microstructures and causes the very rapid age hardening response of this material. Since boundary strengthening is known to be the dominant factor in controlling strength of many Ti<sub>3</sub>Al based alloys, the formation of the O phase as described can lead to very high strength levels [16].

In order to estimate the yield strength of Ti-22-25 after thermomechanical processing tensile tests were correlated with the Vickers hardness. The average ratio of tensile yield strength to Vickers hardness was determined to be 2.8 [11]. This suggests that yield strength levels between 1475 MPa for peak hardening and 700 MPa for a slow cooled stable microstructure can be obtained in Ti-22-25 at room temperature.

In addition to the influence of the aging temperature and time the cooling rate from SHT temperature before aging has also a significant influence on age hardening response. Figure 10 compares the age hardening behavior of Ti-22-25 at 700°C after air cooling and water quenching, respectively. However, water quenching of the  $\beta$ -processed material leads to a lower age hardening response. In addition, the air cooled specimen exhibited a fine basketweave microstructure instead of large colonies with similarly oriented O laths in the water quenched specimen (Figure 11).

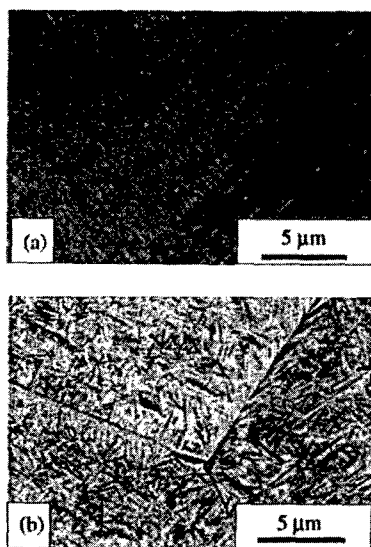


Figure 11: Influence of cooling rate from SHT temperature on microstructure after aging (BEI); (a)  $T_{\beta}+30^{\circ}\text{C}/\text{WQ}+800^{\circ}\text{C}/0.5\text{h}/\text{WQ}$ , (b)  $T_{\alpha}+30^{\circ}\text{C}/\text{AC}+800^{\circ}\text{C}/0.5\text{h}/\text{WQ}$ .

Air cooling was shown to lead to strong streaking and a tweed-like contrast, indicative of displacive shearings in the  $\beta$  phase (Figure 6). However, water quenched specimens did only show a very weak streaking in the diffraction pattern. Therefore it is tempting to assume, that the metastable transition phase formed during air cooling provides numerous nucleation sites for the following decomposition during isothermal aging. Such a transformation path might yield the fine basketweave microstructure of the air cooled specimen and therefore also the higher hardness values due to boundary strengthening effects.

#### Oxidation Behavior

In order to investigate the influence of microstructure and temperature on the oxidation behavior of Ti-22-25, samples in the as-cast (see Figure 1) and as-swaged (see Figure 3 and 4) condition were isothermally oxidized in air between  $650^{\circ}\text{C}$  and  $1000^{\circ}\text{C}$ . Weight gain of the samples follows a parabolic rate law (Figure 12) according to

$$\left(\frac{\Delta m}{A}\right)^2 = k_p \cdot t \quad (2)$$

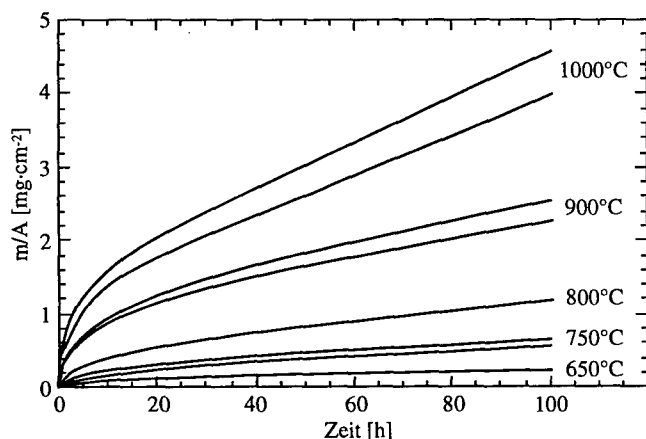


Figure 12: Weight gain vs. time curves for isothermal oxidation of Ti-22-25. Except for  $800^{\circ}\text{C}$  the as-cast samples are more oxidation resistant than the as-swaged specimens (see also Table II).

where  $\Delta m$  and  $A$  represent the mass gain and the surface area of the sample, respectively,  $k_p$  is the parabolic rate constant and  $t$  is the exposure time. Oxidation resistance is higher for the as-cast samples than for the as-swaged ones for all temperatures except for  $800^{\circ}\text{C}$  where weight gain for both microstructures is identical. The influence of microstructure on oxidation resistance slightly increases with increasing temperature (Table II).

Table II: Parabolic rate constant  $k_p$  for isothermal oxidation of Ti-22-25 in the as-cast and as-swaged condition as well as percentage of difference of  $k_p$  between both microstructures  $\Delta k_p/k_{p(\text{as-cast})}$ .

	parabolic rate constant $k_p$ [ $\text{mg}^2\cdot\text{cm}^{-4}\cdot\text{h}^{-1}$ ]				
	$650^{\circ}\text{C}$	$750^{\circ}\text{C}$	$800^{\circ}\text{C}$	$900^{\circ}\text{C}$	$1000^{\circ}\text{C}$
as-cast	$3.91\cdot 10^{-4}$	$3.26\cdot 10^{-3}$	$1.35\cdot 10^{-2}$	$4.75\cdot 10^{-2}$	$1.47\cdot 10^{-1}$
as-swaged	$4.75\cdot 10^{-4}$	$3.93\cdot 10^{-3}$	$1.28\cdot 10^{-2}$	$6.19\cdot 10^{-2}$	$1.97\cdot 10^{-1}$
$\Delta k_p/k_{p(\text{as-cast})}$	+21.5 %	+20.6 %	-5.2 %	+30.3 %	+34.0 %

In comparison with conventional near- $\alpha$  titanium alloys as well as titanium aluminides based on  $\alpha_2\text{-Ti}_3\text{Al}$  and  $\gamma\text{-TiAl}$ , oxidation of orthorhombic Ti-22-25 is considerably less influenced by temperature as shown in Figure 13. The oxidation behavior may be classified into low and high temperature performance. Between  $650^{\circ}\text{C}$  and  $800^{\circ}\text{C}$  the parabolic rate constant corresponds to near- $\alpha$  titanium alloys as well as to  $\text{Ti}_3\text{Al}$ -based titanium aluminides, however, at  $900^{\circ}\text{C}$  and  $1000^{\circ}\text{C}$  oxidation resistance of Ti-22-25 is as high as for  $\gamma\text{-TiAl}$ -based alloys.

One important factor concerning oxidation resistance of Ti-22-25 is the composition of the oxide scale formed at different temperatures. Figure 14 shows the XRD pattern for as-cast material oxidized for 100 hours in air at  $900^{\circ}\text{C}$ . During oxidation a mixed oxide scale forms containing rutile ( $\text{TiO}_2$ ) and  $\text{AlNbO}_4$  rather than protective  $\alpha\text{-Al}_2\text{O}_3$ . Increasing the temperature up to  $1000^{\circ}\text{C}$  leads to higher  $\alpha\text{-Al}_2\text{O}_3$  content in the scale thus making the scale more protective (Table III). By way of contrast, lowering the temperature hinders formation of  $\alpha\text{-Al}_2\text{O}_3$  and  $\text{AlNbO}_4$  and therefore results in poor oxidation resistance. From these results the effectiveness of  $\text{AlNbO}_4$  as a protective oxide is concluded being higher than for  $\text{TiO}_2$  but lower than for  $\alpha\text{-Al}_2\text{O}_3$ .

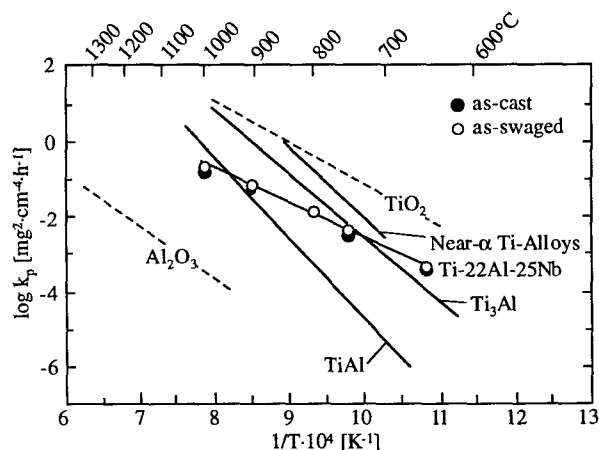


Figure 13: Arrhenius plot of parabolic rate constants for Ti-22-25 compared with literature values [17-19]. The  $\text{TiO}_2$ -line represents oxidation kinetics for pure Ti, whereas the  $\text{Al}_2\text{O}_3$ -line was obtained for  $\beta\text{-NiAl}$  oxidation.

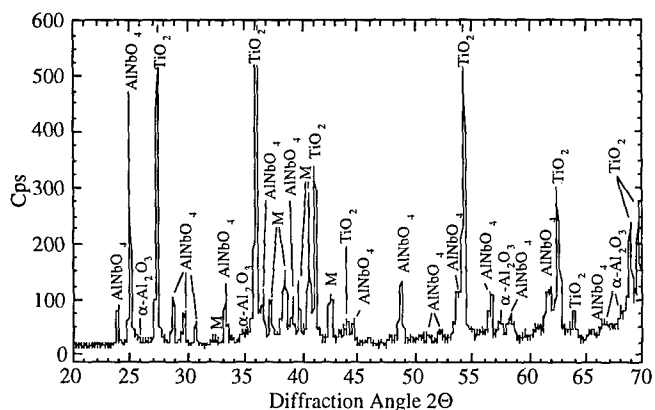


Figure 14: XRD pattern for as-cast Ti-22-25 oxidized in air at 900°C for 100 hr. Metal peaks are labeled with "M".

After oxidation surface topography of the metallic material was found to be reflected and roughness was enhanced leading to deep furrows at the grinding marks of the metal (Figure 15a). However, the surface of the oxide scale is covered by a dense oxide scale (Figure 15b). Higher

Table III: Relative intensities of oxide peaks in the scale formed on as-cast+HIP as well as on as-swaged Ti-22-25 in air after 100 hr.

	650°C	750°C	800°C	900°C	1000°C
TiO <sub>2</sub>	*	medium	high	very high	very high
AlNbO <sub>4</sub>	*	very low	low	high	medium
α-Al <sub>2</sub> O <sub>3</sub>	*	*	very low	low	medium

\* Phase content is too low to be detected by XRD.

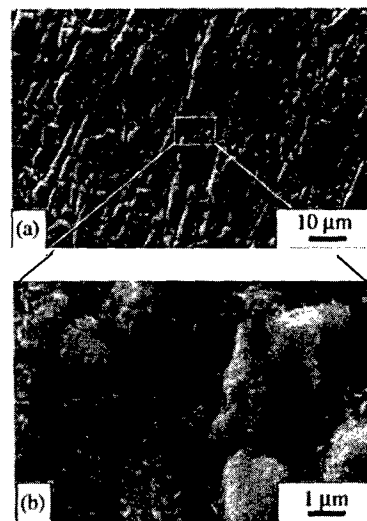


Figure 15: Top view of the oxide scale on Ti-22-25 after 500 hr exposure to air at 900°C.

magnification of the oxide proves the scale being two-phase at least. The oxide morphology observed on the surface considerably differs from the bulk of the scale. Underneath the 1-2 μm thick dense scale a microstructurally homogeneous but rather porous oxide scale follows (Figure 16). The particle size of this fine-grained layer is smaller than 300 nm after exposure to air at 900°C. Further investigations are needed to clarify whether this part of the scale consists of single phase AlNbO<sub>4</sub>, two-phase AlNbO<sub>4</sub>+TiO<sub>2</sub> or even three-phase AlNbO<sub>4</sub>+TiO<sub>2</sub>+α-Al<sub>2</sub>O<sub>3</sub>. Formation of a three-phase oxide layer is most likely as Al-Ti-Nb alloys containing higher Al contents than Ti-22-25 were also found to exhibit this

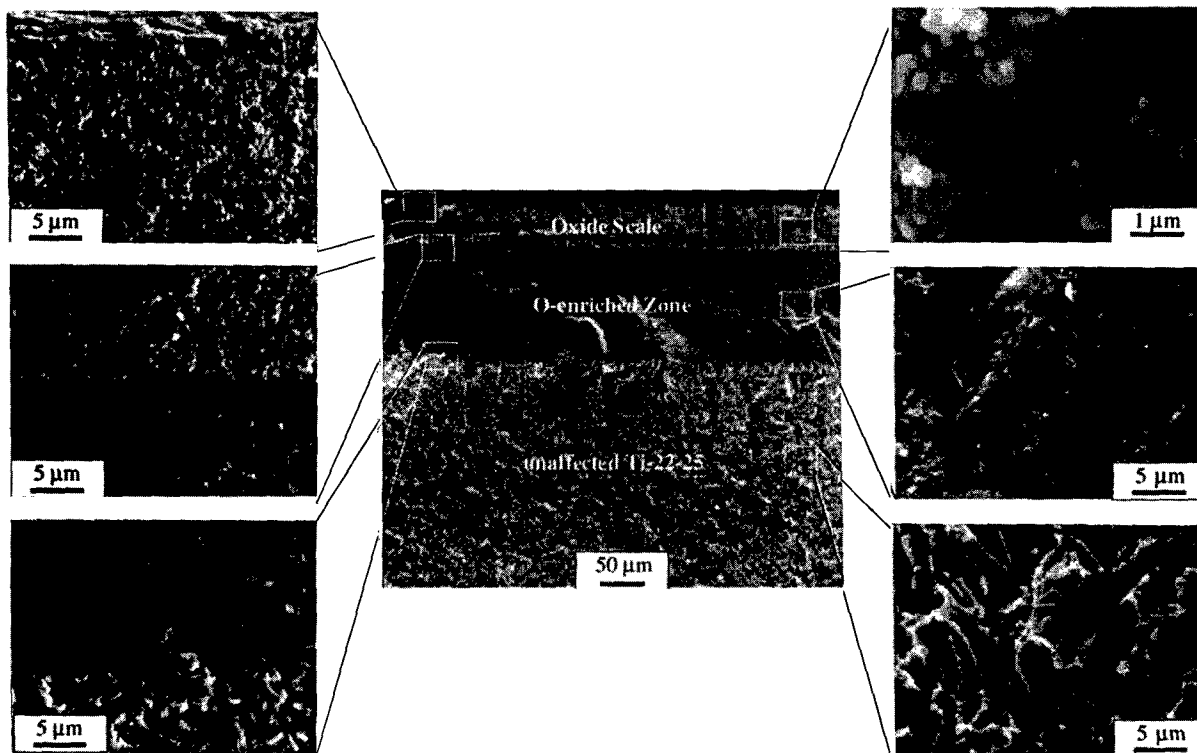


Figure 16: REM fractographs of Ti-22-25 oxidized at 900°C in air for 500 hr.



Figure 17: Cracking of the oxide scale formed during air exposure to 900°C for 500 hr. Under these conditions failure occurred only at the sample edges.

scale composition [20]. The high volume increase of the oxide scale as well as mismatch of the coefficients of thermal expansion (CTE) between the metal and the oxide scale cause scale fracture, delamination and finally spallation only at the edges of the sample. Here considerable stresses are generated perpendicularly to the scale/alloy interface leading to failure when the scale thickness is increased to a critical value (Figure 17). As cracking was observed only after cooling, stresses evolved by CTE mismatch are considered to play a major role for stress generation in the oxide scale. Despite of large stresses excellent adhesion of the oxide scale was found for all samples (except for the edges) even for very thick oxide scales.

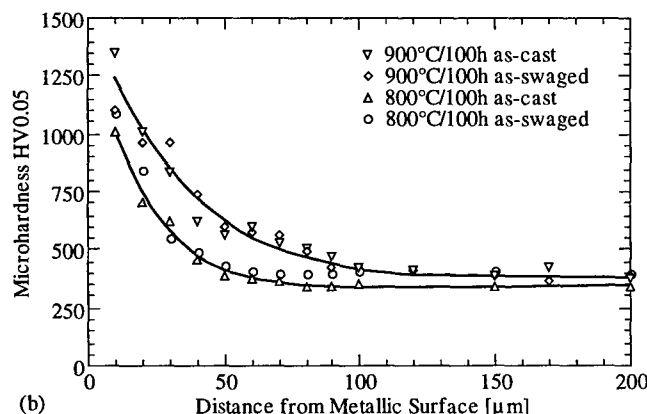
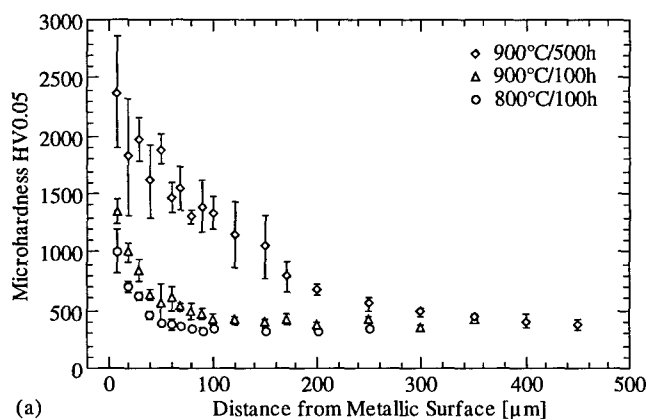


Figure 18: Microhardness curves for oxidized Ti-22-25 determined by using a Vickers indenter. a) Influence of temperature on hardness profiles of as-cast material, b) influence of microstructure on hardness profiles after oxidation at 800 and 900°C.

However, weight gain during oxidation is not only caused by oxide scale formation but also by oxygen solution in the subsurface zone of Ti-22-25. Figure 18 shows a REM fractograph of as-cast Ti-22-25 oxidized in air at 900°C for 500 hours. A 160  $\mu\text{m}$  oxygen-enriched zone is formed during exposure which is estimated to be more than twice as broad as the oxide scale itself (62  $\mu\text{m}$ ) considering fracture morphology. Unlike the unaffected material fracture of the O-enriched zone is characterized by a smooth morphology caused by brittle fracture. The microhardness of the O-enriched zone is drastically increased towards the metal/oxide interface (Figure 18). Maximum hardness of the O-enriched zone even exceeds hardness of the oxide scale which is  $830 \pm 55 \text{ HV0.05}$ . In former investigations on near- $\alpha$  titanium alloys the microhardness profile was found to be correlated with the oxygen diffusion profile [21]. As oxygen penetration is controlled by diffusion, the microhardness profile depends on exposure time as well as on temperature. At 800°C hardness is increased in a 50  $\mu\text{m}$  thick zone after 100 hours. The hardened zone is widened up to 80  $\mu\text{m}$  at 900°C (Figure 18a,b).

The maximum hardness increases with both increasing temperature and time (Figure 18a). As hardness of the unaffected material is identical for all conditions tested, the aforementioned effect is caused by the amount of oxygen dissolved in the alloy rather than by microstructural changes of the bulk alloy. The maximum oxygen solubility, however, is time dependent as can be concluded from the test conditions. Maximum hardness indeed increases with increasing temperature, but the value further rises when exposure time is prolonged at constant temperature thus indicating that oxygen solubility obviously depends on exposure time. Comparing the hardness curves in Figure 18 with the fractograph shown in Figure 16, the fracture morphology is evidently not directly related to the increase of hardness. From hardness measurements the size of the O-enriched zone is determined to be about 250  $\mu\text{m}$  whereas fracture morphology suggest oxygen diffusion only as far as 160  $\mu\text{m}$  for as-cast Ti-22-25 oxidized for 500 hours in air at 900°C. Dary and Pollock, however, revealed by Auger Electron Spectroscopy on Ti-22Al-23Nb that oxygen is enriched up to 175  $\mu\text{m}$  beneath the oxide scale after 100 hours exposure to air at 760°C [22]. Compared to the O-enriched zone detected by hardness measurement after 100 hours at 800°C (50  $\mu\text{m}$ ) shown before, the O-enriched zone is expected to be much broader than detected by the increase of hardness. Therefore, a minimum oxygen content is likely to be necessary in order to alter the fracture behavior of Ti-22-25.

For both microstructures identical microhardness profiles were found at 800 and 900°C (Figure 18b). Different mass gain for both microstructures is therefore caused by growth of the oxide scale rather than by differing oxygen solubility in the subsurface of the alloy.

### Conclusions

In Ti-22Al-25Nb isothermal aging below 950°C and above 600°C leads to a two phase mixture consisting of the ordered orthorhombic O phase and the ordered cubic  $\beta_0$  phase. Between the  $\beta$  transus at 1050°C and temperatures above 950°C only the  $\alpha_2$  phase and  $\beta_0$  phase coexists, while at 960°C a phase mixture consisting of the  $\alpha_2$ , O, and  $\beta_0$  phase was obtained. A rapid transformation of the quenched-in retained  $\beta_0$  phase to a orthorhombic phase was found, which appeared to be metastable between 950°C and 600°C. However, subsequent aging below 600°C up to 500 hours did not lead to transformation of the O phase to an O+ $\beta_0$  phase mixture. The TEM, XRD, and SEM investigations led to a preliminary TTT diagram for Ti-22-25.

Swaging was successful in converting the coarse as-cast lamellar microstructure in a fine recrystallized equiaxed microstructure. However, depending on the deformation ratio, either a wavy contrast or a continuous grain boundary phase has been obtained. While the wavy contrast seems to be related to inhomogeneous deformation of the  $\beta_0$  phase, the grain boundary phase appears to hinder the recrystallization of the  $\beta_0$  phase up to high deformation ratios.

The age hardening behavior of the Ti-22-25 alloy points to a very high strength potential of this alloy. The partitionless transformation of the  $\beta_0$  phase to the O phase leads to rapid transformations and thus to extremely fine microstructures. However, stable microstructures need to be identified with balanced mechanical properties. To achieve high strength, slower cooling rates after solution heat treatment seem to be advantageous over quenching.

Oxidation of Ti-22-25 between 650 and 1000°C leads to the formation of multiphase oxide scales containing  $\text{TiO}_2$ ,  $\text{AlNbO}_4$  and  $\alpha\text{-Al}_2\text{O}_3$ . The portion of specific oxides in the scale depends on exposure temperature. At low temperatures oxidation kinetics are as high as for near- $\alpha$  and  $\text{Ti}_3\text{Al}$ -based titanium alloys, but for high temperatures oxidation resistance of Ti-22-25 is in the order of magnitude of TiAl-based alloys. During exposure to air at high temperatures oxygen dissolves in the subsurface zone of the alloy leading to substantial increase of microhardness. Oxygen diffusion is independent from microstructure as far as detected by hardness profiles. The maximum hardness depends on exposure time rather than on temperature.

#### Acknowledgments

This work was conducted as part of the in-house research activities of the Institute of Materials Research, DLR-German Aerospace Research Establishment. The authors wish to acknowledge the experimental support given by K. Baumann, R. Borath, J. Brien, H. Gedantz, H. Hinderlich, B. Kanka, M. Klaukien, and W.-D. Zimmermann.

#### References

1. D. B. Miracle, P. R. Smith, J. A. Graves, "A Review of the Status and Developmental Issues for Continuously-Reinforced Ti-Aluminide Composites for Structural Applications," *Intermetallic Matrix Composites II*, Eds. J.A. Graves, R.R. Bowman, J.J. Lewandowski (MRS, Pittsburgh, PA, 1994), 133-142.
2. D. B. Miracle, M. G. Mendiratta, *Intermetallic Composites*. in: *Intermetallic Compounds*, Eds. J.H. Westbrook, R.L. Fleischer (John Wiley & Sons, New York, 1994) 287-300.
3. J. Kumpfert, R. Leucht, J. Hemptenmacher, H. J. Dudek, "Effects of Matrix Properties on TMC Properties," *ECCM-7*, (The Institute of Materials, London, UK 1996), 419-424.
4. H. J. Dudek, R. Leucht, W. A. Kaysser, "Development of Metal Matrix Composites by Fiber Coating and HIPing," *Proc. ICCM-10*, Eds. A. Poursartip, K. Street (The Institute of Materials, London, 1995), 695-702.
5. S. A. Singerman, J. J. Jackson, "Titanium Matrix Composites for Aerospace Applications," *Superalloys 1996*, Eds. R.D. Kissinger, et al. (TMS, Warrendale, PA 1996), 579-586.
6. K. Muraleedharan, S. V. N. Naidu, D. Banerjee, "Orthorhombic Distortions of the  $\alpha_2$  Phase in  $\text{Ti}_3\text{Al-Nb}$  Alloys: Artifacts and Facts," *Scripta Metall.*, 24 (1990), 27-32.
7. R. Leucht, K. Weber, H. J. Dudek, W. A. Kaysser, "Processing of SiC-Fibre Reinforced Titanium Parts," *ECCM-7*, (Woodhead Publishing Ltd, Abington, Cambridge, UK 1996), 361-366.
8. J. Kumpfert, "Titanaluminide - eine neue Legierungsklasse für Hochtemperaturanwendungen," *Titan und Titanlegierungen*, Eds. M. Peters, C. Leyens, J. Kumpfert, (DGM, Oberursel 1996), 71-106.
9. M. Thomas, S. Naka, T. Khan, "On the Very High Room-Temperature Ductility Obtained in B2 and/or O-Base Titanium Aluminides," *Titanium '95: Science and Technology*, Eds. P.A. Blenkinsop, W.J. Evans, H.M. Flower (The Institute of Materials, London, UK 1995), 388-395.
10. R. G. Rowe, P. A. Siemers, M. Larsen, "The Effect of Hot Working and Cooling Transformations on the Microstructure and Mechanical Properties of  $\text{Ti}_2\text{AlNb}$ -Based Alloys," *3rd International SAMPE Metals and Materials Processing Conference*, Eds. F.H. Froes, W. Wallace, R.A. Cull, E. Struckholt (SAMPE, Covina, CA 1992), M171-M182.
11. J. Kumpfert, ongoing research, (1997).
12. S. L. Semiatin, P. R. Smith, "Microstructural evolution during rolling of Ti-22Al-23Nb sheet," *Mater. Sci. Eng. A*, A202 (1995) 26-35.
13. L. A. Bendersky, "Modulated Two-Domain Structure of the O Phase Formed in the Ti-25Al-12.5Nb (at.%) Alloy," *Proc. Third International SAMPE Symposium*, Eds. T. Kishi, N. Takeda, Y. Kagawa (Japan Chapter of SAMPE, Japan (1993) 1993), 1507-1512.
14. L. A. Bendersky, W. J. Boettinger, "Phase Transformations in the (Ti, Al)<sub>3</sub>Nb Section of the Ti-Al-Nb System-II. Experimental TEM Study of Microstructures," *Acta Metall.*, 42 7 (1994) 2337-2352.
15. D. B. Miracle, M. A. Foster, C. G. Rhodes, "Phase Equilibria in Ti-Al-Nb Orthorhombic Alloys," *Titanium '95*, Eds. P.A. Blenkinsop, W.A. Evans, H.M. Flower (The Institute of Materials, London, UK, 1995), 372-379.
16. J. Kumpfert, C. H. Ward, M. Peters, W. A. Kaysser, "Thermomechanical Processing, Phase Transformations and Mechanical Properties of Ti-25Al-10Nb-3V-1Mo," *Synthesis/Processing of Lightweight Metallic Materials*, Eds. F.H. Froes, C. Suryanarayana, C.M. Ward-Close (TMS, Warrendale, PA, 1995), 85-96.
17. J. Doychak, "Oxidation Behavior of High-Temperature Intermetallics," *Intermetallic Compounds*, Vol. 1, Principles, Eds. J.H. Westbrook, R.L. Fleischer, (John Wiley and Sons, New York 1994), 977-1016.
18. C. Leyens, M. Peters, W.A. Kaysser, "Oxidation and Protection of Near-Alpha Titanium Alloys," *4th Int. Symp. on High Temp. Corrosion*, (Les Embiez, France, Materials Science Forum, 1996), in press.
19. P. Kofstad, *High Temperature Corrosion* (Elsevier Applied Science, London, New York, 1988).
20. G. Chen, Z. Sun, X. Zhou, "Oxidation and Mechanical Behavior of Intermetallic Alloys in the Ti-Nb-Al Ternary System," *Mater. Sci. Eng. A* 153 (1992), 597-601.
21. C. Leyens, M. Peters, D. Weinem, W.A. Kaysser, "Influence of Long-Term Annealing on Tensile Properties and Fracture of Near- $\alpha$  Titanium Alloy Ti-6Al-2.75Sn-4Zr-0.4Mo-0.45Si," *Metallurgical and Materials Transactions* 27A (1996), 1709-1717.
22. F.-C. Dary, T.M. Pollock, "Effects of High Temperature Air and Vacuum Exposures on the Room Temperature Tensile Behavior of the (O+B2) Titanium Aluminide Ti-22Al-23Nb," *Mater. Sci. Eng. A* 208 (1996), 188-202.



## MICROSTRUCTURE AND MECHANICAL PROPERTIES OF ULTRA SCS<sup>TM</sup> FIBER REINFORCED ORTHORHOMBIC Ti-22Al-26Nb COMPOSITES

A. Chatterjee\*, J.R. Roessler\*, L.E. Brown\*, P.W. Heitman\*, and G.E. Richardson\*\*

\* Allison Engine Company, Indianapolis, IN 46241

\*\* Allison Advanced Development Company, Indianapolis, IN 46241

### Abstract

Titanium aluminide alloys based on the orthorhombic phase Ti<sub>2</sub>AlNb reinforced with silicon carbide fibers have shown promising properties in several metal matrix composite applications. A preliminary study was conducted to assess the mechanical properties of a second generation alloy Ti-22Al-26Nb (atom %) with high strength silicon carbide fibers. Microstructural evaluation showed minimum fiber matrix reactions compared to other composites including titanium aluminides such as Ti-24Al-11Nb and other conventional titanium alloys. Heat treatments studies show that long exposures do not lead to excessive fiber matrix reactions. Tensile, creep, and fatigue tests were conducted on neat and composite specimens. Test results indicate that mechanical properties are superior to other studied titanium metal matrix composite (TMC) systems.

### Introduction

Light, strong, high temperature materials and composites are needed to improve the current thrust to weight ratios, increase performance, and extend the predicted life of compressor and turbine components in advanced propulsion systems. Design analysis and payoff studies have indicated that the use of advanced materials, including titanium based composites, result in weight savings of 30 to 40% in rotating components (compressor and turbine) and up to 20% in static structures such as vanes, cases, liners, and bearing supports.

Significant progress has been made in the development of metal matrix composites with titanium alloys, though application temperatures are currently limited to a maximum use temperature of 550°C. The present technology is inadequate and immature for applications in the 550-750°C range. Orthorhombic titanium composites with high strength fibers are now being proposed as a candidate titanium based composite system capable of achieving the high stress and temperature goals of future aircraft engines.

The advantages of orthorhombic alloys are higher tensile and creep strengths as well as fracture toughnesses compared to  $\alpha_2$  based titanium aluminides. It has been shown that TMC composites having a mixture of the O + B2 +  $\alpha_2$  phases show superior properties over other titanium composites [1]. The most common of the O-TMCs studied has been the

Ti-22Al-23Nb system reinforced with several different silicon carbide fibers like SCS-6<sup>TM</sup>, Amercom<sup>TM</sup>, TriMarc<sup>TM</sup> etc. However, research done at General Electric Company and Allison Engine Company has shown that the Ti-22Al-26Nb alloy would have higher tensile and creep strengths than the Ti-22Al-23 Nb alloy and thus lead to a potentially improved composite material system. In aft compressor disk applications for aircraft engines, burst characteristics are often limited by the tensile and creep properties of the matrix alloy. Therefore, a stronger creep resistant alloy can have a significant impact on the overall engine performance by reducing disk weight and thus specifically impacting the thrust to weight ratios.

### Matrix Microstructures

The high Nb containing Ti<sub>3</sub>Al containing intermetallics were based on the identification of the O phase by Banerjee and co-workers [2] and work at General Electric Company by Rowe et al. [3]. This orthorhombic phase has been shown to be a distortion of the DO<sub>19</sub>  $\alpha_2$  structure, resulting in an ordered orthorhombic symmetry in which the Ti, Al, and Nb atoms occupy specific sub-lattices shown in Fig. 1. Recently Rhodes and Miracle [5] have constructed a pseudo-binary of the Ti-23Al/Nb system shown in Fig. 2. The Ti-22Al-26Nb composition passes through four phase fields as the temperature changes from 1100°C to 650°C. Consequently ingot breakdown and thermomechanical properties are intimately related to the phase evolution and mechanical properties of the individual phases in this complex system. In some instances, such as in the processing of large orthorhombic forgings, which have large amounts of work and are rapidly cooled from above the beta transus, the formation of the  $\alpha_2$  phase may be suppressed and results in a two phase microstructure of an acicular O phase in a B2 matrix [6,7]. However, unlike large forgings that can be rapidly cooled, cold rolling of the Ti-22Al-26Nb foil requires intermediate annealing treatments. Most annealing heat treatments for foil are done in vacuum to prevent oxidation and subsequent grinding losses. This results in slower cooling rates leading to a three phase microstructure in the same Ti-22Al-26Nb alloy and is shown in Fig. 3. The dark, gray, and light phases are the alpha-2, orthorhombic, and beta phases, respectively. The long stringers are presumed to be an  $\alpha_2$  phase that results from microsegregation in the ingot and insufficient ingot breakdown. The kinetics of the phase transformations from the beta phase to the alpha two and orthorhombic phases have been studied and reported by Banerjee et al. [7].

Structural Intermetallics 1997  
Edited by M.V. Nathal, R. Darolia, C.T. Liu, P.L. Martin,  
D.B. Miracle, R. Wagner, and M. Yamaguchi  
The Minerals, Metals & Materials Society, 1997

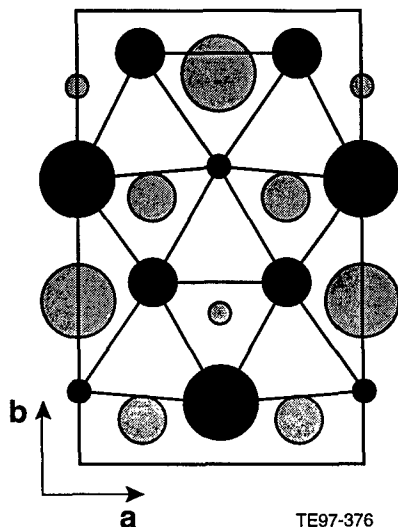


Figure 1: [001] projection of atom layers at  $z=1/4$  (dark) and  $3/4$  (light) of the orthorhombic cell. Small, medium, and large circles represent Al, Ti, and Nb, respectively (from Mozer et al. [4]).

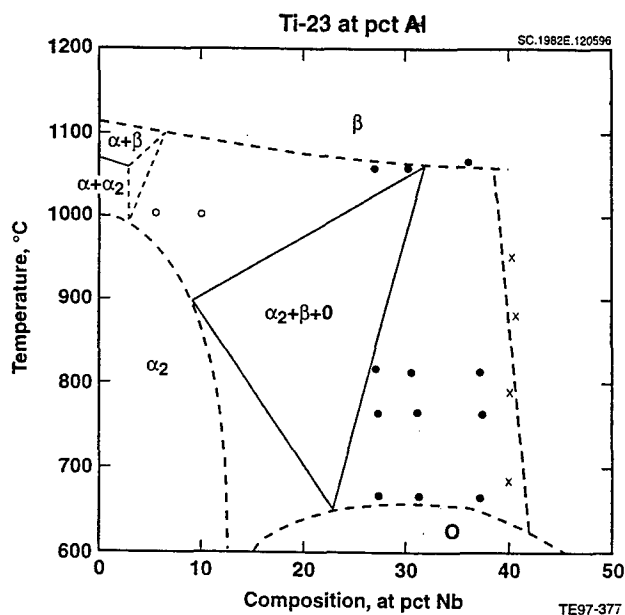


Figure 2: Pseudo-binary phase diagram of the Ti-23Al/Nb system showing the phase boundaries. This diagram is under construction. The dotted lines are mainly speculative at this stage.

#### Materials and Procedure

Fabrication of fiberless ("neat") and composite specimens presented an additional challenge as optimized processing parameters for the conversion of large orthorhombic ingots to foil up to 0.125 mm in thickness have yet to be established. Some of the technical hurdles that needed to be overcome in the rolling of orthorhombic foil are being reported elsewhere in these proceedings [8]. The foil material was made by triple VAR followed by forging into plate, hot rolling to sheet, and then conventional cold mill and Z-Mill rolling to 0.125 mm thick foil.

The silicon carbide based high strength Ultra SCS fiber is manufactured by Textron Specialty Materials. It has a diameter of 0.143 mm and a room temperature ultimate tensile strength of 6.55 GPa [9]. The Ultra

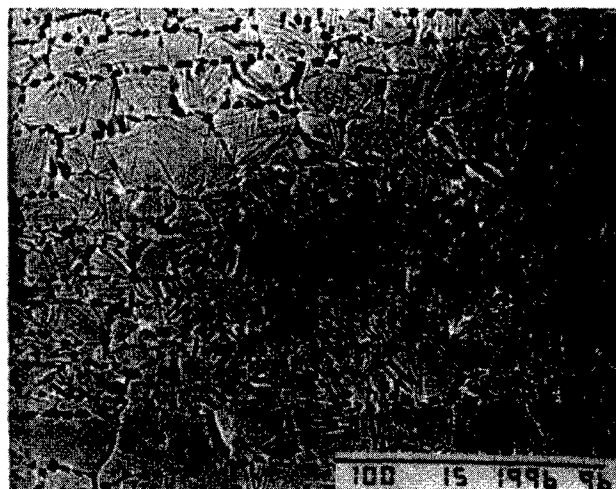


Figure 3: Backscattered SEM microstructure of neat orthorhombic foil showing the three phases. The light, gray, and dark phases are B2, orthorhombic, and  $\alpha_2$ , respectively.

SCS fiber has a 30  $\mu\text{m}$  carbon core and a single pass layer of equiaxed silicon carbide deposited by chemical vapor deposition techniques. This deposition technique is slightly different from the SCS-6 fiber, where the SiC is columnar and deposited in two passes. The surface of the Ultra SCS fiber is then coated with 2-3  $\mu\text{m}$  coating of a proprietary mixture of graphitic carbon and SiC for controlling the interfacial properties. It is the morphology of the CVD silicon carbide and the coating that results in the high strength of this fiber compared to the other available SiC fibers. The modulus of this fiber is 400 GPa, similar to the SCS-6 fiber and most other silicon carbide based fibers. The higher strength, therefore, is a result of the higher strain to failure (1.6% compared to 1% in the SCS-6 fiber). Fig. 4 shows a plot of the strength of the Ultra SCS fiber as a function of temperature. The plot clearly shows that the strength of this fiber exceeds that of the more common SCS-6<sup>TM</sup> fiber at all temperatures.

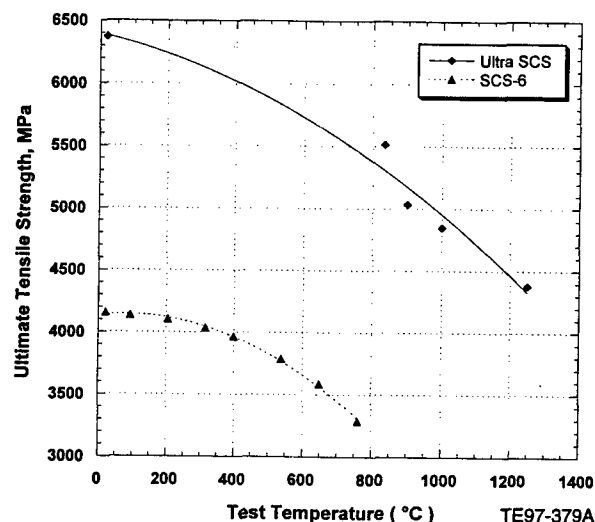


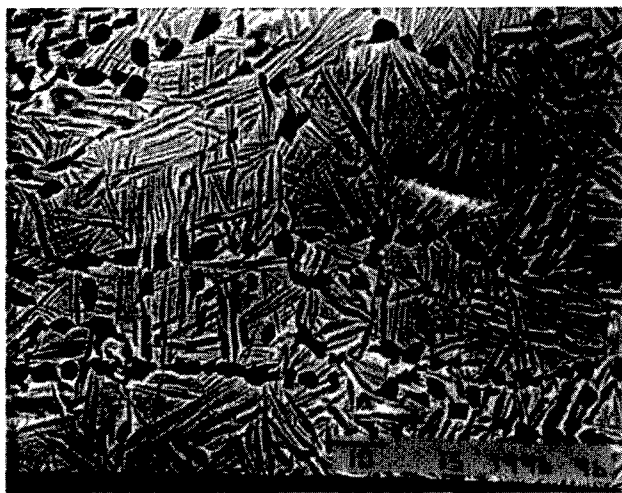
Figure 4: Plot of the tensile strength vs. temperature of the Ultra SCS fiber showing the strength is superior to the SCS-6 fiber at all temperatures.

### Heat Treatment Effects

Typical microstructures of consolidated neat foil and composites are shown in Figs. 5 and 6, respectively. The matrix is a three phase mixture of  $O + \alpha_2 + \beta$  with a distribution of fine and coarse orthorhombic platelets and an ordered B2 phase. The volume fraction of the alpha-two phase was about 15 - 20%. In the Ti-22Al-23Nb system the volume fraction of the three phases seemed to be approximately equal. The fine orthorhombic platelets in the matrix are a result of an aging cycle at 815°C which results in a decomposition of the metastable  $\beta$  phase into the orthorhombic phase. The long stringers are presumed to be  $\alpha_2$  particles that are aligned in the rolling direction of the foil. As shown in Fig. 5, the  $\alpha_2$  particles are stable and seem to decorate the prior beta grain boundaries.

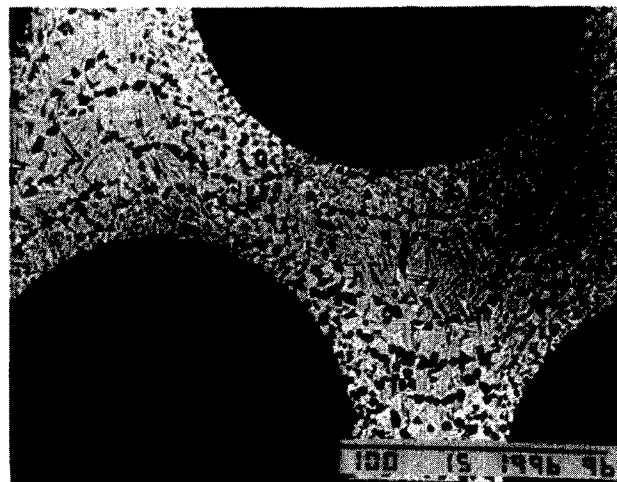
Heat treatment studies have shown that it takes a large excursion into the single phase beta region of the phase diagram shown in Fig. 2 to completely dissolve these  $\alpha_2$  particles. However, on slow cooling from these temperatures, these particles seem to reappear again and are stable at all other intermediate aging and use temperatures. Therefore, getting rid of these stringers involves either very high temperature solution treatments and or fast cooling rates from solution temperatures. However, super transus temperature heat treatments seem to promote excessive beta grain growth and sometimes produced a single grain across the 0.125 mm foil. Past studies in other metal matrix composites have shown that large beta grains result in poor tensile and fatigue properties in the composite. These  $\alpha_2$  bands are also undesirable from a mechanical property standpoint as connected stringers form an easy path for crack nucleation. Efforts are under way at Allison Engine Company to pursue other processing schemes that will avoid the formation of these bands early in the thermomechanical processing of the orthorhombic ingot. Therefore all heat treatment and consolidation studies were conducted in the two and three phase fields of the phase diagram shown in Fig. 2 with corresponding temperatures ranging between 900 and 1050°C.

Similar microstructures to the neat foil were observed in the composite specimens and are shown in Fig. 6. The matrix is a mixture of  $O + B2 + \alpha_2$ . The carbon coating of the SiC fiber promotes the stabilization of the  $\alpha_2$  phase leading to a larger volume fraction of the  $\alpha_2$  phase immediately around the fiber. During heat treatments in the two and three phase fields, the  $\alpha_2$  particles tend to retard beta grain growth by



TE97-380

Figure 5: Higher magnification backscattered micrograph of a consolidated neat foil specimen showing the coarse orthorhombic platelets and the  $\alpha_2$  stringers.

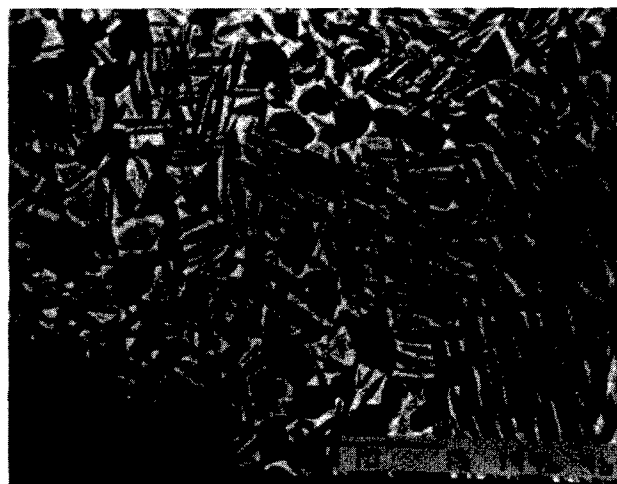


TE97-381

Figure 6: Backscattered photomicrograph of a consolidated composite specimen showing complete bonding. Note a higher concentration of  $\alpha_2$  near the fiber as well as a smaller prior beta grain.

pinning the boundaries. Because of the pinning effects of the  $\alpha_2$  stabilized matrix and larger volume fraction of  $\alpha_2$  particles, the composite specimens had a finer subgrain structure around the fibers. Backscattered photomicrographs shown in Fig. 7 show that the  $\alpha_2$  particles are also surrounded by a rim orthorhombic phase. This rim orthorhombic phase has been observed by other investigators [10]. Away from the fibers, however, the microstructures were similar to the neat specimens. Near surface microstructures had larger prior beta grains than near the fibers as expected due to the reduced stabilization of the  $\alpha_2$  phase and consequent pinning effects.

Fiber matrix reaction studies were conducted on the composite that had been previously consolidated. These specimens were then exposed to a heat treat cycle of 1010°C/4 hours followed by 760°C/10 hours. Other specimens were subjected to similar heat treat cycles and an additional



TE97-382

Figure 7: High magnification photomicrograph showing the decomposition of the  $\alpha_2$  phase forming a "rim" orthorhombic border around the  $\alpha_2$  particles. This rim orthorhombic phase is the gray region around the dark  $\alpha_2$  particles.

heat treatment at 621°C for 300 hours. The reaction zones for the two heat treatments are shown in Figs. 8 and 9. When compared to the as processed structure, there do not seem to be excessive fiber matrix reactions in comparison to the  $\alpha_2 + \beta$  based TMC systems. There were no beta depleted zones or reaction zone cracks that have been observed in the Ti-24Al-11Nb TMC system [11]. After the 300 hour exposure there was additional fiber matrix reaction leading to a larger reaction zone compared to the as processed material. Although a detailed electron microprobe analysis was not carried out of the reaction products, it is expected that the products are complex titanium carbides and silicides, as has been reported extensively in the past [12,13]. The reaction zone size was measured and was approximately 0.48  $\mu\text{m}$  and 0.64  $\mu\text{m}$  for exposures at 760°C /10 hours and 621°C/ 300 hours, respectively. In all these experiments, a portion of the outer graphitic layer of the fiber was consumed after the exposure, but the inner graphitic layer was still intact. It is therefore expected that there would not be any substantial degradation in composite properties if tested after similar exposures.

#### Mechanical Testing

"Neat" and four-ply composite panels were fabricated with Ti-22Al-26Nb (at %) foil and Ultra SCS fiber by hot isostatic pressing. These panels were made by the foil-fiber-foil process whereby alternate layers of foil and fiber are stacked and subsequent hot isostatically pressed for full consolidation. The Ultra SCS fibers were woven into a mat with Ti-Nb as a cross-weave. The foil was oriented such that the rolling direction was perpendicular to the fiber orientation. In the Ti-22Al-23Nb system foil texture has been reported to have a major effect on mechanical properties. The transverse orientation generally has a lower strain to failure compared to the longitudinal rolling direction [14]. All panels had a nominal fiber volume fraction of 0.3. These panels were then sectioned into specimens by electrodischarge machining. The dogboned specimens were 125 mm x 0.9 mm thick. The grip section was 7.5 mm wide and the reduced gage section was 6.25 mm. The specimens were then flash etched to remove the recast layer and then polished by 600 grit paper to remove any scratches and defects prior to testing. Mechanical tests were conducted on dogboned specimens machined from the four-ply neat and composite panels. Miniature ignitor furnaces were used to heat the gage section of the test specimens. Longitudinal tensile tests were conducted at 23°C and 649°C. Low cycle fatigue tests were done at room temperature under load control at a frequency of 0.33 Hz. Creep tests on neat foil and transverse creep tests on composite specimens were also performed as a part of this screening test matrix.

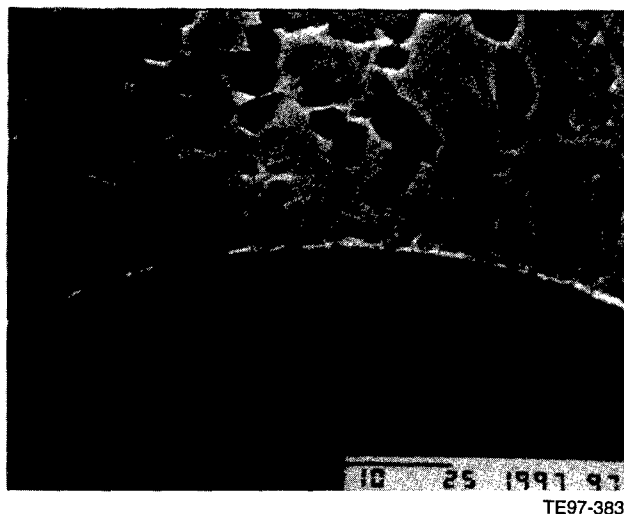
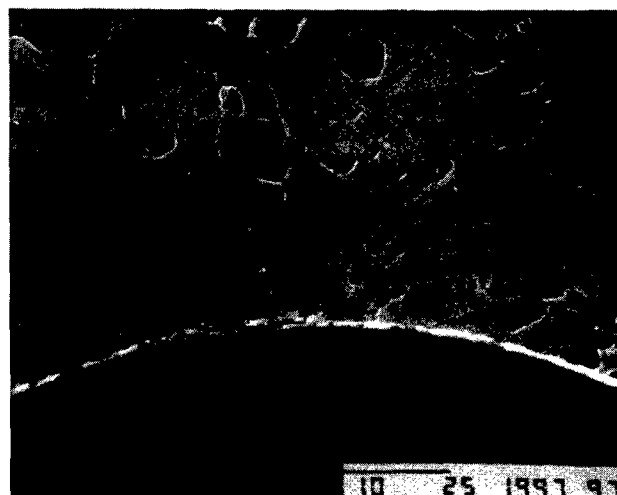


Figure 8: Photomicrograph of the reaction zone between the fiber and matrix after an exposure of 1010°C/4 hours and 760°C/10 hours 2000 X.



a.



b.

TE97-384

Figure 9: Photomicrograph of the reaction zone between the fiber and matrix after an exposure of 1010°C/4 hours and 621°C/300 hours: (a) 2000 X and (b) at 5000 X showing a continuous zone around the fiber; however most of the C/SiC is intact.

#### Tensile Tests

Tensile tests were conducted on the neat foil as well as the composite specimens. All tensile tests were conducted at a strain rate of .001 mm/mm. Fig. 10 shows a plot of tensile strength with temperature for the foil and the composite. In the neat composites the strain to failure was about 19% at room temperature. However, at 649°C the strain at failure decreased to 6%. This loss in ductility has yet to be understood. However, a minimum ductility of only 3% is required for good composite properties. The fracture surfaces of the neat specimens were ductile at both room temperature and 649°C. Figure 11a shows the dimpled fracture surface in a neat specimen tested at 649°C.

The composite specimens had a tensile strength of 1930 MPa at room temperature and 1725 MPa at 649°C. The strain to failure was about 1.25% for both test temperatures, which is a consequence of the higher failure strains of the fiber. Even on a density corrected basis these composites have better tensile properties than the Ti-24Al-11Nb  $\alpha_2 + \beta$  system. Fracture surfaces of the tensile specimens were examined in the

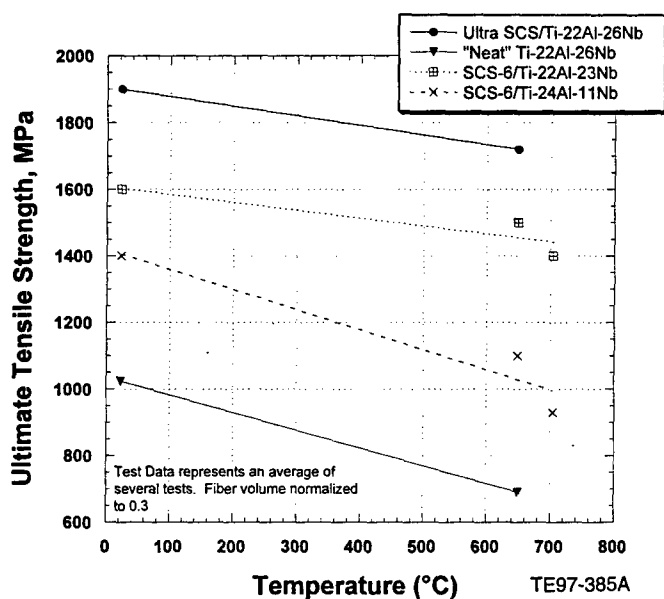
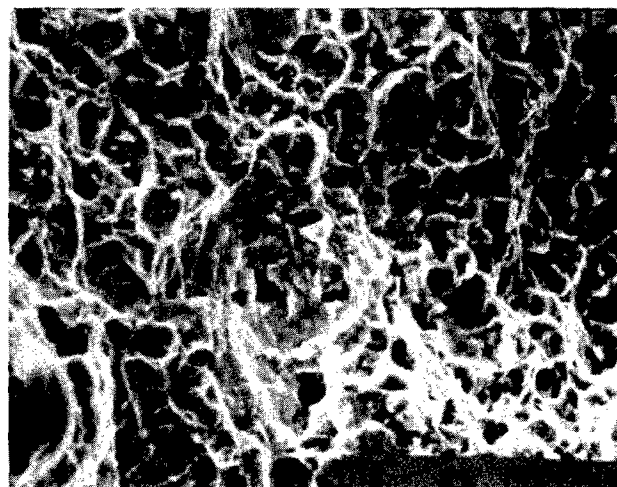


Figure 10: Plot of the tensile data for neat Ti-22Al-26Nb foil and Ti-22Al-26Nb/Ultra SCS composite. The fiber volume fraction is about 0.3.

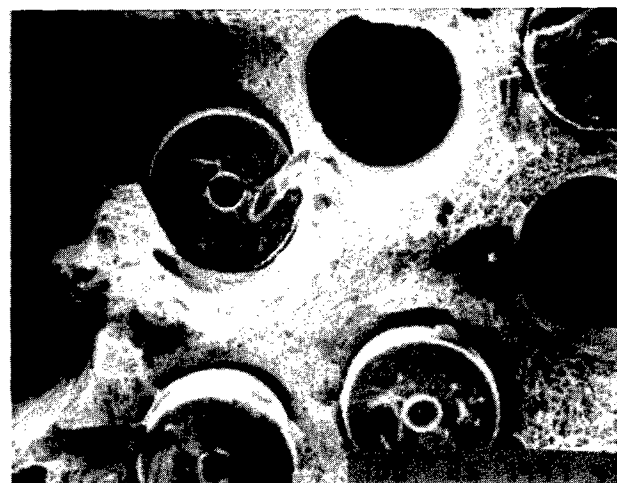
SEM and a typical micrograph is shown in Fig. 11a. There is limited fiber pullout shown in Fig. 11b and the fracture is generally ductile. In situ fiber strengths in the composite were calculated using available micromechanics models. Based on the limited available data on this system, the fiber strength in the composite was calculated to be 4480 MPa at 23°C based on analytical models proposed by He and Curtin [15]. Assuming a Weibull Modulus of  $m = 8$  and single fiber strengths of 6350 MPa and 4140 MPa for Ultra SCS and SCS-6 fibers, the calculated bundle strengths are 4650 MPa and 3175 MPa, respectively. The calculated in situ fiber strengths in this system are clearly higher than any other titanium matrix composite system with ceramic fibers.

#### Low Cycle Fatigue Testing.

An assessment of the low cycle fatigue characteristics of these materials was done by performing load controlled low cycle fatigue (LCF) tests for the "neat" and composite specimens. All tests were conducted at room temperature at an R-ratio = 0 and a frequency of 0.5 Hz. A plot of the stress range vs. life is shown in Fig. 12 for the neat and composite specimens. Fractography showed that there were multiple initiation sites. Most of the initiations were from the surface and the cut fibers on the specimen edges. Fig. 13a and b are lower and higher magnification micrographs showing an initiation site near the surface and evidence of fatigue striations. Since the fracture surfaces were relatively flat with little pullout, there seems to be little evidence of any crack bridging. This is likely because the stress intensity for the uncracked composite region, once the crack front had propagated to the first row, was in a regime where fiber failure would be expected. Thus no fatigue striations were observed once the crack front reached the first row of fibers in this four-ply composite.



a.



b.

TE97-386

Figure 11: Photomicrographs of the fracture surfaces of a tensile specimen tested at 649°C showing (a) a ductile dimpled fracture and (b) limited fiber pullout but generally a ductile failure.

#### Creep Tests

Another key mechanical property that was evaluated was the creep behavior of the foil as well as transverse creep properties of the composite. Creep tests were conducted in air at a temperature and stress ranges of 539 - 648°C and 69 - 414 MPa, respectively. A Larson-Miller plot of the data is shown in Fig. 14. The measured creep behavior is consistent with predictions of the composite creep from "neat" foil data using transverse creep formulations of Crossman and Karlak [16] and Du [17]. In the composite, transverse creep is controlled by the creep properties of the matrix. As shown in Fig. 14, the transverse creep response is independent of the type of fiber (SCS-6 or Ultra SCS). Furthermore, the Ti-24Al-11Nb alloy as well as the orthorhombic alloys have a similar creep response thus resulting in near identical transverse composite creep behavior. The data in this figure has been normalized to a fiber volume fraction of 0.3. Debonding of the fibers from the matrix results in an increase in the matrix stress and corresponding higher creep rates compared to the neat foil. SEM of the failed specimens shows that the fracture is through the matrix as expected. However there seems to be some fiber degradation and coating spallation as shown in Fig. 15.

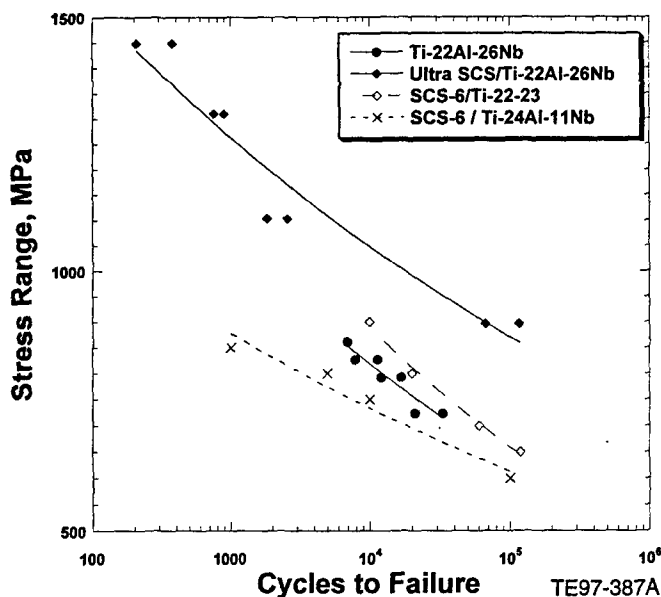


Figure 12: Plot of the low cycle fatigue characteristics of the neat foil and composite at room temperature at R=0 and 0.5 Hz. Fiber volume fraction was 0.3.

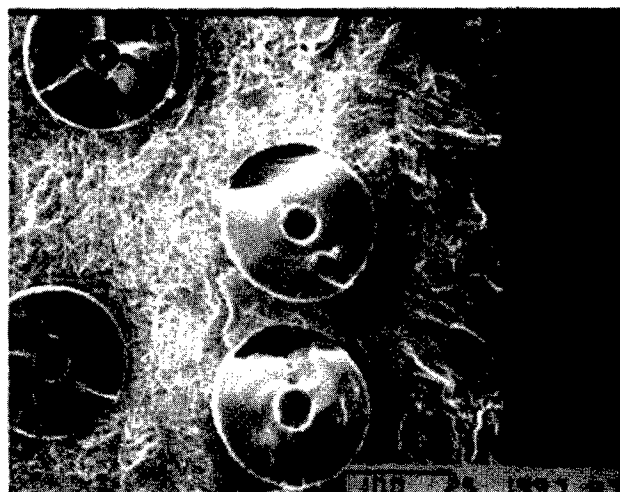
#### Conclusions

A new second generation orthorhombic composite system has been investigated for high temperature turbine engine applications. Some of the results of this study are:

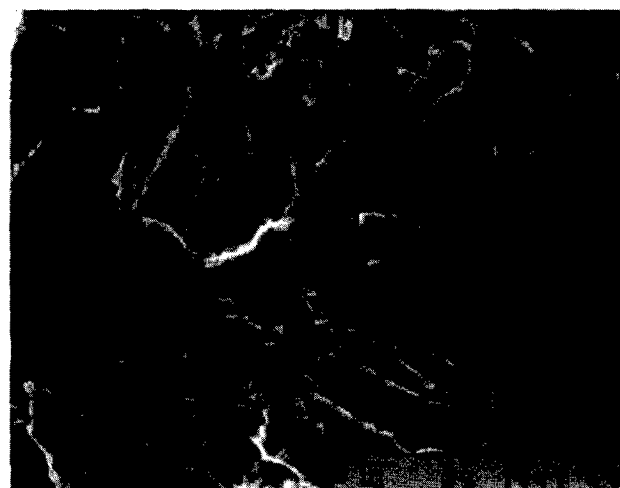
- Neat foil and composite specimens had a three phase microstructure consisting of a mixture of  $\alpha_2 + O + B2$  phases.
- Microstructural evaluation showed minimum fiber matrix reactions compared to other titanium aluminides like the Ti-24Al-11Nb and other conventional titanium alloys.
- After the 300 hour exposure there was additional fiber matrix reaction leading to a larger reaction zone compared to the as processed material. Although a portion of the outer graphitic layer of the fiber was consumed after the exposure, the inner graphitic layer was still intact thus expected to provide adequate composite properties.
- Substantial improvements of properties have been made over the Ti-24Al-11Nb and aluminide systems that have been reported in literature.
- Preliminary mechanical property assessments show adequate properties for aircraft engine applications.

#### Acknowledgments

This work was funded by the Propulsion Directorate of Wright Laboratories, U.S. Air Force under contract F33615-94-C-2410. Capt. Dana Allen is the Contract Monitor.



a.



b.

TE97-388

Figure 13. (a) Fracture surface of a composite specimen that was fatigue tested. One of the surface initiation sites is shown. Note the change in fracture morphology as the crack front reaches the first row of fibers. (b) Fine fatigue striations are visible in the matrix.

#### References

1. P. R. Smith, J. A. Graves, and C.G. Rhodes, Proceedings of the First International Conference on Intermetallics, R. Darolia et al., eds., September 1993, 765 - 771.
2. D. Banerjee, A. K.Gogia, T. K. Nandi and V. A. Joshi, Acta Met, Vol. 36, 1988, 871-882.
3. R. G. Rowe, in High Temperature Intermetallics, S. H.Whang et al. eds., TMS-AIME, Warrendale, PA 1990, 375-401.
4. B. Mozer, L. A. Bendersky, W. J.Boettinger, and R.G. Rowe, Scr. Met., Vol. 24, 1990, 2363-2368.
5. Cecil Rhodes, Rockwell Science Center, and Dan Miracle, USAF; unpublished work.

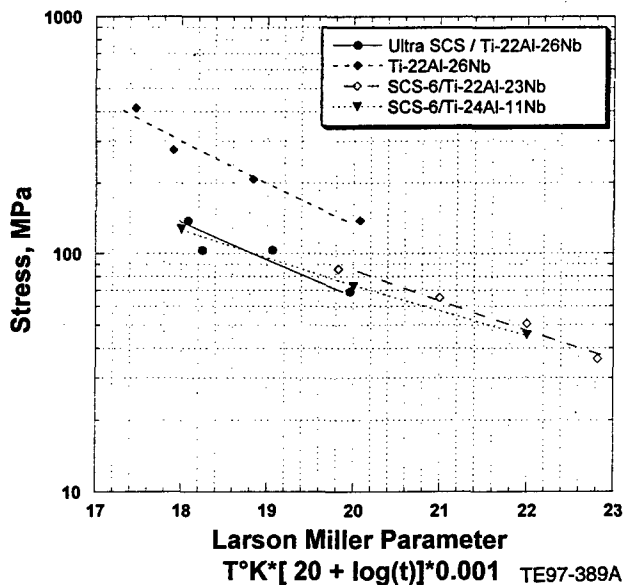
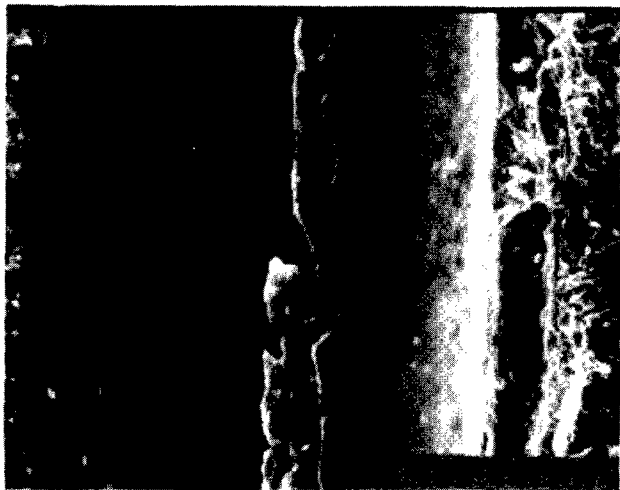


Figure 14: Larson-Miller plot of the creep tests for the neat foil and transverse composites.



TE97-390

Figure 15: Fractograph of a composite specimen tested at 649°C/69 MPa showing damage to the fiber coating at fracture.

6. A. P. Woodfield, Interim Progress Reports, U.S. Navy Contract N686335-93-C-0221.
7. D. Banerjee, A. K. Gogia, T. K. Nandy, K. Muraleedharan, and R.S. Mishra, *Structural Intermetallics*, R Darolia et al. eds., TMS Conference held at Seven Springs, PA, Sept. 26 -30, 1993, 19-34.
8. J. R. Roessler et al., Second International Conference on Structural Intermetallics, Seven Springs, PA 1197, to be published.
9. Al Kumnick, Textron Specialty Materials, private communication.
10. Sheila Woodard, Tresa Pollock, and Francois Dary, WL-TR-95-4068, 124.
11. P.K. Brindley, P.A. Bartollota, and S.J. Klima, NASA TM 100956, 1988.
12. D. Bowden, S. Sastry, and P.R. Smith, *Scripta Met.*, 23, 1989, 407.
13. S. Baumann, P. Brindley, and S. Smith, *Met Trans.*, 21A, 1990, 1559 - 1569.
14. C. G. Rhodes, J. A. Graves, P. R. Smith, and M. R. James, *Structural Intermetallics*, Ram Darolia, ed., TMS Conference held in Seven Springs, PA Sept. 26-30, 1993, 45-52.
15. M. Y. He, A. G. Evans, and W. A. Curtin, *Acta Met.*, 41(3), 871-878.
16. F. W. Crossman, R. F. Karlak, and D. M. Barnett, *Failure Modes in Composites*, TMS-AIME, Warrendale, PA 1974, 8.
17. Z. Z. Du, R. M. McMeeking, and S. Schmauder, submitted to *Mechanics of Materials*.

## MISSION CYCLE BEHAVIOR OF ORTHORHOMBIC TITANIUM MATRIX COMPOSITE

Timothy P. Gabb and John Gayda  
National Aeronautics and Space Administration  
Lewis Research Center  
Cleveland, Ohio

Amit Chatterjee and Robert Ress  
Allison Engine Company  
Indianapolis, Indiana

### Abstract

The objective of this study was to evaluate the fatigue behavior of a unidirectional orthorhombic titanium aluminide matrix composite in realistic compressor conditions. Isothermal fatigue, thermomechanical fatigue, and mission profile fatigue tests were performed at compressor application temperatures and applied stresses. The effects of varying temperature and applied stress on fatigue cyclic response, life, and failure mechanisms were evaluated. The effects of different components of mission cycles were then systematically investigated. It was found that the mission cycles were more damaging than isothermal and classic thermomechanical fatigue tests for a given maximum temperature and maximum applied stress. The thermal and mechanical excursions associated with engine startup and shutdown in the mission cycles combined with the dwell at maximum temperature and stress were found to reduce life. This deficit appeared to be associated with stress relaxation of the matrix and subsequent load shedding to the fibers.

### Introduction

The fatigue failure mechanisms among titanium and titanium aluminide matrix composites (TMC) have many commonalities (ref. 1). In numerous cases, fatigue failure mechanisms in TMCs can be related to the matrix properties. For example, at high applied stresses the composite properties can deviate from rule-of-mixture approximations as matrix plastic yielding shifts additional loads onto the fibers. Similarly, at high temperatures cyclic stress relaxation can

also occur in the matrix during early cycling (ref. 2), shifting additional load to the fibers in load controlled fatigue tests. This can cause early fiber-dominated failures in isothermal fatigue and in-phase thermomechanical fatigue (refs. 3 to 5). In addition, the environment can oxidize and embrittle the matrix surface at high temperatures (ref. 6), promoting accelerated matrix surface cracking in thermal cycling (ref. 7), isothermal fatigue (ref. 8), and out-of-phase thermomechanical fatigue (refs. 3, 5, 8, 9). Based on these observations, one can hypothesize that improved matrix properties could benefit composite fatigue resistance. Orthorhombic titanium aluminide alloys are of particular interest due to their high tensile and creep strength compared to other titanium alloys (ref. 10). Initial evaluations of orthorhombic matrices in TMCs indicated high tensile strength and improved resistance to thermal cycling damage (ref. 11). Based on these encouraging results, orthorhombic alloys could offer benefits as matrix alloys in unidirectional TMCs (refs. 12, 13) for compressor applications.

The use of unidirectional 0° titanium matrix composites (TMC) as reinforcing rings within compressor rotors could result in significantly reduced weight of these components (ref. 12). In service these TMC reinforcing rings would be subjected to complex service mission loading cycles. Since compressor rotor durability is often limited by fatigue damage induced by mission cycle loading, it is imperative that the TMC fatigue failure modes operative in such loading be fully understood. The failure modes of TMCs in such applications are not yet fully characterized. Results to date (ref. 14) indicate missions can produce greater damage and lower life than



isothermal tests at the same maximum temperature and applied stress. Isothermal tests are therefore not conservative predictors of mission life in such applications, and mission cycle tests appear necessary to assess the durability of TMCs in compressor rotors.

The objective of this investigation was to evaluate the fatigue behavior of SCS-6/Ti-22Al23Nb (at. %) orthorhombic TMC in realistic compressor mission conditions. The realistic stress-temperature capabilities of this composite and life limiting material parameters were then determined.

### Materials and Procedure

The composite consisted of Ti-22Al-23Nb(at.%) foil and unidirectional SCS-6 silicon carbide fiber mat containing Ti-Nb ribbon cross weave to hold the fibers in place.  $[0]_4$  layups were consolidated using hot isostatic pressing to produce several panels having 41v/o fiber reinforcement. Specimens having reduced midsections were machined by abrasive water jet or electro-discharge machining. The edges of the gage sections were then diamond polished to remove machining damage. Displacement controlled tensile tests and load controlled isothermal fatigue tests were performed by Allison using a servohydraulic test system employing induction heating. Additional load controlled isothermal fatigue tests and all load controlled mission tests were performed at NASA LeRC using a servohydraulic fatigue test system with quartz lamp heating. Isothermal fatigue tests for initial screening were performed at 0.33 Hz and stress ratios of 0 and 0.1 at temperatures of 428 °C to 705 °C. Failure was defined as complete specimen separation. Fractographic investigations were then performed.

### Results and Discussion

**1. Initial Monotonic and Fatigue Evaluations** A typical cross section of a composite specimen is shown in Fig. 1. The matrix microstructure, shown in the as-consolidated condition tested

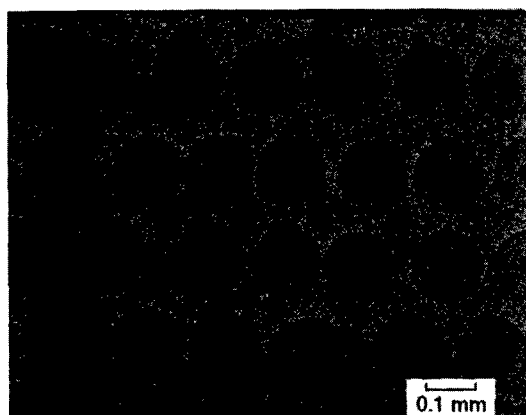


Figure 1.—Typical cross section of a SCS-6/Ti-22Al-23Nb(at.%) composite panel.

here, consisted of about 30%  $\alpha_2$ , 40% orthorhombic, and 30% ordered  $\beta$  phases. Chemical analyses of the composite panel gave an actual composition of Ti-10.4 Al-39.4 Nb-0.105 O-0.011 N- 0.00006 H in wt. % (Ti-20.7Al-22.8Nb in at. %). The results of single tensile tests performed at 25, 427, 566, and 705 °C indicate the composite had good tensile strengths of 1980 MPa at room temperature to 1360 MPa at 705 °C. These tensile results compare well with other tensile data generated on similar orthorhombic TMCs (refs. 10 and 14).

Isothermal fatigue tests were first performed at a frequency of 0.33 Hz to screen fatigue behavior. After initial inelastic yielding on cycle 1, the stress-strain hysteresis loops were nominally elastic at maximum stresses of 70-900 MPa. At stresses of 1035 MPa and higher, inelastic strain was apparent on subsequent cycles. In these load controlled tests, the strain range and maximum amplitude were fairly stable after initial cycling in all tests at 427 °C and low stress tests at 566 °C. However, some increase in maximum strain occurred at high stresses at 538 °C, and at all stresses at 705 °C, as illustrated in Fig. 2 for  $\sigma_{max} = 1100$  MPa. Isothermal fatigue lives are plotted versus maximum applied stress ( $\sigma_{max}$ ) in Fig. 3. Isothermal fatigue life did not exhibit a temperature dependence in tests at 427 and 705 °C near stresses of 750 MPa, but decreased in tests at the higher temperatures of 538 and 705 °C for stresses over 930 MPa, where the strain ratcheting became significant. The fracture surfaces and extent of fatigue cracking were evaluated by optical and scanning electron microscopy. Fatigue cracked areas were macroscopically flat due to matrix cracking, while specimen sections failed in final overload were more irregular due to ductile matrix failure. The strain ratcheting and lower lives were accompanied by a reduction in the percentage of cross sectional area which failed by fatigue cracking, from 61% at 427 °C to 19% at 705 °C in tests at  $\sigma_{max} = 1100$  MPa as

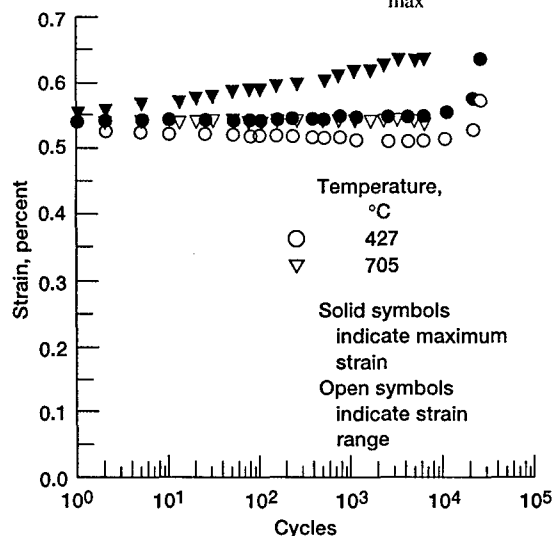


Figure 2.—Strain range and maximum strain versus cycles during isothermal fatigue tests at 427 and 705 °C ( $\sigma_{max} = 1105$  MPa;  $f = 0.33$  Hz).

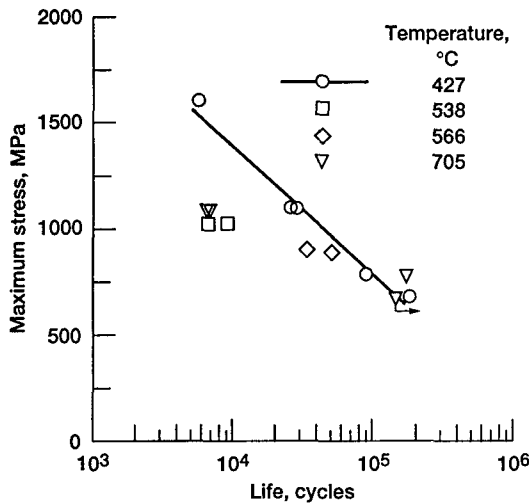


Figure 3—Isothermal fatigue life versus maximum applied stress ( $f = 0.33$  Hz).

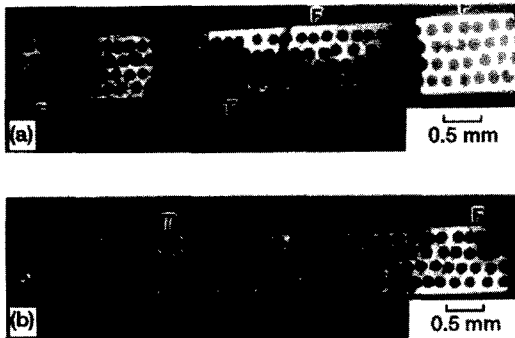


Figure 4.—Fatigue cracking in isothermal fatigue specimens tested at  $\sigma_{\max} = 1105$  MPa: (a) 427 °C, 61 percent fatigue cracking; (b) 705 °C, 19 percent fatigue cracking; F-fatigue cracking and T-tensile failure indicated in figures.

shown in Fig. 4. Evaluation of the fracture surfaces and secondary cracks indicated fatigue cracks initiated in all isothermal tests at damaged fibers exposed along the specimen edges and only infrequently at machining defects along the specimen face. Typical edge-initiated secondary cracks are shown in Fig. 5, from longitudinal sections prepared perpendicular to the thickness of specimens tested at low (a) and high (b) stresses. Both matrix and fibers were cracked in these instances, but matrix cracks were more numerous and often oriented in coincidental lines normal to the load axis, suggesting a continuous macroscopic crack. The lower life in high stress, high temperature conditions appeared related to cyclic stress relaxation of the matrix, which shifts additional load to the fibers (ref. 3). Assuming uniform strain across the composite cross section, the increase in fiber stress produces an increase in maximum fiber and composite strain amplitude. This increased fiber stress can overload the fibers at high applied composite stresses. The edge cracks in these low life, high temperature tests were shorter than that at lower temperatures, with both fiber and matrix cracking.

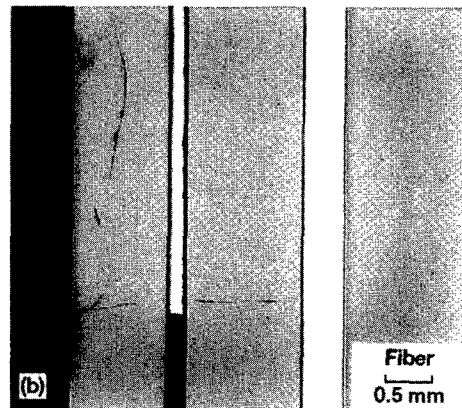
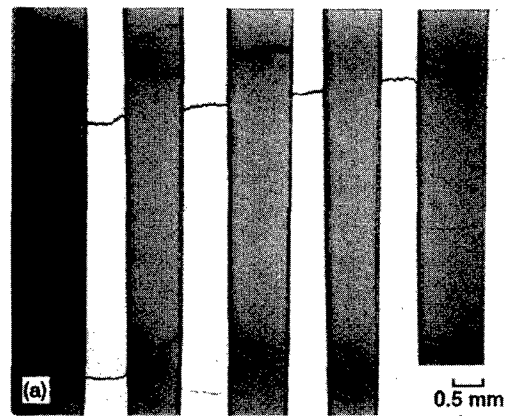


Figure 5.—Secondary fatigue cracks in longitudinal sections of isothermal fatigue specimens tested at (a) 427 and (b) 705 °C,  $\sigma_{\max} = 1105$  MPa. Loading axis oriented vertically.

In summary: 1) fatigue cracks usually initiated at damaged edge fibers in these conventional isothermal fatigue tests; 2) reduced life at higher temperatures and stresses was associated with ratcheting of maximum strain and reduced fatigue cracking.

**2. Baseline Mission** The Allison baseline mission cycle was designed to simulate in a simplified manner aircraft engine operation (ref. 12). The mission, illustrated in Fig. 6, is made up of a "Type I" cycle and "Type III" subcycles. The Type I cycle represents starting the engine, accelerating and stabilizing at maximum engine power at the beginning of an aircraft mission, and later shutting down the engine at the end of an aircraft mission. This cycle is simulated in the mechanical test specimen by an excursion from minimum temperature and zero stress through maximum temperature ( $T_{\max}$ ) and maximum applied stress ( $\sigma_{\max}$ ), with a cyclic stress ratio ( $R_{\sigma}$ ) of zero. Type III subcycles represent going from engine idle to maximum power, stabilizing at maximum power, then returning to idle at different times during a mission. This cycle is simulated in the mechanical test specimen by an excursion from intermediate stress and temperature through  $T_{\max}$  and  $\sigma_{\max}$  with  $R_{\sigma} = 0.5$ . One total mission cycle is composed of one Type I and six Type III subcycles. Baseline conditions of

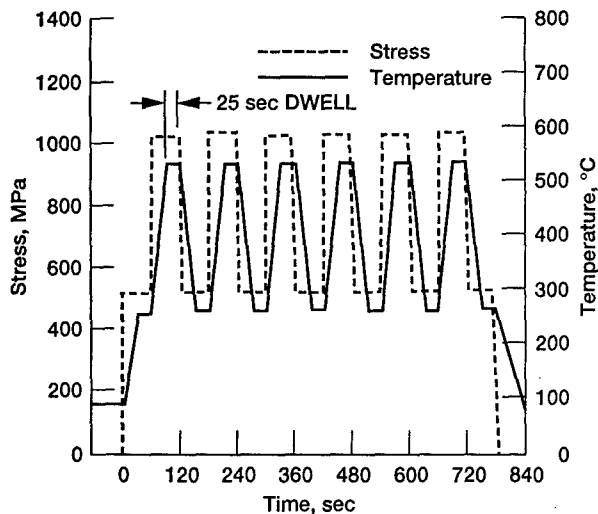


Figure 6.—Applied stress and temperature versus time in the Allison baseline mission cycle.

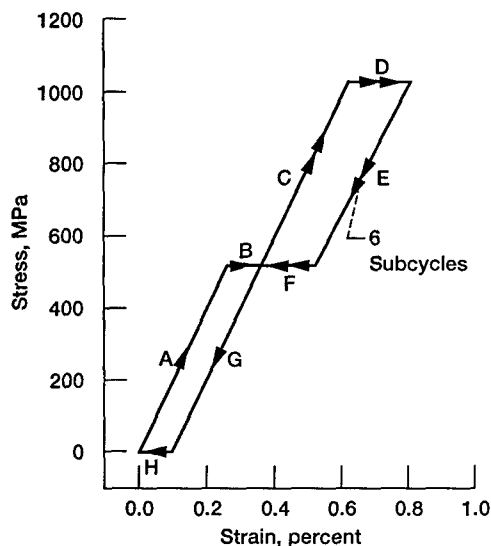


Figure 7.—A typical stabilized stress-strain hysteresis loop of the baseline mission cycle (A: load at 93 °C, B: heat to 260 °C, C: load at 260 °C, D: heat to 538 °C + DWELL at  $\sigma_{max}$ ,  $T_{max}$ , E: unload at 538 °C, F: cool to 260 °C, G: unload at 260 °C, H: cool to 93 °C).

$\sigma_{max} = 1035$  MPa and  $T_{max} = 538$  °C were chosen for detailed evaluations. A typical stabilized stress-strain hysteresis loop is shown with segment descriptions in Fig. 7. The durability target of this mission was 3000 mission cycles, producing 150 hours at  $T_{max}$  and 125 hours at  $T_{max}$  and  $\sigma_{max}$ . Average baseline mission life of triplicate tests was 1235 cycles, which was significantly lower than the average isothermal life of 8149 cycles. The mission encouraged more ratcheting of maximum strain than an isothermal test at  $T_{max} = 538$  °C and  $\sigma_{max} = 1035$  MPa, as shown in Fig. 8. Although fatigue cracks initiated at damaged edge fibers in the mission test, mission cycling reduced the percentage of fatigue cracked area from the isothermal case as shown in Fig. 9. The edge cracks appeared to propagate through both the matrix and fibers, but

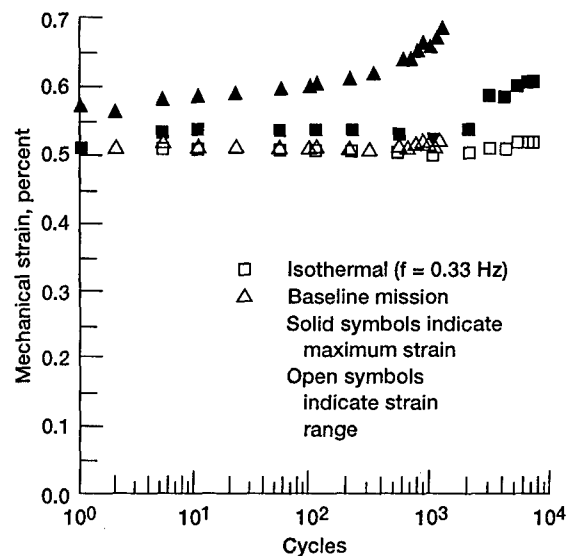


Figure 8.—Mechanical strain range and maximum mechanical strain versus cycles for isothermal and baseline mission tests at  $\sigma_{max} = 1035$  MPa,  $T_{max} = 538$  °C.

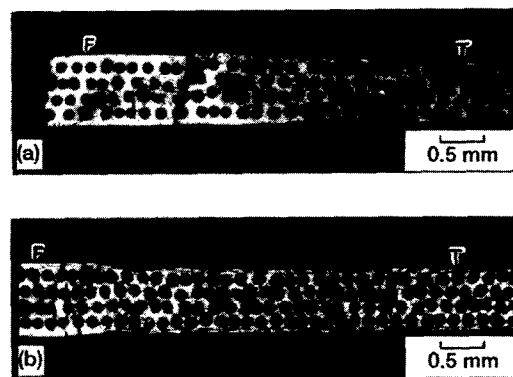


Figure 9.—Fatigue cracking in fatigue specimens tested at  $T_{max} = 538$  °C,  $\sigma_{max} = 1035$  MPa: (a) isothermal fatigue, 29 percent fatigue cracking; (b) baseline mission, 13 percent fatigue cracking; F-fatigue cracking and T-tensile failure indicated in figures.

other independent fiber and matrix cracks were also observed, as shown in Fig. 10.

Design considerations indicated  $T_{max}$  of at least 483 °C and  $\sigma_{max}$  of at least 930 MPa were necessary for this rotor application. Therefore, additional mission tests were performed with  $T_{max} = 483$  °C and 593 °C and  $\sigma_{max} = 930$  MPa and 1035 MPa to determine the temperature and stress dependence of mission life. As shown in Fig. 11, mission life varied with maximum stress and temperature. Mechanical strain range was stable after shakedown in the first two cycles, and did not vary appreciably with  $T_{max}$  in these tests. The ratcheting of maximum mechanical strain with cycling was a strong function of temperature, as shown in Fig. 12. Mission life increased with decreasing  $T_{max}$  and  $\sigma_{max}$ , and the target life could be achieved at 483 °C/1035 MPa and 538 °C/930

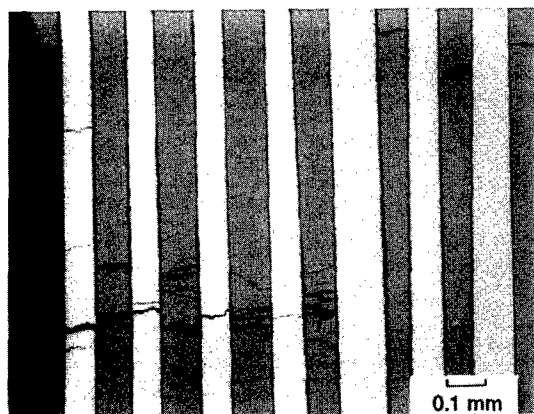


Figure 10.—Secondary fatigue cracks in longitudinal section of a specimen tested in the baseline mission at  $T_{\max} = 538^{\circ}\text{C}$ ,  $\sigma_{\max} = 1035\text{ MPa}$ .

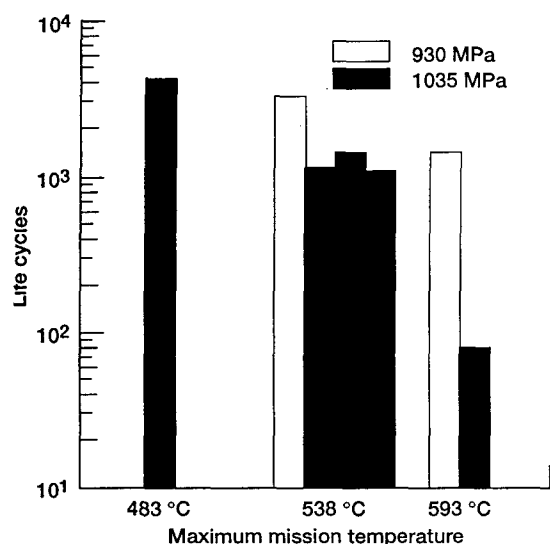


Figure 11.—Variations of baseline mission life with maximum applied stress and maximum temperature.

MPa. The combination of  $483^{\circ}\text{C}/930\text{ MPa}$  should also meet the durability requirements with even greater margin than demonstrated.

In summary: 1) baseline mission life was reduced from conventional isothermal life; 2) baseline mission life increased with decreasing  $T_{\max}$  and  $\sigma_{\max}$ , and could meet the durability targets.

### 3. Effects of Individual Mission Characteristics on Fatigue Life

The baseline mission cycle had many unique characteristics which could cause the reduction in life from isothermal levels. Thermomechanical fatigue, subcycling, and dwells at maximum stress and temperature were present in each mission cycle. Therefore, the effects of each of these characteristics on life were independently evaluated. Thermomechanical fatigue (TMF) effects on life were independently assessed using conventional in-phase and

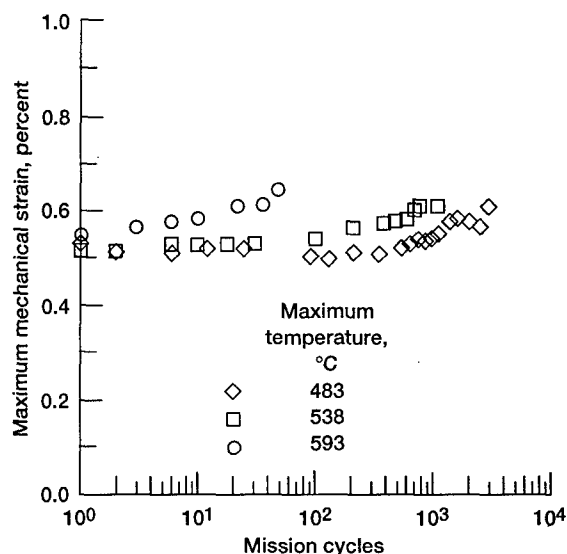


Figure 12.—Maximum mechanical strain versus cycles in baseline mission tests at  $\sigma_{\max} = 1035\text{ MPa}$ .

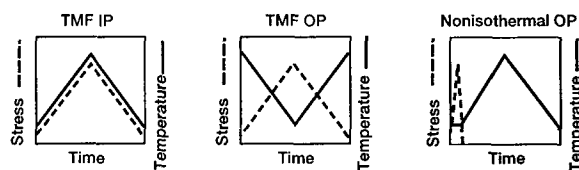
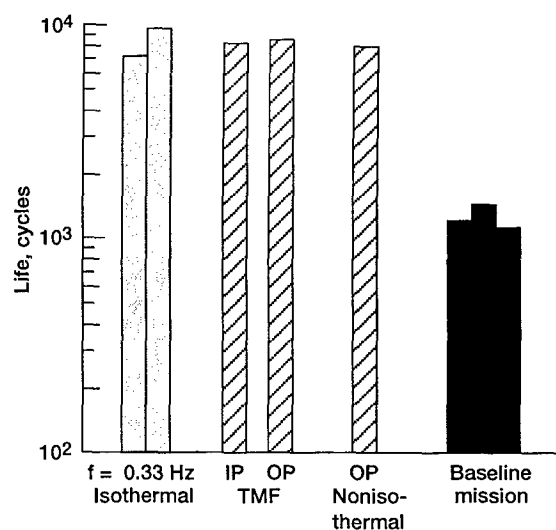


Figure 13.—Comparison of fatigue lives in isothermal, nonisothermal, thermomechanical fatigue, and baseline mission tests ( $\sigma_{\max} = 1035\text{ MPa}$ ,  $T_{\max} = 538^{\circ}\text{C}$ ).

out-of-phase TMF tests with  $\sigma_{\max} = 1035\text{ MPa}$ ,  $T_{\max} = 538^{\circ}\text{C}$ , and minimum temperature of  $93^{\circ}\text{C}$ . A nonisothermal out-of-phase test (ref. 13) was also performed using these same parameters. These lives are compared in Fig. 13 to the baseline mission and isothermal lives. Out-of-phase TMF and nonisothermal lives were comparable to isothermal life, while the in-phase test was interrupted at a comparable number of cycles. Therefore, this composite was not sensitive to

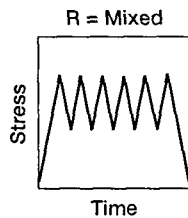


Figure 14.—Applied stress versus time of an isothermal subcycling fatigue experiment at  $T_{\max} = 538^{\circ}\text{C}$ ,  $\sigma_{\max} = 1035\text{ MPa}$ .

conventional TMF effects in these conditions, and TMF effects did not explain the low mission life. The baseline mission had combined Type I and Type III subcycles which mixed the  $R_{\sigma}$  ratio. The effects of mixed  $R_{\sigma}$  were independently assessed in isothermal fatigue test cycles at 0.33 Hz and  $538^{\circ}\text{C}$ , with  $\sigma_{\max} = 1035\text{ MPa}$ . A test with a constant  $R_{\sigma} = 0.5$  had a very long life of 101,332 cycles. A simple isothermal subcycling experiment illustrated in Fig. 14 with one cycle at  $R_{\sigma} = 1$  and six cycles with  $R_{\sigma} = 0.5$  had a life of 6230 blocks. These results indicated load subcycling produced slight additional damage which could be accounted for using Miner's linear fraction damage rule, but did not explain the lower baseline mission life. The baseline mission also had isothermal dwells of 25 sec at  $T_{\max}$  and  $\sigma_{\max}$  within each Type III subcycle. This produced a total time at  $T_{\max}$  and  $\sigma_{\max}$  of 150 sec per mission. The effects of isothermal dwells were independently assessed using an isothermal fatigue test at  $538^{\circ}\text{C}$  with a 150 sec dwell at  $\sigma_{\max} = 1035\text{ MPa}$ . This test produced a life of 2100 cycles, which was longer than the mission life but significantly lower than the standard isothermal life at 0.33 Hz. This result indicated such isothermal dwells significantly reduce fatigue life, but could not in themselves fully explain the baseline mission life.

In summary, 1) no individual mission characteristic could explain the low life of the baseline mission; 2) dwells at  $\sigma_{\max}$  significantly reduced isothermal fatigue life.

**4. Effects of Simple Combinations of Mission Characteristics on Fatigue Life** These relatively simple isothermal and conventional TMF tests indicated no single characteristic of the mission cycle fully accounted for the low mission life. Isothermal dwells were shown to be most damaging to life, while isothermal load subcycling produced only slight life reductions, and conventional TMF produced no clear reductions from isothermal 20 cpm life. Therefore, simple combinations of these mission characteristics needed to be evaluated. The NASA generic mission cycle shown in Fig. 15 was designed to evaluate the combination of the basic Type I cycle with dwells at  $\sigma_{\max}$  and  $T_{\max}$ . This generic mission cycle represents only engine start, acceleration and operation at maximum power, and engine shutdown. This is simulated in the mechanical test specimen by an excursion from minimum temperature and zero stress through  $T_{\max}$  and  $\sigma_{\max}$ , with

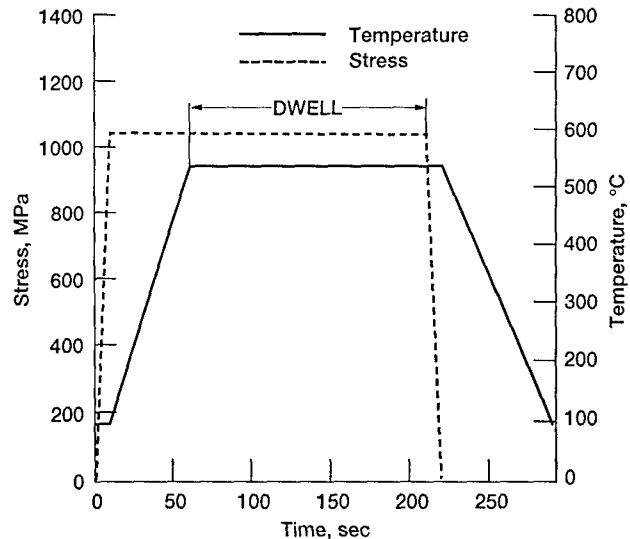


Figure 15.—Applied stress and temperature versus time in the NASA generic mission cycle.

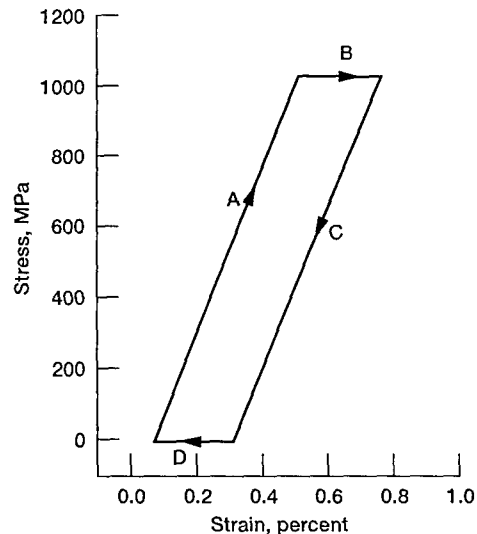


Figure 16.—A typical stabilized stress-strain hysteresis loop of the generic mission cycle with segment descriptions (A: load at  $93^{\circ}\text{C}$ ; B: heat to  $538^{\circ}\text{C}$  + DWELL at  $\sigma_{\max}$ ,  $T_{\max}$ ; C: unload at  $538^{\circ}\text{C}$ ; D: cool to  $93^{\circ}\text{C}$ ).

$R_{\sigma} = 0$ . This cycle begins with TMF out-of-phase loading characteristics ( $\sigma_{\max}$  applied at minimum temperature), and ends with TMF in-phase loading characteristics ( $\sigma_{\max}$  applied at maximum temperature). Dwells at  $\sigma_{\max} = 1035\text{ MPa}$  and  $T_{\max} = 538^{\circ}\text{C}$  of various times were imposed. A typical stabilized stress-strain hysteresis loop is shown in Fig. 16. The lives are compared in Fig. 17. Generic mission life with no dwell was 1843 cycles and strongly decreased with increasing dwell time at  $\sigma_{\max}$  and  $T_{\max}$ . A dwell of 150 sec produced a life of only 100 cycles, compared to a life of 2100 cycles for the isothermal test with the same dwell. This indicated baseline mission life was largely limited by the Type I cycle, in combination with dwells at  $\sigma_{\max}$  and  $T_{\max}$ .

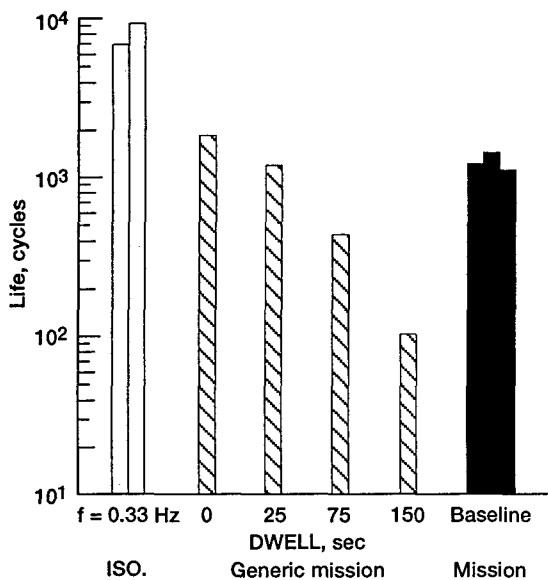


Figure 17.—Comparison of fatigue lives in isothermal fatigue, generic mission, and baseline mission tests ( $\sigma_{\max} = 1035$  MPa,  $T_{\max} = 538$  °C).

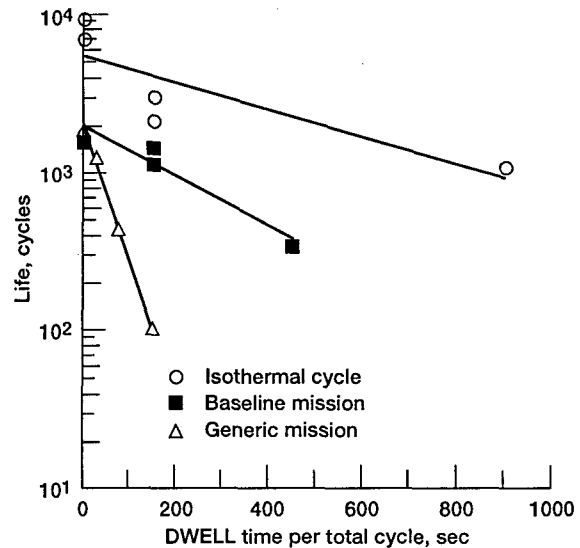


Figure 18.—Fatigue life versus dwell time in isothermal fatigue, generic mission, and baseline mission tests ( $\sigma_{\max} = 1035$  MPa,  $T_{\max} = 538$  °C).

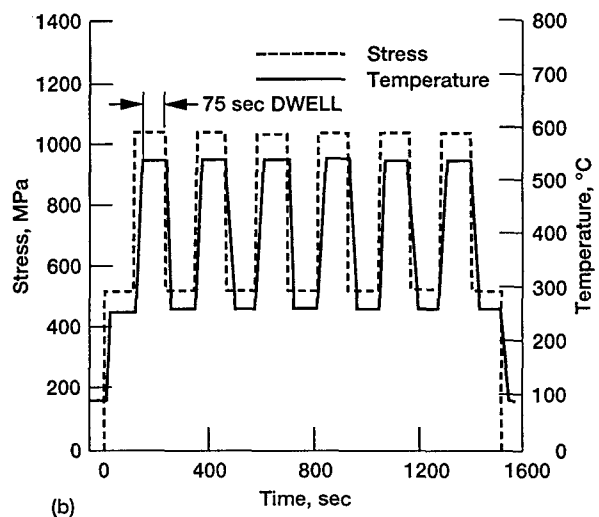
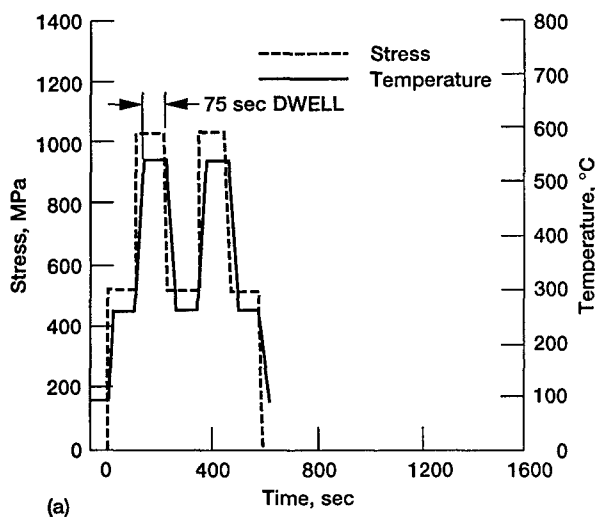


Figure 19.—Applied stress versus time in modified mission tests having two and six Type III subcycles, with a 75 sec dwell at  $T_{\max} = 538$  °C,  $\sigma_{\max} = 1035$  MPa in each subcycle.

In summary, 1) baseline mission life appeared to be largely limited by the Type I cycle; 2) dwells at  $T_{\max}$  and  $\sigma_{\max}$  significantly reduced generic mission life.

**5. Effects of Dwells and Type III Subcycling on Baseline Mission Life** These results indicate a strong impact of dwell time on baseline mission life. Additional baseline mission tests were performed with  $\sigma_{\max} = 1035$  MPa and  $T_{\max} = 538$  °C, with the dwell time changed to 0 or 75 sec in each Type III subcycle. Baseline mission life only slightly improved when the dwell was eliminated. But life sharply decreased to 335 cycles when the dwell in each Type III subcycle was increased to 75 sec. The effects of dwells on isothermal, generic, and

baseline mission lives are compared in Fig. 18. Lives decreased with increasing dwell times according to a semi-log relationship. Dwell effects were more severe in the mission tests than isothermal tests. However, the impact of dwells was less severe in the baseline mission than in the generic mission. This was apparently due to interactions between Type III subcycles and Type I cycle-dwell damage accumulation. Evaluations of the effects of Type III subcycling on mission life were necessary.

The effects of Type III subcycling were first probed by running a baseline mission test incorporating only two Type III subcycles having a dwell time of 75 sec in each subcycle.

This allowed a comparison of mission life with two and six Type III subcycles with the same 75 sec dwell time in each subcycle, as shown in Fig. 19. The NASA generic mission cycle with the 75 sec dwell represented Type I life with a single 75 sec dwell and no subcycling. Life increased from 421 cycles for the generic cycle with one 75 sec dwell to 1517 cycles with the imposition of just two Type III subcycles with 75 sec dwells. The total time at  $T_{max}$  and  $\sigma_{max}$  in this test was  $2 \times 75 = 150$  sec, the same total time at  $T_{max}$  and  $\sigma_{max}$  per mission as that in the generic mission cycle with a 150 sec dwell having a life of only 100 cycles. This surprisingly indicated that the Type III subcycling increased rather than decreased mission life in the presence of dwells. However, the beneficial effects of subcycling were not linearly cumulative. Baseline mission life with six Type III subcycles each having a 75 sec dwell in each subcycle was reduced back down to 335 cycles. These Type III subcycling effects clearly ruled out simple dwell time summation methodologies for predicting mission life.

An important question in evaluating Type III subcycling effects is whether both load and temperature subcycling produce the beneficial effects. Two baseline mission experiments with  $\sigma_{max} = 1035$  MPa,  $T_{max} = 538$  °C, and 25 sec Type III dwell were performed in which Type III load and temperature subcycling effects were isolated, while maintaining the normal Type I load and temperature cycling. In one test, the Type III temperature subcycling was performed while maintaining a constant stress of 1035 MPa. This test had a life of only 205 cycles. In the other test, the Type III load subcycling was performed while maintaining a constant temperature of 538 °C. This test had a life of 1315 cycles, comparable to the normal baseline mission. These results indicated Type III load subcycling had a beneficial effect on mission life, and that the Type III temperature subcycling did not strongly impact mission life.

In summary, 1) baseline mission life decreased with increasing dwell time at  $T_{max}$  and  $\sigma_{max}$ ; 2) Type III load subcycling improved mission life.

**6. Matrix Response During Mission Cycling** Mission life was temperature and dwell time dependent, and induced increased ratcheting of maximum strain and reduced fatigue cracking. This could be associated with matrix relaxation and subsequent load shedding to the fibers. If one assumes constant strain conditions across the composite cross section, axial matrix response within the composite can be inferred by imposing the axial mechanical strains observed in composite tests on unreinforced matrix specimens. Therefore, stress relaxation tests were performed on unreinforced matrix specimens, in order to help understand the behavior of the matrix within the composite in the mission tests. Monotonic constant strain tests were performed at temperatures of 428-595 °C and an imposed strain of 0.54%, which was typical of the maximum

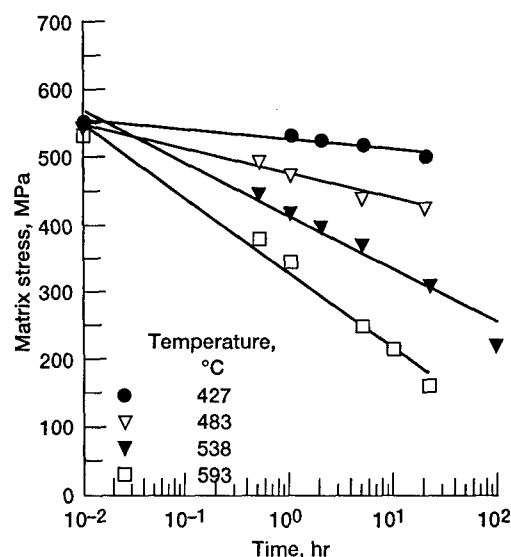


Figure 20.—Stress versus time in monotonic strain-controlled stress relaxation tests of matrix specimens.

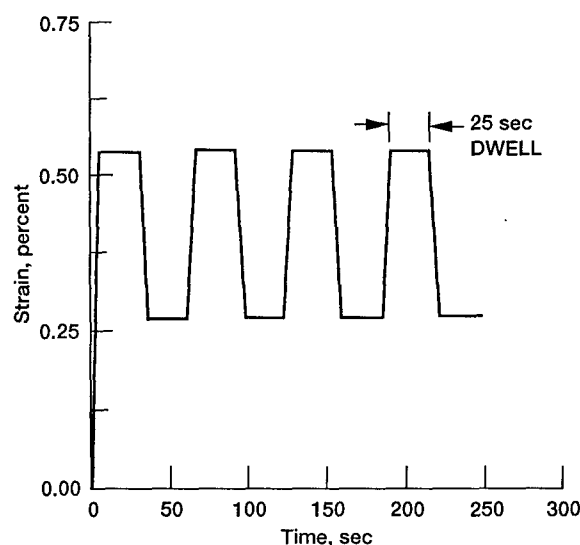


Figure 21.—Imposed strain versus time in cyclic stress relaxation tests of matrix specimens (temperature = 538 °C,  $\epsilon_{max} = 0.54$  percent,  $\epsilon_{min} = 0.27$  percent).

mechanical strain in the composite mission tests. The results of these tests are shown in Fig. 20 and show relaxation to strongly increase with increasing temperature. As Type III subcycling of load appeared to benefit mission life, cyclic strain controlled tests were also performed on unreinforced matrix specimens. These tests imposed the mechanical strains of the composite during Type III subcycling, Fig. 21. Duplicate specimens were subjected to alternating segments of 48 hours cyclic relaxation and 24 hours monotonic relaxation, to compare and reproduce matrix response for equivalent times at maximum strain. Initial stress relaxation for the cyclic test is compared as a function of time to initial monotonic response in Fig. 22(a). Maximum stress is compared as a function of

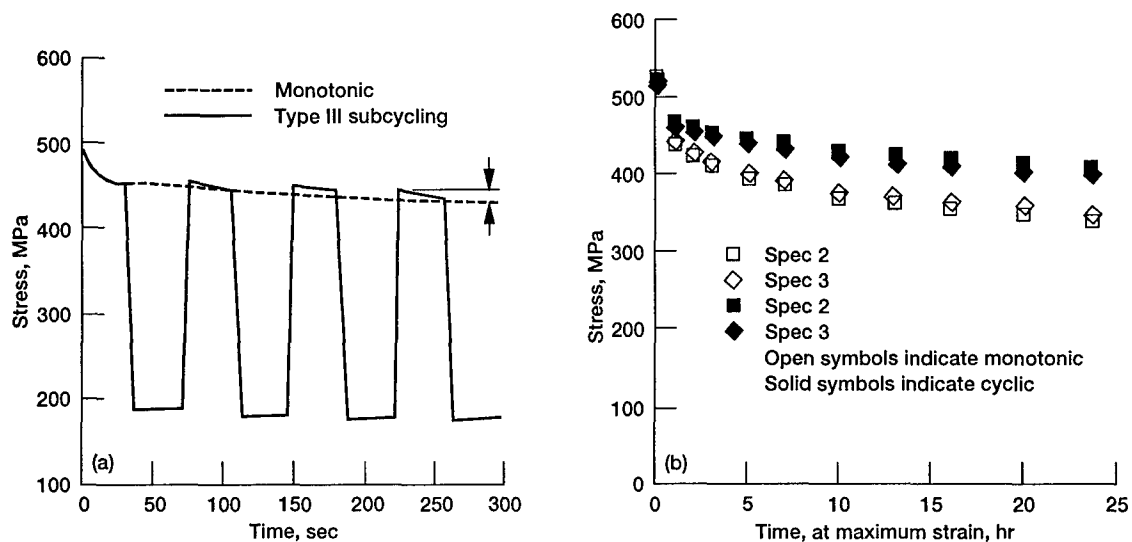


Figure 22.—Comparisons of monotonic and cyclic stress relaxation tests of the matrix: (a) initial stress response versus time in monotonic and cyclic tests; (b) maximum stress versus time at maximum strain for the stabilized third segments of monotonic and cyclic tests (temperature = 538 °C;  $\epsilon_{\max}$  = 0.54 percent,  $\epsilon_{\min}$  = 0.27 percent).

equivalent time at maximum strain in Fig. 22(b) for the stabilized third segments of monotonic and Type III stress relaxation cycling. Matrix stress as a function of time at maximum strain consistently decreased more slowly in the cyclic tests than in monotonic relaxation tests.

The duplicate matrix specimens tested in alternating monotonic and cyclic stress relaxation tests were subjected to a total of at least 120 hours at maximum strain and temperature, and at least 200 hours at maximum temperature. They were subsequently tensile tested at room temperature in order to determine the residual matrix strength and ductility. The specimens had an average yield strength of 770 MPa and tensile strength of 903 MPa, with 4.7% elongation at failure. These results compare well with orthorhombic matrix properties reported elsewhere (refs. 10 and 11), and do not indicate a severely embrittled condition due to the environmental exposure and deformation.

In summary, 1) matrix stress relaxation increased with increasing temperature, but decreased with Type III load subcycling; 2) the environmental exposure and deformation of the baseline mission cycle did not severely embrittle the matrix.

The results of the mission tests, simplified evaluation tests, and unreinforced matrix tests suggest mission life was associated with relaxation of the matrix. Matrix stress relaxation increased with increasing temperature and uninterrupted dwell time at maximum stress and temperature. This would shift more load to the fibers, and could reduce mission life by encouraging a fiber-dominated failure mechanism (ref. 17), as shown in Fig. 23. Type III subcycling interrupts the dwells and reduces matrix stress relaxation rates, and can improve mission life. One can also speculate that

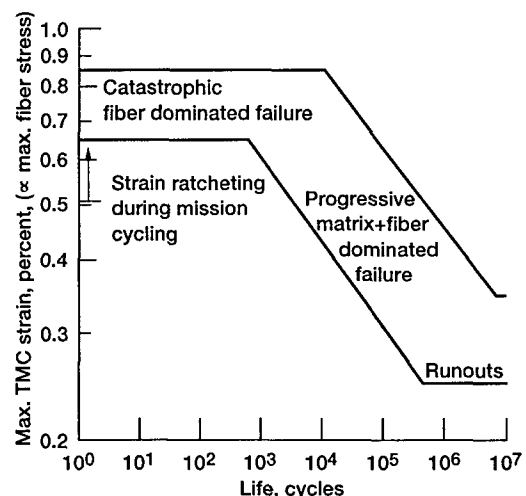


Figure 23—Schematic depiction of the effects of mission cycling on the fatigue failure mode of the composite.

these relaxation related effects could be magnified near crack tips over what was measured in the bulk.

### Summary and Conclusions

In summary, orthorhombic TMC had good tensile strength, isothermal fatigue, and thermomechanical fatigue resistance at temperatures up to 538 °C. However, realistic mission cycling produced lower fatigue lives. Combinations of  $\sigma_{\max}$  and  $T_{\max}$  producing satisfactory mission life were identified. Mission life was limited by Type I cycles combined with dwells at  $\sigma_{\max}$  and  $T_{\max}$ , which encouraged matrix relaxation and a fiber dominated failure mechanism. Longer dwells reduced mission life, by allowing more matrix relaxation. Type III subcycling improved mission life by inhibiting matrix



stress relaxation somewhat. It can be concluded from this work that realistic mission cycles may ultimately limit applications of 0° unidirectional TMCs in compressor rotors. SCS-6/Ti-22Al-23Nb orthorhombic TMC appears to meet mission durability requirements in realistic  $\sigma_{\max} - T_{\max}$  conditions. Mission life is sensitive to sustained dwell time, and can benefit from Type III subcycling to interrupt dwells. Improved matrix creep resistance and fiber strength could improve mission life of TMCs in this application. Fatigue crack initiations occurred at damaged edge fibers in most tests, including the mission tests. The elimination of these damaged fibers on the specimen edges would remove this initiation site, which might also improve life.

### References

1. Gabb, T.P., Gayda, J., Bartolotta, P.A. and Castelli, M.G.: A Review of Thermomechanical Fatigue Damage Mechanisms in Two Titanium and Titanium Aluminide Matrix Composites. *Int. J. Fatigue*, Vol. 15(5), 1993, pp. 413-422.
2. Gayda, J., Gabb, T.P., and Freed, A.D.: The Isothermal Fatigue Behavior of a Unidirectional SiC/Ti Composite and the Ti Alloy Matrix. *Fundamental Relationships Between Microstructures and Mechanical Properties of Metal Matrix Composites*, ed. by M.N. Gungor and P.K. Liaw, The Minerals, Metals & Materials Society, Warrendale, PA, 1990, pp. 497-514.
3. Castelli, M.G., Bartolotta, P.A., and Ellis, J.R.: Thermomechanical Testing of High Temperature Composites: Thermomechanical Fatigue (TMF) Behavior of SiC(SCS 6)/Ti-15-3. *Composite Materials: Testing and Design*, ASTM STP 1120, American Society for Testing and Materials, Philadelphia, PA, 1992, pp. 70-86.
4. Newaz, G.M. and Majumdar, B.S.: Thermomechanical Fatigue Mechanisms in an Unidirectional SCS-6/Ti-15-3 MMC. NASA CR-195482, National Aeronautics and Space Administration, Washington, D.C., 1995.
5. Russ, S.M., Nicholas, T., Bates, M., and Mall, S.: Thermomechanical Fatigue of SCS 6/Ti-24Al-11Nb Metal Matrix Composite. *Failure Mechanisms in High Temperature Composite Materials*, AD-Vol.22/AMD-Vol. 122, ed. by G.K. Haritos, G. Newaz, and S. Mall, American Society of Mechanical Engineers, New York, NY, 1991, pp. 37-43.
6. Brindley, W.J., Smialek, J.L., Smith, J.W., and Brady, M.P.: Environmental Effects on Orthorhombic-Ti Matrix Materials. *Proceedings of the Orthorhombic Titanium Matrix Composites Workshop*, WL-TR-95-4068, ed. By P.R. Smith, Wright-Patterson Air Force Base, OH, 1995, pp. 1-14.
7. Russ, S.M.: Thermal Fatigue of Ti-24Al-11Nb/SCS-6. *Met. Trans. A*, Vol. 21A, 1990, pp. 1595-1602.
8. Gabb, T.P. and Gayda, J.: Matrix Fatigue Cracking of  $\alpha_2$  TMC for Hypersonic Applications. *Life Prediction Methodology for Titanium Metal Matrix Composites*, ASTM STP 1253, American Society for Testing and Materials, Philadelphia, PA, 1995.
9. Brindley, W.J., Gabb, T.P., and Smith, J.W.: Embrittlement of the Surfaces and Crack Faces of TMCs During Fatigue. *Proceedings of the Orthorhombic Titanium Matrix Composites Workshop*, WL-TR-95-4068, ed. by P.R. Smith, Wright-Patterson Air Force Base, OH, 1995, pp. 52-63.
10. Rowe, R.G.: The Mechanical Properties of Titanium Aluminides Near Ti-25Al-25Nb. *Microstructure/Property Relationships in Titanium Aluminides and Alloys*, Y.W. Kim and R.R. Boyer, The Mining, Metallurgy, and Materials Society, Warrendale, PA, 1991, pp. 387-398.
11. Smith, P.R., Graves, J.A., and Rhodes, C.G.: Evaluation of an SCS-6/Ti-22Al-23Nb "Orthorhombic" Composite. *Mat. Res. Soc. Symp. Proc.*, Vol. 273, 1992, pp. 43-52.
12. Chatterjee, A.: Simple Mission Profile Testing of Orthorhombic MMCs. *Proceedings of the Orthorhombic Titanium Matrix Composites Workshop*, WL-TR-95-4068, ed. by P.R. Smith, Wright-Patterson Air Force Base, OH, 1995, pp. 180-200.
13. Russ, S.M., Larsen, J.M., and Smith, P.R.: Mechanical Property Assessment of SCS-6/Ti-22Al-23Nb. *Proceedings of the Orthorhombic Titanium Matrix Composites Workshop*, WL-TR-95-4068, ed. by P.R. Smith, Wright-Patterson Air Force Base, 1995, pp. 162-179.
14. Sait, A.Z., Gayda, J., and Gabb, T.P.: Fatigue Behavior of [0]<sub>g</sub> SCS-6/Ti-6Al-4V Composite Subjected to High Temperature Turbohaft Design Cycles. *Thermo-Mechanical Fatigue Behavior of Materials*, Vol. 2, ASTM STP 1263, American Society for Testing and Materials, 1995.
15. Gabb, T.P. and Gayda, J.: Fatigue Behavior of a Unidirectionally Reinforced Orthorhombic Matrix Composite. *HITEMP Review 1993*, NASA CP-19117, 1993, pp. 33-1 to 33-10.
16. Gabb, T.P. and Gayda, J.: The Effect of  $\alpha_2$  Phase Content on Orthorhombic Titanium Matrix Composite Fatigue Resistance. *HITEMP Review 1994*, NASA CP-10146, 1994, pp. 43-1 to 43-11.
17. Brindley, P.K. and Bartolotta, P.A.: Isothermal Fatigue Behavior of SiC/Ti-24Al-11Nb. *HITEMP Review 1991*, NASA CP-10082, 1991, pp. 46-1 to 46-12.

## MICROSTRUCTURE AND CREEP RESISTANCE OF Nb<sub>3</sub>Al/Nb *in-situ* COMPOSITES

N. Nomura, K. Yoshimi\* and S. Hanada\*

Graduate Student, Department of Materials Processing, Tohoku University, Sendai 980-77, Japan

\*Institute for Materials Research, Tohoku University, Sendai 980-77, Japan

### Abstract

*In-situ* composites of Nb<sub>3</sub>Al/Nb solid solution (Nb<sub>ss</sub>) were produced by hot pressing of prealloyed powder prepared by the rotating electrode process (REP) and by isothermal forging of cast ingots. The microstructure and high temperature creep resistance have been investigated in the present study. Isothermally-forged and annealed Nb-14.1 and 19.5 mol.%Al alloy ingots have homogeneous, equiaxed grain structures, while Nb-16.5mol.%Al alloy made from the REP powder under vacuum hot pressing retains prior powder particle boundaries. Yield stress of the three Nb-Al *in-situ* composites at 1573 K is remarkably dependent on the volume fraction of a ductile Nb<sub>ss</sub> phase; it increases with decreasing the ductile Nb<sub>ss</sub> phase. The isothermally-forged and annealed Nb-19.5mol.%Al alloy exhibits good creep resistance at 1573 K. After creep of the isothermally forged specimens, high densities of dislocations were observed within Nb<sub>3</sub>Al grains, suggesting that Nb<sub>3</sub>Al deforms by dislocation creep at the present test conditions. Also, micro crack formation was observed at triple junctions of boundaries between Nb<sub>3</sub>Al grains. This observation indicates that microcracks are produced in Nb<sub>3</sub>Al grains because of the insufficient slip systems.

### Introduction

Recently, the refractory intermetallic Nb<sub>3</sub>Al has attracted considerable attention as a high temperature structural material for the next generation. This intermetallic can be expected to display excellent strength and creep resistance performance at extra-high temperatures because of its extra-high melting point, and it has been energetically investigated from both viewpoints of basic research and application.

Monolithic Nb<sub>3</sub>Al, however, is very brittle and has little fracture toughness below the ductile-brittle transition temperature (DBTT), which lies above 1300 K. Ductile phase toughening is one of the most applicable techniques for the improvement of poor toughness [1, 2], even in extremely brittle Nb<sub>3</sub>Al alloys. As shown in the binary phase diagram of the Nb-Al system (Fig. 1) [3], ductile Nb solid solution (Nb<sub>ss</sub>) and Nb<sub>3</sub>Al phases coexist at the Al contents between 9 and 20 mol.% at 1773 K. If microstructure of the *in-situ* composites can be controlled by fabrication processing and thermo-mechanical treatment, mechanical properties will be improved.

In this study, Nb<sub>3</sub>Al/Nb<sub>ss</sub> *in-situ* composites are produced by sintering of rotating electrode process (REP) powder and by isothermal forging of cast ingots, and the microstructure was characterized for both materials. Furthermore, creep properties of the isothermally-forged ingots were investigated at 1573 K and are discussed as a function of microstructure.

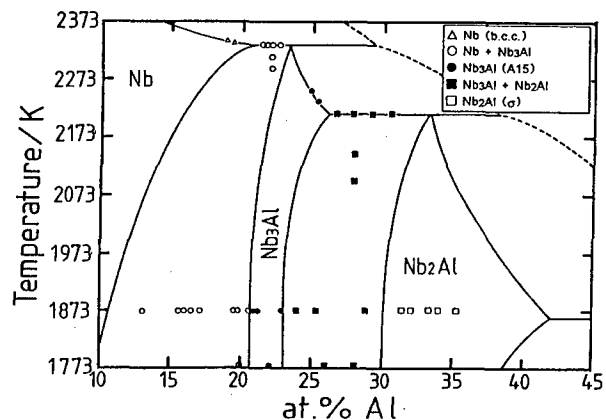


Fig.1 Partial Nb-Al alloy phase diagram[3].

### Experimental Procedure

The rod shaped rotating anode of 8 mm diameter of Nb-16.5mol.%Al alloy was prepared from 99.9 mass%Nb and 99.99 mass%Al by arc melting in an argon atmosphere. The rod anode was homogenized at 2173 K for 3 h in vacuum. Powder was produced by REP with W cathode and the arc current of 85A in the argon atmosphere of  $2.7 \times 10^3$  Pa at the rotating speed of 12000 rpm. The powder was sieved through 355  $\mu$ m mesh. The sieved powder was put into carbon dies, which were coated by BN inside, and hot-pressed at 1873 K and 50 MPa for 2 h. This compact consolidated by hot pressing was then annealed at 1773 K for 24 h. We designate this annealed sample as RHA.

Nb-14.1 and 19.5mol.%Al alloys were also prepared from 99.9 mass%Nb and 99.99 mass%Al by argon arc-melting. The cast button ingots of 40 mm diameter were homogenized at 2173 K for 3 h in vacuum, isothermally forged at 1873 K to the reduction in thickness of 60% in vacuum, and then annealed at 1773 K for 24 h. We designate the annealed samples of Nb-14.1 and 19.5mol.%Al alloys as IF1 and IF2, respectively.

Phase identification was performed by X-ray diffractometry (XRD). Microstructure was observed in a scanning electron microscope (SEM) and a Hitachi H-8100D transmission electron microscope (TEM). The chemical composition of REP powder was

analyzed in a JEOL JXA-8621MX electron probe micro analyzer (EPMA) equipped with an energy dispersive spectrometer (EDS) and a wave length dispersive spectrometer (WDS).

Compression tests and creep tests were conducted in an Instron 8562-type machine. The test samples were about 2 mm × 2 mm × 5 mm. Compression tests were carried out at 1573 K in a vacuum of better than  $2 \times 10^{-4}$  Pa at the strain rate of  $1.6 \times 10^{-4}$  s<sup>-1</sup>. Compressive creep tests were carried out in the same vacuum under constant engineering stresses between 80 - 320 MPa at 1573 K.

## Results and Discussion

### Characterization of REP powder

The size distribution of REP powder of Nb-16.5mol.%Al was bi-modal, and one peak is located around 100 μm and another around 380 μm. Champagne and Angers [4, 5] investigated REP atomization and demonstrated theoretically and experimentally that the size distribution of REP powder becomes bi-modal depending on the fabrication parameters. The size distribution in the present study is in good agreement with their results.

Fig. 2 shows composition distribution of REP powder. Compositions of 79 powder particles were measured at the center of section by EPMA. Mean Al content is about 16 mol.%, and composition varies from 10 to 19 mol.% Al. It is worth noting that 90 % of the particles has the aluminum contents between 15 and 19 mol.%. We can get good powder by REP whose scatter of composition is relatively small.

Microstructures of the surface and cross section of the REP powder are shown in Fig. 3. It is evident from the surface observation (Fig. 3(a)) that nucleation occurs at the beginning of solidification and dendrites grow. From the cross section (Fig. 3(b)), it is found that dendrites grow from surface to center of the powder, and growth of dendrite arms is uniform inside the powder. Since the binary phase diagram (Fig. 1) shows that, during solidification, liquid is enriched with Al, it is expected that fluctuations of Al concentration occur between the interior and the boundary of dendrites.

Fig. 4 shows results of composition analysis performed on a cross section of powder by EPMA. Fig. 4(a) is a SEM micrograph of dendritic structure in the powder and (b) an X-ray image of Al of the same location. From these figures, it is found that Al concentration is considerably enriched at the interdendritic regions.

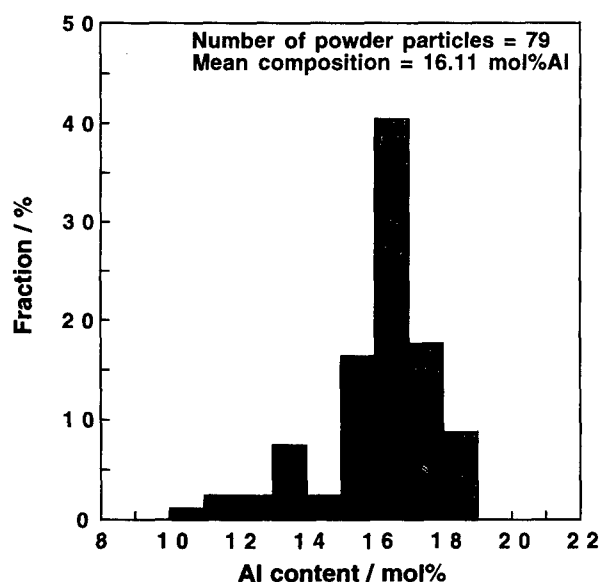


Fig.2 Composition distribution of as-REP powder.

Precipitates, which have a higher Al concentration than the boundary regions, are also observed at the boundaries. On the other hand, within the resolution of this technique Nb is homogeneously distributed in the powder. Thus, the precipitates are compounds with a high Al concentration.

Fig. 5 shows XRD profiles obtained from REP powder. For as-REPed powder, the only peaks of Nb<sub>ss</sub>, which is stable above 2173 K (Fig.1), are detected (Fig. 5(a)). Suppression of the Nb<sub>3</sub>Al phase is due to rapid solidification effect of REP. For annealed REP powder, two groups of peaks reflected from Nb<sub>ss</sub> and Nb<sub>3</sub>Al are detected (Fig. 5(b)), indicating that the powder has the duplex phase.

### Microstructure of hot pressed compact of REP powder and isothermally forged ingot

Fig. 6 shows microstructure of an as-hot pressed compact of Nb-16.5mol.%Al made from REP powder. We obtained a dense compact which has few pores and very fine microstructure. This microstructure is strongly affected by the dendritic structure of REP powder, and delineation of prior powder particles can be seen in places. Based on the phase diagram (Fig. 1) and the results obtained by EPMA (Fig. 7 and Table 1), the elongated phase is identified Nb<sub>ss</sub> and the other phase as Nb<sub>3</sub>Al. Furthermore, the distribution of these two phases is not homogeneous (Fig. 6). This results from the differences in composition between powder particles (Fig. 2).

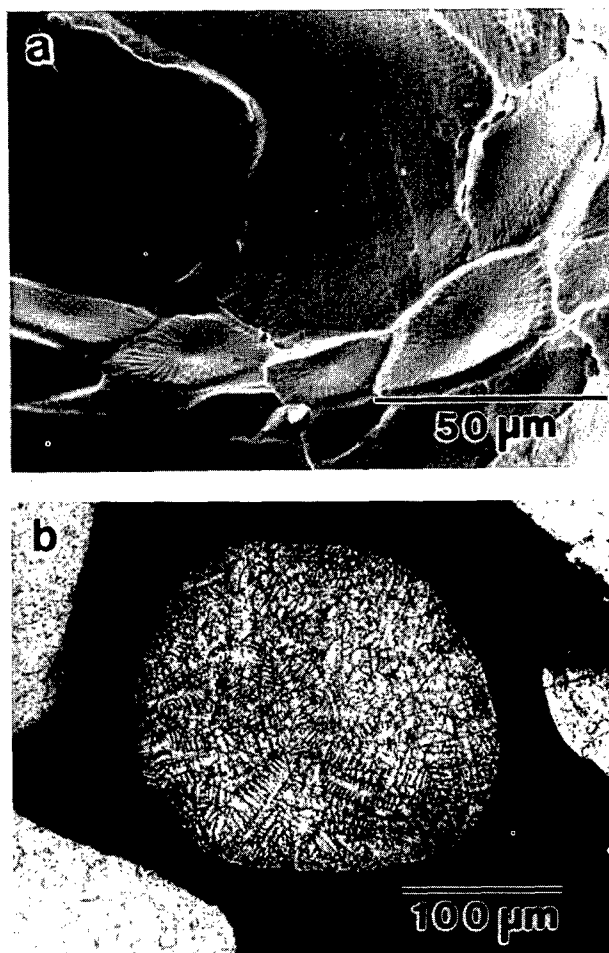


Fig.3 Micrographs of as-REP Nb-Al powder.  
(a) SEM micrograph of the powder surface.  
(b) OM micrograph of the cross section of a powder particle.

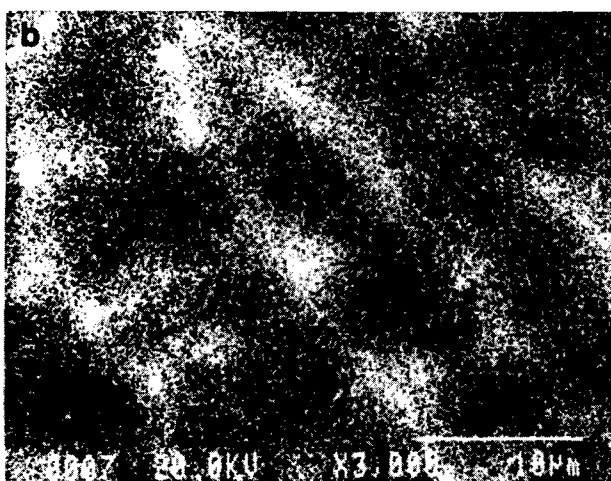
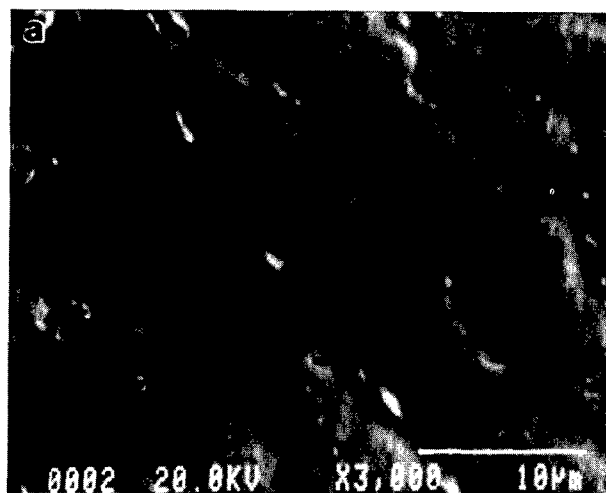


Fig.4 Micrographs of as-REP Nb-Al powder at high magnification.  
(a) SEM micrograph showing the dendritic structures.  
(b) X-ray image for Al.

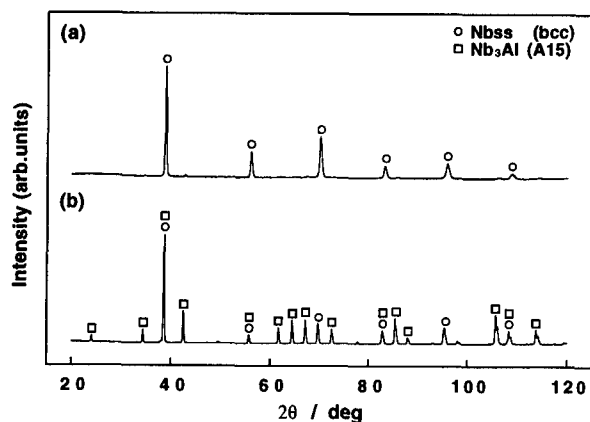


Fig.5 X-ray profiles of Nb-16.5mol%Al REPed powder.  
(a) As REP.  
(b) After annealing at 1273 K for 24 h.

In addition, fine particles are occasionally found at grain boundaries within colonies of  $\text{Nb}_3\text{Al}$  grains. WDS analysis suggests that these particles are  $\text{Al}_2\text{O}_3$ . They were not observed at any boundaries

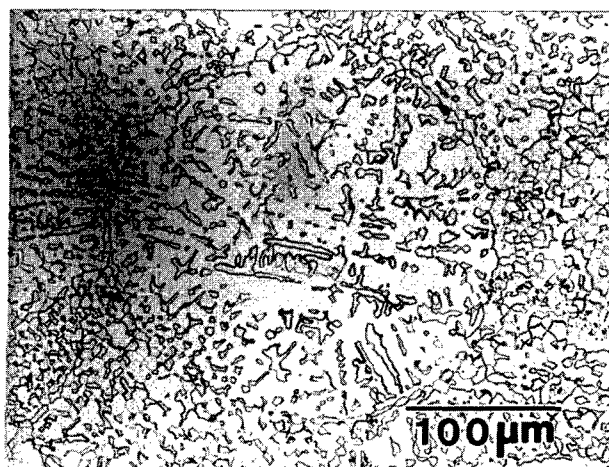


Fig.6 Typical microstructure of as-hot pressed Nb-16.5mol%Al alloy.

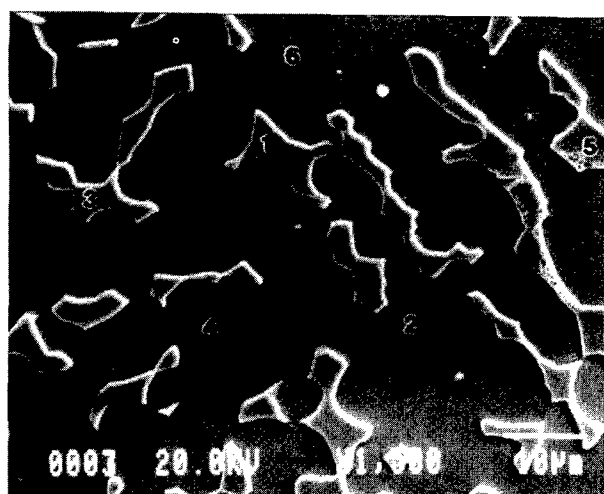


Fig.7 SEM micrograph of as-hot pressed Nb-16.5mol%Al alloy.

Table 1 Results of chemical composition analysis by EPMA.

Region in Fig.7	Nb (mol%)	Al (mol%)	Phase
1	91.4	8.6	Nbss
2	80.1	19.9	Nb <sub>3</sub> Al
3	90.8	9.2	Nbss
4	79.8	20.2	Nb <sub>3</sub> Al
5	90.3	9.7	Nbss
6	79.9	20.1	Nb <sub>3</sub> Al

between  $\text{Nb}_3\text{Al}$  grains in  $\text{Nb}_3\text{Al}/\text{Nb}_{ss}$  duplex phase areas, but only in colonies consisting of  $\text{Nb}_3\text{Al}$  grains. The reason why  $\text{Al}_2\text{O}_3$  is formed only in the  $\text{Nb}_3\text{Al}$  colonies is not clear at present, but one possible explanation is that the solubility limit of oxygen is lower in  $\text{Nb}_3\text{Al}$  than  $\text{Nb}_{ss}$ . Thus,  $\text{Nb}_{ss}$  in the duplex phase areas may act as the oxygen absorbent.

The as-hot pressed compact was annealed at 1773 K for 24 h. Microstructure of the annealed compact (RHA) is shown in Fig. 8.

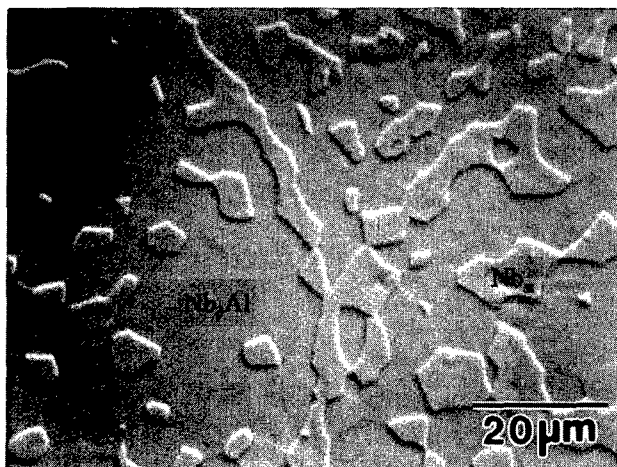


Fig.8 SEM micrograph of Nb-16.5mol%Al alloy after annealing at 1773 K for 24 h (RHA).

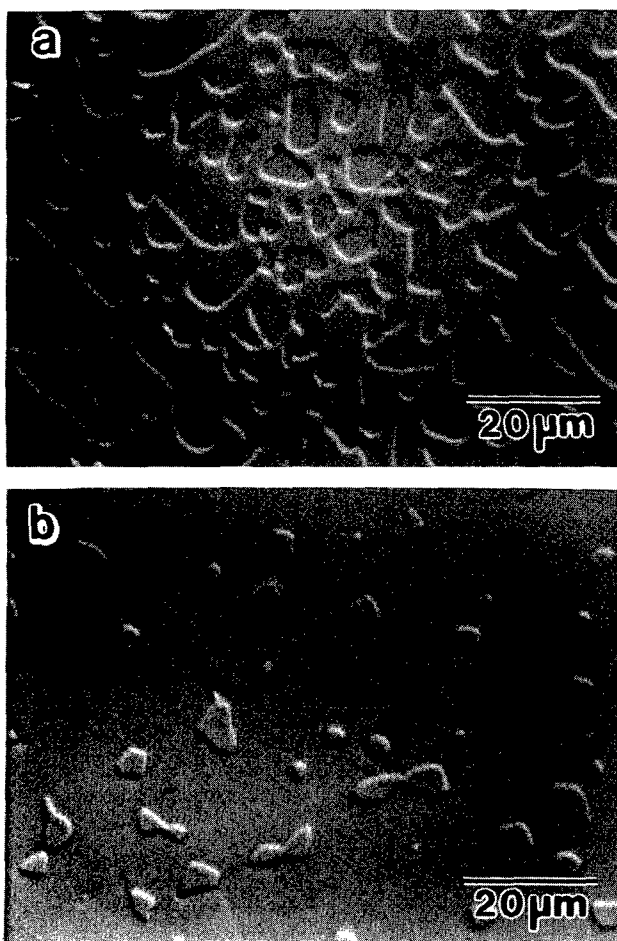


Fig.9 SEM micrographs of isothermally forged Nb<sub>3</sub>Al/Nb composites after annealing at 1773 K for 24 h.  
(a) IF1 (V(Nb<sub>ss</sub>) = 59%)  
(b) IF2 (V(Nb<sub>ss</sub>) = 13%)

In comparison with the as-hot pressed compact, the microstructure is relatively homogeneous, and coarsening of grains occurs slightly. Furthermore, the dendritic structure observed in the as-hot pressed compact is almost completely decomposed in the annealed compact. The isolated phase in Fig. 8 is Nb<sub>ss</sub>, and its volume percent is about 34 %.

Cast ingots of Nb-14.1 and 19.5 mol.%Al alloys after arc-melting have coarse grained or dendritic structure similar to that reported by Kamata et al [6]. These cast ingots were isothermally forged to a reduction in thickness of 60 % and annealed at 1773 K for 24 h. Fig. 9 shows the forged and annealed microstructures of both alloys. The coarse grained or dendritic as cast structure does not remain, and equiaxed, fine duplex structures of Nb<sub>3</sub>Al/Nb having grain size of 10 - 20 μm are obtained, which is similar to the grain size of RHA. The isolated phase of IF1 seen in Fig. 9(a) is Nb<sub>3</sub>Al and the matrix phase is Nb<sub>ss</sub>. By contrast, the isolated phase of IF2 seen in Fig. 9(b) is Nb<sub>ss</sub> and the matrix phase is Nb<sub>3</sub>Al. Volume percent of Nb<sub>ss</sub> of IF1 and IF2 is about 59 and 13 %, respectively.

#### Mechanical tests

Fig. 10 shows yield stresses of RHA, IF1 and IF2 obtained in compression at 1573 K and  $1.6 \times 10^{-4} \text{ s}^{-1}$ . The yield stress is very high for IF2 and decreases rapidly with increasing volume percent of Nb<sub>ss</sub>, indicating that the yield stress is sensitive to the volume percent of Nb<sub>ss</sub> irrespective of the fabrication processes. Although the decrease in yield stress with increasing the volume percent of the ductile phase is unavoidable, this intrinsic problem of the *in-situ* composite can be modified by solid solution strengthening of third elements such as Mo and Ta [7, 8].

Creep tests were performed using isothermally-forged ingots, since homogeneous microstructures were obtained. Fig. 11 shows creep curves of IF1 and IF2 at 1573 K. These creep curves are shown after subtracting the elastic strain of the creep test machine at each stress from the measured creep curves. As shown in this figure, these *in-situ* composites exhibit the S-type creep behavior. The relationship between minimum creep rate and stress obeys a power law for the composites within the present test conditions, as shown in Fig. 12. The stress exponent,  $n$ , is about 5 for IF1 and 6 for IF2. It is worth noting that Nb-19.5mol%Al alloy (IF2) displays better creep performance at high temperatures than MoSi<sub>2</sub> [9] and (Cr, Mo)<sub>3</sub>Si/(Cr, Mo)<sub>3</sub>Si<sub>3</sub> [10], as shown in Fig. 12.

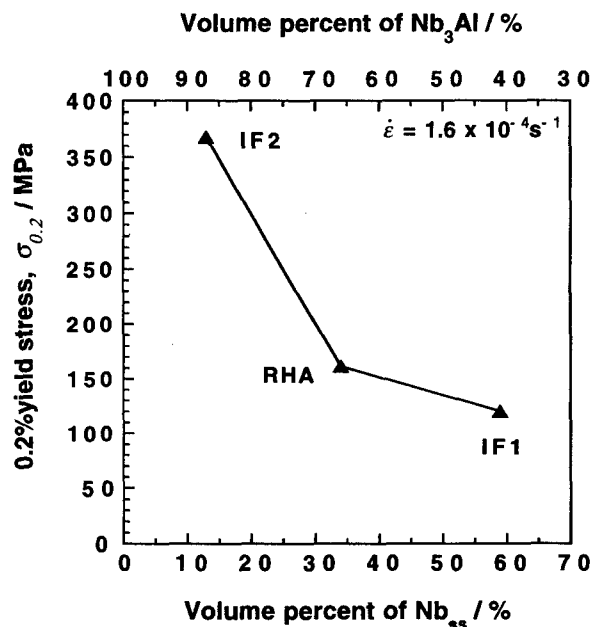


Fig.10 Volume percent dependence of 0.2%yield stress at 1573 K.

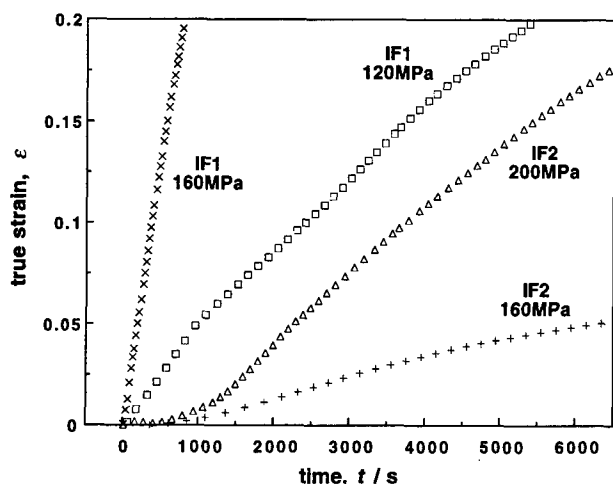


Fig.11 Creep curves for  $\text{Nb}_3\text{Al}/\text{Nb}$  composites at 1573 K.

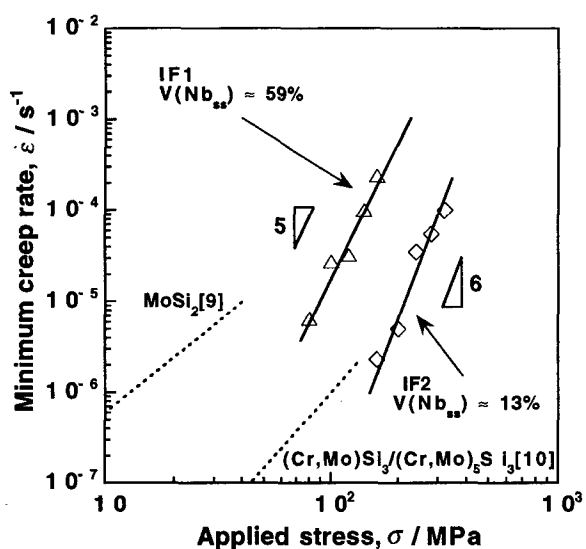


Fig.12 Relationships between minimum creep rate and applied stress at 1573 K.

#### Deformation microstructure

Deformation microstructures on surfaces after creep were observed in SEM, typical micrographs are shown in Fig. 13. Fig. 13(a) illustrates an IF1 specimen crept to  $\epsilon=0.22$  at 100 MPa and (b) an IF2 specimen crept to  $\epsilon=0.23$  at 240 MPa. In both cases, it was observed that  $\text{Nb}_{ss}$  particles are elongated along the direction normal to the compression axis, indicating that  $\text{Nb}_{ss}$  has sufficient deformability at the temperature. On the other hand, many voids looking like cavities are also observed at the grain boundaries and triple junctions between  $\text{Nb}_3\text{Al}$  grains. However, as the deformation in the present work is conducted by compression, it is suggested that these voids are different from cavities formed during diffusional creep in tension. The slip system of  $\text{Nb}_3\text{Al}$  has been reported to be  $\{100\}\langle 010 \rangle$  even at the high temperature [11]. Since this slip system does not satisfy the von Mises criterion, micro cracks would be generated by the insufficient deformability of  $\text{Nb}_3\text{Al}$  at  $\text{Nb}_3\text{Al}$  grain boundaries.

Fig. 14 shows a TEM micrograph taken from an undeformed IF2 specimen. The dislocation density of a  $\text{Nb}_3\text{Al}$  phase is very low, but numerous dislocations are observed in a  $\text{Nb}_{ss}$  phase. These dislocations

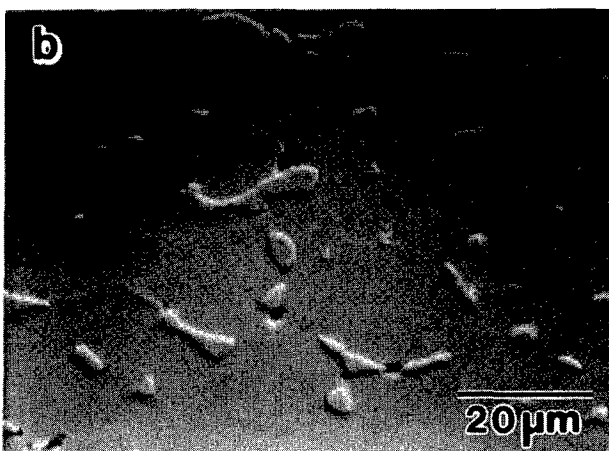
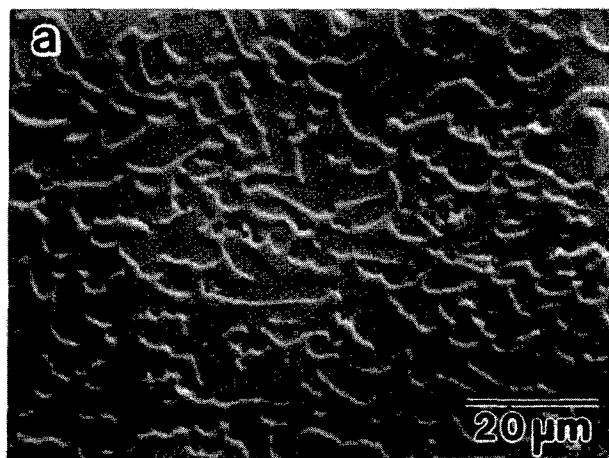


Fig.13 SEM micrographs of the surface deformation structure of  $\text{Nb}_3\text{Al}/\text{Nb}$  composites crept at 1573 K. Compression axis is vertical.

(a) IF1 (100MPa,  $\epsilon = 0.22$ )

(b) IF2 (240MPa,  $\epsilon = 0.23$ )

were probably introduced during the heat treatment due to the difference in thermal expansion coefficient between  $\text{Nb}_3\text{Al}$  and  $\text{Nb}_{ss}$ . Fig. 15 shows deformation microstructure of an IF2 specimen crept to  $\epsilon=0.23$  at 280 MPa. Many dislocations and sub-boundaries are observed in  $\text{Nb}_3\text{Al}$  grains. From this observation, deformation of the  $\text{Nb}_3\text{Al}$  phase is interpreted in terms of a dislocation creep mechanism.

Little has been reported on the creep strength of  $\text{Nb}_3\text{Al}$  because of difficulty in specimen preparation of its single phase alloy. Fortunately, since IF2 contains 87 %  $\text{Nb}_3\text{Al}$  in volume percent, we expect that creep behavior of IF2 is controlled mainly by the  $\text{Nb}_3\text{Al}$  phase. The present results of IF2, for example, creep curves, stress exponent, and SEM microstructure, imply that IF2 deforms by dislocation creep at the test conditions. Furthermore, TEM observation indicates that dislocation creep is dominant in the  $\text{Nb}_3\text{Al}$  phase, as shown in Fig. 15. From the present work, it is suggested that monolithic  $\text{Nb}_3\text{Al}$  has excellent creep performance at high temperatures such as 1573 K. However, creep rate is dependent on the volume fraction of  $\text{Nb}_{ss}$ . With increasing the volume fraction of  $\text{Nb}_{ss}$ , the creep rate becomes faster, and complicated deformation mechanisms become operative in the in-situ composite, which would be responsible for the change of the stress exponent. Unfortunately, numerous dislocations introduced into  $\text{Nb}_{ss}$  phases during thermal history impede examining deformation microstructure in  $\text{Nb}_{ss}$  after creep. Therefore, in the case that  $\text{Nb}_{ss}$  plays a major role for deformation, it is difficult to discuss the creep mechanism of the in-situ composite.

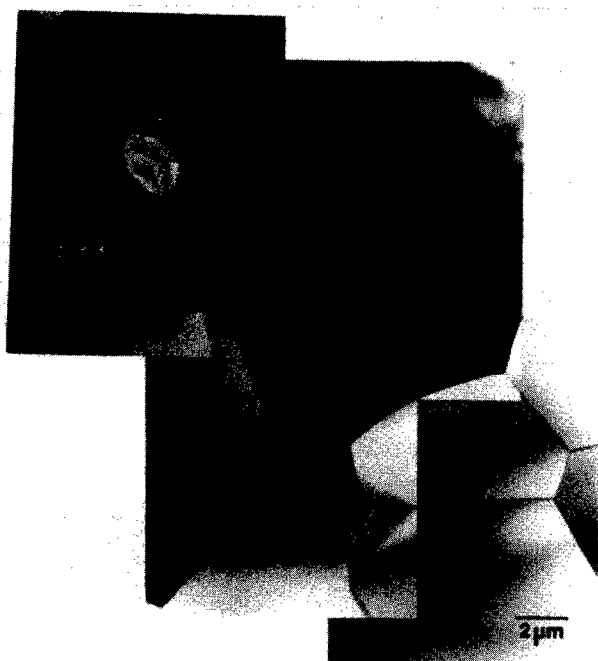


Fig.14 TEM micrograph of non-deformed microstructure of IF2.

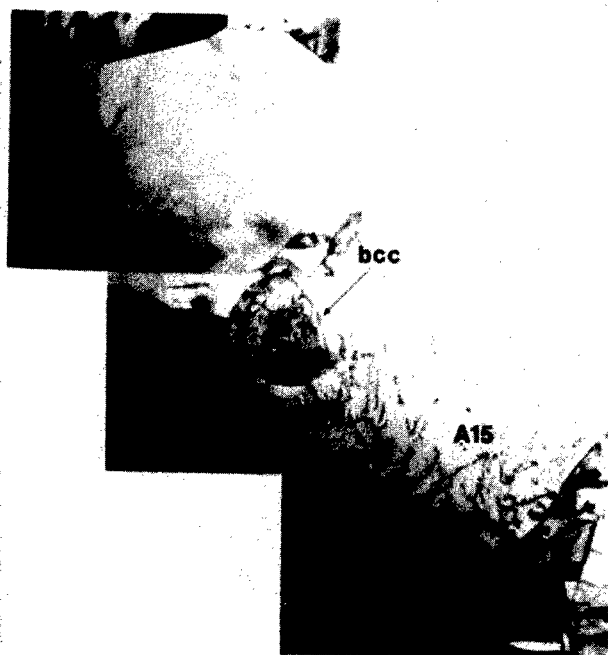


Fig.15 TEM micrograph of microstructure of IF2 crept at 1573 K and 280 MPa. ( $\epsilon = 0.23$ )

### Summary

We could produce  $\text{Nb}_3\text{Al}/\text{Nb}_{ss}$  *in-situ* composites by hot pressing of REP powder and isothermal forging of cast ingots through the present study. The composites produced by isothermal forging (Nb-14.1 and 19.5mol.%Al) have homogeneous, fine, equiaxed grain microstructure without micro cracks. On the other hand, the microstructure of the composite produced by hot pressing (Nb-16.5mol.%Al) is affected by the dendritic structure in the REP powder. Volume fraction of  $\text{Nb}_3\text{Al}/\text{Nb}_{ss}$  is different in places, and traces of the prior powder particles remain. This results from the difference in composition between powder particles. We need to improve the fabrication processing via powder metallurgy.

Yield stress of the  $\text{Nb}_3\text{Al}/\text{Nb}_{ss}$  *in-situ* composites at 1573 K is very sensitive to  $\text{Nb}_{ss}$  content; yield stress is very high in the composite with high  $\text{Nb}_3\text{Al}$  content, while it decreases rapidly with increasing  $\text{Nb}_{ss}$  content. The isothermally-forged  $\text{Nb}_3\text{Al}/\text{Nb}_{ss}$  *in-situ* composite with high  $\text{Nb}_3\text{Al}$  content exhibits good creep resistance at 1573 K compared with  $\text{MoSi}_2$  and  $(\text{Cr}, \text{Mo})_3\text{Si}/(\text{Cr}, \text{Mo})_5\text{Si}_3$ .

The *in-situ* composites of  $\text{Nb}_3\text{Al}/\text{Nb}_{ss}$  used in the present work are binary alloys, and have high potential for increased creep resistance by solid solution strengthening and dispersion strengthening.

### Acknowledgments

The authors would like to thank Dr. T. Tabaru, Mr. S. Watanabe, Mr. H. Tokuno and Mr. Y. Murakami for their partial supports. The present work was supported by the Grant-in-Aid for Scientific Research from the Ministry of Education, Science and Culture, Japan.

### References

1. D. L. Anton and D. M. Shah, in *Intermetallic Matrix Composites*, D. L. Anton, P. L. Martin, D. B. Miracle and R. McMeeking, eds., Mat. Res. Soc. Symp. Proc., 194 (1990), 45.
2. S. Mazdiyashi and D. B. Miracle, in *Intermetallic Matrix Composites*, D. L. Anton, P. L. Martin, D. B. Miracle and R. McMeeking, eds., Mat. Res. Soc. Symp. Proc., 194 (1990), 155.
3. R. Suyama, M. Kimura and K. Hashimoto, in *STRUCTURAL INTERMETALLICS*, R. Darolia, J.J. Lewandowski, C.T. Liu, P.L. Martin, D.B. Miracle and M.V. Nathal, eds., TMS, (1993), 681.
4. B. Champagne and R. Angers, *The International Journal of Powder Metallurgy and Powder Technology*, 16, (1980), 359.
5. B. Champagne and R. Angers, *Powder metallurgy international*, 16, (1984), 125.
6. K. Kamata, T. Degawa and Y. Nagashima, in *STRUCTURAL INTERMETALLICS*, R. Darolia, J.J. Lewandowski, C.T. Liu, P.L. Martin, D.B. Miracle and M.V. Nathal, eds., TMS, (1993), 675.
7. T. Tabaru, "Fabrication and properties of  $\text{Nb}_3\text{Al}/\text{Nb}$  *in-situ* composites as high temperature structural materials," (Ph.D thesis, Tohoku University, 1997).
8. R. Gnanamoorthy and S. Hanada, *Mater. Sci. Eng. A*, 207(1996), 129.
9. K. Sadananda, C. R. Feng, H. N. Jones and J. J. Petrovic, in *STRUCTURAL INTERMETALLICS*, R. Darolia, J.J. Lewandowski, C.T. Liu, P.L. Martin, D.B. Miracle and M.V. Nathal, eds., TMS, (1993), 809.
10. M. Nazamy, C. Nosedá, G. Sauthoff, B. Zeumer and D. Anton, in *High-Temperature Ordered Intermetallic Alloys VI Part2*, J. A. Horton, I. Baker, S. Hanada, R. D. Noebe and D. S. Schwartz, eds., Mat. Res. Soc. Symp. Proc. 364, 1333 (1995).
11. S. Hanada, Y. Murayama and A. Abe, *Intermetallics*, 2 (1994), 155.

## FABRICATION AND MECHANICAL BEHAVIORS OF SiC<sub>CVD</sub> / TiAl COMPOSITE

Youji Mizuhara\*, Keizo Hashimoto\*, Hiroshi Nakatani\*\* and Yukio Shimada\*\*\*

\* Nippon Steel Corporation, Iida, Kawasaki, Kanagawa, 211 Japan

\*\* Kawasaki Heavy Industries, LTD, Kakamigahara, Gifu, 504 Japan

\*\*\* Kawasaki Heavy Industries, LTD, Akashi, 673 Japan

### Abstract

This paper describes the results of fabrication conditions and mechanical properties of SiC<sub>CVD</sub> / TiAl composite using superplastic TiAl thin foil. Fabrication of SiC<sub>CVD</sub> / TiAl composite has not been very successful because of the formation of a brittle layer at high fabrication temperature and the lack of room temperature ductility in TiAl to relax thermal expansion mismatch between SiC fiber and TiAl matrix. In order to solve the above problems, the deformability of a  $\gamma$ -TiAl based alloy has been improved by alloy design and microstructural control applying thermomechanical processing. Superplastic  $\gamma$ -TiAl foils and SiC<sub>CVD</sub> (SCS-6) fibers were consolidated by the vacuum hot pressing process. It was elucidated that the most appropriate condition of consolidating temperature was 1273-1323K through observing the microstructure and testing the mechanical properties of the consolidated composites. A unidirectional SiC<sub>CVD</sub> fiber /  $\gamma$ -TiAl matrix composite exhibits approximately twice the specific strength of Inconel 718 alloy.

### Introduction

The next generation aircraft engines need high performance structural materials which have lighter and higher temperature capabilities(1). Gamma titanium aluminide is promising for aerospace applications due to its low density and high strength at elevated temperatures. However, monolithic titanium aluminides are not necessarily superior to conventional Ni-base superalloys in both specific strength and specific creep properties for the practical usage like compressor discs and low pressure turbine discs (2).

One of the approaches to strengthen TiAl is reinforcement of TiAl alloys with continuous ceramic fibers(3,4). Fabricating SiC<sub>CVD</sub> / TiAl composite has not been perfectly successful for two reasons: high fabrication temperature, which accelerates the formation of a brittle layer by chemical reaction at the interface between SiC fiber and TiAl matrix, and poor ductility of TiAl at room temperature. The residual stresses generated by the thermal expansion mismatch between SiC and TiAl cause cracking of the TiAl matrix during the cooling down process. So fabrication of the TiAl matrix composite requires both decrease of the fabrication temperature and high ductility of the matrix at room temperature.

The deformability of  $\gamma$ -TiAl based alloy can be improved by alloy design and microstructural control applying thermomechanical processing. In the previous studies, it was reported that TiAl-Cr ternary alloy exhibits superplastic deformation above 1273K through  $\beta$  phase deformation at  $\gamma$  grain boundaries (5).

In this paper, the authors will describe improvement of the deformability of  $\gamma$ -TiAl as matrix of SiC<sub>CVD</sub> / TiAl composite and discuss the fabrication conditions and mechanical properties of this composite using superplastic TiAl thin foil.

### Experimental Procedure

#### Superplastic TiAl-Cr foils

Ingots for thin foils were prepared by plasma arc melting methods (PAM) using a plasma arc torch in an argon gas atmosphere for the purpose of reducing impurities like oxygen, followed by homogenization at 1323K for 96 hours in a vacuum.



The chemical composition of Cr added TiAl ternary alloy is given in Table I, noting that the PAM process can reduce the oxygen content to 200 wt. ppm in TiAl.

The  $\beta$  and  $\gamma$  dual phases possessing superplasticity were attainable through isothermal forging (ITF) up to 75% reduction ratio at 1473K with an initial strain rate of  $5 \times 10^{-4} \text{ s}^{-1}$ . After ITF, TiAl-Cr foils with a thickness of 150-200 $\mu\text{m}$  were obtained by electric discharge cutting and surface polishing process.

Table I Chemical composition of superplastic TiAl-Cr  
(Ti, Al, Cr: at.%, O, H, C: wt.%)

Ti	Al	Cr	O	H	C
50.47	44.78	4.74	0.020	0.00076	0.009

### SiC fibers

Continuous SiC fibers (SCS-6) of 140 $\mu\text{m}$  diameter were supplied by Textron Specialty Materials. The SCS-6 fibers were composed of stoichiometric SiC deposited by CVD on a carbon substrate. These fibers have a 3 $\mu\text{m}$  carbon rich coating layer with decreased silicon content show high tensile strength, 3450MPa. A composite preform called "Woven fabric" is a uniweave system in which the SCS-6 monofilaments are held straight and parallel, collimated at about 120 filaments per inch, by a cross-weave of a Ti-Nb metallic ribbon.

### Fabrication of $\text{SiC}_{\text{CVD}}$ /TiAl-Cr composite

$\text{SiC}_{\text{CVD}}$  / TiAl-Cr composite has a sandwich structure consisting of four TiAl-Cr foils and three SCS-6 preforms. In order to determine the most appropriate conditions, these TiAl-Cr foils and SCS-6 preforms were consolidated by vacuum hot pressing for 4 hours at 1223, 1273, 1323 and 1373K and a pressure of 98 MPa. As-fabricated composites were examined by a scanning electron microscope(SEM) and electron micro-probed analyzer (EPMA).

Tensile specimens having a gauge size of (1.5-1.6)mm<sup>l</sup> x 7mm<sup>w</sup> x 20mm<sup>t</sup> were obtained by electric discharge machining in the fiber direction of the composites. They were subsequently polished to remove the surface layer. Tensile tests from room temperature up to 973K were carried out in air at an initial strain rate of  $1.7 \times 10^{-4} \text{ s}^{-1}$ .

## Results and Discussion

### Superplasticity of $\gamma$ + $\beta$ dual phase alloy

In the previous studies, the superplasticity of  $\gamma$ -TiAl was reported for  $\gamma$  single phase (6,7) and  $\gamma$ + $\alpha_2$  phase (8-11) alloys. However, these alloys have not exhibited elongation exceeding 300% below 1473K. The mechanism of superplasticity in these alloys was understood as grain size refinement and dynamic recrystallization at elevated temperatures, which allow grain boundary sliding and nucleation of new grains to relax accumulated strain.

On the other hand, some of the present authors reported high superplasticity of  $\gamma$ -TiAl through microstructural control by thermomechanical processing of the Cr added ternary alloy(5).

This alloy consists of  $\gamma$  and  $\beta$  dual phases, which deform superplastically above 1273K by  $\beta$  phase deformation at  $\gamma$  grain boundary and  $\gamma$  grain rotation. Later, vanadium added TiAl composed of  $\beta$  and  $\gamma$  phases showed superplastic behavior with more than 600% elongation and the strain rate sensitivity factor (m-value) of 0.8 at 1420K(12). These  $\gamma$ + $\beta$  dual phase alloys enable higher superplastic deformation at lower temperature than  $\gamma$  single and  $\gamma$ + $\alpha_2$  dual phase alloys, owing to the higher deformability of  $\beta$  phase. The transformation from  $\beta$  phase to  $\gamma$  and  $\alpha_2$  phases with the same microstructure morphology, which could be obtained by heat treatment, results in decrease of tensile elongation and increase of tensile strength at elevated temperatures(13). Furthermore, the site of  $\beta$  precipitation is an important factor in the deformability of TiAl at elevated temperatures.  $\beta$  precipitation within  $\gamma$  grain cannot improve deformability of TiAl as much as the  $\beta$  phase at  $\gamma$  grain boundary(14,15). As mentioned above, the improvement of superplastic deformation requires the control of grain boundary in addition to grain refinement and phase distribution.

The authors modified the  $\beta$  phase volume fraction at the  $\gamma$  grain boundary in TiAl-Cr alloy through control of the Ti/Al ratio and Cr content and consequently achieved a decrease of the onset temperature of superplasticity. In the present work, Ti-49Al-1Cr, Ti-47Al-3Cr and Ti-45Al-5Cr (at.%) were examined.

Fig.1 shows the microstructures of these alloys through isothermal forging after casting by PAM. The alloy with 1% Cr has coarse grains of 64 $\mu\text{m}$ , while fine grain size of 18.5 $\mu\text{m}$  was observed for 3% Cr and 17.9 $\mu\text{m}$  for 5% Cr alloys. In Fig.1, the white region around the black region of  $\gamma$  phase was identified as  $\beta$  phase with enrichment of Cr element relative to the  $\gamma$  phase by means of X-ray diffraction and EPMA. The volume fraction of  $\beta$  phase at  $\gamma$  grain boundary increases with increasing Cr content.

Fig.2 shows X-ray diffraction patterns for these alloys. The  $\beta$  phase spectra intensities increase remarkably with an increase of Cr content, which is consistent with the result of microstructure observation.

Fig.3 shows the relation between Cr content and tensile elongation from 1073 to 1473K, revealing that increasing Cr content improves tensile elongation. In Fig.3, the elongation at 1473K for 3% Cr ternary alloy and at both 1273K and 1473K for 5% Cr were the upper limits of the testing machine, suggesting their performances were over 400% elongation. The volume fraction of  $\beta$  phase observed at  $\gamma$  grain boundary increases with increasing Cr content up to 5 % Cr addition. In other words, the stability of  $\beta$  phase in TiAl rises with increasing Cr content. The grain boundary occupation ratio by  $\beta$  phase calculated by computational image analysis of micrograph increases with increasing Cr content, as indicated by dotted line in Fig. 3. It was calculated to be 67% for 5 % Cr ternary alloy. It is concluded that the higher volume fraction of  $\beta$  phase at  $\gamma$  grain boundary brings about higher deformability of TiAl at elevated temperatures.

The m-value which is derived from the following equation as a function of true strain rate at 1073-1473K in Ti-45Al-5Cr is illustrated in Fig. 4.

$$\sigma = K \dot{\epsilon}^m$$

where  $\sigma$  is the true stress,  $\dot{\epsilon}$  is the true strain rate and K is a constant. The m value above 1173K exceeds 0.3 which satisfies the criterion of superplastic deformation(16). The increase of Cr shifts the onset temperature of superplasticity to lower temperature. From these results, the matrix composition for  $\text{SiC}_{\text{CVD}}$ /TiAl composite was selected to Ti-45Al-5Cr.

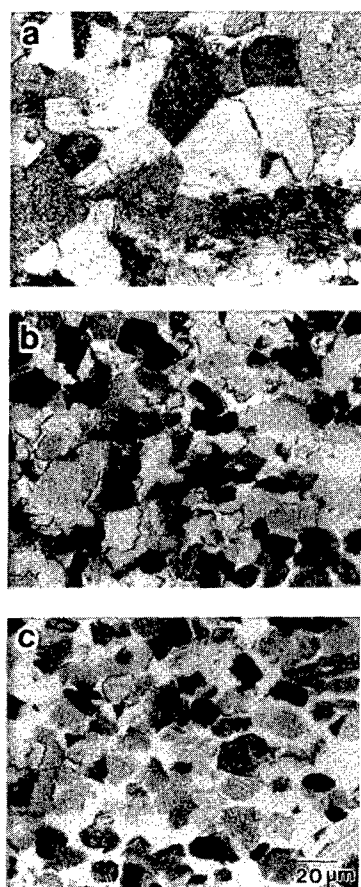


Figure 1: As-forged microstructures of (a) Ti-49Al-1Cr, (b) Ti-47Al-3Cr and (c) Ti-45Al-5Cr (at.%)

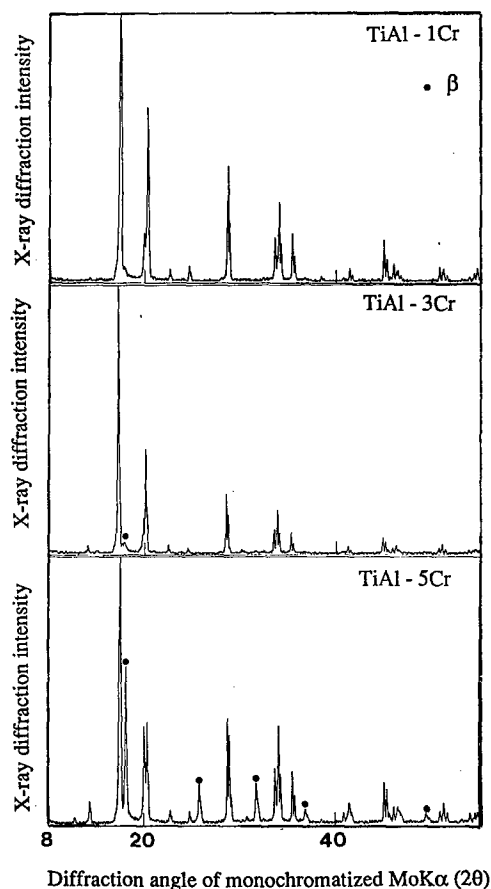


Figure 2: Results of X-ray diffraction patterns in 1, 3 and 5% Cr added TiAl ternary alloy

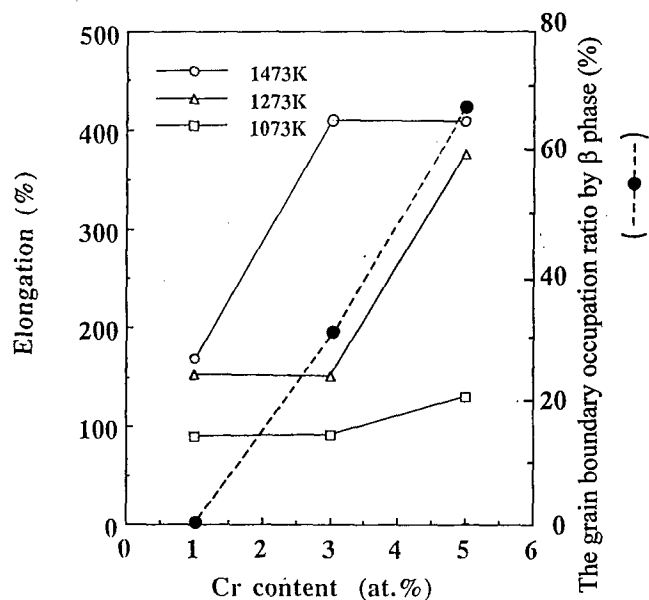


Figure 3: Relation between Cr content and tensile elongation from 1073 to 1473K (dotted line shows the grain boundary occupation ratio of  $\beta$  phase)

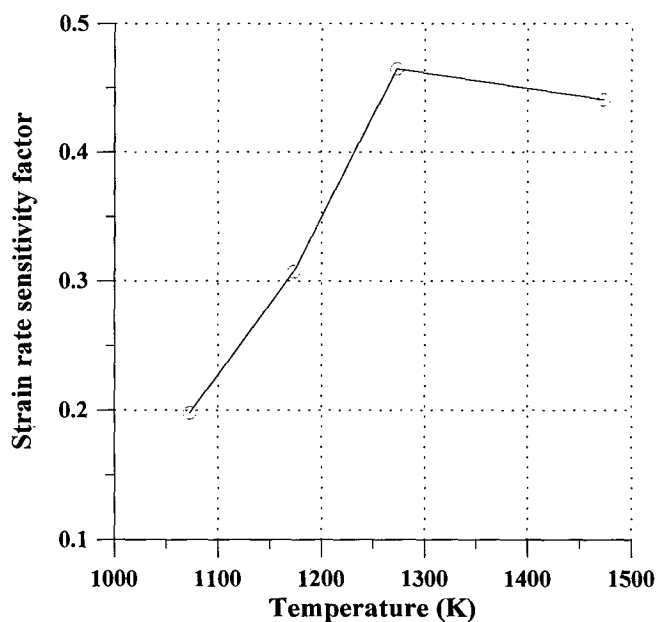


Figure 4: Strain rate sensitivity factor against 0.2% true strain in Ti-45Al-5Cr

On the other hand, the  $\beta$  phase at  $\gamma$  grain boundary also plays a role to inhibit grain growth. From the results of isothermal annealing at 1323K, the grain size does not change even after 96 hours of heat treatment, while grain coarsening occurs in binary for the same condition(13). The stability of the microstructure is expected to be important in the fabrication of composite materials for the prevention of stress concentration in the matrix during consolidation and the maintenance of homogeneity.

#### Oxygen effect on mechanical properties of TiAl-Cr

The oxygen content in TiAl influences the deformation behavior at elevated temperatures. Fig.5 shows testing temperature dependence on tensile elongation in isothermally forged Ti-47Al-3Cr alloy prepared by both PAM and vacuum induction melting method (VIM). The VIM specimen exhibits lower tensile elongation compared with the PAM specimen in the temperature range of 1073-1473K. In the VIM system, the microstructure after ITF is duplex morphology like the PAM system. However, this second phase is identified as  $\beta$  and  $\alpha_2$  phases from X-ray diffraction.

The existence of  $\alpha_2$  phase in a sample by the VIM process is considered to be due to the higher oxygen content of TiAl, resulting in poor ductility at elevated temperatures. The chemical compositions of Ti-47Al-3Cr by both PAM and VIM are given in Table II. The oxygen content of the VIM specimen is higher level (1600 ppm) than that of the PAM specimen (180 ppm). From the experiments by atomic probe field ion microscopy, it is revealed that  $\alpha_2$  phase is stabilized through scavenging oxygen (17,18). The high level of oxygen content in the VIM sample stabilized the  $\alpha_2$  phase, while the very low oxygen content in PAM sample does not result in  $\alpha_2$  phase stabilization. Furthermore, the difference of the second phase of these materials is explained by phase diagram. It is reported that the high oxygen content of TiAl shifts the  $\alpha$  phase to Al rich field since  $\alpha$ -Ti tends to be stabilized by oxygen(19). The interstitial content of the ingot influences not only phase stability but also mechanical properties even if both composition and condition of thermomechanical treatment are the same.

Table II Chemical composition of Ti-47Al-3Cr by both PAM and VIM

	(Ti, Al, Cr: at.%, O: wt.%)			
	Ti	Al	Cr	O
PAM	50.8	46.1	3.1	0.018
VIM	50.5	46.2	3.3	0.160

Fig.6 shows the stress-strain curve of Ti-45Al-5Cr alloy composed of  $\gamma$  and  $\beta$  phases at room temperature, revealing 1.20% elongation slightly lower than the 1.5% for Ti-48.7Al-1.8Cr alloy(20). The improvement of ductility at room temperature is caused by the decrease of the impurity level(20) and fine uniform grain structure(21). The Ti-45Al-5Cr alloy prepared for the matrix of SiC<sub>CVD</sub> / TiAl composite has improved ductility at room temperature and deformability at elevated temperatures.

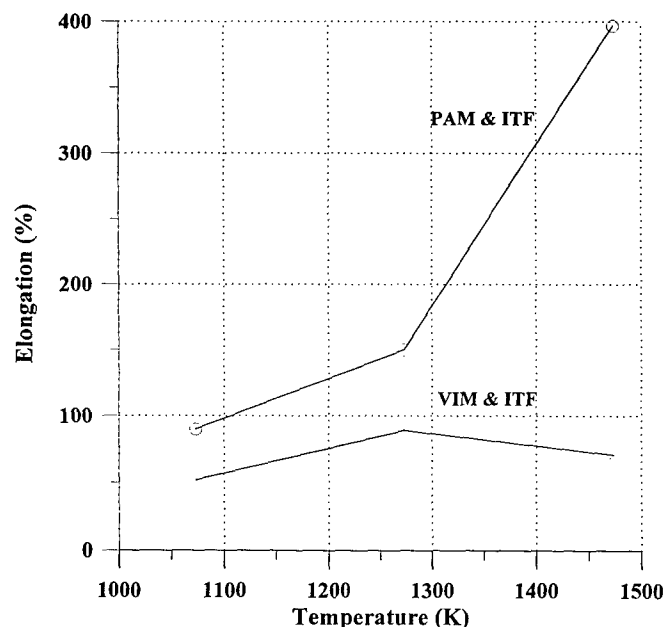


Figure 5: Tensile elongation in isothermally forged Ti-47Al-3Cr prepared by PAM and VIM

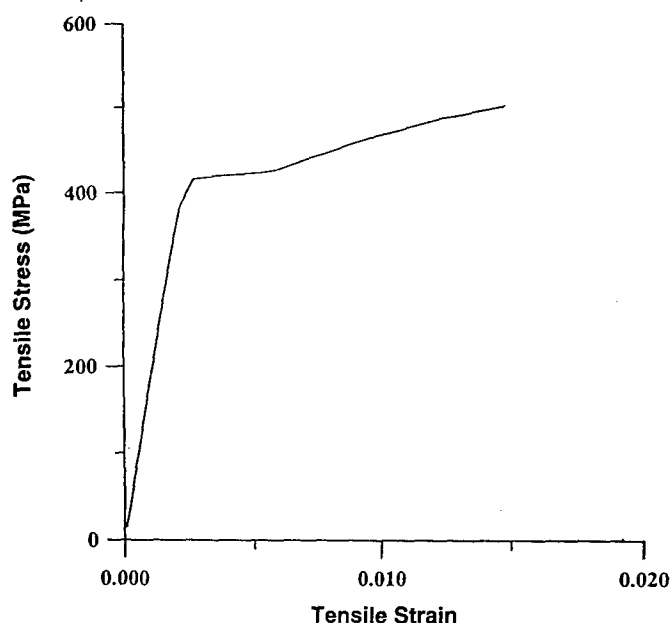


Figure 6: Stress-strain curve at room temperature of Ti-45Al-5Cr exhibiting  $\gamma$  and  $\beta$  dual phases

#### TiAl-Cr foil

Thin foil making process was tried by the ingot metallurgy and the powder method. In ingot metallurgy, forming TiAl sheet is difficult by the conventional process because it requires high temperature, low strain rate and low reduction ratio in either an inert gas atmosphere or a vacuum. Recently, these difficulties have been overcome by isothermal rolling (22) and pack rolling method through prevention of stress concentration in the materials(23,24). Defect free TiAl sheet with thickness up to 1.8 mm has been successfully rolled, but forming foil under 1 mm in thickness has

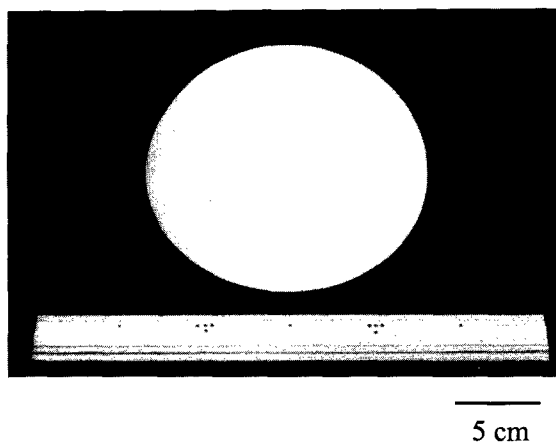


Figure 7: TiAl-Cr foil of 180mm  $\phi$  and 200 $\mu$ m thickness



Figure 8: Microstructure of TiAl-Cr foil

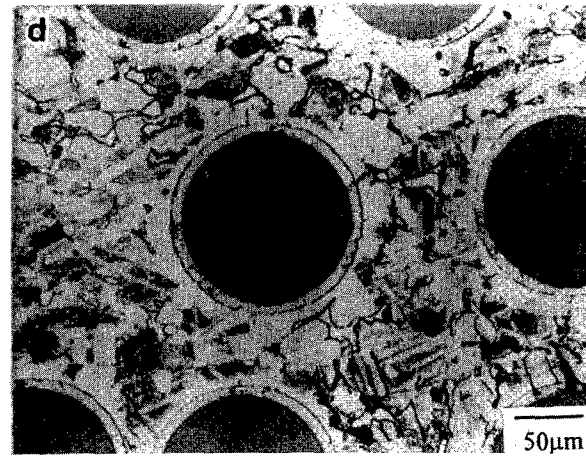
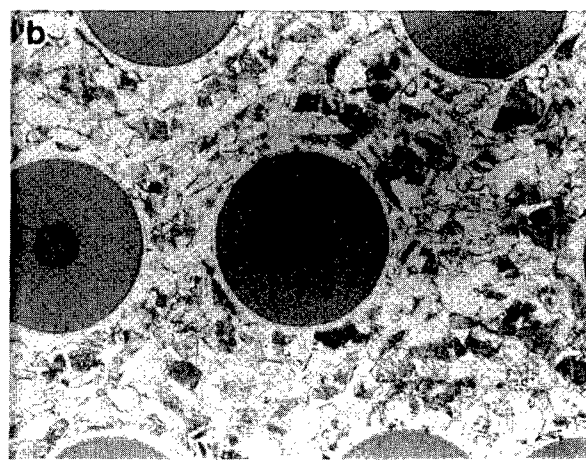
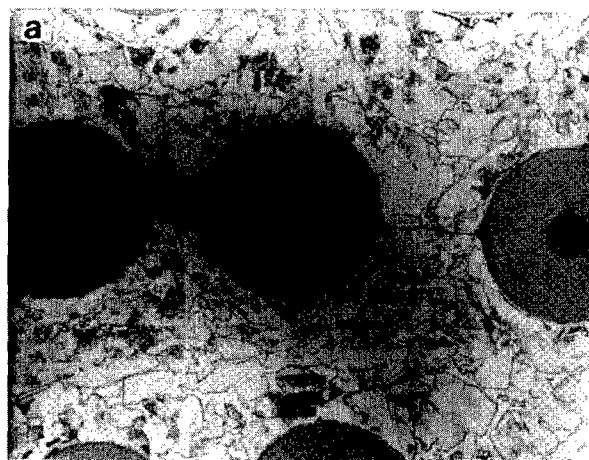


Figure 9: Microstructure of  $\text{SiC}_{\text{CVD}}$  / TiAl-Cr composites consolidated at (a) 1223K, (b) 1273K, (c) 1323K and (d) 1373K

not been achieved. On the other hand, foil-fiber-foil laminates were obtained by rolling elemental Ti-Al powder mixture (4). However, SiC fibers were revealed not to be bonded to TiAl powder foils because of chemical reaction between SiC and TiAl at the higher consolidation temperature.

Foils with the thickness of 100-200  $\mu\text{m}$  are required for the  $\text{SiC}_{\text{CVD}}$ /TiAl composite in order to increase fiber volume fraction, as high volume fraction leads to improved strength of the composite at elevated temperatures. As a practical forming process for foils has not been completed, the present foils were prepared by mechanical grinding. Isothermally forged TiAl-Cr composed of  $\gamma$  and  $\beta$  phases was sectioned to 500 $\mu\text{m}$  thickness by means of the electric discharge cutting process. Foils were finished to 200 $\mu\text{m}$  thickness by grinding with SiC abrasive grit. Fig.7 shows a photograph of TiAl-Cr foil of 180mm  $\phi$  and 200 $\mu\text{m}$  thickness. The foil had a flat surface within 10 $\mu\text{m}$  roughness, and was free of defect like warp or crack. Fig.8 shows the microstructure of foil surface. The surface has the same microstructure as the internal area without either chemical reaction or grain deformation through machining. It was found that TiAl is extremely sensitive to surface cracks (21), therefore careful surface treatment will be necessary. TiAl-Cr foils with no surface crack and homogeneous microstructure were supplied for  $\text{SiC}_{\text{CVD}}$ /TiAl-Cr composites.

#### Consolidation condition of $\text{SiC}_{\text{CVD}}$ /TiAl-Cr composite

In order to determine the optimum conditions for consolidating  $\text{SiC}_{\text{CVD}}$ /TiAl-Cr composites, TiAl-Cr foils and SCS-6 preforms were consolidated by the vacuum hot pressing process at 1223, 1273, 1323 and 1373K. Fig.9 indicates the cross-sectional microstructure of these composites. At the lowest consolidating temperature (1223K), diffusion bonding between each TiAl-Cr foil is not completed. At consolidating temperature higher than 1273K, complete metallurgical and mechanical bonding takes place across both matrix/matrix and matrix/fiber interfaces with the 21% volume fraction of fiber in these composites. These results are in good agreement with the deformability of TiAl-Cr alloy at elevated temperatures. Since TiAl-Cr exhibits excellent superplastic deformation and higher elongation above 1273K as shown in Fig.4, TiAl-Cr foil is sufficient to deform around the fibers. There is no crack in composites consolidated above 1273K as shown in Fig.9. This is attributable to the stability of microstructure morphology, which keeps the deformability of the matrix at room temperature to relax the residual stress by thermal expansion mismatch between matrix and fibers. The reaction zone at the  $\text{SiC}_{\text{CVD}}$ /TiAl-Cr interface becomes thicker with increasing consolidation temperature. Although there isn't sufficient quantitative data about remaining carbon layer on SiC fiber, the diffusion distance of carbon into TiAl-Cr matrix has a tendency to become longer with increasing consolidation temperature. Fig.10 shows SEM image and concentration line profiles by EPMA of the matrix/fiber interface in the composite fabricated at 1323K. The reaction zone with a thickness of 6 $\mu\text{m}$  is thinner than that in composite using elemental powder foil as the matrix(4). The present EPMA line profile is in good agreement with previous results (25,26), which showed fiber - TiC -  $\text{Ti}_2\text{AlC}$  ( $\text{Ti}_3\text{AlC}$ ) -  $\text{Ti}_5\text{Si}$  - matrix. However, Cr is revealed to be enriched in both the TiC and  $\text{Ti}_5\text{Si}$  regions in this system. To explain the formation of these reaction layers in  $\text{SiC}_{\text{CVD}}$ /TiAl-Cr composite, it is necessary to investigate further by means of detailed TEM analysis in addition to measuring diffusivity and solubility of elements.

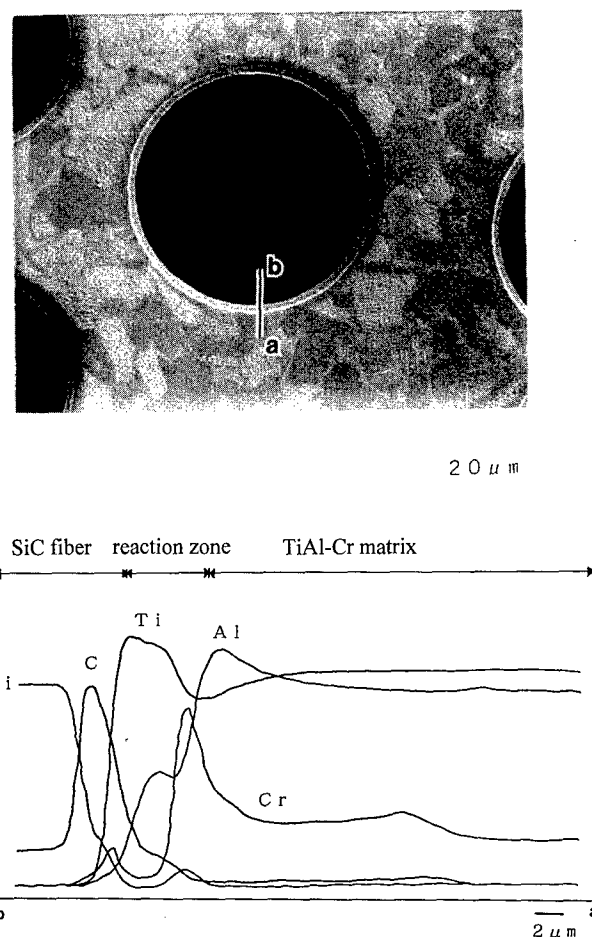


Figure 10: SEM micrograph and EPMA line profile at matrix/fiber interface of TiAl-Cr composite fabricated at 1323K

Fig. 11 shows SEM image and EPMA line profiles of the matrix/matrix bonding zone in the composite fabricated at 1323K. The original matrix/matrix interface disappears by diffusion bonding during fabrication. The microstructure in the bonding area is  $\gamma$  and  $\beta$  dual phases, the same as the matrix. In previous studies on diffusion bonding in  $\gamma$ -TiAl (27,28), equiaxed gamma grains at the bonding interface were formed due to dynamic recrystallization. New recrystallization eliminates the actual bonding interfaces, which improves tensile strength. The formation of dynamic recrystallization at the bonding region was not observed in the present work. However, it is thought that the elimination of the bonding interface provides increased bonding strength.

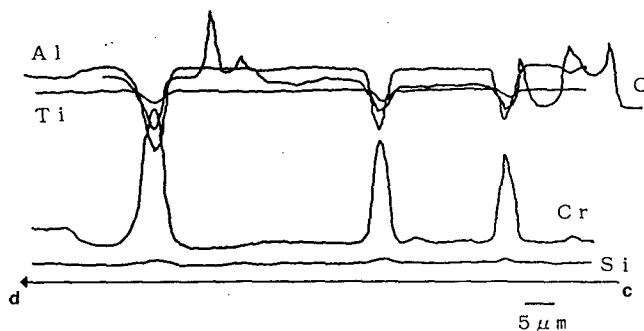
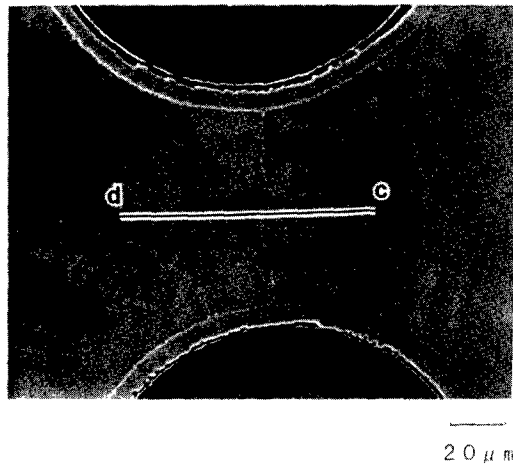


Figure 11: SEM micrograph and EPMA line profile at matrix/matrix bonding zone of TiAl-Cr composite fabricated at 1323K

Fig. 12 shows the dependence of tensile strength of  $\text{SiC}_{\text{CVD}}/\text{TiAl-Cr}$  composite at room temperature on fabrication temperature, indicating the maximum strength in the temperature range from 1273K to 1323K in accord with the microstructure as shown in Fig.9. The stress transmission is insufficient in the composite fabricated at 1123K because of poor diffusion bonding between the matrix and fibers. The fractography of these composites after tensile tests is expressed as a function of consolidation temperature. Although large fiber pull-out can be seen in composite fabricated at 1123K, no fiber pull-out can be observed in the composite fabricated at 1273K and 1323K, indicating strong bonding strength between TiAl-Cr matrix and SiC fiber. However, the thick reaction layer at  $\text{SiC}_{\text{CVD}}/\text{TiAl-Cr}$  interface in the composite fabricated at 1373K was responsible for the poor tensile strength.

As a result, good consistency between the mechanical property and microstructure was obtained in  $\text{SiC}_{\text{CVD}}/\text{TiAl-Cr}$  composite. The appropriate condition for consolidating  $\text{SiC}_{\text{CVD}}/\text{TiAl-Cr}$  composite is a narrow range of 4 hours at 1273-1323K under a pressure of 98MPa.

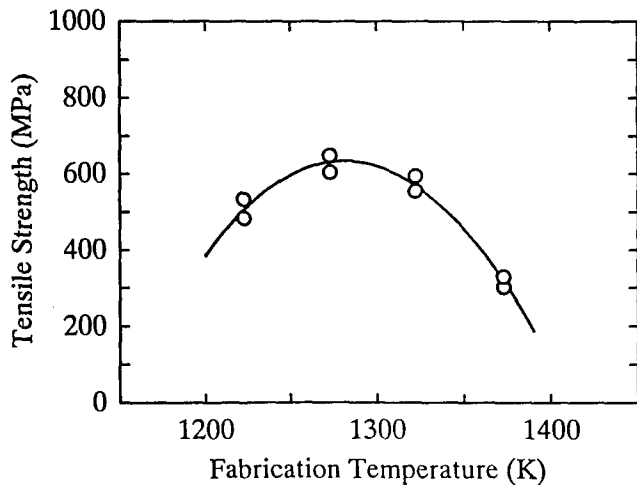


Figure 12: Dependence of tensile strength at room temperature on fabrication temperature

#### Tensile properties of $\text{SiC}_{\text{CVD}}/\text{TiAl-Cr}$ composites

$\text{SiC}_{\text{CVD}}/\text{TiAl-Cr}$  composite was consolidated for 4 hours at 1323K under a pressure of 98MPa. The volume fraction of fiber in this composite is about 22%. Tensile tests along the fiber direction were performed at room temperature, 773, 873 and 973K. The temperature dependence of tensile properties in this composite is shown in Fig.13. Young's modulus is 208 GPa at 773K, which is the same as that at room temperature and slightly decreases with increasing temperature above 773K. Tensile strength indicates a maximum value, 954MPa at 773K and keeps a high value, 852MPa at 973K. It is considered that the residual stress generated by thermal expansion mismatch between SCS-6 fibers and TiAl-Cr matrix during the fabrication process causes temperature inverse dependence of tensile strength from room temperature to 773K (thermal expansion coefficient, SCS-6:  $1.5 \times 10^{-6} \text{K}^{-1}$ , TiAl-Cr:  $11.5 \times 10^{-6} \text{K}^{-1}$ ). So the matrix fractures under quite small strain at room temperature due to the residual stress. At elevated temperatures, the fracture strain of the matrix is larger than that at room temperature, because heating releases the accumulated tensile strain in the matrix. As a result, the tensile strength of  $\text{SiC}_{\text{CVD}}$  is sufficiently reflected in tensile strength at elevated temperatures.

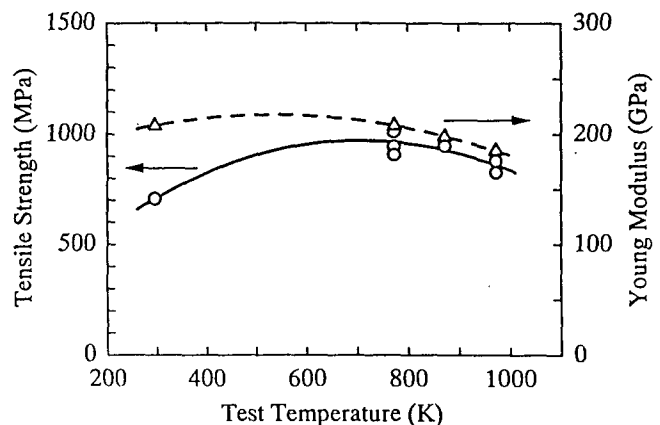
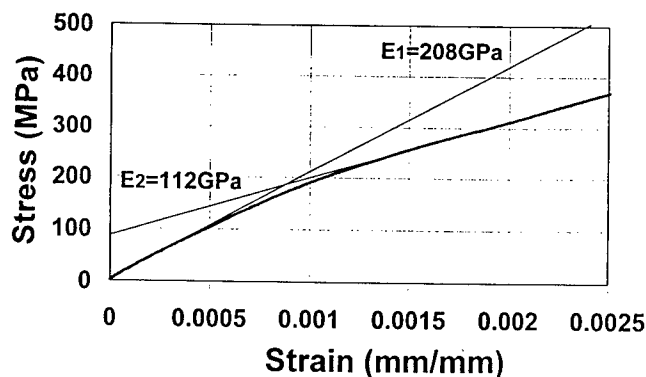


Figure 13: Tensile properties of  $\text{SiC}_{\text{CVD}}/\text{TiAl-Cr}$  composite

This difference is remarkably observed in stress-strain curves. The modulus of elasticity changes at the inflection point in the stress-strain curve for the strain range from 0 to 0.0025 as shown in Fig. 14.

(a) room temperature



(b) 773K

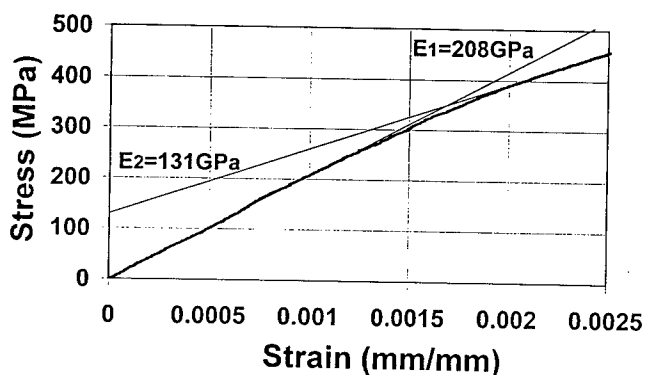


Figure 14: Stress-strain curves of  $\text{SiC}_{\text{CVD}} / \text{TiAl-Cr}$  composite at (a) room temperature and (b) 773K

The inflection point is 0.09% strain at room temperature and 0.17% strain at 773K. It is considered that elastic modulus at room temperature changes at small strain as a result of matrix yielding as above mentioned.

On the other hand, lower tensile strength at room temperature may be due to environmental embrittlement of the matrix, in which tensile properties are influenced by the testing atmosphere. It was revealed that two phase TiAl alloy in polycrystalline form shows lower ductility at room temperature in air than that tested in vacuum(29,30). As tensile tests of the present work were carried out in air, this environmental effect may be responsible for the poor ductility of the matrix at room temperature.

The  $\text{SiC}_{\text{CVD}} / \text{TiAl-Cr}$  composite is slightly inferior in tensile strength to Ni-base superalloys used as conventional engine material. However, this composite shows higher specific strength than that of Inconel 718 alloy from room temperature to 973K (Fig. 15).

We are now investigating practical properties such as fatigue and creep of this composite. Applying the optimum consolidation, an experimental turbine disc of  $\text{SiC}_{\text{CVD}} / \text{TiAl-Cr}$  composite will be manufactured.

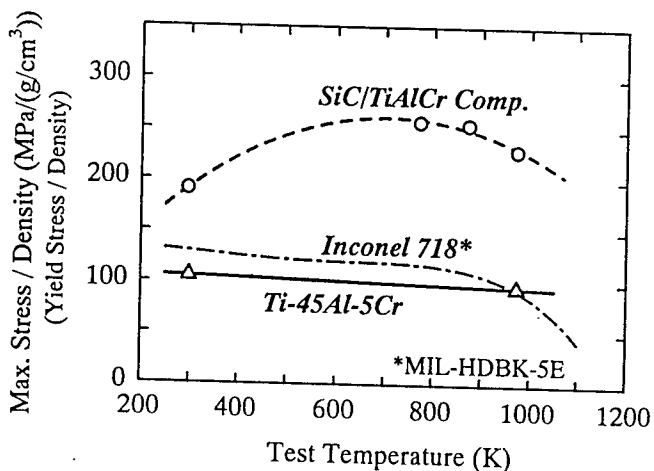


Figure 15: Specific strength of  $\text{SiC}_{\text{CVD}} / \text{TiAl-Cr}$  composite and Ni-base superalloy

### Conclusion

The deformability of  $\gamma$ -TiAl based alloy has been improved by alloy design and microstructure control. The fabrication conditions and mechanical properties of  $\text{SiC}_{\text{CVD}} / \text{TiAl}$  composite using this superplastic TiAl thin foil have been investigated.

It is concluded as follows:

1. The improvement of superplastic deformation requires control of grain boundary in addition to both grain refinement and phase distribution. The higher volume fraction of  $\beta$  phase at  $\gamma$  grain boundary in TiAl-Cr alloy lowers the onset temperature of superplasticity.
2. The oxygen content of TiAl influences the deformation behavior at elevated temperatures. The formation of  $\alpha_2$  phase promoted by oxygen content in  $\gamma$  and  $\beta$  dual phase alloy brings about poor ductility at elevated temperatures.
3. Superplastic TiAl-Cr foils and SCS-6 fibers were consolidated by the vacuum hot pressing process. The volume fraction of fiber in this composite is 21-22%. Good consistency between the mechanical property and microstructure was observed in  $\text{SiC}_{\text{CVD}} / \text{TiAl-Cr}$  composite. The optimum condition of consolidating  $\text{SiC}_{\text{CVD}} / \text{TiAl-Cr}$  composite was determined to be a narrow range of 4 hours at 1273-1323K under a pressure of 98MPa.
4. The tensile properties of  $\text{SiC}_{\text{CVD}} / \text{TiAl-Cr}$  composite have been investigated at elevated temperatures. The measured tensile strength of the composite at 773K is 93% of the value calculated by the rule of mixtures. The specific tensile strength of a unidirectional  $\gamma$ -TiAl matrix composite is roughly double that of Inconel 718 alloy.

### Acknowledgement

The authors would like to acknowledge several discussions and many useful suggestions by Dr. N. Masahashi, Dr. N. Akikawa and Mr. M. Imuta. The authors are also grateful to Mr. S. Sato for technical assistance.

## References

1. J. Sorensen, Structural Intermetallics, eds. by R. Darolia, J.J. Lewandowski, C.T. Liu, P.L. Martin, D.B. Miracle and M.V. Nathal (Warrendale/PA: The Minerals, Metals & Materials Society, 1993), P.717-726
2. J.C. Chesnutt, Superalloys 1992 (1992), P.381-389
3. C. Fujiwara, Proc. of The 4th Symposium on High-performance Materials for Severe Environments, June(1993), P.325-334
4. Th. Jungling, B. Kieback, W. Glatz and H. Clemens, Gamma Titanium Aluminides, eds. by Y-W. Kim, R. Wagner, and M. Yamaguchi (The Minerals, Metals & Materials Society, 1995), P.627-634
5. N. Masahashi, Y. Mizuhara, M. Matsuo, K. Hashimoto, T. Hanamura and H. Fujii, Proc. of MRS Symposium, eds. by L.A. Johnson, D.P. Pope and J.O. Stiegler, Vol.213(1991), P.795-800
6. H. Fukutomi, C. Hartig and H. Mecking, Z. Metallk., 81(1990), P.272-277
7. R. M. Imayev, O. A. Kaibyshev and G. A. Salishchev, Acta metall. mater., 40(1992), P.581-587
8. M. Nobuki and T. Tsujimoto, Advanced Structural Materials, Proc. C-MRS Int., ed. by Y. Han, Vol.2(1991), P.791-796
9. S. C. Cheng, J. Wolfenstine and O. D. Sherby, Metall Trans., 23A(1992), P.1509-1513
10. H. S. Yang, W. B. Lee and A. K. Mukherjee, Structural Intermetallics, eds. by R. Darolia, J.J. Lewandowski, C.T. Liu, P.L. Martin, D.B. Miracle and M.V. Nathal (Warrendale/PA: The Minerals, Metals & Materials Society, 1993), P.69-76
11. R. S. Mishra, W. B. Lee and A. K. Mukherjee, Gamma Titanium Aluminides, eds. by Y-W. Kim, R. Wagner and M. Yamaguchi, (The Minerals, Metals & Materials Society, 1995), P.571-578
12. M. Nobuki, D. Vanderschueren and M. Nakamura, Acta metall. mater., 42(1994), P.2623-2632
13. Y. Mizuhara and N. Masahashi, Scripta Met., 27(1992), P.1079-1084
14. T. Maeda, M. Okada and Y. Shida, Proc. of MRS Symposium, eds. by L.A. Johnson, D.P. Pope and J.O. Stiegler, Vol.213(1991), P.555-560
15. P. L. Martin, H. A. Lipsitt, N. T. Nuhfer and J. C. Williams, Titanium '80 Science and Technology (TES-AIME, Warrendale, PA 1981), P.1245-1254
16. J. W. Edington, Metall Trans., 13A(1982), P.703-715
17. R. Uemori, T. Hanamura and H. Morikawa, Scripta Met., 26(1992), P.969-974
18. N. Masahashi and Y. Mizuhara, Gamma Titanium Aluminides, eds. by Y-W. Kim, R. Wagner and M. Yamaguchi, (The Minerals, Metals & Materials Society, 1995), P.165-172
19. S.C. Huang and P.A. Siemers, Metall Trans., 20A (1989), P.1899-1906
20. T. Kawabata, M. Tadano and O. Izumi, Scripta Met., 22(1988), P.1725-1730
21. K. Hashimoto and M. Kimura, Structural Intermetallics, eds. by R. Darolia, J.J. Lewandowski, C.T. Liu, P.L. Martin, D.B. Miracle and M.V. Nathal (Warrendale/PA: The Minerals, Metals & Materials Society, 1993), P.309-318
22. N. Fujitsuna, Y. Miyamoto and Y. Ashida, Structural Intermetallics, eds. by R. Darolia, J.J. Lewandowski, C.T. Liu, P.L. Martin, D.B. Miracle and M.V. Nathal (Warrendale/PA: The Minerals, Metals & Materials Society, 1993), P.187-194
23. S. L. Semiatin, M. Ohls and W. R. Kerr, Scripta Met., 25(1991), P.1851-1856
24. H. Clemens, P. Schretter, K. Wurzwallner, A. Bartels and C. Koeppel, Structural Intermetallics, eds. by R. Darolia, J.J. Lewandowski, C.T. Liu, P.L. Martin, D.B. Miracle and M.V. Nathal (Warrendale/PA: The Minerals, Metals & Materials Society, 1993), P.205-214
25. D. R. Baker, P. J. Doorbar and M. H. Loretto, Proc. of MRS Symposium, Vol.170(1991), P.85-90
26. Grace K. Goo, Jeffrey A. Graves and Martha L. Mecartney, Scripta Met., 26(1992), P.1043-1048
27. Y. Nakao, K. Shinozaki and M. Hamada, ISIJ International, Vol.31, No.10(1991), P.1260-1266
28. G. Cam, K. -H. Bohm, J. Mullauer and M. Kocak, "Microstructural development during diffusion bonding of  $\gamma$ -TiAl", in International Welding Technology '96 Symposium, Istanbul, Turkey(1996), P.25-35
29. C. T. Liu and Y. W. Kim, Scripta Met., 27(1992), P.599-603
30. T. Takasugi, S. Hanada and M. Yoshida, J. Mater. Res., 7(1992), P.2739-2746



## AN INVESTIGATION OF FATIGUE AND FRACTURE IN NiAl/Mo COMPOSITES

P. Ramasundaram<sup>1</sup>, R. Bowman<sup>2</sup> and W. O. Soboyejo<sup>3</sup>

<sup>1</sup> Wyman-Gordon Forgings, Houston, TX 77095

<sup>2</sup> NASA Lewis Research Center, 21000 Brookpark Road, Cleveland, OH 44135.

<sup>3</sup> Department of Materials Science and Engineering, The Ohio State University, 2041 College Road, Columbus, OH 43210

### **Abstract**

The effects of reinforcement morphology (particulate versus fibers) and particulate volume fraction on the fatigue and fracture behavior of NiAl/Mo composites are discussed. The improved fracture toughness observed in these composites are not associated with improved tensile ductility. The improved fracture toughness levels are explained by quantifying the shielding contributions due to crack trapping mechanisms. Stable crack growth under cyclic loading was observed in all the NiAl/Mo composites studied. The potential implications of the results are discussed for future composite development.

### **Introduction**

NiAl has been investigated for use as a high temperature structural material for over three decades [1,2]. If successful, one potential application of NiAl would be in aeroengine components that are currently fabricated from nickel-based superalloys. Among the range of intermetallic compounds that are being considered as potential alternatives to the Ni-based superalloys, NiAl is especially attractive due to its low density (5.9 g/cc), high melting point (1638°C), high thermal conductivity (40-80 W/mK over a wide temperature range [1]) and excellent oxidation resistance due to the high Al content. However, the major limitation to the application of NiAl is its room temperature brittleness [3]. The room temperature tensile ductility of NiAl ranges from less than 1% to about 2 % for polycrystalline NiAl, and the typical fracture toughness is approximately  $5 \text{ MPa}\sqrt{\text{m}}$  [1]. It is estimated that a minimum room temperature tensile ductility of around 1-2% and a fracture toughness of about  $15\text{-}20 \text{ MPa}\sqrt{\text{m}}$  would be required to

accommodate the contact stresses that can be generated during the assembly of engine components and to retain sufficient damage tolerance respectively [4].

The fracture toughness of brittle ceramics and intermetallics can be improved by reinforcement with ductile phases [5,6]. The fracture toughness increase is typically the result of so-called 'extrinsic' toughening phenomena such as crack-tip blunting, crack bridging, crack trapping and crack deflection by the reinforcement phase [7-9].

The possibility of ductile phase toughening of NiAl by reinforcement with molybdenum (Mo) was considered in this study. Mo was selected as the reinforcement due to its thermodynamic compatibility with NiAl [3], and its attractive room and elevated temperature strength (895 MPa at 20°C, 415 MPa at 1095°C), stiffness (~315 GPa) and high melting point (2610°C) [10]. Since the NiAl-Mo system exhibits a pseudo-binary eutectic equilibrium [11], two phase systems consisting of up to 61 vol. %  $\alpha$ -Mo have been obtained after processing at temperatures up to 1500°C [6].

In this study, artificial composites were fabricated by hot isostatic pressing (HIPing) of phase blended NiAl/Mo powders. The effects of Mo reinforcement morphology and volume fraction on the fatigue crack growth behavior and fracture toughness were investigated. Toughening mechanisms were identified under monotonic and cyclic loading. In the following sections, the materials processing details and the microstructures are presented. The experimental procedure adopted is then described. Results of room temperature fracture toughness and tensile ductility tests are presented and the associated fracture

mechanisms are elucidated. The micromechanisms of stable crack growth are also elucidated, prior to a presentation of salient conclusions arising from this work.

### Materials

Four different NiAl/Mo composites were investigated along with nominally stoichiometric polycrystalline NiAl. These are listed below along with their designations:

- (a) NiAl
- (b) NiAl+10 vol.% Mo (particulate)-designated as NiAl/10 Mo<sub>p</sub>
- (c) NiAl+20 vol.% Mo (particulate)-designated as NiAl/20 Mo<sub>p</sub>
- (d) NiAl+30 vol.% Mo (particulate)-designated as NiAl/30 Mo<sub>p</sub>
- (e) NiAl + 20 vol.% Mo (fiber) - designated as NiAl/20 Mo<sub>f</sub>

The -325 mesh NiAl powder that was used in this study was procured from Homogeneous Metals, Inc., Clayville, NY. The average particle size of the NiAl powder was approximately 25-30  $\mu\text{m}$ . -325 mesh molybdenum (Mo) powder was obtained from CERAC, Inc., Milwaukee, WI. The powder (particulate reinforced) NiAl/xMo<sub>p</sub> (x = 10, 20 and 30 vol. %) composites and NiAl were processed as follows: the component powders were mixed in suitable proportions and ball milled using zirconia milling media for 24 hours. The resulting mixtures were hot pressed at 1093°C/103 MPa/0.5 hours in argon gas followed by hot isostatically pressing (HIP) at 1260°C/138 MPa/4 hours in stainless steel cans. Eight ply NiAl/20 Mo<sub>f</sub> composites were also fabricated using the "powder cloth method" of composite fabrication at NASA, Lewis Research Center, Cleveland [12]. Mo wires were used as reinforcements. Composite monotapes were produced by the powder cloth process. Eight such monotapes were stacked together and hot pressed followed by a HIP cycle that was identical to that used for the particulate reinforced composites.

Typical optical micrographs obtained from the NiAl/10 Mo<sub>p</sub> composite are presented in Fig. 1. The brighter phase consists of the discrete and discontinuous Mo particles (Fig. 1a). The Mo grains are typically 15-20  $\mu\text{m}$  in size while the NiAl grains have an average size of 25-30  $\mu\text{m}$ . An interfacial reaction layer can be seen between the NiAl and Mo particles (Fig. 1b). This layer is about 1  $\mu\text{m}$  thick (Fig. 1b). Prior particle boundaries (PPBs) can also be seen in the NiAl phase (Fig. 1b). The nature of the reaction layer and the PPBs is discussed in greater detail later on in this section. The microstructures of the NiAl/20 Mo<sub>p</sub> and NiAl/30 Mo<sub>p</sub> composites are similar to that of the NiAl/10 Mo<sub>p</sub> composite. The actual volume fractions of the second phase in the NiAl/Mo<sub>p</sub> composites were measured using an image analyzer and found to be close to the nominal volume fractions (Table I).

Table I. Volume fractions of Mo<sub>p</sub> phase in the NiAl/Mo<sub>p</sub> composites

Material	Volume percent Mo (mean)	Standard Deviation ( $\sigma$ )
NiAl/10 Mo <sub>p</sub>	8.95	0.53
NiAl/20 Mo <sub>p</sub>	19.31	2.07
NiAl/30 Mo <sub>p</sub>	28.38	1.50

Typical TEM photomicrographs obtained from the as-processed NiAl/10 Mo<sub>p</sub> and NiAl/20 Mo<sub>p</sub> composites are presented in Figs. 2a and 2b. The particles at the NiAl grain boundaries are shown in Fig. 2a. Fig. 2b includes the reaction layer, which is seen to be polycrystalline with roughly equiaxed grains. The mottled appearance of the Mo phase is an artifact of the ion-milling process that was used to prepare the specimens.

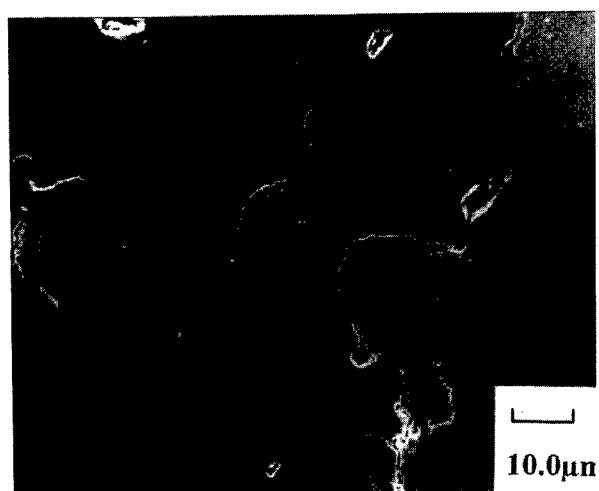
The microstructure of the NiAl/Mo<sub>f</sub> composite is presented in Figs. 3a and 3b. The Mo fibers are about 150  $\mu\text{m}$  in diameter and distributed fairly uniformly within the NiAl matrix (Fig. 3a). A reaction layer is also observed between the NiAl and Mo fiber, as shown in Fig. 3b. The composition of the reaction layer was determined using energy dispersive spectroscopy (EDS) both in the SEM and in the TEM. The interfacial reaction layer consisted of approximately 75 at. % Mo and 25 at. % Al. The Mo-Al phase diagram shows the presence of a non-stoichiometric compound Mo<sub>3</sub>Al, which is stable over a wide range of temperatures [13]. The intermetallic compound, Mo<sub>3</sub>Al, possesses the Al<sub>5</sub> structure (Cr<sub>3</sub>Si prototype) with a lattice parameter,  $a = 0.495 \text{ nm}$  [13]. Selected area electron diffraction patterns were obtained from a single grain in the reaction layer. Comparison of the diffraction patterns with those corresponding to the Mo<sub>3</sub>Al compound confirmed that the reaction layer is in fact Mo<sub>3</sub>Al in both the particulate and fiber reinforced composites [12]. The reaction layer is believed to be a non-equilibrium or intermediate phase in the composites, since the pseudo-binary NiAl-Mo phase diagram indicates that NiAl and Mo form a two-phase eutectic [11].

The composition of the particles comprising the PPBs was determined using EDS in the TEM and found to be rich in zirconium (Zr). These are probably ZrO<sub>2</sub> particles. Zirconia milling media were used in the ball-milling of the NiAl+Mo powder mixtures and is the most likely source of the particles at the prior particle boundaries in the NiAl/Mo<sub>p</sub> composites.

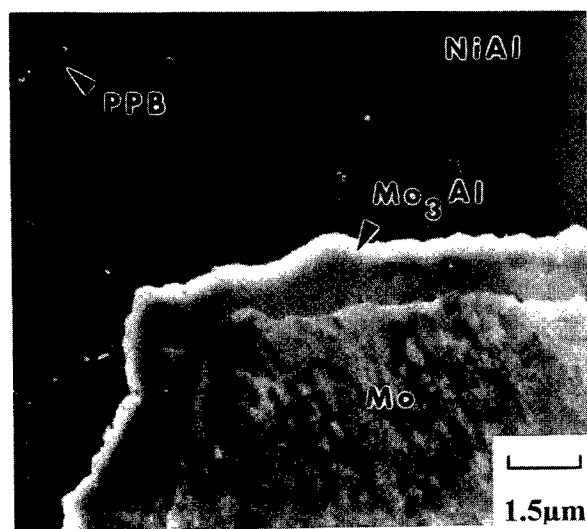
### Experimental Procedure

#### Fracture Toughness and Fatigue Crack Growth

Compact tension (CT) composite specimens of overall dimensions 15mm x 15mm x 3mm were machined by electro-discharge machining (EDM) from the HIPed compacts. CT specimens from the NiAl/xMo<sub>p</sub> (x = 10, 20 and 30 vol. %) and NiAl/20 vol. % Mo<sub>f</sub> composites were tested for fracture toughness at a constant loading rate corresponding to a stress intensity factor increase rate of approximately  $1 \text{ MPa}\sqrt{\text{m}} \text{ s}^{-1}$  according to the ASTM E-399-90 method [14]. The fibers were oriented perpendicular to the notch and the crack-plane in the case of the NiAl/Mo<sub>f</sub> composite. At least two tests were carried out on each composite. Two tests were always conducted using specimens with a "blunt" notch, i.e. notch machined with a wire EDM but without a fatigue pre-crack from the notch. In certain cases, additional tests were carried out on specimens that were pre-cracked under compression and that had sharp fatigue cracks emanating from the notch. The specimens were pre-cracked under cyclic compression using loads that were determined empirically [15]. A schematic illustration of the pre-cracking configuration can be found in [16]. Precracks of length approximately 200  $\mu\text{m}$  were obtained repeatably after 20000 cycles of cyclic compression.



(a)

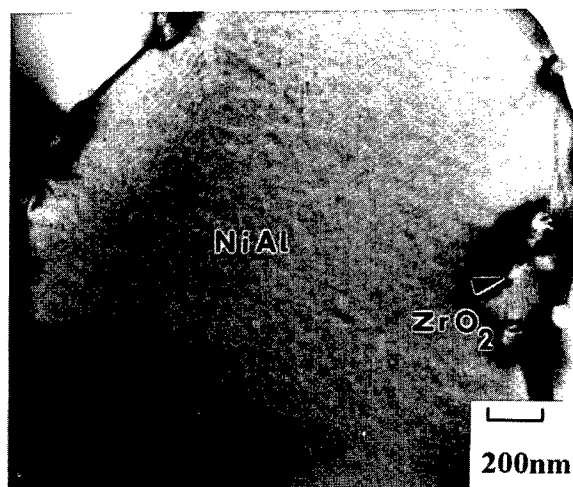


(b)

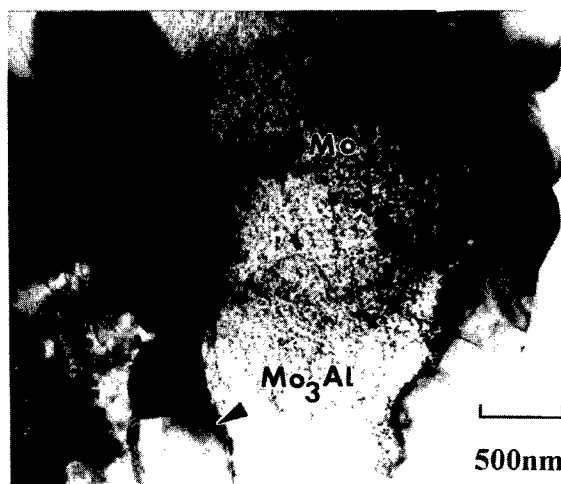
Fig. 1 Typical optical micrographs obtained from as-processed NiAl/10 Mo<sub>P</sub> composite.

Room temperature fatigue crack growth experiments were performed on the NiAl/xMo<sub>P</sub> (x = 10, 20 and 30 vol. %) and NiAl/20 vol. % Mo<sub>f</sub> composites. CT specimens were used for the crack growth studies. Pre-cracked specimens were loaded under cyclic tension at a load ratio,  $R$  of 0.1 ( $R = K_{min}/K_{max}$ ) and a frequency of 10 cycles/sec. The test was stopped periodically (every 100,000 cycles), the specimen was removed from the loading frame and the length of the crack was measured on both sides of the specimen using an optical microscope. Optical micrographs of the crack were also taken in order to obtain the crack profile. This procedure was adopted since the crack length could not be accurately measured *in-situ* while the test was running. Furthermore, the interaction of the crack with the microstructure was also of interest. The average length of the

crack calculated from both sides of the specimen was used to calculate the rate of crack growth ( $da/dN$ ) as a function of the stress intensity factor range ( $\Delta K$ ). The values of the crack lengths on both sides were close to each other indicating that the crack was a through crack.



(a)

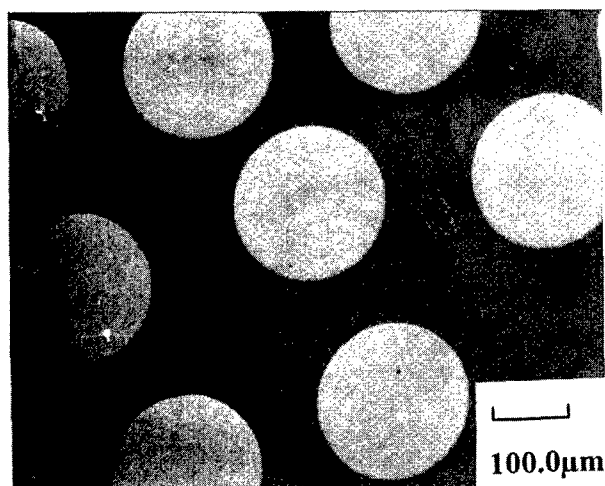


(b)

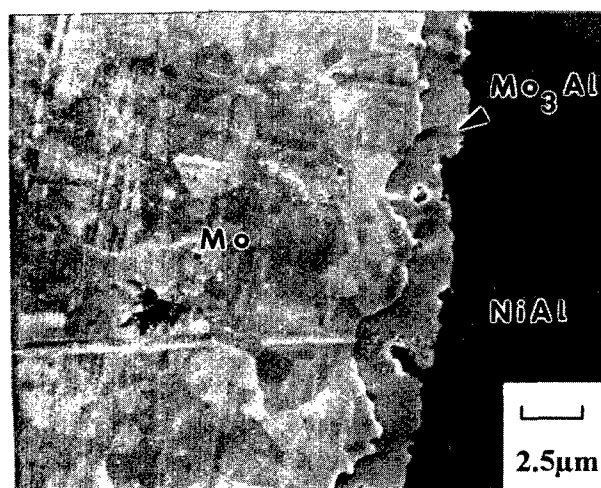
Fig. 2 Typical TEM micrographs from NiAl/x Mo<sub>P</sub> composites. (a) NiAl/10 Mo<sub>P</sub> (b) NiAl/20 Mo<sub>P</sub>.

#### Tensile Tests

Miniature flat tensile specimens of gage length 30 mm and thickness approximately 1.6 mm were machined from the NiAl/20 Mo<sub>P</sub> and NiAl/30 Mo<sub>P</sub> composites for tensile testing. Room temperature tensile tests were carried out on NiAl/20 Mo<sub>P</sub> and NiAl/30 Mo<sub>P</sub> composite specimens to determine the tensile ductility. The specimens were tested at a constant displacement rate of  $2.5 \times 10^{-3} \text{ mm.s}^{-1}$ . This corresponded to an engineering strain rate of approximately  $1 \times 10^{-4} \text{ s}^{-1}$ . The strain was measured using an extensometer mounted on the specimen. The extensometer had a gage length of 25.4 mm and a range of  $\pm 5\%$  strain.



(a)



(b)

Fig. 3 Microstructure of as-processed NiAl/Mo<sub>r</sub> composite.

#### Fractography

The fracture surfaces of the fracture toughness, tensile and fatigue crack growth specimens were examined under a scanning electron microscope (SEM). Secondary electron (SE) imaging mode was used principally, in order to characterize the fracture surface morphology. Occasionally, back-scattered (BS) electron imaging was used to distinguish the different phases on the fracture surfaces.

### Results

#### Fracture Toughness

The fracture toughness,  $K_{Ic}$ , of the NiAl/Mo composites is summarized in Table II. The fracture toughness of the composites is considerably greater than that of monolithic NiAl. The NiAl/Mo<sub>r</sub> composite possesses the highest fracture toughness of  $16.7 \text{ MPa}\sqrt{\text{m}}$ . The fracture toughness measured using specimens with a blunt notch is close to the values measured using specimens with a sharp fatigue crack (see Table

II). Notably, the fracture toughness values do not increase linearly with the volume fraction of the molybdenum phase. The fracture toughness values of the NiAl/20 Mo<sub>p</sub> and the NiAl/30 Mo<sub>p</sub> composites are very similar.

Table II. Fracture toughness values of NiAl/Mo composites

Material	Fracture Toughness, $K_{Ic} \text{ (MPa}\sqrt{\text{m}})$	Nature of notch/crack	Mean Fracture Toughness, $K_{Ic} \text{ (MPa}\sqrt{\text{m}})$
NiAl	5.4 5.2	Blunt notch Blunt notch	$5.3 \pm 0.1$
NiAl/10 Mo <sub>p</sub>	12.0 13.3 11.5	Blunt notch Blunt notch Sharp crack	$12.3 \pm 0.8$
NiAl/20 Mo <sub>p</sub>	16.7 12.2	Blunt notch Blunt notch	$14.4 \pm 2.2$
NiAl/30 Mo <sub>p</sub>	14.8 13.4 13.7	Blunt notch Blunt notch Sharp crack	$14.0 \pm 0.6$
NiAl/Mo <sub>r</sub>	17.0 16.9 16.2	Blunt notch Blunt notch Sharp crack	$16.7 \pm 0.4$

The mechanisms of fracture in NiAl and the NiAl/Mo composites were characterized by SEM fractography (Figs. 4 and 5). Fracture is intergranular in monolithic NiAl (Fig. 4). The predominant mode of fracture of the NiAl grains in the NiAl/Mo<sub>p</sub> composites was transgranular cleavage, with a small fraction of intergranular fracture (Fig. 5). "Dimples" can be seen on the surface of most Mo grains (Fig. 5c). Matching pebble-like features are present on the surface of some NiAl grains (Fig. 5a,b). Based on EDS, it was determined that the "pebbles" are the Mo<sub>3</sub>Al reaction layer grains. Interphase fracture occurs between the Mo grains and the polycrystalline Mo<sub>3</sub>Al layer. Although the dimples and ridges on the surface of the Mo grains suggest plastic deformation (Fig. 5c), it is more likely that these features result from the separation of the Mo<sub>3</sub>Al grains from the Mo grains. In any case, there is no large scale plasticity associated with the Mo grains prior to fracture. It was determined based on back scattered electron images that a small fraction of the Mo grains fractured by transgranular cleavage.

The fracture morphology of the NiAl/Mo<sub>r</sub> composite was a combination of intergranular fracture of the NiAl grains and intergranular fracture of the polycrystalline Mo fibers (Fig. 6). The size of the individual Mo grains in the fibers is approximately 3-5 μm. Once again, there is no appearance of plastic stretching of the Mo fibers prior to fracture.

#### Tensile Ductility

The room temperature tensile properties of the NiAl/20 Mo<sub>p</sub> and NiAl/30 Mo<sub>p</sub> were determined by tensile tests performed on flat dog bone specimens. The tensile ductility of both composites was negligible (<0.3 % - see Table III). Thus, while the fracture toughness of NiAl is significantly improved by the addition of Mo particles, the tensile ductility remains very low. This result is consistent with the observation of negligible plastic deformation of Mo grains in the fracture toughness and tensile

specimens prior to fracture. Alternative toughening mechanisms other than macroscopic plastic deformation are responsible for the improvement in fracture toughness in the NiAl/Mo composites. Discussion of the toughening mechanisms is deferred to a later section.

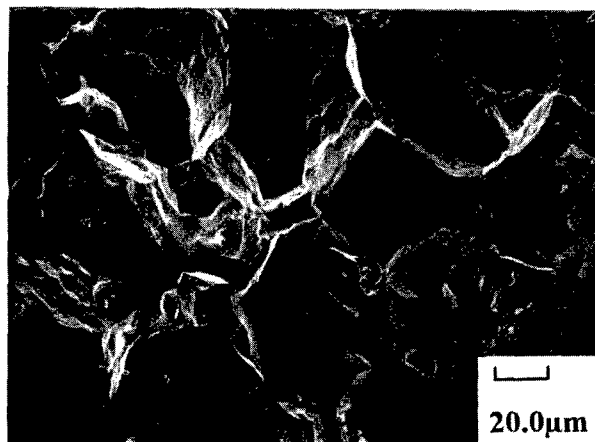


Fig. 4 Intergranular fracture in NiAl

Table III. Tensile properties of NiAl, NiAl/20 Mo<sub>p</sub> and NiAl/30 Mo<sub>p</sub> composites

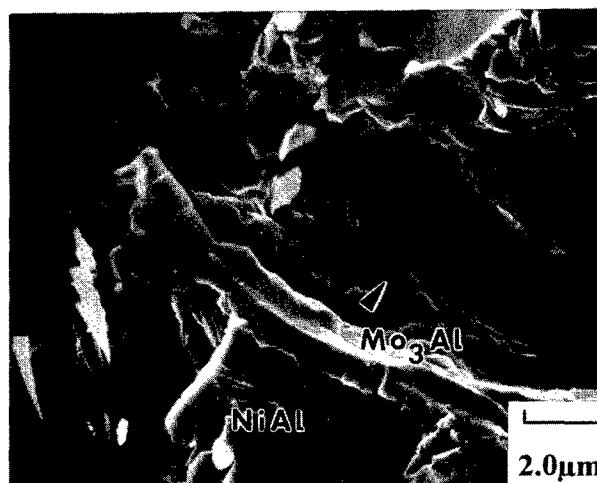
Material	Tensile Ductility (% strain to failure)	Fracture Stress (MPa)
NiAl*	1.4*	257*
NiAl/20 Mo <sub>p</sub>	0.3	250
NiAl/30 Mo <sub>p</sub>	0.3	275

\* Data obtained from [2].

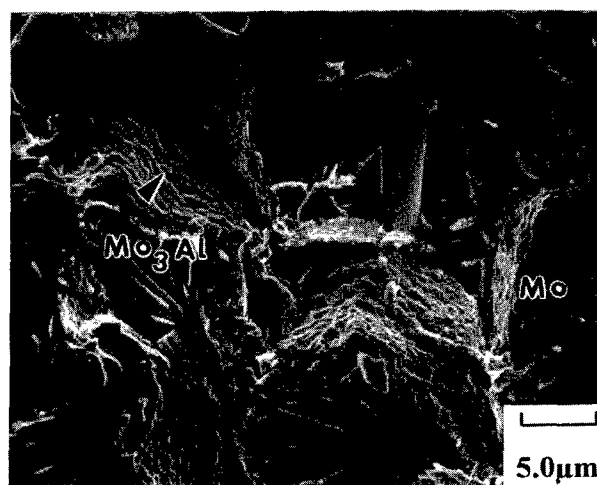
#### Fatigue Crack Growth

Stable fatigue crack growth under tension-tension cyclic loading was obtained in all the NiAl/Mo composites. The fatigue crack growth rate data is plotted in Fig. 7 as a function of the stress intensity factor range,  $\Delta K$ . Fatigue crack growth rates were calculated based on optical micrographs of the crack profile obtained periodically. The fatigue crack growth rates were slowest in the NiAl/Mo<sub>r</sub> composite.

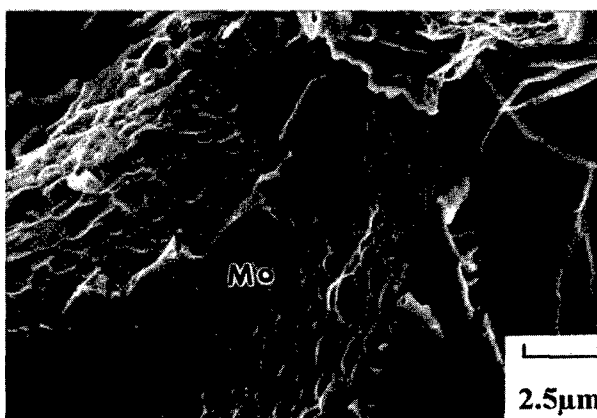
Figure 8 shows a typical fatigue crack profile observed in the NiAl/20 Mo<sub>p</sub> composite. In all the composites, the crack followed a combination of intergranular and transgranular path through the NiAl phase. It was observed that crack growth in all the NiAl/Mo<sub>p</sub> composites was intermittent. Periodically, the crack-tip encountered Mo particles and crack growth was temporarily arrested. This was determined based on a comparison of the optical micrographs of the location of the crack-tip obtained from the sides of the specimen at intervals of 100000 cycles. Subsequently, the crack-tip penetrated the reaction layer and deflected around the Mo grains, resulting in continued crack growth. The spacing of the Mo particles at which the crack-tip apparently arrested was fairly uniform. In all cases, the crack path was predominantly planar without appreciable tortuosity.



(a)

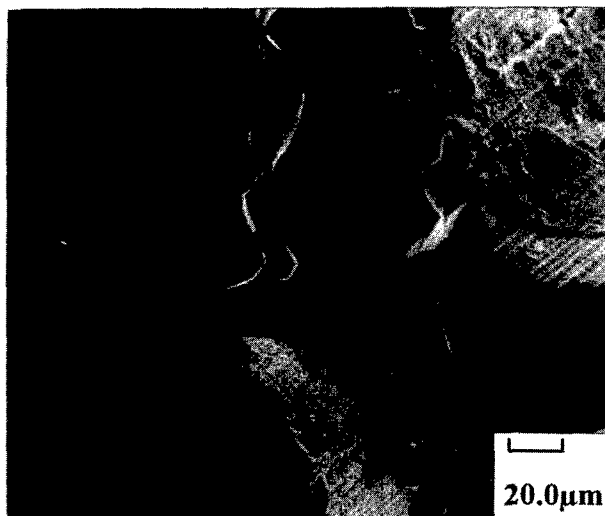


(b)

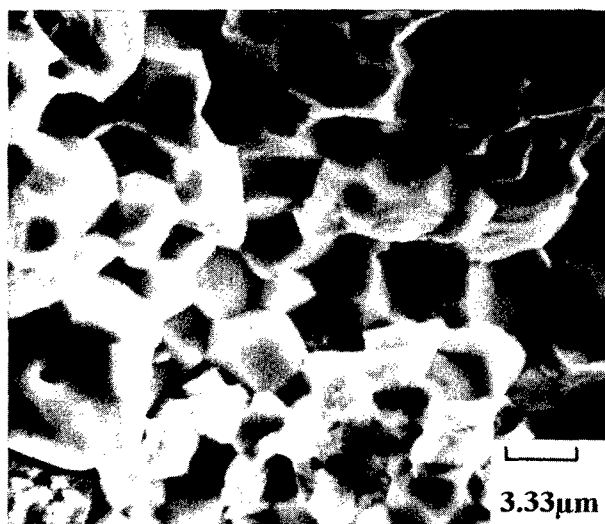


(c)

Fig. 5 Typical fracture surface morphology in NiAl/Mo<sub>p</sub> composites. (a) NiAl/10 Mo<sub>p</sub> (b) NiAl/20 Mo<sub>p</sub> (c) NiAl/30 Mo<sub>p</sub>.



(a)



(b)

Fig. 6 Typical fracture surface morphology of NiAl/Mo<sub>f</sub>.

A typical fatigue crack profile obtained in the NiAl/Mo<sub>f</sub> composite is presented in Fig. 9. The notable feature in the profiles is that the crack propagates across the Mo fibers. However, the rate of crack propagation was retarded whenever the crack-tip approached a Mo fiber. Crack growth then occurred at a fairly uniform rate through the fiber. Since the crack growth rates were determined based on micrographs of the crack profile, these correlations could be made between the crack growth rate and the location of the crack-tip relative to the Mo phase (Table IV). Based on the appearance of the crack profile, it is clear that crack bridging is not observed under cyclic loading in the NiAl/Mo<sub>f</sub> composite.

Fig. 10 shows the shape of the fatigue crack at two early stages of crack growth in the NiAl/Mo<sub>f</sub> composite that suggests a possible toughening mechanism under monotonic loading. In Fig. 10a, the crack-tip appears to have stopped in the middle of

the fiber (indicated by arrow) and renucleated in the NiAl matrix beyond the fiber. At a subsequent stage, the crack has completely cut across the fiber (Fig. 10b). This scenario can occur if the crack front is "trapped" at certain points by the fiber and "bows" between the pinning points. This results in an increase in the stress-intensity factor at the pinning points and a corresponding decrease in the stress-intensity factor along the bowed crack front. When the stress-intensity factor at the trapped locations exceeds the fracture toughness, the crack-front can "burst" through. The effect of crack-trapping on the toughness of the Mo reinforced NiAl composites are discussed in the next section.

The fracture surfaces of the FCG specimens were examined in the SEM. Several grains were observed that possessed characteristic markings or "fatigue striations" (Figs. 11a). The striations were present on several of the NiAl grains and were roughly perpendicular to the overall direction of crack growth. Invariably, cleavage marks intersected the striations, indicating that the striations were formed on crystallographic planes. Similarly, NiAl grains with fatigue striations were found in the NiAl/Mo<sub>f</sub> composite. The fatigue fracture surface of the NiAl/Mo<sub>f</sub> composite also contained a higher fraction of the Mo grains that had fractured in a transgranular fashion when compared to the fracture toughness specimens (Fig. 11b compared to Fig. 6b). Some of the Mo grains also possessed markings reminiscent of fatigue striations (indicated by arrows in Fig. 11b). Therefore, both the NiAl and Mo phases exhibited true, cycle-by-cycle fatigue crack growth behavior in the NiAl/Mo<sub>f</sub> composite.

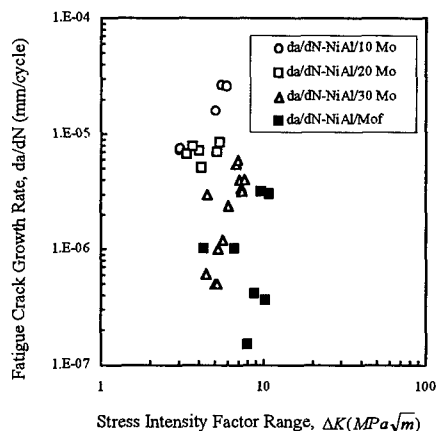


Fig. 7 Fatigue crack growth rates in NiAl/Mo composites.

## Discussion

### Fracture Toughness and Tensile Ductility

The fracture toughness of the NiAl/Mo<sub>p</sub> and NiAl/Mo<sub>f</sub> composites were significantly greater than that of monolithic NiAl (Table II). However, it was clear from the fractographic observations and the crack profiles, that the toughening was not due to crack bridging by plastic stretching of the Mo particles or fibers. Although crack-arrest occurs when the crack-tip is intercepted by the Mo reinforcement, crack-blunting does not appear to result. Crack-tip blunting is typically the result of

interfacial debonding or plastic deformation of the reinforcement phase [7].

The fracture morphology and the crack profiles in the NiAl/Mo composites indicated that the crack path is quite flat without significant tortuosity. Hence, crack deflection does not play a significant role in enhancing the fracture toughness. Large deflections of the crack from a mode I configuration are required for significant improvements in the fracture toughness [9]. For example, a crack that is deflected through 60° from the mode I configuration results in a toughness increase of only around 33%.

Based on the crack-tip - microstructure interactions observed during stable crack growth in the NiAl/Mo<sub>p</sub> and NiAl/Mo<sub>f</sub> composites, crack-trapping appears to be the dominant toughening mechanism. The toughness enhancement due to crack-trapping has been considered theoretically by Bower and Ortiz [8]. Briefly, the crack-front is pinned at several points by particles/fibers that are tougher than the matrix. This results in a "bowed" crack front, with the stress-intensity factor along the bowed segments being lower than the far-field stress-intensity factor, while the stress intensity factor at the pinned points is higher. Crack-growth occurs when the stress-intensity factor at the pinned points exceeds the fracture toughness of the reinforcements. Apart from the fracture toughness, the important variable that determines the shape of the crack front and the overall fracture toughness is the volume fraction of the reinforcement and the average distance between trapping points. Bower and Ortiz [8] derived the following expression for the toughening due to crack trapping:

$$\lambda_{tr} = \frac{K^\infty}{K_{IC}^m} = \left\{ 1 + \frac{2R}{L} \left[ \left( \frac{K_{IC}^{par}}{K_{IC}^m} \right)^2 - 1 \right] \right\}^{1/2} \quad \dots \quad (1)$$

where  $K^\infty$  is the fracture toughness of the composite,  $K_{IC}^m$  is the fracture toughness of the matrix,  $R$  is the radius of the reinforcement,  $L$  is the average distance between the centers of adjacent pinning points (typically the distance between particles where the crack is trapped, but not necessarily the particle spacing, since not all particles may trap the crack front if the crack front is not planar), and  $K_{IC}^{par}$  is the fracture toughness of the reinforcement.

Table IV. Correlation of fatigue crack growth rate in NiAl/Mo<sub>f</sub> with location of crack-tip

$\Delta K$ (MPa√m)	$\left( \frac{da}{dN} \right)$ (mm/cycle)	Crack path
4.28	$1.02 \times 10^{-6}$	Through matrix
6.58	$1.02 \times 10^{-6}$	Fiber + matrix
7.91	$1.52 \times 10^{-7}$	Through matrix, in front of fiber
8.74	$4.13 \times 10^{-7}$	Fiber
9.59	$3.18 \times 10^{-6}$	Matrix
10.19	$3.63 \times 10^{-7}$	Fiber
10.79	$3.05 \times 10^{-6}$	Matrix

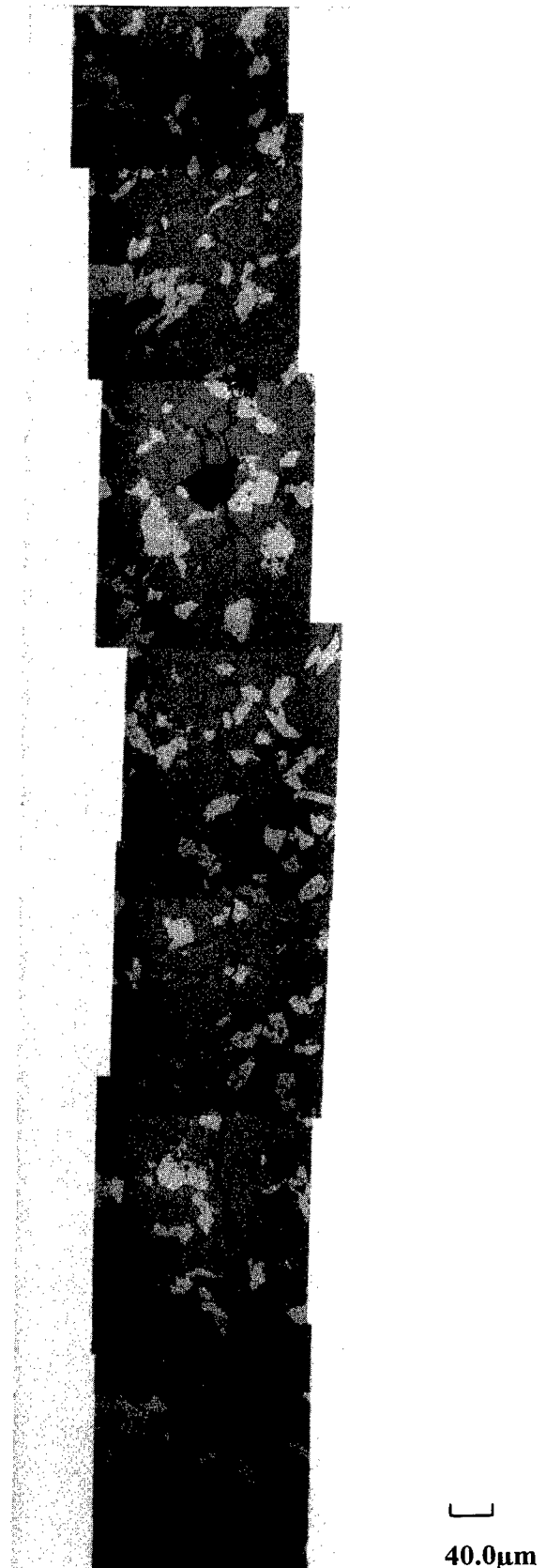


Fig. 8 Typical fatigue crack profile in NiAl/20 Mo<sub>p</sub> composite

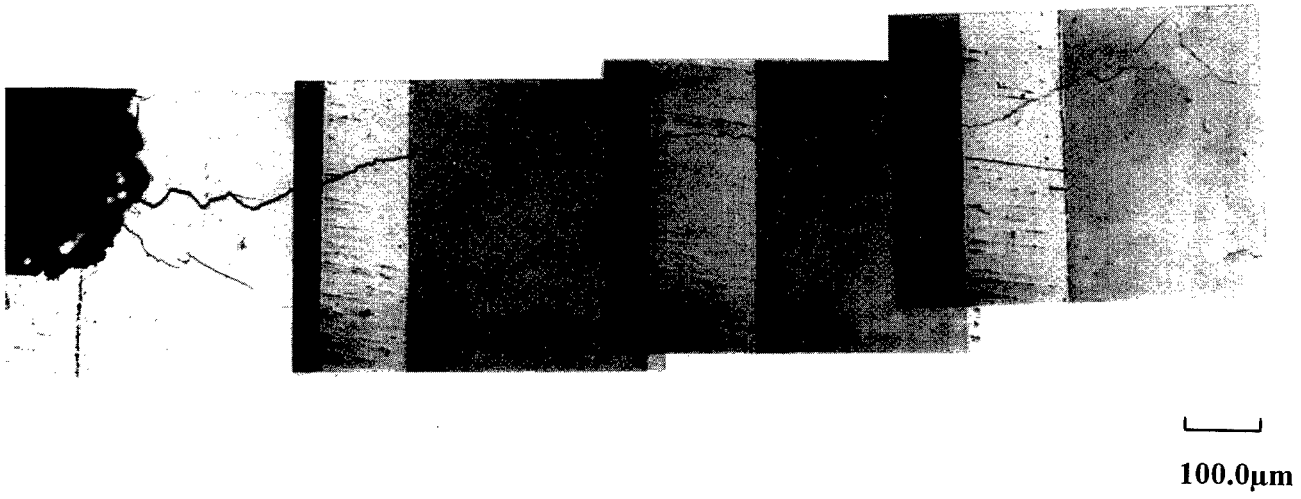


Fig. 9 Typical fatigue crack profile in NiAl/Mo<sub>f</sub>.

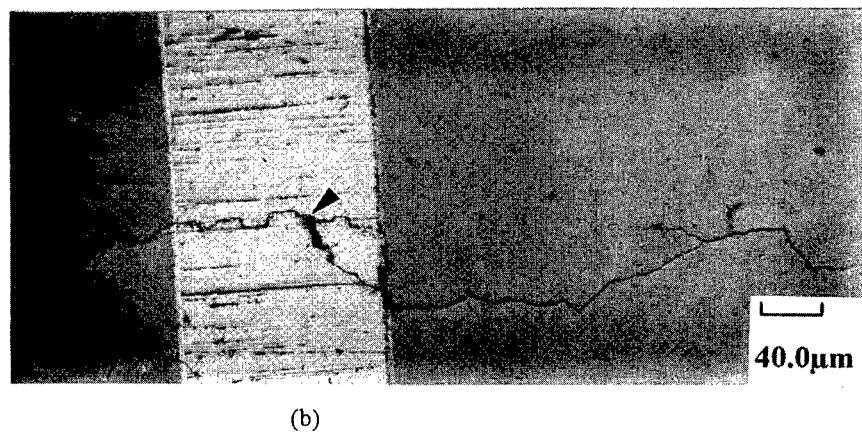
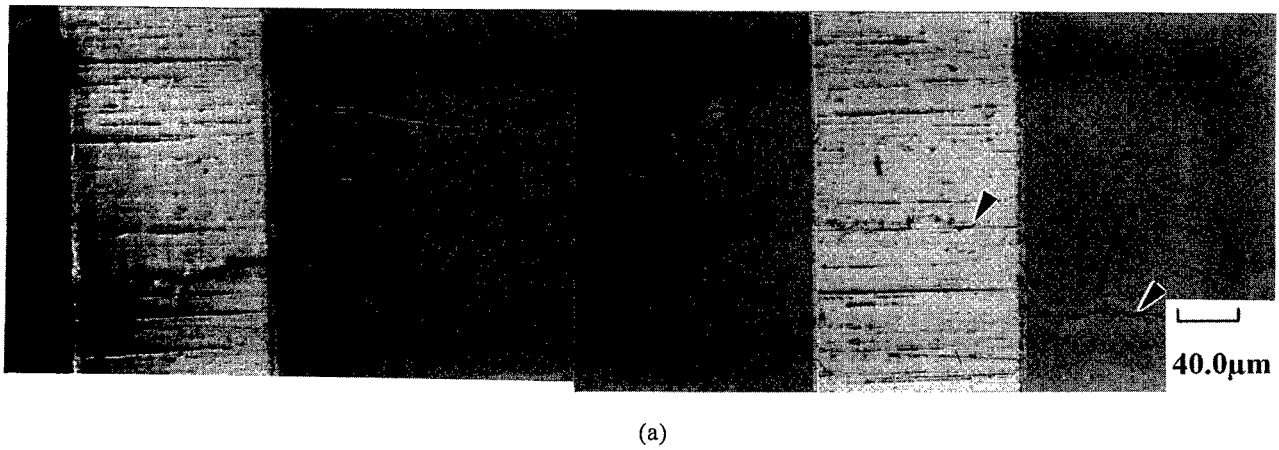
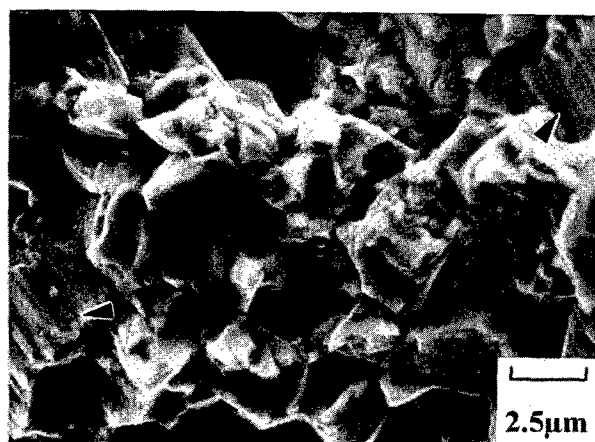


Fig. 10 Fatigue crack profile in NiAl/Mo<sub>f</sub> composite showing possible crack trapping.





(a)



(b)

Fig. 11 Fatigue striations observed on fatigue crack surface. (a) NiAl/30 Mo<sub>p</sub> (b) NiAl/Mo<sub>f</sub>.

In the case of the NiAl/Mo<sub>p</sub> composites studied, it was observed that the crack did not propagate by penetrating through the Mo grains. In most cases, the crack tip was temporarily arrested at a Mo grain and further crack growth occurred by deflection of the crack around the interface between the Mo grains and the Mo<sub>3</sub>Al reaction layer. The local stress intensity factor at which crack propagation occurs therefore depends upon the toughness of the interface. Since this property is not known, an upper bound estimate of the toughening due to crack trapping in the NiAl/Mo<sub>p</sub> composites is made by using the fracture toughness value of Mo as the criterion for crack propagation. In the case of the NiAl/Mo<sub>f</sub> composite, crack growth occurred by fracture of the Mo fibers and the assumptions of Bower and Ortiz's model are satisfied.

The toughening due to trapping calculated based on equation (1) is tabulated in Table V for the different composites. The room temperature fracture toughness of Mo was taken to be  $15 \text{ MPa}\sqrt{\text{m}}$  [5]. The  $(R/L)$  values used for the calculations and recorded in Table V were determined from the crack profiles obtained from the sides of the fatigue tested specimens. It is assumed that the distribution of the Mo particles and fibers in a direction parallel to the crack front (i.e. through the thickness of

the specimens) is similar to that observed on the sides of the specimens. From Table V, it can be seen that the crack trapping mechanism results in a significant increase in the toughness that is comparable to the experimentally measured fracture toughness. The spread in the calculated values of the toughening results from the range of 'L' values measured from the crack profile. Note also that the measured values of  $(R/L)$  for the NiAl/30 Mo<sub>p</sub> and NiAl/20 Mo<sub>p</sub> composites are equal within the measurement spread. This would explain why the measured fracture toughness values of the two composites are roughly the same. Increase in the volume fraction of the Mo reinforcement does not result in a linear increase in the degree of interaction between the crack front and the Mo grains.

Table V. Toughening due to crack-trapping in NiAl/Mo composites - calculated vs. experimental results

Material	$(R/L)$	$\lambda_{tr}$	$\lambda_{exp}$
NiAl/10 Mo <sub>p</sub>	$0.07 \pm 0.02$	$1.44 \pm 0.11$	2.4
NiAl/20 Mo <sub>p</sub>	$0.25 \pm 0.07$	$2.24 \pm 0.27$	2.7
NiAl/30 Mo <sub>p</sub>	$0.30 \pm 0.08$	$2.42 \pm 0.26$	2.7
NiAl/20 Mo <sub>f</sub>	$0.21 \pm 0.007$	$2.08 \pm 0.03$	3.2

Although the fracture toughness of all the NiAl/Mo composites studied were higher than that of the monolithic NiAl, the tensile ductility of the NiAl/20 Mo<sub>p</sub> and NiAl/30 Mo<sub>p</sub> composites was negligible (Table III). In the absence of macroscopic plastic deformation of one or both major phases of the composites, it is unlikely that significant improvements in the ductility can be obtained. The particular microstructure of the NiAl/Mo<sub>p</sub> composites is also partly responsible for the lack of significant ductility. A necklace-type microstructure consisting of NiAl grains surrounded by a continuous Mo phase may result in a greater degree of transgranular fracture of the Mo grains. As it is, fracture in the NiAl/Mo<sub>p</sub> composites occurs predominantly by interphase separation between the Mo grains and the Mo<sub>3</sub>Al reaction layer with a small fraction of the Mo grains fracturing by cleavage.

In this context, a comment about the concept of "ductile phase toughening" is appropriate. Conventionally, composites with brittle matrices (ceramics and intermetallics) were designed to improve the fracture toughness through crack-bridging and plastic dissipation of energy by the reinforcements. Model systems with glass matrix and lead wire reinforcements were considered for experimental validation of theoretical models that considered the effect of matrix constraint on the deformation behavior of the reinforcements [17]. Under most of the constraint conditions studied, the failure of the lead wires was preceded by growth of internal cavities and plastic stretching of the lead wires. However, in the case of intermetallics for high temperature applications, the choice of reinforcement materials is usually limited to the refractory metals, (Nb, Mo, V, Cr or W) and in several instances the refractory metal reinforcement does not exhibit significant ductility at room temperature [6,18]. Fractographic investigations frequently indicate that the refractory metal phase fractures by intergranular or cleavage fracture modes which are not "ductile" fracture modes [6,18].

At the same time, several of these studies have reported substantial improvements in the fracture toughness due to the addition of the refractory metal phase [6,19].

In the case where specific orientation relationships exist between the matrix and the reinforcement phases, toughening has been attributed to plasticity in the matrix with the coherent interfaces acting as dislocation sources [19] or to extensive tortuosity in the crack path which consists of short and highly deflected cleavage steps [20]. In one case where the refractory phase (Mo) was randomly distributed in the NiAl matrix, no single dominant toughening mechanism was identified and a combination of crack-trapping, tortuous crack path and limited plastic deformation of the Mo phase were responsible for the substantial increases in the fracture toughness [6]. The point that is made here is that the fracture toughness of NiAl can be improved by the addition of a refractory metal phase even in the absence of plastic stretching of the reinforcement and in this case the term "ductile phase toughening" is a misnomer.

#### Fatigue Crack Growth

The observation of stable fatigue crack growth at room temperature in all the NiAl/Mo composites was significant because of its implications on the damage tolerance of the composites under cyclic loading. Monolithic NiAl does not exhibit stable crack growth under cyclic loading and failure occurs as soon as a critically sized flaw is nucleated [21]. The presence of fatigue striations on some NiAl grains indicates the operation of a plastic blunting/resharpening process during fatigue loading [22]. Such a mechanism is not possible in monolithic NiAl due to the grain boundary stresses that are generated that lead to catastrophic intergranular fracture. It is suggested that the presence of the Mo grains/fibers accommodates some of the grain boundary stresses and promotes cycle-by-cycle fatigue crack growth through the NiAl phase. The Mo grains also play a part in retarding the rate of crack growth by pinning the crack front.

#### Conclusions

1.) The room temperature fracture toughness of NiAl is substantially improved by additions of Mo particles/fibers. The highest fracture toughness of  $16.7 \text{ MPa}\sqrt{\text{m}}$  was obtained in the NiAl/Mo<sub>r</sub> composite. Crack trapping appears to be the dominant toughening mechanism responsible for the improvements in fracture toughness. A significant result of the study was the lack of plastic dissipation of work by the Mo particles/fibers. As a result, the tensile ductility (plastic elongation to failure) of the NiAl/Mo<sub>p</sub> composites was close to zero.

2.) Stable fatigue crack growth under cyclic tensile loading was observed in all the NiAl/Mo composites. The average rate of crack growth was the slowest in the NiAl/Mo<sub>r</sub> composite. The observation of stable fatigue crack growth implies that the composites possess some measure of damage tolerance under cyclic loading. Monolithic NiAl does not exhibit stable crack growth at room temperature.

3.) Characteristic fatigue "striations" were observed on some NiAl grains in all the NiAl/Mo composites indicating the operation of a plastic blunting/resharpening process during fatigue loading. Based on the appearance of the fatigue

striations, a plastic blunting /relaxation process appears to be responsible for the growth of a stable crack under cyclic loading. It is also suggested that the presence of the Mo phase is responsible for accommodating the grain boundary stresses that cause catastrophic intergranular fracture in monolithic NiAl under cyclic loading.

#### Acknowledgments

The authors (PR and WOS) would like to thank Dr. Mike Nathal for allowing the use of the processing facilities at NASA, Lewis Research Center, Cleveland, during this investigation. PR and WOS also gratefully acknowledge the support of the sponsors of this work, the division of Mechanics and Materials of the National Science Foundation (Dr. Craig Hartley and Dr. Sunil Saigal, program monitors). The authors thank Mr. Mingwei Li for carrying out the image analysis.

#### References

- 1.) D. B. Miracle, *Acta metall. mater.*, 41 (3) (1993) 649-684.
- 2.) R. D. Noebe, NASA Technical Memorandum 106534, Lewis Research Center, Cleveland 1994.
- 3.) R. D. Noebe, A. Misra and R. Gibala, *ISIJ International*, 31 (10) (1991) 1172-1185.
- 4.) D. P. Pope and R. Darolia, *MRS Bulletin*, 21 (5) (1996) 30-36.
- 5.) F. E. Heredia et al., *Acta metall. mater.*, 41 (2) (1993) 505-511.
- 6.) P. R. Subramanian, M. G. Mendiratta and D. B. Miracle, *Metall. Trans. A*, 25A (1994) 2769-2781.
- 7.) K. S. Chan, *Metall. Trans. A*, 23A, (1992) 183-199.
- 8.) A. F. Bower and M. Ortiz, *J. Mech. Phys. Solids*, 39, (1991) 815-858.
- 9.) S. Suresh, *Metall. Trans. A*, 16A (1985) 249-260.
- 10.) *Metals Handbook*, vol. 2 Properties and Selection - Non-Ferrous Alloys and Special-Purpose Materials, (ASM International, U. S. A., 1990) 574-577.
- 11.) H. E. Cline and J. L. Walter, *Metall. Trans.*, 1, (1970) 2907-2917.
- 12.) P. Ramasundaram, "Fatigue and Fracture of Nickel Aluminum (NiAl) - Based Composites" (Ph. D. thesis, The Ohio State University, 1997).
- 13.) *Bulletin of Alloy Phase Diagrams*, 1 (2) (1980) 71-75.
- 14.) *Annual Book of ASTM Standards*, vol. 03.01, (ASTM, Philadelphia, PA, 1991) 485.
- 15.) S. Suresh and J. R. Brockenbrough, *Acta metall.*, 36 (6) (1988) 1455-1470.
- 16.) P. Ramasundaram et al., *Fatigue and Fracture of Ordered Intermetallic Materials II*, ed. W. O. Soboyejo et al. (TMS, Warrendale, PA, 1994) 235.
- 17.) M. F. Ashby, F. J. Blunt and M. Bannister, *Acta metall.*, 37 (7) (1989) 1847-1857.
- 18.) D. L. Davidson, K. S. Chan and D. L. Anton, *Metall. Mater. Trans. A*, 27A (1996) 3007-3018.
- 19.) X. F. Chen et al., *J. Mater. Res.*, 10 (5) (1995) 1159-1170.
- 20.) K. M. Chang, *MRS Symposium Proceedings*, 273 (1992) 191-196.
- 21.) R. D. Noebe and B. A. Lerch, *Scripta metall. mater.*, 27 (1992) 1161-1166.
- 22.) C. Laird, *Fatigue Crack Propagation*, ASTM STP 415, (American Society for Testing and Materials, 1967) 131-168.

## STRONG, TOUGH, AND PEST RESISTANT MoSi<sub>2</sub>-BASE HYBRID COMPOSITE FOR STRUCTURAL APPLICATIONS

M. G. Hebsur\* and M. V. Nathal \*\*

\*NYMA Inc., NASA- LeRC Group, Brookpark OH 44142

\*\*NASA-LeRC, Cleveland, OH 44135

### Abstract

Addition of about 30 to 50 vol % of Si<sub>3</sub>N<sub>4</sub> particulate to MoSi<sub>2</sub> improved resistance to low temperature accelerated oxidation by forming a Si<sub>2</sub>ON<sub>2</sub> protective scale and thereby eliminating catastrophic 'pest failure'. The Si<sub>3</sub>N<sub>4</sub> addition also improved the high temperature creep strength by nearly five orders of magnitude, doubled the room temperature toughness and significantly lowered the CTE of the MoSi<sub>2</sub> and eliminated matrix cracking in SCS-6 reinforced composites even after thermal cycling. The SCS-6 fiber reinforcement improved the room temperature fracture toughness by seven times and impact resistance by five times. The composite exhibited excellent strength and toughness improvement up to 1400 °C. More recently, tape casting was adopted as the preferred processing of MoSi<sub>2</sub>-base composites for improved fiber spacing, ability to use small diameter fibers, and for lower cost. Good strength and toughness values were also obtained with fine diameter Hi-Nicalon tow fibers. This hybrid composite remains competitive with ceramic matrix composites as a replacement for Ni-base superalloys in aircraft engine applications.

### Introduction

Advanced high temperature materials are key to successfully developing the next generation aerospace propulsion and power systems (1). Advanced materials will enhance the performance of these systems by allowing higher speeds, expanded flight ranges, and increased payload capabilities. Due to high specific strength and stiffness, and the potential for increased temperature capability, composite materials are attractive for systems ranging from subsonic commercial aircraft to future space propulsion and power systems. Based on high temperature oxidation behavior, it appears that MoSi<sub>2</sub> is one of the few intermetallics to have potential for further development. Since MoSi<sub>2</sub> is a silica former, it can withstand at least 200 °C higher temperatures (up to 1500 °C) than alumina formers such as NiAl (2). It also has a higher melting point (2023 °C) and lower density (6.2 gm/cc) than superalloys, and has electrical and thermal conductivity advantages over ceramics (3).

However, the use of MoSi<sub>2</sub> has been hindered due to the brittle nature of the material at low temperatures, inadequate creep resistance at high temperatures, accelerated ('pest') oxidation at temperatures between approximately 400 and 500 °C, and its relatively high coefficient of thermal expansion (CTE) compared to potential reinforcing fibers such as SiC. The CTE mismatch between the fiber and the matrix results in severe matrix cracking during thermal cycling.

In the last 12 years, an extensive amount of work has been carried out in efforts to improve the high temperature properties of MoSi<sub>2</sub> by solid solution alloying, discontinuous reinforcement, and fiber reinforcement. Alloying with W (4) or Re (5) has improved high temperature creep strength. Substantial improvements in strength have also been achieved by adding particulates, platelets or whiskers of SiC (6), TiB<sub>2</sub>, and HfB<sub>2</sub> (7). However, the effects of grain refinement may limit the creep strength of these types of composites (8). To date, MoSi<sub>2</sub> alloyed with W and containing 40 vol % SiC has achieved the creep strength superior to that of the superalloys, although not the best monolithic ceramics. The addition of SiC whiskers has also yielded improvements in room temperature toughness (9). However, it appears that the strength and damage tolerance required for high temperature aerospace applications can only be achieved by reinforcement with high strength continuous fibers.

Nb fibers (10) have been shown to improve the strength and toughness but this option is limited by a severe reaction between the Nb fiber and MoSi<sub>2</sub>. Maloney and Hecht (11) have done extensive work on the development of continuous fiber reinforced MoSi<sub>2</sub> base composites to achieve high temperature creep resistance and room temperature toughness. Candidate fibers consisted of fibers, such as SiC, single crystal Al<sub>2</sub>O<sub>3</sub>, ductile Mo, and W alloy fibers. The refractory metal fibers increased both creep strength and fracture toughness, although reaction with the matrix was still a problem. The addition of about 40 vol % of SiC in the form of whiskers and particulate was used to lower the thermal expansion of the MoSi<sub>2</sub> base matrix and prevented matrix

cracking in these composites. However, matrix cracking was still observed in an SCS-6 fiber reinforced composite even with the matrix containing up to 40 vol % SiC whiskers. This composite also suffered catastrophic pest attack at 500 °C. Sapphire fiber reinforced composites showed no evidence of matrix cracking due to the good thermal expansion match between MoSi<sub>2</sub> and Al<sub>2</sub>O<sub>3</sub>. However, the strong fiber-matrix bond did not provide any toughness improvement.

MoSi<sub>2</sub> has been known to be susceptible to pesting, which is usually defined as disintegration into powder, and appears to be most pronounced near 500 °C (12-14). The pesting phenomenon in MoSi<sub>2</sub> is considered to result from accelerated oxidation, which involves the simultaneous formation of MoO<sub>3</sub> and SiO<sub>2</sub> in amounts essentially determined by the Mo and Si concentrations in the intermetallic. The accelerated oxidation is a necessary but not sufficient condition for pesting. In some but not all cases, pesting has been linked to the formation of voluminous Mo oxides in porosity or microcracks. Improvements in fabrication of MoSi<sub>2</sub> have led to materials which had less porosity and were less susceptible to pest attack. Because of increased surface areas and complexities of fabrication from incorporating reinforcement phases in MoSi<sub>2</sub> based composites, pesting of composite materials is still a major concern (11,13). Microalloying with Ge (15) and macroalloying with Cr (16) have also been shown to improve pesting resistance.

In earlier work (17) of developing MoSi<sub>2</sub> suitable for SiC fiber reinforcement, it was found that the addition of about 30 to 50 vol % of Si<sub>3</sub>N<sub>4</sub> particulate to MoSi<sub>2</sub> improved the low temperature accelerated oxidation resistance by forming a Si<sub>2</sub>ON<sub>2</sub> protective scale and thereby eliminated catastrophic pest failure. The Si<sub>3</sub>N<sub>4</sub> addition also improved the high temperature oxidation resistance and compressive strength. The brittle-to-ductile (BDTT) transition-temperature of MoSi<sub>2</sub>-30 vol % Si<sub>3</sub>N<sub>4</sub>, measured in four-point bending, was between 900 and 1000 °C. More importantly, the Si<sub>3</sub>N<sub>4</sub> addition significantly lowered the CTE of the MoSi<sub>2</sub> and eliminated matrix cracking in SCS-6 reinforced composites even after thermal cycling (14,18).

These encouraging preliminary results led to a joint program for further development between Pratt & Whitney, the Office of Naval Research, and NASA Lewis. The overall technical direction of this long range program is to develop these composite system for advanced aircraft engine application as a competitor to both today's superalloys and other advanced materials, primarily ceramic matrix composites. A turbine blade outer air seal for Pratt & Whitney's ATEGG/JTD engine demonstrator was chosen as the first component upon which to focus. This paper briefly describes the progress made so far in developing, processing, and characterizing MoSi<sub>2</sub> base hybrid composites.

#### Materials and Procedures

Attrition milling of MoSi<sub>2</sub> and Si<sub>3</sub>N<sub>4</sub> powder is the first step in composite processing. Several batches containing a mixture of commercially available MoSi<sub>2</sub> and either 30 or 50 vol % of Si<sub>3</sub>N<sub>4</sub> were mechanically alloyed in a Union Process attritor. No densification aids were added to the MoSi<sub>2</sub>-Si<sub>3</sub>N<sub>4</sub> mixtures. The average mean particle size of the mixture after milling was 1.25±0.71 µm at 99 % confidence. The MoSi<sub>2</sub>-Si<sub>3</sub>N<sub>4</sub> powder was consolidated into "matrix-only" plates 12 cm long x 5 cm wide x 0.3 cm thick, or a larger size of 18 cm long x 2.5 cm wide x 1.25 cm thick. The plates were consolidated by vacuum hot pressing followed by hot isostatic pressing to achieve full density. Further consolidation of the hot pressed plate was achieved by hot isostatic pressing (HIP). Composite plates of various thickness consisting of 6, 12, or 56 plies of 30 vol % SCS-6 fibers having 0, 0/90 and 90 orientations in the MoSi<sub>2</sub>-Si<sub>3</sub>N<sub>4</sub> matrix were prepared by the powder cloth technique (15) and consolidated in the same manner as the material without fibers. The two-step consolidation process enabled the use of a lower consolidation temperature than could be used if hot pressing was used alone.

This resulted in a fully dense material without excessive reaction or damage to the fibers.

From the consolidated material, ASTM standard specimens for several tests such as compression, fracture toughness, impact and oxidation were machined by electro discharge machining (EDM) and grinding techniques. Tensile tests were conducted on 1.27 by 15 cm straight or dog bone-shaped specimens machined from 6 ply composite panels. Tests were performed in air between 25 and 1200 °C at constant strain rate of 1.4 x 10<sup>-3</sup> sec<sup>-1</sup>. Constant load compression creep tests were conducted on MoSi<sub>2</sub>-50Si<sub>3</sub>N<sub>4</sub> specimens at 1200 °C in the stress range of 40 to 400 MPa in air. Fracture toughness tests were measured on chevron notched bend specimens made from 12 ply composite panels, tested at a constant strain rate of 1.2 x 10<sup>-5</sup> cm/min. ASTM full size Charpy V-notch impact specimens were machined from 56 ply composites and impact tests were conducted using 356 J Tinius Olsen impact tester with Dynatrup instrumentation. The heating of the specimen was carried out using two oxypropane torches. The temperature was monitored using a laser pyrometer. Tensile creep-rupture tests were performed in vacuum between 1100 to 1200 °C 70 MPa were conducted on hybrid composites using an MTS machine fitted with water cooled grips and a side-contact extensometer. Oxidation coupons typically were 1.2 x 1.2 x 0.25 cm and were ground and polished to final 1 µm diamond polish. In the case of composites, no attempt was made to coat the exposed fibers. Detailed microstructural characterization of as-fabricated and tested specimens were carried out using standard optical and electron microscopic techniques.

#### Results and Discussion

##### Microstructure of as-fabricated materials:

Figure 1(a) shows the microstructure of the as-consolidated MoSi<sub>2</sub>-Si<sub>3</sub>N<sub>4</sub> monolithic matrix. The Si<sub>3</sub>N<sub>4</sub> particles are interconnected and well dispersed in the MoSi<sub>2</sub> matrix. As the volume fraction of Si<sub>3</sub>N<sub>4</sub> particulate increased, the degree of interconnectivity of the Si<sub>3</sub>N<sub>4</sub> phase increased, although even at 50 vol % nitride, the materials could still be machined by EDM. As expected from thermodynamic predictions, the Si<sub>3</sub>N<sub>4</sub> particles appeared to be quite stable, with very little or no reaction with the MoSi<sub>2</sub> even after exposure at 1500 °C. X-ray diffraction of MoSi<sub>2</sub>-Si<sub>3</sub>N<sub>4</sub> showed only the presence of MoSi<sub>2</sub> (tetragonal) and a mixture of α and β Si<sub>3</sub>N<sub>4</sub> phases. Even though there is a significant CTE mismatch between MoSi<sub>2</sub> and Si<sub>3</sub>N<sub>4</sub>, the small particle size prevented thermally induced microcracking. TEM examination, Fig. 1(b), performed on MoSi<sub>2</sub>-Si<sub>3</sub>N<sub>4</sub> also confirmed no reaction between MoSi<sub>2</sub> and Si<sub>3</sub>N<sub>4</sub>. In some isolated areas very fine Mo<sub>5</sub>Si<sub>3</sub> phase was detected. This is believed to have been present in the as-procured MoSi<sub>2</sub> powder. Figure 2 shows the transverse microstructure of the as-fabricated SCS-6/MoSi<sub>2</sub> composite. A reaction zone around the fibers was generally less than 1 µm in thickness and resulted from reaction of the carbon layer to form SiC and Mo<sub>5</sub>Si<sub>3</sub>. Although the fiber distribution is not uniform, Fig. 2 indicates the absence of matrix cracking. The CTE measurements made on the matrix-only plate and composites plotted as a function of temperature are compared with the monolithic constituents in Fig. 3. It is clear from Fig. 3 that the addition of Si<sub>3</sub>N<sub>4</sub> to MoSi<sub>2</sub> has effectively lowered the CTE of the matrix, achieving the desired result of eliminating matrix cracking. Furthermore, no cracks were found in either the matrix or the reaction zone even after 1000 thermal cycles between 1200 and 200 °C. These results show that the use of Si<sub>3</sub>N<sub>4</sub> was much more effective than similar attempts (9) using SiC.

##### Oxidation Behavior of MoSi<sub>2</sub>-Base Composites

Since the low temperature oxidation and pesting phenomenon are limiting factors for structural applications of MoSi<sub>2</sub>-base composites, several critical tests were designed to examine the pesting response. Initially, cyclic oxidation tests were conducted at 400, 500 and 600 °C for 200 cycles. Each cycle consisted of 55 minutes of heating and 5 minutes of cooling. The weight gain at 500 °C was comparatively higher than at 400 and 600 °C, which again

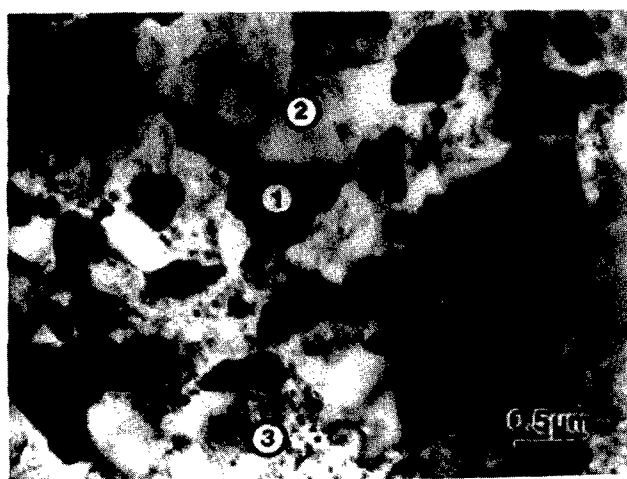
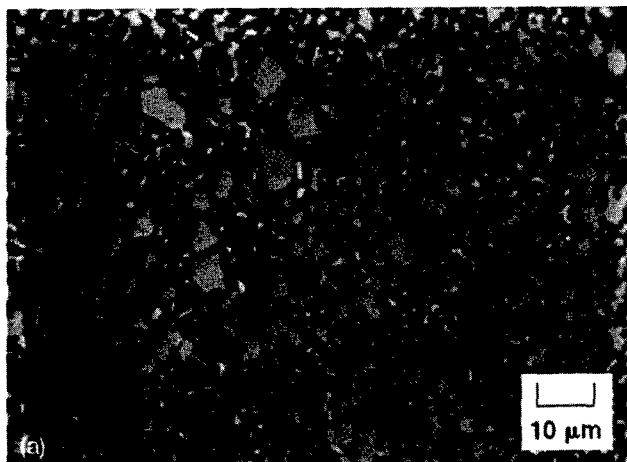


Figure 1.—Micrographs of  $\text{MoSi}_2\text{-Si}_3\text{N}_4$  monolithic matrix (a) SEM micrograph of consolidated  $\text{MoSi}_2\text{-50Si}_3\text{N}_4$  ( $\text{MoSi}_2$  is the light phase). (b) TEM micrograph of HP + HIPed  $\text{MoSi}_2\text{-50Si}_3\text{N}_4$  showing (1)  $\text{MoSi}_2$  phase (2)  $\text{Si}_3\text{N}_4$  phase, and (3) a region containing fine  $\text{Mo}_5\text{Si}_3$  phase.

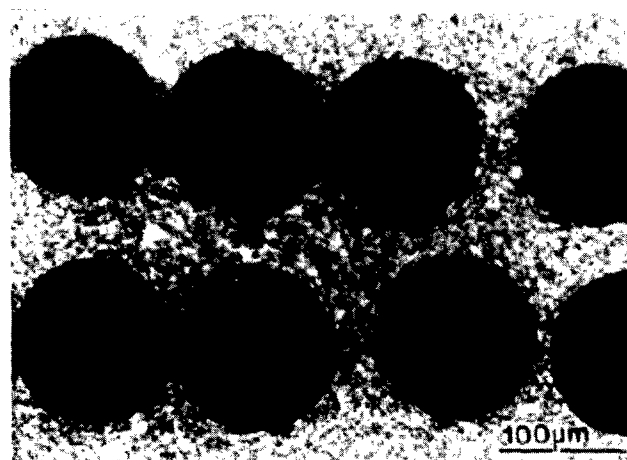


Figure 2.—SEM-BS image of powder cloth fabricated SCS-6/ $\text{MoSi}_2\text{-30Si}_3\text{N}_4$  hybrid composite.

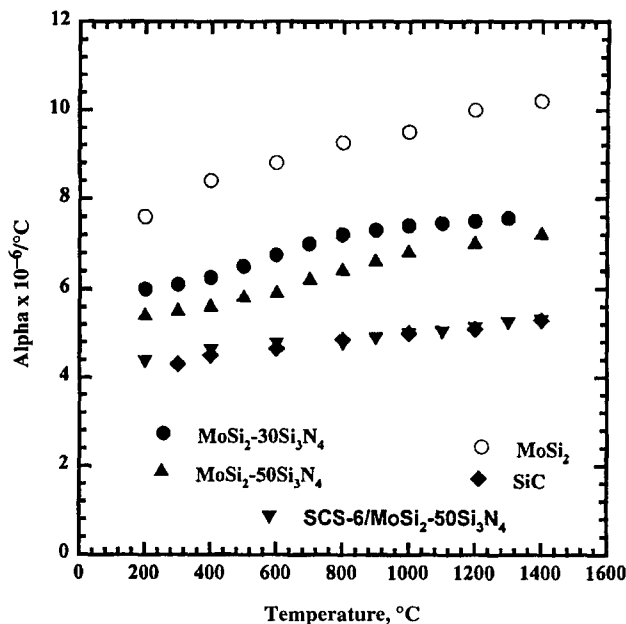


Figure 3.—Thermal expansion data for several  $\text{MoSi}_2$ -base materials and SiC refractory phase.

confirms the previous observation (10) that 500 °C is the temperature for maximum accelerated oxidation/pest for  $\text{MoSi}_2$ -base alloys. It was therefore decided that 500 °C would be used for all subsequent experiments to examine the oxidation behavior in more detail.

Figure 4(a) shows the specific weight gain versus number of cycles at 500 °C. Both  $\text{MoSi}_2\text{-30Si}_3\text{N}_4$  and 50  $\text{Si}_3\text{N}_4$  show very little weight gain indicating the absence of accelerated oxidation. X-ray diffraction analysis of both these specimens indicated strong peaks of  $\text{Si}_2\text{ON}_2$  and the absence of  $\text{MoO}_3$ . The  $\text{MoSi}_2$  exhibited accelerated oxidation followed by pesting. Initial studies on TEM oxidized  $\text{MoSi}_2$  samples indicated that oxide formed on  $\text{MoSi}_2$  is a two phase lamellar structure (Fig. 4(b)) consisting of  $\text{MoO}_3$  and amorphous  $\text{SiO}_2$ . This kind of lamellar structure could provide an easy diffusion path for oxygen, favoring the formation of the  $\text{MoO}_3$ . The TEM examination of a  $\text{MoSi}_2\text{-30 Si}_3\text{N}_4$  specimens oxidized at 500 °C for 1000 hours, Fig. 4(c), showed an order of magnitude decrease in oxide thickness and a disruption of the lamellar oxide structure. However, fine features of the scale in Fig. 4(c) have not analyzed.

Several critical oxidation tests were carried out at 500 °C to examine the influence of pre-existing cracks and superimposed stresses on  $\text{MoSi}_2\text{-30 Si}_3\text{N}_4$  materials. These tests included oxidation of bend bars which were precracked using 250 N load and a Vickers indenter. Both uncracked and precracked specimens were oxidized under unstressed, compressive, or tensile stresses. All these tests were extended to 1000 hours, with no indications of pesting or premature failure. Finally, burner rig tests were conducted using a jet fuel on two specimens with different degrees of surface roughness, and both specimens came out without showing any evidence of pesting.

Under similar conditions the hybrid composite specimens showed much less weight gain than the matrix-only material. However, the carbon layer on the exposed ends of SCS-6 fibers did oxidize, which influenced the weight gain measurement. Figure 5 shows the SCS-6/ $\text{MoSi}_2$  and SCS-6/ $\text{MoSi}_2\text{-30Si}_3\text{N}_4$  composites exposed at 500 °C. The SCS-6/ $\text{MoSi}_2$  specimen, which had matrix cracks, was completely disintegrated into powder within 24 cycles, whereas the SCS-6/ $\text{MoSi}_2\text{-30 Si}_3\text{N}_4$  specimen was intact even after 200 cycles. This is again in strong contrast to previous work (11), where both SCS-6/ $\text{MoSi}_2\text{-40 vol } \%$  SiC and  $\text{Al}_2\text{O}_3/\text{MoSi}_2$  composites were reduced to powder

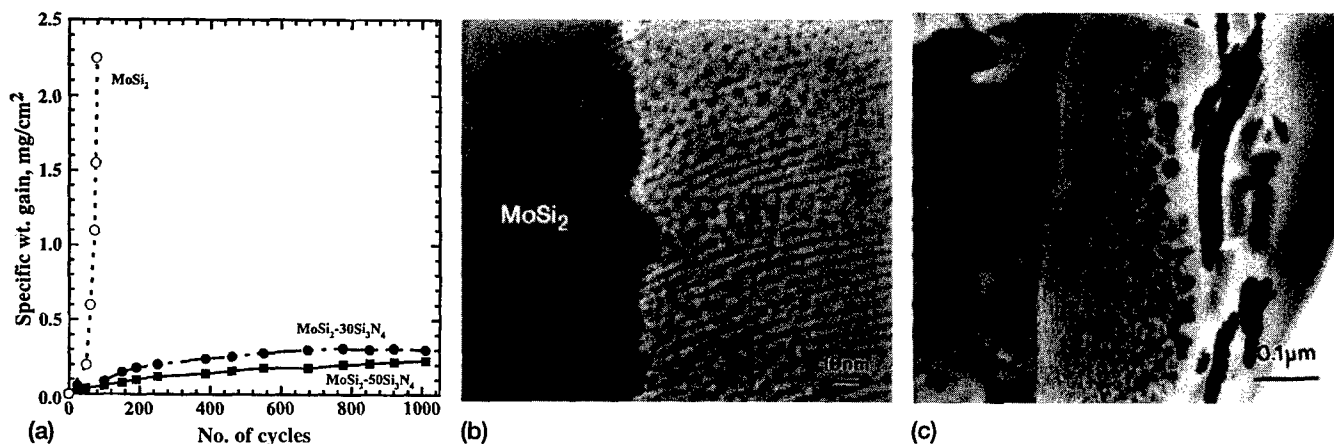


Figure 4.—Oxidation behavior of MoSi<sub>2</sub>-base materials cyclic oxidized at 500 °C in air. (a) Specific weight versus number of cycles for various MoSi<sub>2</sub>-base materials. (b) TEM micrograph of MoSi<sub>2</sub>. (c) TEM micrograph of MoSi<sub>2</sub>-30Si<sub>3</sub>N<sub>4</sub> oxidized for 1000 hours.

after exposure at 500 °C. All of these observations are consistent with the elimination of pest attack in MoSi<sub>2</sub>-Si<sub>3</sub>N<sub>4</sub> composites due to a mechanism involving elimination of the accelerated oxidation associated with a nonprotective MoO<sub>3</sub> oxide scale. The Si<sub>2</sub>ON<sub>2</sub> scale forms rapidly, and is protective even at cracks, pores, and interfaces.

Previous work on high temperature oxidation resistance of this material was restricted to isothermal exposures on the nitride-containing material only. This has now been extended to include cyclic oxidation, on both the matrix and the hybrid composite. The results of cyclic oxidation tests at 1250 °C, which more closely approximates the conditions under which the material would be subjected in a structural application, are shown in Fig. 6. The materials in Fig. 6 were subjected to 1 hour heating cycles to 1250 °C, followed by 20 minutes cooling cycles. It can be seen that the MoSi<sub>2</sub>-50 Si<sub>3</sub>N<sub>4</sub> particulate composite exhibited superior oxidation resistance as compared to MoSi<sub>2</sub> alone. The specific weight gain of MoSi<sub>2</sub>-50Si<sub>3</sub>N<sub>4</sub> was only about 1 mg/cm<sup>2</sup> in 1000 hours, almost comparable to CVD SiC, which is considered the best SiO<sub>2</sub> former available. The composite initially lost weight due to oxidation of the carbon on the SCS-6 fiber. This was followed by steady weight gain, less than 2 mg/cm<sup>2</sup> in 1000 hours. X-ray diffraction of surface oxides on MoSi<sub>2</sub>-50 Si<sub>3</sub>N<sub>4</sub> and hybrid composites indicated strong peaks of  $\alpha$ -cristobalite, which is a crystalline form of SiO<sub>2</sub> and a protective oxide.

#### Mechanical Properties of MoSi<sub>2</sub>-Si<sub>3</sub>N<sub>4</sub>

Previous work (17,18) showed that the nitride additions substantially increased compressive strength at all temperatures. This has been augmented with testing to further characterize this material. Figure 7 shows the results of constant load compression creep tests at 1200 °C on MoSi<sub>2</sub>-50Si<sub>3</sub>N<sub>4</sub> plotted as second stage creep rate versus specific stress. For comparison, several materials such as MoSi<sub>2</sub>, MoSi<sub>2</sub>-40SiC (8), and a single crystal Ni-base superalloy (20) are also included. MoSi<sub>2</sub>-50Si<sub>3</sub>N<sub>4</sub> is almost five orders of magnitude better creep rate than binary MoSi<sub>2</sub> and comparable to MoSi<sub>2</sub>-40SiC. This again confirms the previous observation of beneficial effects of particulate reinforcement. The derived stress exponent,  $n = 5.3$  and the activation energy = 520 kJ/mol calculated from the temperature dependence of creep rate at constant stress, imply a diffusion controlled dislocation mechanism as the rate controlling mechanism.

The fracture toughness of MoSi<sub>2</sub> and MoSi<sub>2</sub>-30Si<sub>3</sub>N<sub>4</sub> base materials were measured on chevron notched four-point bend specimens, and a finite element/slice model was used to calculate the  $K_{IC}$  (21). Figure 8 shows the plot of fracture toughness of MoSi<sub>2</sub>-Si<sub>3</sub>N<sub>4</sub> as a function of temperature. For

comparison, two monolithic ceramics SiC and Si<sub>3</sub>N<sub>4</sub> are also included in the figure (22). The room temperature fracture toughness of both MoSi<sub>2</sub>-30Si<sub>3</sub>N<sub>4</sub> and 50Si<sub>3</sub>N<sub>4</sub> matrix was ~5.2 MPa√m, which is about twice the value measured on monolithic MoSi<sub>2</sub>. Figure 8 also shows that fracture toughness of MoSi<sub>2</sub>-Si<sub>3</sub>N<sub>4</sub> increases with temperature, especially beyond 1000 °C, which is the BDTT for this material. The ceramics chosen for comparison were made by hot pressing techniques that are similar to those used to make MoSi<sub>2</sub>. *In situ* toughened Si<sub>3</sub>N<sub>4</sub> (23) exhibits higher toughness values, approaching 10 MPa√m. But, all of the ceramics maintain the same toughness as temperature is increased.

#### Mechanical Properties of SCS-6/MoSi<sub>2</sub>-Si<sub>3</sub>N<sub>4</sub> Composites

Figure 9 shows the load versus displacement plot for SCS-6/MoSi<sub>2</sub>-30Si<sub>3</sub>N<sub>4</sub> monolithic chevron notched four-point bend specimens tested at room temperature. The composite specimen did not break even after testing for two hours. The apparent critical stress intensity factor,  $K_{IC}$ , calculated from the maximum load data was greater than 35 MPa√m indicated that the hybrid composite specimen was seven times tougher than the monolithic material. The toughness of the hybrid composite also increased with temperature reaching as high as 65 MPa√m, at 1400 °C in argon atmosphere.

Figure 10(a) shows the room temperature tensile stress strain curve for SCS-6/MoSi<sub>2</sub>-Si<sub>3</sub>N<sub>4</sub>, indicating composite-like behavior; and three distinct regions, an initial linear region, followed by a non-linear region and a second linear region. The non-linear region is due to the matrix cracking normal to the loading direction. The second linear region is controlled by fiber bundle strength. Individual SCS-6 fibers were tensile tested at room temperature in the as-received, as-etched and etched-from-composite conditions, and produced average strength values of  $3.52 \pm 0.8$ ,  $3.35 \pm 0.6$ , and  $3.4 \pm 1$  GPa, respectively. Thus, neither etching nor consolidation conditions degraded the strength of the fibers, and SEM examination of the fiber surfaces showed no visible differences among the 3 fiber conditions.

Fiber/matrix interfacial properties play an important role in composite mechanical behavior. In the case of this composite system, the carbon layer on SCS-6 provides an appropriate level of bonding that produces adequate strengthening and toughening. The carbon can react with MoSi<sub>2</sub> to form SiC and Mo<sub>5</sub>Si<sub>3</sub>, although the carbon layer is still retained and the reaction zone thickness is not very large at typical HIP temperatures. The fiber matrix interfacial shear strengths determined from a fiber push out test (24) using thin polished sections produced values near 50 MPa, indicating a weak bond, between the matrix and the fiber. The interfacial shear strength for SCS-6/RBSN is about 30 MPa (24).



Figure 5.—SCS-6 fiber-reinforced specimens cyclic oxidized at 500 °C in air. (a)  $\text{MoSi}_2$  matrix for 24 cycles. (b)  $\text{MoSi}_2\text{-}30\text{Si}_3\text{N}_4$  matrix for 200 cycles.

The ultimate tensile strength increased with an increase in matrix  $\text{Si}_3\text{N}_4$  content from 30 to 50 vol % which may mean that there is a matrix contribution to the tensile behavior, even after cracking has initiated. Alternatively, a different, higher strength lot of fibers could be responsible for this result. It was also found that the room temperature ultimate tensile strength and strain to fracture were reduced by only 20 percent in a specimen with exposed fibers that was pre-oxidized at 1200 °C for 200 hours. High temperature tensile tests were performed in air at temperatures up to 1400 °C. Stress-strain curves for tests at and above 900 °C did not show evidence of matrix cracking. This can be attributed to the plastic nature of  $\text{MoSi}_2$  at these temperatures. This is believed to be an advantage over CMC's which exhibit matrix cracking at all temperatures. Figure 10(b) shows the temperature dependence of ultimate tensile strength, along with the data from competitive materials, namely single crystal PWA1480 (25), and SCS-6/reaction bonded silicon

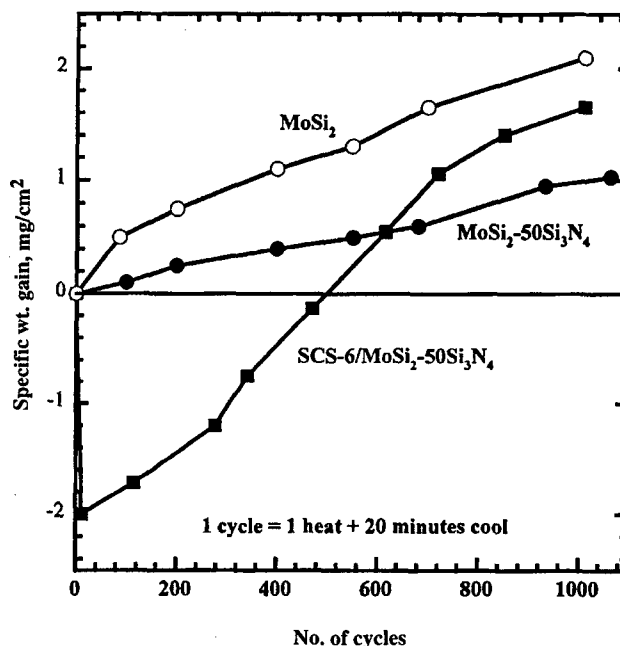


Figure 6.—Specific weight gain versus number of cycles plot for  $\text{MoSi}_2\text{-}50\text{Si}_3\text{N}_4$  monolithic and SCS-6/ $\text{MoSi}_2\text{-}50\text{Si}_3\text{N}_4$  hybrid composite cyclic oxidized at 1250 °C in air.

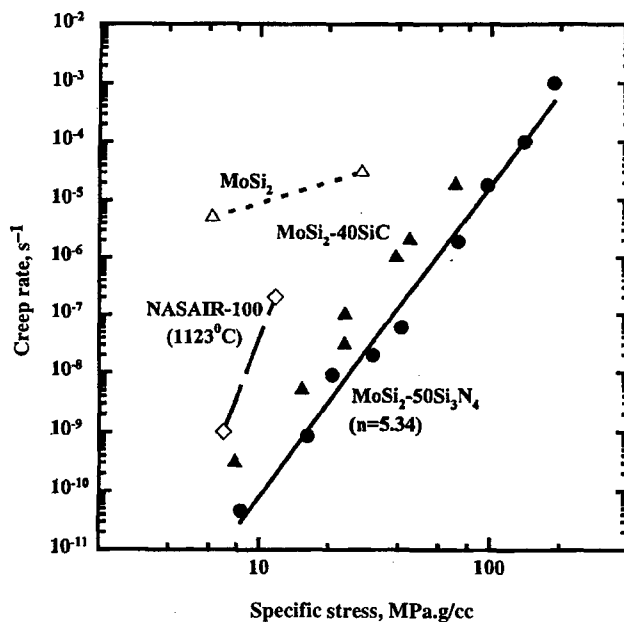


Figure 7.—Second stage creep rate versus specific stress at 1200 °C for  $\text{MoSi}_2\text{-}50\text{Si}_3\text{N}_4$  compared with other materials.

nitride(RBSN) (26). PWA 1480 exhibits higher tensile strength than both  $\text{MoSi}_2$ -base and RBSN-base composites between room temperature and 1000 °C; however, PWA 1480 is almost three times denser than both composites, and hence is at a disadvantage on a specific strength basis. Although not included in Fig. 10(b) because of different fiber and architecture, typical 2D woven SiC-SiC composites (27) exhibit much lower strengths (~200 MPa) between room temperature and 1200 °C. However, SiC-SiC composites retain their strengths beyond 1200 °C. Figure 10(b) also shows the

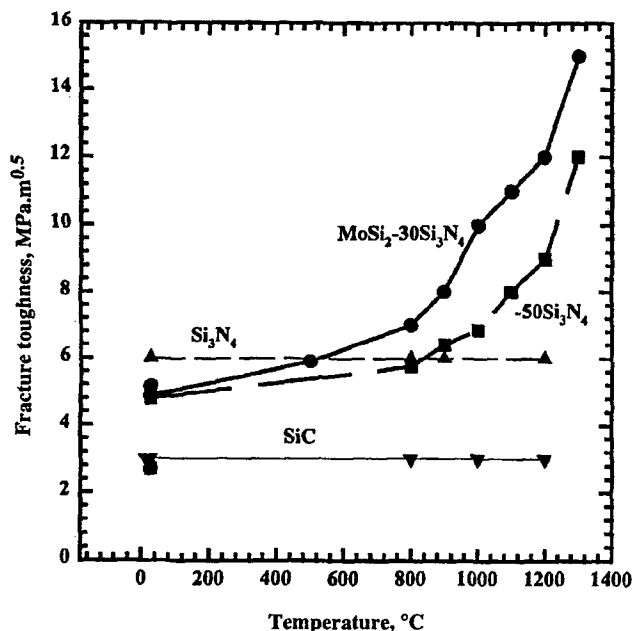


Figure 8.—Temperature dependence of fracture toughness of MoSi<sub>2</sub>-50Si<sub>3</sub>N<sub>4</sub> compared with ceramic matrices.

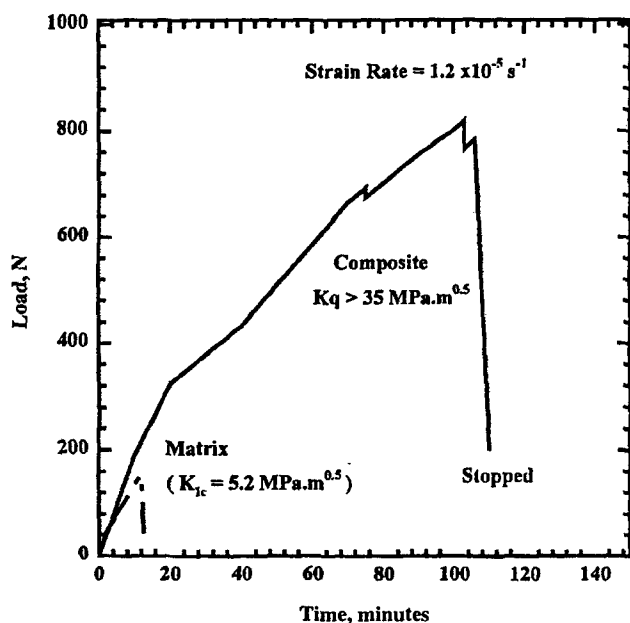


Figure 9.—Load-displacement curves from chevron notched 4 point bend tested SCS-6/MoSi<sub>2</sub>-50Si<sub>3</sub>N<sub>4</sub> and MoSi<sub>2</sub>-50Si<sub>3</sub>N<sub>4</sub> specimen at room temperature.

tensile strength data for the SCS-6 fibers, reemphasizing the fiber-dominated behavior of the composites. The MoSi<sub>2</sub>-base composites also exhibited elastic modulus values of ~290/200 GPa between RT and 1200 °C which were substantially higher than the comparable CMC at all temperatures. Unlike most CMC's which have as much as 20 percent porosity, these MoSi<sub>2</sub>-base composites are fully dense and hence exhibit higher modulus.

Several tensile creep tests were carried out on SCS-6 (0)/MoSi<sub>2</sub>-50Si<sub>3</sub>N<sub>4</sub> composite specimens between 1000 and 1200 °C in vacuum. Unfortunately, it was not possible to get the rupture lives from these specimens due to

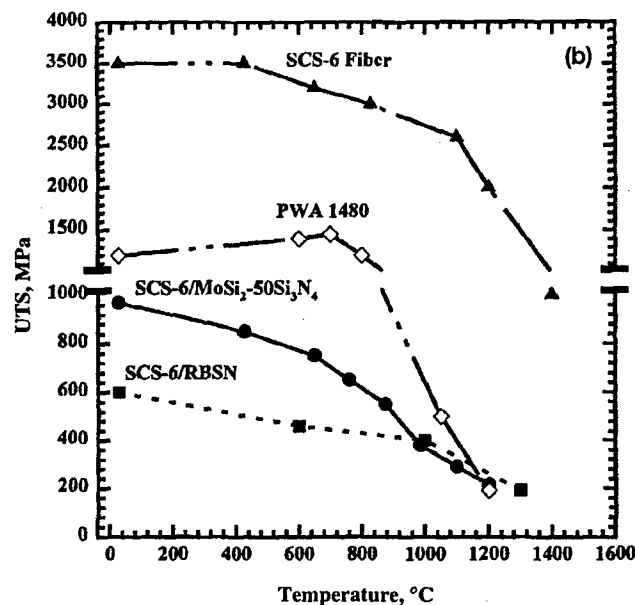
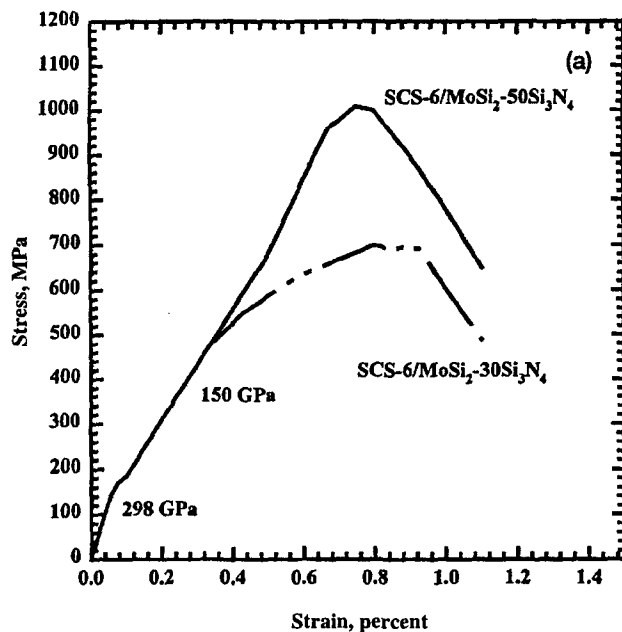


Figure 10.—Mechanical properties of SCS-6/MoSi<sub>2</sub>-50Si<sub>3</sub>N<sub>4</sub> hybrid composites. (a) Room temperature tensile stress-strain curves. (b) Temperature dependence of ultimate tensile strength of SCS-6/MoSi<sub>2</sub>-50Si<sub>3</sub>N<sub>4</sub>-base composites compared with other materials.

accidental power failures. Nonetheless, test durations of ~1000 hours were achieved and some idea of long term durability was obtained. Specimens tested at these temperatures exhibited a short primary creep stage and an extended secondary stage. The minimum creep rates ranged from  $1.0 \times 10^{-9}$  to  $2.0 \times 10^{-9} \text{ sec}^{-1}$  at 70 MPa between 1100 and 1200 °C.

#### Impact Properties

Aircraft engine components require sufficient toughness to resist manufacturing defects, assembly damage, stress concentrations at notches, and foreign and domestic object damage (28). Consultation with engine company designers indicated a strong desire for not only fracture toughness but more importantly, impact resistance to be measured before they would seriously



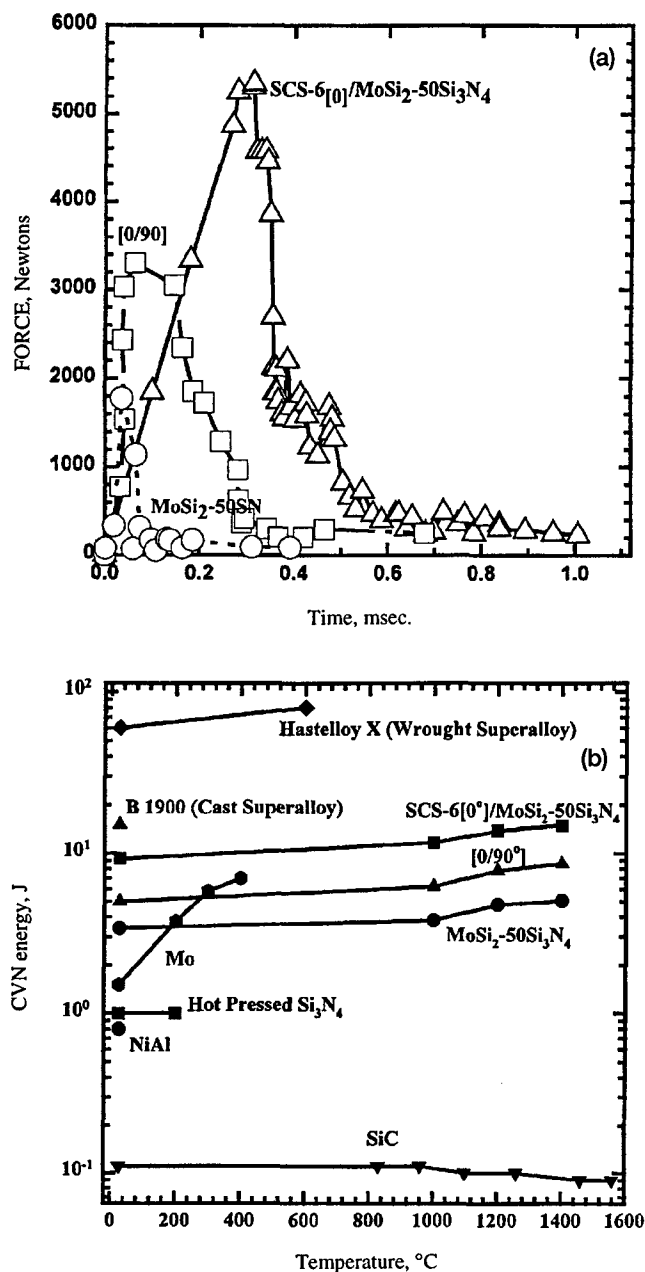


Figure 11.—Impact properties of MoSi<sub>2</sub>-50Si<sub>3</sub>N<sub>4</sub> monolithic and SCS-6/MoSi<sub>2</sub>-50Si<sub>3</sub>N<sub>4</sub> hybrid composites. (a) Force-time curves obtained from Charpy impact tests. (b) CVN energy versus temperature for MoSi<sub>2</sub>-base composites compared with other materials.

consider these types of composites. The Charpy V-notch (CVN) test was chosen to assess impact resistance based on the engine designer's desire to use a relative ranking against more familiar materials, rather than a formal design requirement.

CVN impact tests were conducted on full size specimens of MoSi<sub>2</sub>-50Si<sub>3</sub>N<sub>4</sub> matrix and SCS-6 (0) and (0/90) oriented /MoSi<sub>2</sub>-50Si<sub>3</sub>N<sub>4</sub> hybrid composites between room temperature and 1400 °C in air. Figure 11(a) shows the force time curves obtained from the instrumented impact tests at room temperature for monolithic MoSi<sub>2</sub>-50Si<sub>3</sub>N<sub>4</sub>, SCS-6 (0) and (0/90) /MoSi<sub>2</sub>-50Si<sub>3</sub>N<sub>4</sub> composites. The maximum value of force represents the elastic energy required for crack initiation. The hybrid composite in (0) orientation exhibited the

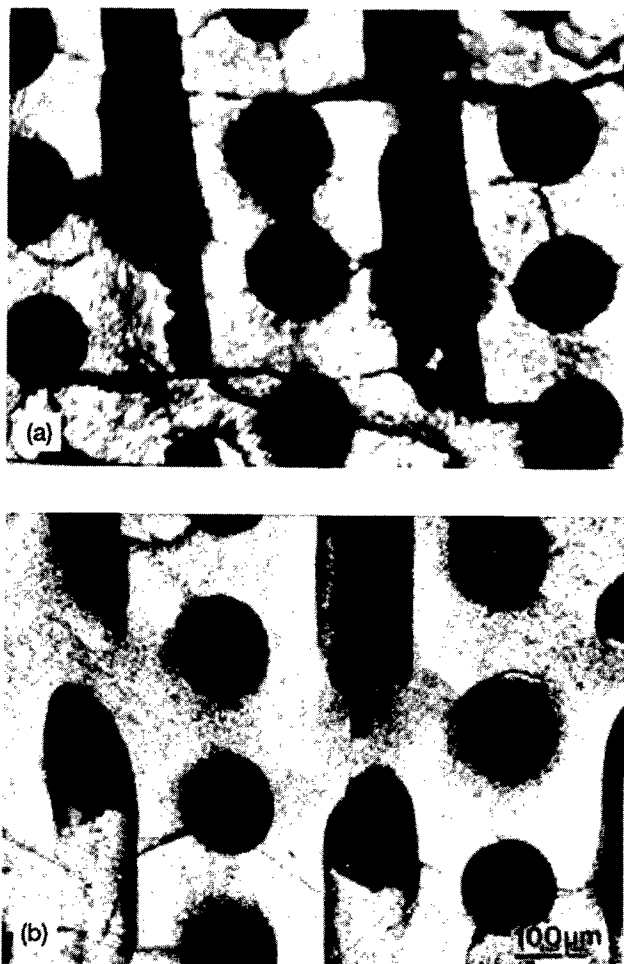


Figure 12.—SEM-BS images of impact tested SCS-6 [0/90]/MoSi<sub>2</sub>-50Si<sub>3</sub>N<sub>4</sub> hybrid composites at (a) room temperature and (b) 1400 °C.

highest peak force values, followed by the cross-ply and finally the monolithic material. At 1400 °C, the peak force values for all three materials were higher than their corresponding values at room temperature. The hybrid composite exhibited a gradual, stepwise decrease in load after the peak force was achieved. This indicates substantial energy absorption during crack propagation, and was especially pronounced in the (0) orientation.

Figure 11(b) shows the temperature dependence of CVN energy for MoSi<sub>2</sub>-base materials compared with other potential materials such as superalloys, and ceramics. The CVN energy for both the monolithic MoSi<sub>2</sub>-50Si<sub>3</sub>N<sub>4</sub> and the hybrid composites increased with increase in temperature. The fiber reinforcement in (0) orientation increased the impact resistance by five times and in (0/90) orientation nearly two times. The CVN energy of SCS-6/MoSi<sub>2</sub>-50Si<sub>3</sub>N<sub>4</sub> was comparable to the cast superalloy B-1900 but substantially lower than the wrought superalloy Hastelloy X. The CVN energy of MoSi<sub>2</sub>-50Si<sub>3</sub>N<sub>4</sub> monolithic was comparable to Mo alloys and was far superior to NiAl (30), and monolithic Si<sub>3</sub>N<sub>4</sub>, and SiC. Unlike MoSi<sub>2</sub>-50Si<sub>3</sub>N<sub>4</sub> which shows increased CVN energy with temperature, SiC shows a slight decrease of CVN energy with temperature. This is probably due to the degradation caused by densification aids used with SiC (29). SEM examination of impact tested SCS-6/ MoSi<sub>2</sub>-50Si<sub>3</sub>N<sub>4</sub> showed substantial fiber pullout in (0) orientation and limited fiber pullout in (0/90) oriented specimens at all temperatures. Additionally, the SEM image (Fig. 12(a)) showed substantial matrix cracking in the room temperature tested specimens, but only limited cracking at 1400 °C (Fig. 12(b)). This again implies that MoSi<sub>2</sub> can behave in a ductile manner at higher temperatures.

#### Technological Needs: Complex Shapes and Low Cost Processing

Most of the attractive strength and toughness values reported so far were achieved with composites reinforced with SCS-6 fibers made by Textron, Inc. This large diameter (145  $\mu\text{m}$ ) fiber was designed primarily for Ti-based composites. This fiber does not have adequate creep strength at the highest temperatures envisioned for  $\text{MoSi}_2$  and is too large to be bent around the sharp radii needed to make complex shapes. However, it is easy to infiltrate matrix powders between these fibers, thus enabling composites to be fabricated routinely. This ease in fabrication was meant to be exploited by further characterization of key properties such as creep resistance, transverse properties, and performance of the composite in an engine test bed. However, finer diameter fibers are preferred on a cost, shape making, creep resistance, and toughness basis. Hi-Nicalon is the best currently available fiber, although Dow Corning's Sylramic® fiber (developed for the High Speed Civil Transport program), is also appropriate for this  $\text{MoSi}_2$ - $\text{Si}_3\text{N}_4$  matrix. A transition in effort to Hi-Nicalon fibers was therefore investigated, first using tow fibers, (i.e., strings of approximately 500 individual filaments that are spread out, wound on a drum and then infiltrated with matrix powder) and ultimately woven cloth (i.e., the tows are woven into two or three dimensional architectures before matrix infiltration).

In earlier studies, the powder cloth technique was used to produce SiC continuous fiber reinforced  $\text{MoSi}_2$ -base composites. The powder cloth process is labor intensive and cannot always produce a uniform fiber distribution. Melt infiltration and chemical vapor infiltration are popular methods for processing of CMC's because of the potential for shape making and lower cost, but are limited to thickness on the order of 5 mm, because segregation

and porosity problems are aggravated in thick specimens. Tape casting was therefore adopted as a powder metallurgy method for composite fabrication. Initially, several casting trials of  $\text{MoSi}_2$ - $\text{Si}_3\text{N}_4$  were carried out to optimize various parameters such as particle size, type and amount of binder and solvent, flow behavior of the slurry, and binder burn-out cycle. A 56 ply composite of SCS-6/ $\text{MoSi}_2$ - $\text{Si}_3\text{N}_4$  was successfully fabricated by tape casting followed by the standard hot press plus HIP consolidation. Composites with small diameter fibers such as SCS-9 (75  $\mu\text{m}$ ) and coated Hi-Nicalon (18 to 20  $\mu\text{m}$ ) were also successfully fabricated. Figure 13 illustrates the range in fiber diameters in this study. Note also the improvement in fiber spacing control between Fig. 13(a) and Fig. 13(b), achieved by switching from powder cloth to tape casting. Fig. 14 displays efficient spreading of the fiber tows and infiltration of  $\text{MoSi}_2$ - $\text{Si}_3\text{N}_4$  powder particles. Although there is still some heterogeneity in the fiber distribution, this microstructure is among the best we have seen on any other study using fine diameter fibers.

Interfacial coatings play a very important role in fiber reinforced composites, and the Hi-Nicalon tow fibers must be coated before compositing. Interfacial coatings that have proven successful in CMC's have been adopted for use with  $\text{MoSi}_2$ . To date, only carbon or BN have been able to provide the level of interfacial bonding required for toughening, but they both exhibit poor environmental resistance. Therefore, a protective coating of SiC or  $\text{Si}_3\text{N}_4$  is required as a second layer on top of the debonding layer. Unfortunately, the state of coating technology for fine diameter tows has still not matured to the state where smooth, crack free and uniformly thick coatings can be produced. This immaturity is also reflected in the high cost and limited facilities nationally available for coating. Therefore, only limited mechanical properties have been generated with these fibers.

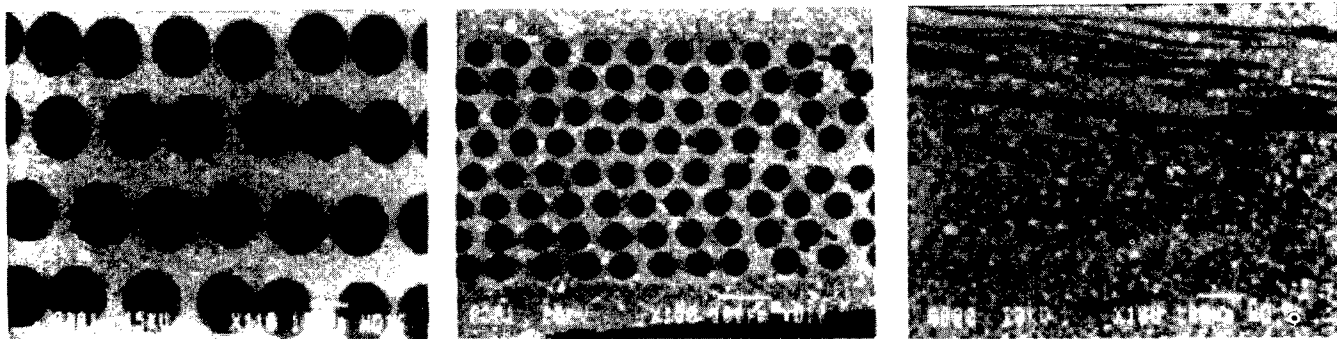


Figure 13.—SEM micrographs of SiC/ $\text{MoSi}_2$ - $\text{Si}_3\text{N}_4$  showing wide range of fiber diameters.

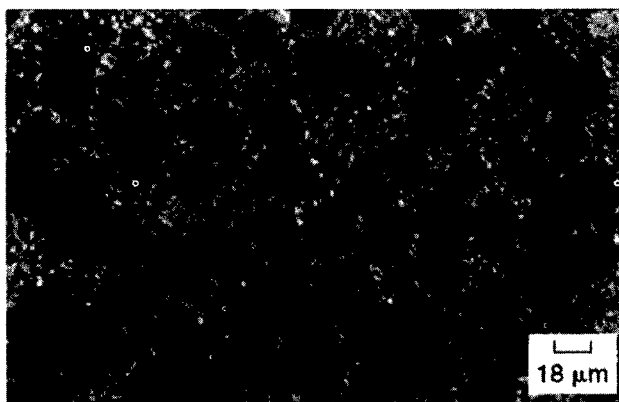


Figure 14.—SEM-SE image of BN/SiC coated Hi-Nicalon/ $\text{MoSi}_2$ - $\text{Si}_3\text{N}_4$  hybrid composite showing good fiber spreading and matrix infiltration.

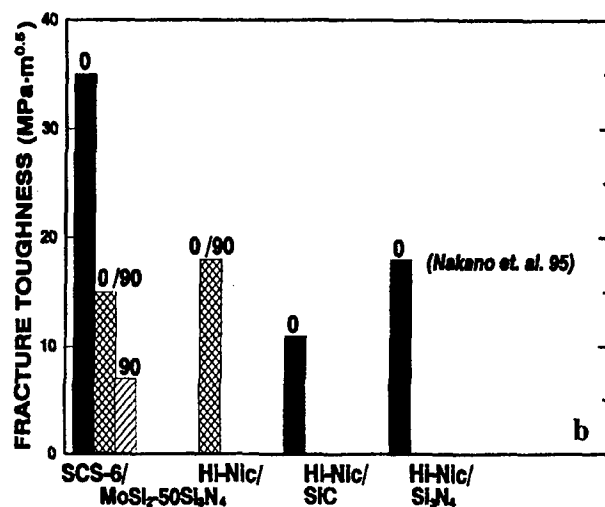
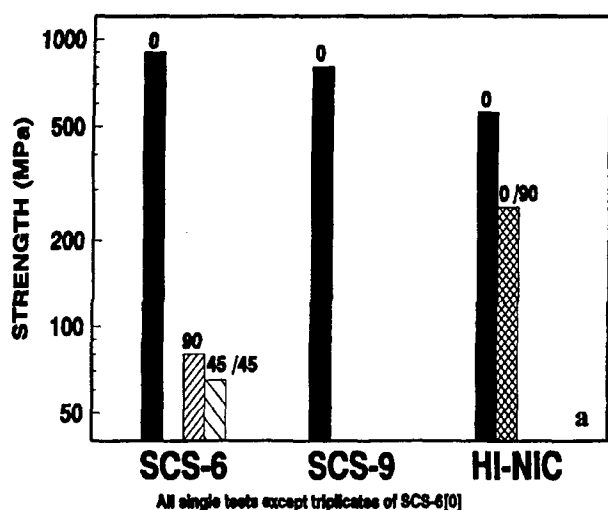


Figure 15.—Influence of fiber diameter and orientation on room-temperature (a) tensile strength and (b) fracture toughness of MoSi<sub>2</sub>-base hybrid composites.

The influence of fiber diameter and architecture on mechanical properties was investigated by conducting room temperature tensile and fracture toughness tests on specimens of SCS-6, SCS-9 and BN/SiC coated Hi-Nicalon/MoSi<sub>2</sub>-50Si<sub>3</sub>N<sub>4</sub> hybrid composites. Testing in the (0) direction (longitudinal) produced the highest strength, (700 to 1000 MPa strength and 1.2 percent total strain) to failure. Testing in the (90) direction produced the lowest ultimate tensile strength of only 72 MPa and 0.04 % strain to failure for SCS-6 reinforced composite. This is not an unexpected result since the fibers cannot bridge matrix cracks in the transverse direction, and cross-plyed laminates or woven 2D or 3D architectures are required to achieve more isotropic properties. For example, the Hi-Nicalon reinforced composite exhibited high strength and strain to failure in the 0/90 architecture, about 60 % of the unidirectional value, Fig. 15(a). Figure 15(b) shows that the Hi-Nicalon/MoSi<sub>2</sub>-Si<sub>3</sub>N<sub>4</sub> in (0/90) direction exhibited higher fracture toughness than the CMC's Hi-Nicalon/SiC and Hi-Nicalon/Si<sub>3</sub>N<sub>4</sub>, even though they were tested in the more favorable (0) direction (31). The CMC's were processed at much higher temperatures, 1600 to 1800 °C, causing more fiber degradation than Hi-Nicalon/MoSi<sub>2</sub>-Si<sub>3</sub>N<sub>4</sub> and therefore exhibited lower toughness. The SEM micrograph of the fracture toughness tested Hi-Nicalon reinforced composite (Fig. 16(a)) showed more fiber pullout than the SCS-6 fiber reinforced composite (Fig. 16(b)).



Figure 16.—SEM-SE images of fracture toughness tested (a) BN/SiC coated Hi/Nicalon [0/90]/ (b) SCS-6 [0/90]/ MoSi<sub>2</sub>-50Si<sub>3</sub>N<sub>4</sub> hybrid composites.

### Conclusions

A wide spectrum of mechanical and environmental properties have been measured in order to establish feasibility of an MoSi<sub>2</sub>-base composite with Si<sub>3</sub>N<sub>4</sub> particulate and SiC fibers. The high impact resistance of the composite is of particular note, as it was a key property of interest for engine applications. Processing issues have also been addressed in order to lower cost and improve shape making capability. These results indicate that this composite system remains competitive with other ceramics as a potential replacement for superalloys.

### Acknowledgments

The authors would like to acknowledge financial support from the Office of the Naval Research, (A.K. Vasudevan) and Pratt & Whitney Aircraft, West Palm Beach, FL (W. Pospisil and R. Hecht), and technical assistance from P. Bartolotta, M. Verrilli, D. Hull and A. Garg.

### References

- (1) J.R. Stephens, Aviation Week and Space Technology, August 1992.
- (2) J. Doychak, Journal of Metals, June (1992), pp. 46-51.
- (3) A.K. Vasudevan and J.J. Petrovic, *High Temperature Silicides*, ed. by A.K. Vasudevan and J.J. Petrovic, North Holland, NY, 1992, pp. 1-17.
- (4) J.J. Petrovic and R.E. Honnell, *Cerm. Eng. Soc. Proc.*, 11 (1990) pp. 734-744.

- (5) D. J. Shah and D.L. Anton, U.S. Airport Report WRDC-TR-90-4122, Feb. 1991.
- (6) S. Bose, High Temperature Silicides, ed., A.K. Vasudevan and J.J. Petrovic, North Holland, NY, 1992, pp. 217-225.
- (7) Robert M. Aikin, Jr., Structural Intermetallics, eds., R. Darolia, J.J. Lewandowski, C.T. Liu, D.B. Miracle, and M.V. Nathal, TMS, Warrendale, PA, 1993, pp. 791-798.
- (8) K. Sadananda, C.R. Feng and H. Jones, High Temperature Silicides, Ed., A.K. Vasudevan and J.J. Petrovic, North Holland, NY, 1992, pp. 227-237.
- (9) J.J. Petrovic R.E. Honnell and W.S. Gibbs, "Moly Disilicide Alloy Matrix Composites", US Patent, 4970, 179.
- (10) E. Fitzer and W. Remmele, 5th Int. Conf. on Composite Materials, ICCM-V, AIME (1985), pp. 515-530.
- (11) M.J. Maloney and R.J. Hecht, High Temperature Silicides, ed., A.K. Vasudevan and J.J. Petrovic, North Holland, NY, 1992, pp. 19-31.
- (12) P.J. Meschter, Met. Trans., Vol. 23A, 1992.
- (13) T.C. Chou and T.G. Nieh, J. Mater. Res. Vol 8, No. 1, 1993, pp. 214-223.
- (14) D.A. Berztiss, R.R. Cerachiara, E.A. Gulbransen, F.S. Pettit and G.H. Meier, Mater. Sci. Eng., A155, 1992, pp. 165-181.
- (15) A. Muller, G. Wang, R.A. Rapp, High Temperature Silicides, Eds., A.K. Vasudevan, J.J. Petrovic, North Holland, Amsterdam, London, NY, 1992, pp. 199-209.
- (16) S.V. Raj, Mat. Sci. Eng., A201, 1995, pp. 229-241.
- (17) M.G. Hebsur, Intermetallic Composites III, Ed. by J.A. Graves, R.R. Bowman, and J.J. Lewandowski, MRS Proc., Vol. 350, 1994, Pittsburgh, PA, pp. 177-182.
- (18) M.G. Hebsur, "Pest Resistant  $\text{MoSi}_2$  Materials and Method of Making" U.S. Patent, No. 5, pp. 429, 997, 1995.
- (19) J.W. Pickens, NASA TM-102060, 44135, 1989 NASA LeRC, Cleveland, OH.
- (20) M.V. Nathal and L.J. Ebert, Metall. Trans., 16 A, 1985 427-439.
- (21) I.J. Blum, Eng. Fract. Mech., 1975 pp. 593-604.
- (22) A. Ghosh, M.G. Jenkins, M.K. Ferber, J. Peussa and J.A. Salem, Eds., R.C. Bradt et al., Plenum Press, New York, 1992.
- (23) A.J. Pyzik and D.R. Beaman J. Am. Ceram. Soc., 76, pp. 2737-2744, 1993.
- (24) J.I. Eldridge, R.T. Bhatt and J.D. Kaiser, NASA TM-103739, 1991, NASA Lewis Research Center, Cleveland, OH.
- (25) M.G. Hebsur and R.V. Miner, NASA TM-88950, 1987, NASA Lewis Research Center, Cleveland, OH.
- (26) R.T. Bhatt., NASA CP-10039, 1989, pp. 57-1-57-13, NASA Lewis Research Center, Cleveland, OH.
- (27) J. Halada, "Enhanced SiC/SiC Ceramic Matrix Composites for Long Life Performance in Oxidizing Environments", Du-Pont Lanxide Composites Report, January 1994.
- (28) P.K. Wright, Structural Intermetallics, eds. R. Darolia, J.J. Lewandowski, C.T. Liu, D.B. Miracle, and M.V. Nathal, TMS, Warrendale, PA, 1993, pp. 885-893.
- (29) R.C. Bradt, NASA CR-165325, 1984, NASA, Washington D.C.
- (30) V.C. Nardone, Met., Trans., Vol., 23A, 1992, pp. 563-572.
- (31) K. Nakano, K. Sasaki, H. Saka, M. Fujikura, and H. Ichikawa, High Temperature Ceramic-Matrix Composites II. Manufacturing and Materials Development, ed. by A.G. Evans, R.N. Nasalin, 1995, pp. 215-229.

## MOLYBDENUM AND TITANIUM SILICIDE BASED COMPOSITES AND ALLOYS

R. Mitra, N. Eswara Prasad, A. Venugopal Rao and Y.R. Mahajan  
Defence Metallurgical Research Laboratory  
Kanchanbagh, Hyderabad 500 058, INDIA

### Abstract

MoSi<sub>2</sub> and Ti<sub>5</sub>Si<sub>3</sub> based alloys and composites have been processed by reaction hot pressing of elemental powders or by hot pressing of commercial grade powders in vacuum. The particle size of Mo or Ti used in reaction hot pressing has a profound effect in determining the grain sizes. Finer grain size in MoSi<sub>2</sub> and Ti<sub>5</sub>Si<sub>3</sub> based materials lead to higher flexural strength and fracture toughness values. Addition of reinforcements to MoSi<sub>2</sub> matrix results in considerable grain refinement and improvement in room and elevated temperature mechanical properties. It is also observed that reaction hot pressed MoSi<sub>2</sub> contains much less SiO<sub>2</sub> as compared to commercial grade MoSi<sub>2</sub> and this is responsible for 25% higher yield strength of the former at 1200°C. Alloying of commercial grade Starck MoSi<sub>2</sub> with 1.5 and 3 wt.% Al forms Al<sub>2</sub>O<sub>3</sub> *in situ* by reaction with SiO<sub>2</sub>, and this leads to a moderate increase in fracture toughness and around 30% improvement in yield strength at 1200°C. Oxidation resistance of MoSi<sub>2</sub>-1.5 and 3 wt.% Al alloy is poorer as compared to pure MoSi<sub>2</sub>. Alloying of Ti<sub>5</sub>Si<sub>3</sub> with 8 wt.% Al forms Al<sub>67</sub>Si<sub>108</sub>Ti<sub>25</sub> and Al<sub>2</sub>O<sub>3</sub> *in situ* as uniformly dispersed phases in the microstructure. As in MoSi<sub>2</sub>, presence of a second phase in Ti<sub>5</sub>Si<sub>3</sub> leads to noticeable improvement in room temperature hardness and fracture toughness properties. Oxidation resistance of Ti<sub>5</sub>Si<sub>3</sub> is however inferior to that of MoSi<sub>2</sub>. Processing-microstructure-property relationship in these materials is discussed in detail in this paper.

### Introduction

Molybdenum and titanium silicide (MoSi<sub>2</sub> and Ti<sub>5</sub>Si<sub>3</sub>, respectively) based materials are promising for their potential for elevated temperature structural applications due to their high melting points (2030 °C and 2150 °C, respectively), outstanding high temperature oxidation resistance and limited ductility at temperatures above 1100°C (1). MoSi<sub>2</sub> has a tetragonal C11<sub>b</sub> crystal structure, whereas Ti<sub>5</sub>Si<sub>3</sub> has a hexagonal D8<sub>8</sub> structure. MoSi<sub>2</sub> has been extensively used for heating elements in furnaces. Other potential applications of silicides include power generation components, high temperature heat exchangers and filters, aircraft engine hot section components like turbine blades, vanes, combustors and nozzles and automotive components such as turbocharger rotors and valves (2). However, one of the major limitations of these materials is the room

temperature fracture toughness, which is reported as 2.6-4 MPa√m for MoSi<sub>2</sub> (2-5) and 2.1 MPa√m for Ti<sub>5</sub>Si<sub>3</sub> (6). Again, the yield and creep strengths decrease sharply above 1200°C, and this trend can be arrested remarkably by presence of ceramic reinforcements in their composites (6-8). Similarly, presence of ceramic reinforcements also improves the room temperature fracture toughness and flexural strength (3,4).

This paper presents a comprehensive study on the effect of processing, presence of ceramic reinforcements (SiC in MoSi<sub>2</sub> and TiC in Ti<sub>5</sub>Si<sub>3</sub>) and alloying with Al on the microstructure and properties of MoSi<sub>2</sub> and Ti<sub>5</sub>Si<sub>3</sub> based materials. SiC is thermodynamically stable in MoSi<sub>2</sub> and TiC is compatible with Ti<sub>5</sub>Si<sub>3</sub>, and this explains the choice of systems for study. It is obvious that the critical mechanical properties can be substantially improved by optimizing the process variables and achieving a desirable microstructure and this investigation is an effort in this direction.

### Processing

#### MoSi<sub>2</sub> Based Composites and Alloys

MoSi<sub>2</sub> based materials were prepared by two processes: (i) reaction hot pressing of elemental powders or (ii) vacuum hot pressing of commercial grade Starck MoSi<sub>2</sub>. Plates of 5-6 mm thickness and 75 mm diameter were obtained from hot pressing the powders.

The Mo powder used in the reaction hot pressed (R.H.P.) monolithic MoSi<sub>2</sub> was obtained from Non-Ferrous Materials Technology Development Centre, Hyderabad, India and had a particle size of about 3.0 μm, while the Mo powder used for MoSi<sub>2</sub>/20 volume percent (v/o) SiC composite was obtained from Johnson Matthey Inc., U.S.A., and had an average particle size of 33.0 μm. The Mo powders were 99.5% pure, with traces of Fe, Ti, V, Cr and Mn and were treated with hydrogen at around 1200°C to remove oxygen. The Si powder, obtained from Johnson Matthey Inc., U.S.A. was 99.8% pure with traces of C, Fe and Mg as impurities, and possessed -325 mesh (about 20 μm) particle size. The oxygen content of Mo and Si powders were also found using vacuum fusion technique, and these values were found to be 0.3 and 0.23 wt.%, respectively. The SiC powder was obtained from Norton Inc., U.S.A. and

had an average particle size of 1.9  $\mu\text{m}$ . In this process, an intimate mixture of Mo and Si powders (in a stoichiometric ratio for  $\text{MoSi}_2$ ) was degassed at 800°C for 4 h and subsequently, hot pressed at 1500°C for 1 h in vacuum using a pressure of 26 MPa, maintaining a heating rate of 15 °C/minute. In this process, atoms of Si in liquid phase diffuse into the Mo lattice, reacting and forming  $\text{MoSi}_2$  *in situ* (9,10) and this reaction assisted densification progresses under pressure. The reaction taking place from surface to core of Mo particles is:

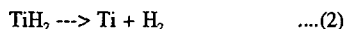


The extent of densification depends on particle sizes, temperature, time and pressure. In case of  $\text{MoSi}_2/20$  v/o SiC composite, appropriate quantity of SiC was mixed with the Mo/Si mixture. Further details of this process has been discussed elsewhere [10].

For the other process, the  $\text{MoSi}_2$  powder was procured from H.G. Starck, Germany. This had a particle size of 5.5  $\mu\text{m}$ , and possessed traces of Fe and Al as impurities. The oxygen content of the powder was found to be about 1 wt.%. Starck  $\text{MoSi}_2$  powder or  $\text{MoSi}_2$  with 20 v/o SiC was hot pressed in vacuum at 1700°C for 1 h using a pressure of 26 MPa.  $\text{MoSi}_2$ -1.5 Al and  $\text{MoSi}_2$ -3 Al alloys were processed by vacuum hot pressing Starck  $\text{MoSi}_2$ -1.5 wt% Al and Starck  $\text{MoSi}_2$ -3 wt% Al powder mixtures, respectively at 1600°C for 1 h using 26 MPa pressure.

#### Ti<sub>5</sub>Si<sub>3</sub> Based Composites

Ti sponge extracted from Ti-ores in this laboratory was hydrided at 1000 °C in hydrogen atmosphere to form  $\text{TiH}_2$ . Chemical analysis of  $\text{TiH}_2$  showed that it contained 1.26% Fe, 0.6% O and 1% O.  $\text{TiH}_2$  was then crushed and ground to fine powder. Si powder was the same as used in processing of  $\text{MoSi}_2$ . A mixture of  $\text{TiH}_2$  and Si powder was prepared by wet and dry blending, and this was subjected to degassing at 800°C for 4 h, when  $\text{TiH}_2$  decomposes to form Ti and  $\text{H}_2$  through the reaction:



The Ti/Si mixture formed in-situ is subsequently hot pressed at 1500°C for 1 h using a pressure of 26 MPa. As in R.H.P.  $\text{MoSi}_2$ , Si atoms diffuse into the Ti lattice forming  $\text{Ti}_5\text{Si}_3$ , and the densification process is assisted by chemical reaction and external pressure. The reaction taking place is:



In case of the  $\text{Ti}_5\text{Si}_3/20$  v/o TiC composite, TiC powder was mixed in an appropriate ratio to  $\text{TiH}_2/\text{Si}$  powder mixture and hot pressed. TiC powder obtained from Johnson Matthey had a particle size of 1  $\mu\text{m}$ .  $\text{Ti}_5\text{Si}_3$ -8 Al alloy was processed by hot pressing of  $\text{TiH}_2/\text{Si}/\text{Al}$  (8 wt%) powder mixture at 1500°C under similar conditions as above.

#### Experimental Procedure

Density measurements were carried out using Archimedes' principle. Microstructural characterization was carried out using optical and scanning electron microscopy (SEM) as well as electron probe microanalysis (EPMA). X-ray diffraction (XRD) was carried out on polished surfaces to identify the phases present. Further microstructural characterization has been carried out using transmission electron microscopy (TEM). TEM samples were prepared using mechanical thinning followed by ion milling and were studied using a Phillips 430T TEM operating at 300 kV.

Room temperature mechanical properties of  $\text{MoSi}_2$  and  $\text{Ti}_5\text{Si}_3$  based materials have been evaluated. Vicker's hardness indentations were taken using loads of 5-30 kg. Indentation fracture behaviour was studied in  $\text{Ti}_5\text{Si}_3$  based materials using the equation proposed by Anstis et al for median cracks (11). The expression for indentation fracture toughness,  $K_Q$

according to Anstis et al is:

$$K_Q = 0.016.(E/H)^{1/2}.P/c^{3/2} \quad \dots(i)$$

where E is the Young's modulus, H is the hardness, c is the crack length and P is the external load applied. Flexural tests were performed on three point bend samples having dimensions as: Breadth (B) = 5 mm, Width (W) = 5 mm, and Span (S) = 40 mm. The flexural strength,  $\sigma$  in a three point bend test is given by the expression:

$$\sigma = 3P_{\max}S/2BW^2 \quad \dots(ii)$$

where  $P_{\max}$  is the maximum load in the load displacement curve. Fracture toughness tests were conducted on the single edge notch bend (SENB) specimens [12] having the dimensions as: B = 5 mm, W = 10 mm, and S = 40 mm in 3-point bend loading. A notch was machined using electro-discharge wire cutting (wire diameter was .15 mm) and depth of the notch was maintained at 0.55W. Three point bend tests were carried out using a loading rate of 0.5 mm/min. on a screw driven Instron 1185 machine on at least 3 specimens of each kind. The fracture toughness,  $K_Q$  is (12):

$$K_Q = (P_{\max}S/BW^{3/2}). f(a/W) \quad \dots(iii)$$

$$3(a/W)^{1/2}[1.99-(a/W)\{(1-(a/W))\} \{2.15-3.93(a/W)+2.7(a/W)^2\}]$$

where  $f(a/W) = \frac{2\{1+(2a/W)\}\{1-(a/W)\}^{3/2}}{2\{1+(2a/W)\}\{1-(a/W)\}^{3/2}}$

For high temperature compression tests, specimens of R.H.P.  $\text{MoSi}_2$ , Starck  $\text{MoSi}_2$  and  $\text{MoSi}_2$ -3 Al alloy with 3 mm diameter and 6 mm height were used. Compression tests were performed in air at temperatures of 1200°C and 1300°C at a strain rate of  $10^{-3}$  per second using a servohydraulic DARTEC test system equipped with  $\text{Al}_2\text{O}_3$  rams. The tests were discontinued after a crosshead displacement of 1.0 mm, which corresponds to around 15% compressive strain.

Oxidation properties of Starck  $\text{MoSi}_2$ ,  $\text{MoSi}_2$ -Al alloys,  $\text{Ti}_5\text{Si}_3$ ,  $\text{Ti}_5\text{Si}_3/\text{TiC}$  composite and  $\text{Ti}_5\text{Si}_3$ -8 wt% alloys were studied at 1200 °C using polished samples of dimension 5mm X 5mm X 10mm. Weight gain due to oxidation was measured at the intervals of 10-15 h. The parabolic rate constant,  $k_p$  was evaluated by measuring the slope of square of weight gain,  $W^2$  versus time plot from the relation:

$$W^2 = k_p.t + C \quad \dots(iv)$$

Oxidized surfaces were characterized using EPMA and XRD analysis.

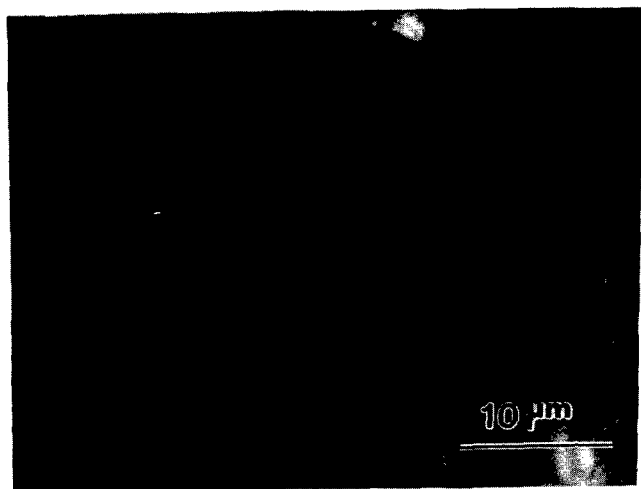
#### Results and Discussion

Relative densities of the  $\text{MoSi}_2$  and  $\text{Ti}_5\text{Si}_3$  based alloys and composites were usually found to be around 98-99% of the theoretical density. Only R.H.P.  $\text{MoSi}_2$  had 95% of the theoretical density.

#### MoSi<sub>2</sub> Based Alloys and Composites

##### Microstructure

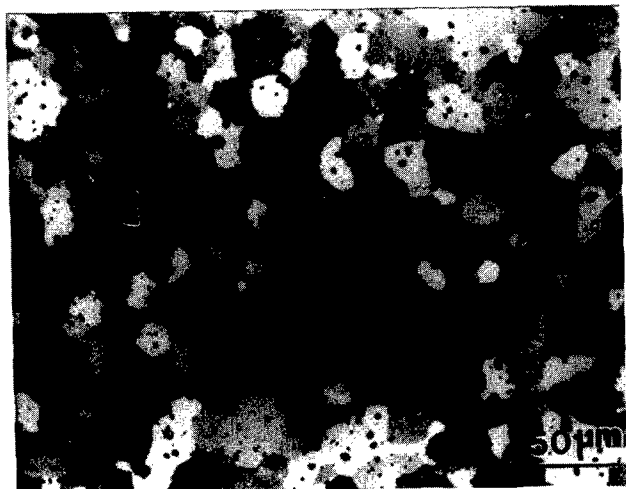
Figures 1(a-e) are representative cross polarized light optical micrographs of R.H.P.  $\text{MoSi}_2$ , R.H.P.  $\text{MoSi}_2/20$  v/o SiC composite, Starck  $\text{MoSi}_2$ , Starck  $\text{MoSi}_2/20$  v/o SiC composite and  $\text{MoSi}_2$ -3 Al alloy.  $\text{MoSi}_2$ -1.5 Al alloy possesses a microstructure similar to that of  $\text{MoSi}_2$ -3 Al alloy (13). The grain sizes in R.H.P.  $\text{MoSi}_2$  and  $\text{MoSi}_2/20$  v/o SiC composite were found to be 5  $\mu\text{m}$  and 18  $\mu\text{m}$ , respectively. The grain size in the latter is coarser, even after the grain boundary pinning action of SiC. This can be explained from much finer Mo particle size (3  $\mu\text{m}$ ) used in case of R.H.P.  $\text{MoSi}_2$ , against 33  $\mu\text{m}$  Mo particle size in case of R.H.P.  $\text{MoSi}_2/20$  v/o SiC composite. As the  $\text{MoSi}_2$  grains form *in situ* from diffusion of Si



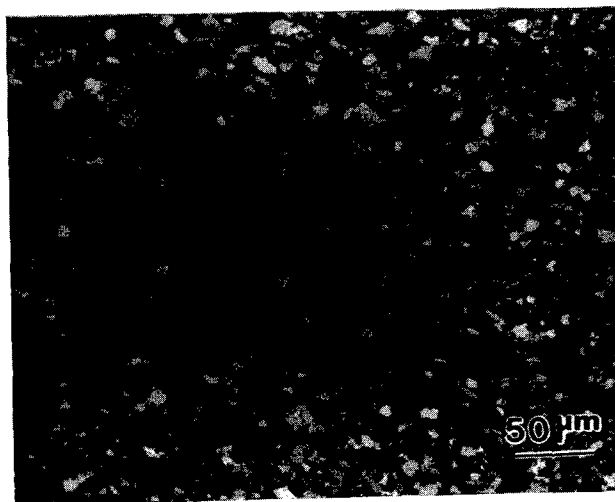
1(a)



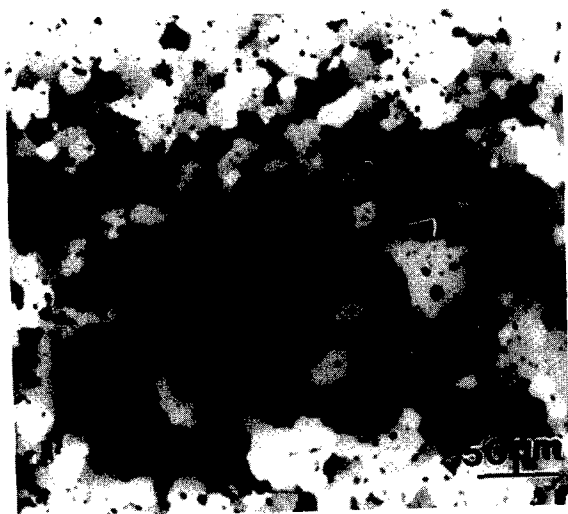
1(b)



1(c)



1(d)

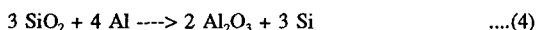


1(e)

Fig. 1. Polarized light optical micrographs of (a) R.H.P.  $\text{MoSi}_2$ , (b) R.H.P.  $\text{MoSi}_2/20$  v/o SiC composite, (c) Starck  $\text{MoSi}_2$  (arrow indicates  $\text{SiO}_2$  phase), (d) Starck  $\text{MoSi}_2/20$  v/o SiC composite, and (e) Starck  $\text{MoSi}_2$ -3 wt.% Al alloy (arrow indicates  $\text{Al}_2\text{O}_3$  phase).

into the Mo particles, prior Mo particle size regulates the grain size. The grain size in Starck MoSi<sub>2</sub> varied between 20-40 µm, whereas Starck MoSi<sub>2</sub>/20 v/o SiC composite possessed a grain size of 5 µm due to strong grain boundary pinning by SiC particles during processing. MoSi<sub>2</sub>-1.5 and 3 Al alloys possess grain sizes of 15-20 µm. The cross polarized light micrograph of Starck MoSi<sub>2</sub> shows a high volume fraction of SiO<sub>2</sub> particles at grain boundaries and inside the grains, which appear bright. The same could not be seen to that extent in R.H.P. MoSi<sub>2</sub> and MoSi<sub>2</sub>/20 v/o SiC composite. This indicates that Starck MoSi<sub>2</sub> contains much higher oxygen as compared to R.H.P. MoSi<sub>2</sub>. This was verified from chemical analysis, which showed oxygen contents in R.H.P. MoSi<sub>2</sub>, R.H.P. MoSi<sub>2</sub>/20 v/o SiC composite and Starck MoSi<sub>2</sub> to be 600 wppm, 2400 wppm and 8900 wppm, respectively. Presence of SiO<sub>2</sub> phase is deleterious at high temperature for its visco-plastic flow beyond 1200°C, and is responsible for softening of MoSi<sub>2</sub> (8,14). Around 3 volume percent Mo<sub>5</sub>Si<sub>3</sub> phase was identified in the microstructure of R.H.P. MoSi<sub>2</sub> and MoSi<sub>2</sub>/20 v/o SiC composite, which contained Fe, Ti, V, Cr and Mn in solution. TEM and HRTEM investigations have shown grain boundaries and interfaces in R.H.P. MoSi<sub>2</sub> and R.H.P. MoSi<sub>2</sub>/20 v/o SiC composite to be free of any amorphous region (10). Figure 2 shows such an MoSi<sub>2</sub>/SiC interface, which is atomically abrupt. But some of the MoSi<sub>2</sub>/SiC interfaces in R.H.P. composite showed an amorphous region possibly due to SiO<sub>2</sub> surface layer on SiC particles, which could not be removed fully even after a treatment with HF.

In MoSi<sub>2</sub>-Al alloys, the Al<sub>2</sub>O<sub>3</sub> particles form *in situ*, which are distributed uniformly throughout the matrix (Fig. 1(e)). The Al<sub>2</sub>O<sub>3</sub> particles formed from the reaction:



The formation of Al<sub>2</sub>O<sub>3</sub> was confirmed using EPMA and X-ray diffraction (XRD) analyses. XRD and TEM electron diffraction analyses have shown that these are α-Al<sub>2</sub>O<sub>3</sub>, similar to the observation of Costa e Silva and Kaufman (15). EPMA analysis of the matrix has shown that 2.5 at% (1.5 wt%) Al goes into solid solution in MoSi<sub>2</sub>-3 Al alloy, and 0.5 at% (0.2 wt%) Al goes into solid solution in MoSi<sub>2</sub>-1.5 Al alloy. Mo-Si-Al ternary isothermal phase diagram at 1600°C shows that about 2 at% Al is expected to be in solution in MoSi<sub>2</sub> (15). MoSi<sub>2</sub>-1.5 Al contains less Al in solid solution than MoSi<sub>2</sub>-3 Al possibly, because α-Al<sub>2</sub>O<sub>3</sub> formation from reaction (4) (consuming the SiO<sub>2</sub> content) precedes solid solution alloying of Al with MoSi<sub>2</sub> and only the balance Al goes into solid solution.

### Mechanical Properties

Table I presents the relative densities, grain sizes and the room temperature mechanical properties of MoSi<sub>2</sub> based materials. R.H.P. MoSi<sub>2</sub> has much finer grain size as compared to R.H.P. MoSi<sub>2</sub>/20 v/o SiC composite, and that explains the slightly higher fracture toughness in the former. Usually, MoSi<sub>2</sub>/SiC composite is expected to have a higher value of fracture toughness than monolithic MoSi<sub>2</sub>, as SiC particles lead to toughening (3,4). As expected, fine grained R.H.P. MoSi<sub>2</sub> showed fully intergranular fracture, whereas the same was both transgranular and intergranular fracture was observed in relatively coarse grained R.H.P. MoSi<sub>2</sub>/20 v/o SiC composite (10). Presence of 20 volume per cent SiC particles however leads to higher flexural strength and hardness in the R.H.P. MoSi<sub>2</sub>/SiC composite. Starck MoSi<sub>2</sub> possesses the lowest flexural strength and fracture toughness, as it has the coarsest grain size. But addition of 20 volume per cent SiC particles leads to considerable grain refinement in the composite. Finer grain size and presence of SiC reinforcements lead to much higher hardness, flexural strength and fracture toughness. The presence of SiC or other ceramic reinforcements in MoSi<sub>2</sub> aids in increasing the fracture toughness values because of finer grain size, crack deflection and bridging effects (3,4). MoSi<sub>2</sub>-1.5 Al alloy demonstrated both an improvement in hardness and flexural strength over monolithic Starck MoSi<sub>2</sub>, but almost similar fracture toughness. MoSi<sub>2</sub>-3

Al alloy has somewhat lower hardness as compared to unalloyed MoSi<sub>2</sub> due to Al in solid solution and this was also observed by Costa e Silva and Kaufman (15). However fracture toughness improved slightly.

The fracture toughness values reported in Table I agree with those found by other investigators, and in some cases are higher due to finer grain size (2-4). Srinivasan and Schwarz (16) found the fracture toughness of MoSi<sub>2</sub>, prepared by mechanical alloying, and having a grain size of about 5.0 µm, to be between 4 and 4.8 MPa√m. The fracture toughness of monolithic MoSi<sub>2</sub> reported in the literature varies between 3.0 MPa√m (2) and 5.3 MPa√m (4). In yet another investigation, Suryanarayana et al have shown that fracture toughness increases with relative density in HIPped MoSi<sub>2</sub>, and the value is around 4.2 MPa√m for MoSi<sub>2</sub> samples having densities above 95% of the theoretical density (5). Average fracture toughness values of 4.0 and 4.4 MPa√m have been reported for MoSi<sub>2</sub>/20 v/o SiC particulate and whisker reinforced composites, respectively by Petrovic in one of the recent publications (2). The variation of fracture toughness values reported in literature is possibly due to differences in processing parameters, densities and grain sizes of MoSi<sub>2</sub> between different investigations.

Figures 3(a) and (b) present engineering stress strain curves of R.H.P. MoSi<sub>2</sub>, Starck MoSi<sub>2</sub> and MoSi<sub>2</sub>-3Al alloys at 1200°C and 1300°C, respectively. Analysis of compressive yield strength values shows that absence of SiO<sub>2</sub> helps in improving the high temperature mechanical behaviour. The strength of R.H.P. MoSi<sub>2</sub> is higher by 25% at 1200°C, as compared to Starck MoSi<sub>2</sub>, inspite of the fact that it possesses a much finer grain size. This can be explained only from the fact that the oxygen content in R.H.P. MoSi<sub>2</sub> was as low as 600 wppm, compared to 8900 wppm in Starck MoSi<sub>2</sub>. It is also obvious that alloying with Al leads to a 30% improvement in yield strength at 1200°C, as SiO<sub>2</sub> is replaced by Al<sub>2</sub>O<sub>3</sub>. It is also obvious that R.H.P. MoSi<sub>2</sub> undergoes more deformation as compared to Starck MoSi<sub>2</sub> and MoSi<sub>2</sub>-3 wt% Al alloy. However at 1300°C, R.H.P. MoSi<sub>2</sub> and MoSi<sub>2</sub>-3 Al have similar yield strength values as Starck MoSi<sub>2</sub> possibly due to the fact that the brittle to ductile transition sets in around 1300°C in absence of SiO<sub>2</sub> (14). It has been earlier reported that all the 5 slip systems in MoSi<sub>2</sub> are activated around 1300°C, when 1/2<111>, <100> and <110> type dislocations are involved and climb mobility is high (17,18). R.H.P. MoSi<sub>2</sub>/20 v/o SiC composite showed remarkable improvement in high temperature compressive yield strength as compared to monolithic Cerac MoSi<sub>2</sub> (8), when the tests were conducted between 1000-1300°C in air at 10<sup>-4</sup>/sec strain rate (Fig. 4) (10). TEM examination of samples of R.H.P. MoSi<sub>2</sub>/20 v/o SiC deformed at 1300°C showed dislocation pile-ups near particle matrix interface and plastic zone formation at transgranular crack tips (10). The strengthening is believed to be due to the non-deformable SiC particles acting as obstacles to the movement of dislocations. As in the case of R.H.P. MoSi<sub>2</sub> and MoSi<sub>2</sub>-3 Al alloy, a sharp drop in the yield strength is noticed in the R.H.P. MoSi<sub>2</sub>/20 v/o SiC composite between 1200°C and 1300°C. TEM observation of high density of dislocations in the matrix of R.H.P. MoSi<sub>2</sub>/20 v/o SiC composite deformed at 1300°C agrees well with the observation of enhanced plastic deformation in the samples at 1300°C. On the other hand, in Cerac or Starck MoSi<sub>2</sub>, softening of SiO<sub>2</sub> particles leads to considerable decrease in yield strength at lower temperatures (8,19).

### Oxidation Resistance

Oxidation resistance of MoSi<sub>2</sub> is due to an impervious and adhesive SiO<sub>2</sub> film, which is stable between 700°C and 1700°C (1,20). Figure 5 shows the variation of weight gained due to oxidation with time for MoSi<sub>2</sub> and MoSi<sub>2</sub>-Al alloys. Comparative oxidation studies of MoSi<sub>2</sub> and MoSi<sub>2</sub>-3Al at 1200°C up to 75 h have shown that the latter has a higher rate of oxidation. MoSi<sub>2</sub>-1.5 Al alloy showed an even higher rate of oxidation. The parabolic rate constants of oxidation for MoSi<sub>2</sub>, MoSi<sub>2</sub>-3Al and MoSi<sub>2</sub>-1.5Al alloy are 2.28 X 10<sup>-14</sup> g<sup>2</sup>cm<sup>-4</sup>s<sup>-1</sup>, 1.3 X 10<sup>-12</sup> g<sup>2</sup>cm<sup>-4</sup>s<sup>-1</sup>, and 2.67 X 10<sup>-12</sup> g<sup>2</sup>cm<sup>-4</sup>s<sup>-1</sup>, respectively. Contradictory reports exist in the



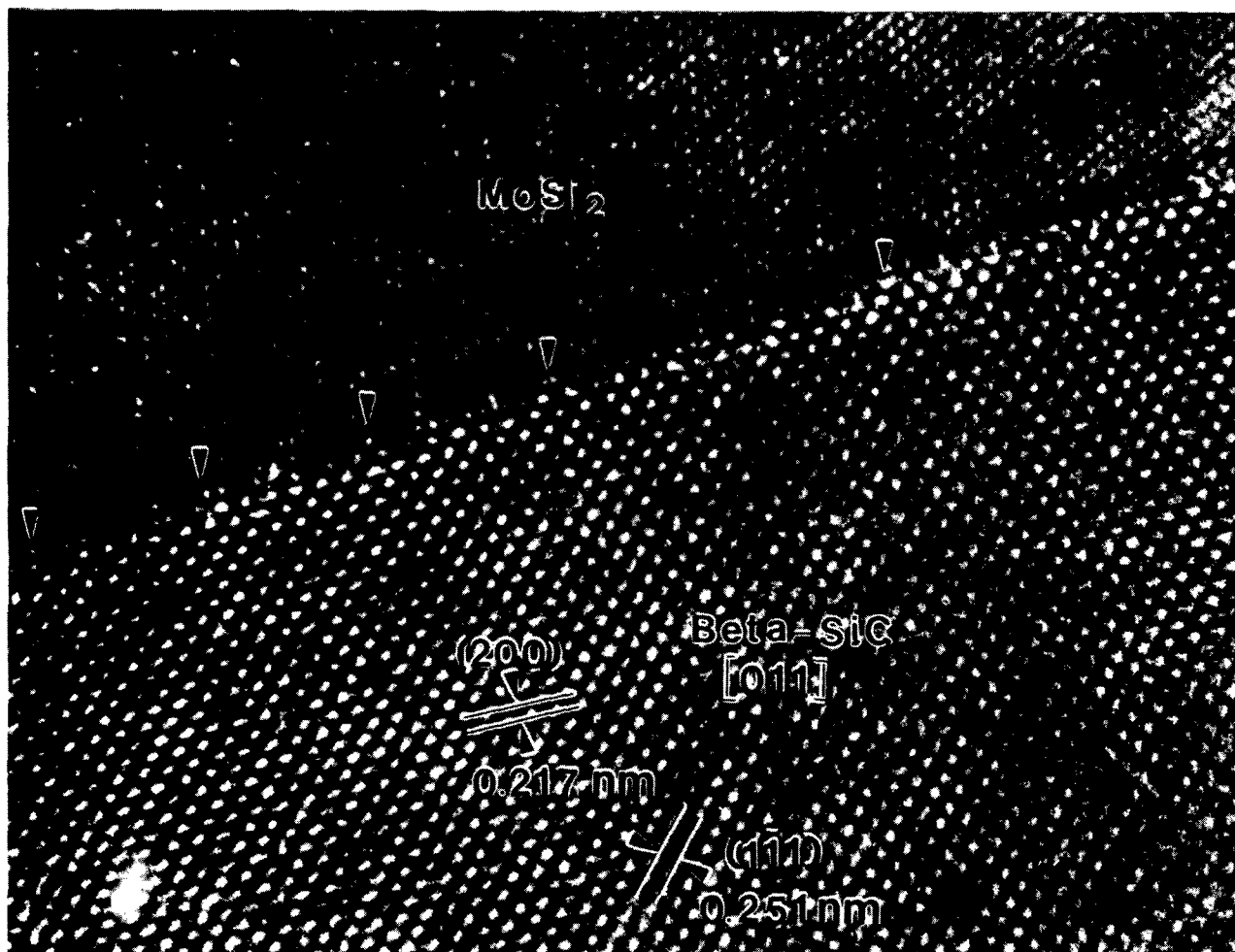


Fig. 2. HRTEM image of an atomically abrupt  $\text{MoSi}_2/\text{SiC}$  interface in the R.H.P. composite. The arrows indicate monatomic steps (10).

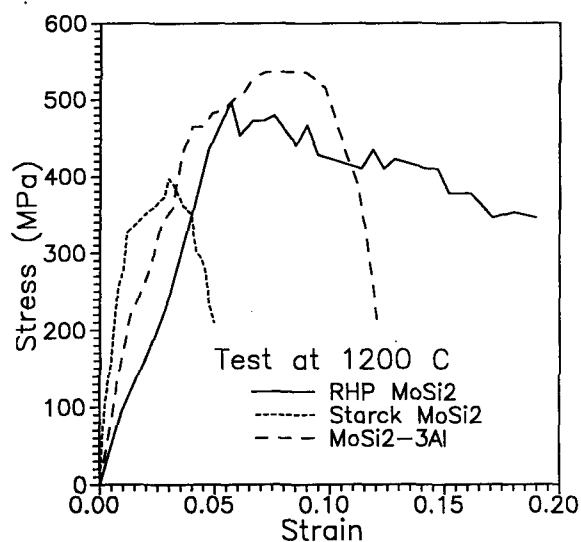


Fig. 3(a). Engineering stress strain curves of R.H.P.  $\text{MoSi}_2$ , Starck  $\text{MoSi}_2$  and Starck  $\text{MoSi}_2$ -3 wt% Al alloy, compression tested at 1200 °C using a strain rate of  $10^{-3}$  per second.

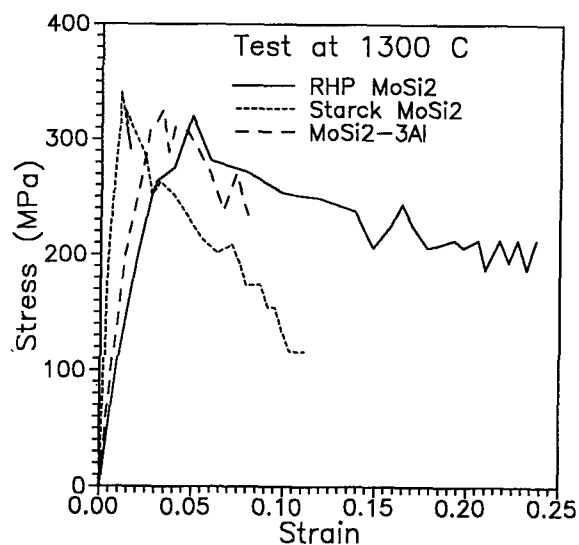


Fig. 3(b). Engineering stress strain curves of R.H.P.  $\text{MoSi}_2$ , Starck  $\text{MoSi}_2$  and Starck  $\text{MoSi}_2$ -3 wt% Al alloy, compression tested at 1300 °C using a strain rate of  $10^{-3}$  per second.

Table I. Mechanical properties of MoSi<sub>2</sub> based materials.

Properties	R.H.P. MoSi <sub>2</sub>	R.H.P. MoSi <sub>2</sub> /SiC	Starck MoSi <sub>2</sub>	Starck MoSi <sub>2</sub> / SiC	MoSi <sub>2</sub> -1.5 Al Alloy	MoSi <sub>2</sub> -3Al Alloy
Relative density	95%	98%	99%	98%	99%	99%
Grain Size (μm)	5.0	18.0	15-40	5.0	15-20	15-20
Vicker's Hardness (GPa)	9.3	11.5	9.8	13.6	11.7	8.7
Flexural Strength (MPa)	193 ± 15	240 ± 20	146 ± 5	290 ± 15	223 ± 4	---
Fracture Toughness (MPa√m) (SENB)	4.8 ± 0.2	4.6 ± 0.1	4.3 ± 0.1	5.2 ± 0.3	4.45 ± .05	4.6 ± .02
Yield Strength (MPa)						
1200 °C	500		405			530
1300 °C	320		325			325

literature about the effect of Al addition on oxidation. It has been reported by Schlichting that Al addition of more than 2 at.% has poorer oxidation resistance as compared to MoSi<sub>2</sub> (21). On the other hand, Kodash et al has reported that resistance to oxidative scaling of Mo(SiAl)<sub>2</sub> is superior to that of MoSi<sub>2</sub> because of formation of mullite coating (22). Stergiou et al have recently shown that Mo(Si<sub>1-x</sub>Al<sub>x</sub>)<sub>2</sub> with 21.8 at% Al gains more weight during oxidation at 1400°C, as compared to monolithic MoSi<sub>2</sub> and Mo(Si<sub>1-x</sub>Al<sub>x</sub>)<sub>2</sub> with 29.3 at% Al due to different operating mechanisms (23). Preliminary analysis of oxidized surface of MoSi<sub>2</sub>-3 Al alloy (after 75 h at 1200°C) has shown that α-Al<sub>2</sub>O<sub>3</sub> accounts for almost all of the surface oxide layer. On the other hand, oxidized surface in monolithic MoSi<sub>2</sub> contains amorphous SiO<sub>2</sub>. The preferential oxidation of Al in the MoSi<sub>2</sub>-Al alloy in comparison to Si can be explained from lower free energy of formation of Al<sub>2</sub>O<sub>3</sub>, as compared to that of SiO<sub>2</sub>. Further work is in progress to understand the oxidation mechanism in the MoSi<sub>2</sub>-Al alloys.

MoSi<sub>2</sub> having poor density undergoes severe oxidation in the temperature range of 400-600°C leading to disintegration as the protective SiO<sub>2</sub> film is not formed, and 500°C is the most critical temperature (24,25). A study of oxidation behaviour of the R.H.P. MoSi<sub>2</sub>/20 v/o SiC composite at 500°C in air showed that the material did not undergo pest disintegration and the oxide layer formed was not more than 10 μm thick after 250 h of exposure (26).

### Ti<sub>5</sub>Si<sub>3</sub> Based Alloys and Composites

#### Microstructure

Formation of Ti<sub>5</sub>Si<sub>3</sub> was verified using X-ray diffraction and EPMA analysis. Representative microstructures of Ti<sub>5</sub>Si<sub>3</sub>, Ti<sub>5</sub>Si<sub>3</sub>/20 v/o TiC and Ti<sub>5</sub>Si<sub>3</sub>-8 wt% Al alloy are shown in Figs. 6(a-c). Ti<sub>5</sub>Si<sub>3</sub> was found to contain about 5 volume percent TiSi phase, which was also noticed in Ti<sub>5</sub>Si<sub>3</sub> processed by self propagating high temperature synthesis (SHS) (27). This indicates that it is a thermodynamically stable phase, and can coexist with Ti<sub>5</sub>Si<sub>3</sub>, if Ti is in excess. The microstructure of Ti<sub>5</sub>Si<sub>3</sub>-8 Al alloy (Fig. 6(c)) shows Al<sub>63</sub>Si<sub>37</sub>Ti<sub>25</sub> and Al<sub>2</sub>O<sub>3</sub> as dispersed phases (chemical composition from EPMA analysis), which formed *in situ*. The volume fraction of these phases is around 15%. Al<sub>2</sub>O<sub>3</sub> formed by reaction between Al and O present in TiH<sub>2</sub> or Si. Vehoff et al have however reported presence of only Al<sub>3</sub>Ti phase in the Ti<sub>5</sub>Si<sub>3</sub>-8 wt% Al studied (28).

Bright and dark field TEM study of grain boundaries in Ti<sub>5</sub>Si<sub>3</sub>,

and Ti<sub>5</sub>Si<sub>3</sub>/TiC interfaces showed that these were free of any amorphous region. Figure 7 shows a typical high angle grain boundary in Ti<sub>5</sub>Si<sub>3</sub>, which is clean. This is expected as Ti<sub>5</sub>Si<sub>3</sub> forms *in situ* in the reaction hot pressing process.

#### Mechanical Properties

The mechanical properties of Ti<sub>5</sub>Si<sub>3</sub> and its composites and alloys are presented in Table II. The grain sizes were measured by observation of fracture surfaces, which were almost fully intergranular. The grain size depends on the size of Ti particles in Ti<sub>5</sub>Si<sub>3</sub>, which again depends on sizes of TiH<sub>2</sub> particles. Ti<sub>5</sub>Si<sub>3</sub> forms at the site of Ti particles by diffusion assisted reaction with liquid Si.

Hardness and fracture toughness values obtained in this investigation are higher than those obtained by Rosenkranz et al (968 VHN and 2.1 MPa√m, respectively) (6, 28-30). This can be appreciated from the fact that grain size of Ti<sub>5</sub>Si<sub>3</sub> studied earlier was 20-50 μm (6), whereas the same was 5 - 10 μm in the present investigation. It has been reported that hardness of Ti<sub>5</sub>Si<sub>3</sub> varies between 9.1 GPa (924 VHN) for coarse grained microstructure (31) and 17.1 GPa (1749 VHN) for submicrometer grain size (32). Thus fine grained monolithic Ti<sub>5</sub>Si<sub>3</sub> shows higher hardness and fracture toughness. These properties are further improved by alloying with Al and addition of TiC reinforcements. Fracture surfaces of these materials were intergranular (13) as is expected in a fine grain size material. Fracture behaviour of these materials was also studied by an indentation technique and this showed increase in fracture resistance with increase in crack length (Fig. 8). The increase in fracture resistance with increase in crack length shows that additional energy is required to propagate the crack as the crack front progresses, resembling R-curve behaviour. This is primarily due to crack bridging and deflection by Ti<sub>5</sub>Si<sub>3</sub> grains or reinforcement particles as shown in Fig. 9. Faber and Evans (33) have discussed in detail the fracture toughness enhancement in ceramics due to crack deflection around second phase particles. As the crack approaches a second phase particle, it tilts out of the original plane of propagation (e.g. D1 in Fig. 9) and as it approaches the next particle, it tilts in the reverse direction, undergoing twist (e.g. D2 in Fig. 9). The stress intensity ahead of the tilted crack has mode I (opening) and mode II (sliding) components, whereas the twisted crack stress intensity possesses mode I and mode III (tearing) components. The local stress intensity factors  $k_I$ ,  $k_{II}$  and  $k_{III}$  are a function of deflection angle and contribute to toughening. In the present investigation, the event of crack

Table II. Mechanical properties of  $\text{Ti}_5\text{Si}_3$  based materials.

Material/ Property	$\text{Ti}_5\text{Si}_3$	$\text{Ti}_5\text{Si}_3/20$ v/o TiC	$\text{Ti}_5\text{Si}_3$ -8 wt% Al
Grain Size	5-10 $\mu\text{m}$	5-10 $\mu\text{m}$	5-10 $\mu\text{m}$
Hardness	12.7 GPa	14.4 GPa	13.5 GPa
Fracture Toughness (SENB)	3.4 $\text{MPa}\sqrt{\text{m}}$	4.1 $\text{MPa}\sqrt{\text{m}}$	4.1 $\text{MPa}\sqrt{\text{m}}$

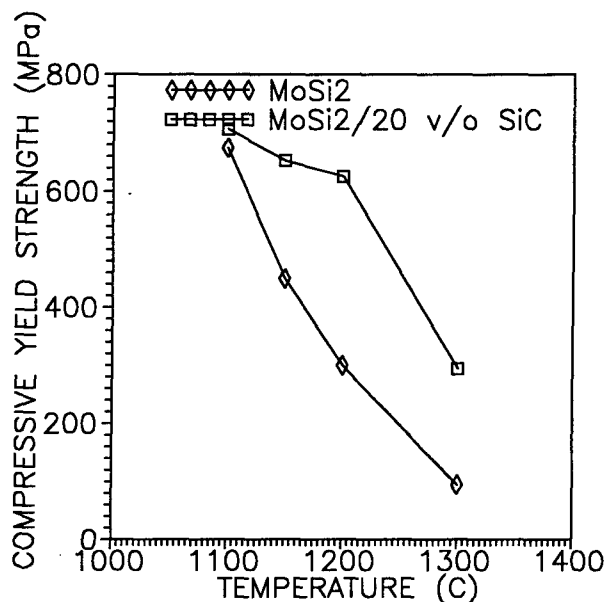


Fig. 4. Variation of high temperature compressive yield strength of reaction hot pressed  $\text{MoSi}_2/20$  v/o SiC composite with temperature (Strain rate =  $10^{-4}$  per second) (10). The data is compared with that of monolithic  $\text{MoSi}_2$  having similar grain size, reported by Aikin in Ref. 8.

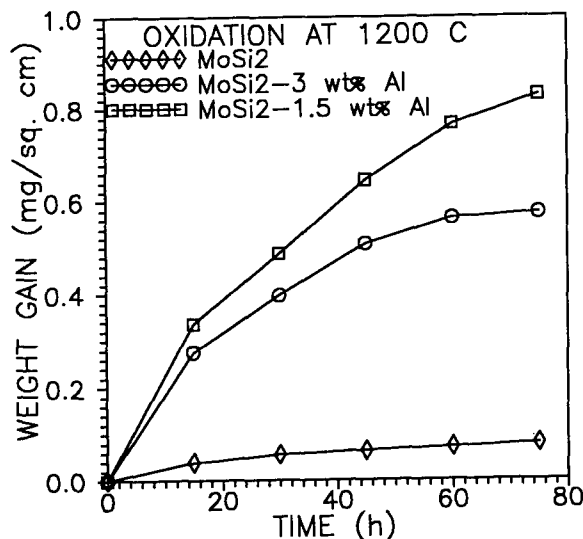


Fig. 5. Variation of weight gain due to oxidation at 1200°C in  $\text{MoSi}_2$ ,  $\text{MoSi}_2$ -1.5 wt% Al and  $\text{MoSi}_2$ -3 wt% Al alloys.

deflection at high angles is much more frequent in case of the  $\text{Ti}_5\text{Si}_3/20$  v/o TiC composite and  $\text{Ti}_5\text{Si}_3$ -8wt% Al alloy than in the monolithic  $\text{Ti}_5\text{Si}_3$ ,

as ascertained by a study of crack paths using SEM. Thus crack deflection plays an important role in toughening of  $\text{Ti}_5\text{Si}_3$  matrix composites. Crack deflection has also been found to be an important toughening mechanism in the  $\text{MoSi}_2/\text{SiC}_w$  composite (34).

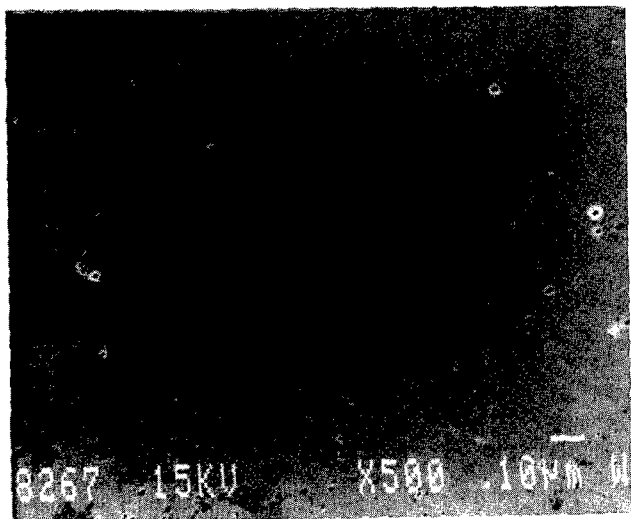
#### Oxidation Resistance

High temperature oxidation studies of  $\text{Ti}_5\text{Si}_3$  have shown that oxidation rate is rapid at temperatures of 1300°C and above, whereas the same is parabolic at 1200°C. The parabolic rate constants at 1200°C and 1300°C are  $1.454 \times 10^{-10} \text{ g}^2\text{cm}^{-4}\text{s}^{-1}$  and  $7.594 \times 10^{-10} \text{ g}^2\text{cm}^{-4}\text{s}^{-1}$ , respectively.  $\text{Ti}_5\text{Si}_3$ -8Al alloy has shown slightly higher weight gain as compared to  $\text{Ti}_5\text{Si}_3$  at 1200°C, whereas  $\text{Ti}_5\text{Si}_3/20$  v/o TiC showed much higher rate of oxidation (Fig. 10). The oxidized surface in  $\text{Ti}_5\text{Si}_3$  comprised of an outer layer of  $\text{TiO}_2$  and an inner layer of  $\text{SiO}_2$  from preliminary EPMA studies (Fig. 11). This is consistent with results of earlier investigation by Frommeyer and Rosenkranz (30), who reported  $\text{TiO}_2$  and  $\text{SiO}_2$  as oxidation products. The oxidation product in  $\text{Ti}_5\text{Si}_3/20$  v/o TiC composite is mainly  $\text{TiO}_2$ . Presence of TiC leads to higher rate of oxidation as TiC oxidizes forming  $\text{TiO}_2$ . Oxidation of Ti precedes that of Si due to lower free energy of formation of  $\text{TiO}_2$ , as compared to that of  $\text{SiO}_2$ , and higher activity of Ti in  $\text{Ti}_5\text{Si}_3$  and in the  $\text{Ti}_5\text{Si}_3/20$  v/o TiC composite. The oxidized surface of  $\text{Ti}_5\text{Si}_3$ -8 wt% Al alloy contained  $\alpha\text{-Al}_2\text{O}_3$  and  $\text{TiO}_2$ , and an EPMA study of the oxide profile showed that the  $\text{Al}_{67}\text{Si}_{108}\text{Ti}$  phase oxidizes preferentially with respect to the  $\text{Ti}_5\text{Si}_3$  matrix (Fig. 12). On exposure to a temperature of 1200°C in air for 80 h, the oxide layer was found to be around 20-30  $\mu\text{m}$  thick in  $\text{Ti}_5\text{Si}_3$  and 30  $\mu\text{m}$  in the  $\text{Ti}_5\text{Si}_3$ -8 wt% Al alloy from EPMA studies. Of course, it was thicker in the  $\text{Ti}_5\text{Si}_3/20$  v/o TiC composite. Further investigation is in progress to understand the oxidation mechanisms in these materials. The oxidation resistance of  $\text{Ti}_5\text{Si}_3$  is obviously much inferior to that of  $\text{MoSi}_2$ , as is clear from comparison of parabolic rate constant values.

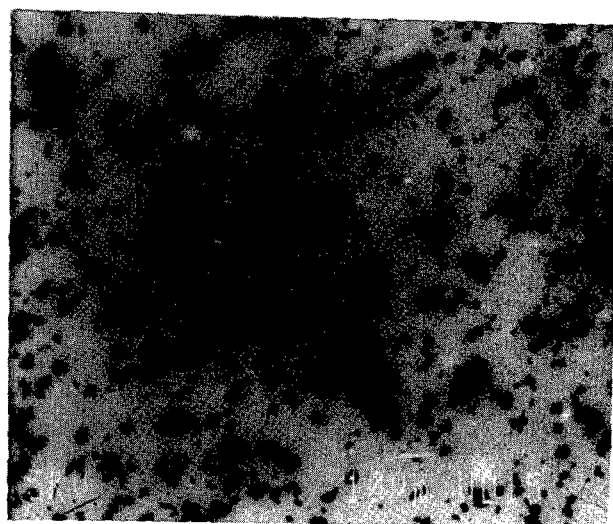
#### Summary

$\text{MoSi}_2$  and  $\text{MoSi}_2/20$  v/o SiC composites have been processed by reaction hot pressing of elemental Mo/Si or Mo/Si/SiC powder mixtures and compared with those prepared by hot pressing Starck  $\text{MoSi}_2$  powder. It was observed that reaction hot pressed  $\text{MoSi}_2$  contained much less oxygen as compared to that contained by Mo and Si powders and Starck  $\text{MoSi}_2$ . On the other hand, hot pressed Starck  $\text{MoSi}_2$  contained almost as much oxygen as the powder. This resulted in a higher strength retention in the R.H.P.  $\text{MoSi}_2$  at 1200°C. The grain size in R.H.P.  $\text{MoSi}_2$  was found to be fine on use of fine Mo particle size. Grain size could also be refined by incorporation of SiC reinforcements into  $\text{MoSi}_2$  matrix. Fine grain size and incorporation of SiC reinforcements led to increase in flexural strength and fracture toughness. Alloying with Al led to a moderate improvement in fracture toughness and high temperature strength with some reduction in oxidation resistance. Yield strength drops sharply in these materials between 1200°C and 1300°C on account of enhanced dislocation activity.

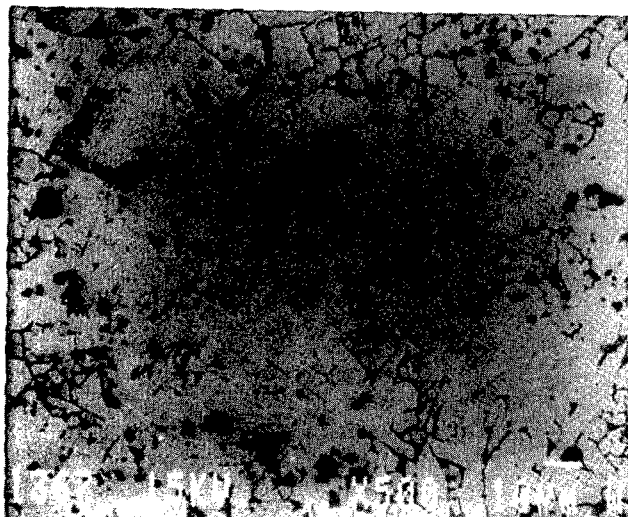
$\text{Ti}_5\text{Si}_3$  based materials were processed by reaction hot pressing



6(a)



6(b)



6(c)

Fig. 6. SEM micrographs of (a)  $Ti_5Si_3$ , (b)  $Ti_5Si_3/20$  v/o TiC composite, and (c)  $Ti_5Si_3$ -8 wt% Al alloy.

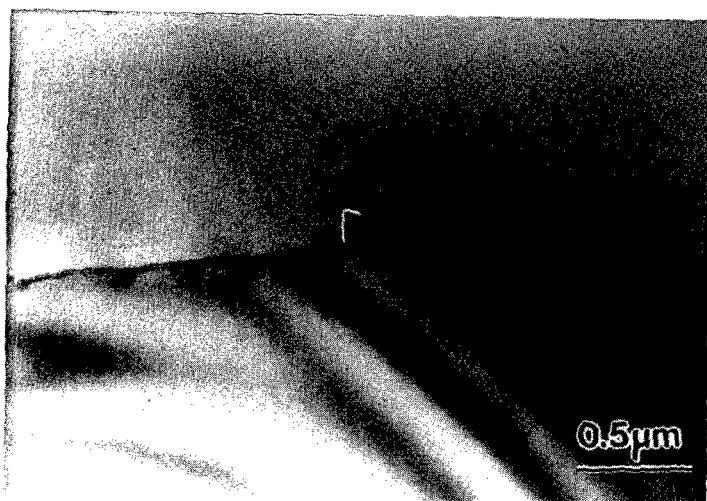


Fig. 7. Bright field TEM micrograph showing a typical grain boundary in  $Ti_5Si_3$  matrix.

of  $\text{TiH}_2/\text{Si}$  powder mixture containing finely ground  $\text{TiH}_2$  particles, and so fine grained microstructure could be obtained. The  $\text{Ti}_5\text{Si}_3/20$  v/o  $\text{TiC}$  composite and  $\text{Ti}_5\text{Si}_3$ -8 wt% Al alloy demonstrated higher hardness and fracture toughness as compared to monolithic  $\text{Ti}_5\text{Si}_3$ , and values reported in earlier investigation [6], but less than those of  $\text{MoSi}_2$ . Oxidation resistance of  $\text{Ti}_5\text{Si}_3$  is much inferior to that of  $\text{MoSi}_2$ .  $\text{Ti}_5\text{Si}_3$ -8Al alloy shows almost similar oxidation behaviour as  $\text{Ti}_5\text{Si}_3$ , whereas  $\text{Ti}_5\text{Si}_3/20$  v/o  $\text{TiC}$  oxidizes at a much higher rate at  $1200^\circ\text{C}$ .

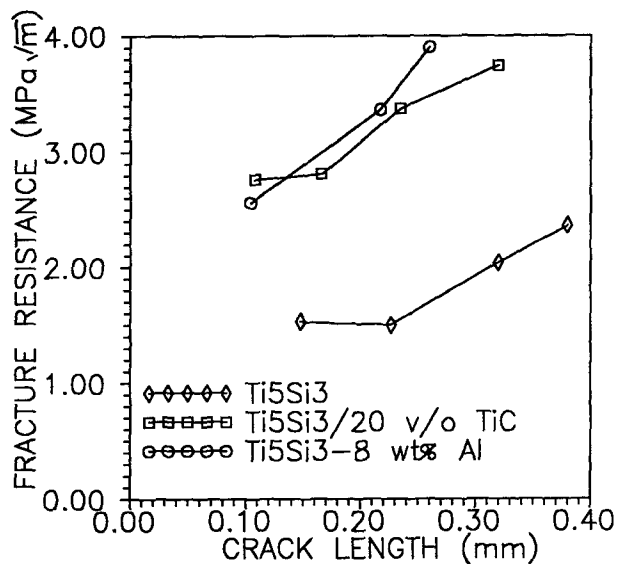


Fig. 8. Variation of indentation fracture resistance with increase in crack length for  $\text{Ti}_5\text{Si}_3$  based materials.

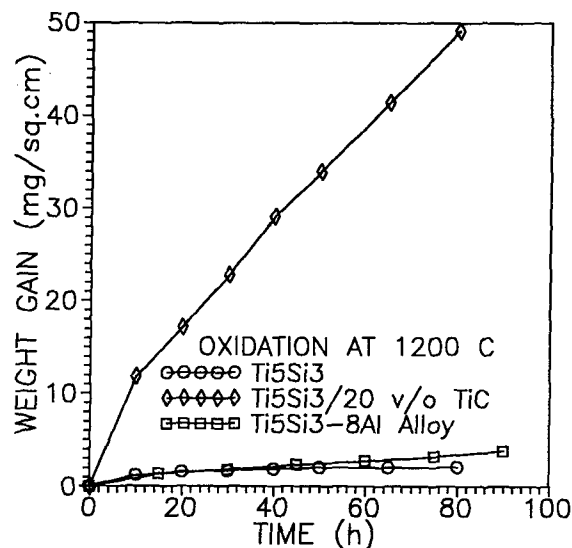


Fig. 10. Variation of weight gain due to oxidation at  $1200^\circ\text{C}$  in  $\text{Ti}_5\text{Si}_3$ ,  $\text{Ti}_5\text{Si}_3$ -8 wt% Al alloy and  $\text{Ti}_5\text{Si}_3/20$  v/o  $\text{TiC}$  composite.

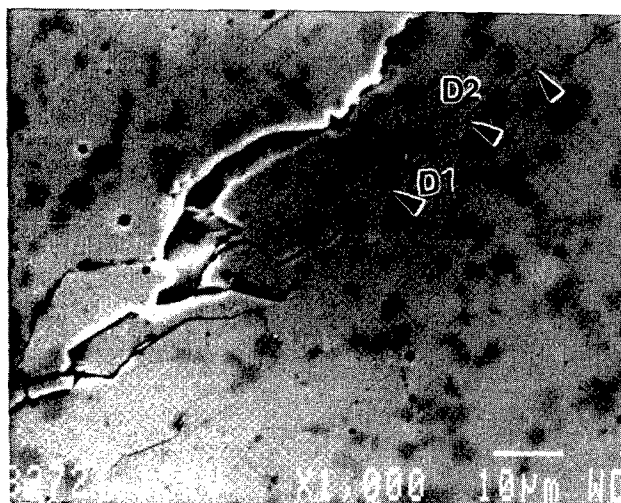


Fig. 9. SEM micrograph showing an indentation crack path in  $\text{Ti}_5\text{Si}_3/20$  v/o  $\text{TiC}$  composite. Arrows show points of crack deflection. D1 and D2 are locations of deflections in opposite directions from neighbouring particles.

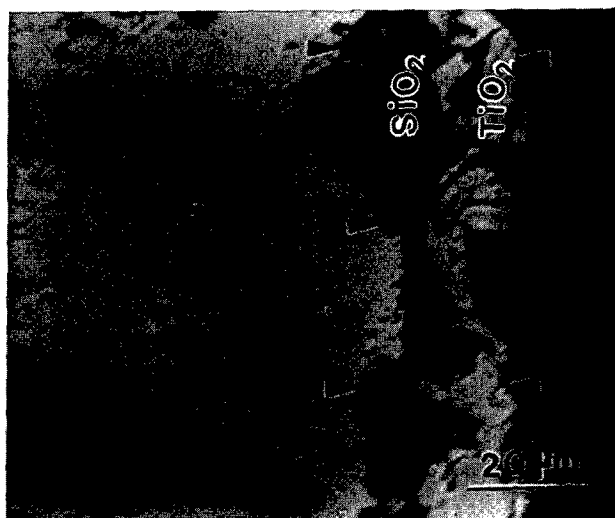


Fig. 11. EPMA backscattered electron image of the oxide layer in  $\text{Ti}_5\text{Si}_3$  oxidized in air at  $1200^\circ\text{C}$  for 80 h.



Fig. 12. EPMA backscattered electron image of the oxide layer in  $\text{Ti}_5\text{Si}_3$ -8 wt% Al alloy oxidized in air at 1200°C for 80 h.

#### Acknowledgement

The authors gratefully acknowledge the financial support from the Defence Research and Development Organisation, India and the Office of Naval Research, U.S.A. through ONR Grant N00014-95-1-0132 for this work. The authors are grateful to Dr. D. Banerjee, Director, D.M.R.L. for all the encouragement and support extended during the progress of this work. Gratitude is expressed to Mr. M. Srinivasa Rao for technical assistance in vacuum hot pressing.

#### References

1. P.J. Meschter and D.S. Schwartz, "Silicide-matrix materials for high temperature applications, JOM, 41 (9) (1989) 52-55.
2. J.J. Petrovic, "Mechanical behaviour of  $\text{MoSi}_2$  and  $\text{MoSi}_2$  composites", Mater. Sci. Engng. A192/193 (1995) 31-37.
3. D.H. Carter, J.J. Petrovic, R.E. Honnell and W.S. Gibbs, "SiC- $\text{MoSi}_2$  composites", Ceram. Eng. Sci. Proc., 10(9/10) (1989) 1121-1129.
4. F.D. Gac. and J.J. Petrovic, "Feasibility of a composite of SiC whiskers in an  $\text{MoSi}_2$  matrix", J. Amer. Ceram. Soc. 68 (1985) C-200.
5. R. Suryanarayanan, S.M.L. Sastry and K.L. Jerina, "Mechanical properties of molybdenum disilicide based materials consolidated by hot isostatic pressing (HIP), Acta Metall. Mater. 42 (11) (1994) 3751-3157.
6. R. Rosenkranz, G. Frommeyer and W. Smarsly, "Microstructures and properties of high melting point intermetallic  $\text{Ti}_5\text{Si}_3$  and  $\text{TiSi}_2$  compounds", Mater. Sci. Engng. A152 (1992) 288-294.
7. K. Sadananda, C.R. Feng, H. Jones and J.J. Petrovic, "Creep of molybdenum disilicide composites", Mater. Sci. Eng., A155 (1992) 227-239.
8. R.M. Aikin, Jr., "Structure and properties of in situ reinforced  $\text{MoSi}_2$ ", Ceram. Eng. Sci. Proc., 12 (9-10) (1991) 1643-1655.
9. S.C. Deevi, "Diffusional reactions in the combustion synthesis of  $\text{MoSi}_2$ ", Mater. Sci. Engng. A149 (1992) 241-251.
10. R. Mitra, Y.R. Mahajan, N. Eswara Prasad and W.A. Chiou, "Processing-microstructure-property relationship in reaction hot pressed  $\text{MoSi}_2$  and  $\text{MoSi}_2/\text{SiC}$  composite" Mater. Sci. Eng. (in press).
11. G.R. Anstis, P. Chantikul, B.R. Lawn, D.B. Marshall, "A critical evaluation of indentation techniques for measuring fracture toughness: Direct crack measurements", J. Amer. Ceram. Soc., 64 (9) (1981) 533-538.
12. ASTM Standard E399-83, Annual Book of ASTM Standards, Section 3 (Philadelphia, U.S.A.: American Society for Testing of Materials, 1990), 500.
13. R. Mitra, Unpublished Research, DMRL, Hyderabad, India
14. R.M. Aikin, Jr., "On the ductile-to-brittle transition temperature in  $\text{MoSi}_2$ ", Scripta Metall. Mater. 26 (1992) 1025-1030.
15. A. Costa e Silva and M.J. Kaufman, "Microstructural modification of  $\text{MoSi}_2$  through aluminum additions", Scripta Metall. et Mater. 29 (1993) 1141-1145.
16. S.R. Srinivasan and R.B. Schwarz, "Synthesis of  $\text{MoSi}_2$ -based alloys by mechanical alloying", Novel Powder Processing: Advances in Powder Metallurgy and Particulate Materials, Vol. 7, (1992) 345-358.
17. O. Unal, J.J. Petrovic, D. Carter and T.E. Mitchell, "Dislocations and plastic deformation in molybdenum disilicide" J. Amer. Ceram. Soc., 73 (1990) 1752-1757.
18. Y. Umakoshi, T. Sakagami, T. Hirano and T. Yamane, "High temperature deformation of  $\text{MoSi}_2$  single crystals with the  $\text{C11}_b$  structure", Acta Metall. Mater., 38 (6) (1990) 909-915.
19. D.A. Hardwick, P.L. Martin, S.N. Patankar and J.J. Lewandowski, "Processing-microstructure-property relationships in polycrystalline  $\text{MoSi}_2$ ", Structural Intermetallics, ed. R. Darolia, J.J. Lewandowski, C.T. Liu, P.L. Martin, D.B. Miracle and M.V. Nathal (Warrendale, PA, U.S.A.: The Minerals, Metals and Materials Society, 1993), 665-674.
20. E.W. Lee, J. Cook, A. Khan, R. Mahapatra and J. Waldman, "The oxidation resistance of  $\text{MoSi}_2$  composites", JOM 43(3) (1991) 54-57.
21. J. Schlichting, Revue Internationale des hautes Temperatures et des Refractories, 16 (1979) 67
22. P.S. Kisly and V.U. Kodash, "The mullite coatings on heaters made of molybdenum disilicide", Ceramics International 15 (1989) 189-191.
23. A. Stergiou, P. Tsakirooulos and A. Brown, "The intermediate and high temperature oxidation behaviour of  $\text{Mo}(\text{Si}_{1-x}\text{Al}_x)_2$  intermetallic alloys", Intermetallics 5 (1997) 69-81.
24. T.C. Chou and T.G. Nieh, "Pesting of the high temperature intermetallic  $\text{MoSi}_2$ ", JOM 45(12) (1993) 15-21.
25. P.J. Meschter, "Low temperature oxidation of molybdenum disilicide", Metall. Trans. 23A (1992) 1763-1772.
26. R. Mitra, V.V. Rama Rao and Y.R. Mahajan, "Oxidation behaviour of reaction hot pressed  $\text{MoSi}_2/\text{SiC}$  composites at 500°C", accepted for publication in Mater. Sci. Tech.
27. S.B. Bhaduri, R. Radhakrishnan and Z.B. Qian, "Combustion synthesis of single phase  $\text{Ti}_5\text{Si}_3$ ", Scripta Metall. 29 (1993) 1089-95.
28. H. Vehoff, S. Reuß, W. Vogt and P. Specht, "Temperature and deformation rate dependence of the fracture toughness of Ti-Si-Al alloys", Structural Intermetallics, ed. R. Darolia, J.J. Lewandowski, C.T. Liu, P.L. Martin, D.B. Miracle and M.V. Nathal (Warrendale, Pennsylvania, U.S.A.: The Minerals, Metals and Materials Society), 657-663.
29. A.J. Thom, M.K. Meyer, Y. Kim, and M. Akinc, "Evaluation of  $\text{Al}_x\text{Si}_{3-x}$  intermetallics for use as high temperature structural materials", Processing and Fabrication of Advanced Materials III, ed. V.A. Ravi, T.S. Srivatsan and J.J. Moore (Warrendale, PA, The Minerals, Metals and Materials Society, 1994), 413-438.
30. G. Frommeyer and R. Rosenkranz, "Microstructure and properties of high melting point intermetallic  $\text{Ti}_5\text{Si}_3$  and  $\text{TiSi}_2$  compounds" International Conference PM Aerospace Mater. Paper 29:1-18, Nov. 4-6, 1991, Lausanne, Switzerland.
31. G. Frommeyer, R. Rosenkranz and C. Ludeke, "Microstructure and properties of the refractory intermetallic  $\text{Ti}_5\text{Si}_3$  compound and the unidirectionally solidified eutectic Ti- $\text{Ti}_5\text{Si}_3$  alloy", Z. Metallkde, 81 (1990) 307.
32. G.V. Samsonov et al, "Relations between the electron work function and certain physical properties in silicides of Group IV transitional metals", Izvestiya Akademii Nauk SSSR, Neorganicheskie Materialy, 12(5) (1976) 850.
33. K.T. Faber and A.G. Evans, "Crack deflection processes - I. Theory", Acta Metall. 31(4) (1983) 565-576.
34. D.H. Carter and G.F. Hurley, "Crack deflection as a toughening mechanism in SiC-whisker-reinforced  $\text{MoSi}_2$ ", J. Am. Ceram. Soc. 70(4) (1987) C79-C81.

## SUBJECT INDEX

### A

$\gamma$ -TiAl, 195, 225, 235, 405  
 $\alpha_2$  Phase Composition, 235  
 $\gamma$ -TiAl, 147  
 $\gamma_2$ -Ti<sub>3</sub>Al, 195  
 48-2-2, 413  
 Activation Energy, 465  
 Aeroengine Application, 713  
 Age Hardening, 895  
 Al<sub>2</sub>Ti, 859  
 ALCHEMI, 649  
 Alloy Design, 655  
 Alloying, 443  
 Alloying Effect on Misfit, 605  
 Alloying Effects in TiAl Alloys, 531  
 AlN, 621  
 Alpha ( $\alpha$ ) Decomposition in TiAl, 531  
 Aluminides, 825  
 Applications, 413  
 Atom Probe Field Ion Microscopy, 53, 877  
 Atomic Force Microscopy, 641  
 Atomic Mobility, 205  
 Atomic Order, 545  
 Atomic Site Occupancy, 545  
 Automobile, 377

### B

B2 Phase, 235  
 B2 FeAl Alloys, 769  
 Ballistic Impact, 613  
 Beta Phase Decomposition, 253  
 Blades, 413  
 Borides, 53, 185  
 Boron, 235  
 Boron Doping, 693  
 Brazing, 323, 395  
 Brittle-to-ductile Transition, 43  
 Brittle-to-ductile Transition Temperature, 885

### C

Calorimetry, 83  
 Carburization, 427  
 Cast, 523, 545  
 Castability, 313  
 Casting, 215, 387, 427, 489, 461  
 CCT Diagram, 253  
 Characterization, 185  
 Cluster Variation Method, 606  
 Coatings, 295, 713

Coherency Stresses, 305  
 Colony Growth, 185  
 Columnar Grain, 215  
 Component Test, 277  
 Component-specific TiAl Alloy Design, 531  
 Composites, 913, 949, 959  
 Compression Strength, 805  
 Compressive Mechanical Properties, 749  
 Constitutional Defects, 815  
     Defect Hardening, 815  
     Vacancy Hardening, 815  
 Constraint Relaxation, 11  
 Continuous Lamellar Coarsening, 235  
 Cooling Rate, 215  
 Crack Closure, 469, 555  
 Creep, 109, 147, 331, 461, 515, 777, 795  
 Creep Behaviour, 885  
 Creep Deformation, 129  
 Creep Regimes, 461  
 Creep Relations in an Orthorhombic  
     Ti-23Al-27-Nb Alloy, 795  
 Creep Resistance, 923  
 Creep Resistance in TiAl Alloys, 531  
     Creep-rupture Strength, 531  
     Effects of Microstructure and  
     Microalloying, 531  
     Larsen-Miller Plot, 531  
     Secondary and Primary Creep, 531  
 Creep Strength, 313  
 Cryomilling, 621  
 CuAu, 83  
 Cubic Titanium Trialuminides, 787

### D

Damage Tolerance, 563  
 Damping, 759  
 Decomposition, 665  
 Defect Formation, 721  
 Defect Interactions, 43  
 Defect Migration, 721  
 Deformation, 225, 505  
 Deformation and Fracture resistance in TiAl  
     Alloys, 531  
     "R-curve" Behavior, 531  
     Ductility-toughness Inverse  
         Relationship, 531  
     Fracture Modes, 531  
     Loading Rate Effect, 531  
 Deformation Mechanisms, 195

- Deformation of Nb-Ti-Al, 851
  - Deformation Processes, 147
  - Deformation Processing, 263
    - Fe<sub>3</sub>Al, 263
    - FeAl, 263
    - Nb<sub>5</sub>Si<sub>3</sub>, 263
    - Ni<sub>3</sub>Al, 263
    - TiAl, 263
  - Deformation Twinning, 129, 545
  - Design, 413
  - Designed Microstructures in TiAl Alloys, 531
  - Diffusion, 43
  - Directional Solidification, 287, 713
  - Directionally-solidified-eutectics, 673
  - Discontinuous Coarsening, 177, 253
  - Dislocation Arrangements, 777
  - Dislocation Creep, 21
  - Dislocation Motion, 147
  - Dispersion Strengthened NiAl, 573
  - Dissociation, 668
  - Double Cross-slip, 157
  - Ductile Phase Toughening, 815
    - Dispersion Strengthening, 815
    - Composites, 815
    - Ductile Phase Strengthening, 815
  - Ductility, 505
  - Duplex, 461, 545
- E**
- Elastic Modulus, 777
  - Elasticity, 759
  - Electron Microscopy, 119
  - Elevated Temperature Fatigue, 555
  - Elevated Temperatures, 469
  - Engine Test, 489
  - Engine Test Experience, 713
  - Engine Valve, 427
  - Environment, 787
  - Environmental Effects, 469, 555,
  - Environmental Embrittlement, 693
  - Extrusion, 395
- F**
- Fatigue, 435, 913
  - Fatigue Crack Growth, 33, 495, 515, 555, 563
  - Fatigue Crack Propagation, 469
  - Fatigue Resistance in TiAl Alloys, 531
    - Damage Tolerance, 531
    - Effects of Microstructure and Grain Size, 531
    - Fatigue Crack Growth, 531
    - Fracture Modes, 531
  - Fatigue Resistance in TiAl Alloys-High-cycle Fatigue Properties, 531
  - Fcc and Ll<sub>2</sub> Two Phase Coherent Structure, 805
  - Fe<sub>3</sub>Al, 741
  - FeAl, 693
  - FeAl Alloys, 735
  - FeAl Intermetallic, 727
  - FeAl System, 721
  - FEM Calculations, 641
  - Forging, 185, 515
  - Formation Volume, 721
  - Fractography, 479, 515
  - Fracture, 413, 683
  - Fracture Mechanisms, 11
  - Fracture Toughness, 11, 673, 787, 859, 959
  - Fully-lamellar (FL) TiAl, 129
- G**
- G-phase, 631
  - Gamma, 109, 413, 523
  - Gamma Alloy, 489
  - Gamma TiAl Alloys, 531
  - Gamma Titanium Aluminides, 267, 295, 353, 469
  - Gamma-TiAl, 205
  - Gas Detonation Coatings, 727
  - Grain Boundary, 53
  - Grain Boundary Sliding, 795
  - Grain Refinement in TiAl Alloys, 531
  - Grain Size, 795
- H**
- Hard Orientation, 665
  - Hardness Test, 395
  - Heat Treatment, 137
  - High Alloying Additions, 405
  - High Pressure Turbine Vanes, 573
  - High Strain Rate Sensitivity, 613
  - High Temperature, 377
  - High-resolution Electron Microscopy, 167
  - Hole Drilling Method, 349
  - Homogeneity of Coatings, 727
- I**
- IC6, 713
  - Image Matching, 545
  - Impact, 413, 435
  - Impact Damage, 613
  - Impact Resistance, 613
  - In-situ Composite, 11



Infrared Joining, 395  
 Ingot Breakdown, 395  
 Interfaces, 53  
 Interfacial Dislocation, 129  
 Intergranular Fracture, 91  
 Intergranular Segregation, 735  
 Intermetallic, 479, 495, 505  
 Internal Friction, 759  
 Interphase Partitioning, 545  
 Interstitial Impurity Effects, 673  
 Intragranular Fracture, 91  
 Investment Casting, 347  
 Ion Implantation, 353  
 Ir, 805  
 Iron Aluminides, 73, 703  
 Iron-aluminum Alloy, 759  
 Irradiation, 205  
 Isothermally Forged, 923

## **J**

Jogs, 157  
 Joining, 323

## **K**

Kinetics, 177, 369

## **L**

L1<sub>0</sub> Long-range Order, 83  
 Lamellar, 215, 461  
 Lamellar Boundaries, 195  
 Lamellar Spacing, 137  
 Lamellar Structure, 109, 177, 495  
 Lamellar Structure Formation, 531  
 Lattice Constant, 769  
 Lattice Dislocation, 129  
 Lattice Misfit, 805  
 Lattice Site Occupation, 63  
 Long Range Order, 205  
 Low Cycle Fatigue, 479, 515  
 Low-Cost, 523

## **M**

MCrAlV, 341  
 Mechanical Behavior, 225  
 Mechanical Properties, 277, 295, 443, 479, 621, 631, 693, 885  
 Mechanical Twinning, 137  
 Microcracks, 225  
 Microhardness, 83  
 Microhardness Joint Properties, 395  
 Microstructural Characterization, 53  
 Microstructural Stability, 795

Microstructure, 167, 235, 323, 331, 361, 395, 443, 461, 479, 495, 505, 631, 703, 877, 923  
 Molybdenum Disilicide, 959  
 Monte Carlo Simulations, 655  
 MoSi<sub>2</sub>, 869, 949  
 Multiphase Microstructure, 831

## **N**

Nb-Al-Mo, 825  
 Nb-Al-V Alloys, 841  
   A15 Phase, 841  
   B2 Phase, 841  
   Cold Rolling, 841  
   Ductility, 841  
   Pseudotwinning, 841  
 Nb-Ti-Al, 851  
 Nb<sub>3</sub>Al/Nb In-situ Composites, 923  
 Ni<sub>2</sub>TiAl, 605  
 Ni<sub>3</sub>Al, 53, 693, 713, 749  
 NiAl, 53, 573, 621, 631, 641, 649, 665, 673, 683  
 NiAl Alloys, 613  
 NiAl Eutectic Alloy, 613  
 NiAl Single Crystals, 585  
   G Phase Strengthening, 585  
   Heusler Phase Strengthening, 585  
   High Temperature Strength, 585  
   Solid Solution Strengthening, 585  
 NiAl-based Eutectics, 573  
 NiAl/AlN, 573  
 NiAl/Mo Composites, 939  
 Nickel Aluminides, 63, 73  
 NiTi, 605  
 NiTi-Ni<sub>2</sub>TiAl Two Phase Alloy, 877  
 Notch Fatigue, 563  
 Numerical Simulation, 347

## **O**

Omega Ordering, 253  
 Omega Phase, 825  
 Ordering, 741  
 Ordering Kinetics, 83  
 Ordering Tie Line, 851  
 Orthorhombic, 913  
 Orthorhombic Alloy, 895  
 Orthorhombic Titanium, 795  
 Oxidation, 295, 405, 859, 869, 895  
 Oxidation Behaviour, 959  
 Oxidation Protective Coatings, 277  
 Oxidation Resistance, 353, 377  
 Oxidation-cyclic, 341  
 Oxidation-Effect of Boron, 815

Oxidation-isothermal, 341

## **P**

Payoff, 413

Penetration, 331

Perovskite Carbides, 703

Phase Diagrams, 73

Phase Equilibria, 885

Phase Evolution, Stability, and Microstructure, 795

Phase Stability, 825, 831

Phase Transformations, 167, 235, 895

Plasma Coatings, 727

Plastic Constraint, 11

Point Defects, 43, 205, 649

Pores, 453

Positron Annihilation, 721

Post-implantation Annealing, 353

Powder Metallurgy, 453

Powder Processing, 263, 859

Fe<sub>3</sub>Al, 263

FeAl, 263

MoSi<sub>2</sub>, 263

Ni<sub>3</sub>Al, 263

NiAl, 263

TiAl, 263

Precipitates, 53

Precipitation, 877

Prestrain, 683

Primary Creep, 137

Process Development in TiAl Alloys, 531

Process Modeling, 331

Processing, 277

Processing-cost Tradeoffs, 263

Properties, 523

Protective Coatings, 341, 713

Pseudogap, 91

PST-crystals, 305

## **Q**

Quenched-in Vacancy Concentration, 769

Quenching and Aging, 703

## **R**

Reaction Hot Pressing, 959

Reactive Sintering, 453

Refined Fully-lamellar (RFL) Microstructures, 531

Alloy K5 (Ti-46.5Al-2Cr-3Nb-0.2W), 531

Fine Fully-lamellar (FFL)

Microstructures, 531

Refractory Metals, 831

Refractory Superalloys, 805

Regression, 443

REP, 923

Residual Stresses, 305

Rh, 805

Room Temperature Brittleness, 735

## **S**

Scatter, 479

Schmid Factor, 137

SCS-6 Fibers, 929

Segregation, 53

Semi-brittle Fracture, 641

Serrated Flow, 851

Shear Strength Joint Properties, 395

Shear-in-compression Test, 395

Sic Fibers, 949

Siccvd/TiAl Composite, 929

Silicide, 949

Silicide Intermetallics, 831

Silicides, 869

Single Crystal, 147, 683, 573, 631, 749

Slip Anisotropy, 11

Slip System, 195, 683

Slip Transfer, 545, 673

Slip Transition, 665

Solid Solution Hardening, 649

Solidification, 831

Solidification Path, 313

Solidification Processing, 263

Fe<sub>3</sub>Al, 263

Nb<sub>3</sub>Al, 263

Nb<sub>5</sub>Si<sub>3</sub>, 263

Ni<sub>3</sub>Al, 263

NiAl, 263

TiAl, 263

Spark-plug Electrode-Erosion Resistance, 815

Spray Forming, 331

Standard Microstructures in TiAl Alloys, 531

Stoichiometry, 749

Strain Aging, 851

Strain Rate, 225

Strength, 453

Stress Exponent, 461

Structural Transformation, 91

Sub-critical Cracks, 573

Substitutional Alloying, 815

Alloy Hardening, 815

Ternary Hardening, 815

Substitutional Strengthening, 815

Substructure Length Scales, 157

Superplasticity, 361

Surface Damage, 683

Surface Treatment, 377

## **T**

Tensile, 479

Tensile Behavior of TiAl Alloys, 531

Dependence on Microstructure, Grain  
Size and Strain-rate, 531

Fracture Modes, 531

Grain-boundary and interface  
weakening, 531

Hall-Petch Relationship, 531

Tensile Properties, 313, 683, 703

Ternary Systems, 73

Texture, 215

Thermal Aging, 235

Thermal Expansion, 759, 859

Thermal Stresses, 347

Thermal Vacancies, 735

Thermo-mechanical Properties, 727

Thermochemistry, 63

Thermomechanical Processing, 369

Thermomechanically Processed Lamellar  
(TMPL) Microstructures, 531

Alpha Forging Process, 531

PM/TMPL Microstructures, 531

TMP Aligned Lamellar (TMPAL)  
Microstructures, 531

Thermomechanically-treated Lamellar (TMTL)  
Microstructures, 531

Ti-47Al-2W-0.5Si Alloy, 515

Ti-48-2-2, 395

Ti-Al Binary Phase Diagram, 531

Ti-Al-Fe Alloys, 885

Ti<sub>2</sub>AlNb, 777, 895

Ti<sub>3</sub>Al, 361

TiAl, 53, 109, 287, 305, 313, 323, 361,  
369, 377, 395, 427, 435, 443, 495,  
523, 545

TiAl Alloy, 119, 157

TiAl Intermetallics, 341

TiAl-Si, 287

Titanium, 913

Titanium Aluminide, 63, 73, 109, 347 167,  
453, 461, 479

Titanium Silicide, 959

Toughness, 949

Transmission Electron Microscopy, 323

TTT Diagram, 369

Turbocharger, 489

Turbocharger Rotor, 427

Twin Boundary, 119

Twin Intersection, 119

Twinning, 119

Two-phase Glass, 295

## **U**

UHV Crack Growth, 555

Ultrafine Lamellar Structure, 235

Unit Dislocations, 157

## **V**

Vacancies, 43, 649

Vacancy Formation Energy, 769

Vacancy-hardness Relation, 769

Vaporization Studies, 63

Volume Fraction, 621

## **W**

Weak-beam TEM, 157

Widmanstätten, 253

Wrought, 185

Wrought Gamma TiAl, 387

Wrought-processing of TiAl Alloys, 531

## **X**

X-ray Diffraction, 305

## **Y**

Yield Strength, 749

Yield Stress, 777

## AUTHOR INDEX

### A

Abe, E., 167  
Aindow, M., 841  
Albers, M., 63  
Annaji, S., 395  
Anton, D.L., 369  
Asokamani, R., 91  
Au, P., 109  
Austin, C.M., 263, 413

### B

Bai, B., 43  
Banerjee, D., 777  
Banerjee, S., 851  
Beddoes, J., 109  
Benci, J.E., 859  
Bendersky, L.A., 177  
Bieler, T.R., 137  
Biermann, H., 305  
Biery, N., 435  
Biscondi, M., 735  
Boehlert, C.J., 795  
Bojar, Z., 727  
Bowman, R., 939  
Bozzolo, G., 655  
Broska, A., 721  
Brown, L.E., 905  
Bystrzycki, J., 727

### C

Chan, K.S., 11  
Chang, Y.A., 649  
Chatterjee, A., 905, 913  
Chaturvedi, M.C., 323, 713  
Chen, C.Q., 353  
Chen, G.L., 119  
Cheng, T.T., 253  
Chesnutt, J.C., 263, 413  
Clemens, D.R., 387  
Clemens, H., 277  
Coetzee, R., 815  
Collins, G.S., 43  
Cornish, L.A., 815  
Couto, A.A., 741  
Cramb, A.W., 215

### D

Dahms, M., 453  
Darolia, R., 585, 613, 631  
Daw, M.S., 665

De Graef, M., 185, 215  
Demura, M., 749  
Dimiduk, D.M., 157,  
235, 531  
Dimitrov, C., 205  
Dimitrov, O., 205  
Dudzinski, D., 109

### E

Eberhardt, N., 277  
Eckert, M., 63

### F

Fackeldey, M., 347  
Fan, J., 43  
Ferrante, J., 655  
Ferreira, P.I., 741  
Forwood, C.T., 545  
Fraczkiewicz, A., 735  
Franz, M., 721  
Fraser, H.L., 195, 851

### G

Gabb, T.P., 913  
Gabdullin, N.K., 505  
Gandelsman, V.Z., 435  
Garg, A., 621, 631,  
655, 665  
Gay, A.S., 735  
Gayda, J., 913  
Gente, C., 453  
George, E.P., 693  
Gibala, R., 673  
Gibson, M.A., 545  
Glass, D.E., 295  
Glatz, W., 277  
Goel, N., 323  
Göken, M., 641  
Golberg, D., 749  
Gong, Z., 361  
Gorzel, A., 885  
Gray, G.T., III, 215, 225  
Grylls, R.J., 851

### H

Han, Y.F., 713  
Hanada, S., 923  
Hansson, T., 495  
Harada, H., 805, 877  
Haraguchi, T., 769

Harding, T., 435  
Hardwick, D.A., 185, 387  
Hashimoto, K., 929  
Hazzledine, P.M., 157  
Hebsur, M.G., 621, 949  
Hehenkamp, Th., 721  
Heitman, P.W., 905  
Hemker, K.J., 21, 147  
Hénaff, G., 469  
Hermann, W., 759  
Hilpert, K., 63  
Hirano, T., 749  
Horspool, D.N., 841  
Hou, D.-H., 851  
Hsiung, L.M., 129  
Humphreys, C.J., 605

### I

Igarashi, M., 595  
Imayev, R.M., 505  
Imayev, V.M., 505  
Inden, G., 73  
Inui, H., 287  
Isobe, S., 427

### J

Jewett, T., 453  
Jia, T., 361  
Jin, Z., 225  
Johnson, D.R., 287  
Jones, J.W., 435

### K

Karlsson, B., 461, 479  
Kath, D., 63  
Kaufman, M.J., 683  
Kawaura, H., 377  
Kelly, T.J., 413  
Khan, T., 313  
Kim, Y.-W., 225, 531  
Kimura, Y., 99  
Knabl, W., 277  
Kogachi, M., 769  
Köhler, B., 721  
Koizumi, Y., 877  
Konkel, W.A., 387  
Kowalewski, R., 305  
Krishnan, M., 235  
Kumagai, T., 167

Kumar, K.S., 703  
Kumeta, T., 877  
Kumpfert, J., 895  
Kurai, S., 495  
Kuznetsov, A.V., 505

## **L**

Larsen, D.E., 137, 523  
Larsen, J.M., 555, 563  
Larson, D.J., 53  
Launois, S., 735  
Lavernia, E.J., 331  
Letzig, D., 885  
Levit, V.I., 683  
Leyens, C., 895  
Li, B., 331  
Li, S., 361  
Li, X.Y., 353  
Lin, R.Y., 395  
Liu, C.T., 245, 649, 693  
Loretto, M.H., 253  
Lu, M., 147  
Lundstroem, D., 461  
Lupinc, V., 515

## **M**

Ma, J.C., 859  
Mabru, C., 469  
Mahajan, Y.R., 959  
Majumdar, B.S., 795  
Manh, D.N., 825  
Marchionni, M., 515  
Martin, P.L., 185, 387  
Martinz, H.P., 277  
Maruko, T., 805  
Maßmann, M., 641  
Masuda, Y., 287  
Maziasz, P.J., 245  
McAllister, K.G., 413  
McQuay, P., 523  
Mercer, C., 443  
Miller, M.K., 53  
Miller, P.R., 545  
Mills, M.J., 665  
Miodownik, A.P., 825  
Miracle, D.B., 795  
Misra, A., 673  
Mitao, S., 177  
Mitra, R., 959  
Mizuhara, Y., 495, 929  
Moriya, T., 495  
Morton, A.J., 545  
Mughrabi, H., 305

Murakami, H., 877  
Muraleedharan, K., 215  
Mutoh, Y., 495

## **N**

Naka, S., 313  
Nakamura, M., 167  
Nakatani, H., 929  
Nandy, T.K., 777  
Natarajan, B., 235  
Nathal, M.V., 949  
Nazmy, M., 515  
Ni, Y., 443  
Nieh, T.G., 119, 129  
Nishino, K., 377  
Nix, W.D., 21  
Noda, T., 427  
Noebe, R.D., 573, 631,  
655, 665, 673  
Nomura, N., 923  
Nunes, C.A., 831

## **O**

Oliver, B.F., 673  
Onofrio, G., 515  
Ort, T., 759

## **P**

Palm, M., 73, 885  
Pang, L., 703  
Partridge, A., 405  
Passa, E., 825  
Perepezko, J.H., 831  
Perungulam, S., 851  
Peters, M.A., 605  
Petit, J., 469  
Pettifor, D.G., 825  
Pfeiler, W., 83  
Pike, L.M., 649  
Pollock, T.M., 215, 435  
Pope, D.P., 99  
Prasad, B.D., 295  
Prasad, N.E., 959  
Przetakiewicz, W., 727

## **R**

Ramasundaram, P., 939  
Rao, A.V., 959  
Recina, V., 479  
Reheis, N., 277  
Remy, L., 515  
Ress, R., 913  
Richards, N.L., 323

Richardson, G.E., 905  
Riemer, M., 305  
Rishel, L.L., 215  
Rita, R., 91  
Ro, Y., 805  
Roessler, J.R., 905  
Rosenberger, A.H., 555,  
563  
Rossouw, C.J., 545  
Rubal, M.P., 435  
Russell, K.F., 53

## **S**

Sahm, P.R., 347  
Saito, T., 377  
Sakidja, R., 831  
Salishchev, G.A., 505  
Sanchez, C., 313  
Sankaran, S.N., 295  
Sattonnay, G., 205  
Sauthoff, G., 815, 885  
Savage, M.F., 665  
Schneider, D., 453  
Seetharaman, V., 263, 795  
Segtrop, K., 453  
Semiatiin, S.L., 263  
Senba, H., 595  
Seo, D.Y., 137  
Shagiev, M.R., 505  
Shao, G., 825  
Shimada, Y., 287, 929  
Soboyejo, A.B.O., 443  
Soboyejo, W.O., 443, 939  
Sockel, H.-G., 759  
Spanl, M., 83  
Sprusil, B., 83  
Srinivasan, R., 665  
Sriram, S., 157  
Staubli, M., 515  
Steif, P.S., 435  
Stergiou, A., 869  
Steyn, H. DeV., 815  
Stoloff, N.S., 33  
Stucke, M.A., 387

## **T**

Tang, Z., 341  
Tappin, D.K., 841  
Tetsui, T., 489  
Thomas, M., 313  
Thome, F., 641  
Tonneau, A., 469  
Triantafillou, J., 109

Tsakiropoulos, P., 825, 869

Zhu, S.J., 495

Zou, D., 361

Zupan, M., 147

## V

Varin, R.A., 727, 787

Vasudevan, V.K., 235

Vehoff, H., 641

## W

Walston, W.S., 573, 585,  
613, 631

Wang, B., 361

Wang, F., 341

Wang, J.G., 119

Warren, P.J., 877

Wheeler, R., 795, 851

Whittenberger, J.D.,  
621, 631

Wiedemann, K.E., 295

Wiezorek, J.M.K., 195

Williams, J.C., 3

Winstone, M.R., 405

Wolff, I.M., 815

Wolff, J., 721

Worth, B.D., 555, 563

Wright, J.L., 245

Wu, W., 341

Wu, Z.L., 673

Würker, L., 347

## X

Xing, Z.P., 713

Xu, Q., 323

## Y

Yamabe-Mitarai, Y.,  
805

Yamaguchi, M., 225, 287

Ye, H.Q., 119

Yin, W.M., 515

Yokokawa, T., 805

Yoshimi, K., 923

## Z

Zbronic, L., 787

Zhang, H.X., 353

Zhang, J., 361

Zhang, J., 361

Zhang, L.C., 119

Zhang, T.H., 353

Zhang, X.-D., 195

Zhang, X.J., 353

Zhang, Y.G., 353

Zhao, L., 109